

AD-A280 386



94-17988



BEST AVAILABLE COPY

Proceedings of the 1993

Particle Acceleration Conference

Volume 1 of 5

Pages: 240 - 393

This document has been approved
for public release and sale; its
distribution is unlimited.



The
American
Physical
Society

Proceedings of the 1993 Particle Accelerator Conference

Volume 5 of 5
Pages 3219-3933

Accession For	
NTIS	<input checked="" type="checkbox"/>
CRA&I	<input type="checkbox"/>
DTIC	<input type="checkbox"/>
TAB	<input type="checkbox"/>
Unannounced	<input type="checkbox"/>
Justification	
By	
Distribution /	
Availability Codes	
Dist	Avail and/or Special
A-1	

Papers from the fifteenth biennial Particle Accelerator Conference, an international forum on accelerator science and technology held May 17-20, 1993, in Washington, D.C., organized by the Continuous Electron Beam Accelerator Facility (CEBAF), jointly sponsored by the Institute of Electrical and Electronics Engineers Nuclear and Plasma Sciences Society and the American Physical Society Division of Physics of Beams, and conducted with support from the U.S. Department of Energy, the National Science Foundation, and the Office of Naval Research.

DTIC QUALITY INSPECTED 1

94 6 10 093

1993 IEEE Particle Accelerator Conference

Abstracting is permitted with credit to the source. Libraries are permitted to photocopy beyond the limits of U.S. Copyright law for private use of patrons those articles in this volume that carry a code at the bottom of the first page, provided the per-copy fee indicated in the code is paid through the Copyright Clearance Center, 27 Congress Street, Salem, MA 01970. For other copying, reprint, or republications permission, write to the IEEE Copyright Manager, IEEE Service Center, 445 Hoes Lane, P.O. Box 1331, Piscataway, NJ 08855-1331. All rights reserved. Printed in the USA. Copyright © 1993 by The Institute of Electrical and Electronics Engineers, Inc.

IEEE Catalog Number: 93CH3279-7

Library of Congress Number: 88-647453

Additional copies of this publication are available from

ISBN Softbound: 0-7803-1203-1

Casebound: 0-7803-1204-x

Microfiche: 0-7803-1205-8

IEEE Service Center

445 Hoes Lane

Piscataway, NJ 08854-4150



The
American
Physical
Society

1993 Particle Accelerator Conference, Washington, D.C., 17-20 May

Conference Chairman
Christoph Leemann, CEBAF
Annie Soltys, Executive Assistant
Telephone: (804) 249-7575
E-mail: soltys@cebaf.gov
Fax: (804) 249-5024

18-May-94
Box 2 of 2

Organizing Committee

M. Allen, SLAC
W. Barletta, LLNL
K. Becker, LBL
D. Berley, NPS
J. Biognano, CEBAF
R. Briggs, SSCL
Y. Cho, ANL
L. Conrath, NBS
M. Craddock, U. of BC
W. K. Dawson, TRIUMF
H. Edwards, FNAL
S. Holmes, FNAL
S. Kinsky, BNL
H. Lustig, APS
C. Roberson, ONR
S. Schriber, LANL
D. Sutter, DOE
S. Tazzari, U. of Rome II & INFN
M. Tigner, Cornell
W. T. Wong, BNL

Program Committee

J. Biognano, Chair, CEBAF
Telephone: (804) 249-7521
E-mail: biognano@cebaf.gov
H. Edwards, Deputy Chair, FNAL

Program Treasurer

Julie Leverenz
Telephone: (804) 249-7642
E-mail: leverenz@cebaf.gov

Conference Editor

Steven T. Corneliusson, CEBAF
Telephone: (804) 249-7582
E-mail: corneliusson@cebaf.gov

Editorial Assistant

Linda Carlton
Telephone: (804) 249-7690
E-mail: carlton@cebaf.gov
Fax: (804) 249-5024

DEFENSE TECHNICAL INFORMATION CENTER
BUILDING 5, CAMERON STATION
ALEXANDRIA, VA 22304-6145

REF.: GRANT NO. N00014-93-1-0623

Dear Sir or Madam:

Enclosed please find two (2) copies of the Proceedings of the 1993 Particle Accelerator Conference (PAC93). The above-referenced \$15,000 grant from the Office of Naval Research helped fund the cost of publishing the Proceedings, enabling us to keep the registration fee to a minimum.

On behalf of the conference organizers and the more than 1300 participants, thank you for supporting PAC93.

Sincerely,

Christoph W. Leemann
Conference Chairman

cc: D. Galicki, IEEE

DTIC QUALITY INSPECTED 1

Five-Volume Contents

Each volume begins with this five-volume table of contents and ends with the five-volume author index. The chairmen's foreword and a list of conference organizers and staff appear as front matter in Volume 1. A list of conference participants precedes the author index in Volume 5.

Volume 1

Opening Plenary

Chair: J. Bisognano

HERA Operations and Physics — B. H. Wiik, U. Hamburg and DESY.....	1
--	---

Single-Particle Beam Dynamics

Chair: W. Weng

Nonlinear Beam Dynamics Experiments at the IUCF Cooler Ring (<i>Invited Paper</i>) — S. Y. Lee, Indiana University	6
The Preservation of Low Emittance Flat Beams (<i>Invited Paper</i>) — T. O. Raubenheimer, SLAC	11
Long-Term Stability Studies for CERN-LHC (<i>Invited Paper</i>) — W. Scandale, CERN	16
Emittance Growth in a Low Energy Proton Beam (<i>Invited Paper</i>) — J. A. Palkovic, SSCL	21
Proton Extraction from the CERN-SPS by a Bent Crystal — S. Weisz and the RD22 Collaboration; CERN	26
Longitudinal Tracking with Phase and Amplitude Modulated RF — D. D. Caussyn, M. Ball, B. Brabson, J. Budnick, J. Collins, V. Derenchuk, G. East, M. Ellison, T. Ellison, D. Friesel, B. Hamilton, H. Huang, W. P. Jones, S. Y. Lee, D. Li, S. Nagaitsev, X. Pei, T. Sloan, Y. Wang, IUCF; A. W. Chao, S. Dutt, M. Syphers, Y. T. Yan, P. L. Zhang, SSCL; M. G. Minty, SLAC; K. Y. Ng, FNAL.....	29
Measurement of Spin Motions in a Storage Ring Outside the Stable Polarization Direction — N. Akchurin, A. Bravar, J. McPherson, F. Olchowski, Y. Onel, U. Iowa; L. Badano, M. Conte, INFN Genova; A. Penzo, INFN Trieste; J. Hall, U. New Mexico; A. Pisent, INFN Legnaro; M. Pusterla, INFN Padova; T. Rinckel, Indiana U.; R. Rossmanith, CEBAF; H. Kreiser, U. Hamburg	32
A Clean Way to Measure Nonlinear Momentum Compaction Factor α_1 — J. P. Shan, I. Kourbanis, D. McGinnis, K. Y. Ng, S. Peggs, FNAL	35
Long-Term Tracking with Symplectic Implicit One-Turn Maps — Y. T. Yan, M. Li, M. J. Syphers, SSCL; P. J. Channell, LANL	38
Injection Method Using the Third Order Resonance at TARN II — M. Tomizawa, Y. Arakaki, K. Chida, S. Watanabe, T. Watanabe, T. Katayama, M. Yoshizawa, INS Tokyo; A. Noda, Kyoto U.	41
Effects of Tidal Forces on the Beam Energy in LEP — L. Arnaudon, F. Bordry, W. Coosemans, B. Dehning, K. Henrichsen, A. Hofmann, R. Jacobsen, J. P. Koutchouk, L. Lawson-Chroco, M. Mayoud, J. Miles, R. Olsen, M. Placidi, G. Ramseier, R. Schmidt, J. Wenninger, CERN; A. Blondel, Ec. Polytech. Paris; R. Assmann, MPI Munich; G. E. Fischer, C. Pan, SLAC; R. Olivier, Lausanne U.	44

Poster presentations:

The Appearance of Beam Lines — D. C. Carey, FNAL	47
Multipole Channel Parameters for Equalization of Beam Intensity Distribution — Y. K. Batygin, MEPI	50
Single Beam Effects Due to Errors in Crab Compensation — D. Sagan, Cornell	53
Lattice Design of the LANL Spallation-Source Compressor Ring — B. Blind, A. J. Jason, F. Neri, LANL	56
Optics Simulations of the 5 MeV NPBSE FOX Telescope — M. F. Reusch, D. L. Bruhwiler, Grumman Corp.	59
Longitudinal Kinetic Energy Spread from Focusing in Charged Particle Beams — N. Brown, M. Reiser, D. Kehne, D. X. Wang, J. G. Wang, U. Maryland	62
Numerical and Experimental Studies of Halo Formation Due to Mismatch in a Space-Charge-Dominated Electron Beam — D. Kehne, M. Reiser, U. Maryland; H. Rudd.....	65
Suppression of the Main LEP Coupling Source — J. Billan, J.-P. Gourber, J.-P. Koutchouk, V. Remondino, CERN	68
Applications of Matrix Optics to Acceptance Studies in Low-Beta Ion Linacs — K. Joh, J. A. Nolen, ANL	71
Analytical Evaluation of the Second Order Momentum Compaction Factor and Comparison with MAD Results — J. P. Shan, S. G. Peggs, S. A. Bogacz, FNAL	74
Chromaticity Compensation Scheme for the Main Injector — S. A. Bogacz, FNAL	77

Proceedings of the 1993 Particle Accelerator Conference

Accelerator Physics Analysis with Interactive Tools — J. A. Holt, L. Michelotti, FNAL	80
The 50 MeV Beam Test Facility at LBL — W. Leemans, G. Behring, K.-J. Kim, J. Krupnick, C. Matuk, F. Sefah, S. Chattopadhyay, LBL	83
Knowledge Rule Base for the Beam Optics Program TRACE 3-D — G. H. Gillespie, P. K. Van Straagen, B. W. Hill, G. H. Gillespie Assoc.	86
Beam Dynamics Studies of Four-Gap Low-Beta Superconducting Resonators — J. A. Nolen, K. Joh, ANL	89
Third-Order Corrections to the SLC Final Focus — N. J. Walker, R. Helm, J. Irwin, M. Woodley, SLAC	92
Global Tuning Knobs for the SLC Final Focus — N. J. Walker, J. Irwin, M. Woodley, SLAC	95
Sigma Matrix Reconstruction in the SLC Final Focus — P. Raimondi, P. J. Emma, N. Toge, N. J. Walker, V. Ziemann, SLAC	98
Beam Based Alignment of the SLC Final Focus Superconducting Final Triplets — P. Raimondi, P. J. Emma, N. Toge, N. J. Walker, V. Ziemann, SLAC	100
A Design of a Quasi-Isynchronous Storage Ring — S. Y. Lee, Indiana U.; K. Y. Ng, FNAL; D. Trbojevic, BNL	102
Optimization Method for Orbit Correction in Accelerators — E. Bozoki, A. Friedman, BNL	105
A Fast Model-Calibration Procedure for Storage Rings — W. J. Corbett, M. J. Lee, V. Ziemann, SLAC	108
Dynamic Accelerator Modeling — H. Nishimura, LBL	111
Procedure for Determining Quadrupole and BPM Offset Values in Storage Rings — W. J. Corbett, V. Ziemann, SLAC	114
Beam Based Alignment of the SLC Final Focus Sextupoles — P. Emma, J. Irwin, N. Phinney, P. Raimondi, N. Toge, N. J. Walker, V. Ziemann, SLAC	116
Analysis of Higher Order Optical Aberrations in the SLC Final Focus Using Lie Algebra Techniques — N. J. Walker, J. Irwin, M. Woodley, SLAC	119
Simulation Support for Commissioning and Operating the SSC Linac — F. W. Guy, J. W. Hurd, C. R. Chang, D. Raparia, C. Y. Yao, SSCL	122
The Provision of IP Crossing Angles for the SSC — Y. Nosochkov, SSCL; D. M. Ritson, SLAC	125
Interactive Simulation of LEB Commissioning Procedure on a Hypercube Parallel Computer — G. Bourianoff, M. Botlo, B. Cole, S. Hunt, N. Malitsky, A. Romero, SSCL	128
Localized Chromaticity Correction of Low-Beta Insertions in Storage Rings — M. Donald, R. Helm, J. Irwin, H. Moshhammer, SLAC; E. Forest, D. Robin, A. Zholents, LBL; M. Sullivan, U. Ca., SLAC	131
Amplitude Function Mismatch — M. J. Syphers, T. Sen, SSCL; D. A. Edwards, DESY/Fermilab	134
SSC Collider Arc Lattice — M. J. Syphers, E. D. Courant, A. A. Garren, S. K. Kauffmann, T. Sen, SSCL	137
Second Order Chromaticity of the Interaction Regions in the Collider — T. Sen, M. J. Syphers, SSCL	140
Chromaticity Correction for the SSC Collider Rings — T. Sen, Y. Nosochkov, F. Pilat, R. Stiening, SSCL; D. M. Ritson, SLAC	143
Effect of Power Supply Ripple on Emittance Growth in the Collider — T. Sen, M. J. Syphers, SSCL	146
The QBA Optics for the 3.2 GeV Synchrotron Light Source ROSY II — D. Einfeld, Res. Ctr. Rossendorf; M. Plesko, Sincrotrone Trieste	149
Dynamic Aperture of the 2.5 GeV Synchrotron Radiation Source LISA — D. Einfeld, Fachhochschule Ostfriesland; D. Husmann, U. Bonn; M. Plesko, Sincrotrone Trieste	152
Four-Cell Third-Order Achromats and Their Application to Multi-Pass Time-of-Flight Spectrometers — W. Wan, M. Berz, MSU-NSCL	155
An Automatic Finder of Field Defects in a Large A.G. Machine — A. Verdier, J. Chappelier, CERN	158
Automatic and Expert Systems for Orbit Analysis — A. Verdier, J. Chappelier, CERN	161
Symplectic Scaling, a DA Based Tool — G. H. Hoffst�tner, M. Berz, NSCL-MSU	164
New Features in DIMAD — R. V. Servranckx, TRIUMF	167
A First Order Matched Transition Jump at RHIC — S. Peggs, S. Tepikian, D. Trbojevic, BNL	168
Comparison of Aperture Determinations on RHIC for Single Particles Tracked 10^6 Turns and 100 Particles, Having Randomly Generated Initial Coordinates, Tracked for 1000 Turns — G. F. Dell, BNL	171
Status of the Variable Momentum Compaction Storage Ring Experiment in SPEAR — P. Tran, A. Amiry, C. Pellegrini, UCLA; J. Corbett, M. Cornacchia, M. Lee, H.-D. Nuhn, H. Winick, D. Wu, SLAC; A. Hofmann, CERN; D. Robin, LBL	173
SSC High Energy Booster Resonance Corrector and Dynamic Tune Scanning Simulation — P. Zhang, S. Machida, SSCL	176
Transport Properties of the CEBAF Cavity — Z. Li, Coll. of William & Mary/CEBAF; J. J. Bisognano, B. C. Yunn, CEBAF	179

Each volume begins with this five-volume table of contents and ends with the five-volume author index. The chairman's foreword and a list of conference organizers and staff appear at front matter in Volume 1. A list of conference participants precedes the author index in Volume 5.

Five-Volume Contents

Global Coupling and Decoupling of the APS Storage Ring — Y. C. Chae, J. Liu, L. C. Teng, ANL	182
Conventional Collimation and Linac Protection — J. Irwin, R. Hehn, W. R. Nelson, D. Walz, SLAC	185
Measurement of Beta-Function and Phase Using the Response Matrix — Y. Chung, G. Decker, K. Evans, Jr., ANL ..	188
MATCH 1.0: The Program for Analytical Matching of Insertion — I. P. Yudin, JINR Moscow	191
The Application Package DeCA for Calculating Cyclic Accelerators — P. I. Gladkikh, A. Yu. Zelinsky, M. A. Strelkov, Kharkov Inst.	194
Echo Effect in Accelerators — G. V. Stupakov, S. K. Kauffmann, SSCL	197
Tune Shift Effect Due to the Sextupole Longitudinal Periodic Structure in the Superconducting Dipole Magnets — G. López, S. Chen, SSCL	200
Decoupling Schemes for the SSC Collider — Y. Cai, G. Bourianoff, B. Cole, R. Meinke, J. Peterson, F. Pilat, S. Stampke, M. Syphers, R. Talman, SSCL	203
Matrix Nonlinear Beam Dynamics in Curvilinear Space-Time — A. Dymnikov, U. St. Petersburg; R. Hellborg, U. Lund	206
A Numerical Check of the Thermal Wave-Model for Particle-Beam Dynamics — R. Fedele, G. Miele, U. Napoli; F. Galluccio, INFN Napoli	209
Longitudinal Dynamics for Electrons in the Thermal Wave Model for Charged Particle Beams — R. Fedele, G. Miele, U. Napoli/INFN Napoli; L. Palumbo, U. Roma/INFN-LNF	212
Experimental Measurement of Dynamic Aperture at the Photon Factory Storage Ring — Y. Kobayashi, T. Mitsuhashi, A. Ueda, KEK; T. Yamakawa, Tohoku U.	215
Lattice and Dynamic Aperture of the Duke FEL Storage Ring — Y. Wu, V. N. Litvinenko, J. M. J. Madey, Duke ...	218
Synchrotron Coupling Effects in Alternating Phase Focusing — W. Cheng, R. L. Gluckstern, H. Okamoto, U. Maryland	221
Experimental Determination of a Betatron Difference Resonance — M. Ellison, M. Ball, B. Brabson, J. Budnick, D. D. Caussyn, J. Collins, V. Derenchuk, G. East, T. Ellison, D. Friesel, B. Hamilton, H. Huang, W. P. Jones, S. Y. Lee, D. Li, S. Nagaitsev, T. Sloan, Y. Wang, IUCF; A. W. Chao, S. Dutt, M. Syphers, Y. T. Yan, P. L. Zhang, SSCL; M. Minty, SLAC; K. Y. Ng, FNAL; L. Teng, ANL; X. Pei, BNL	224
Experimental Results of the Betatron Sum Resonance — Y. Wang, M. Ball, B. Brabson, J. Budnick, D. D. Caussyn, J. Collins, V. Derenchuk, G. East, M. Ellison, D. Friesel, B. Hamilton, H. Huang, S. Y. Lee, W. P. Jones, D. Li, S. Nagaitsev, T. Sloan, IUCF; A. W. Chao, S. Dutt, M. Syphers, Y. T. Yan, P. L. Zhang, SSCL; K. Y. Ng, FNAL; M. Minty, SLAC; X. Pei, BNL.....	227
Chromaticity Compensation and Dynamic Aperture Limitation of SIBERIA-2 — V. Korchuganov, E. Levichev, V. Sajaev, BINP	230
RF Voltage Modulation at Discrete Frequencies, for Application to Proton Extraction Using Crystal Channeling — W. E. Gabella, J. Rosenzweig, UCLA; R. Kick, IMSA; S. Peggs, BNL	233
Modification of the Short Straight Sections of the High Energy Booster of the SSC — M. Li, D. Johnson, P. Kocur, R. Schailey, R. Servranckx, R. Talman, Y. Yan, R. York, V. Yarba, SSCL	236
Dynamic Aperture of the Chromatically Corrected Collider Lattice — F. Pilat, Y. Nosochkov, T. Sen, R. Stiening, SSCL	239
An Optimized Formulation for Deprit-Type Lie Transformations of Taylor Maps for Symplectic Systems — J. Shi, U. Houston; Y. T. Yan, SSCL	242
Symmetric Integrable-Polynomial Factorization for Symplectic One-Turn-Map Tracking — J. Shi, U. Houston; Y. T. Yan, SSCL	243
Recent Results from the Dynamic Aperture Experiment at the SPS — W. Fischer, J. Gareyte, M. Giovannozzi, T. Risselada, W. Scandale, F. Schmidt, CERN	246
Higher Order Tune Derivatives Due to Low- β Insertions — A. Verdier, CERN	249
A Quasi-Isochronous Operation Mode for the LNLS UVX Storage Ring — L. Lin, C. E. T. Gonçalves da Silva, Unicamp/LNLS Brazil	252
Tracking Studies and Machine Performance Simulation of the SSC Low Energy Booster — X. Wu, R. York, R. Servranckx, S. Machida, J. F. Knox-Seith, U. Wienands, SSCL	255
Magnetic Correction of RHIC Triplets — J. Wei, R. Gupta, S. Peggs, BNL	258
Beam-Beam Modulational Diffusion in 2 1/2 Dimensions — T. Satogata, S. Peggs, BNL	261
Preparation of an Experiment to Investigate Nonlinear Beam Dynamics at the Storage Ring DELTA — M. Schürmann, U. Dortmund	264
Statistics of the Half-Integer Stopband — S. Dutt, F. Chautard, R. Gerig, S. Kauffman, SSCL	267
Stochastic Dynamics for Accelerators — A. Pauluhn, DESY	270

Volume 1: 1-747
Volume 2: 748-1640
Volume 3: 1641-2545
Volume 4: 2546-3218
Volume 5: 3219-3933

Proceedings of the 1993 Particle Accelerator Conference

Diffusion Phenomena in Simple Hamiltonian Systems: Some Analytical and Numerical Results — A. Bazzani, S. Rambaldi, G. Turchetti, U. Bologna; M. Giovannozzi, CERN	273
Particle Acceleration in Extremely Strong Electromagnetic Wave Fields — K. O. Thielheim, U. Kiel	276
Laser Powered Beam Conditioner for Free Electron Lasers and Synchrotrons — H. Liu, G. Neil, CEBAF	279
Tracking Studies of Insertion Device Effects on Dynamic Aperture in the APS Storage Ring — Y. Chae, U. Houston; E. A. Crosbie, ANL	282
Particle Diffusion from Resonance Islands in Aladdin at SRC — J. Liu, E. Crosbie, L. Teng, J. Bridges, D. Ciarlette, R. Kustom, D. Voss, F. Mills, M. Borland, ANL; K. Symon, U. Wisc. Madison; W. Trzeciak, SRC Stoughton	285
Alternating-Phase Focusing with Amplitude Modulation — L. Sagalovsky, J. R. Delayen, ANL	288
Full-Turn Symplectic Map from a Generator in a Fourier-Spline Basis — J. S. Berg, R. L. Warnock, R. D. Ruth, SLAC; É. Forest, LBL	291
Synchrotron Resonances Due to Crab Cavities — S. Kurokawa, KEK; D. Pestrikov, KEK/BINP Novosibirsk	294
Third-Order Bending Magnet Optics for Cartesian Coordinates — V. V. Andreev, I. P. Yudin, JINR Moscow	297
Effects of Plane Undulator (Wiggler) Fields on Beam Dynamics at Large Orbit Distortion — S. Efimov, E. Bulyak, Kharkov Inst.	300
Bunching Property of High Current Injector with Subharmonic Prebuncher in Linac — Z. Zhang, Y. Chen, CIAE China	303
Beam Transport Line of CIAE Medical Cyclotron and Its Magnetic Elements Design Studies — T. Zhang, C. Chu, M. Fan, CIAE China	306
Resonant Beam Extraction with Constant Separatrix — K. Hiramoto, M. Tadokoro, J. Hirota, M. Nishi, Hitachi Ltd.	309
The On-Line Control Software for BEPC Beam Transport Lines — X. Zhang, K. Wei, C. Zhang, IHEP China.....	312
About Extraction of 70-GeV Protons by a Bent Crystal from the IHEP Accelerator to the Proza Setup — A. A. Asseev, A. N. Vasil'ev, E. A. Ludmirsky, V. A. Maishev, S. B. Nurushev, Yu. S. Fedotov, IHEP Russia	315
Increase a Bent Crystal Extraction Efficiency by Means of Thin Internal Target — A. A. Asseev, E. A. Myae, S. V. Sokolov, Yu. S. Fedotov, IHEP Russia.....	318
Influence of Thin Internal Target on the Bent Crystal Extraction Efficiency — A. A. Asseev, S. V. Sokolov, IHEP Russia	320
Extraction of 50 GeV Protons from IHEP Accelerator by Bent Crystal — A. A. Asseev, V. A. Maishev, E. A. Myae, IHEP Russia.....	322
On Using the Thin Target at Extraction of Protons from the Accelerators by Bent Crystal — A. A. Asseev, IHEP Russia	324
A Digital Computer Program for the Simulation of Positive or Negative Particle Beams on a PC — J. E. Boers, Thunderbird Simulations	327
Antiproton Extraction in the Fermilab Antiproton Accumulator — M. Church, S. O'Day, FNAL	330
Beam Optics of LEB-MEB Transfer Line for Superconducting Super Collider — N. Mao, J. A. McGill, K. L. Brown, R. E. Gerig, SSCL	333
Acceleration and Bunching by a Gap — S. Kulinski, INFN-LNF	336
The New Slow Extraction System of the CERN PS — Ch. Steinbach, H. Stucki, M. Thivent, CERN	339
Simulation of Slow Extraction in the Main Injector — C. S. Mishra, F. A. Harfoush, J. Johnstone, FNAL	342
Stability of Beam in the Fermilab Main Injector — C. S. Mishra, F. A. Harfoush, FNAL	345
Correction Schemes to Improve the Dynamical Aperture of the Main Injector — C. S. Mishra, F. A. Harfoush, FNAL	348
Defining the Systematic and Random Multipole Errors for Main Injector Tracking — F. A. Harfoush, B. C. Brown, H. D. Glass, C. S. Mishra, S. Peggs, FNAL	351
Experience with the New Reverse Injection Scheme in the Tevatron — S. Saritepe, G. Goderre, J. Annala, B. Hanna, A. Braun, FNAL	354
Injection and Extraction Performance at the SIS/ESR Facility — H. Eickhoff, K. Blasche, U. Blell, B. Franzke, J. Pinkow, GSI Darmstadt	357
The AGS-Booster Complex for the g-2 Experiment and RHIC Injection — M. Tanaka, Y. Y. Lee, BNL	360
First-Turn Losses in the LAMPF Proton Storage Ring (PSR) — R. Hutson, R. Macek, LANL	363

Each volume begins with this five-volume table of contents and ends with the five-volume author index. The chairman's foreword and a list of conference organizers and staff appear as front matter in Volume 1. A list of conference participants precedes the author index in Volume 5.

Five-Volume Contents

Stripper-Foil Scan Studies of the First-Turn Beam Loss Mechanism in the LAMPF Proton Storage Ring (PSR) — R. Hutson, D. Fitzgerald, S. Frankle, R. Macek, M. Plum, C. Wilkinson, LANL	366
Measurement of H^0 Excited States Produced by Foil Stripping of 800-MeV H^- Ions — J. Donahue, D. Clark, S. Cohen, D. Fitzgerald, S. Frankle, R. Hutson, R. Macek, E. Mackerrow, O. van Dyck, C. Wilkinson, LANL; H. Bryant, M. Gulley, M. Halka, P. Keating, W. Miller, U. New Mexico	369
Reducing Phase-Dependent Emittance Growth with Local Flattopping — R. E. Laxdal, T. Kuo, G. H. Mackenzie, L. Root, TRIUMF; A. Papash, INR Kiev	372
An Ion-Source Model for First-Order Beam Dynamic Codes — C. L. Fink, B. P. Curry, ANL	375
Lattice Design and Injection Issues for the 2 TeV SSCL High Energy Booster to Collider Injection Lines — F. Wang, R. Schailey, J. McGill, D. Johnson, SSCL; K. L. Brown, SLAC	378
Detailed Studies on the Beam Transfer Line from Linac to Low Energy Booster Synchrotron for the SSC — R. Bhandari, J. McGill, F. Wang, S. Penner, SSCL	381
200 GeV Beam Transfer Lines at the SSC — F. G. Mariani, J. McGill, SSCL; K. Brown, SLAC	384
Effect of Betatron Motion on the Septum Flux in Superslow Extraction at the SSC — B. S. Newberger, U. Texas, Austin; H.-J. Shih, SSCL; J. A. Ellison, U. NM	387
Study of Energy Ramping Process Applied to the LNLS Synchrotron Light Source (Brazil) — L. Jahnel, C. E. T. Gonçalves da Silva, Unicamp/LNLS Brazil	390
Extraction System Design for the SSC Low Energy Booster — X. Wu, R. York, U. Wienands, T. Hunter, S. Sheynin, SSCL	393
Tests and Analysis for SLC Damping Ring Data — J. E. Spencer, SLAC	396
RF Capture Studies for Injection into a Synchrotron — E. S. Lessner, Y. Cho, ANL	399
Results from Beam Diffusion and Collimation Measurements in Preparation for Fermilab Tevatron Crystal Extraction — G. Jackson, FNAL	402
Operational Experience with Third Harmonic RF Cavity for Improved Beam Acceleration Through Transition in the Fermilab Main Ring — C. M. Bhat, J. Dey, J. Griffin, I. Kourbanis, J. MacLachlan, M. Martens, K. Meisner, K. Y. Ng, J. Shan, D. Wildman, FNAL	405
New Method for Control of Longitudinal Emittance During Transition in Proton Synchrotrons — J. E. Griffin, FNAL (Ret.)	408
Remarks on the Differential Luminosity in the Weak Disruption and the Transition Region — H. Heydari, TUB Germany	411
Flat Beam Studies in the SLC Linac — C. Adolphsen, F.-J. Decker, J. T. Seeman, SLAC	414
Method to Evaluate Steering and Alignment Algorithms for Controlling Emittance Growth — C. Adolphsen, T. Raubenheimer, SLAC	417
Experimental Simulation of Ground Motion Effects — M. J. Syphers, A. W. Chao, S. Dutt, Y. T. Yan, P. L. Zhang, SSCL; M. Ball, B. Brabson, J. Budnick, D. D. Caussyn, J. Collins, V. Derenchuk, G. East, M. Ellison, T. Ellison, D. Friesel, B. Hamilton, H. Huang, W. P. Jones, S. Y. Lee, D. Li, S. Nagaitsev, X. Pei, G. Rondeau, T. Sloan, Y. Wang, IUCF; M. G. Minty, SLAC; W. Gabella, K. Y. Ng, FNAL; L. Teng, ANL; S. Tepikian, BNL	420
Bunch Coalescing Studies for the SSC — N. Mahale, Y. T. Yan, J. Ellison, SSCL	423
Compensation of RF-Induced Energy Spread in the CEBAF Injector Chopping System — M. G. Tiefenback, G. A. Krafft, CEBAF	426
The North Arc of the SLC as a Spin Rotator — T. Limberg, P. Emma, SLAC; R. Rossmannith, CEBAF	429
The Evolution of Tensor Polarization — H. Huang, S. Y. Lee, IUCF, L. Ratner, BNL	432
Even Order Snake Resonances — S. Y. Lee, Indiana U.	435
Wiggler as Spin Rotators for RHIC — A. Luccio, BNL; M. Conte, U. Genova	438
Taylor Map and Calculation of Equilibrium Polarization for Proton Storage Rings — V. Balandin, N. Golubeva, INR Moscow	441
Investigation of Spin Resonance Crossing in Proton Circular Accelerators — V. Balandin, N. Golubeva, INR Moscow	444
Electron Beam Depolarization in a Damping Ring — M. Minty, SLAC	447
SPINLIE: New Computer Code for Polarization Calculation — Yu. Eidelman, V. Yakimenko, BINP	450
IHEP Polarized Proton Beam — V. N. Zapolsky, Yu. A. Chesnokov, A. Dyshkant, N. A. Galyaev, V. I. Kotov, V. I. Kryshkin, R. A. Rzaev, R. M. Sulyaev, S. V. Tsarik, V. G. Zarucheskyy, IHEP Moscow	454
Measurement of Longitudinal Beam Polarization by Synchrotron Radiation — I. P. Karabekov, Yerevan/CEBAF, R. Rossmannith, CEBAF	457

Volume 1: 1-747
 Volume 2: 748-1640
 Volume 3: 1641-2545
 Volume 4: 2546-3218
 Volume 5: 3219-3933

Proceedings of the 1993 Particle Accelerator Conference

The Status of Polarization Studies at HERA — <i>M. Böge, DESY</i>	460
Computer Assisted Accelerator Tuning — <i>J. K. Boyd, LLNL</i>	463
Pulse-to-Pulse Simulation of Orbit Feedback for JLC Final Focus System — <i>N. Yamamoto, K. Hirata, K. Oide, KEK</i>	466
Multi-Dimensional Beam Emittance and β -Functions — <i>J. Buon, LAL Orsay</i>	469
Observation of the Coalescing of Beam into an Asymmetric RF Bucket by Stochastic Cooling — <i>A. M. Halling, X. P. Lu, FNAL</i>	472
Effects of Transverse Coupling on Transverse Beam Size, Simulation and Measurements — <i>A. M. Halling, FNAL</i> ...	474
One of Methods to Extract Truncated Taylor Map for Orbital and Spin Motion in Proton Storage Rings — <i>V. Balandin, INR Moscow</i>	477
Skew Quadrupole Effects in the IBM Compact Synchrotron — <i>C. N. Archie, IBM Semiconductor R&D Ctr.</i>	480
A Simulation Study of Linear Coupling Effects and Their Correction in RHIC — <i>G. Parzen, BNL</i>	483
Eigenfunctions of the Transfer Matrix in the Presence of Linear Coupling — <i>G. Parzen, BNL</i>	486
Emittance and Beam Size Distortion Due to Linear Coupling — <i>G. Parzen, BNL</i>	489
Use of Regularization Method in the Determination of Ring Parameters and Orbit Correction — <i>Y. N. Tang, S. Krinsky, NSLS-BNL</i>	492
Automatic Differentiation of Limit Functions — <i>L. Michelotti, FNAL</i>	495
Corrector Ironing in the SLC Final Focus — <i>V. Ziemann, SLAC</i>	498
General Normal Form Procedure to Correct Tune-Shift and Non-Linear Chromaticity for Large Accelerators like the LHC — <i>M. Giovannozzi, F. Schmidt, CERN</i>	500
Review of Recent Optical Issues in LEP — <i>F. Ruggiero, CERN</i>	503
Emittance and Damping of Electrons in the Neighborhood of Resonance Fixed Points — <i>E. A. Crosbie, ANL</i>	506
Effects of the Third Order Transfer Maps and Solenoid on a High Brightness Beam — <i>Z. Parsa, BNL</i>	509
Simultaneous Cancellation of Beam Emittance and Energy Spread in the CEBAF Nuclear Physics Injector Chopping System — <i>H. Liu, J. Bisognano, CEBAF</i>	512
The Linkage of Zlib to TEAPOT for Auto-Differentiation Map Extraction and Nonlinear Analysis — <i>N. Sun, Y. T. Yan, F. Pilat, G. Bourianoff, SSCL</i>	515
Influence of the Ionization Loss in the Diagnostic Foil on the Phase Motion in the Phasotron — <i>O. N. Borisov, L. M. Onischenko, JINR, Dubna</i>	518

Lepton RF Linacs and Linear Colliders

Chair: *Y. Kimura*

Recent SLC Developments (<i>Invited Paper</i>) — <i>M. Ross, SLAC</i>	522
CEBAF Commissioning Status (<i>Invited Paper</i>) — <i>A. Hutton, CEBAF</i>	527
Overview of Linear Collider Designs (<i>Invited Paper</i>) — <i>R. H. Siemann, SLAC</i>	532
Progress Report on the TESLA Test Facility — <i>H. T. Edwards and the TESLA Collaboration, DESY/FNAL</i>	537
The CERN Linear Collider — <i>The CLIC Study Group, CERN</i>	540
The Next Linear Collider Test Accelerator — <i>R. D. Ruth, C. Adolphsen, K. Bane, R. F. Boyce, D. L. Burke, R. Callin, G. Caryotakis, R. Cassel, S. L. Clark, H. Deruyter, K. Fant, R. Fuller, S. Heifets, H. Hoag, R. Humphrey, S. Kheifets, R. Koontz, T. Lavine, G. A. Loew, A. Menegat, R. H. Miller, J. M. Paterson, C. Pearson, R. Phillips, J. Rifkin, J. Spencer, S. Tantawi, K. A. Thompson, A. Vlieks, V. Vylet, J. W. Wang, P. B. Wilson, A. Yeremian, B. Youngman, SLAC; N. M. Kroll, UC San Diego; C. Nantista, UCLA</i>	543
High Power CW Linac in PNC — <i>S. Toyama, Y. L. Wang, T. Emoto, M. Nomura, N. Takahashi, H. Oshita, K. Hirano, Y. Himeno, PNC Japan; I. Sato, A. Enomoto, M. Ono, KEK</i>	546

Poster presentations:

A mm-Wave Planar Microcavity Structure for Electron Linear Accelerator System — <i>Y. W. Kang, R. Kustom, F. Mills, G. Mavrogenes, ANL; H. Henke, TU Berlin</i>	549
SCANUR: A Subcritical Reactor with Electron Linacs for Transmutation of Nuclear Wastes — <i>A. Krasnykh, Yu. Popov, V. Rudenko, L. Somov, JINR Dubna; L. Men'schikov, V. Prusakov, S. Subbotin, Kurchatov Inst., Moscow</i>	552
New Irradiation Field Shaping Systems of High Voltage Electron Accelerators for Industry — <i>A. S. Ivanov, V. P. Ovchinnikov, M. P. Svinin, N. G. Tolstun, Efremov Inst.</i>	555
A Versatile 2 MeV, 200 mA Compact X-Band Linac — <i>C. E. Clayton, K. A. Marsh, UCLA</i>	558

Each volume begins with this five-volume table of contents and ends with the five-volume author index. The chairmen's foreword and a list of conference organizers and staff appear as front matter in Volume 1. A list of conference participants precedes the author index in Volume 5.

Five-Volume Contents

Emittance Measurements of the 4.5 MeV UCLA RF Photo-Injector — S. C. Hartman, N. Barov, S. Park, C. Pellegrini, J. Rosenzweig, G. Travish, R. Zhang, P. Davis, C. Joshi, G. Hairapetian, UCLA	561
Commissioning of the SIBERIA-2 Preinjector and First Beam Results — V. Korchuganov, G. Kulipanov, E. Levichev, O. Nezhevenko, G. Ostreiko, A. Philipchenko, G. Serdobintsev, E. Shaimerdenov, V. Ushakov, INP Novosibirsk; A. Kadnikov, Yu. Krylov, S. Kuznetsov, V. Ushkov, Yu. Yupinov, Kurchatov Inst.....	564
Emittance Measurement and Modeling of the ALS 50 MeV Linac to Booster Line — J. Bengtsson, W. Leemans, T. Byrne, LBL	567
Extended Version of an S-Band RF Gun — S. Park, C. Pellegrini, UCLA	570
Progress Report on the Commissioning of the Lisa 25 MeV SC Linac — F. Tazzioli, M. Castellano, M. Ferrario, S. Kulinski, M. Minestrini, P. Patteri, INFN-LNF; L. Catani, S. Tazzari, INFN Roma	573
The Plane Wave Transformer Linac Development at UCLA — R. Zhang, S. Hartman, C. Pellegrini, UCLA	575
Nanosecond MOSFET Gun Pulser for the CESR High Intensity Linac Injector — C. R. Dunnam, R. E. Meller, Cornell	578
Progress of PLS 2-GeV Linac — W. Namkung, I. Ko, M. Cho, C. Ryu, J. Bak, S. Nam, H. Lee, POSTECH	581
Lattice Design Principles for a Recirculated, High Energy, SRF Electron Accelerator — D. R. Douglas, CEBAF	584
Commissioning and Operation Experience with the CEBAF Recirculation Arc Beam Transport System — Y. Chao, M. Crofford, N. Dobeck, D. Douglas, A. Hofler, C. Hovater, G. A. Krafft, R. Legg, J. Perry, E. Price, S. Suhring, M. Tiefenback, J. van Zeijts, CEBAF	587
Linac Upgrade Plan for the KEK B-Factory — A. Enomoto, S. Anami, T. Kamitani, H. Hanaki, T. Shidara, I. Sato, KEK	590
Performance Characteristics of the Pulsed High Power Klystron Tube for PLS 2-GeV Linac — M. H. Cho, S. H. Nam, J. S. Oh, S. S. Park, H. S. Lee, J. S. Bak, I. S. Ko, W. Namkung, POSTECH	593
Electron Transport of a Linac Coherent Light Source (LCLS) Using the SLAC Linac — K. L. Bane, T. O. Raubenheimer, J. T. Seeman, SLAC	596
Phasing Schemes for the CEBAF Cavities — S. N. Simrock, R. Kazimi, G. A. Krafft, L. Merminga, L. Ninan, S. Witherspoon, CEBAF	599
Initial Data of Linac Preinjector for Spring-8 — S. Suzuki, H. Yoshikawa, T. Hori, K. Yanagida, A. Mizuno, K. Tamezane, K. Mashiko, H. Yokomizo, JAERI	602
Status of the Advanced Photon Source (APS) Linear Accelerator — M. White, W. Berg, R. Fuja, A. Grelick, G. Mavrogenes, A. Nassiri, T. Russell, W. Wesolowski, ANL	605
200 MeV RF Linac for Brookhaven National Laboratory — K. Whitham, H. Anamkath, S. Lyons, J. Manca, R. Miller, P. Treas, T. Zante, Titan Beta; R. Miller, SLAC; R. Heese, J. Keane, BNL	608
Design of the e^+e^- Frascati Linear Accelerator for DaFne — K. Whitham, H. Anamkath, S. Lyons, J. Manca, R. Miller, T. Zante, P. Treas, D. Nett, Titan Beta; R. Miller, SLAC; R. Boni, H. Hsieh, S. Kulinski, F. Sannibale, B. Spataro, M. Vescovi, G. Vignola, INFN-Frascati	611
The Possibility of Introducing Additional Focusing Caused by the Circular Irises in Iris Loaded Accelerator Sections — M. Kurz, P. Hülsmann, H.-W. Glock, H. Klein, Inst. f. Ang. Physik	614
Disruption Effects from the Collision of Quasi-Flat Beams — P. Chen, SLAC	617
Accelerator and RF System Development for NLC — A. E. Vlieks, R. Callin, H. Deruyter, R. Early, K. S. Fant, Z. D. Farkas, W. R. Fowkes, C. Galloway, H. A. Hoag, R. Koontz, G. A. Loew, T. L. Lavine, A. Menegat, R. H. Miller, D. Palmer, C. C. Pearson, R. D. Ruth, S. G. Tantawi, P. B. Wilson, J. W. Wang, C. Yoneda, SLAC; N. Kroll, UCSD; C. Nantista, UCLA	620
Rise Time of the Amplitudes of Time Harmonic Fields in Multicell Cavities — H.-W. Glock, M. Kurz, P. Hülsmann, H. Klein, Inst. f. Ang. Physik	623
CLIC Drive Beam Generation by Induction Linac and FEL Experimental Studies for the CERN Linear Collider — R. Corsini, C. D. Johnson, CERN; J. Gardelle, J. Grenier, CESTA	626
Beam Instabilities Related to Different Focusing Schemes in TESLA — A. Mosnier, CE Saclay	629
A Large Aperture Final Focus System for TESLA — O. Napoly, CE Saclay	632
Chicane and Wiggler Based Bunch Compressors for Future Linear Colliders — T. O. Raubenheimer, P. Emma, S. Kheifets, SLAC	635
An "NLC-Style" Short Bunch Length Compressor in the SLAC Linac — J. T. Seeman, R. Holtzapple, SLAC	638
Multibunching Studies for CLIC — I. Wilson, W. Wuensch, CERN	641
Linear Collider Systems and Costs — G. A. Loew, SLAC	644
Application of the Monte Carlo Method to Estimate the Tenth-Value Thickness for X-Rays in Medical Electron Accelerators — J. Ródenas, G. Verdú, U. Politénica, Valencia	647

Volume 1: 1-747
 Volume 2: 748-1640
 Volume 3: 1641-2545
 Volume 4: 2546-3218
 Volume 5: 3219-3933

Proceedings of the 1993 Particle Accelerator Conference

Burst-Mode Electron Gun Pulser for FEL with the ISIR Linac — K. Tsumori, Sumitomo Elect. Ind.; S. Okuda, T. Yamamoto, S. Suemine, S. Takamuku, Osaka U.	650
Positron Accumulation Ring for the SPring-8 Project — Y. Miyahara, JAERI-RIKEN	653

High-Current Accelerators

Chair: T. Fessenden

Induction Accelerator Development for Heavy Ion Fusion (Invited Paper) — L. L. Reginato, LBL	656
Generation and Focusing of High Energy, 35-kA Electron Beams for Pulsed-Diode Radiographic Machines: Theory and Experiment — R. L. Carlson, M. J. George, LANL; T. P. Hughes, D. R. Welch, MRC	661
Numerical Investigation of High-Current Ion Beam Acceleration and Charge Compensation in Two Accelerating Gaps of Induction Linac — N. G. Belova, Russian Acad.; V. I. Karas', Kharkov Inst.	664
The Light-Ion Pulsed Power Induction Accelerator for the Laboratory Microfusion Facility (LMF) — M. G. Mazarakis, D. L. Smith, L. F. Bennett, T. R. Lockner, R. E. Olson, J. W. Poukey, J. Boyes, Sandia Nat. Lab.	667

Poster presentations:

First Operation of the LELIA Induction Accelerator at CESTA — Ph. Eyharts, Ph. Anthouard, J. Bardy, C. Bonnafond, Ph. Delsart, A. Devin, P. Eyl, P. Grua, J. Labrousche, J. Launspach, P. Le Taillandier, J. de Mascureau, E. Merle, A. Roques, M. Thevenot, D. Villate, CEA-CESTA	670
An Induction Linac and Pulsed Power System at KEK — J. Kishiro, K. Ebihara, S. Hiramatsu, Y. Kimura, T. Ozaki, K. Takayama, D. H. Whittum, K. Saito, KEK	673
Design and Operation of Inductive Acceleration Modules for FEL with Controlled Voltage Ramp — S. Kawasaki, Saitama U.; H. Ishizuka, Fukuoka Inst.; A. Tokuchi, Nichicon Corp.; Y. Yamashita, S. Nakajima, Hitachi; S. Sakamoto, H. Maeda, M. Shiho, JAERI	676
Study on Induction Accelerator for Industrial Applications — Y. S. Cho, K. H. Baik, K. H. Chung, Seoul Nat. U.; B. H. Choi, Korea Atomic Energy Res. Inst.	679
Linear Induction Accelerators for Industrial Applications — M. I. Demsky, Yu. P. Vakhruhin, A. E. Baranovsky, A. A. Volzhev, A. P. Kuprianov, D. E. Trifonov, Efremov Inst.	682
High Power, High Brightness Electron Beam Generation in a Pulse-Line Driven Pseudospark Discharge — W. W. Destler, Z. Segalov, J. Rodgers, K. Ramaswamy, M. Reiser, U. Maryland	685
Experimental Study of Post-Acceleration and Transport of a Pseudospark-Produced Electron Beam — C. J. Liu, M. J. Rhee, U. Maryland	688
Compound-Lens Injector for a 19-MeV, 700-kA Electron Beam — T. W. L. Sanford, J. W. Poukey, J. A. Halbleib, Sandia Nat. Lab.; R. C. Mock, Ktech Corp.	691
Electron Flow in the SABRE Linear Induction Adder in Positive Polarity — J. R. Smith, Titan/Spectra; J. W. Poukey, M. E. Cuneo, D. L. Hanson, S. E. Rosenthal, M. Bernard, Sandia Nat. Lab.	694
Design and Progress of the AIRIX Induction Accelerator — J. de Mascureau, Ph. Anthouard, J. Bardy, C. Bonnafond, Ph. Delsart, A. Devin, Ph. Eyharts, P. Eyl, P. Grua, J. Labrousche, J. Launspach, P. Le Taillandier, E. Merle, A. Roques, B. Sacepe, M. Thevenot, D. Villate, CEA-CESTA	697
Nuclear Fusion of Protons with Ions of Boron — A. G. Ruggiero, BNL	700
Heavy Ion Fusion Injector Program — S. Yu, S. Eylon, W. W. Chupp, A. Faltens, T. Fessenden, E. Henestroza, R. Hipple, D. Judd, C. Peters, L. Reginato, H. Rutkowski, J. Stoker, D. Vanecek, LBL; J. Barnard, G. Caporaso, Y. J. Chen, F. Deadrick, A. Friedman, D. Grote, D. Hewett, LLNL	703
Ion Pulse Propagation Through a Previously Unfilled Electrostatic Aperture Lens Accelerating Column — H. L. Rutkowski, S. Eylon, D. S. Keeney, LBL; Y. J. Chen, D. W. Hewett, J. Barnard, LLNL	706
LSE-ESQ Injector Scaled Experiment — E. Henestroza, S. Eylon, S. Yu, LBL; D. Grote, LLNL	709
One Dimensional Simulations of Transients in Heavy Ion Injectors — J. J. Barnard, G. J. Caporaso, LLNL; S. S. Yu, S. Eylon, LBL	712
Analysis of Beam Loading in Electrostatic Columns — G. J. Caporaso, J. J. Barnard, LLNL	715
Simulation of Transient Effects in the Heavy Ion Fusion Injectors — Y. Chen, D. W. Hewett, LLNL	718
Electrostatic Quadrupoles for Heavy-Ion Fusion — P. Seidl, A. Faltens, LBL	721
Simulation Studies of Space-Charge-Dominated Beam Transport in Large Aperture Ratio Quadrupoles — W. M. Fawley, L. J. Laslett, C. M. Celata, A. Faltens, LBL; I. Haber, NRL	724

Each volume begins with this five-volume table of contents and ends with the five-volume author index. The chairmen's preword and a list of conference organizers and staff appear as front matter in Volume 1. A list of conference participants precedes the author index in Volume 5.

Three Dimensional PIC Simulation of Heavy Ion Fusion Beams: Recent Improvements to and Applications of WARP — D. P. Grote, A. Friedman, LLNL; I. Haber, NRL	727
Longitudinal Beam Dynamics for Heavy Ion Fusion — D. A. Callahan, A. B. Langdon, A. Friedman, LLNL; I. Haber, NRL	730
Correction of Longitudinal Errors in Accelerators for Heavy-Ion Fusion — W. M. Sharp, D. A. Callahan, J. J. Barnard, A. B. Langdon, LLNL; T. J. Fessenden, LBL	733
System Modeling for the Longitudinal Beam Dynamics Control Problem in Heavy Ion Induction Accelerators — A. N. Payne, LLNL	736
Development of FET-Switched Induction Accelerator Cells for Heavy-Ion Fusion Recirculators — M. A. Newton, W. R. Cravey, S. A. Hawkins, H. C. Kirbie, C. W. Ollis, LLNL	739
Parametric Studies for Recirculating Induction Accelerators as Drivers for Heavy-Ion Fusion — R. L. Bieri, Schafer Assoc.	742
A Fusion Device of the Continuous Electron Beam Confinement Used by the Accumulating Ring with the Continuous Injection — S. Gao, G. Qian, CIAE China	745

Volume 2

RF Structures

Chair: D. Reid

Operating Experience with High Beta Superconducting RF Cavities (<i>Invited Paper</i>) — H. F. Dylla, L. R. Doolittle, J. F. Benesch, CEBAF	748
Perpendicular Biased Ferrite-Tuned Cavities (<i>Invited Paper</i>) — R. L. Poirier, TRIUMF	753
SRF Cavities for Future Applications (<i>Invited Paper</i>) — D. Proch, DESY	758
Preparation and Testing of a Superconducting Cavity for CESR-B — D. Moffat, P. Barnes, J. Kirchgessner, H. Padamsee, J. Sears, Cornell	763
High Power Operation of Single-Cell 352-MHz Cavity for the Advanced Photon Source (APS) — J. F. Bridges, Y. W. Kang, R. L. Kustom, K. Primdahl, ANL	766

Poster presentations:

Development of Crab Cavity for CESR-B — K. Akai, J. Kirchgessner, D. Moffat, H. Padamsee, J. Sears, M. Tigner, Cornell	769
A New 3-D Electromagnetic Solver for the Design of Arbitrarily Shaped Accelerating Cavities — P. Arcioni, M. Bressan, L. Perregrini, U. Pavia	772
Design Study for the ELFA Linac — W. A. Barletta, LBL; G. Bellomo, INFN/ U. Milan; G. Gemme, R. Parodi, INFN Genova; V. Stagno, V. Variale, INFN Bari	775
The RF Cavity for DAFNE — S. Bartalucci, R. Boni, A. Gallo, L. Palumbo, R. Parodi, M. Serio, B. Spataro, INFN-LNF	778
Mechanical Results of the CEBAF Cavity Series Production — J. Mammoser, J. F. Benesch, CEBAF	781
Fabrication of Complex Mechanical Components — Y. Beroud, SICN	784
Measurements of Higher Order Modes in 3rd Harmonic RF Cavity at Fermilab — C. M. Bhat, FNAL	787
POISSON/SUPERFISH on PC Compatibles — J. H. Billen, L. M. Young, LANL	790
Radio Frequency Measurement and Analysis Codes — J. H. Billen, LANL	793
Progress on RF Superconductivity at Saclay — Groupe d'Etudes des Cavités Supraconductrices, CE Saclay and Institut de Physique Nucléaire, Orsay	796
A New Surface Treatment for Niobium Superconducting Cavities — B. Bonin, C. Henriot, C. Antoine, B. Coadou, F. Koechlin, J. P. Rodriguez, E. Lemaitre, P. Greiner, CE Saclay	798
Using the Panofsky-Wenzel Theorem in the Analysis of Radio-Frequency Deflectors — M. J. Browman, LANL	800
The Effects of Temperature and RF Power Level on the Tuning of the Water-Cooled SSC Low-Energy Booster Cavity — C. Friedrichs, LANL; G. Hulsey, SSCL	803
Superconducting Cavities for the LEP Energy Upgrade — G. Cavallari, C. Benvenuti, P. Bernard, D. Bloess, E. Chiaveri, F. Genesio, E. Haebel, N. Hilleret, J. Tuckmantel, W. Weingarten, CERN	806
TESLA Input Coupler Development — M. Champion, D. Peterson, T. Peterson, C. Reid, M. Ruschman, FNAL	809

Proceedings of the 1993 Particle Accelerator Conference

Computer Simulation and Cold Model Testing of CCL Cavities — C. R. Chang, C. G. Yao, D. A. Swenson, L. W. Funk, SSCL	812
Drive Linac for the Argonne Wakefield Accelerator — E. Chojnacki, R. Konecny, M. Rosing, J. Simpson, ANL	815
Choice of the RF Cavity for the SSC Collider — W. Chou, SSCL	818
High Field Conditioning of Cryogenic RF Cavities — M. Cole, T. Debiak, C. Lom, W. Shephard, J. Sredniawski, Grumman	821
Status of the SSC LEB RF Cavity — P. Coleman, F. Brandeberry, C. Friedrichs, Y. Goren, T. Grimm, G. Hulsey, S. Kwiatkowski, A. Propp, L. Taylor, L. Walling, SSCL; J. Averbukh, M. Karliner, V. Petrov, S. Yakovlev, BINP	824
RF Commissioning of the Superconducting Super Collider Radio Frequency Quadrupole Accelerator — R. I. Cutler, G. Arbique, J. Grippe, S. Marsden, O. Marrufo, R. Rodriguez, SSCL	827
Design of a Tuner and Adjustable RF Coupler for a CW 2856 MHz RF Cavity — M. S. de Jong, F. P. Adams, R. J. Burton, R. M. Hutcheon, T. Tran-Ngoc, AECL, Chalk River; A. Zolfaghari, P. T. Demos, MIT-Bates	829
A 2856 MHz RF Cavity for the MIT-Bates South Hall Ring — M. S. de Jong, F. P. Adams, R. J. Burton, R. M. Hutcheon, T. Tran-Ngoc, AECL, Chalk River; A. Zolfaghari, P. T. Demos, MIT-Bates	832
Cavity RF Mode Analysis Using a Boundary-Integral Method — M. S. de Jong, F. P. Adams, AECL, Chalk River ..	835
Design Considerations for High-Current Superconducting RFQ's — J. R. Delayen, C. L. Bohn, W. L. Kennedy, L. Sagalovsky, ANL	838
Commissioning of the CEBAF Cryomodules — M. Drury, T. Lee, J. Marshall, J. Preble, Q. Saulter, W. Schneider, M. Spata, M. Wiseman, CEBAF	841
Design and Fabrication of High Gradient Accelerating Structure Prototype at 36.5 GHz — V. A. Dvornikov, I. A. Kuzmin, MEPI Russia.....	844
The SSC RFQ-DTL Matching Section Buncher Cavities — T. Enegren, C. M. Combs, Y. Goren, M. D. Hayworth, A. D. Ringwall, D. A. Swenson, SSCL.....	846
Bulk Niobium Low-, Medium- and High- β Superconducting Quarter Wave Resonators for the ALPI Postaccelerator — A. Facco, J. S. Sokolowski, INFN Legnaro; I. Ben-Zvi, BNL; E. Chiaveri, CERN; B. V. Elkonin, Weizmann Inst.	849
A Numerical Method for Determining the Coupling Strengths and Resonant Frequencies of a Nonperiodic Coupled Cavity Chain — M. Foley, T. Jurgens, FNAL	852
Thermal Study of HOM Couplers for Superconducting RF Cavities — M. Fouaidy, T. Junquera, IPN Orsay; S. Chel, A. Mosnier, Saclay	855
Very Wide Range and Short Accelerating Cavity for MIMAS — C. Fougeron, P. Ausset, D. de Menezes, J. Peyromaure, G. Charruau, LNS-CE Saclay	858
Fundamental Mode Detuned Travelling Wave Accelerating Structure — J. Gao, LAL Orsay	862
Demi-Disc Travelling Wave Accelerating Structure — J. Gao, LAL Orsay	865
Analytical Formulae for the Coupling Coefficient β Between a Waveguide and a Travelling Wave Structure — J. Gao, LAL Orsay	868
Automated Bead-Positioning System for Measuring Impedances of RF Cavity Modes — D. A. Goldberg, R. A. Rimmer, LBL	871
Measurements of Higher-Order Mode Damping in the PEP-II Low-Power Test Cavity — R. A. Rimmer, D. A. Goldberg, LBL	874
Nonlinear Effects in Ferrite Tuned Cavities — Y. Goren, N. K. Mahale, L. Walling, T. Enegren, G. Hulsey, SSCL; V. P. Yakovlev, V. M. Petrov, BINP	877
Eddy Current Analysis for the SSC Low Energy Booster Cavity — Y. Goren, L. Walling, F. Brandeberry, N. Spayd, SSCL	880
Voltage Counter-Phasing in the SSC Low Energy Booster — Y. Goren, SSCL; T. F. Wang, LANL	883
An Update on High Peak Power (HPP) RF Processing of 3 GHz Nine-Cell Niobium Accelerator Cavities — P. Barnes, J. Kirchgessner, D. Moffat, H. Padamsee, J. Sears, Cornell; C. Crawford, FNAL; J. Graber, P. Schmuizer, DESY	886
Microscopic Investigation of RF Surfaces of 3 GHz Niobium Accelerator Cavities Following RF Processing — P. Barnes, T. Flynn, J. Kirchgessner, J. Knobloch, D. Moffat, H. Muller, H. Padamsee, J. Sears, Cornell; J. Graber, DESY	889
A World Record Accelerating Gradient in a Niobium Superconducting Accelerator Cavity — P. Barnes, J. Kirchgessner, D. Moffat, H. Padamsee, J. Sears, Cornell; J. Graber, DESY	892

Each volume begins with this five-volume table of contents and ends with the five-volume author index. The chairman's foreword and a list of conference organizers and staff appear as front matter in Volume 1. A list of conference participants precedes the author index in Volume 5.

Characterization of NSLS Accelerating Cavities Using Impedance Measurement Techniques — S. M. Hanna, P. M. Stefan, NSLS-BNL	895
In Search of Trapped Modes in the Single-Cell Cavity Prototype for CESR-B — W. Hartung, Cornell; E. Haezel, CERN	898
Envelope Equations for Transients in Linear Chains of Resonators — H. Henke, M. Filtz, TU Berlin	901
A Broad-Band Side Coupled mm-Wave Accelerating Structure for Electrons — H. Henke, W. Bruns, TU Berlin	904
Accelerator Structure Development for NLC — H. A. Hoag, H. Deruyter, C. Pearson, R. D. Ruth, J. W. Wang, SLAC; J. Schaefer, Texas Inst.	907
HOM Damping with Coaxial Dampers in a Pillbox Cavity Without the Fundamental Mode Frequency Rejection Filter — Y. W. Kang, R. L. Kustom, J. F. Bridges, ANL	910
Reduced Length Design of 9.8 MHz RF Accelerating Cavity for the Positron Accumulator Ring (PAR) of the Advanced Photon Source (APS) — Y. W. Kang, J. F. Bridges, R. L. Kustom, ANL	913
Higher Order Mode Damping System in the UNK RF Cavity — V. Katalev, V. Kudryavtsev, I. Sulygin, IHEP	916
Status and Outlook for High Power Processing of 1.3 GHz TESLA Multicell Cavities — J. Kirchgessner, P. Barnes, J. Graber, D. Metzger, D. Moffat, H. Muller, H. Padamsee, J. Sears, M. Tigner, Cornell; L. Bartelson, M. Champion, C. Crawford, H. Edwards, K. Koepke, M. Kuchnir, H. Pfeiffer, FNAL; A. Matheisen, M. Pekeler, P. Schmüser, DESY	918
20 MV/m Accelerating Gradient with Heat Treatment of a Six Cell, 1.5 GHz Cavity for TESLA — J. Kirchgessner, P. Barnes, W. Hartung, D. Moffat, H. Padamsee, D. Rubin, J. Sears, M. Tigner, Cornell; M. Hiller, Babcock & Wilcox; D. Saraniti, SLAC; Q. S. Shu, SSCL	921
A New 50 MHz RF Cavity for Aladdin — K. J. Kleman, SRC Madison	924
Performance of a CEBAF Production Cavity After High-Temperature Heat Treatment — P. Kneisel, M. G. Rao, CEBAF	927
Suppression of Higher-Order Modes in an RF Cavity by Resistive Material — T. Koseki, Y. Kamiya, ISSP Tokyo; M. Izawa, KEK	930
A Coaxial-Type Accelerating System with Amorphous Material — V. A. Krasnopolsky, MRTI Russia	933
Applications and Comparisons of Methods of Computing the S Matrix of 2-Ports — R. M. Jones, K. Ko, S. Tantawi, SLAC; N. Kroll, UCSD/SLAC; D. U. L. Yu, DULY Res.	936
Construction of the CEBAF RF Separator — A. Krycuk, J. Fugitt, A. Johnson, R. Kazimi, L. Turlington, CEBAF	939
RF Cavity for the Medium Energy Booster for SSCL — S. Kwiatkowski, J. Curbow, T. Enegren, A. Propp, SSCL; V. P. Yakovlev, V. M. Petrov, Budker Inst.	941
New Achievements in RF Cavity Manufacturing — G. Lippmann, K. Pimiskern, H. Kaiser, Dornier GmbH	944
Analysis of Mechanical Fabrication Experience with CEBAF's Production SRF Cavities — J. Mammosser, P. Kneisel, J. F. Benesch, CEBAF	947
Microphonic Analysis of Cryo-Module Design — A. Marziali, H. A. Schwettman, Stanford U.	950
The Design of a Pill-Box Cavity with Waveguide HOM Suppressors — A. Massarotti, G. D'Auria, A. Fabris, C. Pasotti, C. Rossi, M. Svandrlík, Sinc. Trieste	953
Power Conditioning of the RF Cavities for ELETTRA — A. Massarotti, G. D'Auria, A. Fabris, C. Pasotti, C. Rossi, M. Svandrlík, Sinc. Trieste	956
High Power Test of a SLED System with Dual Side-Wall Coupling Irises for Linear Colliders — H. Matsumoto, H. Baba, A. Miura, S. Yamaguchi, KEK	959
Performance Tests of a Ferrite-Loaded Cavity Under Operation Conditions — S. Papureanu, Ch. Hamm, A. Schnase, H. Meuth, Jülich	962
CLIC Transfer Structure (CTS) Simulations Using "MAFIA" — A. Millich, CERN	965
Magnetron Sputtering Configuration for Coating 1.3 GHz Cavities with a Nb Film — M. Minestrini, M. Ferrario, S. Kulinski, INFN-LNF; S. Tazzari, INFN Roma	968
Accelerator Structure for Low-Energy Electron Beam — A. V. Mishin, MEPI Moscow	971
Higher Order Mode Dampers for the KAON Booster Cavity — A. K. Mitra, TRIUMF	974
Design and Fabrication of a Ferrite-Lined HOM Load for CESR-B — D. Moffat, P. Barnes, J. Kirchgessner, H. Padamsee, J. Sears, M. Tigner, A. Tribendis, V. Veshcherevich, Cornell	977
High-Beta Linac Accelerating Structure — V. G. Andreev, G. I. Batsikh, B. I. Bondarev, B. P. Murin, MRTI	980
Design of a 90° Overmoded Waveguide Bend — C. Nantista, UCLA; N. M. Kroll, UCSD/SLAC; E. M. Nelson, SLAC	983
Numerical Simulation of Coupler Cavities for Linacs — C.-K. Ng, H. Deruyter, K. Ko, SLAC	986

Proceedings of the 1993 Particle Accelerator Conference

TESLA Vertical Test Dewar Cryogenic and Mechanical Design — T. H. Nicol, D. E. Arnold, M.S. Champion, FNAL	989
Update of the TRISTAN Superconducting RF System — S. Noguchi, K. Akai, E. Kako, K. Kubo, T. Shishido, KEK	992
Cryostat for a Beam Test with the CESR-B Cavity — E. Nordberg, P. Barnes, R. Ehrlich, J. Kirchgessner, D. Metzger, D. Moffat, H. Muller, H. Padamsee, J. Sears, K. She, M. Tigner, Cornell; W. Fox, LANL; H. Heinrichs, U. Wuppertal	995
A Statistical Model for Field Emission in Superconducting Cavities — H. Padamsee, K. Green, W. Jost, B. Wright, Cornell	998
Design and Test of Prototype Cavities for the ELFA Linac — G. Bellomo, R. Parodi, G. Gemme, P. Fabbriatore, R. Musenich, B. Zhang, INFN	1001
Frequency Domain Determination of the Waveguide Loaded Q for the SSCL Drift Tube Linac — J. Petillo, W. Krueger, A. Mondelli, SAIC; J. Potter, AccSys Technology	1004
Some Operational Characteristics of CEBAF RF Windows at 2 K — H. L. Phillips, C. Reece, T. Powers, V. Nguyen-Tuong, CEBAF	1007
Photoemission Phenomena on CEBAF RF Windows at Cryogenic Temperatures — T. Powers, P. Kneisel, M. Vaidya, CEBAF	1010
Fabrication of the APS Storage Ring Radio Frequency Accelerating Cavities — K. Primdahl, J. Bridges, F. Depaola, R. Kustom, ANL; D. Snee, FNAL	1013
Performance of Production SRF Cavities for CEBAF — C. Reece, J. Benesch, P. Kneisel, P. Kushnick, J. Mammoser, T. Powers, CEBAF	1016
A New 15 MHz, 4 MV/m RF-Deflector for the Munich Heavy Ion Recoil Spectrometer (MRS)— K. Rudolph, P. Jaenker, U. Munich	1019
Superconducting Multicell Cavity Development Program at Los Alamos — B. Rusnak, G. Spalek, E. Gray, J. N. DiMarco, R. DeHaven, J. Novak, P. Walstrom, J. Zumbro, H. A. Thiessen, J. Langenbrunner, LANL ..	1021
L-Band Superconducting Cavities at KEK for TESLA — K. Saito, S. Noguchi, E. Kako, M. Ono, T. Shishido, T. Tajima, M. Matsuoka, H. Miwa, T. Suzuki, H. Umezawa, KEK	1024
Design of a HOM Damped Cavity for the ATF Damping Ring — S. Sakanaka, K. Kubo, T. Higo, KEK	1027
Measurement of Microwave Properties of X-Band Accelerating Structure Under Pulsed High-Power Operation at Liquid Nitrogen Temperature — A. J. Saversky, I. S. Shchedrin, MEPI Moscow	1030
RF Systems Engineering for the SSC Collider Rings — G. Schaffer, P. D. Coleman, R. E. Mustaine, J. D. Wallace, X. Q. Wang, Y. Zhao, J. D. Rogers, SSCL	1033
Impedance Calculations for a Coaxial Liner — M. Filtz, T. Scholz, TU Berlin.....	1036
Design of a High-Power Test Model of the PEP-II RF Cavity — H. D. Schwarz, R. A. Bell, J. A. Hodgson, J. G. Judkins, K. Ko, N. Kroll, C. K. Ng, R. P. Pendleton, K. Skarpaas, SLAC; G. Lambertson, R. Rimmer, LBL; M. S. deJong, T. Tran-Ngoc, F. P. Adams, M. G. Lipsett, W. Mellors, AECL	1039
Construction of a Superconducting RFQ Structure — K. W. Shepard, W. L. Kennedy, ANL; K. R. Crandall, AccSys Technology	1042
Niobium Coaxial Quarter-Wave Cavities for the New Delhi Booster Linac — K. W. Shepard, ANL; A. Roy, P. N. Potukuchi, Nuc. Science Ctr., New Delhi	1045
Design of High Power Model of Damped Linear Accelerating Structure Using Choke Mode Cavity — T. Shintake, KEK	1048
Suppression of Longitudinal Coupled-Bunch Instability Using Energy Storage Cavity in B-Factory RF System — T. Shintake, KEK	1051
A Two-Gap Booster Synchrotron RF Cavity — W. R. Smythe, D. C. Van Westrum, U. Colorado	1054
HOM (Higher-Order Mode) Test of the Storage Ring Single-Cell Cavity with a 20-MeV e^- Beam for the Advanced Photon Source (APS) — J. Song, Y. W. Kang, R. Kustom, ANL	1057
Performance of a 1500 MHz Niobium Cavity with 2K-LHe Channel Cooling — J. Susta, P. Kneisel, M. Wiseman, CEBAF	1060
Large Scale Production at Ansaldo of 352 MHz Niobium Coated LEP-CERN Cavities: Development Activities and First Results — A. Bixio, P. Gagliardi, M. Marin, S. Moz, W. Sciutto, F. Terzi, G. Zoni, Ansaldo	1063
RF Hardware Development Work for the CLIC Drive Beam — G. Carron, L. Thorndahl, CERN	1066
Accelerating Frequency Shift Minimization — A. V. Tiunov, V. I. Shvedunov, INP Moscow	1069

Each volume begins with this five-volume table of contents and ends with the five-volume author index. The chairmen's foreword and a list of conference organizers and staff appear as front matter in Volume 1. A list of conference participants precedes the author index in Volume 5.

Five-Volume Contents

Calculations and Model Measurements for the Euterpe Cavity — J. A. van der Heide, M. J. A. Rubingh, W. J. G. M. Kleeven, J. I. M. Botman, C. J. Timmermans, H. L. Hagedoorn, Eindhoven U. of Tech.	1072
APPLE Accelerator Prototype Cavity Fabrication and Low Power Tests — A. M. Vetter, T. L. Buller, T. D. Hayward, D. R. Smith, V. S. Starkovich, Boeing D&S	1075
Mechanically Tuned Accelerating Resonators — F. A. Vodopianov, MRTI	1078
Industrial Fabrication of Superconducting Accelerators — D. Dasbach, R. Fleck, D. Kiehlmann, M. Peiniger, H. Vogel, Siemens AG	1080
Broadband Higher-Order Mode (HOM) Damper for SSC LEB Ferrite-Tuned Cavity — L. Walling, G. Hulsey, T. Grimm, SSCL	1083
Design of the Detuned Accelerator Structure — J. W. Wang, E. M. Nelson, SLAC	1086
Construction of an RF Cavity for the LNLS Synchrotron — D. Wisnivesky, IFGW/ Unicamp/LNLS Brazil; M. A. Remy, R. H. A. Farias, LNLS Brazil	1089
Field Emitted Electron Trajectories for the CEBAF Cavity — B. C. Yunn, R. M. Sundelin, CEBAF	1092
Study on TESLA Cavity Shape — D. Zu, J. Chen, Beijing U.	1095

Power Technology and Miscellaneous Subsystems

Chair: D. Reid

Regulation Loops for the Ring Magnet Power Supplies in the SSC Accelerator Complex (<i>Invited Paper</i>) — E. J. Tacconi, C. F. Christiansen, SSCL	1098
High Power CW Klystron® Amplifier for 267 MHz — M. B. Shrader, D. H. Preist, R. N. Tornoe, Varian	1103
Development of Multimegawatt Klystrons for Linear Colliders — G. Caryotakis, R. Callin, K. Eppley, T. Lee, K. Fant, R. Fowkes, H. Hoag, C. Pearson, R. Phillips, S. Tantawi, A. Vlieks, E. Wright, SLAC; E. Lien, Los Altos, CA; G. Miram, Atherton, CA	1106
CEBAF's New RF Separator Structure Test Results — R. Kazimi, J. Fugitt, A. Krycuk, C. K. Sinclair, L. Turlington, CEBAF	1109
Frequency-Domain Analysis of Resonant-Type Ring Magnet Power Supplies — J. M. S. Kim, U. Victoria; K. W. Reiniger, TRIUMF	1112
The Workshop on Microwave-Absorbing Materials for Accelerators — I. E. Campisi, CEBAF.....	1115

Poster presentations:

Analysis and Applications of Quadrature Hybrids as RF Circulators — S. M. Hanna, J. Keane, NSLS-BNL	1118
Flower-Petal Mode Converter for NLC — H. A. Hoag, S. G. Tantawi, H. Deruyter, Z. D. Farkas, K. Ko, N. Kroll, T. L. Lavine, A. Menegat, A. E. Vlieks, SLAC	1121
Development of an S-Band RF Window for Linear Colliders — A. Miura, Grad. U. for Adv. Studies; H. Matsumoto, KEK	1124
High Power Test of RF Window and Coaxial Line in Vacuum — D. Sun, M. Champion, M. Gormley, Q. Kerns, K. Koepke, A. Moretti, FNAL	1127
Mode Selective Directional Coupler for NLC — S. G. Tantawi, SLAC	1130
Window Design with MAFIA — W. Bruns, H. Henke, B. Littmann, R. Lorenz, TU Berlin.....	1133
Dead-Time Tuning of a Pulsed RF Cavity — P. Balleyguier, CEA, Bruyères le Châtel	1136
Frequency Control of RF Booster Cavity in TRIUMF — K. Fong, M. Lavery, TRIUMF	1139
The Phase Servo Tuner Control System of the ALS 500 MHz Cavity — C. C. Lo, B. Taylor, LBL	1142
The Low Level System for the ELETTRA RF Plants — A. Massarotti, G. D'Auria, A. Fabris, C. Pasotti, V. Rizzi, C. Rossi, M. Svandrlik, Sinc. Trieste	1145
A Pulse Sequencer for the KAON Factory Beam Chopper — G. Waters, D. Bishop, M. J. Barnes, G. D. Wait, TRIUMF	1148
A Dual Frequency Resonator — P. Lanz, M. Lipnicky, M. Zach, TRIUMF	1151
The Los Alamos VXI-Based Modular RF Control System — S. P. Jachim, C. Ziomek, E. F. Natter, A. H. Regan, J. Hill, L. Eaton, W. D. Gutscher, M. Curtin, P. Denney, E. Hansberry, T. Brooks, LANL	1154
General Overview of the APS Low-Level RF Control System — J. D. Stepp, J. F. Bridges, ANL	1157
Operation of New RF Drivers for the Bevatron Local Injector — J. Calvert, J. Elkins, D. Howard, M. Hui, N. Kellogg, A. Lindner, R. Richter, LBL	1160
432-MHz RF Source for the JHP Proton Linac — M. Ono, S. Anami, H. Hanaki, Z. Igarashi, M. Kawamura, T. Kubo, C. Kubota, K. Kudo, E. Takasaki, T. Takenaka, KEK	1163

Volume 1: 1-747
 Volume 2: 748-1640
 Volume 3: 1641-2545
 Volume 4: 2546-3218
 Volume 5: 3219-3933

Proceedings of the 1993 Particle Accelerator Conference

Test Results of the AGS Booster Low Frequency RF System — R. T. Sanders, P. Cameron, R. Damm, A. Dunbar, M. Goldman, D. Kasha, A. McNerney, M. Meth, A. Ratti, R. Spitz, BNL	1166
Design and Test Results of a 600-kW Tetrode Amplifier for the Superconducting Super Collider — D. E. Rees, D. L. Brittain, LANL; J. M. Grippe, O. Maruffo, SSCL	1169
Conceptual Design of the 26.7. MHz RF System for RHIC — J. Rose, D. P. Deng, R. McKenzie-Wilson, W. Pirkel, A. Ratti, BNL	1172
Operation of a High-Power CW Klystron with the RFQ1 Facility — J. Y. Sheikh, A. D. Davidson, G. E. McMichael, L. W. Shankland, B. H. Smith, AECL, Chalk River	1175
Design and Results of a 1.3 MW CW Klystron for LEP — E.-G. Schweppe, R. Bachmor, E. Demmel, Philips RHW	1178
Interleaved Wide and Narrow Pulses for the KAON Factory 1 MHz Chopper — G. D. Wait, M. J. Barnes, D. Bishop, G. Waters, TRIUMF	1181
Considerations Regarding the Efficiency of High Power RF Sources for Particle Accelerators — G. Clerc, C. Bearzatto, M. Bres, G. Faillon, Ph. Guidee, Thomson Tubes Elect.	1184
Initial Commissioning of High Power, Long Pulse Klystrons for SSC Injector Linacs — P. Collet, J. C. Terrien, Ph. Guidee, Thomson Tubes Elect.	1187
Simulation of Traveling-Wave Output Structures for High Power rf Tubes — K. R. Eppley, SLAC	1190
Upgrade of an RF Source of the Linac for the B-Factory Project — S. Fukuda, S. Anami, Y. Saito, S. Michizono, K. Nakao, I. Sato, KEK	1193
High-Power RF Pulse Compression with SLED-II at SLAC — C. Nantista, UCLA; Z. D. Farkas, T. L. Lavine, A. Menegat, R. D. Ruth, S. G. Tantawi, A. E. Vlieks, SLAC; N. M. Kroll, UCSD	1196
Rigid-Beam Model of a High-Efficiency Magnicon — D. E. Rees, P. J. Talerico, LANL; S. J. Humphries, Jr., UNM	1199
High Power Operation Results of the X-Band SLED System — S. Tokumoto, H. Mizuno, KEK; O. Azuma, IHI Japan	1202
Automated Testing of a High-Power RF Microwave Tube — A. Young, D. E. Rees, A. Vergamini, LANL	1205
Two-Klystron Binary Pulse Compression at SLAC — Z. D. Farkas, T. L. Lavine, A. Menegat, A. E. Vlieks, J. W. Wang, P. B. Wilson, SLAC	1208
New Compact Mode Converters for SLAC RF Pulse Power Compression System — G. Luo, SRRRC Taiwan	1211
Performance of Litton 805 MHz, 12 MW Klystrons — Q. Kerns, M. B. Popovic, C. Kerns, A. Moretti, FNAL	1214
Higher-Order Modes in the APS Storage Ring Waveguides — S.O. Brauer, R. L. Kustom, ANL	1217
The Design and Production of the Higher-Order-Mode Loads for CEBAF — I. E. Campisi, L. K. Summers, B. H. Branson, A. M. Johnson, A. Betto, CEBAF	1220
The High Level RF System for Transition Crossing Without RF Focusing in the Main Ring at Fermilab — J. Dey, C. M. Bhat, A. Crawford, D. Wildman, FNAL	1223
RF System of the CW Race-Track Microtron-Recuperator for FELs — V. Arbuzov, S. Belomestnykh, A. Bushuyev, M. Fomin, N. Gavrilov, E. Gorniker, A. Kondakov, I. Kuptsov, G. Kurkin, V. Petrov, I. Sedlyarov, V. Veshcherevich, BINR, Russia.....	1226
Three Years of Operational Experience with the LEP RF System — S. Hansen, CERN	1229
Measured Performance of the GTA RF Systems — P. M. Denney, S. P. Jachim, LANL	1232
Improved RF System for Aladdin — K. J. Kleman, SRC Madison	1235
The ALS Storage Ring RF System — B. Taylor, C. C. Lo, K. Baptiste, J. Guigli, J. Julian, LBL	1238
The Upgrade Project for the RF System for the Brookhaven AGS — J. M. Brennan, D. J. Ciardullo, T. Hayes, M. Meth, A. J. McNerney, A. Otis, W. Pirkel, R. Sanders, R. Spitz, F. Toldo, A. Zaltsman, BNL	1241
Acceptance Test Performance of the Rocketdyne Radio Frequency Power System — M. Curtin, J. Hall, P. Metty, Rocketdyne; E. Gower, J. Manca, K. Whitham, Titan-Beta Corp.....	1244
The LEP II RF Power Generation System — H. Frischholz, CERN	1247
Overview and Status of RF Systems for the SSC Linac — J. Mynk, J. Grippe, R. I. Cutler, R. Rodriguez, SSCL	1250
Possibilities and Limitations for a Fully Digital RF Signal Synthesis and Control — H. Meuth, A. Schnase, H. Halling, Jülich	1253
RF System Analyses for the SSC Collider Rings — J. D. Rogers, P. D. Coleman, G. Schaffer, J. D. Wallace, X. Q. Wang, Y. Zhao, SSCL	1256
PEP-II Prototype Klystron — W. R. Fowkes, G. Caryotakis, T. G. Lee, C. Pearson, E. L. Wright, SLAC	1259

Each volume begins with this five-volume table of contents and ends with the five-volume author index. The chairmen's foreword and a list of conference organizers and staff appear as front matter in Volume 1. A list of conference participants precedes the author index in Volume 5.

Five-Volume Contents

Low Cost Concepts to Reduce the Voltage Ripple of the DC Power Supply — <i>Y. Cheng, K. Liu, SRRC Taiwan</i>	1262
Magnet Power Supply System for the ALS Storage Ring and Booster — <i>L. T. Jackson, K. Luchini, I. Lutz, LBL</i>	1265
Design and Development of Bipolar Power Supply for APS Storage Ring Correctors — <i>Y. G. Kang, ANL</i>	1268
Circuit Description of Unipolar DC-to-DC Converters for APS Storage Ring Quadrupoles and Sextupoles — <i>D. G. McGhee, ANL</i>	1271
PLL Subsystem for NSLS Booster Ring Power Supplies — <i>J. Murray, Stony Brook; R. Olsen, J. Dabrowski, BNL</i>	1274
Control and Performance of the AGS and AGS Booster Main Magnet Power Supplies — <i>R. K. Reece, R. Casella, B. Culwick, J. Geller, I. Marneris, J. Sandberg, A. Soukas, S. Y. Zhang, BNL</i>	1277
Hierarchical Modelling of Line Commutated Power Systems Used in Particle Accelerators Using Saber — <i>J. A. Reimund, SSCL</i>	1280
Independent Resonant System Tracking Considerations — <i>K. W. Reiniger, TRIUMF</i>	1283
Electrical Characteristics of the SSC Low-Energy Booster Magnet System — <i>A. Young, B. E. Shafer, LANL</i>	1285
Analysis and Design of a High-Current, High-Voltage Accurate Power Supply for the APS Storage Ring — <i>M. Fathizadeh, ANL</i>	1288
Design of the HIMAC Synchrotron Power Supply — <i>M. Kumada, K. Sato, A. Itano, M. Kanazawa, E. Takada, K. Noda, M. Sudou, T. Kohno, H. Ogawa, S. Yamada, Y. Sato, T. Yamada, A. Kitagawa, J. Yoshizawa, T. Murakami, Y. Hirao, NIRS; S. Matsumoto, Dokkyo U.; H. Sato, T. Sueno, T. Kato, K. Endo, KEK; K. Utino, Tsukuba Tech.; Y. Takada, U. Tsukuba; A. Noda, Kyoto U.; T. Tanabe, S. Watanabe, INS; S. Koseki, H. Kubo, Hitachi</i>	1291
A 2-Megawatt Load for Testing High Voltage DC Power Supplies — <i>D. Horan, R. Kustom, M. Ferguson, K. Primdahl, ANL</i>	1294
Energy Storage Inductor for the Low Energy Booster Resonant Power Supply System — <i>C. Jach, SSCL; A. Medvedko, S. Petrov, INP Moscow; V. Vinnik, Y. Fishler, UETM Russia</i>	1297
A High Power Water Cooled Resistor for the High Voltage Power Supply in the TRIUMF RF System — <i>K. Jensen, G. Blaker, R. Kuramoto, TRIUMF</i>	1300
Filament Power Supply Improvement of the TRIUMF RF System — <i>A. K. Mitra, J. J. Lu, TRIUMF</i>	1303
Advances in the Development of the Nested High Voltage Generator — <i>R. J. Adler, R. J. Richter-Sand, North Star Res. Corp.</i>	1306
High-Power Klystron Modulator Using a Pulse-Forming Line and Magnetic Switch — <i>M. Akemoto, S. Takeda, KEK</i>	1309
A Compact Modulator for RF Source Development — <i>J. D. Ivers, G. S. Kerslick, J. A. Nation, L. Schachter, Cornell</i>	1312
High Power Pulse Modulator for PLS Linac — <i>S. H. Nam, M. H. Cho, J. S. Oh, S. S. Park, W. Namkung, POSTECH</i>	1315
Pulse Modulator Developments in Support of Klystron Testing at SLAC — <i>R. F. Koontz, R. Cassel, J. de Lamare, D. Ficklin, S. Gold, K. Harris, SLAC</i>	1318
A Blumlein Type Modulator for 100-MW Class X-Band Klystron — <i>H. Mizuno, KEK; T. Majima, S. Sakamoto, Y. Kobayashi, IHI Japan</i>	1321
Noise Reduction Techniques Used on the High Power Klystron Modulators at Argonne National Laboratory — <i>T. J. Russell, ANL</i>	1324
Novel Gigawatt Power Modulator for RF Sources — <i>I. Yampolsky, G. Kirkman, N. Reinhardt, J. Hur, B. Jiang, Integrated App. Physics Inc.</i>	1327
Optimization of Speed-Up Network Component Values for the 30 Ω Resistively Terminated Prototype Kicker Magnet — <i>M. J. Barnes, G. D. Wait, TRIUMF</i>	1330
Test Results of the 8.35 kA, 15 kV, 10 pps Pulser for the Elettra Kickers — <i>R. Fabris, P. Tosolini, Sinc. Trieste</i>	1333
Preliminary Testing of the LEB to MEB Transfer Kicker Modulator Prototype — <i>G. C. Pappas, D. R. Askew, SSCL</i>	1336
A Novel Technique for Pulsing Magnet Strings with a Single Switch — <i>R. J. Sachschaale, C. Dickey, P. Morcombe, Duke</i>	1339
Linac Pulsed Quad Power Supply — <i>L. Bartelson, FNAL</i>	1342
The AGS New Fast Extracted Beam System Orbit Bump Pulser — <i>J. S. Chang, A. V. Soukas, BNL</i>	1345
Experimental Investigation of High Voltage Nanosecond Generators of Injection System for SIBERIA-2 Storage Ring — <i>A. Kadnikov, Y. Matveev, BINP</i>	1348

Volume 1: 1-747
 Volume 2: 748-1640
 Volume 3: 1641-2545
 Volume 4: 2546-3218
 Volume 5: 3219-3933

Proceedings of the 1993 Particle Accelerator Conference

Design and Preliminary Results for a Fast Bipolar Resonant Discharge Pulsar Using SCR Switches for Driving the Injection Bump Magnets at the ALS — G. Stover, L. Reginato, LBL	1351
Design and Preliminary Testing of the LEB Extraction Kicker Magnet at the SSC — D. E. Anderson, L. X. Schneider, SSCL	1354
Development of a High Quality Kicker Magnet System — J. Dinkel, B. Hanna, C. Jensen, D. Qunell, R. Reilly, FNAL	1357
Consequences of Kicker Failure During HEB to Collider Injection and Possible Mitigation — R. Soundranayagam, A. I. Drozhda, N. V. Mokhov, B. Parker, R. Schailley, F. Wang, SSCL	1360
High Efficiency Beam Deflection by Planar Channeling in Bent Silicon Crystals — K. Elsener, M. Clément, N. Doble, L. Gagnon, P. Grafström, CERN; S. P. Møller, E. Uggerhøj, T. Worm, ISA-Aarhus; M. Hage-Ali, P. Stiffert, Strasbourg	1363
Extraction from the Fermilab Tevatron Using Channeling with a Bent Crystal — G. Jackson, FNAL	1366
2 TeV HEB Beam Abort at the SSCL — R. Schailley, J. Bull, T. Clayton, P. Kocur, N. V. Mokhov, SSCL	1369
Electrostatic Septa Design and Performance for Injection and Extraction to and from the MIT-Bates South Hall Ring (SHR) — S. Sobczynski, R. Averill, M. Farkhondeh, W. Sapp, C. Sibley, MIT-Bates	1372
Injection into the Elettra Storage Ring — D. Tommasini, Sinc. Trieste	1375
The Septum Magnets System of Elettra — R. Fabris, F. Daclon, M. Giannini, D. Tommasini, P. Tosolini, Sinc. Trieste	1378
High Voltage Vacuum Insulation in Crossed Magnetic and Electric Fields — W. T. Diamond, AECL	1381
Injection System for the SIBERIA-2 Storage Ring — G. Erg, A. Evstigneev, V. Korchuganov, G. Kulipanov, E. Levichev, Yu. Matveev, A. Philipchenko, L. Schegolev, V. Ushakov, BINP	1384
Fixed Target to Collider Changeover at A0 — K. J. Weber, FNAL	1387
Surface Resistivity Tailoring of Ceramic Accelerator Components — S. Anders, A. Anders, I. Brown, LBL	1390
Compensation of Field Shaking Due to the Magnetic Vibration — Y. Cheng, C. Hwang, SRRC Taiwan	1393
Superconducting Cavity Tuner Performance at CEBAF — J. Marshall, J. Preble, W. Schneider, CEBAF	1396
Test Results and Design Considerations for a 500 MHz, 500 kW Vacuum Window for CESR-B — D. Metzger, P. Barnes, A. Helser, J. Kirchgessner, H. Padamsee, Cornell	1399
An Experimental and Analytical Study of a Buoyancy Driven Cooling System for a Particle Accelerator — B. Campbell, R. Ranganathan, SSCL	1402
Collider Bypass Diode Thermal Simulations and Measurements for the SSCL — C. Rostamzadeh, G. Tool, SSCL ..	1405
Frequency-Feedback Tuning for Single-Cell Cavity Under RF Heating — J. D. Stepp, J. F. Bridges, ANL	1408
A Device of Amplitude and Phase Stabilization for the FEL Injector in the L-Band — Q. Zhang, X. Wang, Y. Sun, S. Bu, M. Zhang, G. Su, CIAE China	1411
A Jet Neutralizer Concept — T. E. Horton, U. Mississippi	1413
Modulator Upgrade of the KEK 2.5-GeV Linac — T. Shidara, H. Honma, S. Anami, I. Sato, KEK	1416
NSLS X-Ray Ring RF System Upgrade — M. G. Thomas, R. Biscardi, W. Broome, S. Buda, R. D'Alsace, S. Hanna, J. Keane, P. Mortazavi, G. Ramirez, J. M. Wang, NSLS-BNL	1419
A Wide Tuning Range Rf Cavity with External Ferrite Biasing — X. Pei, BNL; S. Anderson, D. Jenner, D. McCammon, T. Sloan, IUCF	1421
Longitudinal RF Matching During AGS-RHIC Beam Transfer — X. Pei, BNL	1424
Photon Sources Chair: J. Galayda	
Commissioning and Performance of the ESRF (Invited Paper) — J. L. Laclare and the Project Team, ESRF	1427
Commissioning and Performance of the Advanced Light Source (Invited Paper) — A. Jackson, LBL	1432
Status of BESSY II, a High-Brilliance Synchrotron Radiation Source in the VUV to XUV Range (Invited Paper) — D. Krämer, BESSY	1436
A Superconducting Short Period Undulator for a Harmonic Generation FEL Experiment — G. Ingold, L. Solomon, I. Ben-Zvi, S. Krinsky, D. Li, D. Lynch, J. Sheehan, M. Woodle, X. Z. Qiu, L. H. Yu, X. Zhang, NSLS-BNL; W. Sampson, M. Gardner, K. Robins, BNL; I. Lehrman, R. Heuer, J. Sheehan, D. Weissenburger, Grumman Corp.	1439
UV-VUV FEL Program at Duke Storage Ring with OK-4 Optical Klystron — V. N. Litvinenko, J. M. J. Madey, Duke; N. A. Vinokurov, BINP-Novosibirsk	1442

Each volume begins with this five-volume table of contents and ends with the five-volume author index. The chairman's foreword and a list of conference organizers and staff appear as front matter in Volume 1. A list of conference participants precedes the author index in Volume 5.

Five-Volume Contents

A 2-4 nm Linac Coherent Light Source (LCLS) Using the SLAC Linac — H. Winick, K. Bane, R. Boyce, G. Loew, P. Morton, H.-D. Nuhn, J. Paterson, P. Pianetta, T. Raubenheimer, J. Seeman, R. Tatchyn, V. Vylet, SLAC; C. Pellegrini, J. Rosenzweig, G. Travish, UCLA; D. Prosnitz, T. Scharlemann, LLNL; K. Halbach, K.-J. Kim, M. Xie, LBL	1445
The Vanderbilt University Compton Scattering X-Ray Experiment — P. A. Tompkins, C. A. Brau, W. W. Dong, J. W. Waters, Vanderbilt U.; F. E. Carroll, D. R. Pickens, R. R. Price, VUMC	1448
Observations of Effects of Ion Accumulation in the Maxwell Model 1.2-400 Synchrotron Light Source — R. P. Johnson (now at CEBAF), D. Y. Wang, Maxwell Labs; H. Bluem, LSU	1451
A Progress Report on the Laboratório Nacional de Luz Síncrotron (Brazil) — A. R. D. Rodrigues, C. E. T. Gonçalves da Silva, D. Wisnivesky, LNLS Brazil	1454
An Overview of the PLS Project — T. Lee, POSTECH	1457
Present Status of SRRC — E. Yen, SRRC	1460
 <i>Poster presentations:</i>	
SOLEIL, a New Synchrotron Radiation Source for LURE — M. P. Level, P. Brunelle, P. Marin, A. Nadj, M. Sommer, H. Zyngier, LURE; J. Faure, J. Payet, A. Thatchenko, LNS	1465
Conceptual Design of a Compact Electron Storage Ring System Dedicated to Coronary Angiography — Y. Oku, K. Aizawa, S. Nakagawa, Kawasaki Heavy Ind.; M. Ando, K. Hyodo, S. Kamada, PF, KEK; H. Shiwa, JAERI	1468
Report on DELTA, One Year Before Routine Operation — N. Marquardt, U. Dortmund	1471
Lattice Design for the 1.7-GeV Light Source BESSY II — E. Jaeschke, D. Krämer, B. Kuske, P. Kuske, M. Scheer, E. Wehretter, G. Wüstefeld, BESSY	1474
The Synchrotron Light Source ROSY — D. Einfeld, H. Büttig, S. Dienel, W. Gläser, H. Guratzsch, B. Hartmann, D. Janssen, H. Krug, J. Linnemann, W. Matz, W. Neumann, W. Oehme, D. Pröhl, R. Schlenk, H. Tyrroff, Res. Ctr. Rossendorf; Th. Goetz, M. Picard, U. Bonn; J. B. Murphy, BNL; M. Plesko, D. Tomassini, Sincrotrone Trieste; R. Rossmanith, CEBAF	1477
A Source of Synchrotron Radiation for Research and Technology Applications — E. Bulyak, V. Chechetenko, A. Dovbnya, S. Efimov, A. Gevchuk, P. Gladikh, I. Karnaukhov, V. Kozin, S. Kononenko, V. Likhachev, V. Lyashchenko, V. Markov, N. Mocheshnikov, V. Moskalenko, A. Mytsykov, Yu. Popkov, A. Shcherbakov, M. Strelkov, A. Tarasenko, Yu. Telegin, V. Trotsenko, A. Zelinsky, Kharkov Inst.; V. Baryakhtar, V. Molodkin, V. Nemoshkalenko, A. Shpak, Metallophysics Inst.	1480
Optimum Steering of Photon Beam Lines in SPEAR — W. J. Corbett, B. Fong, M. Lee, V. Ziemann, SLAC	1483
Establishment of a Tolerance Budget for the Advanced Photon Source Storage Ring — H. Bizak, E. Crosbie, E. Lessner, L. Teng, ANL	1485
Study of Transverse Coupled Bunch Instabilities by Using Non-Linear Taylor Maps for the Advanced Light Source (ALS) — M. Meddahi, J. Bengtsson, LBL	1488
Plans to Increase Source Brightness of NSLS X-Ray Ring — J. Safraneck, S. Krinsky, NSLS-BNL	1491
A Design Concept for the Inclusion of Superconducting Dipoles Within a Synchrotron Light Source Lattice — M. W. Poole, J. A. Clarke, S. L. Smith, V. P. Suller, L. A. Welbourne, SERC Daresbury; N. A. Mezentssev, BINP Russia	1494
A Conceptual Design and Thermal Analysis of High Heat Load Crotch Absorber — I. C. Sheng, S. Sharma, E. Rotela, J. Howell, ANL	1497
Thermal Analysis of the Beam Missteering in APS Storage Ring — I. C. Sheng, J. Howell, S. Sharma, ANL	1500
Dynamic Response Analysis of the LBL Advanced Light Source Synchrotron Radiation Storage Ring — K. K. Leung, SSCL	1503
The Study of Seismic Vibration of SR Source "Zelenograd" — S. Kuznetsov, Kurchatov Inst.; E. Levichev, BINP	1506
Measurement of the Orbit Parameters at SOR-RING — H. Kudo, K. Shinoue, H. Takaki, T. Koseki, H. Ohkuma, Y. Kamiya, ISSP Tokyo	1509
Challenging Issues During ESRF Storage Ring Commissioning — A. Ropert, ESRF	1512
Upgrading to 500 mA of the Stored Beam Current at SORTEC 1-GeV Source Facility — M. Kodaira, N. Awaji, T. Kishimoto, K. Mukugi, M. Watanabe, SORTEC; T. Iida, H. Tsuchidate, Mitsubishi Corp.	1515
Performance of Upgraded SORTEC 1-GeV 500-mA SR Source Facility — T. Kishimoto, M. Kodaira, N. Awaji, K. Mukugi, M. Araki, SORTEC; Y. Kijima, M. Haraguchi, Mitsubishi Corp.	1518

Volume 1: 1-747
 Volume 2: 748-1640
 Volume 3: 1641-2545
 Volume 4: 2546-3218
 Volume 5: 3219-3933

Proceedings of the 1993 Particle Accelerator Conference

Design of Test Linac for Free Electron Laser — H. Kang, I. Ko, M. Cho, W. Namkung, POSTECH	1521
The Revised ELFA Project — E. Acerbi, F. Alessandria, G. Baccaglioni, G. Bellomo, C. Birattari, R. Bonifacio, I. Boscolo, A. Bosotti, F. Broggi, R. Corsini, L. De Salvo, D. Giove, C. Maroli, P. Pierini, N. Piovella, M. Pulia, G. Rivoltella, L. Rossi, G. Varisco, INFN/ U. Milan; P. Arcioni, M. Bressan, G. Conciauro, INFN Pavia; W. A. Barletta, LBL; G. Gemme, R. Parodi, INFN Genova; V. Stagno, V. Variale, INFN Bari.....	1524
Design and Construction of a Compact Infra Red Free Electron Laser CIRFEL — J. Krishnaswamy, I. S. Lehrman, J. Sheehan, R. L. Hauer, M. F. Reusch, R. Hartley, Grumman Aerospace Corp.	1527
Coherence and Linewidth Studies of a 4-nm High Power FEL — W. M. Fawley, A. M. Sessler, LBL; E. T. Scharlemann, LLNL	1530
Performance Characteristics, Optimization, and Error Tolerances of a 4 nm FEL Based on the SLAC Linac — K.-J. Kim, M. Xie, LBL; E. T. Scharlemann, LLNL; C. Pellegrini, G. Travish, UCLA	1533
X-Ray Beam Lines and Beam Line Components for the SLAC Linac Coherent Light Source (LCLS) — R. Tatchyn, P. Pianetta, SLAC	1536
Photon Pulse Filtering and Modulation Based on the Extreme Temporal Compression and Correlated Energy Spread of the Electron Bunches in the SLAC Linac Coherent Light Source (LCLS) — R. Tatchyn, SLAC	1539
Infrared (IR) vs. X-Ray Power Generation in the SLAC Linac Coherent Light Source (LCLS) — R. Tatchyn, SLAC	1542
Saturation of a High Gain FEL — R. L. Gluckstern, Maryland; S. Krinsky, BNL; H. Okamoto, Kyoto U.	1545
Numerical Studies of Strong Focusing in Planar Undulators — G. Travish, J. Rosenzweig, UCLA	1548
Generation of High Power 140 GHz Microwaves with an FEL for the MTX Experiment — S. L. Allen, C. J. Lasnier, B. Felker, M. Fenstermacher, S. W. Ferguson, S. Fields, E. B. Hooper, S. Hulsey, M. Makowski, J. Moller, W. Meyer, D. Petersen, E. T. Scharlemann, B. Stallard, R. Wood, LLNL	1551
Burst Mode FEL with the ETA-III Induction Linac — C. J. Lasnier, S. L. Allen, B. Felker, M. E. Fenstermacher, S. W. Ferguson, S. D. Hulsey, E. B. Hooper, M. C. Jackson, M. A. Makowski, W. H. Meyer, J. M. Moller, D. E. Petersen, S. E. Sampayan, B. W. Stallard, W. F. Fields, LLNL; K. Oasa, JAERI	1554
Design and Experiment of SG-1 FEL — Z. Hui, IEE China	1557
Electron Beam Quality Limitations and Beam Conditioning in Free Electron Lasers — P. Sprangle, G. Joyce, NRL; B. Hafizi, Icarus Res.; P. Serafim, Northeastern U.	1560
An Optical Approach to Emittance Compensation in FELs — G. R. Neil, H. Liu, CEBAF	1563
Ultrahigh-Brightness Microbeams: Considerations for Their Generation and Relevance to FEL — H. Ishizuka, Y. Nakahara, Fukuoka Inst. Tech.; S. Kawasaki, Saitama U.; K. Sakamoto, A. Watanabe, N. Ogiwara, M. Shiho, JAERI	1566
The Groove Guide: A Non-Conventional Interaction Structure for Microwave FEL Experiments — P. Arcioni, M. Bressan, G. Conciauro, U. of Pavia; F. Broggi, P. Pierini, INFN Milano	1569
First Undulators for the Advanced Light Source — E. Hoyer, J. Akre, J. Chin, B. Gath, D. Humphries, B. Kincaid, S. Marks, P. Pipersky, D. Plate, G. Portmann, R. Schlueter, LBL; W. Hassenzahl, LLNL	1572
Insertion Device Magnet Measurements for the Advanced Light Source — S. Marks, C. Cork, E. Hoyer, D. Humphries, B. Kincaid, D. Plate, A. Robb, R. Schlueter, C. Wang, LBL; W. V. Hassenzahl, LLNL	1575
Spectral Quality of ALS U5.0 Undulator and Field Error Effects — C. Wang, S. Marks, B. Kincaid, LBL	1578
Modeling and Measurement of the ALS U5 Undulator End Magnetic Structures — D. Humphries, K. Halbach, E. Hoyer, B. Kincaid, S. Marks, R. Schlueter, LBL	1581
Flux Shunts for Undulators — E. Hoyer, J. Chin, LBL; W. V. Hassenzahl, LLNL	1584
Design, Construction and Testing of Insertion Devices for ELETTRA — R. P. Walker, R. Bracco, A. Codutti, B. Diviacco, D. Mollo, D. Zangrando, Sinc. Trieste; C. Poloni, U. Trieste	1587
Performance Optimization of Pure Permanent Magnet Undulators — B. Diviacco, Sin. Trieste	1590
Magnetic Interaction Effects in ELETTRA Segmented Pure Permanent Magnet Undulators — B. Diviacco, R. P. Walker, Sinc. Trieste	1593
Planar Helical Undulator Sources of Circularly Polarized X-Rays — R. Carr, SSRL	1596
Polarized Wiggler for NSLS X-Ray Ring — A. Friedman, X. Zhang, S. Krinsky, E. B. Blum, NSLS-BNL; K. Halbach, LBL	1599
Magnetic Field Measurements of a Superconducting Undulator for a Harmonic Generation FEL Experiment at the NSLS — L. Solomon, G. Ingold, I. Ben-Zvi, S. Krinsky, L. H. Yu, NSLS-BNL; W. Sampson, K. Robins, BNL	1602

Each volume begins with this five-volume table of contents and ends with the five-volume author index. The chairman's foreword, and a list of conference organizers and staff appear as front matter in Volume 1. A list of conference participants precedes the author index in Volume 5.

Five-Volume Contents

Magnetic Performance of the NSLS Prototype Small-Gap Undulator — G. Rakowsky, R. Cover, Rockwell; L. Solomon, NSLS-BNL	1605
Design Considerations for a 60 Meter Pure Permanent Magnet Undulator for the SLAC Linac Coherent Light Source (LCLS) — R. Tatchyn, R. Boyce, K. Halbach, H.-D. Nuhn, J. Seeman, H. Winick, SLAC; C. Pellegrini, UCLA	1608
Adjustment and Measurement of a Hybrid Undulator — B. Wu, Y. Ma, B. Liu, Z. Zhang, CIAE China	1611
Coherent Radiation at Submillimeter and Millimeter Wavelengths — M. Oyamada, R. Kato, T. Nakazato, S. Urasawa, T. Yamakawa, M. Yoshioka, M. Ikezawa, K. Ishi, T. Kanai, Y. Shibata, T. Takahashi, Tohoku U.	1614
Suppression of Coherent Synchrotron Radiation in Conducting Boundaries — R. Kato, T. Nakazato, M. Oyamada, S. Urasawa, T. Yamakawa, M. Yoshioka, M. Ikezawa, K. Ishi, T. Kanai, Y. Shibata, T. Takahashi, Tohoku U.	1617
A Compact Tunable X-Ray Source Based on Parametric X-Ray Generation by Moderate Energy Linacs — X. K. Maruyama, K. Dinova, D. Snyder, Naval Postgraduate School; M. A. Piestrup, Q. Li, Adelphi Tech.; R. B. Fiorito, D. W. Rule, NSWC	1620
Fundamental and Harmonics of Thomson Backscattered X-Rays from an Intense Laser Beam — C. Tang, NRL; B. Hafizi, Icarus Res.; S. K. Ride, UCSD	1623
Generation of Intensive Long-Wavelength Edge Radiation in High-Energy Electron Storage Rings — O. V. Chubar, N. V. Smolyakov, Kurchatov Inst.	1626
The Radiation Emission by a High Energy Electron-Positron Pair and Ultrarelativistic Hydrogen-Like Atom Moving Through Thick Target — A. V. Koshelkin, MEPI	1629
Bremsstrahlung by the Bunch of Ultrarelativistic Charged Particles into a Thick Target — A. V. Koshelkin, MEPI ..	1632
Construction and Commissioning of the SRRC Storage Ring — Y. C. Liu, J. R. Chen, C. C. Kuo, SRRC	1635
Commissioning a Second Superconducting Wiggler in the Daresbury SRS — M. W. Poole, J. A. Clarke, P. D. Quinn, S. L. Smith, V. P. Suller, L. A. Welbourne, Daresbury	1638

Volume 3

Hadron RF Linacs, Cyclotrons, Radioactive Beams

Chair: R. Pollock

An Overview of Radioactive Beam Concepts (Invited Paper) — J. M. D'Auria, TRIUMF	1641
Heavy Ion Beam Accumulation, Cooling, and Experiments at the ESR (Invited Paper) — B. Franzke, K. Beckert, F. Bosch, H. Eickhoff, B. Franczak, A. Gruber, O. Klepper, F. Nolden, P. Raabe, H. Reich, P. Späthke, M. Steck, J. Struckmeier, GSI Darmstadt	1645
The Research Center for Nuclear Physics Ring Cyclotron (Invited Paper) — I. Miura, Osaka U.	1650
The Fermilab 400-MeV Linac Upgrade (Invited Paper) — C. W. Schmidt, FNAL	1655
Use of the Holifield Facility 25-MV Tandem Accelerator in the Oak Ridge Radioactive Ion Beam Project — C. M. Jones, R. C. Juras, M. J. Meigs, D. K. Olsen, ORNL	1660
Realistic Modeling of Radiation Transmission Inspection Systems — K. E. Sale, LLNL	1663
Overview of Accelerators in Medicine — A. J. Lennox, FNAL/Rush U.	1666
Commissioning of the First Drift Tube Linac Module in the Ground Test Accelerator — K. F. Johnson, O. R. Sander, W. H. Atkins, G. O. Bolme, S. Bowling, R. Cole, R. Connolly, P. Denney, J. Erickson, J. D. Gilpatrick, W. B. Ingalls, D. Kersteins, R. Kraus, W. P. Lysenko, D. McMurry, C. T. Mottershead, J. Power, C. Rose, D. P. Rusthoi, D. P. Sandoval, J. D. Schneider, M. Smith, G. Vaughn, E. A. Wadlinger, R. Weiss, V. Yuan, LANL	1669
Acceleration and Isobaric Separation of Radioactive Ion Beams With the Louvain-la-Neuve Isochronous Cyclotrons — M. Loiselet, N. Postiau, G. Ryckewaert, U. Catholique de Louvain; A. Morduev, R. Oganessian, JINR	1672
Linear Accelerator for Plutonium Conversion and Transmutation of NPP Wastes — I. M. Kapchinsky, I. V. Chuvalo, A. A. Kolomiets, N. V. Lazarev, I. M. Lipkin, V. K. Plotnikov, I. A. Vorobjov, ITEP Moscow	1675

Poster presentations:

Acceleration and Transverse Focusing of Ion Beams in Lineondutron — E. S. Masunov, MEPI	1681
Linac Design Study for an Intense Neutron-Source Driver — M. T. Lynch, A. Browman, R. DeHaven, R. Jameson, A. Jason, G. Neuschaefer, P. Tallerico, A. Regan, LANL	1683

Volume 1: 1-747
 Volume 2: 748-1640
 Volume 3: 1641-2545
 Volume 4: 2546-3218
 Volume 5: 3219-3933

Proceedings of the 1993 Particle Accelerator Conference

Design and Operation of the HIMAC Injector — T. Murakami, H. Ogawa, S. Yamada, Y. Sato, T. Yamada, A. Kitagawa, J. Yoshizawa, S. Fu, T. Kohno, K. Sato, A. Itano, M. Kumada, E. Takada, M. Kanazawa, K. Noda, M. Sudou, Y. Hirao, Nat. Inst. of Radiological Sciences; O. Morishita, K. Sawada, Sumitomo Heavy Ind.	1686
Time-of-Flight Measurements of Absolute Beam Energy in the Fermilab Linac — M. B. Popovic, T. L. Owens, T. K. Kroc, L. J. Allen, C. W. Schmidt, FNAL	1689
Phase Scan Signature Matching for Linac Tuning — T. L. Owens, M. B. Popovic, E. S. McCrory, C. W. Schmidt, L. J. Allen, FNAL	1691
Operational Status of the Uranium Beam Upgrade of the ATLAS Accelerator — R. C. Pardo, L. M. Bollinger, J. A. Nolen, K. W. Shepard, P. Billquist, J. M. Bogaty, B. E. Clift, R. Harkewicz, F. H. Munson, J. E. Specht, G. P. Zinkann, ANL	1694
One Year Operation of the 7 MeV Proton Linac — T. Shirai, H. Dewa, H. Fujita, M. Ikegami, Y. Iwashita, S. Kakigi, H. Okamoto, A. Noda, M. Inoue, Kyoto U.	1697
The SSC Linear Accelerator — L. W. Funk, SSCL	1700
Finalized Design of the SSC RFQ-DTL Matching Section — M. Haworth, C. Combs, P. Datte, T. Enegren, W. Funk, Y. Goren, F. Guy, J. Hurd, G. Jamieson, D. Martin, A. Ringwall, R. Sethi, D. Swenson, SSCL; D. Barlow, R. Kraus, R. Meyer, LANL	1703
Accelerator Readiness Review Process for the SSC Linac — J. F. Tooker, T. Benke, L. W. Funk, V. Oliphant, SSCL	1706
Commissioning Status of the Continuous Wave Deuterium Demonstrator — P. Den Hartog, J. Dooling, M. Lorello, J. Rathke, Grumman Aerospace; J. Carwardine, D. Godden, G. Pile, Culham Lab.; T. Yule, T. Zinneman, ANL	1709
Design Study for a Superconducting Proton Linac From 20 to 100 MeV — T. P. Wangler, R. Garnett, F. Krawczyk, J. Billen, N. Bultman, K. Christensen, W. Fox, R. Wood, LANL	1712
Design Considerations for High-Current Superconducting Ion Linacs — J. R. Delany, C. L. Bohn, B. J. Micklich, C. T. Roche, L. Sagalovsky, ANL	1715
Special Design Problems and Solutions for High Powered Continuous Duty Linacs — D. Liska, L. Carlisle, G. McCauley, LANL; S. Ellis, P. Smith, Grumman Aerospace	1718
Status of CIAE Medical Cyclotron — X. Zhang, Z. Li, M. Fan, CIAE China	1721
A 600 MeV Cyclotron for Radioactive Beam Production — D. J. Clark, LBL	1724
Development of a Compact Permanent Magnet Cyclotron for Accelerator Mass Spectrometry — A. T. Young, D. J. Clark, K. Halbach, W. B. Kunkel, K. N. Leung, C. Y. Li, A. Rawlins, R. D. Schlueter, M. E. Stuart, R. P. Wells, LBL; J. X. Yu, Beijing U.; K. J. Bertsch, SSCL	1727
Performance of H ⁺ /D ⁺ Cyclotron Using Internal Source — T. T. Y. Kuo, TRIUMF; G. O. Hendry, Cyclotron Inc.	1730
Operation of the TR30 "Industrial" Cyclotron — K. Erdman, R. Dawson, Ebco Tech./TRIUMF; B. Milton, N. Stevenson, TRIUMF	1733
The First Year with Electron Cooling at CRYRING — K. Abrahamsson, G. Andler, L. Bagge, E. Beche, P. Carlé, H. Danared, K. Ehrnström, M. Engström, Å. Engström, C. J. Herrlander, J. Hilke, J. Jeansson, A. Källberg, S. Leontein, L. Liljeby, A. Nilsson, A. Paál, A. Pikin, K.-G. Rensfelt, U. Rosengård, J. Starker, M. af Ugglas, Manne Siegbahn Inst. Stockholm	1735
Electron Cooling of Heavy Ions at GSI — M. Steck, K. Beckert, H. Eickhoff, B. Franzke, F. Nolden, P. Spädike, GSI Darmstadt	1738
The Aarhus Storage Ring for Ions and Electrons ASTRID — S. P. Møller, Aarhus U.	1741
Recent Developments at the Gustaf Werner Cyclotron and CELSIUS — D. Reistad, Svedberg Lab.	1744
Ion Beam Acceleration and New Operation Modes at the TSR Heidelberg — M. Grieser, D. Habs, R.v. Hahn, B. Hochadel, C. M. Kleffner, J. Liebmann, R. Repnow, D. Schwalm, MPI Heidelberg; G. Bisoffi, INFN Legnaro; E. Jaeschke, BESSY; S. Papureanu, IFIN Bucurest.....	1747
A New Design for an EMIS-CYCLOTRON System, for Direct Production of Gaseous PET Radioisotopes — H. Ayvazian, Ion Beam App. Lab.	1750
The Chandigarh Variable Energy Cyclotron and Its Application for Trace Element Analysis Using PIXE Techniques — I. M. Govil, Panjab U.	1753
Proton Linacs for Boron Neutron Capture Therapy — A. J. Lennox, FNAL/Rush U.	1756
Modeling and System Specifications for an Integrated 3-D Proton Treatment Delivery System — J. W. Staples, B. A. Ludewigt, LBL	1759

Each volume begins with this five-volume table of contents and ends with the five-volume author index. The chairman's foreword and a list of conference organizers and staff appear as front matter in Volume 1. A list of conference participants precedes the author index in Volume 5.

Five-Volume Contents

Shielding and Activation Study for Proton Medical Accelerators — H. B. Knowles, J. L. Orthel, B. W. Hill, G. H. Gillespie Assoc.	1762
Beam Dynamics Studies for Proposed Proton Therapy Facility — D. Raparia, W. Funk, SSCL	1765
Compact Protontherapy Unit Predesign — D. Tronc, G.E.	1768
High Energy Accelerator Technology in Radiology — J. F. Crawford, B. Larsson, H. Reist, U. Zurich/PSI; L. Goldin, ITEP Moscow; H. Condé, K. Elmgren, E. Grusell, B. Nilsson, O. Pettersson, T. Rönngvist, U. Uppsala	1771
The Neutral Particle Beam Space Experiment (NPBSE) Accelerator Designs — C. C. Paulson, A. M. M. Todd, S. L. Mendelsohn, Grumman	1774
The Continuous Wave Deuterium Demonstrator (CWDD) Design and Status — A. M. M. Todd, Grumman; M. P. S. Nightingale, Culham Lab.; T. J. Yule, ANL	1777
Beam Matching Section in the INS Heavy Ion Linac Complex — K. Niki, S. Arai, Y. Hashimoto, H. Masuda, M. Tomizawa, K. Yoshida, INS Tokyo	1780
A Heavy Ion Linac Complex for Unstable Nuclei — S. Arai, M. Doi, Y. Hashimoto, A. Imanishi, T. Katayama, H. Masuda, K. Niki, Y. Takeda, N. Tokuda, M. Tomizawa, E. Tojyo, K. Yoshida, M. Yoshizawa, INS Tokyo; T. Hattori, Tokyo Inst. of Tech.	1783
Interdigital-H Linac for Unstable Nuclei at INS — M. Tomizawa, S. Arai, M. Doi, T. Katayama, K. Niki, M. Yoshizawa, INS Tokyo; T. Hattori, Tokyo Inst. of Tech.	1786
SPIRAL: A Radioactive Ion Beam Facility at GANIL — A. Joubert, R. Anne, P. Bertrand, MP. Bourgarel, C. Bieth, B. Bru, A. Chabert, M. Duval, R. Leroy, Ch. Ricaud, P. Sortais, GANIL	1789
On Line Isotopic Separator Test Benches at GANIL — R. Anne, B. Bru, A. Joubert, R. Leroy, M. Lewitowicz, P. Sortais, M. G. Saint Laurent, C. Tribouillard, GANIL; J. Obert, J. C. Putaux, IPN Orsay; C. F. Liang, P. Paris, CSNSM Orsay; N. Orr, J. C. Steckmeyer, LPC-ISMRA	1792
The Outlook of MPC-10 Cyclotron Use for the Solution of Applied Problems — S. T. Latushkin, V. V. Leonov, A. A. Ogloblin, L. I. Yudin, V. E. Yarosh, D. I. Yartsev, Kurchatov Inst.	1795
ITEP Heavy Ion Alternating Phase Focusing Linac — V. V. Kushin, N. A. Nesterov, I. O. Parshin, S. V. Plotnikov, ITEP Moscow	1798

Accelerator Control Systems

Chair: D. Gurd

Sharing Control System Software (Invited Paper) — P. Clout, Vista Systems	1801
Control System Architecture: The Standard and Non-Standard Models (Invited Paper) — M. E. Thuot, L. R. Dalesio, LANL	1806
Anatomy of a Control System: A System Designer's View — S. Magyary, LBL	1811
Beam Position Monitor Data Acquisition for the Advanced Photon Source — F. R. Lenkszus, E. Kahana, A. J. Votaw, G. A. Decker, Y. Chung, D. J. Ciarlette, R. J. Laird, ANL	1814
New Tevatron Cryogenic Control System — B. Lublinsky, J. Firebaugh, J. Smolucha, FNAL	1817
Control Software for EUTERPE — P. D. V. van der Stok, F. van den Berk, R. Deckers, Y. van de Vijver, J. I. M. Botman, J. L. Delhez, C. J. Timmermans, Tech. U., Eindhoven	1820

Poster presentations:

Network Management of Real-Time Embedded Processors — C. Kalbfleisch, S. Hunt, K. Low, D. Mathieson, SSCL	1823
High Speed Serial Communications for Control Systems — D. Mathieson, C. Kalbfleisch, S. Hunt, K. Low, SSCL	1826
"BUBBANET": A High Performance Network for the SSC Accelerator Control System — S. Hunt, C. Kalbfleisch, K. Low, D. Mathieson, SSCL	1829
Gateway for Inter-Network Connection in the Pohang Light Source Control System — S. C. Won, S. Kwon, POSTECH	1832
The Star, a Dynamically Configured Dataflow Director for Realtime Control — M. Bickley, J. Kewisch, CEBAF	1835
The SSCL Linac Control System — J. Heefner, C. Cuevas, S. Hunt, D. Murray, J. Sage, SSCL	1838
Proposal to Use Failure Prediction as a Means of Meeting Availability Requirements at the SSC — S. Sarkar, W. Merz, F. Meyer, SSCL	1841
Control, Timing, and Data Acquisition for the Argonne Wakefield Accelerator (AWA) — P. Schoessow, C. Ho, J. Power, E. Chojnacki, ANL	1844

Volume 1: 1-747
 Volume 2: 748-1640
 Volume 3: 1641-2545
 Volume 4: 2546-3218
 Volume 5: 3219-3933

Proceedings of the 1993 Particle Accelerator Conference

The High Level Programmer and User Interface of the NSLS Control System — Y. N. Tang, J. D. Smith, NSLS-BNL; S. Sathe, AGS-BNL	1846
NSLS Control Monitor and Its Upgrade — S. Ramamoorthy, J. D. Smith, NSLS-BNL	1849
NSLS Control System Upgrade Status — J. Smith, S. Ramamoorthy, Y. Tang, J. Flannigan, S. Sathe, J. Keane, S. Krinsky, NSLS-BNL	1852
Digital Signal Array Processor for NSLS Booster Power Supply Upgrade — R. Olsen, J. Dabrowski, BNL; J. Murray, Stony Brook	1855
Control System for NSLS Booster Power Supply Upgrade II — R. Olsen, J. Dabrowski, BNL; J. Murray, Stony Brook	1858
Software Environment and Configuration for the DSP Controlled NSLS Booster Power Supplies — R. Olsen, J. Dabrowski, NSLS-BNL; J. Murray, Stony Brook	1861
Control Units for APS Power Supplies — O. D. Despe, C. Saunders, D. McGhee, ANL	1864
High Resolution ADC Interface to Main Magnet Power Supply at the NSLS — M. Bordoley, NSLS-BNL	1867
Design of the Advanced Light Source Timing System — M. Fahmie, LBL	1869
Ring Diagnostics and Consistency Test of the Model for the AGS Booster — A. Luccio, E. H. Auerbach, BNL	1872
Use of Design Codes for On-Line Beam Diagnostics at the MIT-Bates Accelerator — K. D. Jacobs, B. G. McAllister, J. B. Flanz, MIT Bates	1875
A Graphical User-Interface Control System at SRRRC — J. S. Chen, C. J. Wang, S. J. Chen, G. J. Jan, SRRRC Taiwan	1878
Machine Protection System Algorithm Compiler and Simulator — G. R. White, G. Sherwin, SLAC	1881
MPS VAX Monitor and Control Software Architecture — S. Allison, N. Spencer, K. Underwood, D. VanOlst, M. Zelanzy, SLAC	1884
The Continuous and Seamless Replacement of a Running Control System Succeeded — G.v. Egan-Krieger, R. Müller, J. Rahn, BESSY	1887
Control and Data Acquisition System of Electron Accelerator for Radiation Processing — W. Maciszewski, J. Lukasiewicz, W. Migdal, A. G. Chmielewski, Inst. of Nuc. Tech., Warsaw	1890
Expert System for Magnetic Systems Investigations — S. Lima, R. V. Poliakova, F. F. Nodarse, I. P. Yudin, JINR Moscow	1892
Orbit Correction Implementation at CEBAF — M. Bickley, B. A. Bowling, D. Douglas, A. Hofler, J. Kewisch, G. A. Krafft, CEBAF	1895
Controls Interface Protocols for the SSC Correction and 'DC' Magnet Power Supplies — S. Sarkar, J. Gannon, W. Merz, F. Meyer, SSCL	1898
Parametrization of the AmPS Magnets for the Control System — Y. Wu, G. van Garderen, R. Hart, J. van der Laan, R. Maas, F. Schimmel, NIKHEF-K	1901
Global Voltage Control for the LEP RF System — E. Ciapala, A. Butterworth, E. Peschardt, CERN	1903
Designing RF Control Subsystems Using the VXIbus Standard — J. D. Stepp, F. C. Vong, J. F. Bridges, ANL	1906
Automated Measurement of Cavity Frequency and Cavity Tuning at CEBAF — R. Li, S. N. Simrock, B. C. Yunn, CEBAF	1909
A Beam Position Monitor Data Acquisition System for the New Fermilab 400 MeV Line — S. Lackey, J. Firebaugh, C. Johnstone, W. Marsh, J. Smolucha, K. Woodbury, FNAL	1912
A VME Based Quench Protection Monitor for the Tevatron Low Beta Quadrupoles — S. Lackey, C. Briegel, L. Chapman, R. Flora, K. Martin, FNAL; T. Savord, SSCL	1914
Experience with the TRIUMF Main Tank Vacuum Control System — S. Sarkar, D. P. Gurd, SSCL; J. C. Yandon W. Sievers, P. Bennett, P. Harmer, J. Nelson, TRIUMF	1916
Laser Power Stabilization in the TRIUMF Optically Pumped Polarized H ⁻ Ion Source — S. Sarkar, SSCL	1919
MPS Beam Control Software Architecture — K. Krauter, M. Crane, SLAC	1922
The CEBAF Analog Monitor System — K. Crawford, M. O'Sullivan, J. Perry, S. Simrock, CEBAF	1925
Techniques for Increasing the Reliability of Accelerator Control System Electronics — J. Utterback, FNAL	1928
WindoWorks: A Flexible Program for Computerized Testing of Accelerator Control System Electronic Circuit Boards — J. Utterback, FNAL	1931
Switching the Fermilab Accelerator Control System to a Relational Database — S. Shtirbu, FNAL	1934
The Impact of New Accelerator Control Software on LEP Performance — R. Bailey, A. Belk, P. Collier, M. Lamont, G. de Rijk, M. Tarrant, CERN	1937

Each volume begins with this five-volume table of contents and ends with the five-volume author index. The chairmen's foreword and a list of conference organizers and staff appear as front matter in Volume 1. A list of conference participants precedes the author index in Volume 5.

Five-Volume Contents

A Software System for Modeling and Controlling Accelerator Physics Parameters at the Advanced Light Source — L. Schachinger, V. Paxson, LBL	1940
Machine Physics Application Program for Control, Commissioning and Error Findings for Storage Rings — H. P. Chang, C. H. Chang, C. C. Kuo, M. H. Wang, J. C. Lee, J. Y. Fan, H. J. Tsai, SRRC Taiwan; C. S. Hsue, SRRC/Nat. Tsing Hua U.	1943
CATER: An Online Problem Tracking Facility for SLC — R. C. Sass, H. Shoaee, SLAC	1946
Ramping Control Using a Spreadsheet — D. Y. Wang, R. P. Johnson (now at CEBAF), L. S. B. Ng, W. J. Pearce, Maxwell Labs	1949
Easy and Effective Applications Programs Using DataViews — E. S. McCrory, FNAL	1952
The Graphic Environment for Transport Line Control and Beam Diagnostics — S. Kuznetsov, Kurchatov Inst.	1955
An I/O Subnet for the APS Control System: The BITBUS Universal Gateway — G. J. Nawrocki, N. D. Arnold, M. G. Hoffberg, J. R. Winans, S. J. Benes, ANL	1957
Status and Design of the Advanced Photon Source Control System — W. McDowell, M. Knott, F. Lenkszus, M. Krammer, N. Arnold, R. Daly, ANL	1960
Controlling the Third Harmonic Cavity During Focus Free Transition Crossing in the Fermilab Main Ring — M. A. Martens, FNAL	1963
AMS: Area Message Service for SLC — M. Crane, R. Mackenzie, D. Millsom, M. Zelazny, SLAC	1966
Adding PCs to SLC Control System — T. Lahey, S. Levitt, R. MacKenzie, N. Spencer, K. Underwood, SLAC	1969
Precise System Stabilization at SLC Using Dither Techniques — M. C. Ross, L. Hendrickson, T. Himel, E. Miller, SLAC	1972
Thermal Stabilization of Low Level RF Distribution Systems at SLAC — D. McCormick, M. Ross, T. Himel, N. Spencer, SLAC	1975
 Lepton Circular Colliders, Synchrotrons, and Microtrons Chair: A. Sessler	
CESR Luminosity Upgrades and Experiments (<i>Invited Paper</i>) — D. Rice, Cornell	1978
LEP Status and Future Plans (<i>Invited Paper</i>) — L. R. Evans, CERN	1983
Challenges on the High Luminosity Frontier of e^+e^- Factories (<i>Invited Paper</i>) — W. A. Barletta, LBL/UCLA	1988
DAFNE, The Frascati F-Factory (<i>Invited Paper</i>) — G. Vignola, INFN-LNF	1993
Commissioning Results of the Amsterdam Pulse Stretcher/Storage Ring APS — R. Maas, F. Kroes, J. van der Laan, G. Luijckx, J. Noomen, Y. Wu, NIKHEF	1998
 <i>Poster presentations:</i>	
LEP Operation in 1992 with a 90° Optics — R. Bailey, T. Bohl, F. Bordry, H. Burkhardt, K. Cornelis, P. Collier, B. Desforges, A. Faugier, V. Hatton, M. Jonker, M. Lamont, J. Miles, G. de Rijk, H. Schmickler, CERN	2001
Status of TRISTAN-II Project — S. Kurokawa, KEK	2004
The Long Range Beam-Beam Interaction at CERN: Experiments, Simulations and Phenomenology — A. B. Temnykh, INP Novosibirsk; J. J. Welch, D. H. Rice, Cornell	2007
PEP-II Design Update and R&D Results — W. Barletta, M. S. Zisman, LBL; R. A. Bell, J. M. Dorfan, SLAC	2010
Commissioning and Operation of the LEP Pretzel Scheme — R. Bailey, J. M. Jowett, W. Kalbreier, D. Wang, CERN	2013
Progress of the LEP Energy Upgrade Project — C. Wyss, CERN	2016
Flat Beams in the SLC — C. Adolphsen, T. Barklow, D. Burke, F.-J. Decker, P. Emma, M. Hildreth, T. Himel, P. Krejcik, T. Limberg, M. Minty, N. Phinney, P. Raimondi, T. Raubenheimer, M. Ross, J. Seeman, R. Siemann, W. Spence, N. Walker, M. Woodley, SLAC	2019
The Damping Ring For Novosibirsk F- and B-Factories — V. V. Anashin, S. E. Belomestnykh, A. A. Didenko, N. S. Dikansky, B. I. Grishanov, P. M. Ivanov, V. A. Kiselev, V. I. Kudelainen, N. A. Kuznetsov, V. A. Lebedev, B. L. Militsin, S. I. Mishnev, V. V. Parkhomchuk, A. N. Voroshilov, M. N. Zakhvatkin, BINP, Russia	2022
A Possible Redesign of the SLAC SLC Damping Rings — T. O. Raubenheimer, R. Early, T. Limberg, H. Moshhammer, J. Spencer, SLAC	2025
Update on the Argonne Positron Accumulator Ring — M. Borland, ANL	2028
Measurement on the SRRC 1.3 GeV Electron Booster Synchrotron Operation Parameters and the Ramping Behavior — K. K. Lin, K. T. Hsu, T. S. Ueng, SRRC Taiwan	2031

Volume 1: 1-747
 Volume 2: 748-1640
 Volume 3: 1641-2545
 Volume 4: 2546-3218
 Volume 5: 3219-3933

Proceedings of the 1993 Particle Accelerator Conference

1.3 GeV Electron Synchrotron — J. Modér, Scanditronix	2034
Performance of the ALS Injection System — C. H. Kim, LBL	2036
Synchrotron of SPring-8 — H. Yonahara, H. Suzuki, T. Aoki, S. Yoneyama, Y. Ueyama, Y. Sasaki, T. Nagafuchi, S. Hayashi, H. Yokomizo, JAERI	2039
Further Study of JINR Tau-Charm Factory Design — E. Perelstein, V. Alexandrov, V. Antropov, O. Arkhipov, P. Beloshitsky, L. Bobyleva, V. Kazacha, N. Kazarinov, A. Krasnykh, V. Mironov, D. Kalichev, L. Onischenko, A. Sissakian, Yu. Smirnov, Ts. Vylov, JINR Dubna; V. Belov, B. Mudiugin, A. Popov, D. Serebrennikov, SRI St. Petersburg; I. Kvashonkin, E. Petrov, I. Umansky, Russian Inst., St. Petersburg ...	2042
A Versatile Lattice for a Tau-Charm Factory That Includes a Monochromatization Scheme (Low Emittance) and a Standard Scheme (High Emittance) — A. Faus-Golfe, U. Valencia; J. Le Duff, LAL Orsay	2045
DAFNE Interaction Region Design — M. Bassetti, M. E. Biagini, C. Biscari, M. A. Preger, G. Raffone, G. Vignola, INFN-LNF	2048
On an Asymmetric Correlated Flavor Factory — D. Cline, A. Boden, W. Gabella, A. Garren, X. Wang, UCLA	2051
Status of the MIT-Bates South Hall Ring Commissioning — J. B. Flanz, K. D. Jacobs, B. McAllister, R. Averill, S. Bradley, A. Carter, K. Dow, M. Farkondeh, E. Ihloff, S. Kowalski, W. Sapp, C. Sibley, D. Tieger, C. Tschalaer, A. Zolfaghari, MIT-Bates	2054
Current Status of the Design of the Kharkov Pulse Stretcher Ring PSR-2000 — S. Efimov, P. Gladikh, Y. Grigor'ev, I. Guk, I. Karnaukhov, V. Kozin, S. Kononenko, V. Likhachev, V. Markov, N. Mocheshnikov, V. Moskalenko, A. Mytsykov, Yu. Popkov, A. Shcherbakov, M. Strelkov, A. Tarasenko, Yu. Telegin, A. Zelynsky, Kharkov Inst.; M. Nagaenko, Yu. Severgin, ESRI	2057
Moscow State University CW Race-Track Microtron Status — V. I. Shvedunov, A. S. Alimov, A. S. Chepurnov, O. V. Chubarov, I. V. Gribov, B. S. Ishkhanov, I. V. Surma, A. V. Tiunov, INP Moscow	2059
Optical Design of the 75-MeV Eindhoven Racetrack Microtron — G. A. Webers, J. L. Delhez, J. I. M. Botman, H. L. Hagedoorn, Eindhoven U. of Tech.	2062
Example Application for the Hamiltonian Description of an Azimuthally Varying Field Racetrack Microtron — J. L. Delhez, W. J. G. M. Kleeven, H. L. Hagedoorn, J. I. M. Botman, G. A. Webers, Eindhoven U. of Tech.	2065
A 100-MeV Racetrack Microtron — P. Lidbjörk, J. Åström, Scanditronix	2068
Electrostatic Quadrupole Focusing in the AGS g-2 Storage Ring — G. Bennett, R. Larsen, W. Morse, Y. Semertzidis, J. Yelk, BNL; Z. Liu, Boston U.	2070
Design of 8-GeV Rapid-Cycle Booster Synchrotron for the KEK B-Factor — S. Kurokawa, KEK; P. Zenkevich, ITEP Moscow	2073

Instrumentation and Beam Feedback

Chair: R. Shafer

Feedback Control of Coupled-Bunch Instabilities (Invited Paper) — J. D. Fox, N. Eisen, H. Hindi, I. Linscott, G. Oxoby, L. Sapozhnikov, SLAC; M. Serio, INFN Frascati	2076
Electro-Optical Technology Applied to Accelerator Beam Measurement and Control (Invited Paper) — R. J. Pasquinelli, FNAL	2081
RF-Synchronized Imaging for Particle and Photon Beam Characterizations (Invited Paper) — A. H. Lumpkin, ANL....	2086
Diagnostic Instrumentation System for the SRRRC 1.3 GeV Synchrotron Radiation Light Source — K. T. Hsu, G. J. Jan, C. H. Kuo, K. H. Hu, SRRRC Taiwan.....	2091
Overview and Status of Beam Instrumentation at the SSC — R. C. Webber, SSCL	2094
Performance of Advanced Light Source Particle Beam Diagnostics — J. Hinkson, LBL	2097
Damping in the Fermilab Booster — J. M. Steimel, Jr., D. McGinnis, FNAL	2100
Betatron Function Measurement at LEP Using the BOM 1000 Turns Facility — P. Castro, IFIC, Spain; J. Borer, A. Burns, G. Morpurgo, R. Schmidt, CERN	2103
Adaptive Cascaded Beam-Based Feedback at the SLC — T. Himel, S. Allison, P. Grossberg, L. Hendrickson, R. Sass, H. Shoaee, SLAC	2106
Design of the ALS Transverse Coupled-Bunch Feedback System — W. Barry, J. M. Byrd, J. N. Corlett, J. Hinkson, J. Johnson, G. R. Lambertson, LBL; J. D. Fox, SLAC	2109

Each volume begins with this five-volume table of contents and ends with the five-volume author index. The chairman's foreword and a list of conference organizers and staff appear as front matter in Volume 1. A list of conference participants precedes the author index in Volume 5.

Poster presentations:

Results of Prototype Particle-Beam Diagnostics Tests for the Advanced Photon Source (APS) — A. H. Lumpkin, Y. Chung, E. Kahana, D. Patterson, W. Selby, A. Votaw, X. Wang, ANL	2112
Diagnostics Development for High Current Electron Accelerators at CESTA — J. de Mascureau, C. Bonnafond, A. Devin, E. Merle, G. Ployard, D. Villate, CESTA	2115
Beam Instrumentation for the SSC RFQ — P. Datte, G. Jamieson, R. Aiello, D. Beechy, A. Jones, D. Martin, J. Riordon, R. Webber, F. Wood, SSCL	2118
High Density Data Recording for SSCL Linac — A. L. VanDeusen, Allied Signal; C. Crist, SSCL	2121
Physic Requirements of Commissioning Diagnostics for SSCL Linac — J. W. Hurd, G. M. Arbique, C. E. Crist, F. W. Guy, M. Haworth, G. T. Leifeste, K. Saadatmand, SSCL; M. Krogh, K. McGinnis, D. Stittsworth, A. Vandeusen, S. Wright, Allied Signal	2124
Beam Diagnostic Layout Requirements for SSCL Linac — J. W. Hurd, F. W. Guy, G. Jamieson, D. Raparia, K. Saadatmand, SSCL	2127
SSCL Linac Commissioning Diagnostic Cart — C. E. Crist, L. W. Funk, J. W. Hurd, G. T. Leifeste, SSCL; M. Krogh, K. McGinnis, D. Stittsworth, A. Vandeusen, S. Wright, Allied Signal	2130
A Method for LEBT Automation — J. Sredniawski, L. Solensten, R. Schmidt, J. Porter, Y. Ng, C. Lom, Grumman; W. Newman, AMTEX	2133
Beam Energy Measurement Using the Hall C Beam Line — C. Yan, R. Carlini, D. Neuffer, CEBAF	2136
A Wide Range and High Speed Automatic Gain Control — E. J. Tacconi, C. F. Christiansen, SSCL/ UNLP Argentina	2139
A Beamline Design and Data Acquisition with the 20-MeV, 20-ps Electron Beam for the Higher-Order-Mode Studies of the APS SR-RF Cavities — J. Song, A. Nassiri, R. Daly, ANL	2142
A Bunch Killer for the NSLS X-Ray Electron Storage Ring — R. J. Nawrocky, U. Bergmann, D. P. Siddons, NSLS BNL	2145
The Mechanical Design of a Bunched Beam Stochastic Cooling Tank for the FNAL Tevatron — P. Hurh, G. Jackson, FNAL	2148
Design Study of Laser Compton Scattering with Relativistic Electron to Measure the Electron Beam Energy — I. Hsu, H. Chen, C. Cho, Y. Liu, Nat. Tsing Hua U.	2151
Transverse Beam Impedance Measurement: A New Coaxial Method — M. Cardito, F. Galluccio, R. Losito, M. R. Masullo, V. Vaccaro, INFN Napoli; G. Di Massa, U. Calabria	2154
A Novel Method of Noise Suppression in Beam Transfer Function Measurements — F. Caspers, M. Chanel, U. Oeftiger, CERN	2157
Beam Dispersion Measurements with Wire Scanners in the SLC Final Focus Systems — P. Emma, D. McCormick, M. C. Ross, SLAC	2160
Comprehensive Beam Jitter Study for the Commissioning of the Intermediate Matching Section and Drift Tube Linac at Ground Test Accelerator — D. S. Barr, J. D. Gilpatrick, LANL	2163
A New Method of Ion Beam Diagnostics — A. S. Artimov, JINR Dubna	2166
Correlation Method of Measurements of Ion Beam Parameters — A. S. Artimov, JINR Dubna	2169
The Compton Polarimeter at the SLC — G. Shapiro, S. Bethke, O. Chamberlain, R. Fuzesy, M. Kowitt, D. Pripstein, B. Schumm, H. Steiner, M. Zolotarev, LBL; P. Rowson, Columbia; D. Blockus, H. Ogren, M. Settles, Indiana; M. Fero, A. Lath, MIT; D. Calloway, R. Elia, E. Hughes, T. Junk, R. King, T. Maruyama, K. Moffeit, M. Petradza, M. Swartz, M. Woods, SLAC; G. Zapalac, Wisconsin	2172
Measurement of the Spin of a Particle Using Undulator Radiation — A. Luccio, BNL	2175
Quantum Geometrical Phase Signal of NLC Bunch Cross Section Carried by Virtual Photons — J. Shen, IHEP Beijing	2178
Response of Air-Filled Ion Chambers to High-Intensity Radiation Pulses — M. Plum, D. Brown, LANL	2181
The CEBAF Beam Loss Sensors — J. Perry, E. Woodworth, L. Merminga, S. Simrock, R. May, CEBAF; G. Stapleton, SSCL	2184
A Scintillating Fiber Beam Halo Detector for Heavy Ion Beam Diagnostics — M. A. McMahan, A. Assang, S. Herr, F. McCormack, G. Krebs, B. Feinberg, LBL	2187

Proceedings of the 1993 Particle Accelerator Conference

Development and Investigation of the 2π Beam Loss Monitors for Super-High-Energy Accelerators, Part 1: Quad-BLM for "Warm" Machines — S. N. Lapitsky, I. A. Kurochkin, V. S. Seleznev, IHEP Russia	2190
The Design and Performance of a High Sensitivity Loss Monitor System for Use in the Fermilab Antiproton Rings — A. M. Halling, J. R. Zagel, A. Hahn, FNAL	2193
Abort Interlock Diagnostic for Protection of APS Vacuum Chamber — G. Decker, ANL	2196
Experience with Radiation Protection for a Silicon Vertex Detector at a Hadronic Collider — P. F. Derwent, D. Amidei, A. Dunn, T. Song, S. Vejcek, U. Michigan; R. Crouch, R. Ducar, D. Herrup, FNAL; C. Haber, LBL	2199
Design of a New Generation of Collimators for LEP 200 — R. Jung, R. Perret, R. Valbuena, CERN	2202
Synchrotron Radiation Damage Test of Insulating Materials in the TRISTAN MR — H. Mitsui, R. Kumazawa, T. Tani, T. Chugun, Toshiba Corp.; Y. Ohsawa, T. Ozaki, K. Takayama, KEK	2205
Insulating and Metal-Ceramic Materials for Particle Accelerators — Yu. P. Severgin, M. Z. Filimonov, Efremov Inst.	2208
The Advanced Light Source (ALS) Radiation Safety System — A. L. Ritchie, D. E. Oldfather, A. F. Lindner, LBL ..	2210
Radiation Measurements During Cavities Conditioning on APS RF Test Stand — D. M. Grudzien, R. L. Kustom, H. J. Moe, J. J. Song, ANL	2213
Application of a Simple Analytical Model to Estimate Effectiveness of Radiation Shielding for Neutrons — S. Frankle, D. Fitzgerald, R. Hutson, R. Macek, C. Wilkinson, LANL	2216
Monte Carlo Based Formula for Radiation Shielding Assessment in the Forward Direction — C. Wilkinson, D. Fitzgerald, S. Frankle, R. Hutson, R. Macek, LANL	2219
A High Reliability Oxygen Deficiency Monitoring System — R. Parry, G. Claborn, A. Haas, R. Landis, W. Page, J. Smith, SSCL	2222
Programmable Electronic Safety Systems — R. R. Parry, SSCL	2225
A Pseudo Real Time Tune Meter for the Fermilab Booster — G. Wu, V. Bharadwaj, J. Lackey, D. McGinnis, R. Tomlin, FNAL	2228
Measurement Techniques Using the Tektronix® 3052 DSP System — J. M. Steimel, Jr., D. McGinnis, FNAL	2231
Using Transient Waveform Recorders to Measure and Store Beam Parameters — R. E. Stege, Jr., R. K. Jobe, M. Ross, SLAC	2234
Tune Measurement in the APS Rings — W. Selby, E. Kahana, X. Wang, ANL	2237
Integrating Log-Ratio Position Processing for the Los Alamos Proton Storage Ring Extraction Line — T. W. Hardek, A. Band, LANL	2240
Betatron "Ping" Tune Measurement System for the IUCF Cooler Synchrotron/Storage Ring — B. J. Hamilton, M. S. Ball, T. J. P. Ellison, IUCF	2243
Tune Measurement in the NSLS Booster Synchrotron — E. B. Blum, R. Nawrocky, BNL	2246
A Realtime Feedback Microprocessor for the Tevatron — D. A. Herrup, L. Chapman, A. Franck, T. Groves, B. Lublinsky, FNAL	2249
A New Study of the Main Ring Physical Aperture — G. Wu, S. Pruss, D. Capista, FNAL	2252
Electron Beam Stability and Beam Peak to Peak Motion Data for NSLS X-Ray Storage Ring — O. Singh, BNL	2254
Test of Fast-Digital Beamline Feedback Control at the Photon Factory — N. Nakamura, T. Katsura, KEK	2257
Horizontal Movement of the Storage Ring Floor at the Photon Factory — T. Katsura, H. Nakamura, Y. Kamiya, KEK; Y. Fujita, Shimizu Corp.	2260
Closed Orbit Correction Using Singular Value Decomposition of the Response Matrix — Y. Chung, G. Decker, K. Evans, Jr., ANL	2263
Compensation for the Effect of Vacuum Chamber Eddy Current by Digital Signal Processing for Closed Orbit Feedback — Y. Chung, L. Emery, J. Kirchman, ANL	2266
Dynamic Closed Orbit Correction — Y. Cheng, SRRC Taiwan	2269
A Closed-Loop Photon Beam Control Study for the Advanced Light Source — G. Portmann, J. Bengtsson, LBL	2272
Global DC Closed Orbit Correction Experiments on the NSLS X-Ray Ring and SPEAR — Y. Chung, G. Decker, K. Evans, Jr., ANL; J. Safranek, I. So, Y. Tang, BNL; W. J. Corbett, R. Hettel, SSRL	2275
FFT-Oriented Feedback — F.-J. Decker, SLAC	2278
Issues of the Transverse Feedback Systems Design at the SSC — W. Chou, J. Peterson, SSCL	2281
A Digital Feedback System for Orbit Stabilization — A. Friedman, E. Bozoki, O. Singh, J. Smith, BNL	2284
Results from the AGS Booster Transverse Damper — D. Russo, M. Brennan, M. Meth, T. Roser, BNL	2286
Single Board Op-Amp Beam Position Monitors Electronics — M. Ball, T. J. P. Ellison, B. J. Hamilton, IUCF	2289

Each volume begins with this five-volume table of contents and ends with the five-volume author index. The chairman's foreword and a list of conference organizers and staff appear as front matter in Volume 1. A list of conference participants precedes the author index in Volume 5.

Five-Volume Contents

A Single-Passage Beam-Position Monitor in the TRISTAN AR-to-MR Transport Lines — <i>T. Ieiri, M. Arinaga, KEK</i>	2292
Beam Position Monitoring System Using PIN Diode Switches — <i>K. Shinoe, T. Koseki, Y. Kamiya, ISSP Tokyo; N. Nakamura, T. Katsura, T. Ieiri, KEK</i>	2295
Performance of the CEBAF Arc Beam Position Monitors — <i>A. S. Hofler, B. A. Bowling, C. S. Higgins, P. K. Kloeppel, G. A. Krafft, K. L. Mahoney, CEBAF</i>	2298
The Million Turn Data Acquisition System BOSC — <i>A. Burns, W. Fischer, H. Jakob, I. Milstead, F. Schmidt, L. Vos, CERN</i>	2301
Beam Position Monitor Calibration for the Advanced Photon Source — <i>Y. Chung, G. Decker, E. Kahana, F. Lenkszus, A. Lumpkin, W. Sellyey, ANL</i>	2304
Self Triggered Single Pulse Beam Position Monitor — <i>J. L. Rothman, E. B. Blum, NSLS-BNL</i>	2307
A Prototype BPM Electronics Module for RHIC — <i>W. A. Ryan, T. J. Shea, P. Cerniglia, C. M. Degen, BNL</i>	2310
Dynamic Range Extension of BPM at the NSLS — <i>M. Bordoley, NSLS-BNL</i>	2313
Beam Position Monitoring in the 100-MHz to 500-MHz Frequency Range Using the Log-Ratio Technique — <i>F. D. Wells, R. E. Shafer, J. D. Gilpatrick, LANL</i>	2316
Beam Pinging, Sweeping, Shaking, and Electron/Ion Collecting, at the Proton Storage Ring — <i>T. Hardek, R. Macek, M. Plum, T.-S. Wang, LANL</i>	2319
Test Results of the SSC Log-Ratio Beam Position Monitor Electronics — <i>G. R. Aiello, M. R. Mills, R. E. Gonzalez, SSCL</i>	2322
RF Beam Position Monitors for the TESLA Test Facility — <i>R. Lorenz, TU Berlin</i>	2325
RHIC Beam Position Monitor Assemblies — <i>P. R. Cameron, M. C. Grau, W. A. Ryan, T. J. Shea, R. E. Sikora, BNL</i>	2328
Stripline Beam Position Monitor for the MIT-Bates South Hall Ring — <i>J. B. Flanz, R. Averill, E. Ihloff, K. D. Jacobs, D. Wang, A. Zolfaghari, MIT-Bates</i>	2331
Design and Operation of Button-Probe, Beam-Position Measurements — <i>J. D. Gilpatrick, J. F. Power, R. E. Meyer, C. R. Rose, LANL</i>	2334
Design and Calibration of Pickup-Electrodes for Beam Position Monitoring at SOR-RING — <i>K. Shinoe, Y. Kamiya, ISSP Tokyo; N. Nakamura, T. Katsura, KEK</i>	2337
The Position Monitor Using Stretched Wire Technique — <i>T. Mimashi, S. Kuroda, H. Nakayama, K. Oide, R. Sugahara, N. Yamamoto, KEK</i>	2340
An Over-Moded Stripline Beam Position Monitor — <i>J. G. Noomen, J. Bijleveld, F. Kroes, T. Sluijk, NIKHEF-K</i> ...	2343
Loss of Precision in Resonant Beam Position Monitors Due to Finite <i>Q</i> — <i>J. P. H. Sladen, W. Wuensch, CERN</i>	2346
Simulation of the ALS Longitudinal Multibunch Feedback System — <i>J. Byrd, LBL</i>	2349
Analysis of DSP-Based Longitudinal Feedback System: Trials at SPEAR and ALS — <i>H. Hindi, N. Eisen, J. Fox, I. Linscott, G. Oxoby, L. Sapozhnikov, SLAC; M. Serio, INFN</i>	2352
VXI Based Low Level RF System for Fermilab Linac Upgrade — <i>B. E. Chase, R. J. Pasquinelli, FNAL</i>	2355
Longitudinal Feedback in LEP — <i>J. P. Boiteux, P. Brown, E. Ciapala, H. Frischholz, G. Geschonke, J. C. Juillard, E. Peschardt, CERN</i>	2358
Performance of the Upgraded Stacktail Momentum Cooling System in the Fermilab Antiproton Source — <i>R. J. Pasquinelli, D. McGinnis, FNAL</i>	2361
Energy Vernier System for CEBAF — <i>G. A. Krafft, J. J. Bisognano, M. T. Crofford, J. C. Hovater, L. Merminga, S. N. Simrock, S. D. Witherspoon, CEBAF; K. Kubo, KEK</i>	2364
A Digital Approach for Phase Measurement Applied to Delta- <i>t</i> Tuneup Procedure — <i>G. R. Aiello, SSCL</i>	2367
RF Feedback for Beam Loading Compensation in the SLC Damping Rings — <i>P. Krejcik, P. Corredoura, M. Minty, R. Siemann, R. Tighe, SLAC; F. Pedersen, CERN</i>	2370
Simulation and Analysis of RF Feedback Systems on the SLC Damping Rings — <i>M. Minty, T. Himel, P. Krejcik, R. H. Siemann, R. Tighe, SLAC</i>	2373
Improved Impedance Reduction in the CERN SPS Superconducting Cavities for High Intensity Proton Operation — <i>D. Boussard, G. Lambert, T. P. R. Linnekar, CERN</i>	2376
Damping of Phase Errors at Injection in the LHC — <i>D. Boussard, E. Onillon, CERN</i>	2379
A Digital Beam Phase Loop for the Low Energy Booster — <i>L. K. Mestha, V. Brouk, R. C. Webber, J. Mangino, T. Uher, SSCL</i>	2382
General Time-Varying State-Space Control Model and Its Application for Transient Beam Loading Compensation — <i>L. K. Mestha, C. M. Kwan, SSCL; K. S. Yeung, UTA</i>	2385
A Digital Phase and Amplitude Feedforward Correction System — <i>D. Yu, P. Conway, DULY Res. Inc.</i>	2388

Volume 1:	1-747
Volume 2:	748-1640
Volume 3:	1641-2545
Volume 4:	2546-3218
Volume 5:	3219-3933

Proceedings of the 1993 Particle Accelerator Conference

Results of Adaptive Feedforward on GTA — C. D. Ziemek, P. M. Denney, A. H. Regan, M. T. Lynch, S. P. Jachim, L. E. Eaton, E. F. Natter, LANL	2391
Fast Bunch-to-Bunch Current Sampling in the Cornell Electron-Positron Collider — C. R. Dunnam, Cornell; K. B. Unser, CERN	2394
A Method for Measuring Dark Current Electron Beams in an RF Linac — X. K. Maruyama, T. Fasanello, H. Rietdyk, Naval Postgraduate School; M. A. Piastrup, Adelphi Tech.; D. W. Rule, R. B. Fiorito, NSWC	2397
High Bandwidth Beam Current Monitor — R. M. Baltrusaitis, C. A. Ekdahl, LANL; R. G. Cooper, E. Peterson, C. E. Warn, EG&G	2400
Rapid Measurements of Two-Dimensional Ion Beam Current Distribution for Pulsed Neutron Source — A. M. Tron, MEPI	2403
Short Bunch Length Detector for Ion Beam with High Bunch Density — A. M. Tron, V. V. Shako, MEPI	2406
Measurement of Bunch Time-Structure in KEK-PF — M. Tobiyama, T. Kasuga, T. Takeo, T. Obina, K. Tamura, Hiroshima U.; T. Katsura, KEK	2409
A Fifth Harmonic RF Bunch Monitor for the ANL-APS Electron Linac — A. Nassiri, A. Grelick, ANL	2412
Characterization of Subnanosecond Heavy-Ion Bunches at the TASSC Superconducting Cyclotron — G. R. Mitchel, N. A. Towne, AECL	2415
Design, Implementation, and Results from a Longitudinal Phase Space Tomography (PST) Monitor in the Fermilab Main Ring — G. Jackson, FNAL	2418
An Electrostatic Sweep Plate Device for Emittance Measurement of Ion Beams to 2 MeV — T. W. Debiak, J. Porter, R. Heuer, I. Birnbaum, Grumman	2420
Length Monitor for 1 mm SLC Bunches — E. Babenko, BINP Novosibirsk; R. K. Jobe, D. McCormick, J. T. Seeman, SLAC	2423
Bunch Shape Monitor for SSCL Linac — J. W. Hurd, G. M. Arbique, C. E. Crist, F. W. Guy, G. T. Leifeste, D. Raparia, K. Saadatmand, D. A. Swenson, SSCL; S. Esin, A. Feschenko, A. Stepanov, A. Mirzajan, INR Moscow	2426
A Field-Based Technique for the Longitudinal Profiling of Ultrarelativistic Electron or Positron Bunches Down to Lengths of ≤ 10 Microns — R. Tatchyn, SLAC	2429
Performance Limits of a Streak Camera in Real Time Three-Dimensional Measurement of Bunch Oscillation in LEP — E. Rossa, CERN; F. Tecker, RWTH Aachen; J.C. Mathae, ARP Strasbourg	2432
Bunch Length Measurements in the SLC Damping Ring — F.-J. Decker, T. Limberg, M. Minty, M. Ross, SLAC ..	2435
Virtual Photon Impulse of Bunch, Beampipe Response, Coherent RF Beamstrahlung; and BEPC Bunch Length, BES Jam, Virtual Acceleration — J. Shen, IHEP Beijing	2438
Development on Multistrip Monitor for Nonintercepting Measurement of Beam Geometric Moments — Y. Yin, TRIUMF	2441
Wire Scanner Data Analysis for the SSC Linac Emittance Measurement — C. Y. Yao, J. W. Hurd, J. Sage, SSCL	2444
Real-Time Spot Size Measurement for Pulsed High-Energy Radiographic Machines — S. A. Watson, LANL	2447
High Resolution Beam Monitoring with Optical Transition Radiation at 3 MeV Electron Energy — A. Specka, D. Bernard, R. Guirlet, F. Jacquet, P. Miné, B. Montès, R. Morano, P. Poilleux, LPNHE; F. Amiranoff, LULI; J. Morillo, LSI	2450
Beam Profiling with Optical Transition Radiation — D. W. Rule, R. B. Fiorito, NSWCDD	2453
Beam Emittance from Coherent Cherenkov Radiation in a Solid Dielectric — R. D. Richardson, R. C. Platt, SAIC; C. E. Crist, SNL	2456
A 10 μ m Resolution Secondary Emission Monitor for Fermilab's Targeting Station — P. Hurh, S. O'Day, R. Dombrowski, T. Page, FNAL	2459
Construction of a High Resolution Electron Beam Profile Monitor — J. Norem, J. Dawson, W. Haberichter, W. Novak, L. Reed, X-F. Yang, ANL	2462
Design Study of Beam Profile Monitor of Storage Ring by Using Synchrotron Radiation — I. C. Hs, T. H. Huang, Nat. Tsing Hua U./SRRC	2465
Limitations of a Residual Gas Ionization Beam Profile Monitor for the SSC Collider — R. Meinke, W. Nexsen, E. Tsyganov, A. Zinchenko, SSCL	2468
Full Cycle Beam Diagnostics with an Ionization Profile Monitor — A. Stillman, R. E. Thern, BNL	2471
Electron Beam Diagnostics by Means of Edge Radiation — O. V. Chubar, Kurchatov Inst.; E. S. Masunov, MEPI	2474
CEBAF Beam Viewer Imaging Software — B. A. Bowling, C. McDowell, CEBAF	2477

Each volume begins with this five-volume table of contents and ends with the five-volume author index. The chairman's foreword and a list of conference organizers and staff appear as front matter in Volume 1. A list of conference participants precedes the author index in Volume 5.

Prototype Flying-Wire Beam-Profile Monitor — D. B. Barlow, C. M. Fortgang, J. D. Gilpatrick, R. E. Meyer, A. M. Rendon, D. S. Warren, M. D. Wilke, LANL	2480
Emittance Measurement and Data Analysis for the SSC Linac Injector Lab — J. E. Hébert, P. Datte, F. W. Guy, N. C. Okay, K. Saadatmand, J. Sage, D. M. Wetherholt, W. A. Whittenberg, SSCL	2483
Automatic Emittance Measurement at the ATF — X. J. Wang, R. Malone, K. Batchelor, I. Ben-Zvi, BNL	2486
Electron Beam Emittance Monitor for the SSC — E. Tsyganov, R. Meinke, W. Nexsen, S. Kauffmann, A. Zinchenko, A. Taratin, SSCL	2489
Measurement of Vertical Emittance at LEP from Hard X-Rays — H. Akbari, J. Borer, C. Bovet, Ch. Delmère, A. Manarin, E. Rossa, M. Sillanoli, J. Spanggaard, CERN	2492
Performance and Operational Experience of the LEP Synchrotron Light Telescopes — G. Burtin, R. J. Colchester, J. J. Gras, R. Jung, J. M. Vouillot, CERN	2495
High Sensitivity Beam Intensity and Profile Monitors for the SPS Extracted Beams — J. Camas, G. Ferioli, R. Jung, J. Mann, CERN	2498
High Density Harp for SSCL Linac — C. T. Fritzsche, M. L. Krogh, AlliedSignal; C. E. Crist, SSCL	2501
High Resolution Measurements of Lepton Beam Transverse Distributions With the LEP Wire Scanners — J. Camas, G. Crockford, G. Ferioli, C. Fischer, J. J. Gras, R. Jung, J. Koopman, J. Mann, CERN	2504
Beam Size Measurements with Noninterceptive Off-Axis Screens — F.-J. Decker, R. Brown, J. T. Seeman, SLAC ...	2507
Resolution Improvement in Beam Profile Measurements with Synchrotron Light — O. V. Chubar, MEPI	2510
The Orsay Spot Size Monitor for the Final Focus Test Beam — J. Buon, B. Delcourt, J. Jeanjean, F. Le Diberder, V. Lepeltier, P. Puzo, LAL Orsay	2513
Beam Monitor Utilizing Transition Radiation — Y. Ogawa, J. Choi, T. Suwada, T. Kamitani, T. Urano, K. Furukawa, S. Ohsawa, A. Enomoto, I. Sato, KEK	2516
Fermilab Main Ring Low Level RF System Modifications for Focus Free Transition Beam Tests — R. G. Scala, K. Meisner, FNAL	2519
RF Synchronous Transfer into Specific Buckets Between Fermilab Main Ring and Tevatron Accelerators — K. Meisner, FNAL	2522
Main Ring Bunch Length Monitor — K. Meisner, G. Jackson, FNAL	2525
A VXI/LabVIEW-based Beamline Tuner — W. Blokland, FNAL	2528
A Frequency-Domain Directivity Enhancement of Beam Position Stripline Detectors — E. L. Barsotti, FNAL	2531
The Control System of ROSY I — T. Goetz, M. Picard, U. Bonn; M. Plesko, Sinc. Trieste	2534
Measuring Emittance Using Beam Position Monitors — S. J. Russell, B. E. Carlsten, LANL	2537
On the Reliability of Measured Results by Non-Destructive Beam Profile Monitor — T. Kawakubo, E. Kadokura, KEK; T. Ishida, Mitsubishi Elect.	2540
Transverse Feedback System with Digital Filter — V. M. Zhabitsky, JINR; I. L. Korenev, L. A. Yudin, MRTI	2543

Volume 4

Advanced Accelerator Concepts

Chair: C. Joshi

R. R. Wilson Prize Lecture: Adventures with Accelerators (Invited Paper) — J. P. Blewett, BNL (ret.)	2546
Demonstration of Plasma Beat Wave Acceleration of Electrons from 2 MeV to 20 MeV (Invited Paper) — C. E. Clayton, K. A. Marsh, M. Everett, A. Lal, C. Joshi, UCLA	2551
Laser Wakefield Accelerator Experiments Using 1 ps 30 TW Nd:glass Laser — K. Nakajima, H. Nakanishi, T. Kawakubo, A. Ogata, KEK; Y. Kitagawa, H. Shiraga, R. Kodama, T. Zhang, K. Suzuki, Y. Kato, Osaka U.; Y. Sakawa, T. Shoji, Nagoya U.; Y. Nishida, N. Yugami, Utsunomiya U.; T. Tajima, U. Texas, Austin	2556
Photonic Band Gap Resonators for High Energy Accelerators (Invited Paper) — S. Schultz, D. R. Smith, UCSD; N. Kroll, UCSD/SLAC	2559
Update on the ATF Inverse Cherenkov Laser Acceleration Experiment — W. D. Kimura, L. C. Steinhauer, G. H. Kim, S. C. Tidwell, STI Optronics; I. Pogorelsky, K. P. Kusche, BNL/STI Optronics	2564
New Directions in RF Sources (Invited Paper) — L. Schächter, Cornell	2567
Criteria for Comparing the Suitability of Microwave Amplifiers for Driving TeV Linear Colliders — V. I. Granatstein, G. S. Nusinovich, U. Maryland	2572

Proceedings of the 1993 Particle Accelerator Conference

High Gradient Acceleration in a 17 GHz Photocathode RF Gun — S. C. Chen, J. Gonichon, L. C-L. Lin, R. J. Temkin, S. Trotz, B. G. Danly, J. S. Wurtele, MIT	2575
An Inverse Free-Electron-Laser Accelerator — A. S. Fisher, J. C. Gallardo, A. van Steenbergen, S. Ulc, M. Woodle, BNL; J. Sandweiss, Yale; J. Fang, Columbia U.	2578
Phase Control in High-Gradient Laser Particle Accelerators — L. C. Steinhauer, W. D. Kimura, STI Optonics	2581
<i>Poster presentations:</i>	
Beam Quality in a Cyclotron Autoresonance Accelerator — B. Hafizi, Icarus Res.; P. Sprangle, NRL; J. L. Hirshfield, Omega-P Inc.	2584
Superlattice Crystal Accelerator: Acceleration Beyond GeV/m — S. A. Bogacz, FNAL	2587
Design Study of a Microwave Driver for a Relativistic Klystron Two-Beam Accelerator — T. L. Houck, LLNL	2590
The Standing Wave FEL/TBA: Realistic Cavity Geometry and Energy Extraction — J. Kim, A. M. Sessler, LBL; H. Henke, TU Berlin; W. M. Sharp, LLNL	2593
The Argonne Wakefield Accelerator: Overview and Status — P. Schoessow, E. Chojnacki, W. Gai, C. Ho, R. Konecny, J. Power, M. Rosing, J. Simpson, ANL	2596
A Self-Consistent Theory of Ferromagnetic Waveguide Accelerators Driven by Electron Beams — H. S. Uhm, NSWC	2599
Wakefield Accelerator Driven by a Relativistic Electron Beam in a Ferromagnetic Waveguide — H. S. Uhm, NSWC	2602
Magnetic Field-Decay Accelerator Driven by a Relativistic Electron Beam in a Ferromagnetic Waveguide — H. S. Uhm, NSWC	2605
Three-Dimensional Simulation Analysis of the First Sections of a Standing-Wave Free-Electron Laser Two-Beam Accelerator — C. Wang, A. M. Sessler, LBL	2608
Reacceleration Experiment to Demonstrate the Concept of Efficiency Enhancement in a Relativistic Klystron Two-Beam Accelerator — G. A. Westenskow, T. L. Houck, LLNL	2611
Design Analysis for a 100-MeV Inverse Cherenkov Laser Accelerator — J. R. Fontana, UCSB; W. D. Kimura, L. C. Steinhauer, STI Optonics; I. Pogorelsky, BNL/STI Optonics	2614
An Inverse Free Electron Laser Driven Linear Collider Electron-Positron B-Factor — N. Barov, C. Pellegrini, UCLA; J. Sandweiss, Yale	2617
2.5D Numerical Simulation of Relativistic Electron Bunches (REB) Interaction with Underdense and Overdense Plasmas — O. V. Batishchev, Y. S. Sigov, Keldysh Inst.; V. I. Karas', Y. B. Fainberg, Kharkov Inst.	2620
Propagation of Short Electron Pulses in Underdense Plasmas — N. Barov, J. Rosenzweig, UCLA	2623
Numerical Simulations of Driving Beam Dynamics in the Plasma Wakefield Accelerator — G. Joyce, J. Krall, E. Esarey, NRL	2626
Self-Modulated-Laser Wakefield Accelerator — J. Krall, A. Ting, E. Esarey, P. Sprangle, NRL	2629
A 100 MeV Proof-of-Principle Laser Wakefield Accelerator Experiment — A. Ting, A. Fisher, R. Fischer, J. Grun, J. Krall, E. Esarey, P. Sprangle, NRL; D. Umstadter, G. Mourou, U. Michigan	2632
Recent Work on Short Pulse Laser-Plasma Accelerators — T. Katsouleas, T. C. Chiou, USC; W. B. Mori, C. Decker, UCLA; J. S. Wurtele, G. Shvets, MIT	2635
Plasma Lens Experiments at the Final Focus Test Beam — J. Norem, ANL; D. Cline, W. Gabella, P. Kwok, S. Rajagopalan, J. Rosenzweig, UCLA; B. Barletta, UCLA/LBL; R. Williams, Florida A&M; S. Chattopadhyay, W. Leemans, A. Sessler, LBL; G. Westenskow, LLNL; J. Wurtele, MIT; J. J. Su, NCU Taiwan; K. Nakajima, H. Nakanishi, A. Ogata, D. Whittum, KEK; I. Hsu, NTU Taiwan; D. D. Meyerhofer, U. Rochester; T. Katsouleas, P. Lai, R. Liou, USC; P. Chen, W. Craddock, C. K. Ng, J. Spencer, SLAC; Y. Nishida, Utsunomiya U.	2638
A Plasma Lens and Accelerator Based Upon Magnetically Driven Charge Separation — S. Robertson, U. Colorado	2641
The NRL X-Band Magnicon Amplifier Experiment — S. H. Gold, C. A. Sullivan, W. M. Manheimer, NRL; B. Hafizi, Icarus Res.	2644
Theoretical Investigation of Magnicon Efficiency — B. Hafizi, Icarus Res.; S. H. Gold, W. M. Manheimer, P. Sprangle, NRL	2647
First Test of the X-Band Pulsed Magnicon — O. Nezhevenko, I. Kazarezov, E. Kozyrev, G. Kuznetsov, I. Makarov, A. Nikiforov, B. Persov, G. Serdobintsev, M. Tlunov, V. Yakovlev, I. Zapryagaev, BINP Russia	2650

Each volume begins with this five-volume table of contents and ends with the five-volume author index. The chairman's foreword and a list of conference organizers and staff appear as front matter in Volume 1. A list of conference participants precedes the author index in Volume 5.

Five-Volume Contents

TM-FEL With a Longitudinal Wiggler and an Annular Beam — L. Schächter, T. J. Davis, J. A. Nation, Cornell	2653
CARM and Harmonic Gyro-Amplifier Experiments at 17 GHz — W. L. Menninger, B. G. Danly, S. Alberti, C. Chen, E. Giguet, J. L. Rullier, R. J. Temkin, MIT	2656
Stability of Gyrotwistrons — P. E. Latham, G. S. Nusinovich, J. Cheng, U. Maryland	2659
Optimum Operation of Gyrotwistrons — P. E. Latham, G. S. Nusinovich, U. Maryland	2661
Large Orbit Gyroklystron Development at Los Alamos — R. M. Stringfield, R. M. Wheat, D. J. Brown, M.V. Fazio, J. Kinross-Wright, B. E. Carlsen, G. Rodenz, R. J. Faehl, R. F. Hoeberling, LANL	2664
Initial Operation of a High Power, K-Band, Harmonic Gyroklystron for Accelerator Applications — J. P. Calame, H. W. Matthews, W. Lawson, B. Hogan, M. K. E. Lee, J. Cheng, V. L. Granatstein, M. Reiser, C. D. Striffler, U. Maryland	2667
Design of a 100 MW, 17 GHz Second Harmonic Gyroklystron Experiment — W. Lawson, P. E. Latham, V. Specht, M. K. E. Lee, Q. Qian, J. P. Calame, B. Hogan, V. L. Granatstein, M. Reiser, C. D. Striffler, U. Maryland	2670
Some Concepts of Relativistic Gyroamplifiers for Particle Acceleration — G. S. Nusinovich, P. E. Latham, V. L. Granatstein, U. Maryland	2673
Experimental Progress Toward a 1 GW, 1 ns Pulse Length, High Current Relativistic Klystron — M. Fazio, B. Carlsen, R. Faehl, W. Haynes, T. Kwan, R. Stringfield, LANL	2675
Relativistic Plasma Klystron Amplifier in Connection with Application to High Gradient Accelerators — H. S. Uhm, NSWC	2678
Sheet-Beam Klystron RF Cavities — D. Yu, DULY Res. Inc.; P. Wilson, SLAC	2681
Beam-Wave Interaction in a Quasi-Periodic Structure — L. Schächter, J. A. Nation, Cornell	2684
Two-Stage, High Power X-Band Amplifier Experiment — E. Kuang, T. J. Davis, J. D. Ivers, G. S. Kerslick, J. A. Nation, L. Schächter, Cornell	2687
Long-Pulse, High-Power, X-Band Relativistic Traveling-Wave Tube Amplifier — T. Kimura, S. Alberti, B. G. Danly, R. J. Temkin, MIT	2690
Tapered Tube, Microsecond Electron Beam Gyrotron Backward-Wave Oscillators — R. M. Gilgenbach, M. T. Walter, P. R. Menge, T. A. Spencer, U. Michigan	2693
Quiet Start and Autotasking for PARMELA — J. Gonichon, S. C. Chen, L. C.-L. Lin, R. J. Temkin, MIT	2696
Waveguide Side-Wall Coupling in RF Guns — L. C.-L. Lin, S. C. Chen, J. Gonichon, S. Trotz, J. S. Wurtele, MIT	2699
A High-Current Micro-Pulse Electron Gun — F. M. Mako, W. Peter, FM Tech. Inc.	2702
Knife-Edge Thin Film Field Emission Cathodes — B. Lee, H. P. Demoff, M. M. Drew, T. S. Elliot, T. K. Mazumdar, P. M. McIntyre, Y. Pang, D. D. Smith, H.-J. Trost, Texas A&M	2705
The Oxidized Porous Silicon Field Emission Array — D. D. Smith, H. P. Demoff, T. S. Elliott, T. B. Kasproicz, B. Lee, T. K. Mazumdar, P. M. McIntyre, Y. Pang, H.-J. Trost, Texas A&M	2708
Study of Porous Silicon Morphologies for Electron Transport — Y. Pang, H. Demoff, T. S. Elliott, B. Lee, J. Lu, V. B. Madhuri, T. K. Mazumdar, P. M. McIntyre, D. D. Smith, H.-J. Trost, Texas A&M	2711
Cold Test Measurements of a BWO Slow-Wave Structure — W. Main, Y. Carmel, K. Ogura, J. Weaver, S. Watanabe, U. Maryland	2714
Collective Accelerator with Variable Energy and Wide Spectrum of Accelerated Ions — R. Meshcherov, G. Batskikh, V. Krasnopol'sky, V. Rybalko, V. Sazhin, MRTI Moscow; A. Vasiliev, MAE Russia	2717
High Gradient Experiments with Nanosecond Pulses — V. Baglin, H. Haseroth, J. Knott, CERN; F. Chautard, SSCL	2720
Development of the Alternate Entry Port for the ATF — Z. Parsa, BNL	2723
 Magnets, Cryogenics, and Alignment Chair: J. Strait	
Status of Superconducting Magnet Development (SSC, RHIC, LHC) (Invited Paper) — P. Wanderer, BNL	2726
Electrical Performance Characteristics of the SSC Accelerator System String Test (Invited Paper) — W. Robinson, W. Burgett, T. Dombek, J. Gannon, P. Kraushaar, A. McInturff, T. Savord, G. Tool, SSCL	2731
Overview of the Final Focus Test Beam Alignment System — V. E. Bressler, R. E. Ruland, D. Plouffe, SLAC	2736
Long Term Experience with Cryoplant Operation for Superconducting Magnets and RF Cavities at CERN — D. Delikaris, J.-P. Danvergne, P. K. Frandsen, F. Haug, G. Passardi, J.-M. Rieubland, J. Schmid, CERN	2739
Axial Variations in the Magnetic Field of Superconducting Dipoles and Quadrupoles — A. K. Ghosh, K. E. Robins, W. B. Sampson, BNL	2742

Volume 1: 1-747
 Volume 2: 748-1640
 Volume 3: 1641-2545
 Volume 4: 2546-3218
 Volume 5: 3219-3933

Proceedings of the 1993 Particle Accelerator Conference

Large Aperture Quadrupoles for RHIC Interaction Regions — R. Gupta, M. Anerella, G. Ganetis, M. Garber, A. Ghosh, A. Greene, A. Jain, S. Kahn, E. Kelly, E. Killian, G. Morgan, A. Morgillo, J. Muratore, A. Prodell, M. Rehak, W. Sampson, R. Shutt, P. Thompson, P. Wanderer, E. Willen, BNL	2745
---	-------------

Poster presentations:

Design of Superconducting Quadrupole Magnets for CEBAF's Hall A Spectrometer — R. Kreutz, E. Britsch, K. Dreher, H. Gräneberg, H. Lütkehaus, W. Nick, H. Peschel, B. Rzezunka, F. Sommer, P. Schäfer, Siemens AG	2748
Design of a Superconducting Wiggler for the PLS — B. K. Kang, Y. M. Koo, D. E. Kim, H. S. Seo, Y. U. Sohn, Pohang; P. D. Vobly, N. A. Mezentsev, G. N. Kulipanov, BINP	2751
Calculations of Magnetic Field for the End Design of the RHIC Arc Dipole — S. A. Kahn, R. C. Gupta, A. K. Jain, G. H. Morgan, P. A. Thompson, BNL	2754
Collider Scenario Implications of ASST Operation — A. D. McInturff, W. Burgett, M. Christianson, T. Dombek, J. Gannon, D. Haenni, P. Kraushaar, M. Levin, M. McAshan, G. Mulholland, D. Murray, W. Robinson, T. Savord, R. Smellie, F. Spinos, G. Tool, J. Weisend II, J. Zatopek, SSCL	2757
Preliminary Analysis of Coil Wedge Dimensional Variation in SSC Prototype Dipole Magnets — D. Pollock, G. Brown, S. Dwyer, R. Gatta, D. Warner, SSCL	2760
SSC String Test Facility for Superconducting Magnets: Testing Capabilities and Program for Collider Magnets — P. Kraushaar, W. Burgett, T. Dombek, A. McInturff, W. Robinson, V. Saladin, SSCL	2763
"B" Series RHIC Arc Quadrupoles — P. Thompson, M. Anerella, G. Ganetis, M. Garber, A. Ghosh, A. Greene, R. Gupta, A. Jain, S. A. Kahn, G. Morgan, A. Morgillo, J. Muratore, A. Prodell, M. Rehak, W. Sampson, P. Wanderer, E. Willen, BNL	2766
Fermilab-Built SSC Collider Dipoles Using Low Temperature Curing Insulation Systems With and Without Glass Tape — T. S. Jaffery, R. Coombes, A. Devred, J. DiMarco, T. Ogitsu, R. E. Sims, J. C. Tompkins, M. Wake, SSCL; R. Bossert, J. Carson, S. W. Delchamps, I. Gonczy, S. Gourlay, R. Hanft, M. J. Lamm, P. Mazur, D. Orris, J. Strait, FNAL	2769
Design and Tests of UNK Superconducting Correction Magnet Models — E. Rybakov, N. Bogatov, I. Dmitrieva, M. Kosyakina, Yu. Severgin, V. Fedorov, V. Shan'gin, Efremov Inst.; P. Chirkov, S. Kozub, K. Mynnikov, V. Sychev, IHEP Moscow; A. Rychagov, V. Sytnikov, A. Taran, All-Union R&D Inst.	2772
Quench and Quench Protection for the SSC Collider Correctors — A. He, SSCL.....	2775
Variation in a_1 Saturation in SSC Collider Dipoles — R. C. Gupta, A. K. Jain, BNL	2778
Spool Pieces at the SSCL — T. Clayton, Y. Cai, R. Smellie, S. Stampke, SSCL	2781
Quench Simulations of the 40 mm Aperture SSC-Quadrupole Magnet Connected in Series with 50 mm Aperture SSC-Dipole Magnets — G. López, SSCL	2784
Effective Stress of the SSC 80 K Synchrotron Radiation Liner in a Quenching Dipole Magnet — K. K. Leung, Q. S. Shu, K. Yu, J. Zbasnik, SSCL	2787
Improved Cable Insulation for Superconducting Magnets — M. Anerella, A. K. Ghosh, E. Kelley, J. Schmalzle, E. Willen, BNL; J. Fraivillig, J. Ochsner, D. J. Parish, DuPont	2790
Treatment of the Results of Magnetic Mapping of the SIBERIA-2 Magnets — V. Korchuganov, E. Levichev, A. Philipchenko, BINP	2793
Prototype Quadrupole Magnets for the PLS Storage Ring — Y. M. Koo, D. E. Kim, Y. G. Nah, H. S. Han, B. K. Kang, K. H. Park, J. R. Yoon, H. K. Lee, J. E. Milburn, Pohang	2796
Magnetic Measurement Data of the Injector Synchrotron Dipole Magnets for the 7-GeV Advanced Photon Source — K. Kim, S. H. Kim, L. R. Turner, C. L. Doose, R. Hogrefe, R. Merl, ANL	2799
Magnet Measurement Facility for the 7-GeV Advanced Photon Source — S. H. Kim, K. Kim, C. Doose, R. Hogrefe, R. Merl, ANL	2802
Magnetic Measurements of the Storage Ring Quadrupole Magnets for the 7-GeV Advanced Photon Source — S. H. Kim, K. Kim, C. Doose, R. Hogrefe, R. Merl, ANL	2805
Design and Tests of the Injector Synchrotron Magnets for the 7-GeV Advanced Photon Source (APS) — K. Kim, S. H. Kim, K. M. Thompson, L. R. Turner, ANL	2808
Final Analysis of the ALS Lattice Magnet Data — R. Keller, LBL	2811
Design and Measurement of the Sextupole Magnet for the APS Storage Ring — L. R. Turner, K. M. Thompson, S. H. Kim, K. Kim, ANL	2814
A Pulsed Septum Magnet for the APS — L. R. Turner, D. G. McGhee, F. E. Mills, S. Reeves, ANL	2817

Each volume begins with this five-volume table of contents and ends with the five-volume author index. The chairmen's foreword and a list of conference organizers and staff appear as front matter in Volume 1. A list of conference participants precedes the author index in Volume 5.

Five-Volume Contents

The ELETTRA Storage Ring Magnets — G. Petrucci, D. Tommasini, Sinc. Trieste/CERN	2820
Experience with the Source Evaluation Board Method of Procuring Technical Components for the Fermilab Main Injector — D. J. Harding, J. P. Collins, G. R. Kobliska, N. S. Chester, E. G. Pewitt, W. B. Fowler, FNAL ..	2823
Sextupole Magnets for the Fermilab Main Injector — D. J. Harding, N. Chester, R. Baiod, FNAL	2826
Design and Measurements of Prototype Fermilab Main Injector Dipole Endpacks — D. J. Harding, H. D. Glass, J.-F. Ostiguy, B. C. Brown, F. A. Harfoush, C. S. Mishra, FNAL	2829
Magnetic Measurement of Quadrupole and Sextupole Magnets for the MIT-Bates South Hall Ring (SHR) — D. R. Tieger, J. D. Zumbro, W. W. Sapp, MIT Bates	2832
A Permanent Magnet Dipole Correction Element for the Tevatron — J. E. Goodwin, T. Anderson, A. Franck, N. Gelfand, H. Jostlein, FNAL	2835
Precision Measurement of Transport Components — P. Tenenbaum, J. K. Cobb, D. R. Jensen, D. Sawyer, W. Wagner, H. V. Walz, S. H. Williams, SLAC	2838
Measurement and Adjustment of CIAE Medical Cyclotron Magnet — M. Fan, X. Zhang, T. Zhang, C. Liang, Q. Tao, Z. Zhao, C. Chu, T. Li, Y. Hu, Y. Chen, H. Zhang, H. Jia, C. Jiao, J. Liu, W. Zhang, C. Zhou, J. Jiao, Y. Hou, CIAE China	2841
Magnetic Measurement and Alignment of the ELETTRA Storage Ring Quadrupole, Sextupole and Steerer Magnets — D. Zangrando, R. P. Walker, Sinc. Trieste	2844
Measurement and Correction of the ELETTRA Storage Ring Dipole Magnets — R. P. Walker, D. Zangrando, Sinc. Trieste	2847
Magnet Costs for the Advanced Light Source — J. Tanabe, J. Krupnick, E. Hoyer, A. Paterson, LBL	2850
Automatic Bench for Precise Magnetic Measurements of Linac Multipole Focusing Elements — V. S. Skachkov, M. A. Kozchekin, R. P. Koujbida, V. I. Lulevich, A. V. Selin, O. S. Sergeeva, ITEP Moscow	2853
Measurements of Loma Linda Proton Therapy Gantry Dipoles — H. D. Glass, P. O. Mazur, J. W. Sim, FNAL	2856
Techniques for Measurement of Dipole Endfields with a Rigid Integrating Coil — H. D. Glass, FNAL	2859
Lamination and End Plate Design Studies of SSC Low Energy Booster Magnet Prototypes — N. Li, SSCL	2862
Design and Fabrication of a Multi-Purpose Panofsky Magnet — J. Budnick, T. Hall, D. Li, S. Y. Lee, IUCF	2865
Magnetic Septa Design and Performance for Injection and Extraction to and from the MIT-Bates South Hall Ring (SHR) — R. Averill, K. Dow, H. Enge, J. Flanz, E. Ihloff, M. Farkhondeh, C. Sibley, MIT-Bates	2868
Octupole Magnet Design for the 1/2 Integer Resonant Extraction of Electrons from the MIT-Bates South Hall Ring (SHR) — R. Averill, J. Flanz, E. Ihloff, D. Tieger, MIT-Bates	2871
Ramped Quadrupole Design and Performance for the MIT-Bates South Hall Ring (SHR) — R. Averill, J. Flanz, E. Ihloff, D. Tieger, MIT-Bates	2874
Lambertson Upgrade Program — K. J. Weber, FNAL	2877
Computer Studies of a Combined-Function Bend Magnet for a Proposed Redesign of the SLAC SLC Damping Rings — R. A. Early, T. O. Raubenheimer, SLAC	2880
Comparison of Computer Predictions and Magnetic Field Measurements for an Iron Spectrometer Magnet — G. T. Danby, J. W. Jackson, W. Meng, C. Spataro, BNL	2883
Design and Performance of the Dipole Magnet for the SRRRC Storage Ring — C. H. Chang, H. C. Liu, G. J. Hwang, SRRRC Taiwan	2886
Specific Features of Magnet Design for the Duke FEL Storage Ring — B. Burnham, N. Hower, V. N. Litvinenko, J. M. J. Madey, Y. Wu, Duke	2889
Dipole Design for the EUTERPE Storage Ring — J. I. M. Botman, C. J. Timmermans, B. Xi, H. Heller, H. L. Hagedoorn, P. Brinkgreve, E. Dekkers, J. Moerel, Eindhoven,	2892
Design of a Lambertson Injection Magnet for the RHIC Machine — E. Rodger, N. Tsoupas, J. Claus, H. W. Foelsche, BNL	2895
Combined AC Corrector Magnets — A. J. Otter, P. A. Reeve, TRIUMF; N. Marks, Daresbury	2898
Longitudinal Profile and Effective Length of a Conventional Dipole Magnet — J. Ostiguy, FNAL	2901
Magnetic Flux Shielding for the Muon g-2 Storage Ring Superconducting Inflectors — W. Meng, W. B. Sampson, M. Suenaga, BNL	2904
Three Dimensional Field Analysis for the AGS Combined Function Magnets — W. Meng, M. Tanaka, BNL	2907
Survey and Alignment Data Analysis for the ALS Storage Ring — R. Keller, LBL	2910
A Mechanical System for the Positioning of Accelerator Magnets — R. Viola, R. Martin, SSCL	2913
Preliminary Studies on a Magneto-Optical Procedure for Aligning RHIC Magnets — M. A. Goldman, R. E. Sikora, T. J. Shea, BNL	2916

Proceedings of the 1993 Particle Accelerator Conference

RHIC Survey and Alignment — F. X. Karl, R. R. Anderson, M. A. Goldman, F. M. Hemmer, D. Kazmark, Jr., T. T. Mroczkowski, J. C. Roecklein, BNL	2919
Effect of Magnet Sorting Using a Simple Resonance Cancellation Method on the RMS Orbit Distortion at the APS Injector Synchrotron — F. Lopez, R. Koul, F. E. Mills, ANL	2922
Optimal Magnet Sorting Procedure and Application to the APS Injector Synchrotron — R. K. Koul, F. Lopez, F. E. Mills, ANL	2924
Geodetic Concept for the Storage Ring EUTERPE — S. F. C. L. Wetzels, C. J. Timmermans, G. A. Webers, P. H. J. Schellekens, J. I. M. Botman, H. L. Hagedoorn, Eindhoven U. of Tech.	2927
Alignment of CEBAF Cryomodules — W. J. Schneider, J. J. Bisognano, J. Fischer, D. R. Douglas, K. Macha, J. Mammoser, W. Oren, J. Preble, J. Robb, M. Wiseman, CEBAF	2929
The Hydrostatic Levelling System (HLS)/ Servo-Controlled Precision Jacks: A New Generation Altimetric Alignment and Control System — D. Roux, ESRF	2932
Control of Roll in Fiducialization of Quadrupole Magnets for the MIT-Bates South Hall Ring — M. Farkhondeh, K. A. Dow, W. W. Sapp, MIT Bates	2935
Survey and Alignment of the MIT-Bates South Hall Ring — M. Farkhondeh, K. A. Dow, W. W. Sapp, D. R. Tieger, MIT Bates	2938
Magnetic Measurement, Fiducialization and Alignment of Large Dipoles for the MIT-Bates SHR — M. Farkhondeh, K. A. Dow, W. W. Sapp, J. D. Zumbro, MIT Bates	2941
Pulsed Taut-Wire Measurement of the Magnetic Alignment of the ITS Induction Cells — J. G. Melton, M. J. Burns, D. J. Honabarger, LANL	2944
Application of Precision Mechanical Engineering Techniques to the Design of a Moderate Energy Beam Transport for the FAA Explosive Detection System — R. Lujan, K. Christensen, LANL	2947
The Final Focus Test Beam Laser Reference System — V. E. Bressler, R. E. Ruland, SLAC	2950
Thermal Modeling of Cryogenic Accelerator Structures — H. Muller, P. Smith, D. Walend, J. Kirchgessner, Cornell	2953
Cryogenics for the LEP200 Superconducting Cavities at CERN — D. Güsewell, M. Barranco-Luque, S. Claudet, W. K. Erdt, P. Frandsen, Ph. Gayet, J. Schmid, N. Solheim, Ch. Tiscomb, G. Winkler, CERN	2956
Measurements of the Ground Motion Vibrations at the SSC — V. V. Parkhomchuk, BINP; V. D. Shiltsev, H. J. Weaver, SSCL	2959
Particle Sources, Beam Formation, and Matching Chair: J. Fraser	
Performance of Photocathode RF Gun Electron Accelerators (Invited Paper) — I. Ben-Zvi, BNL	2962
First Operation of a High Duty Factor Photoinjector — D. Dowell, K. Davis, K. Friddell, E. Tyson, C. Lancaster, L. Milliman, R. Rodenburg, T. Aas, M. Bemes, S. Bethel, P. Johnson, K. Murphy, C. Whelen, J. Adamski, D. Pistoresi, D. Shofstall, Boeing; G. Busch, D. Remelius, LANL	2967
Operation of the High Brightness LINAC for the Advanced Free-Electron Laser Initiative at Los Alamos — R. L. Sheffield, R. H. Austin, K. D. C. Chan, S. M. Gierman, J. M. Kinross-Wright, S. H. Kong, D. C. Nguyen, S. J. Russell, C. A. Timmer, LANL	2970
Performance of the SLC Polarized Electron Source with High Polarization — J. E. Clendenin, R. K. Alley, H. Aoyagi, J. C. Frisch, C. L. Garden, E. W. Hoyt, R. E. Kirby, L. A. Klaisner, A. V. Kulikov, C. Y. Prescott, P. J. Sáez, D. C. Schultz, H. Tang, J. L. Turner, M. Woods, A. D. Yeremian, M. S. Zolotarev, SLAC	2973
Quantum Efficiency Measurements of a Copper Photocathode in an RF Electron Gun — P. Davis, G. Hairapetian, C. Clayton, C. Joshi, S. Hartman, S. Park, C. Pellegrini, J. Rosenzweig, UCLA	2976
High-Efficiency Target-Ion Sources for RIB Generation (Invited Paper) — G. D. Alton, ORNL	2979
Performance of SSC Linac Injector (Invited Paper) — K. Saadatmand, G. M. Arbique, F. Guy, M. Haworth, J. Hebert, J. Hurd, J. Lenz, N. Okay, D. Raparia, SSCL	2986
Proposal for a Pulsed Optically Pumped Polarized H ⁻ Ion Source for High Energy Accelerators — A. N. Zelenski, INR Moscow; C. D. P. Levy, P. W. Schmor, W. T. H. van Oers, G. Dutto, TRIUMF; Y. Mori, KEK	2991
Design and Performance of the Inter-RFQ Beam Transport and Matching Section for the SAIC PET Isotope Production Accelerator — W. D. Cornelius, SAIC	2994
Electron Cyclotron Resonance Sources of Multiply Charged Ions: Last Developments at Grenoble — G. Melin, F. Bourg, P. Briand, M. Delaunay, A. Girard, D. Hitz, P. Ludwig, T. K. Nguyen, M. Pontonnier, Grenoble	2997

Each volume begins with this five-volume table of contents and ends with the five-volume author index. The chairman's foreword and a list of conference organizers and staff appear as front matter in Volume 1. A list of conference participants precedes the author index in Volume 5.

Poster presentations:

Design and Construction of a Full Copper Photocathode RF Gun — X. J. Wang, K. Batchelor, I. Ben-Zvi, D. Lynch, J. Sheehan, M. Woodle, BNL	3000
Streak Camera Measurements of Electron Bunch Length from a Copper Photocathode in an RF Gun — G. Hairapetian, P. Davis, M. Everett, C. Clayton, C. Joshi, S. Hartman, S. Park, C. Pellegrini, UCLA	3003
Possible Efficiency-Enhancement of Metal Photocathode for DISKTRON Electrostatic Accelerator — T. Tanabe, Y. Kawamura, K. Toyoda, RIKEN; D. Li, Changchun Inst., China	3006
Cold Test of Rocketdyne RF Gun — M. Lampel, Rockwell; R. Zhang, UCLA	3009
Design and Construction of a High-Duty-Factor Photocathode Electron Gun — I. S. Lehrman, I. A. Birnbaum, M. Cole, R. L. Heuer, E. Sheedy, Grumman; I. Ben-Zvi, K. Batchelor, J. C. Gallardo, H. G. Kirk, T. Srinivasan-Rao, BNL	3012
An Improved Thermionic Microwave Gun and Emittance-Preserving Transport Line — M. Borland, ANL	3015
Experience with a Radio Frequency Gun on the SSRL Injector Linac — J. N. Weaver, R. D. Genin, P. Golceff, H. Morales, J. Sebek, SLAC	3018
Design of a High Duty Cycle, Asymmetric Emittance RF Photocathode Injector for Linear Collider Applications — J. B. Rosenzweig, E. Colby, UCLA; G. Jackson, T. Nicol, FNAL	3021
Design of a High Brightness RF Photoinjector for the SLAC Linear Coherent Light Source — J. Rosenzweig, UCLA; L. Serafini, INFN Milan	3024
Performance of the SLC Polarized Electron Source and Injector with the SLAC 3 km Linac Configured for Fixed Target Experiments — A. D. Yeremian, R. K. Alley, J. E. Clendenin, J. C. Frisch, C. L. Garden, L. A. Klaisner, A. V. Kulikov, R. H. Miller, C. Y. Prescott, P. J. Saez, D. C. Schultz, H. Tang, J. L. Turner, M. B. Woods, M. Zolotarev, SLAC	3027
An In-Situ Photocathode Loading System for the SLC Polarized Electron Gun — R. E. Kirby, G. J. Collet, K. Skarpaas, SLAC	3030
High Voltage Processing of the SLC Polarized Electron Gun — P. Sáez, J. Clendenin, C. Garden, E. Hoyt, L. Klaisner, C. Prescott, D. Schultz, H. Tang, SLAC	3033
Study of Non-Linear Photoemission Effects in III-V Semiconductors — H. Tang, R. K. Alley, J. E. Clendenin, J. C. Frisch, C. L. Garden, E. W. Hoyt, R. E. Kirby, L. A. Klaisner, A. V. Kulikov, C. Y. Prescott, P. J. Sáez, D. C. Schultz, J. L. Turner, M. Woods, M. S. Zolotarev, SLAC; H. Aoyagi, Nagoya U.	3036
Photocathode Performance Measurements for the SLC Polarized Electron Gun — C. L. Garden, E. W. Hoyt, D. C. Schultz, H. Tang, SLAC	3039
Electron Quantum Yields from a Barium Photocathode Illuminated with Polarized Light — M. E. Conde, S. Chattopadhyay, K.-J. Kim, K.-N. Leung, A. T. Young, LBL; S.-I. Kwon, Kyonggi U.	3042
The 1992 Polarized Light Source — R. Alley, M. Woods, M. Browne, J. Frisch, M. Zolotarev, SLAC	3045
Operation of a Ti:Sapphire Laser for the SLAC Polarized Electron Source — J. Frisch, R. Alley, M. Browne, M. Woods, SLAC	3047
The Argonne Wakefield Accelerator (AWA) Laser System and Its Laser Pulse Shaper — W. Gai, N. Hill, C. Ho, P. Schoessow, J. Simpson, ANL	3050
CANDELA Photo-injector: The Drive Laser — P. Georges, P. Thomas, Inst. d'Opt. Theor. Appl., Orsay; B. Leblond, C. Travier, LAL Orsay	3053
A Flat-Cathode Thermionic Injector for the PHERMEX Radiographic Facility — T. Kauppila, L. Builta, M. Burns, W. Gregory, D. Honaberger, S. Watson, LANL; T. Hughes, Mission Res. Corp.	3055
The ALS Gun Electronics System — C. C. Lo, LBL	3058
Witness Gun for the Argonne Wakefield Accelerator — J. Power, J. Simpson, E. Chojnacki, ANL	3061
Parametric Studies with PARMELA to Improve SLC Performance — T. A. Jones, A. D. Yeremian, R. H. Miller, SLAC	3063
High Current, Low Energy Electron Beams Produced During the High Current Phase of a Pseudospark — T. Hsu, R. Liou, M. A. Gundersen, USC; G. Kirkman, Integrated App. Phys.	3066
Theoretical and Experimental Study of Pseudospark Electron Beam Generation — L. Pitchford, J. P. Boeuf, U. Paul Sabatier; V. Puech, U. de Paris-Sud; R. Liou, M. Gundersen, USC	3069
A Variable Pulse-Length Electron Beam From the Back-Lighted Thyatron — R. Liou, T. Hsu, G. Roth, M. Gundersen, USC; G. Kirkman, Integrated App. Phys.	3072

Proceedings of the 1993 Particle Accelerator Conference

One-Dimensional Simulation Studies of Breakdown and Electron Beam Generation Processes for a Hollow Cathode Pseudospark Discharge — S. Y. Cai, C. D. Striffler, U. Maryland	3075
A High Brightness Electron Beam Produced by a Ferroelectric Cathode — B. Jiang, G. Kirkman, N. Reinhardt, Integrated App. Physics	3078
The UV-FEL at the NSLS: Straight Injection Configuration — X. Zhang, J. C. Gallardo, BNL	3081
Progress on PEP-II Injection R&D — E. Bloom, F. Bulos, T. Fieguth, G. Godfrey, G. Loew, R. Miller, SLAC	3084
New Pre-Injector of the KEK 2.5-GeV Linac and Its Performance — S. Ohsawa, I. Abe, S. Anami, J.-Y. Choi, A. Enomoto, K. Furukawa, H. Hanaki, K. Kakihara, N. Kamikubota, T. Kamitani, H. Kobayashi, Y. Ogawa, T. Oogoe, I. Sato, T. Suwada, Y. Yamazaki, M. Yokota, KEK; A. Asami, Naruto U.	3087
Hydrodynamic Calculations of 20-TeV Beam Interactions with the SSC Beam Dump — D. C. Wilson, C. A. Wingate, J. C. Goldstein, R. P. Godwin, LANL; N. V. Mokhov, SSCL	3090
First Results Concerning a Crystal Radiator Dedicated to Positron Production by Photons from Channeled Multi-GeV Electrons — R. Chehab, T. Baier, P. Jean, LAL Orsay; X. Artru, M. Chevallier, R. Kirsch, J. C. Poizat, J. Remillieux, IPNL Lyon; A. Jejcic, J. Maillard, J. Silva, LPC Paris; E. Hourany, G. Renou, J. P. Didelez, A. Elayi, L. Rosier, IPN Orsay; V. N. Baier, V. M. Katkov, V. M. Strakhovenko, BINP Novosibirsk; K. Maier, MPI Stuttgart	3093
New Target Results from the FNAL Antiproton Source — S. O'Day, F. Bieniosek, K. Anderson, FNAL	3096
High Current Radioisotope Production with Solid Target System — W. Z. Gelbart, N. R. Stevenson, R. R. Johnson, J. Orzechowski, F. Cifarelli, TRIUMF; F. Nortier, NAC Faure	3099
Isospin Target-Ion Source Shielding — M. M. Barbier, Marcel Barbier Inc.	3102
Beam Raster System at CEBAF — C. Yan, J. Beaufait, P. Brindza, R. Carlini, W. Vulcan, R. Wines, CEBAF	3103
Monitoring Production Target Thickness — M. A. Oothoudt, LANL	3106
Beam Loss Handling at the SSC — I. S. Baishev, A. I. Drozhdin, N. V. Mokhov, SSCL	3109
Analytical Study of RFQ Channel by Means of the Equivalent Charges Model — V. M. Pirozhenko, O. V. Plink, MRTI	3112
Design of an 80-MHz RFQ Linac for Heavy Ions — O. Takeda, Y. Tanabe, K. Satoh, S. Kawazu, Toshiba; Y. Oguri, M. Okamura, T. Hattori, Tokyo Inst. of Tech.	3115
Operational Characteristics of a 100-mA, 2-MeV Radio-Frequency Quadrupole — K. F. Johnson, W. B. Cottingham, G. O. Bolme, C. M. Fortgang, W. Ingalls, J. Marquardt, D. P. Rusthoi, O. R. Sander, M. Smith, G. T. Worth, LANL	3118
Analysis of the End Regions of the CERN Lead-Ion 4-Rod RFQ — V. A. Andreev, ITEP Moscow; A. Lombardi, G. Parisi, INFN Legnaro; M. Vretenar, CERN	3121
90°-Apert-Stem RFQ Structure for Wide Range of Frequencies — V. A. Andreev, ITEP Moscow; G. Parisi, INFN Legnaro	3124
The SSCL RFQ System Integration — G. Arbique, A. Calo, C. Cuevas, P. Datte, D. Evans, J. Hurd, E. Marsden, K. Saadatmand, J. Sage, SSCL	3127
SSC Radio-Frequency-Quadrupole Beam: Comparison of Experimental and Simulated Results — F. W. Guy, J. W. Hurd, D. Raparia, K. Saadatmand, W. A. Whittenberg, SSCL	3130
Mechanical Integration of an RF Volume Source and Einzel Lens LEBT to the SSC RFQ — R. A. Valicenti, J. Lenz, N. C. Okay, L. Plesea, K. Saadatmand, SSCL	3133
Segmented Resonantly Coupled Radio-Frequency Quadrupole (RFQ) — L. M. Young, LANL	3136
Experiments with the High Current RFQ Prototype for GSI — A. Kippert, A. Schempp, H. Deitinghoff, J. Madlung, T. Ludwig, K. Volk, O. Engels, A. Firjahn-Andersch, H. Vormann, Inst. f. Angew. Physik	3139
Transport of Ions in RFQ-Accelerators — J. Dehen, W. Barth, A. Schempp, H. Deitinghoff, Inst. f. Angew. Physik	3142
An ESQ Lens System for Low Energy Beam Transport Experiments on the SSC Test Stand — S. K. Guharay, C. K. Allen, M. Reiser, U. Maryland; K. Saadatmand, SSCL	3145
Test of the Transport Properties of a Helical Electrostatic Quadrupole and Quasi-Octupole — L. Xiu, S. Ohnuma, K. Wang, U. Houston; C. R. Meitzler, Y. Xu, Sam Houston State U.	3148
Comparison of Experimental and Simulated Results for the SSC LEBT — J. W. Lenz, J. Hebert, N. Okay, D. Raparia, K. Saadatmand, SSCL	3151
Axial Magnetic Field Lens with Permanent Magnet — Y. Iwashita, Kyoto U.	3154
Design of a Merging Beamlet Pre-Accelerator for an Electrostatic Quadrupole Accelerator (ESQ) — C. F. Chan, M. C. Vella, LBL	3157
Low Energy H ⁻ Injector Design for SSC RFQ — C. F. Chan, K.-N. Leung, LBL	3160

Each volume begins with this five-volume table of contents and ends with the five-volume author index. The chairmen's foreword and a list of conference organizers and staff appear as front matter in Volume 1. A list of conference participants precedes the author index in Volume 5.

Five-Volume Contents

Lithium Lens for Focusing Protons on Target in the Fermilab Antiproton Source — F. M. Bieniosek, K. Anderson, FNAL	3163
Injector Design for High-Current CW Proton Linacs — R. R. Stevens, Jr., J. D. Sherman, J. D. Schneider, LANL ...	3166
A High Power Long Pulse RF-Driven H ⁻ Source — J. W. Kwan, G. D. Ackerman, W. S. Cooper, G. J. deVries, K. N. Leung, R. P. Wells, LBL	3169
Initial Operation of the CW 8X H ⁻ Ion Source Discharge — H. V. Smith, Jr., P. Allison, C. Geisik, D. R. Schmitt, J. D. Schneider, J. E. Stelzer, LANL	3172
Volume H ⁻ Ion Source Development at LAMPF — R. L. York, D. Tupa, D. R. Swenson, R. Damjanovich, LANL	3175
Further Development with Heavy Ion Sources at Brookhaven National Laboratory's Tandem Van de Graaff Facility — M. J. Zarcone, D. B. Steski, K. S. Smith, P. Thieberger, BNL	3178
A Dual-Optically-Pumped Polarized Negative Deuterium Ion Source — Y. Mori, M. Kinsho, KEK	3181
The IUCF High Intensity Polarized Ion Source Project — M. Wedekind, R. Brown, V. Derenchuk, D. Friesel, J. Hicks, P. Schwandt, IUCF	3184
The High Current Ion Source System HOLCROSS — N. R. Lobanov, MEPI Moscow	3187
Positive Hydrogen Ion Beam Production by an RF-Driven Multicusp Source — K. N. Leung, D. A. Bachman, P. R. Herz, D. S. McDonald, L. T. Perkins, LBL; M. Olivo, PSI	3190
Measurements of Emittance and Species Fractions of a Positive Hydrogen Ion Beam Extracted from an RF-Driven Multicusp Source — G. Gammel, T. W. Debiak, S. Melnychuk, J. Sredniawski, Grumman	3193
A New Design of the Sputter Type Metal Ion Source and Its Characteristics of Ion Beam Extraction — W. Kim, B. H. Choi, J. T. Jin, K.-S. Jung, Korea Atomic Energy Res. Inst.; S. H. Do, Pusan Nat. Fishers U.; K. H. Chung, Seoul Nat. U.	3196
K ⁺ Ion Source for the Heavy Ion Induction Linac System Experiment ILSE — S. Eylon, E. Henestroza, W. W. Chupp, S. Yu, LBL	3199
On the Magnetic Compression and Guiding of Electron Beams in E.B.I. S. or E.B.I.T — J. L. Bobin, E. Mercier, UPMC Paris; G. Giardino, LPAN	3202
Choice of Hexapole Parameters for ECR Ion Source — V. P. Kukhtin, E. A. Lamzin, Yu. P. Severgin, S. E. Sytchevsky, Efremov Inst.	3205
Stripping Efficiencies for 277 MeV/amu Gold Beam on Copper Foils — T. Roser, BNL	3207
Management of High Current Transients in the CWDD Injector 200 kV Power System — J. A. Carwardine, G. Pile, AEA Tech. Culham Lab; T. E. Zinneman, ANL	3210
Design and Results of the Radio Frequency Quadrupole RF System at the Superconducting Super Collider Laboratory — J. Grippe, E. Marsden, O. Marrufo, SSCL; A. Regan, D. Rees, C. Ziomek, LANL	3213
Initial Operation and Beam Characteristics of the UCLA S-Band Photo-Injector — C. Pellegrini, N. Barov, P. Davis, G. Hairapetian, S. C. Hartman, C. Joshi, S. Park, J. Rosenzweig, G. Travish, R. Zhang, UCLA	3216

Volume 5

Multiparticle Beam Dynamics

Chair: M. Reiser

Methods of Impedance Calculation (<i>Invited Paper</i>) — R. L. Gluckstern, Maryland	3219
Space-Charge Calculations in Synchrotrons (<i>Invited Paper</i>) — S. Machida, SSCL	3224
Advanced Computers and Simulation (<i>Invited Paper</i>) — R. D. Ryne, LANL	3229
Measured Optimum BNS Damping Configuration of the SLC Linac — J. T. Seeman, F.-J. Decker, R. L. Holtzapple, W. L. Spence, SLAC	3234
Single Beam Phenomena in BEPC — Z. Y. Guo, X. Bai, G. X. Li, J. Qin, Q. Qin, G. Xu, C. Zhang, X. L. Zhang, Z. T. Zhao, IHEP, Academia Sinica	3237
High Intensity Bunch Length Instabilities in the SLC Damping Rings — P. Krejcik, K. Bane, P. Corredoura, F.-J. Decker, J. Judkins, T. Limberg, M. Minty, R. H. Siemann, SLAC; F. Pedersen, CERN	3240
Investigation on Relaxations in Electron Beams — A. Aleksandrov, N. Dikansky, N. Ch. Kot, V. Kudelainen, V. A. Lebedev, P. Logachov, BINP; R. Calabrese, G. Ciullo, V. Guidi, G. Lamorosa, P. Lenisa, B. Maciga, L. Tecchio, B. Yang, INFN	3243
Studies of Multipass Beam Breakup and Energy Recovery Using the CEBAF Injector Linac — N. S. Sereno, L. S. Cardman, U. Illinois; G. A. Krafft, C. K. Sinclair, J. J. Bisognano, CEBAF	3246

Volume 1: 1-747
 Volume 2: 748-1640
 Volume 3: 1641-2545
 Volume 4: 2546-3218
 Volume 5: 3219-3933

Proceedings of the 1993 Particle Accelerator Conference

Poster presentations:

The Longitudinal and Transverse Beam Dynamics Simulation in the MMF Storage Ring — V. A. Moiseev, INR Moscow	3249
Control of Longitudinal Instabilities in the LEB — T. L. Grimm, P. D. Coleman, SSCL	3252
Simulation of the Transverse Dipole Mode Multibunch Instability for the SSC Collider — S. Chen, G. López, SSCL	3255
HOM RF Cavity Dampers for Suppressing Coupled Bunch Instabilities in the Fermilab Booster — D. Wildman, FNAL; K. Harkay, Purdue	3258
Longitudinal Instabilities in the MEB — J. A. Palkovic, SSCL	3261
A New Formulation of Longitudinal Coherent Instabilities — S. Y. Zhang, W. T. Weng, BNL	3264
Three-Dimensional Simulations for Accelerator Physics Using ARGUS — A. Mondelli, A. Mankofsky, J. Petillo, W. Krueger, C. Kostas, A. Drobot, SAIC; R. Ryne, R. K. Cooper, G. Rodenz, M. J. Browman, LANL	3267
A Higher-Order Moment Simulation Model — K. T. Tsang, C. Kostas, A. Mondelli, SAIC	3270
Collective Effects of the PLS 2 GeV Storage Ring — M. Yoon, J. Choi, T. Lee, Pohang	3273
Nonlinear Evolution of Longitudinal Bunched-Beam Instabilities — A. Gerasimov, FNAL	3276
Multi-Bunch Dynamics in Accelerating Structures Including Interaction with Higher Order Modes — M. Ferrario, F. Tazzioli, INFN-LNF; L. Serafini, INFN Milano	3279
Generation of Space-Charge Waves due to Localized Perturbations — J. G. Wang, D. X. Wang, D. Kehne, M. Reiser, U. Maryland	3282
Three Dimensional Multipole Decomposition of Fields — K. Hahn, LBL	3285
Multi-Bunch Beam-Break-Up Studies for a SWFEL/TBA — J. S. Kim, A. M. Sessler, LBL; D. H. Whistum, KEK; H. Henke, TU Berlin	3288
RF Noise Revisited: The Effect of Coherence — A. Gerasimov, FNAL; S. Y. Lee, Indiana U.	3291
TSD Versus TRL Calibration and Applications to Beam Impedance Measurements — M. Foley, P. Colestock, E. Barsotti, Jr., FNAL	3294
Recent Study of Beam Stability in the PSR — T. Wang, R. Cooper, D. Fitzgerald, S. Frankle, T. Hardek, R. Hutson, R. Macek, C. Ohmori, M. Plum, H. Thiessen, C. Wilkinson, LANL; E. Colton, DOE; D. Neuffer, CEBAF; G. Rees, RAL	3297
Impedance Budget and Beam Stability Analysis of the Fermilab Main Injector — M. A. Martens, K. Y. Ng, FNAL ..	3300
Trapped Ions and Beam Coherent Instability — P. Zhou, P. L. Colestock, S. J. Werkema, FNAL	3303
Comparison of the Coupled-Bunch Mode Theory to Experimental Observations in the Fermilab Booster — K. C. Harkay, Purdue; P. L. Colestock, FNAL	3306
Measurement of Trapped Ion Pockets and Control of Ion Instabilities in the Fermilab Antiproton Accumulator — S. J. Werkema, K. D. Fullett, P. Zhou, FNAL	3309
Study of Possible Energy Upgrade for the ALS and Modeling of the "Real Lattice" for the Diagnosis of Lattice Problems — M. Meddahi, J. Bengtsson, LBL	3312
Study of Coupled-Bunch Collective Effects in the PEP-II B-Factory — J. Byrd, LBL	3315
Study of Coupled-Bunch Collective Effects in the ALS — J. M. Byrd, J. N. Corlett, LBL	3318
Time Domain Solutions for a Coasting Beam with Impedance Feedback — M. Blaskiewicz, BNL	3321
Longitudinal Impedance and Stability Thresholds of the AGS Booster — M. Blaskiewicz, BNL	3324
Calculation of the Bunch Lengthening Threshold — X. T. Yu, J. S. Wurtele, MIT	3327
Computation of Longitudinal Bunched Beam Instability Thresholds — R. Baartman, TRIUMF; M. D'Yachkov, U. British Columbia	3330
Bunch Lengthening Observed Using Real-Time Bunch-Length Monitor in the TRISTAN AR — T. Ieiri, KEK	3333
Transverse Stability in Multibunch Mode for CLIC — G. Guignard, CERN	3336
Simulations of the Longitudinal Instability in the SLC Damping Rings — K. L. F. Bane, SLAC; K. Oide, KEK	3339
Multibunch Beam Break-Up in Detuned Structures — K. A. Thompson, C. Adolphsen, K. L. F. Bane, SLAC	3342
Longitudinal Head-Tail Instability in a Non-Harmonic Potential Well — B. Chen, A. W. Chao, SSCL	3345
Bunch Lengthening Effect and Localized Impedance — B. Chen, A. W. Chao, SSCL	3348
Experimental Reduction of Electron Beam Breakup Instability Using External Coupled Cavities — P. R. Menge, R. M. Gilgenbach, Y. Y. Lau, M. Walter, C. H. Ching, U. Michigan	3351
Beam Breakup in an Annular Beam — Y. Y. Lau, J. W. Luginsland, R. M. Gilgenbach, U. Michigan	3354

Each volume begins with this five-volume table of contents and ends with the five-volume author index. The chairman's foreword and a list of conference organizers and staff appear as front matter in Volume 1. A list of conference participants precedes the author index in Volume 5.

Five-Volume Contents

RF Focusing Effects and Multi-Bunch Beam Breakup in Superconducting Linear Colliders — <i>J. Rosenzweig, S. Hartman, J. Stevens, UCLA</i>	3357
Required Cavity HOM deQing Calculated from Probability Estimates of Coupled Bunch Instabilities in the APS Ring — <i>L. Emery, ANL</i>	3360
Measurement and Analysis of Transverse Beam Transfer Functions in the Fermilab Main Ring — <i>P. J. Chou, G. Jackson, FNAL</i>	3363
Observation of a Short Bunch Train Longitudinal Instability in the Fermilab Main Ring — <i>X. Lu, G. Jackson, FNAL</i>	3366
Suppression of Longitudinal Coupled-Bunch Instabilities by a Passive Higher Harmonic Cavity — <i>R. A. Bosch, C. S. Hsue, SRRC Taiwan</i>	3369
The Longitudinal Coupling Impedance of a Slot on the SSC Collider Liner — <i>V. Thiagarajan, SSCL</i>	3372
Impedance of a Small-Gap Undulator Vacuum Chamber — <i>K. Bane, SLAC; S. Krinsky, NSLS-BNL</i>	3375
A Formula for the High Frequency Longitudinal Impedance of a Tube With Smoothly Varying Radius — <i>R. L. Warnock, SLAC</i>	3378
A Bench Set-Up for Low-Beta Beam-Current Test Measurements with COSY — <i>Ch. Günther, A. Schnase, H. Meuth, IKP Jülich; F. Caspers, CERN</i>	3381
A Generalized Model for Parametric Coupling of Longitudinal Modes in Synchrotrons — <i>P. L. Colestock, L. Klamp, FNAL</i>	3384
Longitudinal Coupling Impedance of a Cavity — <i>I. Gjaja, R. L. Gluckstern, U. Maryland</i>	3387
Transverse Impedance of an Iris in a Beam Pipe — <i>S. Jiang, R. L. Gluckstern, U. Maryland; H. Okamoto, Kyoto U.</i>	3390
RF Characteristics of the APS Storage Ring Isolation Valve — <i>J. J. Song, R. L. Kustom, ANL</i>	3393
Coupling Impedance of Vacuum Pumping Holes for the APS Storage Ring — <i>J. Zhou, J. J. Song, R. L. Kustom, ANL</i>	3396
Impedance Formalism for an Arbitrary Cumulative Instability — <i>X. T. Yu, J. S. Wurtele, MIT; D. H. Whittum, KEK</i>	3399
Longitudinal Impedance of a Prototype Kicker Magnet System — <i>H. J. Tran, M. J. Barnes, G. D. Wait, Y. Yan, TRIUMF</i>	3402
Beam Coupling Impedance Measurements and Simulations of a Beam Pipe Liner with Pumping Holes or Slots — <i>E. Ruiz, L. Walling, Y. Goren, N. Spayd, SSCL</i>	3405
Measurement and Computation of the Higher Order Modes of the ALS 500 MHz Accelerating Cavities — <i>J. N. Corlett, J. M. Byrd, LBL</i>	3408
Impedance Measurements of Components for the ALS — <i>J. N. Corlett, R. A. Rimmer, LBL</i>	3411
Advances and Applications of ABCI — <i>Y. H. Chin, LBL</i>	3414
On Coupling Impedances of Pumping Holes — <i>S. S. Kurennoy, SSCL</i>	3417
Using a Ceramic Chamber in Kicker Magnets — <i>S. S. Kurennoy, SSCL</i>	3420
An Analytical Treatment of Self Fields in a Relativistic Bunch of Charged Particles in a Circular Orbit — <i>J. L. Delhez, J. M. A. Hofman, J. I. M. Botman, H. L. Hagedoorn, W. J. G. M. Kleeven, G. A. Webers, Eindhoven U. of Tech.</i>	3423
Transverse Wake Fields in the CLIC Transfer Structure — <i>G. Guignard, G. Carron, A. Millich, L. Thorndahl, CERN</i>	3426
The LEP Impedance Model — <i>D. Brandt, K. Cornelis, V. Danilov, A. Hofmann, C. Juillard, E. Perevedentsev, E. Peschardt, E. Rossa, F. Tecker, D. Wang, B. Zotter, CERN; L. Rivkin, PSI</i>	3429
Impedance Calculations for the Improved SLC Damping Rings — <i>K. L. F. Bane, C.-K. Ng, SLAC</i>	3432
Broadband Impedance of Azimuthally Symmetric Devices in RHIC — <i>V. Mane, BNL</i>	3435
Software Development with Two Port Calibration Techniques for RHIC Impedance Measurements — <i>V. Mane, T. Shea, BNL</i>	3438
Resistive Wall Wake Function for Arbitrary Pipe Cross Section — <i>K. Yokoya, KEK</i>	3441
Impedance of a Perforated Liner and Its Impact on the SSC Collider — <i>W. Chou, T. Barts, SSCL</i>	3444
A Generalized Method for Calculating Wake Potentials — <i>O. Napoly, Saclay; Y. H. Chin, LBL; B. Zotter, CERN</i> ...	3447
The Interaction of a Beam With a Beam Line Higher-Order-Mode Absorber — <i>W. Hartung, K. Akai, J. DeFord, T. Hays, J. Kirchgessner, D. Metzger, D. Moffat, H. Padamsee, D. Rubin, M. Tigner, A. Tribendis, V. Veshcherevich, Cornell</i>	3450
Persistent Wakefields Associated with Waveguide Damping of Higher Order Modes — <i>N. M. Kroll, X. Lin, UCSD/SLAC</i>	3453

Volume 1:	1-747
Volume 2:	748-1640
Volume 3:	1641-2545
Volume 4:	2546-3218
Volume 5:	3219-3933

Proceedings of the 1993 Particle Accelerator Conference

Perturbation Theory of Broadband Impedances — S. Heifets, SLAC	3456
Broadband Impedance of the B Factory — S. Heifets, SLAC	3459
Study of a Detuned Accelerating Section With the Computer Program PROGON — S. A. Heifets, S. A. Kheifets, SLAC	3462
Estimation of Broad Band Impedance of the SPring-8 Storage Ring — T. Nakamura, JAERI	3464
Head-On and Long Range Beam-Beam Tune Shift Spread in the SSC — G. López, SSCL	3467
Beam-Beam Effects with Errors in the Crab Compensation — D. Sagan, Cornell	3470
A Strong-Strong Simulation on the Beam-Beam Effect in a Linac/Ring B-Factory — R. Li, J. J. Bisognano, CEBAF	3473
Some Aspects of the Long Range Beam-Beam Interaction in Storage Rings — A. B. Temnykh, INP; J. J. Welch, Cornell	3476
Experimental Study of Crossing Angle Collision — T. Chen, SLAC; D. Rice, D. Rubin, D. Sagan, M. Tigner, Cornell	3479
Beam-Beam Experiments in the Tevatron — D. Siergiej, G. Goderre, FNAL	3482
Beam-Beam Effects for the PEP-II B Factory — M. A. Furman, LBL; J. R. Eden, U. Washington.....	3485
Equivalent Equations and Incoherent Lifetime Calculated from e^+e^- Beam-Beam Simulation — Y. Orlov, Cornell	3488
Simulation of Beam-Beam Effects in Electron-Positron Rings — K. Hirata, S. Matsumoto, KEK	3491
Longitudinal Beam-Beam Effects in Circular Colliders — M. Hogan, J. Rosenzweig, UCLA	3494
Strong-Weak Beam-Beam Simulation with a Six Dimension Symplectic Code — Y. Funakoshi, H. Koiso, KEK	3497
Synchrotron Beam-Loading Stability with a Higher RF Harmonic — T. F. Wang, LANL	3500
Compensation of Bunch Position Shift Using Sub-RF Cavity in a Damping Ring — K. Kubo, T. Higo, S. Sakanaka, KEK	3503
Analytic Criteria for Stability of Beam-Loaded RF Systems — S. R. Koscielniak, TRIUMF	3506
Beam Loading Effect in SSCL Coupled Cavity Linac — Yu. Senichev, R. Cutler, J. Hurd, D. Raparia, SSCL	3509
The Ion Core Density in Electron Storage Rings with Clearing Electrodes — E. V. Buljak, Kharkov Inst.	3512
Operation of the CEBAF Linac with High Beam Loading — L. Merminga, J. J. Bisognano, C. Hovater, G. A. Krafft, S. N. Simrock, CEBAF; K. Kubo, KEK	3515
An Idea of Dynamical Cooling of Electron Beam in SR Ring — S. Kato, Osaka U.	3518
The Principle of Ultra-Fast Automatic Cooling for Beams — S. Gao, G. Qian, CIAE	3521
On the Longitudinal Stability of Cooled Coasting Ion Beams — S. Nagaitsev, IUCF.....	3524
Crystalline Beam Ground State — J. Wei, BNL; X. Li, Rutgers; A. M. Sessler, LBL	3527
Confinement and Stability of a Crystal Beam — A. G. Ruggiero, BNL	3530
Bunched Beam Stochastic Cooling in the Fermilab Tevatron Collider — G. Jackson, E. Buchanan, J. Budlong, E. Harms, P. Hurh, D. McGinnis, R. Pasquinelli, D. Peterson, D. Poll, P. Seifrid, FNAL	3533
Longitudinally Space Charge Dominated Beams in a Synchrotron — T. J. P. Ellison, S. S. Nagaitsev, M. S. Ball, D. D. Caussyn, M. J. Ellison, B. J. Hamilton, IUCF	3536
High Density Plasma Source for Plasma Lens Experiments — K. Nakamura, R. Liou, M. Gundersen, USC	3537
Measurement of Escaping Ions in the Fermilab Antiproton Accumulator — P. Zhou, P. L. Colestock, K. Junck, C. A. Crawford, FNAL	3540
Experimental Demonstration of Plasma Lens Focusing — G. Hairapetian, P. Davis, C. E. Clayton, C. Joshi, S. Hartman, C. Pelligrini, UCLA; T. Katsouleas, USC	3543
Numerical Modelling of Time-Space Behavior of High-Current Relativistic Electron Beam in Plasma Waveguide — V. I. Karas', Kharkov Inst.; N. G. Belova, Russian Acad.	3546
IPROP Simulations of the GAMBLE II Proton Transport Experiment — D. R. Welch, Mission Res. Corp.	3549
Plasma Lens and Plasma Wakefield Acceleration Experiments Using Twin Linacs— A. Ogata, H. Nakanishi, K. Nakajima, T. Kawakubo, D. Whittum, M. Arinaga, KEK; Y. Yoshida, T. Ueda, T. Kobayashi, Nucl. Eng. Res. Lab, Tokyo U.; H. Shibata, S. Tagawa, Res. Ctr. Nucl. Sci. Tech., Tokyo U.; N. Yugami, Y. Nishida, Utsunomiya U.	3552
Plasma Focusing of the Final Test Beam — S. Rajagopalan, UCLA	3555
Emittance Growth in MEB and Its Control — Y. Huang, S. Machida, R. Gerig, SSCL	3558
Longitudinal Diffusion as Inflicted by Arbitrary Band-Width Random-Modulated Currents in Feeders of Detuned Cavities — S. Ivanov, IHEP Moscow	3561
Induced Beam Oscillations from Quadrupole Vibrations in the SLC Linac — J. T. Seeman, R. L. Holtzapple, M. C. Ross, SLAC	3564

Each volume begins with this five-volume table of contents and ends with the five-volume author index. The chairman's foreword and a list of conference organizers and staff appear as front matter in Volume 1. A list of conference participants precedes the author index in Volume 5.

Five-Volume Contents

Effects of Magnetic Focusing on Longitudinal Emittance and Energy Dispersion of an Intense Short Accelerating Electron Pulse — J.-M. Doliue, J. C. Coacolo, U. Joseph Fourier/CEA	3567
Measurement and Reduction of Transverse Emittance Blow-Up Induced by Space Charge Effects — R. Cappi, R. Garoby, S. Hancock, M. Martini, J. P. Riinaud, CERN	3570
Transverse Emittance Growth in the Fermilab Antiproton Accumulator with High-Current Antiproton Stacks — S. J. Werkema, D. W. Peterson, P. Zhou, FNAL	3573
Transverse Tails and Higher Order Moments — W. L. Spence, F.-J. Decker, M. D. Woodley, SLAC	3576
Simulation of Emittance Dilution in Electron Storage Ring from Compton Backscattering — L. N. Blumberg, E. Blum, BNL	3579
Transverse Effects of Longitudinal Wakefields at High Dispersion — F. Decker, SLAC	3582
Error and Tolerance Studies for the SSC Linac — D. Raparia, C. R. Chang, F. Guy, J. W. Hurd, W. Funk, SSCL; K. R. Crandall, AccSys	3585
Emittance Growth Due to Dipole Ripple and Sextupole — H.-J. Shih, J. A. Ellison, M. J. Syphers, B. S. Newberger, SSCL	3588
Proton-Proton Scattering Contribution to Emittance Growth — T. Garavaglia, SSCL	3591
Source Size Variation and Ion Effects in the SRS at Daresbury — J. A. Clarke, D. M. Dykes, S. F. Hill, E. A. Hughes, M. W. Poole, P. D. Quinn, S. L. Smith, V. P. Suller, L. A. Welbourne, SERC Daresbury	3594
Global Trajectory Correction Algorithms in CLIC and Main Linac Alignment Tolerances — C. Fischer, CERN	3597
Lattice Scaling and Emittance Control in the CLIC Main Linac — G. Guignard, CERN	3600
Decoherence and Recoherence of Beam in Phase Space — J. Shi, S. Ohnuma, U. Houston	3603
Space-Charge-Induced Emittance Growth in an Elliptical Charged Particle Beam with a Parabolic Density Distribution — T. P. Wangler, LANL; P. Lapostolle, A. Lombardi, CERN	3606
Emittance and Luminosity Evolution During Collisions in the SSC Collider — W. Chou, S. Dutt, T. Garavaglia, K. Kauffmann, SSCL	3609
Emittance Growth in Displaced, Space-Charge-Dominated Beams with Energy Spread — J. J. Barnard, J. Miller, LLNL; I. Haber, NRL	3612
An Injection Scheme for the Brookhaven ATF Utilizing Space-Charge Emittance Growth Compensation — J. C. Gallardo, H. G. Kirk, BNL	3615
A Matrix Theory of the Motion of an Ellipsoidal Bunch in a Beam Control System with a Rectilinear Optical Axis and with Space Charge — A. Dymnikov, U. St. Petersburg; R. Hellborg, U. Lund	3618
Space-Charge Dominated Beam Envelope Transport with Rotatable Axes — E. Y. Tsiang	3621
Effect of Space Charge Forces on Particle Tracking and Generation of High-Order Maps — D. L. Bruhwiler, M. F. Reusch, Grumman	3624
Experimental Study of Longitudinal Dynamics of Space-Charge Dominated Parabolic Bunches — D. X. Wang, J. G. Wang, D. Kehne, M. Reiser, U. Maryland; I. Haber, Naval Res. Lab.	3627
Transition Crossing in the Fermilab Main Ring, Past and Present — I. Kourbanis, K. Y. Ng, FNAL	3630
Observation and Correction of Resonance Stopbands in the AGS Booster — C. Gardner, L. Ahrens, J. W. Glenn, Y. Y. Lee, T. Roser, A. Soukas, W. van Asselt, W. T. Weng, BNL; Y. Shoji, KEK	3633
The Stability of Ions in a Storage Ring in the Presence of Small Gap Insertion Devices — E. Bozoki, BNL	3636
Simulation of Space-Charge Dominated Beam Dynamics in an Isochronous AVF Cyclotron — S. R. Koscielniak, TRIUMF; S. R. Adam, PSI Switzerland	3639
Passage Through a Half-Integer Resonance Due to Space Charge for Different Initial Distributions — A. Budzko, INR; Yu. Senichev, SSCL	3642
Estimation of Collective Effects for the EUTERPE Ring — B. Xi, J. I. M. Botman, J. van Laar, C. J. Timmermans, H. L. Hagedoorn, Eindhoven U. of Tech.	3645
A Moment Method Laplace Solver for Low Energy Beam Transport Codes — C. K. Allen, S. K. Guharay, M. Reiser, U. Maryland	3648
Evolution of Hadron Beams Under Intrabeam Scattering — J. Wei, BNL	3651
Simulation Study of Ion Trapping in PLS Storage Ring — J. Jung, I. Ko, POSTECH	3654
Beam Halo Formation From Space-Charge Dominated Beams in Uniform Focusing Channels — J. S. O'Connell, Booz, Allen & Hamilton; T. P. Wangler, R. S. Mills, LANL; K. R. Crandall, AccSys Tech.	3657
Computer Simulation of the Maryland Transport Experiment — I. Haber, Naval Res. Lab.; D. A. Callahan, A. B. Langdon, LLNL; M. Reiser, D. X. Wang, J. G. Wang, U. Maryland	3660
Integrated Numerical Modeling of a Laser Gun Injector — H. Liu, S. Benson, Y. Bisognano, P. Liger, G. Neil, D. Neuffer, C. Sinclair, B. Yunn, CEBAF	3663

Volume 1: 1-747
Volume 2: 748-1640
Volume 3: 1641-2545
Volume 4: 2546-3218
Volume 5: 3219-3933

Proceedings of the 1993 Particle Accelerator Conference

Halo Formation in Mismatched, Space-Charge-Dominated Beams — C. L. Bohn, J. R. Delayen, ANL	3666
Collective Effects in the VEPP-3 Storage Ring — S. A. Belomestnykh, A. N. Voroshilov, BINP	3669
Single Bunch Effects in the Daresbury SRS — L. A. Welbourn, J. A. Clarke, D. M. Dykes, S. F. Hill, E. A. Hughes, M. W. Poole, P. D. Quinn, S. L. Smith, V. P. Suller, SERC Daresbury	3672
The Effects of Coulomb Beam Interaction in Multiaperture Linac — A. I. Balabin, G. N. Kropachev, I. O. Parshin, D. G. Skachkov, ITEP Moscow	3675
Longitudinal Instability of an Induction Linac with Acceleration — L. Smith, E. P. Lee, LBL	3678
On Solvable Model with Synchrotron Mode-Coupling — D. V. Pestrikov, BINP/KEK	3681
On Limitations on Low- α Rings Performance Due to —Z-Instabilities — N. S. Dikansky, BINP Russia; D. V. Pestrikov, KEK	3684
On Landau Damping of Collective Beam-Beam Modes — D. V. Pestrikov, BINP/KEK	3687
Synchronous Phase Changes Due to the Gap in the Bunch Train — Z. Greenwald, M. Tigner, Cornell	3690
Simulation and Compensation of Multibunch Energy Variation in NLC — K. A. Thompson, R. D. Ruth, SLAC	3693
The Physical Mechanism of Ultra-Fast Automatic Cooling for Beams in the Six-Dimensional Emittance Space — S. Gao, G. Qian, D. Liang, H. Sun, CIAE China	3696
An Exact Expression for the Momentum Dependence of the Space Charge Tune Shift in a Gaussian Bunch — M. Martini, CERN	3699
Stored Beam Lifetime Evaluation Formulae for Electron Storage Rings — A.V. Makulkin, All-Russ. Res. Inst.	3702
A Simulation Study on Beam Bunching in the KEK 2.5-GeV Linac New Pre-Injector — T. Kamitani, J.-Y. Choi, A. Enomoto, S. Ohsawa, Y. Ogawa, T. Urano, T. Suwada, K. Furukawa, I. Sato, KEK	3705
New Outlooks on Bunched Beam Instabilities in Particle Accelerators: A Proposal for a Simple Method to Release a Potential Self-Consistent High Quality Beam — M. Bergher, LURE	3708
Experimental Study of Collective Effects in BEP Storage Ring with High Stored Current — V. Danilov, I. Koop, A. Lysenko, B. Militsyn, I. Nesterenko, E. Perevedentsev, E. Pozdeev, V. Pitsin, Yu. Shatunov, I. Vasserman, BINP	3711
Beam Coupling Impedances of Axial Symmetric Structures — W. Bruns, Technische Universität Berlin	3714

Hadron and e-p Colliders and Hadron Synchrotrons

Chair: D. Edwards

Accelerator Physics Issues at the SSC (Invited Paper) — G. F. Dugan, SSCL	3717
Fermilab Collider Upgrade: Recent Results and Plans (Invited Paper) — D. A. Finley, FNAL	3721
Operation of the Brookhaven AGS with the Booster (Invited Paper) — W. T. Weng, BNL	3726
Overview of Future Spallation Neutron Sources (Invited Paper) — G. H. Rees, Rutherford Appleton	3731
The Heavy Ion Synchrotron SIS: A Progress Report — K. Blasche, B. Franczak, B. Langenbeck, G. Moritz, C. Riedel, GSI	3736
Status of the PSR Improvement Program — R. J. Macek, D. H. Fitzgerald, M. Hoehn, R. Ryder, R. York, LANL	3739

Poster presentations:

First Experience with Colliding Electron-Proton Beams in HERA — R. Brinkmann, F. Willeke, DESY	3742
The Development of a Prototype Multi-MeV Electron Cooling System — D. Anderson, M. Ball, D. Caussyn, T. Ellison, B. Hamilton, S. Nagaitsev, P. Schwandt, IUCF; J. Adney, J. Ferry, M. Sundquist, Nat. Electr. Corp.; D. Reistad, Svedberg Lab.; M. Sedlacek, Alfvén Lab.	3745
The Bevalac Long Spill — C. M. Celata, S. Abbott, M. Bennett, M. Bordua, J. Calvert, R. Dwinell, D. Howard, D. Hunt, B. Feinberg, R. Force, R. Frias, J. Halliwell, J. Kalnins, S. Lewis, M. Nyman, L. Shalz, M. Tekawa, LBL; R. Solomons, RAFAEL, Israel	3748
Capture from Pair Production as a Beam Loss Mechanism for Heavy Ions at RHIC — B. Feinberg, A. Belkacem, R. Bossingham, H. Gould, LBL; W. E. Meyerhof, Stanford U.	3751
Acceleration of Deuteron Beam in the KEK Proton Synchrotron — Y. Mori, KEK	3754
Conceptual Design for a One Megawatt Spallation Neutron Source at Argonne — Y. Cho, J. Bailey, B. Brown, F. Brumwell, J. Carpenter, K. Crawford, D. Horan, D. Jerng, R. Kleb, A. Knox, R. Kustom, E. Lessner, D. McGhee, F. Mills, H. Moe, R. Nielsen, C. Potts, A. Raichas, K. Thompson, ANL	3757
A Los Alamos Design Study for a High-Power Spallation-Neutron-Source Driver — A. J. Jason, R. A. Hardekopf, R. W. Macek, S. O. Schriber, H. A. Thiessen, R. Woods, LANL	3760

Each volume begins with this five-volume table of contents and ends with the five-volume author index. The chairman's foreword and a list of conference organizers and staff appear as front matter in Volume 1. A list of conference participants precedes the author index in Volume 5.

Five-Volume Contents

On the High Intensity Aspects of AGS Booster Proton Operation — R. K. Reece, L. A. Ahrens, E. J. Bleser, J. M. Brennan, C. Gardner, J. W. Glenn, T. Roser, Y. Shoji, W. vanAsselt, W. T. Wang, BNL	3763
Results from Commissioning the AGS Booster Orbit System — E. Bleser, BNL	3766
The Effect of Global Survey Misalignment on the SSC — T. Garavaglia, N. Mahale, J. Peterson, SSCL	3769
Dealing with Abort Kicker Prefire in the Superconducting Super Collider — A. I. Drozhdin, I. S. Baishiev, N. V. Mokhov, B. Parker, R. D. Richardson, J. Zhou, SSCL	3772
Design Status Report on the Collider Utility Straight Insertions — B. Parker, SSCL	3775
Current Design of the SSC Interaction Regions — Y. Nosochkov, A. Garren, T. Sen, R. Stiening, SSCL; E. Courant, BNL; D. M. Ritson, SLAC	3778
The Parameter Spreadsheets and Their Applications — R. Schwitters, A. Chao, W. Chou, J. Peterson, SSCL	3781
Lattice Studies for KAON Factory Accumulator and Booster Rings — A. Iliev, A. V. Budzko, INR-Troitsk; R. V. Servranckx, TRIUMF	3784
Reducing the Coupled-Bunch Oscillation in the Fermilab Booster by Optimizing RF Voltage — J. P. Shan, D. McGinnis, R. Tomlin, FNAL	3787
Beta Measurements and Modeling the Tevatron — N. M. Gelfand, FNAL	3790
The Status of the Fermilab Main Injector Project — D. Bogert, W. Fowler, S. Holmes, P. Martin, T. Pawlak, FNAL	3793
Constructing High Energy Accelerators Under DOE's "New Culture" for Environment and Safety: An Example, the Fermilab 150 GeV Main Injector Proton Synchrotron — W. Fowler, FNAL	3796
Performance and Comparison of the Different Coalescing Schemes Used in the Fermilab Main Ring — I. Kourbanis, G. P. Jackson, X. Lu, FNAL	3799
Operational Experience with Collimators in the Tevatron Collider — S. M. Pruss, FNAL	3802
Reliability of the Fermilab Antiproton Source — E. Harms, Jr., FNAL	3803
Multibunch Operation in the Tevatron Collider — J. A. Holt, D. A. Finley, V. Bharadwaj, FNAL	3806
Operational Experience with the Tevatron Collider Using Separated Orbits — G. Annala, FNAL	3808
Fermilab Antiproton Accumulator in the Main Injector Era — V. Visnjic, FNAL	3811
Study of Betatron Stochastic Cooling in Fermilab Antiproton Debuncher — V. Visnjic, M. Halling, FNAL	3814
Energy and Luminosity Limits of Hadron Supercolliders — W. A. Barletta, LBL/UCLA	3817
Ions Acceleration in the Synchrotrons with Constant RF of Electrical Field — V. P. Belov, Yu. P. Severgin, Efremov Inst.	3820
Ion Storage Ring of the INR Storage-Accelerating Complex — A. V. Dolinsky, A. I. Papash, S. N. Pavlov, A. T. Rudchik, A. E. Val'kov, I. N. Vishnevsky, A. V. Zhmendak, INR Kiev; V. P. Belov, A. A. Kapustin, V. S. Kashihin, A. M. Kokorin, A. A. Makarov, B. G. Mud'jugin, B. V. Rogdestvensky, Yu. P. Severgin, L. A. Schukeilo, M. N. Tarovik, Efremov Inst.	3822
A Compensated Dispersion-Free Long Insertion for an FFAG Synchrotron — P. F. Meads, Jr.	3825
Vacuum Technology Chair: D. Edwards	
Vacuum Technology for Superconducting Colliders (<i>Invited Paper</i>) — A. G. Mathewson, CERN	3828
Dynamic Vacuum in the Beam Tube of the SSCL Collider: Cold Beam Tube and Liner Options — W. C. Turner, SSCL	3833
Distributed Ion Pump Testing for PEP-II, Asymmetric B-Factory Collider — M. Calderon, F. Holdener, W. Barletta, D. Petersen, LLNL; C. Foerster, BNL	3836
High Capacity Getter Pump for UHV Operation — P. Manini, M. Marino, F. Belloni, M. Porro, SAES Getters	3839
<i>Poster presentations:</i>	
ELETTRA Vacuum System — M. Bernardini, F. Daclon, F. Giacuzzo, R. Kersevan, J. Miertusova, F. Pradal, Sinc. Trieste	3842
Vacuum Chamber and Crotch Absorber for the SPring-8 Storage Ring Vacuum System — K. Watanabe, S. H. Be, Y. Oikawa, H. A. Sakaue, C. Y. Xu, S. Yokouchi, Y. Wang, JAERI-RIKEN; S. Takahashi, Kobe Steel; M. Tsuchiya, IHI; Y. Yanagi, Hitachi	3845
SYNRAD, a Montecarlo Synchrotron Radiation Ray-Tracing Program — R. Kersevan, SSCL	3848
Vacuum System Design of the MIT-Bates South Hall Ring — E. Ihloff, R. Averill, J. Flanz, K. Jacobs, S. Sobczynski, D. Wang, A. Zolfaghari, MIT-Bates	3851
Design of Vacuum Chambers for Experimental Regions of Colliding Beam Machines — C. Hauviller, CERN	3854

Volume 1: 1-747
 Volume 2: 748-1640
 Volume 3: 1641-2545
 Volume 4: 2546-3218
 Volume 5: 3219-3933

Proceedings of the 1993 Particle Accelerator Conference

Distributed Non-Evaporable Getter Pumps for the Storage Ring of the APS — R. Dortwegt, R. Banaroya, ANL	3857
Test Fabrication of a Copper Beam Duct for the KEK B-Factor — Y. Suetsugu, K. Kanazawa, KEK	3860
FNAL Main Injector Quadrupole Vacuum Chamber — L. Sauer, FNAL	3863
FNAL Main Injector Dipole Installation Equipment — K. Moravec, F. Lange, J. Leibfritz, L. Sauer, FNAL	3864
Solvents and Pumpdown Characteristics of SRF Nb Cavities — M. G. Rao, P. Kneisel, H. F. Dylla, CEBAF	3867
Leak Checker Data Acquisition System — J. Payns, J. Gannon, SSCL	3870
Theoretical and Experimental Study of Sorption Processes on Non-Evaporable Getters St 707 — J. Miertusova, F. Dacien, Sinc. Trieste	3873
Photodesorption Experiments on SSC Collider Beam Tube Configurations — I. Maslennikov, W. Turner, SSCL; V. Anashin, O. Malyshev, V. Ostrov, V. Nazmov, V. Pindyurin, A. Salimov, BINP; C. Foerster, C. Lanni, BNL	3876
The Heat Load of an 80 K Liner for the SSC — J. Maddocks, A. Yücel, SSCL	3879
Design of Large Aperture, Low Mass Vacuum Windows — W. J. Leonhardt, M. Mapes, BNL	3882
Observation and Analysis for Motions of Trapped Microparticles in the TRISTAN Accumulation Ring — H. Saeki, Japan SRR; T. Momose, Miyagi; H. Ishimaru, KEK	3885
Overview of an 80 K Liner Design for Synchrotron Light Interception in SSCL Collider — Q.-S. Shu, W. Chou, D. Clark, W. G. Y. Goren, R. Kersevan, V. Kovachev, P. Kraushaar, K. Leung, J. Maddocks, D. Martin, D. Meyer, P. Melic, G. Morales, J. Simmons, G. Snitchler, M. Tuli, W. Turner, L. Walling, K. Yu, J. Zbasnik, SSCL	3888
Thermal Model and Associated Novel Approach for Synchrotron Radiation Liner with End Cooling — Q.-S. Shu, K. Yu, W. Clay, J. Maddocks, G. Morales, J. Zbasnik, SSCL	3891
Design of ECR Ion Source Vacuum Systems — J. Pivaric, JINR Dubna	3894
Development of Distributed Ion Pumps for g-2 Beam Vacuum System — H. C. Hseuh, M. Mapes, L. Snyder, BNL	3897
What Joining Method for the New Generation of Accelerators (SSC and LHC) — R. Gillier, Helicoflex; J. Montuclard, M. Lefrancois, Ch. Rouaud, LeCarbone-Lorraine, France	3900
Surface Treatments and Photodesorption of Oxygen Free Copper Used in an Accelerator — T. Kobari, M. Matumoto, S. Ueda, MERL Hitachi; M. Kobayashi, Y. Hori, KEK	3903
The DAFNE Main Ring Vacuum System — V. Chimenti, A. Clozza, H. Hsieh, G. Raffone, C. Vaccarezza, INFN-LNF	3906
Vacuum Tracking — V. Ziemann, SLAC	3909
 Closing Plenary Chair: W. Hess	
Future Accelerators in Japan — N. Toge, KEK	3912
LHC Progress and Status — G. Brianti and the LHC Machine Group, CERN	3917
Status of the SSC — R. J. Briggs, SSCL	3922
Design for Low Beam Loss in Accelerators for Intense Neutron Source Applications — R. A. Jameson, LANL	3926
Is There a Future for High Energy Accelerators? — M. Tigner, Cornell	3931

Each volume begins with this five-volume table of contents and ends with the five-volume author index. The chairman's foreword and a list of conference organizers and staff appear as front matter in Volume 1. A list of conference participants precedes the author index in Volume 5.

Methods of Impedance Calculation*

Robert L. Gluckstern
Physics Department
University of Maryland, College Park, MD 20742

Abstract

We present several analytic techniques to calculate the impedance of an obstacle in a beam pipe in a variety of applications.

I. INTRODUCTION

In the present paper we shall review methods of calculating the longitudinal and transverse coupling impedances of an obstacle (e.g. pillbox, hole) in a beam pipe of radius Q for a point charge traveling at ultra-relativistic speeds ($\beta \simeq 1, \gamma \gg 1$). Since the coupling impedance is the frequency domain equivalent of the wakefield written in the time domain, the drive current in the frequency domain has a sinusoidal dependence on z of the form

$$J_z(x, y, z; k) = I_0 \delta(x - x_1) \delta(y - y_1) \exp(-jkz), \quad (1)$$

where $k = \omega/c$ and where the time dependence is $\exp(j\omega t)$. Here the point charge travels in the z -direction with constant offset $x = x_1, y = y_1$. The definition of the longitudinal coupling impedance is then

$$\begin{aligned} Z_{||}(k) &= -\frac{1}{I_0} \int_{-\infty}^{\infty} dz E_z(x_1, y_1, z; k) e^{jkz} \\ &= -\frac{1}{|I_0|^2} \int dv \vec{E} \cdot \vec{J}^* \end{aligned} \quad (2)$$

where the volume integral is a more general form which will also be used in the transverse impedance. The longitudinal impedance is obtained by setting $x_1 = y_1 = 0$.

We now consider two situations. The first, denoted by the subscript 1, is the lossless pipe and the second, denoted by 2, is the pipe with the obstacle. We then construct

$$|I_0|^2 [Z_{||}^{(2)}(k) + Z_{||}^{(1)*}(k)] = -\int dv [\vec{E}_2 \cdot \vec{J}^* + \vec{E}_1^* \cdot \vec{J}], \quad (3)$$

where $Z_{||}^{(1)}(k)$ is imaginary. (It actually vanishes in the ultrarelativistic limit.) Using

$$\vec{J} = \nabla \times \vec{H}_{1,2} - j\omega \epsilon \vec{E}_{1,2}, \quad \nabla \times \vec{E}_{1,2} = -j\omega \mu \vec{H}_{1,2}, \quad (4)$$

*Work supported by the Department of Energy

Eq. (3) can be converted to a surface integral, leading to [1]

$$|I_0|^2 Z_{||}(k) = \int_{S_2 \neq S_1} dS_2 \vec{n}_2 \cdot \vec{E}_1^* \times \vec{H}_2 = \int_{S_1 \neq S_2} dS_1 \vec{n}_1 \cdot \vec{E}_2 \times \vec{H}_1^*, \quad (5)$$

where the first integral is over the surface of the obstacle different from the beam pipe and where the second integral is over the surface at $r = a$ which is different from the obstacle. For $x_1 = y_1 = 0$, the solution for \vec{E}_1 and \vec{H}_1 in the ultrarelativistic limit is

$$E_{1r} = Z_0 H_{1\theta} = \frac{Z_0 I_0}{2\pi r} \exp(-jkz), \quad E_{1z} = 0. \quad (6)$$

Thus we need to solve Maxwell's equations for \vec{E}_2, \vec{H}_2 , with the drive beam given in Eq. (1), and use Eq. (5) to calculate the longitudinal impedance.

The energy loss of the particle traveling past an obstacle can be obtained directly from the real part of the longitudinal coupling impedance. Specifically it is

$$\Delta W = \frac{I_0 J_0^*}{2\pi c} \int_0^\infty dk \operatorname{Re} Z_{||}(k), \quad (7)$$

where we have used $Z_{||}(-k) = Z_{||}^*(k)$. Contributions to ΔW can come from wall losses, energy radiation to the outside through the obstacle, and generation by the obstacle of outgoing propagating modes in the pipe.

The transverse coupling impedance can be analyzed similarly. Starting with the axial dipole drive current

$$J_z = I_0 \delta(y) [\delta(x - x_1) - \delta(x + x_1)] \exp(-jkz), \quad (8)$$

the transverse impedance can be expressed as the limit for small x_1 of

$$Z_x(k) = -\frac{1}{2k I_0 x_1} \int_{-\infty}^{\infty} dz \frac{\partial E_z}{\partial x} e^{jkz}. \quad (9)$$

Writing the derivative with respect to x as the difference for $x = \pm x_1$ divided by $2x_1$, we find

$$\begin{aligned} Z_x(k) &= -\frac{1}{4k I_0 x_1^2} \int dz [E_z(x_1, 0, z) \\ &\quad - E_z(-x_1, 0, z)] e^{jkz}. \end{aligned} \quad (10)$$

Using the drive current in Eq. (8), the transverse impedance can be written in terms of the same volume integral as before, namely

$$Z_{\perp}(k) = -\frac{1}{4kx_1^2|I_0|^2} \int dv \vec{E} \cdot \vec{J}^* \quad (11)$$

As before the volume integral can be converted to a surface integral, leading to [2]

$$4kx_1^2|I_0|^2 = \int_{S_2 \neq S_1} dS_2 \vec{n}_2 \cdot \vec{E}_1^* \times \vec{H}_2 = \int_{S_1 \neq S_2} dS_1 \vec{n}_1 \cdot \vec{E}_2 \times \vec{H}_1^* \quad (12)$$

In this case, for small x_1 ,

$$\vec{E}_1 = -\exp(-jkz)\nabla_{\perp}\phi_1, \quad Z_0\vec{H}_1 = \hat{z} \times \vec{E}_1, \quad (13)$$

where

$$\phi_1(r, \theta) = \frac{Z_0 I_0}{\pi} x_1 \cos \theta \left(\frac{1}{r} - \frac{r}{a^2} \right) \quad (14)$$

satisfies the boundary condition $\phi_1(a, \theta) = 0$ at the beam pipe radius $r = a$. Here \hat{z} is a unit vector in the z -direction.

In the sections that follow we will apply the formulation outlined above to a variety of different problems.

II. NUMERICAL CALCULATION

For an arbitrary obstacle, the fields \vec{E}_2 and \vec{H}_2 can be written as

$$\vec{E}_2 = \vec{E}_1 + \vec{e}, \quad \vec{H}_2 = \vec{H}_1 + \vec{h}, \quad (15)$$

where the fields \vec{e} and \vec{h} now satisfy Maxwell's equations with no drive current, and the boundary condition along the metallic walls of the pipe and obstacle is

$$\vec{n}_2 \times \vec{e} = -\vec{n}_2 \times \vec{E}_1. \quad (16)$$

Furthermore one can consider only a finite section of the beam pipe and apply an outgoing boundary condition to \vec{e} and \vec{h} at both ends of the truncated pipe. In this way a mesh code can be constructed with given k and the solution for \vec{E}_2 and \vec{H}_2 obtained numerically.

The program SUPERFISH[3] has been adapted to the calculation of the longitudinal coupling impedance for an obstacle of azimuthal symmetry[4]. Clearly one can similarly adapt programs like URMEI and MAFIA[5] to calculate the transverse coupling impedance and the impedances of azimuthally asymmetric obstacles if desired.

The above method appears to be somewhat superior to that used in time domain codes to calculate the wakefields, followed by a Fourier transform to obtain the impedances.

III. RESISTIVE WALL IMPEDANCE

Equation (5) can be used directly to calculate both the longitudinal and transverse resistive wall impedances. Specifically, subscripts 1 and 2 denotes the pipe with infinite and finite wall conductivity respectively. Therefore the term in

\vec{E}_1^* vanishes, and we can express $E_{2\perp}$ in terms of $H_{1\theta}$ and the surface impedance. Specifically

$$E_{2\perp} \simeq -(1+j)(kZ_0\delta/2)H_{1\theta}, \quad (17)$$

where $Z_0 = 377$ ohms is the impedance of free space and δ is the skin depth of the wall material at frequency $kc/2\pi$. Thus the impedance per unit length is given by

$$|I_0|^2 Z_{\parallel}^{RW} = (1+j)(kZ_0\delta/2) \oint ds |H_{1\theta}|^2, \quad (18)$$

where the line integral is over the circumference of the beam pipe. Using Eq. (6) we find for a length of pipe $2\pi R$

$$\frac{Z_{\parallel}^{RW}}{Z_0} = \frac{(1+j)k\delta R}{2a} = (1+j)\frac{\delta}{2a}n, \quad (19)$$

where the second form in terms of $n = kR$, the harmonic of the rotation frequency in a circular accelerator, is the one usually used.

The corresponding analysis for the transverse impedance for a pipe length $2\pi R$, using Eqs. (12)-(14), leads to

$$\frac{Z_{\perp}^{RW}}{Z_0} = (1+j)\frac{\delta R}{a^3}. \quad (20)$$

These results, first obtained by Nielsen, Seasler, and Symon[6], have been extended to pipes of rectangular[7, 2] and elliptical[2] cross section.

IV. IMPEDANCE OF HOLES

Equation (5) is also a natural starting point to calculate the impedance of a small hole in a beam pipe. Taking the integral over the inside surface of the beam pipe we have

$$|I_0|^2 Z_{\parallel}(k) = - \int_{hole} dS E_z H_{1\theta}^* = - \frac{Z_0 I_0^*}{2\pi a} \int_{hole} dS E_z e^{jkz}. \quad (21)$$

For holes whose dimensions are small compared to the wavelength, the integral can be expressed in terms of the fields E_{1r} , $H_{1\theta}$ near the hole and the electric polarizability, χ , and magnetic susceptibility, ψ , of the hole. Specifically, we find

$$\frac{Z_{\parallel}(k)}{Z_0} = \frac{jk}{8\pi^2 a^2} (\psi - \chi)_{inside}, \quad (22)$$

where ψ and χ here are the "inside" susceptibility and polarizability for a wall of finite thickness[8].

It should be noted that the impedance in Eq. (22) is inductive, implying no energy loss by radiation through the hole. This radiation is proportional to the square of the induced dipole moments of the hole, and therefore to ψ^2 and χ^2 . The real part of the impedance of a small hole is therefore much smaller than its imaginary part.

The result for the transverse impedance is obtained in an analogous way, using Eqs. (12)-(14), and is

$$\frac{Z_{\perp}(k)}{Z_0} = j \frac{\cos^2 \theta}{2\pi^2 a^4} (\psi - \chi)_{inside}, \quad (23)$$

where θ is the azimuth of the hole measured from the x -axis.

V. FIELD MATCHING

The impedance of a pill-box has been calculated by many authors using field matching techniques either at the axial locations of the sides of the pill-box[9] or at the inside radius of the beam pipe[10]. In either case, results are obtained by expanding the fields into a complete set of functions in either z or r , matching coefficients in the two regions, truncating the resulting set of matrix equations, and solving for the coefficients by matrix inversion. Results have been given for a variety of parameters (pill-box radius and length) as a function of frequency.

Similar field matching techniques also work for rectangular irises[11] (pill-boxes extending inside the beam pipe radius). Since the driving current on axis is proportional to $\exp(-jkz) = \cos kz - j \sin kz$, the problem is simplified by obtaining results for an even driving current ($\cos kz$) and an odd driving current ($-j \sin kz$) separately. In each case the fields are expanded with appropriate z symmetry into a set of Bessel functions in both the pipe regions and the iris region. One set of coefficients can be eliminated by matching the fields at the axial location of the end of the iris, and the solution is then obtained by truncating and inverting the resulting matrix equations. (Our experience is that the numerical work is more convergent if the final matrix is obtained in terms of the coefficients in the iris region.)

VI. INTEGRAL EQUATION METHOD

We here consider an azimuthally symmetric obstacle which does not extend inside the beam pipe radius, and represent the field E_z for $r \leq a$ as

$$E_z(r, z; k) = \int_{-\infty}^{\infty} dq e^{-jqz} A(q) \frac{J_0(Kr)}{J_0(Ka)}, \quad (24)$$

where $K^2 \equiv k^2 - q^2$ and where the contour in the q plane goes below any poles on the negative real axis and above any poles on the positive real axis[10]. This choice of contour guarantees that the obstacle will only create outgoing waves in the beam pipe. The driving fields are those in Eq. (1) for $x_1 = y_1 = 0$. It is easy to show that the longitudinal impedance defined in Eq. (2) becomes

$$Z_{||}(k) = -\frac{2\pi}{I_0} A(k) = -\frac{1}{I_0} \int dz E_z(a, z; k) e^{jkz}, \quad (25)$$

where the second form is obtained from the Fourier transform of Eq. (24) at $r = a$, and where the integral over z extends only over the obstacle (pill-box) region. This equation corresponds directly to the more general result in the second form of Eq. (5).

The azimuthal magnetic field at the pipe radius can be written as

$$Z_0 H_\theta = \frac{Z_0 I_0 e^{-jkz}}{2\pi a} + \int_{-\infty}^{\infty} dq e^{-jqz} \frac{jka J_1(Ka)}{Ka J_0(Ka)} A(q). \quad (26)$$

Expanding the ratio of Bessel functions in terms of the residues at the zeros of $J_0(Ka)$, we can write

$$\frac{J_1(Ka)}{Ka J_0(Ka)} = \frac{2}{a^2} \sum_{s=1}^{\infty} \frac{1}{q_s^2 - b_s^2/a^2}, \quad (27)$$

where $J_0(p_s) = 0$ and $b_s^2 = k^2 a^2 - p_s^2$. Writing

$$A(q) = \frac{1}{2\pi} \int dz' e^{jqz'} f(z'), \quad (28)$$

where $f(z') = E_z(a, z'; k)$ is the axial electric field in the opening, we can perform the integral over q by properly closing the contour for $z > z'$ and $z < z'$, and obtain

$$Z_0 H_\theta(a, z; k) = \frac{Z_0 I_0}{2\pi a} e^{-jkz} - \frac{jka}{2\pi} \int dz' f(z') K_p(z, z'), \quad (29)$$

where the pipe kernel is

$$K_p(z, z') = \frac{2\pi j}{a} \sum_{s=1}^{\infty} \frac{e^{-jb_s|z-z'|/a}}{b_s}. \quad (30)$$

When b_s^2 is negative, $b_s = -j\beta_s$, with $\beta_s = (p_s^2 - k^2 a^2)^{1/2}$.

We must now write the fields inside the obstacle in terms of E_z at $r = a$. This can be done by expanding the fields in the cavity-like obstacle (shaped like a torus) into a complete set of cavity modes. In this way we find

$$Z_0 H_\theta(a, z; k) = \frac{jka}{2\pi} \int dz' f(z') K_c(z, z'), \quad (31)$$

where the cavity kernel is

$$K_c(z, z') = 4\pi^2 \sum_{\ell} \frac{h_\ell(z) h_\ell(z')}{k^2 - k_\ell^2}. \quad (32)$$

Here $h_\ell(z) = h_\ell^{(\ell)}(a, z)$ is the normalized azimuthal magnetic field in the ℓ^{th} cavity mode with frequency $k_\ell c/2\pi$. Equating the magnetic field in the opening, we then obtain

$$\int dz' F(z') [K_p(z, z') + K_c(z, z')] = j e^{-jkz}, \quad (33)$$

where $F(z) = -ka^2 f(z)/Z_0 I_0$ and

$$Z_{||}(k)/Z_0 = (1/ka^2) \int dz F(z) e^{jkz}. \quad (34)$$

We therefore need to solve the integral equation [Eq. (33)] for $F(z)$ and obtain $Z_{||}(k)$ from Eq. (34).

VII. IMPEDANCE OF A SMALL OBSTACLE

For an obstacle of outer radius b extending from $z = 0$ to $z = g$, with $kg \ll 1$, $k(b-a) \ll 1$, we can obtain approximate values for $K_p(z, z')$ and $K_c(z, z')$. Specifically, the pipe kernel is

$$K_p \simeq \frac{2\pi j}{a} \left[\sum_{s=1}^S \frac{1}{b_s} + j \sum_{s=S+1}^{S_{\text{max}}} \frac{1}{\beta_s} \right], \quad (35)$$

where S is the largest value of s for which $p_s \leq ka$, and where $S_{\max} \sim a/g$ is a logarithmic cutoff needed in the second sum. The cavity kernel is dominated by the mode with $k_z = 0$, for which

$$h_0(z) \simeq [2\pi ga(b-a)]^{-1/2} \quad (36)$$

and is

$$K_c \simeq \frac{2\pi}{ga(b-a)}. \quad (37)$$

Using these values of K_p and K_c , we can obtain $\int dz' F(z')$ from Eq. (33) and are led to the following expression for the admittance

$$Z_0 Y_{\parallel}(k) = 2\pi ka \left[-\frac{j}{k^2 g(b-a)} + \sum_{s=1}^{\infty} \frac{e^{-j b_s s/a}}{b_s} + j \frac{2\ell n 2}{\pi} \right], \quad (38)$$

where the exponential cut-off factor and the third term come from a more careful treatment[12] of the divergent term in Eq. (35). Numerical simulations agree very closely with the result in Eq. (38) for $b = 1.1a$, $g = 0.05a$. [12] Moreover, the corresponding results for the impedance agree very well with the series calculation of Henke.[10]

The result in Eq. (38) is dominated at low frequency by the first term, which is inductive. Clearly the second and third terms provide both an increasing capacitive term and resistive term as the frequency increases. In fact, the familiar broad resonance occurs when the inductive and capacitive contributions cancel.

Another interesting feature of Eq. (38) is its simplicity when expressed as an admittance. In fact the real part is independent of all features of the pill-box for $g \ll a$. It is not hard to show that this term corresponds to the energy which is lost as the pill-box generates outgoing propagating modes in the pipe. Apparently the reactive part arises from the evanescent pipe modes generated by the pill-box.

VIII. IMPEDANCE AT HIGH FREQUENCY

The high frequency behavior of the impedance has been of concern since Lawson's diffraction calculation[13] suggested a $k^{-1/2}$ behavior which, according to Eq. (7) implied an infinite energy loss. This $k^{-1/2}$ behavior (which does not violate energy conservation when we have an ultrarelativistic particle of infinite energy) was confirmed by others[14, 15]. The integral equation of Section VI is a convenient starting point for this calculation.

We write Eqs. (33), (34) for a pill-box as

$$\int_0^g dz' G(z') [\hat{K}_p(z, z') + \hat{K}_c(z, z')] = 2\pi j/a \quad (39)$$

with $F(z) = (a/2\pi) e^{-j k z} G(z)$, and have

$$Z_{\parallel}(k)/Z_0 = (1/2\pi ka) \int_0^g dz G(z). \quad (40)$$

Here

$$\hat{K}_{p,c}(z, z') = e^{jk(z-z')} K_{p,c}(z, z'). \quad (41)$$

Clearly the impedance arises from the smooth part of $G(z)$, which itself will come from the smooth part of the kernel in Eq. (39). Writing

$$\hat{K}_p(z, z') = 2\pi j/a \sum_{s=1}^{\infty} \exp(j\psi_s) / (k^2 a^2 - p_s^2)^{1/2}, \quad (42)$$

where

$$\psi_s = k(z - z') - |z - z'| (k^2 - p_s^2/a^2)^{1/2}, \quad (43)$$

we see that there are rapid oscillations everywhere except near $p_s \ll ka$ for $z > z'$. Expanding $(k^2 a^2 - p_s^2)^{1/2}$ for small p_s/ka , and keeping only the lowest order non-vanishing term in the exponent, we obtain for the average of the smoothed pipe kernel

$$\langle \hat{K}_p(z, z') \rangle \simeq \begin{cases} 0, & z' > z \\ \frac{i-1}{a} \left[\frac{\pi}{k(z-z')} \right]^{1/2}, & z' < z \end{cases}, \quad (44)$$

where we have converted the sum over s to an integral.

The evaluation of the cavity kernel for large ka depends on the cavity geometry, but in the form in Eq. (32), the sum over modes can be approximated by an integral over mode number. This has been done for a pillbox, as well as for several obstacles of triangular cross section and, the results surprisingly depend only on $(z - z')$. In fact the cavity kernel contribution turns out to be exactly the same as that in Eq. (44) for the pipe kernel. Thus the integral equation reduces to

$$\int_0^z \frac{dz' G(z')}{\sqrt{z-z'}} \simeq \frac{(1-j)\sqrt{\pi k}}{2}, \quad (45)$$

whose solution is

$$G(z) \simeq \frac{1-j}{2a} \sqrt{\frac{k}{\pi z}}, \quad (46)$$

leading to the impedance

$$\frac{Z_{\parallel}(k)}{Z_0} \simeq \frac{1-j}{2\pi a} \sqrt{\frac{g}{\pi k}}. \quad (47)$$

Numerical results for the impedance are consistent with the $k^{-1/2}$ average behavior of the impedance, but show a persistent oscillation with frequency as well, suggesting some sort of resonant field behavior within the pillbox.

IX. IMPEDANCE OF MANY OBSTACLES AT HIGH FREQUENCY

We now apply Eq. (39) to a beam pipe containing a large number of obstacles, and assume that they are all identical and separated from each other (center to center) by a constant distance L . Specifically we write the coupled system of integral equations

$$\sum_m \int dz'_m G(z'_m) [\hat{K}_p(z_n, z'_m) + \delta_{mn} \hat{K}_c(z_n, z'_m)] = j, \quad (48)$$

where we recognize that only the m^{th} cavity contributes to the cavity kernel for the purpose of matching the magnetic field at the m^{th} cavity.

If we use the asymptotic values for \hat{K}_p and \hat{K}_e obtained in the last section and approximate $\hat{K}_p(z_n, z'_m)$ for off-diagonal ($n \neq m$) terms as its value when z_n, z'_m correspond to the center of the relevant gaps, we can solve Eq. (48) and obtain the following expression for the admittance per cavity[16]

$$NZ_0Y_{||}(k) \simeq F_0(k) + \alpha\sqrt{N-1}\tan^{-1}(\alpha/2\sqrt{N}), \quad (49)$$

where $F_0(k)/Z_0$ is the admittance of a single cavity and

$$\alpha = (1+j)a\sqrt{\pi k/L}. \quad (50)$$

Once again we have a term independent of the cavity parameters ($g, b-a$) which is added to the admittance.

In the limit of large k with finite N , we find

$$NZ_0Y_{||}(k) \simeq (1+j)\pi a\sqrt{\pi k/g}[1 + \sqrt{gN/4L}] \quad (51)$$

suggesting that the impedance is proportional to $N^{1/2}$ (rather than N) for $Ng \gg L$. This shadowing effect was first suggested by Palmer[17].

If we take the limit for large N with finite k , we find

$$NZ_0Y_{||}(k) \simeq F_0(k) + j\pi a^2 k/L. \quad (52)$$

which is the result for a periodic structure. For large k the imaginary second term dominates. Using the single pillbox impedance in Eq. (47) we obtain an approximate result which shows that real part of the impedance goes as $k^{-3/2}$, a result also obtained by others[18].

The result in Eq. (52) can also be shown to apply to the case of a small obstacle for the parameter range $ka \gg 1, kL \gg 1$, as long as $kg \ll 1, k(b-a) \ll 1$. Specifically we use the result in Eq. (38) for $F_0(k)$, the admittance of a single obstacle. We also believe, although it has not yet been proved, that the same result holds for a periodic array of holes distributed uniformly in azimuth at axial positions separated by L . In this case $F_0(k)$ in Eq. (52) is to be taken as the reciprocal of Eq. (22). Equation (52) is then expected to be valid as long as the wavelength is small compared with a and L , and large compared with the hole dimensions. In all likelihood, it would be valid for wavelengths comparable with or smaller than the hole dimensions if we used a single hole impedance valid in this parameter range.

X. SUMMARY

We have outlined several alternate methods of calculating the impedance of an obstacle (pillbox, hole) in a beam pipe and illustrated the techniques in several applications. The selection is naturally guided by personal taste. Nevertheless there are other techniques often used which offer comparable insights and results.

References

- [1] R.L. Gluckstern and F. Neri, IEEE Trans. Nucl. Sci. NS-32, 2403 (1985).
- [2] R.L. Gluckstern, J.B.J. van Zeijts and B. Zotter, Phys. Rev. E 47, 656 (1993).
- [3] K. Halbach and R.F. Holsinger, Particle Accelerators, 7, 213 (1976).
- [4] R.L. Gluckstern and F. Neri, Proceedings of the Particle Accelerator Conference, Washington, DC, March 1987, p. 1069.
- [5] T. Weiland, Nuclear Instruments and Methods, 216, 329 (1983); T. Weiland et. al., DESY Report M-86-07, June 1986.
- [6] C.E. Nielsen, A.M. Sessler, and K.R. Symon, Proceedings of the International Conference on High Energy Accelerators, CERN, 1959, p. 239.
- [7] V.K. Neil and A.M. Sessler, Rev. Sci. Instrum. 36, 429 (1965); L.J. Lalett, V.K. Neil and A.M. Sessler. Rev. Sci. Instrum. 36, 436 (1965).
- [8] R.L. Gluckstern and J.A. Diamond, IEEE Trans. Microwave Theory Tech. 39, 274 (1991).
- [9] See, for example, E. Keil and B. Zotter, Particle Accelerators 3, 11 (1972).
- [10] See, for example, H. Henke, CERN Report-LEP-RF/85-41.
- [11] See, for example, R.L. Gluckstern and W.F. Detlefs, Proceedings of the Particle Accelerator Conference, San Francisco, CA, May 1991, p. 1600.
- [12] R.L. Gluckstern and F. Neri, Proceedings of Particle Accelerator Conference, Chicago, IL, March 1989, p. 1271.
- [13] J.D. Lawson, Rutherford High Energy Laboratory, Report No. RHEL/M144 (1968).
- [14] See, for example, G. Dôme, IEEE Transactions in Nuclear Science, NS-32, 2531 (1985); S. Heifets and S. Kheifets, Particle Accelerators 25, 61 (1990).
- [15] R.L. Gluckstern, Phys. Rev. D, 39, 2773 (1989).
- [16] R.L. Gluckstern, Proceedings of the Particle Accelerator Conference, Chicago, IL, March 1989, p. 1157.
- [17] R.D. Palmer, A Qualitative Study of Wakefields for Very Short Bunches, SLAC Report SLAC-PUB-4433, October 1987.
- [18] S. Heifets and S. Kheifets, Phys. Rev. D39, 3960 (1989).

Space-Charge Calculations in Synchrotrons

S. Machida

Superconducting Super Collider Laboratory *
2550 Beckleymeade Ave., Dallas, Texas 75237

Abstract

One obvious bottleneck of achieving high luminosity in hadron colliders, such as the Superconducting Super Collider (SSC), is the beam emittance growth, due to space-charge effects in low energy injector synchrotrons. Although space-charge effects have been recognized since the alternating-gradient synchrotron was invented, and the Laslett tune shift usually calculated to quantify these effects, our understanding of the effects is limited, especially when the Laslett tune shift becomes a large fraction of the integer. Using the Simpsons tracking code, which we developed to study emittance preservation issues in proton synchrotrons, we investigated space-charge effects in the SSC Low Energy Booster (LEB). We observed detailed dependence on parameters such as beam intensity, initial emittance, injection energy, lattice function, and longitudinal motion. A summary of those findings, as well as the tracking technique we developed for the study, are presented.

I. INTRODUCTION

One of the challenging issues for proton synchrotrons is to store and accelerate a high brightness beam, that is an intense beam with a very small emittance. In a high energy accelerator complex such as the Superconducting Super Collider (SSC), the luminosity at the final collider directly depends on the brightness in the preceding injector chains. Space-charge effects in the low energy end of an accelerator complex, for instance, the Low Energy Booster (LEB) and possibly the Medium Energy Booster (MEB) at the SSC, could be a potential problem for the emittance and thus brightness preservation.

As a measure of space-charge effects, the Laslett tune shift is usually calculated, that for Gaussian distribution is $\Delta\nu = -(r_p n_t) / (4\pi\beta\gamma^2\epsilon^n B_f)$; where r_p is the classical proton radius, n_t is the total number of particles in a ring, β and γ are the Lorentz factors, ϵ^n is the normalized rms emittance, and B_f is the bunching factor.¹ The conventional design criterion imposes the small Laslett tune shift, such as -0.2 , to keep the entire beam stay away from lower order resonances. Although most of existing machines has been designed in that way, the brightness

has been increased more than the design value experimentally in some machines. An example would be the AGS of BNL and the PS Booster of CERN, and the maximum tune shift like -0.5 to -0.6 has been achieved. The tune shift criterion such as -0.2 is by no means a fixed number.

More importantly, the Laslett tune shift itself does not predict the emittance behavior. If it is small enough, the beam is, for sure, free from any resonances and no emittance growth is expected. When the tune shift becomes large, say -0.5 , some particles in the beam would be at some resonance. Once the amplitude of the particles changes, the particles can escape from the resonances and become stable again. The strong nonlinear nature of the space-charge force, namely detuning, makes it difficult to estimate emittance evolution.

As for a source of resonances, the space-charge force itself, can excite it without lattice imperfections. In late '60s, Montague discussed the importance of zero-th harmonics of the fourth order resonance; $2\nu_x - 2\nu_y = 0$, which is inevitable due to the octupole component of the space-charge force [1]. According to the recent work by Parzen and Machida, non-zero harmonics of the even order resonances should be also avoided because they are excited by the space-charge force coupled with periodicity of lattice functions [2]. One way to weaken those resonances is to make the lattice with higher periodicity. The effect of half-integer resonance excited by lattice imperfections was studied for the coasting beam [2]. A study by Machida shows that maximum tune shift can be more than the distance between the bare tune and the half-integer resonance. The ratio of possible tune shift to the distance depends on the charge distribution and it is about two for Gaussian distribution.

In this paper, we first describe the recent development of the space-charge modelling by multi-particle tracking. Then, we discuss systematic exploration in parameter space; beam intensity, initial emittance, injection energy, lattice function, and longitudinal motion, using the LEB as an example.

II. MODELLING OF THE SPACE-CHARGE IN SYNCHROTRONS

A. The Simpsons Program

The Simpsons program has been developed to study emittance preservation issues in proton synchrotrons [3]. The program consists of two major parts. One is a par-

*Operated by the Universities Research Association, Inc. for the U.S. Department of Energy under Contract No. DE-AC35-89ER40486

¹In this simplified formula, we ignored the effects of image charge and current in surroundings such as magnets and beam pipe.

particle tracking part that tracks macro particles in the 6-D phase space with acceleration. Realistic modelling of longitudinal motion is essential for a rapid cycling synchrotron such as the LEB in which the synchronous momentum rises from 1.219 GeV/c to 12 GeV/c within approximately 26,000 turns. The space-charge force is strongly time dependent. The independent variable is time, in which one can obtain a snapshot of macro particle distribution at each time step. All lattice elements including an RF cavity are represented by thin lenses lattice created by the program TEAPOT [4].

The other part of the program calculates the space-charge force. It is incorporated as a thin lens kick in each time step and typically 100 to 2000 kicks are applied in one turn. We made three different degrees of approximation to compute the space-charge field. The most advanced one, though it is most time consuming as well, employs the Particle-In-Cell method [5]. Three dimensional grids, in real space, are assigned to enclose the entire beam. At every intersection of the grids, a fractional charge is allocated according to location of macro particles nearby, and then the Maxwell equations are solved in a difference form. A boundary condition is imposed such that the scalar potential is zero at the beam pipe radius, which is constant around the ring. Electro-magnetic fields, at the location of macro particles, are interpolated by the fields at neighboring grids and it changes the momentum. Typically, more than 10,000 macro particles are necessary to represent the charge distribution accurately and it takes about 100 Cray cpu hours to simulate the first 10 msec of the LEB, which is one fifth of a cycle. We call it "strong-strong" approximation, because the emittance and charge distribution are updated continuously and it is expected to be self-consistent.

The second approximation assumes that charge distribution is always Gaussian and the image charge and the longitudinal space-charge forces are negligible. By that assumption, the transverse space-charge force can be computed analytically with a certain truncation [6]. By using approximately 1000 macro particles, the rms emittance calculated at the end of each turn and the space-charge field are computed based on that emittance. Although the charge distribution is assumed to remain Gaussian, it is self-consistent that the space-charge force is a function of the instantaneous emittance. We call it "semi strong-strong" approximation. In the longitudinal plane, the emittance is fixed. The bunch shape is, however, fitted on the matched bucket which is a function of the bending field, its derivative, and RF voltage at each time so that the time dependence of a bunching factor is included. It requires 10 Cray cpu hours when 1000 macro particles are tracked to complete the LEB simulation.

The third approximation, which is the most simplified model, assumes that the charge distribution is always Gaussian and the emittance does not change. The same formula is used to calculate the space-charge force of Gaussian distribution as the "semi strong-strong" approxima-

tion without updating the emittance. That approximation should be adequate, when the beam emittance growth is small and when one wants to see either initial behavior of the emittance growth using many macro particles or stability of single particle. We call it "weak-strong" approximation. Most of the following simulation results are based on "semi strong-strong" approximation.

Initial charge distribution was made as Gaussian in both transverse planes, and we examined emittance each turn by two independent definitions. One is the rms emittance calculated from 1000 to 10000 particles. The other is the emittance by fitting a transverse beam profile to Gaussian. In the following exercise, we found that these emittance definitions agree with each other, implying that the charge distribution remains Gaussian throughout one simulation.

B. Fermilab Booster Simulation

A simulation of the Fermilab Booster was performed for comparison with its experimental data that shows the emittance growth as a function of beam intensity [7]. Although our previous study indicated that asymptotic emittance depends on multipoles and misalignment of lattice to some degree [2], we assumed the same magnitude of errors in the Fermilab Booster model as in the LEB because there is no information available on the lattice magnets. (Those are the rms misalignment of 0.4 mm in both horizontal and vertical planes, the rms rotation angle of 1.0 mrad, the rms closed orbit distortion after correction of 1.0 mm, and the same multipole in the dipoles and quadrupoles.) We tested five different lattices with five different seeds to calculate asymptotic emittance of the first 9 msec by "semi strong-strong" and "weak-strong" approximations.

Figure 1 shows the comparison. The error bar of simulation results shows the range due to different seeds. There is apparent discrepancy between the experimental data and the simulation results when the beam intensity is high. The following remarks should be made. First of all, the use of the multipole and misalignment data of the LEB may not be a good model for the Fermilab Booster. Therefore, we do not have rigorous basis for one-to-one comparison. However, a trend such that the emittance start growing when the beam intensity is 1.5×10^{10} per bunch, agrees in the experiment and the simulations. In addition, the simulation shows that the emittance growth lasts about 5 or 6 msec after injection and it agrees with the recent measurement by Graves *et al.*, who took the time dependence of the emittance growth in the Fermilab Booster [8]. The same experimental data also unveils that the emittance evolution has two steps, one is after injection and the other after the transition energy crossing. We may have missed a part of emittance growth at the transition energy crossing which is not included in the simulations. The asymptotic emittance as a sum of the two steps by Graves is more or less equal to experimental data of Figure 1.

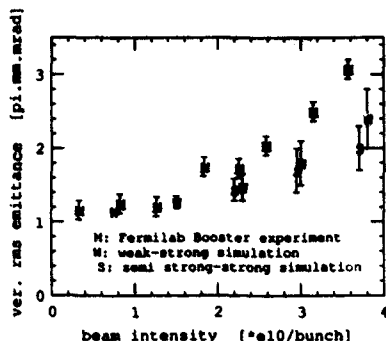


Figure 1. Emittance growth in the Fermilab Booster.

III. SIMULATION RESULTS

A. Beam Parameter Dependence

The design beam parameters of the LEB are 1×10^{10} particles-per-bunch (total number of particles are 1.14×10^{12}) with $0.40 \pi \cdot \text{mm} \cdot \text{mrad}$ rms emittance.² The beam energy rises from 600 MeV to 11.1 GeV in 50 msec with sinusoidal ramping curve. We explored three parameter space, namely beam intensity, initial emittance, injection energy, keeping other two constant. The asymptotic emittance is defined as the emittance about 15 msec after injection, at that time emittance growth has completed. The model lattice has multipoles, misalignment, and closed orbit errors. We used measured multipole data of the AGS Booster magnets [9]. Before doing systematic parameter search, we made a preliminary run to test five different seeds for lattice randomness and picked up the worst lattice in the following simulations.

Figure 2 shows asymptotic rms emittance as a function of beam intensity. Figures 3 and 4 show the emittance evolution and maximum tune shift. There is slight emittance growth already started when the intensity is 1×10^{10} . Below that intensity, no emittance growth is observed. The asymptotic emittance is almost linear with respect to the intensity when the intensity becomes higher.

Figure 5 shows asymptotic rms emittance as a function of initial rms emittance. Figures 6 and 7 show the emittance evolution and maximum tune shift. When the initial emittance is $0.60 \pi \cdot \text{mm} \cdot \text{mrad}$, there is almost no emittance growth. When the initial emittance is less than that, the emittance growth is inevitable and the asymptotic emittance cannot be less than $0.44 \pi \cdot \text{mm} \cdot \text{mrad}$ no matter how small emittance is injected at the beginning. Overshoot phenomena, namely smaller initial emittance ends up with larger asymptotic emittance, is not observed as least within the initial emittance range we explored.

Figure 8 shows the rms emittance as a function of injection energy. Figures 9 and 10 show the emittance evolution and maximum tune shift. If we make the injection energy 1 GeV or higher, almost no emittance growth is observed.

²There is another operational mode called test beam mode, which is supposed to have 5×10^{10} particles per bunch with the rms emittance $4.0 \pi \cdot \text{mm} \cdot \text{mrad}$.

Below 1 GeV, less injection energy is taken, more asymptotic emittance is observed as expected.

B. Lattice Superperiodicity

The present LEB lattice has three fold symmetry with three long straight sections. If the structure resonance dominates the emittance growth, the higher periodicity lattice should help reducing the emittance growth. By taking only arc part of the present LEB lattice, we made a higher superperiod lattice, 16-fold symmetry with almost same circumference and looked at the emittance growth as a function of the beam intensity. Each lattice element has the similar magnitude of multipoles and misalignment as the three-fold symmetry lattice and the closed orbit are corrected as the same level, namely about 1 mm as rms. As shown in Figure 11, not much improvement was obtained.

C. Synchrotron Oscillation Tune

Synchrotron tune becomes as high as 0.05 at 4 msec after injection and gradually decreased toward the final energy. To look at the dependence of the emittance growth on the synchrotron tune, we fixed the energy and rf voltage and tracked particles under constant synchrotron tune. Keeping the peak intensity constant, we varied synchrotron tune under three different conditions, namely with constant $\Delta p/p$, with constant longitudinal emittance, and with constant bunch length. Figures 12 and 13 show the rms emittance after 6000 turns as a function of synchrotron tune. Since there was no energy ramping and the turn number was not enough to have the emittance saturation, they are not asymptotic in value. The horizontal emittance at $\nu_x = 0.20$ and the vertical emittance at $\nu_y = 0.02$ have a bit larger emittance but the overall synchrotron tune dependence is marginal.

IV. DISCUSSIONS

The simulation results described previously indicate that there is a certain limit of the maximum brightness. That can be seen in Figure 14 in which we plotted the brightness defined by the rms emittance divided by beam intensity, as a function of 1) beam intensity, 2) inverse of the initial rms emittance, and 3) the initial $\beta\gamma^2$ which corresponds to injection energy. The horizontal unit is scaled such that the design value of each parameter is one. Figure 14 shows at least two things. One is that the brightness has a certain limit no matter how small initial emittance or intense beam are injected as long as the injection energy is fixed to 600 MeV. That brightness limit is about 10% higher than the design value. The other is that if the injection energy is increased, the brightness can be as high as 20% with the design beam intensity and initial emittance.

A question is then what makes that brightness limit. From Figures 4, 7, and 10, when the tune shift is more than -0.60 or so, beams are not stable. Since the vertical bare tune is 11.80, the maximum loaded tune is about

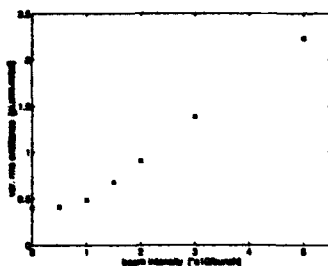


Figure 2. Asymptotic emittance vs. beam intensity. Design beam intensity is 1×10^{10} per bunch.

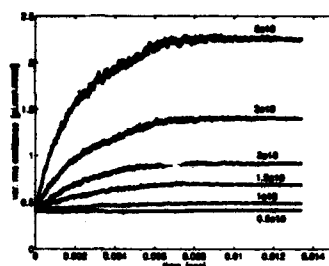


Figure 3. Emittance evolution of Figure 2. Each figure indicates beam intensity.

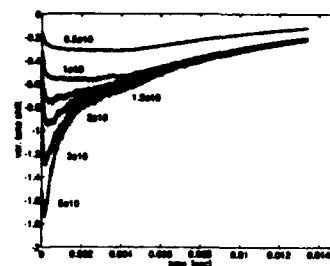


Figure 4. Tune shift evolution of Figure 2. Each figure indicates beam intensity.

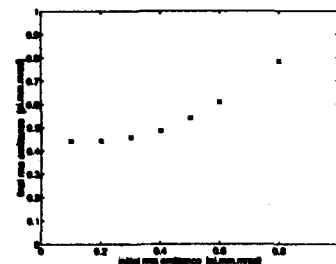


Figure 5. Asymptotic emittance vs. initial emittance. Design initial emittance is 0.4π mm mrad.

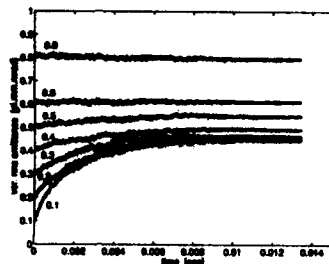


Figure 6. Emittance evolution of Figure 5. Each figure indicates initial emittance in the unit of π mm mrad.

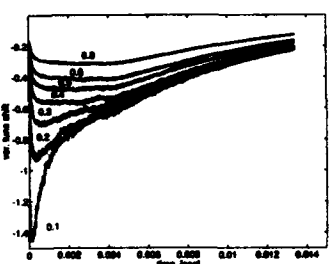


Figure 7. Tune shift evolution of Figure 5. Each figure indicates initial emittance in the unit of π mm mrad.

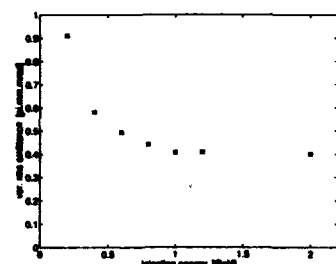


Figure 8. Asymptotic emittance vs. injection energy. Design injection energy is 0.6 GeV.

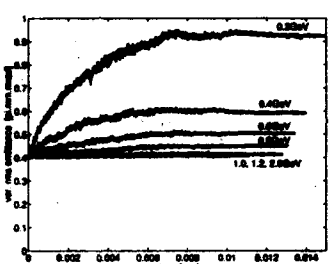


Figure 9. Emittance evolution of Figure 8. Each figure indicates injection energy.

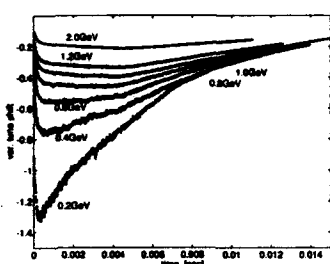


Figure 10. Tune shift evolution of Figure 8. Each figure indicates injection energy.

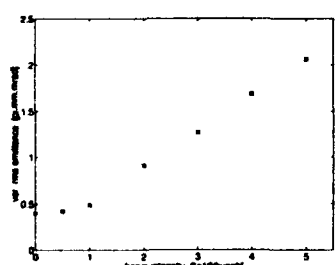


Figure 11. Asymptotic emittance vs. beam intensity in 16-fold symmetry lattice.

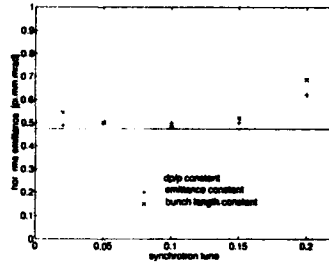


Figure 12. Horizontal emittance after 6000 turns vs. synchrotron tune. There is no energy ramping and the synchrotron tune is kept constant. The horizontal solid line shows the emittance for a coasting beam with the same peak intensity.

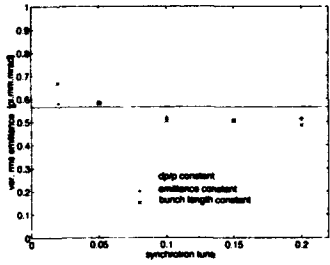


Figure 13. Vertical emittance after 6000 turns vs. synchrotron tune. There is no energy ramping and the synchrotron tune is kept constant. The horizontal solid line shows the emittance for a coasting beam with the same peak intensity.

11.20. According to findings of the previous work, there are two possible mechanism which could explain that limit. One is the structure fourth integer resonance, that is sitting at 11.25. The other is resonances excited by lattice imperfections. Among them, the strongest one is the half-integer resonance at 11.50. By half-integer resonance, emittance growth becomes visible when the maximum tune shift is twice the distance between the resonance and bare tune according to the previous study [2]. Both mechanisms possibly increase the rms emittance because of the superperiodicity of the LEB and lattice imperfections. Similar results in the lattice with 16-fold symmetry implies that the latter is more plausible.

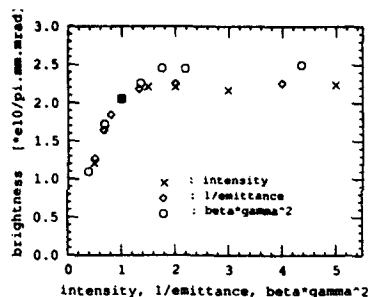


Figure 14. Brightness vs. beam intensity, inverse of initial emittance, and $\beta\gamma^2$.

To confirm that, we looked at the emittance growth in the present LEB and the 16-fold symmetry lattices both without multipole, misalignment, or closed orbit distortion. In these lattice, only the nonlinear elements are chromaticity correction sextupoles. We took 5×10^{10} particles as beam intensity to see the difference if any. Table 1 lists the asymptotic emittance of two different superperiodicity lattices, with and without lattice imperfections. The uncertainty of emittance in the LEB lattice with imperfections indicates the dependence of five seeds. From that table, it is clear that the brightness limit is caused by lattice imperfections in the both lattices. Although the lattice of higher superperiodicity shows the better behavior without lattice imperfections, the difference of the two lattice becomes marginal once the practical imperfections are included.

Table 1
Asymptotic Emittance in the LEB and the 16-fold Symmetry Lattice with and without Lattice Imperfections

	LEB lattice	16-fold lattice
without imperfections	1.2π mm mrad	0.66π mm mrad
with imperfections	$2.0 \pm 0.2 \pi$ mm mrad	2.1π mm mrad

V. SUMMARY

Using the LEB of the SSC as an example, we explored parameter space and investigated space-charge effects. We found that there is brightness limit. The brightness is bound, no matter how small emittance or intense beam is injected. That limit is independent of the lattice superperiodicity and synchrotron tune. The source of the limit is caused by lattice imperfections of the practical magnitude.

VI. REFERENCES

- [1] B. W. Montague, "Fourth-Order Coupling Resonance Excited by Space-Charge Forces in a Synchrotron", CERN 68-38, CERN, 1968.
- [2] G. Parzen, "Space Charge Limits in Proton Synchrotrons", *Nuclear Instruments and Methods*, A281, p.413, 1989. BNL Report 44562, 1990. and S. Machida, "Space-Charge Effects in Low-Energy Proton Synchrotrons", *Nuclear Instruments and Methods*, A309, p.43, 1991.
- [3] S. Machida, "The Simpsons Program: 6-D Phase Space Tracking with Acceleration", Proc. of the Computational Accelerator Physics Conference, 1993.
- [4] L. Schachinger and R. Talman, "TEAPOT: A Thin-Elements Accelerator Program for Optics and Tracking", *Particle Accelerators*, Vol.22, p.35, 1987.
- [5] M. L. Sloan, "Calculation of Electromagnetic Self Forces for LEB Parameter Beams", March 1991, unpublished.
- [6] M. A. Furman, "Practical Approximations for the Electric Field of Elliptical Beams", SSC-N-312, SSC Laboratory, 1987.
- [7] C. Ankenbrandt and S. D. Holmes, "Limits on the Transverse Phase Space Density in the Fermilab Booster", Proc. of the 1987 IEEE Particle Accelerator Conference, p.1066, 1987.
- [8] W. Graves, D. McGinnis, and R. Tomlin, "Measurement and Causes of Emittance Growth in the Fermilab Booster", in these proceedings.
- [9] E. Bleser, private communication

ADVANCED COMPUTERS AND SIMULATION*

Robert D. Ryne
Los Alamos National Laboratory
Los Alamos, NM 87545 USA

Abstract

Accelerator physicists today have access to computers that are far more powerful than those available just 10 years ago. In the early 1980's, desktop workstations performed less than one million floating point operations per second (Mflops), and the realized performance of vector supercomputers was at best a few hundred Mflops. Today vector processing is available on the desktop, providing researchers with performance approaching 100 Mflops at a price that is measured in thousands of dollars. Furthermore, advances in Massively Parallel Processors (MPP) have made performance of over 10 gigaflops a reality, and around mid-decade MPPs are expected to be capable of teraflops performance. Along with advances in MPP hardware, researchers have also made significant progress in developing algorithms and software for MPPs. These changes have had, and will continue to have, a significant impact on the work of computational accelerator physicists. Now, instead of running particle simulations with just a few thousand particles, we can perform desktop simulations with tens of thousands of simulation particles, and calculations with well over 1 million particles are being performed on MPPs. In the area of computational electromagnetics, simulations that used to be performed only on vector supercomputers now run in several hours on desktop workstations, and researchers are hoping to perform simulations with over one billion mesh points on future MPPs. In this paper we will discuss the latest advances, and what can be expected in the near future, in hardware, software and applications codes for advanced simulation of particle accelerators.

Introduction

Today accelerator physicists are finding it possible to perform particle simulations and electromagnetic calculations of unprecedented precision and complexity. Such calculations would have been impractical only two to three years ago, but they are possible now because of two major developments: (1) the availability of very high performance, affordable workstations and (2) the availability of Massively Parallel Processors (MPPs) and distributed computing environments. These topics will be discussed in the first part of this paper.

In the second part of this paper we will discuss simulations we have performed using the Connection Machine 5 at the Advanced Computing Laboratory of Los Alamos National Laboratory. We are developing computer codes that will support efforts related to the design of next-generation,

high current accelerators. We will show preliminary results of beam dynamics calculations with 16,777,216 ($\approx 2^{24}$) particles.

ADVANCED COMPUTERS

Workstations

One of the most significant developments of the late 1980's to early 1990's is the emergence of very high performance workstations. During the early 1980's, desktop workstations generally performed at less than 1 Mflop. The concept of a pipelined machine (which can result in an effective throughput of one result per machine cycle for vector operations) was reserved for multi-million dollar vector supercomputers. Today vector processing and superscalar implementations can be obtained on the desktop for a price measured in thousands of dollars. Typical characteristics of a moderate to high end workstation (in 1993) are as follows:

1. RISC CPU
2. RAM: up to 512 MB (16 SIMMS @ 32 MB/SIMM)
3. Hard Disk: 1 GB to a few GB
4. Performance: 10-40 Mflops
5. Price: \$10,000 to \$80,000

Workstations of this caliber are now in widespread use at many laboratories, universities and institutions. Such machines are often dedicated to running 3D electromagnetics simulation programs such as ARGUS and MAFIA. It is not uncommon for these jobs to require several hours on a high end workstation. Even so, for many problems the turn-around time is faster on a dedicated workstation than that obtained running on a time-shared vector supercomputer. The performance of workstations will likely increase significantly in the near future, with the advent of multiprocessor machines, 64-bit CPUs (for which double precision calculations will be unnecessary), and more CPUs operating around 200 MHz.

Table 1 shows performance benchmarks for a sample of widely used workstations:

* Work supported by the U.S. Dept. of Energy, Office of Energy Research: Office of High Energy and Nuclear Physics, Office of Superconducting Super Collider, Office of Fusion Energy, and Office of Scientific Computing

Table 1 Benchmarks for a sample of workstations

Machine	Spec92Int	Spec92FP	MFLOPS
Intel 486/50	30.1	14.0	
Intel 486/66	32.4	16.1	
Intel P5/66	64.5	56.9	
DEC 3k/400 (Alpha)	65.3	112.2	18.7
DEC 3k/500 (Alpha)	74.3	126.0	
HP 710 (PA RISC)	32.7	56.4	
HP 730 (PA RISC)	52.0	86.7	
HP 735 (PA RISC)	80.0	150.6	40.8
Sun Sparc IPC	26.4	21.0	
Sun Sparc 10/30	44.2	52.9	
Sun Sparc 10/41	52.6	64.7	
IBM RS/6000 320H	20.9	39.4	11.7
IBM RS/6000 350	35.4	74.2	
IBM RS/6000 580	59.1	124.8	38.1
SGI Indigo (R4000)	57.6	60.3	16.0

When choosing a workstation, benchmarks like that shown above should be regarded along with several other factors. For example, it is worth keeping in mind that the performance of workstations from various manufacturers often leap-frog one another in a time span on the order of a year. Long term stability of a workstation manufacturer, and the ability to incorporate a specific machine into one's local network are also important considerations. Finally, benchmarks obtained by running frequently used applications programs are a more valuable indicator of expected performance than SPECmark results, particularly when comparing machines of comparable sophistication from different manufacturers. Table 2 shows the performance of some workstations in running a MAFLA eigenvalue problem [1]:

Table 2 Benchmarks based on a MAFLA eigenvalue problem

Machine	MFLOPS
DEC 3k/500 (Alpha)	22.1
HP 730 (PA RISC)	12.3
Sun Sparc 1	1.36
Sun Sparc IPC	1.71
Sun Sparc 2	3.9
Sun Sparc 10/30	10.4
IBM RS/6000 320	10.1
IBM RS/6000 550	13.4
IBM RS/6000 580	38.1

Massively Parallel Processing and Distributed Processing

Another major advance that has occurred in recent years is the development of computer platforms, software and algorithms for massively parallel processing and distributed processing. These environments are aimed at solving problems that are on the (present) leading edge of high performance computing, and which require performance on the order of 10 Gflops to 1000 Gflops. Typical applications include: global climate modeling, quantum chromodynamics, molecular dynamics, self-consistent electronic structure calculations, 3D seismic calculations, and high resolution simulations in computational fluid dynamics, electromagnetics, and structural analysis, to name a few.

Large scale MPPs typically fall into one of two categories: SIMD (Single Instruction/Multiple Data) and MIMD (Multiple Instruction/Multiple Data). The SIMD model is the least complex and the easiest to utilize from a user standpoint. In this case, all the processing elements operate in synchronism, performing the same operation on different sets of data. Typically, programmers can write code using array constructs like that found in Fortran 90 (for example, $a=b+c$, where a , b and c are arrays); the compiler will recognize this as an operation that can be done in parallel. Thus, from the standpoint of a scientific programmer, it is easy to use MPPs for problems that are inherently *data parallel*. The drawback of this approach is that it is restrictive with respect to the types of calculations that can be implemented (in a straightforward manner). In contrast, in the MIMD approach all the processing elements can be performing different instructions, asynchronously, on different sets of data. While this approach is flexible, it is also far more difficult to make use of from a programming standpoint. In MIMD-style programming, the programmer specifies operations at the level of individual processors and makes use of message passing routines for interprocessor communication.

The implementation of massively parallel processing is complicated by many factors. One factor is the type of memory requirement for a given problem: Do the processors require only local memory, nearest-neighbor communication, or increasingly global communication? If the communication is global, are the required patterns regular or random? Another important factor is the issue of load balancing: It is pointless to allocate a large number of processing elements to a job if only a few processors are working while many others are idle. There are many operations, common to large applications programs, that are not obviously parallelizable and do not lend themselves easily to load balancing. For such operations, it is necessary to devote a great deal of effort to circumvent the difficulties (if it is possible at all). An example of this is the operation of laying down a distribution of charge or mass onto a regular mesh. If the distribution is highly nonuniform (such as a Gaussian distribution), then processors associated with the tails of the distribution will cease to be utilized long before processors associated with the core of the distribution, unless an effort is made to deal with this issue. Researchers in

the field of plasma particle-in-cell (PIC) simulation have made significant progress in this area [2].

For many problems, computational physicists can obtain moderately high performance without having to program at the level of individual processing elements. Two things make this possible: First, many MPP manufacturers are developing scalable software libraries to perform operations of widespread applicability to scientific programmers. Secondly, as mentioned above, many MPP compilers recognize Fortran 90 constructs as operations than are to be performed in parallel. Just as programmers in the 1980's learned to write "clean code" with vectorizable do-loops to achieve high performance on vector supercomputers, scientific programmers of the 1990's will learn to write "clean code" in Fortran 90 to obtain high performance on MPP's. (In addition to Fortran 90, some MPP manufacturers also provide support for the C programming language.) Of course, the very highest performance will still be obtained by researchers who have the time, energy, and need to program at the individual processor level.

Today there are several MPPs available, and many are under development. One of the early successful MPPs was the Intel Touchstone Delta: It consists of 540 i860 CPUs and is capable of a peak performance of 32 Gflops. It has been used very successfully for large scale astrophysical simulations [3]. One of the leading MPPs at this time is the Thinking Machines Corporation Connection Machine 5 (CM-5): It is a tree-connected MIMD machine that consists of a number of Sparc-based CPUs each with 4 vector units. A 1024 node machine is capable of a peak performance of 128 Gflops. A third example of an MPP is the T-3D, which is under development by Cray Research Incorporated. The T-3D is planned to consist of a large number of Digital Equipment Corporation Alpha CPUs, each running at 150 MHz. A 2048-processor system is expected to have a peak performance of 300 Gflops. Many MPP manufacturers believe that performance of a teraflop will be achieved soon after mid-decade.

It is worth pointing out that advances in the workstation market have had a significant impact on the development of MPPs. The goal of an MPP manufacturer is not just to build a high performance machine, but also to build a cost effective, affordable machine. As should be evident from the previous paragraph, MPP manufactures are now building systems around mass produced, inexpensive RISC CPUs. In addition, they make use of inexpensive DRAM memory. A typical MPP will have 16MB to 64 MB per node.

Another approach to high performance computing is to use collections of computers to perform parallel computations. In the simplest case, it consists of a homogeneous collection of machines, such as a cluster of workstations (or workstation "farm"). In a more sophisticated approach, it consists of a heterogeneous collection of computers, including workstations, vector supercomputers, and even the nodes of an MPP; all the processors involved in the computation are connected by a variety of networks. Software such as PVM (Parallel Virtual Machine) is now available to support such calculations. [4]. Distributed processing has been aided by the de-

velopment of high speed networks that operate at nearly a gigabit per second. Many of these are based on the High Performance Parallel Interface (HIPPI), which operates at 0.8 Gbit/sec. Also, 5 Gbit/sec networks are under development. Using high speed networks, it will soon be possible to coordinate the high performance computing platforms at several geographically separated supercomputer centers to run Grand Challenge simulations.

ADVANCED ACCELERATOR SIMULATION

Today there are several important problems in computational accelerator physics that cannot be handled without making use of high performance computing platforms. These include:

1. Self-consistent beam dynamics problems involving very large numbers of particles ($> 10^8$ particles)
2. Electromagnetics simulations involving very large numbers of mesh points ($> 10^8$ points)
3. Long term tracking in circular machines
4. Optimization of beamlines and electromagnetic structures, where each iteration in the simulation is itself difficult or impossible to perform on a single workstation or vector supercomputer

Below we will discuss the simulation of intense beams using large numbers of simulation particles, motivated by the need to predict beam halo in next-generation, high intensity CW accelerators.

During the past several years, many technical advances have been made in the field of Accelerator Technology that are opening up new areas of research and application. Several projects, of major importance to the environment and to international competitiveness, now seem feasible. These include the Accelerator Transmutation of Waste (ATW), Accelerator Production of Tritium (APT), accelerator-based production of 14 MeV neutrons for fusion materials testing, Accelerator Based Conversion of Plutonium (ABC) and the development of a next-generation, high intensity spallation neutron source. These projects are also extremely challenging: They rely on very high intensity, continuous wave accelerators (as opposed to the moderately low intensity, pulsed machines of the past). Adding to the difficulty is the fact that these projects are considered acceptable only if hands-on maintenance of the accelerator is possible. (Remote handling increases the complexity and the cost of these projects significantly.) In order to meet scheduled maintenance requirements and Occupational Safety and Health requirements, the radioactivity level must be a few millirem/hour shortly after shutdown of the accelerator. This corresponds to very strict beam loss requirements: the allowed beam loss is on the order of 0.1 nanoampere/meter, or equivalently, about 1 part in 10 to 100 million. These projects are expensive (some are expected to cost over 1 billion dollars). It will be difficult to get approval for any of them unless one can demonstrate clearly and convincingly that it is possible to meet the beam loss requirements.

Beam losses at this low level are caused by particles in the very sparsely populated beam halo, at a distance of 6 or more standard deviations from the beam axis. Beam halo and resulting beam loss are due to space charge effects coupled with effects such as beam mismatch, machine errors and field nonlinearities. Understanding and predicting beam halo has become a critical issue for many advanced accelerator-based projects. In order to have confidence that we can meet these ultra-low loss requirements, we need to perform particle simulations with on the order of 100 million particles. Consider, for example, that if one simulated a round Gaussian beam with 100 million particles, only about 4 particles would be located in the region beyond six standard deviations. Accelerator simulations of this magnitude are impossible with vector supercomputers, but with the advent of MPPs such simulations are within reach.

We are developing simulations using the CM-5 at the Los Alamos National Laboratory Advanced Computing Laboratory in order to better understand and predict beam halo in high intensity, ultra-low loss accelerators. Ultimately, we expect to be able to perform simulations with on the order of 100 million particles. Accelerator simulations of this magnitude (in which we would propagate a beam in fine detail through up to a kilometer of accelerating structures) are unprecedented in the field and represent a quantum leap beyond what has been accomplished in the past. We hope to be able to accurately predict beam halo, and thereby help demonstrate the soundness of advanced accelerator designs.

In order to learn to utilize the CM-5, we have begun by developing a simulation for a simple test problem. Our program models an intense beam in a periodic focusing channel (in two dimensions). The beam and the external fields are assumed to have cylindrical symmetry (the transport system consists of magnetic solenoids.) Our simulation includes nonlinearities from the beam self-fields and from the external fringe fields of the focusing magnets. The particles are propagated using a 4th order symplectic integration algorithm [5].

Figures 1 and 2 show the initial and final beam density, respectively, from a typical run of an initially mismatched, Gaussian beam propagating in the focusing channel. Figures 3 and 4 show the initial and final horizontal phase space, respectively. The parameters of this CM-5 simulation are shown below:

# of particles	16,777,216 ($=2^{24}$)
# integration steps	100
# processors	512
CPU time	26 min

These results were obtained using beta versions of the operating environment and run time library (CMOST 7.2, Beta 1, patch 4), the CM Fortran compiler (CMF 2.1, Beta 0.1) and the CM Scientific Software Library (CMSSL 3.1, Beta 3).

In the future, we plan to extend our model to perform simulations of 3-dimensional beams propagating through systems of quadrupole magnets and accelerating structures.

Figure 1 Initial Beam Density

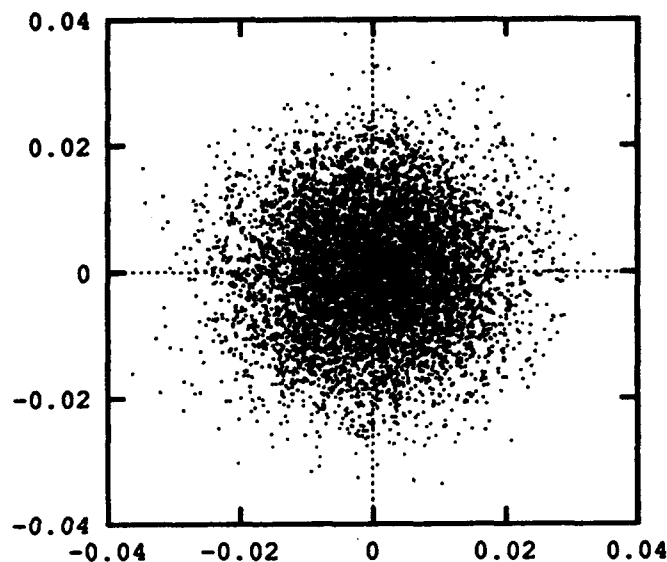


Figure 2 Final Beam Density

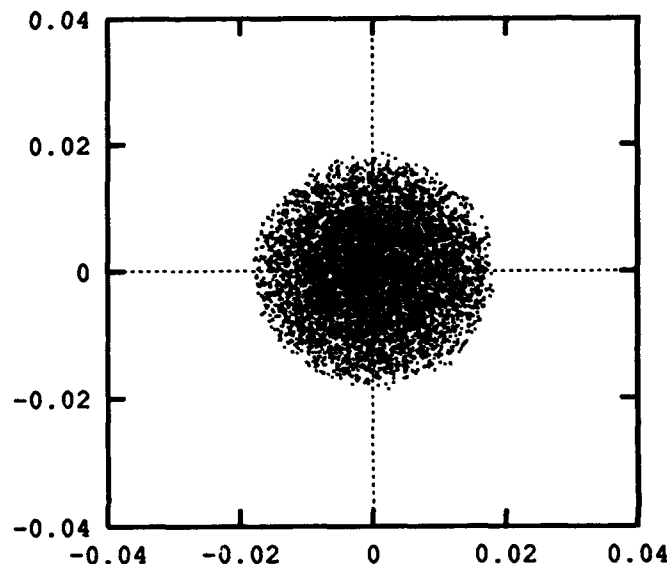


Figure 3 Initial Horizontal Phase Space

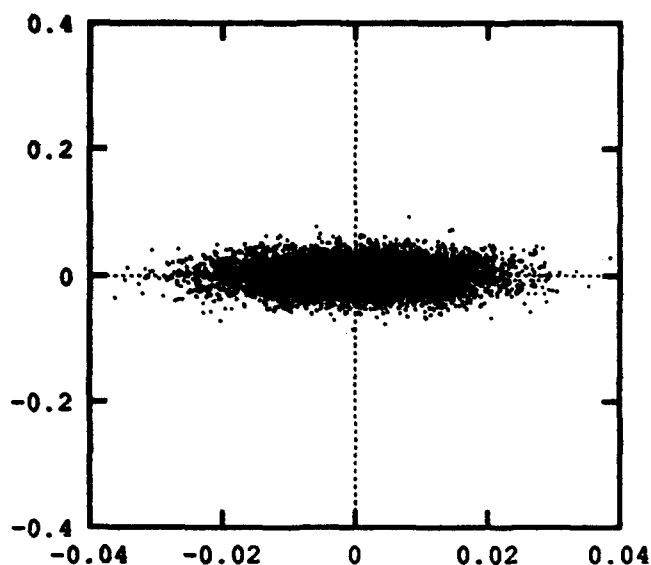
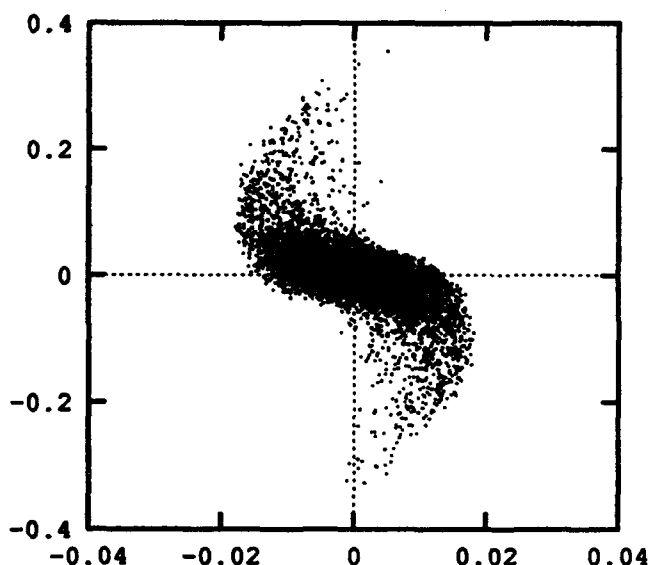


Figure 4 Final Horizontal Phase Space



CONCLUSION

Accelerator physicists presently have access to resources that are far superior to what was available just a decade ago. The performance of desktop workstations now approaches that of the early Cray supercomputers; with the advent of massively parallel and distributed processing, gigaflop performance is becoming increasingly common. By the time of the 1995 Particle Accelerator Conference, many of the participants will have begun to use MPPs, and most will probably program them in a language that resembles Fortran 90. These advances will have an especially profound impact in the area of 3-d modeling. At present, simulations on high end workstations may require many hours, making optimization of structures a difficult task; and though some electromagnetics codes have been ported to MPPs, few researchers have access to these platforms. In the near future, with the advent of 64 bit CPUs operating at very high clock speeds, and with the introduction workstations and several thousand node MPPs based on these structures, researchers will have access to machines of unprecedented performance.

Acknowledgments

This research was performed in part using the resources located at the Advanced Computing Laboratory of Los Alamos National Laboratory, Los Alamos, NM 87545.

REFERENCES

- [1] F. Krawczyk, Private Communication
- [2] P. Liewer and V. Decyk, "A General Concurrent Algorithm for Plasma Particle-in-Cell Simulation Codes," *J. Comp. Phys.* 85, 302 (1989).
- [3] M. Warren and J. Salmon, "Astrophysical N-Body Simulations Using Hierarchical Tree Data Structures," *Proceedings of Supercomputing '92*, September 11, 1992
- [4] J. Dongarra et al., "Integrated PVM Framework Supports Heterogeneous Network Computing," *Computers in Physics* 7, 166 (1993).
- [5] E. Forest and R. Ruth, "Fourth-Order Symplectic Integration," *Physica D* 43, 105 (1990).

Measured Optimum BNS Damping Configuration of the SLC Linac*

J. T. Seeman, F.-J. Decker, R. L. Holtzapple, W. L. Spence

Stanford Linear Accelerator Center
Stanford University, Stanford, California 94309 USA

Abstract

Transverse wakefield (or BNS¹) damping has been successfully used in the linac of the Stanford Linear Collider (SLC) to reduce emittance enlargement from beam trajectory jitter coupled with transverse wakefields². We are presently in the process of raising the bunch intensities from 3×10^{10} particles per bunch to over 4×10^{10} . With these higher currents the RF phasing configuration which produces BNS damping must be improved. Too little "damping" allows excessive emittance growth from jitter but too much damping increases emittance growth from chromatic effects and produces an unacceptable loss of overall energy. Several experiments were performed to find the optimum settings for the present situation. An empirical optimum was found with a combination of 1) somewhat stronger BNS RF phase settings in the upstream section of the linac and 2) a stronger quadrupole lattice in the downstream section.

Transverse (BNS) Wakefield Damping

In the SLC linac high intensity bunches must be accelerated in the 3 km S-Band structure without significant emittance enlargement. Position and angle jitter of the injected beam or beam deflections along the linac can cause significant emittance growth from transverse wakefields. The equation of motion of the particles within a bunch indicates that the head of the bunch will resonantly excite the longitudinal tail of the bunch to ever increasing amplitudes as the bunch makes a betatron oscillation along the linac. A technique to reduce the resonant blowup of the tail by the head is called BNS damping¹ where the energy of the longitudinal tail of the bunch is reduced from that of the head by offsetting the initial RF phases. With this technique, the net "defocusing" transverse wakefield forces on the tail are to a large extent canceled by the increased focusing of the quadrupole lattice for the tail. An analytical model³ gives the condition for "BNS" damping in the discrete focusing case.

$$[\langle \beta \rangle_{\text{lattice}} e^2 N \langle W \rangle_{\text{beam}}] < [2 \langle d^2 \psi / d\delta ds \rangle E \langle \delta^2 \rangle^{1/2}_{\text{beam}}]$$

where β is the lattice betatron function and e is the electron charge. N is the number of particles, W is the transverse wakefield, ψ is the betatron phase advance per cell, δ is the fractional energy offset, s is the distance along the accelerator, and E is the beam energy,

This condition can be expressed for a multi-particle bunch but cannot be easily produced over the bunch length, so that

compromises must be made. Furthermore, several SLC conditions make the matching conditions difficult: the distances between quadrupoles change along the linac, the phase advance per cell changes along the linac, and the energy correlation (spread) is difficult to change rapidly with distance⁴.

To show the trajectory enlargement effect from transverse wakefields without BNS damping, a horizontal oscillation in the beam was made at about the 1.8 km location along the linac and the ensuing beam oscillation was recorded. The oscillation is shown in Figure 1. A rapid growth without BNS damping is very evident.

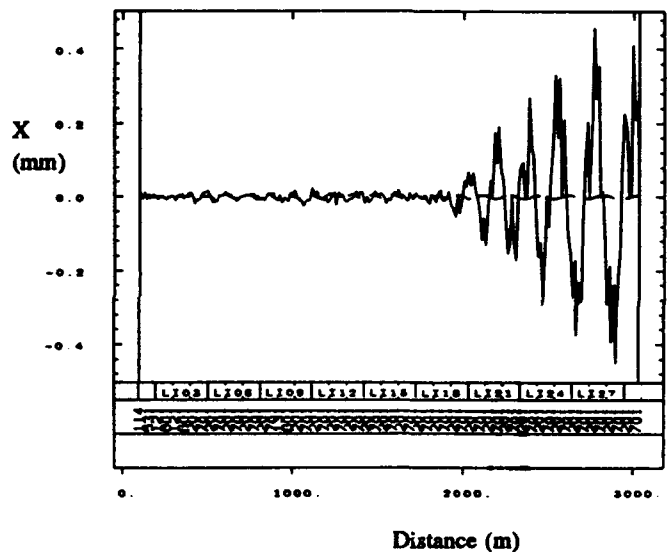


Figure 1 Growth of beam tails and centroid position without BNS damping from a dipole kick starting at about 1800 m.

The present BNS conditions for the SLC linac are listed in Table 1 and are made by (back) phasing the first 56 klystrons at -20 degrees and (forward) phasing the remaining 176 klystrons at +15 degrees. In this way the desired correlated energy spread is produced along the linac as can be seen in Figure 2. One constraint is that the total energy spread be small (0.26% rms or so) at the end of the linac as needed by the final focus system downstream. Horizontal oscillations for a bunch with 3×10^{10} e⁻ generated at three locations along the linac using this nominal BNS configuration are shown in Figure 3. Note the significantly reduced growth effects as compared to Figure 1.

* Work supported by the Department of Energy contract DE-AC03-76SF00515.

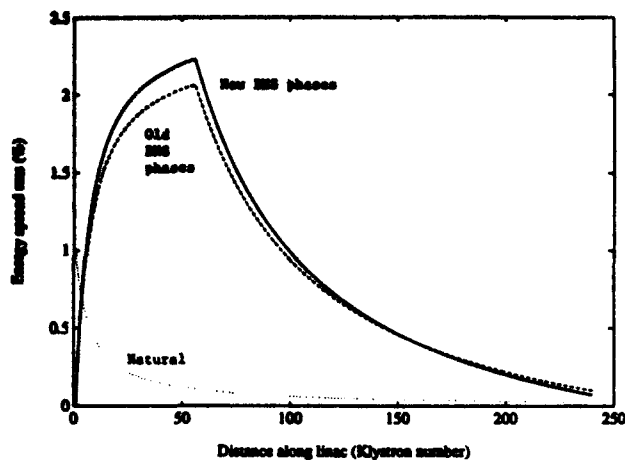


Figure 2 Correlated and uncorrelated energy spreads along the linac for the natural case and for the old and new BNS cases.

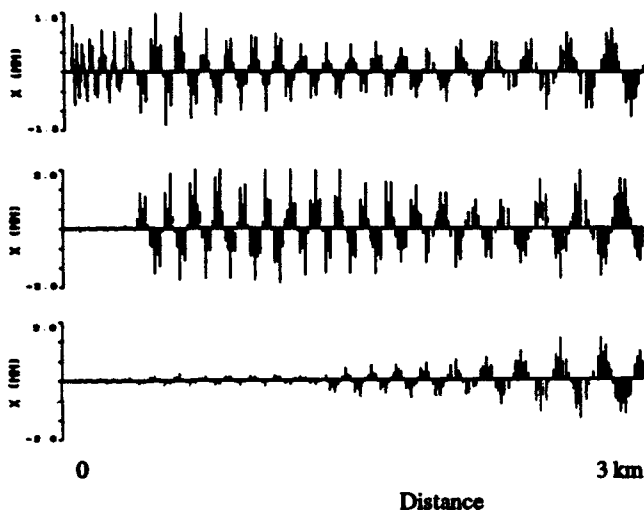


Figure 3 Induced horizontal oscillations at three locations in the linac with the nominal BNS phases: 56 klystrons at -20 degrees and 176 klystrons at +15 degrees.

Optimum BNS Tests

The question we addressed in these tests was: When the beam charge is raised from 3×10^{10} to over 4×10^{10} will a new RF phase configuration be needed? Simulations⁵ indicate that increased energy spreads might help but that issues of energy overhead, stability, and chromatic emittance growth will make the exact optimum choice difficult to predict. Because of these complications, an experimental determination of the best configuration was used.

Several predetermined configurations were studied using the limited accelerator physics time available on the SLC. The measure of comparison was the ratio of the final oscillation amplitude at 47 GeV to the initial amplitude at the source of the dipole change, made at three locations. The studies included four cases: 1) weaker BNS than the present case, 2) the nominal case, 3) a slightly stronger case, and 4) a moderately stronger case. The results of these studies are listed in Table 1. The results indicate that the weaker case is worse

than the nominal for jitter enhanced enlargement. The slightly-stronger case is better than the nominal. The moderately-stronger case appears slightly better than the slightly-stronger case but has too large a chromatic emittance enlargement. Thus, the empirically determined best case is the slightly stronger case. The resulting oscillations are shown in Figure 4, allowing a comparison with the nominal case in Figure 3.

For an exercise, a much stronger BNS condition was tried in the early linac, as is shown in Figure 5. Here, chromatic effects are quite strong and the two nodes in the downstream oscillations show complicated head-tail offset changes.

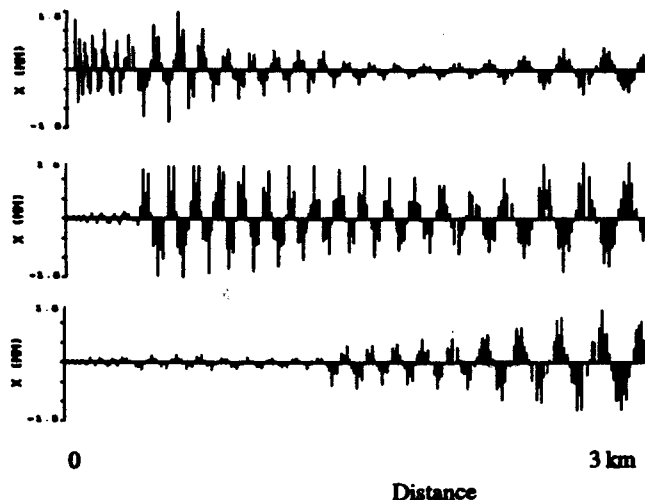


Figure 4 Induced horizontal oscillations at three locations in the linac with the new stronger BNS phases: 56 klystrons at -22 degrees and 176 klystrons at +16 degrees.

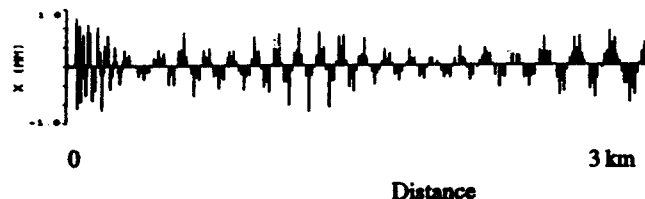


Figure 5 Induced oscillation with a much stronger BNS.

Stronger Quadrupole Lattice

In the downstream half of the linac, BNS damping is no longer very effective against jitter starting midway along the linac. This is because the BNS optimized head-tail energy correlation can no longer be maintained, as can be seen in Table 1 and Fig. 2. Thus, a study of potential improvements suggested stronger quadrupole strengths in that region. By increasing the quadrupole lattice strengths from the present 45 to 60 degrees per cell, the betatron function could be reduced and the phase advance per cell increased. Historically, the quadrupole lattice in this region has been operated somewhat below its maximum so that the lattice could be rescaled to an RF configuration without BNS damping. Since BNS damping is now used continuously, a lattice with an increased strength

is feasible. Reducing the betatron functions helps in two ways: 1) The oscillation amplitude given a source deflection is smaller for the reduced β s and 2) the effects of wakefields from the head of the bunch on the tail are also reduced.

To implement the improved lattice, 1) the quadrupole strengths were increased, 2) the betatron functions were matched at the sector boundaries (every 100 m) with small adjustments, and 3) the chromatic effects on the betatron functions were studied, showing only small sensitivities. A comparison of the vertical betatron functions before and after the change is shown in Figure 6. The horizontal functions are similar. Beam tests of the old and new lattices are shown in Figure 7. The amplitudes of oscillations starting in the middle of the linac (Sector 15) show that the new lattice reduces the resulting oscillation by about 30%, a significant gain.

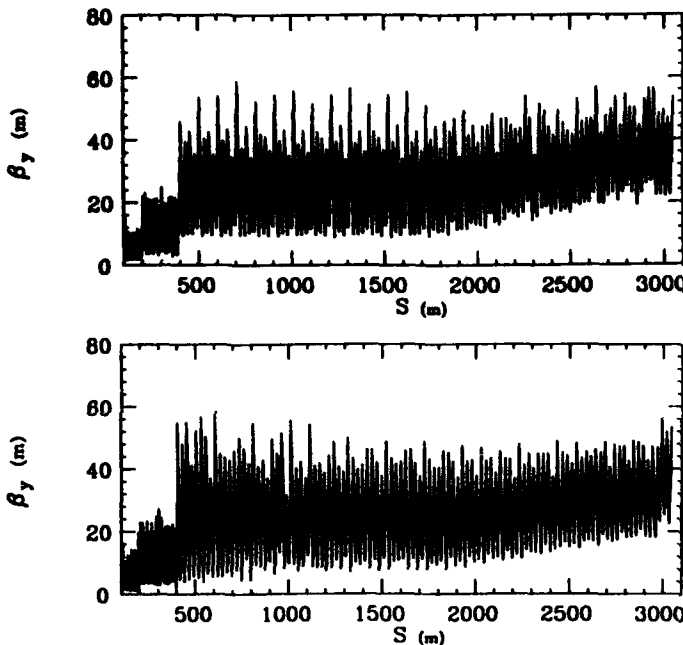


Figure 6 Vertical betatron functions for the old (upper) and new (lower) linac quadrupole lattices. Note that $\langle\beta_y\rangle$ is lower at the end of the linac for the new lattice.

Conclusions

Transverse wakefield (BNS) damping works very well and must be used during high charge per bunch running of the SLC linac. At higher currents (4×10^{10}), the BNS RF phase

offsets must be increased slightly to maintain optimum suppression of injection jitter enlargement of the emittances. In the SLC BNS damping is ineffective in the downstream half of the linac. Here a stronger quadrupole lattice has been generated to reduce the effects of jitter.

Further empirical tests will be made in the next running cycle to determine the fine details of the new BNS configuration including effects of bunch length, luminosity, and detector backgrounds. Tests aiming at higher currents (5×10^{10} or so) are also being considered.

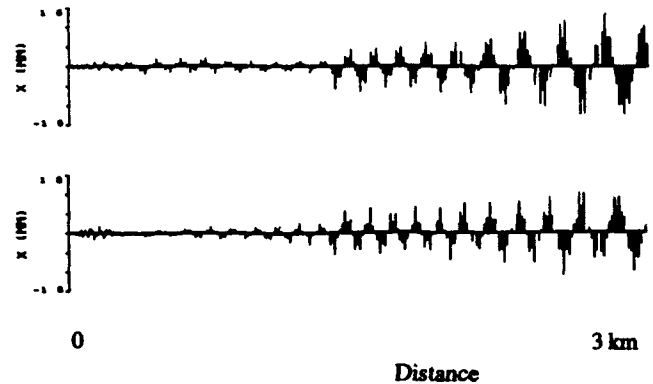


Figure 7 Induced horizontal oscillations at the 1500 m location in the linac with the old (upper) and new (lower) lattices with the new stronger BNS phases: 56 klystrons at -22 degrees and 176 klystrons at +16 degrees.

References

- 1) V. Balakin, A. Novokhatsky, and V. Smirnov, *VLEPP: Transverse Beam Dynamics*, 1983 International Accelerator Conf., FNAL, p. 119 (1983).
- 2) J. Seeman, et al., *Transverse Wakefield Damping in the SLC Linac*, (to be published), SLAC-PUB-4968.
- 3) W. L. Spence, *BNS Damping - "Autophasing" and Discrete Focusing*, Int. Workshop on Emittance Preservation in Linac Colliders, KEK, Tsukuba, April 1993.
- 4) C. Adolphsen, K. Bane, and J. Seeman, *Effect of Wakefields on First Order Transport in the SLC Linac*, IEEE Part. Accel. Conf., San Francisco, p. 3207, (1991).
- 5) K. Bane, *Landau Damping in the SLAC Linac*, IEEE Trans. on Nucl. Sci. Vol. NS-32, No. 5, p. 2389 (1985).

Table 1 Accelerator conditions for several BNS damping measurements at the end of the linac. The last three columns show the ratio of the oscillation amplitudes starting at 10 m, 500 m, and 1500 m and measured at the end of the linac (47 GeV).

Linac Test Condition	# klys A	ϕ (A)	# klys B	ϕ (B)	$x(3\text{km})/x(10\text{m})$	$x(3\text{km})/x(0.5\text{km})$	$x(3\text{km})/x(1.5\text{km})$
Nominal BNS	56	-20 deg	176	+15 deg	1.0	1.6	5.0
Weaker BNS	56	-15 deg	176	+13 deg	1.3	2.5	5.5
Slightly Stronger BNS*	56	-22 deg	176	+16 deg	0.5	1.1	4.7
Moderately Stronger BNS	64	-23 deg	168	+18 deg	0.25	0.8	4.4
New Lattice + BNS of (*)	56	-22 deg	176	+16 deg	0.46	1.0	3.3

SINGLE BEAM PHENOMENA IN BEPC

Z.Y. Guo, X. Bai, G.X. Li, J. Qin

Q. Qin, G. Xu, C. Zhang, X.L. Zhang, Z.T. Zhao

Institute of High Energy Physics, Chinese Academy of Sciences

P.O. Box 918, Beijing 100039, China

Abstract

Beijing Electron Positron Collider (BEPC) is operated as a colliding beam facility as well as a synchrotron radiation source. The maximum single bunch beam currents of 85mA and the maximum multibunch beam currents of 150mA are reached which are stronger than the designed goal^[1]. In this paper the dependence of BEPC single beam phenomena on the beam current and the single beam instabilities are described; the beam current limitations are discussed and the single beam phenomena are analysed.

I. INTRODUCTION

BEPC has been operating stably since the first e^-e^+ collision in 1988. The injection energy is 1.3 GeV for the 2.015 GeV colliding and the 2.2 GeV dedicated synchrotron radiation research at the present operation. No serious beam instability has been observed in BEPC at the present operation level which is attributed to the efforts of making the coupling impedance well controlled. The colliding beam current limit is due to the beam-beam interaction^[2]. As for the synchrotron radiation operation, the limitation is from the RF power that the cavity ceramic windows permit.

Many interesting phenomena are observed, including the bunch lengthening, the energy spread widening, the transverse beam blow up, the tune shift, the head tail instability, the beam-cavity interaction, the longitudinal coherent oscillation and the multibunch effects.

II. COUPLING IMPEDANCE

The coupling impedance expresses the interaction between the beam and the environments. It is a key parameter for the single beam instabilities.

At the beginning of the BEPC construction, we have paid more attentions to making the vacuum chamber as smooth as possible, to reducing the angle of the taper smaller where the dimension of the vacuum chamber is changed, to using two levers bellow to expand the wave length, to designing the injection kickers and the vacuum gates carefully and to forming the flange gaps more narrow and shallow. All of these considerations result in a quite small coupling impedance. For every component, the coupling impedance was estimated by means of the computer code TBCI and UMREL or estimated semi-analytically. During the machine building, the coupling impedance of some typical components such as RF cavities, kickers, bellows, tapers, flanges are measured by the simulation current method^[3]. The whole machine coupling impedance is

also determined by measuring the tune shifts as a function of beam current, which is in the form of:

$$\frac{\Delta Q}{I} = -\left(\frac{eR^2R_T}{2QE}\right)F(\sigma_l)$$

Q is the tune and I , E are the beam current and energy respectively. R_T implies the impedance and $F(\sigma_l)$ is a function of the bunch length. R is the average radius of the storage ring. So the impedance can be easily deduced and it is quite in accord with other methods. The averaged impedance obtained above is: $|Z/n|_0 = 4.0\Omega$.

III. CURRENT DEPENDENT PHENOMENA

A. Bunch Lengthening

The bunch lengthening is one of the most important issues in electron positron collider for the bunch length would influence the achievable luminosity, which could be observed in BEPC^[4].

This phenomenon is explained with two sorts of theories, i.e. potential well distortion and longitudinal turbulence instability. When the beam currents are over certain value, the stronger bunch lengthening as well as the energy widening increases with it. The bunch lengthening effect has been measured in BEPC with the different methods: the synchrotron light monitor and the wall current monitor. The scaling law for the bunch lengthening^[5] predicts that the bunch length is a function as follows:

$$\sigma_l = a\left(\frac{I\alpha_p}{E\nu^2}\right)^b$$

where a and b are constant for a certain machine. The bunch lengths are measured under the different conditions ν_s , I , E , and α_p and the preliminary parameters a and b are obtained for BEPC. The rms bunch length is about 5~10cm. The threshold of turbulence is about 8~10 mA at 1.55 GeV. The measurement errors are caused by the instrument rising time and non-gaussian form of the beam. For the accurate measurement of the bunch length, several methods are being studied under way.

B. Energy Spread Widening

The energy spread increases above a current threshold. It is measured by limiting the longitudinal bucket acceptance^[6] via decreasing the RF voltage until the quantum life time becomes dominant in BEPC. Therefore it can be carried out by measuring the synchrotron frequency and beam life time. The results at 1.7724 GeV are shown in Fig.1. It is obvious that the energy spread widening begins at 8~10mA, which is quite in agreement with the bunch

lengthening measurements and the results detector people obtained in τ mass determination experiments.

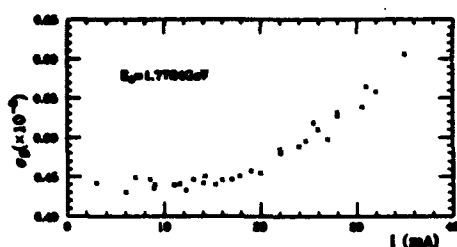


Fig.1 Energy Spread Measurements

C. Transverse Beam Blow-up

The transverse beam blow up is a very important subject especially to BEPC upgrade plans^[7]. The scraper was applied to reduce the beam life time to the transverse quantum life time and therefore the beam sizes σ_x, σ_y can be found. The emittance and the transverse coupling at different energy and different currents have been measured, which are shown in Fig.2. The horizontal beam emittance is proportional to γ^2 as the theory predicted but the vertical beam emittance is almost unchanged with energy. At least 20% increment of the beam emittance occurs if the beam reaches 50mA.

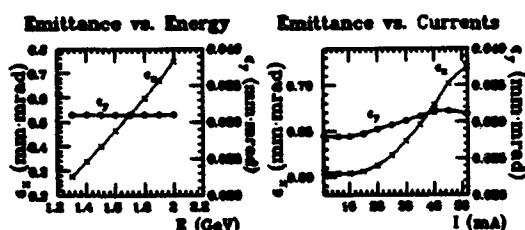


Fig.2 Emittance Measurements

D. Tune Shift

The theory of the single beam effects predicts that the tune will be changed when the beam gets stronger. The measured betatron and the synchrotron frequency as functions of the beam current^[8] are shown in Fig.3.

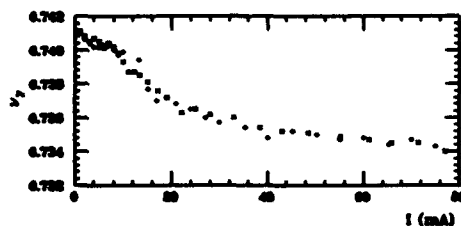


Fig.3 Tune Shift Measurements

The signal is picked up from a monitor with four strip lines. The observation shows that the vertical tune decreases with the beam current in a slope of $-0.00025/\text{mA}$

at 1.3 GeV first, then with a much smaller slope later above 20 mA. The horizontal tune and the synchrotron tune changes slightly with the beam current.

IV. SINGLE BEAM INSTABILITIES

A. Head Tail Instability

The basic theory of this transverse instability is well understood and the phenomenon is observed in many accelerators. The beam current threshold is less than 1mA. The lower mode of the head-tail instability is overcome when the chromaticity is corrected to 0.5. At the normal operating condition we choose it as 2 or 3 by four families of sextupole. The chromaticity is set to 4 or 5 to avoid the beam loss during the energy ramping, detuning and separators turning off.

B. Beam-cavity Interaction

There are two 200MHz RF cavities in BEPC storage ring and two more RF cavities will be installed in the ring for enhancing the RF voltage to shorten the bunch length. Higher order modes can be excited in the cavity. The parameters of the higher order mode have been calculated by the computer program URMEL and compared with the measurement results. The beam could be unstable if the tuner of the idle RF cavity is not put into the correct position. The observation on Robinson effect in BEPC is identical with the theory. The detuning angle of the RF cavity is controlled by tuning loop in normal operation to damp it and the similar effects from the higher order mode and the frequency variation influenced by temperature.

C. Longitudinal Coherent Oscillation

The longitudinal coherent oscillation could be excited in a bunched beam^[9], caused by some noises especially in the RF system. The signals of the oscillations can be observed on the wall current monitor and the spectrum analyser, and also can be picked up from the strip line monitor shown in Fig.4.

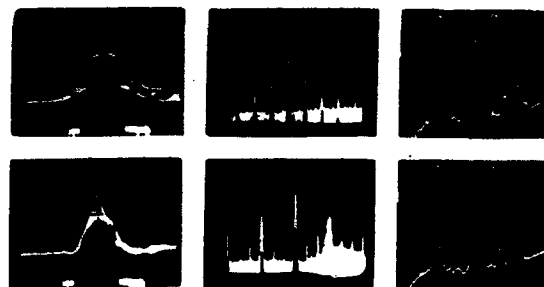


Fig.4 Longitudinal Signal Spectrum

The normal luminosity records are shown in Fig.5a. Occasionally the luminosity decreases during a short period and then returns to the normal level as shown in Fig.5b. When the oscillation occurs, the beam life time

decreases slightly and the significant signal of the longitudinal coherent oscillations especially the dipole mode can be found in three kinds of monitor as mentioned above. The luminosity decreases about 20% usually and the amplitude of the dipole mode oscillation can be estimated about 3° from the signal on the wall current monitor.

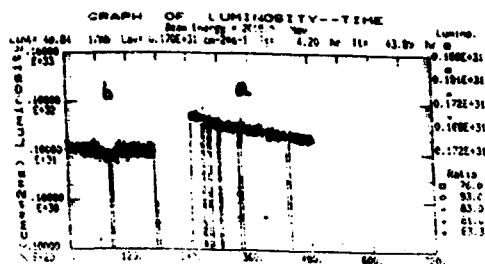


Fig.5 Luminosity Records

When both the electron bunch and positron bunch execute the longitudinal dipole coherent oscillations, there are two possible phases, i.e. in phase or out of phase. If they are in phase, which means the electron bunch and the positron bunch arrive at the designed interaction point in the same time because they advance or delay in the same manner. But in the out of phase oscillation case, the real interaction point of two bunches alternates around the designed interaction point with the same amplitude and the same frequency of the dipole longitudinal oscillation. Because the β function and the transverse beam size are minimized at the designed interaction point, the luminosity should be decreased if the real interaction point deviates from the designed one. In the higher mode cases $m=2, 3, 4, \dots$, the real interaction point does not move from the designed point, but the bunch length will be disturbed and oscillated in the different modes at the different harmonics.

A detail analysis of the luminosity decreasing from the longitudinal coherent oscillation has been done^[10]. The integrated effects of any order longitudinal coherent oscillation have been calculated. For the typical measured parameters of these oscillation, about 15% of the luminosity decrement comes from the dipole mode, 2% from the quadrupole mode, and 2% or 3% from the sum of other higher order modes. This is coincident with the luminosity observation and measurement. Hence the longitudinal feedback system is being developed for damping the dipole mode oscillation.

D. Multibunch Instability

There are 160 RF buckets in which particles can be filled. Multibunch mode is operated for synchrotron radiation research dedicatedly. The multibunch instabilities are driven by narrow band impedance i.e. high order resonators, such as the high order eigenmodes in the RF cavities or in the cavity like objects. The different filling patterns

were tried in BEPC and the multibunch instabilities have been found. The possible multibunch patterns are shown in Fig.6. The results exhibit that the more bunches are, the less particles can be filled in each bucket; the farther distance between the bunches the more particles will be filled in each bunch; it is better that the distances between adjacent bunch are the same and the preferable patterns are 4 or 8 bunches distributed uniformly.

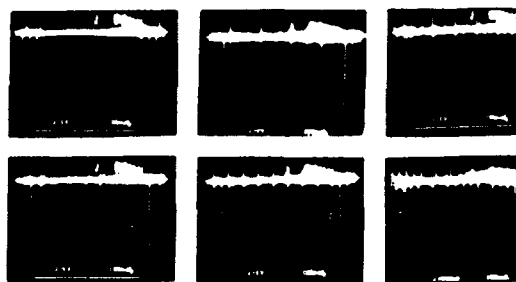


Fig.6 Multibunch Patterns

V. CONCLUSION

Many interesting phenomena have been observed in BEPC. For future luminosity upgrade plans, stronger beam currents are desired and some limitation for the higher luminosity might be come from the single beam effects such as the bunch lengthening, the beam transverse blow up, the energy spread widening and other instabilities. Much more RF power and higher RF voltage are required for adding other two RF cavities to store stronger beam and to suppress the bunch length. The longitudinal feedback system has to be set up effectively for keeping the integrated luminosity at the highest level.

VI. ACKNOWLEDGEMENT

The authors are grateful to other members of BEPC team, with whose efforts our study on beams become practical. Our special thanks go to the instrumentation group for their collaboration.

VIII. REFERENCES

- [1] BEPC Group, *15th Int. Conf. on High Energy Acc.* (1992)
- [2] BEPC AP Group, *5th Chinese Acc. Conf.* (1992)
- [3] G.W. Wang, Ph.D. Thesis (1989)
- [4] L. Ma, *Proc. of the BEPC Workshop* (1984)
- [5] A. Chao et al., *IEEE Trans. Nucl. Sci.*, NS-24 (1977)
- [6] X.L. Zhang et al., BEPC-AP/MD 92-06 (1992)
- [7] C. Zhang, *BEPC Upgrades Plans*
- [8] G.X. Li et al., BEPC-AP/MD 92-08 (1992)
- [9] B. Zotter and F. Sacherer, CERN 77-13
- [10] Z.Y. Guo, *5th Chinese Acc. Conf.* (1992)

High Intensity Bunch Length Instabilities in the SLC Damping Rings*

P.Krejcik, K.Bane, P.Corredoura, F.J.Decker, J.Judkins, T.Limberg, M.Minty, R.H.Siemann
Stanford Linear Accelerator Center
Stanford University, Stanford, California 94305
F.Pedersen
CERN, CH-1211 Switzerland

I. INTRODUCTION

The SLC damping rings function to provide low emittance, short bunches for injection into the linac. As the beam intensity in the rings was raised, as part of the SLC luminosity improvement program[1], we observed a threshold above which beam jitter would occur in the linac. Frequent machine trips, caused by beam loss on some bunches, were associated with the jitter. These erratic "flier" pulses were traced to extraction phase errors from the damping rings. This paper covers the diagnosis of this condition and the observations of the transient bunch length instability phenomena. The evidence of this turbulent (microwave) bunch length instability is seen in both time domain and in frequency domain measurements. The instability has been dubbed the "sawtooth" because of the characteristic time dependent nature of the phase and bunch length signals. It is present in both the SLC electron and positron damping rings at about the same threshold of $3 \cdot 10^{10}$ particles per bunch.

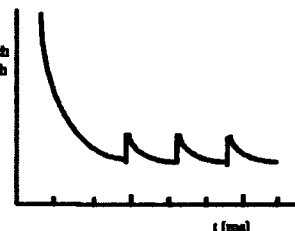
An interim solution to this instability problem has been to exercise control over the bunch length via the RF voltage. The peak current is kept below the instability threshold by ramping the voltage during the store cycle. The blowup in the bunch length as the threshold of peak current (=intensity+bunch length) is crossed, is the result of short-range wake fields. The main contributors to the vacuum chamber impedance are step discontinuities in transition pieces, radiation masks and pump slots. We are at present building a new, smoother vacuum chamber to reduce the impedance and thus increase the intensity in the damping rings.

Earlier measurements of bunch lengthening[2] in the damping rings led us to believe that the lengthening was an equilibrium process. It was the tight tolerance on the phase of the extracted beam that signaled to us the transient behavior of the bunch lengthening. Such tight tolerances on beam phase do not occur in storage rings and so the transient behavior is less important, although there is some evidence that "sawteeth" have been observed elsewhere[3]. There is also some evidence in numerical simulations of transient bunch lengthening phenomena, which is discussed later in this paper.

II. INSTABILITY OBSERVATIONS

The time dependent nature of the bunch length during the 8.3 ms store time in the damping ring is shown diagrammatically in fig. 1. The bunch length decreases rapidly after injection, with a longitudinal damping time of the order of 2 ms. When the bunch length passes below a threshold a sudden blowup in bunch length occurs in a time span comparable to the 10 μ s synchrotron period. The process is

self limiting because of the nonlinear nature of the short range wake fields responsible for blowing up the bunch. Once the blowup ceases the bunch damps down until the threshold is reached again, causing a cyclical repetition of the instability. The time dependent nature is seen in the following two signals.



Bunch length signal

This is derived from the sum signal of a pair of Beam Position Monitor (BPM) electrodes. Passage of the bunch gives a bipolar pulse whose height is proportional to intensity+bunch length. This signal is peak sampled-and-held at the revolution frequency of 8.5 MHz. The sampled output connected through a low pass filter to an oscilloscope gives a real-time display of the inverse of the bunch length during the beam store time. An example is shown in fig. 2.

Bunch phase signal

The behavior of the beam phase is important since it has direct bearing on how the bunch is launched into the linac. The bunch phase can be referenced to either the 714 MHz RF of the damping ring or to the 2956 MHz S-band RF of the linac. The 714 MHz beam phase shown in fig. 2 also exhibits sawtooth-like jumps at the same time that the bunch length signal blows up. The synchronous beam phase angle is given by $\phi_s = \sin^{-1} U_{loss}/V_{rf}$ so the changing phase during an instability reflects a changing energy loss per turn of the bunches. The higher order mode losses of the bunch are a function of the line charge density and so are inversely proportional to bunch length. As the bunch blows up the higher order mode losses decrease and the beam phase shifts. We observe an approximately 0.5° phase shift at 714 MHz during a sawtooth, which implies that at the nominal operating conditions of $V_{rf}=1$ MV and $\phi_s=9^\circ$, the energy loss per turn changes by 9 kV. This is to be compared to the 80 kV radiation losses and the nominally 80 kV higher order mode losses.

The 0.5° phase jump at 714 MHz translates into a 2° jump at S-band in the linac. This magnitude of phase error causes a problem with the RF bunch length compressor in the Ring To Linac beam line. A phase error at extraction transforms to an energy error in the compressor, resulting in both orbit and chromatic errors.

* Work supported by Department of Energy Contract DE-AC03-76SF00515.

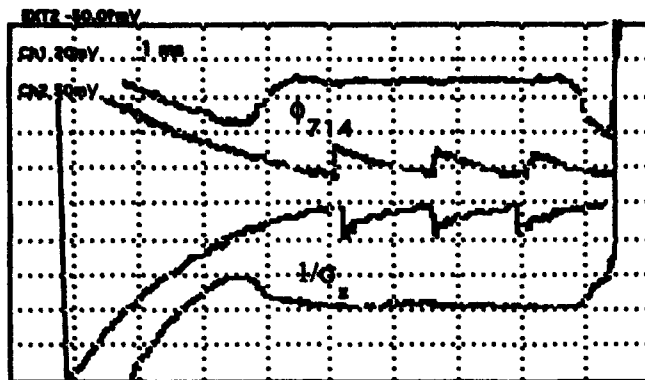


Fig. 2. The inverse bunch length signal and the beam phase signal exhibit sawtooth behavior during the instability. Upper and lower curves (no sawteeth) are with voltage ramp on.

The troublesome feature of the sawtooth behavior is that the timing of the phase hiccups will jiggle around and occasionally occur just at extraction. When this occurs the bunch will be incorrectly launched into the linac and may eventually be lost on the downstream collimators, causing the linac to trip the machine protection circuits.

The beam phase in the damping ring is controlled by an S-band beam-phase feedback loop. The gain-bandwidth of this loop rolls over well below the synchrotron frequency so it is unable to compensate for the rapid phase jumps of the sawtooth. The error signal for the S-band loop shows a series of spikes coincident with the onset of the sawtooth.

Frequency domain measurements

Turbulent bunch lengthening is often referred to as the microwave instability because the bunch length oscillation modes have a characteristic wavelength at some small fraction of the bunch length. For the short (<1 cm) bunch lengths in the damping rings this translates to frequencies in the

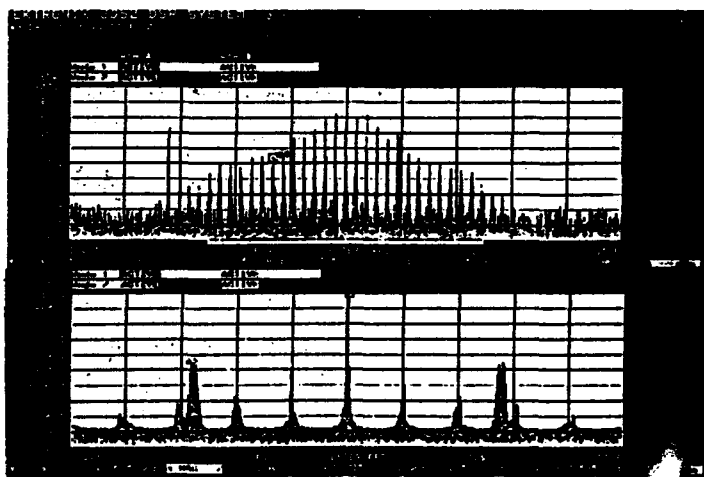


Fig. 3. a. At a harmonic near 20 GHz many modes are visible in the injected beam. (5 MHz span)
b. In the damped beam, with instability, the sextupole mode dominates. (1 MHz span)

100 GHz range, well beyond the reach of our conventional RF measurement equipment. With some care in the setup we have been able to detect useful signatures of the instability at frequencies of up to 20 GHz.

The bunch evolves rapidly during the store time so the emphasis of our measurements has been on separating the frequency spectrum of the turbulent bunch lengthening from the spectrum generated by the bunch at injection. The application of a Digital Signal Processing spectrum analyzer has proven very useful here[4].

When the bunch is injected in the damping ring there is a considerable longitudinal mismatch. The bunch oscillates with many modes as seen by the large number of synchrotron sidebands in fig. 3a. If the spectrum acquisition is triggered later in the store cycle the modes are seen to have damped out. However, if the spectrum acquisition is triggered to occur after the bunch length has damped down to the instability threshold we see a strong signal reappear at the $3\nu_s$ sideband, corresponding to a sextupole mode of oscillation in the bunch length, fig. 3b. Note that although we refer to this sideband as $3\nu_s$ its frequency of ~ 260 kHz is considerably depressed from 3 times $\nu_s = 100$ kHz.

If spectral measurements are done on a stored beam (i.e. by disabling the extraction kicker) the behavior can be recorded as the intensity decays down to the threshold where the instability ceases. The observed behavior is that the $3\nu_s$ line is present during the whole time that the beam is unstable in the damping ring and disappears as soon as the instability stops. Significantly, we observed only a small frequency shift of the $3\nu_s$ mode with changing current (~ 8.6 kHz/ $1 \cdot 10^{10}$). The other weaker modes, up to $6\nu_s$, exhibit similar frequency dependence. We had anticipated an intensity dependence of the mode frequency so that we could account for the instability in terms of longitudinal mode coupling, a phenomena observed at other storage rings[5,6]. An example of mode coupling would have been if the $3\nu_s$ sextupole line had crossed the $2\nu_s$ quadrupole line, but this did not occur.

Since we determined that the instability has its largest observable spectral component at $3\nu_s$, we set up a spectrum analyzer with zero span at this frequency and swept the time span from injection through to extraction. There is an initial large peak in the signal power corresponding to injection transients and then nothing until a sawtooth occurs at which point there is a brief rise in the spectral power. This confirms that the mode is only present during the brief instant that the bunch blows up. The question that is not resolved by these measurements is whether the mode is a symptom or the cause of the instability. It is conceivable that the very rapid bunch blowup is a turbulent process at very high frequencies within the bunch and that when it extinguishes, the mismatch of the bunch length within the RF bucket causes ringing, predominantly at $3\nu_s$.

III. INTENSITY DEPENDENCE

The threshold for the instability occurs at around $3 \cdot 10^{10}$ particles per bunch for a nominal RF voltage of 1 MV. At

higher intensities we observe that the periodicity of the instability increases, i.e. the sawteeth appear closer together in time. The process can be viewed as a relaxation oscillator where the period is a function of the bunch length damping time and the trigger threshold. The damping time is constant but the bunch length at which the bunch goes unstable increases at higher intensities. As the intensity is increased the sawteeth get closer together until a transition occurs at around $4 \cdot 10^{10}$ to a second regime with "continuous sawteeth". The bunch-length and beam-phase signals have noise-like character in this regime. We do not observe that the bunch length ever reaches a quiet, steady state equilibrium between the heating and damping mechanisms.

The thresholds for these regimes also depends on the RF voltage as the equilibrium bunch length is $\propto V^{-1/2}$. At lower RF voltages the bunch takes longer to reach the instability threshold, so the frequency of the sawteeth is reduced. We describe later how to exploit this to avoid the instability altogether.

Bunch lengthening in the damping rings has been the subject of earlier studies[2]. At this time the onset of bunch lengthening was measured by measuring the energy spread of the extracted beam in a high dispersion beam line, as a function of current. Prior to making an impedance reduction in the vacuum chamber by sleeving the bellows, the bunch lengthening threshold was measured at $1.5 \cdot 10^{10}$. The measurement has been repeated since the sleeving was done and the new threshold is close to $3 \cdot 10^{10}$, fig. 4, coincident with the threshold for the sawtooth. The measurement of energy spread is performed over many machine pulses, masking any transient effects related to the sawtooth. Numerical simulations were able to predict the factor 2 improvement in the instability threshold from sleeving the bellows, but remained pessimistic about the absolute threshold value by approximately 30%.

The intensity distribution functions for bunch lengthening have been numerically simulated in several instances. In one example an undershoot phenomena[7] has been seen where the bunch damps below the instability threshold resulting in a sudden blowup. Unlike our sawtooth, these blowups rapidly damp after injection. A simulation of the LEP ring[8] has also shown periodic blowups of bunch length, but on a scale much larger than has ever been observed. A recent simulation with

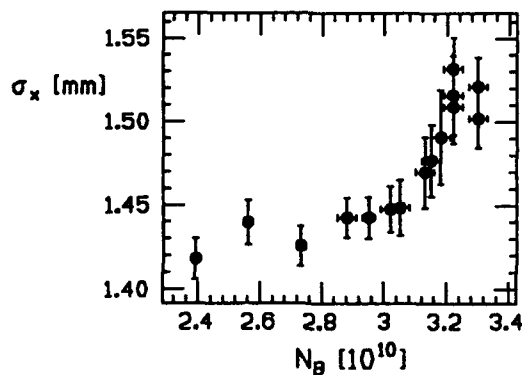


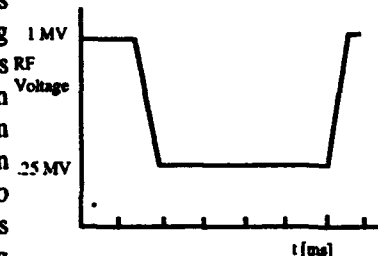
Fig. 4. The energy spread, indicated by the beam size in a dispersive region, shows the onset of turbulent lengthening at $3 \cdot 10^{10}$.

our damping ring parameters[9] has shown evidence of the strong sextupole mode above the threshold, but without any indication of a sawtooth behavior.

IV. BUNCH LENGTH CONTROL THROUGH THE RF

Lowering the RF voltage is a means of increasing the equilibrium bunch length and extending the intensity threshold for the instability. A low RF voltage is not suitable for efficient injection where a large RF bucket is required. A low RF voltage is also unsuitable at extraction, since a very long bunch length at extraction results in an unacceptable energy spread in the compressor, causing the problems alluded to earlier, of beam loss and chromatic errors.

A solution has been implemented for ramping the voltage down approximately 1 ms after injection and ramping it back up around 0.5 ms before extraction as shown in the adjacent fig. 5. In this scheme the injection transients have time to decay but the voltage is soon reduced, preventing



the bunch from damping below the instability threshold. The voltage is ramped up at the end of the store cycle so that the bunch shortens and it is extracted just before it has the chance to go unstable. The programmed voltage changes are made adiabatically so that the bunch remains matched to the RF bucket. A second voltage program (not shown) is used to shorten the bunch further by bunch rotation just before extraction[10]. Lowering of the RF voltage for both these manipulations has severe impact on the beam loading of the RF cavities. The short time scale of the ramp means the cavities can not be retuned for optimal matching at the lower voltage. This combined with the lower cavity power relative to the beam power leads to a beam loading instability at lower voltages. The beam loading has been successfully compensated through the use of RF feedback[11]. We have been able to routinely suppress the onset of instabilities at intensities up to $3.5 \cdot 10^{10}$ per bunch by ramping the voltage from 1 MV down to 250 kV during the beam store time.

V. REFERENCES

- [1] M.C.Ross, "Recent SLC Developments", these procs.
- [2] L.Rivkin et al, Proc 1988 Eur. Part. Accel. Conf., p.634
- [3] G.Rakowsky and L.R.Hughey, IEEE Trans. Nucl. Sci. NS-26, 1979, p. 3845.
- [4] R. Stege et al, Proc. 1992 Accel. Instrumentation Workshop, Berkeley, CA.
- [5] W.Anders, Proc 1992 European. Part. Accel. Conf., p.798
- [6] D.Brandt et al, Proc 1992 European Part. Accel. Conf., p.
- [7] Y. Chin, K.Yokoya, KEK Preprint 83-14, 1983.
- [8] T. Weiland, DESY Report 81-088, December 1981.
- [9] K.Bane, K.Oide, "Simulations of the Longitudinal Instability in the SLC Damping Rings", these Proceedings.
- [10] F.J.Decker et al, Proc. HEACC 1992, Hamburg, p. 148.
- [11] P.Krejčík et al, "RF Feedback for Beam Loading Compensation in the SLC Damping Rings", these procs.

Investigation on Relaxations in Electron Beams

A. V. Aleksandrov¹⁾, R. Calabrese²⁾, G. Ciullo^{2,3)}, N. Dikansky¹⁾, V. Guidi^{2,3)}, N. Ch. Kot¹⁾,
V. I. Kudelainen¹⁾, G. Lamanna^{3,4)}, V. A. Lebedev¹⁾, P. Lenisa³⁾, P. V. Logachov¹⁾, B. Maciga^{2,3)},
L. Tecchio⁵⁾ and B. Yang^{3,6)}

1) Budker Institute of Nuclear Physics, Novosibirsk, Russia

2) Dipartimento di Fisica dell'Università and INFN, I-44100 Ferrara, Italy

3) INFN-Laboratori Nazionali di Legnaro, I-35020 Legnaro, Italy

4) Dipartimento di Fisica dell'Università and INFN, I-70125 Bari, Italy

5) Dipartimento di Fisica sperimentale dell'Università and INFN, I-10125 Torino, Italy

6) PROEL Tecnologie S.p.A, I-50125 Firenze, Italy

Abstract

The achievement of high density very-low energy spread electron beams requires a deep knowledge of this topic. For this purpose longitudinal and transverse beam relaxations are studied for two different sources, a thermo- and a photo-cathode. As a result a plasma parameter greater than 1 has been measured, that may potentially increase the efficiency of the electron cooling technique.

I. INTRODUCTION

Since very-low energy spread provides a higher measurement accuracy and a substantially beam performance improvement, it is the main goal in several research areas.

If the energy broadening at the source is equal to ΔE_{10} , neglecting the interactions between electrons, the relation between ΔE_{11} in the beam rest frame and the kinetic energy W results in:

$$\Delta E_1 = \Delta E_{10}^2 / 4W \quad (1)$$

The charged particle interactions contribute to two effects [1, 2]: the energy transfer from transverse to longitudinal components (Boersch effect), and the relaxation in the longitudinal component. Both could be adequately compensated.

The transverse-longitudinal relaxation can be damped using an axial magnetic field. The magnetic field intensity depends on the condition that the Larmor radius ρ , experienced by the electrons in the magnetic field, has to be less than the minimum inter-particle distance r_{min} . Two regime have to be distinguished: low densities n_e with energy spread ΔE , in which the inter-particle distance is $r_{min} \sim e^2 / \Delta E$, and high densities, in which $r_{min} \sim (4\pi n_e / 3)^{-1/3}$. When the applied magnetic field satisfies both the conditions, the energy transfer from transverse component to the longitudinal one is suppressed.

On the other hand due to the longitudinal relaxation, neglecting the interaction between transverse and longitudinal degrees of freedom, the equation (1) becomes:

$$\Delta E_1 = \Delta E_{10}^2 / 4W + C e^2 / n^{1/3} \quad (2)$$

where the parameter C depends on the accelerating structure.

In such a case with adequate slow acceleration the longitudinal energy spread ΔE_{11} is maintained by plasma oscillations.

If λ is the ratio between the plasma oscillation period and the relaxation time in the beam; then

$$\lambda = (1/\omega_0 \Delta E_{11}) (d\Delta E_{11}/dt) \quad (3)$$

For value of $\lambda \ll 1$, the acceleration is called adiabatic respect to the oscillations and as a result the C value in (2) decreases.

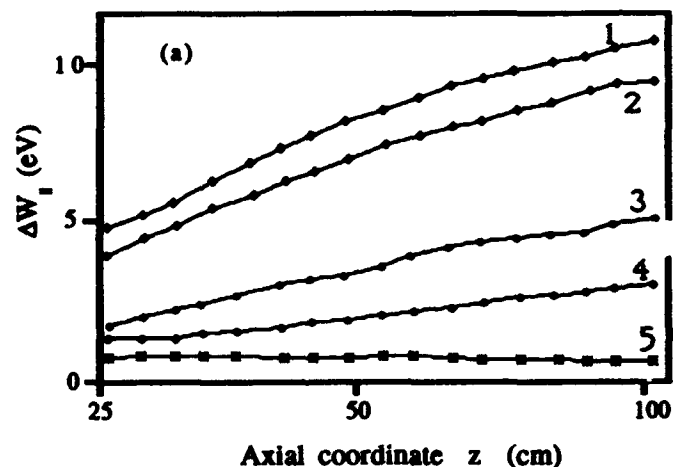
II. APPARATUS AND RESULTS

a) the apparatus

The electron sources, a BaO thermocathode and a GaAs photocathode, the latter activated in NEA condition [3] and illuminated by a 450 mW maximum power single-mode [4] Ti:Al₂O₃ tunable within 750-900 nm, are placed in a Pierce diode at high extraction potential (2 mm of gap between anode and cathode). The continuous electron beams out of the gun enter the adiabatic acceleration section of five 10 mm radius pipes, then they travel along a drift section 1.8 m long [2]. A movable retarding potential analyzer [5] measures the beam energy spread with a 8 meV resolution.

b) transverse-longitudinal relaxation

The energy analyzer allows accurate measurements along the longitudinal direction. The relationship between the energy spread ΔW_{11} , measured by the analyzer, and the longitudinal distance z is illustrated in fig.1 (a) and (b). The electrons, extracted from the thermocathode and rapidly accelerated to 470 eV, generate a beam current ranging from 0.1 to 9.0 mA. The comparison is carried out at 1 and 3 kG magnetic fields.



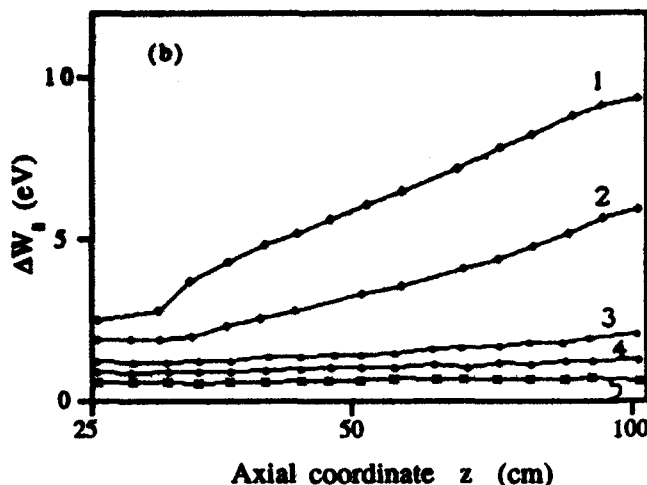


Fig. 1
Energy spread $\Delta W_{||}$ for the oxide thermocathode, versus the longitudinal coordinate z at various beam currents: 1- 9.0 mA, 2- 6.4 mA, 3- 3.2 mA, 4- 1.6 mA, 5- 100 μ A and for different values of magnetic field: a) $B=1$ kG, b) $B=3$ kG. In all cases is $W=470$ eV.

It is evident that the stronger the magnetic field the higher the damping of the transverse-longitudinal relaxation. Actually at 1 kG $\Delta W_{||}$ remains unchanged only for the 100 μ A current level, instead at 3 kG it does not change for current levels up to 3.2 mA.

In fig.2 the energy spreads are compared for the two different sources versus the current density J . For $J \rightarrow 0$, when any contribution due to relaxation is negligible, the energy spread recorded for the photocathode is lower.

While increasing current the transverse-longitudinal relaxation occurs and the benefit provided by photocathode is fully lost.

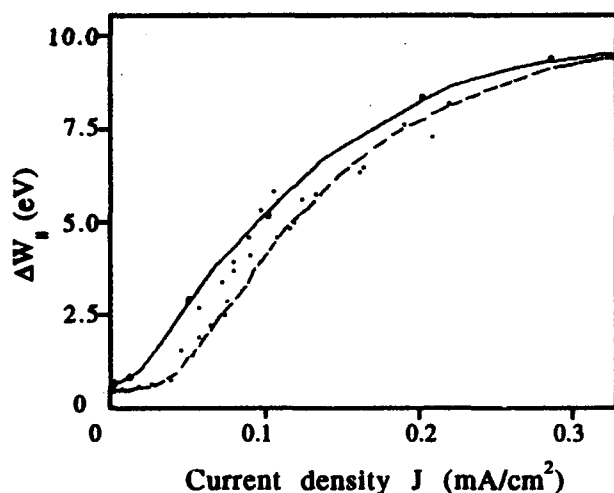


Fig. 2
Energy spread ΔW versus beam current density for (+) thermo- and (•) photo-cathode at 1 kG magnetic field for fast acceleration.

c) longitudinal-longitudinal relaxation and adiabatic acceleration

In fig.3 the measurement of the time taken by the electron beams to develop the relaxation is reported. Herewith it is shown the energy spread $\Delta E_{||}$ versus the flight time, both value are normalized to the average electrostatic energy and the plasma period respectively.

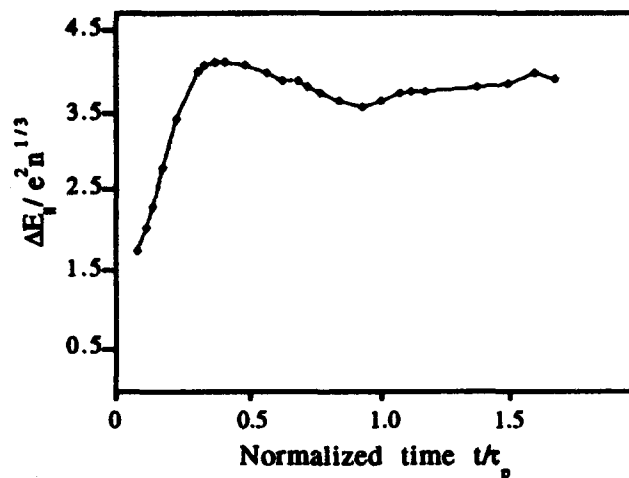


Fig. 3
Experimental trend of normalized longitudinal electron energy spread $\Delta E_{||}$ versus time after a fast acceleration for the oxide thermocathode; $I=300$ μ A, $W=800$ eV, $n=3.73 \cdot 10^7$ cm^{-3} , $B=3$ kG.

This measurement confirms the assumption of the plasma period like relaxation time. The differences on the energy spread between fast and adiabatic acceleration is demonstrated in fig.4. The initial difference at the adiabatic section end is due to the longitudinal-longitudinal relaxation. Then along the z axis the beam experiences the transverse-longitudinal one,

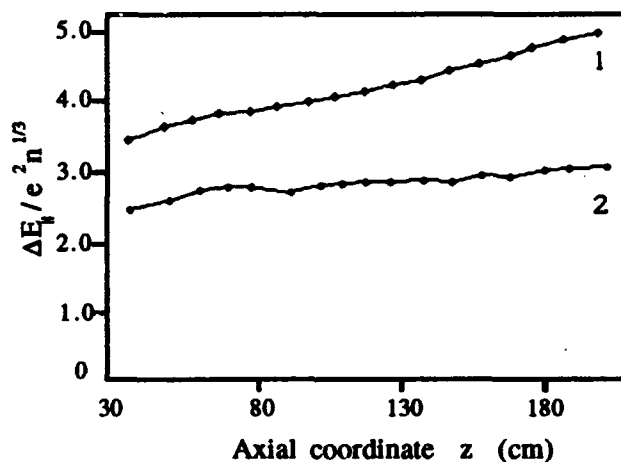


Fig. 4
Normalized energy spread $\Delta E_{||}/e^2 n^{1/3}$ for the thermocathode versus axial z coordinate after (1) fast and (2) adiabatic acceleration; $W=470$ eV, $I=200$ μ A.

resulting in a further increase of the spread. This latter can be only compensated by a stronger magnetic field.

Assembling a photocathode and an adiabatic acceleration better performances should be obtained.

d) Plasma parameter

Considering the electron beam as a one-component plasma confined by the focusing forces of the accelerator device, its macroscopic behavior may be described by the plasma parameter Γ (ratio between interparticle Coulomb energy and average kinetic energy). To measure Γ_H we need to know the particle density n , computable by the current measured in the collector, and ΔE_H in the rest frame of the beam computable by the equation (1). In fig.5 is reported the Γ_H parameter for fast and adiabatic acceleration [6].

Only with a photocathode in an adiabatic acceleration structure is possible to reach a Γ_H values greater than 1, that is the first experimental evidence for an electron beam.

Superimposing this cold electron beam on an ion beams, it should be possible to obtain much colder ion beams.

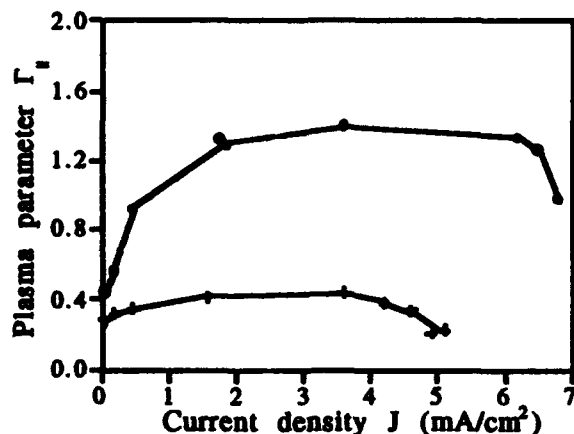


Fig. 5

Plasma parameter as a function of current densities for (+) fast and (o) adiabatic acceleration with $B=3$ kG and $W=900$ eV.

Fig.6 shows the behavior for fast and adiabatic acceleration of beams from the activated GaAs. At low densities the ΔW_H is lower for the adiabatic case, while increasing the current the Boersch effect is dominating. Then the adiabatic acceleration seems disadvantageous for high current beams, unless the magnetic field is adequately strong.

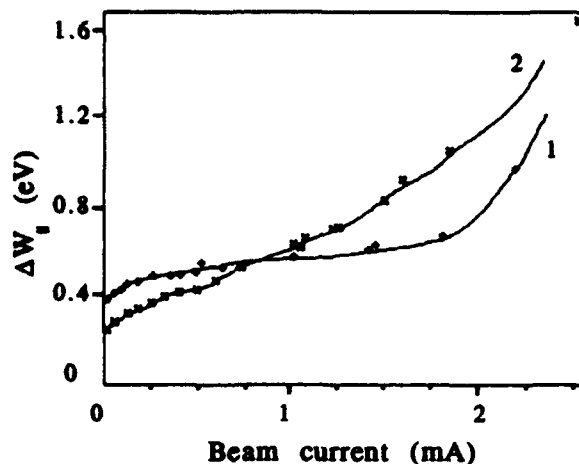


Fig. 6

Longitudinal energy spread ΔW_H for the photocathode versus collector current I at $W=900$ eV and $B=4$ kG: 1- Fast acceleration 2- Adiabatic acceleration.

III. CONCLUSIONS

This paper has examined the differences between a thermo- and a photo-cathode in fast and adiabatic acceleration cases. The best performance of a continuous electron beams is allowed by a photoemission source, which provides a 'cold' beam, an adequately magnetic field, which counteracts the transverse-longitudinal energy transfer, and an adiabatic acceleration structure, which damps the longitudinal-longitudinal relaxation. The maximum value of Γ_H reached is an important step towards the improvement of electron cooling technique and perhaps some hopes for ion beam crystallization.

IV. REFERENCES

- [1] Kudelainen et al.; *Sov. Phys. JETP* **56**(6), 1191 (1982).
- [2] A.V. Aleksandrov et. al.; *Phys. Rev. A* **46**(10), 6628, (1992).
- [3] R.Calabrese et. al.; "Photoelectron source for electron cooling purpose" submitted to *Rev. Sci. Instrum.*
- [4] A.V. Alexandrov et al.; EPAC 92, 1035, Berlin, 24-28 March 1992.
- [5] A.V. Aleksandrov et al.; "Very High Resolution Energy Analyzer for electron beams" to be publ. in *Meas. Sci. Tech.*
- [6] A.V. Aleksandrov et al.; *Europhys. Lett.* **18**(2) 151 (1992).

Studies of Multipass Beam Breakup and Energy Recovery Using the CEBAF Injector Linac

N. S. Sereno and L. S. Cardman †

Nuclear Physics Laboratory and Department of Physics
University of Illinois at Urbana-Champaign, Champaign, IL 61820,

G. A. Krafft, C. K. Sinclair, and J. J. Bisognano ‡

Continuous Electron Beam Accelerator Facility
12000 Jefferson Avenue, Newport News, Va 23606-1909

Abstract

Beam breakup (BBU) instabilities in superconducting linacs are a significant issue due to the potentially high Q values of the cavity higher order modes (HOMs). The CEBAF accelerator, which employs high CW current and 5-pass recirculation through two superconducting linacs, poses unique instability problems. An experimental investigation of multipass BBU along with energy recovery has been completed using a single recirculation through the CEBAF injector linac. Experimental results are compared with computer simulation of multipass BBU.

I. INTRODUCTION

Multipass BBU is characterized by a maximum current (threshold current) above which beam loss occurs. The threshold current is the maximum average current at which the power deposited by the beam into the HOM equals the power dissipated by the HOM through resistive losses. The threshold current for the most unstable mode is the maximum beam current that can be accelerated without beam loss. The HOM Q parameterizes the mode losses and can be the same order of magnitude as the fundamental mode Q (10^9 – 10^{10}). The CEBAF/Cornell cavity design incorporates HOM damping thereby reducing HOM Q values to the range 10^4 – 10^5 [1]. As a result, BBU threshold currents for the full CEBAF linac are calculated to be between 10 and 20 mA [2]—two orders of magnitude above the maximum design current of 200 μ A.

The CEBAF/Cornell cavity design was tested under the conditions of both acceleration and energy recovery of the second-pass beam in the CEBAF injector. The injector offered worst-case conditions (lowest threshold currents) for multipass beam breakup because of the low injection energy of 5.5 MeV (as opposed to the nominal 45 MeV for the full CEBAF linac), the ability to produce in excess of 200 μ A CW current, and the ability to change the transverse optics of the recirculation path to lower the threshold current. The fact that no evidence for multipass beam breakup was experimentally observed for both second-pass

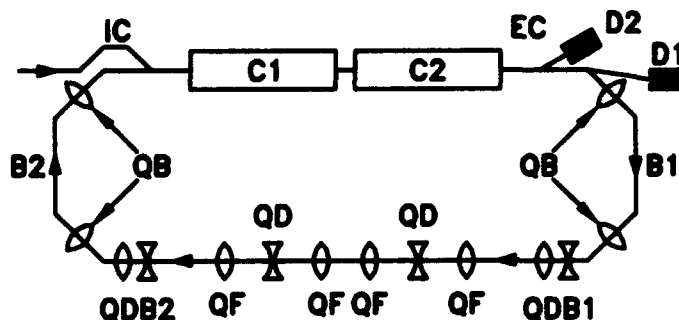


Figure 1: Recirculator layout.

acceleration and energy recovery under these worst case conditions indicates that the HOM damping incorporated in the CEBAF/Cornell cavity design is entirely adequate to prevent multipass BBU in the full CEBAF linac.

II. RECIRCULATOR DESCRIPTION

Figure 1 shows schematically the CEBAF injector linac including the beam recirculation path. The linac consists of two cryomodules C1 and C2, each containing eight 5-cell, 1497 MHz superconducting cavities. The beam is injected into the linac at 5.5 MeV and accelerated to 42.8 MeV after C2. The beam is bent 180° by B1, travels to B2 where it is bent by another 180° and arrives back on the linac axis. Finally it is combined with the injected beam on the linac axis by injection chicane IC and is either accelerated to 80 MeV and dumped at D1 or decelerated to 5.5 MeV and dumped at D2 after the energy recovery chicane EC, which separates the first-pass accelerated beam from the low-energy second-pass beam. Path length adjustment was accomplished by mounting B1 on a movable platform which could be translated along the linac axis by ~ 10 cm ($1/2$ of an RF wavelength at 1497 MHz).

III. TRANSVERSE OPTICS

The recirculation arc transverse optics provided both dispersion-free beam transport and independent adjustment of both x and y plane optics. B1 and B2 were designed to be doubly achromatic in the horizontal plane. Two quadrupoles per bend (QBs) were used to set the

†Supported by N.S.F grant #PHY-89-21146

‡Supported by D.O.E. contract #DE-AC05-84ER40150

Frequency (MHz)	R/Q (Ω)	Q
1899.6	21.9	*90,000
1969.6	48.1	4,000
2086.9	13.1	10,000
2110.5	25.6	*30,000

Table 1: HOM parameters (* from RF measurement).

dispersion and its slope to zero after the bend. Doublets QDB1 and QDB2 were used to match the beam out of B1 and into B2 respectively. The six quadrupoles QD and QF formed a FODO structure that was adjusted to provide various optical settings. As the six quadrupoles were varied the optics of the rest of the recirculator was left unchanged during the experiment. Setting 1 was simply a negative identity matrix (-I) transfer in both x and y planes across the FODO array. For settings 2-4 the y plane optics was changed and the x plane was kept at -I. Settings 5 and 6 were achieved by reversing the polarity of the quads for settings 1 and 2, which resulted in x being varied and y remaining -I. The energy recovery setting was identical to setting 1 except that doublet QDB2 was re-adjusted to provide the smallest beam spot possible at D2.

Calculations of the transverse optics were performed using the code DIMAD. Beam transport calculations were performed for all optical settings including energy recovery. In addition, quadrupole strengths of doublets QDB1 and QDB2 were fit to measurements of the M_{12} and M_{34} matrix elements measured before C1, between C1 and C2 and after C2 for each optical setting. A cavity model was incorporated into DIMAD (and the BBU code TDBBU [2]) which included the cavity focussing by the fundamental accelerating mode at low energy. The calculations did not take into account the small x - y coupling observed at the low energies in the injector [3].

IV. ENERGY RECOVERY

Superconducting cavities have the advantage that high gradients can be maintained under CW operating conditions because of low wall losses. If a beam is decelerated, efficient conversion of beam energy to fundamental mode field energy is possible. Energy recovery of a FEL beam driven by a superconducting linac by means of recirculation is a possible way of greatly increasing the efficiency of the laser since most of the beam energy remains after lasing occurs [4]. The CEBAF energy recovery experiment extended previous experiments [5], [6], [7] to the relatively high gradients (5 MV/m) of CEBAF cavities. In the experiment, the second pass beam was decelerated to 5.5 MeV (at up to 30 μ A CW current) indicating full energy recovery within the 1.8% energy measurement uncertainty.

V. BEAM BREAKUP SIMULATIONS

Setting	I_t (mA)	I_m (μ A)
1	5.3	215
2	6.3	68
3	19.5	120
4	13.2	95
5	15.5	64
6	5.0	67
Energy recovery	.4	30

Table 2: Threshold current and maximum beam current attained for each optical setting.

The beam breakup simulations were performed using the code TDBBU for all optical settings including energy recovery. The cavity HOMs were treated as high Q uncoupled resonators with a strength given by the shunt impedance R/Q . These modes deflect the beam in either the x or y plane. Table 1 lists parameters of the HOMs used in the simulations; the asterisk indicates the Q values for these modes come from RF measurements described in the next section. Reference [1] lists the shunt impedance in terms of the parameter Z'' , which is given by $R/Q = (Z''/Q)(l_e/k^2)$ where k is the HOM wavenumber and l_e is the effective length of the HOM in the cavity (0.5 m). Finally, the code uses the first-order transfer matrix describing the recirculation path from the end of C2 to the beginning of C1 as computed using DIMAD.

Table 2 lists the threshold current I_t computed for each optics setting along with the maximum CW current I_m achieved in the experiment. Similar BBU calculations for the full CEBAF linac indicate threshold currents in the range 10-20 mA [2] so that the injector recirculator is calculated to be more sensitive to multipass BBU by a factor of 2 in the threshold current. For setting 1, over 200 μ A CW was recirculated. This is the CEBAF maximum design current, but is still an order of magnitude below the calculated threshold current for setting 1. The energy recovery setting is seen to have the lowest calculated threshold current due to large recirculation transfer matrix elements. Beam current was primarily limited by large beam sizes on the second pass (with energy recovery having the largest) that resulted in scraping. The beam loss monitoring system shut the beam off when approximately 1 μ A of scraping occurred.

VI. RF MEASUREMENTS

An additional experiment was performed to externally excite the HOMs using an RF kicker that deflected the beam transversely. Figure 2 shows schematically the RF HOM measurement that was performed using a recirculated CW beam. A broadband stripline kicker operating between 350 and 650 MHz was used to deflect the beam transversely. Signals at a particular HOM frequency were detected using the last cavity of C2. Aliasing of the kicker signal by the

Network Analyzer

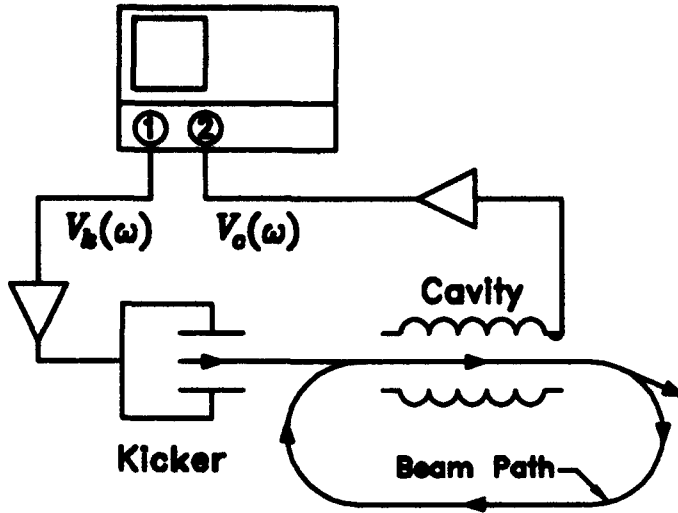


Figure 2: RF HOM measurement schematic.

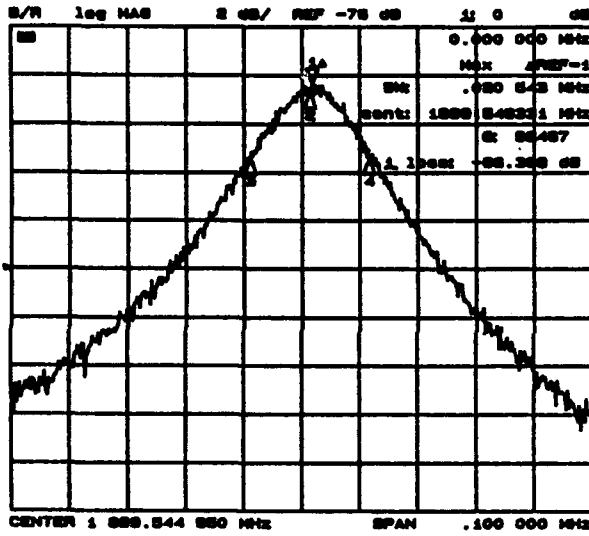


Figure 3: 1899 MHz HOM at 99 μ A CW beam current.

bunching frequency insured that HOMs near 2 GHz were excited. Under recirculation conditions the cavity signal V_c is given in terms of the kicker drive signal V_k by

$$\frac{V_c(\omega)}{V_k(\omega)} = \mathcal{F} \frac{IZ(\omega)}{1 - I/I_t} \quad (1)$$

where $Z(\omega)$ is the total transverse impedance due to all the cavity HOMs and \mathcal{F} is an overall scale factor. The formula shows instability occurring at a particular threshold current. Far from threshold for a particular HOM, the ratio in equation 1 is simply a linear function of the current with the slope proportional to the mode impedance.

Figure 3 shows the 1899 MHz HOM measured using the setup in figure 2. The network analyzer was set up to measure S_{21} (the ratio in equation 1) where port 1 was used to drive the kicker and port 2 was used to detect the cavity signal. For both HOMs measured (at 1899 and

2110 MHz) the height of the peak was plotted as a function of the beam current I for all optical settings including energy recovery. No significant deviation from linearity was observed—a result consistent with the computed threshold currents in table 2.

VII. CONCLUSIONS

From experimental and simulation results, multipass BBU did not prevent high-current operation of the injector recirculator. The main limitation on recirculated current was scraping, primarily due to non-ideal matching of the second-pass beam out of B2. The results indicate that the full CEBAF linac should not be susceptible to multipass beam breakup at the maximum design current of 200 μ A. An FEL driven by a linac that uses energy recovery to increase efficiency would need to incorporate careful optical design aimed at reducing second-pass spot sizes and increasing multipass BBU threshold currents.

ACKNOWLEDGMENTS

The authors express their gratitude to the CEBAF staff and especially to the members of the operations group who put in many long hours during these experiments. We also thank W. Barry who designed and prototyped the stripline kicker used in the RF measurement.

REFERENCES

- [1] J. C. Amato, *Identification and Analysis of TM111 and Schwettmann Cavity Modes*, SRF-850303-EX, (1984).
- [2] G. A. Krafft, J. J. Bisognano, S. Laubach, "Beam Breakup in Superconducting Linear Accelerators," (To be submitted to *Particle Accelerators*).
- [3] M. Tiefenback, Z. Li, L. Merminga, B. Yunn, "Emitance Measurements and Transverse Cavity Transfer Matrix in the CEBAF Nuclear Physics Accelerator," these proceedings.
- [4] R. Rohatgi, H. A. Schwettman, and T. I. Smith, "A Compact Energy Recovered FEL for Biomedical and Material Science Applications," *Proceedings of the 1987 Particle Accelerator Conference*, 230 (1988).
- [5] D. W. Feldman et al., "The Los Alamos Free-Electron Laser Energy-Recovery Experiment," *Proceedings of the 1987 Particle Accelerator Conference*, 221 (1988).
- [6] G. R. Neil, J. A. Edighoffer, and S. W. Fornaca, "Superconducting Linac FEL Technology," *Proceedings of the Beijing FEL Seminar*, 232 (1989).
- [7] T. I. Smith, et al., "Development of the SCA/FEL For Use in Bio-Medical and Material Science Experiments," *Proceedings of the 1986 International FEL Conference*, (1986).

The Longitudinal and Transverse Beam Dynamics Simulation in the MMF Storage Ring

V.A. Moiseev

Institute for Nuclear Research of the Academy of Sciences
60-th October Anniversary Prospect, 7a, Moscow 117312, Russia

Abstract

The computer code has been developed to study both longitudinal and transverse microwave instability problems of an intense beam in synchrotrons and storage rings. The macroparticle method and impedance beam-environment interaction are used in simulation. The beam dynamics have been explored for the Moscow Meson Factory (MMF) storage ring at slow extraction operation mode (SEM). Some results of the numerical simulation are presented.

I INTRODUCTION

The slow extraction mode of the MMF proton storage ring was designed to transform the bunched beam structure during $100\mu s$ accelerator macroimpulse to uniform beam ejected between two successive macroimpulses ($\sim 9.9ms$) [1].

For SEM the ring and beam parameters are [3]:

total intensity	$3.12 \cdot 10^{13} ppp$
average current	$11.3 A$
relativistic parameters	$\beta = 0.792 \quad \gamma = 1.639$
linac rf frequency	$f_{rf} = 198.2 MHz$
total momentum spread	0.002
transition energy	$\gamma_{tr} = 1.720$
momentum slip factor	$\eta_0 = (1/\gamma_{tr}^2 - 1/\gamma^2) = -0.35 \cdot 10^{-1}$
chromaticity	$\xi = -0.534$
revolution period	$T_r \approx 450ns$
betatron tunes	$Q_x = 1.875 \quad Q_y = 1.915$

In the present case the nominal particle energy is below the transition energy. Therefore the capacitive behaviour of the beam-storage ring interaction in the smooth vacuum chamber is expected. But with the space charge dominated impedance the stability of the particle motion might be a problem. However due to operation near transition energy it could be achieved sufficiently long growth time for the instabilities.

II SIMULATION MODEL

Because the changes of the transverse particle parameters are faster than of longitudinal ones the longitudinal dynamics has been taken as basic. The tracking procedure used for longitudinal motion simulation for the MMF storage ring was described in ref.[2].

In betatron phase space $(x_\beta; \dot{x}_\beta)$ the particle motion is governed by differential equation [4]:

$$\begin{aligned} \ddot{x}_\beta + \dot{\varphi} x_\beta &= \frac{F(t, \theta)}{m_0 \gamma} \\ \dot{\varphi} &= Q_0 \omega_0 (1 - \dot{\tau}) + \omega_\xi \dot{\tau} \end{aligned} \quad (1) \quad (2)$$

here x_β and $\dot{x}_\beta = dx_\beta/dt$ are the transverse particle coordinate and velocity with respect to the equilibrium orbit; Q_0 is Q_x or Q_y ; $\omega_0 = 2\pi/T_r$; $\dot{\tau} = \eta(dp/p)$; $\omega_\xi = Q_0 \omega_0 \xi / \eta_0$. Induced electromagnetic force is defined [4]

$$F(t, \theta) = -\frac{i\beta_0}{2\pi R} \int_{-\infty}^{\infty} Z_{tr}(\omega) S_{tr}(\omega, \theta) e^{i\omega t} d\omega \quad (3)$$

$$Z_{tr}(\omega) = Z_{trsc}(\omega) + Z_{trrw}(\omega) + Z_{trbb}(\omega) \quad (4)$$

Here Z_{trsc} , Z_{trrw} , Z_{trbb} are the transverse space charge, resistive wall and broad band impedances defined by standard formulas [4]. And S_{tr} is Fourier spectrum of the transverse dipole-moment current. Applying the macroparticle beam representation and the binning technique which has been used for longitudinal dynamics simulation all spectrum amplitudes of S_{tr} can be determined. Due to computer capability only horizontal transverse motion was studied.

The model parameters are: the total number of macroparticles $N \sim 80000$, the broad band shunt resistance $R_{sh}/n_r = 50\Omega$ and the other parameters are the same which were used for longitudinal dynamics simulation [2].

To estimate the growth time for unstable harmonics the spline approximation for the macroparticle momentum distribution and then the dispersion integral calculation [4] were carried out.

III SIMULATION RESULTS

A Longitudinal Dynamics

In fig.1 the normalized momentum distribution function is shown at the end of injection ($113\mu s$) and during circulation ($165\mu s$ and $215\mu s$). For total stored beam intensity at the beginning of circulation a lot of longitudinal density harmonics close to $mT_r f_{rf} \approx 89m$, where m is integer, have essential growth. The theoretical growth time for these harmonics is $30 \dots 100\mu s$. At the end of injection the momentum spread is insufficient to suppress the microwave instability by Landau damping. During injection the change of the momentum distribution function is negligible, but further the low energy tail of the momentum distribution function is developed drastically. That turns on effectively the Landau damping and leads to saturation of amplitude growth for unstable harmonics. For stabilisation the small number of particles is needed in the momentum tail for low energy intense beams with space charge dominated impedance [5]. In our simulation the saturation times for unstable harmonics are

50...80 μ s. Further all harmonics which have had the essential growth are damped. Unfortunately the ring design parameters restrict the momentum deviation on the value $(\Delta p/p) = -0.75 \cdot 10^{-2}$. That can cause the losses of the particles with lowest energy if the Landau damping will be weak to suppress the unstable harmonics.

Since for simulation the over-pessimistic value for broad band shunt resistance was chosen it has been made the growth time calculation for unstable harmonics for $R_{sh}/n_r = 5\Omega$ expected for MMF storage ring. The particle momentum distribution function which has been resulted from simulation before beam loses (curve for 215 μ s in fig.1) was used. The growth times calculated are greater than 20ms. In fig.2 the instability curve with growth time 24ms and operation impedance for azimuthal harmonic $n = 267$ are shown. For expected ring impedance parameters the simulation results have shown the possibility to avoid beam loses due to the longitudinal microwave instability because of the characteristic times the particles reach the wall are much more the extraction time. Moreover, beam stored current drops linearly with time.

B Transverse Dynamics

In fig.4 the normalised betatron amplitude distribution, the betatron phase space projection and view of the betatron particle distribution function are shown. Here $x = x_p; \dot{x}_p = \dot{x}_p/Q_0\omega_0; A_x = \sqrt{x^2 + \dot{x}_p^2}$. It is evidence that during total stored beam circulation there is rebuilding of the particle distribution function which causes the global changes of the Fourier spectrum of the transverse dipole-moment current. The beam size increasing due to the process mentioned above is not dramatic and can be considered as small addition to beam size growth due to changes of the momentum distribution function.

The growth time calculated for more dangerous low frequency harmonic $n=2$ by standard theory [4] is ~ 1 ms at the end of injection (113 μ s) and ~ 1.6 ms at the end of simulation (215 μ s). Therefore it may be expected there will not problem with transverse stability in the low frequency range for SEM storage ring operation. However if $\eta \rightarrow 0$ the threshold values for transverse impedance will be slightly differ for any harmonics of the dipole-moment current. It means the Landau damping is not effective for that harmonic which has the large value of ReZ_{tr} . Because the great shunt resistance of broad band impedance was chosen for simulation the growth time for high frequency harmonics is less the one for the low frequency range. In fig.3 instability curve with growth time 33 μ s and the impedance parameters are shown for harmonic $n=450$. That situation is dangerous and can result in the transverse beam blow-up on high frequency range for storage rings working in quasi-isochronous mode. However, taking into consideration the over-pessimistic value of the broad band shunt resistance, the dependence of the particle betatron frequency (2) from betatron amplitude and the possibility to change the ring chromaticity the growth time for high frequency harmonics may be done greater the calculated above.

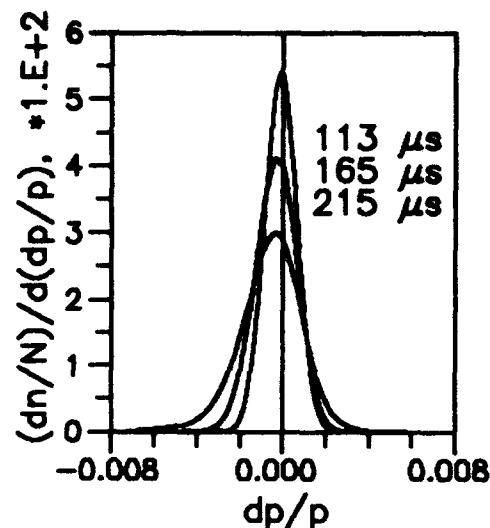


Figure 1: The change of momentum distribution.

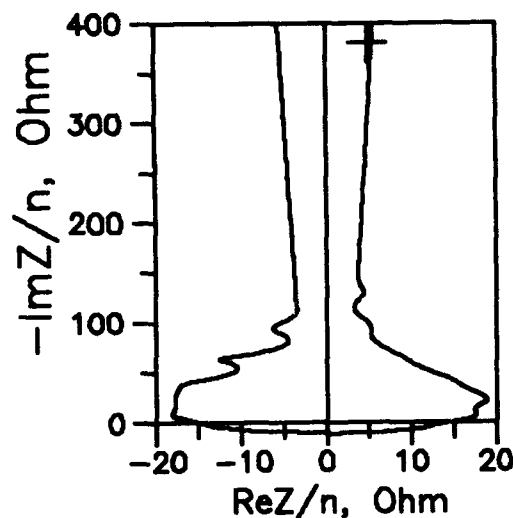


Figure 2: Longitudinal instability diagram for $n=267$.

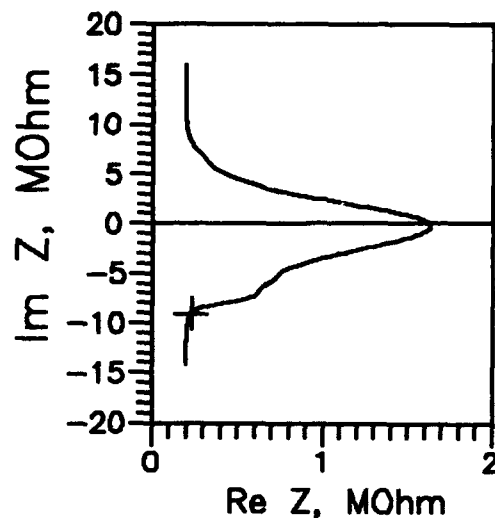


Figure 3: Transverse instability diagram for $n=450$.

The main results of the transverse particle dynamics simulation are the particle re-distribution in the betatron phase space and high frequency transverse microwave instability. The first effect should be taken into account, but second must be cure by adjusting the ring multipole correction elements and eliminating the strong wide-band parasitic resonators in the high frequency domain.

IV REFERENCES

- [1] M.I.Grachev et al, "Moscow Meson Factory Proton Storage Ring", *Proceedings of the XIII International Conference on High Energy Accelerators*, Novosibirsk, vol.1, pp. 264-269 (1987).
- [2] V.A.Moiseev, P.N.Ostroumov, "Longitudinal dynamics simulation of the high intensity beam in the MMF storage ring", *EPAC-2*, Nice, vol.2, pp.1714-1716 (1990).
- [3] V.A.Moiseev et al, "Beam dynamics studies in the MMF storage ring", *EPAC-2*, Nice, vol.2, pp.1673-1675 (1990).
- [4] J.-L.Laclare, "Introduction to coherent instabilities", *CAS*, Geneva, vol.2, pp.377-414 (1985).
- [5] I.Hofmann, "Suppression of microwave instabilities", *Laser and Particle Beams*, vol.3, part 1, pp.1-8 (1985).

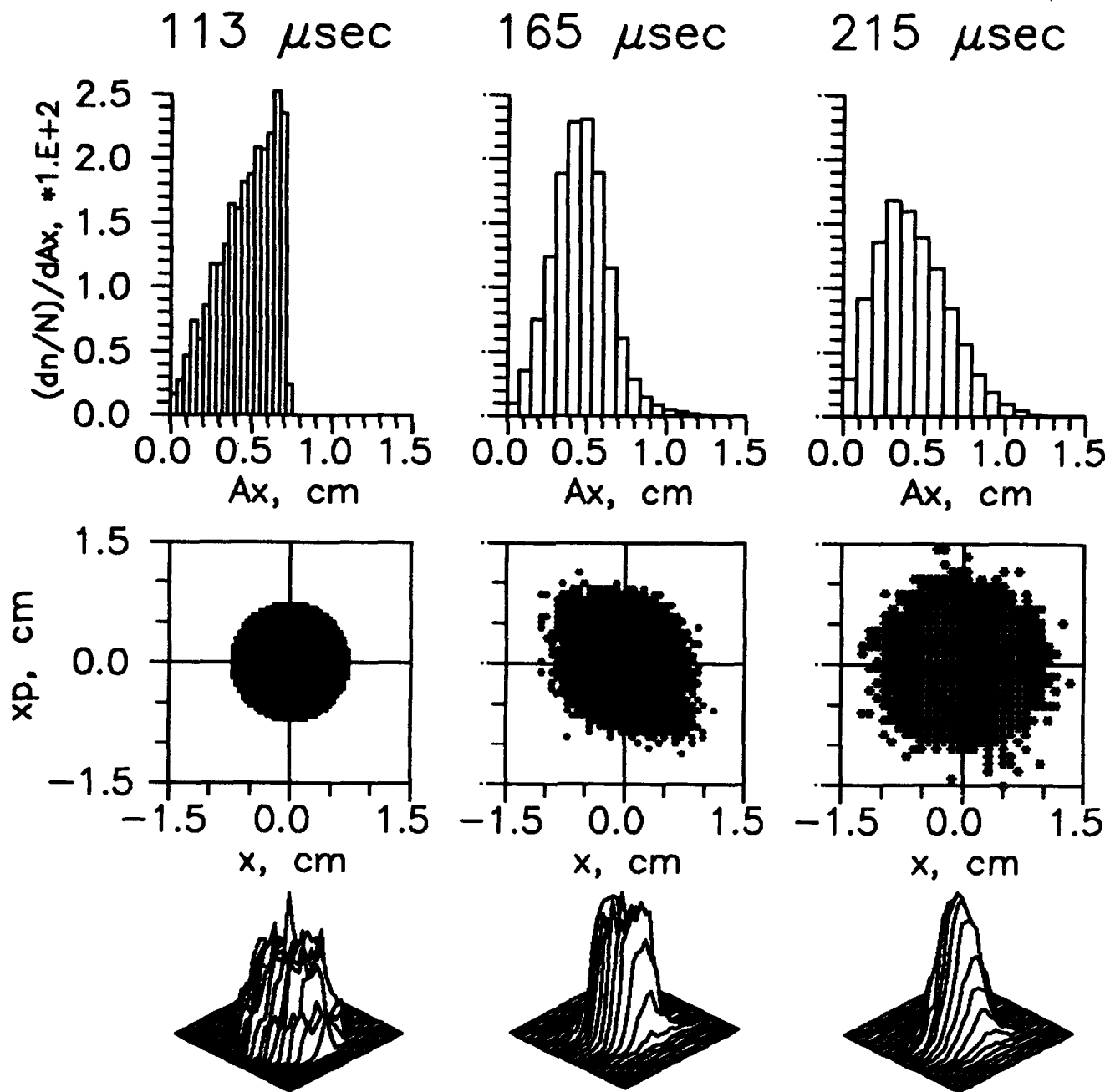


Figure 4: Betatron amplitude distribution, betatron phase space projection, view of the betatron particle distribution function.

CONTROL OF LONGITUDINAL INSTABILITIES IN THE LEB

T.L. Grimm and P.D. Coleman
Superconducting Super Collider Laboratory*
2550 Beckleymeade Avenue
Dallas, TX 75237

Abstract

The potential longitudinal instabilities and their control in the SSC Low Energy Booster are examined. Coasting beam theory shows there is a chance for microwave instabilities at the end of the acceleration period for the maximum design current of 0.5 Adc. The beam is stable to microwave instabilities for the Collider fill current of 0.1 Adc. Single bunch instabilities driven by the RF cavity accelerating mode will be stabilized by beam phase, voltage amplitude, tuner bias and RF feedback loops. The coupled bunch instabilities driven by the cavities' higher order modes and other resonant structures appear to represent the biggest challenge to longitudinal stability. A broadband passive damper on each RF cavity will greatly decrease the chance of any coupled bunch instabilities although other options to aid the damper are investigated. The control of longitudinal instabilities in the LEB appears feasible and should not limit its operation up to the peak design intensities.

I. INTRODUCTION

The SSC Low Energy Booster (LEB) is the first of three booster synchrotrons which supply the proton beam to the Collider. The LEB is a resonant, rapid cycling (10 Hz) machine with 114 bunches spaced 5 m apart[1, 2]. It will boost a maximum beam current of 0.5 Adc, five times Collider fill mode, from 600 MeV to 11 GeV. Six to fourteen quarter-wave ferrite tuned cavities, tuning from 47.5 to 59.8 MHz, will supply a peak ring voltage of 765 kV[3, 4].

The potential longitudinal instabilities and their control are investigated here for the LEB. First, coasting beam instabilities, which are associated with broadband impedances are discussed. Then single bunch instabilities, which are caused by the RF cavity accelerating/fundamental mode, are covered. Finally, coupled bunch instabilities (CBI) which are driven by the RF cavity higher order modes (HOM) and other narrow band impedances, are discussed. A weak instability may stabilize due to nonlinear effects and short interaction times. Thus its only effect would be to increase the longitudinal emittance which would be beneficial because it would simplify matching to the medium energy booster at extraction. If the instability is strong enough to cause beam loss or couples to the transverse direction then it will be

necessary to damp the perturbation.

II. COASTING BEAM

Coasting-beam theory is used to predict the maximum allowable broadband impedance, Z_L/n . Coasting beam theory is derived for a totally debunched beam, although it has been shown to be applicable for a bunched beam provided the perturbation has many periods within a bunch. For the LEB this implies the perturbation index, n , is much greater than the harmonic number and that the instability would occur at frequencies above ~ 1 GHz (ie. microwave instabilities). Fig. 1 shows the threshold Z_L/n given by the Keil-Schnell criterion during the 50 ms beam acceleration for 0.5 Adc. With the use of shielded bellows, shielded pumping ports and smooth tapers at beam pipe transitions the total Z_L/n of the LEB is predicted to be less than $\sim 1\Omega$. This shows there is a possibility for microwave instabilities in the second half of the acceleration period. The growth rate would be fairly small and a large bucket is available later in the cycle, so the only affect anticipated would be an increased longitudinal emittance.

III. SINGLE BUNCH

There will be many RF control loops available to handle Robinson-type single bunch instabilities in the LEB[5]. These instabilities are driven by the RF cavity accelerating mode. The control loops planned are: beam phase, voltage amplitude, tuner bias, and RF feedback. Since all of the RF buckets are equally filled, beam current feedforward will not improve beam loading transients. If necessary, a peak bunch density loop can also be implemented to control bunch length oscillations. For stable operation with these loops, the gap voltage, V_{gap} , must satisfy[6];

$$V_{gap} > \frac{R_{sh} I_B}{2(1 + H)} \quad (1)$$

where $R_{sh} \simeq 100k\Omega$ is the cavity shunt impedance, $I_B = 1$ Aac is the AC beam current, and H is the RF feedback open loop gain. This gives $V_{gap}(kV) > 50/(1 + H)$ which means operating voltages above 50 kV do not require any RF feedback. The design RF feedback loop will easily have an $H = 10 - 20$ which implies operating voltages above 5 kV will be stable. Before a voltage this low is reached multipactoring will have made it necessary to counter-phase the cavities at higher voltages. Thus the RF control loops

*Operated by the Universities Research Association, Inc. for the U. S. Department of Energy under Contract No. DE-AC02-89ER40486.

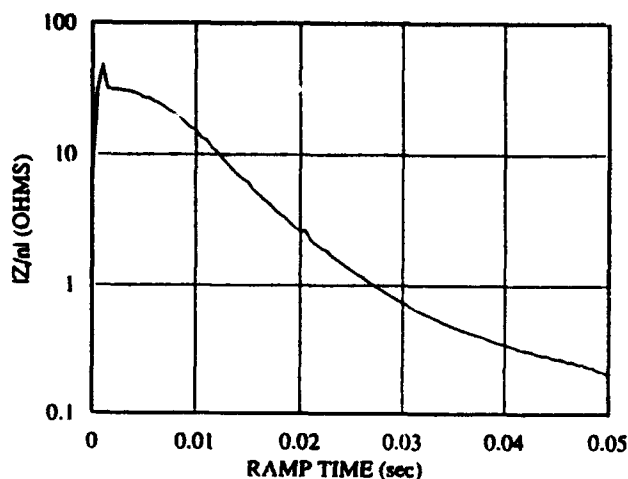


Figure 1. Allowable broadband impedance during LEB cycle.

should not have any trouble controlling the Robinson-type single bunch instabilities.

IV. COUPLED BUNCH

An analysis of CBI in the LEB due to narrowband resonances of the cavity HOMs and other resonant structures (injection and extraction chambers for example) predicts the maximum allowed R_{sh} versus frequency for four e-foldings growth of the instability[7]. Instability due to the cavity's fundamental mode will not be a problem because the cavity bandwidth is much less than the revolution frequency. The total R_{sh} for CBI is about $4k\Omega$ for the $m = 1$ dipole mode at 120 MHz and increases to $28k\Omega$ for the $m = 5$ mode at 1 GHz. HOMs above about 1 GHz should not be a problem for CBIs since the cavity ferrite becomes lossy, the beam current's spectrum will be negligible, and the 8 cm beam pipe is above cutoff to longitudinal modes above 2.9 GHz.

For a given frequency, the total R_{sh} can come from a single beamline component or can be a sum of components such as the cavities. For an undamped cavity the R_{sh} of HOMs will be similar to the fundamental value of $100k\Omega$ which clearly is a problem. Options to correct the cavities' and other structures resonances will be addressed. For now the cavities' R_{sh} will be assumed to be the main contributor to CBIs although the same arguments will apply to other resonant structures.

The options for controlling CBIs can be categorized as either a passive or active system. The passive systems do not require any instability measurement or feedback and the options are: passive dampers, stagger tuning and resonance hiding. The active systems require feedback and possibly measuring the instability, and the options are: active damper, Landau cavity, subharmonic cavity and beam blow-up. If a passive system can eliminate the CBIs then obviously it would be preferable to an active system.

A. PASSIVE SYSTEMS

Because there are so many cavity HOMs from 120 MHz up to 1 GHz, which tune with the fundamental mode, a broadband damper will be the primary method of controlling HOMs. A Smythe-type broadband damper with a high-pass filter between the damping cavity and water cooled loads has been designed[8, 9]. The damper is predicted to damp a single cavity's R_{sh} to less than 600Ω from 120 MHz to 500 MHz and maintains R_{sh} to low enough values above 500 MHz that high frequency CBIs should not be unstable. Thus the most dangerous HOMs will be the first two at about 120 and 190 MHz. For six cavities with the cavities' R_{sh} summing, all CBIs would be predicted to be stable. If more cavities are necessary (the lattice has room for 16) then other methods of damping may be necessary for the first two HOMs. If the CBI occurs at a specific frequency, then a narrowband damper such as a coupling loop or capacitive plate could further damp the mode.

Stagger Tuning shifts the HOM resonant frequency in each cavity so they do not overlap thereby decreasing the total R_{sh} at a given frequency, although this would increase the range of resonant frequencies. This could be accomplished by varying the cavity dimensions. The shift would need to be more than the mode's half bandwidth which has been broadened by the damper. For the 120 MHz HOM with the Smythe damper in place the bandwidth is approximately 4 MHz which would require too large of a change in cavity dimension to be useful. Thus stagger tuning would not be practical when the Smythe damper is used.

Another passive method of eliminating CBIs is to remove the resonance by not allowing the HOM frequency to overlap an integer of the revolution frequency. The LEB revolution frequency is about 0.5 MHz which is much less than the damped HOM bandwidth so resonance hiding will not work for the LEB. Also, because the HOMs tune at a different rate than the fundamental they will cross a revolution frequency sometime during the ramp.

B. ACTIVE SYSTEMS

An active damper would measure the instability and counteract its growth in some manner. Thus the instability must be at a finite level for an active damper to have any effect. The instability measurement can be done in one of two ways. In the first method the beam oscillations are measured directly using a wall current monitor, while the second method will measure the RF which is driving the instability.

For measurement of the beam oscillations, the bunch-by-bunch phase and peak density variation will be measured using a wall current monitor. This will tell the type and magnitude of the CBIs. The same information could be obtained from a Fourier transform of the beam current. To use these measurements in an active feedback system there will need to be a one turn delay circuit whose delay must shift with the RF frequency. For a narrow bandwidth system (100 kHz) the delay circuit error must be less than

2 μ s which should be quite easy, while a wideband system (30 MHz) would require an error less than 8 ns.

A broadband active damper would be needed to damp all possible unstable CBIs. This would require a separate cavity with up to 30 MHz bandwidth, although it could be at high frequency such as 300 MHz and would not need to tune with the RF. If the HOM frequency driving the CBI is known then a narrow band cavity (bandwidth of $2f_s$) or the RF cavity itself could be used at the driving frequency.

For measurement of the RF driving the instability, the overall active damper would be fairly simple. The measured RF would be fed back to the source 180° out of phase. It would be narrowband since the RF comes from HOMs in the cavity. There would be no need for external timing or delay circuits and the measured signal is continuous.

Another way to actively damp the CBIs would be to operate the LEB RF cavity's beam phase and beam amplitude loops from a single bunch instead of the average as is presently envisaged. This would damp the CBIs on that bunch and increase the synchrotron frequency spread between bunches thereby breaking up the coherence of the instability.

A subharmonic cavity operates at a subharmonic of the main RF frequency. This causes a synchrotron frequency shift between bunches which would eliminate the coherence and increase the Landau damping of the CBI[10]. A subharmonic cavity would operate at the RF frequency shifted by a revolution frequency. This small shift relative to the LEB tuning range implies an extra LEB cavity could function as the subharmonic cavity although it would not lead to any acceleration. Since the only additional hardware required (if there is an extra LEB cavity) is the drive frequency and amplitude control system this option will be made available on the LEB. If the instability occurs during a portion of the accelerating ramp where the RF voltage is not maximum then one of the RF cavities in use could be switched to subharmonic operation with the other cavities compensating for it.

A Landau cavity works by applying a harmonic of the RF to the bunches to increase the RF non-linearity seen by the bunches. This increases the synchrotron frequency spread and therefore the Landau damping. The Landau cavity has been shown to work, but requires voltages comparable to the RF and must tune with the RF. Thus the Landau cavity would be as much of an engineering challenge as the present LEB cavity. If a Landau cavity operated over only part of the tuning range its tuning bandwidth could be substantially lower. Due to the complexity and expense of an additional RF system, a Landau cavity will not be designed for the LEB.

Finally, it should be noted that the CBI can be stabilized by purposely increasing the longitudinal emittance or decreasing the bucket size which increases the Landau damping. The increased emittance could be caused by letting an instability grow slowly, driving a microwave instability or intentional noise in the phase loop for example.

V. CONCLUSION

The different types of longitudinal instabilities and their control have been investigated. The beam is stable to microwave instabilities for the Collider fill intensities, but is unstable for peak intensities at the end of the acceleration period. This instability should only increase the longitudinal emittance which is beneficial for matching to the Medium Energy Booster. Robinson-type single bunch instabilities will be controlled by beam phase, voltage amplitude, tuner bias and RF feedback loops. The RF cavity's HOMs will be the principal source of coupled bunch instabilities. Coupled bunch instabilities will be damped primarily with a broadband passive damper on each RF cavity. This will stabilize all modes for Collider fill intensities. For peak intensities the two lowest frequency HOMs will be unstable if there are more than six cavities. This can be controlled with a narrowband passive damper, a subharmonic cavity, cavity beam phase locked to a single bunch or an active damper.

VI. ACKNOWLEDGEMENTS

We would like to thank N.K. Mahale for the use of his simulations of the LEB longitudinal beam dynamics.

VII. REFERENCES

- [1] R.C. York, *et al.* The SSC low energy booster: A status report. In *IEEE PAC*, 1991.
- [2] U. Wienands. Status of the SSC low energy booster. In *IEEE PAC*, 1993.
- [3] C.C. Friedrichs, *et al.* Design of an accelerating cavity for the SSC low energy booster. In *IEEE PAC*, 1991.
- [4] P. Coleman, *et al.* Status of the SSC LEB rf cavity. In *IEEE PAC*, 1993.
- [5] L. Mestha, *et al.* A digital beam phase loop for low energy booster. In *IEEE PAC*, 1993.
- [6] F. Pedersen. A novel rf cavity tuning feedback scheme for heavy beam loading. *IEEE Trans. Nucl. Sci.*, 32:2138-2140, 1985.
- [7] R. Baartman. Allowed narrow-band impedance in the SSC LEB. TRIUMPH Design Note TRI-DN-92-K207, 1991.
- [8] W.R. Smythe, C.C. Friedrichs, and L.S. Walling. Proton synchrotron rf cavity mode damper tests. In *IEEE PAC*, 1991.
- [9] L. Walling, G. Hulsey, T. Grimm, E. Ruiz, and N. Spayd. Investigation of higher-order dampers for the SSC LEB cavity. In *IEEE PAC*, 1993.
- [10] C.M. Ankenbrandt, *et al.* Longitudinal motion of the beam in the fermilab booster. *IEEE Trans. Nucl. Sci.*, 24:1449-1451, 1977.

Simulation of the Transverse Dipole Mode Multibunch Instability for the SSC Collider

S. Chen and G. López
Superconducting Super Collider Laboratory*
2550 Beckleymeade Ave., Dallas, TX 75237 USA

Abstract

We investigate a simulation code to study the transverse dipole mode multibunch instability due to a single RF cavity and the resistive wall for the Superconducting Super Collider. The growth time calculated from our code agrees well with analytical calculations (ZAP code). The code can be used for studying the interplay of wake field, noise and feedback system, i.e. for design the feedback system.

I. INTRODUCTION

The Superconducting Super Collider (SSC) Collider will be the first machine operating with 17424 bunches of protons separated by a relatively short distance [1], 5 m. The bunches are injected from the High Energy Booster (HEB) into the Collider, which requires eight HEB batches to fill almost symmetrically (there is an abort gap) one of its two rings. The batches are injected into the upper and lower ring one at a time. To inject one batch in the same ring requires approximately 515 s, and the eight batches are injected in approximately 1.14 h. Therefore, there is a great deal of concern about possible multibunch instabilities that the beam might suffer during this time. To study the transverse dipole mode (rigid motion) multibunch instability, a computer code was developed to calculate the instability growth time due to Positron-Electron Project (PEP) RF cavity and resistive wall impedance. The results are compared with the analytical approach, and the feedback system design is incorporated to control this instability.

II. TADIMMI CODE AND RF-INSTABILITY

Ignoring the possible coupling of different directions in the motion, the transverse amplitude of motion, Y , of a point-like bunch suffering the electromagnetic wakefield interaction, w , can be described by the differential equation

$$d^2Y/dt^2 + \omega_\beta^2 Y = ww, \quad (1)$$

where ω_β is the free angular betatron oscillation frequency. For simplicity, let us assume the following: there is a single cavity in the ring where there is a point-like interaction, the ring is perfectly linear, and the ring has M equally spaced bunches. With these assumptions the short-range

wakefield can be omitted, and the long-range wakefield is given by the Higher Order Modes (HOM) of the RF cavity. Since the length of the RF cavity is usually much smaller than the betatron wave length, the betatron phase advance within the RF cavity can be ignored. When the k -bunch passes through the RF cavity for $n+1$ turn, the transverse position does not change, $Y(k, n+1) = Y(k, n)$, but its momentum is changed by the wakefield of the RF cavity. For dipole mode wakefield, the change in the transverse momentum is

$$\dot{Y}(k, n+1) = \dot{Y}(k, n) + \frac{Ne^2}{E} \sum_{m=1}^n \sum_{j=1}^M D(j) Y(j, m) W(s/c), \quad (2)$$

where the summation is carried out over the wakefield left behind for all the previous bunches and turns. The variable s can be written in terms of the space between bunches, S_B , as $s = (k-j)S_B + (n-m)MS_B$, where $(k-j)$ and $(n-m)M$ represent the relative bunch and turn numbers. N is the total number of protons in the bunch, e is the proton charge, $E = \gamma m_0 c^2$, c is the speed of light, m_0 is the rest mass of the particle, and $W(s/c)$ is the wake function defined as [2]

$$W(s/c) = \sum_{\lambda} A_{\lambda} \exp(-\alpha_{\lambda} s/c) \sin(\Omega_{\lambda} s/c), \quad (3)$$

if $s > 0$, and it is equal to zero otherwise. The variables A_{λ} , α_{λ} , and Ω_{λ} are defined as $A_{\lambda} = \omega_{\lambda}^2 R_{\lambda} / \Omega_{\lambda} Q_{\lambda}$, $\alpha_{\lambda} = \omega_{\lambda} / 2Q_{\lambda}$, and $\Omega_{\lambda} = \omega_{\lambda} \sqrt{1 - 1/4Q_{\lambda}^2}$, respectively. The summation is carried out over all the transverse HOM of the cavity. Each cavity-mode is characterized by the resonant angular frequency ω_{λ} , the shunt impedance R_{λ} , and the resonant quality factor Q_{λ} . The quantity $c/\alpha_{\lambda} S_B = 2Q_{\lambda} c / \omega_{\lambda} S_B$ gives us the number of bunches that the excited transverse HOM can affect before it decays by a factor of $1/e$. The factor $D(j)$, $0 \leq D(j) = N(j)/N \leq 1$, defines the distribution of bunches and the number of protons per bunch. The bunch is transported from the output to input of the RF cavity using the Courant-Snyder [3] map and together with the Eqs. (2) and (3) comprise the model for simulating transverse multibunch instabilities in the computer program TADIMMI.

A 358.9 MHz PEP cavity will be taken as the test cavity. At the RF location, the dispersion function is zero, and the Courant-Snyder parameters have the following values: $\beta = 112472.0$ mm, $\alpha = 0$, and $\mu = 2\pi \text{frac}(\nu) = 1.759292$. The characteristics of the bunches are $N = 7.5 \times 10^9$, $M =$

*Operated by the Universities Research Association, Inc., for the U.S. Department of Energy under Contract No. DE-AC35-89ER40486.

17424, $E = 2$ TeV, and $S_B = 5$ m.

The calculated growth time was 9 s per cavity. This simulation result for uniform distribution ($D(j) = 1$) is in very good agreement with the analytical approach (ZAP [4]). Studies show that damping several dangerous rf-HOMs of the cavity is not enough to avoid the instability. One way to control the multibunch instabilities rising from the HOM cavities is DE-Q these HOM. For the growth time to be higher than the injection time, the following De-Q quality factor, Q_d , for N_c cavities is deduced: $Q_d \leq 4.8 \times 10^6 \Omega \text{ m}^{-1} / \langle R_L/Q \rangle N_c$, where $\langle R_L/Q \rangle = 125 \Omega/\text{m}$, $N_c = 32$, and $Q_d \leq 1200$ for the PEP cavity model.

A single cell normal cavity with HOM-couplers or a single cell superconducting (sc) cavity with couplers [5] can satisfy this restriction to a large extent. Another way to control multibunch instabilities is to use an active system such as a feedback system [6]. The normal operation of the transverse feedback system is to have a beam position monitor (BPM) that measures the transverse displacement of the bunch. The signal is amplified and transmitted to the kicker (K), located downstream at a phase advance of $\pi/2$, which produces an angular deviation to the bunch given by [7]

$$\Delta Y = g (Y_{BPM} + \delta Y) / \sqrt{\beta_{BPM} \beta_K} \quad (4)$$

where g is the gain of the system, β_{BPM} and β_K are the beta function at the location of the BPM and the kicker, Y_{BPM} and δY are the displacement measured by the BPM and the error transmitted of this displacement (random variable with a Gaussian distribution). This error is called the resolution of the BPM and is due to the electronic noise in the system (white noise). Using the following values of the Collider west utility region $\beta_{BPM} = \beta_K \approx 420$ m, $g = 0.1$, $\delta Y = 10 \mu\text{m}$, and with the bandwidth (BW) of the feedback system assumed to be $BW \geq 30$ MHz, the damping of the dipole mode multibunch instability was verified with the simulations for the same-turn and one-turn delay correction schemes.

III. RESISTIVE WALL INSTABILITY

The resistive wall instability is important for angular frequencies, ω_k , close to the angular revolution frequency, ω_o ; i.e., $\omega_k = \omega_o(\Delta_\beta + k)$, where Δ_β is the fractional part of the tune of the machine such that $-1/2 < \Delta_\beta < 1/2$. Each k corresponds to one possible multibunch mode of oscillation. For lower modes and at the frequency ω_k , the real part of the transverse resistive wall impedance can be approximated by a resonant impedance, where the resonant frequency is ω_k , the shunt impedance is just $\text{Re}[Z_\perp(\omega_k)]$, and the quality factor Q_o can be selected to approximate the shape of the resistive wall impedance. Therefore, the problem is reduced to the previous multibunch instability due to an RF cavity, and the above program can be applied using this new resonator impedance. This is important since the explicit expression of the copper coated resistive

Table 1. Performance for $-1 + \Delta_\beta = -0.75$.

Feedback System	One BPM-One K	TBK
BPM Resolution $\delta Y (\mu\text{m})$	≤ 100	≤ 500
Gain (g)	≥ 0.30	≥ 0.03

wall wakefield is too complicated, and computations would require huge amounts of interactions among the bunches per each turn. Figure 1 shows the phase space generated by the bunches due to this instability. Figure 2 shows the comparison of the simulations with ZAP analytical code.

For the nominal Collider beam tube parameters, the growth time of the instability is 56 ms. To control this instability, a conventional one BPM-one K and a novel two BPM-two K (TBK), configured as B1-K1-B2-K2, feedback systems were used. The kick is given by Eq. (4), but instead of using Y_{BPM} , the p -turns average displacement of the bunches at the BPM,

$$\langle Y \rangle_p = \sum_{i=1}^{pM} Y_i^{BPM} / pM \quad (5)$$

was used. That is, each bunch receives p -times the same correction. This implies that the kicker flat-top time, ft , will be

$$ft = p(C/c) = p \times 2.904 \times 10^{-4} \text{ s} \quad (6)$$

The bandwidth of the feedback system is assumed to equal that defined by the batch-to-batch separation ($\sim 1.7 \mu\text{s}$), $BW \geq 0.3$ MHz. Table 1 summarizes the calculations for the two damper systems.

The copper and stainless steel thicknesses were taken as 0.1 mm and 1.0 mm. The kickers' flat-top was that with $p = 2$. Figure 3 shows the damping effect on average displacement of the bunches, as recorded by the BPM1, using the TBK damping system. The behavior of one particular bunch (number 1000) as seen by the BPM1 in the TBK damping system is shown in Figure 4.

IV. COMMENTS AND CONCLUSIONS

A computer program, TADIMMI, was developed [8] to study the dipole mode multibunch instability in the SSC Collider due to RF cavities. A resonant impedance approximation to the resistive wall impedance at low frequencies allows us to use the same code to study this instability. The design of the feedback system to control these instabilities was incorporated in the code. A two BPM- two K feedback system may be required to control the resistive wall instability since it has much better control of this instability than the conventional one BPM-one K. Study of the feedback system noise effect on the emittance growth is needed.

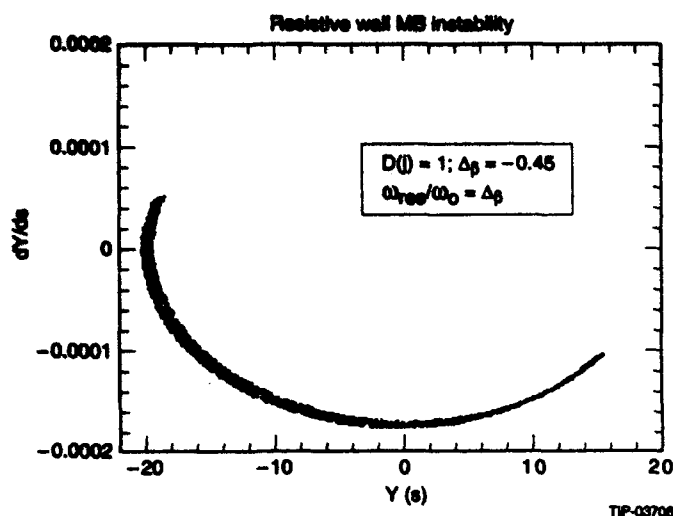


Figure 1. Bunch-generated phase space due to resistive-wall instability.

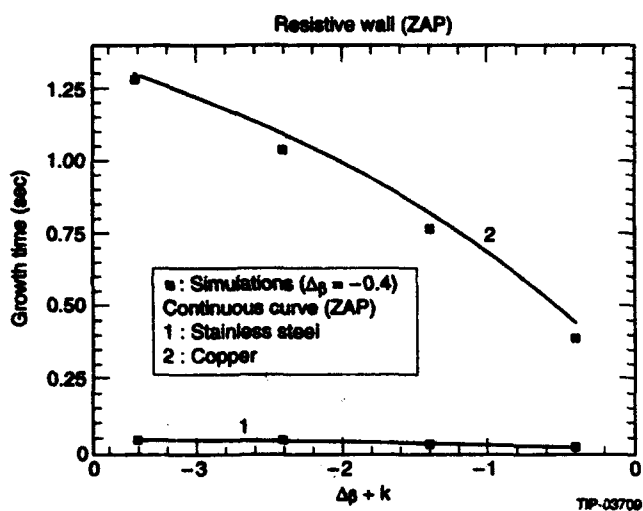


Figure 2. Comparison of simulations and analytical code.

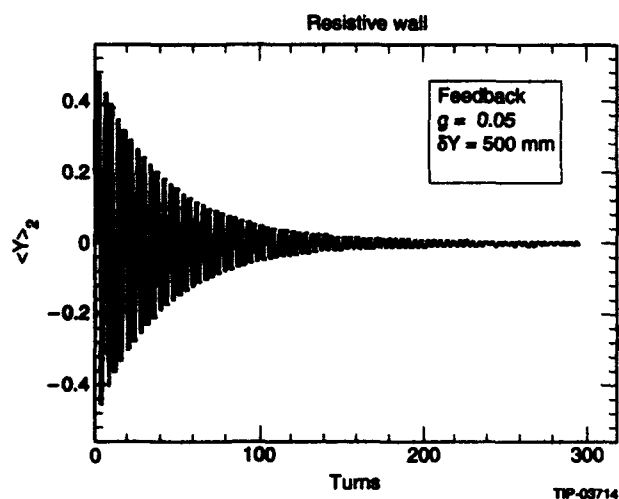


Figure 3. Average displacement in TBK damping system.

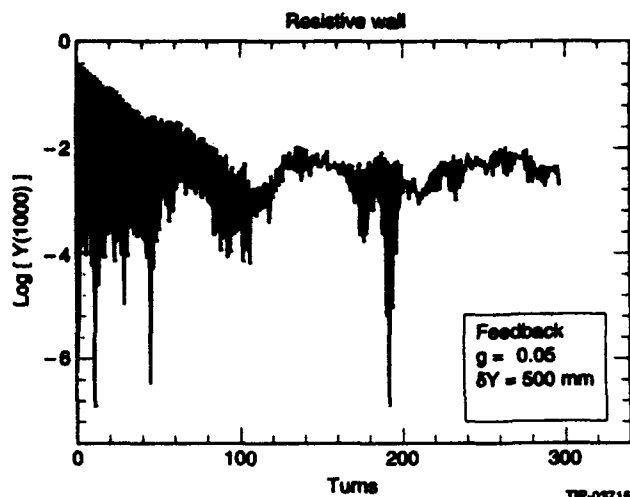


Figure 4. Bunch 1000 in TBK damping system.

V. ACKNOWLEDGEMENTS

We wish to thank Dr. A. Chao for many valuable discussions and suggestions, and Dr. R. Meinke, Dr. R. Gerig, and Dr. R. Schwitters for their support at the SSC.

VI. REFERENCES

- [1] SSCL-SR-1056, July 1990.
- [2] A. W. Chao, *Physics of Collective Beam Instabilities in High Energy Accelerators* (John Wiley & Sons, N. Y., 1993).
- [3] E. D. Courant and H. S. Snyder, *Ann. of Phys.* 3,1 (1958).
- [4] M. S. Zisman, S. Chattopadhyay, and J. J. Bisognano, "ZAP user's manual," LBL-21270 (1986).
- [5] CERN 91-03, section 8.3, May 1991.
- [6] S. van der Meer et al., *Phys. Report* 58, 2, 73 (1980). D. Heins et al., DESY 91-036, April 1991.
- [7] V.A. Lebedev et al., Novosibirsk 91-120, 1991.
- [8] S. Chen and G. López, SSCL-614 (1992).

HOM RF Cavity Dampers for Suppressing Coupled Bunch Instabilities in the Fermilab Booster

D. Wildman, Fermi National Accelerator Laboratory,* Batavia, IL 60510 and
K. Harkay, Purdue University, West Lafayette, IN 47907

Abstract

The coupled bunch mode $n=16$ longitudinal instability observed in the Fermilab Booster has been successfully damped by installing a set of passive higher-order mode (HOM) dampers in the 17 Booster RF cavities. The Booster is a fast cycling 8 GeV proton synchrotron with harmonic number 84. The dampers remove energy from two cavity modes at 165 and 217 MHz. The addition of these dampers to the RF cavities has reduced the longitudinal emittance of high current beams at extraction by a factor of 3. The mode dampers will be described along with beam spectra and data showing the longitudinal emittance reduction.

I. INTRODUCTION

Longitudinal coupled bunch oscillations of bunched beams are often observed in circular accelerators as beam intensities are increased.[1-3] Depending on the growth rate of these instabilities, the amplitude of the oscillations may become large and lead to longitudinal emittance growth due to the nonlinearity of the RF bucket. In the case of the Fermilab Booster, large coupled bunch oscillations are observed to occur after transition for bunch intensities greater than 1.5×10^{10} ppb.[4] The upper curve in Fig. 1 shows the longitudinal emittance growth through the Booster acceleration cycle without damping for an intensity of 2×10^{10} ppb. Values of longitudinal emittance were calculated from measured bunch lengths taken from a wideband resistive wall current monitor.

Coupled bunch oscillations can be stabilized by either increasing the spread in synchrotron frequencies, actively damping the longitudinal motion of each bunch, or reducing the impedances of the resonators responsible for the bunch to bunch coupling. In the case of the Fermilab Booster, the third method of reducing the coupling impedances was chosen because of its simplicity, low cost, and reliability. With this choice the problem could be simplified into three steps: 1) identifying the offending modes in the beam current spectrum, 2) finding the specific higher order RF cavity modes responsible for the coupling, and 3) building a set of HOM dampers to remove energy from the RF cavity higher order modes.

II. IDENTIFYING THE COUPLED BUNCH MODES

Using the same notation as Sacherer[5] for a narrow band resonator at a frequency, f_{res} , the coupled bunch mode number n is excited when:

$$f_{res} = \text{integer} \times M f_0 \pm n f_0$$

*Operated by Universities Research Association, Inc. under contract with the U.S. Department of Energy

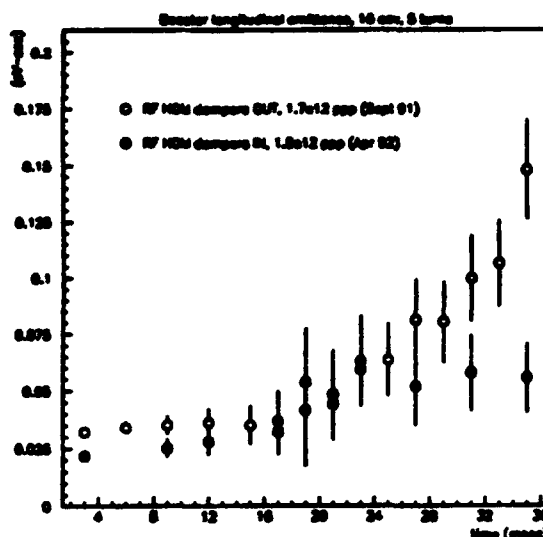


Figure 1. Longitudinal emittance (eV sec) as a function of time (ms) in the Booster cycle with and without HOM dampers.

Here f_0 is the Booster revolution frequency and M is the number of bunches which in our case is equal to the harmonic number $h=M=84$. Figures 2 and 3 show FFTs of the beam current signal taken from a wideband resistive wall monitor using a Tektronix DSA602 digital signal analyzer. The beam current was sampled at 35 ms into the Booster cycle when the coupled bunch oscillations were fully developed. The FFT shows the harmonics of the RF frequency separated by the 84 coupled bunch lines. The dominant coupled bunch mode lines are seen to occur at $n=16$ and $n=36$. The individual bunch motion is predominantly a dipole oscillation. FFT beam spectra taken at 2 ms intervals throughout the acceleration cycle show both the $n=16$ and $n=36$ mode structure appearing shortly after transition. The $n=16$ mode reaches a maximum amplitude at approximately 10 ms before extraction and remains constant or decreases slightly. The amplitude of the $n=36$ monotonically increases after transition reaching its maximum value at the extraction time.

III. HIGHER ORDER RF CAVITY MODES

The HOM of the RF cavities were suspected of providing the coupling between bunches since removing four of the RF cavities resulted in a decrease in the longitudinal emittance growth.[4] The Booster has a total of 17 double gap ferrite tuned cavities.[6] Each cavity consists of two back to back quarter wave coaxial transmission line sections. The electrical length between the two gaps is 140° at the fundamental frequency. The search for the RF cavity modes associated with the beam coupled bunch spectra began with a measurement of the resonant frequency f_{res} of each HOM. Since the fundamental frequency of the cavities $f_{rf}=hf_0$ must

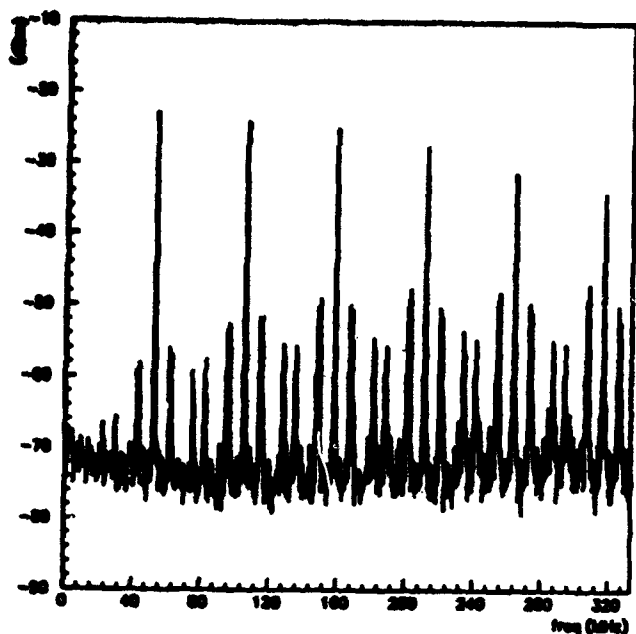


Figure 2. FFT of Booster beam current signal at 1.3×10^{12} ppp without HOM dampers.

sweep from 30 MHz to 52.8 MHz, the majority of the HOM's also tune during the acceleration cycle. The frequency measurements were made on a spare Booster cavity using an RF network analyzer. By varying the bias current to the ferrite tuners on the cavity the HOM spectrum could be measured as a function of the cavity fundamental frequency. This information was then used to calculate the mode number of each HOM as a function of time during the acceleration cycle. One cavity mode at 83 MHz did not tune with ferrite bias current. However, at the extraction energy this mode corresponds to a mode $n=36$.

$$f_{res} = 2 \times 84f_0 - 36f_0 = 83 \text{ MHz}$$

An examination of the tunable modes showed two that pass through mode $n=16$ after transition. The first mode tunes from 127 to 169 MHz while the second mode tunes from 202 to 221 MHz. In all three modes the two cavity gaps oscillate in phase. The impedances of these modes were measured on the test cavity using a standard stretched wire technique. The impedances measured were $Z=10k\Omega$ at 83 MHz, $Z=2.3k\Omega$ at 165 MHz, and $Z=16k\Omega$ at 217MHz.

A complete set of measurements were also made of the beam excitation of the HOMs for each of the 17 Booster RF cavities. A signal from a calibrated, capacitively-coupled, gap voltage monitor from each cavity was fed to the input of an HP8568B spectrum analyzer. Sweeping the spectrum analyzer from 100Hz to 400 MHz and using the maximum hold feature of the instrument, a beam-induced spectrum was obtained over a period of several hours. After the spectral peaks had been identified, the center frequency of the analyzer was set to the peak of each resonance in the zero span mode and triggered at the start of each Booster cycle. This produced a time record of the HOM excitation during the cycle. A typical example of this output for the 217 MHz mode is shown in Fig. 4. The amplitude is seen to reach a maximum

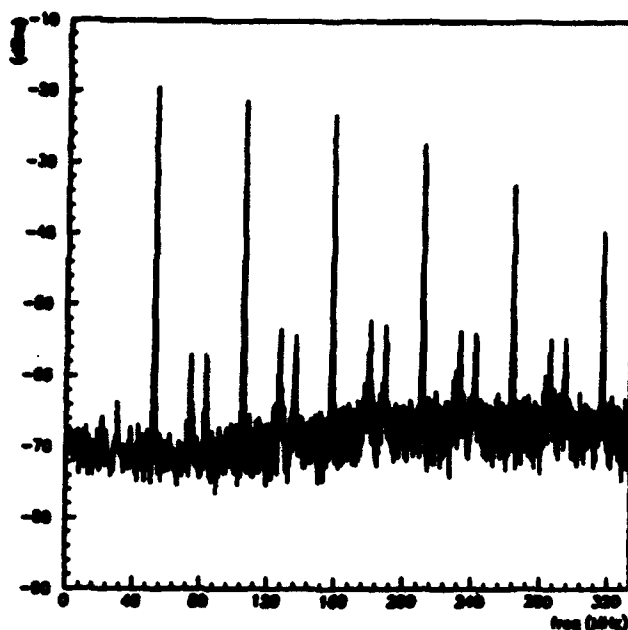


Figure 3. FFT of Booster beam current signal at 1.9×10^{12} ppp with HOM dampers installed.

shortly after transition and then decrease slightly. Data for the 165 MHz mode showed a similar behavior while the 83 MHz mode continually increased after transition. The agreement in the mode numbers between the FFT beam current data and the cavity gap monitor data, along with the same characteristic time dependence, led us to identify these three modes as being responsible for the coupled bunch instabilities.

IV. HOM DAMPERS

The frequency of the non-tunable mode at 83MHz is determined by the physical length of the cavity's drift tube. This mode along with another fixed frequency mode at 79 MHz were already being damped by two coupling loops terminated into 50Ω loads. To increase the damping at 83MHz the loop area was increased with a 0.5" copper spacer and a notch filter was inserted between the loop and the 50Ω

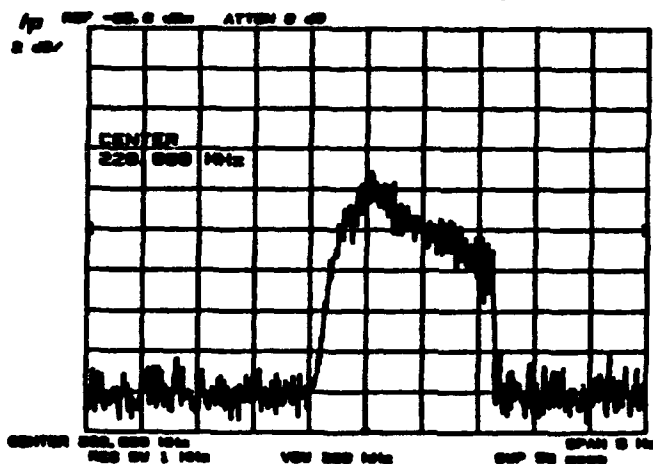


Figure 4. Spectrum analyzer output showing the excitation (2 dB/div) of the 217 MHz RF cavity mode as a function of time (5 ms/div).

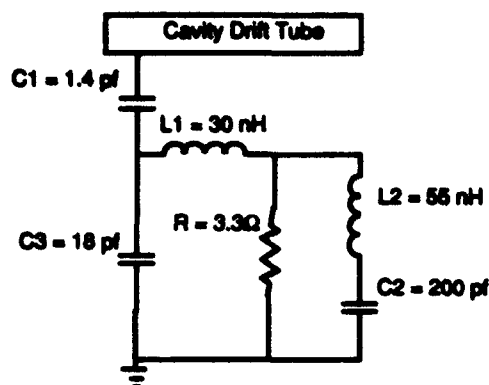


Figure 5. Electrical schematic of 217 MHz HOM damper.

load to reduce the additional power dissipated in the load at the fundamental frequency. This modification produced an additional 10 dB of damping at 83 MHz.

The mode dampers for the 165 and 217 MHz modes are similar in design and are installed on only one half of the cavity. They both consist of capacitively-coupled .125" thick x 6" long x 2"(3.5) wide OFHC copper flaps located at a voltage maximum for each mode. The flaps are curved to be concentric with the outer cavity wall and are supported by a 0.5" dia copper rod which is soldered to the center conductor of an HN type connector. The center pin of the HN connector unscrews from the connector body for easy installation of the damping flaps through the side wall of the cavity. The center pin also acts as the inductor L_1 shown in Fig 5. Outside of the cavity the damping flaps are connected to three 10 Ω , 40W low inductance resistors in parallel, R , and through a short length of .080" dia copper wire, L_2 , to two 100 pF transmitting capacitors, C_2 . L_2 and C_2 are adjusted to be series resonant at 48 MHz with a Q of approximately 25. The center value of 48 MHz was chosen to minimize the total integrated power, over the entire acceleration cycle, dissipated in the resistor R at the fundamental frequency. The entire external damping network is enclosed in a 2" x 3" x 5" shielded aluminum box with a 28 CFM all metal fan attached to the box top to provide extra cooling. Under normal Booster operating conditions the added cooling provided by the fan is not necessary; however, with the additional cooling, the dampers have been tested at the maximum Booster cycle rate of 15 Hz.

The 165 and 217 MHz dampers have a bandwidth of 15 MHz and reduce the HOMs by approximately 20 dB and 25 dB respectively. Fig. 3 is the beam current FFT spectrum taken with dampers installed in all 17 Booster RF cavities. The coupled bunch mode 16 line is no longer present. The reduction in the longitudinal emittance growth with the dampers in place is shown in the lower trace of Fig. 1.

ACKNOWLEDGMENTS

The authors would like to thank D. McGinnis for his help with the early time dependent FFT measurements and A. Heredia-Ocasio for her help in measuring the Booster cavity spectra.

V. REFERENCES

- [1] "Investigation and Cures of Longitudinal Instabilities of Bunched Beams in the ISR," P. Bramham, S. Hansen, A. Hofmann, K. Hübner and E. Peschardt. 9th Int'l Conf. on High Energy Accelerators, (Stanford, Calif., 1974) p. 359.
- [2] "Longitudinal Motion of the Beam in the Fermilab Booster," C. M. Ankenbrandt, J. E. Griffin, R. P. Johnson, J. Lackey, and K. Meisner. IEEE Trans Nucl. Sci. **NS-24** 1449 (1977).
- [3] "Longitudinal Instabilities in the Fermilab 400-GeV Main Accelerator," R.F. Stiening and J. E. Griffin. IEEE Trans. Nucl. Sci. **NS-22** 1859 (1975).
- [4] "Coupled Bunch Instability and Longitudinal Emittance Growth in the Fermilab Booster," V. Bharadwaj, J. Crisp, K. Harkay, J. Lackey, W. Merz, and S. Stahl, proc. 14th Int'l Conference on High Energy Accelerators, Tsukuba, Japan, 1989.
- [5] "A Longitudinal Stability Criterion for Bunched Beams," F. J. Sacherer. IEEE Proc. Nucl. Sci. **NS-20** 825 (1973).
- [6] "NAL Booster and Storage Ring RF Systems," J. A. Dinkel, Q. A. Kerns, L. A. Klaisner, and G. S. Tool. IEEE Trans Nucl. Sci. **NS-16** 510 (1969).

Longitudinal Instabilities in the MEB

John A. Palkovic
Superconducting Supercollider Laboratory *
2550 Beckleymeade Avenue
Dallas, TX 75237

Abstract

In this paper longitudinal instability parameters are calculated for the SSC Medium Energy Booster (MEB). Both single and multiple bunch instabilities are investigated. With a beam intensity of 1.0×10^{10} the longitudinal coupling impedance threshold, $|Z_{||}(\omega)/n|$, is found to be $\sim 60 \Omega$ at the injection momentum 12 GeV/c, and 12Ω at the ejection momentum, 200 GeV/c. Coupled bunch instability growth rates are calculated for the $\lambda/4$ cavity higher order mode (HOM) spectrum.

I. INTRODUCTION

The MEB is a 200 GeV proton synchrotron which is scheduled to be built at the Super Conducting Super Collider Laboratory (SSCL) with first beam in June, 1996. Some of the longitudinal parameters of the MEB are listed in Table 1. The MEB will deliver beam for colliding beam physics and test beam operations. [1]

First the physics of some of the single-bunch instabilities that can occur in the MEB will be discussed. These instabilities arise from the interaction of the beam with the broadband component of the longitudinal coupling impedance $Z_{||}(\omega)$, where ω is the angular frequency in rad/s. A discussion of the multiple bunch instabilities that occur in the MEB follows. A HOM of an accelerating cavity provides a longitudinal coupling impedance which can cause a multi-bunch instability or coupled bunch mode (CBM) if the beam current is above a threshold value. We have used ZAP [2] to calculate CBM growth rates and frequency shifts for the $\lambda/4$ cavity.

II. SINGLE BUNCH STABILITY

The one-dimensional Vlasov equation which describes the evolution of the longitudinal phase-space distribution is written [3, 5, 6]

$$\frac{\partial \psi}{\partial t} + \theta \frac{\partial \psi}{\partial \theta} + \delta \frac{\partial \psi}{\partial \delta} = 0, \quad (1)$$

where $\theta = 2\pi S/R$ is the angular position of the particle around the synchrotron, $\psi = \psi(\theta, \delta, t)$ is the longitudinal distribution function, $\delta = \Delta p/p$, and

$$\delta = -\frac{e\omega_0 I_1 Z_L(\omega)}{2\pi\beta^2 E} e^{i(n\theta - \Omega t)}$$

*Operated by Universities Research Association for the U.S. Department of Energy under Contract No. DE-AC35-89ER40486.

Table 1

MEB Parameters

Injection momentum	12 GeV/c
Extraction momentum	200 GeV/c
Circumference C	3960 m
Harmonic number	792
Momentum "compaction" α	1.85×10^{-3}
Transition γ	23.28
RF frequency at injection	59.776 MHz
RF frequency at extraction	59.958 MHz
95% bunch area, injection	0.04 eV-s
95% bunch area, extraction	0.1 eV-s
Minimum RF Voltage	170 kV
Maximum RF Voltage	1.6 MV
particles/bunch (collider mode)	1×10^{10}

is the term which describes the interaction of the particle distribution with the coupling impedance $Z_L(\omega)$, where Ω is the angular frequency of the perturbation in the lab. The revolution frequency of the synchronous particle is ω_0 , I_1 is the perturbation current, and E is the particle energy.

Using a perturbation analysis we can linearize the Vlasov equation and find the dispersion relation [5]

$$1 = -i \frac{e^2 \omega_0^2 Z_L}{2\pi\beta^2 E} \int \frac{(\partial \psi_0 / \partial \omega)}{\Omega - n\omega} d\omega. \quad (2)$$

The threshold for longitudinal stability is found by solving Eq. 2 with Ω having a small positive imaginary part, $\Omega = \Omega_r + i\epsilon$, $0 < \epsilon \ll 1$. We can evaluate the integral in Eq. 2, solve for the impedance Z_L , and map out the stability boundary in the impedance plane for a given distribution function ψ_0 . If the impedance lies inside the boundary, then any disturbance is damped, which is due to a phenomenon known as Landau damping. [4] In general, these stability boundaries have a somewhat complicated shape (Figure 1). However, the stable region can be conservatively approximated by a semi-circle, a result which we write as

$$\left| \frac{Z}{n} \right| \leq F \frac{\beta^2 E |\eta|}{e I_0} \left(\frac{\Delta p}{p} \right)^2, \quad (3)$$

where $F \approx 1$ is a "form factor" which depends on the radius of the approximating circle, and I_0 is the beam current. This is known as the Keil-Schnell criterion, although an equivalent formulation was published previously by Neil and Sessler. [6] Equation (3) was derived for a

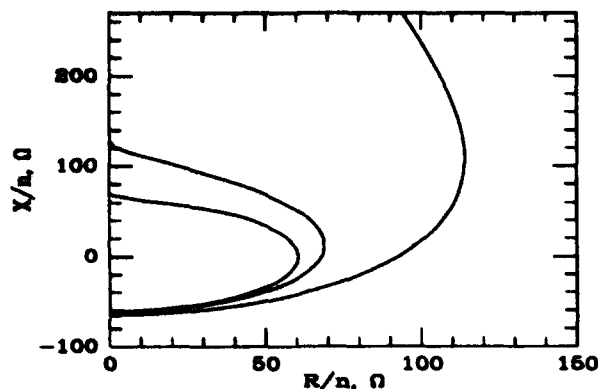


Figure 1. Stability diagrams for the MEB at injection. Positive X/n represents a capacitive impedance. The innermost curve is the boundary for a distribution $f \propto (1-x^2)^{1.5}$; the outermost is for a Gaussian; the intermediate curve is for a quartic, $f \propto (1-x^2)^2$, where x is the normalized rotation frequency.

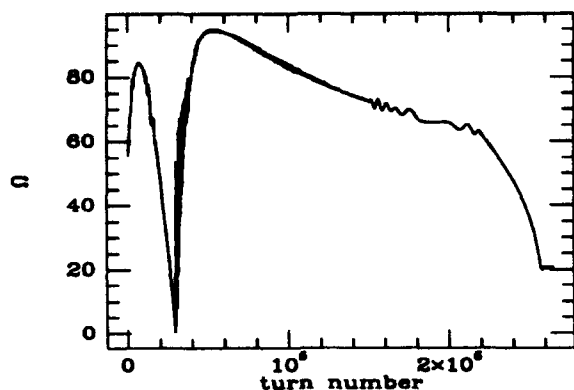


Figure 2. Plot of right hand side of Eq. (3) multiplied by 0.6 vs. turn number in the MEB. The dip in the curve occurs at transition.

coasting beam, but it can be applied to a bunched beam if the growth rate is fast compared to the frequency of synchrotron oscillations, and if the instability occurs at wavelengths short compared to a bunch wavelength. The parameter I_0 is then the peak current in the bunch.

ESME [7], a longitudinal phase-space tracking code, was used to calculate $\Delta p/p$ for an MEB by tracking 2×10^4 pseudo-particles with an amount of charge equivalent to 10^{10} protons/bunch. The ESME output was used to plot Eq. 3 (Figure 2). We see that at injection if, for example, the distribution is similar in shape to a quartic, the MEB bunch will be stable for values of the longitudinal coupling impedance $|Z/n| \leq 60\Omega$. Other than the time spent near transition crossing, it seems unlikely that we will cross the threshold for single-bunch stability, since we expect $|Z/n| \leq 2\Omega$ in the MEB. We will not discuss single-bunch stability at transition crossing.

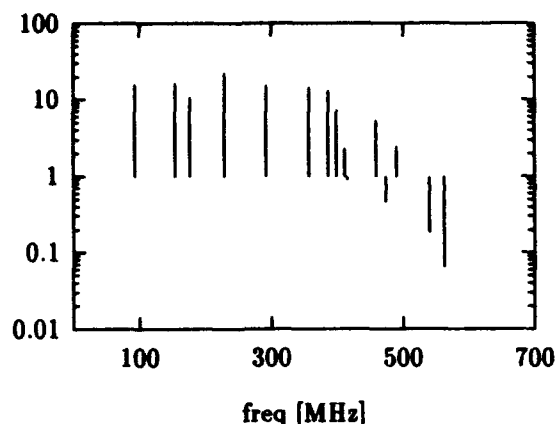


Figure 3. Coupled bunch instability growth rates in s^{-1} at the injection momentum (12 GeV) of the MEB.

III. MULTIPLE BUNCH STABILITY

In Sacherer's formalism [8], the complex frequency shift for coupled-bunch motion is described by

$$\Delta\omega_{m,n} = i\omega_s \left(\frac{m}{m+1} \right) \frac{I}{3B_0^2 h V \cos\phi_s} \sum_p F_m(f_p \tau) \frac{Z_L(f_p)}{p} \quad (4)$$

where

$$F_m(f_p \tau) = \frac{1}{MB_0} \frac{|\tilde{\lambda}_m(p)|^2}{\sum_p |\tilde{\lambda}_m(p)|^2} \quad (5)$$

is another form factor which weights the contributions from the coupling impedance $Z_L(f_p)$. The Fourier transform of the perturbed line density is denoted by $\tilde{\lambda}_m(p)$, ω_s is the synchrotron frequency, m is the synchrotron mode number, B_0 is the bunch length τ_L /the revolution period T , ϕ_s is the synchronous phase angle which is positive below transition and negative above, and

$$f_p = (n + pM)f_0 + mf_s, \quad -\infty < p < +\infty. \quad (6)$$

M is the number of bunches, which are assumed to populate the ring in a symmetric fashion.

ZAP [2], which implements Eq. 4, was used to calculate coupled-bunch instability growth rates for the MEB. The calculation assumes that the bunches have a Gaussian profile in momentum, that the ring is filled with $792 = h$ bunches, and that the beam has an intensity of 10^{10} protons/bunch. The HOM input data was generated with MAFIA, a 3d particle-in-cell code (Table 2). Measured data on a prototype cavity would be preferable, but there is no prototype RF cavity for the MEB as of this writing. The results are plotted in Figures 3 and 4. We see there are many modes with growth rate $> 1s^{-1}$.

Table 2
HOM data for MEB $\lambda/4$ cavity

Frequency MHz	shunt imp. R_s $k\Omega$	quality factor Q
59.8	629	12300
93.0	13	9500
154.7	14	6700
176.5	34	13600
229.2	48	15600
292.3	70	22000
357.1	49	24400
386.5	33	9800
399.3	23	10300
415.6	9	22700
459.3	103	23500
411.6	22	22300
473.4	3	22100
490.2	208	25000
540.1	12	15200
561.8	5	10200

In normal operation, the MEB will be filled with 6 LEB batches approximately once every 8 seconds. The beam will orbit the MEB for ~ 4 seconds. We choose to limit the multi-bunch integrated growth to 4 e-foldings. Hence, we would like for the growth rate $1/\tau$ to be $< 1s^{-1}$. The rates calculated with ZAP almost all exceed this criterion. Therefore the modes must be damped in order to limit the growth. An approximate formula for the growth rate (useful for estimates) due to any particular HOM is

$$\frac{1}{\tau} \sim \frac{\omega_p p}{2 h V \cos \phi_s} \frac{I_0 R}{V \cos \phi_s} \quad (7)$$

The growth rate is proportional to R , the shunt impedance of the HOM. For a given HOM that has $1/\tau > 1s^{-1}$, we can limit the beam to 4 e-foldings (1 e-folding/s) if we damp the mode by a factor equal to the growth rate in the MEB. In fact, we may not need to damp this much, since the Landau stability threshold could be crossed. A given CBM will be Landau damped if $|\Delta\omega_{m,n}| \leq m/2 \cdot (m+1)S$, where

$$S = \frac{1}{8} \left(\frac{\sigma_z}{R} \right)^2 h^2 \omega_s \quad (8)$$

is the synchrotron frequency spread within the bunch. [2] For the MEB at injection, we find $S \simeq 15Hz$ and

$$|\Delta f| = \frac{1}{2\pi} |\Delta\omega_{m,n}| \leq S/8\pi \simeq 0.6Hz. \quad (9)$$

is the condition for Landau damping. However, we require $Im(\omega_{m,n}) \leq 1s^{-1}$ to limit the CBM to 4 e-foldings in the MEB. So there is no need to damp the HOM to the Landau threshold at the injection momentum. At extraction, with $\sigma_z \sim 10cm$ we find $S = 0.4 Hz$, so the Landau damping threshold is correspondingly smaller and the same damping criterion applies. If the beam intensity is increased to

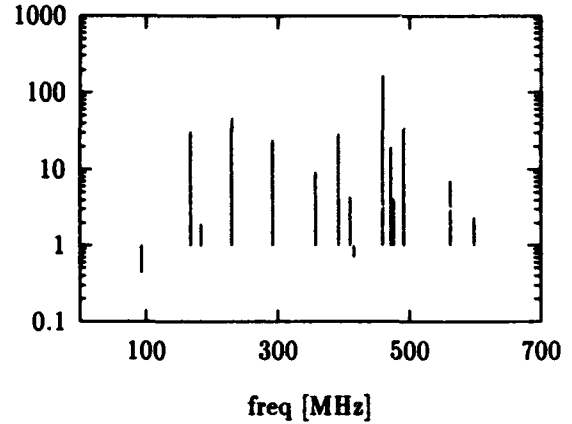


Figure 4. Coupled bunch instability growth rates in s^{-1} at the extraction momentum (200 GeV) of the MEB.

5×10^{10} protons/bunch, then it will be necessary to damp the HOMs by another factor of five; if this is not possible, an active damping system may be required.

IV. ACKNOWLEDGEMENTS

I wish to thank Tai-Sen Wang for the computer program used to calculate single-bunch stability threshold curves, and Slawomir Kwiatkowski for providing the HOM data for the coupled-bunch calculations.

V. REFERENCES

- [1] J.R. Sanford and D.M. Matthews. Site-specific conceptual design report of the superconducting super collider. Technical Report SSCL-SR-1056, Superconducting Super Collider Laboratory, July 1990.
- [2] M.S. Zisman et al. "Zap User's Manual." Lawrence Berkeley Laboratory, December 1986.
- [3] N.A. Krall and A.W. Trivelpiece. *Principles of Plasma Physics*. San Francisco Press (1986).
- [4] L.D. Landau. "On the vibrations of the electronic plasma." *J. Phys. U.S.S.R.* 10:25, (1946).
- [5] D.A. Edwards and M.J. Syphers. *An introduction to the physics of high energy accelerators*. Wiley-Interscience, New York, NY (1993).
- [6] V. Kelvin Neil and Andrew M. Sessler. "Longitudinal resistive instabilities of intense coasting beams in particle accelerators." *Rev. Sci. Instr.* 36(4):429, (1965).
- [7] J. MacLachlan S. Stahl. User's guide to esme. TM 1650, Fermilab, 1990.
- [8] F.J. Sacherer. "Bunch lengthening and microwave instability." *IEEE Transactions on Nuclear Science* NS-24(3), (1977).

A New Formulation of Longitudinal Coherent Instabilities *

S.Y. Zhang and W.T. Weng

AGS Department, Brookhaven National Laboratory
Upton, New York 11973

Abstract - The quadrature response of longitudinal impedance is shown to be the effective impedance for the beam instability. The results of the application of this formulation are compared with that obtained using the Robinson-Pedersen approach and the Sacherer integral equation. The formulation is further generalized to the rigid bunch motion using signal analysis method, where a form factor shows up naturally. Finally, the formulation is applied to solve the coupled bunch instabilities. Examples of the AGS Booster and the AGS coupled bunch instabilities are used to illustrate the applications of the formulation.

I. The New Formulation

In the longitudinal motion, a synchrotron oscillation is modulated by the RF carrier. The beam current induced voltage through the longitudinal impedance may affect the synchrotron oscillation and cause the beam instability.

A. Beam Dynamic Model

A beam dynamic model is shown in Fig.1, where s is the Laplace operator, ω_0 and ω_{RF} are the revolution and RF frequencies, respectively. ΔV_B is the equivalent RF gap voltage deviation caused by the beam motion, and ΔV_{CAV} caused by the cavity voltage variation. I_B is the beam current amplitude of the fundamental frequency, i.e., the RF frequency. Finally, $Z_M(s)$ represents the effective longitudinal impedance with respect to the beam instability. In the block diagram, the upper loop represents the synchrotron oscillation, as shown in [1]. The lower loop represents the effects of the beam current to the cavity voltage through the longitudinal impedance.

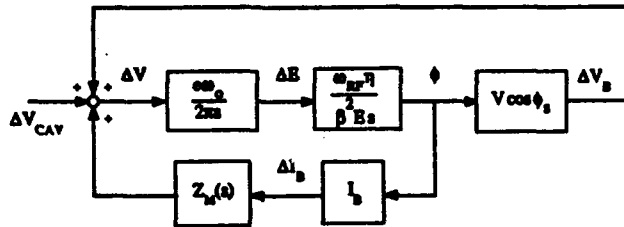


Fig.1. Beam Dynamic Model

B. Impedance

We use both Laplace and Fourier transforms. For instance, an impedance in the Laplace form can be $Z(s+j\omega_{RF})$, and its counterpart in the Fourier form is written as $Z(\omega+\omega_{RF})$. Consider a general situation of the modulated input and output. Let the input signal of a system be $f(t)$ and the output be $g(t)$. The input signal is assumed to be a low frequency signal $f_L(t)$ modulated by an RF carrier, say $\cos\omega_{RF}t$, i.e., we can write, $f(t) = f_L(t) \cos\omega_{RF}t$. Using $f(t) \rightarrow F(\omega)$ and $f_L(t) \rightarrow F_L(\omega)$ to denote the Fourier

pairs, we have,

$$F(\omega) = \frac{1}{2} (F_L(\omega+\omega_{RF}) + F_L(\omega-\omega_{RF})) \quad (1)$$

Also for $f_1(t) = f_L(t) \sin\omega_{RF}t$, we have,

$$F_1(\omega) = \frac{1}{2j} (F_L(\omega+\omega_{RF}) - F_L(\omega-\omega_{RF})) \quad (2)$$

Under the modulation of the frequency ω_{RF} , the in-phase and quadrature responses of the impedance $Z(\omega)$ are determined by [2],

$$Z_P(\omega) = \frac{1}{2} (Z(\omega+\omega_{RF}) + Z(\omega-\omega_{RF})), \quad (3)$$

$$Z_Q(\omega) = \frac{1}{2j} (Z(\omega+\omega_{RF}) - Z(\omega-\omega_{RF})) \quad (4)$$

respectively. We also define $G_P(\omega) = F_L(\omega)Z_P(\omega)$ and $G_Q(\omega) = F_L(\omega)Z_Q(\omega)$. Using $g_P(t) \rightarrow G_P(\omega)$ and $g_Q(t) \rightarrow G_Q(\omega)$ for Fourier pairs, the total response of the modulated signal $F(\omega)$ in (1) through the impedance $Z(\omega)$ is,

$$g(t) = g_P(t) \cos\omega_{RF}t + g_Q(t) \sin\omega_{RF}t \quad (5)$$

Using (1-4), the equation (5) can be shown to be,

$$G(\omega) = F(\omega)Z(\omega) \quad (6)$$

therefore (5) is proved. When the beam passes the cavity gap, the in-phase response due to the cavity impedance, which is modulated by $\cos\omega_{RF}t$, provides an almost constant force in the beam synchrotron oscillation, which has little effect on the beam instability. On the other hand, since the quadrature response is modulated by $\sin\omega_{RF}t$ it is in the same fashion as that of the RF driving wave and functions as the same as the RF driving wave. Therefore, if the instability of synchrotron oscillation is concerned, the quadrature response represented by (4) becomes a dominant effect. Thus the effective longitudinal impedance is,

$$Z_M(s) = Z_Q(s) = \frac{1}{2j} (Z(s+j\omega_{RF}) - Z(s-j\omega_{RF})) \quad (7)$$

Consider an RF cavity with the resonant frequency ω_R , the shunt resistance R , the half-bandwidth σ , and the quality factor Q . Under the conditions of $Q \gg 1$, $\omega_{RF} \approx \omega_R \gg \omega \approx \omega_S$, and also $|\omega_R^2 - \omega_{RF}^2| \gg |s^2| = \omega^2$, the longitudinal impedance of the RF cavity is,

$$Z_M(s) = \frac{-R\sigma^2 \tan\phi_Z}{s^2 + 2\sigma s + \sigma^2(1 + \tan^2\phi_Z)} \quad (8)$$

where the detuning angle $\phi_Z = \tan^{-1}((\omega_{RF} - \omega_R)/\sigma)$.

C. Stability

To study the beam stability under the influence of the longitudinal impedance of RF cavity, we can write the following equation from Fig.1,

$$\phi = \frac{e\omega_0\omega_{RF}\eta V \cos\phi_S}{2\pi\beta^2 E s^2} \phi + \frac{e\omega_0\omega_{RF}\eta}{2\pi\beta^2 E s^2} Z_M(s) I_B \phi \quad (9)$$

* Work performed under the auspices of the U.S. Department of Energy

Using $\omega_s^2 = -e\omega_0\omega_{RF}\eta V \cos\phi_s / (2\pi\beta^2 E)$ and the beam and generator current ratio $Y = I_B/I_{G0} = I_B R/V$, the characteristic equation of the system becomes,

$$s^2 + \omega_s^2 = \frac{\omega_s^2 Y \sigma^2 \tan\phi_s / \cos\phi_s}{s^2 + 2\sigma s + \sigma^2(1 + \tan^2\phi_s)} \quad (10)$$

Using Routh-Hurwitz table, it is straightforward to find the stability conditions as $\tan\phi_s > 0$ and $Y \tan\phi_s \cos^2\phi_s < \cos\phi_s$, which are called the first and second Robinson criteria, respectively.

In deriving the transfer function $Z_M(s)$ in Fig. 1, the in-phase and quadrature transfer functions $Z_P(s)$ and $Z_Q(s)$ are used. In the Robinson - Pedersen approach [3], the beam to cavity phase and amplitude transmissions and their cross transmissions $Z_{PP}(s)$, $Z_{QQ}(s)$, and $Z_{PQ}(s)$ are used to derive the total equivalent transmission from the beam phase variation to the induced cavity voltage phase deviation. In Fig. 2, typical step responses of the transfer functions are plotted, which show the difference between the two types of the transfer functions, and the two approaches as well.

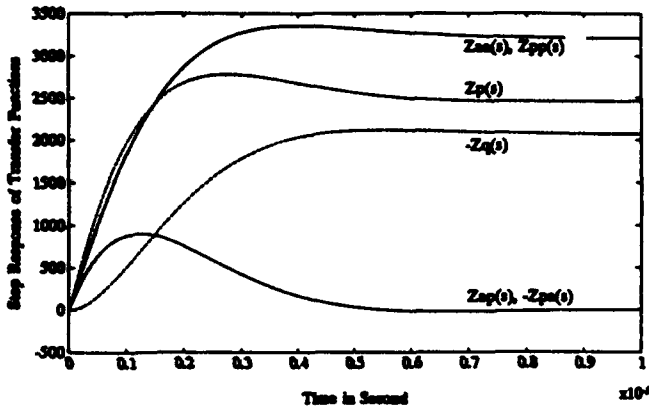


Fig. 2. Step Responses for the Transfer Functions.

Using Sacherer integral equation [4] for the dipole motion, we get the following equation,

$$s^2 + \omega_s^2 = \frac{8\pi\omega_s^2 I_0}{V \cos\phi_s} \left(\int_0^\infty J_1^2(r) \frac{d\psi_0}{dr} dr \right) Z_M(s) \quad (11)$$

where I_0 is the beam average current, ψ_0 is the bunch stationary distribution, and r is the amplitude of the beam phase oscillation. Substituting (8), the equation (11) is shown to be equivalent to (10), except for a scaling difference.

II. Generalize the Formulation

To generalize the formulation to the rigid bunch motion, the beam current signal needs to be analyzed. For each frequency component in the signal, the corresponding effective impedance can be found, which needs only a trivial modification from the results shown in Section I. The summation of the effects of the impedance due to each component in the signal is the force the beam received.

A. Signal of rigid bunch motion

Let T_{RF} be the RF period, $T_{RF} = 2\pi/\omega_{RF}$, a beam longitudinal current signal with N particles in a bunch is,

$$i(t) = Ne \sum_{k=-\infty}^{\infty} \delta(t - kT_{RF} + \tau \cos\omega_s k T_{RF}) \quad (12)$$

where τ is the synchrotron oscillation amplitude in time. The spectrum of this signal is calculated as [1],

$$I(\omega) = 2\pi I_0 \sum_{p,m=-\infty}^{\infty} j^m J_m(\omega\tau) \delta(\omega - p\omega_{RF} - m\omega_s) \quad (13)$$

We further assume that the bunches have a Gaussian distribution, which is chosen for convenience, and with an effective bunch length τ_L . Using the phase oscillation amplitude $\tau = \omega_{RF}\tau$ the equation (13) becomes [1],

$$I(\omega) = 2\pi I_0 \sum_{p,m=-\infty}^{\infty} j^m J_m(\tau\omega/\omega_{RF}) \times e^{-(\tau_L\omega/\omega_{RF})^2/32} \delta(\omega - p\omega_{RF} - m\omega_s) \quad (14)$$

B. Generalization

To compare the rigid bunch signal represented by (14) with the idealized signal, we may write the signal used to develop the formulation in Section I as $i_1(t) = I_B r \cos\omega_s t \sin\omega_{RF} t$, whose spectrum is,

$$I_1(\omega) = 2\pi I_B \frac{r}{4j} \sum_{p,m=-1}^{\infty} (-p) \delta(\omega - p\omega_{RF} - m\omega_s) \quad (15)$$

The first difference between the real rigid bunch motion signal represented by (14) and the idealized signal (15) is that (14) contains not only RF frequency modulation but also RF harmonics modulation, i.e., by the frequencies $p\omega_{RF}$, $|p| > 1$. It is shown [1] that $Z_M(\omega) = Z_Q(\omega)$ is valid not only for the RF frequency modulation, but also for the RF harmonic modulation. For the carrier with the frequency $p\omega_{RF}$, the variable ω_{RF} in (4) should however be replaced by $p\omega_{RF}$. In the system synthesis, firstly these frequency components in the rigid bunch motion signal should be identified, then the corresponding longitudinal impedances should be used to find the induced forces. The combined force is the one the beam received.

The second difference of (14) from (15) is that it contains not only dipole motion but also high mode motion, i.e., $m\omega_s$, $|m| > 1$.

The third difference is that in (14), the spectrum amplitude is affected by the Bessel function, the bunch distribution and the bunch length. The combined influence of these factors can be called a form factor.

C. Form factor

Consider the most important case of dipole motion with RF frequency modulation, where $p = \pm 1$ and $m = \pm 1$. We write (14) as,

$$I(\omega) = 8\pi I_0 J_1(r|\omega|/\omega_{RF}) e^{-(\tau_L\omega/\omega_{RF})^2/32} \times \frac{1}{4j} \sum_{p,m=\pm 1} (-p) \delta(\omega - p\omega_{RF} - m\omega_s) \quad (16)$$

For the delta distribution, $I_B = 2I_0$, the form factor can be written as,

$$F = \frac{I(\omega)}{I_1(\omega)} = \frac{2J_1(r|\omega|/\omega_{RF})}{r} e^{-(\tau_L\omega/\omega_{RF})^2/32} \approx \frac{2J_1(r)}{r} e^{-(\tau_L\omega/\omega_{RF})^2/32} \quad (17)$$

where in the simplification we used $|\omega| \approx \omega_{RF}$.

Consider the longitudinal dipole motion discussed in Section I again. The form factor F in (17) has to be multiplied to the scaling I_B in Fig. 1, and therefore also to $Y = I_B R/V$ in (10). Thus, $Y_1 = FY$ will replace Y in the second stability equation. Since $F < 1$, the stability margin is extended.

III. Coupled Bunch Instabilities

A. Coupled bunch motion

Let there be k bunches, and let n be the coupled bunch mode number. There will be $n = 0, 1, \dots, k-1$ coupled bunch modes [4]. The spectrum of the signal observed from the wall monitor becomes,

$$I(\omega) = 2\pi I_0 \sum_{p,m=-\infty}^{\infty} j^m J_m(r\omega/\omega_{RF}) \times e^{-(r_L\omega/\omega_{RF})^2/32} \delta(\omega - p\omega_{RF} - n\omega_0 - m\omega_S) \quad (18)$$

The coupled bunch mode of $n\omega_0$ can be assumed to be a rigid wave. For an individual bunch, the modulation effect of the beam current signal due to the coupled bunch mode is demodulated. By the same argument as in Section I, the quadrature response represents the effective longitudinal impedance. Therefore we have the following longitudinal impedance,

$$Z_M(\omega) = \frac{1}{2j} (Z(\omega + n\omega_0 + \omega_{RF}) - Z(\omega + n\omega_0 - \omega_{RF})) \quad (19)$$

B. Coupled bunch instabilities

If $n \neq 0$, then the two spectrum lines of the same frequency modulation may be far apart, therefore in general the treatment for the resonator type impedance such as that in Section I cannot be applied, and the spectrum lines may have to be treated separately. Consider the dipole upper sideband at $Z(\omega + \omega_0 + \omega_{RF})$ in (19), and let the real part of the impedance be R_1 . Using $s = j\omega \approx j\omega_S$, the stability equation can be written as,

$$s^2 + \omega_S^2 = \frac{\omega_S^2 I_B F}{2jV \cos\phi_S} Z(\omega + \omega_0 + \omega_{RF}) \approx \frac{-\omega_S I_B F R_1}{2V \cos\phi_S} s \quad (20)$$

Below transition $\cos\phi_S > 0$, therefore the upper sideband is stable because that the coefficient of s is negative. It follows that the lower sideband at $Z(\omega + \omega_0 - \omega_{RF})$, which has a negative sign in (19), is unstable, and the opposite above transition.

It is interesting to revisit the form factor derived in Section II. We rewrite it as,

$$F = \frac{2J_1(r|\omega|/\omega_{RF})}{r} e^{-(r_L\omega/\omega_{RF})^2/32} \quad (21)$$

The simplification of the form factor in (17) cannot be made in the case of the coupled bunch mode, since now $|\omega|$ is not close to ω_{RF} if $n \neq 0$, and both variables have to be considered in the Bessel function. For high frequency, the influence of r shows up, which is shown in Fig.3.

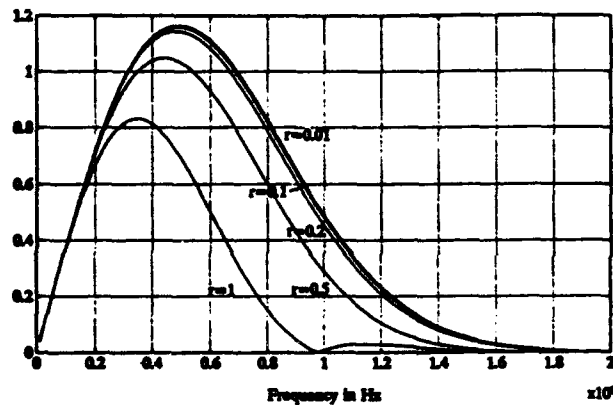


Fig.3. Form Factors with Different r .

In a small range of r , for instance between 0.01 to 0.2 in Fig.3, the form factors are approximately the same. This shows the reason why we can assume that the coupled bunch mode is a rigid wave in the instability study.

C. Examples of the AGS Booster and the AGS

A coupled bunch instability has been excited in the AGS booster by tuning a test RF cavity [5]. In the booster k is 3, and f_{RF} was 2.55 MHz. In the test, the coupled bunch instability of a dipole mode was observed at the first revolution line, i.e., at 850 KHz, which implies that $n = 2$. We have $I_0 = 0.062$ A, $\phi_S = 0$, and $V = 30$ KV, and $r_L = 130$ nS. The RF cavity used to excite the coupled bunch motion has approximately a quality factor 2.5 and a shunt resistance 3 K Ω , it was tuned at the revolution frequency in the test. To estimate the effective resistance FR_1 , the form factor in (21) is used, where the Gaussian distribution is still used allowing minor errors. The effective resistance of the test cavity is found to be 1 K Ω at 850 KHz. The growth rate calculated using (20) is 27.7 mS, which is close to the test result of 30 mS.

In an AGS operation, a coupled bunch instability was observed at the 1.77 GeV front porch, with $f_{RF} = 4.18$ MHz, and $n = 11$ ($k = 12$). To find the location of frequency of the exciting resonator, two tests were performed, with r_L are 46 nS and 70 nS, I_0 are 0.089 A and 0.457 A, V are 260 KV and 184 KV, and f_S are 1.64 KHz and 1.38 KHz, respectively. The observed growth rates are 48 mS and 24 mS, respectively. Using a moderate $r = 0.1r_L$, the resistance required to generate the observed growth rates are plotted in Fig.4, which shows that at 17.6 MHz the required resistances are crossed. The closest unstable coupled bunch mode frequency is at 17.1 MHz, therefore Fig.4 shows a possible location of the exciting resonator. This result agrees to the one obtained by different approaches [6].

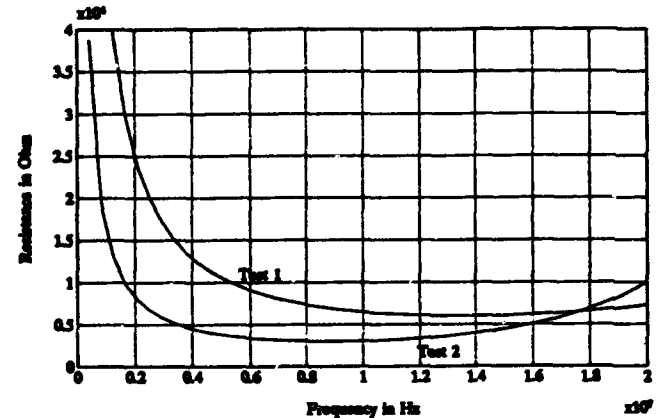


Fig.4. Resistances to Excite the Growth Rates.

Acknowledgment

The authors would like to thank A. Chao, E.C. Raka, and A.M. Sessler for helpful discussions.

References

- [1] S.Y. Zhang and W.T. Weng, BNL Informal Report, No.48905, May, 1993.
- [2] A. Paupolis, 'The Fourier Integral and Its Applications,' New York, McGraw-Hill, 1962.
- [3] F. Pedersen, IEEE Trans. NS-22, 1906, 1975.
- [4] F. Sacherer, IEEE Trans. NS-24, 1393, 1977.
- [5] M. Blaskiewicz, Private communication.
- [6] E.C. Raka, Private communication.

Three-Dimensional Simulations for Accelerator Physics Using ARGUS*

A. Mondelli, A. Mankofsky, J. Petillo, W. Krueger, C. Kostas, and A. Drobot

Science Applications International Corporation, McLean, VA 22102

and

R. Ryne, R.K. Cooper, G. Rodenz, and M.J. Browman

Los Alamos National Laboratory, Los Alamos, NM 87545

Abstract

ARGUS is a three-dimensional, electromagnetic, particle-in-cell (PIC) simulation code that uses a modular code architecture to allow multiple physics modules to share common utilities for grid and structure setup, memory management, disk I/O, differential vector field operators, and diagnostics. The code includes modules for electrostatic and electromagnetic field solutions, electromagnetic eigenvalue problems, and PIC simulation in either a steady-state or a time-dependent algorithm. SAIC and LANL (Accelerator Code Group) are collaborating to release ARGUS to the U.S. accelerator community. The code is available, with documentation, both at LANL and at NERSC (LLNL). Applications of ARGUS to waveguide and cavity problems and wake-field calculations are presented.

I. DESCRIPTION OF ARGUS

The ARGUS code [1], [2] has been under development at SAIC since 1983. The code architecture is designed specifically to handle the problems associated with three-dimensional electromagnetic, PIC simulations. It uses sophisticated memory management and data handling techniques [3] to deal with the large volume of data that is generated in such simulations.

A modular architecture is employed so that all physics modules share code utilities in common. Complicated geometrical structures can be represented on the computational grid, and the grid can be non-uniform in all three directions. Cartesian and cylindrical coordinate systems have been implemented throughout ARGUS. Physics modules are in place to compute electrostatic and electromagnetic fields, the eigenmodes of rf structures, and PIC simulation in either a time-dependent mode or a steady-state (gun code) mode. The PIC modules include multiple particle species, relativistic particle dynamics, and algorithms for creation of particles by emission from material surfaces and by injection onto the grid. A plasma chemistry module allows species to be created or destroyed based on specified rate processes.

Structure input in ARGUS is carried out using combinatorial geometry. The code stores a library of simple solid objects (e.g., a rectangular solid, an elliptical cylinder, an el-

lipsoid, etc.). These objects are combined by the user with logical operations (to either *add* or *delete* the library object) to produce objects of arbitrary shape. The structures so specified are represented on the computational grid by a *structure mask* array, which stores the material and electrical properties of each cell on the grid.

Material properties are associated with structures. The code allows perfectly conducting materials, as well as materials with complex values of both permittivity and permeability; hence lossy materials are allowed. Furthermore, the permittivity and permeability are specified as diagonal tensors to treat certain classes of non-isotropic materials.

ARGUS offers a wide variety of diagnostic plots that are selected by the user and are available at run time. In addition, the user can generate HDF files for exporting data to external visualization tools.

Version 25 of ARGUS is now available, with user support, through the Los Alamos Accelerator Code Group. This paper describes some examples from the ARGUS Primer, which is part of the ARGUS documentation.

II. TOMBSTONE CAVITY

A. Cold Test of the "Tombstone" Cavity

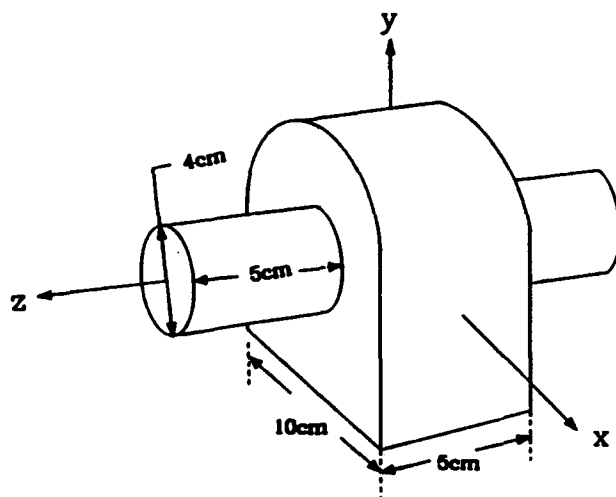


Figure 1. The "Tombstone" Cavity

* Work supported by the Department of Energy under contract number DE-AC05-91ER40625.

An example in the MAFIA User's Guide consists of analyzing the normal modes of the structure shown in Figure 1. The structure is a cylindrical drift tube attached to a cavity made of a rectangular box topped with a half cylinder. MAFIA and ARGUS represent this structure in different ways. ARGUS uses a "stairstep" representation on the grid, while MAFIA allows triangular "half cells".

A comparison of MAFIA and ARGUS cold-test results for the "Tombstone" cavity is given in Figure 2. The ten lowest modes of the structure were computed. The discrepancy is generally in the 1-2% range, and is due to the differences in the structure representation by the two codes. This result is consistent with other comparisons of these codes on comparable meshes. With finer meshing, the codes agree more closely.

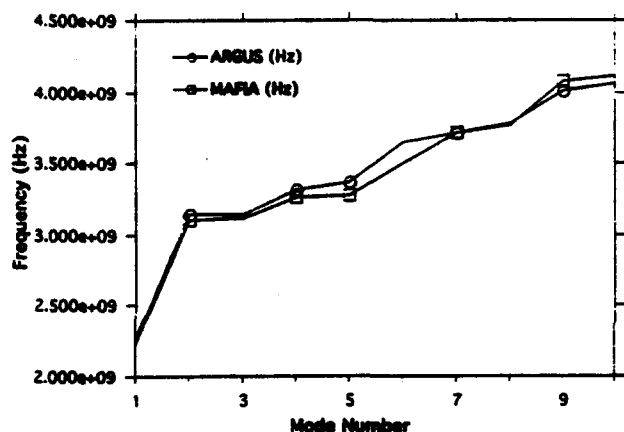


Figure 2. Comparison of ARGUS and MAFIA results for "Tombstone" cavity cold test.

B. Wake Fields in the "Tombstone" Cavity

The time-dependent PIC module in ARGUS can be used to compute wake fields by initializing a Gaussian bunch of heavy particles and allowing them to drift through the structure. This method has been employed to display the wake fields in the "Tombstone" cavity. Figure 3 shows three snapshots of the particles and axial electric field as the bunch traverses the structure. The Gaussian bunch is located on the axis of the cylindrical drift tube and launched into the cavity. The particles are visible in the figure as a line charge on axis. In the first frame, at time step 25, the particles are just entering the cavity from the lower drift tube. The middle frame, at time step 75, shows the particles as they leave the cavity and enter the upper drift tube. In the third frame, at time step 125, they are leaving the upper drift tube (by being absorbed on the upper boundary of the simulation).

III. RADIATING OPEN WAVEGUIDE IN THE TIME DOMAIN

The ability of the ARGUS code to handle open, radiating boundary conditions in the time domain sets it apart from several other codes. Two separate utilities exist for implementing this capability. The first is a "port" boundary condition, which treats a specified opening in the simulation boundary as though it were connected to a waveguide extending to infinity. The second is an implementation of the Lindman [4] algorithm for radiating boundaries. While the port condition only matches the boundary for radiation at a specified frequency, the Lindman condition is a general outgoing-wave boundary condition.

This simulation provides a demonstration of the Lindman algorithm for a rectangular waveguide driven at its lower end, and open at its upper end. Figure 4 shows the radiation fields at two time steps selected to show the phase slippage at the top (open) boundary.

IV. REFERENCES

- [1] A. Mankofsky, *Three-Dimensional Electromagnetic Particle Codes and Applications to Accelerators, Linear Accelerators and Beam Optics Codes*, C.R. Eminheizer, ed., A.I.P. Conf. Proc. No. 177 (American Institute of Physics, New York, 1988), p. 137ff.
- [2] A. Mondelli, C. Chang, A. Drobot, K. Ko, A. Mankofsky, and J. Petillo, *Application of the ARGUS Code to Accelerator Design Calculations*, Proc. 1989 IEEE Part. Accel. Conf. (Chicago, IL, IEEE Cat. No. 89CH2669-0, 1989), p. 877.
- [3] A. Mankofsky, J.L. Seftor, C.L. Chang, K. Ko, A. Mondelli, A. Drobot, J. Moura, W. Aimonetti, S. Brandon, D. Nielsen, Jr., and K. Dyer, *Domain Decomposition and Particle Pushing for Multiprocessing Computers*, Comp. Phys. Commun. 48, 155 (1988).
- [4] E.L. Lindman, "Free-Space" Boundary Conditions for the Time Dependent Wave Equation, J. Comp. Phys. 18, 66 (1975).

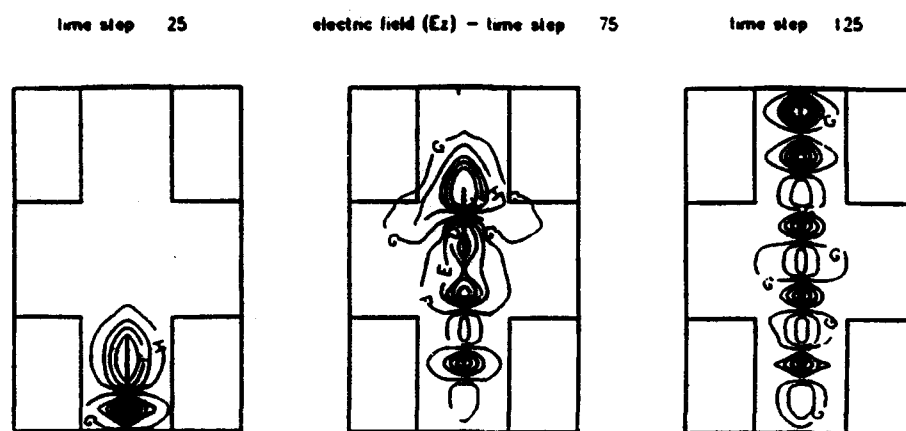


Figure 3. Wake fields due to a Gaussian bunch passing through the "Tombstone" Cavity.

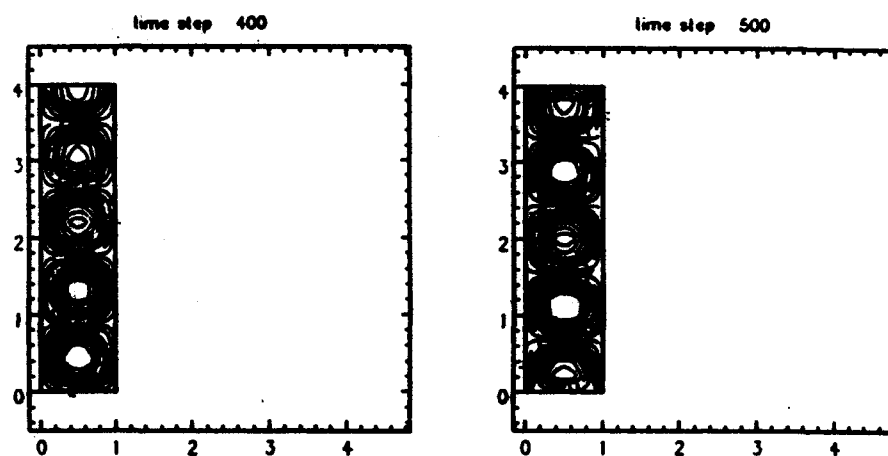


Figure 4. A radiating waveguide in the time domain.

**1993 Particle Accelerator Conference
A High-Order Moment Simulation Model***

K. T. Tsang, C. Kostas, and A. Mondelli

*Science Applications International Corporation
1710 Goodridge Drive, McLean, VA 22102*

1. Introduction

The physical length of accelerator systems presents computational difficulties for three-dimensional discrete-particle simulations of the dynamics and emittance growth in beam transport. An alternative to the discrete-particle approach is a high-order moment equation model, which is an extension of envelope equations formulated first by Kapchinskij and Vladimirovskij¹ and later adapted by Lee, Close and Smith².

Chernin³ has derived a beam envelope equation from the equations of motion for a mono-energetic particle beam in a magnetic field that is linear in the transverse coordinates. In this work we are interested in beams with a spread in energy, and transport systems with a non-linear transverse dependence of the magnetic field. For this type of system the spatial coordinate along the beam motion cannot be used as the time variable; faster particles will overtake the slower particles as time evolves. We present relativistically covariant moment equations for modeling beam transport, based on the work of Newcomb⁴ and Amendt and Weitzner⁵. The beam is described by a set of partial differential moment equations, instead of a set of ordinary differential envelope equations. Our formalism is based on transverse averages of the moment equations obtained from the relativistic Vlasov equation. The spatial coordinate along the beam motion and time are the only independent variables. The moment equations are closed by setting higher order correlation functions to zero. A similar formulation of moment equations by Channel and co-workers⁶ used spatial averaging in all three coordinates to model a bunched beam with time as the only independent variable. For bunch lengths that are large compared to the betatron wavelength, it is impractical to carry sufficiently high longitudinal moments to model the oscillations within the bunch.

2. Formulation

We denote the time t and local Cartesian space coordinate (x^1, x^2, x^3) , replacing the usual coordinate (x, y, z) , where x^3 is measured along the beam motion direction and x^1 and x^2 are the transverse directions. We define $x^4 = ct$, where c is the speed of light, so that space-time is parametrized by $x^\mu, \mu = 1, 2, 3, 4$. We use a summation convention, and assume that Latin subscripts and superscripts, i, j, k, l , are summed from one to three, while Greek subscripts and superscripts are summed from one to four. The space-time metric $(ds)^2 = dx^i dx^i - c^2(dt)^2$ becomes

$(ds)^2 = dx^\mu dx^\nu g_{\mu\nu}$, where the non-zero elements of the metric tensor $g_{\mu\nu}$ are $g_{ij} = \delta_{ij}$ and $g_{44} = -1$. The metric tensors $g_{\mu\nu}$ and $g^{\mu\nu}$, which is defined so that $g_{\mu\nu} g^{\nu\lambda} = \delta_\mu^\lambda$, are used to raise and lower indices covariantly. The usual three velocity v^i is extended to a relativistic covariant four-velocity u^μ by the definitions $\gamma^{-2} = 1 - v^i v^i / c^2$ and $u^i = \gamma v^i, u^4 = \gamma c$ so that $u^\mu u_\mu = -c^2$.

The electromagnetic field tensor $F_{\mu\nu}$ is antisymmetric and is given by

$$E_i = cF_{i4} = -cF_{4i},$$

$$B_1 = F_{23} = -F_{32}, B_2 = F_{31} = -F_{13}, B_3 = F_{12} = -F_{21},$$

while the Lorentz force on a particle of charge q is $q(\vec{E} + \vec{v} \times \vec{B})_i = qF^i{}_\mu u^\mu / \gamma$. The general form of the external magnetic field of interest can be expressed as

$$B_i = B_{i0} + B_{i1}x^1 + B_{i2}x^2 + B_{i11}x^1x^1 + B_{i12}x^1x^2 + B_{i22}x^2x^2,$$

where all the coefficients $B_{10}, B_{20}, B_{30}, B_{11}, \dots, B_{222}$ are functions of x^3 , with B_{i0} the dipole, B_{ij} the quadrupole, and B_{ijk} the sextupole components. The beam distribution function, $f(x^\mu, u^\mu)$, satisfies the relativistic Vlasov equation, which we express in covariant form as:

$$\left(u^\mu \frac{\partial}{\partial x^\mu} + \frac{q}{m} F^i{}_\mu u^\mu \frac{\partial}{\partial u^i} \right) f = 0 \quad (1)$$

where m is the particle mass. The volume element $d\omega = du^1 du^2 du^3 / \gamma$ in the four-momentum space is invariant under a Lorentz transformation. Since the transverse coordinates, x^1 and x^2 , are invariant under a Lorentz transformation, we define an invariant phase space volume element under a Lorentz transformation to be $d\Omega = dx^1 dx^2 du^1 du^2 du^3 / \gamma$, and a phase space average $\langle X \rangle = h^{-1} \int X f d\Omega$, with $h = \int f d\Omega$. We also define a second order correlation function:

$$[u^\mu u^\nu] = h^{-1} \int f(u^\mu - \langle u^\mu \rangle)(u^\nu - \langle u^\nu \rangle) d\Omega, \quad (2)$$

and similar definitions for the third order correlation functions.

The lowest moment of the Vlasov equation gives

$$\frac{\partial}{\partial x^3} h(u^3) + \frac{\partial}{\partial x^4} h(u^4) = 0. \quad (3)$$

With Eq. 2 multiplied by u^ν and $u^\nu u^\lambda$ then integrated over $d\Omega$, we have:

$$\frac{\partial}{\partial x^3} h(u^3 u^\nu) + \frac{\partial}{\partial x^4} h(u^4 u^\nu) = \frac{q}{m} h(F^{\nu\mu} u_\mu), \quad (4)$$

$$\frac{\partial}{\partial x^3} h(u^3 u^\nu u^\lambda) + \frac{\partial}{\partial x^4} h(u^4 u^\nu u^\lambda) = \frac{q}{m} h((F^{\nu\mu} u_\mu u^\lambda) + (F^{\lambda\mu} u_\mu u^\nu)). \quad (5)$$

There are four independent equations represented in Eqs. 4 and ten in Eqs. 5. Equations 3 to 5 are basically the same as the fluid equations of Newcomb⁴ and Amendt and Weitsner⁵, with the additional averaging over the transverse coordinates. Since $F^{\mu\nu}$ depends on the transverse coordinates, Eqs. 4 and 5 cannot be closed without introducing the spatial moment equations:

$$\frac{\partial}{\partial x^3} h(u^3 x^i) + \frac{\partial}{\partial x^4} h(u^4 x^i) = h(u^i), \quad (6)$$

$$\frac{\partial}{\partial x^3} h(u^3 u^\nu x^i) + \frac{\partial}{\partial x^4} h(u^4 u^\nu x^i) = h(u^\nu u^i) + \frac{q}{m} h(F^{\nu\mu} u_\mu x^i), \quad (7)$$

$$\frac{\partial}{\partial x^3} h(u^3 x^i x^j) + \frac{\partial}{\partial x^4} h(u^4 x^i x^j) = h(x^j u^i) + h(x^i u^j), \quad (8)$$

for $i, j = 1, 2$ only.

Physical meanings can be attached to these moments. The first order moments $\langle x^1 \rangle$ and $\langle x^2 \rangle$ denote the centroid position, and $\langle u^1 \rangle, \langle u^2 \rangle, \langle u^3 \rangle$ and $\langle u^4 \rangle$ are associated with the beam current and density respectively. The second order spatial correlations $\langle x^i x^j \rangle$ with $i, j = 1, 2$ define the transverse beam envelope ellipse. The second order momentum correlations $\langle u^\nu u^\mu \rangle$ are the thermal momentum/energy spread. The second order cross correlations $\langle x^i u^\nu \rangle$ are the current and density dipole moments.

To allow easier numerical solution, consider a new general variable y^λ such that $y^1 = 1, y^2 = x^1, y^3 = x^2, y^4 = u^1, y^5 = u^2, y^6 = u^3$, and $y^7 = u^4$. The twenty-eight equations represented in Eq. 3 thru 8 can be obtained by multiplying Eq. 1 by $y^\lambda y^\nu$ and integrating over $d\Omega$.

$$\frac{\partial}{\partial x^3} h(u^3 y^\lambda y^\nu) + \frac{\partial}{\partial x^4} h(u^4 y^\lambda y^\nu) = \Gamma(\lambda, \nu) + \Gamma(\nu, \lambda) \quad (9)$$

where

$$\Gamma(\lambda, \nu) = \begin{cases} 0, & \lambda = 1; \\ \int y^\nu u^{\lambda-1} f d\Omega, & \lambda = 2 \text{ or } 3; \\ \frac{1}{m} \int y^\nu F^{\lambda-3, \mu} u_\mu f d\Omega, & \lambda = 4 \text{ thru } 7. \end{cases} \quad (10)$$

To close the second order system of equations we assume that correlations above second order are zero. This still allows third order moments to be nonzero. The closing condition creates several equivalent families of independent

variables: $\{h(y^\lambda y^\nu u^\lambda)\}$ and $\{h(y^\lambda y^\nu u^\lambda)\}$ where $\lambda = 1$ to 7 and $\nu = \lambda$ to 7, $\{h(y^\lambda y^\nu)\}$ where $\lambda = 2$ to 7 and $\nu = \lambda$ to 7, or $\{h(y^\lambda), [y^\lambda y^\nu]\}$ where $\lambda = 2$ to 7 and $\nu = \lambda + 1$ to 7. Note that each set has twenty-eight elements. The natural set of independent variables to advance in time is $\{h(y^\lambda y^\nu u^\lambda)\}$. At each cell in x^3 these 28 variables describe the moments of f when correlations above second order are zero. To solve this system of equations we need to calculate $h(u^3 y^\lambda y^\nu)$ and $\Gamma(\lambda, \nu)$ after each time advance. We need to relate $\{h(y^\lambda y^\nu u^\lambda)\}$ to the 84 non-zero third order moments, $\{h(y^\lambda y^\nu y^\mu)\}$. We define $[\lambda, \nu] \equiv h(y^\lambda y^\nu u^\lambda)$, and get from the third order correlation functions,

$$[\lambda, \nu] = h[y^\lambda y^\nu u^\lambda] + [1, 1]\langle y^\lambda y^\nu \rangle + [1, \nu]\langle y^\lambda \rangle + [1, \lambda]\langle y^\nu \rangle - 2[1, 1]\langle y^\lambda \rangle \langle y^\nu \rangle. \quad (11)$$

With this a mapping from $[\lambda, \nu]$ to $\{h(y^\lambda y^\nu y^\mu)\}$ is derived. To close the n 'th order system of equations we assume that correlations above order n are zero. Each order has a different closing condition, thus each order has a different mapping from $\{h(y^{\lambda_1} y^{\lambda_2} \dots y^{\lambda_n})\}$ to $\{h(y^{\lambda_1} y^{\lambda_2} \dots y^{\lambda_{n+1}})\}$.

For second and third order systems, the systems have 28 and 84 equations respectively. Currently our computer model allows a fourth order system, which has 210 equations. The general expression for the total number of equations in an n -th order system can be expressed as:

$$1 + \sum_{m=1}^n \sum_{i=1}^{m \ln(6, m)} C_i^6 C_{i-1}^{m-1}.$$

This gives 462 for the fifth order, and 924 for the sixth order systems. The advantage of Eqs.(9)-(11) is that they can be easily manipulated symbolically.

3. Space Charge Model

A space charge model has been implemented to include the image charges of the metallic boundary and the longitudinal component of the space charge fields. The model assumes that the charge density, ρ , can be approximated by a two-dimensional distribution of charged rods inside a cylindrical metallic pipe;

$$\rho = \sum_{i=1}^N q_i(x_3, t) g(\vec{x} - \vec{x}_i), \quad (12)$$

where g is the spatial distribution function for the finite size charged rods whose location are independent of x_3 . Note that g depends on x_1 , and x_2 , while q_i depends only on x_3 . The charges on the rods, q_i , are chosen to be consistent with the spatial moments. In the second order moment system there are six spatial moments, and therefore we have $N = 6$ and a matrix equation to relate the coefficients q_i with the spatial moments: $hX = MQ$, where M is a 6×6 matrix whose elements are of the form $\int x_1^m x_2^n g(\vec{x} - \vec{x}_i) dx_1 dx_2$, with

$k, l = 1, 2$ and $m + n \leq 2$, X and Q are column matrices such that $X^T = (1, \langle x_1 \rangle, \langle x_2 \rangle, \langle x_1 x_1 \rangle, \langle x_2 x_2 \rangle, \langle x_1 x_2 \rangle)$ and $Q^T = (q_1, \dots, q_6)$. Equation (15) can be easily inverted to express q_i in terms of the spatial moments.

The image charges of these rods are easy to determine. For a charge rod located at \vec{x}_i with a charge q_i the image is located at \vec{x}'_i with charge $-q_i$, where \vec{x}'_i is along the same direction outside the metallic cylinder with a magnitude $a^2/|\vec{x}_i|$, and a is the radius of the cylinder. The electric field due to the charged rods inside the cylinder in the beam frame can be written as

$$\vec{E}(\vec{x}) = \sum_{i=1}^N q_i \frac{\vec{x} - \vec{x}_i}{|\vec{x} - \vec{x}_i|^3} - \sum_{i=1}^N q_i \frac{\vec{x} - \vec{x}'_i}{|\vec{x} - \vec{x}'_i|^3}. \quad (13)$$

This result can be transformed back to the laboratory frame. With this simplified model, the self-field contribution to moments involving $F^{\nu\mu}$ can be readily expressed in terms of other moments retained in the system and a close set of equations can be achieved.

5. Results

The High-Order Moment (HOM) model agrees with SAIC's "ABBY"³ code, a linear envelope model for the steady state evolution of a monoenergetic beam. To test the effect of energy spread in the HOM model, we injected two monoenergetic circular beams at $z = 0$ with γ 's of 3 and 3.1, respectively, into a mismatched constant guide field. Each beam will independently exhibit betatron oscil-

lations in the beams radius as a function of the distance of propagation, z . The space charge model has been turned off to eliminate any interaction between the two beams; the addition of the results from an envelope equation will be the exact solution. Figure 1a shows the expected beat pattern in the $\langle x^1 x^1 \rangle$ moment caused by the slight difference in frequencies of the betatron oscillations. The HOM model, when retaining up to third order correlations, does not capture this energy mixing. The average of the two betatron frequencies develops in time as shown in figures 1b and 1c. To capture the effects of this energy spread fourth order correlations must be retained (fig. 1d).

* Work supported by DARPA/DSO

References

- 1 I. M. Kapchinskij and V. V. Vladimirovskij, in *Proceedings of the International Conference High Energy Accelerators* (CERN, Geneva, 1959), P. 274.
- 2 E. P. Lee, E. Close, and L. Smith, in *Proceedings of the 1987 IEEE Particle Accelerator Conference*, edited by E. R. Lindstrom and L. S. Taylor (IEEE, New Jersey, 1987), p. 1126.
- 3 D. Chernin, *Particle Accelerators*, **24**, 29 (1988).
- 4 W. A. Newcomb, *Phys. Fluids*, **25**, 846 (1982).
- 5 P. Amendt and H. Weitzner, *Phys. Fluids*, **28**, 949 (1985).
- 6 P. J. Channell, *IEEE Trans. Nucl. Sci.*, **30**, 2607 (1983); P. J. Channell, L. M. Healy, and W. P. Ly-senko, *IEEE Trans. Nucl. Sci.*, **32**, 2565 (1985).

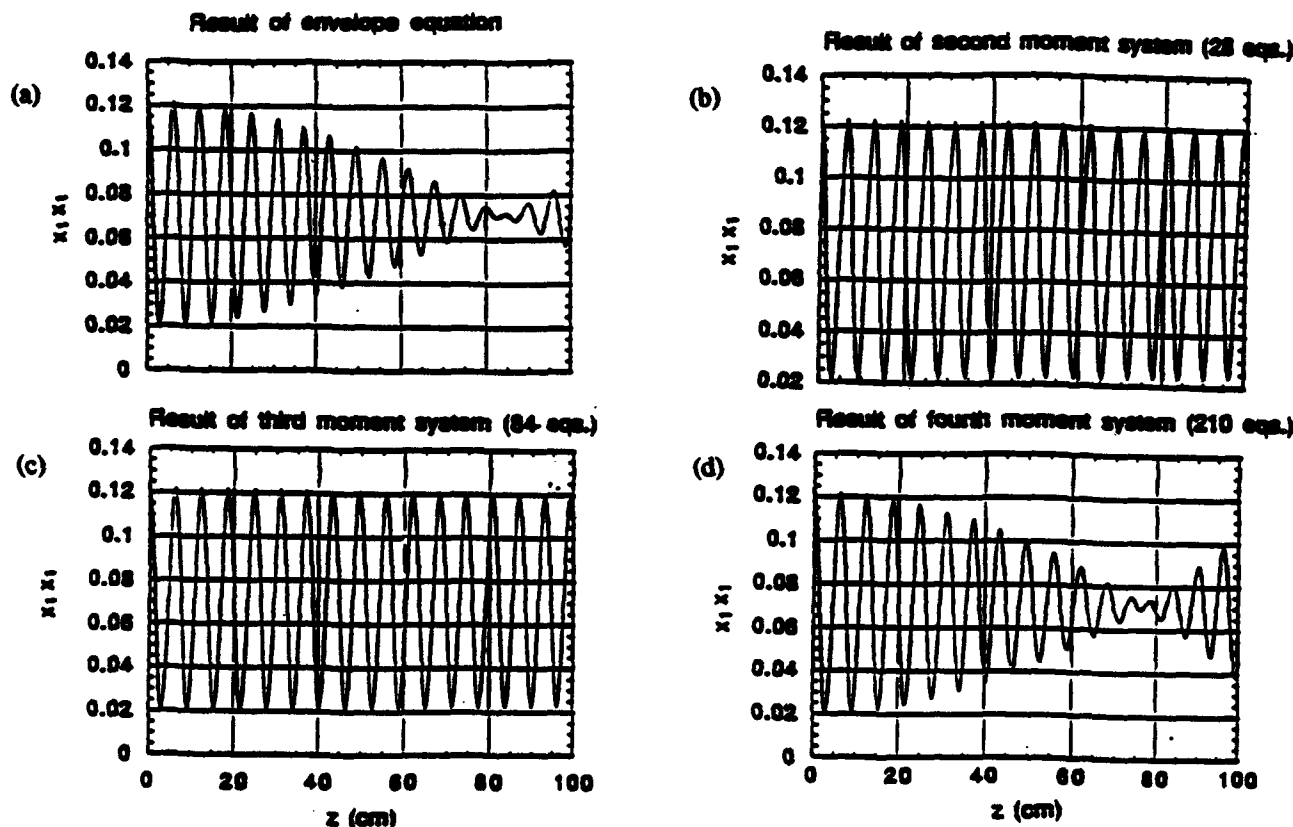


Fig. 1: Envelope solutions for a beam with energy spread.

Collective Effects of the PLS 2 GeV Storage Ring

M. Yoon, J. Choi and T. Lee
Pohang Accelerator Laboratory
Pohang University of Science and Technology
Pohang, Korea 790-660

Abstract

Collective effects of the PLS storage ring are discussed. Evaluation of the PLS storage ring coupling impedances is presented. RF cavity impedances are emphasized. Single-bunch threshold current is studied and longitudinal coupled-bunch instabilities caused by RF narrow-band resonances are analyzed.

I. INTRODUCTION

Charged particles moving very fast feel negligible electrostatic force from other particles. Therefore relativistic bunch of charged particles can maintain its shape and state of motion forever without any disturbance. However, for bunches moving inside a vacuum chamber with finite conductivity and some geometry, the situation is not so perfect. Image charges are induced on the surface of the vacuum chamber and electromagnetic field is generated by the beam bunch and the image charges on the vacuum chamber. This electromagnetic field is called the wake field. Because of the finite conductivity of the vacuum chamber, the wake field is energy consuming and acts as a disturbance to the motion of the bunch. The disturbing effects of the wake field are not only longitudinal but also transversal to the bunched beam motion. To describe these two effects two functions are defined. The longitudinal wake function $W_{||}(s)$ is defined as the amount of energy lost by a unit test charge that follows the wake field generating bunch of unit charge at some longitudinal distance s from a reference position in the bunch. And similarly the transverse wake function $W_{\perp}(s)$ is defined as the total transverse impulse received by a unit test charge that accompanies a bunch of unit charge[1]. Now for the traveling bunches, stable motion is not guaranteed any more. The wake field also causes energy spread of particles in a bunch and increase of the effective emittance of a beam. Since wake fields generated by a bunch do not vanish soon and can spread over a long range, the trailing bunches get influenced. This is why some kinds of coupled bunch instabilities may occur.

Therefore designing accelerators, it is necessary to evaluate these disturbing effects and try to find a way of minimizing them. Sometimes it is useful to work with Fourier transform of wake field to frequency, which is identified as the coupling impedance of the chamber. When the instabilities are described in terms of coherent modes of a beam, the concept of impedance is more convenient.

II. COUPLING IMPEDANCES OF PLS

The frequency description of wake field is given by specifying two impedances, longitudinal impedance $Z_{||}(\omega)$ which is a Fourier transform of $W_{||}(s)$ and transverse impedance $Z_{\perp}(\omega)$ which is a Fourier transform of $W_{\perp}(s)$. All storage ring components are sources of instabilities. In other words they have their own impedances; vacuum chamber resistive wall, RF cavity, bellows, steps, transition pieces, beam position monitors and so on. The total impedance of the storage ring should be as small as possible. In the theories of instabilities, it is not $Z(\omega)$ but $Z(\omega)/n$ that appears, where $n = \omega/\omega_0$ is the frequency divided by the revolution frequency.

The impedance of the resistive wall of the chamber is significant at low frequencies. However at frequencies higher than a few MHzs, the impedance of the resistive wall diminishes and effectively negligible. At these high frequencies, RF cavity is the most important one. The cavity has a fundamental resonant mode and higher frequency resonant modes. The first a few resonant modes are very sharp. These narrow band resonances are equivalent to long range wake fields and therefore origins of coupled bunch instabilities. Each of these sharp resonances is significant and so has to be specified. Higher frequency resonances get broader and at sufficiently high frequencies, one can assume that the impedance is a continuum.

To evaluate the impedance of the storage ring, we performed simplified model calculation for chamber resistive wall, bellows, transition pieces and so on. However for RF cavity we need more rigorous method. The above mentioned sharp resonances will be searched experimentally. And we used TBCI code to evaluate the broad band impedance of RF cavity, which is a big part of the total impedance budget of the storage ring. We adopted resonator model to approximate the broad band impedance. To determine three parameters of the resonator model, we used longitudinal and transverse loss factor, $k_{||}(\sigma)$ and $k_{\perp}(\sigma)$ defined by

$$k_{||}(\sigma) = \frac{1}{\sqrt{2\pi}\sigma} \int_{-\infty}^{\infty} W_{||}(s, \sigma) e^{-s^2/2\sigma^2} ds, \quad (1)$$

$$k_{\perp}(\sigma) = \frac{1}{\sqrt{2\pi}\sigma} \int_{-\infty}^{\infty} W_{\perp}(s, \sigma) e^{-s^2/2\sigma^2} ds. \quad (2)$$

In the above formulas, σ is the *rms* bunch length. By varying σ and running TBCI, we can obtain graph of k 's versus σ . Then we can determine the three parameters of the resonator model by graph fitting.

Table I summarizes the longitudinal impedances for PLS storage ring.

Table I PLS Impedance budget

Item	$ Z_{\parallel}/n $ (Ω)
RF cavity	0.7
Synchrotron radiation	0.16
Space charge	1.3×10^{-4}
Resistive wall	0.02
Steps and transitions	0.17
Bellows (unshielded)	(1.27)
Bellows (shielded)	0.01
Beam position monitors	0.015
Ceramic chamber coatings	1×10^{-4}
Other components and safety margin	1.0
Total	~ 2

The corresponding transverse impedance can be obtained by assuming a circular symmetry of the chamber [2]:

$$|Z_{\perp}| = \frac{2c}{b^2\omega} |Z_{\parallel}| = \frac{2R}{\beta b^2} \left| \frac{Z_{\parallel}}{n} \right| \quad (3)$$

For PLS with $b=2.5$ cm, we get

$$|Z_{\perp}| = 0.286 \text{ M}\Omega/\text{m}.$$

III. THRESHOLD CURRENT FOR SINGLE BUNCH

The peak threshold current for the longitudinal microwave instability (also known as the turbulent bunch lengthening) is given by [3]

$$I_p = \frac{2\pi|\eta|E/c(\beta\sigma_p)^2}{|Z_{\parallel}/n|} \quad (4)$$

where η is the frequency slip factor ($\eta \approx \alpha$ for a highly relativistic particle and α is the momentum compaction factor), E the energy of a stored beam, $\beta = v/c$, σ_p the relative *rms* energy spread of a beam, and $|Z_{\parallel}/n|$ is the longitudinal broad-band coupling impedance divided by the mode number.

Threshold current as a function of $|Z_{\parallel}/n|$ is shown in Fig. 1. Note that the threshold current shown in Fig. 1 is the average beam current I_b . It is related with the peak current via

$$I_b = \frac{\sigma_l}{\sqrt{2\pi}R} I_p, \quad (5)$$

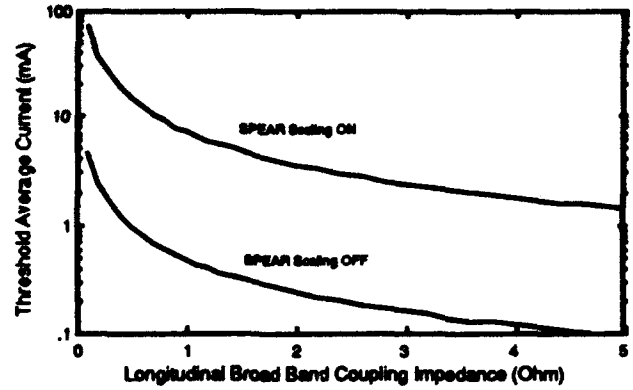


Fig.1 Single bunch longitudinal microwave threshold as a function of coupling impedance

where σ_l is the *rms* bunch length and R is the effective radius of the ring (i.e., $R = C/2\pi$, C =ring circumference). Fig. 1 also compares between with and without SPEAR scaling [4]. It is seen that when the longitudinal broad band impedance is 2Ω , the threshold average current for a single bunch is approximately 0.24 mA without SPEAR scaling and 3.5 mA with SPEAR scaling. The actual threshold current will be some value in between.

IV. LONGITUDINAL COUPLED-BUNCH INSTABILITIES

As is mentioned in section II, narrow-band resonances of RF cavities are origin of coupled-bunch instabilities. The central equation relating impedance resonances and instabilities is that of complex coherent frequency shift, $\Delta\omega_{s,a}$ for small Gaussian bunches [5]:

$$\Delta\omega_{s,a} = i \frac{I_0 \omega_0^2 \eta k_b (\sigma_l/R)^{2(a-1)}}{2\pi E_0 \omega_s} \frac{1}{2^a (a-1)!} (Z_{\parallel})_{eff}^{s,a} \quad (6)$$

where

$$(Z_{\parallel})_{eff}^{s,a} = \sum_{p=-\infty}^{+\infty} (pk_b + s)^{2a} e^{-(pk_b + s)^2 (\sigma_l/R)^2} \frac{Z_{\parallel}[(pk_b + s + a\nu_s)\omega_0]}{pk_b + s + a\nu_s}. \quad (7)$$

In the above equation, k_b represents the number of bunches, s the longitudinal mode number $s = 0, 1, 2, \dots, (k_b - 1)$, a the oscillation mode of the bunch shape in phase space, e.g., the dipole mode $a=1$, the quadrupole mode $a=2$, etc., η the frequency slip factor, I_0 the average beam current, ω_0 the angular revolution frequency, E_0 the nominal beam energy, ω_s the angular synchrotron frequency, R the average radius of a ring, and σ_l is

the rms bunch length in space. At this time of manuscript preparation, the first RF cavity of PLS has been delivered months ago but the full analysis has not been carried out yet. Therefore we used the measured data of Photon Factory, of which cavity is almost the same as that of PLS. To use Eq. (6), the program ZAP has been invoked.

Calculated growth times for the dipole mode (i.e. $a=1$) for each RF cavity mode are summarized in Table II.

Table II Longitudinal dipole ($a=1$) mode growth rate for each higher-order mode of the RF cavity

Frequency (MHz), f_{rf}	Growth time (msec)
758.2	230.8
1,048.0	499.6
1,302.1	1161.2
1,328.0	62.6
1,648.4	0.48
1,707.7	9.04
1,860.5	49.76
1,962.4	381.6
2,121.5	43.08
2,167.7	196.24

In obtaining the growth time of Table II, total number of bunches (k_b) are assumed to be 468 (i.e., fill all RF buckets) and the average beam current was taken to be 100 mA. The rms bunch length was taken arbitrarily to be 5 mm, which is the natural rms bunch length at 2 GeV. The rms energy spread was taken to be 6.8×10^{-4} . It is seen that the mode number 6 (i.e., $f_{rf}=1,648.4$ MHz) gives the worst case. When taking into account the fact that there are total four cavities in the PLS, we expect that the growth times will be smaller than those in Table II. The reason that the mode number 6 gives the smallest growth time is because it is this frequency which is closest to the neighboring coupled-bunch oscillation frequency ($pk_b + s + a\nu_s$) ω_0 , where $p=1$, $s=148$ and $a=1$. Higher-order mode damping or frequency shift of the RF cavity is therefore needed for this mode and others. On the other hand, we believe that the estimation given here is very pessimistic, because in the calculation we have not taken into account the radiation damping and the Landau damping which comes from the frequency spread due to the nonlinear synchrotron oscillation.

The growth times and the tune shifts are tabulated in Table III. Again one RF cavity was assumed in obtaining this table. All the RF buckets were assumed to be filled out and the average beam current was taken to be 100 mA.

Table III shows that for dipole synchrotron mode the coherent growth time increases as the energy increases while for higher synchrotron modes it gets decreasing. This can be easily explained with the help of Eqs. (6) and (7). For dipole mode, the effective impedance decreases as the energy increases because of the increase in bunch length, as seen in Eq. (7). On the other hand, for higher modes

Table III Growth times and tune shifts for the fastest-growing longitudinal coupled-bunch modes for 468 bunches and 100 mA beam current

Energy (GeV)	Mode number (a)	Growth time (msec)	Tune shift
1.5	1	0.34	-2.94×10^{-4}
	2	49.91	-5.86×10^{-5}
	3	1618	-1.98×10^{-5}
	4,...		
2.0	1	0.5	-1.82×10^{-4}
	2	48.7	-3.51×10^{-5}
	3,4,...		
2.5	1	0.57	-1.15×10^{-4}
	2	26.5	-2.48×10^{-5}
	3,4,...		

($a > 1$), the rate of the increase in growth rate rapidly increases as the bunch length increases.

The result indicated that damping mechanism or frequency shift of the RF cavity is required, otherwise the growth time is too small, less than the radiation damping time. It is also seen that dangerous RF modes are mostly located on the high frequency side. The theory employed here has a limitation such that it can not be used for the asymmetric bunch configuration, which will be the actual case for the PLS in order to avoid the ion trapping problem.

V. REFERENCES

- [1] K. Bane and M. Sands, SLAC-PUB-4441 (1987)
- [2] B. Zotter and F. Sacherer, Proc. First Course of Int. School of Particle Accelerators, Erice, CERN 77-13 (1976)
- [3] E. Keil and W. Schnell, CERN ISR-RF 69/48 (1969)
- [4] A. W. Chao and J. Gareyte, SPEAR-197, PEP-224 (1976)
- [5] M. S. Zisman et al, LBL-21270, ESG-15, 1986

Nonlinear evolution of longitudinal bunched-beam instabilities.

A. Gerasimov

Fermi National Accelerator Laboratory;
P.O. Box 500, Batavia, IL 60505, USA

Abstract

Numerical results of the nonlinear evolution of longitudinal instabilities of bunched beams are presented. Saturation effects due to the decoherence (tune spread) are categorized according to the magnitude and type of impedances. New phenomenon of non-saturating instability (beam splitting) is described.

I. INTRODUCTION

Nonlinear stages of development of coherent instabilities have been studied by a few authors [1-3] in relation to the longitudinal instability of the coasting beam. Some numerical simulation studies were carried out for the bunched beam, with the emphasis on the thresholds of instabilities [4]. Numerical simulation results [1] indicated that the longitudinal instability of the coasting beam always saturates and eventually decays due to the effect of decoherence. In the present paper, we undertake a numerical simulation study of the nonlinear development of the longitudinal instability of bunched beams. The saturation effects due to the decoherence from the tune spread are the primary objects of interest. More detailed presentation of this study is available in Ref. [5].

II. THE MODEL.

The simulation is carried out for the model that consists of a single bunch interacting with a localized single-mode longitudinal wakefield under the assumption of the short bunch length relative to the wavelength of the wakefield (Long wavelength/ low frequency approximation in the analysis of Ref. [5]):

$$\begin{aligned} \ddot{x}_i + \omega_s^2 x_i - \lambda x_i^3 &= \sqrt{\frac{\epsilon}{N}} q \delta_{2\pi}(t) \\ \ddot{q} + \alpha \dot{q} + \omega_c^2 q &= \sqrt{\epsilon N} \bar{x} \delta_{2\pi}(t) \end{aligned} \quad (1)$$

*Operated by the Universities Research Association, Inc. under contract with the U.S. Dept. of Energy.

where time is normalized to make the revolution frequency $\omega_0 = 1$, x_i ($i = 1, N$) is the coordinate of the i -th particle, \bar{x} is the coordinate of the centre of gravity of the beam $\bar{x} = \frac{1}{N} \sum_{i=1}^N x_i$, and q is the amplitude of the wakefield. The quantity ϵ measures the strength of interaction in the continuous limit $N \rightarrow \infty$, while $\delta_{2\pi}$ is 2π -periodic δ -function. Frequencies ω_s and ω_c are respectively the synchrotron and resonant impedance frequencies. The constant $\lambda > 0$ measures the nonlinearity of the RF potential well and is always small in our study.

We will assume the interaction strength ϵ together with the tune spread ω_s to be small, $\delta\omega_s \ll \alpha$ (where $\delta\omega_s$ is the tune spread $\delta\omega_s = \frac{\partial}{\partial \omega_s} \lambda(x^2)$), $\epsilon \ll \alpha \omega_s^2 \omega_c$. In the zero tune spread limit, the complex coherent frequency shift $\Delta\omega_s = \omega - \omega_s$ can be found (see, e.g., [5]) to be:

$$\Delta\omega_s = \frac{i\epsilon \tilde{Z}}{2\omega_s} \quad (2)$$

where the complex effective impedance $\tilde{Z} = \tilde{Z}_r + i\tilde{Z}_i$ is defined as $\tilde{Z} = Z(\omega_s)$, with the regular frequency-dependent impedance:

$$Z(\omega) = -\frac{i}{(2\pi)^2} \sum_n \frac{1}{\omega_c^2 + i\alpha(\omega + n) - (\omega + n)^2} \quad (3)$$

For the finite value of the tune spread, the relevant (real) parameters that define the nonlinear evolution are $\delta\omega_s$, $Re(\Delta\omega_s)$ and $Im(\Delta\omega_s)$. One of these parameters defines the units of time, so that the evolution depends essentially on two dimensionless parameters:

$$\begin{aligned} C_r &= -\frac{Re(\Delta\omega_s)}{\delta\omega_s} \\ C_i &= -\frac{Im(\Delta\omega_s)}{\delta\omega_s} \end{aligned} \quad (4)$$

III. SCENARIOS OF EVOLUTION.

The evolution in model (1) is directly simulated by using many particles and implementing the single-turn mapping. In that mapping, the nonlinearity of oscillations λ is treated perturbatively, i.e. the mapping for x_i, \dot{x}_i between the δ -functional "kicks" is that of a linear oscillator with

the shifted frequency. The number of particles N was taken to be large enough to reproduce the continuous limit. We present in Figs.1-4 four characteristic cases of instability evolution. These cases are representative of four different scenarios that we loosely define by the relative strength of instability (distance from the threshold):

I) *Strong instability* $|C_r| \gg C_{rer}$, $|C_i| \gg C_{ier}$

II) *Weak instability* $|C_r| \sim C_{rer}$, $|C_i| \sim C_{ier}$

and by the type of impedance:

a) *Reactive impedance* $|C_r| > |C_i|$ (or $|Z_i| > |Z_r|$)

b) *Active impedance* $|C_r| < |C_i|$ (or $|Z_i| < |Z_r|$)

The quantities C_{rer} , C_{ier} are the critical (i.e. corresponding to the stability border) values defined by the ratio C_r/C_i . Stability border in C_r, C_i plane is shown in Fig.5.

Examples of the time dependencies of centroid position $\bar{x}(t)$ and emittance $\sigma(t) = \langle \langle x^2 \rangle \rangle$ (averaged over the particles and the fast synchrotron oscillations) for four different scenarios are shown in Figs.1-4. Time scale is given in turns, and the scaling factor is the instability rise time in the absence of tune spread $\tau_{gr} = 1/\text{Im}(\Delta\omega_s)$.

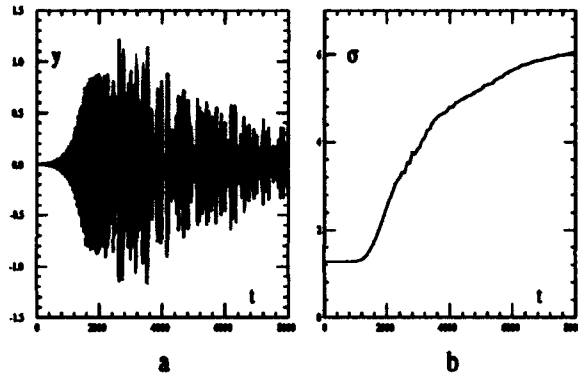


Fig.1. (a) Centroid oscillations $y = \bar{x}(t)$ and (b) Emittance growth $\sigma(t)$ for the case of (Strong instability, Reactive impedance) with $C_r = 4.16$, $C_i = 1.65$, and $\tau_{gr} = 188$.

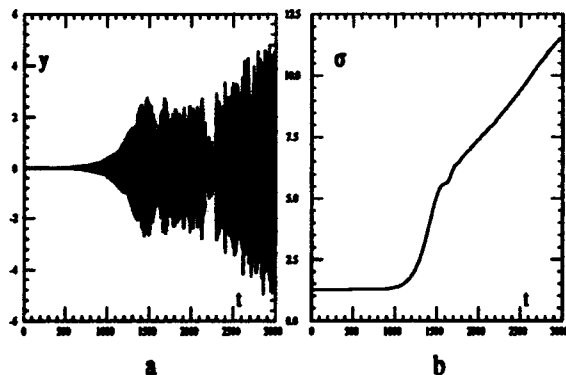


Fig.2. (a) Centroid oscillations $y = \bar{x}(t)$ and (b) Emittance growth $\sigma(t)$ for the case of (Strong instability, Active impedance) with $C_r = 1.18$, $C_i = 4.40$, and $\tau_{gr} = 142$.

The centroid oscillations in Figs.1-4 present itself a

fast-oscillating sinusoidal signal (with the synchrotron frequency) with a slow-changing envelope. The initial growth demonstrates the saturation at some level. After that, one observes some apparently random "turbulent" oscillations. In the *Strong instability* regime the envelope of oscillations grows monotonically until the saturation. For the *Weak instability*, the envelope of oscillations is not a monotonically growing function of time even before the saturation. The first maximum in the envelope of oscillations occurs early before the saturation and is quite small. It is followed by several more maxima of increasing amplitude before the saturation. The maximally attainable amplitudes of centroid oscillations are much smaller than in the case of a strong instability.

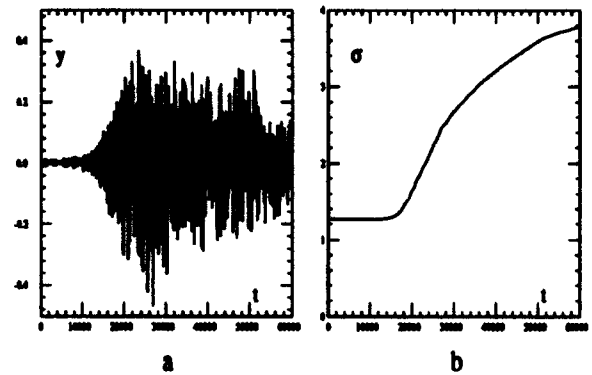


Fig.3. (a) Centroid oscillations $y = \bar{x}(t)$ and (b) Emittance growth $\sigma(t)$ for the case of (Weak instability, Reactive impedance) with $C_r = 1.25$, $C_i = .49$, and $\tau_{gr} = 315$.

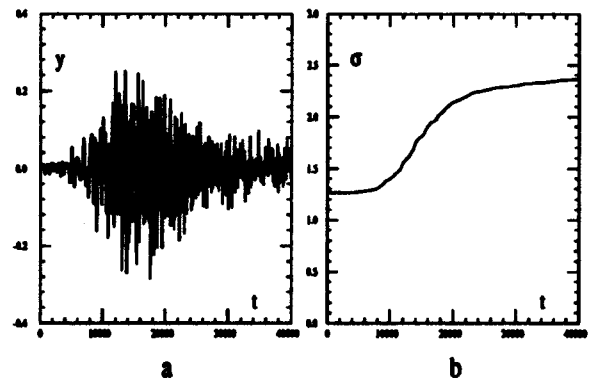


Fig.4. (a) Centroid oscillations $y = \bar{x}(t)$ and (b) Emittance growth $\sigma(t)$ for the case of (Weak instability, Active impedance) with $C_r = .24$, $C_i = .89$ and $\tau_{gr} = 175$.

IV. BEAM SPLITTING.

The *IIb* (*Strong instability, active impedance*) example of Fig.2 shows peculiar non-decaying and even slightly growing oscillations after the saturation. More insight into this behavior is provided by a few phase space snapshots in

Fig.2c. Time labels are in the same scale as in Fig.2a.

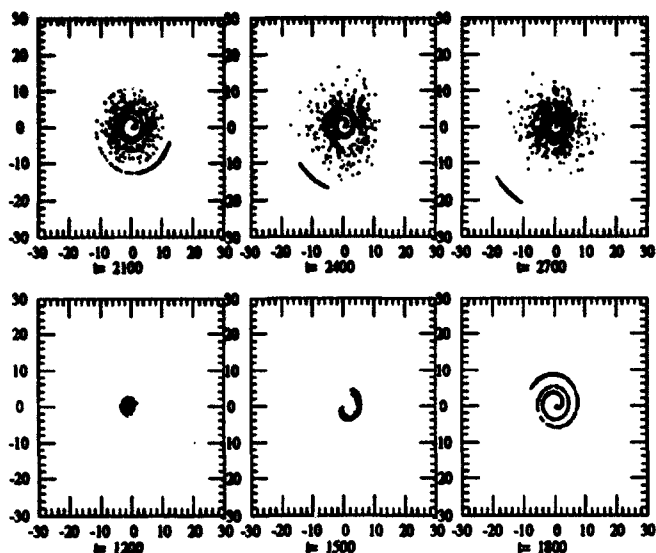


Fig.2c. Phase space snapshots for the parameters of Fig.2a and b.

One can see that the particles that happen to be at the larger radii (amplitude of oscillations) at the moment of saturation start moving toward increasing radii and finally form a distinct beamlet that is separate from the core of the beam. This beamlet does not decohere but oscillates with increasing amplitude as a rigid entity.

The results of a special-purpose series of simulations to explore the onset of beam splitting are presented in Fig.5. The beam splitting was diagnosed by observing a non-decohering beamlet in the phase space.

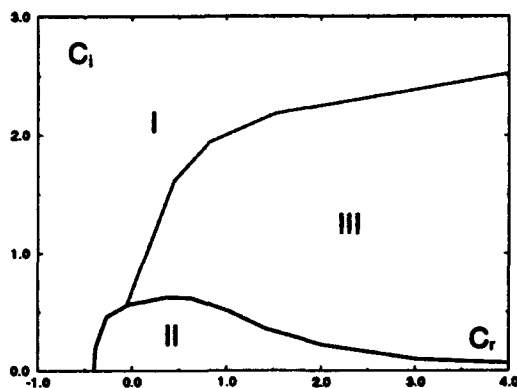


Fig.5 State diagram of instability. I is the beam splitting region, II is stable region and III is unstable, no beam splitting region.

One interesting feature of Fig.5 is the overlap of stability border and splitting border for negative C_r . For large negative C_r one can observe that the beam does not actually split, but rather oscillates as a whole with increasing amplitude without decohering.

The border of the beam splitting is a "soft" one, i.e. the percentage of particles trapped in the "beamlets" is approaching zero when approaching the border. In some cases one can also see several "beamlets" successively splitting from the core of the distribution.

V. DISCUSSION AND CONCLUSIONS.

The most interesting nonlinear effect observed is the beam splitting phenomenon. We suggest to explain, or rather interpret it as the trapped-particles nonlinear modes, in extension of a similar concept of persistent nonlinear (BGK) waves in plasma physics (see, e.g. /6/). We expect by that analogy that in our system a group of particles can be trapped, under certain conditions, near the center of self-driven nonlinear resonance. The elongated shape of the "beamlet" in Fig.2c corroborates that interpretation. The resonant frequency will change in time under the influence of (anti)dissipative impedance component Z_r , carrying the trapped particles towards larger radii. The difference with conventional BGK modes is in this (anti)dissipation in the system causing the frequency sliding. We suggest thus the term "sliding trapped (BGK) modes".

Beam turbulence is another important class of essentially nonlinear phenomena. Even when after the saturation of instability the emittance becomes large enough to make a beam stable for any smooth bell-shaped distribution, the small-scale "microstructure" of the density can persist in the beam for a long time, causing random-like low-level centroid oscillations and slow emittance growth.

In our case of fast synchrotron oscillations $\delta\omega_s \ll \omega_s$, emittance growth can be related to the amplitude of centroid oscillations $\bar{x} = a \sin(\omega_s t)$ through the convenient scaling law:

$$\frac{d\sigma}{dt} = \frac{A^2}{\tau_{gr}} \quad (5)$$

where τ_{gr} is the instability rise time in the absence of the tune spread $\tau_{gr} = \frac{1}{\text{Im}(\Delta\omega_s)}$. A theoretical quasilinear "overshoot" approach /7/ for predicting $\sigma(t)$ and $A(t)$ was developed in Ref./7/ along the same lines as in the coasting beam theory /2-3/.

VI. ACKNOWLEDGEMENTS

I would like to acknowledge many usefull discussions with Pat Colestock. His advice and encouragement were essential.

References 1. E.Keil, E.Meserschmid. Nucl.Instr.

and Meth. 128 (1975) 203.

2. Y.Chin, K.Yokoya. Phys.Rev.D28 (1983) 2141.

3. S.Bogacz, K-Y Ng. Phys.Rev.D36 (1987) 1538.

4. R.H.Siemann. Nucl.Instr.Meth 221 (1984) 293.

5. C.Pelligrini. Proc. of 1991 US School on High En. Part. Accel.

6. A.I.Akhiezer et al., Plazma Electrodynamics, v.2 (1975) p.1.

7. A.Gerasimov. Emittance growth at longitudinal bunched-beam instability: overshoot theory (to appear).

8. A.Gerasimov. Longitudinal bunched-beam instabilities going nonlinear: emittance growth, beam splitting and turbulence (to appear).

Multi-bunch Dynamics in Accelerating Structures Including Interaction with Higher Order Modes.

M.Ferrario *, L.Serafini #, F. Tazzioli *

* INFN Laboratori Nazionali di Frascati

INFN Sezione di Milano

Abstract

The case of interaction of not fully relativistic multi-bunch beams with the fundamental and higher order modes of a cavity is not yet covered by existing codes, nevertheless it is a fundamental problem in the design of RF guns and/or collider cavities. A simple model that couples Newton and Maxwell equations, taking into account also space charge, beam loading and build-up effects of higher order modes under beam-tube cutoff frequency, is presented. This approach is intended to fill that gap, avoiding relativistic approximation. It uses a current density description of the beam and a slowly varying envelope approximation for the time evolution of the modes amplitude. A fast running code (HOMDYN), based on this model has been developed and the application to a few typical examples is illustrated.

Table 1
Symbol definitions

A_n = mode amplitude	L_b = bunch length
\hat{e}_n = mode spatial distribution on axis	q = bunch charge
ω_n = mode radian frequency	$z_{h,t,b}$ = head, tail and bary-center coordinates
ϕ_n = mode phase	R = bunch radius
α_n = mode complex amplitude	c = light velocity
Q_n = quality factor of the mode	m_0 = electron rest mas
U_n = mode stored energy	β = average velocity/light velocity
E_0 = peak electric field	J = beam current density
C.C.= Complex Conjugate	N_b = n. of bunches in train
	ν_r = repetition rate

I. INTRODUCTION

When treating the evolution of high charge, not fully relativistic electron bunches in RF fields of an accelerating cavity, it is necessary to take into account also the field induced by the beam in the fundamental and higher order modes, and the variation of bunch sizes due to both the external fields and space charge.

For single bunches the problem has been already tackled using PIC codes, which describe the bunch as an ensemble of particles and track their motion, coupled to the E.M. field propagation. The case of long bunch trains would consume an unbearable amount of computer time if treated by a mere extension of the single bunch case.

We have therefore devised a simple model that uses a current density description of the beam and slowly varying envelope approximation (SVEA) for the evolution of the cavity modes. The present version deals only with TM

monopole modes: an extended version comprehensive of dipole modes is under development.

The SVEA approximation supposes small field perturbations produced by any single bunch, that add up to give an envelope of any mode field slowly varying on the time scale of its period.

Motion and field equations are coupled together through the driving current term.

II. THE FIELD EQUATIONS

Expressing the electric field E as a sum of normal orthogonal modes:

$$E(z,t) = \sum_n A_n(t) \hat{e}_n(z) \sin(\omega_n t + \phi_n(t))$$

$$= \sum_n \left(\alpha_n e^{i\omega_n t} + \alpha_n^* e^{-i\omega_n t} \right) \hat{e}_n(z)$$

with $\alpha_n = (A_n/2i) e^{i\phi_n}$, $\hat{e}_n(z) = \hat{e}_n(r=0)$ and:

$$\nabla^2 \hat{e}_n = -k_n^2 \hat{e}_n \quad \int_v \hat{e}_n \hat{e}_m dv = \delta_{nm}$$

the equation for the electric field complex amplitude α_n driven by a beam current distribution $J(z,t)$ in the cavity is [1]:

$$\begin{aligned} \frac{d^2 \alpha_n}{dt^2} + \left(2i\omega_n + \frac{\omega_n}{Q_n} \right) \frac{d\alpha_n}{dt} + i \frac{\omega_n^2}{Q_n} \alpha_n = \\ = - \frac{e^{-i\omega_n t}}{\epsilon} \int_v \left(\frac{\partial J}{\partial t} \cdot \hat{e}_n \right) dv \end{aligned}$$

with the normalization relations:

$$|\alpha_n(t)| = \sqrt{\frac{U_n(t)}{2\epsilon}} \quad \hat{e}_n(z) = \sqrt{\frac{\epsilon}{2U_{n,0}}} \hat{E}_{n,0}(z)$$

Applying the SVEA approximation hypotheses:

$$\frac{d\alpha_n}{dt} \ll \omega_n \alpha_n \quad \frac{d^2 \alpha_n}{dt^2} \ll \omega_n^2 \alpha_n$$

we obtain the first order equation:

$$\begin{aligned} \frac{d\alpha_n}{dt} + \left(1 + \frac{i}{2Q_n} \right) \frac{\omega_n}{2Q_n} \alpha_n = \\ = i \frac{e^{-i\omega_n t}}{2\omega_n \epsilon} \left(1 + \frac{i}{2Q_n} \right) \int_v \left(\frac{\partial J}{\partial t} \cdot \hat{e}_n \right) dv + \end{aligned}$$

$$+ \left(1 + \frac{i}{2Q_1}\right) \frac{2\omega_1}{Q_1} K_1$$

The last term is effective only in the fundamental mode equation and accounts for a feeding sinusoidal current of amplitude K_1 representing a power supply.

The current density term can be written as follows:

$$\int_v \left(\frac{\partial J}{\partial t} \cdot \hat{e}_n \right) dv = \frac{q\beta c}{L_b} \left(\hat{e}_n(z_h) \frac{dz_h}{dt} - \hat{e}_n(z_t) \frac{dz_t}{dt} \right)$$

The evolution of the field amplitude during the bunch to bunch interval is given by the analytical solution of the homogeneous equation, which connects successive numerical integrations applied during any bunch transit.

III. THE BEAM EQUATIONS

The basic approximation in the description of beam dynamics lays in the assumption that each bunch is represented as a uniform charged cylinder, whose length and radius can vary under a self-similar time evolution, i.e. keeping anyway uniform the charge distribution inside the bunch. The present choice of a uniform distribution is dictated just by sake of simplicity in the calculation of space charge and HOM contributions to the beam dynamics. A further improvement of the model to include gaussian distributed bunches is under way. According to this assumption, and to the general hypothesis that the space charge and HOM effects on beam dynamics are perturbative, we can write, under a paraxial approximation, the equations for the longitudinal motion of the bunch barycenter:

$$\frac{d\beta}{dt} = \frac{e}{3} \sum_n (\alpha_n e^{i\omega_n t} + \alpha_n^* e^{-i\omega_n t}) \hat{e}_n(z) \quad \frac{dz_b}{dt} = \beta c$$

The evolution of the bunch radius R is described according to a recently proposed envelope equation [2], including RF-focusing and space charge effects, transformed into the time-domain:

$$\frac{d^2 R}{dt^2} + \frac{dR}{dt} \frac{d\beta}{dt} g(\beta) + \frac{R}{4\gamma} \left(\left(\frac{dR}{dt} \right)^2 f(\beta) + K_r \right) - \frac{I_c^2}{I_A R \beta \gamma^3} - \frac{\epsilon_n^2 c^2}{R^3 \gamma^2} = 0$$

$$g(\beta) = \frac{1 - \beta\gamma - 1/\gamma}{\beta} \quad f(\beta) = \frac{1}{\beta^2} (3\beta^2 \gamma^2 - 2\gamma^3 (1+\beta) + \gamma^4 - 1 - \frac{2}{\beta} (1 - \beta^2 \gamma^4))$$

where I_A is the Alfvén current (17 kA), ϵ_n the rms normalized beam emittance and the RF average focusing gradient K_r is given by:

$$K_r = \sum_n \left(\frac{2e^2 |\alpha_n|^2}{m_e c^2} \sum_s \left(a_{s+1,n}^2 + a_{s-1,n}^2 + 2 a_{s+1,n} a_{s-1,n} \cos(2(\phi_n(t) - \phi_{n,s})) \right) \right)$$

where the two sums run over the HOM modes (index n , $n=1$ for the fundamental mode) and over the spatial harmonic coefficients $a_{s,n}$ of each mode form factor $\hat{e}_n(z) = \sum_s a_{s,n} \cos(nk_s z)$.

The bunch lengthening is derived adding to the space charge effect, as given by [3], the first order component coming from fundamental and HOM modes, which is simply given by the head-tail difference of the total RF field acting on the bunch:

$$\frac{d^2 L_b}{dt^2} = \frac{e q}{2\epsilon_0 m_0 \gamma^4 R^2 L_b} \left(\sqrt{(\gamma L_b)^2 + R^2} - (\gamma L_b + R) \right) + \frac{e}{3} \sum_n (\alpha_n(t) e^{i\omega_n t} (\hat{e}_n(z_h) - \hat{e}_n(z_t)) + C.C.)$$

In a similar way we derive the energy distribution inside the bunch by specifying the energy associated to each slice located at a distance s from the bunch barycenter (z_b):

$$\frac{d\gamma_s}{dt} = \frac{e}{m_e c} \beta_s \left(\sum_n (\alpha_n(t) e^{i\omega_n t} \hat{e}_n(z_b+s) + C.C.) + \frac{q s}{\epsilon_0 R^2 L_b^2} \left(\sqrt{(\gamma L_b)^2 + R^2} - (\gamma L_b + R) \right) \right)$$

IV. FIRST RESULTS.

To test the validity of the simulation we have applied the computation to the case of a 500 MHz single cell resonator, computing the mode frequencies and field distributions by the SUPERFISH code. Starting with the case of a train of relativistic rigid bunches and assuming an extreme set of parameters to shorten the time scale of the phenomena ($\gamma=100$, $q=400$ nC, $Q=10^2$, $N_b=10$, $v_r=500$ MHz, $U_{010}=0.138$ J, $U_{012}=0$ J) we show in Fig.1 the evolution of the electric field seen by bunches during transit in the cavity. In Fig.2,3 the stored energies and field phases of TM₀₁₀ are shown for two different injection phases. Notice the transition from absorption to emission regime after 3 bunches in the TM₀₁₀ mode

Induced energy in TM₀₁₀ (Fig.4) and in TM₀₁₂ (Fig.5) are compared for a relativistic ($\gamma=5$) and non-relativistic ($\gamma=2$) beam, ($q=16$ nC, $Q=10^2$, $N_b=200$, $v_r=125$ MHz, $U_{010}=0$ J, $U_{012}=0$ J).

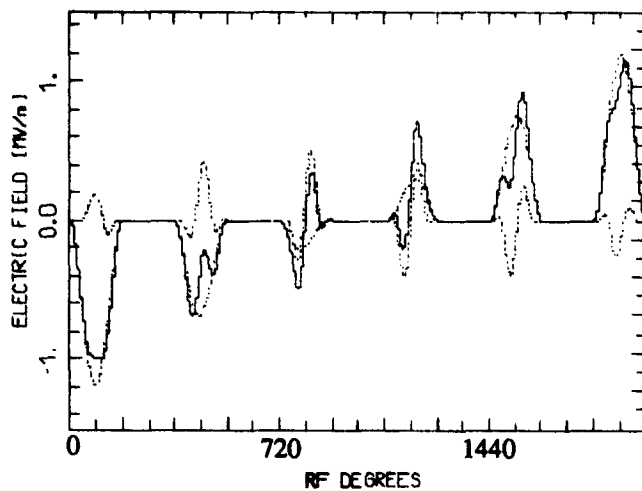


Figure 1 - Electric field seen by bunches, dashed lines are TM_{010} and TM_{012} fields, full line is the superposition of the two modes.

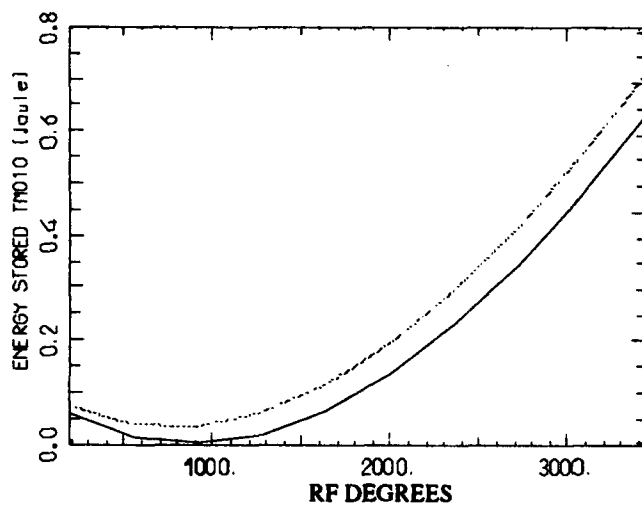


Figure 2 - Stored energies of TM_{010} for two different injection phases, full line $\phi_0 = -90$, dashed line $\phi_0 = -60$.

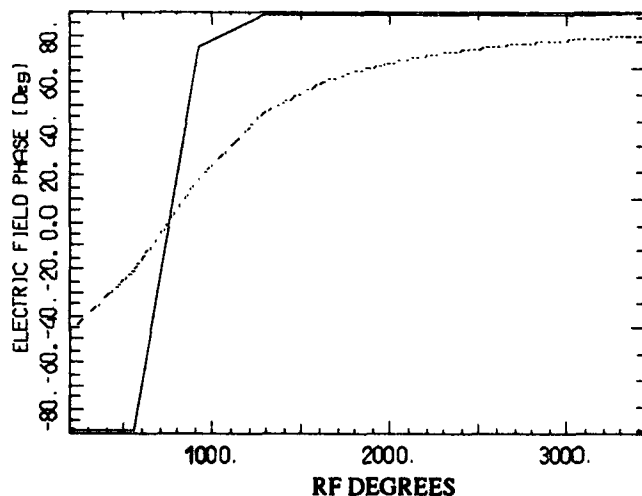


Figure 3 - TM_{010} phase evolution for two different injection phases, full line $\phi_0 = -90$, dashed line $\phi_0 = -60$.

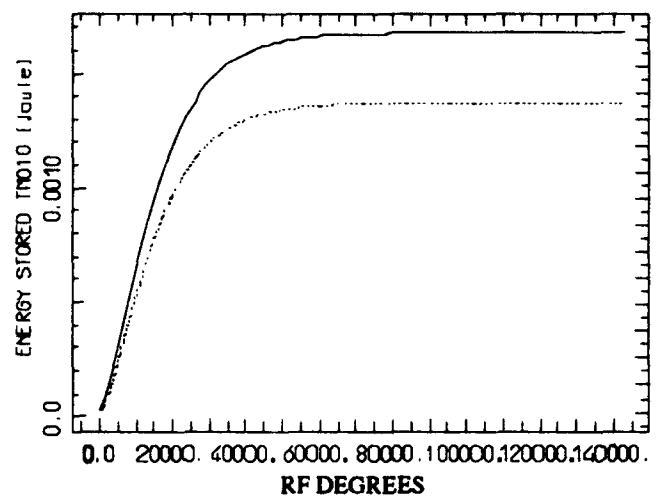


Figure 4 - Induced energy in TM_{010} is compared for a relativistic ($\gamma=5$ full line) and non-relativistic ($\gamma=2$ dashed line) beam.

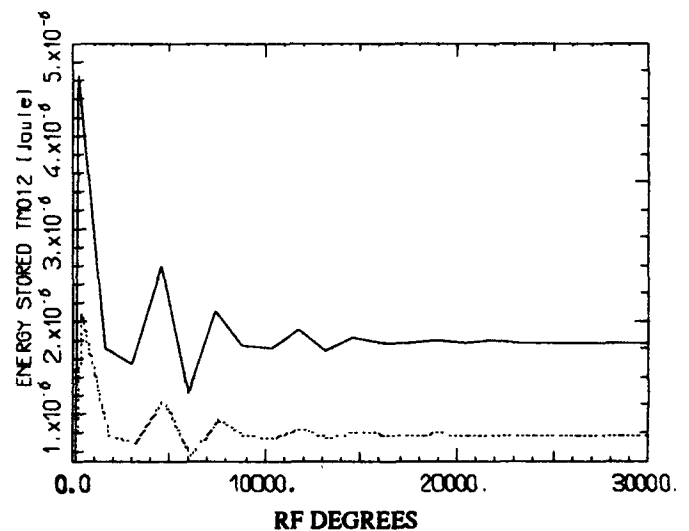


Figure 5 - Induced energy in TM_{012} is compared for a relativistic ($\gamma=5$ full line) and non-relativistic ($\gamma=2$ dashed line) beam. (RF Deg on the scale of TM_{010} period)

V. REFERENCES

- [1] M. Puglisi, "Conventional RF cavity design," *CAS School*, CERN 92-03, (1992).
- [2] S.C. Hartman, J. B. Rosenzweig, "Ponderomotive focusing in axisymmetric RF linacs," *Phys. Rev. E*, Vol. 47, N. 3, (1993).
- [3] G. Mavrogenes, "Space charge effects in high current linac transport systems," *ANL Report*.

Generation of Space-Charge Waves due to Localized Perturbations*

J. G. Wang, D. X. Wang, D. Kehne, and M. Reiser
Laboratory for Plasma Research and Department of Electrical Engineering
University of Maryland, College Park, Maryland 20742

Abstract

Generation of various space-charge waves due to localized perturbations on the beam parameters, namely the velocity, density, and current, is reported. Analytical solutions of one-dimensional fluid equations under such perturbations are presented and compared with the experimental results.

I. INTRODUCTION

The study of longitudinal instabilities in space-charge dominated beams is an on-going research program at the University of Maryland [1]. It has significant importance to high current beam acceleration and transport such as in the case of induction linacs for heavy ion fusion drivers [2]. As the first phase of the program, we study the generation, propagation, and edge reflection of space-charge waves due to localized perturbations in an environment without instability.

The behavior of space-charge waves has been long studied in the fields of microwave generation and particle acceleration [3,4]. The underlying physics is well known when beams are perturbed by sinusoidal signals. In order to study beam physics of longitudinal instability and beam-wave interaction, it is desirable to generate space-charge waves in the form of localized perturbations instead of sinusoidal signals. There is very little information about this in the literature.

In the experiment we found that the space-charge waves generated by localized perturbations have various forms, depending on how specific beam parameters are perturbed. In general two space-charge waves have different amplitude and polarity under the initial velocity and density perturbations. It is only in some special cases, the two space-charge waves are generated with the same amplitudes. There are also conditions under which the two space-charge waves degenerate into one: a fast wave only or a slow wave only. The experimental results, analytical solutions and a comparison between the two are reported in this paper.

II. EXPERIMENTAL RESULTS

The experimental setup consists of a short pulse electron beam injector [5] and a 5-m long periodic solenoid focusing channel [6]. The electron beam is generated by a gridded electron gun. The initial perturbation is introduced to the beam by modulating the grid pulse with a small bump as shown in Fig. 1. This corresponds to a positive velocity perturbation on the beam particles, which in turn produces the initial density, or current perturbations at different values depending on the gun operation conditions. The various space-charge waves in the form of localized perturbations are then generated and propagate on the beam. The beam current and energy can be measured along the channel for analysis.

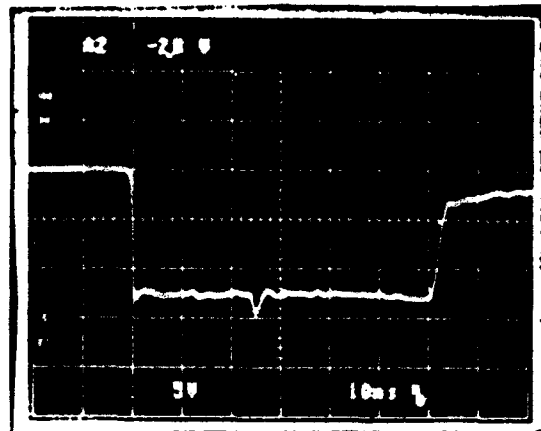


Fig. 1. Grid-cathode pulse of the electron gun, showing a perturbation bump.

Figure 2 shows the beam current waveforms measured at 2 different locations along the transport channel. Two current waves, namely, the slow and fast waves appearing in the beam current waveform, are generated in almost equal amplitudes and opposite polarities, and propagate apart.

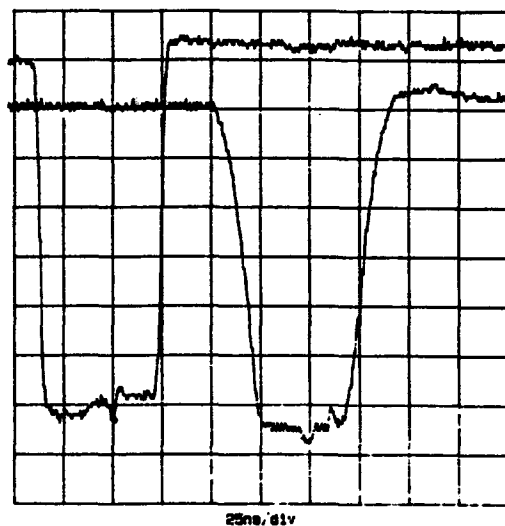


Fig. 2. Beam current waveforms, showing that two current space-charge waves with almost equal amplitudes and opposite polarities propagate away from each other.

Figure 3 shows that only one fast wave with a positive polarity generated on the beam current, which propagates toward the beam front. By contrast, Fig. 4 shows only one slow wave with a negative polarity on the current waveforms, which propagates toward the beam tail.

* Research Supported by the U.S. Department of Energy.

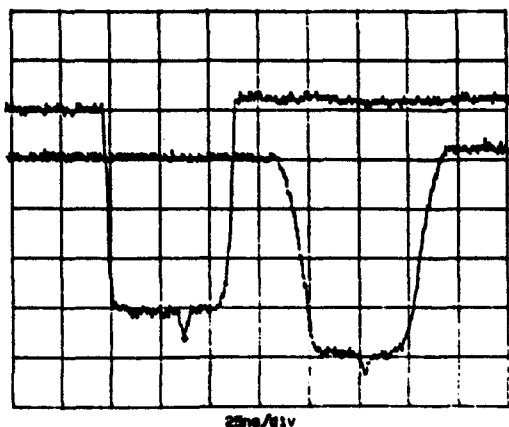


Fig. 3. Beam current waveforms with only one fast wave, propagating towards the beam front.

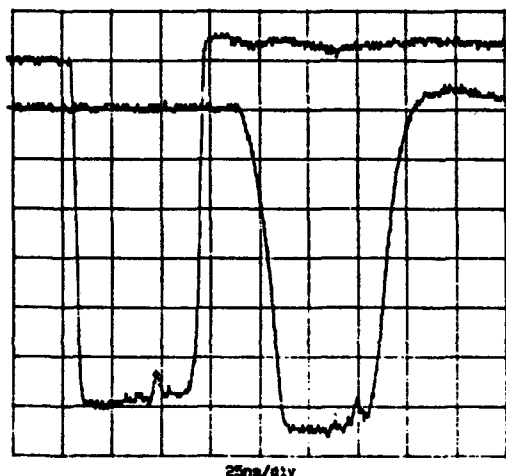


Fig. 4. Beam current waveforms with only one slow wave, propagating towards the beam tail.

Figure 5 shows the space-charge wave signals from an beam energy analyzer, where the beam particles with an energy above the beam average energy pass through the energy analyzer and form the bumps of the traces. On the top trace, only one fast velocity wave appears, corresponding to the case in Fig. 3, while on the bottom trace only one slow wave appears, corresponding the case in Fig. 4. On the fourth trace, two velocity waves with almost the same amplitude appear, that is close to the case in Fig. 2. Other traces show that one velocity wave is dominant over another.

III. ANALYTICAL SOLUTIONS

In order to interpret the experimental observations, the cold fluid model has been employed. The space-charge waves are solved in the time domain for a localized perturbation instead of in the frequency domain for a sinusoidal wave. The specific solutions under the given initial and boundary conditions are obtained instead of eigenmode solutions from dispersion equations. All possible initial conditions of velocity, density, and current perturbations occurred in the experiment are taken into consideration.

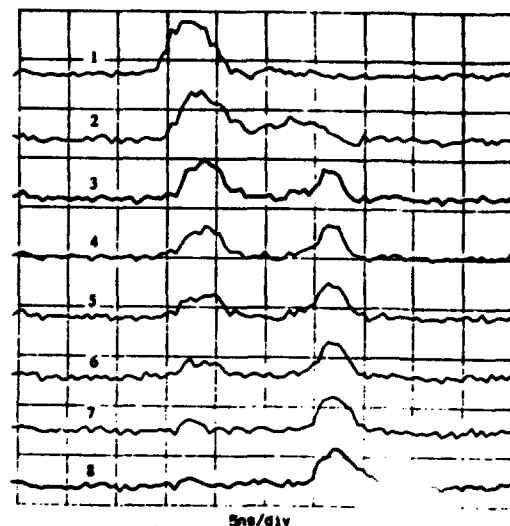


Fig. 5. Velocity waves measured by beam energy analyzer, showing the change from a fast wave to a slow wave when the perturbation conditions vary in the gun.

The one-dimensional fluid model consists of the linearized continuity equation and momentum transfer equation:

$$\begin{cases} \frac{\partial \lambda_1}{\partial t} + v_0 \frac{\partial \lambda_1}{\partial z} + \lambda_0 \frac{\partial v_1}{\partial z} = 0 \\ \frac{\partial v_1}{\partial t} + v_0 \frac{\partial v_1}{\partial z} = -\frac{e}{m\gamma^3} E_z = -\frac{eg}{4\pi\epsilon_0 m\gamma^3} \frac{\partial \lambda_1}{\partial z} \end{cases} \quad (1)$$

where $\lambda(z,t)$ and $v(z,t)$ are the line charge density and the particle velocity, the subscripts 0 and 1 representing the unperturbed and perturbed quantities, respectively, $E_z(z,t)$ is the longitudinal electrical field induced by the a. c. component of the beam current, which equals to $(-g/4\pi\epsilon_0\gamma^2)(d\lambda_1/dz)$ under the long wavelength condition, g is a geometric factor of order unity, and $e/(m\gamma^3)$ denotes the ratio of the charge and the "longitudinal mass" of the charged particles.

By applying the double Laplace transformations both for the space z and time t , defined by

$$\tilde{f}(k, s) = \int_0^\infty dz \int_0^\infty dt f(z, t) e^{-(kz + st)} \quad (2)$$

where $f(z,t)$ is a function representing $v_1(z,t)$, $\lambda_1(z,t)$, or $i_1(z,t)$ - the perturbed beam current, Eq. (1) then can be converted to algebra equations for v_1 , λ_1 and i_1 in the k - s domain.

Further, we consider the following initial and boundary conditions: a). There is no perturbation anywhere along the z -axis when $t < 0$; b). At $z=0$ for $t > 0^+$ a local velocity perturbation is introduced to the beam in the form

$$v_1(0, t) = \alpha v_0 G(\tau) \quad (3)$$

where α is a small quantity to specify the strength of the perturbation, and $G(\tau)$ is the unit gate function defined by the difference of two Heavyside unit step functions

$$G(\tau) = U(t) - U(t - \tau) \quad (4)$$

c). Assume the initial current perturbation has the form

$$i_1(0, t) = \beta i_0 G(\tau) \quad (5)$$

with β as a small quantity to specify the perturbation strength. Therefore, the initial density perturbation is determined by

$$\lambda_1(0, t) = (\beta - \alpha) \lambda_0 G(\tau) \quad (6)$$

Thus, the perturbed beam parameters can be found as

$$\tilde{\lambda}_1(k, s) = \frac{\beta i_0 s + (\beta - \alpha) \lambda_0 \left(\frac{v_0^2 - c_s^2}{c_s^2} \right) k}{(s + kv_0)^2 - k^2 c_s^2} \frac{1}{s} (1 - e^{-s\tau}) \quad (7)$$

$$\tilde{v}_1(k, s) = \frac{[\alpha v_0^2 + (\beta - \alpha) c_s^2] s + \alpha v_0 \left(\frac{v_0^2 - c_s^2}{c_s^2} \right) k}{(s + kv_0)^2 - k^2 c_s^2} \frac{1}{s} (1 - e^{-s\tau}) \quad (8)$$

and

$$\tilde{i}_1(k, s) = v_0 \tilde{\lambda}_1(k, s) + \lambda_0 \tilde{v}_1(k, s) \quad (9)$$

Here c_s is the so called "sound" velocity of space-charge waves and defined as

$$c_s = \sqrt{\frac{eg\lambda_0}{4\pi m\epsilon_0 \gamma^5}} \quad (10)$$

Inverse Laplace transforms yield the perturbed beam density, velocity and current in the real time-space domain as

$$\lambda_1(z, t) = -\frac{\lambda_0}{2} \left[\alpha \frac{v_0}{c_s} - (\beta - \alpha) \right] G_{[z - (v_0 - c_s)t]}(\tau) + \frac{\lambda_0}{2} \left[\alpha \frac{v_0}{c_s} + (\beta - \alpha) \right] G_{[z - (v_0 + c_s)t]}(\tau) \quad (11)$$

$$v_1(z, t) = +\frac{v_0}{2} \left[\alpha - (\beta - \alpha) \frac{c_s}{v_0} \right] G_{[z - (v_0 - c_s)t]}(\tau) + \frac{v_0}{2} \left[\alpha + (\beta - \alpha) \frac{c_s}{v_0} \right] G_{[z - (v_0 + c_s)t]}(\tau) \quad (12)$$

$$i_1(z, t) = \frac{-i_0}{2} \left[\frac{\alpha v_0}{c_s} - \beta + \frac{(\beta - \alpha) c_s}{v_0} \right] G_{[z - (v_0 - c_s)t]}(\tau) + \frac{i_0}{2} \left[\frac{\alpha v_0}{c_s} + \beta + \frac{(\beta - \alpha) c_s}{v_0} \right] G_{[z - (v_0 + c_s)t]}(\tau) \quad (13)$$

Here the two-dimensional unit gate function is defined as

$$G_{[z - (v_0 \pm c_s)t]}(\tau) = U[z - (v_0 \pm c_s)(t - \tau)] - U[z - (v_0 \pm c_s)t] \quad (14)$$

IV. DISCUSSION

According to Eq. (13), the two current waves have the same amplitudes with the opposite polarity only when $\beta=0$, i.e. without an initial current perturbation. This is the case in Fig. 2. When $\beta/\alpha=(1+v_0/c_s)$, only one fast wave is generated as in the case of Fig. 3. When $\beta/\alpha=(1-v_0/c_s)$, only one slow wave survives as shown in Fig. 4.

Fig. 6 shows the relative amplitude of the velocity waves, i.e. the ratio of the velocity wave amplitude over the initial perturbation amplitude αv_0 , versus the quantity β/α for $c_s/v_0=0.1$. It is only at the point A where $\beta/\alpha=1$ indicating the initial density perturbation is zero, the two velocity waves have the same polarity and the same relative amplitude of 1/2. Elsewhere, the two velocity waves have different amplitudes, even different polarity when $|\beta/\alpha|$ is large enough. The sum of the two amplitudes is always 1, i.e. the initial perturbation amplitude, as expected. The slow wave vanishes completely at $\beta/\alpha=11$, while the fast wave vanishes at $\beta/\alpha=-9$. This is compared with the scope traces in Fig. 5.

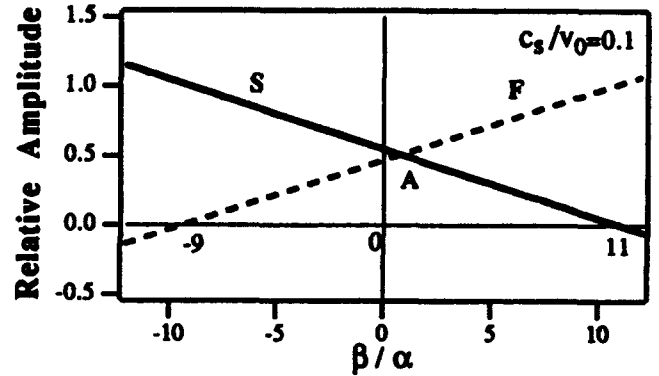


Fig. 6. Relative velocity wave amplitude vs. perturbation parameters.

V. SUMMARY

The generation of space-charge waves due to localized perturbations to the beam parameters is studied experimentally and analytically. Various forms of space-charge waves have been observed and they are the solutions of the fluid model. Good agreement between the theory and experiment has been found.

VI. REFERENCES

- [1] J. G. Wang, M. Reiser, W. M. Guo, and D. X. Wang, Particle Accelerators, Vol. 37-38, 181 (1992).
- [2] E. P. Lee, in the Proceedings of the 1992 Linac Conference, Ottawa, Canada, Aug. 24-28, p. 591.
- [3] A. H. W. Beck, Space-Charge Waves, Pergamon Press, 1958.
- [4] J. D. Lawson, The Physics of Charged Particle Beams, Chapter 6, Oxford University Press, second edition, 1988.
- [5] J. G. Wang, D. X. Wang, and M. Reiser, Nucl. Instr. & Meth. in Phys. Res. A316, 112 (1992).
- [6] D. X. Wang, J. G. Wang, D. Kehne, and M. Reiser, accepted for publication in Applied Physics Letters.

Three Dimensional Multipole Decomposition of Fields*

Kyoung Hahn
Lawrence Berkeley Laboratory
University of California
Berkeley, CA 94720, USA

Abstract

A new method to generate the general multipole representation of the three dimensional static field, electric or magnetic, is obtained via a scalar potential evaluated from the arbitrary specified source. As an application of this formulation, a previously described 3-D electric field decomposition method has been further generalized to the magnetic field.

1. INTRODUCTION

Representing an arbitrary three-dimensional vector field requires enormous amount of information. Multipole expansion is the natural and efficient way of representing a field with symmetry. A good example is the field from a quadrupole magnet which consists of a large quadrupole component with relatively small fringe fields. Then the multipole expansion converges rapidly and from the symmetry of the magnet geometry it can be easily seen that certain multipoles does not occur.

For a static field, electric or magnetic, the Green's function is well known, and the multipole coefficients can be determined from the source of the field. For a electrostatic problems the potential at the electrode is usually given and the charge density can be obtained by the capacity matrix technique[1] without solving for the field everywhere. For the magnetostatic problem, the current source is usually given.

In this report general multipole decomposition method for the static vacuum field from an arbitrary source is presented. In section II, the multipole expansion of the field is defined and the method of generating its coefficients from the Green's function is described. Section III shows the result from its application to a simple magnet geometry. A summary and conclusion is given in Sec. IV.

2. MULTIPOLE EXPANSION

Static vacuum fields, electric or magnetic, can be represented by a scalar potential. The scalar potential can be expressed in terms of multipoles which exploit the polar symmetry of the system. The convergence of the expansion depends on the system of interest, however, most of simple designs such as quadrupoles or sextupoles have a single dominant component in addition to the many small other multipole terms. Then the field can be accurately represented by keeping a few leading terms.

The multipole coefficients $M_{k,l}(z)$ of the potential ϕ are defined in cylindrical coordinates system by

$$\phi(\rho, \theta, z) = \sum_{k=0}^{\infty} \sum_{l=0}^{\infty} M_{k,l}(z) \rho^k \cos(l\theta) \quad (1)$$

for the system of up-down symmetry. No z -axis expansion is performed and $M_{k,l}(z)$ is calculated at numerous locations in z .

The source-free vacuum potential ϕ satisfies the Laplace equation ($\nabla^2 \phi = 0$) and thus the $M_{k,l}$ observe the following recursion relation:

$$M_{k,l} = M''_{k-2,l} / (l^2 - k^2), \quad (2)$$

where double prime denotes the second derivative with respect to z . In order for ϕ be analytic near the origin, the relation $k \geq l \geq 0$ and $k - l = \text{even}$ must be true for non-zero coefficients. The entire ensemble of multipole coefficients can then be determined from $M_{l,l}$ and its z -derivatives.

Since the field can be determined from the Green's function which is analytic away from the source, it is possible to decompose the Green's function into multipoles and the total multipole coefficients are obtained by integration over the source.

Electric potential ϕ from the charge distribution $Q(x')$ is given by (setting $4\pi\epsilon_0 \rightarrow 1$)

$$\phi = \int dx' G_e(x, x') Q(x') \quad (3)$$

where

$$G_e(x, x') = \frac{1}{|x - x'|}. \quad (4)$$

Away from the charges the Green's function G is infinitely differentiable, and it is in principle possible to compute the multipole coefficients $M_{k,j}$ by differentiating equation (1). Hence the multipole coefficient of the electrostatic field at the origin has the form

$$M_{k,l} = \int dx K_{k,l}(x) Q(x) \quad (5)$$

and the explicit expression of $K_{k,l}$ is given in the Table 1.

The magnetic field is determined from the current source I by Biot-Savart's law (setting $\mu_0/4\pi \rightarrow 1$),

$$B = - \int dx' G_m(x, x') \times I(x')$$

*Work supported by the Director, Office of Energy Research, Office of Fusion Energy, U.S. Dept. of Energy, under Contract No. DE-AC03-76SF00008.

where G_m is the Green's function for the magnetic field and its explicit form is given by

$$G_m(\mathbf{x}, \mathbf{x}') = \frac{\mathbf{x} - \mathbf{x}'}{r^3}$$

where

$$r = |\mathbf{x} - \mathbf{x}'|.$$

After some algebra the multipole coefficient $M_{k,l}$ of the magnetic field at the origin can be recast as,

$$M_{k,l} = - \int d\mathbf{x} [K_{k,l}^x I_x(\mathbf{x}) + K_{k,l}^y I_y(\mathbf{x}) + K_{k,l}^z I_z(\mathbf{x})] \quad (6)$$

with the explicit form of the vector coefficients $K_{k,l}$ given in the Table 2.

The zeroth order coefficient $M_{0,0}$ is determined by the integral along the z -axis

$$M_{0,0}(\mathbf{x}) = - \int_0^x B_z(\mathbf{x}') d\mathbf{x}'.$$

3. COMPUTATIONAL RESULTS

It is straight forward to evaluate the multipole coefficients from the expressions (5) and (6). In principle multipole coefficients of all orders, still exact, can be obtained from the method above, however, in the present work the expansion was truncated at 10^{th} order since the number of coefficients increases by the square of the order and the expansion usually converges rapidly for the typical system of interest.

The coefficients are made dimensionless by choosing the scaling length of aperture radius a and the proper scalar potential value at the aperture radius and $\theta = 0$, i.e.:

$$\phi = \phi_0 \sum_{k=0}^{10} \sum_{l=0}^{10} M_{k,l}(z) \left(\frac{\rho}{a}\right)^k \cos(l\theta) \quad (7)$$

Test runs made for an electrostatic quadrupole show an exact match to the previous calculation using the Differential Algebra (DA) technique [1] except the computation time is reduced by at least two orders of magnitude. Typical computation times spent for the extraction of the coefficients up to tenth order is less than 1 second on a Cray computer (XMP) from the charge nodes of 5000 points. Calculation of the charges on the nodes which involves the inversion of the capacity matrix takes about 800 Cray cpu seconds as before. For the magnetic multipole expansion, two test runs are presented for simple geometries. Case one is the simple Helmholtz coil consisting of two identical circular rings of radius a separated by the equal distance a . Axi-symmetry of the field gives zero coefficients except the $M_{k,0}$ for even k . This is an excellent example showing advantage of the multipole expansion since only a few coefficients are needed to describe the 3-D vector field at fixed z . Figure 1 shows the non-zero multipole coefficients up to 10^{th} order. Though not plotted, the axial magnetic field at the axis can be obtained from the z -derivative of $M_{0,0}$

and the slope of the $M_{0,0}$ in the plot is seen to be nearly constant as expected.

A second case is the simple magnetic quadrupole made of current elements shown in Figure 2. A single unit of current is flowing on the arc-shaped current elements of aperture radius a and two units of current are on the straight segment running along the z -axis. The length of the straight section is chosen to be the same as the aperture radius (a) so that a rich content of multipoles from the fringe field is produced. From the symmetry of the current geometry, all the multipole coefficients with l other than $2 + 4k$ for a non-negative integer k are zero. Figure 3 shows the non-zero multipole coefficients of the simple test current distribution of the quadrupole in the Figure 2.

5. CONCLUSION AND DISCUSSION

The general multipole expansion method of the static field is presented. The previous multipole calculation of the three-dimensional electrostatic field from the arbitrary electrode geometry [1] has been generalized to the magnetic field. In addition, using symbolic algebra, instead of differential algebra[2], each multipole coefficient is explicitly calculated, hence the computation time is reduced substantially (by a factor of hundred or greater), which makes this method practical.

6. REFERENCES

- [1] M. Berz, W. Fawley and K. Hahn, Nucl. Inst. and Method, A 307 (1991) 1.
- [2] M. Berz, IEEE Trans. Elec. Dev., 35-11 (1988) 2002.

Table 1. Electric multipole coefficient $K_{k,l}$ at origin from a unit source at \mathbf{x} . Here $r = \sqrt{x^2 + y^2 + z^2}$.

$$\begin{aligned} K_{0,0} &= \frac{1}{r} \\ K_{1,1} &= \frac{x}{r^3} \\ K_{2,2} &= \frac{3(x^2 - y^2)}{4r^5} \\ K_{3,3} &= \frac{5(x^3 - 3xy^2)}{8r^7} \\ K_{4,4} &= \frac{35(x^4 - 6x^2y^2 + y^4)}{64r^9} \\ K_{5,5} &= \frac{63(x^5 - 10x^3y^2 + 5xy^4)}{128r^{11}} \\ K_{6,6} &= \frac{231(x^6 - 15x^4y^2 + 15x^2y^4 - y^6)}{512r^{13}} \\ K_{2,0} &= \frac{x^2 + y^2 - 2z^2}{4r^5} \end{aligned}$$

Table 2. Magnetic multipole coefficient $K_{k,l}^i$ at origin from a unit current source I_i at x . Here $r = \sqrt{x^2 + y^2 + z^2}$.

$$\begin{aligned}
 K_{0,0}^x &= \frac{yz}{(x^2 + y^2)r} \\
 K_{1,1}^x &= K_{3,1}^x = K_{5,1}^x = K_{7,1}^x = K_{9,1}^x = 0 \\
 K_{2,2}^x &= \frac{3yz}{4r^5} \\
 K_{3,3}^x &= \frac{5xyz}{4r^7} \\
 K_{4,4}^x &= \frac{35y(3x^2 - y^2)z}{64r^9} \\
 K_{5,5}^x &= \frac{63xy(x^2 - y^2)z}{32r^{11}} \\
 K_{6,6}^x &= \frac{231y(5x^4 - 10x^2y^2 + y^4)z}{512r^{13}} \\
 K_{2,0}^x &= \frac{3yz}{4r^5}
 \end{aligned}$$

$$\begin{aligned}
 K_{0,0}^y &= -\frac{xz}{(x^2 + y^2)r} \\
 K_{1,1}^y &= \frac{z}{r^3} \\
 K_{2,2}^y &= \frac{3xz}{4r^5} \\
 K_{3,3}^y &= \frac{5(x^2 - y^2)z}{8r^7} \\
 K_{4,4}^y &= \frac{35x(x^2 - 3y^2)z}{64r^9} \\
 K_{5,5}^y &= \frac{63(x^4 - 6x^2y^2 + y^4)z}{128r^{11}} \\
 K_{6,6}^y &= \frac{231x(x^4 - 10x^2y^2 + 5y^4)z}{512r^{13}} \\
 K_{2,0}^y &= -\frac{3xz}{4r^5}
 \end{aligned}$$

$$\begin{aligned}
 K_{0,0}^z &= K_{2,0}^z = K_{4,0}^z = K_{6,0}^z = K_{8,0}^z = K_{10,0}^z = 0 \\
 K_{1,1}^z &= -\frac{y}{r^3} \\
 K_{2,2}^z &= \frac{-3xy}{2r^5} \\
 K_{3,3}^z &= \frac{5y(-3x^2 + y^2)}{8r^7} \\
 K_{4,4}^z &= \frac{35xy(-x^2 + y^2)}{16r^9} \\
 K_{5,5}^z &= \frac{63y(-5x^4 + 10x^2y^2 - y^4)}{128r^{11}} \\
 K_{6,6}^z &= \frac{231xy(-3x^4 + 10x^2y^2 - 3y^4)}{256r^{13}} \\
 K_{3,1}^z &= \frac{3y(-x^2 - y^2 + 4z^2)}{8r^7}
 \end{aligned}$$

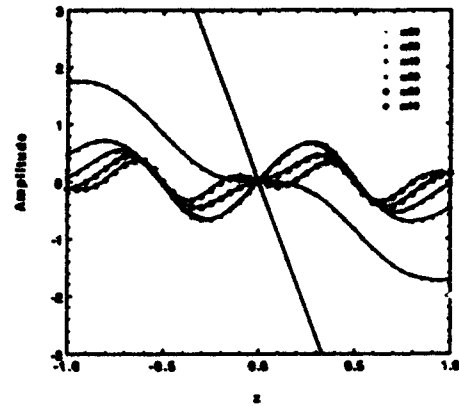


Fig. 1 - Multipole coefficients of the Helmholtz coil up to 10^{14} order. All none-axisymmetric coefficients are zero. In Helmholtz coil, axial separation of the identical rings is equal to their radius (a).

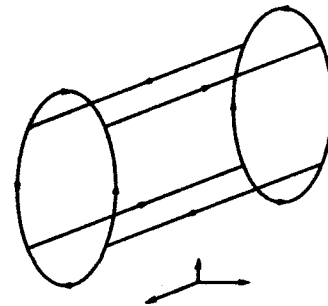


Fig. 2 - Current distribution in a simple quadrupole geometry. A single unit of current is on the arc shaped elements and two units of current is on the straight section in order to prevent charge accumulation.

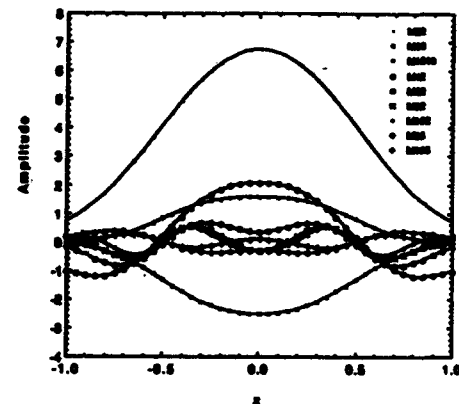


Fig. 3 - Multipole coefficients $M_{k,l}$ for the simple quadrupole geometry in Figure 2. The length of the straight section element is chosen to be the same as the aperture radius. From the symmetry, coefficients of $l = 0, 1, 3, 4, 5, 7, 8$, and 9 are zero.

Multi-Bunch Beam-Break-Up Studies for a SWFEL/TBA*

J.S.Kim, H.Henke^(a) A.M.Sessler and D.H.Whittum^(b)
Lawrence Berkeley Laboratory
University of California, Berkeley, California 94720

Abstract

A set of parameters minimizing BBU is obtained for a high current, low energy "drive beam" in a standing wave free electron laser two-beam acceleration(FEL/TBA). A large reduction in the transverse wake function is obtained by making the cavity-iris junction gradual by means of a cone. BBU is examined under various BBU reduction schemes.

I. INTRODUCTION

Multi-bunch beams have been shown to exhibit unstable transverse beam dynamics due to cumulative transverse wake fields. The purpose of this work is to design a cavity of low transverse wakes and to produce a set of optimized parameters minimizing BBU for a high current, low energy "drive beam" of the SWFEL/TBA[1,2]. The physical set-up is shown in Figure 1.

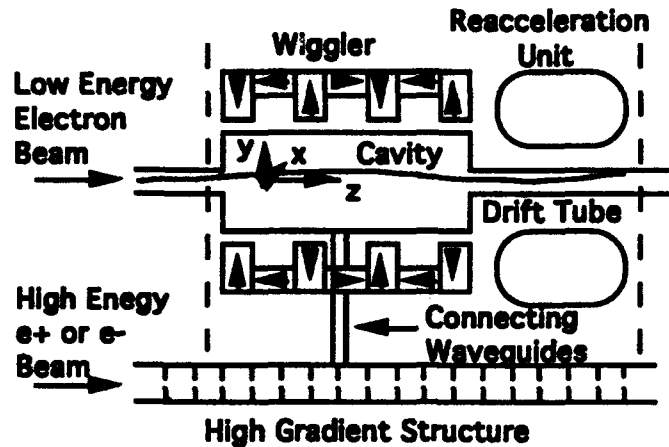


Figure 1. Schematic diagram of SWFEL/TBA

Standing waves can be obtained by making the irises small enough that the FEL mode is below the cutoff frequency of the iris modes. This requires a large change in radius at the junction between the cavity and iris, resulting in large wakes. The wakes can be dramatically reduced by introducing a cone junction (making the junction gradual).

* The work was supported by the Director, Office of Energy Research, Office of High Energy and Nuclear Physics, Division of High Energy Physics, of the U. S. Department of Energy under Contract No. DE-AC03-76SF00098.

(a) Permanent address: Technische Universität Berlin, Institute für Theoretische Elektrotechnik, Einsteinufer 17, D-1000 Berlin 10, Germany

(b) Permanent address: Accelerator Department, National Laboratory for High Energy Physics (KEK), 1-1 Oho, Tsukuba, Ibaraki, 305, Japan

For long cavities the transverse momentum kicks are determined by the junction conditions only, resulting in the same amount of momentum kick for a cavity regardless of the length of the cavity.

BBU calculations were performed, with various BBU reduction schemes, using the parameters in Table 1.

Table 1. Parameters of a SWFEL for 17.1 GHz with cylindrical cavities

cavity	dimension (radius x length) = 1.5 cm x 88 cm iris (radius x length) = 0.4 cm x 3 cm junction = 2 cm length; cone ~30°
beam	energy $\gamma = 16.6$ average current $I = 1$ kA pulse length = 100 ns
focusing	focusing length $\lambda\beta = 52$ cm; ($k\beta = 0.12$ cm ⁻¹)

II. BASIC BEAM-BREAK-UP EQUATIONS

A. The Model

Let the planar wiggler magnetic fields lie in the y-z plane as indicated in Figure 1, with the particle wiggle in the x-z plane. These wiggler oscillations in a cylindrical cavity excite the TE_{11p} FEL mode. The beam dynamics in the wiggler plane and that perpendicular to it can be treated separately as a first order approximation. In this paper we consider BBU in the y-direction, as that is the most severe case.

Assuming one macro particle per bunch and equal spacing between bunches the transverse displacements, ξ_j , of the j-th bunch with energy γ_j can be represented in a standard BBU form.

$$\frac{\partial}{\partial z} \left[\gamma_j(z) \frac{\partial}{\partial z} \xi_j \right] + \gamma_j(z) k_{\beta,j}^2(z) \xi_j = \frac{Is_b}{I_0} \sum_{k=0}^j W((j-k)s_b) \xi_k,$$

where z is the axial coordinate in cm, s_b is the distance between bunches in cm, W is the transverse wake function in cm⁻³, I is the average current in z in kA, and $I_0 = mc^3/e = 17.05$ kA.

B. Analytic Estimates

For a purely sinusoidal wake function, $W = W_0 \sin(\omega_r s/c)$ the oscillation amplitude of displacements of the j-th bunch can be estimated using the discrete Laplace Transformation as in Reference [3]. If only the first bunch is displaced,

$$\frac{\xi_j(s)}{\xi_0} = \left(\frac{1}{5j}\right) A^{1/2} e^A \quad \text{with} \quad A = \left[\frac{I(j\beta) W_0 s}{I_0 \gamma \beta} \right]^{1/2}.$$

Reduction in BBU can be obtained for smaller wakes, higher $\gamma \beta$, smaller charge, and shorter device lengths.

The wakes, in reality, are far from a single sinusoidal wave. Any finite quality factor Q for the cavity, or any spread in frequency of the wakes reduces the amplitude for larger s . In this case, we can reduce BBU for the same output energy FEL by making the pulse length longer, since the output energy of FELs depend on the charge of the pulse. If we take into account the quality factor the wake potential is reduced by

$e^{-(\omega_r/Q)(s/c)}$, where ω_r is the wake modes, and the beam displacements are reduced by the same factor. In the presence of frequency spread $\Delta\omega$ of the wake potential, the displacements are also reduced, although depending on the model, roughly by the factor $e^{-(\Delta\omega)(s/c)}$.

III. TRANSVERSE WAKES

For a Gaussian bunch of 1 Coulomb electrons with width σ , the transverse wake of the dipole ($m=1$) mode in an ideal pill-box cylindrical cavity can be evaluated as following.

$$W(r=a, s) = -\left(\frac{1}{\pi \epsilon_0 L}\right) \alpha^2 e^{-s^2/2\sigma^2} \sum_{n,p} \frac{J_0^2(j_n \alpha) - J_2^2(j_n \alpha)}{J_2^2(j_n)} \\ \times \left[1 - (-1)^p \cos(\nu_{np} L) \right] \frac{1}{2\nu_{np} a} \text{Im} \left\{ w \left(\frac{\nu_{np} \sigma}{\sqrt{2}} - \frac{is}{\sigma\sqrt{2}} \right) \right\},$$

where $\nu_{np} = \omega_{np}/c$, ω_{np} being the cavity mode frequencies, $\alpha = a/R$ and j_n are zeros of the Bessel function J_1 and w is the complex error function. For the cavity of Figure 2(a) with $\sigma = 3$ mm, the wake shown in Figure 2(a') can be reproduced with 50 modes.

Wake functions are obtained for a cylinder of radius 1.5 cm and length 87.5 cm using ABCI [4] for the dipole mode ($m=1$). Transverse wakes for (a) a step junction cavity and (b) a cone junction cavity are shown in Figure 2. By making the junctions gradual, a dramatic reduction in the wakes is achieved for the gradual junction effectively introduces spread in frequencies of wake modes, resulting in similar wake functions as in a de-tuned structure [5]. Smoothing the corners of the step junctions does not adequately reduce the wake. Due to computational limits, we have obtained wakes only up to 3 m. Since with reasonable Q values, the wakes at large s should damp away, we have assumed the wakes beyond 3 m to be negligible.

For long cavities the transverse momentum kicks depend only on the junction conditions and are independent of the cavity lengths. The reason for this is that for long cavities the wakes are superposition of the individual wakes generated due to the two junctions. This has been verified numerically

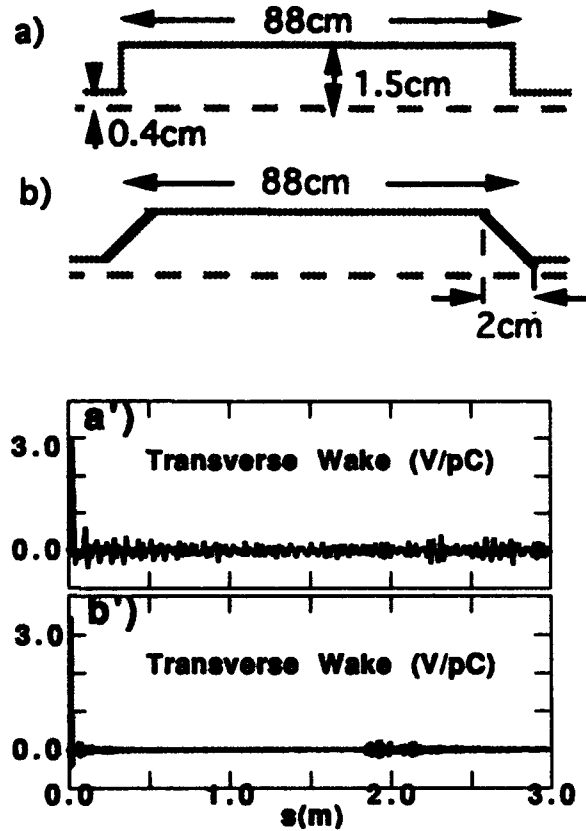


Figure 2. Cylindrically symmetric cavity with abrupt junction (a) and gradual junction with a 2cm cone (b). Also, the transverse wakes for a Gaussian bunch of $\sigma=3$ mm are shown with abrupt junctions (a') and gradual junctions (b').

for the monopole ($m=0$) longitudinal wakes [6]. We believe that the same property applies for the dipole transverse wakes as well. Thus longer cavities reduce the transverse kick per unit length.

A reappearance of the large amplitude wake oscillations near 1.7 m of Figure 2(b') occurs roughly at twice the length of the cavity. That is likely the first wake generated by the signal charge reflected back to the entrance of the cavity. To push the reappearance of the large oscillations further away in s , one might either make the cavity longer or the cone transition longer. The reappearance of these oscillations are commonly observed with discreteness of frequencies and discontinuities in frequency distribution [5].

IV. NUMERICAL BBU RESULTS

Using the wake functions of Figure 2(b'), we have integrated the basic model equation numerically using the 4-th order Runge-Kutta method. Uniform displacements of the pulse were assumed as an initial condition.

The maximum amplitudes of a 100 nsec pulse of 17.1 GHz are shown in Figure 3 with respect to device lengths for the parameters presented in Table 1. Assuming negligible wake beyond 3 m, the beam displacements are small for a 60 m device but become too large for a 100 m device as shown in curve A of Figure 3.

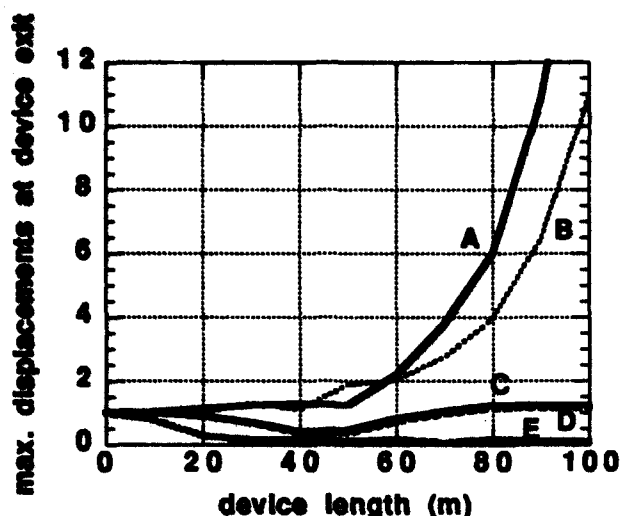


Figure 3. Maximum displacements of a 100 nsec pulse at the time of exiting the device as a function of device length, for the wakes shown in Figure 2(b'). Shown are the displacements (A) with ignoring wakes beyond $s=3$ m, (B) with BNS damping of a 2% increment in $\gamma(s)$, (C) with ignoring wakes beyond $s=1.74$ m, (D) with $Q=100$, and (E) with 2% spread in k_β .

Now we consider some possible damping mechanisms. First consider BNS damping [8]. The idea is to compensate that wake by increasing or decreasing the energy of the bunch, thus introducing a small change to k_β with s . The sign of the slope, k_β with s , is crucial. However, with either an increment (B in Figure 3) or decrement of $\gamma(s)$, we obtain only a slight reduction in BBU.

Next we assumed that the wake beyond 1.74 m is negligible. When we set the wakes beyond 1.74 m to zero (C in Figure 3), then an external $Q=100$ is introduced instead of zeroing the wakes beyond 1.74 m (D in Figure 3). These gave the same good results indicating virtually no growth for 100 m device. Lastly we introduced some spread in k_β . With 2% spread in k_β , all transverse motion are damped out (E in Figure 3).

V. DISCUSSION

The transverse dynamics of the beam depends on γk_β strongly, yielding smaller BBU for larger γk_β . The presented BBU results are for $\gamma k_\beta = 2.0 \text{ cm}^{-1}$. On the other hand the fluctuation level of output power amplitude and phase, in beam energy, depends strongly on k_w . For 17.1 GHz the best sensitivity is obtained around $k_w = 0.16$. For a pulse of 1 kA, 100 nsec, $a_w = 1.4$ is all that is needed to obtain an output energy of about 10 J/m. With such parameters, and with natural FEL focusing alone, the value $\gamma k_\beta = \bar{a}_w k_w$

(where the bar is used for an rms value,) is too small to reduce BBU to an acceptable level. This dilemma can be eliminated by introducing strong focusing in the drift region to minimize BBU (which does not affect the power extraction performance).

The BBU results presented here can be considered as an upper limit since we did not take into account the wiggler motion. Also, we believe that the BBU can be controlled better with rectangular cavities since we have more freedom to change the junction conditions. Nevertheless, even with the excessive estimate of BBU obtained in this work, we can find suitable SWFEL parameters as can be seen in Reference [7].

Acknowledgments

The authors would like to acknowledge to many people who made various codes available for the analysis: D. Chan and R. Ryne, J. Deford and, in particular, Y.H. Chin. Computations were performed at NERSC.

VI. REFERENCES

- [1] A.M.Sessler, in *Laser Acceleration of Particles*, edited by P.J.Channell (AIP, New York, 1982), p.154.
- [2] A.M.Sessler, D.H.Whittum, J.S.Wurtele, W.M.Sharp, and M.A.Makowski, "Standing-wave free-electron laser two-beam accelerator", Nucl. Inst. Method in Phys. Res. A306, pp.592-605 (1991).
- [3] K.Yokoya, "Cumulative beam breakup in large-scale linacs", preprint DESY 86-084 (1986)
- [4] Y.H. Chin, "User's guide for new ABCI Version 6.2", preprint LBL-33091 (1992).
- [5] D.Yu and J.S.Kim, "Wakefield suppression using beatwave structures", IEEE Part. Accel. Conf. Proc., p. 1719 (1991).
- [6] Y.H. Chin, "New features and applications of ABCI", preprint, LBL-33735.
- [7] J.S. Kim, A.M. Sessler, W. M. Sharp, and H. Henke, "Beam Sensitivity to Cavity Geometry and Energy Extraction in a Standing Wave FEL/TBA", This proceeding Ja4, (1993).
- [8] V. Balakin, A. Novokhatsky and V. Smirnov, "VLEPP: transverse beam dynamics", Proc. of the 12th Int. Conf. on High Energy Accelerators, Fermilab, p.119, (1983).

RF noise revisited: the effect of coherence.

A. Gerasimov

Fermi National Accelerator Laboratory,*
P.O. Box 500, Batavia, IL 60510.

S.Y. Lee

Physics Department, Indiana University,
Bloomington, IN 47405.

Abstract

The theory of RF noise-induced diffusion is reconsidered to account for the coherent nature of the noise, when all particle are affected by the same random force. The resulting small-scale spatial fluctuations ("microstructure") of the beam density are analyzed. The power spectrum of the fluctuations is calculated.

I. INTRODUCTION

The theory of the longitudinal density diffusion due to RF noise was studied by several authors [2-5]. That analysis however ignored the fact that all the particles in the bunch(es) are affected by the same realization of the random force (what can be termed a coherent random driving). Instead, a conventional Brownian motion problem, with statistically independent forces for different particles, was considered. In the present paper, we derive the condition when this substitution is justified in the zero-order approximation. We investigate as well the first order effect, which turns out to be the formation of the "microstructure", i.e. the short-wavelength spatial fluctuations, of the beam density. More details of the calculations can be found in [6].

II. MODEL.

We consider the general form of the Hamiltonian of nonlinear oscillator with a random driving:

$$H = \frac{p^2}{2} + g(q) + h(q)\xi(t) \quad (1)$$

where $g(q)$ is an arbitrary nonlinear potential and $\xi(t)$ is, for simplicity yet without loss of generality, chosen to be the white noise, i.e.

$$\langle \xi(t)\xi(t') \rangle = \delta(t - t') \quad (2)$$

*Operated by the Universities Research Association, Inc. under contract with the U.S. Dept. of Energy.

The evolution of the density distribution is governed by the Vlasov equation:

$$\frac{\partial f}{\partial t} - \left(\frac{\partial g}{\partial q} + \frac{\partial h}{\partial q} \xi(t) \right) \frac{\partial f}{\partial p} + p \frac{\partial f}{\partial q} = 0 \quad (3)$$

The statistical properties of the fluctuating quantity f are appropriately defined by the ensemble average of the distribution function:

$$\bar{f}(p, q, t) = \langle f(p, q, t) \rangle_{\{\epsilon\}} \quad (4)$$

and the correlation function of the density fluctuations in the adjacent phase space points:

$$K(p, q, \bar{p}, \bar{q}, t) = \langle (f(p, q, t) - \bar{f}(p, q, t))(f(\bar{p}, \bar{q}, t) - \bar{f}(\bar{p}, \bar{q}, t)) \rangle_{\{\epsilon\}} \quad (5)$$

We limit ourselves with considering only the same-time correlator K and study therefore only the spatial, but not the time, correlation properties of the fluctuations.

The further analysis will be using the action-angle variables J, Ψ of the unperturbed ($h(q) = 0$) Hamiltonian (1), which will be assumed to be known. The perturbed Hamiltonian H in these variables has the form:

$$H = H_0(J) + V(J, \Psi)\xi(t) \quad (6)$$

where $V(J, \Psi) = h(q(J, \Psi))$ and $H_0(J)$ are known functions.

III. EVOLUTION EQUATIONS.

Both the average density \bar{f} and the correlator K are evolving in time. We will derive the evolution equations for both quantities using basically the conventional techniques of the theory of stochastic differential equations [1]. It had been shown previously [2-4] that the evolution of the average density obeys the Fokker-Planck equation. The evolution of the density fluctuations however has never been studied.

In the action-angle variables, the mean and the correlator are given by: $\bar{f} = \bar{f}(J, \Psi, t)$ and $K = K(J, \Psi, \bar{J}, \bar{\Psi}, t)$. We will also use the notation $\bar{\Psi} = \Psi + \varphi$ and compressed

notations for the phase space coordinates (1) = $x_{1i} = (J, \Psi)$ and (2) = $x_{2i} = (\bar{J}, \bar{\Psi})$. Taking the differentially small time increment Δt , one obtains the derivatives of the average density:

$$\frac{\partial \bar{f}(1)}{\partial t} = \lim_{\Delta t \rightarrow 0} \frac{\Delta f(1)}{\Delta t} \quad (7)$$

and the correlator:

$$\begin{aligned} \frac{\partial K}{\partial t} = \lim_{\Delta t \rightarrow 0} \frac{1}{\Delta t} & \{ \langle \Delta f(1) f(2) \rangle + \langle f(1) \Delta f(2) \rangle \\ & + \langle \Delta f(1) \Delta f(2) \rangle - \bar{f}(1) \langle \Delta f(2) \rangle - \\ & - \bar{f}(2) \langle \Delta f(1) \rangle - \langle \Delta f(1) \rangle \langle \Delta f(2) \rangle \} \end{aligned} \quad (8)$$

where the increment of the density $\Delta f = f(t + \Delta t) - f(t)$ can be expressed, due to the conservation of the phase-space density, as

$$\Delta f = \frac{\partial f}{\partial x_i} \Delta x_i + \frac{1}{2} \frac{\partial^2 f}{\partial x_i \partial x_k} \Delta x_i \Delta x_k \quad (9)$$

The increments of the phase-space variables Δx_i in time Δt can be obtained from the stochastic equations of motion. The second order terms in Δx were kept because of the properties of the white noise, where the average of quadratic terms $\Delta x_i \Delta x_j$ produces a linear in Δt terms.

The evolution equation for \bar{f} after the substitution of the averages in equation (8) that can be calculated by standard techniques from the relation (9) and equations of motion, becomes the conventional Fokker-Planck equation:

$$\begin{aligned} \frac{\partial \bar{f}}{\partial t} = & \left(\frac{\partial^2 V}{\partial J \partial \Psi} \frac{\partial V}{\partial J} - \frac{\partial^2 V}{\partial J^2} \frac{\partial V}{\partial \Psi} - \omega(J) \right) \frac{\partial \bar{f}}{\partial \Psi} + \\ & + \left(\frac{\partial^2 V}{\partial \Psi^2} \frac{\partial V}{\partial J} - \frac{\partial^2 V}{\partial \Psi \partial J} \frac{\partial V}{\partial \Psi} \right) \frac{\partial \bar{f}}{\partial J} + \frac{1}{2} \left(\frac{\partial V}{\partial J} \right)^2 \frac{\partial^2 \bar{f}}{\partial \Psi^2} + \\ & + \frac{1}{2} \left(\frac{\partial V}{\partial \Psi} \right)^2 \frac{\partial^2 \bar{f}}{\partial J^2} - \frac{\partial V}{\partial \Psi} \frac{\partial V}{\partial J} \frac{\partial^2 \bar{f}}{\partial \Psi \partial J} \end{aligned} \quad (10)$$

where $V = V(J, \Psi)$. For the correlator K , one obtains an evolution equation that is coupled to the mean \bar{f} :

$$\begin{aligned} \frac{\partial K}{\partial t} = & \left(\frac{\partial^2 V}{\partial J \partial \Psi} \frac{\partial V}{\partial J} - \frac{\partial^2 V}{\partial J^2} \frac{\partial V}{\partial \Psi} - \omega(J) \right) \frac{\partial K}{\partial \Psi} \\ & + \left(\frac{\partial^2 V}{\partial \Psi^2} \frac{\partial V}{\partial J} - \frac{\partial^2 V}{\partial \Psi \partial J} \frac{\partial V}{\partial \Psi} \right) \frac{\partial K}{\partial J} + \frac{1}{2} \left(\frac{\partial V}{\partial J} \right)^2 \frac{\partial^2 K}{\partial \Psi^2} \\ & + \frac{1}{2} \left(\frac{\partial V}{\partial \Psi} \right)^2 \frac{\partial^2 K}{\partial J^2} - \frac{\partial V}{\partial \Psi} \frac{\partial V}{\partial J} \frac{\partial^2 K}{\partial \Psi \partial J} \\ & + \left(\frac{\partial^2 \bar{V}}{\partial J \partial \bar{\Psi}} \frac{\partial \bar{V}}{\partial J} - \frac{\partial^2 \bar{V}}{\partial J^2} \frac{\partial \bar{V}}{\partial \bar{\Psi}} - \omega(\bar{J}) \right) \frac{\partial K}{\partial \bar{\Psi}} \\ & + \left(\frac{\partial^2 \bar{V}}{\partial \bar{\Psi}^2} \frac{\partial \bar{V}}{\partial J} - \frac{\partial^2 \bar{V}}{\partial \bar{\Psi} \partial J} \frac{\partial \bar{V}}{\partial \bar{\Psi}} \right) \frac{\partial K}{\partial J} + \frac{1}{2} \left(\frac{\partial \bar{V}}{\partial J} \right)^2 \frac{\partial^2 K}{\partial \bar{\Psi}^2} \\ & + \frac{1}{2} \left(\frac{\partial \bar{V}}{\partial \bar{\Psi}} \right)^2 \frac{\partial^2 K}{\partial J^2} - \frac{\partial \bar{V}}{\partial \bar{\Psi}} \frac{\partial \bar{V}}{\partial J} \frac{\partial^2 K}{\partial \bar{\Psi} \partial J} \\ & + \frac{1}{2} \frac{\partial V}{\partial \Psi} \frac{\partial \bar{V}}{\partial \bar{\Psi}} \frac{\partial^2 K}{\partial J \partial \bar{\Psi}} - \frac{1}{2} \frac{\partial V}{\partial \Psi} \frac{\partial \bar{V}}{\partial J} \frac{\partial^2 K}{\partial J \partial \bar{\Psi}} \\ & - \frac{1}{2} \frac{\partial V}{\partial J} \frac{\partial \bar{V}}{\partial \bar{\Psi}} \frac{\partial^2 K}{\partial \bar{\Psi} \partial J} + \frac{1}{2} \frac{\partial V}{\partial J} \frac{\partial \bar{V}}{\partial J} \frac{\partial^2 K}{\partial \bar{\Psi} \partial \bar{\Psi}} \end{aligned} \quad (11)$$

where $\bar{V} = V(\bar{J}, \bar{\Psi})$.

On the long time scale, or similarly in the small noise / fast oscillations regime, one can average the dependence of all quantities along the unperturbed trajectories $J = \text{const}$, $\Psi = \omega(J)t$. This approximation is well known under the name of "averaging of fast-oscillating variables" in the theory of Fokker-Planck equations (see, e.g. /1/). It was also implemented in the previous studies of the average density diffusion in the papers /2-4/. The resulting averaged Fokker-Planck equation becomes the well known diffusion equation, /2-4/

$$\frac{\partial \bar{f}}{\partial t} = \frac{\partial}{\partial J} \left(D_J(J) \frac{\partial \bar{f}}{\partial J} \right) \quad (12)$$

where the diffusion intensity D_J is given by:

$$D_J(J) = \langle \langle \Delta J \rangle \rangle = \sum_n n^2 |V_n|^2 \quad (13)$$

where V_n are the harmonic amplitudes in the Fourier expansion of V in the 2π periodic variable Ψ . For the correlator the phase-averaged evolution equation is:

$$\begin{aligned} \frac{\partial K}{\partial t} = & (\omega(J) - \omega(\bar{J})) \frac{\partial K}{\partial \varphi} + \frac{\partial}{\partial J} \left(D_J(J) \frac{\partial K}{\partial J} \right) + \\ & + \frac{\partial}{\partial \bar{J}} \left(D_{\bar{J}}(\bar{J}) \frac{\partial K}{\partial \bar{J}} \right) + (D_{\Psi}(J) + D_{\Psi}(\bar{J})) \frac{\partial^2 K}{\partial \varphi^2} \\ & + F_J(J, \bar{J}, \varphi) \left(\frac{\partial \bar{f}(J)}{\partial J} \frac{\partial \bar{f}(\bar{J})}{\partial \bar{J}} + \frac{\partial^2 K}{\partial J \partial \bar{J}} \right) + F_{\Psi}(J, \bar{J}, \varphi) \frac{\partial^2 K}{\partial \varphi^2} \end{aligned} \quad (14)$$

where we introduced the phase difference $\varphi = \Psi - \bar{\Psi}$ and the functions $D_J, D_{\bar{J}}, F_J, F_{\Psi}$ are:

$$\begin{aligned} D_J(J) &= \sum_n n^2 |V_n|^2 \\ D_{\bar{J}} &= \sum_n \left| \frac{\partial V_n}{\partial \bar{J}} \right|^2 \\ F_J(J, \bar{J}, \varphi) &= \sum_n n^2 V_n(J) \bar{V}_{-n}(\bar{J}) e^{in\varphi} \\ F_{\Psi}(J, \bar{J}, \varphi) &= \sum_n \frac{\partial V_n(J)}{\partial J} \frac{\partial \bar{V}_{-n}(\bar{J})}{\partial \bar{J}} e^{in\varphi} \end{aligned} \quad (15)$$

IV. ASYMPTOTIC SOLUTION.

In the absence of noise, the solution of equation (14) is trivial as only the first term in the r.h.s. survives. The correlation "decay" or rather decohere due to the phase-mixing as $K(t) = \sum_m K_m(I) e^{i(m\varphi + m\omega(I)t)}$ where $K_m(I)$ are the Fourier amplitudes. For nonzero but small noise $\eta \sim V^2$ the time scale of decoherence $\tau \sim 1/\lambda\sigma$ (where $\lambda = \frac{\partial \omega}{\partial J}$ and σ is the r.m.s. value of J for the distribution \bar{f}) is much shorter than diffusion time scale $\tau_d \sim \frac{1}{D_J}$. Furthermore, the correlation "injection", that is provided by the inhomogeneous term in (14), varies only on the slow time scale. As a result, one has a quasistationary equilibrium correlation density that is the balance between the

slowly changing "injection" of correlations and their fast decay.

To analyze the quasistationary solution, we drop the time derivative of K in equation (14). Another simplification comes from noticing that the correlator K is the largest at a small spatial scale $q = J - \bar{J}$, where the "decoherence" term (first term in the r.h.s. of equation (14)) is small. Expanding all the coefficients in the equation (14) to the leading order in q and keeping only the dominant derivatives in q yields:

$$\lambda q \frac{\partial K}{\partial \varphi} + 2D_J \frac{\partial^2 K}{\partial q^2} + \sum_n R_n e^{in\varphi} = 0 \quad (16)$$

where the quantities $\lambda = \frac{\omega(J)}{J}$, $D_J = D_J(J)$ and $R_n = n^2 |V_n(J)|^2 \left(\frac{\partial f(J)}{\partial J} \right)^2$ depend on J as a parameter. For the nonzero harmonics of K in φ one obtains:

$$in\lambda q K_n + 2D_J \frac{\partial^2 K_n}{\partial q^2} + R_n = 0 \quad (17)$$

For the power spectrum of the fluctuations $\tilde{K}_n = \frac{1}{2\pi} \int_{-\infty}^{\infty} dq K_n(q) e^{ikq}$ the resulting equation is of the first order:

$$n\lambda \frac{\partial \tilde{K}_n}{\partial k} - D_J k^2 \tilde{K}_n + R_n \delta(k) = 0 \quad (18)$$

and allows an explicit solution:

$$\tilde{K}_n(k) = \begin{cases} -\frac{R_n}{n\lambda} \exp\left(\frac{D_J}{3n\lambda} k^3\right) & \text{if } nk\lambda < 0 \\ 0 & \text{otherwise} \end{cases} \quad (19)$$

This is the central result of our analysis. The "correlation radius" q_c is $q_c \sim \left(\frac{D_J}{3n\lambda} \right)^{1/3}$. For small noise/large nonlinearity the "correlations radius" is small, which corresponds to the short-wavelength fluctuations ("microstructure") of the beam density.

A special feature of the spectrum (19) is its discontinuity. It is easy to see that this discontinuity is the manifestation of the long $\sim 1/q$ "tail" of the correlator K . Indeed, for large $q \ll q_c$ the second term in equation (17) becomes much smaller than the first, and one obtains $1/q$ tail. It is possible to obtain a more general expression for the "tail" $q \gg q_c$ not limited by the condition $q \ll J$ by keeping the same terms of the primary evolution equation (14) (i.e. the first term in the r.h.s. and the inhomogeneous term) without expanding in q . The resulting expression for the correlator "tail" is:

$$K_n(J, \bar{J}, t) = \frac{iV_n(J)V_n^*(\bar{J})}{n(\omega(J) - \omega(\bar{J}))} \frac{\partial \bar{f}(J, t)}{\partial J} \frac{\bar{f}(\bar{J}, t)}{\partial \bar{J}} \quad (20)$$

The most important quantity characterising the fluctuations is their intensity, which is the value of the correlator K at $q = 0$, and can be calculated by integrating the spectrum \tilde{K}_n . The resulting intensities $P_n = K_n(0)$ are:

$$P_n(J) = \frac{\Gamma(1/3)}{3^{2/3}} \frac{R_n(J)}{(n\lambda(J))^{2/3} D_J^{1/3}(J)} \quad (21)$$

Thus, the fluctuations intensities are of the order $P_n \sim (\eta/\lambda)^{2/3}$ and will be small for small noise /large nonlinearity.

V. CONCLUSIONS.

We presented the evolution equation formalism for the correlation function of the density distribution fluctuations in the nonlinear oscillator under the influence of "coherent" (same for all particles) noise. For the weak noise/large nonlinearity of oscillations the fluctuations are small and short-ranged. The mechanism of the loss of correlations is related to the "decoherence" of oscillations due to amplitude-dependent frequency of oscillations, and since it is not a regular dissipative mechanism, the correlations demonstrate a long $\sim 1/q$ tail in the energy difference.

References

1. K.Gardiner, Handbook of stochastic methods, Springer, 1985. G.E.Uhlenbeck and L.S. Ornstein, On the theory of the Brownian motion, Phys. Rev. 36, 823 (1930).
2. G.Dome, "Theory of RF Acceleration and RF noise", CERN report No.84-15 Accelerator School on Antiprotons for Colliding Beams Facilities, 1984, pp.215-260.
3. S.Krinsky, J.M.Wang, Part.Accel. 12 (1982) 107.
4. J.Ellison, B.S.Newberger, H.-J.Shih "Effect of RF noise on the SSC beam", Proc. 1991 IEEE Particle Accelerator Conf., p.216.
5. S. Hansen, et al., "Longitudinal dilution due to rf noise, IEEE Tran. on Nucl. Sci. 24, 1452 (1977); D. Boussard, G. Dome, C. Graziani, "The influence of rf noise on the lifetime of bunched proton beams", Proc. 11th Conf. on High Energy Accelerators, CERN, p.620 (1980)
6. A.Gerasimov, S.Y.Lee "Random driving of nonlinear oscillator", to appear.

TSD versus TRL Calibration and Applications to Beam Impedance Measurements

M. Foley, P Colestock and E. Barsotti, Jr.
Fermi National Accelerator Laboratory
P.O. Box 500, Batavia, IL 60510 USA

Abstract

At FNAL, bench measurements of the longitudinal impedance of various beam line components have been performed using stretched-wire methods. Two network analyser(NWA) calibration procedures have been implemented and tested in an effort to improve the accuracy of these measurements. The methods, Thru-Short-Delay(TSD) and Thru-Reflect-Line(TRL), each named for their respective calibration standards, are mathematical procedures to extract the S-parameters of a test device from NWA measurements which include the effects of measurement fixtures. The implementation of both these methods has been tested and compared on computer models of the test device and measurement fixtures, whose S-parameters can be exactly computed. The TRL method has been found to be more general and less susceptible to measurement errors. Application of the TRL method to actual stretched-wire impedance measurements has yielded accurate results for a high-Q resonator test device.

1 Introduction

The objective of this work is to recover an equivalent impedance for a given device-under-test(DUT) using a bi-directional reflectometer, otherwise known as a network analyser(NWA). The basic algorithm consists of applying an incident wave to the DUT, which is characterised as a general two-port network, and measuring the vector voltages scattered into the forward and reverse directions. The resulting data are used to calculate S-parameters. The measurements are complicated by the fact that transitions must necessarily occur between the NWA and the DUT, which are known as launchers, since they represent the elements which effectively launch waves at the DUT. The diagram in Figure 1 is a schematic representation of the measurement setup. Launchers A and B

are general, linear networks representing the effect of these transitions, i.e., the errors occurring in the S-parameter measurements of the DUT. The influence of error networks A and B must be calibrated out of the external measurement data in order to accurately evaluate the S-parameters of the DUT. Using standard circuit analysis, it is possible to recover the effective longitudinal impedance of the DUT from the de-embedded S-parameters.

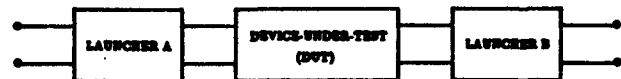


Figure 1: Measurement network

In this work, TOUCHSTONE, an RF/Microwave circuit simulator available from EESof, Inc., is used to simulate an actual DUT with a frequency dependence similar to that expected for a resonant cavity. TOUCHSTONE produces S-parameters for the model cavity, and both the Thru-Short-Delay(TSD)[1] and Thru-Reflect-Line(TRL)[2] de-embedding procedures are employed to recover the model circuit parameters from simulated measurements.

2 Calibration Standards

At FNAL a stretched-wire instrument has been designed to perform bench measurements of the S-parameters of various beam line components. The length of the instrument can be extended easily. Thus, this instrument is appropriate for calibration by the TSD or TRL methods, and so both these methods are implemented at FNAL using FORTRAN codes. The standards required are described below.

THRU(or LINE1) is a length of transmission line with the same characteristic impedance as the DUT

side of A and B. In the simplest case the THRU is a direct connection between A and B.

DELAY(or LINE2) is an identical but longer transmission line. For measurement resolution the difference in length between DELAY(LINE2) and THRU(LINE1) must be less than half a wavelength for the frequency range of interest. Best results are obtained near a quarter wavelength.

SHORT is a perfect short with $S_{11} = S_{22} = -1$ and $S_{12} = S_{21} = 0$.

REFLECT is an unknown reflection (possibly an imperfect short) with no transmission, where $S_{11} = S_{22} = \gamma$ and $S_{12} = S_{21} = 0$.

In order to: (i) Investigate the relative capabilities and restrictions of both methods, and (ii) Test the validity of both FORTRAN codes, the TSD and TRL methods can be applied to computer generated models of the DUT, the launchers and the calibration standards.

3 TOUCHSTONE Model

To accomplish the objectives listed above data files with simulated S-parameter measurements were generated by TOUCHSTONE. These data files contain "measurements" from perfect NWA calibrations using the above standards. Several launcher models with increasing order of complexity were considered. The basic concept was to perform a sensitivity analysis by successively introducing losses and asymmetry in the launcher models and comparing the effect on the simulated TSD and TRL calibrations. Nonideal effects were also introduced in the model calibration standards, shown in Table 1. Line losses and imperfect shorts were investigated in the simulated calibrations.

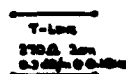
The most complex of these simulated measurements featured models of the stretched wire launchers with asymmetry. This includes a transition from the 50 ohm coaxial cable input to the stretched wire, which forms a coaxial line with characteristic impedance near 280 ohms. Lumped elements incorporate the change in outer conductor diameter and an estimate of matching resistor parasitics from a previous TOUCHSTONE optimisation of a real measurement.

In all of the simulated calibrations the DUT is a model of a cylindrical pillbox cavity with centerwire(TEM mode) plus two modes (850MHz and 1850MHz) relevant to the calibrated frequency range

PERFECT SHORT



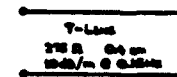
THRU1 (THRU2 = Lossless)



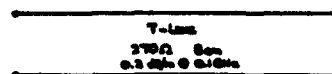
THRU3



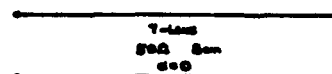
IMPERFECT SHORT



DELAY1 (DELAY2 = Lossless)



DELAY3



THRU4 = Direct connection between launcher networks

Table 1: Calibration Standards

(400MHz-1200MHz). This device exhibits a shunt resonance at 850MHz.

Using the calibration standards from Table 1, a comprehensive set of TOUCHSTONE data files simulating NWA measurements were generated for the launcher models and DUT described above. The S-parameters for the DUT are known directly from TOUCHSTONE. These can be compared to the de-embedded S-parameters obtained by successively applying the TSD and TRL algorithms to the aforementioned TOUCHSTONE data files.

4 Summary of Results

Results of the simulated calibrations yield the following comparison of TSD versus TRL effectiveness in de-embedding the known S-parameters for the model DUT. Neither method is affected by introducing losses in the launchers, while the TSD method shows noticeable performance degradation with the imposition of even minor asymmetry in the launchers. The effects of imposing an imperfect short and simulated losses in the calibration line standards further degrades the performance of the TSD method, whereas the TRL method remains virtually immune and provides accurate results in all cases.

5 TSD vs TRL De-embedding via Cavity Measurements

As a final test, both the TSD and TRL algorithms were applied to data obtained by conducting stretched wire measurements on a RF cavity. In each case, once the S-parameters are extracted, the

impedance of the cavity is calculated based on the method described in [2]. Results for the TSD calibration are shown in Figures 2-3, while those for the TRL calibration are shown in Figures 4-5.

The superiority of the TRL method is most easily evident in the phase of the cavity impedance, which shows a linear phase variation with frequency in the TSD case, but is constant, as expected, in the TRL results. This difference is apparently due to the non-ideal lines, which are more realistically taken into account in the TRL algorithm. Such nonideal effects are most important for the measurement of low loss DUT's, such as the RF cavity chosen, especially off resonance.

6 Conclusions

Implementations of the TSD and TRL algorithms have been investigated by a systematic series of tests using artificial data. The TRL calibration method has proven to be the method of choice for stretched wire impedance measurements of beam line devices. This has been confirmed by applying both methods to measurements on a RF cavity.

References

- [1] D. McGinnis, "Thru-Short-Delay De-Embedding", internal communication, FNAL, April 1991.
- [2] P. Colestock and M. Foley, "A Generalized TRL Algorithm for S-Parameter De-Embedding", FNAL Technical Memo TM-1781, April 1993.

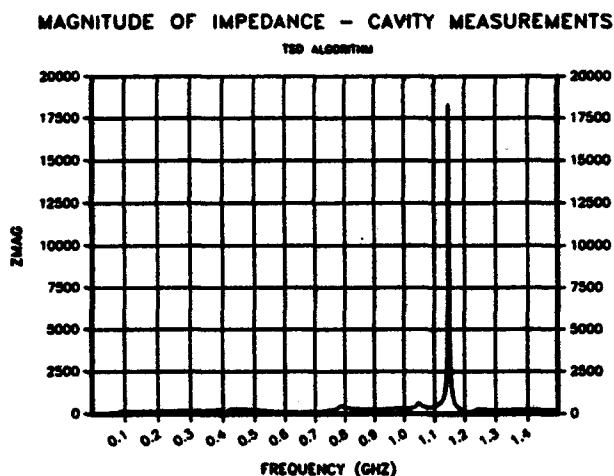


Figure 2

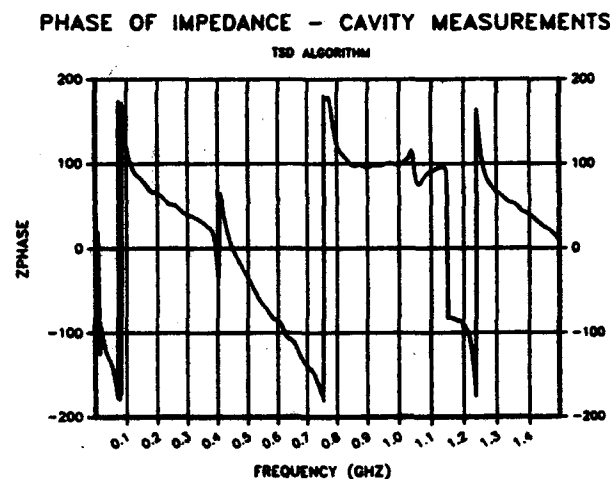


Figure 3

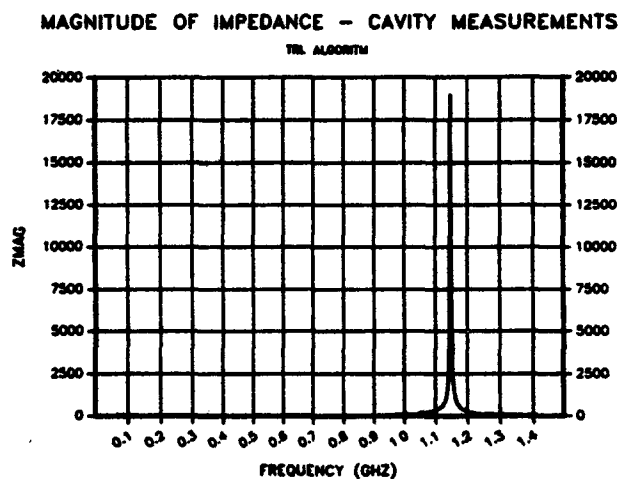


Figure 4

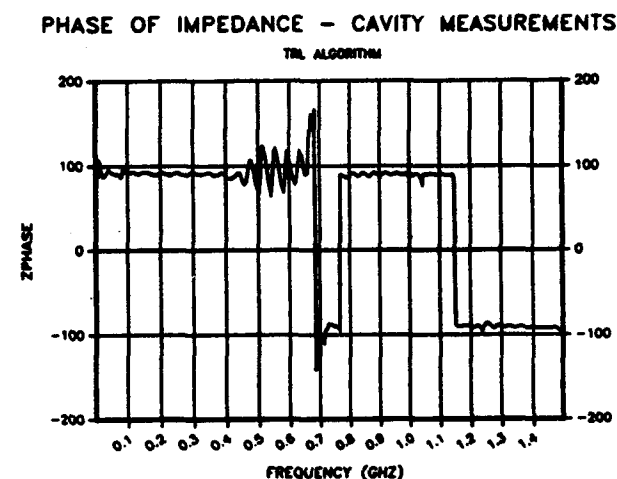


Figure 5

RECENT STUDY OF BEAM STABILITY IN THE PSR*

T. Wang, R. Cooper, D. Fitzgerald, S. Frankle, T. Hardek, R. Hutson
R. Macek, C. Ohmori, M. Plum, H. Thiessen, C. Wilkinson
E. Colton,[†] D. Neuffer,[‡] and G. Rees*

Los Alamos National Laboratory, Los Alamos, New Mexico 87545

Abstract

A fast transverse instability with beam loss has been observed in the 800-MeV Los Alamos Proton Storage Ring (PSR) when the injected beam intensity reaches 2 to 4×10^{13} protons per pulse. Previous observations indicate that the instability is most likely driven by electrons trapped within the proton beam. Theoretical study has shown that beam leakage into the inter-bunch gap leads to electron trapping. Recent experiments were carried out by using the newly installed "pinger" and by varying the machine transition gamma to explore further the "e-p" instability and the nature of the instability. This paper summarizes some of these recent experimental results and theoretical studies.

I. INTRODUCTION

The PSR is a fast-cycling high-current storage ring designed to accumulate beam over a macropulse of the LAMPF linac (~ 1 ms) by multiturn injection through a stripper foil and compress that beam into a short single-turn extracted pulse (~ 0.25 μ s), which drives a neutron source. Key PSR parameters include kinetic energy of 797 MeV, circumference of 90.1 m, revolution frequency of $\Omega/(2\pi) = 2.875$ MHz, betatron tunes ν_x and $\nu_y \approx 3.17$ and 2.13, respectively, and present operating intensity of $N \approx 2.35 \times 10^{13}$ particles. The design intensity is 100 μ A on target at 12 Hz, which implies 5.2×10^{13} protons/pulse. Average and peak intensities have been somewhat less (80 μ A at 20 Hz and 4×10^{13} maximum pulse size). The average current is limited by slow beam losses, and individual pulse intensities are limited by a fast instability [1,2].

The instability occurs when more than $\sim 2 \times 10^{13}$ protons are stored in bunched mode (rf on), and when more than $\sim 5 \times 10^{12}$ are stored in unbunched mode. Transverse oscillations at ~ 100 MHz are seen, and grow exponentially at time scales of 10–100 μ s, causing beam losses. Initially, we suspected that impedance coupling was the cause of the instability. Our searches for a possible impedance source were unsuccessful, although some observations supported our hypothesis that the instability may be caused by the coupled oscillation between the proton beam and the trapped electrons – the "e-p" instability that has been previously observed in some other proton facilities. Supporting observations include the following: degrading

the vacuum makes the beam become more unstable, biasing the foil to a voltage sufficient to clear electrons in the vicinity increases the stability threshold; and moving the halo scrapers into the beam pipe to produce more secondary electrons decreases the threshold. Supporting calculations have also shown that the conditions for e-p instability may occur in the PSR. While there are no clearing electrodes to remove charges, it has been generally observed that varying the conditions that may change the electron production does vary the threshold of the beam instability. However, a dominant electron source has not yet been identified. A possible dominant source is the stripping foil.

We conjectured that electrons have to be stably trapped within the space-charge potential of the circulating beam for more than a revolution period of protons to cause the e-p instability. For an ideally bunched beam in the PSR with a beam-free inter-bunch gap of ~ 100 ns passing through the electrons every turn, trapping enough electrons for instability seems to be difficult. However, calculations and simulations based on the PSR parameter values and the injection process have shown that a small amount of beam may leak into the gap to form a smooth, overall density distribution and an electric potential sufficient for electron trapping [3]. Observations did show that the instability is associated with bunch leakage; with bunched beam (rf on), we observed that instability occurs when the inter-bunch gap has filled in. Measurements taken under various conditions indicate that gap filling occurs either before or simultaneously with the beginning of growing oscillations. In addition, experiments were performed to lower the threshold and to create the instability by deliberately injecting a small amount of beam into the inter-bunch gap. Other experimental evidence supporting the hypothesis of gap-filling-induced instability include (1) beam stabilization by kicking the leakage out of the inter-bunch gap during storage and (2) the storage of a much more stable beam by injecting proton pulses with shorter width deeper into the confining rf bucket to make leakage difficult.

Understanding of this instability and methods of controlling it have taken on new importance as the neutron scattering community considers the next generation of accelerator-driven spallation neutron sources, which call for peak proton intensities of $\sim 2 \times 10^{14}$ per pulse or higher. Recent experimental studies of beam stability in the PSR were carried out by using the newly installed "pinger", a pair of 4-m-long by 7.5-cm-wide electrodes, and by varying the machine transition gamma to understand further the

* Work supported by Los Alamos National Laboratory Institutional Supporting Research under the auspices of the United States Department of Energy. [†] US DOE, [‡] CEBAF, * RAL.

nature of the instability as well as the relation between the gap leakage and the instability. Our theoretical study concentrated on a simple simulation of the e-p instability. This paper reports some of the progress made in these recent studies.

II. EXPERIMENTAL OBSERVATIONS

A. Experiments Using The "Pinger"

We performed experiments using the pinger to keep the gap clean and to "shake" the electrons away from the proton beam. Because the details of the experimental methods are reported in a separate paper in this conference [4], only the results of the stability study will be summarized here.

We first adjusted the fractional part of the vertical to $\sim 1/6$. We then applied pulsed voltage of a few kV, ~ 100 ns long and synchronized with the gap, to the pinger once every six turns. A more than 10% increase of the instability threshold current was possible by resonantly kicking out the protons that leaked into the gap. In another experiment, we tried to shake electrons from the proton beam by applying to the pinger a continuous oscillating voltage (a few kV) of frequencies close to $n\Omega/(2\pi) \pm \nu_y$ (n integer). This experiment also resulted in about a 10% increase in the instability threshold current. The results of both experiments are consistent with the e-p assumption and are similar to those obtained previously by using different instruments [2].

B. Low Transition Gamma Experiments [5]

The purpose of this experiment was to further study the role of gap leakage in the PSR instability. Theoretically, lowering the machine transition gamma (γ_t) in the PSR will decrease the longitudinal mobility of particles. Therefore, at lower γ_t , if the beam is allowed to debunch freely, more time is needed for particles to move into the gap. If the instability is a result of gap leakage, then after switching off the rf during storage, the time period for the beam to remain stable should be longer at lower γ_t .

In this experiment, γ_t was varied between 2.1 and 3.1. For each γ_t , the stability threshold was first examined by varying the amount of injected charges. Then, during the storage of a marginally stable beam, the rf was turned off and the time duration between the rf off and the onset of the instability was measured.

Figure 1 summarizes the observed threshold charges and the stable storage time after the bunching rf was switched off. The results indicate that stable storage time with rf off increases when γ_t is decreased. This result fits well with the theory of gap-leakage-induced e-p instability. Because the γ_t of the PSR cannot be varied without altering the tunes, high current cannot be stored at all values of γ_t . The long storage times at $\gamma_t = 2.129$ and 2.578 correspond to the low currents at these points. At $\gamma_t = 2.129$ only a small amount of beam can be stored

because the momentum spread is much greater than the momentum aperture (0.4 - 0.5 %). At $\gamma_t = 2.293$ and 2.578, the small working areas in the tune space limit the maximum beam currents that can be stored.

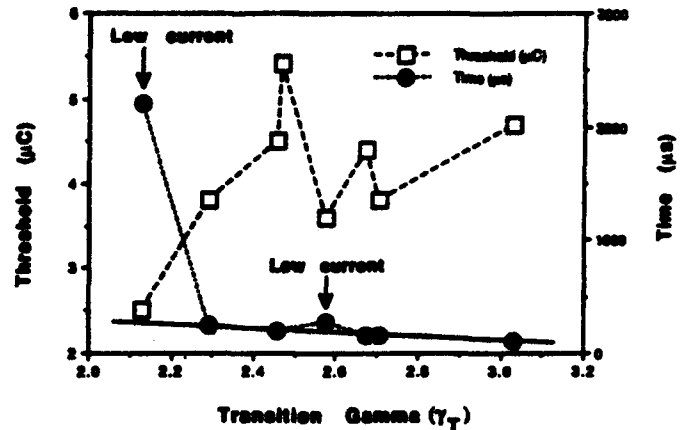


Figure 1. The γ_t dependence of the threshold charge per bunch and the stable storage time after the rf is off.

C. Frequency Spectra Observations

Previous frequency spectrum studies of the beam oscillations were based on measurements using an HP 8563B spectrum analyzer and the Fast Fourier Transforms of digitized position monitor data [2]. Recent studies have employed the autocorrelation method for the power spectra. This method enhances the signal-to-noise ratio in the frequency domain and, hence, allows a better examination of the main peaks of the relatively broad-band spectrum. Similar to the previous observations, spectra of broad bandwidths (10-50 MHz) with peaks near 100 MHz were obtained when instability occurs. The peak location varies between 40 to 200 MHz, depending on beam conditions. These observed variations in peak location and width are consistent with the hypothesis of e-p instability.

III. THEORETICAL STUDY

In our theoretical study, we consider a proton bunch with a round cross-section of radius a propagating inside a perfect conducting pipe of radius b . The transverse focusing force is assumed to vary linearly with the radial distance. We also assume that in the equilibrium state, all the trapped electrons are oscillating inside of the proton beam, and particles are uniformly distributed in the transverse direction. Accordingly, the trapped electrons experience a linear transverse focusing force due to the net charge in the beam. Both the line densities of protons, λ_p , and electrons, λ_e , may vary from the head to the tail of the beam. A Cartesian coordinate system is chosen such that the z -axis is on the symmetry axis of the proton beam, and the y -axis is perpendicular to the plane of the ring. Neglecting all the x -motions and the z -motion of electrons, and adding the damping effect, we formulate the following equations for the motions of the centroids of protons (Y_p)

and electrons (Y_e):

$$\left(\frac{\partial}{\partial t} + v \frac{\partial}{\partial z}\right)^2 Y_p - C_{dp} \frac{dY_p}{dt} + \omega_p^2 Y_p = \left(\frac{2g\lambda_p r_p \chi c^2}{a^2 \gamma}\right) Y_e, \quad (1)$$

and

$$\frac{d^2 Y_e}{dt^2} - C_{de} \frac{dY_e}{dt} + \omega_e^2 Y_e = \left(\frac{2g\lambda_p r_e c^2}{a^2}\right) Y_p, \quad (2)$$

where t is the time, v is the propagation speed of the protons, $g = 1 - (a/b)^2$ is the geometric factor, C_{dp} and C_{de} are the damping constants, $\gamma = (1 - v^2/c^2)^{-1/2}$, c is the speed of light, r_p and r_e are the classical radii of a proton and an electron, respectively, $\chi(z) = \lambda_e(z)/\lambda_p(z)$ is the fraction of neutralization, ω_p is given by

$$\omega_p^2 = \Omega^2 \nu_y^2 + \frac{2\lambda_p r_p c^2}{a^2} \left[\frac{\chi}{\gamma} - \frac{1}{\gamma^3} \left(\frac{a}{b}\right)^2 \right], \quad (3)$$

and $\omega_e = (c/a)\{2r_e \lambda_p [1 - \chi(a/b)^2]\}^{1/2}$ is the bouncing frequency of electrons in the proton beam. Our theoretical study of the e-p instability is based on the numerical solutions of Eqs. (1) and (2).

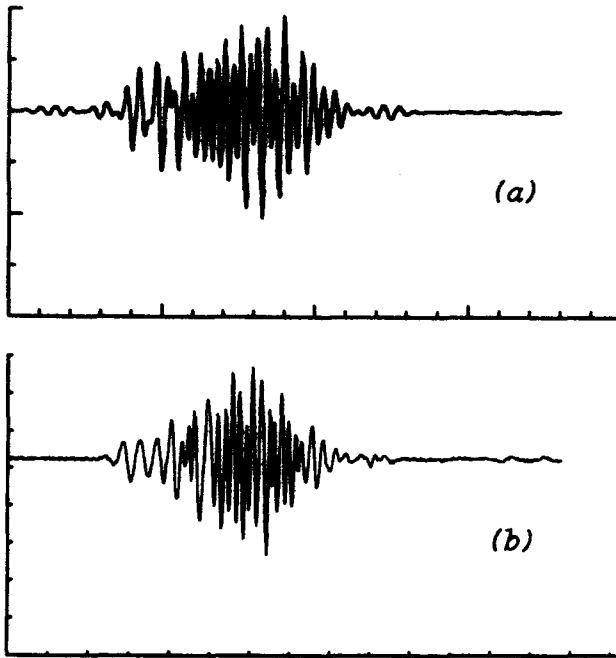


Figure 2. (a) The simulated signal of the vertical beam oscillation by using Eqs. (1) and (2); (b) The experimental data of the vertical beam oscillation.

Only one example of the numerical study will be given here. More details of the theoretical study and results will be included in another report [6]. Figure 2a shows a simulated scope signal of the vertical beam oscillation, and Figure 2b shows real experimental data for comparison. In this case, a cosine square pulse with a small constant density in the gap was assumed for λ_p and λ_e . The computation was initiated with resting electrons and a 100-MHz perturbation in the proton beam. One

percent of neutralization was assumed. Note that in both Figures 2a and 2b, the oscillation frequencies are correlated with the proton line density, i.e., higher at the center of the bunch and lower in the tails. This correlation provides more evidence that the instability is not caused by the machine impedance.

Although this study is still in progress, preliminary investigations have yielded a few notable results. (1) Using the PSR parameter values and reasonably chosen values for the unknown quantities, e.g., C_{dp} , C_{de} and χ , we estimated growth times that are close to those observed in some experiments. (2) When we studied the effect of localized neutralization, i.e., a highly uneven electron distribution around the ring, we found the results are close to those with evenly spread electrons. (3) Gap filling may not be a necessary condition for the e-p instability. The instability may still occur with a clean gap if the beam is sufficiently (a few percent) neutralized by the fresh electrons created in each turn. The instability threshold in the case of a clean gap may be somewhat higher than the threshold in the gap-filled case.

IV. SUMMARY AND CONCLUSIONS

Results from our recent experimental and theoretical studies further support the hypothesis that the observed instability in the PSR is an e-p instability. Recent observations are also consistent with the assumption that the instability is induced by the leakage of protons into the gap, although our theory predicts that gap leakage may not be a necessary condition for instability. We have developed numerical tool based on a simple model that we are using for further study of the instability. Understanding of this instability and methods of controlling it have fundamental importance in both the future operation of the PSR and the design of the next generation of accelerator-driven spallation neutron sources.

One of our future main activities will be to identify dominant electron sources and to clear the electrons. In the forthcoming experiment, we are planning to install clearing electrodes near the injection stripper foil, where the beam losses are relatively large. We expect the theoretical studies and the experiments using pinger to continue into the near future.

V. REFERENCES

- [1] D. Neuffer et al., *Conf. Record of the 1991 IEEE Particle Accelerator Conf.*, Vol. 3, p. 1896.
- [2] D. Neuffer et al., *Nucl. Instr. and Meth.*, **A321**, 1 (1992).
- [3] D. Neuffer, *Conf. Record of the 1991 IEEE Particle Accelerator Conf.*, Vol. 2, p. 1077.
- [4] T. Hardek et al., paper Da50 in these proceedings.
- [5] C. Ohmori et al., Los Alamos PSR Technical Note, PSR-92-012, 1992.
- [6] T. F. Wang, Los Alamos Accelerator Theory Note, in preparation.

Impedance Budget and Beam Stability Analysis of the Fermilab Main Injector

M.A. Martens and K.Y. Ng

Fermi National Accelerator Laboratory,* P.O. Box 500, Batavia, IL 60510

Abstract

The impedance budget of the Fermilab Main Injector (MI) is estimated, which includes the contributions from the resistive walls, bellows, rf cavities, steps, Lambertainons, etc. Beam stability during ramping and bunch coalescence is analyzed. The transverse resistive-wall coupled bunch growth is found to be somewhat worse than the situation in the Main Ring (MR).

IMPEDANCE AND STABILITY

One of the important considerations in the design of the Main Injector is the beam coupling impedances in the vacuum chamber and the stability of the beam. Along with the higher intensities comes the possibility of instabilities which lead to growth in beam emittances and/or the loss of beam. This paper makes estimations of the various impedances and instability thresholds based on calculations and measurements. The Main Injector has a mean radius of $R = 528.30$ m. Its duty is to accelerate a total of 3×10^{13} protons in $h = 588$ rf buckets from the injection energy of 8.9 GeV to the extraction energy of 120 or 150 GeV. The threshold for microwave instability has been estimated [1] to be $Z_{||}/n > 20 \Omega$.

A. Resistive Wall

The shape of the Main Injector beampipe is approximately elliptical with a full width of 4.84 inches and a full height of 2.09 inches. The beampipe is stainless steel, has a thickness of 1.2 mm, and a resistivity of $\rho = 74 \mu\Omega\text{-cm}$.

Using the circular approximation [2] to the MI beampipe with a radius of 1.05 in, we get the results listed in Table 1. The results are expressed as a function of the revolution harmonic number n for both high and low frequencies. We also approximate the beampipe to the rectangular shape with full height and width of $h = 2.09$ in by $w = 4.84$ in. The results can be expressed [3] as the product of a form

	$n < n_c$	$n > n_c$
$Z_{ }/n$	$12.3/n \Omega$	$(1+j)10.2/\sqrt{n} \Omega$
Z_{\perp}	$19.2/n \text{ M}\Omega/\text{m}$	$(1+j)15.4/\sqrt{n} \text{ M}\Omega/\text{m}$

Table 1: Resistive wall impedance as a function of revolution harmonic n for circular beam pipe with radius $b = 1.05$ in. Results are given for frequencies where the skin depth is less (greater) than the thickness of the beampipe $n > n_c$ ($n < n_c$) where $n_c = 1.44$.

factor times the circular result with radius $b = h/2$. The form factors are found to be $F_{||} = 0.989$, $F_{\perp x} = 0.404$, and $F_{\perp y} = 0.822$. We see that except for the horizontal case, the circular approximation is fairly good.

The most important effect of the resistive wall instability is the transverse coupled bunch instability. Since the growth rate is proportional to $\text{Re } Z_{\perp}[(n+\nu)\omega_0]$ where $\omega_0/2\pi$ is the revolution frequency, we are interested in the mode n that gives the lowest frequency. In the vertical plane the tune is 25.4; so the coupled bunch mode $n = -26$ will have the largest growth rate. The relevant frequency is only $0.6\omega_0/2\pi$ which is very small.

Using the low frequency estimates of the Lambertain magnets (see subsection G) and the beampipe, we calculate the growth rate for mode $n = -26$. The beampipe impedance is $32 \text{ M}\Omega/\text{m}$ and the Lambertain is $35 \text{ M}\Omega/\text{m}$. The growth time of the resistive wall impedance at 8 GeV is then 0.32 msec which is very fast. This is, however, only a bare-bone estimate. Octupoles can cause a tuneshift which is a significant way to lower the growth. Also, with a positive vertical chromaticity, there is a suppressing form factor in the growth formula.

We make a comparison of the growth rate with the calculated value of the Main Ring. Using a current in the Main Ring of 0.115 Amp and a transverse impedance of $97.7 \text{ M}\Omega/\text{m}$, the calculated growth rate is 0.65 msec. However, experience has shown that with the higher multipole configuration in the Main Ring lattice, the operation chromaticities, together with the dampers, the Main Ring can operate at this intensity without problem. We therefore expect the present Main Ring dampers (or ones with a higher gain) to be sufficient to damp the transverse resistive wall instability in the Main Injector.

*Operated by the Universities Research Association, under contracts with the U.S. Department of Energy

B. Space Charge

For the space charge impedance estimation, we make estimates based on beampipes with circular and rectangular cross sections. The circular cross section results are well known while those for the rectangular case come from conformal mapping techniques [3].

Using the formula for the circular and rectangular cross sections, the space charge impedance was calculated at 8 GeV for a beam with a total 3×10^{13} particles and 30π mm-mr 95% normalized emittance. With $\beta_{\min} = 10\text{m}$, this corresponds to a cylindrical beam with a radius of $a = 5.6$ mm. The results are shown in Table 2. The space charge impedance is important in contributing to the negative-mass instability at transition and for mismatch of the equilibrium bunch length before and after transition. These issues are not considered in this paper.

	Circular Beampipe	Rectangular Beampipe
$Z_{ }/n$	$-j7.98 \Omega$	$-j9.61 \Omega$
$Z_{\perp s}$	$-j67.0 \text{ M}\Omega/\text{m}$	$-j68.4 \text{ M}\Omega/\text{m}$
$Z_{\perp y}$	$-j67.0 \text{ M}\Omega/\text{m}$	$-j67.6 \text{ M}\Omega/\text{m}$

Table 2: Space charge impedance for both circular and rectangular beampipe. Calculations were made at 8 GeV using a cylindrically uniform beam with transverse radius of 5.62 mm.

We are also interested in the coherent and incoherent tune shifts due to the electric image charges in a rectangular beampipe [3]. For bunched beam at 8 GeV with bunch length of 150 degrees the coherent tune shift in the vertical direction is -0.13 and in the horizontal and vertical directions the incoherent tune shift is ± 0.043 .

Also the incoherent tune shift due to the beam itself was calculated for a round Gaussian beam with a radius of 5.62 mm. The value was found to be 0.014 for the bunched beam. It is possible that the total incoherent tune shift of 0.057 in the horizontal direction might be too large and pose a problem in operation.

C. RF Cavities

Since the Main Injector RF cavities will be transferred from the Main Ring, previous measurements of the cavities can be used for the estimation of the longitudinal impedance. The measurements on the cavities were made using a stretched wire technique [4] and the results are shown in Table 3. The mode at 128 MHz has limited Main Ring performance in the past so a mode damper was designed and installed [5].

We calculate the coupled bunch growth times due to the RF cavities. The nominal parameters for the Main injector are: particles per bunch is 6×10^{10} , the RF voltage is 400 kV, and the bunch area is 0.25 eV-s. As a comparison, we also calculate the growth rates in the Main Ring. The growth times are given in Table 3 for both the Main Ring

Freq (MHz)	$Z_{ }$ (k Ω)	growth time in msec			
		dipole		quadrupole	
		MI	MR	MI	MR
71.0	10.0	16.8	45.0	280	500
100.0	2.5	53.4	151.9	440	810
128.0	6.3	19.2	59.1	93	180
223.0	111.0	1.4	6.8	1.8	4.6
600.0	277.0	5.1	30.0	2.8	12
850.0	49.0	53.2	321.4	38	140

Table 3: Dipole and quadrupole mode growth times for both the Main Injector and the Main Ring due to the longitudinal rf cavity modes.

and the Main Injector. For the Main Ring we used 3×10^{10} particles per bunch.

Experience with the Main Ring has shown that the 128 MHz mode can sometimes be a problem in fixed target operation. Also of concern is the short growth time of the 223 MHz mode. As a result, a set of passive dampers for the cavities is being designed to reduce the shunt impedance of the 223 MHz mode and further damp the 128 MHz mode as well. With this mode damper installed, the 223 MHz impedance is lowered to a value of about 10 k Ω .

Also of concern is the coupled bunch instability with short batches used in coalescing since standard coupled bunch theory is not applicable to a partially filled ring. Presently in the MR there is evidence of an instability with 3×10^{10} particles per bunch. Since this type of instability depends on R/Q and not on R , adding passive dampers will not remove or improve the instability. In the Main Injector there will be 6×10^{10} particles per bunch so there could be substantial difficulty with the short batch operation. The problem will likely require the development of an active damping system.

The growth times for the Main Injector are about one half of those in the Main Ring (Table 4). So far there has not been any evidence of transverse coupled bunch mode observed in the Main Ring.

Freq (MHz)	Z_{\perp} (M Ω/m)	growth time in msec			
		dipole		quadrupole	
		MI	MR	MI	MR
398	3.3	5.1	9.0	5.2	9
454	1.9	9.9	17	20	18
566	0.75	32	56	32	57
700	0.13	230	410	230	410
1260	0.18	290	510	290	520
1270	1.7	31	54	31	54
1290	2.4	23	40	23	40

Table 4: Dipole and quadrupole mode growth times for both the Main Injector and the Main Ring due to the transverse rf cavity modes.

D. Beam Position Monitors (BPM)

The Main Injector BPM consists of 4 stripline pickups which are cut out of the approximately elliptical beampipe. Two pickups are located on each of the top and bottom surfaces of the beampipe and are spaced 40 mm apart from center to center. Each stripline is about 1 cm wide, $\ell = 40$ cm long, and has a characteristic impedance of $Z_0 = 50 \Omega$. The downstream end of each stripline is shorted while the upstream end is connected in parallel with a 50Ω cable which leads to the RF module.

As a bunch passes the BPM, only a tiny fraction of the image current on the beampipe is picked up by the stripline. We estimate this fraction to be $f = 0.055$ and then calculate the power absorbed by the striplines. Since this is the same as the power lost by the beam, we can calculate the beam impedance. For a set of four striplines,

$$Z_{\parallel} = 2f^2 Z_0 \left[1 - \cos\left(\frac{2\ell\omega}{c}\right) + j \sin\left(\frac{2\ell\omega}{c}\right) \right].$$

For 206 sets of BPM in the ring, $Z_{\parallel}/n = 0.050 \Omega$ below ~ 60 MHz, then starts oscillating and rolls off. In the same way, the transverse impedances of the BPM can also be computed. They have the same frequency dependency as Z_{\parallel}/n . For example, the vertical impedance at low frequencies is $Z_{\perp y} = 259 \text{ k}\Omega/\text{m}$. These impedances are much lower than those of other components in the ring. This is mainly due to the relatively narrow width of the stripline pickups. Thus the BPM's are not expected to be a problem.

E. Beam Valve

Although the beam valve design is not yet completed, its general shape is known. Using this general shape, the 3D computer code MAFIA [6] was used to find the longitudinal and transverse impedances. The beam valve is assumed to have the same resistivity as the beampipe, $\rho = 74 \mu\Omega\text{-cm}$.

Calculations for the coupled bunch growth rates show that most of the beam valve modes are benign. This is mainly due to the fact that the cavity modes are at frequencies which are above the beam spectrum frequencies. All modes have a growth time greater than 50 ms except for the quadrupole mode of the 2.46 GHz mode which has a growth rate of 38 ms.

F. Bellows

The beampipe bellows will consist of approximately 10 to 17 convolutions extending over one inch. The inner dimension of the bellows is an ellipse of similar size to the beampipe and the convolutions extend 0.5 inches. To estimate the impedance the elliptical shape was approximated by a circular beampipe with radius 1.05 inches. This was done for both 10 and 17 bellows convolutions using the program TBCI [7].

The longitudinal impedance is very similar for both the 10 and 17 bellows case. The impedance peaks at 120Ω near

8.5 GHz. For 516 bellows in the Main Injector, we have a total of $Z/n = 0.65 \Omega$ at 8.5 GHz. At low frequencies, it is $Z/n = j2.8 \Omega$. According to previous calculations this impedance is below the threshold for the Main Injector except near transition [1].

G. Lambertsons

The main concern of the Lamberton magnets is the low frequency component created by the exposure of the beam to the bare laminations of the magnet. A rough estimation of the Lamberton magnets is made by approximating the magnet as a series of annular laminations of 0.953 mm width. The inner radius is chosen to be $b = 2.54$ cm and the outer radius is $d = 5.08$ cm. We use a resistivity of $\rho = 20 \mu\Omega\text{-cm}$ and a permeability of $\mu = 100$ for the lamination material. The impedance is estimated by integrating the resistance of the low frequency current traveling through the laminations.

With 25.8 meters of Lamberton magnets in the Main Injector the total low frequency resistive wall impedance is calculated to be

$$\frac{Z_{\parallel}}{n} = (1 + j) \frac{16.4}{\sqrt{n}}.$$

And to estimate the transverse impedance, we use the approximate relation

$$Z_{\perp} = \frac{2c}{b^2} \frac{Z_{\parallel}}{\omega} = (1 + j) \frac{26.8}{\sqrt{n}}.$$

It should be noted that the Lamberton magnet was assumed to have a circular geometry with inner radius of $b = 2.54$ cm. The actual shape of the Lamberton is much different, so this estimate can only be approximate. Using a slightly larger inner radius can change the impedance, especially the transverse one, by a significant amount (i.e. if b is 10% larger the impedance drops by 25%).

REFERENCES

- [1] King-Yuen Ng, Fermilab Main Injector Note MI-0029.
- [2] B. Zotter and F. Sacherer, CERN 77-13, pp. 175-218, (1977).
- [3] K.Y. Ng, *Particle Accelerators*, 16, pp. 63-80, (1984).
- [4] R.A. Dehn, Q.A. Kerns, and J.E. Griffin, "Mode Damping in NAL Main Ring Accelerating Cavities", *IEEE Trans. Nucl. Sci.*, NS-18, pp. 260-261, (1971).
- [5] Q.A. Kerns and H.W. Miller, "Fermilab 500-GeV Main Accelerator RF Cavity 128-MHz Mode Damper", *IEEE Trans. Nucl. Sci.*, NS-24, pp. 1704-1706, (1971).
- [6] DESY, LANL and KFA, *MAFIA User Guide*, (1989).
- [7] R. Klatt and T. Weiland, *TBCI Short User Guide*, DESY, (1988).

Trapped Ions and Beam Coherent Instability

P. Zhou, P. L. Colestock and S. J. Werkema
Fermi National Accelerator Laboratory*
P.O. Box 500, Batavia, IL 60510

Abstract

In accelerators with negatively charged beams, ions generated from the residual gas molecules may be trapped by the beam. Trapped ions may interact resonantly with the beam and cause a beam-ion coherent instability. This coherent instability bears many similarities to the resistive wall instability and can present important limitations to these machines' operation. A description of this effect requires a treatment of the beam coherent instability including both the normal machine wake field and the interaction with ions. We present a linear approach incorporating contributions from the machine impedance as well as ion forces. It also includes spreads in beam and ion frequencies and thus Landau damping. The analysis results in a modified stability diagram which will be used together with physical arguments to explain experimental observations in the Fermilab antiproton accumulator.

Introduction

When residual gas molecules are ionized by Coulomb collisions with beam particles, ions are created with little kinetic energy and in a negatively charged beam may be trapped in the beam. In storage rings, since the beam stays in the machine for very long times, the effects of beam-ion interaction sometimes seriously limit machine performance, see [1] and reference therein.

With the most commonly used clearing electrode systems, the neutralization level, defined as the ratio of total trapped ion charge to the total beam charge, can be reduced to e.g. a few percent. Still the beam can develop coherent oscillations. Transverse beam coherent oscillations are routinely observed in the Fermilab Antiproton Accumulator, starting with 10-20 mA of stored beam. Oscillations occur near the $(1 - q)$ and $(3 - q)$ betatron sideband frequencies and also at the $(3 - q)$ frequency with larger beam currents. These oscillations can exist at a stable amplitude for a very long time without disastrous effects, however when the beam is cooled longitudinally, as is required before antiproton transfer from the accumulator to the Main Ring, the transverse emittances experience semi-periodic sudden increases without beam loss.

These instabilities are believed to be either caused or at least worsened by the trapped ions. Theories have been developed to deal with two-stream instability[2][3]. The frequency range of these modes is consistent with the spectrum of trapped ion

bounce frequencies, but this is also where the resistive wall impedance is the largest. It's very likely that both of them will act at the same time, therefore it is necessary for the theory to include both of them simultaneously. We present a treatment modeled after that in [4] and [5], and use it to explain some of the experimental observations in the Fermilab accumulator.

Theory and Ion Impedance

We only consider transverse dipole oscillations here. To include the effects of non-linear focusing we need to make certain approximations. In general with the presence of nonlinearity, the particle motion is no longer a harmonic oscillation and the focusing is a function of particle's position. We will treat the nonlinearity as simply a modulation of the oscillation frequency as a function of their amplitudes only while maintaining the form of harmonic oscillation. This is a good approximation when the nonlinearity is small. When the nonlinearity is not so small, it can be viewed as keeping only the dipole component and ignoring higher order modes of motion, on a time scale much larger than the oscillation period. In this approximation a particle's motion is described by $y = A \cos(\omega_p(A, p)t + \phi_0)$

The Vlasov equations for the beam and trapped ions are

$$\begin{aligned} \frac{\partial \Psi_b}{\partial t} + y_b \frac{\partial \Psi_b}{\partial y_b} + F_b \frac{\partial \Psi_b}{\partial y_b} + \omega_r \frac{\partial \Psi_b}{\partial \theta} &= 0 \\ \frac{\partial \Psi_i}{\partial t} + y_i \frac{\partial \Psi_i}{\partial y_i} + F_i \frac{\partial \Psi_i}{\partial y_i} &= 0 \end{aligned}$$

We will ignore the dependence on the azimuthal angle and take an averaged view of all the distributions and forces for simplicity.

The normalized forces are

$$\begin{aligned} F_b &= -\omega_p^2 y_b - \omega_{bi}^2 \cdot (y_b - \bar{y}_i) + F_w \\ F_i &= -\omega_{bi}^2 \cdot (y_i - \bar{y}_i) \end{aligned}$$

where ω_p depends individual particle's momentum, ω_{bi} is the angular bounce frequency of the beam in the field of trapped ions, and ω_{bi} that of the ions in the field of beam. All of them may be functions of oscillation amplitudes. F_w is the wake force generated by the normal machine impedance. We have neglected the self-force of both the beam and trapped ions, assuming neutralization levels are low.

We define action-angle coordinates as

$$\begin{aligned} y_{b,i} &= A_{b,i} \cos \phi_{b,i} \\ \dot{y}_{b,i} &= \omega_{b,i} A_{b,i} \sin \phi_{b,i} \end{aligned}$$

*Operated by the Universities Research Association under contract with the U. S. Department of Energy

where the subscript b and i are for beam and trapped ions respectively. The phase space area element, on average, is $dy_{b,i} d\phi_{b,i} = \frac{1}{2\pi} d(\omega_{b,i} A_i^2) d\phi_{b,i}$. For simplicity we assume the dependency of the density function Ψ_b on momentum can be separated out, i.e. $\Psi_b(A_b, \phi_b, p) = \Psi(A_b, \phi_b) g(p)$.

Following the normal procedure of separating the density function into an stationary part, for which when there is no coherent oscillation, and a small perturbation,

$$\Psi_b = \Psi_{b0} + \Psi_{b1} e^{i(n\theta - \Omega t)}$$

$$\Psi_i = \Psi_{i0} + \Psi_{i1} e^{i(n\theta - \Omega t)}$$

The coherent oscillations $\bar{\Psi}_{b,i} = Y_{b,i} e^{i(n\theta - \Omega t)}$ have amplitudes of $Y_{b,i} \equiv \frac{1}{2\pi} \int \Psi_{b,i} A_{b,i} \cos \phi_{b,i} d(\omega_{b,i} A_{b,i}^2) d\phi_{b,i}$. The wake force is

$$F_w = i \frac{N e^2}{\gamma m_b T_0 L} Z(\Omega) Y_{b0} e^{i(n\theta - \Omega t)}$$

where $Z(\Omega)$ is the machine impedance[5].

The linearized Vlasov equations

$$\begin{aligned} -i(\Omega - n\omega_r) \Psi_{b1} - \omega_b \frac{\partial \Psi_{b1}}{\partial \phi_b} + \left(\frac{i N e^2}{\gamma m_b T_0 L Z(\Omega)} Y_{b0} + \omega_{bi}^2 Y_i \right) \frac{\partial \Psi_{b0}}{\partial y_b} &= 0 \\ -i\Omega \Psi_{i1} - \omega_i \frac{\partial \Psi_{i1}}{\partial \phi_i} + \omega_{ib}^2 Y_b \frac{\partial \Psi_{i0}}{\partial y_i} &= 0 \end{aligned}$$

lead to the following dispersion equation

$$\begin{aligned} 1 &= i \frac{N e^2 Z(\Omega)}{\gamma m_b T_0 L} \int \frac{\Psi'_{b0}(A_b) \omega_b A_b^2 dA_b g(p) dp}{(\Omega - n\omega_r)^2 - \omega_b^2} \\ &+ \int \frac{\Psi'_{i0}(A_i) \omega_i^2 \omega_b A_i^2 dA_i g(p) dp}{(\Omega - n\omega_r)^2 - \omega_b^2} \int \frac{\Psi'_{i0}(A_i) \omega_i^2 \omega_b A_i^2 dA_i}{\Omega^2 - \omega_i^2} \end{aligned}$$

In general ω_{bi}^2 is a function of A_b and therefore cannot be pulled out of the integration, but if it is only a weak function of A_b , or if ω_r and ω_b are not dependent on A_b , which is almost true, then ω_{bi}^2 , or another quantity of the same order, can be taken out as a constant. This constant, let us call it ω_c^2 , measures the average coupling strength from ions to the beam. In the limit that ω_r and ω_b do not depend on A_b , ω_c is roughly the rms bounce frequency of beam in the field of trapped ions. In this approximation the dispersion equation becomes

$$1 = i \frac{N e^2}{\gamma m_b T_0 L} \int \frac{g(p) dp}{\omega_c^2 - (\Omega - n\omega_r)^2} \cdot [Z(\Omega) + Z_i(\Omega)]$$

where

$$Z_i(\Omega) = -i \frac{\gamma m_b T_0 L \omega_c^2}{N e^2} \cdot \int \frac{\Psi'_{i0}(A_i) \omega_i^2 \omega_b A_i^2 dA_i}{\Omega^2 - \omega_i^2}$$

As we can see, the main effect of trapped ions comes in the form of extra impedance, denoted as "ion impedance", Z_i . The other contribution of ions is to shift the beam oscillation frequency, which is contained in the term $\omega_b^2 = \omega_p^2 + \omega_{bi}^2$. This shift, however, is usually tiny and can be ignored.

It is, however, very difficult to know the details about this ion impedance Z_i , because it depends on the neutralisation profile, ion amplitude distribution, etc. None of these are known in detail. Instead, we will try to get a rough estimation on Z_i and determine a qualitative picture of the effect. For this purpose we assume trapped ions have the same transverse distribution as the beam, and take this distribution as a round Gaussian with an rms size that is the machine average.

The coefficient $\gamma m_b T_0 L \omega_c^2 / N e^2$ in Z_i is independent of the beam intensity and proportional to the machine neutralisation level, e.g. for the Gaussian transverse distribution

$$\omega_c^2 = \frac{\eta N e^2}{L \gamma m_b \sigma_y (\sigma_x + \sigma_y)}$$

and at the stability boundary the ion impedance is

$$\begin{aligned} Z_i &= \frac{\pi T_0}{\sigma_y (\sigma_x + \sigma_y)} \left\{ \frac{\pi}{2} \Psi'_{i0}(\Omega) \Omega^2 A_i^2(\Omega) \right. \\ &\quad \left. - i \frac{\Omega}{2} P.V. \int \frac{\Psi'_{i0}(\omega_i) \omega_i A_i^2(\omega_i) d\omega_i}{\omega_i - \Omega} \right\} \end{aligned}$$

This ion-impedance will tend to damp either the slow wave or fast wave, and anti-damp the other, depending on the ion distribution. Usually, more ions are distributed in the small amplitude, high oscillation frequency region, and the distribution tapers off toward large amplitudes, and consequently we usually have a positive real "ion resistance". This will damp the fast wave and anti-damp the slow wave which is also anti-damped by the normal machine impedance, i.e. the "ion impedance" will reduce the machine impedance budget and may cause beam instability in cases that are otherwise stable. For illustration let us take the simplified picture described above and evaluate some typical numbers from the Fermilab accumulator and plot the stability diagrams with 0% and 1% neutralisation. It can be seen from Fig. 1 that it does not take a high level of ion neutralisation to destabilise an otherwise stable situation, and it is possible to have no stable region at all.

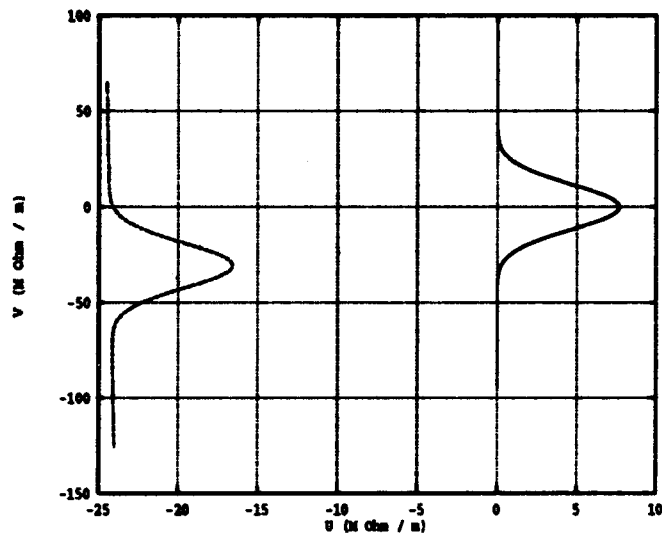


Figure 1: Beam Stability Diagrams with 0 and 1% Neutralisation

We have to point out two points. First, the theory unavoidably overestimates the effect of ions because of the neglect of the longitudinal motion of ions. This motion causes resonant ions to lose the phase information needed to stay resonant. Secondly, this theory is only a perturbative treatment and not a self consistent one. We started with an equilibrium distribution and evaluated the stability of any small perturbation, but the unstable motions may change the "equilibrium" distribution,

especially trapped ions'. To develop a fully self-consistent theory is very difficult. However, we can use an iterative process where the theory together with some physical arguments form a closed loop and we can at least get a qualitative explanation of what we have observed, which we will carry out in the following section.

Experimental Observations

In the Fermilab Antiproton Accumulator, ion trapping has been, at least partly, a limit to the normal operation. To correct the problem an ion clearing electrode system has been installed in the accumulator and it has recently been upgraded from the previous fixed 100V to a variable one with up to 1KV voltage.

Experiments have shown that ion trapping contributes to beam coherent oscillations. Fig. 2 shows the beam coherent oscillation strengths with different amount of neutralisation achieved by varying clearing voltage in one sixth of the machine at 900, 100, 50 and 10 volts, where power in all three coherent lines grows with decreasing clearing voltage. Monitoring the co-

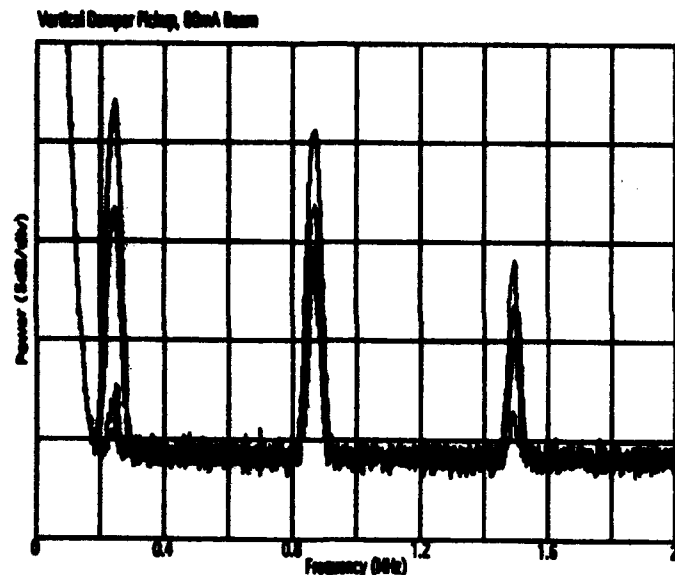


Figure 2: Coherent Power Spectrum with Various Clearing Voltages

herent line power with time shows that they can change rather abruptly. Fig. 3 shows one example.

The above can be explained with the model we presented in the previous section, that as beam current increases the ion impedance will gradually push the otherwise stable beam into the unstable region and cause the beam-ion coherent oscillation to grow. Unlike the normal machine impedance, the ion impedance changes as the beam-ion interaction alters the "equilibrium" ion distribution. When the beam develops an instability, resonant ions also undergo oscillation growth. Since the beam is normally much stronger and more rigid, the initial growth in the coherent oscillation tends to heat the ion distribution and drive the resonant ions to larger amplitudes. As a result, the ion distribution will be distorted so that the beam becomes semi-stable, and the coherent oscillation strength will be reduced, just as shown in Fig. 3. The beam coherent oscillation is needed to maintain this modified ion distribution as

Vertical 2-q line power vs. time

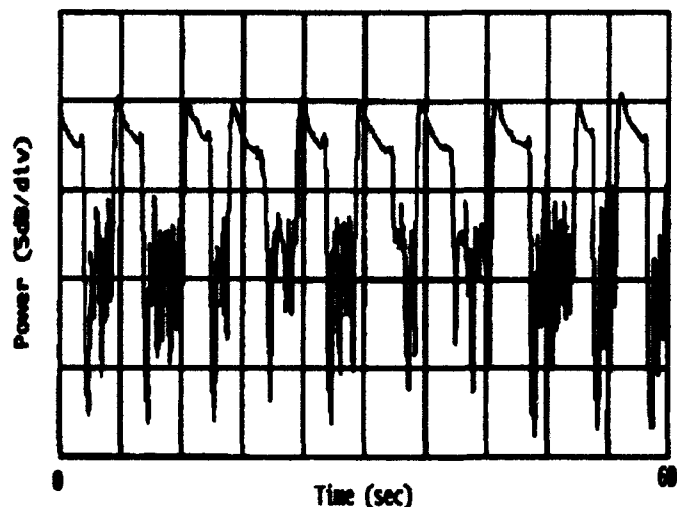


Figure 3: Coherent Oscillation Power Change with Time

the creation of new ions and the natural tendency of ions without heating will bring back the original ion distribution which made the beam to grow in the first place. This process will be enhanced through the increase of beam current and/or the reduction of the beam momentum spread and the increase of ion trapping, where either the beam moves closer to instability intrinsically because of the weakening of Landau damping or trapped ions become stronger or both can occur. When the trapped ions are strong enough and the instability growth is too fast for ions to respond a true instability will develop and beam transverse emittances will suffer explosive growth as has been observed.

Acknowledgment

The authors would like to thank the Fermilab pbar group for their support in the experiments done with the accumulator.

References

- [1] John Marriner, et al. Experiments and practice in beam shaking. *Particle Accelerators*, 30:13-20, 1990.
- [2] D.G. Koshkarev and P.R. Zenkevich. Resonance of coupled transverse oscillations in two circular beams. *Particle Accelerators*, 3:1-9, 1972.
- [3] L.J. Laslett, A.M. Sessler and D. Möhl. Transverse two-stream instability in the presence of strong species-species and image forces. *Nucl. Instr. Meth.*, 121:517-524, 1974.
- [4] L. Jackson Laslett, V. Kelvin Neil, and Andrew M. Sessler. Transverse resistive instabilities of intense coasting beams in particle accelerators. *Rev. Sci. Instr.*, 36(4):436, 1965.
- [5] A.W. Chao. Coherent instabilities of a relativistic bunched beam. *SLAC Internal Note*, SLAC-PUB-2946, June 1982.

Comparison of the Coupled-Bunch Mode Theory to Experimental Observations in the Fermilab Booster

K. C. Harkay

Purdue University, West Lafayette, IN 47907 *

P. L. Colestock

Fermi National Accelerator Laboratory, P.O. Box 500, MS 341, Batavia, IL 60510 **

Abstract

The well-known longitudinal coupled-bunch mode theory is reviewed and evaluated including finite bunch length effects and Landau damping for the parameters of the Fermilab Booster. Predictions of mode growth rates are found to be in general good agreement with experimental observations, both temporally and in frequency space. The inclusion of Landau damping in the stability analysis is required to achieve overall agreement with the observed unstable mode spectrum. Particle simulation using the ESME code are carried out to describe observations of large amplitude oscillations and saturation effects near the end of the acceleration cycle. Finally, a model of the emittance growth, which is valid for growth rates slow with respect to mode frequencies, is explored.

I. INTRODUCTION

Even after installation of RF cavity mode dampers suppressed the long-observed longitudinal coupled-bunch instability [1], questions remained as to whether the behavior scaled as predicted by the theory. Also, the details of the longitudinal emittance growth scaling were unclear. First, we describe the comprehensive comparison of Booster data with the predictions of the linear coupled-bunch mode theory. While there is strong evidence that nonlinear effects are important, we wished to study the unstable mode growth data quantitatively at least to determine the regime for which the linear theory is valid. A rigorous test of and modification of some of the assumptions used in the literature is required for proper application to the Booster. Solutions are found numerically using standard algorithms. It is found that including self-consistently the effects of the beam momentum spread in the nonlinear RF potential (Landau damping) is essential to accurately describe the unstable beam behavior.

The linear theory is completely inadequate in explaining the emittance growth resulting from the instability. Instead, a fully nonlinear simulation is invoked using the longitudinal particle tracking code ESME developed at Fermilab to study the response of the beam in the presence of a high-Q driving impedance. Subsequent analyses of the results produce an qualitative scaling of the emittance growth and a deepened understanding of the subtleties and sensitivities of the instability on various parameters.

I. MEASUREMENTS

Three quantities were measured in the Booster for use in the comparison with the theory. First, the impedance due to the RF cavity higher-order modes (HOM), which drive the instability according to the theory, was measured. [2] Because the RF cycles in 33 msec from 30 to 53 MHz, many of the HOMs also tune, so data were recorded corresponding to several times through the cycle. The beam fluctuation spectra were obtained by detecting the signal from a wideband resistive wall monitor and performing an FFT using a TEK DSA 602. An example of a typical spectrum may be seen in [1]. Before suppressing the instability through the recent installation of RF cavity mode dampers, strong oscillations were seen in coupled-bunch mode (wave) numbers around $n=16$ and 48 (of a possible 84). The spectra were recorded at several times through the cycle and the unstable mode amplitudes were extracted. We see the measured growth of mode $n=16$ plotted in Fig. 2. Finally, the full (95%) bunch lengths τ_L were measured through the cycle in order to calculate the synchrotron frequency spread.

II. LINEAR THEORY

We begin with the linearized Vlasov equation in polar coordinates (r, θ) [3]

$$-i\Omega f_1 + \omega_s \frac{\partial f_1}{\partial \theta} + \frac{\eta \omega_0}{p} F(\phi_0 + r \cos \theta) \frac{\sin \theta}{\omega_s} f_0 = 0 \quad (1)$$

where we assume the particle distribution function f , normalized to unity, may be separated into a stationary and perturbed part given by

$$f(r, \theta, t) = f_0(r) + f_1(r) e^{i\theta} e^{-i\Omega t}, \text{ with } |f_0| \gg |f_1| \quad (2)$$

In this analysis, we consider a pure dipole oscillation only, ie. $m=1$, and no mode coupling. In (2), Ω are the normal modes of the instability. This quantity is complex, therefore a positive $\text{Im}(\Omega)=\Omega_i$ will lead to growth of the perturbation and $\text{Re}(\Omega)=\Omega_r$ gives a frequency shift. The force F in (1) is the self-induced force on the beam due to its wake fields in the beamline environment. This force may be written as the sum of products of the Fourier components of the charge density and the impedance. After substituting F and summing over all bunches, we arrive at

* Current address: Fermi National Accelerator Laboratory, same as above.

** Work supported by the U.S. Department of Energy under Contract No. DE-AC02-76CHO3000.

$$(\Omega - \omega_s(r))f_1(r) = -i \frac{\eta \omega_0^3 h}{\beta^2 E} \frac{1}{r} \frac{\partial f_0(r)}{\partial r} \sum_k \frac{Z_k(\omega)}{k} J_1(kr) \quad (3)$$

$$\times \int_0^{\infty} r' dr' f_1(r') J_1(kr')$$

where J_1 is the Bessel function and Z_k the impedance due to the RF cavity higher-order modes at the frequencies $\omega = k\omega_0 + \omega_s + \Omega$. The index $k = hp + n$, where h is the harmonic number, p the RF harmonic, and n the coupled-bunch mode number. Multiplying by $r J_1(k'r)/(\Omega - \omega_s(r))$ and integrating both sides over r leads to the dispersion relation

$$1 = -i \frac{\eta \omega_0^3 h}{\beta^2 E} \sum_{k,k'} \frac{Z_k(\omega)}{k} \int_0^{\infty} dr \frac{\frac{\partial f_0(r)}{\partial r} J_1(kr) J_1(k'r)}{(\Omega - \omega_s(r))} \quad (4)$$

Normally, we are interested in solving (4) for each coupled-bunch mode $n=0,1,\dots,h$, to find those eigenfrequencies Ω which are unstable. As this is an infinite dimension matrix equation, a number of simplifications are generally made. In the literature, the small-argument expansion is substituted for one or both $J_1(kr)$ terms. This is the short bunch approximation: kr is the ratio of mode amplitude to perturbing wake field wavelength. For the Booster, however, kr is not small. Also, to allow analytical solutions, ω_s is often assumed constant so that Landau damping can be neglected. We studied both regimes, constant ω_s and $\omega_s(r)$, to examine the influence of Landau damping.

For a constant $\omega_s = \omega_{s_0}$, the denominator in (4) may be pulled out of the integral. In the Booster, there are two unstable modes, each driven by two RF cavity parasitic modes. The mode around $n=16$ is driven by 169 and 220 MHz (RF order $p=3,4$). Mode $n=48$ is driven by 83 and 345 MHz ($p=1,6$). For each n , (4) becomes a 2×2 matrix equation with solutions given by $|1 - M_{ij}| = 0$. For a gaussian particle distribution, the matrix elements may be written

$$M_{ij} = i \frac{1}{\Delta\Omega} \frac{\eta I_0 e}{2\pi\beta^2 E} \frac{\omega_0^2}{\omega_{s_0}^2} \frac{1}{L} \frac{Z_{k_i}}{k_i} e^{-\frac{1}{2}(k_i^2 + k_j^2)L^2} I_1(k_i k_j L^2) \quad (5)$$

where $\Delta\Omega = (\Omega - \omega_{s_0})$, $L = \frac{1}{2} \omega_0 \tau_L$ is the bunch half length in radians and I_1 are modified Bessel functions. The matrix elements are evaluated for $n=16,48$ at different times t through the cycle using the measured impedance Z_k . In each case, the larger $\Omega(t)$ of the two solutions is taken to dominate.

In the case of Landau damping, the frequency spread $\omega_s(r)$ must be included. We use the approximation [3]

$$\omega_s(r) = \omega_{s_0} + \Delta\omega_s \approx \omega_{s_0} \left(1 - \frac{r^2}{16}\right), \quad r = hL \quad (6)$$

We eliminate the sum by choosing the dominant Z_k only and write

$$1 = i \frac{\eta I_0 e}{2\pi\beta^2 E} \frac{\omega_0^2}{\omega_{s_0}^2} \frac{16}{\omega_s h^2 L^4} \frac{Z_k}{k} \int_0^{\infty} dx \frac{e^{-x} J_1^2(kL\sqrt{2x})}{x-y} \quad (7)$$

$$y = -\frac{8}{\omega_s h^2 L^4} \Delta\Omega$$

$$\Delta\Omega = (\Omega_r - \omega_{s_0}) + i\Omega_i$$

The integral in equation (7) is solved numerically, fixing Ω_i and varying Ω_r . The curves can be plotted in the complex Z -plane as shown in Fig 1. This example corresponds to Booster parameters at $t=29$ msec in the cycle, $\omega_s = 2\pi(2.2)$ kHz, $\Delta\omega_s = 2\pi(78)$ Hz. The solution for $\Omega(t)$ is found graphically by finding the intersection of one of the curves with the measured Z_k/k . If the impedance falls inside the innermost curve, the system is stable. For a $Z_k/k = (1.4, 2.0)$ k Ω as plotted with a large dot, the growth rate predicted is 0.3 msec^{-1} without Landau damping and only 0.1 msec^{-1} with.

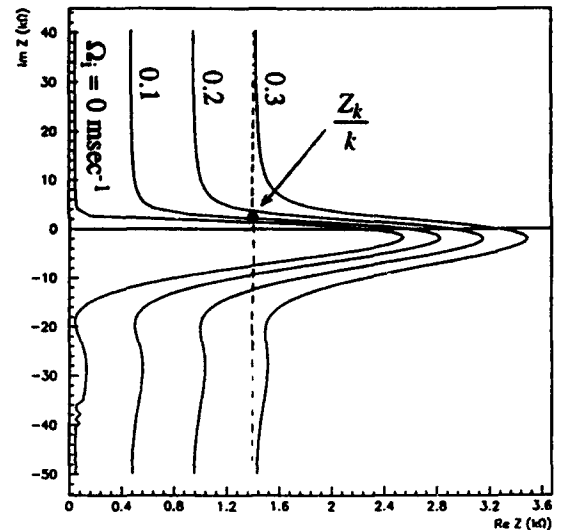


Fig.1. Instability curves showing graphical solution of growth rate.

We may use a WKB approximation, since $\Omega(t)$ is a slow function of time, to get the integrated growth of the instability. The coupled-bunch mode amplitude $\psi(t)$ is calculated using

$$\frac{\psi(t)}{\psi_0(t_0)} = \exp \left(- \int_{t_0}^t |\Omega_i(t)| dt \right) \quad (8)$$

The result, comparing the measured dipole coupled-bunch mode amplitude for $n=16$ in the Booster with the growth predicted by linear instability theory both without and with Landau damping, is shown in Fig 2.

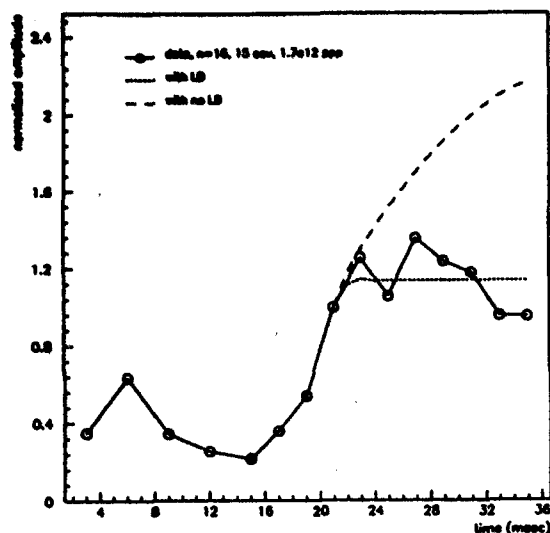


Fig. 2. Linear coupled-bunch theory vs. Booster data, $n=16$.

III. SIMULATION

We used the longitudinal particle tracking code ESME [4] to simulate the Booster using the measured RF cavity HOMs [2]. A full ring of 84 bunches (46k macro particles) were tracked driven in separate runs by 83 and 220 MHz impedances modelled as LRC resonators. The results depend strongly on the initial particle distribution. We reproduced the observed dipole amplitude and emittance growth with a gaussian distribution tracked through transition. In each case, the bunches begin to oscillate rather coherently until, at different radii, they filament in the nonlinear RF potential. The results are shown in Fig. 3. The bunches clearly begin to filament at a larger amplitude on the left. The unstable behavior depends on both the growth rate Ω_i and the frequency shift Ω_r which, for 83 MHz, are a factor of 2 and 100 larger, respectively. The unstable impedance parameter space was explored to determine a scaling for predicting the final maximum amplitude. Additional details are discussed in [5] and [6].

IV. DISCUSSION

Results from the linear coupled-bunch instability theory show good quantitative agreement with the measured growth despite the large amplitude oscillations. It is shown that Landau damping must be invoked to predict the observed saturation. Two additional corrections should be noted. First, the expression for the radial dependence of the frequency ω_s in (6) is strictly true only for a stationary bucket, i.e. when $\phi_s = 0$. A more general expression gives a moving bucket $\Delta\omega_s$ scaling of $(1 + \frac{5}{3} \tan^2 \phi_s)$ [7]. This result, using the same analysis as that leading to (7), predicts growth rates reduced by up to a factor of ten near transition energy, where $\phi_s = 65^\circ$. This seems, however, inconsistent with observations. Second, the measured stationary particle

distributions extracted from the envelope of the RF harmonics in the beam spectra may be used instead in the calculations.

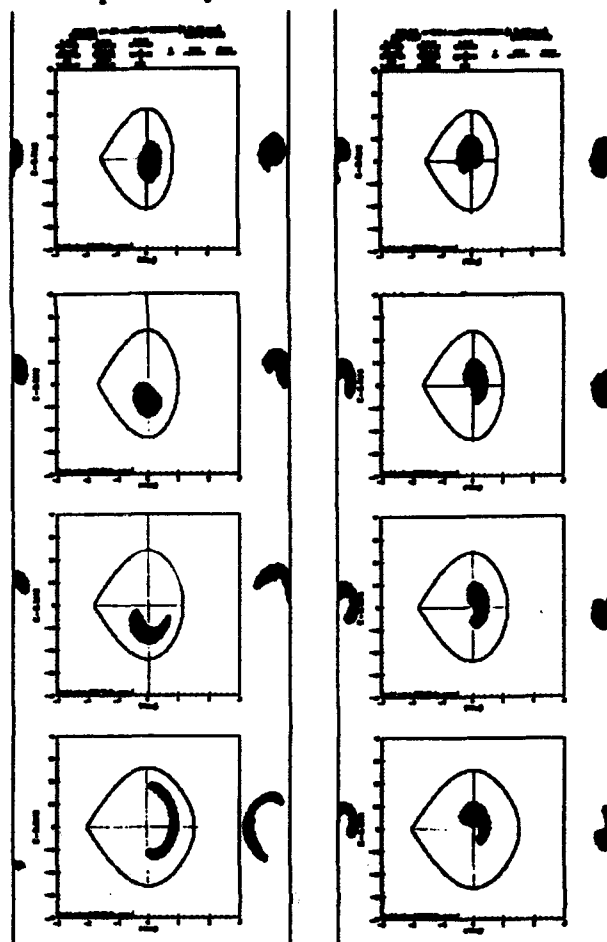


Fig. 3. Phase space plots from ESME simulation for an impedance at 83 MHz (left) and 220 MHz (right) for the last 4 msec in the Booster cycle. The axis scales are $\Delta E = \pm 40 \text{ MeV}$ and $\Delta\phi = \pm 3^\circ$.

The authors would like to thank A. Gerasimov and D. Wildman for productive discussions on emittance growth scaling and RF cavity measurements, respectively.

REFERENCES

- [1] D. Wildman, K. Harkay, "HOM RF Cavity Dampers for Suppressing Coupled-Bunch Instabilities in the Fermilab Booster," These proceedings.
- [2] K. Harkay, P. Colestock, "Calculating Effective Longitudinal Coupling Impedance in the Fermilab Booster from Bench Measurements of RF Cavities," These proceedings.
- [3] J.M. Wang, "Longitudinal Symmetric Coupled Bunch Modes," BNL 51302, Dec 1980.
- [4] S. Stahl and J. MacLachlan, "User's Guide to ESME v. 7.1," FNAL TM-1650, Feb 1990.
- [5] K. Harkay, PhD thesis, Aug 1993.
- [6] A. Gerasimov, "Nonlinear Evolution of Longitudinal Coupled-Bunch Instability," These proceedings.
- [7] R. Baartman, private communication.

Measurement of Trapped Ion Pockets and Control of Ion Instabilities in the Fermilab Antiproton Accumulator

Steven J. Werkema, Kenneth D. Fullett, and Ping Zhou
Fermi National Accelerator Laboratory[†]
P.O. Box 500, Batavia, IL 60510-0500

Abstract

Resonant interaction of positively charged, trapped residual gas ions with a negatively charged, intense antiproton beam has been identified as the primary cause of transverse instability in the Fermilab antiproton accumulator. An upgraded ion clearing system was recently installed. This upgrade yielded a significant improvement in machine performance as well as an enhanced capability for studying trapped ion related phenomena. The operational impact and preliminary results from some initial measurements made with this system are presented herein.

I. INTRODUCTION

Positively charged ions are produced by the coulomb interaction of the highly relativistic \bar{p} beam particles and residual gas molecules in the accumulator vacuum chamber. The ions created by this process acquire only quasi-thermal energies (~ 0.1 eV) and are therefore immediately trapped in the space charge potential of the beam. If no counteractive measures are taken, the trapped ions will accumulate in the beam potential well until the beam is completely neutralized. Even with an extensive clearing electrode system, uncleared sites at local beam potential minima, will result in local neutralization of the beam and potentially hazardous pockets of trapped ions.

Pockets of trapped ions have two detrimental effects. First, the neutralization of the beam can cause significant tune shifts. Figure 1 shows the shift in the vertical tune when the clearing voltage in one of the six accumulator sectors is turned off.

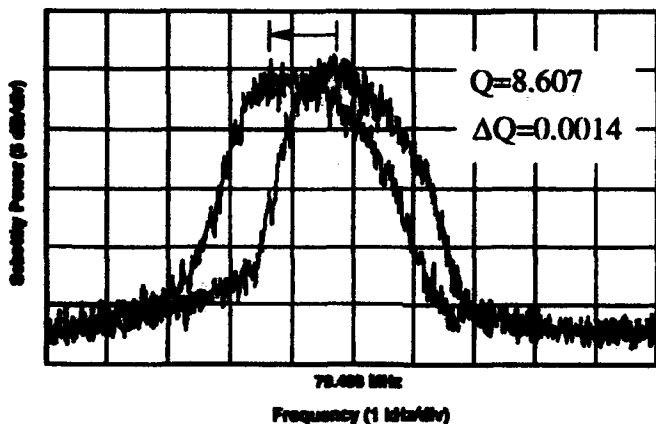


Figure 1. Vertical schottky profile before and after turning off the clearing voltage in accumulator sector 3.

[†] Operated by the Universities Research Association, Inc under contract with the U.S. Department of Energy.

The second undesirable consequence of uncleared pockets of trapped ions is that the ions in these pockets can interact resonantly with the beam resulting in large amplitude coherent oscillations and sudden emittance growth [1]. Figure 2 shows the growth in the first 3 coherent dipole modes as the clearing voltage is decreased from 900 V to 10 V in one sector of the accumulator. Figure 3 shows a typical sequence of ion induced emittance blowups. The operational exigency to clear trapped ions is obvious.

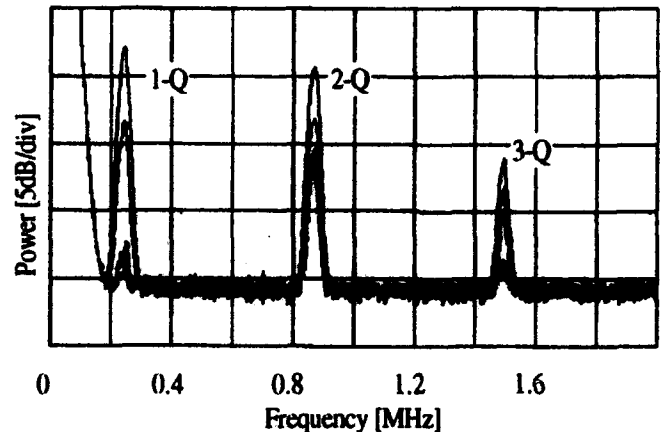


Figure 2. Vertical dipole spectrum showing coherent oscillation at the 1-q, 2-q, and 3-q betatron resonances. As the clearing voltage in accumulator sector 2 is reduced in the sequence - 900 V, 200 V, 100 V, 50 V, and 10 V, the power in each of these lines is seen to grow.

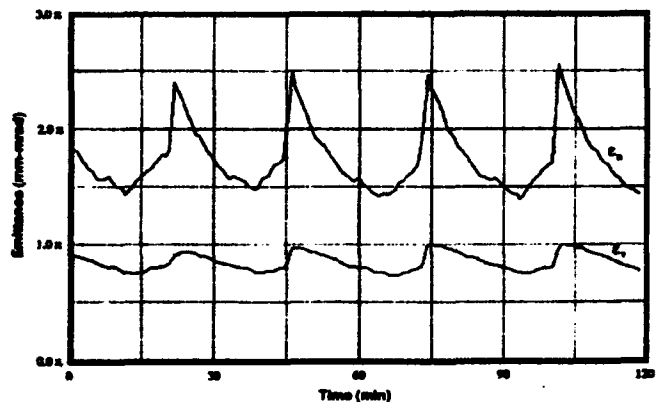


Figure 3. Typical time evolution of trapped ion induced emittance growth.

II. ION CLEARING ELECTRODE HARDWARE

The ion clearing system hardware upgrade consists of six power supplies: one for each of the six sectors in the

Accumulator. The power supplies are individually adjustable through the control system from zero to 1000 volts. Each power supply has ten high voltage output channels. There are an average of two spare channels per sector.

Each channel is connected, by various lengths of coaxial cable, to one or more of the 140 clearing electrodes located throughout the accumulator. Ninety of the electrodes are actually BPM (beam position monitor) pickups; the remaining are dedicated to the ion clearing system. Since the BPM system employs a pre-amplifier at each BPM pickup, it was necessary to insert a one kV DC isolation barrier in front of each BPM pre-amplifier and simultaneously maintain its common-mode rejection performance.

Every channel is capable of monitoring its supply current in the range from zero to ten nA. This current is comprised of both ion clearing current and leakage current. The leakage is due to lengths of coaxial cable and a few clearing electrodes of marginal construction.

The supply current resolution is limited by system noise to 6 pA. External noise (kicker magnets, pulsed power supplies etc.) can further limit the resolution to 50 pA; however, this is dependent upon the operational mode of the accumulator and the location of the clearing electrode and its associated cables.

The clearing electrodes are placed at the most likely locations of trapped ion pockets, which are the minima in the electrostatic potential of the \bar{p} beam. The longitudinal variation of the beam potential well depth depends on the transverse size of the beam and the local dimensions of the vacuum chamber. Figure 4 shows the longitudinal dependence of the beam potential and the deployment of the clearing electrodes for one sector of the accumulator.

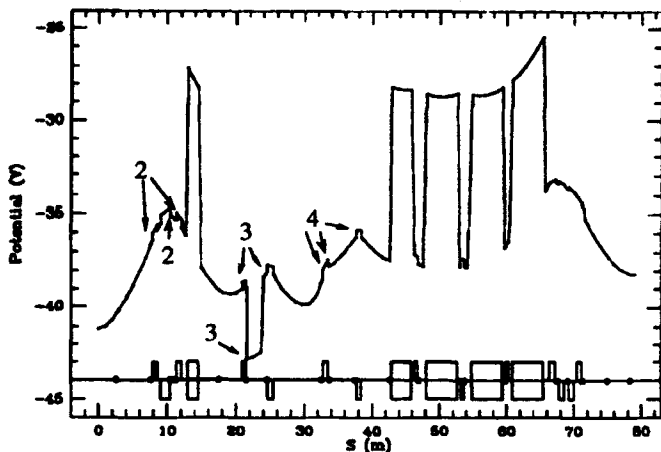


Figure 4. Longitudinal variation of the space charge potential at the center of the beam for accumulator sector 1. This calculation assumed a 200 mA \bar{p} beam and transverse emittances of 2π mm·mrad. The black dots indicate the location of clearing electrodes.

III. OPERATIONAL IMPACT OF THE CLEARING SYSTEM UPGRADE

The deleterious effects of trapped ions are most apparent during the process of extracting \bar{p} 's for use in the collider.

The number of \bar{p} 's transferred to the collider is critically dependent on the extent to which the beam can be cooled in all three dimensions[2]. Prior to the clearing upgrade, relatively small longitudinal densities ($\approx 7 \times 10^{10}$ \bar{p} 's/eV·sec) would result in transverse instabilities. These instabilities would preclude further transverse cooling of the beam. The advent of the ion clearing upgrade increased the achievable longitudinal density by a factor of nearly 2 for horizontal emittances near the threshold for efficient transfer into the collider (see Figure 5).

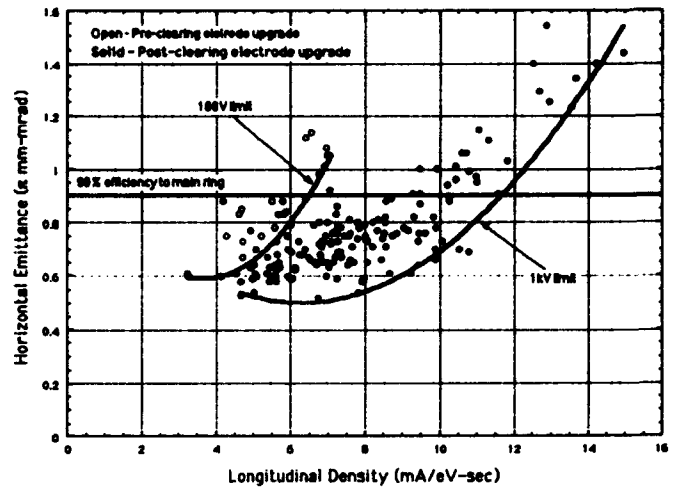


Figure 5. Transverse beam size versus longitudinal density before and after the ion clearing upgrade.

The ion clearing upgrade eliminated the periodic emittance blowup phenomena shown in Figure 3 for \bar{p} stacks of less than 120×10^{10} .

IV. MEASUREMENTS OF TRAPPED ION BEHAVIOR

At the time of this writing, the ion current readback has been in operation for 5 weeks. During this time there have been several opportunities to use this system to study trapped ion phenomena. Some preliminary data from these studies are presented here.

A. Longitudinal Mobility of Trapped Ions

A measurement of the longitudinal mobility of trapped ions is of interest in evaluating the effectiveness of the clearing system and provides an assessment of the validity of the beam space charge potential calculation.

The method used in this study is to turn off the high voltage on one channel of the clearing system. When this is done, the pockets cleared by the clearing electrodes connected to that channel will begin to fill up with ions. As these pockets fill up, the beam becomes partially neutralized at these sites. The local minima in the beam potential quickly disappear and ions produced subsequently will not be locally trapped, but will be free to move in accordance with the longitudinal gradient of the beam space charge potential. The

ion current readback system is used to determine where the ions go when the local pockets are neutralized in this manner.

Figure 6 shows the clearing current readback system response to turning off the high voltage on channel 3 in accumulator sector 1. The clearing current in the adjacent channels (channels 2 and 4) increase; with the greatest increase going to channel 4. Figure 4 shows that there is a large potential barrier between the channel 3 electrodes and the channel 2 electrodes (due to a change in beam pipe diameter). It is, therefore, expected that the majority of ions produced after the pockets at the channel 3 electrodes fill up will indeed go to the channel 4 electrodes.

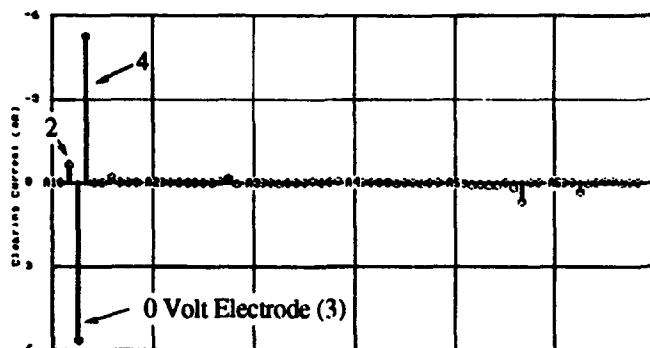


Figure 6. Display of the clearing current readback of all instrumented channels in the accumulator. The current values are differences: Channel 3 OFF - Channel 3 ON. A negative value indicates a net increase in charge cleared.

It is also apparent that the number of ions cleared by the channel 3 electrodes before the voltage was turned off is the same as the number of ions produced at the channel 3 electrode sites but cleared by channels 2 and 4 when the voltage is turned off.

This test was performed on each high voltage channel in the clearing system. The result shown in Figure 6 is typical of what was seen in other channels with a few exceptions. The exceptions include: (1) devices affecting the beam space charge potential which were not incorporated into the potential calculation (e.g. stochastic cooling pickups and kickers), (2) ineffective clearing electrodes, and (3) some genuine mysteries.

The study of trapped ion longitudinal mobility will be continued by attempting to measure the ion longitudinal drift velocities. The bandwidth of the ion current readback system is 10 Hz, which is inadequate for this measurement (the expected velocities are of order several hundred meters/sec). A portable readback system with a bandwidth of 2 kHz is presently being built to facilitate this measurement.

B. Stabilization by Weak RF Bunching

Bunching a small fraction of the accumulator \bar{p} beam with RF has been observed to suppress transverse instability[2]. A study has been initiated to ascertain the mechanism by which

this stabilization occurs. One possibility is that pockets of trapped ions, which are inaccessible to the clearing electrode system, are being cleared by the longitudinal modulation of the beam intensity caused by the RF. The clearing current readback system was used to locate these pockets. Figure 7 shows the clearing current readback response to bunching the beam in a 1.5 eV·sec bucket with an $h=2$ suppressed bucket RF system. Approximately 15% of the beam is contained in the RF bucket.

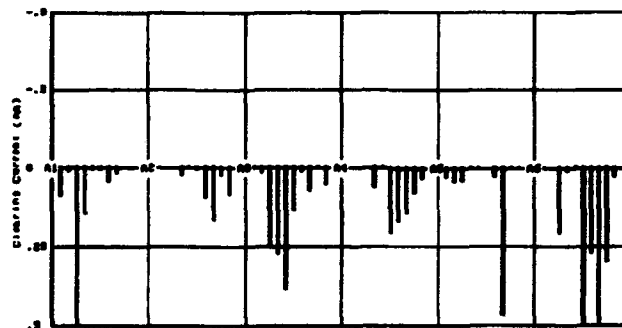


Figure 7. Display of the clearing current readback of all instrumented channels in the accumulator. The current values are differences: RF OFF - RF ON. A positive value indicates a reduction in clearing current.

The clearing current readback indicates a reduction in ion current at roughly the same locations in each sector of the accumulator. A reduction in clearing current is an indication that ions from a nearby site, which were previously drifting to a clearing electrode, are being removed by the effects of RF bunching to the vacuum chamber walls. Generally, it appears that the sites being cleared by RF bunching are in the long straight sections of the accumulator.

Bunching the beam with RF is beneficial even with very small buckets. Applying 5 Volts is nearly as effective as 20 Volts. Moreover, the beam remains stable for a long time (hours) after the RF is turned off.

This effect is far from understood. Much work, both analytical and experimental, remains to be done before any further explanation can be offered.

V. REFERENCES

- [1] P. Zhou, P. Colestock, and S.J. Werkema, Trapped Ions and Beam Coherent Instability. These proceedings (1993).
- [2] S.J. Werkema, D.W. Peterson, and P. Zhou, Transverse Emittance Growth in the Fermilab Antiproton Accumulator with High-Current Antiproton Stacks. These proceedings (1993).

Study of Possible Energy Upgrade for the ALS and Modeling of the "Real Lattice" for the Diagnosis of Lattice Problems*

M. Meddahi and J. Bengtsson
Lawrence Berkeley Laboratory, University of California
1 Cyclotron Road, Berkeley, CA 94720 USA

Abstract

We have studied the change of expected performance of the Advanced Light Source storage ring at LBL for the (design) nominal and maximum energy of 1.5 and 1.9 GeV respectively. Furthermore, we have also studied a possible increase to 2.3 GeV by modeling the change of dynamical aperture caused by saturation of the magnets. Independently, we have also modeled the beam's trajectory at injection. Comparison with bpm data from early storage ring commissioning led to the diagnosis of a major lattice error due to a short in a quadrupole, which was rectified leading to stored beam of 60 turns.

I. INTRODUCTION

Using magnet measurement data, the dynamic aperture was estimated for the ALS storage ring at the nominal energy of 1.5 GeV. By extrapolating magnet currents, multipole errors for quadrupoles were determined and used to estimate the dynamic aperture at 1.9 GeV and 2.3 GeV. Random magnet displacements of 150 μm rms were used as well as random roll errors (100 μrad rms for quadrupoles, 50 μrad rms for bending magnets, 200 μrad rms for sextupoles). The results are discussed in Section 2. Independently, in Section 3, we present the results from modeling of the trajectory of the beam injected into the storage ring. Comparison with bpm data from early commissioning led to the diagnosis of a major lattice error leading to the first circulating beam with 60 turns. All the simulations were done using TRACY [1].

II. DYNAMIC APERTURE AS A FUNCTION OF ENERGY

A. Dynamic aperture at 1.5 GeV

Magnet measurements for 1.5 GeV provide the multipole errors needed to estimate the dynamic aperture. The dynamic aperture shown in Figure 1 is essentially determined by magnet misalignments due to their symmetry breaking effects on the lattice, leading to enhancement of the non-linear effects. This is due to the rather large amplitude dependent tune shifts for the bare lattice together with excitation of resonances linked to the perturbed symmetry. The mechanical aperture is around 21 mm in the horizontal plane and 10 mm in the vertical plane.

B. Dynamic aperture at 1.9 GeV

*This work was supported by the Director, Office of Energy Research, Office of High Energy and Nuclear Physics, High Energy Physics Division, of the U.S. Department of Energy under Contract No. DE-AC-76SF00098.

Rms gradient errors in quadrupoles and bending magnets were obtained by scaling the 1.5 GeV values by a factor of 2, suggested from magnet measurements at 1.9 GeV and similarly for the sextupoles. Systematic multipole errors for bending magnets and quadrupoles were obtained by interpolation of measured values at different currents. Figure 2 shows that the dynamic aperture is reduced mainly in the vertical plane from 11.2 mm to 6.6 mm.

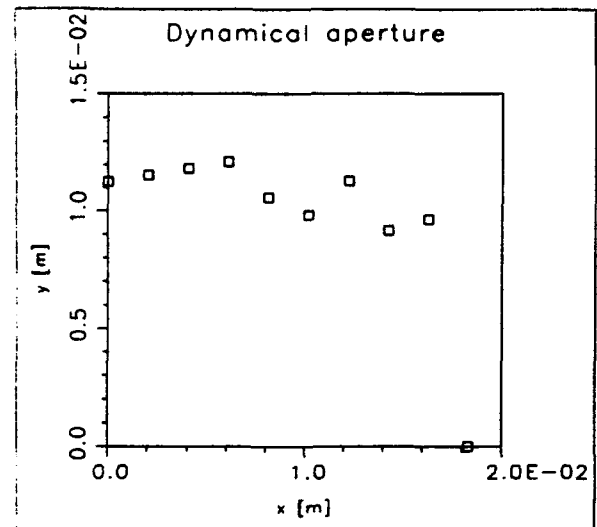


Figure 1. Dynamic aperture at 1.5 GeV.

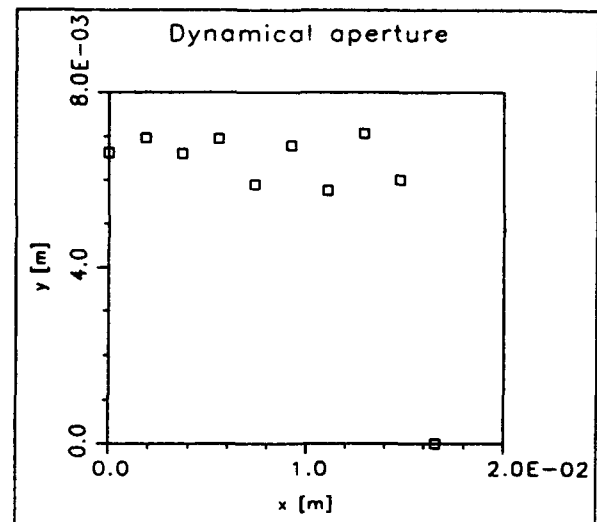


Figure 2. Dynamic aperture at 1.9 GeV.

C. Dynamic aperture at 2.3 GeV

Rms gradient errors in quadrupoles and bending magnets were obtained by scaling the 1.9 GeV values by a factor of 2 and

similarly for the sextupoles. Systematic multipole errors in bending magnets and quadrupoles were obtained by extrapolation of currents and multipole errors using data from measurements at lower energies. The aperture in the vertical plane decreases to 4.8 mm.

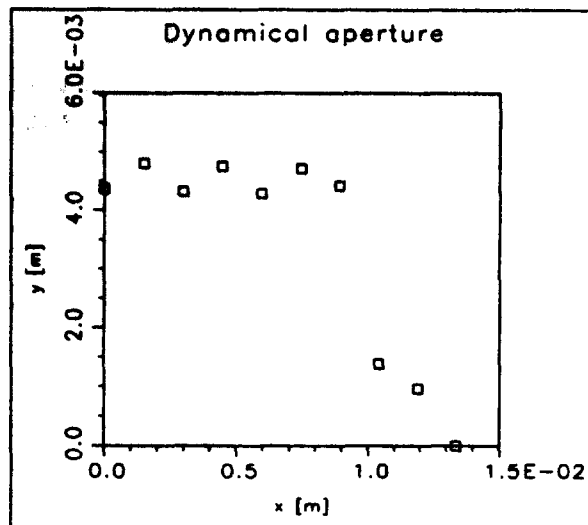


Figure 3. Dynamic aperture for 2.3 GeV.

The three presented cases are using the same pseudo-random number seed. The maximum dynamical aperture was found to be fairly seed independent, which is not the case for the detailed structure of the curve, due to variation of excited resonances.

III. MODELING OF THE REAL LATTICE

At the time bpm data became available the beam in the storage ring was circulating for only a few turns. Since the bpm system has been designed to also record turn by turn data [3] it is possible to analyze the trajectory of the injected beam. Modeling of the data indicated a gradient error at one or possibly two different locations in the lattice. This was confirmed by R. Keller (assisted by the ALS operations team), within a few hours, as a short in a quadrupole magnet. Correction of the error led immediately to the first beam circulating for 60 turns. The following analysis is straightforward but nontrivial due to the limited performance of the bpm:s at this time, i.e. 1-2 mm accuracy down to 5 mm for large displacements in both planes, due to limited dynamical range and input threshold in the electronics.

The model was calibrated by using the bpm:s in sector 1 to 6 (out of 12) since the beam makes it smoothly half a turn but is lost at roughly 2/3 of a turn. An 8 parameter least square fit of the data gives for the initial conditions

$$\begin{aligned}x &= -6.62 \text{ mm, } p_x = -0.259 \text{ mrad} \\y &= -1.29 \text{ mm, } p_y = 0.326 \text{ mrad}\end{aligned}$$

and the for the quadrupole k-values

$$\begin{aligned}k_{q1} &= 2.13 (2.13) \text{ m-2, } k_{q2} = -2.02 (-2.14) \text{ m-2,} \\k_{q3} &= 2.95 (2.98) \text{ m-2, } k_{q4} = -0.802 (-0.714) \text{ m-2}\end{aligned}$$

The k-values estimated from magnet currents are shown within brackets. The rms deviations between bpm data and model are 0.20 mm and 0.21 mm for the horizontal and vertical planes respectively. If we assume a random error of 2 mm rms for each bpm we have

$$\Delta x_{\text{rms}} = \frac{\Delta x}{\sqrt{n}} = 0.29 \text{ mm}$$

since we are using 47 bpm:s, which is consistent with our analysis. The result is shown in Figure 4.

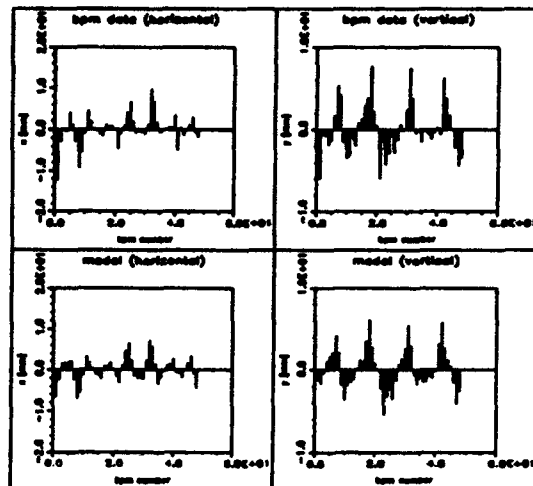


Figure 4: Calibration of model, sector 1-6

Examination of the results show agreement within 1-2 mm on the average and individual disagreements up to 5-6 mm, in particular when the displacements are large in both planes. It is clear that attempts to estimate the initial conditions from the first two bpm:s are futile due to large errors, only statistical analysis can give meaningful results.

One finds little improvement when magnet misalignments based on survey data are added to the model. This is due to the large excursions made by the injected beam. It is therefore irrelevant for the continued analysis.

When sector 7 and 8 are included the rms deviations between bpm data and model increase to 0.28 mm and 0.31 mm. Note that we are adding 16 more data points and would expect the rms values to decrease. Something is clearly wrong within these two sectors, see Figure 5.

We conclude that major deviations between bpm data and model start to show up at bpm number 58. However, a kick of a few mrad has to propagate a few meters to show up as a displacement on the bpm:s. The lattice error might well be upstream of this point. Some simple trials (by adding kicks to the model) confined the problem from the end of sector 7 to the end of sector 8. After some further trial and error we found that only the following kicks have a possibility to reproduce the data. The vertical kicks are

$$\begin{aligned}\theta_{q1}(\text{SR 7 QFA 1}) &= -0.9 \text{ mrad} \\ \theta_{q1}(\text{SR 8 QFA 1}) &= -9.8 \text{ mrad,} \\ \theta_{q1}(\text{SR 8 QFA 2}) &= 31.4 \text{ mrad}\end{aligned}$$

together with a horizontal kick

$$\theta_{q1}(\text{SR 8 QFA 2}) = -4.9 \text{ mrad}$$

This gives rms deviations between bpm data and model of 0.20 mm and 0.18 mm, in agreement with the expected accuracy, see Figure 6.

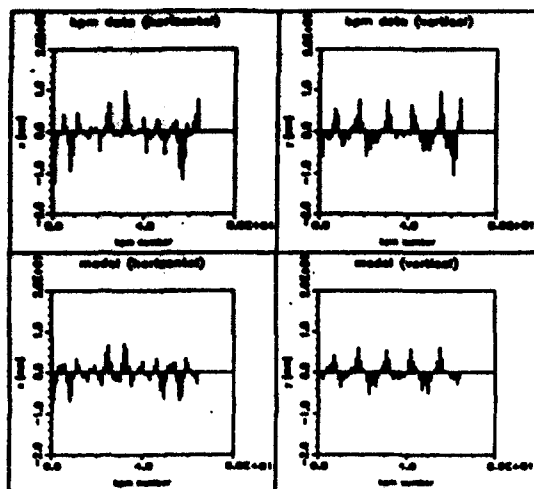


Figure 5: Sector 1-8

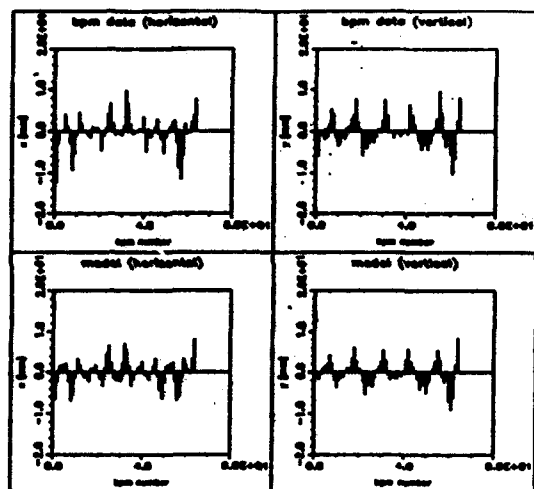


Figure 6: Sector 1-8 with fitted kicks

The first kick is negligible, i.e. no major change of the rms deviations was found (within the expected accuracy) if it was left out. We have therefore located the problem to SR 8 QFA 1 and SR 8 QFA 2. We conclude from the simulations that it is clear that kicks in QF, QD and the bends can not reproduce the bpm data in sector 8. On the other hand, by adding kicks at SR 8 QFA 1 and SR 8 QFA 2 we can restore the agreement between bpm data and model to the expected level. Note, that we have limited statistics downstream of these magnets.

It is possible to obtain some information of the nature of the field error (dipole, gradient etc.) by analyzing a second shot which also provides a consistency check. Injection jitter will slightly change the beam initial conditions so that it follows a different trajectory. We computed the necessary kicks to reproduce the bpm data in this case. If the kicks are significantly different from the previous case the field error is obviously not of dipole type. As before agreement with the model was restored by adding the following vertical kicks

$$\begin{aligned}\theta_{\text{QA}}(\text{SR 7 QFA 1}) &= -2.0 \text{ mrad} \\ \theta_{\text{QA}}(\text{SR 8 QFA 1}) &= -20.2 \text{ mrad} \\ \theta_{\text{QA}}(\text{SR 8 QFA 2}) &= 59.9 \text{ mrad}\end{aligned}$$

and the horizontal kick

$$\theta_{\text{QA}}(\text{SR 8 QFA 2}) = -5.8 \text{ mrad}$$

These kicks differs by a factor of two from the previous. The field error is clearly not of dipole type. The result is shown in Figure 7.

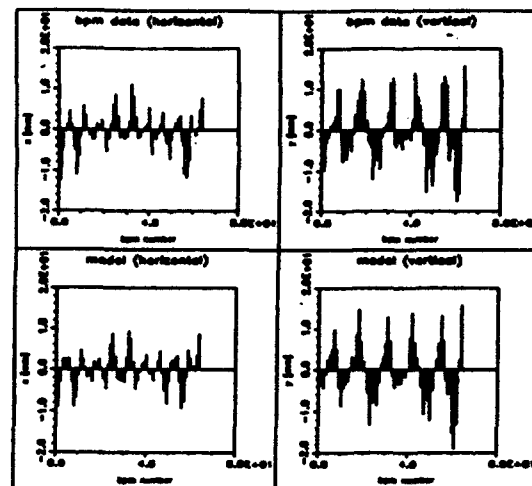


Figure 7: Second shot, sector 1-8 with fitted kicks

IV. CONCLUSION

Dynamic apertures studies show a reduction of the dynamical aperture mainly in the vertical plane when the energy is increased from 1.5 to 2.3 GeV. The study was limited to the transverse dynamics. Analysis of bpm data proved to be useful in diagnosing a major lattice error during early commissioning. The error was diagnosed within a few hours, after presentation of the analysis, as a short circuit between two leads to one of the coils for the quadrupole SR 8 QFA 1 immediately leading to 60 turns.

V. ACKNOWLEDGMENTS

We would like to thank the S. Chattopadhyay and Center for Beam Physics for continuous support and encouragement, R. Keller for providing magnet data and identifying the shorted quadrupole, J. Hinkson, P. Kuske, H. Nishimura, L. Schachinger, C. Timossi and the ALS operations team for providing the bpm data.

VI. REFERENCES

- [1] J. Bengtsson, E. Forest and H. Nishimura, unpublished.
- [2] LBL-Pub-5172 Rev. (1986)
- [3] J. Hinkson, LBL-31526.

Study of Coupled-bunch Collective Effects in the PEP-II B-Factory*

John Byrd
Lawrence Berkeley Laboratory
Berkeley, CA 94720 USA

Abstract

We present an overview of the calculated longitudinal and transverse coupled-bunch (CB) growth rates using the measured RF cavity higher order mode impedance and estimated resistive wall (RW) impedance for the proposed PEP-II B-Factory[1], a dual-ring electron-positron collider. We also describe a visual method of representing the effective beam impedance and corresponding growth rates which is especially useful for understanding the dependence of growth rate on higher order mode frequency and Q, spread of HOM frequencies between cells, and for determining the requirements of the CB feedback systems.

INTRODUCTION

Because of the high beam current and large number of bunches at PEP-II, a proposed dual-ring electron-positron collider, CB instabilities are predicted to be one of the limiting factors in achieving the design beam intensity. Longitudinal and transverse CB feedback systems are currently being designed to combat this problem. This paper provides a detailed estimate of the growth rates in the PEP-II low energy ring (LER) using the measured HOMs of the low-power model of the PEP-II cavity and the resistive wall impedance. The growth rates in the high energy ring (HER) are lower by $\sim 0.7-3$ because of the factor 3 in beam energy. This paper does not include any discussion of the CB effects resulting from the interaction of the beam with the fundamental mode of the cavity.

COUPLED-BUNCH IMPEDANCE

In the case of longitudinal beam oscillations, the RF cavities provide the only sources of impedance strong enough to drive CB instabilities. A series of measurements characterizing the resonant modes of the PEP-II RF cavity cell have been performed on a low-power prototype model. A summary of the properties of the monopole and dipole higher order modes (HOMs) is given in reference [2], in these proceedings.

In the case of betatron oscillations, there are two sources of impedance large enough to drive CB instabilities: the RF cavities and the RW impedance. An estimate of the RW impedance has been made[3], taking into account the variable resistivity, aperture, and cross section of the vacuum chamber around the ring. Because of the narrower vertical aperture in a large part of the vacuum chamber, the vertical RW impedance dominates over the horizontal.

The net vertical RW impedance, scaled by the ratio of the beta function at the RW impedances and the RF cavities, is given by $Z_{\perp, RW} = 0.566 \text{ M}\Omega/\text{m}/\sqrt{f(\text{MHz})}$.

COUPLED-BUNCH GROWTH RATES

Longitudinal Effects—The longitudinal complex frequency shift of CB mode ℓ for a bunched beam with N equally populated and equally spaced bunches is given by[4]

$$\Delta\omega_{\parallel}^{\ell} = \frac{1}{2} \frac{I_0 f_{rf} \alpha}{(E/e)Q_s} i [Z_{\parallel}]_{eff}^{\ell} \quad (1)$$

$$[Z_{\parallel}]_{eff}^{\ell} = \sum_{p=-\infty}^{p=+\infty} \frac{\omega_p}{\omega_{rf}} e^{-(\omega_p \sigma_r)^2} Z_{\parallel}(\omega_p) \quad (2)$$

and

$$\omega_p = (pN + \ell + Q_s)\omega_0. \quad (3)$$

where f_0 is the revolution frequency.

The effective impedance, $[Z_{\parallel}]_{eff}^{\ell}$, represents the sum of the beam spectrum over the actual impedance. The complex frequency shift was evaluated using the measured parameters shown in Table 1 and the measured HOM parameters given in [2]. The imaginary part of Eq. 1 represents a growth or damping of the CB mode and is driven by the real part of the impedance. The growth rates were calculated for the worst case of no spread in HOM frequencies among the RF cells.

Because of the sampling of the cavity wakefields by the beam, the HOM impedances are aliased into a frequency bandwidth given by $1/2T_b$, where T_b is the bunch separation in time. For the case of every other RF bucket filled, the frequency bandwidth is 119 MHz. We consider here the impedances aliased into the frequency band 0-119 MHz. The summation for the effective impedance given in Eq. 2 represents this aliasing. The real part of the effective longitudinal impedance driving the longitudinal coupled bunch modes is shown graphically in Figure 1. The effective impedance is plotted on the left axis and the corresponding growth rates of the unstable beam modes are plotted on the right axis. The dotted line represents the effective impedance resulting in growth for CB modes corresponding to upper sidebands in the frequency band 0-119 MHz. The dashed line is the effective impedance resulting in growth for lower sidebands in the same frequency band. Note that the dashed line represents a damping impedance for the upper sideband modes in the same frequency band. Several of the aliased HOM's are labeled according to their resonant frequency as given in [2].

The CB mode frequencies are closely spaced because of the low revolution frequency. Therefore, there is very little

*This work was supported by the Director, Office of Energy Research, Office of Basic Energy Sciences, Materials Sciences Division, of the U.S. Department of Energy under Contract No. DE-AC03-76SF00066.

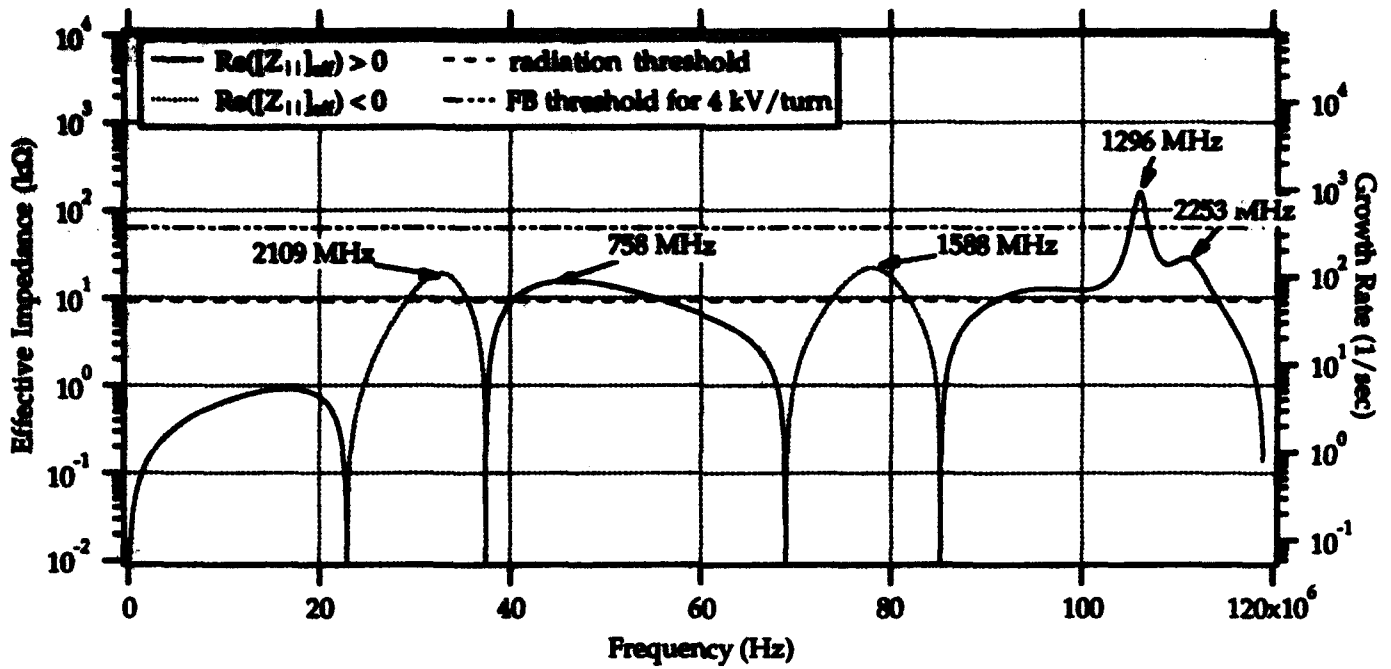


Figure 1: Longitudinal CB growth rates and the effective impedance in the 0-119 MHz frequency band. The largest HOMs have been labeled according to their resonant frequency in MHz. CB mode frequencies are too closely spaced to be resolved on this scale.

Symbol	Description	LER Value
E	Beam energy (GeV)	3.109
C	Circumference (m)	2199.318
f_{rf}	RF Freq.	476 MHz
N	No. of bunches	1746
I_0	Beam current (A)	2.14
α	Mom. compaction	1.49e-3
Q_s	Synchrotron tune	0.05
N_{rf}	No. of RF cells	10
$Q_{s,y}$	x,y β -tron tunes	32.28,35.18
$\langle \beta_{s,y} \rangle$	aver. $\beta_{s,y}(m)$	10.84,9.95

Table 1: PEP-II LER parameters used for calculations.

effect of shifts in the frequencies of the HOMs because they are already heavily damped or in shifts of the CB mode frequencies. However, further "de-Qing" of an HOM would help by bringing down the HOM's shunt impedance even further. This could be accomplished by even more aggressive damping of the HOMs or by a spread in the HOM frequencies between the various RF cells.

Longitudinal Feedback Threshold- A CB feedback (FB) system is being designed to damp the unstable modes plotted in Figure 1. Neglecting any aid from radiation damping, the damping limit of the FB system is reached when the beam-induced voltage/turn equals the maximum FB kick voltage/turn. The magnitude of the beam-induced

voltage/turn is given by

$$V_b = I_0 \Delta \phi Z_{||} = I_0 \Delta \phi_0 Z_{||,eff} \quad (4)$$

where $Z_{||,eff}(\omega) = (\omega/\omega_{rf})Z_{||}(\omega)$ is the where $\Delta \phi_0$ is the amplitude of phase modulation at the RF frequency for a CB mode. The maximum longitudinal kick/turn is 4 kV and a maximum longitudinal CB amplitude of 0.03 rad is assumed.

Transverse Effects- The transverse complex frequency shift of CB mode ℓ for a bunched beam with equally populated and spaced bunches is given by[4]

$$\Delta \omega_{\perp}^{\ell} = -\frac{1}{2} \frac{I_0 f_0}{(E/e)} i [\beta_{\perp} Z_{\perp}]_{eff}^{\ell} \quad (5)$$

where

$$[\beta_{\perp} Z_{\perp}]_{eff}^{\ell} = \beta_{\perp} \sum_{p=-\infty}^{p=+\infty} e^{-(\omega_p \sigma_r)^2} Z_{\perp}(\omega_p) \quad (6)$$

and

$$\omega_p = (pN + \ell + Q_{\perp})\omega_0. \quad (7)$$

I_0 is the DC current and β_{\perp} is the transverse beta function at the location of the impedance. The complex frequency shift was evaluated using the parameters shown in Table 1 and the dipole in reference [2].

The contribution to the real part of the effective transverse impedance from the HOMs is shown graphically in Figure 2. The dotted line represents the effective impedance resulting in growth for CB modes corresponding to upper sidebands in the frequency band 0-119 MHz.

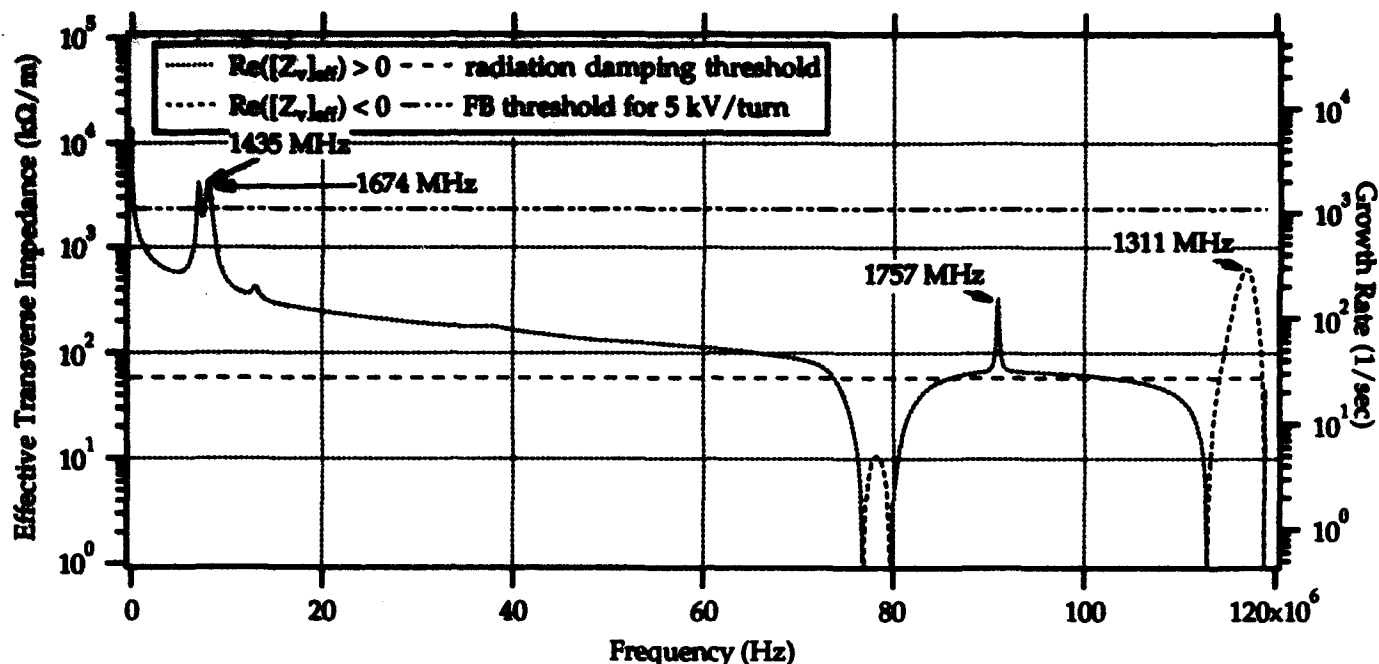


Figure 2: Vertical CB growth rates and the effective impedance in the 0-119 MHz frequency band from the RF cavity dipole HOM and the resistive wall impedance.

The dashed line is the effective impedance resulting in growth for lower sidebands in the same frequency band. Note that the dashed line represents a damping impedance for the upper sideband modes in the same frequency band. The radiation damping rate is also plotted.

Most of the HOMs have been well damped such that they give growth rates below the radiation damping threshold. However, there appears to be two narrowband dipole modes that can cause possible problems. Further investigation of the modes is continuing.

There is relatively little detrimental effect on the growth rates from changes in the betatron tune or changes in an HOM frequencies assuming that all RF cells change equally because of the extent of the damping of the HOMs and the relatively small revolution frequency. If the HOM frequencies in the various RF cells do not shift equally, the net HOM impedance can be reduced, thus lowering the growth rates. However, the RW impedance does not vary significantly over time. It is expected to be the dominant effect in the transverse plane.

Transverse Feedback Threshold—Neglecting any aid from radiation damping, the limit of the transverse feedback system is reached when the beam-induced voltage/turn equals the maximum feedback kick voltage/turn. The magnitude of the beam-induced voltage/turn is given by

$$V_b = I_0 \Delta x Z_{\perp} \quad (8)$$

where Δx is the transverse oscillation amplitude for a CB mode. The maximum vertical kick/turn is 5 kV and a maximum transverse CB amplitude of 1 mm is assumed. As in the longitudinal case, the transverse feedback gain

can be raised to sufficiently stabilize a quiescent beam.

CONCLUSIONS

Most longitudinal CB modes are damped near or below the radiation damping rate. The rest should be damped by the FB system. One remaining monopole HOM requires further damping. The transverse plane is dominated by the RW impedance, and two other dipole HOMs which can potentially drive beam modes at a comparable rate but will likely be reduced because of cell-cell differences. Landau damping from the intrabunch tune spread is not effective in damping any of the fastest growing CB modes at full beam current although it may help at lower currents.

The author would like to thank Glen Lambertson for many useful discussions and members of the Center for Beam Physics at LBL for their general support and encouragement.

REFERENCES

- [1] Design Update for PEP-II, LBL PUB-5303 (1992).
- [2] R. Rimmer, D. Goldberg, *Measurement of Higher-order Mode Damping in the PEP-II Low-Power Test Cavity*, these proceedings.
- [3] J. Byrd, *Resistive Wall Instability at the PEP-II B-Factor*, CBP Tech Note-006, PEP-II AP Note 9-93, May 1993.
- [4] M. Zisman, S. Chattopadhyay, J. Bisognano, *ZAP User's manual*, LBL-21270.

Study of Coupled-bunch Collective Effects in the ALS*

J. M. Byrd and J. N. Corlett
Lawrence Berkeley Laboratory
Berkeley, CA 94720 USA

Abstract

We present an overview of the calculated longitudinal and transverse coupled-bunch (CB) growth rates using the measured RF cavity higher order mode (HOM) impedance for the Advanced Light Source (ALS), a 1.5 GeV electron storage ring for producing synchrotron radiation. We also describe a visual method of representing the effective beam impedance and corresponding growth rates which is especially useful for understanding the dependence of growth rate on HOM frequency and Q , for determining the requirements of the CB feedback system, and for interpreting measured beam spectra.

INTRODUCTION

Because of the high beam current and large number of bunches at the ALS, CB instabilities are predicted to be one of the limiting factors in achieving the design beam intensity while maintaining good beam quality. Longitudinal and transverse CB feedback systems are currently being designed to combat this problem.

COUPLED-BUNCH IMPEDANCE

In the case of longitudinal beam oscillations, the RF cavities provide the only sources of impedance strong enough to drive CB instabilities. A series of measurements characterizing the resonant modes of the ALS RF cavity have been performed. A summary of the measurements is given in reference [3], in these proceedings.

In the case of betatron oscillations, there are two sources of impedance large enough to drive CB instabilities: the RF cavity dipole HOMs and the resistive wall (RW) impedance of the vacuum chamber. A careful estimate of the RW impedance has been made[2], taking into account the variable resistivity, aperture, and cross section of the vacuum chamber around the ring. In addition, the transverse beta functions vary around the ring. Because of the narrower vertical aperture in the chamber, the vertical impedance dominates the horizontal. The net vertical RW impedance, scaled by the ratio of the beta function at the RW impedances and the RF cavities, is given by $Z_{L,RW} = 0.59 \text{ M}\Omega/\text{m}/\sqrt{f(\text{MHz})}$.

COUPLED-BUNCH GROWTH RATES

Longitudinal Effects

The longitudinal complex frequency shift of CB mode ℓ for a bunched beam with N equally populated and equally

spaced bunches is given by[4]

$$\Delta\omega_{\parallel}^{\ell} = \frac{1}{2} \frac{I_0 f_r \alpha}{(E/e)Q_s} i [Z_{\parallel}]_{eff}^{\ell} \quad (1)$$

where

$$[Z_{\parallel}]_{eff}^{\ell} = \sum_{p=-\infty}^{p=+\infty} \frac{\omega_p}{\omega_r f} e^{-(\omega_p \sigma_r)^2} Z_{\parallel}(\omega_p) \quad (2)$$

and

$$\omega_p = (pN + \ell + Q_s)\omega_0. \quad (3)$$

The effective impedance, $[Z_{\parallel}]_{eff}^{\ell}$, represents the sum of the beam spectrum over the actual impedance. The complex frequency shift was evaluated using the measured parameters shown in Table 1 and the measured HOM parameters given in [3]. The imaginary part of Eq. 1 represents a growth or damping of the oscillation and is driven by the real part of the impedance. The growth rates were calculated for the worst case of no spread in HOM frequencies between the two RF cells.

Because of the sampling of the cavity wakefields by the beam, the HOM impedances are aliased into a frequency band of $0-1/2T_b$, where T_b is the bunch separation in time. For nominal ALS conditions, the frequency range is 0-250 MHz. The summation for the effective impedance given in Eq. 2 represents this aliasing. The real part of the effective longitudinal impedance driving the longitudinal coupled bunch modes is shown in Figure 1. The effective impedance is plotted on the left axis and the growth rates of the unstable beam modes larger than radiation damping are plotted on the right axis. The unstable CB modes themselves are represented by solid vertical lines. The dotted line represents the effective impedance resulting in growth for CB modes corresponding to upper sidebands in the frequency range 0-250 MHz. The dashed line is the effective impedance resulting in growth for lower sidebands in the same frequency range. Note that the dashed line represents a damping impedance for the upper sideband modes in the same frequency range. Several of the aliased HOM's are labeled according to their resonant frequency as given in [3]. The radiation damping rate is also shown in the figure.

The plot of the effective impedance clearly shows the dependence of growth rate on HOM parameters such as resonant frequency, Q , and synchrotron tune. For example, if a high- Q HOM is damped, it's width will increase and the peak value of the shunt impedance will decrease. However, as it's width increases, it will drive unstable more CB modes. In addition, the dependence of growth rate on variations of the HOM frequency resulting from cavity tuner position and water temperature or on changes in

*This work was supported by the Director, Office of Energy Research, Office of Basic Energy Sciences, Materials Sciences Division, of the U.S. Department of Energy under Contract No. DE-AC03-76SF00008.

Parameter	Description	Value
E_b	Beam energy	1.5 GeV
C	Circumference	196.8 m
f_{rf}	RF Freq.	499.654 MHz
σ_c	RMS $\delta E/E$	7.1e-4
N	Number of bunches	328
I_0	Total DC beam current	0.4 A
α	momentum compaction	1.594e-3
Q_s	Synchrotron tune	0.009105
σ_t	RMS bunch length	3.9 mm
$Q_{x,y}$	Horizontal betatron tune	14.28, 8.18
$\beta_{x,y,cav}$	$\beta_{x,y}$ at cavity	11.5 m, 5 m

Table 1: ALS parameters used for calculations.

the synchrotron tune is easily found. The plot of the effective impedance is also very useful in interpreting measured spectra of CB oscillations because of the diirect correlation between CB sidebands and HOMs.

Landau damping from the tune spread due to the nonlinearity of the RF voltage is not effective in damping any of the fast-growing CB modes at full current because of the short bunch length.

Longitudinal Feedback Threshold

A CB feedback system is being designed to damp the unstable modes plotted in Fig. 1. Neglecting any aid from radiation damping, the damping limit of the FB system is reached when the beam-induced voltage/turn equals the maximum FB kick voltage/turn. The magnitude of the beam-induced voltage/turn is given by

$$V_b = I_0 \Delta \phi Z_{\parallel} = I_0 \Delta \phi_0 Z_{\parallel,eff} \quad (4)$$

where $Z_{\parallel,eff}(\omega) = (\omega/\omega_{rf})Z_{\parallel}(\omega)$ is the where $\Delta \phi_0$ is the amplitude of phase modulation at the RF frequency for a CB mode. The maximum longitudinal kick/turn is 1.5 kV and a maximum longitudinal CB mode amplitude of 0.03 rad is assumed. For ALS injection conditions, all longitudinal CB modes are excited much less than 0.03 rad. The limit of impedance the longitudinal FB can damp is included in Fig. 1.

Transverse Effects

The transverse complex frequency shift of CB mode ℓ for a bunched beam with equally populated and spaced bunches is given by[4]

$$\Delta \omega_{\perp}^{\ell} = -\frac{1}{2} \frac{I_0 f_0}{(E/e)} i [\beta_{\perp} Z_{\perp}]_{eff}^{\ell} \quad (5)$$

where

$$[\beta_{\perp} Z_{\perp}]_{eff}^{\ell} = \beta_{\perp} \sum_{p=-\infty}^{p=+\infty} e^{-(\omega_p \sigma_r)^2} Z_{\perp}(\omega_p) \quad (6)$$

and

$$\omega_p = (pN + \ell + Q_{\perp})\omega_0. \quad (7)$$

I_0 is the DC current and β_{\perp} is the transverse beta function at the location of the impedance. Using the dipole cavity modes from [3], the complex frequency shift was evaluated the parameters shown in Table 1.

The real part of the effective vertical impedance is shown in Figure 2. The dotted line represents the effective impedance resulting in growth for CB modes corresponding to upper sidebands in the frequency range 0-250 MHz. The dashed line is the effective impedance resulting in growth for lower sidebands in the same frequency range.

Landau damping from the intrabunch tune spread due to the nonlinearity of the transverse restoring force is not easy to evaluate. For the assumed value of the tune spread of 0.01, Landau damping is not effective in damping any of the CB modes at full beam current although it may help at lower currents. Head-tail damping for the expected strength of the broadband impedance is not significant.

Transverse Feedback Threshold

Neglecting any aid from radiation damping, the limit of the transverse FB system is reached when the beam-induced voltage/turn equals the maximum FB kick voltage/turn. The magnitude of the beam-induced voltage/turn is given by

$$V_b = I_0 \Delta x Z_{\perp} \quad (8)$$

where Δx is the transverse oscillation amplitude for a CB mode. The maximum transverse kick/turn is 1.6 kV and a maximum transverse CB amplitude of 1 mm is assumed. As in the longitudinal case, the transverse FB gain can be raised to sufficiently stabilize a quiescent beam. For ALS injection conditions, all transverse CB modes are excited much less than 1 mm. The limit of the transverse FB is shown in Fig. 2.

CONCLUSIONS

Longitudinal CB growth rates in the ALS are $\sim 1/\text{msec}$. Transverse CB growth rates are $0.5-1/\text{msec}$. The growth rates are sensitive to detailed RF cavity conditions and betatron tunes. The proposed CB FB systems can damp all unstable modes for the expected injection conditions.

The author would like thank Glen Lambertson for many useful discussions and members of the Center for Beam Physics at LBL for their general support and encouragement.

REFERENCES

- [1] 1-2 GeV Synchrotron Radiation Source-CDR, LBL PUB-5172 Rev., July 1986.
- [2] J. Byrd, *Resistive Wall Instability at the ALS*, ESG Tech Note-195, LSAP-122, May 1992.
- [3] J. Corlett, J. Byrd, *Measurement of Higher-order Modes of the ALS 500 MHz Accelerating Cavities*, these proceedings.
- [4] M. Zisman, S. Chattopadhyay, J. Bisognano, *ZAP User's manual*, LBL-21270.

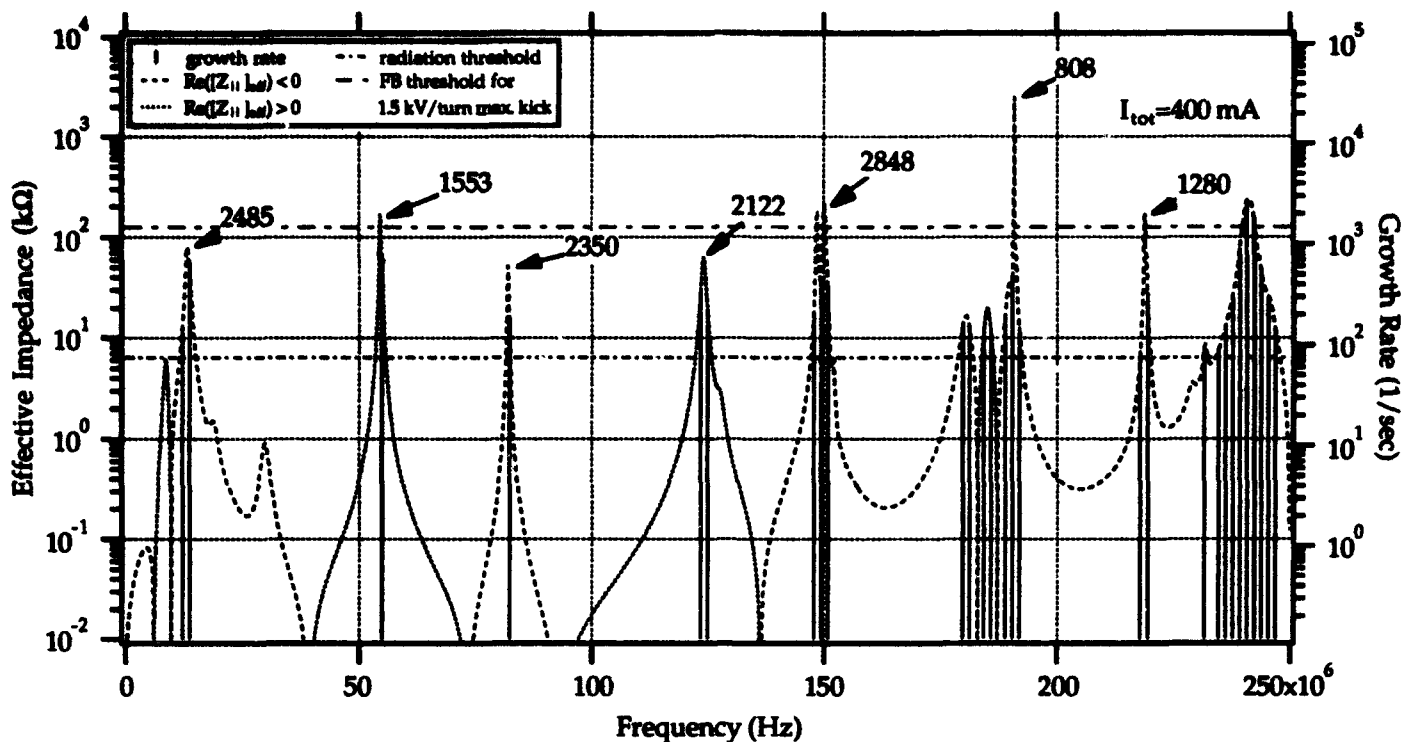


Figure 1: Longitudinal coupled-bunch growth rates and the effective impedance in the 0-250 MHz frequency band. The largest HOMs have been labeled according to their resonant frequency in MHz. Only CB modes with growth rates greater than radiation damping are shown.

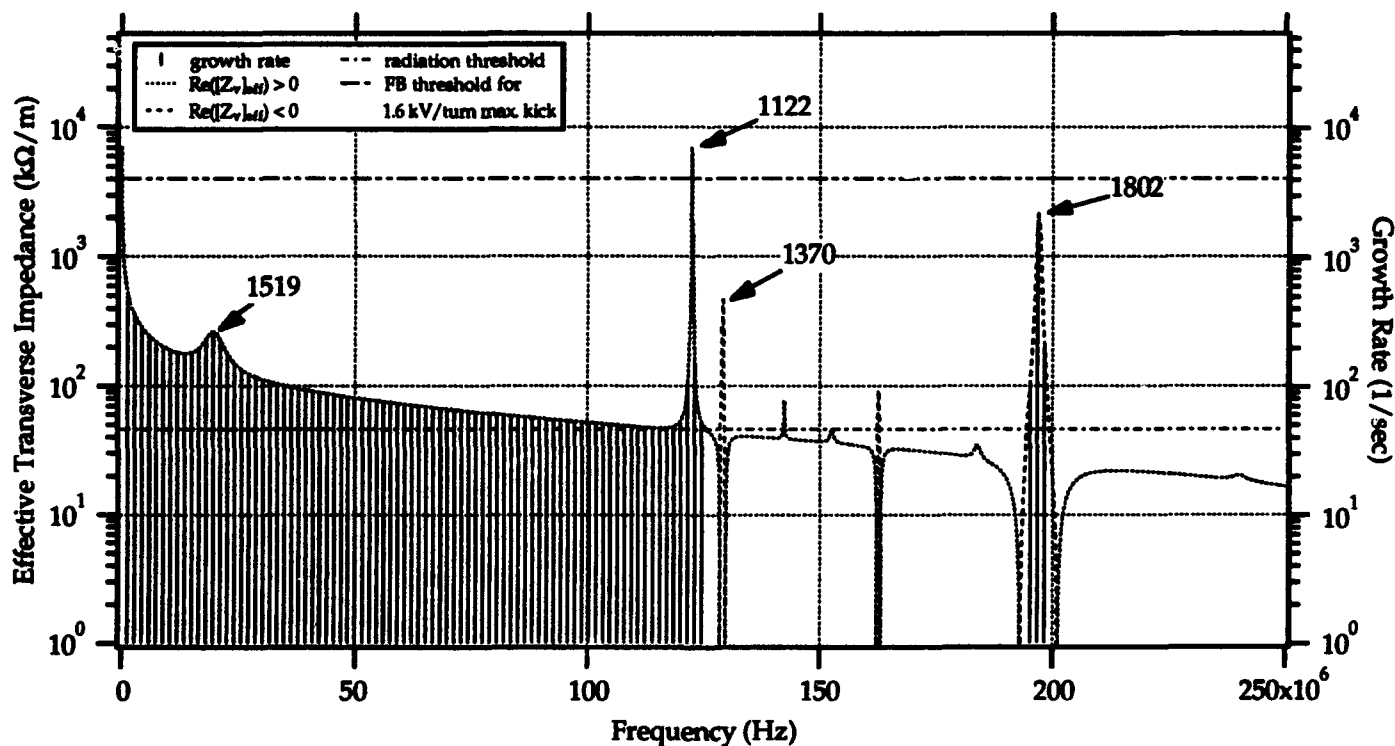


Figure 2: Vertical coupled-bunch growth rates and the effective impedance in the 0-250 MHz frequency band from the RF cavity dipole HOM and the resistive wall impedance.

Time Domain Solutions for a Coasting Beam with Impedance Feedback*

M. Blaskiewicz

AGS Dept. Brookhaven National Lab
BNL 911C Upton, NY 11973

Abstract

Time domain solutions for a coasting beam interacting with a longitudinal or transverse impedance are presented. The treatment is limited to first order perturbation theory, but it includes Landau damping.

I. INTRODUCTION

Analytic treatments of the linearised Vlasov equation are usually posed as eigenvalue problems in the frequency domain [1, 2, 3], while computer codes usually work in the time domain. In this note, a time domain approach to the linearised Vlasov equation is introduced. The technique is applied to both longitudinal and transverse coasting beam instabilities. In both cases, the Vlasov equation is reduced to a one dimensional Volterra equation of the second kind. Analytic solutions for specialised distributions are presented. The solutions are easily expressed in simple functions, allowing for detailed analytic scrutiny, as well as making them easy to include in computer code. The following two sections focus on the longitudinal case. The transverse case is presented in section IV.

II. THEORETICAL DEVELOPMENT

For a coasting beam with self forces due to a longitudinal wake potential, the Vlasov equation reads

$$\frac{\partial \psi(\theta, \delta, t)}{\partial t} + \omega_0(1 - \eta\delta) \frac{\partial \psi(\theta, \delta, t)}{\partial \theta} + \dot{\delta} \frac{\partial \psi(\theta, \delta, t)}{\partial \delta} = 0. \quad (1)$$

In equation (1), θ is the azimuth around the machine, ω_0 is the angular revolution frequency for the ideal particle, $\delta = \Delta p/p_0$ is the fractional momentum deviation, η is the frequency slip factor, and $\psi(\theta, \delta, t)d\theta d\delta$ is the number of particles in $d\theta \times d\delta$ at time t .

The effect of the wake potential is contained in $\dot{\delta}$. In the smooth approximation:

$$\dot{\delta}(\theta, t) = -\frac{q}{2\pi R p_0} \int_{-\infty}^{\infty} W(\tau) I(\theta, t - \tau) d\tau, \quad (2)$$

where q is the charge on a single particle, R is the machine radius, $W(\tau)$ is the wake potential as a function of time

lag, and $I(\theta, t)$ is the beam current as a function of azimuth and time.

As usual, assume that the phase space distribution is given by an unperturbed piece, plus a small perturbation. In the limit of first order perturbation theory, the azimuthal harmonics are orthogonal and may be studied individually:

$$\psi(\theta, \delta, t) = \psi_0(\delta) + \psi_n(\delta, t) e^{in(\theta - \omega_0 t)}. \quad (3)$$

It is assumed that the wake force due to ψ_0 vanishes. Then, the wake force is solely due to the perturbation current. This force is given by

$$\dot{\delta} = -\frac{q^2 \omega_0}{2\pi R p_0} e^{in(\theta - \omega_0 t)} \int_{-\infty}^{+\infty} d\tau W(\tau) e^{in\omega_0 \tau} \rho_n(t - \tau), \quad (4)$$

where,

$$\rho_n(t) = \int_{-\infty}^{+\infty} \psi_n(\delta, t) d\delta. \quad (5)$$

The τ dependence of $\rho_n(t - \tau)$ in the wake force is ignored. This is the only approximation to first order perturbation theory. It assumes that the wake potential decays before ψ_n changes appreciably.

Expressing equation (4) in terms of the longitudinal impedance Z , the first order solution of equation (1) satisfies

$$\frac{\partial \psi_n(\delta, t)}{\partial t} = in\omega_0 \eta \delta \psi_n(\delta, t) + R(\delta) \rho_n(t), \quad (6)$$

$$R(\delta) = \frac{q^2 \omega_0}{2\pi R p_0} \frac{d\psi_0(\delta)}{d\delta} Z(n\omega_0). \quad (7)$$

Equation (6) is easily solved using $\exp(-in\omega_0 \eta \delta t)$ as an integrating factor,

$$\begin{aligned} \psi_n(\delta, t) &= \psi_n(\delta, 0) e^{in\omega_0 \eta \delta t} \\ &+ R(\delta) \int_0^t \rho_n(s) e^{in\omega_0 \eta \delta (t-s)} ds. \end{aligned} \quad (8)$$

Before proceeding with the solution, introduce the total number of particles in the ring N_t and the characteristic

*work supported by US DOE

half width of the momentum distribution σ via

$$\psi_0(\delta) = \frac{N_i}{2\pi\sigma} f(\delta/\sigma). \quad (9)$$

Integrating both sides of equation (8) over δ and switching to the dimensionless time variable $\tau = |\eta|n\sigma\omega_0 t$ results in

$$\rho_n(\tau) = S(\tau) - i \frac{Z(n\omega_0)}{Z_{crit}} \int_0^\tau \rho_n(s) G(\tau-s) ds, \quad (10)$$

$$G(\tau) = \tau \int_{-\infty}^{\infty} f(x) e^{i \operatorname{sgn}(\eta) \tau x} dx, \quad (11)$$

$$Z_{crit} = n \frac{4\pi^2 R p_1 \sigma^2 \eta}{q^2 N_i}. \quad (12)$$

In equation (10), $S(\tau)$ is the source function and is given by the integral, over δ , of the first term on the right of equation (8). For reasonable distributions, $G(\tau)$ is a smooth function that varies over length scales of order unity, and has a maximum value of order unity. For the correct choice of σ , $|Z_{crit}|$ is the Keil-Schnell limiting impedance [1]. The actual stability of the system can be strongly affected by the phase of the impedance as well [3].

III. EXACT SOLUTION

An exact solution to equation (10) may be obtained if the unperturbed distribution is a Lorentzian,

$$f(x) = \frac{1}{\pi(1+x^2)} \quad (13)$$

where $x = \delta/\sigma$. The response function is

$$G(\tau) = \tau e^{-|\tau|}. \quad (14)$$

Since $\tau \geq 0$ in our problem, the absolute value sign is not needed. To solve equation (10), proceed by defining the auxiliary variables

$$\begin{aligned} \alpha(\tau) &= \int_0^\tau e^s \rho_n(s) ds, \\ \beta(\tau) &= \int_0^\tau s e^s \rho_n(s) ds, \\ \rho_n(\tau) &= e^{-\tau} \dot{\alpha}, \\ \dot{\beta} &= \tau \dot{\alpha}, \end{aligned} \quad (15)$$

where dot denotes differentiation with respect to τ , and the second two lines follow from the first two.

Plugging in to equation (10) with equations (14) and (15) gives

$$\dot{\alpha} = S e^\tau + \lambda^2 (\tau \alpha - \beta). \quad (16)$$

The effect of the impedance is fully contained in the constant

$$\lambda^2 = -i \frac{Z(n\omega_0)}{Z_{crit}}. \quad (17)$$

Differentiating equation (16) with respect to τ and using the last line of (15) gives

$$\ddot{\alpha} - \lambda^2 \alpha = \frac{d}{d\tau} [S(\tau) e^\tau]. \quad (18)$$

The boundary conditions at $\tau = 0$ are $\alpha = 0$, and $\dot{\alpha} = S(0)$. For an initial perturbation that is a Lorentzian,

$$S(\tau) = S_0 e^{-\epsilon \tau}, \quad (19)$$

where $\epsilon = \tilde{\sigma} - iz_0$. The width of the perturbation in δ is $\sigma \tilde{\sigma}$, and the perturbation is centered at $\delta = \operatorname{sgn}(\eta) \sigma z_0$. Since the right hand side of equation (18) is an exponential, $\alpha(\tau)$ is readily obtained. I consider the non-degenerate case, so α is a sum of exponential functions. Using the third line of (15) gives $\rho_n(\tau)$,

$$\begin{aligned} \rho_n(\tau) &= \frac{S_0}{(1-\epsilon)^2 - \lambda^2} \left\{ (1-\epsilon)^2 e^{-\epsilon \tau} \right. \\ &\quad \left. - \lambda e^{-\tau} [\cosh(\lambda \tau) + (1-\epsilon) \sinh(\lambda \tau)] \right\} \quad (20) \end{aligned}$$

The motion is stable if and only if $|\Re(\lambda)| \leq 1$. Changing the momentum variable to $z = \operatorname{sgn}(\eta) \delta/\sigma$, and evaluating equation (8) yields,

$$\begin{aligned} \psi_n(z, \tau) &= \frac{S_0 e^{iz\tau}}{\pi} \left\{ \frac{\tilde{\sigma}}{\tilde{\sigma}^2 + (z - z_0)^2} \right. \\ &\quad \left. - i \lambda^2 \frac{2z}{(1+z^2)^2} \frac{F}{[(1-\epsilon)^2 - \lambda^2]} \right\}, \quad (21) \end{aligned}$$

where

$$\begin{aligned} F &= \frac{(1-\epsilon)^2}{(\epsilon + iz)} \left[1 - e^{-(\epsilon + iz)\tau} \right] \\ &\quad - \frac{\lambda(1+\lambda-\epsilon)}{2(1-\lambda+iz)} \left[1 - e^{-(1-\lambda+iz)\tau} \right] \\ &\quad + \frac{\lambda(1-\lambda-\epsilon)}{2(1+\lambda+iz)} \left[1 - e^{-(1+\lambda+iz)\tau} \right]. \quad (22) \end{aligned}$$

As required, equations (20) and (21) are invariant under the substitution $\lambda \rightarrow -\lambda$.

If the system is unstable, the distribution at large τ is given by

$$\psi_n(z, \tau) \approx \frac{C z e^{-(1-\lambda)\tau}}{(1-\lambda+iz)(1+z^2)^2}, \quad (23)$$

where C is a constant that depends on the initial conditions and I have taken $\Re(\lambda) > 1$. Equation (23) is the unstable eigenvector one gets from a frequency domain treatment as may be verified by substitution into (6) with the appropriate change of variables. As one expects, the stability of the system is determined by the eigenvectors.

IV. TRANSVERSE CASE

The solution for a coasting beam subject to a transverse impedance is very analogous to the treatment for the longitudinal impedance, but the treatment is more cumbersome due to the extra phase space dimensions.

Let x be the transverse coordinate and ω_x be the average betatron frequency. Define r as the amplitude of the betatron oscillation and let ϕ be the angle variable. Then

$$\frac{d\phi}{dt} = \omega_x + \Delta\omega_x(r, \delta), \quad (24)$$

$$\frac{dr}{dt} = \frac{\sin \phi F_x}{\gamma m \omega_x}, \quad (25)$$

$$\approx \frac{e^{i\phi} F_x}{2i\gamma m \omega_x}, \quad (26)$$

where $\Delta\omega_x(r, \delta)$ is the amplitude and momentum dependent part of the betatron frequency, F_x is the transverse force due to the beam offset combined with the transverse impedance, γ is the Lorentz factor of the beam and m is the particle mass. The approximation (26) is equivalent to assuming that the betatron tune shift is small compared to the betatron tune.

Assume a solution of the form,

$$\psi(r, \delta, \theta, \phi, t) = \psi_0(r, \delta) + \psi_1(r, \delta, t) e^{i[\phi - \omega_x t + n(\theta - \omega_0 t)]}. \quad (27)$$

By ignoring the variation in ψ_1 over the time scale for the transverse wake potential to decay, the transverse force is given by,

$$F_x(\theta, t) = \frac{iq\beta Z_{\perp}(n\omega_0 + \omega_x)D(t)}{2\pi R} e^{i[n(\theta - \omega_0 t) - \omega_x t]}, \quad (28)$$

where β is the velocity in units of the speed of light and,

$$D(t) = \pi q \omega_0 \int r^2 dr d\delta \psi_1(r, \delta, t), \quad (29)$$

is the dipole moment of the beam.

The first order Vlasov equation is given by,

$$\begin{aligned} \frac{\partial \psi_1}{\partial t} &= -i[\Delta\omega_x(r, \delta) - n\omega_0 \eta \delta] \psi_1 \\ &+ \frac{q\beta Z_{\perp}(n\omega_0 + \omega_x)D(t)}{4\pi\gamma m \omega_x R} \frac{\partial \psi_0}{\partial r}. \end{aligned} \quad (30)$$

Using the same techniques as in the longitudinal case, the Vlasov equation can be reduced to an integral equation for the dipole moment,

$$D(t) = S_x(t) + A \int_0^t D(s) G(t-s) ds, \quad (31)$$

$$A = -\frac{q^2 N_1 Z_{\perp} \omega_0 \beta}{8\pi^2 R \gamma m \omega_x}, \quad (32)$$

$$G(t) = \int r^2 dr d\delta \frac{\partial \psi_0}{\partial r} e^{i(\Delta\omega_x(r, \delta) - n\omega_0 \eta \delta)t}, \quad (33)$$

where $S_x(t)$ is the transverse source function. For the case $\Delta\omega_x = \delta Q' \omega_0$, with Lorentzians for momentum distributions, the equations may be solved.

Define the dimensionless variables $z = \text{sgn}(Q' - n\eta)\delta/\sigma$ and $\tau = i\sigma\omega_0|Q' - n\eta|t$. The unperturbed distribution is given by, $\psi_0(r, \delta) = T_0(r)/(1+z^2)$, and the perturbation at $t = 0$ is $\psi_1(r, \delta, 0) = CT_0'(r)\delta/[\delta^2 + (z - z_0)^2]$. The dipole moment of the beam is given by

$$D(\tau) = S_0 \left\{ \frac{(1-\epsilon)e^{-\epsilon\tau} - \lambda e^{(\lambda-1)\tau}}{1-\lambda-\epsilon} \right\} \quad (34)$$

where $\lambda = A/(\sigma\omega_0|Q' - n\eta|)$, and $\epsilon = \bar{\sigma} + iz_0$. The perturbed distribution is given by,

$$\begin{aligned} \psi_1(\delta, \tau, r) &= C \frac{dT_0(r)}{dr} e^{-iz\tau} \left[\frac{\bar{\sigma}}{\bar{\sigma}^2 + (z - z_0)^2} \right. \\ &\quad \left. + \frac{\lambda F}{(1+z^2)(1-\lambda-\epsilon)} \right], \end{aligned} \quad (35)$$

$$\begin{aligned} F &= \frac{1-\epsilon}{\epsilon - iz} \left[1 - e^{-(\epsilon - iz)\tau} \right] \\ &+ \frac{\lambda}{\lambda - 1 + iz} \left[1 - e^{(\lambda - 1 + iz)\tau} \right]. \end{aligned} \quad (36)$$

V. CONCLUSIONS

Two exact solutions to the initial value problem for the Vlasov equation have been presented. Using fairly simple numerical techniques, solutions for a broad range of momentum distributions could be obtained. These solutions might be useful in the development of computer codes, especially when trying to determine the effect of the granularity produced by particle tracking. Additionally, the simplicity of the solutions may allow for a serious study of the analytic properties of Landau damping. Finally, since momentum distributions in real machines can be measured, a relatively simple comparison of theory and experiment might be possible.

ACKNOWLEDGEMENTS

My thanks to A. Luccio and W.T. Weng for useful discussions and encouragement.

References

- [1] E. Keil & W. Schnell, CERN/69-48 (1969).
- [2] J. L. Laclare, CERN/85-19 (1985) p 377.
- [3] A. G. Ruggiero & V. G. Vaccaro, CERN ISR-TH/68-33 (1968).

Longitudinal Impedance and Stability Thresholds of the AGS Booster *

M. Blaskiewicz

AGS Dept. Brookhaven National Lab
BNL 911C Upton, NY 11973

Abstract

The various sources of longitudinal impedance in the AGS Booster are identified and the effects of the total impedance are estimated. In particular, the parasitic effects of the rf cavities during proton acceleration are explored. Dynamics are treated using a first order Vlasov analysis in the weak synchrotron coupling approximation.

I. INTRODUCTION

The AGS Booster is a fast-cycling proton and heavy ion synchrotron. The Booster will accelerate protons from $E_k = 200$ MeV kinetic energy to $E_k = 1500$ MeV in 60 ms. For heavy ions the acceleration time is about an order of magnitude larger with an output kinetic energy $E_k \sim 500$ MeV per nucleon.

This note is concerned with the collective effects that can appear during proton acceleration. Instability thresholds and growth rates are calculated for fixed bunch length, proton energy, etc. These parameters are varied over appropriate ranges, resulting in an overall picture of beam stability. For simplicity, the root mean square radius of the beam is assumed to be 1.5 cm throughout the cycle. In any case, the longitudinal dynamics depend only logarithmically on the beam radius, via the space charge impedance. The parameters which are assumed constant are given in Table 1

Table 1: Unperturbed Beam Parameters

Machine Radius	32.114 m
Harmonic number	3
Number of bunches	3
Momentum compaction	0.0453
Beam radius	1.5 cm
Pipe radius	6 cm
Protons per bunch	5.0×10^{12}
Synchronous RF phase	13°
RF voltage	80 kV

Table 2: Resonant Impedance Budget

Source	$R(k\Omega)$	f_r (MHz)	Q
Band III rf	40	2.5-4.11	55
Band II rf	5	0.6-2.5	2.5
Kickers	9	60	3
Band III parasitic	5	50	10
PUEs	1	230	5

II. LONGITUDINAL IMPEDANCE

Since the bunches in the Booster are much longer than the radius of the vacuum chamber and the Lorentz factors are small, the impedance above the cutoff frequency of the pipe has a small effect on the general character of the beam dynamics.

For small Lorentz factors, the space charge impedance is important. At injection, the space charge impedance is capacitive with $Z/n = i630\Omega$. The space charge impedance drops as acceleration proceeds and ends up at $Z/n = i80\Omega$ at extraction. The other broad band impedance present is the resistive wall impedance. For these calculations, the resistive wall impedance is negligible. Other than the resistive wall impedance and the space charge impedance, the bulk of the low frequency impedance comes from the rf cavities and, to a lesser extent, modes associated with the kicker magnets and the pick-up electrodes. The resonant impedance budget is summarized in Table 2 [5, 6]. The shunt impedances and quality factors quoted for the band II and band III rf modes are average values, as the cavity is tuned they can change by $\sim 20\%$. The detailed behavior has not been accurately included in the stability calculations and to a large extent has not been measured.

III. STABILITY FORMALISM

Growth rates were calculated using first order perturbation theory on the Vlasov equation in the limit of negligible synchrotron mode coupling with no synchrotron frequency spread [2]. The frequency shifts obtained bear out the assumption of weak coupling. An unperturbed phase space density $\psi_0(r) = K(a^2 - r^2)^{3/2}$ is assumed, where a is the maximum synchrotron amplitude which is also half the

*work supported by US DOE

bunch length, and K is a normalisation factor. It has been noted that actual proton distributions are quite similar to this model [4]. With these assumptions, and taking quantities to vary as $\exp(-i\Omega t)$, the Sacherer integral equation is

$$(\Omega - m\omega_s)R(r) = w(r) \int_0^a G_m(r, r') R(r') r' dr' \quad (1)$$

$$w(r) = \frac{15}{2\pi a^4} \left(1 - \frac{r^2}{a^2}\right)^{1/2} \quad (2)$$

$$G_m(r, r') = im\kappa \sum_k \frac{Z[(kM + s)\omega_0 + \Omega]}{Mk + s} \times J_m[r(Mk + s)] J_m[r'(Mk + s)] \quad (3)$$

$$\kappa = \frac{\omega_0 \eta q \bar{I}}{\beta^2 E_T \nu_s} \quad (4)$$

where \bar{I} is the average current, M is the number of bunches, s is the coupled bunch mode number, r is the amplitude of the oscillation in radians of azimuth, and the rest of the notation is the same as in [7]. For $s = 0$, the $k = 0$ term in the sum is neglected to conserve total charge. The calculation proceeds by expanding $R(r)/w(r)$, and $G(r, r')$ in a basis $\{f_\ell(r) : \ell = 1, 2, \dots\}$ which is orthonormal on $(0, a)$ with weight function $w(r)$. The function $w(r)f_\ell(r)$ is referred to as the ℓ th radial mode. This reduces the integral equation to an (infinite) matrix eigenvalue problem. The formulae are rather cumbersome and are given in Satoh's paper [3]; a computer code was written to evaluate the relevant expressions.

In practice, it is impossible to solve the infinite dimensional matrix equations. For the case at hand, it was found that using the first three radial modes sufficed for determining the largest frequency shift.

Synchrotron frequency spread due to the non-linear portion of the rf force was calculated using [8]

$$\omega_s(r) = \omega_{s,0} \left(1 - \frac{h^2 r^2}{16} \frac{1 + \frac{2}{3} \sin^2 \phi_s}{1 - \sin^2 \phi_s}\right), \quad (5)$$

where $\omega_{s,0}$ is the zero amplitude synchrotron frequency, ϕ_s is the synchronous rf phase, and h is the harmonic number. A plot of equation (5) and the synchrotron frequency obtained using a first order symplectic integration are shown in Figure 1.

Stability diagrams were obtained by setting $\omega_s = \omega_s(r)$, and $G_m(r, r') = C_m(r r')^m$ as in Zotter's analysis [8]. Stability diagrams for the dipole and quadrupole coupled bunch modes are shown in Figure 2

Beam stability is estimated using the frequency shift calculated in the absence of frequency spread $\Delta\Omega$, and the synchrotron frequency spread for the m th synchrotron mode $S = m(\omega_s(0) - \omega_s(a))$. The beam is stable if $\Delta\Omega/S$ is to the left of the stability boundary. Of the three frequency shifts obtained for each coupled bunch mode, the most pessimistic was used in the stability analysis.

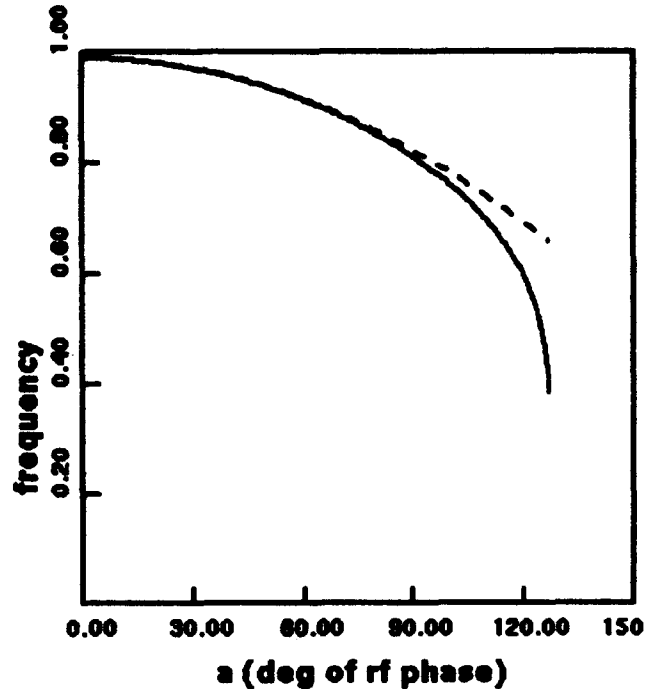


Figure 1: Relative synchrotron frequency for equation (5) (dashed line) and a symplectic integration (solid line) with a synchronous rf phase of 13°

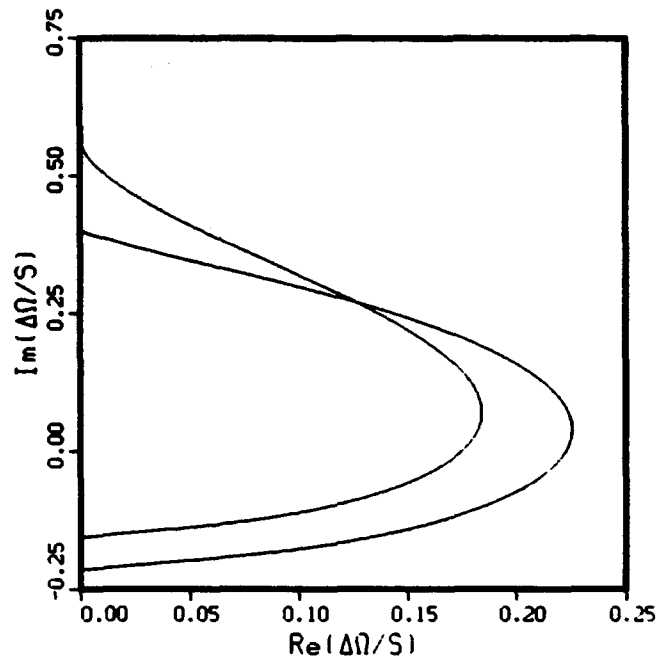


Figure 2: Dipole ($m = 1$) and Quadrupole ($m = 2$) stability boundaries for $\psi_n(r) \propto (a^2 - r^2)^{3/2}$

IV. STABILITY CALCULATIONS

The purpose of the calculations was to determine the beam stability during proton operations. Of the impedances in Table 2 the band II and band III radio frequency modes were by far the most important. For clarity, the other resonant impedances were ignored.

The band III impedance is necessary for acceleration, so calculations with it alone were performed. Depending on bunch length, the $s = 2$ dipole ($m = 1$) mode may be unstable, while the $s = 0, 1$ modes are damped. For $E_k = 200$ MeV the minimum bunch length was $\sim 200^\circ$ of rf phase while at $E_k = 1500$ MeV it was 170° . In both cases the magnitude of the frequency shift was dominated by the real part, which is difficult to control. Ignoring instabilities, the bunch length should decrease by a factor of 2 due to adiabatic damping during acceleration. Taking the extraction length of 170° this implies an injection length of 340° which is significantly larger than the 255° length of the accelerating bucket. However, the growth rate of the instability is very small. Taking a bunch length of 180° of RF phase at injection and assuming adiabatic damping of the synchrotron oscillations throughout the cycle results in a peak growth rate for the dipole mode of 10 s^{-1} . The $s = 2$ quadrupole mode is unstable also with a peak growth rate of 4 s^{-1} . Given the 60 ms cycle time neither of these instabilities should be problematic.

When the band II cavity is included in the calculations, the situation becomes more complicated. While the resonant frequency of the band III cavity is tightly constrained by the RF frequency, the first Robinson criterion and the cavity quality factor, the resonant frequency of the band II cavity is a free parameter. Given the results for the band III cavity alone, the analysis was confined to finding the band II resonant frequency which resulted in the smallest growth rates. The calculations assumed a bunch length of 180° of RF phase at injection and adiabatic damping of the synchrotron oscillations. It was found that by tuning the band II resonant frequency, the dipole instability growth rates could be kept below 18 s^{-1} throughout the cycle. The quadrupole growth rates were less than 10 s^{-1} for the same band II impedance. The required band II resonant frequency varies smoothly from 1.14 MHz at injection to 1.83 MHz at extraction. However, the dipole growth rate depends strongly on the resonant frequency of the band II cavity. At some points in the cycle, mistuning the cavity by 50 kHz results in a growth rate of 50 s^{-1} . Since the impedance is not known accurately the optimal band II tune would need to be found empirically.

V. POSSIBLE CURES

A simple cure to the instability problem is to short out the band II cavity during proton operations. The technology is well known and should not present a problem. Alternately, the band II resonant frequency could be tuned throughout the cycle. An interactive procedure based on beam mea-

surements would be needed, owing to the high precision required.

It has been suggested [1] that the harmonic number of the AGS Booster be switched from 3 to 2. Such a change would have a profound effect on longitudinal instabilities. Consider equation (3) with $M = 2$ and $s = 1$.

$$G_m(r, r') = im\kappa \sum_{k>0, \text{odd}} \frac{Z[k\omega_0 + \Omega] - Z^*[k\omega_0 - \Omega]}{k} \times J_m[kr]J_m[kr'] \quad (6)$$

where the $*$ denotes complex conjugate and the sum is over k positive and odd. For the $s = 0$ mode the sum is over k positive and even. For $\Omega \approx m\omega$, the imaginary part of equation (6) is essentially determined by the derivative of the real part of the impedance at the revolution lines. As with the first Robinson criterion, it then seems possible that all the coherent modes will have a negative imaginary part. Uncertainties are large, but preliminary calculations show that it should be fairly easy to accomplish this as long as the non-accelerating cavity can be tuned by 1.4 MHz; the revolution frequency at extraction.

VI. CONCLUSIONS

In section IV it was found that the AGS Booster will not be able to operate at 1.5×10^{13} protons per pulse and maintain longitudinal stability with the current machine parameters. The growth rates for band III alone are negligible given the cycle time of the machine. If the beam sees the band II impedance, then careful tuning of the band II resonant frequency will be needed. By changing the harmonic number from 3 to 2, it was found that a suitable tuning current for the parasitic cavity should result in exponential damping of all coherent modes.

References

- [1] J. M. Brennan *private communication*.
- [2] F. Sacherer, IEEE Trans. NS 24, 1393 (1977).
- [3] K. Satoh, SLAC-PEP/357 (1981).
- [4] E. C. Raka *private communication*.
- [5] A. Ratti & T.J. Shea, Proceedings of the IEEE PAC p 1803, (1991).
- [6] A. Ratti *private communication*.
- [7] B. Zotter CERN-SPS/81-18 (DI) (1981).
- [8] B. Zotter CERN-SPS/81-19 (DI) (1981).

Calculation of the Bunch Lengthening Threshold

X. T. Yu and J. S. Wurtele

Department of Physics and the Plasma Fusion Center
Massachusetts Institute of Technology, Cambridge, MA 02139

Abstract

A new analysis of the bunch lengthening instability, based on a single synchrotron mode in a distorted potential well, is presented. The nonlinearity of the wakefield plays a critical role: It distorts the equilibrium density from its Gaussian shape, which results in asymmetric corrections to the Sacherer equation. This modified equation will have unstable eigenmodes when the beam current reaches a threshold value. The calculated threshold agrees very well with our multiparticle simulation for SPEAR parameters [1].

I. INTRODUCTION

The performance of modern synchrotron light sources and circular colliders relies on sustaining very short bunches of high peak currents. The bunch lengthening instability, i.e., the sudden increase of both the bunch length and the energy spread at some threshold current, is a serious concern. Much theoretical work has been aimed at explaining this phenomenon [2]. Most notably, mode coupling theory assumes that low order synchrotron modes couple together at the bunch lengthening threshold. However, there is no cogent evidence from experiments that this has actually occurred. In this paper, we investigate the instability mechanism within a particular synchrotron mode in a distorted potential well.

II. LONGITUDINAL DYNAMICS AND EQUILIBRIUM

The mapping for the longitudinal motion in a ring is [3]:

$$\tau_{n+1} = \tau_n - \alpha T_0 \delta_{n+1}, \quad (1)$$

$$\delta_{n+1} = \delta_n + \frac{\omega_{s0}^2 T_0}{\alpha} \tau_n - \frac{\text{wakefield loss}}{E_0}, \quad (2)$$

where τ_n is the arrival time relative to the synchronous particle in the n th turn, δ_n is its relative energy error,

*This work was supported by the U.S. Department of Energy, Division of Nuclear and High Energy Physics.

α the momentum compaction factor of the ring, T_0 the revolution time, ω_{s0} the synchrotron oscillation frequency and E_0 the beam energy.

Since the synchrotron tune is small for most rings and the wakefield loss is distributed throughout the ring, we can then approximate the mapping by the differential equations:

$$\frac{d\tau}{dt} = -\alpha\delta, \quad (3)$$

$$\frac{d\delta}{dt} = \frac{\omega_{s0}^2}{\alpha} \tau - \frac{1}{E_0 T_0} F(\tau). \quad (4)$$

Here $F(\tau)$ is the wakefield loss of the particle:

$$F(\tau) = N e^2 L_0 \int_{\tau}^{+\infty} d\tau' \rho(\tau') W(\tau' - \tau). \quad (5)$$

Eq. 5 involves integrating the wake left by all other charges in front of the particle under consideration. N is the number of particles in the bunch, L_0 the ring circumference, ρ the particle density of the bunch and W the longitudinal wake function [4].

If we identify τ as the coordinate and δ the momentum, then Eqs. 3 and 4 are the dynamic equations of a harmonic oscillator under the influence of the additional force $F(\tau)$. The Hamiltonian of this system is:

$$H = \frac{\delta^2}{2} + \frac{\omega_{s0}^2 \tau^2}{2\alpha^2} - \frac{N e}{E_0 T_0} \int_0^{\tau} d\tau' F(\tau'). \quad (6)$$

For electron machines, synchrotron radiation of electrons and its quantum nature provide damping and diffusion in phase space. The resulting equilibrium state will be a Boltzmann distribution:

$$\psi_0(\tau, \delta) \propto \exp\left(-\frac{H}{\sigma_{\delta 0}^2}\right), \quad (7)$$

where $\sigma_{\delta 0}$, the equilibrium energy spread, is determined by balancing the radiation damping and the diffusion caused by quantum excitation.

It is very useful to observe that, while the wakefield can change the particle distribution in τ , it cannot change the distribution in δ . It will always be a Gaussian distribution with constant energy spread. Experiments show that

the energy spread increases after the current reaches some threshold value. In our simulations, we also observe that the distribution in δ starts to develop a non-Gaussian deformation at the threshold. All these suggest that the equilibrium is unstable as the current reaches the threshold.

III. SACHERER EQUATION

We follow the Vlasov-Sacherer [5] approach to investigate the stability of the equilibrium. The phase space distribution function, $\psi(\tau, \delta, t)$, satisfies:

$$\frac{\partial \psi}{\partial t} - \alpha \delta \frac{\partial \psi}{\partial \tau} + \frac{\omega_{s0}^2}{\alpha} \tau \frac{\partial \psi}{\partial \delta} - \frac{eF(\tau)}{E_0 T_0} \frac{\partial \psi}{\partial \delta} = 0. \quad (8)$$

To introduce the concept of a synchrotron mode, we first neglect the wakefield, i.e., we consider the zero current limit. In polar coordinates, $\tau = r \cos \phi$, $\alpha \delta / \omega_{s0} = r \sin \phi$ and the Vlasov equation reduces to

$$\frac{\partial \psi}{\partial t} + \omega_{s0} \frac{\partial \psi}{\partial \phi} = 0. \quad (9)$$

Thus, the equilibrium distribution, ψ_0 , depends only on r . The eigenmodes of the time dependent solutions are

$$\psi = R_l(r) \exp(i l \phi - i \Omega^{(l)} t), \quad (10)$$

with eigenvalues

$$\Omega^{(l)} = l \omega_{s0}, \quad l = 0, \pm 1, \pm 2, \dots \quad (11)$$

These are called synchrotron modes.

When the current is not zero, different l modes are coupled together by the wakefield. We know from most experiments and simulations that low synchrotron modes are still well separated even when the current reaches the threshold. So we assume the coupling between different synchrotron modes is not critical for the bunch lengthening instability and we will neglect mode coupling henceforth.

Next we keep only the linear term in $F_0(\tau)$:

$$F_0(\tau) = F_0(0) + \frac{dF_0}{d\tau} \tau + O(\tau^2). \quad (12)$$

Here the subscript denotes the wakefield loss from the equilibrium particle density distribution. It is easy to see that all the wakefield effects on the zeroth order Vlasov equation can be incorporated into an incoherent synchrotron frequency shift

$$\omega_{s0}^2 \rightarrow \omega_s^2 \left[1 - \frac{\alpha e}{E_0 T_0 \omega_{s0}^2} \frac{dF_0}{d\tau} \right], \quad (13)$$

and a shift of the center of the bunch:

$$\tau \rightarrow \tau' = \tau - \tau_0, \quad (14)$$

$$\tau_0 = \frac{\alpha e}{E_0 T_0 \omega_s^2} F_0(0). \quad (15)$$

Thus, ψ_0 is still a function of r :

$$\psi_0(r) \propto \exp\left(-\frac{r^2}{2\sigma_r^2}\right). \quad (16)$$

If we project the first order Vlasov equation

$$\frac{\partial \psi_1}{\partial t} + \omega_s \frac{\partial \psi_1}{\partial \phi} - \frac{e}{E_0 T_0} F_1 \frac{\partial \psi_0}{\partial \delta} = 0, \quad (17)$$

into a particular synchrotron mode, we obtain the Sacherer equation:

$$(\Omega - l\omega_s) R_l(r) = \frac{Ne^2}{E_0 T_0} \frac{\psi_0'(r)}{r} \int r' dr' G_l(r, r') R_l(r'). \quad (18)$$

Here, the kernel

$$G_l(r, r') = \int d\omega \frac{Im Z(\omega)}{\omega} J_l(\omega r) J_l(\omega r'), \quad (19)$$

is determined by the imaginary part of the impedance $Z(\omega)$. Since G_l is real and symmetric, there are only real eigenvalues. The single mode Sacherer equation does not provide the instability mechanism we are looking for.

IV. IMPROVED SACHERER EQUATION

The discussion above suggests that it is crucial to keep the nonlinear terms in the wakefield loss $F(\tau)$. The most important consequence is that the wakefield effects cannot be completely incorporated into the incoherent frequency shift and the shift of the center of the bunch. Although ψ_0 is still Gaussian in δ , it is no longer Gaussian in τ . Because of this non-Gaussian deformation, ψ_0 is a function of both r and ϕ : $\psi_0(r, \phi)$.

From Eq. 17, the ϕ dependence of ψ_0 will generate correction terms to the right hand side of the Sacherer equation. Generally, they are not symmetric operators. Since the ϕ dependence in the equilibrium is at least linear in the current, the correction terms to the Sacherer equation are proportional to the square of the current. The improved Sacherer equation will look like:

$$(\Omega - l\omega_s) R_l(r) = I \times \text{symmetric operator on } R_l + I^2 \times \text{asymmetric operator on } R_l. \quad (20)$$

When the current I is small, we don't expect the asymmetric perturbation to be big enough to push the eigenvalues of the symmetric Sacherer operator into the complex plane. When I reaches some critical value, we expect that this will happen and then the system goes unstable.

V. PARAMETERIZATION OF THE EQUILIBRIUM

In order to find the corrections to the Sacherer equation, we need to know the functional form of $\psi_0(r, \phi)$. To accomplish this, Fourier expand ψ_0 :

$$\psi_0(r, \phi) = f_0(r) + f_1(r) \cos \phi + f_2(r) \cos 2\phi + \dots \quad (21)$$

We will determine $f_0(r)$, $f_1(r)$, ... by the following scheme:

The equilibrium density distribution is determined by Haissinski [8] equation:

$$\rho(r) = A_0 \exp \left(-\frac{r^2}{2\sigma_r^2} - I \frac{\alpha e L_0}{\omega_0^3 E_0 \sigma_r^3} \int_0^{+\infty} dt \rho(t+r) g(t) \right), \quad (22)$$

where $g(t)$ is given by:

$$g(t) = \int_0^t dt' W(t'). \quad (23)$$

We can solve this equation numerically and compute the first four cumulants of the particle density distribution $\rho(r)$: τ_0 , average r ; σ_r , standard deviation; γ_1 , normalized skew moment; γ_2 , normalized excess moment. Then we approximate the equilibrium by a cumulant expansion. Denote $x = (r - \tau_0)/\sigma_r$,

$$\rho(r) = [1 + \frac{\gamma_1}{6}(x^3 - 3x) + \frac{\gamma_2}{24}(x^4 - 6x^2 + 3)]n(x). \quad (24)$$

Here $n(x)$ is the standardized Gaussian distribution:

$$n(x) = \frac{1}{\sqrt{2\pi}\sigma_r} \exp(-\frac{x^2}{2}). \quad (25)$$

Based on this approximated distribution, we have only the following five non-zero terms: f_0 , f_1 , f_2 , f_3 , f_4 :

$$f_0(r) = [1 + \frac{\gamma_2}{8}(\frac{r^4}{8\sigma_r^4} - \frac{r^2}{\sigma_r^2} + 1)]f_{00}(r), \quad (26)$$

$$f_1(r) = \frac{\gamma_1}{8}f_{00}(r) \left(\frac{r^3}{\sigma_r^3} - 4\frac{r}{\sigma_r} \right), \quad (27)$$

$$f_2(r) = \frac{\gamma_2}{48}f_{00}(r) \left(\frac{r^4}{\sigma_r^4} - 6\frac{r^2}{\sigma_r^2} \right), \quad (28)$$

$$f_3(r) = \frac{\gamma_1}{24}f_{00}(r) \frac{r^3}{\sigma_r^3}, \quad (29)$$

$$f_4(r) = \frac{\gamma_2}{192}f_{00}(r) \frac{r^4}{\sigma_r^4}. \quad (30)$$

Here

$$f_{00}(r) = \frac{\alpha}{2\pi\omega_r\sigma_r^2} \exp(-\frac{r^2}{2\sigma_r^2}). \quad (31)$$

We are now in a position to write down the explicit form of the improved Sacherer equation:

$$(\Omega - \omega_r)R_l(r) = \frac{Ne^2}{E_0T_0} \frac{g_1(r)}{r} \int r' dr' G_l(r, r') R_l(r') + \frac{Ne^2}{2E_0T_0} \sum_{n=2}^5 g_n(r) \int r' dr' G_l^{(n)}(r, r') R_l(r'). \quad (32)$$

Here, the asymmetric kernels are given by

$$G_l^{(n)} = \frac{1}{\pi^n} \int d\omega Z(\omega) (J_{l-n}(\omega r) - (-1)^n J_{l+n}(\omega r)) J_l(\omega r'), \quad (33)$$

and the functions g are related to functions f by

$$g_n(r) = \frac{r}{2\sigma_r^2} (f_{n+1}(r) - f_{n-1}(r)). \quad (34)$$

The difference between the approximated distribution and the numerically obtained distribution is very small for the SPEAR parameters. For other impedances and equilibrium bunch lengths, the model expansion Eq. 24 may not be valid. The fundamental point is unchanged: nonlinearity of the wakefield loss leads to instability.

VI. RESULTS AND CONCLUSION

We have calculated the threshold current for SPEAR parameters. Since we are most interested in the instability mechanism behind the bunch lengthening, we linearized the RF bucket and neglected the multi-turn wakefield. Rather than comparing the calculated threshold current with experimental results, we compared it with our multiparticle simulation. Approximating the SPEAR impedance by a $Q = 1$ resonator, the simulation gives a threshold current of around 45 mA. Our calculation gives 50 mA. The first unstable modes in our calculation are the dipole mode and quadrupole mode. In the experiment, the quadrupole mode is observed to be the first unstable synchrotron mode.

In summary, we investigated the bunch lengthening instability of an uncoupled synchrotron mode in a distorted potential well. Without the nonlinearity of the wakefield, the Sacherer equation does not have an unstable eigenmode. The nonlinearity of the wakefield gives asymmetric correction terms to the Sacherer equation. The improved Sacherer equation is unstable when the beam current reaches a threshold value. Linear theory gives a threshold current very close to the simulation result and identifies the same unstable mode as seen in the experiment. Future work includes extending the comparison to other rings and impedances and taking into account the nonlinearity of the RF bucket.

ACKNOWLEDGMENTS

We would like to thank Dr. Alex Chao, Dr. Senyu Chen and Mr. Bo Chen for stimulating discussions.

REFERENCES

- [1] P. B. Wilson et al., IEEE-NS 24(1977) p. 1211.
- [2] K. Hirata and T. Suzuki, ed., KEK Report 90-12(1991).
- [3] M. Sands, SLAC Report 121 (1970).
- [4] A. W. Chao, AIP Conf. Proc. No. 87, p. 450.
- [5] F. Sacherer, Trans. IEEE-NS 24(1977) p. 1393.
- [6] J. Haissinski, Nuovo Cimento 18 B(1973) p. 72.

Computation of Longitudinal Bunched Beam Instability Thresholds

R. Baartman

TRIUMF, 4004 Westbrook Mall, Vancouver, B.C. V6T 2A3, Canada

and

M. D'yachkov

Physics Department, University of British Columbia,
6224 Agricultural Road, Vancouver, B.C. V6T 1Z1, Canada

Abstract

An integral equation derived from the linearized Vlasov equation has been used to find the instability thresholds in the case of space-charge impedance alone for various distribution functions. It has been found that the thresholds for the instability which are caused by the coupling between $m = \pm 1$ azimuthal modes may be obtained analytically for many practically used distributions. Moreover, the criterion determining these thresholds appears to be the same as that for thresholds beyond which no stationary distribution can be found.

I. INTRODUCTION

It has been found that in the case of broad-band or space-charge impedance the stationary distribution changes significantly with intensity, and this should be taken into account because the stability thresholds calculated ignoring potential well distortion differ from those obtained in self-consistent calculations [2]. Therefore, the results obtained previously [4] under the assumption of absence of incoherent frequency spread have to be considered critically. However, these results provide us with a clear picture of the physics of the instability and can be used for checking any other new theory.

It has been shown in ref. 4 that the problem of determining the $m = \pm 1$ thresholds (as well as others caused by $\pm m$ coupling) in the absence of synchrotron frequency spread can be formulated as an eigenvalue problem for the Fourier components of the line density. Moreover, analytical expressions for matrix elements for some specific distributions have been found [4].

II. INTEGRAL EQUATION

We normalize the longitudinal coordinate q such that the Hamiltonian of the particle is

$$H(p, q) = \frac{p^2}{2} + V(q), \quad (1)$$

where p is the longitudinal momentum and $V(q)$ is a potential which we assume to be symmetric.

In the case of space-charge impedance, the self-force is proportional to the derivative of the line density and we also can define an intensity parameter I so that

$$F_{SC} = -I \frac{d\lambda}{dq} \text{ and } V = V_0 + I\lambda(q), \quad (2)$$

where $\lambda(q)$ is the line density. I may have either sign: for space-charge it is positive below transition and negative above.

The Vlasov equation can be written in terms of p and q , or, more conveniently, in action-angle variables as

$$\frac{\partial \psi}{\partial t} + \frac{\partial \psi}{\partial \theta} \dot{\theta} + \frac{\partial \psi}{\partial J} \dot{J} = 0, \quad (3)$$

where $\dot{J} = -\partial H / \partial \theta$ and $\dot{\theta} = \partial H / \partial J$.

It can be shown that the stationary distribution ψ_0 is a function of J only. We therefore look for a solution in the form $\psi = \psi_0(J) + \psi_1(J, \theta, t)$, where ψ_1 is a small perturbation. The Hamiltonian of the system can then be written as

$$H(J, \theta, t) = H_0(J) + I \lambda_1(q(J, \theta), t), \quad (4)$$

where $\lambda_1(q, t) = \int \psi_1 dp$. Dropping terms of second order and taking into account that $dH_0/dJ = \omega(J)$, the linearized Vlasov equation becomes

$$\frac{\partial \psi_1}{\partial t} + \omega(J) \frac{\partial \psi_1}{\partial \theta} - I \frac{\partial \lambda_1}{\partial \theta} \frac{d\psi_0}{dJ} = 0. \quad (5)$$

It turns out to be more convenient to take ψ_0 and ω to be a functions of $\epsilon = H(p, q)$ instead of J :

$$\psi'_0(\epsilon) \equiv \frac{d\psi_0}{d\epsilon} = \frac{1}{\omega(J)} \frac{d\psi_0}{dJ}. \quad (6)$$

We look for a solution in the form $\psi_1 = f e^{\nu t}$ (and $\lambda_1 = g e^{\nu t}$). Then with the definition $\Omega(\epsilon) = \nu / \omega(\epsilon)$, we get

$$\Omega f + \frac{\partial f}{\partial \theta} - I \psi'_0(\epsilon) \frac{\partial g}{\partial \theta} = 0. \quad (7)$$

The periodic solution $f(\epsilon, \theta) = f(\epsilon, \theta + 2\pi)$ is

$$f(\epsilon, \theta) = I \frac{\psi'_0(\epsilon)}{e^{2\pi\Omega} - 1} \int_0^{2\pi} e^{\Omega(\theta - \theta')} \frac{\partial g}{\partial \theta'} d\theta'. \quad (8)$$

Note that although this result is formally equivalent to that given by Krinsky and Wang [3, eqn. 3.18], it differs in the sense that the present treatment is a perturbation about the stationary case which includes the space-charge impedance: in ref. 3, the stationary induced potential is ignored.

Integrating eqn. 8 by parts we get

$$f(\epsilon, \theta) = I\psi'_0(\epsilon)g(q) - I\psi'_0(\epsilon)\frac{\Omega}{e^{2\pi\Omega}-1}\int_0^{\theta+2\pi} e^{\Omega(\theta-\theta')}g(q')d\theta'. \quad (9)$$

Integrating eqn. 9 over the momentum and taking into account that $g(q) = \int f(\epsilon, \theta)dp$, we have finally

$$g(q)[1 - I\Lambda'(V)] = I\int_{-\infty}^{\infty} dp\psi'_0(\epsilon)\frac{\Omega}{e^{2\pi\Omega}-1}\int_0^{\theta+2\pi} e^{\Omega(\theta-\theta')}g(q')d\theta', \quad (10)$$

where $\Lambda'(V) = d\Lambda/dV$, and

$$\Lambda(V) = \sqrt{2}\int_V^{\infty} \frac{\psi_0(\epsilon)d\epsilon}{\sqrt{\epsilon-V}} \quad (11)$$

is an auxiliary function for $\psi_0(H)$ which we introduced previously [1] in connection with finding stationary distributions.

Eqn. 11 is non-linear with respect to ν and therefore is not easy to solve in general. In the special case $\nu \rightarrow 0$, however, we have the simple result

$$g(q)[1 - I\Lambda'(V)] = -\frac{I}{\pi}\int_{-\infty}^{\infty} \psi'_0(\epsilon)dp\int_0^{\pi} g(q')d\theta'. \quad (12)$$

The $\nu \rightarrow 0$ limit can be thought of as coupling between $\pm m$ azimuthal modes [4]. Since the dipole mode $m = \pm 1$ is the lowest order antisymmetric eigenmode $g(q) = -g(-q)$, the integral in eqn. 12 vanishes and we find

$$g(q)[1 - I\Lambda'(V)] = 0. \quad (13)$$

III. MODE-COUPLING THEORY

A different method to determine thresholds of longitudinal bunched beam stability in the presence of space-charge was used in ref. 4. The thresholds corresponding to coupling between $\pm m$ azimuthal modes can be formulated as an eigenvalue problem for the Fourier components of the line density. To compare the two techniques we have chosen the family of distributions defined by

$$\psi_0(\epsilon) = \frac{1}{\sqrt{2\pi}}[1 - \alpha(1 - \epsilon)]e^{-\epsilon} \quad (14)$$

This family is very convenient because it contains both the 'gaussian' ($\alpha = 0$) and 'hollow-gaussian' ($\alpha = 1$) cases, and because the matrix elements of the eigenvalue problem can be found analytically. The eigenvalue problem can be written in the form

$$\mu g_k = \sum_{l=-\infty}^{\infty} H_{kl} g_l, \quad (15)$$

where $g(q) = \sum g_k e^{ikq}$ and the matrix elements are

$$H_{kl} = -\frac{1-\alpha}{\sqrt{2\pi}}[1 - \bar{I}_0(kl)] - \frac{\alpha}{\sqrt{2\pi}}\left\{-\frac{k^2+l^2}{2}[1 - \bar{I}_0(kl)] + kl[1 - \bar{I}_1(kl)]\right\}. \quad (16)$$

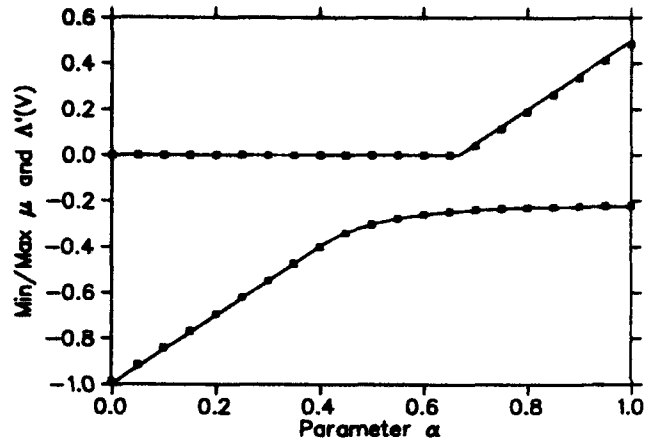


Figure 1: Extreme eigenvalues of eqn. 15 (plotted as squares) and extreme values of $\Lambda'(V)$ (solid lines).

Here $\bar{I}_m(z) = e^{-z}I_m(z)$ is the exponentially scaled modified Bessel function. The lowest thresholds can be found from the condition $\hat{\mu}I_{th} = 1$, where $\hat{\mu}$ are the extreme eigenvalues (of either sign).

In comparison, we have from eqn. 13 that $1 - \Lambda'(V)I_{th} = 0$. With ψ_0 given by eqn. 14, the expression for $\Lambda(V)$ is

$$\Lambda(V) = \left(1 - \frac{\alpha}{2} + \alpha V\right)e^{-V}. \quad (17)$$

Simple analysis allows us to obtain the following expressions for extreme values of $\Lambda'(V)$ for different parameters α .

$$\Lambda'(V)_{\min} = \begin{cases} -1 + \frac{3}{2}\alpha & \text{if } 0 < \alpha < \frac{2}{5} \\ -\alpha \exp\left(\frac{1}{\alpha} - \frac{5}{2}\right) & \text{if } \frac{2}{5} < \alpha < 1 \end{cases} \quad (18)$$

$$\Lambda'(V)_{\max} = \begin{cases} 0 & \text{if } 0 < \alpha < \frac{2}{3} \\ -1 + \frac{3}{2}\alpha & \text{if } \frac{2}{3} < \alpha < 1 \end{cases}$$

Therefore, if one plots $\hat{\mu}$ and $\Lambda'(V)$ vs. α on the same graph, the two curves should be the same. In order to solve numerically eqn. 15, the matrix was truncated at 40×40 . Minimum and maximum eigenvalues obtained in this case are the plotted points in Fig. 1. The solid lines are $\Lambda'(V)$ (18). We can see that the results are in good agreement.

IV. SELF-CONSISTENT CASE

The results discussed in the previous section have been obtained assuming no incoherent synchrotron frequency spread (i.e. $V \propto q^2$). To satisfy this condition in the self-consistent case, the initial potential well should be

$$V_0 = V + I[\Lambda(0) - \Lambda(V)], \quad (19)$$

where $V = q^2/2$, and $\Lambda(V)$ is given by eqn. 11. The necessary $V_0(q)$ to get a self-consistent stationary phase space distribution with $V(q) = q^2/2$ for the 'hollow-gaussian'

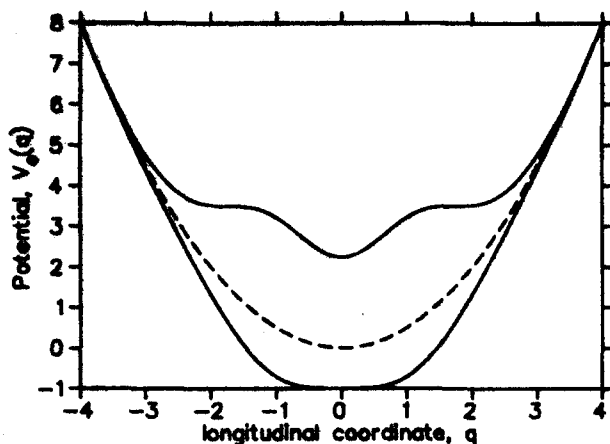


Figure 2: V_0 vs. q at threshold intensities for the 'hollow-gaussian' distribution. $V = q^2/2$ is shown by the dashed curve.

distribution $\psi_0 = e^{-q^2}$ at threshold intensities are shown in Fig. 2. The upper curve shows $V_0(q)$ at the positive mass threshold and the bottom one at the negative mass threshold. As one can see these shapes are far from 'sinusoidal' or 'harmonic'.

Realistically, of course, V_0 is harmonic and $V(q)$ is distorted by space-charge. In this case we can find the thresholds beyond which no stationary distribution exists [1]. Surprisingly, the stationarity criterion found in ref. 1 is the same as we obtained for thresholds corresponding to $m = \pm 1$ mode-coupling! This means that in the case when V_0 is a harmonic potential, $m = \pm 1$ modes do not couple.

It is necessary to mention that this criterion is valid for any $V_0(q)$ for which $dV_0/d(q^2) \neq 0$ (i.e. no local minima). This analysis can be extended to the case when $V_0(q)$ is not symmetric. Unfortunately, in this case we can't use the symmetry of the eigenfunctions to determine the thresholds as has been done earlier in this paper. Numerical solution of the integral equation is required. This has been done for several cases of ψ_0 and the results are consistent with the same threshold, namely $I\Lambda'(V) = 1$. However, no formal proof of the universality of this criterion has been found.

V. CONCLUSION

A simple criterion for the thresholds given by vanishing of the real part of the eigenfrequency (coupling between $m = \pm 1$ azimuthal modes) for the bunched beam in the case of space-charge impedance has been derived from the linearized Vlasov equation. The thresholds obtained from this criterion have been found to be in good agreement with the thresholds obtained by the mode-coupling method for the family of distributions which includes 'gaussian' and 'hollow-gaussian' cases. The method described in ref. 4 neglects the potential well distortion and the incoherent synchrotron frequency spread caused by nonlinear space-charge force. It has been found that when the potential can be approximated by a parabolic one $V_0 = q^2/2$ (or, in

general, when $dV_0(q^2)/d(q^2) > 0$), coupling between $m = \pm 1$ modes cannot occur for any stationary distribution.

We also can make a conclusion about the shape of the eigenfunction $g(q)$ at threshold: since the threshold condition (13) is satisfied in general at only one specific point q_{th} , $g(q)$ can be non-zero only at q_{th} . Indeed, recovering g from the eigenfunction $\{g_k\}$ corresponding to $\mu_n = \hat{\mu}$ [4], we find a very sharp peak at the point where $I_{th} \Lambda'(V) = 1$ and almost zero elsewhere, and the peak becomes sharper with increasing order of the matrix used in eqn. 15.

VI. REFERENCES

- [1] M. D'yachkov, R. Baartman *Methods for Finding Stationary Longitudinal Distributions*, Proc. HEACC'92 (Hamburg), p. 1064.
- [2] K. Oide and K. Yokoya *Longitudinal Single-Bunch Instability in Electron Storage Rings*, KEK Preprint 90-10 (1990).
- [3] S. Krinsky, J.M. Wang *Longitudinal Instability of Bunched Beams Subject to a Non-Harmonic RF Potential*, Particle Accelerators 17, p. 109 (1985).
- [4] R. Baartman, B. Zotter *Longitudinal Stability of Hollow Beams II: Mode-Coupling Theory*, TRIUMF Note TRI-DN-91-K177 (1991).

Bunch Lengthening Observed using Real-Time Bunch-Length Monitor in the TRISTAN AR

Takao Ieiri

KEK, National Laboratory for High Energy Physics
Oho 1-1, Tsukuba-shi, Ibaraki, 305 Japan

Abstract

A new type of a bunch length monitor, detecting two frequency components of a beam spectrum, has been installed in the TRISTAN Accumulation Ring (AR). Calibration of the monitor was carried out with the calculated natural bunch length at a low beam current. Bunch lengthening was measured as a function of the beam current. When the beam current increased, a sudden blowup of the bunch length was observed together with strong coherent oscillations. It was also observed that the blowup exhibited hysteresis when the beam current decreased, which suggested a strong nonlinear force in the bunch lengthening process.

1. INTRODUCTION

Bunch lengthening is one of the most important issues in electron/positron rings from the aspect of beam dynamics. In the AR, bunch lengthening actually occurs. It is expected that the bunch length should be measured dynamically to understand the bunch lengthening. The bunch length has been measured using the synchrotron light by a streak camera, whereby an rms bunch length is obtained from a stored longitudinal profile. This method has an advantage of detecting a charge distribution. However, it is difficult to follow dynamical change of the bunch length. Therefore, a real-time bunch-length monitor has been developed in the AR.

The AR has only one electron or positron bunch. The main parameters of the AR are listed in Table 1.

Table 1 Main parameters of the AR

Beam energy	$E = 2.5 \text{ GeV}$
RF frequency	$F_{rf} = 508.58 \text{ MHz}$
Harmonic number	$h=640$
Average radius	$R=60 \text{ m}$
Number of bunches	$B=1$
Maximum beam current	$I_b=40 \text{ mA}$
Accelerating voltage	$V_c=0.5 - 4.0 \text{ MV}$
Natural rms bunch length	$\sigma_{l0}=0.8 - 2.0 \text{ cm}$
Synchrotron tune	$\nu_{s0}=0.025 - 0.050$
Momentum compaction factor	$\alpha=0.0129$
Energy spread	$\Delta E/E=4.40 \times 10^{-4}$

2. BUNCH LENGTH MONITOR (BLM)

A bunch is picked up by a stripline electrode with a length of $L=30 \text{ cm}$. The pulse is divided into two paths. One is for detecting the 250 MHz component and the other for the 1620 MHz component. The two signals are detected and mixed again. An analog calculator unit (AD538) generates a signal proportional to the bunch length. An imbalance of the gain between the two channels produces an offset at the output of the monitor and is compensated by a variable attenuator inserted in one channel. Details of the electronics are seen in ref.[1].

Calibration of the monitor has been performed using a low-current bunch. When the beam current is sufficiently small, the longitudinal distribution should be Gaussian, and its rms bunch length approaches the natural bunch length (σ_{l0}). The bunch length is controlled by the accelerating cavity voltage (V_c). The bunch length was measured at a beam current of $I_b=0.3 \text{ mA}$ or $N=2.4 \times 10^9$ particles. This current is within the effective range of the monitor. The bunch length at that current will be equal to the natural bunch length from the experiences so far. The measured bunch length is adjusted by using the variable attenuator with a step of 0.25 dB so as to set the measured value by the calculated bunch length. After fixing the attenuation, the bunch length was measured as a function of V_c . V_c was changed from 0.6 to 3.2 MV, which corresponded to the natural rms bunch length of 1.88 to 0.79 cm. Fig. 1 shows the measured bunch length agrees with the calculated natural bunch length within $\pm 10\%$.

This monitor has the following features:

- (1) It has high resolution, and can distinguish a difference of 0.1 mm for 20 mm bunch length, which corresponds time resolution of 0.3 ps.
- (2) It has the wide dynamic range, minimum detectable current is 0.2 mA with an accuracy of $\pm 10\%$.
- (3) It has wide bandwidth of 150 kHz, and can detect coherent oscillations including higher modes, if excited.
- (4) It automatically displays the bunch length.
- (5) Easy to handle and maintain.

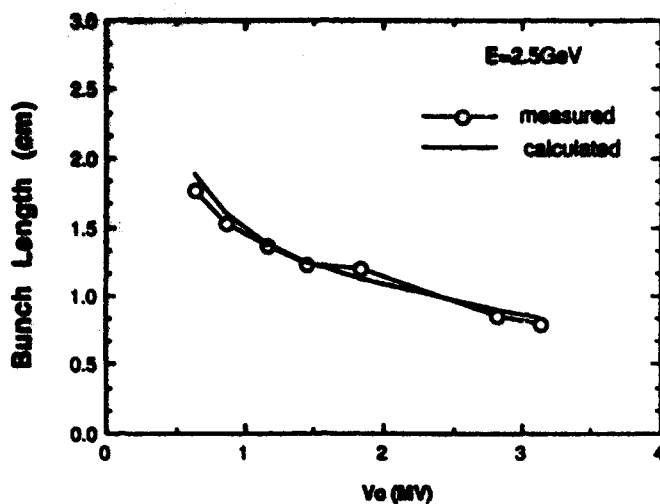


Fig. 1 Measured and calculated bunch length.

3. MEASUREMENT OF BUNCH LENGTH

The measurement was carried out during an injection process under constant V_c . The bunch length was also measured using a streak camera (SC). Bunch lengthening was observed below 1 mA without a clear threshold. No coherent oscillation was observed below 3 mA. On the other hand, the transverse profile obtained from the synchrotron radiation showed a vertical instability [2]. The vertical profile was expanded intermittently, which was not dipole oscillations. The vertical instability is stronger for higher V_c and for shorter bunch length. However, the vertical instability seems to be settled to above 4.0 mA. When the beam current was around 3.2 mA, the monitor showed coherent oscillations with a quadrupole synchrotron frequency ($2f_s$) on a spectrum analyzer. Suddenly, the bunch length increased by 20 to 40%, when the current was 4.8 mA. This jump was also confirmed by the streak camera. A jump of the bunch length makes the pattern of the oscillations different. Though only quadrupole oscillation was excited before a jump, strong oscillations were excited with higher order modes after a jump as seen in Fig.2(a) and Fig.2(b). The synchronous phase angle also jumped by about 2 deg. together with the jump of the bunch length.[3]

A jump in the bunch length exhibited hysteresis as a function of the current as is shown in Fig. 3. When the current was decreased from point <C> after a jump, the bunch length did not return at the same current of 4.8 mA, where the jump-up occurred when the current was increased. The bunch length pursues line <C>-<D>. The pattern of oscillations on line <C>-<D> was the same as that observed at point <C>. While the bunch length was on line <C>-<D>, no vertical oscillation was observed. The longer bunch length on line <C>-<D> fluctuates due to the coherent oscillations as seen in Fig.2(b). As the current was further decreased, jump-down occurred from point <D> to <A>. At the same time, no coherent oscillation was observed, and the bunch length hysteresis disappeared.

There are two jumps in the bunch length, one corresponds to line -<C> and the other <D>-<A>. The current for the jump depends on V_c . A lower V_c or longer bunch length makes the jump-up and the jump-down occur at a lower current. The region between the two jumps is called the hysteresis region, where two bunch lengths are possible. Fig. 4 shows the jump-up and the jump-down values of the current as a function of V_c . The hysteresis region increases as V_c increases.

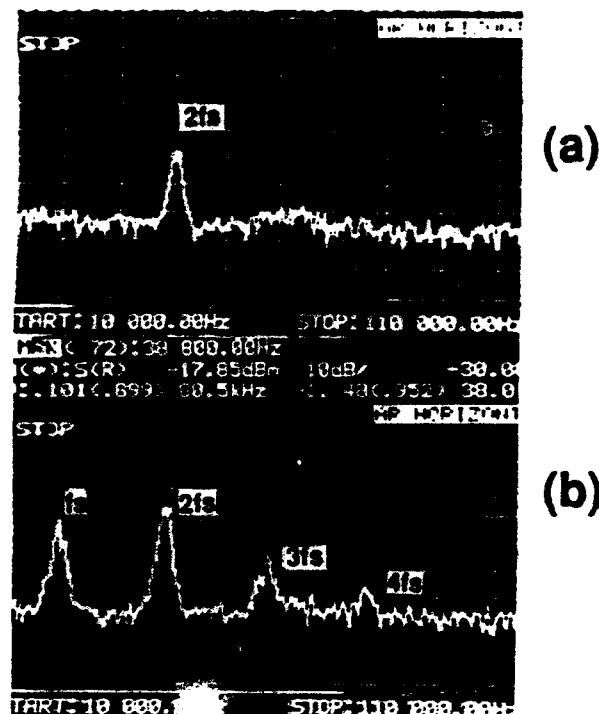


Fig. 2 Coherent oscillations at a shorter bunch length before a jump-up (a), and a longer bunch length after a jump-up (b) at $I_b = 4$ mA. and $V_c = 1.18$ MV. The frequency span is 10 to 110 kHz. The vertical scale is 10 dB/div.

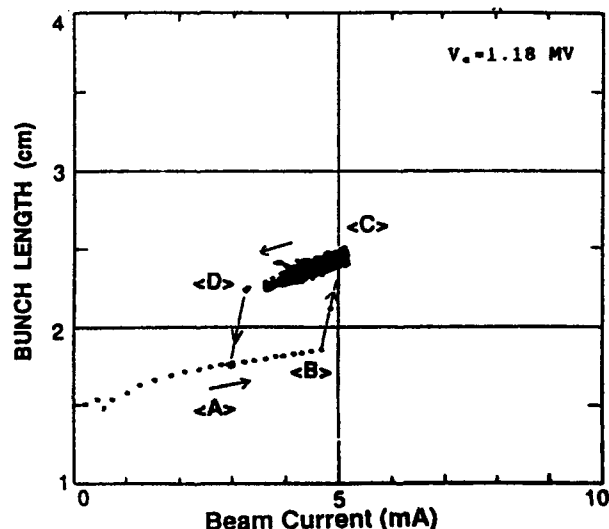


Fig. 3 Hysteresis of a jump in the bunch length as a function of the current at $V_c = 1.18$ MV.

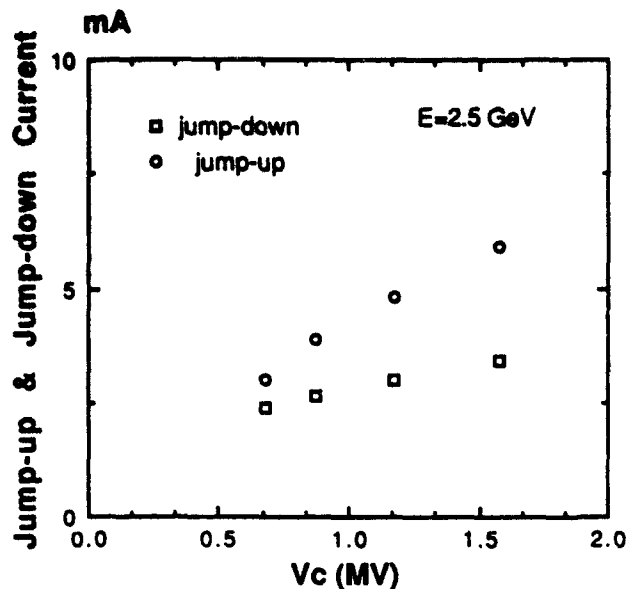


Fig. 4 Jump-up and jump-down currents in the hysteresis as a function of V_c .

4. DISCUSSION

Let's separate the bunch lengthening shown in Fig. 3 into two regions. At a low current region below 3 mA, no coherent oscillation is observed. The bunch length slightly increases. Bunch lengthening data are applied to the potential-well distortion model [4] expressed as

$$\left(\frac{\sigma_l}{\sigma_{l0}}\right)^3 - \left(\frac{\sigma_l}{\sigma_{l0}}\right) = \frac{I_b \cdot \alpha \cdot e}{\sqrt{2\pi} E v_{s0}^2 \sigma_{l0}} \left(\frac{R}{\sigma_{l0}}\right)^3 \left|\frac{Z(\omega)}{n}\right| \quad (1)$$

Here, σ_l is the bunch length, e is the elementary electric charge and $|Z(\omega)/n|$ is the imaginary part of the effective impedance. The effective impedance can be estimated using eq. (1). The measured impedance is 0.9 ± 0.1 and $1.7 \pm 0.2 \Omega$ at $V_c = 1.18$ MV by the BLM and SC, respectively. The difference may be due to a deformation of the bunch shape.

At a higher current region above 3 mA, a bunch is tumbling in the longitudinal phase space and is vertically expanded. One may consider the jump in the bunch lengthening is related to the turbulent instability.[5] The threshold current of the instability is given as

$$I_{th} \equiv \frac{\sqrt{2\pi} E \alpha \left(\frac{\Delta E}{E}\right)^2 \sigma_l}{\text{Re} \left|\frac{Z(\omega)}{n}\right|} \quad (2)$$

The bunch length and the impedance were measured by the two methods. Though there is a difference between their measurements, the threshold current can be estimated using each measured impedance. The calculated energy spread is used in eq. (2). Fig. 5 shows the estimated threshold current

as a function of V_c . One may notice a big difference between Fig. 5 and Fig. 4. In Fig. 5, the threshold current decreases as V_c increases. On the contrary, The jump in the bunch length increases as V_c increases in Fig. 4. The reason of the difference is not clear. The vertical instability which occurs in the hysteresis region may play a mysterious role in this bunch lengthening. Further study is needed.

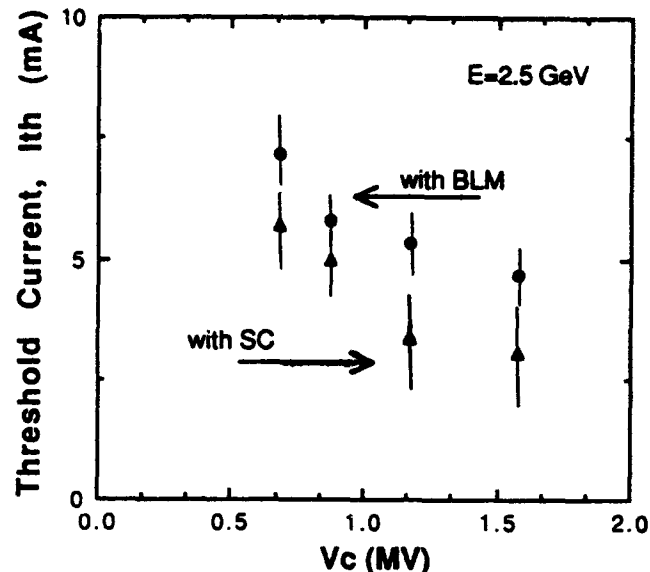


Fig. 5 Estimated threshold current of the turbulent instability using measured bunch lengthening data.

4. SUMMARY

1. The measured bunch length with the BLM agrees with the calculated natural bunch length within 10%. The bunch lengths measured by the BLM and by SC have a slight difference, which may be due to a deformation of the bunch shape.
2. A jump in the bunch length was observed together with coherent oscillations. This jump has hysteresis when the beam current increases and decreases, which suggests a strong nonlinear force in the bunch lengthening.
3. Considering the jumps as the threshold of the turbulent instability, the threshold current is estimated using measured bunch lengthening data. There is a difference between the measured and the estimated thresholds.

5. REFERENCES

- [1] T. Ieiri, KEK Proc. of the workshop on Advanced Beam Instrumentation 91-2, KEK(1991)p.246.
- [2] A. Ogata et. al., IEEE Nucl. Sci. NS-32, No.5 (1985)p.1944.
- [3] K. Ebihara, private communication.
- [4] J. Haissinski, Nuovo Cimento 18B No.1, (1973)p.72.
- [5] J.M.Wang and C.Pellegrini, Proc. of the 11th Int. Conf. on High-Energy Accelerator, CERN (1980)p.554.

Transverse Stability in Multibunch Mode for CLIC

G. Guignard

CERN, 1211 Geneva 23, Switzerland

Abstract

In order to reach the desire luminosity with 250 GeV per beam, multibunch operation (limited to 4 bunches, say) might have to be considered in the CERN linear collider (CLIC). One limitation comes from the coupling of the bunch motion with the long-range transverse wake fields that may induce beam breakup. These wake fields have therefore to be controlled, and means of reducing their effects on the beam are discussed in a companion paper. One possibility consists in detuning the dipole modes in the cells to obtain decoherent contributions and hence reduce the field amplitude at the downstream bunch location. The important question is to know below which value this amplitude must be limited to prevent intolerable beam breakup. In a first attempt at estimating this threshold for CLIC two approaches are considered, i.e. the criterion developed at SLAC and based on the convergence of the multibunch-motion solution [1], and numerical simulations of two-bunch motion in a focusing lattice.

I. INTRODUCTION

Starting with the proposed parameters for the 500-GeV CLIC option [2], i.e. 250 GeV per beam, a single bunch with 6×10^9 particles in each linac leads to a total luminosity of $7.9 \times 10^{32} \text{ cm}^{-2}\text{s}^{-1}$ and a luminosity for energies not lower than 95% of the nominal of $5.3 \times 10^{32} \text{ cm}^{-2}\text{s}^{-1}$. In order to go beyond the target value of 10^{33} at constant repetition rate, one would need either more particles per bunch (thereby increasing the background) or a minimum of two bunches per beam. Reaching sufficient luminosity with lower background might require four bunches per beam with a population reduced to 4.24×10^9 particles per bunch, say. This is the motivation behind the study of multibunch dynamics for CLIC.

The first step in this study is to consider the interaction of two bunches only, through the long-range wake fields induced by the first one. This would not only answer the stability question for two bunches, but also give useful information for a longer train if one assumes that the effect of the wake field generated by each bunch is mainly experienced by its immediate downstream neighbour. This assumption of nearest-neighbour coupling remains to be verified in the specific case of dipole-mode detuning with the CLIC acceleration structure. Nevertheless, one expects interesting indications on beam stability from a two-bunch model, as explained below, knowing that the number of bunches per CLIC beam would always be small anyway.

II. MULTIBUNCH MOTION FORMULATION

Multibunch motion with nearest-neighbour coupling was recently formulated for smooth focusing [1], starting from the basic equation of motion

$$\gamma(s)x'' + \gamma'(s)x' + \gamma(s)k^2x = \int \rho W_T^\delta x(s) dz^* \quad (1)$$

where $\gamma(s)$ is the energy (assumed to increase linearly with distance s like $\gamma = \gamma_0 + Gs$), k the transverse wave number ($= 1/\beta$), ρ the line charge density and W_T^δ the transverse wake field Green's function. To solve the problem, the author [1] looks for an equivalent equation of motion, reduced to one for zero acceleration. Deriving it from (1) requires a change of variables that cancels the s -dependence of γ in the terms $\gamma x''$ and $\gamma k^2 x$. This implies, because of the second derivative, a change of the independent coordinate identical to the change of k , while the amplitude x must be normalized with the β -function that is scaled with γ as $1/k$, i.e.

$$dz = \frac{k}{k_0} ds = \left(\frac{\gamma_0}{\gamma} \right)^{\alpha_b} ds \quad x_n = x \left(\frac{\gamma}{\gamma_0} \right)^{\frac{\alpha_b-1}{2}} \quad (2)$$

The exponent α_b is an arbitrary coefficient that depicts the γ -scaling of the betatron function retained [3]. The transformation (2) does not exactly reduce Eq. (1) to one for constant γ and the approximation that the relative energy gain G/γ is small within a betatron period has to be invoked. Using Eq. (2), the length of the equivalent zero-acceleration linac is given for an arbitrary lattice scaling [3] by

$$L = \int_0^{s_{\text{tot}}} \left(\frac{\gamma_0}{\gamma} \right)^{\alpha_b} ds = \frac{1}{(1-\alpha_b)G} \left[\gamma_f^{1-\alpha_b} \gamma_0^{\alpha_b} - \gamma_0 \right], \quad (3)$$

where G is the energy gain, γ_0 and γ_f the initial and final energies. In the last proposal for CLIC, $\alpha_b \approx 0.4$ [3] and the length becomes equal to 1.2 km about.

The assumption that the wake field is independent of position along the linac allows for the derivation of an exact solution to the equations of motion [1]. The key point is that the amplitude growth is characterized by a power series in $f \cdot z$ and the condition to keep the bunch amplitudes small is

$$f \cdot L < 1 \quad \text{with} \quad f = \frac{W_{Tb} N_e \beta_0}{2 E_0} \quad (4)$$

where W_{Tb} is the wake-field strength at one bunch separation, N_e the charge per bunch, β_0 the initial betatron amplitude and E_0 the injection energy. For the 500-GeV CLIC option

parameters ($N = 6 \times 10^9$, $\beta_0 \approx 6.5$ m, $E_0 = 9$ GeV), condition (4) tells us that W_{Tb} must be smaller than 2.4 MV/m²/nC for the stability. Since the maximum transverse field \hat{W}_T is about 1100 MV/m²/nC in the tail of each bunch [4], this criterion implies an attenuation of approximately 450 of the field at one bunch separation. With a reduced population of 4.2×10^9 particles, an attenuation of 300, say, is required according to (4), for multibunch stability. This already gives a valuable clue about the required reduction of the dipole modes by cell detuning, which remains to be cross-checked with numerical simulations.

III. MULTIBUNCH MOTION SIMULATIONS

The analytical formulation quoted in Section II, leading to a simple stability criterion, is valid for a constant-acceleration linac with smooth focusing and wake fields independent of position along the linac. Although the formalism has been extended to include linac FODO arrays and wake-field variations in the structures [1], numerical simulations have been retained for investigating further the two-bunch motion in an AG focusing lattice of the CLIC linac.

The tracking has been performed with two identical bunches, experiencing the same short-range wake fields whose maximum amplitude \hat{W}_T has been evaluated from 218 transverse modes [4]. In addition, a long-range wake field W_{Tb} has been superimposed in the second bunch, taking it constant within the bunch for simplification. The focusing FODO structure incorporates the most recent lattice scaling with energy [3] that allows, in the single-bunch mode, alignment tolerances of 50 μ m for quadrupoles, 10 μ m for cavities and 2 μ m for beam-position monitors. Microwave quadrupoles are used for BNS damping and autophasing in each bunch.

The procedure for controlling the trajectory is based on the presence of monitors at each girder and possible iterations of the correction [3]. In the two-bunch mode however, the sequence of the successive operations is more complex. One admits the trajectory is first measured and minimized with one bunch only, with sets of RF quadrupoles adjusted for stabilizing transverse oscillations. After an optimum correction, two bunches are injected in the linac, and the trajectory measured using the total integrated signal of both bunches is corrected. During this second operation, RF quadrupoles are tuned again by sectors (700-m long, typically), and iterations are carried out whenever it is worthwhile for emittance control.

Simulations were started with the lower bunch population considered ($N = 4.2 \times 10^9$) for different \hat{W}_T/W_{Tb} ratio. It has been observed that beam breakup always rises strongly over a short distance (200 m, say), after a long and slow buildup of coherent instability (Fig. 1). The physical explanation for such a latent instability has already been proposed in the past [5]. After the initial perturbation, both bunches oscillate with the

same phase and the wake field excitation is in quadrature with the amplitude of the oscillation. Wake fields provoke then a mere phase slip that increases with the distance travelled by the bunches. The oscillations of the second bunch lag behind those of the first and their amplitude spirals slowly towards larger values over a high number of betatron wavelengths depending on field strength. Eventually, when a finite phase lag develops, an in-phase excitation component appears, leading to a rapid amplification of the initial amplitude. For W -ratio of 50, this amplification takes place within the 3-km length of the 250-GeV CLIC linac and for 100, within the 12-km length of the 1-TeV CLIC linac (Fig. 1). In order to have it beyond the exit of the 1-TeV linac, a wake-field ratio of at least 150 is required with this bunch intensity. Having pushed the beam breakup outside the linac, RF quadrupoles can be adjusted to keep the emittance dilution low over the linac length and fight the coherent instability of bunch 2. For that purpose, RFQ strength is reduced, mainly towards the end of the linac, in order to compromise between BNS damping of short-range wake field in both bunches and counteracting long-range constant wake field in bunch 2. This succeeded in limiting emittance growth to tolerable values (average of 2×10^{-7} rad m) for W -ratio equal to 100 (Fig. 2) and 300 (Fig. 3).

Considering then a bunch population of 6×10^9 , a W -ratio of at least 500 is necessary, in order to obtain final normalized emittances (Fig. 4) that lead to about twice the luminosity expected with $\gamma_e = 2 \times 10^{-7}$ rad m and one bunch per beam.

IV. COMMENTS AND PERSPECTIVE

While the analytical formulation suggests a wake-field attenuation on the level of the follower-bunch by 300 and 450 depending on the population, two-bunch tracking shows that careful adjustment of the RF quadrupoles makes it possible to keep both bunches stable within requirements with factors 100 and 500, i.e. in fairly good agreement. These W -ratios look high, however, in the sense that they are difficult to achieve by detuning the dipole modes in the 30-GHz cells, as recent studies show [6]. A possible way out could be the introduction of two dipole modes at different frequencies in every staggered, tuned accelerating section or the introduction of two different types of sections, each with one dipole mode, the two modes being separated by π at the second bunch position. As suggested by W. Schnell, alternating these sections to have a succession of opposite wake-field amplitudes corresponds to a pseudolocal compensation. Tracking with W -amplitudes roughly opposed in two contiguous sections, but with 20% systematic difference and 10% r.m.s. spread, indicates it is possible in a particular case to obtain the target-emittances at the 250-GeV linac end with a \hat{W}_T/W_{Tb} ratio of 40 (Fig. 5). This result and the phenomenology of the latent instability (Section III) suggest the further investigation of what I would call alternate wake-kick damping.

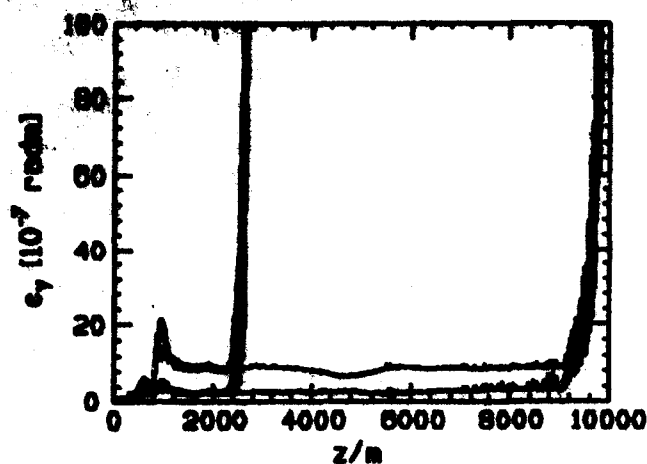


Fig. 1: Beam breakup due to long-range wake fields, with W-ratio of 50 and 100

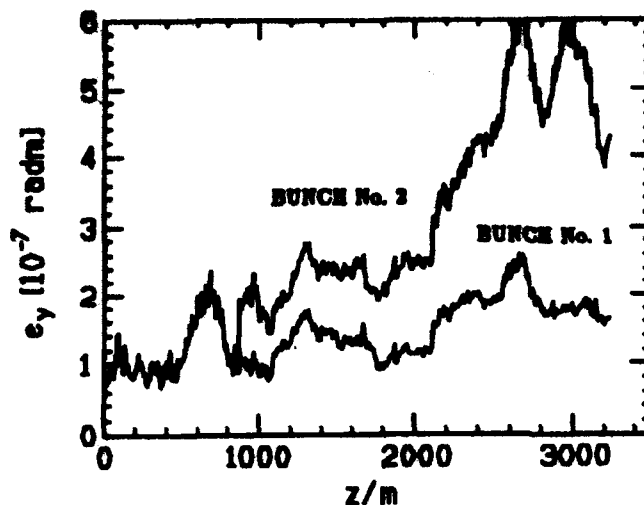


Fig. 4: Emittance growth with $N = 6 \cdot 10^9$ and W-ratio of 500

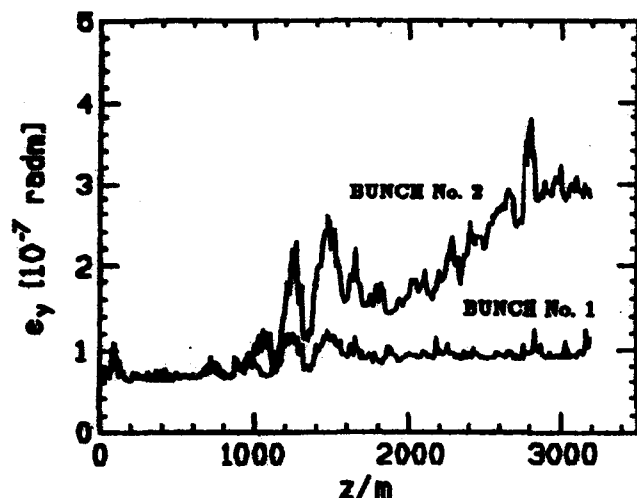


Fig. 2: Emittance growth with $N = 4.2 \cdot 10^9$ and W-ratio of 100

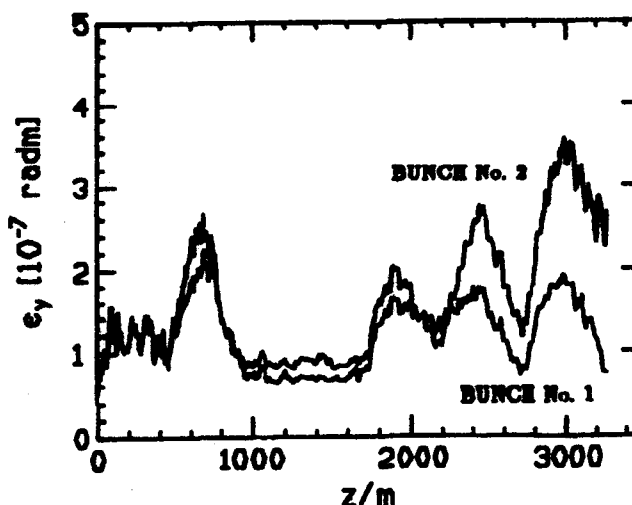


Fig. 5: Two-bunch emittance growth with alternate wake-kick damping, $N = 6 \cdot 10^9$ and W-ratio of 40

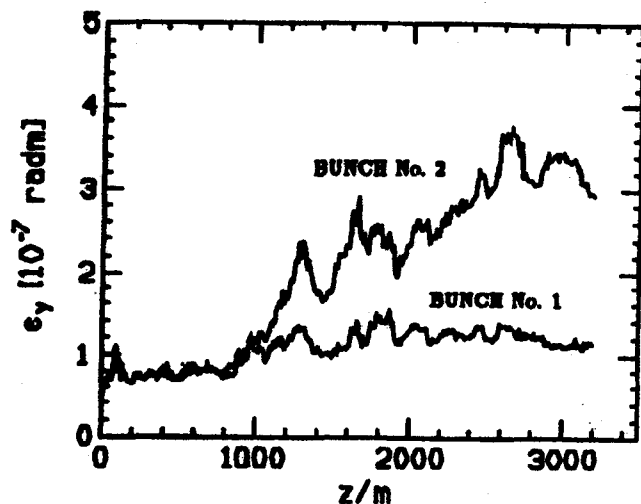


Fig. 3: Emittance growth with $N = 4.2 \cdot 10^9$ and W-ratio of 300

V. REFERENCES

- [1] C. Adolphsen, "Multibunch motion with nearest-neighbor wake-field coupling," *XVth Int. Conf. H. E. Acc.*, Hamburg, 1992.
- [2] G. Guignard, "Beam stability simulations in CLIC linacs," *XVth Int. Conf. H. E. Acc.*, Hamburg, 1992.
- [3] G. Guignard, "Lattice scaling and emittance control in the CLIC main linac," this Conference.
- [4] A. Millich, "Computation of wake fields for the CLIC waveguide," *European Part. Acc. Conf.*, Berlin, 1992.
- [5] H. Henke and W. Schnell, "Analytical criterion for the onset of transverse damping," CERN-LEP-RF/86-18, 1986.
- [6] I. Wilson, W. Wuensch, "Multi-bunch studies for the CERN Linear Collider," this Conference.

K.L.F. Bane and K. Olde^o

Stanford Linear Accelerator Center, Stanford University, Stanford, CA 94309 USA

INTRODUCTION

A longitudinal, single bunch instability has been observed in the SLC damping rings.[1] Beyond a threshold current of 3×10^{10} the energy spread of the beam increases and a "saw-tooth instability" appears. The latter term is meant to describe a rather complicated phenomenon, depending on both current and rf voltage. In one form it describes a cycle that includes a quick increase in bunch length, over a time on the order of a synchrotron period, and then a much slower return to the original length, over a time on the order of a radiation damping time. Although the total relative change in length is only about 10% the resulting unpredictability of the beam properties in the rest of the SLC accelerator makes it difficult, if not impossible, to operate the SLC above the threshold current. With the goal of trying to understand this instability the simulations that are the subject of this paper were begun.

Bunch lengthening calculations have been performed before for the SLC damping rings, to obtain the average bunch shape as function of current.[2] The wakefields of all the important vacuum chamber components were first obtained numerically.[3] The dominant elements were found to be many small discontinuities—bellows, masks, transitions, etc.—elements that are inductive to the beam. Once the total wakefield had been obtained, and the threshold current was known (from measurements), the average bunch shapes were found by means of a potential well calculation. The bunch shapes obtained in this way were found to agree very well with measurement results.[4]

In this paper we investigate the single bunch behavior of the SLC damping rings using time domain tracking and also a Vlasov Equation approach. Since the earlier bunch length calculations the damping ring vacuum chamber has been modified, by sleeving the bellows. Our results will, therefore, include the effects of this modification.

PHASE SPACE TRACKING

The Formalism

We use a now standard tracking method for simulating the effect of the wakefield on the longitudinal phase space of the beam.[5-9] The beam is represented by N_p macro-particles; each particle i has position and energy coordinates (z_i, ϵ_i) , with a more negative value of z more toward the front of the bunch. The properties of particle i are advanced on each turn according to the equations:

$$\Delta \epsilon_i = -\frac{2T_0}{\tau_c} \epsilon_i + 2\sigma_{e0} \sqrt{\frac{T_0}{\tau_c}} r_i + V'_{rf} z_i + V_{ind}(z_i) \quad (1)$$

$$\Delta z_i = \frac{\alpha c T_0}{E_0} (\epsilon_i + \Delta \epsilon_i) \quad , \quad (2)$$

with T_0 the revolution period, τ_c the damping time, σ_{e0} the nominal rms energy spread, V'_{rf} the slope of the rf voltage (a negative quantity), α the momentum compaction factor,

*Work supported by Department of Energy contract DE-AC03-76SF00515.

^oFrom KEK.

and E_0 the machine energy; r_i is a random number obtained from a normally distributed set with mean 0 and rms 1; the induced voltage on any turn is given by

$$V_{ind}(z) = -eN \int_{-\infty}^z W(z-z') \lambda_s(z') dz' \quad , \quad (3)$$

with N the bunch population, $W(z)$ the Green function wakefield, and $\lambda_s(z)$ the longitudinal charge distribution. We approximate Robinson damping of dipole oscillations by adding $-2T_0\langle\epsilon\rangle/\tau_d$ on the right of Eq. (1), with $\langle\epsilon\rangle$ the average energy and τ_d the Robinson damping time.[6]

Practical Considerations

Simulations use only a small fraction of the real number of particles in the beam, and numerical noise can suppress real phenomena or generate its own phenomena. This is particularly true with an inductive impedance, such as the SLC damping rings', since then the induced voltage depends strongly on the slope of the charge distribution. To calculate λ_s on each turn we simply bin the macro-particles in z , without smoothing, and count on the use of a very large number of macro-particles to give us a sufficiently smooth distribution.

The wakefield for the ring with bellows sleeves was calculated as before, using the computer program TBCI,[10] with a short, gaussian driving bunch with $\sigma_z = 1$ mm. To make it causal, the part in front of bunch center (at $z = 0$) was reflected to the back (see Fig. 1). We expect to be able to find beam instabilities down to wavelengths of about 1 cm.

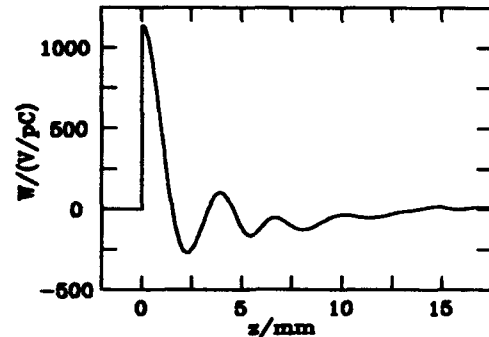


Fig. 1. The Green function wake used to represent the current SLC damping rings.

For the simulations we take $T_0 = 118$ ns, $E_0 = 1.15$ GeV, rf frequency $\nu_{rf} = 714$ MHz, $\sigma_{e0} = 0.07\%$. We choose a peak rf voltage $V_{rf} = 0.8$ MV, where the nominal bunch length $\sigma_{z0} = 4.95$ mm, and synchrotron frequency $\nu_{s0} = 99$ kHz. For practical reasons τ_c was reduced by a factor of 10 to 0.17 ms. Therefore there are 1445 turns per damping time, compared to 85 turns per synchrotron period. We take $N_p = 300,000$, and for calculating λ_s we take 100 bins to extend over $10\sigma_z$ of the bunch. We start the program with the potential well bunch distribution and let it run for 3 damping times.

SIMULATION RESULTS

Average Bunch Properties

On each turn we calculate the lower moments of the distributions. By averaging over the last damping time we obtain the "average" properties of the distributions. Fig. 2a displays the average value of the first (the crosses) and the second (the diamonds) moments in z as functions of current. The ring being inductive, the bunch shapes are more bulbous than gaussians, and the bunch length increases with current.

In Ref. 2 the average bunch shapes are obtained by a modified potential well solution: Haissinski's formula [11] is used to find the bunch shape; above threshold the energy spread, and therefore the natural bunch length used in the formula, are taken to increase as $N^{1/3}$ (since the ring is very inductive). This method applied to the current damping ring, taking the threshold to be 2×10^{10} , are shown by the lines in Fig. 2. This approximate method agrees very well with the tracking results. We should also point out the bunch length for the ring is very similar to that of the old ring, only 10% shorter at 3×10^{10} .

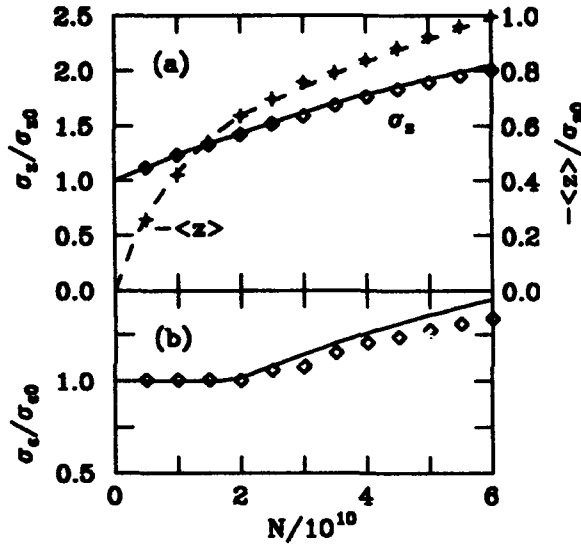


Fig. 2. Average bunch properties vs N .

The Threshold Current

In Fig. 2b we plot the average rms energy spread as function of current. Fitting the results to a power law increase above a threshold we find the power law to be 0.28 and the threshold $N_{th} = 2.0 \times 10^{10}$. A confirmation that this is the threshold current is the fact that the unstable mode (discussed below) first appears at this current, with an uncertainty of -0.25×10^{10} .

P.B. Wilson once hypothesized that one criterion for the onset of the instability is that the slope of the total voltage ($V'_{rf} + V'_{ind}$) goes to zero within the bunch.[12] In our case this criterion holds at 1.9×10^{10} ; at higher currents, as the bunch lengthens, it continues to hold. A related hypothesis by P.B. Wilson is that the Haissinski Equation, a transcendental equation of the form $\lambda_s = f(\lambda_s)$, will, when iterated above threshold, asymptotically give two, alternating solutions.[13] In our case this begins at 2×10^{10} .

Repeating the tracking calculation for the old ring (no bellow sleeves) we find a threshold of 1.1×10^{10} ; repeating

it for a wakefield that represents only the rf cavities (the best impedance we can imagine) we obtain a capacitive wakefield and threshold of 14×10^{10} .

Modes of Instability

Taking a Fourier transform (FT) of one of the moments we find that, beginning at $N = 2 \times 10^{10}$, resonances appear with frequencies above $2.4\nu_s$. Taking the FT(s_z) at 3.5×10^{10} , with s_z the skew in z (see Fig. 3a), we find a very clean signal with only one, very narrow peak (see Fig. 4a). The full width, 1.5%, is given by the limited length of the run and not by any more fundamental limit.

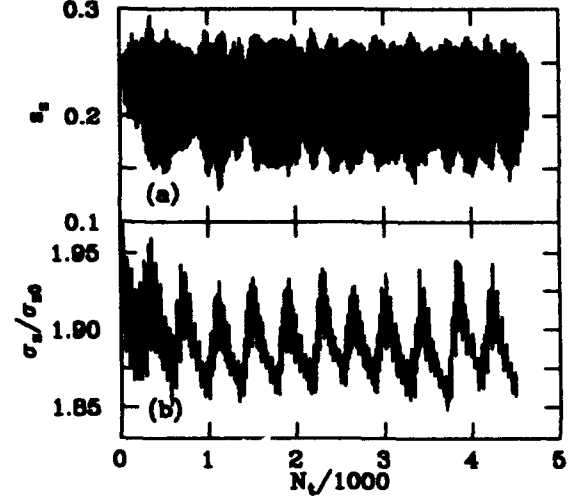


Fig. 3. The turn-by-turn skew when $N = 3.5 \times 10^{10}$ (a), and the rms when $N = 5.0 \times 10^{10}$ (b).

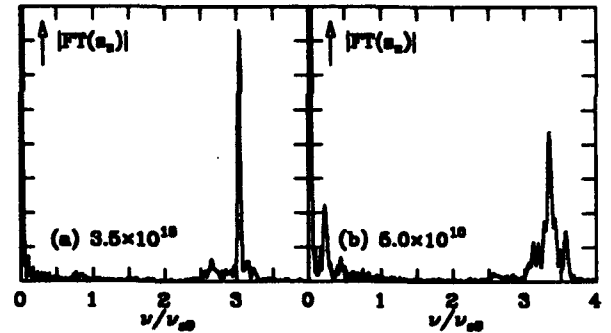


Fig. 4. The absolute value of the Fourier transform of the skew signal for two currents.

At some currents, like 5.0×10^{10} , we find a fairly regular overshoot pattern in the moments as function of time (see Fig. 3b). In this example the bunch length varies by 5% over a cycle: the lengthening time is about $1.5/\nu_{s0}$, the shortening time is maybe twice as long. In the FT we see an extra peak at 22 kHz and sidebands around the instability. At $N = 3.0 \times 10^{10}$ the pattern of the bunch length is more irregular.

Fig. 5 gives two snapshots of the unstable mode when $N = 3.5 \times 10^{10}$. We see that the maximum amplitude of the mode is about 10% and the wavelength about 1.2 cm. We obtain a 3-dimensional mode plot by averaging the distributions at a fixed phase in the oscillation and subtracting from this the average over all phases (see Fig. 6). We see that the mode is a mixture of dipole, quadrupole, and sextupole components. By 5×10^{10} an octupole component can also be seen.

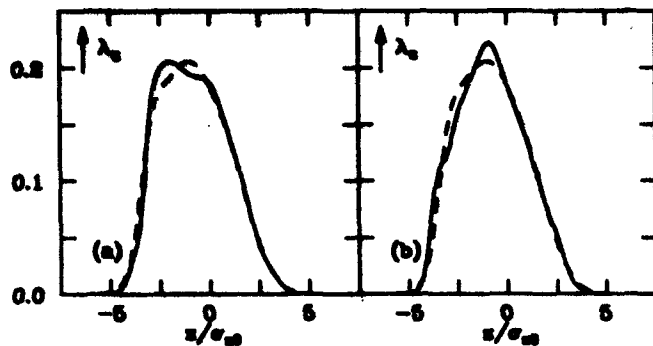
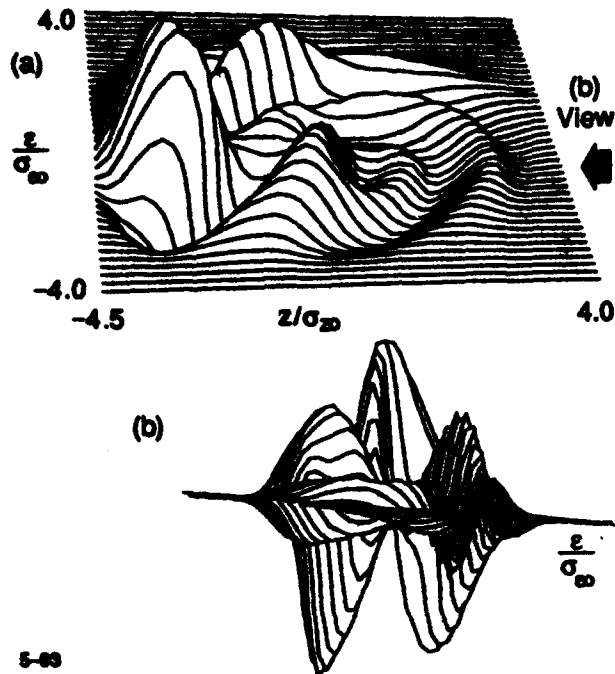


Fig. 5. A snapshot of the beam, at two phases 180° apart, when $N = 3.5 \times 10^{10}$.



5-03
7423A1

Fig. 6. The shape of the unstable mode from two views at $N = 3.5 \times 10^{10}$.

The positions of the major peaks in the spectrum of the skew signal for different currents is shown in Fig. 7. The diamonds show the cases with one narrow spike in the spectrum of s_z , the crosses those with more complicated spectra. We see that the frequency of the unstable mode increases with N ; the dashed line has a slope of $0.27/10^{10}$.

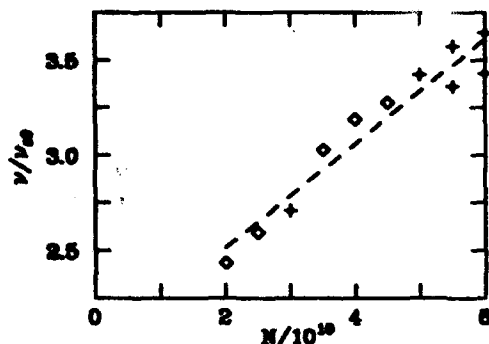


Fig. 7. The positions of the major peaks in the Fourier transform of the skew signal vs N .

A Vlasov Equation Calculation

K. Oide and K. Yokoya have written a computer program to solve the time independent, linearized Vlasov Equation including the effects of potential well distortion.[14] Using the wakefield of Fig. 1 we take 6 azimuthal space harmonics and 60 mesh points in amplitude to represent phase space. We find that, due to the potential well distortion, already by 1×10^{10} the large gaps in mode frequencies have disappeared. The first unstable mode is found at 1.9×10^{10} with a frequency of $2.5\nu_{z0}$ (see Fig. 8).

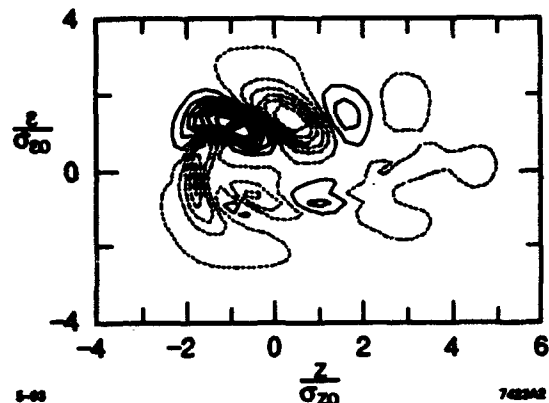


Fig. 8. A contour plot of the unstable mode, obtained by solving the Vlasov Equation.

COMPARISON WITH MEASUREMENTS[1,4]

The agreement with measurements of the average bunch shapes is very good. The calculated threshold currents are about 30% lower than the measurements, which are 3.0×10^{10} in the current ring, 1.5×10^{10} in the old ring. A mode (sometimes call the "sextupole" mode) has been measured above threshold. At 3×10^{10} it has a frequency $2.6\nu_{z0}$; at higher currents the frequency increases at about $0.08/10^{10}$, a much lower slope than calculated here.

ACKNOWLEDGEMENTS

The authors thank M. Sands and the members of the SLC Damping Ring Task Force for helpful discussions.

REFERENCES

- [1] P. Krejčík, et al., "High Intensity Bunch Length Instabilities in the SLC Damping Rings," this conference, Q7.
- [2] K. Bane and R. Ruth, Proc. of the 1989 IEEE Particle Acc. Conf., Chicago, 1989, p. 789.
- [3] K. Bane, Proc. of the 1st European Particle Acc. Conf., Rome, 1988, p. 637.
- [4] L. Rivken, et al., Proc. of the 1st European Particle Acc. Conf., Rome, 1988, p. 634.
- [5] A. Renieri, Frascati, Report No. LNF-75/11R, Feb. 1976.
- [6] P.B. Wilson, et al., IEEE Trans. Nucl. Sci., NS-28, 2525 (1981).
- [7] T. Weiland, DESY 81/088, Dec. 1981.
- [8] R. Siemann, Nucl. Instr. Meth., 203, 57 (1982).
- [9] D. Brandt, CERN-ISR-TH-89-09, May 1982.
- [10] T. Weiland, Nucl. Inst. Meth. 212, 13 (1983).
- [11] J. Haisinski, Il Nuovo Cimento, 18B, No. 1, 72 (1973).
- [12] P.B. Wilson, private communication.
- [13] P.B. Wilson, PEP-232, Feb. 1977.
- [14] K. Oide and K. Yokoya, KEK-Preprint-90-10, 1990.

Multibunch Beam Break-up in Detuned Structures*

K.A. Thompson, C. Adolphsen, and K.L.F. Bane

Stanford Linear Accelerator Center, Stanford University, Stanford, CA 94309 USA

Abstract

A key problem in next-generation linear collider designs utilizing multibunching is the control of multibunch beam break-up. One method of controlling the break-up is detuning, i.e., varying the frequency of the transverse deflecting modes by varying the cell dimensions within the accelerating structures. In this case, the beam break-up is sensitive to the resonances between the bunch frequency and some of the deflecting mode frequencies. It is also sensitive to errors in the fabrication and alignment of the accelerating structures. We examine these effects in the context of the SLAC NLC design.

INTRODUCTION

In the present SLAC design for a Next-generation Linear Collider (NLC), it is planned that a 125 ns train of bunches will be accelerated on each RF pulse. In order to control multibunch beam break-up, we must ensure that the transverse wake is kept sufficiently small over the length of the bunch train. We plan to vary the structure dimensions so that the frequencies of the lowest-passband synchronous modes approximately follow a truncated Gaussian distribution in each structure. This "detuning" of the frequencies provides a strong initial roll-off of the wake before the first bunch spacing is reached. In addition, to maintain sufficient suppression of the longer-range wake, we plan to interleave these detuned frequencies over about four different structure types. This provides a smoother and denser distribution of frequencies than is obtained with just one structure type. However, the success of the method requires that dipole-mode frequency errors and misalignments of the structures be kept sufficiently small; this is the focus of the present paper.

DETUNING STRATEGY AND PARAMETERS

Intuitive understanding of the effects of detuning is most easily obtained by viewing the structure as consisting of a collection of uncoupled oscillators. A more correct treatment includes the effects of the small couplings between the oscillators; the simplest way to do this is via equivalent-circuit models. In this paper we use a "double-band" equivalent-circuit model [1], that takes account of the mixing of the TM_{110} and TE_{111} modes to produce a TM_{11} -like dipole mode, which is the most important mode for multibunch beam break-up.

In the NLC structure design [2] we have the freedom to shape the distribution of the dominant TM_{11} -like dipole mode frequency f_0 between its two end-cell values, while keeping the frequency f_{rf} of the accelerating mode fixed. Let the full-spread be Δf_{tot} , centered on frequency f_0 , and neglect the cell-to-cell coupling for the moment. For a truncated Gaussian distribution with standard deviation σ_f , the spacing between adjacent components is:

$$\delta f_i = \frac{\sqrt{2\pi}}{N-1} \sigma_f \exp \left[\frac{(f_{0,i} - \bar{f}_0)^2}{2\sigma_f^2} \right] \operatorname{erf} \left(\frac{n_\sigma}{2\sqrt{2}} \right) \quad (1)$$

Here $n_\sigma \equiv \frac{\Delta f_{tot}}{\sigma_f}$ is the full width of the truncated distribution in units of σ_f , N is the number of cells in a structure, and $\operatorname{erf}(x) \equiv \frac{2}{\sqrt{\pi}} \int_0^x e^{-u^2} du$ is the usual error function. The fractional spacing in the central core of the distribution is approximately

$$\frac{\delta f}{f_0} \approx \frac{\sqrt{2\pi}}{N-1} \frac{\sigma_f}{f_0} \operatorname{erf} \left(\frac{n_\sigma}{2\sqrt{2}} \right) \quad (2)$$

Including coupling via the equivalent circuit model modifies the distribution, in particular, the core spacing is increased somewhat and the tails of the distribution extend further out. For our parameters, the core frequency spacing in the uncoupled model is $\delta f/f \approx 3 \times 10^{-4}$; for the coupled double-band model, $\delta f/f$ is increased by a factor of about 1.4.

To obtain the overall frequency distribution for n structures with interleaving, we use the distribution as given by Eqn. (1), but we increase N by a factor n . For $n = 4$, the lowest frequency would be assigned to structure type 1, next lowest to type 2, next to type 3, next to type 4, next to type 1, and so on, cycling repeatedly through the structure types. The linac is built by cycling through the n structure types (we have generally used the pattern 1 3 2 4 1 3 2 4...). We have done simulations using "smooth focusing" in which there is a focusing element between each 1.8 meter structure. We have also used a more realistic FODO-type lattice, in which the number of structures between quads increases with energy, while maintaining an approximate $E^{1/2}$ dependence of the average beta function and reasonable magnetic field strengths. In either case, the initial value of the average betatron function β in the NLC main linac will be around 6 meters, and will increase approximately as the square root of the energy going along the linac. Thus, the betatron wavelength $2\pi\beta$ is much greater than the structure length everywhere in the linac. For $n = 4$ interleaved structure types, the effect is much the same as if the wake function $W(z)$ were an average of the wake function over the n structure types.

The NLC structures will have an accelerating frequency of 11.4 GHz (X-band), with irises and inner cell radii tapered to produce a truncated Gaussian before coupling is included. Parameters of this Gaussian are $\sigma_f = 2.5\%$ and $n_\sigma = 4$. The Q 's of all the coupled modes were taken to be 6500 (the variation in Q calculated for the coupled modes was small, and for simplicity we neglected it). The envelope of the single-particle wake function averaged over a single structure is shown in Fig. 1(a). The envelope averaged over four structure types with interleaved frequency distributions is shown in Fig. 1(b); one sees that there is substantial additional suppression of the longer range wake. This is necessary for the 125 ns bunch train design now being proposed for NLC (note that the range shown for z is approximately

* Work supported by Department of Energy contract DE-AC03-76SF00515.

the length of the train). Other parameters are: bunch charge $N = 0.65 \times 10^{18}$, bunch spacing $= 16\lambda_r \approx 42$ cm, initial linac energy 15 GeV, final linac energy $= 250$ GeV, linac length $= 6$ km, initial $\beta \approx 6$ m (and scaling as \sqrt{E}). The energy spread is assumed to be zero in these simulations.

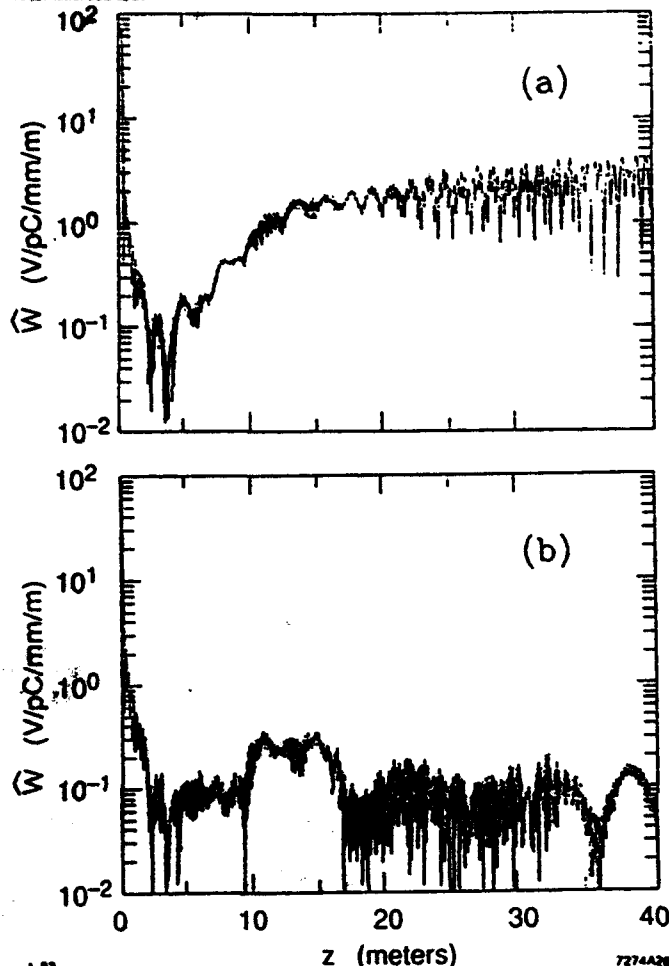


Figure 1. Envelope of the single-particle wake function $W(z)$ (a) for single structure type, (b) for four structure types with interleaved frequency distributions.

INJECTION JITTER

We begin by examining the case of a "perfect" linac (no frequency errors or misalignments), with a uniform initial offset of the beam. The transverse offset of the bunches at the end of the linac (in units of the initial offset, and normalized by factoring out the adiabatic damping due to acceleration) is shown for a single section type in Fig. 2(a) and for four section types with interleaved frequency distributions in Fig. 2(b). The advantage of using the four interleaved section types is mainly the strong suppression of the blow-up from injection jitter, as seen in this figure. For the case of a single section type, keeping the projected emittance growth of the multibunch beam below, say, 25% would require keeping the injection offset to less than 30% of the beam size. Note that it is only in the later part of the train that additional suppression is needed (cf. Fig. 1). For the case of four section types, the emittance growth will be only a few percent even with an injection offset comparable to the beam size.

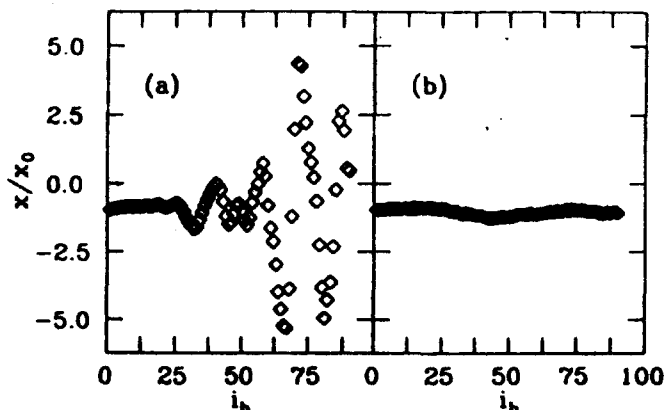


Figure 2. Transverse offset of bunches at end of linac (no errors), in units of initial uniform offset x_0 of train, as function of bunch number i_b , (a) for single section type, (b) for four section types.

FREQUENCY ERRORS

We examined the effects of small random variations in the frequencies, due, for example, to fabrication errors. There are two extreme cases. The first is that in which the error on each frequency in the design distribution is the same in all sections of a given type (but random from cell to cell). This case, which we shall refer to as "systematic" errors generally leads to an increase of the longer range wake field. The second case, which we denote "random" is that in which the errors are independent for each section and each frequency; in this case there is some averaging of the errors over many sections.

The expected rms size of the random frequency errors due to machining precision is $\sigma_{e,ran} = 1 \times 10^{-4}$ (fractional error, i.e. $\delta f/f_0$) [3]. This is comparable to the spacing in the core of the four-interleaved-section frequency distribution, which is one reason why it is not advantageous to have more than about four section types. We hope to keep the systematic component $\sigma_{e,sys}$ smaller than this; for illustration, we look at the cases $\sigma_{e,sys} = 3 \times 10^{-5}$ and $\sigma_{e,sys} = 1 \times 10^{-4}$. Fig. 3 shows histograms of the fractional emittance increase of the multibunch beam compared to that of a single bunch (using four structure types), assuming an initial offset of the beam equal to the bunch size, for fifteen different distributions of systematic errors generated at each value of $\sigma_{e,sys}$. If we also include random errors uncorrelated from section to section, having $\sigma_{e,ran} = 1 \times 10^{-4}$, there is little additional effect on the projected emittance.

RESONANCES

Fig. 4 shows the maximum transverse offset of the bunches, for the point having the largest emittance growth in Fig. 3. The sharp onset of transverse growth at some point in the train is typical of cases with large growth and is due to the fact that the wake function at a number of successive bunches has the same sign. This can happen when frequencies in the detuned distribution are close to a "resonance" with the bunch frequency.

The 21st and 22nd harmonic of the bunch frequency lie within the range of detuned frequencies and have significant kick factors, according to the double-band model. The resonances themselves are not so much a problem as are nonuniformities in the frequency distribution of

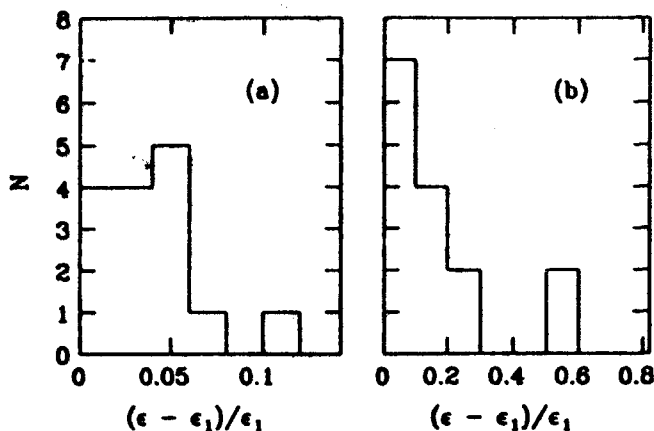


Figure 3. Histogram of fractional emittance increase (w.r.t. accelerator axis) of multibunch beam compared to emittance ϵ_1 of a single bunch, for fifteen different systematic error distributions, (a) at $\sigma_{e,sys} = 3 \times 10^{-5}$, and (b) at $\sigma_{e,sys} = 1 \times 10^{-4}$.

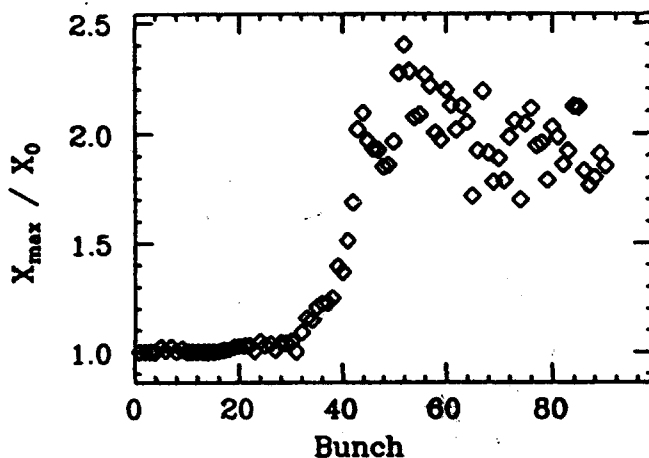


Figure 4. Maximum transverse offset x/x_0 as a function of bunch number i_b , for the $\sigma_{e,sys} = 1 \times 10^{-4}$ distribution with largest emittance growth in Fig. 3.

modes in their vicinity. Note that the resonant wakes are 90° out of phase with the bunches. Even with no frequency errors, a non-symmetric location of the resonant peak relative to neighboring modes can lead to a net wake function sum at a given bunch. This is especially true near the end of the train, where the resonant width starts to become comparable to the mode spacing. Nonuniformities, such as those for frequency errors, can lead to a net resonant wake sum, which is potentially much larger than that for a uniform, symmetric distribution.

MISALIGNMENTS

We have also examined the effects of misalignments of the acceleration structures. As a simple model, we assume each misaligned piece of structure contains i_m cells, (where i_m may vary from 1 to the number of cells in a whole structure), the misalignment within each such piece is uniform, and the misalignments are random with rms size σ_m . Fig. 5 shows the tolerance $t_{25\%}$ on σ_m to produce a 25% emittance blow-up as a function of i_m ,

assuming four interleaved structure types. Here we have assumed a FODO-type lattice, with beam size in the initial focusing quad equal to $3.6 \mu\text{m}$ (comparable results are obtained using smooth focusing). The wake kicks are calculated assuming that the modes themselves are not significantly distorted by the presence of the misalignments.

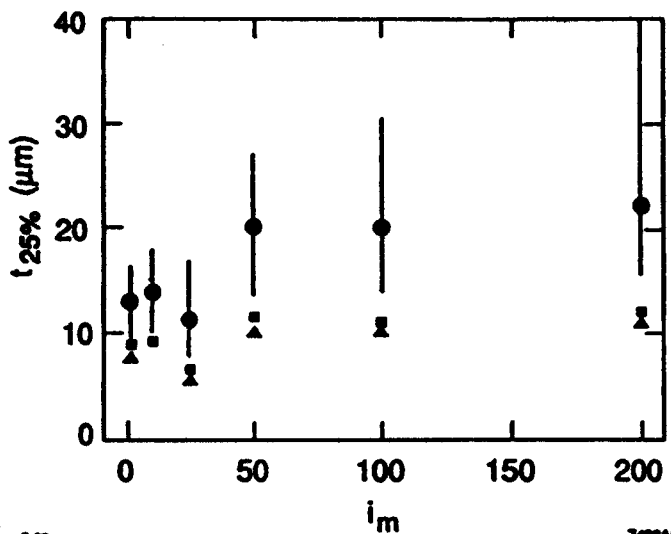


Figure 5. Tolerance (in μm) of rms misalignments for 25% emittance growth (w.r.t. beam centroid) of the multibunch beam as a function of number of cells i_m per uniformly misaligned piece of structure. 174 different random distributions were calculated at each value of i_m . The error bars show the rms on each side of the mean (\odot). The ($\#$) and (Δ) show the 10%, and 5% points respectively.

We see that the tolerance is fairly insensitive to i_m , although it is tightest when i_m is around 20. The loosest tolerance is for misalignment of entire structures, since the coherence of the detuned frequency distribution within a section is preserved. The tolerance for smoother misalignment distributions is less tight than the above case of random uniformly-offset pieces of structures.

CONCLUSIONS

Using four structure types with interleaved frequencies, the jitter tolerance is greater than the beam size, to keep the emittance growth to a few percent. The tolerance on frequency errors that are the same for all sections is a few parts in 10^5 to keep the emittance growth to a few percent. For frequency errors that are uncorrelated in different sections, the tolerance is looser than the expected machining precision of a part in 10^4 . For misalignments, the tolerance to keep the emittance growth below 25% with 95% confidence ranges from 5 to $10 \mu\text{m}$ depending upon the correlation length. It is probably possible to loosen the alignment tolerances using appropriate trajectory correction algorithms; this will be a subject of future work.

We thank the other members of the NLC structures group at SLAC for useful discussions and comments.

REFERENCES

- [1] K.L.F. Bane and R.L. Gluckstern, submitted to *Particle Accelerators*; SLAC-PUB-5783.
- [2] J.W. Wang and E.M. Nelson, this conference.
- [3] H. Hoag, et. al., this conference.

Longitudinal Head-Tail Instability in a Non-Harmonic Potential Well

Bo Chen and Alexander W. Chao
Superconducting Super Collider Laboratory*
2550 Beckleymeade Ave., Dallas, TX 75237

Abstract

A perturbation technique is developed that can be applied to study the collective instability problem when the unperturbed system is not described by a simple harmonic oscillator. The longitudinal head-tail instability effect is well studied as applications of this technique. Applications of the longitudinal head-tail instability effects to the CERN SPS and the SSC are included.

I. INTRODUCTION

The ideal motion of a single particle in a circular accelerator is that of a simple harmonic oscillator. The conventional theory of collective instabilities is developed by imposing the perturbation of collective wake forces on the simple harmonic system.

However, when the new collective longitudinal instability was observed in the CERN SPS[1], the analyses suggested the "longitudinal chromaticity" playing a role. Drawing analogy to the transverse case where the betatron chromaticity causes the head-tail instability, this new instability was named longitudinal head-tail (LHT) instability. The theoretical existence of the LHT instability was pointed out by Hereward[2]; it results from the non-simple-harmonic nature of the system when the longitudinal chromaticity effect is considered. To study the LHT instability, the conventional theory does not suffice because it treats only the simple-harmonic case.

In this paper we develop a new formalism that extends the conventional approach to the non-simple-harmonic Hamiltonian system. The LHT instability is studied as an application to demonstrate the technique. By using the water-bag particle distribution model, it is possible to solve the problem exactly and obtain the growth rates for the various collective modes (the dipole, quadrupole, sextupole modes, etc). Although not discussed below, the potential-well distortion, as well as its effects on collective instabilities, can also be studied with this technique.

II. MECHANISM OF THE LONGITUDINAL HEAD-TAIL INSTABILITY

The LHT instability, like its well-known transverse counterpart, the transverse head-tail instability, is a single bunch effect. The mechanisms of these instabilities are

*Operated by the Universities Research Association, Inc., for the U.S. Department of Energy under Contract No. DE-AC35-89ER40486.

quite similar. They are caused by a dependence of the accumulated betatron or synchrotron phase on the longitudinal position of the particle, coupled with a perturbation due to the collective wake forces.

However, the situation is more subtle in the longitudinal case since longitudinal position z and δ are the dynamic variables which describe the particle motion. The analysis of this problem is therefore more involved.

Consider a circular accelerator whose slippage factor η contains a higher order term in δ , i.e., $\eta = \eta_0(1 + \frac{3}{2}\epsilon\delta)$, where η_0 is the leading contribution of the momentum slippage factor, and ϵ is a parameter that specifies the strength of the higher order contribution. The unperturbed equations of motion of a single particle are given by

$$\frac{dz}{ds} = -\eta_0\delta(1 + \frac{3}{2}\epsilon\delta), \quad \frac{d\delta}{ds} = \frac{\omega_s^2}{\eta_0 c^2} z; \quad (1)$$

where s is the longitudinal coordinate along the accelerator circumference, and ω_s is the unperturbed synchrotron oscillation frequency for small amplitudes.

The coefficient ϵ describes the deviation from the simple harmonicity of the system. We consider small ϵ so that $|\epsilon\delta| \ll 1$. The motion of single particle in the z - δ space follows a constant Hamiltonian contour. One such contour is shown in Fig. 1.

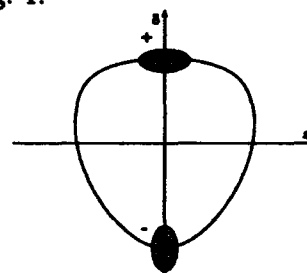


FIG. 1. The phase space trajectory due to the non-simple-harmonic Hamiltonian. The case shown is for $\epsilon > 0$.

The main effect of a non-vanishing ϵ is that it has introduced an asymmetry between the upper and the lower halves of the phase plane. As the beam bunch executes its dipole oscillation in this deformed phase space, the shape of the phase space area occupied by the bunch varies, although its area is conserved. The bunch shape at two instances (marked by + and -) are shown as shaded areas in Fig.1. In particular, the bunch lengths \hat{z}_+ and \hat{z}_- at the two instances are related by the Liouville theorem

according to

$$\frac{\hat{z}_-}{\hat{z}_+} = \frac{|\frac{\hat{z}_-}{\hat{z}_+}|}{|\frac{\hat{z}_+}{\hat{z}_-}|} = \frac{-\delta_-(1 + \frac{3}{2}\epsilon\delta_-)}{\delta_+(1 + \frac{3}{2}\epsilon\delta_+)} \approx \frac{1 - \epsilon\delta_0}{1 + \epsilon\delta_0} \approx \frac{1 + \epsilon\delta_-}{1 + \epsilon\delta_+}, \quad (2)$$

where $\delta_0 = \sqrt{2H_0}/|\eta_0|$, and $\delta_{\pm} \approx \pm\delta_0 - \frac{1}{2}\epsilon\delta_0^2$ are the values of δ at the + and - locations. We conclude from Eq.(2) that, to first order in $|\epsilon\delta_0|$, the bunch length is modulated according to

$$\hat{z} \propto 1 + \epsilon\delta \quad (3)$$

as the bunch executes the dipole oscillation in the phase space. Next we introduce the effect of the collective wake fields. Since the energy loss of the beam bunch depends on the bunch length, the bunch energy loss is also modulated by the same factor of Eq.(3). Adding the energy loss term to Eq.(1),

$$\frac{d\delta}{ds} \approx \frac{\omega_s^2}{\eta_0 c^2} z + \epsilon \frac{\hat{z}}{NEC} \frac{d\Delta\epsilon}{d\hat{z}} \delta, \quad (4)$$

where N is number of particles per bunch, E is the particle energy, C is machine circumference, and $\Delta\epsilon$ is the bunch energy loss per turn (in our convention, $\Delta\epsilon < 0$). We have kept only its leading contribution to first order in δ .

The new equations of motion represent a system with growth (or damping if negative) rate:

$$\tau^{-1} = \epsilon \frac{c\hat{z}}{2NEC} \frac{d\Delta\epsilon}{d\hat{z}}. \quad (5)$$

The Eq.(5) was first obtained in Ref.[1].

III. PERTURBATION APPROACH

From the previous section we knew that to study the LHT instability, we will have to consider an unperturbed system which is described by a non-simple-harmonic Hamiltonian. For such a system, the conventional method of using polar coordinates (the action-angle variables) no longer applies. The technique we develop in this paper is to introduce a new pair of dynamical variables: the Hamiltonian H itself and another variable Q which assumes the role of the time variable. The advantage of using the new variables is we only need to deal with one complicated variable Q . This point will become clear in the later derivation. Having introduced the new dynamical variables, the procedure we use to solve the Vlasov equation then follows basically the conventional treatment.

We start with a general situation when the accelerator is described by a Hamiltonian $H(q, p; s)$. The beam distribution is given by

$$\psi(q, p; s) = \psi_0(H_0) + \psi_1(q, p)e^{-i\eta s/c}. \quad (6)$$

The unperturbed system, ψ_0 must be a function of unperturbed $H_0 = \frac{1}{2}p^2[1 + f(p)] + \frac{\omega_s^2}{2c^2}q^2$ alone.

$$H(q, p; s) = \frac{1}{2}p^2[1 + f(p)] + \frac{\omega_s^2}{2c^2}q^2 - \frac{\eta_0 e}{EC} \int_{-\infty}^q V_1(q') dq' e^{-i\eta s/c}, \quad (7)$$

where the function $f(p)$ represents a small deviation of the system from simple harmonicity, particularly for the system described by Eq.(1) for which $f(p) = -\frac{c}{\eta_0}p$. and V_1 is the retarding wake voltage per turn induced by ψ_1 and is related to the longitudinal impedance $Z_0^{\parallel}(\omega)$ according to

$$V_1 = \frac{e}{2\pi} \int_{-\infty}^{\infty} d\omega Z_0^{\parallel}(\omega) e^{i\omega q/c} \int_{-\infty}^{\infty} dq' e^{-i\omega q'/c} \int_{-\infty}^{\infty} dp \psi_1(q', p), \quad (8)$$

Here the potential-well distortion effect, which is not of interest in the present study, has been ignored. In writing down Eq.(8), we have also ignored multi-turn wake effects.

We now introduce new canonical variables (Q, H_0) , where

$$Q = - \int_0^p \frac{\partial q(H_0, p')}{\partial H_0} dp'. \quad (9)$$

The advantage of using H_0 as dynamical variable lies in the fact that ψ_0 depends on H_0 only.

Notice the period of the motion of a particle is $\Phi = \oint \frac{\partial q(H_0, p')}{\partial H_0} dp'$. This period depends on the value of H_0 for the particle under consideration.

Considering ψ_1 is a small quantity, we use the new variables to obtain the linearized Vlasov equation by keeping the first order terms in ψ_1 ,

$$-i\frac{\Omega}{c}\psi_1 + \frac{\partial\psi_1}{\partial Q} + \frac{\eta_0 e}{EC}V_1(q)\frac{\partial\psi_0}{\partial H_0}\frac{\partial H_0}{\partial p} = 0. \quad (10)$$

To solve the Vlasov equation, we first Fourier expand ψ_1 as

$$\psi_1 = \sum_{l=-\infty}^{\infty} R_l(H_0) e^{i2\pi l Q/\Phi(H_0)}, \quad (11)$$

where the $l = 0$ term in the summation is to be excluded because it violates the total charge conservation for a given H_0 . The Fourier expansion is possible because the motion is periodic in Q with period Φ .

For the l -th mode (for example, $l = 1$ corresponds to the dipole mode),

$$\begin{aligned} & \left[\Omega - \frac{2\pi l c}{\Phi(H_0)} \right] R_l(H_0) + i \frac{\eta_0 e^2 c}{2\pi EC \Phi(H_0)} \int_{-\infty}^{\infty} d\omega Z_0^{\parallel}(\omega) \\ & \times \int_0^{\Phi(H_0)} dQ \frac{\partial\psi_0}{\partial H_0} \frac{\partial H_0}{\partial p} \exp \left[i\omega \frac{q(Q, H_0)}{c} \right] \\ & \times \int_{-\infty}^{\infty} dH'_0 \int_0^{\Phi(H'_0)} dQ' \exp \left[-i\omega \frac{q(Q', H'_0)}{c} \right] \\ & \times \sum_{l'=-\infty}^{\infty} R_{l'}(H'_0) \exp \left[i2\pi l' \frac{Q'}{\Phi(H'_0)} - i2\pi l \frac{Q}{\Phi(H_0)} \right] = 0. \end{aligned} \quad (12)$$

For a general equilibrium distribution ψ_0 (Gaussian, for example), the analysis to solve Eq.(12) is involved. Pursuing along this line would yield the radial modes of the collective oscillation. For one simple beam distribution, the water-bag model, however, the radial modes degenerate and the equation can be solved analytically. In the following, we will assume that the unperturbed beam has a water-bag distribution

$$\psi_0(H_0) = \frac{N}{\int_0^{\hat{H}} \Phi(H_0) dH_0} \Theta(\hat{H} - H_0), \quad (13)$$

where Θ is the step function. $\hat{H} = \omega_s^2 \hat{z}^2 / 8c^2$.

Since any perturbation of a water-bag distribution has to occur around the edge of the bag, we have

$$R_l(H_0) \propto \delta(H_0 - \hat{H}). \quad (14)$$

After adopting the water-bag model, Eq.(12) can be simplified. Also, the coupling among the different modes with $l' \neq l$ are neglected. The validity of this approximation assume the mode frequency shifts are small compared with $2\pi c / \Phi \approx \omega_s$.

We further define an angular variable θ according to

$$q = \frac{c}{\omega_s} \sqrt{2H_0} \cos \theta, \quad p \sqrt{1 - \frac{\epsilon}{\eta_0}} = \sqrt{2H_0} \sin \theta. \quad (15)$$

In terms of the new variable θ , Eq.(12) can be written as

$$\begin{aligned} \Omega^{(l)} - \frac{l\omega_s}{\langle G \rangle} - i \frac{\eta_0 N e^2 c^2}{2\pi^3 E C \omega_s \hat{z} \langle G \rangle} \int_{-\infty}^{\infty} d\omega Z_0^{\parallel}(\omega) \\ \times \int_0^{2\pi} d\theta \sin \theta \exp \left[i \frac{\omega \hat{z}}{2c} \cos \theta + i l \frac{\int_0^{\theta} G(\theta'') d\theta''}{\langle G \rangle} \right] \\ \times \int_0^{2\pi} d\theta' G(\theta') \exp \left[-i \frac{\omega \hat{z}}{2c} \cos \theta' - i l \frac{\int_0^{\theta'} G(\theta'') d\theta''}{\langle G \rangle} \right] = 0. \end{aligned} \quad (16)$$

where

$$\langle G \rangle = \frac{1}{2\pi} \int_0^{2\pi} G(\theta) d\theta, \quad G(p) = \frac{\sqrt{1 - \frac{\epsilon}{\eta_0}} p}{1 - \frac{3}{2} \frac{\epsilon}{\eta_0} p}. \quad (17)$$

If the non-harmonicity is weak, we assume $|\epsilon \sqrt{2\hat{H}} / \eta_0| \ll 1$ and keep the first order terms in ϵ to obtain the mode frequency

$$\Omega^{(l)} = l\omega_s + i \frac{\eta_0 N e^2 c^2}{2\pi^3 E C \omega_s \hat{z}} \left(A + \frac{\epsilon}{2\eta_0} \frac{\omega_s \hat{z}}{c} B \right), \quad (18)$$

where

$$\begin{aligned} A &= \frac{8\pi^2 c}{\hat{z}} l \int_{-\infty}^{\infty} d\omega \frac{Z_0^{\parallel}(\omega)}{\omega} J_l^2 \left(\frac{\omega \hat{z}}{2c} \right), \\ B &= -\frac{32\pi^2 c^2}{\hat{z}^2} l^2 \int_{-\infty}^{\infty} d\omega \frac{Z_0^{\parallel}(\omega)}{\omega^3} \left(\frac{\omega \hat{z}}{2c} J_l \left(\frac{\omega \hat{z}}{2c} \right) J_{l+1} \left(\frac{\omega \hat{z}}{2c} \right) + (1-l) J_l^2 \left(\frac{\omega \hat{z}}{2c} \right) \right) \end{aligned} \quad (19)$$

A is purely imaginary and B is real. If $\epsilon = 0$, only the A coefficient plays a role; the result describes the solution of the conventional longitudinal instability problem. In particular, the fact that A is purely imaginary means the mode frequency Ω is real, and the beam is always stable. This is a well-known result[5][6] when mode coupling and multi-turn effects are ignored, as is presently assumed. If $\epsilon \neq 0$, the B term also contributes to the mode frequency Ω . This contribution, being imaginary, is the cause of the LHT instability. The instability growth rate is

$$\tau_l^{-1} = \epsilon \frac{4N e^2 c^2}{\pi E C \hat{z}} l^2 \int_{-\infty}^{\infty} dx \frac{\text{Re} Z_0^{\parallel}(\frac{2\epsilon}{\hat{z}} x)}{x^2} [x J_l(x) J_{l+1}(x) + (1-l) J_l^2(x)]. \quad (20)$$

For the case $l = 1$, we can recover the result given by the simple physical picture. Eq.(5) applies to dipole mode only, while Eq.(20) is valid for arbitrary l .

For the CERN SPS collider, we estimate that[7] the growth time τ is 5.4 s for the diffraction broad band impedance model. The observed growth rate is 5 ~ 6 s[1]. For SSCL machines, LEB, MEB, HEB and collider, the growth time are found to be 7.0×10^4 s, 3.4×10^3 s, 32 s and 1.2 s, respectively.

The LHT instabilities tend to play a more important role in the lower energy accelerators, particularly those operated close to transition. In all cases studied, however, the LHT instability does not constitute a serious limit on beam intensities.

IV. REFERENCES

- [1] D. Boussard and T. Linnecar, *Proc. 2nd Euro. Part. Accel. Conf.*, (Editions Frontières, France, 1990), pp. 1560-1562.
- [2] G. Hereward, *Rutherford Lab. Report*, RL-75-021 (1975).
- [3] C. Pellegrini, *Nuovo Cimento* 64A, 447 (1969).
- [4] M. Sands, *SLAC Report* TN-69-8, TN-69-10 (1969).
- [5] F. Sacherer, *Proc. 9th Int. Conf. High Energy Accel.*, (SLAC, 1974), pp. 347-351.
- [6] A. Chao, *Physics of Collective Beam Instabilities in High Energy Accelerators*, (John Wiley & Sons, New York, 1993).
- [7] B. Chen and A. Chao, *SSCL Report*, SSCL-Preprint-201 (1993).

Bunch Lengthening effect and Localized Impedance

Bo Chen and Alexander W. Chao
Superconducting Super Collider Laboratory*
2550 Beckleymeade Ave., Dallas, TX 75237

Abstract

The effect of the localized longitudinal impedance is investigated by using the Vlasov equation approach. The motivation is trying to explain the observed discrepancy between the analytical study and numerical simulation on the bunch lengthening phenomenon. The $\nu_s = m/2l$ resonances are found to play a noticeable role. As another application of this treatment, synchro-betatron resonances are also recovered.

I. INTRODUCTION

The discrepancy of the analytical theories (the perturbation techniques, in particular) and the computer simulation on transverse coherent instability has been noticed and was successfully explained by considering the coherent synchro-betatron resonances due to the localized impedance[1][2][3]. When the combination of betatron tune ν_β and synchrotron tune ν_s is close to integer or half-integer, i.e. $\nu_\beta \pm l\nu_s \approx m/2$, the predictions on the mode coupling by two approaches are different. The reason behind this is that the regular Vlasov technique treats the impedance as a distributed one, the wake "force" acts on beam all along the orbit, but a typical computer simulation treats the impedance as a localized one, the wake force just kicks the beam once a turn at the particular location.

The same arguments may be applied to the longitudinal case in the study of the bunch lengthening phenomenon. One possibility to explain the discrepancy between the mode analysis and tracking is tracking uses localized impedance. In this paper, we investigate the longitudinal coherent resonance effect due to the longitudinal localized impedance by using a matrix technique[4]. For one simple particle distribution mode, the water-bag model, the resonance stopbands widths are calculated. The results are what one would expect from the pure analysis side. The further studies on the tracking side is necessary, but are not included in this paper. Also, we extend our studies to the transverse case where the synchro-betatron resonances are re-obtained by our approach.

II. THE VLASOV TECHNIQUE

We consider a single bunch particle beam described by

*Operated by the Universities Research Association, Inc., for the U.S. Department of Energy under Contract No. DE-AC35-89ER40486.

the Vlasov equation[5]

$$\frac{\partial \psi}{\partial s} + \frac{\omega_s}{c} \frac{\partial \psi}{\partial \phi} - \frac{e}{EC} V(z, s) \frac{\partial \psi}{\partial \delta} = 0, \quad (1)$$

where $\psi(r, \phi; s)$ is beam distribution in phase space which consists of a pair of dynamical variables z and δ . The action-angle variables (r, ϕ) are related to (z, δ) through $z = r \cos \phi$, $\frac{\eta c}{\omega_s} \delta = r \sin \phi$; C is the circumference of the ring, E is the beam energy, ω_s is the synchrotron frequency and η is the slippage factor.

We assume the particle beam experiences a localized "kick" due to the interactions between the beam and the surroundings at the location $s = 0$, where s is the distance along the orbit. The particle energy loss in one turn is (here the short range wake field is assumed)

$$V(z, s) = \frac{eC}{2\pi} \delta(s) \int_{-\infty}^{\infty} d\omega \tilde{\rho}(\omega, s) e^{\frac{i\omega s}{c}} Z_0^{\parallel}(\omega), \quad (2)$$

where $\tilde{\rho}(\omega, s)$ is the Fourier transform of $\rho(z)$, the beam distribution in z -axis.

Consider a beam with an unperturbed distribution ψ_0 which is executing collective oscillation due to the interaction of the wake fields. Let the collective oscillation be described by a small distribution perturbation $\psi_1(r, \phi; s)$, i.e.

$$\psi(r, \phi; s) = \psi_0(r) + \psi_1(r, \phi; s). \quad (3)$$

Keeping only the first order terms in ψ_1 , we get the linearized Vlasov equation

$$\begin{aligned} \frac{\partial \psi_1}{\partial s} + \frac{\omega_s}{c} \frac{\partial \psi_1}{\partial \phi} - \frac{e^2 C}{2\pi E} \delta(s) \sin \phi \frac{d\psi_0}{dr} \\ \times \int_{-\infty}^{\infty} d\omega Z_0^{\parallel}(\omega) e^{\frac{i\omega r \cos \phi}{c}} \int_0^{\infty} dr' r' \int_0^{2\pi} d\phi' e^{-i\frac{\omega r' \cos \phi'}{c}} \psi_1 = 0, \end{aligned} \quad (4)$$

Here the potential well distortion effect is not included, the study of which is not the goal of our study.

We consider a simple model of ψ_0 , the water-bag model

$$\psi_0(r) = \frac{4N\eta c}{\pi\omega_s \hat{z}^2} H\left(\frac{\hat{z}}{2} - r\right), \quad (5)$$

where H is the Heaviside step function. The advantage of using the water-bag model is avoiding introducing the radial mode of collective motion, but does not severely limit the generality of the studies.

Observing the fact that the perturbations occur only at the edge of the bag, we can write the perturbation as

$$\psi_1(r, \phi; s) = \delta(r - \frac{\hat{z}}{2}) \sum_{\substack{l=-\infty \\ l \neq 0}}^{\infty} \alpha_l(s) e^{il\phi}. \quad (6)$$

Substituting Eq.(6) into Eq.(4) gives an infinite set of equations describing the coupled motion for all l . We single out the l -th component

$$\frac{d\alpha_l(s)}{ds} + il\frac{\omega_s}{c}\alpha_l(s) - \delta(s) \sum_{\substack{k=-\infty \\ k \neq 0}}^{\infty} K_{lk}\alpha_k(s) = 0, \quad (7)$$

where the matrix K has been defined by

$$K_{lk} = l \frac{2N\eta e^2 c C}{\pi^2 \nu_s E \hat{z}^2} \sum_{\substack{k=-\infty \\ k \neq 0}}^{\infty} i^{l-k} \int_{-\infty}^{\infty} d\omega \frac{Z_0^{\parallel}(\omega)}{\omega} J_l(\frac{\omega \hat{z}}{2c}) J_k(\frac{\omega \hat{z}}{2c}) \quad (8)$$

which has the following properties:

$$K^2 = 0,$$

$$K_{-l,k} = -K_{lk}. \quad (9)$$

We define an infinite dimension vector, whose l -th component is

$$\tilde{X}_l(s) = \alpha_l(s). \quad (10)$$

Then the Eq.(7) becomes

$$\frac{dX_l(s)}{ds} + \sum_k R_{lk} X_k(s) + \delta(s) \sum_k K_{lk} X_k(s) = 0, \quad (11)$$

where

$$R_{lk} = i \frac{2\pi l \nu_s}{C} \delta_{lk} \quad (12)$$

The action of the impedance is obtained by integrating Eq.(11) through $s = 0$, so the map from $s = 0^-$ to $s = 0^+$ is

$$X_l(0^+) - X_l(0^-) = - \sum_k K_{lk} X_k(0^-). \quad (13)$$

Between the location of the impedance, the different α_l 's are decoupled, the map from $s = 0^+$ to $s = C^-$ is

$$X_l(C^-) = \sum_k S_{lk} X_k(0^+),$$

where

$$S_{lk} = e^{-i2\pi l \nu_s} \delta_{lk}. \quad (15)$$

Therefore the total map for one turn is

$$T = S(I - K), \quad (16)$$

Where I is the identity matrix. The diagonal matrix R describes the action between the location of impedance, and K describes the localized "kick".

In the absence of the impedance, the total map $T = R$ whose eigenvalues are

$$\lambda_l = S_{ll} = e^{-i2\pi l \nu_s}. \quad (17)$$

These correspond to the eigen modes of the unperturbed motion and the beam are always stable.

In the presence of the impedance (wake field), as the beam current is increased, the eigenvalues of the total matrix T are more and more perturbed. If one of them acquires an absolute value larger than one, the beam motion becomes unstable.

Without considering the coupling among the different modes, we keep only the l -th and the $(-l)$ -th elements in the transformation matrix. The reason that it is necessary to keep $(-l)$ -th terms is we must observe the property $K^2 = 0$ which guarantees we can use either $X(0^-)$ or $X(0^+)$ on the right hand side of Eq.(14).

The simplified 2×2 matrix becomes

$$T = (-1)^m \begin{pmatrix} e^{-i2\pi l \Delta} (1 + i\epsilon_l) & i e^{-i2\pi l \Delta} \epsilon_l \\ -i e^{-i2\pi l \Delta} \epsilon_l & e^{-i2\pi l \Delta} (1 - i\epsilon_l) \end{pmatrix}, \quad (18)$$

where

$$\Delta = \nu_s - \frac{m}{2l}, \quad (19)$$

and

$$\epsilon_l = l \frac{2N\eta e^2 c C}{\pi^2 \nu_s E \hat{z}^2} \int_{-\infty}^{\infty} d\omega \frac{Im Z_0^{\parallel}(\omega)}{\omega} J_l^2(\frac{\omega \hat{z}}{2c}), \quad (20)$$

which is a real number.

The eigenvalues of the simplified matrix are then determined by the secular equation

$$\lambda^2 - 2(-1)^m [\cos(2\pi l \Delta) + \epsilon_l \sin(2\pi l \Delta)] \lambda + 1 = 0. \quad (21)$$

One of the eigen values has absolute value larger than one and therefore the coherent instability occurs if

$$|\cos(2\pi l \Delta) + \epsilon_l \sin(2\pi l \Delta)| > 1. \quad (22)$$

The stopband width at the region near the resonance $\nu_s = m/2l$ is approximately

$$\delta \nu_l = \frac{|\epsilon_l|}{\pi l} = \frac{2N\eta e^2 c C}{\pi^2 \nu_s E \hat{z}^2} \left| \int_{-\infty}^{\infty} d\omega \frac{Im Z_0^{\parallel}(\omega)}{\omega} J_l^2(\frac{\omega \hat{z}}{2c}) \right|, \quad (23)$$

For the broad band impedance (valid for a diffraction impedance model)

$$Z_0^{\parallel}(\omega) = R_0 \left| \frac{\omega_0}{\omega} \right|^{1/2} [1 + \text{sgn}(\omega) i], \quad (24)$$

the stopband width is

$$\delta \nu_l = \frac{8\sqrt{2}\Gamma(l - \frac{1}{4})}{\pi^2 \Gamma^2(\frac{1}{4}) \Gamma(l + \frac{5}{4})} \frac{\Upsilon}{\nu_s}, \quad (25)$$

where

$$\Upsilon = \frac{\eta e I R_0}{E} \left(\frac{C}{\hat{z}} \right)^{3/2}. \quad (26)$$

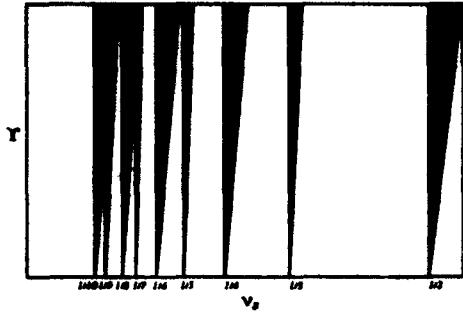


FIG. 1. The longitudinal stopbands. The shaded regions are unstable. Resonance structures are displayed by this diagram.

For SLAC SPEAR ring, $E = 3\text{GeV}$, $\nu_s = 0.042$, $\hat{z} = 2.68\text{cm}$ and $I = 20\text{mA}$, $\delta\nu_s \approx 0.005$.

III. TRANSVERSE CASE AND SYNCHRO-BETATRON RESONANCES

We can also apply the same technique to the transverse case, which has been already extensively studied[1][2][3]. Here we just give some main results. For the transverse motion the Vlasov equation is:

$$\frac{\partial \psi}{\partial s} + \frac{\omega_\beta}{c} \frac{\partial \psi}{\partial \theta} - \frac{e}{EC} V_y(z, s) \frac{\partial \psi}{\partial p_y} + \frac{\omega_s}{c} \frac{\partial \psi}{\partial \phi} = 0, \quad (27)$$

where the transverse dynamical variables, both the regular and the action-angle, are $y = r_y \cos \theta$, $-\frac{cp_y}{\omega_\beta} = r_y \sin \theta$, where ω_β is the betatron frequency. The localized transverse "kick" is defined by

$$V_y(z, s) = -i \frac{eC}{2\pi} \delta(s) \int_{-\infty}^{\infty} d\omega \tilde{\rho}(\omega, s) e^{\frac{i\omega z}{c}} Z_1^\perp(\omega), \quad (28)$$

where the Fourier component $\tilde{\rho}(\omega)$ only comes from the contribution of the longitudinal distribution.

The distribution function is assumed as:

$$\psi(r, \phi; r_y, \theta; s) = f(r_y) \frac{N\eta c}{2\pi\omega_s \hat{z}} \delta(r - \frac{\hat{z}}{2}) - D \frac{df(r_y)}{dr_y} \cos \theta \delta(r - \frac{\hat{z}}{2}) \sum_{p=1, -1} \sum_{l=-\infty}^{\infty} \alpha_l^p(s) e^{il\phi}. \quad (29)$$

where \hat{z} is bunch length.

The first term of right hand side of Eq.(29) is the unperturbed distribution; $f(r_y)$ is its transverse part and the air-bag model is assumed for its longitudinal part. For the perturbed part the index p takes only values 1 and -1. This because only the dipole motion is assumed for the transverse perturbation which is $-D \frac{df(r_y)}{dr_y} \cos \theta$, where D is the dipole displacement of the distribution.

Following the procedures described in the last section, we defined a vector

$$\tilde{Y}_l^p(s) = \alpha_l^p(s), \quad (30)$$

for which the one turn map is

$$T = S(I - K), \quad (31)$$

where

$$S_{lk}^p = e^{-i2\pi(p\nu_s + l\nu_s)} \delta_{lk}, \quad (32)$$

and

$$K_{lk}^d = p \frac{Ne^2 c C}{8\pi^2 \nu_\beta E} \sum_{k=-\infty}^{\infty} i^{l-k} \int_{-\infty}^{\infty} d\omega Z_1^\perp(\omega) J_l(\frac{\omega \hat{z}}{2c}) J_k(\frac{\omega \hat{z}}{2c}). \quad (33)$$

This time only modes represented by α_l^1 and α_{-l}^{-1} contribute significantly. Keeping these two modes, we get the same secular equation for eigenvalues as Eq.(21) except Δ is redefined as

$$\Delta = \nu_\beta + l\nu_s - \frac{m}{2} \quad (34)$$

and the stopband width is

$$\delta\nu_l = \frac{Ne^2 C}{8\pi^2 \nu_\beta E} \left| \int_{-\infty}^{\infty} d\omega Z_1^\perp(\omega) J_l^2(\frac{\omega \hat{z}}{2c}) \right|. \quad (35)$$

For the broad band impedance

$$Z_1^\perp(\omega) = \frac{2cR_0}{b^2\omega_0} \left| \frac{\omega_0}{\omega} \right|^{3/2} [\text{sgn}(\omega) + i], \quad (36)$$

where b is beam pipe radius, the stopband width is

$$\delta\nu_l = \frac{\sqrt{2}}{\pi^2 \Gamma^2(\frac{1}{4})} \frac{\Gamma(l - \frac{1}{4})}{\Gamma(l + \frac{5}{4})} \frac{\Upsilon}{\nu_\beta}, \quad (37)$$

with

$$\Upsilon = \frac{eIR_0}{E} \frac{\hat{z}^{1/2} C^{3/2}}{b^2}. \quad (38)$$

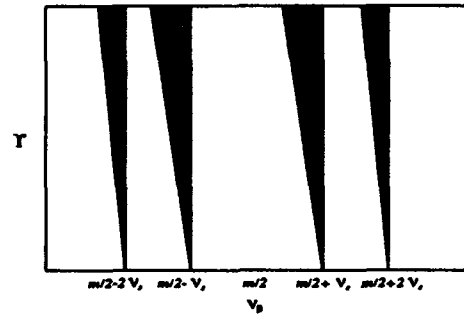


FIG. 2. The transverse stopbands. The shaded regions are unstable. Resonance structures are displayed by this diagram.

IV. REFERENCES

- [1] Y. Chin, *CERN Report*, SPS/85-33 (DI-MST) (1985).
- [2] F. Ruggiero, *Part. Accel.*, Vol. 20, 45 (1986).
- [3] T. Suzuki, *CERN Report*, LEP-TH/87-55 (1987).
- [4] A. Chao and R. Ruth, *Part. Accel.*, Vol. 16, 201 (1985).
- [5] A. Chao, *Physics of Collective Beam Instabilities in High Energy Accelerators* (John Wiley & Sons, New York, 1993).

Experimental Reduction of Electron Beam Breakup Instability Using External Coupled Cavities

P.R. Menge, R.M. Gilgenbach, Y.Y. Lau, M. Walter, and C.H. Ching,
Intense Energy Beam Interaction Laboratory
Nuclear Engineering Dept., University of Michigan, Ann Arbor, MI, 48109-2104

Abstract

Experiments on electron beam transport through 10 RF cavities have shown that BBU growth can be reduced by 6 dB when seven internal beam cavities are coupled by coaxial cable to seven external dummy cavities. The experiment consists of 10 brass pillbox resonant cavities immersed in a solenoidal field. The first cavity has its TM_{110} mode primed at 2.5 GHz by a microwave pulse from an external magnetron. A 200 A e-beam is injected into the transport cavity system by the long pulse MELBA generator ($t = 0.5 - 1.5 \mu s$, $V = -0.7$ to -0.8 MV, diode current = 1-15 kA). Growth (~ 36 dB) of the 2.5 GHz RF is observed between the 2nd and 10th cavities. When seven internal cavities (3rd - 9th) are coupled to seven identical external dummy cavities via coaxial microwave cable, the 2.5 GHz RF growth is reduced to about 30 dB average. These results are shown to be in general agreement with a model using equivalent circuits to determine degree of power sharing between cavities.

Additional BBU growth experiments have been performed using 19 cavities with a propagation distance roughly twice that of the 10 cavity experiments. The experimental BBU growth has been found to scale with distance as expected using a discrete beam-mode coupled theory.

I. INTRODUCTION

The beam breakup instability (BBU) remains a major problem plaguing linear accelerators. The BBU results from an unstable coupling between a misaligned electron beam and non-axisymmetric (dipole) modes associated with the accelerating structure [1-3]. The end results of this coupling can range from brightness degradation to complete beam disruption. Recently, a novel method of BBU reduction was demonstrated at the University of Michigan [4] using coupling between the main beam cavities and separate dummy cavities. This method has been termed "external cavity coupling." The BBU reduction mechanism involves sharing of non-axisymmetric TM_{110} mode energy between the coupled cavities [4-6]. The TM_{110} is the fundamental beam breakup mode associated with the transport structure for these experiments. This power sharing results in a decrease in TM_{110} field strength in the main cavities with a corresponding decrease in the BBU growth rate. A critical parameter governing the magnitude of reduction is the coupling constant, κ [4-6]. In simplest terms κ corresponds to how well the coupled cavities are able to share energy.

This research was supported by SDIO-IST managed through an ONR contract. Support for PRM supplied by a Rackham School of Graduate Studies Fellowship.

This paper presents a review of the external coupled cavity experiments and provides a method of calculating κ that is believed to be more accurate than that presented in [4].

II. EXTERNAL CAVITY COUPLING EXPERIMENTS

The experimental configuration is shown in Figure 1. The MELBA electron beam generator is used for these experiments and is run with diode parameters of: voltage = -750 kV, diode current = 5 kA and pulselength = 0.5 μs . The beam is emitted from a hemispherical velvet field-emission type cathode. An aperture in the anode injects about 200 A into the cavity transport structure region which is immersed in a 3.4 kG solenoidal field. The cavity array generally consists of 10 brass pillbox cavities with an average TM_{110} resonant frequency of $2.5075 \text{ GHz} \pm 0.03 \%$. Each cavity contains a microwave coupling antenna oriented to be sensitive to the TM_{110} beam breakup mode which occurs at 2.5 GHz. The first cavity in the array has its TM_{110} mode primed on resonance by an external magnetron operating at 1 kW and pulselength of 3 μs . This is done to provide initial transverse modulation to the electron beam. The beam coasts through the remaining cavities where it excites the TM_{110} mode in each cavity. The power of the TM_{110} mode grows in the successive cavities as the amplifying BBU disturbance is carried along the beam. The spatial growth of the BBU is determined by measuring the difference in TM_{110} mode microwave power between the 2nd and 10th cavities.

In a typical experiment about 36 dB gain in 2.5 GHz microwave power is observed between the second and tenth cavities, when the external cavities are not connected to the coupling microwave cable. When the cables are connected, the internal and external cavities are coupled, and 30 dB growth in TM_{110} microwave power is typically observed between the second and tenth cavities. This method differs from other BBU suppression techniques in that the control is reactive and not dissipative. Figure 2 shows data from 40 experimental shots in which the uncoupled and coupled cases are alternated every three shots. This figure is reproduced from [4].

III. EXTERNAL CAVITY COUPLING THEORY

Previous analysis [4] has shown that the BBU spatial growth rate, Γ (where total BBU growth is given by $e^{\Gamma z}$), is modified by a factor of $1/(1+\kappa^2 Q^2)$ to account for cavity coupling through a mutual inductance model [5-7]. Thus, the

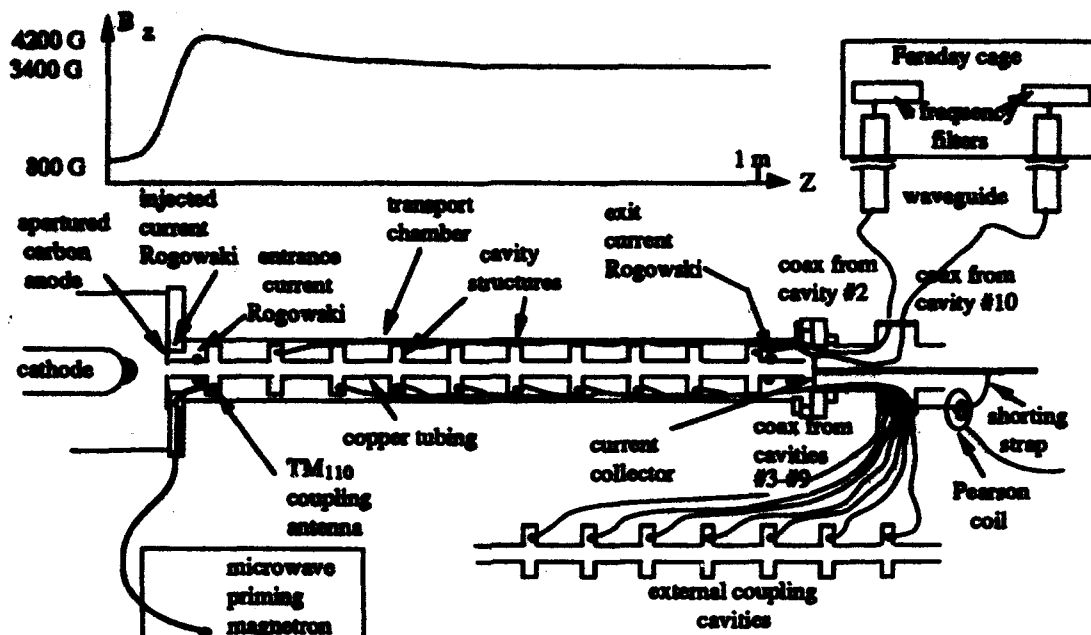


Figure 1. Schematic of experimental configuration (lower) and magnetic field profile (upper).

external coupled cavity growth rate is $\Gamma/(1+\kappa^2Q^2)$. Here, κ is the coupling constant and Q is the cavity quality. This factor of κ^2Q^2 represents the ratio of power leaked to the dummy (external) cavity to the power remaining in the main (internal) cavity [4]. A cold test was performed on a network analyzer (HP-8510) using two model cavities each with two coupling antennas. One antenna in each cavity was used to inject the microwaves and the second was used to transmit the RF power out of the cavity. This cold test experiment indicated that the power sharing ratio for this arrangement is $\kappa^2Q^2 = 0.13$. Using this value in the reduction factor yields an expected experimental reduction to $36 \text{ dB}/(1/1.13) = 32 \text{ dB}$.

However, the cold test of the power sharing ratio differs from the actual experimental configuration. In the experiment, each cavity has only one coupling loop, thus the cold test may underestimate the magnitude of power sharing since the extra antennas provide additional inductance to the overall circuit. An alternative method to determine κ has been developed using an equivalent circuit model similar to those used in coupled cavity klystron analyses [8]. The equivalent circuit representing the experimental configuration is shown in Figure 3. The critical parameter that governs the magnitude of power sharing is the mutual inductance, M , connecting the loop antenna circuits to the cavity circuits. The mutual inductance can be found from the formula [9,10]:

$$\frac{\omega_o^2 M^2}{R} = \frac{2s^2 J_1^2 \left(\frac{3.83 r}{b} \right) Q}{J_0^2 (3.83) \epsilon_o r^2 \pi b^2 \ell Z_o \omega_o},$$

where ω_o is the angular TM_{110} resonant frequency, R is the resistance assigned to the cavity circuit, s is the area of the coupling loop, r is the radial position of the antenna in the

cavity, b is the radius of the cavity, ℓ is the cavity length, and Z_o is the characteristic impedance of the coupling cable. Solving for power in the main and dummy cavities with the circuit program SPICE [11] yields a power sharing ratio of $\kappa^2Q^2 = 0.18$. Use of this value in the reduction factor gives a predicted value of 30 dB growth for the coupled cavity experiments. This results in better agreement between theory and experiment than that reported in [4].

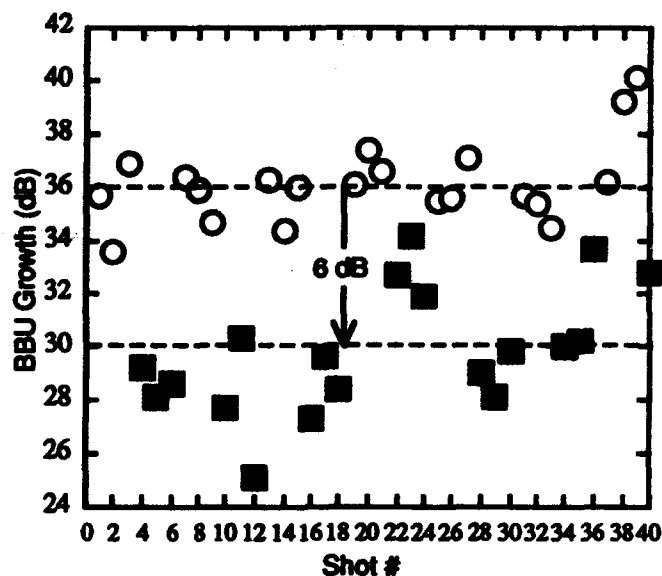


Figure 2. BBU instability growth for uncoupled cavity (open circles) and coupled cavity (black squares) configurations showing an average decrease of 6 dB in growth when cavities are externally coupled. (Reproduced from Ref. [4]).

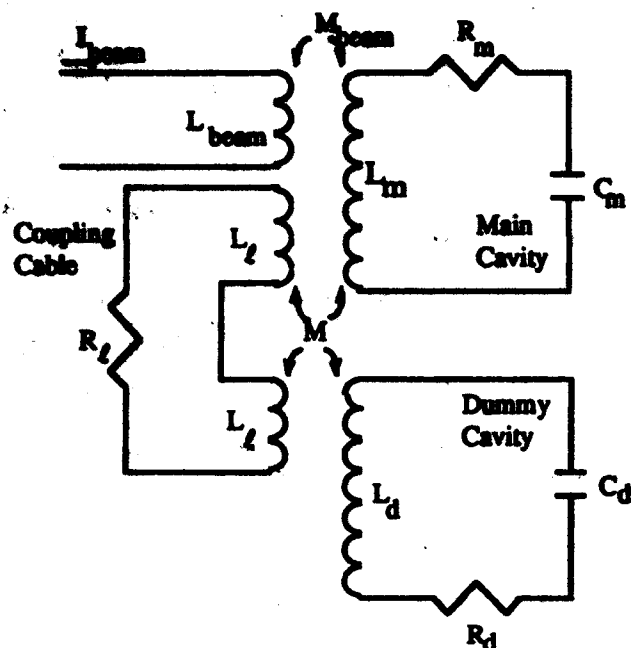


Figure 3. Equivalent circuit representing external cavity coupling configuration.

IV. NINETEEN CAVITY BBU GROWTH EXPERIMENTS

Previously, these University of Michigan experiments examining the BBU growth scaling have been limited to relatively short (~ 1 m) propagation distances using 10 resonant cavities [12]. Recently, experiments designed to study the behavior of BBU growth rates over longer propagation distances have been performed. These experiments use a 2 m solenoidal vacuum chamber using cavities nearly identical to those used above and in [4,12]. The configuration can be represented by Figure 1 without the external cavities and coupling cables, but with a longer transport chamber and nine additional cavities filling the extra length. Most diagnostics and measuring techniques are identical to those used in [12]. The major difference is that in the earlier, 10 cavity experiments the BBU growth was measured between the second and tenth cavities spanning a propagation distance of 68 cm. These 19 cavity experiments measure the BBU growth over the 144.5 cm between the second and nineteenth cavities.

Figure 4 plots the BBU growth versus the ratio of beam current to applied solenoidal magnetic field, I/B (A/kG). The data from the 19 cavity experiments is seen on the left side of the graph. For each experimental growth datum (black squares), the corresponding predicted BBU growth from theory (open squares) is also plotted. A two-dimensional discrete cavity theory is used [13]. For reference, the data from the 10 cavity experiments are seen on the right side of the graph (from Ref. [12]). The lower I/B values for the 19 cavity data are a result of lower transported beam currents. Note that the slope in Fig. 4 for the 10 cavity case is

approximately half that for the 19 cavity case, as expected. The 10 cavity data is reproduced from [12].

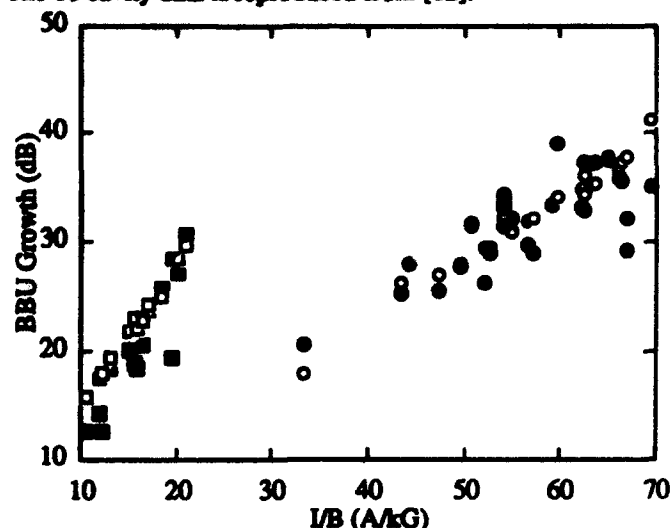


Figure 4. BBU growth (dB) versus ratio of beam current to magnetic field, I/B (A/kG). Experimental data (filled symbols) are plotted with corresponding theoretical growth (open symbols). Two experimental cases are shown: 19 cavities (squares) and 10 cavities (circles).

V. REFERENCES

- [1] W. K. H. Panofsky and M. Bander, *Rev. Sci. Instrum.* **39** (2), 206, 1968.
- [2] V.K. Neil and R.K. Cooper, *Part. Accel.* **1**, 111, 1970.
- [3] Y.Y. Lau, *Phys. Rev. Lett.* **63** (11), 1141, 1989.
- [4] P.R. Menge, R.M. Gilgenbach, and Y.Y. Lau, *Phys. Rev. Lett.* **69** (16), 2372, 1992.
- [5] D. Colombant, Y. Y. Lau, and D. Chernin, *Part. Accel.* **35**, 193, 1991.
- [6] D.G. Colombant and Y.Y. Lau, *J. Appl. Phys.* **72** (9), 3874, 1992.
- [7] D. Colombant and Y. Y. Lau, *Nuclear Instruments and Methods A311*, 1, 1992.
- [8] c.g. R.E. Collin, *Foundations for Microwave Engineering* (McGraw-Hill, Singapore 1966), Chapter 9.
- [9] R.A. Bosch, P.R. Menge, and R.M. Gilgenbach, "Reduction of Beam Breakup Growth by Coupling to External Bleeding Cavities", unpublished (1991).
- [10] P.R. Menge, Ph. D. Dissertation, The University of Michigan, 1993.
- [11] P.W. Tuinenga, *SPICE, A Guide to Circuit Simulation and Analysis Using PSpice* (Prentice Hall, Englewood Cliffs, NJ, 1988).
- [12] P.R. Menge, R.M. Gilgenbach, and R.A. Bosch, *Appl. Phys. Lett.* **61** (6), 642, 1992.
- [13] R.A. Bosch, P.R. Menge, and R.M. Gilgenbach, *J. Appl. Phys.* **71** (7), 3091, 1992.

Beam Breakup in an Annular Beam*

Y. Y. Lau, J. W. Luginsland, R. M. Gilgenbach
Intense Energy Beam Interaction Laboratory and Department of Nuclear Engineering
University of Michigan, Ann Arbor, MI 48109-2104 USA

Abstract

It is shown that an annular electron beam may carry six times as much current as a pencil beam for the same beam breakup (BBU) growth. This finding suggests that the rf magnetic field of the breakup mode is far more important than the rf electric field in the excitation of BBU. A proof-of-principle experiment is suggested, and the implications explored.

I. INTRODUCTION

Annular electron beams have the capability of carrying a much higher current than a pencil beam. Besides the obvious fact that annular beams have a larger cross-sectional area, their limiting currents are significantly higher than those of a pencil beam when placed in a metallic drift tube. For this and other reasons, annular beams have recently been chosen as the preferred geometry to generate coherent, ultra-high power microwaves [1,2]. They have also been used as the primary beam in several "two-beam accelerator" configurations [3,4]. These annular beams either encounter a sequence of modulating gaps, or simply graze a slow wave structure to generate a wake field in the case of two-beam accelerators [3]. Their high current may then lead to the beam breakup instability (BBU) [5-9] and this concern motivates the present study.

II. DISCUSSION

BBU is usually analyzed for a pencil beam propagating along the center axis of a sequence of accelerating cavities. Many BBU calculations of practical interest assume that the accelerating unit is the familiar cylindrical pillbox cavity and that the dominant deflecting mode is the TM_{110} mode [5,6,9]. Extension to an annular beam is straightforward. Nevertheless, this calculation leads to several unexpected results and provides some new insights into BBU, to be reported in this paper.

It is well known that BBU is excited by the combined action of the rf magnetic field (B_1) and the rf electric field (E_1) of the deflecting mode [5]: B_1 causes beam deflection through the Lorentz force and E_1 causes mode amplification through the work done on the mode by the beam current J . Our calculation strongly suggests that B_1 is much more critical than E_1 in contributing to BBU growth. Thus, an annular beam strategically placed near the minimum of the rf magnetic field would suffer far less beam breakup growth than a pencil beam that is centered on the cavity axis, where the magnetic field is large and the axial electric field is small. By

the same argument, placing the annular beam very close to the wall of a metallic drift tube, at which the axial electric field is vanishingly small, cannot eliminate BBU growth because of the substantial deflecting magnetic field generated by the wall current. Toward the end of this paper, we propose an experiment which would unambiguously test the relative importance between the rf magnetic field and the rf axial electric field, as discussed here.

Consider an infinitesimally thin annular beam of radius r_0 inside a cylindrical drift tube of radius b . The beam carries a total current I and coasts at velocity v_0 with the corresponding relativistic factors γ and β . The drift tube is loaded with a slow wave structure, modeled by a series of cylindrical pillbox cavities, each of which supports the nonaxisymmetric TM_{110} mode [3,5,6,9]. The interaction between this mode and the beam causes BBU to be excited. In the limit $r_0 \rightarrow 0$, this is the basic model of BBU for a pencil beam. Since we are comparing the strength of BBU interaction for different values of r_0 , we pretend that magnetic focusing is absent and that the quality factor Q of the deflecting mode is infinite.

Let $A_1 = \hat{z} q(t) (\cos \theta) E(r)$ be the vector potential of the deflecting dipole mode in a cavity. For the fundamental TM_{110} mode, $E(r) = J_1(pr)$ represents the radial dependence of the axial electric field with J_1 being the Bessel function of order one and $p = 3.832/b$. The corresponding magnetic field is $B_1 = \nabla \times A_1$. The action of this mode on the beam is calculated as follows.

We divide the annular beam into N azimuthal segments (N large). The i -th segment is located at $r=r_0$, $\theta = \theta_i = 2\pi i/N$, in the unperturbed state but is displaced radially by ξ_i and azimuthally by η_i when the deflecting mode is present. The linearized force law yields

$$-\gamma(\omega - kv_0)^2 \xi_i = (e/m_0)(v_0/c) q E'(r_0) \cos \theta_i \quad (1)$$

$$-\gamma(\omega - kv_0)^2 \eta_i = (e/m_0)(v_0/c) q [E(r_0)/r_0] \sin \theta_i \quad (2)$$

where the right hand sides represent the components of the Lorentz force that causes beam deflection. In writing Eqs. (1) and (2), we have assumed a wave-like solution $\exp[j(\omega t - kz)]$ for the disturbances, with $j^2 = -1$, and we have used a prime to denote derivative with respect to the argument.

The instantaneous current J on the i -th current filament is

$$J_i(r, t) = \hat{z} \frac{I}{Nr} \delta(r - r_0 - \xi_i) \delta(\theta - \theta_i - \frac{\eta_i}{r_0}) \quad (3)$$

* Supported in part by an SDIO/IST contract managed by ONR.

where δ is the Dirac delta function. The work done by this current filament on the deflecting mode is proportional to

$$W_i = \int dV \vec{A}_i \cdot \vec{J}_i \quad (4)$$

where the volume integral is performed over the cavity. In evaluating W_i , we should retain only the rf component of J_i in Eq. (3), since only the rf current performs work on the breakup mode. Upon substituting Eqs. (1)-(3) into Eq. (4), and summing over all i , we find the total work done $W = \sum W_i$

$$W = \frac{L I e}{m_0} \frac{v_0}{c} q \frac{\left[E'(r_0) \right]^2 + \left[E(r_0)/r_0 \right]^2}{\gamma(\omega - k v_0)^2} \quad (5)$$

apart from a multiplicative constant that is independent of the beam's equilibrium position r_0 . This energy transfer leads to growth of the BBU mode, which is described by the BBU dispersion relation [8]:

$$(\omega^2 - \omega_0^2)(\omega - k v_0)^2 = -2\omega_0^4 \epsilon = -2\omega_0^4 \epsilon_0 \left(\frac{\epsilon}{\epsilon_0} \right) \quad (6)$$

where ϵ is the coupling constant and ω_0 is the breakup mode frequency. In writing the last form of Eq. (6), we normalize ϵ in terms of ϵ_0 , the coupling constant for an on-axis, pencil beam ($r_0 \rightarrow 0$). For the TM_{110} mode, $E = J_1(pr)$ and $\epsilon_0 = 0.422(\beta\gamma)/(1 \text{ kA})$. It is clear from Eq. (5) that

$$\frac{\epsilon}{\epsilon_0} = 2 \left\{ \left[\frac{J_1'(pr_0)}{pr_0} \right]^2 + \left[\frac{J_1(pr_0)}{pr_0} \right]^2 \right\} \quad (7)$$

which compares the BBU strength between an annular beam and a pencil beam of the same current. Note that this ratio reduces to unity in the limit $r_0 \rightarrow 0$.

Equation (7) is plotted in Fig. (1) as a function of r_0/b . It is seen from this figure that ϵ/ϵ_0 may be as small as 0.17 when the annular beam is located at $r_0 = 0.56b$. Note also that this location coincides with the minimum of the rf magnetic field of the deflecting mode. What this means is that an annular beam placed at this location can carry as much as $1/0.17 = 6$ times the current as an on-axis pencil beam, and suffer the same BBU growth. Another point worth noting is that BBU growth retains significant strength even if the annular beam is very close to the wall of the drift tube [cf. $r_0 \rightarrow b$ in Fig. (1)]. This result is unexpected since $E_1 \rightarrow 0$ near a metallic wall. As a result, $J_1 \cdot E_1 = 0$ and there would be little transfer of power from the beam to drive the breakup mode. The finite BBU strength as $r_0 \rightarrow b$ is another strong indication that the deflecting magnetic field is far more important than the axial rf electric field in driving BBU.

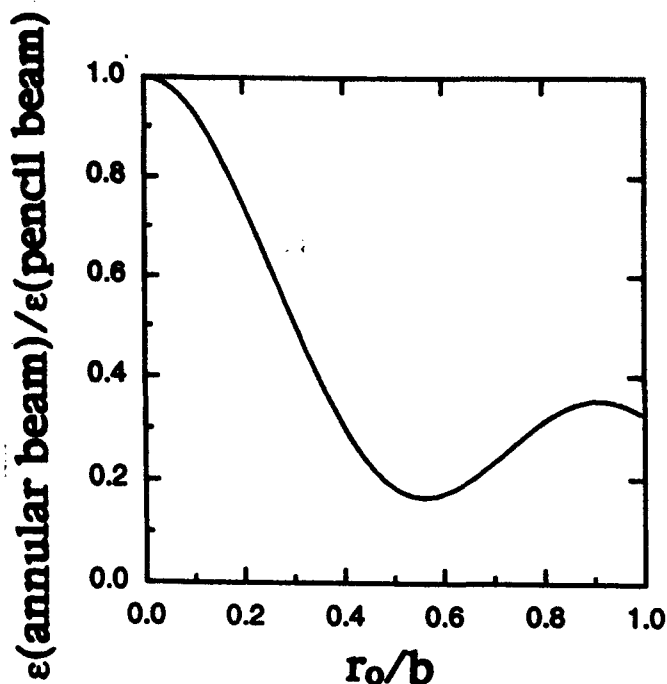


Fig. 1. Comparison of the BBU coupling constant ϵ between an annular beam of radius r_0 and an on-axis pencil beam ($r_0 \rightarrow 0$) with the same total current

III. PROOF OF PRINCIPLE EXPERIMENT

The importance of the rf magnetic field can be tested in an experiment in which a pencil beam is focused by a solenoidal magnetic field and is made to pass through a sequence of pillbox cavities, in which the first cavity is primed with microwaves at the TM_{110} mode [9]. BBU growth is monitored at the last cavity, before the beam exit. The above theory then predicts the *unusual* feature that BBU growth should be *much less* if the pencil beam is placed *off-axis*, than if the pencil beam were on-axis [10]. The BBU growth should be minimum if this pencil beam is placed at a distance of about 0.56 of the pillbox radius, where the rf magnetic field is minimum.

IV. CONCLUSION

We also repeated the calculations for the higher order radial modes: TM_{120} , TM_{130} , TM_{140} , and TM_{150} . Fixing $r_0/b = 0.56$, the ratio ϵ/ϵ_0 equals 0.16, 0.012, 0.037, and 0.013 for these four higher order modes, respectively. Thus, the annular beam still suffers substantially lower BBU growth, in the higher order deflecting modes, than an on-axis pencil beam of the same current.

In conclusion, the rf magnetic field is found to be much more important than the rf electric field in contributing to BBU growth. A simple proof-of-principle experiment is proposed to test this new finding. Annular beams are far more stable than an on-axis pencil beam, as a result.

II. REFERENCES

- [1] M. Friedman, Y.Y. Lau, J. Krall, and V. Serlin, U.S. Patent 5,132,638 (issued July 21, 1992); J. Krall, M. Friedman, Y.Y. Lau, and V. Serlin, *IEEE Trans. EMC-34*, p.22 (1992).
- [2] C. Chen, P. Catraru, and G. Bekefi, *Appl. Phys. Lett.*, (1993).
- [3] G. Voss and T. Weiland, DESY Reports M82-10 (1982); M82-079 (1982).
- [4] M. Friedman, J. Krall, Y.Y. Lau, and V. Serlin, *Phys. Rev. Lett.* **63**, 2468 (1989).
- [5] W.K.H. Panofsky and M. Bander, *Rev. Sci. Instrum.* **39**, 206 (1968).
- [6] V.K. Neil, L.S. Hall, and R.K. Cooper, *Part. Accel.* **1**, 111 (1970); **2**, 213 (1979).
- [7] A.W. Chao, B. Richter, and C.Y. Yao, *Nucl. Instrum. Methods.* **178**, 1 (1980).
- [8] Y.Y. Lau, *Phys. Rev. Lett.* **63**, 1141 (1989).
- [9] P.R. Menge, R.M. Gilgenbach, and Y.Y. Lau, *Phys. Rev. Lett.* **69**, 2372 (1992); P.R. Menge, R. Bosch, and R.M. Gilgenbach, *Appl. Phys. Lett.* **61**, 642 (1992).
- [10] BBU growth on a pencil beam that is placed off-center can be easily calculated by using Eq. (4) instead of Eq. (5). We pretend that the total beam current is carried by the i -th filament that enters Eq. (4). Although the BBU growth of such an off-center beam depends on θ_i , its coupling constant ε is still much less than ε_0 , the value for an on-axis beam.

Rf Focusing Effects and Multi-bunch Beam Breakup in Superconducting Linear Colliders

J. Rosenzweig, S. Hartman and J. Stevens

UCLA Department of Physics, 405 Hilgard Ave., Los Angeles, CA 90024

Abstract

A high gradient standing wave linear accelerator provides axisymmetric transverse focusing due to the presence of strong alternating gradient transverse electromagnetic fields arising from the backward rf wave. This effect is second order in both the field amplitude and in γ^{-1} , so it is of importance only for high gradient, relatively low energy beams. The purpose of the present analysis is to examine the effect of this focusing on multi-bunch beam breakup in a superconducting linear collider, which has both a high accelerating gradient and long bunch train. As an interesting test case, we discuss the beam breakup problem in the TESLA test bed at DESY.

I. RF FOCUSING

The effect of alternating gradient transverse rf fields is to provide net axisymmetric (monopole) focusing to a beam accelerating in a standing wave electron linear accelerator. The focusing strength associated with this effect is, in the smooth approximation,

$$K = \frac{1}{2} \left[\frac{e\bar{E}_\gamma}{\gamma mc^2} \right]^2,$$

where \bar{E}_γ is the average accelerating gradient associated with the resonant component of the wave[1]. This focusing effect has the same form as a solenoidal magnetic field, of strength $B_z = \bar{E}_\gamma / \sqrt{2}c$. Note that for a large average accelerating gradient and a low (by the standard of the linear collider final energy) beam that this can be a very strong effect. For TESLA designs, an average accelerating gradient of 20 MeV/m is often assumed, which yields an effective smooth focusing with equivalent beta-function of $\beta_\gamma(\text{cm}) = 3.5\gamma$. At the TESLA test bed at DESY, the beam will be injected at low energy (approximately 10 MeV), and thus the initial beta-function will be 0.7 m, which is much stronger focusing than the external quadrupole lenses provide. In addition, if the electron beam at TESLA itself is derived directly from an rf gun[2],

the rf focusing will be dominant in the low energy (less than the damping ring energy) section of the linac.

This focusing term can be incorporated into a paraxial ray equation, which has the following simple form in the limit that $\gamma \gg 1$,

$$X'' + \frac{3}{4} \left(\frac{\gamma'}{\gamma} \right)^2 X = 0,$$

where $X \equiv x / \sqrt{\beta\gamma}$ is the reduced transverse position (the derivation of the general form of this equation, and the notation, are due to Lawson[3], and $\gamma' = e\bar{E}_\gamma / mc^2$ is the average rate of change of the beam energy in units of rest energy.

In addition, at the entrance/exit of the cavities, the unmatched iris fields are equivalent to focusing/defocusing lens of focal length $f = 2E_b / E_\gamma = 20 \text{ cm}$ [4].

These effects can be incorporated into a single matrix which describes the passage of a particle through a cavity,

$$\begin{bmatrix} \cos(\alpha) - \sqrt{2} \sin(\alpha) & \sqrt{8} \frac{\gamma_i}{E_\gamma} \sin(\alpha) \\ -\frac{3}{\sqrt{8}} \frac{\gamma'}{\gamma_f} \sin(\alpha) & \frac{\gamma_i}{\gamma_f} [\cos(\alpha) + \sqrt{2} \sin(\alpha)] \end{bmatrix}$$

where $\alpha = \frac{1}{\sqrt{8}} \ln \left(\frac{\gamma_f}{\gamma_i} \right)$ and $\gamma_{i(f)}$ is the normalized beam energy at the beginning (end) of the cavity.

Using this matrix, plus the linear drift and quadrupole matrices in the intercavity regions of the linac, one can construct a full linear transport matrix for the linac.

II. MULTI-BUNCH WAKE FIELDS.

As a bunch which is a member of multi-bunch train passes through a cavity off-axis, it adds a wake-field contribution to the lowest order transverse modes, the dipoles modes. Since the vertical emittance and beam size are much smaller than the horizontal in a linear collider design, we concentrate only on vertical motion, as it will be a more sensitive measure of a wake-field instability. The total vertical kick received at the N-th cavity

by a particle in the i -th bunch due to all bunches which precede it is[5]

$$\Delta p_{x,N} = \frac{e^2 N_b}{2} \sum_m \left(\frac{R'}{Q} \right)_m \sum_{j < i} y_{j,N} S_{ij}, \text{ where}$$

$$S_{ij} = e^{-\frac{(i-j)\omega_m \tau}{2Q_m}} \sin[(i-j)\omega_m \tau].$$

Here the quantities $(R'/Q)_m$ are the transverse shunt impedances of the m -th dipole mode, which has angular frequency ω_m and a loaded quality factor Q_m . These parameters are taken from the work by Mosnier[5], who has studied this problem for the actual TESLA cavities as they are presently designed.

III. SIMULATION

The beam dynamics of the centroid of each bunch in the train can be simulated by using the matrices describing the rf focusing, acceleration, and drifting, adding an additional kick due to the wake-fields at the exit of each cavity. The input parameters for these studies, corresponding to a TESLA-like bunch train, are given in Table 1. The usual TESLA cavity parameters are adopted: $f_{rf}=1.3$ GHz, with nine π -mode cells per cavity.

Bunch spacing τ	1 μ sec
Number e^+ /bunch N_b	5×10^{10}
Number of bunches N	800
Average β -function	83 m
Phase advance/cell	30 degrees
Av. accel. field \bar{E}_{rf}	15 MV/m
Cavity misalignments	1 mm (rms)
Beam injection error	50 microns

Table 1: Parameters for TESLA-like multi-bunch beam breakup simulation studies.

In these studies, the average β -function is kept constant at 41 meters, which means that for energies below a half of a GeV or so, the rf focusing will in fact be stronger than the quad focusing for $\bar{E}_{rf}=20$ MV/m. Note that if a damping ring is not employed, that the electron beam must accelerate through this regime of the transverse dynamics. The bunches are all given a 50 micron initial offset. Following Mosnier[5], we assume an rms misalignment of the cavities of 1 mm.

In a TESLA-like machine, with 10,000 cavities, the excitation of multi-bunch BBU by

misalignments of cavities in the low energy section of the linac were observed to damp (through the mechanism of adiabatic damping), until the amplitude of the beam oscillation was not significantly different when compared to the case when the rf focusing kicks were turned off. The results were, in general, similar to those found by Mosnier.

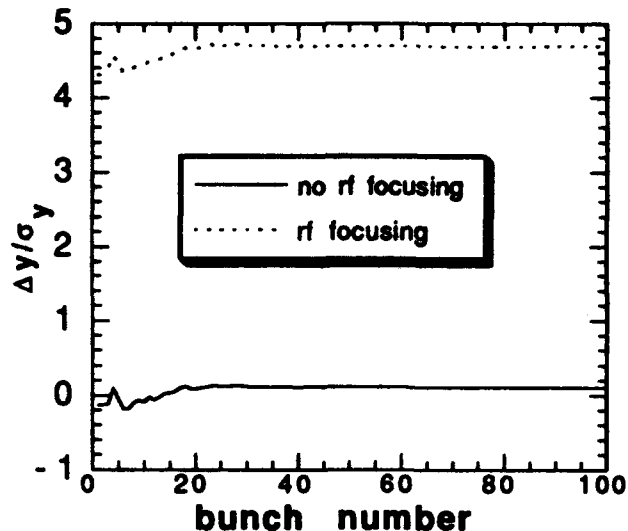


Figure 1: Vertical position as a function of bunch train number, with and without rf focusing for TESLA test bed-like case. The simulation with rf focusing included shows a large, correctable centroid offset.

In the case of the TESLA test bed at DESY, the beam is always in the rf focusing dominated regime, and the results are a bit more interesting. In this case there are only 32 cavities. The first thing that one notices is that the rf focusing kicks move the centroid of the bunch train off axis, as is shown in Figure 1. Since this sort of DC offset is correctable, for the sake of analysis we subtract the leading bunch offset from the coordinates of the remaining bunches, as is shown in Figure 2. The resulting bunch offsets display two notable aspects. First, as expected, the BBU grows faster due to the driving excitation of the rf focusing kicks from misaligned cavities.

The salient feature of the bunch train offset profile is that after an initial transient, the bunches follow each other - they "lock-on" to the position of the bunches which precede. This effect is explained theoretically in the case of a nearest neighbor (daisy chain) model developed by Adolphsen[6]. In this model, only the wake-field from the bunch immediately preceding is included in the calculation. The assumption is that the damping of the mode due to its loaded Q is several e-folds in the time interval between bunches.

While this is not quite the case here, the behavior can be seen to be qualitatively the same.

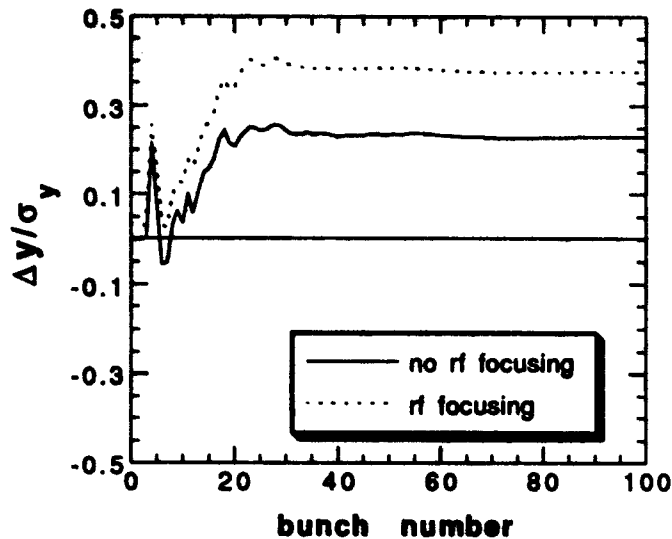


Figure 2: Vertical position as a function of bunch train number, with and without rf focusing for TESLA test bed-like case, with the initial bunch offset subtracted.

It is also clear that the final lock-on offset seen in Fig. 2 is slightly larger for the case which includes the rf focusing kicks. In the daisy chain model the oscillation amplitude is proportional to the average beta-function. Thus a likely explanation for the calculated amplitudes in Fig. 2 is that total amplitude is made smaller by the presence of the additional rf focusing, an effect which cannot, however, overcome the added growth of the instability due to the presence of rf kicks, which provide an additional inhomogeneous driving term in the equations of motion. In both cases, however, the instability amplitude is a relatively small fraction of the bunch height $\sigma_y = 200 \mu\text{m}$. This fraction, as stated above, tends to decrease with additional acceleration in a TESLA-type machine, especially in our case, where the beta-function remains constant.

IV. CONCLUSIONS

The effect of alternating gradient rf focusing has a large effect on the focusing of electrons at low energy in a standing wave linac. This undoubtedly will have some impact on the way one implements external focusing and trajectory correction in an SRF linear collider.

On the other hand, we have found no serious deleterious effects of including rf focusing in a multi-bunch BBU in a long machine. In a low energy machine such as the DESY test-bed,

however, the additional effect of the rf kicks should be observable.

The idea behind pursuing this study was that the rf focusing kicks would contribute a forcing of the motion that is correlated to the wake-fields, since both the kick received by the bunch and the wake-field excited by the bunch are proportional to the bunch offset from the cavity center. The bunches affected by the wake-field, however, do not in general execute subsequent motion which is correlated to the cavity offsets, except to the extent that a dipole mode frequency is commensurate with the bunch spacing frequency. This special case is to be avoided, and in fact the most desirable choice of dipole mode frequency places the zero crossings of the dipole modes at the following bunches.[7] Thus the multibunch BBU is not drastically exacerbated by the presence of rf kicks in cases where the bunch train would be otherwise stable, as can be seen in Figure 2.

REFERENCES

1. S. Hartman and J. Rosenzweig, *Phys. Rev. E* **47**, 2031 (1993).
2. J. Rosenzweig, E. Colby, G. Jackson, and T. Nicol, these proceedings (abstract Ma9).
3. J. D. Lawson, *The Physics of Charged Particle Beams* (Oxford University Press, Oxford, 1977).
4. R. Miller and R. Helm, in *Linear Accelerators*, ed. P.M. Lapostolle and A.L. Septier, 115 (North-Holland, Amsterdam, 1970).
5. A. Mosnier, internal note DAPNIA-SEA-91-16 (Saclay, 1991).
6. C. Adolphsen, SLAC-PUB-5942 (Oct. 1992), to be published in the Proc of the XVth Int. Conf. on High Energy Accelerators.
7. K.A. Thompson and R.D. Ruth, *Phys. Rev. D*, **41**, 41 (1990).

Required Cavity HOM deQing Calculated from Probability Estimates of Coupled Bunch Instabilities in the APS Ring*

L. Emery
Argonne National Laboratory
9700 So. Cass Avenue, Argonne, IL 60439

Abstract

A method of determining the deQing requirement of individual cavity higher-order modes (HOM) for a multi-cavity RF system is presented and applied to the APS ring. Since HOM resonator frequency values are to some degree uncertain, the HOM frequencies should be regarded as random variables in predicting the stability of the coupled bunch beam modes. A Monte Carlo simulation provides a histogram of the growth rates from which one obtains an estimate of the probability of instability. The damping of each HOM type is determined such that the damping effort is economized, i.e. no single HOM dominates the specified growth rate histogram.

I. INTRODUCTION

Previous work [1] on coupled-bunch instability in the APS ring consisted of calculating the growth rate of coupled bunch modes (CBM) assuming that only one HOM from one cavity was shifted to the frequency of the closest CBM. The probability that HOMs from two cavities contributed to the same CBM was deemed small because the HOM frequencies from different cavities were staggered. The required deQing for each monopole and dipole HOM type was derived from these results.

A possibility that should now be considered in a staggered HOM frequency RF system is that once the HOMs are deQed, the impedance functions of two HOMs close in frequency might overlap, thus negating frequency staggering. Another possibility is two or more HOM impedances from different HOM types contributing to the same CBM through frequency aliasing.

In order to cover all possibilities, one has to calculate the CBMs using all of the HOM impedances with staggered frequencies. Since the HOM resonant frequency values have a quasi-random nature, a statistical analysis of the CBM growth rates is used to estimate the amount of required HOM deQing for beam stability. A similar Monte Carlo analysis was first reported by Siemann in [2].

The relevant data in the instability calculation are given in Section II. Section III explains the Monte Carlo method used, and gives a prescription for determining minimum HOM deQing factors. The method is applied to the APS ring in Section IV. As one may expect, the resulting deQing requirement is more stringent than the preliminary one reported in [1].

All coupled bunch growth rates are calculated by the new program *clinchor* [3]. It uses a normal mode analysis based on the theory of Thompson and Ruth [4]. One of *clinchor*'s

features is the possibility of randomizing the HOM frequencies, an idea borrowed from the program PC-BBI [5].

II. RING PARAMETER AND CAVITY HOM DATA

Some of the ring parameters used in the calculations are listed in Table 1. These parameters are constant for all calculations presented here. The β functions at the RF cavities are used instead of the transverse tunes for the transverse growth rate calculation.

Table 1
General parameters for growth rate calculations.

Ring energy	E	7	GeV
Total current	I_t	300	mA
Number of bunches	N	54	
Current per bunch	I_b	5.6	mA
Number of cavities	N_c	16	
Revolution frequency	f_0	271.55	kHz
Synchrotron frequency	f_s	1.5	kHz
Longitudinal damping rate	$1/\tau_z$		sec ⁻¹
Transverse damping rate	$1/\tau_x$	100	sec ⁻¹
β_z at RF cavities		14	m
β_y at RF cavities		10	m

The properties of the APS ring RF cavity HOMs, as calculated by the program URMEL [6], are listed in Table 2. Each HOM type is named after its unperturbed resonant frequency listed in the first column. R_s is the longitudinal shunt impedance, and R_t is the transverse shunt impedance. Later, R will simply refer to the shunt impedance in general. Q_0 is the unperturbed quality factor of the HOM resonator. To explain the last column, staggering the HOM frequencies means separating the frequencies by equal intervals. This is accomplished by designing each cavity longer than the previous one by some small amount. The effect is different for each HOM type because of their distinct field patterns. The staggering interval column in Table 2 lists how much the HOM resonant frequency decreases per cavity using 0.3 mm per cavity as the elongation step. The selection of the elongation step, according to [7], is based on the budgeted tuning range (0.75 MHz) of the cavity tuners to correct for the fundamental mode frequency staggering.

* Work supported by U.S. Department of Energy, Office of Basic Energy Sciences under Contract No. W-31-109-ENG-38.

Table 2
Impedance parameters of HOMs.

Monopole HOMs (MHz)	Q_0 (1000)	R_i (M Ω)	Staggering interval (kHz)
352*	49	5.60	5.1
538	41	1.67	210.
922	107	0.62	330.
939	42	0.23	330.
1172	44	0.18	390.
1210	94	0.49	600.
1509	88	0.40	810.

Dipole HOMs (MHz)	Q_0 (1000)	R_i (M Ω /m)	Staggering interval (kHz)
588.7	68	13.6	24.
761	53	25.6	210.
962	54	6.1	360.
1017	41	2.6	510.
1145	92	2.7	450.
1219	41	3.6	570.

* Fundamental mode included for comparison.

Due to its longitudinal symmetry, the staggering of the 588-MHz dipole HOM is relatively small. The 16 impedance functions of this HOM type will overlap, requiring this HOM type to be damped more strongly than others.

In heavily beam-loaded RF systems, there is a concern that the fundamental mode couple to the longitudinal CBMs of frequencies $f_0 + f_s$ and $(N-1)f_0 + f_s$. In our case, the coupling is negligible. Not included in the transverse CBM growth rates is the effect of the resistive wall impedance. Since this impedance component is not RF related, it is ignored for now.

III. STATISTICAL ANALYSIS OF STABILITY

A multi-bunch beam is predicted to be unstable in a storage ring if the growth rate of any CBM calculated for a given impedance is greater than the natural damping rate (here the radiation damping rate) of the beam. Since the damping rate is fixed for each plane of motion, one only needs to calculate the largest growth rate among the CBMs to determine stability of the beam in each plane.

The growth rate is a highly sensitive function of the HOM frequencies. However, the HOM frequencies are uncertain quantities, since they change during normal operation of a ring. In addition, before the assembly of cavities, one does not know by how much the construction errors will shift the HOM frequencies from their expected staggered values. Thus, the growth rate is an uncertain quantity.

Since beam stability is directly related to growth rate values, one therefore deals with probability of beam stability. One

defines the probability of beam stability to be the number of sets of possible HOM frequencies where the beam is stable divided by the total number of sets of possible HOM frequencies.

Obviously, one must approximate the probability calculation by restricting the infinite set of HOM frequencies to a manageable few. The analysis thus becomes a statistical one.

The Monte Carlo simulation proceeds as follows. One establishes a set of fixed HOM frequencies to which are then added random values in a range given by an error model. A value for the largest growth rate among the CBMs is stored for each set of HOM frequencies generated.

The set of growth rate values can be histogrammed to show their distribution (see Figure 1, for example). The shape of the histogram is a function of the HOM R 's (here, R just means shunt impedance for either plane of motion), Q 's, and f 's and of the random values amplitude. Typically, a sample of 50 random sets of randomized HOM frequencies is sufficient to provide a smooth enough histogram.

A consistent criterion for reasonable certainty of beam stability is now given: if the 95th percentile value of growth rates is greater than the natural damping rate, then the beam is stable (i.e. the beam is stable 95% of the time); otherwise the beam is unstable.

The HOM deQing requirements are obtained as follows, recognizing that each HOM type has differing R/Q values, and one would like to economize the minimum damping effort. As a first step, each HOM type is taken as being the only impedance in the ring. If the beam is predicted by the Monte Carlo calculation to be unstable, the input values of R and Q of the HOMs are reduced such that a repeated Monte Carlo calculation predicts a stable beam. During this step, one observes that growth rates are not necessarily proportional to R since, by reducing Q , the impedance functions spread and couple to more CBMs. Thus a few iterations may be required before determining the deQing factor for each HOM.

In the last step, all HOMs are included together with their new Q 's, and all are further deQed with the same factor for beam stability.

IV. APPLICATION TO APS RING

A simple frequency error model is adopted here because the correct random component of the HOM frequencies attributable to construction errors and operating circumstances is difficult to establish.

A conservative range of $\pm f_0$ (f_0 is the separation of dangerous frequencies) is selected for the random component of all HOMs. That is, it is guaranteed that some frequency values will land very close to a resonance. This prevents the frequency samples from repeating "safe" values of frequency in between resonances. If the actual random component is larger than f_0 , the CBMs that are influenced by the impedances will be different ones. However, the distribution of growth rates is not expected to change much.

Table 3 lists the deQing factors at the first stage of the analysis for dipole HOMs. (Because of space limitations, the table for monopole HOMs is not shown).

Table 3
DeQ factor for each HOM type taken separately.

Dipole HOMs (MHz)	Damping factor Q/Q_0	Resonator width (MHz)	Staggering range (MHz)
588	150	1.300	0.36
761	220	3.100	3.2
962	9	0.161	5.4
1017	2.5	0.045	7.7
1145	2.5	0.031	6.8
1219	3	0.089	8.5

The resonator width is f_{HOM}/Q . The staggering range is the spread of HOM frequencies of the cavities. For the 16 cavities, it is just 15 times the staggering interval in Table 2. For the two lower frequency HOMs, the resonance width is of the order of the staggering range, implying that some of the impedance functions from the 16 cavities overlap, and that damping effort becomes greater. For the other HOMs in the table, there is no obvious overlapping of impedances.

When all HOM types are combined, the probability of two HOM frequencies for contributing to the same CBM is increased through aliasing of the resonant frequencies.

Table 4
Required Q for frequency-staggered cavity HOMs.

Monopole HOM type (MHz)	DeQing factor Q/Q_0	Required Q
538	64	640
922	16	6700
939	6.4	6600
1173	6.4	6900
1210	16	5900
1509	16	5500

Dipole HOM type (MHz)	DeQing factor Q/Q_0	Required Q
588	285	240
761	420	130
962	17	3200
1017	4.8	8500
1145	4.8	19200
1219	5.7	7200

The final values of Q/Q_0 are listed in Table 4. The required Q column is the maximum Q allowed for stability. Figure 1 shows the histogram and its integral of the growth rates for the final set of R_i 's and Q 's for the longitudinal case. The dashed line is the synchrotron radiation damping rate. Note that, for most samples, the growth rate due to the HOM impedances is only about half the damping rate.

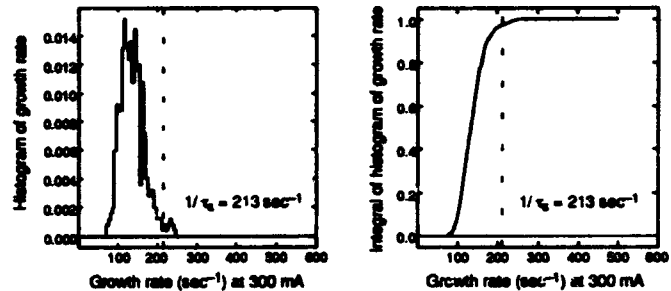


Figure 1
Final histogram and its integral for the longitudinal case.

V. CONCLUSION

The HOM deQing requirements for frequency-staggered cavities have been calculated based on the probability of beam stability using HOM resonator frequencies as random variables.

The deQing requirement for some of the dipole HOMs is stringent because their frequency staggering is small and their R_i/Q is particularly high.

VI. REFERENCES

- [1] L. Emery, "Coupled Bunch Instabilities in the APS Ring," *Proceedings of the 1991 IEEE Particle Accelerator Conference*, 1991.
- [2] R. Siemann, "Instability Growth Rate Calculations for High Energy Storage Rings," *Proceedings of the 1981 IFE Particle Accelerator Conference*, Vol. NS-28, p. 24, June 1981.
- [3] L. Emery, "User's Guide to Program clinchor," ANL technical report, to be published.
- [4] K. Thompson and R. Ruth, "Transverse and Longitudinal Coupled Bunch Instabilities in Trains of Closely Spaced Bunches," *Proceedings of the 1989 IEEE Particle Accelerator Conference*, p. 792, 1989.
- [5] J. Hagel and B. Zotter, "PC-BBI, a Program to Compute Bunch Beam Instabilities on a PC," CERN SL-AP 90-62, CERN, 1990.
- [6] T. Weiland, "On the Computation of Resonant Modes in Cylindrically Symmetric Cavities," *NIM*, Vol. 216, pp. 329-348, 1983.
- [7] Y. Kang, private communication.

Measurement and Analysis of Transverse Beam Transfer Functions in the Fermilab Main Ring

P.J.Chou, G.Jackson
Fermi National Accelerator Laboratory*
MS 341, P.O. Box 500, Batavia, IL 60510 U.S.A.

Abstract

Beam transfer function measurements provide accelerator impedance, beam frequency spread and effective feedback gain information. An analysis technique is used to derive these quantities from beam measurements. Transverse bunched beam measurements in the Fermilab Main Ring are reported.

I. INTRODUCTION

It has been known for many years that the Main Ring suffers from a vertical coupled-bunch instability at injection [1, 2]. An extensive study project is underway to find the offensive modes and the impedance source which causes this instability. Beam transfer function measurements are a useful method for determining the beam impedance, effective damper gain and frequency space distribution. Beam transfer function(BTF) for coasting beam and bunched beam cases are measured. The development of a theory for the bunched beam transfer function is also underway.

II. COASTING BEAM THEORY

A. Closed-Loop BTF Measurements

The beam is a collection of particles, each having its own oscillation frequency $q_i\omega_0$ driven by a common external force amplitude $F(\omega)$ where q_i is the fractional tune and ω_0 is the angular revolution frequency. The equation for each individual particle is

$$\ddot{x}_i + (q_i\omega_0)^2 x_i = F(\omega) \cdot \exp(j\omega t) \quad (1)$$

The BTF is defined as [3]

$$B(\omega) \equiv \frac{j\omega \langle x_i \rangle}{F(\omega)} \quad (2)$$

$$= \frac{1}{2} [\pi \rho(\omega) + j \cdot p v \int \frac{\rho(q_i \omega_0) d(q_i \omega_0)}{q_i \omega_0 - \omega}]$$

where

$$\rho(\omega) = \frac{2}{\pi} \text{Re}[B(\omega)] \quad (3)$$

$j=-i$, $\rho(q_i\omega_0)$ is the normalized distribution of the betatron frequency among the particles.

When there is a self-coupling force due to the transverse impedance[4], eq.(1) is changed to

$$\ddot{y}_i + (q_i\omega_0)^2 y_i = F(\omega) \cdot \exp(j\omega t) - j \frac{e I_0 Z_{\perp}}{m L} \langle y_i \rangle \quad (4)$$

where e and m are the charge and mass of each individual particle respectively, I_0 =total beam intensity, L =accelerator circumference and Z_{\perp} is the transverse impedance. The coupled BTF $B'(\omega)$ is given by $j\omega \langle y \rangle / F(\omega)$ and has the following relation

$$\frac{1}{B'(\omega)} = \frac{1}{B(\omega)} + H(\omega) \quad (5)$$

with $H(\omega) = e I_0 Z_{\perp} / m \omega L$. The above equation represents a feedback loop as depicted in Fig.1.

If a damper system is used to cure an instability, this will add a damping term to the right hand side of eq.(3), say $-j I_0 G \langle y_i \rangle$, where G is complex. Then the equation for the new feedback loop becomes

$$\frac{1}{B'(\omega)} = \frac{1}{B(\omega)} + H(\omega) + D(\omega) \quad (6)$$

with $D(\omega) = G I_0 / \omega$. The new feedback loop is depicted in Fig.2. A plot of $\text{imag}(1/B')$ vs. $\text{real}(1/B')$ gives us the well known stability diagram. The effect of impedance and damper system is to shift the unperturbed stability diagram ($1/B$) by

$$\frac{e I_0 Z_{\perp}}{m \omega L} + \frac{G I_0}{\omega} \quad (7)$$

At lower intensity, an open loop BTF through a damper system can generate the betatron frequency distribution. We can determine the contour shift by comparing with the unperturbed stability diagram from calculation. A plot of contour shift vs. beam intensity provides us the information about the coupling impedance and damper gain.

B. Open-Loop BTF Measurements

The experimental setup is shown in Fig.3 and the corresponding loop diagram depicted in Fig.4. The output signal is

$$V_{out} = B(-D) V_{in} - H V_{out} \quad (8)$$

The measured BTF is

$$B'(\omega) = \frac{-D(\omega)B(\omega)}{1 + H(\omega)B(\omega)} \quad (9)$$

* Operated by Universities Research Association Inc., under contract with the U.S. Department of Energy.

Furthermore, the open-loop stability diagram is described by

$$\frac{1}{B'(\omega)} = \frac{-1}{D(\omega)B(\omega)} - \frac{H(\omega)}{D(\omega)} \quad (10)$$

When the self-coupling effect is very small, the BTF is approximately equal to $-D(\omega)B(\omega)$.

III. MEASUREMENTS

Beam transfer functions are measured with coasting and bunched beam in the Main Ring at 8 GeV flat top. Fig.5, Fig.6 and Fig.7 are results of coasting beam case for $n=1053+q$ betatron sideband. The revolution frequency is 47.4 kHz and vertical tune is 0.4 for the Main Ring. Fig.5 and Fig.6 give the amplitude and phase of BTF respectively. Fig.7 is the distribution of betatron frequency spread derived from eq.(3). Due to limited beam study time, we did not average data from multiple cycles, a process which significantly improves the signal to noise ratio of the results. The presented signals are too noisy to provide a smooth enough stability diagram. We can see a substantial shift in the coherent frequency for different beam intensity from Fig.5 to Fig.7. This frequency change is proportional to the product of beam intensity and transverse impedance. A measurement of coherent frequency shift vs. beam intensity will give the transverse impedance. Fortunately we also do have averaged data for bunched BTFs. The results are depicted in Fig.8, Fig.9 and Fig.10. It is necessary to calibrate the experimental apparatus in order to derive the impedance and damper gain from the stability diagram, see eq.(7). Further work is underway to attain quantitative results from BTF measurements.

IV. REFERENCES

- [1] R. Stiening and E.J.N. Wilson, Nucl. Instr. and Methods 121 (1974) 283-285.
- [2] G. Jackson, Proc. IEEE Part. Acc. Conf., (1991) 1755.
- [3] D. Boussard, CERN SPS/86-11(ARF).
- [4] G. Nassibian and F. Sacherer, Nucl. Instr. and Methods 152 (1979) 21-27.

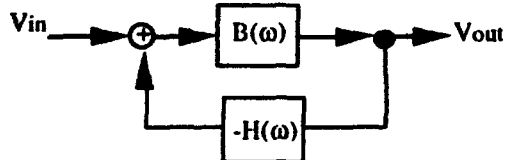


Fig.1: feedback loop with the coupling impedance.

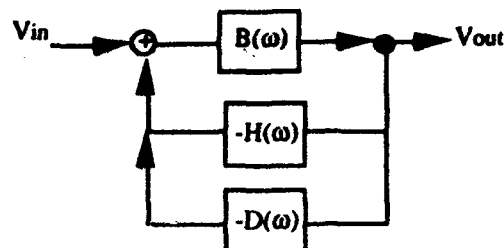


Fig.2: feedback loop with the coupling impedance and damper system.

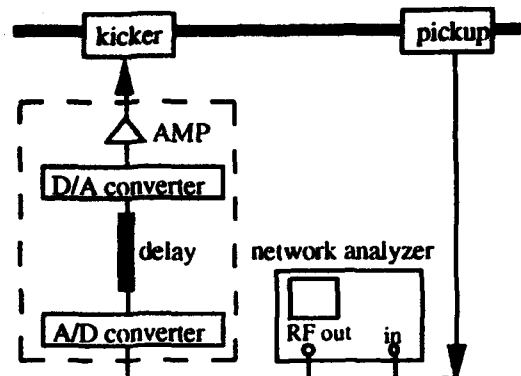


Fig.3: experimental setup for BTF measurements.

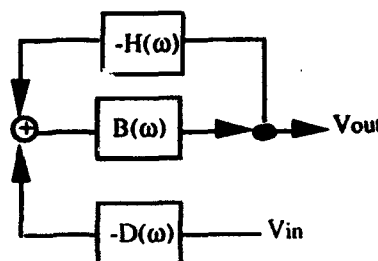


Fig.4: loop diagram corresponding to the BTF measurements.

$N=1053+q$, damper off

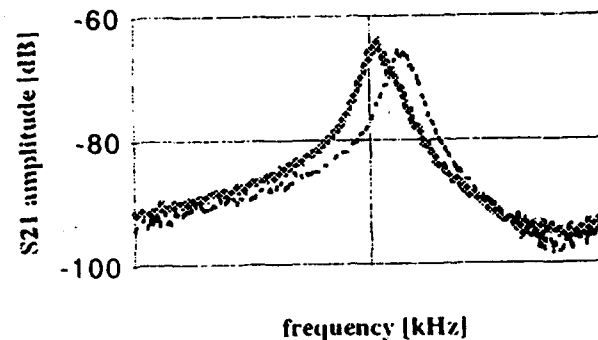


Fig.5: BTF measurement for coasting beam -- amplitude, dashed line corresponds to low beam intensity.

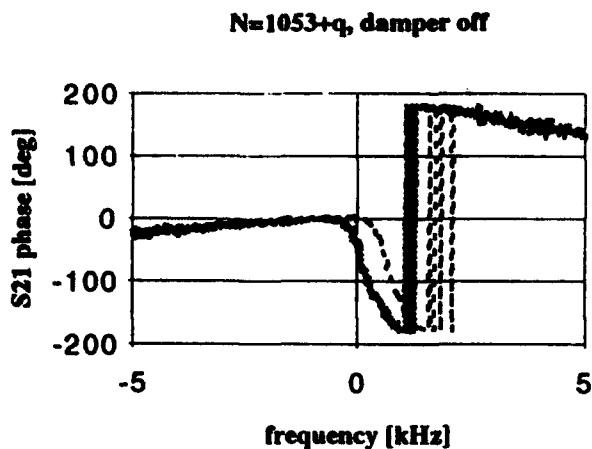


Fig.6: BTF measurement for coasting beam -- phase, dashed line corresponds to low beam intensity.

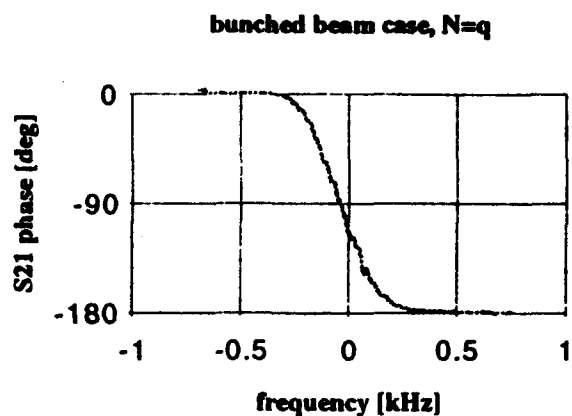


Fig.9: bunched BTF measurement -- phase.

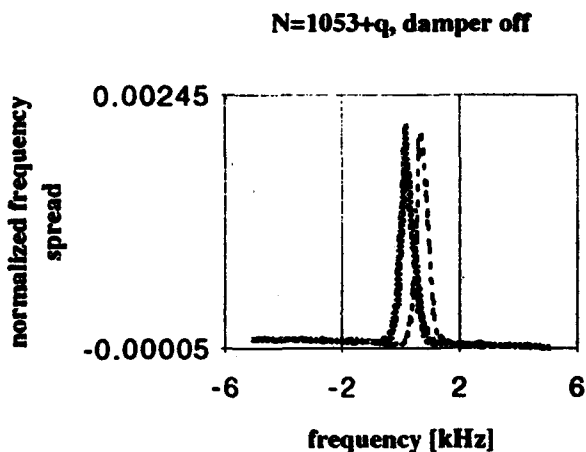


Fig.7: distribution of frequency spread derived from eq.(3), dashed line corresponds to low beam intensity.

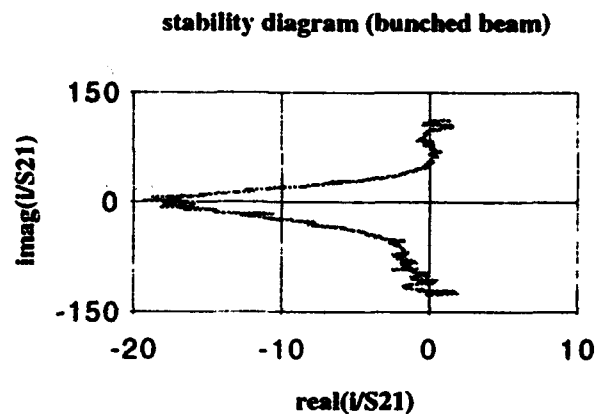


Fig.10: bunched BTF measurement -- stability diagram.

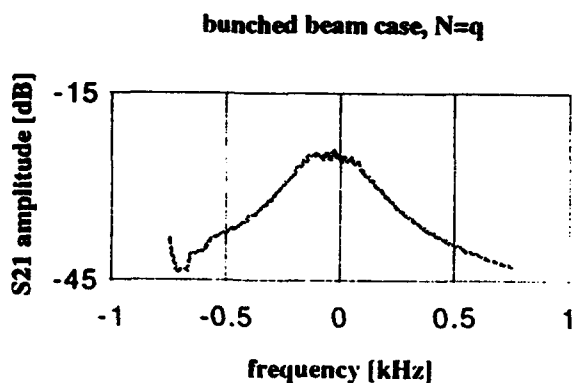


Fig.8: bunched BTF measurement -- amplitude.

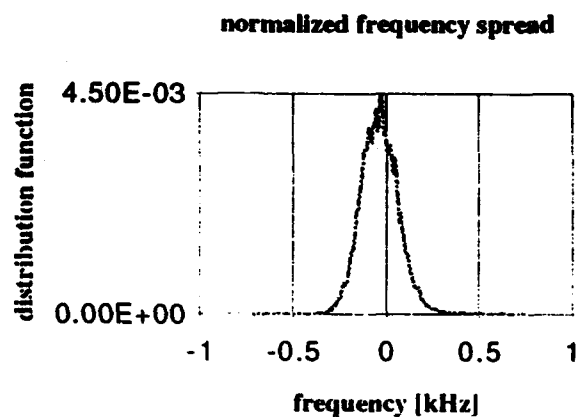


Fig.11: bunched BTF measurement -- distribution of frequency spread derived from eq.(3).

Observation of a Short Bunch Train Longitudinal Instability in the Fermilab Main Ring

X. Lu, G. Jackson
Fermi National Accelerator Laboratory*
P.O. Box 500, MS 341
Batavia, IL 60510

Abstract

Longitudinal coupled-bunch instability has been addressed in many papers. Most of them assume that all bunches are distributed equal-distant from each other. Here we present a different case where a train of 13 bunches is followed by a big gap of 1100 empty buckets in the Fermilab Main Ring. No residual wake fields are left after one revolution for a higher order mode of the RF cavity with Q in the few hundreds. The head bunch of the train cannot feel the wake field left by the previous turn, and classic closed loop instability is not possible, though destructive coherent oscillations are observed in later bunches. However, it has been observed that the beam can still be unstable if the beam intensity is high enough (e.g. $1E10$ per bunch). In this paper we will present some experimental observations along with computer simulation results. They agree with each other quite well. A feedback loop is possible to eliminate these coherent oscillations.

I. INTRODUCTION

This paper is concerned with the subject of longitudinal beam instability observed in the Fermilab Main Ring. During the present collider run, a high intensity proton beam is needed in the Tevatron to provide a high luminosity, described by the equation

$$L = N(p) N(\bar{p}) f n / A \quad (1)$$

Here A is the transverse area, $N(p)$, $N(\bar{p})$ are numbers of protons and antiprotons in one bunch, f is revolution frequency, n is number of proton(antiproton) bunches in the whole ring.

In order to get a high intensity beam, a technique called coalescing[1] is used to get as much charge in a single bunch as possible from 11 to 15 individual bunches in the Main Ring. This coalescing charge efficiency is strongly dependent on longitudinal emittance. It can also be poorer if there is coherent oscillation before coalescing. Based on observations, it is found that the beam is not stable at the coalescing energy of 150 GeV. This instability is caused by a high order mode in the RF cavities.

*Operated by Universities Research Association Inc., under contract with the U.S. Department of Energy.

When a beam passes through a cavity, a voltage is induced (see fig. 1), given by[2]

$$V = q \omega R / Q \quad (2)$$

Here q is bunch charge, ω , R , and Q are resonant frequency, impedance and Q values respectively.

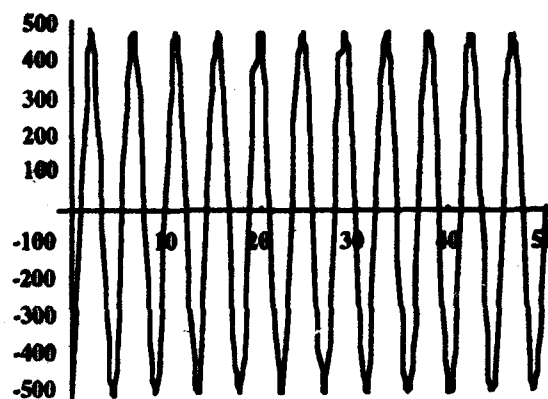


Figure 1 Beam loading voltage(V) as a function of time(nsec) by a bunch with $1E10$ particle

This voltage acts as another external RF voltage. Since we only have 13 consecutive bunches in the ring, the coupled bunch mechanism is different from traditional predictions[3]. The Q of the offending higher order mode is not high enough to let the wake field propagate for one revolution period. The fill time $t = 2Q / \omega_{rf} = 2 \mu\text{sec}$ is a factor of 10 smaller than the revolution period. This is an open loop type of instability[4]. We don't expect any beam oscillations in the front bunches and progressively larger oscillations in the tail bunches. Here we describe the experiment set up, data taking and simulation results.

II. EXPERIMENT SET-UP

In order to record the whole process of beam growth, the proton beam is stored at flattop with an energy of 150 GeV for 10 seconds. During this period, dipole oscillations can be seen quite easily. With higher intensity the situation gets worse. To make analysis easier, a Tektronix RTD720 digitizer is used

to record resistive wall signals turn by turn. The analog bandwidth is 500 MHz and the digitizing rate is 2 Gsamples/sec. Typically the bunch length is about 4 nsec, so there are 8 samples per bunch. The program LabView on a Macintosh is used to read out data stored in the digitizer through GPIB. Some analysis (such as FFT) can also be performed by that program. The time scale is adjusted by a trigger box so that it can take data for any cycle and for any number of turns per trace. This way short and long range phenomenon can be studied.

III. DATA ANALYSIS

Looking at fig. 4, there is a dipole oscillation for later bunches while the front bunches are stationary. The oscillation amplitude varies from bunch to bunch. Typically 2 nsec of oscillation amplitude can be observed, which is close to 1 sigma of the beam. By examining the oscillation closely, a pattern of phase between them is found. A line can be drawn to match oscillation peaks of different bunches. The phase slope is about 70 degrees/bunch for such a line. By doing FFT of this data, beam spectrum is available(see fig. 5). Note that there are modulation sidebands around each RF frequency harmonic line. The frequency is $\Delta\omega=11$ MHz. Thus the driving frequency is determined by $\omega_0=i*\omega_{rf}\pm\Delta\omega$. Here $\omega_{rf}=53.104$ MHz at 150 GeV. To determine the value of i and sign, a more direct measurement is employed. Since the RF cavity is a dominant factor in terms of impedance at such high frequencies, a survey of all possible modes was performed by using a stretched wire method(see fig. 2).

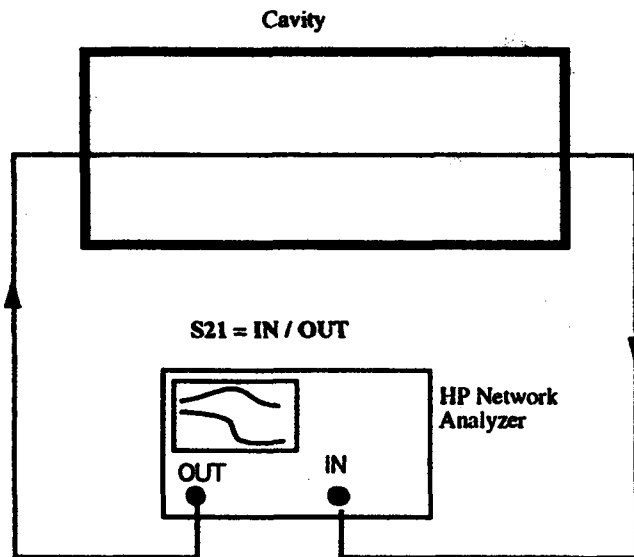


Figure 2 Setup of S21 measurement

This is performed by using a HP8751A network analyzer and a wire is pulled through the cavity center. The two ports of the network analyzer are connected to either wire end, which are impedance matched to 50 Ω using matching resistors[5].

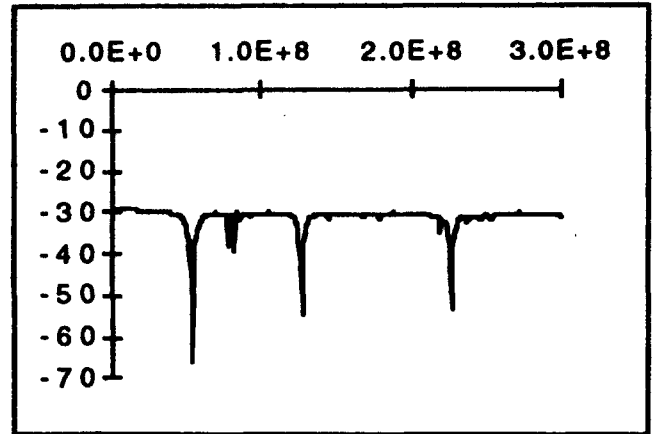


Figure 3 Measured S21(dB) vs. frequency(Hz)

There are three deep notches in S21 (see fig. 3). The first one is the fundamental RF mode. The other two are high order modes. One of them is approximately 225 MHz. This is the mode causing the beam instability. Its frequency corresponds for $i=4$ and has $R/Q=1500$ and $Q=1000$ for a filling time of 2 μ sec. This decay time is relatively short compared to revolution period of 21 μ sec. It explains why the later bunches oscillate with a much bigger amplitude while the front one are still stable.(see fig. 4). While these tail bunches feel a stronger wake field produced by all proceeding bunches, the front bunches see little wake field after one turn. The same behavior can also be seen from our simulation results (see fig.6).

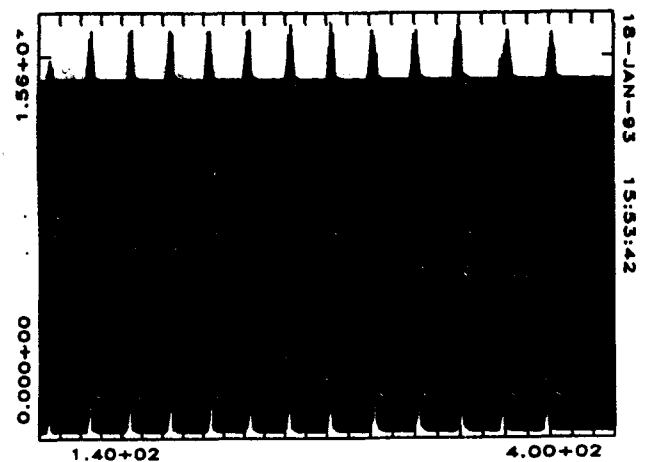


Figure 4 Measured beam motions

this signal into the same higher order mode impedance to nullify the wake field. Another possibility is to make a bunch by bunch feedback system such as done by CERN[6].

V. REFERENCES

- (1) D. Wildman et al., "Bunch Coalescing in the Fermilab Main Ring", 12th Particle Accelerator Conference, 1987.
- (2) P. B. Wilson, "Beam Loading in High-Energy Storage Ring", PEP 100, SLAC, 1974.
- (3) A. Chao, "Coherent Instabilities of A Relativistic Bunched Beam", SLAC-PUB-2946.
- (4) F. Sacherer, Proceedings of the Spring Study on Accelerator Theory, 1972.
- (5) Q. A. Kerns and H. W. Miller, "Fermilab 500-GeV Main Accelerator RF Cavity 128-MHz mode Damper", IEEE transactions on Nuclear Science, Vol. NS-24, No. 3, 1977.
- (6) P. Bramham et al., "Investigation and cures of longitudinal instabilities of bunched beams in the ISR".

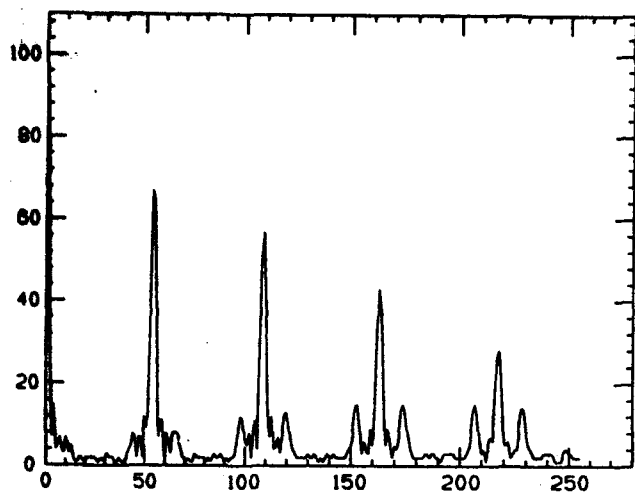


Figure 5 Beam spectrum by FFT

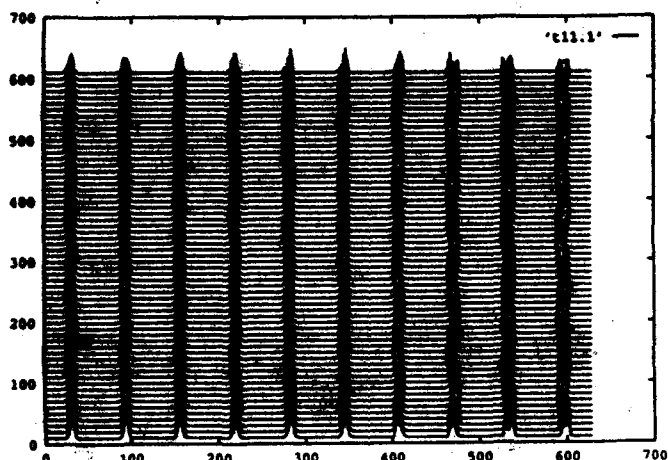


Figure 6 Simulated beam motions

IV. FUTURE WORK

We have studied the short batch coupled bunch phenomenon in the Fermilab Main Ring. A model exists which provides a good description of observed phenomenon. A feedback system must be designed to damp this beam oscillation. We are in the process designing such a system. Beam signals from a current monitor are picked up as a source for this feedback loop. They are amplified and filtered to get the correct component. Then an RF cavity probe delivers

Suppression of Longitudinal Coupled-Bunch Instabilities by a Passive Higher Harmonic Cavity*

R. A. Bosch[†] and C. S. Hsue
Synchrotron Radiation Research Center

Hsinchu Science-based Industrial Park, Hsinchu, Taiwan, R. O. C.

Abstract

A double RF-cavity system with a passive higher-harmonic cavity is considered for the purpose of preventing coupled-bunch instabilities and/or increasing the bunch lifetime. Expressions are presented for the onset of the equilibrium phase instability, the frequency and damping rate of the Robinson instability, the synchrotron frequency, synchrotron frequency spread, and bunch length. An algorithm is presented for evaluating the performance of a passive higher-harmonic cavity, and applied to the SRRC electron storage ring, which is being installed.

1 Introduction

The performance of an electron storage ring may be limited by coupled-bunch instabilities [1] and the Touschek lifetime. A passive RF cavity with resonant frequency near a harmonic of the fundamental RF cavity may be used to increase Landau damping of synchrotron oscillations and/or increase the bunchlength [2, 3], thereby suppressing coupled-bunch instabilities and increasing the Touschek lifetime. However, unwanted side-effects such as the equilibrium phase and Robinson instabilities should be avoided. In Section 2, we present an algorithm which evaluates a higher harmonic cavity [4]. The algorithm is applied to the SRRC storage ring in Section 3. We use the notation of Sands [5].

2 Analysis algorithm

We consider a ring with a passive higher-harmonic cavity in which the fundamental RF-cavity is operated in the "compensated condition" [5] with tuning angle adjusted so that the generator current is in phase with the voltage. The following values must be input to the algorithm: V_{T1} : peak effective RF voltage in Cavity 1; Q_1^o : unloaded quality factor of Cavity 1; R_1^o : unloaded impedance of Cavity 1 at resonance; β : RF-coupling coefficient for Cavity

1; α : momentum compaction; T_o : revolution period; ω_g : generator angular frequency; E : electron energy; σ_E : electron energy spread from synchrotron radiation emission; I : average beam current magnitude; V_s : synchronous voltage; ν : harmonic number of Cavity 2; Q_2 : quality factor of Cavity 2; R_2 : resonant impedance of Cavity 2; ϕ_2 : tuning angle of Cavity 2; τ_L : longitudinal radiation damping time; $Z(\omega_{C.B.})$: parasitic impedance driving coupled-bunch oscillations; and $\omega_{C.B.}$: frequency of the parasitic mode.

Let ω_1 be the resonant frequency of Cavity 1, $Q_1 = Q_1^o/(1 + \beta)$ the loaded quality factor, $R_1 = R_1^o/(1 + \beta)$ the impedance at resonance, and ϕ_1 the tuning angle, defined by $\tan \phi_1 = 2Q_1(\omega_g - \omega_1)/\omega_1$. This tuning angle is the negative of that used by some authors. Robinson oscillations are dependent upon the additional angles $\phi_{1\pm}$ which obey $\tan \phi_{1\pm} = 2Q_1(\omega_g \pm \Omega - \omega_1)/\omega_1$. Cavity 2 is a passive higher harmonic cavity with resonant frequency ω_2 near $\nu\omega_g$, where ν is its harmonic number. ϕ_2 is its tuning angle, given by $\tan \phi_2 = 2Q_2(\nu\omega_g - \omega_2)/\omega_2$. As with Cavity 1, Robinson oscillations involve additional angles $\phi_{2\pm}$ which obey $\tan \phi_{2\pm} = 2Q_2(\nu\omega_g \pm \Omega - \omega_2)/\omega_2$.

Let Ω denote the Robinson instability angular frequency, α_R the instability damping rate (negative for growth), $e > 0$ the electron charge magnitude, while F_1 and F_2 are bunch form factors for the fundamental and harmonic cavities. We initially set $F_1 = 1$ and $F_2 = 0.1$, and iterate until the form factors are consistent with the bunchlength. Our algorithm proceeds as follows:

1. Calculate ψ_1 , the phase angle of the bunch center, which equals zero for a bunch at the voltage peak:

$$V_s = F_1 V_{T1} \cos \psi_1 - 2I R_2 F_2^2 \cos^2 \phi_2 \quad (1)$$

If this equation can only be solved with $|\cos \psi_1| > 1$, then there is no possible equilibrium phase of the bunch in Cavity 1, and the calculation is discontinued.

2. Calculate the tuning angle of Cavity 1 for operation in the "compensated condition" [5]:

$$\tan \phi_1 = \frac{2F_1 I R_1}{V_{T1}} \sin \psi_1 \quad (2)$$

3. Calculate the coefficients of the Taylor expansion of the effective synchrotron potential, $U(\tau) = a\tau^2 + b\tau^3 + c\tau^4$:

*Research supported by the National Science Council, Republic of China

[†]Present address: Synchrotron Radiation Center, University of Wisconsin, 3731 Schneider Drive, Stoughton, WI 53589

$$a = \frac{\alpha \omega_{\perp}}{2ET_0} (V_{T1} \sin \psi_1 + \nu I F_2 R_2 \sin 2\phi_2) \quad (3)$$

$$b = \frac{\alpha \omega_{\perp}^2}{6ET_0} (V_{T1} \cos \psi_1 - 2\nu^2 I F_2 R_2 \cos^2 \phi_2) \quad (4)$$

$$c = -\frac{\alpha \omega_{\perp}^3}{24ET_0} (V_{T1} \sin \psi_1 + \nu^3 I F_2 R_2 \sin 2\phi_2) \quad (5)$$

4. If a is positive and $c < 0.45[a/(\alpha\sigma_B/E)]^2$, then the synchrotron confining potential is mostly quadratic. The synchrotron frequency, bunchlength, and spread in synchrotron frequencies obey:

$$\omega_s = \sqrt{2a} \quad (6)$$

$$\sigma_t = \frac{\alpha\sigma_B}{E\omega_s} \quad (7)$$

$$\sigma_{\omega_s} = \omega_s \sigma_t^2 \left| \frac{3c}{2a} - \left(\frac{3b}{2a}\right)^2 \right| \quad (8)$$

Otherwise, the confining potential is mostly biquadratic so that the bunchlength obeys:

$$\sigma_t = 0.69 \left(\frac{U_0}{c} \right)^{1/4} \quad (9)$$

where $U_0 = \frac{\alpha^2}{2} \left(\frac{eE}{B} \right)^2$. The frequency of a synchrotron oscillation of amplitude σ_t obeys:

$$\omega_{\sigma_t} = 1.17(cU_0)^{1/4} \quad (10)$$

The most unstable frequency is $1.72\omega_{\sigma_t}$.

At the dividing line between quadratic and nonquadratic potentials, the bunchlengths determined by the respective formulas are equal.

5. Use the bunchlengths to determine the form factors (for Gaussian bunches): $F_1 = \exp(-\omega_s^2 \sigma_t^2/2)$ and $F_2 = \exp(-\nu^2 \omega_s^2 \sigma_t^2/2)$. Repeat steps 1-5 if the form factors differ greatly from the previous input values. For new input values, use a weighted average of the two most recent calculations of the form factors. After several iterations of steps 1-5, we have quantities calculated using form factors which are consistent with the bunchlength.

6. Determine if the dipole longitudinal coupled bunch instability is damped. For a mostly-quadratic synchrotron potential, the coherent frequency shift for a resonant dipole interaction with a longitudinal cavity mode of impedance $Z(\omega_{C.B.})$ at frequency $\omega_{C.B.}$ is [1]:

$$|\Delta\omega|_{C.B.} = \frac{eI\alpha\omega_{C.B.}Z(\omega_{C.B.})F_{\omega_{C.B.}}^2}{2ET_0\omega_s} \quad (11)$$

where $F_{\omega_{C.B.}}$ is the bunch form factor at the frequency $\omega_{C.B.}$. To account for radiation damping, subtract τ_L^{-1} from this frequency shift.

The resulting frequency shift may be compared with the calculated synchrotron frequency spread to determine if

Landau damping is sufficient to ensure stability. A growing dipole mode will be Landau-damped [6] when the magnitude of the coherent frequency shift is less than $0.78\omega_{\sigma_t}$. For the case of a nonquadratic synchrotron potential, eq. (11) may be used with the most unstable frequency $1.72\omega_{\sigma_t}$ in place of ω_s . Landau damping is sufficient to prevent the coupled bunch instability [7] if the coherent frequency shift is less than $0.3\omega_{\sigma_t}$.

7. Determine if the equilibrium phase instability will occur. Stability is assured if:

$$F_1 I < \frac{V_{T1} \sin \psi_1}{R_1 \sin 2\phi_1} \quad (12)$$

8. If the previous inequality is satisfied, calculate the Robinson frequency:

$$\Omega^2 = \frac{e\alpha\omega_{\perp}}{T_0 E} \left\{ F_1 V_{T1} \sin \psi_1 - \frac{R_1 F_1^2 I}{2} (\sin 2\phi_{1-} + \sin 2\phi_{1+}) \right. \\ \left. + \nu R_2 F_2^2 I \sin 2\phi_2 - \frac{\nu R_2 F_2^2 I}{2} (\sin 2\phi_{2-} + \sin 2\phi_{2+}) \right\} \quad (13)$$

This calculation requires iteration, and one can start by evaluating the RHS with zero beam current, and then iterate using a weighted average of the most recently computed value of Ω and the previously computed value.

9. Once the Robinson frequency is known, the Robinson damping rate can be calculated; a positive value gives stability:

$$\alpha_R = \frac{4\alpha e I}{ET_0} [F_1^2 R_1 Q_1 \tan \phi_1 \cos^2 \phi_{1+} \cos^2 \phi_{1-} \\ + F_2^2 R_2 Q_2 \tan \phi_2 \cos^2 \phi_{2+} \cos^2 \phi_{2-}] \quad (14)$$

We evaluate a higher harmonic cavity by performing the above calculation for a sequence of values of ring current and tuning angle. In iterated calculations, the iteration is concluded and a flag is set if convergence does not occur within a reasonable number (~ 500) of iterations.

Uncertainty results from the assumption of a resonant coupled-bunch interaction with a parasitic mode, as well as the impedance and frequency of this mode. The bunchlength calculated in the presence of coupled-bunch instability does not include any lengthening resulting from the instability.

3 Application to the SRRC storage ring

To test our algorithm, higher harmonic cavities at MAXlab and BESSY were modeled. The results were in reasonable agreement with experiments when we used a parasitic mode impedance of $0.02 \text{ M}\Omega$, which is an order of magnitude below a typical undamped value, consistent with the presence of spurious mode attenuators.

In the 1.3 GeV storage ring being installed at SRRC, the beam pipe aperture and RF-frequency are nearly the

same as MAX-lab [8]. Thus, we expect a third harmonic cavity at SRRC would have similar properties to that of MAX-lab, so we used the MAX-lab values $R_2 = 0.6 \text{ M}\Omega$, and $Q_2 = 10,000$. For the parasitic mode driving the coupled bunch instability, we used a frequency 1.5 times the fundamental frequency, and an impedance of $0.02 \text{ M}\Omega$. Results are shown in Fig. 1 for the case of two identical passive cavities, which were modeled as a single cavity with $R_2 = 1.2 \text{ M}\Omega$. For a ring current of 60 mA or less, radiation and Landau damping are sufficient to prevent the coupled bunch instability in the absence of a higher harmonic cavity, as shown by the results for passive cavity tuning angles of ± 90 degrees. The coupled-bunch instability can be suppressed at all currents up to the desired maximum current of 200 mA. Similar results were obtained with a single passive cavity.

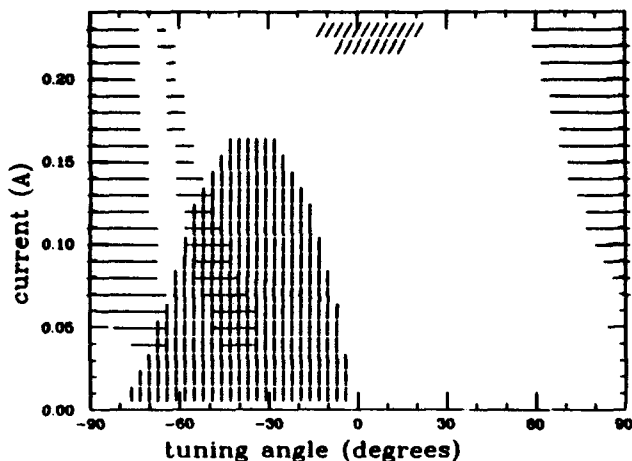


Figure 1. Instabilities are predicted for a range of ring currents and passive cavity tuning angles, for the case of two identical third-harmonic cavities at SRRC.

- : coupled-bunch instability
| : Robinson instability
/ : equilibrium phase instability
\ : there is no equilibrium phase

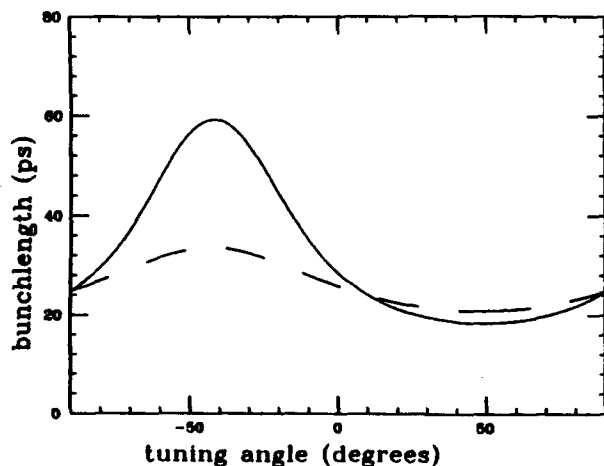


Figure 2: Bunchlength versus passive-cavity tuning angle for a 200 mA current at SRRC. The dashed line shows the results of a single third-harmonic cavity, while the solid line describes two third-harmonic cavities.

In Figure 2, we consider one or two third-harmonic cavities, and show the bunchlength versus the passive cavity tuning angle for a ring current of 200 mA. For stable operation, the bunchlength can be modified in the range of 21–35 ps with a single passive cavity, and 18–60 ps with two identical third-harmonic cavities. With a single passive cavity, a passive cavity power dissipation of 25 kW is required to stabilize the coupled bunch instability. With two passive cavities, about 10 kW per cavity must be dissipated with a tuning angle of -60 degrees. If a tuning angle of -48 degrees is used to maximise the bunchlength, 16 kW per cavity must be dissipated. We estimate that the Touschek lifetime will be proportional to the bunchlength within about 10 percent.

4 Summary

An algorithm has been developed to evaluate instability behavior with a passive higher-harmonic cavity. For the electron storage ring at SRRC, our results support the feasibility of using one or two third-harmonic cavities to suppress coupled-bunch instabilities. Two cavities may be used to substantially increase the bunchlength and the Touschek lifetime.

Acknowledgments

We would like to thank E. Weihrer for suggesting this research topic, many helpful discussions, and critical comments on the manuscript. We would also like to thank Å. Andersson, M. Eriksson, H. P. Chang and H. J. Tsai.

References

- [1] A. W. Chao, SLAC-PUB-2946 (June, 1982).
- [2] E. Weihrer, A. Gaupp, H. G. Hoberg, W. D. Klotz, P. Kuske, H. Lehr, R. Maier, G. Mülhaupt, IEEE Trans. Nucl. Sci. NS-32, 2317 (1985).
- [3] Y. Miyahara, S. Asaoka, A. Mikuni, and K. Soda, Nucl. Instrum. Meth. A260, 518 (1987).
- [4] R. A. Bosch and C. S. Hsue, "Suppression of longitudinal coupled-bunch instabilities by a passive higher harmonic cavity," SRRC/BD/IM/92-04 (1992).
- [5] M. Sands, Institut National de Physique Nucleaire et de Physique des Particules, Rapport technique 2, 3, 4 -76 (1976).
- [6] J. M. Wang, BNL-51302, December 1980.
- [7] S. Krinsky and J. M. Wang, Part. Accel. 17, 109 (1985).
- [8] SRRC Design Handbook (1988).

The Longitudinal Coupling Impedance of a Slot on the SSC Collider Liner

V. Thiagarajan

Superconducting Super Collider Laboratory*
2550 Beckleymeade Ave., Dallas, TX 75237

The submitted manuscript has been authored by a contractor of the U.S. Government under Contract No. DE-AC35-89ER40486. Accordingly, the U.S. Government retains a nonexclusive, royalty-free license to publish or reproduce the published form of this contribution, or allow others to do so, for U.S. Government purposes.

Abstract

The location of a liner inside the collider beam tube is being studied at the SSC Laboratory, in order to provide a synchrotron radiation intercept and to help enhance the vacuum. There will be wake fields propagating inside the liner following the beam fields incident on the pumping holes/slots on the liner. The effect of the wake fields may be expressed through coupling impedances. This paper describes a method to evaluate the longitudinal coupling impedance of slots/holes on the liner for a large range of frequencies (0-60 GHz).

I. INTRODUCTION

The Superconducting Super Collider (SSC) beam is designed to have an energy of 20 TeV. There will be synchrotron radiation to reckon with, even though this is a proton beam. The location of a liner inside the collider beam tube is being studied at the SSC Laboratory. The liner will serve as a synchrotron radiation intercept and also help enhance the vacuum. Suitable pumping holes or slots are required on the surface of the liner. These pumping holes will result in the propagation of wake fields inside the liner, following the incident beam fields. The effect of the wake fields on successive bunches may be evaluated through the coupling impedances, which will depend on the geometry and distribution of slots/holes on the liner. Coupling impedances valid for low frequencies have been presented by Gluckstern [1] and Kurennoy [2]. A semi-analytic expression for the longitudinal coupling impedance of slots/holes valid for a large range of frequencies (0-60 GHz) is derived here and the results are compared with those from Refs. 1 and 2 and with available measurements.

II. DESCRIPTION OF THE PROBLEM

A schematic of the beam pipe and the liner is shown in Figure 1. The liner of inner radius a and thickness Δ is located inside the beampipe of inner radius b . A slot of length w and width d is located on the liner. The center of the slot is at $z = 0$. Our analysis is valid for round holes also, and we will use d to denote the diameter of the hole. The coordinate system is also shown in Figure 1. A single charge q travels along the axis of the liner with the speed of light c , and the field at the slot is given by

$$E_r^b = \frac{q}{2\pi\epsilon_0 a} \delta(z - ct). \quad (1)$$

If we Fourier transform Eq.(1) with $f(\omega) = \int f(t) \exp(j\omega t) dt$, we obtain

$$E_r^b(\omega) = \frac{Z_0 q}{2\pi a} \exp(jkz). \quad (2)$$

In Eq.(2), $Z_0 = 120\pi$ is the impedance of free space. Our task is to calculate the diffracted field and its propagation inside the liner due to the incident field given by Eq.(2).

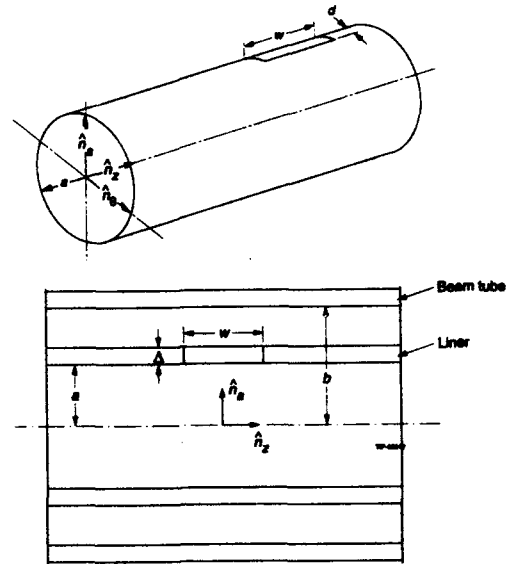


Figure 1. Slot details and coordinate system.

III. DERIVATION OF WAKE FIELDS

The charge relaxation time for our problem is of the order of 10^{-18} s, and the skin depth is of the order of a few microns. We will use the method outlined in Collin [3] for the solution of our problem using the wave guide normal modes and the Lorentz reciprocity theorem. We will follow the notation in Collin [3] and Plonsey and Collin [4]. We will assume a time variation of $e^{j\omega t}$ and a z variation of $e^{-j\beta z}$, with ω and β being the rotational frequency and the propagation factor, respectively. The fields are governed by the Helmholtz equation and can be found in [3] and [4]. The fields for the TM mode, which contributes to the longitudinal coupling impedance, can be expressed in terms of the longitudinal electric field e_z given by

$$e_z = J_n(k_c r) (A \cos(n\theta) + B \sin(n\theta)). \quad (3)$$

*Operated by the Universities Research Association, Inc., for the U.S. Department of Energy under Contract No. DE-AC35-89ER40486.

The J_n is the Bessel function of order n with parameter k_c . The field at the metallic wall at $r = a$ is zero. This implies $J_n(k_c a) = 0$, and there are doubly infinite number of solutions p_{nm} given by

$$J_n(k_c a) = 0, \quad p_{nm} = k_c a, \quad m = 1, 2, 3, \dots \quad (4)$$

The corresponding propagation factor is given by

$$\beta_{nm} = \pm \sqrt{k^2 - \frac{p_{nm}^2}{a^2}}. \quad (5)$$

We will also need the propagation factor for rectangular slots with sides $2a_1, 2b_1$. It is given by [4]

$$\beta_{nm} = \pm \sqrt{k^2 - \left(\frac{n\pi}{a_1}\right)^2 - \left(\frac{m\pi}{b_1}\right)^2}, \quad (6)$$

where k is the wave number given by $\frac{\omega}{c} = k$. The propagation factor for the slot β^s will be high due to the small dimensions of the slot. This implies that the waves inside the slot/hole will be heavily damped. The tangential electric field is zero at the wall everywhere except at the slot/hole, where it is non-zero. We will assume a magnetic wall at the slot, and this implies that the tangential field at the slot/hole will be a maximum and the normal field will be zero. This will result in maximum possible power flow through the slot. Since the normal field is zero, the diffracted electric field at the slot/hole will be equal to the negative of the incident beam field, and the mode inside the slot/hole will be a TE mode. In order to calculate the other components of the diffracted field at the slot, we can use the field continuity criterion given by the following equation:

$$\begin{aligned} \frac{1}{e_{z,nm}} \frac{\partial e_{z,nm}}{\partial r} \Big|_{\text{inner}} &= \frac{J_n'(P_{nm}r/a)}{J_n(P_{nm}r/a)} \Big|_{r=a} \\ &= \frac{1}{e_z} \frac{\partial e_z}{\partial r} \Big|_{\text{slot}} = -\beta^s. \end{aligned} \quad (7)$$

We have used the upper case P_{nm} in Eq.(7) to distinguish it from the lower case p_{nm} used in Eq.(4), which describes the boundary condition at the wall everywhere but at the slot/hole. If we assume the coefficients for the normal modes to be a constant, Eq.(7) will be satisfied for the sums of normal modes. The following equation results, and we can solve it to obtain the P_{nm} :

$$P_{nm} J_n'(P_{nm}) + a\beta^s J_n(P_{nm}) = 0. \quad (8)$$

The magnetic wall at the slot results in the following equation, where a subscript s denotes the diffracted (radiated) fields:

$$E_{sr} = \hat{n}_a \cdot E_s = -E_r^i = \frac{-Z_0 q}{2\pi a} e^{jkz}. \quad (9)$$

Using the ratio of normal modes with P_{nm} in the Bessel argument, we get the following expression for the tangential diffracted electric field:

$$E_{ss} = \frac{Z_0 q}{2\pi a} e^{jkz} \frac{\sum_m J_0(P_{0m})}{\sum_n \sum_m \frac{j\beta_{nm}(P_{nm})}{P_{nm}} J_n'(P_{nm})}. \quad (10)$$

It should be noted that the numerator of Eq.(10) is summed over just $n = 0$ since other modes do not contribute to the longitudinal impedance. The diffracted field given by Eq.(9) will not satisfy the equation $\nabla \times E = 0$. There will be an imbalance, which we will call the magnetic current density J_m , and it will be given by [3]:

$$J_m = -\hat{n}_a \times E_s = \hat{n}_s E_{ss} - \hat{n}_s E_{s\theta}. \quad (11)$$

We can consider the J_m at the slot as an oscillating source and compute the radiated fields in the +ve and -ve directions using the Lorentz reciprocity theorem [3]:

$$\begin{aligned} \int \int (E_n^\pm \times H_s - E_s \times H_n^\pm) \hat{n} ds \\ = \int \int \int (J \cdot E_n^\pm - H_n^\pm \cdot J_m) dv. \end{aligned} \quad (12)$$

The radiated fields in the +ve and -ve directions can be expressed by the normal modes multiplied by appropriate coefficients [3], and we can derive the following coefficients for the wake fields. The coefficients have been generalized with two indices n, m corresponding to the Bessel modes and the roots corresponding to every mode. Further, the field E_{ss} has been multiplied by a factor G_{nm} to decompose it into components corresponding to the n th mode and normalized by a factor f_{nm} :

$$a_{nm} = \frac{1}{2} \int \int H_n^- \cdot \hat{n}_\theta E_{ss} \frac{G_{nm}}{f_{nm}} a d\theta dz \Big|_{\text{slot}}, \quad (13)$$

$$b_{nm} = \frac{1}{2} \int \int H_n^+ \cdot \hat{n}_\theta E_{ss} \frac{G_{nm}}{f_{nm}} a d\theta dz \Big|_{\text{slot}}. \quad (14)$$

The factor G_{nm} is given by

$$G_{nm} = \frac{\frac{P_{nm}}{P_{nm}} J_n'(P_{nm})}{\sum_n \sum_m \frac{\beta_{nm}}{P_{nm}} J_n'(P_{nm})}. \quad (15)$$

IV. THE LONGITUDINAL COUPLING IMPEDANCE

The longitudinal coupling impedance $Z(\omega)$ is defined as follows [1,2]:

$$Z(\omega) = -\frac{1}{q} \int_{-\infty}^{\infty} E_s(r=0, \theta=0) e^{-jkz} dz. \quad (16)$$

Using the expressions for the wake fields derived before, we get

$$Z(\omega) = \sum_m \frac{Z_0 d}{2\pi^2 a} \frac{e^{j\beta_{0m}(P_{0m})w} \sin(kw)}{P_{0m}^2} \times \frac{\sum_m J_0(P_{0m})}{\sum_n \sum_m \frac{-j\beta_{nm}(P_{nm}) a}{P_{nm}} J'_n(P_{nm})} \times \frac{1}{\sum_n \sum_m \frac{\beta_{nm}(P_{nm}) a}{P_{nm}} J'_n(P_{nm})}. \quad (17)$$

In the low frequency limit, $\beta_{nm} = \frac{jP_{nm}}{a}$ and $\sin(kw) \approx kw$, and the impedance is found to be

$$Z(\omega) \approx -j \left[\frac{c_1 Z_0 \omega d k}{2\pi^2 a} + \frac{c_2 Z_0 \omega^2 d k}{2\pi^2 a^2} + \dots \right], \quad (18)$$

where c_1, c_2 are constants. The second term reduces to the expression in [1,2] with $w = d = 2R$ for a round hole with radius R , but for the constant of proportionality.

V. RESULTS AND DISCUSSION

Calculation of the impedance for given slot/hole dimensions involves solution of Eqs.(4) and (8) for the roots p_{nm} and P_{nm} and summing up the series in Eq.(17) for a given k . Computations were carried out for various slots and holes for a liner radius of 0.0165 m. The impedances for 2-, 3-, and 4-mm holes in the frequency range 0–5 GHz are shown in Figure 2; they are compared with the impedance Z_g from [1] and also with measured data from E. Ruiz et al. [5]. The measured values are less than Z_g , and the impedances from the present computations are less than even the measured values. The differences are much less for holes of 2, 3-mm diameter. The impedances of slots of different depths d and same width w are shown in Figure 3. The slot areas have been maintained the same for comparison. The impedance is found to decrease with the depth d . The behavior of the real and imaginary parts of the impedances Z_r and Z_i for 2- and 3-mm square slots for a range of 0–60 GHz is shown in Figure 4. The impedance is inductive for lower frequencies, capacitive for larger frequencies, and reduces to zero for very large frequencies. The impedances decrease as k^{-1} for large frequencies, as shown by Eq.(17). The Z_r is negative for certain frequencies; this is due to the truncation error in the series (with $n = 7$ and $m = 39$) amplified by the term $\sin(kw)$. The advantage of the present formulation is that it is valid for a large range of frequencies and is valid for slots or holes.

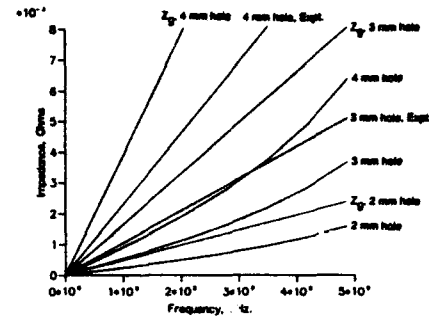


Figure 2. Impedances for 2-, 3-, and 4-mm holes.

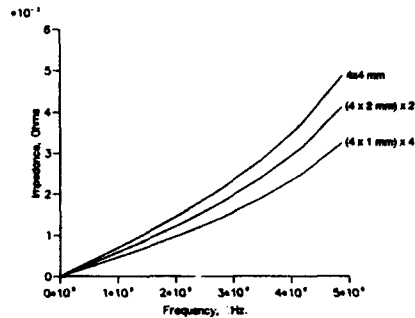


Figure 3. Impedances of slots with different depths.

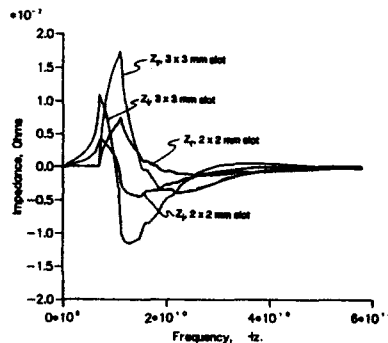


Figure 4. Behavior of the real and imaginary parts of the impedances.

VI. ACKNOWLEDGMENTS

The author acknowledges useful discussions with Weiren Chou and S.S. Kurennoy. The work was performed with encouragement from M.J. Syphers and W. Turner.

VII. REFERENCES

- [1] R.L. Gluckstern, "Coupling Impedance of a Hole in a Thick Wall Beam Pipe," CERN SL/91 (AP), November 1991.
- [2] S.S. Kurennoy, "Beam Chamber Coupling Impedance, Calculation Methods," CERN SL/91-31 (AP), 1991.
- [3] R.E. Collin, *Field Theory of Guided Waves*, IEEE Press, 1991.
- [4] R. Plonsey, and R.E. Collin, *Principles and Applications of Electromagnetic Fields*, McGraw-Hill, 1961.
- [5] E. Ruiz, L. Walling, Y. Goren, N. Spayd, and T. Scholz, "Beam Coupling Impedance Measurements and Simulations of a Beam Pipe Liner with Pumping Holes or Slots," Paper Pa61, IEEE PAC 93.

IMPEDANCE OF A SMALL-GAP UNDULATOR VACUUM CHAMBER*

K. Bane

Stanford Linear Accelerator Center, Stanford, CA 94309

S. Krinsky

National Synchrotron Light Source, Brookhaven National Lab, Upton NY 11973

Abstract

Insertion device performance is limited by the minimum magnet gap allowed by storage ring beam dynamics. In this note, we analyze the impedance of the vacuum chamber for the prototype small-gap undulator being built for the NSLS X-Ray ring, and discuss the consequent beam instability thresholds.

I. INTRODUCTION

In order to optimize insertion device performance, we wish to operate with the minimum magnet gap allowed by the electron beam dynamics. A prototype small gap undulator[1] (PSGU) is under construction for use in the X13 straight section of the X-Ray ring. In this note we consider the impedance of the PSGU variable aperture vacuum chamber and discuss its effect on beam stability.

The PSGU chamber is made of 1 mm thick stainless steel, and is approximately 30 cm in length. It has an inner aperture which can be adjusted from 20 mm down to 2 mm (full). The device is situated at the center of a low- β insertion having values of the betatron functions $\beta_x^* = 1.5$ m and $\beta_y^* = 0.33$ m at the insertion center. The small value of the vertical betatron function significantly reduces the effect of the chamber's transverse impedance on the stability of the vertical betatron oscillations. Our results indicate that beam stability should be maintained with a 4 mm inner vertical aperture. A more detailed description of this work is given in ref. 2.

II. RESISTIVE WALL IMPEDANCE

In the small gap undulator, the vacuum chamber is comprised of 1 mm thick stainless steel, with resistivity $\rho = 80 \times 10^{-8} \Omega\text{-m}$. The circumference of the X-Ray ring is 170 m, so the effective radius $R = 27$ m. At the angular revolution frequency $\omega_0 = c/R = 11$ MHz, the skin depth in the chamber is $\delta_0 = 0.34$ mm and the surface impedance is $Z_s = (1 - i)\mathfrak{R}_s$, where $\mathfrak{R}_s = \rho/\delta_0 = 2.4 \times 10^{-3} \Omega$. The longitudinal resistive wall impedance at the n th harmonic of the revolution frequency, $\omega = n\omega_0$, is[3]

$$Z_n = \left(\frac{\ell}{2\pi a}\right) Z_s \sqrt{n}, \quad (n \geq 0) \quad (2.1)$$

$$Z_{-n} = Z_n^*$$

*Work performed under the auspices of the U.S. Department of Energy under contract DE-AC02-76CH00016.

where ℓ is the length of the small gap chamber and a is the distance of the electron beam to the chamber wall.

A. Power Dissipation

In the case of one bunch with DC current I_0 (Amperes), the power dissipation in the chamber is

$$P = I_0^2 \sum_{n=-\infty}^{\infty} (\text{Re} Z_n) e^{-n^2 \sigma_1^2}, \quad (2.2)$$

where $\sigma_1 = \sigma_y/c$ is the one standard deviation bunch length divided by the speed of light. Approximating the sum by an integral, one obtains[4]

$$P = I_0^2 (\text{Re} Z_1) \frac{\Gamma(3/4)}{(\omega_0 \sigma)^{3/2}}, \quad (2.3)$$

where the gamma function $\Gamma(3/4) = 1.2$ can be approximated by unity. When an average current I_{av} is distributed uniformly in M bunches, the power dissipation is

$$P = M \left(\frac{I_{av}}{M}\right)^2 \left(\frac{\ell}{2\pi a}\right) \mathfrak{R}_s \left(\frac{R}{\sigma_1}\right)^{3/2}. \quad (2.4)$$

We now consider the parameters:

chamber length	$\ell = 0.3$ m
effective radius	$R = 27$ m
bunch length	$\sigma_s = 0.05$ m

In the case of $a = 1$ mm, we find

I_{av}	M	P
0.25 Amp	25	3.5 watt
0.25	5	17.5
0.10	1	14.0

B. Transverse Coupled Bunch Instability

The transverse resistive wall impedance Z_{\perp} is related to the longitudinal impedance Z_{\parallel} by[3]

$$Z_{\perp} = \frac{2R}{a^2} \frac{Z_{\parallel}}{n} = \frac{2R}{a^2} \frac{\ell}{2\pi a} Z_s \frac{1}{\sqrt{n}}. \quad (2.5)$$

The transverse impedance can give rise to a transverse coupled bunch instability. The growth rate of the fastest growing coupled bunch mode is[5]

$$\frac{1}{\tau_{\sigma}} = \frac{ec}{4\pi E} \frac{\beta^*}{R} I_{\omega} \text{Re} Z_{\perp}(n=1) \frac{1}{\sqrt{1-q}}, \quad (2.6)$$

where β^* is the average value of the vertical betatron function in the small gap chamber, which in our case is approximately given by the minimum value in the insertion ($\beta^* \approx 0.33$ m). $E = 2.5$ GeV is the electron energy and $q = 0.2$ is the fractional part of the vertical betatron tune $\nu_y = 6.2$. Taking $\ell = 0.3$ m, $R = 27$ m, we find from Eq. (2.7)

$$\text{Re} Z_{\perp} = \frac{6 \times 10^6}{[\alpha(\text{mm})]^3} \Omega/\text{m}, \quad (2.7)$$

and from Eq. (2.8)

$$\frac{1}{\tau_{\sigma}} = (720 \text{ sec}^{-1}) \frac{I_{\omega}}{[\alpha(\text{mm})]^3}. \quad (2.8)$$

The radiation damping time is 5 msec at 2.5 GeV, hence radiation damping is sufficient to provide stability at 0.25 Amp. In fact, the head-tail damping arising from running with positive chromaticity is stronger than radiation damping, so transverse instability should not be a problem due to coupled bunch effects even for $a = 1$ mm.

C. Strong Head-Tail Instability

The short range part of the transverse resistive wall wakefield can give rise to the strong head-tail instability, a single bunch effect.

The resistive wall wakefield resulting from a Gaussian bunch is

$$W_{\perp}(s, \sigma) = \frac{2}{\pi a^3} \sqrt{\frac{cp}{4\pi e_0}} \sqrt{\frac{2}{\pi \sigma}} g(s/\sigma) \quad (2.9)$$

where

$$g(\xi) = e^{-\xi^2/2} \int_0^{\infty} e^{-t^2/2} e^{-\xi^2 t^2/2} dt \quad (2.10)$$

The function $g(\xi)$ is plotted in Fig. 1 of ref. 2, for $-3 \leq \xi \leq 3$. The maximum value of $g(\xi)$ is $\hat{g} = 1.28$.

Let us define the tune shift

$$\Delta\nu = \frac{eQ\hat{W}_{\perp}\beta^*}{4\pi E} \quad (2.11)$$

where \hat{W}_{\perp} is the maximum value of the wakefield, and $Q = Ne$ is the total charge of the electron bunch. The threshold of the strong head tail instability is expected to occur when[6]

$$\Delta\nu = \nu_s, \quad (2.12)$$

where ν_s is the synchrotron oscillation tune, which in the X-Ray ring has a value $\nu_s = 2 \times 10^{-3}$.

The maximum value \hat{W}_{\perp} of the transverse wakefield is found from Eq. (2.17) to be

$$\hat{W}_{\perp} = \frac{4.7 \times 10^{15}}{[\alpha(\text{mm})]^3} \Omega/\text{m}^2\text{s}, \quad (2.13)$$

for $\sigma_s = 0.05$ m. An average current of 1 Amp in a single bunch corresponds to 3×10^{12} electrons, or a total charge $Q = 480$ nC. Taking $\ell = 0.3$ m, $\beta^* = 0.33$ m, $E = 2.5$ GeV, the tune shift defined in Eq. (2.16) is

$$\Delta\nu = 8 \times 10^{-3} \frac{I_0(\text{Amp})}{[\alpha(\text{mm})]^3} \quad (2.14)$$

For 100 ma in a single bunch and $a = 1$ mm, we find $\Delta\nu = 0.8 \times 10^{-3}$, which is slightly less than the synchrotron tune $\nu_s = 2 \times 10^{-3}$. We should be close to threshold for the strong head tail instability in this case. However, taking $a = 2$ mm, the tune shift is reduced to $\Delta\nu = 10^{-4}$, well below threshold. If in addition, we consider 250 ma uniformly distributed in 25 bunches, then $I_0 = 10$ ma, and the tune shift $\Delta\nu = 10^{-5}$. Therefore, in this operating case, we are very far from the threshold of the strong head tail instability.

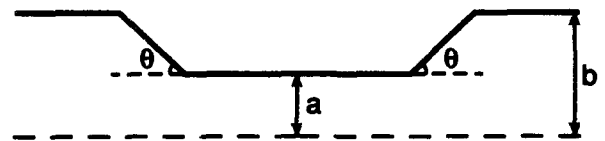


Fig. 1. Profile of cylindrical scraper with inner radius a , outer radius b , and taper angle θ .

III. TRANSVERSE GEOMETRIC WAKEFIELD

Bane and Morton[7] have considered the transverse wakefield of a scraper, as illustrated in Fig. 1. They considered a perfectly conducting cylindrical tube, and found that when $\sigma_s \geq a$, the transverse geometric wakefield for a Gaussian bunch is well approximated by

$$W_{\perp}(s) = \frac{Z_0 c}{\pi a} \left(\frac{2\theta}{\pi} \right)^{1/2} \frac{1}{\sqrt{2\pi\sigma_s}} e^{-\frac{1}{2} \left(\frac{s}{\sigma_s} \right)^2} (b \gg a) (\theta \text{ not too small}) \quad (3.1)$$

where $Z_0 = 377 \Omega$. Taking $\theta = \pi/2$ and $\sigma_s = 0.05$ m, we obtain

$$W_{\perp}(s) = \frac{3 \times 10^{14}}{a(\text{mm})} \Omega/\text{ms} \quad (3.2)$$

The result of Eq. (3.2) can be compared with the maximum of the resistive wall wakefield given in Eq. (2.13), $l = 0.3$ m,

$$W_{\perp} l = \frac{1.6 \times 10^{15}}{[a(\text{mm})]^3} \Omega/\text{ms} \quad (3.3)$$

It is seen that for $a = 1$ mm, the resistive wakefield of Eq. (3.3) is larger than the geometric wakefield of Eq. (3.2). When $a = 2$ mm, the two are approximately of equal magnitude. For $a > 2$ mm, the geometric wakefield of Eq. (3.3) will dominate. We can reduce the geometric wakefield by tapering the ends of the small gap chamber, i.e. choosing θ to be small.

IV. LONGITUDINAL GEOMETRIC WAKEFIELD

When a bunch passes through the small aperture chamber illustrated in Fig. 1, there is a longitudinal effect due to the longitudinal geometric wakefield. This wakefield has a qualitatively different character depending on whether the bunch length is long, $\sigma_s/b > 1$, or short, $\sigma_s/b < 1$. When σ_s/b is small compared to unity, the beam will radiate energy; when σ_s/b is large almost no energy will be radiated and the wakefield will be inductive.

In the case of the X-Ray ring we can restrict our attention to the regime of a long bunch. For a long bunch, it is known that when $(b-a)/a \leq 1$ the inductance is proportional to $(b-a)^2$. For the present application we would like to know the inductance when $(b-a)/a$ is large compared to 1. To determine this, we carried out a study using the computer program TBCI.[9] We first determined the wakefield of a long bunch, and fit the result to the derivative of the (Gaussian) bunch distribution in order to find the inductance L according to

$$W = -L dI/ds \quad (4.1)$$

The result is that asymptotically (for very long bunches), the inductance is well-approximated by

$$L = \frac{Z_0 a}{2\pi c} \left(\frac{b-a}{a} \right)^{3/2} \left(\frac{2\theta}{\pi} \right) \quad (\theta \leq \pi/2) \quad (4.2)$$

Further discussion of this result is given in ref. 2.

We have also considered the sensitivity of the inductance to bunch length. We find that as long as $\sigma_s/b \geq 1$, the numerical result is well-approximated by multiplying Eq. (4.2) by the factor

$$\left[1 + \frac{1}{4} \left(\frac{\sigma_s}{b} \right)^{-2.5} \right] \quad (4.3)$$

To apply these results to the small aperture undulator chamber we consider the parameters $a = 2$ mm, $b = 1$ cm and $\sigma_s = 5$ cm. An inductance of 2 nH ($\theta = 90^\circ$) is insignificant, corresponding to

$$Z/n = \omega_p L = 0.02 \Omega$$

REFERENCES

- [1] P.M. Stefan, L. Solomon, S. Krinsky and G. Rakowsky, Proc. 1991 IEEE Part. Accel. Conf., San Francisco, CA, May 6-9, 1991, p.1096.
- [2] K. Bane and S. Krinsky, Informal report BNL 48792.
- [3] B. Zotter and F. Sacherer, CERN 77-13, p.175.
- [4] P. Morton and P. Wilson, AATF/79/15, SLAC.
- [5] E.D. Courant and A.M. Sessler, Rev. Sci. Instrum. **37** (1966), p.1579.
- [6] R.D. Ruth, Proc. US-CERN School on Part. Accel., Capri, Italy, October 20-26, 1988, Lecture Notes in Physics 343, Springer-Verlag, Berlin, 1989, p.247.
- [7] K. Bane and P. Morton, Proc. 1986 LINAC Conf., SLAC, June 2-6, 1986, SLAC-303, p.490.
- [8] K. Bane, Proc. Impedance and Bunch Instability Workshop, Argonne National Laboratory, October 31-November 1, 1989, ANL/APS/TM-5, p.187.
- [9] T. Weiland, Nucl. Instrum. Meth. **212** (1983), p.13.

A FORMULA FOR THE HIGH FREQUENCY LONGITUDINAL IMPEDANCE OF A TUBE WITH SMOOTHLY VARYING RADIUS*

Robert L. Warnock
Stanford Linear Accelerator Center, Stanford University
Stanford, California 94309

ABSTRACT

A formula for the longitudinal coupling impedance at frequencies above or below the tube cut-off is derived. The round tube is infinite in length, and has an arbitrary, smooth variation of radius over a finite interval.

1. DERIVATION OF THE EQUATION

The method described here may be a useful complement to general purpose programs for computation of fields, especially for high frequency phenomena. Based on a system of integro-algebraic equations, it gives analytic formulas for a first approximation, and also a numerical technique for very accurate solutions. A first report on the analytic and numerical results was given in [1]. Here I review the analytic approach and give an example. The method will be described for the case of the longitudinal impedance in a tube with circular cross section and infinite conductivity. It can be extended to treat transverse fields, wall resistance, and pipes of rectangular cross section.

We take cylindrical coordinates (r, ϕ, z) and suppose that the tube radius is given as $R(z) = b - \epsilon s(z)$, where the function $s(z)$ is zero for $|z| > g$, and not necessarily even in z . We assume that s has a continuous first derivative s' , normalized so that $\max|s'| = 1$; thus $s'(\pm g) = 0$. With this normalization, ϵ measures the effective strength of the wall perturbation; a perturbative method may succeed if ϵ is small compared to 1.

We work in the frequency domain, with the time dependence $\exp(-i\omega t)$. Attention is restricted to positive values of ω , which suffice to express the wake field, thanks to the reflection property of the impedance, $Z(\omega) = Z(-\omega)^*$. The source is assumed to be axisymmetric, a rigid bunch with total charge q and charge density $\rho(r, \phi, z, t) = (q/2\pi)\lambda(z - \beta ct)f(r)$ where $\int \lambda(z)dz = 1$, $\int f(r)rdr = 1$. It follows that the only non-zero fields are (E_z, E_r, H_ϕ) , all independent of ϕ . All fields may be expressed in terms of E_z , which can be written as

$$E_z(r, z, \omega) = \int_{\Gamma} dk e^{ikz} a(k, \omega) \frac{I_0(\chi r)}{I_0(\chi b)} + e_s(r, z, \omega), \quad (1)$$

where $\chi^2 = k^2 - (\omega/c)^2$, and I_0 is the modified Bessel function of the first kind. The Fourier transform \hat{e}_s of the source term e_s is any particular solution of the inhomogeneous radial wave equation for E_z , regular at $r = 0$. The

Fourier amplitude of the radial field is

$$E_r(r, k, \omega) = -\frac{ik}{\chi^2} \frac{\partial E_z(r, k, \omega)}{\partial r}. \quad (2)$$

The function $I_0(\chi b)$ has simple zeros in the k -plane at the points $k = \pm k_s$, $s = 1, 2, \dots$, where $k_s = ((\omega b/c)^2 - j_{0s}^2)^{1/2}$ is defined to be positive for $|\omega b/c| > j_{0s}$ and positive imaginary for $|\omega b/c| < j_{0s}$; the j_{0s} are the positive zeros of the Bessel function J_0 . At any frequency above the lowest cutoff ($\omega b/c = j_{01}$), there are zeros on the real axis. To dodge the corresponding real poles of the integrand in (1), the contour Γ follows the real axis but is indented slightly so as to go above the poles at $k = -k_s$ and below those at $k = k_s$. This choice enforces the outgoing wave boundary condition [2]; (see the discussion in the last section of Ref.[1]). We have assumed that $a(k, \omega)$ is analytic in k ; our construction of solutions will in fact yield an entire function of k .

The boundary condition on the wall is that $\mathbf{E} = (E_r, E_z)$ be perpendicular to the tangent vector $(\partial/\partial z, \partial/\partial r)$, or

$$E_z(R(z), z, \omega) + R'(z)E_r(R(z), z, \omega) = 0. \quad (3)$$

This condition leads to an equation for $a(k, \omega)$ through the following steps: (i) write E_z as in (1), and the corresponding expression for E_r constructed from (2); (ii) take the Fourier transform of (3) with respect to z ; (iii) subtract $I_0(\chi b)$ from $I_0(\chi R(z))$ in the integrand, and notice that the compensating addition gives $\delta(k - l)$. The result is

$$a(l, \omega) = \int_{\Gamma} dk M(l, k, \omega) a(k, \omega) + \hat{S}(l, \omega), \quad (4)$$

where

$$M(l, k, \omega) = \frac{1}{2\pi} \int_{-g}^g dz \frac{e^{i(k-l)z}}{I_0(\chi b)} \cdot [I_0(\chi b) - I_0(\chi R(z)) + \frac{ik}{\chi} R'(z) I_1(\chi R(z))], \quad (5)$$

and \hat{S} is the Fourier transform of

$$S(z, \omega) = - \int_{-\infty}^{\infty} dk e^{ikz} \cdot [e_s(R(z), z, \omega) - \frac{ik}{\chi^2} R'(z) \frac{\partial e_s}{\partial r}(R(z), z, \omega)]. \quad (6)$$

Henceforth we treat only the relativistic limit. In that limit the source term takes on the simple form

$$\hat{e}_s(z, \omega) = \frac{\epsilon Z_0 s'(z)}{2\pi R(z)} \hat{\lambda}(\omega/c) e^{i\omega z/c}. \quad (7)$$

* Work supported by the Department of Energy, contract DE-AC03-76SF00515.

Below cutoff, (4) is an integral equation [3] for $a(k, \omega)$. Above cutoff it is an integro-algebraic equation, since the values $a(k, \omega)$ at the poles on the real axis constitute a discrete set of unknowns to be determined along with the continuous, nonpolar part. These values determine the amplitudes of outgoing waves.

By reversing the order of integrals we see that any solution of (4) may be written in the form

$$a(k, \omega) = \frac{1}{2\pi} \int_{-g}^g e^{-ikz} \Phi(z, \omega) dz. \quad (8)$$

Since the region of integration is finite, $a(k, \omega)$ is an entire function of k , as promised.

2. FORMULA FOR THE IMPEDANCE

An integration by parts on the first two terms of (5) puts the kernel in the form

$$M(l, k, \omega) = \frac{\epsilon}{2\pi} \frac{kl - (\omega/c)^2}{\chi(k-l)} \int_{-g}^g dz e^{i(k-l)z} s'(z) \frac{I_1(\chi R(z))}{I_0(\chi b)}. \quad (9)$$

This shows that the kernel is formally $O(\epsilon)$, and therefore suggests that the equation (4) might be solved by iteration when ϵ is small. The first approximation is obtained by putting $a = \hat{S}$ under the integral in (4). Since the impedance is proportional to $a(\omega/c, \omega)$, and $\hat{S}(\omega/c, \omega) = 0$, the lowest order impedance is $O(\epsilon^2)$.

To evaluate the approximated integral of (4) at the synchronous point $k = \omega/c$ we express \hat{S} in terms of its Fourier transform and reverse integration order to obtain

$$a(\omega/c, \omega) \approx \frac{1}{2\pi} \int_{-g}^g dz e^{-i\omega z/c} R'(z) \int_{-g}^g dz' S(z', \omega) K(z, z', \omega), \quad (10)$$

where

$$K(z, z', \omega) = \frac{1}{2\pi i} \frac{\omega}{c} \int_{\Gamma} dk e^{ik(z-s')} \frac{I_1(\chi R(z))}{\chi I_0(\chi b)}. \quad (11)$$

The integral (11) converges exponentially if $R < b$, but diverges for $R > b$. The divergence is an unwanted limitation since we wish to allow arbitrary R . By performing a contour distortion one can continue the integral analytically from $R < b$ to $R > b$, and incidentally gain other benefits. Taking $R < b$ we let the contour become an infinite semi-circle in the upper (lower) half-plane for $z - z'$ positive (negative). The result is

$$K(z, z', \omega) = \frac{\omega}{c} \sum_{s=1}^{\infty} \frac{J_1(j_{0s} R(z)/b)}{k_s(\omega) b J_1(j_{0s})} e^{ik_s(\omega)|z-s'|}. \quad (12)$$

For $z \neq z'$ the sums converge exponentially, regardless of the value of R . At $z = z'$ and $R = b$ the sum diverges, but if the integral on z' is performed first there will be an extra inverse power of k , and quadratic convergence, uniform in R .

The formula (10) now involves powers of ϵ higher than the second through the presence of $R(z)$ in the denominator of (7) and in (12). To pick out just the ϵ^2 part we put $R(z) = b$ in both locations. Invoking the usual definition of the impedance in terms of the wake potential, we find $Z(\omega) = -2\pi a(\omega/c, \omega)/(q\lambda(\omega/c))$. Then from (7), (10), and (12) we have the impedance to lowest order in ϵ as

$$Z(\omega) = \frac{\omega Z_0 \epsilon^2}{2\pi c b^2} \sum_{s=1}^{\infty} \frac{1}{k_s(\omega)} \int_{-g}^g dz \int_{-g}^g du s'(z) s'(u) e^{ik_s(\omega)|z-u| - i\omega(z-u)/c}. \quad (13)$$

Below cutoff the k_s are all positive imaginary, and the impedance is reactive as required; (the integral is real, since the integrand goes into its complex conjugate on $z \rightarrow u$).

A closer look shows that the formula (13) is actually invalid for the frequency ω in a small neighborhood of each traveling wave cutoff, where $\omega b/c = j_{0s}$. The kernel K has an inverse square-root singularity at such points, owing to the factor $1/k_s$ in (12). It is therefore not small near such frequencies, and the iterative method fails. The same singularity appears in the field expansion (1), from the residue of the pole as it strikes the real axis. It is cancelled by a corresponding zero of $a(k, \omega)$ at $k = \pm k_s$, so that the amplitude of the newly appearing outgoing wave is finite. We have verified that this mechanism operates in the numerical calculation of Ref.[1], but it is a "nonperturbative" effect that cannot take place in a lowest order calculation. In plotting results from (13), we delete small neighborhoods of the bad points, and let the plotting program interpolate nearby values to fill in the gaps. This is justified by the smooth behavior of Z found in the numerical solutions.

As an example for arbitrary frequency, we take $s(z) = d(1 + \cos(\pi p z/g))/2$, where p is an odd integer, thus $\epsilon = \pi p d/(2g)$. An exact evaluation of (13) for this model yields

$$Z(\omega) = \frac{\omega b}{c} Z_0 \frac{\epsilon^2}{2\pi} \left[-i \frac{g}{2b} [h(\omega) + h(-\omega)] + \left(\frac{\pi p b}{g} \right)^2 \sum_{s=1}^{\infty} \frac{1}{b k_s(\omega)} [f(k_s(\omega), \omega) + f(k_s(\omega), -\omega)] \right], \quad (14)$$

where

$$h(\omega) = \frac{I_1(\xi)}{\xi I_0(\xi)}, \quad \xi = \left[\left(\frac{\pi p b}{g} \right)^2 + 2 \frac{\omega b}{c} \left(\frac{\pi p b}{g} \right) \right]^{1/2}, \quad (15)$$

$$f(k, \omega) = \frac{1 - \exp[2i(k - \omega/c)g]}{b^4 [(k - \omega/c)^2 - (\pi p/g)^2]^2}.$$

The first term is imaginary at all ω , and so is the sum for $s > s_m$. The sum for $s \leq s_m$ is complex, and of course present only above cutoff. Its real part is nonnegative as it should be, corresponding to energy lost by the bunch to outgoing waves. The term $h(-\omega)$ has poles, but they are cancelled by corresponding poles in the sum on s .

Figures 1 and 2 show the real and imaginary parts of formula (14) for $p = 5$, $b = 1\text{cm}$, $g = 12\text{cm}$, $d = 0.12\text{cm}$, thus $\epsilon = 0.078$. The frequency range (up to 143 GHz) is sufficient to compute the wake potential of a Gaussian bunch of length $\sigma = 1.2\text{mm}$. Nothing prevents a treatment of still higher frequencies. Figure 3 shows the wake voltage corresponding to the impedance of Figures 1 and 2, as a function of the distance from the center of the Gaussian bunch (positive in front), in units of $\sigma = 1.2\text{mm}$; a positive voltage means energy loss. The persistent "ringing" behind the bunch is due to the narrow low frequency resonance ($\omega b/c \approx 2.865$)

In Ref.[1], accuracy of numerical solutions was tested by checking the boundary condition (3). The same can be done in the analytic approach if we compute $a(k, \omega)$ to order ϵ^2 for general k then construct the fields from (1).

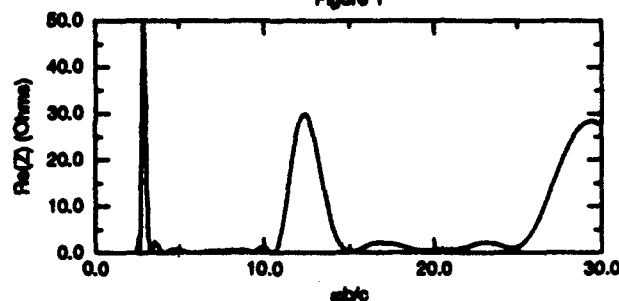
I wish to thank Robert Gluckstern, Karl Bane, and J. Scott Berg for much good advice and technical help.

REFERENCES

1. R. L. Warnock, SLAC-PUB 6038 (1993), to be published in AIP Conference Proceedings.
2. A. Sommerfeld, "Partielle Differentialgleichungen der Physik", p.191 (Dieterich'sche Verlagsbuchhandlung, Wiesbaden, 1947).
3. An equation with the same kernel was derived by S. S. Kurennoy and S. V. Purtov, Particle Accelerators 36 223 (1992). Their form of the source term is incorrect, however, as is their treatment of frequencies above cutoff.

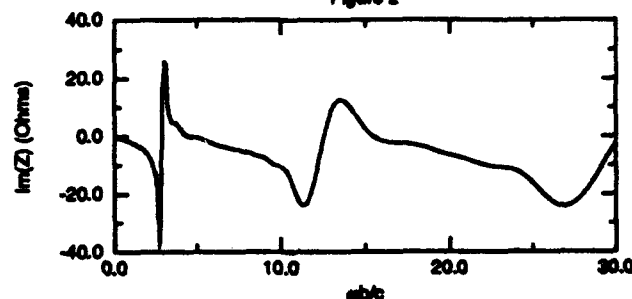
$b=1\text{cm}$ $g=12\text{cm}$ $d=0.12\text{cm}$ $p=5$

Figure 1



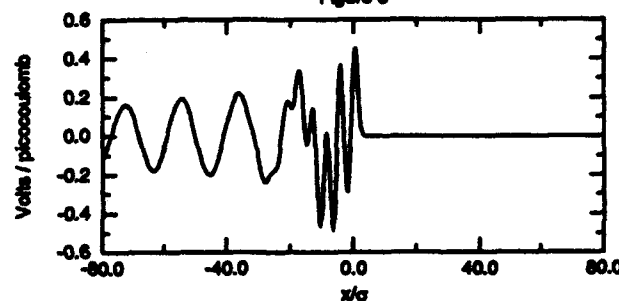
$b=1\text{cm}$ $g=12\text{cm}$ $d=0.12\text{cm}$ $p=5$

Figure 2



Wake Voltage $\sigma=1.2\text{mm}$

Figure 3



A Bench Set-Up for Low-Beta Beam-Current Test Measurements with COSY

Ch. Günther, A. Schnase, and H. Meuth

IKP, Forschungszentrum Jülich GmbH, Postfach 1913, D-52425 Jülich

F. Caspers

PS Division, CERN, CH 1211, Geneva 23

Abstract

Beam current bench tests and simulations, e.g. with beam monitors, are of interest for diagnostic purposes. For highly-relativistic tests, the common coaxial wire method may be used. In contrast, a configuration for non-relativistic beams was devised for transverse impedance measurements. We have combined the two approaches to permit both frequency and time domain low-beta bench tests of the line charge, and of the longitudinal beam impedance. The basic structure is of coaxial 50 Ω geometry, where the outer diameter matches the beam-pipe diameter of COSY, while the inner conductor carries, both around the azimuth and along the axis, suitable pin-and-loop arrays for imposing electric and magnetic fields, respectively. The arrays ensure nearly azimuthal (coaxial) symmetry, and are wired via delay lines such that axially varying field patterns may be generated, permitting the simulation of a broad beta range. We use standard measurement techniques with a network analyzer at a frequency range from 500 kHz up to 100 MHz. A calibration procedure, measuring field pick-up via coupling loops and pins installed in the outer beam pipe wall, ensures the correct $|E|/|B|$ ratio.

1. INTRODUCTION

The coaxial-wire method is commonly employed for simulating a field configuration inside the beam pipe, that is similar to fields generated by a highly relativistic beam, i.e. $\beta \sim 1$, where β is the ratio of the beam velocity to the speed of light in vacuum. In this case fields are closely approximated by modes of TEM-type. Correspondingly, transverse highly relativistic modes are suitably modelled by the common two-wire method, driven in balanced-line, or, respectively, the single-wire-plus-ground-plane method.[1,2] To approximate the situation of transverse modes of a low-beta beam more realistically, a delayed loop-and-pin structure was devised, incorporating in addition a metallic symmetry-plane.[2,3] This structure was used to characterize a meander-shaped slow-wave pick-up structure used for stochastic cooling at low beta.

Here, we present a similar set-up, although topologically different in approach, that aims at the simulation of longitudinal fields of low-beta beams and at the characterization of impedances of structures excited by such beams. The planar geometry of reference [2,3] cannot be used in a straightforward manner for this purpose. Rather, small loops and pins are placed on the inner conductor both around the azimuth and along the axis of the beam pipe. This (quasi-cylindrical) geometry is less accessible to the quantitative description, than is the planar case.[2,3] For instance, an azimuthally symmetric purely azimuthal magnetic field configuration in between inner and outer conductors cannot be produced by an azimuthally symmetric current distribution on the inner conductor alone. The magnetic fields in between inner and outer tube, therefore, essentially depend on the azimuthal array of *discrete* loops.

As an approximate tool to estimate the respective field configurations, we therefore started from single loop and pin properties.

2. MECHANICAL CONFIGURATION

Starting from a basic coaxial structure of a 50- Ω geometry, as it is used for relativistic test measurements, the outer diameter matches the beam-pipe diameter of COSY (150 mm), while the inner conductor must thus measure 66 mm in diameter. The inner conductor is divided into mating modules, each carrying either pins or loops to impose, respectively, electric or magnetic fields. The inner tube serves as the ground/reference surface for the pin-and-loop arrays.

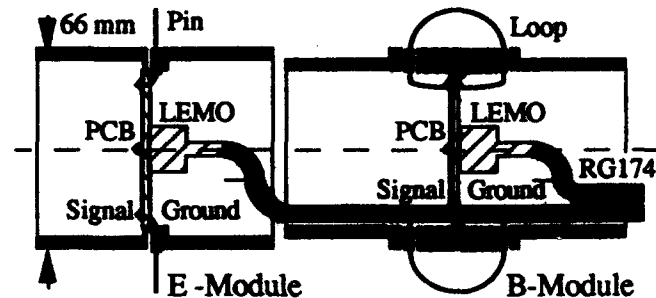


Fig. 1: Schematic of the modules for loops and pins



Fig. 2: Photograph of actually assembled loop and pin arrays

The pins consist of rods of 10 mm length, and the loops of a semi-circle curved of 10 mm radius. Both pins and loops are formed from semi-rigid 1-mm diameter wire, with the teflon insulation (0.5 mm thick) stripped back, where they ex-

tend from the inner conductor. There are 10 pins and 10 loops installed evenly azimuthally into each inner tube module. The modular construction allows for easy assembly and wiring of each station, and for configurational flexibility, achieving a minimum loop-to-pin distance of $\lambda_{\min}/2 = 35$ mm, λ being the structure periodicity (and the field distribution periodicity, if all loops were to be driven in phase). With our module design, this length may arbitrarily be extended by inserting matching extension tubes. Modules are mechanically plugged together; each module features a conical tight fit ensuring mechanical stability of the inner tube without the use of further mechanical fixtures. Conceivably, the minimum distance of 35 mm could be reduced, if a different joining mechanism were to be used. In this respect, we should note, that with these lengths, we roughly fulfill the scale length inequality given by Equ. (9) of [3], which should, at least approximately, also apply to our case. Finally, within each module, pins or loops are connected electrically and mechanically by a suitably shaped printed circuit board (PCB), on which a LEMO connector was installed for attaching the external signal (delay) line.

3. ELECTRICAL CHARACTERIZATION

Electrically, pins are left "dangling" free, while the far end of the loops are connected to the ground/reference plane of the circuit board, to which, in turn, both the inner conductor tube, and the outer conductor/shield of the LEMO is attached (Fig. 1). To characterize a naked pin or loop, they were mounted on the respective PCB, separate from their inner conductor modules. We determined the capacitance and inductance in dependence of the number of loops/pins attached (1 to 10), and found, for the naked $L_{\text{loop}} = 40$ nH, and $C_{\text{pin}} = 2.87$ pF. The loops showed a slightly nonlinear behavior, presumably due to loop-loop coupling. In their final assembly in the module, the value for the single pin capacitance and loop inductance were, at 10 MHz, $C_{\text{pin}} = 3.65$ pF and $L_{\text{loop}} = 39$ nH.

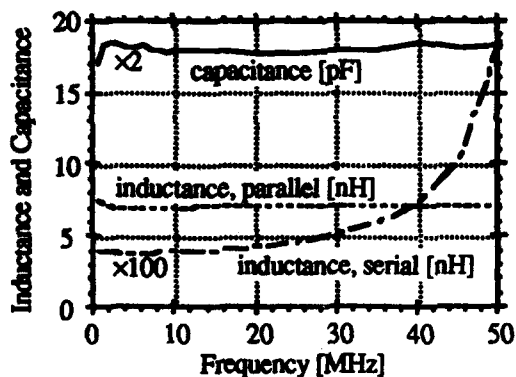


Fig.3: Total loop inductance/pin capacitance of module

The capacitance increases because of the smaller distance between measurement point and ground plane, while the inductance decreases due to the smaller effective area of the loop. Electrically, the 10 pins of each module are connected in parallel, leading to an effective capacitance of the printed circuit of 26 pF including the LEMO socket. For the 10 loops, connections both in parallel and in series were examined. Parallel loops provide superior frequency response to at least 100 MHz, entailing an effective PCB inductance of the printed cir-

cuit of 35.5 nH. Serial loops constitute a more suitable load at frequencies below 20 MHz, but display a resonance above 50 MHz, as can be seen from Fig.3.

4. SINGLE PIN AND LOOP FIELD PROPERTIES

The electric and magnetic fields generated by pins or loops may be rigorously calculated in planar geometry [4,5]. These results, of course, will provide only a rough estimate for the actual situation in cylindrical geometry.

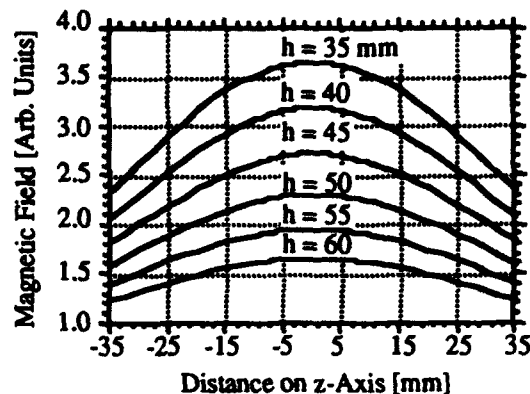


Fig.4: Spatial variation of magnetic field B_ϕ

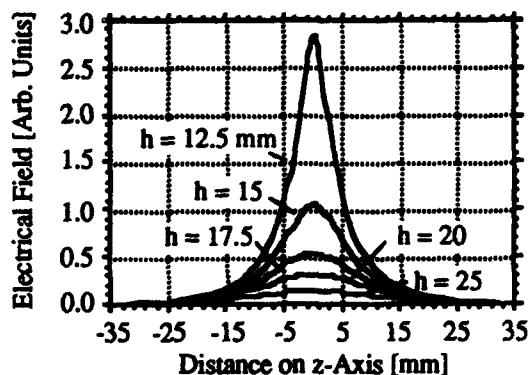


Fig.5: Spatial variation of electric field, E_r

Figures 4 and 5 show the spatial variation of the respective field components E_r and B_ϕ along the axial direction, for various distances h away from the reference plane. Similar variations can be found along the azimuthal direction. However, the loops or pins around the azimuth are spaced such, that the resulting field ripple does not exceed 20%, leading to ten loops or pins. To derive a shape weighting factor for the field variation along the axis, we integrate the area under the curves, $\int F(h)dz / (F_{\text{peak}}(h) \times \lambda)$, from $-\lambda/2$ to $\lambda/2$. For $\lambda_{\min} = 35$ mm and $h \rightarrow 42$ mm, the distance to the outer conductor, we get for this weight factor 0.7 (pins), and 0.9 (loops). These factors will be used for the calibration procedure below.

5. MEASUREMENT SET-UP

We use the standard technique with a network analyzer (HP 8753C) to both generate the signal to be injected into the structure, and to measure and display the transmitted signal,

see "1" of Fig. 6. Both delays and the field strength ratio have to be adjusted so as to match the desired β .

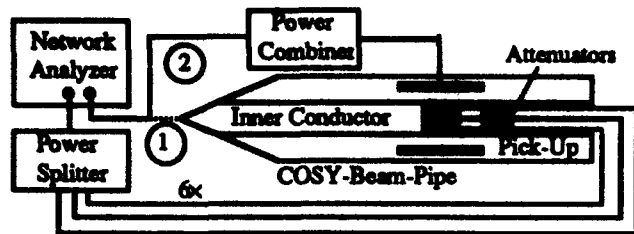


Fig.6: Set-Up

5.1 Delay lines and phase advance

To each of the ten electric field modules and ten magnetic field modules there goes one signal cable, plugged into a LEMO socket on the PCB, as indicated in Fig. 1. The delay length, d , of each signal cable (signal propagation speed c_c) to the various modules is adjusted such that the resulting phase velocity of the generated mode corresponds to the desired beam velocity βc_v , i.e. $d = (\lambda/\beta)(c_c/c_v)$, where, using solid PE insulated RG174 coax, $(c_c/c_v) \sim 0.62$. Thus, for the ($\beta=1$) measurement with loops and pins, one chooses suitable delays of $d(\beta=1) = 0.62(\lambda/2) = 22.3$ mm. An attenuator (6dB) at the LEMO socket of each array reduces reflections (Fig. 6).

5.2 Field calibration and field ratio

We must adjust, according to Faraday's law of inductance, the field ratio to be $B_\phi/E_r = \beta/c_v = 0.33 \times 10^{-8} \times \beta$ [s/m]. [2,4,5] First we may determine the properties of the 50- Ω coaxial configuration without any loops or pins installed, i.e. we impose TEM modes propagating at the speed of light ($\beta=1$). On both ends, the structure is properly matched into type N connectors by conical tapers. Both field types are picked up at the inside of the outer (beam) tube via a test pin and a semi-circular test loop of the same dimensions as in Sect. 2., protruding radially into the space between inner and outer tube. Feed-through and connection is made by SMA sockets.

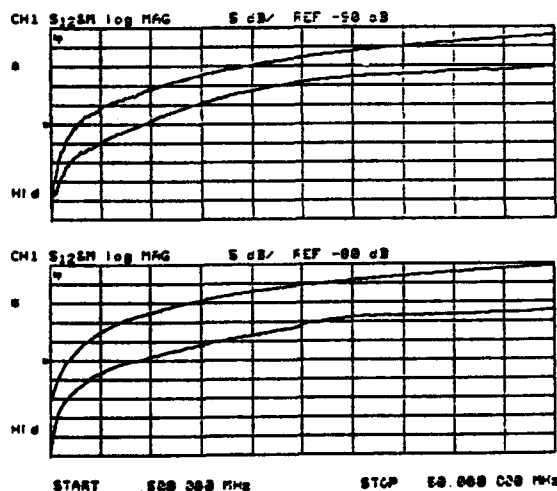


Fig.7: E-field calibration (top); B-field calibration (bottom)

To avoid electrical coupling, i.e. to select exclusively a differential (i.e. magnetic) pick-up from the magnetic test loop, a balanced 180° splitter (center-tapped matched transformer) was used. First, the electric test loop was aligned with an exciting electric loop on the inner conductor. We used pin-and-loop arrays with three modules of each type. The pick up is compared to the result of the coaxial 50 Ω configuration (Fig. 7a). Thereafter, the magnetic test loop was aligned and measured similarly with a magnetic loop (Fig. 7b). Thus, we may generate with the presented pin-and-loop array ($\beta=1$) TEM modes in an empty coaxial structure, if we attenuate the signals into the pins, relative to the signals into the loops, by $|B[dB] - E[dB]| = 2.8$ dB.

5.3 Test-measurements with a beam-position monitor

For arbitrary-beta beam current measurements, a number of current monitors of various geometries are used. For preliminary tests of our low-beta simulation structure ("2" of Fig. 6), we use a standard (spare) COSY beam-position monitor with the common mitre-shaped (diagonally-cut) cylindrical pick-up plate surfaces (diameter as COSY tube). This structure possesses a band pass characteristic to well beyond 100 MHz. A (more interesting) strip-line type pick-up with characteristics that can easily be calculated, is contemplated. However, since no spare exists, such a strip-line pick-up would have to be freed specifically for such tests. For the tests presented here, we aligned the axial center of one electric pin module (with 10 azimuthally mounted pins) and the axial center of the BPM.

To reduce noise, we choose a signal of 10 dBm power at the network analyzer generator, and tune the IF bandwidth to 10 Hz, or use a suitable averaging factor. At a frequency of 500 kHz we observe a transmission loss of about 90 dB; at 50 MHz the transmission loss is 50 dB. Thereafter, the amplitude remains constant to at least 100 MHz. The drop in magnitude at the lower frequency end is due to the capacitive nature of the BPM, in connection with a low impedance measurement. The electrostatic pick-up plates of our BPM can only register electric signals. To measure the magnetic fields as well, we use the same setup as for calibration, Sect. 5.2.

6. CONCLUSION

We have devised a technique to realize coaxial modes with any ratio of electric-to-magnetic field and with arbitrary phase velocity, including greater than the speed of light. Field configurations of the Lienard-Wiechert type [4], which are relevant for longitudinal field modes, can be simulated specifically by a suitable choice of the phase velocity and field ratio. With the presented set-up, low-beta beam simulations are possible, both for line charge and longitudinal impedance measurements. As a next step, we will test with this set-up several of the COSY diagnostic structures, as they are available.

7. REFERENCES

- [1] F. Caspers, Workshop *Impedance and Current Limitations*, Grenoble 1988.
- [2] F. Caspers, US-CERN School Hilton Head Is., SC 1990.
- [3] F. Caspers, D. Möhl, A. Schwinn, EPAC 1990, Nice.
- [4] J.D Jackson, *Classical Electrodynamics*, J. Wiley 1975.
- [5] Ch. Günther, Diploma Thesis, RWTH Aachen, 1993.

A Generalized Model for Parametric Coupling of Longitudinal Modes in Synchrotrons

Patrick L. Colestock, Linda Klump

Fermi National Accelerator Laboratory, P.O. Box 500, MS 341, Batavia, IL 60510 *

Abstract

Observations of nonlinear coupling of longitudinal modes in the Fermilab TEVATRON have been recently identified as a manifestation of parametric coupling.¹ In this model, a spatially uniform, finite-amplitude, longitudinal perturbation is applied to the beam, which then decays into two or more daughter waves as a result of this coupling. Selection rules are derived which are based on frequency and phase matching conditions. These selection criteria are obtained using a multiple time-scale expansion of the weakly non-linear Vlasov equation governing longitudinal motion.

INTRODUCTION

Parametric decay is a wave-wave scattering process whereby a driving wave applied to a system can transfer energy into oscillatory modes of the system. For our case, the driving wave is an external voltage applied to a coasting, unbunched beam. The oscillatory modes are the longitudinal modes of the beam. Only those modes which obey the selection rules of parametric decay are allowed to be excited. This phenomena was observed in the Fermilab Tevatron while doing a longitudinal beam transfer function measurement of 150 Gev beam.

EXPERIMENTAL OBSERVATION

The setup for the beam transfer function measurement was to use a network analyzer to drive the beam via a longitudinal kicker, while monitoring the response with a wideband resistive wall pickup. The return signal from the pickup was passed through a splitter so that the beam spectrum could be observed concurrently on a spectrum analyzer.² During this study the proton beam intensity was 5×10^{12} and σ_p/p was about 2×10^{-3} . The network analyzer scans were done at harmonics of the revolution frequency (47.7 kHz) with a span of 500 Hz. The spectrum shown in Figure 1. is the beam response to a scan with a center frequency of 47.7 MHz. Figure 1a. shows the high frequency end of the spectrum and Figure 1b. shows the low frequency end. There were no excited harmonics in the middle frequency range from 2-45 MHz.

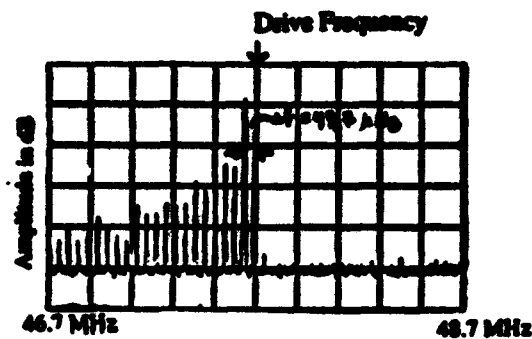


Figure 1a. High Frequency Spectrum

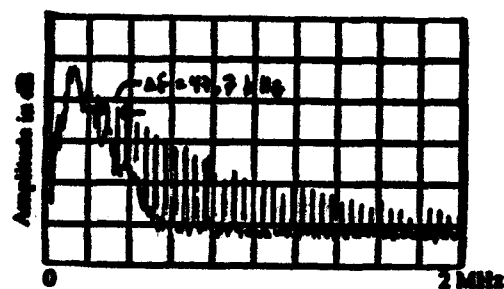


Figure 1b. Low Frequency Spectrum

The observed spectrum shows some remarkable features. The beam has responded to the driving voltage at multiple frequencies, and all of this harmonic content is at frequencies lower than that of the drive. There also appears to be a mirror symmetry between the high and low frequency ends of the spectrum (disregarding the noise at very low frequencies). These properties indicate a nonlinear mechanism, and are a natural consequence of parametric coupling. The overall structure suggests the requirement that energy be transferred from the driving wave to pairs of longitudinal modes whose individual frequencies sum up to the that of the pump wave, $\omega_{m1} + \omega_{m2} = \omega_{drive}$.

THEORY

The system is described with the Vlasov equation written in the conjugate variables of longitudinal motion:

$$\frac{\partial f}{\partial t} + \dot{\theta} \frac{\partial f}{\partial \theta} + \dot{\epsilon} \frac{\partial f}{\partial \epsilon} = 0$$

where $\dot{\theta} = \omega_0 + k_0 \epsilon$ is the revolution frequency, and $\dot{\epsilon}$ is due to wakefield effects. Perturbing the ideal beam distribution

* Operated by the Universities Research Association under contract with the U.S. Department of Energy.

function, the perturbative term can be expressed as an expansion in longitudinal modes:

$$f = f_0 + \sum_m f_m e^{im\theta}$$

The wakefield potential may also be expanded in longitudinal modes:

$$\dot{\epsilon} = \frac{e\omega_0}{2\pi} \sum_m U_m e^{im\theta}$$

The phase matching condition comes from writing the equation for one Fourier component:

$$\frac{\partial f_m}{\partial t} + im\dot{\theta} f_m + \frac{e\omega_0}{2\pi} \frac{\partial f_0}{\partial \epsilon} U_m + \frac{e\omega_0}{2\pi} \sum_{n+k=m} U_n \frac{\partial f_k}{\partial \epsilon} = 0$$

This condition is $n+k=m$, the sum of the phases of the daughter waves must equal the phase of the driving wave.

The system can be naturally broken down into different time scales. The normal modes oscillate relatively rapidly compared to the slower time scale for the growth or decay of power in these modes. Thus, a multiple time scale perturbation expansion can be done, treating the time scales as independent variables.

$$\frac{\partial}{\partial t} = \frac{\partial}{\partial \tau_0} + \lambda \frac{\partial}{\partial \tau_1} + \dots$$

$$f_m = \lambda f_m^1 + \lambda^2 f_m^2 + \dots \quad \text{where } f_m^1 = \hat{f}_m(\tau_1) e^{-i\omega_m \tau_0}$$

$$U_m = \lambda U_m^1 + \lambda^2 U_m^2 + \dots \quad \text{where } U_m^1 = \hat{U}_m(\tau_1) e^{-i\omega_m \tau_0}$$

Making these substitutions, the first order equation is the standard linear dispersion relation³:

$$1 = \frac{(e\omega_0)^2}{2\pi i} Z \int \frac{\frac{\partial f_0}{\partial \epsilon}}{\omega_m - m(\omega_0 + k_0 \epsilon)} d\epsilon$$

The second order equation yields a dispersion relation describing the parametric coupling resonance, as well as the frequency matching condition required for coupling to occur. It also gives an expression for the growth rate of power in a given mode⁴. The complete second order equation contains both resonant and non-resonant terms. The multiple time scale perturbation expansion allows removal of secular behavior from the system by setting the sum of the resonant terms to zero. Identification of resonant terms gives us the frequency matching condition, $\omega_n + \omega_k = \omega_m$. If the frequency of the driving wave is Ω_0 , then $\omega_n + \Omega_0 = \omega_m$ must be obeyed in order to have energy transferred into a pair

of longitudinal modes. The secular equation may be solved for the growth rate of the amplitude of oscillation of mode m :

$$\frac{\partial \hat{I}_m(\tau_1)}{\partial \tau_1} = \frac{-e\omega_0}{2\pi} \hat{I}_n V_0 \times \int \frac{d\epsilon}{\omega_n + \Omega_0 - m\gamma} \frac{\partial}{\partial \epsilon} \left(\frac{\frac{\partial f_0}{\partial \epsilon}}{\Omega_0 - k\gamma} \right) \bigg/ \int \frac{\frac{\partial f_0}{\partial \epsilon} d\epsilon}{(\omega_m - m\gamma)^2}$$

where V_0 is the amplitude of the driving voltage and $\gamma = \omega_0 + k_0 \epsilon$. Note that the growth rate is proportional to V_0 .

The dispersion relation near the resonance can be found if the equation for the growth rate is also written for mode n . Now there are two coupled equations which may be solved using

normal mode analysis. Let $\hat{I}_m(\tau_1) = A e^{\nu \tau_1}$ and $\hat{I}_n(\tau_1) = B e^{\nu \tau_1}$, (ν being the frequency offset from resonance) then:

$$\nu^2 \int \frac{\frac{\partial f_0}{\partial \epsilon} d\epsilon}{(\omega_m - m\gamma)^2} \int \frac{\frac{\partial f_0}{\partial \epsilon} d\epsilon}{(\omega_n - n\gamma)^2} = \left(\frac{e\omega_0}{2\pi} \right)^2 m n (k_0 V_0)^2 \times \int \frac{\frac{\partial f_0}{\partial \epsilon} d\epsilon}{(\omega_m - m\gamma)(\omega_n - n\gamma)^2} \int \frac{\frac{\partial f_0}{\partial \epsilon} d\epsilon}{(\omega_n - n\gamma)(\omega_m - m\gamma)^2}$$

It is possible to get this same result using a different method. The complete dispersion relation can be found by taking the Fourier transform of the Vlasov equation for one Fourier component, substituting a driving voltage for one of the wakefield terms, and then making substitutions to cancel the current terms on both sides of the equation⁵:

$$\left[1 - Z \frac{(e\omega_0)^2}{2\pi i} \int \frac{\frac{\partial f_0}{\partial \epsilon} d\epsilon}{\omega_m - m\gamma} \right] \left[1 - Z \frac{(e\omega_0)^2}{2\pi i} \int \frac{\frac{\partial f_0}{\partial \epsilon} d\epsilon}{\omega_n - n\gamma} \right] = - \frac{(e\omega_0)^3}{(2\pi)^2} n k_0 V_0 Z \int \frac{\frac{\partial f_0}{\partial \epsilon} d\epsilon}{(\omega_m - m\gamma)(\omega_n - n\gamma)^2} \times \frac{(e\omega_0)^3}{(2\pi)^2} m k_0 V_0 Z \int \frac{\frac{\partial f_0}{\partial \epsilon} d\epsilon}{(\omega_m - m\gamma)^2(\omega_n - n\gamma)}$$

If this complete dispersion relation is expanded about the resonant frequency, the final expression is the same as that found using the time perturbation technique.

CONCLUSION

The theory of parametric coupling has been adapted to the accelerator context in order to present a possible explanation for experimental observations. The selection rules which come out of the analysis are consistent with the characteristics of the beam spectra. Pertinent features of the physical system such as the growth rate and the dispersion relation have been calculated. A program is being developed to explore the behavior of the dispersion relation.

REFERENCES

- [1] P. L. Colestock, et al, " Observation and Analysis of Nonlinear Parametric Coupling of Longitudinal Modes in Synchrotrons", EPAC 92, Berlin, Mar 92, Vol. 1
- [2] G. Jackson, "Review of Impedance Measurements at Fermilab", Proc. FIII Instabilities Workshop, Batavia II, Jun 1990
- [3] A. Hofmann, "Single-Beam collective phenomena - Longitudinal", CERN 77-13, Jul 1977.
- [4] Ron C. Davidson, "Methods in Nonlinear Plasma Theory", Academic Press, 1972
- [5] D. G. Swanson, "Plasma Waves", Academic Press, ISBN 0-12-678955-X
- [6] A. G. Sitenko, "Fluctuations & Non-linear Wave Interactions in Plasmas", Pergamon Press, 1982

Longitudinal Coupling Impedance of a Cavity*

I. Gjaja and R. L. Gluckstern

Department of Physics, University of Maryland, College Park, MD 20740

Abstract

We conduct a numerical and analytical study of the longitudinal coupling impedance of a cavity coupled to a beam pipe. The aim of the study is to understand the structure of oscillations of the impedance at high frequency.

INTRODUCTION

There exists an integral equation whose solution describes the behavior of the longitudinal coupling impedance for an azimuthally symmetric obstacle in a circular beam pipe [1]. This equation was the starting point for an analysis that led to an explicit expression for the average behavior of the impedance of a cavity at high frequency [1].

In this paper we describe a numerical solution of the integral equation for the pillbox cavity. The results are compared and found to be in agreement with earlier computations of the impedance that are based on different equations [2,3]. We also confirm the above-mentioned explicit expression for the impedance. Finally, we derive an approximate analytical expression that attempts to account for rapid oscillations at high frequency. While the frequency of oscillations is predicted correctly by our model, the amplitude of oscillations does not agree with numerical results.

NUMERICAL RESULTS

The starting point is the equation [1]

$$\int_0^g dz' G(z') [K_p(z' - z) + K_c(z', z)] = -\frac{2i\pi}{a} \quad (1)$$

for the unknown function $G(z)$, which is related to the impedance $Z(k)$ by

$$\frac{Z(k)}{Z_0} = \frac{1}{2\pi ka} \int_0^g dz G(z). \quad (2)$$

(We use e^{-ikt} for the time dependence, in contrast to e^{jkt} used in ref. 1.) Here $K_p(z' - z)$ is the pipe kernel,

$$K_p(z' - z) = \frac{-2i\pi}{ka^2} e^{ik(z'-z)} \sum_{s=1}^{\infty} \frac{e^{ik\sqrt{1-j_s^2/(k^2a^2)}|z'-z|}}{\sqrt{1-j_s^2/(k^2a^2)}}, \quad (3)$$

*Work supported by the U. S. Department of Energy.

where j_s are the zeroes of $J_0(x)$, and $K_c(z', z)$ is the cavity kernel, which in the case of the pillbox cavity can be written in the form

$$K_c(z', z) = \frac{4\pi}{kag} e^{ik(z'-z)} \sum_{n=0}^{\infty} \frac{\cos(\frac{n\pi z}{g}) \cos(\frac{n\pi z'}{g})}{(1 + \delta_{n0}) \sqrt{1 - (\frac{n\pi}{kg})^2}} \times \frac{P_1(ka\sqrt{1 - (\frac{n\pi}{kg})^2})}{P_0(ka\sqrt{1 - (\frac{n\pi}{kg})^2})}. \quad (4)$$

(Compared to equation (3.12) of ref. 1, we have performed the summation over m .) The symbols $P_1(kay)$ and $P_0(kay)$ stand for

$$P_1(kay) = Y_1(kay)J_0(kby) - J_1(kay)Y_0(kby) \quad (5)$$

and

$$P_0(kay) = Y_0(kay)J_0(kby) - J_0(kay)Y_0(kby). \quad (6)$$

In the expressions (1-6) a denotes the radius of the beam pipe, b the radius of the cavity, g the longitudinal extent of the cavity, and Z_0 the impedance of free space, $Z_0 = 120\pi\Omega$.

In order to solve equation (1) numerically, we Fourier transform it on the interval $[0, g]$, thus replacing the continuous indices z and z' by a pair of discrete indices p and q . The transformed equation reads

$$\sum_{p=-\infty}^{\infty} \tilde{G}_p \tilde{K}_{pq} = -\frac{2\pi i}{a} \delta_{q0}, \quad (7)$$

where the tilde denotes the Fourier transform. In particular, \tilde{K}_{pq} is the sum of Fourier transforms of the cavity and pipe kernels. (The expression is cumbersome and we do not display it here.) The impedance is now given simply by

$$\frac{Z(k)}{Z_0} = -\frac{i}{ka^2} \tilde{K}_{00}^{-1}. \quad (8)$$

Thus all we need to do numerically is to construct the matrix \tilde{K}_{pq} and then to invert it. In order to ascertain that the result is stable, we vary the size of the matrix \tilde{K}_{pq} , as well as the upper limits on the sums in equations (3) and (4). (The upper limits on the sums are chosen such

that for a given size of the matrix \tilde{K}_{pq} all singularities in the sums are included. Except for Figures 1 and 2, where it is smaller, the matrix \tilde{K}_{pq} ranges in size from 81×81 to 121×121 .)

Figures 1 and 2 show the real and the negative of the imaginary part of the impedance as functions of ka for $g/a = 0.05$ and $b/a = 1.1$. These are the same values of parameters as used in Figure 6 of reference 2. The results displayed here are in agreement with those of reference 2.

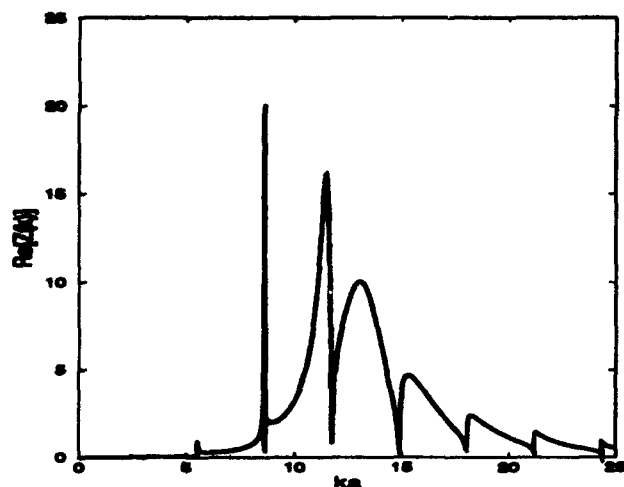


Figure 1: $\text{Re}[Z(k)]$ vs. ka for $b/a = 1.1$ and $g/a = 0.05$.

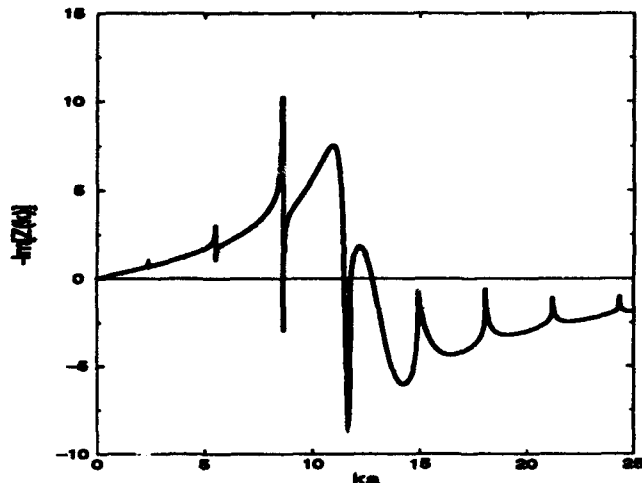


Figure 2: $-\text{Im}[Z(k)]$ vs. ka . Same parameters as Fig. 1.

Our primary interest in this paper is to examine the behavior of $Z(k)$ at high frequency, that is for $ka \gg 1$ and $kg \gg 1$. In this regime, we have compared our results to those obtained in reference 3 and found the two computations to be in agreement.

Figure 3 shows a typical run for $b/a = 1.15$ and $g/a = 0.75$. Superposed on the numerical result is the analytical expression for the average behavior of impedance at high

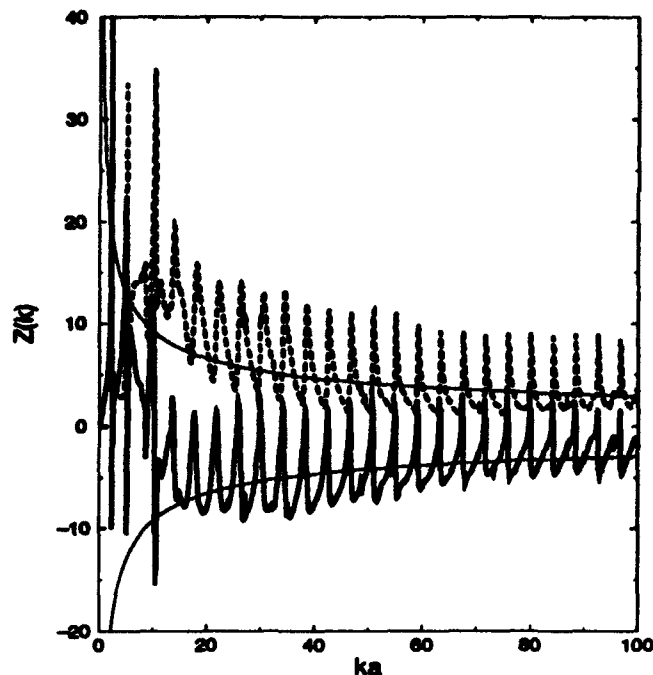


Figure 3: The real part (dashed line) and the negative of the imaginary part (solid line) of $Z(k)$ vs. ka . The thin solid line is the graph of expression (9).

frequency [1]

$$\frac{Z(k)}{Z_0} = \frac{(1+i)}{2\pi a} \sqrt{\frac{g}{\pi k}}. \quad (9)$$

We see that this expression is in satisfactory agreement with the numerical result. Nevertheless, even at large values of ka the behavior of $Z(k)$ is considerably more complicated than $1/\sqrt{k}$. There are large oscillations with an amplitude comparable to the average value of $Z(k)$.

In order to elucidate the structure of the oscillations, we compute the Fourier transform of $\sqrt{k}Z(k)$ for $ka \geq 40$ (using an FFT algorithm). The absolute value of the Fourier transform of Figure 3 multiplied by \sqrt{k} vs. z/a is shown in Figure 4. Apart from the fact that the Fourier transform of $\sqrt{k}Z(k)$ is approximately zero at positive values of z (as it should be by causality), the most striking feature of Figure 4 are the sharp peaks of the graph at the values of $-z$ of $2g, 4g, 6g, \dots$. Therefore, for large values of ka , $Z(k)$ has oscillations with periods corresponding to $\Delta k = \pi/(ng)$, $n \geq 1$. The amplitude of oscillations decreases with frequency.

Motivated by equation (9) and Figure 4, we can surmise that $\sqrt{k}Z(k)$ is of the form

$$\sqrt{k}Z(k) = \sum_{n=0}^{\infty} \alpha_n e^{-2in\pi g}, \quad (10)$$

where the α_n 's are independent of k . The integral under each of the peaks in Figure 4 then gives the value of $|\alpha_n|$. In Figure 5 we plot the integrals under the peaks vs. n for

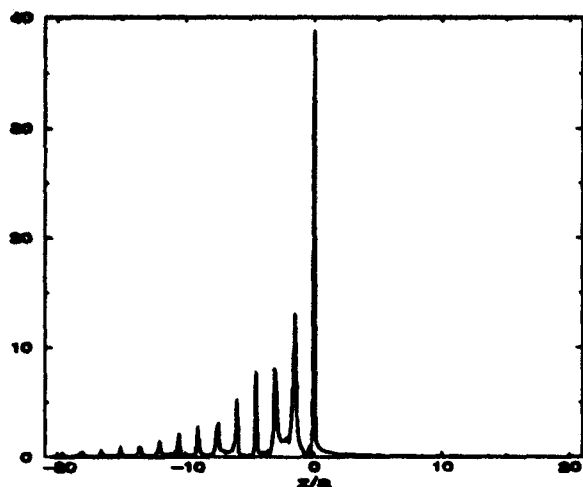


Figure 4: The absolute value of the Fourier transform of $k^{1/2}Z(k)$ vs. z/a ; $b/a = 1.15$ and $g/a = 0.75$.

three different values of b . For comparison, we also plot the number $60\sqrt{2g/(\pi a^2)}$, which is the value of $|\alpha_0|$ obtained from equation (9).

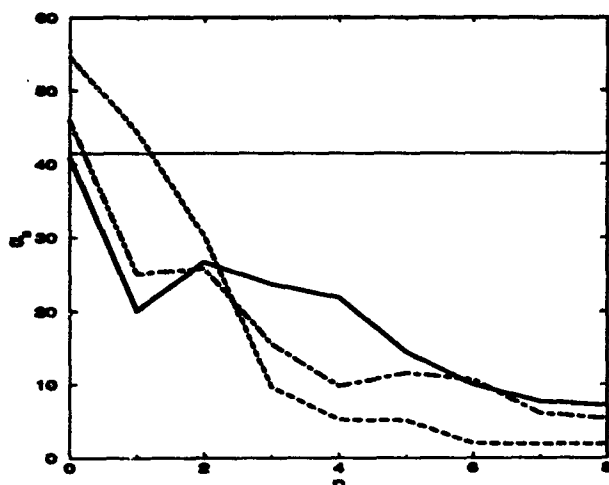


Figure 5: α_n vs. n for $b/a = 1.1$ (dashed line), 1.2 (dash-dot), and 1.5 (solid line). Also shown is the value of α_0 obtained from equation (9) (thin solid line).

From Figure 5 we see that α_n 's in general depend on b/a . (With increasing b/a α_0 approaches the solid line, but the Fourier spectrum analogous to the one in Figure 4 becomes increasingly complicated for nonzero negative values of z . We have observed this trend for values of b/a up to 5.) We are currently conducting additional studies to explore the dependence of α_n 's on b/a and g/a .

ANALYTICAL RESULTS

We begin the track towards an analytical expression for $Z(k)$ by manipulating the pipe and cavity kernels. Under the assumption that $ka/\pi \gg 1$, K_p can be written in the

form

$$K_p(z' - z) \simeq -\frac{i\pi}{a} e^{ik(z'-z)} H_0^{(1)}(k|z' - z|), \quad (11)$$

where $H_0^{(1)}(x)$ is the Hankel function of the first kind. For $K_c(z', z)$ on the other hand, we use the large-argument asymptotic expansions for P_1 and P_0 , and invoke the assumption that $k(b-a)/\pi \gg 1$ to get

$$K_c(z', z) \simeq -\frac{i\pi}{a} e^{ik(z'-z)} \times \left[H_0^{(1)}(k|z' - z|) + H_0^{(1)}(k(z + z')) + \sum_{l=1}^{\infty} [H_0^{(1)}(k(2lg + z - z')) + H_0^{(1)}(k(2lg - z + z')) + H_0^{(1)}(k(2lg + z + z')) + H_0^{(1)}(k(2lg - z - z'))] \right]. \quad (12)$$

It is worthwhile to note that the dependence of K_c on b has disappeared at this stage and so our final expression for $Z(k)$ will be also independent of b . Next, we use the expressions above for K_p and K_c in equation (1), replace the Hankel functions by their large-argument asymptotic expansions, take $G(z')$ of the form

$$G(z') = \frac{A}{\sqrt{z'}} + \frac{B}{\sqrt{g-z'}} e^{-2ikz'}, \quad (13)$$

neglect integrals involving fast-oscillating terms, and replace z and z' by $g/2$ in denominators where they occur summed with $2lg$ ($l \geq 1$), to get

$$\frac{Z(k)}{Z_0} = \frac{1}{2a} \sqrt{\frac{g}{\pi k}} (1+i) \left[\frac{\pi + \lambda(kg)}{\pi^2 + (2\pi-1)\lambda(kg)} \right]. \quad (14)$$

Here

$$\lambda(kg) = \sum_{l=1}^{\infty} \frac{e^{i2klg}}{\sqrt{2l}}. \quad (15)$$

The average over oscillations in equation (14) reproduces the result in equation (9). The oscillations in k , on the other hand, occur with period $\Delta k = \pi/(ng)$, $n \geq 1$, which is in agreement with numerical computations. The limitations of equation (14) are that it is independent of b , which, as we have seen, does not agree with numerical results, and that the amplitudes of oscillation, α_n , are much smaller than the ones observed in simulations for $1.05 \leq b/a \leq 5$. We are currently developing an analytical expression for $Z(k)$ that will remove some of the simplifying assumptions built into equation (14).

REFERENCES

1. R. L. Gluckstern, Phys. Rev. D **39**, 2773 (1989).
2. H. Henke, CERN Report LEP-RF/85-41 (1985).
3. R. Li, PhD Thesis, University of Maryland (1990).

Transverse Impedance of an Iris in a Beam Pipe*

S. Jiang, H. Okamoto,† R.L. Gluckstern
University of Maryland, College Park, MD 20742

Abstract

In an earlier paper the longitudinal impedance of an iris was obtained in the form of an integral equation by matching the fields in the planes perpendicular to the axis at the ends of the iris. This equation was solved by expanding the field components into a complete set of azimuthally symmetric TM modes in the iris region and numerical results were obtained, particularly for large beam pipe radii. The same method is now applied to the calculation of the transverse impedance, where both asymmetric TM and TE modes are needed in the expansions. Once again the results are obtained for large beam pipe radius and a wide range of values of the relative values of the iris radius, the iris thickness, and the wavelength.

I. INTRODUCTION

In previous papers we examined the longitudinal coupling impedance of an iris in a beam pipe. We first treated the case of an iris of zero thickness[1], obtaining a variational form for the impedance, and numerical values by expanding the trial function into a truncated orthonormal set. The results were presented as functions of kb for various values of $(a-b)/b$, where the pipe radius is a , the iris radius is b and the frequency is $kc/2\pi$.

In a subsequent paper[2] we considered the case of finite iris thickness g , again constructing a variational form for the impedance. In this case however, we used a set of matrix equations for the coefficients of the fields in the iris region. In this paper we were particularly interested in the limit $a/b \rightarrow \infty$ corresponding to the impedance of a circular hole of radius b in a transverse conducting wall of thickness g . In all of these studies only TM modes are generated by the drive beam.

In the present paper we examine the transverse (dipole) coupling impedance for an iris of finite thickness. In this case we need both TM and TE modes to satisfy all the boundary conditions. Field matching leads to a set of

equations for the field coefficients in the iris region and the equations resulting from a truncation of the field expansions are solved by matrix inversion. Results are obtained as a function of the three parameters kb , a/b , and g/b .

II. ANALYSIS

The appropriately normalized source fields for an ultrarelativistic beam are

$$E_t^{(s)} = Z_0 H_t \times e_z = (\cos kz - j \sin kz) \nabla_t \phi_0 \quad (1)$$

where we assume a time dependence $\exp(j\omega t)$ and where e_z is a unit vector in the z direction. Here

$$\phi_0(r, \theta) = \left(\frac{r}{a^2} - \frac{1}{r} \right) \cos \theta \quad (2)$$

in the pipe region ($|z| \geq g/2$), and

$$\phi_0(r, \theta) \rightarrow \tilde{\phi}_0(r, \theta) = \left(\frac{r}{b^2} - \frac{1}{r} \right) \cos \theta \quad (3)$$

in the iris region ($|z| \leq g/2$). The separation of the drive current into an even and an odd part in z allows the problem to be treated as the sum of two less complicated problems.

For the even part in Eq. (1), we write the transverse fields in the pipe region as

$$\begin{aligned} E_t = & \sum_{\mu=1}^{\infty} A_{\mu} e^{-j\beta_{\mu}(|z|-g/2)} \nabla_t \phi_{\mu} \\ & + \sum_{\nu=1}^{\infty} B_{\nu} e^{-j\beta_{\nu}(|z|-g/2)} e_z \times \nabla_t \psi_{\nu} \\ & + \cos kz \nabla_t \phi_0 \end{aligned} \quad (4)$$

and

$$\begin{aligned} Z_0 H_t \times e_z = & \pm \sum_{\mu=1}^{\infty} \frac{A_{\mu} k}{\beta_{\mu}} e^{-j\beta_{\mu}(|z|-g/2)} \nabla_t \phi_{\mu} \\ & \pm \sum_{\nu=1}^{\infty} \frac{B_{\nu} \beta_{\nu}}{k} e^{-j\beta_{\nu}(|z|-g/2)} e_z \times \nabla_t \psi_{\nu} \\ & - j \sin kz \nabla_t \phi_0, \end{aligned} \quad (5)$$

*Work supported by the Department of Energy. We also wish to acknowledge the assistance of Dr. Y. Iwashita in performing numerical computations.

†On leave from the Institute for Chemical Research, Kyoto University, Japan

where \pm stand for $z \gtrless g/2$. Here μ, ϕ_μ, β_μ and A_μ are parameters associated with TM modes, with

$$\beta_\mu = (k^2 - p_\mu^2/a^2)^{1/2} = -j(p_\mu^2/a^2 - k^2)^{1/2} \quad (6)$$

and ν, ψ_ν, β_ν and B_ν are parameters associated with TE modes, with

$$\beta_\nu = (k^2 - q_\nu^2/a^2)^{1/2} = -j(q_\nu^2/a^2 - k^2)^{1/2}. \quad (7)$$

The functions ϕ_μ and ψ_ν are products of $\sin \theta$ or $\cos \theta$ and $J_1(p_\mu r/a)$ with $J_1(p_\mu) = 0$, or $J_1(q_\nu r/a)$ with $J_1'(q_\nu) = 0$.

In the iris region we replace a by b and write

$$\begin{aligned} E_t = & \sum_{\xi=1}^{\infty} F_\xi \cos \beta_\xi z \nabla_t \phi_\xi \\ & + \sum_{\eta=1}^{\infty} G_\eta \cos \beta_\eta z e_z \times \nabla_t \psi_\eta + \cos kz \nabla_t \tilde{\phi}_0 \end{aligned} \quad (8)$$

and

$$\begin{aligned} Z_0 H_t \times e_z = & -j \sum_{\xi=1}^{\infty} \frac{F_\xi k}{\beta_\xi} \sin \beta_\xi z \nabla_t \phi_\xi \\ & -j \sum_{\eta=1}^{\infty} \frac{G_\eta \beta_\eta}{k} \sin \beta_\eta z e_z \times \nabla_t \psi_\eta \\ & -j \sin kz \nabla_t \tilde{\phi}_0. \end{aligned} \quad (9)$$

We now equate Eqs. (4) and (8) at $z = g/2$ for E_t over the range $0 \leq r \leq a$ and thereby obtain A_μ and B_ν as a sum over various terms involving $\phi_0, \tilde{\phi}_0, F_\xi$ and G_η . Then we equate Eqs. (5) and (9) at $z = g/2$ for $Z_0 H_t \times e_z$ for $0 \leq r \leq b$ and obtain F_ξ and G_η as a sum over various terms involving $\phi_0, \tilde{\phi}_0, A_\mu$, and B_ν . By eliminating A_μ and B_ν between the two resulting sets of equations, we obtain the matrix equations for F_ξ and G_η

$$\sum_{\xi'} F_{\xi'} U_{\xi\xi'} + \sum_{\eta'} G_{\eta'} V_{\xi\eta'} = P_\xi \quad (10)$$

$$\sum_{\xi'} F_{\xi'} V_{\xi'\eta} + \sum_{\eta'} G_{\eta'} U_{\eta\eta'} = Q_\eta \quad (11)$$

where the parameters U, V, W, P , and Q are explicit sums of integrals involving the Bessel functions. Equations (10) and (11) can then be solved for F_ξ and G_η once we truncate the sums over ξ' and η' . A parallel analysis for the odd part of the source field, yields a similar set of equations.

Finally, we obtain an expression for the impedance as an integral over the three faces of the iris surface ($z = \pm g/2$ and $r = b$). This involves a term independent of F_ξ and G_η as well as ones proportional to F_ξ and G_η for both the even and odd source terms.

III. NUMERICAL RESULTS

We have obtained the transverse impedance for several sets of parameters. In Fig. 1 we show the real and

imaginary parts of the impedance as a function of kb for $a/b = 2, g/b = 1$. A matrix size of 40×40 appears to be sufficient for convergence in this case. The real part of the impedance appears to start at $kb \sim .9$ corresponding to the onset of a propagating TE_{11} pipe mode at $ka = 1.84$. The onset of the propagating TM_{11} mode at $kb \sim 1.9$ corresponding to $ka = 3.83$ also shows clearly.

In Fig. 2 we show the results for $a/b = 10, g/b = 1$. It now appears that the contribution from the TE_{11} mode for $1.84 < ka < 3.83$ is of the order 10^{-3} compared with that from the TM_{11} mode for $ka > 3.83$. For reasons not yet well understood, it appears that the TE modes are suppressed for large a/b . It should be noted that, for large a/b , larger matrices are needed for accurate numerical computation.

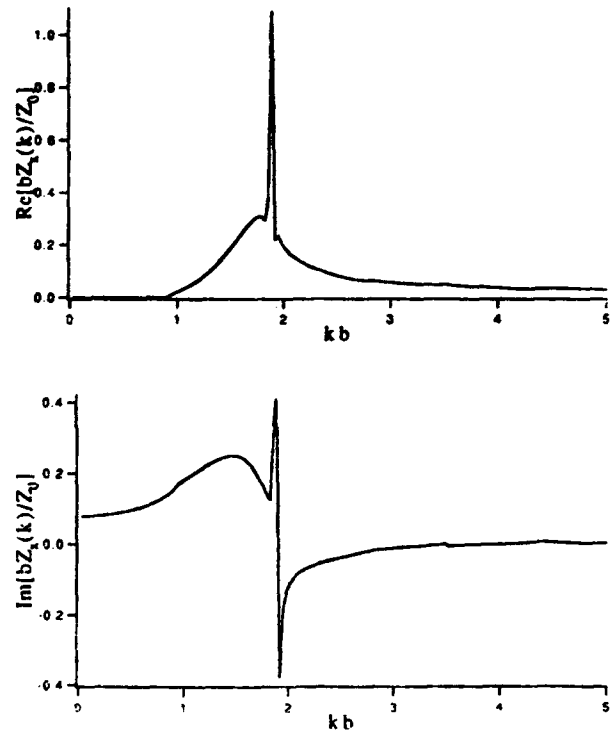


Figure 1: $bZ_x(k)/Z_0$ vs. kb for $a/b = 2, g/b = 1$.

In Fig. 3 we show the results for $a/b = 100, g/b = 1$. The TE_{11} mode is now of order 10^{-5} compared with the TM_{11} mode. And in this case we need a matrix of 250×250 to obtain suitable numerical accuracy.

Finally, we explore the case of a zero thickness wall by doing numerical calculations for $g/b = 0$ as well as for very small g/b . In Fig. 4 we show the result for $a/b = 10, g/b = 0$. Once again the contributions from the TE modes are much less than those for the TM modes.

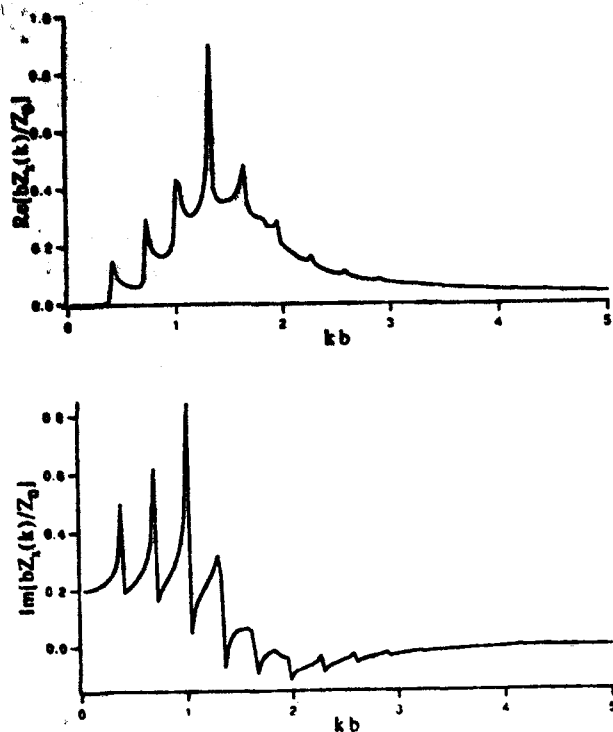


Figure 2: $bZ_s(k)/Z_0$ vs. kb for $a/b = 10$, $g/b = 1$.

IV. SUMMARY

We have briefly outlined the analysis for the transverse coupling impedance of an iris in a beam pipe and have implemented a numerical procedure to obtain values for different parameters. It appears that both TE and TM modes in the pipe region are needed to satisfy the boundary conditions. However the TE contributions fall rapidly to zero as a/b becomes large.

In future work we hope to obtain a variational formulation for the impedance, particularly in the case where $g/b \rightarrow 0$. In addition we would like to obtain the limiting forms for $a/b \rightarrow \infty$ for arbitrary g/b .

References

- [1] R.L. Gluckstern and W.F. Detlefs, Proceedings of the Particle Accelerator Conference, San Francisco, CA, May 1991, p. 1600.
- [2] R.L. Gluckstern and S. Jiang, Proceedings of the Linac Conference, Ottawa, Canada, Aug. 1992, p. 477.

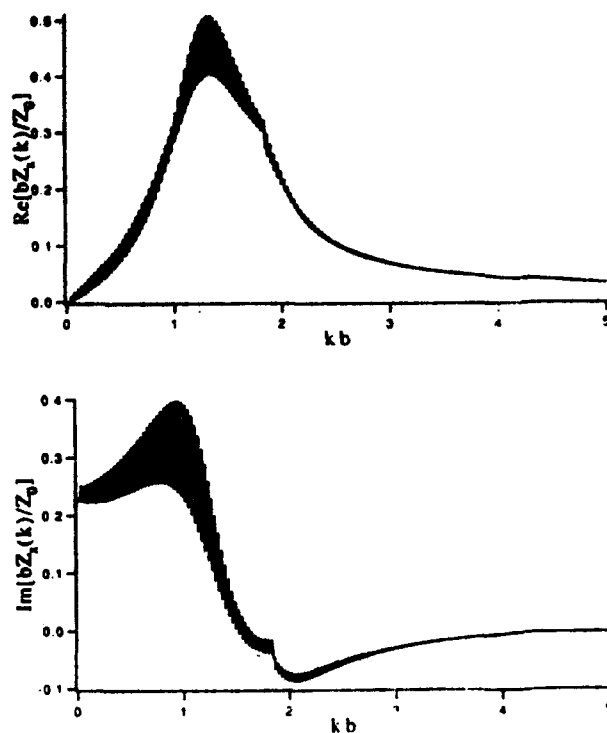


Figure 3: $bZ_s(k)/Z_0$ vs. kb for $a/b = 100$, $g/b = 1$.

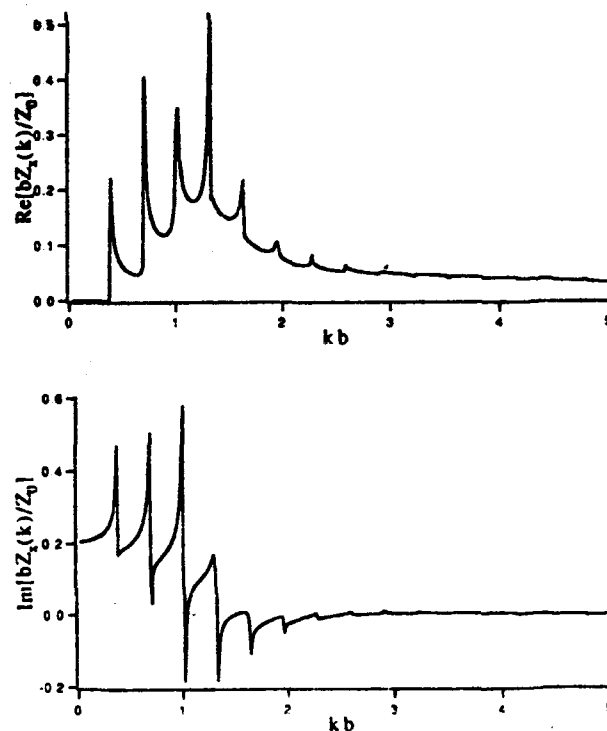


Figure 4: $bZ_s(k)/Z_0$ vs. kb for $a/b = 10$, $g/b = 0$.

RF Characteristics of the APS Storage Ring Isolation Valve*

J. J. Song, R. L. Kustom
Advanced Photon Source
Argonne National Laboratory
9700 S. Cass Ave, Argonne, IL 60439, USA

Abstract

The RF impedance of the isolation valve of the APS storage ring system was measured by the wire method with a synthetic pulse technique. The coupling impedance as well as the energy loss of the sector valve with and without an RF liner or screen, and the flange gap of the various sizes was measured. There appear to be resonances at certain frequencies without an RF liner that might cause an unacceptably large coupling impedance. Data with various sizes of the flange gap show that good RF contact around any flange is necessary. The impedance due to intrusions into the beam chamber was also measured. The results are compared with the computer simulation from MAFIA.

I. INTRODUCTION

The beam coupling impedance must be kept small so that the desired operating current (a maximum of 300 mA with a life-time of at least 10 hrs) can be achieved. To reduce the coupling impedance of the vacuum components in the APS storage ring, there are many places such as bellows, liners, RF isolation valves, RF ion pumps, and screened photon absorbers, that have various RF shielding structures. Among the concerns with RF shielding structures are vacuum, synchrotron radiation, RF heating, and coupling impedance. The photon absorber requires an intrusion into the beam chamber in front of the isolation valve to protect against direct photon radiation.

This paper presents the results of measurements using the wire method with a synthetic pulse technique [1]. A gating technique was applied to obtain the frequency domain reflection. The coaxial wire method is a widespread tool for bench measurements of beam coupling impedance. By sending a short pulse through the center wire of a transmission line or a vacuum chamber, the current distribution on the inner surface of the beam chamber can be obtained which corresponds similarly to the current distribution produced by a passing beam bunch.

The measurement procedure employed here is known as a synthetic pulse technique. Since any pulse defined as a function of amplitude over time can also be defined by its frequency spectrum of amplitude and phase, the synthetic pulse can be generated in the time domain (TD) via inverse fast Fourier transform (IFFT) from measurements taken in the frequency domain (FD). This leads to higher spectral density than real-time pulse measurements, thus giving a higher dynamic range and better repeatability.

* Work supported by US. Department of Energy, Office of Basic Sciences, under contract W-31-109-END-38.

II. LOSS PARAMETER AND IMPEDANCE

For a given particle beam bunch with charge q , the energy loss of the bunch is

$$\Delta E = kq^2 = 2Z_L q^2 \frac{\int I_1(I_1 - I_2) dt}{(\int I_2 dt)^2} \quad (\text{eV}), \quad (1)$$

where Z_L is the characteristic impedance of the transmission line or the wire running through the beam pipe, I_1 is the current flowing through the reference chamber (REF), I_2 is the current flowing through the device under test (DUT), and k is the loss parameter that is physically the energy loss in eV for a bunch with a unit charge passing through the vacuum component. Thus the longitudinal loss parameter, k , can be computed from measurements by the integration of the current over the pulse length such as:

$$k = 2Z_L \frac{\int I_1(I_1 - I_2) dt}{(\int I_2 dt)^2} \quad (\text{V/pc}), \quad (2)$$

It must be pointed out that k is also a function of particle bunch length, σ . The broadband impedance represents the impedance of a non-resonant device (e.g. any little discontinuity around the storage ring), which is given as:

$$Z = \frac{Z(\omega)}{n} \quad (\Omega), \quad (3)$$

assuming that $Q=1$, where $n = \omega/2\pi f_0$ ($f_0 = 1/T_0$ is the revolution frequency of the beam in the storage ring) and $Z(\omega)$ is the individual mode impedance of the DUT in the FD. $Z(\omega)$ can also be computed from the measurements,

$$Z(\omega) = 2Z_L \frac{[I_1(\omega) - I_2(\omega)]}{I_2(\omega)} \quad (\Omega), \quad (4)$$

where $I_1(\omega)$ and $I_2(\omega)$ are the current measured in the FD with the REF and the DUT, respectively. The wake potential is defined as the integrated perturbed electromagnetic energy acting on the beam bunch with a unit charge and can be also derived by transforming Eq. (4) into the TD,

$$W_b(t) = \frac{2Z_L [I_1(t) - I_2(t)]}{q} \quad (\text{V/pc}). \quad (5)$$

III. EXPERIMENTAL SETUP

A. RF Liner

A VAT isolation valve (model S-47) was tested to evaluate the RF characteristics of the RF liner. An RF liner of the model S-47 consists of 64 shielding screens each 1.8 mm wide, 4.3 cm long, 0.1 mm thick with 1.3 mm gap. More detailed specifications can be found in reference [2].

As depicted in Fig. 1, a network analyzer (HP 8510B) was used to measure the two-port S-parameters of the DUT. All the data was transferred to the PC 486 computer for analysis, using the HP Basic 6.0 program language.

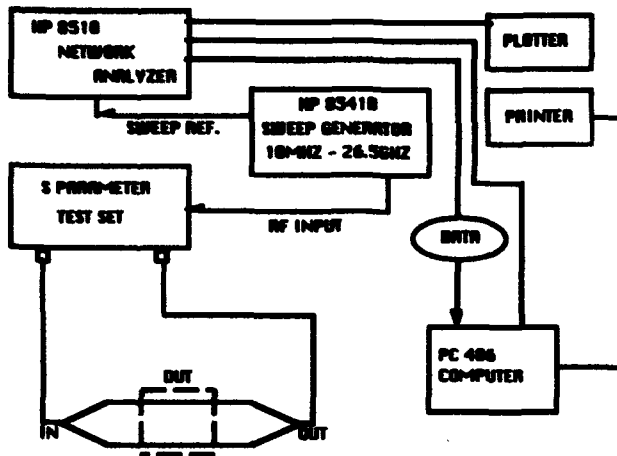


Fig.1 Experimental Setup for Synthetic Pulse Technique

B. Photon Absorber Intrusion

The measurement was done with two different types of intrusions: a round one (7 cm in diameter) and a linear one (10 cm in length). They were inserted from the antechamber through the 1-cm slot into the beam chamber. The intrusion was varied from 0 to 2.5 cm in 0.5 cm steps. The data was taken with the synthetic pulse techniques as mentioned above. To verify the synthetic pulse techniques, the measurement was also done with the real-time pulse.

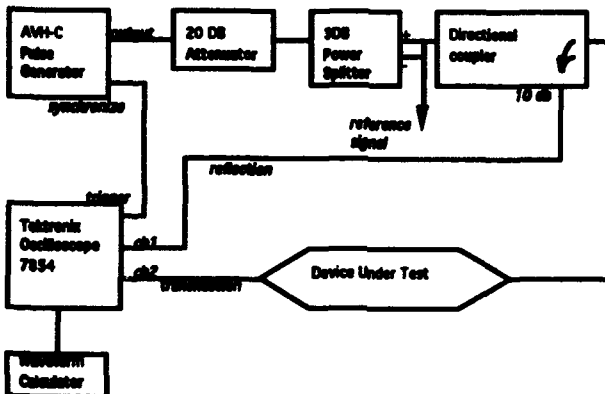


Fig.2 Experimental Setup for Real-Time Pulse Technique.

Figure 2 shows the setup for real-time pulse measurement. The signal is an 8-Volt 140-ps Gaussian pulse generated by an AVH-C pulser. The 20-dB attenuator is used to prevent the pulsar from load mismatch. A Tektronix 7854 sampling oscilloscope that can record data with up to 512 points on one screen was used with its waveform averaging function to significantly reduce the random error. Waveform parameters (area, RMS value, maximum, minimum, etc.) are calculated using the attached calculator.

IV. MEASUREMENTS AND RESULTS

A. RF Liner

The typical transmission data (S21) in the frequency domain is shown in Fig. 3. The top curve comes from the reference beam chamber and the bottom curve is from the standard valve without an RF liner. As seen, there are resonances at 2.3, 5.9, and 9.4 GHz. The Qs of these resonances are high enough to unacceptably lower the thresholds for multibunch beam instabilities. The RF liner in the valve solves the problem as shown in Fig. 4. The cavity-like resonances are eliminated but the broadband impedance of the DUT is still significant (maximum of $Z/n \sim 0.002 \Omega$).

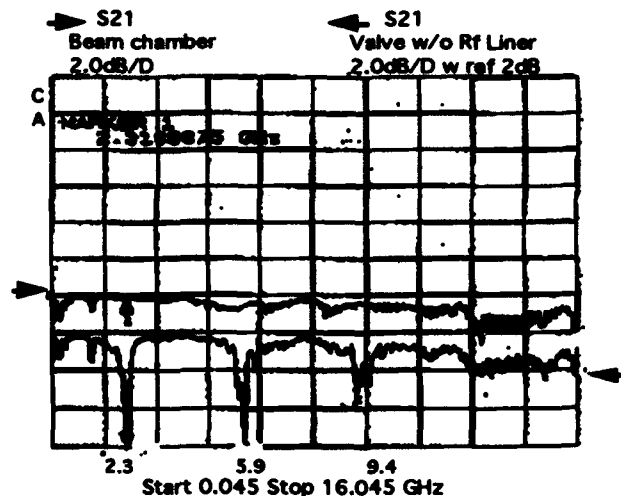


Fig.3 The transmission in FD

A gap existed at the flanges between the isolation valve and the short reference beam chamber. This generated a weak peak around 2 GHz. By filling the gap with an RF gasket for the flange on each side, the impedance due to the whole system was reduced to about $4 \times 10^{-4} \Omega$ (see Fig. 6). Also using the gating function built into the HP 8510, the impedance contribution due to the valve itself is separated from the gasket. More detailed measurement results can be found in reference [3].

The loss factor was measured in the time domain and the results are summarized in Table 1. The bunch length-dependence of the loss factor is plotted in Fig. 4. This was done by varying the frequency span to get a different synthetic pulse length.

Table 1 Impedance and Loss Factor of Isolation Valve

Isolation Valve	Impedance Z/n (Ω)	Loss Factor K (V/pc)
w/o RF Liner, Gasket	0.08	0.1
w RF Liner, but w/o Gasket	0.002	0.01
w RF Liner, Gasket, but no Gating	4×10^{-4}	4×10^{-3}
w RF Liner, Gasket, & Gating	4×10^{-5}	not available

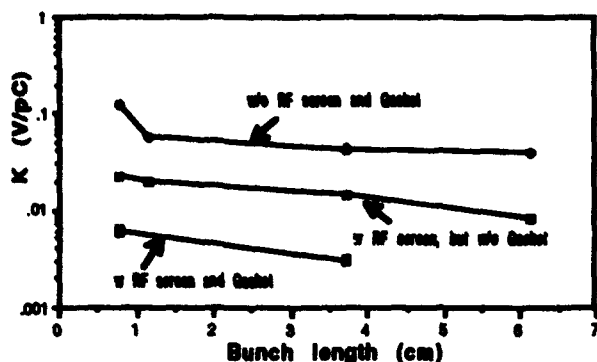


Fig. 4 Loss Factor of Isolation Valve, varying the frequency span to get a different bunch length of the beam

B. Photon Absorber Intrusion

The energy loss due to the intrusion can also be measured with the reflected signal similar to Eq. (1). The loss parameter calculated with the synthetic pulse from S11 is shown in Fig. 5. It can be easily seen that the loss parameter of the linear intrusion is significantly less than the round one with same amount of intrusion. A similar conclusion has been made with MAFIA calculations. [4]

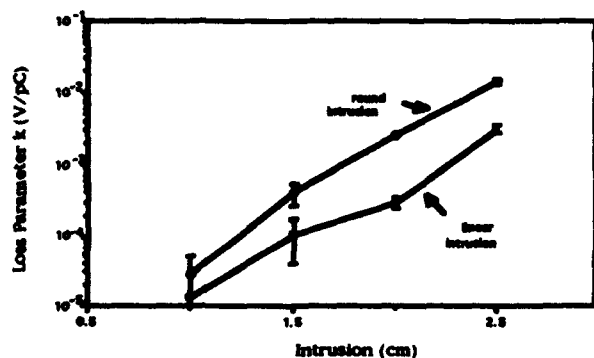


Fig. 5 Loss Parameter for Round and Linear Intrusions Obtained from Synthetic Pulse Measurements

C. Synthetic Pulse vs. Real-Time Pulse

To verify the synthetic pulse techniques, a real-time pulse was employed to measure the loss parameter. The transmission data was measured with the round intrusion, having similar measurement parameters such as pulse length, average number, etc. [5]. As one can see in Fig. 6, the results from the two techniques are in very good agreements. But the measurement error with the real-time pulse is larger because of jitter in the pulse generator. The real-time pulse is not suitable for small loss factor measurement below 1×10^{-3} V/pc.

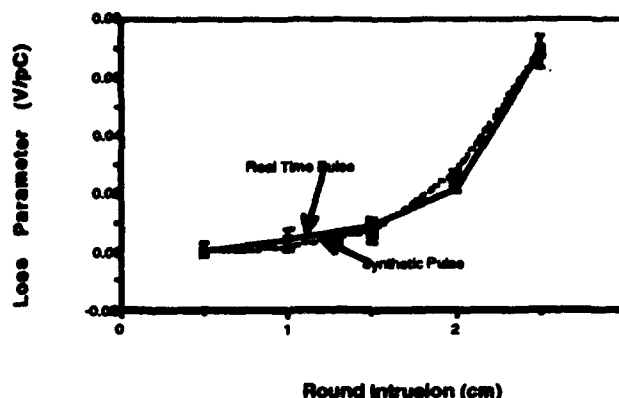


Fig. 6 Synthetic Pulse vs. Real-Time Pulse, S21 measured with the Round Intrusion.

V. CONCLUSION AND DISCUSSION

An RF liner in the isolation valve and a good RF contact between the flanges reduced the coupling impedance to a satisfactorily low level. The measured impedance due to 160 isolation valves was about 0.4 percentage of the total APS impedance budget.

The intrusion due to the photon absorber should not penetrate more than 1.5 cm from the slot into the beam chamber to avoid increasing the coupling impedance. The linear intrusion gives less impedance than the round intrusion.

VI. ACKNOWLEDGMENTS

The author would like to thank J. W. Howell for his mechanical engineering support. Also thanks must be given to D. F. Voss and P. Young for their technical support.

VII. REFERENCES

- [1] J. J. Song, "Experimental Study of Coupling Impedance," APS Light Source Note LS-201, ANL, Oct 11, 1991.
- [2] VALVE DATA SHEET No. e-72453-01 for RF All-Metal Gate Valve from VAT.
- [3] J. J. Song, "RF Characteristics of the APS Storage Ring Isolation Valve," to be published.
- [4] L. Teng, "Single and Multibunch Instability," presented at the Accelerator Advisory Committee Meeting, Nov. 11-12 1991.
- [5] J. H. Zhou, "Intrusion Measurements, Synthetic Pulse vs. Real Pulse," to be published.

Coupling Impedance of Vacuum Pumping Holes for the APS Storage Ring*

J. Zhou**, J. J. Song, R. L. Kestom
Advanced Photon Source
Argonne National Laboratory
9700 S. Cass Ave, Argonne, IL 60439, USA

Abstract

The coupling impedance of a single slot in a thick wall beam pipe was measured. The slot dimension is small compared to the wavelength of interest. The measurements were done by the wire method with the synthetic pulse technique[1]. Gating technique was also applied to obtain the reflection response for a structure that does not have appropriate calibration standards. The measured results are in good agreement with calculated impedance using analytical formulae given by other authors.

I. INTRODUCTION

In the design of storage ring components for the Advanced Photon Source (APS), it is often necessary to open vacuum pumping holes in the beam chamber wall. These holes are long and narrow, located in the longitudinal direction of the beam pipe to minimize their disturbance to the wall current. Since there are a great number of such holes in the storage ring, the impedance induced by these slots is of much concern.

This paper presents the result of a measurement on the coupling impedance due to a single slot using the wire method with synthetic pulse technique. Gating technique was applied to obtain the frequency domain reflection of the slot when calibration standards were not available for the beam chamber. The results show that this method is much more capable in measuring small signals than real pulse measurement. The measured impedance was compared with calculations.

II. THEORETICAL CALCULATION

In the past decades, extensive studies on the aperture coupling problem have been done by many researchers. Most of these studies were based on Bethe's theory of diffraction by small apertures [1]. An aperture is considered small if its dimension is less than a fraction of the wavelength of the excitation signal. Reflected and coupled fields were generated due to the existence of the aperture. These fields can be considered as excited by equivalent sources that consist of an electric dipole, a magnetic dipole, and a magnetic quadrupole[3]. The electric polarizability and magnetic susceptibility of these dipoles are readily available for circular, elliptic, and other common apertures [2], [3]. The beam coupling impedance of an aperture can be expressed in terms of these polarizabilities [3]. A long narrow slot can be approximated by an ellipse with a large eccentricity. The coupling impedance of such a rectangular slot is given by [4]:

$$Z(\omega) = \frac{jZ_0\pi w^4}{96\pi c b^2 \ell} \left(\ln \frac{4\ell}{w} - 1 \right) \quad (1)$$

where Z_0 is the characteristic impedance of the beam pipe and center wire structure; ω is the angular frequency of excitation; c is the speed of light; ℓ and w are the length and width of slot; and b is the radius of cylindrical beam pipe.

In Eq.(1), the slot is considered to be of zero thickness. According to R. Gluckstern [5], the coupling impedance of a circular hole in an infinitely thick wall will have a value which is 56 % of that for zero thickness. We can take this value as a reasonable estimation on the impedance reduction for the rectangular slot.

Note that the coupling impedance is purely imaginary below cut-off frequency of the beam pipe and is linearly proportional to the angular frequency ω .

In this measurement, the beam pipe has a rectangular cross section. Since Eq.(1) only applies to circular beam pipes, we use an estimated radius of the rectangular pipe for the calculation. The parameters for the test chamber are: $Z_0=88 \Omega$; $\ell=5$ cm; $w=0.4$ cm; $b=2$ cm. The calculated result is shown in Fig. 3.

III. EXPERIMENTS

3.1 Coupling Impedance by Reflection

The experimental setup is shown in Fig. 1. The test chamber has a rectangular cross section with a dimension of 7 x 4 cm. A narrow slot is placed longitudinally in the middle of the common wall. The slot dimension is 5 x 0.4 cm. The thickness of the beam pipe is 0.64 cm. The measurements were made in the frequency domain (0.045–4.545 GHz) using a HP 8510B network analyzer. There are 201 data points measured for the reflection S_{11} . The average function of the analyzer was applied to reduce the noise level. The results were transformed into time domain by the built-in IFFT routine. Since there are no calibration standards available for the rectangular pipe, the calibration can only be made up to the end of the connecting cables. In order to eliminate all the reflections from the tapers and adapters, the Gating function was applied to the reflected synthetic pulse. In this way, the reflection due to the slot itself was obtained in the time domain as well as in frequency domain. This result can be used directly to estimate the coupling impedance of the single narrow slot.

There are two things one has to consider in this Gating technique. One is the influence of the taper on the magnitude of the pulse. The typical reflection coefficient of the taper is $\Gamma = 0.3$. Since the reflected pulse travels twice through the taper, its magnitude is reduced by a factor of $1 - \Gamma^2 = 90\%$. The other thing is that there is a DC current component contained in the synthetic pulse, which is the offset due to systematic error. If this component is not eliminated in the time domain

* Work supported by U.S. Department of Energy, Office of Basic Sciences, under contract W-31-109-END-38.

** Dept. of ECE, Illinois Institute of Technology.

data, then the resulting S_{11} in the frequency domain would be distorted dramatically at low frequencies. In order to eliminate this error, a reference chamber which has no slot in the chamber wall, was used. The time domain response of the reference chamber was subtracted from that of the slot. The obtained results in the time and frequency domains are shown in Fig. 2. The reflection detected by this method is on the order of 10^{-4} . This is far beyond the capability of real pulse measurement for detecting such a small reflection.

Suppose the conduction and radiation loss in the slot is negligible. After some derivation, we obtain the beam coupling impedance in terms of S_{11} :

$$\frac{Z}{n} = \frac{Z_L |S_{11}|^2}{n} \quad (2)$$

where $n = \ell/f_0$, f_0 is the revolution frequency of the beam in the storage ring (271.55 KHz for APS) and Z_L is the characteristic impedance of the test chamber and center wire structure.

The coupling impedance of one slot obtained using Eq. (2) is plotted in Fig. 3. It can be seen that the result is in good agreement with the calculation of Eq.(1). The $\frac{Z}{n}$ of the slot is estimated to be $2 \times 10^{-8} \Omega$. The measured result deviates from the calculation when $f > 1.5$ GHz. This implies that the small hole approximation is valid for $f < 1.5$ GHz ($\ell < 0.2\lambda$).

3.2 Coupling Impedance by Radiation

In the previous section we obtained the coupling impedance due to the reflection under the assumption that the radiated energy loss through the slot is negligible. While the reflected energy corresponds to the imaginary part of the impedance $\text{Im}(Z)$, the radiation energy loss contributes to the real part of the coupling impedance $\text{Re}(Z)$. According to the derivation of S. Kurennoy [3], for a small hole ($\ell/\lambda \ll 1$), we have the relation:

$$\frac{\text{Re}Z}{\text{Im}Z} \sim \left(\frac{\ell}{\lambda}\right)^3 \ll 1 \quad (3)$$

Figure 4 shows the result for coupling measurement. The top two curves are S_{41} , S_{31} , which represent the signal coupled through the slot from port 1 to ports 4 and 3, respectively. These frequency domain responses are obtained by applying Gating function to the time domain synthetic pulse. Observe that S_{31} is about 20 dB higher than S_{41} ; the slot behaves like a directional coupler in the measured frequency range. The bottom two curves are time domain synthetic pulse responses for ports 3 and 4. The second peak in S_{41} is from the multiple reflection of port 3 because the matching tapers do not have very good characteristic at these low frequencies. This can be verified from the 4-ns time delay between the two peaks which exactly corresponds to the length of the chamber. From the time domain result, we can see that the coupling signal, S_{31} , is 53 μUnits while the reflected signal is 520 μUnits (see Fig. 3). Thus the energy radiated through the slot is about only 1 percent of that reflected by the slot. This verified the estimation of Eq.(3).

It is also observed from Fig. 4 that S_{31} has a linear dependence on frequency, since the top curve, which is for S_{31} ,

is quite similar to a logarithm curve on the semi-log plot. This conclusion holds only for a small slot ($\ell/\lambda \ll 1$). Figure 5 is the measurement result of the same slot for S_{31} up to a higher frequency (4 GHz). The linearity of S_{31} is only seen for $f < 1$ GHz. A resonance at 3 GHz is observed. Recall that the slot length is 5 cm; this resonance happened at half wave-length ($\ell = \lambda/2$). Similar resonance was also observed for reflection (S_{11}) at the same frequency (not shown here). Since both reflection and coupling were observed to have a reduced amplitude at resonance, one should anticipate that the transmission (S_{21}) has a maximum value when the half wavelength equals the slot length. Until now, we were not able to observe this directly from measurement.

Fig. 6 shows the measured coupling for different wall thicknesses. From top to bottom, the three curves are for wall thicknesses of 0.4, 3.2, and 6.4 mm, respectively. On this semi-log plot, the three curves are equally spaced by a 20-dB difference. This suggests that the coupling depends on wall thickness exponentially. This agrees with the prediction of M. Sands [6].

IV. CONCLUSION AND DISCUSSION

The beam coupling impedance of a single slot has been measured using the wire method with synthetic pulse technique. Gating was applied to eliminate the influence of tapers and adapters. The systematic error in the time domain response was corrected using a reference chamber. The measured results agree quite well with analytical formulae given by other authors. The impedance Z/n of a single slot was measured to be $2 \times 10^{-8} \Omega$. For small holes, the impedance is dominated by its imaginary part which is due to reflection. Its real part, which is due to radiation loss through the hole, is negligible. The small aperture approximation is valid when slot length is less than one-fifth of the wavelength. Both reflection (S_{11}) and coupling (S_{31}) have a linear dependence on frequency for small holes. Resonance was observed when the half wavelength equals slot length ($\ell = \lambda/2$). The influence of the wall thickness on reflection and coupling was also examined from measured results.

V. ACKNOWLEDGMENTS

The authors would like to thank F. Caspers for his valuable discussions on this measurement. Thanks must also be given to P. Young and D. Freeman for their help in measurements.

VI. REFERENCES

- [1] J. J. Song, "Experimental Study of Coupling Impedance Part I Longitudinal Impedance Measurement Techniques," LS-Note-201, 1991.
- [2] H. A. Bethe, "Theory of diffraction by small holes," Phys. Rev., Vol. 66, p. 163, 1944.
- [3] R. E. Collin, "Field Theory of Guided Waves," p.499-533, IEEE Press, 1991.
- [4] S. S. Kurennoy, "Beam Coupling Impedance of Holes in Vacuum Chamber Walls," CERN Report SL/91-29(AP) Rev., July, 1991.

- [5] R. L. Gluckstern, "Coupling Impedance of a Single Hole in a Thick Wall Beam Pipe," CERN SL/92-05(AP), Jan., 1992.
 [6] M. Sands, "Energy Loss from Small Holes in the Vacuum Chamber," FEP-253, Sept., 1977.

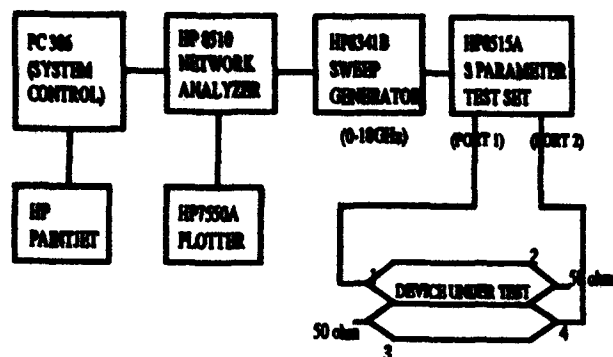


Fig. 1 Experimental setup for single slot measurement

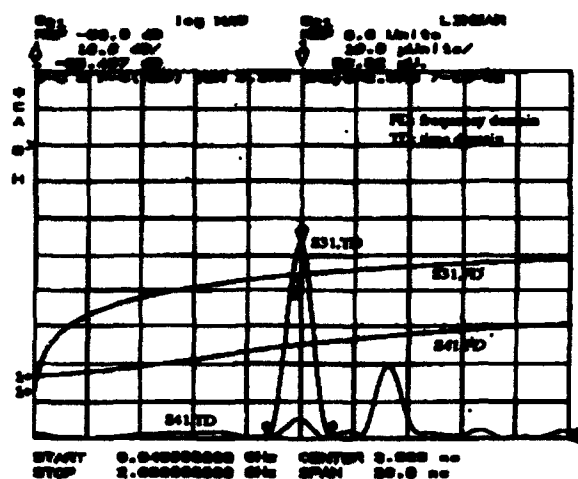


Fig. 4 Coupling of single slot in frequency and time domains

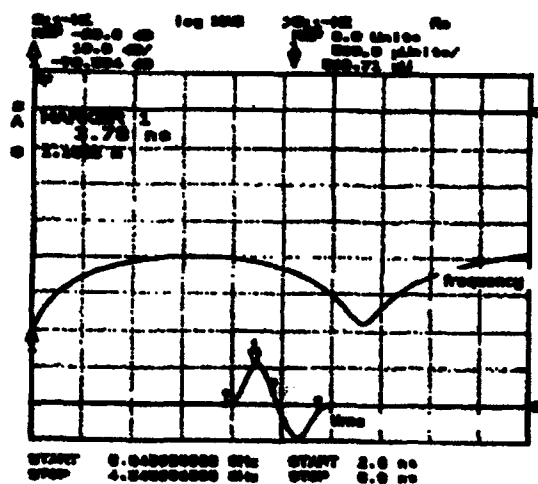


Fig. 2 Reflection of single slot measured in frequency and time domains

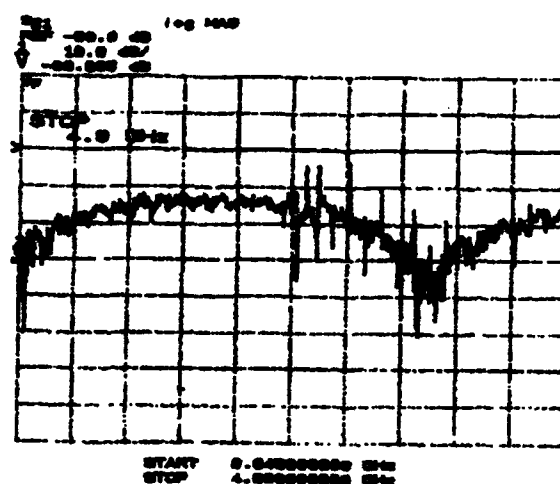


Fig. 5 Wide band characteristics of single slot.

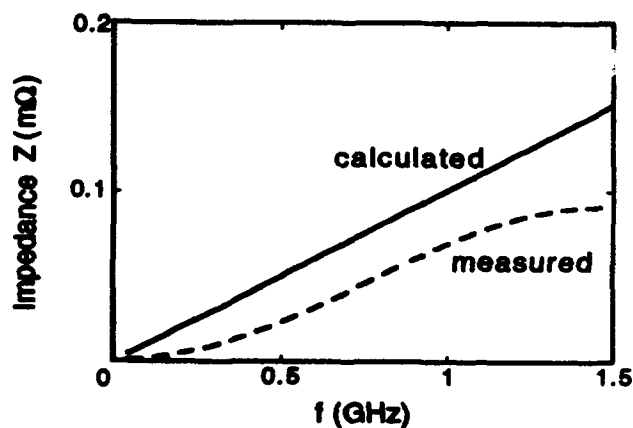


Fig. 3 Measured and calculated impedance of single slot.

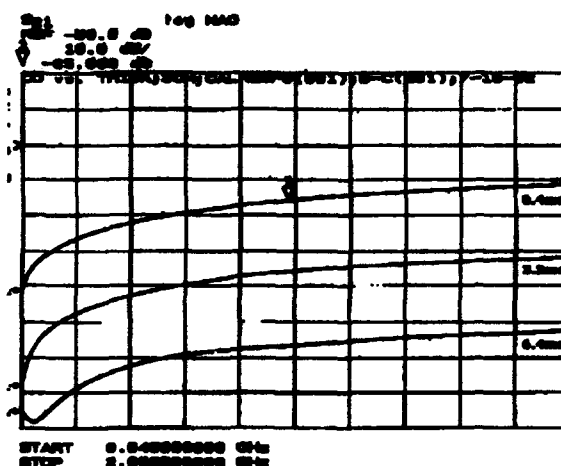


Fig. 6 Coupling of single slot in different wall thicknesses

Impedance Formalism for an Arbitrary Cumulative Instability

X.T. Yu and J.S. Wurtele*

Department of Physics and the Plasma Fusion Center
Massachusetts Institute of Technology, Cambridge, MA, 02139

and

D.H. Whittum†

National Laboratory for High Energy Physics (KEK), Tsukuba, Oho, Ibaraki, Japan 305

Abstract

A formalism is developed for the analysis of collective instabilities in standing-wave systems. The analysis permits a unified treatment of the coupled-cavity free-electron laser, relativistic klystrons and other high power microwave sources. Coupling from both transverse and longitudinal beam motion is included in the calculation of the transverse and longitudinal impedances.

I. INTRODUCTION

An understanding of high-power microwave sources and their scalings is crucial to the future of high-energy electron-positron colliders. In fact, the tradeoffs between rf breakdown and beam break-up scalings [1] is responsible for the current consensus that future linear colliders should be powered by sources with an operating frequency in the 10-20 GHz range. Slow-wave devices are expected to produce the power levels required at the lower frequencies. However, they have also exhibited, at higher frequencies, what is, in fact, an intrinsic problem for such rf sources: when the structure is small enough to couple effectively to the longitudinal beam motion, it also couples effectively to the transverse motion. This results in, among other undesirable phenomena, beam break-up and pulse shortening [2].

To circumvent this scaling, the "coupling impedance" [3] of the desired longitudinal mode should scale independently from that for those TM modes which produce beam break-up. In effect, this requires circumventing the Panofsky-Wenzel theorem [4]. One method of accomplishing this has been proposed in the form of a "standing-wave" free-electron laser, in which transverse oscillatory motion is induced by a magnetic wiggler. Since the design orbit takes the beam off-axis, the premise of the Panofsky-Wenzel theorem fails, as does its conclusion.

*Work supported by U.S. Dept. of Energy, Division of Nuclear and High Energy Physics

†Work supported by the Japan Society for the Promotion of Science and the US National Science Foundation.

In this work we derive a formalism for quantifying such effects in an idealized cavity immersed in an arbitrary plane polarized magnetic field. The formalism in essence extends the wealth of work on longitudinal [6] and transverse [7] instabilities to include systems where the design particle orbit is curved within the cavity. In such "magnetized cavities" the coupling impedance describing longitudinal bunching can depend on the applied field. This permits one to enlarge the rf structure, so as to reduce undesirable transverse wakefields, while maintaining the desired longitudinal coupling. Previous workers [8] have calculated the coupling impedances in a cyclotron resonance maser with a traveling wave interaction region and a single cavity.

In the SWFEL, the power is produced in a series of uncoupled cavities (the rf is cutoff between the cavities), each of which is of order one wiggler oscillation in length. The FEL thus operates as a standing-wave device. The propagating beam provides the only coupling between the cavities. Numerical studies [9] of the SWFEL have examined phase sensitivity and longitudinal particle stability. In fact, the standing wave FEL has many similarities to the relativistic klystron, the main difference between them being that the FEL produces power through the coupling of the transverse wiggler oscillation with the transverse E field, while the klystron couples the longitudinal components (E_z with v_z).

II. COUPLING IMPEDANCES

Assume that a bunch with unit charge enters a cavity at $t = 0$. The particles move transversely as well as longitudinally, due the presence of a magnetic field. Their trajectory and velocity inside the cavity is

$$\mathbf{r}(z) = z_1(z)\hat{x} + z_2(z)\hat{y}, \mathbf{v}(z) = v_1(z)\hat{x} + v_2(z)\hat{y}. \quad (1)$$

As the bunch moves through the cavity, it excites cavity modes. Without loss of generality, we may consider a single cavity mode. The vector potential of the mode can be represented as

$$\mathbf{A} = \frac{mc^2}{e} q(t) \mathbf{a}(\mathbf{r}), \quad (2)$$

where $a(r)$ satisfies the appropriate boundary conditions on the wall and is normalized to the volume V of the cavity:

$$\int d^3r |a(r)|^2 = V. \quad (3)$$

Also, $q(t)$ is the amplitude of the cavity excitation and can be determined from a knowledge of trajectory and velocity of the bunch:

$$q(t) = \frac{4\pi c}{V} \frac{e}{mc^2} \int_0^L dz' G(t - \frac{z'}{v_s}) a(x_1(z'), 0, z') \cdot \frac{v_1(z')}{v_s}. \quad (4)$$

Here $G(t)$ is the cavity response Green function:

$$G(t) = \frac{1}{\Omega_\lambda} \sin \Omega_\lambda t e^{-\Omega_\lambda/2 Q_\lambda} \theta(t), \quad (5)$$

where $\Omega_\lambda^2 = \omega_\lambda^2 - (\frac{\omega_\lambda}{Q_\lambda})^2$, with ω_λ the resonant frequency in the absence of damping and Q_λ the quality factor of the excited mode. $\theta(t)$ is the step function.

We assume a unit charge test particle enters the cavity at time $t = t_0$ with trajectory $r_2(z)$ and velocity $v_2(z)$. The test particle will experience the cavity mode excited by the first bunch. The longitudinal wakefield, defined to be the total energy loss of the test particle, is then

$$W^\parallel(t_0) = \frac{4\pi}{V} \int_0^L dz \int_0^L dz' G'(t_0 + \frac{z-z'}{v_s}) a(x_1(z'), 0, z') \cdot \frac{v_1(z')}{v_s} a(x_2(z), 0, z) \cdot \frac{v_2(z)}{v_s}. \quad (6)$$

We are interested in the cases where the initial offsets for both the leading and trailing bunches are small. Then, the dominant contributions to the longitudinal wakefield can be computed assuming both bunches follow the same orbit:

$$W^\parallel(t_0) = \frac{4\pi}{V} \int dz e^{i\Omega_\lambda z/v_s} a(x(z), 0, z) \cdot \frac{v(z)}{v_s} |G'(t_0)|^2. \quad (7)$$

The longitudinal coupling impedance is

$$Z_\lambda^\parallel(\omega) = \int_{-\infty}^{+\infty} dt e^{i\omega t} W^\parallel(t) = R_\lambda^\parallel \frac{1}{1 + iQ_\lambda(\frac{\omega}{\omega_\lambda} - \frac{\omega}{\omega_\lambda})}. \quad (8)$$

In Eq. 8, the longitudinal shunt impedance R_λ^\parallel is given by

$$\frac{R_\lambda^\parallel}{Q_\lambda} = \frac{4\pi}{\omega_\lambda V} \left| \int dz e^{i\Omega_\lambda z/v_s} a(x(z), 0, z) \cdot \frac{v(z)}{v_s} \right|^2. \quad (9)$$

This expression is valid for any particle orbit in the cavity, and includes both the transverse and longitudinal coupling.

As an example, consider the SWFEL in the limit that the betatron motion can be ignored (i.e., the betatron phase advance per cavity is small). The one-dimensional vector potential for a planar wiggler, $A_w = \frac{m c^2}{e} a_w \cos k_w z \hat{x}$, can be used to find the particle motion:

$$\begin{aligned} r_\perp(z) &= [x(0) - \frac{c a_w}{\gamma v_s k_w} \sin k_w z] \hat{x} + O(\frac{a_w}{\gamma})^2, \\ v(z) &= -\frac{c a_w}{\gamma} \cos k_w z \hat{x} + v_s \hat{z} + O(\frac{a_w}{\gamma})^2. \end{aligned} \quad (10)$$

Further calculations of the shunt impedance require a knowledge of the cavity mode. Here we take the modes of a rectangular cavity with transverse dimensions a and b , and longitudinal dimension d . $x(0) = a/2$ is at the center of the cavity. For the operational mode TE_{01p} , the shunt impedance is

$$\frac{R_{01p}^\parallel}{Q_{01p}} = \frac{4\pi}{\omega_{01p} V} (\frac{a_w d}{2\gamma \beta_s})^2. \quad (11)$$

For other modes (TE and TM), the shunt impedance is non-zero only if n is odd. With m even, and a TE mode,

$$\frac{R_{mnp}^\parallel}{Q_{mnp}} = 2 \frac{R_{01p}^\parallel}{Q_{01p}} \frac{(\frac{n}{2})^2}{(\frac{m}{2})^2 + (\frac{n}{2})^2} (\frac{\sin \theta}{\theta})^2. \quad (12)$$

Here $\sin \theta/\theta$ is the largest transit time factor with $\theta = (\frac{\Omega_\lambda}{v_s} \pm \frac{p\pi}{d} \pm k_w) d/2$. When m is odd,

$$\frac{R_{mnp}^\parallel}{Q_{mnp}} = 2 \frac{R_{01p}^\parallel}{Q_{01p}} \frac{(\frac{n}{2})^2}{(\frac{m}{2})^2 + (\frac{n}{2})^2} A_m^2 (\frac{\sin \theta}{\theta})^2. \quad (13)$$

Here $A_m = (m\pi a_w / \gamma \beta_s k_w) a$, and $\theta = (\frac{\Omega_\lambda}{v_s} \pm \frac{p\pi}{d} \pm 2k_w) d/2$. When the mode is TM and m is even,

$$\frac{R_{mnp}^\parallel}{Q_{mnp}} = \frac{4\pi}{\omega_{mnp} V} \frac{2\delta^2 d^2}{\delta^2 + (\frac{p\pi}{d})^2} (1 \pm \frac{k_w}{2} \frac{p\pi}{\delta^2})^2 A_m^2 (\frac{\sin \theta}{\theta})^2. \quad (14)$$

Here, $\delta^2 = (\frac{m\pi}{2})^2 + (\frac{n\pi}{2})^2$ and the $\theta = (\frac{\Omega_\lambda}{v_s} \pm \frac{p\pi}{d} \pm k_w) d/2$. When m is odd,

$$\frac{R_{mnp}^\parallel}{Q_{mnp}} = \frac{4\pi}{\omega_{mnp} V} \frac{2\delta^2 d^2}{\delta^2 + (\frac{p\pi}{d})^2} (\frac{\sin \theta}{\theta})^2, \quad (15)$$

and $\theta = (\frac{\Omega_\lambda}{v_s} \pm \frac{p\pi}{d}) d/2$.

The transverse impedance is found from the Fourier transform of the transverse kick per unit charge. For simplicity, we present results only for particle motion in x -direction (the wiggle plane). The transverse force experienced by a unit charge test particle is:

$$F_x = -\frac{1}{c} \frac{dA_x}{dt} + \frac{\partial}{\partial x} (\frac{v}{c} \cdot A). \quad (16)$$

The net transverse kick is

$$K(t_0) = \int_{t_0}^{t_0+L/v_s} dt F_x. \quad (17)$$

Assuming the front and end walls of the cavity are perpendicular to the axis, we can drop the surface term and find

$$K(t_0) = \frac{4\pi}{V} \int_0^L dz \int_0^L dz' G(t_0 + \frac{z-z'}{v_s}) a(x_1(z'), 0, z') \cdot \frac{v_1(z')}{v_s} \frac{\partial}{\partial x} a(x_2(z), 0, z) \cdot \frac{v_2(z)}{v_s}. \quad (18)$$

Expanding $K(t)$ with respect to an initial offset x_0 of the leading bunch yields $W^\perp(t_0) = K(t_0)/x_0$:

$$W^\perp(t_0) = \frac{4\pi}{V} \left| \int_0^L dz e^{i n_\lambda z / v_s} \frac{\partial}{\partial x} a(x(z), 0, z) \cdot \frac{v(z)}{v_s} \right|^2 G(t_0). \quad (19)$$

Using Eqs. 5 and 19,

$$Z_\lambda^\perp(\omega) = -ic \int_{-\infty}^{+\infty} dt e^{i\omega t} W^\perp(t) = R_\lambda^\perp \frac{\omega_\lambda / \omega}{1 + iQ_\lambda(\frac{\omega_\lambda}{\omega} - \frac{\omega}{\omega_\lambda})}. \quad (20)$$

In Eq. 20, the transverse shunt impedance is given by

$$\frac{R_\lambda^\perp}{Q_\lambda} = \frac{4\pi c}{\omega_\lambda^2 V} \left| \int dz e^{i n_\lambda z / v_s} \frac{\partial}{\partial x} a(x(z), 0, z) \cdot \frac{v(z)}{v_s} \right|^2. \quad (21)$$

Comparing with the longitudinal shunt impedance, Eq. 9, we note a derivative of the vector potential with respect to the transverse position. Thus, we can read off the results for the transverse impedance. For the TE modes, when both n and m are odd,

$$\frac{R_{mnp}^\perp}{Q_{mnp}} = 2 \frac{c}{\omega_{mnp}} \left(\frac{m\pi}{a} \right)^2 \frac{R_{01p}^\parallel}{Q_{01p}} \frac{(\frac{n}{b})^2}{(\frac{m}{a})^2 + (\frac{n}{b})^2} \left(\frac{\sin \theta}{\theta} \right)^2. \quad (22)$$

When n is odd and m is even,

$$\frac{R_{mnp}^\perp}{Q_{mnp}} = 2 \frac{c}{\omega_{mnp}} \left(\frac{m\pi}{a} \right)^2 \frac{R_{01p}^\parallel}{Q_{01p}} \frac{(\frac{n}{b})^2}{(\frac{m}{a})^2 + (\frac{n}{b})^2} A_m^2 \left(\frac{\sin \theta}{\theta} \right)^2. \quad (23)$$

For the TM modes, when both n and m are odd,

$$\frac{R_{mnp}^\perp}{Q_{mnp}} = \left(\frac{m\pi}{a} \right)^2 \frac{4\pi c}{\omega_{mnp}^2 V} \frac{2\delta^2 d^2}{\delta^2 + (\frac{e\pi}{d})^2} \left(1 \pm \frac{k_w}{2} \frac{p\pi}{d\delta^2} \right)^2 A_m^2 \left(\frac{\sin \theta}{\theta} \right)^2. \quad (24)$$

When n is odd and m is even, we get the well-known transverse BBU impedance:

$$\frac{R_{mnp}^\perp}{Q_{mnp}} = \left(\frac{m\pi}{a} \right)^2 \frac{4\pi c}{\omega_{mnp}^2 V} \frac{2\delta^2 d^2}{\delta^2 + (\frac{e\pi}{d})^2} \left(\frac{\sin \theta}{\theta} \right)^2, \quad (25)$$

For TM modes there is off-resonant DC deflection, which will be examined in a future paper.

Using the above definitions for the impedances, BBU calculations proceed in the usual manner. For example, in the long beam, high Q limit, both transverse ($y = x$) or longitudinal ($y = r$, the delay in arrival time with respect to the synchronous electron) BBU from a single cavity mode can be found from the coupled equations:

$$\left(\frac{\partial}{\partial t} + v_s \frac{\partial}{\partial z} \right)^2 y = a(z, t), \quad (26)$$

$$\frac{\partial^2 a}{\partial t^2} + \frac{\omega_\lambda}{Q_\lambda} \frac{\partial a}{\partial t} + \omega_\lambda^2 a = C y(z, t), \quad (27)$$

where, with a beam current I and a single cavity transit time T_0 , the constant C is given by

$$C = \begin{cases} \frac{eI}{\gamma m c T_0} \omega_\lambda^2 \frac{R_\lambda^\parallel}{Q_\lambda^2} & \text{longitudinal,} \\ \frac{eI}{\gamma m c T_0} \omega_\lambda^2 \frac{R_\lambda^\perp}{Q_\lambda^2} & \text{transverse.} \end{cases} \quad (28)$$

III. CONCLUSIONS

In a typical SWFEL design, the interaction cavity is highly overmoded. As a consequence, a realistic wake consists of a number of superimposed modes. These modes will not be given by the idealized cavity modes described herein, but rather need to be calculated numerically for the particular structure. These more realistic modes will produce some BBU growth through the conventional mechanism (that a particle slightly off axis couples to an E_s field), and will also generate BBU through the magnetized cavity mechanism described herein. An analysis of BBU which includes both realistic cavity modes and wiggling particle trajectories is a topic for future research.

REFERENCES

- [1] R.B. Palmer in New Developments in Particle Acceleration Techniques, edited by S. Turner (CERN, Geneva, 1987), Vol. 1, pp. 80-120.
- [2] G. Westenskow et al., Proc. 1991 IEEE Particle Accelerator Conference, Loretta Lizama and Joe Chew, eds., (IEEE, New York, 1991) pp. 646-648.
- [3] S.A. Heifets and S. A. Kheifets, The Physics of Particle Accelerators, American Institute of Physics Conf. Proc. **249**, Melvin Month and Margaret Dienes, eds., (American Institute of Physics, New York, 1992), pp. 154-235.
- [4] W.K.H. Panofsky and W.A. Wenzel, Rev. Sci. Instrum. **27**, 967 (1956).
- [5] A. M. Sessler, et al., Nucl. Instr. and Meth. in Phys. Res. **A306**, 592 (1991).
- [6] V.K. Neil and R.K. Cooper, Part. Accel. **1**, 111 (1970); E. Keil, et al., Nucl. Instr. and Meth. in Phys. Res. **127**, 475 (1975).
- [7] W.K.H. Panofsky and M. Bander Rev. Sci. Instr. **39**, 206 (1968); V.K. Neil, L.S. Hall and R. K. Cooper, Part. Accel. **2**, 213 (1970); A.W. Chao, B. Richter, and C.Y. Yao, Nucl. Instr. and Meth. in Phys. Res. **178**, 1 (1980); R.L. Gluckstern, R.K. Cooper and P.J. Channell, Part. Accel. **16**, 125 (1985).
- [8] R.J. Briggs, S. F. Paik, and A.H. Gottfried, IEEE Trans. on Electron Devices, **ED-18**, 511 (1971).
- [9] W.M. Sharp et al., Proc. Conf. on Intense Microwave and Particle Beams, Int. Soc. for Optical Engineering (SPIE, to be published); J.S. Kim, et al. (these proceedings).

Longitudinal Impedance of a Prototype Kicker Magnet System

H. J. Tran, M. J. Barnes, G. D. Wait, Y. Yan
TRIUMF, 4004 Wesbrook Mall, Vancouver, B.C., Canada V6T 2A3

Abstract

The longitudinal impedance of a kicker magnet system for the proposed KAON factory has been measured from 0.3 to 200 MHz. The measurement was done by transforming the kicker magnet under test into a coaxial line in order to measure the transmission parameter S_{21} through the line. The measurement was performed in two frequency ranges. From 0.3 to 50 MHz the magnet was transformed into a 50 Ω coaxial line, and from 45 to 200 MHz into a 180 Ω coaxial line. Resonances in the longitudinal impedance spectrum are due to the electrical resonant modes of the kicker magnet system. The effect on the longitudinal impedance of a speed-up network and a saturating inductor, installed on the input to the kicker magnet to improve its kick performance, was determined. The speed-up network can damp some of the resonances whereas the saturating inductor can eliminate the resonances due to the input cable of the kicker magnet. Above 45 MHz where attenuation in the LC cells of the kicker magnet is strong, external components connected to the kicker magnet have negligible influence on the longitudinal impedance. Hence the longitudinal impedance spectrum of the kicker magnet in the 45 to 200 MHz frequency range does not depend on external components such as the speed-up network, the saturating inductor and the input and output cables.

I. INTRODUCTION

In the proposed KAON factory a high intensity beam of 100 μ A is accelerated to 30 GeV step by step in a series of 5 accelerator rings. Kicker magnets will be used to inject and extract the beam. A 1 MHz beam chopper [1,2] will be used to create gaps in the beam during which the field in the kicker magnet must rise or fall from 1% to 99% in order to minimize beam losses. The time interval of the gap created is approximately 108 ns long. The required rise (fall) time of each kicker magnet varies from ring to ring. The fastest rise (fall) time will be 82 ns [2]. The design of these kicker magnets is based on those of CERN PS Division. Each kicker magnet consists of many LC cells. Each cell consists of ferrite C-cores sandwiched between high voltage capacitance plates. Hence a characteristic impedance for a kicker magnet can be defined in terms of the inductance and capacitance of its LC cells. The injection and extraction kicker magnets in the KAON factory will have a designed characteristic impedance of 25 Ω with the exception of those in the booster ring which will be 16.7 Ω [2].

Longitudinal impedance characterizes the interaction of the beam with accelerator components in the frequency do-

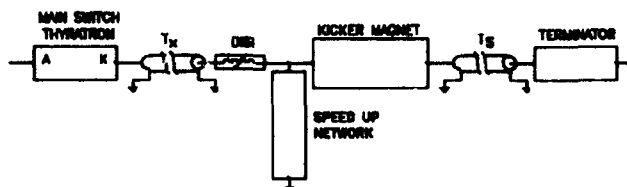


Figure 1: Block diagram of the kicker magnet system.

main. In terms of equivalent circuit representation, this interaction can be described as mutual coupling between the beam and accelerator components. In order to achieve high beam intensity and energy, collective instabilities driven by longitudinal impedances must be minimized or carefully controlled. Thus all accelerator components which can give a large contribution to the total longitudinal impedance have to be carefully designed and measured before installation. Due to the large number of kicker magnets required in the proposed KAON factory, their contribution to the total longitudinal impedance should be determined.

II. KICKER MAGNET SYSTEMS

A kicker magnet system consists of pulse-forming networks, transmission cables, several kicker magnet modules with speed-up networks and saturating inductors, and resistive or short terminations. Speed-up networks and saturating inductors are components which improve the performance of the kicker magnets [4,5]. To avoid reflections in the system, the characteristic impedance of all the components is matched as close as possible. The input cable from the kicker magnet (T_x in Fig.1) is connected to the main-switch thyatron of the pulse-forming network. Thus when the main-switch thyatron is in the off state, this end of the cable is effectively open circuit (see Fig.1). The output cable (T_s in Fig.1) is usually connected to a resistive load. For the extraction kicker magnets in the booster ring, the outputs of the magnets may be shorted [2] and there are no output cables needed.

As part of the KAON Factory project definition study a prototype kicker magnet has been designed and built at TRIUMF. PSpice modelling [3,4] has been done to determine optimal values of circuit elements for the speed-up networks and saturating inductors. The prototype magnet [2] is wired up for each electrical configuration in which it would operate and then the transmission parameter S_{21} is measured to determine the longitudinal impedance. The effect of the cables, the speed-up network and the displacement-current suppression saturating

inductor (DISI) on the total longitudinal impedance is determined.

III. TRANSFORMED COAXIAL LINES

We performed longitudinal impedance measurements by transforming the kicker magnet under test into a coaxial line by putting in a central wire in order to measure the transmission parameter S_{21} through the line. The central conductor emulates the charged particle beam. From coaxial transmission theory we can calculate the longitudinal impedance from the transmission parameter S_{21} . In order to minimize the presence of unwanted reflections in the line, matching sections are used to maintain as much as possible a constant characteristic impedance throughout the line. We measured the transmission parameter from 0.3 to 200 MHz in two steps. From 0.3 to 50 MHz we transformed the kicker magnet into a 50 Ω coaxial line and from 45 to 200 MHz into a 180 Ω coaxial line. Semi-rigid 50 Ω test cables were used to connect the transformed coaxial lines to the HP network analyzer. For the 50 Ω line, HP standards and calibration procedures were used to eliminate the systematic errors of the test cables. Similarly for the 180 Ω line, we used the TSD (Through, Short, Delay) calibration method, which can calibrate the measurement assembly from the network analyzer up to the transformed coaxial line [6]. The TSD calibration standards consist of a Through pipe, a Short plate, and a Delay pipe. Error parameters are calculated from the TSD calibration and then used to extract corrected transmission parameter S_{21} .

IV. LONGITUDINAL IMPEDANCE AND TRANSMISSION COEFFICIENT

To obtain the longitudinal impedance, transmission parameter through the transformed coaxial line is measured and compared to that through a section of reference pipe. A series impedance Z_l , which can be extracted from the transmission parameter, represents the longitudinal impedance of the kicker magnet in the circuit model of the transformed coaxial line. For the reference pipe and the transformed coaxial line, the conductance can be neglected. Thus the resultant propagation constant γ' of the transformed coaxial line is

$$\gamma' = \sqrt{(R + j\omega L + Z_l)(j\omega C)}. \quad (1)$$

The transmission parameter S_{21} through a line with propagation constant γ' is $\exp(-j\gamma'l)$ where l is the length of the line. S_{21} can be separated into the real and imaginary parts explicitly to first order as follows [6],

$$\text{phase} \left[\frac{S_{21}}{S_{21}^{ref}} \right] \cong -\frac{lX_l}{2Z_c} \quad (2)$$

$$\text{mag.} \left[\frac{S_{21}}{S_{21}^{ref}} \right] \cong 1 - \frac{R_l l}{2Z_c} \quad (3)$$

where $Z_c = \sqrt{L/C}$ is the characteristic impedance of the transformed line. These two equations can be used to calculate the longitudinal impedance $R_l + jX_l$ of the magnet under test after transmission measurements are taken for the transformed line and the reference pipe.

V. MEASUREMENTS

To confirm that a calibration is successful, the longitudinal impedance of the brass reference pipe is measured first. The reference pipe should have very low longitudinal resistance since brass is a very good conductor in this frequency range. Typical maximum longitudinal impedance of the brass reference pipe is less than $0.3 + j0.2 \Omega$ from 0.3 to 50 MHz and less than $1 + j3 \Omega$ from 45 to 200 MHz. The longitudinal reactance for both frequency ranges increases slightly as the frequency increases. This is due to the phase instability of the long test cables caused by a slight variation in length.

The prototype magnet is 345 mm in length and has ten LC cells with a characteristic impedance of 30 Ω . In the proposed KAON factory, kicker magnets will be short circuited or resistively terminated [2]. For a short termination the output of the magnet is electrically shorted and for a resistive termination the output is connected to a matched resistor by a cable.

Below 45 MHz resonances in the impedance spectrum are produced by electrical resonant modes of the kicker magnet system. These resonances are evident in Fig. 2 and correspond to that of a half-wavelength resonator. The maximum longitudinal impedance for the shorted magnet is $32 + j34 \Omega$ and for the resistively terminated magnet is $26 + j34 \Omega$. Above 45 MHz the central conductor, which emulates the particle beam, does not couple strongly to other components, which are connected to the magnet, due to the onset of strong attenuation in the LC cells of the magnet. Hence the impedance spectrum from 45 to 200 MHz does not depend much on the termination of the magnet nor on other components of the kicker magnet system.

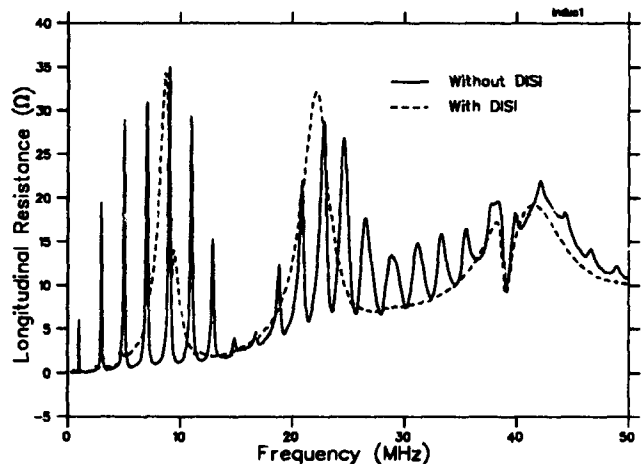


Figure 2: Longitudinal impedance of shorted kicker magnet with and without DISI (No speed-up network, $T_s=192$ ns).

The maximum impedance is $30 + j125 \Omega$ in the 45 to 200 MHz range for both short and resistively terminated kicker magnets. In the 45 to 200 MHz range, the impedance spectrum exhibits small resonances and a rising slope.

It has been proposed that a saturating inductor be connected in series between the input of the magnet and the cable T_s (Fig.1) to absorb small displacement current pulses before the main power pulse so as to improve the rise time of the magnet [4]. For small magnitudes of current the saturating inductor has a high impedance, hence effectively terminating the input cable as an open circuit. Resonances due to the input cable are eliminated when the saturating inductor is connected (Fig.2). The resulting impedance spectrum has the same features as that of a magnet with its input open circuit. Fig.2 shows the impedance spectrum of a shorted magnet with and without the saturating inductor (DISI).

The effect of various speed-up networks with different values of capacitance and resistance is shown in Fig. 4. A speed-up network is connected on the input of the magnet to improve its performance [3,4]. A capacitor and a resistor in series make up a speed-up network. Besides shifting the resonances slightly, the resistor of the network can damp some of the resonances. Hence it is beneficial to connect the speed-up network between the kicker magnet and the saturating inductor. In the proposed KAON factory, a gap may be present between the kicker magnet, which is in a vacuum tank, and the beam pipe which is connected to the tank. Such a gap can contribute additional low and high Q resonances with large values compared to the longitudinal impedance of the magnet system (see Fig.4).

VI. CONCLUSION

We have determined the longitudinal impedance of a kicker magnet system with short and resistive terminations and the effect on the longitudinal impedance of saturating inductors and speed-up networks, which are installed to improve the kick performance. When a saturating induc-

tor (DISI) is connected between the input of the magnet and the input cable, the longitudinal impedance spectrum does not contain the resonances which are otherwise produced by the input cable. The resistor of the speed-up network, which is connected to the input of the magnet, has a beneficial damping effect on some of the resonances. However, in the frequency range from 45 to 200 MHz, the longitudinal impedance spectrum does not depend much on the termination of the magnet nor on other components connected to it due to the onset of strong attenuation in its LC cells. Air gap between the kicker magnet and the beam pipe can contribute very large resonances to the longitudinal impedance spectrum of the kicker magnet system.

VII. REFERENCES

- [1] G. D. Wait, M. J. Barnes, D. Bishop, G. Waters, "Interleaved Wide and Narrow Pulses for the KAON Factory 1 MHz Beam Chopper" Proceedings of this Conference.
- [2] M. J. Barnes, G. D. Wait, "Kickers for the Kaon Factory" Proceedings of XVth International Conference of High Energy Accelerators (HEACC'92), Hamburg, July 1992.
- [3] M. J. Barnes, G. D. Wait, "Optimization of Speed-Up Network Component Values for the 30 Ω Resistively Terminated Prototype Kicker Magnet" Proceedings of this Conference.
- [4] M. J. Barnes, G. D. Wait, "Improving the Performance of Kicker Magnet Systems" Proceedings of XVth International Conference of High Energy Accelerators (HEACC'92), Hamburg, July 1992.
- [5] M. J. Barnes and G. D. Wait, "A Mathematical Model of a Three-Gap Thyatron Simulating Turn-on" to be presented at the Ninth IEEE Pulsed Power Conference, June 1993. Albuquerque
- [6] L.S. Walling et al, "Transmission Line Impedance Measurements for an Advanced Hadron Facility" LANL 1988.

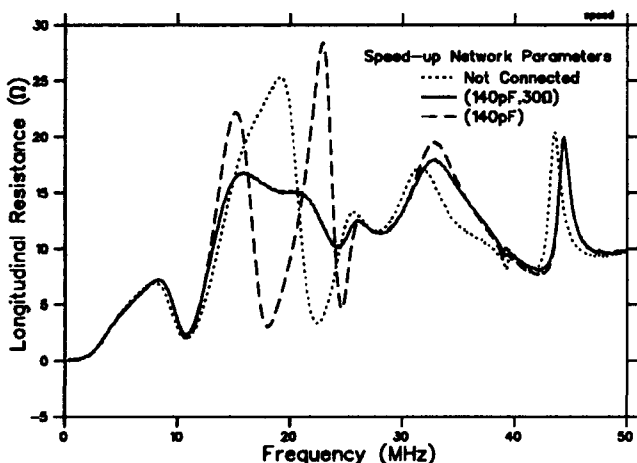


Figure 3: Longitudinal Resistance of kicker magnet with speed-up networks (no DISI, $T_s=30$ ns).

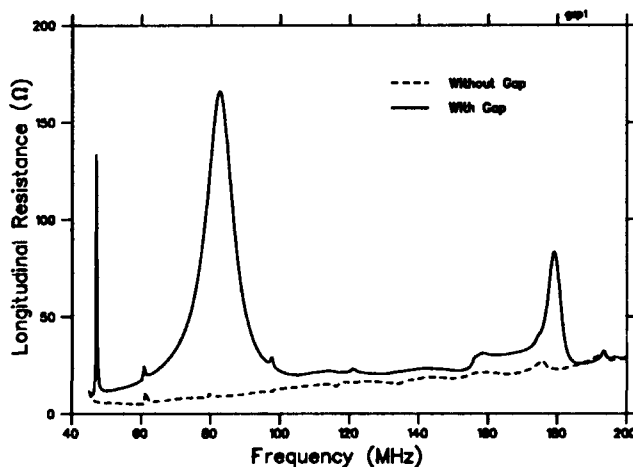


Figure 4: Resonances due to gap.

Beam Coupling Impedance Measurements And Simulations Of A Beam Pipe Liner With Pumping Holes Or Slots*

E. Ruiz, L. Walling, Y. Goren, N. Spayd
Superconducting Super Collider Laboratory
2550 Beckleymeade Ave., MS-4010, Dallas, TX 75237

Abstract

We report the results of measurements using the wire method and numerical simulations using the code HFSS (High-Frequency Structure Simulator) of the beam coupling impedance of the proposed liner for the collider ring of the SSC. We compare the results of the measurements and simulations to analytical estimates by R. Gluckstern[1] and S. Kurennoy[2], and conclude that the additional coupling impedance introduced by a liner with pumping holes can be acceptable.

I. INTRODUCTION

To avoid reduction of beam lifetime due to photodesorption and to shield the SSC collider ring bore tube from synchrotron radiation, it is proposed to include a holed liner within the bore tube which intercepts the synchrotron radiation while allowing required vacuum to be achieved. Discontinuities in the liner, such as pumping holes or slots interrupt the beam image currents, resulting in beam coupling impedance. In addition, electromagnetic coupling through the holes in the liner allow power to circulate between the liner and bore tube in synchronism with the beam. This TEM wave would couple back into the beam pipe, thereby possibly presenting an unacceptably high impedance. The coupling impedance of pumping holes and slots is estimated analytically, and numerical and measurement results are presented.

II. ANALYTICAL ESTIMATION

Analytical determination of the coupling impedance of small apertures in metallic walls has been studied extensively, but only recently has their collective coupling impedance in a beam tube liner been described analytically. The pumping holes or slots in the liner excite electric and magnetic dipoles which scatter energy back into the beam pipe and couple some energy through the aperture into the coaxial region formed between the liner and bore tube. Gluckstern calculates the impedance due to holes in a liner including the effect of wall thickness and the outer coaxial region:

*Operated by the University Research Association, Inc. for the U.S. Department of Energy under contract No. DE-AC35-89ER40486

$$Z_{\parallel} = \frac{jZ_0 k P}{8\pi^2 b^2} \left[\psi_{in} - \chi_{in} - \frac{(\psi_{out} - \chi_{out})^2}{\psi_{in} - \chi_{in} - j8\pi b^2 \left(\frac{\alpha}{k}\right) L \ln\left(\frac{a}{b}\right)} \right] \quad (1)$$

and

$$Z_{\perp} = \frac{Z_{\parallel}}{n} \left(\frac{2R}{b^2} \right) \quad (2)$$

where

$$\frac{\alpha}{k} \ln\left(\frac{a}{b}\right) = \frac{1}{4} \left(\frac{\delta_a}{a} + \frac{\delta_b}{b} \right)$$

and ψ_{out} , χ_{out} , ψ_{in} , and χ_{in} are the magnetic susceptibility and electric polarizability for the inside and outside of the liner, Z_0 is 377 ohms, $k=2\pi f/c$, P is the number of holes, b is the liner radius, a is the bore tube radius, δ_a and δ_b are the skin depth for the bore tube and outer surface of the liner, respectively, L is the average axial hole spacing, and R is the ring radius. For small pumping holes, the contribution to the coupling impedance due to power circulating outside the liner is shown by Gluckstern to be negligible.

III. SIMULATION AND MEASUREMENT

First, the triaxial geometry for low-frequency longitudinal impedance was simulated. The beam pipe had a radius of 16.5 mm and thickness of 1 mm. We found that the outer coax contributed insignificantly to the coupling impedance, so to speed up the simulations the outer coax was eliminated. Since holes this size represent a very small impedance, it was necessary to detect minute phase shifts due to the holes. The simulations were converged until the uncertainty in the phase was much smaller than the phase shift ($\theta - \theta_0$), where θ_0 , the electrical length of the reference liner, was calculated using c specified to about 5 decimal places. However, there was an error that could not be extracted by further adaptive passes when merely subtracting the length of the reference liner. This phase shift is due to small errors in the mapping of the 3-D tetrahedrons to the 2-D port surfaces. Another order of magnitude in phase accuracy was obtained by modeling the holes and the beam tube as separate elements, meshing and running the problem with both specified as vacuum, then, without changing the mesh, re-specifying the holes as metal and re-running over the frequency range. This was used as the "reference pipe" to normalize the data, and removed the port mapping errors as well as the baseline transmission.

The submitted manuscript has been authored by a contractor of the U.S. Government under Contract No. DE-AC35-89ER40486. Accordingly, the U.S. Government retains a nonexclusive, royalty-free license to publish or reproduce the published form of this contribution, or allow others to do so, for U.S. Government purposes.

Table 1: Longitudinal Impedance of Various Hole and Slot Geometries at 5.0 GHz (b=16mm, thickness=1mm)

Slot Shape	Longitudinal Impedance per Slot (Ω)	Z/n scaled to number required for vacuum (Ω)
Rectangular (2x6mm)	0.0023	4.7×10^{-2}
Rounded (2x6mm)	0.0020	4.3×10^{-2}
Rounded (3.2x31mm)	0.0172	4.0×10^{-2}
Elliptical (2x6mm)	0.0012	3.0×10^{-2}
Square Hole (2x2mm)	0.0021	14×10^{-2}
Hole (dia=3.0mm)	0.0075	27×10^{-2}
Hole (dia=2.0mm)	0.0012	11×10^{-2}
Hole (dia=1.5mm)	0.00050	9.0×10^{-2}
Hole (dia=1.0mm)	0.00015	7.5×10^{-2}

A. Longitudinal Impedance

Measurements were made of a liner 2 meters in length with 1010 pumping holes or 160 rounded slot using the wire technique[3]. Initially, these were made with a center conductor of diameter 12.7 mm, however, simulation of the measurement using HFSS revealed that a 3.2 mm diameter center conductor yielded more accurate results. For this reason, the longitudinal impedance data shown in Figure 1 was made with the 3.2 mm center conductor. In addition, measurements confirmed that the presence of the outer triaxial region did not significantly affect the observed impedance data so later measurements were made without a bore tube.

Many variations of liner holes were simulated. These included variation in the number of holes axially from 2 to 20, variation of the number of holes longitudinally from 2 to 20, and varying the depth of the holes. These simulations confirmed that for low frequencies, the longitudinal impedance of the holes add, and the impedance is reduced by the wall thickness, as theory predicts. Simulations were also performed with small and large center conductors and compared to measurement results for the same parameters. We found very good agreement between HFSS' simulation of the wire technique and wire measurements. Extensive simulations were also performed for comparison with MAFIA simulations done by Chou and Barts[4].

To reduce the low-frequency beam impedance, short slots are being considered. Simulations were run to study the influence of the shape of the slot and measurements were performed using the wire technique on 3.2 x 31 mm rounded slots. The results of longitudinal impedance measurements and simulation at 5.0 GHz for holes and slots are shown in Table 1. A large savings in low-frequency impedance is achieved by using slots; the high-frequency behavior should be acceptable for short slots.

B. Transverse Impedance

The transverse impedance was measured using two paral-

Table 2: Transverse Impedance of Various Hole and Slot Geometries (b=16mm, thickness=1mm)

Slot Shape	Transverse Impedance per Slot (Ω/m)	Z ₀ /meter scaled to number required for vacuum (Ω/m^2)
Rectangular (2x6mm)	0.21	71
Rounded (2x6mm)	0.14	50
Rounded (3.2x31mm)	0.88	34
Elliptical (2x6mm)	0.14	58
Square Hole (2x2mm)	0.17	185
Hole (dia=3.0mm)	0.31	186
Hole (dia=2.0mm)	0.087	135
Hole (dia=1.5mm)	0.037	111
Hole (dia=1.0mm)	0.011	92

lel center conductors driven 180° out of phase relative to each other (odd mode). The spacing between the 3.2 mm-diameter conductors is 16 mm. Holes and slots are distributed in rings with 10 holes or slots azimuthally per ring.

Transverse impedance for various hole and slot geometries was also simulated and compared to calculations by Kurennoy for a zero-thickness liner. Kurennoy predicts a factor of 2 reduction in transverse impedance when there are 3 or more holes in one radial cross-section. We find results half of Kurennoy's predictions, which is consistent when the reduction due to wall thickness is taken into account. Simulation results are shown in Table 2 while measurement results are shown in Figure 2.

IV. LINER LEAKAGE

Measurements of leakage were made using a triaxial impedance measurement technique[5]. The test liner is 2 meters long, with 1010 holes in the center 1 meter, and 0.5 meters of solid pipe on both ends. The outer bore tube has a radius of 23 mm, while the liner has an inner radius of 16 mm and is 1 mm thick. The center conductor diameter was 12.7 mm for the leakage measurements. To measure leakage, the center conductor is placed on axis within the liner and the transmission through the pumping holes, S_{41} , is measured. A transmission measurement is also made through the coaxial regions formed between the liner and bore tube (S_{43}), and between the center conductor and liner (S_{21}), to correct the effects of hardware mismatches and multiple reflections in the triax on the S-parameters. S_{41} is time-gated, and divided by the square root of gated S_{43} and S_{21} . Liners with holes of diameter 1 mm, 2 mm, and 3 mm were measured. Results of leakage measurements and simulation are shown in Figure 3.

To estimate the contribution to the coupling impedance of the TEM wave traveling in the region outside the liner and 'feeding back' on to the beam, a two-step calculation was per-

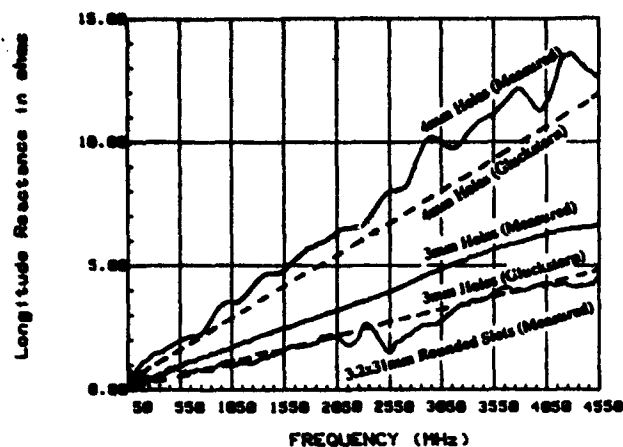


Figure 1. Measured Longitudinal Reactance of 1010 3 mm and 4 mm diameter holes and 160 rounded slots.

formed. A triaxial model representing 20 holes axially and 22 longitudinally, was driven at the inner coax on one side. The other side has enough blank pipe forming the outer coax such that the maximum radial electric field, E_r , due to forward-leaked power could be determined. Thus, the ratio E_r/I was determined where I is the current on the center conductor within the liner. Then, the center conductor is removed from the model, the outer coax is driven, and the ratio of E_z , the maximum longitudinal electric field on axis, to the radial electric field in the outer coax is determined. This ratio is then multiplied by the scaling ratio l_{att}/l to yield the coupling impedance, where l is the length of the liner segment with holes in it, and l_{att} is the attenuation length in the outer coax. Numerical simulations were performed for holes of 2mm, 3mm, and 4mm diameter. This inquiry confirmed that this contribution was much smaller than the inductive impedance for reasonably-sized holes at low frequencies.

V. DISCUSSION OF RESULTS

The simulations and the measurements both yielded low-frequency longitudinal impedances which are in good agreement with Gluckstern's thickness corrected estimate for the longitudinal impedance of round holes. Transverse impedance for round holes fit Kurennoy's theory well. Slots reduce the impedance but must be kept short to avoid the potentially large coupling impedance caused if the slots themselves become resonant.

We have investigated the high-frequency coupling impedance using TM_{01} excitation[6]. Because of disagreement between HFSS and MAFIA simulations done by Chou and Barts, we plan to measure the high-frequency impedance[7].

VI. CONCLUSION

We have performed measurements and simulation of the coupling impedance of a liner in the collider ring of the SSC. Using HFSS we were able to study various hole and slot configurations. Good agreement has been demonstrated between

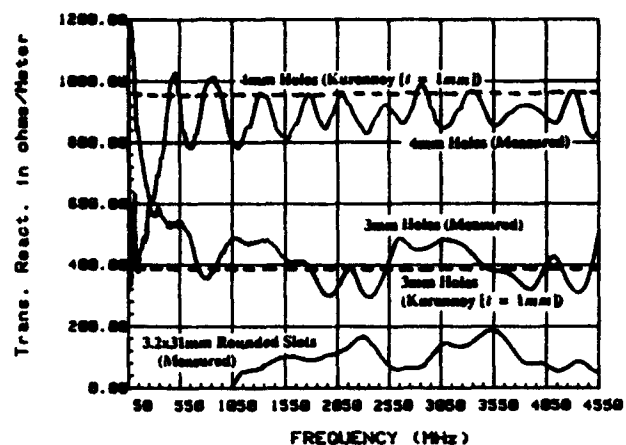


Figure 2. Measured Transverse Reactance of 1010 3 mm and 4 mm diameter holes and 160 rounded slots.

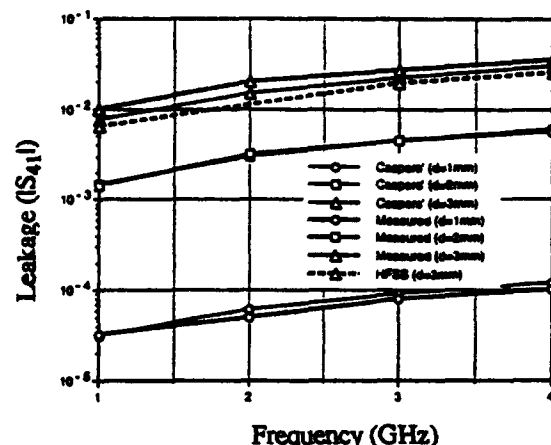


Figure 3. Leakage through a 1 mm thick liner with 1010 holes of various diameters.

HFSS, laboratory measurements, and theory. Based on these simulations and measurements, the coupling impedance of a liner in the collider ring can be acceptable.

VII. REFERENCES

- [1] R. L. Gluckstern, "Coupling impedance of many holes in a liner within a beam pipe," CERN SL/92-05 (AP) (1992).
- [2] S. Kurennoy, "Beam Coupling Impedance of Holes In Vacuum-Chamber Walls," IHEP, Protvino. No.92-84, 1992.
- [3] "Transmission-Line Impedance Measurements for an Advanced Hadron Facility," L. S. Walling, D.E. McMurtry, D.V. Neuffer, and H.A. Thiessen, *Nucl. Instr. and Meth.* A281 (1989) 433
- [4] W. Chou and T. Barts, "Wakefield and Impedance Studies of a Liner Structure Using MAFIA," *Proc. of the 1993 Computational Accelerator Physics Conference*, Pleasanton, CA.
- [5] F. Caspers, "Triaxial line technique," in *Proc. of the Coupling Impedance Measurement Workshop*, Argonne National Laboratory-APS, August 12-13, 1991
- [6] E. Ruiz, L. Walling, Y. Goren, "Liner Impedance Calculations Using HFSS," *Proc. of the 1993 Computational Accelerator Physics Conference*, Pleasanton, CA.
- [7] G. Lambertson, A.F. Jacob, R.A. Rimmer, and F. Voelker, "Techniques for Beam Impedance Measurements Above Cut-off," LBL-28190

Measurement and Computation of the Higher Order Modes of the ALS 500 MHz Accelerating Cavities*

J. N. Corlett and J. M. Byrd,
Lawrence Berkeley Laboratory
1 Cyclotron Road, Berkeley, CA 94720, USA

Abstract

Higher order modes in the accelerating cavities are expected to drive coupled bunch instabilities in the ALS, which will be overcome by a bunch-by-bunch feedback system. Computations of the cavity higher order modes using the URMEL-T and MAFLA codes are presented. Damping of the higher order modes is achieved by filters in the high power feeder waveguide which is aperture coupled to the cavity. Measurements of the modes in an ALS 500 MHz cavity are presented and compared with the computed values for an isolated, un-damped cavity. The resources of the Lamberton Beam Electrodynamics Laboratory of the Center for Beam Physics at LBL were used to perform these studies.

I. INTRODUCTION

The design current of the ALS storage ring is 400 mA in multibunch mode, leading to coupled bunch instabilities with growth rates faster than the radiation damping rate for typical RF cavity higher order mode (HOM) impedances [1].

Suppression of coupled bunch instabilities will be achieved by a bunch-by-bunch feedback system, described elsewhere [2]. The required gain of the feedback system is determined by the strongest driving impedance, and for nominal operation it has been assumed that the longitudinal HOM's can be damped such that the total shunt impedance R_s at frequency ω_p is:

$$R_s \frac{\omega_p}{\omega_{rf}} \leq 120 \text{ k}\Omega$$

where ω_{rf} is the frequency of the RF system (500 MHz). In the transverse case a maximum transverse impedance of $4 \text{ M}\Omega \text{ m}^{-1}$ is assumed.

Calculations using the URMEL-T electromagnetic design code suggest that without damping a single ALS cavity would have higher order modes of up to $1.9 \text{ M}\Omega$ shunt impedance (at 800 MHz) and $30 \text{ M}\Omega \text{ m}^{-1}$ transverse impedance.

In order to better quantify the impedance of the cavities, measurements were made of a spare cavity, identical to the cavities in the storage ring, with waveguide coupler and higher order mode filters included in the measurements.

Higher order modes were identified using a perturbation method, and Q-values measured. Impedance was determined

from multiplying the measured Q by the R/Q determined by URMEL-T computations.

II. HOM DAMPING IN THE FEEDER WAVEGUIDE

The ALS radiofrequency accelerating system uses two 500 MHz cavities with reentrant nosecone geometry, aperture coupled to the feeder waveguide. A detailed description is given elsewhere [3]. A single klystron feeds the cavities, via a magic-tee junction, and in the waveguide sections between magic-tee and each cavity are H-plane and E-plane low-pass filters. These filters consist of right-angle tee-junctions with one arm of the tee a bifurcated waveguide section. A metal plate along the center of the broad wall prevents propagation of the 500 MHz wave, but allows higher frequency waveguide modes to pass on either side. At the ends of these bifurcated tee sections are placed loads made of absorbing material cast into a section of bifurcated waveguide. A similar arrangement exists behind the bifurcated matching stub. The system is designed to absorb higher order mode power coupled out of the cavity into the waveguide, providing damping of those HOM's that couple to the filters.

III. NUMERICAL COMPUTATIONS

Since there is no simple method of modelling the cavity with feeder waveguide and loads included, the longitudinal and transverse (dipole) modes were computed using the URMEL-T code [4] for the basic cavity geometry. This two-dimensional model computes modes in an isolated cavity with cylindrical symmetry, with no feeder waveguide or coupling aperture. The results are shown in table 1 for longitudinal modes and in table 2 for transverse (dipole) modes, up to the cut-off frequencies of the beam tubes (2.5 GHz for dipole modes, 3.3 GHz for longitudinal (monopole) modes).

The required damping factor indicates the reduction in impedance necessary to ensure that higher order modes in the cavities do not drive coupled bunch instabilities beyond the capabilities of the feedback system to damp the motion. This makes the conservative assumption that the two cavities in the storage ring have exactly the same higher order mode spectrum and thus HOM's coincide in frequency.

MAFLA computations of a three-dimensional cavity model including coupling aperture were useful in identifying HOM's. In particular the three-dimensional modelling allows determination of the orientation of the two polarizations of the dipole modes, and also gave some indication of which modes would couple most effectively into the waveguide.

*This work was supported by the Director, Office of Energy Research, Office of Basic Energy Sciences, Materials Sciences Division of the U.S. Department of Energy under Contract No. DE-AC03-76SF00098.

Table 1
Longitudinal Higher Order Modes Computed by URMEL-T

Frequency (MHz)	R/Q (Ω)	Q	R ($M\Omega$)	Required damping factor
797.61	50.95	37526	1.912	50.8
1024.0	1.189	38997	0.046	1.6
1295.1	15.53	36473	0.566	24.5
1343.1	9.724	81292	0.791	35.4
1559.6	7.679	37260	0.286	14.9
1785.8	4.551	55690	0.253	15.1
1870.7	0.418	103768	0.043	2.7
1871.9	3.215	47754	0.154	9.6
2108.1	4.191	39387	0.165	11.6
2246.9	0.248	76392	0.019	1.4
2324.9	3.497	87683	0.307	23.8
2423.5	0.786	99820	0.078	6.3
2427.3	3.507	41225	0.145	11.7
2611.7	0.094	52421	0.005	
2743.9	0.090	89671	0.008	
2781.8	1.602	54646	0.088	8.1
2808.1	4.689	80873	0.379	35.5
2968.0	0.054	107891	0.006	
2979.2	0.047	44478	0.002	
3149.2	0.747	83910	0.063	6.6
3183.6	1.235	61187	0.076	8.0
3243.0	0.020	74974	0.001	
3252.4	0.539	56151	0.030	3.3
3256.0	7.693	27527	0.212	23.0
3257.6	8.055	27948	0.225	24.5

IV. MEASUREMENTS OF THE TEST CAVITY

A spare cavity identical to the storage ring cavities was used for the measurements of the higher order modes. A coupling waveguide together with cylindrical ceramic window was mounted onto the cavity, and the higher order mode filters, created by bifurcated waveguide sections, were attached to either end of the coupling waveguide. The layout used in the measurement is a reasonably accurate simulation of the real configuration, although neglecting the effects of waveguide bends, tee-junctions, magic-tee and the circulator.

Modes were excited in the cavity by using electric probes inserted into the beam pipes, one on either side of the cavity. The probes were held near to the beam pipe wall on an acrylic support structure which allowed rapid adjustment of the position of the probes. By adjusting the azimuthal position of these probes while monitoring the S_{21} signal the longitudinal and transverse cavity modes were excited. The frequencies at which to look for particular modes were found in the URMEL-T and MAFIA computations. The Q-value of each mode was measured from the width of the S_{21} resonance curve, at the half power points.

In order to identify the modes a perturbation method was used. A hollow cylindrical needle was threaded onto a nylon

Table 2
Dipole Higher Order Modes Computed by URMEL-T

Frequency (MHz)	R/Q*1/(kr ²) (Ω/m)	Q	R ($M\Omega/m$)	Required damping factor
705.55	4.91	51229	0.25	
815.57	307.0	57906	17.78	8.9
1118.8	528.9	53646	28.37	14.2
1182.4	5.06	52833	0.27	
1243.8	2.51	103047	0.26	
1388.8	70.76	66585	4.71	2.4
1513.9	220.5	44481	9.81	4.9
1592.0	47.09	102317	4.82	2.4
1645.2	16.91	59163	1.00	
1781.6	2.15	116675	0.25	
1788.1	550.2	52854	29.08	14.6
1850.5	2.61	89109	0.23	
1943.3	5.38	38636	0.21	
2044.1	47.60	108366	5.16	2.6
2138.0	2.26	112062	0.25	
2138.7	1.82	115129	0.21	
2196.0	166.1	78218	12.99	6.6
2202.3	58.36	37136	2.17	1.1
2338.2	13.45	81679	1.10	
2375.8	6.78	121562	0.82	
2448.2	44.81	38486	1.72	
2504.3	23.58	113974	2.69	1.4
2537.1	19.67	37545	0.74	
2539.5	5.77	23015	0.13	

line strung inside the cavity between adjustable supports mounted on the beam pipe flanges. The needle was drawn through the cavity at various displacements with respect to the cavity axis (on-axis, horizontally and vertically off-axis), with the long dimension of the needle parallel to the cavity axis. Using a needle of aspect ratio (length to diameter) 29:1 the longitudinal electric field was perturbed. Qualitative observations of the perturbation patterns allowed identification with the corresponding computed mode. A longitudinal mode would exhibit no significant difference in perturbations when the needle was on axis or any position off axis. A dipole mode would show maximum perturbation off axis at one azimuth, with negligible perturbation either on axis or off axis displaced 90°.

Since the asymmetry of the real cavity splits the degeneracy of the dipole modes, we have two modes for each dipole mode predicted by URMEL-T. These modes are found at slightly different frequencies and with different azimuthal orientations of the fields. For most dipole modes measured the field distributions were such that the mode would couple principally to either horizontal or vertical motion of the beam, hence the modes were designated as H or V.

Although the R/Q for the HOM's in the real cavity may vary from the idealistic case of cylindrical symmetry, the error involved in assuming that R/Q is unchanged with the addition of the aperture coupled waveguide is generally small [5].

Measurements were made at the nominal operating temperature of 40°C, with the fundamental mode tuned to the RF frequency. For those modes driving the strongest coupled bunch motion the frequency over a range of 5 mm tuner movement was recorded at 40 °C, and the frequency variation with temperature was also measured over $\pm 5^\circ\text{C}$.

V. RESULTS

Measurement results are given in table 3 for the longitudinal modes, and table 4 for dipole modes. Almost all of the predicted modes were found, and a comparison with tables 1 and 2 shows that the damping via the feeder waveguide is very effective for most modes.

The Q values of modes above 2.8 GHz were difficult to measure due to the presence of fields at the ends of the beam pipes, and conservative estimates of the Q values are given.

Table 3
Measured Longitudinal Higher Order Modes

Frequency (MHz)	Q	Δ	kHz/°C	kHz/mm	Required damping factor
808.44	21000	1050	-20	37	28
1007.96	840	1.76	70		
1280.10	3000	33.0	-45	276	1.4
1309.34	810	5.51	35		
1553.55	3400	26.52	-28	-118	1.4
1807.68	2900	13.34	-33		
1846.72	2200	0.88	-15		
2122.61	1800	7.56	10	-155	
2266.6	2200	0.55			
2349.8	5100	17.8	-31	-35	1.4
2416.3	7000	5.53	-27	-78	
2484.94	2400	8.40	19		
2625.9	1500	0.14			
2769.1	1500	0.14			
2817.4	≤ 1000	1.60			
2847.82	≤ 4000	18.8	-32	-6	1.8
2968	< 1500	0.08			
2979	< 1500	0.08			
3149	< 1500	1.125			
3183	< 1500	1.86			
3243	< 1500	0.03			
3252	< 1500	0.81			
3256	< 1500	11.54			1.2
3257	< 1500	12.1			1.3

The longitudinal mode at 808 MHz (TM_{011}) does not couple strongly into the feeder waveguide and may drive coupled bunch instabilities beyond the damping capabilities of the feedback system. Six other longitudinal modes have impedances marginally greater than the feedback design criteria. Three transverse modes remain with impedance greater than $2 \text{ M}\Omega \text{ m}^{-1}$.

Table 4
Measured Dipole Higher Order Modes

Frequency (MHz)	Q	R (k Ω /m)	kHz/°C	kHz/mm	*	**
810.08	48000	14800	-12	-23	H	7.4
1121.77	7000	3700	-21	34	V	1.8
1122.72	17000	9000	-18	-3	H	4.5
1183.20	800	4			V	
1189.85	1800	92	-18	-3	H	
1369.83	3700	260	-17	-13	V	
1518.60	300	67			V	
1529.00	1800	200	-22		H	
1597.36	8400	400	-16	-38	H	
1648.00	600	10			H	
1726.90	900	2			H	
1739.00	500	1			V	
1796.64	1200	660	-23		H	
1801.61	2000	1100	-17	-52	V	
1966.11	4000	22	-31		H	
2136.97	16000	36	-31		H	
2141.08	9000	20	-20		V	
2151.34	2500	5	70		V	
2156.70	2400	4			H	
2178.98	1700	280	-32	-110	H	
2335.56	4800	65	-48		45°	
2504.20	500	12			H	

* orientation

** required damping factor

Variations of cavity temperature and tuner position may overcome coupled bunch instabilities driven by these modes, however it may be difficult to solve the problem for all modes simultaneously. The stability of coupled bunch motion in the ALS is discussed elsewhere [2].

Damping of the strongest HOM's using probes in the cavity pumping port will be investigated as a solution to this problem.

VI. ACKNOWLEDGEMENTS

Thanks to B. Taylor who conceived of the waveguide filter damping scheme, and to J. Julian for assistance in making the measurements.

VII. REFERENCES

- [1] "1-2 GeV Synchrotron Radiation Source Conceptual Design Report", LBL PUB-5172, July 1986.
- [2] "Coupled-bunch Stability at the ALS", J. M. Byrd and J. N. Corlett, this conference.
- [3] "The ALS Storage Ring RF System", B. Taylor, C. Lo, K. Baptiste, J. Guigli, and J. Julian, this conference.
- [4] U. Laustroer, U. van Rienen, T. Weiland, "URMEL and URMEL-T Userguide," DESY M-87-03, Feb 1987.
- [5] "Higher Order Modes in the SRS 500 MHz Accelerating Cavities", J. N. Corlett, Proc. 1989 Particle Accelerator Conference, Chicago, March 20-23, 1989.

Impedance Measurements of Components for the ALS*

J. N. Corlett and R. A. Rimmer
Lawrence Berkeley Laboratory
1 Cyclotron Road, Berkeley, CA 94720, USA

Abstract

The high current and short bunch length of the ALS beam make the machine susceptible to beam instabilities over a frequency range extending to 13 GHz and beyond. All components of the storage ring have been carefully designed to minimize the impedance presented to the beam, and assemblies have been laid out to avoid resonant enclosures between components. Novel bellows shields allowing considerable mechanical movement while maintaining a low impedance are described. Results are presented of impedance measurements of ALS components and assemblies of components, using a precision coaxial wire technique in frequency domain, extending to frequencies beyond cut-off. All measurements were performed at the Lambertson Beam Electrodynamics Laboratory of the Center for Beam Physics at LBL.

I. INTRODUCTION

The ALS storage ring consists of twelve straight sections containing transitions from curved section to straight section aperture, bellows, vacuum valves, injection equipment, RF cavities, feedback equipment and transitions into the insertion device apertures. The design current is 400 mA in 250 bunches (there is a gap of 78 RF buckets for ion clearing) in multibunch mode, and 7 mA per bunch in single bunch or few-bunch mode. With a natural bunch length of 12 ps (sigma) the significant frequency content of the bunches extends to approximately 13 GHz, and such high currents over a broad frequency spectrum lead to concerns about multi-bunch and single bunch instabilities, and heating of vacuum vessel components by the beam.

In order to minimize the impedance of vacuum vessel components in the ALS, the designs of all transition sections and devices in the vacuum vessel have been carefully developed to minimize the beam impedance. Impedance measurements of components have been made during the engineering design process, using the coaxial wire method.

II. IMPEDANCE MEASUREMENT METHOD

Using the coaxial wire method a thin wire is placed along the beam path through the device under test, supported by styrofoam guides [1]. Fields at the surrounding wall induced by

the currents carried by the wire are assumed to be equivalent to those of a relativistic beam. Tapers from 50 Ω cables transform into the higher impedance of the test setup to minimize reflections of the TEM waves over the frequency range of interest.

Unlike the TEM waves, travelling waveguide modes can reflect off the tapers, and in order to minimize these reflections absorptive material (Emerson & Cuming Eccosorb AN73) is placed on the walls of the transition tapers. Although attenuating the TEM signal as well as the unwanted TM waveguide modes, this can be accommodated by the dynamic range of modern network analyzers.

A normalizing measurement through a smooth reference pipe allows the calculation of beam impedance Z_b from the characteristic impedance of the device Z_1 and the measured S_{21} :

$$Z_b = 2 Z_1 \left(\frac{S_{21, \text{reference}}}{S_{21, \text{object}}} - 1 \right)$$

III. FLEXIBLE RF BELLOWS SHIELDS

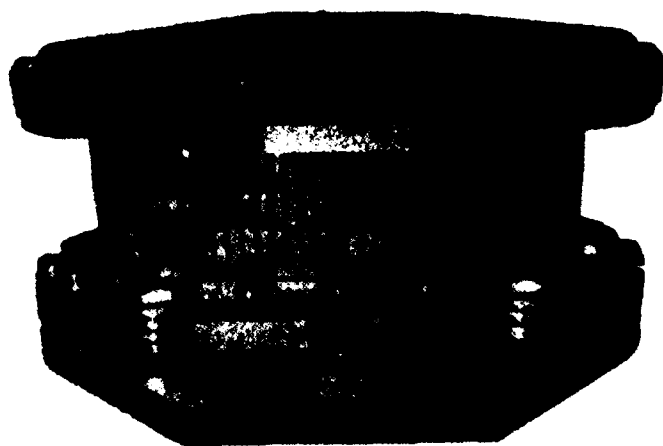
A. Description

Bellows sections are located at either end of the straight sections, to allow for movement due to thermal expansion during normal operations and during bakeout of the vacuum vessels. To minimize the beam impedance the cross section of the adjacent beam tube is extended across the bellows by an RF shield as shown in figure 1. This consists of flexible strips, that can be seen, and spring fingers between the flanges at one end. The strips are of beryllium copper foil 0.003 inch thick with longitudinal slits to allow bowing without damage. This bowing accommodates the 5 - 10 mm compression of the bellows during bakeout. During normal operations the bowed shape must be avoided because it would support resonant modes excited by the beam. This is achieved by a spring arrangement which maintains the strips in tension up to a temperature of 29°C. The normal operating temperature of the chamber is 24°C \pm 1°C, with an expected movement of approximately 0.1 mm. This small movement is absorbed by the spring fingers.

The beryllium copper foil section does not have strips at the horizontal extremes to avoid interference with the bellows during contraction. This does not deteriorate the impedance properties since there is little image current in this region.

*This work was supported by the Director, Office of Energy Research, Office of Basic Energy Sciences, Materials Sciences Division of the U.S. Department of Energy under Contract No. DE-AC03-76SP00098.

Figure 1. Elliptical section bellows shield.

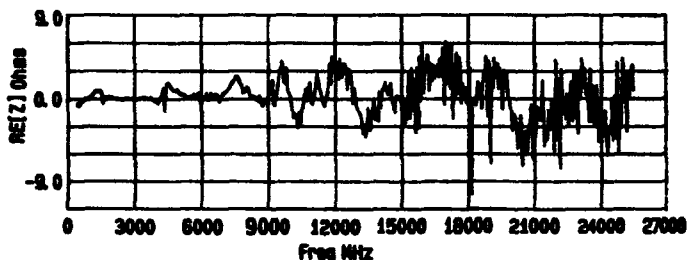


If the chamber cools to 17°C the spring fingers will lose contact and the impedance will increase due to the gap created, however this is significantly below the nominal operating temperature and is not likely to occur.

B. Measurements

Impedance measurements of the RF shield have been made in frequency domain up to 26 GHz, using the coaxial wire method. A number of small resonances have been observed, and a typical impedance measurement result is shown in figure 2, all are below 5 Ω shunt impedance and of low Q values. The corresponding Z/n values are less than 1 mΩ. Cut-off occurs at 9 GHz for the TM modes. Above approximately 15 GHz the uncertainty in the measurement becomes appreciably worse, with reproducibility of the order of ± 10 Ω.

Figure 2. Impedance measurement of bellows shield.



Summing the loss parameters for the measured resonances below 13 GHz we have

$$k = \sum_i \frac{\omega_i}{2} \left(\frac{R}{Q_i} \right) e^{-(\omega_i \sigma)^2} = 0.03 \text{ V pC}^{-1}$$

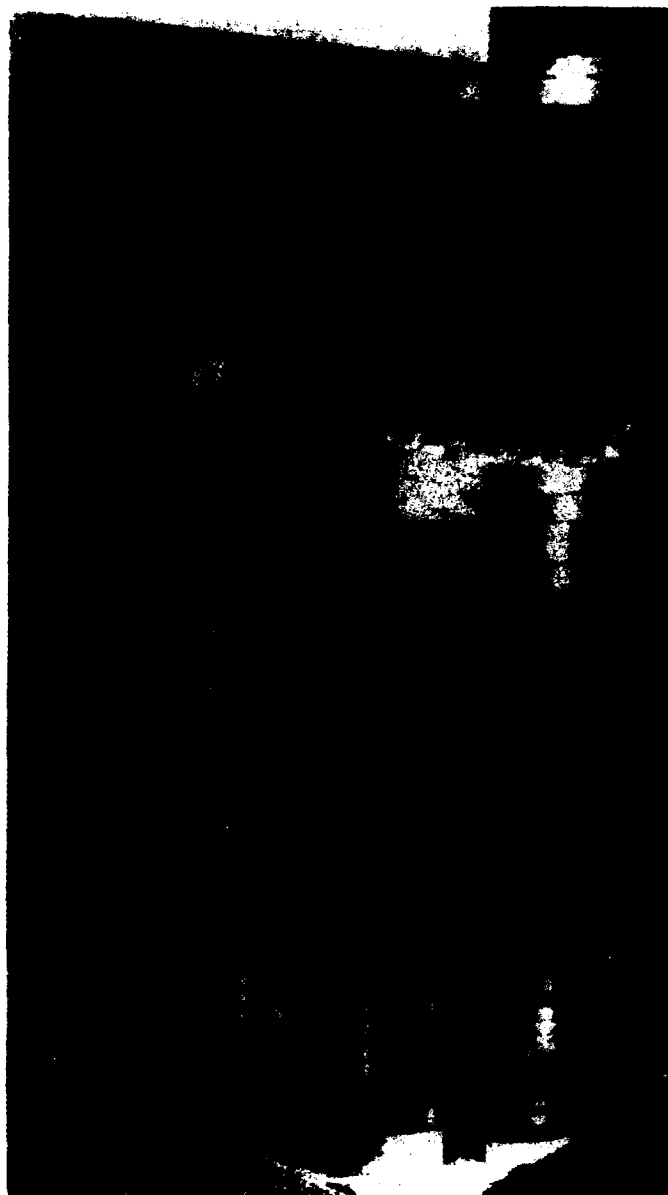
The strength of these resonant modes increased rapidly with compression of the shield, leading to a criterion of 1 mm maximum deviation from flat (i.e. bowing) during operation with beam.

IV. FLEXIBLE SECTIONS FOR TRANSVERSE DISPLACEMENT

A. Description

The injection straight is moveable in the transverse direction to allow optimization of the injection process by moving the the injection septum relative to the closed orbit. This movement is permitted by bellows sections at the ends of the straight. In this case the bellows shield must also be free to move transversely, with one flange allowed to be displaced with respect to the other.

Figure 3. Flexible cage and bellows shield assembly.



To accommodate this motion a cage of wires was built which maintains the racetrack cross-section of the injection straight and has sufficient flexibility to accommodate a transverse displacement of ± 10 mm of one flange with respect to the other. Figure 3 shows the cage, in an assembly including the foil and spring finger sections which allow for longitudinal motion and are similar to those described above. As the cage is displaced, the longitudinal movement is accommodated in a double set of spring fingers designed to accommodate the additional longitudinal motion required in this section.

B. Measurements

Measurements of the cage section with displaced ends were complicated by length changes in the apparatus, but showed the generation of resonant modes as one end was displaced. As the cage is displaced a pair of modes are observed around 2.4 GHz, with impedance $< 20 \Omega$ at 4.75 mm offset, corresponding to $Z/n < 12.5 \text{ m}\Omega$. The total loss parameter for these modes is 0.003 V pC^{-1} .

V. TRANSITIONS, VACUUM VALVES AND SUB-ASSEMBLY OF COMPONENTS

Transitions between vacuum vessels of different cross-section occur predominantly at the ends of the straight sections, since the curved vessels and the major part of the straight sections are made from single pieces of aluminum and have uniform beam apertures. Measurements of the curved sector tank impedance are described in [2]. From the curved vessel to the straight section the beam aperture transforms from a diamond shape to an ellipse, over a distance of approximately 50 mm. With the future installation of insertion devices some further transitions will be introduced to accommodate a more reduced vertical aperture.

Vacuum valves with RF shields have been used at both ends of all straight sections. These valves have metal foil inserts which bridge the gap between the valve flanges to provide a smooth, continuous path for beam induced wall currents when the valve is open. Visual inspections indicated considerable variations in quality from valve to valve, with the RF shield being bowed, and/or a step of up to a millimeter between the shield and the body of the valve in some cases. Measurements were performed on a typical valve, indicating few resonances, however all valves were visually inspected and the worst cases were corrected by adjusting the foil to reduce bowing and displacements of the RF shield.

An assembly consisting of a transition from a diamond shape to an ellipse, an elliptical bellows shield, a dummy vacuum valve, and a second elliptical bellows shield was measured. In addition to the effects of the bellows shields a broad resonance centered at 13 GHz was observed, shunt impedance 15Ω and Q value approximately 8. For this mode the loss parameter k is 0.03 V pC^{-1} .

VI. INJECTION BUMP MAGNETS

Ceramic vacuum vessels are used in the injection bump magnets to allow penetration of the pulsed magnetic field. The inside surface of the tubes is coated with a thin layer of titanium to allow passage of the beam image current. The metallization is arranged in strips to minimize perturbations of the pulsed magnetic field while reducing the beam impedance. The impedance of this device is expected to peak at low frequencies, due to resonant effects in the arrangement of metallized strips. A low frequency impedance measurement was made using a coaxial wire resistively matched to 50Ω at the ends.

Measurements show broad resonances at 50 MHz and 190 MHz as predicted [3], with impedance $< 20 \Omega$.

VII. RF CAVITIES

Measurements of the RF cavity modes have been made using a spare cavity, with higher order mode damping filters in the feeder waveguide, as described elsewhere [4]. The strongest higher order longitudinal mode has a measured shunt impedance of $1.05 \text{ M}\Omega$, with other modes less than $33 \text{ k}\Omega$. The sum of loss parameters for the longitudinal modes below cutoff frequency of the beam pipe (3.3 GHz) is 0.40 V pC^{-1} . By equating this loss parameter to that of a single $Q=1$ resonator centered at the beam pipe cut-off frequency gives a shunt impedance of 40Ω , and a corresponding estimate of $Z/n = 18 \text{ m}\Omega$ per cavity.

VIII. ACKNOWLEDGEMENTS

Thanks are due to J. Meneghetti for conceiving and developing the flexible bellows shields, to T. Henderson and K. Kennedy, and to G. Lambertson for helpful advice on all impedance issues.

IX. REFERENCES

- [1] "Techniques for Beam Impedance Measurements Above Cutoff", G.R. Lambertson, A.J. Jacob, R.A. Rimmer, and F. Voelker, Proc. 1990 European Particle Accelerator Conference, Nice, France, June 12-16, 1990.
- [2] "Beam Impedance Measurements on the ALS Curved Sector Tank", R.A. Rimmer, D.A. Goldberg, A.J. Jacob, G.R. Lambertson, and F. Voelker, Proc. 1990 European Particle Accelerator Conference, Nice, France, June 12-16, 1990.
- [3] "Conductive Coating in Bump-Magnet Tubes", G.R. Lambertson, LBL internal note ESG Tech Note-201, June 1992.
- [4] "Measurements of the Higher Order Modes of the ALS 500 MHz Accelerating Cavities", J.N. Corlett and J.M. Byrd, these proceedings.

Advances and Applications of ABCI*

Y. H. Chin

Lawrence Berkeley Laboratory
University of California
Berkeley, CA 94720

Abstract

ABCI (Azimuthal Beam Cavity Interaction) is a computer program which solves the Maxwell equations directly in the time domain when a Gaussian beam goes through an axi-symmetrical structure on or off axis. Many new features have been implemented in the new version of ABCI (presently version 6.6), including the "moving mesh" and Napoly's method of calculation of wake potentials. The mesh is now generated only for the part of the structure inside a window, and moves together with the window frame. This moving mesh option reduces the number of mesh points considerably, and very fine meshes can be used. Napoly's integration method makes it possible to compute wake potentials in a structure such as a collimator, where parts of the cavity material are at smaller radii than that of the beam pipes, in such a way that the contribution from the beam pipes vanishes. For the monopole wake potential, ABCI can be applied even to structures with unequal beam pipe radii. Furthermore, the radial mesh size can be varied over the structure, permitting to use a fine mesh only where actually needed. With these improvements, the program allows computation of wake fields for structures far too complicated for older codes. Plots of a cavity shape and wake potentials can be obtained in the form of a Top Drawer file. The program can also calculate and plot the impedance of a structure and/or the distribution of the deposited energy as a function of the frequency from Fourier transforms of wake potentials. Its usefulness is illustrated by showing some numerical examples.

I. INTRODUCTION

The first version (version 2.0) of ABCI [1] was written in 1984, however, its manual was published only in 1988. It used the FIT method [2] to discretize the Maxwell equations, similar to TBCI [3]. However, in addition to some internal differences, it was preferable to TBCI mainly due to capability to change dimensions of arrays to make a larger mesh if necessary and the possibility of different mesh sizes in r - and z -directions. Furthermore, one could input the mesh sizes rather than the number of mesh lines, and could use CONTINUE cards to calculate with different bunch lengths and/or mode numbers ($m=0$ or 1) in a single job. In this program, the beam was assumed to be hollow, with surface charges azimuthally distributed either in an uniform or sinusoidal way. In the first version of ABCI, the radius of the hollow beam was always chosen to be equal to that of a beam pipe so that no fields were

brought with it into the structure of concern. The wake fields were integrated at the radius of the beam pipe, which left the integration across the cavity gap as the only contribution to the wake potentials and thus made long beam pipes unnecessary. The program was compact, and simply structured so that users could easily change important parameters such as an array size for the number of mesh points, and modify the program for their special needs. Since the main body of the program was small, relatively large arrays could be allocated to mesh points in a limited memory space. Furthermore, permitting unequal mesh sizes in the axial and radial directions helped to reduce the number of mesh points.

However, if one tried to apply the program to long structures and/or very short bunches, the total number of mesh points easily becomes of the order of many hundred thousands or more. For example, the recently proposed "stagger-tuned" structure for the NLC of SLAC [4] consists of a disc-loaded waveguide with a large number of cells with slightly different dimensions of the order of μm or less. In order to correctly represent such tiny differences, many million mesh points would be needed.

Not all of these mesh points are simultaneously necessary at each time step for the calculation of fields. If we are only interested in the wake potentials not too far behind the beam, the fields need to be calculated only in the area called, "window". The window is defined by the area of the structure which starts at the head of the bunch and ends at the last longitudinal coordinate in the bunch frame (which is often the tail of the bunch) up to which we want to know the wake potentials. The fields in front of the bunch are always zero. The fields behind the window can never catch up with the window, which is moving forward with the speed of light, and thus do not affect the fields inside the window. Since the calculation is confined to the area inside the window, the "mesh" is needed only for this frame and moves together with it. One of main new features of ABCI is the implementation of this "moving mesh" in lieu of the conventional static mesh. Since the window is usually much smaller than the total structure, the number of mesh points can be drastically reduced. In addition, since the window length is determined only by the last longitudinal coordinate of the wake potentials, the number of mesh points does not change as the structure length increases.

Another main new feature of ABCI is the implementation of "Napoly's integration method" of fields

* This work was supported by the Director, Office of Energy Research, Office of High Energy and Nuclear Physics, High Energy Physics Division, of the U.S. Department of Energy under Contract No. DE-AC03-76SF00098.

to calculate wake potentials [5,6]. The conventional integration method at the radius of the beam pipe breaks down when a part of the structure comes down below it, or when the radii of the two beam pipes at both ends are unequal. The only alternative was to integrate over a straight line at an allowable radius and with beam pipes long enough to allow the fields to catch up with the beam far behind the structure. Napoly's integration method is a solution to this classical problem (the integration along the structure surface was already described by Gluckstern and Neri [7] in 1985). It relies on the expression of the wake potentials, at any multiple order, as an integral of electromagnetic fields along any one dimensional contour spanning the structure longitudinally. For the particular case of the contours parallel to the r - and z -axes, the integration is considerably simplified [6]. For this reason, ABCI has an option which uses a path of integration ("Napoly-Zotter contour") that starts as usual along the beam pipe, then descends radially to pass underneath the smallest material structure radius. It then rises again to the radius of the outgoing beam pipe and moves along it to the end of the structure (Napoly's method and a proper integration contour are actually automatically chosen as soon as a material point has a radius smaller than the beam pipe). This path is shown in Fig. 1 by the broken curve.

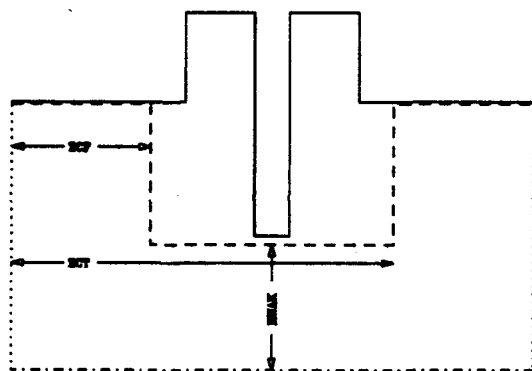


Fig. 1. Napoly-Zotter integration contour for computation of wake potentials.

The first axial coordinate where the path descends, the radius to which it goes, and the second axial coordinate where it rises again can also be chosen as input commands. In particular for structures with a complicated boundary extending to the inside of the beam pipes, this technique leads to a considerable saving in computing time. For the monopole (longitudinal) wake potential case, this method permits a structure with unequal beam radii at both ends. For the dipole (transverse and longitudinal) wake potential case, the beam pipe radii must be equal.

In addition to these two new main features mentioned above, ABCI has a completely new mesh generator, which permits circular and elliptical inputs just as TBCI. The program allows variable radial mesh sizes for different radial intervals for the better fitting of mesh and reducing the total number of mesh points by permitting to use a fine mesh only where actually needed. In addition to the conventional method of inputting the shape of the structure by giving the absolute coordinates of points, users can now

input the structure by giving the increments of coordinates from the previous positions (incremental input). In this method, one can use repetition commands to repeat input blocks which saves time and labor when the same structure repeats many times. Any bunch shape supplied by an user can be used (default=Gaussian). The new ABCI also has better plotting facilities. It can show on a separate page each the input and actual shape of a cavity used for calculation, electric field lines (or total current lines) at subsequent time steps for the monopole case, the wake potentials, and finally the impedance of a structure from Fourier transforms of wake potentials. ABCI creates a "Top Drawer" file [8] for the corresponding figures. By this method, ABCI's graphical output becomes independent of computers and graphic devices. One can easily import/export the graphical output to other computers, and/or edit it if desired.

II. APPLICATIONS

In this section, we show two typical examples of structures which demonstrate the usefulness of the new version of ABCI.

A. Collimator

A Saclay collimator shown in Fig. 2 is a simple constriction of a beam pipe, which can be computed easily with the new version of ABCI using Napoly's method. The beam pipes at both sides have 5 cm length. The integration contour used is shown by the broken curve. The rms bunch length is chosen to be 0.5mm. The longitudinal loss factor was then found to be -1.755×10^{13} V/C. For comparison, longitudinal loss factors were also computed by the integration along a straight line at the inner radius of the collimator and subtracting the contribution of the beam pipe from it (similar to the "WAKCOR" option in TBCI). The results are shown by the solid curve in Fig. 3 as a function of the beam pipe length L at both sides. The dotted line denotes the loss factor obtained by Napoly's method. They agree when a quite long beam pipe ≥ 30 cm compared to the beam pipe radius of 1 cm is used for the WAKCOR method. However, Napoly's method provides results much easier and faster.

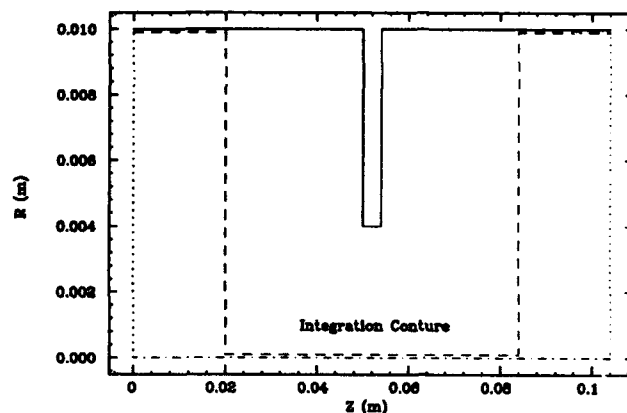


Fig. 2. Saclay collimator.

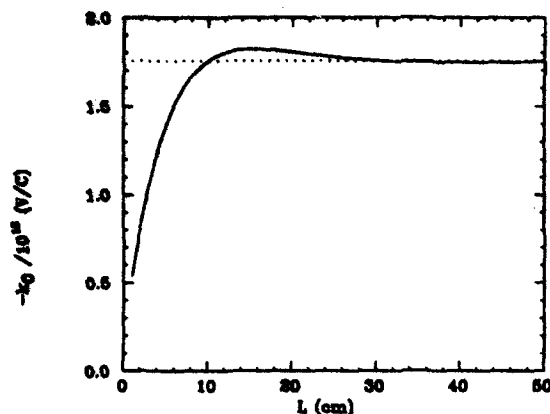


Fig. 3. Comparison of the longitudinal loss factor obtained by Napoly's method (dotted line) with that obtained by the "WAKCOR" method (solid line) as a function of beam pipe length L at both sides.

B. CLIC stagger-tuned disk-loaded waveguide

A "stagger-tuned" structure of the CLIC (CERN Linear Collider) [9] is a disk-loaded waveguide composed of many cells with slightly different dimensions in such a way that the mode frequencies of each cell are distributed around the average values. Then, wake fields from each cell are expected to cancel each other so that the total wake fields will damp away rather quickly. Figure 4 shows an example of the CLIC stagger-tuned structure with 20 cells. The computed (normalized) transverse wake potential is plotted in Fig. 5 up to 1cm behind the head of the bunch (the bunch length in this case is only 0.17 mm). A clear damping of the transverse wake potential can be seen.

If TBCI is used instead in this example, it would have required about 4.6 million mesh points of uniform mesh size for required mesh sizes of $10\text{ }\mu\text{m}$ and for almost 7.2cm long structure of over 6.4mm radius. That would probably not fit any computer. With the moving, variable and unequal meshes, ABCI requires only 84 thousands mesh points, by factor ~ 60 less than TBCI does.

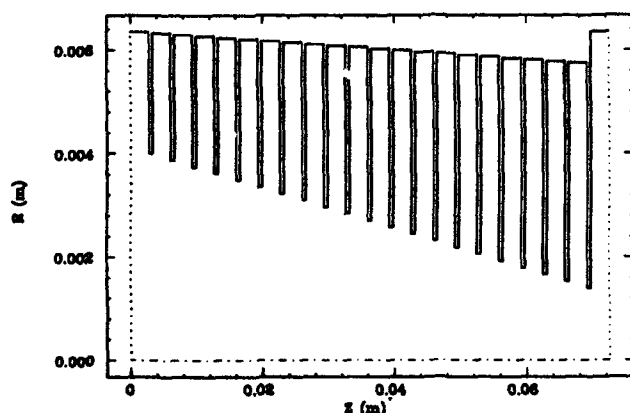


Fig. 4. Stagger-tuned disk-loaded waveguide of CLIC.

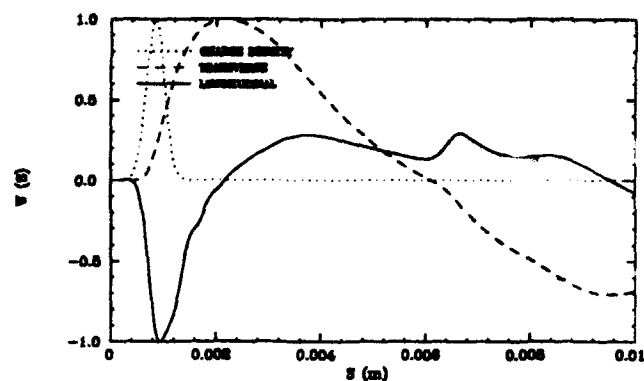


Fig. 5. Normalized transverse wake potential for CLIC stagger-tuned structure up to 1cm behind the head of bunch. The rms bunch length is 0.17mm.

III. CONCLUSIONS

The implementation of the moving mesh and Napoly's method for computing wake potentials, together with the option of variable radial mesh sizes, permits a large saving in memory and computing time, and thus drastically enhances the computational power of ABCI. It is now possible to compute wake potentials in much more complicated structures than before. The numerical examples shown in this paper demonstrate the usefulness and the remarkable advances in the new version of ABCI.

The author would like to thank B. Zotter and O. Napoly for helpful discussions and Center for Beam Physics at LBL for general support and encouragement.

IV. REFERENCES

- [1] Y. H. Chin, CERN LEP-TH/88-3, 1988.
- [2] K. S. Yee, IEEE Trans. Antennas Propagat., Vol. AP-14, 302 (1966).
- [3] T. Weiland, DESY 82-015, 1982.
- [4] K. L. F. Bane, and R. L. Gluckstern, SLAC-PUB-5783, 1992.
- [5] O. Napoly, Part. Accelerators, 36, 15 (1991).
- [6] O. Napoly, Y. H. Chin and B. Zotter, DAPNIA/SEA/93-01, 1993, and to be published in Nucl. Instrum. Methods.
- [7] R. L. Gluckstern, and F. Neri, IEEE NS-32, 5, 2403 (1985).
- [8] Top Drawer Manual, SLAC Computation Group, CTGM-189, 1980.
- [9] B. Zotter, private communications.

On Coupling Impedances of Pumping Holes

Sergey S. Kurennoy

Superconducting Super Collider Laboratory*
2550 Beckleymeade Ave., Dallas, TX 75237 USA

Abstract

Coupling impedances of a single small hole in vacuum-chamber walls have been calculated at low frequencies. To generalize these results for higher frequencies and/or larger holes one needs to solve coupled integral equations for the effective currents. These equations are solved for two specific hole shapes. The effects of many holes at high frequencies where the impedances are not additive are studied using a perturbation-theory method. The periodic versus random distributions of the pumping holes in the Superconducting Super Collider liner are compared.

I. INTRODUCTION

Pumping holes and slots are very typical and numerous discontinuities of the vacuum chamber in accelerators. The contributions of a small hole to the beam-chamber coupling impedances at low frequencies (below the chamber cut-off) have been calculated analytically [1, 2], and the results coincide well with subsequent simulations and measurements, e.g. [3]. The approach is based on the Bethe theory of diffraction by small holes [4], which can be applied when the wavelength is large compared to a typical hole size, and the hole size is small compared to that of the beam-pipe cross section. Due to the impedance additivity below cut-off, this theory gives reasonable estimates for many holes at low frequencies.

In the present paper we attempt to generalize this approach for a single hole with dimensions comparable to or larger than those of the chamber cross section. This leads to integral equations that are solved for two particular cases.

At frequencies above cut-off the problem is more complicated since there is no additivity of contributions to the coupling impedance from different discontinuities. To study the impedance of many holes above cut-off we use a model based on the perturbation method. This model allows us to compare the impedance for periodic and random distributions of pumping holes in the Collider liner.

II. INTEGRAL EQUATIONS

To calculate the coupling impedance we have to find the fields induced in the chamber by a given current perturbation, e.g., by a relativistic point charge. Taking as a zeroth

approximation the fields in the chamber without hole, one can consider them as incident electromagnetic waves on the hole. According to the Bethe theory [4], the fields diffracted by the hole can be obtained as those radiated by effective surface "magnetic" currents, which have to be introduced to satisfy the boundary conditions on the hole. Then integrating the fields along the beam path one can obtain coupling impedances. As a result, the longitudinal impedance of an arbitrary hole in the chamber with the circular cross section of radius b can be written as

$$Z(\omega) = -\frac{1}{2\pi b q} \iint_{hole} dS e^{-ikz} J_\varphi, \quad (1)$$

where $k = \omega/c$ and J_φ is the Fourier-harmonic of the azimuthal component of the effective "magnetic" current induced by charge q in the hole. The impedance for an arbitrary chamber cross-section can be obtained using an expansion over eigenfunctions, e.g., [5], and for the longitudinal case it also includes only the effective-current component, which is transverse to the chamber axis. The effective surface current \vec{J} and charge ρ should satisfy integral equations

$$\begin{aligned} \frac{1}{2} E_r(\vec{r}) &= \frac{1}{4\pi} \iint_{hole} dS' (J_v \nabla_u G - J_u \nabla_v G), \\ \frac{1}{2} Z_0 H_\varphi(\vec{r}) &= \frac{1}{4\pi} \iint_{hole} dS' (c\rho \nabla_u G - ik J_u G), \end{aligned} \quad (2)$$

and the continuity condition $\text{div} \vec{J} = i\omega\rho$, where $Z_0 = 120\pi\Omega$, $G(R) = \exp(ikR)/R$, $R = |\vec{r} - \vec{r}'|$; $\vec{r}, \vec{r}' \in S$, $\vec{J} = \vec{J}(\vec{r}')$, and (u, v) are the local coordinates on the hole, with \vec{e}_v being parallel and \vec{e}_u transverse to the chamber axis z . According to [4], E_r and H_φ here are Fourier-harmonics of the beam fields on the wall in the chamber without hole, which are equal to $E_r = Z_0 H_\varphi = Z_0 q \exp(ikz)/(2\pi b)$ in the round pipe.

In the case of a small hole ($h \ll b$) at low frequencies ($\omega \ll c/b$) one can consider the beam fields to be the same everywhere on the hole and reduce the problem to an electrostatic one [4]. Then the impedance can be obtained analytically in terms of hole polarizabilities [1, 2, 5]. In the case of a long slot (length $l \gg b$) or when the transverse hole size is larger than the pipe radius, it does not work.

However, one can solve the general problem for two special cases. The first one is mostly of academic interest, namely, the infinitely long narrow slot, width $w \ll b$, in a perfectly conducting pipe. The only dependence on z

*Operated by the Universities Research Association, Inc., for the U.S. Department of Energy under Contract No. DE-AC35-89ER40486.

for such a slot is $J_z \propto \exp(ikz)$. Substituting $J_z = c\rho$, $J_\varphi = 0$, one can reduce Eqs. (2) at frequencies $\omega \ll c/b$ to a single equation for J_z , which has a solution

$$J_z(u, z) = \frac{Z_0 q}{\pi b} e^{ikz} \frac{u}{\sqrt{(w/2)^2 - u^2}},$$

where $|u| < w/2$. Since $J_\varphi = 0$, the impedance of such a slot vanishes, cf. Eq. (1). This answer follows as a limiting case from results for an elongated elliptic hole [1], and was also obtained in [6]. From the physical point of view, the charge drags the static field pattern along the chamber without producing any distortions. The field distortions could only be produced by the slot ends. It means that the low-frequency impedance of a long ($l \gg b$) narrow slot is independent of slot length.

The second case is a narrow transverse gap of length $g \ll b$ separating two pieces of the infinite beam pipe. Due to the axial symmetry there is no current dependence on φ when the beam goes along the axis. In the case of $kg \ll 1$, Eqs. (2) after integrating over φ are reduced to

$$\frac{1}{2} H_\varphi(z) = -ik \int_{-g/2}^{g/2} dz' e^{ikz'} K(z - z') J_\varphi(z'), \quad (3)$$

where $K(2bx) = (1 + x^2)^{-3/2} {}_2F_1[1/2, 3/2, 1, (1 + x^2)^{-1}]$. Eq. (3) has a solution

$$J_\varphi(x) \simeq \frac{4Z_0 q}{\pi k^2 g^2 \ln(16b/g)} \frac{x}{\sqrt{(g/2)^2 - x^2}},$$

which gives the low-frequency impedance of the gap

$$Z(\omega) = i \frac{Z_0 c}{2\omega b \ln(16b/g)}, \quad (4)$$

i.e., the capacitance $C = 2\epsilon_0 b \ln(16b/g)$. This result is natural since the gap cuts the image low-frequency currents in the wall and works as a capacitance. In a real accelerator chamber there are usually some electrical connections of chamber pieces separated by gaps, e.g., cavity walls or through the ground. Low-frequency currents flow through these connections, which have lower reactance in this frequency range than the gap.

A similar answer for C can be obtained from the plane electrostatic problem: find a capacitance per unit length of a gap g separating two half-planes. The problem can be easily solved by conformal mapping, and the result is $2\epsilon_0 \ln(4\Lambda/g)/\pi$. It includes the log-dependence on a cut-off parameter, $\Lambda \gg g$. Comparing to our cylindrical problem it seems natural to put $\Lambda \simeq 2b$, while the length is $2\pi b$. It gives us impedance (4) up to a factor of the order of 2.

To compare with numerical results we computed wakes in the chamber $b = 2$ cm with a narrow gap g surrounded by a cavity with length l and depth h , by means of the code ABCI [7]. The cavity inductance is $L = \mu_0 l h / (2\pi b)$, and such a cavity-gap system will have resonances at $\omega_r = 1/\sqrt{LC}$, i.e., with wavelength $\lambda_r = 2\sqrt{lh \ln(16b/g)}$. Figure 1 shows a good agreement of this formula with ABCI results.

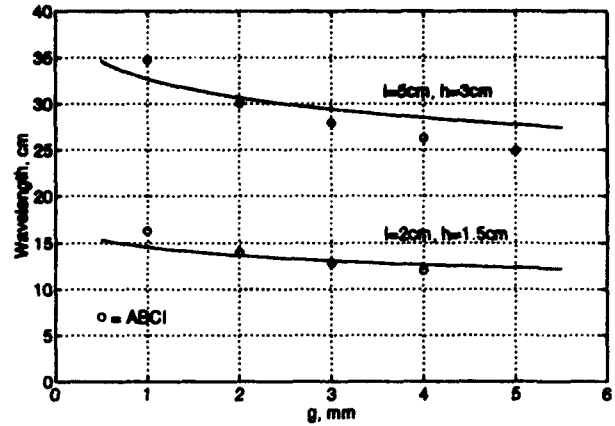


Figure 1. The resonance wavelength versus gap width.

III. PERIODIC OR RANDOM STRUCTURE

The design of the liner inside the Superconducting Super Collider (SSC) Collider beam tube, which has to screen the cold chamber walls from the synchrotron radiation, anticipates a lot of small pumping holes. With the hole radius $r = 1$ mm and $b = 1.5$ cm the number of holes should be nearly 1500 per meter, and their total number in the ring is about 10^8 . There will be $M = 15$ holes in one cross section, and such rows will be spaced by distance $D = 1$ cm. The low-frequency impedances produced by these holes can be calculated as in Refs. [1, 2]: $Z/n \simeq -i0.15 \Omega$ and $Z_\perp \simeq -i18 \text{ M}\Omega/\text{m}$ for this specific case with the liner wall thickness 1 mm. To study effects of periodicity of liner holes at frequencies above cut-off we introduce a model that works for wavelengths large compared to the hole size, i.e., below $f \sim c/(2h) \simeq 150$ GHz. Namely, we replace a row of M holes in one chamber cross section, which has a discrete axial symmetry, by an axisymmetric small enlargement with the triangular (in the longitudinal direction) cross section of depth $h = r/2$ and base $g = 2r$. We will assume that the impedance of M holes in a row is that of such a discontinuity multiplied by azimuthal factor $\phi = Mr/(\pi b)$, cf. Ref. [1]. The model has small parameter $\epsilon = h/(2b)$, which is $1/60$ in our case. So, one can apply the perturbation method for periodic structures of small discontinuities that was developed in [8], and its generalization to broken periodicity [9]. It makes use of an expansion over ϵ in boundary conditions and gives the impedance at low frequencies and at resonances in an analytical form. The low-frequency impedance due to enlargements is

$$Z/n = -iZ_0 \epsilon^2 G/2 \sum_{p=1}^{\infty} p C_p^2 I_1(pG)/I_0(pG) + O(\epsilon^3), \quad (5)$$

where D is the structure period, $G = 2\pi b/D$, $I_m(x)$ are modified Bessel functions, and C_p are Fourier coefficients of the boundary shape,

$$C_p = (-1)^p 2g/D [\sin(\pi p g/2D)/(\pi p g/2D)]^2 \quad (6)$$

for triangular perturbations. The resonant frequencies $f_{p,r}$ of the r -th radial mode, bandwidths $(2\Delta f)_{p,r}$, and impedances $Z_{p,r}$ are

$$\begin{aligned} f_{p,r} &= c/(4\pi b) (pG + j_{0r}^2/pG), \\ (2\Delta f)_{p,r} &= f_{p,r} \delta f_{p,r} / (2b) \left[1 + (j_{0r}/pG)^2 \right], \\ Z_{p,r}/n &= Z_0 \epsilon^2 C_p^2 2b / \delta f_{p,r} \left[1 + (j_{0r}/pG)^2 \right]^{-2}, \end{aligned} \quad (7)$$

where j_{0r} are roots of the Bessel function $J_0(x)$ and δf is the skin-depth at frequency f . From Eq. (5) $(Z/n) \cdot \phi = -i0.17 \Omega$, which is close to the exact answer for holes at low frequencies and justifies the choice of the model parameters. An important point is that Eqs. (5) and (7) work for an arbitrary distribution of perturbations on the ring; one has only to replace period D by the ring circumference $2\pi R$ and take proper C_p . In this case $N = 2\pi R/D$ identical perturbations are distributed along the ring. To take into account various insertions that violate the periodicity, e.g., interaction regions and warm pipe sections without holes, we consider the number of perturbations $K \leq N$. In general, new coefficients $C_p^{(K)}$ are related to those C_p for a single perturbation on the ring. Let us assume that perturbations are randomly displaced from their positions in exactly periodic (period $D = 2\pi R/N$) structure and the deviations have the Gauss distribution with dispersion $(\delta D)^2$. Then the averaged over distribution coefficients are

$$\begin{aligned} [C_p^{(K)}]^2 &= F_p^{(K)}(\delta) C_p^2, \\ F_p^{(K)}(\delta) &= K(1 - \zeta_p) + \zeta_p F_p^{(K)} - \zeta_p(1 - \zeta_p) \frac{\sin 2\pi p K/N}{\sin 2\pi p/N} \end{aligned} \quad (8)$$

where C_p are given by Eq. (6) with $D \rightarrow 2\pi R$, $\zeta_p = \exp[-(2\pi p\delta/N)^2]$ and $F_p^{(K)} = [\sin(\pi p K/N)/\sin(\pi p/N)]^2$. In the case of the exactly periodic structure, $\delta = 0$, we have $\zeta_p = 1$ and $F_p^{(K)}(0) = F_p^{(K)} \in [0, K^2]$, with maxima K^2 for $p = Nl$, $l = 0, 1, 2, \dots$. If $K = N$ in addition, $F_p^{(K)} = N^2 \delta_{p, Nl}$, i.e., all resonances $p \neq Nl$ vanish, and the case of the structure with short period $D = 2\pi R/N$ is recovered. Figure 2 shows the hole impedance for this case. The wall conductivity of copper at room temperature $\sigma = 6 \cdot 10^7 (\Omega \text{ m})^{-1}$ was taken just for reference. Resonance values should be scaled $\propto \sqrt{\sigma} \propto \sqrt{R/R_0}$. Certainly, it gives the worst and, fortunately, unrealistic case, since for the real design the exact periodicity is broken.

Let us consider a more realistic model: blocks of length $L = 15$ m containing the periodic hole structure (magnets with a regularly perforated liner inside) are separated by short insertions without holes (rf joints). Using the method of Ref. [9], one can calculate the damping of resonances in Figure 2 due to periodicity violation; it is by a factor 0.03–0.05. So, the maximal resonance values of $\phi Z/n$ are 8–12 Ω , according to the block model.

One can go further and destroy periodicity inside blocks by placing holes not exactly in one transverse row, changing steps between rows, etc. The impedance estimate for this case ("random" hole distribution) can be obtained

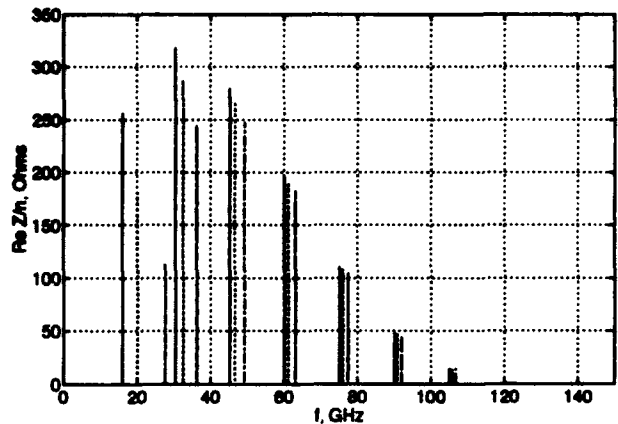


Figure 2. Resonances of the exactly periodic structure

from Eq. (8) with $\zeta_p \rightarrow 0$. Then $F_p^{(K)}(\delta) \rightarrow K$; that means the incoherent sum of contribution from different perturbations, and due to overlapping of small resonances we get $\text{Re } Z/n \simeq 0.2 \Omega$, i.e., approximately the constant value in the frequency range above cut-off (7–50 GHz). In this case we have something like a broad-band impedance with $Q = 1$, since $\phi \text{Re } Z/n(f > f_{\text{cut}}) \simeq \phi |\text{Im } Z/n|(f < f_{\text{cut}}) \simeq 0.2 \Omega$.

IV. CONCLUSIONS

The integral-equation approach allows one to calculate the impedance for two examples when the hole is not small. Unfortunately, these cases are of mostly academic interest.

The impedance of many small holes in the SSC Collider liner is studied at frequencies above cut-off using a model. It is shown that random hole distributions give lower impedance than periodic ones in this frequency range. It is reasonable to introduce some periodicity violation in the hole pattern.

V. REFERENCES

- [1] S.S. Kurennoy, *Part. Acc.*, Vol. 39, pp.1–13 (1992).
- [2] R.L. Gluckstern, Reports CERN SL/92-05,06(AP), Geneva (1992).
- [3] W. Chou and T. Barts, *Proceed. of this Conference*; E. Ruiz, et al., *ibid.*
- [4] H.A. Bethe, *Phys. Rev.*, Vol. 66, pp.163–182 (1944).
- [5] S.S. Kurennoy, Report IHEP 92-84, Protvino (1992); *Proceed. of EPAC*, Berlin (1992).
- [6] S.A. Heifets, SLAC-AAS-Note-76, Stanford (1992).
- [7] Y.H. Chin, Report CERN SL/92-49 (AP), Geneva (1992).
- [8] S. Krinsky, *Proceed. of 11th Int. Conf. on Part. Accel.*, Geneva (1980), p.576.
- [9] S.S. Kurennoy, Report IHEP 88-10, Serpukhov (1988) and *Proceed. of EPAC*, Rome (1988), p.761.

Using a Ceramic Chamber in Kicker Magnets

Sergey S. Kurennoy
Superconducting Super Collider Laboratory*
2550 Beckleymeade Ave., Dallas, TX 75237 USA

Abstract

A ceramic chamber inside kicker magnets can provide the relevant field risetime. On the other hand, some metallic coating inside has to prevent static charge buildup and shield the beam from ceramic and ferrite at high frequencies to avoid possible resonances. The issues concerning the metallized ceramic chamber, such as coupling impedances and requirements on the coating, are studied to find a compromise solution for kickers of the Medium Energy Booster at the Superconducting Super Collider.

I. INTRODUCTION

There are two reasons for using ceramic chambers in kickers: (1) to avoid shielding of a fast-changing external magnetic field by metallic chamber walls; and (2) to reduce heating due to eddy currents. On the other hand, such a chamber can produce large coupling impedances, since it works as a slow-wave structure, and can lead to accumulation of static charges on the ceramic surface. The natural way to avoid these unwanted effects is to put a thin metallic coating on the inner surface of the ceramic chamber. However, shortcomings of such a coating are obvious. It will again shield fast-changing external magnetic fields and heat the chamber walls due to eddy currents, cf. the reasons for the ceramic chamber. To find a compromise solution we have to estimate quantitatively both the effects of shielding and impedances.

II. RISETIMES AND HEATING

The length of the front of the magnetic field pulse, τ_k , should be about 50 ns for the Medium Energy Booster (MEB) injection kicker and 2 μ s for abort and extraction kickers. Even if we have a step-like external magnetic field, the risetime of the magnetic field inside a vacuum chamber with a metallic layer on the wall would be finite because of (1) shielding due to eddy-currents and (2) skin-depth effect.

A. Shielding by Eddy Currents

Continuous coating. For a round metallic tube of radius b and wall thickness d the risetime τ_s due to shielding of

a step-like external magnetic field by eddy currents in the wall is [1, 2, 3]

$$\tau_s = \mu_0 b \sigma d / 2. \quad (1)$$

The cross section of the vacuum chamber in MEB and Low Energy Booster (LEB) kickers is more similar to a rectangle 10×5 cm with rounded angles. One can easily calculate risetime τ_s for such a geometry as $\tau_s \simeq L/R$, where L and R are characteristic inductance and resistance. For metal-wall thickness d in a chamber with length l and rectangular cross section $w \times h$ ($d \ll w$, vertical magnetic field) we get $L = 4\mu_0 l / \pi$; $R = 4l / (\sigma w d)$, and hence

$$\tau_s \simeq L/R \simeq \mu_0 w \sigma d / \pi. \quad (2)$$

This estimate is approximately the same as that of Eq. (1) if $w = 2b$ is assumed.

Applying Eq. (2) with $w = 10$ cm, we try to satisfy condition $\tau_s < \kappa \tau_k$, where $\kappa = 0.1-0.2$ is a numerical factor. For $\kappa = 0.2$ this gives 99% of B_{max} inside the chamber after τ_k for a step-like external magnetic field. This leads to the following restriction

$$\sigma d < \frac{\pi \kappa \tau_k}{\mu_0 w},$$

which gives for the injection kicker with $\kappa = 0.2$

$$\sigma d < 0.25 \Omega^{-1}; \quad \text{or} \quad R_\square > 4 \Omega;$$

and for the extraction/abort ones with $\kappa = 0.1$

$$\sigma d < 5 \Omega^{-1}; \quad \text{or} \quad R_\square > 0.2 \Omega.$$

Here $R_\square = 1/(\sigma d)$ is the surface resistivity per square. Then the allowed thickness of the coating by stainless steel or titanium ($\sigma \simeq 1.43 \cdot 10^6 (\Omega)^{-1}$) is $d < 0.17 \mu\text{m}$ for the injection kicker and $d < 3.4 \mu\text{m}$ for extraction/abort ones. For more accurate calculations that take into account the shape of the pulse of the external magnetic field see [4].

Coating by stripes. The shielding effect due to eddy currents can be reduced essentially if the coating by longitudinal stripes is applied instead of the continuous one, e.g. [5]. For a rectangular cross section if we have N stripes with width $w_1 = w/N$ and thickness d , $d \ll w_1$ (we neglect here the width of small gaps between stripes) on horizontal chamber walls, the resistance with respect to eddy currents is N times higher than for continuous coating, and as a result, $\tau_s \rightarrow \tau_s/N$, and the allowed value of thickness

$$d \rightarrow Nd.$$

The coating of side walls does not affect the shielding.

*Operated by the Universities Research Association, Inc., for the U.S. Department of Energy under Contract No. DE-AC35-89ER40486.

B. Skin-Depth Effect

It is well-known that the skin-depth in a metal is equal to $\delta = \sqrt{2/(\mu_0 \sigma \omega)}$. If the metal-wall thickness is d and frequency ω_{sd} is defined by the equation $\delta(\omega_{sd}) = d$, all frequencies higher than ω_{sd} will be screened by the wall. It gives us the risetime due to skin-depth effect

$$\tau_{sd} = \omega_{sd}^{-1} = \mu_0 \sigma d^2 / 2. \quad (3)$$

To satisfy condition $\tau_s < \kappa \tau_h$, it is necessary to restrict

$$\sigma d^2 < 2\kappa \tau_h / \mu_0.$$

For the injection kicker we get $\sigma d^2 < 0.016 \text{ m}/\Omega$ and for stainless steel $d < 100 \mu\text{m}$. The limitation from the skin-depth effect is weak in comparison with those from the eddy currents.

C. Heating Due to Eddy Currents

The energy produced by eddy currents during time τ in the wall of length l , width w and thickness d can be estimated as

$$E \simeq \frac{B_0^2 \sigma d w^3 l}{12\tau}, \quad (4)$$

where $\dot{B} \simeq B_0/\tau$ is taken. The relevant temperature rise is

$$\Delta T \simeq \frac{E}{CM} \simeq \frac{B_0^2 \sigma w^2}{12\tau c_m \rho_m}, \quad (5)$$

where c_m and ρ_m are specific heat and density of the wall material. If we take them as 450 J/kg/K and 7800 kg/m^3 for stainless steel, $B_0 = 0.015 \text{ T}$, $\tau = 50 \text{ ns}$, we get $E/l = 0.5 \text{ J/m}$ for $d = 1 \mu\text{m}$, and $\Delta T = 1.5 \text{ K}$. That is not too much. It should be noted also that ΔT is independent of the thickness of the coating.

For N metallic stripes instead of a solid coating, the induced eddy current in each stripe is $I_1 = I/N^2$ and the resistance of a stripe is $R_1 = NR$. The total energy released is only $E_N = E/N^2$ and, hence, $\Delta T_N = \Delta T/N^2$. It means that in the case of $N = 20$ stripes we have the temperature rise $\Delta T = 0.004 \text{ K}$ only.

D. Effects of Slots in Metallic Coating

Let us consider what width w_1 of stripes and g of gaps between them are reasonable if the metallic coating is performed as stripes. If there are N stripes on a horizontal chamber wall, then $w_1 + g = w/N$ and the allowed thickness of coating is $d = Nd_0$, where w is the width of chamber and d_0 is the allowed thickness of continuous coating. When $d_0 \simeq 0.15 \mu\text{m}$ for stainless steel and $w = 10 \text{ cm}$ we would get reasonable figures $d = 3 \mu\text{m}$ and $w_1 + g = 5 \text{ mm}$ for $N = 20$. As for ratio g/w_1 , it can be estimated as follows. A narrow ($g \ll w_1$) gap between two thin stripes ($d \ll g$), which are in one plane, has capacitance

$$C \simeq \frac{\epsilon + 1}{2} \frac{4\epsilon_0 l}{\pi} \ln(2w_1/g),$$

where l is the gap length. If g is very small, this capacitance is big, and eddy currents at high frequencies would easily flow between stripes, shielding the external magnetic field strongly, as it occurs with a continuous coating. At $\omega \simeq 5/\tau_h = 10^8 \text{ s}^{-1}$ and $l = 26 \text{ cm}$ (the length of one section of the MEB injection kicker), $Z_C = 1/(\omega C) \simeq 300 \Omega$ for $w_1/g = 4$. It should be compared with the resistance of a stripe $R \simeq 60 \Omega$ and its reactance $Z_L = \omega L \simeq 42 \Omega$. It is clear that from the point of view of shielding we have to restrict the ratio $w_1/g \leq 10-15$ in this case. It means that reasonable values for the stripe and gap width are $w_1 = 4.5 \text{ mm}$ and $g = 0.5 \text{ mm}$ for the case of $N = 20$.

III. COUPLING IMPEDANCES OF CERAMIC CHAMBER

To estimate impedances of ceramic chamber we will use a model with a circular cross section of inner radius b and multi-layer wall: inner metal coating of thickness d (conductivity σ), ceramic of thickness Δ (permittivity ϵ), and thick outermost layer (perfect conductor or magnet). For such a geometry, it is possible to calculate em-fields produced by a given current perturbation and to derive explicit expressions for coupling impedances. The longitudinal impedance was done by B. Zotter [6].

A. Low-Frequency Impedances

The real part of the longitudinal impedance of a chamber piece with length L is

$$\text{Re } Z(\omega) = \frac{L}{2\pi b} \mathcal{R}$$

where at low frequencies ($\delta > d$) $\mathcal{R} = \mathcal{R}_\square = 1/(\sigma d)$. Since it works when $f < f_{rev} = 75.7 \text{ kHz}$, the ratio of the kicker resistive-wall impedance to that of the ring is

$$r = \frac{\text{Re } Z_{kicker}}{\text{Re } Z_{ch}} = \frac{L}{2\pi R} \frac{d_{ch} \sigma_{ch}}{d \sigma},$$

where $2\pi R = 3960 \text{ m}$ is the MEB circumference and $d_{ch} = 2 \text{ mm}$ is the wall thickness. The transverse impedance can be obtained making use of the relation $Z_\perp = (2R/b^2)Z/n$. With $L = 3 \text{ m}$ as the total length of the injection kicker, $\sigma_{ch} = \sigma$ and $d = 0.15 \mu\text{m}$, we get $r \simeq 13$ (!). Certainly, it is the worst case since we assume the image current flows only through the coating. In fact, some part of it will flow through external circuits. Nevertheless, for N stripes this ratio would be N times lower since the allowed thickness is N times higher. Otherwise, in the case of a solid coating it is reasonable to connect two pieces of the beam pipe, those upstream and downstream the kicker, by a good external conductor to prevent the essential reduction of the resistive-wall instability risetime.

In the so-called low-frequency limit, i.e., when $\omega \ll c\gamma/(\sqrt{\epsilon}b)$, the longitudinal impedance of the uncoated chamber ($d = 0$) is [6]

$$\frac{Z}{n} = \frac{Z_0 L}{2\pi R} \left[\frac{1}{\epsilon} \tan \delta_\epsilon - i(\beta^2 - \frac{1}{\epsilon}) \right] \ln \left(1 + \frac{\Delta}{b} \right), \quad (6)$$

where $\tan \delta_e$ is the loss-tangent (10^{-4} for alumina), and a perfect conductor outside ceramic is assumed.

From similar calculations the transverse impedance of the uncoated ceramic chamber with a perfect conductor outside ceramic is

$$Z_{\perp} = \frac{Z_0 L}{2\pi b^2} \left[\frac{2\epsilon \tan \delta_e}{(\epsilon + \alpha)^2} - i \left(\frac{\epsilon - \alpha}{\epsilon + \alpha} - \frac{\beta^2 b^2}{(b + \Delta)^2} - \frac{1}{\gamma^2} \right) \right],$$

where

$$\alpha = \frac{(b + \Delta)^2 - b^2}{(b + \Delta)^2 + b^2}.$$

The transverse impedance in the case when a perfect magnet is outside ceramic is

$$Z_{\perp} = \frac{Z_0 L}{2\pi b^2} \left[\frac{2\epsilon \tan \delta_e}{(\epsilon + 1/\alpha)^2} - i \left(\frac{\alpha\epsilon - 1}{\alpha\epsilon + 1} + \frac{\beta^2 b^2}{(b + \Delta)^2} - \frac{1}{\gamma^2} \right) \right].$$

For the case of inner continuous coating we have simple expressions in the low-frequency limit $\omega < c/(\sqrt{\epsilon}b)$ when $\gamma \gg 1$ and, in addition, $\epsilon\epsilon_0\omega b/\sigma \ll d \ll \delta$. For stainless steel at frequency $f = 60$ MHz it means 10^{-9} m $\ll d \ll 5.4 \cdot 10^{-8}$ if $\epsilon = 10$, i.e., the interval of practical interest. The transverse impedance is

$$Z_{\perp} = Z_0 \frac{L}{2\pi b^2} \frac{s - i\zeta}{s^2 + \zeta^2}, \quad (7)$$

where $s = bd/\delta^2$ and $\zeta = (b + \Delta)^2/[(b + \Delta)^2 \mp b^2]$, the upper sign corresponds to the case when a perfect conductor is outside ceramic, and the lower one to a perfect magnet.

Now one can make some estimates. Let us take $b = 2.5$ cm for a pessimistic estimate and $b = 5$ cm for an optimistic one, $\Delta = 3$ mm, $\epsilon = 10$, $\gamma = 13$ –213, $R = 630$ m and $L = \sum N_i L_i = 21$ m, the total length of all MEB kicker magnets. The impedance values at $f = 60$ MHz, which corresponds to the bunch spacing 5 m, are shown in Tables 1 and 2.

Table 1
Longitudinal Impedance

	$(Z/n)/\text{m}\Omega$		
$d, \mu\text{m}$	0	1	5
$b = 2.5$ cm	?-i202	88 - i51	23 - i3
$b = 5$ cm	?-i104	46 - i25	12 - i1

Table 2
Transverse Impedance

	$Z_{\perp}/(\text{k}\Omega/\text{m})$		
$d, \mu\text{m}$	0	1	5
injection kicker			
$b = 2.5$ cm	?-i243	34 - i2	7 - i0.1
$b = 5$ cm	?-i44	4 - i0.1	0.9 - i0.005
extraction & abort kickers			
$b = 2.5$ cm	?-i310	152 - i89	40 - i5
$b = 5$ cm	?-i42	20 - i11	5 - i0.5

Here “?” in the first column means that the real part of impedance for an uncoated chamber is defined mostly by losses in external conductors or ferrite.

At frequencies below 1 MHz $\text{Im } Z/n$ and $\text{Im } Z_{\perp}$ are nearly frequency- and d -independent: -0.17Ω and $-0.35 \text{ M}\Omega/\text{m}$ for the extraction and abort kickers together; -0.26Ω and $-0.52 \text{ M}\Omega/\text{m}$ for the injection one, when $b = 2.5$ cm is taken. With $b = 5$ cm (optimistic estimate), we get the same values of $\text{Im } Z/n$, and $-0.09 \text{ M}\Omega/\text{m}$ and $-0.13 \text{ M}\Omega/\text{m}$ for $\text{Im } Z_{\perp}$, respectively.

B. Resonances

Since the ceramic chamber works as a slow-wave structure, some resonances can occur at high frequencies. If we consider $\tan \delta_e \ll 1$ and frequency range $c/(\sqrt{\epsilon}b) \ll \omega \ll c\gamma/b$, the resonance condition is simplified to [6]

$$\cot |\nu| \Delta = b|\nu|/(2\epsilon), \quad (8)$$

where $\nu = \omega\sqrt{1 - \epsilon\mu\beta^2}/c$. If, in addition, $b/(2\epsilon\Delta) \ll 1$, the p -th resonance is approximately defined by $z_p \equiv |\nu_p| \Delta \approx \pi(p - 1/2)$. The maximal value of the longitudinal impedance at the resonance can be estimated as

$$\left(\frac{Z}{n} \right)_p = \frac{L}{2\pi R \tan \delta_e} \frac{8Z_0 \beta^2 \Delta^3 (\epsilon - \beta^{-2})^2}{z_p^2 b^3 z_p^2 + C}, \quad (9)$$

where $C = x[x + 2/(\epsilon\beta^2) - 1]$ with $x = 2\epsilon\Delta/b$. For the parameters cited above we get the lowest ($p = 1$) resonance frequency $f_1 \approx 8.6$ GHz and corresponding maximal impedance $(Z/n)_1 \approx 16 \text{ k}\Omega$ if $L = 21$ m.

The metallic coating damps these resonances drastically. The impedance value is approximately

$$\frac{Z}{n} = Z_0 \frac{L}{2\pi R} \frac{\delta^2}{2bd}, \quad (10)$$

which gives $(Z/n)_1 \approx 1.2 \text{ m}\Omega$ for $d = 1 \mu\text{m}$.

IV. CONCLUSIONS

The inner metallization of the ceramic chamber in kickers helps to avoid resonances and static charge buildup. For very fast kickers the coating by stripes has some advantages.

V. REFERENCES

- [1] R. Shafer, Report SSC-SR-1017 (1985); FNAL Report TM-991 (1980).
- [2] K.-Y. Ng, Report SSC-N-22 (1985).
- [3] A. Piwinski, *IEEE Trans. NS*, NS-24, p. 1364, (1977).
- [4] J.M. Peterson, SLAC Note CN-49 (1981).
- [5] L.S. Walling, et al., *NIM*, Vol. A281, pp. 433–447, (1989).
- [6] B. Zotter, *Part. Acc.*, Vol. 1, pp. 311–326. (1970).

An Analytical Treatment of Self Fields in a Relativistic Bunch of Charged Particles in a Circular Orbit

J.L. Delhez, J.M.A. Hofman, J.I.M. Botman, H.L. Hagedoorn, W.J.G.M. Kleeven and G.A. Webers,
Eindhoven University of Technology, P.O. Box 513, 5600 MB Eindhoven, Netherlands.

Abstract

It is known that the electromagnetic field caused by a moving charge depends on its acceleration. Therefore, if a bunch of charged particles has a circular trajectory, the self fields in the bunch depend on the radius of curvature. We will treat these self fields analytically for a one-dimensional bunch, using the Liénard-Wiechert potentials. These depend on the retarded positions of the charges in the bunch. We will show that one only has to determine these positions explicitly for the endpoints of the bunch. The one-dimensional model predicts non-zero tangential and radial forces in the middle of the bunch which depend on its angular width and on its angular velocity. Expressions for these forces are presented. A comparison between the power loss due to coherent radiation and the tangential force exerted on the central electron of the bunch shows that there is a definite relation between these quantities.

I. INTRODUCTION

We consider a charge q in an arbitrary orbit. At time t' , the charge is located at \vec{r}' , has velocity $\vec{\beta}$ and acceleration $\dot{\vec{\beta}}$. The electromagnetic field caused by this charge, experienced at time $t > t'$ and position \vec{r}_1 can be derived from the Liénard-Wiechert potentials [2] and reads

$$\vec{E}(\vec{r}_1, t) = \frac{q}{4\pi\epsilon_0} \left[\frac{\vec{n} - \vec{\beta}}{\gamma^2(1 - \vec{\beta} \cdot \vec{n})^3\Lambda^2} + \frac{\vec{n} \times \{(\vec{n} - \vec{\beta}) \times \dot{\vec{\beta}}\}}{c(1 - \vec{\beta} \cdot \vec{n})^3\Lambda} \right]$$

$$\vec{B}(\vec{r}_1, t) = (\vec{n}/c) \times \vec{E}(\vec{r}_1, t),$$

with $\Lambda = c(t - t') = ||\vec{r}_1 - \vec{r}'||$ and $\vec{n} = (\vec{r}_1 - \vec{r}')/\Lambda$. The first term in the equation for \vec{E} represents the usual Coulomb-like 'space charge field,' the second term the 'synchrotron radiation field' (containing the acceleration $\dot{\vec{\beta}}$ and being perpendicular to \vec{n}). The fact that the above equations relate the EM field at t to quantities at retarded time t' makes it difficult to express the total field at t for a bunch with arbitrary charge distribution in a general orbit. The retardation condition, which depends on the orbit path and observer position \vec{r}_1 , must be solved to express the relation between $\vec{r}(t)$ and $\vec{r}'(t')$.

II. ONE-DIMENSIONAL BUNCH

The treatment presented in this paper is an overview of work reported in reference [1]. We look at the electromagnetic field for the specific case of a homogeneously

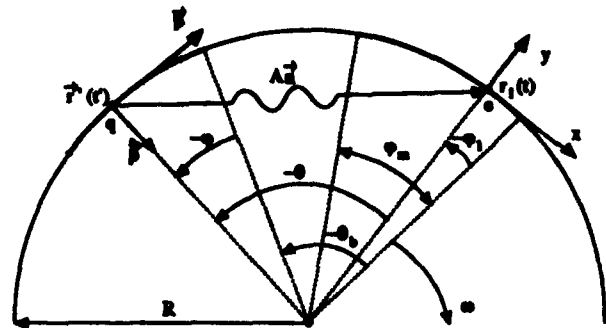


Figure 1: 1D bunch in a circular orbit.

charged 1D bunch in a circular orbit with radius R (see Fig. 1). The 'bunch angle' is denoted $\varphi_m = l/R$ with l the (longitudinal) size of the bunch. The (constant) rotation frequency is ω and the linear charge density is λ . We consider a reference charge e at an angular position φ_1 relative to the front side of the bunch, i.e. $-\varphi_m < \varphi_1 < 0$ (all angles will be taken positive in the direction of rotation). The force exerted on e is caused by all other charges in the bunch. One of those other charges is q , at angular position φ ($-\varphi_m < \varphi < 0$). At retarded time t' , charge q emits a photon that reaches charge e at time t . Meanwhile, the bunch has rotated over an angle $-\theta_b = \omega(t - t')$, $\theta_b < 0$. The angular distance between q at t' and e at t is denoted $\theta = \theta_b + \varphi - \varphi_1$ (can be positive or negative). The retardation condition expresses the relation between θ_b and $(\varphi - \varphi_1)$. We obtain (for the case $\varphi_m < \pi - 2\beta$)

$$\varphi - \varphi_1 = |\theta_b| \pm 2 \arcsin \left(\frac{|\theta_b|}{2\beta} \right), \quad -2\beta \leq \theta_b < 0.$$

Note that charges both to the left and to the right of e contribute to the field, hence two values for $(\varphi - \varphi_1)$ exist for given θ_b .

We now consider an infinitesimal charge $dq = \lambda R d\varphi$ at angular position φ . It causes an electric field $d\vec{E}$ at the position of reference charge e and a force $d\vec{F}$ given by

$$d\vec{F} = e\{d\vec{E} + \beta \vec{e}_s \times (\vec{n} \times d\vec{E})\},$$

where the force contribution by the magnetic field has also been taken into account (note that β is constant). Here, the coordinate system (x, y) has been used, with \vec{e}_s the unit vector at \vec{r}_1 in the tangential direction, and \vec{e}_r in the radial direction. The total force on e caused by the entire

bunch is then found via integration

$$\vec{F} = \int_{\text{bunch}} d\vec{F} \equiv \lim_{\epsilon \downarrow 0} \left(\int_{-\varphi_m}^{\varphi_1 - \epsilon} \frac{d\vec{F}}{d\varphi} d\varphi + \int_{\varphi_1 + \epsilon}^0 \frac{d\vec{F}}{d\varphi} d\varphi \right).$$

In the limit $\epsilon \downarrow 0$, the separate integrals are not finite, but only their sum is relevant. The x and y components of the force are given by

$$\begin{aligned} \mathcal{F}_x &= \varphi_m \int_{\text{bunch}} \mathcal{E}_x d\varphi, \\ \mathcal{F}_y &= \varphi_m \int_{\text{bunch}} \{\beta n_y \mathcal{E}_x + (1 - \beta n_x) \mathcal{E}_y\} d\varphi, \end{aligned}$$

where the dimensionless quantities \mathcal{E} and \mathcal{F} are defined according to

$$\mathcal{E} = \frac{4\pi\epsilon_0 R^2}{q} E, \quad \mathcal{F} = \frac{4\pi\epsilon_0 l}{e\lambda} F.$$

In order to find analytical expressions for \mathcal{F}_x and \mathcal{F}_y , it would be convenient if \mathcal{E}_x , \mathcal{E}_y and \vec{n} could be expressed as functions of φ . However, these quantities are only known as a function of θ and are given by

$$\begin{aligned} n_x &= -(\sin \theta)/\mathcal{W}, \quad n_y = (1 - \cos \theta)/\mathcal{W}, \\ \mathcal{W} &= \sqrt{2 - 2 \cos \theta}, \\ \mathcal{E}_x &= \frac{(2\beta^2 - 1) \sin \theta - 2\beta^2 \sin(2\theta) + \mathcal{W}\beta(\beta^2 - \cos \theta)}{(\beta \sin \theta + \mathcal{W})^3}, \\ \mathcal{E}_y &= \frac{(1 + \beta^2 \cos \theta)(1 - \cos \theta) + \mathcal{W}\beta \sin \theta}{(\beta \sin \theta + \mathcal{W})^3}. \end{aligned}$$

The retardation condition expresses θ as an implicit function of φ , with φ_1 and β as parameters. It turns out that it is impossible to express θ as a finite number of explicit functions in φ . As a solution to this problem, we simply choose θ_b as new integration variable. This is a very useful method, since both θ and φ are explicit functions of θ_b . The relation between θ and θ_b reads

$$\cos \theta = 1 - \frac{\theta_b^2}{2\beta^2}, \quad \sin \theta = \pm \frac{|\theta_b|}{\beta^2} \sqrt{\beta^2 - \frac{1}{4}\theta_b^2}.$$

As an example, the equation for the tangential force component becomes

$$\mathcal{F}_x = \varphi_m \lim_{\epsilon \downarrow 0} \left(\int_{\theta_{b1}}^{\theta_{b2}} \mathcal{E}_x \frac{d\varphi}{d\theta_b} d\theta_b + \int_{\theta_{b3}}^{\theta_{b4}} \mathcal{E}_x \frac{d\varphi}{d\theta_b} d\theta_b \right).$$

By having changed the integration variable from φ (longitudinal position) to θ_b (representing time), the retardation condition now only has to be solved explicitly for the four endpoints of the integrals rather than for every single position within the bunch. We have for given β and φ_1

$$\begin{aligned} \theta_{b1} &= \theta_b(\varphi = -\varphi_m), & \theta_{b2} &= \theta_b(\varphi = \varphi_1 - \epsilon), \\ \theta_{b3} &= \theta_b(\varphi = \varphi_1 + \epsilon), & \theta_{b4} &= \theta_b(\varphi = 0). \end{aligned}$$

III. TANGENTIAL FORCE

The expression for the tangential force \mathcal{F}_x can now be found analytically. For this purpose, the variable v is introduced

$$v(\theta_b) = \left(1 - \frac{\theta_b^2}{4\beta^2} \right)^{-1/2},$$

and the tangential force reads (still assuming $\varphi_m < \pi - 2\beta$)

$$\mathcal{F}_x = \varphi_m \{ \mathcal{P}_x(v_4, \beta) - \mathcal{P}_x(v_1, -\beta) \}, \quad v_i = v(\theta_{bi}),$$

with

$$\begin{aligned} \mathcal{P}_x(v, \beta) &= \frac{1+\beta}{4} \sqrt{1 - \frac{2}{v+1}} + \frac{1-\beta}{4} \sqrt{1 + \frac{2}{v-1}} \\ &+ \frac{\beta^2}{2} \sqrt{1 - \frac{2\beta}{v+\beta} + \frac{\beta^2-1}{(v+\beta)^2}}. \end{aligned}$$

Note that v_2 and v_3 do not appear in the expression for \mathcal{F}_x because their contributions cancel in the limit $\epsilon \downarrow 0$. This implies that the retardation condition only has to be solved for the two edges of the bunch.

In practice, we are mainly interested in forces near the centre of the bunch (denoted '0' for convenience). In case $\frac{1}{2}\varphi_m \ll 1 - \beta$ (i.e. $\beta \ll 1$), we obtain for the tangential force in the middle of the bunch

$$\mathcal{F}_x(0) = -\frac{2}{3}\beta^3\gamma^4\varphi_m^2 + O(\varphi_m^4).$$

It is seen that the force is *unequal zero and negative*, i.e. points in a direction opposite to the bunch velocity. It can be shown that the minus sign is caused by a negative contribution originating from the synchrotron field. The space charge field gives a (three times smaller) positive contribution, which is also unequal zero as a result of the orbit curvature ($\varphi_m \neq 0$). In case $\gamma \gg 1$, the above approximation is not valid. Instead, the following expression must be used

$$\mathcal{F}_x(0) = -\left(\frac{4\varphi_m}{\sqrt{3}}\right)^{2/3} + \frac{1}{120}(12\varphi_m)^{4/3} + O(\varphi_m^2).$$

Again, the large negative term is caused solely by the synchrotron field. In this expansion we see that $\mathcal{F}_x(0)$ is mainly proportional to $R^{-2/3}$ and independent of γ . However, γ -dependency appears in higher order terms.

Both the above expressions for $\mathcal{F}_x(0)$ (based on expansions of v_1 and v_4) are in good agreement with numerical calculations, which solve v_1 and v_4 exactly.

IV. TANGENTIAL FORCE VS. POWER LOSS

The above results show that $\mathcal{F}_x(0) < 0$ over the full energy range $0 < \beta < 1$ and that the resulting bunch deceleration is caused entirely by the synchrotron field component. This leads to the thought that there could be a relation between the force $\mathcal{F}_x(0)$ and the power loss due to (synchrotron) radiation. The general relation between

the power P_b lost by a bunch in circular motion and the average force $\langle F_s \rangle$ exerted on the particles in the bunch reads

$$P_b = -N\omega R \langle F_s \rangle,$$

with N the total number of particles. The power P_e radiated by a single charge e in circular motion is given by $P_e = \sum_{n=1}^{\infty} P_n$ with [3]

$$P_n = \frac{n\omega e^2}{4\pi\epsilon_0 R} \left[2\beta^2 J_n'(2n\beta) - (1 - \beta^2) \int_0^{2n\beta} J_{2n}(x) dx \right],$$

and J_n the Bessel function of order n . The total power P_b radiated by a bunch with given charge distribution can be split into incoherent (P_{inc}) and coherent (P_{coh}) contributions. For the subsequent calculations, we assume $P_{inc} \ll P_{coh}$, which is valid for high current, low energy, bunched beams (e.g.: $\gamma = 10$, $\varphi_m = 0.2$ rad and $N = 2 \cdot 10^{10}$ gives $P_{inc}/P_{coh} \approx 2 \cdot 10^{-8}$). We then get for the scaled, average force representing the decelerating 'radiation reaction' caused by the coherent power loss of a homogeneously charged 1D bunch

$$\langle F_s \rangle = \begin{cases} -\frac{2}{3}\beta^3\varphi_m^2 + O(\beta^5\varphi_m^4) & \text{for } \beta \ll 1, \\ -(3\varphi_m)^{2/3} + O(\varphi_m^{4/3}) & \text{for } \gamma \gg 1. \end{cases}$$

So, apart from a numerical factor close to 1, the average radiation reaction force $\langle F_s \rangle$ is equal to the total tangential force $\mathcal{F}_s(0)$ exerted on the central electron in the bunch. In general, there is no *a priori* relationship between the average force and the force experienced by the central electron, but such a relation seems to exist in the present case.

V. RADIAL FORCE

The expression for the radial force \mathcal{F}_r is found in a similar way as for the tangential force. We get

$$\mathcal{F}_r = \varphi_m [\mathcal{P}_r(v_1, -\beta) - \mathcal{P}_r(v_2, -\beta) - \mathcal{P}_r(v_3, \beta) + \mathcal{P}_r(v_4, \beta)]$$

$$\mathcal{P}_r(v, \beta) = \frac{1 + \beta^2}{4} \ln \left(\frac{v - 1}{v + 1} \right) + \frac{\beta^2(1 - \beta^2)}{2(v + \beta)},$$

and v_i defined as before. Contrary to the case of the tangential force, we cannot take the limit $\epsilon \downarrow 0$ here since \mathcal{F}_r is divergent. This is caused by the fact that the bunch has no radial dimension. As a solution, we think of the bunch as a sector (angle φ_m) of a 3D torus with major radius R (orbit radius) and minor radius a (bunch radius, $a \ll R$). Then, we must set [4]

$$\epsilon \approx \frac{a}{2R}.$$

So, we calculate \mathcal{F}_r according to the 1D model, but we use a finite value for ϵ that approximately takes the properties of a 3D bunch into account.

We now consider the value of \mathcal{F}_r in the centre of the bunch. Assuming $\epsilon \ll \varphi_m \ll 1$, expansions are used to find the most important contributions. We get

$$\mathcal{F}_r(0) = \begin{cases} (1 + \beta^2)\varphi_m \ln(\varphi_m/2\epsilon) + O(\varphi_m^2) & \text{for } \beta \ll 1, \\ \frac{2}{3}\varphi_m \ln(\varphi_m/2\epsilon) + O(\varphi_m^{5/2}) & \text{for } \gamma \gg 1. \end{cases}$$

In the first case ($\beta \ll 1$), it turns out that the force is entirely due to the electric part of the space charge field. The magnetic force and the synchrotron field contribution can be neglected. Additionally, the expression for $\mathcal{F}_r(0)$ is in perfect agreement with results obtained from an EM-statics approach. In the second case ($\gamma \gg 1$), the force is mainly caused by the synchrotron field. In both cases, we see that $\mathcal{F}_r(0)$ is positive, i.e. points in a direction away from the centre of curvature. Moreover, $\mathcal{F}_r(0)$ is inversely proportional to R and almost independent of γ . Finally note that the above expressions for $\mathcal{F}_r(0)$ are in good agreement with numerical calculations, which solve v_1 through v_4 exactly.

VI. CONCLUSIONS

Self forces in a 1D bunch were calculated using Liénard-Wiechert field expressions. By choosing a convenient coordinate transformation, an analytical expression for the force vector has been found and it is shown that the retardation condition only needs to be solved explicitly for the two endpoints of the bunch. This can be done numerically or by making an analytical expansion in terms of the bunch angle. It follows that the self force in the middle of the bunch has non-zero radial and tangential components. For low energy bunches ($\beta \ll 1$), the tangential force is almost zero while the radial force has a finite value that is in perfect agreement with the result of EM statics. For high energy bunches ($\gamma \gg 1$), these forces reach a limiting value. Over the entire energy range, the tangential force points in a direction opposite to the bunch velocity and seems to be closely related to the coherent radiation reaction force.

VII. REFERENCES

- [1] J.M.A. Hofman, internal report TUE (in Dutch), VDF/NK-93.09 (1993).
- [2] J.D. Jackson, "Classical Electrodynamics," 2nd edition, John Wiley & Sons, New York, Chapter 14, pp. 654 (1975).
- [3] J. Schwinger, "On the Classical Radiation of Accelerated Electrons," *Phys. Rev.* Vol. 75, No. 12, pp. 1912 (1949).
- [4] J.D. Lawson, private communications and "The Physics of Charged Particle Beams," 2nd edition, Clarendon Press, Oxford, Section 4.9.2, pp. 231 (1988).

Abstract

The transfer structure for generation of microwave power from the bunched drive beam presently consists of a smooth beam tube and a periodically loaded wave guide running in parallel and coupled to it by a slot. The bunches are in synchronous interaction with a forward $2\pi/3$ -mode. Both the coupling from the beam to the output wave guide and the wave propagation down the tube have been measured on a scaled model at 8.6 GHz with the wire method, giving the longitudinal beam impedance and wake field. Transverse wake fields can be calculated from the longitudinal ones measured with the wire close to a shorting plate introduced in the centre of the structure. Quantitative estimates are then deduced for the real-scale transfer structure at 30 GHz and compared with results obtained from the three-dimensional MAFIA package, both being in good agreement. While the longitudinal wake fields from leading bunches are in phase with the following bunches, the transverse wake fields have a 90° phase offset. The wake field functions resulting from these studies have been inserted into the tracking program DTRACK and the transverse beam blow-up obtained seems to indicate that the effects of such wake fields remain tolerable.

I. INTRODUCTION

CERN Linear Collider (CLIC) studies are based on a two-linac scheme. The main linac accelerates the beam towards the experimental collision point, while the drive linac carries the strong beam to generate the required power. The drive beam is made of trains of intense bunchlets and its dynamics includes specific features [1]: the energy differences between bunchlets are unusually large due to increasing decelerating field, the energy spread within individual bunchlets is strong since the bunch length σ_z is assumed to be 10% of the 30 GHz wavelength, and the wake fields may endanger beam stability.

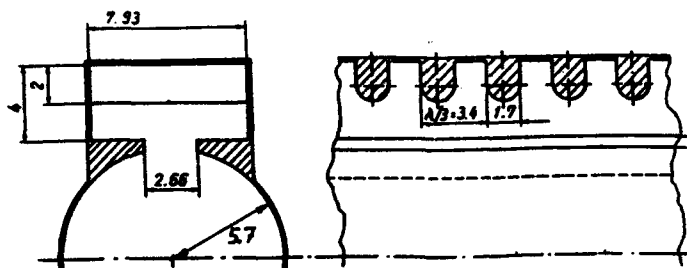


Fig. 1 Upper half of the vertically symmetric CTS showing the round beam chamber and the upper periodically loaded wave guide with $\lambda/3$ cells. The wave guides are charged with EM energy through constructive interference at the passage of bunch trains.

The impact of these features in the presence of misalignments, trajectory corrections and magnetic focusing has been studied by tracking with the code DTRACK [1]. Since tracking requires a wake field description as realistic as possible, these fields were actually measured and calculated for a recent model (Fig 1) of the CLIC transfer structure (CTS). Simulations include ever since synchronous transverse fields and focus on the option of CLIC with a c.m. energy of 500 GeV and an RF frequency of 30 GHz [2].

II. CTS MODEL MEASUREMENT AND MAFIA SIMULATION

The Wenzel-Panofsky relation $j\omega\Delta p_x = -\partial(\Delta E)/\partial x$ [3] (x transverse co-ordinate, Δp_x transverse momentum kick, ΔE energy change at x caused by modes associated with the transverse kick only) together with the usual definitions

$$\Delta E = -Z_{||}ei(\omega) \text{ and } \Delta p_x = -jZ_{\perp}edi(\omega)/c$$

(d transverse beam offset, $i(\omega) = q(\text{Exp}(-\omega\sigma)^2/2)$ spectral beam current for a gaussian bunch with charge q , σ RMS length) and with a linearity assumption $\Delta E(x, \omega) = \Delta E(d, \omega)x/d$ yields the simple relation

$$Z_{\perp}(\omega) = cZ_{||}(\omega, d)/\omega d^2$$

between the longitudinal impedance at d and the transverse one. In practice a measurement of the transmission S_{21} along a traversing wire of characteristic impedance Z_0 , offset by d from a shorting mid-plane (suppressing all parasitic E_{0N}/H_{0N} modes), allows the evaluation first of

$$Z_{||}(\omega, d) = 2Z_0(1-S_{21})/S_{21}$$

and then of $Z_{\perp}(\omega)$ from $Z_{||}(\omega, d)$ as described above. The transverse kick $\Delta p_x(t)$ is subsequently calculated via inverse Fourier transformation of $-jedi(\omega)Z_{\perp}(\omega)/c$ (see Fig. 2). The cumulative wake from many bunches is obtained by superposition. The wake is shown at time intervals of 5 RF cycles (167 ps) after the passage of the single bunch that created the wake. The wake exhibits zero crossings at the centres of subsequent bunches. This wake results from a non-centred bunch inducing unequal fields in the 2 opposite wave guides. It fades away as the energy in the wave guides propagates out of the CTS.

The CLIC transfer structure was simulated using the code MAFIA 3D on a SUN IPX workstation [4]. A twelve-cell section of the structure with some 120'000 mesh points was used in the time domain processor T3310 to find the wake fields induced by a bunch of charge 1 pC with a longitudinal dimension $\sigma_z = 1$ mm. The longitudinal wake field was

found placing the bunch on the axis of the cylindrical beam chamber, while for the transverse wake the bunch was offset 1 mm vertically away from the axis.

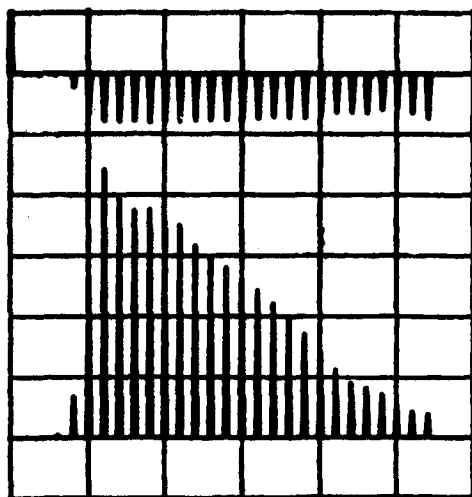


Fig. 2 Phase (90°/div.) and amplitude (12.2 V/pCm/div) of the CTS wake obtained from inverse Fourier transformation of measured wire transmission data $S_{21}(\omega)$

The transverse wake field is the most dangerous for beam stability. Its calculated shape is shown in Fig. 3

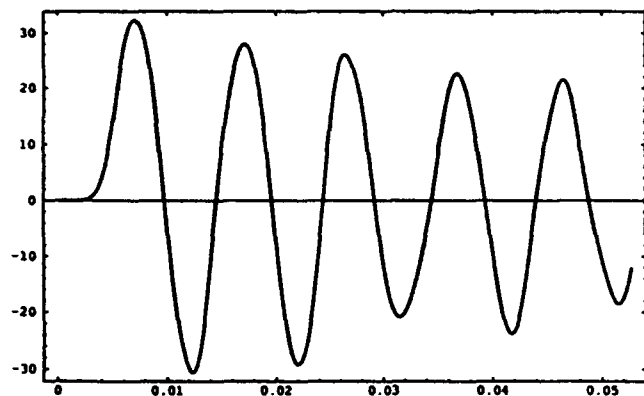


Fig. 3. Transverse wake field of one bunch with charge 1pC traversing one CTS structure. (Vertical scale: V/pCm, horizontal scale: m).

The peak value of the transverse wake field found in the simulation corresponds to a peak deflecting field of 32 V/pCm for one CTS structure with 144 cells. This value is slightly lower than the one found by model measurement.

III. BEAM DYNAMICS

Unavoidable acceleration at low frequency and 30 GHz power transfer force the use of several trains with bunchlets separated by λ_{RF} . The difficulty of generating short and intense bunchlets pleads for a relatively large number of these with lower population. A proposal to use, beside the super-

conducting (SC) 352 MHz cavities, harmonic cavities 2 and 4 [5] makes it possible to lengthen the pre-acceleration ramp such as to accelerate up to 43 bunchlets instead of 11 as in the simplest arrangement (reducing the bunchlet charge from 160 to 40 nC). In order to partly counterbalance beforehand the beam energy deposition, the bunchlets may have different injection energies, increasing from the beginning to the end of a train following the pre-acceleration ramp. Using harmonics, this ramp can last 180° at 352 MHz but have the shape of a sinus function between 45° and 90° at 88 MHz for instance (Fig. 4, thick curve). Since the focusing drops with energy in the last part of the linac and the phase advance increases monotonously, the last bunchlet has to be injected at about 3.5 GeV to avoid betatron instability. This implies an energy of about 2.3 GeV for the first bunchlet.

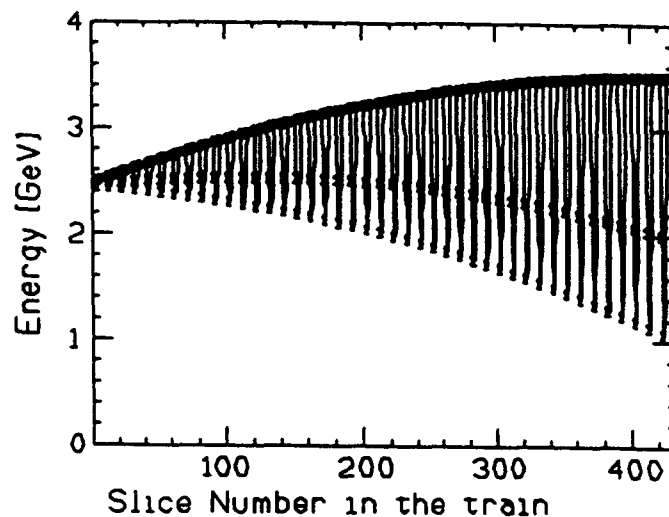


Fig. 4 Initial (thick curve) and final (thin curves) bunchlet energies in the drive beam.

Hence, in a 3.5 km drive linac, the energy of the train tail falls to ~1 GeV, which satisfies the two conditions [6]

$$\langle \gamma^2 \rangle \geq \frac{L_t}{2\sigma_z} \quad \langle \gamma \rangle \geq \frac{\gamma \epsilon_y L_t}{4\sigma_z} \left\langle \frac{1}{\beta} \right\rangle$$

that velocity spread due to finite energy and path length spread due to transverse emittance do not make bunches drift apart. If the linac length $L_t = 3500$ m and $\sigma_z = 1$ mm, the first condition (the most restrictive) gives an energy threshold of approximately 0.7 GeV. The second condition is less restrictive mainly because we assume an r.m.s. normalised emittance $\gamma \epsilon_y$ of $5 \cdot 10^{-4}$ rad m for $2.5 \cdot 10^{11}$ particles per bunch. Such a value prevents intermediate re-acceleration in the 3.5 km long linac (500 GeV c.m. option).

The wake field model includes now two components: i) the fundamental modes that are synchronous with the beam at 30 GHz and come from model measurements and computations, ii) the asynchronous part that is calculated for a circular and smooth resistive pipe. With a charge of 40 nC the decelerating field per bunchlet is about 17 kV/m and the worst transverse wake field (measured peak value) is $\sim 2 \cdot 10^6$

V/m . The synchronous wakes increase linearly from bunchlet to bunchlet, but the longitudinal amplitude has peaks at every bunch centre while the transverse one is shifted by 90° and has zeros at bunch centres. Wake field effects have been investigated for misalignments of $50\mu m$ r.m.s. for quadrupoles and transverse structures and of $5\mu m$ r.m.s. for the position monitors. Trajectory is corrected on the basis of measurements integrated over the whole train and with a one-to-one algorithm. Focusing has to begin with a phase advance of 30° at 3.5 GeV (last bunch) in order to avoid a core instability near the linac exit at ~ 1 GeV. Betatron functions must however remain low so that the emittances stay confined within the linac acceptance. This is achieved by having quadrupoles every 2 m, i.e. a total of ~ 1750 .

Longitudinal wake fields induce strong energy variations as shown in Fig. 4. Bunchlet cores have energies between 2.3 and 1 GeV while heads and tails maintain their injection energies (from 2.3 to 3.5 GeV). If the Twiss functions remain constant for the first bunch whose energy does not change much, they may vary a lot for the last one. Its phase advances rise from 30° to close to 180° and its β -function, which decreases initially, increases when $\mu > 90^\circ$ (Fig. 5) and the beam sizes blow-up. When β_{min} reaches zero, focusing instability occurs and this point has to be kept beyond the linac exit (Fig. 5).

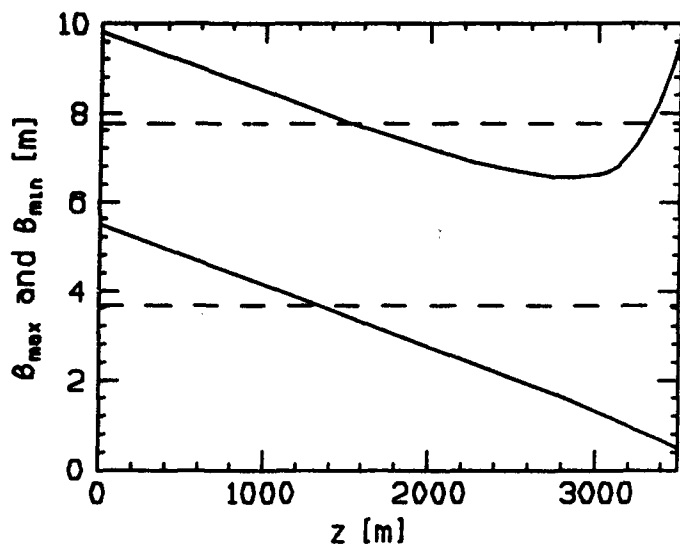


Fig. 5 Betatron functions for the first (dotted line) and the last (full line) bunchlet.

Furthermore, β -functions differ between the head, the core and the tail of the bunchlets because of strong energy variations. Hence, when the contribution to emittance blow-up of transverse wake fields is calculated, the emittances of these different parts of the bunches are tracked and normalised separately. They are eventually compared to the pipe acceptance to verify that the beam gets through the linac. Fig. 6 shows a plot of the vertical core emittances at the end of the linac, which are confined within the acceptance represented by a circle tangential to the frame.

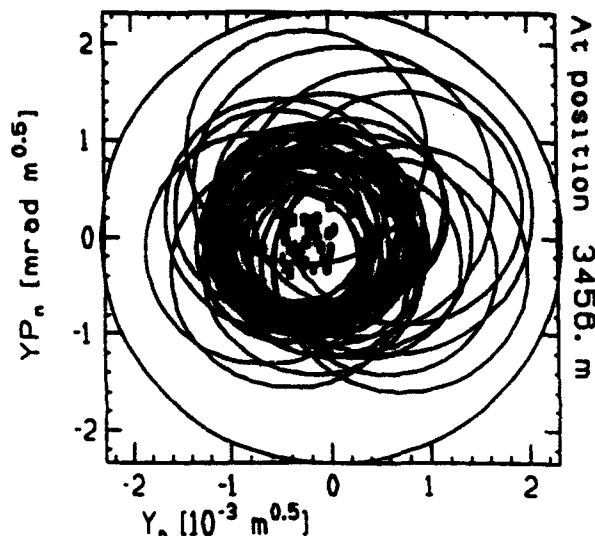


Fig. 6 Vertical bunchlet emittances at the linac exit.

IV CONCLUSIONS

Transverse wake fields of CTS have been actually measured on a model and calculated with MAFIA, both results being in good agreement. Beam tracking in these conditions indicates that all the bunchlets remain inside the linac aperture over the required 3.5 km, provided the injection energy is adjusted along the train. With the retained parameters the stability limitation comes not so much from the wake fields due to the transfer structure as from the drop of the focusing with energy.

REFERENCES

- [1] G. Guignard, Tracking Code for the Bunchlet Trains in a Drive Linac, HEACC92, Hamburg, 1992.
- [2] G. Guignard, Beam Stability Simulations in the Two CLIC Linacs, HEACC92, Hamburg, 1992.
- [3] G. Lambertson, Dynamic Devices Physics of Particle Accelerators, AIP Conf. Proc. 153, p.1414, 1987.
- [4] A. Millich, Simulation of the CLIC Transfer Structure by Means of MAFIA, CAP93, Pleasanton, 1993.
- [5] L. Thorndahl, A Multi-Frequency Preacceleration System for the CLIC Drive Linac, HEACC92, Hamburg, 1992.
- [6] W. Schnell, The Drive Linac for a Two Stage RF Linear Collider, CERN-LEP-RF/88-59, 1988.

The LEP Impedance Model

D. Brandt, K. Cornelis, V. Danilov*, A. Hofmann, C. Juillard, E. Perevedentsev*,
E. Peschardt, E. Rossa, F. Tecker, D. Wang, B. Zotter, CERN and L. Rivkin PSI

Abstract

The bunch current in LEP is limited by collective effects slightly below its design value. To understand this limitation, a set of experiments has been carried out to obtain a model of the impedance seen by the circulating beam. From measurements of the current dependence of the synchrotron and betatron frequencies information about the longitudinal and transverse reactive impedance has been obtained. The growth rate of the $m=1$ head-tail instability has been observed to gain some knowledge of the resistive transverse impedance. The dependence of the transverse mode-coupling threshold on bunch length has been measured. The energy loss per turn of a stable bunch is given by the longitudinal resistive impedance and has been measured by recording the change of the synchronous phase angle with current. All these quantities represent integrals over products of bunch mode spectra and impedances. By measuring them for different bunch lengths the frequency dependence of the impedances can be estimated. From these results a model of the LEP impedance has been obtained which can be used to estimate the current limitation under different operating conditions.

I. INTRODUCTION

Single bunch instabilities, in particular transverse mode coupling at injection energy, are limiting the current and hence the luminosity of LEP[1]. To understand - and possibly overcome - this limitation, we have computed the impedances of various components of the vacuum chamber wall. Their interaction with charged particle bunches can be described quite well by a number of broad-band resonators.

The largest impedance in LEP is due to the RF cavities, in particular the 5-cell copper cavities, of which 128 were installed originally. Their transverse broad-band impedance is computed from the dependence of the transverse loss factor on bunch length [2], which yields a value for R/Q of about 11.8 $K\Omega$ per cavity, with a resonant frequency slightly above 2 GHz.

Eight of the 350 MHz copper cavities have since been replaced by four 1 GHz feedback cavities (7 cells each). in

our calculations. Furthermore, a small number (2 modules of 4 cavities each) of superconducting (SC) 4-cell cavities have been added so far, with many more to come for LEP200. The transverse broad-band impedance of these cavities is much lower ($R/Q = 1.88 K\Omega$ per cavity), as well as their resonant frequency (0.71 GHz), due to the larger beam tube holes and smoother shapes. For simplicity we just retain the original number of cavity cells

The second most important impedance in LEP is caused by the vacuum chamber bellows, of which there are a very large number because of the large circumference of the machine. All of those which connect oval chambers with small height (70 mm) have been shielded with sliding finger contacts to reduce their effect on the beam (2800). There are also almost 400 unshielded bellows between circular chambers of larger diameter (100 mm). Their transverse impedance, inversely proportional to the third power of the beam hole is hence smaller, and we simply increase the number of shielded bellows to 3000.

Due to the small size of the cross-section variations, the broad-band impedance of the bellows is expected to have a rather high resonant frequency. In principle, it can be estimated from the position of the maximum of the transverse loss factor. However, until recently the size limitations of our mesh codes (a few 100.000 mesh cells) did not permit us to find this maximum, and thus only a lower limit of 8 GHz could be given for the resonant frequency[4]. A recent improvement of the code ABCI, introducing a so-called "moving mesh", permits the use of much finer meshes. With a mesh size corresponding to 7 million mesh cells in a static mesh code, the maximum of the loss factor was finally found, corresponding to a frequency of almost 120 GHz, ten times above the previous limit. However, this value is important only for extremely short bunches which are of little interest in LEP.

For the longitudinal impedance, the contribution of the unshielded large bellows is also important. Nevertheless, the total longitudinal loss factor is some 20% too small for bunches of $\sigma_z \leq 10mm$, probably due to many other small impedances which have been neglected. Such components include the electro-static separator plates, (about 40 pairs), pick-up buttons, collimators, flange gaps, pump connections etc. For the transverse threshold calculations, it is sufficient to include the RF cavities and bellows to

*Visitor from BINP, Novosibirsk

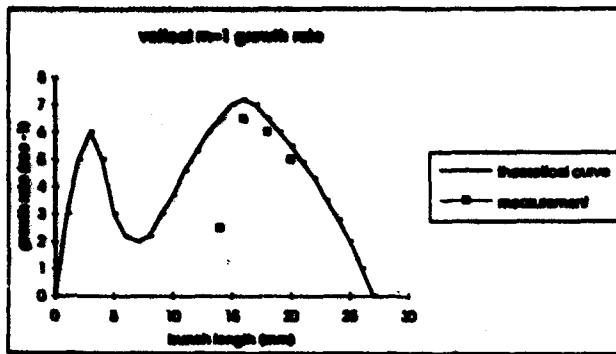


Figure 1: Growth rate of the m=1 head-tail mode

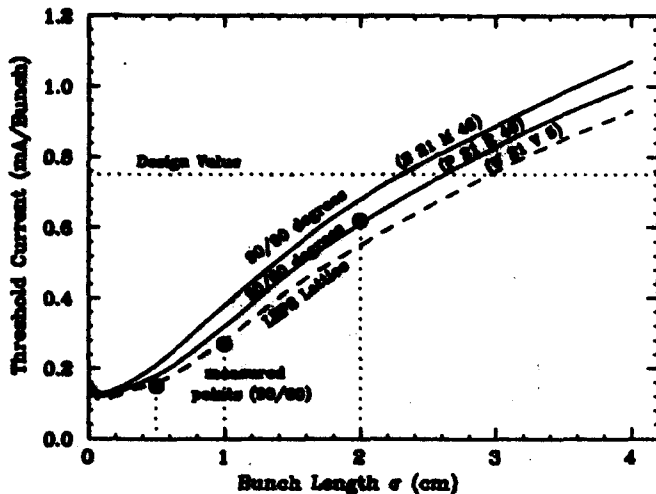


Figure 2: TMC threshold current vs. bunch length

obtain satisfactory agreement with measurements.

II. CURRENT DEPENDENCE OF BETATRON TUNES

A simple measurement which yields the imaginary part of the transverse impedances is that of the change of the betatron tunes with current[3]. However, the measurement should be made at constant bunch length in order to get a model-independent result. Fortunately, the bunch length is (almost) independent of current when the bunches are lengthened by excitation of the wigglers, and longer bunches can be measured up to quite high currents. For shorter bunches one has to stay below the "turbulent threshold". We have thus obtained a set of values for the "tune-slopes" dQ/dI , in both the horizontal and the vertical planes, over a range of bunch lengths of interest for LEP (5 - 20 mm).

The tune-slopes are proportional to the sum of the prod-

ucts of the beta functions and "effective" impedances

$$\frac{\Delta Q}{\Delta I} = \frac{R}{2\pi\sigma_z E} \sum (\beta)_i Z_{1,eff}^{(i)} \quad (1)$$

where the effective impedances are given by the overlap integrals of the impedance and the spectrum of the bunch oscillations. For gaussian bunches oscillating in a dipole mode, and a broad-band resonator impedance, one can approximate the result for short bunches ($\omega_r \sigma_z/c \ll 1$) by $Z_{1,eff} = 2(\omega_r \sigma_z/c)^2 (R/Q)$, while $Z_{1,eff} \approx R/Q$ for longer ones.

The difference between the tune-slopes in the horizontal and vertical directions also permits an estimate of the contributions of the RF-cavities - which have circular beam holes - and of the bellows (resp. the rest of the oval vacuum chamber), where the vertical dimension is about a factor two smaller than the horizontal one.

The measured "slopes" (depending on bunch length) are of the order $(\frac{\Delta Q}{\Delta I})_H \approx 60-70 A^{-1}$, $(\frac{\Delta Q}{\Delta I})_V \approx 100-130 A^{-1}$. These values agree quite well with the predictions, and were thus a first confirmation of the impedance model.

III. GROWTH RATE OF M=1 HEAD-TAIL MODES

At injection, LEP is normally operated with a slightly positive ($Q'=1$) chromaticity in order to avoid the m=0 head-tail instability. For a chromaticity of $Q'=2$ or higher, the vertical m=-1 mode becomes unstable before the transverse-mode-coupling threshold is reached. Due to eddy currents, the chromaticity is hard to control to a precision better than ± 1 at the start of the ramp. Hence it was important to determine the growth rate of the m=-1 mode as a function of bunch length.

The experiment was performed in two steps. For each bunch length (the bunch length was varied using wigglers) the single particle damping time was measured. A bunch with very low intensity (50 μA) was used and the chromaticity was rigorously set to zero. In this way any Landau damping or space charge effects could be ignored. We then measured the response of the beam to an excitation with a single frequency that was swept through the betatron frequency. From the width of the response we could determine the damping time. Then the chromaticity was set to +4 and the intensity was slowly increased until the m=-1 mode became unstable. In this way we could determine the intensity at which the m=-1 growth rate was equal to the measured damping time.

Assuming a linear dependence of the growth rate on intensity, we could normalize the measured growth rates to a fixed intensity of 250 μA per bunch, for which current

the calculations had been done with the LEP impedance model. The measurements and calculations are compared in fig.1.

IV. TRANSVERSE MODE COUPLING THRESHOLD

At 20 GeV, the current in LEP is limited by the vertical transverse-mode-coupling instability. For the nominal synchrotron tune Q_s of .083 and a bunch length σ_s of 20mm, this instability occurs at $640\mu A$ per bunch. The closest approach between the $m=-1$ and $m=0$ modes then equals about 0.022, before they merge into a broad peak. With a Q_s of 0.04, the two modes could approach each other down to a tune difference of 0.006.

We also did measurements on the lattice that is going to be used during 1993 (90/60 degrees). The vertical TMC threshold in this lattice was found to be slightly lower than in the 1992 lattice (90/90 degrees). The smallest tune approach of the $m=-1$ and $m=0$ modes was 0.025, and the maximum current of $600\mu A$ per bunch. This is in agreement with the predictions of the LEP impedance model as shown in fig.2.

V. ENERGY LOSS PER TURN

The resistive part of the longitudinal impedance $Z_r(\omega)$ leads to an energy loss U_{pm} per turn for each particle in a bunch. It is given by the integral over the impedance times spectral power of the bunch current. The latter is usually close to a Gaussian with a width determined by the bunch length σ_s . This energy loss normalized by the bunch charge gives the parasitic mode loss parameter $k_{pm} = U_{pm}/q_s$. It was measured by observing the change of the synchronous phase angle as a function of bunch current I_b . A first method uses a streak camera with a trigger derived from the RF-system and gives the bunch position in time and its width[5]. In a second method, the bunch signal observed with an intensity monitor is filtered at a revolution harmonics and compared to a corresponding signal derived directly from the RF-system, [6] To gain in sensitivity this was done at a high frequency of 1 GHz. Such a measurement is shown in Fig. 3 where the change in synchronous phase (referred to the RF-frequency of 352 MHz) and the bunch length are plotted against the bunch current. The parasitic mode loss factor is obtained from the slope of the phase change. A set of five measurements was carried out with different values for the bunch length as controlled by the polarization (PW) and the damping (DW) wigglers of LEP. For the analysis we considered only bunches with currents below the turbulent threshold which have Gaussian form. The results summarized in Fig. 4 show the dependence of the mode loss factor k_{pm} on σ_s . It can be

fitted by a power law of the form $k_{pm} \propto \sigma_s^{-1.12}$.

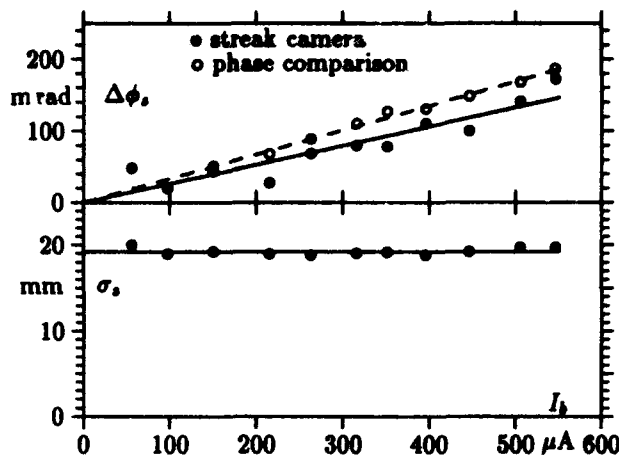


Figure 3: RF-phase and bunch length vs. current

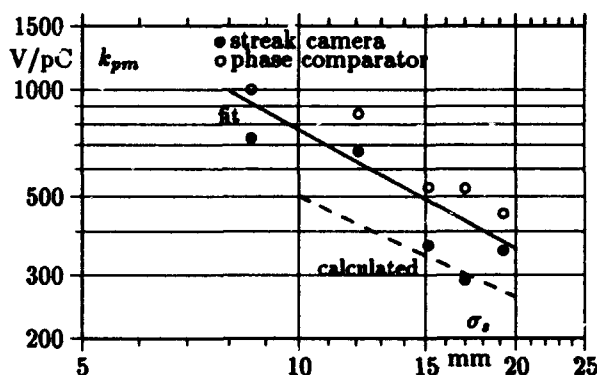


Figure 4: Parasitic mode loss parameter vs. bunch length; fit: $k_{pm} [V/pC] = 10070 \sigma_s^{-1.12} [mm]$

VI. CONCLUSIONS

The LEP impedance model, consisting of 2 broad-band resonators for the copper RF cavities and the shielded bellows, is sufficient to explain the measured behaviour of single bunch stability.

Acknowledgements

We would like to thank all the engineers in charge of the machine during our experiments for their help and support.

VII. REFERENCES

- [1] S. Myers, CERN Divisional report 93-08 (1993)
- [2] B. Zotter, CERN Divisional report 87-34 (1987)
- [3] D. Brandt et al, LEP Performance Note 75 (1992)
- [4] B. Zotter, Proc. EPAC 92, Berlin, vol.1, p.273 (1992)
- [5] E. Roosa, F. Tecker, J. Mathae, this Conference
- [6] M. Allen et al., IEEE Trans. on Nucl. Sci. NS 22-3 1838 (1975)

IMPEDANCE CALCULATIONS FOR THE IMPROVED SLC DAMPING RINGS*

K.L.F. Bane and C.-K. Ng

Stanford Linear Accelerator Center, Stanford University, Stanford, CA 94309 USA

INTRODUCTION

A longitudinal, single bunch instability is observed in the damping rings of the Stanford Linear Collider (SLC).[1] Beyond a threshold bunch population of 3×10^{10} particles the bunch energy spread increases and a "saw-tooth" variation in bunch length and synchronous phase as functions of time is observed. Although the relative amplitude of the saw-tooth variation is small—only on the order of 10%—the resulting unpredictability of the beam properties in the rest of the SLC accelerator makes it difficult, if not impossible, to operate the machine above the threshold current. An additional problem at higher currents is that the bunch length is greatly increased: according to earlier measurements the rms length is increased by 60% at 3×10^{10} . [2] When the bunch is very long in the ring it becomes difficult or impossible to properly compress it after extraction. We want to solve both of these problems so that the SLC can run at higher currents to increase the luminosity. In order to solve these problems the vacuum chambers of both damping rings are being rebuilt with the aim of reducing their impedance.[3]

According to previous calculations the impedance of the SLC damping rings is dominated by the many small discontinuities that are located in the so-called QD and QF vacuum chamber segments—elements such as transitions, masks, bellows—that are inductive to the beam.[4] Since these earlier calculations were performed the bellows of the QD segments have been sleeved, yielding a factor of 2 increase in the instability threshold.[1] In this paper we begin by discussing the gains that might be achieved if we can reduce the impedance of the rings even further. Then we estimate the effect on the total impedance of the actual design changes that are being proposed. Three important elements—the bend-to-quad transitions, the distributed ion pump slots, and the beam position monitor (BPM) electrodes are fully 3-dimensional and will be studied using T3 of the MAFIA computer programs.[5]

EXPECTED GAINS

Since the QD and QF vacuum chamber segments are the dominant contributors to the impedance of the damping rings the main effort of the redesign project is being applied to reducing their contributions to a negligible quantity. The vertical profile of the QD and QF segments are shown in Fig. 1. In the QD segments, for example, we find a bend-to-quad transition (2), a BPM (3), a bellows [now sleeved] (4), a serf gasket (5), a synchrotron radiation mask (6), and a transition to the next bend (7). Both types are cylindrically symmetric except for the transitions and the BPM electrodes. Both segment types are repeated 20 times in the ring. Also being redesigned are the distributed ion pump slots in the bend chambers, and the kicker bellows will be sleeved.

*Work supported by Department of Energy contract DE-AC03-76SF00515.

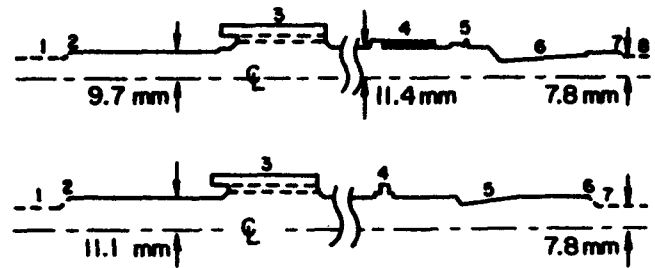


Fig. 1. The vertical profile of a QD segment (top) and a QF segment (bottom). Non-cylindrically symmetric objects are given by dashes.

Tracking simulations have been performed before to obtain the bunch shapes and instability threshold for the current damping rings.[6] The Green function wake needed for these calculations was obtained in the following manner: The wakefield for a short bunch passing through a cylindrically symmetric approximation to the QD and QF segments was carefully calculated numerically.[4] Combining these results with the wakefields for other ring objects—such as the rf cavities, kicker bellows, straight section BPM's, etc.—a wakefield representing the entire ring was obtained. To see what might be gained from the rebuilt vacuum chamber we have repeated the tracking simulations, at the nominal peak voltage of 0.8 MV, but with a wakefield that does not include the contributions of the QD/QF segments nor of the kicker bellows.

The instability threshold obtained from the simulations is compared with other calculations and measurements in Table 1 (Note: by "old ring" we mean the ring before the QD bellows were sleeved). We see that the calculated threshold is a factor of 2.5 higher for the improved ring than for the present one. In Fig. 2 we plot the rms bunch length σ_z obtained by the simulations for the improved ring (the solid line) and for the current ring (the dashes). We see that at 3×10^{10} the bunch length increase for the improved ring is only 10%, instead of the 60% for the current ring.

Version	Calculated	Measured
Old ring	1.1×10^{10} [6]	1.5×10^{10} [2]
Present ring	2.0×10^{10} [6]	3.0×10^{10} [1]
Improved ring	4.8×10^{10}	

Table 1. The calculated and measured thresholds currents for different ring versions.

What evidence do we have that we can believe in the simulation results? From Table 1 we see that although the absolute threshold values as calculated are 30% lower than the measured ones, the relative improvement in the present and old ring results of the calculations matches that of the measurements. In addition, the bunch shape calculations for the old ring were found to be in very good agreement with the measurements.[7]

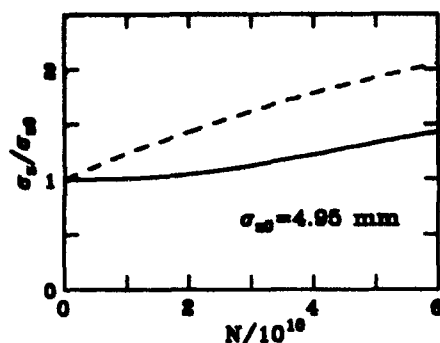


Fig. 2. Calculated rms bunch length if the QD/QF segment impedance is made negligible and the kicker bellows are sleeved.

IMPEDANCE REDUCTION

The SLC damping ring impedance is very inductive at the typical rms bunch length $\sigma_z \gtrsim 0.5$ cm. In Table 2, we reproduce a list from Ref. 4 of the approximate contributions at low frequency of the important inductive elements to the impedance of the old ring. (The "Factor" in the table represents an azimuthal filling factor, used in the calculation of non-cylindrically symmetric objects; N gives the number of objects.) The only difference in the current ring is that the QD bellows contribution has been eliminated by their sleeving; therefore, the total now is about 38 nH. Since the ring circumference is 35 m the quantity $|Z/n|$ is 2.0Ω . This should be compared with the impedance of the rf cavities, which is resistive/capacitive to the bunch and contributes approximately $|Z/n| = 0.44 \Omega$. One must be aware that Table 2 is an approximation to be used only as a rough guide. Note, for example, that the QD bellows contribute only 25% of the Table 2 total, whereas the calculated threshold increased by 80% when they were eliminated from the simulations.

Ring element	$L(\text{nH})$ single	Factor	N	$L(\text{nH})$ total
QD bellows	0.62	1.0	20	12.5
QD & QF masks	0.47	1.0	20	9.5
Transitions	0.26	0.9	40	9.3
Ion pump slots	1.32	0.1	40	5.3
Kicker bellows	2.03	1.0	2	4.1
Flex joints	0.18	1.0	20	3.6
1" BPM transitions	0.10	0.8	40	3.3
Other				2.4
Total				50.0

Table 2. The contribution to the impedance of the old ring of the major inductive elements.

From Table 2 it is clear that there are many objects that contribute to the impedance, and completely new versions of the QD and QF vacuum chamber segments will be required for their contribution to become negligible. Unfortunately, there are many practical reasons why these segments cannot just be replaced by simple smooth tubes. For example, bellows are needed in a ring so that the whole vacuum chamber can be assembled. The impedance of the bellows can be reduced by sleeving, but then masks are needed to protect the sleeves from synchrotron radiation. More specific to SLAC, the bend vacuum chambers have a rather rectangular cross-section whereas the quad cham-

bers are circular; therefore transitions are required. This situation cannot be changed without heroic efforts, such as rebuilding the bend magnets. Finally, replacing our electrode and cavity type of BPM's by the buttons type would also require a major effort that will not be done now.

The major changes to the damping rings will be:[3] the number of QD bellows will be reduced to 12, and their sleeves will include a 1.5 mm step (for protection against synchrotron radiation); the QD/QF masks will be removed, the bend-to-quad transitions will be tapered more gently, the distributed ion pumping slots will be narrowed, the 1" BPM transitions will be removed, and the flex joints, the serf gaskets, and the kicker bellows will all be sleeved.

IMPEDANCE CALCULATIONS

To estimate the impedance of an inductive element we first find the wakefield for a gaussian bunch of typical length numerically using a time domain MAFIA program (T2 or T3). If the element is inductive the wake will be similar to the derivative of a gaussian. Fitting to $W = -L dI/dt$, with W the wake and I the bunch shape, we obtain the inductance L . For some simple objects—such as a small cavity, shallow iris, shallow transitions, small hole in the beam tube—analytical formulas are known and can be used.[4,8]

For 3-dimensional objects T3 was used to obtain the impedance (Note: $\sigma_z = 1$ cm):

The Bend-to-Quad Transitions

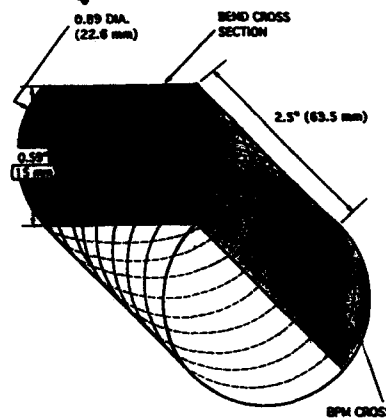


Fig. 3. The new bend-to-quad transition.

The change from the bend to the quad chamber requires a transition from a rather rectangular cross-section to a circular one. Presently the angle of transition is roughly 45° . An approximate formula that can be used for a pair of shallow, cylindrically symmetric transitions is[4]

$$L = \frac{3Z_0 a \Delta^2}{2\pi c b^2} \left(\frac{2\theta}{\pi} \right)^{1/2}, \quad (1)$$

with $Z_0 = 377 \Omega$, c the speed of light, a and b , respectively, the small and large radius, $\Delta = b - a$, and θ the transition angle.

A solution that has a very shallow angle in y (3.5°) and no transition in x is sketched in Fig. 3. The resulting wakefield is inductive, with $L = 0.05$ nH per transition pair, or $L = 2$ nH for all 40 transition pairs. Note that using Eq. (1) with the vertical dimensions, and then dividing the result by 2, we get the same answer.

The Distributed Ion Pumping Slots and the BPM's

For a long, narrow, longitudinal slot we expect the beam to interact only with the ends. The impedance will be inductive and we expect it to be given by the impedance of a hole with radius $r_0 = w/2$, with w the width of the slot, times a factor α on the order of 1. The inductance of a hole in a round chamber is given by [8]

$$L = \frac{Z_0 r_0^3}{6\pi^2 b^2 c} \quad (2)$$

with b the chamber radius. For a hole deeper than $r_0/2$ the above result is multiplied by 0.57. [9]

We have run T3 for deep, longitudinal slots in a round pipe, for different slot lengths l . We have chosen $w = 1.5$ mm and $b = 10$ mm. Fig. 4 gives the ratio of the numerical result to the analytical solution for a deep, round hole with $r_0 = w/2$, L_0 , for slots with squared ends (the diamonds) and also for slots with rounded ends (the crosses). We see that the impedance approaches a constant value when the length of the slot is 1-2 times its width, and that the asymptotic value for a slot with rounded ends is only 2/3 that of one with squared ends. Thus tapering the ends of the slots helps. Fig. 5 shows the wakefield for a long slot (squared ends). It can be seen that the impedance is very inductive (bunch center is at $s = 0.05$ m).

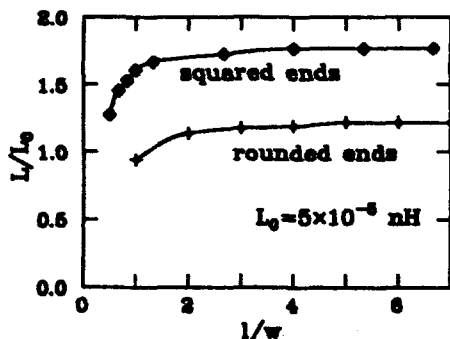


Fig. 4. The inductance of a slot; $w = 1.5$ mm.

The distributed ion pumping slots of the damping rings are located in the bend chambers. They are very long, have a width $w = 5$ mm, and are located 11 mm (in x) from the beam path; 5 mm beyond the slots are the pump electrodes. The slots have squared ends and are deep. From the foregoing (taking $\alpha = 1.75$) we estimate each slot to contribute 0.005 nH, and all 40 to contribute 0.2 nH to the ring impedance. According to this calculation the entry for ion pump slots in Table 2 is greatly overestimated. In the new vacuum chamber each of the current slots will be replaced by 3 slots: one with $w = 3$ mm and two with $w = 1.5$ mm. For the new slots, assuming they are deep and have squared ends, the total impedance contribution is 0.03 nH.

A BPM consists of four symmetrically spaced electrodes separated by gaps of 3.7 mm. At one end of the electrodes there is a 0.15 mm gap (small enough so that its impedance can be neglected). Radially reaching 4.5 mm beyond the electrodes is a cavity. Currently the BPM's are set back 2 mm by means of a pair of 45° transitions. These transitions will be removed. The new BPM's appear to the beam as 4 deep slots with squared ends in a round tube of radius 11 mm. The MAFIA mesh of 1/4 of a BPM is shown in Fig. 6. From a T3 simulation we find that to a

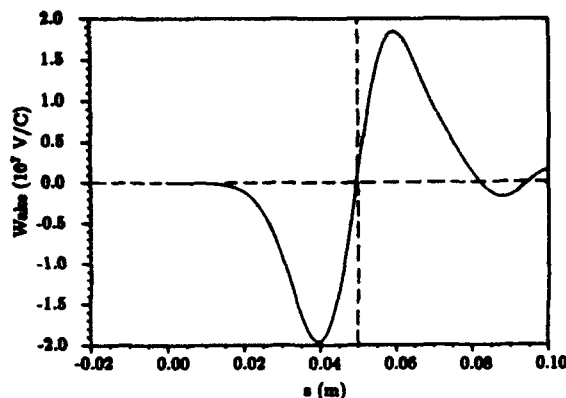


Fig. 5. The wakefield of a slot (squared ends) with width 1.5 mm and length 8 mm; $\sigma_z = 1$ cm.

1 cm bunch the BPM is inductive with $L = 0.0042$ nH for each BPM, or $L = 0.17$ nH for the entire ring. The above analytical method yields the same answer.

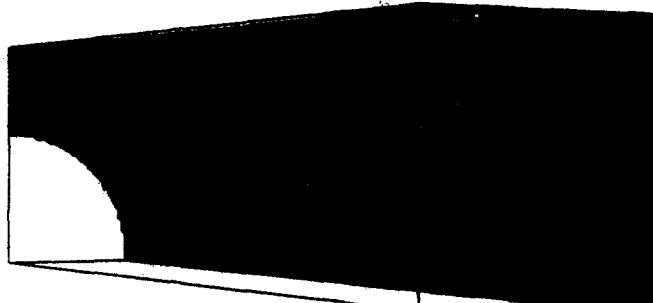


Fig. 6. MAFIA mesh for the BPM.

CONCLUSION

With the new vacuum chamber we can expect to reduce the impedance of the inductive elements from a current total of about 33 nH to about 5 nH, or $|Z/n|$ from 1.75 Ω to about 0.25 Ω . The ring should become resistive, the bunch lengthening will decrease, and the instability threshold should increase significantly.

ACKNOWLEDGEMENTS

We thank J. Bowers, T. Limberg, B. Siemann, and the other members of the New Damping Ring Vacuum Chamber Design Group for explaining the practical problems in the design.

REFERENCES

- [1] P. Krejcik, *et al.*, "High Intensity Bunch Length Instabilities in the SLC Damping Rings," this conference, Q7.
- [2] L. Rivken, *et al.*, Proc. of the 1st European Particle Acc. Conf., Rome, 1988, p. 634.
- [3] The New Damping Ring Vacuum Chamber Design Group.
- [4] K. Bane, Proc. of the 1st European Particle Acc. Conf., Rome, 1988, p. 637.
- [5] F. Ebeling *et al.*, MAFIA User Guide, 1992.
- [6] K. Bane and K. Oide, "Simulations of the Longitudinal Instability in the SLC Damping Rings," this conference.
- [7] K. Bane and R. Ruth, Proc. of the 1989 IEEE Particle Acc. Conf., Chicago, 1989, p. 789.
- [8] S. Kurennoy, *Part. Accel.* **39**, 1 (1992).
- [9] R. Gluckstern, *Phys. Rev. A* **46**, 1106 (1992).

Broadband Impedance of Azimuthally Symmetric Devices in RHIC*

Vibha Mani

Brookhaven National Laboratory, Upton, NY 11973, USA

Abstract

The interaction between the beam and its environment leads to beam instabilities, and is characterized by coupling impedance. The longitudinal coupling impedance of some RHIC devices with azimuthal symmetry such as bellows, pipe transition, gate valve and collimator have been calculated numerically using the time domain code TBCI [1]. The objective is to keep the broadband impedance below a threshold so that it satisfies the microwave stability criteria [2]; and make sure there is no contribution to narrowband impedance from any of these structures.

I. DETERMINING COUPLING IMPEDANCE

Let $W(t)$ is the wakepotential of a δ -function charge. The coupling impedance is given by [3]

$$Z(\omega) = - \int_{-\infty}^{\infty} dt W(t) e^{-i\omega t}$$

The broadband impedance has been calculated in time domain, as the excited wakefields decay in a short time. The calculations are done for a Gaussian charge distribution traversing a cavity with $\beta = 1$, perfectly conducting walls and monopole mode ($m=0$). The wakepotential is obtained as a function of distance behind the leading charge. The impedance is given by the Fourier Transform of the wakepotential divided by the Fourier Transform of the charge distribution.

II. IMPEDANCE OF RHIC DEVICES

In RHIC, there is transition in pipe radius from 3.5 cm in the cold region to 6 cm in the warm region. The cutoff frequency of the 3.5 cm pipe is 3.3 GHz and that of the 6 cm pipe is 1.9 GHz. There are bellows in the cold and the warm regions and gate valves in the warm region. The results of numerical calculations, for pipe transitions, gate valves, bellows and a circular collimator are given below. The σ of the Gaussian pulse is 5 mm for the bellows and collimator, and 4 cm for the pipe transition and gate valve. $\sigma = 10\Delta z$ for all the calculations. The collimator calculation was also verified for $\sigma = 20\Delta z$. The results are valid upto a frequency of $c/(2\sigma)$

A. Pipe Transition

The pipe changes radius from 3.5 cm to 6 cm over a length of 5 cm. Figure 1 gives a plot of the wakepotential and impedance. The impedance has resistive and inductive components at low frequencies. The inductance is 1.24×10^{-9} henry. The resistance is 31 ohm. There is a sharp jump near 1.9 GHz, the TM_{01} mode of the 6 cm pipe. Above 1.9 GHz higher order modes of the 6 cm pipe give broad impedance as energy is radiated into the pipe.

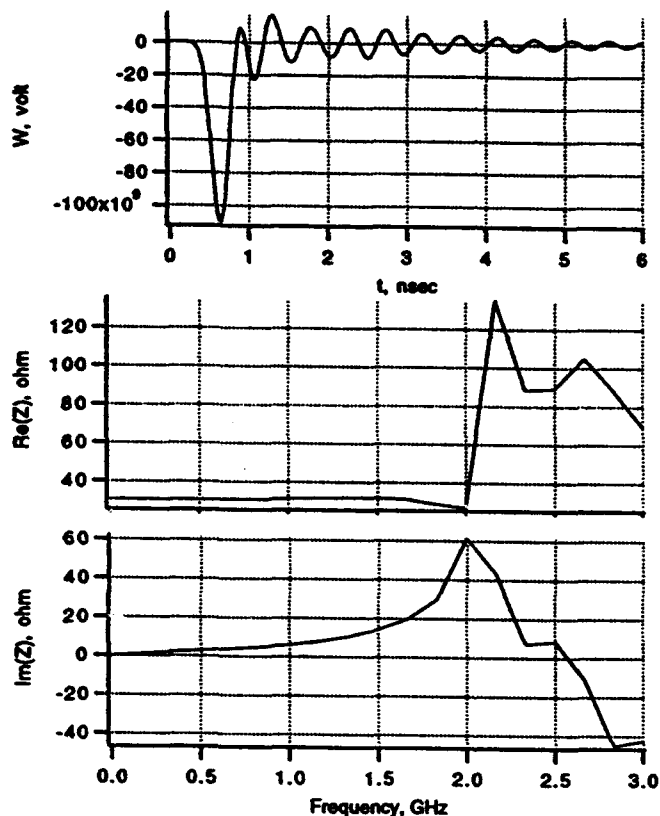


Figure 1. Pipe Transition, Wakepotential and impedance

B. Gate Valve

The gate valve is a rectangular cavity and is approximated by a cylindrical cavity of the same volume. The pipe radius is 6 cm, cavity radius is 9.9 cm and the length of the cavity is 4.2 cm. Figure 2 gives a plot of the wakepotential and impedance. It shows one resonance below cutoff at 1.38 GHz with infinite R and Q, as perfectly conducting walls are assumed. The Q will be finite when the finite conductivity of

* Work supported by the U.S. Department of Energy

steel is taken into account. The calculation was verified in frequency domain with Superfish, giving a mode at 1.37 GHz. The gate valves will be shielded, in order to avoid coupled bunch instabilities.

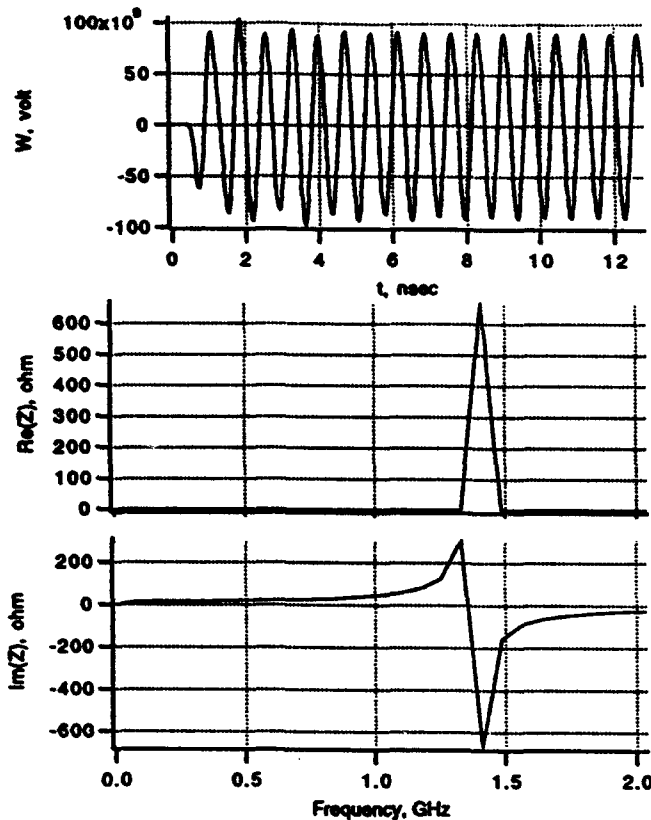


Figure 2. Gate Valve, Wakepotential and Impedance

C. Bellows

The parameters of the bellows are its total length (l), number of corrugations (N) and the depth of the corrugation (Δ). The bellows show a broad resonance at frequency which is a strong function of the depth of the corrugation. The impedance was calculated from the wakepotential and fitted to a resonator response of the form

$$Z(\omega) = \frac{R}{1 + iQ \left[\frac{\omega}{\omega_r} - \frac{\omega_r}{\omega} \right]}$$

where R is the shunt impedance, Q is the quality factor and ω_r is the resonance frequency.

Figure 3 shows wakepotential and impedance of 3.5 cm bellows with $\Delta = 1$ cm, $l = 15$ cm and $N = 30$. There is a resonance at 4.7 GHz with $R = 850$, $Q = 7$ and $R/Q = 121$. As the depth Δ is decreased to 0.5 cm, the resonance frequency increases to 7 GHz with $R = 360$, $Q = 3.2$ and $R/Q = 112$.

$$\frac{R}{Q} = \sqrt{\frac{L}{C}} \text{ and } f_r = \frac{1}{\sqrt{LC}}, \text{ both } L \text{ and } C \text{ have decreased by a}$$

factor of 1.5 and f_r has increased by a factor of 1.5 keeping R/Q approximately constant.

For the 3.5 cm bellows with $\Delta = 1$ cm, the resonance at 4.7 GHz is above the pipe cutoff of 3.3 GHz. If Δ is increased to say 1.5 cm, there will be resonance and very large impedance around 3 GHz. Therefore Δ should be kept below 1 cm.

The 6 cm bellows with $\Delta = 1$ cm, $l = 15$ cm and $N = 30$ show resonance at 3.6 GHz, with $Q = 2.5$ and $R = 170$. The resonance frequency is above the cutoff frequency. Therefore for the 6 cm bellows as well, Δ should be kept below 1 cm.

The following empirical relation satisfied by the resonance frequency agrees with that in [4].

$$f_r = \frac{1.69}{2\pi} \left(\frac{c}{\Delta} \right) \left(\frac{\Delta}{b} \right)^{0.43}$$

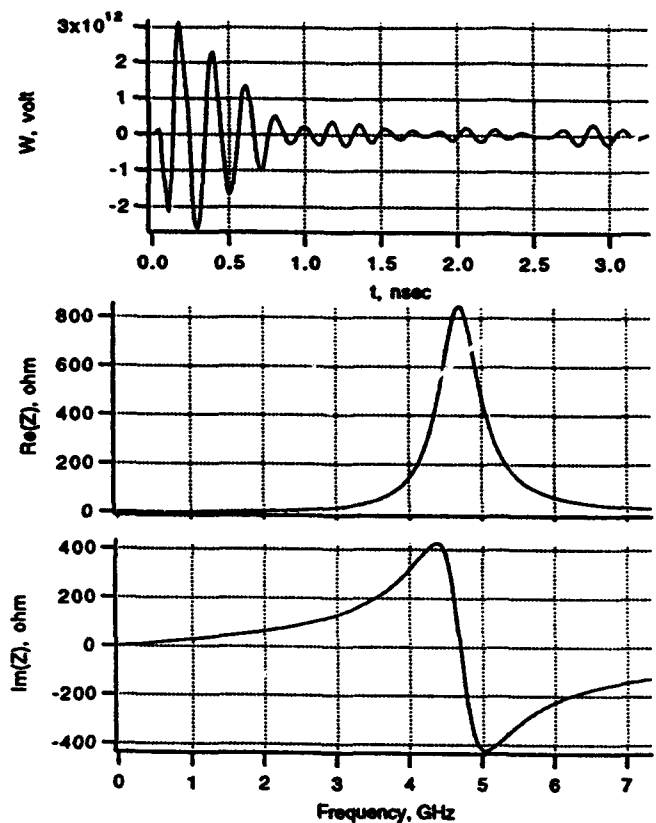


Figure 3. Bellows, Wakepotential and Impedance

D. Collimator

The impedance and wakepotential of a circular collimator with radius 1 cm, length 50 cm and beam pipe radius 3.5 cm was determined. Figure 4 gives a plot of its wakepotential and impedance. The impedance is similar to that of the pipe transition. At low frequencies there is an inductive response, with inductance 8.6×10^{-9} henry. At 3.3 GHz, there is a resonance due to the TM_{01} of the 3.5 cm pipe. Above the 3.3 GHz there is broad impedance due to the high modes of the 3.5 cm pipe.

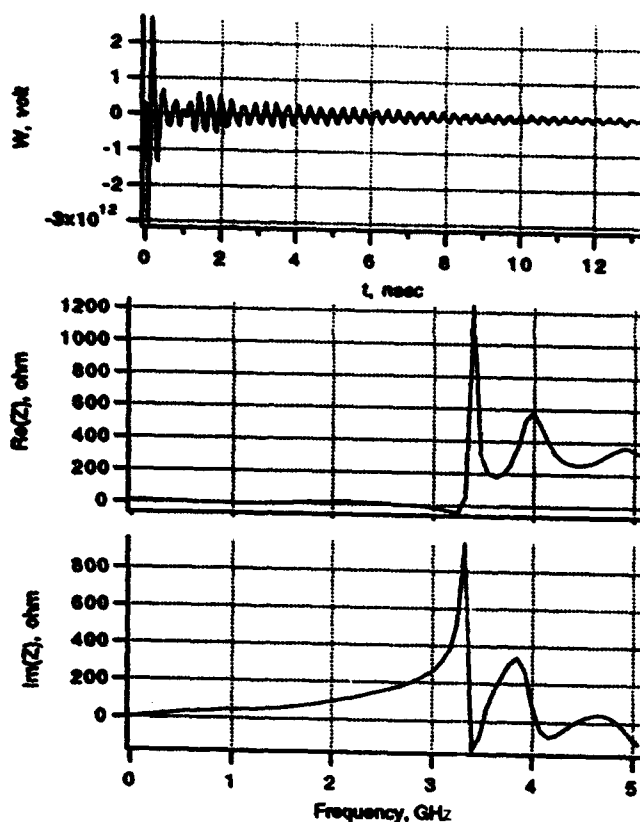


Figure 4. Collimator, Wakepotential and Impedance

III. CONCLUSION

In order to satisfy the microwave stability criteria, the broadband impedance should be below a threshold, upto 3.3 GHz. Of the above mentioned structures, the largest contribution to broadband impedance, comes from the bellows. In addition beam position monitors, wall resistance and injection and extraction kickers also contribute to the broadband impedance. The kickers would also have resonances which have to be determined.

IV. REFERENCES

- [1] T. Weiland, Particle Accelerators 15 (1984), pp.245-292
- [2] A. Hoffman, CERN 77-13.
- [3] A. Chao, SLAC-PUB-2946, June 1982.
- [4] K. Bane, R. Ruth, SSC Impedance Workshop Report SSC-SR-1017, p.10 (1985).

Software Development with Two Port Calibration Techniques for RHIC Impedance Measurements*

Vibha Mane and Tom Shea
Brookhaven National Laboratory, Upton, NY 11973

Abstract

The coupling impedance of accelerator devices is measured by simulating the beam with a central wire and measuring the scattering parameters of the system. The wire pipe system forms a mismatch with the 50 ohm transmission line. An integrated software environment has been developed in LabVIEW, for the Macintosh. The program measures the scattering parameters of some known standards, determines the correct scattering parameters of a device using TRL calibration technique and gives the impedance of the device. Its performance has been tested for some known microwave devices.

I. INTRODUCTION

The Thru-Reflect-Line (TRL) algorithm deembeds the scattering parameters and hence the impedance of a Device Under Test (DUT). A LabVIEW program with user interface is written to implement this algorithm. The program acquires data from HP8753 Network Analyzer via GPIB bus, or reads it from a file, and obtains the impedance of a device placed between mismatched ports. The algorithm is reproduced here [1],[2]; and the implementation is described in detail.

The nonideal port at each end of the two-port DUT is modeled by an ideal port in cascade with an error box [Figure 1]. The scattering parameters are measured for three known conditions between the measurement planes M1 and M2, using the Network Analyzer. The scattering parameters of the Error Boxes A and B are then determined, and the scattering parameter and the impedance of the DUT is calculated.

II. SCATTERING PARAMETERS AND IMPEDANCE

The scattering parameters of a microwave network give the relationship between the incident waves and the reflected waves at its terminals[3].

$$\begin{bmatrix} b_1 \\ b_2 \end{bmatrix} = \begin{bmatrix} S_{11} & S_{12} \\ S_{21} & S_{22} \end{bmatrix} \begin{bmatrix} a_1 \\ a_2 \end{bmatrix}$$

a_1, a_2 are the incident waves; b_1, b_2 are the reflected waves;

$$S = \begin{bmatrix} S_{11} & S_{12} \\ S_{21} & S_{22} \end{bmatrix} \text{ is the Scattering Matrix}$$

Also defined is the transmission matrix which gives the relationship between the input quantities and the output quantities. This is useful when two ports are connected in cascade, because the transmission matrix of the cascaded ports is equal to the product of the transmission matrix of each port.

$$\begin{bmatrix} b_2 \\ a_2 \end{bmatrix} = \begin{bmatrix} R_{11} & R_{12} \\ R_{21} & R_{22} \end{bmatrix} \begin{bmatrix} b_1 \\ a_1 \end{bmatrix}$$

$$R = \begin{bmatrix} R_{11} & R_{12} \\ R_{21} & R_{22} \end{bmatrix} \text{ is the Transmission matrix}$$

For the measurement of the longitudinal coupling impedance of accelerator devices, the beam is simulated by a current in a wire placed at the axis of the pipe. The longitudinal impedance is given by [4]

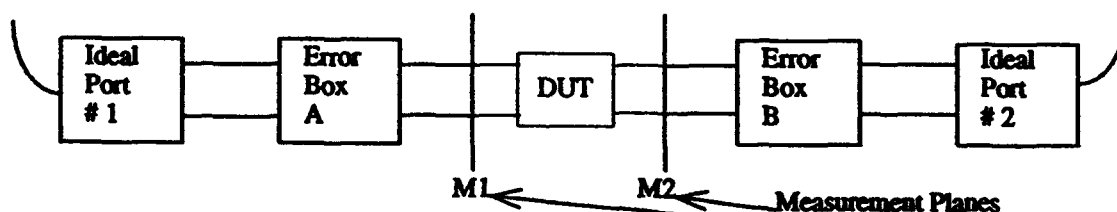


Figure 1. Model for Two Port Calibration, with mismatches represented by error boxes.

* Work supported by the U.S. Department of Energy

$$Z(\omega) = 2Z_0 \frac{(S_{21}(\text{ref}) - S_{21}(\text{DUT}))}{S_{21}(\text{DUT})}$$

where $S_{21}(\text{ref})$ is the scattering parameter with DUT replaced by a reference pipe, Z_0 is the characteristic impedance of the pipe wire system.

III. PROGRAM ALGORITHM

A. Measurements

The scattering parameters between the measurement planes M1 and M2 are measured for the following four cases:

- (i) Thru Measurement: The measurement planes M1 and M2 are connected and all the S parameters are measured.
- (ii) Reflect Measurement: A reflective load of unknown reflection coefficient Γ is connected at the measurement plane M1 and S_{11} is measured. The reflective load is connected at measurement plane M2 and S_{22} is measured.
- (iii) Line (Delay) Measurement: A nonreflecting transmission line of arbitrary length is connected between M1 and M2 and the S parameters are measured.
- (iv) Device Measurement: The device is placed between the measurement planes M1 and M2, and the S parameters are measured.

B. Determining Error Matrices

The transmission matrices R_A and R_B of the error ports A and B are determined as follows:

$$R_T = R_A R_B \quad (1)$$

R_T is the transmission matrix obtained from the thru measurement

$$R_D = R_A R_I R_B \quad (2)$$

R_D is the transmission matrix obtained from the line measurement

$R_I = \begin{bmatrix} e^{-\gamma l} & 0 \\ 0 & e^{\gamma l} \end{bmatrix}$ is the transmission matrix of the nonreflecting delay line.

From (1) and (2)

$$R_M R_A = R_A R_I$$

$$\text{where } R_M = R_D R_T^{-1} = \begin{bmatrix} m_{11} & m_{12} \\ m_{21} & m_{22} \end{bmatrix}$$

$$\text{For Port A, write } R_A = \begin{bmatrix} ka & pb \\ k & p \end{bmatrix}$$

Solve for a and b,

$$a, b = -\frac{(m_{22} - m_{11})}{2m_{21}} \pm \sqrt{\left(\frac{m_{22} - m_{11}}{2m_{21}}\right)^2 + \frac{m_{12}}{m_{21}}}$$

Select a and b such that $|a| > |b|$.

Similarly for Port B

$$R_B R_N = R_I R_B \text{ where } R_N = R_T^{-1} R_D = \begin{bmatrix} n_{11} & n_{12} \\ n_{21} & n_{22} \end{bmatrix}$$

$$R_N^T = \begin{bmatrix} n_{11} & n_{12} \\ n_{21} & n_{22} \end{bmatrix}$$

$$R_N^T R_B^T = R_I^T R_B^T$$

$$\text{write } R_B^T = \begin{bmatrix} rc & sd \\ r & s \end{bmatrix}$$

Solve for c and d,

$$c, d = -\frac{(n_{12} - n_{11})}{2n_{21}} \pm \sqrt{\left(\frac{n_{12} - n_{11}}{2n_{21}}\right)^2 + \frac{n_{12}}{n_{21}}}$$

Select c and d such that $|c| > |d|$.

The reflection coefficient Γ is determined as follows

With Port A connected to the load,

$$p = \pm \sqrt{\frac{\Gamma(a - w_1)}{(a - b)(w_1 - b)}} \quad (3)$$

$w_1 = S_{11}$ when Port A is connected to the reflective load, Γ is the reflection coefficient of the load.

Also for a reciprocal network $|R_A| = 1$ gives

$$k = \frac{1}{p(a - b)} \quad (4)$$

With Port B connected to the load,

$$s = \pm \sqrt{\frac{\Gamma(w_2 + c)}{(c - d)(w_2 + d)}} \quad (5)$$

$w_2 = S_{22}$ when Port B is connected to the reflective load.

For the reciprocal network B, $|R_B| = 1$ gives

$$r = \frac{1}{s(c - d)} \quad (6)$$

From $R_T = R_A R_B$

$$R_T = \begin{bmatrix} karc + pbsd & kar + pbs \\ krc + psd & kr + ps \end{bmatrix}$$

Therefore

$$S_{11T} = \frac{p^2 \left(\frac{s}{r}\right) (a - b) b + a}{p^2 \left(\frac{s}{r}\right) (a - b) + 1} \quad (7)$$

From equations (3), (5) and (7)

$$\Gamma = \pm \sqrt{\frac{(S_{11T}-a)(w1-b)(w2+d)}{(S_{11T}-b)(w1-a)(w2+c)}}$$

After determining Γ , p and s are determined from equations (3) and (5); k and r are determined from (4) and (6). In the Thru-Short-Delay (TSD) algorithm, Γ is set to -1.

The sign of p , k and r , s is selected by comparing the sign of $R_A R_B$ with that of R_T . The sign of Γ is determined by knowing whether the load is closer to a short or an open.

C. Determining the Scattering matrix of the device

$$R_{MDUT} = R_A R_{DUT} R_B$$

R_{MDUT} is the transmission matrix of the measured device. R_{DUT} is the transmission matrix of the calibrated device.

D. Length of delay

The frequencies at which the length of the delay line is an integer multiple of half wavelength, i.e.

$$l = \mp \frac{\lambda}{2}, \text{ both } e^{j\pi} \text{ and } e^{-j\pi} = \pm 1; R_M = \mp 1 \begin{bmatrix} 1 & 0 \\ 0 & 1 \end{bmatrix} \text{ at these}$$

values. Therefore, at these frequencies, measurements from the second delay are used. The length of the second transmission line should not be a multiple of the length of the first transmission line. The difference between the diagonal elements of R_M gives a criteria for switching to the second delay.

IV. EXPERIMENTAL RESULTS

Measurements were done with a 400 MHz filter as a device. The device is connected to the two ports of the Network Analyzer and a large mismatch is placed at Port B. Figure 2 shows the S_{21} parameter of the uncalibrated device. Fig 3 shows the S_{21} parameter of the device obtained from the above calibration algorithm. This matches with S_{21} parameter measured with the Network Analyzer and no mismatches at either Port. The Network Analyzer cannot in general give the desired accuracy, as it requires gating of the mismatches and also requires precision standards (short, open and matching load) which are not easy to construct for a pipe wire system.

The above described software will help measure small impedances, provided the transformer from the 50 ohm cable to the wire pipe geometry gives sufficient transmitted signal. The measurements can be further enhanced using attenuation pads. Results of some measurements using similar algorithm are described in [5].

V. REFERENCES

- [1] R. A. Soares, P. Gouzien, P. Legaud and G. Follot, IEEE Trans. Microwave Theory Tech, vol. 37, pp. 1669-1673, Nov 1989.
- [2] G. F. Engen and C. A. Hoer, IEEE Trans. Microwave Theory Tech., vol. MTT-27, pp. 987-998, Dec 1979.

- [3] S. Ramo, J. Whinnery, John Wiley & Sons, 1956.
- [4] H. Hahn, F. Pedersen, BNL 50870, April 1978.
- [5] L.S. Walling, D.E. McMurray, D.V. Neuffer, H.A. Thiesen, Nucl. Instr. and Meth in Phys Res. A281 (1989) 433-447.

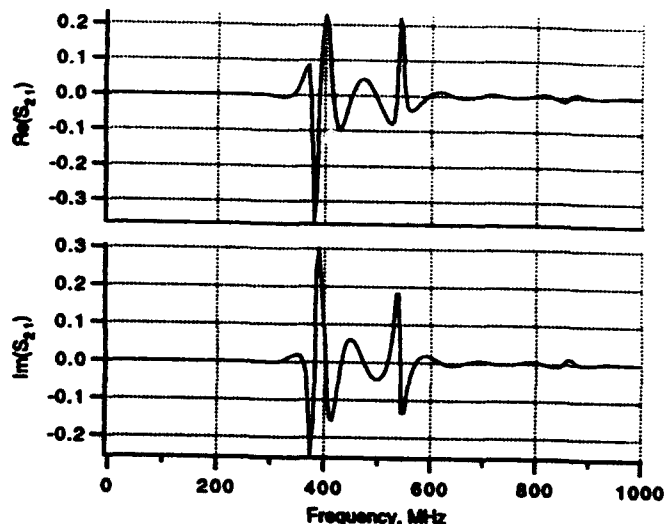


Figure 2. S_{21} Parameter of Uncalibrated Device

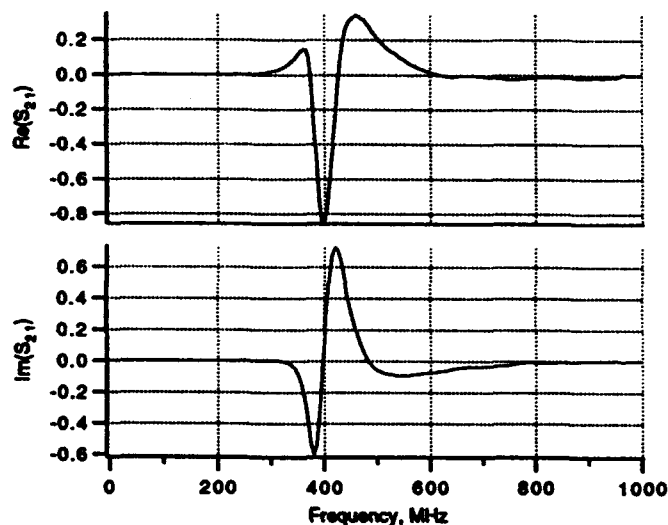


Figure 3. S_{21} Parameter of Device Calibrated with TRL

Resistive Wall Wake Function for Arbitrary Pipe Cross Section

Kaoru Yokoya

National Laboratory for High Energy Physics, Oho, Tsukuba-shi, Ibaraki, 305, Japan

Abstract

A method for calculating the impedance and the wake function of resistive beam pipes is given. It allows an arbitrary shape of the crosssection, and arbitrary location of the source and witness particles, including the short-range behavior of the wake function. The pipe is uniform longitudinally and the beam is assumed to be ultra-relativistic. A simple computer code has been written using the boundary element method. Some results for elliptical, rectangular and hyperbolic pipes are presented.

I. METHOD OF COMPUTATION

The resistive wall impedance has been a topic in accelerator physics since 1960's and is thought to be well known but, in fact, it calls for further investigation still now as the recent papers show [1,2,3,4,5]. The aim of the present paper is to give a method of computing the impedance/wake function for arbitrary shape of the beam pipe, arbitrary location of the particles including the short range behavior of the wake. The detail of our method is described in [6].

A. Assumptions and notation

We assume a longitudinally uniform pipe and an ultra-relativistic beam. The z -axis is parallel to the pipe. In the (x, y) plane, the vacuum region surrounded by the wall is denoted by Ω . The coordinate s is the length measured along the wall surface $\partial\Omega$. The unit normal (outward from Ω) and tangential vectors at s are denoted by $\mathbf{n}(s)$ and $\boldsymbol{\tau}(s)$, respectively, and the unit vector along z by \mathbf{e}_z . The source and the witness charge (unit charge) are located at $\mathbf{r}_s = (x_s, y_s)$ and $\mathbf{r}_w = (x_w, y_w)$, respectively. All the field quantities are proportional to $\exp i(kz - \omega t)$ ($k = \omega/c$) because of the longitudinal uniformity.

We write the electric and magnetic fields as $\mathbf{E} + \mathbf{E}^{(0)}$ and $\mathbf{H} + \mathbf{H}^{(0)}$, where the superscript (0) denotes solutions for the perfectly conducting wall with the same wall shape. Since the transverse Lorentz force $\mathbf{F}_\perp = \mathbf{E}_\perp + Z_0 \mathbf{e}_z \times \mathbf{H}$ satisfies $\mathbf{F}_\perp = -i/k \nabla_\perp E_z$, all the needed information is obtained from E_z .

B. Kirchhoff integral formula

Since (\mathbf{E}, \mathbf{H}) obeys the sourceless Maxwell equation, it satisfies the Kirchhoff integral formula, which, when the field is proportional to $e^{ik(z-ct)}$, can be written as

$$E_z(\mathbf{r}) = \oint ds' [ik(E_n - Z_0 H_\tau)G - E_s \mathbf{n}' \cdot \nabla'_\perp G], \quad (1)$$

$$\mathbf{E}_\perp(\mathbf{r}) = \oint ds' [ik(\boldsymbol{\tau}' Z_0 H_s - \mathbf{n}' E_z)G - E_n \nabla'_\perp G - E_\tau \mathbf{e}_z \times \nabla'_\perp G], \quad (2)$$

Here, \oint is the integral along $\partial\Omega$ and the prime refers to the quantities evaluated on the wall at s' . The function

$G = G(\mathbf{r}, \mathbf{r}')$ is the Green function satisfying the Laplace equation $\Delta_\perp G(\mathbf{r}, \mathbf{r}') = -\delta(\mathbf{r} - \mathbf{r}')$. The simplest choice is $G(\mathbf{r}, \mathbf{r}') = -(1/2\pi) \log |\mathbf{r} - \mathbf{r}'|$.

The limit that $\mathbf{r} \rightarrow \partial\Omega$ gives integral equations where only the fields on the wall appear. For numerical calculation, we divide the wall surface $\partial\Omega$ into short segments and express the field as column vectors $|\cdot\rangle$. Then, the integrals appearing in eqs.(1) and (2) can be represented by matrices. Thus, we obtain matrix equation

$$\mathcal{D} |E_z\rangle = -ik \mathcal{G} |Z_0 H_\tau - E_n\rangle, \quad (3)$$

$$\mathcal{N} |E_n\rangle - \mathcal{T} |E_\tau\rangle = -ik [\mathcal{C} |E_z\rangle + \mathcal{S} |Z_0 H_s\rangle], \quad (4)$$

$$\mathcal{T} |E_n\rangle + \mathcal{N} |E_\tau\rangle = -ik [\mathcal{S} |E_z\rangle - \mathcal{C} |Z_0 H_s\rangle]. \quad (5)$$

C. Approximate boundary condition

When the skin depth is much smaller than the typical transverse scale L of the pipe, the boundary condition is:

$$Z_0(H_\tau + H_\tau^{(0)}) = -\frac{\kappa}{k} E_z, \quad Z_0 H_s = \frac{\kappa}{k} E_\tau. \quad (\text{on } \partial\Omega) \quad (6)$$

$$\kappa \equiv e^{\pi i/4} \sqrt{\mu_0 c k \sigma} = (1+i)/\delta_{skin} = e^{\pi i/4} \sqrt{k/\rho_0}, \quad (7)$$

$$\delta_{skin} = \sqrt{2/\mu_0 c k \sigma}, \quad \rho_0 = 1/\mu_0 c \sigma \quad (8)$$

where μ_0 is the permeability of vacuum and σ the conductivity of the wall material. ($\rho_0 \approx 0.5 \times 10^{-10} \text{m}$ for copper at room temperature.)

D. Solution of the integral equation

The E_τ terms on the l.h.s. of (4) and (5) can be ignored when $\delta_{skin} \ll L$. Then, eqs.(4) and (5) can formally be solved as

$$|E_n\rangle = -ik \mathcal{M} |E_z\rangle, \quad (9)$$

where \mathcal{M} is a matrix defined by

$$\mathcal{M} = (\mathcal{N} + \mathcal{S} \mathcal{C}^{-1} \mathcal{T})^{-1} (\mathcal{C} + \mathcal{S} \mathcal{C}^{-1} \mathcal{S}). \quad (10)$$

Using eq.(9) and the boundary condition (6), we can solve eq.(3), under the same condition $\delta_{skin} \ll L$, as

$$|E_z\rangle = \frac{k}{\kappa} \left[1 - i \frac{k^2}{\kappa} \mathcal{M} \right]^{-1} |Z_0 H_\tau^{(0)}\rangle. \quad (11)$$

The solution $Z_0 H_\tau^{(0)}$ for the perfectly conducting case, appearing on r.h.s. of this equation, can be found using the matrices \mathcal{G} and \mathcal{D} defined in (3) as

$$|u\rangle \equiv |Z_0 H_\tau^{(0)}\rangle = \mathcal{G}^{-1} \mathcal{D} |g_s\rangle - \left| \frac{\partial g_s}{\partial n} \right\rangle, \quad g_s(\mathbf{r}) = G(\mathbf{r}, \mathbf{r}_s) \quad (12)$$

E. The field at the witness particle

To find E_z at the witness particle, we go back to the Kirchhoff formula (1), which can formally be written as

$$E_z(\mathbf{r}_w) = -ik \langle g_w | Z_0 H_\tau - E_n \rangle - \langle g'_w | E_z \rangle, \quad (13)$$

where g_w and g'_w are functions on $\partial\Omega$ defined by

$$g_w(s) = G(\mathbf{r}_w, \mathbf{r}) \quad \text{and} \quad g'_w = \partial g_w / \partial n = \mathbf{n} \cdot \nabla_\perp G(\mathbf{r}_w, \mathbf{r}).$$

The brackets $\langle | \rangle$ denote the integral over the circumference of the cross section: $\langle u | v \rangle \equiv \oint ds u^*(s) v(s)$. Using eq.(3), we can rewrite eq.(13) as $E_s(\mathbf{r}_w) = \langle v | E_s \rangle$ where $\langle v | \equiv (g_w | G^{-1} \mathcal{D} - (g'_w |$.

Thus, finally we find E_s at the witness particle

$$E_s(\mathbf{r}_w) = Z_0 \frac{k}{\kappa} \langle v | \left[1 - i \frac{k^2}{\kappa} \mathcal{M} \right]^{-1} | u \rangle. \quad (14)$$

F. Eigenvalues and eigenfunctions of the matrix \mathcal{M}

We denote the eigenvalue (always real) of \mathcal{M} by μ_α and the eigenfunction by $|\alpha\rangle$, which is normalized as $\langle \alpha | \alpha \rangle = 1$. Then, eq.(14) can be written as

$$E_s(\mathbf{r}_w) = Z_0 \frac{k}{\kappa} \sum_\alpha \frac{c_\alpha}{1 - i(k^2/\kappa)\mu_\alpha}, \quad (15)$$

with $c_\alpha(\mathbf{r}_w, \mathbf{r}_s) = \langle v | \alpha \rangle \langle \alpha | u \rangle$. The transverse force is then given by

$$\mathbf{F}_\perp(\mathbf{r}_w) = -i \frac{Z_0}{\kappa} \sum_\alpha \frac{\partial c_\alpha / \partial \mathbf{r}_w}{1 - i(k^2/\kappa)\mu_\alpha}, \quad (16)$$

where the coefficients $\partial c_\alpha / \partial \mathbf{r}_w$ can be calculated simply by using $\partial g_w / \partial \mathbf{r}_w$ instead of g_w . From eqs.(15) and (16), we can calculate any physical quantities like the wake function, loss parameters, wall heating etc. Note that \mathcal{M} depends only on the wall shape but is independent of the particle location, the frequency, and the conductivity.

G. Asymptotic form for $k \ll (L^2 \rho_0)^{-1/3}$

In the asymptotic region $k \ll (L^2 \rho_0)^{-1/3}$, μ_α in eqs.(15) and (16) can be ignored. Since $\sum_\alpha |\alpha\rangle \langle \alpha|$ is identity, we get

$$E_s = \frac{Z_0 k}{\kappa} \langle v | u \rangle = \frac{Z_0 k}{\kappa} \oint ds v^*(s) u(s), \quad (k \ll (L^2 \rho_0)^{-1/3}). \quad (17)$$

When $\mathbf{r}_s = \mathbf{r}_w$, we have $u = v$ and, consequently, the integrand becomes $|u(s)|^2$, giving rise to a formula identical to the longitudinal impedance formula obtained in [5]. Similar formulas can be found for the transverse impedance. Thus, if one is interested only in the asymptotic form, the operator \mathcal{M} is not needed.

H. Wake function

Since all the terms in eqs.(15) and (16) have the same wave number dependence, the wake function can easily be computed from two basic functions f_L and f_T

$$W_L(z) = \sum_\alpha \frac{c Z_0}{\mu_\alpha} c_\alpha f_L(z/z_\alpha), \quad z_\alpha = [(2\mu_\alpha)^2 \rho_0]^{1/3} \quad (18)$$

$$\mathbf{W}_\perp(z) = \sum_\alpha \frac{c Z_0 z_\alpha}{\mu_\alpha} \frac{\partial c_\alpha}{\partial \mathbf{r}_w} f_T(z/z_\alpha), \quad (19)$$

(See [6] for the explicit form of f_L and f_T .) The asymptotic forms for large $z \gg (L^2 \rho_0)^{1/3}$ are found to be

$$W_L \approx \frac{c Z_0 \sqrt{\rho_0}}{2\sqrt{\pi} z^{3/2}} \sum_\alpha c_\alpha, \quad \mathbf{W}_\perp \approx \frac{c Z_0 \sqrt{\rho_0}}{\sqrt{\pi} z} \sum_\alpha \frac{\partial c_\alpha}{\partial \mathbf{r}_w}. \quad (20)$$

I. The AC Conductivity at High Frequencies

As pointed out by Bane [3], the AC conductivity is no longer equal to the DC conductivity at very high frequencies and is approximately expressed by $\sigma/(1-i\omega\tau)$, τ being the relaxation time of the metal. Our formulas in the frequency domain are still valid in such a case. The wake function, however, cannot be expressed by the two functions $f_L(\zeta)$ and $f_T(\zeta)$.

II. APPLICATIONS

Results of the application to various pipes are given in [6], such as the transient behavior of the wake, influence of the AC conductivity, dependence on the source/witness particle location for round, elliptic, rectangular, and hyperbolic pipes. Here, we shall show some of them and some more structures.

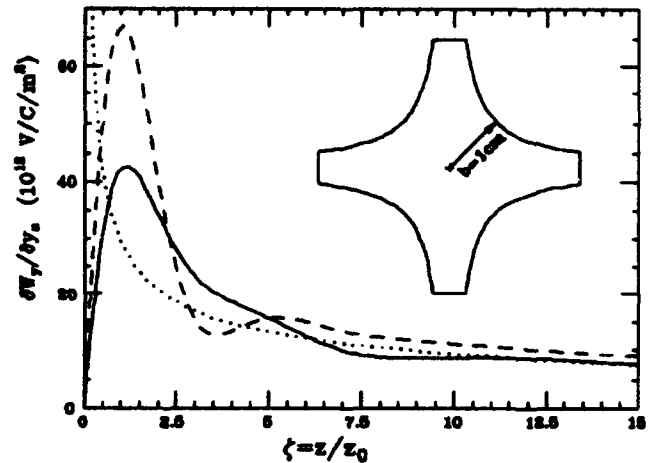


Figure 1: Transverse wake function (solid line) for a hyperbolic pipe with $b=1\text{cm}$. The dotted line is the asymptotic form and the dashed line is for the round pipe with radius 1cm.

Fig. 1 shows the transverse wake function for a hyperbolic pipe having a shape like the pole of a quadrupole magnet. The radius at the pole tip is $b=1\text{cm}$. (The area is cut at 2cm but the result is almost independent of the cut if it is larger than 1.5cm.) The horizontal axis is the normalized distance $\zeta = z/z_0$ with $z_0 = (b^2 \rho_0)^{1/3}$ ($= 17\mu\text{m}$ for copper). The solid line is $\partial W_y / \partial y_s$ for the hyperbolic pipe. The dotted line is the asymptotic form ($\propto 1/\sqrt{z}$). For comparison, the wake for the round pipe with radius 1cm is plotted in the dashed line. One finds the wake for the hyperbolic pipe is considerably smaller than that for the round pipe in the short-range region but the difference is only slight in the asymptotic region (factor 0.835).

Next, let us discuss the dependence of the transverse asymptotic wake on the location of the witness particle \mathbf{r}_w with $\mathbf{r}_s = 0$. The transverse wake is absent in the case of round pipes but this is not true in general.

The vertical asymptotic wake is plotted in Fig. 2 as a function of y_w for rectangular and elliptic pipes. The aspect ratio is indicated by the line modes as shown in the figure with crosses for the curves for rectangular pipes. The

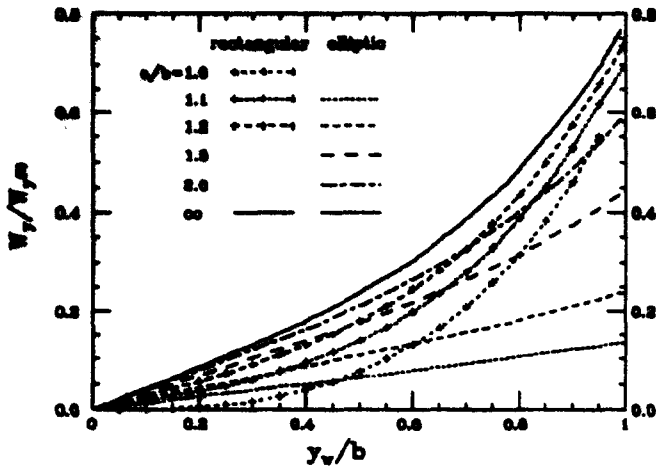


Figure 2: Vertical asymptotic wake vs. the location of the witness particle for rectangular and elliptic pipes of various aspect ratio with fixed vertical aperture.

vertical half aperture b is fixed in all cases. The wake W_y is normalized by $W_y^{(0)} = b[\partial W_y/\partial y_s]_{\text{round pipe}, r_s=0}$, which is the dipole wake for a round pipe when the source particle is near the pipe wall. From this figure we find the following facts. Firstly, W_y increases as y_w in rectangular pipes more rapidly than in elliptic pipes. Even for the square pipe $a/b=1.0$, W_y is almost the same as that for $a/b = \infty$, when the witness particle is close to the wall. Secondly, the y_w dependence is almost linear for elliptic pipes if $a/b \lesssim 1.5$ but W_y is still large near the wall unless a/b is very close to unity. For example, when $a/b=1.2$, W_y is about one quarter of the dipole wake of a round pipe with $y_s = b$.

These facts strongly suggest that the collimator for linear colliders has to be round.

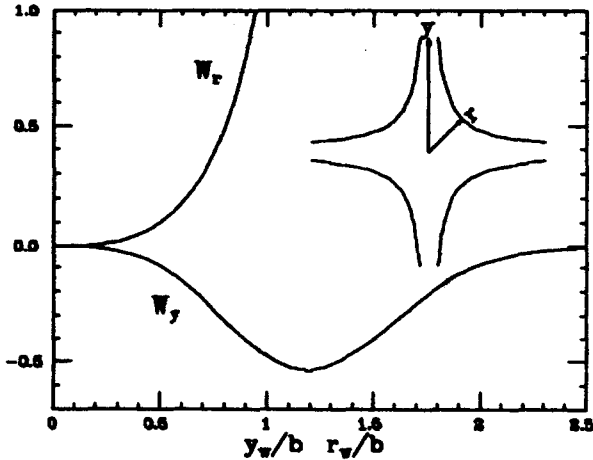


Figure 3: Transverse asymptotic wake for a hyperbolic pipe for r_w on the y -axis (W_y) and on the 45-degree line (W_r). The distance from the center to the pole is b .

Fig. 3 is a similar plot for hyperbolic pipe. Plotted is the transverse asymptotic wake for $r_s = 0$ with the witness particle along the y -axis (W_y) and that along the 45-degree

line (W_r). They are normalized by the same $W_y^{(0)}$ as in the previous plot. W_r becomes large near the pole face.

As we have seen in Fig. 1, the asymptotic wake for a hyperbolic pipe is nearly the same as that in a round pipe tangent at the pole face. This means that the wall current is concentrated on a part of the wall close to the beam. We have computed the asymptotic wake for a flat-face scraper with finite horizontal width $2a$ and the gap height $2b$. The result is shown in Fig. 4. Both the source and witness particle are at the center. The longitudinal wake W_L (long-dash) and four transverse wakes, $\partial W_x/\partial x_s$ (dot-dash), $\partial W_y/\partial y_s$ (dash), $\partial W_y/\partial y_w$ (dot), and $\partial W_y/\partial y_s + \partial W_y/\partial y_w$ (solid) are plotted against the width a . W_L is normalized by W_L of a round pipe of radius b , and the transverse wakes are normalized by $\partial W_y/\partial y_s$ for the round pipe. The limit $a \rightarrow \infty$ corresponds to the two parallel pipes. One finds that the wake is rather insensitive to the scraper width a and is even large when a is small.

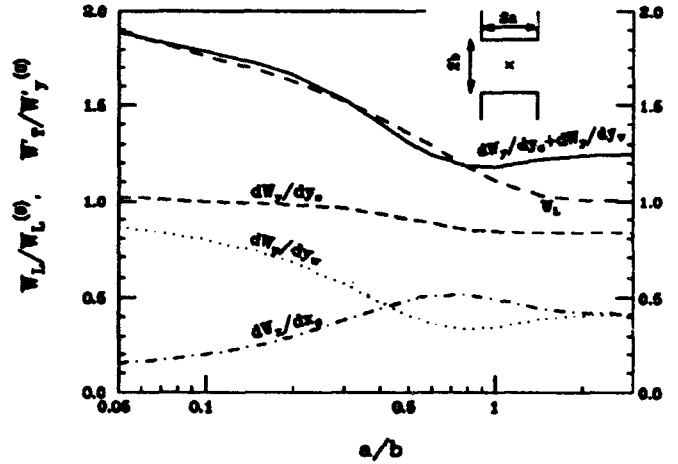


Figure 4: Asymptotic wake for finite width parallel collimator for $r_w = r_s = 0$. (width $2a$, gap height $2b$) Normalized by the corresponding wake for a round pipe with radius b .

References

- [1] H. Henke and O. Napoly, Proc. 2nd EPAC, June 12-16, 1990, Nice, France, page 1046. Also, CERN-LEP-RF 89-71, 1989, Geneva, Switzerland.
- [2] O. Henry and O. Napoly, Part. Acc. 35 (1991) 235.
- [3] K. Bane, *The Short Range Resistive Wall Wakefields*, SLAC-AP-87, June 1991.
- [4] A. Piwinski, *Wake Fields and Ohmic Losses in Round Vacuum Chambers*, DESY, HERA 92-11, Jan. 1992, Hamburg. *Wake Fields and Ohmic Losses in Flat Vacuum Chambers*, DESY, HERA 92-04, May 1992, Hamburg.
- [5] R. L. Gluckstern, J. van Zeijts and B. Zotter, *Coupling Impedance of Beam Pipes of General Cross Section*, CERN SL/AP 92-25, 18 June 1992, Geneva.
- [6] K. Yokoya, *Resistive Wall Impedance of Beam Pipes of General Cross Section*, KEK preprint 92-196, Feb. 1993, to be published in Part. Acc.

Impedance of a Perforated Liner and Its Impact on the SSC Collider

W. Chou and T. Barts
Superconducting Super Collider Laboratory*
2550 Beckleymeade Ave., Dallas, TX 75237

Abstract

Various approaches (analytical, numerical, and experimental) have been tried to investigate the impedance and wakefields of a liner. At low frequencies, the results obtained from different approaches are in agreement. At high frequencies, the simulations show that the resonance peaks and the associated long term wakes are related to the periodicity of the hole distribution. The dependence of the impedance on the size, shape and pattern of the holes and slots has been studied. The rounded short slots of random distribution is recommended for minimising the impedance. The rf coupling between the area inside the liner and the annulus is negligibly small in the frequency range of interest. The impact of the liner on the safety margin and resistive wall instability has been studied.

I. INTRODUCTION

The synchrotron radiation in the SSC Collider will cause a large amount of gas load from the photon-induced desorption process and may result in a poor vacuum in the beam tube. A possible solution to the problem is to install a perforated liner inside the bore tube [1]. The introduction of the liner brings up a number of issues that need to be studied. Among them, one is the increase of the rf impedance. The increments come from the holes (or slots) as well as from the smaller ID of the liner.

The impedance of the holes and slots has been studied by means of 3D simulations (MAFIA [2] and HFSS [3]), analytical modeling [4], wire measurements [3] and electron beam measurement [5]. The impedance increments of the bellows, beam position monitors and other components due to a smaller liner ID have also been computed. The increase of the impedance implies the decrease of the safety margin, which is defined as the ratio of the instability threshold impedance to the machine impedance. This is now under study to determine the minimum allowable ID of the liner.

II. LOW FREQUENCY REGION

A. Analytical Model

For some structures, such as a pipe attached to a small pillbox or a pipe with small holes on its surface (i.e., the perforated liner), the longitudinal and transverse impedances can be approximated by a pure inductance L

at low frequencies (below the cutoff):

$$Z_{\parallel}(\omega) = i\omega L, \quad Z_{\perp}(\omega) = i \frac{2c}{b^2} L \quad (1)$$

in which b is the radius of the pipe, c the velocity of light. When a Gaussian bunch traverses the pure inductance, it will generate the longitudinal and transverse wake potentials [2]:

$$W_{\parallel}(z) = \frac{c^2 L}{\sqrt{2\pi}\sigma^3} z e^{-\frac{z^2}{2\sigma^2}}, \quad W_{\perp}(z) = \frac{2c^2 L}{\sqrt{2\pi}\sigma b^2} e^{-\frac{z^2}{2\sigma^2}} \quad (2)$$

in which σ is the rms bunch length. The magnitudes and locations of the peaks of the wake potentials are:

$$W_{\parallel}^{max(min)} = \pm \frac{c^2 L}{\sqrt{2\pi}\sigma^2} e^{-1/2}, \quad \text{at } z = \pm\sigma \quad (3)$$

$$W_{\perp}^{max} = \frac{2c^2 L}{\sqrt{2\pi}\sigma b^2}, \quad \text{at } z = 0 \quad (4)$$

B. MAFIA Results

The inductance of a small hole with diameter d at low frequency has been worked out [4]:

$$L = \frac{Z_0}{48\pi^2 c} \frac{d^3}{b^2}, \quad (5)$$

in which $Z_0 = 377 \Omega$. Therefore, the peak of the wakes of each hole are given by (all dimensions in meters):

$$W_{\parallel}^{max} = \frac{Z_0 c}{48\pi^{5/2} \sqrt{2} e} \frac{d^3}{\sigma^2 b^2} = 0.0577 \times \frac{d^3}{\sigma^2 b^2} \left(\frac{V}{nC} \right) \quad (6)$$

$$W_{\perp}^{max} = \frac{Z_0 c}{24\pi^{5/2} \sqrt{2}} \frac{d^3}{\sigma b^4} = 0.00019 \times \frac{d^3}{\sigma b^4} \left(\frac{V}{nC \cdot mm} \right) \quad (7)$$

Eqs. (6)-(7) can be compared with the MAFIA results as shown in Figs. 1a-b. When the hole size is small and bunch length large, the theory and simulations agree with each other. However, when the hole becomes larger ($d \geq 4$ mm) or the bunch becomes shorter ($\sigma = 0.25$ and 0.6 cm), the simulation results appear to be larger than what the theory would predict. This probably indicates the breakdown of the low frequency assumption.

The hole shape in the simulations is a square rather than a circle. It would thus give an inductance larger than that of a circular one as predicted by Eq. (5). On the other hand, Eq. (5) is derived from a zero-thickness liner. The finite thickness (1 mm) used in the simulations would lead to a smaller inductance [6]. It is interesting to see from Fig. 1 that these two effects seem to cancel each other and result in a good agreement between Eqs. (6)-(7) and the MAFIA results.

*Operated by the Universities Research Association, Inc., for the U.S. Department of Energy under Contract No. DE-AC35-89ER40400.

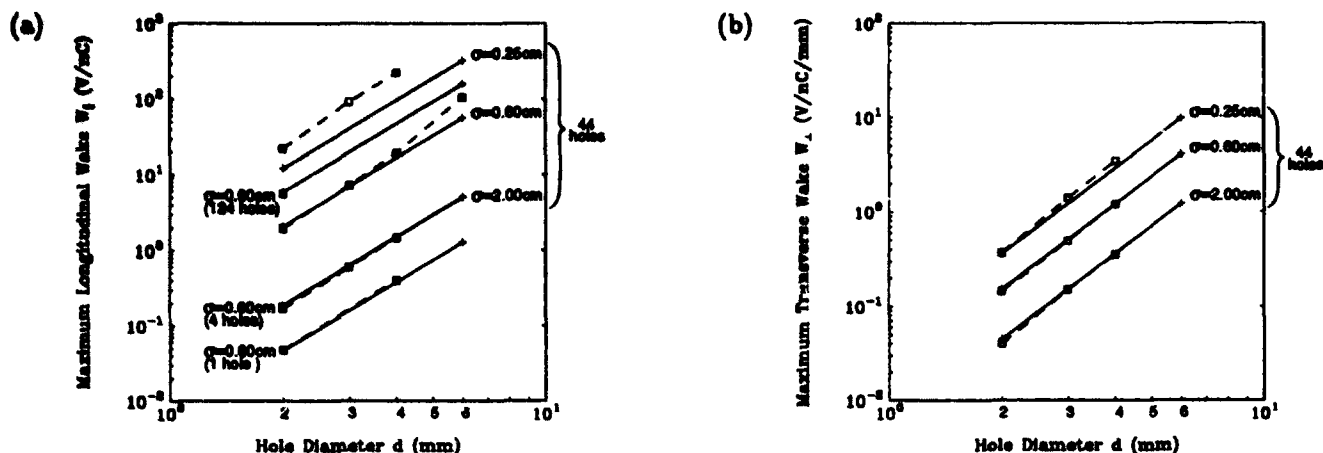


Figure 1. The solid lines are computed using Eqs. (6)-(7). The squares and dashed lines are the MAFIA results. (a) $W_{||}^{max}$, (b) W_{\perp}^{max} .

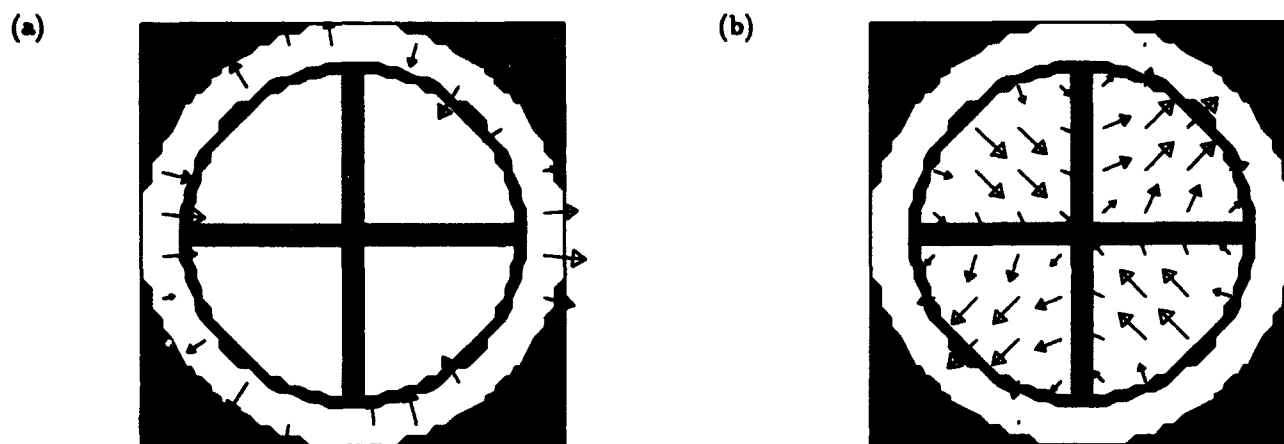


Figure 2. Electric field vectors for: (a) The TE31 mode (10.4 GHz) and (b) The TE21 mode (11.5 GHz).

III. HIGH FREQUENCY REGION

A. Fields in the Annulus

The annulus region allows the existence and propagation of a TEM wave, which has zero cutoff and travels with the speed of the light. In order to understand whether this should be a concern, the frequency domain simulation with periodic boundary conditions was carried out. Many modes have been identified and compared with the theoretical values of the frequencies. The errors are in general less than 1%. Two of them are shown in Fig. 2a-b. Up to 30 GHz, no coupling is seen between the inner and outer regions. Therefore, the impact of the co-axial structure to the impedance is considered to be insignificant.

B. Periodic Distributions of Holes on a Liner

When the holes are periodically arranged along the axis with 1 cm spacing, resonance peaks above the cutoff (~ 7 GHz) are observed in the longitudinal impedance spectrum as shown in Figs. 3a-b. Below the cutoff, the spectrum agree with the analytical value (5) within a few percent. Similar results have also been obtained for the transverse impedance.

C. Random distribution of Holes on a Liner

One effective way to reduce the resonance impedance is to destroy the periodicity of the hole distribution. This is demonstrated in Figs. 4a-b, when the spacing between two neighboring holes in the axial direction is randomised. Compared with Figs. 3a-b, the low frequency impedance remains about the same (as it should be due to the additivity), whereas the resonance peaks at high frequencies are greatly suppressed. However, by using the same technique, the reduction in the transverse direction is less dramatic. This needs further study.

D. Slots vs. Holes

When the holes are replaced by the slots that have the same area and have the major axis parallel to the pipe axis, the low frequency impedance is reduced, whereas the long term wakes and high frequency resonances are enhanced because it becomes easier to resonate [2]. Therefore, the trade off should be studied carefully. The short slots with rounded edges seem to be a good compromise.

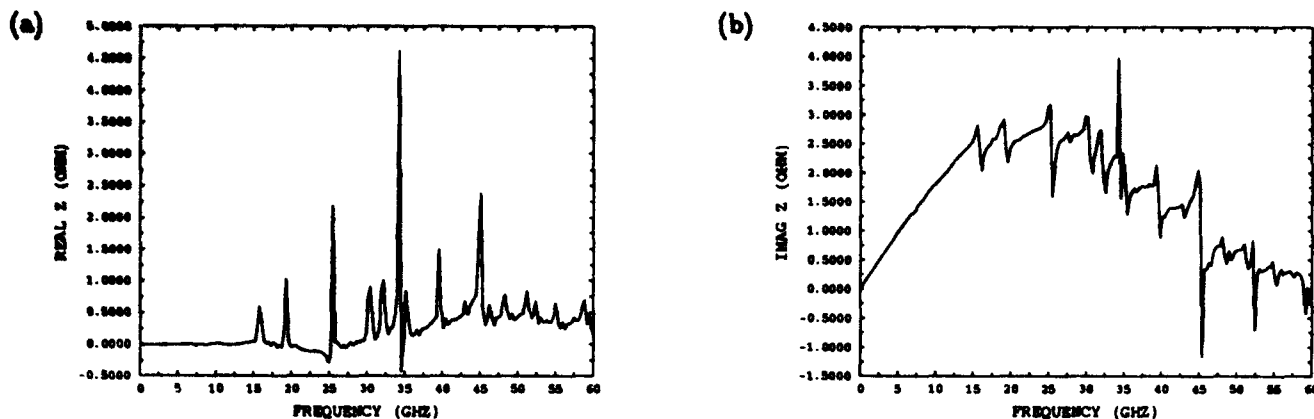


Figure 3. The longitudinal impedance for a liner with 420 square holes (2mm), periodically distributed.

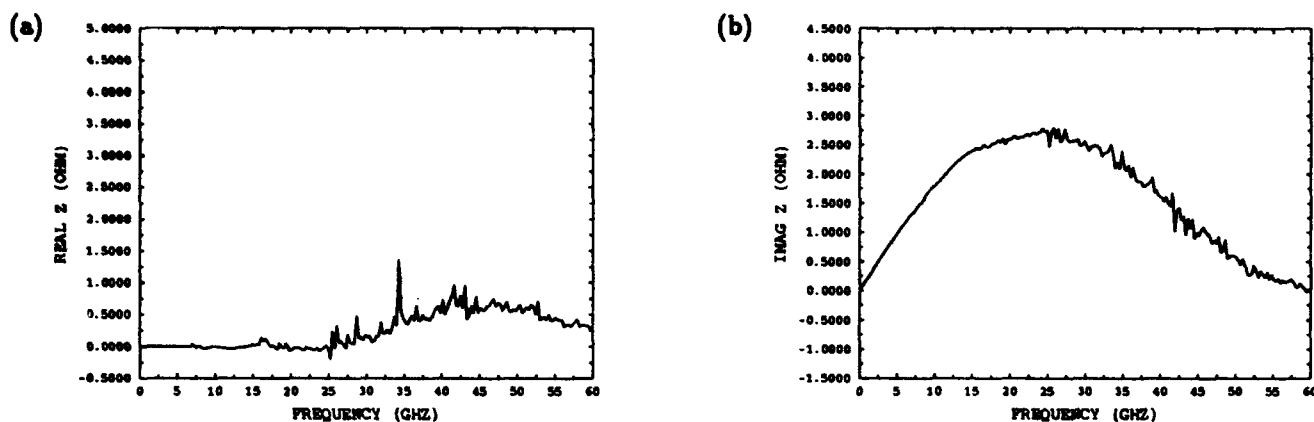


Figure 4. The longitudinal impedance for a liner with 420 square holes (2mm), randomly distributed.

IV. SAFETY MARGIN

The baseline beam tube ID is 33 mm. The impedance threshold before any coherent transverse instability could occur is 270 M Ω /m. Assuming the liner ID be 25.3 mm (as designed for the string test), hole diameter 2 mm, and 4% area coverage of the holes on the liner surface, then the safety margin will be reduced by a factor of 3, as listed in the table below.

Case	$Z_{\perp}^{(liner)}$ M Ω /m	$Z_{\perp}^{(others)}$ M Ω /m	$Z_{\perp}^{(total)}$ M Ω /m	Safety Margin
Baseline	-	40	40	6.7
With liner	37	80	117	2.3

There are several possible measures that will increase the safety margin: (a) To increase the threshold impedance by increasing the longitudinal emittance and rf voltage at injection of the Collider; (b) To reduce the machine impedance by maximising the liner ID and optimising the size and shape of the holes or slots.

V. RESISTIVE WALL INSTABILITY

The growth time of the resistive wall instability is proportional to ID^{-3} . The baseline specification is 110 turns. When a liner of 25.3 mm ID is installed, the growth time will be reduced to 50 turns. It will be further reduced if the stainless steel pieces are introduced near the BPM

for thermal insulation purposes. As a consequence, the requirement of the feedback system becomes more demanding.

VI. REFERENCES

- [1] H. T. Edwards, SSCL-N-771 (1991).
- [2] W. Chou and T. Barts, "Wakefield and Impedance Studies of a Liner Using MAFIA," *Proc. Computational Accelerator Physics Conference (CAP93)*, San Francisco, February 22-26, 1993; also see SSCL-Preprint-204 (1993).
- [3] L. Walling, private communication.
- [4] S. Kurennoy, CERN Report SL/91-29; R. L. Gluckstern, CERN Report SL/92-05.
- [5] Measurements of the liner impedance with large size holes have been made by J. Simpson's group using the short electron pulses of AATF at ANL. The results show that a better resolution is required in order to perform quantitative analysis.
- [6] R. L. Gluckstern and J. A. Diamond, *IEEE MTT*, v. 39, p. 274 (1991).

A Generalized Method for Calculating Wake Potentials

Olivier Napoly*, Yong H. Chin† and Bruno Zotter‡

* DAPNIA-SEA, CE Saclay, F-91191 Gif/Yvette, France

† Lawrence Berkeley Laboratory, 1 Cyclotron Road, Berkeley, CA 94720, USA

‡ CERN, SL/AP, CH-1211 Geneva, Switzerland

Abstract

We describe a generalized method to compute wake potentials created in axisymmetric structures. It relies on expressing the wake potentials, of any multipole order, as integrals over the e.m. fields along an arbitrary one-dimensional contour spanning the structure longitudinally. For perfectly conducting structures, the integration along the axis can then be replaced by choosing a contour beginning and ending on the beam tubes. Thus it generalizes the former method of calculating the wake potentials by integrating along a straight line at the beam tube radius. Its usefulness is illustrated with the computer code ABCI which permits calculation of wake potentials in structures extending to the inside of the beam tube radius, or having unequal beam tube radii at the two sides.

I. INTRODUCTION

The determination of the wake potentials and impedances created by metallic structures surrounding the beam trajectory is an important issue in the design of accelerators. In most practical cases, the wake fields must be calculated with computer codes. For cavity-like structures symmetric about the beam axis, using the known radial dependence of the monopolar ($m=0$) longitudinal and dipolar ($m=1$) transverse potentials, the integration of the wake fields can be performed along a straight line parallel to the axis at the beam tube radius [1]. For perfectly conducting walls, the boundary conditions ensure that the integral along the beam tube vanishes for the tangential (longitudinal or azimuthal) components of the wake potential. This leaves the integral across the cavity gap as the only contribution to the wake potentials. This simplification is essential for computer calculations, in particular for long structures and short bunches requiring small mesh size and where long beam tubes would require excessive computer memory and cpu time. However, this technique does not work when the two beam tubes have unequal radii, or when part of the cavity extends to a smaller radius. If it is the case, for instance for tapers, steps, collimators or cavities with small aperture irises, the only alternative is to integrate along a straight line at an allowable radius, and with beam tubes as long as possible. Usually one must also subtract the wake potential of the beam tubes without structure ("numerical noise") which is different from zero due to the discretization of the geometry.

In this paper, we generalize the above straight-line integration method, by showing that the longitudinal and transverse wake potentials, at all orders m in the multipolar expansion, are given by a wakefield integral along any arbitrary contour, like (C) in Figure 1, starting and ending on the beam tubes. This integral is such that the contribution of the beam

tubes vanishes. One can therefore treat more general structures by passing underneath the lowest radius material without having to introduce long beam tubes. The detailed derivation of this method is given in [2]. Its only limitation is, for $m \geq 1$, that the two beam tubes have equal radii.

This method has been implemented in the computer code ABCI [3] where the integration path is made of straight line segments defined by the 3 parameters ZCF, ZCT and RWAK as shown in Figure 1. Results from this code are presented.

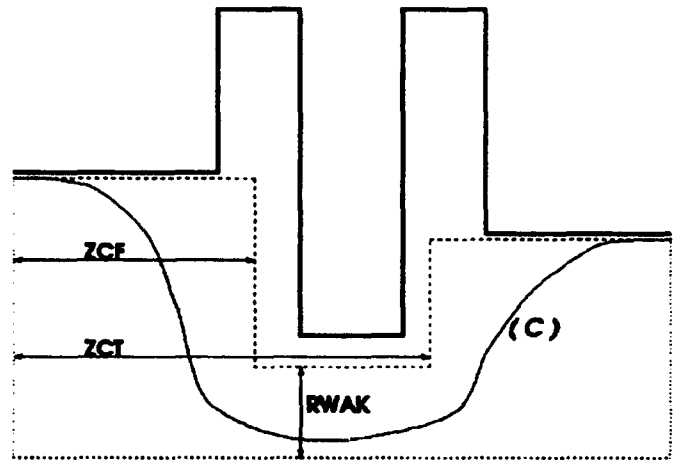


Figure 1 Contours and contour parameters in program ABCI

II. CALCULATION OF THE WAKE POTENTIALS

The longitudinal and transverse wake potentials are defined by

$$W_z(r, \theta, s) = -\frac{1}{Q} \int_{-\infty}^{+\infty} dz E_z(r, \theta, z, t(z, s)) \quad (1)$$

and

$$W_{\perp}(r, \theta, s) = \frac{1}{Q} \int_{-\infty}^{+\infty} dz (E_{\perp} + v \times B)(r, \theta, z, t(z, s)) \quad (2)$$

where s is the distance behind the exciting charge Q of velocity $v=c$.

$$t(z, s) = (z + s)/c \quad (3)$$

It is convenient to decompose the electromagnetic fields as $E = E^{(0)} + E^{(r)}$ and $B = B^{(0)} + B^{(r)}$ where $(E^{(0)}, B^{(0)})$ are the

fields generated by Q in free space, and $(E^{(r)}, B^{(r)})$ are the fields radiated by the structure and contributing to the wake potentials W_z and W_\perp . Assuming $\theta = 0$ for the exciting charge, these fields obey the following Fourier expansion

$$\begin{aligned} (E_r, B_\theta, E_z)(r, \theta, z, t) &= \sum_{m=0}^{\infty} (e_r, b_\theta, e_z)^{(m)}(r, z, t) \cos(m\theta) \\ (B_r, E_\theta, B_z)(r, \theta, z, t) &= \sum_{m=1}^{\infty} (b_r, e_\theta, b_z)^{(m)}(r, z, t) \sin(m\theta) \end{aligned} \quad (4)$$

Defining the 2d-vectors $S^{(m)}$ and $D^{(m)}$ in the (r, z) -plane, as

$$S^{(m)} = \begin{pmatrix} r^m [e_r^{(r)} + cb_\theta^{(r)} - e_\theta^{(r)} + cb_r^{(r)}]^{(m)} \\ r^m [e_z^{(r)} + cb_z^{(r)}]^{(m)} \end{pmatrix} \quad (5)$$

$$D^{(m)} = \begin{pmatrix} r^{-m} [e_r^{(r)} + cb_\theta^{(r)} + e_\theta^{(r)} - cb_r^{(r)}]^{(m)} \\ r^{-m} [e_z^{(r)} - cb_z^{(r)}]^{(m)} \end{pmatrix} \quad (6)$$

one can show, using the homogeneous Maxwell's equations satisfied by the fields $(E^{(r)}, B^{(r)})$, that the one-forms defined by these vectors are closed in the (r, z) -plane, i.e.

$$\begin{aligned} \partial_r S_z^{(m)}(r, z, s, t(z, s)) - \partial_z S_r^{(m)}(r, z, s, t(z, s)) &= 0 \\ \partial_r D_z^{(m)}(r, z, s, t(z, s)) - \partial_z D_r^{(m)}(r, z, s, t(z, s)) &= 0 \end{aligned} \quad (7)$$

This implies that the vectors $S^{(m)}$ and $D^{(m)}$ derive from a potential and that their integral along a closed contour (enclosing the vacuum) vanishes. This property allows one to deform the wakefield integration path from the straight line (L_r) at constant radius r used in definitions (1) and (2), to any contour (C) .

A. The $m=0$ case

In this case the radiated fields $(E^{(r)}, B^{(r)})$ vanish at both ends of the beam tube, and the integrals of $S^{(0)}$ along (L_r) and along the path (C) , are equal:

$$\int_{L_r} S^{(0)}(r, z, s) \cdot d\mathbf{l} = \int_C S^{(0)}(r', z, s) \cdot d\mathbf{l} \quad (8)$$

The right-hand side of this equation is proportional to the longitudinal potential $W_z^{(0)}(s)$, which is therefore given by

$$\begin{aligned} W_z^{(0)}(s) &= -\frac{1}{Q} \int_C [E_z dz + (E_r + cb_\theta) dr]^{(m=0)}(r, z, t(z, s)) \\ &\quad + \frac{1}{\pi \epsilon_0} \ln \left[\frac{a_{in}}{a_{out}} \right] \delta(s) \end{aligned} \quad (9)$$

where the log term comes from the integration of the free fields $E_r^{(0)} + cb_\theta^{(0)}$, and a_{in} and a_{out} are the tube radii.

B. The $m>0$ case

In that case we assume that $a_{in} = a_{out} = a$, as will be justified later. Then

$$\int_{L_r} S^{(m)}(r, z, s) \cdot d\mathbf{l} = \int_C S^{(m)}(r', z, s) \cdot d\mathbf{l} \quad (10)$$

$$\int_{L_r} D^{(m)}(r, z, s) \cdot d\mathbf{l} = \int_C D^{(m)}(r', z, s) \cdot d\mathbf{l} \quad (11)$$

since the radial integrals at $z = \pm\infty$ cancel each other. The first equation, evaluated on the z -axis, implies that the integral of $S^{(m)}$ along any contour vanishes. It is then easy to show that

$$W_z^{(m)}(r, \theta, s) = -\frac{\cos(m\theta)}{2Q} r^m \int_C D^{(m)} \cdot d\mathbf{l} \quad (12)$$

Adding to the integral of $D^{(m)}$ the (vanishing) integral of $S^{(m)}$ along (C) divided by a^{2m} , leads to an expression of the longitudinal wake potential where the integral along the beam tube vanishes due to the metallic boundary conditions. This is however only possible when the tube radii are equal. Evaluating the resulting expression in terms of the e.m. fields in the structure, leads to

$$W_z^{(m)}(r, \theta, s) = \frac{r^m \cos(m\theta)}{2Q a^m} w^{(m)'}(s) \quad (13)$$

with

$$\begin{aligned} w^{(m)'}(s) &= - \int_C dz \left[\left(\frac{a^m}{r^m} + \frac{r^m}{a^m} \right) e_z - \left(\frac{a^m}{r^m} - \frac{r^m}{a^m} \right) cb_z \right] \\ &\quad + dr' \left[\left(\frac{a^m}{r^m} + \frac{r^m}{a^m} \right) (e_r + cb_\theta) + \left(\frac{a^m}{r^m} - \frac{r^m}{a^m} \right) (e_\theta - cb_r) \right] \end{aligned} \quad (14)$$

The transverse potential can be written, using the Panofsky-Wenzel theorem, as

$$W_\perp(r, \theta, s) = \sum_{m=1}^{\infty} \frac{mr^{m-1}}{2Q a^m} (\cos(m\theta)\hat{r} - \sin(m\theta)\hat{\theta}) w^{(m)}(s) \quad (15)$$

with

$$\begin{aligned} w^{(m)}(s) &= \frac{-1}{m} \int_C r' dr' \left[\left(\frac{a^m}{r^m} - \frac{r^m}{a^m} \right) e_z - \left(\frac{a^m}{r^m} + \frac{r^m}{a^m} \right) cb_z \right] \\ &\quad + r' dz \left[\left(\frac{a^m}{r^m} + \frac{r^m}{a^m} \right) (e_\theta + cb_r) - \left(\frac{a^m}{r^m} - \frac{r^m}{a^m} \right) (e_r - cb_\theta) \right] \end{aligned} \quad (16)$$

In equations (14) and (16), it is understood that the electromagnetic fields are projected on their multipolar component of order m , and that their argument is $(r', z, t(z, s))$.

III. COMPUTER IMPLEMENTATION

The possibility of integrating along a non-straight path, using Equations (9), (14) and (16), has been implemented in the time-domain program ABCI [3] as discussed in the introduction. We illustrate the interest of this method with the calculation of wake potentials for two cases. We first consider a 1 cm long collimator of 4 mm radius in a beam tube of 1 cm radius. Figure 2 shows a comparison of the loss factor of a Gaussian bunch with $\sigma_z = 5$ mm calculated with two different methods:

1. the wakefield integration along a straight line at 4 mm constant radius (solid line). The calculated wake potential and loss factor then depend on the length L of the tube on both sides of the collimator. The result is given, after subtraction of the wake of the tube alone ("numerical noise correction" similar to the WAKCOR method in TBCI [5]), by the asymptotic value.
2. the wakefield integration along the boundary of the collimator, using Equation (9). In this case the result is independent of the length of the tube and gives directly the value of the loss factor (dotted line).

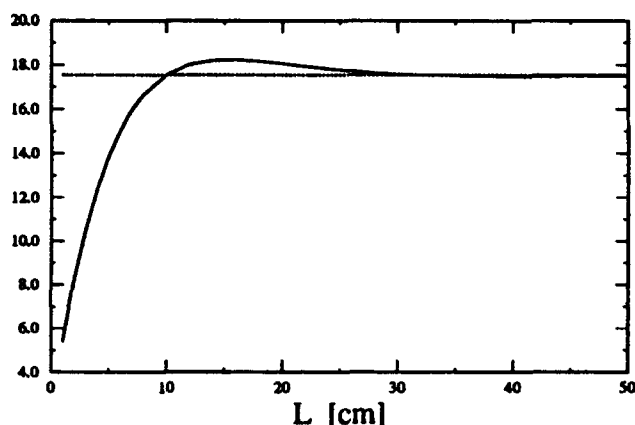


Figure 2 Longitudinal loss factor [V/pC] of a collimator as a function of the beam tube length

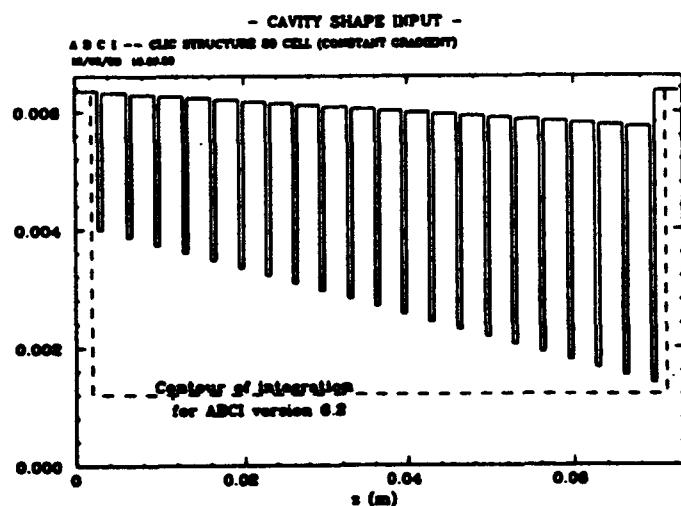


Figure 3 Constant gradient structure for CLIC

Finally Figure 4 plots the $m=1$ wake potentials of a 20 cell 30 GHz constant gradient structure, as shown in Figure 3, where the inner and outer radii of each cell are different. The contour of integration chosen by the program is given by the dashed line.

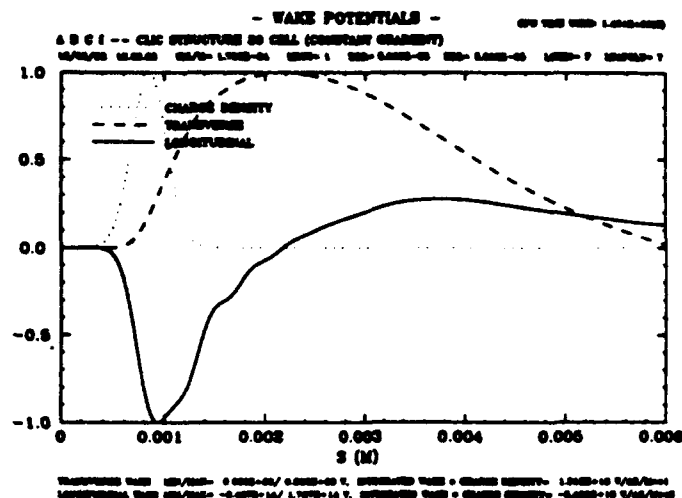


Figure 4 Dipolar wake potential ($m=1$)

IV. CONCLUSION

In practical calculations of the wake potentials created by axisymmetric cavities, one usually evaluates them by integrating along the cavity gap at the beam tube radius. We have generalized this method by showing that the wake potentials, of any multipole order, are given by integrals over the wake fields along any arbitrary contour spanning the structure longitudinally. By so doing we have extended the range of applications to structures of more complicated shape. The integration of wake fields along well chosen contour permits a large savings in computer capacity. In particular, the integration along a structure extending to the inside of the beam tubes - such as a collimator or iris - has become much easier with this method. Also the $m=0$ wake potential of structures with unequal beam tubes can be calculated in this manner. The new method of integration has been implemented in the code ABCI (versions 5 or higher) which can choose the proper contour automatically or as selected by the user.

V. REFERENCES

- [1] T. Weiland, NIM 216 (1983), 31
- [2] O. Napoly, Y.H. Chin, B. Zotter, DAPNIA/SEA/93-01 and CERN-SL/AP 93-14, to appear in NIM A
- [3] Y.H. Chin, Report LBL-33091, CERN-SL/AP 92-49 (1992), and these proceedings
- [4] W. Panofsky and W. Wenzel, Rev. Sci. Instrument, 27 967 (1956)
- [5] T. Weiland, Report DESY 82-015 (1982)

The Interaction of a Beam with a Beam Line Higher-Order Mode Absorber*

W. Hartung, K. Akai, J. DeFord, T. Hays, J. Kirchgasner, D. Metzger, D. Moffat, H. Padamsee, D. Rubin, M. Tigner, A. Tribendis, & V. Veselcherevich[‡]

Laboratory of Nuclear Studies, Cornell University, Ithaca, New York 14853

"Round and 'round and 'round and 'round."
N. Cherry

I. INTRODUCTION

Plans for CESR-B, the proposed upgrade of the CESR e^+e^- storage ring to a B -factory [1], call for beam currents of ~ 1 A. Studies indicate that the beams will be unstable unless the higher-order modes (HOMs) in the superconducting cavities are strongly damped; $Q \leq 100$ is required for the dangerous modes [2]. The cavity is designed to enable all HOMs to propagate into the beam pipe, where a layer of microwave-absorbing ferrite is to provide the damping. The load geometry is shown in Figure 1. RF measurements with a full-size mock-up of the cavity and loads made of two types of ferrite, TT2-111-series and Ferrite-50,¹ indicate that this scheme provides the required damping [3]. The HOM loads can also interact directly with the beam. Preliminary predictions for the effect of loads made of TT2-111V² ferrite on beam stability in CESR-B are given in this paper.

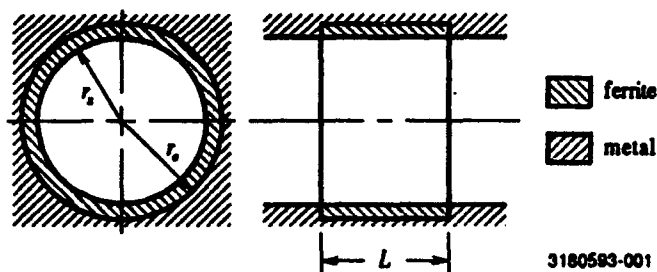


Figure 1. Load geometry. For a full-size load, $L = 150$ mm, $r_s = 118.4$ mm, and $r_o = 121.6$ mm.

II. COUPLING IMPEDANCE PREDICTIONS

The beam coupling impedance of a load was predicted using (i) AMOS, a program which calculates wake fields in the presence of absorbing materials [4], and (ii) analytic formulae for the coupling impedance of a conducting pipe with a material layer. The formulae were derived using an approach previously applied to multi-layer pipes [5, 6]; a detailed explanation of the technique and its application

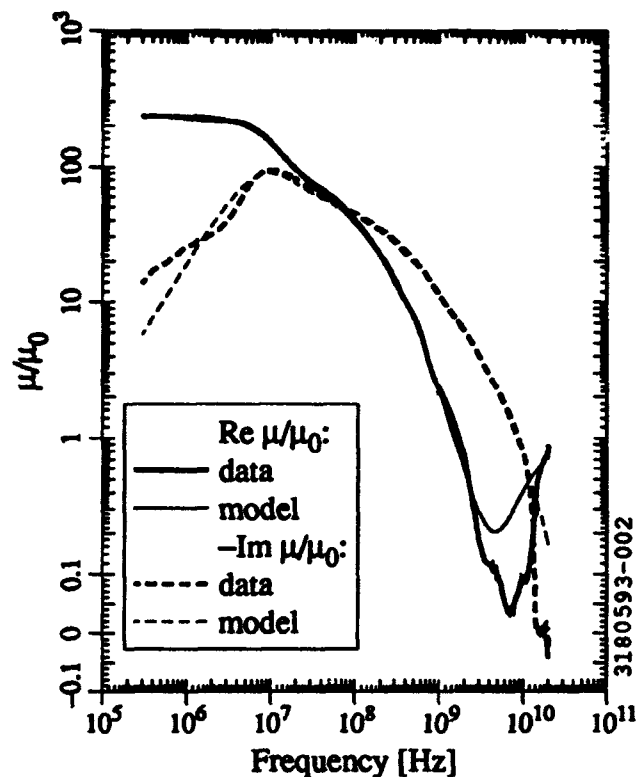


Figure 2. Measured and fitted values of the real and imaginary (times -1) parts of μ for TT2-111V.

to the resistive wall can be found in [7]. In the analytic calculation, the beam pipe is assumed to be homogeneous in the axial direction, so that end effects are neglected.

Prediction of the impedance requires knowledge of the microwave properties (complex permeability μ and permittivity ϵ) of the absorbing material. The properties of TT2-111V and some other absorbing materials were measured using the coaxial transmission line technique [8]. Measured values of μ are shown in Figure 2. The 6-pole "relaxation" model fit used in AMOS is also shown. The measured ϵ/ϵ_0 has a real part of about 14 and an imaginary part corresponding to a DC conductivity of about $0.0023 (\Omega\text{m})^{-1}$; these are the values that were input to AMOS.

Predictions for the monopole longitudinal impedance Z_0^{\parallel} are shown in Figure 3. There is a significant difference between the AMOS and analytic predictions above 1 GHz, possibly due to the fact that the analytic calculation neglects end effects. The "broad-band" longitudinal and transverse impedances are shown in Figure 4. More information on the impedance predictions and on additional

*Work supported by the National Science Foundation, with supplementary support from U. S.-Japan collaboration.

¹present address: KEK, Tsukuba-Shi, Ibaraki-Ken 305, Japan

²Lawrence Livermore National Lab, Livermore, California 94550

³present address: Institute of Nuclear Physics, 630090 Novosibirsk, Russia

⁴TT2-111-series ferrite and Ferrite-50 are products of Trans-Tech, Inc.

⁵We use "TT2-111V" to refer to a variety of TT2-111R ferrite with enhanced DC conductivity.

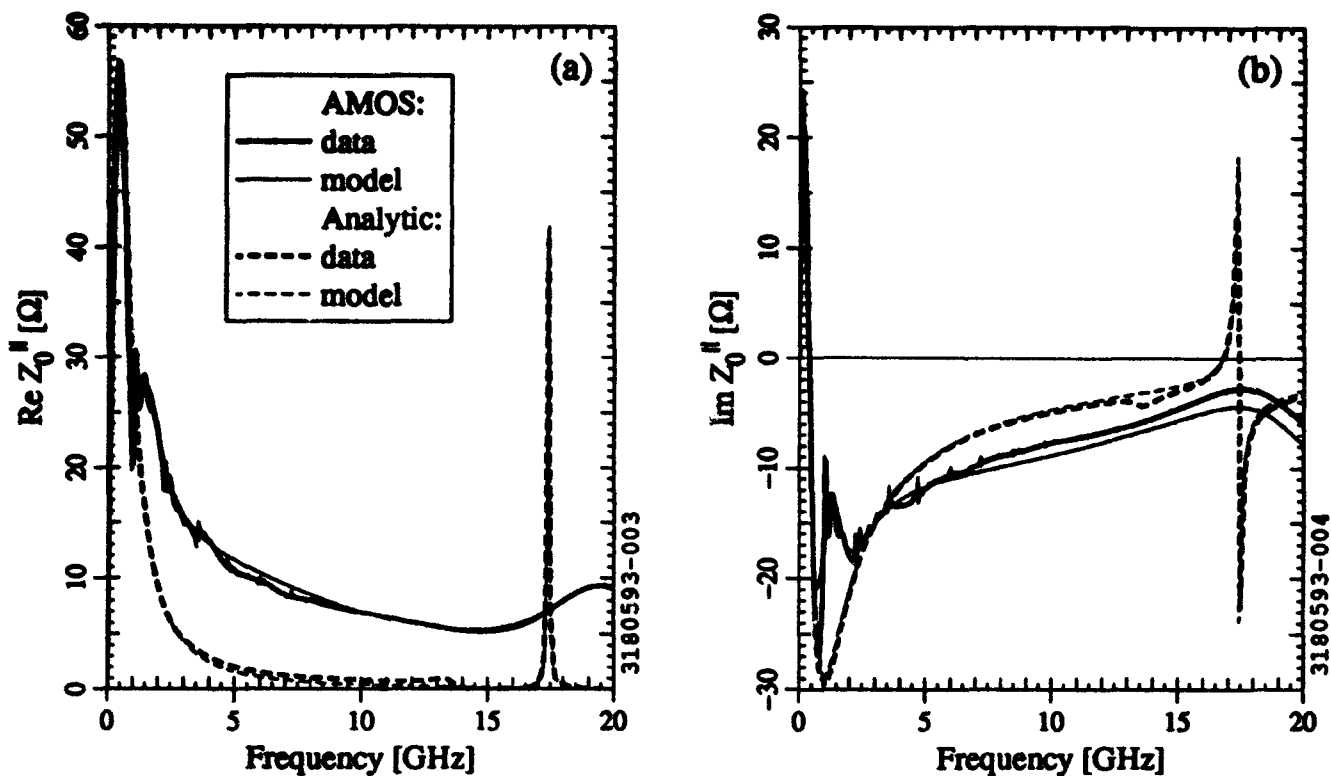


Figure 3. Predicted (a) real part and (b) imaginary part of the longitudinal monopole coupling impedance for a full-size TT2-111V load, along with model values used for ZAP. The complex conjugates of the AMOS values are shown.

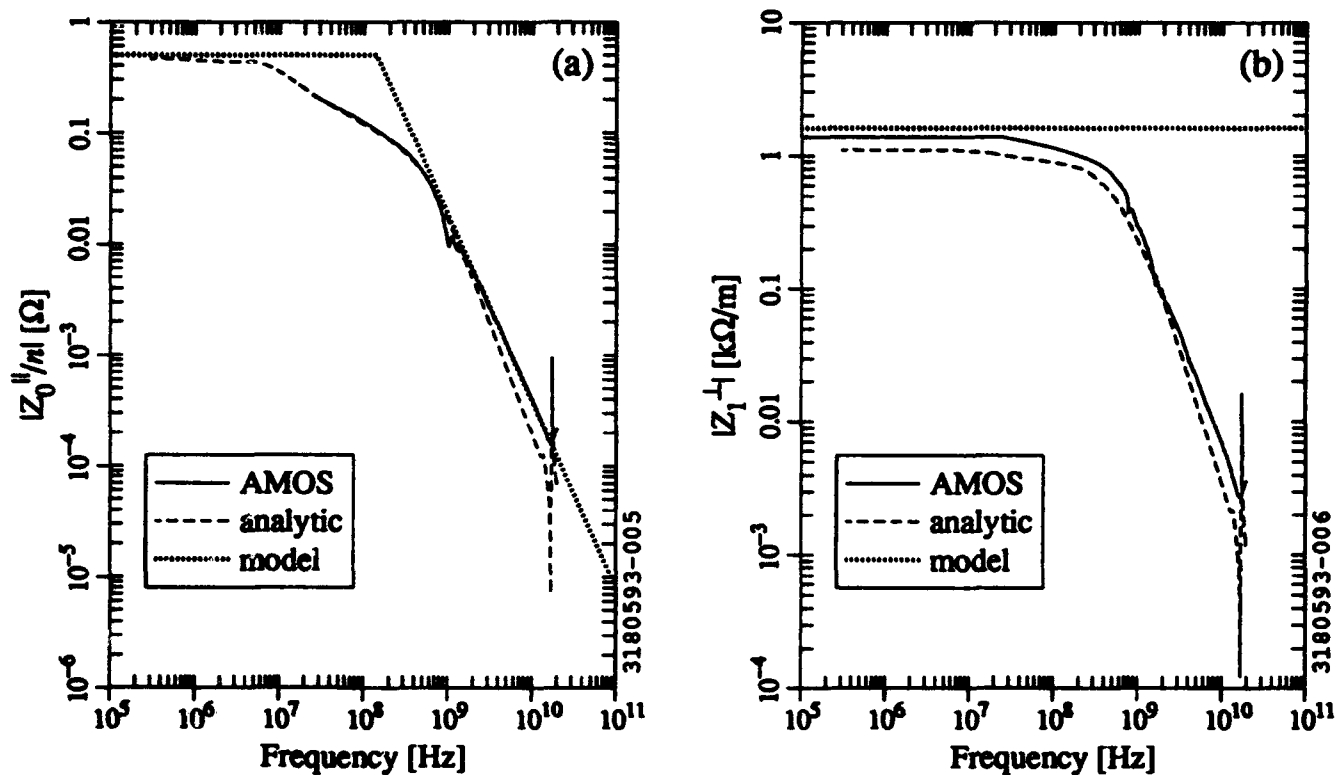


Figure 4. Predicted (a) $|Z_0^H/n|$ and (b) $|Z_1^H|$ for a full-size TT2-111V load, along with model values used for ZAP.

wire measurements may be found elsewhere [9, 10].

III. BEAM STABILITY PREDICTIONS

The ZAP program [11] was used to predict the effect of the ferrite loads' coupling impedance on CESR-B beams. Relevant machine parameters are given in Table 1.

Table 1. Selected CESR-B Machine Parameters.

Parameter	Low-Energy Ring	High-Energy Ring
Ring circumference	764.84 m	
Beam energy	3.5 GeV	8 GeV
Beam current	1.98 A	0.87 A
Particles per bunch	$1.92 \cdot 10^{11}$	$0.84 \cdot 10^{11}$
Longitudinal bunch size	1 cm	
Total RF voltage	11.64 MV	33.82 MV
RF Frequency	500 MHz	
Momentum compaction	0.011	0.0084
Momentum spread	$6.44 \cdot 10^{-4}$	$8.30 \cdot 10^{-4}$
Horizontal betatron tune	11.56	12.56
Vertical betatron tune	8.63	
Horizontal tune spread	$2 \cdot 10^{-4}$	
Chromaticity	1	
Number of HOM loads	5	14

Single-bunch thresholds were predicted from the calculated broad-band impedances. A constant $|Z_1^{\perp}|$ and a SPEAR-like $|Z_0^{\parallel}/n|$ was assumed (see Figure 4). SPEAR scaling was used to obtain the effective $|Z_0^{\parallel}/n|$. The results are given in Table 2. ZAP predicts no bunch lengthening due to potential well distortion.

Growth rates for longitudinal and transverse coupled-bunch instabilities were predicted with ZAP, after fitting Z_0^{\parallel} and Z_1^{\perp} to a multi-mode resonator model. Because the AMOS and analytic impedances are somewhat different, they were fitted separately. The model impedances used for Z_0^{\parallel} are shown in Figure 3. There was a significant disagreement between the predictions from the two possible formalisms (Wang and Zotter) in some cases. The worst-case results are given in Table 3. The $\alpha = 1$ mode has the fastest growth time in all cases. As can be seen, all modes are predicted to be stable in the presence of radia-

Table 2. Predicted single bunch thresholds.

Instability type	Threshold particles/bunch	
	Low-Energy Ring	High-Energy Ring
Transverse fast blow-up or mode coupling	$1.9 \cdot 10^{13}$	$1.5 \cdot 10^{13}$
Microwave / turbulent bunch lengthening	$7.9 \cdot 10^{12}$	$7.5 \cdot 10^{12}$

Table 3. Predicted worst-case growth times for coupled-bunch instabilities. CESR-B radiation damping times are also given for comparison.

Instability type	Fastest growth time	
	Low-Energy Ring	High-Energy Ring
Longitudinal	44 s	106 s
Transverse	4 s	6 s
Type of damping	Radiation damping time	
	Low-Energy Ring	High-Energy Ring
Longitudinal	12 ms	4.2 ms
Transverse	25 ms	8.5 ms

tion damping.

The loss factor was calculated from the predicted Z_0^{\parallel} . In the worst case (the AMOS prediction for the low-energy ring), the direct power transfer from the beam to the load is 11.5 KW per load, which corresponds to an average power dissipation of 0.102 W/mm².

IV. CONCLUDING REMARKS

The ZAP results indicate that the single-bunch instability thresholds from the loads are at least a factor of 40 above the design beam current for CESR-B and the coupled-bunch growth times due to the loads are at least a factor of 100 longer than the radiation damping times. We plan to design a scaled load with appropriately magnified effects and test our understanding of its interaction with a beam in the existing CESR storage ring.

V. REFERENCES

- [1] M. Tigner, *Conference Record of the 1991 IEEE Particle Accelerator Conference*, p. 132-134.
- [2] H. Padamsee *et al.*, *ibid.*, p. 786-788.
- [3] V. Veshcherevich *et al.*, *Proceedings of B Factories: The State of the Art in Accelerators, Detectors, and Physics*, SLAC-400/CONF-9204126, p. 177-180.
- [4] J. DeFord *et al.*, *Proceedings of the 1989 IEEE Particle Accelerator Conference*, p. 1181-1183.
- [5] B. Zotter, *Particle Accelerators* 1, 311 (1970).
- [6] A. Piwinski, *IEEE Trans. Nucl. Sci.* NS-24, 1364 (1977).
- [7] A. Chao, in AIP Conf. Proc. no. 105, M. Month, Ed., (AIP, New York, 1983), p. 353-523.
- [8] W. Hartung *et al.*, "Measurements of the Microwave Properties of Some Absorbing Materials," presented at the Microwave-Absorbing Materials for Accelerators Workshop, CEBAF, 22-24 February 1993.
- [9] W. Hartung *et al.*, "Assessment of the Coupling Impedance of Beam Line Higher-Order Mode Loads," *ibid.*
- [10] J. DeFord *et al.*, these proceedings.
- [11] M. Zisman, *Particle Accelerators* 23, 289 (1988).

PERSISTENT WAKEFIELDS ASSOCIATED WITH WAVEGUIDE DAMPING OF HIGHER ORDER MODES*

Norman M. Kroll and Xintian Lin
University of California, San Diego, La Jolla, CA 92093
Stanford Linear Accelerator Center, Stanford University, Stanford, CA 94309

Abstract

By means of an analytic model and numerical simulations we demonstrate that the wake of a waveguide damped cavity contains a persistent component which decays as $t^{-3/2}$ and thus is dominant at sufficiently large values of t . Because there are scenarios for which the effect gives rise to unacceptable beam instability, it cannot be ignored, but it seems likely that such an outcome can be avoided with proper design.

1 Introduction

The passage of a bunch of charged particles through an accelerator cavity generates a wakefield which may have a deleterious effect on the motion of subsequent bunches which pass through the cavity. The effect is often cumulative from bunch to bunch and from cavity to cavity and may lead to beam breakup [1]. One solution to this problem which has received extensive study is to drain the wakefield energy out of the cavity by means of waveguides coupled to the cavity and feeding into matched terminations [2]. The effectiveness of this procedure has typically been assessed by evaluating the resultant Q_{ext} of higher order cavity modes, thereby determining their exponential damping rate. The purpose of this paper is to point out the existence of an additional effect which leads to a wakefield which falls off as $t^{-3/2}$ rather than exponentially. Because this effect always dominates at sufficiently long times, we refer to it as the persistent wake. It consists of a superposition of the frequencies of the various waveguide cutoff frequencies and may be understood as arising physically from the fact that the group velocity of each waveguide mode vanishes at its cutoff frequency. As we shall see below, for sufficiently heavy damping, it may dominate before the arrival of the second bunch. A similar phenomenon with essentially the same physical origin which occurs in the decay of unstable quantum states has received extensive study.

2 The Dielectric Cavity Model

As a simple model of a cavity heavily damped by waveguides, we consider a waveguide which has a finite section of length h filled with dielectric. The configuration is illustrated in Fig. 1.

For brevity, we confine our attention to fields whose transverse configuration is that of the TE_{10} waveguide mode. There is always at least one trapped cavity mode in the dielectric, symmetric with respect to the y - z plane,

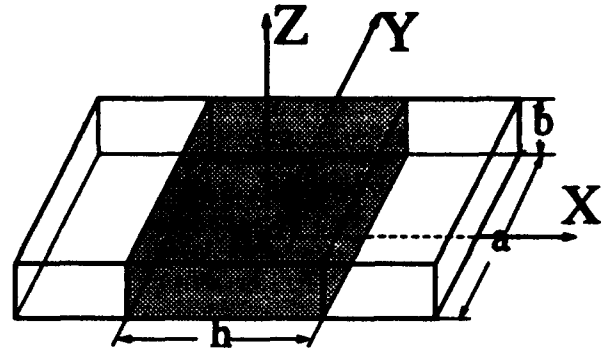


Figure 1: Dielectric cavity model

and with resonant frequency below the cutoff frequency of the dielectric free portion of the waveguide. This mode has an electric field distribution suitable for accelerating particles in the z direction along the z axis. There are also damped modes associated with multiple reflections between the two dielectric-free space interfaces which have frequencies above the cutoff of the free space portion of the waveguide. Hence it provides us with a reasonable model of a waveguide damped accelerator cavity.

To further simplify the problem we look only at the on axis transverse deflecting field B_y generated by a unit charge moving relativistically in the z direction and displaced by the infinitesimal distance d_z from the z axis, as shown in Fig. (1). Defining the transverse wake function W_{\perp} as B_y/d_z evaluated on the z axis, and solving Maxwell's equations for our configuration we find

$$W_{\perp} = \int \frac{2}{ab} (e^{\frac{i\omega t}{c}} - 1) \frac{k D_2}{\omega D_1} e^{-i\omega t} d\omega \quad (1)$$

$$D_1 = \left(1 + \frac{1}{\mu} \frac{k}{l}\right) - \left(1 - \frac{1}{\mu} \frac{k}{l}\right) e^{ikh}, \quad l = \frac{1}{c} \sqrt{\omega^2 - \omega_c^2}$$

$$D_2 = \left(1 + \frac{1}{\mu} \frac{k}{l}\right) + \left(1 - \frac{1}{\mu} \frac{k}{l}\right) e^{ikh}, \quad k = \frac{1}{c} \sqrt{\epsilon \mu \omega^2 - \omega_c^2}$$

The integrand of Eq. (1) has a pair of branch points where l vanishes, corresponding to the cutoff frequency in the dielectric free waveguides, and the Riemann surface of the integrand therefore has two sheets. In addition to the branch points the integrand has poles where D_1 vanishes. Causality and time reversal invariance tell us that we can choose the sign of l so that there are no complex singularities in the complex plane cut along the real axis to the left and right of the branch points and extending to plus and minus infinity. These specifications define what is referred to as the physical sheet of the Riemann surface. We choose the parameters of the cavity so that there are no

*Work supported by U.S. Department of Energy grant DE-FG03-92ER40759 and contract DE-AC03-76SF00515

trapped deflecting modes in order that we may expect W_1 to decay rapidly after the passage of the charge. Hence the only singularities on the physical sheet are the two branch points. The integral in Eq. (1) is taken along the entire real axis of the physical sheet with infinitesimal detours above them.

The second sheet of the Riemann surface is reached by crossing the branch cuts from the physical sheet. It has an infinite number of complex poles. These occur in groups of four, symmetrically distributed with respect to both axes. There may also be pairs of real poles between the branch points.

After the particle leaves the cavity ($t > b/c$), the integral over the semi-circle at infinity in the lower half plane vanishes. We use it to close the integration path of Eq. (1) and shrink it to the form shown in Fig. (2). Here the upper half plane and the region between the two indicated branch cuts is a part of the physical sheet, while the remainder of the lower half plane is on the second sheet. In shrinking the contour integral to the two discontinuity integrals along the branch cuts, we must pass through the poles which have been exposed on the second sheet, and we must retain a residue from each of them. Thus we have expressed W_1 as an expansion in terms of the discrete exponentially damped cavity modes plus a contribution from the branch cut integrals. It is this latter contribution which provides the persistent wake.

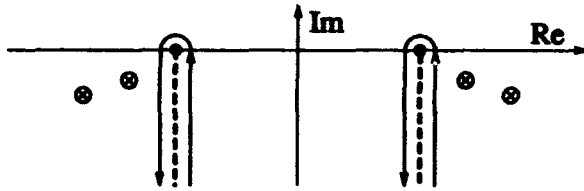


Figure 2: Contour for Calculating W_1

We define the persistent wake function W_p as the contribution from the branch cut discontinuity integrals, and to simplify the discussion we redefine t as $\omega_c t$ and ω as ω/ω_c . The cut discontinuity can then be written as $\sqrt{\omega^2 - 1}F(\omega)$ where F is analytic in the neighborhood of the branch point. Making use of partial integration, we obtain the large t asymptotic behaviour as follows:

$$\begin{aligned} W_p(t) &= \int_1^{1-i\infty} \sqrt{\omega^2 - 1} F(\omega) e^{-i\omega t} d\omega \\ &= \frac{1}{it} \int_1^{1-i\infty} e^{-i\omega t} d\omega \frac{d}{d\omega} \sqrt{\omega^2 - 1} F(\omega) d\omega \\ &= \frac{1}{it} \int_1^{1-i\infty} e^{-i\omega t} \frac{F(1)}{\sqrt{\omega^2 - 1}} d\omega + \\ &\quad \frac{1}{it} \int_1^{1-i\infty} e^{-i\omega t} \sqrt{\omega^2 - 1} G(\omega) d\omega + c.c. \quad (2) \end{aligned}$$

Here G , which has the same analyticity properties as F , is given by

$$G(\omega) = \frac{F(\omega)\omega - F(1)}{\omega^2 - 1} + \frac{dF}{d\omega} \quad (3)$$

The dominant asymptotic behavior comes from the first term. Carrying out the integral we find

$$W_p(t) = -\frac{\pi}{2i} H_0^{(2)}(t) F(1) + c.c. \quad (4)$$

which decays as $t^{-3/2}$. Here $H_0^{(2)}$ is the zeroth order Hankel function of the second kind. Because the second term is subject to the same manipulations as the first, it falls off as $t^{-5/2}$, and by repeating the process one can get a sequence terms falling off with increasing powers of $1/t$.

The full expression for W_1 has been evaluated numerically. Highly damped successive reflections from the interfaces appear at early time, but as shown in Fig. (4) the asymptotic limit takes over quite rapidly.

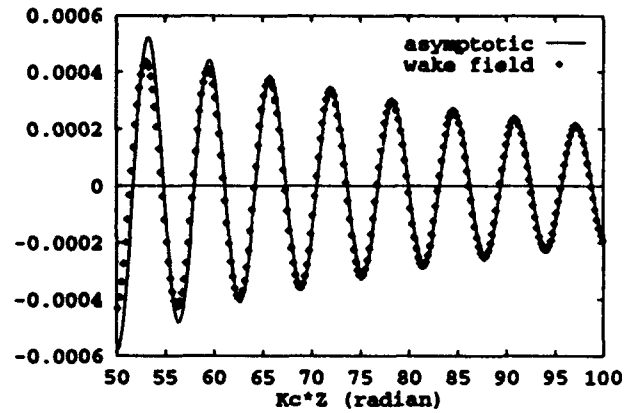


Figure 3: Asymptotic behavior of the wake field

3 2-D simulation

For our simulation structure we have taken a cavity with four damping waveguides with the cross section shown in Fig. (4a). The scale is chosen so that the cavity has an accelerating mode at 11.424 GHz. The waveguide cutoff for the lowest mode is 14.27 GHz. Two damped dipole modes were identified with MAFIA frequency domain calculations. Their frequencies, 17.365 and 34.297 GHz, and Q 's, 3.74 and 9.0 were determined using Kroll-Yu [3] and Kroll-Lin [4] for the former, and because the latter was above cutoff for two waveguide modes, Kroll-Kim-Yu [5] was required. A MAFIA time domain computation determined the wakefield excited by a Gaussian line charge bunch displaced from the origin. The wakefield obtained for a σ_z of 2.6 mm is described by Figs. (4 b,c,d). The abscissa represents the distance of a synchronous trailing bunch behind the excitation bunch, a typical value being 42 cm. Fig. (4b) shows the persistent wake dominating after 25 cm. The logarithmic plot of the averaged amplitude shown in Fig (4c) exhibits perhaps three exponential damping rates. The straight line fit shown determines a damping rate of 44.33 m^{-1} . This is to be compared with the unresolved pair of decay rates of 48.64 m^{-1} and 39.92 m^{-1} from the first and second dipole modes. The second

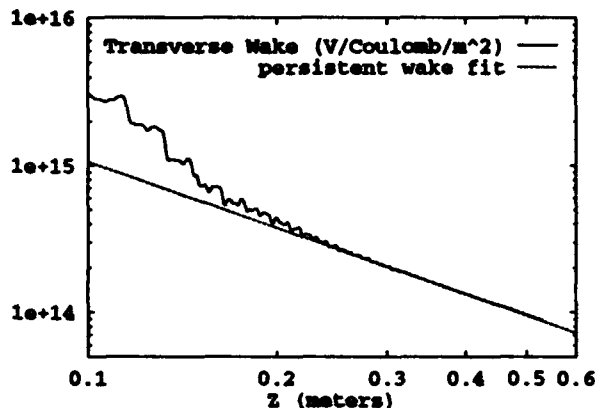
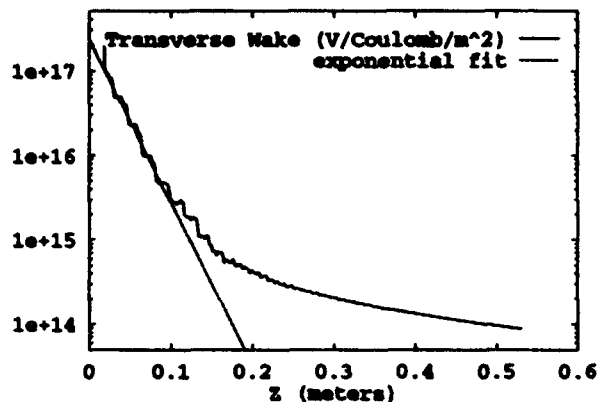
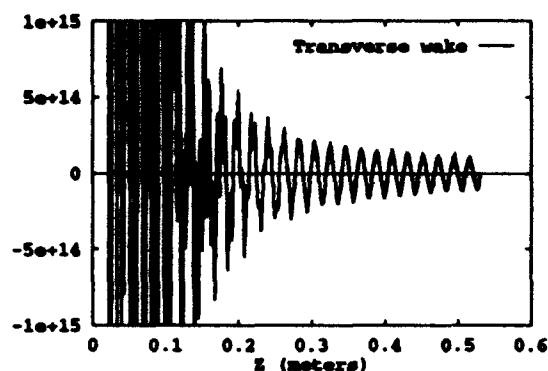
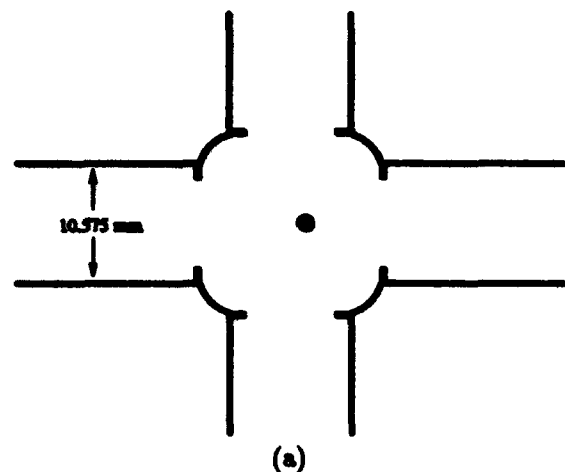


Figure 4: (a): 2D strongly damped structure, the dot refers to beam path in third dimension. (b): Dipole wake field as a function of distance $= t * c$. (c): log plot of the same wake field, dashed line refers to the best exponential fit. (d): log-log plot, dashed line is $t^{-3/2}$

slope of 27.6 m^{-1} (straight line is not shown) was associated with a high frequency mode beyond the range of our frequency domain simulation. The log-log plot of Fig (4.2d) compares the persistent wake with a $t^{-3/2}$ straight line.

4 Concluding Remarks

The magnitude of the wake at 42 cm appears to be large enough to cause some beam blow up. We have also studied the extreme case of the cavity formed by two waveguides intersecting at right angles. While no damped dipole resonances could be identified, indicating extreme higher order mode damping, the persistent wake was four times as large, and the beam blow up would be disastrous. This suggests that an iris which decreases the damping tends to decouple the cavity from the persistent wake, and hence that better results could be obtained by further decreasing the damping. Detuning the persistent wake by distributing the waveguide cutoff frequencies, which should be simpler than detuning the HOM's, would also be expected to be effective. It is also likely that the effect would be negligible in the choke mode cavity damping scheme [6].

References

- [1] K. Thompson and R. Ruth, *Phys Rev D* 41, 964 (1990)
- [2] R. Palmer, *High Energy Physics in the 1990's*, S. Jenson, Ed. (World Scientific, Singapore, 1989), pp.638-641
- [3] N. Kroll and D. Yu, *Part. Accel.* 34, 231 (1990)
- [4] N. Kroll and X. Lin, *Proc. 1990 Linac Conf.*, Albuquerque, NM, June 10-14 (1990) p. 238
- [5] N. Kroll, J. Kim, and D. Yu *Proc. 1992 Linac Conf.* Ottawa, Ontario, August 24-28 (1992) AECL-10728 217 (1992)
- [6] T. Shintake, *Jpn. Jour. of Appl. Phys.* 31 p. L1567 (1992)

PERTURBATION THEORY OF BROADBAND IMPEDANCES*

S. Heifets

Stanford Linear Accelerator Center
Stanford University, Stanford, CA 94309 USA

Abstract

A perturbation theory for broadband impedance calculations has been developed, allowing evaluation of impedances for an accelerating structure of a rather arbitrary shape. General formulas are given for the longitudinal and transverse impedances. The method is checked by calculating impedances and comparing results with those for structures previously studied. Several new results, including impedance of a taper, are presented.

I. INTRODUCTION

The interaction of a beam with the beam environment in accelerators is usually described in terms of the coupling impedances, with most of the impedance calculations performed using numeric codes. This paper describes a perturbation theory for the impedance calculations based on Kirchhoff's equations, analogous to the Born series in the scattering theory. A perturbation theory of this kind was used in the time domain by Novokhatsky [1], and by the author [2] for more general structures in the frequency domain. A cylindrical symmetry is implied in most cases, unless it is stated otherwise, although the method also may be applied to study impedances of structures without cylindrical symmetry. ring.

II. ILLUSTRATION: THE METHOD

Consider a well known electrostatic problem: find the field of a point-like charge e placed at distance $z = a$ from an ideal conducting x, y plane. The field potential for $z > 0$ is a superposition of the potential ϕ_{ext} of a charge in free space and the potential of the image charge $-e$ at $z = -a$. This result may be obtained using Green theorem [3] volume:

$$\begin{aligned} \phi(\vec{R}) &= \phi_{\text{ext}}(\vec{R}) + \int \frac{d\vec{S}'}{4\pi} \\ &\times [G(\vec{R}, \vec{R}') \vec{\nabla}' \phi(\vec{R}') - \phi(\vec{R}') \vec{\nabla}' G(\vec{R}, \vec{R}')] . \end{aligned} \quad (1)$$

Solve (1) by iterations: $\phi = \phi^{(0)} + \phi^{(1)} + \dots$. In the zeros approximation, $\phi^{(0)} = \phi_{\text{ext}}$. In the n th approximation

$$\begin{aligned} \phi(\vec{R}) &= \phi_{\text{ext}}(\vec{R}) - e/[(z+a)^2 + r^2]^{1/2} \\ &\times \left[\frac{1}{2} + \left(\frac{1}{2}\right)^2 + \left(\frac{1}{2}\right)^3 \dots \right] , \end{aligned} \quad (2)$$

giving the correct answer.

*Work supported by Department of Energy contract DE-AC03-76SF00515.

Note that although the final result satisfies the boundary condition, the result of any finite number of iterations does not. Hence, the solution is exact for each iteration, but the boundary conditions are satisfied only approximately.

The perturbation method based on Kirchhoff's integral equation gives [4] the impedances for the monopole and dipole modes

$$\begin{aligned} Z_l^0(k) &= -\frac{ikZ_0}{2\pi} \int dz a'(z) \int dz' a'(z') \int d\phi' \\ &\times [G_k(\vec{R}, \vec{R}')]_{r=a(z), r'=a(z')} \cos(\phi - \phi') e^{-ik(z-z')} . \end{aligned} \quad (3)$$

$$\begin{aligned} Z_l^{(1)}(k) &= -Z_0 \frac{ikrr_0 \cos \phi}{2\pi} \int d\phi \cos 2(\phi - \phi') \int dz dz' \\ &\times e^{-ik(z-z')} \left\{ \frac{a'(z) a'(z')}{a(z) a(z')} \right\} [G_k(\vec{R}, \vec{R}')]_{r=a(z), r'=a(z')} . \end{aligned} \quad (4)$$

The transverse impedance then is given by the Wenzel-Panofsky theorem.

Equations (3) and (4) give a close form of the longitudinal and transverse impedances for a cylindrically symmetric beam pipe, with an arbitrary variation of the pipe radius $a(z)$. From these equations it is also easy to obtain the longitudinal and transverse wakefields.

III. EXAMPLES OF LONGITUDINAL IMPEDANCE

For a hole in a beam pipe, the imaginary part of the impedance

$$\text{Im} Z_l(k) = \frac{w^2}{(2\pi)^2 a^2 c} \int_0^{2kL} \frac{dx}{x} \sin(x) . \quad 5$$

If the slot is short $kL \ll 1$, then

$$\text{Im} Z_l(k) = Z_0 \frac{kLw^2}{(2\pi)^3 a^2} \quad (6)$$

reproduces the Kurennoy's result [4]. The impedance increases with L for short slots $kL \ll 1$, and goes to a constant for $kL \gg 1$.

For a shallow cavity $(b-a) \ll a$, $g \ll a$, $k[g^2 + (b-a)^2]^{1/2} \ll 1$ the longitudinal impedance obtained from simulations with the code TBCI for long bunches is inductive [5]. We obtain for this case

$$L = \frac{Z_0(b-a)^2}{(2\pi)^2 a} f(\lambda) , \quad (7)$$

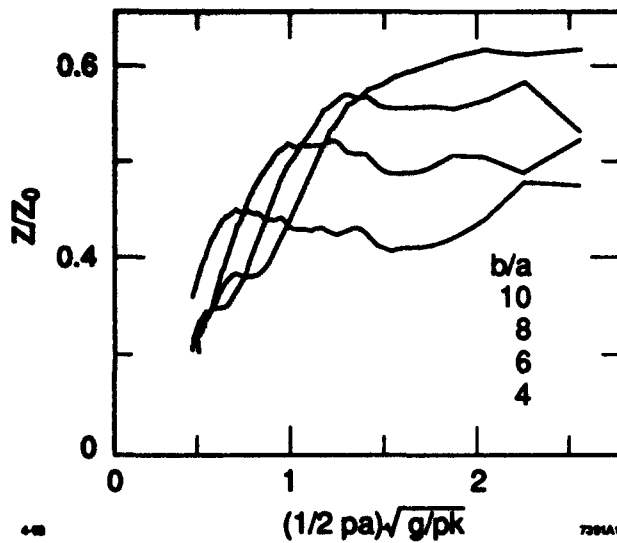


Figure 1. The real part of the longitudinal impedance of a cavity as a function of the Dome-Lawson parameter: $g/a = 3.0$, b/a in the range 2.0 – 6.0. The transition from the regime of a cavity to the regime of a step is shown.

where $\lambda = g/(b-a)$ and $f(\lambda) \approx 1$. For small $\lambda \ll 1$ it gives K. Baue's result.

For a shallow collimator the inductance

$$L = \frac{Z_0(b-a)^2}{4\pi a} \ln \left[\frac{2\pi a}{(b-a)} \right] + (3/2), \quad (8)$$

which is similar to the TBCI result

$$L = \frac{Z_0(b-a)^2}{(\pi a)}.$$

Impedance of a cavity in the high-frequency limit $kg \gg 1$, $ka \gg 1$, has been studied before [7]. The real part of the impedance is

$$\text{Re} Z_l = \frac{Z_0}{2\pi a} \left(\frac{g}{\pi k} \right)^{1/2}. \quad (9)$$

For this geometry, the general formula for the real part of the impedance is given by the interval $-k < p < k$:

$$\text{Re} Z_l^{(0)}(k) = \frac{kZ_0}{2\pi} \int_{-k}^k \frac{dp}{(k^2 - p^2)} \sin^2$$

$$\times \frac{g}{2} (k-p) [J_0(\Omega a) - J_0(\Omega b)]^2.$$

At high frequencies, $ka \gg 1$, $kb \gg 1$, we obtain the Dome-Lawson result (9).

For very large gaps g , the impedance does not depend on g , but depends on both radii. Transition from the regime of a cavity to the regime of a step occurs [7] at $g \approx k(b-a)^2$.

The result of the numerical integration of Eq. (10) is shown in Fig. 1.

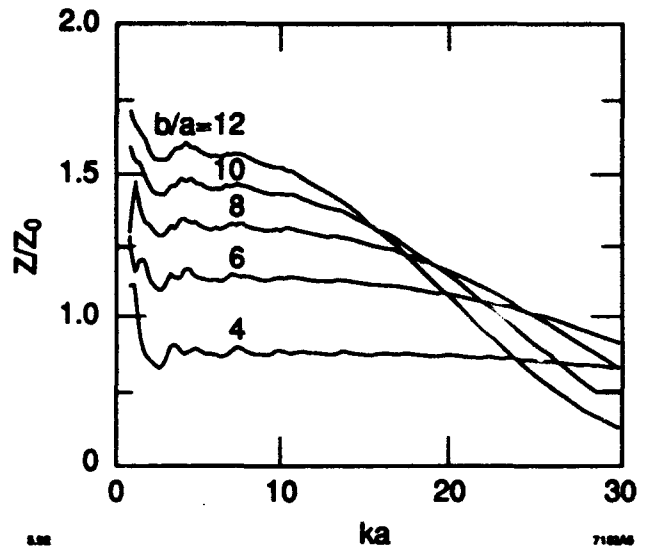


Figure 2. The frequency dependence of the impedance of a collimator. The impedance is constant for small ka and rolls off at large frequencies. The roll-off starts at frequencies dependent on the ratio of the radii.

The impedance of a collimator can be derived similarly to the impedance of a cavity. The impedance calculated from this formula is shown in Fig. 2.

The radius of a taper varies linearly from a to $b > a$ at distance L . The longitudinal impedance is

$$Z_l^{(0)}(k) = \frac{Z_0}{\pi} \ln \left(\frac{b}{a} \right) + \frac{kZ_0(a')^2}{8\pi} S(k), \quad (11)$$

where

$$S(k) = \int dp \int_0^L dz dz' \exp\{i(p-k)(z-z')\} \times [G_{1,p}(z, z')]_{r=a(z), r'=a(z')}. \quad (12)$$

The integral (12) can further be reduced to a single integral.

Results of the numerical integration of Eq. (12) are shown in Figs. 3, 4, and 5.

IV. CONCLUSION

The perturbation method described above reproduces numerous previously known analytical results. This method allows us to obtain all these results in a unified way as extreme cases of the same formula, and to demonstrate the transition from one case to another; for example, from the regime of a cavity to the regime of a step, or from a single cavity to a periodic array. The method can be generalized to more complicated geometries.

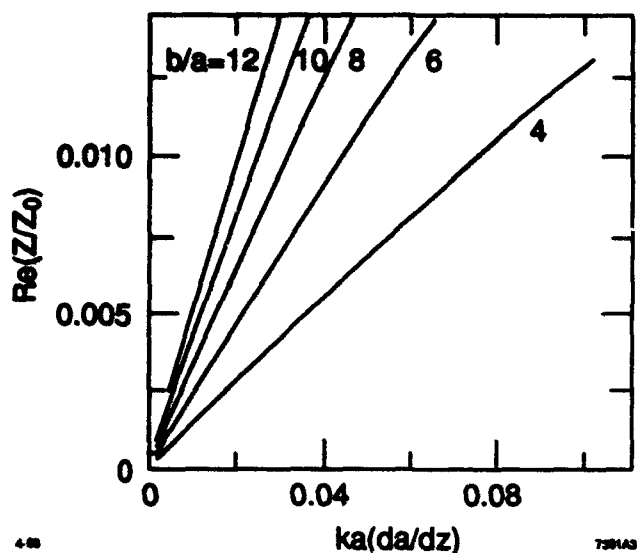


Figure 3. The real part of the longitudinal impedance of a taper, with large $p = b/a$.

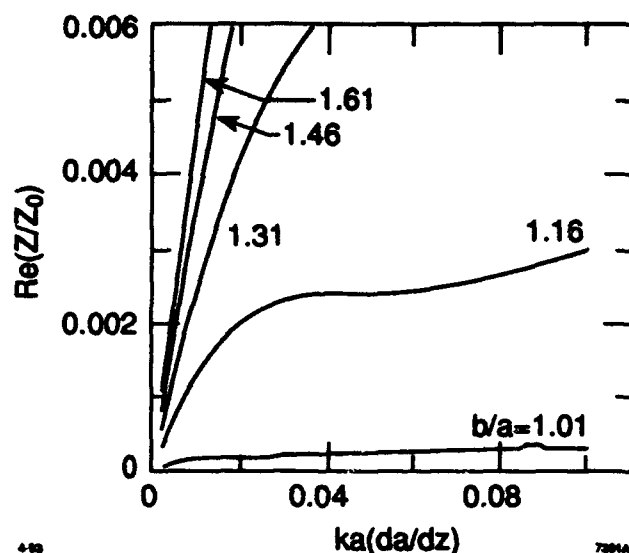


Figure 5. The transition from $(p-1) \ll 1$ to $(p-1) \simeq 1$.

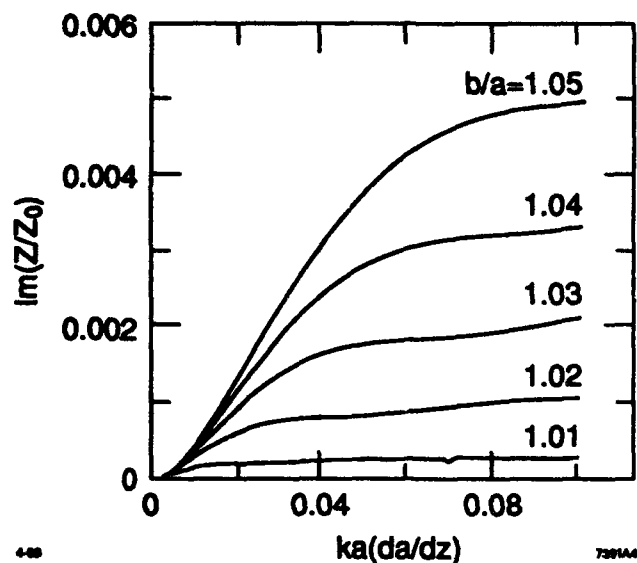


Figure 4. The real part of the longitudinal impedance of a taper, for small $(p-1) \ll 1$.

ACKNOWLEDGMENTS

I am thankful for discussions with K. Bane, S. Kheifets, M. Sands, M. Zolotarev, and B. Zotter.

REFERENCES

- [1] A. V. Novokhatsky, preprint INP, Novosibirsk (1989).
- [2] S. Heifets, "Diffraction Model of the High-Frequency Impedance," *Phys. Rev. D* **40**, 9, 3097-3106 (1989).
- [3] J. D. Jackson, *Classical Electrodynamics* (Wiley, New York, 1975).
- [4] S. S. Kurennoy, "On the Coupling Impedance of a Hole or Slot," CERN SL/91-29 (AP)/rev (1991).
- [5] K. L. F. Bane, "The Calculated Longitudinal Impedance of the SLC Damping Ring," SLAC-PUB-4618 (1988).
- [6] S. Heifets and S. Kheifets, "High Frequency Limit of the Longitudinal Impedance," *Part. Accel.* **25**, 2-4, 61-72 (1990).
- [7] J. J. Bisognano, S. Heifets, and B. C. Yunn, "The Loss Parameters for Very Short Bunches," CEBAF-PR-88-005 (1988); P. B. Wilson, LEP-70/62 (1978).

BROADBAND IMPEDANCE OF THE B FACTORY.

S. Heifets

Stanford Linear Accelerator Center
Stanford University, Stanford, CA 94309 USA

Abstract

The broadband impedance is described phenomenologically by expansion over $\sqrt{\omega}$. It is shown that different terms of the expansion correctly describe particular impedance-generating elements. The broadband impedance and the wake function of the B factory [1] are reconstructed with numeric code TBCI. The losses at the interaction region due to excitation of the higher order modes (HOM) are estimated.

I. INTRODUCTION

Impedance can be constructed as a sum of narrow-band and broad-band impedances. The narrow-band impedance is typical for the rf cavities and described in the modal analysis as the sum

$$Z(\omega) = i \sum \chi_l \left(\frac{1}{\omega - \omega_l + i\gamma_l} + \frac{1}{\omega + \omega_l + i\gamma_l} \right), \quad (1)$$

where χ_l and ω_l are the loss factor and the frequency of the l th mode and the width $\gamma_l = \omega_l/2Q_l$.

Broadband impedance often has been described empirically as the impedance of a single low-Q mode, but this is no more than data fitting, and has no other justification. Here, we further develop the approach used by K. Bane in his analysis of the impedance of the SLC damping ring [2].

Broadband impedance may be represented in the form of the expansion over $\sqrt{\omega}$ (we imply the time dependence $\exp\{-i\omega t\}$):

$$Z(\omega) = -i\omega L + R_\Omega + (1-i)\sqrt{\omega}B + (1+i)Z_C\sqrt{\omega_0/\omega} + \dots \quad (2)$$

The coefficients $L, R, B, Z_C \dots$ are real, as they follow from the analytic property of the impedance.

The first term represents inductive impedance. This behavior of the impedance at low frequencies also can be expected from Eq. (1) in the limit $\omega \rightarrow 0$, giving $L = -i\omega \sum (\chi_l/\omega_l^2)$. Impedance remains inductive for small discontinuities at rather high frequencies.

The second term in the expansion (2) is the low-frequency resistive impedance; the third term has the structure of the impedance of the resistive walls; and the last term describes the high-frequency tail of the impedance of the rf cavities. At high frequencies, the narrow-band impedance rolls off as ω^2 , and is small compared to the high-frequency tail,

$$\frac{Z(n)}{n} = (1+i) \frac{Z_{cav}}{n^{3/2}}.$$

At the bunch frequencies $\omega/c \simeq 1/\sigma$, this is very close to the SPEAR scaling

$$Z/n \propto \left(\frac{\sigma}{b}\right)^{1.68}, \quad (3)$$

where b is assumed to be equal to the beam-pipe radius.

*Work supported by Department of Energy contract DE-AC03-76SF00515.

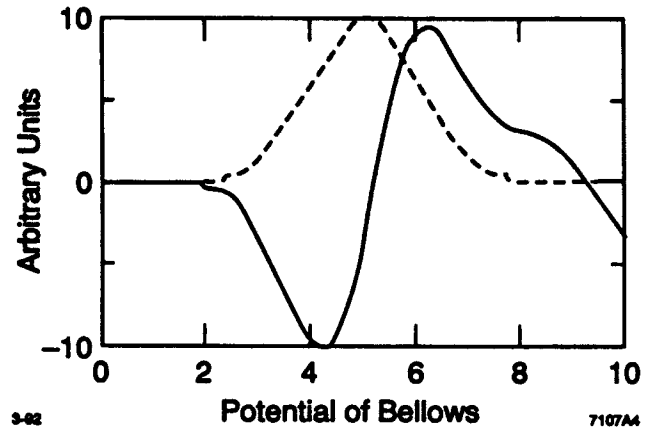


Figure 1. The wake potential of a bellow, as given by TBCI. The wake is typical for the discontinuities, giving inductive impedance.

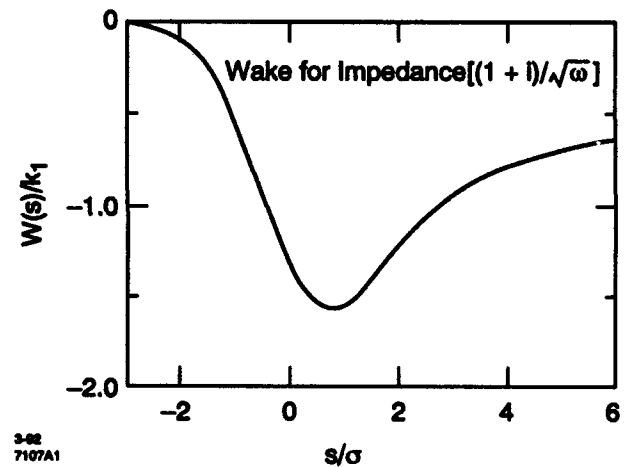


Figure 2. Wake $W(s)$ in units $\chi/(V/pC)$ for the model impedance.

Simulations show that, for the B factory, it is sufficient to describe the impedance by three parameters: inductance L , resistivity R_Ω , and the parameter Z_C . The wake function for these cases is quite different, being proportional to the bunch density $\rho W(s) = 4\pi(R_\Omega/Z_0)\rho(s)$ for constant $Z(\omega) = R_\Omega$, and to the derivative $W(s) = L(\partial\rho(s)/\partial s)$ for the inductive impedance [see Fig. 1]. The wake function in the last case has maximum and minimum at $s = \pm\sigma$:

$$W_{\max} = -W_{\min} = \frac{L}{\sqrt{2\pi e} \sigma^2}, \quad (4)$$

and the loss factor is zero. The dependence $W(s)$ for the last term in (2) [see Fig. 2] is quite similar to the behavior of the wake of the rf cavity given by TBCI [see Fig. 3].

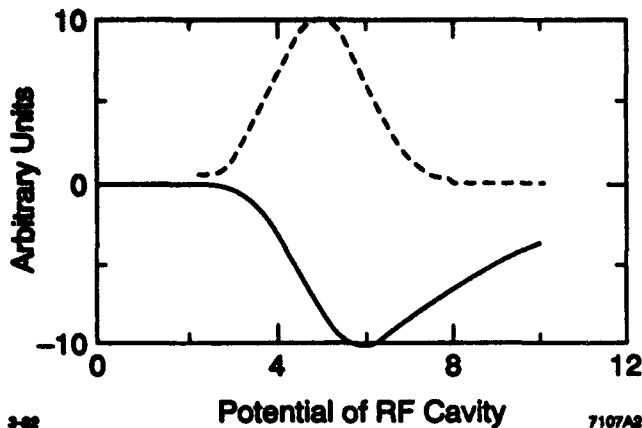


Figure 3. Wake $W(s)$ of the re-entrant rf cavity, given by TBCI.

In the following, we assume $R = 350$ m and $\sigma = 1$ cm.

II. IMPEDANCE GENERATING ELEMENTS

The main sources of the impedance are 20 re-entrant rf cavities. The rest comes from any variations of the cross-section of the beam pipe in the ring. Impedance-generating elements per 1/12 of the ring (12 cells of an arc and a straight section) are summarized in Table 1 (rf cavities, a feedback system, injection system, collimators, and the interaction region (IR) have to be taken into account, in addition to the elements given in the table). Some elements (for example, diagnostics) certainly will be added later. More details of the vacuum chamber may be found in the Conceptual Design Report (CDR) [1].

Table 1
Average number of the impedance-generating elements in 1/12 of the ring

Flanges	60
BPM	12
Vacuum ports	24
Bellows	12
Clearing electrodes	4
Valve	1
Taper	1
Slots of the distributed pumps	3.0×10^3 .

The parameter Z_C has been found from the known loss-factors of the low-frequency modes and the total loss factor given by TBCI for the re-entrant rf cavity. Resistive-wall impedance was found as the average over the copper elliptical pipe in the arcs and the round stainless steel pipe in the straight sections. The impedance of inductive elements were calculated using TBCI, Kurrenroy's formula for slots [3], and the analytic formula for shallow transitions,

$$L = 2g \frac{b-a}{a}.$$

Kickers for the feedback system and four-button BPMs were described using results of measurements [4]. The IR API-

ARY7.5E, generated by M. Sullivan, is a 3-dimensional structure with a number of tapers asymmetrically placed in the horizontal and vertical planes. The impedance was estimated using TBCI with proper azimuthal averaging. The wake field found by TBCI corresponds to the inductive impedance with $Z(n)/n = 1.8 \times 10^{-3} \Omega$, or $L = 2$ nH. The real part is small: $\text{Re}Z/n = 12.5 \Omega$. The total power deposition in the IR by two beams is

$$P_{\text{tot}} = e\langle\chi\rangle(I_{\text{avg}}^+ N_B^+ + I_{\text{avg}}^- N_B^-)$$

with the averaged currents specified in the CDR, $P_{\text{tot}} = 1.77$ KW. The contribution from the low-energy beam is about two times the contribution of the high-energy beam. This is very small compared to the power deposited by the synchrotron radiation (about 94 kW, M. Sullivan [1]).

The Ohmic losses are much smaller. The power deposition per unit length by a beam with n_B bunches in the ring is

$$\frac{dP}{dz} = n_B f_{\text{rev}} \left(\frac{e^2}{2\pi b} \right) \frac{N_B^2}{\sigma_z^{3/2}} \sqrt{\frac{2}{\sigma Z_0}} \Gamma\left(\frac{3}{4}\right).$$

For a beryllium pipe, $\sigma = 3.1 \times 10^5 \Omega^{-1}\text{cm}^{-1}$, $b = 2.5$ cm, that gives 0.86 W/cm for two bunches with CDR parameters $n_B = 1658$, $f_{\text{rev}} = 136$ KHz, $N_B = (4.08 \text{ and } 5.91 \times 10^{10})$. The power deposited in HOM will be absorbed mostly outside of the IR. The waves generated outside of the IR and absorbed within IR deposit very little energy, because the average loss factor per unit length outside of the IR (excluding rf cavities) is much smaller than that of the IR. Energy deposition could be enhanced substantially if there were trapped modes in the IR, provided their wave length is a multiple of the bunch spacing. We tried to find the trapped modes in the structure which reproduces the real structure within ± 25 cm from the IP and then is continued with the straight pipes. The MAFIA code (Kwok Ko simulations) failed to find trapped modes, although a single mode resembles such a mode [see Fig. 4]. This is not surprising in an open structure such as APIARY7.5E.



Figure 4. A candidate for a trapped mode at the IR; MAFIA output (Kwok Ko).

The total impedance is

$$Z(\omega) = -in \text{Im} \left(\frac{Z}{n} \right) + R_0 + 2.55 (1-i) \sqrt{n} + 5.55 \times 10^3 \frac{1+i}{\sqrt{n}} (\Omega).$$

The real part [see Fig. 5] is dominated by rf cavities and the stainless steel resistive walls. The rest of the ring gives a small contribution that can be described as a constant resistive impedance $R_0 = 117 \Omega$ given by bellows (75Ω), tapers (29.5Ω), and IR (12.5Ω).

The contributions to the inductive part of the parameter $\text{Im}(Z(n)/n)$ are given in Table 2.

With the contingency $Z(n)/n = 0.03 \Omega$ for the injection system and collimators, the total inductive impedance is $Z(n)/n = 0.10 \Omega$.

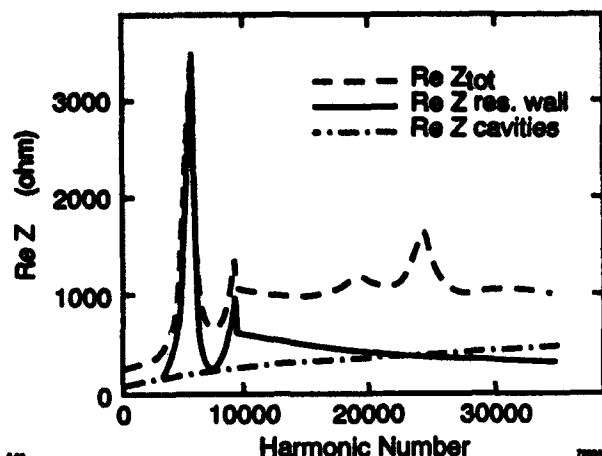


Figure 5. The real part of the longitudinal impedance.

Table 2
The impedance budget

BPMs	0.13×10^{-4}
Vacuum ports	0.5×10^{-4}
Bellows	0.62×10^{-2}
Flanges	0.001
Valves	0.006
Taper	0.016
DIP screen	0.030
Feedback system	0.0035
Interaction region	0.002
Injection crotches	3.6×10^{-3}
Total	<u>0.07</u>

The wake function is shown in Fig. 6. Figure 7 gives the partial contribution to the total wake from the impedances of resistive walls and the cavity, and correspondingly, the inductive and real parts of the impedance generated by discontinuities, from the Table 2.

ACKNOWLEDGMENTS

I am very thankful to Kwok Ko for simulations with MAFIA, and to K. Bane for useful discussions.

REFERENCES

- [1] "An Asymmetric B Factory, Conceptual Design Report," BL PUB-5303, SLAC-372 (1991).

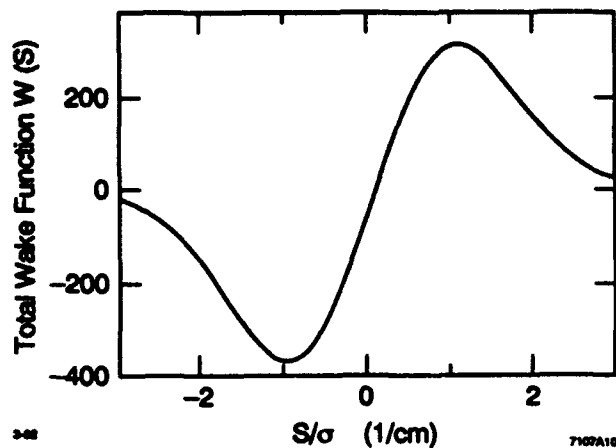


Figure 6. The total wake function.

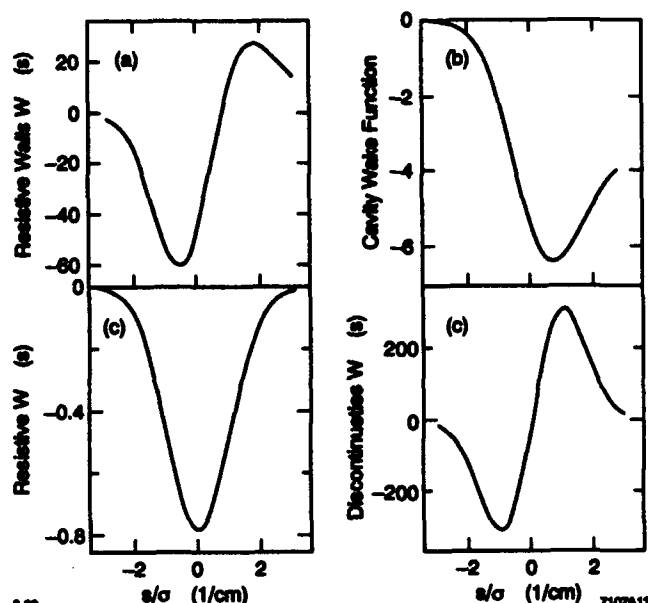


Figure 7. Partial contribution to the total wake from the impedances of (a) resistive walls, (b) cavity, (c) inductive, and (d) real parts of the impedance generated by discontinuities, correspondingly.

- [2] K. Bane, "The Calculated Longitudinal Impedance of the SLC Damping Ring, SLAC-PUB-4618 (1988).
- [3] S. S. Kurennoy, "On the Coupling Impedance of a Hole or Slot," CERN-SL/91-29 (AP) (1991).
- [4] A. Jacob and G. R. Lambertson, "Impedance Measurements on Button Electrodes," E-4, LSAP-46, LBL-25955.

STUDY OF A DETUNED ACCELERATING SECTION WITH THE COMPUTER PROGRAM *PROGON**

S. A. Heifets, S. A. Kheifets

Stanford Linear Accelerator Center, Stanford University, Stanford, CA 94309 USA

Abstract

The longitudinal coupling impedance for a number of lower passbands, bunch to bunch energy variation due to longitudinal wake fields, the beam loading compensation, some effects of production errors, and the rf pulse transmission through a detuned disk loaded accelerating section with finite wall conductivity have been studied using the computer program *PROGON*.

MOTIVATION AND METHOD

The detuned accelerating section [1] designed to diminish the undesirable effects of the transverse wake field has been studied previously using approximate methods. [2] [3] Here these results are confirmed by employing the new computer code *PROGON* [4] which is based on the field matching technique for the Fourier harmonics of the longitudinal electromagnetic (EM) travelling waves. The geometry of the considered 204 cell section is presented in Fig. 1a.

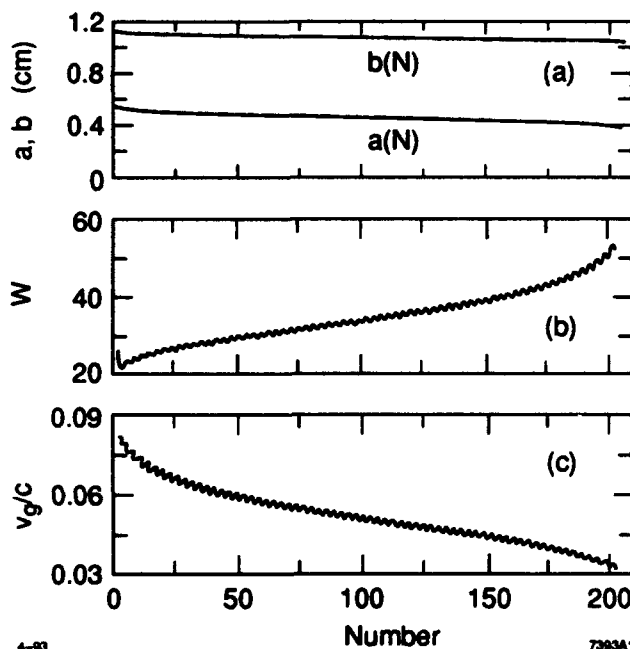


Figure 1. (a) The radii of the N th cavity $b(N)$ and iris $a(N)$ for the considered 204 cell section. The gaps $g(N) = 0.729$ cm, the iris thicknesses $l(N) = 0.149$ cm. (b) The stored energy in the N th cell $W(N)$. (c) The relative group velocity in the N th cell $v_g(N)/c$.

* Work supported by Department of Energy contract DE-AC03-76SF00515.

ACCELERATING FIELD

First, the EM fields in the structure, the corresponding stored energy $W(N)$ per cell and the power flow $S_z(N)$ through the cavity cross section are found. These quantities define the relative group velocity $v_g/c = S_z d/W$, where d is the cell length. The stored energy W and the group velocity v_g are plotted in Figs. 1b,c, respectively.

ERRORS AND DAMPING

Next, the effect of fabrication errors for infinite and finite wall conductivity on the excitation of and propagation through the section of a cylindrical accelerating wave with frequency f has been studied. The absolute values of the reflection $R(f)$ and the transmission $T(f)$ coefficients are plotted in Fig. 2 for 'small' relative random radii er-

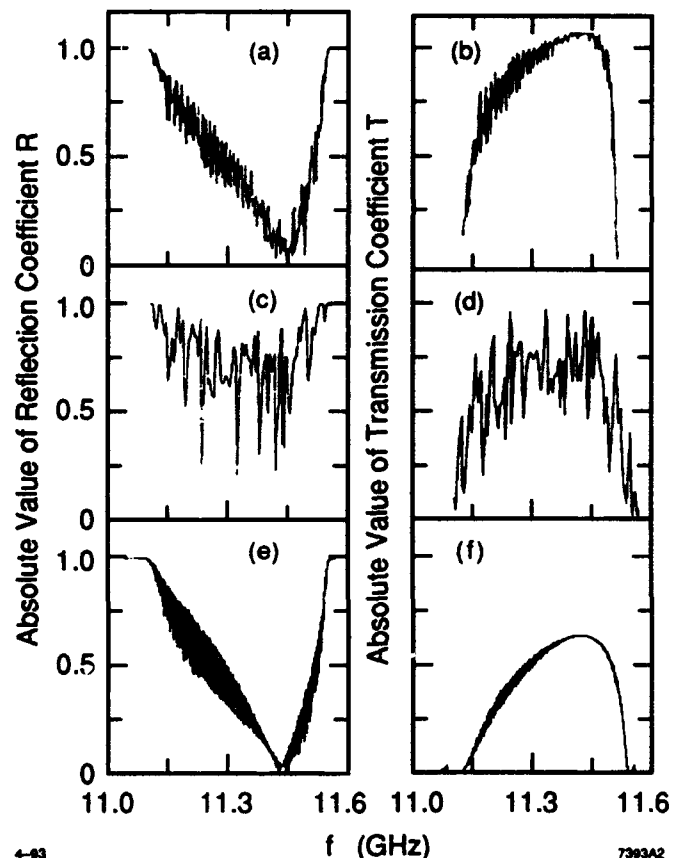


Figure 2. The absolute values of the reflection $R(f)$ and the transmission $T(f)$ coefficients: (a),(b) 'small' relative random radii errors in the range $\Delta a/a = \Delta b/b = \pm 2.5 \cdot 10^{-4}$; (c),(d) 'large' errors $\Delta a/a = \Delta b/b = \pm 2.5 \cdot 10^{-3}$; (e),(f) the finite conductivity of the copper walls.

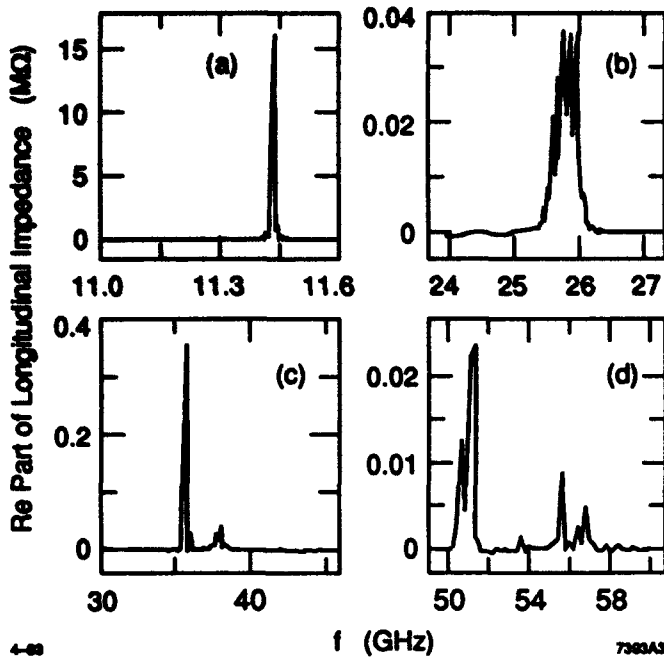


Figure 3. The real part of the longitudinal coupling impedance $Z_c(f)$ for a few lowest passbands.

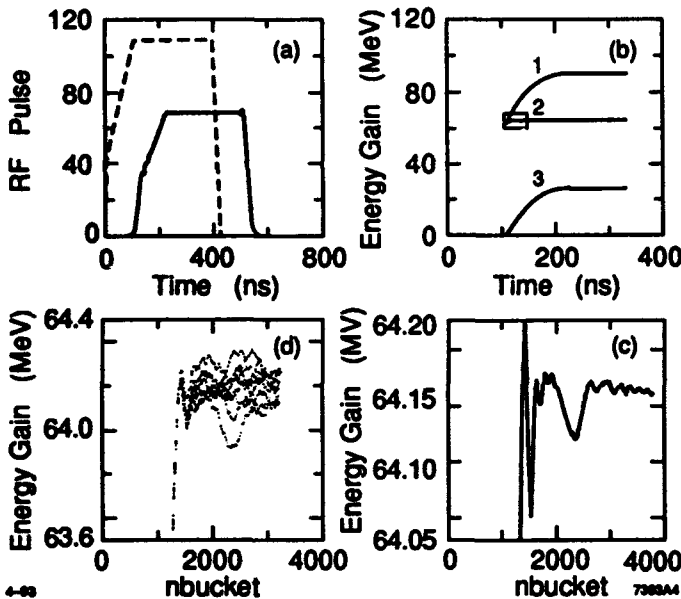


Figure 4. (a) The envelopes of the rf pulse at the entrance (dashed curve) and exit (solid curve); (b) The energy gain by a bunch in an accelerating wave with power $70.56 MW$ (curve 1), the energy loss due to wake fields of the previous bunches (curve 3) and their difference (curve 2) versus the bunch number. The number of electrons is $N_p = 0.7 \cdot 10^{10}$ per bunch. (c) A close up of part of curve 2 in Fig. 4b. (d) The effect of the random bunch population in the range $\Delta N_p/N_p = \pm 3\%$. This plot was obtained using ten different sets of random numbers for the same conditions as in Fig. 4b,c.

rors (Figs. 2a,b), for 'large' errors (Figs. 2c,d), and for the copper wall conductivity (Figs. 2e,f) without errors.

COUPLING IMPEDANCE

The real part of the longitudinal coupling impedance $Z_c(f)$ is presented in Fig. 3 for a few lower passbands.

PULSE TRANSMISSION

The distortion of an rf pulse transmitted through the detuned section with finite wall conductivity is illustrated in Fig. 4a where the envelopes of the rf pulse at the entrance (dashed curve) and the exit (solid curve) are plotted [5].

BEAM LOADING

The beam loading [6] for a long train of bunches is illustrated in Fig. 4b [7]. The energy gain by a bunch in an accelerating wave with power $70.56 MW$ (curve 1), the energy loss due to wake fields of the previous bunches (curve 3) and their difference (curve 2) are plotted versus the bunch number for the number of electrons $N_p = 0.7 \cdot 10^{10}$ per bunch. The impedance of the first passband only is taken into account for the wake field calculations. Fig. 4c is a close up of part of curve 2 in Fig. 4b. Fig. 4d illustrates the effect of the random bunch population in the range $\Delta N_p/N_p = \pm 3\%$.

ACKNOWLEDGEMENTS

We are grateful to K. Bane, R. Miller, R. Ruth and J. Wang for useful discussions.

REFERENCES

1. J.W. Wang, B.W. Littmann, "Design Study on Quasi-Constant Gradient Accelerating Structure," SLAC/AP-32, 1991.
2. R. Helm, "Computation of the properties of traveling-wave linac structures," SLAC-PUB-813 (1970).
3. K. Thompson, R. Ruth "Controlling Transverse Multi-bunch Instabilities in Linacs," Phys. Review D41, 964 (1990).
4. S.A. Heifets, S.A. Kheifets "Longitudinal Electromagnetic Fields in an Aperiodic Structures," SLAC-PUB-5907, 1992.
5. S.A. Heifets, S.A. Kheifets "RF Pulse Transmission through an Accelerating Section," SLAC Note AAS-74, September 1992.
6. R. Ruth, "Multi-bunch Energy Compensation," SLAC-PUB-4541, 1988.
7. S.A. Heifets, S.A. Kheifets "Study of the Energy Gain and the Beam Loading of the Detuned Structures with a Simple Model," SLAC/AP-96, January 1993.

Estimation of Broad Band Impedance of the SPring-8 Storage Ring

T. Nakamura
RIKEN-JAERI SPring-8 Project Team
Hirosawa 2-1, Wako-shi, Saitama JAPAN

Abstract

The broad band impedance of the vacuum chamber of the SPring-8 storage ring was estimated with several analytical equations and the numerical simulation with MAFIA T2. The estimated value of the total impedance is a few $10^{-1}\Omega$.

The vacuum chamber consists of the beam chamber and the slot-isolated antechamber. The effect of the obstacles in the slot is estimated numerically, which shows that the designed shape is effective to reduce the impedance of them.

I. INTRODUCTION

The broad band impedance of the vacuum chamber of the SPring-8 storage ring, which is a 8GeV electron/positron ring for a high brilliance light source, should be low enough to get the design current of 5mA/bunch with less than 2 times higher value of the energy spread than the natural. To meet this requirement, the vacuum chamber is carefully designed to reduce the discontinuities in the beam chamber.

The estimation of the impedance is performed with some theoretical and approximated equations and with the simulations by MAFIA[2] T2.

In numerical simulation with MAFIA T2, the approximation that the beam chamber has round shape of 20mm radius while the real shape is ellipse of 20mm \times 35mm, and several models of the wake factions such as cavitylike, inductive and resistive are assumed.

There exist obstacles in the slot and antechamber such as absorbers, pumping holes and NEG stripes. The effect of them are also estimated numerically with MAFIA T3 and S3.

II. MODEL WAKE FUNCTIONS

The models of the wake functions adopted here are cavitylike, inductive and resistive.

A. cavitylike

A cavitylike element is a groove with a larger gap and depth compared with the wave length of the wake field of interest.

The theoretical impedance of a cavitylike element of inner radius a and gap g is[3, 4, 5]

$$Z = \frac{Z_0}{2\pi} \frac{1}{a} \sqrt{\frac{cg}{\pi\omega}} (1+i) \quad (1)$$

,where $Z_0 = 377\Omega$.

The impedance can be obtained with MAFIA T2, assuming above frequency dependence of the impedance,

Elements	Number	Total Impedance $\frac{Z}{n} [\Omega]$	
		Equations	MAFIA T2
RF cavities	32	$1.5 \times 10^5 \frac{1+i}{n\sqrt{n}}$	$1.3 \times 10^5 \frac{1+i}{n\sqrt{n}}$
weldments	2000	$-0.005i$	$-0.006i$
flanges	700	$-0.005i$	$-0.005i$
offsets	2700	$-0.013i$	$-0.019i$
BPMs	300	$-$	$\frac{360}{n}$
pump slots	6000	$-\frac{72}{n}i$	$-$
bellows	400	$-$	$-0.040i$
valves	100	$-0.03i - \frac{2.3}{n}i$ $+ \frac{20}{n}$	$-$
BPMs	300	$\frac{1.2}{n}$	$-$
ID sections	40	$-0.018i$	$-0.012i$
resistive	$-$	$1.9 \frac{1-i}{\sqrt{n}}$	$-$
wall	$-$	0.026	$-$
synchrotron radiation	$-$	$-$	$-$

Table 1: Impedance of SPring-8 storage ring

with[6]

$$Z = \frac{1}{\frac{\Gamma(1/4)}{4} \frac{2\sqrt{e}}{\pi}} \sqrt{\sigma} k_l \frac{1+i}{\sqrt{\omega}} \quad (2)$$

,where σ is the bunch length(r.m.s.) and k_l is the loss parameter which MAFIA T2 can calculate.

B. inductive

The impedance of elements which have the discontinuities of the scale smaller than the wave length of the wake field of interest are inductive.

The theoretical impedance of a small rectangular groove is[7, 8]

$$Z = -i\omega \frac{Z_0}{2\pi c} \frac{g(b-a)}{a} \quad (3)$$

, where b is an outer radius of the groove.

The impedance of a pair of shallow transitions is approximated with the formula[9]

$$Z = -i\omega \frac{3Z_0}{2\pi c} \frac{a(b-a)^2}{b^2} \left(\frac{2\theta}{\pi} \right)^{\frac{1}{2}} \quad (4)$$

,where θ is the tapering angle.

The impedance can be obtained with MAFIA T2, assuming above frequency dependence, with[6, 10]

$$Z = -i\omega \frac{2\pi e}{c^2} \sigma^2 W_{max} \quad (5)$$

, where σ and W_{max} are the bunch length(r.m.s.) and the maximum value of the wake function which MAFIA T2 can calculate, respectively.

C. resistive

The simulation with MAFIA T2 shows that a groove which is deep compared with the wave length of the wake field of interest has resistive impedance of the form

$$Z = R \quad (6)$$

, and with this impedance, R can be obtained with MAFIA T2 with [6]

$$R = 2\sqrt{\pi} \frac{\sigma}{c} k_l \quad (7)$$

III. THE IMPEDANCE OF ELEMENTS

A. An RF cavity

An RF cavity has the beam pipe of 50mm radius and the acceleration gap of 220mm wide. The wake function obtained with MAFIA T2 shows that it has a cavitylike impedance as expected.

B. A flange

The gap of a flange is shielded with RF contact fingers. The residual discontinuity is a triangle groove of 0.5mm wide \times 1mm deep. The wake function calculated with MAFIA T2 shows that its impedance is inductive and the value of the impedance obtained with the Eq.(5) is almost half of the theoretical value of the impedance of the rectangular groove of 0.5mm wide \times 1mm deep, obtained with Eq.(3).

C. A weldment

A weldment is designed to be a rectangular groove smaller than 0.2mm wide \times 1mm deep.

D. An offset

The offset at the flange or at the weldment are designed to be less than 0.5mm. This is modeled as a step change of the radius of the beam pipe and estimated analytically with Eq.(4) and numerically with Eq.(5).

E. An insertion device section

An insertion device(ID) section consists of a pair of 5 degree taper transitions which connects the normal section of 35mm radius and the ID section of 10mm. The impedance is estimated analytically with Eq.(4). The wake function calculated with MAFIA T2 shows that the impedance is inductive.

F. A pump slot

The pumping slot is a longitudinal slot of 2mm wide \times 9mm long. The theoretical impedance is inductive and estimated with [3]

$$Z = -i \frac{Z_0 \pi w^2}{4(2\pi)^3 a^2} \quad (8)$$

, where w is the width of the slot.

G. A valve

The gap of a valve is shielded by RF contact fingers.

The valve consists of a triangle groove of 3mm wide \times 1mm deep, a deep groove of 0.5mm wide and 30 longitudinal slots of 0.5mm wide \times 100mm long between the

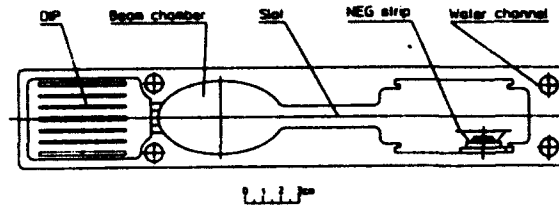


Figure 1: Cross section of the vacuum chamber.

RF contact fingers. the impedance of the triangle groove is estimated with Eq.(3) as in the case of the flange and the impedance of the slot is estimated with Eq.(8). and the slots is The wake function of the deep groove calculated with MAFIA T2 shows that its impedance is resistive. The total impedance is estimated by the sum of them.

H. Shielded bellows

Bellows are shielded with RF contact fingers. The shape of shielded bellows consists of an outward taper transition of 105mm long and 4mm high, an outward step of 1mm high and an inward taper transition of 50mm long and 5mm high.

The wake function calculated with MAFIA T2 shows that the impedance is inductive.

I. A beam position monitor

The button beam position monitor(BPM) is coaxial line with 0.5mm wide gap. This structure is modeled with a deep groove of 0.5mm wide The upper limit of the effect of BPM can be estimated with this model.

The wake function obtained with MAFIA T2 shows that its impedance is resistive and obtained with Eq.(7).

J. Resistive wall

The resistive wall impedance is estimated with the equation

$$Z = Z_0 \frac{1 - i \delta}{2 b} \quad (9)$$

,where $\delta = \sqrt{2/\omega \mu \sigma}$ is the skin depth.

K. Synchrotron radiation

The synchrotron radiation impedance is estimated with the equation

$$\left| \frac{Z}{n} \right| = 300 \frac{b}{R} \quad (10)$$

,where b, R is the radius of the vacuum chamber and the average radius of the machine.

IV. EFFECT OF OBSTACLES IN SLOTS AND ANTECHAMBERS

In the slot, there exist absorbers and pumping holes.

The effect of these obstacles in the slot and antechamber is estimated numerically with MAFIA T3 and S3.

The typical crosssection of a vacuum chamber are shown in Fig.1.

The structures used in this simulation with MAFIA T3 and S3 are shown in Fig.2 and Fig.3 ,respectively.



Figure 2: Model structure for MAFIA T3.

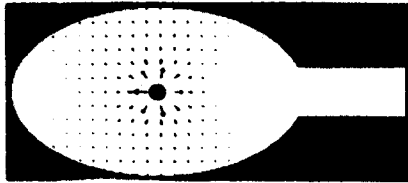


Figure 3: Model structure for MAFIA S3.

With MAFIA T3, which solves in time domain, the wake function was calculated for a test obstacle, which is a hole of 10mm long \times 10mm deep \times slot height high opened to the end wall of the slot.

The disturbance of the wall current causes the wake field hence the strength of the wake field can be estimated with the strength of the wall current.

With S3, which solves the electro-static problems, the wall current flowing at the end wall of the slot was calculated. The charge are placed at the beam axis and the induced charge on the end wall of the slot was calculated for several height and depth of the slot. This induced charge is proportional to the wall current.

The result for several height of slot (10mm, 12mm, 14mm) are shown in Fig.4. The relative strength of the wake field is parameterized by the peak value of the wake functions.

This result shows that the strength of the wake field and the wall current both depends only on $d = \text{depth/height}$ and the strength of the wake field and the strength of the wall current are proportional to $1/d^2$ and $1/d$, respectively.

V. CONCLUSION

The total impedance of the SPring-8 storage ring is estimated to be of the order of $10^{-1}\Omega$ for $n = \omega/\omega_{rev} \sim (c/\sigma)/\omega_{rev} \sim 2 \times 10^4$.

The numerical simulation shows that the obstacles in the slot should be at least $2 \times$ height apart from the beam chamber surface to reduce their effect and the design of the vacuum chamber fulfills this requirement. In this design, the width of the slot fulfills height/width > 4 , which is enough that the effect of the pumping system in the antechamber is negligible.

ACKNOWLEDGMENT

The author thanks the vacuum group of the SPring-8 storage ring and Bob Rimmer, LBL for helpful discussions on the chamber structures.

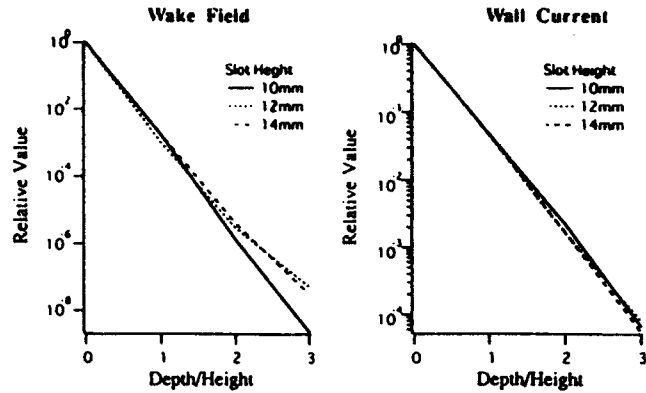


Figure 4: Relative strength of the wake functions(left) and the wall current on the end wall of the slot(right). Depth/Height is the depth from the beam chamber normalized by the slot height.

REFERENCES

- [1] W. Watanabe, et al., "Vacuum Chamber and Crotch Absorber for the SPring-8 Storage Ring Vacuum Chamber," this conference.
- [2] R. Klatt and T. Weiland, "Wake Field Calculations with Three-Dimensional BCI," Proc. of Linear Accelerator Conference, SLAC, (1986) 282.
- [3] S. Heifets, "Broad Band Impedance of Accelerating Structures: Perturbation Theory," SLAC-PUB-5792(1992).
- [4] G. D. Dôme, "Wake Potentials of a Relativistic Point Charge Crossing a Beam-Pipe Gap: An Analytical Approach," *IEEE Trans. Nucl. Sci.*, NS-32, No.5, 2531(1985).
- [5] R. L. Gluckstern, "High-frequency behavior of the longitudinal impedance for a cavity of general shape," *Phys. Rev. D* **39**, 2773(1989).
- [6] S. Heifets, "Broad Band Impedance of The B-Factory," SLAC/AP-93(1992).
- [7] K. L. F. Bane and M. Sands, "Wakefields of Very Short Bunches in an Accelerating Cavity," SLAC-PUB-4441(1987).
- [8] E. Keil and B. Zotter, *Particle Accelerators* **3** 11(1972).
- [9] K. L. F. Bane, "Bunch Lengthening in The SLC Damping Rings," SLAC-PUB-5177(1990)
- [10] M. Takao, T. Higo and K. L. F. Bane, "Estimation of the Longitudinal Impedance of the ATF Damping Ring," *Conference Record of the 1991 IEEE Particle Accelerator Conference*, Vol. 2, pp.506-508.

Head-On and Long-Range Beam-Beam Tune Shift Spread in the SSC

G. López

Superconducting Super Collider Laboratory*
2550 Beckleymeade Ave., Dallas, TX 75237 USA

Abstract

The head-on and long-range incoherent tune shifts for the Superconducting Super Collider (SSC) are estimated using the numerical integration of the analytical expression coming from the first order in the perturbation strength. The variation of the tune shift as a function of the displacements of the charged particle in the vertical and horizontal planes is studied with the nominal parameters for the SSC. A scaling expression is obtained for the parameters involved in the beam-beam tune shifts, which allows us to predict the effect in the incoherent tune shift spread under changes in these parameters.

I. INTRODUCTION

The tune shift spread (TSS) in a collider machine is one of the most important parameters in its design and operation. The spread must be limited to those values that avoid crossing dangerous resonances in the operation tune space of the machine. This crossing may produce instabilities in the beam, limiting the performance of the machine (beam lifetime and luminosity [1]), and creating radiation problems in the detectors themselves (beam-halo [2]). Therefore, it is desirable to keep the TSS as small as possible at the SSC. The most important contribution to the TSS comes from the beam-beam interaction (head-on and long-range). This TSS is due to the kicks given to the particles in one bunch by another bunch because of the nonlinear (in general) force felt by the particles of the two interacting bunches. One kick corresponds to the head-on collision (when actually the two interacting bunches are in the same line), which produces a negative TSS in both transverse directions. The other kick comes from the long range interaction in the intersection region (IR), where the beams have not yet been separated into different beam tubes. Assuming the crossing angle is in the vertical plane (y), this kick produces a negative tune shift in the horizontal plane (x) and a positive tune shift in the vertical plane, for y -amplitudes oscillate a little less than the separation of the close orbits of the two bunches, D_y . For a beam with Gaussian density distribution in both transversal planes, the exact expression for the tune shift experienced by a test particle due to head-on collision is well known [3]. This expression will be used in the study of the TSS.

*Operated by the Universities Research Association, Inc., for the U.S. Department of Energy under contract No. DE-AC35-80ER40486.

II. ANALYTICAL APPROXIMATION FOR HEAD ON AND LONG RANGE TSS

In general, the kick given to a particle (which has horizontal (x) and vertical (y) displacement from its own closed orbit) due to beam-beam interaction is given in the horizontal and vertical planes by

$$\Delta x' = -\left(\frac{4\pi\xi}{\beta}\right)\frac{2\sigma^2}{r^2} (1 - \exp(-r^2/2\sigma^2)) x \quad (1a)$$

and

$$\Delta y' = -\left(\frac{4\pi\xi}{\beta}\right)\frac{2\sigma^2}{r^2} (1 - \exp(-r^2/2\sigma^2)) (y + D_y), \quad (1b)$$

where β is the Courant-Snyder beta function, σ is the standard deviation in the Gaussian distribution of the particles, r is defined by $r^2 = x^2 + (y + D_y)^2$, and ξ (called the tune shift parameter) is defined as $\xi = -Nr_p\beta/4\pi\gamma\sigma^2$. N is the number of particles in the bunch, r_p is the classical radius of proton (e^2/mc^2), which has the value $1.5348 \times 10^{-18}m$, and γ is the relativistic factor, $\gamma^{-1} = \sqrt{1 - v^2/c^2}$.

Out of any resonance, the tune shifts are given at first order in the perturbation strength by Reference [4]:

$$\frac{\Delta\nu_x}{\xi} = \int_0^1 du e^{-pu} [I_0(\alpha_1 u) - I_1(\alpha_1 u)] \left[I_0(\alpha_2 u) + \sum_{n=1}^{\infty} \frac{(a_y d_y u)^{2n} n!}{2^n (2n)!} \sum_{k=0}^n \frac{(-1)^k}{k!(n-k)!} \frac{d^k I_0(\alpha_2 u)}{d(\alpha_2 u)^k} \right] \quad (2a)$$

and

$$\frac{\Delta\nu_y}{\xi} = \int_0^1 du e^{-pu} I_0(\alpha_1 u) \left[I_0(\alpha_2 u) - I_1(\alpha_2 u) + \sum_{n=1}^{\infty} \frac{(a_y d_y u)^{2n} (n+1)!}{2^n (2n)!} \sum_{k=0}^{n+1} \frac{(-1)^k}{k!(n+1-k)!} \frac{d^k I_0(\alpha_2 u)}{d(\alpha_2 u)^k} - \sum_{m=1}^{\infty} \frac{a_y^{2m-2} d_y^{2m} u^{2m-1} m!}{2^{m-1} (2m-1)!} \sum_{k=0}^m \frac{(-1)^k}{k!(m-k)!} \frac{d^k I_0(\alpha_2 u)}{d(\alpha_2 u)^k} \right] \quad (2b)$$

where $d_y = D_y/\sigma$ is the relative separation between the orbits of the colliding bunches, $s_i = \sin(\psi_i)$ and $\psi_i = \phi_i + 2\pi\nu_i t$ for $i = x, y$. $I_\nu(z)$ are the Bessel functions of imaginary argument; p and α_i 's are defined as $p = \alpha_1 + \alpha_2 + d_y^2/2$ and $\alpha_i = a_i^2/4$, $i = x, y$.

III. HEAD-ON AND LONG-RANGE TUNE SHIFT FOR THE LOW- β IR

Using the above analytical approximation and making a numerical integration of these expressions, the TSS can be calculated for the nominal parameters of the SSC collider. These calculations will be made mainly for the low- β IR, but the medium- β IR will be considered at the end of this section and in the next section.

A. Head-On and Long-Range Tune Shift

Making $d_y = 0$, the relative horizontal head-on tune shift predicted by Eq. (2) is shown in Figure 1 (for the vertical case, A_x and A_y are inverted). as a function of the amplitudes. Using the relation between the beam size and the Courant-Snyder parameters, the beta function (β) and the relative emittance (ϵ), $\sigma = \sqrt{\epsilon\beta/\gamma}$, the tune shift parameter is expressed as

$$\xi = -\frac{Nr_p}{4\pi\epsilon} \quad (3)$$

With the nominal values for the SSC, $N = 7.5 \times 10^9$ and $\epsilon = 10^{-6}m$, the value of the tune shift parameter obtained is $\xi = -0.000916$. Figure 2 shows the TSS due to the head-on case.

For the long-range tune shift, $d_y \neq 0$ and the tune shift parameter (3) has to be multiplied by the number of long-range interactions for the two low- β IRs, $2(2L/S_B)$, where S_B is the separation between the colliding bunches. This defines a new parameter, $\xi_L = \frac{4L}{S_B}\xi$, for the long-range tune shifts. Using the relation between the separation, D_y , the long-range interaction length, L , and the crossing angle, α ($D_y = \alpha L$), the relative closed orbits separation can be written in terms of the crossing angle, α ($D_y = \alpha L$), the long-range interaction length, L , the energy, γ , and the Courant-Snyder parameters, β and ϵ , as $d_y = D_y \sqrt{\gamma/\epsilon\beta} = \alpha L \sqrt{\gamma/\epsilon\beta}$. In addition, assuming a pure drift space during the long-range interaction, where the beta function is given by $\beta(L) = \beta^* + L^2/\beta^* \simeq L^2/\beta^*$, then, the relative closed orbit separation can be written in the form $d_y = \alpha \sqrt{\beta^* \gamma \epsilon}$. For the low- β IR, $\beta^* = 0.5$ m, and at the highest energy, $\gamma = 2 \times 10^4$, this parameter has the simple expression

$$d_y = 10^5 \alpha \quad (4)$$

Using the nominal crossing angle, $\alpha = 75 \mu\text{rad}$, Figure 3 and Figure 4 show the relative (with respect to ξ_L) tune shifts as a function of the amplitudes a_x for some a_y 's. Finally, for the nominal values, $L = 75$ m and $S_B = 5$ m ($4L/S_B = 60$ long-range collisions),

the total TSS (head-on plus long-range) is shown in Figure 5 for the above nominal values.

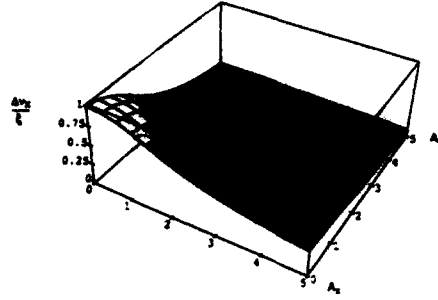


Figure 1. Relative horizontal head-on tune shift.

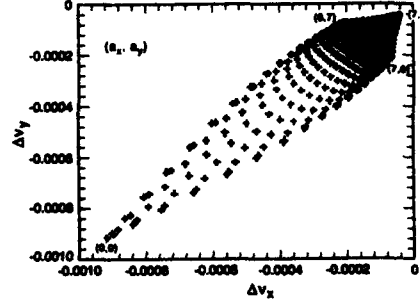


Figure 2. Head-on tune shift with the nominal SSC low- β IR parameters.

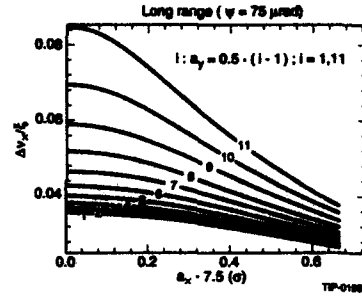


Figure 3. Relative horizontal long-range tune shift.

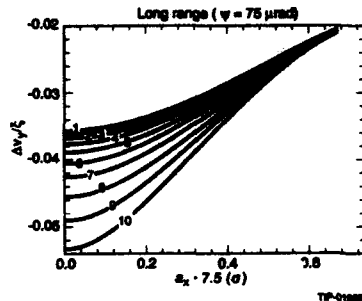


Figure 4. Relative vertical long-range tune shift.

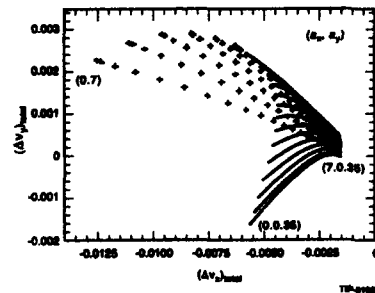


Figure 5. Total TSS with one low- β IR, $\alpha = 75 \mu\text{m}$.

B. Maximum Long Range Tune Shift

The relative horizontal long-range tune shift reaches its maximum value when the horizontal amplitude is zero and the vertical amplitude (almost true for the vertical plane) has its maximum allowed value ($a_x = 0$ and $a_y = a_y^{max}$). This observation helps to simplify the analysis of the maximum relative tune shift as a function of the crossing angle, since the maximum tune shifts can be calculated from the following expressions. (See Reference [4].)

$$\left(\frac{\Delta\nu_x}{\xi}\right)_L^{max} = \frac{1}{\pi} \int_0^{2\pi} \frac{(1 - e^{-s_{xy}/2})}{s_{xy}} d\psi_y \quad (5a)$$

and

$$\left(\frac{\Delta\nu_y}{\xi}\right)_L^{max} \simeq \frac{2}{\pi} \int_0^{2\pi} \frac{(1 - e^{-s_{xy}/2}) (s_y^2 + \frac{d_y}{a_y^{max}} s_y)}{s_{xy}} d\psi_y, \quad (5b)$$

where s_{xy} is defined as $s_{xy} = -(a_y^{max} s_y + d_y)^2$.

The maximum long-range tune shifts expected for the SSC as a function of d_y and for several maximum amplitudes a_y^{max} are shown in Figure 6. In the same way, the maximum tune shifts expected as a function of the maximum vertical amplitude are shown in Figure 7.

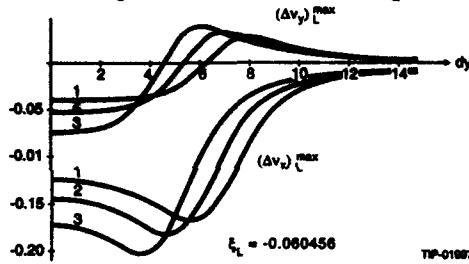


Figure 6. Maximum LRTS in one low- β IR, $a_x = 0$; and 1: $a_y=7$; 2: $a_y=6$; 3: $a_y=5$.

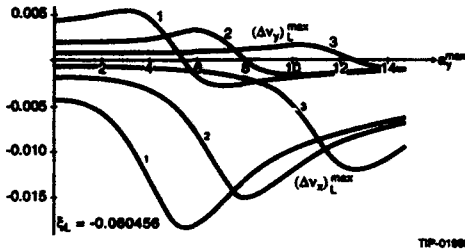


Figure 7. Maximum LRTS in one low- β IR, $a_x = 0$; and 1: $\alpha=50 \mu\text{rad}$; 2: $\alpha=75 \mu\text{rad}$; 3: $\alpha=120 \mu\text{rad}$.

IV. MAXIMUM TUNE SHIFT SCALING

The maximum head-on tune shift has the following dependence: $(\Delta\nu_{x,y})_{ON}^{max} \sim -\frac{N}{\epsilon}$. The maximum long range tune shifts vary, for not very high vertical amplitudes ($a_y \leq 5d_y/6$), as $(\Delta\nu_x)_L^{max} \sim -N\beta(L)/LS_B\gamma\alpha^2$ and $(\Delta\nu_y)_L^{max} \sim +N\beta(L)/LS_B\gamma\alpha^2$. Therefore, the total maximum tune shifts in the horizontal and vertical planes are

$$(\Delta\nu_x)_T^{max} = -N \left(\frac{f_1}{\epsilon} + \frac{f_2\beta(L)}{LS_B\gamma\alpha^2} \right) \quad (6a)$$

and

$$(\Delta\nu_y)_T^{max} = -N \left(\frac{f_1}{\epsilon} - \frac{f_2\beta(L)}{LS_B\gamma\alpha^2} \right), \quad (6b)$$

where f_1 and f_2 are integration factors. Using the approximation $\beta(L) \simeq L^2/\beta^*$ and the nominal values for the SSC collider, and considering two low- β and two medium- β IR ($n_{low\beta} = n_{med\beta} = 2$), the following scaling relation is obtained for the maximum horizontal tune shift (similar relation for the vertical):

$$(\Delta\nu_x)_T^{max} = -0.000916 n_o^* N_o / \epsilon_o - \frac{0.0125 N_o}{S_{Bo}\gamma_o} \left[\left(\frac{n_o L_o}{\beta_o^* \alpha_o^2} \right)_{low\beta} + \frac{1}{10} \left(\frac{n_o L_o}{\beta_o^* \alpha_o^2} \right)_{med\beta} \right], \quad (7)$$

where the subindex (o) in $N_o, \epsilon_o, S_{Bo}, \gamma_o, L_o, \beta_o^*, \alpha_o$, and $n_o^* = n_{low\beta} + n_{med\beta}$, means its relative values with respect to the nominal ($N = 7.5 \times 10^9$, $\epsilon = 10^{-6}$ m, $S_B = 5$ m, $\gamma = 2 \times 10^4$, $L_{low\beta} = 75$ m ($L_{med\beta} = 150$ m), $\beta_{low\beta}^* = 0.5$ m ($\beta_{med\beta}^* = 10$ m), $\alpha = 75 \mu\text{rad}$, and $n_o^* = 4$).

Making $\alpha_o \geq 1.6$ ($\alpha \geq 120 \mu\text{rad}$) and keeping all other parameters equal to one, the maximum TSS can be reduced to a tolerable value for the SSC (Figure 8). Notice from these expressions that collision at lower energies worsens the long-range tune shift.

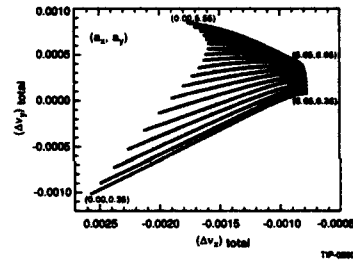


Figure 8. Total TSS with one low- β IR, $\alpha=120 \mu\text{rad}$.

V. CONCLUSIONS

Using the first approximation in the incoherent perturbative beam-beam strength, the tune shift spread was estimated for the SSC collider. The results suggests that this TSS may be large for the SSC collider with the nominal SSC parameters, and the beam-beam tune shift moves toward or outward the line $\nu_x = \nu_y$ in the tune shift space (depending of the location of the selected operational point). They establish that by increasing the crossing angle up to at least $120 \mu\text{rad}$, it is possible to bring down the TSS to tolerable values for the SSC.

VI. REFERENCES

- [1] L. R. Evans and J. Gareyte, "Beam-Beam Effects," CERN-SPS/86-8 (1986).
- [2] S. Peggs, *Particle Acc.*, Vol. 17, 11-50 (1985).
- [3] J. Le Duff, *VII Int. Acc. Conf.*, CERN (1971).
- [4] G. López, SSCL-442 (1991).

Beam-Beam Effects with Errors in the Crab Compensation*

David Sagan

Laboratory of Nuclear Studies, Cornell University, Ithaca, NY 14853

Abstract

The effect of the beam-beam interaction in the presence of errors in the crab compensation for a crossing angle is shown to be asymmetric with respect to both beams. A comparison with experience at CESR with colliding beams with dispersion indicates that the tolerances for the crab compensation are not stringent.

Introduction

In terms of the beam-beam interaction, the parameters under which the Cornell B-factory CESR-B would operate correspond approximately to parameters under which the present CESR storage ring is currently running. There is, however, one exception. The CESR-B design calls for a 24 mrad full crossing angle θ_{cross} with transverse 'crab' compensation in which a pair of RF cavities are used to give a time-varying sideways kick to a bunch as it passes through either cavity[1]. With 'perfect' crab compensation the bunches of each beam would be tilted at the IP by an angle $\theta_{crb} = \theta_{cross}/2$. In this case, the beam-beam kick is modified by a factor $\cos^2(\theta_{cross})$ [2]. This change in kick is independent of position and thus with perfect crab compensation an angle crossing would not excite any additional synchrotron resonances. The problems with a crab compensation scheme are therefore caused by imperfections in the compensation. These errors can come from various sources. Possibilities include errors in the betatron phase advance from the crab cavities to the IP, the finite wavelength of the crab cavity RF, etc. The purpose of this paper is to explore the effect upon the beam-beam interaction due to imperfections in the crab compensation scheme proposed for CESR-B.

Theory

In the 'weak-strong' picture of the beam-beam interaction one beam (the 'strong' beam) is held fixed in shape while particles of the 'weak' beam are allowed to interact with the first beam. The beam-beam interaction can be described by an Interaction Hamiltonian H_I . For head-on collisions with zero angle crossing and no crabbing

$$H_I(x, p_x, y, p_y, t) = \bar{\epsilon} \sum_{n=-\infty}^{\infty} \bar{V}(x, y) \frac{2c}{\sqrt{2\pi\sigma_s^2}} \exp[-(2s_n(t) + z)^2/(2\sigma_s^2)], \quad (1)$$

where σ_s is the strong bunch length, n is the revolution number, x , y , and z are the transverse and longitudinal displacements of a weak beam particle, \bar{V} is the normalised potential, and $s_n(t)$ is the offset of the center of the weak bunch from the IP on the n^{th} revolution

$$s_n(t) = ct - ns_0, \quad (2)$$

with s_0 being the ring circumference. The normalisation factor $\bar{\epsilon}$ is given by $\xi_x \sigma_x^2 / \beta_x$ with ξ_x being the horizontal beam-beam strength parameter, σ_x is the strong beam horizontal width, and $\beta_x(s)$ is the horizontal beta function.

The arguments of $\bar{V}(x, y)$ are the transverse offsets from the centerline of the strong bunch. With head-on collisions these offsets are just due to the betatron oscillations displacements x_β and y_β . With a finite crossing angle or a finite crab angle in the horizontal plane the horizontal offset is now dependent upon s_n and z as shown in Figure 1. The potential \bar{V} in equation (1) must be replaced by

$$\bar{V}(x, y) \rightarrow \bar{V}(x_\beta + \theta_{cross} \cdot (s_n + z) - \theta_{crb,s} \cdot (2s_n + z) - \theta_{crb,w} \cdot z, y_\beta), \quad (3)$$

where $\theta_{crb,s}$ and $\theta_{crb,w}$ are the crab angles of the strong beam and weak beam respectively. V is now dependent upon z which indicates that synchrotron resonances will be excited. Perfect crabbing is seen to be achieved when the z dependence is eliminated in V . This is achieved when

$$\theta_{crb,s} = \theta_{crb,w} = \frac{1}{2} \theta_{cross}. \quad (4)$$

Simulation Program

The simulation program used for this report is a version of the program developed by Bob Siemann and Srinivas Krishnagopal[3] modified to include crab compensation. Briefly, the program is a full 3-dimensional tracking simulation. Outside of the IR transport is linear with fluctuation and radiation damping effects included. At the IR the dependence of the strong beam size upon the quadratic variation of the horizontal and vertical betas is taken into account. For the beam-beam interaction the strong beam is divided into 5 equal charge slices. Particles of the weak beam are kicked as they move past the centers of the slices and between kicks particles are propagated freely. At the crab cavities the finite wavelength of the RF is taken into account. Between the crab cavities and the IP and in the arc horizontal chromaticity effects are included. A partial input parameter list used by the simulation program is given in Table 1. With the given parameters the tune

*Work supported by the National Science Foundation

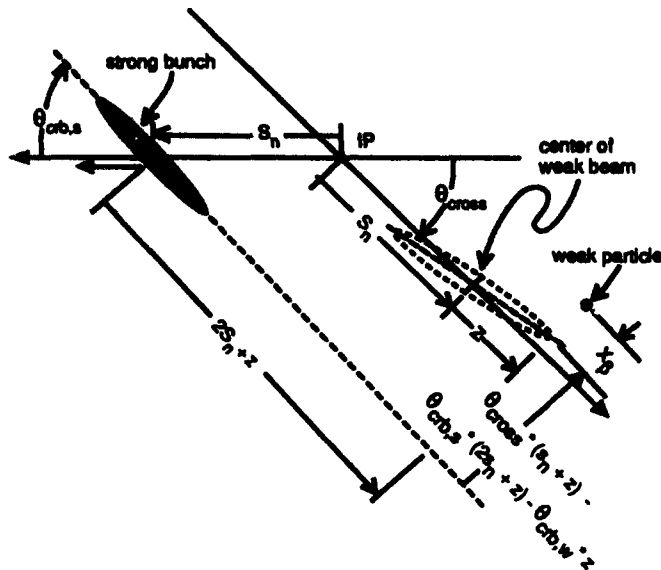


Figure 1: Beam-Beam interaction with a crossing angle and crabbing.

shifts due to the strong beam were $\xi_x = \xi_y = 0.03$. 200 particles were tracked in the simulation. The particles were allowed to equilibrate for 3 transverse damping times (15,000 turns) and after this the average weak beam sizes in the horizontal and vertical planes were calculated using the particle's coordinates over the next 7,000 turns.

Figures 2 and 3 show the effect of varying the weak and strong crabbing angles in the presence of a 24 mrad crossing angle. In the figures $V_{crb,w}$ is the normalized voltage of the crab cavities for the weak beam. $V_{crb,w}$ is proportional to $\theta_{crb,w}$ with the normalisation such that that with no other compensation errors $V_{crb,w} = 1$ gives a perfect crab angle of $\theta_{cross}/2$. In each figure the beam sizes have been normalised by the initial beam sizes σ_{x0} and σ_{y0} that the weak beam would have without the beam-beam interaction.

Figure 2 shows the effect of varying the weak crab angle while the strong beam is maintained at a perfect crab angle of 12 mrad. Figure 2 shows a steady increase in beam size with increasing deviation of $V_{crb,w}$ from a value of 1. This is to be compared with Figure 3 in which $V_{crb,w}$ is held constant at 1 and the strong crab angle is allowed to vary. Figure 3 shows that the beam sizes are virtually independent of $\theta_{crb,s}$. This result can be explained in part with the help of equation (3): Consider the horizontal offset of a particle from the strong beam centerline as it passes a given section of the strong beam located a longitudinal distance z_s from the center of the strong beam. When the particle passes this section one has (cf. Figure 1)

$$z_s = 2s_n + z. \quad (5)$$

Thus the horizontal offset term in equation (3) involving $\theta_{crb,s}$ can be rewritten as

$$\theta_{crb,s} \cdot (2s_n + z) = \theta_{crb,s} \cdot z_s. \quad (6)$$

Parameter	Symbol	Nom. Value
Trans. damping	δ_{damp}	$2 \cdot 10^{-4}/\text{turn}$
Horis. emittance	ϵ_x	$1.3 \cdot 10^{-7} \text{ m}$
Vert. emittance	ϵ_y	$1.95 \cdot 10^{-9} \text{ m}$
IP Horis. beta	$\beta_x(ip)$	1.00 m
IP Vert. beta	$\beta_y(ip)$	0.015 m
Synch. tune	Q_s	0.085
Horis. tune	Q_x	0.632
Vert. tune	Q_y	0.587
Strong bunch length	$\sigma_{z,strong}$	0.01 m
Weak bunch length	$\sigma_{z,weak}$	0.01 m
Crossing angle	θ_{cross}	0.024 rad
Crab RF wavelength	λ_{RF}	0.6 m
IP Dispersion	$\eta(ip)$	0.0 m
Strong beam Current	I_{strong}	3.78 mA
Test particle number	$n_{particle}$	200
Horis. chromaticity	$Q'_{x,tot}$	2
IP to cavities chrom.	$Q'_{x,crb \rightarrow ip}$	-6

Table 1: Simulation Program Partial Parameter List

This part of the horizontal offset is independent of z . That is to say, as far as the strong crab angle is concerned, the synchrotron motion does not produce any amplitude modulation of the beam-beam interaction. There is, on the other hand, betatron phase modulation of the beam-beam interaction due to the $\theta_{crb,s}$ term and this does lead to synchrobetatron resonances. For CESR-B conditions, however, these phase modulation driven resonances only have a small effect on the beam. In fact, in the limit of large β_x , where the phase advance across the IR is negligible, there are no first order resonances associated with $\theta_{crb,s}$ [4]. Of course, the above results do not preclude the possibility of the resonances associated with $\theta_{crb,s}$ having an appreciable effect under different conditions (e.g. with small beta's, etc.). However, for CESR-B, the above results show that there will be an asymmetry between the effect that a crabbing error of one beam will have upon the two beams.

Comparison with Dispersion

One important question to answer is how the synchrobetatron resonances scale with variations in beam sigmas, etc. An analysis of the interaction Hamiltonian (eq (1)) shows that for equally sized beams there are 6 independent parameters that determine the resonance strengths[4]. In practice one would like to have a single overall 'figure of demerit' for imperfections in a crab compensation scheme. For beams of equal size and equal crab angles, a 'natural' scaling parameter is κ_c defined by

$$\kappa_c \equiv \frac{\theta_{err} \sigma_z}{\sigma_x} = \frac{(\theta_{cross} - 2\theta_{crb}) \sigma_z}{\sigma_x}. \quad (7)$$

The numerator of the RHS of equation (7) is the length scale of the (time varying) displacement of a particle of

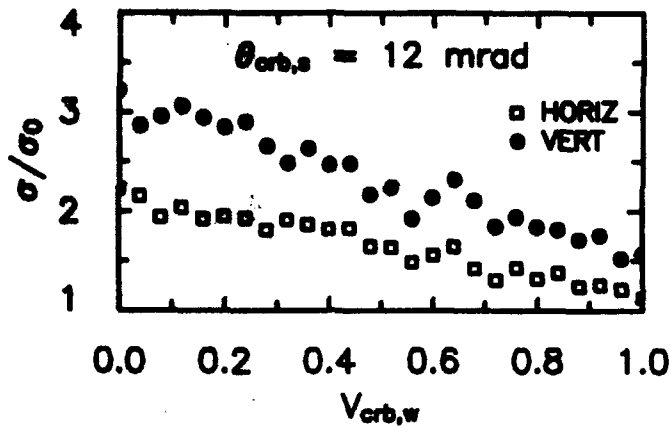


Figure 2: Weak beam sizes as a function of the weak beam crab cavity voltage with no error in the strong beam crab angle.

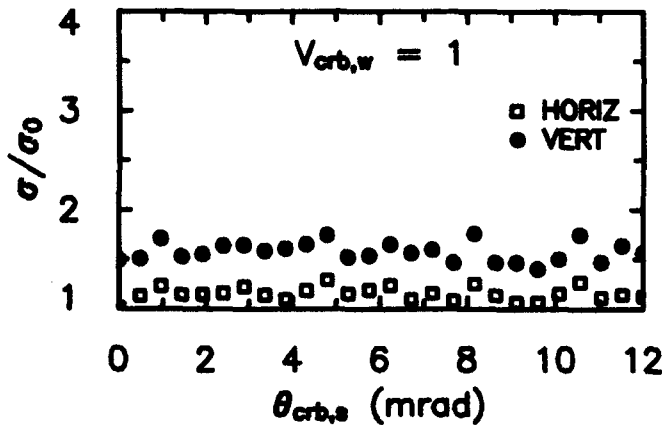


Figure 3: Weak beam sizes as a function of the strong beam crab angle with no error in the weak beam crab cavity voltage.

one bunch from the centerline of the other bunch due to errors in the crab compensation. The denominator of the RHS of (7) is the characteristic length scale upon which the beam-beam force varies. κ_c is thus a measure of the modulation of the beam-beam force due to any compensation errors.

An analysis of figures 2 and 3 show that in the simulations if the crab compensation errors obey $\kappa_c \lesssim 0.1$ the effect on the beam sizes of imperfections in the compensation is small. Additional evidence for setting a bound of $\kappa_c \lesssim 0.1$ comes from the operating experience of the CESR ring with a finite dispersion at the IP. While there is, in general, no strict equivalence between the effect of finite dispersion and the effect of a finite crossing angle, there is a special case within the weak-strong framework where there is a direct proportionality between the two. This happens when both beams are crabbed at the same angle and

$$(\theta_{cross} - 2\theta_{crb}) \cdot \sigma_{z,strong} \ll \sigma_{z,strong}, \text{ and} \quad (8)$$

$$\sigma_{z,strong} + \sigma_{z,weak} \ll \beta_x, \quad (9)$$

Param	Typ. Value	Param	Typ. Value
$\beta_x(ip)$	1.00 m	σ_{p_x}	$6 \cdot 10^{-4}$
$\beta_y(ip)$	0.015 m	σ_z	1.7 cm
$\eta_x(ip)$	0.5 m	$\sigma_x(ip)$	$5 \cdot 10^{-4}$ m
$\xi_{x,max}$	0.03	$\sigma_y(ip)$	$1.2 \cdot 10^{-6}$ m
$\xi_{y,max}$	0.02	ϵ_z	$2 \cdot 10^{-7}$ m
δ_{damp}	$1 \cdot 10^{-4}/\text{turn}$	ϵ_y	$1 \cdot 10^{-8}$ m

Table 2: 'Typical' CESR Parameters for operation With Dispersion at the IP

where equation (8) is needed so that the beam-beam interaction can be treated as a single kick and equation (9) is needed so that one can neglect the phase advance across the IR. In this case the correspondence between dispersion and a crossing angle is given by[5]

$$\theta_{err} = \frac{\sigma_{p_x,weak}}{\sigma_{z,weak}} \eta(ip). \quad (10)$$

where $\sigma_{p_x,weak}$ is the weak beam energy sigma. Using values 'typical' for CESR conditions with dispersion at the IP as given in Table 2, equation (10) gives an equivalent θ_{err} of about 17 mrad. For CESR one then finds the equivalent κ_c to be 0.5. Considering that the inequalities in equations (8) and (9) are not satisfied one is cautioned to take the above comparison with a grain of salt. Imperfect as the comparison is, however, does give one greater confidence that a bound of $\kappa_c \lesssim 0.1$ is sufficient to ensure the operation of CESR-B.

Given the bound $\kappa_c \lesssim 0.1$ with CESR-B conditions this gives an allowable crab angle error $\delta\theta_{crb}$ of

$$\frac{|\delta\theta_{crb}|}{\theta_{crb}} \lesssim 0.3. \quad (11)$$

This bound can be translated into an error budget for parameters such as betatron phase advances, etc. An analysis [4] shows that rather large parameter errors are needed to violate equation (11).

References

- [1] K. Berkelman et. al, CESR-B Conceptual Design Report, Cornell CLNS 91-1050 (1991).
- [2] K. Oide and K. Yokoya, Phys. Rev. A, 40, p. 315 (1989).
- [3] D. Sagan, S. Krishnagopal and R. Siemann, 2nd European Part. Acc. Conf, pg. 1649 (1990). Cornell CBN 91-01 (1991).
- [4] D. Sagan, Cornell CBN 91-01 (1991).
- [5] D. Sagan, Cornell CON 91-05, (1991).

A Strong-Strong Simulation on the Beam-Beam Effect in a Linac/Ring B-Factory*

Rui Li and Joseph J. Bisognano

CEBAF, 12000 Jefferson Ave., Newport News, VA 23606

Abstract

The beam-beam effect in a linac/ring B factory is studied here using strong-strong simulation based on a macro-particle model. Included in the ring dynamics are the linear betatron oscillation and synchrotron motion, as well as the transverse and longitudinal damping and quantum excitation. As a benchmarking test, the coherent quadrupole effect in a ring/ring collider was observed by the simulation. The simulation shows that in a linac/ring collider, the stability of the storage ring bunch is strongly affected by the synchro-betatron coupling induced by the deep envelope modulation of the highly disrupted linac bunch. However, with the initial conditions for the linac bunch properly chosen, the beam-beam tune shift limit of the ring bunch can be made comparable with that for a ring/ring collider.

Introduction

The intrinsic nonlinearity in the beam-beam interaction sets a limit on the achievable beam-beam tune shift, which is typically around 0.06 for ring/ring colliders, above which the beam will start to blow up to larger equilibrium bunch sizes in a few damping times. This beam-beam effect is primarily responsible for the limitation on the observed luminosity. The idea of a linac/ring B factory is proposed[1] such that the e^+ beam is stored in a ring, and the e^- bunches in the linac are not recycled after each collision. It is expected that the limits on the beam-beam tune shifts for the e^- beam can then be loosened. However, at the required luminosity, the relatively low average-beam-current capability of linacs compared to a storage ring's implies low emittance[2] and hence leads to high disruption for the e^- beam. The beam-beam dynamics experienced by the positron bunch is therefore disparate from that in a ring/ring collider. Thus it is important to study the beam-beam tune shift limit for the e^+ beam in the linac/ring dynamical system.

Beam-Beam Interaction Model

In this study, the finite size macro-particle model[3, 4] is employed to simulate the beam-beam interaction in a strong-strong manner. This model does not impose any restriction on the charge distribution of the beams under study.

At the IR of an e^+e^- collider, the two relativistic beams exert Lorentz forces on each other only in the transverse directions. This allows us to divide each bunch longitudinally into many slices, with the width of a slice corresponding to

the longitudinal step size over which the charged particles are advanced in the collisions. In the simulation, each slice is populated with macro-particles. The macro-particles in the two colliding beams experience mutual forces only when their corresponding slices overlap. For the simulation of interactions of elliptical beams, the macro-particles in a beam themselves have Gaussian charge distribution, with their aspect ratio comparable to the aspect ratio of the beam. The number and sizes of the macro-particles in each slice should be chosen to ensure sufficient overlap of the macros in order to suppress the collisional effect due to the finite number of macro-particles used in the simulation.

In the code, the force on each macro-particle is computed by direct Coulomb sum over the forces acting on the macro generated by all the macros in the overlapping slice of the approaching beam. The total luminosity is then obtained by the sum over the luminosity for each interaction pair at each time step[5]. Here, the electric fields on a two-dimensional grid, generated by a Gaussian macro-particle with given aspect ratio, are obtained in terms of the complex error functions[6] and stored in a table. The mutual force for each interaction pair of macros is then readily calculated by interpolating data from the lookup table. To properly describe the evolution of beam sizes with time, especially the pinching effect of the e^- beam from the linac, the sizes of the macros in each slice of a bunch are set to vary proportionally as the rms sizes of the slice evolve in each step of a collision. Here the ratio of the macro-particle size to the corresponding slice size is chosen to be $r = 0.5$. Smaller macro size has been used occasionally for error estimation. Simulation results are insensitive to the macro size as long as $r^2 \ll 1$.

A Benchmarking Test

The coherent quadrupole beam-beam effect in a ring/ring collider is a proper candidate for the benchmarking of beam-beam simulation codes[7]. The phenomenon was predicted by Chao and Ruth using a linearized Vlasov equation, and was first observed by Krishnagopal and Siemann in beam-beam simulation. It has the remarkable feature that at tunes just below the quarter-integer, the beam distributions oscillate in an anti-correlated manner with period 2.

As a benchmarking test for our simulation, we use parameters shown in Table 1. Here the two beams are round in the transverse plane and have no longitudinal length. The anti-correlated oscillation of beam sizes with period 2 is clearly demonstrated in Fig. 1. These results agree well with the previous results[8] obtained using completely different simulation algorithms.

*Supported by D.O.E. contract #DE-AC05-84ER40150

Table 1: Parameter List in Simulation of Coherent Quadruple Effect as a Benchmarking Test

Energy (E_0)	5.3 GeV
Revolution Period (T_0)	2.56 μ s
Transverse Emittances ($\epsilon_x = \epsilon_y$)	1×10^7 m
Amplitude Functions ($\beta_x^* = \beta_y^*$)	3 cm
Betatron Tunes ($Q_x = Q_y$)	0.72
Damping Decrement (δ)	1×10^{-3}
Current (I)	35 mA
Nominal Beam-Beam Parameter (ξ_0)	0.121
Number of Test Particles	300

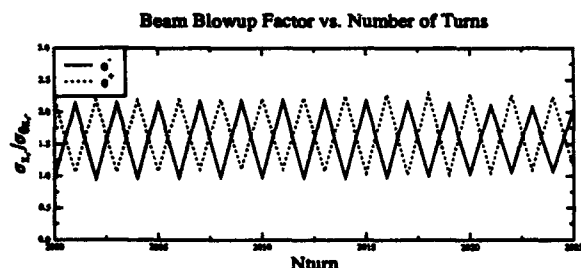


Figure 1: Results of coherent quadruple effect in a ring/ring collider with parameters given in Table 1.

Beam-Beam Effects in a Linac/Ring Scheme

The parameter list shown in Table 2 [9] is used in our simulation for the study of the beam-beam effect in a linac/ring colliding scheme. Notice that the proposed nominal luminosity is $\mathcal{L}_0 = 1 \times 10^{34}$, with the nominal vertical beam-beam tune shift for the e^+ beam being $\xi_{y+,0} = 0.056$ and the nominal vertical disruption parameter for the e^- beam being $D_{y-,0} = 273.7$. The simulation-related parameters are listed in Table 3.

In the simulation, the e^+ beam is circulated in the storage ring, experiencing beam-beam collisions at IP once a turn with a new e^- bunch. The ring dynamics includes linear betatron oscillations, synchrotron oscillations, as well as damping and diffusion in all three dimensions [10]. The initial distribution of macro-particles in the e^+ bunches is 3-D Gaussian with the nominal beam sizes. The pre-collision charge distributions for the e^- bunches are transversely Gaussian and longitudinally parabolic. In Fig. 2 we show the variation of the vertical rms size for each e^- slice through the e^+ bunch during the first collision. The formation of pinches when the e^- macros oscillate through the e^+ bunch can be clearly seen as the effect of the high disruption of the e^- beam. This will induce (1) stronger nonlinearity and (2) stronger synchro-betatron coupling compared to the case of a ring/ring collider. The consequent blowup of the vertical bunch size for the e^+ beam is shown in Fig. 3, which reaches an equilibrium value in about three damping times.

Table 2: Linac/Ring B-Factory Parameter List

Linac(e^-)	Storage Ring(e^+)
$E_- = 3.5$ GeV	$E_+ = 8.0$ GeV
$N_- = 0.544 \times 10^9$	$N_+ = 6.1 \times 10^{11}$
$f_c = 20.0$ MHz	$n_B = 30$
$\epsilon_{x-,0} = 5.75$ nm	$\epsilon_{x+,0} = 5.75$ nm
$\epsilon_{y-,0} = 0.37$ nm	$\epsilon_{y+,0} = 0.057$ nm
$\beta_{x-,0}^* = 3.32$ mm	$\beta_{x+,0}^* = 3.33$ mm
$\beta_{y-,0}^* = 3.33$ mm	$\beta_{y+,0}^* = 21.55$ mm
$\sigma_{x-,0}^* = 4.37 \mu$ m	$\sigma_{x+,0}^* = 4.37 \mu$ m
$\sigma_{y-,0}^* = 1.11 \mu$ m	$\sigma_{y+,0}^* = 1.11 \mu$ m
$\sigma_{z-,0} = 2.64$ mm	$\sigma_{z+,0} = 3.3$ mm
$D_{x-,0} = 69.6$	$\nu_s = 0.07$
$D_{y-,0} = 273.7$	$\tau_x = 0.9$ msec
	$\tau_y = 2.4$ msec
	$\tau_\delta = 6.9$ msec
	$\xi_{x+,0} = 0.002$
	$\xi_{y+,0} = 0.056$
$\mathcal{L}_0 = 1.1 \times 10^{34} \text{ cm}^{-2} \text{ sec}^{-1}$	

Table 3: Parameters for Simulation Model

	e^-	e^+
Number of Slices		45
Number of Macros	360	1000
Aspect Ratio of Macros		3.93
Size of Macros		$0.5 \times \text{beam sizes}$

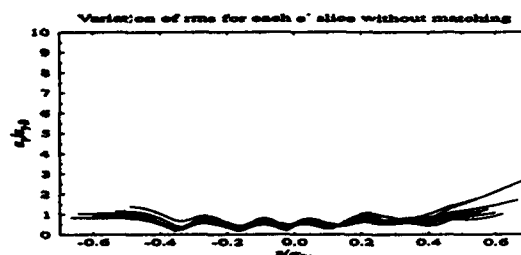


Figure 2: Variation of the vertical rms size for the e^- slices in the $y-z$ plane in the rest frame of the e^+ bunch without matching.

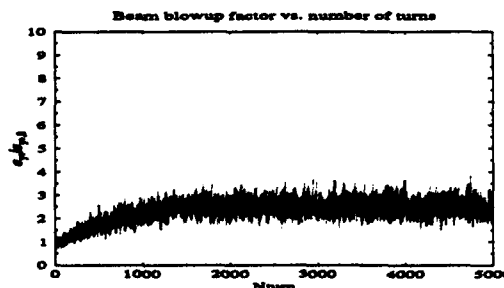


Figure 3: Beam blowup for the e^+ beam during 5000 turns for parameters in Table 2.

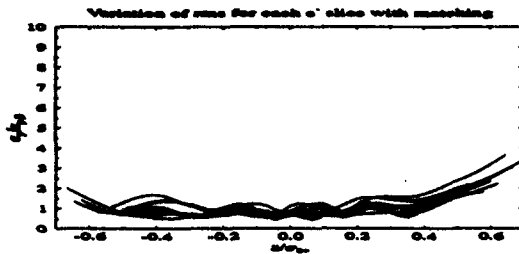


Figure 4: Variation of the vertical rms size for the e^- slices in the $y-z$ plane in the rest frame of the e^+ bunch with matching.

To reduce the effect of pinches, a matching scheme was developed by S. Heifets[9], where the transverse bunch sizes for the e^- and e^+ beam are set to be equal at IP and then the matched e^- bunches are tracked back to the beginning of the interaction region. The pre-collision phase space distribution of the e^- macros thus chosen allows the spreading out of the focusing points and produces a much smoother envelope distribution for the e^- bunches, as shown in Fig. 4. The long-term behavior of the e^+ beam, similar to that in Fig. 3, can also be obtained in the case of matching.

We then proceed to study the beam-beam effect for both matched and unmatched cases by varying $\xi_{y+,0}$ while fixing $D_{y-,0}$. The dependence of the equilibrium values of the beam blowup factor and the luminosity with respect to $\xi_{y+,0}$ is shown in Fig. 5. As shown in Fig. 5(a), for the non-matching case, the beam starts to blowup around $\xi_{y+,0} = 0.02$, whereas the blowup takes place around $\xi_{y+,0} = 0.05$ if matching applies. In Fig. 5(b), it is shown that for $\xi_{y+,0}$ above the value of 0.06, the luminosity in the matching case increases slowly with values larger than the saturated value in the non-matching case. The above comparison of the beam-beam effect with and without matching manifests the effect of envelope modulation of the e^- beam.

The above results are obtained for the fractional betatron tune $(Q_x, Q_y) = (0.64, 0.54)$ for the e^+ beam in the storage ring. Further investigation shows that for the high-disruption case without matching, the above beam blowup occurs over almost all the tune plane. This agrees with the results obtained by Gerasimov [11] using weak-strong simulation with envelope-modulated electron bunches.

Effect of Jitter

The effects of the white noise jitters for the linac beam has been estimated analytically[12] using a linear model, and simulated[13] using weak-strong simulation without damping. Previous results shows that the required jitter tolerances are at the margin of the precision of the measurement. Here the effect of 10% intensity jitter in the linac beam on the stability of the storage ring beam is also tested using our strong-strong simulation. With the inclusion of all the possible dynamics in the simulation, the predicted extremely unstable situation for the positron bunch is not observed.

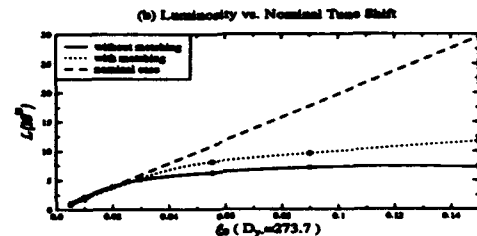
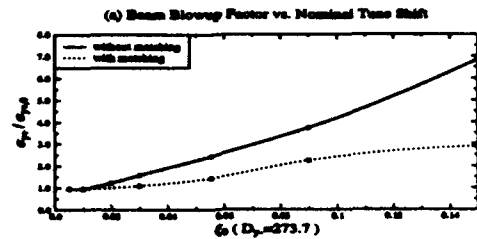


Figure 5: Results of beam-beam effect for a linac/ring B factory using parameters in Table 2. Here $\xi_{y+,0}$ is changed by varying only the electron current.

Acknowledgement

We have benefited greatly from the conversations with G. A. Krafft on the macro-particle model, and the code SWARM written by J. R. Boyce.

References

- [1] P. Gross-Wiesmann, SLAC-PUB-4545, 1988.
- [2] J. J. Bisognano, *et al.*, 1988 Linear Accelerator Conference, Williamsburg, 1988.
- [3] G. A. Krafft, private communication.
- [4] J. R. Boyce, *et al.*, 1990 Linear Accelerator Conference, 1990.
- [5] G. A. Krafft, CEBAF TN-92-032, 1992.
- [6] M. Bassetti and G. A. Erskine, CERN-ISR-TH/80-06, 1980.
- [7] S. Krishnagopal and R. H. Siemann, LBL-32581, 1992.
- [8] S. Krishnagopal, private communication.
- [9] S. A. Heifets, *et al.*, *Nucl Instrum. Methods*, A295, p286, 1990.
- [10] S. Krishnagopal and R. H. Siemann, Cornell Internal Note, CBN/88-1, 1988.
- [11] A. Gerasimov, CEBAF-TN-90-243, 1990.
- [12] Y. Baconnier, CERN PS/91-02(LP), 1991.
- [13] C. D. Johnson, AIP Conference Proceedings No.261, p198, 1991.

Some Aspects of the Long Range Beam-Beam Interaction in Storage Rings *

Alexander B. Temnykh [†] and James J. Welch, Wilson Lab. Cornell University, Ithaca NY

Introduction

In this paper we develop a linear model of the long range beam-beam tune shift for cases when the electron and positron orbits are separated at all crossing points [4]. Theoretical considerations show that the tunes of coherent beam-beam modes depend crucially on the betatron phase advance between crossing points. Under certain conditions the tune split may be reduced, or even made equal to zero in spite of a strong beam-beam interaction. Measurements of coherent beam-beam modes were made at CESR. In most cases, the experimental results are in good agreement with the linear model.

The behavior of coherent beam-beam modes was examined theoretically, taking into account the coherent tune shift caused by impedance effects. As in [2] we form the single turn matrix describing the bunch centroid motion and evaluate the eigenvalues. In the simplest case, this motion includes the linear transport through the magnetic lattice, for which betatron phase advance does not depend on a bunch current, followed by a long range beam-beam 'kick' in the linear approximation. The measurements and comparisons with model predictions are discussed in the final section.

This work was motivated by the CESR upgrade program [1]. A central part of this program is to increase the average stored beam current by forming multiple trains of bunches. However, it is not possible to get large enough separation at all crossing points to be able to ignore the long range beam-beam interaction because the length of each train is comparable with a half betatron wavelength.

Long range beam-beam interaction in the linear approximation

We assume the separation distances at the crossing points are large enough compared with the beam sizes that the linear approximation of the beam-beam kick angle does not contain terms significant terms coupling vertical and horizontal motion. Likewise, we assume the linear transport between crossing points does not include coupling and therefore develop only a one dimensional model.

Consider the simplest case of one bunch per beam and refer to figure 1. The electron and positron bunches should

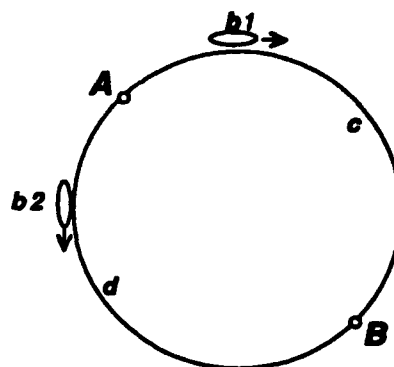


Figure 1: Electrons in bunch b_1 interact with positrons in bunch b_2 at positions A and B. The phase advance along arc c may be different from the phase advance along arc d.

interact with each other only at two points A and B located at the opposite sides of the storage ring. If these points are not on a symmetry axis of the lattice, the betatron phase advance from A to B on side c would not in general be equal to the phase advance on side d. This kind of asymmetry leads to some unexpected behavior of coherent modes.

Lets form the vector (X_1, X'_1, X_2, X'_2) , where $X_{1,(2)}$ and $X'_{1,(2)}$ are the horizontal coordinates and associated angles of bunch $b_{1,(2)}$, appropriately normalised by the horizontal beta function. The matrix that transports both bunches simultaneously (in opposite directions) through the magnetic structure from A to B is,

$$M_{A,B} = \begin{pmatrix} \cos \mu_c & \sin \mu_c & 0 & 0 \\ -\sin \mu_c & \cos \mu_c & 0 & 0 \\ 0 & 0 & \cos \mu_d & \sin \mu_d \\ 0 & 0 & -\sin \mu_d & \cos \mu_d \end{pmatrix} \quad (1)$$

where μ_c and μ_d are the absolute values of phase advance from A to B along side c and d accordingly. For simplicity we have assumed that magnitude of horizontal beta function is equal to one and its derivative is equal to zero at both points A and B.

To get the matrix describing the long range beam-beam interaction consider the kick angle produced by the electromagnetic field of b_2 on b_1 . If distance between centers of bunches is much larger than the bunch size, then the change of angle will be $\delta X'_1 = 2N_2 r_0 / \gamma d$, where N_2 is

* Work supported by the National Science Foundation

[†] On leave from BINP, Novosibirsk

the number of particles in bunch 2, r_0 the classical electron radius, γ , the Lorents factor, and d is the distance between bunch centers. Note that d is composed of a closed orbit separation, d_0 , and $X_{1,2}$ which are the displacements of bunches $b_{1,2}$ relative to the closed orbit, i.e., $d = d_0 + X_1 - X_2$. Assuming $|X_{1,2}| \ll d_0$ we can rewrite formula for angle change as:

$$\delta X'_1 = \frac{2N_2 r_0}{\gamma d_0} - \frac{2N_2 r_0}{\gamma d_0^2} (X_1 - X_2) \quad (2)$$

Here the first term is a dipole kick, which gives a very small orbit distortion that does not depend on X_1 or X_2 . The second term is proportional to bunch displacements. It is like a gradient error and couples the motion of the two beams to produce coherent motion. In what follows, we will ignore the first term and only take into account the gradient term. Conceptually this means we must include the effects of the dipole error as a distortion of the closed orbit. In practice, the distortion of the closed orbit is too small to matter.

The long range beam-beam interaction matrix from just before the kick to just after kick will be

$$M_{int} = \begin{pmatrix} 1 & 0 & 0 & 0 \\ 4\pi\delta\nu_1 & 1 & -4\pi\delta\nu_1 & 0 \\ 0 & 0 & 1 & 0 \\ -4\pi\delta\nu_2 & 0 & 4\pi\delta\nu_2 & 1 \end{pmatrix} \quad (3)$$

where $\delta\nu_{1,2} = N_{2,1} r_0 \beta / 2\pi \gamma d^2$ is the tune shift for a single crossing point and $N_{2,1}$ is the number of particles in bunch 2,1. To get a single turn matrix M_{tot} we must make a matrix multiplication:

$$M_{tot} = M_{int} M_{B,A} M_{int} M_{A,B} \quad (4)$$

where $M_{B,A}$ describes the bunch motion from B to A. Eigenvalues and eigenvectors of M_{tot} characterize the coherent modes.

In figure 2 we present results of numerical calculation of beam-beam coherent modes as described above. We can see that at low total current, where one bunch is very weak, the tune of the higher frequency mode doesn't depend on bunch intensity, but the lower tune goes down with increasing bunch current. The resulting tune split is proportional to bunch intensity. This picture has a simple interpretation. The unaffected tune belongs to the strong bunch, while the decreasing tune is associated with the motion of the weak bunch. The fact that the tune is decreasing means there is a defocussing effect by large bunch. The tune shift or tune split, both are the same in this case, is the sum of the tune shifts calculated for each of the single crossing points, i.e., $2\delta\nu_1$. An asymmetry in phase advance between c and d does not matter.

A different situation arises in the case where both bunches have significant intensity. Here the asymmetry in phase advance $\mu_{as} = |\mu_c - \mu_d|$ plays an important role. In figure 2 we see that if the phase advance is zero, i.e., ($\mu_{as} = 0$), the dependence of mode tunes resembles that

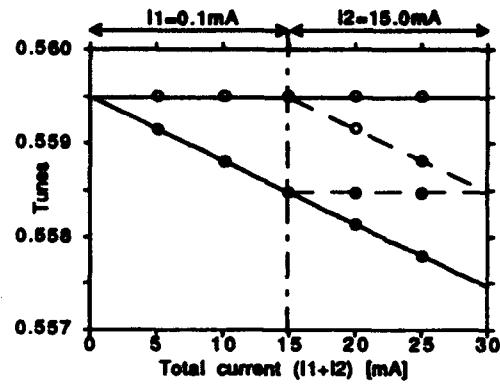


Figure 2: Calculated mode tunes. Open and solid circles refer to the two different modes. Here the effects of asymmetries in the phase advance are evident. Dotted and continuous lines are for the cases of $|\mu_c - \mu_d| = \pi$ or 0. The calculation was done for $\gamma = 10^4$, $d = 29$ mm, $\beta = 40$ m, $N_b = 1.6 \times 10^{11} \times I$ [mA].

of the strong-weak case. The tune shift of the lower mode is proportional to sum of bunch intensities and tune split equals to sum of tune shifts at both crossing points. However, if $\mu_{as} = \pi/2$, the higher tune goes down with increasing bunch intensities, while the lower tune remains constant. At the point where the bunch intensities become equal one to another, both coherent beam-beam modes have the same tune shift, which is equal one half the tune split in the $\mu_{as} = 0$ case. Moreover the tune split equals zero in spite of beam-beam interaction.

To get a more realistic model which can be compared with experimental data, the beam-wall coherent tune shift and multiple bunches must be taken into account. The beam-wall coherent tune shift should be introduced as an extra phase advance $\delta\mu_{b-w}$ for each bunch. The magnitude of $\delta\mu_{b-w}$ is proportional to bunch intensity and is taken from single beam measurements. To describe a configuration with k bunches per beam, the eigenvalues of matrices of order $2k$ must be evaluated.

Measurements

Three machine studies were carried out at CESR to measure long range tune shifts under different conditions as a function of beam current. The choice of bunches and the pretzel configuration insured that there were no head-on collisions at the normal interaction points. Betatron tune shifts were measured on a spectrum analyser connected to beam pickup electrodes. For an accurate measurement of the frequency it was necessary to artificially spread the tunes of the two beam enough that the peaks would not overlap. This was done by varying sextupole strengths in the region of separated orbits. The betatron resonance widths were about 1 kHs wide which is larger than many of the tune shifts. Signal averaging and careful attention

to the frequency measurement were paid – not always successfully – resulting in a variance of the frequency shift measurements of order 0.1 kHz. The optics used were the same as those used during normal operation of CESR.

The first measurement consisted of one bunch of positrons circulating against one bunch of electrons. The electron bunch was used as a ‘probe’ beam. Its betatron tunes were measured and its current held constant at 2 mA/bunch while the positron bunch current was reduced from 12 mA to 2 mA. One of the nicer features of this technique is that there is no confusion introduced by frequency shifts due to impedance as the measured beam is held at constant current. The results are summarized in the table below:

Crossing points	Bunch #		measured	theory
	e^+	e^-	$\nu_y \left[\frac{Hz}{mA} \right]$	$\nu_y \left[\frac{Hz}{mA} \right]$
2,7	1	7	-15 ± 7	-0.5
3,6	1	6	-8.6 ± 5	-8
4,5	1	5	56.6 ± 6	53.8

The theoretical values of β_x and the betatron phase ϕ_A at the parasitic crossing points are probably only good to about 15% and constitute the main uncertainty in the theoretical values. The variance in the experimental values is dominated by the variance in the frequency measurements. Within these uncertainties the measurements are consistent with the theoretical predictions.

The second set of measurements was quite similar to the first except that ‘improved’ techniques for frequency measurement and data taking were used, and data was taken at two different pretzel amplitudes. The results are given below:

Bunch		$\nu_x \left[\frac{Hz}{mA} \right]$		$\nu_y \left[\frac{Hz}{mA} \right]$		pretzel
e^+	e^-	data	theory	data	theory	
1	5	-6 ± 2	-16.4	60 ± 2	66.3	1200
1	5	-42 ± 5	-36.9	183 ± 3	149	800
1	6	-10 ± 1	-20	14 ± 2	9.3	1200
1	6	-28 ± 2	-44	35 ± 3	21	800

Here there is substantial disagreement between the theory and experiment. The experimental horizontal tune changes are substantially less than the predicted values, while the experimental vertical tune changes are generally somewhat greater than the predictions. If this is to be explained by errors in the assumed beta function values, the horizontal beta functions must be in error by about a factor of 2. More likely is the possibility that the “improved technique” was in fact worse.

In the third machine studies we measured the tuneshifts generated by two trains of 7 bunches each. In this configuration, each bunch undergoes 14 crossings with opposing bunches, each at a different separation distance and beta function [3]. The total tune shift received may be different for different bunches. We measured the only the tune shifts for the highest and lowest frequency modes. The total current in the positron beam was held constant while

the current in the electron beam was varied. An attempt was made to keep the individual bunch currents more or less equal for each beam. The results are also summarised in the following table.

Mode	$\nu_x \left[\frac{Hz}{mA} \right]$		$\nu_y \left[\frac{Hz}{mA} \right]$	
	measured	theory	measured	theory
highest	-3.2 ± 1	-12	$21.1 \pm .4$	21
lowest	-25 ± 2	-22	$-32.9 \pm .8$	-33

The tune shift due to impedance was measured during earlier machine studies opportunities and added to the theoretical prediction. In most cases the theoretical and measured slopes of frequency versus total electron current are in good agreement. However, for the data with the highest horizontal frequency, the measured slope is less negative than the theoretical indicating less long range tune shift than expected. One possible reason for the discrepancy is betatron phase errors. Another possible reason for the discrepancy may arise from the implicit assumption that the change of position of the peak in the betatron spectrum is exactly representative of the tune change. This would not be the case when two peaks are overlapping since the peak of the sum of the signals would not follow the tune of each mode independently. This is particularly relevant to the horizontal tune because the frequency spread of the modes is not large and does not increase with higher currents as much as for the vertical modes.

Conclusions

The use of tune splits of coherent beam-beam modes to test parasitic interaction points, analogous to the use of π - mode and σ - mode for head-on collisions, may lead to confusing results. Under certain conditions the tune split may be reduced, moreover it may be zero in spite of a strong beam-beam interaction. The best way to study the tune shifts due to the long range beam-beam interaction is to use one bunch per beam and measure the dependence of the coherent tunes on the intensity of one of the bunches keeping the intensity of the other bunch fixed and quite small. Only in this case can you be sure that the tune shift of smallest bunch will be equal to sum of tune shifts for the single interaction points.

References

- [1] J. Welch, *CESR Upgrade and Conversion to a B Factory*, proc. KEK BFWS92, Nov. 1992
- [2] E. Keil, LEP Performance Note 83 (1992)
- [3] D. Rice, et. al. *Symmetric Beam-Beam Experience* CBN 92-10 Cornell U., proc. SLAC B Factory Workshop, April 1992
- [4] CBN 92-13

Experimental Study of Crossing Angle Collision†

T. Chen

SLAC, MS26, P.O.Box 4349, Stanford, CA94309

D. Rice, D. Rubin, D. Sagan, and M. Tigner

Newman Laboratory, Cornell University, Ithaca, NY 14853.

Abstract

The non-linear coupling due to the beam-beam interaction with crossing angle has been studied. The major effect of a small ($\sim 12\text{mrad}$) crossing angle is to excite $5Q_x \pm Q_y = \text{integer}$ coupling resonance family on large amplitude particles, which results in bad lifetime. On the CESR, a small crossing angle ($\sim 2.4\text{mr}$) was created at the IP and a reasonable beam-beam tune-shift was achieved. The decay rate of the beam is measured as a function of horizontal tune with and without crossing angle. The theoretical analysis, simulation and experimental measurements have a good agreement. The resonance strength as a function of crossing angle is also measured.

I. INTRODUCTION

A primary objective of modern e^+e^- collider development is to achieve very high luminosity to meet the requirements of high energy physics. The design luminosity of these colliders, so called B-Factories, Φ -Factories, etc., is about 50 times as high as that achieved in current colliders. To obtain this luminosity, the new designs employ two rings, with each ring being filled with large number of bunches to make the collision rate at the single interaction point large. The natural way to bring the two beams into collision and separating them thereafter is to have a small crossing angle. However, studies^[1] show that synchrotron resonances are excited by crossing angle beam-beam interaction. This paper analyzes this problem, and provides the results of an experimental measurement. The conclusion of analysis, simulation, and experiment agrees reasonably well.

II. ANALYTICAL ANALYSIS AND SIMULATION

The reason why synchrotron coupling is introduced by a crossing angle is that, due to the angle, the distance between a particle and the center of the counter bunch is modulated by the particle's longitudinal position. As a result, the beam-beam kick, which is a function of the distance, is modulated by the longitudinal motion too.

A resonance analysis method can be developed based on difference equations^[2]. Considering horizontal and longitudinal planes, particle motion in a linear ring with a thin, nonlinear kick can be described by

$$\begin{aligned} x_{t+1} - 2\cos\mu_x x_t + x_{t-1} &= -\beta_x \sin\mu_x F(x_t + \tan\Phi \cdot s_t) \cos^2\Phi, \\ s_{t+1} - 2\cos\mu_s s_t + s_{t-1} &= 0. \end{aligned} \quad (1)$$

Where $F(r)$ is the beam-beam kick, Φ is the crossing angle, and t stands for turn number. For small crossing angle, the longitudinal component of the kick is neglected. It is easy to see that the linear solutions of (1) are:

$$x_t = A_x \cos(\mu_x t), \quad s_t = A_s \cos(\mu_s t). \quad (2)$$

As the first step approximation, insert (2) into the right-

hand side of (1), and do a Fourier expansion. Then, the right-hand-side of first equation of (1) is written as:

$$\frac{1}{2} \sum_{m,n} c_{m,n} \cos[(m\mu_x + n\mu_s)t] + d_{m,n} \cos[(m\mu_x - n\mu_s)t] \quad (3)$$

Naturally, a similar form of solution of (1) is expected:

$$x_t = \frac{1}{2} \sum_{m,n} a_{m,n} \cos[(m\mu_x + n\mu_s)t] + b_{m,n} \cos[(m\mu_x - n\mu_s)t] \quad (4)$$

Substitute (3), (4) into (1), the relation between driving terms and response terms is found:

$$(a,b)_{m,n} = \frac{(c,d)_{m,n}}{2\sin\frac{1}{2}[(m+1)\mu_x \pm n\mu_s] \sin\frac{1}{2}[(m-1)\mu_x \pm n\mu_s]} \quad (5)$$

Near resonances $(m \pm 1)Q_x \pm nQ_y = \text{integer}$, the denominator is small. Then, $(a,b)_{m,n}$ has strong response to $(c,d)_{m,n}$. Therefore, we can say that $c_{m,n}$ and $d_{m,n}$ drive these resonances.

Spectrum of crossing angle beam-beam kick

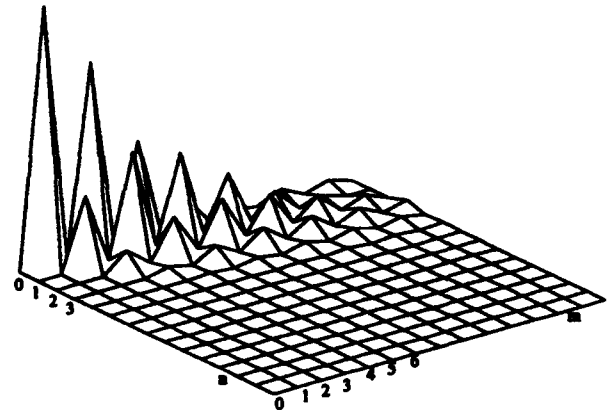


Figure (1). The power spectrum of the crossing angle beam-beam kick.

Figure (1) shows the two-dimensional FFT power spectrum of the beam-beam kick. From the picture, one can easily see that the strongest driving terms are at $m=4, n=1$ and $m=6, n=1$. According to the previous analysis, both these two terms will drive $5Q_x \pm Q_y = \text{integer}$ resonances. It is natural to conclude that the $5Q_x \pm Q_y = \text{integer}$ resonances are the strongest coupling resonances.

In order to analyze the effect of a crossing angle, a computer simulation similar to Piwinski's work^[3] was made. The storage ring was model by a linear ring and a thin-kick beam-beam interaction with crossing angle. Three dimensional motion is simulated. Particles are launched in 6 dimensional phase space with 6σ amplitudes. The program scans the horizontal fractional tune from 0 to 1. The maximum amplitude of all particles ever reached during the 1000-turn tracking is recorded as a function of horizontal tune. Figure (2) plots the maximum horizontal amplitude versus

† Supported by the National Science Foundation.

fractional tune. It shows that, besides the one-dimensional resonances which exist also in head-on collision, the strongest coupling resonances are $5Q_x \pm Q_y = \text{integer}$ family.

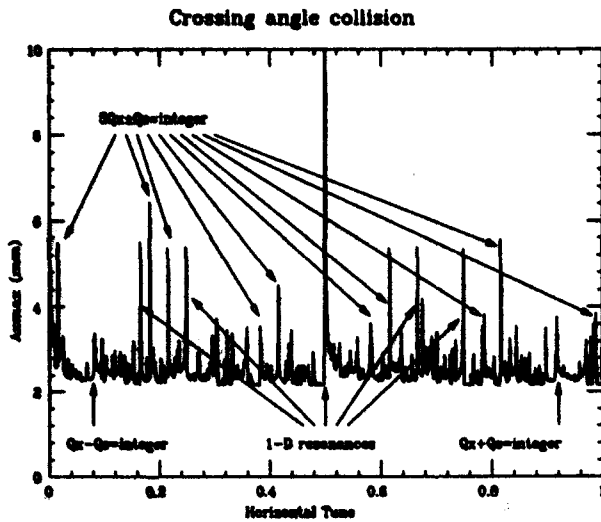


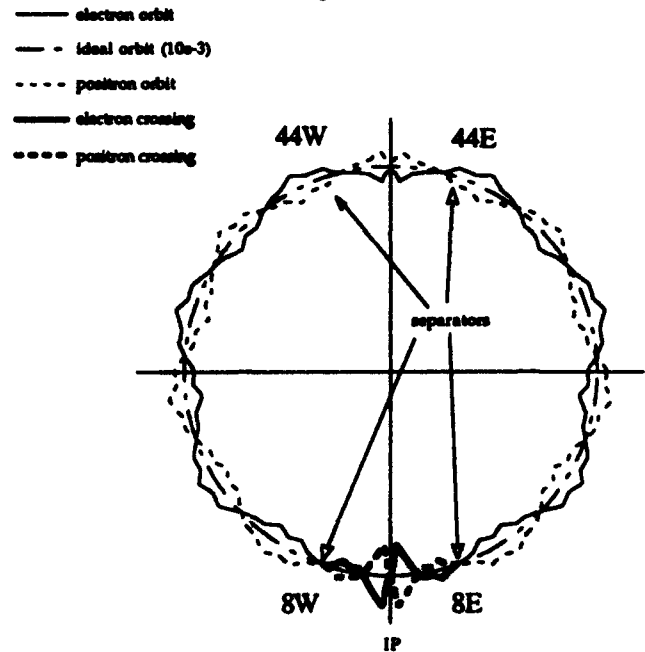
Figure (2) Maximum horizontal amplitude vs. tune for crossing angle collision. ($Q_y=0.081$)

III. EXPERIMENTAL MEASUREMENT

The experiment is designed to observe the $5Q_x + Q_y$ resonance excited by the crossing angle collision, which is predicted by the theory in previous section. The experiment is based on the setup of the CESR crossing angle experiment^[4]. CESR has been running with multi-bunch mode (7 bunches of e^- on 7 bunches of e^+). The key point of making multi-bunch mode possible is to separate bunches at crossing points around the ring except at the interaction point where the detector is located. In CESR, four electrostatic separators are used to separate electron and positron orbits at parasitic crossing points. As shown in figure (3), the orbits (thin lines) are separated at 13 would be collision points, but merged between the two south (lower) separators, including the IP where the collision takes place. The crossing angle lattice is essentially a modified version of the normal operation lattice with the bunches separated at the collision points except the IP. An anti-symmetric voltage applied to the south separators will create anti-symmetric orbits about the IP. This is displayed in figure (3) as the thick lines.

The experiment was performed in a way similar to the simulation. The strong-weak beam-beam interaction is achieved by colliding a 2mA beam on 10mA beam. The beam size and beam current decay rate is measured while scanning the horizontal tune in the $5Q_x + Q_y$ resonance region. A high decay rate peak was observed on the resonance when the crossing angle was turned on. However, the peak disappeared when the crossing angle was turned off. Figure (4) shows the tune scan data with and without crossing angle. For comparison, the simulation results are shown in figure (4) too. One can easily see the agreement between them. Note that the vertical axis represents different quantities in experimental data and simulation. The reason is that the calculation is only qualitative. Nevertheless, they both reflect

the same physical phenomena. Meanwhile, the vertical beam size is measured. No beam blow up is observed at the same resonance, with or without crossing angle. This implies that this effect applies only on beam tail, which is what the theoretical analysis and simulation predicted.



Figure(3). Diagram of the orbits for crossing angle experiment

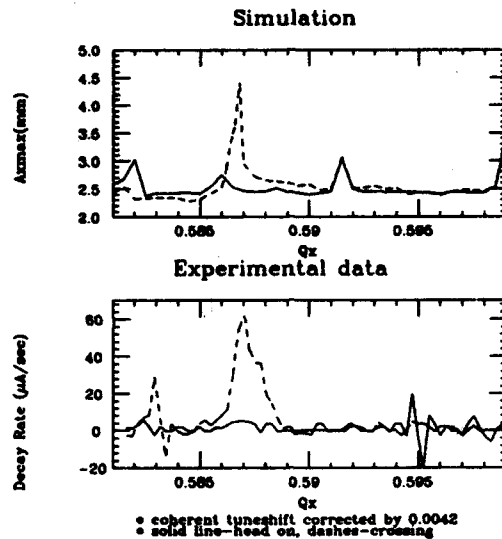


Figure (4). (a)upper: Simulation result, maximum amplitude versus horizontal tune. (b)lower: Experimental data, decay rate as a function of horizontal tune.

A two dimensional tune scan was also performed to check the resonance. The result with crossing angle on is shown in figure (5). In this part of experiment, strong-strong beam-beam interaction was employed, because, a weak beam cannot survive after crossing the resonance many times. The $5Q_x + Q_y$ resonance corresponds to the light vertical line on the left. With this result, the resonance is better identified due to its consistent appearance and independent of vertical tune.

The resonance strength, in terms of peak decay rate, is

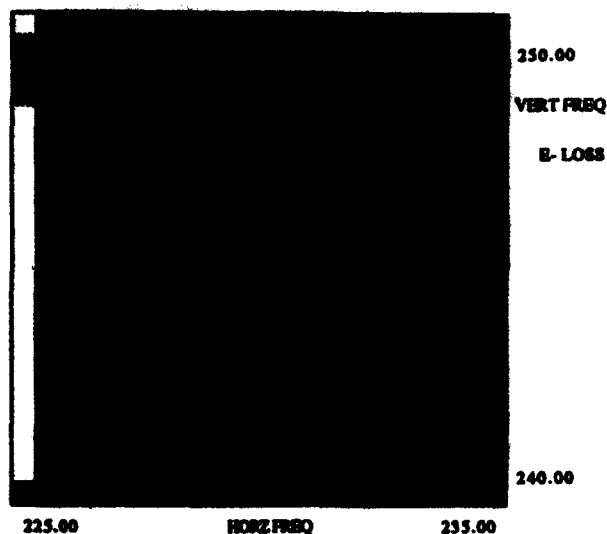


Figure (5) Electron decay rate measured in two dimensional tune scan with 2 mrad crossing angle. The lighter shade indicates higher decay rate. The horizontal and vertical tune frequencies, the product of the tune and the revolution frequency, are in kHz. (The revolution frequency is 390 kHz). also measured as a function of crossing angle. Figure (6) plots the measured result. Each line in the picture is from a single tune scan with certain crossing angle. The crossing angle ranges from about ± 1.4 mrad to ± 2.5 mrad. For crossing angle smaller than ± 1.4 mrad, there is no clear decay rate peak being measured.

Crossing Angle Experiment

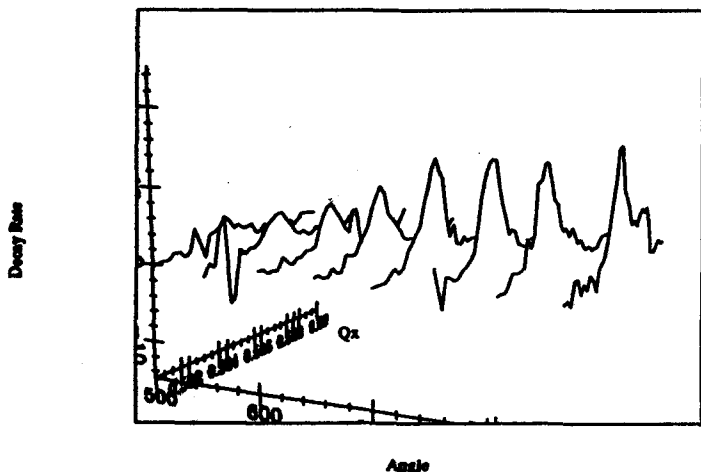
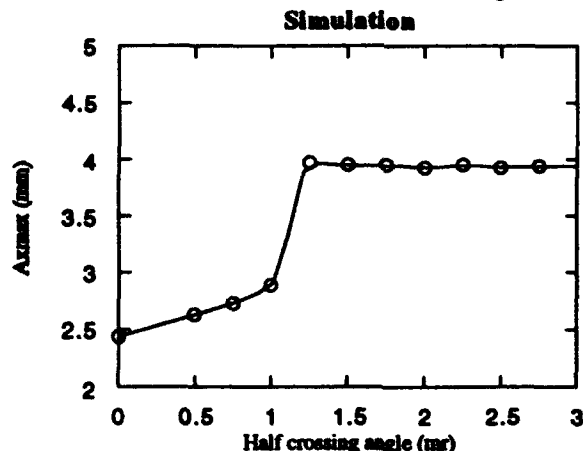


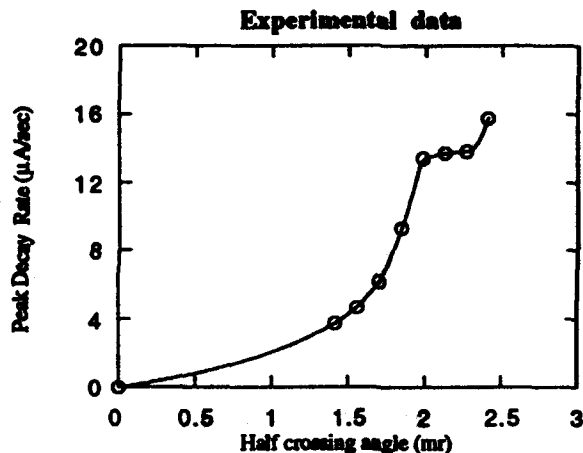
Figure (6). Tune scans versus crossing angle.

The maximum decay rate from figure (6) is plotted as a function of the half crossing angle in figure (7), one can easily see the rise of the resonance strength as the crossing angle increases. The simulation result is also plotted for comparison. Again, the quantities in vertical axis are different, so that the comparison is only qualitative. However, from both plots, a saturation effect can be seen. Simulation shows that the saturation goes up to ± 12 mrad.

Unfortunately, the crossing angle in the experiment cannot go larger, because it is limited by machine aperture. The last data point raises again. The reason may be that the crossing angle has been pushed to the limit of the physical aperture at this angle. The tight physical aperture certainly enhances the decay rate. We also cannot exclude other driving sources.



(a) Maximum amplitude on the resonance vs. crossing angle.



(b). Peak decay rate on the resonance vs. crossing angle Figure (7). Resonance strength as a function of crossing angle.

IV. CONCLUSIONS

The study shows a good consistency among analytical analysis, computer simulation and experiment on the strongest coupling resonance family excited by the crossing angle beam-beam interaction. This resonance family, $5Q_x \pm Q_s = \text{integer}$, will result in a bad lifetime in operation.

V. ACKNOWLEDGMENT:

Authors would like to sincerely thank CESR accelerator physicists and operation group for their help for the experiment.

VI. REFERENCES

- [1] A. Piwinski, IEEE Trans. NS-24, p1408 (1977).
- [2] Peggs, S. and Talman, R., "Nonlinear Problems in Accelerator Physics," *Ann. Rev. Nucl. Part. Sci.*, vol. 36, 287, 1986.
- [3] Piwinski, A., "Simulations of Crab Crossing in Storage Rings," SLAC-PUB-5430, Feb. 1991.
- [4] Rubin, D. and *et al*, "Beam-beam Interaction with a Horizontal Crossing Angle," *to be published in Nuclear Instruments and Methods A* or CLNS 92/1183.

Beam-beam Experiments in the Tevatron

D. Siergiej and G. Goderre
Fermi National Accelerator Laboratory*
P.O. Box 500
Batavia, Illinois 60510

Abstract

The working point tunes in the Tevatron at 900 GeV are nominally in an area in betatron tune space that borders the 7th and 5th order resonances. An attempt will be made in this 1992 collider run to measure whether the beam-beam interaction plays an important role in driving resonances in this region of tune space. Experimental results which identify the beam-beam driven resonances are presented. An experimental method of ensuring head-on collisions in order to minimize odd-ordered resonance effects in the Tevatron is also presented.

INTRODUCTION

The tune shift and the tune spread caused by the beam-beam interaction dictated the installment of separators in the Tevatron for the 1992 collider run. The electrostatic separators separate the proton and antiproton orbits such that head-on collisions occur only at the location of the two high energy physics detectors. This reduced the tune shift for a store of 6 protons colliding with 6 antiprotons by a factor of 6. The analytical beam-beam tune footprint shown in Figure 1 represents the tune shift and tune spread of the antiprotons colliding head-on at the two collision sites in the Tevatron. The proton base tune is 20.58 in the horizontal plane and 20.575 in the vertical plane. The tune footprint is calculated using parameters representing the normal operating conditions of the collider run. A normalized emittance of 20π mm-mrad (using the 95% definition of emittance) for the protons and 16π mm-mrad for the antiprotons was used in the calculation, along with a momentum spread of 124 MeV for the 900 GeV beam. Bunch intensities of 120×10^{11} and 50×10^{11} are typical intensities for the protons and antiprotons, respectively.

This is the first collider run where the Tevatron collides protons and antiprotons at two interaction regions and separates the beams in two dimensions at all other crossing

*Operated by the Universities Research Association under contract with the U.S. Department of Energy

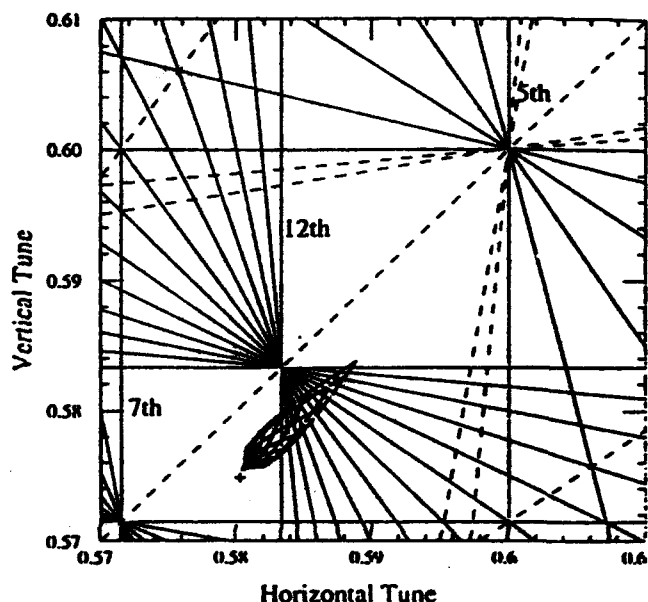


Figure 1: Antiproton beam-beam tune footprint in the Tevatron

points in the storage ring. The experiments presented below were done in an effort to understand what adverse effects the beam-beam interaction may have in this new operational state of the Tevatron.

BEAM-BEAM DRIVEN RESONANCES

In order to identify resonances driven by the beam-beam interaction, the proton tune was moved across resonances in both a proton only store and a store in which protons and antiprotons were colliding. Proton background losses were measured as a function of proton tune. The focusing and defocusing correction quadrupole circuits were used to change the tunes linearly at a constant rate of 0.01 tune units per minute. The tune signals were measured using Shottky plate signals sent into a spectrum analyzer.¹ Measurements of the tunes were taken at both end points of the tune scan. Loss monitors located at the physics detectors were used to measure proton background losses. The

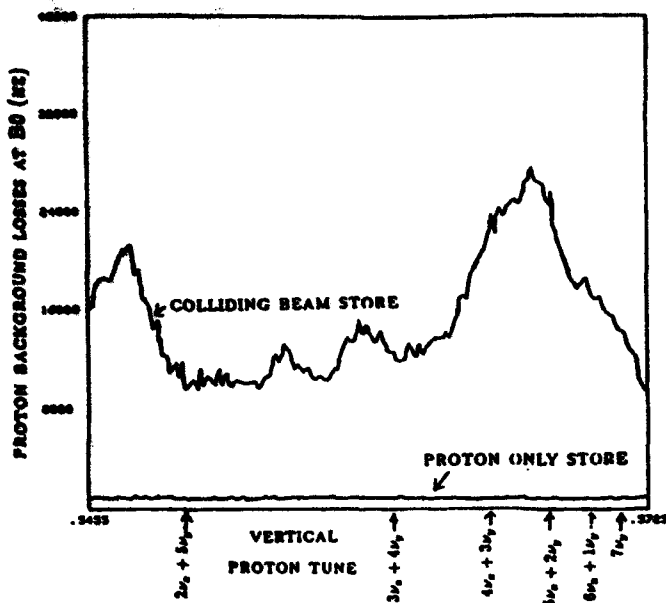


Figure 2: Proton losses crossing 7th order resonances for a proton only and a colliding beam store

colliding beam tune scans were done at the end of stores, when the proton and antiproton emittances were 25π and 18π , respectively.

A typical comparison of tune scans in which the proton vertical tune was moved across the 7th order resonance is shown in Figure 2. The horizontal tune of 20.58 was held constant during the scan. The result of the vertical tune scan show background losses to be large when the tune scan is done with protons and antiprotons in the machine, and negligible when protons only cross the 7th order resonance. Thus, in the Tevatron, the 7th order resonance gives measurable losses only when the beam-beam interaction is present.

When similar tune scans were done across 5th order resonances, background losses were seen when crossing some 5th order resonances during the proton only store. The losses became much larger when protons and antiprotons were colliding. This indicates that, along with a beam-beam driven response, there are nonlinearities in the Tevatron lattice which drive 5th order resonances.

A tune scan across the 12th order resonance, located in the midst of the Tevatron operating region, was found to cause minimal background losses under either proton only or colliding beam conditions. Proton and antiproton lifetimes, though, may be affected by the 12th and were not measured in this experiment.

ENSURING HEAD-ON COLLISIONS

The theory of the beam-beam interaction predicts that beams colliding with a separation or crossing angle will excite odd-ordered resonances². The results of the tune scans, indicating that the $\frac{1}{2}$ resonance is strongly driven by the beam-beam interaction, led us to investigate the possibility that the beams were colliding with a small separation or crossing angle at the interaction points. In order to measure the effects of collisions which were not quite head-on, separator four bumps were used to control the proton and antiproton orbits as they crossed the interaction regions.

The separators provide an electrostatic field which causes the protons and antiprotons to get kicked in opposite directions. By using four separators as elements in a closed bump (one that is local to the region between the bump elements), we are able to control both the separation and crossing angle at which the protons and antiprotons collide. The locality of the bump and the location of the separators in the Tevatron enabled collisions at each of the physics detectors to be controlled individually. This is the method by which head-on collisions are obtained in the Tevatron.

An experiment was done in which separator four bumps were used to vary the transverse separation of the colliding protons and antiprotons. The luminosity was measured as a function of the beam-beam separation. A simple one-dimensional dependance of luminosity, \mathcal{L} , on the transverse separation, d , of the centroids of two gaussian particle distributions can be written as³

$$\mathcal{L} = \mathcal{L}_0 \exp \left(-\frac{d^2}{2(\sigma_p^2 + \sigma_{\bar{p}}^2)} \right) \quad (1)$$

\mathcal{L}_0 is the luminosity when the collisions are head-on and σ_p and $\sigma_{\bar{p}}$ are the transverse rms beam size of the proton distribution and antiproton distribution, respectively.

A typical separation scan is shown in Figure 3. In this separation scan, the magnitude of a separator four bump across B0 is varied to allow the vertical separation of the centroid of colliding protons and antiprotons to change. The magnitude of the bump is smaller than the resolution of the beam position monitors in the ring. It is predicted here using a model of the Tevatron, TEVCONFIG⁴, which calculates an orbit for a given lattice configuration of the ring. By including the angular kicks of the separators used in the four bump, a predicted orbit is calculated. The magnitude of the voltage change of the separators can thus be translated into a beam-beam separation at B0. The luminosity is plotted in Figure 3 as a function of the beam-beam separation. A gaussian fit to the data calculates an rms σ of 62μ , where $\sigma = \sqrt{\sigma_p^2 + \sigma_{\bar{p}}^2}$ as seen in equation 1. The separation scans were done both in the horizontal and vertical planes at each of the interaction sites.

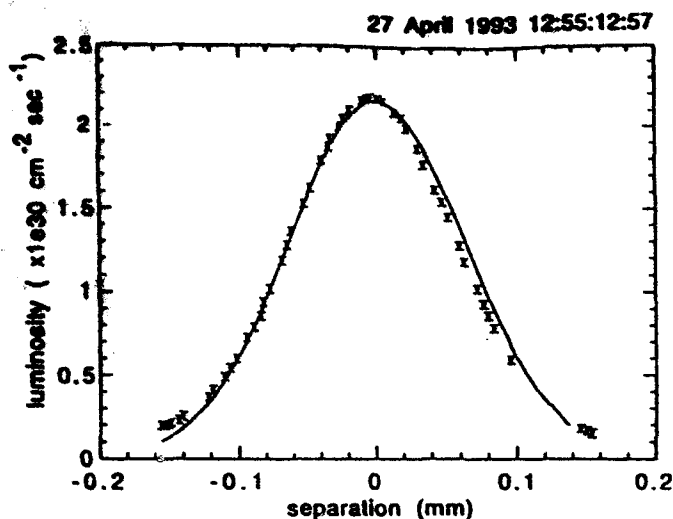


Figure 3: Separation Scan in the Vertical Plane at B0

The measurement of σ can be compared to one which is done using the flying wires in the Tevatron.⁵ Using the rms beam sizes which are obtained by this method, an rms σ of 57μ was calculated. The 8% discrepancy may be due to an inaccuracy in the lattice functions used in the calculations.

The luminosity was then measured as a function of the crossing angle at each of the interaction sites. A typical crossing angle scan is shown in Figure 4. In this case, the orbit distortion in the arcs is of the order of 1 mm, and the real orbit in the Tevatron can be compared to the TEVCONFIG prediction of the orbit. The data agrees within one LSB of the beam position monitors. A fit to the data is also shown, using a one-dimensional formula for the luminosity as a function of crossing angle⁶.

$$\mathcal{L} = \mathcal{L}_0 \left(\sqrt{1 + \frac{\sigma_z^2}{\sigma_x^2} \delta^2} \right)^{-1} \quad (2)$$

The crossing angle, δ , is defined as one half of the total crossing angle. The transverse sigma, $\sigma_x = \frac{1}{2} \sqrt{\sigma_{p_x}^2 + \sigma_{\bar{p}_x}^2}$, used as a parameter in the fit is 57μ . The longitudinal sigma, $\sigma_z = \frac{1}{2} \sqrt{\sigma_{p_z}^2 + \sigma_{\bar{p}_z}^2}$, is dependant on the longitudinal rms beam size of the protons and antiprotons. The value of σ_z used in the fit is 65 cm, comparable to a typical measurement of the rms of the longitudinal distribution in the Tevatron.

The results of the crossing angle scans indicate that under normal operation, the protons and antiprotons collide at the minimum measurable separation, but that there is a crossing angle of 50 urads (full crossing angle) at B0. This 50 urad crossing angle corresponded to a 5 percent loss in luminosity. After the separator voltages were adjusted for head-on collisions, a 5 percent increase in the initial luminosity was achieved.

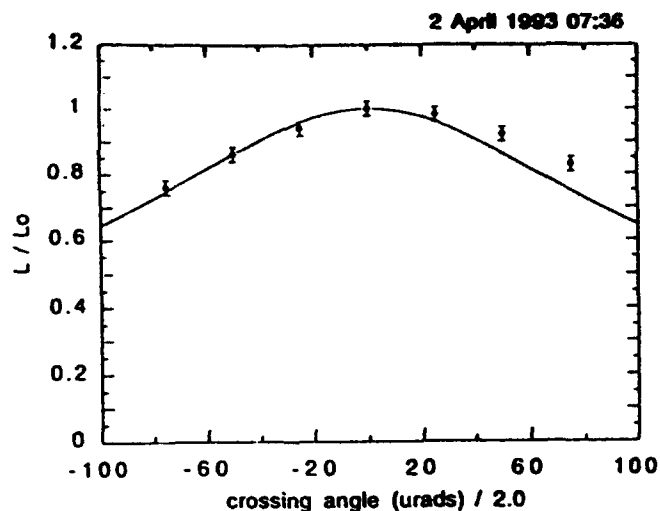


Figure 4: Crossing Angle Scan in the Horizontal Plane at B0

CONCLUSIONS

We have found that when operating the Tevatron with two-dimensional helical orbits, the luminosity is optimized by varying the separation and crossing angle at each individual interaction region. In the future, we plan to use this method of orbit control to investigate how the $\frac{4}{3}$ resonance is driven by beam-beam effects when the protons and antiprotons collide with small separations or crossing angles.

REFERENCES

- [1] D. Martin, et.al, A Shottkty Reciever for Non-Perturbative Tune Monitoring in the TEVATRON, FERMILAB-Conf-89/73, March 1989.
- [2] see, for example, S.G. Peggs and R.M. Talman, Non-linear Problems in Accelerator Physics, Ann. Rev. Nucl. Part. Sci., 36, pg. 287 (1986).
- [3] R. Dubois et. al., Beam Separation Experiments at the SPS Collider, CERN SPS/85-5 (DI-MST), January 1985.
- [4] Glenn P. Goderre, Online Model of the Tevatron, to be published. This will include our current understanding of the Tevatron lattice.
- [5] J. Gaunon, et. al., Flying Wires at Fermilab, Proc. IEEE Accelerator Conference, Chicago, IL, 1989, pg. 68.
- [6] M. Sands, The Physics of Electron Storage Rings; An Introduction, SLAC-121 UC-28, November 1970.

We would like to acknowledge David Finley for his helpful discussions and Paul Derwent for his help with the data analysis.

Beam-Beam Effects for the PEP-II B Factory†

Miguel A. Furman
Center for Beam Physics
Accelerator & Fusion Research Division
Lawrence Berkeley Laboratory, Berkeley, CA 94720, U.S.A.
and
Jennifer R. Eden
Department of Geophysics
University of Washington, Seattle, WA 98195, U.S.A.

Abstract

We present a summary of a fairly extensive study of beam-beam issues that arise in the design of PEP-II. Most of these studies are carried out with "strong-strong" multiparticle tracking simulations. We focus on: choice of nominal beam-beam parameter, strength of the parasitic collisions, injection issues, performance and tradeoffs with unequal beam-beam parameters. We comment only briefly on beam lifetime. We conclude that: the beams are sufficiently well separated so that the parasitic collisions are effectively weak; that small inequalities in the beam-beam parameters may imply more comfortable performance margins; and that vertical injection with vertical beam separation is more comfortable than horizontal.

1. INTRODUCTION

The proposed PEP-II B Factory is an asymmetric e^+e^- collider with a design luminosity of $3 \times 10^{33} \text{ cm}^{-2} \text{ s}^{-1}$ whose primary purpose is the detailed study of the B meson system. The two rings have the same circumference and intersect at only one interaction point (IP). In its present conception the low-energy ring (LER) contains the positrons, with an energy of 3.1 GeV, while the high-energy ring (HER) contains the electrons, with an energy of 9 GeV. Although the interaction region (IR) design allows for the possibility of crab crossing with a finite angle, in the current design the beams collide head-on and are magnetically separated in the horizontal plane. Full details of the design are contained in the Conceptual Design Report [1] and in the Design Update Report [2]. The current PEP-II design is slightly different from that described in these reports: the beta functions of the HER at the IP are now $\beta_x^*/\beta_y^* = 50/2 \text{ cm}$ rather than $75/3 \text{ cm}$, and the beam orbit separation at the first parasitic collision is now $d = 3.5 \text{ mm}$ rather than 2.8 mm .

The bulk of the beam-beam studies carried out to date have set a priority on demonstrating the feasibility of attaining or exceeding a short-time-average luminosity of $3 \times 10^{33} \text{ cm}^{-2} \text{ s}^{-1}$. The short-time-average luminosity is determined by the dynamics of the beam core, which is studied effectively with

"strong-strong" or "weak-strong" simulations neglecting all lattice nonlinearities. This linear-lattice approximation is legitimate for these purposes on account of the good dynamic-aperture properties of the PEP-II. Previous experiments and simulations [3] provide justification for this approximation once a good working point is adopted. On the other hand, the beam lifetime is determined by the long-time dynamics of the tails of the beam. This dynamics is far more complicated, and is generally expected to be sensitive to lattice nonlinearities. For this reason, and because it is impossible to have good average luminosity with poor peak luminosity, we have concentrated first on the dynamics of the beam core. Recent preliminary results [4], however, indicate acceptable lifetime.

In our simulations we typically represent the bunches by 256 "superparticles" that are initially Gaussian-distributed in 6-dimensional phase space, and we run for five damping times (we have carried out spot-checks with more superparticles). Thick-lens effects during the beam-beam collision are taken into account by dividing up the bunches into five slices. As time progresses, the distributions deviate a bit from Gaussian; however, for the purposes of computing the beam-beam kick, the time-dependent rms beam sizes are fed into the formula for the kick corresponding to a Gaussian distribution [5].

Due to the necessary approximations that are made, we cannot, in general, take our results to be quantitatively accurate. However, we believe that qualitative comparisons between results for different parameter values do provide valid guidance for desirable or undesirable changes in parameters. This is the philosophy that underlies the interpretation of our beam-beam studies, particularly multiparticle simulations.

2. BEAM-BEAM PARAMETER

The PEP-II design specifies a rather conservative value for the nominal beam-beam parameter, namely $\xi_0 = 0.03$ (all four beam-beam parameters are equal). The subscript 0 denotes "nominal," by which we mean "in the limit when the beam-beam interaction is negligible." Simulation results in the absence of parasitic collisions (PCs) [1,2] indicate that the dynamics behaves close to nominal (i.e., beam blowup is relatively small) up to $\xi_0 \sim 0.06$ – 0.08 provided a "good" working point is adopted (limited tune scans have suggested a working point with fractional tunes (0.64, 0.57) for both beams, which we have adopted for the present purposes; we have not tried to optimize the working point methodically).

†Work supported by the Director, Office of Energy Research, Office of High Energy and Nuclear Physics, High Energy Physics Division, U.S. Dept. of Energy, under Contract No. DE-AC03-76SF00098.

3. PARASITIC COLLISIONS

The large value required for the luminosity, coupled with other constraints, implies the need for many bunches, each of which has "normal" bunch current and emittance. This, in turn, implies short bunch spacing; thus, if the main collision is head-on, the bunches experience parasitic collisions in the IR. To be precise, each bunch experiences four PCs on either side of the IP (the optics and the geometry is symmetric about the IP in this region). The PCs on either side of, and closest to, the IP overwhelm the others, so we have only taken into account these first PCs in our simulations. The separation of the beam orbits at this point is $d = 3.5$ mm, corresponding to a normalized separation $d/\sigma_{0x,+} = 11.8$, where $\sigma_{0x,+}$ is the local nominal horizontal rms beam size of the LER (a normalization to the local HER beam size would yield the larger value of 14.4). In general, PCs induce tune shifts and tune spreads that can cause significant beam blowup. On the other hand, if the separation d is large enough, all effects from the PCs disappear. Simulations [1,2,6,7,8,9] in which the PC separation d is taken as a free parameter show that the PC becomes essentially weak provided $d/\sigma_{0x,+} \geq 7$. Thus the actual separation in the PEP-II design is comfortably large and the PCs are effectively weak. For the nominal value of the PC separation, the beam blowup has an inconsequential reduction of the luminosity to a dynamical value $\mathcal{L} \leq 2.9 \times 10^{33} \text{ cm}^{-2} \text{ s}^{-1}$.

When d is varied as an independent parameter, the tunes sampled by the beam core also vary due to the d -dependence of the PC tune shift. This spurious effect can be compensated for by appropriate changes in the bare lattice tunes. Simulations show that, when this compensation is in effect, the blowup curves look smoother, although the qualitative shape is the same [10], and the conclusions drawn from the uncompensated simulations remain unaltered.

4. VARIANTS

4.1 Larger ξ_0

We have examined [1,2,6,8,9] the consequences of increasing ξ_0 to 0.05. We have done this in two ways: (a) by increasing the bunch current by a factor of 5/3 at fixed nominal emittance, and (b) by decreasing the emittances by a factor of 3/5 at fixed bunch current. In case (a) the simulations show that the onset of substantial beam blowup occurs for $d/\sigma_{0x,+} \leq 9$ as d decreases. The beam blowup factor at the nominal value of d is larger than for 0.03; however, although the degradation of the luminosity relative to its nominal value, $\mathcal{L}_0 = 8.33 \times 10^{33} \text{ cm}^{-2} \text{ s}^{-1}$, is more significant, the resultant absolute dynamical value, $\mathcal{L} \leq 7 \times 10^{33} \text{ cm}^{-2} \text{ s}^{-1}$, is quite substantial. In case (b) the resultant nominal luminosity is $\mathcal{L}_0 = 5 \times 10^{33} \text{ cm}^{-2} \text{ s}^{-1}$, the beam sizes are a factor $\sqrt{3/5}$ smaller, and the normalized parasitic separation is thus $d/\sigma_{0x,+} = \sqrt{5/3} \times 11.8 = 15.2$. The simulation shows that the beam blowup in this case reduces the luminosity to a

dynamical value $\mathcal{L} \geq 4 \times 10^{33} \text{ cm}^{-2} \text{ s}^{-1}$. In this approach, the onset of substantial beam blowup also occurs for $d/\sigma_{0x,+} \leq 9$ as d decreases. We conclude that increasing ξ_0 by decreasing the emittance at fixed bunch current is safer, although less effective, than increasing the bunch current at fixed emittance.

4.2 Larger bunch spacing

One can increase the bunch spacing by 50% by filling every third RF bucket rather than every second bucket. In order to maintain ξ_0 and \mathcal{L}_0 at their original values, one must require that the bunch currents and nominal emittances of both beams also be increased by 50%. The total beam current remains unchanged but the beam separation at the new parasitic crossing point is $d = 10.1$ mm instead of 3.5 mm, and $d/\sigma_{0x,+} = 20.1$ instead of 11.8, which implies a much weaker parasitic collision. Simulations [1,2,8,9] show that the beam blowup is slightly less for this case than for the previous case at the nominal value of $d/\sigma_{0x,+}$. What is more important is that the comfort margin for d is significantly larger, since the value of 20.1 for $d/\sigma_{0x,+}$ is much larger than the "threshold" value of 7.

If the bunches are injected every third bucket but the emittances and bunch currents have nominal values instead of being 50% larger [8], then the first PC is such that $d/\sigma_{0x,+} = 24.6$ and therefore it is truly negligible. In this case the beam-beam parameter at the IP is still $\xi_0 = 0.03$, but the luminosity is $\mathcal{L}_0 = 2 \times 10^{33} \text{ cm}^{-2} \text{ s}^{-1}$. This operating configuration might be used as a comfortable intermediate stage in the commissioning of the machine, if necessary.

4.3 Unequal beam-beam parameters

We have also explored consequences of breaking the equality of the beam-beam parameters [11]. To this end we have carried out simulations in two cases: in approach (a) we set $\xi_{0x,+} = \xi_{0y,+} = \xi_{0+}$ and $\xi_{0x,-} = \xi_{0y,-} = \xi_{0-}$ with $\xi_{0+} \neq \xi_{0-}$. In approach (b), $\xi_{0x,+} = \xi_{0x,-} = \xi_{0x}$ and $\xi_{0y,+} = \xi_{0y,-} = \xi_{0y}$ with $\xi_{0x} \neq \xi_{0y}$ (the subscripts $+$ and $-$ refer to the e^+ or e^- beams, respectively). In both cases we have maintained the pairwise equality of the rms beam sizes at the IP, and kept the nominal luminosity fixed at $3 \times 10^{33} \text{ cm}^{-2} \text{ s}^{-1}$. Other constraints were in effect. The simulations show that: (1) In both approaches only the vertical beam blowup is significant, and this blowup behaves smoothly as the beam-beam parameters move away from full equality. (2) In approach (a), the dynamics favors (i.e., beam blowup is lesser) $\xi_{0+} = 0.024$, $\xi_{0-} = 0.04$ over $\xi_{0+} = \xi_{0-} = 0.03$. (3) In approach (b), the dynamics favors $\xi_{0y} = 0.023$, $\xi_{0x} = 0.04$ over $\xi_{0x} = \xi_{0y} = 0.03$. In both cases the dynamical value of the luminosity is slightly increased from the values corresponding to $\xi_{0x,+} = \xi_{0y,+} = \xi_{0x,-} = \xi_{0y,-} = 0.03$. We conjecture that, if the beam-beam parameters were chosen according to the preference expressed by the dynamics, the operation of the machine would perhaps be smoother. Of course, there are unfavorable implications for other areas of the design associated with these

changes. For example, in both of these approaches, the total current in the LER is higher than in the nominal case.

5. INJECTION SIMULATIONS

The transient effects that follow the injection of the first 20% batch of the low-energy beam when the high-energy beam is fully stored have been studied by Chin [12]. If the beam is injected in the horizontal plane, the centroid oscillations can lead to almost head-on collisions at the PC locations, with substantial beam blowup, during the transient time. If injection is in the vertical plane, the effects from the PCs are weak. The conclusion is that vertical injection is favored over horizontal.

Assuming that a temporary orbit bump will be required for smooth injection, we have [13] looked at the effects on the dynamics of the fully stored beams after all injection transients have died down but before the orbit bump is turned off. The optics of the PEP-II lattice is such that the kicking elements of a traditional orbit bump must be located at a distance ≥ 2.5 m from the IP. This happens to be true for both rings whether the separation is vertical or horizontal. This means that all four parasitic collisions on either side of the IP would be encompassed by such an orbit bump. If the beams are separated horizontally, the simulation results indicate that the closed orbit bump must be tightly constrained by the lattice functions and phase advances of all the PC locations in order to maintain the beams well separated, while there is no such constraint in the vertical-separation case. In the unlikely event that an orbit bump encompassing only the IP and the first PC could be designed, a horizontal separation $3\leq d_x/\sigma_{0x}\leq 10$ seems to be adequate for smooth injection. If the beams are vertically separated the dynamics is essentially determined by the main collision at the IP. In this case, a separation $d_y\geq (1-2)\sigma_{0x}$ is probably adequate for smooth injection. As a practical matter, the orbit separation must be \sim a few σ_{0x} 's in magnitude whether it is vertical or horizontal, for it to be effective; this conclusion from our simulations is consistent with available experience.

The horizontal-separation alternative does have the advantage that the simulations show no significant beam blowup when the beams are slowly brought into collision. In the vertical-separation case, on the other hand, the simulations show beam blowup of $\sim 75\%$ in the vertical dimension when the beam centers come together by a distance $d_y\sim (1-2)\sigma_{0y}$. Since PEP-II has conservative beam-stay-clear specifications, this temporary beam blowup seems a small price to pay, if any, for the added safety and simplicity of the vertical separation option.

6. CONCLUSIONS

(1) None of the simulation results show any indication that the energy asymmetry is a problem *per se*. Thus PEP-II (or any other asymmetric collider) does not seem to be qualitatively different from a single-ring, symmetric machine from the perspective of beam-beam dynamics provided the beam-beam effects are properly balanced [14]. (2) A beam-

beam parameter of 0.03 seems quite conservative for PEP-II. (3) The beams are sufficiently well separated that the PCs are effectively weak. (4) Small inequalities in the nominal beam-beam parameters may imply more comfortable performance margins but not substantially better luminosity performance. (5) Vertical injection with vertical beam separation is more comfortable than horizontal.

7. ACKNOWLEDGMENTS

We are grateful to NERSC for supercomputer support.

8. REFERENCES

- [1] "An Asymmetric B Factory Based on PEP: Conceptual Design Report," LBL PUB-5303/SLAC-372/CALT-68-1715/UCRL-ID-106426/UC-IIRPA-91-01, Feb. 1991.
- [2] "PEP-II: An Asymmetric B Factory Design Update," Feb. 1992, unpublished.
- [3] G. Jackson and R. Siemann, *Nuclear Instruments and Methods A286*, 17 (1990).
- [4] T. Chen and J. Irwin, unpublished results.
- [5] M. Bassetti and G. A. Erskine, CERN-ISR-TH/80-06.
- [6] Y.-H. Chin, Proc. 1991 Part. Accel. Conf., San Francisco, May 1991, p. 213.
- [7] J. L. Tennyson, ABC-29, April, 1991 (draft).
- [8] J. R. Eden and M. A. Furman, ABC-62/ESG Tech. Note 186, May, 1992.
- [9] J. R. Eden and M. A. Furman, PEP-II/AP Note 2-92/ESG Tech-Note 210, October, 1992.
- [10] J. R. Eden and M. A. Furman, PEP-II/AP Note 4-92/ESG Tech-Note 213, January, 1993.
- [11] J. R. Eden and M. A. Furman, PEP-II/AP Note 6-92, ESG Tech Note-216, February, 1993.
- [12] Y.-H. Chin, ABC-51/LBL-31434/ESG-158; LBL-32468; Proc. *Intl. Conference on B Factories: The State of the Art in Accelerators, Detectors, and Physics*, Stanford, California, April 6-10, 1992, p.130.
- [13] M. A. Furman, PEP-II/AP Note 14-93/CBP Tech Note-011, April 1993.
- [14] Y.-H. Chin, in *Beam Dynamics Issues of High Luminosity Asymmetric Collider Rings*, Ed. Andrew M. Sessler, AIP Conference Proceedings 214, p. 424 (1990); A. Garren et al, Proc. 1989 Particle Accelerator Conf., Chicago, March 20 - 23, 1989, p. 1847.

Equivalent Equations and Incoherent Lifetime Calculated from e^+e^- Beam-Beam Simulation

Y. Orlov

Newman Laboratory of Nuclear Studies
Cornell University, Ithaca, New York 14853, USA

Abstract

For given tunes (ν_x, ν_y, ν_s), the influence of different terms $x^h y^l s^m$ in the nonlinear beam-beam forces is different, so only some of them are important as sources of regular (nonstochastic) effects. As for irregular effects, it seems that in e^+e^- colliders the simultaneous action of both quantum fluctuations and three-dimensional nonlinearities creates effectively an additional stochastic force. The developed program of beam-beam simulation including Fourier analysis of different moments $M^{hlm}(t) = x^h(t) y^l(t) s^m(t)$ permits us to identify both regular and stochastic effective forces in the equivalent equations of the particles' motion. These differential equations can be used, for example, for the calculation of the particles' lifetime.

I. INTRODUCTION

The idea of extracting equivalent differential equations for particle coordinates x, y and s from incoherent spectrum densities calculated in the course of beam-beam simulations has been described in detail earlier [1,2]. The scheme of calculating the equivalent equations is the following.

The individual spectrum of a single particle # j is:

$$m_j^{hlm}(\nu) = \frac{1}{n_{\max}} \sum_n x_j^h(n) y_j^l(n) s_j^m(n) e^{-2\pi i \nu n}$$

$\Delta\nu = 1/n_{\max}$; n = the number of revolutions.

Incoherent "Schottky noise":

$$|F_{\text{incoh}}^{hlm}(\nu)|^2 = \frac{1}{N} \sum_j^N |m_j^{hlm}(\nu)|^2$$

N = the number of particles. x, y, s are taken in the IP (interaction point).

An example of the effective equation for the particles' vertical movement (as explained in [2]):

$$\begin{aligned} \ddot{y} + \gamma \dot{y} + \omega^2(x, y)y &= \\ &= a_1 y + b(x^2 - \langle x^2 \rangle)y + \\ &+ (c_0 + c_B) \sum_{t_k < t} \delta(t - t_k) \end{aligned}$$

(we can use the term $a_1 s y$ instead of $a_1 y$). Analogous equations can be written for x and s oscillations.

II. DIFFUSION

c_0 corresponds to the radiation fluctuations without BB interactions.

c_B describes the result of the combined effect of the radiation fluctuations and stochastic nonlinear diffusion.

For $\sigma^2 = \beta\epsilon$ we get

$$\frac{d\sigma^2}{dt} = -2\gamma\sigma^2 + \text{const} \cdot (c_0^2 + c_B^2) \approx 0$$

$$\sigma^2 = \sigma_0^2 + \sigma_B^2 = \beta(\epsilon_0 + \Delta\epsilon_B)$$

$$\frac{\sigma_B^2}{\sigma_0^2} = \frac{c_B^2}{c_0^2} \approx \frac{\Delta\epsilon_B}{\epsilon_0}; \quad c_B \cong c_0 \sqrt{\frac{\Delta\epsilon_B}{\epsilon_0}}$$

$$\Delta\epsilon_B = \text{const} \cdot \int \Delta d\nu$$

(see Fig. 1).

$$\epsilon_0 = \text{const} \int |F_0^s(\nu)|^2 d\nu$$

(Using real, not logarithmic scales!)

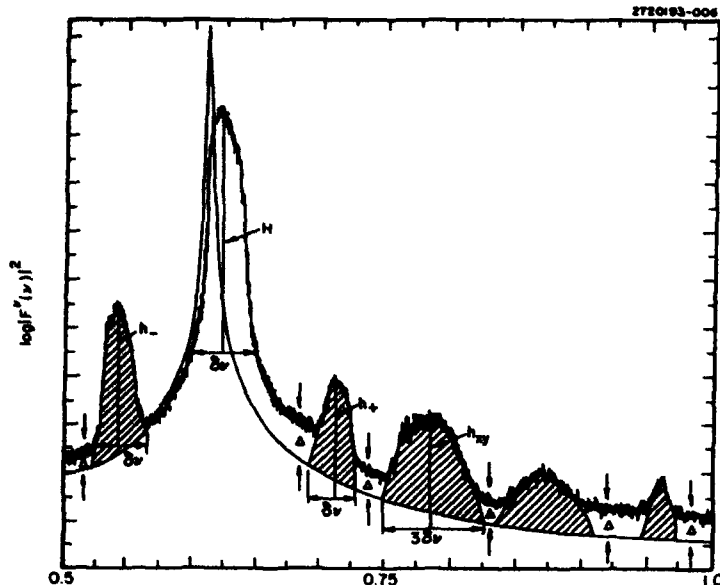


Fig. 1: Vertical spectrum density with and without b-b interaction. $\nu_{s0} = 0.568$, $\nu_{y0} = 0.610$.

III. LONGITUDINAL-VERTICAL COUPLING

Let us consider the equation (after the beginning of the BB interaction):

$$\ddot{y} + \omega^2 y = asy$$

$$y = y_0 + y_s; \quad y_0 = Ae^{i\omega t} + A^*e^{-i\omega t};$$

$$s = Be^{i\Omega t} + B^*e^{-i\Omega t}$$

$$y_s = \frac{-a}{\Omega(2\omega + \Omega)} \left(AB e^{i(\omega + \Omega)t} + A^* B^* e^{-i(\omega + \Omega)t} \right) +$$

+(the analogous term for $-\Omega$).

$$\frac{\langle y_s^2 \rangle}{\langle y_0^2 \rangle} = \frac{h_{\pm}}{H} \approx \frac{a^2 \sigma_s^2}{8\omega_0^4 \nu_y^2 \nu_z^2}$$

(ω_0 = revolution frequency)

$$a \approx \frac{2\sqrt{2}\omega_0^2 \nu_y \nu_z}{\sigma_s} \sqrt{\frac{\langle h_{\pm} \rangle}{H}} \quad (\sigma_s \equiv \sigma_L)$$

IV. HORIZONTAL-VERTICAL COUPLING

$$b \approx \frac{8\omega_0^2 \nu_s (\nu_s + \nu_y)}{\sigma_s^2} \sqrt{\frac{h_{sy}}{H}}$$

V. FAST LOSS OF PARTICLES IN THE BEGINNING OF BB INTERACTION

The distribution before BB interaction:

$$\phi_0 = e^{-\frac{A^2}{2\sigma_s^2}}, \quad A^2 = y^2 + \dot{y}^2/\omega_y^2$$

In the beginning of the BB, after $\Delta t \sim \tau_{\text{rad}} \sim \frac{1}{\gamma}$

$$\phi_B = e^{-A^2/2\sigma_B^2}$$

The technique previously used in [3] is used here. The number of particles $n = \text{const} \int \phi dA^2$. ϕ_B is the new distribution of the particles that survive after the beginning of BB plus Δt . After that the slow loss begins.

The fast loss of particles (during $\Delta t \sim \tau_{\text{rad}}$)

$$\delta_y = \int_0^\infty \frac{dA^2}{2\sigma_0^2} (e^{-A^2/2\sigma_0^2} - e^{-A^2/2\sigma_B^2}) = 1 - \frac{\sigma_0^2}{\sigma_B^2}$$

The full fast loss is

$$\delta = 1 - \frac{\sigma_{s0}^2 \sigma_{y0}^2 \sigma_{z0}^2}{\sigma_{sB}^2 \sigma_{yB}^2 \sigma_{zB}^2}$$

VI. LIFETIME OF THE BEAM CENTER DENSITY, $n(o)$

Here we give only an approximate estimation. We take into account only the diffusion mentioned in II. In this approximation, the lifetime τ_D depends mainly (and very strongly) on ξ , $\tau_D = f(\xi)$, [3]

$$\xi = \frac{A_{(\text{permit.})}^2}{2\sigma^2}$$

$A_{(\text{permit.})}$ is the permitted amplitude (the distance to the physical border, or to the dynamic aperture).

σ is rather uncertain. For big vertical amplitudes, when $A_y \sim A_{\text{permit}}$, $x - y$ coupling is essential; so, $\sigma \sim \sigma_x$ (and not σ_y).

According to [3]

$$\frac{n(\sigma, t)}{n(\sigma, 0)} \approx \xi(\xi e^{-t}) \cdot e^{-2\gamma t \xi e^{-t}}$$

Here $t = 0$ means just after the fast loss. For $t = \tau_D = 4$ hours, $\gamma = 1/400T$, $\frac{n(\sigma, \tau)}{n(\sigma, 0)} = 1/e$ we get $\xi \sim 24$; $A_{(\text{permit.})}/\sigma \sim 7$.

VII. REFERENCES

1. [1] Y.F. Orlov, C.M. O'Neill, A. Soffer. Fourier Analysis of $x^k y^l$ Moments in Beam-Beam Simulations. XV International Conference on High Energy Accelerators. Int. J. Mod. Phys. A (Proc. Suppl.) 2B (1993).
2. [2] Yuri Orlov and A. Soffer. Fourier Analysis of High Order Coherent and Incoherent Resonances in B-B Interaction. (I. Incoherent Spectroscopy). CLNS 92/1178
3. [3] Yu. F. Orlov and S. A. Kheifets. Losses of Particles in Ring Accelerators Taking Damping Into Account. Proceedings of the International Conference on High-Energy Accelerators and Instrumentation, CERN, 1959.

Simulation of Beam-beam Effects in Electron-positron Rings

Kohji HIRATA and Shuji MATSUMOTO

KEK, National Laboratory for High Energy Physics, Oho, Tsukuba, Ibaraki 305, Japan

Abstract

We examine the coherent beam-beam effects for the case of a very flat beam by multi-particle tracking. On resonances, the coupling between coherent dipole mode and higher modes plays an important role.

1 Introduction

Multi-particle tracking(MPT) is a powerful tool to evaluate the beam-beam effects accurately[1,2]. In MPT, beam is represented by a cluster of particles and each particle motion is pursued numerically. The aim of this report is to examine the significant effects on the coherent dipole motion by MPT. To this end, it is valuable to consider the problem in a simplified situation: both beams are *very flat*. In this case, the dominant beam-beam effect will appear in the vertical motion only. If we neglect the modulation on the vertical beam-beam force by the horizontal betatron motion, we can consider the beam-beam problem in one dimensional space. While this is a rather drastic simplification and an ideal mathematical limit, the result of this approach should be useful for further study on the beam-beam problem. In our approach, it is important that we evaluate the beam-beam kick without any kind of assumption for beam distribution.

When estimating the beam-beam force in a tracking study, sometimes, the beam barycenter motion is neglected (both beams are forced to be always in head-on collision)[1] or the beam envelope is approximated as a Gaussian[2]. The former scheme artificially eliminates the contribution from the dipole mode and the latter from some part of other higher order modes. However this may give a great influence on the beam motion. In fact, as for the latter, the importance of non-Gaussian effect was already pointed out[1]. In the present paper, we will see that we should also pay attention to the dipole motion.

MPT with these two schemes are less realistic than that with ours. We call the scheme of the former, MPT with Gaussian approximation, the Error-function Scheme (EFS) since the beam-beam force is described by the error function. As for the latter, MPT which does not include dipole mode, we call it the No-Dipole Scheme (NDS). Our scheme is called the Sorting Scheme (SS) since the beam-beam force calculation is executed based on the sorting algorithm.

2 MPT in one dimensional space

We consider a simple model ring that has only one interaction point(IP) and consists of only linear elements. The beam-beam kick at the IP is $\Delta Y_1 = 0$ and

$$\Delta Y_2 = -2\pi^{3/2}\eta \int dY_1^* \rho_*(Y_1^*) E(Y_1 - Y_1^*), \quad (1)$$

where $E(y) = \pm 1$ for $y \geq 0$, the quantity with * refers to the encountering bunch, ρ is the distribution function and η is the nominal beam-beam parameter. Here we use the canonical variables of an e^\pm , $Y_1^\pm = y_\pm/\sigma_{0y}$ and $Y_2^\pm = \beta_{0y} y'_\pm/\sigma_{0y}$, where σ_{0y} is the nominal vertical beam size and β_{0y} is the nominal betatron function at the IP. We can calculate the beam-beam force by counting the number of particles[3]. From Eq.(1), $\Delta Y_2 = -2\pi^{3/2}\eta(N_*^u - N_*^d)/(N_*^u + N_*^d)$, where $N^{u(d)}$ is the number of particles in the encountering bunch which are above (below) Y_1 . Any approximation in evaluating the beam distribution ρ is not necessary.

In the arc, the beams are transported with linear betatron motion perturbed by the effects of synchrotron radiation[4]: $(Y_1, Y_2)^t$ changes to

$$\lambda \begin{pmatrix} \cos \mu & \sin \mu \\ -\sin \mu & \cos \mu \end{pmatrix} \begin{pmatrix} Y_1 \\ Y_2 \end{pmatrix} + \sqrt{(1-\lambda^2)} \begin{pmatrix} r_1 \\ r_2 \end{pmatrix}$$

Here $\mu = 2\pi\nu$ (ν being the tune), $\lambda = \exp(-1/T)$ (T being the vertical damping time divided by the revolution time) and r_i is a Gaussian random number with zero mean and the unit r.m.s.

We define the beam coherent quantities as usual: for dipole modes, $\bar{Y}_i^\pm = \langle Y_i^\pm \rangle$ and for quadrupoles, $M_{ij}^\pm = \langle (Y_i^\pm - \bar{Y}_i^\pm)(Y_j^\pm - \bar{Y}_j^\pm) \rangle$, where $\langle \rangle$ means the average over the particles in a bunch and $i, j = 1, 2$.

3 Result and Discussion

We study the head-on collision only. The two beams have the same design orbit. We use a rather large beam-beam parameter, $\eta = 0.10$, in order to enhance the beam-beam effects.

3.1 Equilibrium behavior

We employ following three average quantities to specify it: the average distance of two barycenters $D \equiv \langle |\bar{Y}_1^+ - \bar{Y}_1^-| \rangle_{av}$, the average effective beam size $\Sigma \equiv$

$\langle \sqrt{M_{11}^+ + M_{11}^-} \rangle_{av}$ and the luminosity reduction factor:

$$R = \langle \sqrt{\frac{2}{M_{11}^+ + M_{11}^-}} \exp \left[-\frac{1}{2} \frac{(\bar{Y}_1^+ - \bar{Y}_1^-)^2}{M_{11}^+ + M_{11}^-} \right] \rangle_{av}.$$

Here $\langle \rangle_{av}$ means average over many turns. The real luminosity L is $L_0 \times R$ where L_0 is the nominal luminosity[5].

At first, we compare SS with EFS. The result is shown in Fig.1. Generally speaking, the equilibrium

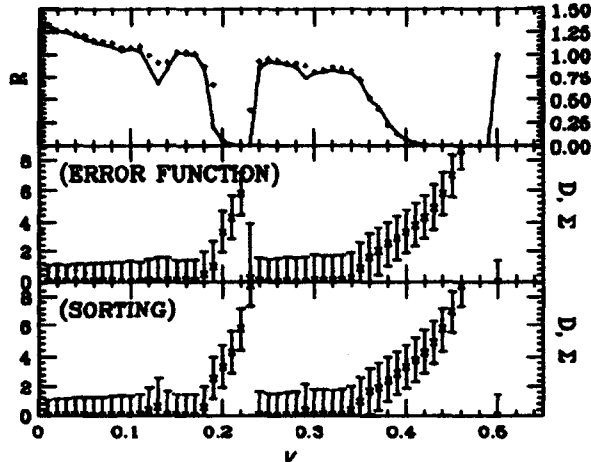


Figure 1: The tracking results of SS and EFS. (Top) the luminosity reduction factor R by SS (line) and EFS (+). (Middle) The barycenter difference D (×) and the effective beam size Σ (as error bars) by EFS. (Bottom) D and Σ in SS. Parameters: $\eta = 0.10$ and $T = 1000$. We started from $M = I$ and $\bar{Y}_1^+ - \bar{Y}_1^- = 0.0$ and tracked for 10000 turns. 1000 particles were used for each beam.

state predicted by EFS is very similar to the one by SS at almost all tunes. This is a surprising and interesting fact. As far as the equilibrium property is concerned, the Gaussian approximation for beam envelope seems to be good. There, however, are some exceptions.

We have a large dip in R below $\nu = 0.5$ (half-integer resonance). This is due to the coherent dipole instability[6, 7]. Another large dip is seen below $\nu = 0.25$ (the fourth order resonance) both in SS and EFS. We naturally expect the quadrupole instability[6], however SS and EFS show the appearance of dipole oscillation instead of beam size enhancement. The particle distribution in phase space is shown in Fig.2. We have tiny dipole excitation at the sixth order and the third order resonances in SS, while it does not exist in EFS.

To study these properties of nonlinear resonances, we will observe what occurs on the beam motion in a way to the equilibrium.

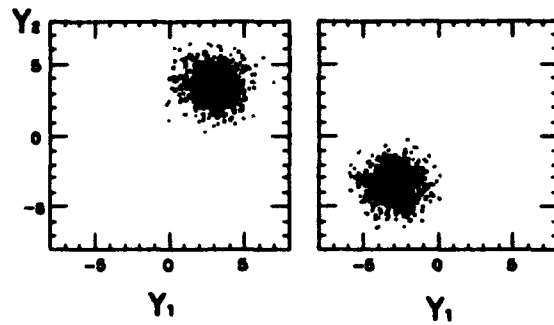


Figure 2: The phase space equilibrium distribution of e^+ and e^- bunches (Y_1^\pm, Y_2^\pm) on the fourth order resonance in SS. We have similar beam distribution in EFS. $\nu = 0.22$ The system moves in period-4.

3.2 Transition properties

Let us see the fourth order resonance first. See Fig.3. In

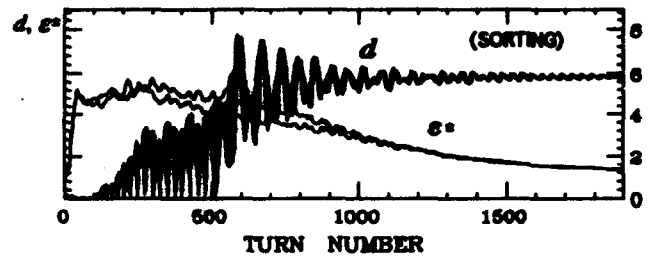


Figure 3: The change of the barycenter difference, $d = |\bar{Y}^+ - \bar{Y}^-|$ and two beam emittances, $\epsilon^\pm = (\det M^\pm)^{1/2}$, by every turn. For (first) 2000 turns in SS. $\nu = 0.22$.

SS, we have rapid growth of both beam sizes in the beginning. However, the dipole oscillation becomes prominent gradually and the beam sizes are slowly damped to the nominal one. The similar behavior was observed in EFS.

The same mechanism seems to work at the sixth order resonance (around $\nu = 0.16$) but not apparently. We have beam size enhancement first, but the excitation of the dipole mode is extremely slow: we tracked for 90000 turns (for 90 damping time), but the system does not seem to be in equilibrium. The phase space distribution in SS is shown in Fig.4. It seems that $\eta = 0.10$ is too small to excite a rapid and large dipole oscillation at the sixth order resonance. We observe a very small dipole excitation in EFS but it does not grow at all.

On the third order resonance, a similar mechanism seems to work. We found the dipole oscillation was excited only in SS. The origin of this excitation may attribute to the skewness of ρ , which makes the odd order

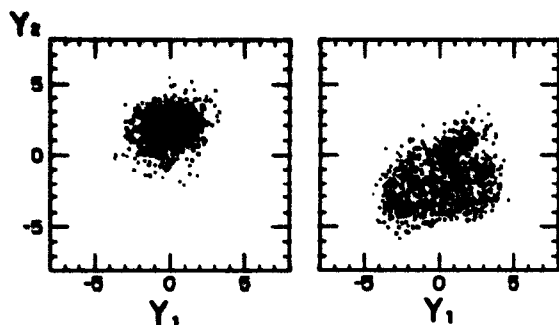


Figure 4: The particle distribution in phase space on the sixth order resonance after 90000 turns in SS. $\nu = 0.13$. The system may not still be in the equilibrium. Two beam envelopes are asymmetric ($(M_{11}^+/M_{11}^-)_{av} = 2.76$). Dipole mode is excited ($D = 2.0$).

components in beam-beam force with respect to Y_1 even with head-on collision. We found the flip-flop states in the equilibrium in SS only. In EFS, because of this assumption, the skewness is zero, so that the dipole excitation does not occur. On the contrary, in the collision with the primordial offset at IP, third order resonance can be excited even in EFS.

Above results indicate the importance of the coupling between dipole and higher order modes. In this sense, NDS is a special scheme since it assumes the existence of feed-back system that eliminates completely the beam dipole excitation. Especially, in the case where the dipole mode plays a dominant role, NDS will give a very different result. Let us see it.

3.3 No-Dipole Scheme

In NDS, a completely different motion appears on above nonlinear resonances, since the barycenter motion is completely eliminated before the two beams collide. See Fig.5 and compare it with Fig.2. In NDS, each beam splits into two pieces in phase space. Notice that the beam sizes change by period-2 and *out of phase* with each other. The assumption of a very fast and powerful feed-back system makes this difference.

4 Conclusion

We have realized that the coupling of coherent dipole mode and some other modes is important in the beam-beam dynamics. Its prominent effect was seen on the fourth order resonance, where the quadrupole mode was unstable first, but the dipole mode was excited gradually and finally beam separation took place. On the sixth order resonance, the same mechanism seems to work but not so obvious. Another example was seen at the third order resonance. It seems that a flip-flop phenomenon and a small dipole excitation coexist in the equilibrium.

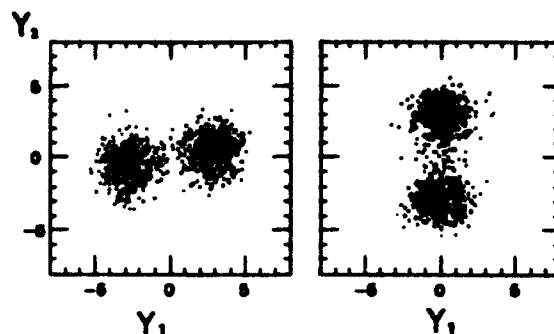


Figure 5: The equilibrium particle distribution in phase space in NDS. $\nu = 0.22$. The system moves in period-4, but the distribution is drastically different from that of SS. See Fig.2.

As stressed in [1], we should not use any assumption in calculating the beam-beam force. This applies for the dipole mode. The NDS treats the very special situation: ring with an extremely fast feed-back system.

References

- [1] S. Krishnagopal and R. Siemann, Phys.Rev.Lett., 67, 2461 (1991).
- [2] A.Piwnski, in Proc. 11 th Int. Conf. on High Energy Accelerators, Genève-July 1980, 751 (Birkhäuser,1980); E.Keil, Nucl. Instrum. Methods 188, 9 (1981); S. Myers, Nucl. Instrum. Methods 211, 263(1983).
- [3] K. Hirata, KEK Preprint-92-83 (1992), to appear in Particle Accelerators.
- [4] K. Hirata and F. Ruggiero, Particle Accelerators 28, 137 (1990).
- [5] Strictly speaking, the calculation of luminosity (reduction factor) by this method is not correct for non-Gaussian beam.
- [6] N. S. Dikanski and D. V. Pestrikov, Particle Accelerators 12, 27 (1982); A.W. Chao and R.D. Ruth, Particle Accelerators 16, 201 (1985); P. Zenkevich and K. Yokoya, KEK Preprint 92-116 (1992).
- [7] K. Hirata and E. Keil, Nucl. Instrum. Methods A292, 156 (1990).

Longitudinal Beam-Beam Effects in Circular Colliders

M. Hogan and J. Rosenzweig
Department of Physics
University of California, Los Angeles, CA 90024

Abstract

The longitudinal beam-beam interaction, which can lead to incoherent heating, synchrotron coupling, and coherent longitudinal instabilities in circular colliders, is examined. This analysis discusses two types of energy kicks, those due to the transverse particle motion coupling to the electric portion of the transverse kick, and those derived from the inductive electric field induced near the interaction, which is obtained from the transverse kick through use of a generalization of the Panofsky-Wenzel Theorem. Implications for low energy e^+e^- colliders (ϕ & B factories) with beams crossing head-on, and at finite angles, with and without crab crossing, are discussed.

I. INTRODUCTION

Table 1: Notation used in this paper.

e	electron charge
r	radial position
x, y	transverse coordinates
z	longitudinal coordinate
c	speed of light
$s = z - ct$	beam coordinate
p	particle momentum
d/ds	
σ_i	rms. beam size in i dim.
β	Beta-function
a	Courant-Snyder amplitude
N	# electrons in bunch
$*$	denotes evaluation at IP

An ultra-relativistic particle with longitudinal coordinate s_0 has E-M fields which are nearly normal to the direction of motion, and may be approximated as [1]

$$E_{\perp} = \frac{2e}{r} \delta(s - s_0) \quad (1)$$

where the notation is given in Table 1. Since particles do not all collide head on there is some longitudinal kick given during the beam-beam interaction. The net longitudinal kick can be obtained for a single particle by taking the projection of the transverse fields from the opposing beam onto the design orbit of the particle and integrating over the betatron phase space of the opposing beam. The resulting energy kick can be thought of as arising from two sources: a) longitudinal fields, and b) the work done by the transverse motion of the particle against the transverse fields.

For beams that do not collide at the nominal interaction point (IP), there is a time dependent beta function, $\beta(s)$, and the beam size variation gives rise to an inductive longitudinal field. The longitudinal momentum has been previously derived from a straight forward retarded relativistic calculation [2]. In the limit that the beams are shorter than β^* (this limit is assumed Ed throughout this paper), these kicks can also be

derived from a form of the Panofsky-Wenzel Theorem which is generalized to include fields arising from free charges [see Appendix].

$$\bar{V}_{\perp}(\Delta p_z) = \frac{\partial(\Delta \bar{p}_{\perp})}{\partial s} \quad (2)$$

We will employ the Panofsky-Wenzel theorem method in this paper, as it is simpler and more powerful than doing the straight forward calculation, especially for off-axis particles.

II. THE LONGITUDINAL BEAM-BEAM INTERACTION

The longitudinal kick due to transverse motion is the sum of the individual kicks a particle receives traversing the opposing bunch, calculated by integrating over the phase space of the opposing bunch. The resulting differential equation for the transverse acceleration involves complex error functions for elliptical beams.

A focused gaussian beam is described by a time dependent charge density and has associated transverse currents given by the continuity equation. By integrating the charge and current densities we obtain the corresponding scalar and vector potentials, which then describe associated electric and magnetic fields. The Lorentz force law may then be used to compute the instantaneous acceleration felt by a test particle traversing these fields. The resulting equations contain very tedious integrals that may be solved numerically [2].

Both cases yield results that are not intuitive and do not allow for an estimate of the size of these kicks which could determine the importance of this analysis for circular colliders. Therefore we will now consider certain limiting cases.

A. Round Beams

The energy change (ΔE) an off-axis test particle which travels at a nonzero angle with respect to the axis receives passing through an opposing beam is given by projecting the orbit of the particle onto the field of the opposing beam particles, as given by Eq. (1). Assuming a round beam with a gaussian distribution, Eq. (1) can be integrated to give the total energy change per passage:

$$\Delta E = -\frac{Ne^2}{r^2} \left[1 - \exp\left(-\frac{r^2}{2\sigma_r^2}\right) \right] (xx' + yy'). \quad (4)$$

Averaging over a betatron oscillation (which is assumed to be much shorter than a synchrotron oscillation), and expanding equation (4) for $r < \sigma_r$, reduces this to

$$\Delta E = \frac{Ne^2 \beta'(\frac{s}{2})}{2\beta(\frac{s}{2})} \left[\frac{a_x + a_y}{2\epsilon} \right], \quad (5)$$

where we have introduced the Courant-Snyder amplitudes of the particle. Note that if the beams do not collide at the nominal IP, implying that $\beta' \neq 0$, the energy kick averaged over a betatron oscillation is non-vanishing.

The energy kick due to the inductive field is computed using the Panofsky-Wenzel Theorem:

$$\frac{\partial(\Delta p_z)}{\partial r} = \frac{\partial(\Delta p_r)}{\partial s} \quad (6)$$

For round beams the transverse kick is, from equation (4),

$$\Delta p_r = \frac{2Ne^2}{cr} \left[1 - \exp\left(-\frac{r^2}{2\sigma_r^2}\right) \right] \quad (7)$$

Since

$$\sigma_r = \sigma_0 \left[1 + \left(\frac{s}{2\beta^*} \right)^2 \right] \quad (8)$$

has an s dependence, the longitudinal kick is obtained using Eqs. (7) and (8), and integrating the Panofsky-Wenzel expression (taking the boundary condition $\Delta p|_{r=0} = 0$) to yield

$$\Delta E = \Delta p_z c = \frac{Ne^2 \beta^* (\frac{1}{2})}{2\beta(\frac{1}{2})} \exp\left(-\frac{r^2}{2\sigma_r^2}\right) \quad (9)$$

Averaging over a betatron oscillation for $r < \sigma_r$, we have

$$\Delta E \equiv \frac{Ne^2 \beta^* (\frac{1}{2})}{2\beta(\frac{1}{2})} \left[1 - \frac{a_x + a_y}{2\epsilon} \right],$$

and the amplitude dependence of this kick is canceled by the term found in Eq. (5). Previous analysis[1] has not included this cancellation, which makes the energy kick more uniform as a function of position. The resulting total energy kick for round beams is

$$\Delta E = \Delta p_z c = \frac{Ne^2 \beta^* (\frac{1}{2})}{2\beta(\frac{1}{2})} \quad (10)$$

This energy kick, which is now correlated only to the relative longitudinal position of the oncoming bunch, can contribute to a coherent instability, as discussed in section III.

B. Flat Beams

Other relevant aspects of the beam-beam interaction can be analyzed in the limit that $\sigma_x \gg \sigma_y$. In this quasi-one dimensional case the Panofsky-Wenzel theorem reads

$$\frac{\partial(\Delta p_z)}{\partial y} = \frac{\partial(\Delta p_y)}{\partial s} \quad (11)$$

The transverse kick in a gaussian beam is given by

$$\Delta p_y = \frac{\sqrt{2\pi} Ne^2}{c\sigma_x} \operatorname{erf}\left(-\frac{y}{\sqrt{2}\sigma_y}\right), \quad (12)$$

where

$$\sigma_y = \sigma_0 \left[1 + \left(\frac{s}{2\beta_y^*} \right)^2 \right]^{\frac{1}{2}} \quad (13)$$

The contribution to the energy kick is now due to transverse motion can be found in analogy to Eq. 4. Also, the inductive energy kick is, using Eq. (11),

$$\Delta E = \Delta p_z c = \frac{Ne^2 \sigma_y \beta_y^* (\frac{1}{2})}{2\sigma_x \beta_y (\frac{1}{2})} \exp\left(-\frac{y^2}{2\sigma_y^2}\right) \quad (14)$$

Again, the transverse dependence is proportional to the current density, a variation which is canceled exactly by the energy kick due to transverse motion derivable from Eq. 12 for small amplitude ($y < \sigma_y$) particles. Note that this expression is smaller than the equivalent round beam formula (Eq. (10)) by a factor of $R = \sigma_y/\sigma_x$. This factor is due to larger average distances between particles ($R/2$) and weaker focusing in the x -dimension (2).

III. COHERENT BEAM-BEAM OSCILLATIONS

Longitudinal beam-beam effects can drive a coherent longitudinal oscillation. While this subject has been analyzed before[1], it has never been understood that the longitudinal beam-beam kick is nearly independent of x and y . The coupled equations of motion for the beam centroids ($s_{1,2}$) are

$$\begin{aligned} \ddot{s}_1 + \omega_s^2 s_1 &= (\pm) k_{bb} (s_1 - s_2) \\ \ddot{s}_2 + \omega_s^2 s_2 &= (\pm) k_{bb} (s_2 - s_1) \end{aligned} \quad (15)$$

Here, $k_{bb} \equiv V'_{bb}/V'_{rf}$, the rf gradient $V'_{rf} = k_{rf} V_{rf}$, and V'_{bb} (the effective beam-beam gradient) includes components due to both parallel and transverse motion of the beam particles:

$$eV'_{bb} = \frac{Ne^2}{2R\beta^{*2}} \quad (16)$$

The + (-) sign refers to operation above (below) transition. Above transition, we obtain the dispersion relation

$$\omega = \omega_s (1 - 2k_{bb})^{\frac{1}{2}} \quad (17)$$

Thus the instability threshold, which occurs when $\omega=0$, is given by $2V'_{bb} = V'_{rf}$. If the vertical beta function is lowered by a factor η , then V'_{bb} will increase by a factor of $\eta^{\frac{1}{2}}$. This is a strong dependence and may indicate trouble with higher luminosity designs.

If the machine is run below transition, the frequency of the coupled mode becomes

$$\omega = \omega_s (1 + 2k_{bb})^{\frac{1}{2}} \quad (18)$$

and there is no possibility of this coherent longitudinal instability.

IV. IMPLICATIONS FOR LOW ENERGY COLLIDERS

A. ϕ Factories

For the UCLA ϕ -factory design parameters, the expected energy kick for a one σ_x particle is ~ 1 keV. The rf voltage gradient $V'_{rf} = 1$ MeV/m is quite small due to the quasi-isochronous condition being employed. With $N=1.6 \times 10^{11}$, $R=7$, $\beta_y^* = 4$ mm, and emittances of 1.1×10^{-6} m-rad in both x and y , the effective beam-beam gradient is

$$eV'_{bb} = \frac{Ne^2}{2R\beta^{*2}} = 1 \text{ MeV/m} \quad (19)$$

If the machine is run above transition, this gradient is longitudinally defocusing, and one would expect serious bunch lengthening, since to first order there is complete longitudinal defocusing.

$$\frac{\sigma_z}{\sigma_{z0}} = \left(1 - \frac{V'_{bb}}{V'_{rf}}\right)^{-1} = \infty \quad (20)$$

This system is also above threshold for the longitudinal instability by a factor of two in beam charge.

If the machine is designed to operate below transition, the beams have stable coherent longitudinal motion. The beam-beam effects reinforce the rf focusing because

$$\frac{\sigma_z}{\sigma_{z0}} = \left(1 - \frac{V'_{bb}}{V'_{rf}}\right)^{-1} = \frac{1}{\sqrt{2}}. \quad (21)$$

This implies that the bunches could be shortened allowing shorter bunches than present designs indicate.

B. B Factories with Crab Crossing

Crab crossing schemes (Figure 1) may be necessary to provide the high luminosity's ($\sim 3 \times 10^{33}$) required for B-factories.

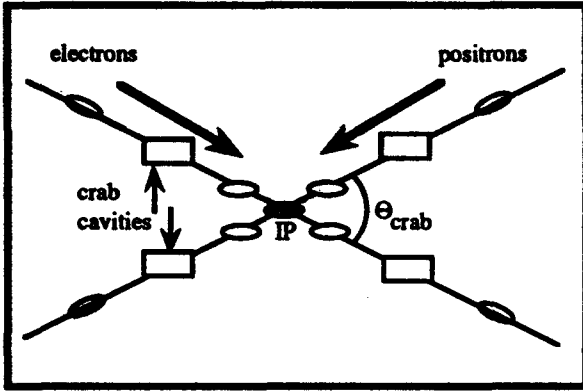


Figure 1: Schematic representation of crab crossing. Crab cavities apply time dependent rf kicks which tilt the bunches. After the collision, another set of crab cavities kick the beams back to there original orientations.

The longitudinal beam-beam interaction could become important in this type of scheme. Recall that the energy kick due to transverse motion for round beams contains terms proportional to xx', yy' . For crab crossing the angle x' is now essentially to the crossing angle. The resulting energy kick may again lead to large longitudinal effects. This issue needs to be investigated further.

V. CONCLUSION

This paper has analyzed two types of longitudinal kicks arising from the longitudinal beam-beam interaction: those due to the transverse particle motion coupling to the transverse portion of the electric kick, and those derived from the inductive electric field induced near the interaction point. These effects may become important in low energy or high luminosity colliders (ϕ & B factories) since they may lead to coherent longitudinal instabilities. These effects can be minimized by the use of flat beams. In addition, if coherent instabilities become a problem, it may be necessary to operate below transition. The effect on low energy colliders such as B-factories which may utilize crab crossing to improve luminosity needs to be addressed further.

Appendix: Generalized Panofsky-Wenzel Theorem

The Panofsky-Wenzel theorem gives a relationship between the integrated longitudinal and transverse momentum kicks a particle receives as it traverses a medium or device excited in the wake of another particle [4]. This appendix will generalize this theorem to include fields arising from free charges, assuming that fields and potentials vanish at infinity, and that the particle receiving the kick travels parallel to the z axis. In general, an electric field \vec{E} may be described in terms of a scalar potential (Φ) and vector potential (\vec{A}):

$$\vec{E} = -\frac{1}{c} \frac{\partial \vec{A}}{\partial t} - \vec{\nabla} \Phi. \quad (22)$$

Inserting (22) into the Lorentz force equation

$$\vec{F} = q \left(\vec{E} + \frac{\vec{v}}{c} \times \vec{B} \right) \quad (23)$$

and noting that for a particle traveling parallel to the z-axis

$$\frac{1}{c} \vec{v}_b \times \vec{B} = \beta_b \hat{z} \times (\vec{\nabla} \times \vec{A}) = \vec{\nabla}(\beta_b A_z) - \beta_b \frac{\partial \vec{A}_z}{\partial z} \quad (24)$$

we obtain the following expression for W, the force per unit charge q:

$$\vec{W} = -\frac{1}{c} \frac{\partial \vec{A}}{\partial t} - \vec{\nabla} \Phi - \left[\vec{\nabla}(\beta_b A_z) + \hat{z} \beta_b \frac{\partial A_z}{\partial z} \right]. \quad (25)$$

By noting that

$$\frac{1}{c} \left(\frac{\partial \vec{A}}{\partial t} + v_b \frac{\partial \vec{A}}{\partial z} \right) \Leftrightarrow \frac{1}{c} \frac{\partial \vec{A}}{\partial t} = \beta_b \frac{\partial \vec{A}}{\partial z}, \quad (26)$$

equation (25) can be rewritten as

$$\Delta \vec{p} = \frac{q}{c} \int_R \left[\beta_b \frac{\partial \vec{A}}{\partial z} + \vec{\nabla}(\beta_b A_z - \Phi) \right] dz. \quad (27)$$

Outside of region R, $\vec{A} = 0$, leaving

$$\Delta \vec{p} = \vec{\nabla} \left[\frac{q}{c} \int_R (\beta_b A_z - \Phi) dz \right]. \quad (28)$$

Since it can be derived from a potential, $\Delta \vec{p}$ satisfies the relation

$$\vec{\nabla} \times (\Delta \vec{p}) = 0. \quad (29)$$

In shorthand notation, this can be written as

$$\vec{\nabla}_\perp (\Delta p_z) = \frac{\partial (\Delta \vec{p}_\perp)}{\partial z}. \quad (30)$$

REFERENCES

- [1] V.V.Danilov, et. al., *Longitudinal Effects in Beam-Beam Interaction for an Ultra-High Luminosity Regime*, in *Beam-Beam and Beam-Radiation Interactions* p.1-10, Eds. C. Pellegrini, J. Rosenzweig and T. Katsouleas, (World Scientific Publishing Co., Singapore, 1991)
- [2] G. Jackson and R. H. Seimann, *Nucl. Instr. and Meth.* A286 (1990) p.17-31.
- [3] W. K. H. Panofsky and W. A. Wenzel, *Rev. Sci. Inst.*, 27, 967, 1956.

Yoshihiro Funakoshi and Horuyo Koiso
National Laboratory for High Energy Physics
1-1 Oho, Tsukuba-shi, Ibaraki, 305, Japan

Abstract

By using a symplectic code in the six dimensional phase space, we have tried to study beam blow-up due to the combined effect of the beam-beam force and the other non-linear forces from the lattice. Tune dependence of beam blow-up was studied. With the nominal beam-beam parameters of the KEK B factory (0.05), some beam blow-up was observed in the simulation. The simulation showed that the beam-beam interaction does not affect dynamic aperture.

I. INTRODUCTION

The motivation of this study arises mainly from designs of future B factories. The designers of B factories want to know the answers to the following questions; (1)How fast damping rate is required to keep the effects of the beam-beam interaction within a tolerable region? (2)Which tunes should we choose to minimize the harmful effects of the beam-beam interaction? (3)How long bunch length should we use? (4)How large (horizontal) crossing angle for the purpose of beam separation is allowable from the viewpoint of the beam-beam interaction? and so on. In studying the above issues, we should study not only the effects of the beam-beam interaction alone but also non-linearity of a lattice in conjunction with the beam-beam interaction. In this study we aimed at simulating beam behavior taking both effects of the beam-beam interaction and non-linearity of the lattice into consideration simultaneously. For this purpose we added the beam-beam force to the tracking code "SAD"[1] which has been developed at KEK. As for the beam-beam interaction we followed the method proposed by K. Hirata et al.[2] where both of the bunch length effect on the collision points and the energy change caused by the electric field of the counter-rotating beam are considered. The energy change is necessary to keep the map symplectic in the six dimensional phase space.

Our study is still at an early stage and in this paper some preliminary results on the head-on collision case are described. We used the lattice of the KEK B factory which is being designed for its low energy ring[3]. Although this study has been done on the KEK B factory ring, our method is, of course, in principle applicable to any ring collider.

II. FORMULA FOR THE BEAM-BEAM MAP

In this simulation a strong bunch is divided into some slices so that each slice contains the same number of particles. Each slice is represented by a infinitesimally thin disc which is located at the barycentre of the particles. We assume that the strong bunch has gaussian distribution in the six dimension. In the following, we consider a map for a weak particle affected by the strong (thin) slice. As is mentioned above, we used a beam-beam map proposed by K. Hirata et al.[2]. Here, we briefly describe this beam-beam map.

The motion of a particle belonging to the weak beam is described by the coordinate

$$x = (x, p_x, y, p_y, z, \epsilon)$$

as a function of the distance, s from the IP. (The values for the strong slice are specified by asterisks in subscript.) Here, x and y are the transverse position deviations from the nominal orbit. And p_x and p_y are associated momenta normalized by p_0 (the absolute value of three-momentum p for a reference particle; i.e.

$$(p_x, p_y) = \frac{m\gamma}{p_0} \left(\frac{dx}{dt}, \frac{dy}{dt} \right)$$

where γ is the Lorentz factor for the considered particle. In the longitudinal direction, we use

$$z = c(t_0 - t)$$

where c is the light velocity and $t_0 - t$ is the difference in the arrival times at s between the relevant particle and the reference particle. And we also use

$$\epsilon = \frac{p - p_0}{p_0} = \frac{E - E_0}{E_0}$$

where we assumed the ultra-relativistic beam for briefness. The map has the following form;

$$\begin{aligned} x^{new} &= x + S(z, z_*) f_X(X, Y, Z), \\ p_x^{new} &= p_x - f_X(X, Y, Z), \\ y^{new} &= y + S(z, z_*) f_Y(X, Y, Z), \\ p_y^{new} &= p_y - f_Y(X, Y, Z), \\ z^{new} &= z \\ \epsilon^{new} &= \epsilon - \frac{1}{2} f_X(X, Y, Z) [p_x - \frac{1}{2} f_X(X, Y, Z)] \end{aligned}$$

$$-\frac{1}{2}f_Y(X,Y,Z)[p_Y - \frac{1}{2}f_Y(X,Y,Z)] - g(X,Y,Z). \quad (1)$$

In these expressions, we use the usual Bassetti-Erskine formula for a gaussian bunch which gives the transverse (2 dimension) beam-beam kick[4];

$$f_y(x,y,\sigma_x(s),\sigma_y(s)) + if_x(x,y,\sigma_x(s),\sigma_y(s)) = -\frac{N_e r_e}{\gamma_0} \sqrt{\frac{2\pi}{\sigma_x^2 - \sigma_y^2}} \left\{ w\left(\frac{x+iy}{\sqrt{2(\sigma_x^2 - \sigma_y^2)}}\right) - \exp\left(-\frac{x^2}{2\sigma_x^2} - \frac{y^2}{2\sigma_y^2}\right) w\left(\frac{\frac{\sigma_x}{\sigma_y}x + i\frac{\sigma_x}{\sigma_y}y}{\sqrt{2(\sigma_x^2 - \sigma_y^2)}}\right) \right\}. \quad (2)$$

One should note that the arguments of f_x, f_y in the map are different from the above. We have to replace x, y and s in eq. (2) by X, Y , and S that are defined as follows:

$$S(z, z_*) = (z - z_*)/2, \\ X = x + p_x S(z, z_*), \\ Y = y + p_y S(z, z_*), \\ Z = z$$

The last term in eq.(1) comes from the longitudinal electric field due to the strong slice and are expressed for a gaussian distribution as

$$g(X,Y,\sigma_x(S),\sigma_y(S)) = (-\alpha_x + \gamma_x S)A_x + (-\alpha_y + \gamma_y S)A_y$$

where α and γ are twiss parameters at the IP and $A_{x,y}$ are defined by

$$A_{x,y}(X,Y,\sigma_x(S(Z)),\sigma_y(S(Z))) = \frac{1}{2(\sigma_x^2 - \sigma_y^2)} \{Xf_X + Yf_Y + \frac{2N_e r_e}{\gamma_0} \left[\frac{\sigma_{y,x}}{\sigma_{x,y}} \exp\left(-\frac{X^2}{2\sigma_x^2} - \frac{Y^2}{2\sigma_y^2}\right) - 1 \right] \}.$$

III. CHOICE OF BASIC TRACKING PARAMETERS

By using the tracking program, we have mainly studied beam blow-up and its (betatron) tune dependence. We also studied the effect of the beam-beam interaction on dynamic aperture. Prior to the tracking studies, we examined some basic parameters used in the trackings. To see beam blow-up multiple particles are tracked simultaneously. In this study we tracked 100 super particles which represent the weak bunch for each case. (Although we compared a case that 100 particles are tracked to a case of 1000 particles for one damping time (8000 turns), we found no essential difference between them.) In our simulation code, the strong bunch is composed of some thin slices. With some different number of slices we tracked 100 weak particles for five damping times (40000

turns). In the tracking we included the effects of radiation damping and quantum excitation. Fig. 1 shows the vertical beam size as a function of the number of turns. (In this condition beam blow-up in the horizontal or longitudinal direction was not remarkable.) As is seen in the figure beam blow-up does not depend significantly on the number of slices except in the case of one slice. However, in the following simulation we used 20 slices, since almost all computing time is devoted to the tracking in the lattice and increasing the number of the slices does not contribute to the total computing time. As is also seen in Fig. 1, 10000 or 20000 turns is maybe enough to estimate roughly the equilibrium beam size. In the following simulation we tracked 100 particles for 10000 turns for economy of time. The initial distribution for weak bunch is generated by a random number method with 6 dimension gaussian distribution. We use nominal machine parameters for the standard deviations of the distributions.

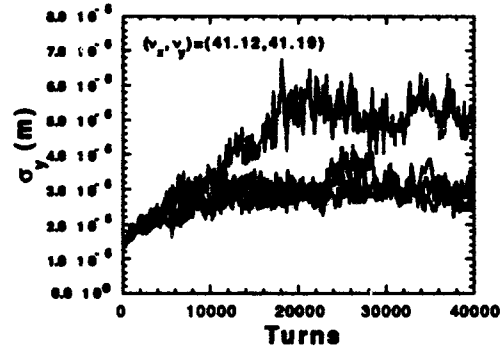


Figure 1: The vertical beam size as a function of the number of turns with different number of slices. The cases of 1, 3, 5, 10 and 20 slices were examined.

IV. SOME RESULTS OF THE SIMULATION

A. Dependence of beam size on betatron tunes

The nominal tune of the KEK B factory of the present design is $(\nu_x, \nu_y) = (41.12, 41.19)$. With some different vertical tunes we made trackings and observed equilibrium beam sizes under the condition that the horizontal tune was fixed at 41.12. The result of the tune survey is shown in Fig. 2. The solid line denotes the case that the beam-beam interaction exists. The dotted line designates the case that the beam-beam interaction is removed. Even without the beam-beam interaction, the vertical beam size increases around the coupling resonance. With the beam-beam interaction there are three peak. They might be assigned to the resonances of $\nu_x = \nu_y, 4\nu_y = 165$ and $2\nu_x + 2\nu_y = 165$. The nominal tune was chosen considering dynamic aperture and the coupling correction. Fortunately this tune is also good from the viewpoint of the beam-beam interaction. However, even with this good tune some beam blow-up is

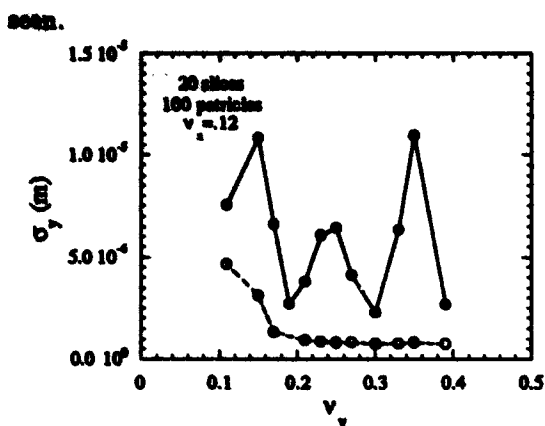


Figure 2: Tune dependence of the equilibrium beam size.

B. Dependence of beam size on the beam-beam parameters

At the nominal tune of $(\nu_x, \nu_y) = (41.12, 41.19)$, dependence of beam size on the beam-beam parameters were examined. The result is shown in Fig. 3. If the beam-beam parameter is small, the vertical beam size decreases as time goes by. This is because the initial beam size for which we used the nominal value of x-y coupling (1%) is different from the value which is determined by the lattice. In this study we did not consider any machine error and the calculated emittance ratio (ϵ_y/ϵ_x) was 0.1%. With the nominal beam-beam parameters of 0.05, some beam blow-up was observed in the simulation.

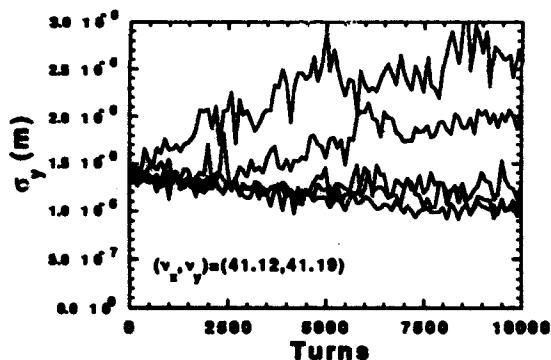


Figure 3: The vertical beam size as a function of the number of turns with different number of particles in the strong bunch. The cases with $\xi_x = \xi_y$ of 0, 0.01, 0.03, 0.04 and 0.05 are shown.

C. Dynamic aperture

At the nominal tune, we investigated dynamic aperture in two cases; with and without the beam-beam interaction. For each case, both the horizontal and the vertical apertures were studied. We found that dynamic aperture in both directions is not affected by the beam-beam interaction almost at all. In Fig. 4 the horizontal aperture is depicted as a function of momentum deviation. As is shown in the figure, there is no signature that dynamic aperture is influenced by the beam-beam inter-

action as far as the present case is concerned. However, this seems to be not so surprising, since unlike usual non-linear forces the beam-beam force decreases rapidly as the amplitude of the betatron oscillation becomes large.

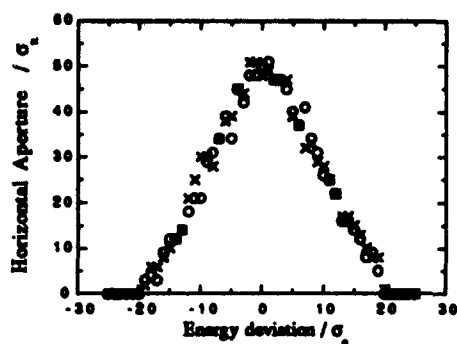


Figure 4: Horizontal dynamic aperture as a function of momentum deviation.

V. SUMMARY AND REMAINING PROBLEMS

By using a symplectic code in the six dimensional phase space, we have tried to study beam blow-up due to the combined effect of the beam-beam force and the other non-linear forces from the lattice. Beam blow-up depends on betatron tunes and the resonance lines which seem to induce the beam blow-up were found. However, to what extent the lattice non-linearity is responsible to the beam blow-up is not clear from the present study. To see this, it is important to compare the present results with the case that the non-linearity of the lattice is removed from the simulation and only the beam-beam force is a non-linear element in the ring. With the nominal beam-beam parameters of the KEK B factory (0.05), some beam blow-up was observed in the simulation. Aiming at suppression of this beam blow-up, shortening the radiation damping time may be helpful. The effect of the damping can be and should be simulated using the present code. The simulation showed that the beam-beam interaction does not affect dynamic aperture so far as the present case is concerned. Other interesting issues such as relationship between synchro-betatron resonance and crossing angle or bunch length can also be dealt with the present method and will be investigated shortly.

VI. REFERENCES

- [1] K. Oide, Nucl. Instr. Meth. **A276** 427(1989).
- [2] K. Hirata, H. Moshhammer and F. Ruggiero, KEK Preprint 92-117(1992).
- [3] B-Factory Accelerator Task Force, KEK Preprint 90-24(1990).
- [4] M. Bassetti and G. Erskine, CERN-ISR-TH/80-06(1980).

SYNCHROTRON BEAM-LOADING STABILITY WITH A HIGHER RF HARMONIC*

Tai-Sen F. Wang

AT-7, MS H825, Los Alamos National Laboratory
Los Alamos, New Mexico 87545, USA

Abstract

This work extends Robinson's stability studies [1] to include a higher rf harmonic. Using an equivalent circuit model, the stability of the "0-mode" coherent dipole oscillation of bunched beams is studied for synchrotrons or storage rings with rf systems operated at the fundamental and a higher harmonic, i.e., a second or third harmonic. Analytical expressions of the stability criteria are derived from the linearized circuit equations. Numerical solutions of the fully nonlinear equations are provided to compare with the analytical results. A simple feedback model for stabilisation is discussed.

I. INTRODUCTION

Higher-harmonic rf systems are frequently used in synchrotrons and storage rings to increase bunch length in order to reduce the space charge effects, and to damp the longitudinal instability by increasing the synchrotron frequency spread [2,3]. Under the circumstance of heavy beam-loading, instability may occur due to the beam-induced voltage on the cavities. For a single-frequency rf system, this kind of instability has been well studied [1,4]. However, few documents can be found on the theory of the stability of rf systems with higher harmonics [3,5]. A rigorous study of this subject requires either complex calculations using kinetic theory and nonlinear particle dynamics or substantial computer simulations for exploring the parameter space. Because some future accelerators may use a higher-harmonic rf system, a theoretical understanding of and methods for estimating the stability of double-harmonic rf system are needed before rigorous theory and computational data become available. Simple conditions for stability were obtained by Miyahara et al. [3]; however, these results are applicable for some specific cases only. In the followings, we discuss the beam loading stability in an rf system with a higher harmonic by directly investigating the equations derived from the equivalent circuit model. An example of controlling the system stability by using the "rf feedback" [6] will be given. Details of the mathematical derivations and part of the following materials have been included in a few recent reports [7,8].

II. THEORETICAL MODEL

*Work supported by the US Department of Energy, Office of High Energy and Nuclear Physics.

In the equivalent circuit model, an rf cavity is envisioned as a parallel *RLC* circuit. The applied rf power source and the circulating beam current can be modeled as currents i_g and i_b , respectively. We consider a system having two cavities: a "fundamental cavity" operated at the frequency ω_1 , which is equal to the h th harmonic of the revolution frequency of beam particles, and a "harmonic cavity" operated at the frequency ω_2 , which is equal to $n\omega_1$. For systems run with both frequencies of rf power in one type of cavity, the following formalism still is applicable.

By Kirchhoff's law, the total voltage on each cavity v_k satisfies the differential equation

$$\frac{d^2 v_k}{dt^2} + 2\alpha_k \frac{dv_k}{dt} + \omega_{rk}^2 v_k = 2\alpha_k \mathcal{R}_k \frac{d(i_{gk} + i_{bk})}{dt}, \quad (1)$$

where $k = 1$ (for the fundamental cavity) or 2 (for the higher harmonic cavities); t is the time, $\alpha_k = \omega_{rk}/(2Q_k)$, $\omega_{rk}^2 = 1/(L_k C_k)$; \mathcal{R}_k , L_k , C_k and Q_k are the shunt resistance, the inductance, the capacitance, and the quality factor of each cavity respectively. For high- Q cavities, only those Fourier components of i_k with frequencies near ω_{rk} need to be considered. In the steady state, v_k is maintained at the phase ψ_{vk} with respect to the beam current. Our interest here is the stability of the small oscillations of the phase deviations in cavity voltages ϕ_{vk} and beam current ϕ_{bk} ($\phi_{b2} = n\phi_{b1}$) around their steady states. Thus, making the substitutions of $v_k = V_k(t) \exp\{-j[\omega_k t + \psi_{vk} + \phi_{vk}(t)]\}$, $i_b \approx I_{b1} \exp\{-j[\omega_1 t + \phi_{b1}(t)]\} + I_{b2} \exp\{-j[\omega_2 t + \phi_{b2}(t)]\}$, and $i_{gk} = I_{gk} \exp\{-j(\omega_k t + \psi_{gk})\}$ in Eq. (1), we derive

$$\frac{1}{\alpha_k} \frac{dV_k}{dt} + V_k = \mathcal{R}_k [I_{gk} \cos \phi_{vk} - I_{bk} \cos(\phi_{bk} - \phi_{vk} - \psi_{vk})], \quad (2)$$

and

$$\frac{1}{\alpha_k} \frac{d\phi_{vk}}{dt} = \frac{\omega_{r1} - \omega_{gk}}{\alpha_k} - \mathcal{R}_k [I_{gk} \sin \phi_{vk} + I_{bk} \sin(\phi_{bk} - \phi_{vk} - \psi_{vk})]/V_k, \quad (3)$$

where $j = \sqrt{-1}$. Some approximations were used to derive Eqs. (2) and (3). First, we assumed that the bandwidths of the impedances of these two types of cavities are much smaller than the separation between their resonant frequencies, so only one of the beam current's harmonics is considered for each cavity. Second, because $\alpha_k \ll \omega_k$ for high- Q and high frequency cavities, we neglected the time derivatives of V_k and dV_k/dt when comparing with the products of these quantities and the rf frequencies. For

simplicity, we assumed $\psi_{sk} = \psi_{vk}$, i.e., the system is tuned for the rf sources to see real impedances. In obtaining Eq. (3), we also used the approximation $\omega_k + \omega_{rk} \approx 2\omega_k$.

The equations of beam motion are those of synchrotron motion:

$$\frac{d\Delta E}{dt} = \frac{q\omega_1}{2\pi h} [V_1 \sin(\psi_{s1} + \phi_{v1} - \phi_{b1}) - V_{s1} \sin \psi_{s1} + V_2 \sin(\psi_{s2} + \phi_{v2} - n\phi_{b1}) - V_{s2} \sin \psi_{s2}] , \quad (4)$$

and

$$\frac{d\phi_{b1}}{dt} = -\frac{\eta\omega_1}{\beta^2} \left(\frac{\Delta E}{E_0} \right) , \quad (5)$$

where E_0 is the total energy of the reference particle, ΔE is the energy deviation from E_0 , β is the speed of the reference particle divided by the speed of light, ψ_{sk} is the synchronous angle between the beam current and the cavity voltages, V_{sk} is the value of V_k at steady state, and $\eta = \gamma_t^{-2} - \gamma^{-2}$. In this paper we consider the case of $\gamma < \gamma_t$. However, the case of $\gamma > \gamma_t$ can be treated with the same procedures. Note that in the steady state $V_{sk} = \mathcal{R}_k(I_{gk} - I_{bk} \cos \psi_{vk})$, and

$$-(\mathcal{R}_k I_{bk} \sin \psi_{vk})/V_{sk} = (\omega_{rk} - \omega_k)/\alpha_k = \tan \phi_{yk} , \quad (6)$$

where ϕ_{yk} is referred to as the detuning angle.

III. LINEAR STABILITY CONDITIONS

Applying Routh's criteria [9], we obtain the following necessary and sufficient conditions for a stable system:

$$F_1 = b_0 > 0,$$

$$F_2 = b_3(b_4b_5 - b_3) - b_5(b_5b_2 - b_1) > 0,$$

$$F_3 = (b_4b_5 - b_3)(b_2b_3 + b_0b_5 - b_1b_4) - (b_2b_5 - b_1)^2 > 0,$$

and

$$F_4 = [b_3(b_4b_5 - b_3) - b_5(b_5b_2 - b_1)][b_1(b_2b_5 - b_1) - b_0b_3b_5] - [b_1(b_4b_5 - b_3) - b_0b_5^2]^2 > 0,$$

where

$$b_0 = \omega_s^2(1 - \xi)\rho_1\rho_2 - \lambda_1\rho_2 - \lambda_2\rho_1,$$

$$b_1 = 2\omega_s^2(1 - \xi)(\alpha_1\rho_2 + \alpha_2\rho_1) - 2(\alpha_1\lambda_2 + \alpha_2\lambda_1),$$

$$b_2 = \rho_1\rho_2 + \omega_s^2(1 - \xi)(\rho_1 + \rho_2 + 4\alpha_1\alpha_2) - \lambda_1 - \lambda_2,$$

$$b_3 = 2(\alpha_1\rho_2 + \alpha_2\rho_1) + 2\omega_s^2(1 - \xi)(\alpha_1 + \alpha_2),$$

$$b_4 = \rho_1 + \rho_2 + 4\alpha_1\alpha_2 + \omega_s^2(1 - \xi),$$

$$b_5 = 2(\alpha_1 + \alpha_2),$$

$$\xi = -(nV_{s2} \cos \psi_{s2})/(V_{s1} \cos \psi_{s1}),$$

$$\lambda_k = (\alpha_k^2 \omega_s^2 \mathcal{R}_k I_{bk} \tan \phi_{yk})/(V_{s1} \cos \psi_{s1}),$$

$$\rho_k = \alpha_k^2 \sec^2 \phi_{yk},$$

where $\omega_s = [(-q\eta h V_{s1} \cos \psi_{s1})/(2\pi m R^2)]^{1/2}$, is the synchrotron frequency without the higher harmonic rf field; q and m are the charge and the relativistic mass

of a beam particle respectively; and R is the averaged machine radius. All these conditions must be satisfied for the system stability. Condition $F_1 > 0$ can be rewritten as

$$\frac{I_{b1} \mathcal{R}_1}{V_{s1} \cos \psi_{s1}} < \frac{2(1 - \xi)}{\sin(2\phi_{y1}) - n\vartheta(\mathcal{R}_2/\mathcal{R}_1) \sin(2\phi_{y2})} , \quad (7)$$

where $\vartheta = I_{b2}/I_{b1}$. Equation (7) is similar to the result obtained by Miyahara et al. [3] except for the factor of ϑ on the right hand side. When $\xi = \vartheta = 0$, the above inequality reduces to the Robinson stability criterion [1]

$$\sin(2\phi_{y1}) < (2V_{s1} \cos \psi_{s1})/(\mathcal{R}_1 I_{b1}) . \quad (8)$$

The other Robinson stability condition, $\sin \phi_{y1} > 0$, can be obtained from the condition $F_4 > 0$ by letting $\xi = \vartheta = 0$ and $\alpha_2 \rightarrow 0$.

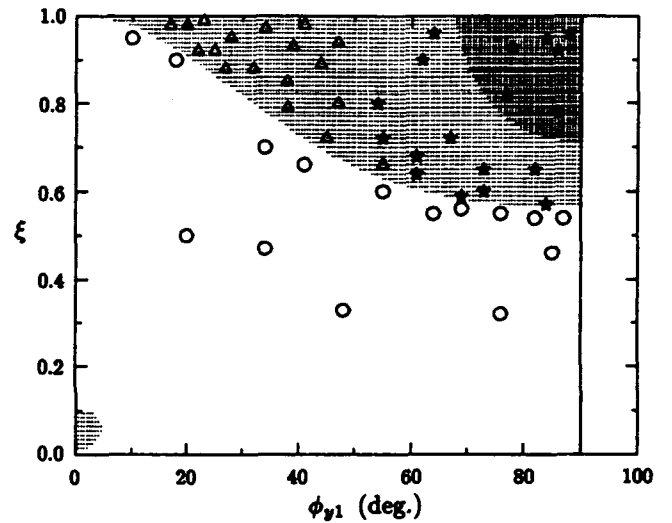


Figure 1. Comparison of the analytical and the numerical solutions for Eqs. (2)–(5). Shaded areas correspond to the unstable regions: $F_4 > 0$ at the lower left corner; $F_1 > 0$ and $F_4 > 0$ (heavily shaded) at the upper right corner. Numerical solutions of Eqs. (2)–(5) are shown by circles for stable and damped oscillations, stars for unbounded unstable solutions, and triangles for initially unstable but asymptotically bounded solutions.

The nonlinear equations (2)–(5) have been solved numerically to compare with the results evaluated from the linear stability conditions. In general, solutions of Eqs. (2)–(5) can be roughly grouped into three categories: (i) stable and damped oscillations, (ii) unbounded unstable solutions, and (iii) initially unstable but asymptotically bounded solutions. A comparison of the numerical with the analytical solutions is given in Figure 1. In this case, both the fundamental and second harmonic rf are used for bunching. The unstable zones are shown in the shaded areas on the $\xi - \phi_{y1}$ plane for the parameter values of $n = 2$, $\psi_{s1} = 0$, $\psi_{s2} = \pi$, $(\omega_s/\alpha_1)^2 = 0.1$, $\mathcal{R}_2/\mathcal{R}_1 = 0.3$, $Q_1 = Q_2$, and $\vartheta = 0.7$. The cavity detunings are related by $\tan \phi_{y2} = -(n\vartheta \mathcal{R}_2/\xi_1) \tan \phi_{y1}$. Conditions $F_2 > 0$ and $F_3 > 0$ are always satisfied in this region. Also

shown in Figure 1 are the qualitative results of more than fifty numerical solutions of Eqs. (2)–(5). The agreements between the analytical and the numerical solutions seem very good in describing the local stability.

IV. FEEDBACK CONTROL

We consider an example of increasing stability by using the “rf feedback” [6]. More control examples will be included in another paper [10]. In the rf feedback, a fraction of the rf gap voltage is subtracted from the driving signal at an appropriate point in the amplifier chain. When using this kind of feedback with an open loop gain of H , the effective cavity impedance will be reduced by a factor $(1+H)$. For a single-harmonic system, if the rf feedback is the only control used, the threshold current in Eq. (8) can be raised by a same factor. For a double-harmonic system equipped with separate rf feedbacks for each harmonic, the linear stability conditions derived in the last section are modified by the substitution of $\mathcal{R}_k \rightarrow \mathcal{R}_k^* = \mathcal{R}_k/(1+H_k)$ for $k=1$ and 2, where H_k is the open loop gains of the rf feedbacks. Analytical relations between the stability limits and H_k are difficult to obtain in this case and a numerical evaluation is necessary.

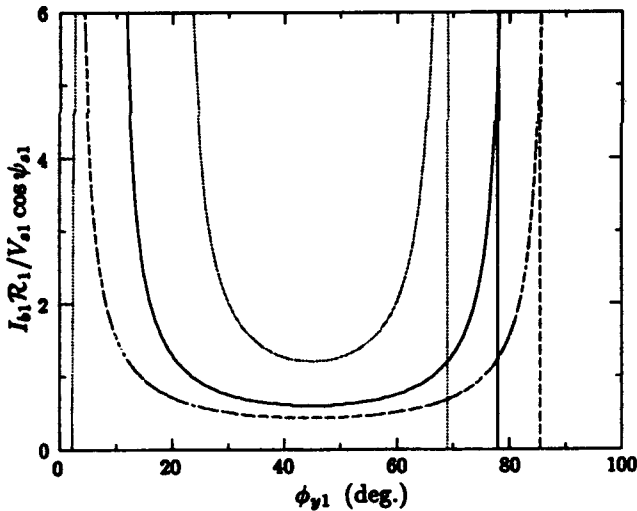


Figure 2. Plot of the threshold beam current versus ϕ_{y1} for $\mathcal{R}_2^*/\mathcal{R}_1^* = 0.8$ (dotted curves and lines), 0.4 (solid), 0.1 (dashed), and the system parameter values given in the text. The curves correspond to the solutions of $F_1 = 0$. The almost vertical lines on both sides of the curves are the solutions of $F_4 = 0$ (the LHS and the RHS solutions). For $\mathcal{R}_2^*/\mathcal{R}_1^* = 0.1$ and 0.4, the LHS solutions coincide with the line $\phi_{y1} = 0$. The stable zones are these regions below the curves and between the LHS and the RHS solutions. The thresholds derived from $F_2 > 0$ and $F_3 > 0$ are higher than 100.

As an example, consider an rf system operated at both the fundamental and the second harmonics. We assume that, in the absence of feedback, the system is characterized by $\xi = 0.8$, $Q_1 = Q_2$, $\phi_{y2} = 70^\circ$, $\vartheta =$

0.65, $(\omega_s/\alpha_1)^2 = 0.1$, and $\mathcal{R}_2/\mathcal{R}_1 = 0.4$. With the feedback on, the threshold beam currents normalized by $(V_{s1}/\mathcal{R}_1) \cos \psi_{s1}$, are shown in Figure 2 as functions of ϕ_{y1} for the cases of $\mathcal{R}_2^*/\mathcal{R}_1^* = 0.8, 0.4$, and 0.1.

As shown in Figure 2, the stability limit given by the vertical line on the right hand side of the figure moves towards a higher detuning angle when the ratio $\mathcal{R}_2^*/\mathcal{R}_1^*$ decreases. In the medium and low ϕ_{y1} regions, the stability limit given by the curve increases as the ratio $\mathcal{R}_2^*/\mathcal{R}_1^*$ increases. Thus, for systems operated at high ϕ_{y1} , H_2 needs to be higher than H_1 in order to increase the system stability. For the systems operated at medium and low ϕ_{y1} , it may be more desirable to have higher H_1 for higher stability.

V. CONCLUSIONS

Using an equivalent circuit model and linearized circuit equations, we derived the stability conditions for the beam-loading in synchrotrons or storage rings with a higher rf harmonic. We found that, when compared with the beam-loading stability limit of a single-frequency system, the addition of higher-harmonic rf without any external control may decrease the stability threshold. Numerical examples of the stability limits were given and compared with the analytical results. The agreements between the analytical and the numerical solutions in describing the local stability are very good. Finally, we gave an example of the use of the “rf feedback” control was discussed by using an example.

VI. REFERENCES

- [1] K. W. Robinson, Report No. CEA-11, Cambridge Electron Accelerator, Cambridge, Mass. (1956).
- [2] H. Frichholtz et al., CERN Internal Report CERN-ISR-RF-TH/DL/77-41 (1977).
- [3] Y. Miyahara et al., *Nucl. Instrum. and Methods*, **A260**, 518 (1987).
- [4] See the references in: T. F. Wang, *Particle Accelerators*, **34**, 105 (1990).
- [5] A. Hofmann and S. Myers, *Proc. of the XIth Intl. Conf. on High Energy Accelerators*, 610 (1980).
- [6] F. Pedersen, *IEEE Trans. Nucl. Sci.*, Vol. NS-32, No. 5, 2138 (1985).
- [7] T. F. Wang, *Proc. of the XVth Intl. Conf. on High Energy Accelerators*, 1097 (1992).
- [8] T. F. Wang, Los Alamos National Laboratory Accelerator Theory Note AT-7:ATN-92-11 (1992).
- [9] E. J. Routh, *A Treatise on the Dynamics of a System of Rigid Bodies* (Macmillan, 1877).
- [10] T. F. Wang, Los Alamos National Laboratory Accelerator Theory Note. In preparation.

Compensation of Bunch Position Shift Using Sub-RF Cavity in a Damping Ring

K. KUBO, T. Higo and S. Sakanaka
KEK, National Laboratory for High Energy Physics
1-1 Oho, Tsukuba, Ibaraki, 305 Japan

Abstract

In the damping rings of future linear colliders, bunches will be filled along the ring in a bunch-train configuration, where spacing between trains is much larger than bunch-to-bunch spacing in a train. Because of this configuration, beam loading in RF cavities will cause the shift of bunches from their nominal longitudinal positions. The shift can be compensated with an active or a passive RF cavity whose resonance frequency is well controlled. By tracking simulations, the method is demonstrated for ATF damping ring at KEK.

I. INTRODUCTION

In order to achieve high luminosity, a train of many bunches with narrow spacing is accelerated in a long RF pulse. In the damping rings for this type of operation, beams should have bunch-train configurations. Beams in the ring will consist of some trains which contain many bunches with narrow spacing. Spacing between trains in a ring should be longer than rise and fall time of kicker magnets for injection and extraction and will be much longer than spacing of bunches in a train. In the present design of JLC(Japan Linear Collider), spacing between bunches in a train is less than 6 nsec and spacing between trains is more than 60 nsec.

Bunches in this configuration induce transient beam loading in RF cavities varying from bunch to bunch in a train; a bunch in tail of a train feels higher wake field than a bunch in head of a train. This non uniformity causes shift of bunch positions according to where the bunches are in a train. Without any cure, the maximum amount of shift from nominal positions can be more than bunch length resulting in a significant deterioration of the quality of the multibunch beam.

In order to compensate different beam loading from bunch to bunch in the main RF cavities, sub-RF system is proposed here.

The effect of the system is demonstrated by tracking simulations for the ATF(Accelerator Test Facility at KEK) damping ring. Longitudinal bunch motions were simulated taking account the generator induced voltage, wakefield of the accelerating mode and wakefield of some higher order modes. Each bunch was assumed to be a point charge. Used parameters of the ring are as follows.

Beam energy	1.54 GeV
Revolution frequency	2.16 MHz
RF frequency	714 MHz
Maximum beam current	0.6A
Radiation loss	0.20MeV/turn
Momentum compaction α	0.003
Damping partition number	1.78
RF cavity : Total voltage	1.2 MV
Shunt impedance	14.4 M Ω
Unloaded Q	22000
Coupling	2.34

Various scheme of bunch configurations (number of trains, number of bunches in a train and charge of a bunch) will be tested in the ATF within the maximum total current of 0.6A. In this paper, two extreme cases were examined as examples:

Case (a). 5 trains/ring,

20 bunches/train and 2×10^{10} e/bunch

Case (b). 3 trains/ring,

68 bunches/train and 1×10^{10} e/bunch

II. EQUILIBRIUM POSITION SHIFT

Accelerating field in RF cavities will be controlled by feedback loop to keep the field strength and phase constant. Because speed of the feed back will be much slower than the transient time of a train, field induced by non uniformly filled bunches can not be compensated. This will cause time dependent modulation of the amplitude and phase of accelerating field within a train.

Fig. 1 shows change of amplitude and phase of total cavity voltage vs. time which are calculated by tracking simulation for the case (a). The trajectory of the voltage on complex plane can be seen in Fig. 2 where reference phase is the phase of nominal bunch position. During passage of a bunch train, bunches induce voltage of opposite direction to themselves. Between trains, the field decays and rotates according to the Q-value and frequency detuning of the cavities.

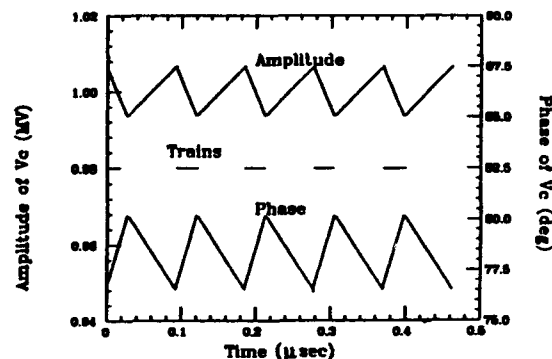


Fig. 1, Amplitude and phase of cavity voltage with non uniform bunch population.

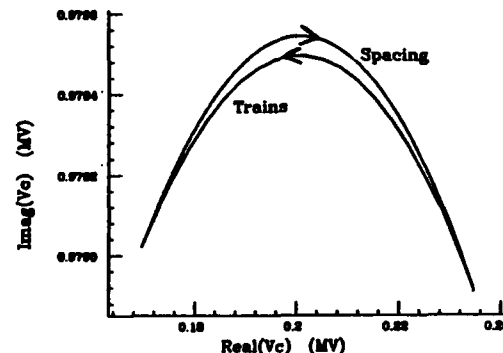


Fig. 2, Trajectory of cavity voltage on complex plane.

Because all bunches have the equal revolution time, the energy must be equal and radiation loss of all bunches along the ring should have the same value. This means all bunches should gain the same voltage at the RF cavities. To be accelerated by the same amount from the field of different amplitude and phase, bunches will change their timing of passage at the cavities or the equilibrium position of bunches will shift from their nominal positions. Fig. 3 shows time delay from nominal positions of 1st, 10th and 20th bunches in a train which are calculated by tracking simulations for the case (a). The horizontal axis shows number of turns along the ring. The equilibrium position of the head bunch is delayed and tail bunch is advanced from the nominal positions. Initial condition was that all bunches have the same longitudinal position error of 10 psec. Fig. 4 (a) and (b) show the equilibrium positions of bunches vs. bunch number in a train for the case (a) and (b), respectively. Bunch number 1 means the head bunch in a train and the last number means the tail of a train. The values of the shift are almost linear to the bunch number. Nonlinearity of the first bunch is caused by the wakefield of the higher order mode.

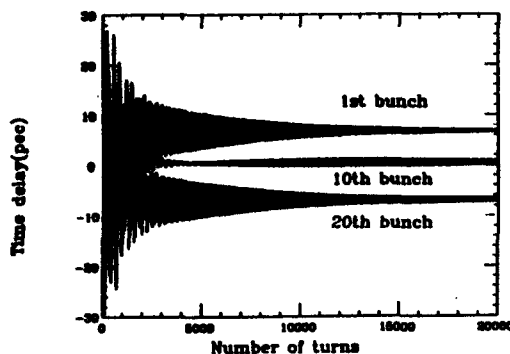


Fig. 3, Time delay from nominal positions of 1st, 10th and 20th bunches in a train versus number of revolution.

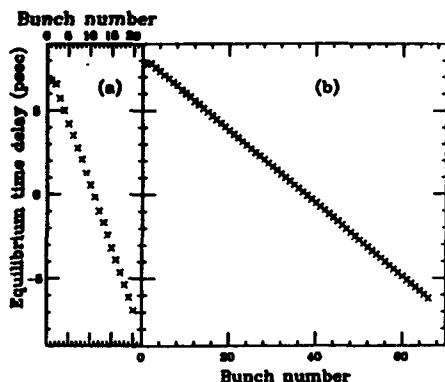


Fig. 4, Equilibrium positions of bunches vs. bunch number for case (a) and case (b).

The maximum values of the shift in both cases are comparable of the bunch length of the order of 10 psec. After extracted from the ring, the position difference means different RF phases along the main linac of the linear collider. The resulting significant energy difference may easily deteriorate the emittance of multibunch beam through bunch compressor, main linac and final focus region.

III. COMPENSATION BY ACTIVE SUB-RF SYSTEM

To correct the shift of the bunch positions, sub-RF system is proposed. RF field with frequency of

$$f_{\text{sub}} = f_{\text{RF}} - N_t f_{\text{rev}}$$

can compensate the difference of the field of the main RF, where f_{RF} is the frequency of the main RF, f_{rev} the revolution frequency and N_t the number of trains. Adjusting the phase of the sub-RF field so that the voltage is zero at the nominal timing of the passage of the center bunch in a train, bunches in head of a train will be decelerated and bunches in tail of a train will be accelerated. If length of a bunch-train is short enough compared with the bunch spacing, as in the case (a), the compensation can be almost linear. But if the length is not short, as in the case (b), the nonlinearity of the compensation field may be important.

As is shown in Fig. 2, required strength of compensation field is several tens of kilovolts and can be obtained by introducing one cavity (sub-RF cavity).

The total voltage is vector sum of generator (external power source) induced voltage and beam induced voltage. Here, shunt impedance, unloaded Q and loaded Q of the sub-RF cavity are assumed to be $2M\Omega$, 20000 and 10000, respectively. Amplitude and phase of the total voltage is assumed to be fixed by controlling cavity tuning and RF input. In the case of (a), in order to obtain total voltage of 40 kV and the phase of 90 degree respect to the nominal phase of the center bunches in trains, detuning angle (detuning from sub-RF frequency f_{sub}) is -86.1° and required power is 0.8 kW.

Fig. 5 shows time delay from nominal positions of 1st, 10th and 20th bunches in a train with sub-RF, which are calculated by tracking simulations for the case (a). This can be compared with the result without compensation in Fig. 3. Fig. 6(a) shows the equilibrium positions of bunches vs. bunch number in a train for the case (a) with sub-RF whose voltages are set to be 30 kV, 40 kV, 50kV and 60 kV. Fig. 6(b) shows the equilibrium positions of bunches vs. bunch number in a train for the case (b) with sub-RF voltages are set to be 20 kV, 30 kV, 40kV and 50 kV. This shows voltage of about 30 ~ 40 kV is optimum. In the case (a), the residual shift is much smaller than the bunch length (about 5 mm in r.m.s.). In the case (b), the residual is several percent of the bunch length in r.m.s.

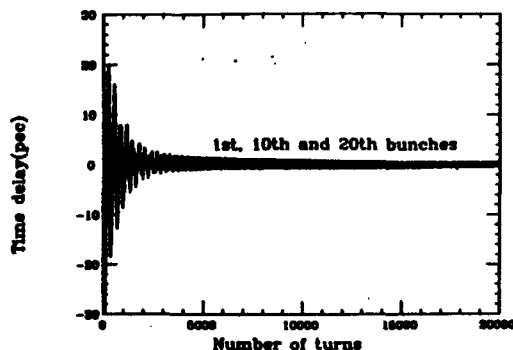


Fig. 5, Time delay from nominal positions, 1st, 10th and 20th bunches in a train for case (a) with active sub-RF.

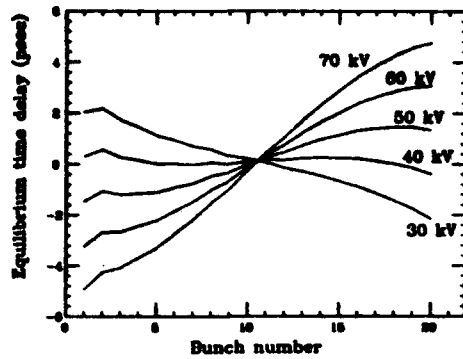


Fig. 6(a) Equilibrium positions of bunches vs. bunch number for case (a) with active sub-RF.

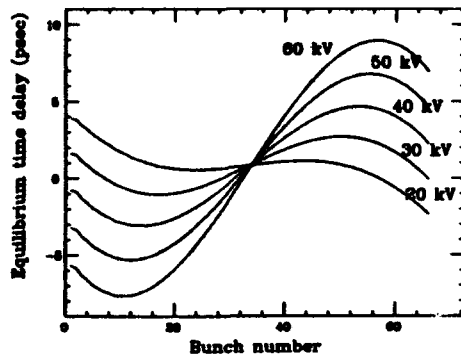


Fig. 6(b) Equilibrium positions of bunches vs. bunch number for case (b) with active sub-RF.

IV. COMPENSATION BY PASSIVE SUB-RF SYSTEM

If detuning angle (ϕ) of sub-RF cavity is near -90° , the phase of beam induced voltage is near by 90° with respect to the center beam and the generator induced voltage is very small ($\cos\phi$ of the total voltage). Without generator power, the voltage in the sub-RF cavity is only beam induced voltage. It means that the compensation will be possible without input power. For a passive RF cavity, only resonance frequency can be controlled in operations in order to obtain appropriate compensation.

With the same parameters as in section III but without input power, tracking simulations were performed with some cases of detuning of the cavity. Fig. 7 shows time delay from nominal positions of 1st, 10th and 20th bunches in a train with passive sub-RF for the case (a) where cavity detuning angle is -86.0° or detuning from f_{sub} is -500 kHz. Fig. 8(a) and (b) show the equilibrium positions of bunches vs. bunch number in a train with passive sub-RF with several detuning frequencies. These figures show that a frequency controlled passive sub-RF cavity can be used for the compensation. With appropriate detuning, residual shift is as small as that with active sub-RF compensation in each case.

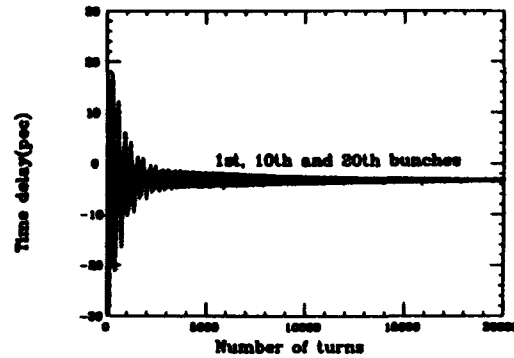


Fig. 7, Time delay from nominal positions, 1st, 10th and 20th bunches in a train for case (a) with passive sub-RF.

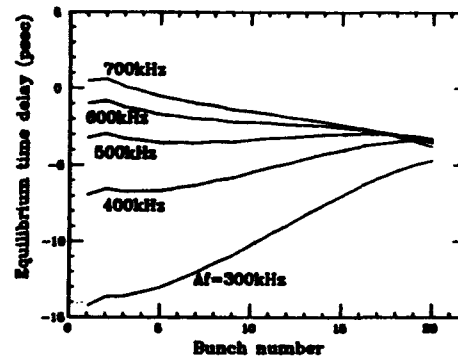


Fig. 8(a) Equilibrium positions of bunches vs. bunch number for case (a) with passive sub-RF.

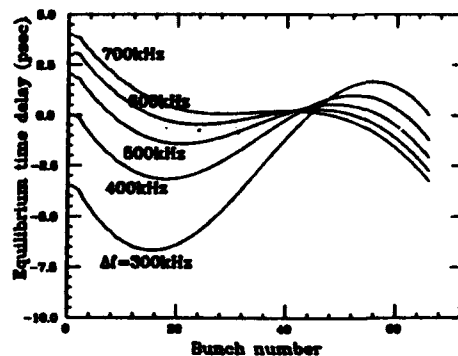


Fig. 8(b) Equilibrium positions of bunches vs. bunch number for case (b) with passive sub-RF.

V. SUMMARY AND DISCUSSION

It was found that equilibrium position shift in damping rings for future linear colliders with bunch-train configuration can be compensated by active or passive sub-RF system.

As the case (b), if length of a train is longer than spacing between trains, residual shift may be significant. If necessary, adding higher order sub-RF with frequency of $f_{RF} - nN_t f_{rev}$ ($n=2,3, \dots$), this residual shift will be compensated.

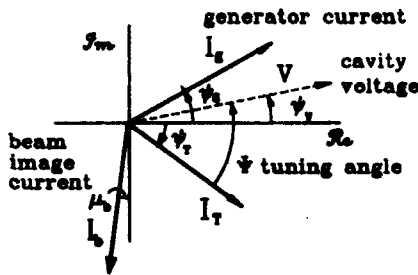
Analytic Criteria for Stability of Beam Loaded R.F. Systems

Shane R. Koscielniak, TRIUMF Vancouver B.C. Canada

Abstract

This paper presents the instability analysis of a beam-loaded radio-frequency system with beam phase-loop and cavity tuning-loop for both accelerating and non-accelerating beams. The case of voltage-proportional feedback around the cavity is also included. The symbolic manipulation program SMP [1] was used to expand and simplify the Routh determinantal conditions for a fifth order characteristic polynomial. The paper is a much abridged version of an internal design note [2].

I. BEAM LOADING EQUATIONS



The disposition of steady state phasors is as shown above. We adopt the notation of Reference [2]. The cavity voltage is $V(t)e^{j\omega t}$ and the total current driving the cavity is $I_T(t)e^{j\omega t}$, where t indicates time and ω is the drive angular frequency. Bold face indicates complex quantities, and ordinary type denotes scalars. We employ dot notation for time derivatives. The cavity fundamental resonance is modelled as a parallel resonance LCR circuit. Let $\Omega_{res} = 1/\sqrt{LC}$ be the resonance frequency and $\alpha = \Omega_{res}/(2Q) = 1/(2RC)$ be the half-bandwidth. We write the voltage and current as the sum of steady state parts $V^0 = V^0 e^{j\psi_V}$ and $I_T^0 = I_T^0 e^{j\psi_T}$, and small time dependent perturbations. We use ψ to denote steady state phases and ϕ perturbation phases. Let $\Psi = \psi_V - \psi_T$.

A. Steady state

We must specify the steady state generator current $I_g^0 = I_g^0 e^{j\psi_g}$ and beam image current $I_b^0 = I_b^0 e^{j\psi_b}$ which sum to form the total current I_T^0 . The beam current is $\approx 90^\circ$ out of phase with the cavity voltage; depending on the synchronous phase angle μ_b . We set $\mu_b = 0$ for a non-accelerating beam. Hence $\psi_b = \pm(\pi/2 + \mu_b)$ and the - sign applies below transition energy and the + above. We adopt the dimensionless current ratios $Y_g = I_g^0/I_V^0$ and $Y_b = I_b^0/I_V^0$, where $I_V^0 = V^0/R$. The components obey:

$$1 = Y_g \cos \psi_g - Y_b \sin \mu_b$$

$$\tan \Psi = Y_b \cos \mu_b - Y_g \sin \psi_g$$

From this follows the detuning $\tan \Psi = (\Omega^2 - \omega^2)/2\alpha\omega$. Until we choose a definite value for ψ_g , there is no direct relation between $\tan \Psi$ and (Y_b, μ_b) .

B. Non steady state

Let us assume the "slow approximation" $\ddot{V} \ll \omega \dot{V}$ and $\dot{I}_T \ll \omega I_T$. We allow for a varying resonance frequency $\Omega(t) = \Omega_0(t) + \Delta\Omega(t)$. We introduce the perturbation vectors e as follows: $V = V^0(1 + e_V)$ and $I_T^0(1 + e_T) = I_g^0(1 + e_g) + I_b^0(1 + e_b)$. The dimensionless components z_r and ϕ_r of the vector $e_r = (z_r + j\phi_r)$ are amplitude and phase modulations, respectively. The cavity response is modelled by:

$$z_V(1 + s\tau_c) + \phi_V \tan \Psi + Y_g(\phi_g \sin \psi_g - z_g \cos \psi_g) + Y_b(z_b \sin \mu_b - \phi_b \cos \mu_b) = 0,$$

$$\phi_V(1 + s\tau_c) - z_V \tan \Psi - Y_g(\phi_g \cos \psi_g + z_g \sin \psi_g) + Y_b(z_b \cos \mu_b + \phi_b \sin \mu_b) = \tau_c \Delta\Omega.$$

Here $\tau_c = \alpha^{-1}$ is the cavity time constant, and time derivatives are replaced by the Laplace operator s .

C. Beam rigid bunch dipole motion

Suppose the ideal drive frequency is synchronous with a particle travelling with the equilibrium. However, as a result of modulations the cavity phase may advance or lag by an amount ϕ_V . Likewise, the beam centroid may differ from the ideal phase by an amount ϕ_b . Suppose the cavity has relative amplitude modulation z_V .

To first order in perturbation amplitudes, the Laplace transform, of the beam energy deviation δE is:

$$s \delta E = K_1 [z_V \sin \mu_b + (\phi_V - \phi_b) \cos \mu_b].$$

Because of the energy deviation, the phase error ϕ_b will advance at the rate: $s \phi_b = K_2 \delta E$. The product $\sqrt{K_1 \times K_2} = \Omega_s$, the synchrotron frequency sans the usual $\cos \mu_b$ term.

D. Stability conditions

The system response contains only self-damped oscillations, when all zeros of the characteristic polynomial lie in the left half of the complex plane. Necessary conditions are for the coefficients of s^n and the Routh-Hurwitz criteria [RH(i) for $i = 1, 2, \dots, n+1$] for combinations of the coefficients to be greater than zero. We shall omit trivial conditions such as $\tau_c > 0$.

II. CAVITY AND BEAM DIPOLE MODE

This is the case originally treated by Robinson [3]. The model assumes that the generator current is maintained by an ideal feed-forward.

Characteristic polynomial

$$\Omega_s^2 [\cos \mu_b \sec^2 \Psi - Y_b \tan \Psi] + 2\Omega_s^2 \cos(\mu_b) \tau_c s + [\sec^2 \Psi + (\Omega_s \tau_c)^2 \cos \mu_b] s^2 + 2\tau_c s^3 + \tau_c^2 s^4.$$

Routh determinants

RH(4): $\tan \Psi \geq 0$, hence $\Psi \geq 0$. If RH(4) < 0, then the cavity is detuned in the wrong sense.

RH(5): $\cos \mu_b \sec^2 \Psi - Y_b \tan \Psi > 0$ implies the Robinson limit: $Y_b < 2 \cos \mu_b / \sin 2\Psi$. If RH(5) < 0, the bunch simply wanders. Substituting the matched generator condition ($\psi_g = 0$) gives the special case $Y_b < 1 / \sin \mu_b$.

III. CAVITY, BEAM DIPOLE MODE, PHASE-LOOP

The model of section II is supplemented with a beam phase-loop intended to damp bunch dipole oscillations. We assume that the feedback has the response of a pure integrator, and modifies the generator phase ϕ_g , that is $\phi_g = (K_p/s) \times (\phi_b - \phi_v)$. If there is an r.f. feedback around the cavity, this loop modifies the demand phase ϕ_d .

Characteristic polynomial

$\Omega_s^2 [\cos \mu_b \sec^2 \Psi + K_p \tau_c \sin \mu_b Y_g \sin \psi_g - Y_b \tan \Psi] +$
 $+ [K_p \sec^2 \Psi + K_p Y_b (\sin \mu_b - \cos \mu_b \tan \Psi) + 2\Omega_s^2 \cos(\mu_b) \tau_c] s +$
 $+ [\sec^2 \Psi + K_p \tau_c (1 + Y_b \sin \mu_b) + (\Omega_s \tau_c)^2 \cos \mu_b] s^2 + 2\tau_c s^3 + \tau_c^2 s^4$
 A necessary condition for stability is that the coefficient of s^1 be > 0. Unless $\tan \Psi \leq \tan \mu_b$ and $K_p > 0$, we find a condition for Y_b which resembles the Robinson limit;

$$Y_b < \frac{2}{\sin 2\Psi} + \frac{2\Omega_s^2 \tau_c}{K_p \tan \Psi} \quad \text{if } \mu_b = 0.$$

In most cases this limit is subordinate to RH(5) below.

Routh determinants

RH(3): $2 + K_p \tau_c [\cos 2\Psi + Y_b \cos \Psi \sin(\Psi + \mu_b)] > 0$.

This condition allows a domain of stability with $\Psi + \mu_b < 0$. The damping provided by the phase-loop can overcome (partially) the instability caused by incorrect detuning.

RH(5): $\cos \mu_b \sec^2 \Psi + K_p \tau_c \sin \mu_b Y_g \sin \psi_g - Y_b \tan \Psi > 0$. Unless $\psi_g \times \mu_b > 0$ there is no change to the Robinson limit.

RH(4): $0 \leq 2K_p \sec^2 \Psi [\sec^2 \Psi + Y_b (\sin \mu_b - \cos \mu_b \tan \Psi) +$
 $+ (\Omega_s \tau_c)^2 \cos \mu_b (\cos 2\Psi + \tan \mu_b \sin 2\Psi)] +$
 $+ 2K_p (\Omega_s \tau_c)^2 \cos \mu_b Y_b (\cos \mu_b \tan \Psi - \sin \mu_b) + 4\Omega_s^2 \tau_c Y_b \tan \Psi +$
 $+ \tau_c K_p^2 [(1 + Y_b \sin \mu_b)^2 - (Y_g \sin \psi_g \tan \Psi)^2]$.

A sufficient condition for RH(4) > 0 is $\tan \Psi = \tan \mu_b$. Alternatively, we may substitute $\psi_g = 0$ and so find RH(4) > 0 at all points on the matched generator curve. Finally, we note that $\mu_b = 0$, $\tan \Psi < 1 / \tan \psi_g$ and RH(5) > 0 are sufficient conditions for RH(4) > 0.

IV. CAVITY, BEAM DIPOLE MODE, AND TUNING LOOP

A feedforward (or program) accomplishes the bulk of the cavity tuning. The tuning loop endeavours to bring the generator current and gap voltage vectors in-phase by modifying the cavity resonance frequency. The feedback, for small oscillations about the program set-point, is modelled by a pure integrator: $\tau_c \Delta \Omega_{res} = (K_t/s) \times (\phi_g - \phi_v)$. Since there are no other loops present, $\phi_g = 0$ for all time. The loop will tend to reduce the phase error to zero (i.e. $\phi_g = \phi_v$) provided K_t is positive.

Characteristic polynomial

$\Omega_s^2 \cos \mu_b K_t (1 - Y_b \sin \mu_b) + 2\tau_c s^4 + \tau_c^2 s^5 +$
 $+ \Omega_s^2 [\cos \mu_b (\sec^2 \Psi + \tau_c K_t) - Y_b \tan \Psi] s +$
 $+ [K_t + 2\Omega_s^2 \cos(\mu_b) \tau_c] s^2 + [\sec^2 \Psi + \tau_c K_t + (\Omega_s \tau_c)^2 \cos \mu_b] s^3$.
 A necessary condition for stability is that the coefficients of s^1 be greater than zero, and this implies

$$Y_b < \cos \mu_b \left[\frac{2}{\sin 2\Psi} + \frac{K_t \tau_c}{\tan \Psi} \right] \quad \text{if } \Psi > 0.$$

However, this condition is subordinate to RH(5).

Routh determinants

RH(3): $2 \sec^2 \Psi + K_t \tau_c \geq 0$.

RH(4):

$K_t (2 \sec^2 \Psi + K_t \tau_c) + Y_b \Omega_s^2 \tau_c [4 \tan \Psi - K_t \tau_c \sin 2\mu_b] \geq 0$.
 This condition is usually unimportant for positive detuning ($\Psi > 0$), and is subordinate to RH(5) for negative detuning.

RH(5): This expression can be solved for the beam current Y_b , and is found to factor:

$$Y_b < [0.5 K_t \sin 2\mu_b (\sec^2 \Psi + \tau_c K_t) - K_t \tan \Psi +$$

 $+ \Omega_s^2 \cos(\mu_b) \tau_c (2 \tan \Psi - 0.5 K_t \tau_c \sin 2\mu_b)] \times$
 $(2 \sec^2 \Psi + K_t \tau_c) / \Omega_s^2 \tau_c (2 \tan \Psi - 0.5 \tau_c K_t \sin 2\mu_b)^2$.

Since the beam current (Y_b) is positive, this leads to a quadratic constraint on the tuning loop gain.

We now simplify the expressions to a non-accelerating beam, to make a correspondence with Reference [4]. In the limit $\mu_b \rightarrow 0$ the stability criterion can be written:

$$Y_b < \left[1 - \frac{K_t}{2\Omega_s^2 \tau_c} \right] \left[\frac{2}{\sin 2\Psi} + \frac{K_t \tau_c}{\tan \Psi} \right].$$

The tuner gain condition, for +ve and -ve tuning angles, can be summarized $(K_t - 2\Omega_s^2 \tau_c) \times \Psi < 0$. The instability regime where $Y_b \ll 1$, $\Psi > 0$ and $K_t > 2\Omega_s^2 \tau_c$ has been experimentally observed in the PSB [4].

V. TUNING LOOP AND BEAM PHASE-LOOP

We supplement the previous model with the ideal phase-loop; $s\phi_g = K_p(\phi_b - \phi_v)$. Because $s\tau_c \Delta \Omega_{res} = K_t(\phi_g - \phi_v)$ there is the possibility for cross-coupling to the tuning loop through the cavity-voltage phase-perturbation ϕ_g .

Characteristic polynomial

$\Omega_s^2 \cos \mu_b K_t (1 - Y_b \sin \mu_b) + 2\tau_c s^4 + \tau_c^2 s^5 +$
 $+ \{ \Omega_s^2 [\cos \mu_b (\sec^2 \Psi + \tau_c K_t) - Y_b \tan \Psi] +$
 $K_p [K_t + \Omega_s^2 \tau_c \sin \mu_b (Y_b \cos \mu_b - \tan \Psi)] \} s + \{ K_t + 2\Omega_s^2 \cos \mu_b \tau_c +$
 $+ K_p [\sec^2 \Psi + \tau_c K_t + Y_b (\sin \mu_b - \cos \mu_b \tan \Psi)] \} s^2 +$
 $+ [\sec^2 \Psi + \tau_c K_t + (\Omega_s \tau_c)^2 \cos \mu_b + \tau_c K_p (1 + Y_b \sin \mu_b)] s^3$.

The coefficients of s^1 and s^2 have the possibility to change sign when $\Psi > 0$. For brevity we give the limit $\mu_b = 0$.

$$Y_b < \frac{2}{\sin 2\Psi} + \frac{K_t (\tau_c + K_p / \Omega_s^2)}{\tan \Psi} \quad \text{when } \mu_b = 0, \Psi > 0.$$

The coefficient of s^2 is automatically positive if $\tan \Psi \leq \tan \mu_b$; alternatively,

$$Y_b < \frac{2}{\sin 2\Psi} + \frac{2\Omega_c^2 \tau_c + K_t(1 + \tau_c K_p)}{K_p \tan \Psi} \quad \text{if } \mu_b = 0, \Psi > 0.$$

Routh determinants

RH(3) factors and simplifies to: $2 + \tau_c K_p \cos 2\Psi + Y_b \tau_c K_p \cos \Psi \sin(\Psi + \mu_b) + \tau_c K_t(1 - K_p \tau_c) \cos^2 \Psi \geq 0$.

This condition is reminiscent of RH(3) in section III and has the effect of allowing some negative detuning. We should also like RH(3) to be satisfied in the limit $Y_b \rightarrow 0$; and for $K_p \tau_c \gg 1$ this implies the approximate condition: $K_t \tau_c < 2 - \sec^2 \Psi \leq 1$.

RH(4): The Routh determinant has many terms, but simplifies under the substitution $\tan \Psi \Rightarrow Y_b \cos \mu_b$, as occurs when the generator is matched ($\psi_g = 0$); one finds a cubic condition in Y_b . A sufficient stability condition is that the coefficients of Y_b^0 , Y_b^1 , Y_b^2 , Y_b^3 be greater than zero. Only the coefficients of Y_b^0 and Y_b^1 have the possibility to change sign; and so, by inspection, sufficient conditions for RH(4) > 0 are $\tau_c K_t \leq 1$ and $K_p \geq K_t$.

RH(5): The Routh determinant has many decades of monomial terms. Under the condition $\psi_g = 0$, there results a quintic polynomial in Y_b . The condition $\mu_b = 0$ reduces the system to a quadratic in Y_b^2 ; the coefficient of Y_b^4 is unavoidably negative, and so limits the maximum beam current. The allowed domain of Y_b will be maximized when the coefficients of Y_b^0 and Y_b^2 are positive. By inspection, $K_t \tau_c \leq 1$ and $K_p \geq K_t$ is a sufficient condition for both coefficients to be positive.

RH(6): $1 - Y_b \sin \mu_b > 0$ imposes a further constraint on the beam current, which is the same as the no-loop case for a matched generator.

A. R.F. feedback around the cavity

Including a voltage proportional feedback around the cavity modifies the equations. This type of feedback, as discussed in Reference [5], requires a high power summing junction since it is the entire r.f. signal which is fed back. The current I_g becomes the sum of the demand current I_d^0 and the feedback current $I_f = -hI_v$. It is found that the characteristic polynomials are identical with those of sections II, III, IV, V except with the substitutions: $\tau_c \Rightarrow \tau_c/(1+h)$, $\tan \Psi \Rightarrow \tan \Psi/(1+h)$, $Y_b \Rightarrow Y_b/(1+h)$ made throughout. This being so, we can take over all previous results regarding the polynomial coefficients and Routh-Hurwitz determinants. Generally, the stability limit is enhanced by a factor $(1+h)$.

VI. CAVITY, BEAM DIPOLE AND QUADRUPOLE MODES

Robinson type stability for dipole-quadrupole mode coupling has been investigated in Reference [6], for the case $\mu_b = 0$. We generalize to the case of an accelerating beam.

A. Rigid bunch quadrupole motion

Let bunch half-length be $\Theta = \Theta_0 + \theta$, the sum of a steady state part Θ_0 and a small perturbation $\theta(t)$. The Laplace transform of the envelope oscillation can be derived from:

$s\theta = \Omega_c^2 \delta W$ and $s\delta W = -4 \cos \mu_b \times \theta - z_v \Theta_0 \cos \mu_b$, where the variable δW is conjugate to θ . To complete our description of the beam coupling to the cavity, we give the relation between θ and amplitude modulation of the beam current z_b . To first order $z_b + F_0 \times \theta = 0$. The form factor F_0 depends on the bunch shape, λ . Let J_n be Bessel functions. For the functions $\lambda = (\Theta_0^2 - x^2)^\alpha$ with $\alpha > 0$,

$$F_0(\Theta_0) = (2\alpha + 1)/\Theta_0 - J_{\alpha-1/2}(\Theta_0)/J_{\alpha+1/2}(\Theta_0).$$

For example, if $\alpha = 1$ then $F_0 \approx \Theta_0/5$ when $\Theta_0 < 1$.

Characteristic polynomial

The polynomial is too lengthy to reproduce here. We consider $\mu_b > 0$, in which case only the coefficient of s^2 has the possibility to change sign when $\Psi > 0$; this implies a beam current limit, but the condition is subordinate to those below.

Routh determinants

RH(3): $2 \sec^2 \Psi - Y_b F_0 \Theta_0 (\Omega_c \tau_c)^2 \cos \mu_b \sin \mu_b > 0$.

This constraint is quite severe for small tuning angles and long bunches, but is subordinate to RH(6).

If RH(3) > 0 then a sufficient condition for RH(4) > 0 is:

$$\tan \Psi \geq \sin 2\mu_b F_0 \Theta_0 (1 + 2\Omega_c^2 \tau_c^2 \cos \mu_b) / 2(1 + F_0 \Theta_0 \cos^2 \mu_b).$$

RH(5) simplifies very slightly to a condition with 24 monomial terms, and there is no simple interpretation. In the limit of large tuning angle, short bunch length, and $\Omega_c \tau_c$ order of or less than unity, we find the approximation:

$$2 \tan \Psi [2 \cos \mu_b - Y_b \sin 2\Psi] + F_0 \Theta_0 \cos \mu_b [16 \cos^2 \mu_b \tan \Psi + 4 \sin 2\mu_b \sec^2 \Psi + 2Y_b(2 \cos \mu_b - \sin \mu_b \tan \Psi - 4 \sin^2 \Psi)] > 0.$$

The leading term in $\tan \Psi$ contains the Robinson limit.

RH(6) factors; if RH(3) > 0 and RH(4) > 0 this leaves the new condition $Y_b < 3 \tan \Psi / [F_0 \Theta_0 \cos \mu_b]$ which poses a severe constraint at small tuning angles unless μ_b is large or the bunches are short.

RH(7): $4(\cos \mu_b \sec^2 \Psi - Y_b \tan \Psi) + Y_b F_0 \Theta_0 \cos \mu_b (\sin \mu_b - \cos \mu_b \tan \Psi + Y_b) > 0$. The term in Y_b^2 in this quadratic will favourably modify the stability compared with the Robinson limit. However, for small tuning angles condition RH(6) supersedes RH(7).

VII. REFERENCES

- [1] SMP: A Symbolic Manipulation Program; Inference Corporation, Los Angeles, California.
- [2] S. Koscielniak: Analytic Criteria for Stability of Beam Loaded R.F. Systems; Triumf TRI-DN-92-K204.
- [3] K. Robinson: Stability of beam in radio-frequency system; Internal Report CEAL-1010, Feb. 1964.
- [4] F. Pedersen: Beam loading effects in the CERN PS Booster, IEEE Trans. Nucl. Sci. Vol. NS-22, No. 3, June 1975, p. 1906-1090.
- [5] D. Boussard: Control of cavities with high beam loading; CERN/SPS/85-31 (ARF).
- [6] Tai-Sen Wang: Bunches beam longitudinal mode coupling and Robinson type instabilities, Particle Accelerators Vol.34, p.105, 1990.

Beam Loading Effect in SSCL Coupled Cavity Linac

Yu. Senichev, R. Cutler, J. Hurd, D. Raparia
Superconducting Super Collider Laboratory*
2550 Beckleymeade Ave., Dallas, TX 75237

I. INTRODUCTION

The Superconducting Super Collider Accelerating Complex consists of a cascade of accelerator and each one of them accelerates the beam to some energy and then transfers it to the next stage. The design luminosity of $10^{33} \text{ cm}^{-2} \text{ s}^{-1}$ is obtained by the high efficiency of all stages and the ability to accelerate beam with as minimum emittance growth as possible. For this purpose the Linac pulse length is specified as $9 \mu\text{s}$ in order to minimise the number of target crossings and so to minimise the emittance growth during charge exchange injection into the LEB booster.

However, the transient caused by switching on the beam makes up a significant part of the pulse length and can influence the characteristics of beam. In this paper we present the results of the transient study of the coupled cavity linac and discuss the model that predicts the parametric resonance between the beam and the field distortion setup during transient.

II. RF TRANSIENT IN CAVITY

CCL structure consists of 9 modules and each one of them has 8 tanks [1]. Each CCL tank is formed by brasing together 16 identical accelerating cells and 17 identical coupling cells with 7% coupling coefficient. The tanks are connected with bridge couplers that have 16% coupling coefficient. The power from the generator is input into the central bridge.

The excitation of the module can be described by a system of normal modes for the periodical chain of coupled cells (accelerating and coupling). Every cell is considered in a single mode approximation. We shall solve the problem of beam loading and compensation of beam's electromagnetic field perturbation by the generator. It is assumed that at the moment $t = 0$ the beam enters the resonator (in our case module). Simultaneously, the generator gives the additional power required to compensate for beam loading. In common form, the total electromagnetic field is described by the equation:

$$E(x, y, z, t) = \text{Re} \left[\sum_s \frac{Q_s}{N_s \omega_s} a_s(t) e^{i k_s z} \right] \\ E_0(x, y, z) \left[\int_V j^s E_s^* dv - \int_V j^e E_s^* dv e^{-i \omega_s t} \right], \quad (1)$$

where

$$a_s(t) = \frac{1 - e^{-i \frac{\omega_s^2 - \omega^2}{\omega_s} t} e^{-\frac{\omega_s^2}{2Q_s} t}}{1 + i \frac{\omega_s^2 - \omega^2}{\omega_s^2} Q_s} \quad (2)$$

$$\omega_s^2 - \omega^2 = K_j \cos(h_s) \quad (3)$$

$$N_s = \epsilon \int_V E_s E_s^* dv \quad (4)$$

where j^s and j^e are the generator and beam currents, K_j is the coupling coefficient. N_s is a norm, Q_s is a quality factor, h_s is a wave number and ω_s is a frequency of s -th mode. The first integral describes the additional power of the generator and the second one is the excitation by beam. The coefficients outside the integrals are the same, so the beam loading compensation in the trivial case is when the integrals cancel. However, in practice it is possible to compensate only for one mode since the character of the interaction of the beam and of the generator with the resonator is quite different. Actually the beam and the generator currents can be written as

$$j^s(z, t) = j_1(z) e^{-i(\omega t - h_1 z)} \quad (5)$$

$$j^e(z, t) = j_1 \delta(z - z_0) e^{-i \omega t}, \quad (6)$$

where $h_1 = \omega/v_b$, v_b is beam velocity, z_0 is point of power input into the resonator, j_1 means first harmonic and the frequency of the beam and the generator equal each to other. Here the magnitude of the currents is taken as an average over the cross section of the beam and the loop (or hole) since we study the excitation of axial symmetrical modes only. It is obviously that the integral of the beam interaction for a constant first harmonic along the resonator doesn't equal to zero except for fundamental mode ($s = s_1$) under the condition when $h_s = h_1$. At the same time the integral for generator doesn't equal zero for any mode if the coupling coefficient $\text{Re}[e^{i h_s z_0}]$ has a "nonzero" magnitude. In other words, in order to compensate the beam perturbation of the fundamental mode, we have to input power which equals the beam power but simultaneously this local input of power excites all modes. Let's rewrite the expression (3) for the field induced by beam, taking into account that only the fundamental mode will be excited:

$$E_{b1} = \text{Re} \left[(1 - e^{-\frac{\omega^2}{2Q_0} t}) e^{i h_1 z} E_0(x, y, z) e^{-i(\omega t + \phi_s)} RP \right], \quad (7)$$

where $RP = \frac{P_{beam}}{P_{0s} \cos \phi_s}$.

Here we have taken $P_{0s} = \frac{N_s \omega_s}{3Q_0}$, Q_0 is the loaded quality factor of the resonator for the fundamental mode,

*Operated by the Universities Research Association, Inc., for the U.S. Department of Energy under Contract No. DE-AC35-89ER40496.

$P_{beam} = \frac{1}{2} \cos \phi_s \int_0^L j E_1^* dv$, and ϕ_s is the synchronous phase of beam. Now since we are interested in the effect of the interaction of the beam with the perturbed field by itself, let's represent the field of the generator in the view of the travelling harmonics $E_1 = 0.5E_0$ with the phase velocity equal the beam velocity:

$$E(x, y, z, t) = R_s \left[\sum_i^N B_i(z, t) 2E_1 e^{-i(\omega t - h_i z + \phi_s)} \right] RP \quad (8)$$

where

$$B_i(z, t) = e^{-i[(\omega_s - \omega)t - (h_s - h_i)z]} \times \begin{cases} (1 - e^{-\frac{v^2}{2\omega Q_0} t}) & \text{if } z = s_j \\ -\frac{e^{-\frac{v^2}{2\omega Q_0} t}}{1 + i\frac{\omega^2 - \omega_s^2}{\omega Q_0}} & \text{otherwise} \end{cases} \quad (9)$$

From this expression one can see that the space-time distortion (front) of the electromagnetic field with the carrier resonant frequency moves along the resonator with a velocity equal to average velocity for all modes:

$$v_{front} = (\omega_s - \omega) / (h_s - h_i) \quad (10)$$

Since

$$\lim_{\omega_s - \omega \rightarrow 0} (\omega_s - \omega) / (h_s - h_i) = v_{group}, \quad (11)$$

then it means that the front of perturbation which the beam "sees" moves with the group velocity. It is obviously that each mode has its own group velocity and moreover, it damps slightly differently. Due to this the front will change shape as it moves along the resonator. $B_i(z, t)$ for $z = s_j$ is the average of the electromagnetic field over the

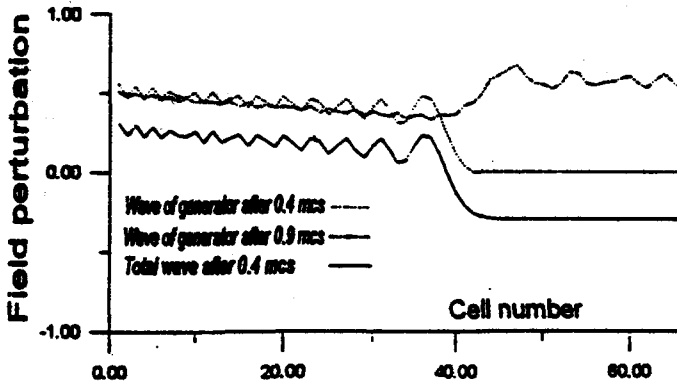


Figure 1. Field perturbation along module

length of the resonator at any moment in time. It is exactly equal to the field induced by beam, when $P_{beam} = P_{gener}$. So if this term subtracted from equation(9) then we shall get field which the beam sees. Knowing the dispersion function of the structure, it is possible to calculate what the distribution of electromagnetic field will be during the transient. Figure 1 shows the field of generator at the moments $t=0.4\mu s$ and $0.9\mu s$ and total field at the moment

$t=0.4\mu s$. This picture explains what will happen in the cavity during injection of beam and simultaneous input of power. The origin of coordinates corresponds to the point of the power input. In the case of the SSC, this is the middle of the resonator. Physically, it means that the beam moves with the phase velocity and fills the resonator $1/K$, as fast as the wave front from generator. So after first tens of ns the beam interacts with the whole resonator and the average level of field will decrease in accordance with the exponential law $\sim (1 - e^{-\omega t/2Q_0})$. The generator creates a wave which radiates in both directions from the middle and divides the resonator into three parts with alternative drops of field. The overfall change in time goes as $\sim e^{-\omega t/2Q_0}$. The main contribution to the distortion of the field in resonator is done by harmonics which are reflected with coefficients $|\rho|=1$. The incident and reflected waves give standing wave:

$$e^{ih_s z} + e^{-ih_s z} = 2\cos(h_s z), \quad (12)$$

which means that the distribution is described by $\cos \frac{\pi}{N} n$, where N is the total number of cells in module and n is number of cell. One can say that the integral over module of the total distortion (except the fundamental mode) equals zero. However, the front of the wave can have significant impact. For the simplest case, when we use linear dispersion, $\omega_s - \omega = \frac{\pi \omega K_L}{2N}$, it is possible to get an analytical expression for the height of the wave [2]:

$$\delta E_1 = 2E_1 RP \frac{L_{cav}}{v_{group}} \frac{\omega}{2Q_0} e^{-\omega t/2Q_0}, \quad (13)$$

or using $P_{beam} = \frac{1}{2} I_1 E_1 \cos \phi_s$, one gets the expression by taking $R_{shunt} = E_1^2 L_{cavity} / P_{losses}$:

$$\delta E_1 = I_1 R_{shunt} \frac{\tau_{gr}}{\tau_i} e^{-t/\tau_i}, \quad (14)$$

where $\tau_{gr} = L_{cav}/v_{gr}$ and $\tau_i = 2Q_0/\omega$. The value $K_r = \frac{\tau_{gr}}{\tau_i}$ defines the ratio between the front of the wave at the initial time and the final magnitude of the electromagnetic field obtained when we excite the resonator by a generator with the vector $I_1 R_{shunt}$. For SSC case $K_r=0.35$. This means inputting a generator power into resonator with a shunt impedance $R_{shunt} = 50 M\Omega$ to compensate the beam loading with first a harmonic $I_1 = 2I_0 = 2 \cdot 0.02$ mA, then a wave is excited with a front amplitude equals to 0.7 Mv/m. This is 10% of the accelerating harmonic.

III. BEAM DYNAMICS

Thus, during the transient the beam sees almost rectangular wave which radiates from the point of power input and damps simultaneously. In this section we shall do the analyse of the beam dynamics in this perturbed field.

The CCL structure has some features and one of them is a constant cell size in each tank which implies a constant phase velocity along the tank. So the equations for longitudinal motion are:

$$\frac{dp}{d\phi} = \frac{eE_p \sin \phi}{2\omega}$$

$$\frac{d\phi}{d\psi} = 1 - \frac{\beta_w}{\beta}, \quad (15)$$

where E_p is field which the particle sees, p is the momentum of the particle, β and ϕ are the relative velocity and phase of particle, β_w is the phase velocity of the wave and ψ is the normalized longitudinal coordinate which connects the longitudinal coordinate z as $\psi = z/l_{cell}$, l_{cell} is length of cell.

This system of equations can be represented by the second order, nonlinear, inhomogeneous, differential equation:

$$\frac{d^2\phi}{d\psi^2} + \frac{d(\ln\beta)}{d\psi} \frac{d\phi}{d\psi} + \Omega_0^2(\sin\phi - \sin\phi_s) = \Omega_0^2 \sin\phi_s \frac{\delta E_1}{E_1} Re \sum_i 2B_s(z, t) + \sum_k 2 \frac{\delta\beta_w}{\beta_w} \cos \frac{2\pi k}{T} \psi \quad (16)$$

where $\Omega_0^2 = \frac{eE_1 \lambda \beta_w}{m_e c^2 2\pi T \delta\beta_s}$ is the synchronous frequency for particles near the origin of the separatrix, T is the periodicity of the tanks, $\delta E_1/E_1$ is the perturbation amplitude of the electromagnetic field during the transient, $\delta\beta_w/\beta_w$ is the jump of stepwise function of the phase velocity from tank to tank. One can see that even in an ideal structure we have the inhomogeneous equation what means that in the structure with constant cell size, the quasi-synchronous particle oscillates along the structure. During the transient the synchronous frequency becomes a function of the longitudinal coordinate ψ . Using (10) we can write the expression for the variable synchronous frequency Ω :

$$\Omega^2 = \Omega_0^2 [1 + Re \sum_i 2B_s(z, t)] \quad (17)$$

Each harmonic has a distribution along the resonator of $\cos(\frac{\pi}{N} - \frac{\pi}{2})n$. Taking into account that we have parametric and external resonances simultaneously the motion becomes unstable in the case when

$$\nu = \frac{2\Omega}{m}, \quad (18)$$

where ν is the frequency of the perturbation and m is the order of resonance. However, one should remember that Ω here is the average synchronous frequency which depends on amplitude of oscillation (nonlinear resonance). In other words, we have many resonant conditions. The effective side band of resonance is defined by the perturbation amplitude and the degree of nonlinearity. Figure 2 shows the behavior of the quasi-synchronous frequency along the CCL accelerator. The vertical lines show the possible resonance frequency. Oscillation of the frequency is due to the constant phase velocity of the tank. If particles go through a resonance losses will be observed. Figure 3a shows the separatrix if we go through resonance. It is clear that this situation is unacceptable for the accelerator. To avoid this effect we need to increase periodicity of the electromagnetic field perturbation. One solution is to input power in two symmetrical points at 1/4 and 3/4 of the module

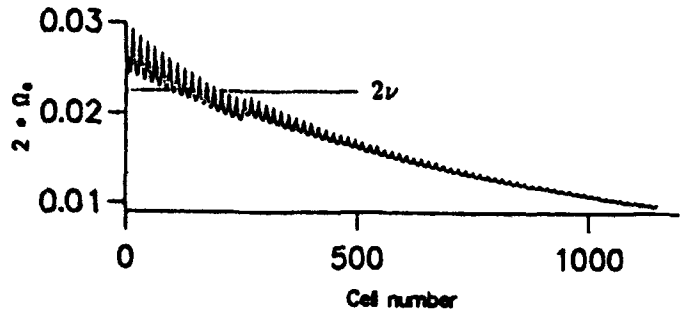


Figure 2. Synchronous frequency versus on cell number

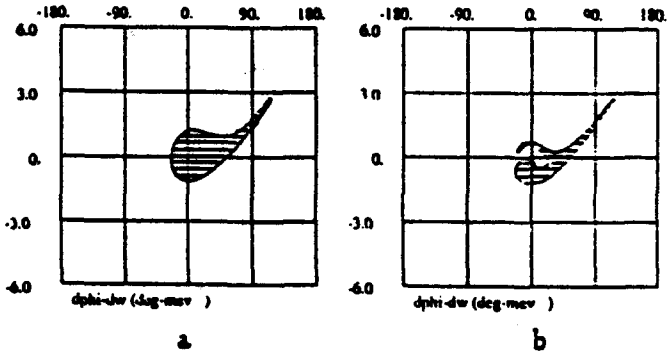


Figure 3. Corrected (a) and uncorrected (b) separatrix

length. Then the amplitude of the wave will decrease two times and the frequency of perturbation will increase two times giving the possibility of avoiding the resonant condition. On the same picture the case when we input the power in two points is shown (fig.3b). The separatrix has a quit perfect shape.

IV. CONCLUSION

In conclusion we would like to make a general comment concerning accelerator design. Increasing the rate of acceleration increases the probability of resonance crossing. For the SSCL linac we pass through resonance in the second module. The maximum acceptable perturbation of electromagnetic field for our case is 2-3%. To reduce the strength of a perturbing resonance, we have considered the method of resonance damping by "two points" power input. In conclusion the authors would like to thank to Dr. W.Funk for his helpful discussion and support of this work.

V. REFERENCES

- [1] L.Warren Funk, The SSC Linac, Linear Accelerator Proceedings, pp.8-12, 1992
- [2] Yu.V.Senichev, Study of Injection Transient in Coupled Cell Linac Cavities, Third European Particle Accelerator Conference, pp.774-776, Berlin, 1992

The Ion Core Density in Electron Storage Rings with Clearing Electrodes

Eugene V. Bulyak

Kharkov Institute of Physics and Technology
1 Academicheskaya St., Kharkov 310108, Ukraine

Abstract

The low density of the ion core is required for efficient performance of electron storage rings. One of the effective methods of decreasing the density of ions in the electron beams circulating in storage rings is the application of electrostatic clearing electrodes. This report presents the results of analytic investigations of the ion core density distribution versus the magnetic field, the beam current, the density of the residual gas in the vacuum chamber and the distance between the sequential clearing sets. The numerical simulation of self-consistent evolution of the ion core has also been carried out. The results of simulation are in agreement with the theoretical predictions.

I. INTRODUCTION

The extraction efficiency of clearing electrodes depends on the longitudinal motion of ions because the electrodes do not cover all the ring circumference. They cannot be inserted inside the magnets of the ring. Hence, the parameters of the ion core trapping by the electron beam are dependent on ion motion between the clearing sets. As a rule, the clearing electrostatic electrodes are installed at dipole magnet ends. So, the present results for the ion core parameters are given just for this layout.

II. ION MOTION IN COMBINED MAGNETIC AND ELECTRIC FIELDS

The drift of charged particles in crossed electric and magnetic fields has been studied rather thoroughly [1]. However, implementation conditions for the drift theory significantly differ from those existing in storage rings, namely, the initial kinetic energy of ions is about the thermal energy of gas molecules (≈ 0.03 eV), whereas the electrostatic potential of the beam reaches several hundred volts per ampere of the beam current. Therefore, the ion momentum changes significantly during a cyclotron period [2]. The cyclotron motion of ions can not be used for perturbation treatment. Here we shall derive ion trajectories in combined fields.

The ion trajectory in dipole magnets

Consider a singly charged ion born at rest in the uniform magnetic field $B_z = B_0$ and the normal to it electric field E_x . Let the electric field be expanded around the initial coordinates of the ion (x_0, y_0) :

$$E = E_0 + (x - x_0)E' \quad (1)$$

This field is related to the normal component of the potential

$$\Phi = -(x - x_0)E_0 - \frac{(x - x_0)^2}{2}E'. \quad (2)$$

The trajectory of the ion of mass M in these fields has the form

$$x = x_0 + \frac{P_0}{M\Omega}(1 - \cos\Omega t)$$

$$y = y_0 - \frac{\omega P_0}{\Omega M}t + \frac{\omega P_0}{\Omega^2 M} \sin \Omega t \quad (3)$$

$$P_0 = -\frac{eE}{\Omega}; \quad \Omega^2 = \omega^2 + \frac{eE'}{M}; \quad \omega = \frac{eB_0}{Mc}.$$

These expressions show the ion describing an ellipse that moves along the y axis with a direct velocity

$$v_y = -\frac{\omega P_0}{\Omega M}. \quad (4)$$

It should be noted that v_y is the same as the drift velocity is (see [1]), but the trajectory (3) differs from the drift one.

The amplitude of the x -oscillations is

$$a_x = \frac{|P_0|}{M\Omega} = \frac{v_y}{\omega}. \quad (5)$$

It can be easily found that for a small nonuniformity of the electric field ($|a_x E' / E_0| \ll 1$), the direct velocity v_y is determined by the electric field strength in the center of x -oscillations:

$$v_y = \frac{E_0 + a_x E'}{B_0} c = \frac{E_c c}{B_0} = -\frac{c}{B_0} \frac{d\Phi}{dx} \Big|_{x=x_0 - a_x}. \quad (6)$$

Analysis of the ion motion

In the reference frame turned around the z -axis by an arbitrary angle, the direct ion velocity can be written in the canonical form:

$$v_x = \dot{x} = \frac{c}{B_0} \frac{\partial \Phi}{\partial y}; \quad v_y = \dot{y} = -\frac{c}{B_0} \frac{\partial \Phi}{\partial x}. \quad (7)$$

The coordinates (x, y) of the direct motion are canonically conjugated, Hamilton function is independent of time

$$H = \frac{c\Phi}{B_0}. \quad (8)$$

Using the hamiltonian treatment of direct ion motion we come to the conclusion that in a uniform magnetic field the ions move along the curves of a constant electrostatic potential Φ . Expression (8) is very useful as a basic solution for the perturbation treatment. By this way one can easily obtain the gradient drift at the magnet ends:

$$v_x = \frac{\partial H}{\partial y} = -\frac{c\Phi}{B^2} \frac{\partial B}{\partial y} \quad (9)$$

It explains the acceleration of ions moving out and reflection of ions moving into a magnet. Similar effects occur if the longitudinal electric field is applied (asymmetric electrodes, etc. [3]). Examples of the direct trajectories of ions are presented in Fig.1. The magnet edge and the clearing electrode are at the right hand side. The isolines in this figure have been drawn at regular intervals of the Hamiltonian, so the velocity is inversely proportional to the spaces between the lines. The repulsion of ions by a positive electrode (bottom figure) has been observed and obtained in the simulations [3].

Kinetic description

The above-written Hamilton function (8) generating ion trajectories allows us to describe the evolution of the ion core by the Vlasov-like kinetic equation:

$$\frac{\partial n_i}{\partial t} + \{H, n_i\} = \sigma n_b n_0 c; \quad \Delta \Phi = 4\pi e |(n_b - n_i)|. \quad (10)$$

Here σ is the ionization cross section; n_b is the beam density averaged over the period of the bunch sequence; n_0 is the density of residual gas; $\{ \}$ represent the Poisson brackets.

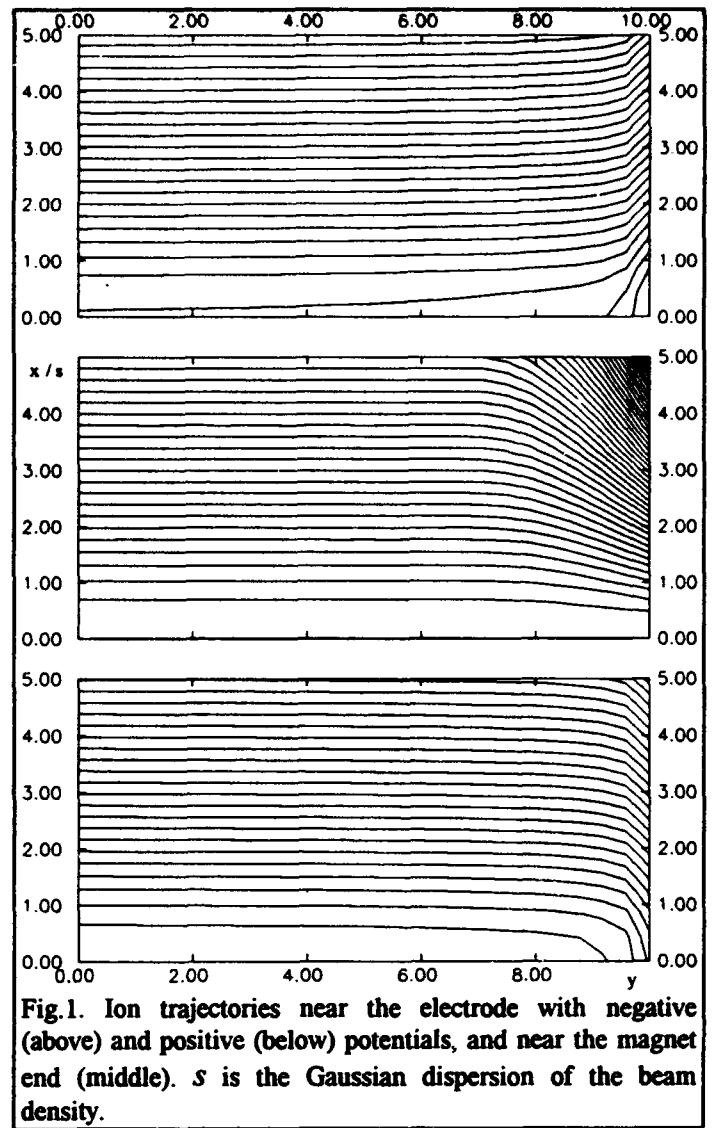


Fig.1. Ion trajectories near the electrode with negative (above) and positive (below) potentials, and near the magnet end (middle). s is the Gaussian dispersion of the beam density.

For the case of a low core density $n_i/n_b \ll 1$ and the azimuthally uniform electron beam, one obtains the core density at a distance y downstream the clearing electrodes:

$$n_i = \sigma n_0 B_0 y \frac{n_b}{E_x}. \quad (11)$$

In this case, the density of the ion core is independent of the beam current, because the electric field E_x is proportional to the beam density n_b . Taking into account both the upstream and the downstream ion flows, we can easily obtain that the number of ions between two clearing sets is proportional to the distance between these sets, to the residual gas pressure and the magnetic field strength for any beam current. For an arbitrary neutralization, when all ions reach the clearing electrodes, the neutralization factor cannot exceed one half

$$\eta = \frac{N_L}{N_b} \leq 0.5 \quad (12)$$

as can be derived from (11). This is twice as small as that for the absence of clearing. It should be noted that the near-axis ions, that move slowly, cannot reach the electrodes. So the ion core density at $x \approx 0$ is limited by the conditions of ion confinement by the beam in the magnet-free space [3].

The core-to-beam density ratio is presented in Fig.2 for the Gaussian distribution of the x beam density.

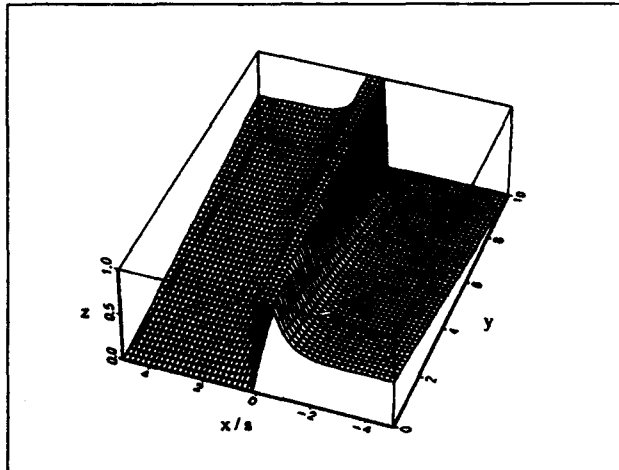


Fig.2. The relative core density. y and z axes are in arbitrary units.

The shape of the ion core density differs from that of the beam both in transverse and longitudinal directions.

III. SIMULATIONS

Simulation of the ion core evolution has been carried out. The code is based on equation (10) without the RHS in the kinetic equation. The initial density shape of the ion core was the same as the beam -- Gaussian transverse density distribution and the uniform longitudinal one. The neutralization factor for singly charged nitrogen ions was 0.1. The clearing electrodes are placed at both sides. Fig.3 depicts the density distribution after time interval of 6.6 μ sec. As it can be seen from this figure, the longitudinal density shape becomes 'three-angular,' the transverse shape differs from the Gaussian one.

IV. CONCLUSIONS

Here we have studied some aspects of ion core formation between the clearing sets in the magnetic field. The results presented can be summarized as follows.

- i -- The longitudinal velocity of ions in the magnets is independent of the initial momentum and can be sufficiently higher than the thermal velocity of the residual gas atoms.

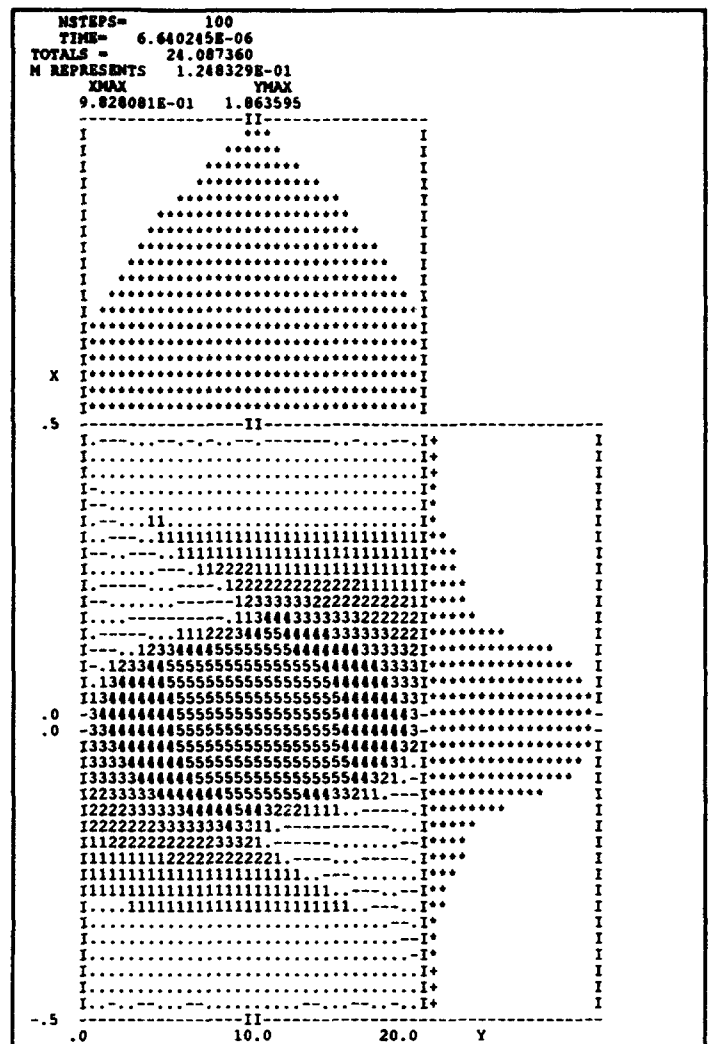


Fig.3. Simulated ion core density distribution, x -axis is directed vertically.

- ii -- The neutralization factor is limited from above by the value of one half comparing to unity in the free space.
- iii- At a low neutralization, the density of the ion core is independent of the beam current.

V. REFERENCES

- [1] B. Lehnert, "Dynamics of charged particles," *N-H Pub., Amsterdam, 1964.*
- [2] A. Poncet, "Ion clearing in EPA," *CERN PS/ML/Note 83-1.*
- [3] E. Bulyak, P. Gladkikh, I. Karnaukhov, A. Shcherbakov, "Ion core density confined in negative particle beams," *HEPACC-92 Proceedings (Hamburg, 1992)*

Operation of the CEBAF Linac With High Beam Loading*

L. Merminga, J. J. Bisognano, C. Hovater, G. A. Krafft, S. N. Simrock,
Continuous Electron Beam Accelerator Facility
12000 Jefferson Avenue, Newport News, VA 23606-1909 USA
and K. Kubo,
National Laboratory for High Energy Physics (KEK)
Oho, Tsukuba-shi, Ibaraki-ken, 305, Japan

Abstract

The superconducting RF, CW CEBAF accelerator will use a pair of antiparallel 400 MeV linacs connected by recirculation arcs for nominal 4 GeV in five passes. Single-pass, high power testing of the first linac has been conducted during the months preceding the conference. The RF control system [1] has been designed to control cavity gradient and phase under a wide range of gradients and significant beam loading. At full beam current, accelerating gradient is approximately equal to accelerating voltage in the superconducting RF cavities. Even though the beam current during the high power testing is one-fifth of the full current, beam loading is substantial. Operational experience of the response of the RF system is presented. A tuning algorithm which compensates for beam loading effects has been developed and tested. Heavy beam loading, corresponding to five-pass operation, was studied by increasing the loaded Q of the cavities. A current modulation experiment addressed the issue of energy spread increase due to current fluctuations, and the effect of by-passed cavities on beam properties was investigated.

I. INTRODUCTION

The superconducting RF, CW CEBAF accelerator consists of two antiparallel 400 MeV linacs connected by recirculation arcs for nominal 4 GeV in five passes. At full beam current of 1 mA the beam loading is significant, resulting in a beam induced voltage approximately equal to the accelerating voltage in the RF cavities, $V_{br} = I_b(R/Q)Q_{ext}$. For the CEBAF cavities $(R/Q) = 960 \text{ } \Omega/\text{m}$, nominal $Q_{ext} = 6.6 \times 10^6$, thus $V_{br} = 6.3 \text{ MV/m}$.

To achieve the low specification on the beam energy spread of $\sigma_E/E = 2.5 \times 10^{-5}$, strict amplitude and phase control of the RF field in the 338 cavities is required. The RF control system has been designed to control the cavity gradient and phase under a wide range of gradients and significant beam loading.

During the months preceding the conference, single-pass, high power testing of the first linac was conducted. Even

though the beam current during the high power testing is one-fifth of the full current, beam loading is substantial. A number of tests aiming towards gaining operational experience of the response of the RF system were carried out and are presented here: the beam loading algorithm, RF performance with heavy beam loading, current modulation and cavity by-passing experiments. More tests were carried out during the high power testing which are described elsewhere [2], [3], [4], [5].

II. BEAM LOADING ALGORITHM

To demonstrate the necessity of beam loading compensation of the tuning algorithm, we start with Fig. 1, which is a vector representation of the generator V_g , beam loading V_b , and total cavity V_c voltages in an RF cavity [6]. The generator and beam induced voltages for an on-resonance cavity are represented by V_{gr} and V_{br} respectively. The three angles noted on the figure are: the phase angle ϕ between beam current and the crest of the RF voltage wave, the detuning angle ψ between generator (beam loading) voltage on and off resonance, and the angle α between cavity voltage and generator voltage on resonance. In reality the detuning angle is modulated by microphonic noise in the frequency range of 1 to 200 Hz with a typical amplitude of $\pm 5^\circ$. In the CEBAF accelerator the tuning mechanism allows only for slow corrections; therefore the detuning angle is controlled on average. The average detuning angle has to be maintained to better than $\pm 3^\circ$ in order to meet the specifications for amplitude and phase regulation and minimise power requirements.

The phase detector in the RF control system can not measure directly the detuning angle, but the phase difference between incident and transmitted (probe) signals, which is the angle α in Fig. 1. For zero beam current, the detuning angle is equal to angle α . However, for finite beam current the two angles are different. For example, for $I_b = 1 \text{ mA}$, $\phi = 30^\circ$ and $\psi = 10^\circ$, $\alpha = 20.07^\circ$. Thus the purpose of the algorithm is to find the true detuning angle in terms of α , ϕ , V_c and V_{br} and use this as the signal to which the tuners respond. From Fig. 1,

$$\tan \psi = \frac{\tan \alpha [V_c + V_{br} \cos \phi] - V_{br} \sin \phi}{V_c} \quad (1)$$

*Supported by U.S. DOE contract DE-AC05-84ER40150

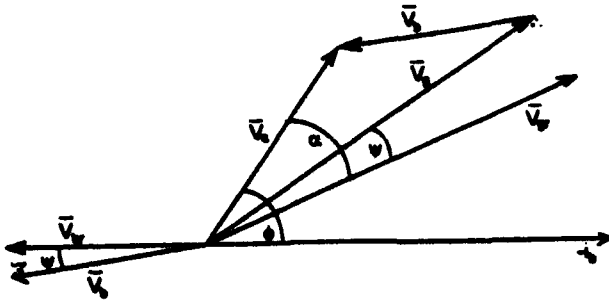


Figure 1: Vector representation of the generator, beam induced and total cavity voltages in an RF cavity.

where V_{be} is given in the Introduction.

The algorithm was tested in the Injector cavities IN04-6 and IN04-8 with $Q_{ext} = 5 \times 10^6$ and 1.6×10^7 correspondingly. CW beam was on crest and the accelerating gradient in these cavities was 2.5 MeV/m. The cavities were initially detuned by 20° at zero beam current. Current was then varied from 200 to 0 μA in steps of 20 μA , and the angle α was measured (at each step) with the algorithm turned off and on. For cavity IN04-6 the algorithm succeeded in returning the correct detuning angle within 0.5° , while for IN04-8, with Q_{ext} 3 times higher, the largest error was 2° , due to the fact that the detuning angle is 3 times more sensitive to frequency changes of the cavity.

III. HEAVY BEAM LOADING

The purpose of this test was to measure the effect of beam loading on the quality of cavity gradient and phase regulation and to verify that RF controls are stable under heavy beam loading. The test took place in the Injector cavities IN04-7 and IN04-8 where waveguide transformers increased the external Q to 1.9×10^7 and 1.6×10^7 respectively. The above Q values provide matching at 300 μA . CW beam current of 30 MeV run in the Injector and residual gradient and phase fluctuations in the two cavities mentioned above were measured as functions of beam current. The set-up for the measurements is shown in Fig. 2. An external Schottky diode with DC-block was used to measure gradient fluctuations independently of noise generated in the electronics of the controls module. The similarity of the spectra of the gradient fluctuations at different beam currents (0, 40, 80, 160 μA), shown in Fig. 3, demonstrates that residual amplitude noise does not depend on beam current. Furthermore, a more quantitative measurement was conducted: the integral of the rms gradient error signal in the frequency range of 10 to 100 Hz was calculated (using a LeCroy type scope) for 0, 40 and 80 μA . These values were found to be -33.92 dBV, -34.22 dBV and -33.78 dBV. Taking into account the 60 dB preamplifier (see Fig. 2), the relative rms gradient error is

$$\frac{\Delta V}{V} \approx \frac{2 \times 10^{-5} V}{600 \text{ mV}} \approx 3.3 \times 10^{-5} \quad (2)$$

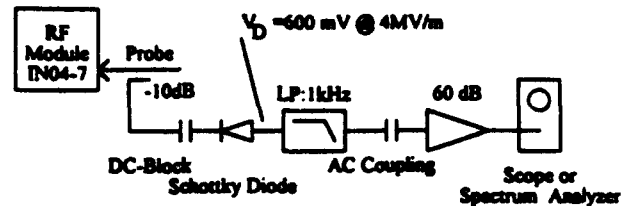


Figure 2: Experimental set-up for testing the RF performance under heavy beam loading.

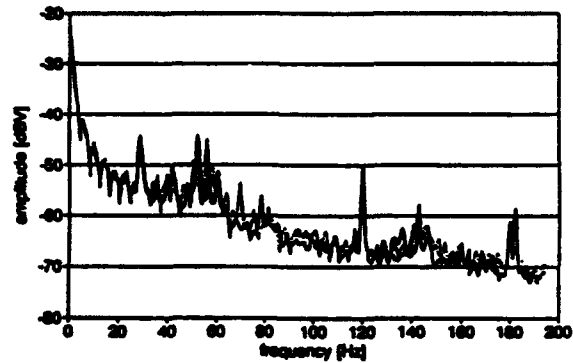


Figure 3: Spectra of gradient error for 0, 40, and 80 μA beam current.

in the 10 to 100 Hz frequency range. The specification for uncorrelated amplitude fluctuations is 2×10^{-4} up to 1 MHz; however, it has been observed before that the contribution from the higher frequencies is negligible.

IV. CURRENT MODULATION

In order to determine whether beam current fluctuations cause energy spread in the beam, a current modulation experiment was completed. The experiment consisted of fully modulating a high current beam, and correlating with the voltage fluctuations in the IN04-6 superconducting cavity. Two hundred microamp CW beam was square-wave modulated at 150 Hz by amplitude modulating the chopper power (the average current after modulation was 100 μA). The response of the RF control system was measured in two locations.

Firstly, the gradient modulator drive in the gradient controls was observed. The gradient mod drive controls the klystron power; it exhibited the same square wave modulation. Comparing the spectra of the beam current and the mod drive revealed that the spectra were identical at harmonics of the modulation frequency up to more than 10 kHz. They also exhibited the $1/f$ frequency dependence at odd harmonics, a characteristic of square wave modulation. The scales of the modulation peaks were consistent with the known properties of the RF controls.

Secondly, the gradient fluctuations in the cavity were also observed using the Schottky diode described previ-

only. The spectrum of the diode output had peaks at harmonics of the modulation frequency. A one parameter theoretical calculation was done using the formula

$$\delta V(\omega) = \frac{R(\omega)I(\omega)}{1 + G(\omega)}$$

to calculate the peak locations based on the current spectrum and the Bode plot of the RF controls. The Bode plot shows that the loop gain $G(\omega)$ falls as $1/f^2$ in the region between 1 and 10 kHz, accounting for the flat peak values observed in this frequency range.

The smallness of the voltage fluctuations induced by the ambient current fluctuations in the CW beam combined with the relatively large noise in the RF controls (at the $\delta V/V \approx 10^{-4}$ level) made it difficult to directly measure the ambient voltage fluctuations due to beam loading effects. However, these modulation measurements, along with measurements that show that the ambient current fluctuations are less than 1.5%, demonstrate that the beam induced relative voltage fluctuations are under 10^{-6} . Because the correlated relative amplitude error specification is 10^{-6} , beam loading should be a negligible contributor to the energy spread in the final beam.

V. CAVITY BY-PASSING

Hardware failures such as defective klystrons or high voltage power supplies may require the shutdown of individual cavities or cryomodules. In this case the failing system needs to be by-passed until the defective subsystem is repaired. Non-operational cavities need to be detuned to reduce the beam induced voltage. An experiment [7] was carried out during the high power testing of the north linac in order to a) verify the validity of calculation of the beam induced voltage V_b , and its fluctuations δV_b , due to microphonic noise in a by-passed cavity, b) determine the effect of by-passing a cavity on the beam energy and energy spread and c) specify an optimum off resonance frequency for by-passing. Injector cavity IN04-6 was by-passed while the Injector was operated with 30 MeV, CW beam and up to 80 μ A beam current. Cavity 6 was detuned by approximately 100, 200 and 1500 Hz, and V_b and δV_b were measured from the cavity probe. Data was recorded from both the spectrum analyzer and the oscilloscope and is plotted in Fig. 4 together with the theoretically expected values of V_b (straight lines) and δV_b (dotted lines). The bars represent the experimental fluctuations of V_b . The theoretical values are derived from the LCR circuit model of a resonant cavity. There is a good agreement between measured data and predicted values for V_b . However, the fluctuations of V_b are bigger, experimentally, than one would expect simply due to microphonics. A beam position monitor (BPM) in a high dispersion region was also used to measure energy changes at different detuning angles and beam currents. The energy changes observed are consistent with the values of V_b ; however, it was not possible to estimate the effect of microphonic noise on the energy spread due

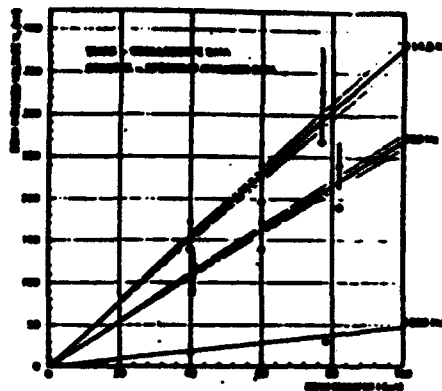


Figure 4: Measured data and predicted values of beam induced voltage and its fluctuations in a by-passed cavity.

to insufficient accuracy of our measurements. Finally at 200 μ A CW beam, a detuning frequency of 1 kHz appears to provide the required energy stability of the beam.

VI. CONCLUSIONS

Results of the single-pass, high power tests during the CEBAF north linac commissioning have been reported. A tuning algorithm which provides compensation for beam loading effects has been developed and successfully verified in the machine. Heavy beam loading was simulated by increasing the loaded Q of a cavity, and the performance of the RF control system was measured. The RF control system can regulate within specifications independently of beam current. A current modulation experiment showed unambiguously that beam current fluctuations at the expected 1.5% level will have a negligible effect on the energy spread of the beam. Good agreement between predicted values and measured data of the beam induced voltage were obtained from a by-passed cavity. The optimum detuning frequency for by-passing was determined to be at least 1 kHz at 200 μ A.

ACKNOWLEDGMENTS

The authors would like to sincerely thank the machine operations crew and the RF maintenance group for their enthusiastic support during the high power tests, and Ken Crawford for help with the current modulation experiment.

REFERENCES

- [1] S. Simrock, *Conference Record of the 1991 IEEE PAC*.
- [2] Y. Chao *et al.*, these proceedings.
- [3] S. Simrock *et al.*, these proceedings.
- [4] G. A. Krafft *et al.*, these proceedings.
- [5] A. Hutton, these proceedings.
- [6] P. Wilson, AIP Conf. Proc. No. 87, 450 (1981).
- [7] O. Bashenov *et al.*, CEBAF-TN-93-032.

An Idea of Dynamical Cooling of Electron Beam in SR Ring

Syohei KATO

Laboratory of Nuclear Studies, Faculty of Science,
Osaka University, Toyonaka, Osaka 560, Japan

A beam cooling method which uses a stimulated emission of radiation by relativistic electrons in a magnetic field, is proposed to apply to an electron beam in synchrotron radiation rings. The stimulation is produced by a traveling RF electric field in a transmission line against the beam. Averaging the emission power over electron energy distributions, the net emission from the beam is taken place in a certain frequency region. Some conditions for the energy emission are discussed. The emission power is shown to be enough large to decrease the horizontal emittance of the beam to a very small value in typical synchrotron radiation rings.

I. Introduction

The equilibrium horizontal emittance of the electron beam in a synchrotron radiation (SR) ring is determined by competition of the quantum excitation and radiation damping [1]. The emittance scales like θ^3 where θ is a deflection angle per bending magnet [2]. Therefore, in principle, an arbitrarily small value of the emittance can be reached if the deflection angle is chosen small enough. This trend, however, is inevitably limited by the inability to correct chromaticities which restrict beam stability.

II. Principle of the method

As a possible alternate method to decrease the emittance, we propose a method based on a stimulated emission of radiation from a cyclotron motion of electrons in a magnetic field. The emission is caused by a relativistic quantum effect in a certain frequency condition of an incident radiation [3].

The cyclotron motion of an electron in a uniform magnetic field B is relativistically described by Dirac equation [4] which leads the kinetic energy levels

$$W_i = m_e c^2 \sqrt{1 + \frac{2(i + \frac{1}{2})\hbar\omega_c}{m_e c^2}} - m_e c^2$$

for the motion in a perpendicular plane to the magnetic field, where m_e is the electron mass and $\omega_c = eB/m_e$ is the cyclotron frequency of the non-relativistic electron. The transition frequency $\omega_{i,i+1}$ between state $i+1$ and i can be obtained by expanding the square root up to the second order as

$$\omega_{i,i+1} = \omega_c \left(1 - \frac{i\hbar\omega_c}{m_e c^2} \right)$$

The matrix element for the electric dipole transition between the states i and $i+1$ is

$$\mu_{i,i+1} = e \sqrt{\frac{(i+1)\hbar}{2m_e\omega_c}}$$

The transition probability $w_{i,i+1} = w_{i+1,i}$ between the state i and $i+1$ is given as

$$w_{i,i+1} = \frac{E^2 (\mu_{i,i+1})^2}{\hbar^2} g(\omega, \omega_{i,i+1})$$

where E is the amplitude and ω the frequency of the applied electric RF field. The frequency response function $g(\omega, \omega_{i,i+1})$ of applied RF electric field can be assumed to be Lorentzian for a rather large debunching time τ as

$$g(\omega, \omega_{i,i+1}) = \frac{\tau}{1 + (\omega_{i,i+1} - \omega)^2 \tau^2}$$

The net power transfer is

$$P_i = \hbar(\omega_{i,i+1} w_{i,i+1} - \omega_{i,i-1} w_{i,i-1})$$

which can be either plus or minus depending on the ω . The negative value means the emission of power from the electron. In the formula, the frequency between state i and $i-1$ is slightly larger than $\omega_{i,i+1}$ and can be written as $\omega_{i,i-1} = \omega_{i,i+1} + \alpha\omega_c$. Summarizing above relations, the net transfer of power per electron with kinetic energy W is written as

$$p(\omega) = \frac{e^2 \tau E^2 W}{m_e 2 \hbar \omega_c} \left(\frac{1 + \frac{\hbar\omega_c}{W} - \alpha}{1 + x^2} - \frac{1}{1 + (x + \alpha Q)^2} \right) \quad (1)$$

where $Q = \tau\omega_c$, $\alpha = \hbar\omega_c/m_e c^2$ and

$$x = \left(\omega_c \left(1 - \frac{W}{m_e c^2} \right) - \omega \right)$$

Originally the power transfer (1) is not for single electron but for an ensemble of monoenergetic electron. However if electrons gyrate the cyclotron orbit in same phase, it may be used for single electron. A phase bunching mechanism is shown classically to arise from the frequency change due to the relativistic mass effect on the cyclotron gyration [5]. The mechanism is shown to be justified by numerical calculation of the phase history of an electron gyration. The bunched electrons emit their energy coherently.

Hereafter we consider an electron in a beam bunch in an application of the phenomena to SR rings. In the application, the magnetic field is applied longitudinally and the RF field transversally to the electron beam. The quantities in the co-moving frame with the electron bunch are specified by the upper bar of them.

III. Average over energy spreads

In order to obtain an effective power transfer of an electron in a synchrotron radiation ring, the power transfer have to be averaged over longitudinal and transverse energy spreads of the electrons in the beam. The longitudinal energy

spread fields a spread $\Delta\bar{\omega}$ of the applied frequency $\bar{\omega}$. The frequency spread is given as $\Delta\bar{\omega}/\bar{\omega} = \Delta\gamma/\gamma$ where γ is the Lorentz factor for the central electron energy and $\Delta\gamma$ is the spread. Because of the energy spread, an electron feels an RF field with a frequency $\bar{\omega}$ which distributes around $\bar{\omega}$. We take a uniform distribution

$$f(\bar{\omega}) = 1/2\Delta\bar{\omega} \quad \text{for } \bar{\omega} - \Delta\bar{\omega} < \bar{\omega} < \bar{\omega} + \Delta\bar{\omega}$$

$$= 0 \quad \text{otherwise}$$

to make the calculation easy. The power transfer averaged over the frequency distribution is

$$\langle \bar{p}(\bar{\omega}) \rangle = \int \bar{p}(\bar{\omega}) f(\bar{\omega}) d\bar{\omega}.$$

Furthermore, the power transfer has to be average over the transverse kinetic energy \bar{W} . The distribution function of \bar{W} in an electron ring is an exponential one as [1]

$$g(\bar{W}) = (1/\bar{T}) \exp(-\bar{W}/\bar{T}),$$

where \bar{T} is some mean transverse kinetic energy of electrons in the beam. The average power transfer at $\bar{\omega}$ is

$$\langle \bar{p} \rangle = \int_0^\infty \langle \bar{p}(\bar{\omega}) \rangle g(\bar{W}) d\bar{W}.$$

The power transfer is function of the frequency of applied field $\bar{\omega}$ and can be plus or minus depending on the frequency. It is complicated to express the function at an arbitrary frequency. At the frequency $\bar{\omega} = \bar{\omega}_c + \Delta\bar{\omega}$, where $\bar{\omega}_c = eB_L/m_e$, B_L the longitudinal magnetic field, the power transfer is simplified to

$$\langle \bar{p} \rangle = \frac{e^2 E^2}{2m_e} \frac{1}{\hbar\bar{\omega}_c} \frac{1}{2\Delta\bar{\omega}\bar{T}} \times$$

$$\times \int_0^\infty \bar{W} \left[\left(1 + \frac{\hbar\bar{\omega}_c}{\bar{W}} - \alpha \right) \left\{ -\tan^{-1} \frac{\tau\bar{\omega}_c\bar{W}}{m_e c^2} + \tan^{-1} \tau \left(2\Delta\bar{\omega} + \frac{\bar{\omega}_c\bar{W}}{m_e c^2} \right) \right\} \right.$$

$$\left. + \tan^{-1} \tau \left(\frac{\bar{\omega}_c\bar{W}}{m_e c^2} - \alpha\bar{\omega}_c \right) - \tan^{-1} \tau \left(2\Delta\bar{\omega} + \frac{\bar{\omega}_c\bar{W}}{m_e c^2} - \alpha\bar{\omega}_c \right) \right] \exp\left(-\frac{\bar{W}}{\bar{T}}\right) d\bar{W}.$$

Since in electron rings, the condition $\alpha\bar{\omega}_c\tau = \alpha Q \ll 1$ is always satisfied, we can expand the integrand function to the Taylor series. We take up to second order terms in the series, then power transfer is lead to for $\tau\Delta\bar{\omega} \gg 1$

$$\langle \bar{p} \rangle = -\frac{\pi e^2 E^2 \hbar\bar{\omega}_c}{16m_e \bar{T} \Delta\bar{\omega}} \left[1 - \frac{2m_e c^2}{\pi \hbar\bar{\omega}_c Q} z e^z E_1(z) \right] \quad (3)$$

where $\bar{Q} = \tau\bar{\omega}_c$,

$$z = 2m_e c^2 \Delta\bar{\omega} / \bar{T}\bar{\omega}_c. \quad (4)$$

$$E_1(z) = \int_z^\infty \frac{e^{-t}}{t} dt.$$

Otherwise for small value of $\tau\Delta\bar{\omega}$, the power transfer at $\bar{\omega} = \bar{\omega}_c$ is calculated directly using eq. (1) to be

$$\langle \bar{p} \rangle = \frac{e^2 E^2 \tau \hbar\bar{\omega}_c}{4m_e \bar{T}} \left[1 - \frac{2(m_e c^2)^2}{\hbar\bar{\omega}_c \bar{T} Q^2} \log\left(\frac{\bar{T}}{m_e c^2} - 0.577\right) \right].$$

This is not in actual cases however. Either way, the characteristic cooling time of the betatron oscillation in the co-moving frame is

$$\bar{\tau}_c = \bar{T} / \langle \bar{p} \rangle.$$

A negative value of $\bar{\tau}_c$ indicates the beam is cooled rather than heated.

IV. Estimation of the parameters

Now we express \bar{T} as a function of some ring parameters. Here we take a usual coordinate system s, x and z to specify the position of an electron. Then the width of transverse kinetic energy \bar{T} in the moving frame is given by

$$\bar{T} = T_x + T_z$$

In actual ring, T_z is much smaller compared to T_x . The typical value of T_x is expressed as [6]

$$T_x = m_e c^2 \gamma^2 e_x / 2\pi\beta_x$$

where β_x is the horizontal betatron function in the region of the RF field. We give typical values of the quantities for Advanced Light Source (ALS) ring at Lawrence Berkeley Laboratory [7]. The T_x is 8.6×10^2 eV for the beam energy $m_e c^2 \gamma = 1.5$ GeV for $e_x = 4.08 \times 10^{-9}$ m.radian and $\beta_x = 11$ m for the ring. The value of T_x is taken to be the mean energy \bar{T} of the transverse motion in the beam.

The RF electric field is produced as a traveling wave in the parallel plate transmission line in the beam tube against the electron beam as shown in Fig. 1. The fields in the laboratory frame are, so to speak, compressed in the co-moving frame and the strengths are amplified by a factor 2γ for extremely relativistic electron energy [8].

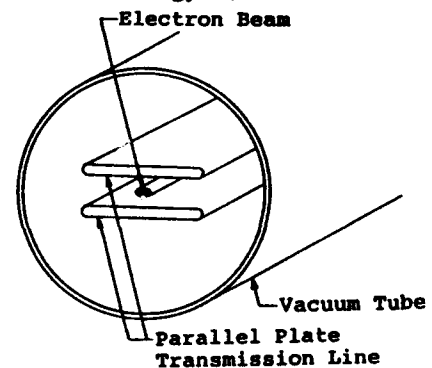


Fig.1. Inside view of the vacuum tube in the longitudinal solenoidal magnet with the parallel plate transmission line. The frequency of the RF field in the laboratory frame ω is multiplied also by the same factor in the co-moving frame as

$\bar{\omega} = 2\gamma\omega_c$. The cooling time in the co-moving frame is elongated by a factor γ in the laboratory system by a relativistic effect.

Next we will consider the value of the phase breaking time $\bar{\tau}$ of the cyclotron motion in the transverse plane. The main source to reduce the phase breaking time comes from a spread of cyclotron rotation angle produced by energy spread of electron in the beam. The source is represented as the first term of the following equation of the breaking time $\bar{\tau}$ [9]

$$\frac{1}{\bar{\tau}} = \frac{\bar{\omega}_c}{\pi B_L L} \left\{ -\frac{\Delta\gamma}{\gamma} \oint B_z(0,0,s) ds + \oint \Delta B_z(x,z,s) ds \right\} \quad (5)$$

for extremely relativistic electron beam, where L is the length of the longitudinal magnetic field and $B_z(x,z,s)$ the variation of the field. Since the first term in the bracket is too much large for usual relative energy width $\Delta\gamma/\gamma$ of electron beam in a ring in application to the master cooling, we propose to cancel out the term by introducing a compensating solenoidal magnet in the ring. We make the field direction of the compensating magnet to be opposite with that of the longitudinal magnet field shown as Fig. 1 of ref. [9].

The second term denotes the small field variation of longitudinal field components of the two magnet. The field variation has an appreciable effect on the debunching of the cyclotron motion. However any beam dynamical effects of the field may not cause the pile up of the field integral for a ring which has a symmetric lattice structure. Debunching of the motion may occur from the longitudinal component in the fringing fields of the solenoidal and lattice magnets. However the electron receives the fields within a very short time duration in the co-moving frame and the effect on the cyclotron motion may be much attenuated by an adiabatic consideration of the motion. Further, the sum of the effect cancels out for each magnet. Intra-beam scattering in the bunch is estimated to give an insignificant effect on the debunching.

Finally we will estimate the lower limited of the $\bar{\tau}$ required. In the first place, the parameter z of eq. (4) is calculated to be 0.358 for the ALS ring parameters $\bar{T} = 860$ eV, $\Delta\bar{\omega}/\bar{\omega}_c = 3 \times 10^{-4}$ and $m_e c^2 = 5.11 \times 10^5$ eV and it leads the value of the function $ze^2 E_1(z)$ of 0.4. We adopt 10 Tesla for B_L . It leads the cyclotron frequency $\bar{\omega}_c = 1.76 \times 10^{12}$ rad/sec and the corresponding quantum energy $\hbar\bar{\omega}_c = 1.16 \times 10^{-3}$ eV. The condition of energy emission is that the value in the square bracket of eq. (3) is positive. It leads a lower limit of $\bar{\tau}$. The lower limited of $\bar{\tau}$ which leads energy emission can be derived from eq. (3) with above parameters to be

$$\bar{\tau} > 10^{-4} \text{ sec}$$

for the typical example. The condition may be fulfilled when the compensation less than 10^{-4} . This may be technically possible. The condition is almost independent of \bar{T} and $\Delta\bar{\omega}/\bar{\omega}_c$ for $z \geq 0.5$.

V. Conclusions and remarks

We are now in position to estimate the cooling time $\bar{\tau}_c$ of the betatron oscillation. A rough estimate of the time is the first factor of $\langle \bar{\beta} \rangle$ in eq. (3) as

$$\begin{aligned} \bar{\tau}_c &\sim \frac{16m_e \bar{T}^2 \Delta\bar{\omega}}{\pi e^2 E^2 \hbar \bar{\omega}_c} \\ &= -1.1 \times 10^4 \frac{\bar{T}^2 (\text{eV})}{\gamma^2 E^2} \frac{\Delta\bar{\omega}}{\bar{\omega}_c} \text{ sec} \end{aligned} \quad (6)$$

where E is the amplitude of RF electric field in laboratory system in V/m. In our example, the values of quantities in eq. (6) are $\bar{T} = 860$ eV, $\gamma = 3 \times 10^3$, $\Delta\bar{\omega}/\bar{\omega}_c = 3 \times 10^{-4}$ and the cooling time is estimated to be 2.7×10^{-9} sec for $E = 10^4$ V/m. The time is enough short to decrease the transverse emittance in particle electron rings. For the electron field, the power transmitted through the parallel plate transmission line is some 10 0W and the loss is about 0.01 W/m in usual design of the line. The loss of this extent will be tolerated in the superconducting solenoidal magnet.

Though the cooling time of the dynamic method seems to be able to be short as much as one like using as RF field of large amplitude, the time in the laboratory frame cannot decrease below an inverse electron frequency $1/\omega_c = 2\gamma/\bar{\omega}_c$, which is order of 10^{-9} sec in this example by an adiabatic condition.

The electron beam is cooled only in the RF field with the longitudinal magnetic field. The electron motion in the remainder of the ring does not affect the transition between the Landau levels in the solenoid. Consequently the transition rate reduce by a factor L/C where L is the solenoid length and C the circumference of the ring. Thus the cooling time constant $\bar{\tau}_c$ has to be multiplied by a factor C/L to obtain the effective cooling time constant. The factor is 100 if the length L is assumed to be 1% of the C . In order to continue the cyclotron rotation successively, a suitable phase locking consideration is necessary to the betatron motion in the ring.

Though the cooling time constant in the co-moving frame has to be multiplied by the product of two factors γ (3×10^3) and C/L (10^2) to obtain the laboratory one, the time is yet much shorter than the radiation damping time which is typically some 10 msec in usual SR rings. Since the transverse emittance of the beam decrease in proportional to the cooling time [1], we can obtain an electron beam of very small emittance in an electron ring by the dynamical method.

VI. References

- [1] M. Sands, SLAC Report 121 (1970).
- [2] A. Wulrich, Particle Acc. 22 257 (1988).
- [3] L. Schneider, Phys. Rev. Lett. 2 504 (1959).
- [4] V. B. Berestetskii, E. M. Lifshitz and L. P. Pitaevskii, Quantum Electrodynamics, Pergamon Press p.121 (1982).
- [5] P. Sprangle and A. T. Drobot, IEEE MTT 25 258 (1977).
- [6] E. D. Courant and H. S. Snyder, Ann. Phys. (N. Y.) 3 1 (1958).
- [7] 1-2 GeV Synchrotron Radiation Source, Conceptual Design Report, LBL PUB-5172 Rev. (1986).
- [8] J. D. Jackson, Classical Electrodynamics, 2nd. ed., John Wilkey & Sons, Inc. (1975).
- [9] H. Ikegami, Phys. Rev. Lett. 64 1737 (1990).

THE PRINCIPLE OF ULTRA-FAST AUTOMATIC COOLING FOR BEAMS^①

Gao Shuyang Qian Guang^②

China Institute of Atomic Energy, P.O.Box 275(3)

Beijing 102413, P. R. China

Abstract

This paper is to illustrate that the transverse emittance of a beam with constant energy can be automatically shrinked in the particular static magnetic field, which can be used as an ultra-fast "cooler" to accelerators or storage rings. The analytical solution for the nonlinear equation of motion is obtained. The exact proof of the problem is given by means of the precisely analytical representation of Jacobean determinant corresponding to the nonlinear transformation of emittance.

1. INTRODUCTION

Concerning the motion for particles with constant energy under the influence of static magnetic fields, the beam emittance is an invariant[1], which was strictly proved in the linear approximation in 1958. It has not only become a fundamental principle in the modern beam dynamics and optics, but also been used to the classical and quantum optics[2]. Therefore in 1991 V.V. Parkhomchuk and A.N. Skrinsky pointed out: "the phase density of the beam can not be increased by using any set of external electromagnetic fields, independent on the motion of specific particles of the beam." [3] In other words, in the modern beam dynamics the conservation of the beam emittance seems not to be changed forever.

In order to overcome the above severe restriction, people could not help looking for other ways reducing the beam emittance. The electron beam cooling was proposed by G.I. Budker in 1966[3]. After then, the cooling time was contracted to 0.1s. Hence it is so-called "fast electron cooling"[4]. In 1968, Simon van der Meer proposed stochastic cooling[5], which played an extremely important role in the discovery of W and Z bosons. So he was awarded 1984 Nobel Prize for physics[6]. But both electron and stochastic cooling were so slow that people were forced to look for other even faster cooling method. In 1989 H. Iwagami proposed the cyclotron maser cooling[7], which

is on the way to be investigated. Hence it is still in great need of looking for an ultra-fast cooling method.

D.E. Edwards and M.J. Syphers pointed out: "Since x' is not the conjugate momentum to x , we can't make statements about phase space and energy, but is not a concern at present." [8] However, that is not the case in nonlinear motion. In order to distinguish it from the canonical phase space, we call the $x-x'$ space as Courant-Snyder (C-S) phase space or the emittance phase space in this paper. F.J.N. Wilson pointed out that Liouville's theorem in the emittance phase space is just to prove that the corresponding Jacobean determinant equals unity[9]. It is worth pointing out that the emittance conservation in the nonlinear case has never been proved exactly, although none of exceptions have ever been found out in all accelerators or storage rings in the world at present. Hence, this problem has never been made any progress in several decades.

Fortunately, in the nonlinear case, we have found out a particular static magnetic field in which the emittance conservation is not true any longer, so the transverse emittance of a beam with constant energy will be shrinked rapidly. Of course, that is distinguished from both adiabatic and synchrotron radiation damping arising from the field or the energy change. Such a magnet with ultra-fast automatic cooling can be treated as a "cooler", which can be used to accelerators, storage rings and so on[10]. As compared with the stochastic cooling or "fast electron cooling", its cooling rate is much more rapid by six or seven orders of magnitude[10]. It is technically simple and remarkably feasible. Its application fields are much more widespread than the others, especially to the fusion device of the continuous electron beam with intense current and so on.[10]

2. THE MOTION IN THE MEDEAN PLANE

^①Supported by the National Science Foundation of China.

We are interested in the motion in the axis-symmetrical field, which in the median plane is only dependent on ζ . There is a Cartesian coordinate set of ζ, x, ζ . The Hamilton equations in the median plane are represented[11]

$$\dot{\zeta} = \frac{p_{\zeta}}{\sqrt{1-p_{\zeta}^2}} \quad (2.1)$$

$$\dot{p}_{\zeta} = -(1-\delta) \cdot \frac{e}{p_0} \cdot B,$$

$$p_{\zeta} = \frac{\dot{\zeta}}{\sqrt{1+(\dot{\zeta}')^2}}$$

$$H(\zeta, p_{\zeta}, \zeta) = -\sqrt{1-p_{\zeta}^2} - (1-\delta) \cdot \frac{e}{p_0} \cdot A$$

Because H does not contain the independent variable ζ explicitly, Hamilton H is a constant. As well known

$$\dot{\zeta} = \tan\left(\frac{\pi}{2} - \theta\right) \quad (2.2)$$

where θ is an angle between the velocity vector and the ζ -axis. From the formulas (2.1) we obtain

$$p_{\zeta} = \cos(\theta) \quad (2.3)$$

$$\sin(\theta) = f(\zeta, \zeta, \theta_1)$$

$$f(\zeta, \zeta, \theta_1) = \sin(\theta_1) + (1-\delta) \cdot \frac{e}{p_0} \cdot [A(\zeta_1) - A(\zeta)]$$

$$\frac{d\zeta}{d\zeta} = -\frac{f}{\sqrt{1-f^2}}$$

$$\zeta - \zeta_1 = -\int_{\zeta_1}^{\zeta} \frac{f}{\sqrt{1-f^2}} \cdot d\zeta$$

Let us consider the motion of two particles with differently initial conditions, there are two invariants

$$\sin(\theta + \delta\theta) - \sin(\theta) = \sin(\theta_1 + \delta\theta_1) - \sin(\theta_1) \quad (2.4)$$

$$\delta\zeta = \delta\zeta_1$$

When the particles from free space pass through the magnetic field region, by means of the transformation from Cartesian coordinate system to the natural coordinate set of x, y, s , as shown in Fig.1, the solution is represented

$$x_k = \left\{ \frac{x_1}{\cos(\theta_{a1}) + x_1' \cdot \sin(\theta_{a1})} \right. \quad (2.5)$$

$$+ \int_{\zeta_1}^{\zeta_k} \left[\frac{f}{\sqrt{1-f^2}} - \frac{f_1}{\sqrt{1-f_1^2}} \right] \cdot d\zeta \}$$

$$\cdot [\cos(\theta_{ak}) + x_k' \cdot \sin(\theta_{ak})]$$

$$x_k' = -\frac{\sin(\delta\theta_k)}{\sqrt{1-\sin^2(\delta\theta_k)}}$$

$$\sin(\delta\theta_k) = [C_1 + \sin(\theta_{a1})] \cdot \cos(\theta_{ak})$$

$$- \sin(\theta_{ak}) \cdot \sqrt{1 - (C_1 + \sin(\theta_{a1}))^2}$$

$$C_1 = \frac{\sin(\theta_{a1})}{\sqrt{1+(x_1')^2}} - \cos(\theta_{a1}) \cdot \frac{x_1'}{\sqrt{1+(x_1')^2}}$$

$$- \sin(\theta_{a1})$$

$$f = \sin(\theta_{a1} + \delta\theta_1) + (1-\delta) \cdot \frac{e}{p_0} \cdot [A(\zeta_1) - A(\zeta)]$$

$$f_1 = \sin(\theta_{a1}) + (1-\delta) \cdot \frac{e}{p_0} \cdot [A(\zeta_1) - A(\zeta)]$$

$$\sin(\theta_{a1} + \delta\theta_1) = \sin(\theta_{a1} + \delta\theta_1) + \sin(\theta_{a1}) - \sin(\theta_{a1})$$

$$x_1' = -\tan(\delta\theta_1)$$

That is the exactly analytical solution of the nonlinear motion in the natural coordinate system.

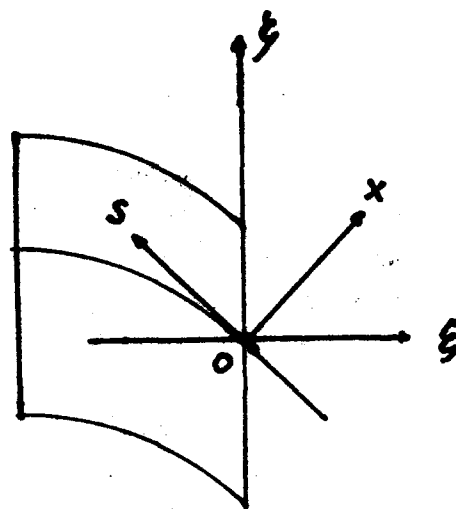


Figure 1. Cartesian and natural coordinate

3. THE PROOF FOR THE COOLING

According to the fundamental method given by F.J.N.Wilson[9], it is the necessary condition for the cooling that the corresponding Jacobean determinant must be smaller than unity. By means of differentiating the above formula, the Jacobean determinant can be obtained. From the above formula we know

$$J_{21} = \frac{\partial x_k'}{\partial x_1} = 0 \quad (3.1)$$

Then we have

$$J = J_{11} \cdot J_{22} \quad (3.2)$$

$$J_{11} = [\cos(\theta_{a1}) + x_1' \cdot \sin(\theta_{a1})]^{-1} \cdot [\cos(\theta_{ak}) + x_k' \cdot \sin(\theta_{ak})]$$

$$J_{\pi} = \{ \cos(\theta_{\pi}) + \sin(\theta_{\pi}) \cdot \frac{C_1 + \sin(\theta_{\pi})}{\sqrt{1 - [C_1 + \sin(\theta_{\pi})]^2}} \} \\ \cdot [\cos(\theta_{\pi}) + x'_1 \cdot \sin(\theta_{\pi})] \\ \cdot [\cos(\delta\theta_{\pi})]^{-1} \cdot [1 + (x'_1)^2]^{-\frac{1}{2}}$$

When $\theta_{\pi} = \pi$, The above formula becomes

$$J = [\cos(\delta\theta_{\pi})]^{-1} \cdot [1 + (x'_1)^2]^{-\frac{1}{2}} \quad (3.3)$$

$$\cos(\delta\theta_{\pi}) = 1 - \sin(\theta_{\pi}) + \frac{x'_1 \cdot \cos(\theta_{\pi}) + \sin(\theta_{\pi})}{\sqrt{1 - x'^2_1}}$$

When we select the parameters for the equilibrium orbit

$$\theta_{\pi} - \frac{\pi}{2} = \frac{\pi}{6}; \frac{\pi}{4}; \frac{\pi}{3}; \frac{5\pi}{12} \text{ and } \theta_{\pi} = \pi$$

and $x'_1 = -0.01 + 0.01$ Radian, the results for calculus of J are illustrated in Figure 2. That suggest us:

1. The Jacobean determinant J is not dependent on the initial coordinate x_1 , but on x'_1 .

2. It is only when $x'_1 = 0$ that J is equal to 1. By other words, it is only when the beam emittance equals zero that such emittance can really becomes an invariant of motion. Therefore, in a general way, the emittance conservation is not true any longer.

3. If $x'_1 \neq 0$, the Jacobean determinant J is always smaller than 1. In that case, after a beam passes through such magnetic field region, its transverse emittance must be shrinked automatically. That results in the ultra-fast automatic cooling for the beam.

4. The bigger the angular width of the bending magnet is, the smaller the Jacobean determinant J is.

5. The decisive factor for the ultra-fast automatic cooling is only dependent on the proper edge-focusing angle of the bending magnet rather than the field distribution. The necessary conditions are $\theta_{\pi} = \pi$ rather than the field distribution. The necessary conditions are $\theta_{\pi} = \pi$ and the two edges of the bending magnet are parallel. Therefore it is technically simple and remarkably feasible.

6. That "cooler" is fitted for ions, electron, especially for the ultra-low energy fields. It can be used to accelerators, storage rings and so on.

7. An example of its application has been given in the forthcoming paper [10]. As compared with the stochastic cooling or the fast electron cooling, its cooling rate is much

more rapid by six or seven orders of magnitude.

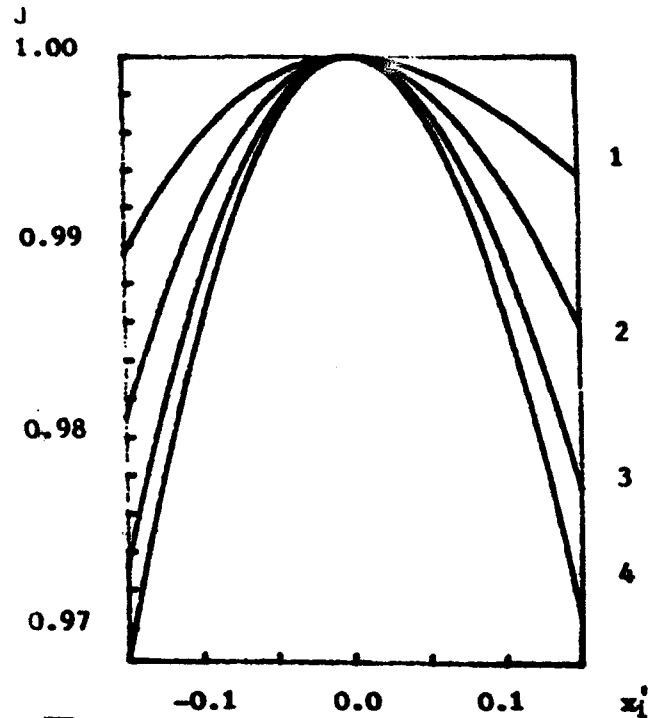


Figure 2. Jacobean determinant corresponding to the nonlinear transformation of emittance

References

- [1] E.D.Courant, H.S.Snyder, *Ann. Phys.*, 3, 1, (1958)
- [2] G.Dattoli et al, *Proc. Workshop on Nonlinear Problems in Future Particle Accelerators*, Ed. W.Scandale and G.Tarchetti, 402 and 18, (1990)
- [3] V.V.Parkhomchuk, A.N.Skrinsky, *Reports on Progress in Physics*, Vol. 54, 7, 919, (1991)
- [4] V.V.Parkhomchuk, 1984 physics of fast electron cooling, *Proc. Workshop on Electron Cooling and Related Application*, Ed. H.Poth (1984)
- [5] I.Mohl, G.Petrucci, Simon van der Meer, *Phys. Rep.* 58, 7 5-119, (1978)
- [6] CERN Courier, 1984 Nobel Prize, December, 419, (1984)
- [7] H.Ikegami, 12-th Intern. Conf. Cycl. their Appl., 55, (1989)
- [8] D.A. Edwards and M.J. Sypher, *AIP Conf. Proc.* 184, 2, (1989)
- [9] F.J.N. Wilson, *AIP Conf. Proc.* 153, 3, (1987)
- [10] Gao Shuyang, Qian Guangyu, a Fusion Device of the Continuous Electron Beam Confinement Used by the Continuous Injection, (the same proceedings)
- [11] F.Willeke and G.Ripker, *AIP Conf. Proc.* 184, 758, (1989)

On the Longitudinal Stability of Cooled Coasting Ion Beams

Sergei Nagaitsev
Indiana University Cyclotron Facility
2401 Milo B. Sampson Ln., Bloomington, IN 47405 USA

Abstract

The longitudinal stability of intense, low momentum spread ion beams is of great interest today, especially in electron-cooled storage rings. Stability conditions are usually formulated as the limitations on the allowed value of beam-chamber coupling impedances. In the case of cooled beams, the effect of cooling can not be neglected if the cooling rate is comparable with the revolution frequency spread. The effect of the electron cooling can be described by the Fokker-Planck equation. In this paper we present a simple analytical method to derive dispersion relations for the longitudinal coasting beam instabilities using a perturbative approach. Numerical examples applied to 45 MeV protons in the IUCF cooling ring are presented.

I. INTRODUCTION

The interest in the longitudinal stability of the coasting cooled ion beams was stimulated by the number of publications [1], [2] reporting measured stability diagrams significantly different from what one could expect for the coasting beams with Gaussian momentum distributions in the absence of any cooling mechanism. In Ref. [3] two possible reasons of this difference were suggested: deviation of the momentum distribution from Gaussian and the influence of the electron cooling on the coherent stability of the ion beam. Both the non-Gaussian distributions and the influence of the cooling have been studied elsewhere [3], [4]. This paper elaborates on the derivation of dispersion relation in the presence of cooling in the closed analytical form. It is also oriented towards practical application for the IUCF cooler ring.

II. DISPERSION RELATION

A. Fokker-Planck Equation

The influence of the cooling on the particle distribution function ψ can be described by the Fokker-Planck equation [4], [5]:

$$\frac{\partial \psi}{\partial t} + \theta \frac{\partial \psi}{\partial \theta} + \delta \frac{\partial \psi}{\partial \delta} = \frac{\partial}{\partial \delta} \left(\lambda \delta \psi + \frac{D}{2} \frac{\partial \psi}{\partial \delta} \right) \quad (1)$$

Here $\theta = s/(2\pi R)$ is the longitudinal coordinate, $\delta = \Delta p/p$ is the conjugate momentum variable and t is time. The cooling rate λ and diffusion coefficient D are assumed to be constant in (1). For coasting beams the stationary distribution $\psi_s(\delta)$

satisfies the equation:

$$\lambda \delta \psi_s + \frac{D}{2} \frac{d \psi_s}{d \delta} = 0 \quad (2)$$

The solution of (2) is the Gaussian distribution function:

$$\psi_s(\delta) = \frac{N}{(2\pi)^{1/2} \sigma} e^{-\delta^2/2\sigma^2} \quad (3)$$

where $\sigma = (D/2\lambda)^{1/2}$ is the rms momentum spread of the beam and N is a number of particles. One can now describe the perturbed particle distribution function as:

$$\psi(\delta, \theta, t) = \psi_s(\delta) + \psi_1(\delta) e^{i(n\theta - \Omega t)} \quad (4)$$

where ψ_1 is a small perturbation of the stationary distribution function, n is a positive integer and Ω is the complex frequency of this coherent perturbation. Let us now assume that $\psi_1(\delta)$ is normalized to the number of particles involved in the perturbation:

$$\int_{-\infty}^{\infty} \psi_1(\delta) d\delta = N_1 = \frac{2\pi I_1}{e\omega_s} \quad (5)$$

where ω_s is the revolution frequency of the synchronous particle and e is the ion charge. Taking into account that

$$\delta = \frac{1}{\beta^2} \frac{\Delta E}{E} = -\frac{e\omega_s I_1 Z_{||}}{2\pi \beta^2 E} e^{i(n\theta - \Omega t)} \quad (6)$$

where $Z_{||}$ is the longitudinal coupling impedance, E is the energy of the beam and β is the usual relativistic parameter, Eq. (1) can be rewritten to the first order as:

$$i(n\omega - \Omega) \psi_1 - \frac{d\psi_s}{d\delta} \frac{e\omega_s I_1 Z_{||}}{2\pi \beta^2 E} = \frac{d}{d\delta} \left(\lambda \delta \psi_1 + \frac{D}{2} \frac{d\psi_1}{d\delta} \right) \quad (7)$$

Here ω is the revolution frequency of the particle with momentum δ : $\omega(\delta) = \omega_s(1 - \eta\delta)$, where η is the phase slip factor ($\eta = -\Delta\omega/\omega_s\delta$).

B. Dispersion relation

Since ψ_1 vanishes at the infinity, the natural way to solve

equation (7) is by the Fourier transform method:

$$f(k) = \frac{1}{\sqrt{2\pi}} \int_{-\infty}^{\infty} \psi_1(\delta) e^{ik\delta} d\delta \quad (8)$$

which decreases the order of the differential equation (7) by one. The transformed equation can be solved by simple integration. Introducing the new notations:

$$a_n = \frac{n\omega_0 - \Omega}{\lambda}; \quad q_n = \frac{n\eta\sigma\omega_0}{\lambda} \quad (9)$$

the dispersion relation can be written as follows:

$$1 = i \frac{eI_0}{2\pi\beta^2\sigma^2\eta E} \frac{Z_1}{n} \int_0^{q_n} \left(1 - \frac{x}{q_n}\right)^{a_n+q_n^2-1} e^{q_n x} dx \quad (10)$$

where I_0 is the beam current. Equation (10) can also be expressed in analytical form as [6]:

$$1 = iA \frac{Z_1}{n} q_n^2 B(a_n + q_n^2, 2) \Phi(2; a_n + q_n^2 + 2; q_n^2) \quad (11)$$

where A is given by:

$$A = \frac{eI_0}{2\pi\beta^2\sigma^2\eta E} \quad (12)$$

and $B(x, y)$, $\Phi(\alpha; \gamma; z)$ are the beta function and the degenerate hypergeometric function respectively.

C. Asymptotic Behavior

In the case of vanishing cooling ($\lambda \rightarrow 0$) the dispersion relation (10) has to become the well-known dispersion relation for a Gaussian beam without cooling. In fact, recalling that the ratio a_n/q_n remains finite, after some algebra one can write:

$$1 = iA \frac{Z_1}{n} J\left(\frac{\Omega - n\omega_0}{n\eta\sigma\omega_0}\right) \quad (13)$$

where $J(u)$ is given by the expression:

$$J(u) = \int_0^{\infty} e^{-x^2/2 + iux} x dx = \frac{1}{\sqrt{2\pi}} \int_{-\infty}^{\infty} \frac{u}{u-u_0} e^{-u^2/2} du \quad (14)$$

Another limiting case is the coherent perturbation with a high harmonic number ($n \rightarrow \infty$). This case is almost identical to the previous one. Cooling is too "slow" for such oscillations and the only stabilizing mechanism is Landau damping. For high harmonic numbers the dispersion relation

reduces to (13).

D. Stability Diagram

Figure 1 shows the stability diagrams, calculated using Eq. 10, for the first three harmonics of a proton beam (45 MeV) in the IUCF cooler ring. The cooling rate was taken to be 70 Hz [7] and momentum spread $4 \cdot 10^{-5}$. The stability diagram for the Gaussian beam, given by (13), is also shown on Fig. 1.

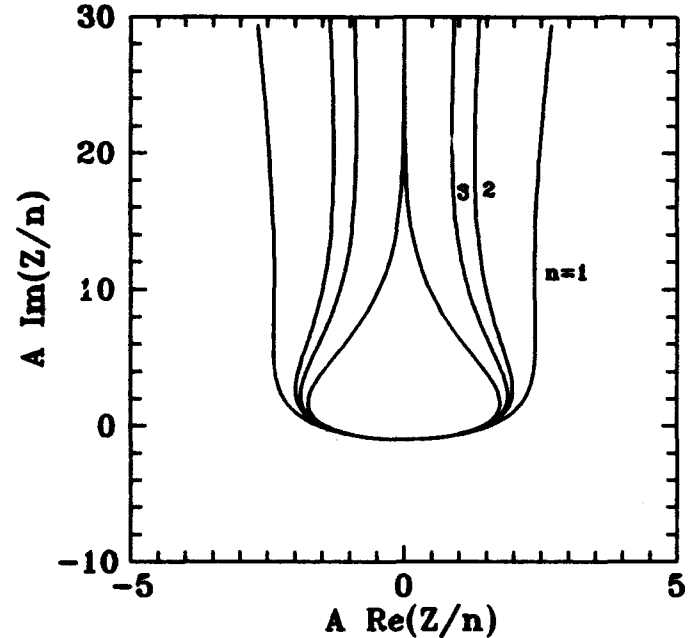


Figure 1. Variations of the stability diagram with harmonic number ($q_1 = -2.5$) for the cooled beam and stability diagram for the Gaussian beam without cooling.

III. SCHOTTKY SPECTRUM

The dielectric permeability function of the beam corresponding to the dispersion relation (10) can be written as:

$$\epsilon_n = 1 - iA \frac{Z_1}{n} \int_0^{q_n} \left(1 - \frac{x}{q_n}\right)^{a_n+q_n^2-1} e^{q_n x} dx \quad (15)$$

For a given n , equation (10) yields the frequency (generally complex) at which a perturbation can exist in the beam without an external source. For vanishing impedance or current the effect of polarization of the medium is negligible and we have $\epsilon_n = 1$. The Schottky noise power spectrum then can be written, using the dielectric function [1]:

$$P_n(\Omega) = \frac{e^2 N}{\pi n} \frac{\psi_n(\Omega/n)}{|\epsilon_n|^2} \quad (16)$$

The main feature of this Schottky spectrum is that at high

am intensities, it is strongly deformed into a double-peak shape [8], corresponding to the excitation of the slow and the fast coherent longitudinal waves by the external electric field by beam current fluctuations. The frequency of this wave depends solely upon the beam current and the value of coupling impedance. Although it is generally a nontrivial problem to calculate the coupling impedance, one can make reasonable assumptions for the low energy electron-cooled rings. First, assume that $|Im Z_1/n| \gg |Re Z_1/n|$ and second, that Z_1/n is independent of harmonic number n . These two assumptions correspond to the case of space-charge dominated impedance, given by:

$$\frac{Z_1}{n} = -i \frac{Z_0}{2\beta\gamma^2} \left(2 \ln \left(\frac{b}{a} \right) + 1 \right) \quad (17)$$

where $Z_0 = 377 \Omega$, a and b are diameters of the beam and vacuum chamber respectively. For the IUCF cooler ring at 1 MeV expression (17) gives $|Im Z_1/n| \approx 4 k\Omega$, whereas the real part of the impedance (resistive wall and broad-band) is typically less than 5Ω for any harmonic. Having made these assumptions and neglecting the momentum spread of the beam, we can obtain for the coherent frequencies in the presence of the cooling:

$$\Delta\Omega = \Omega - n\omega_0 = \pm n\omega_0 \left| \frac{e\eta I_0}{2\pi\beta^2 E} \right|^{1/2} \left| \frac{Z_1}{n} \right|^{1/2} \quad (18)$$

As we can notice, that the value of $\Delta\Omega/n\omega_0$ is independent on n . This can be also seen directly from (13) after some algebraic transformations. For a cooled beam this is no longer true. In fact, the deviation of $\Delta\Omega/n\omega_0$ from a constant value for different harmonics is the easiest way to observe the influence of the cooling on coherent stability. Fig. 2 shows the frequency for coherent oscillations, given by (18) as well as the frequency in the presence of cooling for a 0.5 mA, 45 eV proton beam in the IUCF cooler ring.

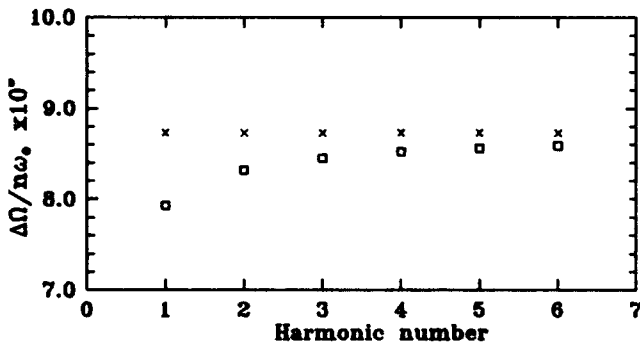


Figure 2. Frequency of coherent oscillations as a function of harmonic number for the beam with Gaussian momentum distribution in the absence (x's) and in the presence (□'s) of cooling.

IV. CONCLUSION

We have calculated the dispersion relation for cooled coasting beams. The influence of the cooling on the coherent beam stability can be observed by measuring the separation of the two coherent peaks in the Schottky spectrum as a function of harmonic number. The momentum distribution function of the beam can be deduced from the shape of the Schottky power spectrum using (16). Beam transfer function measurements [1] can be also performed to obtain stability diagrams directly.

V. ACKNOWLEDGMENTS

We would like to thank S.Y. Lee, D.V. Pestrikov and T. Ellison for useful discussions. We also would like to point out that the Fokker-Planck approach for the electron cooled beams was initially developed by D.V. Pestrikov in Ref. [4], [8].

VI. REFERENCES

- [1] I. Hofmann, "Beam dynamics of cooled heavy ion beams", *Conference Record of the 1991 IEEE Particle Accelerator Conference*, Vol. 4, pp. 2492-2496.
- [2] J. Bossert et al., "Electron beam cooling and beam instability studies at LEAR", *CERN/PS 92-45(AR)*, 1992.
- [3] S. Cocher and I. Hofmann, "On the stability and diagnostics of heavy ions in storage rings with high phase-space density", *Particle Accelerators*, 1990, Vol. 34, pp. 189-210.
- [4] D.V. Pestrikov, "The longitudinal Schottky noise of intense beam", *Proceedings of the Workshop on Electron Cooling and New Cooling Techniques*, Legnaro, Padova-Italy, 15-17 May, 1990, pp. 165-180.
- [5] H. Risken, "The Fokker-Planck Equation", 2nd edition, Springer-Verlag, 1989, p. 7.
- [6] I.S. Gradshteyn and I.M. Ryzhik, "Table of Integrals, Series, and Products", New York: Academic Press, 1980, p. 318, formula 3.383.1
- [7] Tim Ellison, "Electron cooling", *Ph.D. Thesis*, Indiana University, 1990, p. 77.
- [8] V.V. Parkhomchuk and D.V. Pestrikov, *Sov. Phys. Tech. Phys.*, Vol. 25(7), p. 818 (1980).

Crystalline Beam Ground State*

Jie Wei, Brookhaven National Laboratory, Upton, New York 11973

Xiao-Ping Li, Rutgers University, and Andrew M. Sessler, Lawrence Berkeley Laboratory

Abstract

In order to employ Molecular Dynamics method, commonly used in condensed matter physics, we have derived the equations of motion for a beam of charged particles in the rotating rest frame of the reference particle. We include in the formalism that the particles are confined by the guiding and focusing magnetic fields, and that they are confined in a conducting vacuum pipe while interacting with each other via a Coulomb force. Numerical simulations have been performed to obtain the equilibrium structure. The effects of the shearing force, centrifugal force, and azimuthal variation of the focusing strength are investigated. It is found that a constant gradient storage ring can not give a crystalline beam, but that an alternating-gradient (AG) structure can. In such a machine the ground state is, except for one-dimensional (1-D) crystals, time-dependent. The ground state is a zero entropy state, despite the time-dependent, periodic variation of the focusing force. The nature of the ground state, similar to that found by Rahman and Schiffer[1], depends upon the density and the relative focusing strengths in the transverse directions. At low density, the crystal is 1-D. As the density increases, it transforms into various kinds of 2-D and 3-D crystals. If the energy of the beam is higher than the transition energy of the machine, the crystalline structure can not be formed for lack of radial focusing.

I. INTRODUCTION

The ground states of crystalline beams were first studied, in seminal work, by J. Schiffer[1] and his colleagues. Their work assumed a storage ring model in which particles are subject to time-independent harmonic forces in both transverse directions. Subsequently, they studied the crystallization in a time-dependent, AG focusing potential.[2]

In order to employ Molecular Dynamics method for quantitative studies, we first derive in section 2 the equations of motion for the particles in the rotating rest frame of the reference particle. Qualitative studies pertaining to the crystallization in the weak and AG focusing rings are presented in section 3. Section 4 describes the molecular dynamics calculation and the numerical results.

II. ROTATING BEAM FRAME HAMILTONIAN

The motion of the particles under Coulomb interaction

*Work performed under the auspices of the U.S. Department of Energy, supported by NSF Grant DMR-91-15342, and by the DOE, Office of Energy Research, Office of High Energy and Nuclear Physics, under Contract No. DE-AC03-76SF00098.

and external electromagnetic (EM) forces can be most conveniently described in the rotating rest frame (x, y, z, τ) of the reference particle of which the orientation of the axes are constantly aligned to the radial (x), tangential (z) and vertical (y) direction of the motion, and τ is the proper time. The equations of motion are derived using the general relativity formalism. First, we express the equations of motion in a general tensor formalism applicable to any arbitrary coordinate system. The Lorentz force experienced by the particle is constructed as a product of the EM field tensor and the four-velocity. Starting from the laboratory frame, the EM field tensor is written by means of the components of the EM fields. Then, tensor algebra is used to transform this field tensor into the rest frame. With a similar transformation, the metric tensor of the rest frame is also obtained. The equations of motion and the Hamiltonian can thus be constructed in the rest frame.

Consider the case that the beam is guided by a bending field B_0 , and focused by a quadrupole field of gradient B_1

$$B_x = B_1 y, \quad B_y = B_0 + B_1 x, \quad B_z = 0, \quad (1)$$

where the magnet end effect is neglected. Assume that there exists no electric field so that the beam is not focused azimuthally. The magnitude of B_0 is determined by the velocity βc and the bending radius R of the reference particle $eB_0 R = m_0 c^2 \beta \gamma$. Let $n = -B_1 R/B_0$ represent the strength of the focusing field. The Hamiltonian $H(x, P_x, y, P_y, z, P_z; t)$ of the particle system is derived as

$$H = \frac{1}{2} (P_x^2 + P_y^2 + P_z^2) - \gamma x P_z + \frac{1}{2} [(1-n)x^2 + ny^2] + V_C, \quad (2)$$

where V_C is the Coulomb potential, the time t is in unit of $R/\beta \gamma c$, the space coordinates x, y, z are in unit of ξ ($\xi \equiv (r_0 R^2/\beta^2 \gamma^2)^{1/3}$ with $r_0 = e^2/m_0 c^2$), and the energy is in unit of $\beta^2 \gamma^2 e^2/\xi$. Here, ξ is a characterization of the inter-particle distance in the presence of Coulomb interaction. The equations of motion are given by the Hamilton's equations.

III. CONDITIONS FOR CRYSTALLIZATION

In a weak-focusing machine, the constant n provides pure focusing (and defocusing) in the vertical (and radial) direction. Typically, radial (or horizontal) focusing emerges from the difference in the centrifugal forces experienced by the particles of different radial displacements. Among particles of the same energy, the difference in the centrifugal force always focuses the particles towards the reference orbit. The effective radial focusing is $1 - n$, and ^{1,2} if $0 < n < 1$, there is focusing in both planes.

The situation becomes different when the beam is crystallized. In the ground state, particles circulate around with the same angular velocity. Contrary to the conventional case, the centrifugal force provides a defocusing force. Using the equations in the rest frame, it has been proven in general that crystalline beam can not exist in any dimension in a weak-focusing machine.

In the case of AG focusing, however, the amount of magnetic net focusing can easily prevail over the centrifugal defocusing caused by crystallization. Qualitatively, the conditions of crystallization can be estimated using the smooth approximations. Consider a ring consisting of N_c identical lattice cells. In the rest frame, the potential produced by the external magnetic field varies periodically with period $T_c = 2\pi/N_c$ in the reduced unit. The equilibrium state is defined as the one when the motions of all the particles are periodic in T_c . After linearizing the Coulomb force by expanding around the equilibrium orbit (x_j, y_j, z_j) of each particle i , the transverse equations become

$$\begin{aligned} \ddot{x} + \left\{ \nu_x^2 - \gamma^2 - \sum_j \left[\frac{1}{r_{ij}^3} - \frac{3(x_i - x_j)^2}{r_{ij}^5} \right] \right\} x &= \sum_j \frac{x_i - x_j}{r_{ij}^3}, \\ \ddot{y} + \left\{ \nu_y^2 - \sum_j \left[\frac{1}{r_{ij}^3} - \frac{3(y_i - y_j)^2}{r_{ij}^5} \right] \right\} y &= \sum_j \frac{y_i - y_j}{r_{ij}^3}, \end{aligned} \quad (3)$$

where r_{ij} is the distance between i and j , and ν_x and ν_y are the horizontal and vertical tunes in the absence of the Coulomb interaction. Similar to the weak focusing case, the crystal can only exist when the effective transverse focusing is sufficiently strong i.e. $\nu_x^2 > \gamma^2$ and $\nu_y^2 > 0$. Since typically $\nu_x \approx \gamma_T$, it is implied that the AG machine has to operate below the transition energy.

When the particle density is low, the equilibrium state is a 1-D chain where all the particles are aligned along the $x = y = 0$ axis and uniformly distributed in z . As the density increases, it transforms into 2-D. If the net radial focusing is weaker (or stronger) than the vertical one i.e. $\nu_x^2 - \gamma^2 < \nu_y^2$ (or $\nu_x^2 - \gamma^2 > \nu_y^2$), the 2-D structure lies in the horizontal (or vertical) plane. As the density is increased further, the equilibrium state eventually becomes 3-D.

To estimate the threshold density at which the 1-D crystal becomes 2-D, consider a 1-D crystal chain with the nearest-neighbor azimuthal distance Δ_z . The vibrational frequencies $\omega_x(k)$ in x direction can be expressed as

$$\omega_x^2(k) = (\nu_x^2 - \gamma^2) - \frac{2}{\Delta_z^3} \sum_m \frac{1}{m^3} + \frac{2}{\Delta_z^3} \sum_m \frac{\cos(mk)}{m^3}, \quad (4)$$

where k is the crystal momentum. Apparently $\omega_x(k)$ takes its minimum at $k = \pi$, which corresponds to two neighboring particles moving in the opposite direction. The transition from 1-D to 2-D occurs in x direction at the Δ_z value where the smallest $\omega_x(k)$ becomes imaginary. Therefore, in the case that $\nu_x^2 - \gamma^2 < \nu_y^2$, the condition for a stable 1-D crystal is given by the equation

$$\nu_x^2 - \gamma^2 > 4.2/\Delta_z^3. \quad (5)$$

IV. MOLECULAR DYNAMICS RESULTS

When Coulomb interaction and AG focusing are present, it is impossible to solve the Hamiltonian in Eq. 2 analytically. We therefore seek numerical solutions using molecular dynamics. Since the Coulomb interaction is long ranged, an Ewald-type summation has to be performed to calculate the energy and the forces. Rahman and Schiffer[1] used periodic boundary conditions in all three directions in order to utilize the standard Ewald summation method. However, in a realistic accelerator, the system may be considered infinite only in z direction. Also, the infinitely long collection of positively charged particles give a logarithmically diverging energy. In general, a negatively charged background has been added to the system to cancel this infinity. To simulate a real accelerator, we consider instead a bunch of charged particles confined in a perfectly conducting, infinitely long pipe. The periodic boundary condition is used only in the z direction, where the "supercell" of length L (in unit of ξ) repeats itself to infinity. The energy $\phi(\mathbf{x}_i, \mathbf{x}_j)$ due to two particles at \mathbf{x}_i and \mathbf{x}_j , after all the image charges and equivalents in other supercells are included, is

$$\begin{aligned} \phi &= \frac{1}{r_{ij}} + \frac{4}{L} \int_0^\infty \frac{\cosh(2z_{ij}k/L) J_0(2\rho_{ij}k/L) - 1}{\exp(2k) - 1} dk + \\ &+ \frac{2}{L} [\log(\pi b/L) + C], \end{aligned} \quad (6)$$

where $z_{ij} = z_i - z_j$, $\rho_{ij} = \sqrt{(x_i - x_j)^2 + (y_i - y_j)^2}$, $r_{ij} = \sqrt{z_{ij}^2 + \rho_{ij}^2}$, b is the radius of the pipe. The condition $\rho_{ij} \ll b$ is used and z_{ij} is understood to be between $-L/2$ and $L/2$. Apart from the last term which is an unimportant constant, Eq. (6) is the same as the formula given by Avilov[4], but the physical environments are different.

The integration in Eq. (6) is performed by a 15th order Gauss-Laguerre method. The equations of motion is integrated by the 4th order Runge-Kutta algorithm. The storage ring is assumed to consist of 10 identical FODO cells. Within each cell, the lengths of the F, O, D, and O elements are assume to be 15%, 35%, 15%, and 35% of the cell length, respectively. The focusing and defocusing gradients n are set to be 50 and -50, respectively. This arrangement results in $\nu_x = 2.7$, $\nu_y = 2.3$, and γ_T is about 2.5. γ is set to 1.4. The time step for the integration is 1/20 of the period T_c of the focusing field.

Notice that the Hamiltonian we are solving is time dependent, therefore the total energy is not a constant of motion, and the "temperature" as conventionally defined is no longer meaningful. Initially, the positions and momenta of the particles are randomly chosen. At the end of each FODO period, a periodic condition is imposed on all positions and momenta. The "drifting velocity" $v_z = [z(T_c) - z(0)]/T_c$ is then subtracted from P_z for each particle to correct "shearing" in the beam. Our experience shows that this is a very effective method to "cool" the system down to reach the ground state.

Here, we report the preliminary results with $L = 10$ and number of particles N in the supercell ranging from 5 to 100. When $N = 5$, the crystal is 1-D, and does not change

with time in spite of the change of the focusing force. When $N = 10$, the crystal is 2-D — a zig-zag chain in the $x - z$ plane. The reason that the crystal is in the $x - z$ plane instead of the $y - z$ plane is because of the relatively stronger vertical focusing. Now the particles move with time — a symmetrical breathing in x direction. The crystal transforms from 1-D to 2-D when N goes from 8 to 9.

With the current lattice and beam energy, the critical density at which the crystal transforms from 2-D to 3-D is approximately twice that from 1-D to 2-D. It is trivial to change the parameters in the simulation as well as in a real accelerator so that these effective focusing strengths are different, and therefore the crystal remains 2-D at a much higher density.

Fig. 1 show the plots for $N = 40$. The crystal is 3-D. Basically the particles form elliptical cylinders. They fall on ellipses when projected onto the $x - y$ plane, and form spirals on the cylinders. At lower densities (e.g. $N = 40$), one cylinder is formed, but at higher densities (e.g. $N = 60$), a second one is formed in the center.

Many of the features discussed above are similar to those found by Schiffer *et al.*[1,5] with static focusing and without the shearing force. However, the ground state we found is time dependent. The shape of the crystals and the position of the particles are both periodic in time. The foci of the ellipses move as functions of time, and the principal axes can be either the x or the y axis. To show the dramatic change of the crystal shape in one period of time, we take $N = 60$ as an example and plot four snap shots of the particle positions (projected onto the $x - y$ plane) in Fig. 2. The particles move as much as one hundred percent of their coordinates in the $x - y$ plane and then all move back to their previous locations after one period. The crystal "breathes" transversely with no drifting and almost no oscillation in z .

V. CONCLUSION

We have studied the ground state of a crystalline particle beam under time-dependent, realistic storage ring environment. The equations of motion for the particles are derived in the rest frame of the reference particle that circulates around the ring with constant velocity. It has been shown that in a weak-focusing storage ring, the crystalline beams can not be formed for lack of transverse focusing. In an AG focusing ring, on the other hand, the crystalline beams can exist in spite of the variation in the focusing strengths, as long as the energy of the beam is less than the transition energy of the machine. If γ is higher than γ_T , the crystalline structure can not be formed for lack of radial focusing.

The quantitative investigation is performed using the molecular dynamics method. The ground state is obtained by, at the end of each focusing period, imposing the periodic condition on all the positions and momenta of the particles and then subtracting the "drifting velocity" from the z component P_z of the canonical momentum for each particle.

The nature of the crystalline beam is determined by the density of the particles and the effective strengths of the transverse focusing. When the density is low so that Eq. 5 is approximately satisfied, the beam is a 1-D crystal. When the density is increased, the crystal becomes a 2-D zig-zag chain in the plane of relatively weaker transverse focusing. The critical density at which the crystal transforms from 2-D to 3-D depends on the ratio of the effective focusing strengths between radial and vertical directions. In both 2-D and 3-D cases, the time-dependent crystalline structure has the same periodicity as that of the focusing forces. The crystal "breathes" transversely with no shearing and almost no oscillation in the azimuthal direction.

REFERENCES

- [1] A. Rahman and J.P. Schiffer, Phys. Rev. Lett. 57,1133 (1986).
- [2] J.P. Schiffer and A. Rahman, Z. Phys.A 331, 71-74 (1988); J.P. Schiffer, Proc. Workshop on Crystalline Ion Beams, Werheim, 2 (1988).
- [3] C. Moller, *The Theory of Relativity*, Oxford, 1952.
- [4] V. V. Avilov, Solid State Comm. 44, 555 (1982).
- [5] J. P. Schiffer, Phys. Rev. Lett. 61, 1843 (1988).

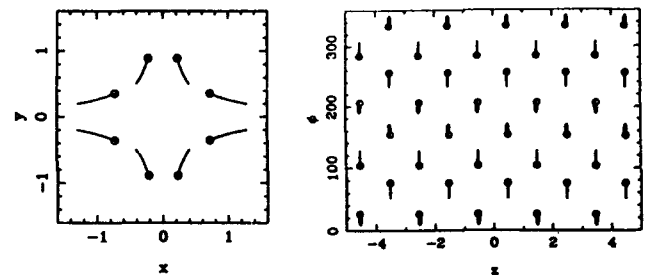


Fig. 1 Particle positions for $N = 40$. (a) Projected onto the $x - y$ plane. (b) The $\phi - z$ plot (ϕ is the polar angle). Circles are the positions at beginning and end of the focusing period. Solid lines are the trajectories within one period.

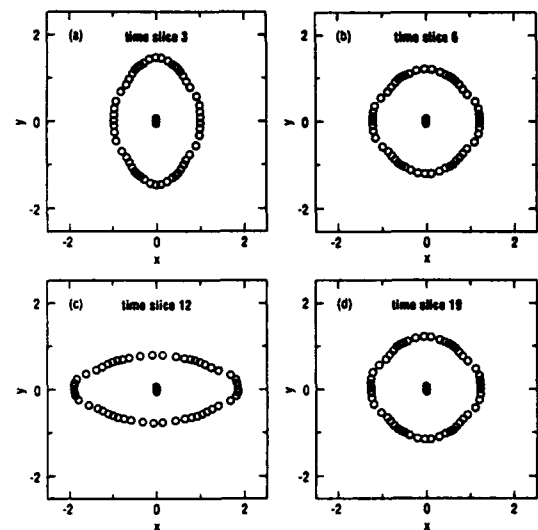


Fig. 2 Snap shots of the particle positions (projected onto the $x - y$ plane) in one time period for $N = 60$ (20 time slices per focusing period).

Confinement and Stability of a Crystal Beam*

Alessandro G. Ruggiero
Brookhaven National Laboratory
Upton, Long Island, New York 11973, USA

Abstract

The following is an analysis of the confinement and stability issues of a Crystal Beam. A method is described to determine the equilibrium configuration of a beam of highly charged particles. It is required that the beam has a uniform distribution in the direction of motion, which is stable and does not need therefore confinement with external means. It is shown that this can be obtained only for a relatively longitudinally compact beam. Confinement in the plane transverse to the direction of motion is obtained with external means, which also provide stability. It is important that particles are distributed so that the resulting space charge forces are linear with respect to the particle transverse coordinates.

I. INTRODUCTION

A Crystal Beam [1-3] is an ensemble of charged particles, all identical to each other, with the same electric charge Qe and mass at rest Am , where e is the electron charge and m the proton mass at rest. The charge state Q and mass number A are integer. Particles are treated point-like, with no internal structure. Only interaction among each other is the electromagnetic interaction. It is assumed that there is an equilibrium configuration where particles occupy a rigid position with respect to each other while all together move in one direction. Particles are allowed to oscillate around their equilibrium positions as long as the amplitude of the oscillations is small.

Confinement and stability questions are best described with the rectangular and infinite Crystal Beam model which is introduced in section II. We consider next the case of a cylindrical beam, infinitely long in the longitudinal direction, but having finite transverse dimensions. Section III defines this beam, whereas section IV discuss the requirement for the longitudinal stability and section V and VI the confinement and stability respectively in the transverse plane. It is seen that, in order to keep the beam confined transversely, a magnet with a profile providing focussing simultaneously in both transverse directions is required. This could be the case of a Betatron magnet. The field profile is also required to maintain the beam stable against transverse oscillations. Since the external restoring force is linear with the particle transverse coordinates, it is also important that the equilibrium configuration places particles in such a way that the resulting space charge forces are also linear.

Section VII defines quantitatively the limits of the beam spreads in momenta as evidence of crystallization. Finally section VIII is an analysis of the effects introduced by the insertions of drifts. The resulting storage ring lattice is to show stability at the two extremes: when the space charge is ignored and for the final state of the Crystal Beam.

* Work performed under the auspices of U.S. DOE

II. THE RECTANGULAR MODEL

The number of particles is infinite. They all move with the same velocity in the same direction. Particles are uniformly distributed, extending to infinity in all three dimensions. They are equally spaced from each other, sitting at the knots of a rectangular grid with step size λ_{\parallel} in the longitudinal direction and λ_{\perp} in the plane transverse to it. The field experienced by a particle is the sum of all the fields generated by the other particles. Because of the symmetry arrangement, the field is the same for all particles and identically equal to zero. Thus there is no interaction between particles and they are perfectly screened from each other. This is an equilibrium configuration which obviously does not need to be confined with external forces.

To determine if this configuration is also stable, we add a longitudinal perturbation of motion [3] to any particle and calculate the resulting field. For a small perturbation, after linearizing the field expression, we obtain that the particle perturbed performs longitudinal oscillations with angular frequency given by

$$\Omega_{\parallel}^2 = \frac{Q^2 e^2 g_{\parallel}(w)}{\lambda_{\perp}^3 \gamma^2 m A} \quad (1)$$

where $w = \lambda_{\parallel} \gamma / \lambda_{\perp}$ and, with $j = (j_1, j_2, j_3)$,

$$g_{\parallel}(w) = \sum_{j \neq 0} \frac{2 w^2 j_3^2 - j_1^2 - j_2^2}{(j_1^2 + j_2^2 + w^2 j_3^2)^{5/2}} \quad (2)$$

A similar result is obtained when a transverse perturbation is added. The resulting angular frequency Ω_{\perp} has the same expression of Eq. (1) but the response function $g_{\parallel}(w)$ is replaced by $g_{\perp}(w) = -g_{\parallel}(w) / 2$. Stability requires that both g_{\parallel} and g_{\perp} are positive; this cannot be satisfied at the same time. We choose $g_{\parallel} > 0$, so that the beam is stable longitudinally, and let the beam to be unstable in the transverse plane. An external restoring force is then required to recover the beam stability also in the transverse plane. The condition $g_{\parallel} > 0$ is satisfied for $w < 1$, that is for a longitudinally compact beam.

III. THE CYLINDRICAL MODEL

We continue assuming an infinitely long beam but with a more realistic finite cross-section. Particles are still uniformly distributed in the longitudinal direction, where they are separated again by the period λ_{\parallel} so that no confinement is required and the motion is stable in that direction. We assume there is an equilibrium configuration where the beam is made of a number n_s of shells of elliptic cross-sections of the same aspect ratio. Each shell is made of n_h particles equally spaced by the same angle $\theta = 2\pi / n_h$. The innermost shell is a string where the particles are aligned, equally spaced, on the beam axis.

It can be seen that the longitudinal component of the field vanishes identically, whereas the transverse component is zero on the beam axis and increases in amplitude toward the edge of the beam. Its magnitude and direction is independent on the longitudinal position along the beam. In the limit of a large number N of particles distributed over a length L , and for a round beam of radius b , the transverse field is actually linear with the distance r from the beam axis [4], that is

$$E_{\perp} = 2QeNr/Lb^2 = kr \quad (3)$$

as long as the i -th shell is located at the radius $b_i = b\sqrt{i/n_s}$. In particular the *string* has vanishing radius, that is $b_0 = 0$.

Clearly this configuration needs to be confined with transverse external restoring forces, also linear.

IV. LONGITUDINAL STABILITY

As for the previous model, we determine the longitudinal stability by adding a small longitudinal perturbation to the motion of any particle. After linearizing the field expression, we derive that the particle performs longitudinal oscillations with angular frequency Ω_{\parallel} given by

$$\Omega_{\parallel}^2 = \frac{Q^2 e^2 g_{\parallel}(w) n_s^{3/2}}{b^3 \gamma^2 m A} \quad (4)$$

where now $w^2 = \gamma^2 \lambda_{\parallel}^2 n_s / b^2$ and $(i = 0, 1, \dots, n_s)$

$$g_{\parallel}(w) = \sum_{j \neq i} \frac{2w^2 j_3^2 - i - j_1 + 2\sqrt{ij_1} \cos(\theta j_2)}{[i + j_1 - 2\sqrt{ij_1} \cos(\theta j_2) + w^2 j_3^2]^{5/2}} \quad (5)$$

In order for the beam to be stable against longitudinal perturbations it is required that $g_{\parallel}(w) > 0$, that is the compactness parameter w is to be less than a limiting value which depends on the number n_s of shells and on the separation angle θ . For instance [3], for a single shell $w < 1.9\theta$ and for ten shells $w < 6.0\theta$.

V. TRANSVERSE CONFINEMENT

Let us consider the motion of the i -th particle in the transverse plane by adding a radial perturbation [3]. We shall still assume a round beam, for simplicity. Its position can be written as $r_i = r_{0i} + u$. The equation of motion can be written as follows

$$\begin{aligned} m A \ddot{r}_i &= Q e E_i(r_i) \\ &= Q e E_i(r_{0i}) + Q e \left. \frac{dE_i(r_i)}{dr_i} \right|_{r_{0i}} u + \dots \\ &= m A \ddot{r}_{0i} + m A \ddot{u} \end{aligned} \quad (6)$$

where E_i is the field acting on the particle. This can be broken down into two equations

$$m A \ddot{r}_{0i} = Q e E_i(r_{0i}) \quad (7)$$

and

$$m A \ddot{u} = Q e \left. \frac{dE_i(r_i)}{dr_i} \right|_{r_{0i}} u \quad (8)$$

The field is made of two contributions: the *internal*, due to the beam proper, and the *equivalent external* due to the restoring forces. In particular,

$$E_i = (k - k_{ext}) r_{0i} \quad (9)$$

where k is given by Eq. (3) and k_{ext} corresponds to the restoring forces.

The following *confinement condition* is to be satisfied

$$k_{ext} = k \quad (10)$$

This condition is fulfilled by having the beam circulating in a Betatron which provides focusing in both transverse directions at the same time. The magnetic field profile is measured by the field index n , a positive quantity, less than unit. For a round beam, a suitable choice is $n = 0.5$ in which case

$$k_{ext} = \beta B_0 / 2\rho \quad (11)$$

where B_0 is the bending field and ρ the bending radius.

The confinement condition can be expressed in terms of the magnet and beam parameters as follows

$$A \beta^2 \gamma^2 \pi b^2 = 2 Q^2 r_0 N \rho \quad (12)$$

VI. TRANSVERSE STABILITY

The stability of motion in the transverse plane is investigated by solving Eq. (8) where

$$\left. \frac{dE_i(r_i)}{dr_i} \right|_{r_{0i}} = -k_{ext} - Q e g_{\perp}(w) n_s^{3/2} / b^3 \quad (13)$$

The first term at the right-hand side is the contribution from the external restoring forces whereas in the second term, proper of the beam, $g_{\perp}(w) = -g_{\parallel}(w) / 2$. We recover thus the result we have already obtained for the rectangular Crystal Beam model. Therefore the same considerations made before will also apply here.

The following *stability condition* is to be satisfied

$$k_{ext} > Q e g_{\parallel}(w) n_s^{3/2} / 2b^2 \quad (14)$$

which can also be written as

$$w g_{\parallel}(w) < 4 n_h \quad (15)$$

Particles will then perform transverse oscillations with an angular oscillation frequency Ω_{\perp} given by

$$\Omega_{\perp}^2 = \frac{2Q^2 e^2 (N/L)}{m A \gamma^3 b^2} \varepsilon(w) \quad (16)$$

where

$$\varepsilon(w) = 1 - w g_{\parallel}(w) / 4 n_h \quad (17)$$

which ranges between 0 and 1 for the motion to be stable in the transverse plane.

VII. BEAM CRYSTALLIZATION

With a perturbation added, the beam will perform stable longitudinal oscillations provided that the amplitude a_{\parallel} of the oscillations is small enough. The beam momentum spread is

then measured by the maximum velocity encountered during the oscillations, that is

$$\Delta p_1 = m A \gamma a_1 \Omega_1 \quad (18)$$

where Ω_1 is given by Eq. (4). Since the condition for crystallization can be taken as

$$a_1 < \lambda_1 \quad (19)$$

the same condition can be expressed as follows

$$\Delta p_1 / p < \lambda_1 \Omega_1 / \beta c \quad (20)$$

A similar condition ought also to be satisfied for the transverse momentum spread, that is

$$\Delta p_\perp < m A \gamma \theta b \Omega_\perp \quad (21)$$

which is obtained by requiring that transverse oscillations have an amplitude $a_\perp < \theta b$, and where Ω_\perp is given by Eq.(16).

VIII. INSERTION OF DRIFT SPACES

Circulation of the beam in a betatron magnet will introduce the effect of *curvature* that we shall not investigate here. Drifts are required for beam manipulation like injection, abort and cooling. The betatron magnet will thus be broken in M identical periods each of length $\ell_B = 2\pi p / M$ and separated by drifts of length ℓ_D . The insertion of drifts will disrupt the equilibrium configuration and it will not be possible to maintain the beam cross-section constant. The motion remains periodic with the period length equal to $2\pi p / M + \ell_D$.

Let z_j denote either the horizontal or the vertical coordinate of the j -th particle. It is more convenient to replace the time as the independent variable with the curvilinear length s travelled along the reference closed orbit. The equation of motion can now be written as

$$z_j'' + [Qe(k_{ext} - k) / m A \gamma \beta^2 c^2] z_j = 0 \quad (22)$$

where $k_{ext} = 0$ in the drifts and takes a constant value in the sector magnets. For convenience let us write

$$K = Qe k_{ext} / m A \gamma \beta^2 c^2 \quad (23)$$

The term k which is proper of the beam itself, includes a dependence on the beam size b and therefore will also vary periodically. It is convenient to write the dependence with the beam size explicitly

$$Qe k / m A \gamma \beta^2 c^2 = \frac{2Q^2 e^2 (N/L)}{m A \gamma^3 b^2 \beta^2 c^2} = h / b^2 \quad (24)$$

The solution of the equation above of course has to be periodic with the period given by $\ell_B + \ell_D$. In particular, the equation of motion can be written for the particle at the edge of the beam, thus deriving the equation of the beam envelope

$$b'' + K b - h / b = 0. \quad (25)$$

We shall assume that the drifts are not too long so that the beam dimension remains almost constant with a little periodic modulation added. Let $b = b_0 (1 + \Delta)$ where b_0 is the beam size in absence of drifts. We shall expand and retain

only terms linear in Δ . In the drift regions $K = 0$ and the envelope equation reduces to

$$\Delta'' + K_D \Delta = K_D \quad (26)$$

with $K_D = h / b_0^2$. The equation for the sector magnet, letting $K_B = K + K_D$, is simply

$$\Delta'' + K_B \Delta = 0 \quad (27)$$

The periodic solution of these equations, which are linear, can be searched with the conventional 3×3 matrix notation [3].

To determine the stability on the transverse plane, as usual, we add a small perturbation u to any particle along one of the two transverse directions. After linearization, the equation of motion is

$$u'' + q u = 0 \quad (28)$$

where, in the sector magnets,

$$q = \Omega_\perp^2 / \beta^2 c^2 = q_B \quad (29)$$

and, in the drifts,

$$q = -q_B w g_1(w) / 4 n_h \varepsilon(w) = -q_D \quad (30)$$

As usual, we can search the solution with a matrix notation [3]. Only 2×2 matrices are required. The motion is stable if the trace of the transfer matrix corresponding to a period has an absolute value not exceeding 2, that is

$$|2 \cos \xi_B \cosh \xi_D + (\sqrt{q_D/q_B} - \sqrt{q_B/q_D}) \sin \xi_B \sinh \xi_D| < 2 \quad (31)$$

where $\xi_B = \ell_B \sqrt{q_B}$ and $\xi_D = \ell_D \sqrt{q_D}$. A similar condition is to be satisfied also for the stability of motion in the storage ring in the limit of zero space-charge forces, that is

$$|2 \cos (\ell_B/p) - (\ell_D/p) \sin (\ell_B/p)| < 2 \quad (32)$$

IX. ACKNOWLEDGMENTS

The author wishes to thank the scientific staff of the Laboratori Nazionali di Legnaro (Padua, Italy) for many useful and informative discussions. This work is a contribution to the CRYSTAL collaboration.

X. REFERENCES

- [1] J.P. Schiffer and A. Rahman, "Feasibility of a Crystalline Condensed State in Cooled Ion Beams of a Storage Ring", PHY-5121-ME-88, Feb. 1988, Argonne National Laboratory.
- [2] Proceedings of the Workshop on Crystalline Ion Beams, Werheim, Germany, Oct. 1988. GSI-89-10 Report.
- [3] A.G. Ruggiero, "Confinement and Stability of a Crystal Beam", BNL Formal Report, in preparation, May 1993. AGS Department, Brookhaven National Laboratory.
- [4] A.G. Ruggiero, "Review of Space Charge Calculations", Booster Technical Note No. 104, January 1988. AD Department, Brookhaven National Laboratory.

Bunched Beam Stochastic Cooling in the Fermilab Tevatron Collider

G. Jackson, E. Buchanan, J. Budlong, E. Harms, P. Hurh,
D. McGinnis, R. Pasquinelli, D. Peterson, D. Poll, P. Seifrid
Fermi National Accelerator Laboratory*
P.O. Box 500 MS 341
Batavia, IL 60510

Abstract

In order to double the integrated luminosity of the Tevatron collider in the next running period, a 4-8 GHz bunched beam betatron stochastic cooling system has been designed. The horizontal and vertical emittances of the protons and antiprotons will be cooled to counteract the effects of power supply noise, beam-beam interaction, and intrabeam scattering. A vertical proton prototype system has been installed in the Tevatron and tested. In addition, measurement results and details of the hardware are reviewed.

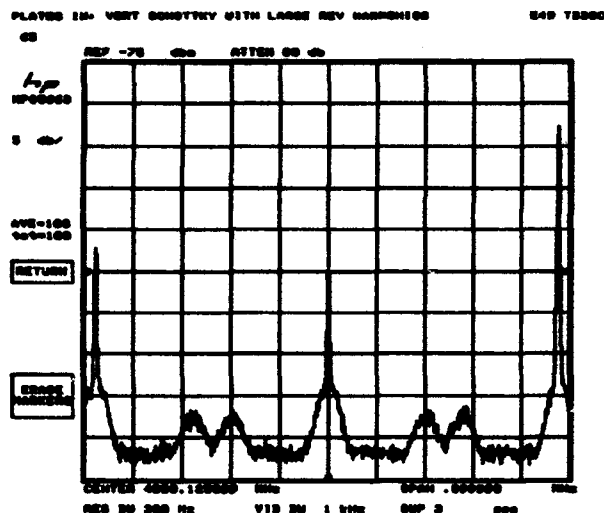


Figure 1: Measured beam spectrum from a vertical proton pickup. Note the large coherent lines at revolution harmonic frequencies at the left, center, and right. The betatron Schottky lines are clearly visible above the noise floor. The center frequency is 4 GHz and the scale is 10 kHz/div.

I. INTRODUCTION

A great deal of measurement, calculation, design, and construction work has gone into the Tevatron bunched beam stochastic cooling system [1] in the last two years. Based on beam measurements made with the first proton vertical cooling system [2], a second pickup tank was fabricated with improvements aimed at solving the problem of large

revolution harmonic power saturating amplifiers (see figure 1). In addition, a new repetitive notch filter was designed and built [3] to further combat the power at harmonics of the revolution frequency. System phasing and timing adjustments have been completed.

II. COHERENT POWER MEASUREMENTS

One of the mysteries associated with bunched beam cooling in the Tevatron Collider was the existence of larger than expected coherent revolution harmonic power. Given that the longitudinal distribution of the beam is roughly Gaussian [4], one would expect that the revolution harmonic power should drop quadratically when viewed on a logarithmic scale. Figure 2 contains the measured revolution harmonic power as a function of frequency (where the beam power at each harmonic of the RF frequency was measured). Note that instead of a downward parabolic shape, the spectrum actually exhibits something like a $1/f$ shape.

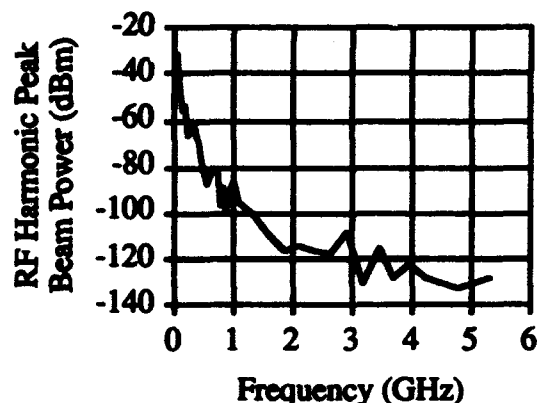


Figure 2: Beam current power spectrum, measured at each harmonic of the RF frequency.

If one were to Fourier transform this distribution back into the time domain, the required beam profile would scale as the K_1 Bessel function, which is undefined at the bunch center! Therefore, this excessive power at high frequency must be due to a small, high frequency modulation of the beam profile. This high frequency structure could possibly be due to filamentation from a small coherent oscillation [5].

A study was undertaken to find such a coherent oscillation. Figure 3 contains a closeup view of a revolution harmonic line. By fitting the amplitudes of the various synchrotron sidebands on either side of the revolution frequency to a Bessel

*Operated by the Universities Research Association under contract with the U.S. Department of Energy.

function distribution describing FM modulation, a coherent dipole oscillation of amplitude 60 psec is calculated. Therefore, a plausible explanation for these lines now exists.

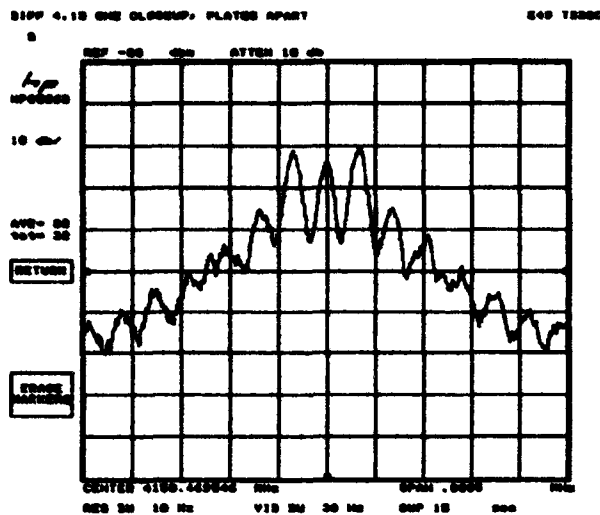


Figure 3: Closeup of the power spectrum of a single revolution harmonic line near 4.15 GHz. The frequency scale is 50 Hz/div.

III. PROTOTYPE PICKUP IMPROVEMENTS

In order to balance the phase from the top and bottom detector arrays, both a Petter hybrid [2] and a Burleigh inchworm motor [6] were installed to adjust their relative vectorial alignment. The inchworm motor, which has a step size of 1 micron, was required because a longitudinal misalignment of the plates as small as 60 microns could ruin the common mode rejection required to suppress the coherent revolution harmonic power.

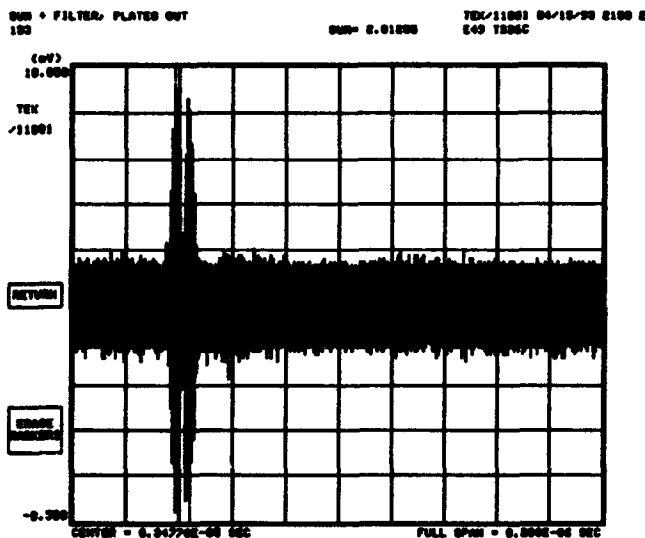


Figure 4: Max/min hold sampling oscilloscope image of the sum signal from the 180° hybrid. The time scale is 20 nsec/div.

With the original pickup array it was noted [2] that microwave signals trailed the bunch signal on an oscilloscope image of the pickup signal. This microwave burst was found to be caused by the response of the tunnel preamplifier to shock excitation by a large voltage burst of beam signal. With the above improvements reducing the coherent power (and hence voltage), this phenomenon is no longer visible (see figures 4 and 5). What remains is a small microwave signal on only the hybrid difference port which is independent of coherent beam power.

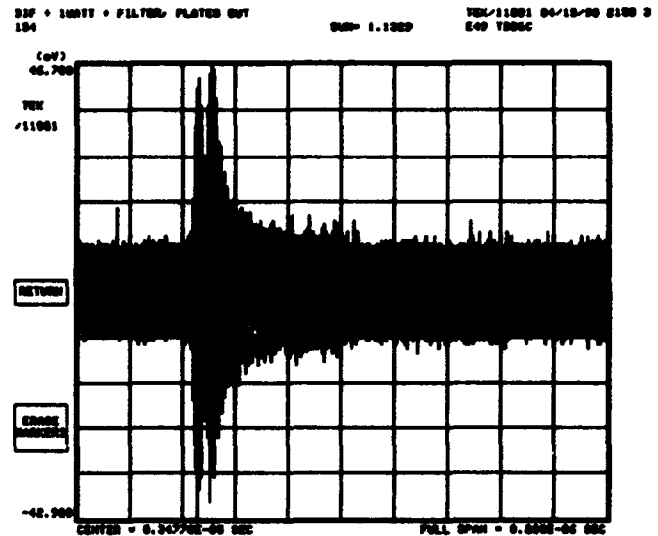


Figure 5: Max/min hold sampling oscilloscope image of the difference signal from the 180° hybrid. The time scale is 20 nsec/div. Note the small amount of microwave power trailing the beam signal which is still present in the new prototype.

III. REPETITIVE NOTCH LOOP FILTER

A typical single turn delay notch filter produces a $\text{lsin}(x)$ response which repeats each revolution period. The unfortunate aspect of this filter is that the phase linearly progresses through 180° every revolution period. In the case of small mixing factor where the betatron Schottky signals are spread over a large portion of each revolution band, a large portion of the particles see either no damping or antidamping.

The purpose of the loop notch filter is to overcome this phase change per band. The phase change comes from the fact that betatron oscillation information is being applied to the kicker one turn too late, thereby giving the particles the wrong kick. If one injects a bunch signal into a storage loop each turn, where the fraction of the signal which survives one turn of the loop is described by the variable α , the betatron information is exponentially averaged away and the transfer function of the full filter becomes

$$T(\omega) = \frac{1 - e^{-i\omega\tau}}{1 - \alpha e^{-i\omega\tau}} \quad (1)$$

where τ is the revolution period (see figures 6 and 7).

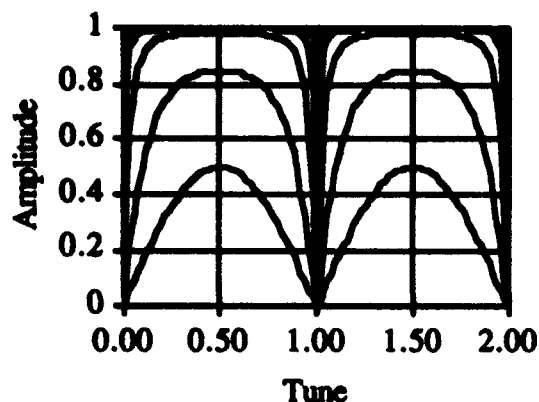


Figure 6: Calculated amplitude response of a loop notch filter. The lowest curve is for the limiting case of a single turn delay notch filter ($\alpha \ll 1$). The value of $1-\alpha$ for the other curves are 0.3, 0.1, 0.03, and 0.01 (in order of progressively improved notch width and phase change filter characteristics).

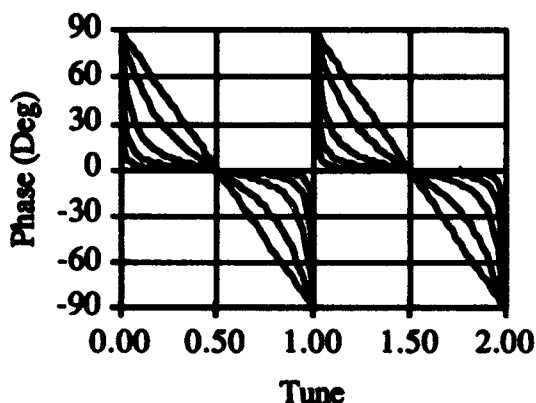


Figure 7: Phase corresponding to the above amplitudes. The straight diagonal lines are in the limiting case of a single turn delay notch filter.

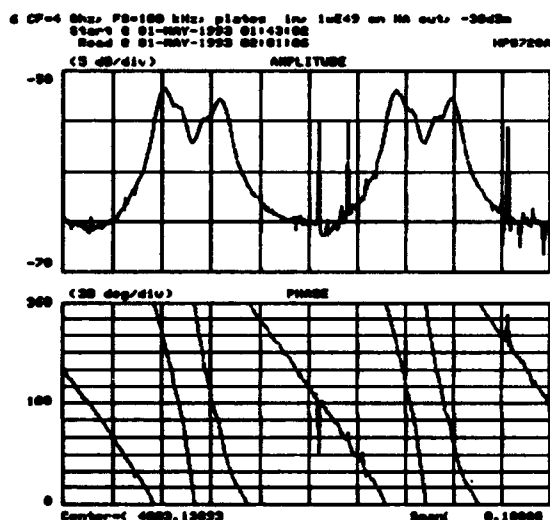


Figure 8: Open loop transfer function measurement across two revolution harmonic bands at 4 GHz. Note the phase rolls through $3 \times 360^\circ$ per band.

IV. PHASING & TIMING MEASUREMENTS

When the second prototype pickup tank was installed, the relative position of the pickup and kicker tanks in the lattice was reversed (pickup now upstream). This was done because the fractional tune of the accelerator was changed from 0.4 to 0.6, and the change was necessary to keep the phase advance between the pickup and kicker at an odd multiple of 90° . The implications of this change on open loop transfer function measurements was both dramatic and unexpected (see figure 8).

Compared with the previous measurements [2], which exhibited a destructive interference in the amplitude at a fractional tune of 0.5, the amplitude at that point now adds the signals from both betatron lines. In the phase, while previous measurements showed a phase advance of $2 \times 360^\circ$ per revolution harmonic band, $3 \times 360^\circ$ is now observed.

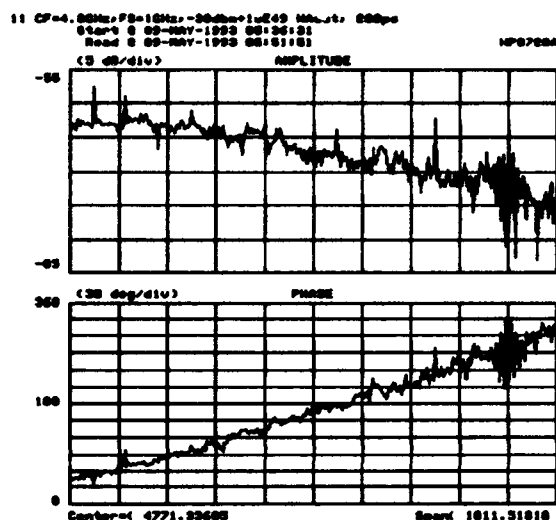


Figure 9: Timing measurement where the phase and amplitude at a fractional tune of 0.5 is measured every 205 revolution harmonic bands with a center frequency of 4.77 GHz. The phase slope indicates that the electrical length is too short.

V. REFERENCES

1. G. Jackson, "Bunched Beam Stochastic Cooling", Proc. IEEE Part. Acc. Conf., San Francisco (1991) 2532.
2. G. Jackson, et al., "A Test of Bunched beam Stochastic Cooling in the Fermilab Tevatron Collider", Proc. IEEE Part. Acc. Conf., San Francisco (1991) 1758.
3. R. Pasquinelli, "Electro-Optical Technology Applied to Accelerator Beam Measurement and Control", Proc. IEEE Part. Acc. Conf., Washington D.C. (1993).
4. G. Jackson, "Results form Beam Diffusion and Collimation Measurements in Preparation for Fermilab Tevatron Crystal Extraction", Proc. IEEE Part. Acc. Conf., Washington D.C. (1993).
5. A. Gerasimov, "Saturation and Turbulent Dynamics of Longitudinal Instabilities of Bunched Beams", Proc. IEEE Part. Acc. Conf., Washington D.C. (1993).
6. P. Hurh, G. Jackson, "The Mechanical Design of a Bunched Beam Stochastic Cooling Tank for the FNAL Tevatron", Proc. IEEE Part. Acc. Conf., Washington D.C. (1993).

LONGITUDINALLY SPACE CHARGE DOMINATED BEAMS IN A SYNCHROTRON*

Timothy J.P. Ellison, Sergei S. Nagaitsev, Mark S. Ball, David D. Caussyn, Michael J. Ellison, Brett J Hamilton
The Indiana University Cyclotron Facility (IUCF) 2401 Milo Sampson Lane, Bloomington IN 47405 USA

Abstract

For a given rf cavity voltage amplitude, V_{rf} , there is a maximum attainable peak current in an ion storage ring. This occurs when the electric field from the beam space charge balances the rf cavity field. In this limit, the linear charge density distribution, $\lambda(s)$, is parabolic and incoherent synchrotron motion is suppressed. The beam energy spread cannot be determined from the bunch time spread, T_{FWHM} , which depends only upon the beam current, I , and V_{rf} .

This work has recently been published [1]; no beam time is been available since for further results. This 1 page paper summarizes this work, discusses planned measurements, conjectures about possible results, and does its small part to mit the explosive growth of the PAC proceedings!

I. SUMMARY OF PREVIOUS WORK

Electron cooling can reduce the beam emittance so that the electrostatic potential energy spread across the bunch exceeds the rest frame kinetic energy spread. In this regime $\lambda(s)$ is:

$$\lambda(s) = \frac{\gamma^2}{8\pi \ln(r_v/r_b)} \frac{h e V_{rf}}{m c^2} \frac{e}{r_e} \frac{(L_b^2 - s^2)}{R^2} \quad (1)$$

here $|s| \leq L_b$ and $2L_b$ is the bunch length; γ the usual relativistic parameter; h the harmonic number; e , m , and r_e the electron charge, mass, and classical radius; R the ring radius; and $\ln(r_v/r_b) \approx 3.2$ in the IUCF Cooler, the logarithm of the ratio of the vacuum chamber to cooled beam radius.

Integrating $\rho_f(s)$ over s , where $\beta = v/c$ yields $K(T_{FWHM} V_{rf})$:

$$I = \frac{h^2 \beta^4 \gamma^2}{24 \sqrt{2} \pi^2 \ln(r_v/r_b)} \frac{e V_{rf}}{m c^2} \frac{e c}{r_e} \frac{c^3 T_{FWHM}^3}{R^3} \quad (2)$$

The time structure of an electron-cooled 45 MeV proton beam was measured by recording the signal from a beam position monitor. Comparisons between Eq. (2), and measured T_{FWHM} are summarized in Fig. 1. The observed increase in T_{FWHM} with I has been previously attributed to an increase in the beam momentum spread, δ , due to intrabeam scattering. These theories, however, predict δ , and consequently T_{FWHM} , increase as $I_{peak}^{1/3}$. With such scaling, T_{FWHM} should increase as $I^{2/9}$ rather than $I^{1/3}$ (Eq.(2)). This model clearly disagrees with our data.

In Figs. 2a and 2b Eq. (1) is compared with the measured $\lambda(s)$ for two different cases. The theoretical $\lambda(s)$, dashed curve, is modified to include the measured pickup RC time constant (212 ns) and filtering due to cable loss ($\sim e^{-f/66 \text{ MHz}}$).

supported by the Nat. Sci. Found. (Grant No. NSF PHY 90-15957).
* T. Ellison et al., Phys. Rev. Lett. 70 No. 6 (8 Feb '93) p. 790.

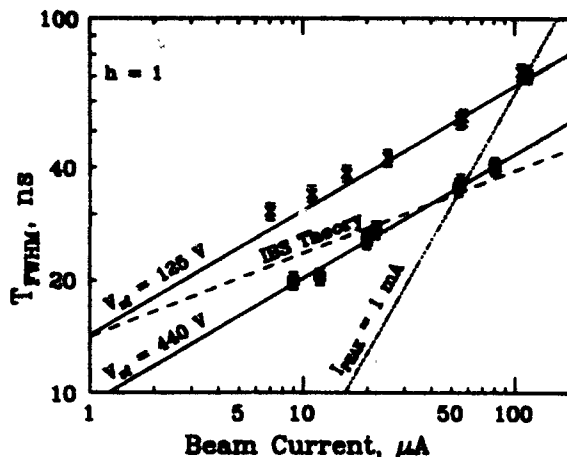
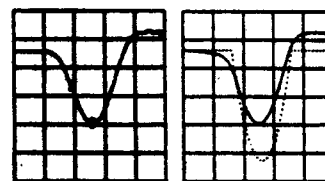


Fig. 1. Measured (x's, □'s) and theoretical (Eq. 2, solid lines) values for $T_{FWHM}(I)$; dashed curve is (IBS) theory.

(a) $I = 107 \mu A$ $V_{rf} = 125 \text{ V}$



(b) $I = 55 \mu A$ $V_{rf} = 437 \text{ V}$

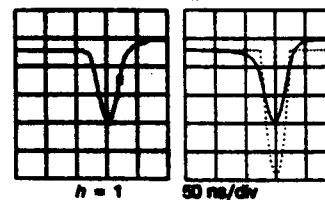


Figure 2. Measured (left) and theoretical (right) $\lambda(s)$, dashed curve is theory, solid includes filtering effects.

DISCUSSION

Since the synchrotron frequency, f_s , within the bunch is reduced, coherent oscillations do not decohere, but instead damp in accordance with the measured cooling force.

The space charge model predicts a bunch shape oscillation frequency of $\sqrt{3}$ times the unperturbed frequency, f_{so} and the emittance dominated model predicts $2f_{so}$. We, however, consistently measure $1.84f_{so}$ -- a mystery.

We conjecture that the transverse beam distribution may also be space charge dominated, having a uniform distribution with a radius increasing also as $I^{1/3}$. This will be measured.

We also conjecture that the transverse shape oscillation frequency may not be twice the coherent betatron oscillation frequency as predicted by the emittance dominated model but instead determined by the beam plasma frequency.

High Density Plasma Source for Plasma Lens Experiments*

K. Nakamura**, R. Liou and M. Gundersen
University of Southern California
Los Angeles, CA 90089-0484

Abstract

Experimental results of the study of a candidate source for high-energy particle beam underdense plasma lens experiments are presented. The high density plasma is based on the operation of the back-lighted thyatron. A 100% ionized hydrogen plasma with density of $1.7 \times 10^{16} \text{ cm}^{-3}$, homogeneous in space and monotonically varying in time with a time scale on the order of μsecs is straightforwardly achievable. The desired plasma density for lens experiments can be achieved very simply by controlling either the applied voltage, the beam entry time or other parameters. This scheme presents a simple device with the ability to support a plasma with density ranging from 10^{12} cm^{-3} to above 10^{16} cm^{-3} . The structure also facilitates the particle beam entry and the components are vacuum compatible. The device is small, simple, robust, easy to adjust, can be operated at high repetition rates, and has a long life time.

I. INTRODUCTION

It has been proposed to use a layer of plasma as a final focusing lens for high energy particle beams. The scheme is usually termed "plasma lens".[1-5] The advantage of this approach lies in the exceptional focusing strength provided by plasma; several orders higher than conventional quadrupole magnets (10^5 T/m with plasma density of 10^{16} cm^{-3} compared with conventional quadrupole focusing lens of 10^2 T/m). Presently various plasma lens schemes have been proposed, namely, thin, thick, adiabatic and optimal plasma lens.[6,7] For both thin and thick lenses, the plasma density is uniform within the plasma slab. Adiabatic lens and optimal lens require a tailored density profile in the beam propagation direction. The adiabatic lens also offers the potential of overcoming the Oide limit on final spot size which limits all other lens designs.[8] In this paper the application of a back-lighted thyatron (BLT) or a Pseudospark is presented. The intent is to utilize the homogeneous BLT high density plasma as a plasma source for the final focusing plasma lens.

There are two regions in a passive, self-focusing plasma lens, namely underdense and overdense. In the underdense regime where the plasma density is lower than the beam density ($n_b > n_e$), the plasma electrons respond to the incoming beam by total rarefaction from the beam volume. The result is a nearly uniform focusing of the beam due to the less mobile ions. The focusing strength κ for the underdense plasma lens can be written as

$$\kappa \equiv \frac{F_r}{r} = \frac{n_e e^2}{2\epsilon_0} \quad (1)$$

* This work was supported in part by the U.S. Army Research Office, SDIO through the U.S. Office of Naval Research.

** K. Nakamura is with USHIO, Inc., Himeji, Japan.

where F_r is the radially focusing force, n_e is the plasma density and ϵ_0 the permittivity. The focusing strength of a underdense plasma lens is proportional to the plasma density. The focusing mechanism of a positron beam can be described similarly with a major difference that the plasma electrons are now being pulled into the a positron beam instead of being rejected.[1] The space charge neutralization is provided with the incoming plasma electrons.

Experiments in Argonne National Laboratory (ANL) and University of Tokyo have confirmed that the plasma do focus low-energy ($\approx 20 \text{ MeV}$), low-density ($\approx 10^{10} \text{ cm}^{-3}$) electron beams.[9,10] In the ANL experiment a 35 cm long DC hollow cathode arc plasma source with density on the order of 10^{13} cm^{-3} is used to focus the beam size from $\sigma=1.4 \text{ mm}$ to $\sigma=0.91 \text{ mm}$. In the University of Tokyo, a 36 cm plasma with density on the order of 10^{11} cm^{-3} is used. It has been confirmed that plasma certainly has a lens effect, even though the reduction of transverse emittance is not yet fully understood.

Presently the challenge of plasma lens experiments is to demonstrate the plasma focusing effect with high energy (10 's of GeV) and high density (on the order of 10^{17} cm^{-3}) particle beams like Stanford Linear Accelerator Center (SLAC) Final Focus Test Beam (FFTB). From equation (1) a plasma with the highest possible density is required to achieve strong focusing for an underdense plasma lens design. The BLT is a potential candidate for plasma lens experiment due to its high-density plasma and other favorable features.[11] The plasma density in a typical BLT operation with a discharge current of several kA is on the order of 10^{15} cm^{-3} . Results presented in this paper indicate that plasma densities in the range of several times 10^{16} cm^{-3} can be readily achieved.

II. RESULTS AND DISCUSSION

Figure 1 shows the experimental setup for BLT high plasma density operation and density measurement. A single stage, UV flash lamp (EG&G, FX-265) triggered BLT is typically operated with a $2 \mu\text{F}$ capacitor and ultra-high purity hydrogen gas.[12] The BLT, being optically triggered Pseudosparks, can also be electrically triggered.[13] Both cathode and anode are made of molybdenum. The electrode separation is $\approx 3 \text{ mm}$. A quartz window behind the cathode allows UV light to illuminate the cathode back surface and initiates the discharge. Stark broadening spectroscopic technique was chosen to measure the plasma density.[14] With the expected plasma density variable to several times 10^{16} cm^{-3} the broadened line width (FWHM) of Balmer lines are on the order of several \AA . An accuracy within 30% is expected with this measurement. The SPEX 1302 series spectrometer (f/7) has a resolution $\approx 0.9 \text{ \AA}$ with a $150 \mu\text{m}$ entrance slit width. A two-lens imaging system collects and focuses the plasma light emission onto the spectrometer

entrance slit with matched f number. The measurement is taken at the mid-plane in between cathode and anode. The spatial resolution is $\approx 150 \mu\text{m}$. Together with Hamamatsu streak camera a time-resolved plasma density measurement can be achieved. In this present experiment the jitters of BLT is $\leq 20 \text{ nsec}$ when operated at above 7.5 kV. The triggering of BLT and streak camera were controlled separately by two different channels from a single pulse generator. The streak camera streak time setting allows one to look at a specific time interval of interest during the discharge. Not shown in the figure are the supporting vacuum and gas supply system.

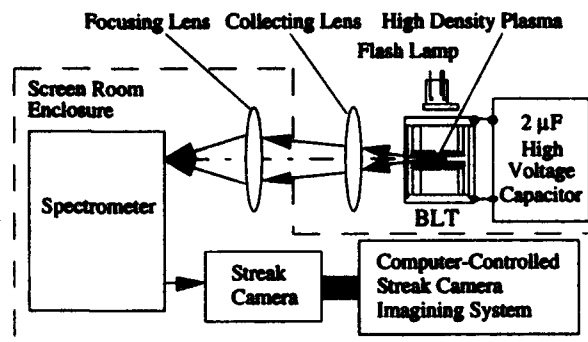


FIG. 1 Schematic for BLT high density plasma measurements

Figure 2 shows the time-resolved plasma density with two different applied voltages (7.5 kV and 10 kV). The oscillating discharge current has period $\approx 4.8 \mu\text{sec}$ and peak current proportional to the applied voltage (18.75 kA corresponding to 7.5 kV, 25 kA to 10 kV and 31.25 kA to 12.5 kV). A lumped circuit inductance of 300 nH is estimated. With a working gas of 275 mTorr hydrogen the maximum plasma density is $\approx 1.76 \times 10^{16} \text{ cm}^{-3}$. The streak camera streak time was set at $20 \mu\text{sec}/15 \text{ mm}$ with a full screen time of $13.3 \mu\text{sec}$. With a $100 \mu\text{m}$ entrance slit the temporal resolution is $\approx 150 \text{ nsec}$. The plasma density is measured through H_{α} line broadening. As shown in Figure 2, the plasma density increases with increasing

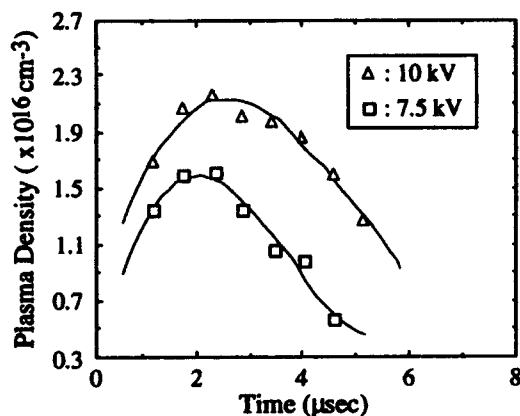


FIG. 2 Time-resolved plasma density measurements

applied voltage from 7.5 kV to 10 kV. The electron temperature is estimated to be of the order of 1 eV.[11] With 10 kV applied voltage a peak density of $2.0 \times 10^{16} \text{ cm}^{-3}$ is measured with ions assumed mobile.[15] With the possible 30% error, the plasma is believed to be fully

ionized. Another supporting evidence is that when the voltage is further increased to 12.5 kV the peak plasma density did not increase accordingly. Theories assuming ions immobile tend to over-estimate the plasma density and is not suitable for the present measurement since the time scale of discharge is long compared with the ion plasma period.[14]

There are different ways to achieve the desired plasma density during lens experiments. One is to vary the discharge current through different applied voltage as has been done in this present experiment. Figure 3 shows the peak plasma

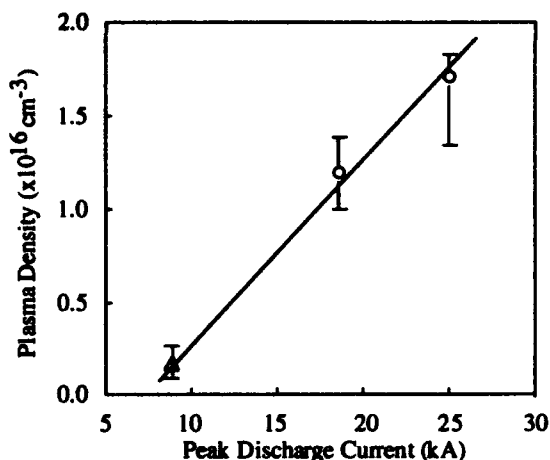


FIG. 3 Peak plasma densities with various discharge currents. Δ was taken with a slightly different discharge condition (180 mTorr hydrogen, $C=0.7 \mu\text{F}$, $R=0.5 \Omega$, $L=400 \text{ nH}$ at 12 kV). The error bar represents the intrinsic accuracy of the measurement method, not the reproducibility of the plasma.

density obtained with various peak discharge current. With a single device the plasma density can be varied to above 10^{16} cm^{-3} . A second way is by injecting the particle beam at different time during the discharge with a fixed applied voltage since the particle beam bunch length (typically on the order of psec) is much shorter than the time scale of density variation so within the beam bunch the plasma density can be regarded as constant. It is also possible to vary the pressure, gas, and geometry thus achieving a broad range of operating conditions for a uniform, pulse repeatable, homogeneous plasma.

As indicated above the maximum plasma density is determined by the available neutral density. For this reason a circuit with one switching BLT (low pressure gas) and one lens BLT (high pressure gas) has been constructed and tested. The results indicate that the plasma density increases with increasing neutral density when operated with same discharge current. The measurements at two different positions (on discharge axis and 3 mm away from axis) also indicate a homogenous plasma, with a macroscopic density variation $\approx 15\%$. For a μm beam size the plasma can be regarded as uniform. Thus operating the lens with a modulator is a simple way to achieve variable plasma density.

As a numerical example of this plasma source in SLAC FFTB underdense plasma lens experiment it has been shown that, for a round beam, the final beam size can be reduced

from $4.1 \mu\text{m}$ to $1.9 \mu\text{m}$ by a 2 cm thick plasma of density $6 \times 10^{15} \text{ cm}^{-3}$ inserted at 6 cm before the natural beam waist.[16] The normalized beam emittance is assumed to 30 mm-mrad. With a three times higher density ($1.8 \times 10^{16} \text{ cm}^{-3}$) the same electron beam can be focused to less than $1 \mu\text{m}$.

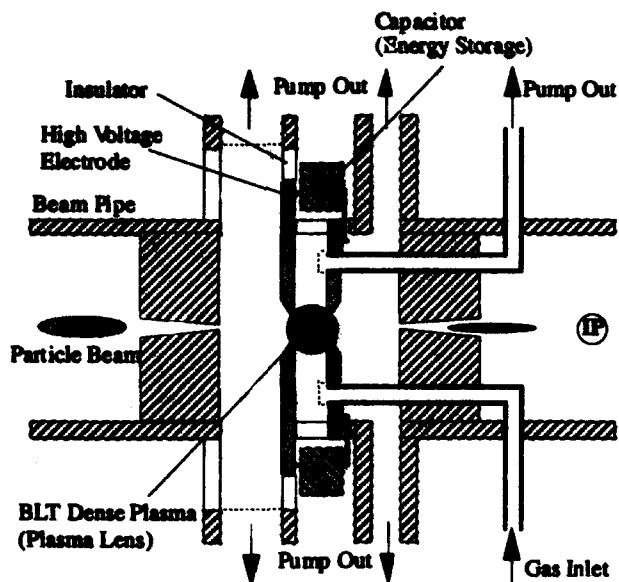


FIG. 4 Conceptual design for the BLT-based SLAC FFTB plasma lens experiments.

Figure 4 shows a conceptual design of BLT-based plasma lens design for SLAC FFTB. Many other geometries are also possible. An intuitive choice will be using the electrode central holes for beam entry and exit. Working gas will flow into the cathode-anode gap and be pumped out through electrode holes. The beam line apertures (for both beam entry and exit) need to be small enough to minimize the gas flow conductance while large enough (for example, $\geq 20\sigma$) to avoid a vacuum wake field. The pumping requirement can also be significantly reduced if a puff gas valve is used.

III. CONCLUSION

In conclusion, the results of a study of BLT high plasma density operation and proposed application to SLAC FFTB plasma lens experiment are presented. A homogeneous, reproducible hydrogen plasma with variable density from 10^{12} cm^{-3} up to $1.7 \times 10^{16} \text{ cm}^{-3}$ was achieved. At density $1.7 \times 10^{16} \text{ cm}^{-3}$ the plasma is believed to be fully ionized.

With this single device the density can be easily varied by changing the applied voltages or by various other means. The plasma source is suitable for underdense plasma lens experiments. The operation and the structure of BLT have several features which are optimal for plasma lens experiments. These include (a) central holes to facilitate beam entry and exit, (b) vacuum compatible components that will not degrade the FFTB vacuum system, (c) precision timing and reproducibility, (d) variable plasma density and thickness. The device is robust and extremely simple in structure, and long lived.

IV. REFERENCES

- [1] P. Chen, *Particle Accelerators*, **20**, 171 (1987).
- [2] P. Chen, S. Rajagopalan and J. B. Rosenzweig, *Phys. Rev. D*, **40**, 932 (1989).
- [3] J. B. Rosenzweig and P. Chen, *Phys. Rev. D*, **39**, 2039 (1989).
- [4] J. J. Su, T. Katsouleas, J. Dawson and R. Fidele, *Phys. Rev. A*, **41**, 3321 (1990).
- [5] P. Chen, *Phys. Rev. A*, **45**, R3398 (1992).
- [6] P. Chen, K. Oide, A. M. Sessler, and S. S. Yu, *Particle Accelerator*, **31**, 7 (1990).
- [7] T. Katsouleas and C. Lai, *Third Workshop on Advanced Accelerator Concepts*, Port Jefferson, NY, 14-20 July, 1992.
- [8] K. Oide, *Phys. Rev. Lett.*, **61**, 1713 (1988).
- [9] J. B. Rosenzweig, B. Cole, C. Ho, W. Gai, R. Konecny, S. Mtingwa, J. Norem, M. Rosing, P. Schoessow and J. Simpson, *Physica Scripta*, **T31**, 110 (1990).
- [10] H. Nakanishi, Y. Yoshida, T. Ueda, T. Kozawa, H. Shibata, K. Nakajima, T. Kurihara, N. Yugami, Y. Nishida, T. Kobayashi, A. Enomoto, T. Oogoe, H. Kobayashi, B. Newberger, T. Tagawa, K. Miya, and A. Ogata, *Phys. Rev. Lett.*, **66**, 1870 (1991).
- [11] W. Hartmann, V. Dominica, G. Kirkman, and M. Gundersen, *J. Appl. Phys.*, **65**, 4388 (1989).
- [12] G. Kirkman, W. Hartmann, and M. A. Gundersen, *Appl. Phys. Lett.* **52**, 613 (1988).
- [13] *Physics and Applications of Pseudosparks*, edited by M. A. Gundersen and G. Schaefer, Plenum Press, New York, 1990.
- [14] G. Bekefi, *Principles of Laser Plasmas*, edited by G. Bekefi, John Wiley and Sons, New York, 549 (1976).
- [15] J. Seidel, *Z. Naturforsch.* **32a**, 1195 (1977).
- [16] D. Betz, P. Chen, D. Cline, M. Gundersen, C. Joshi, T. Katsouleas, J. Norem, S. Ragaopalan, J. Rosenzweig, J. J. Su, and R. Williams, *Proc. IEEE Particle Accelerator Conference*, 619 (1991).

Measurement of Escaping Ions in the Fermilab Antiproton Accumulator

P. Zhou, P. L. Colestock, K. Junck and C. A. Crawford
Fermi National Accelerator Laboratory*
P.O. Box 500, Batavia, IL 60510

Abstract

Positively charged ions trapped in the negatively charged beam of the Fermilab antiproton accumulator pose a limit to beam stability and density. To better understand the dynamics and the consequences of the beam-ion interaction, we have built and installed a low energy ion detector and energy analyser in the Fermilab accumulator. This analyser is capable of energy analysis of the escaping ions using a probe with energy retarding grids and may also be scanned in the pitch angle of the escaping ions. Measurements have been made in both longitudinal and transverse planes under a variety of machine operating conditions. The experimental measurement results will be presented together with attempts to model the ion dynamics and explain observations.

Introduction

Ion trapping in accelerators with negatively charged beams occurs when ions created through Coulomb collisions with beam particles are not energetic enough to escape the beam electric field. This is a very complex process as it involves the constant creation, interaction with the beam and the background gas molecules, and escape of the ions. A direct measurement of the ions would provide some of the information needed to understand the interaction process.

Fermilab Antiproton Accumulator is a DC storage ring of antiprotons where ion trapping is a major problem if uncorrected. The average vacuum in the accumulator is 2×10^{-10} torr. Calculations using Bethe theory with experimentally measured constants [1] and by clearing current measurements both show a neutralisation time, in which beam will completely neutralise its own charge, of about 2 seconds. While the incoherent effects due to trapped ions are small and can be ignored when the ion clearing system maintains the overall neutralisation level to few percent, the coherent interaction between the beam and trapped ions are still causing noticeable effects on the beam quality. An ion detector and energy analyser, IDEA, is installed in

the Fermilab accumulator and has been used to observe escaping ions with various beam conditions.

Detector setup

The overall system is shown schematically in Fig. 1. The

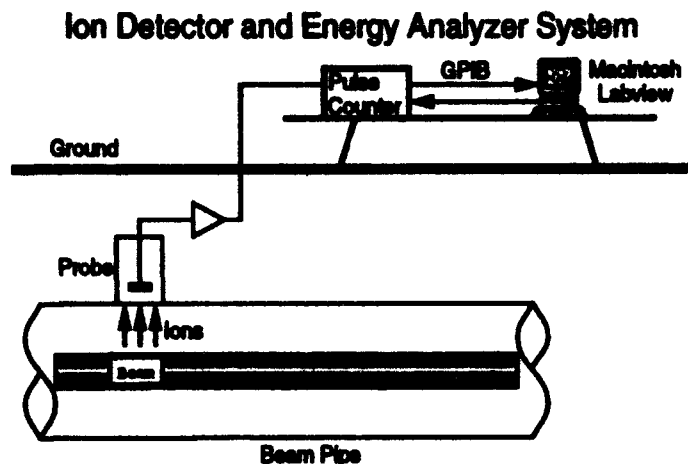


Figure 1: IDEA layout

probe construction is shown in Fig. 2. In the center of the probe is a three stage Micro Channel Plate (MCP) assembly which has a gain of up to a few 10^7 which enables the probe to detect single ions. The front of the MCP assembly is at a negative high voltage, usually 2kV for our operation. This provides the operating voltage for the MCP assembly, but also serves as an acceleration for the ions entering the probe and increases their detection efficiency[2]. Another benefit of this voltage is the exclusion of electrons with energy below 2keV, which should be the majority if not all of the electrons present, from being detected. Voltages can be applied to the plates in front of the MCP to repel lower energy ions, by varying which energy distribution of ions can be measured. The orientation of the probe can be changed nearly 180°. The signal pulses out of the probe, which is mounted in beam pipe vacuum, are then amplified and sent to a pulse counter. Control and count rate measurement are done by a Macintosh computer running Labview®[3].

*Operated by the Universities Research Association under contract with the U. S. Department of Energy

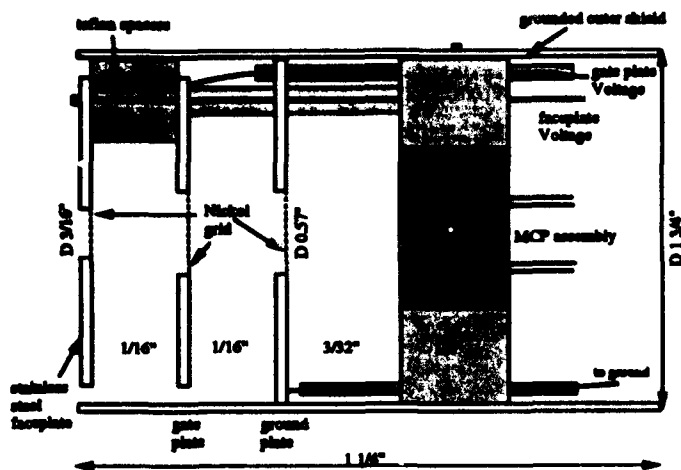


Figure 2: Schematic drawing of IDEA probe

The detector is installed in a drift section, about 1.5 meters to a quadrupole magnet. The lattice functions have the following values, $\beta_x = 22m$, $\beta_y = 2m$, $D = 1.7m$. The pointing angle of the probe is defined such that at 0 it points in the direction of movement of the antiproton beam.

Measurement results

Angular distributions of escaping ions are measured with both antiproton and proton beams, see Fig. 3. The accu-

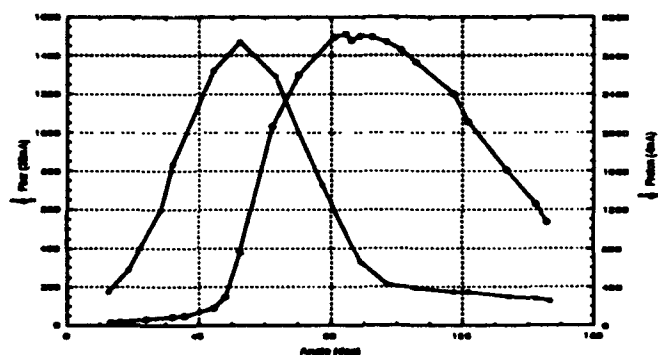


Figure 3: Angular distribution measured with IDEA

mulator sometimes runs with a few mAs of proton beam for the purpose of machine study and tune up. Most of the time proton beams are run in the opposite direction of the antiproton beam, however the proton beam usually has different momentum and therefore passes the detector at a different horizontal position relative to the antiproton beam. Furthermore, protons may have a small crossing angle with the probe because of installation errors, which is estimated at $\pm 5^\circ$. The observed difference in angular distribution between proton and antiproton beams is consistent with the hypothesis that horizontally antiproton

and proton beams pass the probe on the two sides and a crossing angle causes the probe to face the two beams at different angles and therefore a differently peaked and shaped angular distribution. The crossing angle is within the possible installation tolerance.

The energy distributions measured by IDEA are qualitatively as expected. For the proton beam the electric field of the beam itself pushes positive ions out and therefore should result in a distribution with an mean drift. For the antiproton beam, only ions that have acquired sufficient transverse kinetic energy can escape the beam potential and be detected by our detector. The energy distribution should thus be Maxwellian-like. Fig. 4 shows the comparison of the measured ion energy distribution from a 4mA proton beam and one from calculation using a simple model where ions are created without any kinetic energy from an round Gaussian beam. It can be seen from Fig. 4 that they agree reasonably well. Fig. 5 shows the ion energy distribution from a 20mA pbar beam. The

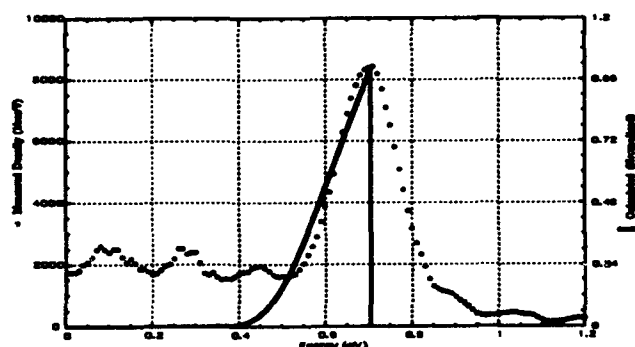


Figure 4: Ion energy distribution from a 4mA proton beam

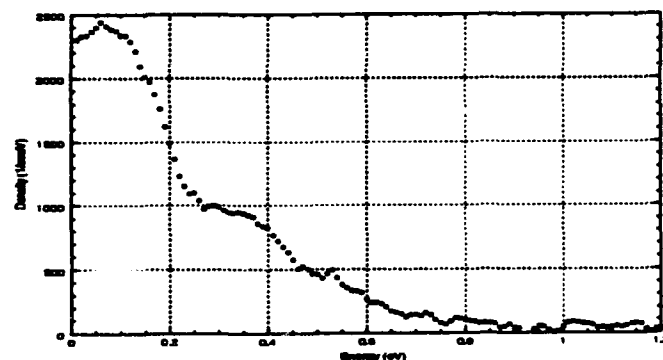


Figure 5: Ion energy distribution from a 20mA pbar beam

distribution with antiproton beam shows a very hot ion energy distribution, considering the residual gas temperature. Some ions have energies extending to 1eV level. This "temperature" seems to be insensitive to the beam current and other conditions of beam. The energy source and transfer mechanism will be discussed later.

One important motive of making the detector was to establish the positive link of beam coherent oscillations and emittance growths with the activity of ions. This is best illustrated as the beam becomes unstable and the emittances undergoes semi-periodic explosive growth. Accompanying the emittance growth there are bursts of coherent oscillation observed on the coherent pickup. Fig. 6 shows one example. From the figure it can be clearly seen that the large coherent oscillation coincides with the emittance growth and illustrates the cause of that emittance growth. The count rate measured for that period by IDEA, in Fig. 7, shows a very good match to the beam coherent oscillation strength.

One interesting, and still not completely understood, problem is the source of energy of the escaping ions. The usual count rate observed by IDEA is on the order of $10^3/\text{sec}$. Electron-ion pairs are created through collision of beam particles, antiprotons in this case, with residual gas molecules. An ion created in this process usually has little kinetic energy ($\lesssim 0.1\text{eV}$). The electric potential well depth in eV, on the other hand, can be roughly written as $0.2 \times I(\text{mA})$ for typical accumulator conditions. This will mean a 10eV deep potential well. Therefore, ions have far less initial energy needed to escape the beam trapping field and drift to e.g. IDEA probe. With the detector and beam pipe geometry, the energy flux carried by the flow of ions is estimated to be on the order of $100\text{GeV}/\text{sec}$. Since residual gas is at room temperature, or "tunnel temperature" to be exact, which at the hottest is about $40\text{--}50^\circ\text{C}$, ion-gas collisions are, on average, energy depleting interactions for the ions. Other interactions with the environment include charge exchange with neutral molecules or atoms, re-combination with electrons. For accumulator conditions, the former is estimated to have an lifetime of $10\text{--}100\text{sec}$, while the latter has an estimated lifetime orders of magnitudes higher and can thus be ignored. The charge exchange process essentially causes the ion to lose almost all of its kinetic energy to an escaping neutral particle, for which the IDEA probe has a very small detection efficiency[2]. However, a potentially energy gaining interaction for ions is that with the beam. Beam particles have an rms transverse energy of a few MeV, and they have both longitudinal and transverse Schottky noise which can potentially heat the trapped ions relatively fast. A more quantitative investigation of this mechanism is in progress.

Conclusion

The Ion Detector and Energy Analyser has been used to successfully detect ions escaping the pbar beam potential well and measure their energy distribution. Ions have unexpectedly high temperatures and their source of energy needs more explanation. Ions have been directly observed participating resonantly with the beam coherent oscillations which have led to emittance growth. The observa-

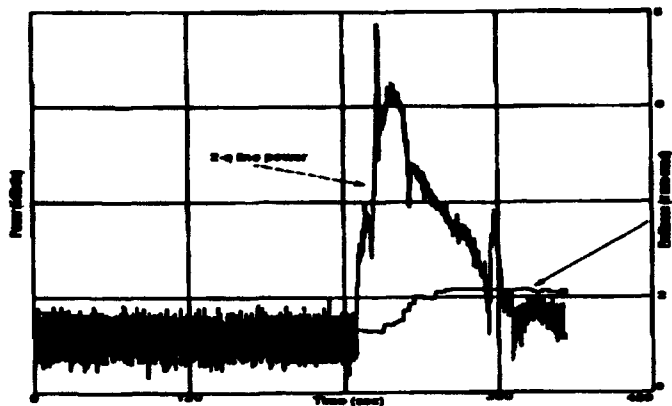


Figure 6: Coherent 2-Q line power at emittance blowup

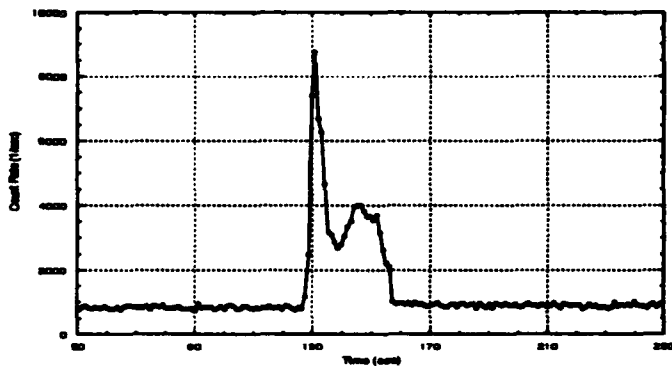


Figure 7: IDEA count rate at emittance blowup

tion of the effect of ions' longitudinal motion is however obstructed by the crossing angle of the detector and the beam.

Acknowledgment

We would like to thank Dr. Shao Yuan Hsueh for very helpful discussions on energy transfer mechanisms from the beam to trapped ions. We are also indebted to the Fermilab pbar group for their support and assistance in the installation and setup of IDEA.

References

- [1] Foster F. Rieke and William Prepejchal. Ionisation cross sections of gaseous atoms and molecules for high-energy electrons and positrons. *Physical Review A*, 6(4):1507, October 1972.
- [2] Hamamatsu Corporation. *Technical Information: MCP Assembly*, September 1991.
- [3] Labview® is a commercial product and a trademark of National Instruments Corporation.

Experimental Demonstration of Plasma Lens Focusing

G. Hairapetian, P. Davis, C. E. Clayton, C. Joshi

Department of Electrical Engineering, UCLA, 405 Hilgard Avenue, Los Angeles, CA 90024 USA

S. Hartman, C. Pellegrini

Department of Physics, UCLA, 405 Hilgard Avenue, Los Angeles, CA 90024 USA

T. Katsouleas

Department of Electrical Engineering, USC, Los Angeles, CA 90089 USA

Abstract

The magnetic self-focusing of a relativistic electron beam propagating through a plasma is demonstrated. The plasma which is produced by an RF discharge in a glass tube with no externally applied magnetic field, focuses a 3.5 MeV, 25 ps (FWHM) long electron beam from an initial size of 2.5 mm (FWHM) to about 0.5 mm (FWHM) at a focal length of 18 cm.

I. INTRODUCTION

A relativistic electron beam propagating through a plasma can self pinch due to its self generated azimuthal magnetic field[1]. In vacuum, the beam generated Lorentz force counteracts the radial space charge force and the beam propagates with an equilibrium radius. As the beam enters the plasma, the plasma electrons re-distribute themselves to charge neutralize the beam. If the beam radius is small ($r < c/\omega_p$ = collisionless skin depth), most of the plasma return currents will flow outside of the beam. As a result, the beam magnetic field will not be reduced appreciably within the beam, and it will focus under its own radial Lorentz force. This mechanism can be used to generate focusing gradients exceeding MG/cm which is several orders of magnitude greater than the strength of conventional quadrupole magnets[2].

While a large number of theoretical studies[2],[3] of this effect have been performed, there have been only two experimental studies[4],[5]. In the first experiment[4], the plasma length (35 cm) was much longer than the focal length

(8 cm), and the spot size was measured outside of the plasma column. In the second experiment[5], the beam focused outside of the plasma column but the amount of radial focusing was very limited (in some cases the spot size variations were within the experimental errors). In this paper, we report on a plasma lens experiment at UCLA, where a 3.5 MeV electron beam was focused from an initial spot size of 2.5 mm (FWHM) to about 0.5 mm, well outside of the plasma column.

II. EXPERIMENTAL SETUP

The experiment was performed with the UCLA's 4.5 MeV, laser driven RF gun[6]. The gun is capable of producing very short ($\tau < 10$ ps) electron bunches ($Q > 1$ nC, $I_{\text{peak}} > 100$ A) at 1 Hz. In order to simplify the diagnostics, the electron bunches were stretched to about 25 ps (FWHM) by illuminating the cathode with a longer laser pulse. The photo electrons are accelerated to about 3.5 MeV in the 1.5 cell RF gun and transported using a focusing solenoid and four steering magnets to the plasma chamber 2 m downstream of the gun (Figure 1). The plasma chamber which is filled with Ar gas up to a pressure of 30 mTorr is connected to the RF gun ($p < 5 \times 10^{-8}$ Torr) through a windowless, two stage differential pumping system (Figure 1). Each pumping stage consists of a low conductance tube followed by a turbomolecular pump. The first stage maintains a pressure differential of three orders of magnitude; while the second, a differential of two orders of magnitude. The electron beam which initially contains up to 1.5 nC of charge, is scraped by

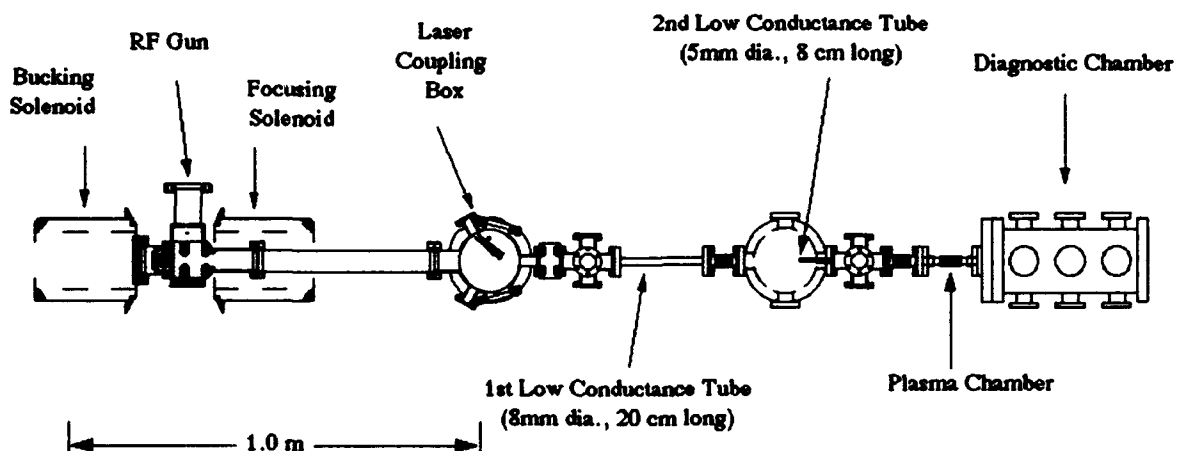


Figure 1. Experimental Setup

the two low conductance tubes, and a maximum charge of 0.6 nC is transported to the plasma chamber. Beam diagnostics include: phosphor screens both upstream and downstream of the plasma chamber, retractable faraday cups, a current transformer for non-destructive measurement of beam charge, and a Cerenkov radiator downstream of the plasma chamber.

The plasma is produced by an RF discharge in a glass tube (diam. = 1.7 cm, length = 10 cm) with no external magnetic field. The RF amplifier (10-20 MHz, 800 W) is connected via a capacitive tuning circuit to a helical antenna wrapped on the outside of the glass tube filled with Argon gas. The helical antenna (5 cm long, 12 turns) induces large azimuthal electric fields inside the tube where the Ar gas is ionized by impact ionization. Under optimum tuning, about 75% of the input RF power is coupled to the plasma. The RF plasma density is diagnosed by a small cylindrical (diam. = 0.76 mm, length = 2.5 mm) Langmuir probe. Figures 2(a) and (b) show typical radial and axial density profiles. The radial profile, measured at an axial position 0.5 cm away from the edge of the antenna, has a flat profile in the middle and decreases sharply near the tube wall. Axially, the plasma density peaks under the antenna and falls rapidly away from

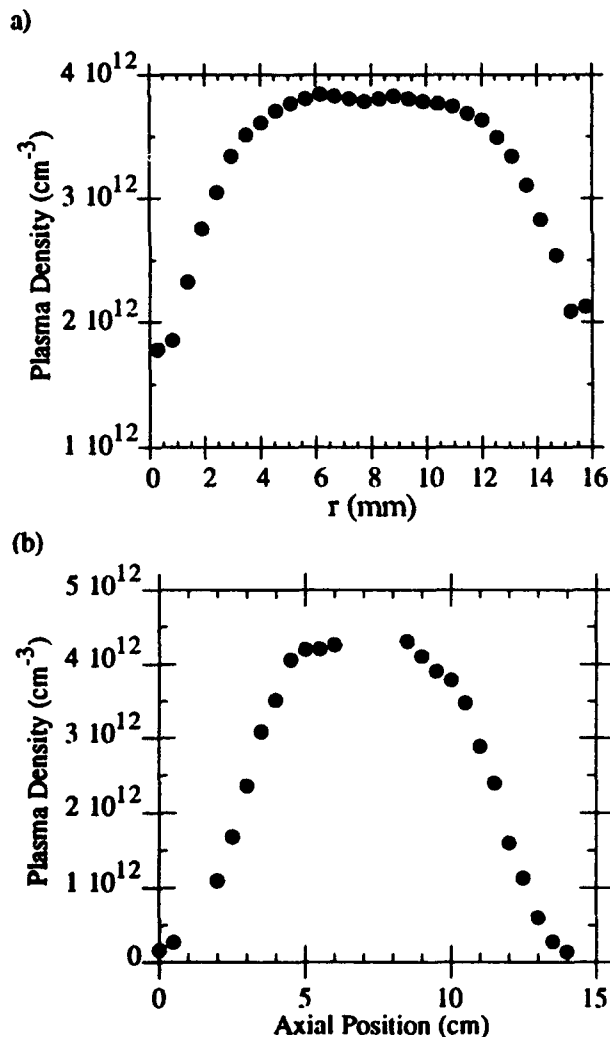


Figure 2. (a) Radial profile of plasma density. (b) Axial profile of plasma density.

the antenna ($n/\nabla n \approx 5$ cm). The density directly underneath the antenna cannot be measured because the Langmuir probe perturbs the RF discharge. The plasma density can be varied over an order of magnitude by varying the gas pressure and the RF power.

The plasma density has to be high enough to charge neutralize the beam in a time less than the electron bunch length $\tau = 25$ ps; i.e. $\tau\omega_p > 1$ where $\omega_p = (4\pi ne^2/m)^{1/2}$. Hence, the minimum required plasma density is $n = 5 \times 10^{11}$ cm⁻³ which can easily be attained by this source. The transverse beam size is about 3 mm FWHM ($< c/\omega_p$) at the entrance of plasma which implies that the beam density is approximately $n_b < 4 \times 10^{10}$ cm⁻³ ($n_b < n_{\text{plasma}}$); i.e., the lens operates in "overdense" plasma regime. One can roughly estimate the focal length of the lens from the "thin" lens approximation, which is given by [2]

$$f = (c/\omega_{bp})^2(2\gamma/l)$$

where f is the focal length, l is the plasma length, c is speed of light, and ω_{bp} is the beam plasma angular frequency. For a 5 cm long plasma and a typical beam density of 3×10^{10} cm⁻³, the predicted focal length is about 27 cm. The focal length

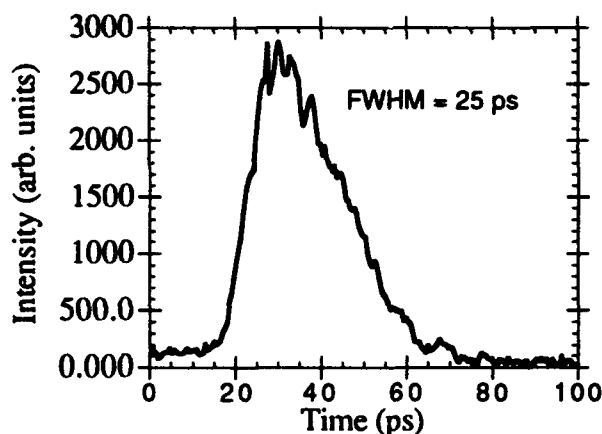


Figure 3. Temporal Profile of the electron beam.

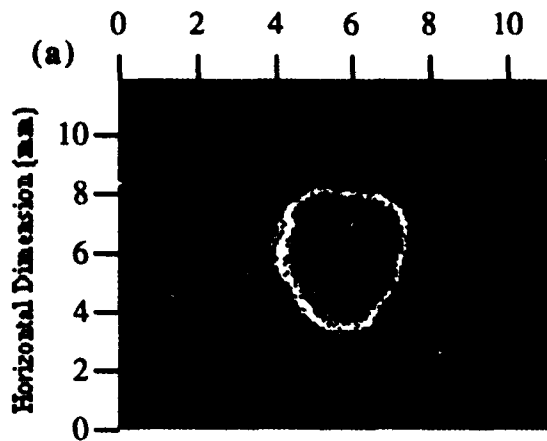
calculation is for a beam with uniform density in space and time. In reality, the focal strength of the lens is not constant and has both longitudinal and radial variations.

III. EXPERIMENTAL RESULTS

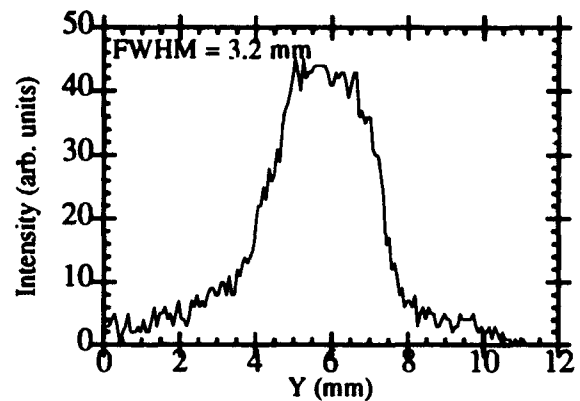
The time integrated electron beam size and the total charge were measured 22 cm upstream of the plasma. The beam is about 2.5 mm FWHM in the vertical dimension, and contains up to .6 nC of charge. The electron bunch length is measured 27 cm downstream of plasma source by streaking the Cerenkov light from a 0.5 mm thick fused silica [7]. Figure 3 shows the temporal profile of the electron bunch. It has a sharp rise and a fairly long tail. The electron beam propagates through the plasma and hits the first phosphor screen 18 cm downstream of the plasma. Figure 4(a) shows the time integrated beam size at the first phosphor screen with no

No Plasma

Vertical Dimension (mm)



(b)



Plasma on

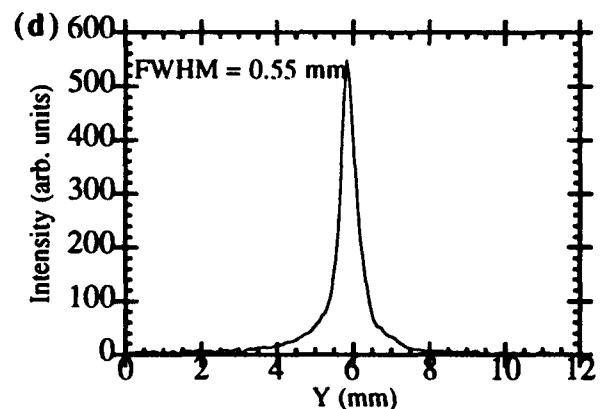
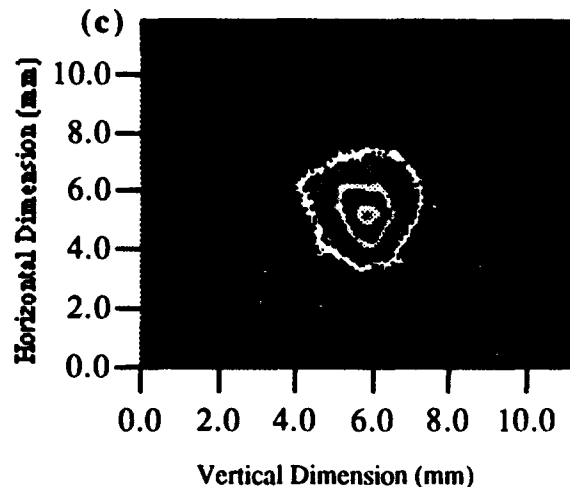


Figure 3. (a) Unfocused beam image 18 cm downstream of plasma source. (b) Vertical line out of image (a). (c) Focused beam image. (d) Vertical line out of image (c).

plasma. The beam dimensions are measured by taking either a vertical or horizontal line-out through the pixel with the highest intensity. As Figure 4 (b) shows, the vertical dimension of the unfocused beam is about 3.2 mm FWHM. When the plasma is turned on, the beam focuses down to about 0.55 mm (Figs. 4 (c) and (d)). The spot size increases to about 1.1 mm at a second phosphor screen, 22 cm downstream of the first. The apparent plasma focal length (18 cm) is shorter than that predicted from the thin lens approximation (27 cm). This can be attributed in part to the finite length of the plasma. As the beam propagates through the plasma, it begins to focus within the lens, increases its density, and shortens the lens focal length.

IV. FUTURE WORK

To learn more about the time dependent focusing of the beam, the Cerenkov radiation from the focused electron beam has been streaked using a fast streak camera (temporal resolution = 3.5 ps). Currently, we are in the process of analyzing these results which will be reported elsewhere. We also plan to investigate the effects of beam and plasma density

on the focusing. Furthermore, experimental results will be compared with both particle simulation and analytical calculation results.

VI. ACKNOWLEDGMENTS

The authors acknowledge helpful discussions with J.B. Rosenzweig, J.J. Su, and H. Zwi. Also, expert technical assistance from N. Barov, M. Fauver, M. Hogan, P. Kwok, S. Park, G. Travish, and R. Zhang is greatly appreciated. This work is supported by SDIO/IST through ONR Grant N00014-90-J-1952 and US DOE Grant DE-FG03-92ER-40493.

V. REFERENCES

- [1] P. Chen, *Part. Accel.* **20**, 171 (1987).
- [2] J.J. Su et. al., *Phys. Rev. A* **41**, 3321 (1990), and References therein.
- [3] P. Chen, *Phys. Rev. A* **45**, r3398 (1992).
- [4] J. B. Rosenzweig et. al., *Phys. Fluids B* **2** (6), 1376 (1990).
- [5] H. Nakanishi et. al., *Phys. Rev. Lett.* **66**, 1870 (1991).
- [6] C. Pellegrini et. al., these proceedings.
- [7] G. Hairapetian et. al., these proceedings.

Numerical Modelling of Time-Space Behavior of High-Current Relativistic Electron Beam in Plasma Waveguide

Vyacheslav I. Karas'

Kharkov Institute of Physics and Technology Ukrainian Academy of Sciences

310108 Akademicheskaya Str. 1, Kharkov-108, Ukraine

Nadya G. Belova

Institute of Physics and Technology Russian Academy of Sciences

117218 Krasikov Str. 25a, Moscow, Russia

Abstract

The physical processes in the magnetized plasma waveguide, in which the high-current relativistic electron beam (Sudan parameter $S > 1$) is injected, are investigated by the developed 2.5-D relativistic electromagnetic code. The computer study has shown that the charge and current compensations of the high-current beam are considerably different from those of the low-current beam. In addition the self-consistent electromagnetic fields generated by a beam at the initial state radically alter both the linear and the nonlinear instability stages.

I INTRODUCTION

The advantages of a use of the high-current relativistic electron beam (HCREB) for development of a powerful electromagnetic radiation sources, and the new type accelerators based on the collective methods of the particles acceleration, and etc. are presented in [1]–[3]. It was noted that the simultaneous growth both of the beam energy and the non-equilibrium degree of a system defining by the Sudan parameter $S = (n_b/n_e)^{1/3}\gamma$ (n_b , n_e are the beam and plasma densities, γ is the relativistic factor) is a very important fact. In the unbounded systems this can results in the decrease of the energy (at $S > 1$) transferring from a beam to the plasma for the oscillations excitation. In the system bounded in the radial direction this fact decreases the efficiency of the electromagnetic waves radiation due to the oscillations excitation with the small ratio between the transverse and longitudinal components [3, 4]. Čerenkov mechanism was proved to be changed to the anomalous Doppler mechanism for HCREB [5]. This allows to remain the high efficiency of the electromagnetic radiation at the certain parameters of a system such as the magnetized plasma waveguide (MPW) – HCREB.

The equilibrium and stability conditions of HCREB were investigated in many works (see Refs. in [1]–[5]). The injection of the low-current ($S \ll 1$) stringent REB is also studied in detail both with the magnetic field and without field. It was shown if the beam radius a to be greater than the skin-depth $\lambda_E = c/\omega_e$ (c is the light velocity, ω_e is the Langmuir plasma frequency) the beam current is compensated by a return plasma current damping in a plasma with the finite conductivity. The external magnetic field modifies the current compensation condition to the form $a \gg \lambda_E(1 + \Omega_e^2/\omega_e^2)$ (Ω_e is the Larmor electron frequency).

In this work both the charge–current compensation and the stability of HCREB ($S > 1$) in MPW are investigated. The hollow narrow beam of the a radius and of the Δ_b thick-

ness (so that $\Delta_b < c/\omega_e$, but $a > c/\omega_e$) is considered, and the hollow wide beam with $\Delta_b \approx r_L$ (r_L is the waveguide radius) is also. In the both cases the Čerenkov resonance condition of the beam with the plasma wave is not valid i.e. $\gamma > \omega_e/(ck_\perp)$ (k_\perp is a transverse wave number). For comparison, the study of the low-current beam is also presented.

II MODEL AND EQUATIONS

In order to study the dynamics of a collisionless plasma with the relativistic electron beam in both the self-consistent and the external electromagnetic fields in axisymmetric ($\partial/\partial\theta = 0$) geometry, we use the set of relativistic Vlasov's equations for the distribution functions of the given type of particles $f_s(\vec{p}, \vec{R}, t)$. Here $\vec{p} = m_s \vec{v}\gamma$, $\vec{v} = \{\dot{r}, r\dot{\theta}, \dot{z}\}$, $\gamma = [1 - (|\vec{v}|/c)^2]^{-1/2}$ is the relativistic factor, $\vec{R} = \{r, z\}$. The self-consistent electromagnetic fields in Vlasov's equation are determined by Maxwell's equations in the form of wave equations for the dimensionless scalar ϕ and vector \vec{A} potentials in which the right side is defined by the total charge and current densities [6].

We will consider the infinite value of the uniform external magnetic field $H \rightarrow \infty$ then the motion of the particles can be treated as the one-dimensional. Thus we have the only equation of the motion and the equations for the potentials $\phi(r, z)$ and $A_z(r, z)$.

In these equations the quantities involved are used in the dimensionless form: $[v] = c$; $[r, z] = c/\omega_e$; $[t] = \omega_e^{-1}$; $[n] = n_{0e}$; $[q] = e$; $[m] = m_0$; $[\phi, A] = \mathcal{E}_{ch}/e$; $[E, B] = (4\pi n_{0e} \mathcal{E}_{ch})^{1/2}$; $[J] = en_{0e}c$, where $\omega_e = (4\pi n_{0e}e^2/m_0)^{1/2}$ is the electron plasma frequency, $\mathcal{E}_{ch} = m_0c^2$ is the rest energy of the beam electron, n_{0e} , m_0 , e are the initial density, rest mass and charge of the electrons respectively.

The dimensionless equation of motion, obtained as characteristic equation of Vlasov's equation, was written as

$$\frac{du_z}{dt} = -\frac{q}{m} \left(\frac{\partial A_z}{\partial t} + \frac{\partial \phi}{\partial z} \right)$$

where $u_z = \gamma v_z$, $\gamma = [1 + u_z^2]^{1/2}$.

The boundary conditions for the potentials are

$$r = 0: \quad \partial\phi/\partial r = \partial A_z/\partial r = 0;$$

$$r = r_L: \quad \phi = A_z = 0;$$

$$\left. \begin{array}{l} z = 0 \\ z = z_L \end{array} \right\}, \quad \phi = \frac{\partial A_z}{\partial z} = 0$$

The initial conditions for the self-consistent fields are $\Delta\phi = -\rho$, $A_z = 0$. Here Δ is Laplacian.

The boundary conditions for the distribution functions set the Maxwellian distribution for plasma particles with the temperature T at $(z = 0, z = z_L)$ and the hollow electron beam injection at $z = 0$: $f_b(m_0 u_z, \vec{R}, t) = \delta(u_z - u_{0b})$ at $r_{\min} \leq r \leq r_{\max}$ and $u_z > 0$, they are equal to zero at $z = z_L$. Here, r_{\min} and r_{\max} are the minimum and maximum beams radii respectively, $u_{0b} = V_b / (1 - V_b^2)^{1/2}$, V_b is a beam velocity. At the initial time, the distribution functions are equal to Maxwellian for the plasma particles and equal to zero for the beam electrons.

The present model is a particular case of the general 2.5-dimensional cylindrical model [6]. We have used the version of the general computer code for the investigation of a relativistic beam dynamics in the plasma waveguide.

III COMPUTER SIMULATION

Let a hollow magnetized electron beam with velocity V_b be injected along the z -axis into the plasma waveguide under the external magnetic field. The beam current density is equal to $q_b n_b V_b$. In the calculations we assumed the mass ratio to be $m_i/m_e = 100$, $m_e = 20m_0$, $m_b = n_0$, the number of particles in the cell was $N_e = N_i = 4$, $N_b = 100$ for narrow beam and $N_b = 20$ for wide beam. The electron beam velocity was supposed $V_b \approx 0.995$, i.e. $\gamma = 10$. The length and radius of the waveguide were $z_L = 127.5$ and $r_L = 7.5$. The plasma temperature is equal to $T = 2 \cdot 10^{-3}$. The number of points and the time step for solving Maxwell's equations were $(J_r \times J_z) = (16 \times 256)$ and $\Delta \tau = 0.025$. The time step for solving of the equation of the motion is equal to $\Delta t = 0.1$. Three variants were run with the following parameters:

No. of case	1	2	3
r_{\max}	2.	7.	2.
Δ_b	0.5	7.	0.5
n_{0b}/n_{0e}	0.5	0.5	0.05
$S = (n_b/n_e)^{1/3} \gamma$	7.94	7.94	3.68
$(n_b/(n_e \gamma))^{1/3}$	0.37	0.37	0.17
$\mu = ((n_b \gamma)/n_e)^{1/3}$	1.71	1.71	0.79

The results of the computer simulation are presented in figures 1,2,3 according to the number of variants. In the figures it is shown the longitudinal section of the cylindrical system at the line $r = 1.75$ i.e. along the beam line. It is clearly seen that the beam front excites the plasma and the disturbances are high i.e. the plasma is nonlinear both in the cases of the narrow beams and in the case of the wide beam. The development of the beam instability occurs only for the wide beam (see fig.2) as the Čerenkov resonance condition $\gamma < \omega_e/(ck_{\perp})$ is not valid but the beam current is greater the threshold value. The fact is important that the instability development takes place without the charge and current compensations and this essentially influences on both the excitations dynamics and the electromagnetic fields spectrum. The almost entire charge compensation occurs for the narrow beams ($\Delta_b < c/\omega_e$) as the potential distributions show in fig.1a,3a at $t = 160$. No current compensation are available both in the case of the high density beam (fig. 1b) and in the case of low density beam (fig. 3b).

Thus the self-consistent electromagnetic fields generated by a beam at the initial state radically alter both the linear and the nonlinear instability stages.

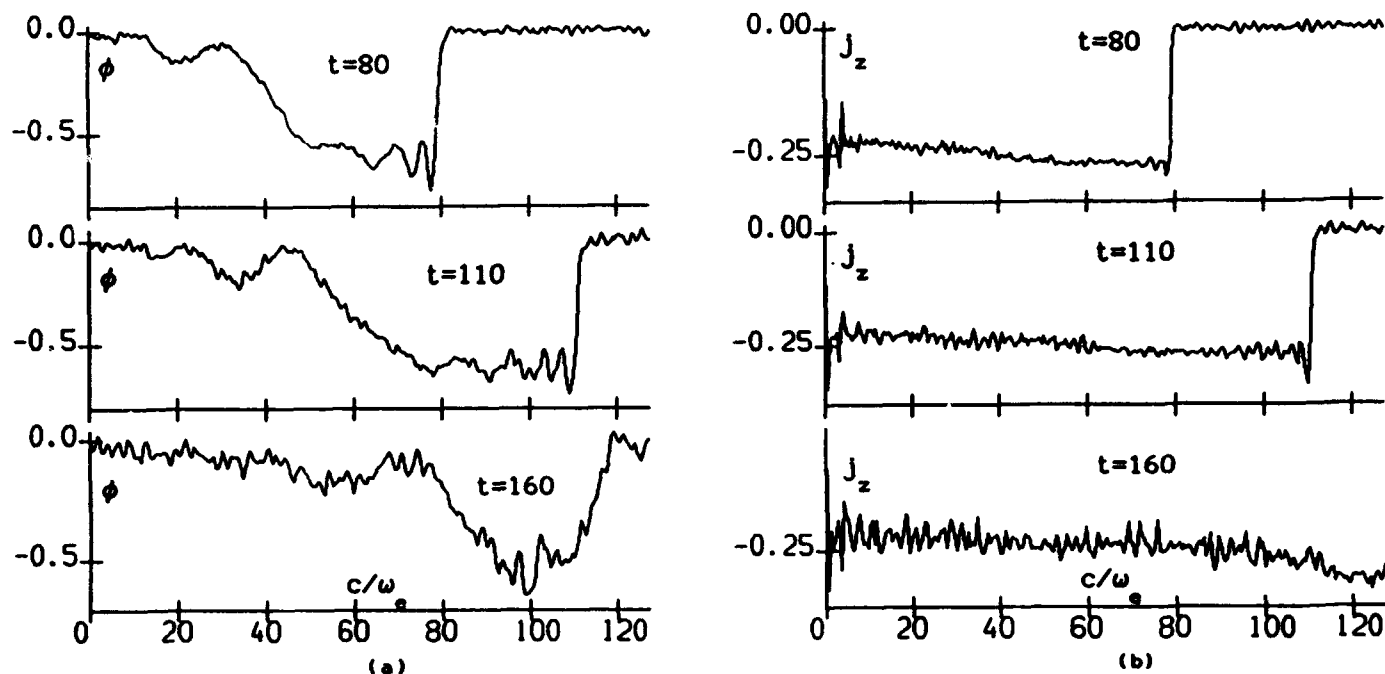


Figure 1: The longitudinal section ($r_b = 1.75$) of (a) the scalar potentials $\phi(r_b, z)$ and (b) the axial current density $j_z(r_b, z)$ for the narrow high-current beam along the beam line at $t = 80$, $t = 110$, $t = 160$.

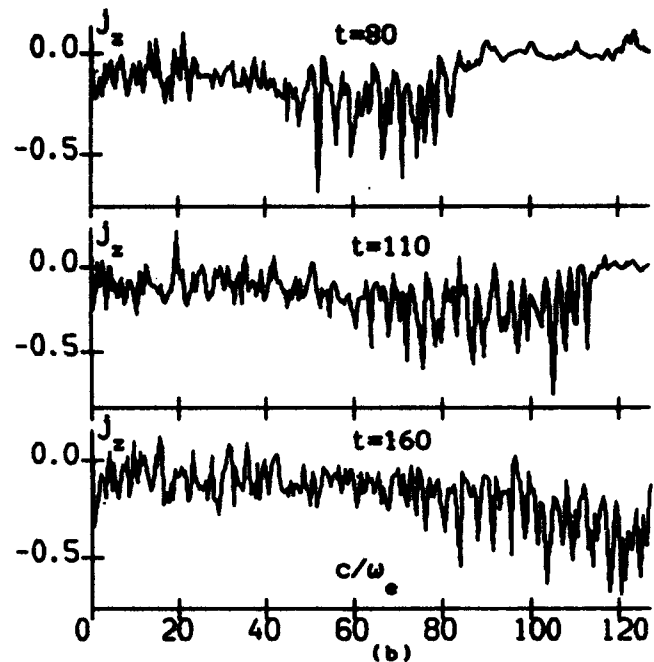
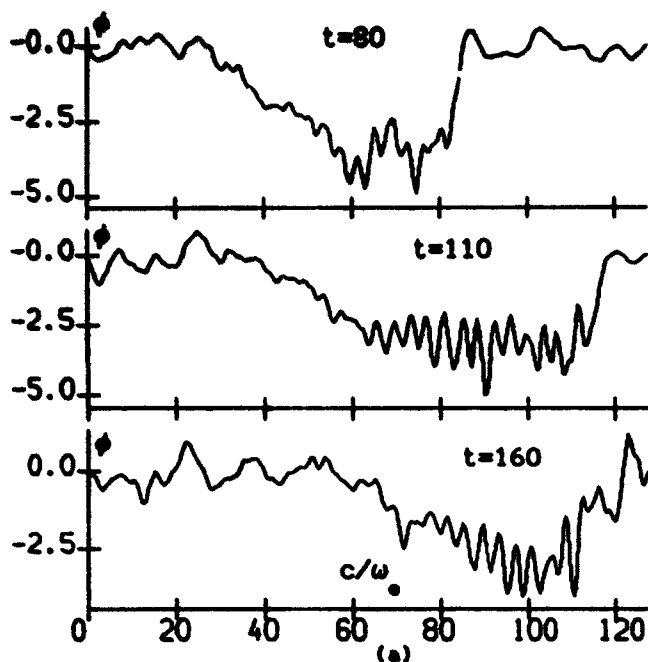


Figure 2: The longitudinal section ($r_b = 1.75$) of (a) the scalar potentials $\phi(r_b, z)$ and (b) the axial current density $j_z(r_b, z)$ for the wide high-current beam along the beam line at $t = 80$, $t = 110$, $t = 160$.

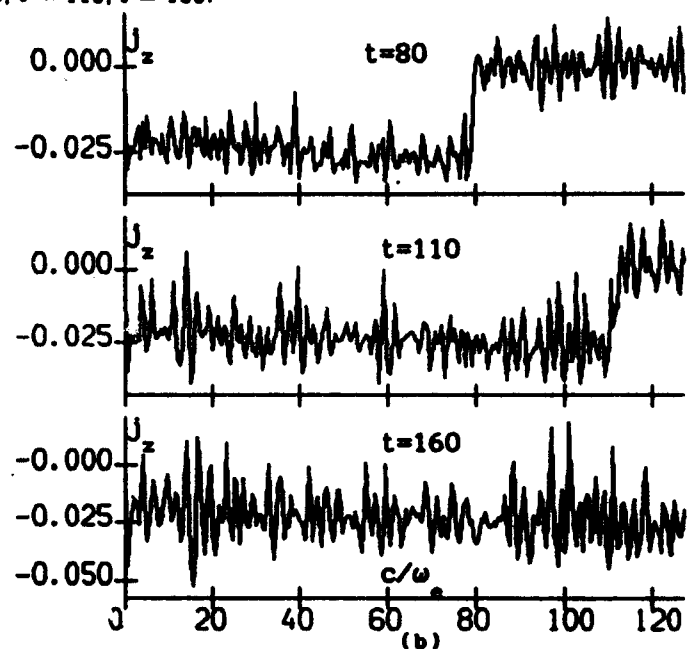
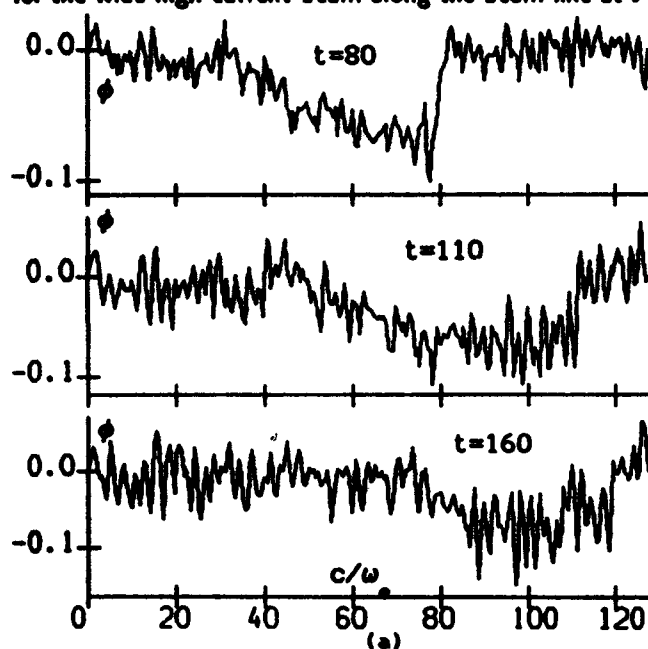


Figure 3: The longitudinal section ($r_b = 1.75$) of (a) the scalar potentials $\phi(r_b, z)$ and (b) the axial current density $j_z(r_b, z)$ for the narrow low-current beam along the beam line at $t = 80$, $t = 110$, $t = 160$.

IV REFERENCES

- [1] Ya. B. Fainberg, "Some problems of plasma electronics," *Fiz. Plasmy* 11, No. 11, 1398 (1985)
- [2] R. N. Sudan, "Collective interaction of beam with plasmas," *Foundations of Plasma Physics*, M., 1984 (Osnovy fiziki plazmy, Dopolnenie k T.2, Moscow, Energoatomizdat, 1984)
- [3] M.V. Kuzelev, A. A. Rukhadze, "Electrodynamics of dense electron beams in plasma," *Nauka*, (Moscow publ., 1990)
- [4] V. A. Balakirev, E. A. Galst'yan, N. I. Karbushev, A. O. Ostrovsky, G. V. Sotnikov, A. D. Shatkus, "Wave excitation in plasma system by high-current relativistic electron beams," *Relativistic high-frequency electronics*, Issue 6, 127 (1990).
- [5] Yu. P. Bliokh, V. I. Karas', M. G. Lyubarskij, I. N. Onishchenko, Ya. B. Fainberg, "On the theory of interaction of the high-current relativistic electron beam with the magnetized plasma waveguide," *DAN SSSR* 275, No. 1, 56 (1984).
- [6] N. G. Belova, V. I. Karas', these proceedings.

IPROP Simulations of the GAMBLE II Proton Transport Experiment*

D. R. Welch

Mission Research Corporation

1720 Randolph Road SE, Albuquerque, NM 87106 USA

Abstract

We have simulated the proton transport of the 6-kA, 1-MV GAMBLE II experiment using a modified version of the IPROP particle-in-cell code. IPROP now uses a hybrid model in which plasma electrons are divided into high-energy macro particle and thermal-fluid components. This model includes "knock-on" bound-electron collision and runaway sources for high-energy electrons. Using IPROP, we have calculated net currents in reasonable agreement with the experiment ranging from 5–11% of the total current in pressures from 0.25–4 torr helium. In the simulations, the pinch current sample by the 1.5-cm beam was 2–3 times larger than the net current at 4-cm radius. The attenuation of net current at larger radii was the result of a highly-conductive energetic component of plasma electrons surrounding the beam.

Having benchmarked IPROP against experiment, we have examined higher-current ion beams with respect to possible transport for inertial confinement fusion. We present some preliminary findings.

I. INTRODUCTION

The efficient transport and focusing of intense ion beams is essential for ion-driven inertial confinement fusion (ICF).^{1,2} Research in the area of ion-beam transport is just beginning. Two of the basic concepts considered for ion beams are ballistic¹ and self-pinched³ transport. In the ballistic mode, a low-pressure gas provides near ballistic transport by effectively neutralizing all self fields. The most exciting concept is self-pinched transport where the gas and gas pressure (~1 torr) are chosen to provide only partial current neutralization so that the residual magnetic field confines the beam. If sufficiently-high magnetic fields can be attained, even a hot beam can be pinched and the demands on accelerator emittance becomes somewhat less stringent.

The physics of the ballistic and self-pinched transport is complex, characterized by nanosecond breakdown of the gas.² Extremely rapid gas breakdown is necessary for the >99% current neutralization desired for good ballistic transport. For self-pinched transport, sufficient magnetic field must penetrate the plasma generated in the gas to provide the confinement before the gas becomes highly conductive. The breakdown process is dominated by an electric-field driven avalanche of secondary electrons which may involve sufficient fields to produce electron runaway.⁴

The transport of these plasma electrons into the ion beam to provide neutralization may be hindered by applied or beam-generated magnetic fields. In addition, at the pressures near a torr, electron $E \times B$ drift may be as important as Ohmic current (σE), where the conductivity $\sigma = en_e/m_e v_m$, n_e is the plasma electron density and v_m is the momentum transfer frequency. We have modified the IPROP charged-particle beam propagation code,⁵ which had used a simple scalar conductivity model for plasma electrons, into a hybrid code which assumes plasma electrons have both fluid and high-energy particle components. This model includes a formalism for electron runaway.

In this paper, we first discuss the modifications to the IPROP code necessary to model breakdown in a low-pressure gas. Using the new modeling, we present simulations of the GAMBLE II proton transport experiment at Naval Research Laboratory (NRL). Energetic plasma electrons are shown to greatly attenuate net currents (beam plus plasma current) outside the ion beam. We then proceed to discuss preliminary findings for high-current ion beams with respect to ballistic and self-pinched transport for ICF.

II. HYBRID PLASMA-ELECTRON MODEL

The behavior of the secondary plasma electrons is the key to quantifying the gas breakdown driven by an intense ion beam. If the plasma-electron population remains highly collisional with a thermal distribution, plasma electrons drift and diffuse slowly. However, energetic electrons (>100 eV) have much longer mean-free paths. The non-local energy deposition of these fast secondaries carries conductivity away from or even ahead of the beam. In addition, these electrons have a much smaller collision frequency and, thus, contribute more to conductivity. The energetic electrons attempt to decrease the net current as they co-move with the ion beam. Thus, a non-thermal component to the plasma-electron distribution has a significant impact on gas breakdown.

The two sources of energetic electrons are "knock-on" collisions and runaway. The velocity distribution of knock-on bound electrons is forward-directed in an impact ionization event. The energy distribution is roughly as $1/E^2$ with the maximum secondary velocity that of the impacting electron or twice the impacting ion velocity. If an electron in an electric field increasingly gains momentum between

* Work supported by Sandia National Laboratories.

collisions, it is said to be in runaway. Runaway in a given gas typically occurs above some E/p threshold. As the gas breaks down, the rising current drives an inductive electric field which attempts to resist further net-current rise. This field pushes electrons ahead of the ion beam. For a weakly relativistic ion beam, the beam space charge precedes the beam front which draws in electrons. These trapped electrons have a strong effect on both net current, and possibly, instability growth.

We have characterized the runaway phenomenon with the PIC code IPROP. By turning off the electromagnetic field solver and substituting uniform electric (and/or magnetic) fields, we allow swarms of electrons to drift in the field and scatter elastically and inelastically (including ionization, which creates new particles) with various gases (Ar, N₂, and He). The elastic scattering is assumed to be isotropic with momentum-transfer cross sections taken from experimental data. Using an initial 10,000 particles, we approximate the full velocity distribution and characterized drift velocities, electron average energies, and collision frequencies.

To determine the source of runaway electrons as a function of E/p , we define a cutoff energy, E_c , above which an accelerating electron is assumed to be in runaway. We typically choose $E_c = 100$ eV for two reasons. First, electrons below 100 eV cannot move far on the nanosecond time scale of gas breakdown. Second, for $E > 100$ eV, electron binding energies become less important and v_m declines rapidly. The steady-state depletion rate (α_r) of low-energy plasma electrons accelerating past E_c scales as $(E/p)^2$ for nitrogen and helium. The runaway depletion exceeds the avalanche production rate for electrons below 100 eV when $E/p > 2$ MV/cm-atm in N₂ and > 0.5 MV/cm-atm for He. The velocity distribution of the runaways as they exceed E_c is peaked in the direction of E . The root-mean squared (RMS) velocity perpendicular to E is roughly that of the velocity parallel to E with only a slight dependence on E/p . At very high E/p , the velocity becomes more strongly peaked in the E direction. The runaway electrons can be incorporated into a simulation code as a volumetric source of new macro particles emitted from a colder fluid of electrons.

Having characterized the runaway source, in IPROP we now divide plasma electrons into two components: a low-energy electron fluid and a mobile high-energy macro particle group. We model the bulk of the electrons as a fluid, particularly late in time when the plasma is collisional and densities are high, to avoid temporal resolution of the plasma oscillations which should physically damp. Plasma electrons with energies $E < E_c$ eV are treated as a fluid with T_e , v_m , and α — all functions of E/p and p . Electrons can either be removed from the fluid through the runaway sink or be added to the fluid due to electrons slowing down below E_c . Macro-particle electrons are created due to runaway and energetic forward scattering of a bound electron from a neutral gas molecule, which produces an electron with energy above E_c .

In IPROP, Maxwell's equations are solved with two current-density sources J_b and J_p (macro particles and fluid plasma). J_b is simply the sum of all macro-particle current including that of plasma-electron ($E > E_c$), beam and wall emission particles. The fluid plasma motion is the sum of Ohmic currents and electron $E \times B$ drift (ions can not move on breakdown time scales).

III. GAMBLE II SIMULATIONS

When plasma-electron motion is not inhibited by strong external magnetic fields, the net current produced by an ion beam in an ~ 1 -torr gas may be quite small as described in Section II. The GAMBLE II proton beam experiment at NRL produced net currents that were only a few percent of the 4–8 kA (30 ns rise time) proton current.⁶ The experimental and simulation geometry consisted of a 20-cm long, 7.6-cm radius metal pipe and a 1.5-cm proton beam with a 50 milliradian divergence. We assume constant energy (0.7–1 MV) and a shot-dependent current rise to a constant current. The total beam pulse length was 68 ns. For direct comparison with experiment, we positioned a B_θ probe at $z = 11$ cm and a 4-cm radius. The net current measured at $r = 4$ cm is not necessarily the pinch current sampled by the ion beam. The simulations suggest that significant plasma current exists between the beam and the monitor, reducing the observed net current up to a factor of 3. For three helium shots, IPROP and experimental net current fractions (net current to beam current ratio, f_{net}) at $r = 4$ cm were compared. We find agreement of the IPROP code calculations at $r = 4$ cm to within 30% of the measurements with 0.047–0.106 net current fractions.

The effect of energetic secondaries, of which electron runaway is the primary source early in time and knock-ons late in time, is to further attenuate magnetic fields outside the beam radius. In Fig. 1, we compare the radial dependence of the net current for IPROP simulations with and without the energetic electron component for shot 5479 at 1 torr. Although the net current at 4 cm in the full IPROP simulation is only half that of the simulation without runaways (and knock-ons), the net current at the beam radius is actually enhanced 20%. In the full simulation, hot electrons diffuse outwardly in radius and produce additional secondary electrons in the runaway simulation. These electrons attenuate the net current greatly at larger radii. In the beam region where self-magnetic fields are significant, the hot electrons are less collisional than the thermal fluid electrons with $\omega_c/v_m = 2$ –4 at 1 torr. Any further decrease in collisionality degrades the conductivity across the magnetic field lines. Thus, the IPROP simulations, which include energetic electrons, yield a greater net current at smaller radii (10–20% of beam current) than the simulations without energetic electrons.

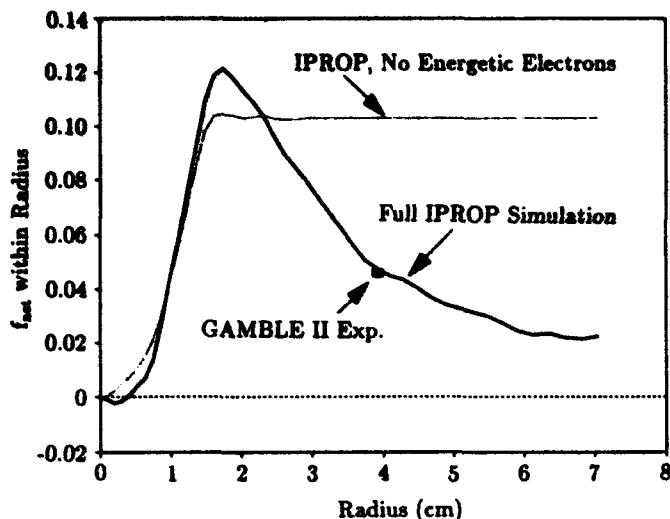


Fig. 1. The net current fraction calculated at all radii is plotted for IPROP simulations of GAMBLE II shot 5479 in 1 torr helium with and without energetic electrons. The values were calculated 68 ns into the simulations 10 cm from injection. The maximum experimental value at 4-cm is also plotted.

IV. INITIAL HIGH-CURRENT RESULTS

We have begun examining transport of more intense proton beams (50–500 kA, 0.75–3 cm radii) with IPROP and now present some preliminary results. Simulations show a trend to higher net current fractions for more intense beams in lower-pressure helium gas with fraction ranging from 1–12% near the injection plane. Prospects for good ballistic look promising for large radius beams (>1 cm) in helium near 1 torr. The net current may actually drop with propagation distance as energetic co-moving electrons build up near the beam front. Pre-ionization and a higher atomic number gas such as argon reduced net current fractions to <1%.

We simulated a 100 kA, 5-MeV proton beam which exhibited adequate self-pinch propagation. The beam was propagated 40 cm showing a pinching radius for beam slices more than 4 ns into the beam pulse. This time corresponds to the point at which the effective pinch current exceeded 2 kA. This current roughly matches the 20-milliradian divergence of the beam. Although the maximum pinch current declined away from the injection point, a pinch current of 5 kA (7 ns into the beam pulse) was calculated 20 beam radii from injection.

Another promising configuration for self-pinch transport involves pre-ionization of an annular plasma channel with inner radius roughly that of the beam radius (annular plasma transport, APT) in a <100 mtorr gas. IPROP and IVORY (a pure PIC electromagnetic cousin of IPROP) simulations predict a 6–20 kA pinch current for a 50 kA, 45-MeV proton beam in 10–100 mtorr nitrogen. The plasma provides excellent charge neutralization early in time. The gas provides enough collisionality to reduce the current neutralization and improve the charge neutralization at the higher pressures. The beam self-fields reached an equilibrium 2 ns into the pulse for 100 mtorr pressure. At pressures of <100 mtorr, the plasma channel is necessary to provide the conditions for self-pinch transport.

V. CONCLUSIONS

The IPROP code has been modified to include a hybrid model for plasma electrons in which plasma electrons have fluid and high-energy particle components. The high current neutralization of the GAMBLE II proton beam was found to be caused by a halo of highly conductive electrons and their secondaries surrounding the beam. Preliminary examination of ion-beam transport for ICF shows good ballistic transport for >1 torr gas. Sufficient net currents for self-pinch transport looks possible for lower pressures and intense beams. The use of an annular plasma has yielded 10–40% net current fractions in 1–100 mtorr nitrogen. In future work, we will examine long-distance ion-beam equilibrium and stability.

VI. REFERENCES

- [1] P. F. Ottinger, D. V. Rose, J. M. Neri, and C. L. Olson, *J. Appl. Phys.* 72, 395 (1992).
- [2] C. L. Olson, *J. Fusion Energy* 1, 309 (1982).
- [3] S. Yu and E. Lee, *Proc. Heavy Ion Fusion Workshop*, Edited by W. B. Herrmannsfeldt (Lawrence Berkeley Laboratory, LBL-10301, 1980) p. 504.
- [4] C. L. Olson, *Phys. Rev. A* 11, 288 (1975).
- [5] B. B. Godfrey and D. R. Welch, in *Proceedings of the Twelfth Conference on Numerical Simulation of Plasma, San Francisco, California* (Lawrence Livermore National Laboratory, Livermore, CA, 1987) Paper No. CM1.
- [6] F. C. Young, D. D. Hinshelwood, R. F. Hubbard, M. Lampe, J. M. Neri, C. L. Olson, P. F. Ottinger, D. V. Rose, S. P. Slinker, S. J. Stephanakis, and D. R. Welch, *Phys. Rev. Lett.* 70, 2573 (1993).

Plasma Lens and Plasma Wakefield Acceleration Experiments Using Twin Linacs

A. Ogata, H. Nakanishi, K. Nakajima, T. Kawakubo, D. Whittum, M. Arinaga

National Laboratory for High Energy Physics (KEK), Oho, Tsukuba, Japan

Y. Yoshida, T. Ueda, T. Kobayashi

Nuclear Engineering Research Laboratory, Faculty of Engineering, The University of Tokyo, Tokai-mura, Ibaraki-ken, Japan

H. Shibata and S. Tagawa

Research Center for Nuclear Science and Technology, The University of Tokyo, Tokai-mura, Ibaraki-ken, Japan

N. Yugami and Y. Nishida

Department of Electrical and Electronic Engineering, Utsunomiya University, Utsunomiya, Japan

Abstract

A collinear wakefield test facility using two linacs with a common test section is constructed. Beams from one linac excite wakefields in a test medium such as a plasma, while beams from the other linac witness the wakefields. The time interval between the two beams is controllable with an accuracy of ~ 1 psec. Plasma wakefield acceleration and plasma lens experiments were conducted using this facility.

1 INTRODUCTION

Plasma wakefield acceleration and plasma lens experiments were conducted using a collinear wakefield test facility[1]. This facility is unique in that it consists of two identical but independent linacs which are called twin-linacs, while in other wakefield accelerators one linac generates both the driving and witness beams. Beams from one linac excite wakefields in a plasma, while beams from the other linac witness the wakefields. The time interval between the two beams is controllable with an accuracy of ~ 1 psec. The plasma lens experiments were conducted using one of the linacs, while the acceleration experiments were conducted using both of them.

2 EXPERIMENTAL APPARATUS

A schematic diagram of the twin linacs is shown in Fig. 1. The part depicted by thick lines has been newly constructed. Each linac can generate beams in three schemes; an isolated single bunch, a 476 MHz bunch train or a 2856 MHz bunch train. Only single isolated bunches were used in these experiments. Because the two beams have different energies, the beamlines were joined in a configuration inverse to that of an energy analyzer. They consist of achromatic lines as shown in Fig. 1, each of which has two dipole magnets and one quadrupole magnet. The two lines share one dipole magnet BM3, i.e., the two lines merge at BM3. Particles with the design energy are focused

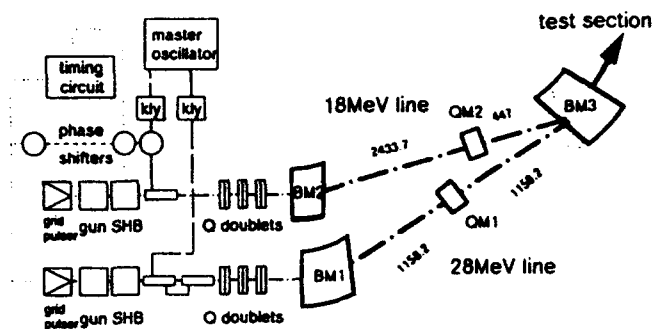


Figure 1: Schematic diagram of the wakefield accelerator. The part depicted by thick lines is newly constructed. Distances between magnets are given in mm. The length of each quadrupole magnet QM_n ($n=1,2$) is 80mm. The distance between two linacs is 750 mm where they are running in parallel.

on the quadrupole magnets (QM1 and QM2 in Fig. 1). The off-energy particles are dispersed by the first dipoles (BM1 and BM2 in Fig. 1), and focused again by QM1 and QM2 onto BM3. Each line has three pairs of doublet quadrupoles upstream, permitting fine tuning of the lattice. The fringe angles of the dipoles are designed so that the β, β' variables at the entrance of the BM1 and BM2 are transposed as $\beta, -\beta'$ at the exit of the BM3. This configuration transports the entire drive beam into the test region without loss due to energy dispersion. It is also possible to introduce witness beams with good energy resolution by inserting a vertical slit at the position of the quadrupole magnet.

To isolate the linacs from the test section, we adopted differential pumping. Previous experience on plasma lens experiments informs us that argon gas is quite harmful to the ion pumps used in the linac main ducts[4]. Nitrogen was adopted as a working gas in these experiments.

Plasmas are produced in a chamber with .3m in diam-

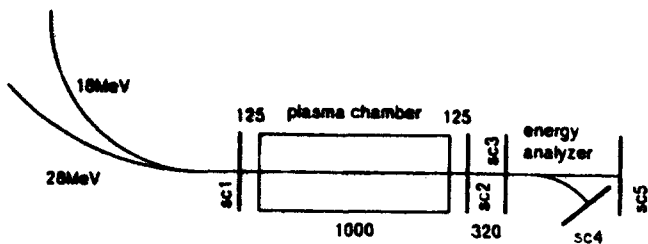


Figure 2: Positioning of phosphor screens.

eter and 1m in length by pulse discharges between four lumps of LaB₆ cathodes and the chamber[2]. The cathodes are heated by a 10V-80A direct current source. The discharge pulse has a voltage of 80-100V, a current of 10-20A, a duration of 2ms and a rate of 6.25Hz equal to the linac beam repetition rate. The multi-dipole field of permanent magnets, 1kG at the inner surface of the water-cooled chamber, is applied to confine the plasma. The base pressure of the chamber is typically 10^{-6} torr. The plasma density was controlled both by the gas flow controller and the discharge current. The plasma density and temperature are measured by a Langmuir probe. Though we have no measurement of the density distribution, the measurement on a similar confinement device shows that it is fairly homogeneous both in longitudinal and transverse directions[3].

A 45° bending magnet at the end of the plasma chamber measured the beam energy, giving a displacement of -55.8keVmm^{-1} . Five phosphor screens measured transverse profiles, whose positions are given in Fig. 2.

3 EXPERIMENTAL RESULTS

3.1 Single Beam Experiments

Plasma lens experiments in the overdense regime already have been reported[4]. Here we report those in underdense regime. Experimental conditions were as follows; beam energy was 16MeV, charge of a bunch was 300pC, beam sizes at the first screen (SC1 in Fig. 2) were $1.27\text{mm} \times 3.13\text{mm} \times 3\text{mm}$, electron density n_b at SC1 was 10^{10}cm^{-3} . vertical β, γ functions at SC1 were 0.99m and 1.4m^{-1} , and vertical emittance was 1.64mm mrad . Transverse beam sizes were measured on SC2 and SC3 as a function of plasma density n_p .

Fig. 3 gives the results of experiments and calculations; the solution of

$$\beta''/2 + K\beta - (1 + \beta'^2/4)/\beta = 0,$$

where $K = 2\pi r_e n_p / \gamma$. This focusing is stronger than that predicted by simulation.

3.2 Two Beam Experiments

The beam energies of drive beams and test beams were 26.76 MeV and 15.98 MeV, respectively, and the respective

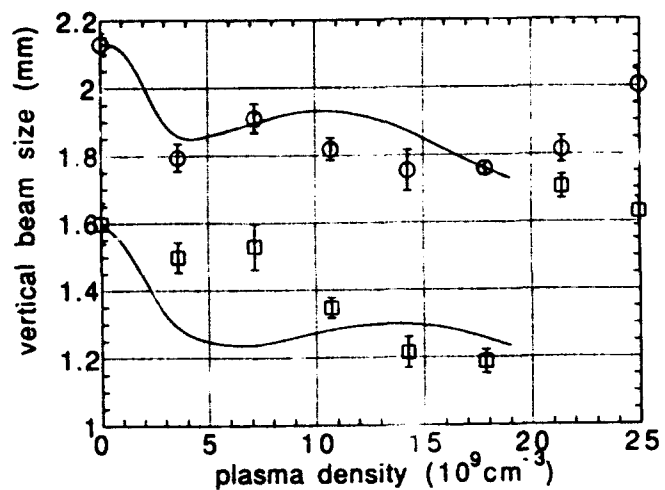


Figure 3: Plasma density dependence of beam sizes on SC2 and SC3. The lines show results of analytical calculation.

charges in each bunch were 300 pC and 15-30 pC. Vertical and horizontal beam sizes of the drive bunch at SC1 are 1.99mm and 0.94mm, respectively, and those of the test bunch were 0.79mm and 0.70mm. Transverse centroids of the two beams coincided at SC1, but they differed 0.5mm vertically and 0.2mm horizontally at SC2.

Beam images on SC5 were observed as a function of time delay between drive and test bunches. A remarkable observation is a periodical, horizontal split of the test bunch, which is shown in Fig. 4. Such an effect would be expected given the incomplete overlap of the two beams. The horizontal distribution is assumed to be sum of two Gaussian distributions. Delay dependence of the centroids of the two components obtained by the least square fit is given in Fig. 5. As for the vertical distribution, the mean and the standard deviation are calculated, which are given in Fig. 6 as position and spread.

The delay dependences were fit to the equation

$$f(t) = e^{-t/\tau} [a_1 \sin(\omega t + \phi_1) + a_2 \sin(2\omega t + \phi_2)].$$

The $\sin 2\omega t$ term is phenomenological, included to improve the fit. The following is a discussion of the parameters in this equation.

1) ω gives the plasma frequency. The plasma density derived from the ω value of the delay dependence of the vertical position is $1.46 \times 10^{11}\text{cm}^{-3}$. This is quite consistent with the value given by the Langmuir probe, $1.5 \times 10^{11}\text{cm}^{-3}$.

2) τ gives the damping time of the oscillation. The same curve gives 3.69nsec. This is very fast.

3) The vertical position is varied only by the transverse wakefield, while the horizontal positions are varied both by the transverse and longitudinal wakefields. Panofski-Wentzel theorem tells there should be $\pi/2$ difference between these two wakefields. Let us consider only the $\sin(\omega t + \phi_1)$ term. The vertical position of Fig. 6 is approximated as $\sin(21.96t - 0.249)$, where t is in nsec. The

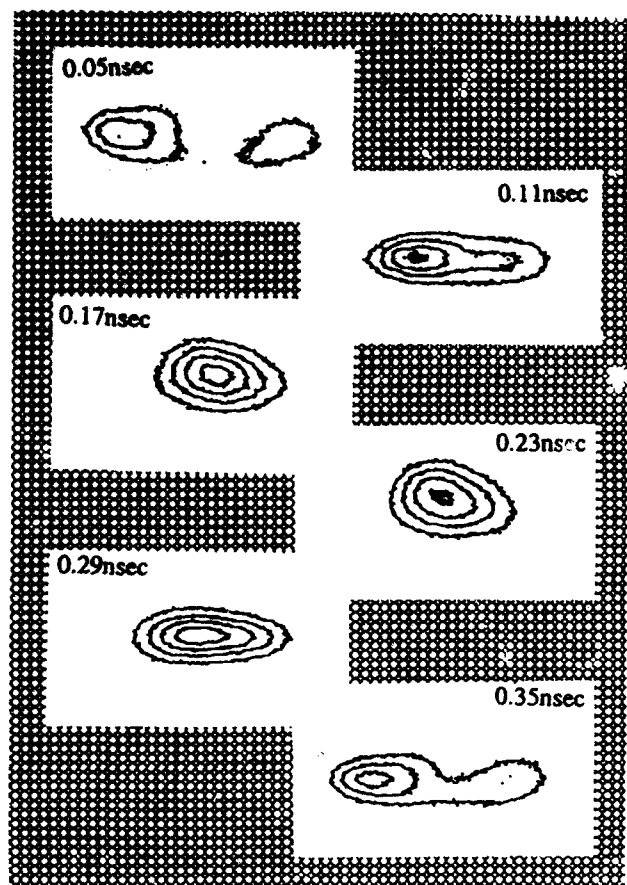


Figure 4: Typical images on SC.

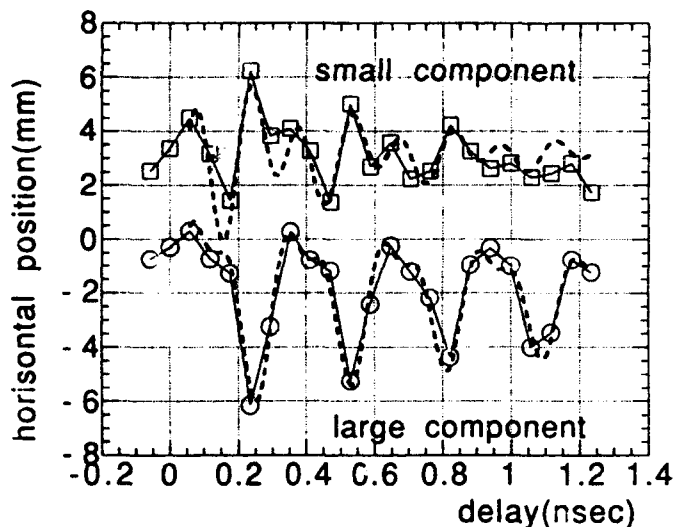


Figure 5: Delay dependence of the horizontal centroid shift of two components.

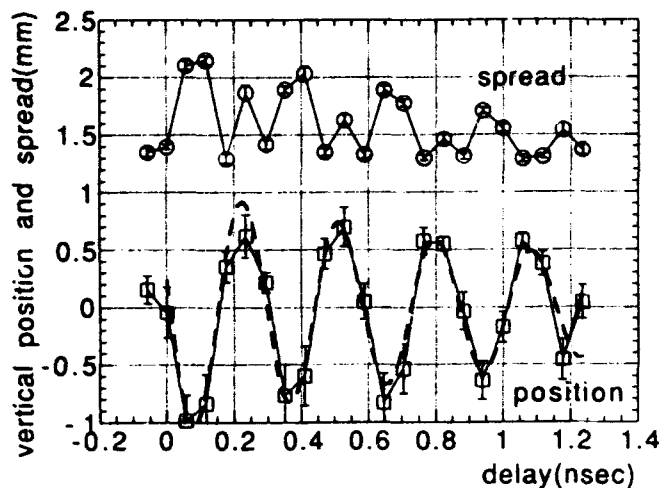


Figure 6: Delay dependence of the vertical position and spread.

small component of Fig. 5 is approximated as $\sin(21.15t - 1.22) = \sin(21.96t - 0.249 - 0.97)$ while the large component is $\sin(22.47t - 0.85) = \sin(21.96t - 0.249 - 0.60)$. The coefficients of t are regarded as the same values. Using the equality $a_i \sin(\omega t + \phi_1) + a_l \cos(\omega t + \phi_1) = (a_l^2 + a_i^2)^{1/2} \sin(\omega t + \phi_1 + \psi)$, $\tan \psi = a_l/a_i$, we can derive the ratio between longitudinal and transverse wakes a_l/a_i from the ψ values. The small component gives $a_l/a_i = \tan(-0.97) = -1.45$ while the large component gives -0.684 .

4) We can derive amplitudes of longitudinal wakefields from a_l and a_i values, which are around 100keV, consistent with the predictions of linear theory.

4 CONCLUSION

Plasma lens and plasma wakefield acceleration experiments were conducted on colinear wakefield test facility. Plasma focusing in the underdense regime was demonstrated. In the acceleration experiments, beam images were observed as a function of time delay between drive and test bunches at the end of an energy analyzer. A periodic, horizontal split of the test bunch is observed. The plasma oscillation decayed with a very short time constant; a few ns. A $2\omega_p$ component also appeared in the oscillation.

5 REFERENCES

- [1] H. Nakanishi *et al.*, Nucl. Instr. Meth., in press.
- [2] K. Nakajima *et al.*, Nucl. Instr. Meth. A292(1990)12.
- [3] Y. Nishida *et al.*, IEEE Trans. Plasma Sci. PS-15(1987)243.
- [4] H. Nakanishi *et al.*, Phys. Rev. Lett. 66(1991)1870; Y. Yoshida *et al.*, Part. Accel. 39(1992)77.

Plasma Focusing of the Final Focus Test Beam*

S. Rajagopalan*

Stanford Linear Accelerator Center, Stanford University, Stanford, CA 94309

Abstract

The focusing of the Final Focus Test Beam by means of a plasma is studied by means of models, based on theory and simulation. A set of parameters for a test of various aspects of plasma focusing is presented with attention to the limitations of diagnostic schemes available presently at the FFTB.

I. INTRODUCTION

Plasma focusing devices are compact, simple, and very strong focusing elements. The focusing strengths for typical parameters are equivalent to $\sim 10^9$ Gauss/cm focusing magnets. In principle, such strong fields are capable of focusing beams to very small spot sizes. Several proof-of-principle experiments using low density particle beams have demonstrated plasma focusing. The goal in this paper is to define a set of parameters for a plasma lens test using the FFTB. The results will be of interest for SLC and the next generation high energy linear colliders.

For our purposes, the focusing nature of the interaction can be understood using the following arguments without detailed mathematical analysis: The beam particles carry charge and current. For a relativistic beam in vacuum the electric repulsion is almost neutralized by the magnetic attraction among the particles. The introduction of the beam into the plasma results in a response that neutralizes the intrusion as much as possible. The charge neutralization takes place primarily by the fast motion of the plasma electrons and the current neutralization occurs due to the development of the "return current" in the plasma. The resulting large electric and magnetic fields both accelerate and focus trailing particles. For a single bunch the head can excite the plasma and focus the main body of the bunch.

II. Model of Focusing

The focusing strength of a plasma lens depends on whether it is underdense or overdense. When ignoring the effects due to the return current, the focusing strength for underdense lenses is governed by the plasma density n_p ,

$$K = \frac{2\pi r_e}{\gamma} n_p,$$

* Work supported by the U.S. Department of Energy under contract DE-AC03-76SF00515 and grant DE-AS03-88ER40381.

* Visitor from Department of Physics, UCLA, Los Angeles, CA 90024.

whereas for overdense lenses the strength is determined by the beam density n_b ,

$$K = \frac{2\pi r_e}{\gamma} n_b.$$

However the formula for an overdense plasma is true only in the extreme where the period of plasma oscillations is much smaller than the time of passage of the beam and the amplitude is much smaller than the beam radius. The change in beam density is taken into account as the beam propagates in the plasma. The equation used for the beta function is

$$\beta''' + 4K\beta' + 2K'\beta = 0$$

The boundary conditions are that β and β' are continuous and at the boundary of the lens the quantity $\beta'' + 4K\beta$ jumps by $2\Delta K\beta$, where ΔK is the discontinuity in K . The beta function can be found by numerically integrating with the proper boundary conditions and plasma regimes.

The longitudinal variation of beam density is taken into account by calculating the beta functions of different slices of the beam. In the regime where the focusing dynamics changes from underdense to overdense there is a transition where the oscillation of the plasma gives rise to focusing beyond the limit imposed by the beam density. This is seen to be true upto a density ratio of plasma to beam of 2. Therefore a conservative model limits the focusing strength to twice that from a plasma of density twice the beam. This is true for the range of beam densities under study.

The transverse variation in focusing strength due to incomplete expulsion of plasma electrons is not included in this model. Like the longitudinal effects this affects only the tails of the distribution. One transverse effect, that of return currents in the extreme overdense case is included and the effect for Case C is in Table 1. This flows outside the beam in all other cases and can be ignored except in case C where the plasma oscillations are much faster than the time of passage of the beam and the current penetrates the beam volume.

The evolution of the integrated beam sizes in Case A thru E are calculated with the effects of the longitudinal variation included, as shown in Figures 1 thru 5 respectively.

III. Round Beam Focusing

The plasma is created by an intense laser beam before the arrival of the particle beam bunch. The gas target density will be varied to cover all regimes of the plasma lens from underdense to overdense and to the

regime where the effect of current neutralization can be observed in the focusing. The optimized lens conditions will be capable of demonstrating the focusing of a $5\text{ }\mu\text{m}$ round beam to a final spot size of about $2\text{ }\mu\text{m}$. A fully coupled "round beam" in the FFTB line is assumed to have the normal FFTB population of 1×10^{10} per bunch at 10 Hz. The results are summarised in Table 1 below.

Table 1

Beam	A	B	C
$\mathcal{E}[\text{GeV}]$	50	50	50
$N[10^{10}]$	1.0	1.0	1.0
$\epsilon_n[10^{-5}\text{m} - \text{rad}]$	3.0	3.0	3.0
$\beta_0^*[cm]$	7.5	7.5	7.5
$\sigma_{r0}^*[\mu m]$	4.74	4.74	4.74
$\beta_0[cm]$	8.03	8.03	8.03
$\sigma_0[\mu m]$	4.91	4.91	4.91
$\sigma_z[mm]$	0.47	0.47	0.47
$n_{b0}[10^{16}\text{cm}^{-3}]$	5.3	5.3	5.3
Lens			
$n_p[10^{17}\text{cm}^{-3}]$	0.2	1.0	10
$k_p\sigma_z$	12.5	28.0	88.5
$s_0[cm]$	-2.0	-2.0	-2.0
$l[cm]$	0.3	0.3	0.3
$f[cm]$	3.80	2.92	3.60
Focused Beam			
$\beta_r^*[mm]$	3.7	2.1	3.4
$\sigma_r^*[\mu m]$	3.35	2.55	3.23
$s^*[cm]$	1.95	1.07	1.75

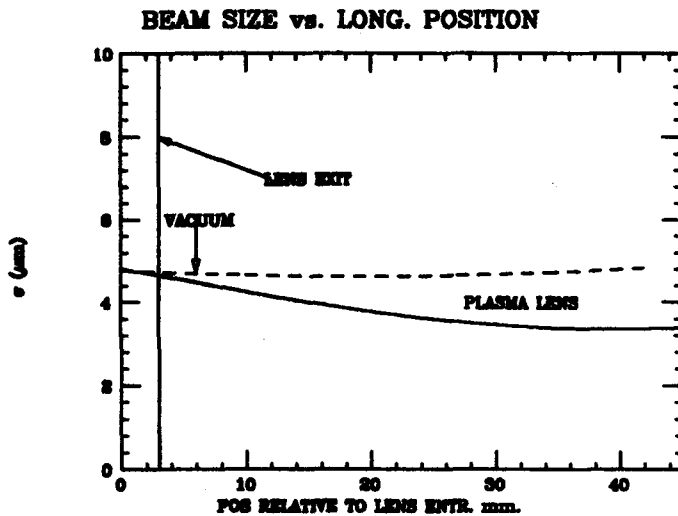


Figure 1. Underdense lens. Solid line includes long. effects. Dashed line is vacuum and dotdash is plasma lens without aberrations.

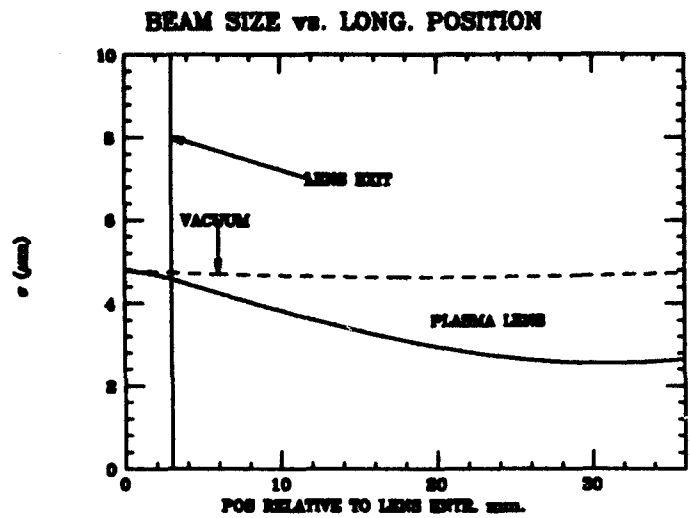


Figure 2. Mostly undersense lens. Solid line includes long. effects. Dashed line is vacuum and dotdash is plasma lens without aberrations.

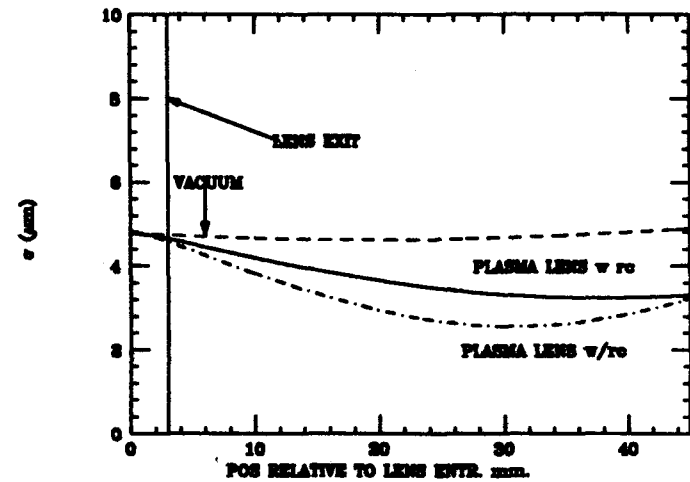


Figure 3. Overdense lens. Solid line includes long. effects. Dashed line is vacuum and dotdash is plasma lens without aberrations. The spot size is degraded due to return currents from $2.55\text{ }\mu\text{m}$ to $3.23\text{ }\mu\text{m}$.

IV. Flat Beam Focusing

This is to study the focusing of the beam with a laser-ionized plasma and also a beam-ionized plasma. The bunch population is increased to 2.5×10^{10} per bunch while maintaining the aspect ratio of the FFTB i.e., $\epsilon_{nz}/\epsilon_{ny} = 3 \times 10^{-5}\text{m} - \text{rad}/3 \times 10^{-6}\text{m} - \text{rad}$. This will help to improve the impact ionization probability and to reach the tunneling ionization threshold. Two cases are presented for testing focusing by tunnelling ionization and to focus better than the FFTB. The former case has a relaxed beta function for the y direction to prevent a rapid blowup of the beam. The results are summarised in Table

2 below.

Table 2

Beam	D	E
$N[10^{10}]$	2.5	2.5
$\epsilon_{ns}/\epsilon_{ny}[10^{-5}\text{mrad}]$	3.0 / 0.3	3.0 / 0.3
$\beta_{s0}/\beta_{y0}[\text{mm}]$	3.0 / 3.0	3.0 / 0.12
$\sigma_{s0}^*/\sigma_{y0}^*[\text{nm}]$	1000 / 333	1000 / 60
$\beta_{s0}/\beta_{y0}[\text{mm}]$	4.33 / 4.33	4.33 / 33.5
$\sigma_{s0}/\sigma_{y0}[\text{nm}]$	1200 / 400	1200 / 1000
$n_{s0}[10^{18}\text{cm}^{-3}]$	7.7	2.8
Lens		
$n_p[10^{18}\text{cm}^{-3}]$	2.0	2.5
$s_0[\text{mm}]$	-2	-2
$l[\text{mm}]$	1	1
Focused Beam		
$\beta_s^*/\beta_y^*[\text{mm}]$	0.90 / 0.90	0.75 / 0.047
$\sigma_s^*/\sigma_y^*[\text{nm}]$	520 / 165	480 / 38
$s_s^*/s_y^*[\text{mm}]$	0.10 / 0.10	-0.12 / -0.63

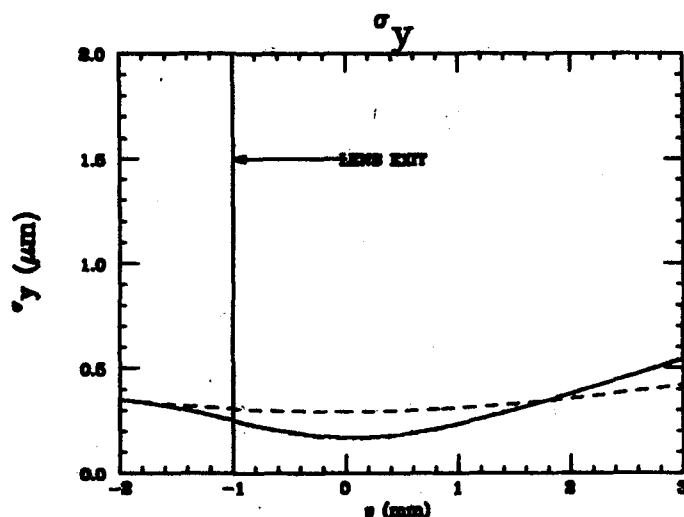


Figure 4. Focusing with a beam-ionized plasma produced with a relaxed β_y .

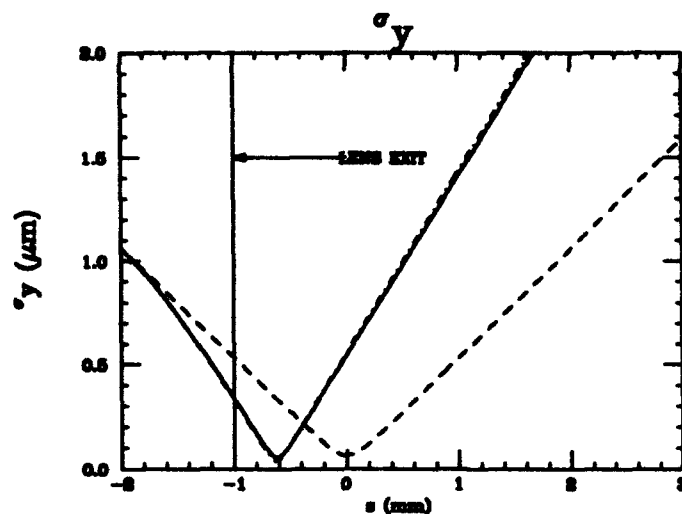
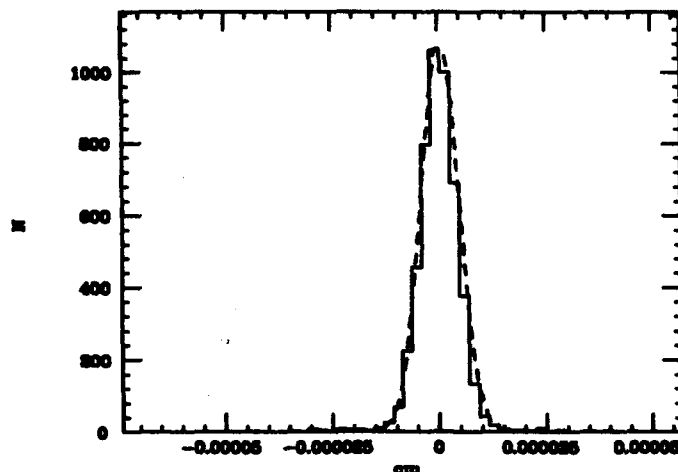


Figure 5. Focusing to improve on the FFTB. Longitudinal effects degrade σ_y^* to 55 nm. But a plot of the particles shows the core is best fitted by a Gaussian with σ between 40 and 45 nm. This can be distinguished from 60 nm by the Compton backscattering monitor. Histogram of particles at Focal Point



V. Comments

The plasma lenses in our experiments produce beam sizes in the range of $\sim 40 \text{ nm} - 4 \text{ }\mu\text{m}$, thus beam size and profile measurements over this range will be required. For Case A thru C the focused beam sizes are in the $\sim 2 - 4 \text{ }\mu\text{m}$ range and can be conveniently measured with a wire scanner. The beam sizes are determined from the bremsstrahlung yields as the electron beam is scanned across micron sized fibers. The sub-micron focused beam sizes for Case D and E can be measured with a Compton Backscattering monitor. I would like to acknowledge help and comments from P. Chen, R. Ruth, P. Kwok, D. Cline and others whom space precludes mention.

VI. REFERENCES

All the references contained in "Plasma lens Experiments at the Final Focus Test Beam" in these same proceedings.

Emittance Growth in MEB and Its Control

Y. Huang, S. Machida, and R. Gerig
Superconducting Super Collider Laboratory*
2550 Beckleymeade Ave., Dallas, TX 75237

Abstract

There are effects in the Medium Energy Booster (MEB) of SSC which will lead to growth of the transverse beam emittance. Among them are space charge, decoherence due to residual chromaticity and nonlinearity of field, coherent instabilities, etc. This paper numerically estimates the strength of these effects on the beam stability and the emittance growth. To ensure that the emittance growth is within the stringent emittance budget of the SSC accelerator complex, a few feasible cures have been planned. Their improvements on beam quality are also described in this paper.

I. INTRODUCTION

The transverse emittance preservation in the SSC accelerator complex is essential to achieve the luminosity goal. A very stringent emittance budget has then been imposed on the MEB; namely 0.6π mm-mrad (rms. normalized) at injection and 0.7π mm-mrad at extraction. The allowed increase is only 17%. Therefore, care must be taken in our design study to: include all possible sources which might contribute to the emittance growth, predict their strength, and implement some precautions to control this growth within the above limitation. Table 1 lists the main beam parameters of MEB.

In general, the following factors in the MEB should be included in the study for the emittance growth control:

- A) multipoles in magnetic field;
- B) space-charge tune spread at injection and transition;
- C) decoherence due to residual chromaticity and nonlinearity of fields when the beam is injected with transverse errors;
- D) coherent instabilities, etc.

A computer simulation of the beam has been performed to examine the effect of the factor A on the emittance growth. Five thousands particles in the six-dimensional Gaussian distribution are tracked up to four thousands turns after injection. All multipoles in the dipoles and quadrupoles as well as alignment errors, which are specified by SSC documents[1], are included in the calculation. The result does not show any significant increase in either horizontal or vertical emittances. The discussions of other

Table 1
Main beam and machine parameters of MEB

Parameters	Value
Injection Momentum	12 GeV/c
Extraction Momentum	200 GeV/c
Harmonic Number	792
Bunch Spacing	5 m
Bunch Density	1×10^{10} proton
95% Bunch Area at Injection	0.038 eV-Sec.
Bucket Area at Injection	0.43 eV-Sec.
Chromaticity Natural	-31.0
$\frac{\partial p}{p}$ at injection	2.16×10^{-4}
Transition Gamma	23.28
Betatron Tune(H)	25.43
Betatron Tune(V)	25.46

factors (B, C, D) will be the subjects of the following paragraphs, which are based on either computer modeling or scaling law.

II. SPACE CHARGE TUNE SPREAD AND CHOICE OF OPERATING POINT

The repulsive electric force produced by the beam itself often can not be ignored, resulting in the betatron tune of the particles being depressed. The maximum tune shift from the bare tune is given by Laslett formula for the Gaussian distribution:

$$\Delta\nu = -\frac{r_p n_t B_f}{4\pi\beta^2\gamma^3\epsilon^{un}}$$

where, r_p is the classical proton radius, n_t is the total number of particles in the ring, β and γ are the Lorentz factors, ϵ^{un} is the unnormalized beam emittance, and B_f is the bunching factor, which is the ratio of peak beam intensity to the average around the ring. For MEB the value is -0.083 at injection and becomes smaller at higher energy. This shift may make the beam cross lower-order resonances. In a real machine, where errors exist, the particles can be lost, or the beam emittance can grow when the tune approaches one of these resonances. Fig. 1 shows the tune diagram near the fractional operating points of MEB. The initial operating point was tentatively set to (25.42, 25.38). The location on the tune diagram is marked by the top square. Due to space charge effects the tunes of the particles spread

*Operated by the Universities Research Association, Inc., for the U.S. Department of Energy under Contract No. DE-AC35-80ER40486.

out downward on the plane. The particles near the center of bunch are depressed the most, reaching point on the diagram (25.34, 25.30); very close to the horizontal third-order resonance. While some outer particles in the beam would fall in the vertical third-order region. The beam simulation code, SIMPSONS[2] indicates that there is an increase in both horizontal and vertical emittances, and this increase in the vertical plane can reach approximately 10% when the MEB injection process is finished. In addition, there is another problem found with the operating point. That is, the tune distribution with particle amplitude is spread downward along the diagonal on the diagram due to the effect of the difference resonance $\nu_x - \nu_y = 0$, where, ν_x and ν_y are the horizontal and vertical tunes, so that the linear aperture is reduced much.

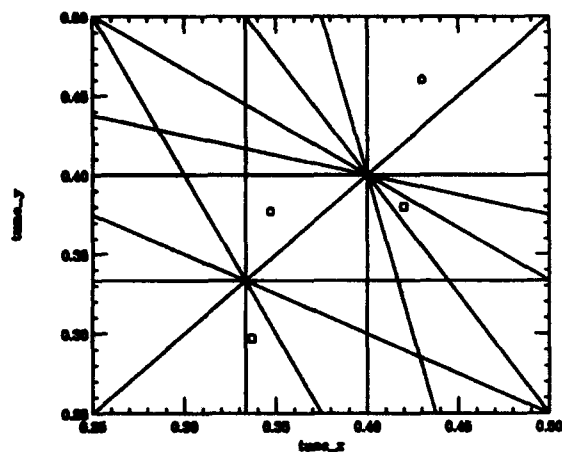


Figure 1. Tune diagram near the operating points

To solve the above problems, the operating point has been adjusted from (25.42, 25.38) to (25.43, 25.46) as marked by the circle on the diagram. Third integer resonances are hereby avoided, even with space charge included. The simulation shows no significant growth in emittances.

When the beam crosses the transition energy, the bunches become much shorter. The bunching factor increases from 8.1 to about 65. Using the Laslett formula expressed above, the maximum tune shift due to space charge is 0.19, twice the value at injection. However, this expression does not recognize the component of the beam size due to the combination of dispersion and momentum spread. At transition this contribution to beam size is larger than the contribution from betatron motion. Otherwise the shift is even smaller than the injection value according to our calculation. Fig. 2 shows the transverse emittance evolution around transition with space charge and its image force included. Both horizontal and vertical emittance are stable except that there are compensatory emittance oscillations between the two planes. It is obviously caused by difference resonance.

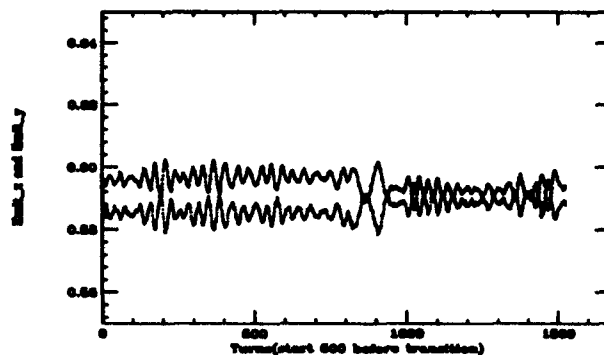


Figure 2. Transverse emittance around transition

III. DECOHERENCE AND SUPPRESSION OF INJECTION ERROR

When a beam is injected with a departure from the closed orbit, it begins making betatron oscillations about the closed orbit. If the beam contains a spread of tunes, the motion will decohere as the individual betatron phases of the particles disperse. The phase space distribution of the beam spreads from a localized bunch to an annulus which occupies all betatron phases[3]. In MEB, the injection errors come from the LEB extraction system(kicker, septum), MEB injection kicker and other elements on the beam transition line. The statistical errors at the injection point are 0.7 mm in horizontal plane and 1.1 mm in vertical plane. The emittance dilution factors, which are defined by

$$F \equiv \frac{\delta\epsilon}{\epsilon} = \frac{\pi}{2} \frac{\Delta x^2 (\beta\gamma)_{Lorenz}}{\beta\epsilon},$$

will be 20% in horizontal plane and 85% in vertical plane. Here, Δx is the equivalent injection error given above. The β function at the injection point are 51 m and 14.4 m in the both planes, respectively.

A damper has been specified for killing the coherent oscillation due to the injection errors. The damping speed should be much faster than the dilution time which is expressed by $\tau_D = \frac{1}{\Delta\nu}$. Where $\Delta\nu$ is the tune spread in the beam. In MEB, there are two sources of the betatron tune spread: transverse nonlinearity (tune as a function of particle amplitude) and nonzero chromaticity (tune as a function of momentum spread through $\Delta\nu_c = \xi \frac{\Delta p}{p}$). According to our simulation, the latter effect dominates. Suppose residual chromaticity is -5.0, then the emittance will be diluted completely within 310 turns. So an damping period of 25 turns is good enough for limiting the emittance dilution.

IV. COHERENT INSTABILITIES AND CURES

The interaction between the charged beam and the environment (wake field) might excite many different coher-

ent oscillations in the beam. In some case it can lead to the transverse emittance growth and even a beam loss. By their original mechanism, the coherent instabilities in MEB may be classified into three categories: single bunch caused by the broad band impedance, couple bunch by the high-Q impedance of RF cavity and resistive wall by the non-purely conductive vacuum pipe. A code ZAP[4] has been used to estimate the threshold value or growth time of these instabilities. Around transition, where the theoretical mode used in ZAP no longer works well, the six-dimensional tracking code SIMPSONS is used, as well as the two-dimensional code ESME[5].

Many efforts have been made in the design to reduce the broad band impedance of MEB. These include shielded bellows and screened pump ports, etc. As a result of these efforts, the broad band impedance is expected to be reduced to 1.65 MOhm/m. Our study indicates that there is big margin of the impedance budget in comparison with the threshold value of the single instability(36 MOhm/m at the injection).

However, the beam in MEB does have a problem with the coupled bunch instability which is caused by the transverse high-mode impedance inside RF cavity. Fig. 3 gives the growth time of the instability over the full RF cycle. As denoted by the bottom curve in the figure, the growth time is about 1 second. This obviously can not be tolerated, considering the beam will circulate in the ring for 5 second. A HOM damping scheme is then proposed. A significant improvement on growth time can be seen in the top curve in Fig. 3 where a few major impedance peaks have been damped by a factor of 10.

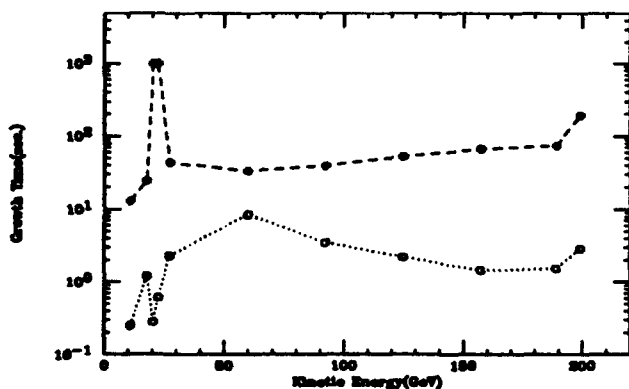


Figure 3. Transverse couple bunch instability growth time

The resistive-wall instability belongs to family of the coupled bunch instabilities. It may be triggered in many different modes. For MEB, the lowest mode frequency is 41KHz with the fastest growing time of 2.5ms and the highest mode is about 30MHz. To suppress this instability, a feed-back system has been planned. It will consist of beam position monitor, electronic processing, time delay, filter and kicker. To guarantee the functionality, the main properties of the system have been set as follows:

bandwidth: 30KHz-15MHz
deflection: $3.2\mu\text{rad/turn}$, at $P_{inj}=12\text{GeV}/c$
damping period: 25 turns
acceptance: 2mm
peak power: 700W

Special attention has been paid to the transition region of the MEB where the dynamic process is nonadiabatic. As the phase slip factor, $\eta \equiv \frac{1}{\gamma^2} - \frac{1}{\gamma_0^2}$, approaches zero, less Landau damping is provided. Since the chromaticity is not zero in a real machine, a large shift in coherent mode frequencies, which is estimated through $\omega_\xi \equiv \xi \omega_0 \nu_0$, occurs, where ξ is chromaticity, ω_0 is the revolution frequency and ν_0 is the betatron tune. So a strong coupling of $m=0$ mode to the resistive part of the broad band impedance can be expected, as indicated by Jacques Gareyte[6]. One cure to this head-tail instability is a chromaticity-jump. By reversing the sign of the chromaticity before and after transition correctly, one can guide the shift to the right direction so to avoid the coupling. This technique has been successfully implemented in both the main ring of Fermilab and the PS at CERN.

V. CONCLUSION

In the MEB, there will be many different sources which might lead to a transverse emittance growth. To limit this growth within a stringent tolerance is very challenging. Studies indicate that, with a good machine design and some necessary precautions it is still possible to achieve the goal of the SSC: high luminosity with a low transverse emittance.

VI. REFERENCES

- [1] SSCL, "Element specification for the medium energy booster accelerator of the superconducting super collider," (1992).
- [2] S. Machida, "The Simpsons Program, 6D phase space tracking with acceleration." Proceedings of the Computational Accelerator Physics Conference, (San Francisco), 1993.
- [3] R. E. Meller, A. W. Chao, etc., "Decoherence of kicked beams," SSC-N-360, (1987).
- [4] Michael S. Zisman, etc., "ZAP USER's Manual", LBL-21270, (1986).
- [5] S. Stahl and J. MacLachlan, "User's guide to ESME v.7", (1991).
- [6] Jacques Gareyte, "Observation and correction of instabilities in circular accelerators", CERN SL/91-09(AP).

Longitudinal Diffusion as Inflicted by Arbitrary Band-Width Random-Modulated Currents in Feeders of Detuned Cavities

Sergei Ivanov
Institute for High Energy Physics
Protvino, Moscow region, 142284, Russia

Abstract

Diffusion coefficient for a bunched p-beam in a synchrotron is presented with two technically imposed items included into the scheme. (1) The role of basic external noises is attributed to random envelopes $i^{(a,\varphi)}(t)$ carried by two modulated time-quadrature RF-currents. These represent amplitude, (a) or (small) phase, (φ) noises of forward current in cavity feeders. (Commonly, the (a, φ)-noise voltages $v^{(a,\varphi)}(t)$ at the accelerating gaps are taken as the basic ones.) Phase shifts between spectral components $v(\omega)$ vs. $i(\omega)$ are inevitable due to both, the transfer function from feeder current to the detuned-cavity gap voltage, and the phasor diagram of the gap voltages maintained under beam loading. None of the 'pure' noises $v^{(a)}(t)$ or $v^{(\varphi)}(t)$ is observable practically. Only their mixture is. (2) The possibility of an arbitrary ratio of the noise correlation time to the revolution period (i.e., the effect of noise spectrum to stretch over many revolution frequency harmonics) is incorporated, which is important to treat the noise-induced diffusion in the large rings (UNK, LHC, SSC).

I. INTRODUCTION

A. Diffusion Equation

Longitudinal dilution of a proton bunch subjected to noise obeys a diffusion equation which according to, say, ref.[1] reads

$$\frac{\partial \langle F_0 \rangle(\mathcal{J}, t)}{\partial t} = \frac{\partial}{\partial \mathcal{J}} \left(D(\mathcal{J}) \frac{\partial \langle F_0 \rangle(\mathcal{J}, t)}{\partial \mathcal{J}} \right). \quad (1)$$

Here t is time; \mathcal{J} is action; F is bunch distribution; $\langle \dots \rangle$ is statistical average over noise ensemble; subscript '0' denotes the mathematical average over phase ψ , the canonical conjugate of \mathcal{J} . Variables (ψ, \mathcal{J}) are introduced in the phase-plane $(\vartheta, \vartheta' \equiv d\vartheta/dt)$, where $\vartheta = \Theta - \omega_s t$ is azimuth in a co-rotating frame; Θ is azimuth around the ring in the laboratory frame; ω_s is the angular velocity of a reference particle synchronous to the nominal RF. The origin $\vartheta = 0$ is put on the unperturbed reference particle of the bunch in question.

The diffusion coefficient is

$$D(\mathcal{J}) = A \sum_{m=-\infty}^{\infty} (mq)^2 \sum_{k, k_1=-\infty}^{\infty} \frac{I_{mk}^*(\mathcal{J}) I_{mk_1}(\mathcal{J})}{k k_1} \times \quad (2)$$

$$\times \int_{-\infty}^{\infty} \langle \Delta V_k(t) \Delta V_{k_1}^*(t - \tau) \rangle \exp(im\Omega_s(\mathcal{J})\tau) d\tau.$$

The beam is subjected to a random voltage $\Delta V(\vartheta, t)$ which is decomposed into $\sum_k \Delta V_k(t) e^{ik\vartheta}$, and eq.2 embeds time correlations of random amplitudes $\Delta V_k(t)$. Functions $I_{mk}^*(\mathcal{J})$ are the coefficients of series which expand a plane wave $e^{ik\vartheta(\mathcal{J}, \psi)}$ into sum over multipoles: $\sum_m I_{mk}^*(\mathcal{J}) e^{im\psi}$. Factor A is equal to

$$A = \frac{1}{2} \left(\frac{\Omega_0^2}{q^2 V_{\text{ext}} \sin \varphi_s} \right)^2. \quad (3)$$

Here Ω_0 is the small-amplitude synchrotron frequency (circular); q is the acceleration frequency harmonic number; V_{ext} is the nominal amplitude of accelerating voltage; φ_s is the stable phase angle ($\varphi_s > 0$ below transition, the synchronous energy gain being $eV_{\text{ext}} \cos \varphi_s$); $\Omega_s(\mathcal{J}) = d\psi/dt$ is the non-linear synchrotron frequency.

B. Representative Time Scales

The bunch had been matched and stationary until $t = 0$ when the noise was switched on. Diffusion approximation implies fluctuations $\Delta V(\vartheta, t)$ to be fast and weak:

$$\tau_{\Delta V} \ll \tau_{\text{diff}}, \quad (4)$$

where τ_{diff} is a rate measure of the noise-induced bunch dilution; $\tau_{\Delta V}$ is a correlation time of $\Delta V(\vartheta, t)$. Bunch evolution is pursued at $t \gg \tau_{\Delta V}$.

In general, $\Delta V_k(t)$ is a periodically unstationary stochastic process: its moments $\langle \Delta V_k(t) \Delta V_{k_1}^*(t - \tau) \rangle$ are periodic functions of t , $2\pi/\omega_s$ being a period. The slow diffusion is governed by the non-oscillating terms in $\langle \Delta V_k(t) \Delta V_{k_1}^*(t - \tau) \rangle$, these being extracted by t -averaging the latter over a turn (over-line in eq.2). The correlations thus smoothed depend on τ solely, and can hence be treated in terms of spectral intensities. Function $\langle F_0 \rangle(\mathcal{J}, t)$ is as well smoothed over a turn, being a slowly varying one:

$$2\pi/\omega_s \ll \tau_{\text{diff}}. \quad (5)$$

Refs.[2, 3, 4] study stationary noise $\Delta V(\vartheta, t)$ as given in the co-moving frame directly, which implicitly conjectures the noise's low-frequency and narrow-band features:

$$2\pi/\omega_s \ll \tau_{\Delta V} \ll \tau_{\text{diff}}. \quad (6)$$

However, with the orbit perimeters L growing (UNK, LHC, SSC) feasible are the relationships

$$2\pi/\omega_s \sim \tau_{\Delta V} \ll \tau_{\text{diff}}; \quad \tau_{\Delta V} \ll 2\pi/\omega_s \ll \tau_{\text{diff}}. \quad (7)$$

This paper presents formulae which hold true not only within the range given by eq.6, but well beyond it, eqs.7.

II. NOISES OF VOLTAGE

A. Accelerating Voltage

This field is imposed by N accelerating cavities (gaps),

$$E(\Theta, t) = L^{-1} \sum_{n=1}^N G_n(\Theta) V_n \cos(q' \omega_s t - \varphi_n). \quad (8)$$

Here V_n , φ_n are the amplitude and phase of voltage across the n -th gap; $q' \omega_s$ is the nominal RF — a (higher) harmonic of the acceleration frequency $q \omega_s$, $q'/q = 1, 2, \dots$

Functions $G_n(\Theta)$ specify the field localization. They can be decomposed into Fourier series $\sum_k G_{n,k} e^{ik\Theta}$. Given $\int_0^{2\pi} |G_n(\Theta)| d\Theta = 2\pi$, quantities $|G_{n,k}|$ grow into transit-time factors at $\omega = k \omega_s$. Variables V_n , φ_n are adjusted so as to provide propagating wave $V'_{\text{ext}} \cos(q' \vartheta + \varphi'_s)$, stationary w.r.t. the co-rotating frame. The main RF system drives a wave whose $(V'_{\text{ext}}, q', \varphi'_s) = (V_{\text{ext}}, q, \varphi_s)$.

B. Random Voltages

Put down the random field by analogy with eq.8 as

$$\Delta E(\Theta, t) = L^{-1} \sum_{n=1}^N G_n(\Theta) u_n(t) \quad (9)$$

with $u_n(t)$ being the noise voltage. Take the latter as

$$u_n(t) = \sum_{\zeta} v_n^{(\zeta)}(t) \cos(q' \omega_s t - \varphi_n^{(\zeta)}). \quad (10)$$

Here ζ is a noise type index. Carrier phase $\varphi_n^{(\zeta)}$ is, generally, other than φ_n from eq.8. Modulating voltages $v_n^{(\zeta)}(t)$, $\langle v_n^{(\zeta)}(t) \rangle = 0$ are the stochastic processes, mutually stationary w.r.t. the laboratory frame.

The particular option of indices $\zeta = a, \varphi$ and phases

$$\varphi_n^{(a)} = \varphi_n; \quad \varphi_n^{(\varphi)} = \varphi_n - \pi/2 \quad (11)$$

allows one to interpret eq.10 as a decomposition of $u_n(t)$ into a sum of its inphase ($\zeta = a$) and quadrature ($\zeta = \varphi$) components w.r.t. the reference signal, eq.8. The inphase component represents the noises of amplitude, while the quadrature one — those of phase,

$$v_n^{(a)}(t) = \Delta V_n(t); \quad v_n^{(\varphi)}(t) = V_n \Delta \varphi_n(t), \quad (12)$$

of the gap voltages. Either may be driven in a relatively independent way (noises in a master oscillator, an amplitude modulator, a phase shifter).

Adopting $q' = \varphi_n^{(\zeta)} = 0$ and, e.g., $\zeta = 1$ results in a particular case of gap noise voltage $u_n(t) = v_n^{(\zeta)}(t)$, stationary w.r.t. the laboratory frame (a shot noise of anode DC current in the tube, a ripple of its power supply).

C. Diffusion as Inflicted by Random Voltages

Inserting eq.10 into eq.2 yields

$$D(\mathcal{J}) = A \sum_{n,n_1=1}^N \sum_{\zeta, \zeta_1} \sum_{k, m=-\infty}^{\infty} \times \quad (13)$$

$$\times P_{nn_1}^{(\zeta, \zeta_1)}(k \omega_s + m \Omega_s(\mathcal{J})) V_{n;mk}^{(\zeta)}(\mathcal{J}) V_{n_1;mk}^{(\zeta_1)*}(\mathcal{J}).$$

The (mutual) spectral power densities $P_{nn_1}^{(\zeta, \zeta_1)}(\omega)$ are the Fourier transforms of voltage cross-correlations,

$$P_{nn_1}^{(\zeta, \zeta_1)}(\omega) = \int_{-\infty}^{\infty} \langle v_n^{(\zeta)}(t) v_{n_1}^{(\zeta_1)}(t - \tau) \rangle e^{i\omega \tau} d\tau. \quad (14)$$

Weight factors $V_{n;mk}^{(\zeta)}(\mathcal{J})$ specify the bunch excitation at the m -th multipole caused by spectral components of noise $v_n^{(\zeta)}(t)$ at frequency $\omega \simeq k \omega_s$:

$$V_{n;mk}^{(\zeta)}(\mathcal{J}) = (mq/2) \times \quad (15)$$

$$\times \left(\frac{I_{m,k+q'}^*(\mathcal{J})}{k+q'} G_{n;k+q'} e^{+i\varphi_n^{(\zeta)}} + \frac{I_{m,k-q'}^*(\mathcal{J})}{k-q'} G_{n;k-q'} e^{-i\varphi_n^{(\zeta)}} \right).$$

These functions depend on the carrier frequency $q' \omega_s$ and its phase $\varphi_n^{(\zeta)}$ w.r.t. the bunched beam. The presence of expansion coefficients $I_{m,k \pm q'}^*$ accompanied by transit-time factors $G_{n;k \pm q'}$ is quite explainable. Multiplication of $v_n^{(\zeta)}(t)$ by a high-frequency oscillation $\cos(q' \omega_s t - \varphi_n^{(\zeta)})$ translates spectral components $v_n^{(\zeta)}(t)$ from $\omega \simeq k \omega_s$ into a region of (higher) frequencies $\omega \simeq (k \pm q') \omega_s$ from which these affect the beam by driving its multipole oscillations.

For example, consider one gap ($n = N = 1$), a single noise source $v_n^{(\zeta)}(t)$ with $\zeta = a$ or φ whose spectrum is localized in a lower-frequency domain within a bandwidth $\Delta \omega_v \ll \omega_s$ so as to comply with eq.6:

$$P_{nn_1}^{(\zeta, \zeta_1)}(k \omega_s + \Omega) \simeq P_n^{(\zeta)}(\Omega) \delta_{nn_1} \delta_{\zeta \zeta_1} \delta_{k0} \quad (16)$$

with δ_{ij} being the Kronecker's delta-symbol. In this case eqs.13, 15 yield the results of refs.[2, 3, 4].

III. NOISES OF CURRENT

Noises of accelerating voltage are excited by those of RF-drive current in the gap feeders. The latter noises are more logical to deal with while specifying the noise tolerances on a practical, RF-engineering level.

A. Drive Current and Beam Loading Effect

To excite accelerating field, eq.8, the RF-generator drives a forward wave of current in the gap feeder. Let this wave be presented by a current

$$I_n \cos(q' \omega_s t - \phi_n) \quad (17)$$

which flows through, say, a coupling device between the feeder and the n -th gap. (Reflected-wave current does not enter this definition.)

The following phasor diagram of voltages is maintained under beam loading of the narrow-band gap

$$V_n e^{i\varphi_n} = T_n(q' \omega_s) I_n e^{i\phi_n} - 2T_n'(q' \omega_s) G_{n;-q'} J_{q'}. \quad (18)$$

Here $T_n(\omega)$ is a transfer function between Fourier transforms of the feeder current and the gap voltage thereby

excited. Transfer function $T_n^*(\omega)$ from the beam current to beam-induced voltage is such as to have $\text{Re} T_n^*(\omega) > 0$, and $T_n^*(\omega)|G_{n,q'}|^2$ to become a standard beam-gap coupling impedance at $\omega \simeq q'\omega_s$. Coefficient $J_{q'}$ is the one from Fourier series $J(\vartheta) = \sum_k J_k e^{ik\vartheta}$ with $J(\vartheta)$ being the stationary beam current. Given short bunches, $J_{q'} \simeq J_0$, where J_0 is the average beam current. Phase ϕ_n required to calculate $D(J)$ is readily extracted from eq.18:

$$\phi_n = \arg \frac{V_n e^{i\varphi_n} + 2T_n^*(q'\omega_s) G_{n,-q'} J_{q'}}{T_n(q'\omega_s) I_n}, \quad (19)$$

and $\phi_n \rightarrow \varphi_n - \arg T_n(q'\omega_s)$ when $J_{q'} \rightarrow 0$.

Standing-wave accelerating cavities are the most widely used ones, in which case

$$T_n(\omega) = \frac{2}{g} T_n^*(\omega); \quad T_n^*(\omega) = R_n \left(1 - i \frac{\omega^2 - \omega_{0n}^2}{2\omega \Delta\omega_n} \right)^{-1}, \quad (20)$$

where R_n , $\Delta\omega_n$ are the shunt impedance and bandwidth (both loaded ones); ω_{0n} is the resonant frequency; g is the gain in coupling-loop to accelerating-gap voltage transformation. An optimal cavity detuning ($\omega_{0n} \neq q'\omega_s$) exists which would offer a resistive load to the RF-generator and, hence, result in $\phi_n = \varphi_n$.

B. Random Currents

Noises in RF-feeding circuitry induce random addition $j_n(t)$ to the main current, eq.17. It drives voltage $u_n(t)$ across the n -th gap, eq.9. A feeder, a coupler and a gap are a linear and stationary circuit. Hence, the relation between $j_n(t)$ and $u_n(t)$ is linear and time-invariant:

$$u_n(\omega) = T_n(\omega) j_n(\omega) \quad (21)$$

with $T_n(\omega)$ being the same as in eqs.18, 20. To comply with eq.10, consider random-modulated current

$$j_n(t) = \sum_{\zeta} i_n^{(\zeta)}(t) \cos(q'\omega_s t - \phi_n^{(\zeta)}) \quad (22)$$

with $i_n^{(\zeta)}(t)$, $\langle i_n^{(\zeta)}(t) \rangle = 0$ being the stochastic processes, mutually stationary w.r.t. the laboratory frame.

Technically imposed system of basic perturbations is that of the amplitude and phase noises of drive current, eq.17, their cross-uncorrelated performance being quite feasible practically. To get these noises take $\zeta = a', \varphi'$ along with

$$\phi_n^{(a')} = \phi_n; \quad \phi_n^{(\varphi')} = \phi_n - \pi/2, \quad (23)$$

$$i_n^{(a')}(t) = \Delta I_n(t); \quad i_n^{(\varphi')}(t) = I_n \Delta \phi_n(t). \quad (24)$$

By taking $q' = \phi_n^{(\zeta)} = 0$ and, e.g., $\zeta = 1$ one arrives at the noise current $j_n(t) = i_n^{(\zeta)}(t)$, stationary w.r.t. the laboratory frame.

C. Diffusion as Inflicted by Random Currents

Using eq.21 one finds relation between the Fourier transforms of $v, i_n^{(\zeta)}(t)$:

$$v_n^{(\zeta)}(\omega) e^{\pm i\varphi_n^{(\zeta)}} = T_n(\omega \pm q'\omega_s) i_n^{(\zeta)}(\omega) e^{\pm i\phi_n^{(\zeta)}}. \quad (25)$$

A 'weak' stationarity of $v, i_n^{(\zeta)}(t)$ implies:

$$\langle v_n^{(\zeta)}(\omega) v_{n_1}^{(\zeta_1)*}(\omega_1) \rangle = 2\pi P_{nn_1}^{(\zeta\zeta_1)}(\omega) \delta(\omega - \omega_1); \quad (26)$$

$$\langle i_n^{(\zeta)}(\omega) i_{n_1}^{(\zeta_1)*}(\omega_1) \rangle = 2\pi Q_{nn_1}^{(\zeta\zeta_1)}(\omega) \delta(\omega - \omega_1). \quad (27)$$

Here $P_{nn_1}^{(\zeta\zeta_1)}(\omega)$ is the voltage noise spectrum, eq.14, while $Q_{nn_1}^{(\zeta\zeta_1)}(\omega)$ is that for the current noise; $\delta(\omega)$ is the delta-function. Eqs.25, 26, 27 allow one to express $P_{nn_1}^{(\zeta\zeta_1)}(\omega)$ through $Q_{nn_1}^{(\zeta\zeta_1)}(\omega)$. Inserting them into eqs.13, 15 yields

$$D(J) = A \sum_{n,n_1=1}^N \sum_{\zeta,\zeta_1} \sum_{k,m=-\infty}^{\infty} \times \quad (28)$$

$$\times Q_{nn_1}^{(\zeta\zeta_1)}(k\omega_s + m\Omega_s(J)) U_{n;m}^{(\zeta)}(J) U_{n_1;m}^{(\zeta_1)*}(J)$$

with 'current-wise' weight factors, cf. eq.15,

$$U_{n;m}^{(\zeta)}(J) = (mq/2) \times \quad (29)$$

$$\times \left(\frac{I_{m,k+q'}^{*}(J)}{k+q'} G_{n,k+q'} T_n [(k+q')\omega_s + m\Omega_s(J)] e^{+i\phi_n^{(\zeta)}} + \right.$$

$$\left. + \frac{I_{m,k-q'}^{*}(J)}{k-q'} G_{n,k-q'} T_n [(k-q')\omega_s + m\Omega_s(J)] e^{-i\phi_n^{(\zeta)}} \right).$$

Commonly, in beam dynamics studies, refs.[2, 3, 4], amplitude and phase noises of the gap voltages are treated as the basic ones, in which case eq.11 and $P_{nn_1}^{(a\varphi)} = P_{nn_1}^{(\varphi a)} = 0$ should be inserted into eqs.13, 15. However, from a practical standpoint the use of eqs.28, 29 with eq.23 and $Q_{nn_1}^{(a'\varphi')} = Q_{nn_1}^{(\varphi'a')} = 0$ looks more adequate. Thus, quite different expressions for $D(J)$ are arrived at.

For stationary noises $u, j_n(t)$, whose $q' = 0$, $\varphi_n^{(\zeta)} = 0$, and $\zeta = 1$, the entire distinction between eqs.13, 15 and eqs.28, 29 is reducible to a mere noise filtering: $P_{nn_1}^{(\zeta\zeta_1)}(\omega) = T_n(\omega) T_{n_1}^*(\omega) Q_{nn_1}^{(\zeta\zeta_1)}(\omega)$.

The author thanks Drs. V. Balbekov and G. Gurov for the instructive discussions on the subject.

IV. REFERENCES

- [1] S. Ivanov, *Preprints IHEP 92-43 & 93-14*, Protvino, 1992-93.
- [2] D. Boussard, G. Dôme, C. Graziani, *Proceed. of 11-th Int. Conf. on High-Energy Accel.*, CERN, Geneva, 1980, pp. 620-626.
- [3] G. Dôme, *CAS Proceed.*, CERN/84-15, Geneva, 1984, pp. 215-260.
- [4] S. Krinsky, J.M. Wang, *Part. Accel.*, 1982, Vol. 12, pp. 107-117.

Induced Beam Oscillations from Quadrupole Vibrations in the SLC Linac*

J. T. Seeman, R. L. Holtzapple, M. C. Ross

Stanford Linear Accelerator Center
Stanford University, Stanford, California 94309 USA

Abstract

Linac beams in the Stanford Linear Collider (SLC) were driven into oscillation by transverse vibration of lattice quadrupoles at about 7 Hz. These quadrupoles are centered on 12-meter support girders located early in the linac. The vibrations were caused by ground motion at the $0.06 \mu\text{m}$ level which was amplified in the accelerator supports up to $5 \mu\text{m}$. Seismic and support vibration measurements were Fourier analyzed and a strong correlation with beam observations was observed. Subsequent modifications of the supports have eliminated these oscillations.

Introduction

In the spring of 1992 the SLC positron beam exhibited a coherent betatron oscillation in the vertical plane apparently emanating from the damping ring or early linac. These oscillations had an amplitude of about one half the beam size at the end of the linac with a frequency of about 7 Hz. These oscillations caused occasional accelerator trips, prompting a search for the source. Since it was a positron beam problem and not electron, the positron damping ring and ring-to-linac transport line were investigated first for power supply, kicker, or vibration problems; but none were found. This result led to the investigation of the vertically focusing quadrupoles in the early linac. But again, no quadrupole power supply instabilities were found. Finally, the connection to vertically vibrating linac girders was made.

In the bulk of the linac the quadrupoles are placed at the end of the support girders (12 m long). The vibration for these quadrupoles mounted over the supports was measured and found to be about $0.06 \mu\text{m}$, which was safely under the desired tolerance^{1,2}. However, in the early linac additional quadrupoles were added in the center of the girders to increase the focusing and reduce the betatron functions. Thus, these quadrupoles (necessarily stronger because of the smaller spacing) were placed where vibration amplitudes could be larger. The reason the positron vertical measurements showed the largest effects is that the quadrupoles at the center of the girders had the largest vertical offsets and these quadrupoles are vertically focusing for positrons. Horizontal oscillations should have been visible for electrons, but other upstream difficulties clouded the observations.

Measured Beam Oscillations

The key beam evidence that the girders were vibrating came from position measurements from adjacent monitors early in the linac. Figure 1 shows beam oscillations of about $50 \mu\text{m}$ on two position monitors. The two monitors are very nearly 180° apart in betatron phase and should show identical but inverted oscillations. A frequency spectrum of this data shows a strong peak at a frequency of about 7 Hz as can be seen in Figure 2. The two data in Figure 1 are similar but definitely not just inversions of each other. Thus, the differences arose from changes between the two monitors located 24 m apart. For this region of the linac, the differences could only be explained by local quadrupole vibrations.

Measured Girder Vibrations

The girder which supports the lattice quadrupoles and

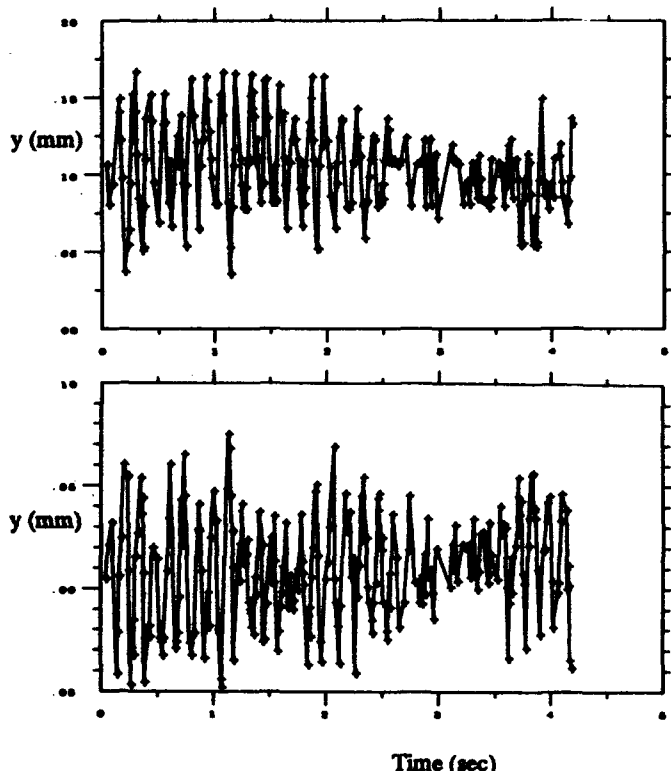


Figure 1 Observed positron vertical beam oscillations on two position monitors (LI03-321, LI05-521) with time. The two monitors are 180° apart in betatron phase about 120 m downstream of the damping rings. The energy is 2.8 GeV.

* Work supported by the Department of Energy contract DE-AC03-76SF00515.

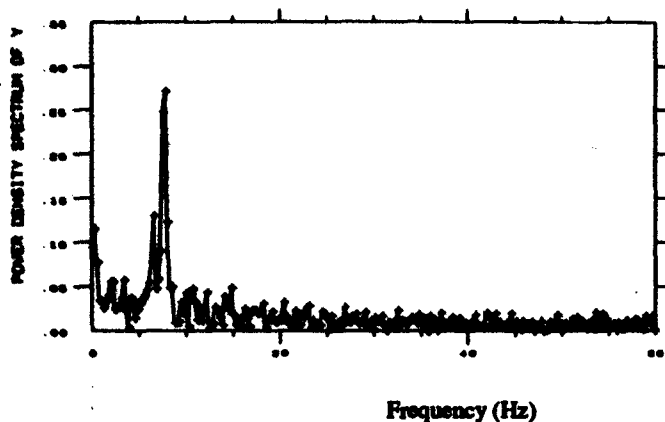


Figure 2 Frequency spectrum of the beam oscillation in the upper plot of Figure 1. Note the resonance at about 7 Hz.

accelerating structures is schematically shown in Figure 3. The ends are rigidly attached to the floor and wall but the center is free to vibrate, modified somewhat by loose connections to the tunnel from RF power feeds, cooling water connections, quadrupole power connections, vacuum pumping lines, and diagnostic cables.

To measure the girders, access to the tunnel was made under near running condition with the water pumps, helium compressors, and cooling towers operating. The vibrations of the girders were measured using a light-weight ICPTM 308B02 accelerometer³ with a 1v/g sensitivity and a frequency range of 1 to 3000 Hz. The signals were analyzed using an Hewlett-Packard Dynamic Signal Analyzer⁴ HP3560A. A typical signal measurement versus time is shown in Figure 4 and the frequency spectrum of that measurement is shown in Figure 5. Many girders were measured and the data are summarized in Table 1. The girder amplitudes and frequencies change slightly depending on their location. This is due in part to the changing driving forces from the tunnel which, in turn, depend on the distance and orientation from the sources (heavy pumps, etc.) and from external connections (RF feeds, water connection,...). Also note that the lightly loaded girders have slightly higher frequencies, e.g. Girders 2-1, 3-1, 3-2, and 3-3.

The combined effects of these vibrating girders on the beam trajectory can be calculated. The vertical position ΔY at a position monitor, say monitor LI03-321 as in Figure 1, is the sum of the contributions of the vibrations of all the quadrupoles upstream and the effects of the lattice transport.

$$\Delta Y(t) = \sum_{\text{quads}} R_{12} Q \Delta y \sin(2\pi f t) / B\rho$$

where R_{12} is the angle-to-position TRANSPORT element from the location of the vibrating quadrupole to the position monitor including energy changes. Q is the integrated strength of the vibrating quadrupole, Δy is the quadrupole vibration

amplitude, f is the vibration frequency, t is time, and $B\rho$ is the beam's magnetic rigidity. A calculation was done using the data in Table 1 to predict the beam data in the upper plot in Figure 1. The result of the calculation is shown in Figure 6. The amplitude and variability of the predicted beam position resemble strongly those seen with the real data.

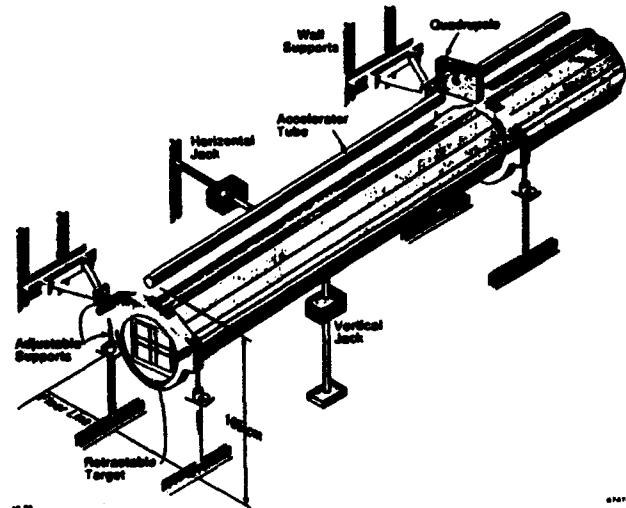


Figure 3 Schematic overview of the accelerator support girder.

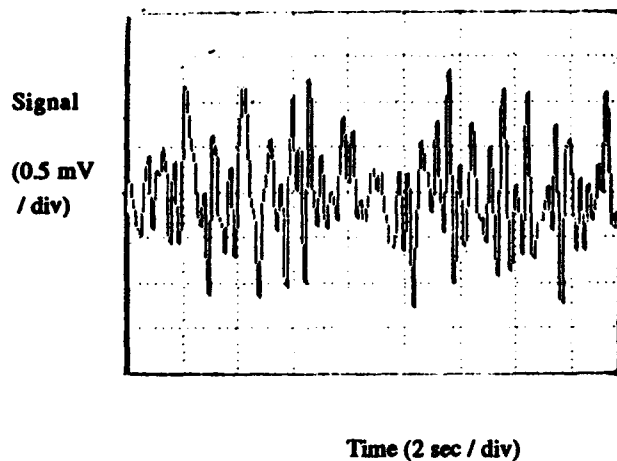


Figure 4 Measured vertical vibration of Girder 2-4 vs time.

The Cure: Girder Struts

The cure for these vibrations was to install horizontal and vertical mechanical struts (clamps) attached to the floor and wall near each quadrupole on the affected girders. A schematic view showing these struts at the girder center can be seen in Figure 3. After the strut installation the measured girder vibrations at 7 Hz were no longer visible as can be seen in Figure 7. However, vibrations appeared at higher frequencies

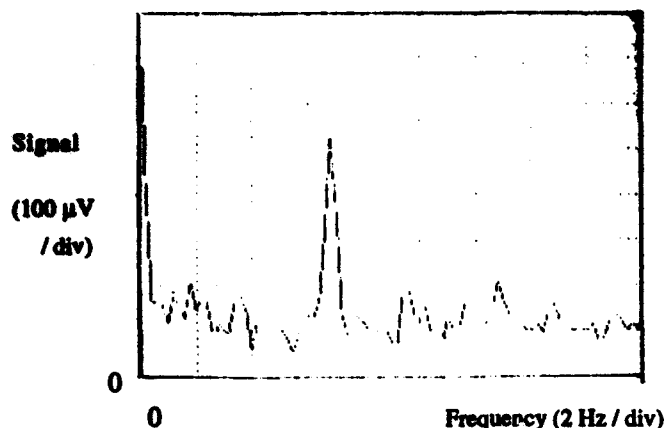


Figure 5 Vertical frequency spectrum of Girder 2-4 (Fig. 4).

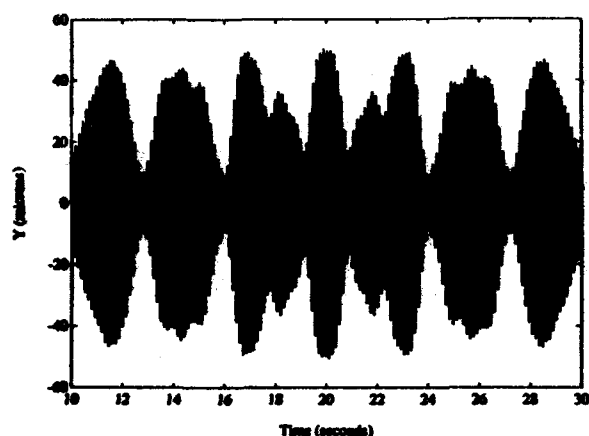


Figure 6 Predicted beam oscillation with time from the girder vibration data in Table 1 and the quadrupole lattice at the beam monitor in Fig. 1.

Table 1 Measured vibration frequencies and amplitudes of the centers of the first 11 girders (12 m each) of the linac using an accelerometer.

Girder number	Horizontal Frequency (Hz)	Horizontal amplitude (nm)	Vertical frequency (Hz)	Vertical amplitude (nm)
2-1	6.4	---	7.1	---
2-2	5.6	4000	6.4	1920
2-3	5.5	---	6.8	3200
2-4	5.6	1400	6.45	2000
2-5	5.4	1400	6.75	4000
2-6	5.7	680	6.6	2520
2-7	5.4	1200	6.7	3200
2-8	---	1600	6.6	2040
3-1	7.2	2800	7.75	4800
3-2	---	---	7.4	5600
3-3	---	---	8.0	7600

due to other modes of the structure and the installation orientation of the struts. Fortunately, the amplitudes of the vibrations at these higher frequencies are below the required tolerances. The consequences of the installation of the struts on the motion of the beam was immediate. The beam oscillations at 7 Hz were gone.

With the success of this linac effort, a search is now underway to look for smaller oscillations with signals at different frequencies coming from sources upstream of the linac.

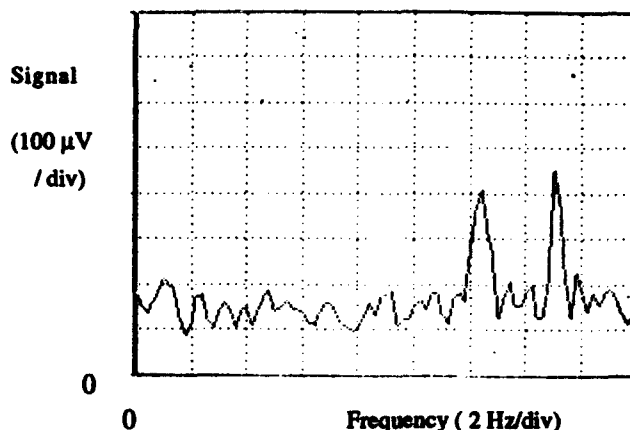


Figure 7 Measured vertical frequency spectrum of a girder with a center strut (clamp) installed. Note that higher frequencies appeared at 12-15 Hz, about twice the old resonant frequency.

Acknowledgments

The authors wish to thank the SLC Operations Staff for helping with the beam measurements. R. Pennacchi, K. Burrows, and members of the Mechanical Fabrication Department installed the girder struts.

References

- 1) R. Stiening, *How straight is the linac and how much does it vibrate?*, SLAC Note CN-42, Stanford, January 1981, (unpublished).
- 2) K. McLagan, *SLC Intergirder Quad Vibrations*, SLAC Note CN-271, Stanford, June 1984, (unpublished).
- 3) Piezotronic, Inc., 3425 Walden Ave., Depew, NY 14043.
- 4) Hewlett-Packard, Page Mill Rd, Palo Alto, CA 94305

Effects of Magnetic Focusing on Longitudinal Emittance and Energy Dispersion of an Intense Short Accelerating Electron Pulse

J.-M. DOLIQUE and J.C. COACOLO

Université Joseph Fourier-Grenoble I and CEA, Centre d'Etudes de Bruyères-le Châtel. France.

Abstract

Magnetic focusing by coils appropriately disposed and fed has been widely proposed and used as a transverse emittance recovering technique. In particular for the accelerating electron beam of FEL RF-photoinjectors. After a new investigation of the effect on radial emittance, we address the question of the consequences of magnetic focusing on longitudinal emittance and energy dispersion. With the theoretical method described in a previous article, the radial, transverse, longitudinal, and 3D- rms emittances of the whole beam pulse are computed from the cathode onwards, for sample beam parameters, and various magnetic field intensities. Obviously beneficial in terms of beam radius, magnetic focusing seems to induce only a moderate and transitory radial emittance reduction and, on the other hand, a strong degradation of longitudinal emittance and energy dispersion.

I. INTRODUCTION

The situation under consideration is the one which occurs for instance in the photoinjector of a high-intensity RF-FEL (e.g. [1]). A short (10-100 ps) intense (some hundred of A) electron beam, extracted from the cathode, is accelerated in a first RF cell, about 0.1 m long, from thermal energy to a few MeV. During extraction and at acceleration beginning, the beam undergoes radial expansion and radial emittance growth under the influence of strong self-field effects (often called space charge effects though they are not electrostatic but in fact intricate electromagnetic effects).

To focus the beam and remedy the emittance growth, a magnetic lens is often placed at photoinjector exit, before the beam enters further accelerating cavities. The beneficial effect on radial emittance of such magnetic focusing has been studied in various publications (e.g. [2]). We propose on the one hand to come back to this effect, and on the other hand to investigate the consequences of magnetic focusing for longitudinal emittance and energy dispersion.

II. THEORETICAL TOOLS

A. Self-field calculation

The theory has been described in [3],[4]. With view of an analytical study, the electromagnetic field introduced in the electron motion equation is calculated as a direct relativistic electron-electron interaction field obeying the Liénard-

Wiechert formulas. Retardation and acceleration field effects, which play an important role, are thus taken into account more simply and transparently than in the way generally followed by computer simulations, which consists in solving the set of Maxwell's equation. Boundary conditions on the cathode are satisfied using images.

B. Definitions used for the emittances

The emittances are normalized rms emittances, linked to the first symplectic linear invariant [5]

$$I = \sum_{i,j} \langle \Delta x_i \Delta x_j \rangle \langle \Delta p_{x_i} \Delta p_{x_j} \rangle - \langle \Delta x_i \Delta p_{x_j} \rangle \langle \Delta x_j \Delta p_{x_i} \rangle$$

where $\langle \rangle$ means an average taken over the whole beam

$$\langle G \rangle = \int G(x, p|t) f(x, p|t) d^3x d^3p$$

where x is the position, p the impulsion. The distribution function f is normalized to 1. $\Delta x = x - \langle x \rangle$, $\Delta p = p - \langle p \rangle$, where $\langle x \rangle$ and $\langle p \rangle$ are the centroid position and impulsion respectively.

In the absence of magnetic field :

$$I = \left(\frac{mc}{4}\right)^2 [\epsilon_x^2 + \epsilon_y^2 + \epsilon_z^2]$$

where ϵ_x and ϵ_y are the two usual transverse emittances :

$$\epsilon_x = 4 \left[\langle x^2 \rangle \langle \left(\frac{p_x}{mc}\right)^2 \rangle - \langle x \frac{p_x}{mc} \rangle^2 \right]^{1/2}$$

(similar expression for ϵ_y), and ϵ_z the longitudinal emittance :

$$\epsilon_z = 4 \left[\langle \Delta z^2 \rangle \langle \left(\frac{\Delta p_z}{mc}\right)^2 \rangle - \langle \Delta z \frac{\Delta p_z}{mc} \rangle^2 \right]^{1/2}$$

And for an axisymmetric beam :

$$\epsilon_x = \epsilon_y = \epsilon_r = 2 \left[\langle r^2 \rangle \langle \left(\frac{p_r}{mc}\right)^2 \rangle - \langle r \frac{p_r}{mc} \rangle^2 \right]^{1/2}$$

When a magnetic field is present, there is an azimuthal motion. Again for an axisymmetric beam, besides the radial emittance, one has to consider a transverse emittance ϵ_1 given by :

$$\epsilon_1^2 = \epsilon_x^2 + \epsilon_y^2 = 2\epsilon_r^2 + 8 \langle r^2 \rangle \langle \left(\frac{p_\theta}{mc}\right)^2 \rangle.$$

In any case, it is interesting to consider I itself, conveniently reduced to the dimension of a length, as a 3D emittance :

$$4\sqrt{I}/mc = (\epsilon_x^2 + \epsilon_y^2 + \epsilon_z^2)^{1/2} = \epsilon_{3D}$$

III. EFFECT OF MAGNETIC FOCUSING ON RADIAL EMITTANCE

A. Evolution of the emittances inside the magnetic field zone

Figures 1 and 2 show the evolution of the emittances along the beam (t is the time passed from the beginning of the photoemission : at time 0 the beam front is at $z=0$), without magnetic focalisation (1), or with (2). The parameters are : RF electric field on the cathode $E_0=15$ MV/m, beam current, section, and length $I=100$ A, $S=1$ cm², $\tau=50$ or 100 ps.

The photoinjector exit is at $z=10$ cm, which corresponds to $t=430$ ps.

The magnetic lens center is at $z=12,5$ cm, which corresponds to $t=516$ ps.

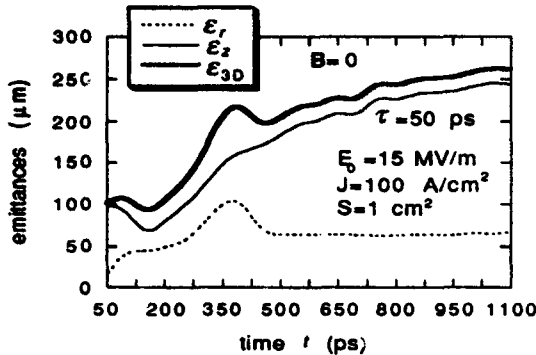


Figure 1a ($\tau=50$ ps)

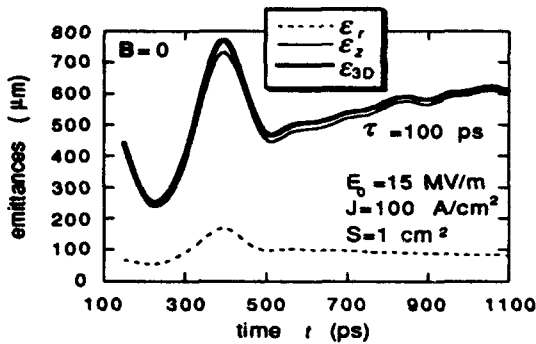


Figure 1b ($\tau=100$ ps)

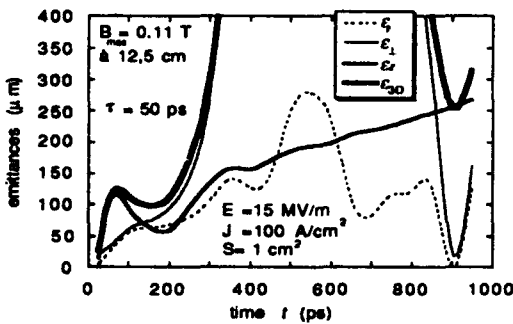


Figure 2a ($\tau=50$ ps)

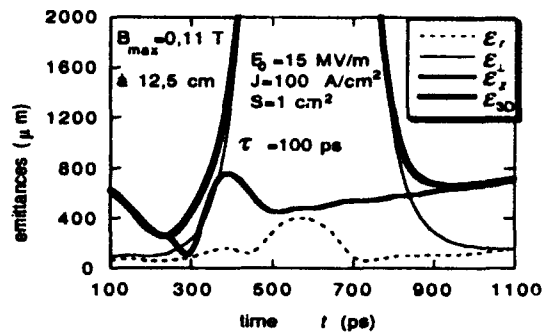


Figure 2b ($\tau=100$ ps)

Figure 1 (no magnetic field), shows that the emittances grow and oscillate inside the photoinjector, where electrons are accelerated ($0 < t < 430$ ps), whereas in the following ballistic phase ϵ_r remains practically constant, while ϵ_z (and therefore ϵ_{3D}) keeps on growing but slower and slower. This corresponds : a) in the photoinjector accelerating phase, to an electromagnetic self-field strongly non-linear in both radial and axial directions ; b) in the ballistic phase, to a radial dynamics decoupled from the longitudinal one, and with negligible non-linear effects, while for the longitudinal dynamics the latter remain and slowly decrease.

In Figure 2, ϵ_z and ϵ_{3D} exhibit, as expected in consideration of the azimuthal motion, a strong maximum around the lens center. Radial and azimuthal dynamics coupling drives ϵ_r oscillations. As expected again $\epsilon_r(t)$ remains unchanged.

B. Influence of the lens magnetic field intensity on radial emittance downstream from the lens

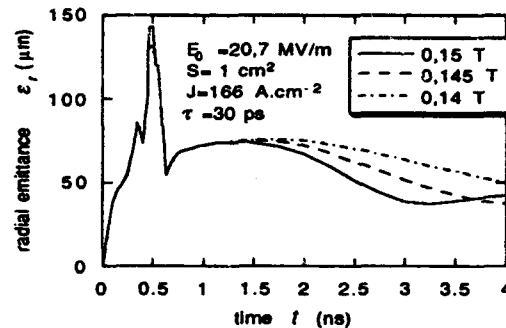


Figure 3

Figure 3 shows the evolution of ϵ_r downstream from the lens, in a region of ballistic propagation, as a function of the magnetic field intensity. The beneficial effect observed from $t=1.5$ to 3.2 ns (for the above particular values of the parameters), i.e. from $z=0.4$ to 0.9 m, disappears later : in the more strongly focused beam, non-linear effects drive a new emittance growth. In actual RF-FEL further accelerating cavities are not so distant from the lens center. But taking a

new acceleration into account does not modify the above result : the beneficial effect on ε_r of a stronger B_0 is only transitory.

IV. EFFECTS OF MAGNETIC FOCUSING ON LONGITUDINAL EMITTANCE AND ENERGY DISPERSION

Figures 4, 5 and 6 show the influence of the magnetic field intensity on the longitudinal and 3D emittances ε_z and ε_{3D} , as also on the energy dispersion $\sigma_\gamma / \langle \gamma \rangle$, where σ_γ is the γ standard deviation.

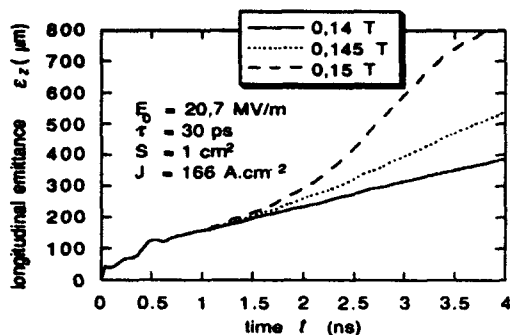


Figure 4

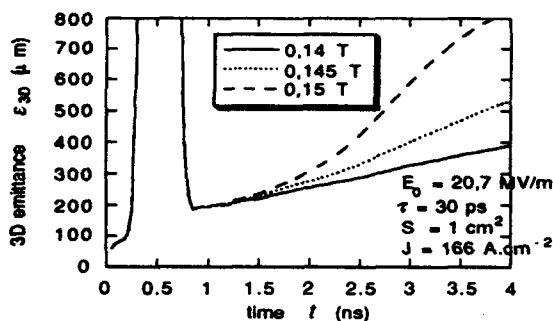


Figure 5

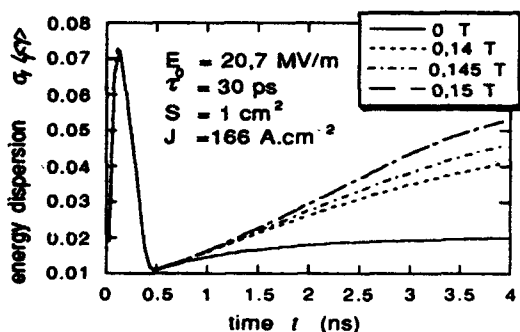


Figure 6

The meaning of these curves is clear : magnetic focusing drives strong growths for both longitudinal emittance and energy dispersion. The larger the magnetic field intensity, the stronger the growth.

V. CONCLUSION

If magnetic focusing has an evident practical interest to avoid an unacceptable radial expansion, its beneficial effect on emittance, sometime emphasized, seems to be questionable. For radial emittance it is moderate and transitory. For longitudinal emittance (and for energy dispersion), magnetic focusing induces a strong growth.

VI. REFERENCES

- [1] R.Dei-Cas, S. Joly *et al.*, Nucl. Instr. and Meth. A318,121 (1992)
- [2] B.E. Carlsten, Nucl. Instr. and Meth. A285, 313 (1989)
- [3] J.-M. Dolique and J.C. Coacolo, Proc. 1991 IEEE Particle Accelerator Conf., San Francisco, 233 (1991).
- [4] J.-M. Dolique and J.C. Coacolo, Proc. 1992 European Particle Accelerator Conf., 771, Berlin (1992)
- [5] A.J. Dragt, F. Neri, G. Rangarajan, Phys. Rev. A, vol. 45, 2572 (1992).

Measurement and Reduction of Transverse Emittance Blow-up Induced by Space Charge Effects

R. Cappi, R. Garoby, S. Hancock, M. Martini, J.P. Riinaud
CERN, CH-1211 Geneva 23

Abstract

The CERN PS, as part of the LHC injector chain, will have to keep a high intensity, high brilliance beam for 1.2 s at the injection energy. The transverse particle density will exceed, by a factor of three, the highest currently attained. Careful experimental studies have recently been carried out in the PS to investigate transverse emittance blow-up in such a severe space charge regime. In addition, a new controlled longitudinal blow-up technique has been developed to produce bunches with flat-topped density profiles and, accordingly, reduced peak current. The results achieved so far are presented and discussed.

I. INTRODUCTION

Transverse emittance conservation is a major concern in the LHC injector chain of LINAC, PS Booster (PSB), PS and SPS [1, 2]. In the PS, for example, the total transverse emittance blow-up must be less than 20%.

One of the peculiarities of the beam for the LHC is that the PSB cannot deliver sufficient intensity to the PS within the required transverse emittances in a single cycle. Consequently, the PS beam will be made up of two PSB batches (each of four bunches) separated by the 1.2 s PSB cycle time. The first batch transferred to the PS will have to circulate at the injection energy of 1 GeV during this time in a strongly space charge dominated regime, leading to an incoherent tune shift, $|\Delta Q_{x,s}| > 0.4$.

For bunches with Gaussian transverse distributions, the space charge detuning at the centre of the bunch may be written

$$\Delta Q_{x,s} = -\frac{r_0}{ec} \frac{I_p R^2}{Q_{x,s} \beta^3 \gamma^3} \frac{1}{\sigma_{x,s}(\sigma_x + \sigma_s)} \quad (1)$$

where $Q_{x,s}$ are the horizontal and vertical tunes, r_0 is the classical proton radius and e its charge, c is the speed of light, R is the machine radius, and β and γ are the usual relativistic factors; I_p is the peak bunch current which, for a parabolic line charge density, is equal to $3N_b e / 2\tau_b$, with N_b the number of particles in the bunch and τ_b the full bunch duration. The rms transverse betatron beam sizes are

$$\sigma_{x,s} = \sqrt{\beta_{x,s} \mathcal{E}_{x,s} + \left(D_{x,s} \frac{\sigma_p}{p}\right)^2} \quad (2)$$

where $\mathcal{E}_{x,s}$ are the rms transverse emittances, $\beta_{x,s}$ and $D_{x,s}$

are the average beta and dispersion functions, and σ_p/p is the relative rms momentum spread.

Large $|\Delta Q_{x,s}|$ leads to the beam crossing betatron resonances and can cause transverse emittance blow-up. For a given beam intensity and transverse emittance, Eqn.1 shows that $|\Delta Q_{x,s}|$ can only be reduced by increasing the energy of the beam and/or by decreasing I_p . How much the PS injection energy should be raised and what can be done to reduce the peak bunch current are the two points addressed here.

II. SPACE CHARGE INDUCED TRANSVERSE BLOW-UP

A. Blow-up Evaluation Method

Refined tracking programs exist [3, 4] to evaluate beam blow-up, but simulation of the PS beam during 1.2 s would require excessive computing time. Instead, several experiments simulating LHC beam conditions have been conducted in the PS [5]. These tests were performed at the present injection energy of 1 GeV and the space charge tune shift was modified by varying the bunch length by means of the RF voltage. After injection in the PS, the RF voltage was raised and maintained at an elevated value for 800 ms, then returned to its original value as shown in Fig.1. Beam emittances before and after the voltage

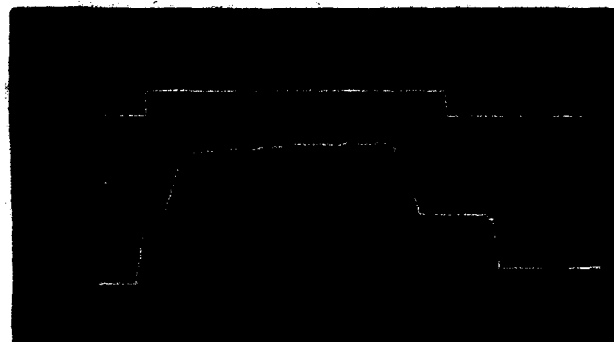


Figure 1: Beam current (2×10^{12} protons/div.) and RF voltage (50 kV/div.) versus time (200 ms/div.).

increase were measured by flying-wire scanner and compared. The experiment was performed at two different working points. As expected, slightly raising Q_x improves the situation as the beam moves away from the integer resonance $Q_x = 6$. However, in order to avoid the third-order resonance $Q_x = 6.33$, Q_x was not set above 6.28.

B. Experimental Results

The results shown in Fig.2 are plotted as a function of the detuning calculated from the measured beam dimensions. The detuning expected from Eqn.1 for the LHC beam at 1 GeV in the PS is $|\Delta Q_{x,s}| > 0.4$, so that Fig.2 can be used to estimate that the resultant transverse emittance blow-up would exceed 30%. An acceptable emittance increase requires $|\Delta Q_{x,s}| < 0.3$ which, from Eqn.1, implies that the PS injection energy must be raised to 1.4 GeV.

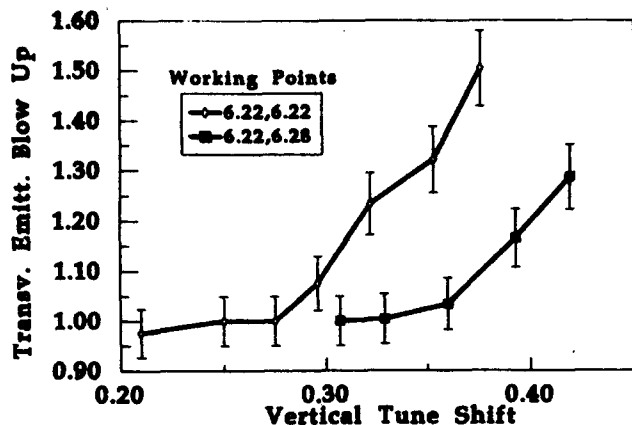


Figure 2: Mean emittance blow-up versus vertical space charge tune shift, $\Delta Q_{x,s}$, for two different working points: $Q_{x,s}^{(1)} = 6.22, 6.22$ and $Q_{x,s}^{(2)} = 6.22, 6.28$. The emittance blow-up is evaluated as $1 + \Delta\epsilon/\epsilon$ with $\epsilon = (\epsilon_x + \epsilon_z)/2$. $\Delta Q_{x,s}$ is calculated from the initial beam dimensions.

Beam blow-up has also been measured as a function of time and this is plotted in Fig.3. No alteration of the shape of the transverse distributions was observed.

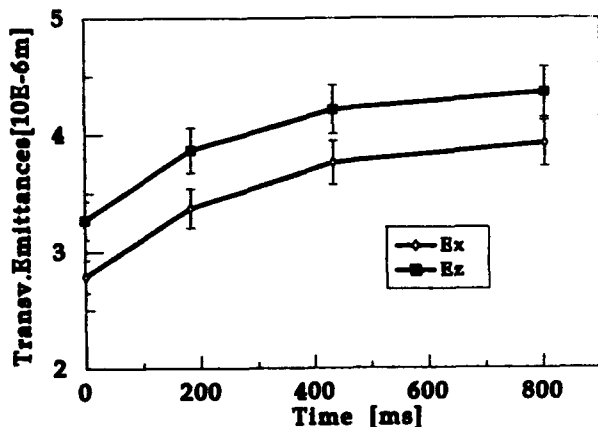


Figure 3: Transverse emittances, $\epsilon_{x,s}$, versus time in a strong space charge regime ($|\Delta Q_{x,s}| = 0.45$) at 1 GeV with $Q_{x,s} = 6.22, 6.28$. Injection is at $t = 0$.

In order to reduce further the harmful effects of space charge, τ_b could be increased to lower I_p . However, there is little margin for this in the PS as the constraints imposed by the injection kicker rise time and by the available RF bucket confine τ_b within a 200 ns bound.

III. FLAT-TOPPED BUNCHES

A. Principle

For the same τ_b , proton bunches with flat-topped density profiles have lower I_p than the more usual quasi-parabolic bunches. Reduction of the space charge induced tune shift is then expected (from Eqn.1), for the same transverse particle distributions, and has indeed been obtained using second harmonic cavities [6]. Although effective, the latter technique has the disadvantage of requiring an additional RF system throughout the low-energy stages of acceleration.

However, flat-topped bunches can be matched to a single RF system given a suitable distribution of particles in longitudinal phase space. Experiments performed in the past to capture a LINAC beam with a hollow energy distribution have been inconclusive [6].

B. Method

A new method has been developed to transform bunch profiles from quasi-parabolic to flat-topped using two basic ingredients:

- a depopulation of the bunch centre by a dipolar excitation of the bunch within the bucket (peak phase excursion A_{mod} at modulation frequency f_{mod} for n_{mod} periods),
- a "smoothing" of the resulting filamentation by a high frequency RF voltage slightly offset (Δf) from a harmonic of the main RF.

Fig.4 shows the buckets of the two RF components drawn independently in phase space for the parameters in Table 1.

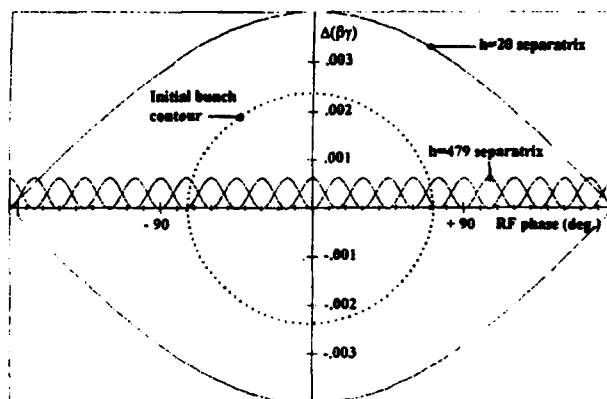


Figure 4: Longitudinal phase space during the production of flat-topped bunches.

$V_{h=20}$ [kV]	A_{mod} [deg]	f_{mod} [kHz]	n_{mod}	$V_{h=479}$ [kV]	Δf [kHz]
44	27	1.65	7	6.5	9.9

Table 1: Parameters to produce flat-topped bunches.

C. Experimental Results

The extent to which flat-topped bunches combat transverse blow-up has been measured in the PS in an experiment very similar to that described above at a working point of $Q_{s,x} = 6.22, 6.22$. By applying the parameters of Table 1 to a quasi-parabolic bunch like that of Fig.5, the flat-topped bunch of Fig.6 was produced. The entire process lasted 10 ms and caused some longitudinal blow-up. The transverse emittances of such a bunch were measured before and after a four-fold increase in RF voltage, as described above. These measurements were repeated with the same voltage programme applied to a quasi-parabolic bunch whose length had been increased by a conventional controlled longitudinal blow-up [7], without modifying its shape, to match that of Fig.6. The overall emittance growth ($\Delta\epsilon/\epsilon$) due to the 800 ms at elevated tune shift was 29% in the case of quasi-parabolic bunches compared with only 17% for the flat-topped ones.

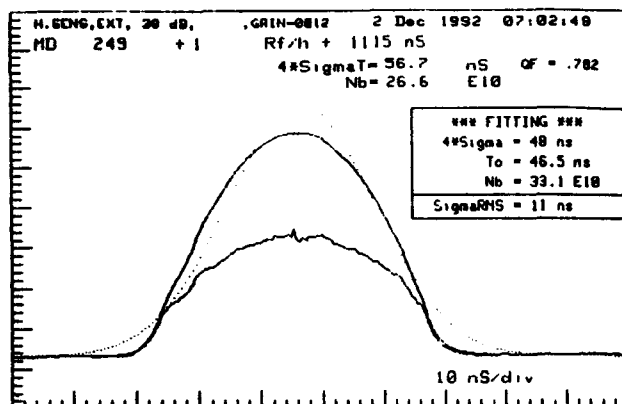


Figure 5: Quasi-parabolic bunch. The dotted curve is a Gaussian fit to the 1-D density profile (upper trace). The lower trace is the 2-D phase space density derived from the profile by an Abel transform [8].

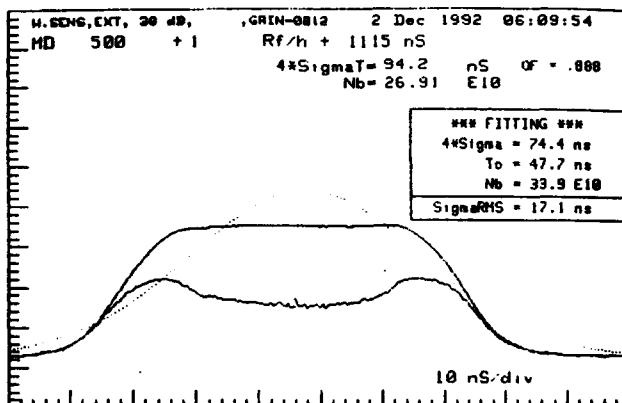


Figure 6: Flat-topped bunch. The Abel transform reveals the depopulation at low synchrotron amplitude.

A "bunch shape quality factor", Q_f , has been devised in analogy with the familiar bunching factor and defined as the ratio of the mean to peak line charge density, where the mean is taken over $\pm\sqrt{3}$ rms standard deviations about

the centre of the bunch rather than over the entire bucket length or machine circumference. This makes Q_f largely insensitive to the aspect ratio of the bucket while the factor of $\sqrt{3}$ was chosen so that Q_f is unity for a perfectly rectangular profile. An increase in Q_f from 78% in Fig.5 to 89% in Fig.6 is achieved.

Flat-topped bunches have been produced at 1 GeV and 3.5 GeV/c, at intensities in the range $2-6.5 \times 10^{11}$ protons per bunch, and have proved stable under closed-loop conditions: they have remained flat for ~ 1 s at constant energy and even after acceleration across transition.

IV. CONCLUSIONS

Experiments at 1 GeV in the PS under conditions similar to those that will prevail for the beam for the LHC indicate that the energy of the PSB-to-PS transfer should be raised to 1.4 GeV to preserve the transverse emittance of quasi-parabolic bunches.

A new method for creating flat-topped bunches has been developed and tested. Such bunches are longitudinally stable and are less prone to transverse blow-up due to space charge induced tune shift. The method will be employed in the PSB for the benefit both of the PSB itself and of the downstream PS. It could be of interest in other space charge limited synchrotrons.

V. ACKNOWLEDGEMENTS

The authors wish to thank H. Charmot, C. Hill, F. Nitsch, K. Schindl and H. Schönauer for their various contributions to this work.

VI. REFERENCES

- [1] The LHC Study Group, "Design study of the Large Hadron Collider (LHC)", CERN 91-03 (May 1991).
- [2] R. Cappi, R. Garoby, S. Hancock, M. Martini, N. Rasmussen, J.P. Riinaud, K. Schindl, H. Schönauer, E.J.N. Wilson, 1991 IEEE PAC, p. 171.
- [3] S. Machida, NIM A309, pp. 43-59, (1991).
- [4] M. Martini, O. Ponomarev, 1991 IEEE PAC, p. 1890.
- [5] R. Cappi, M. Martini, J.P. Riinaud, K. Schindl, H. Schönauer, "Production and measurements in the PS Complex of a high brilliance proton beam in view of the LHC", LHC Note 209, CERN/PS 92-52 (PA), (1992).
- [6] J.P. Delahaye, G. Gelato, L. Magnani, G. Nassibian, F. Pedersen, K.H. Reich, K. Schindl, H. Schönauer, "Shaping of proton distribution for raising the space-charge limit of the CERN PS Booster", CERN/PS/BR 80-14 (June 1980).
- [7] R. Cappi, R. Garoby, E.N. Shaposnikova, "Experimental study of controlled longitudinal blow-up", CERN/PS 92-40 (RF) (1992).
- [8] P.W. Krempf, "The Abel-type integral transformation with the kernel $(t^2 - x^2)^{-1/2}$ and its application to density distributions of particle beams", CERN MPS/Int.BR/74-1 (March 1974).

Transverse Emittance Growth in the Fermilab Antiproton Accumulator with High-Current Antiproton Stacks

Steven J. Werkema, David W. Peterson, and Ping Zhou
Fermi National Accelerator Laboratory[†]
P.O. Box 500, Batavia, IL 60510-0500

Abstract

Transverse emittance growth due to coherent instabilities in the Fermilab antiproton accumulator imposes a limit on the number of antiprotons which can be stacked and subsequently transferred to the collider. Consequently, the diagnosis and control of these phenomena has been required to further increase the luminosity of the collider. In this paper we present an overview of the techniques by which these instabilities have been studied and the methods by which they are controlled.

I. INTRODUCTION

The Fermilab antiproton accumulator was designed to deliver intense \bar{p} bunches at 8 GeV kinetic energy to the main ring for acceleration and injection into the Tevatron p - \bar{p} collider. The intensity of the \bar{p} bunches extracted from the accumulator is a principal determiner of the luminosity of the collider.

The \bar{p} bunches are extracted by capturing some fraction of the \bar{p} stack in a 1.25 eV·sec RF bucket, accelerating the captured beam across the accumulator momentum aperture to an extraction orbit, and kicking the beam on the extraction orbit into the transfer line connecting the accumulator to the main ring accelerator. The intensity of the extracted \bar{p} 's is therefore determined by two things: (1) the longitudinal density of the beam in the \bar{p} stack (i.e. the number of \bar{p} 's captured in a 1.25 eV·sec bucket), and (2) the efficiency of the transfer from the accumulator to the main ring. However, optimizing either or both of these can lead to transverse instabilities in the \bar{p} stack.

The criteria for transverse stability can be written in terms of the longitudinal density[1]:

$$\frac{\Delta p/p}{I_0} > \frac{eR}{4\pi\eta cQ} \left| \frac{Z_T}{(n-Q)\eta + \xi} \right| \quad (1)$$

The longitudinal density of the \bar{p} stack is increased by increasing the beam intensity (I_0) and/or decreasing the momentum spread ($\Delta p/p$) of the beam. It is evident from equation (1) that attempting to increase the intensity of the extracted \bar{p} bunches by doing either of these decreases the margin to transverse instability.

In addition one can increase the intensity of the extracted \bar{p} bunches by endeavoring to increase the transfer efficiency into the main ring. This can be accomplished by reducing the

transverse size of the extracted \bar{p} bunches below the admittance of the transfer line and the main ring. To this end, the accumulator is equipped with betatron stochastic cooling with sufficient gain to achieve smaller than 1.0π mm·mrad absolute emittance horizontally and vertically for a stack size of 10^{12} \bar{p} 's (101 mA). There are, however, limitations to the transverse emittance reductions which can be achieved. First, the small momentum spread of the \bar{p} bunches causes a degradation in the stochastic cooling pickup to kicker mixing factor[2]. Secondly, a reduction in the transverse size of an intense negatively charged beam increases the depth of the beam space charge potential well for trapping positively charged ions, which decreases the margin to ion induced instabilities.

The combined effect of excessively increasing the longitudinal density and decreasing the transverse beam size to increase the intensity of the extracted \bar{p} bunches during collider operation is illustrated in Figure 1. This Figure shows the time evolution of the horizontal and vertical emittances after the beam has been cooled below the trapped ion instability threshold.

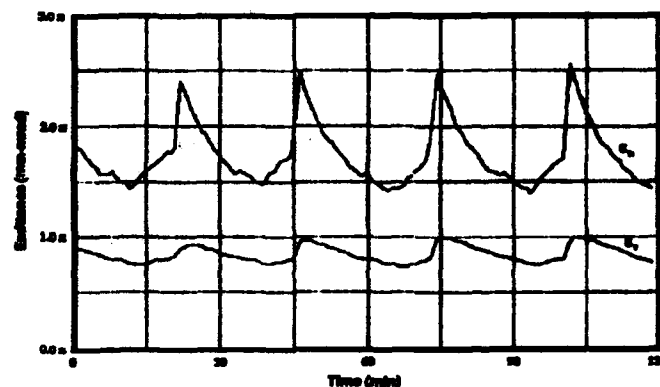


Figure 1. Transverse core emittances versus time.

The horizontal emittance undergoes a rapid 70% growth at approximately 25 minute intervals. The vertical emittance shows a similar pattern; in phase with the horizontal plane, albeit with a much smaller amplitude. The emittance growth is small enough to preclude beam loss, however the horizontal excursions give rise to emittances which are much larger than the admittance of the transfer line or the main ring. The long recovery times present serious operational difficulties during \bar{p} extraction.

A variety of techniques to simultaneously stabilize the \bar{p} stack and maximize the number of extracted \bar{p} 's have been successfully employed. These techniques include: (1) optimization of the accumulator operating point, (2) the use of wide band active dipole dampers, and (3) various trapped ion

[†] Operated by the Universities Research Association, Inc under contract with the U.S. Department of Energy.

clearing methods. A very brief survey of these techniques is given in what follows.

II. ACCUMULATOR OPERATING POINT

There are three basic considerations vis-à-vis the accumulator operating point: (1) chromaticity, (2) the location of the tunes, and (3) coupling.

The conventional wisdom regarding the chromaticity is that it be positive to increase Landau damping of unstable coherent dipole modes, but not so large as to cause the tune spread to span a resonance. Currently the allowed accumulator chromaticity is highly constrained by the requirement that the tunes be "reasonable" throughout the 170 MeV/c (2%) momentum aperture and excellent on the extraction orbit. This requirement is due to the fact that the accumulator injection/extraction orbits and the \bar{p} core orbit are on the opposite sides of the momentum aperture; therefore, during both \bar{p} stacking and extraction, the beam is moved across the most of the momentum aperture. Also, during extraction the \bar{p} bunch remains on the extraction orbit for an appreciable amount of time (~ 500 msec) prior to being kicked out of the accumulator.

Because of these constraints, the accumulator is currently operated with $\xi_H = 0.05$, and $\xi_V = -0.5$ ($\xi = dQ/d(\Delta p/p)$). In the future there are two items which may improve the chromaticity situation: (1) an upgrade in the octupole circuit power supplies which will allow more compensation for the tune excursion due to chromaticity, and (2) a redesign of the accumulator extraction lambertson which currently has an appreciable effect on the extraction orbit tunes.

There is some small evidence that the horizontal and vertical tunes have an impact on beam stability. A beam transfer function measurement capability to obtain a quick, real-time determination of the dependence of the beam stability diagram on the tunes is being developed. To date, the systematic scan of the tunes which would be necessary to understand any relationship of the tune working point to the stability of the beam has not been completed.

The introduction of tune coupling by means of skew quadrupoles has been observed to have a stabilizing effect on the beam. A possible explanation of this may have to do with the fact that the horizontal chromaticity is close to zero; therefore horizontal coherent oscillation will see minimal Landau damping. When coupling is inserted, the horizontal plane now benefits from the much greater vertical tune spread. In practice, the accumulator is operated with the tunes uncoupled. This is done to simplify various routine diagnostic measurements. The detrimental effects of uncoupling the tunes are more than compensated for by employing any of the beam stabilizing techniques described below.

III. ACTIVE DAMPERS

Calculations of the accumulator transverse impedance[3] indicate that a stack of 10^{12} \bar{p} 's will be unstable at a $\Delta p/p$ of 0.07% (FWHM) and $(n-Q) \leq 3$. Therefore, the necessity of actively damping coherent transverse oscillations of the beam was recognized early in the design of the accumulator.

In practice, a horizontal and vertical damper are required for operation of the accumulator with \bar{p} stacks greater than approximately 20 mA.

The principle design requirements of the damper systems are to continuously damp transverse coherent oscillation during antiproton accumulation and extraction, and provide a flexible diagnostic tool for the study of the transverse behavior of the beam. The damper systems sense the transverse center of mass motion of the beam, amplify the resultant electrical signal, insert a delay to match the transit time of the beam and apply a correcting kick.

The damper systems consist of 0.5 meter long stripline pickups back terminated in high impedance capacitive loads to flatten the low frequency response, high input impedance differential preamplifiers, phase compensation filters and diagnostic switches, correlator notch filters to reject revolution harmonics, and power amplifiers driving 50 Ω stripline kickers. The system phase response is flat from 240 kHz (which is just below the 1-Q beam resonance) to over 50 MHz. The system gain peaks below 240 kHz due to the phase compensation filters and is flat from 3 MHz to over 50 MHz [4].

A damper system upgrade is planned for the summer of 1993. The upgrade plans include; higher impedance preamplifiers to provide flatter gain and phase below 1 MHz, rearrangement of the medium level electronics to provide for more reliable operation, and additional coupled input and output ports for improved diagnostics and closed loop beam measurements.

IV. TRAPPED ION CLEARING

Positively charged ions trapped in the \bar{p} beam potential have been identified as the primary cause of the transverse instabilities which have been observed to date [5]. This identification prompted a concentrated investigation into a variety of ion clearing methods. The implementation of some of these methods resulted in a marked improvement in the operational performance of the antiproton source[6].

A. Clearing electrodes

The most fundamental and effective way to remove trapped ions is the clearing electrode. Recently the accumulator ion clearing electrode system underwent a significant upgrade. The high voltage limit was extended from -100 Volts to -1000 Volts. Clearing electrodes were added to the system to clear trapped ion pockets which had previously not been cleared. There are now 140 clearing electrodes installed throughout the accumulator. The level of multiplexing in the clearing current readback has been reduced from one clearing current sum for each of the six accumulator sectors to a single readout for each two or three electrodes. The sensitivity of the current readback is at the 10 pA level, providing a powerful tool for the diagnosis of ion related phenomena. A more detailed description of the hardware upgrade is given in reference [6].

The consequent improvement in the performance of the antiproton source can be measured by comparing the minimum beam size achievable (in three dimensions) before and after the

upgrade. Figure 2 shows a plot of the minimum horizontal emittance achieved versus the longitudinal density of the \bar{p} stack.

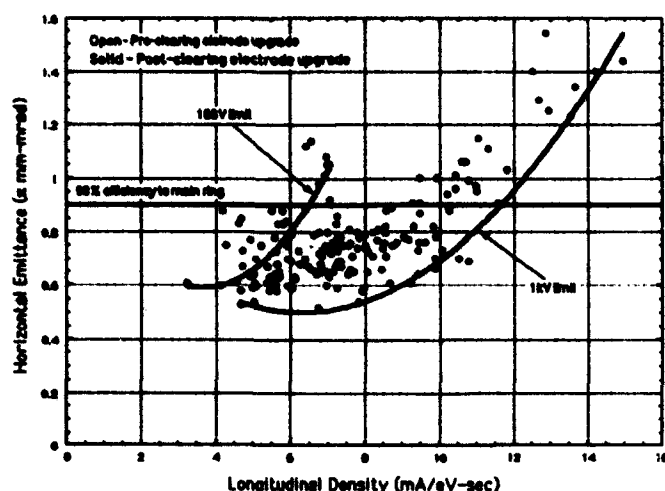


Figure 2. Transverse beam size versus longitudinal density before and after the ion clearing upgrade.

Prior to the clearing upgrade, relatively small longitudinal densities ($\approx 7 \times 10^{10}$ \bar{p} 's/eV-sec) would result in transverse instabilities. These instabilities would preclude further transverse cooling of the beam. The advent of the ion clearing upgrade increased the achievable longitudinal density by a factor of nearly 2 for horizontal emittances near the threshold for efficient transfer into the main ring.

The ion clearing upgrade prevented the periodic emittance blowups for \bar{p} stacks of less than 120×10^{10} . However, as is evident in Figure 2, the transverse beam size is too large for efficient transfer into the main ring at longitudinal densities in excess of 11×10^{10} \bar{p} 's/eV-sec.

B. Beam Shaking

Prior to the clearing electrode system upgrade, stable operation of the accumulator, during both stacking and \bar{p} extraction, required the use of beam shakers[7]. To date, this ion clearing technique involves shaking the beam at a fixed frequency which are simultaneously close to one or more of the betatron dipole resonances of the beam and the bounce frequency of trapped ions.

Since the clearing electrode upgrade the beamshakers have had no observable operational impact and are normally turned off. There is an effort in progress to implement swept frequency beam shaking in the accumulator[8]. So far this undertaking has not progressed far enough to achieve a measurable improvement in beam stability.

C. Longitudinal modulation of beam intensity

Bunching a small fraction (5% - 15%) of the \bar{p} beam with RF has been observed to have a stabilizing effect on the beam. This stabilization is manifested in three ways: (1) beam with emittances in equilibrium will exhibit a finite cooling rate when the RF is turned on (see Figure 3), (2) periodic emittance

blowups are eliminated for intense beams (up to 135 mA), and (3) the amplitude of the coherent betatron dipole oscillations is damped (see Figure 3).

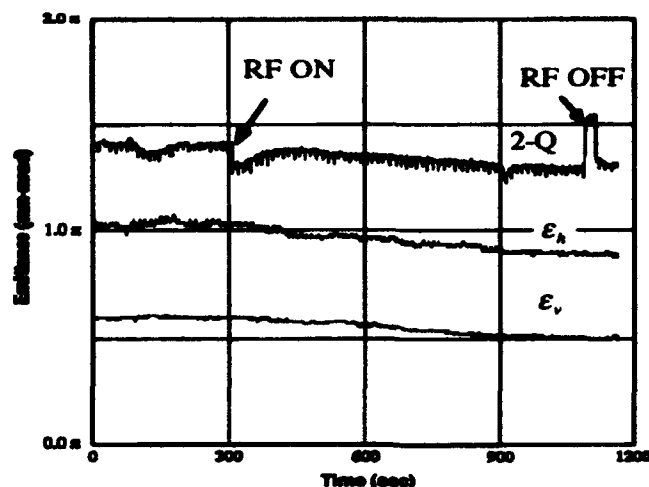


Figure 3. Time evolution of the \bar{p} beam transverse emittances and the power in the 2-Q dipole oscillation after the beam is bunched with RF.

Figure 3 shows about a 20% reduction in the transverse emittance after the RF is turned on. The lower emittance is preserved for several hours after the RF is turned off. This effect is the subject of an ongoing study[6].

V. REFERENCES

- [1] B. Zotter and F. Sacherer, Transverse Instabilities of Relativistic Particle Beams in Accelerators and Storage Rings. CERN Report 77-13, p.175.
- [2] J. Marriner and D. McGinnis, An Introduction to Stochastic Cooling. AIP Conference Proceedings #249 (1992).
- [3] J. Marriner, et.al., Stability Criterion and Wall Impedance for the Antiproton Accumulator. Fermilab Antiproton Source Department internal memo #422.
- [4] J. Petter, J. Marriner, and J. McCarthy, Transverse Beam Dampers for the FNAL Antiproton Rings. Proceedings of the 1987 IEEE Particle Accelerator Conference, p.791.
- [5] J.B. Rosenzweig and P. Zhou, Coherent Beam-Ion Instabilities in the Fermilab Antiproton Accumulator. Proceedings of the Fermilab III Instabilities Workshop, June 25-29 (1990), p.9.
- [6] S.J. Werkema, K. Fullett, and P. Zhou, Measurement of Trapped Ion Pockets and Control of Ion Instabilities in the Fermilab Antiproton Accumulator. These proceedings (1993).
- [7] J. Marriner, et.al., Experiments and Practice in Beam Shaking. Particle Accelerators, 30 (1990) p.13.
- [8] R. Alves-Pires, Beam Shaking for the Fermilab Antiproton Accumulator. Proceedings of the Fermilab III Instabilities Workshop, June 25-29 (1990), p.18.

Transverse Tails and Higher Order Moments*

W. L. SPENCE, F.-J. DECKER and M. D. WOODLEY

Stanford Linear Accelerator Center, Stanford University, Stanford, California 94309 U. S. A.

The tails that may be engendered in a beam's transverse phase space distribution by, e.g., intrabunch wakefields and nonlinear magnetic fields, are an important diagnostic and object of tuning in linear colliders. Wire scanners or phosphorescent screen monitors yield one dimensional projected spatial profiles of such beams that are generically asymmetric around their centroids, and therefore require characterization by the third moment $\langle x^3 \rangle$ in addition to the conventional mean-square or second moment. A set of measurements spread over sufficient phase advance then allows the complete set $\langle x^3 \rangle$, $\langle xx'^2 \rangle$, $\langle x'^3 \rangle$, and $\langle x^2 x' \rangle$ to be deduced—the natural extension of the well-known 'emittance measurement' treatment of second moments. The four third moments may be usefully decomposed into parts rotating in phase space at the β -tron frequency and at its third harmonic, each specified by a phase-advance-invariant amplitude and a phase. They provide a framework for the analysis and tuning of transverse wakefield tails.

Third Moments

The totally symmetric tensor of third moments $\langle x_i x_j x_k \rangle$ ($i = 1, \dots, d$, the number of phase space dimensions) evolves in a linear beamline [1] with transfer matrix R according to

$$\langle x_i x_j x_k \rangle \rightarrow R_{ii'} R_{jj'} R_{kk'} \langle x_{i'} x_{j'} x_{k'} \rangle \quad (1)$$

In normal coordinates for 2-dimensional phase space $\hat{x} = \frac{1}{\sqrt{\beta}} \begin{pmatrix} 1 & 0 \\ \alpha & \beta \end{pmatrix} x$, and

$$\langle \hat{x}_i \hat{x}_j \hat{x}_k \rangle \rightarrow O_{ii'} O_{jj'} O_{kk'} \langle \hat{x}_{i'} \hat{x}_{j'} \hat{x}_{k'} \rangle \quad (2)$$

where O is a 2×2 rotation matrix.

In two phase space dimensions $\langle x_i x_j x_k \rangle$ has 4-components, viz.,

$$\langle x^3 \rangle, \langle xx'^2 \rangle, \langle x'^3 \rangle, \langle x^2 x' \rangle \quad (3)$$

Four skew $\langle \hat{x}^3 \rangle = \langle x^3 \rangle / \beta^{3/2}$ measurements are necessary and sufficient to determine the four independent components $\langle \hat{x}_i \hat{x}_j \hat{x}_k \rangle_0$ at some reference point defined as being at phase advance $\Delta\psi = 0$

$$\begin{aligned} \langle \hat{x}^3 \rangle &= \cos^3(\Delta\psi) \langle \hat{x}^3 \rangle_0 + 3 \cos(\Delta\psi) \sin^2(\Delta\psi) \langle \hat{x} \hat{x}'^2 \rangle_0 \\ &\quad + \sin^3(\Delta\psi) \langle \hat{x}'^3 \rangle_0 + 3 \sin(\Delta\psi) \cos^2(\Delta\psi) \langle \hat{x}^2 \hat{x}' \rangle_0 \quad (4) \\ &= \frac{1}{4} \cos(3\Delta\psi) (\langle \hat{x}^3 \rangle_0 - 3 \langle \hat{x} \hat{x}'^2 \rangle_0) \end{aligned}$$

$$\begin{aligned} & - \frac{1}{4} \sin(3\Delta\psi) (\langle \hat{x}'^3 \rangle_0 - 3 \langle \hat{x}^2 \hat{x}' \rangle_0) \\ & + \frac{3}{4} \cos(\Delta\psi) (\langle \hat{x}^3 \rangle_0 + \langle \hat{x} \hat{x}'^2 \rangle_0) \\ & + \frac{3}{4} \sin(\Delta\psi) (\langle \hat{x}'^3 \rangle_0 + \langle \hat{x}^2 \hat{x}' \rangle_0) \end{aligned} \quad (5)$$

The second, Fourier series expression, shows that first and third β -tron harmonics enter.

The linear combinations

$$\langle \hat{x}^3 \rangle + \langle \hat{x} \hat{x}'^2 \rangle = \tau \sin \Psi \quad (6)$$

$$\langle \hat{x}'^3 \rangle + \langle \hat{x}^2 \hat{x}' \rangle = \tau \cos \Psi \quad (7)$$

transform analogously to $\langle x_i \rangle$, i.e., $\Psi \rightarrow \Psi + \Delta\psi$ along the beamline and $\tau \geq 0$ is invariant. The complementary linear combinations

$$\langle \hat{x}^3 \rangle - 3 \langle \hat{x} \hat{x}'^2 \rangle = -\kappa \sin \Phi \quad (8)$$

$$\langle \hat{x}'^3 \rangle - 3 \langle \hat{x}^2 \hat{x}' \rangle = \kappa \cos \Phi \quad (9)$$

rotate at three times the normal phase advance, i.e., $\Phi \rightarrow \Phi + 3\Delta\psi$ along the beamline, with $\kappa \geq 0$ invariant.

There are no symplectic invariants (like emittance) for odd-order moments, but there are useful phase-advance-invariants (i.e., invariants with respect to the rotational sub-group of the full symplectic group), analogous to $\frac{1}{2} \text{tr} \langle \hat{x} \hat{x}^T \rangle = \bar{\epsilon}$, the matched-equivalent emittance. They are in correspondence with the irreducible representations of the rotation group $SO(2)$ contained in the moments tensor.

The components can then be parameterized

$$\langle \hat{x}^3 \rangle = \frac{3}{4} \tau \sin \Psi - \frac{1}{4} \kappa \sin \Phi \quad (10)$$

$$\langle \hat{x} \hat{x}'^2 \rangle = \frac{1}{4} \tau \sin \Psi + \frac{1}{4} \kappa \sin \Phi \quad (11)$$

$$\langle \hat{x}'^3 \rangle = \frac{3}{4} \tau \cos \Psi + \frac{1}{4} \kappa \cos \Phi \quad (12)$$

$$\langle \hat{x}^2 \hat{x}' \rangle = \frac{1}{4} \tau \cos \Psi - \frac{1}{4} \kappa \cos \Phi \quad (13)$$

$\langle \hat{x}'^3 \rangle$ and $\langle \hat{x}^3 \rangle$ are related by a 90° phase shift, and

$$\langle \hat{x} \hat{x}'^2 \rangle = -\frac{1}{3} \frac{d}{d\psi} \langle \hat{x}'^3 \rangle \quad (14)$$

$$\langle \hat{x}^2 \hat{x}' \rangle = \frac{1}{3} \frac{d}{d\psi} \langle \hat{x}^3 \rangle \quad (15)$$

analogous to the 2nd moment relation $\langle \hat{x} \hat{x}' \rangle = \frac{1}{2} d \langle \hat{x}^2 \rangle / d\psi$.

* Work supported by the Department of Energy, contract DE-AC03-76SF00515.

Sampling the observable

$$\frac{\langle x^3 \rangle}{\beta^{3/2}} = \frac{3}{4} \tau \sin(\Delta\psi + \Psi) - \frac{1}{4} \kappa \sin(3\Delta\psi + \Phi) \quad (16)$$

at at least 4 appropriate phases then makes possible the determination of the two invariants and two phases that are equivalent to knowing the 4 independent moments at a point.

A 'simple' asymmetric phase space tail is characterized as having 4 third moments with the property that there is some (rigid) phase rotation that reduces 3 of them simultaneously to zero. The rotation can be chosen such that the non-vanishing moment is $\langle x'^3 \rangle$, and the associated beam-line phase regarded as an effective phase at which the skew or asymmetric tail originated in an impulse or kick. In invariant terms a 'simple' tail has $\kappa = \tau$ and some phase where $\Phi = \Psi = 0$, i.e., $\Phi = 3\Psi$ (modulo 2π).

More generally it is useful to identify a 'principal axis' phase P at which $\langle \hat{x}'^3 \rangle$ is maximized, and hence $\langle \hat{x}\hat{x}'^2 \rangle_P = 0$; the magnitude of the $\langle \hat{x}^3 \rangle_P$ and $\langle \hat{x}^2\hat{x}' \rangle_P < \langle \hat{x}'^3 \rangle_P$ moments then measures how 'simple' the tail is. For a 'simple' tail $\langle \hat{x}'^3 \rangle_P = \kappa = \tau$.

In 4-dimensional phase space there are 12 additional third moments ($\langle x^2y \rangle$, $\langle xy^2 \rangle$, etc.), that are in principle accessible through the observable

$$\langle x^2y \rangle + \langle xy^2 \rangle = \frac{1}{3} \left[\langle u^3 \rangle - \frac{\sqrt{2}}{4} (\langle x^3 \rangle + \langle y^3 \rangle) \right] \quad (17)$$

containing Fourier components for $\Delta\psi_x$, $\Delta\psi_y$, $2\Delta\psi_x \pm \Delta\psi_y$, and $\Delta\psi_x \pm 2\Delta\psi_y$, and corresponding to irreducible representations of $SO(2) \times SO(2)$. Thus observations must be made at at least 12 phase-advance-incommensurate beamline locations for a complete 4-dimensional analysis to be made. There are 5 4th moments in 2 phase space dimensions, and 35 in 4 dimensions.

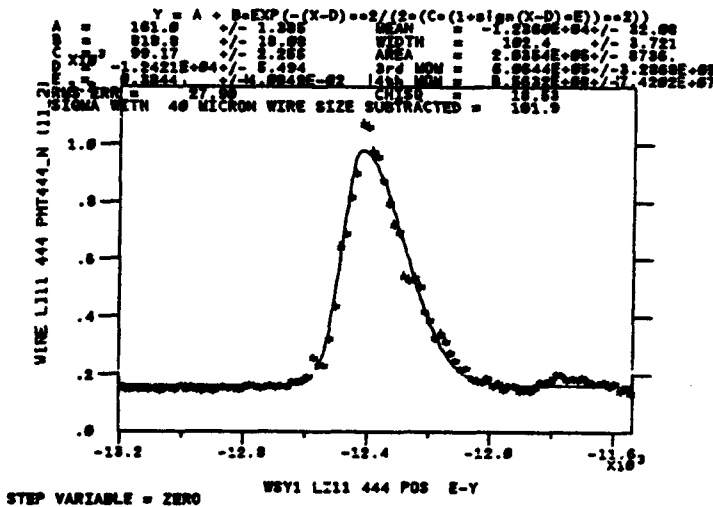


FIG. 1 An 'asymmetric Gaussian' fit to SLC wire scanner data, indicating a wakefield tail.

Asymmetric Gaussian-like Function

A simple and useful beam profile fitting function can be constructed by allowing the width of a Gaussian function to be different on the right from on the left

$$\sigma_L = \sigma_0(1 - E), \quad \sigma_R = \sigma_0(1 + E) \quad (18)$$

($\sigma_L + \sigma_R$)/2 = σ_0 as for a (symmetric) Gaussian, and the asymmetry $(\sigma_R - \sigma_L)/(\sigma_R + \sigma_L) = E$ is bounded: $-1 \leq E \leq 1$. Fitting (Fig. 1) to the five parameter function (including a background offset)

$$f(x) = A + B \exp \left\{ -\frac{1}{2} \left[\frac{x - D}{C(1 + \text{sgn}(x - D) E)} \right]^2 \right\} \quad (19)$$

$$\text{yields } \langle (x - \langle x \rangle)^3 \rangle = 2\sqrt{\frac{2}{\pi}} [1 + (\frac{16}{\pi} - 5) E^2] EC^3.$$

Phenomenology of Transverse Wakefield Tails

In the case of wakefields the asymmetry arises from the fact that kicks are longitudinally differential, i.e., $\Delta x'_r = (e^2/E) \int dN_{r_0} W_\perp(\tau - \tau_0)(x_{r_0} - \xi)$, where the impulsive point dipole wakefield $W_\perp(\Delta\tau)$ depends on the longitudinal coordinate difference $\Delta\tau$, N is the bunch population, E the beam energy, and ξ the structure offset. A 'simple' tail corresponds to a single impulsive excitation or series of multiple excitations that are sufficiently weak that, being dominantly first order or 'two-particle' like, they obey vector addition in phase space (Fig. 2a).

The exact relationship between third moments or tails and rms emittance depends on the details of the mechanism—second and third moments are *a priori* independent. In the simple though qualitatively representative model in which the wakefield coefficient depends linearly on longitudinal distance $W_\perp = W'_\perp \theta(\tau - \tau_0)(\tau - \tau_0)$, the matched-equivalent emittance $\bar{\epsilon}$ [2] of a 'simple' wakefield tail

$$\bar{\epsilon} \cong \left(\frac{0.29069}{4/15} \right) \frac{\beta}{2} \left(\frac{e^2 N}{E} W'_\perp \xi \right)^2 \langle \tau^2 \rangle \quad (20)$$

$$\cong \left(\frac{0.39010}{(70/67)^{2/3} \cdot 4/5} \right) |\langle \hat{x}'^3 \rangle_P|^{2/3} \quad (21)$$

The upper geometric factor corresponds to a Gaussian and the lower to a uniform (step) longitudinal distribution, and $\langle \tau^2 \rangle$ is the mean square bunch length.

For a prior emittance ϵ_0 , the net prompt emittance $\bar{\epsilon} = \sqrt{\epsilon_0^2 + 2\epsilon_0\bar{\epsilon}}$, growing still further to $\bar{\epsilon} = \epsilon_0 + \bar{\epsilon}$ if filamentation subsequently occurs. The significance of relating the emittance due to wakefields to the third moments is that it connects observable quantities—the third moment, unlike the second, can be expected to be due entirely to the transverse wakefield.

The Lorentz invariants $\gamma^{3/2} \langle \hat{x}_i \hat{x}_j \hat{x}_k \rangle$, and $\gamma^{3/2} \tau$, $\gamma^{3/2} \kappa$ are usually most convenient to deal with. It is useful to note that for $\gamma^{3/2} \langle \hat{x}^3 \rangle_P = 10^{-7} \text{ m}^{3/2} = 10^{11} (\mu\text{m} \cdot \mu\text{rad})^{3/2}$, the maximum fractional skew $|\langle x^3 \rangle_{\text{max}} / \langle x^2 \rangle^{3/2}| = \gamma^{3/2} \langle \hat{x}'^3 \rangle_P / (\gamma\bar{\epsilon})^{3/2} = 1$ for an invariant emittance $\gamma\bar{\epsilon} \cong 2.15 \cdot 10^{-6} \text{ m}$, and that $\gamma\bar{\epsilon} \cong 0.84 \cdot 10^{-6} \text{ m}$ for a 'simple'

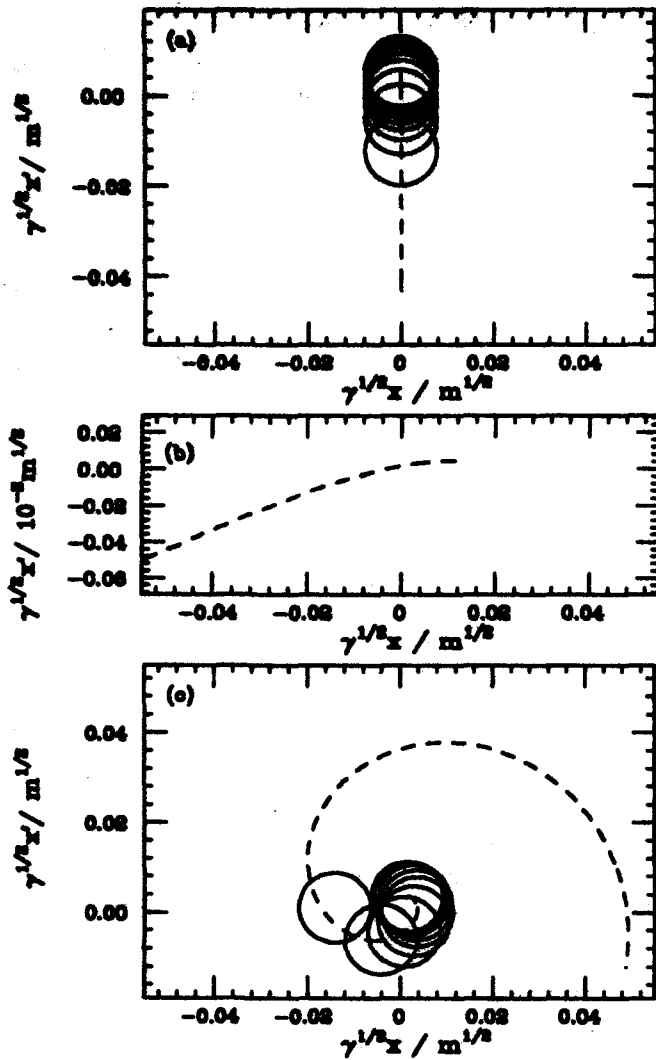


FIG. 2 Phase space distributions in beam centroid subtracted normal coordinates in which the transverse centroids for definite longitudinal 'slices' are indicated by dashed lines, and longitudinal segments, each containing $1/9$ of the total beam charge, are shown as circles corresponding to a transverse emittance $\gamma\epsilon_0 = 3 \cdot 10^{-5}$ m.

(a) $\gamma^{3/2}\kappa = \gamma^{3/2}\tau = 2.3 \cdot 10^{-7} \text{ m}^{3/2}$, $\gamma\bar{\epsilon} = 1.4 \cdot 10^{-5}$ m, and $\gamma\epsilon = 0$ [3].

(b) $\gamma^{3/2}\kappa \approx \gamma^{3/2}\tau = 18 \cdot 10^{-7} \text{ m}^{3/2}$, $\gamma\bar{\epsilon} = 5.8 \cdot 10^{-5}$ m, and $\gamma\epsilon = 0.02 \cdot 10^{-5}$ m.

(c) $\gamma^{3/2}\tau = 4.8 \cdot 10^{-7} \text{ m}^{3/2}$, $\gamma^{3/2}\kappa = 0.9 \cdot 10^{-7} \text{ m}^{3/2}$, $\gamma\bar{\epsilon} = 2.4 \cdot 10^{-5}$ m, and $\gamma\epsilon = 2.3 \cdot 10^{-5}$ m.

tail. Fractional skew and emittance are in general related by

$$\left(\frac{0.39010}{(70/67)^{2/3} \cdot 4/5} \right) \left[\frac{\gamma^{3/2} \langle \hat{x}'^3 \rangle_p}{(\gamma\bar{\epsilon})^{3/2}} \right]^{2/3} = \frac{1}{2} \left(\frac{\bar{\epsilon}}{\epsilon_0} - \frac{\epsilon_0}{\bar{\epsilon}} \right) \rightarrow \begin{cases} (\bar{\epsilon} - \epsilon_0)/\epsilon_0, & \bar{\epsilon} - \epsilon_0 \ll \epsilon_0 \\ \frac{1}{2}\bar{\epsilon}/\epsilon_0, & \bar{\epsilon} \gg \epsilon_0 \end{cases} \quad (22)$$

If the transverse offsets relative to the bunch centroid of significant fractions of the charge become comparable to

the offset of the centroid relative to the center of cylindrical symmetry of the structure, the tail will deviate from the 'simple' form (Fig. 2b). Nevertheless for a (linearly) increasing point wakefield function, the tensor of third moments will appear 'simple' in as much as the third moments will be dominated by particles that get deflected to large phase space distances—far from the bulk of the charge—and are thus insensitive to its precise distribution relative to the center of the structure. However, the cumulative transverse phase advance differential that will arise in the presence of magnetic lattice chromaticity if the bunch has an energy spread correlated with longitudinal position (as in BNS damping [4]), creates significant departures from the 'simple' form (Fig. 2c). The third moments will be Landau damped, although when taken about the beam centroid they may manifest transient increases as the first moment vector (i.e., the centroid) damps. The Fourier component $\tau > \kappa$ (becoming $\tau \gg \kappa$) is characteristic of this process, since the κ component oscillates and hence damps at three times the rate for τ (i.e., three times the β -tron frequency).

At the SLC we have recently implemented on-line analysis of third moments using the fit (19) to wire scanner profiles, and eqn. (16). The use of linac orbit bumps to cancel wakefield excitation [5], [6] can be enhanced both in speed and efficacy by knowing the 'tail' phase and amplitude changes resulting from test variations in the orbit. Knowledge of the tail nature ('simple' or not?) is important in that bumps that fail to drive the tail closer toward 'simplicity' are too distant (downstream) from the source to remove it fully. First efforts at automating the tuning procedure using digital feedback are in progress.

We thank Chris Adolphsen, Tom Himel, and John Seeman for useful discussions throughout the course of this work.

1. There are no wakefield or chromaticity effects in the beamline considered here, as is usually true to a good approximation in a high energy linac if it is sufficiently short.
2. $\bar{\epsilon} = \frac{1}{2} \left[\langle (\hat{x}'_{\perp})^2 \rangle_{\tau} + \langle (\hat{x}'_{\perp})^2 \rangle_{\tau} \right]$ here. $\langle \rangle_{\perp}$ represents a transverse phase space average, i.e., $\langle x \rangle_{\perp}$ and $\langle x' \rangle_{\perp}$ are the longitudinal 'slice' centroids, and $\langle \rangle_{\tau}$ the longitudinal beam average.
3. The emittance due to wakefields, or emittance if the emittance in the absence of wakefields is zero, $\epsilon = \left[\langle (\hat{x}'_{\perp})^2 \rangle_{\tau} \langle (\hat{x}'_{\perp})^2 \rangle_{\tau} - \langle (\hat{x}'_{\perp})_{\tau} \rangle_{\tau}^2 \right]^{1/2} \leq \bar{\epsilon}$. In general the net prompt emittance $\bar{\epsilon} = \sqrt{\epsilon_0^2 + 2\epsilon_0\bar{\epsilon} + \bar{\epsilon}^2}$, and $\epsilon \rightarrow \bar{\epsilon}$ under the influence of filamentation.
4. V. Balakin, A. Novokhatskii, and V. Smirnov, *Proc. Intl. Conf. High Energy Accel.*, Fermilab, 1982.
5. A. Chao, B. Richter, and C. Yao, *Nucl. Inst. Meth.* 178(1980)1.
6. J. T. Seeman, F.-J. Decker, and I. Hsu, *Proc. Intl. Conf. High Energy Accel.*, Hamburg, 1992.

Simulation of Emittance Dilution in Electron Storage Ring from Compton Backscattering*

L. N. Blumberg and E. Blum

National Synchrotron Light Source, Brookhaven National Laboratory
Upton, New York 11973

Abstract

A Monte-Carlo simulation of Compton backscattered $\lambda_L = 3.2\text{-}\mu\text{m}$ ($E_L = .38494\text{ eV}$) photons from an IR-FEL on 75-MeV electrons in a storage ring yields an RMS electron energy spread of $\Delta_E = 11.9\text{-keV}$ for a sample of 10^7 single scattering events. Electrons are sampled from a beam of natural energy spread $\sigma_E = 5.6\text{-keV}$ and damped transverse angle spreads $\sigma_x = .041\text{-mrad}$ and $\sigma_y = .052\text{-mrad}$ (100% coupling), scaled from the 200-MeV BNL XLS compact storage ring. The Compton-scattered X-Rays are generated from an integral of the CM Klein-Nishina cross-section transformed to the lab. A tracking calculation has also been performed in 6-dimensional phase space. Initial electron coordinates are selected randomly from a Gaussian distribution of RMS spreads $\sigma_{x0} = .102\text{-mm}$, $\sigma_{x'0} = .041\text{-mrad}$, $\sigma_{y0} = .018\text{-mm}$, $\sigma_{y'0} = .052\text{-mrad}$, $\sigma_{\phi0} = 22\text{-mrad}$ and $\sigma_{E0} = 6\text{-keV}$. A sample of 10000 electrons were each following for 40000 turns around the ring through an RF cavity of $f_{rf} = 211.54\text{-MHz}$ and peak voltage $V_m = 300\text{-keV}$. Preliminary results indicate that the resulting energy distribution is quite broad with an RMS width of $\Delta_E = 124\text{-keV}$. The transverse widths are only slightly increased from their original values, i.e. $\Delta_x = .106\text{-mm}$ and $\Delta_x = .043\text{ mrad}$. The scaled energy spread of $\Delta_E \sim 360\text{-keV}$ for $\sim 350,000$ turns desired in a 10-msec X-Ray angiography exposure is well within the RF bucket used here; even $V_m < 50\text{-keV}$ is adequate. Further, the electron energy spread adds a negligible RMS X-Ray energy spread of $\Delta_{EX} = .32\text{-keV}$. The electron energy damping time of $\tau_E = 379\text{-msec}$ at 75-MeV in an XLS-type ring allows for damping this induced spread and top-off of the ring between heart cycles.

1. INTRODUCTION

The production of X-Rays by Compton backscattering of laser photons by electron beams has been considered recently by several laboratories. At BNL we have numerically studied scattering of an infrared photon beam produced by a Free Electron Laser (IRFEL) from an electron beam in a low energy (75-570 MeV) Storage Ring [1-3]. Sprangle, et al. at NRL have proposed a configuration based on a 1- μm terawatt Nd:YAG laser beam scattering from low energy ($\sim 40\text{ MeV}$) electrons from a rapid-cycling betatron [4]. An experiment using another approach, an electron-linac-driven IRFEL photon beam scattered from a linac electron beam is underway at Vanderbilt [5]. The Compton backscattering studies at

BNL have been directed specifically at the medical problem posed by trans venous digital subtraction coronary angiography at the Iodine K-edge ($E_x = 33.17\text{-keV}$). This problem has heretofore been pursued experimentally using high field wiggler radiation from high energy electron storage rings by the Stanford-BNL group [6,7] and the DESY group [8] and there have been proposals for a somewhat lower ($\sim 1.3\text{ GeV}$) storage ring using a superconducting 8-T wiggler [9] or a pulsed $\sim 15\text{T}$ wiggler [10]. Previous BNL studies of Compton backscattering sources [2,3] have considered an in-ring FEL; however, it is clear for the intensities needed in angiography that the required FEL power exceeds the Renieri limit [11] and gives an electron energy spread too large for the FEL to operate. Renieri's estimate has been confirmed in numerical simulations by Luccio and Pellegrini [12]. In the present study we consider Blum's proposal [1] of an external, Linac-driven IRFEL in an optical resonator configuration colliding with a storage ring beam at the low-beta interaction region of the ring straight section. The model for the ring is the compact, 8.5-m circumference, 200-MeV XLS ring operated at BNL with peak currents in excess of 1A [13]. The ring parameters used here are scaled down to 75-MeV. The calculations were performed in two parts, (1) calculations of the angle and energy distributions resulting from a sample of 10^7 randomly selected single scattering events, and (2) a full 6-dimensional tracking calculation of 10000 randomly selected initial electron coordinates, with each electron followed for 40000 turns around the ring. The collision probability on each encounter of the electron with the photon bunch is computed from the total (Thomson) cross section σ_0 and the number of photons per bunch N_L . For the present calculation there are an average of 87 collisions per electron.

2. FORMULATION

Initial electron phase space coordinates are computed using a random Gaussian generator [14] and input values of the RMS widths of the damped distributions, σ_{x0} , $\sigma_{x'0}$, σ_{y0} , $\sigma_{y'0}$, $\sigma_{\phi0}$, and σ_{E0} of the XLS storage ring [13], scaled down to 75-MeV for the present application. The scattering angle Θ of the X-Ray relative to the electron direction is then obtained by random selection from a table of the normalized integrated Compton differential cross section vs. polar angle Θ [15],

$$\sigma_N(\Theta) = 2\pi \int_0^\pi (d\sigma/d\Omega)_{cm} J(\Theta) \sin\theta d\theta / \sigma_0 \quad (1)$$

*Work performed under the auspices of the U.S. Department of Energy, under contract DE-AC02-76CH00016.

where σ_0 is the total cross section from the integral of Eq. 1

from 0 to π . For the energies considered here $\sigma_e \approx 665$ mb. The expressions for $(d\sigma/d\Omega)_{cm}$ and the Jacobian transformation $J(\Theta)$ from the electron rest frame to the lab were taken from Sandorfi, et al. [16]. The energy of the X-Ray is then evaluated as

$$E_s(\theta) = 4\gamma^2 E_L / (1 + 4\gamma E_L / mc^2 + \gamma^2 \theta^2) \quad (2)$$

and the recoil electron energy is then $E = E_0 - E_s$. A random azimuthal angle ϕ is then generated in the interval $0 \leq \phi \leq 2\pi$. New momentum coordinates of the recoil electron are then obtained in the transverse (X-Y) and longitudinal (z) direction and new angle projections of the electron are computed as $x' = P_x/P_z$, $y' = P_y/P_z$. It is not necessary to modify the position coordinates x, y since we assume (unlike the XLS) that the interaction point is at the center of a dispersionless straight section with $\eta = \eta' = 0$. The electron is then transported around the ring by the one-turn transport matrix M_o to obtain new transverse coordinates x, x', y, y'

$$M_o = \begin{pmatrix} \cos 2\pi\nu & \beta_o \sin 2\pi\nu \\ -(\sin 2\pi\nu)/\beta_o & \cos 2\pi\nu \end{pmatrix} \quad (3)$$

and then passes through an RF cavity prior to re-entering the interaction region. The electron phase angle relative to the RF phase is also modified by the one-turn phase advance

$$\Delta\phi = 2\pi\alpha h(E - E_0)/E_o \quad (4)$$

where $\alpha = (\Delta C/C_o)/(\Delta p/p_o)$ is the momentum compaction factor and h is the harmonic number. We take $\alpha = .32$ and $h = 6$ from the XLS [13]. The RF cavity energy increment $E_c = eV_m \sin \phi$ also changes the longitudinal momentum component p_z ; we therefore modify the angles x' and y' after passage through the cavity. Finally, when the electron re-enters the interaction region, the probability of another collision with a photon of the laser bunch is evaluated as

$$P_c = N_L \sigma_e / A_{eff} \quad (5)$$

where N_L is the number of laser photons per bunch and A_{eff} is the effective overlap area of the electron and photon bunches. Here we assume equal transverse size of the bunches and $A_{eff} = 4\pi\sigma_x\sigma_y$.

3. RESULTS

For the single scattering case we show the resulting x' electron angle distribution in Fig. 1 for 10^7 scattering events and the corresponding electron energy distribution in Fig. 2. The resulting RMS width of the x' distribution, $\Delta x' \approx .041$ -mrad, is unchanged from the input width σ_x within the accuracy of this calculation. The resulting electron energy distribution is decreased by $\delta E = 16.7$ -keV, as expected since this calculation has no mechanism for restoring the electron energy lost in the electron-photon collisions. The resulting

RMS width of the electrons is $\Delta_e = 11.85$ -keV, a modest increase from the initial RMS spread of $\sigma_e = 5.6$ -keV. The double peak exhibited in Fig. 2 is not understood.

The realistic estimate of beam emittance dilution requires a multiturn calculation in which the six-dimensional phase volume (x, x', y, y', ϕ, E) is tracked for the desired ~ 10 msec duration of the X-Ray pulse. For the $f_r = 35.257$ -MHz rotation frequency of the ring model used here this is 352,570 turns. The collision probability per turn from Eq. 5 using $N_L = 3.24 \cdot 10^{18}$ photons/bunch (0.2-J/bunch) previously estimated [3] to obtain the required X-Ray flux for coronary angiography, is $P_c = 2.0757 \cdot 10^3$. Thus, each electron will suffer about $N_c = 732$ collisions on average. Since the energy of this ring is relatively low there is insignificant radiation damping during the 10 msec spill, and we have indeed not included synchrotron radiation loss in the calculation. The preliminary results quoted here are only for 40000 turns due to computer time limitations but we feel that the RMS spreads can be scaled by $\sqrt{N_c}$. The results for the ϕ and E distributions from a 10000 electron sample are shown in Fig. 3 and 4 and yield RMS spreads $\Delta\phi = .1155$ rad and $\Delta_e = .124$ -MeV. The E distribution is surprisingly uniform perhaps due to the limited statistical sample.

4. ACKNOWLEDGMENTS

Helpful comments on storage ring FELs and IR laser optics from K. Robinson, A. Luccio, G. Williams and A. Fisher were much appreciated. We thank D. Chapman, H. Zeman, and W. Thomlinson for numerous discussions of their angiography experiments, and A. Sandorfi for enlightenment on the physics of electron-photon scattering. Finally, We are grateful to E. Rubinstein for stimulating interest in this work and M. Blume for support of the present effort.

5. REFERENCES

- [1] E. B. Blum, NSLS unpublished report (April 1992).
- [2] L. N. Blumberg, BNL Report 47503 (May, 1992).
- [3] L. N. Blumberg, poster paper PD11, 12th Int. Conf. on Appl. of Accel. in Res. and Industry, Denton, TX. (Nov. 1992); BNL report 40816 (Nov. 1992).
- [4] P. Sprangle, A. Ting, E. Esarey and A. Fisher, NRL Report NRL/MR/4790-92-6973 (April, 1992), and J. Appl. Phys. 72 (11) 5032 (Dec. 1992).
- [5] P. Tompkins, W. Andrews, C. Brau, J. Waters, F. Carroll, D. Pickens and R. Price, paper F8, this conference. See also M. Mendenhall, paper BL3, 12th Int. Conf. on Appl. of Accel. in Res. and Industry, Denton, TX (Nov, 1992).
- [6] E. Rubinstein, J. C. Giacomini, H. J. Gordon, A. C. Thompson, G. Brown, R. Hofstadter, W. Thomlinson, and H. Zeman, Nucl. Instr. & Meth. A291 (1990) 80 and prior references therein.

- [7] W. Thomlinson, N. Gmur, D. Chapman, R. Garrett, N. Lazarz, H. Moulin, A. C. Thompson, H. D. Zeman, G. S. Brown, J. Morrison, P. Reiser, V. Padmanabahn, L. Ong, S. Green, J. Giacomini, H. Gordon and E. Rubinstein, Rev.Sci.Instr. 63(1) 1992.
- [8] W. R. Dix, W. Graeff, J. Heuer, M. Lohmann, B. Reime, R. Reumann, K. Engelke, C. Hamm, W. Kupper and B. Kaempf, DESY report SR 91-01(1991).
- [9] L. N. Blumberg, Stanford U. unpublished HEPL report (1983), reissued as BNL report 47356 (March, 1992).
- [10] H. Wiedemann, IEEE Trans. Nucl. Sci. NS-32 (1985) 3308.
- [11] A. Renieri, Il Nuovo Cim., Vol. 53B, 1 (Sept 1979) 160, and G. Dattoli and A. Renieri, Il Nuovo Cim., Vol. 59B(1), (Sept 1980) 1.
- [12] A. Luccio and C. Pellegrini, J. Appl. Phys. 55(3), (Feb 1984) 670.
- [13] J. B. Murphy, et al., Proc. of 1991 IEEE Part. Accel Conf., Conf. Record 91CH3038-7 (May, 1991) 1107.
- [14] L. Blumberg, RANGAUSS, unpublished (1992).
- [15] L. Blumberg, COMPTSIG, unpublished (1992).
- [16] A. M. Sandorfi, M. J. Levine, C. E. Thorn, G. Giordano, G. Matone and C. Schaerf, Proc. 1983 Part. Accel Conf., Santa Fe, NM, IEEE Trans. Nucl. Sci. NS-30 (1983) 3083. See also BNL report 32717 (1982).

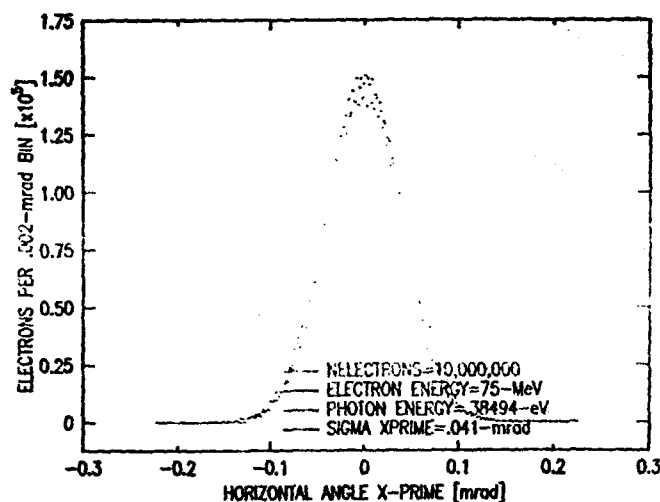


Fig. 1. ELECTRON HORIZONTAL ANGLE DISTRIBUTION

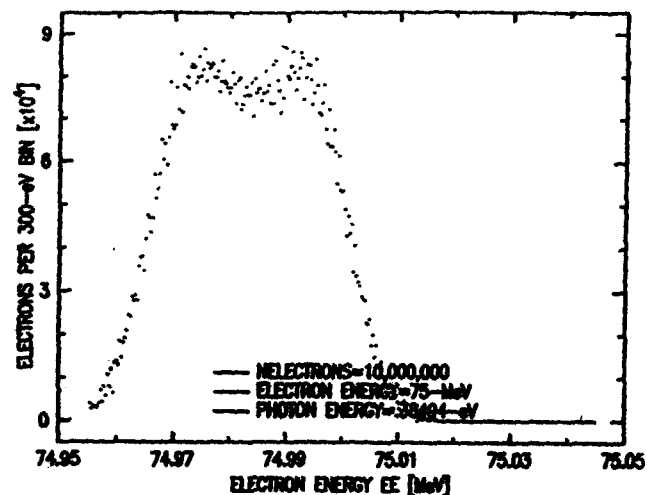


Fig. 2. ELECTRON ENERGY DISTRIBUTION IN COMPTON BACKSCATTERING

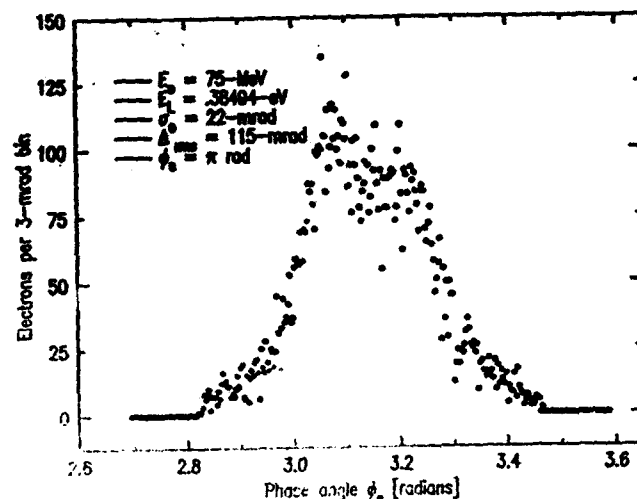


Fig. 3. ELECTRON PHASE DISTRIBUTION AFTER 40000 TURNS IN XLS

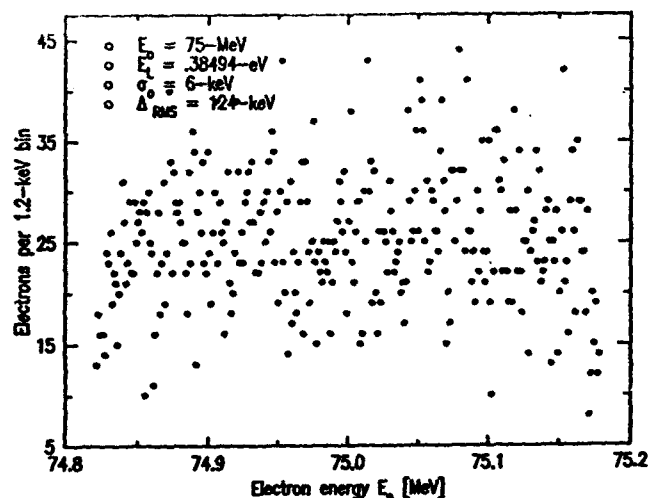


Fig. 4. ELECTRON ENERGY DISTRIBUTION AFTER 40000 TURNS IN XLS

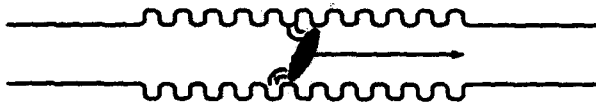
Transverse Effects of Longitudinal Wakefields at High Dispersion

Franz-Josef Decker

Stanford Linear Accelerator Center*, Stanford, California 94309

Abstract

In high energy linear colliders the transverse beam emittance has to be preserved in order to achieve small interaction spots. Beams with trajectory offsets in cavities excite transverse wakefields which kick the tail of the beam leading to an undesired emittance growth. Here we will concentrate on the longitudinal wakefield creating an energy deviation ΔE_W within the beam. At high dispersion η the beam will be spread out corresponding to its initial (and/or correlated) energy spread ΔE_e (or ΔE_{rf}) and is therefore very sensitive to energy changes. The energy variation ΔE_W will cause a transverse emittance blow up in the high dispersion regions. The effect can be estimated by comparing the betatron size $\sigma_x = \sqrt{\beta\epsilon}$ with displacement $\Delta x = \eta \Delta E_W / E$. Some kicks and displacements will compensate each other along the beam line. Simulation results are presented showing how much is really compensated and the final emittance contribution of this effect for the SLC Ring-To-Linac transport line. To minimize it, any vacuum pipe irregularities, like bellows, diameter steps, collimators, etc. should be smoothed or avoided at higher dispersion areas.



1 Introduction

At the SLC, the 10 mm long bunch of the damping ring (DR) is compressed in the RTL section down to the necessary 1 mm length for the main linac. The compression is achieved by introducing an longitudinal energy correlation with a compressor cavity followed by a high dispersive region (η), where particles of different energy travel along different trajectories. Particles at $\pm\sigma_l$ (bunch length $\sigma_l \approx 10$ mm) get an energy difference of $\Delta E/E = \pm 1.4\%$ and therefore at $\eta = 1.0$ m $\Delta x = \pm 14$ mm is about 100 times bigger than the betatron size.

$$\Delta x = \eta \cdot \frac{\Delta E}{E} \quad \text{and} \quad \Delta E = E_{rf} \sin(2\pi\sigma_l/\lambda), \quad (1)$$

with an energy $E = 1200$ MeV, rf-amplitude of $E_{rf} = 30$ MeV and $\lambda = 105$ mm. Additionally to the intended

*Work supported by the Department of Energy contract DE-AC03-76SF00515.

path length difference, the off axis particles also experience any nonlinear kicks coming from transverse wakefields or higher order magnetic fields causing an emittance blow up [1].

Besides these transverse kicks which are most severe at high beta points, there is a mechanism with longitudinal wakefields creating an effective beam offset which is worse for low beta points ("longitudinicity"). The indirect effect over several phase space axes and the compasion with the transverse effect are given at the example of the RTL.

2 Direct and Indirect Phase Space Correlation

Wakefields introduces normally a direct curved correlation between the longitudinal axis z and the energy E by the longitudinal wakefield, or x and the transverse position x or y by the transverse wakefield. These first order linear (e.g. linear in z) excitations are the most common source of emittance blow up for instance in the linac. A correlation to another phase space axis (say x , E e.g. by BNS phasing) starts a filamentation of x, x' which makes the initial emittance blow-up practically unrecoverable. Indirect effects need more than one correlation for instance E, x at high dispersion plus z, E from the longitudinal wakefield.

2.1 Sensitivity to Direct Effects

Direct effects in the transverse are most sensitive to big offsets e.g. at high dispersion or wrong off-axis steering, and where the disturbed phase space axis (x' or y') is small which is at high beta points (RTL lattice and final focus are sensitive). At high dispersion even the higher order wakefields near the aperture have to be considered. The longitudinal correlation between z, E is given by the induced wakefield and energy gain and therefore a constant over the acceleration if no other correlation (like BNS) are involved. It is not easy possible to cancel the correlation by the same technique since there is no longitudinal focussing.

2.2 Indirect Effects

Indirect correlations are in some way different and their effect might not be as obvious as in the direct case where big offsets and sensitive areas are the reasons. Let's take the RTL as an example andh a beam with no energy spread

(compressor cavity off). The beam emittance is expected to be unchanged at the end. The high dispersion area enlarges the beam not very much and it stays on axis away from non-linear fields. The longitudinal phase space seems to be decoupled. But on the other hand, the longitudinal wakefields introduce an energy spread ΔE , creating an offset at high dispersion $E, \Delta E$, which will blow-up the emittance! (Therefore the name "longitudinicity" to keep indirect effects in mind).

Other indirect effects might be some coupling type correlation between e.g. x, y , where a wide x distribution produces different kicks over z, y wakefields, which is even more severe for flat beam emittance ratios. This has not been studied further.

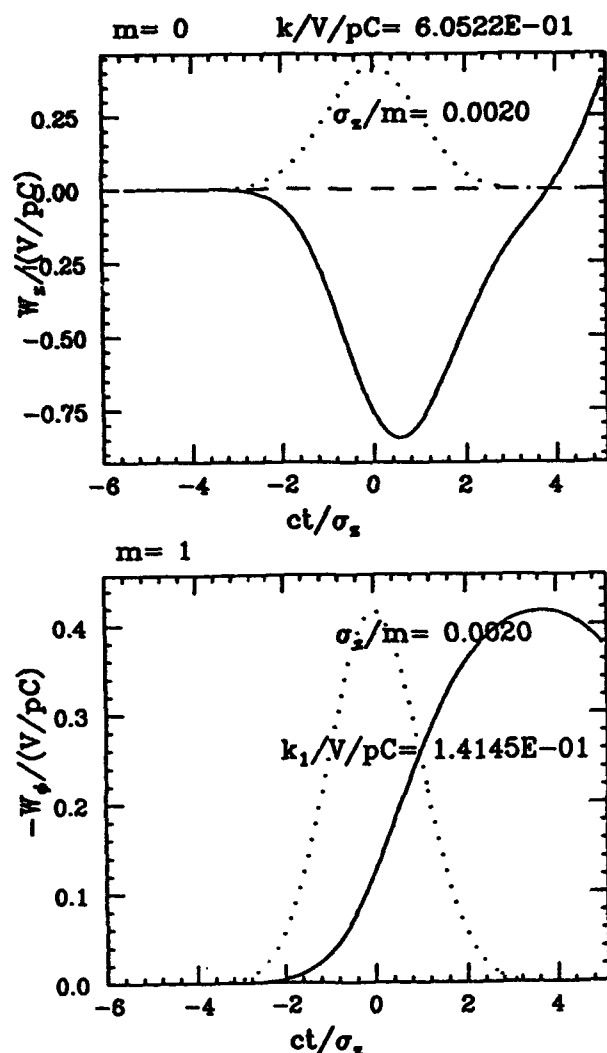


Figure 1: Wakefield Calculation.

The calculated longitudinal W_z and transverse W_ϕ wake potentials for the lowest transverse order and $\sigma = 2$ mm is shown.

3 Sources of Wakefields

First of all there is no reason to put unsleeved bellows at a high dispersion region. Even pump-outs, profile monitors, BPMs and other beam pipe transitions can be designed in a way to avoid any significant wakefield generation [2]. The only problem might be collimators which need to be close to the beam to fulfill their duty. The finals remaining parts should be the smaller resistive-wall wakefields.

But since the RTL was not designed with this in mind, we have 30 bellows in the high dispersion region of the north RTL and 25 in the south. The mostly used bellows have a diameter of $2a = 49$ mm with 20 convolutions each 6 mm high and 2.5 mm wide which gives an overall length of 3 m active bellows. Fig. 1 shows simulation results with TBCI [3] for 1/5 of a bellow with a 2 mm (σ) long bunch. The results of these and higher order wakefields are discussed and summarized in the next section.

4 Quantitative Kicks and Offsets

4.1 Single and Combined Excitations

The sizes and effects are summarized in Tab. 1. The transverse and longitudinal wakefields are taken at about one σ_z (transverse) or at their maximum (longitudinal) and multiplied by 8 nC ($5 \cdot 10^{10}$ particles). The higher order wakefields are scaled to an offset of a two and one $\sigma_z = 10$ mm particle at about $\eta = 0.9$ m (21 mm and 12 mm). Since two betatron oscillations share 30 bellows, the effect of 5 are combined. Their kicks or offsets are calculated and compared with high and low beta function values. As reference also the size due to dispersion is shown.

Comparison of Transverse and Longitudinal Wakefields							
Order m	Transverse			Longitudinal			
	1	2	3	0	1	2	3
$W_{\phi,z}$ [V/pC]	1.5	3.0	4.5	4	8	8	8
$W \cdot 8$ nC [kV]	12	24	36	32	64	64	64
at $r = 0.85a$ [kV]	10	15	16	32	46	33	24
at $r = a/2$ [kV]	6	3	1	32	16	4	1
5 bellows [kV]	30	15	5	160	80	20	5
$p = 1.2$ GeV/c	25			133			
$x' = p_\perp / p$ [μ rad]							
$\eta = 1$ m							
$z = \eta \Delta E / E$ [μ m]							
$\gamma c = 16 \mu\text{m}-\mu\text{rad}$	12 μ rad			580 μ m			
z, x' at $\beta = 50$ m							
z, x' at $\beta = 1$ m	83 μ rad			83 μ m			
$z = \eta \Delta E / E$ [mm]				14			

Table 1: Summary of Bellow Wakefield Effects.

Transverse wakefields induce a kick, while longitudinal wakefields cause indirectly an offset. Both have different sensitivities at different beta functions.

4.2 Cancellation

The offsets and kicks are about 1.5 to 2 times bigger than σ_x or σ'_x at the corresponding sensitive beta functions. Since some of the kicks cancel out (see Fig. 2), the emittance blow-up might be not too bad, but to rely on a cancellation of big numbers is always a risk. The observed emittance blow-up with $3 \cdot 10^{10}$ particles was about from $\gamma\epsilon = 1.6 \cdot 10^{-5}$ m-rad to $1.8 \cdot 10^{-5}$ m-rad in 1992 with round beams.

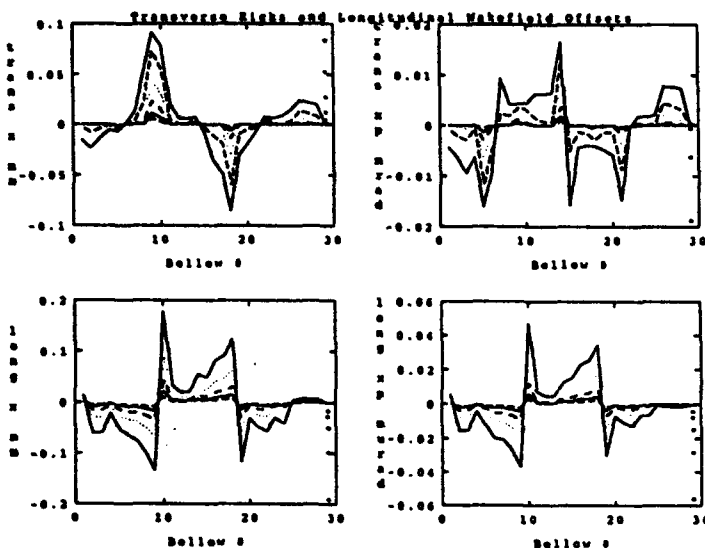


Figure 2: Summarized Kicks and Offsets.

There are 30 bellows in the north RTL which cause different kicks or offsets of a part of the beam. Here the result of each bellow is shown as a position x and angle xp variation at the entrance to the linac where $\sigma_x = 160 \mu\text{m}$ and $\sigma'_x = 45 \mu\text{rad}$. The transverse and longitudinal effect are studied separately since they influence different parts of the bunch. The different curves are the effects of higher orders m at an offset which corresponds to an energy offset of a particle at σ_1 . At the end (29) there are the sums for each order indicated by dots.

4.3 Less and More Sensitivity in 1993/94

With flat beams in 1993 we expected an emittance of about $3.2 \cdot 10^{-5}$ m-rad and achieved it also at the end of the RTL measured in the linac. The bigger emittance in x is less sensitive to emittance blow-ups either from wakefields or non-linear magnetic fields. In the 1994 run we will probably run with higher currents due to a new damping ring vacuum chamber against microwave instability oscillations [4], and we might reduce the horizontal emittance by creating combined functions in magnets [5]. This will make a sleeving of the RTL bellows even more urgent than now.

5 Conclusion

The transverse wakefields of a beam at high dispersion lead to dispersive aberrations of higher order, which can be mainly compensated by magnetic elements, like for higher order magnetic errors. The longitudinal wakefield has a small effect on the compression process, but has an indirect effect on the transverse beam size. This chromatic like effect ("longitudinicity") should be avoided by reducing the amount of generated wakefields, e.g. with sleeves in the bellows.

Acknowledgement

I would like to thank T. Raubenheimer for some helpful discussions and his interest in "longitudinicity" especially for future compressor schemes.

References

- [1] F.-J. Decker, *Transverse Wakefield at High Dispersion*, EPAC'92, Berlin, March 1992, p. 759.
- [2] Like the recent new damping ring vacuum chamber design, (to be published later).
- [3] T. Weiland, *Transverse Beam Cavity Interaction, Part I: Short Range Forces*, NIM 212 (1983), 329-348.
- [4] P. Krejcik, K. Bane, P. Corredoura, F.-J. Decker, J. Judkins, T. Limberg, M. Minty, R. Siemann, SLAC; F. Pedersen, CERN, *High Intensity Bunch Length Instabilities in the SLC Damping Rings*, PAC'93, Washington, May 1993.
- [5] T. Raubenheimer, R. Early, T. Limberg, H. Moehammer, *A Possible Redesign of the SLC Damping Rings*, PAC'93, Washington, May 1993.

Error and Tolerance Studies for the SSC Linac

D. Raparia, Chu Rui Chang, F. Guy, J. W. Hurd, W. Funk
Superconducting Super Collider Laboratory*
2550 Beckleymeade Ave., Dallas, Texas 75237

and

K. R. Crandall
AccSys Technology, Inc

Abstract

This paper summarizes error and tolerance studies for the SSC Linac. These studies also include higher-order multipoles. The codes used in these simulations are PARMTEQ, PARMILA, CCLDYN, PARTRACE, and CCLTRACE.

I. INTRODUCTION

The SSC Linac [1] will deliver a 600 MeV H^- beam with pulse lengths of 2 to 35 μsec at a nominal current of 21 mA for injection into the low energy booster (LEB) with transverse normalized rms emittance of $\leq 0.3\pi$ mm-mrad. Emittance from the magnetron ion-source is about 0.18π mm-mrad for 30 mA and the requirement at the end of the CCL is 25 mA with an emittance of $\leq 0.3\pi$ mm-mrad. This means that emittance growth budget for the entire linac is only about 67% ! The purpose of this work was to find out the tolerance limits to meet the challenge of preserving emittance through the linac.

The errors were divided into the three groups. Beam related errors e.g. displacements of beam with respect to accelerator axis at injection into the accelerator, mismatched beam in phase space, energy shift, energy spread etc. falls into the first group. Since steering is provided in each degree of freedom before each type of accelerator, this group of errors will not be presented here except the radio frequency quadrupole (RFQ). The second group of errors include time independent errors. This group of errors includes manufacturing errors e.g. errors in tank length, cell-length, coupling-slot-length, quad gradient, higher order components in the quad fields, tuning errors e.g. field-flatness, field-amplitude, field-phase, and alignment errors e.g. tank displacements, quad displacements, quad tilt and yaw, quad rotation etc. The third group of errors consists of time dependent errors e.g. amplitude and phase errors from rf source including feed back, mechanical vibrational errors etc. This group of errors is responsible for the jitter in the beam. The tolerance limits presented for these errors are not the limits on rms errors but the tolerance limits which are uniformly distributed between the limits.

II. LOW ENERGY BEAM TRANSPORT (LEBT)

The low energy beam transport (LEBT) works like the matching section for the Radio-Frequency Quadrupole

*Operated by the Universities Research Association, Inc. for the U.S. Department of Energy, under contract No. DE-AC02-89ER40486

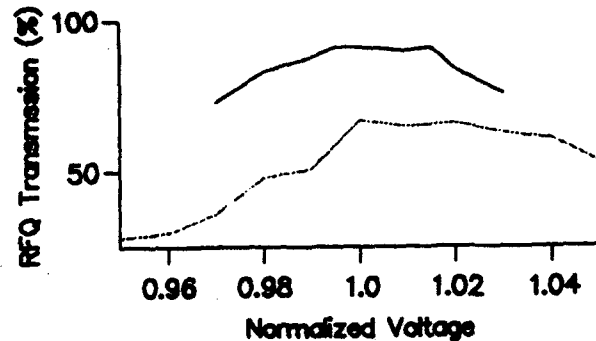


Figure 1: RFQ Transmission vs Voltage normalized to design voltage. solid line: HESQ, dotted line: einzel lens.

(RFQ), therefore the first and second groups of errors are not considered. Only time dependent errors were considered, to find the voltage tolerance on the einzel lens and helical electrostatic quadrupole (HESQ). First using AXCEL [2] and HESQT, optimum voltages were determined; then voltages on einzel lens and HESQ were varied by $\pm 5\%$ and the transmission through the RFQ was calculated using PARMTEQ. Figure 1 shows the curve for transmission vs voltage normalized to design voltage. The tolerance limit on the voltage was set to 0.3%.

III. RADIO FREQUENCY QUADRUPOLE (RFQ)

Since the RFQ bore radius is small and there are not enough steering elements in the LEBT, the first group of errors which includes misalignment in the injection of the beam, mismatched beam in the phase space, beam energy fluctuations and energy spread from the ion source were considered [3]. PARMTEQ was revised to include the higher order multipole expansion for the vane tip field [4]. Figure 2a shows the transmission vs x displacement of the beam and figure 2b shows the transmission vs beam angle offset. Figure 3a shows the transmission vs the mismatch factor as defined in TRACE3D. For each mismatch factor there are infinite different sets of twiss parameters (α, β) which lie on the ellipse. However for each mismatch factor, only two sets of α and β lie at the two vertices of the ellipse. In figure 3a, the upper curve corresponds to the choice of α and β such that the initial beam radius is smaller than the matched radius while the lower curve corresponds to the initial beam radius bigger than the matched beam. Figure 3b shows the transmission vs the energy shift from 35 keV in the injected beam. The time dependent errors were

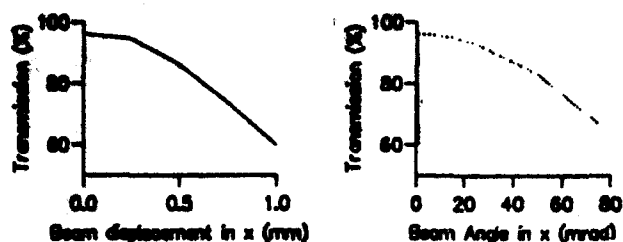


Figure 2: (a) Transmission vs Beam Displacement in x (mm). (b) Transmission vs Beam Angle in x (mrad)

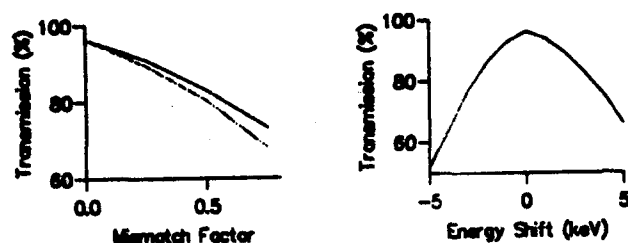


Figure 3: (a) Transmission vs the mismatch factor. Upper curve, the initial mismatched beam radius is smaller than matched beam. Lower curve, the initial mismatched beam radius is bigger than matched beam. (b) Transmission vs energy shift from 35 keV

amplitude (vane voltage) and phase of accelerating field. Their tolerance limits are 0.5% and 0.5 deg respectively.

IV. DRIFT TUBE LINAC (DTL)

In the case of the DTL, the second group of errors includes time independent errors e.g. tank displacement, cell-to-cell phase and field errors, accelerating field tilt, quad displacements, quad tilt and yaw, quad gradient errors, quad rotation and higher-order multipoles. The third group of errors includes time dependent errors e.g. field amplitude and phase errors from the klystrons. Since the drift tubes are mounted on stem they may vibrate. The time dependent and time independent error tolerances are listed in Table 1. Figure 5 shows the probability distribution of the emittance growth for the errors listed in Table 1. This curve was obtained by using PARTRACE [5]. The most sensitive error for emittance growth is quad rotation; the tolerance limit on this error is 0.5 deg. The tolerance limits on the multipoles were obtained using PARMILA. An upper bound was assigned to the amplitude of the $n = 3, 4$ and 5 components and values are chosen at random between zero and this tolerance limit for each multipole. The phase of each of these multipole components was chosen at random. The $n = 6$ component was assumed to be systematic, and its amplitude was set at the tolerance limit and phase angle to zero. For this study to be realistic, alignment errors as well as multipoles were included. The

Error	Tol. Limit
Time Independent	
Tank disp	± 0.25 mm
Quad disp	± 0.1 mm
Quad Pitch and Yaw	± 1.0 deg
Quad Roll	± 0.5 deg
Quad Strength	0.- 5% (Graded)
Multipoles, $n=3,4,5,6$	1.5% @ 6 mm
Tank Field Tilt	$\pm 3\%$
Cell-to-Cell Field	$\pm 3\%$
Cell-to-Cell Phase	± 0.5 deg
Time Dependent	
Tank Field	$\pm 3\%$
Tank Phase	± 0.5 deg
DT vibration amp(rms)	6.0 μ m

Table 1: Tolerance Budget for the SSC DTL.

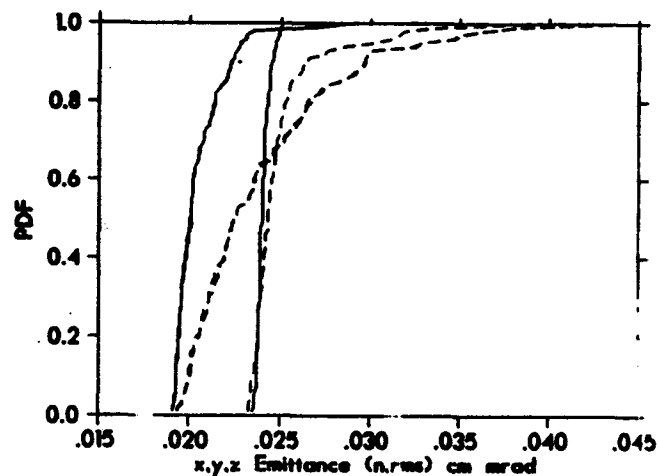


Figure 4: Probability distribution of the emittances (x,y and z) out of the DTL for errors listed in Table 2., dotted curves show the emittances when the errors were twice as large as given in Table 2. Curves show the probability that the emittances will at or below the plotted value.

M %	QR								
	0.00 deg			0.25 deg			0.50 deg		
	ϵ_x	ϵ_y	ϵ_z	ϵ_x	ϵ_y	ϵ_z	ϵ_x	ϵ_y	ϵ_z
0.0	.21	.20	.28	.22	.21	.28	.23	.22	.28
1.0	.21	.20	.28	.22	.21	.28	.23	.22	.28
1.5	.21	.20	.28	.22	.21	.28	.23	.22	.28
2.0	.21	.20	.28	.22	.21	.28	.23	.22	.28

Table 2: Output (average of 50 runs) normalized rms emittances ϵ_x , ϵ_y and ϵ_z are in units of π mm-mrad.

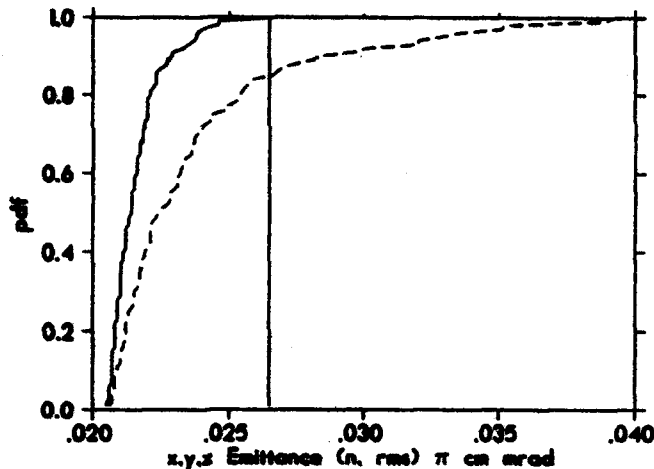


Figure 5: Probability distribution of the emittances (x,y and z) out of the CCL for errors listed in Table 3., dotted curves show the emittances when the errors were twice as large as given in Table 3. Curves show the probability that the emittances will at or below the plotted value.

results of 12 cases, where each case consisted of 50 runs, are summarized in Table 2. The twelve cases were for all combinations of clocking errors (QR) of 0., 0.25, 0.5 degrees and multipole errors (M) of 0.0, 1.0, 1.5, and 2.0% @ 6 mm. The quadrupole displacements of 0.1 mm and tank displacement tolerance of 0.25 mm were used in all cases, and the beam was "steered" back on the axis after each tank.

V. COUPLED CAVITY LINAC (CCL)

The second group of errors for the CCL includes time independent errors in tank displacements, cell-length (cell-to-cell phase) coupling-slot-size (cell-to-cell field), bridge-coupler -slot-size (tank-to-tank field), bridge-coupler-length (tank-to-tank phase), quad displacement, quad tilt and yaw, quad rotation, quad-to-quad field gradient and high order multipoles. The third group of errors includes time dependent errors e.g. amplitude and phase error from the klystron and quad gradient error due to the power supplies. These tolerance limits are listed in Table 3. Figure 6 shows the probability distribution of the transverse emittance for the tolerance limit listed in Table 3. These calculations were done using CCLTRACE [6]. In the case of the CCL, higher order multipoles which are achievable in

Error	Limits
Time Independent	
Tank disp	± 0.1 mm
Quad disp	± 0.1 mm
Quad Pitch and Yaw	± 1.0 deg
Quad Roll	± 0.5 deg
Quad Strength	$\pm 0.10\%$
Tank Field	$\pm 0.5\%$
Tank phase	± 0.5 deg
Cell-to-Cell Field	$\pm 1.0\%$
Cell-to-Cell Phase error	$\pm 0.5\%$
Time Dependent	
Quad Strength	$\pm 0.1\%$
Klystron Field	$\pm 0.5\%$
Klystron Phase	± 0.5 deg

Table 3: Tolerance Budget for the SSC CCL.

the electromagnet quad are 0.056, 0.005, 0.0056, 0.00022% for $n=3,4,5$, and 6 respectively, at the radius of 1 cm. CCL-DYN [6] simulations shows these multipoles have no effect on the emittance growth. The quad and tank displacement used in these simulations are listed in Table 3.

VI. CONCLUSIONS

These studies show that if we can achieve specified tolerances, we can meet the challenging requirement of emittance of $\leq 0.3 \pi$ mm mrad at 600 MeV. The most sensitive error for the emittance growth is quad rotation.

We would like to thank to Jun Wu for his help in PARMTEQ simulations.

VII. REFERENCES

- [1] L. W. Funk, "The SSC Linear Accelerator," these proceedings.
- [2] E. F. Jaeger and I. C. Whitson, "Numerical Simulation for Axially Symmetric Beamlets in the Duopigatron Ion Source," ORNL/TM-4990, Oak Ridge, TN (1975)
- [3] A. Cuccheti, "Beam Dynamics Error Study on RFQ for SSC", Los Alamos National Laboratory memorandum, AT-1:91-241.
- [4] F. W. Guy, *et al*, "Simulation Support for Commissioning and operating the SSC LINAC", these proceedings.
- [5] K. R. Crandall, "Error Studies using partrace, A New Program that Combines PARMILA and TRACE 3-D," 1988 Linear Accelerator Conference Proceedings, CEBAF-Report-89-001, p 335, Newport News, Virginia, Oct 3- 7 1988.
- [6] K. R. Crandall, Private Communication.

Emittance Growth Due to Dipole Ripple and Sextupole

H.-J. Shih, J.A. Ellison, M.J. Syphers, and B.S. Newberger
Superconducting Super Collider Laboratory*
Dallas, TX 75237

Abstract

Ripple in the power supplies for storage ring magnets can have adverse effects on the circulating beams: orbit distortion and emittance growth from dipole ripple, tune modulation and dynamic aperture reduction from quadrupole ripple, etc. In this paper, we study the effects of ripple in the horizontal bending field of the SSC in the presence of nonlinearity, in particular, the growth in beam emittance.

I. INTRODUCTION

For simplicity, we will assume that dipole ripple is localized, i.e., it affects only one dipole magnet. An element-by-element tracking simulation using the program ZTRACK¹ with a localized dipole ripple yields the results shown in Figure 1. In the simulation, 192 particles are tracked, the ripple has a frequency of 743.29 Hz and an amplitude of 10 Gauss, the nominal bending field is 6.684×10^4 Gauss, and the horizontal betatron tune is 123.7821548. Note that the revolution frequency at the SSC is 3441 Hz. We observe from Figure 1 that dipole ripple causes the beam emittance to oscillate between the initial value (3.0×10^{-10} m) and a much larger value ($\approx 2.5 \times 10^{-7}$ m), and that this oscillation is damped with emittance leveling off around an intermediate value ($\approx 1.0 \times 10^{-7}$ m). The beam emittance here is defined as the emittance averaged over the whole beam. Thus it appears that dipole ripple causes the beam to go from one equilibrium state to another where the beam has a larger emittance. In this simulation, we have chosen the ripple frequency to be close to the betatron frequency of 748.62 Hz ($\approx 3441 \times .21785$) and a large ripple amplitude so that we can observe the final equilibrium state in a short time.

One can easily imagine the physics possibly at work here: dipole ripple causes the whole beam to wobble around the design orbit, and nonlinearity, which is built in the full lattice and results in betatron tune dependent on betatron amplitude, then smears the whole beam over a larger phase space area. Our motivation for this work is to understand this quantitatively. In particular, we want to explain the following regarding the beam emittance: the existence of an apparent equilibrium, the amplitude and period of initial oscillations, the final equilibrium value, and how much time it takes to reach the final equilibrium state. To this end, we have constructed a theoretical model using a second-order perturbation theory and the method of averaging. Since the nonlinearity, which is present in the full lattice simulation above, was found to produce a quadratic dependence of betatron tune on betatron amplitude, we represent it in our model by a single sextupole. Our theoretical calculations are in excellent agreement with results from

the simple tracking simulations using a linear lattice plus kicks from a single sextupole and a localized dipole ripple.

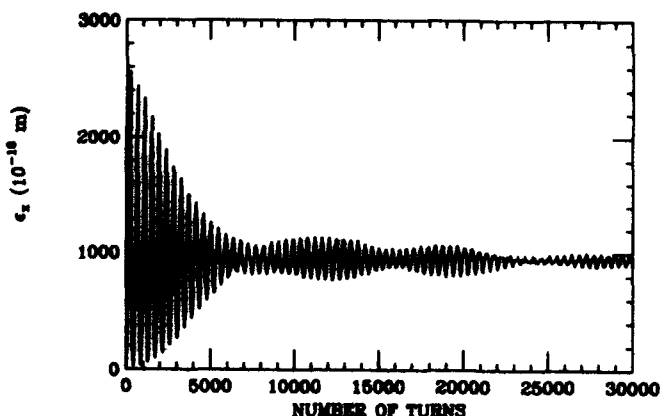


Figure 1. Variation of beam emittance in time from a full lattice simulation.

II. THEORETICAL MODELS

The perturbed beam dynamics is described by the Hamiltonian

$$H(x, x', s) = H_0(x, x', s) + \epsilon H_1(x, s) \quad (1)$$

where $H_0 = \frac{1}{2}(x'^2 + K(s)x^2)$. Here s is the path length along the design orbit, x the horizontal coordinate, $x' = dx/ds$, $K(s)$ the focusing or defocusing function, and ϵ the smallness parameter of the perturbation. For perturbation from a single sextupole and a localized dipole ripple, we have

$$\epsilon H_1(x, s) = \frac{1}{6}S(s)x^3 - F(s)x \quad (2)$$

$$S(s) = S_0 \delta_p(s - s_1) \quad (3)$$

$$F(s) = A_0 \cos(\omega_r \tau + \phi_r) \delta_p(s - s_0) \quad (4)$$

where S_0 is the sextupole strength, δ_p is the periodic Dirac delta function, s_1 the position of the sextupole, $A_0 = (B_r/B_0)\theta_0$, B_r the ripple amplitude, B_0 the nominal bending field, θ_0 the nominal bending angle, ω_r the angular ripple frequency, τ the time, and s_0 the position of the localized dipole ripple.

To explain initial periodic oscillations, we will consider only the dipole ripple perturbation. Using the independent variable $t = \int ds (\nu \beta(s))^{-1}$ and the dependent variable $\eta = x/\sqrt{\beta(s)}$ where $\beta(s)$ is the betatron function, and ν the betatron tune, the equation of motion becomes

$$\frac{d^2 \eta}{dt^2} + \nu^2 \eta = \nu \beta_0^{\frac{1}{2}} A_0 \cos(Q_r t + \theta_r) \delta_p(t - t_0) \quad (5)$$

where $Q_r = \omega_r/\omega_0$, ω_0 is the revolution frequency, and β_0 the betatron function at the dipole ripple. Since the right-hand side of (5) can be expressed in the form

$$\sum_{n=-\infty}^{\infty} (A_n e^{i(n+Q_r)t} + B_n e^{-i(n+Q_r)t}),$$

*Operated by the Universities Research Association, Inc., for the U.S. Department of Energy under Contract No. DE-AC35-89ER40486.

¹L. Schachinger and Y. Yan, SSCL Report SSCL-N-664, September, 1989.

we seek a particular solution of the same form. The particular solution we find can be written as

$$\eta_p = \left(\frac{\nu}{2\pi}\right) \beta_0^{\frac{1}{2}} A_0 \sum_{n=-\infty}^{\infty} \frac{\cos((n+Q_r)t - n t_0 + \theta_r)}{\nu^2 - (n+Q_r)^2}. \quad (6)$$

With initial conditions $\eta(0) = \eta_0$ and $\xi(0) = \xi_0$, where $\xi = d\eta/dt$, the solution to (5) is then given by

$$\eta = (\eta_0 - \eta_p(0)) \cos \nu t + (\xi_0 - \xi_p(0)) \sin \nu t + \eta_p(t). \quad (7)$$

The results on beam emittance calculated using (7) with $B_r = .322$ Gauss and $\omega_r = (2\pi)(743.29)$ rad sec⁻¹ are shown in Figure 2 by a solid curve, which agrees well with results from a full lattice simulation indicated by circles. The crosses are results from a simple tracking simulation, to be described in Section III.

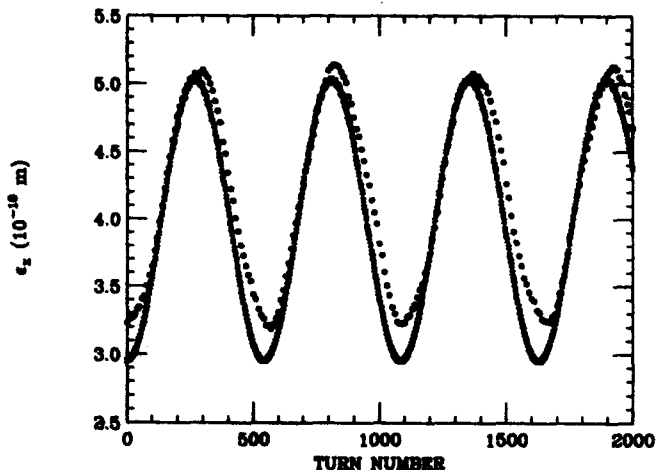


Figure 2. Variation of beam emittance in time. Curve: exact theory; circles: full lattice tracking; crosses: simple tracking.

To explain the final equilibrium state, we will consider both dipole ripple and sextupole perturbations. We will carry out the second-order perturbation calculation in the action-angle representation. The action-angle variables J and ϕ are defined through the following transformation

$$\eta = \left(\frac{2J}{\nu}\right)^{\frac{1}{2}} \cos \phi, \quad \xi = -(2J\nu)^{\frac{1}{2}} \sin \phi. \quad (8)$$

The new Hamiltonian for the action-angle variables is given by

$$\mathcal{H}(J, \phi, t) = \nu J + \epsilon \nu^2 \beta(s) H_1 \left(\beta^{\frac{1}{2}}(s) \left(\frac{2J}{\nu}\right)^{\frac{1}{2}} \cos \phi, s \right). \quad (9)$$

Here s is understood to be a function of t . From (9) one obtains the Hamiltonian equations of motion

$$\dot{J} = \epsilon f(J, \phi, t), \quad \dot{\phi} = \nu + \epsilon g(J, \phi, t). \quad (10)$$

To find approximate solutions of (10) with initial conditions $J(0) = J_0$ and $\phi(0) = \phi_0$, we look for a special autonomous system given by

$$\dot{J} = \epsilon F_1(I) + \epsilon^2 F_2(I) \quad (11)$$

$$\dot{\theta} = \nu + \epsilon G_1(I) + \epsilon^2 G_2(I) \quad (12)$$

with initial conditions $I(0) = J_0 + \epsilon u(J_0, \phi_0)$, $\theta(0) = \phi_0 + \epsilon v(J_0, \phi_0)$, and a near identity transformation

$$J = I + \epsilon P_1(I, \theta, t) + \epsilon^2 P_2(I, \theta, t) \quad (13)$$

$$\phi = \theta + \epsilon Q_1(I, \theta, t) + \epsilon^2 Q_2(I, \theta, t) \quad (14)$$

such that J and ϕ satisfy (10) to $O(\epsilon^3)$ with initial conditions $J(0) = J_0 + O(\epsilon^2)$ and $\phi(0) = \phi_0 + O(\epsilon^2)$. It can be shown that $J(t)$ and $\phi(t)$ approximate $J(t)$ and $\phi(t)$ to an accuracy of $O(\epsilon^2)$ over a time interval of $O(\frac{1}{\epsilon})$. Thus the task of finding solutions to (10) is then reduced to that of finding F_1, F_2, G_1, G_2, P_1 , and Q_1 . (We don't need to find P_2 and Q_2 if we are concerned with an $O(\epsilon^2)$ accuracy.) Because f and g are periodic in ϕ and quasi-periodic in t , (two periods are involved: one is associated with the beam revolution and the other associated with ripple) we require that P_1, P_2, Q_1 and Q_2 are also periodic in θ and quasi-periodic in t .

For dipole ripple and sextupole perturbations, one can write $f = f^{(r)} + f^{(s)}$ and $g = g^{(r)} + g^{(s)}$ where the superscripts (r) and (s) stand for contributions from dipole ripple and sextupole respectively. A lengthy calculation involving expansion in ϵ to the second order and averaging over θ and t yields $F_1 = 0$, $G_1 = 0$, $F_2 = 0$, $G_2 = G_2^{(s)} = (g_1^{(s)} P_1^{(s)} + g_2^{(s)} Q_1^{(s)})$ where $\langle \rangle$ denotes the average over θ and t , the subscripts I and θ denote the derivatives with respect to I and θ respectively, and $P_1^{(i)}$ and $Q_1^{(i)}$ ($i = r, s$) satisfy the homological equations $P_{1t}^{(i)} + \nu P_{1\theta}^{(i)} = f^{(i)}$ and $Q_{1t}^{(i)} + \nu Q_{1\theta}^{(i)} = g^{(i)}$ respectively. We refer the readers to the paper by H. Dumas et al.² for more information on our averaging procedure. In summary, our approximate solutions J and ϕ are given by

$$\dot{J} = 0, \quad \dot{\theta} = \nu + \epsilon^2 G_2^{(s)}(I) \quad (15)$$

$$J = I + \epsilon (P_1^{(r)}(I, \theta, t) + P_1^{(s)}(I, \theta, t)) \quad (16)$$

$$\phi = \theta + \epsilon (Q_1^{(r)}(I, \theta, t) + Q_1^{(s)}(I, \theta, t)) \quad (17)$$

with $u(J, \phi) = -P_1(J, \phi, 0)$, $v(J, \phi) = -Q_1(J, \phi, 0)$, and $G_2^{(s)}, P_1^{(s)}, Q_1^{(s)}, P_1^{(r)}$ and $Q_1^{(r)}$ given by

$$G_2^{(s)}(I) = \frac{3}{64\pi^2} I \beta_1^3 S_0^2 \times \left\{ -\frac{10}{9} + \nu \left(\psi(1+\nu) - \psi(1-\nu) + \frac{\psi(1+3\nu) - \psi(1-3\nu)}{3} \right) \right\} \quad (18)$$

$$P_1^{(s)}(I, \theta, t) = -\left(\frac{\nu}{32}\right)^{\frac{1}{2}} I^{\frac{1}{2}} \beta_1^{\frac{3}{2}} S_0 \times \left\{ \frac{\cos(\nu([t'_1] - \pi) - \theta)}{\sin(\pi\nu)} + \frac{\cos(3\nu([t'_1] - \pi) - 3\theta)}{\sin(3\pi\nu)} \right\} \quad (19)$$

$$Q_1^{(s)}(I, \theta, t) = -\left(\frac{\nu}{128}\right)^{\frac{1}{2}} I^{\frac{1}{2}} \beta_1^{\frac{3}{2}} S_0 \times \left\{ 3 \frac{\sin(\nu([t'_1] - \pi) - \theta)}{\sin(\pi\nu)} + \frac{\sin(3\nu([t'_1] - \pi) - 3\theta)}{\sin(3\pi\nu)} \right\} \quad (20)$$

$$P_1^{(r)}(I, \theta, t) = \left(\frac{\nu}{8}\right)^{\frac{1}{2}} I^{\frac{1}{2}} \beta_0^{\frac{3}{2}} A_0 \times \left\{ \frac{\cos((\nu - Q_r)([t'_0] - \pi) - (\theta - Q_r t - \theta_r))}{\sin \pi(\nu - Q_r)} + \frac{\cos((\nu + Q_r)([t'_0] - \pi) - (\theta + Q_r t + \theta_r))}{\sin \pi(\nu + Q_r)} \right\} \quad (21)$$

²H.S. Dumas, J.A. Ellison and A.W. Sáenz, *Annals of Physics* 209, 97 (1991).

$$Q_1^{(r)}(I, \theta, t) = \left(\frac{\nu}{32}\right)^{\frac{1}{2}} I^{-\frac{1}{2}} \beta_0^{\frac{1}{2}} A_0 \times \left\{ \frac{\sin((\nu - Q_r)([t'_0] - \pi) - (\theta - Q_r t - \theta_r))}{\sin \pi(\nu - Q_r)} + \frac{\sin((\nu + Q_r)([t'_0] - \pi) - (\theta + Q_r t + \theta_r))}{\sin \pi(\nu + Q_r)} \right\} \quad (22)$$

where $\psi(x) \equiv \Gamma'(x)/\Gamma(x)$, β_1 is the betatron function at the sextupole, $t'_0 \equiv t - t_0$, $t'_1 \equiv t - t_1$, and $[\]$ denotes the modulus between 0 and 2π . Our perturbation calculations indicate that, up to the second order, dipole ripple contributes only in the near-identity transformations (16) and (17). The vector field, (15), is still given by sextupole perturbation.

Figure 3 shows the phase space distribution of a beam after 50000 turns calculated using (15)–(22). The beam consists of 500 particles and is initially uniformly distributed in the ranges of $0.1 < x < 0.3$ mm and $-2.4 < x' < -2.0$ μ rad. In this calculation, the ripple has a frequency of 720 Hz and an amplitude of 0.322 Gauss, and the sextupole strength is $S_0 = -0.55580$, which reproduces the relationship $G_2^{(s)} = (1.0567 \times 10^3)I$ obtained from a fit to the dependence of betatron tune on betatron amplitude in the full lattice mentioned in Section I. For an initial beam whose distributions in x and x' are Gaussian (and thus the distribution in the angle variable is uniform in the linear approximation), the averages of the second order terms over the angle variable are zero, and one has to go to a third-order perturbation calculation. However, a serious drawback of the action-angle approach is that $\epsilon P_1^{(r)}/I$ is proportional to $I^{-\frac{1}{2}}$, and the perturbation calculation breaks down for small I . We are now working on a new set of variables which doesn't have this problem.

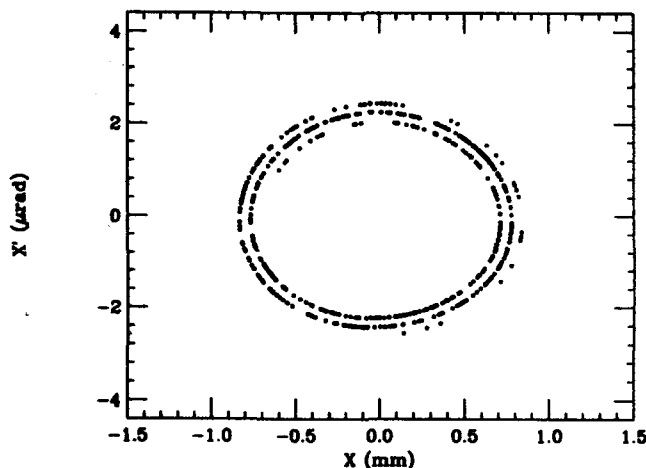


Figure 3. Phase space distribution of a beam after 50000 turns from a perturbation calculation.

III. TRACKING SIMULATIONS

To check our theoretical models, we have tracked particles using linear transfer matrices with kicks from a single sextupole and a localized dipole ripple. This simple tracking method has produced the results indicated by crosses in Figure 2, and reproduced those shown in Figure 3. It also gives results very similar to those shown in Figure 1. The results from a run following 500 particles with $B_r = 1$ Gauss, $\omega_r = 2\pi(720)$ rad sec^{-1} , and

$\nu = 123.78677$ is shown in Figure 4. Because the computing time with the simple tracking simulation is greatly reduced, we can now more easily determine the dependence of the final equilibrium emittance on a few relevant parameters, e.g., ripple amplitude. Figure 5 summarizes our study on the dependence of relative emittance growth on ripple amplitude and betatron tune. The ripple frequency is fixed at 720 Hz.

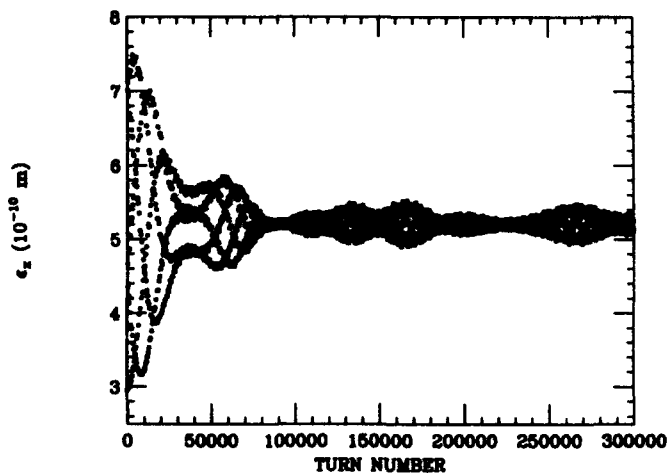


Figure 4. Variation of beam emittance in time from a simple tracking simulation.

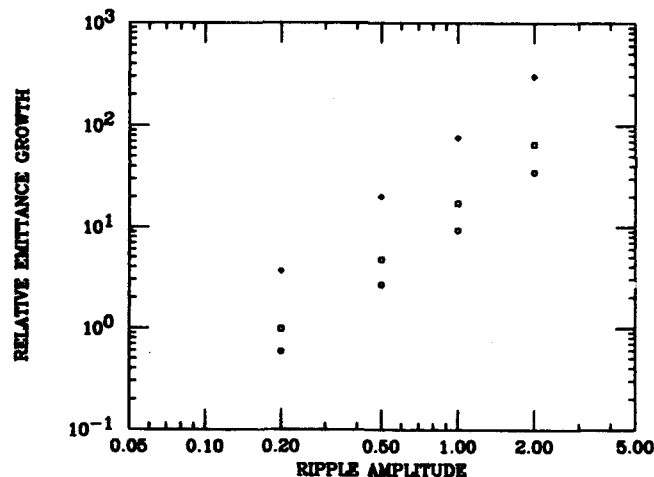


Figure 5. Relative growth in beam emittance as a function of ripple amplitude. Circles: $\nu = 123.77877$; squares: $\nu = 123.78215$; diamonds: $\nu = 123.78677$.

IV. CONCLUSIONS

Theoretical models have been developed to explain the features of emittance evolution observed from the full lattice simulation in the presence of dipole ripple. Our calculation with just dipole ripple is exact and explains the observed initial oscillations of beam emittance. Our model for the apparent existence of final equilibrium state is based on a second-order perturbation calculation involving both dipole ripple and sextupole. Its predictions agree very well with results from simple tracking simulations using a linear lattice plus kicks from dipole ripple and sextupole. The simple tracking method that we have developed is very fast and very suitable for exploring final equilibrium states by changing relevant parameters over a wide range.

J.A.E. gratefully acknowledges discussions with M. Kummer.

Proton-Proton Scattering Contribution to Emittance Growth

T. Garavaglia
Superconducting Super Collider Laboratory*
2550 Beckleymeade Ave., Dallas, TX 75237 USA

Abstract

Proton-proton scattering contributes to the emittance growth of the SSC. A formulation is given and used to estimate the mean scattering angle, which is used to determine the contribution to SSC emittance growth resulting from elastic pp scattering. The method is based upon Lorentz invariants, and it permits the determination of the cross-section for scattering in the center of mass (c.m.) system, as well as scattering from a fixed target (f.t.). Also an example is given for the case of electromagnetic pp scattering, which results from single virtual photon exchange.

I. INTRODUCTION

The contribution from pp elastic scattering to transverse emittance growth is determined for the SSC. Elastically scattered protons with a small scattering angle will remain within the Collider proton beam. These scattered particles contribute to the growth of the beam's transverse emittance. Numerical results for emittance growth resulting from pp scattering and other sources are given in [1]. In this paper, a summary is given of the analytical methods that are used to determine the mean scattering angle resulting from pp elastic scattering. Lorentz invariants and cross-sections are defined in Appendix A.

II. PROTON-PROTON ELASTIC SCATTERING

The contribution to transverse emittance growth, for one degree of freedom, resulting from pp elastic scattering is given by

$$\left(\frac{d\epsilon_x}{dt}\right) = (\beta_{1s}^* \mathcal{L}_1 + \beta_{2s}^* \mathcal{L}_2) \sigma_{el} \langle \theta_s^2 \rangle / (MN_B), \quad (2.1)$$

where β_i^* and \mathcal{L}_i are, respectively, the beta function and the luminosity at the i^{th} interaction point. In this expression N_B is the number of protons per bunch, M is the number of bunches, σ_{el} is the pp elastic scattering cross-section, and $\sqrt{\langle \theta_s^2 \rangle}$ is the rms value of the pp elastic scattering angle in the center of mass system, which is projected onto the transverse x -direction. A similar expression occurs for the transverse y -direction. The mean scattering angle can

be estimated from the differential elastic scattering cross-section

$$\left(\frac{d\sigma_{el}}{d\Omega}\right)_{c.m.} = \frac{S}{4\pi} \left(\frac{dT}{dT}\right)_{c.m.}, \quad (2.2)$$

where S and T are Lorentz invariants. These invariants, defined in (A1), are $S \approx 2E_{c.m.}$, and $T \approx -S \sin^2(\theta/2) \approx -S(\theta_x^2 + \theta_y^2)/4$. The invariant differential cross-section for pp elastic scattering is [2]

$$\frac{d\sigma_{el}}{dT} \approx \frac{\sigma_T^2}{16\pi} (1 + \rho^2) e^{bT}, \quad (2.3)$$

where σ_T is the total pp cross-section, b is the slope parameter, and $\rho \approx 0$ is the ratio of the real part to the imaginary part of the scattering amplitude. Assuming that the slope parameter is a constant, one can integrate the differential cross-section to obtain $b \approx \sigma_T^2 / 16\pi \sigma_{el}$. With the approximation $\sigma_{el} \approx (1/4)\sigma_T$, one finds $b \approx \sigma_T / 4\pi$.

Using the approximations above, the differential cross-section in the c.m. system becomes

$$\left(\frac{d\sigma_{el}}{d\Omega}\right)_{c.m.} \approx \frac{S\sigma_T^2}{64\pi^2} e^{\left(\frac{\theta_x^2}{2} + \frac{\theta_y^2}{2}\right)}, \quad (2.4)$$

where

$$\sigma_{\theta_s} = \sqrt{\langle \theta_s^2 \rangle} = (bS/2)^{-1/2}. \quad (2.5)$$

This is the expression to be substituted into (2.1) to find $d\epsilon_x/dt$. For colliding proton beams with $\sqrt{S} = 40$ TeV and $\sigma_T \approx 130$ mb, one finds $b \approx 26.6$ GeV⁻² and

$$\sigma_{\theta_s} = \sqrt{\langle \theta_s^2 \rangle} = 6.9 \mu\text{rad}. \quad (2.6)$$

In the above, the value of the total pp scattering cross-section is determined from

$$\sigma_T = 38.5 + 1.33 \ln^2\left(\frac{\sqrt{S}}{10 \text{ GeV}}\right), \quad (2.7)$$

which is obtained from cosmic ray data [3]. Theoretical models giving values for the total and elastic pp cross-sections can be found in [4].

Using the above techniques, one can estimate the rms scattering angle $\sqrt{\langle \theta^2 \rangle}$ for the scattering of a proton in a 20 TeV beam from a fixed proton. The scattering angle in the c.m. system for high energy pp scattering is found from

$$\cos(\theta) \approx \frac{2T}{S} + 1. \quad (2.8)$$

*Operated by the Universities Research Association, Inc., for the U.S. Department of Energy under Contract No. DE-AC35-89ER40486.

The scattering angle for a proton of energy $\omega = S/2m$ from a proton at rest is found from

$$\cos(\tilde{\theta}) \approx 1 - \frac{2\sin^2(\theta/2)}{(S/m^2)} - \frac{4}{(S/m^2)^2}. \quad (2.9)$$

Using $\cos \tilde{\theta} \approx 1 - (1/2)\sin^2 \tilde{\theta}$, the fixed target scattering angle is related to the c.m. scattering angle θ through

$$\tilde{\theta} \approx \frac{\sqrt{2}}{(\omega/m)} \sqrt{\left(\frac{\theta^2(\omega/m)}{4} + 1\right)}. \quad (2.10)$$

For the scattering of a 20 TeV proton from a proton at rest, the rms scattering angle in the c.m. system is found from (2.5), with $\sqrt{S} = 193$ GeV, $\sigma_T = 50.2$ mb and $b \approx 10.3 \text{ GeV}^{-2}$, to be $\sqrt{\langle \theta^2 \rangle} \approx 3.2$ mrad. The corresponding angle in the fixed target system is found to be $\sqrt{\langle \tilde{\theta}_s^2 \rangle} \approx 47 \mu\text{rad}$.

III. PROTON-PROTON ELECTROMAGNETIC SCATTERING

In this example, pp scattering is treated as an electromagnetic event, and the scattering of two fermions of initial four-momenta a and b to a final state of four-momenta c and d results from the exchange of a single virtual photon. The system of units $\hbar = c = m = 1$ is used. Since both the initial and final states involve identical particles, these states must be antisymmetrical. The initial state $|I\rangle$ and the final state $|F\rangle$ are represented as

$$|I\rangle = \frac{|ab\rangle - |ba\rangle}{\sqrt{2}} \quad |F\rangle = \frac{|cd\rangle - |dc\rangle}{\sqrt{2}}. \quad (3.1)$$

The matrix element for this process is

$$\begin{aligned} (F|M|I) &= [(cd|M|ab) - (cd|M|ba) + \\ &\quad (dc|M|ba) - (dc|M|ab)]/2 \\ &= e^2 [J^\mu(d, b) D_{\mu\nu}(a - c) J^\nu(c, a) - (d \leftrightarrow c)], \end{aligned} \quad (3.2)$$

where the fermion current is $J^\mu(c, a) = \bar{u}_c \gamma^\mu u_a$. The photon propagator is $D_{\mu\nu}(a - c) = 4\pi g_{\mu\nu} / ((a - c)^2 + i\epsilon)$. We use the fermion density matrix $\rho_{ij}(a) = u_{ai} \bar{u}_{aj}$, which has the property $\text{Tr} \rho(a) = 2$.

The invariant differential cross-section for this process is

$$\frac{d\sigma_{el}}{dT} = \frac{1}{16\pi f(S, a, b)} \mathcal{M}(S, T), \quad (3.3)$$

where $\mathcal{M}(S, T) = |(F|M|I)|^2$. For the scattering of unpolarized fermions when the polarization of the final state fermions is not observed, the initial state spin density matrices for a and b are of the form $\rho_0(a) = (\not{1} + 1)/2$. For the final states $|c\rangle$ and $|d\rangle$, which include a summation over the final spin states, the corresponding density matrices are

multiplied by two. The invariant differential cross-section for this case is now found to be

$$\begin{aligned} \frac{d\sigma_{el}}{dT}(ab \rightarrow cd) &= \frac{\pi e^4}{64S(S/4 - 1)} [A(S, T, U) + A(S, U, T) \\ &\quad - B(S, T, U) - B(S, U, T)]. \end{aligned} \quad (3.4)$$

The invariant functions are

$$A(S, T, U) = \frac{4}{T^2} T^{\mu\nu}(d, b) T_{\mu\nu}(c, a) \quad (3.5)$$

$$B(S, T, U) = \frac{4}{TU} T^{\mu\nu}{}_{\mu\nu}(b, c, a, d), \quad (3.6)$$

where

$$T^{\mu\nu}(c, a) = \text{Tr}[(\not{c} + 1)\gamma^\mu(\not{a} + 1)\gamma^\nu], \quad (3.7)$$

$$T^{\mu\nu\lambda\sigma}(b, c, a, d) = \text{Tr}[\gamma^\mu(\not{b} + 1)\gamma^\nu(\not{c} + 1)\gamma^\lambda(\not{a} + 1)\gamma^\sigma(\not{d} + 1)]. \quad (3.8)$$

Upon evaluation of the traces, the invariant functions become

$$A(S, T, U) = \frac{32}{T^2} [S^2 + U^2 + 8T - 8] \quad (3.9)$$

$$B(S, T, U) = -\frac{32}{TU} [S^2 - 8S + 12]. \quad (3.10)$$

In the high energy limit when S becomes large, one finds

$$\frac{d\sigma_{el}}{dT}(ab \rightarrow cd) \approx \frac{4\pi e^4}{T^2}. \quad (3.11)$$

The rms value of the c.m. scattering angle associated with (3.11) can be found using (2.8) in the form

$$\langle \cos \theta \rangle \approx 1 - \langle \theta^2 \rangle / 2 = 2 \langle T/S \rangle + 1, \quad (3.12)$$

where

$$\langle T \rangle = \int_{T_{\min}}^{T_{\max}} T(d\sigma_e/dT) dT / \sigma_e, \quad (3.13)$$

and $\sigma_e = \int (d\sigma_e/dT) dT$. The rms value of the scattering angle is written in terms of the projection on the transverse direction as $\sqrt{\langle \theta^2 \rangle} = \sqrt{2 \langle \theta_x^2 \rangle}$. The integration limits are found from $T \approx \theta^2/4$, where θ_{\max} and θ_{\min} are found from the uncertainty principal, $\Delta r \Delta \theta \approx \hbar/p$, and r_{\max} and r_{\min} are found from the beam size and proton radius, respectively. One finds for $\sigma_{el} < \theta^2 >$, which appears in (2.1), $1.6 \times 10^{-40} \text{ m}^2$ from (2.3) and $1.8 \times 10^{-42} \text{ m}^2$ from (3.11), which is smaller.

APPENDIX A: Kinematics and Cross-Sections

In this appendix, the kinematical variables and cross-sections used in the analysis are given. Particles characterized by four-momenta a and b interact elastically to yield particles characterized by four-momentum c and d . For this process, energy-momentum conservation is represented as $a + b = c + d$, where a typical four-vector is represented as $a = (a^0, \mathbf{a})$, such that $a^2 = (a^0)^2 - \mathbf{a} \cdot \mathbf{a} = m_a^2$. The

interaction channels are defined according to the Lorentz invariants

$$S = (a+b)^2, T = (a-c)^2, U = (a-d)^2, \quad (A1)$$

which satisfy $(S+T+U) = a^2 + b^2 + c^2 + d^2$.

In the c.m. system, one finds the invariant expressions for energy, momentum, and scattering angle

$$\mathcal{E}_a = \mathcal{E}(S, a, b) = (S + a^2 - b^2)/4(S/4)^{1/2}, \quad (A2)$$

$$\mathcal{E}_b = \mathcal{E}(S, b, a), \mathcal{E}_c = \mathcal{E}(S, c, d), \mathcal{E}_d = \mathcal{E}(S, d, c),$$

$$|a| = |b| = [f(S, a, b)/4S]^{1/2}, |c| = |d| = [f(S, c, d)/4S]^{1/2}, \quad (A3)$$

and

$$\cos \theta_{ac} = (T - a^2 - c^2 + 2\mathcal{E}_a \mathcal{E}_c)/2|a||c|, \quad (A4)$$

with

$$f(S, a, b) = [S - (m_a + m_b)^2][S - (m_a - m_b)^2]. \quad (A5)$$

In the fixed target system, the corresponding relations are

$$\omega_a = \omega(S, a, b) = (S - a^2 - b^2)/2m_b,$$

$$\omega_b = m_b, \omega_c = -\omega(U, c, b), \omega_d = -\omega(T, d, b), \quad (A6)$$

$$|a| = f^{1/2}(S, a, b)/2m_b, |b| = 0,$$

$$|c| = f^{1/2}(U, c, b)/2m_b, |d| = f^{1/2}(T, d, b)/2m_b, \quad (A7)$$

and

$$\cos \bar{\theta}_{ac} = [2b^2(T - a^2 - c^2) - (S - a^2 - b^2)(U - b^2 - c^2)]/[f(S, a, b)f(U, c, b)]^{1/2}. \quad (A8)$$

The differential cross-sections are found from the definition of the invariant total cross-section for the interaction of two particles initially in the states $|a\rangle$, and $|b\rangle$ and the subsequent production of an n -particle final state, where each particle is characterized by a momentum state $|p_i\rangle$.

This cross-section is defined as

$$\sigma(S, T) = \frac{1}{2f^{1/2}(S, a, b)(2\pi)^{3n-4}} \times \int dp_1 dp_2 \dots dp_n$$

$$\prod_{i=1}^n \delta(p_i^2 - m_i^2) \theta(p_i) \times \delta(a+b - \sum_{i=1}^n p_i) \mathcal{M}(S, T, U), \quad (A9)$$

with $\theta(p) = [(p^0/\omega) + 1]/2$, $\omega = (|p|^2 + m^2)^{1/2}$, and

$$\mathcal{M}(S, T, U) = |\langle f | \mathcal{M} | a, b \rangle|^2,$$

where $\langle f | \mathcal{M} | a, b \rangle$ is the transition amplitude from the initial to the final state. In (A9), one uses an invariant definition of the flux, which is represented as the magnitude of the relative velocity $|\mathbf{v}_a - \mathbf{v}_b|$ in the c.m. system. The flux becomes $F = f^{1/2}(s, a, b)/2\mathcal{E}_a \mathcal{E}_b$.

Particular differential cross-sections may now be obtained from (A9). Of special interest is the differential cross-section defined formally as

$$\frac{d\sigma}{dT} = \sigma(S, T) \delta[T - (a-c)^2]. \quad (A10)$$

For scattering into the solid angle $d\Omega_{ac}$, one finds for elastic scattering in the c.m. system

$$\frac{d\sigma}{d\Omega_{c.m.}} = \frac{1}{4\pi S} f^{1/2}(S, a, b) f^{1/2}(S, c, d) \frac{d\sigma}{dT}. \quad (A11)$$

The corresponding differential cross-section in the f.t. system may be found from (A8) and (A10) to be

$$\frac{d\sigma}{d\Omega_{f.t.}} = \frac{2f^{1/2}(S, a, b)f^{3/2}(U, c, b)}{\pi g(S, T, 1, m, 1, m)} \frac{d\sigma}{dT}. \quad (A12)$$

For the elastic scattering of a particle of unit mass with a particle of mass m , one finds the expression

$$g(S, t, 1, m, 1, m) = 128m^2[(S/4)^2 + ST/16 - (S/4)(m^2+1)/2 - (T/4)(m^2-1)/4 + (m^2-1)^2/16]. \quad (A13)$$

The integration indicated in (A9) and (A10), when there is a two-particle final state characterized by four-momenta c and d , is performed in the c.m. system using the momentum-space measure

$$dcdd = |c|^2 d|c| d\Omega_c \frac{dc^2}{2c^0} dd \frac{dd^2}{2d^0} \quad (A14)$$

to find (3.3).

IV. REFERENCES

- [1] W. Chou, S. Dutt, T. Garavaglia, and S. K. Kauffmann, these proceedings.
- [2] K. Goulianos, "Diffractive and rising cross-sections," *Comments on Nucl. Part. Phys.* 17, No. 4, pp. 177-193 (1987).
- [3] M. Honda et.al., *Phys. Rev. Lett.* 70, 525 (1993).
- [4] P.V. Landshoff, "Soft hadron physics," *Joint International Lepton-Photon & Europhysics Conference on High Energy Physics*, Vol. 2, pp. 365-373 (World Scientific, 1991).

Source Size Variation and Ion Effects in the SRS at Daresbury

J. A. Clarke, D. M. Dykes, S. F. Hill, E. A. Hughes, M. W. Poole, P. D. Quinn, S. L. Smith, V. P. Suller, L. A. Welbourne
SERC Daresbury Laboratory, Daresbury, Warrington, WA4 4AD, UK.

Abstract

Source dimensions in the electron storage ring are routinely monitored on a diagnostic beam line. During recent recommissioning of the SRS, following the installation of a second wiggler magnet, relatively poor vacuum conditions were experienced. Large step changes in source size have been measured and broad tune signals have been seen, together with other effects characteristic of ion influences. Changes of source size and beam stability as a function of ion clearing electrode voltage have also been observed. This paper summarises all such effects observed and comments on their probable causes. It also includes other data on source dimensions, such as measured emittance coupling and the effect of insertion devices in the lattice.

I. INTRODUCTION

The source size of the stored electron beam in the SRS is monitored routinely and now uses a fully automated computer data acquisition system. Recording the beam profiles during every stored beam has brought to light some interesting patterns of source size behaviour. This paper summarises some of the results obtained recently. Of particular interest is the way in which positive ions appear to affect the beam. This paper emphasises the results that show such ion dependent phenomena. After a recent vacuum system let-up, for the installation of a second superconducting wiggler magnet [1], relatively poor vacuum conditions existed as the vacuum system reconditioned. The opportunity was taken to study alternative methods of controlling ion behaviour.

II. SOURCE SIZE DIAGNOSTICS

The SRS has a dedicated diagnostic beamline which monitors the visible synchrotron radiation emitted by the stored electron beam. This diagnostic facility has been described in detail elsewhere [2]. The beam profiles are measured by imaging the visible synchrotron radiation onto a pair of photodiode arrays, one for each axis. Recently the system has been expanded to include computer controlled data acquisition. The output of the arrays is read into a Macintosh computer controlling a range of instruments. This allows accurate curve fitting to be carried out on the data. The system is fully automated and is generally allowed to run for periods of approximately 24 hours. All of the software is written using the commercial software package LabVIEW [3]. LabVIEW is a graphical programming system for data acquisition, analysis and presentation. By assembling graphical software modules in the form of block diagrams the programmer avoids the need for cumbersome text-based code.

III. SOURCE SIZE VARIATION

A. Typical Beam Behaviour

The beam profiles are recorded routinely during every operational stored beam period. On the SRS typical starting currents are of the order of 250 mA after being ramped to the full energy of 2 GeV. The beam lifetime is generally around 25 hours. All of the 160 rf buckets are filled.

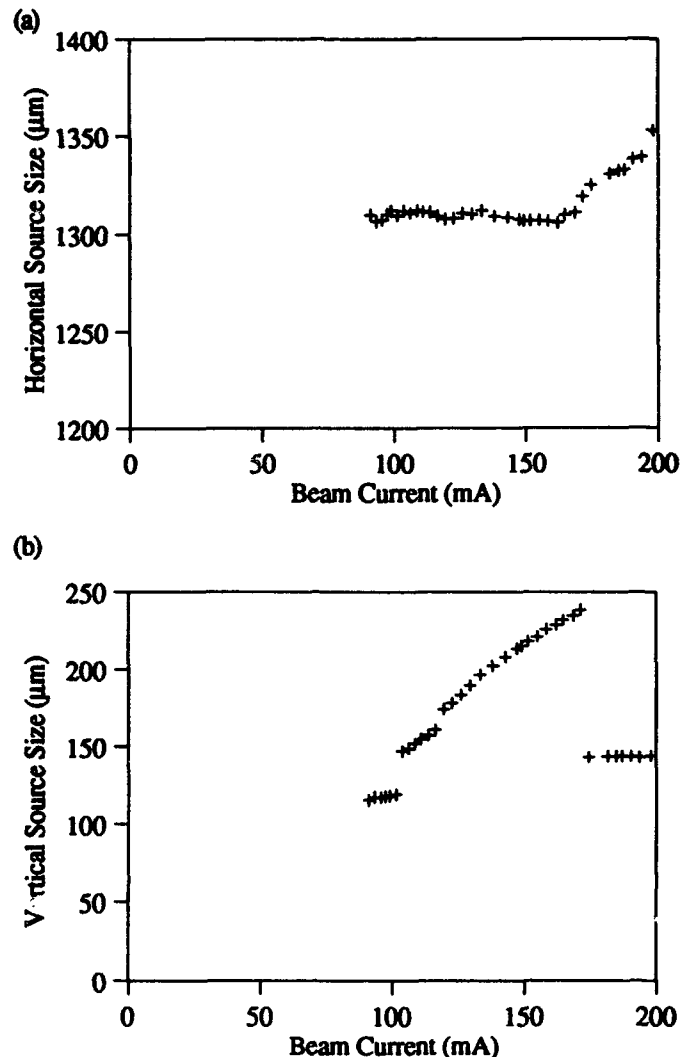


Figure 1. Typical horizontal (a) and vertical (b) source size measurements on the SRS at 2 GeV.

After opening the vacuum system to install the second superconducting wiggler magnet in early 1992 the residual gas pressure in the SRS was relatively high ($\approx 7 \times 10^{-9}$ Torr). This led to some interesting changes in profile during periods of stored beam. A typical example of how the profile varied as the current decayed is shown in Figure 1. Note how the

vertical step change appears to coincide with a levelling off of the horizontal profile. The step like changes apparent in the vertical profile are thought to be due to ion species trapping and detrapping. This behaviour has been observed to become less common as the vacuum has improved ($\sim 3 \times 10^{-9}$ Torr). It is usual for the vertical profile to decrease in a smooth fashion as the beam current decays at lower pressures and presumably less ions, however the horizontal profile does still show some unpredictable behaviour.

Clearly unusual behaviour cannot be automatically attributed to ions. A rigorous exercise was undertaken to identify and eliminate other possible causes. On the SRS there are two well established working points in betatron tune space (one for high emittance and one for low). The unpredictable beam profile behaviour has been observed at both working points. No coherent signals are associated with the phenomena which points away from certain instabilities. Also, the betatron tune signals observed with a pick-up are relatively wide at higher residual gas pressures, particularly in the vertical plane (± 0.008 compared with ± 0.001 at lower pressures).

B. The Influence of Ion Clearing Electrodes

Ion clearing electrodes are installed above and below the beam orbit in each of the sixteen dipole vessels. These are used routinely during operations. To demonstrate the necessity to operate with the electrodes on, the electron beam profiles have been recorded during the decay of a 2 GeV beam under typical operating conditions with and without the clearing voltage applied. The vertical source size for the two cases is shown in Figure 2. In this case a clearing voltage of -500 V has produced a significant reduction in vertical profile and with lower point to point scatter. Clearly the ion clearing electrodes are necessary for minimising the influence of ions on the electron beam.

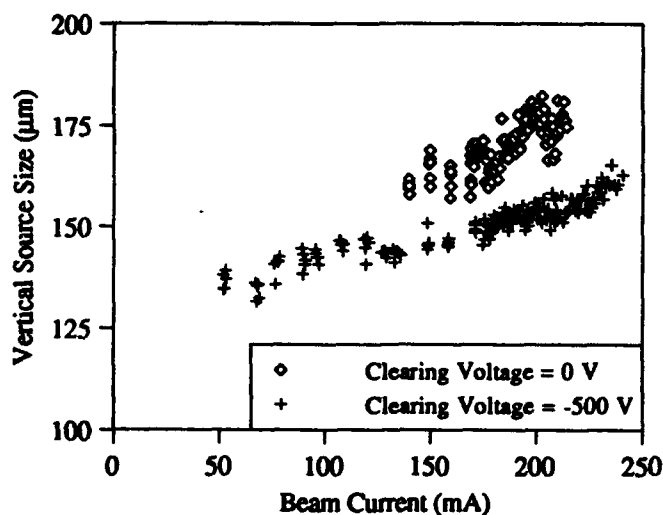


Figure 2. Vertical source size as a function of beam current for different ion clearing voltages.

A more extensive optimisation than can be detailed here has been undertaken of the actual routine value to be used for the clearing voltage. This has found that most of the benefit is gained from the first -100 V but additional voltage does have a useful effect. In general the ion clearing electrodes are used at a level of -600 V.

C. Different Fill Structures

It is well known that the trapping of ions depends greatly upon the fill structure employed. By leaving a number of consecutive rf buckets empty during injection the threshold current for ion capture can be greatly reduced. The influence of the fill structure on the beam dimensions has been investigated on the SRS. A beam was injected with approximately 30 of the possible 160 rf buckets filled consecutively. At 2 GeV typical operational conditions were applied and the beam was allowed to decay naturally. The source dimensions were compared with those of the next two normal operational beams which both had all 160 bunches filled. Note that for all of these beams the ion clearing electrodes were employed at their nominal value of -600 V. The vertical profiles obtained are shown in Figure 3. It is clear that the vertical source size is highly influenced by the fill structure as expected. Simple linear theory has confirmed that with all buckets filled then all ions can be trapped whereas with a large gap of around 130 buckets only ions with a mass to charge ratio greater than ~ 50 will be readily trapped by the electron beam at over 100 mA.

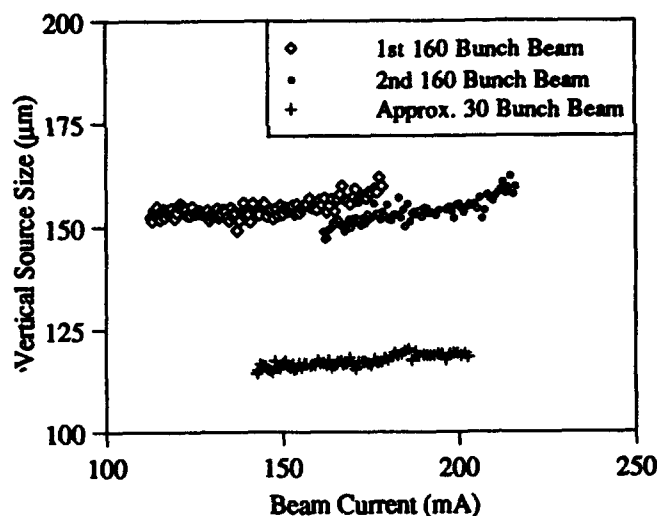


Figure 3. Vertical source size as function of beam current for different fill structures.

D. Insertion Devices

There are now three insertion devices installed in the SRS, one undulator and two superconducting wigglers. The undulator has a minimal effect on the source size but the wigglers should have a significant effect. The beam profiles have been recorded as the 5 T wiggler is energised. The wiggler ramp was paused at a number of field values and several sets of profiles recorded at each one. The betatron tune change induced by the wiggler was minimal since a

compensation scheme is in use although this does leave some residual beta function modulation [4]. The results of the experiment are shown in Figure 4. Unexpectedly the vertical source size actually decreases as the wiggler field is increased to 5 T.

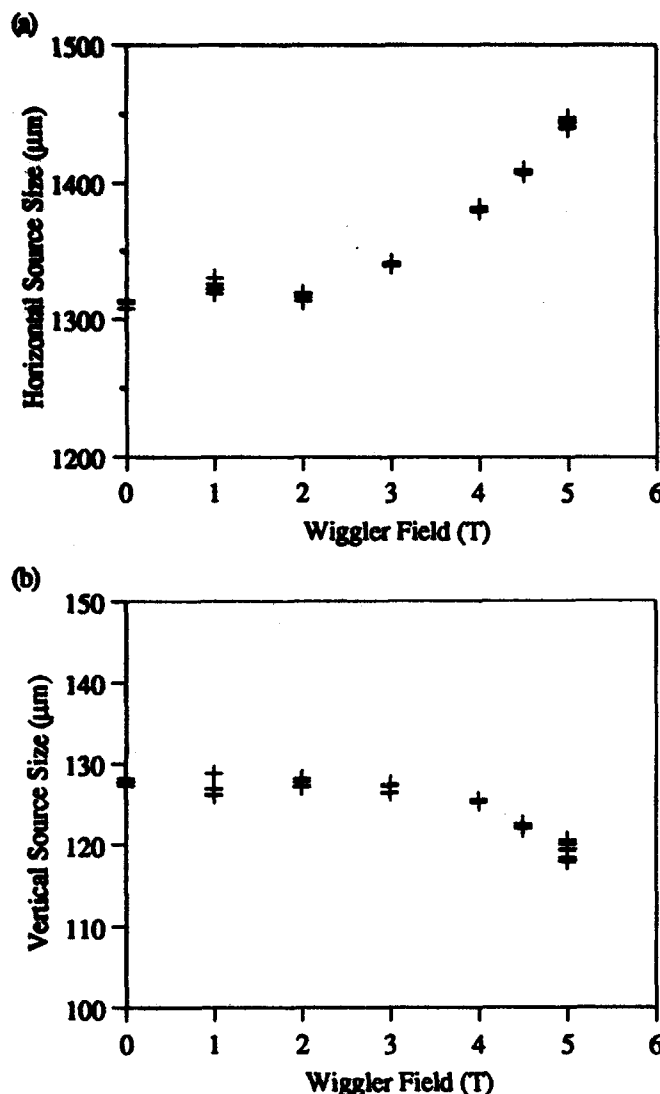


Figure 4. Horizontal (a) and vertical (b) source size variation as a function of wiggler field. The beam current was 100 mA.

A lattice model has been used to predict the theoretical effect of the wiggler. Our in-house code ORBIT [5] predicts that the emittance should increase by ~25%. In a simple model the emittance increases with the integral of the B-field cubed. This is clearly reflected in the figure. Since the vertical beam profile actually reduces it is assumed a slight decrease in the emittance coupling must be induced by the wiggler. By using values of beta functions and dispersion function from the lattice model it is possible to estimate the change in the apparent emittance coupling. The coupling with the wiggler off is 2.8% whereas with the wiggler on at its full field of 5 T it is 2.3%. The newly installed 6 T wiggler has now been commissioned [1] and early indications are that the source size changes will be of the same order as for the 5 T wiggler.

IV. CONCLUSIONS

It has been demonstrated that under relatively poor vacuum conditions the source size exhibits step like changes which have been attributed to ion trapping and detrapping. Following these observations several experiments have been carried out to study the influence of the ion clearing electrodes and the beam fill structure on the source dimensions.

It has been shown that the influence of ions is significantly reduced, in terms of source size, by the application of the ion clearing electrodes. The fill structure of the beam has also been demonstrated to be an efficient method of reducing the influence of ions. A roughly 25% reduction in vertical profile has been demonstrated by reducing the number of consecutive rf buckets from the full complement of 160 to approximately 30. Simple linear ion theory agrees that such a change in the fill structure should severely restrict ion trapping. However it would not be feasible to run the SRS operationally in this mode since the lifetime would be too short. This is due to the Touschek effect at such relatively high bunch currents. To maintain a long lifetime it will be necessary to increase the number of buckets, whilst still having sufficient gap to reduce the influence of the ions. Different fill structures will be investigated in the near future.

The 5 T wiggler has been shown to reduce the vertical profile although the radial emittance is increased. This is thought to be due to a slight change in the emittance coupling from 2.8% to 2.3%. It appears from early commissioning work that the effect of the 6 T wiggler on the source dimensions will be of the same order as that of the 5 T insertion device.

Although experiments on ion effects in storage rings are notoriously difficult to assess, it has been demonstrated that ion influences are significant on the SRS. However by using simple techniques, such as ion clearing electrodes and different fill structures, the effect of the ions on the source size can be minimised. At the moment the standard operational stored beam uses all of the rf buckets. More research is required before a new operating regime can be introduced for normal operations.

V. REFERENCES

- [1] M. W. Poole et al, these proceedings.
- [2] J. S. Mackay, "Electron beam profile, position systems and measurements on the Daresbury SRS," *Proceedings of the European Particle Accelerator Conference, Rome, 1988*, p43.
- [3] National Instruments, Austin, Texas.
- [4] M. W. Poole et al, "Wiggler tune shift compensation on the Daresbury SRS," *Proceedings of the IEEE Particle Accelerator Conference, Chicago, 1989*.
- [5] S. L. Smith, "ORBIT Users Guide," DL internal report.

Global Trajectory Correction Algorithms in CLIC and Main Linac Alignment Tolerances

C. Fischer

CERN, 1211 Geneva 23, Switzerland

Abstract

Alignment tolerances in linear colliders are closely dependent on the expertise in beam trajectory handling, particularly in CLIC where wake fields dominate. Control of the on-momentum trajectory only can be considered as in a straightforward one-to-one scheme. However, more sophisticated processes can be contemplated, involving several correctors and beam position monitors. Moreover, it is possible to apply gradient variations from the nominal values in order to simulate and better compensate dynamical effects, as first suggested at SLAC. The present paper describes various methods applied with assumptions reflecting the most recent characteristics of the CLIC main linac and beam. Calculations for several sets of parameters are presented. Alignment requirements are alleviated and fall in the feasibility domain while maintaining the previously mentioned key parameters within specifications.

I. INTRODUCTION

Global trajectory correction algorithms were first successfully proposed at SLAC for the NLC [1], their advantage being to better cope with misalignments affecting magnets and accelerating structures of a linac than a straightforward one-to-one scheme. These global schemes aim at the minimization of an expression of the form:

$$\phi = \sum_j \frac{(x_j + X_j)^2}{\sigma_x^2 + \sigma_b^2} + \frac{(\Delta x_j + \Delta X_j)^2}{2 \sigma_x^2} \quad (1)$$

The first term is related to the nominal momentum trajectory and x_j and X_j are the measured and calculated deflections at j , whereas the second one deals with off-momentum phenomena. In the case of the Dispersion-Free (D.F.) algorithm, Δx_j and ΔX_j are the measured and predicted trajectory differences between particles with energy excursion $\delta = \Delta p/p_0$ and particles at nominal momentum p_0 . A customary weighting of both terms is applied considering σ_x the r.m.s. pick-up reading resolution and σ_b their r.m.s. alignment error which disappears in the second term where only trajectory differences are involved. Instead of a D.F. process, one can try to simulate and hence correct for the influence of wake fields experienced by particles having off-centred trajectories in the accelerating structures; these wake field kicks always have the same direction on a given side of the machine axis. A Wake-Free (W.F.) algorithm tries to mimic them by generating an anti-symmetrical gradient variation of the focusing and defocusing lattice quadrupoles; the induced trajectory differences are then minimized. Both the D.F. and W.F. methods require one to vary the strength of

lattice quadrupoles, but in the former process the F and D chains are moved in synchronism, whereas in the latter case they are affected in opposite directions. Measuring the trajectory at each pick-up for nominal setting and every perturbed configuration provides the quantities x_j and Δx_j . The determination of X_j and ΔX_j requires the knowledge of all transfer matrix coefficients $R_{12}(i,j)$ from any kick i to a pick-up $j > i$, again at nominal setting and for every detuned situation. When these coefficients only reflect the basic machine FODO model, they exhibit non-linearities with energy deviation which can be treated [2]. However, in the case of CLIC, with wake fields at full strength, this description is not sufficient for good convergence, and they have to be determined by measurement in the presence of the wakes and of the beam-energy dispersion along the linac. Their behaviour is then much more linear. In practice a given kick is generated at i , looking at the response at the subsequent locations j . With the beam-energy dispersion, the effect of a kick is damped after some distance. Good accuracy requires therefore the regeneration of these kicks regularly along the linac [3].

II. APPLICATION TO THE CLIC MAIN LINAC

Both D.F. and W.F. algorithms have been tested in the case of the CLIC main linac. CLIC (stage 1) with final c.m. energy of 0.5 TeV is considered, which implies an accelerating structure length of 3200 m and 320 quadrupoles per linac. Beam parameters are described in [4]; an injection energy of 5 GeV is considered with a 90° phase advance FODO lattice; the usual $(E/E_0)^{1/2}$ scaling is applied for B.N.S. damping considerations; external focusing by means of RF quadrupoles located at each lattice quadrupole is used with a relative strength of a few per cent.

Only the vertical plane is considered. With a nominal aspect ratio of 29 [4], emittance preservation is much more critical in this plane, the aim being to maintain the emittance blow-up below a factor of four at the linac end, starting with a normalized emittance of $5 \cdot 10^{-8}$ nm at injection. Relative gradient variations δ of 3.5% in amplitude are used. These perturbations induce trajectory differences of several hundred microns, Figure 1, larger by two orders of magnitude than the expected alignment errors, and are also above the beam-energy dispersion one wants to cope with. Pick-ups and kicks are localized at every F and D quadrupole. Tests revealed that the correction processes are more efficient when pick-ups are distributed along the beam axis rather than attached to their adjacent quadrupole [2]; the number of pick-ups and correctors to be considered in a single application of the algorithm is of the order of 10 for the best efficiency.

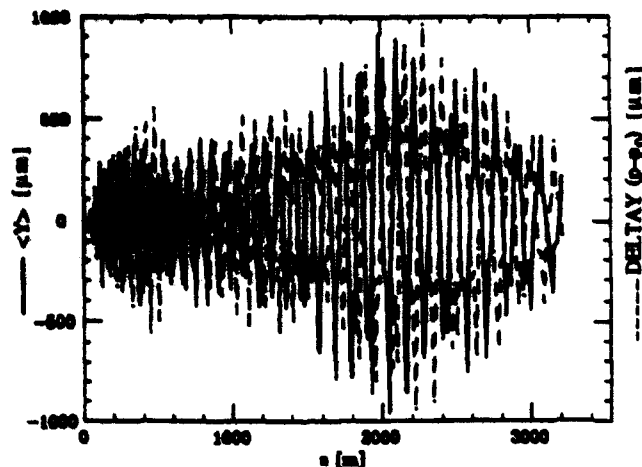


Figure 1. Vertical beam trajectory (solid line) and vertical dispersion for $\delta = +3.5\%$ (dashed curve) of the non-corrected CLIC linac in the 5-2-2 case.

Results are presented for r.m.s alignment errors of 5-2-2 μm and 5-5-5 μm respectively on quadrupoles, pick-ups, and accelerating cavities. The first set is so far considered realistic in CLIC alignment studies [5]. Pick-up resolution errors are expected to fall in the sub-micron range [6].

III. DISPERSION-FREE ALGORITHM RESULTS

In the 5-2-2 case the beam follows the vertical trajectory represented in Figure 1 (solid line). Dispersion effects for an energy excursion $\delta = +3.5\%$ from the nominal momentum are also shown (dashed curve).

Without correction the initial normalized emittance of $5 \cdot 10^{-8}$ nm blows up by three orders of magnitude.

The same data are given in Figure 2 after application of the D.F. process. A reduction of the trajectory peak-to-peak amplitude by two orders of magnitude is obtained, whereas the dispersive term is damped by about a factor 30. Figure 3 shows the normalized emittance evolution along the corrected linac reaching a value of $17 \cdot 10^{-8}$ nm at the exit.

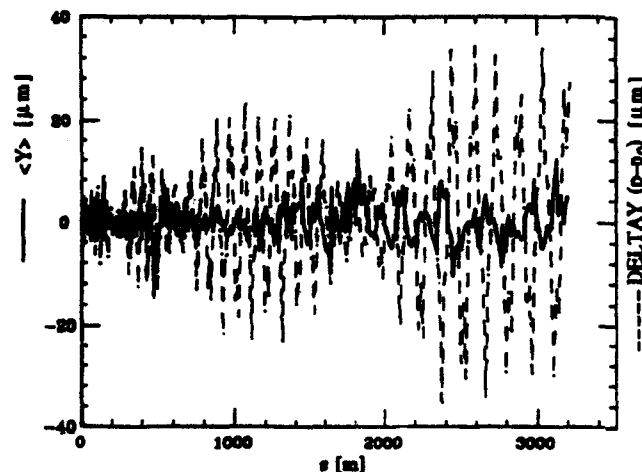


Figure 2. Vertical beam trajectory (solid line) and vertical dispersion for $\delta = +3.5\%$ (dashed curve) after D.F. correction in the 5-2-2 case.

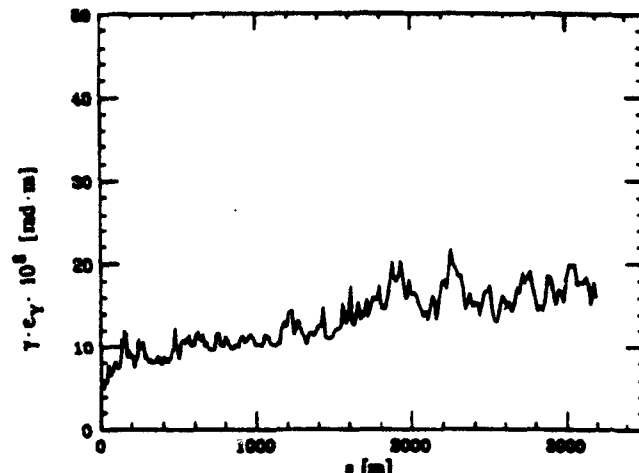


Figure 3. Normalized vertical emittance evolution after D.F. correction in the 5-2-2 case.

The application of the process is, however, not completely straightforward. Using 6 to 10 pick-up and corrector bins several iterations are required on the same region and a total number of more than 200 iterations is reached along the 3.2 km. Another striking feature is the weighting strategy to apply. Considering expression (1) and in agreement with the working hypothesis ($\sigma_b = 2 \mu\text{m}$ and $\sigma_\xi \approx 0.5 \mu\text{m}$ [6]) one ought to weight the dispersive term 10 times more than the trajectory. If such a strategy is applied the process efficiency is much reduced as far as the transverse emittance is concerned; on the contrary, good results are consistently obtained by stressing first the basic trajectory contribution by a factor of 10 or more. When acceptable results are thus obtained, they can be further improved by a factor 2 to 5 by resuming the iterative process with the two terms equally weighted. Any attempt to stress the dispersive term with respect to the trajectory leads quite systematically to bad results.

Requirements on the nominal vertical emittance are met, but a one-to-one scheme gives similar results [7] for this misalignment configuration.

IV. WAKE-FREE ALGORITHM RESULTS

This next section presents the results achieved when applying a W.F. algorithm with alignment tolerances relaxed to an r.m.s value of 5 μm for the three types of components (5-5-5 case). The trajectory and 'wake-free' term are represented in Figure 4 after this application, and the evolution of the vertical emittance along the corrected linac is given in Figure 5.

A total number of roughly 200 iterations were also necessary in that case; again, instead of stressing the 'wake-free' term in expression (1) 50 times more than would have been suggested by pick-up misalignment errors, a first pass was performed with equal weighting of the two terms, and then reinforcing again the basic trajectory contribution with respect to the other one: stressing this second term 10 times more was, however, found useful to better preserve the

emittance during the first half-kilometre of the linac, i.e. at low energy when the disturbing wake-field forces are the most harmful. This is reflected on Figure 4: trajectory distortion amplitudes are kept within $\pm 10 \mu\text{m}$, in agreement with expectations made on misalignment errors and are worsened at the beginning by the emphasis put on the wake-free term; this latter is, on the contrary, well controlled in the first part of the linac and then deteriorates progressively.

A normalized vertical emittance value of $16 \cdot 10^{-8} \text{ nm}$ is obtained—Figure 5. Considering the longitudinal bunch distribution between $+3\sigma_z$ and $-2\sigma_z$ brings the final emittance value down to $14 \cdot 10^{-8} \text{ nm}$ (dots).

With respect to a one-to-one scheme, a factor of more than three is now gained on the final emittance value [7].

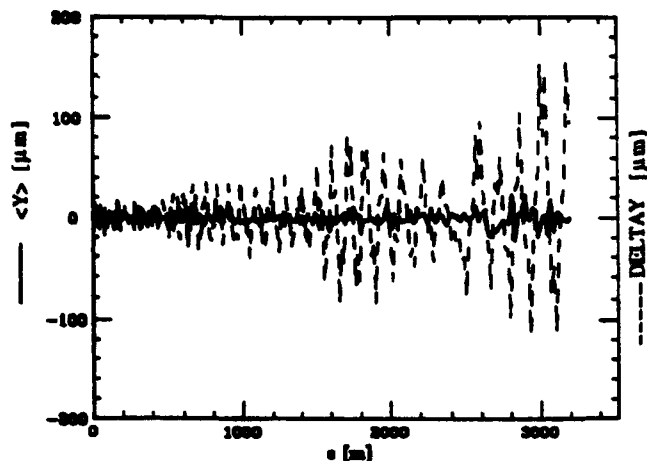


Figure 4. Vertical trajectory (solid line) and 'wake-free' term for a relative strength modulation of $\pm 3.5\%$ applied respectively on the QD and QF chains (dashed curve) after W.F. correction in the 5-5-5 case.

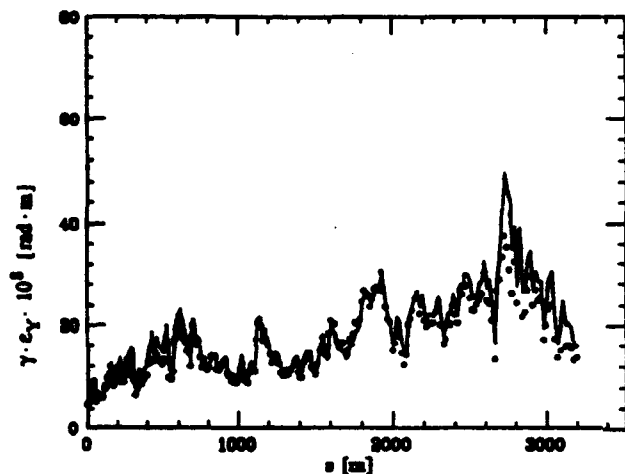


Figure 5. Normalized vertical emittance evolution after W.F. correction in the 5-5-5 case.

V. DISCUSSION

It is shown that, for CLIC, a global correction method can be contemplated as soon as alignment tolerances of pick-ups have to be relaxed beyond an r.m.s. value of $2 \mu\text{m}$; below this value, a one-to-one scheme is as good at finding a solution. A W.F. algorithm looks more efficient than a D.F. one. This is not surprising when considering the huge wake fields of CLIC, and corroborates the conclusions of [1]. The application of such processes is not straightforward: in some cases the strategy to apply relies on the observation of the emittance behaviour as well as on the minimization of quantities provided by the signal of pick-ups located at lattice quadrupoles only. This can probably be attenuated by adding more pick-ups in the accelerating sections in order to better centre the trajectory in the R.F. cavities where wake fields are generated.

The contribution of the nominal trajectory term had to be made predominant most of the time for the best process efficiency; therefore a 'natural' weighting strategy relying only on pick-up misalignment errors and resolution was not adequate. The strategy to follow might depend on the machine which is considered and on the application of the method. Indeed, the relative importance of both terms in expression (1) varies with wake-field levels as well as with the energy or gradient excursions applied to evaluate quantities coming into the second term. In the case of CLIC, with a modulation amplitude of 3.5% , the importance of the two terms was roughly balanced, as can be observed in Figure 1.

VI. CONCLUSION

For CLIC, by virtue of a global algorithm, alignment contingencies can be alleviated by more than a factor of two, whilst the nominal value of the normalized vertical emittance is preserved; misalignment r.m.s. errors of $5 \mu\text{m}$ can be tolerated on pick-ups. This figure can probably approach $10 \mu\text{m}$ when applying these global correction methods to a machine with higher injection energy and new scaling laws [8]. Work is continuing in this direction.

VII. ACKNOWLEDGEMENTS

I had many helpful discussions with G. Guignard in the course of this study.

VIII. REFERENCES

- [1] T. Raubenheimer, R. Ruth, *2nd EPAC, Nice, June 1990*.
- [2] C. Fischer, G. Guignard, *3rd EPAC, Berlin, March 1992*.
- [3] C. Fischer, CLIC Note to be published.
- [4] G. Guignard, *XVth Int. Conf. H. E. Acc., Hamburg, 1992*.
- [5] I. Wilson, *Linear Acc. Conf., Ottawa, 23-28 August 1992*.
- [6] W. Schnell, J.P.H. Sladen, I. Wilson, W. Wuensch, *XVth Int. Conf. H. E. Acc., Hamburg, 1992*.
- [7] G. Guignard, private communication.
- [8] G. Guignard, these proceedings.

Lattice Scaling and Emittance Control in the CLIC Main Linac

G. Guignard
CERN, 1211 Geneva 23, Switzerland

Abstract

For the main linac of the CERN linear collider (CLIC), emittance degradation due to wake fields and misalignments was previously investigated at unvarying injection energy and scaling of the betatron function. In particular, to keep a constant stability margin along the linac, the scaling retained was such that β^2/γ was constant. Recent developments suggest that the lattice scaling along the linac should be modulated differently in order to better balance the effects of the wake fields with respect to the chromatic dispersion. This may help to reduce the emittance dilution as would also a reasonable increase of the injection energy compatible with a bunch compressor. In the case of 250-GeV CLIC linacs, it was found that independent scaling of the cell length and focusing strength, and scaling laws different from the one mentioned above allow a better control of the growth of the small emittances foreseen, especially in the vertical plane. This approach, combined with a simultaneous adjustment of the injection energy and an improvement of the trajectory mastering, has made it possible to relax the alignment tolerances on the quadrupoles and the cavities while keeping the final emittances at their required level.

I. BETATRON SCALING WITH ENERGY

Scaling assumptions different from the one that keeps constant the stability margin [1] can be made when including, besides the wake fields, the emittance and trajectory chromaticity as another source of emittance dilution. One of those, which involves a variation of the phase advance per cell μ along the linac, can for instance be defined by [2]

$$\frac{1}{4f(s)}(\beta(s) - \check{\beta}(s)) = \tan \frac{\mu}{2} = \left[\frac{\gamma_0}{\gamma(s)} \right]^\alpha \quad (1)$$

where f is the focal distance of the quadrupoles, and $\check{\beta}$ and β the minimum and maximum of the β -functions. The basic relation between f , μ and the distance L_c separating two successive quadrupoles

$$\sin \frac{\mu}{2} = \frac{L_c}{2f} \quad (2)$$

implies that a modulation of μ requires different scaling laws for f and L_c . Having found that constant focusing up to a given energy followed with a scaling according to (1) with $\alpha = 1$ gives no improvement in emittance control with respect to the $\sqrt{\gamma}$ -law for β , we decided to try independent scalings of the cell length $2L_c$ and focal distance f [3]. Giving the preference

to continuous and smooth variations of these quantities with s , they can be characterized by

$$\frac{L_c(s)}{L_{c0}} = \left(\frac{\gamma(s)}{\gamma_0} \right)^{\alpha_a} \quad \frac{f(s)}{f_0} = \left(\frac{\gamma(s)}{\gamma_0} \right)^{1-\alpha_q} \quad (3)$$

which mean that $\sin \mu/2$ varies with γ to power $\alpha_a + \alpha_q - 1$ by virtue of (2) and β -average with γ to power α_b , close to α_a since $\beta \sim L_c$. The hope was to be able to reduce μ with the distance along the linac and simultaneously limit the increase of the β -functions. This comes from the observation [2] that emittance dilution due to chromatic effects decreases when α increases from 0 to 1, while the blowup due to wake fields favours $\alpha = 0$. Since wake fields dominate in the first part of the linac and chromaticity rises with energy if the focusing is not relaxed, there must be an optimum balance between these two effects that depends on the choice of α_a and α_q for the linac considered. In CLIC (30 GHz, 80 MV/m), we found such a balance for $\alpha_a = 0.3$ and $\alpha_q = 0.6$. This means that μ decreases gently from the initial 95° with $\alpha \equiv 0.2$ (Eq. (1)), while β -average rises with γ to power 0.4 about, instead of $\sqrt{\gamma}$ (Fig. 1).

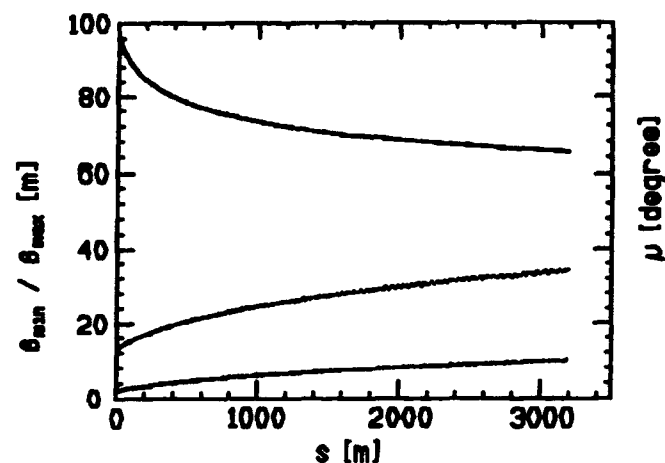


Fig. 1: CLIC Twiss functions with scaling of Eq. (3)

II. CHOICE OF INJECTION ENERGY

Raising the injection energy would reduce the wake-field impacts while increasing the pre-acceleration cost. But acceleration is necessary between the damping ring and the linac owing to the need for bunch compression. Therefore, the injection energy will only be known after a detailed study of the bunch compressors, but a first guess may come from the simple arguments given below.

At the exit of the 3-GeV damping ring [4], the bunch length σ_z and energy spread σ_E are about 2.2 mm and 1.5%, while at the entrance of the linac σ_z should be of the order of 0.17 mm and σ_E between 0.5 and 1%, say. The bunch must then be compressed by a factor ~ 13 and this would correspond to an energy spread close to 2% in a one-stage compressor. Accelerating the beam to 9 GeV would subsequently reduce σ_E by a factor 3, to about 0.65%, i.e. within the interval assumed to be tolerable. However, $\sigma_E = 2\%$ at the end of such a compressor would enhance chromatic effects and it might be better to have two compressors of a factor 3.6 with intermediate acceleration to 9 GeV. Thereby, σ_E would never exceed 0.65% in the compressors. More studies are required to define both the number of stages and the tolerable (in view of emittance preservation) energy spread at injection; however, it seems today that the injection energy should be about 9 GeV rather than 5 GeV, as previously selected.

III. MASTERING OF BEAM TRAJECTORY

Since the kicks on the trajectory are linear with the misalignment amplitudes and the correction is obtained by moving quadrupoles, a single one-to-one correction should converge to the same final trajectory independently of the initial size of the quadrupole displacements. Nevertheless, if the numerical model in the simulations is not perfect, and if real-life inaccuracies in the correction setting or quadrupole jitter are included, the quality of the correction depends weakly on this initial size. In order to remedy this dependence, the possibility to iterate the one-to-one correction as many times as required has been added in the main-linac tracking program [5]. This procedure tends to realign the quadrupoles with the beam, towards the linac ideal line.

Since the wake fields are strong in CLIC, it is important to have beam-position monitors associated with the cavities rather than with the quadrupoles. The present idea consists of installing these monitors at the beginning of each girder (about 1.3-m long) supporting four accelerating sections. The additional information acquired between quadrupoles can be exploited for the correction, while keeping the idea of local correction. It is only a matter of determining every correcting kick by minimizing all the trajectory deviations measured downstream but only as far as the next quadrupole, i.e. the function

$$\Phi = \sum_{j < i < j+1} \left(\langle x \rangle_i - \frac{b_i}{f_j} dx_j \right)^2, \quad (4)$$

where j is the quadrupole index and i the monitor index. f_j and dx_j are the focal length and the quadrupole displacement that reduce the average bunch position $\langle x \rangle_i$ at all monitors between quadrupoles j and $j+1$. b_i is the transfer coefficient

from quadrupole j to monitor i (separated by a distance ℓ_i and an energy difference $E_i - E_j$),

$$b_i = \ell_i \frac{E_j}{E_i - E_j} \log \frac{E_i}{E_j} \quad (5)$$

generalized to include the wake fields [5]. The solution which annuls the derivatives of Φ with respect to dx_j and thereby minimizes Φ can be written as follows, once the errors on the monitor signals $\xi_{m,i}$ and on the quadrupole displacements $\xi_{d,j}$ are included

$$dx_j = \frac{\sum_i (\langle x \rangle_i + \xi_{m,i}) \frac{b_i}{f_j}}{\sum_i \left(\frac{b_i}{f_j} \right)^2} + \xi_{d,j}. \quad (6)$$

This algorithm aims at reducing the deviations in all the cavities rather than centring the beam in the next quadrupoles and relaxing the cavity tolerances at same performance.

Combining the iteration procedure with the one-to-few algorithm described above allows a trajectory reduction by almost three orders of magnitude after two iterations (Fig. 2) and a realignment of the quadrupoles on the beam path within less than 5 μm r.m.s. (Fig. 3), starting from 50 μm .

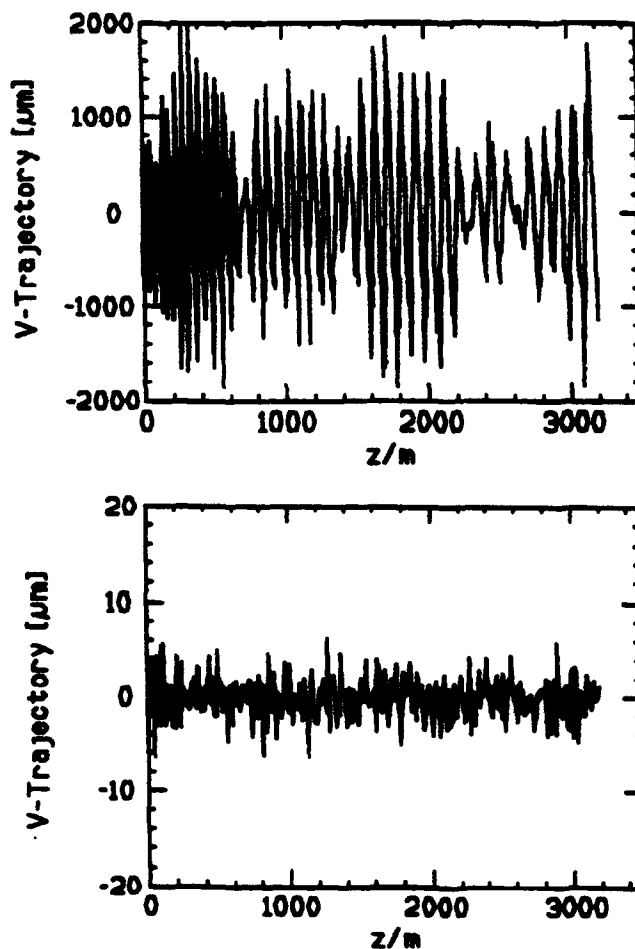


Fig. 2: Trajectory reduction after two iterations

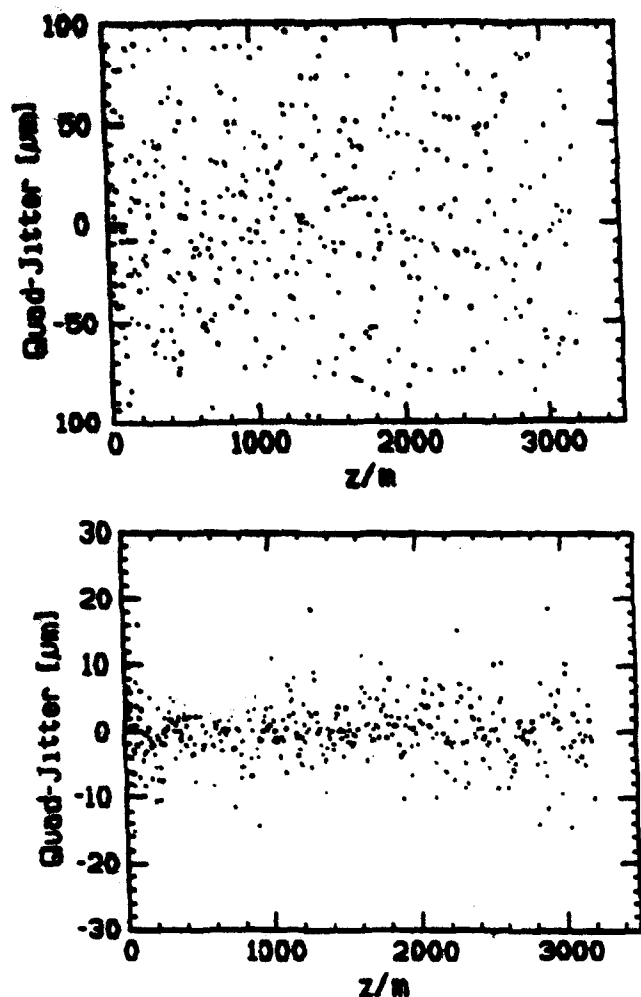


Fig. 3: Reduction of quadrupole scattering after two iterations of the correction

IV. RESULTS AND CONCLUSIONS

Emittance dilution calculations have been carried out for the CLIC main linac with 500-GeV centre of mass [6]. Adopting the independent scaling of Section I (with $\alpha_a = 0.3$, $\alpha_q = 0.6$) instead of the $\sqrt{\gamma}$ -law gave a vertical blowup reduction of 33%, all other parameters being constant. Another gain of 25% came from raising injection energy from 5 to 9 GeV (Section II). The correction of the trajectory used iterations when needed and the one-to-few method described in Section III. All these improvements have been made with a view to relaxing the alignment tolerances, while aiming at normalized emittances of $1.8 \mu\text{rad m}$ horizontally and $0.2 \mu\text{rad m}$ vertically as required by the performance [6]. The r.m.s. quadrupole misalignments are limited to $50 \mu\text{m}$, not by the correction efficiency, but by the trajectory excursion (Fig. 2 top) in cavity irises with 4-mm diameter. An r.m.s. spread of $10 \mu\text{m}$ in cavity positions is tolerable with position monitors in front of every girder. By contrast, these monitors

which define the beam path have to be aligned within $2 \mu\text{m}$ r.m.s. Starting from emittances of $1.5 \mu\text{rad m}$ and $0.05 \mu\text{rad m}$ at linac injection, dilution reaches on average (statistics over eight machines) 20% horizontally and a factor four vertically (Fig. 4), giving emittances at the linac exit in agreement with the target values. It was checked also that tolerances of the order of $0.5 \mu\text{m}$ for the resolution and jitter of quadrupole displacements do not increase the emittance dilution by more than $\sim 10\%$. These results show that we progressively succeeded in relaxing tolerances while keeping constant the emittance target values.

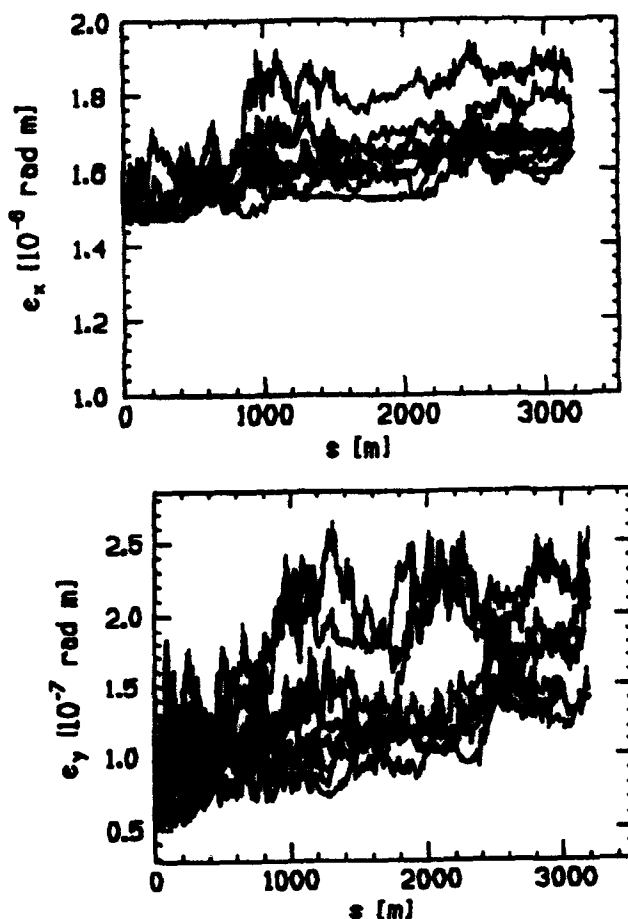


Fig. 4: Horizontal and vertical emittance dilution with new independent scalings

V. REFERENCES

- [1] H. Henke and W. Schnell, CERN LEP-RF/86-18, 1986.
- [2] V. Tsakanov, *ICFA Workshop on Linear Colliders*, Garmisch-Partenkirchen, 1992.
- [3] G. Guignard, CERN-SL/93-12 (AP), 1993.
- [4] J.P. Delahaye, J.P. Potier, CERN-PS/91-10 (LP), 1991.
- [5] G. Guignard, CERN-SL/91-19 (AP), 1991.
- [6] G. Guignard, "Beam stability simulations in CLIC linacs," *XVth Int. Conf. on H. E. Acc.*, Hamburg, 1992.

Decoherence and Recoherence of Beam in Phase Space

Jicong Shi and Sho Ohnuma

Department of Physics, University of Houston, Houston, TX 77204-5506, USA

Abstract

Using the particle distribution in phase space, we introduce a new approach to study the decoherence and recoherence of a kicked beam when betatron tunes are far from any resonance. With this method, the decoherence and the recoherence of a beam can be analyzed easily in both 2-dimensional and 4-dimensional cases with any form of the tune spread. We have also studied the decoherence of a beam initially trapped in a resonance island. Due to the tune modulation, the separatrix of island develops a chaotic layer and particles within the island can drift out of the island along the layer. Consequently, the beam decoheres gradually. The rate of decoherence is shown to be proportional to the modulation amplitude. As a function of the modulation frequency, it reaches a peak near the tune of trapped particles before decreasing to zero.

I. DECOHERENCE IN THE NEAR-LINEAR REGIME

In the presence of amplitude dependence of betatron tunes (tune spread), an off-centered beam will gradually dilute from a localized bunch to an annulus in transverse phase-space which results in a disappearance of coherent signal. Due to a finite energy spread, the beam may also oscillate between the localized bunch and the annulus which results in a periodic oscillation of the coherent signal. These decoherence and recoherence of a kicked beam have been studied experimentally as well as analytically [1,2]. Previous studies based on a single-particle picture were however limited to quadratic amplitude-dependence of the tunes. Since the decoherence and recoherence are basically multiparticle phenomena, a more suitable as well as easier description should be based on a study of the particle distribution in phase space. In this note, we shall introduce this approach to study the decoherence and recoherence. With our method, these phenomena can be analyzed in both 2 and 4-dimensional cases with any form of amplitude dependence of the tunes.

In general, the Hamiltonian of 4-dimensional betatron oscillations can be written as

$$H = \bar{\nu} \cdot \bar{J} + U_0(\bar{J}) + U(\bar{J}, \bar{\phi}, \theta), \quad (1)$$

where $\bar{\nu} = (\nu_1, \nu_2)$ are betatron tunes, θ the independent variable which is the path length of the central orbit divided by the average machine radius. $(\bar{J}, \bar{\phi}) =$

$(J_1, \phi_1, J_2, \phi_2)$ are action-angle variables:

$$\sqrt{2J_k} \cos \phi_k = z_k / \sqrt{\beta_k}, \quad (2)$$

$$\sqrt{2J_k} \sin \phi_k = -\sqrt{\beta_k} z'_k + \beta'_k z_k / (2\sqrt{\beta_k}), \quad (3)$$

where $k = 1, 2$ and (z_1, z_2) denote (x, y) . $U_0(\bar{J}) + U(\bar{J}, \bar{\phi}, \theta)$ represents the nonlinear perturbation of which $U_0(\bar{J})$ depends on \bar{J} only and $\langle U \rangle_{\bar{\phi}, \theta} = 0$. The transverse distribution of the beam particle $f_T(\bar{J}, \bar{\phi}, \theta)$ satisfies the equation

$$\frac{\partial f_T}{\partial \theta} = [H, f_T], \quad (4)$$

where $[]$ is the Poisson bracket. Since the time scale we are interested in is much shorter than the diffusion time scale, as betatron tunes are far from any major resonance, we consider U_0 only and Eq. (4) is reduced to

$$\frac{\partial f_T}{\partial \theta} + \left[\bar{\nu} + \frac{\partial U_0}{\partial \bar{J}} \right] \cdot \frac{\partial f_T}{\partial \bar{\phi}} = 0. \quad (5)$$

The solution of this equation is easily found to be

$$\begin{aligned} f_T(\bar{J}, \bar{\phi}, \theta) &= f_T \left(\bar{J}, \bar{\phi} - \int_0^\theta \bar{\nu}(\tau) d\tau - \frac{\partial U_0}{\partial \bar{J}} \theta, 0 \right) \\ &= f_T(\bar{J}, \bar{\psi}, 0) \end{aligned} \quad (6)$$

where $f_T(\bar{J}, \bar{\psi}, 0)$ is the initial distribution and

$$\bar{\psi} = \bar{\phi} - \int_0^\theta \bar{\nu}(\tau) d\tau - \theta \frac{\partial U_0}{\partial \bar{J}} = \bar{\phi} - \bar{\chi}. \quad (7)$$

If the synchrotron motion is assumed to be linear,

$$\bar{\nu} = \bar{\nu}_0 + \bar{\xi} \sqrt{J_L / \beta_L} \sin(\nu_s \theta + \phi_L), \quad (8)$$

where $\bar{\xi}$ is chromaticity, (J_L, ϕ_L) the action-angle variable for synchrotron motion, and ν_s the synchrotron tune, and

$$\bar{\chi} = \bar{\nu}_0 \theta + \frac{2\bar{\xi}}{\nu_s} \left(\frac{J_L}{\beta_L} \right)^{\frac{1}{2}} \sin \left(\frac{\nu_s \theta}{2} \right) \sin(\nu_s \theta + \phi_L) + \theta \frac{\partial U_0}{\partial \bar{J}}. \quad (9)$$

Let $f_L(J_L, \phi_L)$ denote the beam particle distribution in the longitudinal phase-space. The beam centroid can be calculated from

$$\begin{aligned} &\langle \sqrt{2J_k} e^{-i\phi_k} \rangle_{\bar{J}, \bar{\phi}} \\ &= \int \sqrt{2J_k} e^{-i\phi_k} f_T(\bar{J}, \bar{\phi}, \theta) f_L(J_L, \phi_L) d\bar{J} d\bar{\phi} dJ_L d\phi_L \end{aligned}$$

¹Supported by TNRLC under award FCFY9221 and the U.S. Department of Energy under grant DE-FG05-87ER40374.

$$\begin{aligned}
&= \int \sqrt{2J_k} e^{-i\phi_k} f_T(\vec{J}, \vec{\phi} - \vec{\chi}, 0) f_L(J_L, \phi_L) d\vec{J} d\vec{\phi} dJ_L d\phi_L \\
&= \int \sqrt{2J_k} e^{-i(\phi_k + \chi_k)} f_T(\vec{J}, \vec{\phi}, 0) f_L(J_L, \phi_L) d\vec{J} d\vec{\phi} dJ_L d\phi_L \\
&= e^{-i\nu_k \theta} \int \exp(-i\phi_k \sqrt{J_L} \sin \phi_L) f_L(J_L, \phi_L) dJ_L d\phi_L \\
&\times \int \sqrt{2J_k} \exp\left[-i\left(\phi_k + \theta \frac{\partial U_0}{\partial J_k}\right)\right] f_T(\vec{J}, \vec{\phi}, 0) d\vec{J} d\vec{\phi}, \quad (10)
\end{aligned}$$

where $k = 1, 2$.

Assume that initially the beam has a Gaussian distribution with its centroid located at $(x, x', y, y') = (x_{01}, x'_{01}, x_{02}, x'_{02})$ in the transverse phase-space,

$$f_T(\vec{J}, \vec{\phi}, 0) = f_1(J_1, \phi_1) f_2(J_2, \phi_2), \quad (11)$$

where

$$\begin{aligned}
f_k(J_k, \phi_k) &= \frac{1}{2\pi\sigma_k^2} \\
&\times \exp\left\{-\frac{1}{\sigma_k^2} \left[J_k + J_{0k} - 2\sqrt{J_{0k}J_k} \cos(\phi_k - \phi_{0k})\right]\right\},
\end{aligned} \quad (12)$$

and

$$\sqrt{2J_{0k}} \cos \phi_{0k} = z_{0k} / \sqrt{\beta_k}, \quad (13)$$

$$\sqrt{2J_{0k}} \sin \phi_{0k} = -\sqrt{\beta_k} z'_{0k} + \beta'_k z_{0k} / (2\sqrt{\beta_k}) \quad (14)$$

with $k = 1, 2$. We also assume that the beam has a Gaussian distribution in the longitudinal phase-space,

$$f_L(J_L, \phi_L) = \frac{1}{2\pi\sigma_L^2} \exp\left(-\frac{J_L}{\sigma_L^2}\right). \quad (15)$$

Substitution of Eqs. (11)–(15) into Eq. (10) yields

$$\begin{aligned}
\langle \sqrt{2J_k} e^{-i\phi_k} \rangle_{\vec{J}, \vec{\phi}} &= \exp\left[-i(\phi_{0k} + \nu_{0k}\theta) - \frac{J_{0k}}{\sigma_k^2} - \frac{J_{0j}}{\sigma_j^2}\right] \\
&\times \exp\left[-\frac{\xi_k^2 \sigma_L^2}{\nu_s^2 \beta_L} \sin^2\left(\frac{1}{2}\nu_s \theta\right)\right] \\
&\times \frac{1}{\sigma_k^2 \sigma_j^2} \int dJ_j I_0\left(\frac{2\sqrt{J_{0j}J_j}}{\sigma_j^2}\right) \exp\left(-\frac{J_j}{\sigma_j^2}\right) \\
&\times \int dJ_k \sqrt{2J_k} I_1\left(\frac{2\sqrt{J_{0k}J_k}}{\sigma_k^2}\right) \exp\left(-\frac{J_k}{\sigma_k^2} + i\theta \frac{\partial U_0}{\partial J_k}\right), \quad (16)
\end{aligned}$$

where I_0 and I_1 are modified Bessel functions of order 0 and 1 respectively. (k, j) is any permutation of 1 and 2. After knowing the amplitude dependence of the betatron tunes, the time evolution of beam centroid can be obtained by integrating J_k and J_j in Eq. (16) analytically or numerically.

If we consider only the lowest-order amplitude dependence of the tunes:

$$U_0 = \frac{1}{2} b_1 J_1^2 + b_3 J_1 J_2 + \frac{1}{2} b_2 J_2^2, \quad (17)$$

the beam centroid is found from Eq. (16) as

$$\begin{aligned}
\langle \sqrt{2J_k} e^{-i\phi_k} \rangle_{\vec{J}, \vec{\phi}} &= \frac{\sqrt{2J_{0k}}}{[1 + (\sigma_k^2 b_k \theta)^2] [1 + (\sigma_j^2 b_j \theta)^2]^{1/2}} \\
&\times \exp\left\{-\frac{J_{0k}(\sigma_k b_k \theta)^2}{1 + (\sigma_k^2 b_k \theta)^2} - \frac{J_{0j}(\sigma_j b_j \theta)^2}{1 + (\sigma_j^2 b_j \theta)^2}\right\} \\
&\times \exp\left\{-\frac{\xi_k^2 \sigma_L^2}{\nu_s^2 \beta_L} \sin^2\left(\frac{1}{2}\nu_s \theta\right)\right\} \exp(-i\phi_{ck}), \quad (18)
\end{aligned}$$

where

$$\begin{aligned}
\phi_{ck}(\theta) &= \phi_{0k} + \nu_{0k}\theta + 2 \tan^{-1}(b_k \sigma_k^2 \theta) + \tan^{-1}(b_j \sigma_j^2 \theta) \\
&+ \frac{J_{0k} b_k \theta}{1 + (\sigma_k^2 b_k \theta)^2} + \frac{J_{0j} b_j \theta}{1 + (\sigma_j^2 b_j \theta)^2}, \quad (19)
\end{aligned}$$

and (k, j) is any permutation of 1 and 2. The amplitudes of the beam centroid are thus

$$\begin{aligned}
A_k(\theta) &= \left| \langle \sqrt{2J_k} e^{-i\phi_k} \rangle_{\vec{J}, \vec{\phi}} \right| \\
&= \frac{\sqrt{2J_{0k}}}{[1 + (\sigma_k^2 b_k \theta)^2] [1 + (\sigma_j^2 b_j \theta)^2]^{1/2}} \\
&\times \exp\left\{-\frac{J_{0k}(\sigma_k b_k \theta)^2}{1 + (\sigma_k^2 b_k \theta)^2} - \frac{J_{0j}(\sigma_j b_j \theta)^2}{1 + (\sigma_j^2 b_j \theta)^2}\right\} \\
&\times \exp\left\{-\frac{\xi_k^2 \sigma_L^2}{\nu_s^2 \beta_L} \sin^2\left(\frac{1}{2}\nu_s \theta\right)\right\}. \quad (20)
\end{aligned}$$

If $\partial^2 U_0 / \partial J_j \partial J_k = 0$, i.e. the betatron tunes are independent of \vec{J} , we have

$$A_k(\theta) / A_k(0) = \exp\left\{-\frac{\xi_k^2 \sigma_L^2}{\nu_s^2 \beta_L} \sin^2\left(\frac{1}{2}\nu_s \theta\right)\right\}. \quad (21)$$

Eq. (21) shows that the coherent signal slowly oscillates with the frequency of the tune modulation ν_s . The smallest coherent signal occurs at $1/(2\nu_s)$ turns with

$$A_k\left(\frac{1}{2\nu_s}\right) / A_k(0) = \exp\left\{-\frac{\xi_k^2 \sigma_L^2}{\nu_s^2 \beta_L}\right\}. \quad (22)$$

After each $1/\nu_s$ turns a coherent signal with original magnitude reappears.

For $\partial^2 U_0 / \partial J_j \partial J_k \neq 0$, Eq. (20) describes the decrease of magnitude of the coherent signal due to a finite tune spread. It shows that:

1. The rate of this decrease is independence of ν_s .
2. The larger the amplitude dependence of the tunes and the transverse beam size, the larger the rate.
3. Since the oscillation part of A_k has a period of $1/\nu_s$ turns, for

$$\frac{\sigma_k^2}{\nu_s} \left| \frac{\partial^2 U_0}{\partial J_k^2} \right| \ll 1, \quad \text{and} \quad \frac{\sigma_j^2}{\nu_s} \left| \frac{\partial^2 U_0}{\partial J_j \partial J_k} \right| \ll 1, \quad (23)$$

the first minimum of A_h is around $\theta = \pi/\nu_s$ and the next maximum is around $\theta = 2\pi/\nu_s$. The ratio of the next maximum and first minimum is

$$\frac{A_{h,max}}{A_{h,min}} = \frac{[\nu_s^2 + (\pi\sigma_h^2 b_h)^2] [\nu_s^2 + (\pi\sigma_j^2 b_j)^2]^{1/2}}{[\nu_s^2 + (2\pi\sigma_h^2 b_h)^2] [\nu_s^2 + (2\pi\sigma_j^2 b_j)^2]^{1/2}} \times \exp \left\{ -\frac{3J_{0h}(\pi\nu_s\sigma_h b_h)^2}{[\nu_s^2 + (2\pi\sigma_h^2 b_h)^2] [\nu_s^2 + (\pi\sigma_h^2 b_h)^2]} - \frac{3J_{0j}(\pi\nu_s\sigma_j b_j)^2}{[\nu_s^2 + (2\pi\sigma_j^2 b_j)^2] [\nu_s^2 + (\pi\sigma_j^2 b_j)^2]} + \frac{\xi_h^2 \sigma_h^2}{\nu_s^2 \beta_L} \right\}. \quad (24)$$

If this ratio is larger than 1, a weaker coherent signal will reappear after $1/\nu_s$ turns.

II. DECOHERENCE OF BEAM IN A RESONANCE ISLAND

Consider a beam kicked into a resonance island. If this resonance is isolated, and there is no tune modulation, the beam will be trapped inside the island "forever". With a tune modulation, the separatrix of island develops a chaotic layer. Particles within this chaotic layer will eventually drift out of the island along the layer. Consequently, the beam decoheres gradually. For a beam kicked into the neighborhood of the chaotic layer (part of beam overlap with the layer), more particles will drift out of the island once the layer becomes wider. If the drifting speed of particles is assumed to be uniform within the chaotic layer, the rate of decoherence of the beam is proportional to the width of the chaotic layer. Therefore, by estimating this width, the decoherence rate of a beam in the island can be understood at least semi-quantitatively. Here we only consider the motion in $x-x'$ plane.

As we consider a n th-order resonance, $n\nu_0 = k$, the Hamiltonian can be written as

$$H_0 = \delta\nu J + U_0(J) + U_1(J) \cos(n\phi + \phi_0), \quad (25)$$

where $\delta\nu = \nu - \nu_0$, ϕ_0 is a phase constant, and (J, ϕ) is the action-angle variable of (x, x') . The tune modulation $\delta\nu = \delta\nu_0 + D \cos(\nu_s \theta)$ is treated as a periodic perturbation,

$$H = [\delta\nu_0 + D \cos(\nu_s \theta)]J + U_0(J) + U_1(J) \cos(n\phi + \phi_0) \\ = H_0 + JD \cos(\nu_s \theta) \quad (26)$$

Near the resonance, the Hamiltonian can be expanded with $(J - J_r)$ where J_r is the value of J for the resonance. Let $t = n\theta$, $r = U_0''(J_r)(J - J_r)$, $\omega_0^2 = -U_0''(J_r)U_1(J_r)$, $\psi = n\phi + \phi_0$, and $r_r = J_r U_0''(J_r)$, the new Hamiltonian is then

$$\tilde{H}(r, \psi, t) = \frac{1}{2}r^2 - \omega_0^2 \cos \psi + D(r_r + r) \cos\left(\frac{\nu_s}{n}t\right) \\ = \tilde{H}_0 + D(r_r + r) \cos\left(\frac{\nu_s}{n}t\right). \quad (27)$$

This is the Hamiltonian for the pendulum with a periodic driving force. The motion in a vicinity of the separatrix can be described by the whisker map [3],

$$\begin{cases} w_{n+1} = w_n + W \sin \psi_n \\ \psi_{n+1} = \psi_n + \lambda \ln(32/|w_{n+1}|) \end{cases} \quad (28)$$

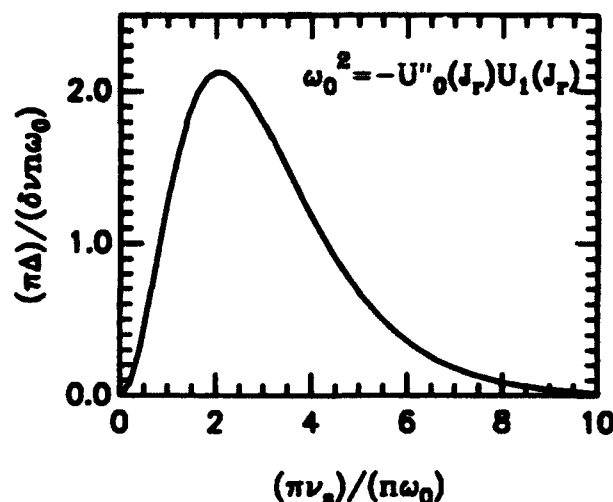


Figure 1: Δ as a function of ν_s .

where

$$w_n = \frac{\tilde{H}_0 - \omega_0^2}{\omega_0^2}, \quad \lambda = \frac{\nu_s}{\omega_0},$$

$$W = \frac{2\pi\nu_s D}{n\omega_0^2 \cosh[\pi\nu_s/(n\omega_0)]}.$$

The width of the chaotic layer is [3]

$$\Delta = \omega_0^2 \lambda W = \frac{2\pi\nu_s^2 D}{n\omega_0 \cosh[\pi\nu_s/(n\omega_0)]}. \quad (29)$$

Eq. (29) shows that :

1. The width of the chaotic layer, that is, the rate of decoherence is proportional to the modulation depth D .
2. Δ takes the maximum value at the modulation tune ν_s^m which is the solution of the equation,

$$\frac{\pi\nu_s^m}{n\omega_0} = 2 \coth\left(\frac{\pi\nu_s^m}{n\omega_0}\right). \quad (30)$$

$$\nu_s^m \simeq \frac{2n}{\pi}\omega_0 = \frac{2n}{\pi} |U_0''(J_r)U_1(J_r)|^{\frac{1}{2}}. \quad (31)$$

3. For $\nu_s \ll 1$, $\Delta \propto \nu_s^2$. For $\nu_s \rightarrow \infty$, $\Delta \rightarrow 0$ (see Fig. 1).

REFERENCES

- [1] F. Willeke, Fermilab Report TM-1309, (1985).
- [2] R. E. Meller *et al*, SSCL Report SSC-N-360, (1987).
- [3] Chirikov, B. V., Phys. Rep. 52, 265(1979).

SPACE-CHARGE-INDUCED EMITTANCE GROWTH IN AN ELLIPTICAL CHARGED PARTICLE BEAM WITH A PARABOLIC DENSITY DISTRIBUTION

Thomas P. Wangler, Pierre Lapostolle*, and Alessandra Lombardi*
Los Alamos National Laboratory, Los Alamos, NM 87545
*PS Division, CERN, CH-1211, Geneva 23, Switzerland

Abstract

We present a simple analytical model of emittance growth caused by nonlinear space-charge forces using a laminar, parabolic-density beam. The model allows us to explain a surprising and important result that space-charge-induced emittance growth is larger in the plane with the larger semi-axis.

I. INTRODUCTION

We consider a model, which describes the process in a short drift space, in which the particles experience a space-charge impulse, but do not propagate far enough for their positions to change appreciably. Thus the spatial distribution is assumed to remain unchanged as the beam propagates. We consider a continuous beam of elliptical cross section, propagating in the z direction. The horizontal semi-axis is a and the vertical semi-axis is b . The beam current is given by $I = qN_1v$, where q is the charge per particle, v is the beam velocity, and N_1 is the number of particles per unit length.

For an assumed particle density $n(x,y)$, Poisson's equation provides the basis for obtaining the space-charge field components (assuming nonrelativistic beams and ignoring magnetic forces). The solution for the electric-field components from a distribution with elliptical symmetry has been given by Sacherer¹. If the density function has the form

$$n(x,y) = n \left(\frac{x^2}{a^2} + \frac{y^2}{b^2} \right),$$

the x and y components of the field are given by

$$E_x = \frac{qabx}{2\epsilon_0} \int_0^\infty ds \, n \left(\frac{x^2}{a^2+s} + \frac{y^2}{b^2+s} \right) (a^2+s)^{-3/2} (b^2+s)^{-1/2},$$

and

$$E_y = \frac{qaby}{2\epsilon_0} \int_0^\infty ds \, n \left(\frac{x^2}{a^2+s} + \frac{y^2}{b^2+s} \right) (a^2+s)^{-1/2} (b^2+s)^{-3/2}.$$

From the field components the transverse momentum impulse can be calculated as a function of position. This results in a new phase-space distribution (changed in momentum space), and a new rms emittance. For the x plane the change in the momentum component is

$$\Delta p_x = \frac{qE_x L}{v},$$

Work supported in part by Los Alamos National Laboratory Institutional Supporting Researches under the auspices of the United States Department of Energy.

where L is the length of the drift space. The impulse can also be expressed as a change in the divergence angle, given nonrelativistically in the paraxial approximation by

$$\Delta x' = \frac{qE_x L}{mv^2},$$

where m is the mass of the beam particles.

Suppose the initial beam is idealized by assuming the particle distribution is described by a straight line in phase space, given by

$$x'_0 = A \frac{x_0}{a}.$$

The rms emittance is defined as

$$\epsilon = \left[\overline{x^2 x'^2} - [\overline{xx'}]^2 \right]^{1/2}.$$

If the final second moments of the particle distribution can be evaluated from the expression for x and x' , the final rms emittance can be obtained. The positions are assumed to remain fixed so

$$x = x_0.$$

The final divergence is

$$x' = A \frac{x_0}{a} + \frac{qE_x L}{mv^2}.$$

To go further, we need to specify the transverse spatial-density distribution. The uniform density beam, which gives a linear defocusing space-charge force, leads to defocusing effects with no rms emittance growth². The parabolic-density beam leads to a nonlinear space-charge force, and growth of the rms emittance.

II. PARABOLIC DENSITY ELLIPTICAL BEAM

Suppose that the density is parabolic, given by

$$n(x,y) = \frac{2N_1}{\pi ab} \left[1 - \frac{x^2}{a^2} - \frac{y^2}{b^2} \right],$$

within the boundary of the ellipse defined by

$$\frac{x^2}{a^2} + \frac{y^2}{b^2} = 1.$$

Outside the ellipse, the density is assumed to equal zero. In this section we will treat the problem in the x plane; the

y-plane result can be obtained in a similar way. The x component of the electric field is given by

$$E_x = \frac{qN_1 x}{\pi \epsilon_0} I_x,$$

where

$$I_x = \int_0^\infty ds \left(1 - \frac{x^2}{a^2 + s} - \frac{y^2}{b^2 + s} \right) (a^2 + s)^{-3/2} (b^2 + s)^{-1/2}.$$

The integral I_x can be evaluated to obtain the expression for the field.²

The x component of the space-charge electric field is

$$E_x = \frac{2qN_1}{\pi \epsilon_0} \left[\frac{x}{a(a+b)} - x^3 \left[\frac{(2a+b)}{3a^3(a+b)^2} \right] - xy^2 \left[\frac{1}{ab(a+b)^2} \right] \right].$$

By symmetry, the y component is

$$E_y = \frac{2qN_1}{\pi \epsilon_0} \left[\frac{y}{b(a+b)} - y^3 \left[\frac{(2b+a)}{3b^3(a+b)^2} \right] - yx^2 \left[\frac{1}{ab(a+b)^2} \right] \right].$$

The field components contain a linear term, a cubic term, and a coupling term that depends on both coordinates. For the uniform density case, we have²

$$E_x(a,0) = E_y(0,b).$$

For the parabolic density this result is not true. Instead, we have

$$E_x(a,0) = \frac{2qN_1}{\pi \epsilon_0(a+b)} \left[1 - \frac{2+b/a}{3(1+b/a)} \right],$$

and

$$E_y(0,b) = \frac{2qN_1}{\pi \epsilon_0(a+b)} \left[1 - \frac{2b/a+1}{3(1+b/a)} \right].$$

Curves of $E_x(a,0)$ and $E_y(0,b)$ in relative units versus the ratio a/b are shown in Fig. 1. We see from the curves that, although these fields are not exactly equal except when the beam is round, they are within about 20% over a large range of a/b ; thus these electric field components are generally comparable in magnitude. We will see later that this approximate symmetry affects the scaling of emittance growth with beam size.

In the round beam limit one obtains

$$E_x = \frac{qN_1}{\pi \epsilon_0 b^2} \left[x - \frac{x^3}{2b^2} - \frac{xy^2}{2b^2} \right],$$

and the round-beam expression for E_y is

$$E_y = \frac{qN_1}{\pi \epsilon_0 b^2} \left[y - \frac{y^3}{2b^2} - \frac{yx^2}{2b^2} \right],$$

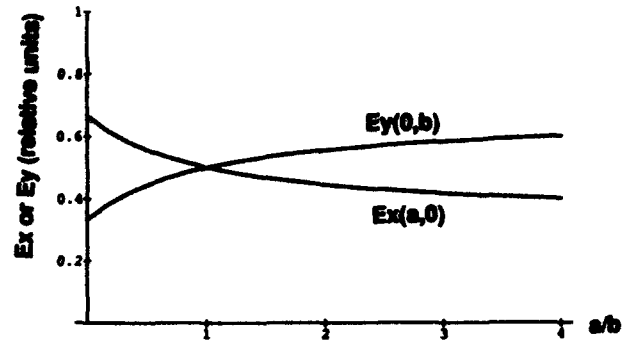


Figure 1. $E_x(a,0)$ and $E_y(0,b)$ in relative units versus ellipse aspect-ratio a/b for the parabolic-density distribution.

Now consider the effect of the coupling term for E_x . For any x value, the y value ranges from $-b(1-x^2/a^2)^{1/2}$ to $+b(1-x^2/a^2)^{1/2}$. The minimum value of E_x corresponds to $y^2=b^2(1-x^2/a^2)$, and the maximum value of E_x occurs when $y^2=0$. These limiting curves are plotted versus x/a in Fig. 2. We see that the coupling of the y coordinate into the x field component results in a range of E_x values for any x coordinate.

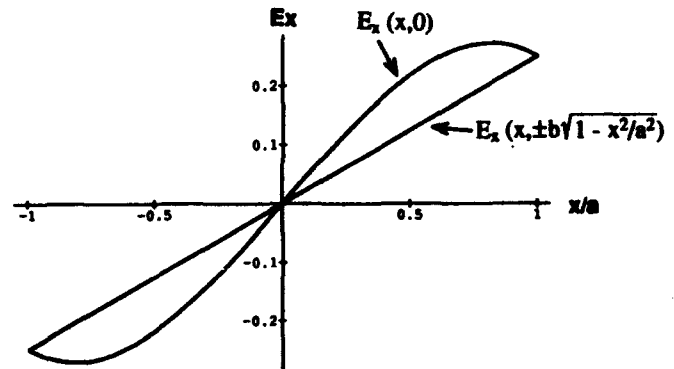


Figure 2. E_x versus x/a for a parabolic-density beam. The curves corresponding to $y=0$ and $\pm b\sqrt{1-x^2/a^2}$ define the maximum and minimum values of the space-charge electric field.

The space-charge kick in the x plane produces a divergence change, which depends on both x and y . The final divergence can be written, using the expression for the field. The rms emittance, calculated from the second moments of the distribution, is²

$$\epsilon_x = KL \frac{a}{b} \sqrt{\frac{1}{432} \left(\frac{2a}{b} + 1 \right)^2 \left\{ 1 + \frac{a}{b} \right\}^4 + \frac{7}{720} \frac{1}{\left\{ 1 + \frac{a}{b} \right\}^4} - \frac{1}{360} \left(\frac{2a}{b} + 1 \right) \left\{ 1 + \frac{a}{b} \right\}^4}.$$

The emittance expression for the y plane is obtained by interchanging a and b . The first term corresponds to the filamentation effect caused by the cubic term in the field, and represents the rms-emittance increase from the resulting

curvature in phase space. The second term comes from the coupling, i.e. the dependence of the x component of the field on the y coordinate, which produces the spreading of the initial filament. The last term is a cross term between the filamentation term and the coupling term.

For the round beam, where $a = b$, this reduces to

$$\epsilon_x = \frac{KL}{\sqrt{720}} = \frac{KL}{26.833},$$

which is independent of beam size. The initial and final phase-space configurations are shown in Fig. 3. The nonlinearity has changed the initial straight line into a distribution with an average curvature, which represents the beginning of the filamentation process where the phase-space distribution begins to bend. Of course as time increases the beam distribution also changes and for longer drifts, this must also be taken into account. The coupling has produced the spreading effect, which changes the initial line in phase space into a finite area. The spreading is zero at the origin and at the edge of the beam.

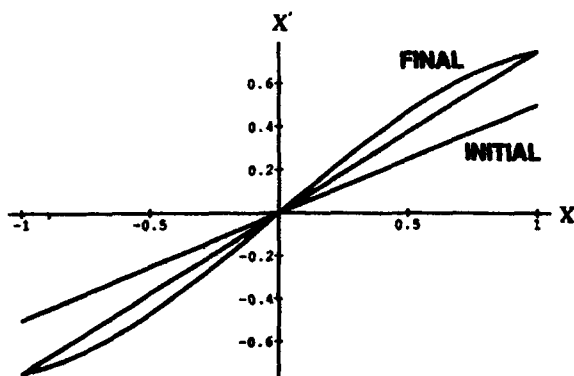


Figure 3. Effect of space charge from a parabolic density on an initial zero-emittance beam. The initial and final phase-space distributions are shown.

III. DEPENDENCE OF THE RMS EMITTANCE ON ELLIPSE ASPECT RATIO

In Fig. 4 we show the plot of the x and y final emittances versus the semiaxis ratio a/b . The final x emittance increases and the y emittance decreases with increasing a/b . That the emittance growth increases as the semiaxis length increases may seem surprising for an effect that arises from space-charge force, which increases as the beam size becomes smaller, rather than larger. The explanation is that the relative field components, and therefore the relative divergence kicks in x and y, are insensitive to the semiaxis sizes, as we saw earlier (see Fig. 1). However, emittance is an area in phase space, and is essentially a product of the divergence spread times the spatial extent of the beam in that plane. Therefore, if the divergence kicks are comparable in the two planes, the emittance growth is larger in the plane that has the larger semiaxis length.

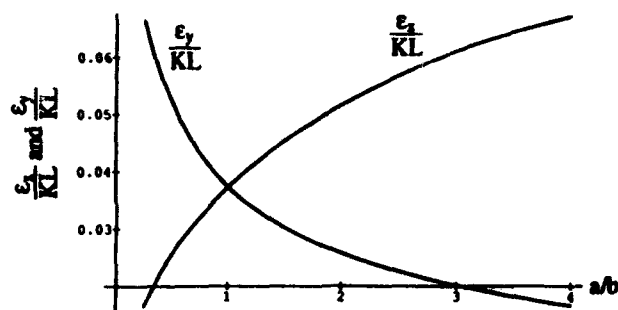


Figure 4. Final rms emittance values versus ellipse-aspect ratio a/b for a beam with parabolic density.

A closer examination of the effects of the different terms in the expression for ϵ_x^2 can be made by plotting each of these three terms versus the semiaxis ratio a/b , as shown in Fig. 5. The filamentation term dominates for $a/b > 1$. The coupling or spreading term dominates in the region given approximately by $a/b < 0.5$. The third or cross term is never the dominant term. One sees that the coupling term does decrease with increasing a/b when $a/b > 1$, but this occurs when the dominant term is the filamentation term.

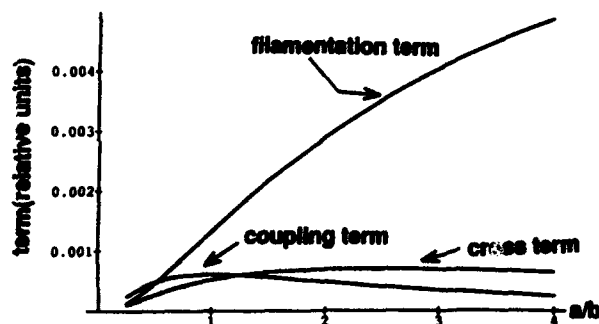


Figure 5. The three terms in the expression for ϵ_x^2 versus ellipse aspect ratio a/b .

IV. ACKNOWLEDGMENTS

We acknowledge some valuable discussions with our colleagues M. Weiss and E. Tanke at CERN.

V. REFERENCES

- [1] Frank J. Sacherer, "RMS Envelope Equations With Space Charge", IEEE Trans. Nucl. Sci. 18, 1105 (1971).
- [2] T. P. Wangler, P. Lapostolle, and A. Lombardi, "A Model of Non-Linear Space-Charge Forces in a Charged Particle Beam", CERN report CERN/PS 93-11 (H1), March 1993, and Los Alamos AT-Division Technical Note No. AT-1:92-416, December 15, 1993.

Emittance and Luminosity Evolution during Collisions in the SSC Collider

W. Chou, S. Dutt, T. Garavaglia and S. Kauffmann
Superconducting Super Collider Laboratory*
2550 Beckleymeade Ave., Dallas, TX 75237

Abstract

The nominal beam storage time in the SSC Collider is 24 hours. During this period, there are many co-existing effects that have impacts on the luminosity — intrabeam scattering, synchrotron radiation, pp collisions, beam-gas scattering and beam collimation. A computer program has been written which takes these effects into account simultaneously, and calculates the emittances and luminosity as a function of time. These evolution curves are compared for different operation scenarios (i.e., different initial conditions of the beam current, emittances, and beam energies.)

I. INTRODUCTION

The luminosity profile during the 24-hour or so collision period in the SSC Collider is an important issue that needs to be carefully studied. The luminosity is a function of a number of parameters. Among them are the number of particles per bunch (N_b), the beam emittances (ϵ_x , ϵ_y and ϵ_L), and the reduction factor (R) due to the crossing angle. These parameters vary with time. The number of particles will decrease due to beam-beam collisions, beam-residual gas collisions, and beam collimation. The beam emittances will be damped by the synchrotron radiation, but will be blown up by intrabeam scattering, beam-gas scattering, collective instabilities and external perturbations (e.g., ground motion and power supply ripple). The reduction factor (R) is a function of the beam emittances. This picture is further complicated by the fact that the emittance growth rates due to some processes, such as intrabeam scattering and pp elastic collisions, are by themselves evolving with time.

In order to model the luminosity evolution accurately, a computer program is written. Based on the best knowledge that we have about the complex processes that will occur during the beam storage time, the program considers pp collisions (elastic and inelastic), synchrotron radiation, intrabeam scattering, residual gas scattering and beam collimation simultaneously. It calculates the evolution of the emittances, particle numbers, reduction factors and luminosity. It is interesting to notice that the originally round-shaped beam gradually becomes flat because of the asymmetric feature of intrabeam scattering. The luminosity profile obtained is similar to that of a preliminary study [1].

*Operated by the Universities Research Association, Inc., for the U.S. Department of Energy under Contract No. DE-AC35-89ER40486.

II. EVOLUTION CALCULATIONS

A. Basic Formulae and Parameters

The luminosity per interaction point (IP) is computed from:

$$\mathcal{L} = \frac{N_b^2 M f_0}{4\pi\beta^* \sqrt{\epsilon_x \epsilon_y}} \cdot R \quad (\text{per IP})$$

in which M is the number of bunches (17424), f_0 the revolution frequency (3.441 kHz) and β^* the beta-function at the IP. The reduction factor is derived from the crossing angle ϕ :

$$R_{x,y} = \left(1 + \left(\frac{\phi \sigma_{x,y}}{2\sigma_{x,y}}\right)^2\right)^{-1/2}$$

in which $\sigma_{x,y,z}$ are the rms beam size in the horizontal, vertical and longitudinal directions, respectively. In the present design, there are two high luminosity IP's, where β^* is 0.5 meters. The nominal full crossing angle ϕ is 135 μ rad. One IP is horizontal crossing, the other vertical.

The emittance is a function of time:

$$\left(\frac{d\epsilon}{dt}\right)_{\text{total}} = \epsilon \left(\frac{1}{\tau_{\text{ibs}}} - \frac{1}{\tau_{\text{rad}}}\right) + \left(\frac{d\epsilon}{dt}\right)_{\text{gas}} + \left(\frac{d\epsilon}{dt}\right)_{pp}$$

in which τ_{ibs} and τ_{rad} are the emittance growth (damping) time of the intrabeam scattering and synchrotron radiation, respectively. The last two terms are for the elastic residual gas scattering and elastic pp collisions and will be discussed in detail later.

The number of protons per bunch decreases with time:

$$\left(\frac{dN_b}{dt}\right)_{\text{total}} = \frac{\mathcal{L}_{\text{total}}}{M} \cdot \sigma_{\text{inel}} + \left(\frac{dN_b}{dt}\right)_{\text{gas}} + \left(\frac{dN_b}{dt}\right)_{\text{others}}$$

in which σ_{inel} is the inelastic pp cross-section at 20 TeV (100 mb) and the last two terms are the beam loss due to the residual gas nuclear scattering and other effects (e.g., collimation).

B. Intrabeam scattering

The intrabeam scattering in the SSC has been studied elsewhere [2]. The growth times in the three bunch dimensions are given below [3]:

$$\frac{1}{\tau_s} \equiv \frac{1}{\sigma_s} \frac{d\sigma_s}{dt} = \left\langle A \frac{\sigma_h^2}{\sigma_p^2} f(a, b, c) \right\rangle$$

$$\frac{1}{\tau_z} \equiv \frac{1}{\sigma_{z\beta}} \frac{d\sigma_{z\beta}}{dt} = \left\langle A \left(f\left(\frac{1}{a}, \frac{b}{a}, \frac{c}{a}\right) + \frac{D_z^2 \sigma_p^2}{\sigma_z^2} f(a, b, c) \right) \right\rangle$$

$$\frac{1}{\tau_y} \equiv \frac{1}{\sigma_{y\beta}} \frac{d\sigma_{y\beta}}{dt} = \left\langle A \left(f\left(\frac{1}{b}, \frac{a}{b}, \frac{c}{b}\right) + \frac{D_y^2 \sigma_p^2}{\sigma_y^2} f(a, b, c) \right) \right\rangle$$

with

$$A = \frac{r_p^2 c_l N_b}{64\pi^2 \sigma_p \sigma_p \epsilon_x \epsilon_y \gamma^4}$$

$$\frac{1}{\sigma_h^2} = \frac{1}{\sigma_p^2} + \frac{D_x^2}{\sigma_x^2} + \frac{D_y^2}{\sigma_y^2}, \quad \sigma_{x,y}^2 = \sigma_{x,y,p}^2 + D_{x,y}^2 \sigma_p^2$$

$$a = \frac{\sigma_h}{\gamma \sigma_{x,p}}, \quad b = \frac{\sigma_h}{\gamma \sigma_{y,p}}, \quad c = \sigma_h \sqrt{\frac{2d}{r_p}}$$

The brackets denote the average over the whole circumference. The function f can be found in Ref [2]. The other quantities are: r_p = classical proton radius, c_l = velocity of light, γ = relativistic parameter, $D_{x,y}$ = dispersion functions, σ_x = rms bunch length, σ_p = rms relative energy spread and d = impact parameter $\approx \min\{\sigma_x, \sigma_y\}$.

It should be pointed out that what is computed here are the growth times of the beam amplitudes. They are a factor of two greater than the growth times of the beam emittance.

C. Synchrotron Radiation

The energy lost by a 20 TeV proton in the SSC due to synchrotron radiation is 0.126 MeV per turn. The damping time for energy oscillations works out to be 12.81 hours at the nominal circulation frequency of 3.441 kHz. Over the 24 hour beam storage time of the SSC, this allows for two e-foldings in the longitudinal emittance. The damping partition numbers for the collider are $J_x = J_y = 1$, and $J_z = 2$, so that both the horizontal and vertical transverse emittance would also suffer two e-foldings in a 24 hour period [4].

D. Elastic Proton-Proton Scattering

The contribution to transverse emittance growth, for one degree of freedom, resulting from proton-proton elastic scattering is given by

$$\frac{d\epsilon_x}{dt} = \frac{N_b f_0}{4\pi \sqrt{\epsilon_x \epsilon_y}} \cdot \sigma_{el} \langle \theta_x^2 \rangle \quad (\text{per IP})$$

In this expression σ_{el} is the proton-proton elastic scattering cross-section, and $\sqrt{\langle \theta_x^2 \rangle}$ is the rms value of the pp elastic scattering angle in the center of mass system, which is projected onto the transverse x -direction. A similar expression occurs for the transverse y -direction. The integrated and center-of-mass-system-differential pp elastic cross-sections are approximately related to the total pp cross-section by the formulae,

$$\sigma_{el} \approx (1/4)\sigma_T,$$

and

$$\left(\frac{d\sigma_{el}}{d\Omega}\right)_{c.m.} \approx \left(\frac{E_{c.m.}\sigma_T}{2hc_l}\right)^2 \exp\left(-\frac{\theta_x^2}{2\sigma_x^2} - \frac{\theta_y^2}{2\sigma_y^2}\right),$$

where h is Planck's constant and

$$\sigma_{\theta_x} = \sqrt{\langle \theta_x^2 \rangle} = \frac{hc_l}{E_{c.m.} \sqrt{2\pi\sigma_T}}.$$

For colliding proton beams with $E_{c.m.} = 20$ TeV and $\sigma_T \approx 130$ mb [5], one finds

$$\sigma_{\theta_x} = \sqrt{\langle \theta_x^2 \rangle} = 6.9 \mu\text{rad}.$$

E. Elastic Residual Gas Scattering

Following the approach set forth in Ref [6], we have that the scattering of an ultra-relativistic proton beam from the residual gas produces an average emittance growth rate of

$$\frac{d\epsilon}{dt} = \bar{\beta} \frac{d(\theta_x^2)}{dt} = \bar{\beta} \pi c_l \left(\frac{2e^2}{E}\right)^2 \sum_r n_r Z_r^2 \ln(a_r/R_r)$$

where $\bar{\beta}$ is the average β -function (180 m), E is the energy of the proton beam (20 TeV), e is the elementary unit of charge (esu), and the summation index r labels atomic (not molecular) species present in the residual gas, with Z_r the atomic number, a_r the orbital-electron-shielded atomic "radius", R_r the atom's nuclear "radius", and n_r the total number per unit volume of this type of atom which is present in the residual gas.

Partial pressures (as normalized to 0°C) of residual gases in the SSC Collider are projected to be 8×10^{-9} torr of H_2 , 10^{-10} torr of CO, and 2×10^{-11} torr of CO_2 [7]. We now assume that for all the atomic types involved (H, C, and O) we may take $\ln(a_r/R_r) \approx \ln(10^5) = 11.5$. With these assumptions we obtain,

$$\frac{d\epsilon}{dt} \approx 4.2 \times 10^{-17} \text{ m/s}.$$

F. Particle Loss

The main causes of particle loss are the nuclear interaction between the proton beam and the residual gas, and the inelastic pp collisions at the IP's. For the former, one can define an equivalent luminosity as

$$\mathcal{L}_{gas} = N_b M c_l \cdot n_{H_2} = 1.2 \times 10^{33} \text{ cm}^{-2}\text{s}^{-1}$$

in which $n_{H_2} = 3 \times 10^8 \text{ cm}^{-3}$ is the density of the residual H_2 in the beam vacuum and $N_b = 0.75 \times 10^{10}$. From the measured data of other laboratories (BNL and CERN) it is known that heavy species in the residual gas (CO and CO_2) make a significant contribution to the particle loss. Therefore, the value of \mathcal{L}_{gas} above is multiplied by a factor of 3 in the calculations [8]. Other causes of particle loss are beam collimation, collective beam-beam interactions, and noise in the RF system. They account for about 10% of the total particle loss.

III. RESULTS AND DISCUSSION

A. Initial Conditions and Evolution Curves

The initial conditions of the baseline design are: $\mathcal{L} = 1 \times 10^{33} \text{ cm}^{-2}\text{s}^{-1}$ per IP, $N_b = 0.75 \times 10^{10}$, $\gamma = 21315.8$ (20

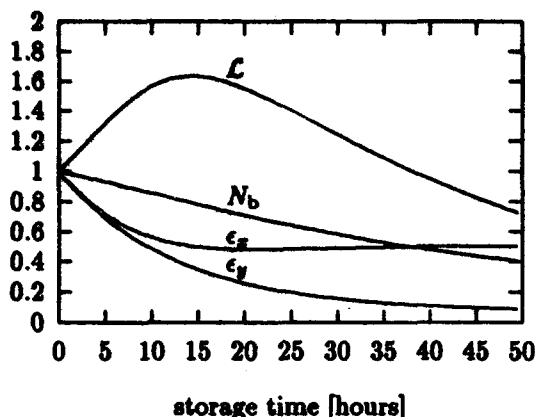


Figure 1. Evolution curves for luminosity, number of protons per bunch, and horizontal and vertical emittances. Parameters used are for baseline design.

TeV), the normalized transverse emittances $\epsilon_{Nx} = \epsilon_{Ny} = 10^{-6}$ m-rad, $\sigma_s = 6$ cm, $\sigma_p = 0.58 \times 10^{-4}$. The evolution curves are shown in Fig. 1.

- The luminosity curve first rises because the emittances decrease due to synchrotron radiation. It reaches a peak, and then drops because of particle loss and intrabeam scattering. This feature is qualitatively similar to that in Ref [1].
- The transverse emittance in the x -direction gradually becomes larger than that in the y -direction. This is because the average dispersion function D_x (1.5 m) is much bigger than D_y (which is virtually zero). This results in different intrabeam scattering growth rates in x and y . Therefore, the round beam will become flat. After 24 hours, the aspect ratio is about 2.4 to 1; after 50 hours, 5.7 to 1.
- The transverse emittances converge toward equilibrium values where damping effects are balanced by antidamping effects.

B. Different Operational Scenarios

The Collider may be operated under different initial conditions for various reasons. Fig. 2 is for the case when the luminosity is upgraded by a factor of 10 (by increasing N_b by a factor of $\sqrt{10}$), whereas Fig. 3 shows the curves for an energy upgrade from 20 TeV to 23 TeV, while keeping the same beam current.

IV. ACKNOWLEDGEMENTS

We thank Nikolai Mokhov and John Palkovic for helpful discussions and comments.

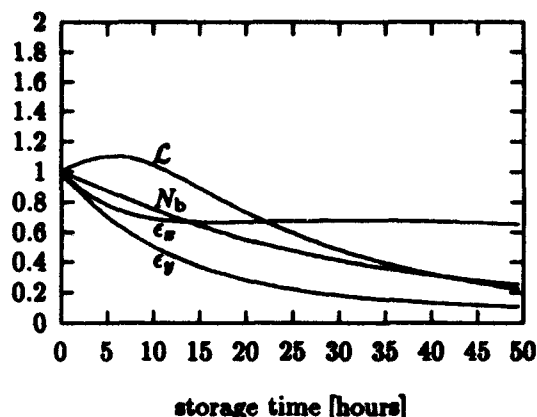


Figure 2. Evolution curves for luminosity upgrade by a factor of 10.

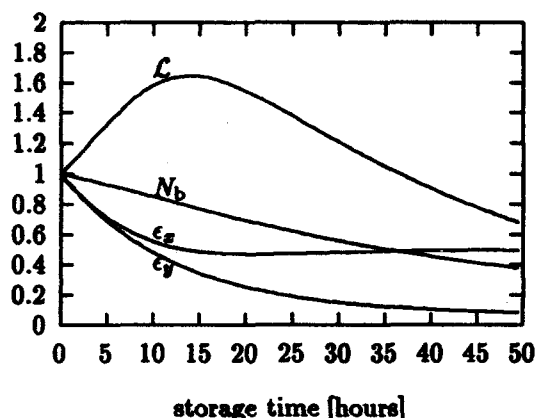


Figure 3. Evolution curves for energy upgrade from 20 TeV to 23 TeV.

V. REFERENCES

- [1] *Site Specific Conceptual Design*, SSCL-SR-1056, p. 258, (July 1990).
- [2] W. Chou and A. Piwinski, "Intra-Beam Scattering in the SSC Collider and in the Boosters," SSCL-574 (June 1992).
- [3] A. Piwinski, *Proc. 9th Conf. on High Energy Accelerators*, SLAC, May 2-7, 1974, p. 405.
- [4] S. K. Dutt, "Synchrotron Radiation from Protons," *Workshop on Fourth Generation Light Sources*, SSRL 92/02 (1992), pp. 170-177.
- [5] M. Honda et al., *Phys. Rev. Lett.* **70**, 525 (1993).
- [6] D.A. Edwards and M.J. Syphers, *An Introduction to the Physics of High Energy Accelerators*, Wiley, New York, 1993, pp. 249-252.
- [7] Same as Ref 1, p. 479.
- [8] N. Mokhov, private communication.

Emittance Growth in Displaced, Space-Charge-Dominated Beams with Energy Spread*

J.J. Barnard, J. Millert†

Lawrence Livermore National Laboratory, L-440, Livermore, CA 94550

I. Haber

Naval Research Laboratory, Washington, D.C. 20375

Abstract

Conversion of transverse energy associated with the coherent motion of displaced beams into thermal energy, and thus emittance growth, has been predicted theoretically by a number of authors. Here, we show, using 2-D particle-in-cell simulations, that emittance growth is inhibited for tune depressed beams, if the energy spread of the beam is not too large. Further, using a uniform density model to calculate the space charge field of the beam, we numerically determine the criteria for emittance growth as a function of tune depression, energy spread, and beam displacement over a wide range of parameters. A theoretical interpretation of our results is presented.

I. INTRODUCTION

In an inertial fusion energy reactor, driven by a heavy ion accelerator, the ion beam must be focused down to a small (2-3 mm) spot at the target. The normalized emittance, (which is a measure of the transverse phase area occupied by the beam) must be sufficiently small in order to meet the spot size requirement. An understanding of emittance growth is thus of paramount importance to ensure optimum performance of a driver. One source of emittance growth is the conversion of the energy associated with coherent oscillation of the beam centroid into thermal energy of the beam. These oscillations may arise from initially non-aligned beams or accumulated from small misalignments in the focusing quadrupoles, for the case of a linear accelerator. In addition, centroid oscillations may arise from errors in the field strength in bending magnets, or voltage errors in the acceleration modules in accelerators in which bends are present.

It is well known, that a beam with a KV distribution in the transverse direction [1] and monoenergetic in the longitudinal direction, and subject to strictly linear focusing forces will undergo no emittance growth, even if the beam is initially displaced. It is also well known that for emittance dominated beams (in which space charge is negligible), a small spread in the longitudinal velocity gives rise to a spread in the betatron frequency of individual particles, and this spread mixes the phase of the oscillating particles, removing the coherent oscillation of the centroid as a whole and increasing the effective transverse area of

phase space occupied by the beam. For emittance dominated beams, the smaller the energy spread, the smaller the rate at which the emittance grows to its final phase-mixed value. However, the asymptotic value of the emittance is nearly independent of energy spread, and can be estimated by using the conservation of transverse energy.

In this paper, we examine the effect of energy spread on beams with finite space-charge-depressions in linear focusing channels and find behavior which is qualitatively different from the emittance dominated case. In particular, we find that for large initial centroid displacements there exists a threshold in energy spread, below which, no significant emittance growth occurs, and above which, the beam approaches the asymptotic phase mixed state. For small beam displacements, the transition is not sharp but the same general trend occurs.

II. 2-D PARTICLE-IN-CELL RESULTS

The effect was first observed numerically, using the 2-D slice code SHIFTX [2]. Here x and y are the transverse coordinates, and prime indicates derivative with respect to z the longitudinal coordinate. The beam is assumed to be displaced $x_c = \langle x \rangle$ in the x direction only, where $\langle \rangle$ indicates average over particles in a slice. The beam widths in both x and y directions were matched for the emittance and current of the beam.

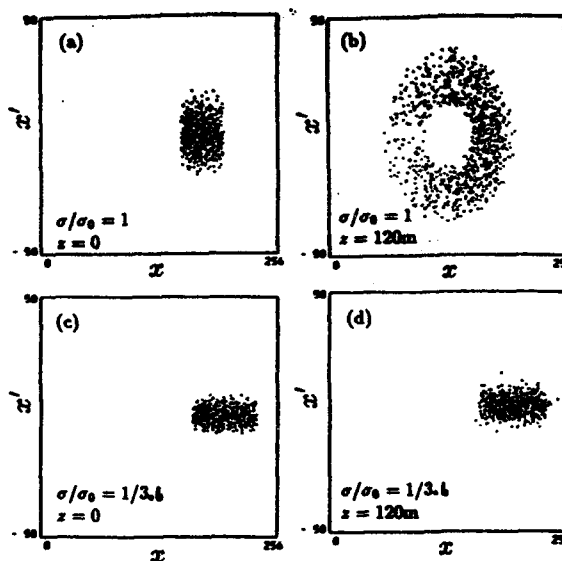


Fig. 1. $x-x'$ phase space plots for two beams as indicated.

Fig. 1 illustrate the effects. In fig. 1a, the $x-x'$ phase space is shown for an undepressed beam ($\sigma/\sigma_0 = 1$), initially at $z = 0$ and in fig. 1b, eight betatron periods later ($z = 120$ m). Here σ_0 and σ are the undepressed

*Work performed under the auspices of the U.S. D.O.E. by LLNL under contract W-7405-ENG-48 and by NRL under contracts DE-AI05-92ER54177 and DE-AI05-83ER40112. †Presently at Harvard University.

and depressed phase advances, respectively. The beam had fractional momentum spread of halfwidth $\Delta = 0.01$, and the initial centroid displacement $x_{c0} = 2a$, where a is the initial beam radius in x . The beam fills a ring in $x - x'$ space of nearly uniform density, as different particles with different betatron frequencies, phase mix, damping the coherent centroid oscillation. In figure 1c and 1d, the initial and final phase spaces are shown for $\sigma/\sigma_0 = 1/3.4$ with the same momentum spread. Note the transverse area is nearly unchanged from the initial area. This reduction in emittance growth (in this case by two orders of magnitude) is an unexpected benefit of space-charge dominated beams.

III. MODEL RESULTS

In order to obtain an understanding of this behavior we may adopt model equations of motion which simplify the physics of the space-charge force. We assume that the equations of motion of for each ion are given by,

$$x_i'' = (-k_{\rho 0}^2 x_i + k_{xx}^2(x_i - x_c))/(1 + \delta_i)^2. \quad (1)$$

$$y_i'' = (-k_{\rho 0}^2 y_i + k_{yy}^2(y_i - y_c))/(1 + \delta_i)^2. \quad (2)$$

Here, subscript i indicates the coordinates of the i th particle in a particular slice in z , which is traveling in the $+z$ direction; $k_{\rho 0} \equiv \sigma_0/(2L)$ represents magnetic FODO focusing in the smooth approximation, and L is the lattice half-period; $\delta_i = \delta p_i/p$ is the fractional difference between the momentum of the i th particle and the average momentum; $K \equiv 2qI/(\beta^3 A I_0)$ is the perveance, where q is the charge state of the ions, A is the atomic mass of the ions, β is the average longitudinal ion velocity in units of c , $I_0 \equiv m_p c^3/e$ is the proton Alfven current (≈ 31 MA). Also,

$$k_{xx}^2 \equiv K/[2(\Delta x^2 + (\Delta x^2 \Delta y^2)^{1/2})],$$

$$k_{yy}^2 \equiv K/[2(\Delta y^2 + (\Delta x^2 \Delta y^2)^{1/2})]. \quad (3)$$

Here $\Delta x^2 = \langle x^2 \rangle - \langle x \rangle^2$, and $\Delta y^2 = \langle y^2 \rangle - \langle y \rangle^2$. Eqs. (1) and (2) represent in an approximate way, the effects of magnetic focusing and space charge, and the $(1 + \delta_i)^{-2}$ factor indicates the velocity dependence of these forces when z is the independent variable. The physical approximations that have been made include the following: (1) Focusing is smooth and not a function of z ($k_{\rho 0}$ is constant). (2) In eqs. (1) and (2) terms through first order in the small quantities $k_{\rho 0} x_i$, $k_{\rho 0} y_i$ have been kept. Non-linearities arise through the dependence of k_{xx} and k_{yy} on Δx^2 and Δy^2 and phase mixing can occur because of the $(1 + \delta_i)^{-2}$ factors. (3) Space charge forces depend only on lowest order moments. (We have used the electrostatic potential of a uniform density elliptical beam, allowing variation with z of the centroid position and semi-major axes.) (4) The beam is not undergoing acceleration: (p , β , and δp_i are constants). (5) The beam is non-relativistic: ($\beta \ll 1$).

It has been shown [3,4], that when the factor $(1 + \delta_i)^{-2}$ is set to unity in equations (1) and (2), a transverse energy H may be defined which is constant in z :

$$2H = k_{\rho 0}^2(\Delta x^2 + \Delta y^2) + \Delta x'^2 + \Delta y'^2 - K \ln[(\Delta x^2)^{1/2} + (\Delta y^2)^{1/2}]$$

$$+ k_{\rho 0}^2 x_c^2 + k_{\rho 0}^2 y_c^2 + x_c'^2 + y_c'^2 \quad (4)$$

When the factor $(1 + \delta_i)^{-2}$ is included, H is no longer precisely constant, but the fluctuations in H are small when Δ is small.

Phase mixing can lead to a final state in which the beam centroid has decayed to zero, at the expense of a larger phase space area. Two final states of the beam are of interest. When the x and y equations of motion are sufficiently uncoupled (as for example when $\sigma \cong \sigma_0$) the beam width and displacement in the y direction are unaffected by the initial displacement in x . The final state of the beam evolves to $x_{cf} = y_{cf} = x'_{cf} = y'_{cf} = 0$ and $\Delta y_f^2 = \Delta y_0^2$, where subscripts 0 and f stand for initial and final, respectively. Conservation of the transverse energy, yields:

$$2H_0 = k_{\rho 0}^2(\Delta x_f^2 + \Delta y_0^2) + k_{xxf}^2 \Delta x_f^2 + k_{yyf}^2 \Delta y_0^2 - K \ln[(\Delta x_f^2)^{1/2} + (\Delta y_0^2)^{1/2}] \quad (5)$$

Here $2H_0 = 2(k_{\rho 0}^2 + k_{xx0}^2)\Delta x_0^2 - K \ln[2(\Delta x_0^2)^{1/2}] + k_{\rho 0}^2 x_{c0}^2$. Equation (5) may be solved (numerically) for Δx_f^2 . The root mean square width in x' is given by $\Delta x_f'^2 = k_{xxf}^2 \Delta x_f^2$ and similarly the width in y' is given by $\Delta y_f'^2 = k_{yyf}^2 \Delta y_f^2$ (ref. 4). The final x emittance is given by $\epsilon_{xf} = 4(\Delta x_f^2 \Delta x_f'^2)^{1/2}$ and similarly in y , $\epsilon_{yf} = 4(\Delta y_f^2 \Delta y_f'^2)^{1/2}$.

The second final state of interest is the case where the x and y equations of motion are sufficiently coupled so that the final state of the beam is the same in both x and y . In that case, $\Delta x_f^2 = \Delta y_f^2$ and

$$2H_0 = 2(k_{\rho 0}^2 + k_{xxf}^2)\Delta x_f^2 - K \ln[2(\Delta x_f^2)^{1/2}] \quad (6)$$

Again, eq. (6) may be solved numerically for Δx_f^2 , and then $\Delta x_f'^2$, $\Delta y_f'^2$, ϵ_{xf} , and ϵ_{yf} may be calculated as in the first case above.

We have integrated the model eqs. (1) and (2), over a distance of 33 betatron periods for an ensemble of particles, for a variety of ratios of beam radius $a = 2(\Delta x_0^2)^{1/2}$ to initial beam displacements x_c , space charge depressions σ/σ_0 , and halfwidth Δ of distribution in δ . The difference between final and initial x -emittance is shown in figures 2 and 3 for $a/x_c = 1$. Note the sharp threshold for emittance growth. The threshold may be heuristically derived by a consideration of equation (1). In the case of no energy spread the centroid oscillates sinusoidally, $x_c = x_{c0} \cos k_{\rho 0} z$, and the beam widths are constant $\Delta x^2 = \Delta y^2 = \Delta x_0^2$. If we integrate eq. 1, assuming these values for x_c , Δx^2 and Δy^2 respectively, we find the solution to eq. (1):

$$x_i = (x_{i0} - \frac{k_{xx}^2 x_{c0}}{k_{\rho 0}^2 - k_{xx}^2}) \cos k z + \frac{x'_{i0} \sin k z}{k} + \frac{k_{xx}^2 x_{c0} \cos k_{\rho 0} z}{k_{\rho 0}^2 - k_{xx}^2} \quad (7)$$

Here $k^2 \equiv (k_{\rho 0}^2 - k_{xx}^2)/(1 + \delta_i)^2 \equiv (\sigma/2L)^2/(1 + \delta_i)^2$. Also, $k_{xx}^2 \equiv k_{xx}^2/(1 + \delta_i)^2$. Note that because of the energy spread, the assumption that Δx^2 is constant breaks down. A necessary condition for eq. (7) to be nearly self-consistent is that the difference between the assumed x_c and a particle position x at the edge of the distribution in δ_i be much less than some fraction f of a beam radius. This condition leads to the equation:

$$\left(\frac{\delta_i^2}{\delta_i^2 - \delta_c^2} - 1\right)x_{c0} \leq fa \quad (8)$$

Eq. 8 defines a critical δ_i below which (i.e. for large negative values) the equations of motion become very non-linear, but above which the linear solution (eq. 7) remains approximately valid. When we substitute the half-width Δ of a uniform distribution in δ_i for $-\delta_i$ into equation (8) that threshold may be written

$$\Delta = 1 - \left(\frac{1 + (\sigma^2/\sigma_0^2)f/a/x_{c0}}{1 + f/a/x_{c0}}\right)^{1/2} \quad (9)$$

This threshold closely matches the threshold found in the numerical integration of eqs. 1 and 2 for emittance growth, when the value of $f = 0.6 + 0.5(a/x_{c0})$. This formula for f was found by fitting to the numerical plots. When the threshold is exceeded the emittance growth is given closely by that calculated from eq. (5) (see fig. 4). This threshold is sharp when $a/x_{c0} < 1$, but the simulations show that the threshold is much broader when $a/x_{c0} \gg 1$. In that case, the asymptotic emittance is close to the initial matched emittance, and the transition from zero emittance growth to asymptotic emittance growth is gradual, so that the precise value of f is not well defined.

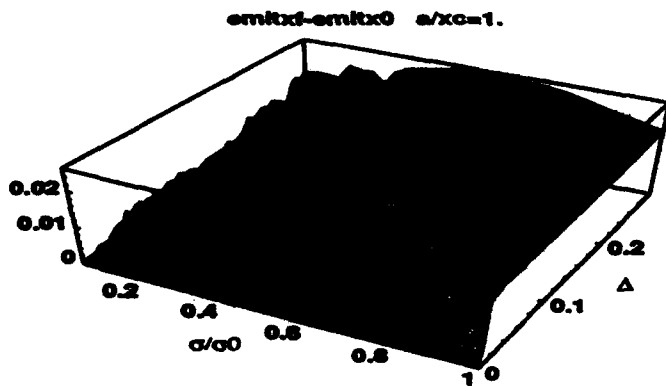


Figure 2. Model equation results of $\epsilon_{xf} - \epsilon_{x0}$ for $a/x_{c0} = 1.0$.

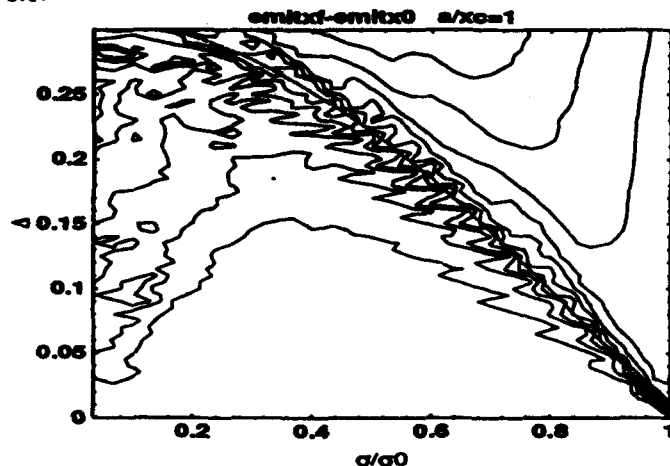


Figure 3. Contour plot of figure 2, ($\epsilon_{xf} - \epsilon_{x0}$ for $a/x_{c0} = 1.0$). Dotted line is the threshold, (eq. 9).

IV. DISCUSSION AND CONCLUSION

Although, use of eqs. 1 and 2 simplify the actual forces experienced by the particles, threshold predicted by

eq. 9 is qualitatively obtained in the particle-in-cell (PIC) results, and the final emittance predicted by eq. 5 is also approximately obtained in the PIC results, although

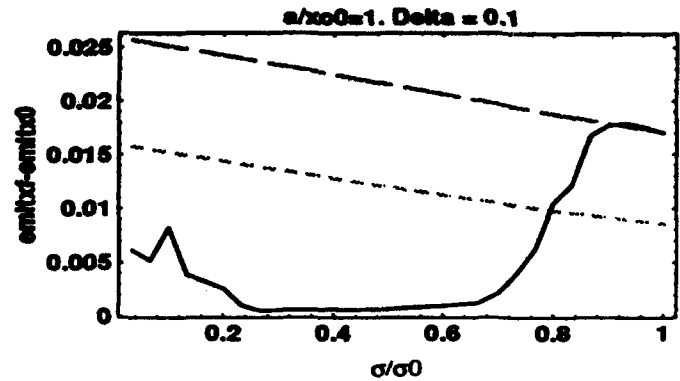


Figure 4. Model equation results of $\epsilon_{xf} - \epsilon_{x0}$ vs. σ/σ_0 for $\Delta = 0.10$. Dashed line is asymptotic emittance found using eq. 5. Short dashed line is found using eq. 6.

additional phase mixing to the final state predicted by eq. 6 is seen for smaller σ/σ_0 . The result that space-charge depression reduces chromatic aberration in an alternating gradient lattice was observed by Lee [5] and is physically related to the reduction of phase mixing for displaced beams. The coherence of centroid oscillations of highly depressed beams over many betatron periods was unexpected and was not predicted in previous studies of emittance growth from displaced beams [3,6]. Also, as indicated above, sufficiently large longitudinal velocity spreads will give rise to non-linearities which may become fully phase mixed. These results will have applications in determining error tolerances in possible drivers for heavy-ion inertial fusion.

V. REFERENCES

- [1] I. M. Kapchinskij and V.V. Vladimirkij, in Proc. Intl. Conf. High-Energy Accelerators (CERN, Geneva, 1959), p 274.
- [2] I. Haber, "High Current Simulation Codes," in High Current High Brightness and High Duty Factor Ion Injectors, AIP Conf. Proc. 139, (AIP, New York, 1986) p. 107.
- [3] M. Reiser "Free Energy and Emittance Growth in Non-stationary Charged Particle Beams," Journal of Applied Physics 70, 1919 (1991).
- [4] J.J. Barnard, H.D. Shay, S.S. Yu, A. Friedman, D.P. Grote, "Emittance Growth in Heavy Ion Recirculators," 1992 Linear Accelerator Conference Proceedings 1992 August 24-28 Ottawa, Ontario, Canada AECL-10728 1, p. 229 (1992).
- [5] E.P. Lee, "Partial Cancellation of Second Order Chromatic Aberration of a Quadrupole Focussing System by Space Charge Forces," Bull. Amer. Phys. Soc. 35, p. 1022 (1990). (Abstract).
- [6] O. A. Anderson, "Emittance Growth Rates for Displaced or Mismatched High Current Beams in Nonlinear Channels," Proc. of the Fourth NPB Techn. Symp., Argonne National Laboratory, (1992).

AN INJECTION SCHEME FOR THE BROOKHAVEN ATF UTILIZING SPACE-CHARGE EMITTANCE GROWTH COMPENSATION

Juan C. Gallardo and Harold G. Kirk

Physics Department
Brookhaven National Laboratory
Upton, New York 11973

Abstract

We consider possible configurations for injection of photocathode-produced electron beams straight into linear accelerating sections. A slightly convergent beam into the linac is required for maximum transmission through the linac sections and therefore a solenoid pair is considered. We describe strategies for placing the rf gun injector and the strength of the solenoids so as to minimize the emittance growth of the beam as it traverses the linac sections. The simulation codes PARMELA and TRACE 3-D were used for this design study.

I. INTRODUCTION

The Brookhaven Accelerator Test Facility consists of a photocathode loaded rf gun, a double-bend, low-energy transport system, two traveling-wave accelerating sections and a high-energy transport to an experimental hall [1]. Our goal in this paper is to examine beam line configurations which will permit straight injection into the linac sections without having to resort to bending magnets. The control of emittance growth is a primary design objective.

The issue of emittance growth and containment in high-brightness electron beams has been studied extensively. It has been argued that to study the physical phenomena that produces emittance dilution in the transport and acceleration of a high-brightness electron beam it is desirable to divide the electron bunch in longitudinal slices. These slices provide a tool to probe and extract the different dynamical behavior of the slices of the electron pulse. It is well known that emittance dilution due to the rf dynamics within the rf gun [2] is quite different from that due to space charge [3] within the bunch structure of the electron beam.

Using the code PARMELA [4], we track each slice through the system and observe that the intrinsic emittance within each slice can be very small ($\epsilon_n \approx 1 \pi$ mm-mrad) but the projection on the phase space of all slices give rise to a larger global emittance. Although, the area in phase space (emittance) swept by each slice is small, the area covering all the slices is significantly larger and consequently, the emittance of the total beam is larger in

magnitude. Since the space-charge effects are greater at the longitudinal center of the beam than at the ends, the core tends to develop larger values of $\langle s \rangle$ and $\langle s' \rangle$. This leads to each slice evolving differently in phase space as time evolves.

II. NUMERICAL ANALYSIS AND RESULTS

2.1 Long Drift Solution

Injecting beam straight into the linacs entails placing an rf gun inline with the linacs and utilizing a solenoid-gun-solenoid arrangement while possibly incorporating the present inline triplet for matching beam into the linac. The solenoid preceeding the gun is used so as to buck the magnetic field of the second solenoid, thus insuring that an emittance degrading magnetic field is not present at the photocathode. In this configuration the cathode plane is located 2.5 meters from the linac entrance. The advantage of this approach is that it preserves the present double-bend for injection into the linac [5] thus providing for valuable redundancy thereby reducing program downtime.

Matching the beam into the linac so as to encounter no beam loss after traversing the two linac sections requires the electron beam to be slightly converging as it enters the first linac section. We have checked that this is not possible for a 1 nC, 10 ps beam if we wish to rely exclusively on the focusing of a solenoid. By utilizing the inline triplet, it is possible to present a properly matched beam to the linac. We find, however, that a solenoid placed immediately after the gun is still required in order to contain the beam during the 70 cm drift to the triplet entrance. We used TRACE 3-D [6] to develop the initial conditions for matching the electron beam into the linac and then used PARMELA to calculate the full beam dynamics from the plane of the photocathode through to the emergence from the two linac sections.

We show in Fig. 1 a typical solution for delivering full beam through the linac. The electron beam parameters for this solution entail beginning at the photocathode with a beam with a uniform radial distribution of $r = 0.9$ mm and a uniform longitudinal pulse length of 10 ps. The use of a uniform distribution was found to offer significant advantages over gaussian distributions in terms of minimising the final beam emittance. The beam emerges from the linac sections with an rms radius of 1.6 mm and a transverse emittance of 3.5π mm-mrad.

2.2 Close-in Solution

We explore placing the rf gun inline as close as possible to the linac entrance. Matching into the linac, however, requires at a minimum a solenoidal focusing magnet between the gun and the linac entrance. The principal variables explored for this study are: the strength of the solenoid field, the gun-to-linac distance, and the phase of the linac sections relative to the rf gun. The length of the solenoid was fixed at 16 cm and the average accelerating gradient of the linac sections was set at 7 MV/m. While we did vary the radius of the initial electron beam, the bunch charge was fixed at 1nC and the bunch length was fixed at 10 ps.

Fig. 2 shows the solution of the $s=62$ cm case, presenting a beam identical to the previous example displayed in Fig. 1. The beam emerges from the two linac sections with an rms radius of 0.28 mm, an rms divergence of 0.050 mrad, and an invariant emittance $\epsilon_n = 0.75 \pi$ mm-mrad. We find that the energy spread of the emerging beam is particularly sensitive to the phasing of the linac sections while the final beam emittance is rather insensitive to this variable (see Fig. 3). The optimum setting of the phase delivers a beam with an rms dp/p of 2×10^{-3} . In Fig. 4, we display the results of varying the drift distance between the gun-solenoid and the linac entrance. We find that the optimum distance from the photocathode plane to the linac is 70 cm.

2.3 Electron Bunch Dynamics

We have examined the process whereby the emittance of the electron first grows then diminishes as the beam drifts then accelerates after it leaves the rf gun. The emittance growth experienced during the drift period immediately after the beam leaves the rf gun results from defocusing forces due to space charge within the electron bunch. These defocusing forces are stronger in the center of the bunch than on the leading and trailing edges of the beam. This results in a time-dependent, phase-space structure which can be neutralized if the space charge forces are inverted so as to make the defocusing forces stronger in the ends of the electron bunch than the center. This can be achieved through a focusing action on the beam followed by a drift. In Fig. 5, we see the trajectories in $x-x'$ phase space of an ensemble of electrons first at the longitudinal ends of the bunch and then at the longitudinal center of the bunch. Notice that after the focusing action is complete both ensembles move toward the left (toward negative x) due to drift and simultaneously up (toward positive x') due to defocusing space-charge forces. The interesting feature observed in this plot is that a cross-over occurs going from negative to positive x' (defocusing action) instead of the standard positive to negative x (drift action). Clearly seen in the figure is that the end sections of the electron bunch are spatially compressed more than the center of the bunch. This results in an increase of the space-charge defocusing forces in the ends relative to the center thus compensating in part the global emittance growth observed before the focusing action.

III. CONCLUSIONS

We observe an increase of the electron beam emittance ϵ_n , immediately after the gun and a subsequent reduction to a rather broad minimum (in some cases there is a gentle asymptotic decrease) located inside the linac sections. This behavior of ϵ_n reflects the interplay of focusing, drifting and defocusing space charge fields [7]. The net result is to close the fan in phase space which results in a decrease of the global emittance of the beam. If at this point the beam is accelerated, then the phase spaces of the slice ellipses are locked in with respect to each other due to the decrease of the space charge forces ($F_1 \approx O(\frac{1}{\gamma^2})$). The electron beam emerging from the linac exhibits a high-brightness characterized by, $B = \frac{I_b}{\pi \epsilon_n \sigma_x \sigma_y} = 6 \times 10^{13}$.

We give in Table I a summary of the parameters for the beam entering the high-energy transport system following the linacs. We find that the optimum photocathode plane to linac entrance distance for our initial conditions is 70 cm.

IV. ACKNOWLEDGEMENT

The authors wish to thank D. Yeremian and R. Miller of SLAC for providing the PARMELA input parameters for the traveling-wave accelerating sections. This research was supported by the U.S. Department of Energy under Contract No. DE-ACO2-76-CH00016.

TABLE I. Parameters used in the PARMELA simulations for an axially symmetric $1 \frac{1}{2}$ -cell gun in a π -mode configuration with a solenoid pair.

RF frequency [MHz]	2856
Radius of aperture [cm]	1.0
Field on cathode [MV/m]	100.0
Initial phase [degree]	43.0
Laser spot size* [mm]	0.9
Laser pulse full width* [ps]	10.0
Charge [nC]	1.0
B_0 [kG]	2.2
Average linac accelerating gradient [MV/m]	7.0
ϵ_n , π mm-mrad	0.75
dp/p [%]	0.2

*Uniform profile

- [1] K. Batchelor, et al, The Brookhaven Accelerator Test Facility, Proceedings of the 1988 Linear Acceleration Conference, CEBAF report 89-001, 540 (1988)
- [2] K.-J. Kim, Nucl. Instr. and Meth. A278, 201 (1989).
- [3] Juan C. Gallardo and Robert B. Palmer, Nucl. Instr. and Meth. A304, 345 (1991).
- [4] L. M. Young, private communication.
- [5] K. Batchelor, et al, Performance of the Brookhaven photocathode rf gun, Proceedings of the Thirteenth International Free Electron Conference, Santa Fe, NM, USA, August 25-30, 1991, Nucl. Instr. and Meth. A318, 373 (1992).
- [6] K.R. Crandall, TRACE 3-D Documentation, Los Alamos Accelerator Code Group, LA-UR-90-4146 (1990)
- [7] B.E. Carlsten, New photoelectric injector design for the Los Alamos National Laboratory XUV FEL accelerator, Nucl. Instr. and Meth. A285, 313 (1989)

FIG. 1. Normalised transverse emittance ϵ_n vs. distance z utilising a solenoid and quadrupole triplet

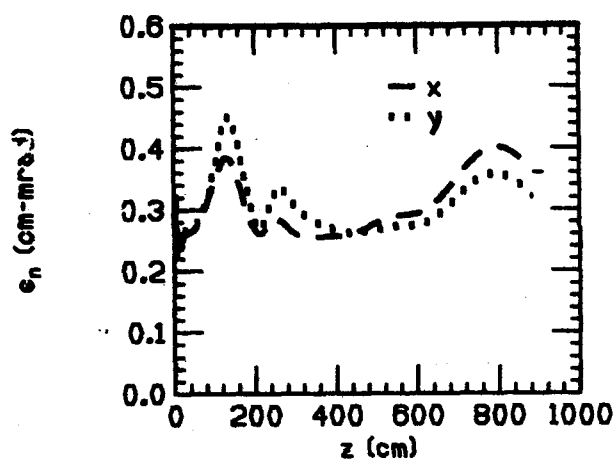


FIG. 2. Normalised transverse emittance ϵ_n vs. distance z utilising only a solenoid pair—the plane of the photocathode is 62 cm from the linac entrance

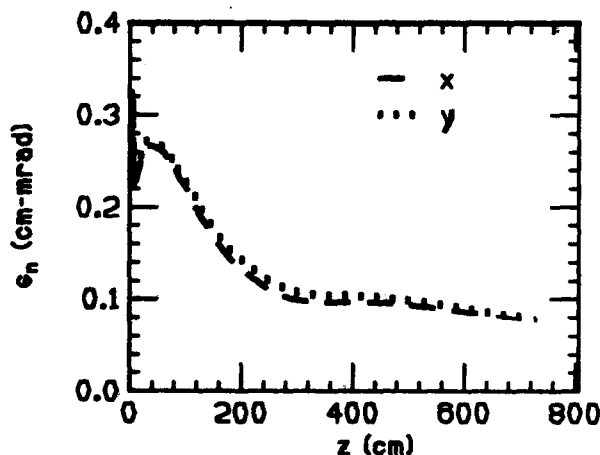


FIG. 3. The dp and normalised emittance of the electron beam exiting the two linac sections as a function of phase relative to the electron beam launch phase at the photocathode

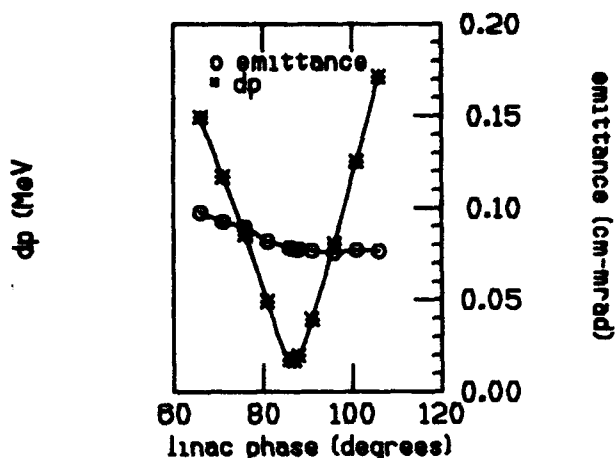


FIG. 4. The normalised emittance of the electron beam exiting the linac sections as a function of the longitudinal distance between the photocathode plane and the linac entrance

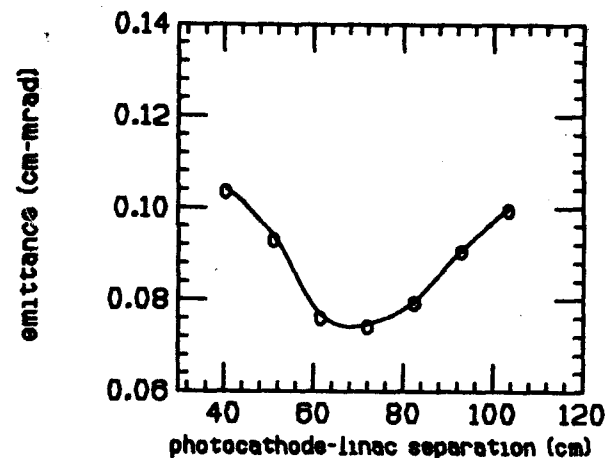
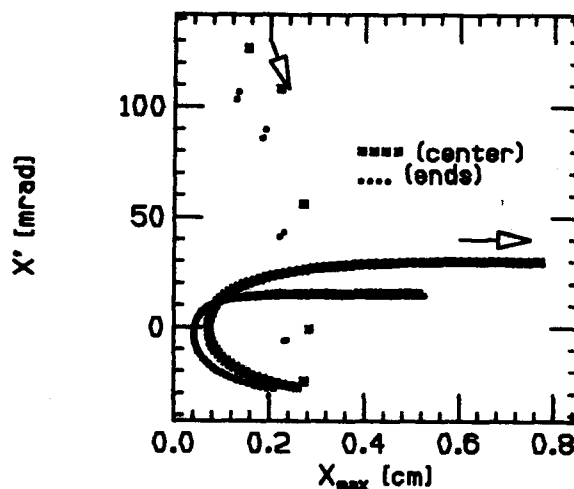


FIG. 5. The trajectories of the end and center slices of the electron beam in $x-x'$ phase space



A MATRIX THEORY OF THE MOTION OF AN ELLIPSOIDAL BUNCH IN A BEAM CONTROL SYSTEM WITH A RECTILINEAR OPTICAL AXIS AND WITH SPACE CHARGE

Alexander Dymnikov
Institute of Computational Mathematics
University of St. Petersburg
Stary Petergof 198904
St. PETERSBURG, Russia

Ragnar Hellborg
Department of Physics
University of Lund
Sölvegatan 14
S-223 62 LUND, Sweden

ABSTRACT

The motion of a 3-dimensional ellipsoidal bunch of charged particles in an arbitrary external electromagnetic field is considered taking into account the effect of space charge. The first approximation of the electromagnetic field within the bunch due to space charge has been found. The nonlinear matrix equation in the envelope variable space is written. An effective recursive computational method for the solution of the nonlinear beam envelope evolution is proposed.

1 INTRODUCTION

A time-varying field can be used for the transverse focusing of particles and in some cases a high-frequency focusing system can be constructed more simply and cheaply than a strong-focusing system [1]. The possibility to use a high-frequency focusing field in nuclear microprobes [2] opens up possibilities for the analysis of high-frequency or rapidly moving processes. Most advanced accelerator and microprobe applications require high-brightness beams [3]. In some cases -like a narrow beam through the whole system or a very bright beam- the beam is dominated by space-charge forces throughout the entire system from source to target.

In this paper the electromagnetic field inside a beam bunch due to the space-charge is presented. The paraxial, nonlinear equations of motion of this bunch in an arbitrary external electromagnetic field, as well as a new, recursive technique for solving these equations, have been constructed and are presented. A more detailed report on this theory is to be found in [4]. In two recent papers [5] and [6], this theory has been applied to a special case with an infinitely long beam (i.e. a DC-beam) and with an elliptical beam cross-section in a static electromagnetic field.

2 THE COORDINATE SYSTEM AND NOTATIONS

The motion of the particles of a bunch is described relative to a single particle, the *reference particle*, which follows a *reference trajectory*. The equations of motion and of the 4-vector electromagnetic potential A are written in a coordinate frame x , moving with the reference particle. All symbols and notations in this paper will follow the same conventions as used in ref. [7]. The coordinates of the reference particle are described by the four vector z_m . This is chosen such that $z_{m1} = z_{m2} = 0$, $z_{m4} = ct_m$. In this paper we restrict ourselves to first-order (paraxial) focusing with a rectilinear reference trajectory $z = z(t_m)$. An arbitrary particle is described by a 4-vector x , where the components of x are the deviation of any particle from the reference particle [7]. Here x_1 and x_2 are the transverse coordinates, x_3 is the longitudinal coordinate and $x_4 = c(t - t_m)$, i.e. the time coordinate. All the particles in a bunch are detected at the same time $t = t_m$. This means that the observer is located in the plane $x_4 = 0$ and that $x_4 = z_{m4} = ct_m$.

The quantities B , E , ρ , I and j denote magnetic field induction, electric field strength, charge density, beam current and current density, respectively. The quantities p and γ denote momentum and total energy of the reference particle. The 3-dimensional vectors B and E are expressed in the inverse of the units used to measure x and z (i.e. m^{-1}). The 4-dimensional vector A and the quantities γ , p and I are dimensionless. The quantities ρ and j are expressed in m^{-2} .

As notated above, $x_4 = 0$. Therefore, instead of the notation \bar{x} for the three dimensional vector, we will use

for convinience the notation x , i.e. $\bar{x} = \begin{pmatrix} x_1 \\ x_2 \\ x_3 \end{pmatrix} = x$.

The following notations are also used:

$$x' = \frac{dx}{dz_{m4}}, d\{x\} = dx_1 dx_2 dx_3, d\{x'\} = dx'_1 dx'_2 dx'_3$$

$$x'_1 = x'_1, x'_2 = x'_2, x'_3 = x'_{3m} + x'_3, x'_4 = 1$$

3 THE ELECTROMAGNETIC POTENTIAL A INSIDE THE ELLIPSOIDAL BUNCH DUE TO THE SPACE CHARGE

Let us consider the motion of a bunch of particles which is the canonical central, 3-dimensional ellipsoid $\Omega(x)$. This ellipsoid is described by the following equation:

$$0 \leq \alpha(x) = \frac{x_1^2}{a_1^2} + \frac{x_2^2}{a_2^2} + \frac{x_3^2}{a_3^2} \leq 1 \quad (1)$$

Here a_1, a_2 and a_3 are functions of x_{m4} .

The 4-vector potential A is written in the form:

$$A(x, x_{m4}) = \int_{\Omega(x^*)} \frac{j(z(x^*), x_{m4} - \tilde{z}^* x^*) d\{x^*\}}{4\pi \sqrt{(\tilde{z} - \tilde{z}^*)(x - x^*)}}$$

We suppose that the bunch of particles in the space (x') is also the canonical, central, 3-dimensional ellipsoid. Therefore $A_1 = 0$ and $A_2 = 0$.

Let a, b, c be any three unequal, positive, real numbers which we suppose to be arranged in descending order of magnitude:

$$a > b > c > 0$$

where:

$$a = \max_i a_i, c = \min_i a_i,$$

$$b = a_i, \text{ if } a_i \neq a \text{ and } a_i \neq c$$

Assuming that $\rho = \rho_m$ is constant inside the ellipsoid we obtain the components A_3 and A_4 in the following forms [8]:

$$A_3 = \frac{p}{\gamma} \rho_m \psi, A_4 = \rho_m \psi$$

where:

$$\psi = \frac{1}{2} (M_0 - M_1 x_1^2 - M_2 x_2^2 - M_3 x_3^2)$$

$$M_0 = \frac{abc}{\sqrt{a^2 - c^2}} F(\phi, k)$$

$$M_1 = \frac{abc}{(a^2 - b^2)\sqrt{a^2 - c^2}} [F(\phi, k) - E(\phi, k)]$$

$$M_2 = -\frac{abc}{\sqrt{a^2 - c^2}} F(\phi, k) + \frac{abc\sqrt{a^2 - c^2} E(\phi, k)}{(a^2 - b^2)(b^2 - c^2)} \quad (2)$$

$$-\frac{c^2}{b^2 - c^2}$$

$$M_3 = -\frac{abc}{(b^2 - c^2)\sqrt{a^2 - c^2}} E(\phi, k) + \frac{b^2}{b^2 - c^2}$$

$$\phi = \arccos \frac{c}{a}, k = \sqrt{\frac{a^2 - b^2}{a^2 - c^2}}$$

$$a^2 M_1 + b^2 M_2 + c^2 M_3 = M_0$$

Here $F(\phi, k)$ and $E(\phi, k)$ are incomplete elliptic integrals of the first and the second kind.

Using the expressions for A we obtain, in the first approximation, the following expressions for the electromagnetic field inside the elliptical bunch of particles due to the space charge:

$$B_1 = -\frac{p}{\gamma} \rho_m M_3 x_2, B_2 = \frac{p}{\gamma} \rho_m M_1 x_1, B_3 = 0$$

$$E_1 = \rho_m M_1 x_1, E_2 = \rho_m M_2 x_2, E_3 = \rho_m M_3 x_3$$

4 PARAXIAL EQUATIONS OF MOTION

The motion of the elliptical bunch of charged particles in arbitrary space-time is described by the following paraxial equation:

$$y' = Py \quad (3)$$

where:

$$y_1 = x_1, y_2 = x_2, y_3 = x_3, y_4 = \frac{p}{p_0} x'_1, y_5 = \frac{p}{p_0} x'_2,$$

$$y_6 = \frac{p_0^3}{p^3} x'_3, P = \begin{pmatrix} 0 & C \\ F & D \end{pmatrix}$$

$$C_{ik} = 0, i \neq k, C_{11} = C_{22} = \frac{p_0}{p}, C_{33} = \frac{p^3}{p_0^3}$$

$$F_{1k} = \frac{1}{p_0} \left(-\nabla_k B_{m2} + \frac{\gamma}{p} \nabla_k E_{m1} + \delta(k, 1) \frac{\rho_m}{p\gamma} M_1 \right)$$

$$F_{2k} = \frac{1}{p_0} \left(\nabla_k B_{m1} + \frac{\gamma}{p} \nabla_k E_{m2} + \delta(k, 2) \frac{\rho_m}{p\gamma} M_2 \right) \quad (4)$$

$$F_{3k} = \frac{p_0^3}{p^3 \gamma} (\nabla_k E_{m3} + \delta(k, 3) \rho_m M_3)$$

$$D_{kk} = 0, k = 1, 2, 3; D_{12} = -D_{21} = \frac{B_{m3}}{p}$$

$$D_{31} = \frac{p_0^4}{\gamma p^6} E_{m1}, D_{13} = -\frac{\gamma p^2}{p_0^4} E_{m1}, D_{32} = \frac{p_0^4}{\gamma p^6} E_{m2}$$

$$D_{23} = -\frac{\gamma p^2}{p_0^4} E_{m2}$$

$$\nabla_k B_{mj} = \frac{\partial B_j}{\partial x_k} \Big|_{x=0}, \nabla_k E_{mj} = \frac{\partial E_j}{\partial x_k} \Big|_{x=0}$$

Here B and E are external electromagnetic fields and p_0 is the initial value of p at $z_{m4} = z_{m40}$. The Kronecker delta is defined as $\delta(i, j) = 1$ if $i = j$ and $\delta(i, j) = 0$ if $i \neq j$. Assuming that the charge of the bunch is given by:

$$Q = \int_{\Omega(\sigma)} \rho^* dx_1 dx_2 dx_3 = \frac{4}{3} \pi a_1 a_2 a_3 \rho_m^*$$

we obtain:

$$\rho_m^* = \frac{I}{\frac{4}{3} \pi a_1 a_2 a_3 \nu} = \frac{I}{\frac{4}{3} \pi a b c \nu}$$

where ν is the frequency of the beam current impulses.

5 THE RECURSIVE σ -METHOD OF SOLUTION

The solution of the matrix equation of motion eq. (3) is written in terms of the matrizant in the form:

$$y = R y_0, \quad R_0 = I_6$$

where R is a 6×6 matrix, I_6 is a 6×6 unit matrix and R_0 and y_0 are the initial values of R and y , resp. A continuous, generalized, analogue of the Gauss brackets or the method of shuttle integrals, refs. [2] and [9], can be used to calculate the matrizant for an arbitrary coefficient matrix $P(z_{m4})$ with rigorous conservation of the phase volume of the beam at each stage of the calculation.

We are considering the bunch of particles which is the 6-dimensional ellipsoid in phase space. It is convenient to use the envelope matrix σ , where:

$$\sigma = R \sigma_0 \tilde{R}$$

Here R is the matrizant and σ is the matrix characterizing the shape of the initial 6-dimensional ellipsoid in the phase space. We note that:

$$\sigma_{11} = a_1^2(z_{m4}), \quad \sigma_{22} = a_2^2(z_{m4}), \quad \sigma_{33} = a_3^2(z_{m4})$$

$$\sigma_{44} = \left(\frac{p}{p_0} x'_{1\max} \right)^2, \quad \sigma_{55} = \left(\frac{p}{p_0} x'_{2\max} \right)^2$$

$$\sigma_{66} = \left(\frac{p_0^2}{p^3} x'_{3\max} \right)^2$$

where $x'_{j\max}$ is the maximum value of x'_j in the phase set with an ellipsoid boundary.

The matrix σ satisfies the differential equation:

$$\sigma' = P\sigma + \sigma\tilde{P}$$

where the coefficient matrix P is described by the eqs. (4). It is to be noted that the matrix P depends of the elements σ_{11} , σ_{22} and σ_{33} .

6 SUMMARY

We have considered the motion of the 3-dimensional elliptical bunch of particles in an arbitrary, external, electromagnetic field, taking into account the effect of space-charge. The space-charge effect is important for a high beam current I , for a bunch of small volume and for beam current impulses of low frequency ν . In the first approximation we have found the electromagnetic field inside the bunch due to the space charge. This is given in eq. (2). A new recursive technique has been proposed for the solution of the non-linear equations of motion in the first approximation, given by eq. (3) where, in each step of the numerical integration, the phase volume of the beam is strictly conserved.

Acknowledgement

This work was supported by the Swedish-Soviet Research Cooperation, established between the former USSR Academy of Sciences and the Royal Swedish Academy of Sciences.

REFERENCES

1. J.D. Lawson, The physics of charged-particle beams (Clarendon Press, Oxford, 1988).
2. A. D. Dymnikov and G. N. Osetinskij, Sov. J. Part. Nucl., Vol. 20, No 3 (1989) p. 293-310.
3. F. Watt and G.W. Grime (eds.), Principles and Applications of High-Energy Ion Microbeams (Adam Hilger, Bristol, 1987).
4. A. Dymnikov and R. Hellborg, The influence of space charge on the motion of a bunch of particles in an ion optical system, submitted to Nucl. Instr. Meth. part B.
5. A. Dymnikov, R. Hellborg, J. Pallon, G. Skog, C. Yang and G. Ohlén, Nucl. Instr. Meth. A 328 (1993) 164.
6. A. Dymnikov, R. Hellborg, J. Pallon, G. Skog and C. Yang, Calculations of the beam transport through the low energy side of the Lund Pelletron accelerator, accepted for publication in Nucl. Instr. Meth. part A.
7. A. Dymnikov and R. Hellborg, Matrix theory of the motion of a charged-particle beam in curvilinear space-time. Part I and II, Nucl. Instr. Meth. part A in press.
8. A.P. Prudnikov, Ya.A. Brychkov and O.I. Marichev, Integrals and Series, vol. 1, Gordon and Breach Science Publishers, 1986.
9. A.D. Dymnikov, Problems in Mechanics and Control Processes, No 2, Control of Dynamical Systems (in Russian) (Leningrad State University, Leningrad 1978) p. 64.

Space-charge Dominated Beam Envelope Transport with Rotatable Axes

Eugene Y. Tsiang

400 Davey Glen Road, #4629, Belmont, CA 94002 USA

Abstract

In normal paraxial studies of self-interacting accelerator beams, coupling between x- and y-motions that rotate the elliptical beam envelope is considered undesirable. Yet in some applications, such as electron beam lithography and electron beam transmission X-ray computed tomography, external focussing elements cause this coupling by design. To meet this need, the classical 4th order Kapchinskii-Vladimirsky (KV) differential equations have been generalized to include beam envelope rotation. This set of 10th order generalized envelope equations based on the KV distribution were applied to a 600 mA, 130 keV beam moving through a low-pressure nitrogen gas, where the absence and presence of complete plasma neutralization along its path cause the beam to diverge and converge.

I. INTRODUCTION

The standard equations for the beam envelope are the Kapchinskii-Vladimirsky equations for the principal axes of an ellipse that does not rotate, because the x- and y- motions are decoupled. However, for certain applications, the x and y motions are coupled deliberately, in order to align the ellipse axes with desired directions. The generalized envelope equations described here allow for rotating elliptical envelopes.

II. THE ELECTRON OPTICS

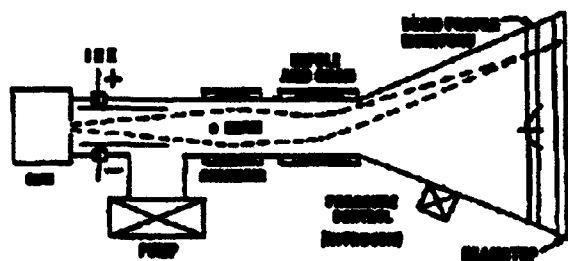


Figure 1. Electron optical system.

A steady space charge limited beam is produced by the gun (Figure 1). By adjusting the nitrogen pressure in the drift tube, the beam is made to ionize the gas in its path on a timescale short compared to its transit time. The ion clearing

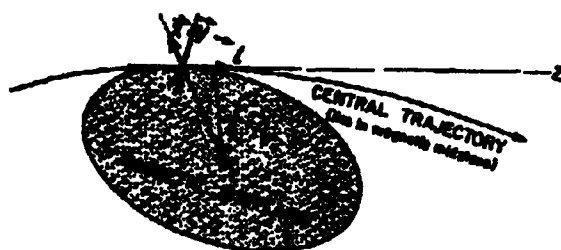


Figure 2. Local beam coordinates.

electrodes[1] sweep the ions out of the beam. The electron beam expands by self-repulsion until it leaves the ICE, when it becomes neutralized and focussed by the solenoid and quadrupole fields, and its own magnetic self-field. The beam is deflected by dipole coils, which add their own inherent focussing fields along its path. The bend plane and beam path constitute a natural coordinate system (Figure 2).

III. ENVELOPE EQUATIONS

The condition that the beam has a uniform elliptical profile means that the particles be uniformly distributed over the surface of a 4-dimensional ellipsoid in its phase space, according to the Kapchinskii-Vladimirsky (KV) micro-canonical ensemble ρ :

$$\rho = \delta(1 - I(x, y, p_x, p_y, t)) \quad (1)$$

where

$$I(x, y, p_x, p_y, t) = a_{11} x^2 + 2 a_{12} x y + 2 a_{13} x p_x + 2 a_{14} x p_y + a_{22} y^2 + 2 a_{23} y p_x + 2 a_{24} y p_y \quad (2)$$

is a quadratic function of the phase variables and δ is the Dirac delta function. Let the paraxial Hamiltonian be

$$H = (k_1 x(t)^2 + (p_y(t) + q x(t))^2 / p_0 + 2 m x(t) y(t) + k_2 y(t)^2 + (p_x(t) - q y(t))^2 / p_0) / 2 \quad (3)$$

Then the condition that $I(x, y, p_x, p_y)$ be a phase invariant is

$$a_{11}'(t) = 2 (k_1 a_{13}(t) + (-q a_{12}(t) + q^2 a_{13}(t)) / p_0 + m a_{14}(t))$$

$$a_{12}'(t) = m (a_{13}(t) + a_{24}(t) + k_2 a_{14}(t) + k_1 a_{23}(t) + (q (a_{11}(t) - a_{22}(t)) + q^2 (a_{14}(t) + a_{23}(t))) / p_0$$

$$a_{13}'(t) = k_1 a_{33}(t) + (-a_{11}(t) - q (a_{14}(t) + a_{23}(t)) + q^2 a_{33}(t)) / p_0 + m a_{34}(t)$$

$$a_{14}'(t) = k_1 a_{34}(t) + (-a_{12}(t) + q (a_{13}(t) - a_{24}(t)) + q^2 a_{34}(t)) / p_0 + m a_{44}(t)$$

$$a_{22}'(t) = 2 (m a_{23}(t) + k_2 a_{24}(t) + (q a_{12}(t) + q^2 a_{24}(t)) / p_0)$$

$$a_{23}'(t) = m a_{33}(t) + k_2 a_{34}(t) + (-a_{12}(t) + q (a_{13}(t) - a_{24}(t)) + q^2 a_{34}(t)) / p_0$$

$$a_{24}'(t) = m a_{34}(t) + k_2 a_{44}(t) + (q a_{14}(t) - a_{22}(t) + q a_{23}(t) + q^2 a_{44}(t))/p_0$$

$$a_{33}'(t) = -2(a_{13}(t) + q a_{34}(t))/p_0$$

$$a_{34}'(t) = -(a_{14}(t) + a_{23}(t) + q(a_{44}(t) - a_{33}(t)))/p_0$$

$$a_{44}'(t) = -2(a_{24}(t) - q a_{34}(t))/p_0 \quad (4)$$

where the solenoidal focussing strength q^2/p_0 is external, while the quadrupole strengths k_1 , k_2 and m are given by a sum of external (k_{1ext} , k_{2ext} , m_{ext}) and self-forces:

$$k_1 = k_{1ext} + (-2\pi^2 r_d^2/\epsilon)(a_{11} - (a_{14}^2 a_{33} - 2 a_{13} a_{14} a_{34} + a_{13}^2 a_{44})/(-a_{34}^2 + a_{33} a_{44}) + (\pi^2/\epsilon)/\sqrt{a_{33} a_{44}(t) - a_{34}^2})/\Delta$$

$$k_2 = k_{2ext} + (-2\pi^2 r_d^2/\epsilon)(a_{22} - (a_{24}^2 a_{33} - 2 a_{23} a_{24} a_{34} + a_{23}^2 a_{44})/(-a_{34}^2 + a_{33} a_{44}) + (\pi^2/\epsilon)/\sqrt{a_{33} a_{44}(t) - a_{34}^2})/\Delta$$

$$m = m_{ext} + (-2\pi^2 r_d^2/\epsilon)(a_{12} + (-a_{14} a_{24} a_{33}) + a_{14} a_{23} a_{34} + a_{13} a_{24} a_{34} - a_{13} a_{23} a_{44})/(-a_{34}^2 + a_{33} a_{44})/\Delta$$

$$\Delta = (- (a_{14}^2 + a_{24}^2) a_{33} + 2 a_{13} a_{14} a_{34} + 2 a_{23} a_{24} a_{34} - (a_{13}^2 + a_{23}^2) a_{44})/\sqrt{a_{33} a_{44}(t) - a_{34}^2} + (a_{11} + a_{22})/\sqrt{a_{33} a_{44}(t) - a_{34}^2} + 2\pi^2/\epsilon \quad (5)$$

By Liouville's theorem, the emittance ϵ is conserved.

$$\epsilon = \iiint \delta(1 - I(x, y, p_x, p_y, t)) dx dy dp_x dp_y$$

where

$$\begin{aligned} \pi^2/\epsilon = & (a_{14}^2 a_{23}^2 - 2 a_{13} a_{14} a_{23} a_{24} + a_{13}^2 a_{24}^2 - \\ & a_{14}^2 a_{22} a_{33} + 2 a_{12} a_{14} a_{24} a_{33} - a_{11} a_{24}^2 a_{33} \\ & + 2 a_{13} a_{14} a_{22} a_{34} - 2 a_{12} a_{14} a_{23} a_{34} - 2 a_{12} a_{13} a_{24} a_{34} + \\ & 2 a_{11} a_{23} a_{24} a_{34} + a_{12}^2 a_{34}^2 - a_{11} a_{22} a_{34}^2 - a_{13}^2 a_{22} \\ & a_{44} + 2 a_{12} a_{13} a_{23} a_{44} - a_{11} a_{23}^2 a_{44} - a_{12}^2 a_{33} a_{44} + \\ & a_{11} a_{22} a_{33} a_{44})^{1/2} \end{aligned} \quad (6)$$

In these equations:

$r_d^2(t) = (1.36J(1 - (1 + 0.00196 E)^2 f))/(2 + 0.00196 E) E^{3/2}$, the relativistic perveance term, which can be positive (defocussing) or negative (focussing); E = energy of beam in keV; f = neutralization fraction; $f = 1$, complete neutralization; $f = 0$, no neutralization; J = total current in Amps;

$$p_0 = \beta_1 \beta_2 / \sqrt{1 - \beta^2} = 0.0442372 \sqrt{(2 + 0.00195693 E) E}$$

IV. NUMERICAL EXAMPLE

The equations above were applied to the system in Sec. II.

A. System parameters

The dipole that bends the beam around runs from 57 to 82.57 cm. The beam enters and leaves the quadrupole at $t = 59.45$ and 79.93 cm. The focal plane is at 219.67 cm. The beam is deflected 22.67° away from the gun axis. Deliberate mixing of x- and y- motions is imposed by a non-zero m_{ext} . The location of various optical elements splits the beam path into 8 regions, as shown in Table 1.

Table 1. Separation of beam path into regions.

Region	Start (cm)	External focus power (cm ⁻²)
1 ICE	0	0
2 ICE + Solenoid	31.25	$q^2/p_0 = .00063$ to $.0018$
3 ICE	48.75	0
4 Drift	55.	0
5 Dipole	57	$k_{1ext} = .00024$
6 Dipole + Quad	59.45	$k_{1ext} = .00024 \pm 7.5 \cdot 10^{-4}$ (Max); $-k_{2ext} = \pm 7.5 \cdot 10^{-4}$ (Max); m_{ext}
7 Dipole	79.93	$k_{1ext} = .00024$
8 Drift	82.57	0
Image	219.7	NA

We assume no partial neutralization on the path. Within the ICE, we take $f = 0$ (no neutralization); outside of the ICE, we take $f = 1$. We assume that the bending magnet field is uniform. All pole face effects are ignored. Other beam parameters are $E = 130$ keV beam, $p_0 = 0.76$, $\epsilon_x / (\pi p_0) = 8 \cdot 10^{-4}$ cm radian, and $\epsilon_y = 0.00060585 \pi$ cm radian. The initial envelope radius $r(0) = 0.18$ cm and the slope $r'(0) = 0.01$ radian. It is convenient to work with a natural unit of transverse length = $\epsilon_x / \sqrt{\pi p_0 k_d^2(1)} = 0.072$ cm, a unit slope = $\sqrt{|r(0) r'(0)|} / p_0 = 0.011$ radian, and t is normalized w.r.t. a unit longitudinal length = 219.67 cm. A Mathematica® electron beam CAD package SIBER (Self Interacting Beam Envelope Rotator [10]) has been written for interactive integration of the envelope equations.

B. Results

The envelope equations were first integrated with 45° quadrupole field $m_{ext} = 0$, from $t = 0$ to $t = 2$ for different solenoid q^2/p_0 and k_{1ext} . The image plane ($t = 1$) ellipse amplitudes are shown in Figures 3 and 4.

For a good focus in the y-direction (perpendicular to the dipole bend plane) it is necessary to stay in the black strip in Figure 4. We chose $q^2/p_0 = 0.018 \text{ cm}^{-2}$ and $k_{1\text{ext}} = -0.064 \text{ cm}^{-2}$ for the integration with nonzero m_{ext} . The march of the x- and y-amplitude with path parameter is shown in Figure 5.

We next imposed a 45° quadrupole $m_{\text{ext}} = 5 \times 10^{-4} \text{ cm}^{-2}$ in region 6. The x- and y-amplitudes remain substantially unchanged, but the orientation of the principal axes of the ellipse jumps from 0° to about 2° within the quadrupole and increases only slowly after that (Figure 6).

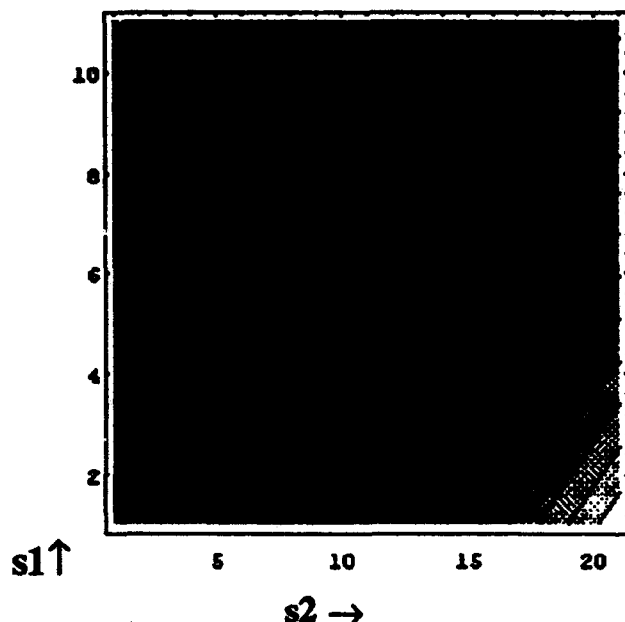


Figure 3. Contour plot of ellipse x-amplitude as a function of focus and quadrupole parameters s_1 and s_2 respectively. Solenoid focussing strength $q^2/p_0 = 1.2 \times 10^{-4} s_1 + 5.1 \times 10^{-4} \text{ cm}^{-2}$. Quadrupole focussing strength $k_1 = 7.5 \times 10^{-5} s_2 - 8.25 \times 10^{-4} \text{ cm}^{-2}$. 10 equally spaced contours between 0.46 (black) and 86.91 (white) $\times 0.72 \text{ mm}$.

V. CONCLUSIONS

A set of 10th order envelope equations was applied to a space-charge dominated electron beam system. Mixing was introduced by imposing a 45° quadrupole strength, and the change in orientation of the elliptical envelope followed through to the image plane and beyond. A electron beam optical CAD program SIBER now exists for investigating basic electron beam design and beam tuning sensitivities.

VI. REFERENCE

- [1] R. E. Rand and E. Y. Tsiang, U. S. Patent 5,193,105, March 9, 1993.

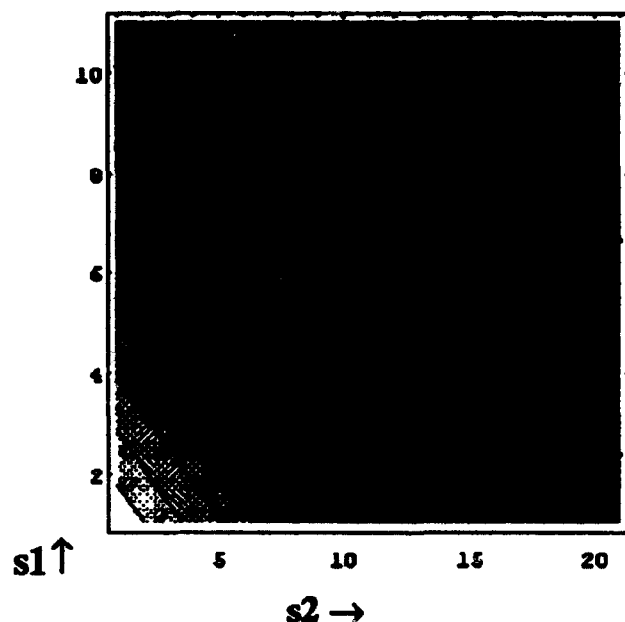


Figure 4. Same as Figure 3. Contour plot of ellipse y-amplitude in units of 0.72 mm. 10 equally spaced contours between 0.46 (black) and 117.64 (white) $\times 0.72 \text{ mm}$.

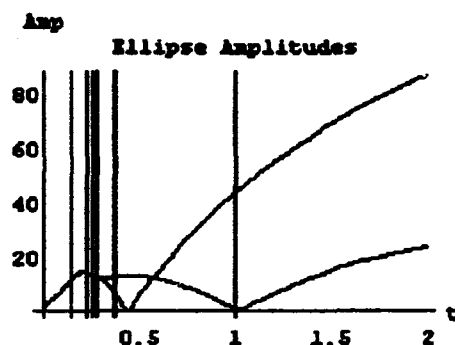


Figure 5. X and y amplitudes (upper and lower), in units of 0.072 cm, as a function of path parameter t . 0° quad strength = $6.375 \times 10^{-4} \text{ cm}^{-2}$, solenoid strength = $1.8 \times 10^{-3} \text{ cm}^{-2}$. Vertical lines divide regions.

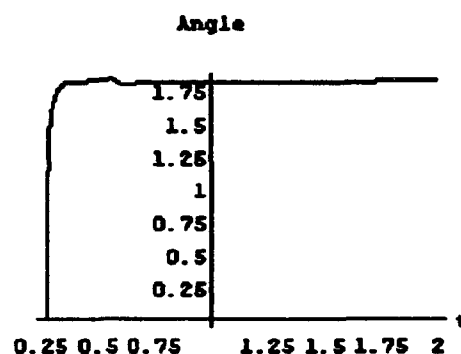


Figure 6. Ellipse orientation in degrees, from regions 6 to 8 of Table 1. 0° quad strength = $6.375 \times 10^{-4} \text{ cm}^{-2}$, solenoid = $1.8 \times 10^{-3} \text{ cm}^{-2}$, 45° quad strength = $5 \times 10^{-4} \text{ cm}^{-2}$.

Effect of Space Charge Forces on Particle Tracking and Generation of High Order Maps*

David L. Bruhwiler and Michael F. Reusch
Grumman Corporate Research Center
4 Independence Way, Princeton NJ 08540-6620 USA

Abstract

TOPKARK is a beam optics program consisting of two Fortran codes developed in parallel: a 3-D high-order mapping code and a particle tracking code; both utilize a space charge model which treats the particle bunch as a uniformly-filled 3-D ellipsoid. The map code uses the differential algebra library DA [1] to generate an arbitrary-order Taylor map describing a given lattice, then the Lie algebra library LIELIB [2] is used to obtain the Dragt-Finn factorization [3] of the corresponding Lie polynomial. The Lie polynomial generated by TOPKARK without space charge has been successfully benchmarked through third order against MARYLIE 3.0 [4] and through fifth order against TLIE [5]. With space charge on, TOPKARK generates a linear map that agrees well with TRACE 3-D [6]. The tracking code uses a symplectic integration scheme [7] when space charge is off, and it includes a more general space charge model [8] which assumes only ellipsoidal symmetry of the spatial distribution.

I. GENERAL FEATURES OF THE CODE

TOPKARK has evolved from an earlier code, which was developed during a collaboration between Grumman, LBL and BNL [9]. The mapping version is a useful design tool, while the tracking version is a useful diagnostic which resolves any ambiguities regarding very high order effects that might be missed by Lie algebra or mapping codes and is also required for dynamic aperture studies.

A. Mapping Version

TOPKARK employs a fourth-order, adaptive-step-size, Runge-Kutta integration scheme [10] which provides good accuracy and reasonable computational speed. The differential algebra library DA [1] is used to generate a high-order Taylor map expansion of the dynamical variables about the design trajectory (in practice up to fifth order has been used) step by numerical step along the length of the lattice. This map is used to propagate the spatial moments of the (assumed) initial particle distribution from one integration step to the next.

At each integration step, a 3-D uniformly-filled ellipsoid is constructed according to the calculated spatial moments. The exact linear electric fields associated with this ellipsoid are calculated [11] and, in combination with any magnetic fields, are used to advance to the next step. At the end of the lattice, the final Taylor map is used to calculate the emittance and Twiss parameters of the final distribution. The Lie algebra library LIELIB [2] is used to obtain the Dragt-Finn [3] factorization of the Lie polynomial corresponding to this final Taylor map.

*Supported by IR&D funds of Grumman Aerospace Corp.

The code includes two optimizing routines, one based on the downhill simplex method [10] and another based on Powell's method [10]. Either of these algorithms can be used by a matching routine that sets the final transverse Twiss parameters to specified values by modifying any four of the lattice parameters. This matching routine has been successfully used both with and without space charge.

Another type of matching routine, which can also use either of the optimizing algorithms, is used to zero specified terms in the Lie polynomial, sometimes while simultaneously satisfying other imposed constraints. For example, TOPKARK can determine the required strengths of three (or more) octupoles in order to eliminate third-order geometric aberrations.

B. Tracking Version

This version currently exists as a test-particle tracking code which integrates the full equations of motion, using a Hamiltonian formalism and an explicitly symplectic fourth-order integration scheme [7]. The code has been used and tested extensively; in particular, the second moments obtained at the end of example beam lines often agree well with the second moments propagated by the mapping version.

TOPKARK can generate a six-dimensional phase space ellipsoid of initial conditions, which yields the desired Twiss parameters in each of the two-dimensional phase planes. Distributions currently supported include a) uniformly-filled ellipsoid in space with gaussian distribution in momentum and b) gaussian distribution in space and momentum. The code can also read in a file of initial conditions for tracking, and it outputs the Twiss parameters and particle positions as desired.

Three distinct space charge models (described below) are being implemented in the tracking version of TOPKARK. Each imposes ellipsoidal symmetry on the spatial distribution. The Hamiltonian formalism and symplectic integration will be abandoned for space charge calculations--the equations of motion and the fourth-order adaptive-step-size Runge-Kutta [10] integrator of the mapping version will be used.

C. Features Common to both Versions

TOPKARK currently implements a number of "hard edge" or uniform-field magnet elements, including a dipole (i.e. a normal entry and exit sector bend) and quadrupole through duodecapole. Also available are "thin fringe" elements for dipole and quadrupole magnets. All of these elements, including the fringe fields, have been successfully benchmarked against MARYLIE 3.0 [4] through third order. The fringe

field models, although calculated independently, were based on ideas developed previously by Forest [12].

TOPKARK also employs one extended-fringe magnet model. This is a line-dipole model for large-bore magnets constructed from a cylindrical array of magnetized rods, including quadrupole, octupole and duodecapole configurations [13]. TOPKARK was successfully benchmarked against TLIE [5] through fifth-order in a single test-case where these extended-fringe quadrupole and octupole models were used. New element types are easily added to the list above.

Both codes use MKS units, with all momenta normalized to the longitudinal design momentum p_0 . We define the longitudinal variables $\delta\tau = c(t-t_0)$ and $\delta p_\tau = (E_0 - E)/p_0 c$, and the magnetic rigidity $B\rho = p_0/c$. For straight elements, the equations of motion are:

$$\frac{dx}{dz} = \frac{\beta_x}{\beta_z}; \quad \frac{dy}{dz} = \frac{\beta_y}{\beta_z}; \quad \frac{d\delta\tau}{dz} = \frac{1}{\beta_z} - \frac{1}{\beta_0}; \quad (1a)$$

$$\frac{dp_x}{dz} = \frac{1}{B\rho} \left(\frac{\beta_y}{\beta_z} B_z - B_y + \frac{1}{\beta_z c} E_x \text{ eff} \right); \quad (1b)$$

$$\frac{dp_y}{dz} = \frac{1}{B\rho} \left(-\frac{\beta_x}{\beta_z} B_z + B_x + \frac{1}{\beta_z c} E_y \text{ eff} \right); \quad (1c)$$

$$\frac{d\delta p_\tau}{dz} = -\frac{1}{B\rho c} \left(\frac{\beta_x}{\beta_z} E_x \text{ eff} + \frac{\beta_y}{\beta_z} E_y \text{ eff} + E_z \text{ eff} \right). \quad (1d)$$

The electric field components $E_x \text{ eff}$, etc. include the self-magnetic field of the particles and relativistic effects (see below). The corresponding equations of motion for bending elements have been given elsewhere [14].

II. SPACE CHARGE MODELS

We consider only models with ellipsoidal symmetry, meaning that the spatial density distribution has the form

$$\rho(x, y, \delta z) = \rho_0 f(u), \quad (2a)$$

where the function $u(x, y, \delta z)$ is defined by the equation

$$u^2(x, y, \delta z) = \frac{x^2}{a^2} + \frac{y^2}{b^2} + \frac{\delta z^2}{c^2}, \quad (2b)$$

with $a^2 = \langle x^2 \rangle$, etc. Thus the one-parameter family of 3-D ellipsoids defined by Eq. (2b) are isodensity contours.

Such models yield electric fields of the following form (for all points *within* the distribution) [15], [8]:

$$E_{xB} = \frac{q\rho_0}{2\epsilon_0} abc x \int_0^\infty ds \frac{f[u(x, y, \delta z)]}{(a^2+s)^{3/2} (b^2+s)^{1/2} (c^2+s)^{1/2}}, \quad (3)$$

with analogous results for E_{yB} and E_{zB} . These electric fields are calculated in the *bunch* frame, then relativistically transformed to the laboratory frame.

The length of the bunch as observed in the lab frame is shortened due to relativistic length contraction, so the lab frame distribution is first stretched out in the z -direction before

calculating the fields: $\delta z_B = \gamma_0 \delta z_L$. This reduces the particle density: $n_B = n_L/\gamma_0$, so E_{xB} , E_{yB} , E_{zB} are all reduced by a factor γ_0 from what one would naively calculate in the lab. However, the fact that the distribution is stretched out in z effectively increases the value of E_{zB} by γ_0 at the position of each particle, thus negating the decrease in E_{zB} noted above. This stretching of the bunch also alters the geometry of the distribution, which affects the values of all three components of E_B accordingly.

Particle velocities are neglected in the bunch frame, so the Lorentz transformations yield:

$$E_L^\parallel = E_B^\parallel; \quad E_L^\perp = E_B^\perp; \quad (4a)$$

$$B_L^\parallel = B_B^\parallel = 0; \quad B_L^\perp = \gamma_0 B_B \times E_B/c. \quad (4b)$$

The Lorentz force equation is:

$$\frac{1}{q} F_L = E_L + v \times B_L. \quad (4c)$$

Combining these results yields an *effective* electric field:

$$E_L \text{ eff} = E_B^\parallel + E_B^\perp/\gamma_0. \quad (4d)$$

This is the quantity used to advance the particles. The longitudinal field is altered by geometric effects only, while the transverse fields are *also* reduced by a factor of γ_0^2 .

A. Mapping Version

TOPKARK works with a Taylor-series expansion about the design trajectory, so the obvious question arises: How then does one propagate a particle distribution down the beam-line? This has been explained in detail elsewhere [14], but essentially one calculates the second moments at a given point in the lattice by using second and higher moments of the initial distribution.

Of course, we must assume a *convenient* initial distribution function, and one that is consistent with our assumption of a uniformly-filled 3-D ellipsoid in space. Such a distribution has been found and implemented [14]. The projection of this distribution in the x - p_x plane has the form:

$$g(x, p_x) = \frac{3}{4\sqrt{10}\pi \epsilon_x} \left(1 - \frac{x^2}{5\epsilon_x \beta_x} \right) \exp \left[-\frac{\beta_x}{2\epsilon_x} \left(p_x + \frac{\alpha_x}{\beta_x} x \right)^2 \right], \quad (5)$$

for $x^2 \leq 5\epsilon_x \beta_x$ (otherwise, $g=0$). We are using RMS Twiss parameters, which means that $\langle x^2 \rangle = \epsilon_x \beta_x$, $\langle x p_x \rangle = -\epsilon_x \alpha_x$, and $\langle p_x^2 \rangle = \epsilon_x \gamma_x$. The linear bunch frame electric fields can be found analytically in terms of complete elliptic integrals [11].

B. Tracking Version

Three distinct space charge models are being implemented in the tracking code. One assumes a uniformly-filled ellipsoid in space, for which $f(u)=1$. Another assumes a gaussian ellipsoid in space, for which $f(u)=\exp(-u^2/2)$. The third is a more

general scheme developed by Garnett and Wangler [8] in which $f(u)$ is Fourier expanded.

The uniform model will start with the same distribution function as is assumed by the mapping code. This general form will continue to be imposed on the actual particle distribution, with only the second moments being determined directly from the particles. The extent to which this imposed form is actually preserved by the particles will provide a direct check on the validity of the mapping code.

For particles within the bounds of the assumed 3-D ellipsoid, the purely linear space charge forces can be found analytically in terms of complete elliptic integrals [11]. For those few particles outside these bounds, the now-nonlinear fields can be calculated analytically in terms of incomplete elliptic integrals [11], requiring the phase-like quantity λ , which is the real positive root of the following equation:

$$\frac{x^2}{5a^2+\lambda} + \frac{y^2}{5b^2+\lambda} + \frac{\delta z^2}{5c^2+\lambda} = 1. \quad (6)$$

The gaussian model has been used previously [15], although not in a beam optics code like TOPKARK. Here, the integrals cannot be evaluated in closed form. The favored numerical method [8], [15] is to use ten-point gaussian quadrature [10]. In this model, the space charge forces will have strong nonlinear components. The extent to which an initial gaussian distribution is preserved and the extent to which the results of this model differ from those of the uniform model will help to clarify the relative importance of how one models the beam distribution for high-brightness high-order beam optics applications.

For the more general scheme of Garnett and Wangler [8], $f(u)$ is left arbitrary. One Fourier expands $f(u)$, obtaining the expansion coefficients directly from the particle positions. It was shown [8] that keeping the first six terms of the expansion is probably adequate. Again, ten-point gaussian quadrature will be used to evaluate the electric fields.

III. DISCUSSION

The mapping code has already demonstrated [14] that three-dimensional space charge forces cause a new class of geometric aberrations to appear. These aberrations result from the introduction by space charge of an asymmetry in the longitudinal variable $\delta\tau$. This result is contrary to the physical intuition developed from the use of linear codes with 3-D space charge models and high-order optics codes with 2-D models. This result was partially confirmed [14] in a given example by comparison with the PARMILA code, and the results are consistent [14] with analytic considerations based on a Green's function approach to estimating nonlinear effects [16].

Our approach is faster and simpler than a particle-in-cell (PIC) or point-to-point particle code, and it is free of the strong numerical noise associated with such codes. On the other hand, because we impose a *smooth* form on the distribution, we must be in a regime where the combined field of the particles is predominantly smooth and individual collisions are a secondary effect. This condition is generally satisfied [17] if there are many particles within a Debye sphere.

The algorithms used by TOPKARK cannot follow the development of any structure within a bunch (unless, in the case of the Garnett and Wangler scheme, such structures preserve ellipsoidal symmetry), such as might arise due to plasma waves or instabilities. Thus the transit time through a lattice should not be much longer than a plasma period [17].

IV. CONCLUSIONS

The mapping version of TOPKARK is a tested and reliable high-order optics code in which a TRACE3D-like space charge model has been successfully implemented. Implementation of three distinct space charge models--uniform, gaussian and more general--into the tracking version is currently under way.

Used in a complementary fashion, the mapping and tracking versions of TOPKARK will provide a unique tool for investigating basic physics issues associated with space charge. These codes will also serve as powerful design and diagnostic tools for high-brightness beam optics applications.

V. ACKNOWLEDGEMENTS

The authors wish to acknowledge many fruitful discussions with Alan Todd of Grumman, with Etienne Forest of LBL and with Tom Mottershead, Filippo Neri, Walter Lysenko and Paul Channell of LANL.

VI. REFERENCES

- [1] M. Berz, *Part. Accel.* 24, 109 (1989).
- [2] E. Forest, M. Berz, J. Irwin, *Part. Accel.* 24, 91 (1989).
- [3] A. Dragt and J. Finn, *J. Math. Phys.* 17, 2215 (1976).
- [4] A. Dragt, L. Healy, F. Neri and R. Ryne, *IEEE Trans. Nucl. Sci.* 5, 2311 (1985).
- [5] J. van Zeijts and F. Neri, "New Features in the Design Code TLIE," to appear in *Computational Accelerator Physics Conference Proceedings* (February, 1993).
- [6] K. Crandall and D. Rusthoi, *TRACE3D Documentation*, (Los Alamos Accelerator Code Group, 1990).
- [7] E. Forest and R. Ruth, *Physica D* 43, 105 (1990).
- [8] H. Yoshida, *Phys. Lett. A* 150, 262 (1990).
- [9] R. Garnett and T. Wangler, 1991 *IEEE Particle Accelerator Conference Proceedings* 1, 330 (1991).
- [10] M. Reusch, E. Forest and J. Murphy, 1991 *IEEE Particle Accelerator Conference Proceedings* 3, 1651 (1991).
- [11] W. Press, B. Flannery, S. Teukolsky and W. Vetterling, *Numerical Recipes* (Cambridge University Press, 1990).
- [12] O. Kellogg, *Foundations of Potential Theory*, (Dover Publications, 1954).
- [13] E. Forest, "The Absolute Bare Minimum for Tracking in Small Ring (Minus Radiation), unpublished (1989).
- [14] M. Reusch and D. Bruhwiler, "Optics Simulations of the 5 MeV NPBSE FOX Telescope," this proceedings.
- [15] D. Bruhwiler and M. Reusch, "High-Order Optics with Space Charge: The TOPKARK Code," to appear in *Computational Accelerator Physics Conference Proceedings* (February, 1993).
- [16] M. Martini and M. Promé, *Particle Accelerators* 2, 289 (1971).
- [17] D. Carey, *The Optics of Charged Particle Beams*, (Harwood Academic Publishers, 1987).
- [18] J. Lawson, *Applied Charged Particle Optics*, ed. A. Septier, (Academic Press, 1983).

Experimental Study of Longitudinal Dynamics of Space-Charge Dominated Parabolic Bunches *

D. X. Wang, J. G. Wang, D. Kehne, and M. Reiser
Laboratory for Plasma Research and Department of Electrical Engineering
University of Maryland, College Park, Maryland 20742

I. Haber
Naval Research Laboratory, Washington D.C. 20375

Abstract

Longitudinal dynamics of space-charge dominated parabolic beams has been studied at the University of Maryland Electron Beam Transport Facility. In this paper we report results which emphasize experiment, while numerical simulation studies are presented in another paper in this proceedings [1]. Excellent agreement is found between experiment, simulation and theoretical prediction.

I. INTRODUCTION

The longitudinal dynamics of space-charge dominated beams has been theoretically, experimentally and numerically studied at the University of Maryland. One of the objectives is to study the parabolic bunch which is important to both theory and application. The longitudinal bunch model with parabolic line charge density has been developed by L. Smith and D. Neuffer [2,3]. Since the self-forces are linear this model plays a similar role for the longitudinal dynamics as the uniform density K-V distribution for the transverse dynamics. We note that a parabolic beam was observed as the final equilibrium state at the Indiana University Cyclotron Facility [4]. A systematic experimental and numerical study will check the validity of the theoretical model and can contribute to better understanding of the beam physics.

II. THEORETICAL MODEL

The longitudinal space-charge field can be approximately calculated as follows [5,6]

$$E_z(z, s) = - \frac{g}{4\pi\epsilon_0\gamma^2} \frac{\partial \Lambda(z, s)}{\partial z}, \quad (1)$$

where z is the distance from the center of the beam bunch, $\Lambda(z, s)$ is the line charge density at a longitudinal distance s traveled by the beam bunch center, and the geometry factor g is a function of the ratio of the pipe radius b over the beam radius a , where $2Z$ is the bunch length. g can also depend on the ratio Z/a when Z/a become comparable to unity [6]. Neuffer found a self-consistent distribution function of the longitudinal phase space that gives a linear force and velocity distribution and a preserved parabolic bunch shape. It is a solution of the Vlasov equation. The evolution of the bunch length is described by the longitudinal envelope equation:

$$\frac{d^2 Z}{ds^2} - \frac{2gZ_i I_p(0)}{\beta^3 I_0} \frac{1}{Z^2} - \frac{\epsilon_L^2}{Z^3} = 0, \quad (2)$$

where $2Z_i$ and $I_p(0)$ are the initial bunch length and peak current, respectively, $I_p = 1.7 \times 10^4$ amperes is the characteristic current for electrons, $\beta_0 = v_0/c$, v_0 is the beam center velocity, c is the speed of light, and ϵ_L is the longitudinal emittance of the beam. If the space-charge term is dominant over the emittance term, (20 times larger in this experiment), then an analytical expression for Z is given in Ref. [7]. If the initial velocity is a linear function of z , then it remains linear and its slope is determined by Z' .

In this one-dimensional model the longitudinal and transverse dynamics can be coupled through the geometry factor g , which reflects the boundary condition and bunch dimensions.

III. EXPERIMENTAL SETUP AND METHOD

The experimental configuration is illustrated in Ref. [7]. The electron bunch is produced by a newly developed electron beam injector which consists of a variable-perveance electron gun, an induction acceleration module, and three matching lenses. The parabolic beam profiles can be generated by controlling the pulse shape applied to the grid of the gun. An initial velocity tilt can be imparted to the beam by the time-varying acceleration voltage of the induction gap, as shown in Fig. 1. Then, the beam is matched into a 5-m long periodic focusing channel consisting of 36 short solenoidal lenses.

The typical initial beam parameters in this experiment are 2.5 keV energy, 20 mA peak current, 26 ns pulse duration. The beam current profiles are measured by fast beam current monitors and a fast Digitizing Signal Analyzer. The beam center velocity $c\beta_0$ and energy can be obtained by the time of flight method. The acceleration gap voltage at the beam center can be calculated by subtracting the 2.5 keV beam energy before the gap. Matching it in Fig. 1, one can figure out the initial velocity tilt.

The parabolic beam is produced and matched into the channel. Without the induction acceleration the bunch expands and the current reduces, while with the acceleration the bunch is compressed to a waist then expands after that.

IV. EXPERIMENTAL RESULTS

A. Longitudinal envelope measurement

To verify the envelope equation, the beam current profiles are measured at 5 different locations, shown in Fig. 2 for the expansion case and in Fig. 3 for the compression case. They are fitted by ideal parabolic curves to obtain the bunch width, i.e. the longitudinal envelope. The envelope evolution is plotted in Fig. 4 for different initial velocity tilts in comparison with the calculation of the envelope equation. They are in very good agreement.

* Research Supported by the U.S. Department of Energy.

B. Velocity distribution measurement

To check the linearity of the space-charge force and velocity distribution the beam energy is measured at 3 different locations. A typical beam velocity vs. time is plotted in Fig. 5 and fitted by a straight line. The slopes are plotted and compared with the envelope calculation in Fig. 6 for the expansion case and in Fig. 7 for the compression case. Again, good agreement is found.

C. The transverse coupling

To explore the transverse coupling effect we have done the measurements with the same longitudinal conditions but different transverse focusing, i.e. different beam radius. The experimental results plotted in Fig. 8 show that due to different transverse focusing the envelope evolution changes but still obeys the envelope equation, however g values are different for each case.

In calculating the theoretical curves we assumed that the g -factor remains constant along the channel. This assumption gave surprisingly good agreement with the experimental data. However, since the beam radius varies along the bunch and also along the channel one does not expect g to remain constant. In practice it is not an easy task to determine the g factor without experimental measurement or 2-D computer simulation. Nevertheless, work is underway to calculate the g factor by numerical methods.

We also have looked into how critical the transverse matching condition is to the longitudinal beam behavior. In the experiment we deliberately mismatched the beam by changing the matching lens focusing. We found that the current profiles showed very little change over quite a wide range of mismatch conditions. When the mismatch became too large we started losing beam. These results are confirmed by a 2-D simulation. In the simulation the longitudinal dynamics remains almost the same though there is a very significant transverse mismatch.

VI. CONCLUSION

An experimental study of a space-charge dominated parabolic beam has been carried out. Excellent agreement has been achieved between the experiment and the longitudinal envelope model. In the experiment we have demonstrated that the parabolic current profile is preserved and the velocity distribution remains linear as a result of the linear space-charge force. A constant g along the transport channel used in the 1-d model was found to be a good approximation. However, g changes significantly when the transverse focusing changes and can be measured or calculated by a 2-D code. The experiment shows that the transverse mismatching has little effect on the longitudinal dynamics, and this was confirmed by the 2-D simulation.

V. REFERENCES

1. I. Haber, D.A. Callahan, A.B. Langdon, M. Reiser, D.X. Wang, and J.G. Wang, "Computer Simulation of the Maryland Transport Experiment", these proceedings.
2. L. Smith, "ERDA summer study for heavy ion inertial fusion" (ed. R. O. Bangerter, W. B. Herrmannsfeldt, D. L. Judd, and L. Smith), LBL-5543 (1976), pp. 77-79.
3. D. Neuffer, IEEE Trans. on Nuclear Science, 26(3), pp. 3031-3033, June 1979.

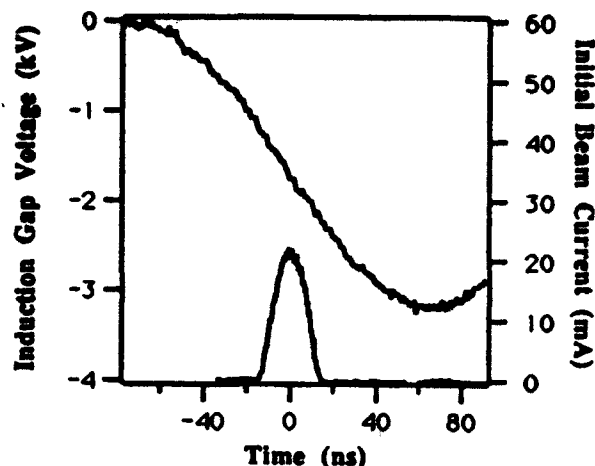


Fig. 1 Voltage waveform of induction gap (top) and current pulse shape of initial parabolic beam (bottom).

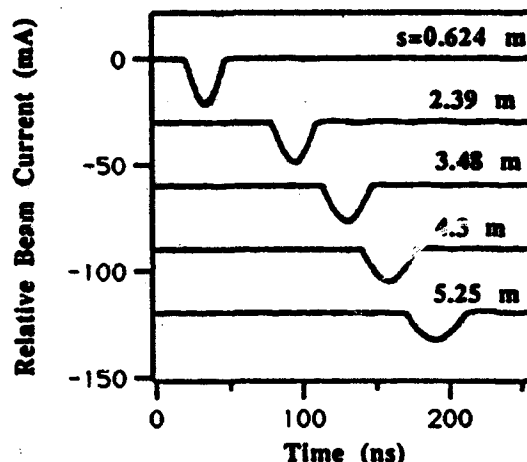


Fig. 2 Current profiles of parabolic bunch without initial velocity tilt at five different locations of the channel.

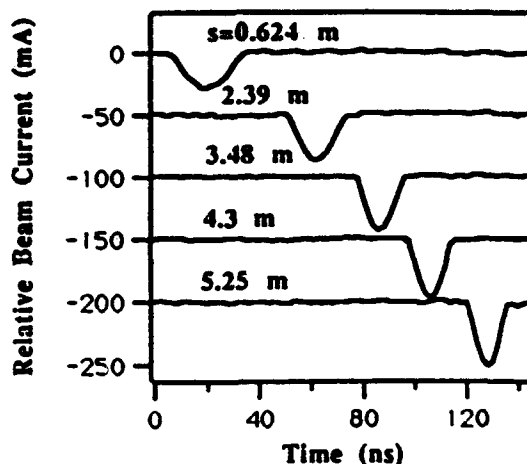


Fig. 3 Current profiles of parabolic bunch with initial velocity tilt at five different locations of the channel.

4. T. Ellison, S. Nagaitsev, M. Ball, D. Caussyn, M. Ellison, and B. Hamilton, Phys. Review Letters Vol. 70, Num. 6 pp. 790-793, Feb. 1993
5. D.A. Edwards and M.J. Syphers, "An Introduction to the Physics of High-Energy Accelerators", J. Wiley & Sons, N.Y., 1993, Ch.6.2.
6. M. Reiser, "Theory and Design of Charged Particle Beams" (Wiley & Sons, New York, to be published in Fall 1993), Ch. 5.4.
7. D.X. Wang, J.G. Wang, and M. Reiser, accepted for publication in Applied Physics Letters, July, 1993.

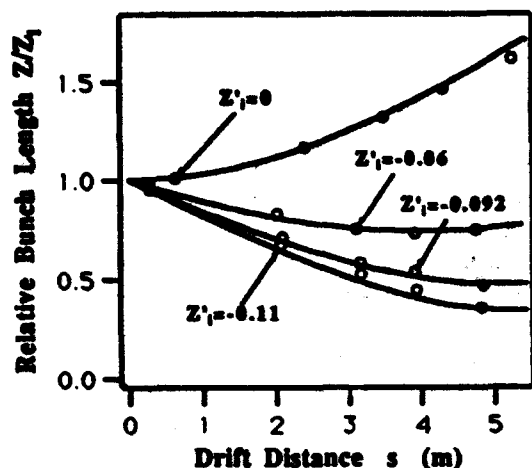


Fig. 4 Relative parabolic bunch lengths Z/Z_i vs. drift distance with different initial velocity tilts, where the circles represent experiment and the solid curves theory.

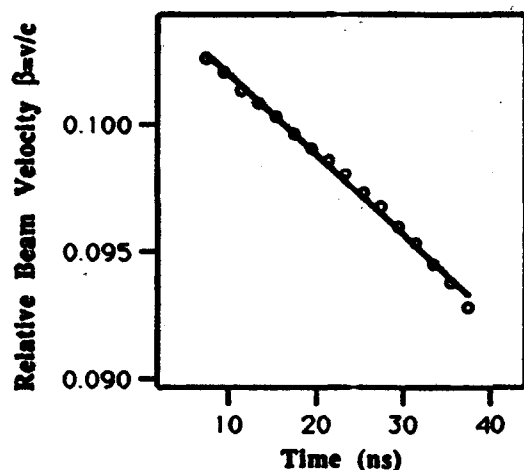


Fig. 5 Velocity distribution of parabolic bunch without initial velocity tilt measured at $s=3.746$ m, where the circles represent experiment and the solid line is linear fitting.

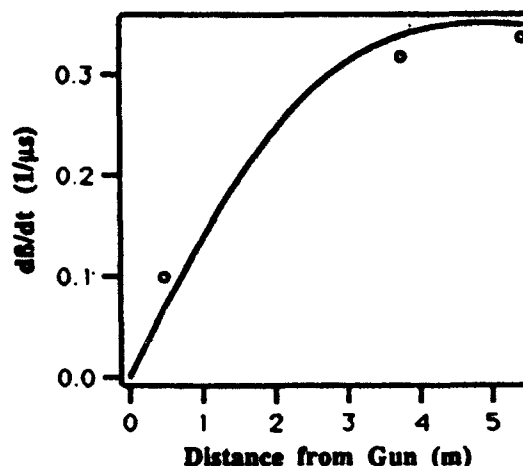


Fig. 6 Slopes of linear velocity distribution without initial velocity tilt, measured at $s=0.473, 3.746$, and 5.42 m. The circles represent experiment and the solid curve theory.

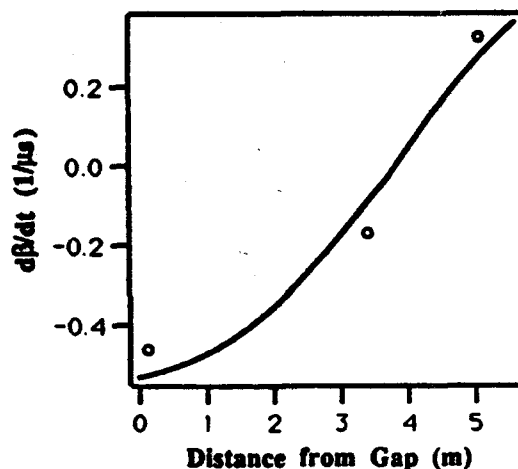


Fig. 7 Slopes of linear velocity distribution with initial velocity tilt $Z'_i=-0.06$, where the circles represent experiment and the solid curve theory.

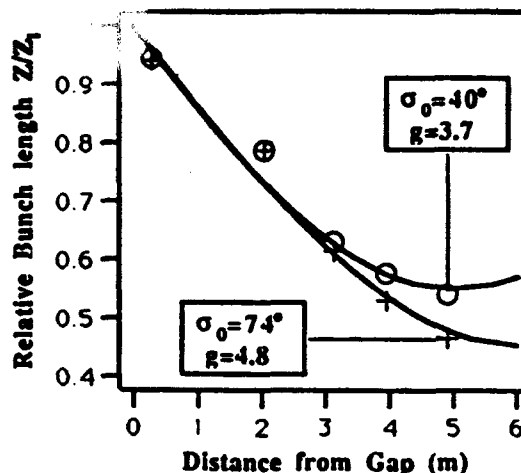


Fig. 8 Relative bunch length vs. drift distance with $Z'_i=-0.092$ for different transverse focusing strength, where the circles represent experiment and the solid curves theory.

Transition Crossing in the Fermilab Main Ring, Past and Present.

I. Kourbanis and K.Y. Ng

Fermi National Accelerator Laboratory, P.O. Box 500, Batavia, IL 60510*

Abstract

A recent installation of passive mode dampers in the Booster [1] has eliminated most of the longitudinal emittance blowup of intense bunches due to coupled-bunch instabilities. As a result, high intensity effects (negative-mass instability) dominate the present transition crossing in the Main Ring for the high-intensity cycles. A negative-mass stability limit is derived for transition crossing in the Main Ring and recent observations of high frequency signals around transition is presented. Finally, some predictions about the effect of the negative mass instability on the transition in the Main Ring with the future upgrades are attempted.

I. INTRODUCTION

In past years, coupled-bunch instabilities in the Fermilab Booster were responsible for longitudinal emittance blowup in very intense bunches. As a result, high intensity (larger than 2.0×10^{10} p) Booster bunches transferred to the Main Ring had large longitudinal emittance (0.18–0.20 eV-sec). In that case, our measurements showed that nonlinear phenomena were responsible for the emittance blowup around transition in the Main Ring [2]. Recent installation of passive mode dampers in the Booster cavities has eliminated most of the longitudinal emittance blowup. In fact, the longitudinal emittance blowup in the Booster has been reduced by a factor of 3. Now, a 2.5×10^{10} Booster bunch transferred to the Main Ring has an emittance of 0.06 eV-sec. In this case, the blowup at transition in the Main Ring has increased to a factor of 2.8–3.2 resulting in final longitudinal emittances of 0.18–0.22 eV-sec after transition. We attribute this emittance blowup to a negative-mass instability at transition. High frequency negative-mass signals have been observed up to 7 GHz.

*Operated by the Universities Research Association under contracts with the U.S. Department of Energy.

II. EXPERIMENTAL OBSERVATIONS

For the experimental observation of the high frequency signals, we used a wall-current monitor with a flat frequency response up to 6 GHz located in the Main Ring tunnel. The signal from the wall monitor was brought upstairs and was amplified with a 4–8 GHz amplifier. It was then brought to an rf switch panel with a switch gate determined by an HP 8112A pulse generator triggered by a Main Ring beam synchronised clock. This was necessary in order to reduce the noise in the signal since there were only 84 consecutive bunches out of 1113 in the Main Ring cycle used for our observations. Finally, the signal was viewed on a HP8566B spectrum analyser set at the zero-span mode.

In Fig. 1, we display the observed signals around transition at frequencies 4, 5, and 6 GHz for proton bunches with initial emittance 0.07 eV-sec and 2.3×10^{10} p. The units on the vertical axis are 5 db per division and on the horizontal axis 2 msec per division. The transition time is marked with an arrow. As seen in Fig. 1, the signals are getting stronger and more persistent with increasing frequency as expected from the negative-mass instability. In this case, the longitudinal emittance after transition was 0.25 eV-sec corresponding to a blowup of 3.6. Next we used a phase mismatch at injection to blowup the longitudinal emittance of the bunches with initial emittance of 0.06 eV-sec and intensity 1.8×10^{10} p. In Fig. 2, we display the signals observed at 5.0 GHz, with two different longitudinal emittances before transition. As expected, the 5.0 GHz signal is smaller for the bigger longitudinal emittance, and dies away faster compared to the signal in the case with the smaller emittance. The emittance blowup at transition is also much smaller for the bigger initial emittance (a factor of 2 compared with 3.7).

III. NEGATIVE-MASS BLOWUP

Hardt [3] proposed a theory of negative-mass blowup that takes into account of Landau damping. In the absence of space charge, the spectral coefficient of the bunch for revolution harmonic k is $|c_k| = N_b^{-1/2}$ due to the statistical fluctuation of the N_b particles in the bunch. As a result of

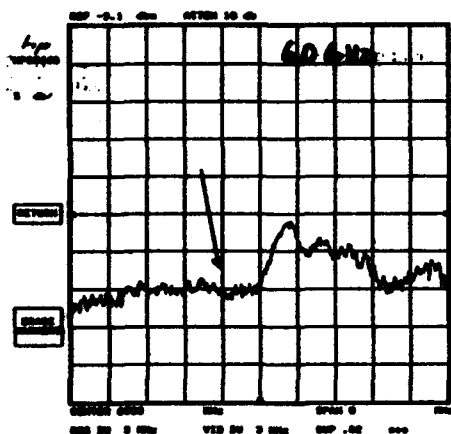
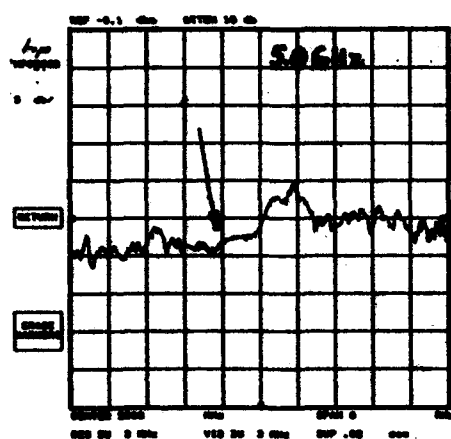
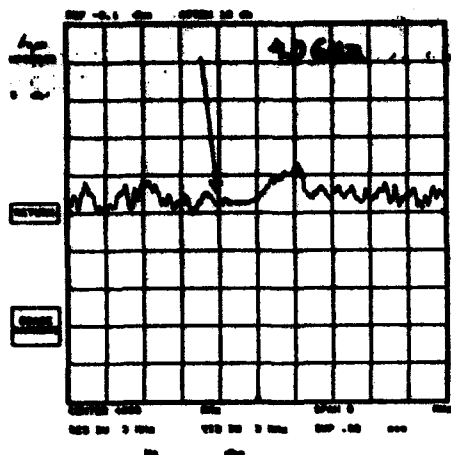


Figure 1: Negative mass signals at different frequencies for bunches with emittance of 0.07 eV-sec and 2.2×10^{10} p.

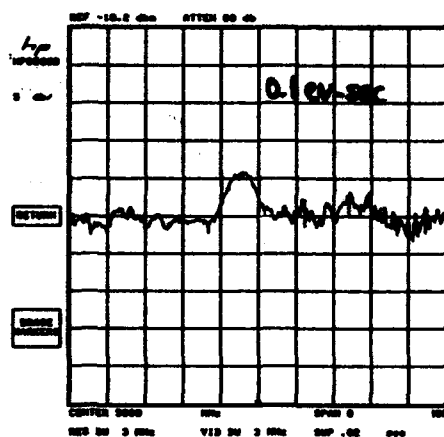
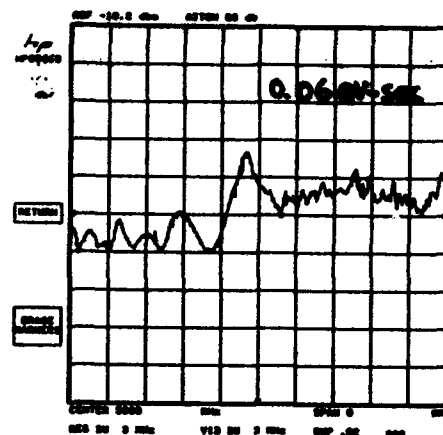


Figure 2: Negative mass signals observed around transition at 5.0 GHz for bunches with the same intensity and different longitudinal emittances.

space charge, a blowup becomes significant when $\sum |c_k|^2$ grows to unity. Here the summation is over all the longitudinal modes of the bunch when the total bunch length 2ϕ in rf radius at transition is an integral number of the harmonic wavelength. As is well-known, the time-integral growth due to space charge after transition for revolution harmonic k is proportional to k . However, the space-charge parameter $g_0 = 1 + 2 \ln(b/a)$, where $a \approx 0.5$ cm and $b \approx 3.5$ cm are, respectively, the beam and beam pipe radii, starts to drop when $k \sim \gamma R/b$, $R = 1000$ m being the mean radius of the Main Ring. In fact, it drops to one-half of its value when $k_1 \approx \gamma R(1.6/b + 0.52/a)$. Therefore the integrated growth has a maximum, which occurs at $k_c = k_1/\sqrt{3}$. In our case, this corresponds to 1.6×10^6 or 78 GHz. After summing up all the bunch modes, we have

$$\xi k_{\text{eff}} \left(\frac{r_p}{R} \right)^2 \left(\frac{E_0^{5/2}}{h^{1/3} \omega_0^{4/3} \gamma^{2/3}} \right) \left(\frac{N_b^2 g_0^2 |\tan \phi_s|^{1/3}}{A^{5/2} \dot{\gamma}^{7/6}} \right) = c E_c, \quad (1)$$

where E_c is the maximum allowable time integrated growth at harmonic $k_1/\sqrt{3}$, and is given by

$$E_c = \frac{1}{2} \left[\ln N_b - \ln \left(\frac{k_1 \sqrt{8\pi}}{3 \sqrt{\frac{1}{2} \ln N_b}} \right) \right], \quad (2)$$

$k_1 = k_1 \phi / \pi h$, and $k_{\text{eff}} = 3\sqrt{3} k_1 / 16$. When the critical coefficient $c < 1$, there is no blowup due to negative-mass instability. In the above, the coefficient $\xi = 2^{-17/6} 3^{13/6} \pi^2 \Gamma(2/3) (1 - \pi/4)$, A is the bunch area in eV-sec, E_0 is the proton rest energy, and r_p is the classical proton radius.

The highest intensity in our measurement was $N_b = 2.2 \times 10^{10}$ protons per bunch. The transition gamma is $\gamma = 18.85$, the rate of acceleration across transition is $\dot{\gamma} \approx 90 \text{ s}^{-1}$ at the synchronous angle $\phi_s = 60^\circ$. The blowup coefficient c for various bunch areas at such high bunch intensity are given in Table 1. The non-adiabatic time is 3.4 msec.

IV. CONCLUSION

A negative-mass instability is dominating the transition crossing in the Main Ring with the present emittances and intensities. The experimental data are in agreement with the negative mass instability threshold. In the next collider run, Main Ring is expected to accept bunches with intensity up to 4.0×10^{10} p. The emittance of these bunches is expected to be 0.11–0.12 eV-sec. (following the Booster longitudinal emittance vs intensity curves). In this case, the calculation in Table 2 shows that the instability threshold c remains about 1; i.e., things will not become worse than now. If the Booster emittance remains at 0.06 eV-sec, however, c becomes 5. Then, the blowup around transition will become much worse than now and there will be more beam loss.

Bunch Area (eV-s)	Bunch Length (ns)	c	E_c
0.040	0.438	4.07	9.88
0.050	0.490	2.34	8.83
0.060	0.537	1.49	9.78
0.070	0.580	1.02	9.74
0.080	0.620	0.73	9.71
0.100	0.693	0.42	9.66
0.120	0.759	0.27	9.61
0.140	0.820	0.18	9.57
0.160	0.876	0.13	9.54
0.180	0.929	0.10	9.51
0.200	0.980	0.08	9.48
0.220	1.027	0.06	9.46
0.240	1.073	0.05	9.44

Table 1: Negative-mass blowup coefficient vs bunch area at bunch intensity 2.2×10^{10} per bunch.

Bunch Area (eV-s)	Bunch Length (ns)	c	E_c
0.040	0.438	13.06	10.19
0.050	0.490	7.52	10.13
0.060	0.537	4.79	10.09
0.070	0.580	3.27	10.05
0.080	0.620	2.35	10.02
0.100	0.693	1.35	9.96
0.120	0.759	0.86	9.91
0.140	0.820	0.58	9.88
0.160	0.876	0.42	9.84
0.180	0.929	0.32	9.81
0.200	0.980	0.24	9.79
0.220	1.027	0.19	9.76
0.240	1.073	0.15	9.74

Table 2: Negative-mass blowup coefficient vs bunch area at bunch intensity 4.0^{10} per bunch.

ACKNOWLEDGMENT

The authors would like to thank Kathy Harkay for supplying the Booster longitudinal emittance figures and Jerry Jackson for his help in the experimental setup.

REFERENCES

- [1] D. Wildman and K. Harkay, *HOM RF Cavity Dampers for Suppressing Coupled-Bunch Instabilities in the Fermilab Booster*, these proceedings.
- [2] I. Kourbanis, K. Meisner, and K.Y. Ng, *Experimental Study of the Main Ring Transition Crossing*, IEEE Particle Accelerator Conference, San Francisco, May 6-9, 1991, p.111.
- [3] W. Hardt, *Gamma-transition-jump scheme of the CPS*, Proc. 9th Int. Conf. on High Energy Accelerators, Stanford 1974.

Observation and Correction of Resonance Stopbands in the AGS Booster*

C. Gardner, Y. Shoji†, L. Ahrens, J.W. Glenn, Y.Y. Lee, T. Roser

A. Soukas, W. van Asselt, and W.T. Weng

AGS Department, Brookhaven National Laboratory

Upton, New York 11973

Abstract

At the design intensity of 1.5×10^{13} ppp, the space charge tune shift in the AGS Booster at injection has been estimated to be about 0.35. Therefore, the beam is spread over many lower order resonance lines and the stopbands have to be corrected to minimize the amplitude growth by proper compensation of the driving harmonics resulting from random errors. The observation and correction of second and third order resonance stopbands in the AGS Booster, and the establishment of a favorable operating point at high intensity are discussed.

I. INTRODUCTION

The AGS Booster began operation [1] in 1992, delivering beam at one third the design intensity of 1.5×10^{13} ppp. An important part of the ongoing effort to reach the design intensity has been the correction of the second and third order resonance lines encountered by the beam during injection and early acceleration. The Booster operates with the horizontal and vertical tunes (Q_x and Q_y) between four and five, and at the design intensity the space charge tune shift has been estimated to be about 0.35 at injection. With the nominal operating point at $Q_x = 4.82$, $Q_y = 4.83$ several of the second and third order lines shown in Figure 1 are therefore encountered and the associated stopbands must be corrected in order to minimize beam loss. The second and third order resonances and the types of field which excite them are listed below:

Second Order (excited by quadrupole fields):

$$2Q_x = 9, \quad 2Q_y = 9 \quad (1)$$

Second Order (excited by skew quadrupole fields):

$$Q_x + Q_y = 9, \quad Q_x - Q_y = 0 \quad (2)$$

Third Order (excited by sextupole fields):

$$3Q_x = 14, \quad Q_x + 2Q_y = 14 \quad (3)$$

$$3Q_x = 13, \quad Q_x + 2Q_y = 13 \quad (4)$$

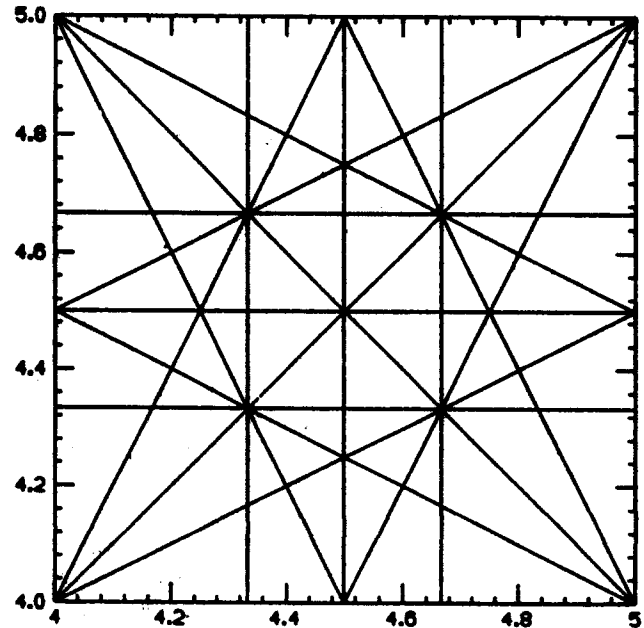


Figure 1: 2nd and 3rd Order Resonances

$$2Q_y - Q_x = 5, \quad 2Q_y - Q_x = 4 \quad (5)$$

Third Order (excited by skew sextupole fields):

$$3Q_y = 14, \quad Q_y + 2Q_x = 14 \quad (6)$$

$$3Q_y = 13, \quad Q_y + 2Q_x = 13 \quad (7)$$

$$2Q_x - Q_y = 5, \quad 2Q_x - Q_y = 4 \quad (8)$$

The resonance correction system [2, 3] employs auxiliary windings placed on quadrupoles and sextupoles whose main windings serve to adjust the machine tunes and chromaticities. Special windings on the correction dipoles produce the required skew quadrupoles, and passive windings on the dipole vacuum chambers compensate the sextupole fields produced by eddy currents [4]. The various windings are excited so that appropriate azimuthal harmonics are produced which compensate the resonance driving harmonics resulting from random magnetic field errors. The system is capable of correcting resonances (1-4) simultaneously, i.e. it can correct each of these resonances without

*Work performed under the auspices of the U.S. Dept. of Energy.

†Permanent address, KEK

affecting the correction of the others. The remaining resonances (5-8) are either difference resonances or resonances excited by skew sextupole fields. These were not considered in the development of the correction schemes because they were thought to be relatively weak. However, during the course of our studies we found that the skew sextupole resonances (6) are actually quite strong, and as a result, windings were placed on existing magnets in the ring to produce four skew sextupoles. Subsequent excitation of these magnets reduced losses significantly. Another unexpected source of beam loss was the presence of a strong ninth harmonic in the sextupole fields around the machine which, due to radial displacement of the orbit in the sextupoles, drives the quadrupole resonances (1). The loss was reduced by exciting available sextupole windings to produce a ninth harmonic sextupole field.

Resonances (1-3) and (6) were observed by programming the tunes to pass through each resonance at various times during the magnetic cycle. The beam intensity was reduced to ensure that the area occupied by the beam in tune space was as small as possible, and the loss upon traversal of each resonance was measured by observing a circulating beam current transformer. Figure 2 shows a typical trace of the beam current as a resonance is crossed. Here the upper and lower traces are respectively the beam current transformer and the current in the tune quadrupoles. The amount of loss was measured for several different correction settings in order to accurately determine the setting required to minimize the loss. These measurements were made at several different values of the field, B , and dB/dt to determine the dependence of the required correction on these parameters. The results of the measurements and the effects of the corrections on the overall beam intensity are summarized in the following sections.

II. QUADRUPOLE CORRECTION

The corrections required for resonances (1) were found to have the following dependence on B and dB/dt :

$$C_x = 25 + 110B + 6.0\dot{B}, \quad S_x = -172 + 160B - 1.9\dot{B} \quad (9)$$

for the $2Q_x = 9$ resonance, and

$$C_y = 147 + 90B + 5.0\dot{B}, \quad S_y = -192 + 54B - 6.0\dot{B} \quad (10)$$

for the $2Q_y = 9$ resonance. Here C and S are proportional to the cosine and sine components of the 9th harmonic quadrupole field and the units of B and dB/dt are kG and kG/s. The units of correction have been chosen for tuning convenience.

During the course of determining these corrections we found that we could not completely eliminate the loss as the resonances were crossed, and with a crossing speed of 0.01/ms the residual loss was about 20%. We initially thought that an 18th harmonic octupole field might be responsible for the loss, but then found that the required corrections vary linearly with the orbit radius which strongly

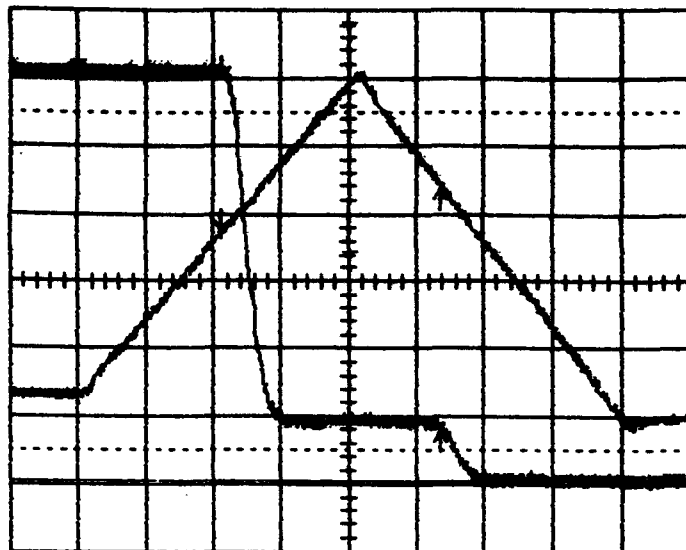


Figure 2: Beam Loss upon Crossing a Resonance.

suggested a ninth harmonic sextupole field. Beam particles whose momentum differs by δp from the central momentum would then see a ninth harmonic quadrupole field which is proportional to δp and this could produce the observed loss. We found that by introducing a ninth harmonic with available sextupole windings we could eliminate the dependence of the required correction on radius and reduce the residual loss to about 4%. It is possible that the remanent fields of the sextupole magnets used to adjust the chromaticities are responsible for the ninth harmonic sextupole field.

III. SKEW QUAD CORRECTION

The corrections required for resonances (2) were found to depend on B but not on dB/dt :

$$C_{xy} = 40 + 50B, \quad S_{xy} = -100 + 30B \quad (11)$$

for $Q_x + Q_y = 9$ resonance, and

$$C = -180 + 140B \quad (12)$$

for the $Q_x - Q_y = 0$ resonance. Here C_{xy} and S_{xy} are proportional to the cosine and sine components of the 9th harmonic skew quadrupole fields and C is proportional to the zeroth harmonic of these fields. As before, the units of correction have been chosen for tuning convenience.

As with the corrections for resonances (1) we found that we could not completely eliminate the loss as the $Q_x + Q_y = 9$ resonance was crossed, and with a crossing speed of 0.01/ms the residual loss was about 20%. We suspect that the residual loss is due to a ninth harmonic skew sextupole field, but we have not yet confirmed this hypothesis.

IV. SEXTUPOLE CORRECTION

The corrections required for resonances (3) were found to depend on dB/dt but only weakly on B :

$$C_x = 30 + 0B + 3.5\dot{B}, \quad S_x = -90 + 20B + 6.0\dot{B} \quad (13)$$

for the $3Q_x = 14$ resonance, and

$$C_{xy} = 0 + 13B + 4.7\dot{B}, \quad S_{xy} = 120 + 9B + 2.6\dot{B} \quad (14)$$

for the $Q_x + 2Q_y = 14$ resonance. Here C and S are proportional to the cosine and sine components of the 14th harmonic sextupole fields.

V. SKEW SEXT CORRECTON

As previously mentioned, resonances (6) were found to be quite strong and as a result, additional windings were placed on existing magnets to produce four skew sextupoles. These were excited to produce the required 14th harmonic correction which was found to depend on B and dB/dt :

$$C_{xy} = 35 + 0B + 0\dot{B}, \quad S_{xy} = 40 - 7.0B + 0.3\dot{B} \quad (15)$$

for the $Q_y + 2Q_x = 14$ resonance. Here C and S are proportional to the cosine and sine components of the 14th harmonic skew sextupole fields. With this correction the loss upon traversal of the resonances at a crossing speed of 0.01/ms was reduced from 20% to 4%.

VI. INTENSITY GAINS

To see the effect of the corrections at high intensity, the corrections were programmed on the high intensity machine cycle according to their measured dependencies on B and dB/dt . On this cycle beam is injected at $B = 0.15T$ with $dB/dt = 3T/s$. Shortly after injection, dB/dt increases to 7 T/s and then decreases to 1 T/s near extraction where $B = 0.52T$. The effect of the skew sextupole corrections is shown in Figure 3 where the upper and lower traces show the beam current with these corrections turned ON and OFF. Here the peak intensity at injection was 14×10^{12} and with the operating point of $Q_x = 4.78$, $Q_y = 4.94$ the final intensity just before extraction with the skew sextupole corrections turned ON was 9.6×10^{12} . With these corrections turned OFF the final intensity decreased to 7.6×10^{12} ppp. Turning off the sextupole corrections for resonances (3) further reduced the intensity by 0.7×10^{12} ppp. The quadrupole and skew quadrupole corrections had very little effect on the intensity at this operating point, which is consistent with the estimated space charge tune shift.

ACKNOWLEDGMENTS

The authors would like to thank G. Danby and J. Jackson for their help and advice concerning the skew sextupole

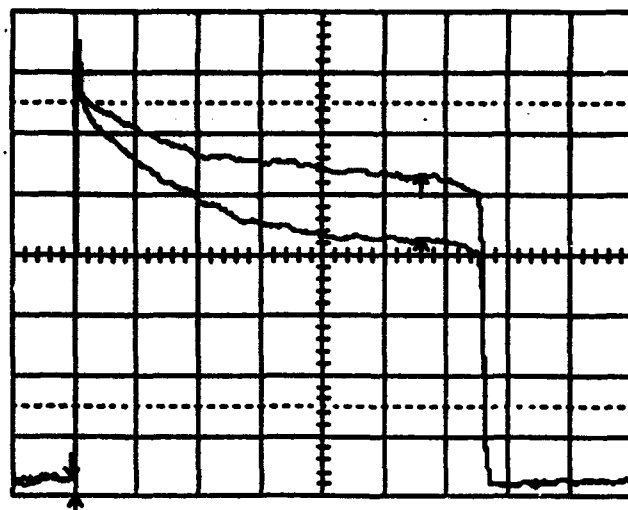


Figure 3: Beam Current with and without Skew Sextupole Correction. Time per division is 10 ms.

corrections and the vacuum chamber self-correction windings. The addition of the skew sextupole and ninth harmonic sextupole corrections would not have been possible without the dedicated and enthusiastic support of the power supply group.

REFERENCES

- [1] L. Ahrens, et al., "The Operational Status of the Booster Injector for the AGS Accelerator Complex at BNL", XVth Int. Conf. on H.E. Accel., Hamburg, Germany, July 1992, pp. 109-111.
- [2] J. Milutinovic, et al., "AGS Booster Orbit and Resonance Correction", Proceedings of the 1989 Particle Accelerator Conference, March 20-23, 1989, pp. 1367-69.
- [3] C. Gardner, "Booster Stopband Corrections", Booster Technical Note No. 217 (unpublished report), AGS Dept., Brookhaven National Laboratory, January 6, 1993.
- [4] G. Danby and J. Jackson, "Vacuum Chamber Eddy Current Self-Correction for the AGS Booster Accelerator", *Particle Accelerators*, 1990, Vol. 27, pp. 33-38.

THE STABILITY OF IONS IN A STORAGE RING IN THE PRESENCE OF SMALL GAP INSERTION DEVICES*

Eva Bozoki

National Synchrotron Light Source, BNL, Upton, New York, 11973

1. INTRODUCTION

With more and more insertion devices in storage rings, where the vacuum chamber size can be suddenly different, ionization pockets may develop, thus ions may be trapped leading to beam blow up, beam instabilities or even beam loss.

One have to take a closer look at the stability conditions of the ions in these longitudinal potential wells. For equidistant bunches: are the ions above or below the Ac critical mass? For a bunch train followed by a gap: is the ion of mass A stable or unstable for a given current at a given azimuthal location in the ring? Are the ions longitudinally mobile and be able to get to an unstable region? If the ions proved to be stable in that region and if their longitudinal kinetic energy is less then the depth of the potential well, then they have to be statically cleared at that location.

We are going to investigate the question of ion stability in the NSLS X-ray ring with a .32 m long variable gap (4-18mm) undulator [1] and a .95 m long 27 mm gap undulator [2] in it. We will concentrate our attention to CO ions (A=28) since they are the most bothersome in the ring (H₂, being much lighter, they are always more unstable). We will show the effect of gap in the bunch train, the effect of non-linearity in the beam kicks and the effect of restricted longitudinal mobility of ions. The methods used and the calculations performed are general enough to be applied to any other storage ring or accelerator, thus representing general interest.

2. BEAM POTENTIAL

The smaller the beam size or the larger the diameter of the vacuum chamber is, the deeper the beam potential will be at that location. This is easy to see for the simple case of round beam of radius a and round chamber of radius r_0 , when the beam potential is $V = -(\lambda/2\pi\epsilon_0) \ln(a/r_0)$, but it is also true in general (elliptic beam in elliptic chamber [3]). Therefore longitudinal potential wells will be found at either side of the small gap undulators, which will prevent ions (with longitudinal kinetic energy less then the depth of the well - which is the majority of the ions) entering the undulator from either direction. If the ions are stable in that regions, then ionization pocket occurs.

The beam in the X-ray ring is flat ($\sigma_x > \sigma_y$), therefore the vertical beam and vacuum chamber size is more critical than the horizontal. They are plotted together with the calculated beam potential at the center of the beam. The potential was calculated for $I = 250$ mA beam current. The figure shows, that the depth of the potential wells are $\Delta U = 50$ and 10 MeV for the two undulators, respectively.

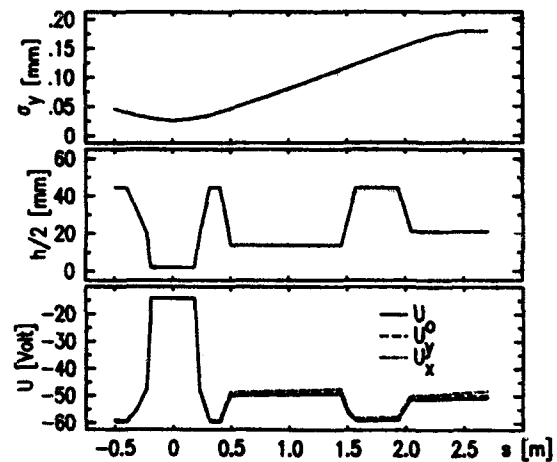


Fig. 1. Vertical beam size (σ_y), half height of the vacuum chamber ($h/2$) and beam potential at the center of the beam (U_0) in the 2 undulator region for $I = 250$ mA beam current.

3. CRITICAL MASS

In a simplified, linear model of ion trapping by a bunched electron beam the ions are "kicked" by the electron bunches and they drift freely between the kicks. (In this linear approximation the beam's electric field is assumed to be linear with the distance from the middle of the beam.) The effect of kick and drift can be described in the usual matrix formalism [4]. When the bunches are uniformly distributed, that is for equidistant bunches, then the stability condition imposed on the Trace of the matrix ($\text{Trace}(M) \leq 2$) yields a critical ion mass, above which the ion motion is stable:

$$A_c = \frac{C^2 r_p I}{2\epsilon_0 c n_g^2} \frac{1}{\sigma_y (\sigma_x + \sigma_y)}$$

where r_p is the classical proton radius and I is the beam current.

The critical mass with 5, 15 or 30 equidistant bunches is plotted in one superperiod of the the ring for $I = 250$ mA on Figs. 2. The location of dipoles (-[]-), quadrupoles (- -) and undulators (-[]-) are also shown. One can see that with 5 bunches, practically all ions are instable anywhere in the ring. With 15 bunches only H₂ is unstable anywhere, CO and CO₂ is unstable only in the straight sections, where the undulators are. With all 30 buckets filled in the ring, even the H₂ ions are stable everywhere except in the straight sections and heavier ions are stable practically everywhere (except in a very small region around the middle of the straights).

*Work performed under the auspices of the U.S. Dept. of Energy.

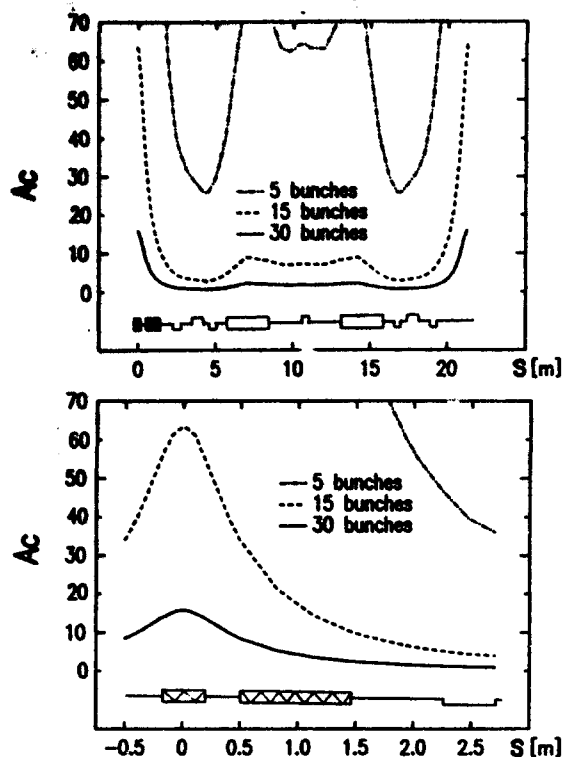


Fig. 2. Critical mass with 5, 15 or 30 equidistant bunches, for $I = 250$ mA shown in (a) one superperiod of the ring and (b) in the 2 undulator region.

4. NON EQUIDISTANT BUNCHES

In this section, we are still assuming linear beam-ion forces. When there are N uniformly distributed bunches

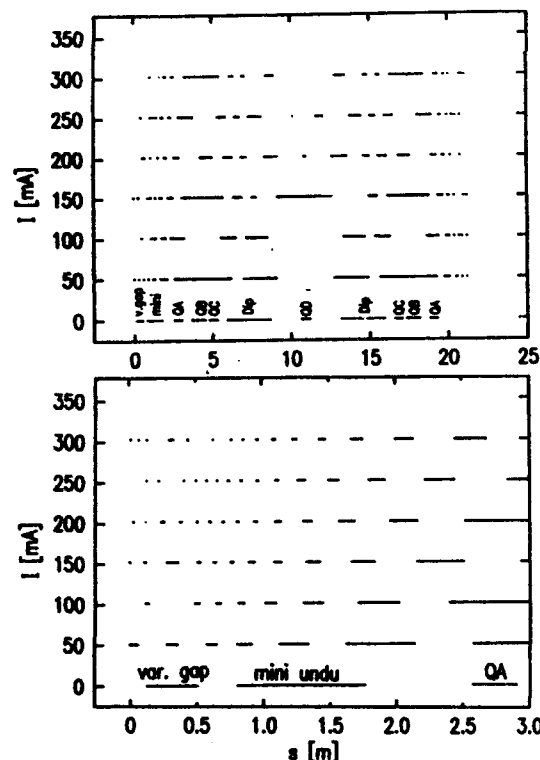


Fig. 3. Linearly stable regions of $A=28$ ions with 25 consecutive bunches are shown for different beam currents in (a) one superperiod (with $ds=10$ cm resolution) (b) the $0 \leq s \leq 2$ m undulators region (with $ds=1$ cm resolution)

(bunch train) followed by M empty bunches (gap) in the ring, then the stability condition imposed on the Trace of

the matrix yields a N -th order nonlinear equation and instead of a critical mass, there are bands of stable regions of A for any given current and longitudinal location. This can be "mapped" into stable/unstable longitudinal (s) regions around the ring for a given ion, beam current and gap length.

We calculated the stable longitudinal regions for the CO ions with 25 consecutive bunches ($M=5$) in the ring at different beam currents and plotted them on Figs. 3. One can see, that even at $I = 50$ mA beam current, there are enough unstable regions in/around the undulator that the ions would not build up. This is also true around the ring.

5. NONLINEAR BEAM-ION FORCES

Let us now consider the nonlinear nature of the beam-ion force. We track ions [5] with different initial conditions for (x, y, s, v_x, v_y, v_z) , and examine the relative number (%) of "living ions", that is ions still in and around the beam, as a function of the number of turns in the machine (time). 100 CO ions were tracked with initial Gaussian random distribution in (x, y, v_x, v_y, v_z) while the initial s_0 was uniformly distributed in $0 \leq s \leq 2.0$ m (the region where the 2 undulators are) and $0 \leq s \leq 21$ m (one superperiod of the ring). In either case, linear and nonlinear tracking were performed with longitudinally mobile ions, as well as nonlinear tracking with longitudinally immobile ions. This latter is important to see, whether or not ions longitudinally confined in the potential wells around the undulators can escape from the beam. $A=28$ ions in 25 consecutive bunches for $I=250$ mA beam were used in the tracking.

The results are shown on Fig. 4. One can see that (a) nonlinearity of kicks makes the ions (initially) more stable but even so, $\approx 100\%$ of the ions created in the undulator region and $\approx 80\%$ of all ions will hit the vacuum chamber after only 250 turns, that is .14 msec, (b) ions created in the undulator region are slightly more unstable than those created anywhere else in the ring and (c) longitudinal ion mobility or lack of it does not influence the stability of ions. Consequently, with $I=250$ mA in 25 consecutive bunches, the ions do not build up around the undulators.

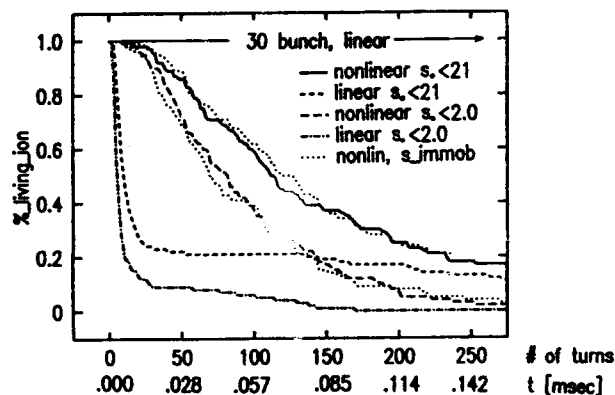


Fig. 4 % of living ions vs. number of turns with $N = 25$ consecutive bunches in the ring and $A = 28$, $I = 250$ mA.

Next, we looked at the effect of increasing the number of consecutive bunches in the ring. Fig. 5a shows the % of

living ions when 100 Gaussian random ions, created uniformly in the full superperiod, were tracked with linear beam-ion forces for $N = 25 - 30$, while Fig. 5b is for nonlinear beam-ion forces and $N = 25 - 27$. One can see, that even for linear forces, the ions are rapidly getting stable with increasing N , and with 30 bunches all ions are stable. In the realistic case of nonlinear forces all ions disappear after .17 msec when there are 25 bunches in the ring, but $\approx 40\%$ are still "alive" with 27 bunches.

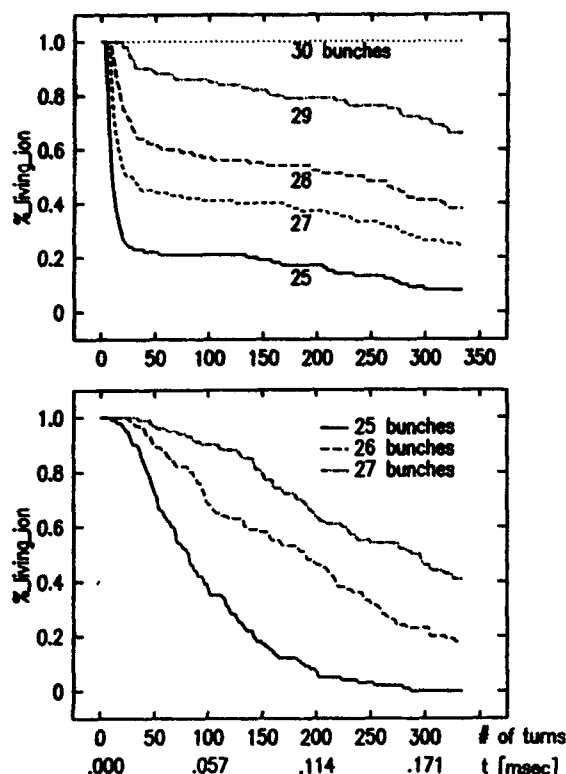


Fig. 5 Life-curve of $A = 28$ ions with $I = 250$ mA and different number of consecutive bunches in the ring when assuming (a) linear and (b) nonlinear beam-ion forces.

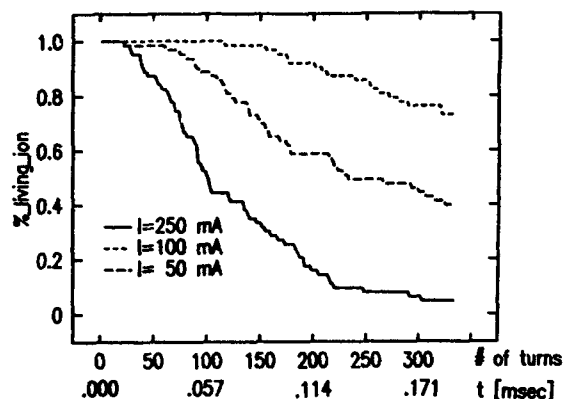


Fig. 6 % of living ions vs. number of turns with $A = 28$, $I = 50-250$ mA and $N = 25$, assuming nonlinear beam-ion forces.

We already pointed out the current dependence of the critical mass and the linearly stable regions. The next figure shows the dependence of the nonlinear 'lifetime' of the ions on the beam current. The % of living ions is plotted on Fig. 6 when tracking was done with nonlinear beam-ion forces, $N = 25$ and $I = 50, 100$ and 250 mA beam currents. The same 100 ions were tracked as for Figs. 5. The figure

shows a strong dependence on current. Even with only 25 bunches in the ring, the ions are almost stable at $I = 50$ mA.

6. EFFECT of POTENTIAL WELLS

We turn our attention now to the effect of the potential wells due to the narrowing vacuum chamber in the undulators and how do they effect the (un)stability of the ions.

Fig. 7 shows the "life-curve" of 100 CO ions in 25 consecutive bunches for $I = 250$ mA beam assuming nonlinear beam-ion forces and under the following conditions. The ions were tracked with initial s_0 uniformly distributed in $0 \leq s_0 \leq .15$ m (before the variable gap undulator) with longitudinally mobile ions and (a) neglecting the effect of the potential well, (b) taking the effect of the potential well into consideration. 100 ions were tracked with initial s_0 uniformly distributed in $0 \leq s_0 \leq 2$ m (from before the variable gap undulator until after the mini undulator) with longitudinally mobile ions and (c) neglecting the effect of the potential well, (d) taking the effect of the potential well into consideration, as well as (e) with longitudinally immobile ions ($v_z = 0$ and no longitudinal kicks) and without the effect of the potential well. All ions were created Gaussian random in (x, y, v_x, v_y, v_z) , except where $v_z = 0$ was assumed.

One can see that the potential well caused by the narrow vacuum pipe in the undulators have no considerable effect on the lifetime of ions (all 5 curves are identical!), and that the ions are unstable in the two undulator region. The effect of the narrow cross section is that the ions will drift towards the deeper part of the potential well, away from the undulators. But since the whole area is unstable, the ions will get lost.

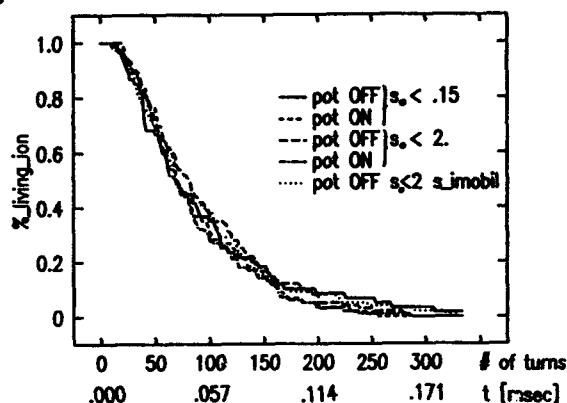


Fig. 7 % of living ions vs. number of turns with $A = 28$, $I = 250$ mA and $N = 25$ assuming nonlinear beam-ion forces with and without the effect of beam potential.

Acknowledgement

The author is grateful to David Sagan for the many discussions and for the use of his ion tracking program.

References

- [1] P.M.Stefan et al., Proc. IEEE PAC, p.1096, 1991.
- [2] H.Rarback et al., NIM A266 p.96, 1988.
- [3] G.Grober, K.Hubner, CERN/ISR-TH-VA/75-27, 1975.
- [4] M.Barton, NIM A243 p.278, 1986.
- [5] D. Sagan, NIM A307, 1991.

Simulation of Space-Charge Dominated Beam Dynamics in an Isochronous AVF Cyclotron

Shane R. Koscielniak, TRIUMF Vancouver B.C. Canada
Stefan R. Adam, PSI Villigen Switzerland.

Abstract

This paper describes a beam dynamics code 'PICN' for simulation of high current proton beams in an isochronous azimuthally-varying-field cyclotron. It is assumed that the median plane and vertical motions are decoupled, so that the internal space-charge forces can be calculated by a particle-in-cell method applied to the median plane charge distribution. We assume operation in a regime where vertical focusing is not weak. This paper details the simulation method and approximations, including a summary of the equations of motion. Results of the code, when applied to the P.S.I. Injector II cyclotron are presented, and compared with results from an earlier code that treated the beam as composed of a distribution of rigid spheres.

I. INTRODUCTION

As has been noted by several authors [1] [2] [3], space-charge is important in isochronous cyclotrons for the following reason: there is no longitudinal focusing and there is strong radial-azimuthal coupling. Because the space-charge electric fields are severely non-linear, practical investigation must proceed by numerical methods [4] [5].

The original code 'PICS' [3] considered the beam to be formed of charged spheres, and completely neglected the internal motions within these spheres. The main argument to justify this simplification was that the betatron oscillations are much faster movements than the deformations of a beam bunch due to space charge forces.

The new simulation code, to be called PICN, assumes that the radial and the vertical betatron motions are decoupled, just as in the code PICS. However, the median plane internal motions within a charged sphere are now to be included explicitly. The sphere is decomposed into cylinders and the cylinders are divided into vertical rods or needles. There are now new freedoms in the motion: rods within the same initial sphere need not have the same centre nor the same oscillation frequency, and individual time-dependent modulations of tune and betatron amplitude are now allowed. The new model assumes that all needles have the same, fixed height; i.e. the spheres are replaced by full cylinders. The artificial force law used in PICS is replaced by the force between two uniformly charged vertical rods.

A. Elementary force law between two needles

Consider two parallel rods of length $2b$ separated by a distance a with charges Q_1 and Q_2 respectively. Then the mutual repulsive force is

$$F(a, b) = \frac{Q_1 \times Q_2}{2\pi\epsilon_0 a (2b)^2} \left[\sqrt{(2b)^2 + a^2} - a \right].$$

II. MOTION EQUATIONS IN THE LABORATORY FRAME

The centre of charge (and mass) moves with velocity u . An arbitrary particle in the bunch has some velocity v . We should like to find an equation for $\frac{d}{dt}(v - u)$. We use the energy equations to eliminate the time derivatives of the γ -factors from the momentum equations. For the reference particle: $m_0\gamma_u du/dt = F_0^{ex} - u(u \cdot F_0^{ex})/c^2$. For the general particle: $m_0\gamma_v dv/dt = F_2^{sc} + F^{ex} - v[v \cdot F^{ex}]/c^2$, where $F_2^{sc} = F^{sc} - v[v \cdot F^{sc}]/c^2$. F^{ex} is an externally applied force due to magnets and cavities, say. F^{sc} is the force due to space-charge; i.e. from the whole assembly of which the 'test' particle is a member.

A. An expression for space-charge force

The space-charge term can be expressed in terms of the Coulombic electric fields, due to the assembly of particles, as measured (or calculated) in the frame co-moving with the centre of mass of the group. We now define \parallel and \perp to mean parallel and perpendicular to u . Let the electric field be E'_{sc} in a frame which is co-moving with u . It is assumed that in this rest frame (of the bunch) there is an electric field E'_{sc} but no magnetic field B'_{sc} . The electric field is resolved into components transverse and longitudinal to the reference motion: $E' = E'_\perp + E'_\parallel$. In the laboratory frame the space-charge force on a test particle is:

$$F^{sc} = q \left[E'_\parallel + \gamma_u E'_\perp + v \wedge (u \wedge E'_\perp) \gamma_u / c^2 \right]. \quad (1)$$

The vector $v \wedge (u \wedge E'_\perp)$ occurring in the space-charge force term, F^{sc} equation (1), is perpendicular to v and so the magnetic field due to the beam cannot alter the energy.

We now substitute $v = v_\parallel + v_\perp = u + \Delta v$ and note that

$$\frac{1}{q} F_2^{sc} = (E'_\parallel + \gamma_u E'_\perp) \left(1 - \frac{uv_\parallel}{c^2} \right) - \frac{\Delta v}{c^2} (v_\parallel E'_\parallel + v_\perp \gamma_u E'_\perp) \quad (2)$$

is an exact expression. Now, to first order $(1 - uv_\parallel/c^2) \approx 1/\gamma_u \approx 1/\gamma_v$. Also note that the final term of (2) in $\Delta v/c^2$ is negligible. Hence, now approximately,

$$F_2^{sc} = (q/\gamma_u) \left[E'_\perp + E'_\parallel/\gamma_u \right].$$

B. Explicit Representation

We acknowledge the cylindrical symmetry of the cyclotron applied E^{ex} and B^{ex} fields, and adopt cylindrical polar coordinates (ρ, ϕ, z) for the reference particle position $x_0 = \rho e_\rho(\phi)$. We note that with space-charge there are preferential directions parallel and perpendicular to u ,

and take a local cartesian (rectangular) coordinate system (r, s, z) for the position vector of a general particle, $\mathbf{x} = \mathbf{x}_0 + \mathbf{e}_r r + \mathbf{e}_s s + \mathbf{e}_z z$. The velocity increment is $\Delta \mathbf{v} = (\dot{r} - s\dot{\phi})\mathbf{e}_r + (\dot{s} + r\dot{\phi})\mathbf{e}_s + \mathbf{e}_z \dot{z}$. ϕ is a reference coordinate, and we specify this to be isochronous so that it rotates at constant angular velocity $\dot{\phi} = \omega_c = (q/m_0)B_c^0$. In this case,

$$\Delta \dot{\mathbf{v}} = \mathbf{e}_r [\ddot{r} - 2\dot{s}\omega_c - \omega_c^2 r] + \mathbf{e}_s [\ddot{s} + 2\dot{r}\omega_c - \omega_c^2 s] + \mathbf{e}_z \ddot{z}.$$

We must compare the above identity for acceleration with the equation for forces. For brevity, we set (q/m_0) equal to unity. For simplicity we write the form appropriate to no external electric field $\mathbf{E}^{ex} = 0$.

$$\gamma_u \Delta \dot{\mathbf{v}} = [\Delta \mathbf{v} \wedge \mathbf{B}_0 + \mathbf{v} \wedge \Delta \mathbf{B}]^{ex} + (1/\gamma_u) [\mathbf{E}_H'/\gamma_u + \mathbf{E}_\perp']^{ex}.$$

Here $\mathbf{B}_0^{ex} = (B_\rho = 0, B_z^0, B_\phi = 0)$ is the reference field in the median plane, and $\Delta \mathbf{B}$ the field increment at (r, s, z) .

C. Almost Flat field, $\Delta \mathbf{B} = 0$

For the almost flat magnetic field $B_z^0(\rho) = \gamma(\rho)B_c^0$, where B_c^0 is the magnetic field at the cyclotron centre, there is a single Lorentz force term expressible as $\Delta \mathbf{v} \wedge \mathbf{B}_0^{ex}$.

Since time and turns accumulate equally, there is a simple transformation between derivatives. Let $\theta = \omega_c t$, so one turn corresponds to $\theta = 2\pi$. Under the approximation $\gamma_u = \gamma(\rho)$, the motion equations become:

$$\begin{aligned} (r' - s)' &= (1/\omega_c^2)(q/m_0) E_r'(r, s, z)/\gamma_u^2 \\ (s' + r)' &= (1/\omega_c^2)(q/m_0) E_s'(r, s, z)/\gamma_u^3, \end{aligned}$$

where the superfix prime denotes the derivative with respect to radian-turns.

D. An approximation for AVF

It is no simple matter to find equations of motion in the median plane so as to describe a smooth focusing due to the combination of radial field gradients and sectorized azimuthal variations of the magnetic field.

Let the angle formed between radius vectors to the general and reference particles be θ . We take a force proportional and perpendicular to the 'extra' azimuthal velocity $\Delta v_\theta = \dot{s} \cos \theta - \dot{r} \sin \theta$ and to the 'extra' radial velocity $\Delta v_\rho = \dot{r} \cos \theta + \dot{s} \sin \theta$, at point (s, r) . Thus we take a focusing force $\mathbf{F}_{focus} = m[\mathbf{e}_\rho \Delta v_\theta - \mathbf{e}_\theta \Delta v_\rho]$. In terms of the cartesian unit vectors $\mathbf{e}_r, \mathbf{e}_s$, we find $\mathbf{F}_{focus} = m(\mathbf{e}_r s' - \mathbf{e}_s r')$, and the space-charge term $\mathbf{F}_2^{sc} = \mathbf{e}_s F_s + \mathbf{e}_r F_r$. Hence the equations of motion are:

$$(s' + \nu r)' = F_s, \quad (r' - \nu s)' = F_r. \quad (3)$$

The radial betatron tune ν is given by $\nu = (m + 1)$. There are two constants of motion if $F_s = F_r = 0$; however the speed is not exactly conserved. These equations yield betatron motion in the form of circles in the median plane, which property lends itself to finding self-consistent matched charge distributions under internal space-charge forces. Further, these equations are formally identical with those presented by Kleven [6].

III. STARTING ENSEMBLE

The overall density of points (in real space) will be the convolution of an elementary disc composed of concentric rings of short vertical rods convolved with the distribution of disc centres, which may be distributed homogeneously over a rectangular grid. Each particle point $[s, r, s', r']$ may carry a different charge.

A. Matched elementary disc - no space charge

The elementary ensembles are circular in position and in velocity space, and made as follows. From a uniformly populated disc (in r, s -space) generate the correlated velocities for betatron motion according to $r' = \nu s$ and $s' = -\nu r$.

B. Matched elementary disc - with space-charge

It is desirable that elementary charge clouds be stationary under the action of the internal space-charge force; this facilitates comparison with the sphere model in PICS.

The disc consists of concentric rings, and our matching scheme will be to adjust the velocity coordinates of particles on each ring so as to give a self-consistent distribution under space-charge. We take a system of local polar coordinates (ρ, θ) with centre at the reference particle, such that $s = \rho \cos \theta$ and $r = \rho \sin \theta$. The equations (3) become:

$$\rho'' - \rho(\theta')^2 + \nu(\rho\theta') = F_\rho; \quad -2\rho'\theta' - \rho\theta'' + \nu\rho' = -F_\theta. \quad (4)$$

Here F_ρ, F_θ are the radial and azimuthal (with respect to centre of cloud) components of \mathbf{F}_2^{sc} . We look for an equilibrium circular solution of (4) with $\theta', \rho = \text{constants}$. For the rods at radius, ρ , the angular velocity θ' is given by:

$$2\theta'(\rho) = \nu + \sqrt{\nu^2 - 4F_\rho/\rho}.$$

The matched disc is found as follows. (i) Generate a uniformly populated disc. (ii) Numerically solve for the space-charge forces F_s, F_r and transform to F_ρ, F_θ . (iii) Ring by ring evaluate $\theta'(\rho)$. (iv) Generate the correlated velocities according to $r' = \theta' s$ and $s' = -\theta' r$.

IV. EXAMPLE CASES

The mutual forces between the elementary charge discs are not compensated for and will cause a perturbation of the matched circular betatronic motion and also cause the cloud centres to move. These effects were studied for a coasting beam in PSI Injector II. All cases are for a 1 mA, 5 MeV beam with vertical height 2 mm. The integration algorithm is a fourth order time explicit Runge-Kutta integrator, used with a 0.05 turns integration step size and the program working fully in double precision.

Fig. 1: A round starting distribution, not matched under space-charge, of one centre and 5000 needles in a single cloud remains round, but "breathes", expanding and shrinking; it performs a monopole mode oscillation. Plotted are the r.m.s. radial and azimuthal width as a function of turn number. The oscillation frequency is lower than ν_ρ due to space charge forces. This beam has a longitudinal extension only from coupled radial-longitudinal betatron oscillations, but no phasewidth.

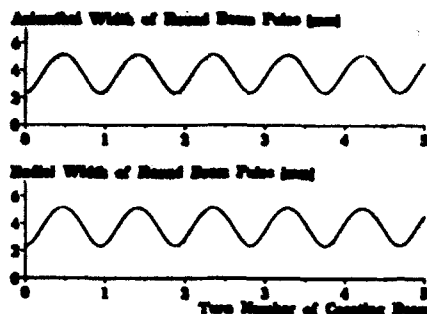


Fig. 1: Initial unmatched, round ensemble.

Fig. 2: Radial and azimuthal r.m.s. width of a bunch of 7.5 degree initial phase width, showing the increase of the radial width and the decrease of the azimuthal width followed by a small, slow rise towards a common value for both widths at a round beam (seen from the top); rather a 'disk' than a ball as the height is 2 mm.

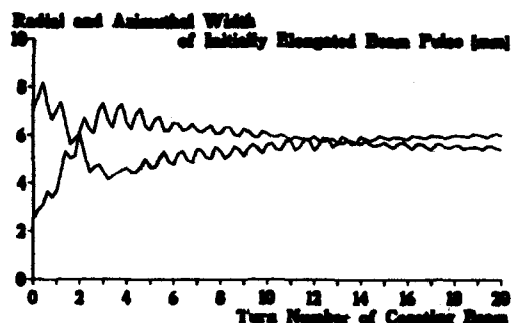


Fig. 2: Initial unmatched, oblong ensemble.

The initial increase of radial width and decrease of azimuthal width arises from rotation of the bunch. At an angle of 90° of the rotation, the beam is wider in the radial direction than in the azimuthal one. As this rotation carries on, it slows down with the approach of the two widths towards the matched case at about 75% of the initial length. The initial rotation is faster than the 15° case.

Fig. 3: The PICN simulation shows five successive top views of a bunch with initial phase width 15° (Injector II is on 10th harmonic) on turn numbers 0, 2, 4, 6, 8.

Fig. 4: The same case as PICN, but with the earlier program PICS. It really looks quite similar to previous case; the basic mechanism of forming an S-shape and then gradually a galaxy-like distribution is present in both models. However, the deformation is generally about 20 to 25 percent weaker for the needle model PICN.

Since it is clear that the phenomena are basically mismatching, the interesting question is whether a round charge distribution (not necessarily a sphere) is stable (i.e. matched). The test was a 'flying saucer' with an r.m.s width of 8 mm azimuthally and radially. This case, Fig. 5, shows almost constant radial and azimuthal width over many turns. From the way the centres are initialized it was a little 'squarish' at the beginning, and so probably this case did not have a precise matching; therefore it shows a small partial monopole mode as well.

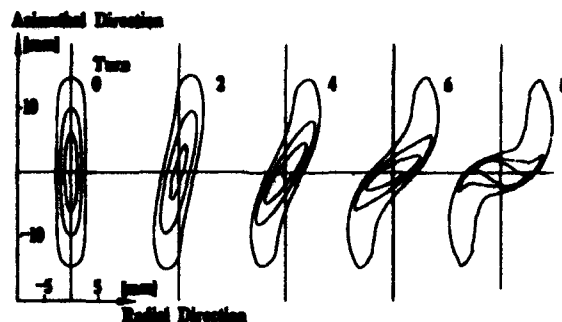


Fig. 3: PICN simulation of 15° phase width beam.

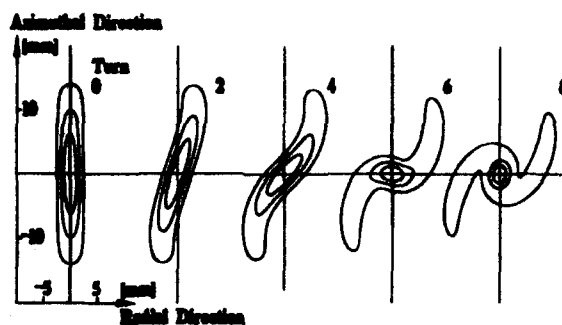


Fig. 4: PICS simulation of 15° phase width beam.

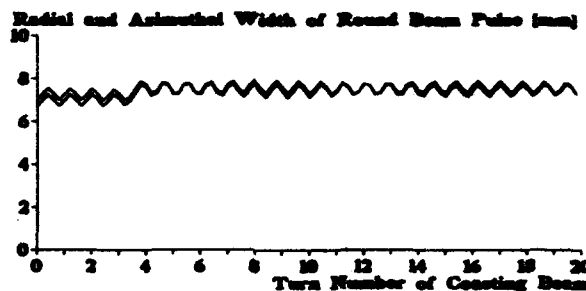


Fig. 5: Initial matched, round ensemble.

V. REFERENCES

- [1] M.M. Gordon: The Longitudinal Space Charge Effect and Energy Resolution; Proceedings of the 5th International Cyclotron Conference, Oxford 1969, pgs 305-317.
- [2] C. Chasman and A.J. Baltz: Space Charge Effects in a Heavy Ion Cyclotron; Nuclear Instruments and Methods in Physics Research 219 (1984), pgs 279-283.
- [3] S.R. Adam: Method for Calculating the Longitudinal Space-Charge Effect in Isochronous Cyclotrons; Doctoral Thesis, Swiss Federal Institute of Technology, Zurich, 1985.
- [4] S.R. Adam: Calculation of Space Charge Effects in Isochronous Cyclotrons; IEEE Trans. on Nuclear Science, Vol. NS-32, No.5, October 1985.
- [5] V. Cazoll: Theoretical and Numerical Study of a Sector Focused Cyclotron under Space-Charge; Doctoral Thesis, University Paris-Sud, 1988.
- [6] W.J.G.M. Kleeven: Theory of Accelerated Orbits and Space-Charge Effects in an AVF Cyclotron; Doctoral Thesis, Technical University of Eindhoven, 1988.

Passage through a Half-Integer Resonance due to Space Charge for Different Initial Distributions

A. Budzko

INR,* 7-A 60th Oktober Anniversary Prospect, Moscow, Russia 117312

and Yu. Senichev

SSC Laboratory† 2550 Beckleymeade Ave., Dallas, TX 75237, USA

I. INTRODUCTION

The problem of space charge continues to be interesting in connection with the development of Kaon and Neutron Facilities and Superconducting Super Collider Projects. In the first, a high average proton beam intensity can be reached by super-high peak currents in each acceleration cycle, so a painting procedure is required. In colliders, as is well known, super luminosity can be reached by minimising the emittance growth during acceleration. In other words, the task consists of accelerating beam with the maximum attainable current density and with minimum achievable emittance growth. This is why this task arises when new accelerator projects are developed.

At least two possibilities exist how to investigate the space charge effects at the design stage: analytical and numerical simulation [1-3]. Each of them has its own advantages and disadvantages. Numerical simulation using the macro-particle approximation is very well developed but requires a lot of computer time and so little flexibility in variation of the initial conditions. Because of this numerical methods are restricted in their optimisation capability.

Analytical investigations gives a clearer picture of the physical phenomena but the necessarily simplified the physical model sometimes gives an incorrect interpretation of the results. Analytical research can be divided in two types: the envelope equation method for self-consistent distributions and the nonlinear equation for higher distribution moments. In our work we use numerical simulation as the base to achieve the correct results, but for interpreting the results, the simplified analytical model is used as well.

II. PROBLEM STATEMENT

In almost any accelerator emittance growth is observed during beam injection. This is due to resonance crossing and mismatch between the beam and the acceptance. But this growth depends on what distribution is chosen during injection. In this paper we study the emittance growth under resonance crossing for different initial beam distributions. To eliminate the reasons for emittance growth

*On leave at TRIUMF, Vancouver, B.C.

†Permanent address is INR of Russian Academy of Sciences, Moscow

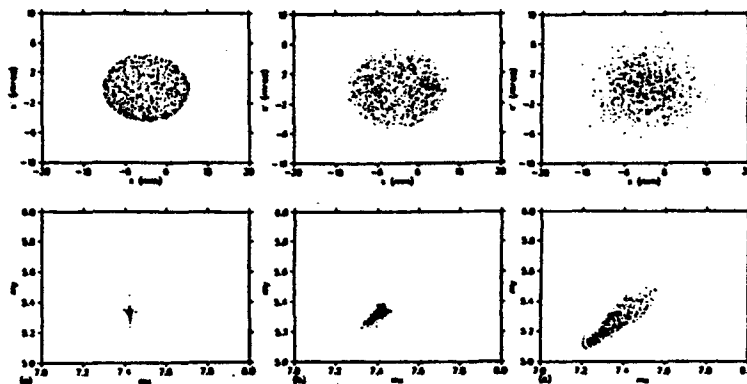


Figure 1: Phase space and tune diagram for K-V (a), waterbag(b) and Gaussian (c) distributions.

we consider a linear lattice without errors. In this case the emittance should grow only because of the intrinsic resonances, or in other words, the envelope oscillation.

III. NUMERICAL CALCULATION

The problem is solved for three different initial distributions: K-V, waterbag and Gaussian. To simulate self-consistent beam motion a two-dimensional tracking program is used. Space-charge forces are found by solving the Poisson equation with zero boundary conditions. Longitudinal motion effects and beam bunching are not taken into consideration. The particle oscillation frequency is found from the rotation angle in the normalised phase space. As a test lattice, we use the racetrack structure for TRIUMF Booster with two arcs and working point 7.65/5.6 although these results could be useful for the SSC LEB and AGS as well.

The initial phase space projections and the advanced phase diagram are shown in Figs. 1(a), 1(b) and 1(c) for K-V, waterbag and Gaussian distributions respectively. For each distribution we take the same *rms* emittance. One can see that all distributions have the same centroid, indicating the same coherent tune shift.

Figure 2 shows the emittance growth versus the number of turns for different distributions. The maximum emittance growth (a factor 2.8) was observed for K-V and waterbag at only a factor 1.25 for the Gaussian distribution.

Figures 3(a), 3(b) and 3(c) show the phase space for all observed distributions after five turns. It is obvious that

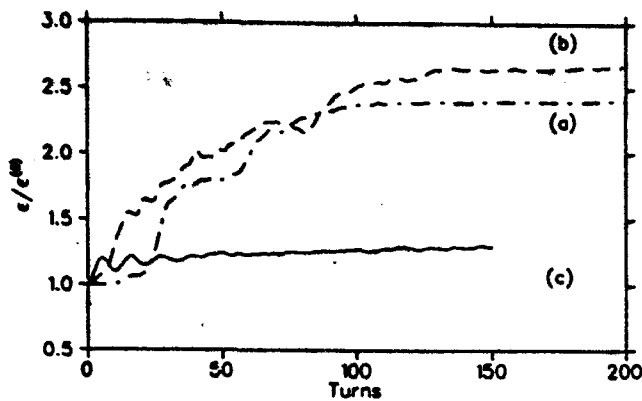


Figure 2: Emittance growth vs the turn number for K-V (a), waterbag (b) and Gaussian (c) distributions.

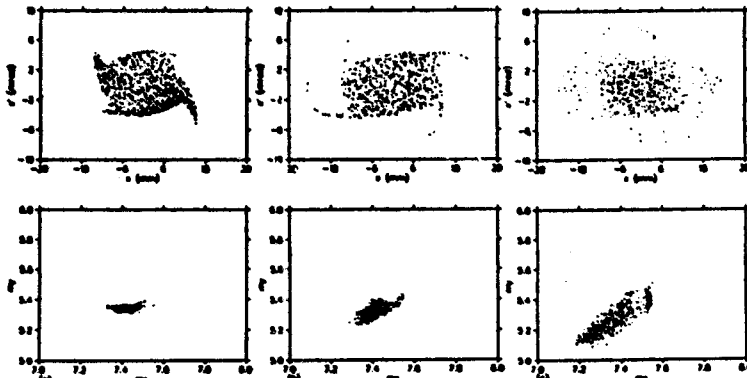


Figure 3: Phase space for K-V (a), waterbag (b) and Gaussian (c) distributions after 5 turns.

the beam passes through half-integer and fourth-order resonances. In all cases the amplitude of oscillation is finite.

Figures 4(a), 4(b) and 4(c) show the distributions after 45 turns. For waterbag and K-V distributions we can observe a half-integer resonance which is stabilized by a fourth-order resonance. For the Gaussian distribution we observe the distribution stabilised by a fourth-order resonance.

Figures 5(a), 5(b) and 5(c) show the final distributions for the same cases. The instability does not grow. They are stabilised, but the particles are still in the half-integer resonance excited by the envelope oscillation. This self-stabilisation phenomenon is known for nonlinear system,

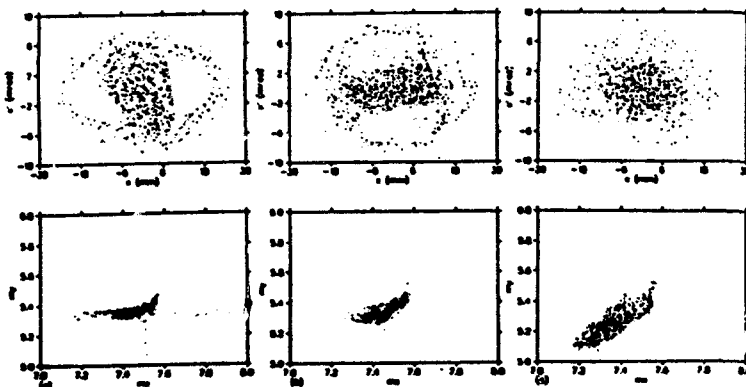


Figure 4: Phase space for K-V (a), waterbag (b) and Gaussian (c) distributions after 45 turns.

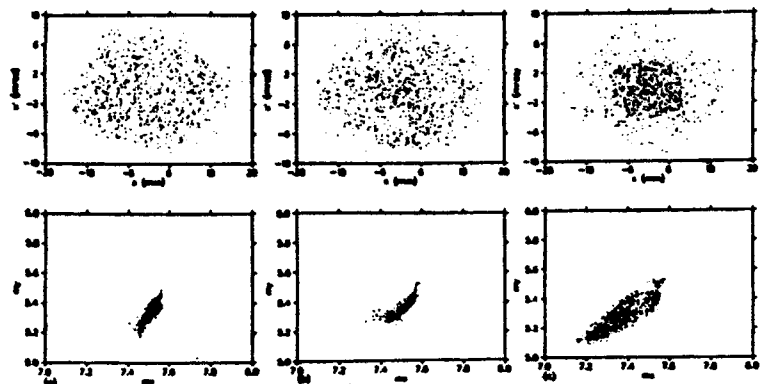


Figure 5: Stabilized distribution for initial K-V. (a), waterbag (b) and Gaussian distributions.

but in the space-charge problem we observe a system where the nonlinearity changes with time.

We now try to explain the phenomenon using a simplified analytical model which describes the resonance interaction.

IV. ANALYTICAL DESCRIPTION

Taking into account that we treated the two planes separately in the numerical experiment, the analytical study has been performed for a symmetrical cylindrical beam. The Maxwell equation for the symmetrical beam with density distribution ρ is:

$$\frac{1}{r} \frac{\partial(rE_r)}{\partial r} = \frac{1}{\epsilon_0} \rho(r) \quad (1)$$

We choose the m -order binomial distribution, which includes in itself the three types of distribution considered: Kapchinskij-Vladimirskij ($m=0$), the waterbag ($m=1$) and the Gaussian ($m \rightarrow \infty$):

$$\rho(r) = \frac{m}{\pi b^2} \left[1 - \frac{r^2}{b^2}\right]^{m-1}, \quad (2)$$

where b is the maximum size of the beam. Then the dispersion function σ is defined as $\sigma = \frac{b}{\sqrt{2m+2}}$ and the rms emittance $\epsilon_{rms} = \sigma^2/\beta$. The equation of motion for any particle will be:

$$\frac{d^2 r}{ds^2} + \kappa(s)^2 r - \frac{r_0 N}{\pi R \beta_0^2 \gamma^3} \frac{r}{2\sigma^2} \mathcal{F}(r) = 0, \quad (3)$$

or using the smooth approximation $r = \eta\sqrt{\beta}$ and the new longitudinal coordinate $d\theta = \nu_0 \beta ds$

$$\eta'' + \nu_0^2 \eta = 2\nu_0 \frac{r_0 N}{4\pi \beta_0^2 \gamma^3 \epsilon_{rms}} \eta \left[1 + \sum_p b_p \cos p\theta\right] \mathcal{F}(\eta), \quad (4)$$

where we use the Fourier expansion for $\beta = \bar{\beta}(1 + \sum_p b_p \cos p\theta)$ and the mean β -function $\bar{\beta} = \frac{R}{\nu_0}$, R being the average radius of the accelerator.

$$\mathcal{F}(r) = \begin{cases} 1/2 & \text{for K-V} \\ \frac{2}{3} - \frac{2}{9} \frac{1}{21} \frac{r^2}{\epsilon_{rms}^2} & \text{for waterbag} \\ 1 - \frac{1}{21} \frac{r^2}{2\epsilon_{rms}^2} + \frac{1}{3!} \left(\frac{r^2}{2\epsilon_{rms}^2}\right)^2 - \dots & \text{for Gaussian} \end{cases} \quad (5)$$

Usually one denotes the value $\nu_0 N / 4\pi\beta^2 \gamma^3 \epsilon_{rms}$ as the tune shift $\delta\nu$. Bogolubov's method can be used to solve this nonlinear equation:

$$\begin{aligned}\eta &= \sqrt{\epsilon} \cos \Phi \\ \eta' &= -\nu_0 \sqrt{\epsilon} \sin \Phi,\end{aligned}\quad (6)$$

or passing to new variables

$$\begin{aligned}\epsilon &= \eta^2 + \left(\frac{\eta'}{\nu_0}\right)^2 \\ \Phi &= -\arctan(\eta'/\nu_0\eta).\end{aligned}\quad (7)$$

Differentiating the new variables ϵ and Φ with respect to θ and substituting (6), we get:

$$\begin{aligned}\frac{d\epsilon}{d\theta} &= -2\delta\nu\epsilon \sin 2\Phi \left[1 + \sum_p b_p \cos p\theta\right] \mathcal{F}(\epsilon) \\ \frac{d\Phi}{d\theta} &= \nu_0 - 2\delta\nu \cos^2 \Phi \left[1 + \sum_p b_p \cos p\theta\right] \mathcal{F}(\epsilon)\end{aligned}\quad (8)$$

The function $\mathcal{F}(\epsilon)$ has the same meaning as (6), but with a new argument $\frac{\epsilon}{2\epsilon_{rms}} \cos^2 \Phi$. In the absence of any resonances we can average (9) over the whole cross section of the beam:

$$\begin{aligned}\overline{\frac{d\epsilon}{d\theta}} &= 0 \\ \overline{\frac{d\Phi}{d\theta}} &= \nu_0 - \Delta\nu,\end{aligned}\quad (9)$$

where $\Delta\nu$ is the average tune shift. It may be shown that equals $\frac{5}{8}\delta\nu$ for Gaussian, $\frac{5}{9}\delta\nu$ for waterbag and $\frac{1}{2}\delta\nu$ for K-V. This means that in a resonanceless system ($b_p = 0$) the emittance does not grow and the coherent tune shift does not depend on the distribution with the same rms emittance. On other hand the tune spread is a maximum for the Gaussian and equals zero for the K-V.

In fact, for any lattice the Fourier expansion of the envelope β -function involves in itself all harmonics which could give the resonance condition for emittance growth. Consider the case when \mathcal{F} involve just two terms and can be represented as $\mathcal{F} = f_0 - \epsilon f_1 \cos^2 \Phi$. Then

$$\begin{aligned}\overline{\frac{d\epsilon}{d\theta}} &= \delta\nu \epsilon b_m f_0 \sin(2\Phi - m\theta) - \\ &\delta\nu \epsilon^2 f_1 b_m \left[\frac{1}{2} \sin(2\Phi - m\theta) - \frac{1}{4} \sin(4\Phi - m\theta)\right] \\ \overline{\frac{d\Phi}{d\theta}} &= \nu_0 - \delta\nu f_0 + \frac{3}{4} \delta\nu \epsilon f_1 + \frac{1}{4} \delta\nu f_0 b_m \cos(2\Phi - m\theta) - \\ &\delta\nu \epsilon f_1 b_m \left[\frac{1}{8} \cos(4\Phi - m\theta) + \frac{1}{2} \cos(2\Phi - m\theta)\right],\end{aligned}\quad (10)$$

where m is the resonant harmonic number with amplitude b_m . One can see from these equations that any square nonlinearity in distribution gives the half-integer and the fourth-order resonances simultaneously. They can

exist only together. The main question is only whether the fourth-order resonance stabilises the half-integer resonance. The trajectories of particles on the phase plane are described by the equation:

$$\begin{aligned}&\frac{1}{2} \delta\nu b_m f_0 \epsilon \cos 2\Phi - \frac{1}{4} \delta\nu b_m f_1 \epsilon^2 \cos 2\Phi \\ &-(\nu_0 - \delta\nu f_0) \epsilon - \frac{3}{8} \delta\nu f_1 \epsilon^2 - \frac{1}{4} \delta\nu f_0 b_m \epsilon \cos 2\Phi + \\ &\frac{1}{4} \delta\nu f_1 b_m \epsilon^2 \cos 2\Phi = C(\epsilon, \Phi),\end{aligned}\quad (11)$$

where $\Phi = \phi - m\theta/n$ is the "slow phase" in the n -th order resonance. The terms with ϵ^2 stabilise parametric resonance. So for the distribution where the square term is absent, the half-integer resonance will give sufficient growth. Of course we should explain here that our analytical model doesn't allow us to take into account the self-consistent redistribution, which could create the term with ϵ^2 for any distribution after passing through the resonance. At least this explanation gives the answer why the emittance grows so strongly in the resonance for the K-V distribution.

Using more high-order terms of the binomial distribution it is possible to show that any order resonance will be stabilized by the next order distribution. Since the envelope β -function has all harmonics we will always have the resonant condition for one or more harmonics. So maximum stabilisation will be observed for the Gaussian, where any perturbation will be distributed over an unlimited number of harmonics.

V. CONCLUSION

We have studied in this paper a beam passing through the grid of intrinsic envelope resonances, where the half-integer resonance is maximum. At the initial stage a beam with any kind of distribution is very sensitive to the half-integer and fourth-order resonances. During 60-100 turns the distribution becomes self-stabilised and very similar to Gaussian. Maximum growth is observed for maximum uniform distribution in real space. For intrinsic resonances selfstabilisation occurs when most particles remain in resonance.

In conclusion we would like to thank Dr. A. Iliev for helpful discussions during this work.

VI. REFERENCES

- [1] S. Machida, "Space-charge effects in low-energy proton synchrotron", Nuclear Instruments and Methods in Physics Research, A309(1991)
- [2] I. Hofmann, "Simulation of space-charge and integer resonance crossing in storage rings and its application to heavy ion fusion", Particle Accelerators, 1992, v.39, pp.169-184
- [3] A. Budsko and Yu. Senichev, "Study of space charge effects close by half-integer resonances", Proc. 15th Int. Conf. on High Energy Accelerators, Hamburg, 1061 (1993)

Estimation of Collective Effects for the EUTERPE Ring

Boling Xi, J.I.M. Botman, J. van Laar, C.J. Timmermans, H.L. Hagedoorn
Eindhoven University of Technology, P.O. Box 513, 5600 MB Eindhoven, Netherlands.

Abstract

In low energy storage rings with a high current, collective effects can make the real bunch length, transverse emittances and beam lifetime notably different from the ones designed on the basis of single particle dynamics. The storage ring EUTERPE is a low energy ring with a nominal beam energy of 400 MeV and with an injection energy of 75 MeV. The estimation of collective effects in this ring is reported in this paper. The dependence of several collective effects on various machine parameters, limiting effects on the bunch size and current for several optical options and possible improving measures are discussed. The results indicate that an equilibrium transverse emittance of 8.5 nm.rad with a beam current of 100 mA in a high brilliance mode is achievable, which is near the natural emittance. Collective effects have no obvious adverse effects on low energy injection in the EUTERPE ring.

I. INTRODUCTION

A beam current is expected of more than 100 mA for the storage ring EUTERPE with a nominal beam energy of 400 MeV and an injection energy of 75 MeV. Collective effects can not be ignored in that case. With the demands of studies on particle beam dynamics and applications of synchrotron radiation, the realization of different optical options, such as the HBSB (high brightness, small beam), the SBL (short bunch length) and the HLF (high light flux) modes, is required in the EUTERPE ring [1]. In this paper, we examine the dependence of collective effects on various machine parameters and the performance limitations caused by collective effects, especially by the turbulent bunch lengthening, the intra-beam scattering and background gas scattering, in the different modes. Since the EUTERPE ring will operate with a single bunch or up to six bunches, we concentrate the discussion on the single bunch instability effects.

II. BUNCH CURRENT THRESHOLD AND BUNCH LENGTH

On the basis of single particle dynamics, the natural bunch length σ_{L0} can be calculated by [2]

$$\frac{\sigma_{L0}}{R} = C_{qe} (hV_0 \cos \phi_s)^{-1/2} \left(\frac{\alpha}{\rho_0 J_E} \right)^{1/2} \gamma^{3/2}, \quad (1)$$

where $C_{qe} = 1.11 \times 10^{-3} (\text{meter.volt})^{1/2}$, R is the average machine radius, h the RF harmonic number, V_0 the peak RF voltage, ϕ_s the synchronous phase angle, α the momentum compaction, J_E the damping partition number for energy oscillations, ρ_0 the bending radius of magnets and γ the normalized energy.

Considering the "turbulent bunch lengthening effect" [3], the energy spread and the bunch length will both increase with the stored current in the bunch above a threshold bunch current $I_{b,th}$. It can be determined by [4]:

$$I_{b,th} = \frac{\sqrt{2\pi\alpha}(E/e)}{|Z/n|_{eff}} \left(\frac{\sigma_E}{E} \right)^2 \left(\frac{\sigma_{L0}}{R} \right), \quad (2)$$

where σ_E/E is the energy spread and $|Z/n|_{eff}$ the effective longitudinal broad band impedance which represents the interaction between the bunch and the surroundings. Above the threshold, the bunch length will be given by [4]:

$$\left(\frac{\sigma_L}{R} \right)^3 = \frac{\sqrt{2\pi} I_b}{hV_0 \cos \phi_s} \left| \frac{Z}{n} \right|_{eff}, \quad (3)$$

where I_b is the bunch current. The parameters of the bunch character with the bunch current below and above the threshold have been examined separately for the EUTERPE ring. There, a value of 3Ω for the total broadband impedance $|Z/n|_0$ has been taken for the sake of simplification. For getting a good estimation, we have taken the SPEAR scaling of the effective impedance [4] and the limitation of the free space impedance [5] into account. The results indicate that the single bunch current can not be larger than 1 mA if several mm bunch length is required with a 45 MHz RF frequency and with 100 kV RF voltage. However, if a RF system with 300 MHz and 400 kV is used, a single bunch current can be achieved of several mA at a bunch length of the order of 1 mm.

From Eq.1, it seems no problem to get a very small bunch length by selecting a very small momentum compaction factor. However, in practice, when a bunch current is beyond the limitation given by Eq.2, the bunch length will mainly be determined by the effective longitudinal broad band impedance and RF parameters, but will not be influenced by the momentum compaction.

III. SELECTION OF RF VOLTAGE AT 45 MHZ FREQUENCY

What is a suitable RF voltage at a certain RF frequency? This issue concerns the assurance of several hours of beam lifetime with 100 mA beam current under 400 MeV operating energy.

For the storage ring, the beam lifetime is mainly limited by three factors: quantum fluctuations, residual gas and intra-beam scattering. Considering the effective aperture of the vacuum chamber with 2.3 cm in vertical direction in bending magnets and 4.7 cm in any transverse direction elsewhere [1], the quantum lifetime will be more than 1000 hours for the transverse oscillation. In order

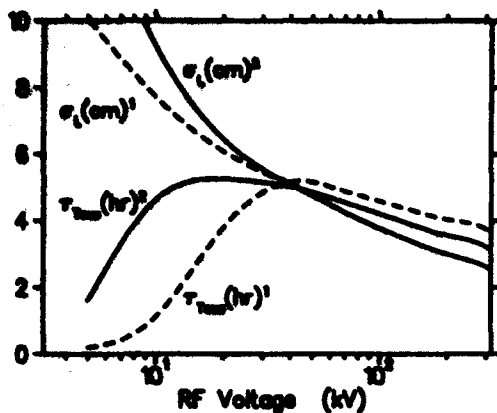


Figure 1: Bunch length and Touschek lifetime versus RF voltage with frequency of 45 MHz. Beam current is 100 mA with 400 MeV. 1: HBSB mode; 2: HLF mode.

to obtain the same quantum lifetime for the longitudinal oscillation, the RF voltage needs to be larger than 10 kV at 45 MHz frequency.

Single, large-angle Coulomb scattering within a bunch will reduce the beam lifetime by causing particle momenta to exceed the momentum acceptance, which is determined by the RF bucket momentum height, the transverse dynamical aperture and the physical aperture. Using the Touschek scattering formulae [3,4] and considering the bunch lengthening, the equilibrium emittance (resulted from a balance among the quantum excitation, intra-beam scattering and radiation damping processes) and the effect of the dispersion on the beam dimensions, we calculate the scattering lifetime in the EUTERPE ring. Fig.1 shows the bunch length and Touschek lifetime as a function of the RF voltage. The suitable RF voltage appears to be somewhere between 10~100 kV, where the Touschek lifetime can be longer than four hours and the equilibrium emittance is almost constant.

Furthermore, for a certain RF frequency, the optimum operating voltage ought to give a RF bucket height which is near the transverse momentum acceptance of the ring. In order to get a long Touschek lifetime and not to cause an obvious increase in the transverse emittance, it looks reasonable to choose 60 kV as a suitable voltage in the EUTERPE ring. This selection of the RF voltage is also good enough for getting a long gas scattering lifetime, which will be seen in later discussion.

IV. EMITTANCE GROWTH AND MINIMUM EMITTANCE

The natural emittance is 5.4 nmrad for the HBSB mode and 168 nmrad for the HLF mode [1]. We have examined the equilibrium emittance with the computer code ZAP [4]. The results are shown in Fig.2. When the energy increases, the radiation damping increases quickly and the emittance tends to the natural value. At the same time the Touschek lifetime increases up to 5 hours. The interesting thing is that the smallest emittance appears

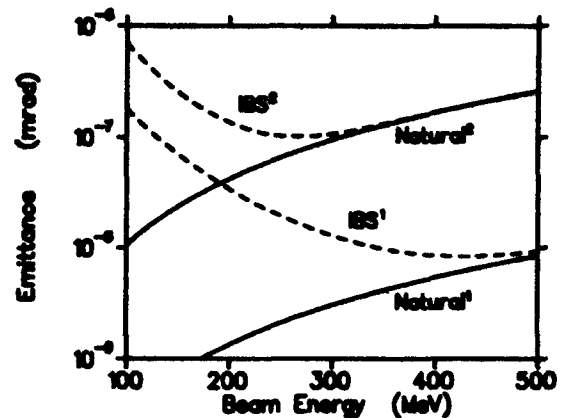


Figure 2: Horizontal emittance versus beam energy. Beam current is 100 mA and RF voltage is 60 kV at 45 MHz. 1: HBSB mode; 2: HLF mode.

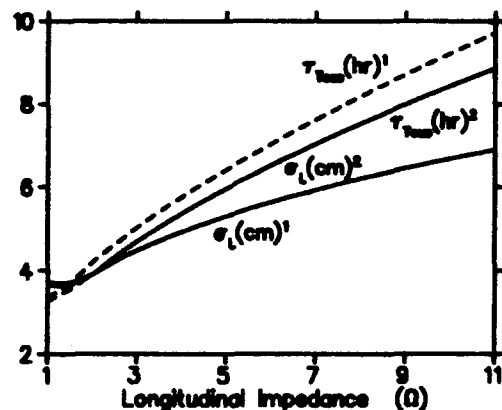


Figure 3: Bunch length and Touschek lifetime versus longitudinal impedance. Beam current is 100 mA with 400 MeV energy and RF voltage is 60 kV at 45 MHz. 1: HBSB mode; 2: HLF mode.

just near the 400 MeV region which is the expected operating region for the EUTERPE ring (It is favourable to a high spectral brilliance). This shows that the designed parameters of the lattice and RF cavity are reasonable. On the other hand, the beam size in the horizontal direction (injection region) is about 4 mm for the HLF mode and is 3 mm for HBSB mode when the beam energy is 75 MeV with the same RF parameters. The Touschek scattering lifetime is longer than one hour for both modes. Hence, this gives no problem for the electron accumulation and acceleration using low-energy injection.

V. EFFECTS OF DIFFERENT IMPEDANCE

From section II, we know that the influence of the turbulent bunch lengthening mainly depends on the effective impedance of the ring. As the impedance increases, the beam bunch becomes longer and wider. This results in intra-beam scattering weakening and Touschek lifetime increase. The bunch length σ_L is almost same in the two different modes except when $|Z/n|_0$ is smaller than 2 Ω , which can be seen clearly from Fig.3. On the other hand,

the impedance has little influence on the emittance in transverse direction except that a short bunch length will cause more intra-beam scattering when the impedance is small. Hence, when the bunch length is not important for the synchrotron radiation, a big longitudinal impedance seems useful to get a long bunch at a certain current and to get a long lifetime.

VI. INFLUENCE OF BEAM INTENSITY ON BUNCH CHARACTER

When the beam current increases up to the threshold I_{th} , the beam bunch length starts to increase and the energy spread also starts to increase. For the HLF mode, the emittance is almost constant with increasing beam current, which indicates that multiple small angle Coulomb scattering is not serious in that case. However for the HBSB mode, the emittance will become large as the beam current increases, which is because the charge density of the bunch current in the HBSB mode is much higher than that in the HLF mode. The emittance with 200 mA beam current is near the double of the natural emittance. Then, the beam lifetime drops by one hour.

VII. GAS SCATTERING LIFETIME

There are essentially four processes on the beam-gas interaction [2], i.e., the elastic scattering on nuclei (ESN), the bremsstrahlung on nuclei (BSN), the elastic scattering on electrons (ESE) and the inelastic scattering on electrons (ISE). At "room temperature", the gas-scattering (GS) lifetime is given by

$$\tau_g = \frac{2.16 \times 10^{-19}}{n_s P \sigma_t} (\text{hours}), \quad (4)$$

where P is the residual gas pressure in Pascal, n_s the number of atoms per gas molecule and σ_t the cross section for the electron losses. It tells us that the GS lifetime is inversely proportional to n_s , P and σ_t . σ_t is mainly determined by the aperture of the ring and by the atomic number for residual gas components. Fig.4 shows the relative contribution of the different types of scattering to the lifetime in the case of the HLF mode, where the RF voltage is 60 kV at 45 MHz. There, the ESN gives the main contribution to $1/\tau_g$. Because the ESN is strongly dependent on the β function of the lattice, the loss of the electron is more serious in the HBSB mode and the GS lifetime is only about half of the value in the HLF mode.

The vacuum in a running electron storage ring is limited by the photon stimulated desorption (PSD) originating from the synchrotron radiation. The vacuum design of EUTERPE is chosen in such a way that we can expect a partial CO pressure of 100 nPa at 400 MeV with 200 mA. We assume that the residual gas mainly consists of hydrogen and CO. Generally, the GS from hydrogen can be neglected. Thus, the expected GS lifetime is 10 hours in the HLF mode, see Fig.4. During the injection, the critical energy of the synchrotron radiation is far below the

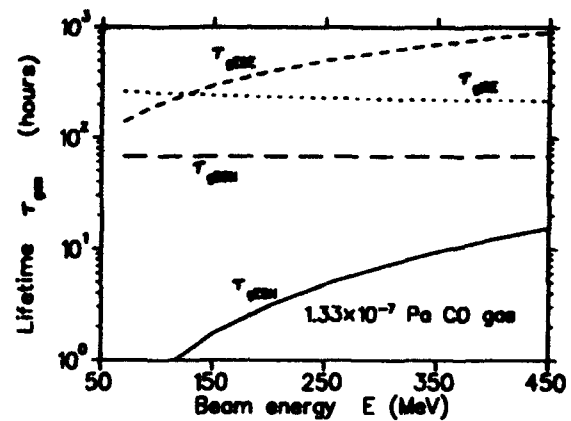


Figure 4: Lifetime resulted from the different processes of beam-gas interactions for HLF mode.

10 eV threshold for PSD. Then, the pressure in the machine will be limited only by the thermal gas desorption of the chamber walls with the expected CO partial pressure lower than 10 nPa corresponding to about 4 hours GS lifetime in the HLF mode. At present, experiments are carried out in our laboratory to find the best material and surface treatment for the vacuum chamber.

VIII. CONCLUSION

The estimation of collective effects in the EUTERPE ring indicates that:

1. Using a 45 MHz and 20-100 kV RF cavity and taking the designed parameters of the lattice, the value of the horizontal emittance at 400 MeV with 100 mA beam current is near the value of the natural emittance and the smallest emittance is 8.5 nmrad in the high brilliance mode.
2. Under these conditions, the Touschek lifetime is longer than four hours in the high light flux mode and high brilliance mode.
3. It is necessary to take a 300 MHz RF system if a high intensity single bunch (with single bunch current more than 1 mA) with a length of the order of 1 mm is needed.
4. When the beam energy is 75 MeV, the gas scattering lifetime and Touschek lifetime can be more than one hour. Therefore, collective effects have no obvious adverse effects on low energy injection in the ring.

IX. REFERENCES

- [1] Boling Xi, J.I.M. Botman, C.J. Timmermans and H.L. Hagedoorn, Nucl. Instr. and Meth. B68 (1992) 101.
- [2] M. Sands, SLAC-121, may, 1979.
- [3] J. Le Duff, Nucl. Instr. and Meth. A239 (1985) 83.
- [4] M. S. Zisman, S. Chattopadhyay and J. J. Bisognano, "ZAP User's Manual", LBL-21270, Dec., 1986.
- [5] A. Faltens and L. J. Laslett, Particle Accelerators, 4 (1973) 151.

A Moment Method Laplace Solver for Low Energy Beam Transport Codes*

Christopher K. Allen, Samar K. Guharay, and Martin Reiser
Laboratory for Plasma Research
University of Maryland, College Park, MD 20742

Abstract

A moment method technique for solving Laplace's equation is presented. The technique is then extended to Poisson's equation to include space charge. The procedure is implemented on a PC and applied to the cases of an electrostatic quadrupole (ESQ) lens and an ellipsoidal bunch in a grounded pipe.

I. INTRODUCTION

Currently we are engaged in the design and development of a Low Energy Beam Transport (LEBT) section for H^- ion beams [1]. We have chosen to employ electrostatic lenses in this design, since for low ion velocities magnetic lenses fail to provide enough focusing for intense beams while gas focusing is intrinsically stochastic. The current prototype consists of 6 ESQ lenses. In order to model the action of such a lens it is necessary to solve Laplace's equation for the particular lens geometry. Once the lens is characterized electrically, the information may be used in other simulation tools to aid in design.

In general, numerical methods must be utilized to solve Laplace's equation. We present a technique which is fully three dimensional yet is efficient enough for implementation on a PC. The efficiency of the technique arises from the fact that it is based on an integral formulation rather than the more common differential form. Instead of solving for electrostatic potential directly, we solve for the surface charge density on conducting bodies. This results in a reduced dimensionality of the problem domain. The integral formulation also readily extends itself to Poisson's equation. Thus, we can model lenses in the presence of charge distributions. Also, since we know the surface charges, we may evaluate capacitances between various lens elements.

II. NUMERICAL TECHNIQUE

A. Laplace's Equation

Letting ϕ denote electrostatic potential, the problem is usually seen in the mathematical form

$$\begin{aligned}\nabla^2 \phi(x) &= 0 & \forall x \in \Omega, \\ \phi(x) &= f(x) & \forall x \in \Gamma.\end{aligned}\quad (1)$$

Here Ω is the 3D region of interest and Γ is its boundary (i.e. $\Gamma = \partial\Omega$). The function f represents the given boundary values and constitutes the data of the problem. Usually Ω represents the beam line and Γ is the surface of a focusing lens, thus f would be the lens voltage. A finite differencing method would typically attack this problem directly. However, we prefer to work with an integral representation of the problem rather than the differential form [2].

$$f(x) = \int_{\Gamma} G(x, \xi) \sigma(\xi) d^2 \xi, \quad (2)$$

where

$$G(x, \xi) = \frac{1}{4\pi |x - \xi|} \quad (3)$$

is the free space Green's function for Poisson's equation. The function σ is introduced as the new unknown for the problem. It is recognized as the surface charge density on the boundary Γ . Once σ is known, ϕ may be recovered via

$$\phi(x) = \int_{\Gamma} G(x, \xi) \sigma(\xi) d^2 \xi \quad \forall x \in \Omega. \quad (4)$$

Note that the dimensionality of the problem has been reduced. In (1), ϕ must be solved on Ω , a 3D subset of E^3 , while (2) is defined only on the 2D manifold Γ .

We employ the method of moments to solve (2), the details of which are presented in [3]. Qualitatively, the technique is very similar to the representation of a quantum mechanical operator in matrix form. We choose a set of expansion functions $\{u_n\}$ on Γ which is used to approximate σ , that is $\sigma(x) = \sum a_n u_n(x)$, for some set of $a_n \in \mathbb{R}$. Another set of functions called weighting (or testing) functions $\{v_m\}$ is also selected. After expanding (2) in $\{u_n\}$ we take the inner product with each of the v_m 's. We end up with a series of linear equations where the a_n 's are the unknowns. This system may be solved by standard matrix methods. We apply a conjugate gradient algorithm to this end [4]; this is an iterative method which seems to provide fastest convergence.

For our moment method we chose for $\{u_n\}$ a set of piecewise constant functions, constant over the face of a triangle. Specifically, Γ is triangulated (approximated by triangles, for example see figure 1) and σ is assumed constant

*Supported by ONR/SDIO

over each triangle. This selection results in a finite element representation to (2). For the weighting functions we selected Dirac delta functions located at the centroid of each triangle (this is known as point-matching). This allows fastest evaluation of the inner products and yields good results as long as the triangles are sufficiently regular.

B. Extension to Poisson's Equation

If we wish to model a charge distribution ρ in the presence of our boundary Γ , it is convenient to exploit the linearity of the integral operator in (2). That is the potential at the boundary must be the sum of that due to both σ and ρ .

$$f(x) = \int_{\Gamma} G(x, \xi) \sigma(\xi) d^2\xi + \int_{\Omega} G(x, \xi) \frac{\rho(\xi)}{\epsilon_0} d^3\xi \quad (5)$$

or

$$f(x) - \phi_p(x) = \int_{\Gamma} G(x, \xi) \sigma(\xi) d^2\xi \quad (6)$$

where ϕ_p is the free space potential due to the charge distribution ρ , given by the second integral in (5). Equation (6) is similar in form to (2) and may be solved by applying the method of moments as before to the boundary data $f - \phi_p$. Therefore, it is only necessary to determine ϕ_p , the free space potential due to ρ , in order to apply the method to Poisson's equation. This may be done numerically or analytically (if available).

III. APPLICATIONS

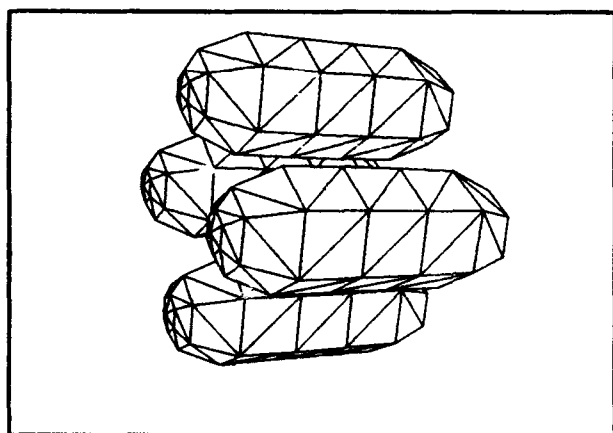


Figure 1: Triangulated ESQ Lens

The preceding technique was implemented with a computer program written in Borland C++ 3.1. The platform was an i486 PC operating at 33 MHz and running Windows 3.1 operating system. All examples were run in double precision arithmetic.

A. ESQ Lens

A 3D potential problem is the modeling of an electrostatic quadrupole lens. Figure 1 shows the computer model of an ESQ lens similar to the type used in [1]. It is formed from 4 cigar-shaped electrodes, the beam would enter from the left. Each electrode is 59 mm long and has a radius of 12 mm. The aperture of the entire lens is 10.5 mm. Two grounding shunts are located at $z = \pm 31$ mm (they are not

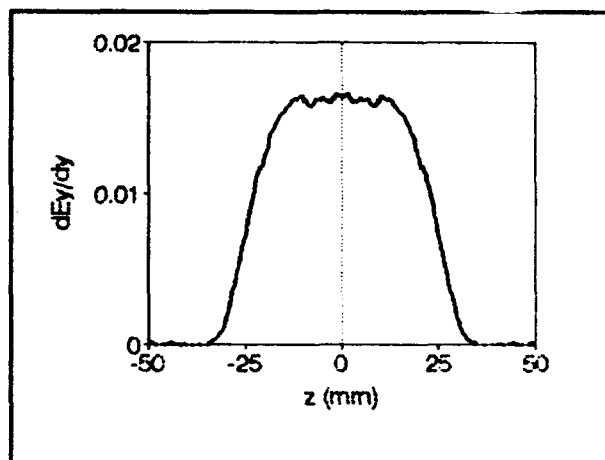


Figure 2: ESQ Lens Focusing Function

shown in figure 1 to avoid clutter) which provide isolation from adjacent lenses.

The single particle focusing effect (the kappa function $\kappa(z)$) from such a lens can be determined from the derivatives dE_x/dx and dE_y/dy on axis. Figure 2 shows the computed data for the y-plane for the case in which the x-plane electrodes are driven to 1V and the y-plane electrodes are held at 1V. The grounding shunt at either end of the lens cause the rapid decay in dE_y/dy .

B. Ellipsoidal Bunch in a Pipe

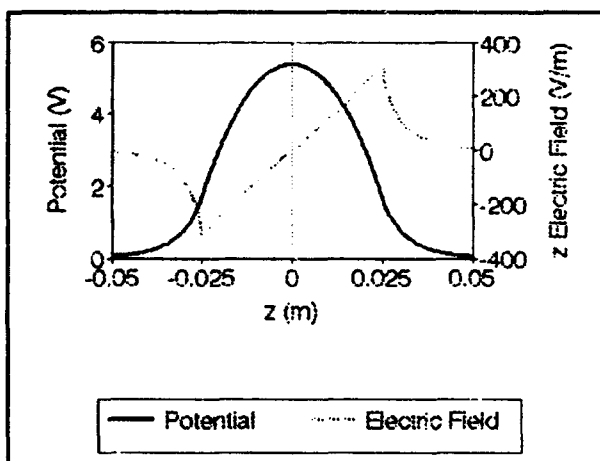


Figure 3: 2.5:1 Ellipsoid in Pipe

We can use the Poisson extension to simulate a uniform charge density ellipsoid in a conducting cylinder. This situation is useful in modeling cold bunched beams propagating through a beam pipe. There exists an analytic solution for the potential of such an ellipsoid in free space [5]. Thus, it is only necessary to model the pipe (surface charge) numerically.

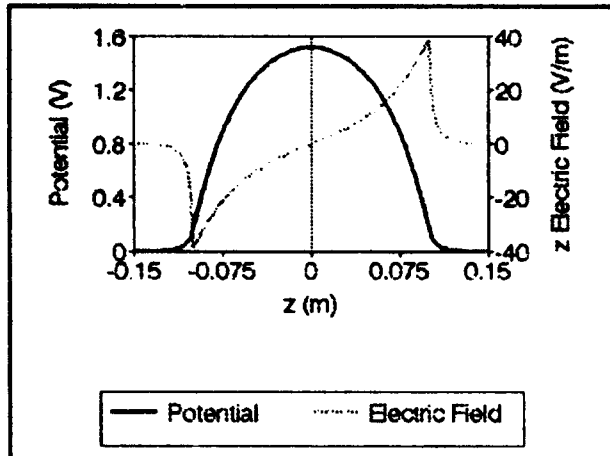


Figure 4: 10:1 Ellipsoid in Pipe

Figure 3 shows the axial potential and z component of electric field for the case of an axis-symmetric ellipsoid with major axis 2.5 cm and minor axis 1 cm inside a pipe of radius 2 cm. In this case the fields are still relatively linear, the image effects from the pipe are slight. However, in figure 4 we see a very nonlinear field for the case of an ellipsoid with major axis 10 cm and minor axis 1 cm. We find that after the bunch length becomes comparable to the pipe radius the image effects play an increasing role. The total charge in both cases is 10^{-11} C.

The above simulations can be used to determine the so called "g-factor" for bunched beams in cylindrical pipes. A detailed discussion of these results can be found in [6].

IV. CONCLUSION

The method of moment technique has several advantages and disadvantages. The overall advantage of the technique stems from the fact that only surfaces are considered, rather than 3D regions. Hence, it is a good method to model complicated or otherwise arbitrary geometries. For the same system order, we get a higher boundary resolution as compared to finite differencing on a grid. Also, since the surface charges are solved for it is possible to calculate the fields anywhere in space, without interpolation. This fact allows us to apply the method to unbounded situations.

When dealing with the situation of conductors in a vacuum the moment technique is in general quite successful. However, if many dielectrics are present it is probably best to use finite differencing. Also, when it is necessary to know the fields over a large set of points, say when doing many particle simulations, it is probably best to use finite differencing. Computing the potential is a moderately expensive process, since we must evaluate (4) at each point, while finite differencing solves for the potential directly.

For the situations discussed the technique is well suited. We need full 3D solutions, yet only for the case of conductors in a vacuum. Also, we are only concerned with the solution data along the beamline axis. Therefore, the number of data points to compute is a minimum.

V. REFERENCES

- [1] S. K. Guharay, C. K. Allen, M. Reiser, K. Saadatmand, and C. R. Chang, "An ESQ Lens System for Low Energy Beam Transport Experiments on the SSC Test Stand", (this conference).
- [2] I. Stakgold, *Green's Functions and Boundary Value Problems* (Wiley, NY, 1979) pp. 508-517.
- [3] C. K. Allen, S. K. Guharay, and M. Reiser, "Solution of Laplace's Equation by the Method of Moments with Applications to Charged Particle Transport", *AIP Conf. Proc. on Computat. Accelerator Physics*, Pleasanton, CA (1993) (to appear).
- [4] T. K. Sarkar and E. Arvas, "On a class of Finite Step Iterative Methods (Conjugate Directions) for the Solution of an Operator Equation Arising in Electromagnetics", *IEEE Trans. Antennas Propagat.*, vol. AP-33, no. 10, pp. 1058-1066, Oct. 1985.
- [5] R. L. Gluckstern, "Scalar Potential for Charge Distributions with Ellipsoidal Symmetry", Fermilab Report TM-1402 (1986).
- [6] M. Reiser, *Theory and Design of Charged Particle Beams* (John Wiley & Sons, NY, to be published in fall 1993), Ch. 5.

Evolution of Hadron Beams under Intrabeam Scattering*

Jie Wei
Brookhaven National Laboratory
Upton, New York 11973

Abstract

Based on assumptions applicable to many circular accelerators, we simplify into analytical forms the growth rates of hadron beams under Coulomb intrabeam scattering (IBS). Because of the dispersion that correlates the horizontal closed orbit to the momentum, the scaling behavior of the growth rates are drastically different at energies low and high compared with the transition energy. At high energies, the rates are approximately independent of the energy. Asymptotically, the horizontal and longitudinal beam amplitudes are linearly related by the average dispersion. At low energies, the beam evolves such that the velocity distribution in the rest frame becomes isotropic in all the directions.

1 INTRODUCTION

During the last decade, many theories have been developed on the subject of intrabeam Coulomb scattering¹⁻⁴ of the hadron beam. These theories assume that the particle distribution remains Gaussian in the six-dimensional phase space. The rates of growth in the rms beam amplitudes are expressed in complex integral forms.

This paper attempts to describe the principle scaling behavior of the growth rates and, based upon which, the evolution of the beam at different energy regimes. In section 2, the previous expressions for the rates are simplified into analytical forms, provided that the lattice of the accelerator mainly consists of regular cells. The dependence of the growth rates on the beam charge state, mass, energy, phase-space area, and the machine transition energy is obtained. Based on these formulae, we derive the scaling laws of the beam evolution in different dimensions under various circumstances. In particular, the results for the high-energy and low-energy regimes are discussed in Sections 3 and 4, respectively.

2 BEAM GROWTH RATES

The growth of the particle beam under intrabeam scattering is usually described by the relative time derivatives of the rms horizontal betatron amplitude σ_x , vertical amplitude σ_y , and fractional momentum deviation σ_p , respectively. Assume that the scatterings mostly occur at small scattering angles, and that the particle distribution remains Gaussian in six-dimensional phase space. When the transverse motions are not coupled, these rates are

obtained at any location of the machine⁴

$$\begin{bmatrix} \frac{1}{\sigma_p} \frac{d\sigma_p}{dt} \\ \frac{1}{\sigma_x} \frac{d\sigma_x}{dt} \\ \frac{1}{\sigma_y} \frac{d\sigma_y}{dt} \end{bmatrix} = \frac{A_0}{2} \int e^{-Dz} \ln(1+C^4 z^2) \begin{bmatrix} n_s(1-d^2)g_1 \\ a^2 g_2 + (d^2 + \bar{d}^2)g_1 \\ b^2 g_3 \end{bmatrix} \times \sin \theta d\theta d\phi dz \quad (1)$$

$$\text{where } A_0 = \frac{cr_0^2 N Z^4 \beta_x \beta_y}{32\pi^2 A^2 \sigma_x^2 \sigma_y^2 \sigma_p \sigma_s \beta^3 \gamma^4}, \quad r_0 = \frac{e^2}{m_0 c^2},$$

$$d = \frac{D_p \sigma_p}{(\sigma_x^2 + D_p^2 \sigma_p^2)^{1/2}}, \quad \bar{d} = \frac{\bar{D}_p d}{D_p}, \quad \bar{D}_p = \alpha_x D_p + \beta_x D'_p,$$

$$a = \frac{\beta_x d}{D_p \gamma}, \quad b = \frac{\beta_y \sigma_x}{\beta_x \sigma_y} a,$$

and

$$D = \cos^2 \theta + b^2 \sin^2 \theta \sin^2 \phi + (a \sin \theta \cos \phi - \bar{d} \cos \theta)^2,$$

$$C = 2\beta \sigma_p [\sigma_y(1-d^2)/r_0]^{1/2},$$

$$g_1 = 1 - 3 \cos^2 \theta,$$

$$g_2 = \cos^2 \theta - 2 \sin^2 \theta \cos^2 \phi + \sin^2 \theta \sin^2 \phi + 6\bar{d} \cos \theta \sin \theta \cos \phi / a,$$

$$g_3 = \cos^2 \theta + \sin^2 \theta \cos^2 \phi - 2 \sin^2 \theta \sin^2 \phi.$$

Here, the prime denotes the derivative with respect to the azimuthal displacement, D_p is the horizontal dispersion, $\alpha_{x,y}$ and $\beta_{x,y}$ are the Courant-Snyder parameters, γ is the Lorentz factor, n_s is equal to 1 if the beam is azimuthally bunched, and is equal to 2 if it is not. For bunched beams, σ_s is the rms bunch length and N is the number of particles per bunch; for un-bunched beams, N is the total number of particles and $\sigma_s = L/2\sqrt{\pi}$, where L is the circumference of the machine. The quantity $d < 1$ is the effective ratio between the longitudinal and horizontal total amplitude. The actual growth rates observed over a time long compared with the revolution period, are calculated by averaging Eq. 1 over the circumference. This averaging process is implicitly implied in almost all the following equations.

Eq. 1 can in many cases be simplified into analytical forms. Firstly, the quantity $\ln(1+C^4 z^2)$ in Eq. 1 has a weak dependence on the beam configuration. It can be substituted² by a constant $2L_c$, where L_c is about 20. With this simplification, the integration over z can be performed. Secondly, we assume that the accelerator consists mostly of regular cells, so that the variation in $D_p/\beta_x^{1/2}$ is small along the circumference. Terms including \bar{D}_p and \bar{d}

*Work performed under the auspices of the U.S. Department of Energy.

in Eq. 1 are thus negligible. Replacing $\sin^2 \phi$ and $\cos^2 \phi$ with their average value $1/2$, Eq. 1 is simplified by integrations over x , θ and ϕ

$$\begin{bmatrix} \frac{1}{\sigma_p} \frac{d\sigma_p}{dt} \\ \frac{1}{\sigma_x} \frac{d\sigma_x}{dt} \\ \frac{1}{\sigma_y} \frac{d\sigma_y}{dt} \end{bmatrix} = 4\pi A_0 L_c F(\chi) \begin{bmatrix} n_b(1-d^2) \\ -a^2/2 + d^2 \\ -b^2/2 \end{bmatrix}, \quad (2)$$

where

$$\chi = (a^2 + b^2)/2 \geq 0. \quad (3)$$

As shown in Fig. 1, the function

$$F(\chi) = \frac{-3 + (1 + 2\chi)I(\chi)}{1 - \chi} \quad (4)$$

with

$$I(\chi) = \begin{cases} \frac{1}{\sqrt{\chi(\chi-1)}} \text{Arth} \sqrt{\frac{\chi-1}{\chi}} & \chi \geq 1; \\ \frac{1}{\sqrt{\chi(1-\chi)}} \arctan \sqrt{\frac{1-\chi}{\chi}} & \chi < 1 \end{cases} \quad (5)$$

is a smooth function of χ . It is positive when $\chi < 1$, zero when $\chi = 1$, and negative when $\chi > 1$. $F(\chi)$ has the asymptotic expression

$$F(\chi) = \begin{cases} \frac{\pi}{2\sqrt{\chi}} & \chi \ll 1; \\ -\frac{\ln \chi}{\chi} & \chi \gg 1. \end{cases} \quad (6)$$

In terms of the normalized transverse emittance $\epsilon_{x,y} = \beta\gamma\sigma_{x,y}^2/\beta_{x,y}$ and longitudinal bunch area $S = \pi m_0 c^2 \gamma \sigma_x \sigma_y / \beta^3 c A$ in phase space, Eq. 2 can be rewritten

$$\begin{bmatrix} \frac{1}{\sigma_p} \frac{d\sigma_p}{dt} \\ \frac{1}{\sigma_x} \frac{d\sigma_x}{dt} \\ \frac{1}{\sigma_y} \frac{d\sigma_y}{dt} \end{bmatrix} = \frac{Z^4 N}{A^2} \frac{r_0^2 m_0 c^2 L_c}{8\beta^4 \gamma \epsilon_x \epsilon_y S} F(\chi) \begin{bmatrix} n_b(1-d^2) \\ -a^2/2 + d^2 \\ -b^2/2 \end{bmatrix}. \quad (7)$$

Except for the form factors χ , d , a , and b that depend on the ratio of the beam amplitudes in different dimension, the rates are linearly proportional to the density in the six-dimensional phase space, and are strongly dependent ($\sim Z^4/A^2$) on the charge state of the particle.

The growths in the longitudinal and vertical amplitudes are both caused by the variation of the velocity in the corresponding direction. The growth in the horizontal amplitude, on the other hand, is caused partly by the variation in the horizontal velocity, and partly by the change in the betatron closed orbit when the momentum of the particle is varied during the collision. It can be easily verified that the first (or second) part dominates when the beam is below (or above) the transition energy of the machine.

The coupling between the horizontal and vertical motion averages the growth rates in the transverse dimension.

If the motion is fully coupled⁴ within time periods much shorter than the IBS diffusion time, the average rates become

$$\begin{bmatrix} \frac{1}{\sigma_p} \frac{d\sigma_p}{dt} \\ \frac{1}{\sigma_{x,y}} \frac{d\sigma_{x,y}}{dt} \end{bmatrix} = \frac{Z^4 N}{A^2} \frac{r_0^2 m_0 c^2 L_c}{8\beta^4 \gamma \epsilon_x \epsilon_y S} F(\chi) \begin{bmatrix} n_b(1-d^2) \\ (-\chi + d^2)/2 \end{bmatrix} \quad (8)$$

3 BEAM EVOLUTION AT HIGH ENERGIES

In a typically circular accelerator, the transition energy γ_T is approximately equal to the average value of β_x/D_p in the regular cells. When the beam energy is high $\gamma \gg \gamma_T$, the growth in horizontal direction results mostly from the variation of the betatron closed orbit during the exchange of the particle momentum ($a^2 \ll d^2$). The growths in horizontal and longitudinal amplitudes are therefore proportional to each other (Eq. 2).

Consider the case that the vertical σ_y is very small, i.e. on the average

$$\frac{\sigma_y}{\sigma_x} < \frac{d}{2} \frac{\gamma_T}{\gamma}, \quad \gamma \gg \gamma_T. \quad (9)$$

It may be verified that $\chi > 1$, and $F(\chi) < 0$. According to Eq. 2, both the horizontal and longitudinal amplitudes shrink, while the vertical one grows. The beam evolves until Eq. 9 is no longer satisfied.

When the vertical amplitude is no longer small so that $\chi < 1$, both horizontal and longitudinal amplitudes grow.⁴ Consider the effective ratio between the horizontal betatron amplitude and longitudinal amplitude, $C_H \equiv n_b n_c \sigma_x^2 / D_p^2 \sigma_p^2$ where n_c is equal to 1 if the horizontal and vertical motions are not coupled, and is equal to 2 if they are fully coupled. Using Eq. 2, the rate of change of C_H can be derived on the average

$$\frac{dC_H}{dt} = 4\pi A_0 L_c d^2 C_H F(\chi) (1 - C_H). \quad (10)$$

This rate is positive if C_H is less than 1, and is negative if C_H is larger than 1. Therefore, σ_x and σ_p grow such that asymptotically the quantity C_H approaches 1, or

$$n_b n_c \sigma_x^2 \approx D_p^2 \sigma_p^2, \quad \gamma \gg \gamma_T. \quad (11)$$

σ_x and σ_p are related only by the average dispersion D_p .

In a typical storage ring like the Relativistic Heavy Ion Collider (RHIC), the beams are stored at energies much higher than the transition energy. Due to coupling and injection conditions, the horizontal and vertical betatron amplitudes are about the same. The growth rates can be explicitly written from Eq. 2 by using Eq. 6

$$\begin{bmatrix} \frac{1}{\sigma_p} \frac{d\sigma_p}{dt} \\ \frac{1}{\sigma_x} \frac{d\sigma_x}{dt} \end{bmatrix} = \frac{Z^4 N}{A^2} \frac{\pi r_0^2 m_0 c^2 L_c}{16\beta^4 \gamma_T \epsilon_x \epsilon_y S} \begin{bmatrix} n_b(1-d^2)/d \\ d/n_c \end{bmatrix}. \quad (12)$$

Their dependence on the energy of the beam, which appears only in the form factor d , is usually weak. After the initial stage of storage, the asymptotic configuration Eq. 11 will be approximately reached ($d \approx n_s n_c / (1 + n_s n_c)$).

4 BEAM EVOLUTION AT LOW ENERGIES

Beam evolution at energies much lower than the transition energy of the machine can be studied similarly. At low energies, $a^2 \gg d^2$, the growth in horizontal amplitude is mostly caused by the variation in the horizontal velocity alone. Eq. 2 indicates that the growths in horizontal and vertical amplitudes are proportional to each other.

Consider the case that the longitudinal σ_p is very small, i.e. on the average

$$\frac{D_p \sigma_p}{\sigma_s} < \frac{\gamma}{\gamma_T} \sqrt{\frac{2}{1 + C_L}}, \quad \gamma \ll \gamma_T, \quad (13)$$

where $C_L \equiv \beta_x^2 \sigma_x^2 / \beta_y^2 \sigma_y^2$ is the betatron velocity ratio between horizontal and vertical directions. It may be verified that $\chi < 1$, and $F(\chi) > 0$. According to Eq. 2, both horizontal and vertical amplitudes shrink, while the longitudinal one grows. The beam evolves until Eq. 13 is no longer satisfied.

When the longitudinal amplitude is no longer small so that $\chi > 1$, both horizontal and vertical amplitudes grow. Using Eq. 2, the rate of change of C_L can be derived

$$\frac{dC_L}{dt} = -4\pi A_0 L_e a^2 C_L F(\chi)(1 - C_L). \quad (14)$$

σ_x and σ_y grow in such a way that asymptotically the quantity C_L approaches 1. Combining with Eq. 13 and the previous results, we therefore obtain the asymptotic beam configuration at low energies

$$\frac{\sigma_x}{\beta_x} \approx \frac{\sigma_y}{\beta_y} \approx \frac{\sigma_p}{\gamma}, \quad \gamma \ll \gamma_T. \quad (15)$$

The three quantities in Eq. 15 are proportional to the horizontal, vertical, and longitudinal velocities in the rest frame of the particles, respectively. Eq. 15 implies that the beam evolves such that the velocity distribution in the rest frame becomes isotropic in all the three directions.

5 CONCLUSIONS AND DISCUSSIONS

Based on assumptions applicable to many circular accelerators, we simplified the general integral expressions (Eq. 1) of the IBS growth rates into analytical forms (Eq. 2). The rates are expressed in terms of the beam charge state, mass, energy, phase-space area, and the machine transition energy, both for the un-coupled (Eq. 7) and fully coupled (Eq. 8) cases. They have been shown to be linearly proportional to the particle density in the six-dimensional phase space. Because of the dispersion that correlates the horizontal closed orbit to the momentum, the effect of intrabeam scattering is different at different energy regime. At energies much higher than the transition energy, the growth rates have been shown to be approximately independent of the energy (Eq. 12).

Quantitative comparisons have been performed on the average growth rates between the simple estimate (Eq. 7) and the detailed evaluation (Eq. 1) including⁴ lattice variation using the actual RHIC lattice. For both the injection (low energy) and storage (high energy) cases, the relative deviation between them is about 20%.

The evolution of the beam in different dimensions has been investigated at energies both much higher and much lower than the transition energy. At high energies, the asymptotic beam amplitudes in horizontal and longitudinal direction are shown to be linearly related by the average dispersion (Eq. 11). At low energies, on the other hand, the beam evolves such that the velocity distribution in the rest frame becomes isotropic in horizontal, vertical, and longitudinal directions (Eq. 15).

During the entire analysis it has been assumed that the beam distribution remains Gaussian in the phase space. This assumption is valid only when the beam amplitudes are small compared with the machine aperture. In the case that beam loss occurs due to aperture limitation, different approaches⁵ have to be adopted.

6 ACKNOWLEDGEMENTS

The author thanks G. Parzen for the helpful discussions and tutoring, and S. Peggs for the stimulating discussion.

REFERENCES

1. A. Piwinski, Proc. CERN Accelerator School, 1984, p405; 1991, p.226.
2. J. Bjorken and S. Mtingwa, Particle Accelerators, 13, 115 (1983).
3. M. Martini, CERN PS/84-9 (AA) (1984).
4. G. Parzen, Nucl. Instr. Meth. A256, 231 (1987); Proc. 1988 EPAC, Rome, p.821.
5. J. Wei and A. G. Ruggiero, Proc. 1991 Particle Accelerator Conference, San Francisco, p.1869.

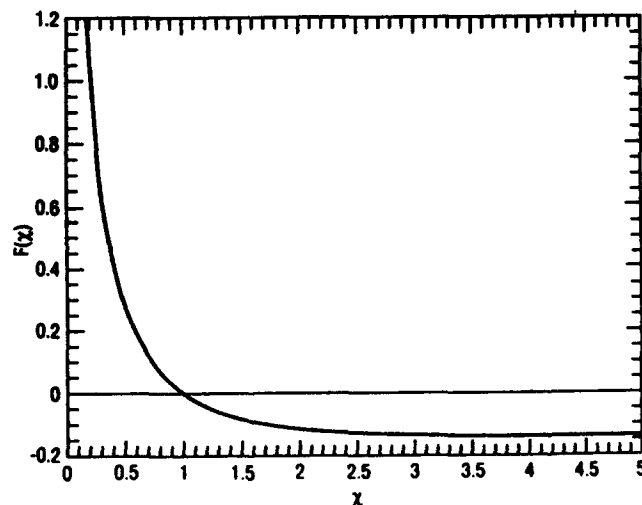


Fig. 1. Function $F(\chi)$ with $0 \leq \chi < \infty$.

Simulation Study of Ion Trapping in PLS Storage Ring*

J. Jung and I. Ko

Pohang Accelerator Laboratory, POSTECH

P. O. Box 125, Pohang 790-600, Korea

Abstract

Ion trapping phenomena in the PLS storage ring have been studied by computer simulation in the view point of tune shift effect of the electron beam. Ions created by strong synchrotron radiation in the vacuum chamber are trapped and accumulated in the electron beam potential, and then the beam and the ions move in the potential of each other. Tune shifts in terms of various beam currents show a stable-unstable band structure representing the relationship of the tunes. For the unstable tune values, a partial beam filling and clearing electrodes are used to clear the ions.

1 INTRODUCTION

Circulating electron beams in the storage ring generate strong synchrotron radiation. Even though the storage ring maintains an ultra-high vacuum condition, strong radiation and beam itself ionize the residual gas molecules. These ions can be trapped in the electron beam path. This phenomenon, called ion trapping, can lead to degradation of beam performances, and sometimes, can cause beam instability or beam blow-up. Earlier studies on the motion of single ions implied many things about the mechanism and consequences of the ion trapping phenomenon. In this report, the simulation results using many ions and various filling patterns are presented, especially with respect to the tune shift.

2 THEORY

2.1 Electric Field

A circulating electron beam has the following charge distribution:

$$\rho(x, y) = -\frac{eN_e}{2\pi\sigma_x\sigma_y} e^{-\left(\frac{x^2}{2\sigma_x^2} + \frac{y^2}{2\sigma_y^2}\right)}, \quad (1)$$

where σ_x and σ_y are beam sizes in x and y direction, respectively, and N_e for the number of electrons in the beam bunch. This leads to the electric fields such as:

$$E_x - iE_y = -\frac{ieN_e e^{(b-ia)^2}}{2\epsilon_0 \sqrt{2\pi\Delta\sigma^2}} [\text{Erf}(b-ia) - \text{Erf}(b/r - iar)], \quad (2)$$

*Work supported by Pohang Iron & Steel Co. and Ministry of Science and Technology, Korea

where the error function $\text{Erf}(z)$ is defined as

$$\text{Erf}(z) = \frac{2}{\sqrt{\pi}} \int_0^z e^{-t^2} dt. \quad (3)$$

Here,

$$\Delta\sigma^2 = \sigma_x^2 - \sigma_y^2, a = \frac{x}{\sqrt{2\pi\Delta\sigma^2}}, b = \frac{y}{\sqrt{2\pi\Delta\sigma^2}},$$

and $r = \sigma_x/\sigma_y$. Instead of using the complex error function in Ref. [1], we used a real error function. Thus, the result is numerically calculable by the Mathematica™ program.

2.2 Equation of Motion

The typical length of the electron beam is about 32 ps for PLS storage ring. This is much shorter than the minimum interaction interval t_b which is 2 ns. The interaction between ions and electron beams can, thus, be considered to be instantaneous. Ions experience impulse due to the passing electron beam such as

$$\begin{aligned} m_i \Delta \dot{x}_i &= q_i/c E_x(x_i - x_b, y_i - y_b), \\ m_i \Delta \dot{y}_i &= q_i/c E_y(x_i - x_b, y_i - y_b). \end{aligned} \quad (4)$$

At the same time, the motion of the electron bunch is also affected by these ions by

$$\begin{aligned} \gamma m_e N_e \Delta \dot{x}_b &= -q_i/c E_x(x_i - x_b, y_i - y_b), \\ \gamma m_e N_e \Delta \dot{y}_b &= -q_i/c E_y(x_i - x_b, y_i - y_b). \end{aligned} \quad (5)$$

Here, m_i , m_e are masses for the ion and the electron, respectively. q_i is the electric charge of the ion, and γ is the relativistic factor. x_i (y_i) and x_b (y_b) are x (y) locations for the ion and the center of electron beam, respectively. After the instantaneous interaction, ions drift freely during t_b or until the next electron bunch arrives in the case of partial filling. The electron beam moves along the beam trajectory with a constant speed c . During the time interval t_b , the phase advances of the electron beam are $\Delta\phi_x = \nu_x c t_b$ in x direction and $\Delta\phi_y = \nu_y c t_b$ in y direction. Here ν_x and ν_y are tunes in x and y direction.

2.3 Tune

Tunes of the electron beam can be calculated by Fourier transform of the beam motion. In y direction, for example, we define the Fourier amplitude as

$$A(\omega) = \int_{-\infty}^{\infty} y(t') e^{-i\omega(t'-t)} W(t-t') dt', \quad (6)$$

where the weight function W is

$$W(t - t') = \frac{1}{\tau} e^{-(t-t')/\tau}. \quad (7)$$

The weight function is introduced to save computational time. The ω resolution is given as $d\omega \sim 2\pi/\tau$. If we choose $\tau \sim 10 \mu\text{sec}$, about 0.1 MHzs frequency resolution can be obtained in the simulation. The tune is obtained by plotting $A(\omega)$ in terms of the frequency.

3 SIMULATION

3.1 Parameters

The simulation is based on PLS storage ring parameters, which are summarized in Table 1. Since ions move very slowly compared to the electron beam, the interaction between ions and electron beams is assumed to be confined to the xy plane. The electron beam size is also fixed during the simulation. There is no external electric or magnetic field, so the ion trapping takes place in the area such as long insertion straight section where the vacuum pressure is relatively poor. Some important values used in the simulation are listed in Table 2.

Table 1: Parameters for PLS storage ring

Beam Energy	2 GeV
Circumference	280.56 m
Beam Current	400 mA (multibunch)
Natural Emittance	12.1 nm-rad
Natural Energy Spread	6.8×10^{-4}
Harmonic Number	468 ($= 2^2 \times 3^2 \times 13$)
RF Frequency	500.087 MHz
Betatron Tunes	
Horizontal	14.28
Vertical	8.18
Synchrotron Tune	0.011
Momentum Compaction	1.81×10^{-3}
Natural Bunch Length	5.04 mm (rms)
Beam Size†	
Horizontal	348 μm
Vertical‡	66 μm
Damping Time	
Horizontal	16.6 msec
Vertical	16.6 msec
Longitudinal	8.34 msec

† at the center of insertion straight section.

‡ 10% emittance ratio is assumed.

3.2 Ions

Number of ions created due to the synchrotron radiation can be determined by the neutralisation η which is defined as a ratio of ions to the electrons. Here, we assume that η is 0.5%. In the simulation, 117 ions of charge Zq_e are used. The multiplication factor Z is determined by the neutralisation η and the electron beam current I . The

mass number of the ion is 28 which represents a nitrogen ion (N_7^+) or a carbon monoxide ion (CO^+). These are usual background ions found in the storage ring vacuum chamber.

Table 2: Simulation parameters

Beam Size (rms)	
Horizontal (σ_x)	0.35 mm
Vertical (σ_y)	0.16 mm
No. of Ions	117
Ion Mass	28
Neutralisation	0.5%
Time Step (t_0)	1/500.087 μsec

3.3 IONTRAP Code

The simulation code IONTRAP is written in the C++ language. Before the code calculates equations of motion, electric fields shown in Eq. (2) are calculated by Mathematica, and the results are used as an input to the IONTRAP. This reduces computational time drastically, so the code runs on an ordinary personal computer. The electric field profile is shown in Figure 1.

4 RESULTS

Effects due to the ion-beam interaction can be observed when the beam circulates the storage ring within 100 turns. One hundred turns are equivalent to about 0.1 msec for the PLS storage ring. It is well known that leaving gaps between consecutive bunches can cure ion trapping phenomena [2]. Figure 2 shows tune changes in terms of different gap sizes for different beam currents. The tune change is as bad as 0.1 in this simulation. As expected, the tune change is significant when the gap is not large enough. For a fixed beam current, the tune shift is smaller as the gap is larger, as shown in Figure 4. When the gap size is larger than 5% of the whole bucket, the tune change is reduced to within 0.01. However, Figure 4 shows that there is still a certain range of beam currents which gives relatively larger tune shifts when the gap size is fixed. It suggests that a sequential bucket filling is better than stacking electrons into the partially filled buckets during the injection period when the ion trapping phenomena are considered. A clearing electric field is applied in order to reduce the tune change further as shown in Figure 5. About 1 kV/m DC potential is necessary to decrease the tune change to less than 0.001.

5 REFERENCES

- [1] M. Bassetti and G.A. Erskine, "Closed Expression for the Electrical Field of a Two-dimensional Gaussian Charge," CERN-ISR-TH/80-06 (1980).
- [2] M. Q. Barton, "Ion Trapping with Asymmetric Bunch Filling of the NLS VUV Ring," *Nucl. Inst. and Methods*, A243, p. 378 (1986).

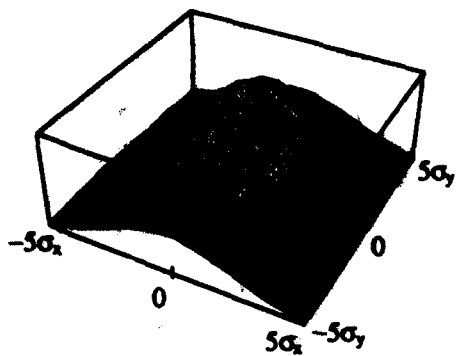


Fig. 1: Electric field profile.

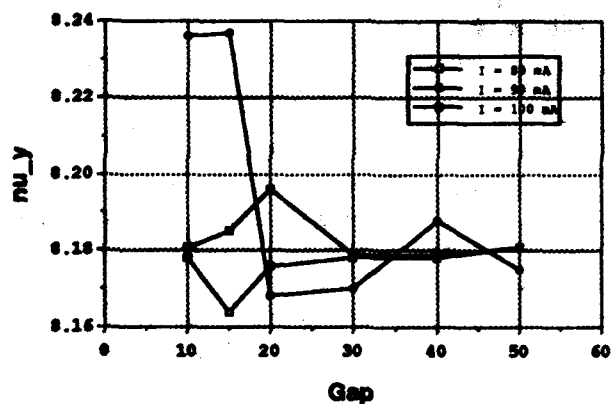
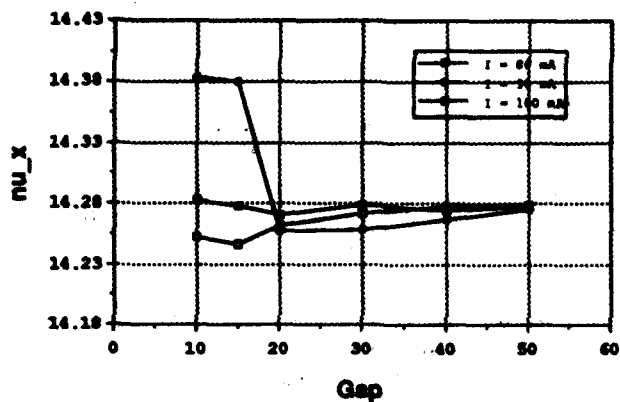


Fig. 2: Tune changes in x(upper) and y(lower) direction.

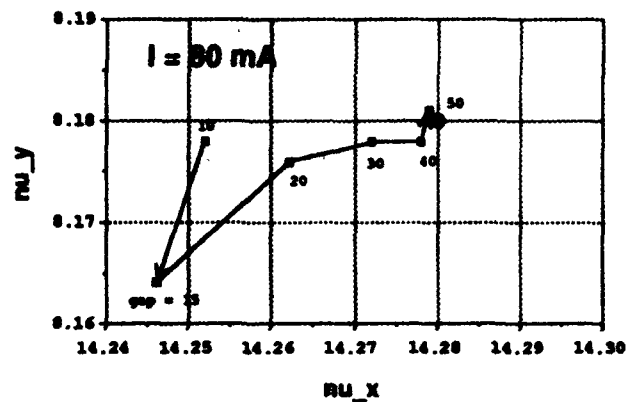


Fig. 3: Tune change in terms of gap size at $I=80$ mA. The open circle is the operating point.

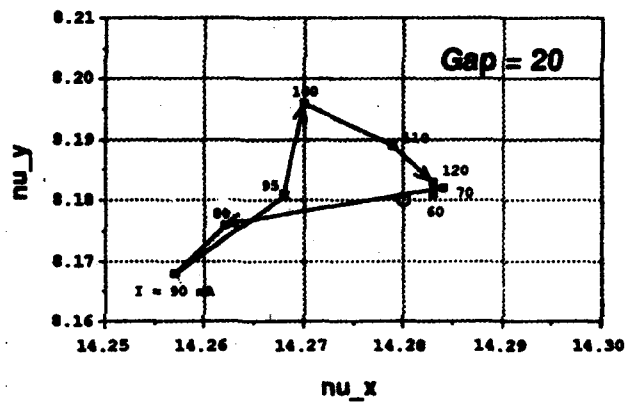


Fig. 4: Tune change in terms of beam current at gap size is 20. The open circle is the operating point.

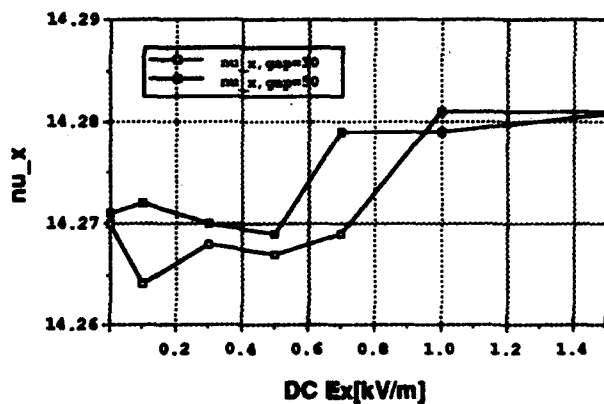


Fig. 6: Tune changes when the clearing voltage is applied.

BEAM HALO FORMATION FROM SPACE-CHARGE DOMINATED BEAMS IN UNIFORM FOCUSING CHANNELS

J. S. O'CONNELL*, T. P. WANGLER, R. S. MILLS, and K. R. CRANDALL†

Los Alamos National Laboratory, Los Alamos, NM 87545

*Booz, Allen and Hamilton, Inc., Arlington, VA 22202

†AccSys Technology, Inc., Pleasanton, CA 94566

Abstract

In space-charge dominated beams the nonlinear space-charge forces produce a filamentation pattern, which results in a 2-component beam consisting of an inner core and an outer halo. The halo is very prominent in mismatched beams¹⁻³ and is a concern because of the potential for accelerator activation. We present new results about beam halo and the evolution of space-charge dominated beams from multiparticle simulation of initial laminar beams in a uniform linear focusing channel, and from a model consisting of single particle interactions with a uniform-density beam core. We study the energy gain from particle interactions with the space-charge field of the core⁴, and we identify the resonant characteristic of this interaction as the basic cause of the separation of the beam into the two components⁵. We identify three different particle-trajectory types, and we suggest that one of these types may lead to continuous halo growth, even after the halo is removed by collimators.

I. PHASE-SPACE DYNAMICS FROM MULTIPARTICLE SIMULATION

We use multiparticle simulation to study a round continuous beam in a uniform linear focusing channel with purely radial focusing. For the studies described in this paper, the computer code has been run with 3000 simulation particles through 56 steps per plasma period. We have chosen to study the dynamics of initially Gaussian, laminar (zero-emittance) beams, where the initial density distributions are truncated at three standard deviations. In Fig. 1a we show the radial or $r - r'$ phase space at 20 plasma periods for an initial mismatch parameter $M = 1.5$, where the mismatch parameter gives the ratio of the initial beam radius to the matched radius. We assign an initial positive radius to all particles, but if during the simulation a particle crosses the axis, we change the sign of the radius before plotting a point in $r - r'$ space. Fig. 1a shows the inner core and the outer halo filament as distinct structures. At present there is no established criterion for defining the halo. We define the core and the halo by choosing a core ellipse in $r - r'$ space with the same Courant-Snyder ellipse parameters as the rms ellipse with an emittance that we think encloses most of the core and excludes most of the halo.

*Work supported in part by Los Alamos National Laboratory Institutional Supporting Researches under the auspices of the United States Department of Energy.

†Supported in part by SDIO-84-92-C-0025

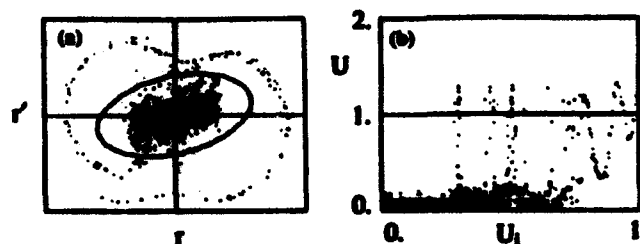


Figure 1. Results at 20 plasma periods from multiparticle simulation of an initial Gaussian-density laminar beam in a uniform linear focusing channel. The initial rms size in x is larger than the matched value by a factor $M = 1.5$. We show a) $r - r'$ phase space, b) particle energy U versus the initial particle energy U_i .

Fig. 1b shows the distribution at 20 plasma periods of zero-current particle energy U versus initial U_i . The core appears as the concentration of particles at small U . All particle energies are normalized so that the particle with the maximum initial energy (largest initial radius) has $U_i = 1$. Fig. 1b shows that after 20 plasma periods, the beam does contain particles with $U > 1$, which have more energy than the most energetic initial particle. The halo is mostly populated by the particles that have large initial energy, i.e., have large initial radius. However, a small fraction of particles with small initial radius (only one such particle is present in the 3000 particle run and it is not visible in Fig. 1) also populate the halo, and the fraction of these halo particles with small initial energy increases rapidly with increasing mismatch parameter.

The characteristics of the beams after 20 plasma periods are shown in Table 1. All particle energies in Table 1 are normalized in the same way, to unity for the initial matched beam case. Column 1 shows the initial mismatch parameter M . Column 2 shows the values of the core emittance to rms emittance ratio. Column 3 shows that the maximum particle energy increases from the initial value by 10% for the matched case, and increases by 50% for a mismatch of $M = 2.5$. The last two columns show the percentage of final particles in the halo and the percentage of final particles with energy that exceeded the maximum initial particle energy. We see again that the percent of particles in the halo increases rapidly with increasing mismatch, and reaches a value of over 30% for an initial mismatch parameter of 2.5. We are unable to define the halo unambiguously for $M=1$.

Table 1
Beam Halo Characteristics at 20 Plasma Periods for
Beams with Different Initial Mismatch

M	$\epsilon_{\text{core}}/\epsilon_{\text{rms}}$	$U_{i,\text{max}}$	U_{max}	$U_{\text{max}}/U_{i,\text{max}}$	% in halo	% $U > 1$
1.0	—	1.00	1.10	1.10	—	0.1
1.5	7	2.25	2.97	1.32	5.4	2.2
2.0	3	4.00	5.90	1.48	16.	1.7
2.5	2	6.25	9.38	1.50	31.	2.0

II. PHASE-SPACE DYNAMICS FROM UNIFORM-DENSITY CORE MODEL

A. Energy Transfer Between a Single Particle and an Oscillating Core.

To gain some physical insight into what we observe in the simulation, we consider the model of a zero-emittance, uniform-density beam core of radius R , propagating in a uniform linear focusing channel. The transverse equation of motion of the beam radius is given by the envelope equation

$$\frac{d^2 R}{dt^2} + \omega_0^2 R - \frac{K}{R} = 0,$$

where ω_0 is the natural frequency at zero current of a single particle, and nonrelativistically $K = qI/2\pi\epsilon_0 m v$, where q , m , and v are the charge, mass, and axial velocity of the particles, I is the beam current, and ϵ_0 is the permeability of free space. For the matched beam $d^2 R/dt^2 = 0$, and the matched beam radius is $R = R_0 = \sqrt{K}/\omega_0$. The transverse equation of motion of a single test particle is

$$\frac{d^2 x}{dt^2} + \omega_0^2 x - F_{sc} = 0,$$

where F_{sc} is the space charge force, given for a uniform density by

$$F_{sc} = \begin{cases} Kx/R^2, & x < R. \\ K/x, & x > R. \end{cases}$$

The $I=0$ particle energy is not constant because of the space-charge repulsion of the core. For a matched core radius, there is no net change in energy averaged over a complete period of particle motion. For an oscillating, mismatched core there can be a net change in particle energy. For a small, radially symmetric core mismatch δR about the equilibrium radius R_0 , we can write for $x < R$,

$$\frac{d^2 x}{dt^2} + A\Omega^2 x \cos \Omega t \equiv 0,$$

where $\delta R/R_0 = A \cos \Omega t$ and $\Omega = \sqrt{2}\omega_0$. This approximate result is a special case of the Mathieu equation, which suggests periodic solutions in x for particle frequencies below half the core frequency Ω . When the particle frequency is half the core oscillation frequency, we expect a resonant growth of the x amplitude. The resonant condition requires a constant phase relationship between the particle and the core. We expect that the effect of the nonlinearity outside the core

is to create a self limit to the resonance because of the change of frequency with amplitude, which causes a loss of phase coherence. The core oscillation causes a rate of energy gain for a particle with velocity \dot{x} within the beam core, given by

$$\frac{dU}{dt} = \vec{F} \cdot \vec{\dot{x}} = -A\Omega^2 x \dot{x} \cos \Omega t.$$

A particle that passes through the beam core can either gain energy, lose energy, or have no net energy change, depending on the relative phases of the particle displacement, the transverse velocity, and the core radius oscillation.

B. Trajectory Classification

A study of the trajectories of individual particles has been helpful for understanding the dynamics of the halo formation. The uniform-core model described above provides an important reference point for such a study. We have numerically integrated the trajectories of particles through the field of the uniform core for the $M = 1.5$ case, launching particles with different initial x values, and with $R = 1.5$, $\dot{R} = 0$, and $\dot{x} = 0$. We find three distinct classes of trajectories, which for the $M = 1.5$ case, we describe in terms of the initial x displacement as follows: a) For $x < 1.5$ the particles oscillate in phase with the core radius about their own equilibrium radius. These are stable radial plasma oscillations within the core, and we refer to these orbits as plasma trajectories. b) For $x > 2.0$ the particles oscillate about the origin with an orbit in phase space that looks like an ellipse that is pinched inward along the velocity axis (the pinching is caused by the space-charge force of the core). The amplitudes are variable and each orbit is confined to a narrow band in phase space. These particles occupy the halo and we call these orbits betatron trajectories. c) Finally, for $1.5 < x < 2.0$ the particles execute a more complex motion. They may initially spend part of the time executing plasma-like oscillations within the core, after which they move into the proper phase relationship with respect to the core oscillations such that they can gain energy and move into an outer betatron-like orbit in the halo. These particles can also reverse the pattern and return from the outer betatron-like orbit in the halo to a plasma-like orbit within the core. We refer to these as hybrid trajectories, and we find that these particles are strongly affected by resonant energy transfer with the oscillating core, which can cause either energy loss into the core, or energy gain into the halo. Figure 2 shows examples of these trajectories in phase space traced for 20 core oscillation

periods using the uniform core model, with $\omega_0 = 1$, and $K = 1$, launched with the following initial conditions: $R = 1.5$, $\dot{R} = 0$, and $\dot{x} = 0$, and a) $x = 1.0$, b) $x = 1.55$, c) $x = 1.65$, and d) $x = 2.2$. The outlines of the core-radius oscillation are shown on each of the plots, extending from $x = \pm 0.5743$ to $x = \pm 1.50$. These examples show a pure plasma trajectory in Fig. 2a, a hybrid trajectory that has not yet left the core in Fig. 2b, a hybrid trajectory in the halo in Fig. 2c, and a periodic betatron trajectory in the halo in Fig. 2d.

The discovery of the hybrid trajectories is important because of the implications for the effectiveness of collimation. Suppose at a given time the beam is collimated to remove the existing halo. Any such collimation procedure, even if carried out under the most ideal of circumstances, would be able to remove only the particles with betatron trajectories and the particles with hybrid trajectories, which at that time populate the halo. Any hybrid orbits that are within the core at the time of collimation may be expected to gain energy at some later time and repopulate the halo. Therefore, while collimation does some good, its effectiveness would be limited by the percentage of hybrid particles that would repopulate the core within the time scale of interest. Although this may appear to be a serious limitation of the collimation, it appears in the uniform beam model that the hybrid amplitudes in the halo are bounded. For this example collimation at a radius of 1.5 units could still be effective in limiting all hybrid amplitudes to less than $x = \pm 2.7$.

III. ACKNOWLEDGMENTS

We would like to thank George Lawrence and Jim Stovall for their support at Los Alamos of this work.

IV. REFERENCES

- [1] A. Cucchetti, M. Reiser, and T. P. Wangler, "Simulation Studies of Emittance Growth in RMS Mismatched Beams," Proceedings of 1991 Particle Accelerator Conference, San Francisco, California, May 6-9, 1991, IEEE Conf. Record 91CH3038-7, p 251.
- [2] T. P. Wangler, "Emittance Growth from Space-Charge Forces," High-Brightness Beams for Advanced Accelerator Applications, AIP Conf. Proc. 253,21(1991).
- [3] T. P. Wangler, "Beam Halo in High-Intensity Beams", presented at the Computational Accelerator Physics Conference (CAP93), Pleasanton, CA, February 22-26, 1993.
- [4] R. A. Jameson has developed this idea independently. See R. A Jameson, "Beam-Halo from Collective Core/Single-Particle Interactions", Los Alamos Report LA-UR-93-1209, March, 1993.
- [5] R. L. Gluckstern suggested in an informal note "Possible Model for Halo Formation", March, 1993, the idea that a resonant nonlinear interaction between individual particles and an oscillating core could lead to a depopulation of a region of phase space and that would explain the absence of particles between the core and the halo.

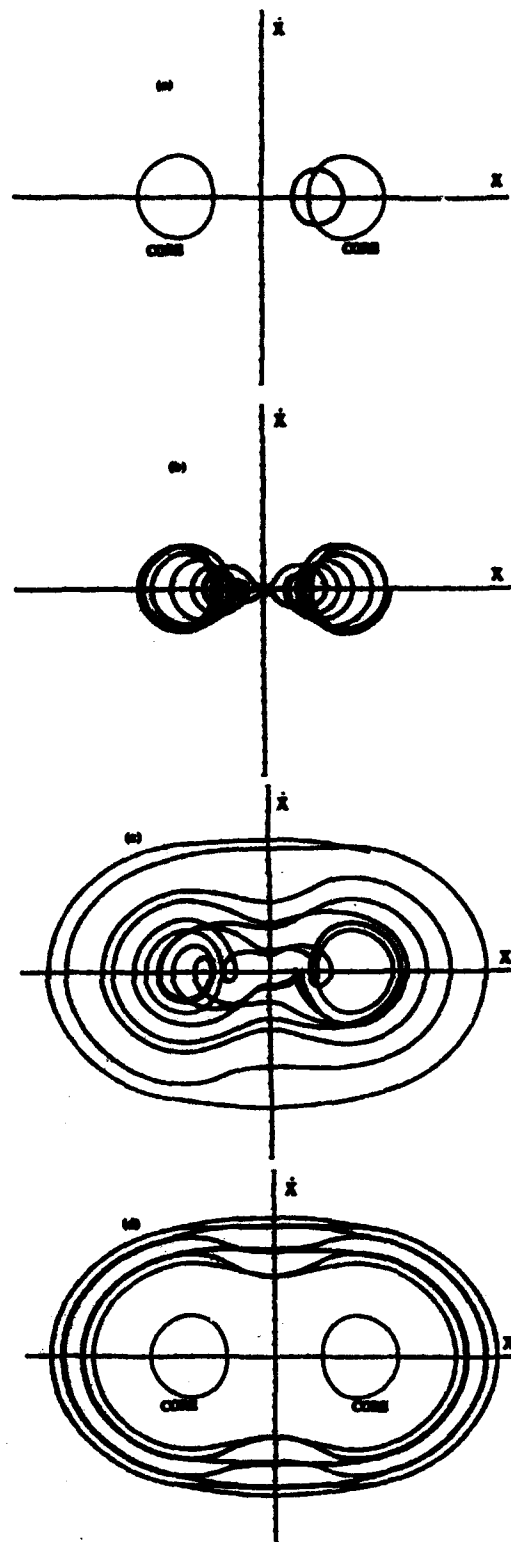


Fig. 2. Trajectories in phase space traced for 20 core oscillation periods using the uniform core model, with $\omega_0 = 1$, and $K = 1$, launched with the following initial conditions: $R = 1.5$, $\dot{R} = 0$, and $\dot{x} = 0$ and a) $x = 1.0$, b) $x = 1.55$, c) $x = 1.65$, and d) $x = 2.2$. The outlines of the core-radius oscillation are shown on each of the plots, extending from $x = -1.50$ to $x = -0.5743$ and from $x = 0.5743$ to $x = 1.50$.

Computer Simulation of the Maryland Transport Experiment.*

I. Haber

Plasma Physics Division, Naval Research Laboratory
Washington, DC 20375 USA

D. A. Callahan, A. B. Langdon

Lawrence Livermore National Laboratory, University of California
Livermore, CA 94550 USA

M. Reiser, D. X. Wang, J. G. Wang

Laboratory for Plasma Research, University of Maryland
College Park, MD 20742 USA

Abstract

The longitudinal dynamics of the high-perveance long-pulse electron beam in the Maryland Transport Experiment is examined for the special case of an initially parabolic bunch. Because the longitudinal dynamics can depend on details of time-dependent transverse beam parameters which are difficult to measure, sensitivity studies using r - z simulations have been used to demonstrate that the details of longitudinal beam evolution are insensitive to transverse mismatch, and the bunch length evolution can be accurately described by the one-dimensional envelope equation with the "geometry factor" appropriately chosen. Comparison of experimental data to r , z simulation and to the envelope solution is presented.

I. INTRODUCTION

The University of Maryland Transport Experiment is a flexible apparatus designed to explore the fundamental physics of space-charge-dominated beam transport. In the current configuration, a high perveance gridded gun injects an electron beam into a transport line with 38 interrupted solenoid focusing elements. Details of recent experiments, concentrated primarily on studying longitudinal and multi-dimensional beam physics, are described elsewhere[1-3]. One of the features of the apparatus which is important to the work described here is the gridded gun which is used to program the current waveform. This permits examination of longitudinal beam physics, which can be nonlinear and multi-dimensional, as the initial bunch shape is varied.

In view of past success in obtaining agreement between experiments, and simulation and theory, on the nonlinear transverse beam dynamics in the Maryland Experiment[4], comparisons are being extended to include the longitudinal and multi-dimensional physics in the recent experiments. However, it is difficult in the current apparatus to obtain detailed time-resolved data on the transverse beam characteristics. We therefore describe below the use of simulations to demonstrate, for the simple case of an expanding parabolic bunch, insensitivity of the longitudinal dynamics to the details of the transverse match. The r , z simulations, which have been performed using the WARP[5,6] PIC code, are compared to the experimental data as well as to the simple one-dimensional envelope model which can be used to describe the special case of a parabolic bunch.

II. DYNAMICS OF A PARABOLIC BUNCH

For a beam bunch which is long compared to the radius of the beam pipe, the beam longitudinal self-electric field can be approximated by[7] $E_z \propto g \partial \lambda / \partial z$, where λ is the line density and g is a geometry factor which depends on the ratio of beam radius to pipe radius. If the bunch shape is parabolic, the longitudinal self-field is then a linear function of the distance from the bunch center. If the longitudinal velocity distribution of the bunch is appropriately chosen, an envelope equation[8] can then be derived to describe the bunch dynamics. In the experiment, the longitudinal beam temperature is sufficiently low that the thermal pressure, or emittance, contribution to the beam expansion is negligible compared with the space-charge contribution. Details of the longitudinal velocity distribution do not then significantly influence the bunch expansion.

If the one-dimensional description of the beam were adequate, an initially parabolic bunch would retain its parabolic bunch shape and its expansion would be well described by the longitudinal envelope equation. However, even in the one-dimensional description, the self-electric field depends on the beam radius through the geometry factor g , which multiplies the derivative of the line density. This "g-factor" can be written in the form $g = C + 2 \ln(b/a)$ where b and a are the pipe and beam radius respectively, and C is a factor, generally between zero and unity, which will be further discussed below. It should be noted that, in general, g will vary along the bunch, as well as along the transport system, as the beam expands longitudinally and its radius decreases in order to remain in equilibrium with the transverse focusing forces.

Despite the possible influence of the beam radius on the longitudinal beam dynamics, no direct data are presently available on the time-resolved variation in the beam radius as the beam propagates down the transport line. However, the beam is approximately matched to the transport line by adjusting the matching lenses until some current loss is observed, presumably associated with the mismatched beam hitting the beam pipe, and then setting the matching lens values in the middle of the broad minimum for which little loss is observed.

If the beam is assumed matched to the transport line however, previously obtained experimental data on the magnet characteristics[9], as well as extensive data on transverse beam dynamics[4], allow confident prediction of the matched beam

*Supported by U. S. Department of Energy.

radius, if the average magnetic field is known. The average magnetic field can, in turn, be accurately related to the coil currents. For the 26.3 mA peak beam current, and the 1.91 A coil current used in the experiment described here, the calculated matched beam radius at the peak current is 6 mm. The beam pipe radius is 19 mm.

This estimate of the matched radius along with the measured initial peak current and bunch length can be used to run an r, z WARP simulation which can be used to compare with the experiment. Lacking time-resolved data about the transverse beam characteristics, however, some assumption must still be made regarding the axial variation of transverse beam conditions away from the bunch center. The beam in the simulation is assigned a local emittance proportional to current and is therefore assumed to have a constant tune depression along the beam. The beam is matched along its length to the focusing force in the simulation, which is applied uniformly along the transport line, by adjusting the local radius so that the charge density is a constant. Once these conditions are met there are no free parameters in comparing the simulation to the experiment.

The top curve in Fig. 1 shows the evolution of the rms bunch length, from the simulation, as a function of distance propagated. Also plotted on the same axes are the experimental bunch widths measured at each of the five current monitors. Both rms bunch length and the bunch length of a best fit parabola are shown. In both cases a small tail in the current distribution at the edge of the bunch shape has been neglected.

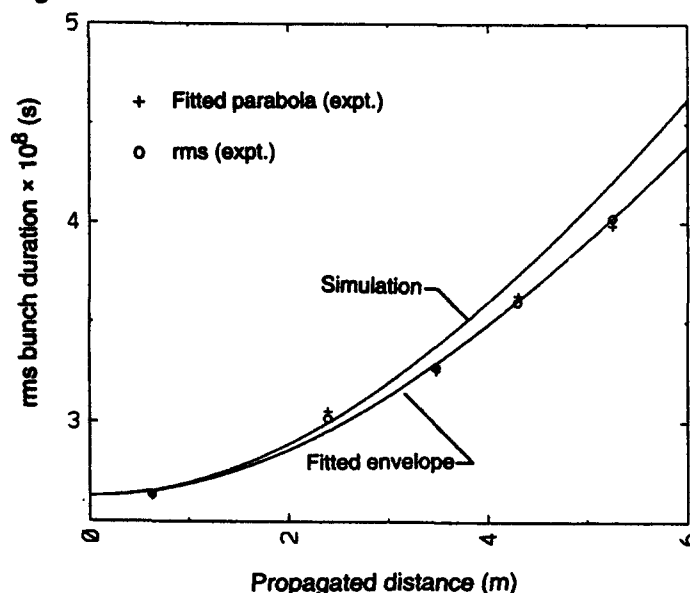


Fig. 1. Bunch length vs. distance propagated for a bunch with initially parabolic shape. Data from an r, z WARP simulation is plotted, as the top curve, on the same axes as experimental measured points, as well as, an envelope solution fitted to the expansion data.

In view of the lack of data on the transverse beam dynamics, it is difficult to say whether any of the difference between simulation and experiment is a consequence of an inappropriate choice of the initial transverse beam distribution.

Simulations were therefore performed to examine the sensitivity of the longitudinal beam expansion rate to a transverse mismatch. When the beam is initially mismatched, transverse betatron oscillations are observed which, as expected, vary in frequency along the bunch as the expansion results in a differential in the beam velocity between the head and tail of the bunch. Even when the beam is initialized with a 50% mismatch that varies along the bunch, and which is sufficient to cause halo formation along the beam, only a 0.6% change is observed in the rms bunch expansion after the bunch has propagated six meters. Furthermore, the insensitivity to transverse mismatch observed for the rms average, also extends to local details of the longitudinal beam evolution. Examination of the longitudinal phase space and various projections of that phase space, such as the line density variation along the bunch, show almost no evidence of the transverse mismatch.

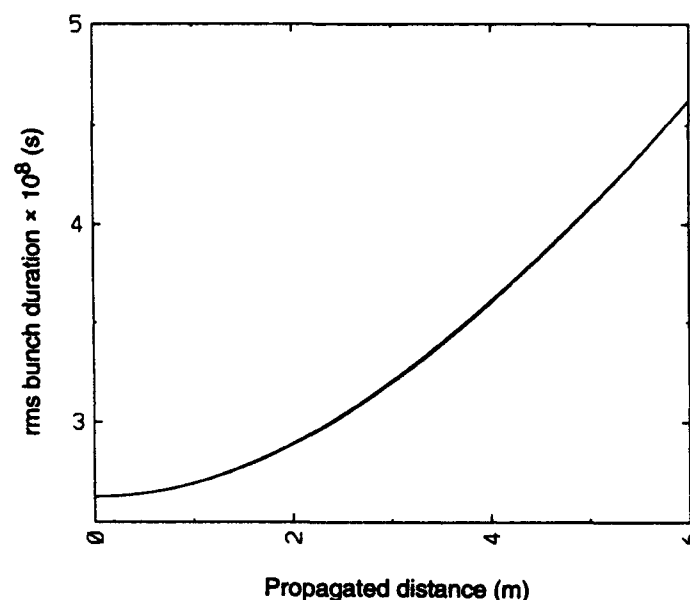


Fig. 2. Solution of the one-dimensional envelope equation overlaid onto the curve of rms bunch length obtained from the r, z simulation.

Because of the degree of insensitivity of the bunch expansion to substantial transverse mismatch, a comparison was undertaken to determine how well the bunch length in the simulation would conform to the envelope equation prediction. Since it is difficult to calculate what g -factor is appropriate for a nonuniform bunch whose radius varies with time as the beam expands, the procedure which was employed was to consider g to be a free parameter, and to find the value of g which would result in a beam expansion which matches the r, z simulation at the end points of 6 m in the simulation. The curves of rms bunch length from the simulation, and the bunch length calculated using the g value which matches the end points, were then plotted on the same set of axes as shown in Fig. 2. As can be seen from the curves, the intermediate points coincide to approximately the width of the line on the plot. If the value of g is written in the form $g = C + 2 \ln(b/a)$, then the value of C is found to be 0.791. This comparison between envelope solution and simulation was also performed

for a bunch with the same current, but with the externally applied transverse focusing lowered, so that the matched radius at the beam center is doubled to 12 mm. In this case, the envelope solution and simulation curves also agreed closely and a value of 0.775 was obtained for C . This weak dependence means that the rms bunch dynamics for an initially parabolic bunch may be accurately predictable using a simple envelope model, although whether this procedure remains valid over a larger range of parameters or whether it breaks down if the beam is given an initial inward (bunching) head-to-tail differential velocity, and is then allowed to compress longitudinally, remains to be tested.

Since the expansion calculated by the envelope solution closely matches the simulation, it becomes convenient to use the envelope equation to compare against the experimental data. The bottom curve in Fig. 1 is from a solution of the envelope equation with $g = 2.7$, chosen to match the data points. This compares to the value of 3.11 used in Fig. 2 to match to the simulation curve. This is the value of g which would be calculated if the beam matched radius were approximately 23% larger than the 6 mm matched radius calculated from the strength of the externally applied magnetic field. Because only the product of g and the initial current appears in the envelope equation, this curve would also be generated by a 15% reduction in the intimate peak current from what was measured.

The difference in expansion rate between simulation and experiment appears to be larger than the uncertainty in either the equilibrium matched radius or the initial beam current. However, under other experimental conditions much closer agreement has been obtained. Further experimental uncertainty can also arise from the degree to which the bunch tail, whose amplitude approaches the ripple in the current waveform, is included in the definition of the bunch length. As more of the tail is included, the bunch expansion comes somewhat closer to the simulation.

Another possible source of measurement uncertainty is possible loss in beam as the bunch propagates. There is in fact some evidence that part of the beam is lost, and particularly if this loss occurs primarily at the bunch ends, can account for a decrease in the expansion rate compared to what is predicted in the simulation. The fact that the current measured at the monitor 2.39 m from the gun consistently is above the expansion curve which fits the other data points, may in fact be evidence that beam particles are being lost.

In addition to the difference in expansion rate between the simulation and the experiment there are several details of the observed bunch behavior which are not the same as the simulation. For example, the initial current waveform is not precisely a parabola and this effects the evolution of the bunch pulse shape which shows deviations from parabolic shape, including the formation of tails not seen in the simulation, as the beam propagates. There is also a noticeable difference between the phase space in the simulation and the observed variation in beam velocity along the bunch. The simulations, shortly downstream from the gun show an "s" shape in the phase space not observed experimentally.

III. CONCLUSIONS

The description above is concentrated on the use of simulations, together with experiment, to examine evolution of the bunch length during free expansion of an initially parabolic bunch. Many details of the comparisons between simulation and experiment must await a more comprehensive description of the work conducted. The use of simulation, as described here, in the conduct of the relatively simple investigation of a relatively simple experiment has nevertheless yielded interesting insight into the bunch dynamics. It was found that the longitudinal dynamics is insensitive to the details of transverse beam match, and the bunch length evolution is well described by a simple envelope equation, notwithstanding the expectation that the "g-factor," which multiplies the current in that description, would vary along the beam and along the transport line as the beam expands, so that the envelope description would not be accurate. As the comparisons are expanded to include beams which fill a greater fraction of the beam pipe, whose shapes deviate substantially from the parabolic shape employed here, and which are subject to an initial velocity "tilt" which causes the bunch to compress, a very rich set of phenomena can be explored.

IV. REFERENCES

- [1] D. X. Wang, J. G. Wang, D. Kehne, M. Reiser, I. Haber, "Experimental Studies of Longitudinal Beam Dynamics of Space-Charge Dominated Beams," these proceedings.
- [2] J.G. Wang, D.X. Wang, D. Kehne, and M. Reiser, "Propagation of Local Perturbation in Space-Charge Dominated Electron Beams," these proceedings.
- [3] N. Brown, M. Reiser, D. Kehne, D. X. Wang, and J. G. Wang, "Longitudinal Kinetic Energy Spread From Focusing in Charged Particle Beams," these proceedings.
- [4] I. Haber, D. Kehne, M. Reiser, and H. Rudd, "Experimental, Theoretical and Numerical Investigation of the Homogenization of Density Nonuniformities in the Periodic Transport of a Space-Charge Dominated Beam," *Phys. Rev. A* **15**, 44, 5194 (Oct. 15, 1991).
- [5] A. Friedman, D. P. Grote, I. Haber, "Three Dimensional Particle Simulation of Heavy Ion Fusion Beams," *Physics of Fluids B: Plasma Physics*, **4**, 2203 (1992).
- [6] D. Callahan, A. Langdon, A. Friedman, I. Haber, "Longitudinal Beam Dynamics for Heavy Ion Fusion," these proceedings.
- [7] A. Hofmann, "Single-Beam Collective Phenomena - Longitudinal," *Theoretical Aspects of the Behavior of Beams in Accelerators and Storage Rings*, CERN 77-13, 139 (CERN, Geneva, 1977).
- [8] David Neuffer, "Longitudinal Motion in High Current Ion Beams - A Self-Consistent Phase Space Distribution with an Envelope Equation," *IEEE Trans. Nucl. Sci.* **NS-23** No. 3, 3031 (1979).
- [9] P. Loschialpo, W. Namkung, M. Reiser, J. D. Lawson, "Effects of Space Charge and Lens Aberrations in the Focusing of an Electron Beam by a Solenoid Lens", *J. Appl. Phys.* **57**, 10 (1985).

Integrated Numerical Modeling of a Laser Gun Injector *

H. Liu, S. Benson, J. Bisognano, P. Liger, G. Neil, D. Neuffer, C. Sinclair and B. Yunn
CEBAF, 12000 Jefferson Ave., Newport News, VA 23606

Abstract

CEBAF is planning to incorporate a laser gun injector into the linac front end as a high-charge cw source for a high-power free electron laser and nuclear physics. This injector consists of a DC laser gun, a buncher, a cryounit and a chicane. The performance of the injector is predicted based on integrated numerical modeling using POISSON, SUPERFISH and PARMELA. The point-by-point method incorporated into PARMELA by McDonald is chosen for space charge treatment. The concept of "conditioning for final bunching" is employed to vary several crucial parameters of the system for achieving highest peak current while maintaining low emittance and low energy spread. Extensive parameter variation studies show that the design will perform better than the specifications for FEL operations aimed at industrial applications and fundamental scientific research. The calculation also shows that the injector will perform as an extremely bright cw electron source.

I. INTRODUCTION

CEBAF has been studying an IR FEL and a UV FEL utilizing the superconducting accelerator technology that has been developed at CEBAF, aimed at industrial applications and fundamental scientific research[1-4]. An FEL injector based on a DC laser gun will be used as a high-brightness cw source. The schematic of the injector is shown in Fig. 1. The DC laser gun produces a cw train of electron bunches at 400 ~ 500 keV with bunch lengths of 60 ~ 100 ps. Then electrons are bunched using a room-temperature buncher to provide suitable injection into a cryounit containing two standard CEBAF SRF cavities. The cryounit accelerates the electrons up to ~ 10 MeV while providing suitable tilt in longitudinal phase space distributions. Then the electrons are finally bunched using a chicane with a $R_{56} = -0.085$ cm/%.



Fig. 1 Schematic of the FEL injector

The specifications for our FEL injector are summarized in Table 1. Throughout the paper, the bunch length and energy spread are represented using $4\sigma_z$ and $4\sigma_E$, which correspond to 95% particles for ideal Gaussian distributions. For non-Gaussian distributions, they generally still correspond to ~ 90% particles.

*Supported by Virginia Center for Innovative Technology

Table 1 FEL Injector Specifications

Energy	10 MeV
Charge per bunch	120 pC
Bunch length ($4\sigma_z$)	2 ps
Energy spread ($4\sigma_E$)	400 keV
Normalized rms emittance (ϵ_n)	15 mm mrad
Average beam current	900 μ A
Repetition frequency	7.677 MHz

In this paper, we present our injector performance predictions based on integrated numerical modeling using POISSON, SUPERFISH and PARMELA.

II. CHICANE BUNCHING

Chicane bunching is not a new method for compressing electrons, and it has been clearly described, e.g., in Ref. 5. However, as will be shown later in this paper, it fits our injector design quite well when it is used together with two standard CEBAF SRF cavities. Therefore we introduce this bunching mechanism first instead of going to the numerical results immediately.

The bunching process using a chicane with two SRF cavities in our injector design is shown in Fig. 2. Using the

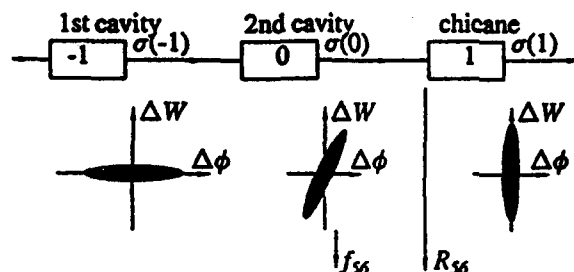


Fig. 2 Bunching using a chicane with two SRF cavities
standard σ matrix representation, we have the following mathematical description

$$\sigma_{55}(1) = \sigma_{55}(0)(1 - R_{56}/f_{56})^2 + R_{56}^2\sigma_{00}(-1),$$

where $\sqrt{\sigma_{55}(0)}$ is the bunch length at the entrance of the chicane, $\sqrt{\sigma_{55}(1)}$ the bunch length at the exit of the chicane, $\sqrt{\sigma_{00}(-1)}$ the momentum spread at the entrance of the second SRF cavity, $R_{56} = \delta l/(\delta p/p)$ the parameter of the bunching property of the chicane, δl the path difference between electrons having a momentum spread of

$\delta p/p$, and $f_{se} = -\sigma_{se}(0)/\sigma_{se}(0)$ the tilt of the longitudinal phase space distribution of the bunch at the exit of the second SRF cavity. It is seen that when $f_{se} \approx R_{se}$, the final bunch length depends only on the product of the momentum spread and R_{se} of the chicane. We call the above condition the *conditioning for final bunching*, which is a term borrowed from Ref. 6. It has been built into PARMELA so that f_{se} can be calculated statistically from all the particles at the exits of the SRF cavities, and by comparison with R_{se} of the chicane, the matching of longitudinal phase space distributions from the second SRF cavity to the chicane can be accurately predicted accordingly. This has turned out to be an indispensable means for optimising the design efficiently.

III. NUMERICAL MODELING

Based on the previous calculation[4], the performance of the FEL injector has been thoroughly investigated and optimised using time-consuming but accurate integrated numerical modeling. The beam dynamics is calculated using a version of PARMELA with the point-by-point method for space charge treatment[7,8]. The code POISSON was used to generate the DC electric fields in the photocathode gun, and the code SUPERFISH was used to generate the 2-D RF fields in the buncher and two SRF cavities in the cryounit. In each integrated simulation (~ 10 cpu-hours on an HP 9000/730 UNIX workstation), the same electrons are followed from emission at the photocathode through the gun, the buncher, the cryounit and the chicane.

a) Baseline Design

The injector performance was optimised at first for the baseline design which corresponds to 500 kV gun voltage, 100 ps (4σ) laser pulse length and 3 mm (4σ) laser spot size defining the emission diameter. The distance from the gun to the buncher is reduced to account for the divergence (~ 20 mrad) of the beam out of the gun, and the distance from the buncher to the cryounit is increased to meet the optimum bunching requirement. The performance of the baseline design is shown in Table 2. It is seen that the injector performance stays well within the specifications by a factor of 2 \sim 3. Various distributions of the bunch are shown in Fig. 3.

Table 2 Performance of the Baseline Design

Bunch charge	120 pC
Bunch length ($4\sigma_z$)	0.96 ps
Energy spread ($4\sigma_E$)	290 keV
Mean energy (E_m)	9.492 MeV
Norm. rms emit. ($\epsilon_{ns}/\epsilon_{ny}$)	4.44/4.73 (mm mrad)

b) Robustness of the Baseline Design

The robustness of the baseline design has been investigated against the laser intensity fluctuation and consequently the bunch charge fluctuation. A series of inte-

grated simulations were conducted with all the system parameters fixed while the bunch charge was varied from 120 pC to 160 pC. The variations of the bunch performance at

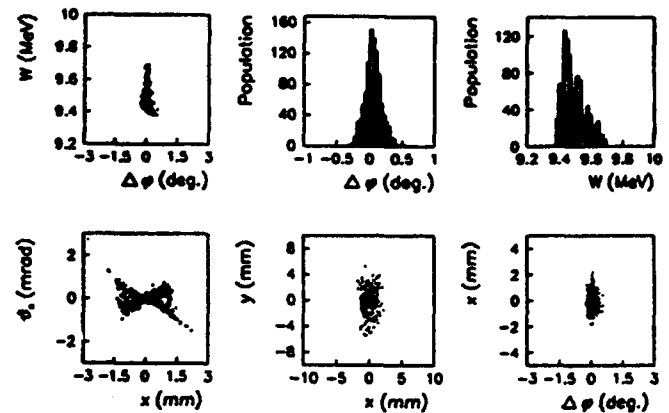


Fig. 3 Various distributions of 1000 superparticles at the exit of the chicane, showing the optimised baseline design performance listed in Table 2. *upper left*: longitudinal phase space distribution (W - energy; $\Delta\phi$ - relative phase); *upper middle*: phase profile; *upper right*: energy profile; *lower left*: horizontal trace space distribution (x - horizontal position; θ_x - horizontal divergence angle); *lower middle*: cross-sectional distribution; *lower right*: horizontal snapshot.

the exit of the chicane are listed in Table 3, where δE_m and $\delta\phi_m$ represent the mean energy shift and the phase shift of the bunch centroid. The units are pC for bunch charge, ps for bunch length, keV for energy spread, mm mrad for emittance, keV and degree for centroidal energy and phase shifts throughout the paper. It is seen that the mean energy shift and the phase shift of the bunch centroid caused by the charge fluctuations are negligible.

Table 3 Robustness of the Baseline Design

Q	$4\sigma_z$	$4\sigma_E$	$\epsilon_{ns}/\epsilon_{ny}$	δE_m	$\delta\phi_m$
120	0.96	290	4.44/4.73	0	0 (baseline)
140	1.04	281	4.99/5.31	-1	-0.0048
150	1.11	277	5.25/5.58	-1	-0.0075
155	1.17	275	5.37/5.71	-2	-0.0092
160	1.21	273	5.50/5.84	-2	-0.0092

c) Sensitivity of the Baseline Design

The sensitivity of the baseline design has been investigated on the basis of $\delta\phi = \pm 2^\circ$ for the RF phase change and $\delta E/E = \pm 2\%$ for the RF amplitude change in the buncher and the two RF cavities in the cryounit. For each case only one parameter was varied with all the others being the same as for the optimised baseline design stated in Table 2. The results are listed in Table 4. It is found that the most sensitive performance is the bunch length. The most sensitive system parameters, in sequence, are

the RF phase of the second SRF cavity, the RF amplitude of the second SRF cavity, the RF amplitude of the first SRF cavity and the RF phase of the first SRF cavity. The sensitivity comes from the resultant mean energy shift of the particles and the small value of R_{45} of the chicane. However, no case is found to be out of the specifications.

Table 4 Sensitivity of the Baseline Design

Element	$\delta\phi$	$\delta E/E$	$4\sigma_t$	$4\sigma_E$	$\epsilon_{ns}/\epsilon_{ny}$	δE_m	$\delta\phi_m$
(Baseline)	0.0	0.0	0.96	290	4.44/4.73	0.0	0.0
Buncher	+2	0.0	1.57	306	4.69/4.98	-51	+0.42
Buncher	-2	0.0	1.37	261	4.23/4.50	+56	-0.47
Buncher	0.0	+2	1.05	309	4.52/4.81	-1	+0.025
Buncher	0.0	-2	1.21	257	4.34/4.63	+3	-0.053
1 st cavity	+2	0.0	1.53	260	4.30/4.58	-75	-0.22
1 st cavity	-2	0.0	1.23	306	4.60/4.90	+78	+0.42
1 st cavity	0.0	+2	1.22	296	4.45/4.75	+106	-1.81
1 st cavity	0.0	-2	1.52	269	4.41/4.69	-102	+2.04
2 nd cavity	+2	0.0	1.63	269	4.41/4.70	+114	-1.94
2 nd cavity	-2	0.0	1.89	295	4.45/4.74	-117	+2.33
2 nd cavity	0.0	+2	1.18	288	4.42/4.71	+85	-1.47
2 nd cavity	0.0	-2	1.41	277	4.45/4.73	-84	+1.63

d) Gun Parameter Variations

To evaluate the maximum operational flexibilities, the injector performance under different gun operating conditions has been investigated. These conditions include the voltage V_0 (keV), the field gradient E_0 (MV/m) at the cathode, the laser pulse length $4\sigma_t$ (ps) and the diameter d_0 (mm) of the active cathode area. The corresponding beam parameters at the exit of the chicane are shown in Table 5. The low gradient of 6 MV/m was obtained by increasing the cathode-anode gap while holding the cathode and anode shapes unchanged. Low-gradient operation would be favorable for avoiding vacuum breakdown and cathode poisoning. It is seen that the design will function over a quite wide range of operating conditions.

Table 5 Gun Parameter Variations

V_0	E_0	$4\sigma_t$	d_0	$4\sigma_t$	$4\sigma_E$	$\epsilon_{ns}/\epsilon_{ny}$
500	10	100	3	0.96	290	4.44/4.73 (baseline)
500	10	60	3	2.00	109	3.65/3.85
500	10	60	5	1.54	118	3.78/3.97
500	10	100	5	0.79	287	4.07/4.44
400	8	100	3	1.24	272	5.32/5.02
400	8	60	5	0.91	260	6.12/6.08
500	6	100	3	0.91	330	6.49/6.12

e) Emission Phase Fluctuations

Emission of electrons is controlled by the laser pulses regularly illuminating the photocathode. Arrival time spread $\delta\phi_0$ (deg.) of the laser pulses will cause bunch-to-bunch energy spread δE_m and bunch-to-bunch centroid phase shift $\delta\phi_m$. As is shown in Table 6, the effects on both mean energy and centroid phase are negligible.

Table 6 Emission Phase Fluctuations

$\delta\phi_0$	$4\sigma_t$	$4\sigma_E$	$\epsilon_{ns}/\epsilon_{ny}$	δE_m	$\delta\phi_m$
0	0.96	290	4.44/4.73	0	0 (baseline)
+2	1.06	276	4.50/4.80	-14	+0.039
-2	0.94	303	4.32/4.61	+15	-0.029

f) Space Charge Effects

The setup procedure is one of our major concerns. To investigate the possibility of using a low-current beam to guide the injector to its full-charge (120 pC) operation, an integrated simulation was conducted, in which the space charge was simply turned off, in the case of 400-kV gun voltage, 60-ps laser pulse length and 5-mm cathode diameter[9].

In this specific case, the bunch length changes from 0.96 ps with space charge on to 1.92 ps with space charge off. This is because the system parameters are for a matched space-charge-dominated bunch in longitudinal phase space. The normalized rms emittance $\epsilon_{ns}/\epsilon_{ny} = 3.53/3.47$ mm mrad with space charge on or 0.66/0.66 mm mrad with space charge off, at the exit of the gun. $\epsilon_{ns}/\epsilon_{ny} = 6.12/6.08$ mm mrad with space charge on or 2.19/1.83 mm mrad with space charge off, at the exit of the chicane.

Our numerical calculations show that on a step-by-step basis, a lower current beam can be used to guide the injector to its full-charge operation, which will greatly simplify the setup procedures.

IV. SUMMARY

Extensive careful integrated computer simulations have demonstrated that our injector design will perform better than the specifications over a quite wide range of operating conditions.

REFERENCES

1. J. Bisognano et al, *Nucl. Instrum. Methods* A318, 216 (1992).
2. G. R. Neil et al, *ibid.*, p. 212.
3. C. K. Sinclair, *ibid.*, p. 410.
4. P. Liger et al, *ibid.*, p. 290.
5. T. Raubenheimer, Workshop on Fourth Generation Light Sources, SSRL, 263 (1992).
6. A. M. Sessler et al, *Phys. Rev. Lett.* 68, 309 (1992).
7. K. T. McDonald, *IEEE Trans. ED*, 35, 2052 (1988).
8. H. Liu, to be published.
9. H. Liu, CEBAF-TN-93-009.

HALO FORMATION IN MISMATCHED, SPACE-CHARGE-DOMINATED BEAMS*

C.L. Bohn and J.R. Delayen,
Argonne National Laboratory,
Engineering Physics Division, Argonne, Illinois 60439

Abstract

A semianalytic formalism was recently developed for investigating the transverse dynamics of a mismatched, space-charge-dominated beam propagating through a focusing channel. It uses the Fokker-Planck equation to account for the rapid evolution of the coarse-grained distribution function in the phase space of a single beam particle. A simple model of dynamical friction and diffusion represents the effects of turbulence resulting from charge redistribution. The initial application was to sheet beams. In this paper, the formalism is generalized to fully two-dimensional beams.

I. INTRODUCTION

We recently introduced a semianalytic formalism describing the dynamics of transverse emittance growth and halo formation in nonrelativistic, mismatched beams arising as a consequence of nonlinear space-charge forces [1, 2]. The formalism is based on the Fokker-Planck equation governing the evolution of the coarse-grained distribution function of beam particles. The Fokker-Planck equation incorporates coefficients of dynamical friction and diffusion in velocity space. Turbulence excited as a consequence of charge redistribution enhances these coefficients and converts free energy due to mismatch into thermal energy. If the local free-energy density is sufficiently high, microinstabilities may cause turbulent fluctuations to grow to large amplitudes during a fraction of a plasma period [3]. The fluctuations attenuate, however, via Landau damping on the same time scale [3], and heating can therefore occur very rapidly. Relaxation toward Maxwell-Boltzmann equilibrium ensues on a time scale determined by weak residual turbulence. These processes generate emittance growth and halo by injecting particles into high-amplitude orbits. They also dissipate any fine structure present in

the beam at injection. Heating and relaxation of space-charge-dominated beams can occur during beam transport, as observed in laboratory experiments and numerical simulations [4].

To develop methods for inhibiting emittance growth and halo-induced radioactivation of the accelerator walls, we must first know the associated dynamics and time scales in realistic beams. Our initial application of the formalism was to sheet beams. We now generalize it to enable ready investigation of fully two-dimensional beams.

II. GOVERNING EQUATIONS

In a turbulent beam, the simultaneous interactions of a particle with many rather distant particles dominate binary coulomb interactions with nearby particles. This circumstance generates dynamical friction and diffusion in velocity space. We discuss beam evolution from the perspective of a comoving coordinate system. According to the Fokker-Planck equation, the evolution of the coarse-grained distribution function $W(\mathbf{x}, \mathbf{u}, t)$, in which \mathbf{x} , \mathbf{u} , and t denote position, velocity, and time, respectively, is determined from

$$\partial_t W + \mathbf{u} \cdot \nabla_{\mathbf{x}} W + \mathbf{K} \cdot \nabla_{\mathbf{u}} W = -\nabla_{\mathbf{u}} \cdot (\mathbf{F} W) + \nabla_{\mathbf{u}} \cdot [\nabla_{\mathbf{u}} \cdot (\mathbf{D} W)], \quad (1)$$

in which \mathbf{K} is the net force per particle mass M in the comoving frame,

$$\mathbf{F} = -\frac{\langle \Delta \mathbf{u} \rangle}{\Delta t}, \quad \mathbf{D} = \frac{1}{2} \frac{\langle \Delta \mathbf{u} \Delta \mathbf{u} \rangle}{\Delta t} \quad (2)$$

are the dynamical-friction vector and diffusion tensor, respectively, and Δt is a short time during which the fluctuations modify the distribution function [5]. Both the distribution function and the net force are regarded to be smoothed out.

The spectrum of electric-field fluctuations determines \mathbf{F} and \mathbf{D} [5]. We do not know these coefficients a priori; however, it should be possible to infer them by studying individual particle orbits in N -body simulations [6]. In general, the coefficients may be expected to be functions of position, velocity, and time. We shall ignore the position and velocity dependencies and model the beam as a fluctuating fluid in which particles execute Brownian motion. We

*This work was supported by the U. S. Department of Energy under contract W-31-109-ENG-38 and by the Strategic Defense Initiative Organization.

take $F = -\beta(t)u$ and $D = D(t)I$, where β and D are the time-dependent relaxation-rate and diffusion coefficients, respectively, and I is the identity tensor. This simplification, which says the beam has uniform "temperature", is likely to be most appropriate for particles moving with velocities not much exceeding the thermal velocity, just as it is when only binary coulomb collisions drive relaxation [5]. It may therefore be expected to apply to "typical" particles comprising the central region of the beam. In actuality, the relaxation rate is slower for fast particles because they have less time to interact with localized field fluctuations. Consequently, because halo particles either move rapidly through the core or do not sample the core, the halo may be expected to thermalize more slowly than the core. This is seen in simulations [4]. Despite this shortcoming, our simplified coefficients should be useful both for studying the evolution of fine structure in the beam and for investigating halo generation from the core. By design, the formalism developed here can be adapted to accommodate coefficients with spatial and velocity dependencies once they are known.

The dynamics we have described obviously operate in three dimensions. In what follows, we consider only the two-dimensional dynamics in a plane orthogonal to the accelerator axis. The Fokker-Planck equation in cylindrical coordinates $(r, \theta, u_r, u_\theta = r d\theta/dt)$ is

$$\begin{aligned} \frac{\partial W}{\partial t} + u_r \frac{\partial W}{\partial r} + \frac{u_\theta}{r} \frac{\partial W}{\partial \theta} + \left(K_r + \frac{u_r^2}{r}\right) \frac{\partial W}{\partial u_r} \\ + \left(K_\theta - \frac{u_r u_\theta}{r}\right) \frac{\partial W}{\partial u_\theta} = 2\beta W \\ + \beta \left(u_r \frac{\partial W}{\partial u_r} + u_\theta \frac{\partial W}{\partial u_\theta}\right) + D \left(\frac{\partial^2 W}{\partial u_r^2} + \frac{\partial^2 W}{\partial u_\theta^2}\right), \quad (3) \end{aligned}$$

where K is given by the superposition of the focusing force and the space-charge force found from the coarse-grained potentials Φ_f and Φ_s , respectively, in the manner

$$K = -\frac{Q}{M} \nabla_x (\Phi_f + \Phi_s), \quad (4)$$

where Q is the particle charge. According to Poisson's equation, the coarse-grained space-charge potential is determined from the smoothed-out charge density, which in turn is determined from the coarse-grained distribution:

$$\frac{1}{r} \frac{\partial}{\partial r} \left(r \frac{\partial \Phi_s}{\partial r}\right) + \frac{1}{r^2} \frac{\partial^2 \Phi_s}{\partial \theta^2} = -\frac{NQ}{\epsilon_0} \int_{-\infty}^{+\infty} du_r \int_{-\infty}^{+\infty} du_\theta W, \quad (5)$$

where N is a normalization parameter related to the particle density, and ϵ_0 is the permittivity of free space.

Although the problem is formulated for arbitrary external focusing potential, in the following section we specialize to a harmonic external potential, i.e. $\Phi_f = M\omega^2 r^2/2Q$, where ω is the betatron frequency. In so doing, we ignore effects from, for example, cyclotron motion and beam rotation in an axial magnetic focusing field, which is to say we assume coriolis and centrifugal forces are small.

III. POLYNOMIAL EXPANSION

To solve the coupled Fokker-Planck and Poisson equations self-consistently, we decompose the distribution function into complete sets of orthogonal polynomials:

$$W = \sum_{m=0}^{\infty} \sum_{n=0}^{\infty} \sum_{p=-\infty}^{+\infty} \sum_{q=0}^{\infty} A_{mn}^{pq} \psi_m(u_r) \psi_n(u_\theta) \phi_q^p(r) e^{ip\theta}, \quad (6)$$

where ψ_m are Gauss-Hermite polynomials,

$$\psi_m(u) = \left[\frac{1}{2^m m! \pi}\right]^{\frac{1}{2}} e^{-\alpha u^2} H_m(\sqrt{\alpha} u), \quad (7)$$

and ϕ_q^p are Gauss-Laguerre polynomials,

$$\phi_q^p(r) = \frac{a}{\pi} \left[\frac{q!}{(|p|+q)!}\right]^{\frac{1}{2}} (ar^2)^{\frac{|p|}{2}} e^{-ar^2} L_{|p|}^q(ar^2). \quad (8)$$

In these polynomials, we require $\alpha = \alpha(t) = \beta(t)/2D(t)$, while $a = a(t)$ is a free time-dependent variable.

Two considerations motivate the use of these sets of polynomials. The first is that both sets begin with Gaussians at zeroth order. This is desirable because the Maxwell-Boltzmann distribution of a beam in the absence of space charge is Gaussian in both velocity and position (Gaussian ψ_0 and Gaussian ϕ_0^0). The second is that this choice of polynomials gives $A_{00}^{00} = 1$ for all t , an expression which is convenient for numerical calculations. This expression follows directly from the particle density

$$n(r, \theta) = N \sum_{p=-\infty}^{+\infty} \sum_{q=0}^{\infty} A_{00}^{pq} \phi_q^p e^{ip\theta}, \quad (9)$$

which, when integrated over r and θ , must always yield N . Upon evaluating the mean-square radius, we find $\langle r^2 \rangle = a^{-1}(1 - A_{00}^{01})$. It is therefore convenient to let $a \equiv 1/\langle r^2 \rangle$, so that $A_{00}^{01} = 0$ for all t . The coefficients A_{mn}^{pq} are complex, and $A_{mn}^{-pq} = (A_{mn}^{pq})^*$.

After solving Poisson's equation for the space-charge potential, we find the components of acceleration to be

$$\begin{aligned} K_r = -\omega^2 r + \frac{NQ^2}{M\epsilon_0} \left(\frac{1}{2\pi r} (1 - e^{-ar^2}) - \sum_{p=-\infty}^{+\infty} \right. \\ \times \left\{ \frac{A_{00}^{p0}}{2\pi r} \frac{(ar^2)^{\frac{|p|}{2}}}{\sqrt{|p|!}} \left[e^{-ar^2} - \frac{|p|}{2} (ar^2)^{-\frac{|p|}{2}} \gamma(|p|, ar^2) \right] \right. \\ \left. \left. - \sum_{q=1}^{\infty} \frac{A_{00}^{pq}}{2ar} \left[\phi_q^p - \frac{|p|+2q}{2\sqrt{q(|p|+q)}} \phi_{q-1}^p \right] \right\} e^{ip\theta} \right), \quad (10) \end{aligned}$$

$$\begin{aligned} K_\theta = -\frac{NQ^2}{M\epsilon_0} \sum_{p=-\infty}^{+\infty} \left\{ \frac{A_{00}^{p0}}{4\pi r} \frac{(ar^2)^{-\frac{|p|}{2}}}{\sqrt{|p|!}} \gamma(|p|, ar^2) \right. \\ \left. + \sum_{q=1}^{\infty} \frac{A_{00}^{pq}}{4ar} \frac{1}{\sqrt{q(|p|+q)}} \phi_{q-1}^p \right\} i p e^{ip\theta}. \quad (11) \end{aligned}$$

Here, the prime on the sum over p means $p = 0$ is to be excluded from the summation, and $\gamma(p, s)$ is the incomplete gamma function.

After inserting the components of acceleration into the Fokker-Planck equation (3), we derive a set of coupled differential equations for the coefficients $A_{mn}^{pq}(t)$ using recurrence relations and normalization properties of the polynomials. We let α_0 and a_0 denote $\alpha(t=0)$ and $a(t=0)$, respectively, and we introduce a reference frequency $\omega_0^2 = a_0/\alpha_0$ and plasma frequency $\omega_p^2 = NQ^2 a_0/2\pi M\epsilon_0$. The result, expressed in terms of the dimensionless time $\zeta = \omega_0 t$ and the dimensionless quantities $\hat{\alpha} = \alpha/\alpha_0$ and $\hat{a} = a/a_0$, is

$$\begin{aligned} \frac{d}{d\zeta} A_{mn}^{pq} = & \frac{1}{2\hat{\alpha}} \frac{d\hat{\alpha}}{d\zeta} \left[\sqrt{m(m-1)} A_{m-2,n}^{pq} + (m+n) A_{mn}^{pq} \right. \\ & + \sqrt{n(n-1)} A_{m,n-2}^{pq} \left. \right] + \frac{1}{2\hat{a}} \frac{d\hat{a}}{d\zeta} \left[(|p|+2q) A_{mn}^{pq} \right. \\ & - 2\sqrt{q(|p|+q)} A_{mn}^{p,q-1} \left. \right] - (m+n) \frac{\beta}{\omega_0} A_{mn}^{pq} \\ & + \sqrt{\frac{\hat{a}}{2\hat{\alpha}}} \sqrt{m} \sum_{q'=0}^{\infty} A_{m-1,n}^{pq'} \left\{ [|p|+2(q'+1)+n] J_{qq'}^p \right. \\ & - 2\sqrt{(q'+1)(q'+|p|+1)} J_{q,q'+1}^p \left. \right\} \\ & + \sqrt{\frac{\hat{a}}{2\hat{\alpha}}} \sqrt{m+1} \sum_{q'=0}^{\infty} A_{m+1,n}^{pq'} \left\{ [|p|+2(q'+1) \right. \\ & - (n+1)] J_{qq'}^p - 2\sqrt{(q'+1)(q'+|p|+1)} J_{q,q'+1}^p \left. \right\} \\ & + \sqrt{\frac{\hat{a}}{2\hat{\alpha}}} \sum_{q'=0}^{\infty} J_{qq'}^p \left\{ \sqrt{m(n+1)(n+2)} A_{m-1,n+2}^{pq'} \right. \\ & - \sqrt{n(n-1)(m+1)} A_{m+1,n-2}^{pq'} \\ & - ip \left[\sqrt{n} A_{m,n-1}^{pq'} + \sqrt{n+1} A_{m,n+1}^{pq'} \right] \left. \right\} \\ & - \sqrt{\frac{2\hat{\alpha}}{\hat{a}}} \frac{\omega^2}{\omega_0^2} \sqrt{m} \sum_{q'=0}^{\infty} A_{m-1,n}^{pq'} K_{qq'}^p \\ & - \sqrt{\frac{\hat{a}}{2\hat{\alpha}}} \frac{\omega_p^2}{\omega_0^2} \sum_{p'=-\infty}^{+\infty} \sum_{q'=0}^{\infty} \sum_{p''=-\infty}^{+\infty} \sum_{q''=0}^{\infty} A_{00}^{p'q''} \delta_{0,p''+p'-p} \\ & \times \left\{ 2\sqrt{m} A_{m-1,n}^{p's'} M_{qq's''}^{pp'p''} - i\sqrt{n} A_{m,n-1}^{p's'} N_{qq's''}^{pp'p''} \right\}; \quad (12) \end{aligned}$$

$$\frac{1}{\hat{a}} \frac{d\hat{a}}{d\zeta} = \sqrt{\frac{\hat{a}}{2\hat{\alpha}}} \sum_{q=0}^{\infty} A_{10}^{0q} [(2q+1)J_{1q}^0 - 2(q+1)J_{1,q+1}^0], \quad (13)$$

in which δ_{ij} is the Kronecker delta, and

$$I_{qq'}^{pp'p''} = \frac{2\pi^2}{a^{5/2}} \int_0^{\infty} dr e^{-ar^2} \phi_q^p \phi_{q'}^{p'} \phi_{q''}^{p''}, \quad (14)$$

$$J_{qq'}^{pp'}(0) = \frac{2\pi^2}{a^{3/2}} \int_0^{\infty} dr e^{-ar^2} \phi_q^p \phi_{q'}^{p'}, \quad J_{qq'}^p = J_{qq'}^{pp}(0), \quad (15)$$

$$\begin{aligned} J_{qq'}^{pp'}(p'' \neq 0) = & \frac{2\pi^2}{a^{3/2}} \frac{|p''|}{2\sqrt{|p''|!}} \int_0^{\infty} dr e^{-ar^2} (ar^2)^{-\frac{|p''|}{2}} \\ & \times \gamma(|p''|, ar^2) \phi_q^p \phi_{q'}^{p'}, \quad (16) \end{aligned}$$

$$K_{qq'}^p = \frac{2\pi^2}{a^{1/2}} \int_0^{\infty} dr r^2 e^{-ar^2} \phi_q^p \phi_{q'}^p, \quad (17)$$

$$M_{qq'0}^{pp'p''} = I_{qq'0}^{pp'p''} - J_{qq'0}^{pp'}(p'') \quad (18)$$

$$M_{qq'q''}^{pp'p''} = I_{qq'q''}^{pp'p''} - \frac{2q'' + |p''|}{2\sqrt{q''(|p''|+q'')}} I_{qq'q''-1}^{pp'p''}, \quad (19)$$

$$N_{qq'0}^{pp'p''} = 0, \quad N_{qq'q''}^{pp'p''} \neq 0 = 2J_{qq'q''}^{pp'}(|p''|), \quad (20)$$

$$N_{qq'q''}^{pp'p''} \neq 0 = \frac{|p''|}{\sqrt{q''(|p''|+q'')}} I_{qq'q''-1}^{pp'p''}. \quad (21)$$

These constants, which are independent of a , may be tabulated and stored for future numerical calculations.

The system of equations (12) is equivalent to the coupled Fokker-Planck and Poisson equations (3)-(5) in cylindrical coordinates for a general, i.e. not necessarily axisymmetric, beam. It is valid for Fokker-Planck coefficients of arbitrary time dependence, which are required as inputs. It is clearly nonlinear in the coefficients, a property which is a signature of the nonlinear space-charge force, and must therefore be solved by numerical integration rather than by matrix methods. The number of nonzero coefficients will generally shrink in the presence of symmetries. In addition, $A_{00}^{00}(t) = 1$ follows from the conservation of the total number of particles, and $A_{00}^{01}(t) = 0$ identifies the free variable $a(t) \equiv 1/\langle r^2 \rangle$. The initial conditions are determined by decomposing the input beam into its polynomial components. A generalized emittance can be defined which is appropriate for use with beams in which the Cartesian components of the motion are coupled [7]. It is straightforward to express this generalized emittance in terms of the coefficients of the polynomial expansion. Examples of solutions will be discussed in future papers.

REFERENCES

- [1] C.L. Bohn, *Proc. 1992 Linear Accelerator Conf.*, AECL Report No. 10728, pp. 471-473 (1992).
- [2] C.L. Bohn, *Phys. Rev. Lett.*, **70**, 932 (1993).
- [3] M.V. Goldman, *Rev. Mod. Phys.*, **56**, 709 (1984).
- [4] D. Kehne, M. Reiser, H. Rudd, in *High-Brightness Beams for Advanced Accelerator Applications*, ed. W.W. Destler and S.K. Guharay, AIP Conf. Proc. 253, (AIP, NY, 1992), pp. 47-56; T.P. Wangler, *ibid.*, pp. 21-40.
- [5] S. Ichimaru, *Basic Principles of Plasma Physics*, (W.A. Benjamin, Reading, MA, 1973).
- [6] J.M. Dawson, *Rev. Mod. Phys.*, **55**, 403 (1983).
- [7] W.P. Lysenko and M.S. Overley, in *Linear Accelerator and Beam Optics Codes*, ed. C.R. Eiminshizer, AIP Conf. Proc. 177, (AIP, NY, 1988), pp. 323-335.

Collective Effects in the VEPP-3 Storage Ring

Sergey A. Belomestnykh and Alexey N. Voroshilov
Budker Institute of Nuclear Physics
630090, Novosibirsk, Russia

Abstract

Lengthening of a single bunch has been investigated in the VEPP-3 storage ring at different energies for beam current up to 100 mA. The bunch length was measured using optical diagnostic system. The current dependences of the transverse beam size, synchronous phase shift, coherent and incoherent synchrotron tune shift have been measured. The experimental data are in agreement with the model of longitudinal potential well distortion. The real and imaginary parts of the longitudinal coupling impedance are deduced from measured data.

I. INTRODUCTION

The VEPP-3 storage ring is a 2 GeV electron and positron storage ring, which is multiarmed facility [1]. This storage ring is operating with routine current up to 100...150 mA.

Two RF systems - at 2nd and 18th harmonics of a revolution frequency - are used at the VEPP-3 operation. The injection of particles takes place when the first one is working. The injection energy is 350 MeV. At the energy of 600 MeV, the second RF system is switched on to provide the acceleration of particles to the energy of experiment and to compensate synchrotron radiation energy losses. The maximum RF voltage is equal to 600 kV. During the experiment the 2nd harmonic cavity stays passive.

The bunch lengthening and incoherent synchrotron tune shift in the VEPP-3 storage ring has been measured [2], but that experiments was made only at injection energy and with low value of 1st harmonic RF voltage.

In this paper we present the measurements of collective effects, i.e. current dependences of the bunch length, width, synchronous phase shift and coherent and incoherent synchrotron tune shifts at the beam energies of 600, 1200 and 2000 MeV and at the maximum RF voltage.

II. INSTRUMENTATION AND RESULTS

The applied method for observation of beam parameters is based on using of a synchrotron radiations light emitted by the bunch of charged particles at one of the bending magnets [3]. We used two dissectors: for measuring longitudinal and transverse profile of a beam.

To decrease the statistical spread, the results of 16 measurements are accumulated and averaged at the each current point. The longitudinal resolution is 13 mm. This value have been obtained by measuring dependence of a beam length on RF voltage at a low current (less than 100 μ A). One has to obtain a voltage dependence of a beam length at this current value like square root. The transverse resolution less than 0.17 mm has been obtained.

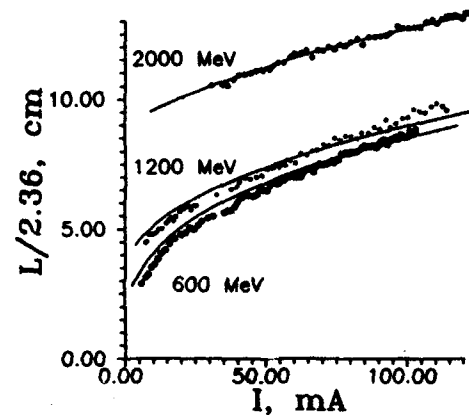


Figure 1: Bunch length versus current (L - halfwidth bunch length, $s = L/2.56$).

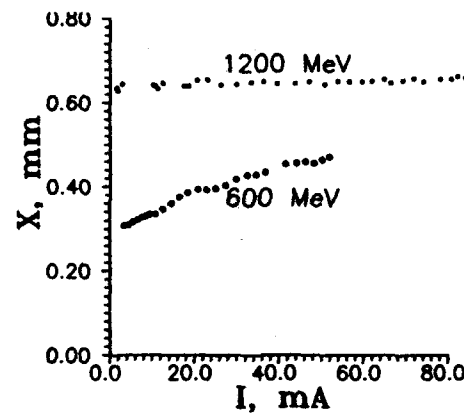


Figure 2: Current dependence bunch horizontal transverse size.

A. Bunch lengthening measurements

In Table 1 measured zero current length of a bunch at different energies is presented. The current dependence of bunch length at these energies is shown in Figure 1.

Table 1
Bunch length at zero current

Beam energy	MeV	600	1200	2000
rms bunch length	cm	1.4	3.8	9.0

The bunch length may increase due to different mechanisms with increasing of a beam intensity. At low energies beam transverse and longitudinal sizes could increase due

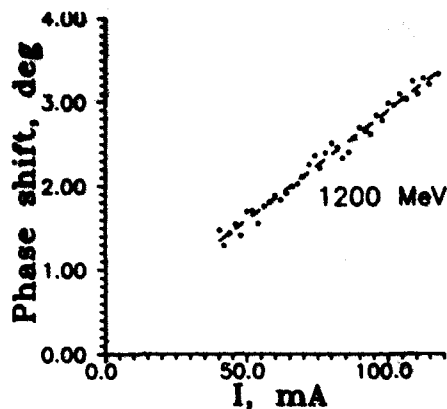


Figure 3: Current dependence synchronous phase shift.

to intrabeam scattering effect, which is suppressed at high energy with the law: $\sigma_e, \sigma_x \sim 1/\gamma$, where $\sigma_e = \sigma_E/E$ is the energy spread, σ_x - the horizontal beam size, and γ - the relativistic factor. At a high current, the beam length increases due to potential well distortion and so called microwave instability. The behavior of a bunch lengthening due to potential well distortion can be described as [4]

$$\left(\frac{\sigma_l}{\sigma_{l0}}\right)^3 - \frac{\sigma_l}{\sigma_{l0}} = \frac{\sqrt{2\pi} I_0 |Z_n/n|}{qU_0} \left(\frac{R}{\sigma_{l0}}\right)^3, \quad (1)$$

where I_0 is the average beam current, q is the RF harmonic number, U_0 is accelerating voltage, $|Z_n/n|$ is the longitudinal coupling impedance at the n -th harmonic number of the revolution frequency, R is the mean radius of the ring, and σ_{l0} is the beam length at zero current. In the case of potential well distortion there is no increase of energy spread but incoherent synchrotron tune shift can be very large.

On the other hand, the bunch lengthening due to microwave instability is accompanied by energy spread increasing. For the case $|Z_n/n|$ has no frequency dependence (pure inductance), we have scaling law [5] $\sigma_l \sim I^{1/3}$ above threshold current of instability.

The value of longitudinal coupling impedance at the n -th harmonic of the revolution frequency, determined by the eq. (1), is equal to 11.3 Ohm at 600 MeV. At energies of 1200 and 2000 MeV these values are equal to 12.1 and 15.4 Ohm respectively. Besides we observed a length dependence of the value $|Z_n/n|$. The continuous curves in Figure 1 correspond to a theoretical dependence, determined by (1) for given values of an impedance. Note, no microwave instability threshold current was noticed.

At low currents the bunch has gaussian longitudinal shape. At high currents the bunch longitudinal shape changes from Gaussian to parabolic profile. Besides an asymmetry of bunch shape takes place. This asymmetry could be provided by the contribution of real part of impedance.

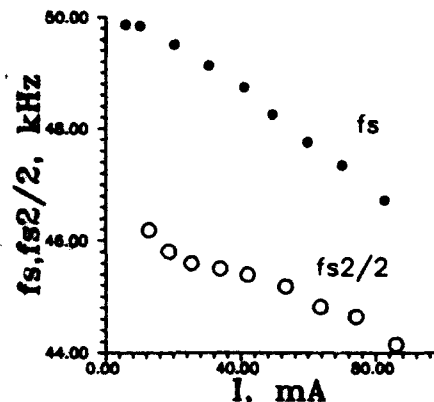


Figure 4: Current dependence synchrotron frequencies at 600 MeV.

B. Bunch energy spread measurement

To obtain an information about energy spread, we measured a current dependence of bunch horizontal transverse size. But this value is determined by both betatron and synchrotron bunch sizes. In our case the betatron horizontal size is a little bit larger than the synchrotron one at the point of light emitting. In Figure 2 the current dependence of bunch horizontal transverse size is shown. At the energy of 1200 MeV (and 2000 MeV, which case is not presented at this graph) there is no change of a bunch transverse size. At the energy of 600 MeV there is a weak changing of this value with the current. Computer simulation shows that this dependence could be provided by the intrabeam scattering effect (for given bunch length current dependence).

C. Synchronous phase shift measurement

The synchronous phase shift is being determined as a difference between phase of beam longitudinal distribution center of mass and phase of RF system reference signal. The phase difference between reference signal phase and RF cavity phase is kept constant by phase feedback system. The accuracy is less than 0.1 degree.

The measurements of synchronous phase shift were done for energies of 1200 and 2000 MeV and results coincide. At the energy of 600 MeV this measurement haven't be obtained, probably due to phase oscillation of a beam. The results are shown in Figure 3. Experimental data allowed to determine a value of a bunch coherent energy loss. At current 100 mA this value is equal to 35 kV. This corresponds to the real part of impedance $R = \text{Re} |Z_n| = 1300 \text{ Ohm}$.

D. Synchrotron tune shift measurement

It is possible to obtain some information about incoherent synchrotron tune shift by observing the behavior of longitudinal quadrupole mode frequency. In these experiments we excited dipole and quadrupole mode oscillations by phase and amplitude modulation of RF voltage, and then observed a response from a beam position monitor.

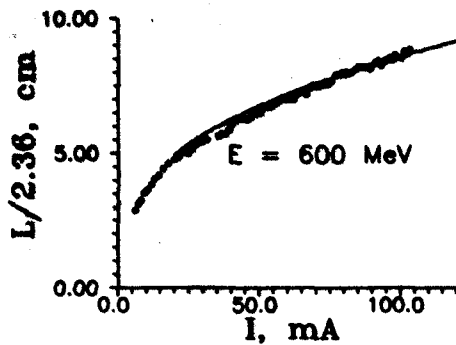


Figure 5: Calculated current dependence bunch length.

In Figure 4 the current dependence of the frequencies of dipole and quadrupole synchrotron modes at energy of 600 MeV are presented. We see that both the quadrupole and dipole modes frequencies decrease, and tune shift for the quadrupole mode is more than 10% at current 80 mA. At energy of 600 MeV we couldn't measure a quadrupole mode shift at current less than 10 mA because of exiting the coherent phase oscillations.

III. ANALYSIS

When the bunch wake fields damp during one revolution period, we have so called broad band impedance, which is provided by different discontinuities of a vacuum chamber. Otherwise, when the bunch interacts with self-fields supplied by the elements, having high quality factor Q , say about narrow band impedance. In our experiment the bunch lengthening was insensitive to the position of the cavity higher order modes tuners (apart from narrow bands where we observed coherent longitudinal instabilities) and to the position of the passive cavity tuner. So we conclude only single turn effects take place, which are described by broad band impedance model.

In the Figure 1 we see there is no good agreement of experimental data with the theoretical curve, calculated using eq. (1). Besides the bunch length arises steeper than $1/3$ power of a beam current at energies 600 and 1200 MeV, provided pure inductive impedance. We suppose both parts of impedance - inductance and resistance - contribute the potential well distortion. To analyze beam lengthening due to potential well distortion we solved balance equation using a condition of full compensation of external RF voltage by fields produced of a bunch itself. For this condition the potential well has a flat bottom for all bunch lengths. The analysis of stability with this condition have been done at [6]. Let L and R are the inductive and the resistive parts of effective longitudinal coupling impedance. Equations for potential, produced a bunch itself is given:

$$L \frac{dI(t)}{dt} + RI(t) = U_s(t), \text{ where } U_s = -q\omega_0 U_0 t. \quad (2)$$

Here and further ω_0 is the revolution frequency, $\tau = L/R$, t_h , t_t - the displacement of a head and a tail of a bunch, N - number of particles, e - the electron charge. Let $\Delta = (t_t - t_h)$ is the bunch length and $t_m = \frac{1}{2}(t_t + t_h)$ is the bunch mass center displacement (for simplification we ignore here the bunch shape asymmetry). Using boundary condition for the bunch tail we get an equation for bunch length current dependence, which can be solved numerically:

$$\Delta = 2 \cdot \left(\frac{T^2}{\Delta} + \tau - \left(\tau + \frac{\Delta}{2} + \frac{T^2}{\Delta} \right) \cdot \exp \left(-\frac{\Delta}{\tau} \right) \right), \quad (3)$$

where $T^2 = \frac{RNq}{q\omega_0 U_0}$. Equation (3) describes quite correctly a bunch behavior for strong lengthening case, when it is possible to ignore zero current bunch longitudinal size (so called case of the frozen bunch [6]). In Figure 5 the calculated curve of a bunch length current dependence for $R = 1300$ Ohm and $L = 600$ nH (continuous curve) together with the experimental data points at the energy 600 MeV are presented.

IV. CONCLUSIONS

The current dependence of bunch length was measured. This dependence is in a quite good agreement with that obtained from solution of balance equation if real and imaginary parts of broad band impedance are of the same order.

Also a change of the bunch longitudinal shape has been observed. To separate the single turn (broad band impedance) and multiturn effects, the current dependence of bunch length was measured at different positions of both cavities tuners and no difference of bunch lengthening have been observed. Hence observed effects are single turn ones.

V. ACKNOWLEDGMENTS

The authors wish to thank S.Mishnev and E.Zinin for useful discussions and help in the installation of measurement technique. Also we wish to acknowledge N.Vinokurov, A.Burov and E.Perevedentsev for very useful discussions on the subjects of this paper.

REFERENCES

- [1] S.A.Belomestnykh et al., *Proc. of the XI All Union Conf. on Part. Accel.*, Dubna, 1989, Vol.1, p.410.
- [2] N.A.Vinokurov et al., *Proc. of the V All Union Conf. on Part. Accel.*, Dubna, 1977, Vol.2, p.16.
- [3] E.I.Zinin, *Nucl. Instr. Meth. A* 208, No.1/3, 439(1983).
- [4] B.Zotter, CERN/ISR-TH/78-16 (1978).
- [5] A.W.Chao and J.Gerate, PEP-224 (1976).
- [6] A.V.Burov, *Sov. JTP.* 56, No.10, 1941 (1986).

Single Bunch Effects in the Daresbury SRS

L A Welbourne, J A Clarke, D M Dykes, S F Hill, E A Hughes, M W Poole, P D Quinn, S L Smith, V P Suller.

SERC Daresbury Laboratory, Daresbury, Warrington, WA4 4AD, UK.

Abstract

Single bunch currents in the SRS have now been increased to over 100 mA injected at 600 MeV, with user beams of 50-60 mA at 2 GeV routinely obtained. Such high currents in short (500 MHz) bunches have necessitated attention to ensuring adequate lifetimes, including deliberate control of bunch volume to reduce Touschek losses. At lower energies substantial bunch lengthening has been experienced which has been compared with standard theoretical models. The associated prediction of chamber impedance has been compared with results obtained from mode shift experiments. Other aspects of single bunch behaviour in the SRS are also mentioned.

I. INTRODUCTION

During a recent shutdown to install a second superconducting wiggler magnet [1] a new injection septum and kicker magnets were installed in the SRS. This has led to greatly improved single bunch injection with over 110 mA being accumulated at 600 MeV. Much higher current per bunch is achieved than in the normal (all 160 bunches filled) multibunch mode of operation. At these high current densities the beam lifetime is limited by Touschek losses even at 2 GeV. In order to alleviate this effect the lattice is operated close to a working point with betatron tunes $Q_r=4.25$, $Q_v=3.25$ which has higher emittance [2]. Experiments have been carried out to increase the lifetime by varying the emittance coupling and hence the bunch volume with a view to minimising Touschek losses.

The high currents obtained have enabled a thorough investigation of bunch lengthening effects. Bunch lengthening behaviour has been assessed as a function of beam current at a range of energies up to 1.8 GeV and in particular detail at 600 MeV. A determination of the effective broadband impedance has been made from these results and also from measurements of vertical tune shift with beam current at 600 MeV.

II. MEASUREMENT SYSTEM

Beam profile and bunch length measurements are made on a dedicated optical diagnostic beam line on the SRS [3]. Profile measurements in the horizontal and vertical plane are made using photodiode arrays and captured with a Macintosh computer using the data acquisition software LabVIEW [4]. Bunch length measurements are made using a stroboscopically synchronised image dissector tube [5] and are also analysed using the LabVIEW system.

III. BEAM LIFETIME

Measurements of beam lifetime dependence on current in single and multibunch modes have been used to calculate the Touschek lifetime, which has a dominant contribution to the

overall single bunch beam lifetime. Touschek lifetimes as short as 12 hours for 40 mA at 2 GeV have been measured, rising to 56 hours at 10 mA.

The bunch volume is dependent on proximity to the coupling resonance $Q_r-Q_v=1$. Small changes to the vertical tune have been made such that the horizontal/vertical tune split causes the beam to approach or avoid this resonance. Tune splits of 26 - 200 kHz which corresponds to 0.008-0.048 in non-integer tune space have been assessed. The orbit frequency is 3123 kHz. Experiments were carried out under conditions close to those during user beam i.e. with the superconducting wiggler magnet energised at 5 T and the undulator magnet at minimum gap. The variation of bunch volume as a function of tune split is shown in Figure 1.

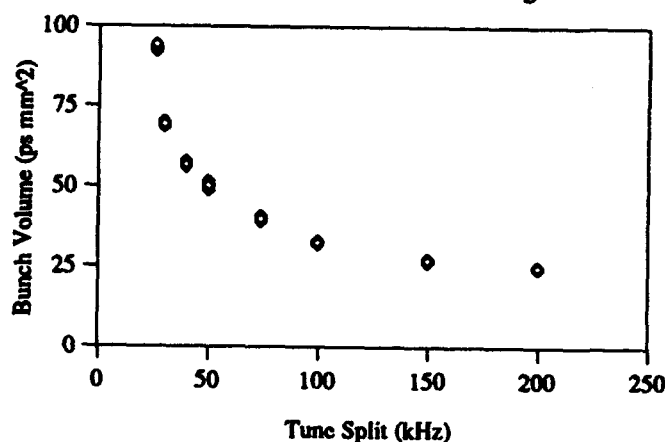


Figure 1. Bunch volume as a function of tune split for 30 mA single bunch beam.

The subsequent lifetime variation with tune split is shown in Figure 2. It is clear that a significant increase in the beam lifetime can be gained at increased coupling. Nominally a tune split of 40 kHz is used during operations.

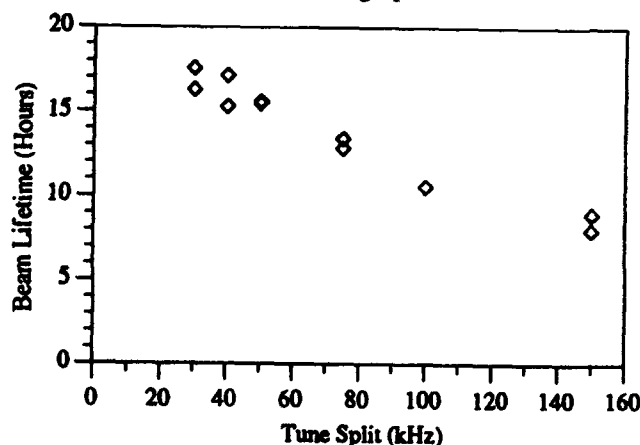


Fig 2. Total beam lifetime as a function of tune split.

IV. IMPEDANCE EFFECTS AT 600 MeV

Bunch Lengthening Effects

The longitudinal microwave instability threshold in the SRS has been calculated to be ~ 1.5 mA using the program ZAP [6]. All of the bunch length data collected has been in excess of that current, and hence it is assumed that bunch lengthening is predominantly due to this effect. Provided the bunch length is greater than the beam pipe radius, the dependence of bunch length σ_l on beam current I_b is given by [7]

$$\sigma_l = \left[\frac{I_b \alpha e}{\sqrt{2\pi E} V_s^2} \left| \frac{Z_{||}}{n} \right|_{0}^{BB} \right]^{1/3} R \quad (1)$$

where α is the momentum compaction, e the electronic charge, E the beam energy, V_s the synchrotron tune, R the ring average radius and the longitudinal broadband impedance denoted by

$$\left| \frac{Z_{||}}{n} \right|_{0}^{BB}$$

Several experiments have been carried out to measure bunch length as a function of beam current at 600 MeV. Previously two state bunch lengths have been reported [8] but this phenomena has recently been uncommon. For the few points where two state bunch length was observed, the shorter bunch length has been used. The results were fitted to equation 1 which yielded a value for the longitudinal effective broadband impedance of $8.6 \Omega \pm 0.6 \Omega$.

Above the microwave instability threshold, both bunch length and momentum spread are increased. Bunch lengthening behaviour at 600 MeV has been modelled using the lattice simulation program ZAP, and a comparison made with the experimental results. From the results presented above, an impedance of 8.6Ω was assumed for the modelling. The experimental data along with the theoretical model is shown in Figure 3.

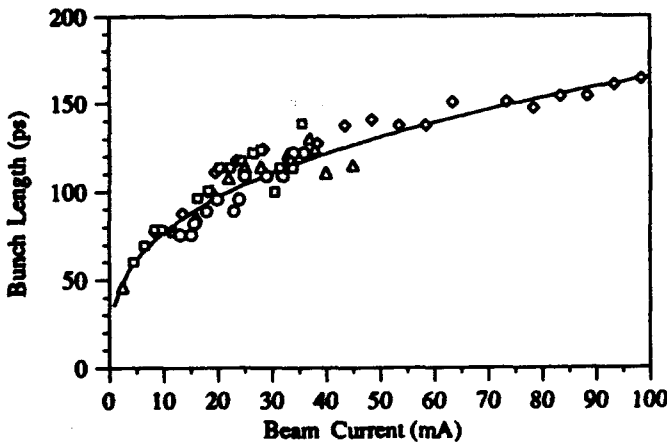


Figure 3. Measured and theoretical bunch length as a function of current.

Previous results from bunch lengthening and independently from direct vessel impedance measurements have indicated that the impedance is of the order $10-15 \Omega$ [8]. These earlier measurements were made with different septum and kicker magnets which would be expected to have slightly higher impedance. At high currents the bunch-length may be increased by potential well distortion, however the effects of this are small over the current range normally seen in the SRS.

Radial Beam Size

The increase in momentum spread in the beam causes an increase in the beam size at points of finite dispersion in the ring. The SRS is of a FODO design, and has finite dispersion all around the lattice.

In conjunction with bunch length, measurements have been made of beam sizes. Horizontal beam size as a function of beam current has been measured between 10 and 50 mA. The program ORBIT [9] has been used to calculate radial beam size as a function of beam current. The results are inconsistent with an assumed impedance of 8.6Ω . The modelled beam size behaviour for an impedance of 6.4Ω together with experimental data is shown in Figure 4.

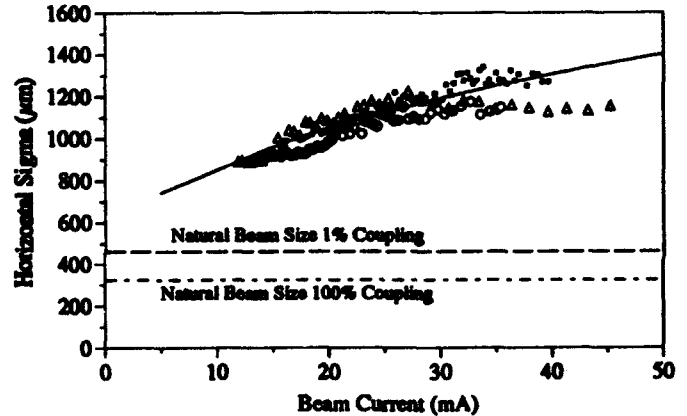


Figure 4. Horizontal beam size as a function of current showing modelled and measured beam sizes.

Clearly the revised estimate of 6.4Ω gives a good fit to the experimental points. It should be noted however that the coupling is assumed to be 100% in the modelled case in order to give an upper estimate of Z/n . It is difficult to assess the real emittance coupling at 600 MeV as the vertical beam size is blown up to a greater extent than would be found with 100% coupling of the natural horizontal emittance.

Betatron Tune Shift

Vertical tune shift as a function of beam current has also been measured. The results are illustrated in Figure 5. The data has been fitted to the lowest head-tail mode in the following form [7];

$$\Delta \nu_v = - \frac{e \hat{\beta}_v R}{4 \sqrt{\pi E} \sigma_l} Z_v I_b \quad (2)$$

where β_v is the average vertical beta function, equal to 5.8 m and Z_v the effective vertical impedance. The transverse impedance is related to the longitudinal broadband impedance by

$$\left| \frac{Z_{\perp}}{n} \right| = \frac{b^2}{2R} Z_{\parallel} \quad (3)$$

for a round beam pipe of radius b .

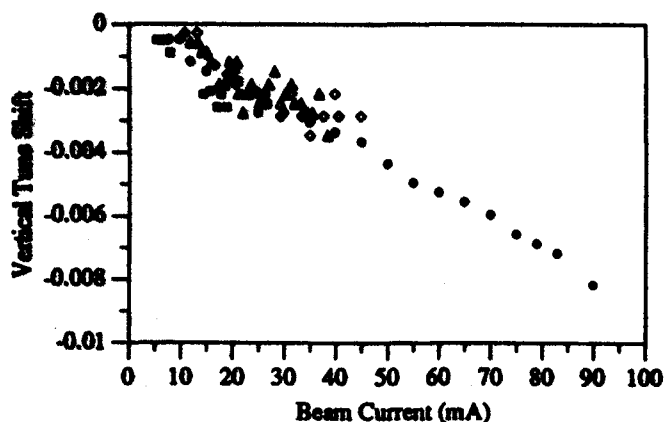


Figure 5. Tune shift as a function of beam current.

If the assumption is made that $Z_{\perp} = Z_v$ and the average geometrical beam pipe radius is ≈ 30 mm, the measured data gives a value for the broadband impedance of 6.8Ω - similar to that predicted by the horizontal beam size increase.

V. BUNCH LENGTH VARIATION WITH ENERGY

Bunch length has also been measured as a function of beam current at 1.0, 1.5 and 1.8 GeV. At injection energy measurements have been made with currents up to 100mA, however rather lower currents were measured at higher energies due to current losses during the energy ramp. The experimental data is shown in Figure 6.

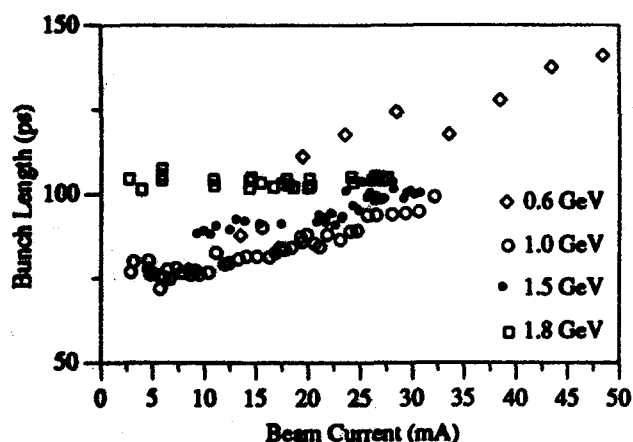


Figure 6. Bunch length variation at different energies.

A fit to the experimental data using equation 1 gave results largely in agreement with previous experiments. An impedance of 8.9Ω was calculated from the 1.0 GeV data. At 1.5 GeV however, the calculated 14.1Ω is more questionable, but this contains a large error since only a few points were obtained above threshold. No bunch lengthening was observed at 1.8 GeV as the beam current was well below threshold.

VI. CONCLUSIONS

Experiments to vary the emittance coupling have shown that beam lifetime can be significantly increased at lower tune splits due to the reduction of Touschek effects. It is possible that in future operations this result could be used to improve lifetime such that current losses during the energy ramp from 0.6 to 2.0 GeV are minimised, and operational lifetimes are improved.

The behaviour of bunch length as a function of current has been studied at 600 MeV and at higher energies up to 1.8 GeV. An estimate of the longitudinal broadband impedance was made from the bunch lengthening work of 8.6Ω . A fit to the radial beam size experimental data required coupling to be set to 100%. Because of uncertainties in the true coupling at 600 MeV it is not clear whether this is a realistic simulation. This data predicted an impedance of 6.4Ω . Calculation of impedance from mode shift measurements at 600 MeV implies that the impedance is 6.8Ω .

Bunch length as a function of current at different energies has given a number of different results for broadband impedance. However the best fits to the experimental data gave results of 8.9Ω and 14.1Ω , which are not too far removed from previous experiments.

VII. REFERENCES

- [1] L A Welbourne 'A Second Superconducting Wiggler Magnet for the Daresbury SRS.' *Synchrotron Radiation News* Vol.5 No.5.
- [2] V P Suller et al., 'Performance of the Daresbury SRS with an Increased Brilliance Optic.' *Proc. European Particle Accelerator Conference 1988* pp 418-420.
- [3] J S MacKay 'Electron Beam Profile, Position Systems and Measurements on the Daresbury SRS.' *Proc. European Accelerator Conference 1988* pp 43-45.
- [4] National Instruments, Austin, Texas.
- [5] G S Brown et al., 'Measurement of Bunch Length with an Image Dissector Tube' *IEEE Trans. Nuc. Sci. NS-30* No.5 pp2348-2350, Aug. 1983.
- [6] M Zisman et. al., *ZAP Users Manual* LBL-21270 Dec. 1986.
- [7] Nakamura N et. al., 'Collective Effects in Single Bunch Mode at the Photon Factory Storage Ring' *Proc. IEEE Particle Accelerator Conference 1991* Vol. 1 pp 440-442.
- [8] M W Poole et. al., 'Beam Instability Characteristics of the Daresbury SRS.' *Proc. European Accelerator Conference 1988* pp 830-832.
- [9] S L Smith, 'ORBIT user Guide' Daresbury Laboratory Internal Report.

The Effects of Coulomb Beam Interaction in Multiaperture Linac

A.I. Balabin, G.N. Kropachev, I.O. Parshin and D.G. Skachkov
ITEP, Bolshaja Chertomushkinskaja 25, 117259 Moscow, Russia

Abstract

In a multiaperture linac the Coulomb coherent beam oscillations are excited and thus stimulate particle losses. To analyse the coherent oscillations the model is proposed, in that the Coulomb fields of surrounded beams in relation to the considered bunch train are approximated by the fields of uniformly charged threads. The low order mode equations are derived by linearisation of Coulomb and external fields. The beam interaction effects in the multiaperture alternating phase focused linac are studied. The dipole mode is shown to influence mainly the beam dynamics in this linac, and increasing of bunch sizes by the quadrupole mode is negligible.

1 INTRODUCTION

The basic method of total current increasing in ion linac is a use of multiaperture accelerating systems [1]. In a multiaperture linac the Coulomb coherent beam oscillations are excited and thus stimulate particle losses. The dipole and quadrupole modes are the low order modes of these oscillations. The dipole mode excites the bunch centre oscillations, and the quadrupole mode increases the bunch sizes. To analyse the coherent oscillations the model is proposed, in that the Coulomb fields of surrounded beams in relation to the considered bunch train are approximated by the fields of uniformly charged threads. The equations for dipole and quadrupole modes of coherent oscillations are derived by linearisation of Coulomb and external fields. The beam interaction effects in the multiaperture alternating phase focused linac (APF) are studied.

2 THE EQUATIONS FOR DIPOLE AND QUADRUPOLE MODES OF COHERENT BEAM OSCILLATIONS

We derive the equations for dipole and quadrupole modes of coherent oscillations of a bunched beam in the given channel of a multiaperture drift tube linac. The considered beam is represented by a sequence of uniformly charged ellipsoids with semiaxes r_x, r_y, r_z following each other at distance L . The Coulomb fields of surrounded beams in relation to the considered bunch train are approximated by the fields of uniformly charged threads. The Coulomb field potential inside a beam propagating in the given channel is

$$U(x, y, z) = U_i(x, y, z) + U_e(x, y, z),$$

where x, y, z are coordinates originated from the given channel axis; U_i is the beam self-field potential; U_e is the field

potential created by all other beams of the multiaperture linac.

The potential U_i is determined by the field superposition of all ellipsoidal charges. If we neglect the metal boundary influence the self-field potential inside the considered bunch in linear approximation to space-charge forces is described by the quadratic form

$$U_i(x, y, z) = -\frac{\rho}{2\epsilon_0} [M_x^2(x-x_0)^2 + M_y^2(y-y_0)^2 + M_z^2(z-z_0)^2] \quad (1)$$

Here ρ is the space-charge density; ϵ_0 is the electric constant; x_0, y_0, z_0 are coordinates of the given bunch centre; M_x^2, M_y^2, M_z^2 are ellipsoid form factors with mutual influence of the bunches [2].

Within the framework of the accepted model the potential defining the beam interaction in the accelerating gaps has the form

$$U_e(x, y, z) = -\frac{1}{4\pi\epsilon_0\beta c} \sum_{\substack{j=1 \\ j \neq j_0}}^N I_j \ln[(x-x_j)^2 + (y-y_j)^2] + \text{const}, \quad (2)$$

where β is the ratio of synchronous particle velocity to the speed of light; c is the speed of light; N is the number of channels of the multiaperture linac; j_0 is the number of the given channel; I_j and (x_j, y_j) are current and centre coordinates of the beam in the j th channel (fig. 1).

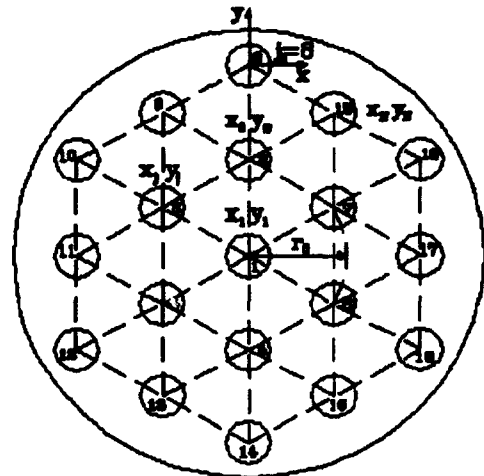


Figure 1: The arrangement of channels in the proton multiaperture APF linac.

We neglect the coupling between transverse degrees of freedom arising from the beam interaction. Then the linear equations of particles motion with the potential of the

beam self-field (1) and the potential of the beam interaction (2) may be written as follows

$$\begin{aligned}\frac{d^2x}{d\tau^2} + Q_x^*(\tau)x - \frac{\alpha M_x^*}{r_x r_y r_z}(x - x_0) &= f_x(\tau), \\ \frac{d^2y}{d\tau^2} + Q_y^*(\tau)y - \frac{\alpha M_y^*}{r_x r_y r_z}(y - y_0) &= f_y(\tau), \\ \frac{d^2(z - z_s)}{d\tau^2} + Q_z^*(\tau)(z - z_s) - \frac{\alpha M_z^*}{r_x r_y r_z}(z - z_s) &= 0.\end{aligned}\quad (3)$$

Here $\tau = t/T_F$; T_F is the transition time of the focusing period; $Q_{x,y}^*(\tau) = Q_{x,y}(\tau) - g_{x,y}(\tau)$; the functions $Q_{x,y,z}(\tau)$ are proportional to the external force gradients with opposite sign; $\alpha = \frac{2\lambda^2}{\gamma^2} \frac{I}{I_0} k_F^2$; I is the beam pulsed current in the given channel; λ is the wavelength of the accelerating field; γ is Lorentz factor; I_0 is the characteristic current; $k_F = S_F/\beta\lambda$; S_F is the length of the focusing period. The functions $f_{x,y}(\tau)$ and $g_{x,y}(\tau)$ caused by mutual influence of beams are determined by the expressions in the accelerating gaps

$$\begin{aligned}f_i(\tau) &= -\frac{1}{\beta(\tau)} \sum_{\substack{j=1 \\ j \neq i_0}}^N \alpha_j^* \frac{t_j}{x_j^2 + y_j^2}, \\ g_i(\tau) &= -\frac{1}{\beta(\tau)} \sum_{\substack{j=1 \\ j \neq i_0}}^N \alpha_j^* \frac{2t_j^2 - x_j^2 - y_j^2}{(x_j^2 + y_j^2)^2}, \quad (i = x, y)\end{aligned}$$

and equal zero in drift tubes of a multiaperture linac. The parameters α_j^* are $\alpha_j^* = \frac{2\lambda^2}{\gamma^2} \frac{I_j}{I_0} k_F^2$. Note that factor $1/\gamma^2$ is added in the formulas for α , α_j^* to take into account influence of the magnetic fields created by beam currents.

We introduce coordinates originating from the beam centre in the given channel: $\tilde{x} = x - x_0$, $\tilde{y} = y - y_0$, $\tilde{z} = z - z_s$. Then from (3) we receive equations of motion of the bunched beam centre

$$\begin{aligned}\frac{d^2x_0}{d\tau^2} + Q_x^*(\tau)x_0 &= f_x(\tau), \\ \frac{d^2y_0}{d\tau^2} + Q_y^*(\tau)y_0 &= f_y(\tau),\end{aligned}\quad (4)$$

and also equations for bunch semiaxes ($r_s < \frac{1}{2}L$)

$$\begin{aligned}\frac{d^2r_x}{d\tau^2} + Q_x^*(\tau)r_x - \frac{F_x^2}{r_x^3} - \frac{\alpha M_x^*}{r_y r_z} &= 0, \\ \frac{d^2r_y}{d\tau^2} + Q_y^*(\tau)r_y - \frac{F_y^2}{r_y^3} - \frac{\alpha M_y^*}{r_x r_z} &= 0, \\ \frac{d^2r_z}{d\tau^2} + Q_z^*(\tau)r_z - \frac{F_z^2}{r_z^3} - \frac{\alpha M_z^*}{r_x r_y} &= 0,\end{aligned}\quad (5)$$

where F_x and F_z are transverse and longitudinal beam emittances on the phase planes $(\tilde{x}, \frac{d\tilde{x}}{d\tau})$ and $(\tilde{z}, \frac{d\tilde{z}}{d\tau})$ respectively.

Transverse beam sizes in the channel are connected with bunch semiaxes by relations

$$\begin{aligned}R_{x,\max}(\tau) &= \pm r_x(\tau) + x_0(\tau), \\ R_{y,\max}(\tau) &= \pm r_y(\tau) + y_0(\tau).\end{aligned}\quad (6)$$

Table 1: APF linac design parameters

Ion	H^+
Input energy	60 keV
Output energy	3 MeV
Frequency	148.5 MHz
Number of channels	19
Aperture radius of one channel	3.3 mm
Pulse current limit in one channel	13 mA
Phase acceptance	120°
Longitudinal phase advance	62°
Normalised transverse acceptance of one channel	0.13 $\pi \text{ cm} \cdot \text{mrad}$
Transverse phase advance	67°
Number of focusing periods	7
Focusing period length	$3\beta\lambda$
Number of accelerating gaps	28
Peak field in gap	180 kV/cm
Accelerator length	1.45 m

Thus, in multiaperture accelerating systems the coherent beam oscillations caused by Coulomb beam interaction are excited. The proposed model of this interaction enables to study the dipole and quadrupole modes of coherent oscillations. The dipole mode excites the beam centre oscillations and obeys equations (4), and the quadrupole mode increases the bunch sizes according to (5).

3 THE COHERENT BEAM OSCILLATIONS IN THE ALTERNATING PHASE FOCUSED LINAC

We consider the coherent beam oscillations in the proton multiaperture alternating phase focused linac containing 19 channels (fig. 1). The main linac parameters are given in table 1.

In the central channel the Coulomb fields created by peripheral beams are compensated completely. The beam dynamics in the central channel of the multiaperture linac is studied by means of a set of equations (5). The periodic solutions of equations (5) in the first focusing period at $g_{x,y}(\tau) \equiv 0$ were accepted as injection conditions. The transverse beam emittance is chosen equal to 0.4 of the acceptance value. The transverse bunch sizes as functions of the longitudinal coordinate are shown in fig. 2 for zero and 7 mA injection currents.

As is seen in fig. 2, the envelope maximums are oscillated along the accelerator. Modulation of beam envelope maximums is caused by discontinuities of instantaneous values of transverse tunes at the joint points of focusing periods. In spite of existing beam mismatching the accelerated particle losses are absent in the central channel for injection currents not exceeding 7 mA.

The peripheral beams located in the vicinity of the drift tube boundary suffer the largest influence of Coulomb in-

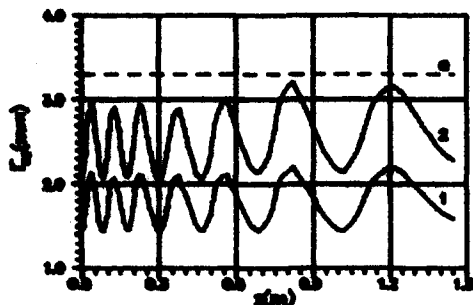


Figure 2: The transverse bunch semiaxes $r_{x,y}$ in the central channel 1 vs the longitudinal coordinate s for zero (1) and 7 mA (2) injection currents.

teraction forces. Due to the symmetry of channels arrangement in the multiaperture linac it is enough to consider the dynamics of interacting beams in channels 8 and 17 (fig. 1). We neglect displacement of bunch centres in the electrostatic injector of a multiaperture linac and accept beam emittances and initial bunch sizes equal to the corresponding values for the 7 mA central beam. The results of the solution of equations (4),(5) are plotted in fig. 3 for peripheral 7 mA beams propagating in channels 8 and 17.

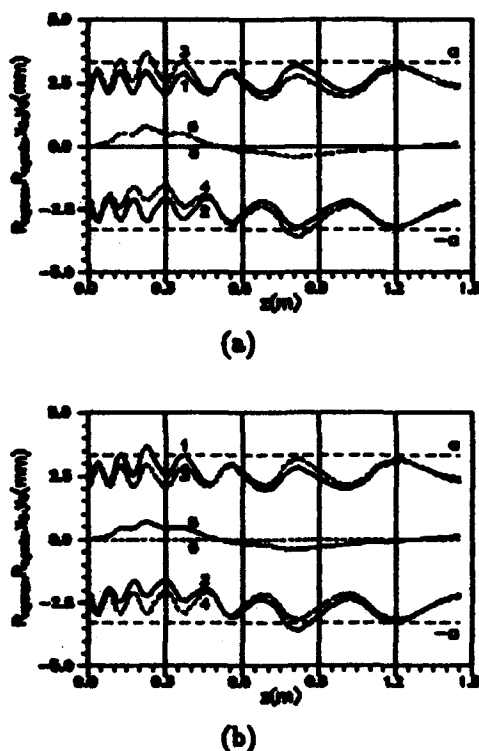


Figure 3: The transverse sizes $R_{x,max}$ (1), $R_{x,min}$ (2), $R_{y,max}$ (3), $R_{y,min}$ (4) and bunch centre position s_0 (5), y_0 (6) in peripheral channel 8 (a), 17 (b) vs the longitudinal coordinate s for 7 mA current in each beam.

The distance between the centres of channels is chosen equal to $r_c = 7.6 \text{ mm} = 2.3a$, where a is an aperture

radius of the channel. The given packing of channels provides high density of their arrangement and sufficient construction rigidity of multiaperture drift tubes. As is seen in fig. 3, the bunch centre oscillations (dipole oscillations) are stable and are accomplished in the radial plane passing over the centre of the considered channel. This polarization of dipole oscillations is accounted for by the fact that in the direction perpendicular to the radial plane the forces of beam interaction are compensated completely because of the channels symmetrical arrangement. For the given packing of channels the amplitudes of peripheral beam centre oscillations in channels 8 and 17 are 0.79 mm (0.24a) and 0.72 mm (0.23a) respectively.

The comparison of the curves in figs. 2,3 shows that increasing of semiaxes of peripheral bunches relative to the central ones is less than 0.5%. Therefore influence of the quadrupole mode on the beam dynamics in the linac is negligible.

The dipole mode of coherent oscillations mainly contributes in the effect of the beam size growth $|R_{x,y,min}|$, $R_{x,y,max}$ (6) in the channels of the multiaperture linac. For the given packing of beams the dipole mode excitation results in particle losses in peripheral channels (fig. 3).

One of the possible ways of particle loss reduction in linac is decreasing of the channel arrangement density. In particular, to transport beam in the considered multiaperture linac without particle losses the distance between the channels must be increased approximately 2.6 times [2].

4 CONCLUSION

To analyse coherent oscillations in a multiaperture linac the model is proposed, in that the Coulomb fields of surrounded beams in relation to the considered bunch train are approximated by the fields of uniformly charged threads. The equations for the low order modes of coherent oscillations are derived by linearisation of Coulomb and external fields. The beam interaction effects in the multiaperture alternating phase focused linac are studied. The Coulomb beam interaction is shown to be substantial for packing of channels with high density ($r_c = 2.3a$). The dipole mode of coherent oscillations mainly influences the beam sizes in the channel. In the considered accelerating structure the bunch centre oscillations result in particle losses in peripheral channels. To decrease particle losses in a multiaperture linac it is necessary to depress the dipole mode.

5 REFERENCES

- [1] B.P. Murin, B.I. Bondarev, V.V. Kushin, A.F. Fedotov, "Linear Ion Accelerators" /Edited by B.P. Murin, Moscow (1978), v.1, pp. 208-208.
- [2] A.I. Balabin, G.N. Kropachev, I.O. Parshin, D.G. Skachkov, "Coulomb Coherent Beam Oscillations in Multiaperture Linac", Nucl. Instr. and Meth. in Phys. Res., to be published.

Longitudinal Instability of an Induction Linac with Acceleration*

Lloyd Smith and Edward P. Lee
Lawrence Berkeley Laboratory
Berkeley, California 94720 USA

Abstract

The question arises as to what effect acceleration, which so far has been ignored, has on the longitudinal instability of an induction linac. The answer is not much for the anticipated acceleration rate (1 - 2 MeV/m) and minimum e-folding distance for the instability (50 - 500 meters). However, total unstable growth is significantly reduced over distances which are long enough for appreciable acceleration to occur. The purpose of this note is to record a calculation of the instability, including a constant acceleration rate. Some interesting features emerge -- for example, the velocity of the head is a more convenient independent variable than axial position and, for an initial sinusoidal perturbation of velocity in time, the number of oscillations along the pulse is constant; as the pulse shortens in time the frequency increases.

I. BASIC EQUATIONS AND UNPERTURBED SOLUTION

We start, as in previous work, with the one-dimensional cold fluid equations, neglecting the space charge force, and adopting a parallel R-C circuit for the perturbed electric field from the induction modules:

$$\partial \lambda / \partial t + \partial I / \partial z = 0 \quad (1)$$

$$\partial v / \partial t + v \partial v / \partial z = E_0 + E \quad (2)$$

$$\partial E / \partial t + E / \tau = -e \Delta I / mC \quad (3)$$

where E_0 is the applied field (multiplied by e/m), C is the circuit capacity and $\tau = RC$. The circuit parameters, R and C , might in general depend on axial position. E and ΔI are the perturbed components of electric field and beam current, while I , λ , and v are total beam current line charge and velocity.

The velocity of the head is given by:

$$v_H^2 = v_i^2 + 2az \quad (4)$$

where a is the constant acceleration and v_i is the head velocity at $z = 0$, where the initial perturbation occurs.

We change the independent variables (z , t) to $\bar{z} = z$ and:

$$\bar{t} = t - \int_0^z \frac{dz}{v_H} \quad (5)$$

Eliminating λ , the fluid equations become:

$$\frac{\partial}{\partial \bar{t}} \left(\frac{1}{v} - \frac{1}{v_H} \right) I + \frac{\partial I}{\partial \bar{z}} = 0 \quad (1')$$

$$v \left(\frac{1}{v} - \frac{1}{v_H} \right) \frac{\partial v}{\partial \bar{t}} + v \frac{\partial I}{\partial \bar{z}} = E_0 + E \quad (2')$$

$$\frac{\partial E}{\partial \bar{t}} + \frac{E}{\tau} = -\frac{e \Delta I}{mC} \quad (3')$$

II. CASE OF INCREASING CURRENT

For the unperturbed pulse, we take $I = v_H I_1 / v_i$, independent of time during the pulse and lasting for a time, $T = v_i T_1 / v_H$. The velocity during the pulse is given by (1'):

$$v = \frac{v_H}{1 - \frac{a\bar{t}}{v_H}} \quad (6)$$

Note that aT/v_H is the velocity tilt $\Delta\beta/\beta$. In the GeV energy range, this quantity is quite small. The required voltage wave shape as a function of z and t is given by (2'):

$$E_0 = a \frac{\left(1 - \frac{3a\bar{t}}{v_H} \right)}{\left(1 - \frac{a\bar{t}}{v_H} \right)^3} = a \left[1 - 3 \left(\frac{a\bar{t}}{v_H} \right)^2 \right] \quad (7)$$

III. INSTABILITY

*This work supported by the Director, Office of Energy Research, Office of Fusion Energy, of the U. S. Department of Energy under Contract No. DE-AC03-76SF00098.

The next step is to find equations for a linearized perturbation of the unperturbed quantities. This process is rather messy because the unperturbed quantities also depend

on \bar{z} and \bar{t} . However, the equations are greatly simplified by replacing \bar{z} and \bar{t} by v_H and a scaled time:

$$v_H = \sqrt{v_i^2 + 2a\bar{z}} \quad (8)$$

$$\bar{t} = \frac{v_H}{v_i} \bar{t} \quad ,$$

and taking the perturbed quantities to be of the form:

$$I + \Delta I = \frac{v_H}{v_i} I_i (1 + u) \quad (9)$$

$$\Delta v = \left(1 - \frac{a\bar{t}}{v_H}\right) \hat{v} \quad .$$

The equations for u , \hat{v} , and E are:

$$\frac{\partial u}{\partial v_H} = \frac{1}{av_i} \frac{\partial}{\partial \bar{t}} \left(1 - \frac{av_i}{v_H^2} \bar{t}\right)^3 \hat{v} \quad (10)$$

$$\frac{\partial \hat{v}}{\partial v_H} = \frac{1}{a} E \quad (11)$$

$$\frac{\partial E}{\partial \bar{t}} + \frac{v_i}{v_H} \frac{E}{\tau} = -k^2 v_i^3 u \quad (12)$$

$$k^2 = \frac{eI_i}{mCv_i^3} \quad (13)$$

These equations are of the same form as those for the unaccelerated case except for the cubed parenthesis in (10) and the factor, v_i/v_H in (12). The equations are exact in the sense that $a\bar{t}/v$ is not yet assumed to be small. The duration in \bar{t} is:

$$T' = \frac{v_H}{v_i} T = T_i \quad ,$$

which means that a disturbance maintains the same relative position in time as the pulse shortens and the rate of change in real time increases. In particular, a sinusoidal perturbation would retain the same number of cycles over the pulse duration, as mentioned above.

Equation (12) is simplified if we assume that the gap capacity is independent of position but that the matched resistance is inversely proportional to the current (directly proportional to pulse duration). Equation (12) is then:

$$\partial E / \partial \bar{t} + E / \tau_i = -k^2 v_i^3 u \quad ,$$

where τ_i is the time constant at $z = 0$.

Furthermore, the extra terms in the cubed parenthesis in (10) appear to give corrections of order $\Delta\beta/\beta$ and can be neglected. The equations then have the same form as for the unaccelerated case; if the initial perturbation is:

$$\hat{v}(z=0) = \delta e^{i\omega\bar{t}} \quad ,$$

a particular solution for \hat{v} is:

$$\begin{aligned} \hat{v} &= \delta e^{i\omega\bar{t}} \cos \left[\frac{kv_i}{a} \sqrt{\frac{i\omega\tau_i}{1+i\omega\tau_i}} (v_H - v_i) \right] \\ &= \delta e^{i\omega\frac{v_H}{v_i}\bar{t}} \cos \left[kz \sqrt{\frac{i\omega\tau_i}{1+i\omega\tau_i}} \frac{2v_i}{v_H + v_i} \right] \end{aligned} \quad (14)$$

For $a = 0$, we have $v_i = v$ and the e-folding rate with z is the imaginary part of $\sqrt{i\omega\tau/(1+i\omega\tau)} k$. The maximum growth rate is $k/\sqrt{8}$, which occurs when $\omega\tau = 1/\sqrt{3}$. For $a \neq 0$ and z large, $v_H \sim \sqrt{2az}$ and the perturbation only grows exponentially with $z^{1/2}$. However, if $k \sim (50 \text{ meters})^{-1}$, the accelerating gradient $\sim 1 \text{ MeV/meter}$ and a perturbation occurs at $\sim 1 \text{ GeV}$, there are many e-foldings before v_H is significantly greater than v_i . The coasting beams assumption is then good enough to show the nature of the problem, however it is of interest to examine the breakdown of this approximation over long distances.

IV. CASE OF CONSTANT CURRENT

So far we have computed the instability growth rate for a pulse where the current increases proportional to $v_H(z)$, i.e. approximately fixed pulse length in meters. It is also of interest to compute growth for the case of constant current, where pulse length increases proportional to v_H but pulse duration T is constant. This could be the preferred approach at high energy if a practical lower limit on pulse duration for the synthesis of acceleration waveforms is observed (say $T > 100 \text{ ns}$). In this case the unperturbed velocity of the entire pulse is $v(z) = v_H(z) = \sqrt{v_i^2 + 2az}$, and in place of eqns. (1') - (3') we have for the perturbed components Δv , ΔI , E :

$$v^2 \partial \Delta I / \partial \bar{z} = \partial \Delta v / \partial \bar{t} \quad (1'')$$

$$\partial (v \Delta v) / \partial \bar{z} = E \quad (2'')$$

$$\partial E / \partial \bar{t} + E / \tau = -e \Delta I / mC \quad (3'')$$

Since E_0 and I are both constant it is reasonable to assume R and C are separately constant, since for efficient energy transfer we scale

$$R \propto E_0/I \text{ and } RC = \tau \propto T \propto I^{-1} \quad .$$

With these assumptions eqns. (1" - 3") yield an equation for Δv :

$$\left(\frac{\partial}{\partial t} + \frac{1}{\tau}\right) \frac{\partial^2}{\partial z^2} (v\Delta v) = - \frac{eI}{mC} \frac{1}{v^3} \frac{\partial}{\partial z} (v\Delta v) \quad (15)$$

Taking an initial perturbation, $\Delta v = \delta e^{i\omega t}$, with ω real, we have

$$\frac{\partial^2 v\Delta v}{\partial z^2} = -k^2 \frac{i\omega\tau}{1 + i\omega\tau} \left(\frac{v_1}{v}\right)^3 (v\Delta v) \quad (16)$$

where k is given by eqn. (13).

In general, eqn. (16) is solved by the bessel functions J_2 and N_2 of the argument x :

$$x = k\sqrt{\frac{i\omega\tau}{1 + i\omega\tau}} \frac{2v_1^{3/2}}{a} (\sqrt{v} - \sqrt{v_1}) \quad (17)$$

A convenient asymptotic form, obtained by the WKB method, is

$$\Delta v = \delta e^{i\omega t} (v_1/v)^{1/4} \cos(x) \quad (18)$$

Again, for small z growth is identical with that of the coasting beam. However, for large z a perturbation increases exponentially with $z^{1/4}$. This reduced rate of growth reflects the dilution of line charge density during acceleration at constant current. Note that the number of wavelength within the pulse ($= \omega T/2\pi$) remains constant, as before.

V. SUMMARY

In order to compare growth formulas for the three cases we have examined (drifting beam, constant line charge

density, and constant current), it is convenient to define a scale length proportional to v_1^2 :

$$z_0 = v_1^2/2a, \quad v_H = v_1 \sqrt{1 + z/z_0}$$

$$\text{Coasting Beam: } \Delta v \propto \cos kz \sqrt{\frac{i\omega\tau}{1 + i\omega\tau}}$$

Current proportional to v :

$$\Delta v \propto \cos \left[kz \sqrt{\frac{i\omega\tau}{1 + i\omega\tau}} \frac{2}{1 + (1 + z/z_0)^{1/2}} \right]$$

Constant Current:

$$\Delta v \propto \left(\frac{1}{1 + z/z_0}\right)^{1/8} \cos \left[kz \sqrt{\frac{i\omega\tau}{1 + i\omega\tau}} \frac{2}{1 + (1 + z/z_0)^{1/2}} \cdot \frac{2}{1 + (1 + z/z_0)^{1/4}} \right]$$

Keeping in mind that z_0 will be in the range 100 m - 2000 m, the following table gives the predicted reductions in the exponential of growth.

Note that for short distances of a few hundred meters ($z \leq z_0$) the coasting beam growth rate is an adequate approximation. At most, a few e-folds of growth are expected in this distance, and feedforward correction might be applied to eliminate further growth. However, when long distances ($z \gg z_0$) without use of corrections are considered, it is seen from Table I that very substantial reductions of total growth are predicted.

V. REFERENCES

- 1) Edward Lee, Proc. 1997 Linear Accelerator Conference at Ottawa, Ontario, Canada, AECL-10728, Vol. 2, pg. 591.

$I \propto v$		$I = \text{constant}$	
$\frac{z}{z_0}$	$\frac{v}{v_1} = \sqrt{1 + \frac{z}{z_0}}$	$\frac{2}{(1 + v_H/v_1)}$	$\frac{4}{(1 + v_H/v_1)(1 + \sqrt{v_H/v_1})}$
0.00	1.0000	1.0000	1.0000
0.30	1.1402	0.9345	0.9038
1.00	1.4142	0.8284	0.8013
3.00	2.0000	0.6677	0.5523
10.00	3.3166	0.4633	0.3285
30.00	5.5678	0.3045	0.1813

Table I. Reduction of growth with acceleration for current proportional to velocity and constant current. The tabulated factor is the reduction of exponential growth rate compared with that of a coasting beam.

On Solvable Model with Synchrotron Mode-Coupling

D.V. Pestrikov¹

KEK, National Laboratory for High Energy Physics,
1-1 Oho, Tsukuba-shi, Ibaraki, 305, Japan

Abstract

Typically the study of the collective stability of a bunch with the strong coupling of the synchrotron modes demands the solution of the infinite set of integral equations. The paper reports two cases, when these mode-coupling equation can be solved directly for synchrotron and for synchrotron collective modes.

I. INTRODUCTION

It is well known that in many cases the possibility of increasing the beam current in a storage ring is limited by coherent interaction of the beam bunches with their environment. In the case of a single-turn interaction, when the bunch wakes decay faster than the revolution period in the ring, the specific features of coherent instabilities significantly depend on the ratio of the bunch coherent frequency shift Ω_m to the frequency of synchrotron oscillations of particles in this bunch ω_s . If this ratio is high, the calculation of the increments of coherent modes and stability criteria demands the solution of a system of integral equations, which generally couple the harmonics of the bunch distribution function over the phases of synchrotron oscillations (see, for instance in [1,2]). The solvable examples of such problems except for their heuristic worth can be used to test the codes, designed for numerical study mode-coupling problems.

Here we report a simple model, when these equations can be solved directly for the synchrotron and synchrotron modes. However, the resulting dispersion equations are very complicated and, except for the case of a weak mode-coupling, still require a numerical solution.

II. SYNCHROBETATRON OSCILLATIONS

We describe the unperturbed vertical betatron and synchrotron oscillations of a particle near the closed orbit by usual formulae:

$$\begin{aligned} z &= a_s \cos \psi_s, \quad \theta = \omega_s t + \varphi, \quad \varphi_s = \varphi \cos \psi_s, \\ \dot{\varphi} &= -\omega_s \varphi_s \sin \psi_s, \quad \dot{\psi}_s = \omega_s = \omega_0 \nu_s, \\ \dot{\psi}_s &= \omega_0 \nu_s, \quad I_s = \frac{p}{2R_0} \nu_s a_s^2, \quad I_s = \frac{\mathcal{E} \nu_s}{2\omega_0 \alpha} \varphi_s^2. \end{aligned} \quad (1)$$

Here, $\Pi = 2\pi R_0$ is the perimeter of the orbit, ($\mathcal{E} \simeq pc$) is the energy of a particle. We neglect Landau damping

due to the nonlinearity of the particle synchrotron oscillations and we do the calculations for the case of the dipole betatron coherent oscillations, which are described by the expansion of the distribution function ($f_0 = F_0(I_s)\rho(\varphi)$)

$$f = f_0 + \sqrt{I_s} e^{i\psi_s} \sum_{m_s=-\infty}^{\infty} \chi_m(\varphi) e^{im_s \psi_s - i\omega t} + c.c. \quad (2)$$

Then, for a single-turn interaction the amplitudes χ_m satisfy the system of integral equations ($\omega = \pm\omega_s + \Delta\omega_m$) [2]

$$\begin{aligned} (\Delta\omega_m - m_s \omega_s) \chi_m &= \rho(\varphi) \int_{-\infty}^{\infty} dn \Omega_{m,n} J_{m_s}(n\varphi) \chi(n), \\ \chi(n) &= \sum_{m_s=-\infty}^{\infty} \int_0^{\infty} d\varphi \varphi J_{m_s}(n\varphi) \chi_m(\varphi). \end{aligned} \quad (3)$$

Here, the bunch wake is described by the value $\Omega_{m,n}$, giving the coherent frequency shift of the coasting beam. Eqs(3) can be solved exactly for the simplified model, where ($\Omega_m = m_s \Omega$, $m_s = \pm 1$)

$$\rho(\varphi) = \delta(\varphi_0^2 - \varphi^2), \quad \Omega_{m,n} = \frac{i\Omega_m}{\pi(n + i\Delta)}. \quad (4)$$

In the region $|\Delta\omega_m| \ll \omega_s$, the quantity Ω defines the coherent frequency shift of the betatron mode ($m_s = 0$). According to Eqs(3) and (4) we write $\chi_m(\varphi) = C_m \delta(\varphi_0^2 - \varphi^2)$, which replaces Eqs(3) by an equivalent system of the algebraic equations

$$\begin{aligned} (\Delta\omega_m - m_s \omega_s) C_m &= \frac{i\Omega_m}{\pi} \sum_{m'_s=-\infty}^{\infty} Q_{m,m'} C_{m'}, \\ Q_{m,m'} &= \begin{cases} -i\pi, & m_s = m'_s = 0, \\ \frac{4 \sin(\pi[m - m'])}{\pi(m^2 - m'^2)}, & m_s, m'_s \neq 0. \end{cases} \end{aligned} \quad (5)$$

Using $x = \Delta\omega_m/\omega_s$, $w = \Omega_m/\omega_s$, we rewrite Eqs(5) in the following form ($W = 4w/\pi^2$)

$$(x - w)C_0 = iW \sum_{k=0}^{\infty} \frac{C_{2k+1}^-}{(2k+1)^2}, \quad C_{2p}^+ = \frac{2iW x S^-}{x^2 - 4p^2}, \quad (6)$$

$$C_{2k+1}^- = \frac{2iW x}{x^2 - (2k+1)^2} \left[\frac{C_0}{(2k+1)^2} + S^+ \right]. \quad (7)$$

¹ On leave of absence from Budker Institute of Nuclear Physics, 630090 Novosibirsk, Russia.

Here,

$$S^+ = \sum_{p=1}^{\infty} \frac{C_{2p}^+}{(2k+1)^2 - 4p^2},$$

$$S^- = \sum_{k=0}^{\infty} \frac{C_{2k+1}^-}{(2k+1)^2 - 4p^2},$$

$$C_{2k}^+ = C_{2k} + C_{-2k}, \quad C_{2k+1}^- = C_{2k+1} - C_{-(2k+1)}.$$

Substituting C_{2p}^+ from Eqs(6) into Eq.(7), we obtain

$$C_{2k+1}^- = \frac{2iWx}{x^2 - (2k+1)^2} \left[\frac{C_0}{(2k+1)^2} + \sum_{k'=0}^{\infty} S_{k,k'} C_{2k'+1}^- \right],$$

$$S_{k,k'} = \sum_{p=1}^{\infty} \frac{2iWx}{[x^2 - 4p^2][(2k+1)^2 - 4p^2][(2k'+1)^2 - 4p^2]}.$$

The calculation of the sum over p in $S_{k,k'}$ results in:

$$S_{k,k'} = -\frac{1}{2x^2(2k+1)^2(2k'+1)^2} + \frac{\pi}{4x} \frac{\cot(\pi x/2)}{[x^2 - (2k+1)^2][x^2 - (2k'+1)^2]}.$$

Using this expression, we find

$$C_{2k+1}^- = -\frac{2W^2}{(2k+1)^2[x^2 - (2k+1)^2]} \frac{w}{x-w} \times \sum_{k'=0}^{\infty} \frac{C_{2k'+1}^-}{(2k'+1)^2} - W^2 \frac{\pi x \cot(\pi x/2)}{[x^2 - (2k+1)^2]^2} S^-.$$

The solutions of Eqs(10) read:

$$C_{2k+1}^- = \frac{A(x)/(2k+1)^2}{x^2 - (2k+1)^2} + \frac{B(x)}{[x^2 - (2k+1)^2]^2}. \quad (11)$$

The substitution of C_{2k+1}^- from Eq.(11) in Eq.(10) yields the dispersion equation

$$1 - \frac{x}{w} = 2W^2 F_1(x) - \frac{2W^4 F_2^2(x) \pi x \cot(\pi x/2)}{1 + W^2 \pi x \cot(\pi x/2) F_3(x)}, \quad (12)$$

where

$$F_1(x) = \sum_{k=0}^{\infty} \frac{1}{(2k+1)^4[x^2 - (2k+1)^2]},$$

$$F_2(x) = \sum_{k=0}^{\infty} \frac{1}{(2k+1)^2[x^2 - (2k+1)^2]^2},$$

$$F_3(x) = \sum_{k=0}^{\infty} \frac{1}{[x^2 - (2k+1)^2]^3}.$$

III. SYNCHROTRON OSCILLATIONS

Similar model can be used to describe the mode-coupling instability of the coherent synchrotron oscillations, if we take as $\rho(\varphi)$ the so-called water-bag distribution

$$\rho(\varphi) \propto \begin{cases} 1, & \varphi \leq \varphi_0, \\ 0, & \varphi > \varphi_0 \end{cases}$$

and the longitudinal wake from a pure resistive impedance, which does not depend on n . With these assumptions the synchrotron collective modes are defined by the system of equations, which can be written in the form, similar to that of Eqs(3)

$$(x - m_s) \chi_m = im_s w \delta(\varphi^2 - \varphi_0^2) \int_{-\infty}^{\infty} \frac{dn J_{m_s}(n\varphi) \chi(n)}{n + m_s \nu_s + i\Delta}, \quad (14)$$

or, after the substitution $\chi_m = C_m \delta(\varphi - \varphi_0)$,

$$(x - m_s) C_m = im_s w \sum_{m'} C_{m'} \int_{-\infty}^{\infty} \frac{dn J_{m_s}(n) J_{m'}(n)}{n + m_s \nu_s \varphi_0 + i\Delta}. \quad (15)$$

Since typically $\nu_s \varphi_0 \ll 1$, we can expand the integrand in Eq.(15) in the power series of $m_s \nu_s \varphi_0$. Taking into account in Eq.(15) the first two terms of this expansion, we obtain

$$(x - m_s) C_m = im_s w \sum_{m'} Q_{m,m'} C_{m'} - iw m_s^2 \nu_s \varphi_0 \sum_{m'} C_{m'} \int_{-\infty}^{\infty} \frac{dn J_{m_s}(n) J_{m'}(n)}{n^2}. \quad (16)$$

The second term in this equation couples the modes with the same parity. In the region $|w| \ll 1$, when the mode-coupling is negligible small, this term gives a leading contribution in the decrements (or increments) of the synchrotron modes

$$- \text{Im} x = \delta/\omega_s \simeq w \nu_s \varphi_0. \quad (17)$$

The oscillations will be unstable, when $w < 0$.

On the contrary, in the region $|w| \sim 1$, the leading contribution in the r.h.s. of Eq.(16) gives the first term, while the second describes small perturbations. Neglecting in this equation the values, proportional to $\nu_s \varphi_0 \ll 1$ and using the definitions from Eq.(8), we rewrite Eq.(16) in the following form

$$C_{2p}^+ = \frac{8Wp^2 S^+}{x^2 - 4p^2}, \quad C_{2k+1}^- = \frac{2Wx(2k+1) S^-}{x^2 - (2k+1)^2}. \quad (18)$$

Substituting here the first equation into the second, we find

$$C_{2k+1}^- = \frac{4xW^2(2k+1)}{x^2 - (2k+1)^2} \sum_{k'=0}^{\infty} \Sigma_{k,k'} C_{2k'+1}^-, \quad (19)$$

where

$$\Sigma_{k,k'} = \sum_{p=1}^{\infty} \frac{1}{[(2k+1)^2 - 4p^2][(2k'+1)^2 - 4p^2]} - x^2 S_{k,k'}.$$

Now, simple calculations result in the dispersion equation

$$1 = -W^2 \pi x^2 \cot \frac{\pi x}{2} \sum_{k=0}^{\infty} \frac{2k+1}{[x^2 - (2k+1)^2]^3}. \quad (20)$$

V.V. Denisov and E.A. Perevedentsev are acknowledged for their stimulating discussions. I indebted to K. Hirata, S. Kurohawa, N. Yamamoto and K. Yokoya for their valuable help during the preparation of this report. It is my pleasure to thank KEK and its B-factory group for their hospitality.

IV. REFERENCES

- [1] G.Benier, D.Brandt, B.Zotter. CERN LEP-TH/84-11, CERN, (1984).
- [2] N.S.Dmitriyev, D.V. Pestrikov. Physics of Intense Beams in Storage Rings. Nauka, Novosibirsk 1989.

On Limitations on Low- α Rings Performance Due To ∇Z -Instabilities

N.S. Dikansky,
Budker Institute of Nuclear Physics, 630090 Novosibirsk, Russia
D.V. Pestrikov¹
KEK, National Laboratory for High Energy Physics,
1-1 Oho, Tsukuba-shi, Ibaraki, 305, Japan

Abstract

We analyze collective instabilities of a bunch due to the radial gradient of the longitudinal impedance. One of the specific features of these collective effects is that decrements of collective synchrotron modes do not depend on the value of momentum compaction factor of the ring. This effect can limit the performance of the so-called low- α storage rings. It can be used for the damping of unstable modes of the synchrotron coherent oscillations as well.

I. INTRODUCTION

To decrease the bunch length, it was suggested in [1] to use the rings with abnormally small value of the momentum compaction factor α . The performance of such low- α rings can be very sensitive to collective instabilities, when the dependence of the increments on α is weak. Usually, the analysis of these issues is focused on the cases, when the beam interacts with devices producing the nonzero impedance $Z(\omega)$ on the particle trajectory. In this case, the rates of unstable modes decrease with a decrease in α . The different type of collective effects may occur due to radial gradient of the coherent energy losses. If, for example, the bunch interacts with a matched plate, the increments of coherent modes do not depend on α but are determined by the local value of the dispersion function η [2,3]. With the suitable sign for the gradient of the energy losses, this fact can be used to enhance the damping of the synchrotron coherent oscillations of bunches. However, if such a gradient appears accidentally, the collective interaction redistributes the increments between the synchrotron, or horizontal coherent modes [4] and the instability gets the global character. This instability is one of the simplest results of the theorem of the sum of the decrements for collective modes [4]. If the bunch wake is described in terms of the coupling impedance, the radial gradient of the coherent energy losses is described by the radial gradient of $Z(\omega)$. Apart from the use of special devices [2,3], the gradient Z can occur due to nonsymmetric position of the closed orbit inside the vacuum chamber of the ring. The last case is specific, for instance, for the future B-factories. In this report we use a simple example to describe the main features of such ∇Z - collective instabilities.

¹ On leave of absence from Budker Institute of Nuclear Physics, 630090 Novosibirsk, Russia.

II. SYNCHROTRON OSCILLATIONS

Let us consider the single-turn interaction of the bunched beam with a low-Q system of electrodes, which has a radial gradient of the coupling impedance. Therefore, we take the relationship between the harmonics of the longitudinal wake field $E_z(n, \omega)$ and the azimuthal harmonics of the bunch distribution function $f_{n, \omega}$ in the form

$$E_z(n, \omega) = -\frac{N e \omega_0}{\Pi} \int d\Gamma Z_n(x, \omega) f_{n, \omega}. \quad (1)$$

Here, $\Pi = 2\pi R_0$ is the perimeter of the orbit. If the unperturbed oscillations of the particle are described by the equations ($\mathcal{E} \simeq pc$)

$$\begin{aligned} x &= x_s + \eta \frac{\Delta p}{p}, \quad x_s = a_s \cos \psi_s, \\ \theta &= \omega_0 t + \varphi, \quad \varphi = \varphi_s \cos \psi_s, \quad \dot{\varphi} = -\omega_s \varphi_s \sin \psi_s, \\ \dot{x}_s &= \omega_s = \omega_0 \nu_s, \quad \dot{\psi}_s = \omega_0 \nu_s, \\ I_s &= \frac{p}{2R_0} \nu_s a_s^2, \quad I_s = \frac{\mathcal{E} \nu_s}{2\omega_0 \alpha} \varphi_s^2, \end{aligned}$$

the integral equation for synchrotron coherent oscillations ($f(I_s, \psi_s, t) = f_0(I_s) + f_m \exp(im_s \psi_s - i\omega t)$, $\omega \simeq m_s \omega_s + \Delta\omega_m$) reads

$$\begin{aligned} \Delta\omega_m f_m &= \frac{N e^2 \omega_0 m_s}{2\pi} \frac{\partial f_0}{\partial I_s} \int_{-\infty}^{\infty} dn J_{m_s}(n\varphi_s) \int_0^{\infty} d\varphi'_s \varphi'_s \times \\ &\left\{ \frac{i Z_n(x, n\omega_0 + m_s \omega_s)}{n + m_s \nu_s} \exp(in\varphi_s \cos \psi_s) \right\}_{m_s} f_m. \end{aligned} \quad (2)$$

For the sake of simplicity, we assume that $Z_n(\omega)$ is a pure resistive impedance, which linearly depends on x

$$Z_n(x, \omega) = (\partial Z_n / \partial x)_0 x = (\nabla Z_n)_0 \eta \frac{\Delta p}{p},$$

and that for typical harmonics $|\partial Z_n / \partial \omega| \ll |Z_n / \omega|$. Then, the calculation in Eq.(2) of the harmonics over ψ_s results in

$$[\Delta p / p \exp(in\varphi_s \cos \psi_s)]_{m_s} = \frac{m_s \nu_s}{\alpha n} J_{m_s}(n\varphi_s),$$

Neglecting in Eq.(2) the higher powers of $m_s \nu_s$, we trans-

from Eq.(2) into

$$\Delta\omega_m f_m = i \frac{Ne^2\omega_0}{2\pi} \frac{m_s^2\nu_s}{\alpha} \frac{\partial f_0}{\partial I_s} \eta \int_{-\infty}^{\infty} \frac{dn}{n^2} (\nabla Z_n)_0 \times \quad (3)$$

$$\times J_m(n\varphi_s) \int_0^{\infty} d\varphi'_s \varphi'_s J_m(n\varphi'_s) f_m, \quad |m_s\nu_s| \ll 1.$$

Substituting here $u = \sqrt{\varphi_s^2/2}$ and

$$\Delta\omega_m = -i\Lambda m_s^2 \frac{Ne^2\omega_0}{2\pi p}, \quad f_m = \sqrt{-\frac{\partial f_0}{\partial u}} \chi_m, \quad (4)$$

we transform Eq.(3) into an integral equation with a symmetric kernel

$$\Lambda \chi_m = \eta \int_{-\infty}^{\infty} \frac{dn}{n^2} (\nabla Z_n)_0 \int_0^{\infty} du' K_m(u, u') \chi_m(u'), \quad (5)$$

$$K_m(u, u') = \sqrt{\frac{\partial f_0}{\partial u} \frac{\partial f_0}{\partial u'}} J_m(n\sqrt{u}) J_m(n\sqrt{u'}).$$

The kernel $K_m(u, u')$ will be positively defined, and hence, all its eigennumbers Λ will be real positive numbers if

$$\eta \int_{-\infty}^{\infty} dn (\nabla Z_n)_0 > 0. \quad (6)$$

Due to Eq.(4) the last condition yields the criterion, when synchrotron coherent oscillations decay. This has the obvious physical sense. The interaction with electrodes damps the coherent synchrotron oscillations if the coherent energy losses increase with the amplitude of oscillations. In our case, this takes place if condition (5) is satisfied.

Eq.(5) is too complicated for direct solution. In fact, it is not necessary, since the general conclusion concerning the collective stability of a bunch can be obtained by the calculation of the relevant sums of the decrements [4]. The sum of decrements of the synchrotron modes near the given m_s is

$$\delta_{m_s} = -\eta \frac{Ne^2\omega_0^2}{2\pi p v} \int_0^{\infty} du \frac{\partial f_0}{\partial u} \int_{-\infty}^{\infty} \frac{dn}{n^2} (\nabla Z_n)_0 m_s^2 J_m^2(n\sqrt{u}). \quad (7)$$

Using the identity

$$\sum_{m=-\infty}^{\infty} m^2 J_m^2(x) = \frac{x^2}{2},$$

we obtain

$$\delta_{\Sigma}^{(s)} = \sum_{m_s=-\infty}^{\infty} \delta_{m_s} = \eta \frac{Ne^2\omega_0^2}{2\pi p v} \int_{-\infty}^{\infty} dn (\nabla Z_n)_0. \quad (8)$$

III. HORIZONTAL OSCILLATIONS

Apart from the effect on synchrotron coherent oscillations the interaction with such an element of the vacuum chamber will modify the increments of radial coherent modes. The variation of the sum of the decrements for the dipole horizontal coherent oscillations ($m_s = \pm 1$) can be calculated using the relationship

$$i_s = \int_0^{2\pi} \frac{d\tau}{2\pi} \frac{\partial I_s}{\partial \Delta p} e E_\theta(\tau + \varphi, t), \quad \tau = \omega_0 t.$$

Substituting this expression and

$$f = f_0(I_s, I_s) + f_m \exp(im_s \psi_s + im_s \psi_s - i\omega t),$$

$$f_0(I_s, I_s) = F_0(I_s) \rho(\varphi_s)$$

in the linearized Vlasov equation, we obtain the integral equation for horizontal collective modes

$$(\omega - m_s \omega_s - m_s \omega_s) f_m = -i(I_s)_{m_s, m_s} \rho(\varphi_s) \frac{\partial F_0}{\partial I_s}. \quad (9)$$

Using here $(\partial I_s / \partial \Delta p) = -(\nu_s \eta a_s \cos \psi_s / R_0)$, $\Delta\omega_m = \omega \pm \omega_s - m_s \omega_s$ and $f_m = \chi_m(\varphi_s) \sqrt{I_s} \partial F_0 / \partial I_s$, we find that χ_m obeys the following equation

$$\Delta\omega_m \chi_m = i \rho(\varphi_s) \frac{Ne^2\omega_0 \eta}{2\pi p} \int_{-\infty}^{\infty} dn (\nabla Z_n)_0 \times \quad (10)$$

$$J_m(n\varphi_s) \int_0^{\infty} d\varphi'_s \varphi'_s J_m(n\varphi'_s) \chi_m(\varphi'_s).$$

The direct calculation of the trace of the kernel in Eq.(10) yields the total sum of decrements ($\delta = -\text{Im}\omega$) of the horizontal betatron and synchrobetatron modes

$$\sum_{m_s=-\infty}^{\infty} (\delta_{1, m_s} + \delta_{-1, m_s}) = -\eta \frac{Ne^2\omega_0^2}{2\pi p v} \int_{-\infty}^{\infty} dn (\nabla Z_n)_0. \quad (11)$$

The comparison of Eqs.(8) and (11) gives the sum rule

$$\delta_{\Sigma} = \delta_{\Sigma}^{(s)} + \sum_{m_s=-\infty}^{\infty} (\delta_{1, m_s} + \delta_{-1, m_s}) = 0. \quad (12)$$

This equation describes a particular case in a more general statement concerning the sum of the decrements of coherent oscillations, which previously was found in [4]. Eq.(12) shows that without special efforts the interaction of the beam with a device producing the horizontal gradient of the coupling impedance results in a global coherent instability of the bunch, when the synchrotron, or the horizontal synchrobetatron collective modes, are unstable.

Let us also mention an example, where Eq.(10) can be solved directly. The model, which will be described below, can be useful for analysis of many others single-bunch

instabilities [5]. We take as $\rho(\varphi_s)$ a Lorents distribution: $\rho = \sigma_s / (\sigma_s^2 + \varphi_s^2)$ and assume that ∇Z does not depend on s . Then, we can find from Eq.(10) that a function

$$w(z) = \sqrt{z} \int_0^\infty dt J_{m_s}(2zt) \chi_m(2t), \quad t = \frac{\varphi_s}{\sigma_s} \quad (13)$$

satisfies the equation [5]

$$\frac{d^2 w}{dz^2} + \left\{ -\frac{1}{4} + \frac{\Lambda}{z} - \frac{m_s^2 - 1/4}{z^2} \right\} w = 0. \quad (14)$$

Here, $z = n\sigma_s/2$ and

$$\Lambda = 2i\eta \frac{Ne^2\omega_0}{2\Delta\omega_m \Pi p} (\nabla Z)_0. \quad (15)$$

The solution of Eq.(14) reads

$$w = z^{|m_s|+1/2} e^{-z/2} F(|m_s| + \Lambda + \frac{1}{2}, 2|m_s| + 1, z), \quad (16)$$

where $F(\alpha, \gamma, z)$ is the confluent hypergeometric function. The eigenfunctions w do not grow at $z \rightarrow \infty$ if

$$|m_s| + \Lambda + 1/2 = -l, \quad l = 0, 1, \dots$$

The substitution of Λ from this equation in Eq.(15) yields the increments of modes

$$\delta_{m_s, l} = -\frac{Ne^2\omega_0^2}{2\pi p v} \left(\eta \frac{\partial Z}{\partial x} \right)_0 \frac{1}{2(|m_s| + l) + 1}. \quad (17)$$

In contrast with the "ordinary" instabilities, the increments in Eq.(17) and relevant decrements of the synchrotron modes do not depend on the momentum compaction factor of the ring. In particular, this fact will limit the performance of rings with very low α .

Described instability occurs due to a redistribution of decrements between the synchrotron and horizontal coherent modes. If, for some reason, the decrements of the horizontal coherent oscillations exceed the increments due to such a redistribution, the wideband systems of the electrodes with a proper sign for the horizontal gradient of the longitudinal impedance can be used to damp synchrotron coherent oscillations of a single bunch. For instance, this can be done using systems of the matched plates [2]-[5].

We thank prof. A. Skrinsky, who originally drew our attention to these problems. One of the authors (D.V.P.) is indebted to KEK and its B-factory group for their hospitality.

IV. REFERENCES

- [1] C.Pellegrini, D.Robin, *NIM A* 301, (1991), 27.
- [2] Ya.S.Derbenev, N.S.Dikansky. In Proc. of the 7-th Intern. Conf. on High Energy Accel., v. 2, p. 294, Yerevan 1970.

[3] N.S.Dikansky. Ph.D. Thesis. Novosibirsk 1969.

[4] Ya.S.Derbenev, N.S.Dikansky, D.V.Pestrikov. In Proc. of the 2-nd All Union Part. Accel. Conf., v. 2, p. 62, Moscow, Nauka 1970.

[5] N.S.Dikansky, D.V. Pestrikov. Physics of Intense Beams in Storage Rings. Nauka, Novosibirsk 1989.

On Landau Damping of Collective Beam-Beam Modes

D.V. Pestrikov¹

KEK, National Laboratory for High Energy Physics,
1-1 Oho, Tsukuba-shi, Ibaraki, 305, Japan

Abstract

In this paper we report a simplified model, where collective beam-beam oscillations can be described by a differential equation similar to the Schrödinger equation in quantum mechanics. In this case, the stability criteria can be obtained inspecting the behaviour of effective potential well curves.

I. INTRODUCTION

It is well known, that a study of collective beam-beam instabilities typically demands a solution of a very complicated system of integral equations. Usually, if we neglect a nonlinearity of the beam-beam kicks, produced by the stationary motion of the colliding bunches, these equations predict (see, for instance, [1]) a resonance instability of the betatron coherent oscillations with increments of the order of $\omega_0\xi$, where ω_0 is the revolution frequency, and ξ beam-beam strength parameter. Since such an initial assumption eliminates Landau damping of unstable modes, we may expect that such models overestimate the strength of the collective beam-beam instability.

Here we briefly report a model, which enables the evaluation of the effect of the Landau damping on the collective beam-beam modes. More detailed calculations can be found in [2]. For the sake of simplicity, we assume one interaction point (IP), identical colliding bunches and zero dispersion function at the IP.

II. SHORT BUNCHES

The description of Landau damping of the collective beam-beam modes can be simplified within the framework of the model described in [1]. Namely, we calculate the eigenmodes of the horizontal coherent oscillations, assuming that colliding bunches have very flat unperturbed distribution functions in amplitudes of betatron oscillations

$$f_0(J_x, J_z) = N\delta(J_z)F_0(J_x)/\epsilon. \quad (1)$$

If F_0 is a Gaussian distribution, ϵ has the sense of the bunch horizontal emittance, N is the number of particles in the bunch. We consider, first, the case when the lengths of colliding bunches $\sigma_z \ll \beta_z^*$, where β_z^* is the value of the horizontal β -function at the IP. Then, the incoherent horizontal betatron oscillations of a particle in the interaction

region (IR) are given by

$$x = \sqrt{J_x} \cos \psi_x, \quad R_0(p_x/p) = dx/d\tau = x', \quad (2)$$

$$\tau = \omega_0 t, \quad \psi'_x = \nu_x + \Delta\nu_x(J_x).$$

Here, $2\pi R_0$ is the perimeter of the orbit and p is the momentum of the particle, $\Delta\nu_x(J_x)$ is the incoherent beam-beam tune shift. Near an isolated resonance ($\nu_x + \Delta\nu_x(J_x) = n/m$) a linearized system of Vlasov's equations written for the horizontal coherent betatron oscillations ($f^{(1,2)} = f_0 + \delta f^{(1,2)}$, $f_0 \gg |\delta f^{(1,2)}|$)

$$\delta f^{(1,2)}(J_x, \psi_x, \tau) = \sum_{m \neq 0} f_m^{(1,2)}(J_x) e^{im_x \psi_x - i\nu \tau} \quad (3)$$

yields the following system of integral equations [1]

$$f_m^{(1,2)} = \frac{m_x \xi}{\nu - m_x \Delta} \int_0^\infty du' u' F'_0(u') G(u, u') X_m^{(2,1)}(u'). \quad (4)$$

Here, $u^2 = J_x/\epsilon$, $\xi = Ne^2/(2\pi p c \epsilon)$, $X_m^{(1,2)} = f_m^{(1,2)} + f_{-m}^{(1,2)}$, $F'_0 = dF_0/d(u^2/2)$, $\Delta = \nu_x + \Delta\nu_x(J_x) - n/m$ and

$$G(u, u') = \int_{-\infty}^\infty \frac{dk}{|k|} J_{m_x}(ku) J_{m_x}(ku'), \quad (5)$$

where $J_m(x)$ is the Bessel function. The calculation of the integral in Eq.(5) results in [3] ($m = |m_x|$)

$$G(u, u') = \frac{1}{m} \begin{cases} (u/u')^m, & u \leq u' \\ (u'/u)^m, & u > u' \end{cases} \quad (6)$$

As can be seen, Eq.(4) separates the so-called π - and σ -modes (the sign $(-)$ corresponds to π -mode)

$$\chi^\pm = X_m^{(1)} \pm X_m^{(2)}, \quad (7)$$

which satisfy independent equations

$$\chi^\pm = \frac{\pm 1}{m} \int_0^\infty du' u' V(u') G(u, u') \chi^\pm, \quad (8)$$

where

$$V(u) = \frac{2\xi \Delta(u)}{(\nu/m)^2 - \Delta^2(u)} \frac{dF_0}{d(u^2/2)}, \quad \text{Im} \nu > 0. \quad (9)$$

¹On leave of absence from Budker Institute of Nuclear Physics, 630090 Novosibirsk, Russia.

The substitution $\chi^\pm = w_\pm/\sqrt{u}$ and subsequent double differentiation of Eq.(8) over u transform it into the following differential equation:

$$w_\pm'' + \left[\pm 2V(u) - \frac{m^2 - 1/4}{u^2} \right] w_\pm = 0. \quad (10)$$

Eq.(10) can be used to study stability of various stationary distributions F_0 . For instance, for a water-bag distribution function when $dF_0/du = -2\delta(u-1)$ and $(\Delta_0 = \nu_s - n/m)$

$$\Delta(u) = \Delta_0 + \xi' \begin{cases} 1, & u \leq 1, \\ 1/u, & u > 1, \end{cases} \quad \xi' = \frac{Ne^2}{\pi p c \epsilon}, \quad (11)$$

Eq.(10) results in

$$w_\pm(u) = \begin{cases} u^{1/2+m}, & u \leq 1, \\ u^{1/2-m}, & u > 1, \end{cases} \quad 1 = \frac{\mp 2\xi' \Delta/m}{(\nu/m)^2 - \Delta^2}. \quad (12)$$

These equations predict unstable coherent oscillations within the stopbands $|\Delta \mp \xi'/m| \leq \xi'/m$ with the maximum increments $(\text{Im}\nu = \xi')$ independent of the mode number m_s . Note, that in these equations Δ is calculated at $u = 1$. This fact causes general shifts of the centers of the stopbands when ξ' increases.

For a more realistic Gaussian distribution when

$$\frac{dF_0}{d(u^2/2)} = -e^{-u^2/2}, \quad \Delta = \Delta_0 + \frac{2\xi[1 - \exp(-u^2/2)]}{u^2},$$

Eq.(10) cannot be solved directly. However, in the case of unstable oscillations ($\text{Re}\nu = 0$), general properties of eigenfunctions and spectra can be predicted using the analogy of Eq.(10) and the Schrödinger equation, which is written for a particle with zero energy moving in effective potential well

$$U_{eff}(u) = \frac{m^2 - 1/4}{u^2} \mp 2V(u). \quad (13)$$

Since $U_{eff}(u)$ is a real function and, therefore, the operator in Eq.(10) is a self-adjointed one, Eq.(10) can have non-trivial solutions, if a potential curve ($U_{eff}(u)$) has a negative minimum ($dU_{eff}(u_0)/du = 0$, $U_{eff}(u_0) < 0$) between the stop-points ($U_{eff}(u_{1,2}) = 0$, $u_1 < u_0 < u_2$). As seen from Eqs(9) and (13) for π -modes U_{eff} can be negative, if $\Delta_0 < 0$, and for σ -modes, if $\Delta_0 > 0$. This determines a usual location of the stopbands of π - and σ -modes relative to the point $\Delta_0 = 0$. Stability of coherent oscillations can be studied inspecting the behaviour of U_{eff} . For example, Fig.1 shows the possibility for unstable solutions with increments of 0.7ξ for dipole oscillations at least within the stopband $-2 \leq \Delta_0 \leq -1$. Fig.2 shows an increase in the depth of U_{eff} for dipole oscillations if $\text{Im}\nu$ decreases. This figure also shows that slow modes ($\text{Im}\nu \ll \xi$) can penetrate in the core of the bunch which, generally, may cause stronger perturbations of incoherent oscillations. Fig.3 illustrates the possibility for unstable sextupole modes with increments of 0.08ξ within the stopband $-0.8 \leq \Delta_0 \leq -0.7$. Figs1-3 indicate that Landau

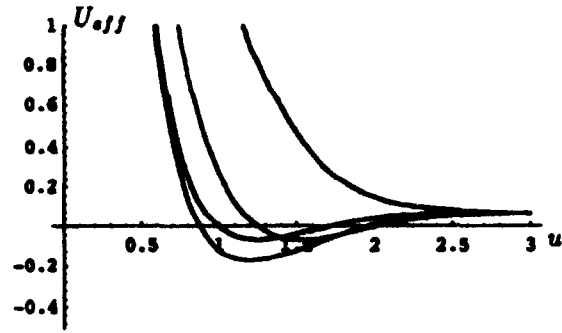


Figure 1: U_{eff} vs u ; $m = 1$, $\nu = 0.7i\xi$, from top to bottom: $\Delta_0/\xi = -0.5, -1, -2, -1.5$.

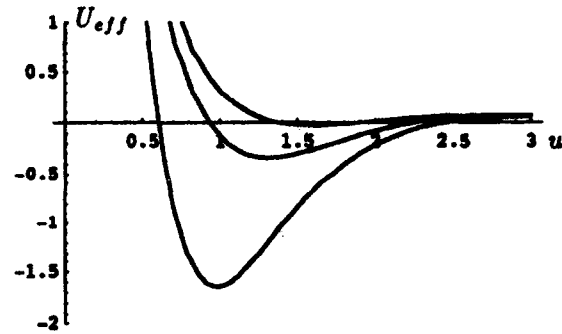


Figure 2: U_{eff} vs u ; $m = 1$, $\Delta_0 = -\xi$, from bottom to top: $\nu/i\xi = 0.25, 0.5, 0.75$.

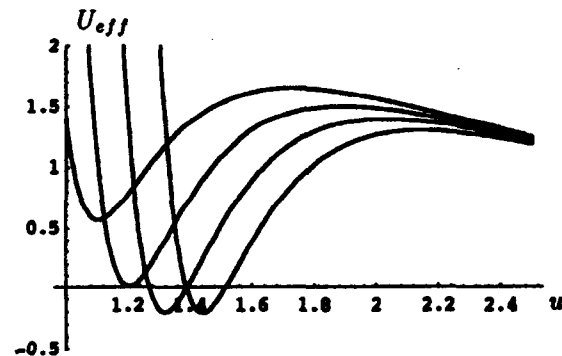


Figure 3: U_{eff} vs u ; $m = 3$, $\nu = 0.08i\xi$, from top to bottom (at $u = 1.6$): $\Delta_0/\xi = -0.85, -0.8, -0.75, -0.7$.

damping due to a non-linearity of the beam-beam kick does not stabilize at least the dipole, quadrupole and sextupole beam-beam modes of short bunches [2]. This result was recently confirmed [4] by the numerical solution of Eqs(4).

III. LONG BUNCHES

As was shown in [5] the collective beam-beam instability of long bunches (in our model, $\sigma_s \approx \beta_x^*$) can be strongly suppressed by the so-called phase-averaging effect [6]. This suppression occurs due to strong modulation of the β -function and of the phase of betatron oscillations in IR:

$$\begin{aligned} x &= \sqrt{J_x \beta(\tau)} \cos \psi_x(\tau), \\ \beta(\tau) &= \beta_x^* + \frac{(R_0 \tau)^2}{\beta_x^*}, \quad \psi_x(\tau) = \arctan(s/\beta_x^*). \end{aligned} \quad (14)$$

For coherent oscillations the effect of the bunch length is described by a simple redefinition of the beam-beam parameter [5]

$$\xi \rightarrow \xi_{eff} = \xi Y_m(\zeta), \quad \zeta = \frac{\sigma_s}{\beta_x^*}. \quad (15)$$

For this reason, for long bunches Eq.(9) takes the form:

$$V(u) = \frac{2\xi Y_m \Delta(u)}{(\nu/m)^2 - \Delta^2(u)} \frac{dF_0}{d(u^2/2)}, \quad \text{Im} \nu > 0. \quad (16)$$

The suppressing factors (Y_m) in Eqs(15) and (16) depend on the ratio of β^* to β_x^* and on the mode-number (m). As an illustration, we can assume, for instance, $\beta^* = \beta_x^*$ when [5]

$$Y_m = \int_{-\infty}^{\infty} \frac{du}{\sqrt{\pi}} e^{-u^2} \left(\frac{1+i\zeta u}{1-i\zeta u} \right)^m. \quad (17)$$

Figs4 and 5 show that, in the region $\sigma_s \approx \beta_x^*$, the phase-

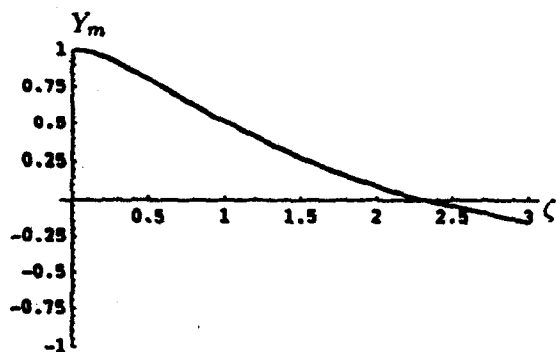


Figure 4: Dependence of Y_m on the bunch length; $m = 1$.

averaging effect roughly twice decreases the value of $V(u)$ for dipole modes and, practically, eliminates the instability of the sextupole modes. Note, that the dependence of Y_m on the bunch length for the sextupole (as well as for higher modes [5]) is rather sharp. This means that a suppression of the higher-order coherent resonances can occur

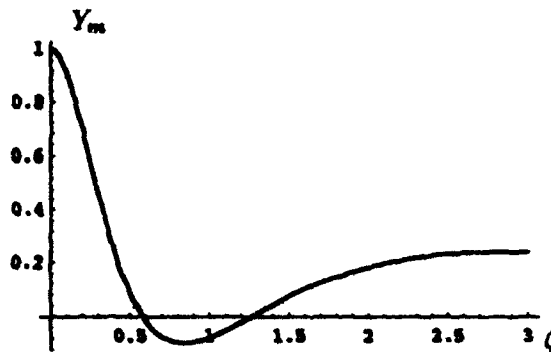


Figure 5: Dependence of Y_m on the bunch length; $m = 3$.

for rather short bunches. As seen in Fig.5, the strength of the sextupole resonance decreases twice when $\sigma_s \approx 0.25\beta_x^*$.

I am indebted to K. Hirata, S. Kurokawa and K. Yokoya for the valuable discussions and comments. It is my pleasure to thank KEK and its B-factory group for their hospitality.

IV. REFERENCES

- [1] N. Dikansky and D. Pestrikov. *Part. Acc.* 12, 27, (1982).
- [2] D. Pestrikov. SLAC-PUB-5510, SLAC, 1991.
- [3] I.S. Gradshteyn, I.M. Ryzhik. *Table of Integrals, Series and Products*. Academic Press, New York, (1965).
- [4] P. Zenkevich and K. Yokoya. KEK Preprint 92-116. KEK, (1992).
- [5] D. Pestrikov. SLAC-PUB-5575, SLAC, 1991; see also D.V. Pestrikov. KEK Preprint 92-208, KEK, (1993).
- [6] S. Krishnagopal, R. Siemann. *Phys.Rev. D* 41, 2312, (1990).

Synchronous Phase Changes Due to the Gap in the Bunch Train *

Z. Greenwald, M. Tigner

Laboratory of Nuclear Studies, Cornell University, Ithaca, NY 14853

Introduction

The B Factory bunch train in both beams is designed with a 250 nsec gap in order to minimize ion trapping. Possible differences in the synchronous phase between the bunches due to this gap in the bunch train are studied. Such an unequal phase shift between the bunches could lower the luminosity.

1 Synchronous Phase Calculation

The synchronous phase, which is the angle between the cavity voltage and the beam current, can be found from the beam loading vector diagram as seen in Figure 1. For a ring with evenly spaced bunches the synchronous phase ϕ_o is given by:

$$\phi_o = \arccos \left(\frac{V_o}{V_{co}} \right) = \begin{cases} 81.4^\circ \text{ H.E.R.} \\ 86.37^\circ \text{ L.E.R.} \end{cases}$$

where V_{co} is the cavity voltage and V_a is the loss per turn. The values of these parameters for both rings are given in Table 1. For strong coupling, like in super conducting cavities, the optimum tuning angle is $\psi_o \cong \phi_o$ [1] with the generator voltage V_g :

$$V_g = V_{co} \frac{\sin(\pi - 2\phi_o)}{\sin(\psi_o)} = \begin{cases} 10.46 \text{ MV H.E.R.} \\ 1.52 \text{ MV L.E.R.} \end{cases}$$

For a bunch train with a gap, the induced voltage is expected to change with time.

Ring and Cavity Parameters	H.E.R	L.E.R
N_b No. of bunches	230	230
I_o Beam current (Amp)	0.9	2.0
Number of RF cavities	12	4
V_{co} Total cavities voltage	35.	12.
V_a Energy Loss (MeV)	5.23	0.76
f_r Cavity Res. Freq. (MHz)	500.	499.9923
$\frac{\omega_r - \omega}{\omega_r}$	$1.4 \cdot 10^{-5}$	$2.94 \cdot 10^{-5}$
$\frac{R}{Q}$ per cavity	89.	89.
Q_L Loaded quality factor	$2.4 \cdot 10^5$	$2.68 \cdot 10^5$
β_{opt} Coupling parameter	$4.1 \cdot 10^3$	$3.74 \cdot 10^3$
T_b time between bunches nsec	9.99986	9.99986

*Work supported by the National Science Foundation

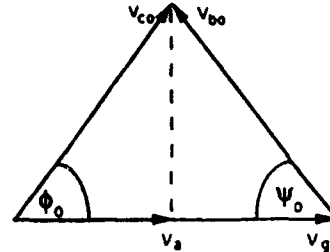


Figure 1: Vector Diagram Showing the cavity voltage as a superposition of the RF generator voltage V_g and the beam induced voltage V_{bo} .

1.1 Beam Induced Voltage

The beam induced voltage for a continuous train of bunches (see P. Wilson [1]) can be found by taking the vectorial sum of the voltage induced by each bunch V_{bo} , including its decay by a time constant τ and rotation of an angle δ where

$$V_{bo} = \frac{\omega_r R}{2 Q} I_o T_b$$

$$\tau = \frac{T_b}{T_f}$$

$$\delta = T_b(\omega_r - \omega)$$

T_b is the time between bunches, T_f is the filling time, and ω_r is the cavity resonance frequency.

$$T_f = \frac{2 \cdot Q_o}{\omega(1 + \beta)}$$

As time evolves, each bunch induced voltage can be represented by a vector $V_{bo}e^{n\xi}$ where $\xi = (-\tau + j\delta)$, n is the number of T_b passed since the bunch went through the cavity. The total induced voltage V_b is the vectorial sum $V_b = \sum_{n=0}^{N_b-1} V_{bo}e^{n\xi}$. To include the effect of the gap we note that during the gap $n = [N_b, N_t - 1]$ (N_b number of bunches in the train, N_t number of evenly spaced bunches in one revolution-no gap) the train of bunches continues to propagate, but there are not any new bunches going through the cavity and the induced voltage given by

$$\sum_{n=N_b}^{N_t-1} V_{bo} (e^{n\xi} - e^{(n-N_b)\xi})$$

starts to decay. In general for one revolution R_o of the bunch train

$$\begin{aligned}
\frac{V_t}{V_{b0}} &= \quad (1) \\
&= \sum_{R_0 N_t}^{R_0 N_t + N_b - 1} e^{n\ell} [1 - e^{-N_b \ell} + e^{-N_t \ell} \\
&\quad - e^{-(N_t + N_b)\ell} + e^{-2N_t \ell} - \dots] \\
&= \sum_{R_0 N_t}^{R_0 N_t + N_b - 1} e^{n\ell} \left[\frac{e^{-N_t \ell (R_0 + 1)} - 1}{e^{-N_t \ell} - 1} - e^{-N_b \ell} \frac{e^{-N_t \ell R_0} - 1}{e^{-N_t \ell} - 1} \right]
\end{aligned}$$

and in the gap interval:

$$\begin{aligned}
\frac{V_t}{V_{b0}} &= \quad (2) \\
&= \sum_{R_0 N_t + N_b}^{(R_0 + 1)N_t - 1} e^{n\ell} [1 - e^{-N_b \ell} + e^{-N_t \ell} - e^{-(N_t + N_b)\ell} \\
&\quad + e^{-2N_t \ell} - e^{-(2N_t + N_b)\ell} + \dots] \\
&= \sum_{R_0 N_t + N_b}^{(R_0 + 1)N_t - 1} e^{n\ell} [1 + e^{-N_t \ell} + e^{-2N_t \ell} + \dots] \\
&\quad - e^{-N_b \ell} [1 + e^{-N_t \ell} + e^{-2N_t \ell} + \dots] \\
&= \sum_{R_0 N_t + N_b}^{(R_0 + 1)N_t - 1} e^{n\ell} \frac{e^{-N_t \ell (R_0 + 1)} - 1}{e^{-N_t \ell} - 1} [1 - e^{-N_b \ell}]
\end{aligned}$$

The vectorial sum of the induced voltage of a train of 230 bunches with a gap of $25T_b$ for the high energy ring is seen in figure 2a. The saw tooth shape of the line is due to voltage decay during the gap. The voltage seen by the bunches is:

$$\bar{V}_b = V_b + \frac{1}{2} V_{b0} \quad (3)$$

and its absolute value is shown in figure 2b. This voltage is not constant even at steady state as for the case of continuous train, but changes with time. Figure 3 shows the high energy ring and Figure 4 shows the low energy ring. The oscillations during the build up time are due to the difference between the RF driving frequency ω_{rf} and the resonance frequency of the cavity ω_r . The larger the difference $\omega_{rf} - \omega_r$, the amplitude of oscillation of the transient response is larger, but the steady state value is smaller.

1.2 Cavity Voltage Calculation

Since the generator voltage V_g and the tuning angle ψ can not be regulated on a time scale of 10 nsec (time between bunches) the voltage on the cavity V_c is temporarily changed when V_b is changed.

$$\bar{V}_c = \bar{V}_g - \bar{V}_b$$

The change in $|V_c|$ corresponding to the changes in V_b is also shown in Figures 3 and Figure 4.

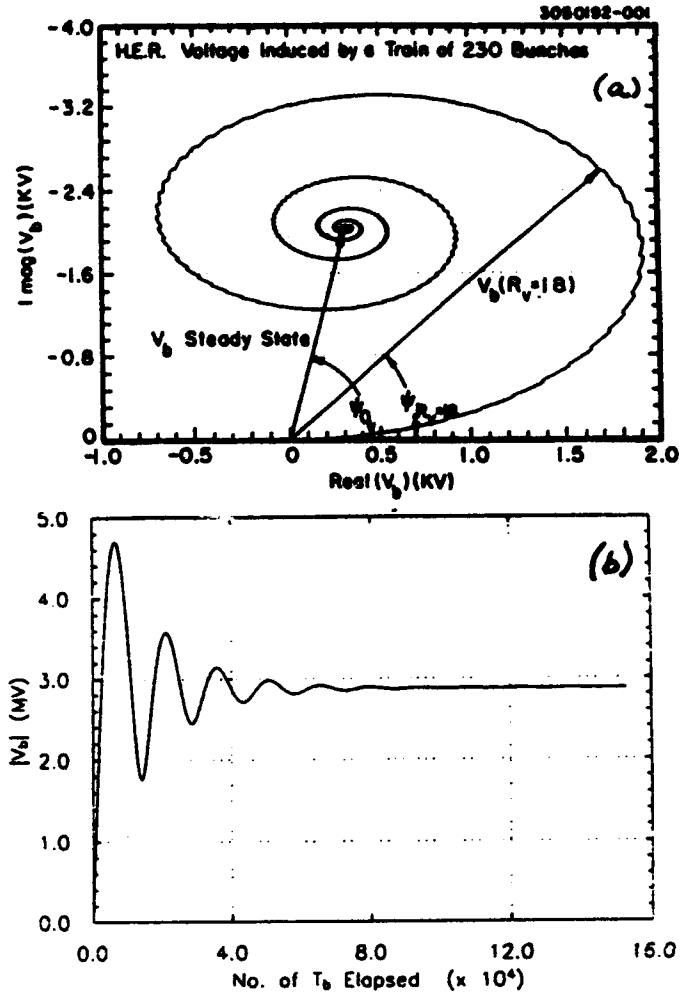


Figure 2: Evolution of the Beam Induced Voltage. a) As vectorial propagation. b) As function of time passed.

By looking at figure 3 and figure 4 one can follow the changes of the vector diagram of a bunch train with a gap. The beam induced voltage $|V_b|$ increases during $n = [R_0 N_t, R_0 N_t + N_b - 1]$ and reaches its maximum at the end of the train, while the cavity voltage decreases to its minimum during this period. Figure 5a and Figure 5b shows the position of $|V_c|$ and $|V_b|$ at the beginning of the train $|V_{ci}|$, $|V_{bi}|$ and at the end of the train (beginning of the gap) $|V_{ce}|$, $|V_{be}|$ correspondingly, both imposed on a diagram of a continuous train with equal current.

In reality the bunch spacing will be slightly different to keep the loss V_a constant in the steady state for all the bunches. Allowing this change on the vector diagram, while keeping $V_a = \text{constant}$, creates a new direction for the current. The associated synchronous phase measured relative to this new direction is:

$$\phi_b = \arccos \left(\frac{V_a}{V_c} \right)$$

Assuming that the change in V_c due to the change in the spacing is very small and using the values obtained in Fig-

Assuming that the change in V_b due to the change in the spacing is very small and using the values obtained in Figures 3 and Figure 4, the change in the synchronous phase $\Delta\phi_b = \phi_b - \phi_o$ was calculated. The result is shown in Figure 6.

H.E.R.—Voltage Induced by a Train of 230 Bunches

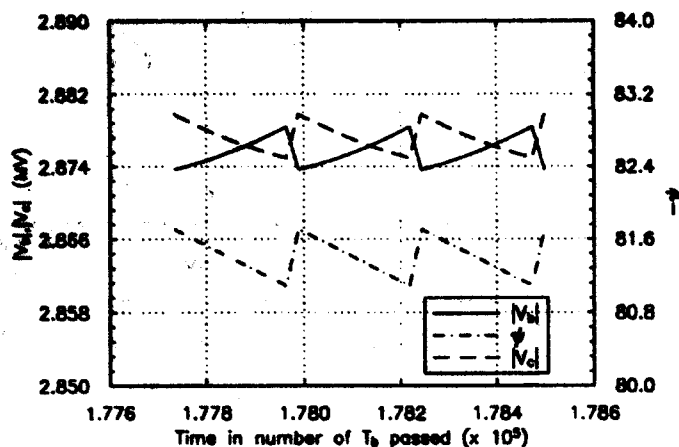


Figure 3: Beam Induced Voltage seen by the bunch train at steady state for H.E.R., its phase ψ and the corresponding cavity voltage.

L.E.R.—Voltage Induced by a Train of 230 Bunches

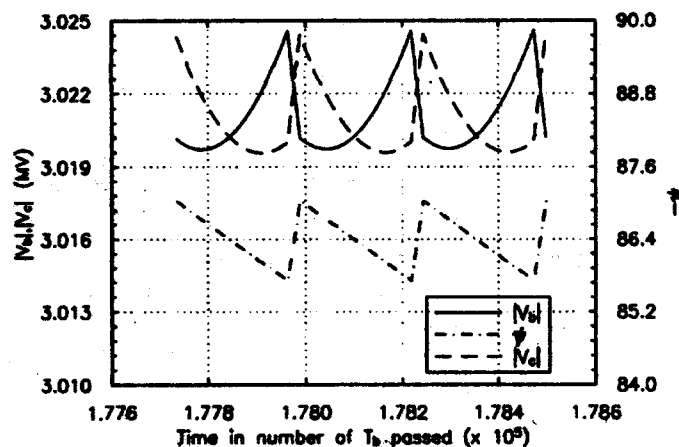


Figure 4: Beam Induced Voltage seen by the bunch train at steady state for L.E.R., its phase ψ and the corresponding cavity voltage.

2 Conclusions

A maximum change of $\Delta\phi_b = \pm 0.007^\circ$ and $\pm 0.0025^\circ$ was obtained for the H.E.R. and L.E.R. respectively which is equivalent to deviation of $1.2 \cdot 10^{-3} \text{ cm}$ and $4 \cdot 10^{-4} \text{ cm}$. Since the change in phase for both rings goes in the same direction, the maximum relative deviation between the bunches in the two rings is $8 \cdot 10^{-4} \text{ cm}$ compared to the 1 cm bunch length. Since there are only 4 cavities in the L.E.R. as opposed to 12 in the H.E.R. this leads to a smaller induced voltage even though the current is more than twice as large. The reason that a gap of 250 nsec does not cause

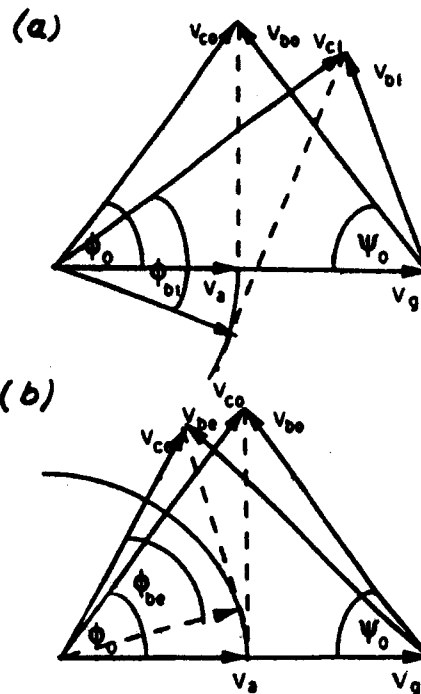


Figure 5: Vector diagram of a bunch train with a gap. a) at the end of the train. b) At the beginning of the train.

Synchronous Phase Change of a Train of 230 Bunches

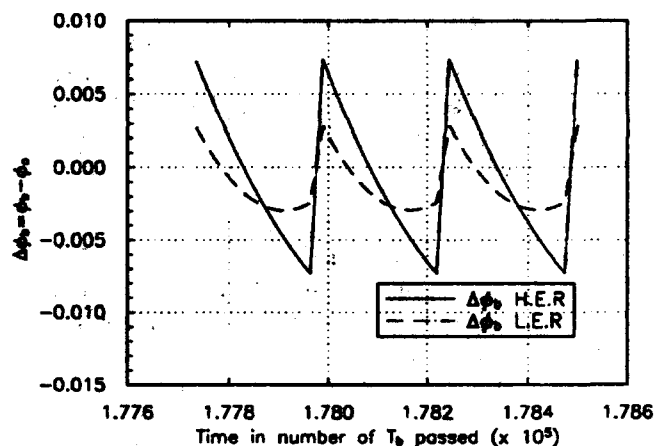


Figure 6: Change in the synchronous phase $\Delta\phi_b = \phi_b - \phi_o$.

a measurable change in the synchronous phase is that the time constant of each cavity $\frac{2\omega_r}{Q_L} = 38.2 \mu \text{ sec}$ is much larger than the $0.25 \mu \text{ sec}$ gap length which means that the cavity voltage does not discharge significantly during the gap causing only small change in ΔV_b .

Acknowledgment

I'd like to thank S. Greenwald for helpful discussions.

References

- [1] P. Wilson, SLAC-PUB-2884, February 1982.

Simulation and Compensation of Multibunch Energy Variation in NLC*

K. A. Thompson and R. D. Ruth

Stanford Linear Accelerator Center, Stanford University, Stanford, CA 94309 USA

Abstract

The SLAC NLC design for a next-generation linear collider utilizes multibunching (acceleration of a train of bunches on each RF fill) to increase the luminosity and energy efficiency. It is necessary to control the energy spread of the beam, in order to minimize chromatic emittance dilution and be within the energy acceptance of the final focus. It is anticipated that the NLC may run with bunch trains having length equal to a substantial fraction of the filling time. Multibunch energy simulation methods and compensation schemes appropriate to this regime are presented.

INTRODUCTION

Utilizing multibunching in a next-generation linear collider (NLC) requires that the energies of the bunches be tightly controlled. To be within the acceptance of the final focus system and to control chromatic emittance dilution in the linac, $\delta E/E$ needs to be less than about 0.15%.

By adjusting the timing of injection of the bunch train with respect to the RF pulse, and choosing the bunch spacing appropriately, one may cancel most of the energy variation between bunches in the train. The basic idea is to have the RF structure fill with sufficient extra energy between bunch passages to make up for the energy lost in accelerating the preceding bunches in the train.

However, with the simplest form of this "matched-filling" scheme [1], there is a "sag" in energy at the middle of the bunch train, and the longer the bunch train the greater the sag. In this paper we shall focus on compensation that permits running longer bunch trains (\sim a filling time) while maintaining an acceptable energy spread. Long trains are under consideration as a way of obtaining the maximum possible luminosity and energy efficiency.

We begin by discussing the factors that affect the energy spread of the beam. A detailed simulation program has been written, the elements of which are outlined here. In this simulation, one may take account of input RF pulse shaping and timing, the dispersion of the RF pulse as it transmits the structure, the longitudinal distribution of charge within the bunches, the long range wake (LRW) including both the fundamental (accelerating) mode and higher order modes (HOM's), the short range wake (SRW), and phasing of the bunches with respect to the crests of the RF. We shall focus only on the inter-bunch energy spread in the present paper.

BASIS OF SIMULATION

We begin by considering a single accelerating section, fed at its upstream end by an input RF waveform that travels to the other end and is absorbed in a load. At some specified time with respect to the entry of the RF pulse, a train of relativistic ($v = c$) bunches enters the structure, and the electrons in each bunch are accelerated by the fields (sum of RF pulse and wake fields) they encounter in the structure. The total charge in each bunch is divided into a finite number of longitudinal slices, small enough that the longitudinal position and the energy gain of the electrons in a given slice may be taken to be equal.

The total voltage gained in the section by slice r of bunch n may be broken down into

$$\Delta V_{n,r} = \Delta V_{n,r}^{rf} + \Delta V_{n,r}^{lrw} + \Delta V_{n,r}^{srw} \quad (1)$$

We denote the time of entry of this slice into the section by $t_{n,r}$, and longitudinal position in the section by s , where s runs from 0 to the structure length L , and consider each of these three contributions to the total section voltage gain.

The voltage $\Delta V_{n,r}^{rf}$ due to the RF pulse is

$$\Delta V_{n,r}^{rf} = \int_0^L E^{rf}(s, t_{n,r} + s/c) ds \quad (2)$$

where $E^{rf}(s, t)$ is the field of the RF waveform at location s and time t , obtained by propagating the input RF pulse $E^{rf}(0, t)$ down the structure. Let us specify the input RF pulse as

$$E^{rf}(0, t) = \hat{E}_0(t) \cos(\omega_{rf}t + \varphi_0) \quad (3)$$

The accelerating frequency ω_{rf} is assumed to have phase velocity in the structure equal to c and thus is synchronous with the charges to be accelerated.

If we neglect dispersion, i.e., assume the group velocity v_g is the same for all frequency components in the pulse (though it may in general still depend on s), we have

$$E^{rf}(s, t) = \hat{E}_0 \left(t - \int_0^s \frac{ds'}{v_g(s')} \right) \cdot \exp \left(- \int_0^s \alpha(s') ds' \right) \cos[\omega_{rf}(t - s/c) + \varphi_0] \quad (4)$$

* Work supported by Department of Energy contract DE-AC03-76SF00515.

In reality, dispersion makes the shape of the RF pulse change as it propagates through the structure, particularly for a sharply varying envelope $\hat{E}_0(t)$. Thus, one should Fourier analyze the input pulse,

$$E(\omega) = \int_{-\infty}^{\infty} E^{rf}(0, t) e^{-i\omega t} dt, \quad (5)$$

and propagate each of its frequency components according to the dispersion relation $\Gamma(\omega, s) = \alpha(\omega, s) + i\beta(\omega, s)$ for the structure:

$$E^{rf}(s, t) = \frac{1}{2\pi} \int_{-\infty}^{\infty} E(\omega) \exp[i\omega t - \int_0^s \Gamma(\omega, s') ds'] d\omega. \quad (6)$$

Here we assume that the structure can be modelled locally as a band-pass filter, though its properties may change gradually with s .

For a narrow-band structure with small attenuation [2], α may be assumed independent of ω , and a good approximation to $\beta(\omega, s)$ is

$$\beta(\omega, s) = \frac{1}{d} \cos^{-1} \left[-\frac{\omega - \omega_0(s)}{\omega_{hw}(s)} \right], \quad (7)$$

where d is the structure period (cell length), $\omega_0(s)$ is the mid-band frequency, and $\omega_{hw}(s)$ the half-width of the passband. In the usual situation, the accelerating mode lies in the range of β between 0 and π/d ; it is common to choose $\beta(\omega_{rf}, s)d = \frac{2\pi}{3}$.

The long range wake voltage $\Delta V_{n,r}^{lrw}$ felt by the slice is

$$\Delta V_{n,r}^{lrw} = \sum_{j=1}^{n-1} \int_0^L E^{lrw}(s, t_{n,r} + s/c, j) ds, \quad (8)$$

where $E^{lrw}(s, t, j)$ is the field at location s and time t , due to the wake left by bunch j .

There are two simpler special cases of particular interest. One is the constant-impedance (CZ) structure, made of identical cells so that its properties such as v_g , α , etc., are independent of s . For the CZ structure, we have

$$E^{rf}(s, t) = \frac{1}{\pi} \int_{\omega_{lo}}^{\omega_{up}} \left[\text{Re} E(\omega) \cos[\omega t - \beta(\omega)s] - \text{Im} E(\omega) \sin[\omega t - \beta(\omega)s] \right] e^{-\alpha(\omega)s} d\omega. \quad (9)$$

The other special case is the constant-gradient (CG) structure, which when unloaded has constant electric

field along the structure when fed with a constant amplitude input pulse. Thus the attenuation coefficient α for the electric field is zero. For such a structure

$$v_g(s) = \frac{\omega_{rf}}{Q} [L' - s], \quad (10)$$

where $L' \equiv \frac{L}{1-s/r}$. We assume r (shunt impedance per unit length) and Q are approximately independent of s . For the CG structure,

$$E^{rf}(s, t) = \frac{1}{\pi} \int_{\omega_{lo}(s)}^{\omega_{up}(s)} \left[\text{Re} E(\omega) \cos[\omega t - B(\omega, s)] - \text{Im} E(\omega) \sin[\omega t - B(\omega, s)] \right] e^{-\alpha(\omega)s} d\omega, \quad (11)$$

where $B(\omega, s)$ may be derived analytically [3]. The limits ω_{lo} and ω_{up} are the lower and upper passband boundaries of the fundamental mode. The CG structure is a fairly good representation of the detuned structures being contemplated for the SLAC NLC design.

Denoting the time when bunch j enters the structure by t_j^{ent} , and neglecting dispersion, we have for the LRW voltage in the CZ case:

$$E^{lrw}(s, t, j) = \sum_m -2\kappa_m q_j F_{m,j} \exp[-(t - t_j^{\text{ent}} - \frac{s}{c}) \frac{\omega_m}{2Q_m}] \cdot \cos[\omega_m(t - t_j^{\text{ent}} - \frac{s}{c})] \cdot H(t - t_j^{\text{ent}} - \frac{s}{c}) H(t_j^{\text{ent}} + \frac{s}{v_{g,m}} - t). \quad (12)$$

Here the sum m runs over the modes in the wake (fundamental and HOM's); κ_m is the loss factor, Q_m the quality factor, and $v_{g,m}$ the group velocity of mode m . $F_{m,j}$ is a form factor that depends on the charge distribution of bunch j ; for a Gaussian distribution, $F_{m,j} = \exp(-\omega_m^2 \sigma_{t,j}^2 / 2)$. In future linear collider designs, the bunch length is very short, and we may take $F_{m,j} = 1$. $H(t)$ is the unit step function.

The contribution of the fundamental mode to the LRW in the CG case is

$$E_1^{lrw}(s, t, j) = -2\kappa_1 q_j F_{1,j} \cos[\omega_1(t - t_j^{\text{ent}} - \frac{s}{c})] \cdot H(t - t_j^{\text{ent}} - \frac{s}{c}) H(t_j^{\text{ent}} + t_s - t). \quad (13)$$

where

$$t_s = -\frac{Q_{rf}}{\omega_{rf}} \ln(1 - \frac{s}{L'}) \quad (14)$$

and κ_1 is assumed to be independent of s . The HOM's in non-CZ structures may be treated by equivalent circuit models [4], but this is beyond the scope of the present paper.

Table 1: Parameters

RF frequency, $f_{rf} = 11.424$ GHz
Section length = 1.8 m
Attenuation $\tau = 0.505$
Fundamental mode $Q = 7107$
Fund. mode loss factor, $\kappa_1 = 203.75$ V/pC
Filling time, $T_f = 100$ ns
Bunch spacing = $16\lambda_{rf} \approx 42$ cm
Bunch charge = 1×10^{10}

COMPENSATION SCHEMES AND EXAMPLES

We model the linac as made up of CG sections (as defined above), with $2\pi/3$ phase advance per cell. bunch charge = 1×10^{10} . Parameters are as shown in Table 1.

The most promising strategy useful for bunch trains of length a filling time or longer, is to pre-fill the structure in such a way that the energy gain of each bunch during the transient period approximates the energy gain of each bunch in the steady state[5]. In the simplest form of this scheme, the amplitude of the input RF field $[\pm]$ is linearly ramped during the first filling time, then the bunch train is injected at the beginning of the second filling time. The input RF pulse used in our example is shown in Fig. 1. However, since dispersion creates large amplitude variations on the front of the RF pulse, it is desirable to wait an additional 10 nsec before injecting the bunch train, to allow the worst of these dispersion "wiggles" to propagate out of the structure. The resulting fractional energy deviation, for a 90-bunch train is shown in Fig. 2. Were it not for the effects of dispersion, the steady state would be reached at about bunch 70, as can be seen in Fig. 2(a), where dispersion is not included in the calculation. Fig. 2(b) shows the result with dispersion included, but with its effects diminished by allowing the front 10 nsec of the pulse to propagate out of the structure before injecting the bunch train.

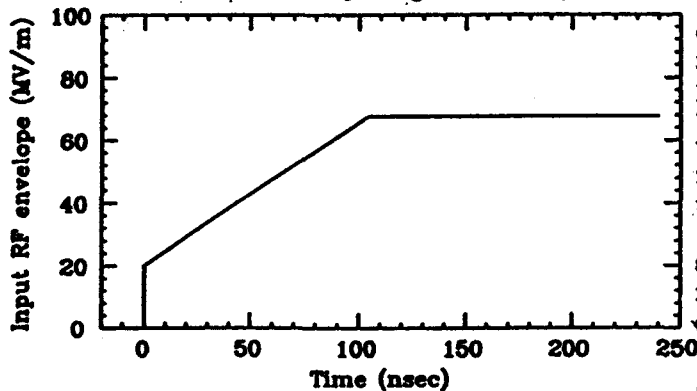


Figure 1. Envelope of input RF pulse, used in long-pulse pre-filling compensation scheme.

Another possible scheme for long bunch trains involves staggering the timing of the RF pulses in different sections[6]. Space prevents a detailed discussion of this scheme here; the overall energy compensation (net effect over a sum of sections) obtained with this scheme is similar to that of the preceding scheme. It does not, however, keep the energy as well compensated locally.

$\delta E / E$

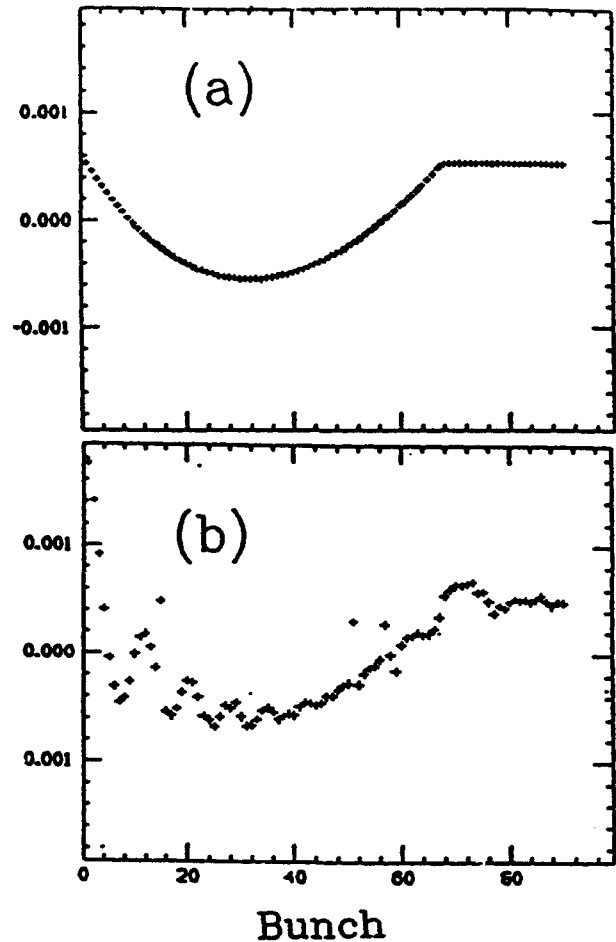


Figure 2. Fractional energy deviations of bunches in long-pulse pre-filling compensation scheme, (a) ignoring dispersion, (b) including dispersion.

Finally, we mention a related strategy[7], in which one approximately equalizes the bunch energies via the matched-filling method, and then modulates the RF input during the time when the train is passing through the structure, to compensate the "sag" one would otherwise get in the middle of the bunch train. Such a scheme may be the best for trains which are of order a half of the filling time in length.

We thank D. Farkas, R. Miller, and R. Palmer for suggestions regarding compensation schemes, and the members of the NLC structures group for other helpful discussions.

REFERENCES

- [1] R.D. Ruth, in Proceedings of ICFA/INFN Workshop on Physics of Linear Colliders, Capri, Italy (1988), and SLAC-PUB-4541.
- [2] J. Leiss, in *Linear Accelerators*, ed. by P. Lapostolle and A. Septier, (North-Holland, 1970).
- [3] K.A. Thompson and R.D. Ruth, to be published.
- [4] K. Bane, private communication.
- [5] R. Palmer and R. Miller, private communication.
- [6] R. Miller, private communication.
- [7] Z.D. Farkas, 16th International Linac Conference, Ottawa, Ontario, (23-28 August 1992); SLAC-PUB-5879.

THE PHYSICAL MECHANISM OF ULTRA-FAST AUTOMATIC COOLING FOR BEAMS IN THE SIX-DIMENSIONAL EMITTANCE SPACE^①

Gao Shuyang, Qian Guangyu, Liang Dongqi and Sun Hancheng
China Institute of Atomic Energy
P. O. Box 275(3), P. R. C. 102413, Beijing, P. R. China

Abstract

This paper is to illustrate that the four-dimensional emittance is automatically shrunked in the particular static magnetic field, while the vertical emittance is still a constant. It is the physical mechanism that the transverse velocity of any particles is not only decreased but also makes the longitudinal velocity approximate to the velocity of the equilibrium particle.

1. INTRODUCTION

The ultra-fast automatic cooling for beams (UFACB) was found out [1]. In the work followed [2], the damping phase diagrams in the emittance space were obtained. Such show that UFACB of the emittance space in the transverse direction is true indeed. In this paper the result of UFACB in six-dimensional emittance space will be given, so we are sure that the phase density of the emittance space is increased indeed. By means of the simply and explicitly physical picture of the transfer between both of the transverse and longitudinal energy, the mechanism of UFACB is illustrated. The transverse cooling is due to the energy transferring to the longitudinal direction, which also results in the longitudinal cooling, so the six-dimensional cooling rate is much faster than the transverse cooling rate.

2. THE TRANSFORMATION OF THE PHASE VOLUME

The relativistic Hamiltonian for a charged particle moving under the influence of an electromagnetic field [3] is

$$H = c \left[\frac{1}{(1+kx)^2} (p_x - eA_x)^2 + (p_z - eA_z)^2 + (p_y - eA_y)^2 + m^2 c^2 \right]^{1/2} + eV \quad (2.1)$$

Since the particle velocity $v = \text{const}$, let us introduce the relative velocity

$$\frac{d}{dt} = v \cdot \frac{d}{vdt} \quad (1+kx)^2 \cdot s^2 + x^2 + y^2 = 1 \quad (2.2)$$

The corresponding canonical momentum can be represented by [3]

$$p_x = \vec{p} \cdot \vec{s} \cdot (1+kx) \quad (2.3)$$

$$= m\gamma v (1+kx)^2 \cdot s + eA_x$$

$$p_z = m\gamma v x + eA_z$$

$$p_y = m\gamma v y + eA_y$$

in the uniform field, let

$$\frac{e}{m\gamma v} B = k \quad (2.4)$$

the corresponding vector potentials are

$$A_z = \vec{A} \cdot \vec{s} \cdot (1+kx) \quad (2.5)$$

$$= -\frac{1}{2} \cdot \frac{B}{c} (1+kx)^2$$

$$A_x = A_y = 0$$

the eq. (2.3) becomes

$$H = c \left\{ \frac{1}{(1+kx)^2} \left[p_x + \frac{1}{2} p_z (1+kx)^2 \right]^2 + p_z^2 + p_y^2 + m^2 c^2 \right\}^{1/2} \quad (2.6)$$

Let us consider the four-dimensional emittance on the horizontal direction. In the canonical phase space, we have

$$du = dx \cdot dp_x \cdot ds \cdot dp_s \quad (2.7)$$

in the emittance space, there is

$$dv = dx \cdot dx \cdot ds \cdot ds \quad (2.8)$$

they are related to each other by Jacobian determinant J ,

$$du = J dv \quad (2.9)$$

$$J = \frac{\partial(x, p_x, s, p_s)}{\partial(x, \dot{x}, s, \dot{s})}$$

performing a derivative to eq(2.5), we know,

$$J = (m\gamma v)^2 (1+kx)^2 \quad (2.10)$$

then

$$du_x = (m\gamma v)^2 (1+kx)^2 dv_1 \quad (2.11)$$

$$du_z = (m\gamma v)^2 (1+kx)^2 dv_z$$

Liouville's theorem tell us,

$$du_z = du \quad (2.12)$$

therefore

$$dv_z = \frac{(1+kx)^2}{(1+kx_z)^2} dv_1 \quad (2.13)$$

Which shows that the emittance element is not a con-

① Supported by the National Science Foundation of China

stant. In other words, the necessary and sufficient condition for the six-dimensional emittance conservation can not be obtained.

3. THE MOTION ON THE MEDIAN PLANE

In the case of the uniform field, the vertical motion is equivalent to the motion in the free space, so that the vertical emittance is an invariant. In this way, we need only to discuss the motion in the median plane of the magnet.

Under the hard-edge approximation, as shown in Fig 1, when the initial conditions of the incident particles are x_i, x'_i, s_i, s'_i respectively, where dot means the derivative with respect to t over v , the straight line equation of the particle's orbit in free space is written as

$$x - x_i = x'_i \cdot (s - s_i) \quad (3.1)$$

where $x' = \frac{dx}{ds} = x/s$, the ζ -axis equation is

$$x = s \cdot \tan\left(\frac{\pi}{2} - \theta_u\right) \quad (3.2)$$

$$= -s \cdot \tan(\theta_u)$$

performing the solution of the above two linear algebraic equation, we get the coordinate at the magnet entrance

$$\zeta_i - \zeta_u = -\left[\frac{s_i \cdot x_i - s_i \cdot s_i}{s_i \cdot \cos(\theta_u) + x_i \cdot \sin(\theta_u)}\right] \quad (3.3)$$

$$\Delta s_i = [(s_i - s_u)^2 + (x_i - x_u)^2]^{1/2} \\ = \frac{x_i \cdot \sin(\theta_u) + s_i \cdot \cos(\theta_u)}{x_i \cdot \sin(\theta_u) + s_i \cdot \cos(\theta_u)}$$

where Δs_i stands for the travelling distance in the edge region.

Let us consider the transformation of the beam going through the uniform magnetic field region, as shown in Fig 1, the particle's orbit in the uniform field is a circle. In the conditions given by the paper [1][2] the edge at the magnet exit is parallel to that at the entrance, and the center of the equilibrium orbit places on the exit edge. In that case, no one of the velocity is not parallel to each other at any place while they are parallel at the entrance.

By means of the similar relation, the increased quantity of the distance of travels in the magnet region can be written as [1,2]

$$\Delta S_m = \int_{\zeta_i}^{\zeta_u} \left[\frac{1}{\sqrt{1-f^2}} - \frac{1}{\sqrt{1-f_e^2}} \right] d\zeta \quad (3.4)$$

we know

$$x'_i = -\sin(\delta\theta_i) \quad (3.5)$$

$$\sin(\delta\theta_i) = [1 - s_i \cdot \sin(\theta_u) + x_i \cdot \cos(\theta_u) + \sin(\theta_u)]$$

since the coordinates and the velocity are continuous, by means of the similar ways to the paper [1], the final results can be written as

$$x_u = -\left[\frac{s_i \cdot x_i - x_i \cdot s_i}{s_i \cdot \cos(\theta_u) + x_i \cdot \sin(\theta_u)}\right] + \delta x \quad (3.6)$$

$$x'_u = -[1 - (\sqrt{1-x_i^2}) \cdot \sin(\theta_u) + x_i \cdot \cos(\theta_u) + \sin(\theta_u)]$$

$$s_u = \Delta s_i + \Delta s_m$$

$$= \frac{x_i \cdot \sin(\theta_u) + s_i \cdot \cos(\theta_u)}{x_i \cdot \sin(\theta_u) + s_i \cdot \cos(\theta_u)} + \Delta S_m$$

$$s_i = \sqrt{1 - \sin^2(\delta\theta_i)}$$

$$\sin(\delta\theta_i) = -[1 - s_i \cdot \sin(\theta_u) + \sqrt{1-s_i^2} \cdot \cos(\theta_u) + \sin(\theta_u)]$$

$$\delta x = -\int_{\zeta_i}^{\zeta_u} \left[\frac{f}{\sqrt{1-f^2}} - \frac{f_e}{\sqrt{1-f_e^2}} \right] d\zeta$$

$$f = \sin(\theta_u + \delta\theta_i) + k \cdot \zeta$$

$$f_e = \sin(\theta_u) + k \cdot \zeta$$

$$k = \frac{e}{p_0} \cdot B$$

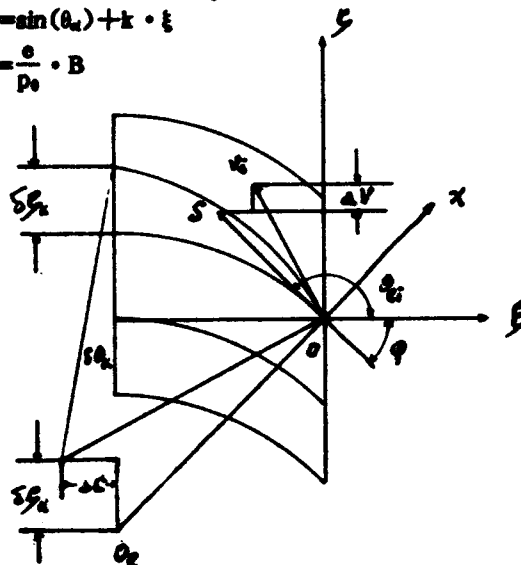


Fig. 1, Diagram of Particle's Motion in the Influence of Uniform Field

they are the precise solutions in the four dimensions. In the case of the two dimensions, those become the same as eq. (3.9) in the paper [1]

4. JACOBIAN TRANSFORMATION OF THE EMITTANCE SPACE IN THE FOUR DIMENSIONS

By means of differentiating the above precise formulas, the corresponding Jacobian determinant in the four dimensions can be obtained. Since x_i is only dependent on s_i , and s_i is only dependent on s_i , we know $dx_i \cdot dx'_i \cdot ds_i \cdot ds'_i = J \cdot dx_i \cdot dx'_i \cdot ds_i \cdot ds'_i$

$$J = \begin{vmatrix} J_{11} & J_{12} & J_{13} & J_{14} \\ 0 & J_{22} & 0 & 0 \\ J_{31} & J_{32} & J_{33} & J_{34} \\ 0 & 0 & 0 & J_{44} \end{vmatrix} \quad (4.1)$$

$$= J_{22} \cdot J_{44} \cdot (J_{11} \cdot J_{33} - J_{13} \cdot J_{31})$$

$$J_{11} = \frac{\partial x_i}{\partial s_i} = -s_i / [s_i \cdot \cos(\theta_u) + x_i \cdot \sin(\theta_u)]$$

$$J_{13} = \frac{\partial x'_i}{\partial s_i} = x_i / [s_i \cdot \cos(\theta_u) + x_i \cdot \sin(\theta_u)]$$

$$J_{22} = \frac{\partial x_2}{\partial x_1} = -[\cos(\theta_0) + \frac{x_1}{\sqrt{1-x_1^2}} \cdot \sin(\theta_0)]$$

$$J_{21} = \frac{\partial x_2}{\partial x_1} = \sin(\theta_0) / [x_1 \cdot \cos(\theta_0) + x_1 \cdot \sin(\theta_0)]$$

$$J_{22} = \frac{\partial x_2}{\partial x_1} = \cos(\theta_0) / [x_1 \cdot \cos(\theta_0) + x_1 \cdot \sin(\theta_0)]$$

$$J_{44} = \frac{\partial x_4}{\partial x_1} = -\frac{\operatorname{tg}(\theta_0)}{\operatorname{tg}(\theta_0)} [\cos(\theta_0) + \frac{x_1}{\sqrt{1-x_1^2}} \cdot \sin(\theta_0)]$$

we have

$$J = \frac{\operatorname{tg}(\theta_0)}{\operatorname{tg}(\theta_0)} \cdot \frac{1}{(1-x_1^2)} [x_1 \cdot \cos(\theta_0) + x_1 \cdot \sin(\theta_0)]$$

$$\operatorname{tg}(\theta_0) = \frac{\sin(\theta_0)}{\sqrt{1-\sin^2(\theta_0)}} \quad (4.2)$$

$$\sin(\theta_0) = 1 - x_1 \cdot \sin(\theta_0) + x_1 \cdot \cos(\theta_0) + \sin(\theta_0)$$

this result gives us such inspirations as follows.

1. Jacobian J is less than unity 1. while $x_1 \neq 0$, the emittance in the four dimensions will be always shrunk. In other words, it is cooling indeed.

2. From the formula (4.1) we know, $J_{11} \cdot J_{22} = 1$, which signifies that the extended rate of the transverse coordinate x is just equal to the shrunk rate of the transverse velocity x' . so the transverse emittance in the six dimensions is an invariant, too. Therefore, the beam cooling is only taken place in the longitudinal direction.

3. Since the vertical emittance is an invariant, but one of the four degree daughter space is shrunk, it is sure that the emittance in the six dimensions is decreased.

5. THE PHYSICAL MECHANISM

The physical mechanism of the cooling can easily be seen. It is the basic characteristics of the motion that all of the transverse velocity not to equal zero are always decreased and transferred to the longitudinal. Firstly, $J_{11} > 1$, the dimension of the transverse amplitude for the parallel incident particles is increased; secondly, $J_{22} < 1$, the transverse velocity is decreased; and thirdly, $J_{11} J_{22} = 1$, the transverse emittance for the six dimensions is an in-

variant. In that case, the transverse velocity is continuously transferred to the longitudinal direction to make the longitudinal velocity continuously approximate to the equilibrium one. However, J_{22} is approximately equal to unity 1, but $J_{44} < 1$, the longitudinal dimension is approximately invariant, while the longitudinal emittance is obviously decreased. Since the longitudinal cooling comes from that the transverse velocity is transferred to the longitudinal direction, we can call it the transfer cooling.

In the paper [1][2], in the case of simplifying the problem to the four-dimensional one, transverse emittance is decreased, which is led by the longitudinal velocity transferred to the transverse. we know, $\frac{dx_1}{ds} = \frac{dx_1}{vdt} \cdot \frac{ds}{vdt}$

$= x_1/s_1 = -\operatorname{tg}(\theta_0)$, and we have seen that the decreased rate of the transverse velocity x_1 is equal to the increased rate of x_1 , also we think about that the longitudinal velocity x' is increased because x is transferred to the longitudinal direction, so the decreased rate of x' must be less than the decreased rate of x because of the increase of the denominator s . Therefore, in this case, the transverse cooling comes from the longitudinal transfer.

the mechanism gives us an inspiration to find a way of improving the cooling rate. If we make the edge focusing angle φ at the exit become minus, which plays a role in focusing for the transverse motion, the x_1 at the exit is rather approximating to zero, so that the cooling rate must be improved, which will be tested latter.

REFERENCES

- [1]. Gao Shuyang, Qian Guangyu, Principle of Ultra-Fast Automatic Cooling for Beams, (the same proceedings)
- [2]. Gao Shuyang, Qian Guangyu. A Fusion Device of the continuous Electron Beam confinement used by the Accumulating Ring with the continuous Injection. (the same proceedings)
- [3]. D. A. Edwards and M. J. Syphers, AIP Conf. Proc. 184,2,(1989)

An Exact Expression for the Momentum Dependence of the Space Charge Tune Shift in a Gaussian Bunch

Michel Martini
CERN, CH-1211 Geneva 23

Abstract

An analytical approach to calculate the incoherent tune shift in the presence of non-linear space charge forces is described in this paper. Closed form expressions to evaluate the dependence of the space charge detuning on betatron amplitude have been derived previously for a beam of elliptic cross section with Gaussian distribution in transverse dimensions, under the condition that each particle has the same momentum. The present computation considers in addition the dependence of the space charge detuning on momentum, for a beam with Gaussian momentum distribution. Two effects are taken into account for an exact calculation: the widening of the beam due to momentum spread and the variation of the tune shift with the longitudinal position in the bunch. Application to the present high intensity beams in the CERN PS machine and to the foreseen beam for LHC is discussed.

I. INTRODUCTION

The understanding of the space charge effects is of primary importance for low energy circular accelerators and storage rings especially for beams of high intensity and brightness as required for the LHC [1]. Theoretical models which permit reliable numerical simulation are desirable to analyze the beam behaviour. An analytical approach to calculate the incoherent tune shifts in circular accelerators and storage rings in the presence of nonlinear space charge forces is described hereinafter. The model takes into account the dependence of the space-charge induced detuning on betatron amplitude and momentum, for a beam with Gaussian distributions in transverse dimensions and momenta.

II. EQUATIONS OF MOTION

In a linear lattice the synchro-betatron motion for a charged particle in the presence of space charge forces can be derived from the Hamiltonian [2]

$$H(x, z, \sigma, p_x, p_z, p_\sigma) = \frac{eU(x, z, \sigma)}{m_0 c^2 \beta^2 \gamma} + \frac{p_\sigma^2}{2\gamma^2} - (K_x x + K_z z) p_\sigma + \frac{1}{2} (g_x x^2 + g_z z^2 + p_x^2 + p_z^2) + \frac{L}{2\pi k} \frac{eV(\sigma)}{m_0 c^2 \beta^2} \cos\left(\frac{2\pi h}{L} \sigma + \varphi\right) \quad (1)$$

in which $x, p_x, z, p_z, \sigma \stackrel{\text{def}}{=} s - \beta c t$, $p_\sigma \stackrel{\text{def}}{=} \Delta E / \beta^2 E$ describe the synchro-betatron oscillations, s is the arc length, E is

the total energy of the particle and β, γ the relativistic parameters. $U(x, z, \sigma)$ is the potential generated by the beam, $g_{x,z}$ is the quadrupole strength, $K_{x,z}$ the curvature of the reference orbit, L its length, $V(s)$ and φ are the accelerating field and the phase, h the harmonic number, m_0 and e the rest mass and the charge of the particle.

The off-momentum trajectory may be placed at the center of phase space by means of a canonical transformation with generating function [2]

$$F_2(x, z, \sigma, \tilde{p}_x, \tilde{p}_z, \tilde{p}_\sigma) = \tilde{p}_x(x - D_x \Delta) + \tilde{p}_z(z - D_z \Delta) + (D'_x x + D'_z z) \Delta - (D'_x D_x + D'_z D_z) \frac{\Delta^2}{2} + \tilde{p}_\sigma \sigma \quad (2)$$

where $\Delta \stackrel{\text{def}}{=} \Delta p / p$ is the momentum deviation, $D_{x,y}$ is the dispersion function and a prime implies differentiation with respect to s . The transformation equations lead to the known expressions

$$\tilde{y} = y - D_y \Delta \quad \tilde{p}_y = p_y - D'_y \Delta \quad (3)$$

$$\tilde{\sigma} = \sigma + \left(1 - \frac{\tilde{p}_\sigma}{\gamma^2}\right) (-D_x \tilde{p}_x - D_z \tilde{p}_z + D'_x \tilde{x} + D'_z \tilde{z}) \quad (4)$$

and $\tilde{p}_\sigma = p_\sigma$, where y stands either for x or z . Assuming that there is no dispersion in the cavities ($V(s)D_y = 0$, $V(s)D'_y = 0$) and using the "oscillator model" for the synchrotron motion [2], with expansion of the cosine term to the second order, the Hamiltonian reduces to

$$\tilde{H}(\tilde{x}, \tilde{z}, \tilde{\sigma}, \tilde{p}_x, \tilde{p}_z, \tilde{p}_\sigma) = \frac{eU(\tilde{x}, \tilde{z}, \tilde{\sigma})}{m_0 c^2 \beta^2 \gamma} + \frac{\eta}{2} \tilde{p}_\sigma^2 - \frac{1}{2} (g_x \tilde{x}^2 + g_z \tilde{z}^2 + \tilde{p}_x^2 + \tilde{p}_z^2) + \frac{\Omega_\sigma^2}{2\eta \beta^2 c^2} \tilde{\sigma}^2 \quad (5)$$

where $\eta = 1/\gamma^2 - \alpha_p$ is the phase slip factor, with the momentum compaction factor and the synchrotron frequency

$$\alpha_p = \frac{1}{L} \int_{s_0}^{s_0+L} (K_x D_x + K_z D_z) ds \quad (6)$$

$$\Omega_\sigma^2 = \frac{2\pi h \eta c^2 \cos \varphi}{EL^2} \int_{s_0}^{s_0+L} eV(s) ds \quad (7)$$

We introduce the action-angle variables $I_{x,z,\sigma}$, $\psi_{x,z,\sigma}$ and $\tilde{I}_{x,z,\sigma}$, $\tilde{\psi}_{x,z,\sigma}$ use two consecutive canonical transformations, transforming first \tilde{H} into K and then K into \tilde{K} ,

with generating functions [2]

$$F_1(\bar{x}, \bar{z}, \bar{\sigma}, \psi_s, \psi_z, \psi_\sigma) = -\frac{\bar{x}^2}{2\beta_s} (\alpha_s + \tan \psi_s) - \frac{\bar{z}^2}{2\beta_z} (\alpha_z + \tan \psi_z) - \frac{\bar{\sigma}^2}{2\beta_\sigma} (\alpha_\sigma + \tan \psi_\sigma) \quad (8)$$

$$F_2(\bar{I}_s, \bar{I}_z, \bar{I}_\sigma, \psi_s, \psi_z, \psi_\sigma, s) = \bar{I}_s \left(\psi_s + \frac{Q_s s}{R} - \int_0^s \frac{ds}{\beta_s} \right) + \bar{I}_z \left(\psi_z + \frac{Q_z s}{R} - \int_0^s \frac{ds}{\beta_z} \right) + \bar{I}_\sigma \left(\psi_\sigma + \frac{Q_\sigma s}{\eta R} - \int_0^s \frac{\eta ds}{\beta_\sigma} \right) \quad (9)$$

Then the equations of motion can be written as

$$\dot{y} = \sqrt{2I_y \beta_y} \cos \psi_y \quad \dot{\bar{y}} = -\sqrt{\frac{2I_y}{\beta_y}} (\alpha_y \cos \psi_y + \sin \psi_y) \quad (10)$$

with

$$\bar{I}_y = I_y \quad \bar{\psi}_y = \psi_y + \frac{Q_y s}{R} - \int_0^s \frac{F_y ds}{\beta_y} \quad (11)$$

in which $R = L/2\pi$, y now stands either for x , z , or σ , and $F_x = F_z = 1$, $F_\sigma = \eta$. The Hamiltonian \bar{K} after substituting the transformed variables becomes

$$\bar{K}(\bar{I}_s, \bar{I}_z, \bar{I}_\sigma, \bar{\psi}_s, \bar{\psi}_z, \bar{\psi}_\sigma) = \frac{\bar{I}_s Q_s}{R} + \frac{\bar{I}_z Q_z}{R} + \frac{\bar{I}_\sigma Q_\sigma}{R} + \frac{e}{m_0 c^2 \beta^2 \gamma} U(\bar{I}_s, \bar{I}_z, \bar{I}_\sigma, \bar{\psi}_s, \bar{\psi}_z, \bar{\psi}_\sigma) \quad (12)$$

Using perturbation theory a final canonical transformation to new action-angle variables $\bar{I}_{s,z,\sigma}$ and $\bar{\psi}_{s,z,\sigma}$ may be further applied so that to first order the transformed Hamiltonian \bar{K} is the average of the old Hamiltonian \bar{K} over the old angle variables [2]. Moreover, assuming that the disturbing potential is small, the new action variables may be replaced by the old ones so that the transformation equation for the angle variable is

$$\bar{\psi}_y = \frac{\partial \bar{K}}{\partial I_y} = \frac{Q_y}{R} + \frac{e F_y}{m_0 c^2 \beta^2 \gamma} \frac{\partial \langle U \rangle}{\partial I_y} \quad (13)$$

where the average is taken over both the $\bar{\psi}_{s,z,\sigma}$ and s .

III. SPACE CHARGE POTENTIAL

Bunched beams of ellipsoidal shape with half-dimensions a , b , c defined as $\sqrt{2}$ times the r.m.s. beam sizes σ_x , σ_z , σ_σ , and with Gaussian charge density in the ellipsoid

$$\rho(x, z, \sigma) = \frac{N_b e}{\pi^{3/2} abc} \exp \left(-\frac{x^2}{a^2} - \frac{z^2}{b^2} - \frac{\sigma^2}{c^2} \right) \quad (14)$$

yield non-linear space charge forces generated by the scalar potential [3]

$$U(x, z, \sigma) = -\frac{N_b e}{4\pi^{3/2} \epsilon_0 \gamma^2} \times \int_0^\infty \frac{1 - \exp \left(-\frac{x^2}{a^2+t} - \frac{z^2}{b^2+t} - \frac{\sigma^2}{c^2+t} \right)}{\sqrt{(a^2+t)(b^2+t)(c^2+t)}} dt \quad (15)$$

where N_b is the number of particles per bunch and ϵ_0 the dielectric constant of vacuum. The effects of image fields due to the conducting vacuum pipe have been ignored.

Combining Eqs. 3-4 and Eqs. 10-11, and considering the "smooth approximation" $\beta_y \approx R/Q_y$ and $\beta_\sigma \approx \eta R/Q_\sigma$ gives, replacing $\bar{\psi}_{s,z,\sigma}$ by $\bar{\psi}_{s,z,\sigma}$ to first approximation

$$y = \hat{y} \cos \psi_y - \bar{D}_y \hat{\Delta} \sin \psi_y \quad (16)$$

$$\sigma = \hat{\sigma} \cos \psi_\sigma - \bar{D}_\sigma Q_\sigma \hat{x} \sin \psi_\sigma - \bar{D}_z Q_z \hat{z} \sin \psi_\sigma \quad (17)$$

in which $\hat{y} = \sqrt{2I_y R/Q_y}$, $\hat{\sigma} = \sqrt{2I_\sigma Q_\sigma/\eta R}$, $\hat{\Delta} = Q_\sigma \hat{\sigma}/\eta R$ denote the amplitudes of the synchro-betatron oscillations, \bar{D}_y is the mean dispersion function. Then, expanding $U(x, z, \sigma)$ in series and using the above expressions yields

$$\langle U \rangle = \frac{N_b e}{4\pi^{3/2} \epsilon_0 \gamma^2} \left\langle \sum_{n=1}^{\infty} \frac{(-1)^n}{n!} \sum_{j_1+j_2+j_3=n} J(j_1, j_2, j_3) \times \left(\frac{\hat{x} \cos \psi_x - \bar{D}_x \hat{\Delta} \sin \psi_x}{a} \right)^{2j_1} \left(\frac{\hat{z} \cos \psi_z - \bar{D}_z \hat{\Delta} \sin \psi_z}{b} \right)^{2j_2} \times \left(\frac{R \hat{\sigma} \cos \psi_\sigma - \bar{D}_\sigma Q_\sigma \hat{x} \sin \psi_\sigma - \bar{D}_z Q_z \hat{z} \sin \psi_\sigma}{Rc} \right)^{2j_3} \right\rangle \quad (18)$$

with the elliptic integral

$$J(j_1, j_2, j_3) = \int_0^\infty \frac{dt}{(1 + \frac{t^2}{a^2})^{j_1+1/2} (1 + \frac{t^2}{b^2})^{j_2+1/2} (1 + \frac{t^2}{c^2})^{j_3+1/2}} \quad (19)$$

When the longitudinal dimension of the bunch is much larger than the transverse dimensions, Eq. 19 may be approximately evaluated using the recursion formula [4]

$$J(0, 0, n) \approx \ln \left(\frac{4\gamma c}{a+b} \right)^2 - 2 \sum_{i=1}^n \frac{1}{2i-1} \quad (20)$$

$$J(1, 0, j_3) \approx \frac{2}{\alpha + 1} \quad (21)$$

$$J(j_1, 0, j_3) \approx \frac{\alpha - (n-1)J(j_1-1, 0, j_3)}{(n-1/2)(\alpha^2-1)} \quad (22)$$

$$J(j_1, j_2, j_3) \approx \frac{\alpha - \alpha^2(j_1+1/2)J(j_1+1, j_2-1, j_3)}{j_2-1/2} \quad (23)$$

where $\alpha = b/a$. Eqs. 21-23 are independent on j_3 .

IV. TUNE SHIFT FORMULAE

Integrating Eq. 13 through one machine turn gives an additional phase advance which is identified with the space charge detuning

$$\Delta Q_y = \frac{e R F_y}{m_0 c^2 \beta^2 \gamma Q_y \hat{y}} \frac{\partial \langle U \rangle}{\partial \hat{y}} \quad (24)$$

Assuming that the machine tune is removed from non-linear and coupling resonances Eq. 18 may be averaged individually over the phase advances. The resulting calculations yield a potential which depends only on the synchro-betatron amplitudes \hat{x} , \hat{z} , and $\hat{\Delta}$. Hence, differentiating

this potential and inserting the result into Eq. 24 gives the betatron and momentum amplitude dependence of the incoherent tune shift. Thus, the horizontal space charge tune shift is

$$\begin{aligned} \Delta Q_x(\hat{x}, \hat{z}, \hat{\Delta}) = & -\Delta Q_{0,x} \left(1 + \frac{b}{a}\right) \\ & \times \sum_{n=1}^{\infty} \frac{(-1)^n}{2^{2n}} \sum_{j_1=0}^n \sum_{j_2=0}^{n-j_1} \frac{(2j_1)!(2j_2)!(2j_3)!}{j_1!j_2!j_3!} J(j_1, j_2, j_3) \\ & \times \sum_{i=0}^{j_1} \sum_{k=0}^{j_2} \sum_{l=0}^{j_3} \sum_{m=0}^{j_3-l} \frac{(2(j_1-i)+2(j_2-k))!}{(2(j_1-i))!(2(j_2-k))!} \frac{1}{i!k!l!m!} \\ & \times \frac{i+m}{(i+m)!(j_3-l-m)!(j_3+k-l-m)!(j_1+j_2-i-k)!} \\ & \times \frac{1}{(j_1+j_2-i-k+l)!} \left(\frac{\hat{x}}{a}\right)^{2(i+m-1)} \left(\frac{\hat{z}}{b}\right)^{2(j_3+k-l-m)} \\ & \times \left(\frac{\hat{\Delta}}{\delta}\right)^{2(j_1+j_2+k-l-m)} \left(\frac{\bar{D}_x Q_x a}{Rc}\right)^{2m} \left(\frac{\bar{D}_x Q_x b}{Rc}\right)^{2(j_3-l-m)} \\ & \times \left(\frac{\bar{D}_x Q_x c}{\eta R a}\right)^{2(j_1-i)} \left(\frac{\bar{D}_x Q_x c}{\eta R b}\right)^{2(j_2-k)} \end{aligned} \quad (25)$$

in which $\delta = Q_x c / \eta R$ and $\Delta Q_{0,x}$ is the Laslett tune shift in the center of a Gaussian beam

$$\Delta Q_{0,x} = -\frac{k_b N_b R r_0}{\pi B_f Q_x \beta^2 \gamma^3} \frac{1}{a(a+b)} \quad (26)$$

where $B_f = k_b \sigma_z / \sqrt{2\pi} R$ is the bunching factor defined as the ratio of the mean to peak line charge density, k_b being the number of bunches and $r_0 = e^2 / 4\pi\epsilon_0 m_0 c^2$ the classical particle radius. Expressions for the vertical and the longitudinal tune shifts can be written similarly. Eq. 25 reduces to the Keil formula when $c \gg a, b$ and $\hat{\Delta} = 0$ [4].

V. RESULTS AND CONCLUSION

The foregoing formulae have been applied at the 1 GeV injection into the PS to the present high intensity beam delivered to the SPS, and at the 1.4 GeV injection into the PS to the high brilliance beam required for the LHC [1]

- SPS: 20 bunches of 10^{12} protons, 1 GeV, 55 ns long, 1σ -momentum spread $\sigma_\Delta = 0.75 \times 10^{-3}$, 1σ -normalized emittances $\epsilon_{x,s}^* = 12.5, 6.25 \mu\text{m}^2$.
- LHC: 8 bunches of 1.75×10^{12} protons, 1.4 GeV, 190 ns long, 1σ -momentum spread $\sigma_\Delta = 1.25 \times 10^{-3}$, 1σ -normalized emittances $\epsilon_{x,s}^* = 3.5, 1.75 \mu\text{m}^2$.

Figures 1-2 show the amplitude dependence of the space charge tune shifts for these two beams. The nominal tunes are $Q_{x,s} = 6.22, 6.28$. Calculations have been performed for amplitudes varying between 0 to $2\sigma_{x,s,\Delta}$ with the series expansions pushed to the 15th order. The Laslett tune shifts are $\Delta Q_{x,s}^{\text{SPS}} = -0.21, -0.30$ and $\Delta Q_{x,s}^{\text{LHC}} = -0.18, -0.31$.

¹The beam half-dimensions are $a = \sqrt{2} \sqrt{\epsilon_{x,s}^* R / \beta \gamma Q_x + D_{x,s}^2 \sigma_\Delta^2}$, $b = \sqrt{2} \sqrt{\epsilon_{y,s}^* R / \beta \gamma Q_y + D_{y,s}^2 \sigma_\Delta^2}$ and $c = \sqrt{2} \eta R \sigma_\Delta / Q_x$, $Q_x = \Omega_x R / \beta c$.

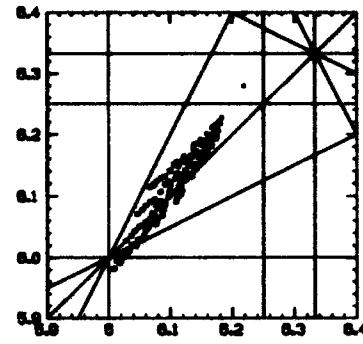


Figure 1: Tune diagram at the 1 GeV PS injection for the present beam for SPS.

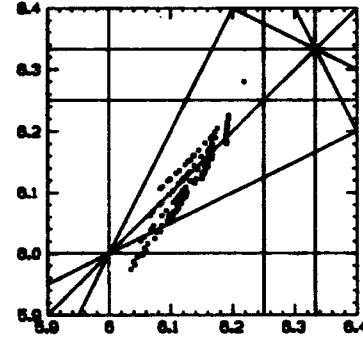


Figure 2: Tune diagram at the 1.4 GeV PS injection for the future beam for LHC.

The betatron and momentum amplitudes having Rayleigh distributions [4], the mean tune shifts have been computed from Eq. 15 by averaging Eq. 24 over all the amplitudes using Monte-Carlo integration. The results are $\langle \Delta Q \rangle_{x,s}^{\text{SPS}} = -0.09, -0.13$ and $\langle \Delta Q \rangle_{x,s}^{\text{LHC}} = -0.08, -0.13$. Thus, the weighted average of the detuning is less than half the Laslett tune shift.

The tune diagrams $Q_x - Q_y$ for the LHC and the SPS beams look almost similar. Thus, by raising the PS input energy to 1.4 GeV the tune spreads of the LHC beam will be maintained at the present limiting level.

VI. REFERENCES

- [1] R. Cappi, R. Garoby, S. Hancock, M. Martini, N. Rasmussen, J.P. Riinaud, K. Schindl, H. Schönauer, "The CERN PS Complex as part of the LHC injector chain", Proc. 1991 IEEE PAC, p. 171.
- [2] D.P. Barber, H. Mais, G. Ripken, F. Willeke, "Non-linear theory of coupled synchro-betatron motion", DESY report 86-147 (1986).
- [3] K. Takayama, "A new method for the potential of a 3-dimensional nonuniform charge distribution", Lettere al Nuovo Cimento, Vol. 34, p. 190 (1980).
- [4] E. Keil, "Non-linear space charge effects I", CERN report ISR-TH/72-7 (1972).

STORED BEAM LIFETIME EVALUATION FORMULAE FOR ELECTRON STORAGE RINGS

A.V. Makulkin.

All-Russian Research Institute for Optophysical Measurements.
Ozernaya 46, 119361, Moscow, Russia.

Abstract

Two simple analytical formulae to evaluate a lifetime of a stored electron (positron) beam at storage ring have been derived. Comparison between the lifetimes measured under typical operation conditions and calculated values has been carried out.

I. INTRODUCTION

Traditionally, to calculate a beam lifetime along with a bunch volume, revolution frequency, harmonic number, electron energy, bending radius and current, the external parameters such as a vacuum chamber aperture, residual gas pressure and RF voltage have been used. [1], [2], [3]. However, discrepancies more than an order of magnitude may be observed between a calculated and experimental data [2], [4]. In our case we tried to obtain a lifetime estimations based only on beam parameters. Previously, such kind situation has experimentally acknowledged at TANTALUS [5] ring.

II. THE FORMULAE DERIVATION

Consider train of electron bunches moving throughout a magnetic field media supplied by bending magnets. It has been known that in plasma physics the relation of a plasma to magnetic pressure is commonly used to describe plasma behavior. By analogy of plasma pressure we introduce a single bunch electrons pressure P_e as:

$$P_e = \frac{N \cdot E}{V \cdot K_b}$$

Where: N – number of beam electrons, E – electron energy, V – bunch volume, K_b – number of used bunches. Magnetic pressure P_m can be written as:

$$P_m = \frac{B^2}{2\mu_0}$$

Where: B – magnetic induction of bending magnets, μ_0 – permeability of free space.

Then relation of electrons to magnetic pressure β can be written as:

$$\beta = \frac{2 \cdot N \cdot E \cdot \mu_0}{V \cdot B^2 \cdot K_b}$$

Furthermore, let an electron be considered as a sphere of radius r , such as:

$$r = \frac{\lambda_c}{2\gamma}$$

Where: λ_c – Compton wavelength, $\lambda_c = 2.42 \cdot 10^{-12}$ m, γ – relativistic factor, $\gamma = E/E_0$, E_0 – rest energy.

Also, let a scattering crosssection of an electron be dependant on only this radius.

Finally, let for β larger than the unit electron bunch behavior be similar to that of ideal gas cloud. When β is lower than the unit a separate spherical electron moving throughout a «medium» whose density is product of a single bunch density and number of used bunches must be considered. The latter condition, in turns, requires a some kind of density memory in a relativistic orbit region. $\beta > 1$. Lifetime is calculated by means of a commonly used formula [6]:

$$\tau = \frac{1}{n \cdot \sigma \cdot c},$$

Where: τ – beam $1/e$ lifetime, n – density of particles, σ – scattering crosssection of a single spherical electron, c – speed of light.

$$\sigma = \pi d^2 = \frac{\pi \lambda_c^2}{\gamma^2},$$

$$d = 2 \cdot r,$$

$$n = \frac{N}{V \cdot K_b},$$

$$V = (4\pi)^{\frac{3}{2}} \cdot \sigma_x \cdot \sigma_z \cdot \sigma_L$$

Where: σ_x , σ_z , σ_L – bunch sizes measured in bending magnets,

$$\sigma_{xzL} = \frac{S_{xzL}}{2.35}$$

$$\sigma_L = c \cdot \tau_L,$$

Where: S_{xzL} – bunch FWHM sizes, τ_L – bunch duration.

The followings relations also taken into account:

$$\gamma = 1957 \cdot E(\text{GeV}),$$

$$R(\text{m}) \cdot B(\text{T}) = 3.34 \cdot E(\text{GeV}),$$

$$I(\text{A}) = 1.6 \cdot 10^{-10} \cdot N \cdot \omega_0 (\text{Hz}),$$

Where: R – bending radius, I – stored beam current, ω_0 – bunch revolution frequency.

On transforming the formula and β for practical use, we have:

$$\tau(\text{hours}) = \frac{1.41 \cdot K_b \cdot \omega_0 (\text{MHz}) \cdot \sigma_x (\text{mm}) \cdot \sigma_z (\text{mm}) \cdot \sigma_L (\text{mm}) \cdot E^2 (\text{GeV})}{I(\text{mA})}$$

$$\beta = \frac{5 \cdot R^2 (\text{m}) \cdot I(\text{mA})}{\sigma_x (\text{mm}) \cdot \sigma_z (\text{mm}) \cdot \sigma_L (\text{mm}) \cdot K_b \cdot \omega_0 (\text{MHz}) \cdot E (\text{GeV})}$$

$\beta < 1$. Write a total drag force F , which is applied to spherical electron moving in a medium of the density ρ as [7]:

$$F = C_D \cdot A \cdot \frac{1}{2} \rho \cdot c^2$$

Where: A – characteristic area, C_D – coefficient of drag.

According to the above suppositions:

$$\rho = \frac{N \cdot E}{V \cdot c^2}$$

$$A = \pi \cdot \left(\frac{\lambda_c}{2\gamma} \right)^2$$

Approximately constant over transcritical region of its dependence on a Reynolds number Re , coefficient of drag C_D [8], [9] equal to 0.15 has been choosen.

Energy E_i , which the electron lost during one turn in a storage ring magnetic field is:

$$E_i = 2\pi \cdot R \cdot F$$

Full energy loss E_i during lifetime τ is:

$$E_i = E_0 \cdot \omega_0 \cdot \tau$$

Due to this process a bending radius R become smaller. It is supposed that the electron should be finally lost when it has come full measured bunch width $3\sigma_r$ in the radial direction.

Energy change ΔE due to bending radius reduction is:

$$\Delta E = \frac{3\sigma_r E}{R}$$

We obtain τ equating E_r to ΔE :

$$\tau = \frac{1.5\sigma_r \cdot E}{\pi \cdot R^2 \cdot C_0 \cdot A \cdot \rho c^2 \omega_r}$$

$$\tau(\text{hours}) = \frac{10.46 \cdot \sigma_r^2(\text{mm}) \cdot \sigma_r(\text{mm}) \cdot E^2(\text{GeV})}{I(\text{mA}) \cdot R^2(\text{m})}$$

III. COMPARISON WITH EXPERIMENTAL DATA

In the table storage rings parameters, maximum achieved beam lifetime - τ , calculated lifetime - τ_c , discrepancies between these lifetimes - $\Delta\%$ are listed.

Ring name	E GeV	R m	ω MHz	K_0	σ_r mm	σ_z mm	σ_L mm	I mA	τ hours	β	τ_c hours	$\Delta\%$
ACO	0.54 [10]	1.10 [11]	13.60 [11]	2.00 [10]	1.50 [10]	0.30 [10]	300.00 [10]	100.00 [10]	16.00 [10]	55.00	15.10	5.60
ADONE	1.50 [12]	5.00 [11]	2.85 [11]	3.00 [12]	0.80 [12]	0.40 [12]	45.00 [12]	100.00 [12]	4.00 [12]	6.70	3.90	2.50
ALLADIN	0.80 [11]	2.08 [11]	3.36 [11]	15.00 [11]	0.55 [13]	0.07 [14]	255.00 [11]	100.00 [11]	3.90 [11]	5.37	4.53	16.00
AURORA	0.65 [15]	0.50 [15]	95.40 [15]	2.00 [15]	1.20 [15]	0.14 [15]	30.00 [16]	4.00 [15]	20.00 [15]	0.01	26.60	33.00
BESSY	0.77 [17]	1.78 [17]	4.80 [17]	104.00 [17]	2.00 [17]	1.00 [17]	70.00 [4]	100.00 [17]	6.00 ⁴⁾ [17]	0.03	5.50	7.50
	0.75 [18]	1.78 [17]	4.80 [17]	104.00 [18]	0.20 [18]	0.50 [18]	45.00 [11]	600.00 [18]	3.00 [18]	5.60	3.00	1.00
CHESR	5.44 [19]	32.00 [19]	0.39 [19]	6.00 [19]	1.08 [19]	0.19 [19]	16.00 [19]	80.00 [19]	4.00 [19]	9800.0	4.00	1.00
DCI	1.85 [11]	3.82 [11]	3.17 [11]	1.00 [11]	2.72 [20]	1.06 [20]	300.00 [11]	300.00 [11]	40.00 [11]	4.30	44.10	10.00
MAX	0.55 [11]	1.20 [11]	9.26 [11]	54.00 [11]	0.20 ⁵⁾ [21]	0.20 ⁵⁾ [21]	45.00 [11]	150.00 [11]	2.00 [11]	1.90	2.95	48.00
N-100	0.07 [22]	0.50 [22]	52.24 [22]	1.00 [22]	1.00 [23]	0.75 [23]	600.00 [24]	700.00 [22]	0.14 [22]	0.52	0.13	6.00
NEJI-I	0.16 [25]	0.70 [25]	22.60 [25]	7.00 [25]	1.10 [26]	1.80 [25]	170.00 [27]	200.00 [25]	0.85 [25]	0.05	1.05	27.00
NSLS-VUV	0.75 [28]	1.90 [28]	5.88 [11]	1.00 [29]	0.85 [29]	1.00 [29]	84.00 [30]	155.00 [29]	1.85 [29]	8.90	2.12	15.00
	0.75 [28]	1.90 [28]	5.88 [11]	6.00 [29]	0.51 [29]	1.30 [29]	102.00 [30]	286.00 [29]	5.35 [29]	2.90	6.46	21.00
	0.75 [31]	1.90 [11]	5.88 [11]	7.00 [31]	0.58 [32]	0.20 [32]	255.00 [31]	800.00 [33]	1.66 [33]	16.00	1.19	28.00
NSLS-XRAY	2.50 [11]	6.87 [11]	1.75 [11]	25.00 [29]	0.38 [28]	0.12 [28]	90.00 [11]	57.00 [29]	22.50 [29]	2631.00	28.40	26.00
PEP	7.10 [34]	165.00 [11]	0.14 [34]	68.00 [34]	0.29 [35]	0.08 [35]	5.00 [35]	34.00 [34]	1.66 [34]	4·10 ⁵	2.30	39.00
PF-RING	2.50 [37]	8.66 [37]	1.61 [37]	208.00 ⁶⁾ [37]	1.70 [37]	0.25 [38]	15.00 [37]	300.00 [37]	55.00 [37]	14.70	58.40	6.20
SIBERIA-I	0.45 [39]	1.00 [40]	34.50 [40]	1.00 [40]	1.82 [39]	0.13 [39]	300.00 [39]	100.00 [39]	2 [39]	0.32	2.10	5.00
SOR	0.38 [41]	1.10 [41]	17.20 [41]	1.00 [41]	0.98 [41]	0.16 [41]	81.00 [41]	10.00 [41]	1.66 [41]	0.72	1.55	7.00
	0.38 [42]	1.10 [42]	17.20 [42]	7.00 [42]	1.95 [42]	0.80 [42]	170.00 [42]	200.00 [42]	4.00 [42]	0.10	3.25	20.00
SORTEC	1.00 [43]	2.78 [43]	6.55 [43]	18.00 [43]	1.00 [44]	1.00 [44]	90.00 [43]	200.00 [44]	56.00 [44]	0.70	74.30 ⁴⁾	32.70
SRS-2	2.00 [45]	5.55 [45]	3.12 [45]	160.00 [45]	1.35 [45]	0.12 [45]	20.00 [45]	150.0 [45]	45.00 [45]	7.13	61.00	35.00
SUPER ALIS	0.60 [46]	0.66 [46]	17.80 [46]	7.00 [43]	1.26 [46]	0.19 [46]	72.00 [43]	100.00 [46]	1.94 [46]	0.17	1.88	3.00
SURF-2	0.28 [47]	0.84 [48]	57.00 [48]	2.00 [48]	0.64 [48]	0.04 [48]	300.00 [48]	200.00 [47]	0.33 [47]	2.60	0.52	57.00
	0.28 [48]	0.84 [48]	57.00 [48]	2.00 [48]	1.30 [49]	0.76 [48]	300.00 [48]	200.00 [48]	2.50 [48]	0.07	2.34	6.40

Ring name	E GeV	R m	ω MHz	K_L	σ_x mm	σ_y mm	σ_L mm	I mA	τ hours	β	τ_{half} hours	$\Delta\%$
TANTALUS	0.24 [50]	0.63 [50]	32.00 [50]	1.00 [50]	0.73 [50]	0.25 [50]	300.00 [50]	20.00 [50]	3.00 [50]	0.09	3.17	5.00
TERAS	0.60 [51]	2.00 [51]	9.55 [51]	10.00 [51]	0.65 [51]	0.21 [51]	115.00 [51]	70.00 [51]	29.00 ¹⁾ [52]	0.60	25.60 ²⁾	11.00
TRISTAN AR	3.70 [53]	23.20 [11]	0.80 [11]	1.00 [53]	1.24 [54]	0.12 [54]	20.00 [53]	30.00 [53]	2.66 [53]	6000.0	3.60	35.00
UVSOR	0.75 [55]	2.20 [55]	5.60 [55]	16.00 [55]	0.41 [55]	0.29 [55]	60.00 [55]	150.00 [55]	4.00 [55]	7.50	3.40	15.00
VEPP-1	0.04 [56] 0.13 [56]	0.43 [56] 0.43 [56]	110.00 [56] 110.00 [56]	1.00 [56] 1.00 [56]	1.20 [56] 0.35 [56]	0.40 [56] 0.05 [56]	60.00 [56] 40.00 [56]	100.00 [56] 100.00 [56]	0.03 [56] 0.01 [56]	0.67 [56] 9.00 [56]	0.04 [56] 0.02 [56]	28.00 [56] 42.00 [56]
VEPP-2M	0.70 [57]	1.22 [57]	16.60 [57]	1.00 [57]	0.97 [57]	0.40 [57]	40.00 [57]	200.00 [57]	1.2 [57]	6.70	1.33	11.00
VEPP-3	2.00 [58] 0.35 [60]	6.16 [58] 6.16 [61]	4.00 [59] 4.00 [61]	2.00 [58] 1.00 [61]	0.90 [58] 0.45 [60]	0.06 [58] 0.20 [60]	300.00 [58] 100.00 [60]	250.00 [58] 20.00 [61]	3.4 [58] 0.20 [61]	182.00 [58] 301.00 [61]	2.92 [58] 0.31 [61]	16.00 [58] 55.00 [61]

1) half-time, 2) calculated size, 3) partial filling, 4),5) calculated assuming $\beta > 1$

Dependence of σ_x , σ_y , σ_L on current I has been taken into account using the beam sizes observed in presence of the current subjected to estimation, provided that such dependence was found. For SORTEC and TERAS rings the formulae give correct results if the gaseous model is applied. We believe that β can be properly changed in these special cases. It should be also mentioned that for TERAS calculated lifetime equal to only the expected one, which five times longer the achieved values if a residual gas wall desorption is suppressed. In many cases the results are in accordance with previously estimated one on the base of the Touschek scattering.

The discrepancies between the experimental and calculated data have been found for SuperACO, SPEAR, PEP (15 GeV), VEPP-4, SPS-1, DORIS, C.E.A. storage rings. These machines were not included in the table. About fifteen new rings were not mentioned because of shortage in the presently available data set.

The uncertainty of measurements of each beam size was evaluated in 5% r.m.s. The mean table uncertainty is 20%.

IV. REFERENCES

- [1] T.Tomimasu et al. Rev.Sci.Inst. 60(7), 1630 (1989).
- [2] Y. Miyazawa. J.Vac.Sci.Tech.A4(1), 111 (1986)
- [3] R.P.Walker. Proc. 1987 IEEE Part. Accel. Conf. p. 491.
- [4] G.V.Egan-Krieger et al. IEEE Trans.Nucl.Sci. NS-30(4), 3094(1983).
- [5] E.M.Rowe et al. Part. Accel. 4(4), 211 (1973).
- [6] J.Le Duff. Nucl. Inst. Meth. A239,83(1985).
- [7] Encyclopedia of Fluid Mechanics. v.1, p.441 (Gulf Publishers 1986).
- [8] E.Achenbach. J.Fluid Mech. 54(3), 565(1972).
- [9] E.Achenbach. J.Fluid Mech. 65(1), 113(1974).
- [10] P.Fierffe-Prevost et al. Rev. de Phys. Appl. 12(6), 913 (1977) (in French).
- [11] Y.Kobayakawa et al. Rev. Sci. Inst. 60(7), 2548(1989).
- [12] F.Boscherini. Synchrotron Radiation News Compendium. 1991. Facility information, p.11.
- [13] T.Yin et al. Nucl. Inst. Meth. A246, 413 (1986).
- [14] W.S.Trzeciak et al. Nucl. Inst. Meth. A291, 416 (1990).
- [15] H.Yamada. The Rev. Laser Eng. 25(5), 31 (1990) (in Japanese).
- [16] K.Mima et al. IEEE J.Quant. Electr. 27(12), 2572 (1991).
- [17] W.Peatman. Nucl. Inst. Meth. 222, 6 (1984).
- [18] S.Bernstorff et al. Phys. Scr. 36, 200 (1987).
- [19] E.B.Blum. Proc. 1989 IEEE Part. Accel. Conf. p.473.
- [20] J.Goulon. Nucl. Inst. Meth. 208, 625 (1983).
- [21] M.Erikson. Proc. 6All Union Conf. on Syn. Rad. Inst. p. 49 (1984).
- [22] I.A.Grihaev et al. Instrum. and Exp Tech 19(6) pt. 1, 1611 (1976)
- [23] Yu.N.Grigoriev et al. Vopr. Atom. Nauki Tech N1, 38 (1972) (in Russian).
- [24] Yu.N.Grigoriev et al. Proc. 8 AllUnion Conf. on. Char. Part. Accel. v.2. p.238 (1983) (in Russian).
- [25] H.Takada et al. Opt. Eng. 27(8), 550 (1988).
- [26] H.Takada et al. Trans. IEE Jap. C 108(8), 547 (1988) (in Japanese).
- [27] H.Takada et al. Nucl. Inst. Meth. A294, 373 (1990).
- [28] R.Heese. Proc. 1987 IEEE Part. Accel. Conf. p.400.
- [29] T.S.Chou et al. Proc. 1987 IEEE Part. Accel. Conf. p.1773.
- [30] J.Galayda et al. Nucl. Inst. Meth. A239, 106 (1985).
- [31] A.M.Fauchet et al. Nucl. Inst. Meth. A319, 8 (1992).
- [32] S.L.Hulbert et al. Nucl. Inst. Meth. A319, 25 (1992).
- [33] H.J.Halama. AIP Conf. Proc. 236(1), 99 (1991).
- [34] S.L.Kramer et al. Proc 1989 IEEE Part Accel. Conf. p.1208.
- [35] H.Wiedemann. Proc. 1987 IEEE Part. Accel. Conf. p.395.
- [36] J.M.Paterson. Proc. 1989 IEEE Part. Accel. Conf. p.456.
- [37] Photon Factory Activity Report (8) (1990).
- [38] S.Sagaki et al. Rev.Sci.Inst.60(7),1859(1989).
- [39] S.Kusev et al. Nucl.Instr.Meth. A308, 464(1991).
- [40] A.Artemiev et al. Nucl.Instr.Meth. A308, 61(1991).
- [41] Y.Miyahara et al. IEEE Trans.Nucl.Sci. NS-32(5), 3821(1985).
- [42] S.Asaoka et al. IEEE Trans.Nucl.Sci. NS-30(4), 2944(1983).
- [43] H.Hirabayashi. Nucl.Inst.Meth.A291, 493(1990).
- [44] O.Asai et al. Jap.J.Appl. Phys.Pt.1, 30(11B),3043(1991).
- [45] V.P.Suller et al. Proc.1989 IEEE Part.Accel.Conf. p.467
- [46] T.Hosokawa et al. NTT R&D 39(4), 543(1990) (in Japanese)
- [47] M.L.Furst et al. Proc. SPIE 932, 548(1988).
- [48] R.P.Madden et al. Rev.Sci.Inst. 63(1), 1594(1992).
- [49] L.R.Hughey Proc. 1989 IEEE Part. Accel. Conf. p.461
- [50] E.M.Rowe et al. Proc. 9 Int.Conf. on High Energy Accel. p. 759(1974).
- [51] S.Sugiyama et al. Rev. Sci.Inst. 60(7), 1748(1989).
- [52] T.Tomimasu et al. Rev.Sci.Inst. 60(7), 1744(1989).
- [53] H.Saeki et al. Rev.Sci.Inst. 62(4), 874(1991).
- [54] X.Zhang et al. Rev.Sci.Inst. 63(1), 404(1992).
- [55] W.Watanabe. Synchrotron Radiation News Compendium. 1991. Facility information. p.31.
- [56] G.N.Kulipanov et al. I.N.F. Preprint N69. Novosibirsk. 1966. (in Russian).
- [57] A.Prokopenko. Synchrotron Radiation News Compendium. 1991. Facility information. p.21.
- [58] N.A.Mezentsev. Synchrotron Radiation News Compendium. 1991 Facility information. p.22.
- [59] N.A.Mezentsev. Dissertation. p.96 (I.N.P. Novosibirsk. 1981) (in Russian).
- [60] I.B.Drobyazko et al. Nucl.Inst.Meth. A282, 424(1989).
- [61] G.Mulhaupt et al. Nucl.Inst.Meth. A246, 845(1986).

A Simulation Study on Beam Bunching in the KEK 2.5-GeV Linac New Pre-Injector

T. Kamitani, J. -Y. Choi, A. Enomoto, S. Ohsawa, Y. Ogawa, T. Urano, T. Suwada, K. Furukawa and I. Sato

National Laboratory for High Energy Physics (KEK)

1-1 Oho, Tsukuba-shi, Ibaraki-ken, 305, Japan

Abstract

We have performed a simulation study on beam bunching in the KEK 2.5-GeV linac new pre-injector comprising double prebunchers and a buncher. Dependence of the bunching performance upon the rf powers and the phases of the prebunchers is discussed. We obtained an optimum bunch length of 4 ps with the simulation.

I. INTRODUCTION

The pre-injector of the KEK 2.5-GeV linac was upgraded in the summer of 1992 [1]. The bunching system was improved in order to accelerate more intense electron beams required for the production of positrons for the KEK B-factory [2], which is under consideration as a future project of KEK. A short bunch is essential for the injection efficiency to the B-factory ring, since the bunch length of the electrons determines that of the positrons and it set the limit of the narrowness of the energy spectrum. Besides, the emittance degradation by the transverse wake-field is larger for a longer bunch. To achieve good bunching performance, we adopted a system comprising double prebunchers and a buncher. The system was designed to be flexible; the rf input power and the relative rf accelerating phase of each buncher are independently tunable for optimum bunching. The parameters of the system are adjusted according to the change of the beam conditions such as the currents and the pulse length. The dependence of the bunch length upon the relative phases and the rf input powers of the prebunchers is studied using a beam dynamics simulation code.

II. BUNCHING SYSTEM

In bunching an intense beam, it is important to minimize the effect of the debunching due to space-charge forces. We thus adopted a system of double prebunchers and a buncher. The first prebuncher (PB1) provide the d-c beam from the gun with the velocity modulation and the beam is slightly bunched in the drift space to the second prebuncher (PB2). The rf phase for PB2 is adjusted for the electrons to enter PB2 in accelerating phase, causing further bunching and acceleration as well. The debunching of the beam is significant at low energy, it is desirable to accelerate the electrons in earlier stage of the bunching. Acceleration of the

electrons by PB2 before entering the buncher is effective for improving the bunching performance. The electrons are finally bunched in the strong accelerating field of the buncher.

A schematic diagram of the system is shown in Figure 1. Parameters of the bunchers are summarized in Table 1. All three bunchers are traveling-wave structures operated in the $2\pi/3$ mode of 2856 MHz. An array of the Helmholtz coils encompasses the bunchers. They produce a uniform solenoidal focusing field of 1.0 kG. A new high-power attenuator-and-phase-shifter system is used for the independent adjustment of the rf input power and the accelerating rf phase [3]. This flexibility of the bunching system is expected to enhance the capability of the parameter tuning.

Table 1
Bunching system design values

Prebuncher 1 (PB1)	
maximum field	0.4 MV/m
available input power	0.1 MW
cavity number	7
cavity size D	24.318 mm
Prebuncher 2 (PB2)	
maximum field	2.0 MV/m
available input power	2.3 MW
cavity number	5
cavity size D	24.318 mm
Buncher	
maximum field	15 MV/m
available input power	13 MW
cavity number	6
buncher section	29
normal section	27.01 ~ 34.99 mm
cavity size D	
Focusing magnetic field	
Helmholtz coils	1.0 kG

We have estimated the performance of the system to search for the optimum values for these operation parameters with the simulation code PARMELA.

III. SIMULATION

The PARMELA code is widely used for designing bunching systems of electron linear accelerators [4]. In this code, an electron beam is represented by a few hundreds

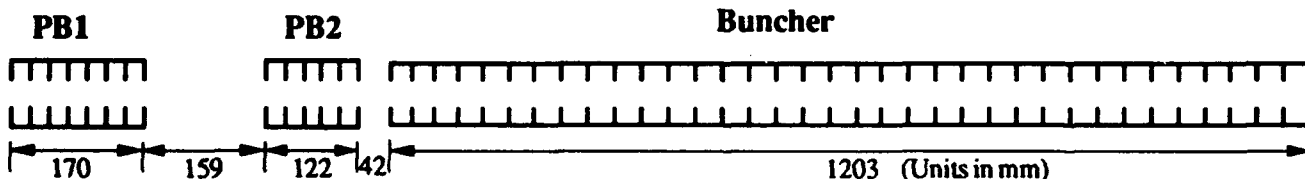


Figure. 1 Layout of the first and second prebuncher and the buncher

(~300 in our calculations) of macroparticles. They are traced in consecutive finite time-steps under the influence of the accelerating electric fields, the focusing magnetic fields and the space-charge forces. Effects due to the wake-field in the cavities are not taken into account. As an initial condition, these macroparticles were assumed to be distributed randomly within the specified volume in the 4-dimensional transverse phase space. The initial transverse r.m.s. emittance was taken to be 7π mm.mrad. In the longitudinal direction, they have a uniform distribution within the range corresponding to one wave length $\beta\lambda$ ($= 73.5$ mm) of the 2856 MHz rf acceleration, where $\beta=v/c$. Their initial energies were 200 keV. All the calculations were made for the beam current of 4 A.

To estimate the bunching performance of our double prebuncher system, we have studied the dependence of the bunch lengths upon the rf parameters of PB1 and PB2. The shapes of the bunches are dependent upon these parameters. In certain conditions, bunches have very irregular forms as shown in Figure 4(a). To discuss the bunch lengths of such irregular bunches, FWHM's or r.m.s. widths are not suitable. Instead, we used a fraction of the particles which lie in the rf phase width of 4 degrees around the peak of the distribution (Bunch Core). We chose this criterion because the optimum bunch width obtained by the calculations was about 4 degrees as shown later. This reflects well not only the sharpness of the bunch shapes but the extent of the tail or sub-peaks, regardless of forms of the bunches. We, therefore, used this criterion as an index evaluating the bunching performance in the following discussion.

In studying the dependence of the bunching performance upon the rf parameters, we took high and low field cases of PB1. The dependence upon the rf field and input phase of PB2 was mainly studied with those of the buncher fixed. Table 2 gives the range of the rf fields varied in the calculations.

Table 2
Range of the rf fields

PB1	0.15, 0.40 MV/m
PB2	0.1 ~ 2.5 MV/m
Buncher	15 MV/m

IV. RESULTS & DISCUSSION

The bunching performance is dependent not only on the electric field of the prebunchers but also their relative phases. The effect of their electric fields was studied first. The relative rf phase of PB2 to that of PB1 was fixed, such as the incident phase at PB2 to be 30 degrees for the reference particle which was at the zero phase in PB1. The incident phase at the buncher was also fixed to 50 degrees in the case that the field of PB2 is 2.0 MV/m. Figure 2 shows the dependence of the bunching performance upon the electric field of PB2. It was evaluated with the index defined in the previous section.

It can be shown that the better performance is obtained for the weaker field (0.15 MV/m) of PB1 in the whole range in Figure 2. The optimum value of the electric field of PB2 is 2.0 MV/m for both cases.

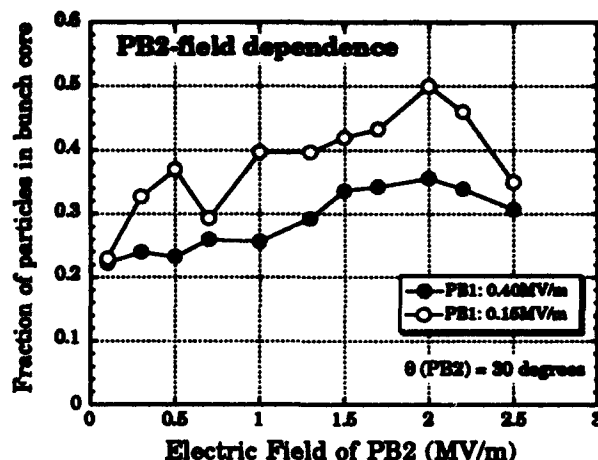


Figure 2. Dependence of the bunching performance upon the electric field of PB2.

Concerning the bunching performance upon the phase of PB2, we have studied for the cases of PB2's fields of 1.0 and 2.0 MV/m (Figure 3). The relative phase of the buncher to that of PB1 was not changed.

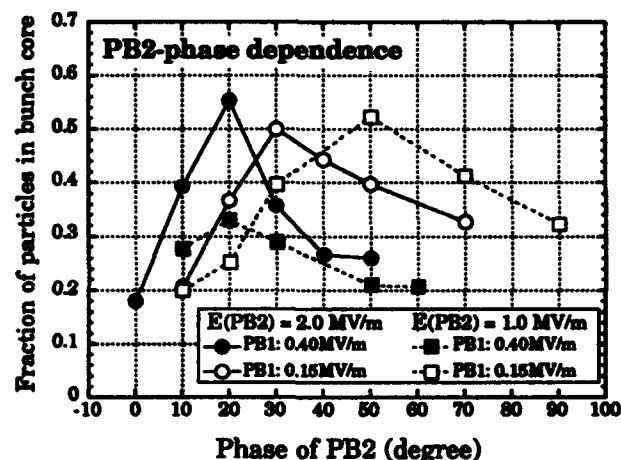


Figure 3. Dependence of the bunching performance upon the rf phase of PB2.

For the weaker field (0.15 MV/m) of PB1, the good performances are obtained for the wide range of the phase of PB2. The range is narrower for the stronger field (0.40 MV/m) of PB1 and the two-peak structures of the bunches were observed for the conditions a little away from the optimum value as shown in Figure 4 (a). The similar structures were also observed in experiments as shown in Figure 4 (b). The structure is believed to be caused by the over-bunching due to the excessive field of PB1.

With the optimum condition obtained for the stronger field of PB1, the two peaks are expected to be coalesced. Calculated trajectories for this case are shown in Figure 5. It shows that the two sub-bunches, formed by the over-bunching, coalesce in such a particular phase relation that the preceding sub-bunch is decelerated while the subsequent sub-bunch is accelerated in the rf field of PB2. The discontinuity of the trajectories shown in the figure is because the positions

of the particles are expressed with the references to the rf phase of each buncher. Though the condition gives a good performance, the tolerance of the relative phase of PB2 is small as shown in Figure 3.

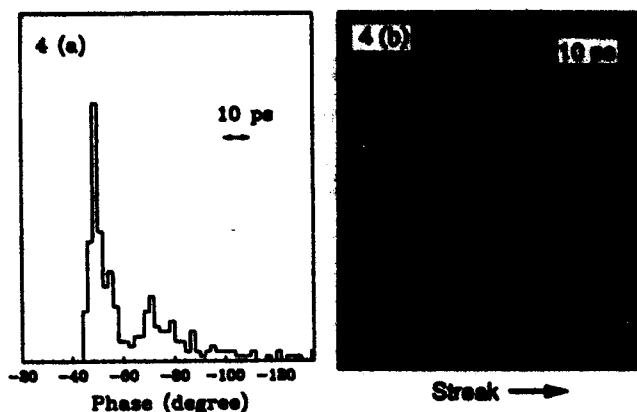


Figure 4. Bunches with two-peak structure by the calculation (a) and by the measurement (b) [5].

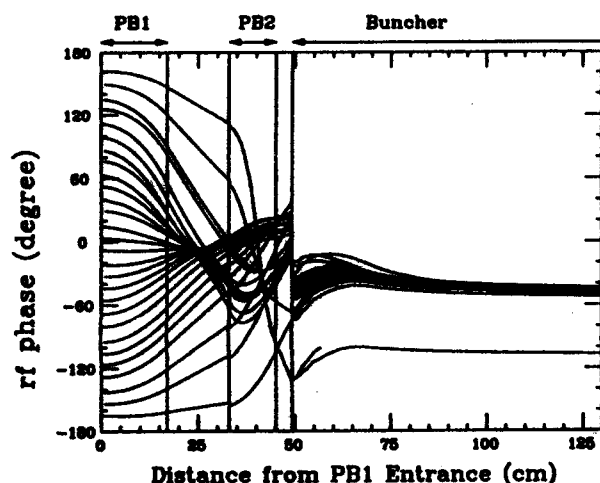


Figure 5. Typical trajectories for the optimum condition with the field of 0.4 MV/m for PB1.

For the optimum condition for the weaker field (0.15 MV/m) of PB1, calculated trajectories are shown in Figure 6. This optimum bunching results from the moderate bunching by PB1 and the further bunching by PB2 and the buncher. The bunch shape with this condition is shown in Figure 7. The FWHM bunch width is estimated to be about 4 degrees, which corresponding to the time duration of 4 ps.

V. SUMMARY

We have studied the bunching performances of our new bunching system with the simulation code PARMELA. The bunch length of 4 ps is obtained as a preliminary optimum value. Further extensive optimization of the parameters with the simulation will be performed. The effects due to the longitudinal wake-field will be included there. The experimental studies measuring the bunch length with the optical transition radiation monitor [5] will also be performed.

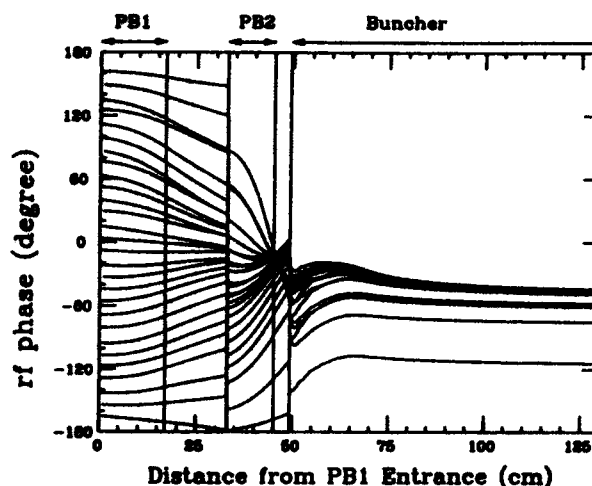


Figure 6. Typical trajectories for the optimum condition with the field of 0.15 MV/m for PB1.

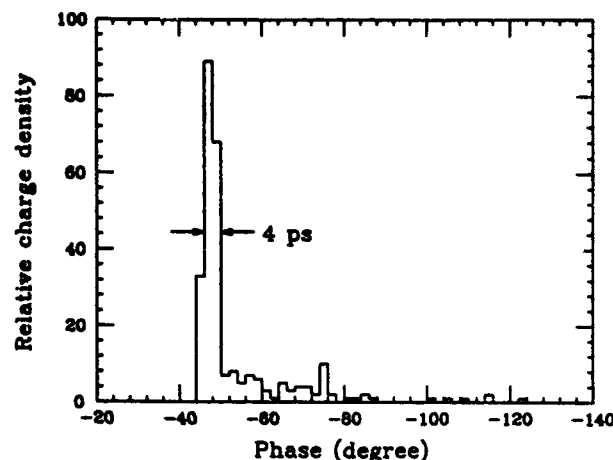


Figure 7. Bunch shape calculated for the optimum condition with the field of 0.15 MV/m for PB1.

VI. REFERENCES

- [1] S. Ohsawa et al., "Improvement to the Injection system of the KEK 2.5-GeV Linac," *Conference Record of the 16th International Linac Conference*, 1992, pp. 91-93.
- [2] S. Ohsawa et al., "New Pre-injector of the KEK 2.5-GeV Linac and its Performance," these proceedings.
- [3] A. Enomoto et al., "Linac Upgrade Plan for the KEK B-Factor," these proceedings.
- [4] S. Ohsawa et al., "High-Power Hybrid Attenuator & Phase-Shifter Systems," *Conference Record of the 15th International Linac Conference*, 1990, pp. 159-161.
- [5] R. Miller et al., "Design of a Bunching System for a High Intensity Electron Linac," LBL-25237-mc, Jun. 1988. 3pp.; Proceedings of the first European Particle Accelerator Conf., Rome, Italy, Jun. 7-11, 1988.
- [6] Y. Ogawa et al., "Beam Monitor Utilizing Transition Radiation," these proceedings.

New Outlooks on Bunched Beam Instabilities in Particle Accelerators. A Proposal for a Simple Method to Release a Potential Self-Consistent High Quality Beam

M. Bergher

LURE, Bat. 209 D, Centre Universitaire Paris-Sud, 91405 ORSAY CEDEX FRANCE,

Abstract

Several hypotheses have been proposed to explain bunched beam instabilities under increasing intensity. In fact, the cause of these instabilities can be used to generate a very high quality beam. Total coherent synchrotron radiation brings the bunches to plasma density by self-consistent supercooling in the three bunch dimensions i.e. by reduction of energy dispersion. Maximal density and minimal residual instabilities can be controlled by feedback loops. Thus, more efficient machines can be made available, opening new possibilities in many fields.

I. INTRODUCTION

In bunched beam instabilities, if "practice" agrees with "theory" within some limits, there is divergence outside. The cause of these instabilities can be used to transform this "natural" disadvantage into a mean to generate a very high quality beam [1].

A specific example for a lepton ring is given below.

II. BUNCH "LENGTHENING"

First, let us assume that there is an unique bunch in the ring vacuum chamber. This bunch is not perturbed by any other accelerating voltage than the monopole generated by the main RF cavity without higher multipole modes. Below the beam current threshold, where instabilities appear, classical beam dynamic studies give gaussian shape for the three dimensions and for particle energy which depends only on ring characteristics. No other instability than synchrotron radiation noise can be given if Robinson criterion is satisfied. Let us now place an other ideal cavity in the ring. The choice of the frequency of the accelerating monopole is close to the cutoff of the vacuum chamber and the harmonic number of the rotation frequency corresponds to the inverse of the bunch-length before the effect of the new cavity. The field produced by the circulating beam excites this cavity and then, if Q and the shunt impedance are sufficient, at the new turn, the composite accelerating voltage seen by particles leads to a different longitudinal shape of the bunch. In other words, the second cavity is a passive or idle cavity. By self-consistent effect, the

bunch can split up into microbunches (MB) partially or totally. This effect depends on the bunch intensity and becomes stronger at low energy of the ring. It is boosted by the other effects described in the following section. All MB do not have the same density. The bunch length average density appears identical after and before the installation of the new accelerating cavity.

If we inject into the ring more particles, two opposite forces act in concert: on one hand, the main RF voltage brings the new particles to the same place, and on the other hand, for each injected particle, preexistent MB contained in the micro-buckets becomes like a macroparticle whose Coulomb force prevents new particles to go into these buckets. They go preferentially into the nearest empty buckets. This is sufficient to explain the observed "lengthening" of the bunch, especially if we do not have an apparatus of sufficient bandwidth to observe the micro-temporal structure.

Usually, for one accelerating voltage, the synchrotron oscillating coupled mode number is equal to the number of bunches, but for only one frequency of synchrotron oscillation. With two accelerating cavities, the synchrotron oscillation frequencies are not identical for the different MB [2]. Another reason jumbles up explanation of the phenomenon: groups of MB have one more mode of synchrotron oscillation which depends on the main RF voltage and is near the frequency oscillation given by the main RF voltage alone. If the second high frequency cavity is tuned to the first, in order to fulfil Robinson's criterion for two cavities [3], the MB are stable. If not, MB are unstable and can strongly be subjected to multi-mode synchrotron oscillations. As shown in Figure 1, this depends on the second RF voltage and therefore on the beam current. This explains the discrete and multiple longitudinal oscillations measured in two rings of very different sizes [4,5]. When the beam current increases, the synchrotron oscillation frequency of a few MB goes to the same value. Thus, these MB can have strongly coupled oscillations and therefore they disappear above a new current threshold. When the MB oscillate with strong amplitude at the synchrotron oscillation frequency, giving a broad FM swing modulation, their fields

can excite the nearest transverse modes and then produce transverse instabilities, the later leading to total loss of the concerned MB. When multimode synchrotron oscillations are present without beam lost, at the same current threshold, the beam shows bunch "lengthening" and apparent widening of energy dispersion [6]. In summary, the preceeding explanations are sufficient to account for the bunched beam "lengthening" and the instabilities which come with it. But in reality, this leads to a self consistent shortening!

Among the superior accelerating modes of the main cavity or open accelerating structure like multifianges or winding corrugations between two pipes [7], one single mode can emerge owing to a self-consistent effect if its frequency is at the rotation frequency harmonic or is near to it, and has the highest Q and the highest shunt impedance. Then, the other modes can no more be excited because the spectral field changes and many harmonics disappear. If we can adjust the frequency, amplitude and phase in accordance with the main RF cavity, MB become stable. The later has important consequences, as seen below.

III. COHERENT BEAMS

The harmonic oscillating fields produced by the MB are coherent below a borderline frequency corresponding to the inverse of the temporal MB length. The oscillating fields propagate into the beam-pipe beyond its cutoff frequency. As a consequence, the self micro-bunching can be very strong and the micro-bunching length very short.

Four phenomena act together on the beam.

In the bending magnet, since the orbit is curved, two new favorable consequences arise :

An enhancement of coherent synchrotron radiations takes place at all harmonics of the rotation frequency until the inverse of the MB length is reached. The radiation intensities have a quadratic dependence on the number of particles in the MB [8].

1) For a beam above the ring transition energy, the trailing particles are those with the highest energy. They emit more energy, and this energy is provided to the leading particles in the same MB. The particles are moving on the arc of circle and the emitted energy following the cord path. In other words, a stimulated absorption for the leading particles is present. A new gradual and strong shortening appears for every MB.

2) Because of the coherent synchrotron radiations, the beam quickly reaches the point of zero energy dispersion. The

noise due to incoherent synchrotron radiations disappears.

On straight line , two other phenomena are present:

3) When each MB shortens, it follows the propagating azimuthal electric fields and it lags behind the crest of the electric field. A particle in front of the MB acquires more energy than the one at the back. This is valid for particles above the ring transition energy [9,10] and the complex electric field is equivalent to the accelerating voltage given by multiple cavities at every harmonic frequency.

4) Particles with higher energy go faster than those with less energy; this phenomenon has the same effect than that given by optical klystron in a FEL and acts in agreement with the above effect. This is valid only if the MB becomes very short.

Additional effects :

- The dynamic reduction of energy dispersion and of particle momentum lead to cumulative effects at each turn, and turn after turn.

- By synchrotron-betatron effect, the transverse dimensions reach zero.

- The beam quality limit depends on the perfect agreement of the couples of relative voltages and phases of one accelerating cavity to the next one, i.e. correct tune of both cavities.

- A very fast self-consistent supercooling in the three bunch dimensions is obtained and may thus conduct to plasma density. Raman radiations replace Compton radiations. Strong superradiant effect can arise [11].

- We observed once coherent synchrotron radiations in visible light in the ACO ring, under particularly favorable circumstances. Meanwhile, Touchek and beam-beam effects were also strongly modified. The large aperture of the vacuum chamber (15 cm by 6.5 cm) and the low radius of the curvature in the bending magnet (1.1 m) of this small ring give a wavelength cutoff of 3.2 cm, according to the rate formula, Eq. 1 in [12]. This can explain, when the micro structures [13] become stable, all the beneficent effects observed in ACO.

Consequences :

The particles have the same energy; the beam has very low longitudinal and transversal dimensions; the emittance is also very low; the Touchek effect disappears; beam-beam effect also disappears, and as a result, luminosity becomes very high; the multiple waves of synchrotron radiation light are coherent harmonics of the rotation frequency; the synchrotron beam light is enhanced by the number of particles in MB and totally

polarized.

IV. CONCLUSION

All current particle accelerators could be transformed into far more efficient machines with only moderate investments.

The very high beam quality generated by these improvements would lead to new outcomes in many fields.

V. REFERENCES

- [1] Patent, PCT/FR92 n°00315.
- [2] D. Potaux, LAL, ORSAY, NI-22, (1972).
- [3] M. Bergher, J.C. Bourdon, P. Brunet, *I E E E Trans. Nucl. Sci.*, NS-24, N.3, pp.1784-1785, (1977).
- [4] G. Da Silva R. Bernier, M. Bergher, and R. Belbeoch, LAL, ORSAY, NI-46 (1973).
- [5] D. Brandt, K. Cornelis, and A. Hofmann, Experimental observations of instabilities in the frequency domain at LEP, Proc. 3rd EPAC Conf., Berlin, (1992), in press
- [6] M.S. Zisman, LBL-28820, ESG 94, (1990).
- [7] S.S. Kurennoy, S.V. Purlov, *Particle Accelerators*, Vol. 34, pp. 155-167, (1990).
- [8] F.C. Michel, *Physical Review Letters*, vol. 48, pp.581, (1982).
- [9] J.D. Lawson, *Physics of Charged Particle Beams*, p. 319, Clarendon Press, Oxford. (1977)
- [10] J. Wei, S.Y. Lee, *Particle Accelerators*, vol. 28, p. 557, (1990).
- [11] R. Bonifacio and al. *Revisita Del Nuovo Cimento*, N-9, Vol. 13, pp. 1-69, (1990)
- [12] R.L. Warnock, *I E E E P.A.C.* 91, Vol. 3, pp. 1824-1826, (1991).
- [13] M. Bergher, M. Velghe and J.C. Mialocq, *Nuclear Instruments and Methods A*. 237, pp. 259-262, (1985).

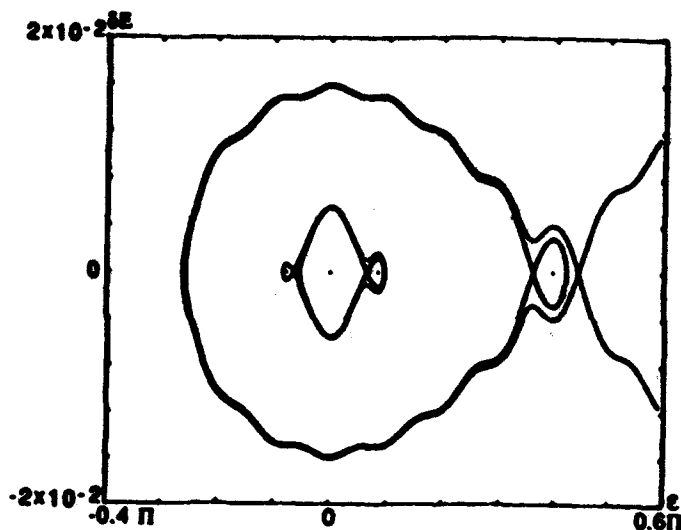


Fig.1a

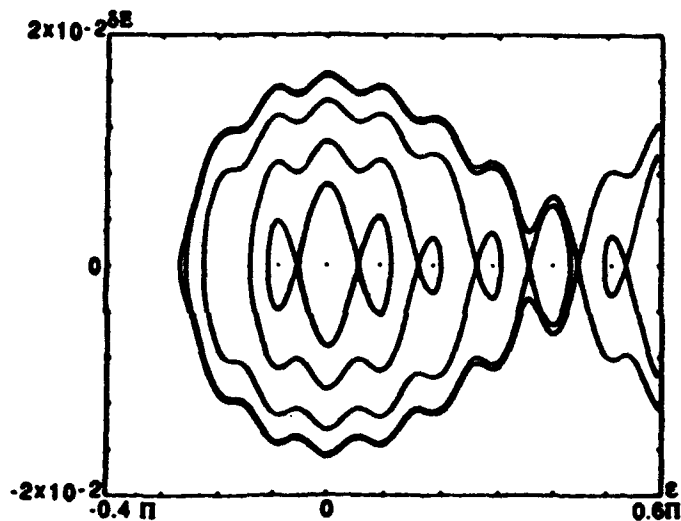


Fig.1b

Evolution of the complex separatrix for two significant values of the second RF voltage .

Both in Fig.1a, where $\alpha=0.5$ and Fig.1b, where $\alpha=1$, we have $V_2 = \alpha V_1$, $h_2 = 10 h_1$, $h_1 = 2$, $\phi_1 = \phi_0$, $\phi_2 = \pi$, h , corresponding to the harmonic of the rotation frequency and ϕ_0 to the energy loss for one cavity with $eV \sin \phi_0 = \Delta E \gamma$. Separation between the two cavity frequencies has been limited for a clear view. According to these curves, it is evident that the different possible synchrotron oscillations would be more and more complicated if the harmonic of the second cavity is very high. They are often interpreted as bunch multipole turbulences by many machine specialists.

EXPERIMENTAL STUDY OF COLLECTIVE EFFECTS IN BEP STORAGE RING WITH HIGH STORED CURRENT

V. Danilov, I. Koop, A. Lysenko, B. Militsyn, I. Nesterenko,
E. Perevedentsev, E. Pozdeev, V. Ptitsin, Yu. Shatunov and I. Vasserman
Budker Institute of Nuclear Physics, Novosibirsk, 630090, Russia

Abstract

The results of extensive investigation of beam dynamics with high current in BEP booster are presented. Strong bunch lengthening due to the potential well distortion by the inductive impedance was observed on the background of the multiple intrabeam scattering and of the ion accumulation (in the e^- beam). The octupole and sextupole corrections enabled control of collective damping of the head-tail modes. Fast damping is also observed at zero chromaticity, this is attributed to the injection kickers acting as transmission lines. The proper tuning of the non-linearity corrections cures the transverse instabilities and enables capability to store up to 0.8A current in a single bunch.

I. INTRODUCTION

The electron and positron accumulator ring BEP is recently built to upgrade performance of the e^+e^- collider VEPP-2M [1]. Electrons and positrons are accumulated alternately at the energy of 120 MeV. The injection repetition rate is 0.7 Hz, the machine is capable to capture 150 μ A ($0.75 \cdot 10^8$) of positrons and 150 mA of electrons in a single-turn injection. The maximum accumulated currents are 0.2 A of positrons and 0.8 A of electrons.

Energy ramping time in BEP is about 8 s, its lower limit is mostly due to the effect of eddy-currents in the aluminum beam pipe. The maximum energy achieved is 775 MeV, and its upper limit currently results from shifting of the vertical betatron tune down to the integer resonance, while the available gradient correction strength is insufficient to oppose this tuneshift during the ramp.

The beam parameters were measured at the energies of 120, 360 and 510 MeV.

II. BEAM PARAMETER MEASUREMENT TECHNIQUES

For measurement of both transverse and longitudinal bunch dimensions we used the system of optical dissectors, as described in [2]. The resolution of the longitudinal disector was ~ 2 cm, while the transverse disector gave ~ 0.25 mm. In a series of measurements we also imaged the beam onto a CCD matrix, and obtained the same transverse resolution, which resulted from the realistic quality of the available mirror, window and lens optics, rather than from the image-scanning device.

Indirect measurements of the vertical beam size below that resolution were enabled by monitoring of the particle loss rate (from intra-beam scattering), which was performed with the scintillation counter and resulted in ~ 60 μ m of the vertical beam size FWHM at the energy of 510 MeV. The count rate was calibrated against the vertical beam size directly measured with the disector, when the machine was operated at the betatron coupling resonance, and the disector could reliably resolve the enhanced beam height. Direct measurement of the beam energy spread is described in [2].

III. DYNAMIC APERTURE STUDY

The correct choice of the machine operating point is important for accumulation of intense beams. Due to low radiative damping at injection ($\tau_r \simeq 1$ s) the particle motion is subject to influence of weak non-linear resonances, even those of the 6th order and above. Fig. 1 shows the positron beam capture efficiency as a function of the operating point. The injected positron beam has a large transverse emittance, so it is suitable for testing the dynamic aperture. The design operating point of $\nu_x = 3.18$, $\nu_z = 3.61$ proved to be bad because of the neighbouring strong sum coupling resonances.

Changing the lattice for $\nu_x = 3.2$, $\nu_z = 3.45$ resulted

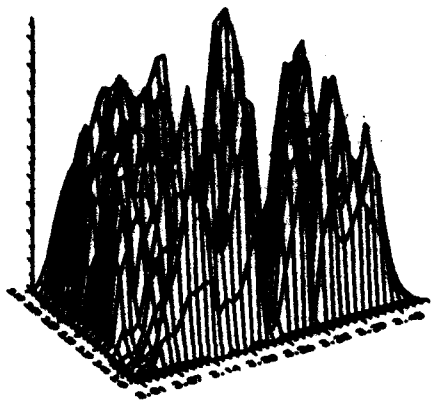


Figure 1: Positron beam capture efficiency.

in capability to use practically whole beam stay clear sizes of the vacuum chamber. For this lattice the horizontal injection kicker pulse lasts during two turns and serves as a pre-kicker at once. The lattice with $\nu_x \approx \nu_y = 3.27$ also provides for a large dynamic aperture, however it requires a separate pre-kicker (which is also installed in BEP).

Scanning of the operating point in a wider range demonstrated relatively safe operation closely to the integer resonances $\nu_{x,y} = 3$, and revealed wide stopbands surrounding the resonances $\nu_{x,y} = 4$. The latter combine the effect of integer resonances with the non-linear 12/3 ones, which are enhanced in the 12-fold symmetry of the machine lattice.

IV. ION ACCUMULATION IN BEP BEAM

The positive ion accumulation in the electron beam of the BEP storage ring was mostly pronounced during the first days of the machine commissioning, resulting in the stored current limitation at a few milliamp level with the subsequent shift of this limit up to dozens of milliamps. With an upgrade of the vacuum in the machine due to cleaning the vacuum pipe walls by irradiation with the synchrotron light, the current limitation was no more imposed by the ions, other reasons were predominant, as outlined above. However, the presence of a small positive ion concentration in the electron beam trace can be detected even after a three-year period of practically continuous operation with the average pressure of $\sim 10^{-8}$ Pa.

Fig. 2 shows the vertical beam sizes for electrons and positrons as functions of the operating point ν_z . The positron curve responds to the sum and difference resonances only, while the electron curve exhibits numerous one-dimensional resonances, which have a natural explanation in the framework of the ion accumulation hypothesis. With the current ramping the vertical beam size of the electron bunch grows much stronger than the positron beam size, the latter scales as $I^{1/6}$ due to the multiple intrabeam scattering effect. Above 300 mA the vertical beam size shrinks (see Fig. 3) that is likely to result from

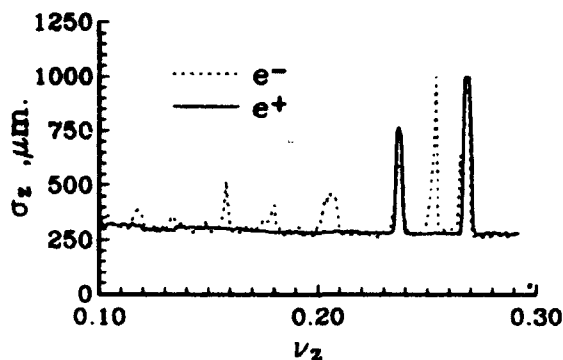


Figure 2: Vertical beam sizes for electrons and positrons.

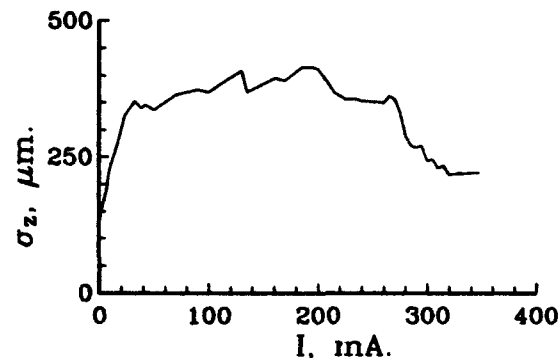


Figure 3: Current dependence of vertical beam size.

ion rejection out of the beam because of trespassing the ion stability limit. This threshold current value agrees with the assumption that single charge Ar^+ or CO_2^+ molecules dominate in the ion contents.

The effect of ion rejection from the beam can also be observed when the resonance excitation of the vertical betatron oscillations is switched on with a certain small tune offset with respect to the exact resonance tune.

The estimate for the degree of the beam space charge compensation of $\sim 5 \cdot 10^{-3}$ at 20 mA current has been obtained from the measured coherent tunes shift of $\sim 2 \cdot 10^{-4}$ at the injection energy of 120 MeV. This corresponds to the ion Ar^+ partial pressure of $6 \cdot 10^{-7}$ Pa. At the energy of 510 MeV we did not observe any effect from ions on the beam dynamics.

V. CURRENT DEPENDENCE OF BUNCH DIMENSIONS IN BEP

Experimental data on the current-dependent bunch dimensions in BEP at the energy of 360 MeV are presented in Fig. 4. We saw, that:

- with ramping the current the longitudinal bunch profile was observed to deviate from the Gaussian and to approach the parabolic shape (Fig. 5);
- the bunch length scaled as the 1/3 power of the beam current, while the beam energy spread scaled as the current to the 1/6 power (Fig. 4), the latter dependence was

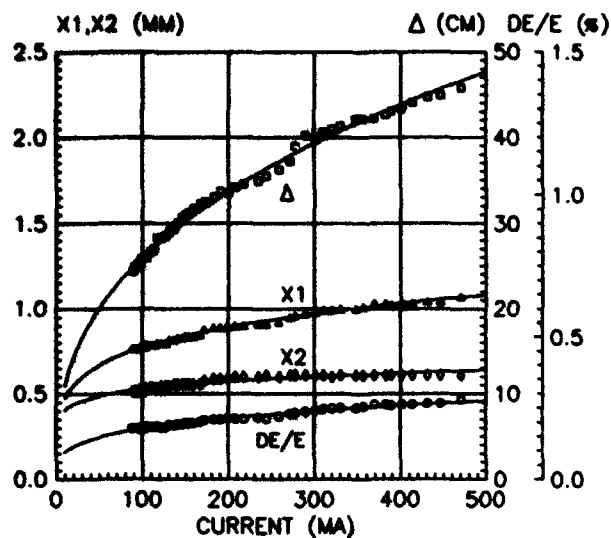


Figure 4: Current dependencies of total horizontal size $X1$, betatron size $X2$, beam energy spread DE/E and bunch length (FWHM) Δ ; the curves are $I^{1/6}$ and $I^{1/3}$ fits to the measured data.

due to the multiple intrabeam scattering effect (IBS);
 c) the bunch equilibrium phase shift was small (practically undetectable);
 d) the synchrotron tune shift with current was small ($\sim 10\%$ at 300mA) if measured with the coherent excitation, but the *large incoherent tunes* shift was observed by a special technique [3] and proved to be in agreement with the longitudinal potential well flattening;
 e) the longitudinal bunch size was independent of the revolution frequency displacement and insensitive to the position of the cavity higher order modes' tuners (apart from narrow bands where we had coherent longitudinal instabilities), so the multi-turn wakes were ruled out.

All this is consistent with the assumption of the static bunch lengthening due to the longitudinal potential distorted by the inductive wake. For a quantitative analysis we used the Haisinski equation, and the inductance value deduced from these measurements was about 50 cm. The incoherent synchrotron tunes shift resulting from the longitudinal well flattening was measured for currents up to 470 mA. The data agree with the bunchlength behavior.

The data taken at the injection energy of 120 MeV showed that:

- a) the bunch length below ~ 10 mA currents follows the $I^{1/6}$ relation, i.e. this lengthening results from IBS;
- b) at the currents of ≥ 150 mA that slow energy spread blow-up due to IBS is negligible, and the bunch length scales with the beam current as $I^{1/3}$.

The collective damping rates $\propto I$ were measured [3] using the blinded PMT technique. At positive chromaticity the damping rate was proportional to its value. However at zero chromaticity the collective damping did not vanish at BEP, one should set $\partial\nu/\partial\ln\gamma = -0.3$ to eliminate the effect. At zero chromaticities it is due to the x' terms in the

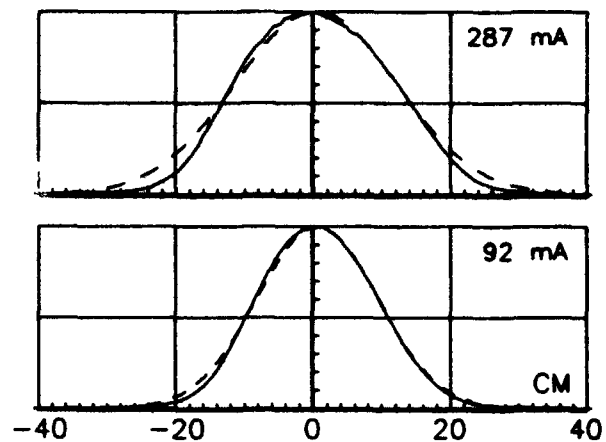


Figure 5: Evolution of the bunch longitudinal profile with current; solid line - the profiles from the disector; dashed lines are the Gaussians with the same height and same FWHM.

transverse wake, resulting from the two injection kickers which are the transmission lines in their design. The reliable evidence for this was given by the two-fold reduction of the measured damping rates resulting from the elimination of one of the two kickers by a special mechanism envisaged in its design: the transmission line was grounded over its total length. This fast damping proved to be independent of the bunch length and the betatron tune.

At the energy of 510 MeV the measurements of transverse beam emittances gave $2.5 \cdot 10^{-8}$ cm-rad for the vertical emittance and $6 \cdot 10^{-6}$ cm-rad, which fairly well agree with their design values.

REFERENCES

- [1] V.V.Anashin et al. *Proc. XIII Int. Conf. on High Energy Accelerators*, Novosibirsk, Nauka, 1 (1987) 159.
- [2] V.V.Danilov et al. "Current Dependence of Bunch Dimensions in BEP Storage Ring." *Proc. of the XVth Int. Conf. on High Energy Accelerators, Hamburg, Germany, July 20-24, 1992*, 2, 1115.
- [3] V.V.Danilov et al. "Measurement of Betatron Coherent Tunes Shifts and Collective Damping Rates in BEP Storage Ring with the Optical Technique." *ibid.*, 1, 230.

Beam Coupling Impedances of Axial Symmetric Structures

W. Bruns

Technische Universität Berlin, EN-2, Einsteinufer 17, D-1000 Berlin 10, Germany

Abstract

The transverse and longitudinal coupling impedances of axial symmetric geometries with an arbitrary number of cross section jumps are calculated. Field matching with renormalized wave amplitudes is applied at planes $z = z_n$. The resulting linear equations are solved straightforward, leading to good numerical stability. The Dirac-like pulses of the impedances below cut-off or of structures with trapped modes are avoided using a complex permittivity. Numerical results are presented for a sample detuned structure with more than 400 different radii.

I. Introduction

The structure under consideration is a beam pipe with an arbitrary number of different cross section jumps. Parallel to the axis a charge Q travels with a constant velocity $\vec{v} = \vec{e}_z \beta c$. This charge excites a field that is scattered by the inhomogeneous boundary. The scattered field acts on a test charge following behind the exciting charge.

In this paper, the Fourier transformed field is expanded in orthogonal functions, each a solution of Maxwell's equations. The continuity and boundary conditions at the planes of the cross section jumps are fulfilled by mode matching. The mode matching is applied at all cross section jumps simultaneously, leading to a single linear system of equations. The effect of the scattered field is expressed in terms of coupling impedances.

In previous studies [2]..[5], similar problems were examined. In [2] no azimuthal dependence was allowed. In [3] the azimuthal dependence $m = 1$ was considered, but with other expansion functions. In [4] a similar problem with azimuthal dependence, but without a current was calculated using scattering matrices. In [5] an even more general problem is considered, where there are jumps also in the φ -direction and with TEM-waves in coaxial segments. Their calculation also uses scattering matrices.

II. Geometry

Consider an infinitely long beam pipe with N cross section jumps. The jumps lie in the planes $z = z_n$, $n = 0..N-1$. The charge travels at a distance $\rho = \rho_q$ off axis, at the azimuthal angle $\varphi = 0$.

Inside the cylinder $\rho = \rho_q$ is the area $A_n^{(1)}$, outside the area $A_n^{(2)}$. Left of the plane z_n is the area $A_n^{(i)}$ with radius r_n , right of it the area $A_{n+1}^{(i)}$ with radius r_{n+1} .



III. The excitation

The moving charge represents a current density $\vec{J}[\text{Am}^{-2}]$.

$$\vec{J}(t) = \vec{v} \rho = \vec{e}_z \int_{-\infty}^{+\infty} J(\omega) e^{+j\omega t} d\omega = \vec{e}_z \int_{-\infty}^{+\infty} Q e^{-jk_z \rho} \frac{\delta(\rho - \rho_q)}{\rho} \sum_{m=0}^{\infty} \frac{\cos(m\varphi)}{\pi(1 + \delta_m^0)} e^{+j\omega t} d\omega$$

In the following only the Fourier transformed entities and only the m^{th} component of the Fourier series are considered.

IV. Field representation

The tangential fields in the n^{th} area A_n at the plane $z = z_n$ are represented by

$$\begin{aligned} \mu_n \vec{e}_z \times \vec{H}_{tn} &= \sum_{s=1}^{\infty} \left[k^2 \vec{F}_{ns}^{TM} Z_{ns}^{TM} - \vec{F}_{ns}^{TE} \frac{\partial}{\partial z} Z_{ns}^{TE} \right]_{z=z_n} + \\ &\quad + \vec{e}_z \times \vec{E}_{tn}^{TMS(i)}(z_n) \\ \frac{\vec{E}_{tn}}{-j\omega} &= \sum_{s=1}^{\infty} \left[\vec{F}_{ns}^{TM} \frac{\partial}{\partial z} Z_{ns}^{TM} + \vec{F}_{ns}^{TE} Z_{ns}^{TE} \right]_{z=z_n} + \\ &\quad + \frac{1}{-j\omega} \vec{E}_{tn}^{TMS(i)}(z_n) \\ \vec{F}_{ns}^{TM} &= \vec{e}_\rho \frac{d}{d\rho} J_m(j_{m,s} \rho / r_n) \cos(m\varphi) + \\ &\quad + \vec{e}_\varphi \frac{1}{\rho} J_m(j_{m,s} \rho / r_n) \frac{d}{d\varphi} \cos(m\varphi) \\ \vec{F}_{ns}^{TE} &= \vec{e}_\rho \frac{1}{\rho} J_m(j'_{m,s} \rho / r_n) \frac{d}{d\varphi} \sin(m\varphi) - \\ &\quad - \vec{e}_\varphi \frac{d}{d\rho} J_m(j'_{m,s} \rho / r_n) \sin(m\varphi) \\ TX &\in \{TM, TE\} \\ Z_{ns}^{TX}(z) &= C_{ns}^{TX} e^{+j\epsilon_{ns}^{TX}(z-z_{n-1})} + D_{ns}^{TX} e^{-j\epsilon_{ns}^{TX}(z-z_n)} \\ q_{ns}^{TX} &= \sqrt{\omega^2 \mu_n \epsilon_n - p_{ns}^{TX^2}} \\ p_{ns}^{TM} &= \frac{j_{m,s}}{r_n}; p_{ns}^{TE} = \frac{j'_{m,s}}{r_n}; J_m(j_{m,s}) = J'_m(j'_{m,s}) = 0 \end{aligned}$$

The exponential factors are chosen to be one at the planes $z = z_n$ and in magnitude less or equal one in the areas A_n .

The source fields are represented by:

$$\begin{aligned} \vec{e}_z \times \vec{B}_{in}^{TMS(i)}(z_n) &= k^2 e^{-jhz_n/\beta} \times \\ &\left\{ \vec{e}_\rho \frac{d}{d\rho} R_n^{(i)}(\rho) \cos(m\varphi) + \vec{e}_\varphi \frac{1}{\rho} R_n^{(i)}(\rho) \frac{d}{d\varphi} \cos(m\varphi) \right\} \\ \frac{1}{-j\omega} \vec{E}_{in}^{TMS(i)}(z_n) &= \left[\frac{d}{dz} e^{-jhz_n/\beta} \right]_{z=z_n} \times \\ &\left\{ \vec{e}_\rho \frac{d}{d\rho} R_n^{(i)}(\rho) \cos(m\varphi) + \vec{e}_\varphi \frac{1}{\rho} R_n^{(i)}(\rho) \frac{d}{d\varphi} \cos(m\varphi) \right\} \end{aligned}$$

(abbreviations: $\gamma = 1/\sqrt{1-1/\beta^2}$; $\zeta_q = \frac{\rho_q k}{\gamma}$; $\zeta_n = \frac{\rho_n k}{\gamma}$):

$$R_n^{(1)}(\rho) = A_n^{(1)} J_m\left(\frac{\rho k}{\gamma}\right)$$

$$R_n^{(2)}(\rho) = A_n^{(2)} J_m\left(\frac{\rho k}{\gamma}\right) + B_n^{(2)} Y_m\left(\frac{\rho k}{\gamma}\right)$$

The amplitudes A , B of the source fields are given through

$$\begin{pmatrix} -J'_m(\zeta_q) & J'_m(\zeta_q) & Y'_m(\zeta_q) \\ -J_m(\zeta_q) & J_m(\zeta_q) & Y_m(\zeta_q) \\ 0 & J_m(\zeta_n) & Y_m(\zeta_n) \end{pmatrix} \begin{pmatrix} A_n^{(1)} \\ A_n^{(2)} \\ B_n^{(2)} \end{pmatrix} = \left(\frac{\gamma \mu_n Q}{\rho_q k^3 \pi (1 + \delta_m^0)}, 0, 0 \right)^T$$

V. Mode Matching

At the common boundary of two areas A_n , A_{n+1} , the tangential fields have to be continuous. At the metallic walls the tangential E -field must vanish:

$$r_s = \min(r_n, r_{n+1}); \quad r_g = \max(r_n, r_{n+1})$$

$$\begin{aligned} \vec{H}_{in}(z_n) &= \vec{H}_{i,n+1}(z_n); & 0 \leq \rho \leq r_s \\ \vec{E}_{in}(z_n) &= \vec{E}_{i,n+1}(z_n); & 0 \leq \rho \leq r_s \\ \vec{E}_{is}(z_n) &= 0 & r_s \leq \rho \leq r_g \end{aligned}$$

Expansion of the continuity- and boundary conditions on the tangential components yields a linear system of equations for the unknown C_{ns}^{TX} , D_{ns}^{TX} :

$$i \in \{1 \dots \infty\}; \quad TX \in \{TM, TE\}$$

$$r_s = \min(r_n, r_{n+1}); \quad r_g = \max(r_n, r_{n+1});$$

$$\begin{aligned} \frac{1}{\mu_n} \int_0^{2\pi} \int_0^{r_s} [\vec{e}_z \times \vec{B}_{in}] \vec{F}_{si}^{TX} \rho d\rho d\varphi &= \\ \frac{1}{\mu_{n+1}} \int_0^{2\pi} \int_0^{r_s} [\vec{e}_z \times \vec{B}_{i,n+1}] \vec{F}_{si}^{TX} \rho d\rho d\varphi & \\ \int_0^{2\pi} \int_0^{r_s} \vec{E}_{in} \vec{F}_{si}^{TX} \rho d\rho d\varphi &= \int_0^{2\pi} \int_0^{r_{n+1}} \vec{E}_{i,n+1} \vec{F}_{si}^{TX} \rho d\rho d\varphi \end{aligned}$$

The occurring integrals $\int \int \vec{F}_{nj}^{TX} \vec{F}_{li}^{TY} \rho d\rho d\varphi$ can be evaluated in closed form. Sorting the equations yields a linear system for the unknown C_{ns}^{TX} , D_{ns}^{TX} :

$$\begin{pmatrix} LC_n^H & LD_n^H & RC_n^H & RD_n^H \\ LC_n^E & LD_n^E & RC_n^E & RD_n^E \end{pmatrix} \begin{pmatrix} \vec{C}_n \\ \vec{D}_n \\ \vec{C}_{n+1} \\ \vec{D}_{n+1} \end{pmatrix} = \begin{pmatrix} \vec{H}S_n \\ \vec{E}S_n \end{pmatrix}$$

The matrices LC_n^H , LD_n^H come from the expansion of the source free H -field in the n^{th} area at the plane $z = z_n$ (left of it), the matrices RC_n^H , RD_n^H from the source free field in the $(n+1)^{\text{th}}$ area (right of z_n). Similar are LC_n^E , LD_n^E , RC_n^E , RD_n^E matrices containing the coupling integrals for the source free E -field. The vectors \vec{C}_n , \vec{D}_n contain the unknown amplitudes of the waves travelling forward or backward respectively. The vectors $\vec{H}S_n$, $\vec{E}S_n$ contain the expansion integrals of the source fields.

There are N such equations for the N cross section jumps. The submatrices are of order infinity, so are the column vectors. After truncation of the submatrices to a size M , all equations together constitute $N \times 2M$ equations for the $(N+1) \times 2M$ unknown C_{ns}^{TX} , D_{ns}^{TX} . The C_{0s}^{TX} of the leftmost area A_0 have to be zero, as they represent waves coming from a nonexistent source at $z = -\infty$. A similar argument holds for the D_{Ns}^{TX} . Half of the submatrices are diagonal due to the orthogonality of the expansion functions. The equations can be swapped to a structure as (\backslash means a diagonal matrix, X means a dense matrix)

$$\begin{pmatrix} \backslash & X & X \\ X & \backslash & \backslash \\ & X & X & \backslash & \backslash \\ & & X & X & \backslash & \backslash \\ & & & X & X & \backslash & \backslash \\ & & & & X & X & \backslash & \backslash \\ & & & & & X & X & \backslash & \backslash \\ & & & & & & X & X & \backslash \end{pmatrix} \vec{x} = \vec{b}$$

This linear system can be transformed by scaling to a very well conditioned one with the diagonal elements being unity and the off-diagonal elements all less than unity.

VI. Coupling Impedances

A test charge Q_p travelling behind the exciting charge at an azimuthal angle φ_p experiences a force by the scattered field. This force changes the impulse of the test charge. Under the assumption, that the velocity of both the exciting charge and the test charge is near the velocity of light, the change in the impulse will not change the velocity but the mass. The integrated impulse deviation (the kick) of the test charge travelling with the same velocity as the exciting charge at a distance $\Delta z = \tau v$ behind is a function of this time τ .

$$\begin{aligned} \vec{w}(\tau) [V] &= -\frac{1}{c\beta Q_p} \int_{-\infty}^{+\infty} \frac{d}{dt} (m\vec{v}) dt \\ &= -\frac{1}{c\beta Q_p} \int_{-\infty}^{+\infty} [Q_p \vec{E}(\vec{s}(t), t) + Q_p \vec{v} \times \vec{B}(\vec{s}(t), t)] dt \end{aligned}$$

The Fourier transform of the kick is proportional to the longitudinal- and transverse coupling impedances.

$$Z_L [V/A] = W_z(\omega) \frac{1}{Q(\rho_q/r_0)^m (\rho_p/r_0)^m \cos(m\varphi_p)}$$

$$\begin{aligned}
&= \frac{-\int_{-\infty}^{+\infty} E_z(\rho_p, \varphi_p, z, \omega) e^{+jks/\theta} dz}{Q(\rho_q/r_0)^m (\rho_p/r_0)^m \cos(m\varphi_p)} \\
Z_T[V/A] &= W_p(\omega) \frac{-j}{Q(\rho_q/r_0)^m (\rho_p/r_0)^{m-1} \cos(m\varphi_p)} \\
&= \frac{-\int_{-\infty}^{+\infty} [E_z(\rho_p, \varphi_p, z, \omega) - c\beta B_\varphi(\rho_p, \varphi_p, z, \omega)] e^{+jks/\theta} dz}{jQ(\rho_q/r_0)^m (\rho_p/r_0)^{m-1} \cos(m\varphi_p)}
\end{aligned}$$

The factors are chosen to make the Fourier transforms impedances and to make the impedances in the ultrarelativistic case independent of the radii ρ_p and ρ_q .

VII. Numerical results

In [1] a design algorithm for a detuned accelerator is proposed. This procedure was used to generate the geometry data of a detuned accelerator with 204 cells. The cells are designed to have the same resonance frequency for the monopole mode ($m = 0$) and a Gaussian frequency distribution for the dipole resonances ($m = 1$) with a mean of 15.39 GHz and a variance of 0.39 GHz. This expected resonance density is shown in Fig. 3. The iris radii vary from $0.39\text{cm} \leq a_n \leq 0.54\text{cm}$, the cavity radii are between $1.05\text{cm} \leq b_n \leq 1.12\text{cm}$. The iris thickness and gap width are held constant at $t = 0.146\text{cm}$ and $g = 0.729\text{cm}$. In [2] the longitudinal impedance ($m = 0$) of the same geometry was computed. They had designed coupling cavities at the left and right of the structure. These coupling cavities also were used here.

The resulting structure has 413 cross section jumps. The calculation was performed with 10 TM and 10 TE modes per area, thus, the order of the linear system was $2 \times 20 \times 413$. The normalisation radius was $r_0 = 1\text{cm}$.

The structure has trapped modes. The impedance at their resonances has a characteristic like Dirac pulses. This behaviour is circumvented by using a complex permittivity $\epsilon_r = 1 + j10^{-4}$. The impedance gets a Gaussian shape. The resulting transverse impedance ($m=1$) is shown in Fig. 2.

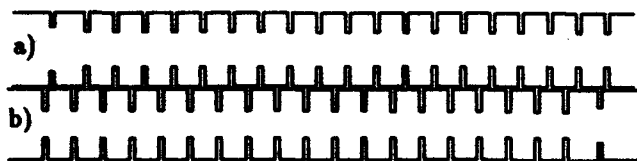


Figure 1: a) The left coupler and the first 18 cells of the detuned structure; b) The last 18 cells and the right coupler.

VIII. Acknowledgement

I like to thank Manfred Filtz for giving me first insights in mode matching.

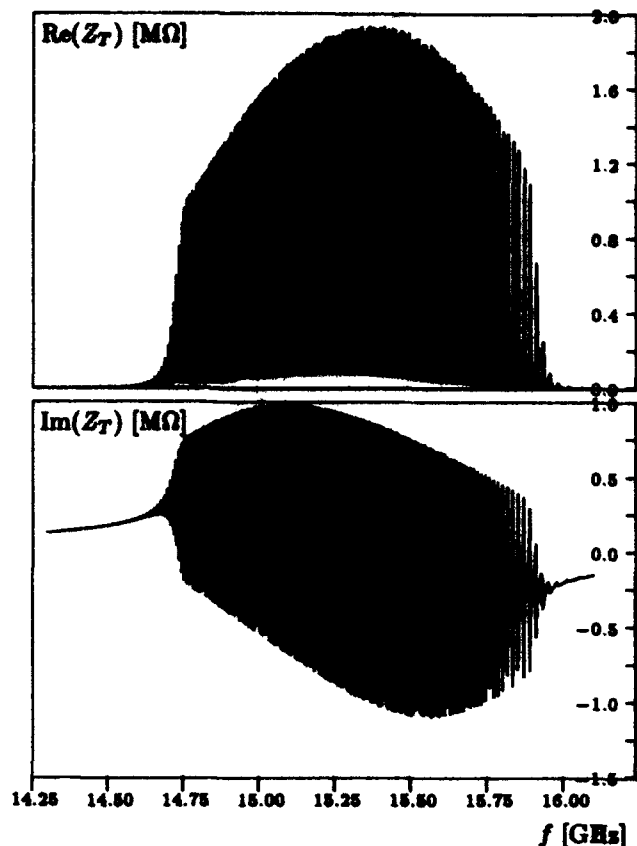


Figure 2: Transverse impedance in the detuned structure

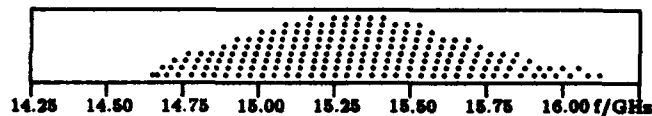


Figure 3: Expected locations of the 204 dipole resonances in the detuned structure

References

- [1] J.W. Wang, and B.W. Littmann, Design Study on Quasi-Constant Gradient Accelerator Structure SLAC/AP-92 September 1991
- [2] S.A. Heifets, S.A. Kheifets, LONGITUDINAL ELECTROMAGNETIC FIELDS IN AN APERIODIC STRUCTURE, SLAC-PUB-5907 September 1992
- [3] S.A. Kheifets, K.L.F. Bane, H. Bizek, TRANSVERSE IMPEDANCES OF CAVITIES AND COLLIMATORS, SLAC-PUB-4097 March 1987 (A)
- [4] H.G. Beyer, N. Holtkamp, U. van Rienen, K. Steinigke, V. Tsakanov, R. Wansenberg, T. Weiland, M. Witting, Zang M., MODAL FIELD MATCHING IN TAPERED MULTICELL STRUCTURES, ECFA WORKSHOP e^+e^- LINEAR COLLIDERS, Garmisch Partenkirchen July 25 to August 2, 1992
- [5] M. Filtz, T. Scholz, Impedance Calculation for a Coaxial Liner, these proceedings

ACCELERATOR PHYSICS ISSUES AT THE SSC

Gerald F. Dagan
Superconducting Super Collider Laboratory†
2550 Beckleymeade Ave., Dallas, TX 75237

I. INTRODUCTION

Realization of the design energy and luminosity goals of the Superconducting Super Collider (SSC) will require proper resolutions of a number of challenging problems in accelerator physics. The status of several salient issues in the design of the SSC will be reviewed and updated in this paper. The emphasis will be on the superconducting accelerators.

II. LATTICE AND BEAM LINE DESIGN

A. Collider

A new configuration for the lattice of the Collider^[1] has been adopted, in which space has been created in the north and south arcs, by the removal of a small number of dipole magnets. The magnets have been removed in pairs separated by 180° in phase advance, so that the perturbation to the dispersion function is local and minimal. The rest of the dipoles in the ring will be operated at a slightly higher field to attain the same energy, and the margin will be retained by lowering the operating temperature by about 0.1°K. Some of the resulting free space provided in the arcs has been utilized to allow cryogenic and electrical feed point placement consistent with surface land acquisition sites for utility buildings. Additional free space will be filled with empty cryostats initially, but will be available for use in the future for purposes such as beam scraping, polarization preserving devices, damping systems, and other as yet unspecified needs. An additional modification to the lattice now being studied is the option of a larger aperture ($\geq 48\text{mm}$) quadrupole in the Collider arcs. This is motivated by a desire for uniformity with larger aperture quadrupoles in the utility and IR regions; simplification of quench protection for a larger bore quadrupole; and ease of magnetic measurements with an increased bore tube inner diameter in both dipoles and quadrupoles. The larger aperture quadrupole would develop a smaller gradient, and so would require a larger slot length, which is provided by the space previously allocated to mid-half-cell correction systems (see below).

In addition to the modifications described above for the arcs of the Collider, parts of the straight sections (specifically the West Utility Region and the East Interaction Region) have undergone significant design evolution.

The current design^[2] of the East Interaction Region incorporates three additional families of independently powered quadrupoles. These quadrupoles are used to change the optics from injection to collision while the final triplet quadrupoles

are held constant. This feature of the design allows the two rings to be "squeezed" independently. The new design has two secondary foci where the IP is imaged, located symmetrically on both sides of the IR. Additional changes from the previous design include: 1) A significant reduction in the peak value of β at injection, 2) larger bore (5cm) triplet quadrupoles, 3) a standard design for the vertical bends, 4) a reduced total length of magnets. The design can accommodate different β^* 's at the two IP's, and a range of values between 40 and 180m is possible for the space allocated to a detector at each IP.

Crossing angle control is achieved through local steering dipoles. This introduces undesirable anomalous dispersion due to the necessarily large orbit excursions through the high beta triplets. A scheme has been proposed^[3] to correct this dispersion, using opposite polarity quadrupole pairs separated by 180° in phase and located in the arcs, just prior to entry into and after exit from the IR's. The IR design incorporates a phase advance between these quadrupoles and the IR triplet such that the anomalous dispersion from the triplet is fully canceled.

The Collider West Utility region has also undergone considerable design development^[4]. The maximum β values have been reduced by a factor of two to about 600m. The complexity and plurality of different components (quadrupoles, spools, warm-to-cold transitions) in the region has been reduced. The abort line admittance has been increased, and specific locations for damping systems have been identified.

B. High Energy Booster

The lattice of the High Energy Booster (HEB) has also been modified in order to increase its dynamic aperture. The cell length has been decreased from 78 to 64m. The stronger focusing increases the dynamic aperture from 9σ to 11σ at injection. Additional minor modifications to the lattice in the short straight sections are under consideration to obtain further increases in dynamic aperture.

C. Beam Lines

The optics of several of the beam lines which interconnect the synchrotrons has also been redesigned, in order to increase simplicity, reduce cost and improve operability. These include the 12 GeV/c LEB-MEB transfer line^[5], the 200 GeV/c MEB-HEB transfer lines^[6], and the 2 TeV HEB-Collider transfer lines^[7]. All these transfer lines are fabricated from resistive magnets. The general guidelines in these redesigns have been to minimize sensitivity to magnet and alignment errors, and to provide flexibility, and orthogonality, for amplitude and dispersion function matching between the rings. In the case of the higher energy transfer lines, for which the beam transfer

† Operated by the Universities Research Association, Inc., for the U.S. Department of Energy under Contract No. DE-AC35-89ER40486.

takes place into or between superconducting accelerators, provision for control of beam loss and considerations of component failure scenarios (particularly kicker misfires/prefires) are incorporated into the designs^[8].

III. COLLIDER CORRECTION SYSTEMS

A. Linear Coupling

A decoupling scheme has been proposed^[9] which utilizes 44 skew quadrupole correctors, located within the arcs in missing dipole spaces, and in the utility straight sections. The system can be operated to achieve global decoupling in two families of 12 skew quadrupoles or in four families of 24 skew quadrupoles. Alternately, all 44 skew quadrupoles can be independently set if desired to achieve both global and local decoupling. The strengths of the quadrupoles will be sufficient to achieve $\Delta v < 0.003$ with the expected sources of coupling in the ring (systematic $a_1 = 0.1 \times 10^{-4} \text{ cm}^{-1}$ in the dipoles, random $a_1 = 1.25 \times 10^{-4} \text{ cm}^{-1}$ in dipoles, and 0.5 mrad rms quadrupole roll.)

B. Chromatic Correction^[10]

The sextupole correctors in the Collider arcs are intended to compensate for both the natural chromaticity of the machine and the high field systematic sextupole of the dipoles. In addition, the system must compensate for chromatic effects introduced by the IR's in collision optics. The IR's can make a significant contribution not only to the first order chromaticity, but also to the second order chromaticity^[11]. Because of cancellation between adjacent IR's, the second order effects are small if the IR's are separated by an odd multiple of $\pi/2$ and they are operated at the same value of β^* . However, large second order chromatic effects can arise if the adjacent IR's are operated at different values of β^* , or if the tune departs substantially from the design value. To ameliorate this problem, a local sextupole correction scheme is planned, utilizing four families of sextupoles in the arc sections next to the IR regions. Global chromatic correction is achieved through the bulk of the arc sextupoles; local control is achieved by these four families near the IR's. The strength of the global and local sextupoles is planned to be adequate for correcting natural chromaticity, that from $b_2 = 0.8 \times 10^{-4} \text{ cm}^2$ in the dipoles, and that from the two low- β and two high- β IR's.

C. Dipole/Quadrupole/Decapole/Octupole Correctors

The dipole corrector system is planned to be sufficient to correct, at the 4σ level, quadrupole misalignments of 0.4mm rms, and dipole rolls of 0.5 mrad rms. The quadrupole correction system has two principal functions. It will correct the differential dipole-quadrupole saturation, and will also allow tune adjustments of up to ± 3 units.

In the previous designs for the Collider, octupole, decapole, and skew quadrupole correctors were envisioned for some mid-half-cell locations. As noted above, the current plan for skew quadrupoles utilizes space in the arcs provided in the

current lattice design, which eliminates the need for skew quadrupoles in mid-half-cell locations. Recent analysis has indicated that if the dipoles meet the specifications for systematic and random octupole and decapole harmonics, then octupole and decapole correctors in the spool pieces will be sufficient. A separate system in mid-half-cell locations is not needed. All the prototype dipole magnets manufactured to date have met the required specifications. Hence, it has been decided to eliminate all mid-half-cell correctors, which will result in considerable simplification and cost savings.

IV. EMITTANCE CONTROL

One of the principal challenges in achieving the SSC design luminosity is that of preserving the beam brightness throughout the accelerator chain and during storage in the Collider.

A. Emittance Growth in the Accelerator Chain

In the accelerator chain, there are several threats to brightness; one of these occurs in the LEB due to the strong space-charge effects at injection. This has been extensively studied^[12] and it is believed that the current design of the LEB can cope with these effects without excessive emittance dilution. Another threat to brightness occurs during each beam transfer, where injection oscillations, and amplitude and dispersion function mismatches, can lead to emittance dilution due to phase space filamentation. The recent redesign of the beam lines noted above, which has emphasized ease of matching from one ring to another and reduced sensitivity to errors, should lessen this threat. Another significant issue in the accelerator chain is that of coupled bunch instabilities, which can lead to emittance growth if not properly controlled. Damping systems^[13] are planned for each accelerator to provide multi-bunch stability control and reduce sensitivity to dipole mode injection errors.

B. Long-Term Emittance Growth

In the Collider, during storage, additional issues arise related to sources of long-term emittance growth. These include the effects of power supply ripple and possible ground motion effects.

The low revolution frequency of the Collider causes the lowest betatron sideband to occur at a frequency in the range of 700 - 900 Hz, depending on the exact value of the fractional part of the tune. The amplitude of ground motion or power supply noise in general grows as the frequency is lowered, so the effect of these perturbations on the beam's betatron motion can be expected to be relatively more important in the Collider than in existing machines with larger revolution frequencies. These are difficult issues to study, and particularly to quantify accurately, although some progress has recently been made^[14]. Measurements of ground motion and vibration in the tunnel environment are planned, and the damping of such motion will be considered in the design of the Collider components and their support systems. The effect of power supply ripple has been simulated, and it is believed that the

baseline power supply filter system^[15] will be adequate to limit emittance growth due to power supply ripple to less than 20 percent per 24 hours. Provision for retrofit of an active filter system has been allowed.

C. Field Quality

Field quality is primarily an issue in the higher energy machines. In the MEB, field quality requirements dictate the specifications on the dipoles, particularly at the lowest fields. However, these specifications are not difficult to meet with some care in magnet fabrication. In the superconducting machines, field quality is tied directly to the requirements (principally aperture) on the superconducting dipoles. For both the HEB and the Collider, dipoles with a 5cm diameter coil will have adequate static field quality to meet the requirements. For the HEB, there is a special problem related to the rapid ramp rate (0.062T/sec): the field harmonics due to transient eddy currents arising during the ramp must be small enough that sufficient linear and dynamic aperture is maintained during acceleration. The bipolar ramp cycle of the HEB makes for a particularly challenging environment in which to meet this demand.

V. BEAM LOSS CONTROL

Beam loss control is of particular concern in the superconducting accelerators, in which even small amounts of beam-related energy deposition can cause quenching of the superconducting magnets. As noted above, this issue has been kept in mind during the design of beam injection, extraction, and abort systems for these machines. In addition, control of the beam halo and localized beam loss in the vicinity of the Collider IP's is crucial to maintaining a relatively low background environment for the Collider detectors. An extensive system^[16] of collimators and beam scrapers has been proposed for the Collider in order to achieve the necessary low beam loss conditions.

A. Collider Vacuum

A particularly thorny problem related to beam loss control is that of maintaining an adequately high level of vacuum in the Collider. Degradation of the Collider vacuum is directly related to the presence of synchrotron radiation in the machine^[17]. The Collider will be the first proton synchrotron for which the beam energy is high enough to produce significant amounts of synchrotron radiation. The major effect of this radiation, which is absorbed by the cold beam tube walls, is to place a significant dynamic heat load on the Collider's cryogenic system. This is handled in a straightforward way by proper sizing of the 4°K refrigeration system. However, as in electron synchrotrons, the synchrotron radiation will also desorb gas (primary H₂) from the beam tube walls. Unlike in electron synchrotrons, this gas will be cryopumped onto the walls of the beam tube. Since it is very loosely bound, the effective cross-section for photodesorption of this cryosorbed gas is quite high. Thus, there is a constant "recycling" of gas molecules from the

surface into the beam tube vacuum, which produces a "dynamic" gas density^[18]. If sufficiently dense, this gas can lead to substantial beam loss and even local overload of the cryogenic system due to scattered high energy radiation. At this point, machine operation stops and the beam tube wall must be warmed to ~20°K to allow the H₂ to be pumped out.

Several approaches are available as potential solutions to this problem. The simplest is to ensure that the total hydrogen gas flux evolved from the surface is low enough that the time associated with surface buildup of cryosorbed H₂ gas is long (~one year).

The gas flux evolved is determined by the effective photodesorption coefficient and the amount of gas initially trapped on the surface or in the bulk of the beam tube material. Recent experiments^[19] have indicated that the effective photodesorption coefficient is substantially suppressed (relative to its room temperature value) at cryogenic temperatures, which will limit the total amount of gas evolved. The gas load may also be reduced by proper fabrication and cleaning of the beam tube. An extensive series of investigations into possible options in this area is underway at SSCL and its subcontractors.

If this approach does not succeed in limiting the gas density evolved by photodesorption, another technique is the introduction of a liner^[20]. This solution involves the use of an insert in the magnet bore tube, with holes to allow photodesorbed gas to be pumped by cryosorbent material located between the liner and the beam tube. The cryosorber, shielded from the photons by the liner, would accumulate gas for a long period before warm-up was required. An engineering design of an 80°K^[21] liner has recently been completed. Engineering design is planned for a liner operating at 4°K, which has advantages in simplicity and reduced photodesorption coefficient, and disadvantages in pumping speed and cryogenic efficiency, relative to the 80°K solution. The increased bore tube size mentioned above in the first section provides sufficient physical aperture to adopt this solution if it is required.

VI. COLLIDER RF SYSTEMS

The baseline RF system for the Collider is a 20 MV, 360 MHz room temperature 5-cell cavity system. Recently, the possibility of the utilization of superconducting RF for the Collider has come under consideration^[22]. Superconducting RF has advantages in the areas of reduced higher-order-modes, a smaller number of cavities, and reduced RF power (and window power) requirements. Disadvantages relative to room temperature systems lie in the areas of increased development and support requirements at SSCL, possibly lower reliability, and possibly larger initial capital costs (vs lower operating costs). A decision of which path to proceed along is expected in the near future.

VII. REFERENCES

- [1] M. Syphers, et al., "SSC Collider Arc Lattice",

contribution to this conference.

- [2] Y. Nosochkov, et al., "Design of the Interaction Regions at the SSC," contribution to this conference.
- [3] Y. Nosochkov and D. Ritson, "Provision of IP Crossing Angles for the SSC," contribution to this conference.
- [4] B. Parker, "Design Status Report on the Collider Utility Straight Insertions," contribution to this conference.
- [5] N. Mao, et al., "Beam Optics of LEB-MEB Transport Line for Superconducting Super Collider," contribution to this conference.
- [6] F. Mariani, et al., "200 GeV Beam Transfer Lines at the SSC," contribution to this conference.
- [7] F. Wang, et al., "Lattice Design and Injection Issues for the 2 TeV SSCL High Energy Booster to Collider Injection Lines," contribution to this conference.
- [8] I. Balshov, et al., "Dealing With Abort Kicker Prefire and Misfire in the Superconducting Super Collider," contribution to this conference.
- [9] Y. Cai, et al., "Decoupling Correction for the SSC Collider," contribution to this conference.
- [10] T. Sen, et al., "Chromaticity Correction for the SSC Collider Rings," contribution to this conference.
- [11] F. Pilat, et al., "Dynamic and Momentum Aperture of the SSC Collider in Presence of the Sextupole System for the Local Correction of the Interaction Region Chromaticity,"; T. Sen, et al., "Second Order Chromaticity of the Interaction Regions in the SSC," contributions to this conference.
- [12] S. Machida, "Space-Charge Calculations in Synchrotrons," contribution to this conference.
- [13] T. Grimm and P. Coleman, "Control of Longitudinal Instabilities in the Low Energy Booster"; J. Palkovic, "Longitudinal Instabilities in the MEB"; W. Chou and J. Peterson, "Issues of the Feedback Systems Design at the SSC"; contributions to this conference.
- [14] T. Sen and M. Syphers, "Effect of Power Supply Ripple on Emittance Growth in the Collider"; H. Weaver, "Vibrational Studies at the SSC"; M. Syphers, et al., "Experimental Simulation of Ground Motion and Power Supply Ripple in IUCF Cooler Ring"; H. Shih, et al., "Transverse Emittance Growth Due to Dipole Field Ripple and Noise"; contributions to this conference.
- [15] E. Tacconi and C. Christiansen, "Ring-Magnet Power-Supply Regulation Loops for the SSC Accelerator Complex," contribution to this conference.
- [16] I. Bashiev, et al., "Beam Loss Handling at the SSC," contribution to this conference.
- [17] A. Mathewson, "Vacuum Technology for Superconducting Colliders," contribution to this conference.
- [18] W. Turner, "Dynamic Vacuum in the Beam Tube of the SSCL Collider - Cold Beam Tube and Liner Options," contribution to this conference.
- [19] I. Maslennikov, et al., "Photodesorption Experiments on SSC Collider Beam Tube Configurations," contribution to this conference.
- [20] J. Zbasnik, et al., "Design of the Superconducting Super Collider Beam Tube: Baseline and Liner Approaches," contribution to this conference.
- [21] Q. Shu, et al., "Prototype Liner System for the Interception of Synchrotron Radiation in a Half Cell of the SSCL Collider," contribution to this conference.
- [22] W. Chou, "Choice of the RF Cavities for the SSC Collider"; G. Schaffer, et al., "RF Systems Engineering for the SSC Collider Rings"; contributions to this conference.

Fermilab Collider Upgrade: Recent Results and Plans

D. A. Finley
Fermi National Accelerator Laboratory*
P.O. Box 500
Batavia, Illinois 60510

Abstract

The Fermilab collider program has entered its first physics run with two major detectors, CDF and D0. Recent results on the performance of the accelerators are presented, along with plans to improve the luminosity of the collider. The peak luminosity routinely exceeds the goal of $5 \times 10^{30} \text{ cm}^{-2} \text{ sec}^{-1}$, and the integrated luminosity routinely exceeds 1 pb^{-1} per week to each detector. The Tevatron has been successfully upgraded to include electrostatic separators which provide helical orbits which overcome the beam-beam tune shift limitations of previous runs by only allowing bunch crossings at the two detectors. The installation of two matched low beta inserts in the Tevatron has allowed for the simultaneous operation of two high luminosity interaction regions. The Antiproton Source has increased its performance over the previous run as measured by stack size and stacking rate. The Linac will be upgraded from 200 MeV to 400 MeV in order to lessen the space charge tune shift upon injection into the Booster. Additional improvements to the Antiproton Source are required to meet the luminosity projections. Higher luminosity requires more bunches in the Tevatron in order to keep the number of interactions per bunch crossing acceptably small. The present plan is to increase the number of bunches from 6 to 36 per beam. Until it is replaced with the Main Injector, the Main Ring will remain as the most significant bottleneck on the performance of the collider.

Current Performance

Initial and Integrated Luminosity

The initial luminosity delivered to the detectors has routinely exceeded $5 \times 10^{30} \text{ cm}^{-2} \text{ sec}^{-1}$ which is the goal for the present run. This is demonstrated in Figure 1 which shows the initial luminosity for both the present run and the previous run. The "10X

Running Average" means that the initial luminosities for a particular store and the nine previous stores are summed, divided by ten, and plotted. This averaging removes much of the scatter from store to store and presents a clearer picture of the actual accelerator performance. Some of the variations in the average are due to various failure modes - particularly those which result in dropping the antiproton stack - and some are due to differences in emphasis between operating for peak luminosity and other machine improvements. For the present run, the initial luminosity is taken after scraping which is done on the beams to reduce the backgrounds at the two detectors. The peak initial luminosity for the run has been $8.79 \times 10^{30} \text{ cm}^{-2} \text{ sec}^{-1}$. The luminosity displayed is for CDF; the luminosity for D0 is comparable. The luminosity lifetime at the beginning of a store is typically 12 to 16 hours. It increases about 0.2 hours per hour during the store.

Figure 2 shows the integrated luminosity for the present and previous runs for each week and for the entire run. The figure shows the integrated luminosity for the present run approaching 30 pb^{-1} . The goal for the run is 25 pb^{-1} . The plateau near week 22 is due to a scheduled shutdown. The goal for the run of 1000 nb^{-1} per week has been exceeded several times, and one week exceeded 2 pb^{-1} .

Figure 2 shows the integrated luminosity delivered to CDF. Approximately 70% of this is logged to tape. D0 logs about 20% less than this primarily due to the blanking required when Main Ring beam passes through the D0 detector during antiproton stacking. The concern that the D0 detector may not be able to run at all during stacking has been put to rest.

Beta* and the CDF SVX

The design for the minimum beta function at the interaction regions (beta*) is 50 cm. However, for the nominal current settings of the low beta

*Operated by the Universities Research Association under contract with the U.S. Department of Energy

quadrupoles, a beta beat is created which results in an effective beta* of about 35 cm at both interaction regions. This beta beat appears to be the result of errors in the field gradient of the low beta quadrupoles of about 1 part in 1000. This has been corrected with trim supplies on individual quadrupoles. The power supplies and low beta quadrupole magnets are designed to provide a beta* of 25 cm. The initial measurements with the 25 cm beta* lattice have produced the expected increase in the specific luminosity. (Specific luminosity is the luminosity divided by the product of the number of protons and antiprotons.) In addition, the length of the luminous region decreased to an rms of about 26 cm as measured by the CDF SVX (Silicon Vertex Detector).

Separators and Feeddown Sextupoles

In the previous run, with no separators and 6 bunches per beam, the beams collided 12 times per revolution. This resulted in a beam-beam tune shift which severely limited the proton brightness, and consequently the luminosity. (Brightness is the intensity divided by the emittance.) The implementation of separators in the Tevatron allow the beams to collide only at the two detector locations. The subsequent increases in the proton brightness and the luminosity are given in the table. (The previous run is "1989" and the present run is IA.) The separators in the Tevatron provide two-dimensional helical orbits, not one-dimensional pretzel orbits (in the horizontal plane only) as in other accelerators. The separators have been used to scan the beams through one another, and a summary of these results is presented at this conference by D. Siegiej et al.

The presence of the helical orbits allow the use of families of trim sextupoles (both normal and skew) for adjusting the tunes and coupling of the proton and antiprotons beams independently. When sextupoles are used in this manner, they are called "feeddown sextupoles".

Pbar Improvements

The improvements in the Antiproton Source - especially the Accumulator stacktail system - have resulted in increased stacking rates. The production rate exceeds 14 antiprotons per 10^6 protons on target. The stacking rate is typically 4.5×10^{10}

antiprotons / hour at modest stacks and 3.5×10^{10} antiprotons / hour at stacks exceeding 10^{12} .

The development of techniques for stabilizing large antiproton stacks has been necessary. Clearing electrodes have been used to help expel trapped ions which are the primary problem. However, the clearing electrodes alone are not enough. Counter circulating protons, and bunching of the antiproton core have also been found to have a stabilizing influence. P. Zhou and P. Colestock, S. Werkema et al., and A. Gerasimov, all have presented at this conference some of the observations of the effects of trapped ions in the Antiproton Source.

Coalescing Improvements

Longitudinal instabilities in the Main Ring limit the efficiency of coalescing. (Coalescing is the process by which several - typically 11 - bunches are combined into a single high intensity bunch.) By speeding up the process of coalescing, so that the instability does not have time to develop, the intensity of the coalesced bunches has been increased from 80×10^9 to greater than 125×10^9 . The "speeded up process" is called "snap coalescing". Refer to X. Lu and G. Jackson, and I. Kourbanis et al., at this conference, for details.

Collider Upgrade Plans

Overview

The table presents the overall plan for the upgrade of the collider. The previous run (called 1989 in the table) provided 0.32 inverse picobarns per week on the average, with a typical initial luminosity of $1.6 \times 10^{30} \text{ cm}^{-2} \text{ sec}^{-1}$, which exceeded the Tevatron I design goal of $1 \times 10^{30} \text{ cm}^{-2} \text{ sec}^{-1}$. As noted previously, the present run (Run IA) provides 1 inverse picobarn per week at each detector, with a typical initial luminosity in excess of $5 \times 10^{30} \text{ cm}^{-2} \text{ sec}^{-1}$. Run IA is scheduled to end June 1, 1993 to allow the final installation and commissioning of the Linac upgrade, and the installation of the cold compressors in the Tevatron. The integrated luminosity per week is expected to double in Run IB which is scheduled to begin in the fall of 1993. Run II is not expected to provide much more integrated luminosity per week, but the energy of the Tevatron will be raised and number of interactions per crossing will be greatly reduced. Finally, a factor of

five increase in the integrated luminosity will be provided by the Main Injector.

The form factor in the table describes the reduction in the luminosity which occurs when the bunch length is comparable to the beta function. It approaches 1.00 if the beta function is much larger than the bunch length. However, this is not the case for the actual case presented in the Tevatron as seen in the table where typically one only obtains about 2/3 of the luminosity one would naively expect from the bunch intensities, emittances and crossing rate.

Linac Upgrade

This summer, the Linac upgrade project will be completed. The kinetic energy of the H^- ions provided by the Linac will be increased from 200 MeV to 400 MeV. This is accomplished by replacing the last four sections of the present drift tube linac with seven side coupled cavity sections. The first 100 MeV of energy will still be provided by the original (20+ year-old) drift tube linac tanks. The beam will be transported to the Booster with a new 400 MeV beam transfer line. The calculated reduction in the space charge tune shift limit for injection into the Booster decreases by a factor of 1.75 which in principle allows for an equivalent increase in the proton intensity delivered by the Booster. However, the full realization of this factor is not expected to be attained until the Main Ring is replaced with the Main Injector.

Lower Temperature

This summer, cold compressors and new valve boxes are to be installed in the 24 helium refrigerators for the Tevatron. These allow for subatmospheric operation of the helium system and a subsequent reduction of the temperature of the superconducting cable in the Tevatron magnets from 4.5 °K to 3.5 °K. This is expected to raise the short sample limit of the cable and allow the beam energy of the Tevatron to be raised from 900 GeV to 1 TeV for collider operations. Run IB will be used to gain experience with lower temperature operation, and the increase in energy is expected to become operational for Run II as shown in the table.

Multibunch Kickers

As the table shows, the Main Injector will result in typical initial luminosities in excess of

$5 \times 10^{31} \text{ cm}^{-2} \text{ sec}^{-1}$. The present collider operates with 6 proton and 6 antiproton bunches colliding at the two detectors, CDF and D0. For the present configuration, the minimum spacing between bunches is 185 buckets. For the present typical initial luminosity, $5 \times 10^{30} \text{ cm}^{-2} \text{ sec}^{-1}$, the number of interactions in the detectors per bunch crossing is 0.79 (assuming a cross section of 45 mbarns). For the upcoming collider run, typical initial luminosities are expected to exceed $1 \times 10^{31} \text{ cm}^{-2} \text{ sec}^{-1}$. Since the number of bunches per beam will remain at 6 for that run, the number of interactions per crossing will exceed 1.57. Certain types of physics - not including the discovery of the top quark - are done more efficiently if the number of interactions per crossing is kept below one. The number of bunches per beam will be increased to 36, in order to reduce the number of interactions per crossing to 0.26. For this configuration, the minimum spacing between bunches will be 21 buckets.

With the Main Injector, the typical initial luminosity will exceed $5 \times 10^{31} \text{ cm}^{-2} \text{ sec}^{-1}$, and the number of interactions per crossing will exceed 1.31, again exceeding one. If necessary for the types of physics to be done, some modest improvements to the Antiproton Source and the Tevatron can provide 99 bunches per beam with 7 bucket spacing. This would keep the number of interactions per crossing near one for luminosities of $1 \times 10^{32} \text{ cm}^{-2} \text{ sec}^{-1}$.

Additional details of bunch loading schemes can be found in J. Holt et al., this conference.

Antiproton Source

There are several improvements needed in the Antiproton Source to realize the upgrades given in the table. An $h=4$ rf system in the Accumulator will allow the delivery of 36 rather than 6 bunches. Improvements in Debuncher cooling include rebuilding the pickups to allow for 2 - 4 GHz operation and cooling the pickups to 20 °K. Increases in the apertures of the Accumulator, Debuncher and the beam transfer lines are also being considered. Finally, the Main Injector will deliver sufficient intensity at 120 GeV to the antiproton production target that the target is not expected to survive the shock. R&D on a beam sweeping system has begun.

Table of Fermilab Collider Upgrade Parameters

	1989	IA	IB	II	Main Injector	
Protons/bunch	7.0×10^{10}	1.2×10^{11}	1.5×10^{11}	1.5×10^{11}	3.3×10^{11}	
Pbars/bunch	2.9×10^{10}	3.6×10^{10}	4.5×10^{10}	7.5×10^9	3.7×10^{10}	
Proton emittance	25	16	16	16	30	mm-mrad
Pbar emittance	18	16	16	16	22	mm-mrad
Beta at IP	0.55	0.50	0.35	0.35	0.5	m
Beam Energy	900	900	900	1000	1000	GeV
Number of Bunches	6	6	6	36	36	
Bunch length (rms)	0.65	0.5	0.5	0.5	0.65	m
Form Factor	0.71	0.76	0.65	0.65	0.68	
Luminosity*	1.60×10^{30}	5.37×10^{30}	1.03×10^{31}	1.15×10^{31}	5.60×10^{31}	$\text{cm}^{-2}\text{sec}^{-1}$
Integrated Luminosity	0.32	1.08	2.08	2.31	11.28	$\text{pb}^{-1}/\text{week}$
Bunch spacing	3000	3000	3000	396	396	nsec
Interactions / crossing (@ 45 mbarn)	0.25	0.84	1.62	0.30	1.47	
Antiproton tune shift	0.025	0.011	0.014	0.014	0.016	
Proton tune shift	0.014	0.003	0.004	0.001	0.002	
What's New?		Separators, D0 Detector, Pbar Improvements	Linac	Faster Kickers and Cold Compressors	Main Injector	

*Typical luminosity at the beginning of a store; translates to integrated luminosity with a 33% duty factor.

Main Injector

The purpose of the Main Injector is to remove the Main Ring bottleneck in the delivery of high intensity proton and antiproton beams to the Tevatron. The Main Injector will remove backgrounds from the CDF and (especially) the D0 detector, since the Main Ring - which shares the tunnel with the detectors - will no longer be used. The Main Injector will allow for test beams and fixed target physics year round.

Most of the wetlands mitigation has been completed. Civil construction for the MI-60 enclosure and service building has begun. This building is at the point of tangency between the Tevatron and the Main Injector and will contain the rf for the new accelerator. This building also services the principle

access point to the Main Injector tunnel. The R&D for the project has produced several dipoles which have met the required field quality.

The funding profile in the President's FY94 Budget Request allows initiation of operations with the Main Injector in the summer of 1998.

Final Note

The author wishes to thank all the many accelerator and high energy physics collaborators who have contributed to the work summarized in this paper, although only a few of their contributions are mentioned by name. Each individual's professional contributions to the team effort have made it a pleasure to describe an ongoing success story as stunning as the Fermilab Collider.

Figure 1. 1992 & 1988 Initial Tevatron Luminosity
(10X Running Average)

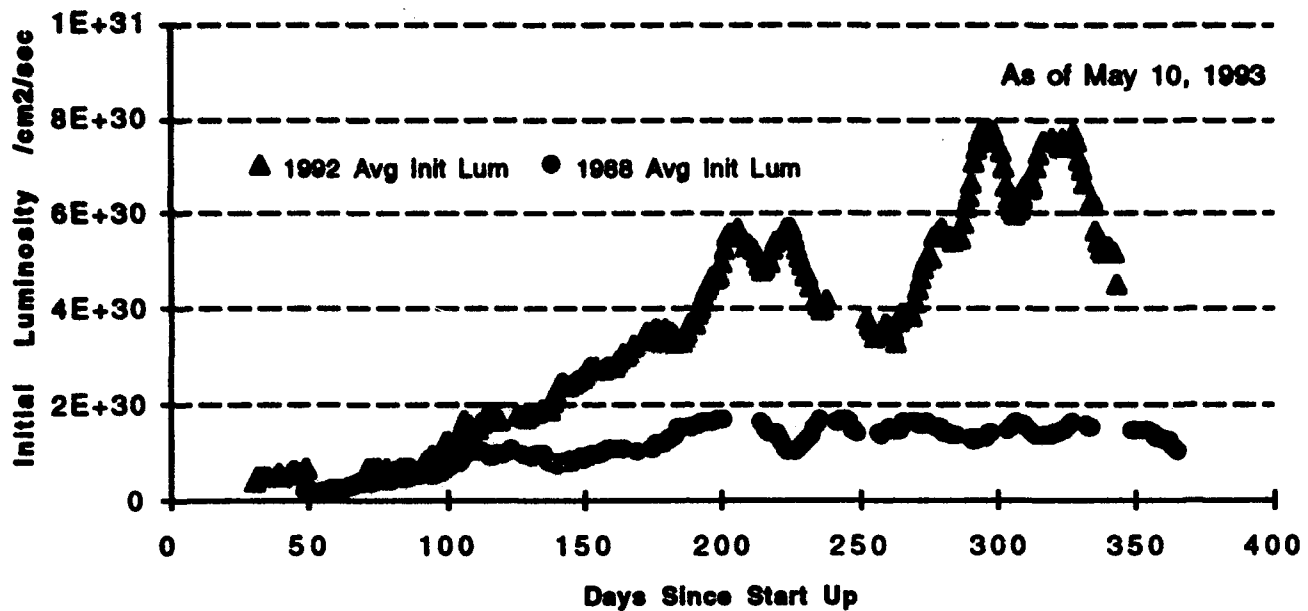
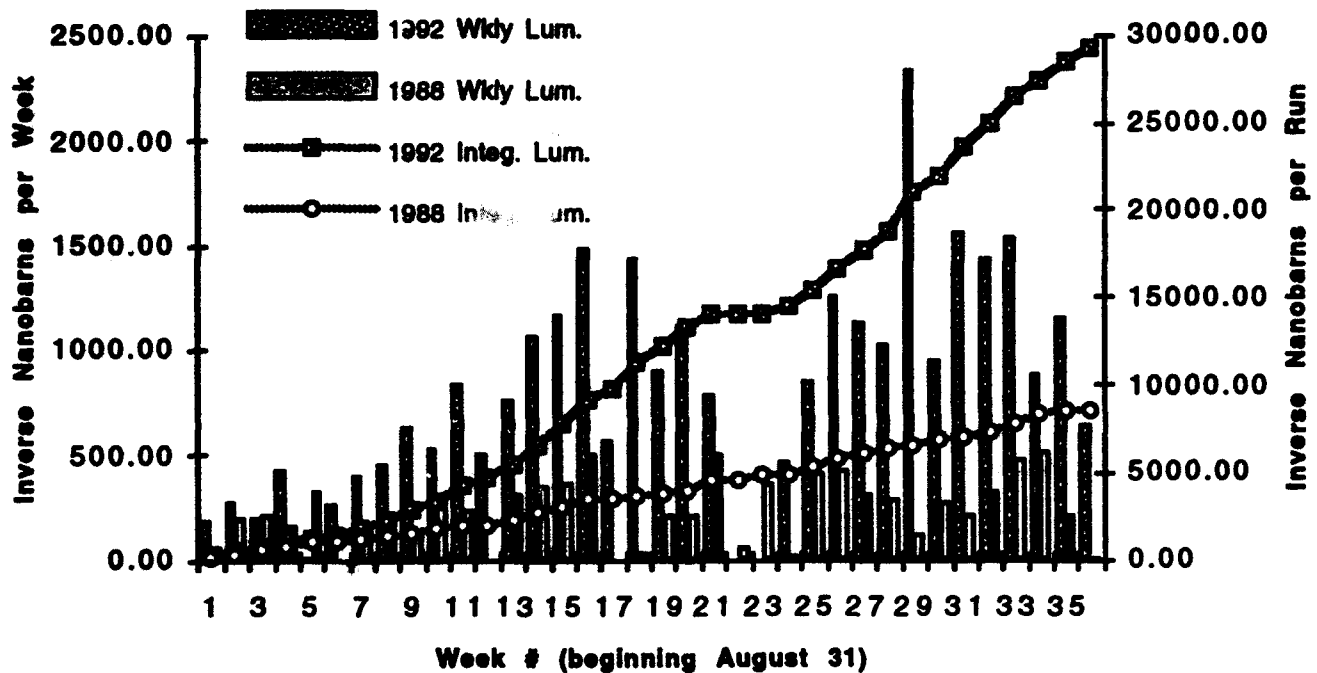


Figure 2. 1992 & 1988 Tevatron Integrated Luminosity



OPERATION OF THE BROOKHAVEN AGS WITH THE BOOSTER*

W.T. Weng (for the Accelerator Division Staff)
AGS Department, Brookhaven National Laboratory
Associated Universities, Inc.
Upton, New York 11973

Abstract

The Brookhaven Alternating Gradient Synchrotron (AGS) received protons directly from a Linac and heavy ions directly from a Tandem Van de Graaff before 1992. The newly constructed Booster has been brought on line to serve as an injector for the AGS. The operational status of the acceleration of proton and heavy ions through the Booster and the AGS is reviewed. Accelerator improvement programs to increase proton intensity for physics research and to prepare heavy ion beams for RHIC injection are discussed.

I. INTRODUCTION

The Booster construction was completed in April of 1991, followed by a short commissioning period in May and June to accelerate 200 MeV beam to a top energy of 1.2 GeV and to successfully extract the beam out of the machine. The Booster was brought on line to serve the high energy physics program using proton beam from February to April, and nuclear physics research from May to June, 1992. In 1993, eight weeks of dedicated machine studies was performed from March to May. This paper will summarize the performance of the Booster and the AGS up to May of 1993.

In Section II, the results of the measurement of basic machine functions of the Booster are presented. In Section III, the status of proton acceleration and intensity performance are reviewed. In Section IV, the status of heavy ion acceleration will be presented. Finally, in Section V, plans for future AGS upgrades for high intensity proton acceleration and preparation for heavy ion beams for RHIC injection will be discussed.

II. MACHINE FUNCTIONS OF THE BOOSTER

A schematic layout of the AGS complex is shown in Figure 1 [1, 2]. Working MAD-based computer models now exist for the LTB, Booster, and BTA. The models correctly predict the transfer matrixes and beta functions of all three areas. In the following, selected measurements will be discussed.

A. Booster Orbits

The Booster bare orbits indicate RMS horizontal errors of about 5 mm and RMS vertical error of about 3 mm, which

can be corrected to about 0.5 mm and 0.2 mm, respectively[3]. The relatively large errors of uncorrected orbit are not consistent with the alignment reading of 0.2 mm RMS misalignment of quadrupoles and the amplification factor of 15. A total re-survey, including survey monuments, will be carried out in the summer of 1993.

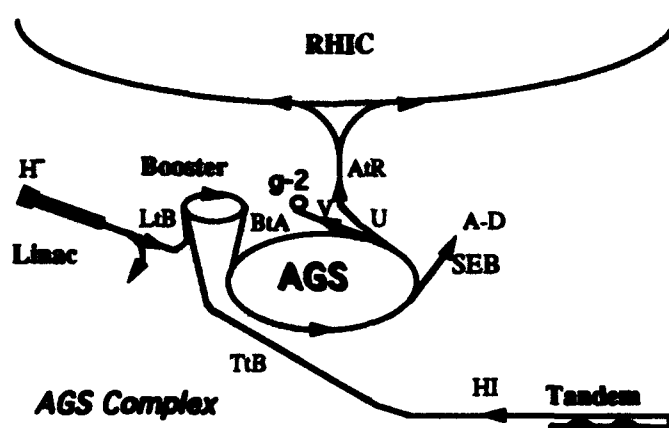


Figure 1. AGS Complex.

B. Tunes and Chromaticities of the Booster

Using the time function of the orbit signal obtained at one BPM, an automatic tune display is provided through a Fast Fourier Transform (FFT) analyzer. The orbit signal and the tune display are shown in Figure 2. The measured uncorrected tunes of $\nu_x = 4.56$ and $\nu_y = 4.60$ are very close to the prediction of the MAD program using the measured quadrupole strength. Trim power supplies have been provided to adjust the tunes within one unit for proton acceleration and 0.5 unit for heavy ion acceleration.

The natural chromaticities of the accelerator are $\xi_x = -5.1$ and $\xi_y = -5.5$. Both are measured and confirmed by measuring the tunes of various energy beams in the Booster. During acceleration, the eddy current correction coil has to be provided to compensate the sextupole field produced by the vacuum chambers. Again, trim supplies have been provided to control the chromaticity within ± 5 units. For stable operation, the chromaticity is set at a small negative value.

C. X-Y Coupling

One application of the tune measurement device is to detect the existence of the X-Y coupling and to confirm its minimization by coupling correction skew quadrupoles. If there is little coupling, a sizable orbit oscillation in the horizontal plane cannot excite the oscillation in the vertical

*Work performed under the auspices of the U.S. Department of Energy.

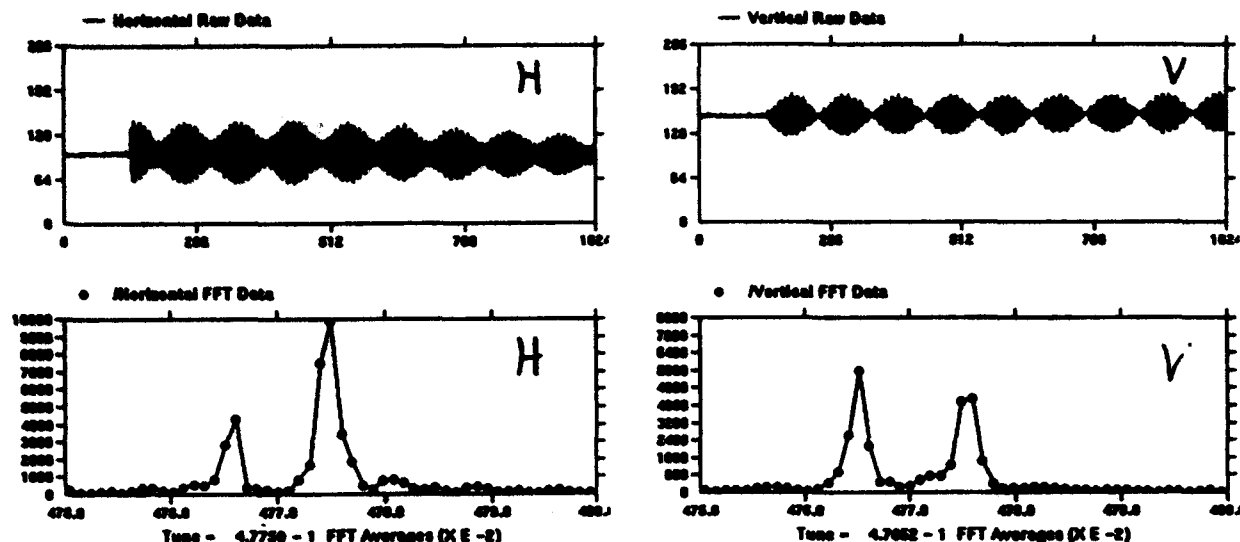


Figure 2. Horizontal and vertical orbit signals and tune display.

plane, and the horizontal and vertical tunes assume their well defined values with a single peak in the FFT display. When there is coupling between the horizontal and vertical planes, a sizable oscillation in the horizontal plane will excite visible oscillations in the vertical plane, as shown in of Figure 2. At this time, both horizontal and vertical tunes display double peaks indicating the existence of the normal modes and the separation between two peaks is a measure of the strength of the coupling. Such X-Y coupling can be minimized by powering the skew quadrupole correction system to eliminate the oscillation in the vertical plane.

D. Emittance Growth by the Foil

The RMS horizontal beam emittance of the Linac beam is about 1.2π mm-mrad. After proper steering, matching of beta-function and dispersion function, the minimum beam emittance achievable inside the Booster is about 2.3π . Such a factor of two increase in beam emittance can be explained by the multipole Coulomb scattering of the proton beam through the H^- stripping foil. The way we inject into the Booster, the proton beam passes through the foil about 30 to 50 turns. According to a six-dimensional tracking simulation [4], such a multipole transverse of the foil will increase the beam emittance by a factor of two. After the initial fast growth, the emittance will grow at a much reduced rate. At the foil location, the vertical beta function is close to minimum; hence, the perturbation in divergence caused by the foil is comparatively smaller in the vertical plane. To minimize emittance growth in the stacked horizontal plane, it may be a better choice to place the foil at the horizontal beta minimum. With such a pencil beam, the Booster horizontal aperture has been confirmed to be about ± 4 cm instead of ± 5 cm as required. Further correction of the orbit and avoidance of obstructions are needed to restore the available aperture to ± 5 cm. Furthermore, the aperture of the extraction channel is found to be about ± 2.2 cm, corresponding to a normalized emittance of 52π .

III. PERFORMANCE WITH PROTON BEAM

Once the linear machine properties are determined, the acceleration of proton beam requires injection and acceleration of over 200 turns of Linac beam. To accomplish such a task, understanding of rf capture, space charge tune spread, stopband correction, and coherent instabilities play an important role. Some of the experiences will be discussed in this section.

A. Beam Size and Emittance Tracking

The ionization profile monitor (IPM) [5] is used to measure the beam size and emittance over the acceleration cycle. Shown in Figure 3 is the horizontal and vertical profiles taken from the IPM.

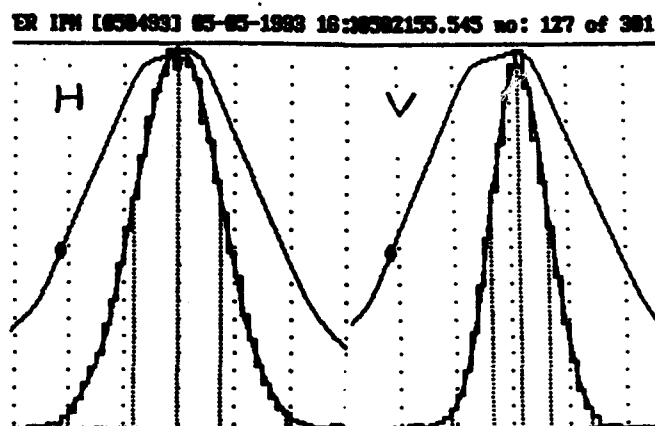


Figure 3. Beam profiles from the IPM.

The traces show the beam profiles taken at the dotted moment in the acceleration cycle. The evolution of the beam emittances over one cycle, including deceleration, are recorded.

Horizontal emittance tends to grow more both by the foil transverse and the non-linear resonance, which will be explained below. Many machine operation modes were devised to minimize the emittance growth gathered from such a display. Absolute beam size calibration will be accomplished by comparison with external SEM readings.

B. Working Point, Space Charge Tune Shift and Stopband Correction

The Booster working points are chosen to be about $v_x = 4.85$ and $v_y = 4.90$ at injection and the estimated space charge tune shift at full intensity is $\Delta v_x = 0.25$ and $\Delta v_y = 0.35$. At high intensity, the tune of some of the particles can cross $2v_x = 9$, $2v_y = 9$, $v_x - v_y = 0$, $v_x + v_y = 9$, $3v_x = 14$, $3v_y = 14$, $v_x + 2v_y = 14$, $2v_x + v_y = 14$ lines. Examples of particle losses due to some resonance lines and the survival of beam after correction are shown in Figure 4 [6].

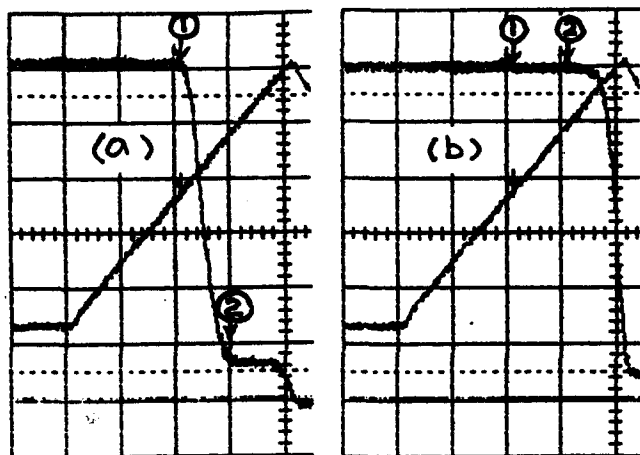


Figure 4. Stopband Correction; (a) without correction and (b) with correction, (1) $2v_x = 9$ and (2) $v_x + v_y = 9$.

The left trace shows the beam intensity decrease when it encounters the first resonance of $2v_x = 9$ and further decreases when it encounters the second resonance $v_x + v_y = 9$. The right trace shows that the total beam intensity is almost constant in crossing those two resonances after the correction system is turned on. The same process is repeated for all the resonances listed above. Such a correction study is carried out at flattop by varying the tune. During acceleration, with or without correction, this can make a 5-10% difference for weak resonances and a 30-50% difference for strong resonances[6].

C. Transverse Coupled-Bunch Instability

It has been estimated that the threshold for transverse coupled bunch instability excited by the resistive wall is at about $4-5 \times 10^{12}$ ppp. A damper system has been constructed to damp such an instability when it occurs. Shown in Figure

5 is the signal of the instability. The suppression of coherent motion had been tried successfully with a prototype system. The new system will be available in June. The actual threshold of vertical instability has been found to be about 7×10^{12} ppp, when $v_x = 4.94$ and $\xi_x = -0.25$, which can be avoided by adjusting the tune and chromaticity of the machine. Active damping is necessary when the beam intensity is larger than 10^{13} ppp [7]. By supplying a constant amplitude of damping, instead of proportional to the oscillation, the power requirement of the damping system can be reduced by a factor of four. The effectiveness of the constant amplitude method has been tested in the Tevatron [8].

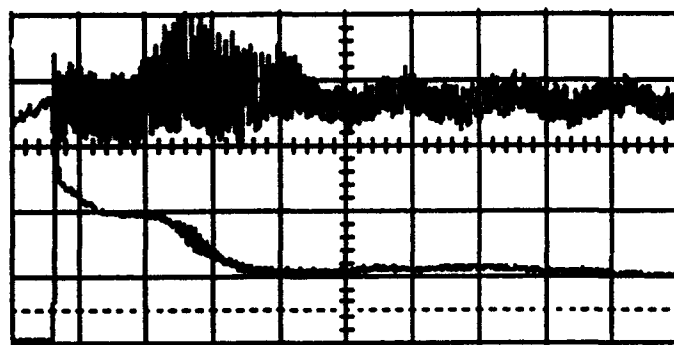


Figure 5. Signal of transverse instability and intensity.

D. Summary of Performance

After acceleration to the top energy of 1.5 GeV, the Booster beam is extracted and transported to the AGS. Four batches are needed to fill up the whole AGS ring as shown in Figure 6. At this time, the performance record of the four-batch Booster intensity and AGS intensity are summarized in Table I. In 1993, the AGS is limited by the capabilities of the old rf system. An accelerator improvement plan is in progress to replace the power amplifier system and low level system, which will be described in Section V.A. This new system will be installed in the summer of 1993.

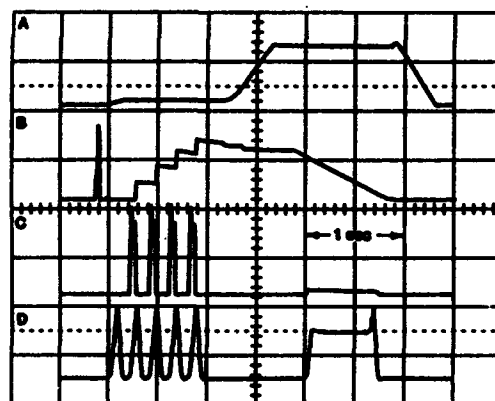


Figure 6. Proton acceleration with a study cycle: (A) AGS and (D) Booster magnetic field cycles, and (B) AGS and (C) Booster beam intensities.

About 3×10^7 npp has been accelerated and used for heavy ion research.

TABLE I Booster and AGS Intensities ($\times 10^{13}$ ppp)				
	Design	May 1993	1994	1995
Booster	7	4.0	6	7
AGS Injected	6.5	2.4	4	6
AGS Acceleration	6	1.5	3.5	5

IV. PERFORMANCE WITH HEAVY ION BEAM

The AGS vacuum is about 10^{-8} Torr. The heavy ion beam from the Tandem Van de Graaff with masses higher than sulfur cannot survive due to their partially stripped state. The Booster vacuum is designed to be in the 10^{-11} Torr range [10] where any heavy ion beam can survive without loss from charge exchange or the electron stripping process. In the past, the fully stripped Si^{14+} beam has been injected into the AGS directly. At the end about 10^8 nucleons were extracted from the AGS. Now the Booster can accept Si^{8+} from the Tandem and accelerate it to 2 GeV/nucleon, extracted, stripped to Si^{14+} and injected into the AGS. The final intensity achieved is 2×10^9 nucleons, a factor of 20 better than direct injection into the AGS. This gain is due to the much better efficiency of stripping into Si^{8+} , instead of Si^{14+} , after the Tandem.

Another price to pay in accelerating Si^{8+} is that its injection energy is much lower than Si^{14+} and hence the rf frequency at injection is about 500 kHz instead of 2 MHz. The solution to this problem is to run the rf cavity at a harmonic number of 12 instead of 3 at injection and switch to a harmonic number of 6 one-third of the way through acceleration and to 3 two-thirds of the way through acceleration. During the switch from the higher harmonic to the lower one, two rf bunches have to be properly controlled and coalesced into one[9]. The bunch coalesce from two into one is shown in Figure 7.

After successful acceleration of Si^{8+} , the gold beam Au^{33+} was injected into the Booster and accelerated to the energy of about 350 MeV/nucleon and extracted, stripped, and injected into the AGS. At the running time, no reliable knowledge was available for the proper foil thickness to optimize for either Au^{79+} or Au^{78+} . After stripping, the profile monitor showed two equal peaks, each with about 40% efficiency [10]. In the next running period, several foils will be provided to find the optimal stripping efficiency for Au^{79+} and Au^{78+} . In accelerating Au^{33+} in the Booster, five harmonic switches have been performed and the overall efficiency is about 70%. There certainly is room for improvement in future running. The final gold beam of 11 GeV/nucleon is the first ever achieved in the laboratory.

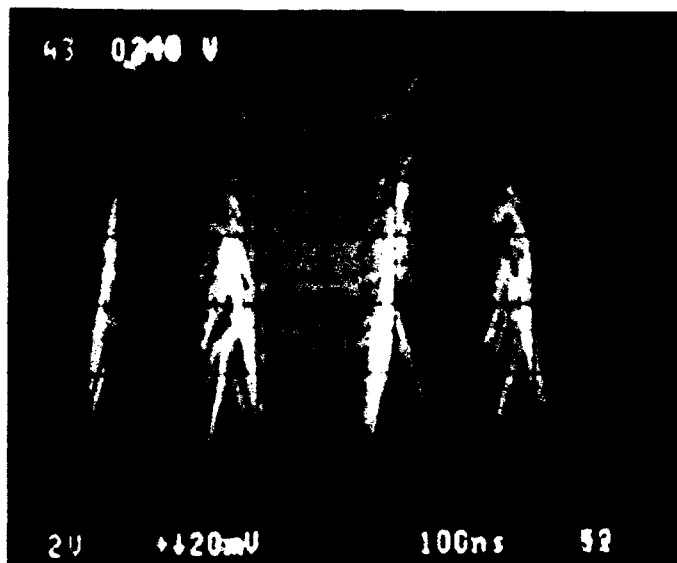


Figure 7. Bunch coalesce.

For RHIC injection, 3×10^9 npp from the AGS is needed. The current performance and future plan for gold intensity in the AGS is shown in Table II.

TABLE II Gold Intensity from the AGS				
	1992	1993	1994	1995
Tandem Beam	Au^{33+}	Au^{33+}	Au^{14+}	Au^{14+}
Intensity	3×10^7	10^8	5×10^8	10^9

V. AGS UPGRADE PROGRAMS

A. AGS RF System

The current AGS rf system was designed and installed in 1970. The original design was to accelerate 10^{13} ppp with a power amplifier system capable of delivering 60 kW. With the Booster as the injector, the expected beam intensity will be more than 6×10^{13} ppp, which requires a system capable of delivering 200 kW to drive the rf cavities. Therefore, the plan is to replace the existing 10 Philips 8752 tubes with the new Thomson 573 tubes, which also presents much less impedance to the beam [11].

In the existing AGS, the high level power amplifier system and the low level beam control system are integrated into one system for all ten acceleration stations, sharing the same frequency tuning loop, the AGC and phase loop. Therefore, there is no freedom for tuning each station individually and often times, the output voltage varies from

station to station. In the new arrangement, both the high level and the low level system will be independently adjusted. Such a capability is crucial for beam loading compensation, which would include transient, periodic, and steady state cases. An rf feedback system with loop delay of less than 200 nsec will be provided for each driver to counteract the strong beam loading effect created in the injection process from the Booster. A factor of 15 reduction in the induced voltage has been achieved by the rf feedback method on a prototype cavity. All ten stations will be replaced in the summer of 1993. This is the reason that the final AGS intensity can go beyond 2×10^{13} ppp after 1993.

B. Gamma-Transition Jump

With high intensity beam, during the transition crossing in the AGS, the non-linear space charge force can blow up the beam emittance when the bunch length reduces beyond a certain critical length. One way to combat such an effect is to modify the gamma-transition parameter of the synchrotron in such a way that the beam energy crosses the gamma-transition as fast as possible. The figure of merit of this fastness of crossing can be increased by a factor of twenty by quickly pulsing special quadrupoles provided for such a purpose. Calculations have been done to show that with an initial longitudinal emittance of 1 eV-sec, such a gamma-transition jump system can reduce the emittance growth from 5 eV-sec to 3 eV-sec. If the initial emittance is increased to 2 eV-sec, such a system can reduce the emittance growth to less than 15% even at an intensity of 10^{14} ppp [12]. A 96 MHz VHF system has been built to control the beam emittance before transition crossing and the gamma-transition jump system will be installed in the summer of 1993.

C. Heavy Ion Intensity and Emittance

Using Au beam as an example, the RHIC collider requires an Au^{79+} beam of 3×10^9 npp with a transverse emittance of $10 \pi \text{ mm-mrad}$ and a longitudinal emittance of 0.3 eV-sec. During the 1992 running period, the AGS produced 3×10^7 npp Au^{79+} with a transverse emittance of 25π and a longitudinal emittance of 1 eV-sec. One way to increase the Au intensity is to inject Au^{14+} into the Booster instead of Au^{33+} . This will increase the Au^{14+} intensity by a factor of 5 inside the Booster. Another factor of 5 can be gained by minimizing the number of harmonic switches in the Booster by using lower frequency rf systems and by increasing the Tandem current and lengthening its pulse. A final factor of 4 can be gained by improving the acceleration and extraction efficiencies in the AGS. Further possible gains can be obtained by running Au^{77+} , instead of Au^{79+} , in the AGS which will be tried in 1994.

The Au^{79+} suffered a factor of three emittance growth in the AGS during transition crossing. Careful machine studies are needed to minimize such a growth. The charge density of Au^{79+} inside 0.3 eV-sec longitudinal phase space is high enough to suffer space charge blow up during transition crossing. The newly provided gamma-transition jump

system will be used to minimize the emittance growth both in the transverse and longitudinal planes.

D. SEB Spill Servo

In the AGS, sextupole excitation is used to generate third-order resonance and extract the large amplitude beam from the ring to the experimental area over a 1 second flat-top. The performance so far is satisfactory in terms of efficiency and beam emittance delivered. The only drawback is in the uniformity of the spill over the 1 second period. The intensity fluctuation can be as large as 50%, which is undesirable from the experimental point of view. Sources of such a fluctuation include power supply ripples, non-uniform energy distribution and space charge tune spread. A system is under design to sense the extracted beam intensity and feedback on the strength of the sextupole field to control the spill uniformity to better than 10%.

Other ongoing AGS upgrade projects, not covered here, include longitudinal damping system, Linac power transmission system, new beam position monitor system, and polarized proton acceleration system. If the space charge tune shift becomes excessive, a second harmonic cavity can be employed in the Booster.

VI. REFERENCES

- [1] W.T. Weng, L. Ahrens, R. Damm, and A. McNerney, "Construction and Early Commissioning Results of the AGS Booster", 1991 IEEE PAC Conf. Proc., p. 52-56.
- [2] L. Ahrens, et al., and W.T. Weng, "The Operational Status of the Booster Injector for the AGS Accelerator Complex at BNL", XVth Int. Conf. on H.E. Accel., Hamburg, Germany, July 1992, pp. 109-111.
- [3] D.J. Ciardullo, et al., "Design and Performance of the Booster Beam Position Monitor System", XVth Int. Conf. on H.E. Accel., Hamburg, Germany, July 1992, pp. 245-247.
- [4] S.Y. Lee and S. Tepikian, "Six-Dimensional Tracking Simulation for H⁻ Injection", BNL-48950, 1989.
- [5] A. Stillman, R. Thern, and R. Witkov, "An Ultra-High Vacuum Beam Profile Monitor", Rev. Sci. Instrum., Vol. 63, No. 6, pp. 3412-3416, 1992.
- [6] C. Gardner, et al., "Observation and Correction of Resonance Stopbands in the AGS Booster", these proceedings.
- [7] D. Russo, J.M. Brennan, M. Meth, T. Roser, "Results from the AGS Booster Transverse Damper", these proceedings.
- [8] G. Jackson, D. McConnell, B. Fellenz, E. Raka, and S.P. Yamin, "Tevatron Studies Report", BNL-48906, 1992.
- [9] J.M. Brennan, "The RF Beam Control System for the BNL AGS Booster Synchrotron", XVth Intl. Conf on H.E. Accel., Hamburg, Germany, July 1992, pp. 275-277.
- [10] T. Roser, "Stripping Efficiencies for 277 MeV/amu Gold Beam on Copper Foils", these proceedings.
- [11] J.M. Brennan, et al., "The Upgrade Project of the RF System for the BNL AGS", these proceedings.
- [12] P. Yamin, et al., "A γ_{tr} -jump Scheme for the Brookhaven AGS", BNL-48894, 1986.

Overview of Future Spallation Neutron Sources

G. H. Rees

Rutherford Appleton Laboratory, Chilton, Didcot, U.K.

Abstract

Initiatives have commenced, both in Europe and in the U.S.A., towards studies of very intense pulsed spallation neutron sources. Average proton beam powers of up to 5 MW are under consideration, representing an extrapolation of a factor of about 30 over the most intense existing source, ISIS (U.K.). Various options are discussed, and important design areas of the accelerators and targets are outlined.

I. INTRODUCTION

First generation spallation neutron sources now contribute significantly to slow neutron scattering studies of condensed matter, and their success has led to proposals for higher power, second generation sources. Traditionally, neutron scattering experiments have been made at research reactors, but a number of advantages arise in the use of pulsed neutron beams [1] at spallation sources, making them serious competitors to the reactors. The spallation sources cannot compete, however, in the areas of isotope production and high flux irradiation and activation studies.

Early neutron scattering experiments with pulsed beams used an electron linac target, but studies at ANL [2] showed the advantages of lower power dissipation in proton spallation targets. Four pulsed sources, using such targets, have since been developed, three based around a rapid cycling proton synchrotron (RCS), and the fourth, that at LANL, around a compressor ring fed from the 800 MeV LAMPF linac:

Table 1

Parameters of Existing Pulsed Spallation Sources
(Av. is a typical daily output beam power average)

Facility	Energy	Rep.Rate	Av.	Pk.
KENS (Japan)	500 MeV	20 Hz	2,	2 kW
IPNS (US)	450 MeV	30 Hz	6,	7 kW
LANSCe (US)	800 MeV	20 Hz	40,	60 kW
ISIS (UK)	800 MeV	50 Hz	145,	160 kW

In addition to these pulsed sources, there is a c.w. spallation source (SINQ) under construction at PSI in Switzerland [3]. It is based on the existing cyclotron,

with 1 MW proton beam power at 570 MeV. The target is a vertical cylinder, with injection from below.

A second generation of pulsed sources has been under consideration for a number of years, but there has been a new emphasis after recent initiatives:

1. The 5 MW SNQ project at KFA, Julich, 1984;
2. ISIS in a European context, 1986;
3. FFAG studies at KFA and ANL, 1986-88;
4. Japanese Hadron Facility, JHP, 1988-93;
5. U.K. - German European initiative, 1991-93;
6. AUSTRON initiative in C. Europe, 1991-93; and
7. Studies at ANL, BNL and LANL, 1992-93.

The European and U.S. initiatives hope to become formal conceptual design reviews (CDR) in 1994, with the former seeking funding from the Commission of the European Community (CEC), and the latter drawing on expertise from ANL, BNL and LANL, but to be centred at LBL. The beam powers selected for the European and U.S. sources are 5 and 1 MW respectively, but with a 5 MW upgrade potential also for the latter.

The repetition frequency of the European source is to be 50 Hz, but with 2 target stations, one at 50 Hz and 4 MW, and the other at 10 Hz and 1 MW. The idea of a 10 Hz target, for the lower energies of the neutron spectrum, first arose at the 1986 Rapallo Workshop [4] for the study of ISIS in a European context.

Source studies have broadened since 1990, following experimental results from JINR [5] which showed that, for a given beam power, the useful neutron yield versus proton energy remains approximately constant in the energy range 1 to 3.7 GeV. This has led to a wider range of spallation sources being considered, e.g:

	Linac	Ring(s)	Power
AUSTRON	0.07 GeV	1.6 GeV RCS	0.1 MW
ANL	0.4 GeV	2.2 GeV RCS	1.0 MW
HMI	0.46 GeV	1.6 GeV FFAG	5.0 MW
RAL (3)	0.8 GeV	0.8 GeV COMP	5.0 MW
LANL (1)	0.8 GeV	0.8 GeV COMP	1.0 MW
INR	0.6 GeV	45 GeV K.FAC	5.0 MW
LBL (IND)	1.0 GeV		5.0 MW

AUSTRON [6] is a projected regional research centre for Austria, Croatia, Czechoslovakia, Hungary, Italy, Poland and Slovenia. Envisaged is a spallation source of the scale of ISIS, but using a higher energy RCS to reduce the repetition rate to 25 Hz, and with the possible addition of a storage ring to reduce further the 25 to 12.5 Hz. JHP [7] also proposes a power level comparable to ISIS, but it is now being reassessed.

The remaining source options are all for 1 MW beam power or above. Two are for high power H^- linacs and proton compressor rings: RAL [8] considers an 800 MeV linac and 3 rings or a 1200 MeV linac and 2 rings; LANL [9] considers an 800 MeV linac and 1 ring for a 1 MW source, and either increasing the linac energy or adding more rings for a 5 MW upgrade. In Germany, a source based on a H^- linac and an FFAG accelerator is favoured. Initially, an energy of 3.2 GeV was proposed for the FFAG [8], but HMI now considers lowering the energy to 1.6 GeV and making use of beam stacking techniques. At ANL, the 1 MW proposal [10] is based around a 2.2 GeV RCS, at a repetition frequency of 30 Hz. BNL has recently commenced studies, and all the sources of power ≥ 1 MW now plan to use 2 target stations, as proposed at Rapallo.

Two different types of source complete the options. INR, Troitsk, suggests the use of the proton beams available at the KAON Factory projects, either at the highest energy (eg 45 GeV) of the main ring synchrotron or that of its booster injector [11]. The engineering of the target stations is very different for this approach. Finally, there is the suggestion to use an induction linac accelerator [12], at 0.8 or 1 GeV, to create the required proton pulse at the target without any associated ring. This approach has had the least attention to date, but is likely to receive detailed assessment at the CDR in LBL.

II. SOURCE CONSIDERATIONS

The most important initial consideration is the choice of kinetic energy for the high power proton beam. This choice impinges on the designs of the accelerator, targets and moderators, and so involves neutron scatterers, and accelerator and target designers. A range of energies appears acceptable, which extends the task of finding an overall cost and reliability optimisation.

For the European source study, target designers from SINQ, KENS, RAL, IPNS and LANSCE recommended restricting the proton kinetic energy to the range between 0.8 and 3 GeV. Within this restricted energy range, the

following comments may be made for the targets T, moderators M, and accelerator A, assuming 5 MW of proton source power in each case:

T: the material needs to be W, Ta, Pb or U238; the target is horiz. or vert. and may be split; the required length has to increase with energy; the power in the input window falls with energy; the useful neutron yield per MW is \sim constant, but with some enhancement around 1.1 GeV; the peak target power density falls with energy, but with more power in escaping secondaries; the neutron backgrounds increase with energy; shutters are more extensive for higher energies; stationary H_2O cooled plates may work at 5 MW.

M: the design is integrated for target - M - reflector; the layout is slab, wing, fluxtrap or backscatter, the last two of which require a split target; there is some downstream adjustment with energy; the materials are ambient temp. H_2O , liquid H_2 , liquid CH_4 , or a liquid H_2 cooled metal hydride; use is made of poisoning, coupling and decoupling; heating from target secondaries rises with energy, as does the radiolysis for some materials eg CH_4 ; radiation damage and heat deposition need study.

A: the FFAG and RCS options favour 1.6 to 3 GeV; the induction linac favours an energy ≤ 1 GeV; the compressors proposed are 3 rings at 0.8 GeV, or 2 rings at 1.2 GeV, or 1 ring at 2 - 2.4 GeV; the injection energy depends on ring/source power; low loss in the linac and rings is a key issue; optimised H^- ring injection schemes are essential; collection of beam lost in the rings is required; ring activations vary with local power loss level; the activated volume rises somewhat with energy; the cost of beam line to target rises with energy; and overall T-M-A availability of $> 90\%$ is required.

The technology of a 5 MW target was assessed at a 1992 PSI workshop [13]. The highest power density case was studied, that for an 800 MeV target. It was concluded that, "Of the options considered, the stationary water cooled plate target was considered to offer the best overall prospects. Its design will be a technical challenge, but the working group felt there was every prospect for success. A rotating target based on the SNQ design [14] was recognised as a viable option, which could be adapted for the new source if the difficulties of the stationary target proved insurmountable."

At the same PSI workshop, three conceptual target-moderator-reflector layouts were discussed, one for a horizontal, one for a vertical and one for a split vertical target; the last of these is shown schematically in Figure 1. A neutronic analysis for all three options was recommended, including an evaluation of radiation damage and heat deposition in moderators, reflectors and decouplers. Also recommended was R & D towards a viable high hydrogen density cold moderator.

At this stage, engineering solutions appear to be within reach for the targets, moderators and reflectors of a 5 MW source throughout the 0.8 to 3 GeV range. It seems therefore that the choice of proton energy will be set mainly by detailed accelerator considerations.

III. ACCELERATOR CONSIDERATIONS

The simplest concept is a 1 GeV induction linac with no associated ring. It has the longest length at ~ 1 km, however, so it may prove too costly. Also, its design is based on very high space charge detunings and exact matching, so the effect of variations in ion source current (50A, 1 MeV, 2 μ s) needs careful assessment.

The most challenging option is the FFAG. Initial studies at KFA and HMI have shown that a 0.46 to 3.2 GeV, wide aperture, superconducting magnet FFAG is overexpensive. This has led HMI to studies of a higher frequency, 1.6 GeV ring, using beam stacking at high energy to build up the beam current. An alternative has been suggested by ANL, with a 100 Hz low energy FFAG feeding 2 successive pulses for each 50 Hz cycle of a higher energy ring.

For a 1 MW source, ANL prefers a 30 Hz, 0.4 to 2.2 GeV, RCS, with the high output energy reducing the number of protons to be handled each pulse. The design will have the potential for a 5 MW upgrade. An RCS has also been considered in Europe, with the parameters 50 Hz, 0.8 to 3 GeV, and 5 MW. The 0.8 GeV injection is the same as in one compressor ring option, which is favoured due to its shorter beam storage, lower beam power per ring and more rugged design (an RCS has a low impedance, uncooled, shield and capacitor in its ceramic vacuum chamber).

The H⁻ linac-compressor ring options of RAL and LANL have already been outlined, and the individual pros and cons are as follows. The H⁻ ion source performance is a limiting factor, so 2-stage funneling is assumed, with the same linac peak current in all options.

The linac duty cycle then increases with the number of rings, so favouring a high linac energy. Nearly all other factors favour a low energy, however, eg. cost, linac length, debunching, momentum ramping, shielding, H⁻ injection, reliability (losing a ring leads only to lower intensity), beam loss collimation, lower beam power per ring (with more loss acceptable per ring), beam extraction, high energy transport, and previous experience with spallation targets. A possible exception is that of beam instabilities, which have been relatively benign at ISIS, but not so at the PSR, LANL.

Another factor linked to the choice of energy is the cost of the H⁻ linac, which may be room temperature, RT, or superconducting, SC. Initial designs have assumed frequencies of ~ 350 and 700 MHz for the pre and post funneling stages of a RT linac, with half these values for the SC case. Q values of $2 \cdot 10^4$ have been taken for the former, and loaded Q's of 10^6 for the latter, values typical for cavities used in e⁻ storage rings. The pulsed nature of the linac leads to revised SC parameters, however, as the 1 ms cavity filling time is too long. This would give slow rise and fall times for the cavity fields, with added cryogenic and generator power; high power klystrons, with circulator and load, are assumed for the generators. A factor of 10 reduction in filling time is obtained by using the RT frequencies, and lowering the loaded Q to $2 \cdot 10^5$. Comparisons then, between a RT and SC linac, include a reduced linac length and lower power for the latter, as against its complexity, enhanced maintenance, less reliable windows, and probably larger activation (gamma danger parameters for Nb are ~ 4 times those for Cu).

The most important accelerator considerations are: ion source performance, overall induction linac and H⁻ linac optimisations; RFQ, chopper and funneling characteristics; and the ring designs for H⁻ injection, beam loading compensation, extraction and beam loss collimation and protection. H⁻ injection and ring collimators are discussed further.

Low loss injection is such an important feature that the lattice for the rings has to be designed around the preferred arrangement of the injection components. This, together with the constraint of obtaining specific lattice parameters at a stripping foil location, result in a low superperiodicity, S, for the rings. It is very desirable, however, to choose $S > 2$, to reduce the number of betatron resonances, close to the working point, that may be excited by space charge forces.

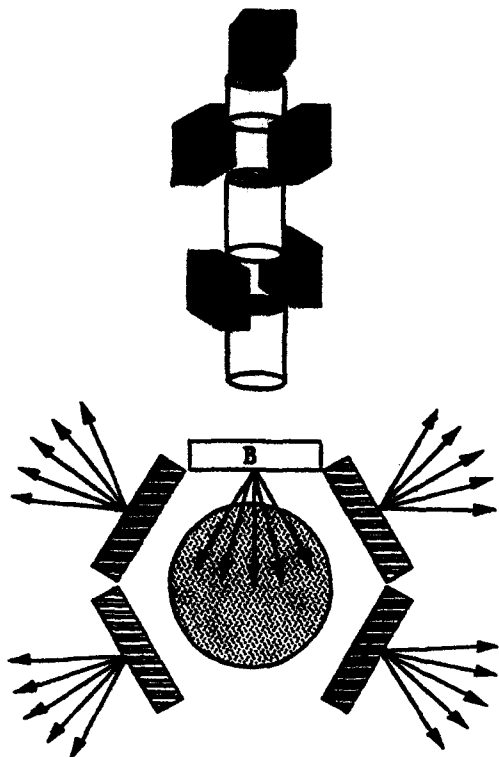


Fig. 1 SCHEMATIC OF FLUX-TRAP AND BACK-SCATTER (B) MODERATORS

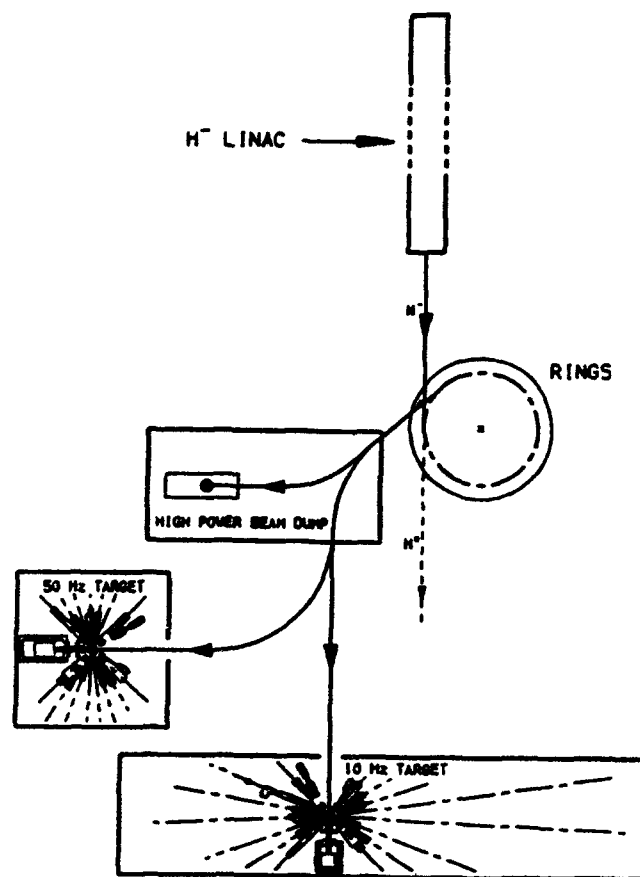


Fig. 2 SCHEMATIC OF 5 MW SOURCE

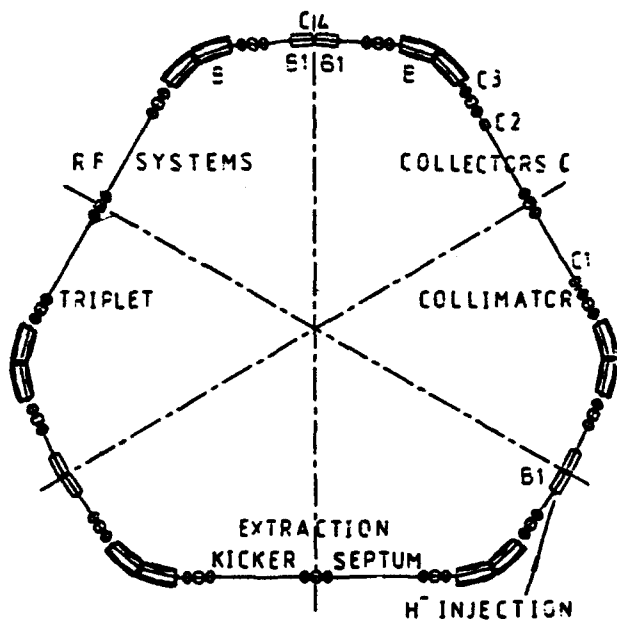


Fig. 3 COMPRESSOR RING

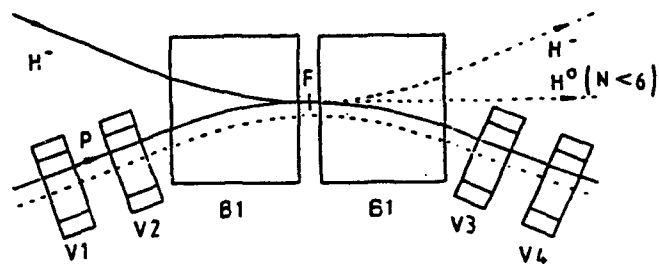
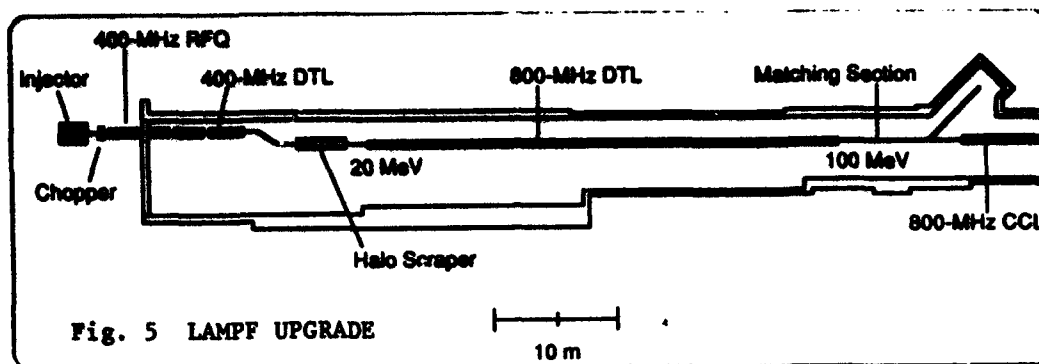


Fig. 4 OPTIMISED H^- INJECTION SYSTEM



Schematics are shown of a 5 MW source layout in Fig. 2, a 0.8 GeV compressor lattice in Fig. 3, an optimised H^- injection system in Fig. 4, and the low energy part of the LAMPF upgrade in Fig. 5. The ring of Fig. 2 may be an FFAG, an RCS, or one or more compressors. The lattice of Figs. 3, 4 has $S = 3$, zero dispersion for rf systems, collimation and extraction, and the betatron and dispersion parameters at the B1 dipoles for optimised injection. In B1, the H^- beam merges with the protons that circulate after charge exchange stripping. For Fig. 5, there may be 2 ion sources and linacs, funneling into 1 at 20 MeV.

Optimised H^- injection involves simultaneous 'painting' in all 3 phase planes. There is momentum ramping of the input beam for longitudinal and horizontal betatron painting, and programming of 4 bump fields for vertical painting. Large horizontal amplitudes are correlated initially with small vertical and energy amplitudes, and the correlations are slowly reversed during injection. The use of a foil with 2 free edges then reduces the foil traversals by protons. Fields near the foil, F , are chosen to allow collection of stripped e^- , and to control the partially stripped metastable H^0 states; the scheme proposed by RAL is given in [15]. On injection, the equipartition of energy in the 3 phase planes is lost, with a larger increase of longitudinal than transverse emittances.

Collimators and loss collectors are essential for the high power beams. Betatron collimation is important for the FFAG and compressors, and momentum collimation for the RCS. Primary collimators are followed by collectors, with equal horizontal and vertical phase shifts to the downstream units. The system must limit the areas of activation and also protect the rings, particularly the chamber of the RCS. Angled, not straight, collimators are used as they result in greater penetration depths and reduced outscatter. Such an angled unit is to be tested soon in ISIS.

IV. REFERENCES

- [1] H. Grunder et al, Report of the Working Group on Spallation Neutron Sources, BESAC PANEL, Oakbrook, Sept. 1992.
- [2] J. M. Carpenter and D. L. Price, An Intence Pulsed Neutron Source for ANL, Proc. US Nat. Acc. Conf., IEEE Trans. Nucl. Sc. NS-22, No. 3, 1975.
- [3] G. S. Bauer, SINQ Status Report Oct. 1990, Proc. ICANS XI, Vol. 1, KEK, 1990, p.41.
- [4] B. Dreyfus, Report of the ISIS Project Group, RAL and Rapallo Workshops, 1986.
- [5] V. A. Nikolaev et al., Neutron Production in Thick Lead Target by 1-3.7 GeV Protons and Deuterons, Proc. ICANS XI, Vol. 1, KEK, 1990, p.612.
- [6] K. Schindl et al., AUSTRON, A Pulsed Spallation Neutron Source in Central Europe, Proc. of 3rd. EPAC, Berlin, 1992, p. 432.
- [7] Japanese Hadron Project, JHP, Institute for Nuclear Study, University of Tokyo Report, 1989.
- [8] S. Martin and C. Planner, Accelerator Design Parameters for a European Pulsed Spallation Source, Proc. of 3rd. EPAC, Berlin, 1992, p.435.
- [9] LANSCE, The Los Alamos '1 MW' Spallation Source, LANL Report, Sept. 1992.
- [10] Y. Cho, IPNS Upgrade Accelerator Plan, IPNS reports submitted at BESAC PANEL, 1992, and at Santa Fe Spallation Source Workshop, 1993.
- [11] Y. Stavisky et al., Superintensive Pulse Slow Neutron Source SIN based at KAON Factory, Proc. ICANS XI, Vol. 1, 1990, p.628.
- [12] A. Faltens, Induction Linac Design, Santa Fe Spallation Source Workshop, 1993.
- [13] Technology of Targets and Moderators for Medium to High Power Spallation Neutron Sources, PSI Workshop Proc. 92-03, 1992.
- [14] SNQ Project Proposal for a Spallation Neutron Source, KFA, Dec. 1984.
- [15] G. H. Rees and H. Zhang, RAL Design Notes for ESS, EPNS/RAL/A2-91 and A4-92, 1991-92.

The Heavy Ion Synchrotron SIS - A Progress Report

K. Blasche, B. Francsak, B. Langenbeck, G. Morits, C. Riedel
GSI, Postfach 110 552, D-64220 Darmstadt 11, Germany

Abstract

A brief description is given of the Heavy Ion Synchrotron SIS, which is part of the new SIS/ESR facility at GSI. A survey of the ions that were accelerated in 1992 is presented showing the respective beam energies and intensities. Plans to increase the available beam intensities are shortly discussed. Progress in the supercycle operation for a time-shared use of up to 16 machine settings and commissioning of the beam line from the ESR back to the SIS with storage and future postacceleration of cold ESR beams are summarised. In addition, the results of recent machine experiments are presented: they include new data on Q-values for the dynamic change-over from triplet focusing at injection to doublet focusing at extraction and on machine chromaticity as well as beam profile measurements for the circulating SIS beam, which yield information on the transverse beam emittances. Finally some aspects of the present and future experimental program are discussed.

1 INTRODUCTION

The heavy ion synchrotron SIS is part of the new GSI accelerator facility [1], [2]. As shown in the plan view of Fig. 2 the Unilac, which is in operation since 1975, provides low energy beams up to 20 MeV/u. The new SIS/ESR facility was conceived for acceleration, storage, and cooling of high energy heavy ion beams. Construction of the new facility had begun in December 1986. Since January 1990 it is fully used for experiments.

The SIS is designed for the acceleration of all kinds of heavy ions to maximum energies between 1 and 2 GeV/u. The high energy beams can be delivered either directly to several experiments in the target area or to the ESR via a beam line with stripper target and charge separator. A third way for the SIS high energy beams leads to a production target at the fragment separator (FRS), where secondary beams can be produced by projectile fragmentation. The FRS prepares pure beams of any interesting nuclear fragment, which can either be studied at the final focal plane or can be injected into the ESR for ring experiments.

The Unilac was up-graded for its role as SIS injector. A new injector with an ECR ion source, a short RFQ section, and an IH linac was installed midway in order to provide two ion beams of different species: one for a low energy experimental program and another one for SIS injection.

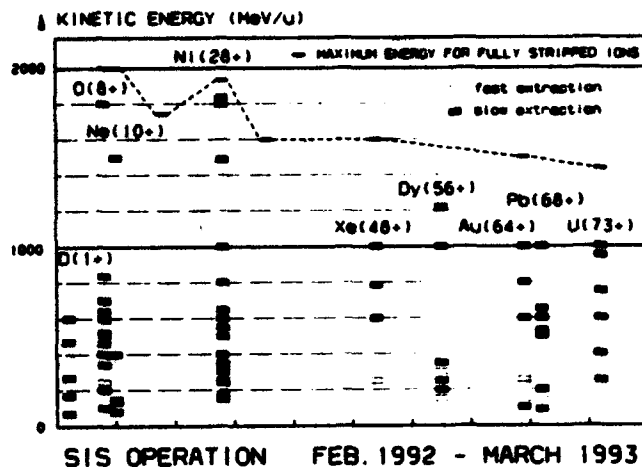


Figure 1: SIS operation from February 1992 until March 1993. The dashed line indicates the maximum energies for fully stripped ions.

2 ENERGIES AND INTENSITIES

In Fig. 1 the status of SIS operation is summarised for the last year until March 1993. It can be seen that slow resonance extraction was used in a broad energy range, while fast extraction mostly for the ESR storage ring took place between 150 and 300 MeV/u. The maximum energies at $(B\rho)_{\text{max}} = 18.4 \text{ Tm}$ are 2 GeV/u for light ions with $q/A = 0.5$ and about 1 GeV/u for heavy ions, e.g. U(73+), according to the charge state after stripping at 11.4 MeV/u SIS injection energy. For fully stripped ions, which will be stored and cooled in the ESR, higher energies will be available, e.g. 1430 MeV/u for U(92+).

As shown in Fig. 3 maximum intensities range from 10^7 ions per spill for heavy ions up to $1 \cdot 10^{10}$ for neon or oxygen. These intensities, which were reached until end of 1992, are restricted by the available Unilac currents, typically about 100 μA for Neon (10+) or 1 μA for uranium (73+).

It is planned to raise the available SIS intensities roughly by a factor of 20 until the end of 1994. This goal shall be approached with an improvement program for ion source operation, Unilac transmission and SIS injection. In the course of this program the SIS space charge limit will be tested for light ions up to $2 \cdot 10^{11}$ ions per cycle. For very heavy ions new developments are necessary. One way to increase intensities by a factor of 100 would be the construction of a new RFQ injector and a 35 m long IH linac

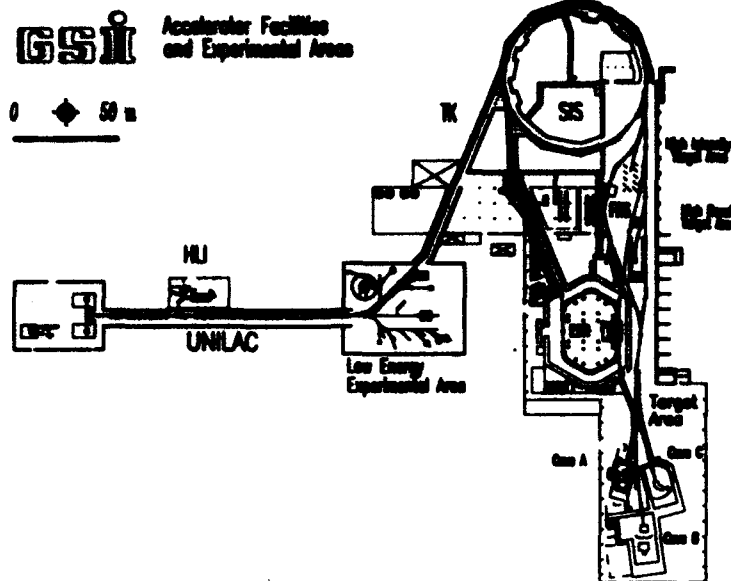


Figure 2: Plan view of the GSI accelerator facility

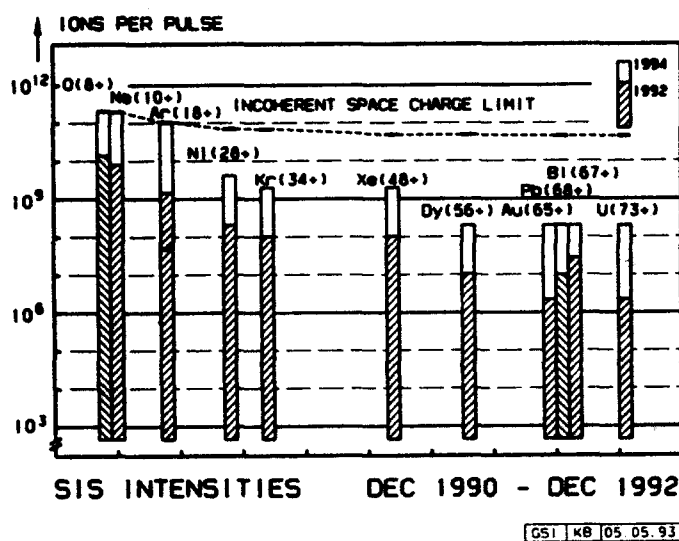


Figure 3: SIS beam intensities at the end of 1992 and prospective intensities for the end of 1994. The incoherent space charge limit is indicated for $\Delta Q = 0.25$.

for the acceleration of low charge ion beams like uranium (3+) up to 1.4 MeV/u [3]. It was shown that such a linac should accelerate uranium (3+) up to about 10 pA, while filling of the SIS to the space charge limit of $4 \cdot 10^{10}$ ions would require only 10 pA of uranium (73+) and 2 pA of uranium (3+) respectively.

3 STATUS OF MACHINE OPERATION

Usually the SIS has been used in a time-shared mode with slow extraction of ion beams for target station experiments at the same time as fast extraction to feed the ESR. These modes are combined on a pulse-to-pulse basis, so that with ESR filling usually needing only a few hundred pulses every

hour, most of the SIS capacity was available for target station experiments. It is also possible to run several machines with slow extraction in a time-shared mode, e.g. four machines with energies of 200, 270, 330, and 400 MeV/u have been used to provide depth variation of the Bragg peak in a thick PMMA plastic block (Fig. 5).

In January 1993 commissioning of the reinjection line ESR/SIS was started. The following uses are planned: (1) Acceleration of fully stripped heavy ions to maximum energies above 1430 MeV/u. (2) Slow standard and stochastic extraction of cold ion beams. (3) Transfer of intense short and cold ESR ion bunches through the SIS to the target station for high energy density experiments.

In the first round of commissioning it was possible to transfer ESR beams and to store them in the SIS. It is foreseen to optimise the operation of the reinjection line in a second round with argon ions in July 1993 and to store the reinjected ESR beam in the SIS with high efficiency. In addition, it will be tried to test acceleration and slow resonance extraction for cooled low emittance beams.

4 RECENT MACHINE EXPERIMENTS

The standard focusing scheme for acceleration is pure triplet focusing at injection with a change-over to doublet focusing at high energy keeping the Q-values constant. During the last year the Q-measurement system has been improved [4]. Narrow band measurements of the beam transfer function (BTF) provide an accuracy of 10^{-4} for the tunes, and signal processing at a fixed intermediate frequency of 50 MHz will allow dynamic tune measurements within less than 1 ms for each data point along the acceleration ramp. In Fig. 4 first results at three energies are plotted, which show that the precision of tune setting

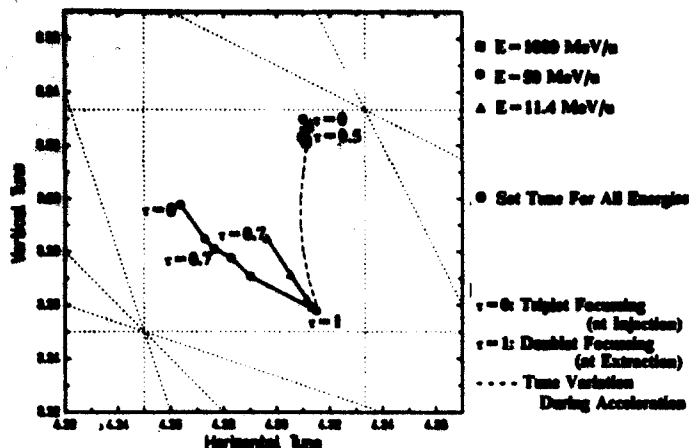


Figure 4: Tune measurements for three SIS energies with different settings for triplet($\tau=1$)/doublet($\tau=0$) focusing.

is not yet perfect at low energies. At injection energy the measured vertical tunes Q_v are about 0.06 below the set tunes while the horizontal tunes deviate mainly for doublet focusing. The variation of the tunes on the acceleration ramp is small for Q_h and rather large for Q_v . The observed tuning errors at low energy are probably due to a linear approximation of the magnetisation curve, which has to be refined according to the magnetic measurements for the SIS quadrupoles.

The BTF method was also used to study chromatic effects. The observed values of $\xi_h = -0.74(T), -1.77(D)$, $\xi_v = -2.13(T), -2.11(D)$, were compared to the calculated natural machine chromaticity $\xi_{h,n} = -0.95(T), -1.54(D)$ and $\xi_{v,n} = -1.88(T), -1.43(D)$. It was necessary to include a sextupole term of $B''/B\rho = 0.04\text{m}^{-2}$ in all 24 SIS dipole magnets, which is larger than the measured sextupole term, in order to achieve good accordance of the theoretical data with the measured chromaticities.

For chromaticity correction two families of sextupole magnets are foreseen, which can be used to correct horizontal and vertical chromaticity separately. It was shown that the observed chromaticity correction is in good agreement with machine theory.

In another machine experiment movable beam scrapers were used to measure the current on the scraper jaw as a function of its position with respect to the beam axis. From the beam width and height the horizontal and vertical beam emittances were deduced. At injection energy of 11.4 MeV/u a horizontal beam emittance of $120\pi\text{mm}\cdot\text{mrad}$ was observed, which corresponds to the machine acceptance with the present positions of the injection and extraction septa. The vertical emittance of $20\pi\text{mm}\cdot\text{mrad}$ after multi turn injection was larger by a factor of 4 than the Unilac beam emittance. Probably the beam matching to the vertical machine acceptance was inadequate, since the beam profiles at high energy show a broad shoulder and a high intensity core of $0.5\pi\text{mm}\cdot\text{mrad}$, which corresponds to the Unilac beam emittance with the correct $\beta\gamma$ transformation. The high energy horizontal emittance of

$7\pi\text{mm}\cdot\text{mrad}$ is even smaller than the expected value of 10, which may be explained with beam losses and corresponding emittance reduction during rf beam capture.

5 EXPERIMENTAL FACILITIES

It is planned to extend the experimental facilities shown in Fig. 2 in the following way: (1) A direct beam line from the FRS to the target hall is under construction. It will provide a direct way for secondary FRS beams to the target hall. (2) A dilepton spectrometer HADES was proposed. It shall be installed in the north east area of the target hall. (3) In front of the new HADES cave a detector test facility is foreseen, where SIS beams and also secondary beams will be available. (4) North west of cave A a new radiotherapy cave is planned. It will have direct access from a new building west to the target hall, which can be used for the medical care of patients.

For the radiotherapy program the development of an active three-dimensional scanning technique is underway. In a first step it had been demonstrated that a homogeneous two-dimensional dose distribution could be achieved with magnetic scanning. The second step was energy variation of the SIS and the beam transport system on a pulse-to-pulse basis. It was also shown that the three-dimensional dose distribution can be well controlled using the PET technique to spot positron emitters produced by projectile fragmentation in the target volume [5]. Fig. 5 shows the dose distribution in a plastic block (PMMA) for an ^{16}O beam.

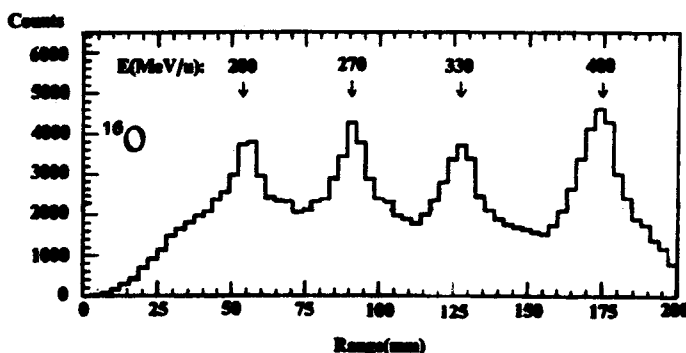


Figure 5: Dose distribution in a plastic block (PMMA) for an ^{16}O beam with four different energies.

6 REFERENCES

- [1] P.Kienle, The SIS/ESR Project of GSI, GSI-report GSI 85-16 (1985).
- [2] K.Blasche et al, The Heavy Ion Synchrotron SIS, EPAC 92.
- [3] U.Ratsinger, Low Energy IH-Linac, GSI-Unilac-WT/92-02.
- [4] P.Moritz et al, Narrowband Measurements of Beam Position, Tune, and Chromaticity, DIPAC Workshop, Montreux (1993).
- [5] W.Enghardt et al, priv. comm., FZ Rossendorf (1993).

Status of the PSR Improvement Program*

R. J. Macek, D. H. Fitzgerald, M. Hoehn, R. Ryder, and R. York

Medium Energy Physics Division, Los Alamos National Laboratory, Los Alamos NM, 87545

Abstract

A program of improvements to increase intensity and improve reliability of the Los Alamos Proton Storage Ring (PSR) has been under way for several years. Reduction of stored beam loss rates by a factor of 4.6 since 1987 through exploitation of H^0 injection has allowed the average intensity to increase by a factor of two to $75 \mu A$. Reliability of the PSR and associated beam delivery systems has been improved by extensive rework of numerous subsystems. Radiation protection has been improved by additional shielding of Line D and extensive use of relatively fail-safe radiation detectors incorporated into an improved radiation security system.

I. INTRODUCTION

PSR was designed as an 800 MeV pulse compressor ring to accumulate a large fraction of a LAMPF macropulse ($\sim 800 \mu s$) and provide short ($0.25 \mu s$), intense pulses to a spallation neutron target. After two years of commissioning and initial operation, the limitations on performance due to beam losses and hardware reliability were evident. Radioactivation of the ring components limited the average current to about $30 \mu A$. Peak intensity was and still is limited to $\sim 3.5 \times 10^{13}$ protons per pulse by a transverse instability, now thought to be caused by coupled e-p oscillations. [1] Concerns about the adequacy of the shielding required exclusion of users from the LANSCE (Los Alamos Neutron Scattering Center) experimental hall (ER-1) when beam was on. Overall beam availability on target was $\sim 55\%$ (1988) and judged to be inadequate for a national users program.

By 1988, the mechanisms for the stored beam losses had been identified, the potential for significant improvement recognized, and an improvement program initiated which had as its main goals safe, reliable, $100\text{-}\mu A$ operation at 20-Hz repetition rate. Longer term, there was the possibility to increase the repetition rate to 60 Hz and thereby achieve average currents up to $300 \mu A$.

II. INTENSITY IMPROVEMENTS

The initial intensity upgrade plan was to first exploit H^0 injection by a number of incremental improvements and an upgrade of the H^- ion source before undertaking more fundamental and costly changes to PSR injection or the full aperture extraction upgrade.

Injection into PSR is a two-step process, as depicted in Figure 1. The 800-MeV H^- beam is completely stripped to H^0 in a high-field stripping magnet then passes through a hole in the yoke of a ring dipole. The H^0 beam strikes a 200-mg/cm^2 carbon foil where most of it ($\sim 93\%$) is stripped to H^+ and captured in the ring. Beam is accumulated for typically 1700

turns and extracted in a single turn.

A. Beam Losses

The requirement for hands-on-maintenance limits localized losses (over distances of ~ 1 m) to about 100-200 nA average. For the loss patterns in PSR, this implies keeping the total losses to less than 500 nA.

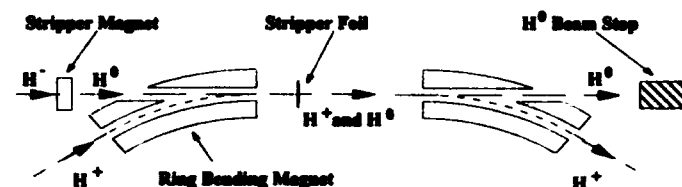


Figure 1. Layout of injection region in the PSR.

The "slow" beam-loss current is well described by two terms: a constant term (1st turn) proportional to the injected current, I_{in} , and a term increasing linearly in time and proportional to the stored beam current, $I_{in} \cdot N(t)$, where N is the number of turns injected. The losses of 0.2-0.3% on the first turn after injection are now thought to be predominately caused by production of excited states of H^0 with principle quantum number ≥ 3 , which subsequently strip part way through the fringe field of the first dipole downstream of the stripper foil and fall outside the acceptance of the ring. [2] Stored beam losses arise primarily from nuclear and Coulomb scattering of the protons through repeated traversals of the stripper foil and from the increase in beam size due to the increase in momentum spread produced by action of the RF buncher. [3]

The key to reducing the stored beam losses is to minimize beam scattering at the stripper foil. Most options for increasing the current aim to reduce the number of times the stored protons hit the foil; many use an improved scheme of phase-space "painting" at injection to reduce foil hits.

B. Exploitation of H^0 Injection

Offset injection in the vertical plane exploited the unfilled vertical acceptance in the PSR and used betatron oscillations to paint in the (y, y') phase plane, as shown in Figure 2. The stripper foil material need only cover the area of the H^0 beam; any extra foil material adds to the losses by intercepting more of the stored beam. To exploit this idea, a minimum area carbon foil supported by thin (5 micron) carbon fibers, the so-called "postage stamp" foil, was developed and has been used successfully for several years.

Studies of beam losses as a function of the betatron tunes, ν_x and ν_y , showed increased loss when crossing the 5th-order resonances. Operating below the 5th-order resonances reduced the stored beam loss rate by about 30%.

Halo collimation concepts were studied and tests performed with tungsten scrapers in the ring. Preliminary

* Work performed under the auspices of the U.S. D.O.E.

results were discouraging. Two problems were recognized: (1) Scattering from the edges of the scraper/collimator produces losses elsewhere; thus, for collimators to be beneficial, slit scattering must be less than the losses prevented elsewhere by the collimator. (2) A good optics location for the collimator, where the limiting aperture (septum magnet) is shadowed by a dispersion-free image of the collimator, was not found in the existing lattice.

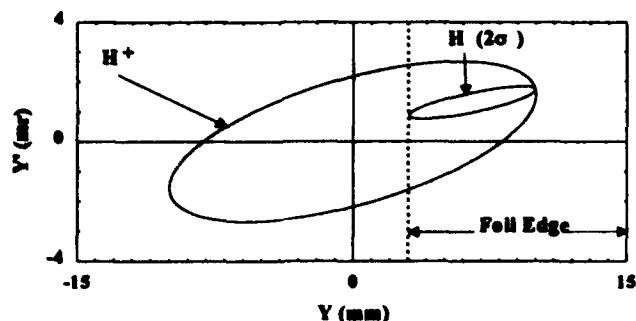


Figure 2. Y, Y' phase-space ellipses at the stripper foil.

Reductions in the stored beam-loss rate for various measures implemented since 1987 are listed below.

Measure	Loss Reduction Factor
Vertical Offset Injection	~1.7
"Postage Stamp" Foil	~1.5
Lower Operating Point	~1.3
Miscellaneous Improvements	~1.4
Overall Improvement	~4.6

C. H^- Ion Source Upgrade

Injection of higher peak current into the PSR will reduce the number of turns needed to accumulate a given charge and the number of foil traversals. Development of a volume H^- source with twice the peak intensity and half the emittance of the present cusp-field source was judged to be feasible and considered to be the most cost-effective next step toward increased intensity. It has the added benefit of reducing the linac duty factor needed to serve the LANSCE program. A major effort is under way at Los Alamos to test and evaluate two promising options (a design from Berkeley and a version of the BNL design engineered for high duty factor operation) and the use of RF to excite the source plasma. Results to date are encouraging; details can be found in a companion paper at this conference. [4]

D. Direct H^- Injection

The H^0 injection method at the PSR suffers from two problems: growth of emittance (factor of ~3) in the bend plane of the stripper magnet and the large horizontal mismatch, which arises from fundamental constraints (small beam spot size) at the stripper magnet and lack of flexibility in tuning the beam parameters at the injection foil. A way around both of these difficulties is to inject the H^- directly, as shown in the proposed layout of Figure 3.

The H^- beam enters a low-field (0.38 Tesla), 6° dipole in

the ring at a position and angle such that it will emerge on the same trajectory as the stored H^+ beam. A foil stripper to convert H^- to H^+ follows. Bump magnets in the ring provide a programmed closed-orbit bump for optimized injection painting. Some H^0 will emerge from the stripper foil; in addition, some H^- will miss the foil and be stripped to H^0 in the fringe field of the ring dipole. Provisions are made to transport both H^0 beams to the existing H^0 dump. Of all the upgrades considered, the direct H^- injection option was expected to provide the greatest reduction in beam losses, but lack of funding has prevented its implementation.

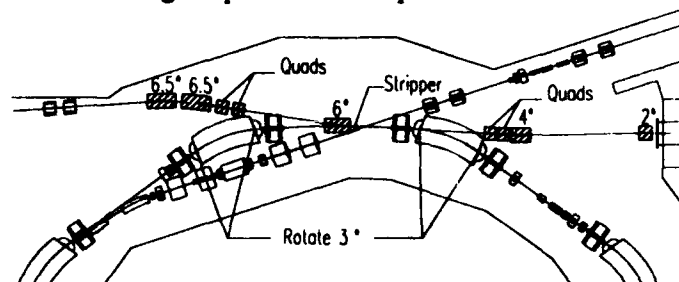


Figure 3. Layout for direct H^- injection.

E. Full-Aperture Extraction

The horizontal acceptance of the PSR is limited by the existing extraction system; 50% more horizontal aperture (2 times larger horizontal phase space acceptance) is available with more powerful extraction kickers. The larger aperture would have three main advantages: more of the beam scattered in the foil can be captured, thus reducing losses; injection painting can be made more effective in keeping the beam off the foil with either H^0 or direct H^- injection; and the increased horizontal beam size will reduce the beam density and associated space-charge effects.

R&D was started on a ferrite kicker system that would provide the larger kick needed for full-aperture extraction. A prototype pulser was designed and fabrication begun but was halted just short of completion for lack of funds.

III. RADIATION PROTECTION UPGRADES

Shielding and radiation protection issues have been among the most difficult problems to solve, in part because of the difficulty in developing lasting criteria in an environment of changing standards, but also because shielding retrofits are very difficult and expensive in the highly built up area around Line D (the H^- transfer line) and LANSCE. It would have been far easier and less costly to provide more shielding in the initial construction at the green-field site.

The problems originate with the criteria used for construction of LANSCE (WNR at the time) and Line D beam transport which was based on design losses of 0.04 nA/m (fractional loss $2 \times 10^{-6}/m$) from a 20- μ A beam. Shielding was designed to keep the radiation levels in occupied areas below 2.5 mrem/h for the postulated beam loss. Beam-loss monitors interlocked with the beam were used to shut off the beam quickly in the event of errant beam spills. The criteria were accepted at Los Alamos at the time. The difficulty with these criteria is the extensive (critics claim excessive) reliance on

instrumentation to prevent lethal doses in the event of a worst-case, full-power beam spill. Should the instrumentation fail during a full-power spill, dose rates as high as $10\text{--}50 \times 10^3$ rem/h are possible at the shielding surface for indeterminate lengths of time. Much of the Line-D shielding was not upgraded with the advent of the PSR and an upgraded WNR.

Improvement of radiation protection systems proceeded on several fronts. Reliability of the active protection system was greatly enhanced by the development and implementation of a three-layered radiation interlock system consisting of fail-safe beam-current limiters for the normally low-current portions of Line D, fail-safe spill monitors for all beam tunnels, and neutron radiation detectors in occupied areas. These were incorporated into an improved radiation security and beam shut-off system. LAMPF prompt radiation protection criteria were developed that called for a non-lethal cap on the maximum potential doses possible in occupied areas under worst-case accident scenarios, including failure of all the protection instrumentation. A comprehensive shielding assessment was undertaken, which included extensive beam-spill tests of shielding effectiveness. Most importantly, major augmentations of the shielding were implemented in Line-D where it passes over the LANSCE experimental room (ER-1) and in the region around the proton beam transport (1L Line) just before the beam enters the LANSCE target (see Figure 4). More shielding was added over the Line-D tunnel under a heavily traveled road, and at the Line-D entrance maze to the beam switchyard.

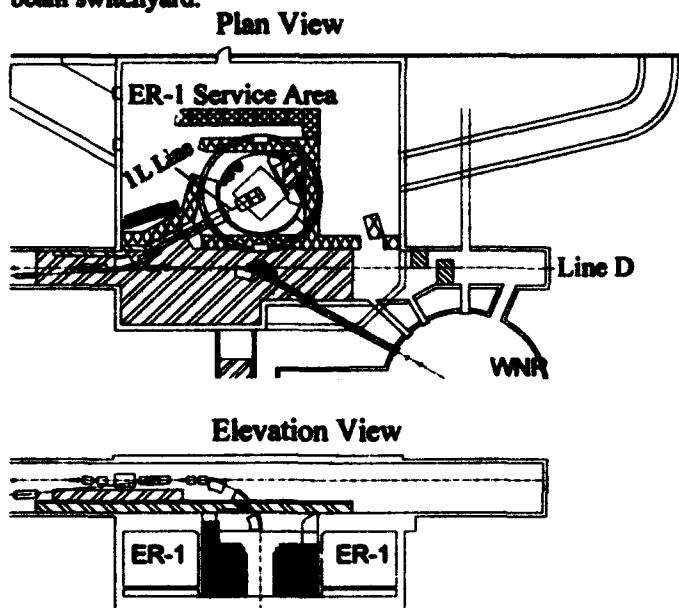


Figure 4. LANSCE target cell shielding.

The most pressing radiation protection issue remaining is the continuing need to exclude personnel access to ER-1 with beam on. The shielding added to the target cell was not sufficient to reduce the potential levels in ER-1 from a full-power beam spill to below 100 rem/h, as can be seen from the data displayed in Figure 5 for a spill at the top of the 90° bend. Calculation indicate that spills further down the bend lead to even higher levels. Time and funding limitations prohibit a

retrofit that would reduce the potential hazard to levels that permit occupancy while beam is on.

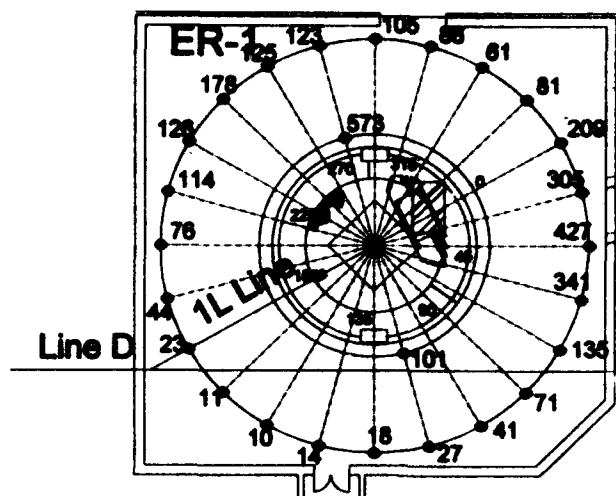


Figure 5. Radiation levels (rem/h) in ER-1 from a full-power spill (from data scaled to a 100 μ A spill).

IV. RELIABILITY/AVAILABILITY

Availability of the PSR and the LANSCE beam delivery systems has improved greatly since 1988 through extensive rework of numerous subsystems, including magnet power supplies, deionized water, vacuum, pulsed power, beam diagnostics, and computer controls systems. Overall availability of beam (including the linac) to the users rose from ~55% in 1988 to ~75% in 1989 but has declined to ~65% in the past two years, primarily because of declining availability of the linac. The situation is complicated but is essentially caused by funding shortfalls for the LAMPF nuclear physics program, which funds the operation of the linac.

V. CONCLUSIONS

We conclude that there are no technical barriers to reliable, 100 μ A operation of PSR which is the same conclusion reached by the external PSR Review Board. The menu of proposed improvements contains enough to reach the goal. We acknowledge the contributions of the entire PSR development and operations staff in the progress to date.

VI. REFERENCES

- [1] D. Neuffer et al, "Observations of a fast transverse instability in the PSR", Nucl. Instrum. Meth. A321 (1992) pp. 1-12.
- [2] R. Hutson and R. Macek, "First Turn Losses in the LAMPF Proton Storage Ring (PSR)," and J. Donahue et al, "Measurement of H^0 Excited States Produced by Foil Stripping of 800-MeV H^- Ions", these proceedings.
- [3] R. Macek et al, "Analysis of Beam Losses at PSR," Conference record of the 1988 EPAC Conference, Vol. 2, pp. 1252-1254.
- [4] R. York et al, "Volume H^- Ion Source Development at LAMPF," these proceedings.

First Experience with Colliding Electron-Proton Beams in HERA

R. Brinkmann and F. Willeke
Deutsches Elektronen Synchrotron
Notkestr. 85, 2000 Hamburg 52, Germany

Abstract

We report on first experience with colliding electron and proton beams in HERA (see also [2]). In 1992, the first year of operation, HERA has delivered some $60(\text{nb})^{-1}$ of e-p Luminosity to the experiments H1 and ZEUS. The beam energies amounted to 26 GeV and 820 GeV. A maximum luminosity of $2.2 \cdot 10^{29} \text{cm}^{-2} \text{s}^{-1}$ has been achieved by colliding a train of nine electron bunches against nine proton bunches. A complete collection of data is contained in reference [1]. The beams could be brought into and held in collision without problems. The lifetime of the proton beam in collision is as long as 50 h. This requires both careful matching of the electron and proton beam cross sections and also that the two orbits coincide within $\approx 0.2\sigma$ beam size at the interaction point. The proton beam suffered a beam-beam tune shift of up to $\Delta Q_x \approx 0.0018$. This is close to the limit which was assumed in the design of HERA. Nonetheless, there is only little degradation in the proton beam quality in collision. Under these conditions, the proton beam fills could be stored and be made available for collision for some 24 h in HERA.

I. Introduction

On October 20, 1991, a 480 GeV proton beam and a 12 GeV electron beam have been collided for the first time in the double storage ring HERA. Good colliding beam conditions had been accomplished in the last weeks of 1991 so that the machine could be made available for a luminosity production run in 1992. Operations started with a test run during which the procedures to inject into the machine, to accelerate the beams to full energy and to bring them into collision were established and set up for routine operation. The two experiments ZEUS and H1 were able to start data taking almost immediately after the start up on May 31. This test run was followed by a 7-week production run in the fall in which the experiments collected approximately $53(\text{nb})^{-1}$.

There were a number of concerns during the design of the double ring electron-proton collider. Above all was the question about the stability of the proton beam when colliding with a high intensity electron beam. Other interesting questions were also how difficult it is to bring the two beams into collision, and how to maintain stable operation during collision.

Meanwhile, answers to these questions are available which are discussed below.

The scope of this report will be as follows:

In the first section we will summarize the parameters and the results of the 1992 luminosity run.

In the second section we will discuss practical aspects of electron proton collision such as beam finding algorithms, stability and reproducibility of collision orbits.

Finally we will analyse the proton beam stability. We discuss the relevant parameters and we will make comparisons with predictions.

We will conclude with a short outlook on 1993 beam-beam operation.

II. Overview of the 1992 Luminosity Operation

The luminosity operation in the fall of 1992 included 80 colliding beam runs. 820 GeV protons collided with 26.6 GeV electrons. Each run lasted on average $\approx 5 \text{h}$. A total luminosity of $53(\text{nb})^{-1}$ has been acquired by each of the two experiments. The operation was limited to nine colliding bunches. A tenth proton and electron bunch respectively were also present to allow for background discrimination. The reason for the restriction to a relatively small number of colliding bunches (design value is 210) was originally to ease the start up of the experiment especially in view of the complex trigger system. Later, however, it turned out that the beam intensity of the electrons was limited to $\approx 3 \text{mA}$ due to a breakdown of the beam lifetime. This problem was only resolved by the end of the year by exchanging a small section of beam pipe.

The bunch intensity of the proton beam was limited by the preaccelerators. In 1992, bunches with up to $3 \cdot 10^{10}$ protons have been delivered by PETRA, this is about 30% of the design goal.

For other parameters it could be demonstrated that the design goals can be reached.

The transverse emittance of the proton beam suffered in some cases from a horizontal excitation which increased the transverse beam size. This is why average and best achieved values of the proton emittance differ by a factor of more than two. The values of the β -function have been increased intentionally for the electron beam whereas they have been squeezed beyond the design values for the proton beam. The reason is to obtain a better match of the beam cross sections, which turned out to be crucial for the proton beam stability. This will be discussed below.

The specific luminosity which was obtained with these parameters exceeded in some cases the design goal. In all cases, the specific luminosity as measured by the luminosity monitor (see below) compares well with the values calculated from the measured beam dimensions. The stability of operations is reflected in the fact that the specific luminosity remained nearly constant over a whole luminosity run of 5 h. This indicates that there were no difficulties to bring the beams into collision and to maintain good con-

ditions for collision.

Table 1 reviews the beam parameters of the 1992 luminosity run.

Table 1: Parameters of the 1992 Luminosity Run			
	Mean	Best	Goal
Beam Energy/GeV			
Electrons	26.6	26.6	30.
Protons	820	820	820
Number of Bunches	9	9	210
N_e/Bunch [10^{10}]	3.3	4.3	3.6
N_p/Bunch [10^{10}]	2.5	3.2	10
Emittance			
$\epsilon_{x,p}/\pi\text{mm}$	0.015	0.0062	0.007
$\epsilon_{y,p}/\pi\text{mm}$	0.015	0.0046	0.007
$\epsilon_{x,e}/\pi\text{mm}$	0.039	0.039	0.039
$\epsilon_{y,e}/\pi\text{mm}$	0.002	0.002	0.002
β -Function Values at IP			
$\beta_{x,p}/\text{m}$	7.0	7.0	10.0
$\beta_{y,p}/\text{m}$	0.7	0.7	1.0
$\beta_{x,e}/\text{m}$	2.2	2.2	2.0
$\beta_{y,e}/\text{m}$	1.4	1.4	0.7
Beam Size at IP			
$\sigma_{x,p}/\text{mm}$	0.324	0.210	0.265
$\sigma_{y,p}/\text{mm}$	0.102	0.052	0.084
$\sigma_{x,e}/\text{mm}$	0.29	0.29	0.27
$\sigma_{y,e}/\text{mm}$	0.053	0.053	0.036
Beam-Beam Tuneshift/IP			
$\Delta Q_{x,p}$	0.0007	0.0009	0.0013
$\Delta Q_{y,p}$	0.0004	0.0005	0.0010
$\Delta Q_{x,e}$	0.003	0.011	0.018
$\Delta Q_{y,e}$	0.007	0.020	0.020
Luminosity			
per Bunch [$10^{28}\text{cm}^{-2}\text{s}^{-1}$]	1.2	2.4	7.14
Spec. [$10^{29}\text{cm}^{-2}\text{s}^{-1}\text{mA}^{-2}$]	2.3	4.4	3.4

III. Operational Aspects of e-p Collisions

Routine operation could be established after a few weeks of colliding beam operation. The following played an important role in this successful start up

- Beam Position Pickups Available Close (7m) to the IP
- Availability of Fast Luminosity Monitoring
- Reproducibility of Collision Orbits after a Magnetic Cycle

Pairs of capacitive pickups are located on both sides of the interaction points. The position of the two beams is measured independently (one after the other). Due to the reproducibility of the beam orbits within 0.1mm for a particular setting of the magnets, this measurement allows us to bring the two beams as close as $1 - 2\sigma$ of the beam cross section. This can be repeated for many magnetic cycles before a new set up becomes necessary. The orbit of the protons need some 120min to become stable

after thermal equilibrium is reached in the normal conducting magnets. The fine steering, to obtain complete overlap between the beams, is performed by observing the rates from the luminosity monitors. This device detects Bremsstrahlung emitted by electrons scattered at the protons. The off-energy electron is detected in coincidence. Beam-gas Bremsstrahlung is discriminated by the use of a non-colliding electron bunch (see also [3]). Every 30sec these monitors provide a luminosity value with a precision of $\approx 4\%$ (for luminosities in the range of $10^{29}\text{cm}^{-2}\text{s}^{-1}$). Optimum collision orbits are found quickly (20min) by horizontal and vertical scans using closed orbit bumps. The life time of the proton beam usually drops from 50h to 1-5 hours during this scan. A few percent of beam loss is taken into account. In case the beams are separated by several σ , finding the collision orbits was eased by observing and maximising the betatron frequency signal from one beam in the transverse spectrum of the other beam. This becomes a good collision monitor if the excitation signal for one beam is used as a reference for the lock-in amplifier of the beam signal of the other beam [5]. Due to the good orbit reproducibility this more sophisticated method was only rarely used in routine operation. During a colliding beam run, the beam orbits drift only very slightly and slowly. Manual corrections from time to time turned out to be adequate. This behaviour is expected from estimates of diffusive ground motion which predicts a separation of 1σ after 10h. (using the ATL-law [6] with $\langle \Delta y^2 \rangle = A \cdot T \cdot L$, where $A = 10^{-4}\mu\text{m}^2\text{s}^{-1}\text{m}^{-1}$, T is the time and L the value for a β -tron wavelength in HERA). Experience shows that dynamic beam separations are not important for HERA. This is in agreement with earlier investigations [4] which predicted a separation of only 0.1σ due to magnet vibrations, the most prominent contribution.

IV. Stability of the Proton Beam

The crucial issue in e-p interaction is the stability of the proton beam in collision. Due to the lengthy cycling, injection and ramp procedure of the proton machine (minimum turn around time is 60min) proton beam lifetimes of more than 20h are required. Proton lifetime is also correlated with the background picked up by the experiments. and which becomes a problem if the lifetime drops below this number.

Necessary conditions for good proton beam lifetime in collision are to keep the tunes in a narrow window of $\Delta Q_{x,y} \leq 0.005$ at the working point of $Q_x \approx Q_y - 1 = 31.295$ to stay clear from the nearby 7-th order and 10-th order resonances at 31.286 and 31.3 respectively. Besides a well corrected orbit and a compensated chromaticity ($\xi_{x,y} \approx +1$) it turned out to be important to compensate the width κ of the coupling resonance $Q_x - Q_y = 1$ to about $\kappa \leq 0.005$ in order to place the working point close to the main diagonal in the tune diagram.

The most important parameter for achieving high proton beam stability in collision, however, was found in the ratio of proton and electron beam sizes.

If the electron beam cross section is considerably smaller than the proton beam size, the proton beam life time may

deep by two orders of magnitude (from 100h to 1h) for beam-beam tune shift values as moderate as $\Delta Q = 0.001$. Such effects have been observed earlier in the SpS collider [8]. In HERA, the beam optics has been modified in sev-

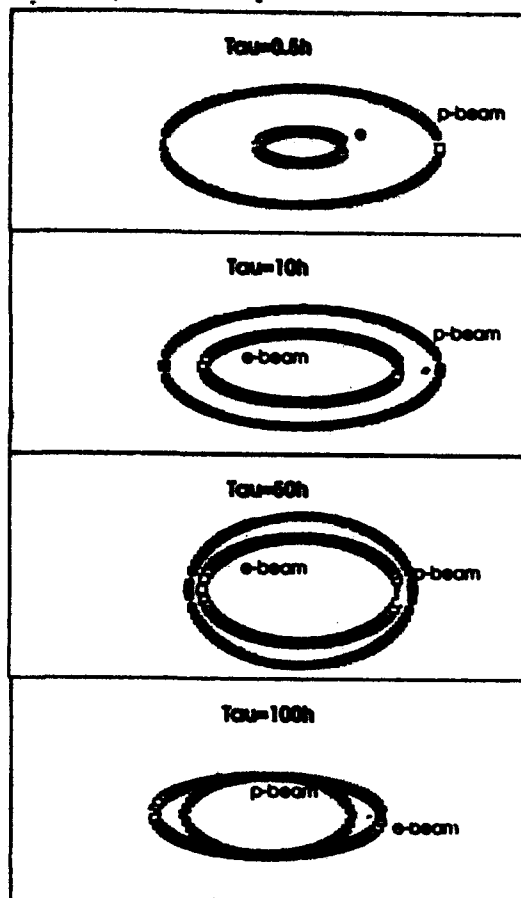


Figure 1: p-Beam Lifetime for different e/p Beam Cross Sections, Beam-Beam Tuneshifts $\Delta Q_{x,y} \simeq 0.0015$; from up to down:

$$\sigma_{px}/\sigma_{py}/\sigma_{ex}/\sigma_{ey} = 0.41/0.12/0.13/0.033\text{mm} \rightarrow \tau_p = 0.5h$$

$$\sigma_{px}/\sigma_{py}/\sigma_{ex}/\sigma_{ey} = 0.41/0.12/0.28/0.07\text{mm} \rightarrow \tau_p = 10h$$

$$\sigma_{px}/\sigma_{py}/\sigma_{ex}/\sigma_{ey} = 0.33/0.10/0.29/0.070\text{mm} \rightarrow \tau_p = 50h$$

$$\sigma_{px}/\sigma_{py}/\sigma_{ex}/\sigma_{ey} = 0.21/0.05/0.29/0.053\text{mm} \rightarrow \tau_p = 100h$$

eral steps. At the cost of increased beam-beam tune shift for the electron beam, the β -function values of the electron beam at the IP have been increased by almost a factor of two and the ones of the proton beam have been reduced by 30%. At each step, considerable improvement of the proton beam lifetime was achieved which is illustrated in Figure 1.

Attempts have been made to understand this behaviour. Emittance growth rates have been calculated for protons colliding with an electron beam in HERA[9]. A tune modulation of 10^{-3} (which is somewhat stronger than expected from magnet power supply ripple) leads to strong threshold-like enhancement of emittance growth for particles with oscillation amplitudes larger than two standard deviations of the electron beam cross section.

Simulations of collision of protons with a flat electron beam ($\sigma_{y,p} = 2.75 \times \sigma_{y,e}$) have been performed which include os-

cillatory as well as random tune changes [7]. The result is also a rather strong emittance growth for protons with amplitudes larger than the electron beam size. This analysis at least qualitatively explains, what is observed in e-p collision.

Another important ingredient of good operating conditions is that the two beams are well centered with respect to each other at the interaction point. We estimate the critical value for transverse beam separation to be in the order of 0.2σ which corresponds to about $(10-20)\mu\text{m}$. For larger values we observe reduced proton beam lifetime. This is explained with the enlargement of the width of the nearby 7-th order resonance. An estimate of the maximum tolerable separation of the emittance growth threshold for large amplitude protons ($8\sigma_e$) on the 7th order resonance results in a separation of only $0.1\sigma_e$ (assuming a round electron beam and a 50Hz tune modulation with a depth of 0.001). Due to this effect, the process of bringing the beams into collision is critical and delicate. However, beam loss and emittance growth can usually be avoided by careful adjustment of the tunes. The optimization procedure should not take more than about 20min which was usually the case.

V. Conclusion

HERA had a successful start up of luminosity operation. No unpleasant surprises have been encountered in electron proton collision and beam-beam interaction. E-p collisions are delicate but well under control. All effects observed so far can be understood, at least qualitatively, by single particle models of the motion of the proton beams. In the just starting 1993 operation, 84 bunch pairs are being collided. We expect a considerable increase of luminosity in the near future.

REFERENCES

- [1] W. Bialowons, in Proceedings of the HERA Seminar 1993, Bad Lauterberg
- [2] B. Wiik, this conference
- [3] S. Levonian, DESY HERA 92-07 (1992) ZEUS Luminosity Monitor Group, DESY 92-066 (1992)
- [4] J. Rossbach, DESY 89-023 (1989)
- [5] S. Herb and F. Zimmermann, Proc. of the XV Int. Conf. on High Energy Acc Hamburg (1992), p227
- [6] B.A. Baklakov et al, INP Novosibirsk preprint 91-15 (1991)
- [7] R. Brinkmann, DESY-HERA 89-24 (1989)
- [8] L. Evans and J. Gareyte, Cern82-8(DI-MST)(1982)
- [9] F. Zimmermann, thesis, University of Hamburg (1993) unpublished

The Development of a Prototype Multi-MeV Electron Cooling System*

D. Anderson, M. Ball, D. Causyn, T. Ellison, B. Hamilton, S. Nagaitsev, P. Schwandt
Indiana University Cyclotron Facility, 2401 Milo Sampson Ln, Bloomington, IN USA 47405

J. Adney, J. Ferry, M. Sundquist
The National Electrostatics Corporation, Graber Rd, Middleton, WI USA 53562

D. Reistad
The Svedberg Laboratory, Box 533 S-751 21 Uppsala Sweden

M. Sedlacek
The Alfvén Laboratory, S-100 44 Stockholm Sweden

Abstract

Next generation electron cooling systems require a multi-MeV, 2 A DC electron beam source. Such electron cooling systems can reduce the emittances of proton and heavy ion beams leading to corresponding increases in luminosity. The technology needed to produce the necessary DC electron beams is being developed by the MEBEC group and tested at the National Electrostatics Corporation (NEC). This paper will outline the design considerations behind the system, improvements made over previous systems and the current status of the project.

I. INTRODUCTION

Although electron cooling has now become a routine tool in many laboratories, its use has been restricted to lower energy accelerators (<500 MeV). This is unfortunate, as it could prove to be very effective in higher energy accelerators as well. For example, the emittance of fully-stripped 7 GeV/nucleon gold beams in the proposed PS collider (KEK lab, Japan) could be reduced by an order of magnitude resulting in a factor of 10 increase in the machine luminosity. Other examples have been described in a previous paper [1]. Above electron energies of about 500 keV the traditional approach of using a Cockcroft-Walton power supply and magnetically-confined electron beams becomes impractical. A Pelletron electrostatic accelerator is well-suited to such an application requiring the acceleration of electron beams without subsequent emittance blow-up. NEC has made their 3 MV test Pelletron available for the construction and testing of a prototype 2 MeV, 2 A DC electron recirculation system. An increase in energy above 2 MeV should not pose a problem since it would involve no fundamental changes in technology. The goal of this project is to develop the technology to the point where such a system could be purchased commercially and used as a tool to significantly enhance accelerator performance.

II. BEAMLINE DESIGN AND OPTICS

A. Design Principles

Figure 1 shows the beamline layout for the electron recirculation system tests [2]. The beamline joins a pair of Pelletron acceleration/deceleration tubes (not shown). Both the electron gun and collector are located inside the high voltage terminal of the Pelletron accelerator.

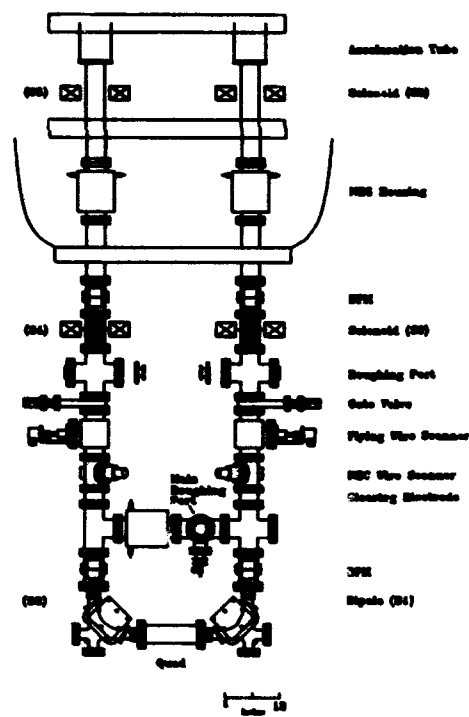


Figure 1. Recirculation test system beamline.

The beamline is symmetric about the center of the quadrupole. The quadrupole strength is adjusted to make the entire 180° bend achromatic, thus relaxing the stability requirements for the dipole magnet power supplies. The dipole magnets have a field index $n = 1/2$ to provide equal

*This work was supported by the TNRLC under grants RGFY9158 & RGFY9258. Additional support by Indiana Univ. and NEC.

focussing in both the horizontal and vertical planes. There are six beamline solenoids in the recirculation test apparatus; one in the acceleration tube, four more in the external beamline, and the last one in the deceleration tube. Solenoidal focussing was chosen over quadrupole doublets or triplets due to the beam cylindrical symmetry at the exit of the Pelletron acceleration tube.

B. Electron Optics

The optics for this beamline have been modelled using both a version of TRANSPORT [3] which includes the effects of space charge and SCAT [4], a code that integrates the Twiss parameters and includes the effects of finite emittance, space charge and acceleration. The transfer line produces a beam waist at the middle of the 180° bend, and the beam envelope shape is consequently symmetric about that point. Figure 2 shows a typical optics plot obtained from SCAT. Additional waists occur prior to the first dipole, B1, and after the second dipole, B2. The position of these foci depend somewhat on beam current, moving slightly away from the dipoles with increasing current. A set of clearing electrodes has been placed at these focal points to sweep away any ions produced.

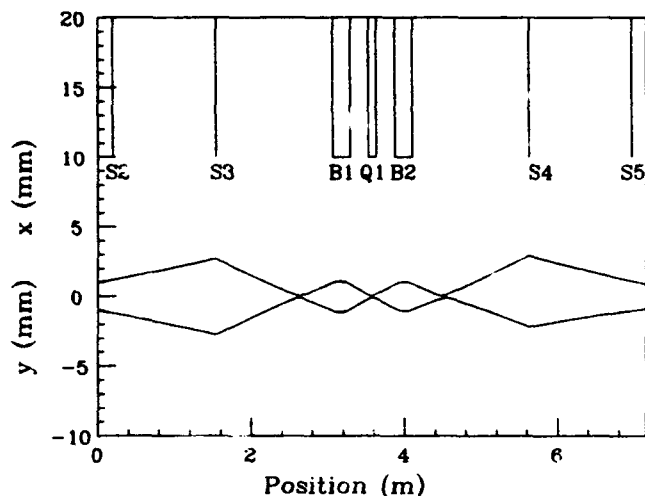


Figure 2. Horizontal and vertical beam envelopes. The slight asymmetry is due to the quadrupole.

As the beam current increases, space charge effects require that the solenoid field strengths change to compensate for the resulting defocussing. Changes in focussing must occur smoothly, to allow them to follow the increasing beam current without passing through a point where the beam can be lost. The optics are also constrained by the maximum solenoid field strengths and periodic 1 inch apertures within the transfer line.

A solution was found that utilized S3 and S4 together (with S2 and S5 off), for the full range of expected beam currents. The search for the calculated solenoid settings was automated, and carried out for over twenty different beam currents. The results are shown in Figure 3, where the solenoid currents, as

a fraction of the maximum solenoid current, are plotted versus the electron beam current. This is a solution which changes relatively slowly with increasing beam current, and satisfies all the applicable constraints. This is also a rather elegant solution, considering that the total number of beam waists changes from 5 to 3 as the electron beam current varies from 0 to 2 A. These settings will be tabulated for automatic computer control.

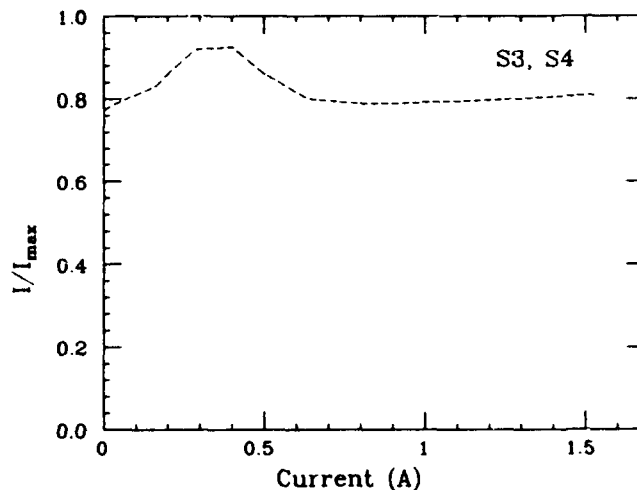


Figure 3. Calculated solenoid currents as a function of electron beam current.

III. DESIGN IMPROVEMENTS

A. General

Many changes have been made to the design of the recirculation test system as it first appeared during the UW/C/FNAL collaboration [5]. A much greater emphasis has been placed on magnet alignment. The magnets themselves have been designed specifically for this project, unlike those from various sources for the previous experiment. They have all been carefully field-mapped and have known focussing properties. Hall probes located inside the dipoles will ensure reproducible fields. Clearing electrodes will be placed at the positions of the three beam waists for ion sweeping to prevent space charge neutralization of the beam, which would greatly affect the electron optics. There will be greatly increased pumping capabilities available from a combination of non-evaporable getter (NEG) and ion pumps. The previous system had no ion clearing, and much less pumping. Other improvements include better radiation shielding of the Pelletron itself (to reduce SF_6 ionization leading to premature breakdown and voltage instability) and corona needles replaced by resistors.

B. Diagnostics

There are a total of eleven diagnostic stations (5 horizontal and vertical nonintercepting Beam Position Monitors (BPMs), 2 NEC wire scanners, 2 single-pass flying wire scanners and 2 residual gas beam profile monitors) included in the present design. The previous system had only two wire scanners which were limited to operation with beam currents below 100 μ A due to high beam power and excessive beam loss. The BPM's are designed to operate over the full range of beam currents ($< 20 \mu$ A to 2 A), while the flying wire scanners have a current limit of 200 mA. For higher currents, a residual gas beam profile monitor is being developed. Use of these monitors will enable the operators to verify correct electron optics throughout the transfer beamline.

C. Enhanced Collection Efficiency

High collection efficiency is important for three reasons. First of all, the Pelletron can only source approximately 400 μ A (limited by charging chain current), any further losses lead to a droop in terminal voltage and subsequent loss of beam. Secondly, since the secondary (backscattered) beam will have a much larger emittance than the primary (incident) beam, it can lead to voltage discharges in the deceleration tubes and gas desorption. Finally, any beam loss will produce x-rays which can ionize the SF₆ insulating gas and lead to premature breakdown and voltage instabilities.

The collector design incorporates two systems which prevent nearly all the backscattered electrons from the collector from re-entering the deceleration tubes. The first is a standard Faraday-cup type collector with electron suppression which limits the backscattered electron current to a few parts in 10⁴ of the incident beam current. This collector is preceded by a 90° dipole magnet which will deflect the remaining backscattered current in the opposite direction of the primary current. The insulated vacuum chamber for this magnet will then serve as a secondary collector, collecting virtually all the remaining electrons.

IV. CURRENT STATUS

A. Pelletron Accelerator

The Pelletron accelerator has been raised to allow for semi-permanent alignment apparatus to be installed beneath the beamline. A two foot thick concrete vault was then poured around the beamline for radiation shielding. The electrical service and ground end feedthroughs have been reconnected, as well as the main SF₆ gas transfer line. The closed-loop charging system electronics have been reinstalled, and the refurbished light link fiber control cable has been connected to the terminal electronics. Once the control system was tested, the Pelletron column was conditioned (without tubes) to 2.3 MV in approximately 1 hour.

B. Magnets and Alignment Structure

The dipole magnets have been assembled and field-mapped, and their vacuum chambers have been welded and leak-checked. Two of the four external beamline solenoids have been assembled and field-mapped. The acceleration tube lenses (from the previous project) have also been field-mapped. Power supplies for the above magnets have been procured and installed. A beamline support and alignment structure has been designed utilizing standard off-the-shelf components. The dipoles and quadrupole will be mounted on a single frame and have the capability to be pre-aligned.

C. Diagnostics

Components for the Beam Position Monitor (BPM) electrode assembly have been designed and partially procured. The BPM pre-amp and synchronous detection electronics have been prototyped. The pre-amp electronics for the residual gas beam profile monitor have also been built and tested. The single-pass flying wire beam profile monitor design has been simplified and components have been procured and tested. The computer control software has also been modified and simplified.

D. Vacuum Hardware

The majority of the off-the-shelf beamline vacuum components have been procured. The NEG pump housing components have been fabricated and await welding. The associated NEG power supplies have been built and tested.

V. REFERENCES

- [1] T. Ellison, et al., "Multi-MeV electron cooling -- a tool for increasing the performance of high energy hadron colliders?", submitted for the Fifth Annual 1993 International Industrial Symposium on the Super Collider (IISCC) and Exhibition (San Francisco, CA, May 1993).
- [2] Design Report, *Feasibility of decreasing the emittance of beam in the SSC by electron cooling in the SSC Medium Energy Booster* (IUCF Publication, October 1992).
- [3] U. Rohrer, "The present state of the VAX-Transport at SIN [now PSI]" (SIN internal report, May 1982).
- [4] SCAT code written by Del Larson (SSCL).
- [5] D.J. Larson, J.R. Adney, D.R. Anderson, F.E. Mills and M.L. Sundquist, "Operation of a prototype intermediate-energy electron cooler", NIM A311, pp. 30-33 (1992).

The Bevalac Long Spill*

C.M. Celata, S. Abbott, M. Bennett, M. Bordua, J. Calvert, R. Dwinell, D. Howard, D. Hunt, B. Feinberg, R. Force, R. Frias, J. Halliwell, J. Kalnins, S. Lewis, M. Nyman, L. Shalz, M. Tekawa

Lawrence Berkeley Laboratory
Berkeley, California 94720 USA

R. Solomons
RAFAEL
M.O.D. Israel

Abstract

The Bevalac extraction time was increased from 1 to a maximum of 9.5 seconds, thus increasing the synchrotron duty factor and the data rate for experiments by a factor of 2-3, depending on the magnetic field. This slow rate of extraction required improved control of beam time structure, since magnet ripple remained approximately constant while the spill rate was decreased. Measurements of spill structure for the long spill are presented. Changes made to the accelerator systems are described, as well as tuning procedures found to be necessary, and the ultimate hardware limits found for the spill length.

I. INTRODUCTION

One measure of the efficiency of a synchrotron is the "duty factor", i.e., the percent of the pulse cycle time during which beam is being extracted for the use of the experimenters. Until July of 1992, the duty factor of the Bevalac ranged from 17% at full field (12575 G; 2.09 GeV/amu for $Z/A=1/2$) to 25% at low field (2500 G; 0.161 GeV/amu for $Z/A=1/2$). The normal pulse cycle included 1-1.5 seconds for extraction. As described in this paper, in July the timing cycle was changed so that for all but the highest magnetic fields the beam could be extracted for up to 9.5 seconds, with the rest of the cycle unchanged. This increased the duty factor to 34% at full field, 60% at 10 kG, and 80% at low field-- a factor of 2 - 3. The increase was reflected in an increased data rate for experiments performed in the last few months of Bevalac operation.

The circulating beam intensity was increased in proportion to the duration of extraction, so that average intensity remained the same. This meant that experiments already using the full intensity available from the source could not profit from the longer extraction time. In practice, this was not a problem for the experiments running when the long spill capability was available.

Ultimately the extraction time was limited by hardware constraints. These are described in Section II. In Section III we discuss measurements of the time structure of the extracted beam for the old (1 s) spill and the long spill, and describe changes made to the feedback systems which improved this structure.

II. HARDWARE LIMITS TO THE EXTRACTION TIME

The stated goal of this project was to extend the extraction time to 9.5 seconds for main synchrotron fields up to 10 kG. However, every effort was made to increase the duty factor for all energies to the limit given by available hardware. As will be described below, the complete 9.5 second spill was not possible for fields at and slightly below 10 kG due to motor-generator synchronization, but the duty factor increases cited above were certainly sufficient to justify the project.

The limits to the extraction time were set by: (1) main magnet heating, (2) rms input power of the motor-generators powering the main magnet, and (3) synchronization of the motor generators. The first of these limits refers to the fact that on hot days the main magnet was not adequately cooled by the wind tunnel-fan-cooling tower system, and for any fields above 7 kG the extraction length could be limited by the main magnet temperature. However, given the climate, this occurred rarely.

Limits (2) and (3) refer to capabilities of the motor-generator system. The main magnet for the Bevatron was powered by two 12-phase half-wave-rectified motor-generator sets (MG's) with two 67 ton flywheels for energy storage. The input power for these motors was limited by fabrication specification to 3.3 MVA per motor, rms. A normal value for the power factor was 0.8, giving a limit of 2.64 MW per motor. It proved possible, using data obtained in 1949, to calculate quite accurately the rms power required of the motors. This included friction and windage losses, power losses in the rectifier ignitrons, I^2R losses in the motors and generators, and power loss in the main magnet. The motor power limit affected the possible extraction time for fields above about 12 kG, limiting extraction time to 5 seconds at full field.

For fields between about 8 kG and full field, synchronization of the two motor-generators provided an unexpected limit on the extraction time. At high fields (≥ 7600 G for 1 s spills), the power required for the main magnet exceeded what could be produced by one motor. The load was then balanced between the two motor-generators, with uncomfortable mechanical consequences if a sufficient imbalance occurred. Insufficient operating time was available to investigate the phenomenon, but somewhere between 8 and 10 kG this load imbalance began to occur for the longer extraction times. At 10 kG this effect limited the extraction

* This work supported by the U.S. D.O.E. under contract #DE-AC03-76SF00098.

time to 6.5 seconds. The load-balancing was performed by the "Kramer system", a system of two induction motor-generators used to supplement power from the public power line when flywheel speed dropped during peak power use. It was hypothesized that this system could not supply enough power for long pulses. Since the motors would slow at slightly different rates, this would lead to a phase difference between the two MG's, creating a load imbalance.

It should be noted that at low fields the extraction time could have been extended further than 9.5 seconds. This was not attempted, but the only limitations revealed by our work were the amount of charge available from the source, and, at very low extraction rates, the spill time structure. This latter factor will be discussed below. There is one precedent for near-dc beams in the Bevalac. As a prelude to construction of the PEP accelerator, beam was circulated in the Bevatron for 30 minutes without incident. However no extraction was attempted.

III. EXTRACTED BEAM TIME STRUCTURE

Increasing the length of extraction was expected to increase time variation of the extracted intensity. This is due to the fact that regardless of the length of the spill, the same fraction of the circulating beam, limited by extraction physics to approximately 25%, was extracted. Doing this over a longer time meant that a smaller percent of the beam (by almost an order of magnitude) was extracted per unit time, requiring much finer control of the magnetic field. For many experiments, degradation of the beam time structure could quickly undo gains due to increasing the synchrotron duty factor. "Count-rate-limited" nuclear physics experiments, for instance, use electronics or data acquisition systems which cannot tolerate intensities above a given value. Increases in the amplitude of beam intensity oscillations would necessitate decreasing the average intensity, to bring the highest amplitudes below this threshold. This could bring the data rate back to the values obtained with the old 1 second spill. Early trials with a low rate of extraction showed that for the Bevalac this did not occur-- though the spill structure deteriorated somewhat with lengthening extraction time, there was a net gain in projected data rate. However improvements in the spiller feedback system, described below, kept the quality of the spill somewhat constant as the extraction time was increased, enabling gains for the experiments commensurate with duty factor increase.

Beam extraction was accomplished using resonance extraction. Just before extraction the beam tune was brought close to $2/3$ by a perturbation magnet, P1. A (mainly) sextupole winding, S1, on the same magnet then was used to drive orbit growth by ramping the sextupole, thus moving the unstable fixed points into the beam. Normally 20 - 30% of the beam could be extracted.

Variations in the intensity could be caused by time structure in the main magnetic field or the extraction (perturbation or sextupole) magnet fields. In practice, the currents of the extraction magnets could be better controlled, and measurements of the extracted beam intensity vs. time, to be described below, show that the main magnet ripple contributed most of the structure which was due to magnetic field ripple. Because of the large dispersion of the machine,

ripple in the main magnetic field, $\Delta B/B$, as small as $\sim 2 \times 10^{-7}$ could produce bursts of beam [1].

Several feedback systems were in place to minimize magnet ripple. These included: feedback control of the generator voltage and phasing (effective for low frequency: 0-5 Hz), LC filters across the main magnet (170, 354, 658, 1008, 1345 Hz), and the "Ripple Reduction" feedback system (10 Hz - 20 kHz). The Ripple Reduction system measured dB/dt using a one-turn loop in each quadrant of the machine, and made use of extra pole-face windings to compensate for field ripple. It should be noted that due to the load on the motor-generators, main magnet ripple did not occur at multiples of power line frequencies, but rather at multiples of a frequency somewhat lower which depended on the value of the main field. This is reflected in the filter frequencies given above.

A final feedback system directly controlled the beam extraction rate in order to minimize variation of the intensity. The "spiller feedback system" [2,3] measured extracted beam intensity vs. time using a scintillator and photomultiplier tube, then adjusted the current in the S1 magnet in order to keep the beam intensity constant. The bandwidth of this system was approximately 0-2 kHz. Though effective at these frequencies, the system actually introduced an oscillation into the extracted intensity at approximately 2.5 kHz, due to delay in the feedback loop. Beam destabilized due to an increase in S1 current required approximately 100 μ s to reach the septum magnet and leave the synchrotron. Thus the information available to the feedback system about the condition of the beam was essentially delayed by 100 μ s. As the control system began extraction, S1 current would rise until the intensity measured by the PM tube was at the right value, then attempt to stabilize the level. Due to the delay, the beam intensity would continue to increase (following the previous increase in S1 current), causing the feedback system to decrease the S1 current enough to actually stop the extraction. Thus the beam spill occurred in ~ 2.5 kHz bursts¹, modulated by lower frequency structure at harmonics of the MG fundamental. As noted in reference [3], very low frequency (~ 5 Hz) variation of the intensity was also seen, and traced to the voltage regulation feedback loop of the generators.

An improvement was made to the spiller feedback system by one of the authors (M.N.) which greatly improved its quality for experiments. As noted above, this was of particular importance for long spills, where the beam was extracted over several seconds. A 10 kHz oscillation induced in the S1 current by a malfunctioning power supply was observed to decrease the amplitude of the feedback oscillations in the beam intensity. So an open-loop oscillation at approximately this frequency was introduced into the S1 current. This had the effect of terminating the feedback oscillations in the beam intensity before the feedback system could, lowering the amplitude of the bursts. The beam then emerged with ~ 10 kHz structure rather than 2.5 kHz. It was found that varying the frequency of the applied oscillation

¹Note: Oscillation occurs at the frequency where the delay = 180° . Since the loop includes an integrator to produce the time average, which contributes 90° to the delay, the oscillations occur at 2.5 kHz, where 100 μ s gives a quarter-period delay.

either up or down from the approximate frequency fortuitously applied by the faulty power supply increased the amplitude of the bursts. This is assumed to be because this frequency has a period equal to the information delay time in the loop. If the applied oscillation is at higher frequency, beam destabilized during one oscillation may add to the next burst. If the oscillation is slower, the system will not catch the intensity overshoot due to the delay. The optimal waveform for the oscillation appeared to be approximately a sawtooth.

The beam time structure was measured by two different systems, both using the signal from a scintillator-PM tube system at the first focus of the beam in the extraction channel. One system Fourier analyzed the signal (bandwidth ≤ 20 kHz), and the other sampled the signal for intervals of 0.5 s at 1 MHz. As a measure of beam quality, the ratio of rms to average intensity for each of the 0.5 s intervals was computed from the data obtained from the latter system. This will be referred to as the "spill duty factor", or SDF. Though very little time was available in the last months of Bevalac operation for making accelerator measurements, extensive data-taking was done over one two-day period (Sept. 15-16, 1992), and at other times experimenters were consulted as to the quality of the beam they received. The data quoted below derives from the measurements of Sept. 15, 16. The main field strength was 7650 G, or 1.05 GeV/amu for $q/m=1/2$.

The SDF varied with the tuning of the synchrotron. But it was not found to degrade significantly as the extraction time lengthened. For a 1 s extraction time the SDF was 1.6. At the beginning of the long (9.1 s) spill, the SDF was worse (2.3), though such an increase is more than compensated by the increased length of extraction. However measurements of 0.5 seconds at the middle of the spill produced an SDF of 1.5, and the SDF near the end of the spill was found to be 1.4. Thus in some average sense the time structure of the long spills was better than that of the 1 second spills, at least on the days when our measurements were permitted. This was born out, as mentioned above, by an increase in data rate for the experimenters at least commensurate with the increase in synchrotron duty factor.

Fourier analysis of the beam time structure revealed the usual components due to MG ripple below about 2 kHz, as described in reference [3], plus the ~ 10 kHz (actually, 8.8 kHz) oscillations inserted by the oscillation applied to S1, and harmonics of this frequency. Sidebands occurred for the 8.8 kHz structures and their harmonics whose spacing was given by the MG frequencies. The frequency domain data was examined to try to find some reason for the improvement in the time structure with time during the long spill. dB/dt due to the MGs, as measured by the dB/dt loops, actually increased during this time, both at harmonics and subharmonics of the MG frequency and for the ~ 5 Hz structure. Oscillations in the Ripple Reduction feedback system were somewhat less, but it is not at all clear that this can account for the improvement. Figure 1 shows the signal from the PM tube (in arbitrary units) vs. time for typical 5 ms intervals of spill. The upper trace is taken from the last third of the spill, and the lower from the first third. The difference in structure is notable. The

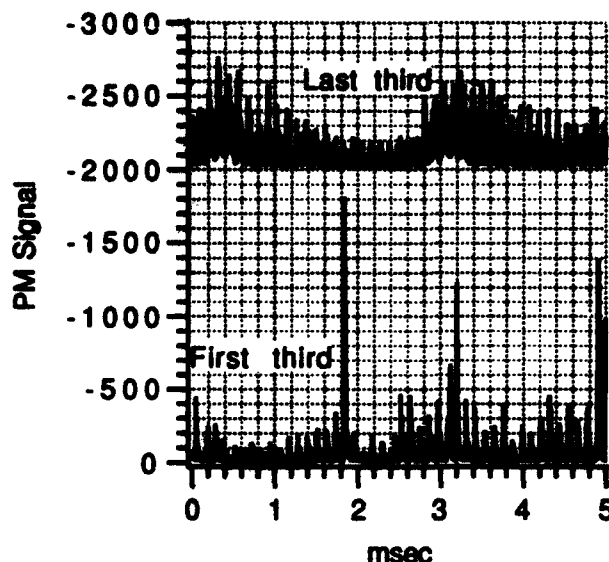


Figure 1. Photomultiplier signals vs. time showing extracted beam intensity from 5 ms of the first (lower trace) and third (upper trace) third of the spill. The upper trace has been offset by -2000 of the (arbitrary) units for clarity.

improvement seems not to be due to the difference in the distribution function of the particles extracted at the beginning vs. the end of the spill, since a similar change in time structure does not occur for 1 s spills. It is possible that the increased field ripple, plus the slowing of the MG's due to the prolonged load, made the effect of the 8.8 kHz oscillation more favorable. As can be seen from Figure 1, at the end of the spill the S1 oscillation was not able to completely shut off the spill.

IV. SUMMARY

The maximum Bevalac extraction time was increased from 1 to 9.5 seconds for its last few months of running. This increased the synchrotron duty factor by a factor of 2 to 3 depending on the beam energy. Time structure of the extracted beam was as good or better than with the shorter extraction time. Due to the lack of time to study this phenomenon, the cause is not known.

V. REFERENCES

- [1] J. Staples, private communication.
- [2] M. Nyman et al., *IEEE Trans. Nucl. Sci.* NS-32, No. 5, 2177(1985).
- [3] C.M. Celata et al., *Conference Record of the 1991 IEEE Particle Accelerator Conference.*, Vol. 3, pp.1401-1403.

Capture From Pair Production as a Beam Loss Mechanism for Heavy Ions at RHIC*

B. Feinberg, A. Belkacem, R. Bossingham, Harvey Gould

Lawrence Berkeley Laboratory

1 Cyclotron Rd., Berkeley, CA 94720 USA

W.B. Meyerhof

Stanford University

Stanford, CA 94305 USA

Abstract

Electron capture from electron-positron pair production is predicted to be a major source of beam loss for the heaviest ions at RHIC. Achieving the highest luminosity thus requires an understanding of the capture process. We report the first observation and measurement of this process, in Bevalac experiments using 1 GeV/u U^{92+} projectiles on Au targets. Capture from pair production is a process in which the very high electromagnetic field involved in the collision of two relativistic heavy ions polarizes the vacuum, resulting in the production of an electron-positron pair and the capture of the electron by one of the ions. There are many theoretical papers published on capture from pair production with very large discrepancies between predicted cross sections. The experimental results are compared to theory, and the implications of extrapolations to RHIC energies are presented.

I. INTRODUCTION

At relativistic energies, the capture of electrons by ions (recombination) occurs by the well-understood collisions processes of Radiative Electron Capture (REC) and Non-Radiative Capture (NRC). These processes, which require an electron in the initial state, have cross sections that decrease rapidly with increasing collision energy. REC is the capture of a target electron by the ion with the simultaneous emission of a photon (to balance momentum and energy). NRC is the capture of an electron that is initially bound to a target atom or ion. Until recently, REC and NRC were thought to be the dominant processes for electron capture at all relativistic energies.

The large transient fields produced in relativistic charged particle atomic collisions (no nuclear contact) have long been known to produce electrons through electron-positron pair production [1]. But, in 1984, Gould pointed out that for bare heavy ions, the probability for pair creation with simultaneous capture of the electron from the pair into the K-shell, was

significant [2]. The cross section for this "capture from pair production" mechanism is expected to increase with energy (as does the cross section for producing free electron-positron pairs), making it the dominant electron capture mechanism at highly relativistic energies. And since capture from pair production requires no electron in the initial state, it can take place between two bare ions, possibly limiting the lifetime of stored beams of bare heavy ions in relativistic heavy ion colliders.

A number of theoretical papers aimed at calculating the cross sections for electron capture from pair production have been published since 1984 [3]. Different calculational techniques were used, and several results, in disagreement with each other, have been reported. Until recently, no experimental measurement to check the validity of these different theoretical predictions, or even the existence of electron capture from pair production, has existed.

In this article we report the observation and measurement of electron capture from electron-positron pair production in relativistic heavy ion collisions, and discuss the possible implications for the lifetime of heavy ions in the Relativistic Heavy Ion Collider (RHIC) now being constructed at Brookhaven National Laboratory [4]. The experiment has been performed at the Bevalac accelerator at Lawrence Berkeley Laboratory, using 956 MeV/u bare uranium ions (U^{92+}) incident on thin, fixed targets of Au.

II. EXPERIMENT DESCRIPTION

Figure 1 shows a diagram of the Advanced Positron Spectrometer (APS) used to detect positrons. The U^{92+} ion passes through a fixed target located inside the APS, described below. In the case of capture from pair production, the electron is created directly bound to the uranium ion, changing its charge by one unit to U^{91+} . The experimental signature is the detection of the positron emitted during the collision, in coincidence with the charge-changed U^{91+} . The U^{91+} is magnetically separated from the main beam of U^{92+} and each charge state is detected by a scintillator-photomultiplier tube detector.

*Supported by the Director, Office of Energy Research, Office of Basic Energy Sciences, Chemical Sciences Division and (BF) Office of High Energy and Nuclear Physics, Nuclear Physics Division, U.S. Department of Energy under contract DE-AC03-76SF00098. One of us (WEM) was partially supported by NSF grant No. PHY8614650.

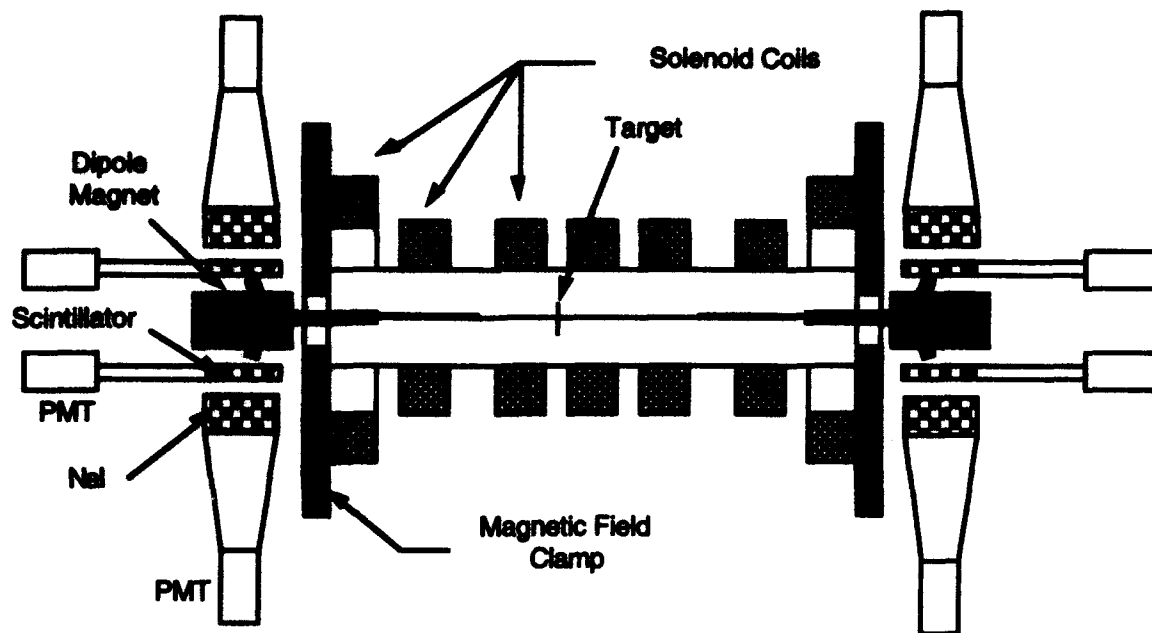


Figure 1 - Schematic diagram of the apparatus (top - sectional view). The solenoid field decreases adiabatically from the center towards the ends causing the particle orbits to grow and their divergence to decrease, allowing them to be swept by the dipole magnets into the detectors. Only one positron detector (and no electron detector) is shown. The target is located near the center of the solenoid and the heavy ion beam travels horizontally through the apparatus.

The target is placed inside and slightly upstream from the center of the APS. The APS is used to detect and measure the energy distribution and angular distribution of the electrons and positrons emitted from the target. It contains a solenoid magnet in the center and a dipole magnet at each end. The solenoid generates a strong magnetic field ($B=0.8$ T max.) that adiabatically decreases toward the ends. The field transports the electrons and positrons away from the target, and converts much of the positron (electron) transverse motion into longitudinal motion. The positrons and the electrons are efficiently deflected in opposite transverse directions at each end of the solenoid by the dipoles. There they strike plastic scintillator-photomultiplier tube detectors.

This combination of magnetic fields, results in a very high acceptance for electrons and positrons emitted both forward and backward with respect to the beam direction. Without the adiabatically decreasing field, the acceptance of the spectrometer would be very low because most of the positrons, upon reaching the end of the solenoid field, would have a large transverse motion causing them to strike the walls of the apparatus rather than to be deflected into the spectrometer detectors. Tests of the APS using beams and radioactive sources have shown a detection efficiency close to unity for emission angles of up to 75 degrees forward and backward. The acceptance is independent of the positron or electron energy in the energy range investigated (from 0.1 to 2.5 MeV).

The emission angle with respect to the beam direction is measured using the time of flight of the positrons (electrons) through the solenoid. Four plastic scintillator-detectors (see figure 1) are used to detect the positrons (electrons) and to measure their energy and time of flight. The magnetically separated U^{91+} ion that produced the positron, detected in its scintillator-detector at the end of the beamline, is used for the timing reference.

The dipole magnets that deflect electrons and positrons in opposite directions are used for the initial discrimination between electrons and positrons. However, at 1 GeV/u, a large number of knock-on electrons are ejected from the target by collisions with the uranium ion. Approximately 3 to 4 electrons with an energy above 100 keV are ejected from a 1 mg/cm² gold target for every uranium ion, while only one positron from the same target is expected for every 10⁶ uranium ions. Roughly two or three per thousand knock-on electrons backscatter from the electron scintillator-detector into the positron scintillator-detector, thus simulating a positron.

To discriminate against these scattered electrons we require the detection of one of the two 511 keV photons that are emitted back-to-back when the positrons annihilate at rest in the plastic scintillator. The 511 keV photon is detected by a NaI scintillator-photomultiplier detector (see figure 1). The detection efficiency of the photon (by the 12.5 cm diameter by 15 cm long active area) NaI detector has been measured to be 42%, with roughly 60% of the photons appearing as a narrow

single peak at 511 keV, and the rest as a broad Compton distribution. In our data analysis only the narrow peak is used. This sets the overall efficiency of the APS for the detection of a positron at 25%.

III. RESULTS

We integrate the spectra over the positron energy and angle to obtain the total cross section for capture from pair production. We correct for the angular region between 75 and 105 degrees, not accounted for by the spectrometer, and for the energy range above 2.5 MeV. Making these small corrections, we measure the total cross section for capture from pair production by a 956 MeV/u U^{92+} on a gold target to be 2.19 (0.25) barns.

We obtain a cross section of 3.3 (0.65) for the free pair process by assuming that a similar fraction of free pairs are not detected by the spectrometer (The error we make, in estimating the fraction between 75 and 105 degrees for free pair production is well within our error bars, even though the angular distributions for capture from pair production and free pair production are expected to be different.)

IV. DISCUSSION

At 1 GeV/u the electron of the $e^+ - e^-$ pair is almost as likely to emerge from the collision bound to the U^{92+} , changing its charge state to U^{91+} , as it is to emerge free. Perturbation theory predictions [5] underestimate the measured total cross section for capture from pair production by about a factor of 2.5, and underestimate the ratio of capture to free pair production by about a factor of 3 [6].

Calculations of the cross section for both free pair production and capture from pair production have been made for Au at RHIC collider energies of 100 + 100 GeV/u. These perturbative calculations indicate that the free pair production cross section increases to the order of 3×10^5 barns for Au ions, while the fraction of pair electrons that are captured is predicted to decline to a part per thousand at RHIC energies [4,7]. The fraction of electrons that are captured may be sensitive, however, to several effects such as multiple pair production, combined charges of projectile and target, and other effects enhancing capture. As has been seen, the fraction at 1 GeV/u is observed to be considerably larger than that predicted by perturbation theory.

Capture from pair production (resulting in the loss of the charge-changed ion in the collider ring) has been predicted to be the dominant beam loss mechanism for colliding Au + Au beams at RHIC and a significant loss mechanism for lighter ions [4]. Small effects that might enhance capture, as discussed above, could have a significant impact upon the ratio of captured electrons, and thus upon the operation of RHIC. If the fraction of captured electrons is an order of magnitude higher than predicted at RHIC energies, then the current after 10 hours will decrease to about 20% of the initial value, instead of 77%, after taking into account intrabeam Coulomb scattering.

Measurements of the cross section for capture from pair production at Bevalac energies indicate that current calculations based upon perturbation theory underestimate the fraction of electrons captured by a factor of three. These results indicate the need for better calculations and measurements over a wide range of energies to understand the useful lifetime of heavy ions in RHIC.

V. REFERENCES

- [1] G. Racah, *Nuovo Cimento* 14, 93 (1937) and references therein.
- [2] H. Gould, Lawrence Berkeley Laboratory Report No. LBL-18593 (1984).
- [3] See references in A. Belkacem, Harvey Gould, B. Feinberg, R. Bossingham, and W.E. Meyerhof, "Measurement of Electron Capture From $e^+ - e^-$ Pair Production in Relativistic Heavy Ion Collisions," submitted to *Phys. Rev. Lett.* (1993).
- [4] "Conceptual Design of the Relativistic Heavy Ion Collider - RHIC", BNL Report BNL-52195 pp 117-121.
- [5] U. Becker, *J. Phys. B* 20, 6563 (1987); values for U on Au were computed by K. Momberger.
- [6] U. Becker, N. Grün and W. Scheid, *J. Phys. B* 19, 1347 (1986).
- [7] C. Bottcher, M.R. Strayer, *Phys. Rev. D* 39, 1330 (1989).

Acceleration of Deuteron Beam in the KEK Proton Synchrotron

Yoshiharu Mori and the crew of the heavy ion acceleration group in the KEK PS

National Laboratory for High Energy Physics(KEK)

Oho 1-1, Tsukuba-shi, Ibaraki-ken 305, JAPAN

(abstract)

Deuteron beam has been successfully accelerated in the KEK PS up to the energy of 11.2GeV(5.6GeV/u), the limiting energy of the ring. The first physics experiment with deuteron beams was carried out in April of 1992 after this success. Helium beam acceleration is scheduled in April in 1994.

I. INTRODUCTION

Acceleration of heavy ion beams in the KEK PS was discussed about more than 8 years ago. However, the project was stopped by several reasons and heavy ion acceleration in the KEK PS has not been realized so far. Very recently, as one of the possible candidates among the future plans of the KEK PS, the PS-Collider, which aims to accelerate and collide heavy ion beams with the beam energy of up to 7GeV/u for a gold beam, has been proposed.[1] The PS-Collider is designed to use the present KEK PS as its injector, therefore a much more simple scheme compared with the previous one for accelerating heavy ions in the PS has been examined carefully for ease of operation. Simultaneously, possibility of a polarized deuteron beam acceleration in the PS has been also studied.[2]

In November of 1990, the PAC(Programme Advisory Committee) of the KEK PS has conditionally approved an experiment using a high energy deuteron beams of 2 ~ 5 GeV. According to the request from the PAC, a task force for aiming deuteron beam acceleration in the PS has been initiated in the accelerator department. On Jan. 31 in 1992, deuteron beam has been successfully accelerated in the KEK PS up to the energy of 11.2GeV(5.6GeV/u), the limiting energy of the ring. The first physics experiment with deuteron beams was carried out in April after this success.[3] In this paper, the outline of the deuteron acceleration scheme and the experience of the first long term operation are described and the future plan for heavy ion beam acceleration is also presented.

II. MODIFICATIONS FOR DEUTERON BEAM ACCELERATION

Earnest studies of examining the beam behaviors in deuteron acceleration according to the newly proposed scheme has been carried out for each part of the KEK PS. [4] Some components of the accelerator were replaced or modified for this purpose.

(a) *Injector:* The injector consists of the 750-keV Cockcroft-Walton preinjector and the 40-MeV Alvarez linac. The ion source which has been used at the KEK PS is a plasma-sputter type of negative hydrogen ion source. It generates more than 20 mA negative hydrogen ion beam with the 90% normal-

ized emittance of 1.5 mm.mrad.[5] This type of ion source can be converted to produce negative deuterium ions by changing a gas species from hydrogen to deuterium. The negative deuterium ion beam extracted from the ion source is accelerated by the Cockcroft-Walton preinjector and injected into the linac. The acceleration energy is 375-keV, which is a half of that for proton acceleration, because the linac is operated in 4π mode acceleration for deuteron acceleration. In order to accelerate heavy ions whose $Q/A = 0.5$ in an Alvarez type of proton linac, $4p$ mode acceleration can be used. When deuteron acceleration is performed in 4π mode, the energy gain in each (ΔW_d) cell should be half of that for proton(ΔW_p). Thus,

$$\Delta W_d = m_p/m_d \Delta W_p = 1/2 \Delta W_p, \quad (1)$$

where m_p and m_d are the masses of proton and deuteron, respectively. Since the transit time factor of each cell for 4π mode acceleration is almost a half of that for 2π mode acceleration, the condition of eq.(1) is satisfied.

(b) *Booster* Beam parameters of deuteron acceleration in the booster is summarized in Table 1.

Table 1 Beam parameters of deuteron acceleration in the booster

	injection	extraction
Energy(MeV)	19.28	293.8
Bp(Tm)	0.8994	3.636
$\beta\gamma$	0.1438	0.5812
harmonic number	1	
RF frequency(MHz)	1.132	3.996
RF voltage(max. kV)	~25	
emittance(pmm.mrad)		
horizontal	90	22
vertical	40	10
$\Delta P/P$	+0.5%	+0.4%
bunch width(nsec)		100

There are two RF cavities in the booster at the moment. In deuteron acceleration, the RF frequency at the beam injection is 1.132MHz, which is almost a half of that for proton acceleration. The capacitance of each RF cavity is about 1000pF and the maximum inductance of each RF cavity is about 6 mH when the ferrite DC bias current is zero, respectively. Therefore, another capacitance of about 2000pF should be added for each RF cavity so as to tune the injection RF frequency to

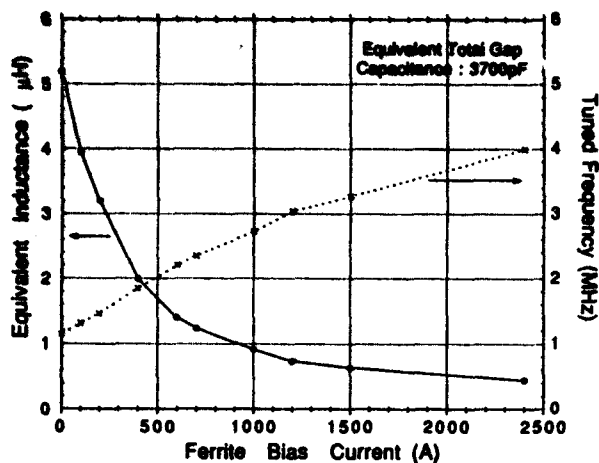


Fig. 1 Measured variations of inductance and tuned frequency as a function of the ferrite DC bias current of the cavity, when the vacuum capacitor of 2000pF was attached to the RF cavity.

each RF cavity so as to tune the injection RF frequency to 1.132MHz. Practically, this can be made by attaching a vacuum capacitor to the accelerating gap of each cavity. Figure 1 shows measured variations of inductance and tuned frequency as a function of the ferrite DC bias current of the cavity, when the vacuum capacitor of 2000pF was attached to the RF cavity. The inductance was changed for more than 13 times. This might be enough for deuteron acceleration. The shunt impedance of the cavity was also measured. The shunt impedance was about 400 W at the beam injection, which was approximately 40 % of the minimum shunt impedance for proton acceleration. However, since the RF voltage at the beam injection has to keep small to raise a longitudinal capture efficiency by an adiabatic process, the power loss in the ferrite of the cavity due to the low shunt impedance can be eliminated. The bucket height at the beam injection is relatively large for deuteron acceleration compared with proton acceleration. This is caused by the fact that the velocity of the deuteron beam at injection is a half of that for proton acceleration.

(c) Main ring: Beam parameters for deuteron acceleration in the main ring are summarized in Table 2. In deuteron acceleration in the main ring, the RF frequency range is as follows: $f_{inj} = 3.996\text{MHz}$, $f_{ext} = 7.869\text{MHz}$ and $f_{ext}/f_{inj} = 1.97$. For proton acceleration, $f_{inj} = 6.027\text{MHz}$. The RF frequency can be lowered by adding extra capacitance to the accelerating gap of each RF cavity used in the main ring. Since the maximum inductance of the present RF cavity is approximately 6mH, the total capacitance of about 260 pF is required for deuteron acceleration. The present total capacitance of each cavity is about 110 pF, so another 150 pF should be added. The variations of the RF frequency as a function of the ferrite DC bias current were measured when the vacuum capacitor of 150 pF was attached to the accelerating of the RF cavity. It was observed that the frequency increased up to 7.9MHz when the ferrite DC bias current was raised to 1100A. The variations of the shunt impedance were also measured carefully and no serious power loss in the ferrite of the cavity due to the shunt impedance reduction was not observed.

Table 2 Beam parameters of deuteron acceleration in the Main Ring.

	injection	extraction
Energy(GeV)	0.294	5.6
Bp(Tm)	3.636	43.04
harmonic number	9	
transition energy	5.32GeV/u	
betatron wave number	7.11(H), 7.25(V)	
RF frequency(MHz)	3.996	7.9
RF voltage(max. kV)	~69	
dP/P	+0.35%	
bunch width(nsec)	100	

III. ACCELERATION OF DEUTERONS

The first trial for deuteron acceleration in the main ring of the KEK PS has been performed from July 17 in 1991 and on July 19, the deuteron beam was successfully accelerated in the main ring up to the energy of 7.2GeV(3.6GeV/u). In this acceleration test, only one RF cavity of the main ring was available in accelerating deuteron beam. There was just only one ferrite bias power supply which was capable to swing its current up to 1100 A. Therefore, the maximally attainable RF voltage in this test was about 23 kV. The RF voltage of at least 50 kV is necessary for beam acceleration in the main ring when a field ramping rate of the bending magnets (dB/dt) equals to 3.17 T/sec as used in normal proton acceleration. In this acceleration test, we have reduced dB/dt to one third of the normal value, although the attainable deuteron beam energy was somewhat decreased to 7.2GeV(3.6GeV/u). In December of 1991, another two ferrite bias power supplies were ready for use in operation. On January 31 in 1992, deuterons was accelerated to 11.2GeV(5.6GeV/u), the limiting energy of the ring. In April of 1992, the first physics experiment with deuteron beams was carried out. Characteristics and performance of each part of the accelerator in the deuteron acceleration are briefly described in the following.

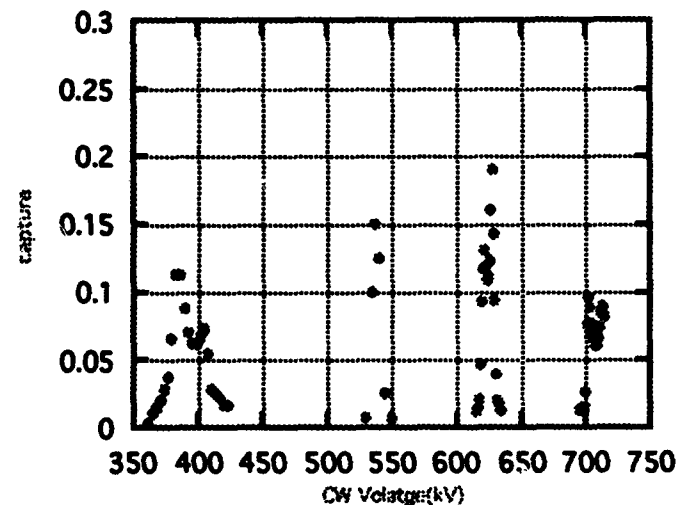


Fig. 2 Variations of the beam capture efficiency of the linac for 4π mode acceleration as a function of the injection energy.

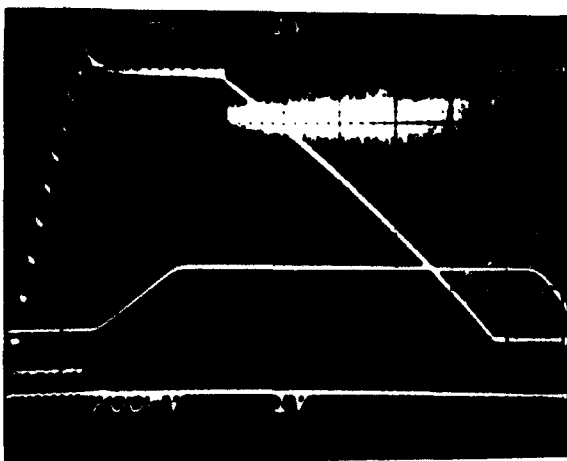


Fig. 3 Accelerated deuteron beam intensity in the main ring is shown simultaneously with a magnetic field pattern.

The ion source has produced negative deuterium ions by feeding a deuterium gas instead of a hydrogen gas. More than 15 mA negative deuterium ion beam from the ion source was accelerated by the Cockcroft-Walton preinjector and 12mA negative deuterium beam was injected into the linac. One of the most different operating parameters of the ion source compared with proton beam operation was a cesium consumption rate. The cesium consumption rate was relatively large for negative deuterium ion beam operation. In this type of ion source, negative ions are generated on the cesium covered molybdenum surface by ion sputtering in the plasma. Thus, the large cesium consumption was probably caused by a mass effect of sputtering ions.

In 4π mode acceleration of deuteron in the linac, the possible injection energy is not only 375 keV, which is a just half of that for proton. A relatively high energy of 540keV is also possible.[6][7] In Fig. 2, variations of the beam capture efficiency of the linac for 4π mode acceleration are shown as a function of the injection energy. It is found that not only the

beam energy of 375 keV but the higher energies such as 540keV can be acceptable for the linac. In normal operation, 540keV injection was chosen and the optimized beam capture efficiency in the linac was reached to about 30 %.

The injected beam momentum of the booster for deuteron acceleration is about 3% less than that for proton acceleration. Not only the magnetic field of the booster at beam injection was decreased but the beam transport elements between the linac and the booster were re-tuned to match the deuteron beam momentum. By tuning them carefully, almost 90 % injection efficiency was achieved in the booster. More than 95 % of the beam was extracted from the booster and transported to the main ring. The typical beam intensity in the booster is about 4×10^{11} ppp.

In Fig. 3, the accelerated deuteron beam intensity in the main ring is simultaneously shown with a magnetic field pattern. The typical accelerated deuteron beam intensity at the maximum energy in the main ring was 2×10^{12} ppp. According to the requests from physics experimentalists, the variable energy beam extraction from 2GeV(1GeV/u) to 11.2GeV(5.6GeV/u) has been tried for the deuteron beams so far. In Fig.4, the beam intensity variations for one-month operation in deuteron beam acceleration of April in 1992 is summarized.

IV. CONCLUSION

Deuteron acceleration is added to the routine operation of the KEK PS from April in 1992. The intensity of accelerated deuteron beam reached to about 2×10^{12} ppp at the beam energy of 11.2GeV(5.6GeV/u). The variable energy beam extraction from 2GeV(1GeV/u) to 11.2 GeV(5.6GeV/u) is also available. In April of 1994, the helium beam acceleration is scheduled.

The authors would like to express their sincere appreciation to Director General of KEK, H. Sugawara, and Profs. M.Kihara and Y.Kimura for their continuous encouragement. They are also indebted to Drs. M.Numaziri and K.Kondo for their helps on radiation estimations in deuteron acceleration.

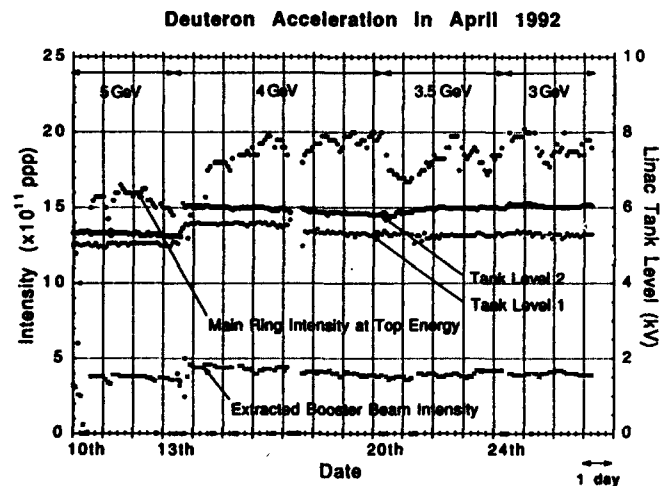


Fig.4 Beam intensity variations for one-month operation in deuteron beam acceleration of April in 1992 is summarized.

[1]PS-Collider design group;KEK Report 89-20,1990(in Japanese),KEK Report 90-13,1990(in English).

[2]H.Sato,Y.Mori,S.Ninomiya,T.Toyama,S.Hiramatsu;Accelerator Study Note,ASN 293(KEK),1988.

[3]J.Chiba et al.;

[4]Proc. of the Workshop on Deuteron Beam Acceleration in the KEK 12GeV PS:edited by Y.Mori, KEK-Proc. 91-12,1991(in Japanese).

[5]Y.Mori,A.Takagi,K.Ikegami,S.Fukumoto;Proc. of the fourth International Symp. on Production and Neutralization of Negative Ions and Beams,AIP Conf. Proc. Series No.158,1987,page378.

[6]S.Ohnuma, Th.Sluyters;Proc. 1972 Linac Conf.,Los Alamos,1972,page 191.

[7]T.Kato;KEK Report 86-5(1986).

Conceptual Design for One Megawatt Spallation Neutron Source at Argonne*

Y. Cho, J. Bailey, B. Brown, F. Brumwell, J. Carpenter, K. Crawford, D. Horan, D. Jerng, R. Kelb, A. Knox, R. Kustom, E. Lessner, D. McGhee, F. Mills, H. Moe, R. Nielsen, C. Potts, A. Rauchas, and K. Thompson
Argonne National Laboratory
Argonne, IL 60439

Abstract

A feasibility study of a spallation neutron source based on a rapid cycling synchrotron which delivers a proton beam of 2 GeV in energy and 0.5 mA time-averaged current at a 30-Hz repetition rate is presented. The lattice consists of 90-degree phase advance FODO cells with dispersion-free straight sections, and has a three-fold symmetry. The ring magnet system will be energized by 20-Hz and 60-Hz resonant circuits to decrease the dB/dt during the acceleration cycle. This lowers the peak acceleration voltage requirement to 130 kV. The single turn extraction system will be used to extract the beam alternatively to two target stations. The first station will operate at 10 Hz for research using long wavelength neutrons, and the second station will use the remaining pulses, collectively, providing 36 neutron beams. The 400-MeV negative-hydrogen-ion injector linac consists of an ion source, rf quadrupole, matching section, 100-MeV drift-tube linac, and a 300-MeV coupled-cavity linac.

I. INTRODUCTION

During the past two years there have been several studies on accelerator-based pulsed spallation sources in Europe, the United States, and elsewhere. Studies in Europe include a 5-MW source called the European Spallation Source (ESS) [1] and the Austron Project [2] for the eastern European countries. The ESS concept consists of an 800-MeV linac and three pulse compressor rings capable of accumulating and compressing pulse length to the order of 1 microsec and delivering over 2 mA of time-averaged current in each ring for a total of 6.25 mA. Studies in the United States include Los Alamos National Laboratory's LANSCE-II and Argonne National Laboratory's IPNS (Intense Pulsed Neutron Source) Upgrade. These two U.S. studies center around 1 MW of beam power.

For over a dozen years the IPNS facility has been providing research opportunities for the neutron scattering research community. The IPNS facility consists of a 50-MeV negative-hydrogen-ion linac and a 30 Hz rapid-cycling synchrotron (RCS) which accelerates 50-MeV injected

beams to 500 MeV. The RCS accelerates 3×10^{12} protons per pulse with a repetition rate of 30 Hz resulting in a time-averaged current of some 15 μ A. The 1-MW study described here is for upgrading the IPNS system.

With respect to the choice of the accelerator's peak energy, several studies have shown that the neutron yield is proportional to beam power almost independent of beam energy up to several GeV beam energy [1]. This fact provides an opportunity to compare the lower-energy/higher-current case with a higher energy/lower-current machine. That is to say, for a 1-MW facility, the choice of beam energy can be traded with choice of the beam current.

A decision was made to study initially a higher-energy/lower-current configuration of the accelerator system with a majority of the acceleration taking place in a circular machine. The other study option was to perform all acceleration in a linac with a circular machine acting as a pulse compressor. Since the cost of a high energy linac is relatively expensive, the latter scheme usually tends to have lower energy and high current. The decision to accelerate in a circular machine was based on past experiences with a high intensity circular proton accelerator; that beam loss always occurs during injection and capture processes and not during acceleration or extraction processes. Furthermore, the lost particles create residual radiation around the accelerator components. This residual radiation created by beam loss can be alleviated by injecting lower energy protons and handling fewer particles.

A. Choice of Repetition Rate

For a given-time averaged current, a higher repetition rate would provide an easier condition by lowering the number of particles to be accelerated per pulse. On the other hand, a higher repetition rate necessitates higher acceleration voltage. Repetition rates commonly used in this kind of setting range from 30 Hz at IPNS to 50 Hz at the ISIS facility in the U.K. Discussions with the user communities indicate that many experimental programs require lower repetition rates in order to avoid the so called "frame overlap" problem. A repetition rate of 30 Hz was chosen. In order to facilitate those experiments requiring an even lower repetition rate, it is proposed to have two target stations: one receiving a 10-Hz beam and the other using the remainder of the pulses.

*Work supported by U. S. Department of Energy, Office of Basic Energy Sciences under Contract no. W-31-109-ENG-38.

B. Choice of Machine Type

RCS technology is a mature technology. There are several operating proton machines of this type. Since the plan is to inject a lower energy beam and accelerate to a higher energy, using a proven technology provides the advantage of reliability. Furthermore, IPNS personnel have accumulated over 10 years of experience in operating a 30-Hz RCS. If the desired repetition rate was much higher than 30-Hz, another type of machine, such as the FFAG (Fixed Field Alternating Gradient), would be appropriate.

C. Use of Existing Infra-structure

The IPNS facility occupies a small fraction of the former ZGS (Zero Gradient Synchrotron) complex area, and nearly all of about 500k square ft. of space is available for 1-MW upgrade of IPNS. The ZGS ring building, which is heavily shielded, can accommodate a synchrotron 200 m in circumference, and several of the former ZGS experimental area buildings can house the two target stations mentioned earlier.

II. SYNCHROTRON

A. Lattice Type

The FODO-type lattice was chosen for simplicity and flexibility. A 90-degree phase advance was chosen to facilitate a missing-magnet-scheme dispersion suppression for the straight section area, and to provide relatively high transition gamma. Lattice functions are shown in Figure 1, which shows the normal cells, dispersion suppressor cell, and long straight section cells which are missing-magnet-normal cells. After having decided on the normal cells and the dispersion cells, the straight section cells can be added or removed as the length of the straight section requires. (One half of the super-period is shown in the figure with the dispersion function displaced by 10 m for clarity.) For example, around the 1-MHz radio-frequency range, a typical cavity system provides about 10 kV rf voltage per meter of cavity. Thus if the required rf voltage is 120 kV, then there should be some 12 m of straight sections for the rf system.

B. Choice of $B(t)$ and dB/dt

The lattice shown in Figure 1 can accelerate protons up to 2.2 GeV if the maximum magnetic field is about 1.5 T, which is commonly used value for this type of machine. It was decided to design a 2.2-GeV machine and to operate at 2 GeV for reliability reasons. The space charge limit discussed below implies the injection energy of the machine would be 400 MeV; this corresponds to the injection field of 0.417 T. A 30-Hz sinusoidal excitation of the ring magnets would require 180 kV of peak rf voltage. However, utilizing two (one 20-Hz and another 60-Hz) resonant power supplies for energizing the ring magnet with 20-Hz excitation and 60 Hz de-excitation enables the peak voltages to be lowered to some 120 kV.

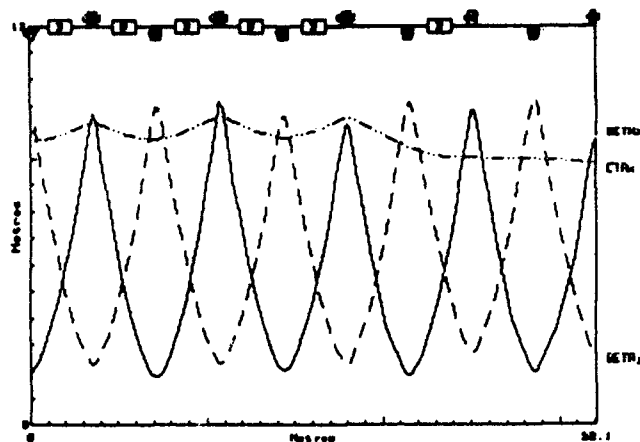


Figure 1. Lattice Functions (see text for detail)

C. Space Charge Limit and Injection Energy

Typical transverse phase space acceptance of this type of accelerator varies from 200 pi mm.mr to 500 pi mm.mr. An iterative study using the beta-function shown in Figure 1 and reasonable apertures of quadrupole magnets showed that a choice of 375 pi mm.mr in both transverse planes is about optimum for the quadrupole magnet designs. The number of protons per pulse required to make a 0.5-mA time-averaged current is 1.04×10^{14} . If the injection energy is 400 MeV, the acceptance of 375 pi mm.mr in both planes together with an assumption that the allowed space charge tune shift is 0.2, gives about 1.4×10^{14} protons per pulse. Therefore, the 400-MeV injection energy is chosen.

D. Injection

In order to facilitate a multi-turn-acceptance filling injection into the synchrotron, a phase-space-painting scheme is used which incorporates a negative-hydrogen-ion beam and a "stripper foil" system. The stripper foil system which changes the negative-hydrogen-ions to positive-hydrogen-ions (charge exchange injection).

III. INJECTOR

A. Injector Requirements

To facilitate 0.5 mA of the time-averaged current, the negative-hydrogen-ion source must deliver 1.04×10^{19} per pulse at a 30-Hz rate. This corresponds to a pulse current of 33 mA if the pulse width is 0.5 msec. If the available pulse current is 50 mA, then the pulse width could be 0.33 msec. Another implication here is that if the revolution period is about 1 micro-second, 300 to 500 turns could be injected depending on the pulse width. The space charge limit requires that the final energy of the injector should be around 400 MeV.

B. Injector Configuration

The injector system consists of the negative-hydrogen-ion source, a 2-MeV rf quadrupole, a beam chopper to

facilitate loss less capture, a 100-MeV drift-tube linac, and a 300-MeV coupled-cavity linac. It is contemplated that the frequency for both the rf quadrupole and the drift-tube linac will be 400 MHz and 1200 MHz for the coupled-cavity linac. This choice was made to take advantage of recent progress in linac technology from the SSC Laboratory and Fermilab.

IV. SUMMARY

Table 1 shows the parameters of the accelerator system, and the facility layout is shown in Figure 2. Figure 2 also shows the existing IPNS facility as well as the proposed two target stations. Further R&D work on various hardware performances as well as a simulation study on

injection and capture [3] are in progress. The study team concludes that RCS technology is suitable for a 1-MW pulsed spallation source.

V. REFERENCES

- [1] S. Martin and C. W. Planner, "Accelerator Design Parameters for a European Pulsed Spallation Neutron Source," 3rd European Particle Accelerator Conference, pp. 435-437 (1992).
- [2] "AUSTRON" Machine Study Team, "A Pulsed Spallation Source in Central Europe," 3rd European Particle Accelerator Conference, pp. 432-434 (1992).
- [3] E. S. Lessner and Y. Cho, "RF Capture Studies for Injection into a Synchrotron", these proceedings.

Table 1 Major Parameters

Circumference	192.6	(m)	Vertical Tune	6.21
Injection Energy	400	(MeV)	Transition Gamma	6.04
Maximum Energy	2.2	(GeV)	Peak Rf Voltage	120 (kV)
Nominal Energy	2.0	(GeV)	Harmonic Number	1
No. of Protons/pulse	1×10^{14}		rf Frequency @Injection	1.103 (MHz)
Average Current	0.5	(mA)	rf Frequency @Extraction	1.456 (MHz)
Injection Field	0.417	(T)	Number of Cavities	6.
Extraction Field	1.341	(T)	Maximum Beam Current @Extraction	61 (A)
Bending Magnet Length	1.3	(m)	Average Power Delivered to Beam	900 (kW)
Quadrupole Max. Gradient	8.6	(T/m)	Number of Extraction Ports	2
Quadrupole Length	0.5	(m)	Number of Target Stations	2
Horizontal Tune	7.28			

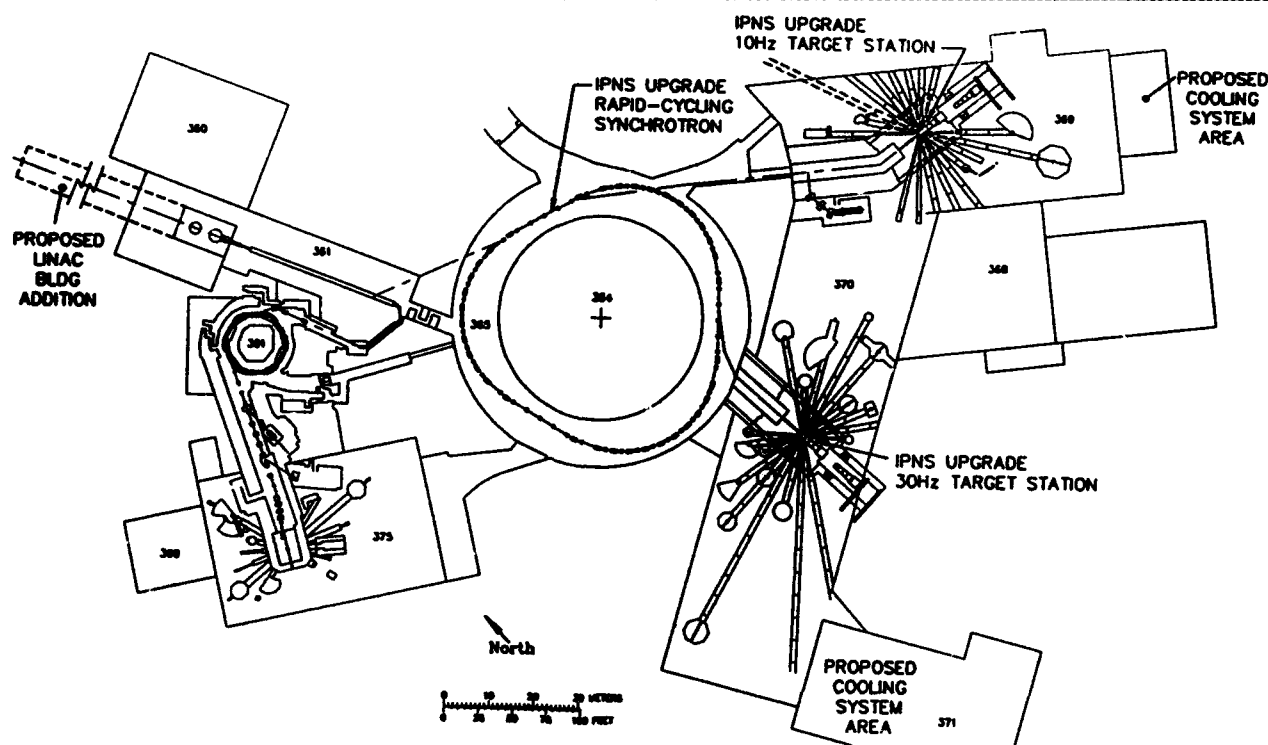


Figure 2. IPNS Upgrade Facility Layout

A Los Alamos Design Study for a High-Power Spallation-Neutron-Source Driver*

A. J. Jason, R. A. Hardekopf, R. W. Macek, S. O. Schriber, H. A. Thiessen, and R. Woods
Los Alamos National Laboratory
Los Alamos, NM 87545

Abstract

A design study for an accelerator-driven spallation-neutron source is underway at Los Alamos. The driver, based on the LAMPF facility, produces a 1-MW proton beam and is upgradable to 5 MW. After linear acceleration to full energy, an H^+ beam is accumulated for approximately 1.2 ms in an accumulator ring and then extracted to produce an intense proton burst, less than 1 μ s long, onto a spallation-target system with a 60-Hz pulse rate. The design uses existing infrastructure insofar as possible while maintaining project goals. This paper summarizes the system specifications and design status.

I. INTRODUCTION

Since the construction of the Los Alamos Proton Storage Ring (PSR) [1], there has been a strong program for neutron research at the Manuel Lujan, Jr. Neutron Scattering Center (LANSCE). The PSR was designed to provide 80 kW of beam power to the LANSCE spallation target. In view of a possible upgrade for this facility, we have undertaken a study to delineate a system capable of delivering 1 MW of beam power to an upgraded LANSCE facility with provision for a further increase in power to 5 MW. The project is known as the National Center for Neutron Research (NCNR).

The concept emerging from these studies features acceleration of H^+ ions to an energy of 800 MeV and subsequent multi-turn injection into an accumulator ring. The compressed pulse is then extracted in a single turn and transported to the spallation target.

In all the studies we have stressed reliability and low beam loss as well as technical performance.

II. GENERAL DESCRIPTION

The proposed scheme is shown in Figure 1. The existing side-coupled linac (SCL), which accelerates beam from 100 MeV to 800 MeV and comprises about 90% of the LAMPF linac, is retained as an integral part of the proposal. The present front end consists of three ion sources that provide H^+ , H^- , and polarized H^- accelerated by Cockcroft-Walton generators to 750 MeV. The three beams are merged, bunched, and matched to a 201.25-MHz drift-tube linac (DTL) for acceleration to 100 MeV. Our concept replaces the three sources with a single H^+ source capable of providing up to 40-mA peak current at 100 keV. Beam is then matched to a 402.5-MHz radio-frequency-quadrupole linac that bunches and accelerates beam to 7.0 MeV. The next stage of acceleration is provided by a 402.5-MHz DTL to 20 MeV and subsequent acceleration by an 805-MHz DTL to 100 MeV for matching into the 805-MHz SCL. The many choices in this specification involved considerations of beam dynamics, reliability, and cost. Additionally, the configuration can be upgraded in current by funneling into the 805-MHz DTL.

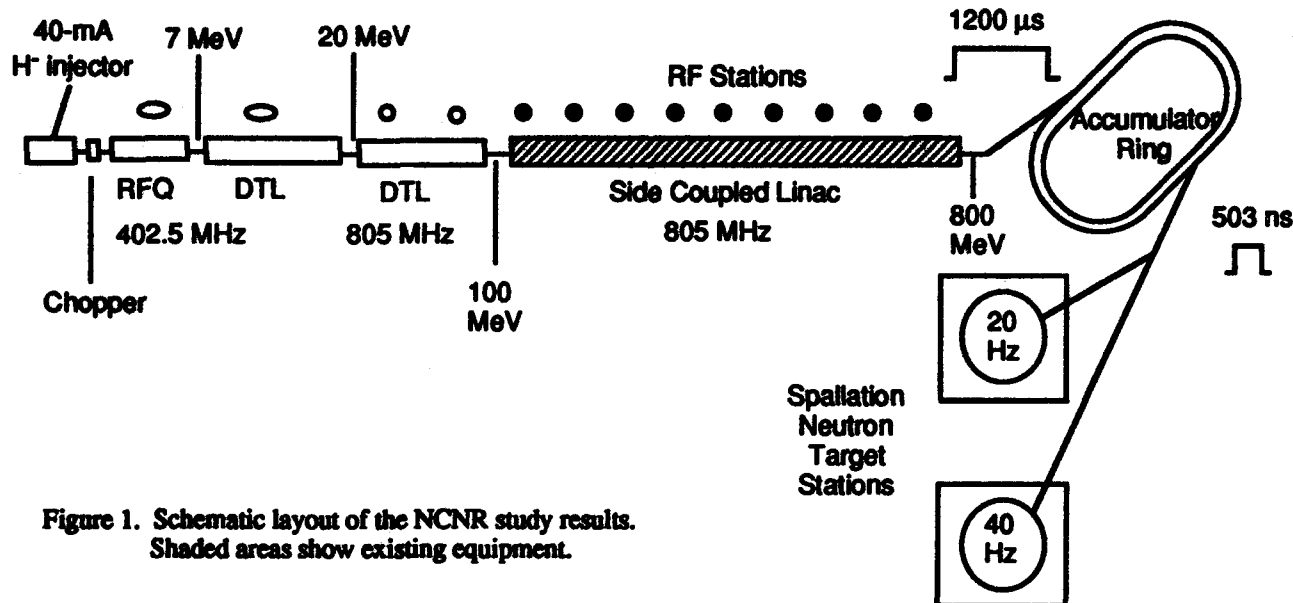


Figure 1. Schematic layout of the NCNR study results. Shaded areas show existing equipment.

*Work Supported by the US Department of Energy, Office of Defense Programs.

An achromatic transport line takes the beam north-east to the accumulator ring. The line also performs the function of dispersion scraping to remove off-momentum beam particles and contains magnets properly sized to avoid appreciable field stripping of the H⁻ beam. Beam is injected by single-stage stripping through a foil and, after accumulation for some 1790 turns, is immediately extracted. Beam is then transported to two spallation sources and inserted vertically upwards into the targets. Experiments at the neutron source generally require a regular pulse rate. Hence, pulsed equipment in the linac and ring must be capable of an 8.3 ms pulse repetition time to provide a uniform 20 and 40 Hz to the respective targets.

III. INJECTOR

Extensive development of high-current, high-brightness H⁻ ion sources has taken place at Los Alamos both for use at LAMPF [2] and for other projects such as the Ground Test Accelerator (GTA) [3]. We require currents near 40 mA with an rms normalized emittance of below 0.020π cm mrad and a duty factor near 9%. No existing ion source meets all these requirements although there are several applications for which one or more of the requirements has been exceeded. The 4X ion source developed for GTA has produced, for example, over 60 mA at about a third of the required emittance. However, the nominal duty factor for which it has been developed is 1%. The LAMPF ion source performs with adequate duty factor and emittance but produces a current of 20 mA. Similar comments also apply to sources developed at other institutions. With a modest development program, it is reasonable to extrapolate to the required performance.

A more difficult problem, for which no entirely satisfactory solution now exists, is that of chopping the beam at a 1.49-MHz rate (436 ns on, 235 ns off) to maintain an extraction gap in the compressor-ring stored beam. This is currently done for the PSR by a slow-wave deflector in the LAMPF injector region at 750-keV beam energy. Such a scheme will be difficult at the low matching energy of the RFQ in the NCNR scheme. Several other options are being explored, among them fast beam switching at a source plasma electrode with modest pulsed-power requirements.

IV. LINAC

Specifications for the linac are given in Table 1

Table 1
Linac Parameters

Average current	1.4 mA
Average power	1.4 mA x 800 MeV=1.12 MW
Peak current	30 mA
Repetition rate	20 + 40 Hz
Beam duty factor	7.2 %
Macropulse length	1.2 ms
Micropulse frequency	402.5 MHz
Chopping frequency, duty factor	1.49 MHz, 65%

The RFQ selected is similar to previous four-vane designs constructed or proposed at Los Alamos [4]. The high output energy of 7 MeV requires an unusual length of 6.9 m. The RFQ features an integral copper vacuum, rf, and structural envelope and is constructed in eight electroformed sections. Each pair of sections forms a loop-driven rf segment resonantly coupled to the others in a coupled-cavity structure. The average structure power is 140 kW with a peak power (including beam) of 1.54 MW. Proven tuning algorithms have been developed for this type of device. Dynamics calculations show that the structure will have over 95% transmission with an emittance of 0.02π cm mrad (rms normalized) at 38 mA.

The 402.5-MHz DTL is designed with two tanks and a total length of 5.43 m. Permanent-magnet quadrupoles are used in an FFDD configuration. Drift-tube bores are 1.8-cm diameter, approximately 10 times rms beam size. The DTL is similar to designs tested at Los Alamos on GTA and other projects. The total peak power needed is 1.48 MW. This is to be supplied by a two-tube klystron module with each tube providing a nominal 1.25 MW of rf peak power. Beam-dynamics calculations show little emittance growth with a test current of 38 mA.

The 805.0-MHz DTL is similarly constructed with a total length of 54.7 m and consists of 15 tanks. The lattice is a FFFOODODDOOO configuration using 1.8-cm-bore permanent-magnet quadrupoles. From our loss estimates and extensive testing of magnetic material, we do not believe that radiation-induced deterioration of the magnets will be appreciable over a period of many years. The ratio of aperture radius to beam rms size is greater than the factor of seven generally used at LAMPF as a "safe" value. Beam-dynamics calculations show small emittance growth with a current of 75 mA. The total peak rf power required is 5.8 MW to be supplied by a klystron module similar to that used for the 402.5-MHz DTL.

Matching between the four linac sections is done transversely with variable permanent-magnet quadrupoles and longitudinally with pairs of buncher cavities. The buncher systems require a total of 50-kW peak power and are supplied by six tetrode-driven supplies.

Studies and experimental results have shown that the LAMPF SCL (100 to 800 MeV) is quite adequate for NCNR purposes. Note that the LAMPF facility has functioned as a provider of beam at 1-MW levels at a repetition rate of 120 Hz with a micropulse frequency of 201.25 MHz. At these levels, it operates under low stress and has had a long history of high reliability. Our proposal nearly doubles the peak current. However, the increase in micropulse frequency to 402.5 MHz results in a similar charge per beam bunch; the single-bunch beam dynamics is hence unchanged. Because of the 65% chopping duty factor, the peak-average current is 19.5 mA, slightly above the present nominal current of 17 mA. Total peak power is then nearly 41 MW, to be supplied by the existing 44-klystron system. Taking into account the ratio of total supplied power to structure losses ($\sim 4/3$), the additional average power to be supplied is some 4%, well within the present rf-system reserve capacity. Hence, no substantial upgrade is needed.

A remaining question is the SCL response to the chopping pattern. Beam to the PSR is currently supplied at about one-third the NCNR peak-current requirement and at twice the chopping frequency with no perceived perturbation to performance. Combined structure and beam-dynamics calculations show that, under NCNR conditions, the cavity fields will vary uniformly in each tank by about 1% during the chopping cycle but will have little effect on beam quality. This point will be tested in an upcoming series of experiments. Further discussion of the linac stability is found elsewhere in these proceedings [6].

Recent advances in fast adaptive feed-forward control techniques [7], proven on operating systems, will be very useful in achieving low-loss beam control in the linac and will soon be tested on the SCL. Studies are underway for high-current adaptations to tuning techniques such as the Δt method. Programs are also in place to study halo growth and develop techniques that minimize beam loss [8].

V. ACCUMULATOR RING

The accumulator ring will be given short treatment here; it is described more extensively in an accompanying paper [9]. The major parameters are however listed in Table 2.

Table 2
Accumulator-Ring Parameters

Ring circumference	168.9 m
Accumulated turns	1790
Extracted-beam-bunch length	503 ns
Stored protons	1.3×10^{14}
Peak stored current	57 A
Average extracted current	1.25 mA

The ring is designed in a racetrack configuration as implied by Figure 1 and has dispersionless straight sections and arcs configured as second-order achromatic bends. Injection is non-Liouvillian with a single-stage foil-stripping process and has an efficiency of better than 90%. First-turn losses by field stripping of excited neutrals are minimized by placing the foil in a specially configured magnetic field. Injection painting is done to minimize foil interaction and to control the transverse distribution. This, along with an adjustable chromatic contribution to Landau damping and introduced anharmonicities, is used to control ring stability by tune-spread damping. A clean extraction gap is maintained by a five-harmonic barrier bucket to minimize extraction losses and to avoid the electron-proton instability as well as to provide adequate matching to the injected-beam longitudinal phase-space structure. The injected beam is swept in energy to control the longitudinal distribution. High-order studies are underway to assess space-charge nonlinearities and to map the tune space spanned by the beam. Correction of high-order stop bands will be done by introduction of nonlinear elements. A continuing program of theoretical and experimental studies is underway to refine the design. Here we are particularly challenged to maintain low losses ($<10^{-3}$) and the design will include halo collimators.

VI. UPGRADE OPTIONS

Although the major thrust of our study has been toward the 1-MW scenario, several options have been proposed for an upgrade to 5 MW and we have included features needed by these options in our design. The new linac front end is highly adaptable to funneling for increasing the current by the needed factor of 5 if a final energy of 800 MeV is retained. In this case further work is needed to establish the current-carrying capacity of the SCL and a multiple ring system would be needed.

The alternative, a higher beam energy of up to 2 GeV, is very attractive. Here a single ring, but with a substantially different lattice, appears feasible. Replacement of the CCL with a superconducting linac would use the existing LAMPF infrastructure and would ensure insensitivity to the chopping pattern that poses problems for a low-stored-energy room-temperature structure. Studies on upgrade alternatives are continuing.

VII. ACKNOWLEDGMENTS

We wish to thank the many individuals from LANSCE and AT and MP Divisions who contributed to this study.

VI. REFERENCES

- [1] G. P. Lawrence, R. A. Hardekopf, A. J. Jason, P. N. Clout and G. A. Sawyer, "Los Alamos High-Current Proton Storage Ring; a Status Report," *IEEE Trans. Nucl. Sci* NS-32, No. 5, 2662 (1985).
- [2] R. York, D. Tupa, and D. Swenson, "Volume H⁻ Source Development at LAMPF," these proceedings.
- [3] H. V. Smith, J. D. Sherman, P. Allison, "Pulsed H⁻ Ion Beams from Penning SPS Sources Equipped with Circular Emitters," *Proceedings of the 1988 Linear Accelerator Conference*, Newport News, October, 1988, p 164.
- [4] L. Young, "Segmented Resonant Coupled Radio Frequency Quadrupole," these proceedings.
- [5] K. Johnson, et al., "Commissioning of the First Drift Tube Linac Module in the Ground Test Accelerator," these proceedings.
- [6] M. Lynch, et al., "Linac Design Study for an Intense Neutron-Source Driver," these proceedings
- [7] C. D. Ziomek, "Adaptive Feedforward in the LANL RF Control System," *Proceedings of the 1992 Linear Accelerator Conference*, Ottawa, August, 1992, p 685.
- [8] R. Jameson, "Design for Low Beam Loss in Accelerators for Intense Neutron Applications," these proceedings.
- [9] B. Blind, A. J. Jason, F. Neri, "Lattice Design of the LANL Spallation-Source Compressor Ring," these proceedings.

ON THE HIGH INTENSITY ASPECTS OF AGS BOOSTER PROTON OPERATION*

R.K. Reece, L.A. Ahrens, E.J. Blester, J.M. Brennan, C. Gardner, J. W. Glenn, T. Roser,
Y. Shoji,¹ W. vanAsselt, W.T. Weng
AGS Department, Brookhaven National Laboratory
Upton, NY 11973

SUMMARY

Observations of high intensity effects on the proton performance of the AGS Booster are presented, including present operational limits and correction methods. The transverse emittances, optimum tune working points, damping of coherent transverse oscillations and correction of stopband resonances through third-order are discussed in addition to the observed tune spread due to space charge forces. The initial longitudinal phase space distribution, capture and acceleration parameters and measurements are also given. Operational tools and strategies relevant to the high intensity setup are mentioned.

OVERVIEW OF ACCELERATOR

The present high intensity proton mode of operation of the Booster synchrotron is as a rapid cycling (5Hz) machine which accepts the 200 MeV Linac beam and delivers a nominal 1.5 GeV beam to the AGS accelerator. The Booster circumference was designed to be $\frac{1}{4}$ that of the AGS so that four Booster cycles fill the AGS. By requiring the extraction rf frequency of the Booster to be the same as the injection rf frequency of the AGS (with the ratio of harmonic numbers = $\frac{1}{4}$), precise bunch to bucket transfer is achieved. Details of early commissioning have been given in previous proceedings [1,2].

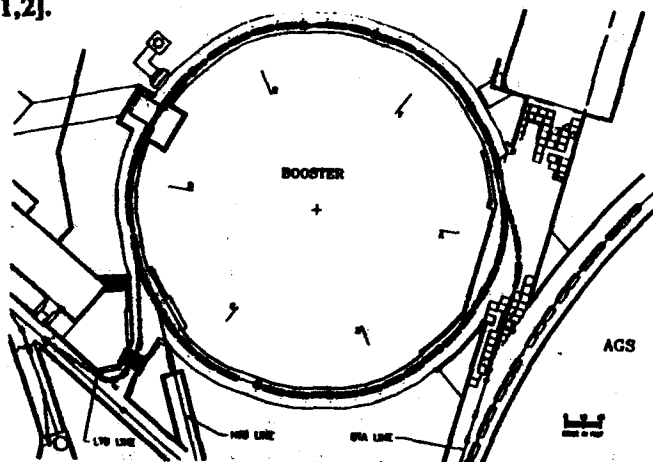


Figure 1. Booster layout.

*Work performed under the auspices of the U.S. Dept. of Energy.

¹Permanent address, KEK.

INJECTION STRATEGIES

Injection of the Linac H^- beam is accomplished using a 200 μg carbon stripping foil in the Booster vacuum chamber. This foil is located to the inside (small radius) of the machine. The beam from the Linac is initially matched to the Booster lattice and steered onto the locally distorted equilibrium orbit at the foil using the transfer line magnetic elements. The transverse emittance roughly doubles during this process which leaves it still small (12π mm-mr, 95% normalized) relative to the Booster aperture (80π mm-mr) and also relative to the emittance needed for high intensity acceleration.

The local orbit distortion is obtained using four fast injection ring magnets that allow orthogonal time-dependent position and angle control of the equilibrium orbit at the injection point. This bump is used to compensate for the -12.3mm radial motion of the orbit at the foil during the 250 μs injection period caused by the 3T/sec dB/dt at injection, and to relax the orbit away from the foil after injection. An additional slow outward bump assures that the equilibrium orbit is completely off the foil once the fast bump has collapsed.

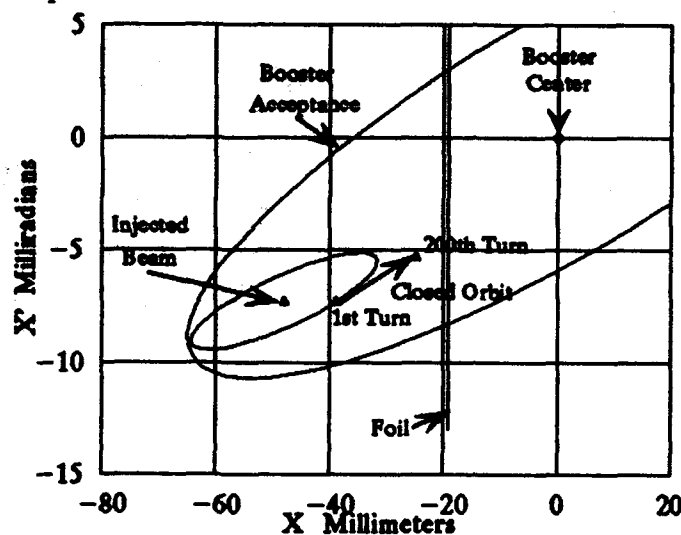


Figure 2. Booster injection phase space showing the component of closed orbit motion due to the fast injection bumps.

In order to minimize the emittance growth due to multiple passes through the foil, the fast bump is trimmed to offset the equilibrium orbit slightly toward the outside edge of

the foil (relative to the incoming beam). This process was quantified using absolute injected beam position from a PUE located immediately downstream of the foil, and trajectory (relative to the equilibrium orbit) information from the on-line analysis of digitized multiturn data from a second PUE [3]. Both of these measurement techniques have continued to give valuable benchmarks for operations in maintaining stable injection conditions.

LONGITUDINAL CONSIDERATIONS

The rf cycle begins with bunch-to-bucket injection of the fast chopped Linac beam into a moving 1.4 eV-s bucket at 3T/sec with 90 kV of rf voltage. The energy distribution of the 200 MeV H⁻ Linac beam was measured by bunch rotation in a mis-matched bucket to be $\Delta p/p = \pm 3 \times 10^{-3}$ for 90% of the beam. This energy spread, together with the change in synchronous energy of the moving bucket for the 250 μ s injection pulse length is approximately equal to the bucket height. The result is an essentially uniformly filled bucket, leading to a bunching factor (average/peak current) of 0.47. Figure 3 shows a mountain range oscillograph of a longitudinal pickup for the first 3 ms of the cycle. Using the maximum available rf voltage at injection alleviates beam loading problems and provides a capture efficiency of > 80%.

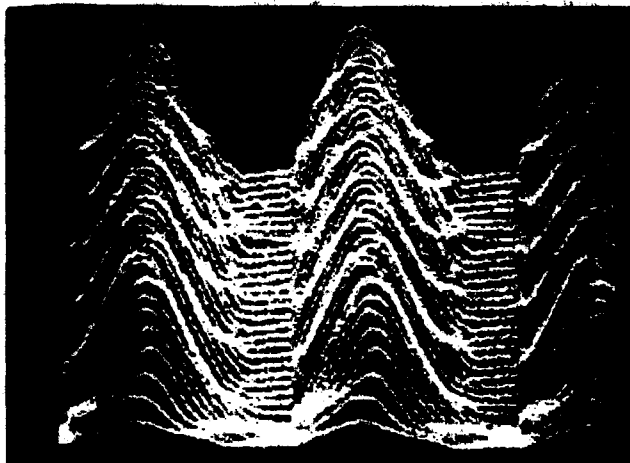


Figure 3. Mountain range through the capture process.

TRANSVERSE CORRECTION

Much of the control of the Booster machine parameters is done from a high level perspective. The main dipoles and quadrupoles are powered in series from the Main Magnet power supply. Bare machine functions (e.g., tune and chromaticity) have been measured as a function of main field and dB/dt. Variations of the bare tunes simply scale with (dB/dt)/B. An overlay of incremental tune and chromaticity can be mapped onto these bare machine functions allowing the user to deal only with the final tune. The uncorrected machine closed orbit is nearly field independent. Correction of the transverse closed orbit distortions is accomplished by measuring the orbit harmonics (primarily 4th, 5th and 6th) and

correcting them at one momentum, usually at or near injection. These corrections are then scaled programmatically with the main guide field B(t) function to extrapolate and correct throughout the cycle.

Second and third order stopband corrections have been successfully parameterized as simple functions of B, dB/dt and radial position through extensive study with low intensity beams on main magnet cycles tailored to give a variety of time dependences[4]. This work also identified two potentially important third order lines driven by skew sextupole fields which were not originally correctable, but for which corrections have been added to the lattice, allowing the stopbands to be efficiently compensated for.

The injection dB/dt was increased to 3T/sec (a factor of five over that used last year) and the transition to full dB/dt (7T/sec) was shortened to reduce the time spent at lower energies (largest tune spreads) in order to reduce the impact of the peripheral stopbands on the beam.

HIGH INTENSITY TECHNIQUES

For high intensity operation, the transverse aperture of the machine is fully utilized at injection. The differentiation of beam loss due to the transverse and longitudinal techniques invoked to get to high intensity (e.g., fast bump program, rf voltage and radial steering programs) from losses driven by the high intensity itself (e.g., stopband losses far from the operating point, rf beam loading) is critical in refining these techniques. An invaluable aid in defining this separation is the 750 keV chopper [5], the primary function of which is to "chop" the Linac beam "in time" to fit into the Booster RF buckets. This chopper can also eliminate a precise fraction of this pre-bunched beam altogether and therefore reduce the intensity while preserving the overall time development of the injection process. In this mode, the rf chopper behaves like a "longitudinal sieve". See Figure 4. By reducing the normal 200 turn injection to 20 dilute turns, non-intensity dependent beam loss sources were cleanly identified. Alternately, this rf chopper permits injection of a few turns at any time during the injection interval which then allows observation of the survival of that part of the process; again, in the absence of high intensity effects.

With the tools available, it has been possible to define operationally starting values for the injection trajectory, injection field, injection fast bump program, and rf capture parameters independent of intensity measurements. Stopband corrections were also defined from low intensity studies. These setups have required little adjustment when intensity optimization is added as a constraint.

Referring again to the injection trajectory match, experiments are in progress to explore the intentional mismatch of the injection and equilibrium orbits, leading to a known transverse dilution or "smoke ring". While this is expected to be more effective in the vertical plane, it has been applied to the horizontal plane as a by-product of reducing foil losses. Documentation of the beam size throughout the cycle

was done using the Ionization Profile Monitor (IPM), and a low intensity benchmark was established to be compared to in the high intensity cases. Preliminary results indicate that although the initial emittance is larger with the "smoke ring" configuration, emittance growth at high intensities may be less and lead to a net smaller emittance at extraction.

BOOSTER MORE - LEFT FAST CHOPPER Wed May 5 13:17:43 1993
 V_{core}: 85.0 KeV/turn I_{dot}: 3.2 I/sec Inj turns: 200 I_{beam}: 20.000 mA
 K.E.: 200.0 MeV F_{dot}: 35.2 kHz/sec phi_i: 110.0 deg
 Moving Bkt Bunch Stationary Bkt
 Area: 1.23 eVns 1.14 eVns 1.62 eVns phi_{stable}: 5.96 deg
 Height: 2.95 MeV 2.83 MeV 3.22 MeV
 Height: 13.85 kHz 12.50 kHz 14.22 kHz delta R: 0.01 cm
 Injection time: 236.7 msec Synch Freq: 7.000 kHz #Synch osc: 1.00
 Fill fraction: 31.2 % of bunch height #inj particles: 1.95e+12

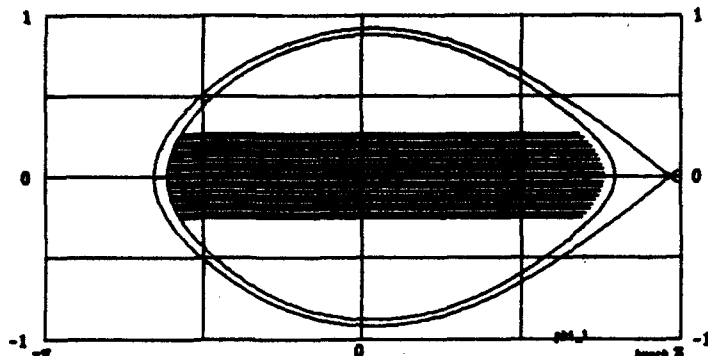


Figure 4. Longitudinal phase space: "dilute" population of 20 turns injected over the period of 200 turns.

The ability to damp transverse coherent instabilities has been incorporated into the Booster and is discussed elsewhere in these proceedings [6]. First evidence of these instabilities has been seen at an intensity of 5-7TP with the vertical chromaticity set to -0.25 and a vertical tune of 4.94. At this intensity, the instability was eliminated by decreasing the chromaticity toward -1.

With an injected beam intensity of 1.5×10^{13} protons, 9×10^{12} protons have been accelerated to extraction energy. To achieve this intensity it was necessary to move the vertical betatron tune up to near the integer ($Q_v = 4.94$) during the early part of the acceleration cycle (bare machine tunes are $Q_{H,V} = 4.6$). A calculation of the incoherent tune spread using the relation below [7] yields a value of 0.3 with the following parameters; $r_p = 1.535E-18m$, $N = 9E12$ protons, $e_N(95\%) = 60 \pi$ mm-mr, $\beta = 0.5662$, $\gamma = 1.2132$ and B (bunching factor) = 0.47. It is assumed for this estimate that the beam is round and has a Gaussian density distribution where the emittance enclosed 95% of the beam.

$$\Delta Q = \frac{3 r_p N}{2\pi e_N(95\%) \beta \gamma B}$$

Given the nominal working point and that most of the 2nd and 3rd order stopbands in the operating quadrant of tune space are corrected (linear coupling is small and corrected), and that there was an uncorrected stopband at $Q_v = 4.67$,

beam loss at intensities greater than 9×10^{12} protons is consistent with that expected from the incoherent tune spread of this high intensity beam.

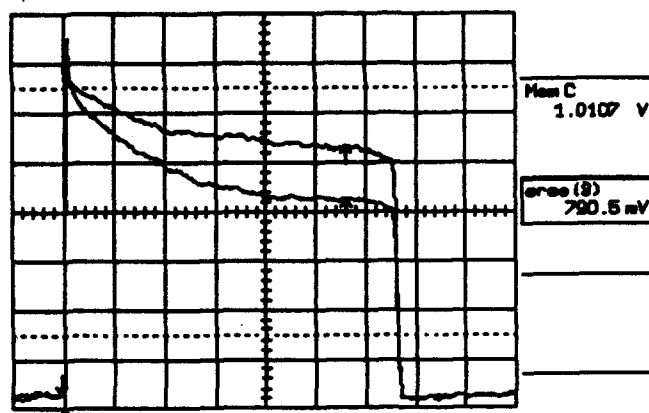


Figure 5. Circulating beam intensity (10 ms/div.) with and without a particular stopband correction applied. Upper trace yields 9.6 TP late in the cycle.

ACKNOWLEDGMENTS

The progress made in improving our understanding of the high intensity Booster came as a result of more than two months of totally dedicated study time this spring. The AGS Operations Group under A. McNerney and P. Ingrassia participated actively in the study work itself, in preparing and maintaining the machines, and in coping with the safety environment. The continuing enthusiastic involvement of several of the Booster designers and builders including G. Danby, Y. Y. Lee, and A. Soukas provided ideas and solutions as problems became defined. The entire exercise was only possible due to the administrative and scientific support of the AGS Department Chairman D. Lowenstein.

REFERENCES

- [1] L. Ahrens, et al., "The Operational Status of the Booster Injector for the AGS Accelerator Complex at BNL", XVth Int. Conf. on H.E. Accel., Hamburg, Germany, July 1992, pp. 109-111.
- [2] W.T. Weng, "Operation of the Brookhaven AGS with the Booster", these proceedings.
- [3] C. Gardner, L. Ahrens, "A Method for Determining the Position, Angle and Other Injection Parameters of a Short Pulsed Beam in the Brookhaven AGS", 1985 IEEE PAC Conf. Proc. pp. 1888-1890.
- [4] C. Gardner, et al., "Observation and Correction of Resonance Stopbands in the AGS Booster", these proceedings.
- [5] J.M. Brennan, et al., "A Fast Chopper for Programmed Population of the Longitudinal Phase Space of the AGS", 1989 IEEE PAC Conf. Proc., pp. 1154-1156.
- [6] D. Russo, et al., "Results from the AGS Booster Transverse Dumper", these proceedings.
- [7] L.J. Laslett, "On Intensity Limitations Imposed by Transverse Space Charge Effects in Circular Particle Accelerators", BNL-7534 (1963).

RESULTS FROM COMMISSIONING THE AGS BOOSTER ORBIT SYSTEM*

E. Bleser

AGS Department, Brookhaven National Laboratory
Upton, NY 11973

I. INTRODUCTION

This note reports results from the commissioning of three systems in the AGS Booster [1]: the beam position monitor system, which works to a relative accuracy of 0.36 millimeters; the uncorrected Booster orbit, which has quite large excursions; and the passive eddy current correction system, which eliminates all but a few percent of the eddy current dipole effect.

II. RESULTS FROM THE BEAM POSITION MONITOR SYSTEM

Figure 1 shows an uncorrected orbit in the Booster as measured by the beam position monitor (BPM) system [2]. It has excursions of ± 15 mm where ± 5 mm would have been excessive. This orbit is fully correctable by the steering magnet system so it is not deleterious to machine operation but it does raise several questions as to the validity of the BPM system, the quality of the magnets, and the accuracy of the survey. In a new machine all problems are possible.

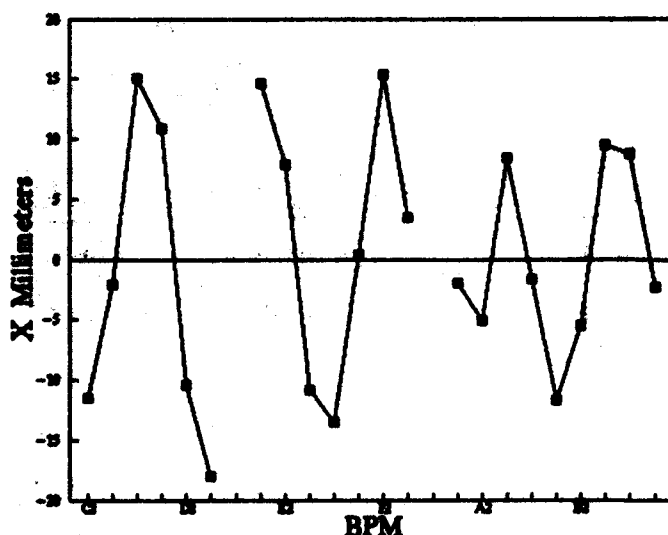


Figure 1.

A measurement of the uncorrected orbit of the proton beam in the AGS Booster. BPM's D6 and F6 do not exist because of the requirements of the dump and extraction systems.

*Work performed under the auspices of the U.S. Dept. of Energy.

In order to check out the BPM system the four extraction bump magnets were each powered individually and a difference orbit was found by subtracting the unperturbed orbit from the bumped orbit. A typical result is shown in Figure 2.

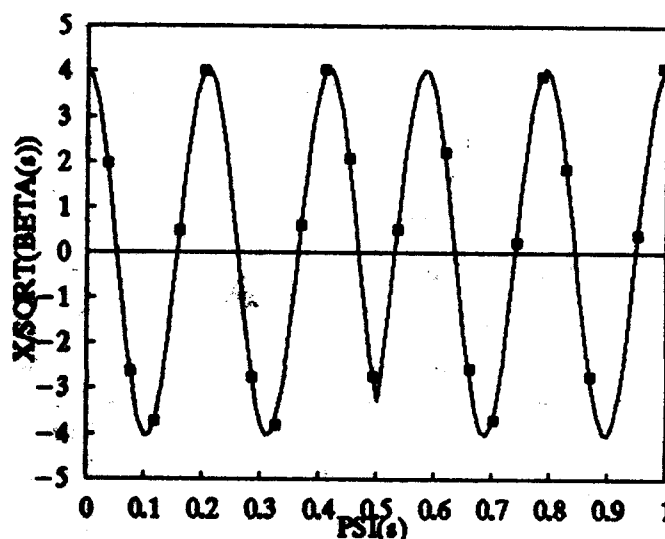


Figure 2.

A difference orbit showing the effect of a bump magnet. The Y-axis is the difference, X , in millimeters divided by the square root of the local Twiss beta function in meters. The X-axis is ψ , the phase advance around the machine divided by $2\pi Q$, where Q is the tune. The bump magnet is located at $\psi = 0.5$. The formula: [3] $X(s) = K \cos(2\pi Q \cdot \psi)$ is fitted over the range $-0.5 < \psi < +0.5$.

We can assume that the output of a BPM is given by:

$$X = a + b \cdot x$$

where a and b are constants, preferably 0 and 1, and x is the actual position of the beam in the BPM. We can evaluate each BPM by powering each of the four magnets at two different currents, assuming the actual beam position, x , is that given by the curve fitted to all twenty-two points, and then compar-

ing the measured position against that called for by the fit. Figure 3 shows a typical result. In sum the BPM's are linear over a range of ± 25 mm, the average value of b is $1.006 \pm .03$, and for difference orbits the BPM measures a change in position to an accuracy of 0.36 mm. In addition this process calibrates the extraction bumps in situ to an accuracy of 1%.

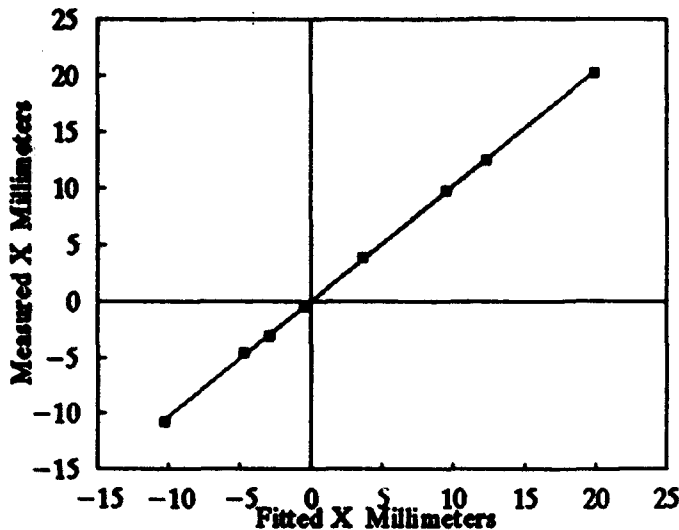


Figure 3.

A plot for one BPM of X measured for various bumps versus the beam position predicted by fitting the formula of Figure 2 to all 22 BPM's.

III. EDDY CURRENT EFFECTS

We can conclude that the BPM system is very good for difference orbits but we still do not have any information on the absolute orbit, shown in Figure 1, which can have many possible sources - field errors, survey errors, or offset terms, a , in the BPM's. Before pursuing this question we can evaluate the absolute orbit as a function of magnetic field strength, B , and as a function of rate of change of field, dB/dt .

The Booster is a rapid cycling machine, going from 600 to 5000 gauss in 60 milliseconds, and it has stainless steel vacuum chamber in the field. To compensate for the high eddy currents produced in the vacuum chamber, a passive correction system [4] has been installed which consists of field windings placed on the chamber, which windings are powered by windings around the magnet poles. The system is designed to balance the sextupole component induced by currents in the vacuum chambers. Thus there are four contribution to the dipole field: 1. The main field of the magnets, by far the largest; 2. The dipole field produced by the currents induced in the vacuum chamber, which retards the main field; 3. The dipole field produced by the currents induced in the windings around the magnet poles, which also retards the main field; 4. The dipole field produced by the windings placed on the

vacuum chamber, which are connected so as to add to the main field. As long as these effects are uniform from magnet to magnet they are of no consequence and there should be no observable orbit dependence on dB/dt . However, comparing orbits at two different values of dB/dt gives the result shown in Figure 4, a significant effect. The orbit can be nicely fit by assuming a dipole, proportional to dB/dt , located at the injection magnet, a special magnet with a special vacuum chamber. Subsequent, unrelated work discovered that the correction system for this special case was miswired. After fixing this case there still remained a small dependence on dB/dt , which we attribute to random errors in the eddy currents. In particular for the Booster this orbit corresponds to random bend errors of 0.01 milliradians or .2 Gauss. Table 1 summarizes the expected eddy current fields. We can conclude that the individual elements are good to 3% to produce this small an orbital effect. These effects are not significant for the Booster orbit but they do enable us to project that the eddy current sextupoles are corrected to 3%.

Table 1.
DIPOLE EDDY CURRENT FIELDS

SOURCE	FIELD GAUSS
Vacuum Chamber (7 G/ms)	-20
Correction Winding	+ 5
Random Error from Orbit	0.2

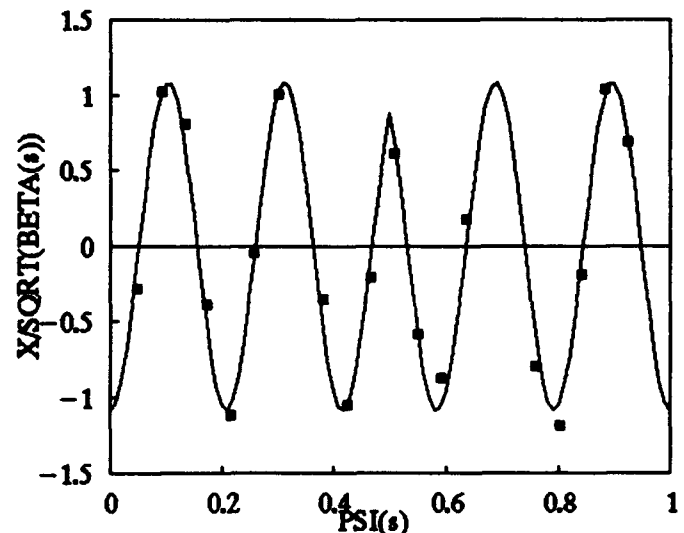


Figure 4

A difference orbit comparing uncorrected orbits as in Figure 1 taken at dB/dt values of 5 G/ms and 70 G/ms. The original orbits look quite similar and a significant difference becomes apparent only on subtraction. The curve is generated as in Figure 2 by assuming a bump at the injection magnet.

IV. CONCLUSION

Because several aspects of the orbit were easily explained, a fair effort was made to find a simple source for the orbit of Figure 1, but without success. In the Booster design manual, random survey errors for quadrupoles of 0.3 millimeters rms were assumed and 20 random distributions were calculated. The worst result is shown in figure 5, and it agrees remarkably well with our measured orbit. Apparently the simplest explanation for our observed orbit is that the random alignment errors have occurred in such a way that we have built a machine with an orbit in the fifth percentile. To maintain our professional pride we shall realign it in the next major shutdown, and hope that the gods of chance are more favorably disposed toward us.

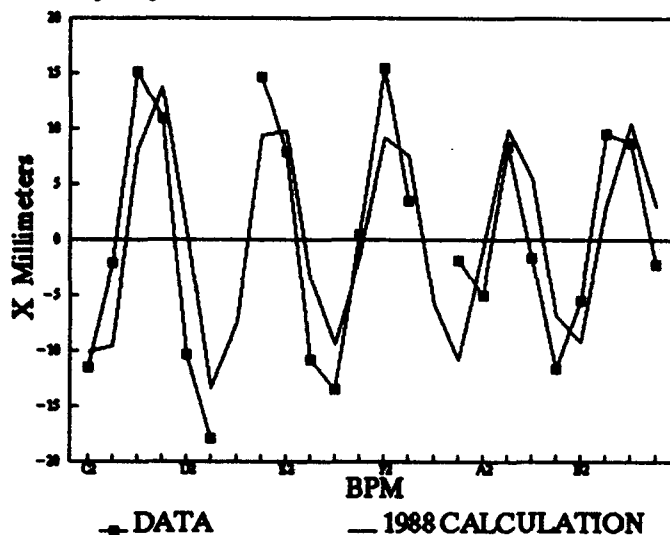


Figure 5.

The measured data of Figure 1 plotted along with a curve generated in the 1988 design study which assumed a random distribution of survey errors. The conclusion is that the measured orbit could well result from a random distribution of survey errors, which were within our rms tolerances of 0.3 millimeters.

REFERENCES

- [1] W.T. Weng, "Operation of the Brookhaven AGS with the Booster", these proceedings.
- [2] D.J. Ciardullo et.al, "Design and Performance of the Booster Beam Position Monitor System", Proc. XVth Intern. Conf. High Energy Accelerators, Hamburg, Germany, July 20-24, 1992, Ed. J. Rossbach, Int. J. Mod. Phys. A, 2A, Vol. I, 245-247 (1993).
- [3] E. Wilson, "Transverse Beam Dynamics", p.78; CERN Accelerator School, CERN85-19, Geneva, 1985
- [4] G. Danby and J.W. Jackson, "Vacuum Chamber Eddy Current Self-Correction for the AGS Booster Accelerator", Proc. XIV Intern. Conf. High Energy Accelerators, Tsukuba, Japan, August 22-26, 1989, Ed D. Keefe, Particle Accelerators 27, Part II, 33-38 (1990).

The Effect of Global Survey Misalignment on the SSC

T. Garavaglia, N. Mahale, and J. Peterson
Superconducting Super Collider Laboratory*
2550 Beckleymeade Ave., Dallas, TX 75237 USA

Abstract

Survey errors in the global alignment of the SSC can affect its performance. These errors can result in an uncertainty in the circumference of the Collider, and this can produce a mismatch in the transfer of bunches from the HEB to the SSC. An uncertainty in the half-circumference of the Collider will reduce the luminosity. To estimate this effect, an expression is given for the luminosity as a function of crossing angle and half-circumference difference. In addition, estimates are given for closed orbit distortion, vertical dispersion, and tune shift, resulting from circumferential errors. Suggestions are made for correcting the effects resulting from global survey errors. Further details may be found in [1].

I. INTRODUCTION

Performance of the Superconducting Super Collider (SSC) will require precision in global and local survey consistent with the survey precision required of individual components guiding the beam. Local transverse misalignment gives rise to a closed orbit error and a tune shift, and these effects should be within the range of the correctors. Survey errors also lead to an error in the circumference of the Collider, which has two consequences. The first is a mismatch in the circumferences of the High Energy Booster (HEB) and the Collider. Either this has to be compensated by moving the orbit of the HEB or the concomitant increase in longitudinal emittance has to be acceptable. The second is an error in the location of the detectors (half-circumferential error) on opposite sides of the ring. The bunch crossing, if perfect on one side, will be mismatched on the other side, and this will lead to a reduction in luminosity, which has to be corrected by moving the interaction point where the mismatch occurs.

There are two principal contributions to survey errors. The first is the uncertainty in the location of the principal survey monuments, approximately 4.3 km apart, at the tunnel level. This uncertainty, resulting from the Global Positioning System and transfer to the tunnel level, is of the order $3\sigma \sim 15(22)$ mm, with(without) sight pipes. The second is the positioning of the secondary monuments. Between the principal transfer monuments there are secondary monuments spaced at 30 m to 45 m apart. The

locations of the secondary monuments have random errors with $\sigma \sim 0.5$ mm. Even after the initial survey, other misalignment errors can occur. Tunnel survey shows that the LEP transverse alignment is deteriorating approximately 140 μ m per year [2]. In addition there can be a systematic radial error, as observed in HERA [3], due to horizontal refraction during angular measurement and inaccuracies in the self-centering of the theodolite and targets. This error, maximum value for HERA being 16 mm, is estimated to be 30-50 mm for the SSC.

II. CIRCUMFERENTIAL ERRORS

The arc length between two transfer monuments can be represented by

$$S(\theta_0) = \int_0^{\theta_0 \pm \delta\theta_0} \rho(\theta) [1 + (\frac{d\rho}{d\theta}/\rho(\theta))^2 + (\frac{dz}{d\theta}/\rho(\theta))^2]^{1/2} d\theta, \quad (1)$$

with radius $\rho(\theta) = \rho_0 + \epsilon_1 + \epsilon_2 \sin(\pi\theta/\theta_0)$, where ϵ_1 (radial) and $\delta\theta_0$ (angular) are random errors, and ϵ_2 is the maximum systematic radial deviation. To first order, the error in the part of the circumference between two monuments is,

$$\Delta C(\theta_0) = \pm[(\epsilon_1\theta_0)^2 + (\rho_0\delta\theta_0)^2]^{1/2} \pm 2\epsilon_2\theta_0/\pi, \quad (2)$$

where $\theta_0 \sim \pi/N$ for N transfer monuments in each arc. The total uncertainty in the circumference resulting from the two Collider arcs is at least

$$\Delta C_{arcs} = \pm(\sqrt{2N}[(\epsilon_1\theta_0)^2 + (\rho_0\delta\theta_0)^2]^{1/2} \pm 4\epsilon_2). \quad (3)$$

With $\rho_0\delta\theta_0 \sim \epsilon_1\theta_0$, and $\epsilon_2 = 0$, (3) gives

$$\Delta C_{arcs} = 2\pi\epsilon_1/\sqrt{N}. \quad (4)$$

For $N = 8$, and $\epsilon_1 = 3\sigma$, one finds at the three sigma level $\Delta C_{arcs} = 33(49)$ mm, with(without) sight pipes. The random error could be reduced with additional transfer monuments. The systematic errors, however, could be the major source of circumferential error. For the case with $\epsilon_2 = 30 \rightarrow 50$ mm, one finds a systematic circumferential error $4\epsilon_2 \sim \pm(120 \rightarrow 200)$ mm, which should be added to the random error.

In a straight section, the ideal distance between transfer monuments is R_1 . If one assumes an error vector \vec{a} at each ideal location, then the vector distance between monument locations i and j is $\vec{r} = \vec{R}_1 + \vec{a}_i - \vec{a}_j$. When averaged over

*Operated by the Universities Research Association, Inc. for the U. S. Department of Energy under Contract No. DE-AC35-80ER40498.

the angles between the vectors, one finds the change in the distance between transfer monuments to be

$$r - R_1 \sim \frac{a^2}{R_1}. \quad (5)$$

For each straight section, the maximum systematic distance error resulting from the misalignment of N_1 pairs of transfer monuments would be $N_1 a^2 / R_1$.

Between the transfer monuments, there are secondary monuments spaced at $R_2 \sim 30$ m apart. For N_2 pairs of secondary monuments with error vectors \vec{b} , the estimated distance error would be $N_2 b^2 / R_2$. For both straight sections, the change in the circumference of the Collider resulting from systematic monument alignment error, would be

$$2N_1 a^2 / R_1 + 2N_2 b^2 / R_2.$$

For random alignment errors, N_1 and N_2 are replaced with $\sqrt{N_1}$ and $\sqrt{N_2}$, respectively. For values $a = 10$ mm, $b = 1.0$ mm, $R_1 = 4.3$ km, $R_2 = 30$ m, $N_1 = 20$, and $N_2 = 72$, there is a one sigma circumferential uncertainty of $\Delta C_{\text{systematic}} = 4.9 \mu\text{m}$ and $\Delta C_{\text{random}} = 0.63 \mu\text{m}$.

III. CLOSED ORBIT ERROR

The closed orbit error due to transverse misalignment for N transfer monuments can be estimated from the formula, applicable to both transverse directions,

$$\Delta x_{rms} = \frac{\beta_{max}^{1/2} (\beta_{max} + \beta_{min})^{1/2}}{2\sqrt{2}\sin(\pi\nu)} [\theta_{rms}] \sqrt{N/2}, \quad (6)$$

where θ_{rms} is the rms angular deflection resulting from monument alignment errors, and ν is the machine tune. With a three sigma alignment error, the deflection angle would be

$$\theta_{rms} = \frac{\sqrt{2} \times 3\sigma}{(C/N)}. \quad (7)$$

With $N = 20$, one finds $\theta_{rms} = 4.8(7) \mu\text{rad}$, with(without) sight pipes. For $\beta_{max} = 305$, $\beta_{min} = 54$, $\nu = 123.28$, and $N = 20$, one finds the random closed orbit error $\Delta x_{rms} = 2.3(3.4)$ mm, with(without) sight pipes, at the three sigma level for monument alignment errors.

As a result of surveying methods, systematic tilt errors in the alignment of the magnets are not expected; however, there is a possibility of systematic radial alignment error in the location of the monuments and the magnets. If there is a transverse systematic radial change along the ideal orbit of the form $\rho = \rho_0 + \epsilon_2 \sin(\pi s / s_0)$, where s is the ideal orbit length and s_0 is the length over which the systematic error of maximum deviation ϵ_2 occurs, then the angle which must be corrected is

$$\theta_c \sim 2d\rho/ds|_{\theta=0} = \epsilon_2 2\pi / s_0. \quad (8)$$

For $s_0 = 4.3$ km and $\theta_c \sim 45 \mu\text{rad}$, this permits a maximum deviation of $\epsilon_2 \sim 30$ mm. There are corrector magnets in each cell to correct for this effect.

If there is a systematic uncertainty in the vertical alignment of the transfer monuments, a vertical correction bend of order

$$\theta_c \sim 4D/s_0$$

would be required. For a systematic vertical error of ϵ at each of N monuments, the maximum vertical deviation would be $D = N\epsilon/2$. For an arc, $N \sim 10$, $\epsilon \sim 10$ mm, and $s_0 = 35$ km; thus a correction of $\theta_c \sim 5.7 \mu\text{rad}$ would be required. Between transfer monuments of separation $s_0 \sim 4.3$ km there are approximately 143 secondary monuments. If $\epsilon \sim 1.0$ mm for each secondary monument, then a vertical steering correction of $67 \mu\text{rad}$ would be required. One sees that systematic vertical alignment errors require steering correction; however, there are steering correctors in each cell to correct for this effect.

With vertical misalignment we expect a contribution to vertical dispersion. The equation for the dispersion is,

$$D''(s) + K(s)D(s) = 1/\rho. \quad (9)$$

If $\rho_y = Q_0 \rho_0$, then $D_y(s) \sim Q_0^{-1} D_x(s)$. For a vertical arc of sagitta d and length s_0 , the radius of curvature is $\rho_y \sim \frac{s_0^2}{8d}$. With $d \sim 100$ mm, $s_0 \sim 4.3$ km, and $\rho_0 \sim 12$ km, we find $Q_0 \sim 2 \times 10^3$, which is negligible.

The tune shift associated with a circumferential error is

$$\delta\nu \sim \frac{\Delta C}{2\pi\beta} = .44 \times 10^{-4}, \quad (10)$$

where $\beta = 180$ m and $\Delta C = 5 \times 10^{-2}$ m.

IV. LUMINOSITY

We assume gaussian bunches of distribution $\rho(x, y, z)$ with standard deviations σ_x , σ_y and σ_z , with z along the orbit. For n_b bunches of circulation period T_0 , with N_B protons in each bunch, crossing angle 2α , and speed v relative to the interaction point, the luminosity, which depends on the difference in half-circumference δ , is

$$\mathcal{L}(\alpha, \delta) = 2v \cos(\alpha) \frac{n_b}{T_0} \int \rho_1(x_1, y_1, z_1) \rho_2(x_2, y_2, z_2) dx dy dz dt. \quad (11)$$

For bunches, which cross at an angle α relative to the z axis and which have a distance δ between their centers when one bunch center is at the interaction point, the coordinates of the two bunches are

$$x_1 = x_2 = x$$

$$y_1 = z \sin(\alpha) + y \cos(\alpha)$$

$$y_2 = -z \sin(\alpha) + y \cos(\alpha)$$

$$z_1 = z \cos(\alpha) - y \sin(\alpha) - vt$$

$$z_2 = z \cos(\alpha) + y \sin(\alpha) + vt - \delta. \quad (12)$$

Integration gives,

$$\mathcal{L}(\alpha, \delta) = \frac{N_B^2 n_b}{T_0} \frac{e^{-[(\frac{\delta}{2\sigma_z})^2 (1 + (\frac{\sigma_x \cos(\alpha)}{\sigma_z})^2)^{-1}]}}{4\pi \sigma_x \sigma_y \cos(\alpha) \sqrt{1 + (\frac{\sigma_x \tan(\alpha)}{\sigma_y})^2}}. \quad (13)$$

As a measure of the overlap of the bunches we define the luminosity efficiency $R(\delta) = \mathcal{L}(\alpha, \delta)/\mathcal{L}(\alpha, 0)$, which is

$$R(\delta) = 100 \times \exp\left[-\left(\frac{\delta}{2\sigma_z}\right)^2 \left(1 + \left(\frac{\sigma_y \cot(\alpha)}{\sigma_z}\right)^2\right)^{-1}\right] \%. \quad (14)$$

For $\beta^* = 0.5$ m, $R(\delta = 50 \text{ mm}) = 97.13\%$ and $R(\delta = 100 \text{ mm}) = 89.14\%$. For $\beta^* = 10$ m, $R(\delta = 50 \text{ mm}) = 99.8\%$ and $R(\delta = 100 \text{ mm}) = 99.3\%$.

The luminosity can be restored at one interaction point, preferably low β , with RF manipulations. The final focusing quadrupole magnets can move the interaction point approximately one meter within the detector.

V. BEAM TRANSFER FROM THE HEB

To match the bunches from the HEB to the buckets in the Collider, it may be necessary to move the closed orbit from its center. The Collider circumference (87.12 km) is approximately eight times the HEB circumference (10.8 km). It is better to move the HEB orbit and to keep the Collider orbit at its center. If the error in the Collider circumference is ΔC_{HEB} , then the error in the mean radius is $\Delta \bar{r}_{HEB} = \Delta C_{Coll}/16\pi$. For $\Delta C_{Coll} = 50$ mm, one finds $\Delta \bar{r}_{HEB} = 1.5$ mm. Since $\alpha_{HEB} = 9.1 \times 10^{-5}$, and $(\Delta p/p)_{HEB} \sim 4.9 \times 10^{-4}$, the peak radial excursion of the closed orbit of the HEB would be $\delta \bar{r}_{HEB} \sim 1.5$ mm, with $\eta_{HEB} = 3.1$ m. This is marginally acceptable.

Alternatively we may use the circumferential discrepancy to accomplish fine cogging. If the circumferences of the two machines are perfect, assigned buckets in the two machines can be brought within a distance of 360 meters. Further alignment, called fine cogging, is accomplished by introducing a mismatch, made zero at extraction, in the machine circumferences. Mismatch in the central orbit could be used to do this fine cogging with a difference that it is not brought to zero at extraction. If the slippage rate, due to surveying error, is comparable to 114 buckets/sec, which corresponds to a slippage rate of one-half bucket in fifteen turns in the Collider, then the fine cogging can be done in ~ 1.3 seconds.

Here we have to accept the mismatch and resulting dilution of the longitudinal emittance. The latter is found from

$$\Delta \epsilon_l / \epsilon_l = \frac{1}{2} (\Delta z / \sigma_z)^2. \quad (15)$$

If the central bunch in a train from the HEB is centered on an RF bucket in the Collider, then there will be an error in the position of the end bunches relative to a bucket center in the Collider of the order

$$\Delta z = \Delta C_{Coll} (C_{HEB} / C_{Coll}). \quad (16)$$

For $\Delta C_{Coll} = 50$ mm, and $\sigma_z = 70$ mm, the longitudinal emittance dilution is $\Delta \epsilon_l / \epsilon_l \sim 0.39\%$, which is a small effect.

The change in the RF frequency due to the circumferential error is $\Delta f / f = \Delta C_{Coll} / C_{Coll}$. For $\Delta C_{Coll} \sim 50$

mm, one finds $\Delta f / f = 0.57 \times 10^{-6}$. For the Collider RF cavity, the nominal operating frequency is 360 MHz, and $\Delta f \sim 205$ Hz, which is within the tuning range, 50 kHz, of the RF cavity.

VI. CONCLUSIONS

It appears that a global tunnel survey with the use of sight pipes would be desirable in achieving the ideal design requirements for the Collider. Although random errors of the order of $3\sigma \sim 15 \rightarrow 22$ mm in the transverse alignment of the transfer monuments at the tunnel level would appear to contribute not more than a 50 mm error at the three σ level to the circumference of the Collider, a systematic error of the type observed at HERA could contribute as much as $120 \rightarrow 200$ mm to the circumference. The detectors can accommodate an uncertainty of the order of $\sigma_z \sim 70$ mm in the location of the interaction point, and the interaction point can be moved up to one meter with tuning of the final focusing quadrupole magnets.

If sight pipes are used for the global survey, certain locations of these pipes would aid in the precision achieved in alignment. Sight pipes located at the ends of the straight sections would reduce the initial angular errors, which can occur in surveying the arcs. In addition, it would be helpful to locate sight pipes at arc midpoints and at the interaction points.

We have received valuable technical suggestions from D. Larson, M. Syphers, and R. Wilkins.

VII. REFERENCES

- [1] T. Garavaglia, J. Peterson, and N. Mahale, "The Effect of Global Alignment Survey Errors on the Performance of the Super Collider," SSCL-N-803, December 1992.
- [2] LEP Status Report, in *Proceedings of the XV International Conference on High Energy Accelerators*, Hamburg, July 20-24 1992. To appear.
- [3] F. Löffler, and W. Schwarz, "The Geodetic Approach for HERA," in *Proceedings of the First International Workshop on Accelerator Alignment*, SLAC-375, CONF. -8907190, UC-414, (A), pp. 101-127, October 1990.

Dealing With Abort Kicker Prefire in the Superconducting Super Collider

A.I.Drozhdin, I.S.Baishev, N.V.Mokhov, B.Parker, R.D.Richardson, and J.Zhou
Superconducting Super Collider Laboratory*
2550 Beckleymeade Ave., Dallas, TX 75237 USA

The submitted manuscript has been authored by a contractor of the U.S. Government under Contract No. DE-AC05-85SF00065. Accordingly, the U.S. Government retains a nonexclusive, royalty-free license to publish or reproduce the published form of this contribution, or allow others to do so, for U.S. Government purposes.

Abstract

The Superconducting Super Collider uses a single-turn extraction abort system to divert the circulating beam to a massive graphite absorber at normal termination of the operating cycle or in case of any of a number of predefined fault modes. The Collider rings must be designed to be tolerant to abort extraction kicker prefires and misfires because of the large circulating beam energy. We have studied the consequences of beam loss in the accelerator due to such prefires and misfires in terms of material heating and radiation generation using full scale machine simulations and Monte-Carlo energy deposition calculations. Some results from these calculations as well as possible protective measures for minimizing the damaging effects of kicker prefire and misfire are discussed in this paper.

I. INTRODUCTION

The Superconducting Super Collider beam[1,2] contains approximately 420 MJ of circulating beam energy per ring at the operating design point, proton momentum equal to 20 TeV/c and a circulating current of 70 mA. This amount of circulating beam energy is equivalent to about 100 kg of high explosives and must be dealt with by a reliable abort system.

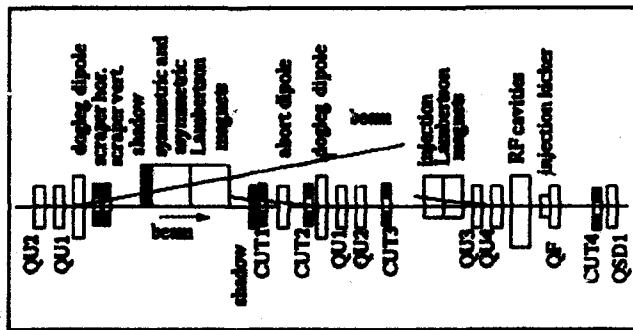


Figure 1. Collimators Locations in the West Utility

The abort system consists of 24 pulsed kicker magnets which direct the beam through the field free region of a series of Lambertson magnets on to a massive graphite absorber[3,4,5]. The abort kickers have a risetime of about 3 μ s. Normally this system is triggered during the 4 μ s abort gap in the circulating beam and takes 290 μ s to extract

*Operated by the Universities Research Association, Inc., for the U.S. Department of Energy under Contract No. DE-AC35-80ER40486.

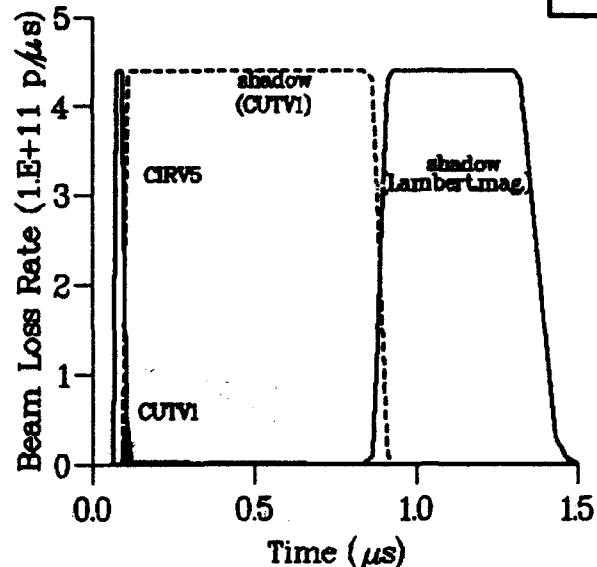


Figure 2 Beam Loss During the 3 μ s Kicker Rise Time

beam from the full 87 km circumference of the Collider. If one or more kicker module either prefires or misfires, some fraction of the beam may not reach the absorber. The consequences of such a beam loss on accelerator components are discussed in the next section. In this paper particle tracing is done with STRUCT program[6]. Beam loss induced cascades and corresponding temperature rise is simulated with MARS12 code[7].

II. ABORT PREFIRE PROBLEM

An abort kicker prefire causes large amplitude coherent betatron oscillation of the beam and results in halo particles being intercepted by the collimators positioned around the ring. These particles can induce overheating of the collimator jaws up to hundreds of degrees. The most severe situation takes place at 20 TeV/c before or during collisions.

Simulations of this process have been done for the following assumptions. We assumed that the circulating beam is cleaned to the 10 σ level by a scraper which leaves 99% of the circulating beam inside of 4 σ and 1% of the beam between 4 and 10 σ . Collimators are located in West Utility, as shown in Figure 1 and in the Interaction Region (IR) of the Collider (not shown) to protect low-beta quadrupoles against irradiation. For our initial simulations we assumed

that these collimators are placed 4σ inside the physical aperture of Collider. With an admittance of machine of 729 mm.mrad or 27σ of the circulating beam at top energy, the collimators were therefore positioned at 23σ with respect to the Collider closed orbit.

For the worst case, when abort kicker prefire takes place just after the longitudinal abort gap passes, one needs to wait one full turn to resynchronize with the abort gap in order to cleanly remove beam from the Collider. For this case the overheating of IR collimator CIR5 considerably exceeds the melting point of iron. In order to avoid overheating this collimator one could arrange to immediately fire the next 23 kickers; however, according to our simulations one would have to limit the interval of time between the prefire and the start of the rest of the kickers to be less than about $5\mu\text{s}$. Unfortunately the full abort kicker pulse is unlikely to be contained within the abort gap and one has an unsynchronized abort. Results of a simulation of beam loss around the Collider during the $3\mu\text{s}$ kicker rise time are presented in Figure 2. At low kicker field levels, halo particles are intercepted by a collimator in the IR and by the first collimator in West Utility. The temperature rise of these collimators are 400°C and 40°C respectively.

At the level of about 10% of full kicker strength the deflected beam is intercepted by the first collimator in the West Utility. We must protect this collimator by a graphite shadow and temperature rise in shadow is 250°C . At the level of about 40% of kicker strength the beam is intercepted by the graphite shadow of Lambertson magnet[8] and the shadow overheating is a tolerable 800°C .

III. PREFIRE PROTECTIVE MEASURES

There are two ways we have investigated to avoid overheating of collimators and shadows:

- decreasing of the abort kicker rise time from $3\mu\text{s}$ to $1\mu\text{s}$ and
- compensating a prefired kicker by another kicker with opposite magnetic field (antikicker).

Decreasing the abort kicker rise time yields a three fold decrease in heating. For sufficiently short antikicker delay the full beam abort can be delayed until synchronization with the abort gap and thereby eliminating beam loss during the kicker risetime.

Recent simulations[9] suggest that the dynamic aperture of Collider at the top energy is around 12σ and the lifetime of the particles with large betatron amplitudes, from 12 to 20σ , varies from 50 to 2 turns. The lifetime is less than one turn for amplitudes greater than 20σ . For this case collimator jaws would have to be installed between 16 - 20σ from the circulating beam axis to protect superconducting magnets irradiation and the collimator jaws would then intercept a more dense part of the circulating beam. This closer position would lead to an additional overheating about 20 times greater than for the 23σ positions. The overheating of the collimator CIRV5 jaw during an unsynchronized abort increases to an inadmissible 900°C . The

first method of overheating reduction is ineffective in this case and only via an antikicker is it possible to eliminate the danger of collimator and shadows damage.

The collimator jaw overheating is also strongly dependent upon the delay between prefire and start of antikicker. The resulting kick and beam loss versus time for different delays ($1.2\mu\text{s}$ and $1.65\mu\text{s}$) are presented in Figure 3,4. At $1.8\mu\text{s}$ delay the result kick exceeds 75% of one kicker strength and collimator CIRV5 overheating exceeds melting point. Collimator jaws overheating versus antikicker delay is shown in Figure 5. An acceptable level of temperature rise of about 300°C is exceeded at $1.5\mu\text{s}$ delay between prefire of abort kicker and start of antikicker. Providing a short ($< 1.5\mu\text{s}$) delay is an important antikicker design requirement.

IV. CONCLUSIONS

Our simulations show that for large ($> 20\sigma$) Collider collimators settings an unsynchronized abort is allowed if graphite shadows are used upstream of the first abort Lambertson magnet and at a few critical collimator locations. For smaller collimator settings (between 14σ and 20σ) an antikicker with less than $1.5\mu\text{s}$ delay appears to be needed to limit Collider equipment overheating to tolerable levels; however, further study is required in order to understand multi-kicker prefire and other failure scenarios.

V. REFERENCES

- [1] Site-Specific Conceptual Design of the Superconducting Super Collider, SSCLab, July 1990.
- [2] Collider Accelerator Arc Section, Element Specification (Level 3B), SSCL Document Control # E10-000027, August 1992.
- [3] Collider Accelerator Utility Section, Element Specification (Level 3B), SSCL Document Control # E10-000073, March 1993.
- [4] "Collider Preliminary Design Requirements Review (PDRR): Copy of Presented Transparencies," Available SSCL Library, January 1993.
- [5] "Collider Abort Subsystem Conceptual Scheme and Optics: Copy of Transparencies", Brett Parker, Available SSCL Library, May, 1993.
- [6] I.S. Baishev, A.I. Drozhdin, and N.V. Mokhov, SSCL-306, Dallas (1990).
- [7] N.V. Mokhov, The MARS12 Code System, Proc. of SARE Workshop, Santa Fe, 1993, See also N.V. Mokhov, Fermilab FN-509, 1989.
- [8] N.V. Mokhov, Collider Utility Section PDRR, SSCL, Jan. 1993.
- [9] Y. Cai, Private Communication, Available SSCL Library, April 1993.

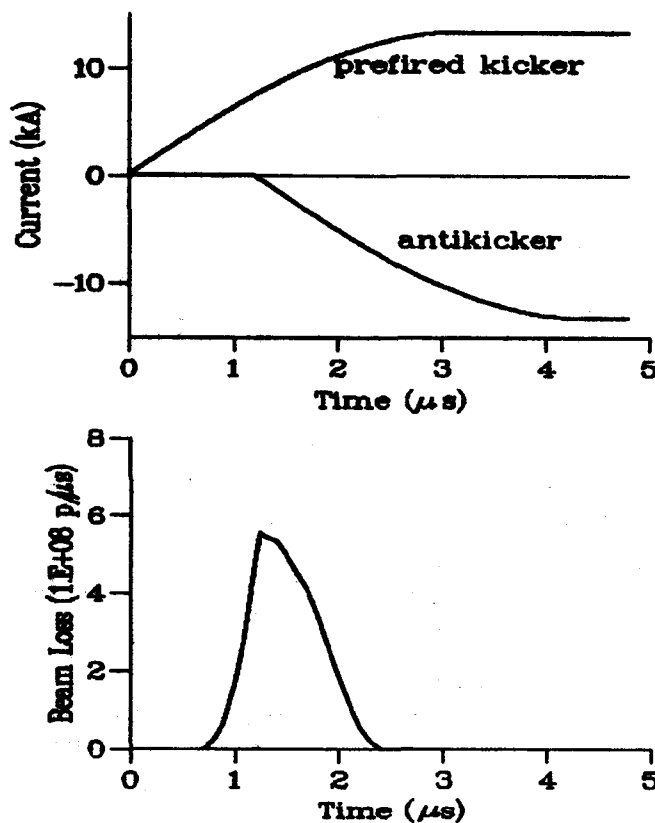


Figure 3. Kicker/Antikicker Pulse Shape (top) and Beam Loss Versus Time (bottom) for 1.2 μs Delay

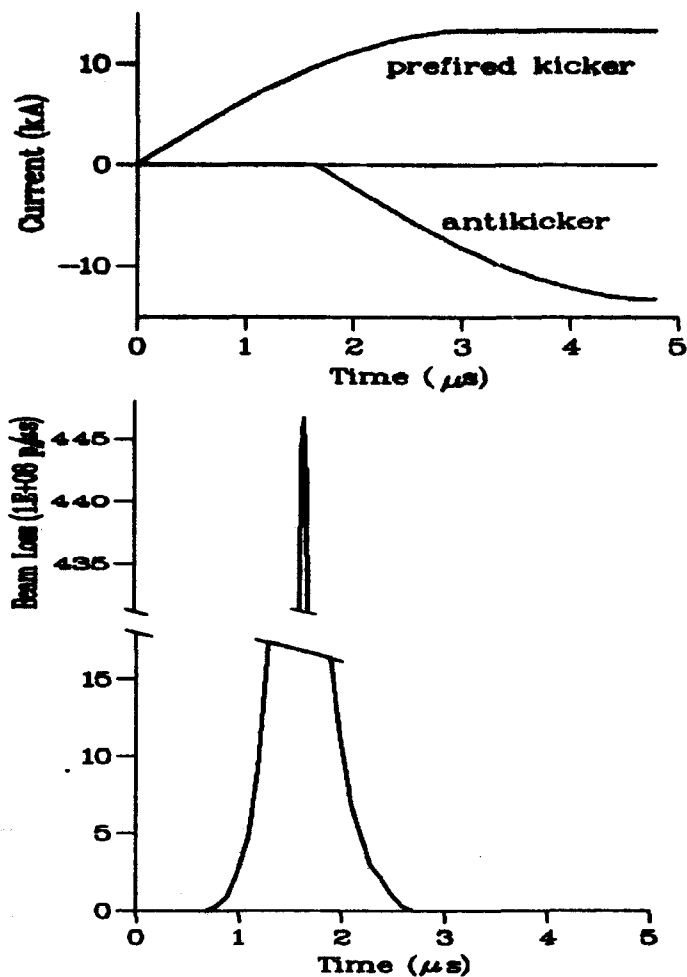


Figure 4. Kicker/Antikicker Pulse Shape (top) and Beam Loss Versus Time (bottom) for 1.65 μs Delay

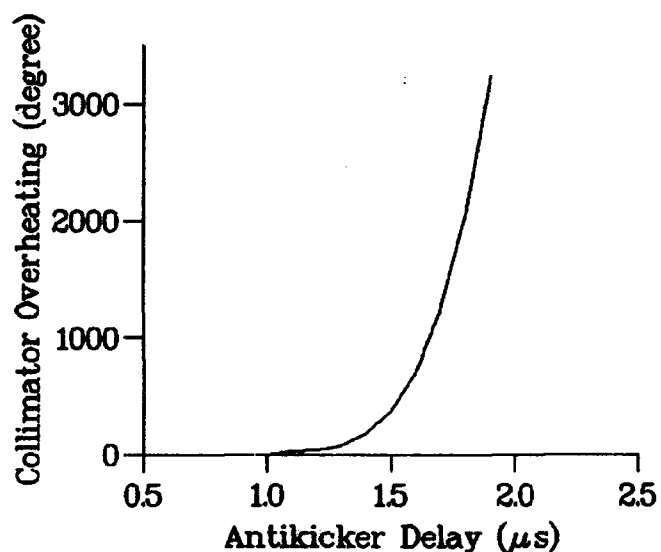


Figure 5. Collimator Jaws Overheating Versus Antikicker Delay

Design Status Report on the Collider Utility Straight Insertions

Brett Parker

Superconducting Super Collider Laboratory*
2550 Beckleymeade Ave., Dallas, TX 75237, USA

Abstract

The lattice for the rings of the Superconducting Super Collider is divided into arcs, a FODO array of superconducting quadrupoles and dipoles; interaction regions, places where the beams are focused and brought into collision within physics detectors; and utility sections, places where injection, acceleration, abort, halo-scraping, and other control and diagnostic functions are performed [1-3]. Recent modifications to the utility region design are reported here. Briefly these include lowering injection β -maxima by 40%; reducing the lengths and varieties of superconducting quadrupoles; improving conditions for injection matching; increasing abort admittance; mitigating component interferences; and identifying places for dampers and other beam instrumentation [4].

I. INTRODUCTION

The rings of the Superconducting Super Collider are divided geographically into east and west clusters and north and south arcs, as shown in Figure 1. The east and west clusters are in turn subdivided by function into optics modules, as shown in Figure 2. The design requirements for the interaction regions (IR) and hinge (HI) sections are discussed elsewhere. The utility sections that are described below include eight dispersion suppressor (DS) sections, four transition to interaction region (TI) sections, two transition to utility (TU) sections, and the east and west utility straight (EU and WU) sections. After reviewing the design of the TU, TI, and DS sections, we describe recent lattice changes associated with optimizing the design of the utility straight sections.

II. TRANSITION SECTIONS

The TU section, which provides a region of beam to separate the muon vectors from the IR and utility straight regions, is essentially a short (12 standard 90-m arc half cells) piece of arc with arc-like Twiss functions, as shown in Figure 3. Note that as with the arcs, a few dipole pairs are removed at π phase advance separation in order to provide contingency space for future technical systems.

The TI lattice (not shown) functions are very similar to those for the TU. The TI consists of a single cell in which

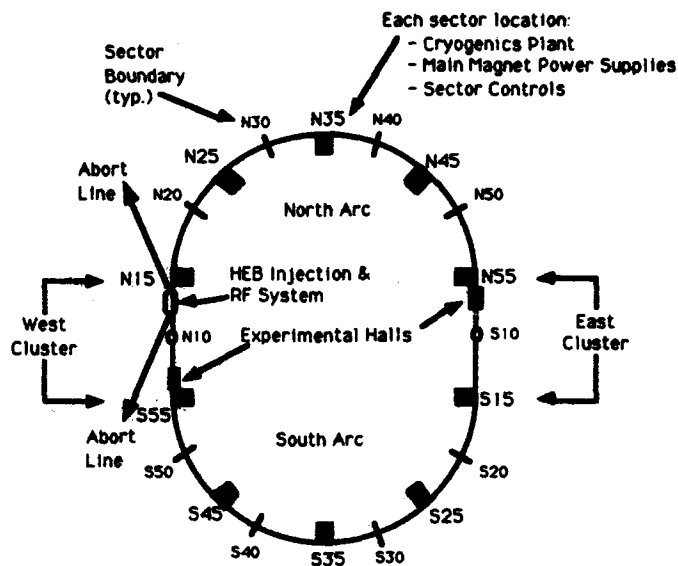


Figure 1. Layout schematic of Superconducting Super Collider.

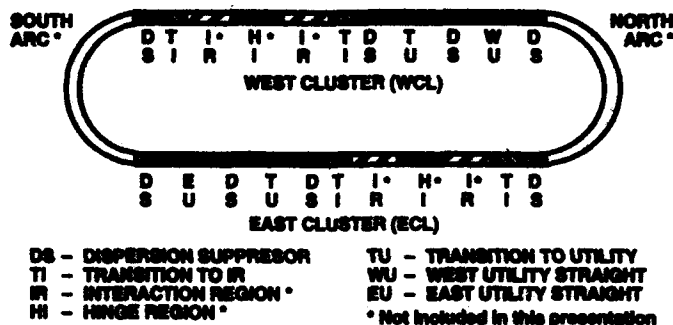


Figure 2. Section layout schematic.

*Operated by the Universities Research Association, Inc., for the U.S. Department of Energy under Contract No. DE-AC35-80ER40486.

The submitted manuscript has been authored by a contractor of the U.S. Government under Contract No. DE-AC35-80ER40486. Accordingly, the U.S. Government retains a nonexclusive, royalty-free license to publish or reproduce the published form of this contribution, or allow others to do so, for U.S. Government purposes.

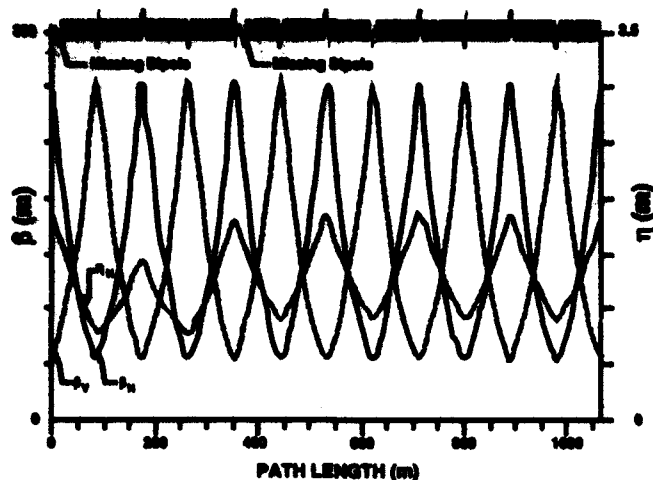


Figure 3. TU lattice functions.

all bending is omitted; however the dispersion, $\eta \approx 0$ across the TI sections due to the neighboring DS sections. Each TI has skew quadrupole convector magnets at mid-half cell locations that are part of the global decoupling scheme. The TI sections are potential take-off and return points for a diamond bypass configuration.

III. DISPERSION SUPPRESSOR SECTIONS

The DS section, shown in Figure 4, is composed of cells with three-quarters the length and two-thirds the bending of an arc cell. This gives an $L \times \theta$ of half that of a standard arc cell, and enables matching from full to zero dispersion over the 270-m extent of the four DS half cells. There are DS sections surrounding the utility straight and IR sections (the HI performs as back-to-back DS sections) in order to kill the dispersion in these regions. It is anticipated that a controlled amount of dispersion will be introduced into the east utility straight in order to enable off-momentum scraping in the EU.

IV. UTILITY STRAIGHT SECTIONS

While the main superconducting quadrupole lattices are identical for the EU and WU utility straight sections, the two sections are quite different in nature due to the inclusion of extended warm regions in the WU for beam injection, acceleration and abort. The Twiss functions for the baseline (TOP-REV0) WU lattice are shown in Figure 5 for comparison to the current (TOP-REV1) lattice shown in Figure 6. The EU and WU straight in section are both equal in length to 15 standard 90 m half cells.

In the central warm bend region of the WU is a series of symmetric and asymmetric Lambertson-style magnets that provides a means for dispatching a collider ring fill to an external backstop by firing a series of abort kicker magnets. Note that the beam scraper system (i.e., high-intensity collimators) shares the same central dogleg with the abort system in order to point the neutral vector and

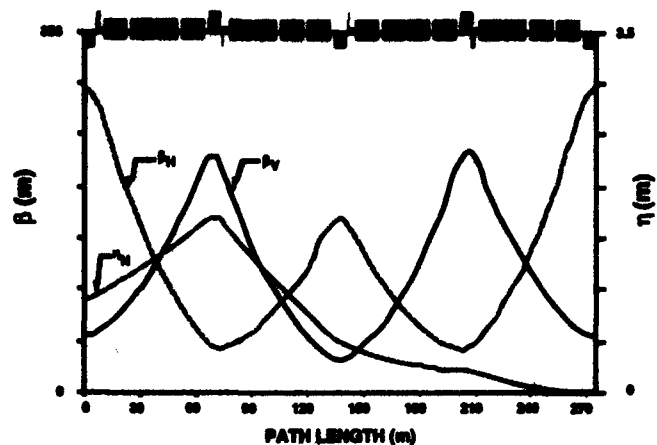


Figure 4. Dispersion suppressor lattice functions.

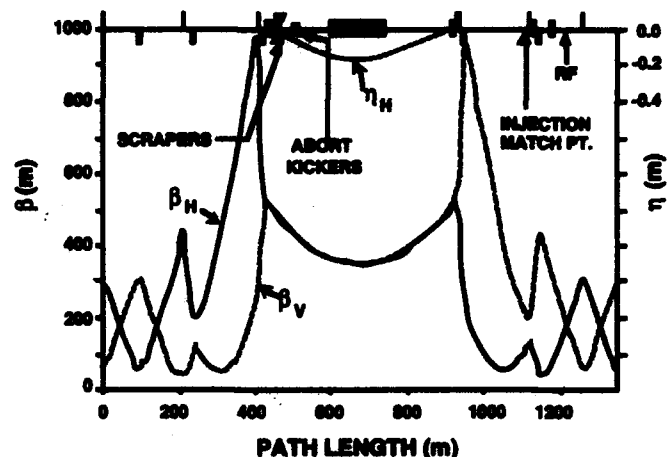


Figure 5. Baseline TOP-REV0 lattice functions for west utility.

secondary charged particles escaping from the scraper away from downstream superconducting magnet apertures.

One significant change involved moving the abort kickers upstream of the central quadrupole doublet, both to avoid the intense radiation field near the scrapers and to keep the abort kicker $\int B \cdot dl$ at a manageable level. To accomplish this the polarity of these quadrupole doublets on either side of the central dogleg was flipped. With the new polarity it is possible to reduce both the β -maximum and the lengths and number of distinct types of main superconducting quadrupole magnets as shown in Figure 6.

At the request of the IR design team, the utility straight transfer matrix was further constrained to have a unit map as this simplifies the scheme for IR chromaticity correction in the north and south arcs. Also we reduced by half the $\int B \cdot dl$ required for the injection kicker magnets by providing lattice space for these kickers near to $\pi/2$ phase advance from the injection Lambertson magnets. Favorable FODO-like lattice functions were maintained at the injection matching point.

The design and review process for the WU has been greatly facilitated through an ability we have developed

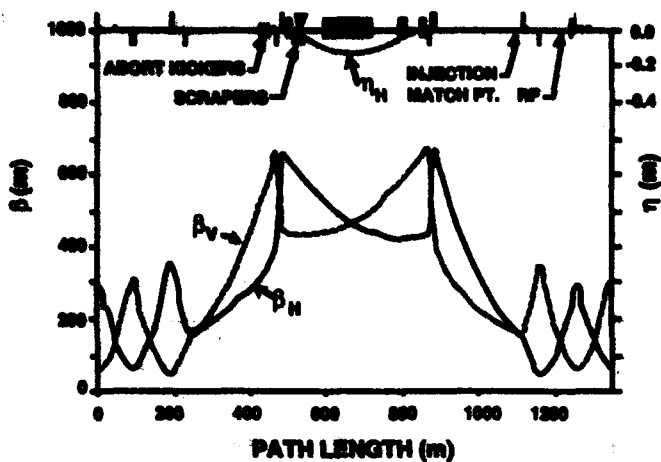


Figure 6. Current TOP_REV1 lattice functions for west utility.

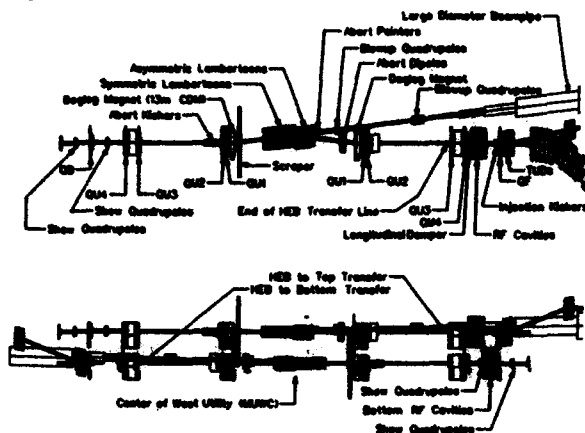


Figure 7. West utility layout.

to rapidly and automatically build a 3-dimensional CAD model of all major technical components and beamlines almost directly from the survey output of accelerator design programs (MAD, TRANSPORT, SYNCH, etc.). This facility, which allows one to "try out" a new lattice component configuration and to "see" points of interference, has been found critical in laying out and verifying abort and tune-up beamline components [5].

With the technical component layout in hand it is much easier to wrap tunnel across sections, underground galleries, and access shafts around the various beamlines and subsystems with considerable confidence [6]. For instance we have determined locations where a single shaft provides access to High Energy Booster (HEB) extraction kickers and an underground gallery housing Collider abort kicker power supplies. Design studies indicate that it should be possible to excavate the tunnels for the HEB-to-Collider beam transfer lines so as to provide sufficient cover to enable operation of the HEB while maintaining access to the Collider. Earlier concepts for this region, based upon opening up a large underground "cathedral" connecting the HEB and Collider rings, would have required the introduction of a prohibitive amount of mass shielding.

We are currently midway through the Title I phase for the WU underground tunnel design. It is anticipated that the data base driven nature of the CAD model will be important in future studies of construction, installation, operation and maintenance. The CAD model forms a complementary tool to the component data interface (CDI) in facilitating accelerator design work [7].

V. SUMMARY

In summary the TU, TI, and DS sections have undergone minor design tuning which involved reducing the number of different spool types and empty cryostat lengths. The EU and WU have undergone significant changes during the process of determining their detailed layout. We concluded that early 3D CAD modeling has proved invaluable to this effort. Continued modeling will be critical in future efforts, which include special magnet, component stand, cryogenic bypass, LCW, cable tray, and RF waveguide design and installation work.

VI. ACKNOWLEDGEMENTS

These results are the product of work from many people: Al Garren, David Johnson, and YunHai Cai for optical design fitting; Mike Syphers, Dave Ritson, Karl Brown, and Ron Schailey for many important discussions and suggestions; Dale Orth for putting together his macro/database solution for creating 3D CAD models; and, finally, Rainer Meinke and Lindsay Coffman for their continued support and encouragement.

VII. REFERENCES

- [1] Site-Specific Conceptual Design of the Superconducting Super Collider, SSC Lab, December 1989.
- [2] "Collider Accelerator Arc Sections Level 3B Element Specification," SSC Lab Document Control #E10-000027, August 1992.
- [3] "Collider Accelerator Utility Sections Level 3B Element Specification," SSC Lab Document Control #E10-000073, Draft, January, 1993.
- [4] "Collider Preliminary Design Requirements Review (PDRR): Copy of Presenters' Transparencies," SSC Lab, Available SSCL Library, January 1993.
- [5] "Facility Modeling of West Utility Straight Tunnel Sections," SSCL-Preprint-339, M. Butalla, B. Parker, D. Orth, and A. Elioff, presented to IISCC, May 1993.
- [6] "SSC NIS to N10 Basic Tunnel Design Requirements (Including West Utility Straight)," SSC Lab Document Control #Y16-00188.
- [7] "Accelerator Design Using Databases and Graphical User Interfaces," SSCL-620, M. Popp, April 1993.

Current Design of the SSC Interaction Regions

Y. Nosochkov, E. Courant[†], A. Garren, D.M. Ritson[‡], T. Sen and R. Stiening
Superconducting Super Collider Laboratory *
Dallas, TX 75237

[†] Visitor from Brookhaven Lab

[‡] SLAC, Stanford University, Stanford, CA 94309

Abstract

We review the important changes made to the optics of the Interaction Regions (IRs) in the collider since the conceptual design (SCDR) of 1990. The most significant modification is a new procedure for the β squeeze. Three additional families of independently powered quadrupoles change the optics from injection to collision while the strengths of the final focus triplet quadrupoles are held constant. The phase advance from the interaction point (IP) to the arc quadrupoles is optimized to provide more effective positions of the local correctors for the IR. Two secondary foci where the IP is imaged have been incorporated symmetrically on both sides of the IP. Other changes include a significant reduction in the β_{peak} at injection, optimised configuration of the $M = -I$ section, quadrupoles with 5 cm bore, minimized number of quad families, standard design of the vertical bends and reduced total length of the magnets. The optics allows for a wide range of values for a detector space at each IP. The time scenario for the β squeeze is considered as well.

I. INTRODUCTION

The design of the IRs at the SSC has undergone several modifications since the SCDR design [1]. At present there are four IRs in the collider, two in the East cluster and two in the West. Present plans call for the detectors in the East IRs to operate at lower β^* than those in the West cluster. The modifications of the IR optics are the following:

- exclusion of the final triplet quadrupoles from the β squeeze between injection and collision optics, thus providing an independent squeeze for each ring;
- including a secondary focus on either side of the IP;
- providing a specific value of the phase advance across half an IR to simplify local IR corrections;
- providing a wide range of possible values for detector space with minimal optical modifications;
- use of standard 5 cm bore magnets in the IR.

Here we review the above changes and discuss the optical and geometrical properties of the various IR configurations. The above modifications to the IR have not affected the rest of the machine.

II. MAIN IR MODULES

Figure 1 shows a vertical schematic view of a complete IR. The dipoles straddle the horizontal lines, the focussing

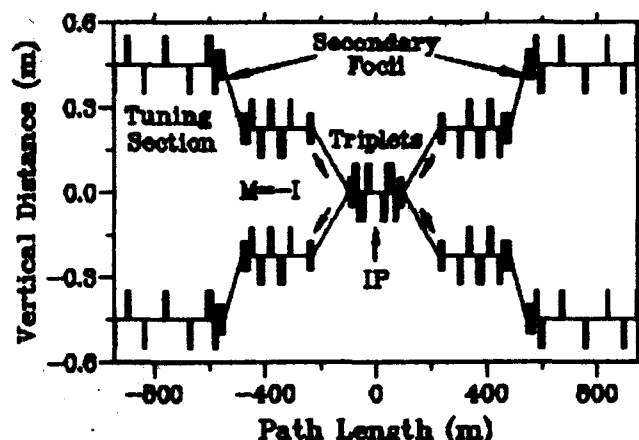


Figure 1. Vertical view of an IR.

quadrupoles are shown above the line and the defocussing quadrupoles below. As before, the optics is antisymmetric with respect to the IP. Each half IR is composed of three modules: the final triplet, the $M = -I$ section and the tuning section. Besides the quadrupoles there are vertical dipoles placed in two steps, which bring the beams into collision. The final triplet quadrupoles and adjacent splitting dipoles are common to both rings. The beams share the same beam pipe inside these magnets. There is a vertical separation of 45 cm between the beams in the $M = -I$ sections, which requires a 2-in-1 magnet design. The magnets in the tuning section in the two rings are separated by the standard vertical distance of 90 cm.

The triplets focus the beams to extremely small sizes at the IP. Therefore, these magnets are quite strong and the beam is very sensitive to field errors in them. The most important change made in the present design is to keep these quadrupoles at fixed gradients during the β squeeze. The advantages are that the squeeze can be done independently for each ring and no additional field errors are introduced in the triplets during the squeeze. To keep the same number of controls for the β squeeze, another 3 families of quadrupoles, now labelled QL7, QL8, QL9, from the regions outside the previous IR were included into the IR. The 6 tuning quadrupoles QL4, QL5, ..., QL9 form the tuning section. This change has increased the length of the IR from 1350 m to 1890 m.

Another new feature is the inclusion of a secondary fo-

* Operated by the Universities Research Association Inc., for the U.S. Department of Energy, under contract DE-AC35-89ER40486

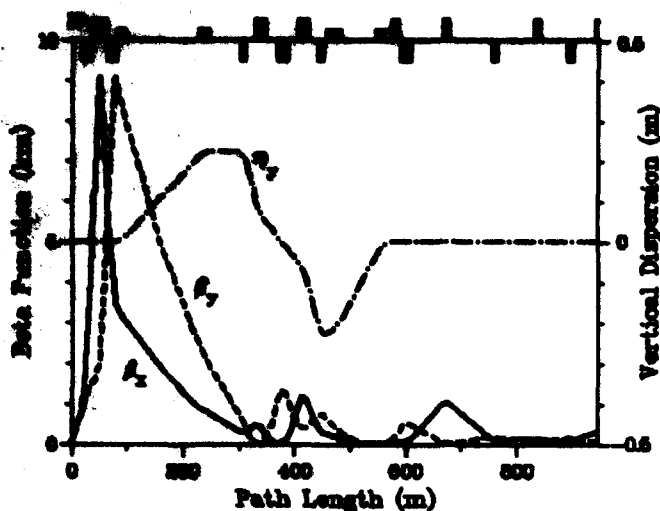


Figure 2. Lattice functions in one-half of the IR with magnets at the top.

cus, a point at which the IP is imaged. This image can be used for diagnostics, and protection collimators can be placed here to reduce the background at the IP. Two secondary foci are located at 541 m from the IP, symmetrically on each side of the IR, with fixed 2π phase advance from the IP. They optically separate the two tuning sections which have variable transfer matrices from the central region (comprised of the two $M = -I$ and two triplets) with constant gradients.

Between the triplets and the tuning section is a module of 8 quadrupoles, known as the $M = -I$ section. The transfer matrix across this section is the negative of the identity matrix, hence the name. This section causes a cancellation of the vertical dispersion η_y , induced by the adjacent pairs of dipoles, at the IP. The length of these quadrupoles was significantly reduced by use of the FODO configuration instead of FOFDOD. The $M = -I$ section can be placed anywhere between the two sets of dipoles without affecting the rest of the IR. To reduce the chromaticity at collision and provide the most detector space, this section was moved as far as possible from the IP.

III. OPTICAL PROPERTIES

A primary optical goal is to provide a broad range of accessible low β^* values. In the present design, the variable gradient quadrupoles can be tuned to a minimum $\beta^* = 0.25$ m for a detector free space of $L^* = 20.5$ m, which is defined to be the distance between the IP and the triplet. However, the baseline design requires only $\beta^* = 0.5$ m at collision. This corresponds to a β_{peak} in the triplets of 9 km. This is the maximum value allowing a region of a good field quality in the 5 cm bore triplet quadrupoles. Figure 2 shows the lattice functions across one-half of the IR at collision with $\beta^* = 0.5$ m. It is envisaged that future upgrades will increase the triplet bore thus allowing $\beta^* = 0.25$ m to be achieved.

At injection, β^* is chosen to be 7 m which is when the chromaticity of the IR and the β_{peak} are a minimum. The β_{peak} at injection is significantly reduced, from 1.3 km in the SCDR design to 670 m at present, by reversing the polarity of the doublet quadrupoles QL4, QL5.

In the earlier design the phase advance across an IR was kept constant during the squeeze so that only the sum of phase advances, $\mu_x + \mu_y$, across half an IR was held constant, but not each of the terms. Present plans include a set of local trim quadrupoles and sextupoles, correcting for the crossing angle [2] and IR chromaticity [3], located next to the quadrupoles in the arc cells adjacent to the IR. To optimize the above corrections, we require that μ_x and μ_y be separately constant during the β squeeze. The specific values chosen are $\mu_x = 3.75\pi$ and $\mu_y = 3\pi$ across half an IR and exchanged due to antisymmetry on the other side of the IP. With 90° phase advance per cell in the arcs, this makes the phase advance between the IP and the outside cell quadrupoles to be a multiple of $\pi/2$, i.e.

$$\mu_x^F - \mu_x^{IP} = n_x \pi/2; \quad \mu_y^D - \mu_y^{IP} = n_y \pi/2$$

where for instance μ_x^F is the horizontal phase at an arbitrary F quad in the arcs. The above correctors are now at optimal positions with respect to the triplet quadrupoles, the main sources of IR perturbations. This choice also keeps the phase advance between adjacent IPs to be $\pi/2$ (mod 2π) which minimizes the higher order chromaticity of the two IRs combined.

IV. MAGNET PARAMETERS

In the present design we use optimized, realistic parameters of the IR magnets. All the quadrupoles have 5 cm bore and maximum gradient of 191 T/m. The quadrupole gradients in the triplets and $M = -I$ sections are not changed during the β squeeze while the tuning quadrupoles have variable gradients. The 5 cm bore vertical dipoles have the same design as the horizontal dipoles in the arcs. Only the dipoles located next to the triplets need the larger aperture of 8.5 cm to provide enough space for the separated beams.

The positions of the quadrupoles in the tuning section and configuration of the $M = -I$ section were optimized to reduce the total length of magnets and number of different quad lengths. Excluding the triplets, there are only 3 different lengths of IR quadrupoles: 8.0 m, 8.6 m and 10.2 m. Compared to the previous IR design, the total length of magnets is reduced by 12%, which is about 392 m for 4 IRs.

V. BETA SQUEEZE

The characteristic feature of the low- β optics is an extremely high β_{peak} value in the final triplets at collision optics. A much lower β_{peak} value is allowed at injection energy because of the larger beam emittance. A smooth transition between the two optical configurations is achieved by

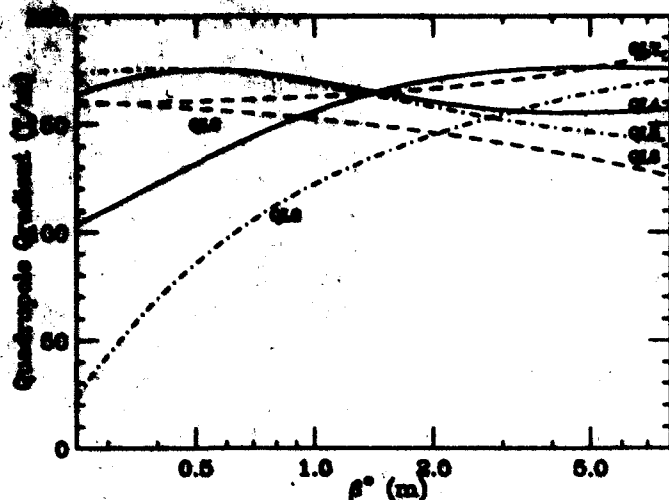


Figure 3. Tuning curves for a low- β IR ($L^* = 20.5\text{m}$).

varying the gradients of the six quadrupoles in the tuning section. This requires that each tuning quad have an independent power supply. The variation of gradients during the β squeeze is shown in Figure 3. It is seen that only the power supply across QL8 will have a large swing from injection to collision and the other quadrupoles may use weaker power supplies. In contrast to the SCDR design, there is no reversal of polarity during the β squeeze which makes the present design more robust.

The transfer matrix across the IR and the phase advance across each half IR stay constant during the squeeze. This guarantees that the rest of the machine is unaffected in the absence of errors.

Figure 3 shows a slow change of the gradients in the high β^* part of the β squeeze and a fast change in the low β^* part. The chromaticity of the IR quadrupoles behaves similarly during the squeeze. A non-uniform time dependence of β^* must be specified to make the variations more uniform in time. Minimizing both the rate of change of current in the tuning quadrupoles and the rate of change of chromaticity through the IR leads to the following exponential variation,

$$\beta^*(t) = 6.8 \exp(-t/20.36) + 0.2.$$

The duration of the squeeze is chosen to be 100 seconds which is the least time consistent with magnet specifications for dI/dt and it is also the duration used at Fermilab. Figure 4 shows the rate of change of current through each quadrupole during the squeeze.

VI. DIFFERENT L^*

The four IRs envisaged in the collider might have different experimental requirements, such as space for the detector and beam size at the IP. Any L^* in the range between 20.5 m and 90 m can be obtained in the present design by a simple modification. To achieve a specific value of L^* , the

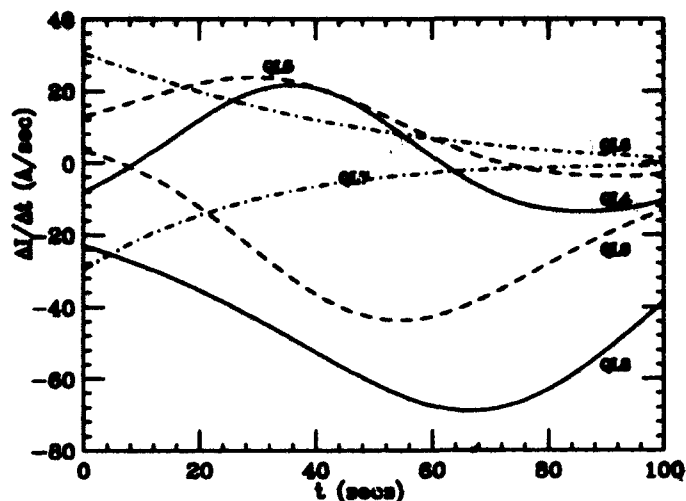


Figure 4. Rate of change of current during the squeeze ($L^* = 20.5\text{m}$).

triplet and adjacent pair of the dipoles are moved together by an appropriate distance from the IP while the other magnets stay at the same positions. The lengths of the triplet quadrupoles are adjusted to keep the secondary focus at the same distance from the IP and to minimize β_{peak} in the triplet. As L^* increases, the triplets get shorter because of the longer focal length. Slight changes are required for the gradients of the tuning quadrupoles.

For any given L^* , the lowest β^* at collision corresponds to $\beta_{peak} = 9\text{ km}$ in the triplet. Injection optics requires a minimum of both β_{peak} and chromaticity over the IR. With these conditions, the range of the tuning gradients is about the same for any L^* . The following table shows the relevant parameters for the four values of L^* chosen.

L^* (m)	β^* (m)		Triplet Quad Lengths (m)		
	Inj.	Coll.	QL1	QL2	QL3
20.50	7.0	0.5	15.5650	11.8545	13.1715
34.55	11.0	0.7	12.6064	11.1793	12.6064
56.90	23.0	1.1	10.2948	10.2948	11.8835
90.00	40.0	1.95	8.6890	9.4405	11.2051

The values of 34.55 m and 56.90 m were chosen since in these cases two of the quadrupoles in the triplet could be made to have the same length. The two smaller values of L^* can be used for the low- β IRs in the East cluster, and possibly the other two values might be used for the IRs in the West cluster.

VII. REFERENCES

- [1] J.R. Sanford, D.M. Mathews, Eds., *Site-Specific Conceptual Design*, SSCL Document SSCL-SR-1056 (1990).
- [2] Y. Nosochkov and D. Ritson, "The Provision of IP Crossing Angles for the SSC", these proceedings.
- [3] T. Sen et. al., "Chromaticity Correction for the SSC Collider Rings", these proceedings.

The Parameter Spreadsheets and Their Applications

R. Schwitters, A. Chao, W. Chou and J. Peterson
Superconducting Super Collider Laboratory*
2550 Beckleymeade Ave., Dallas, TX 75237

Abstract

This paper is to announce that a set of parameter spreadsheets, using the Microsoft EXCEL software, has been developed for the SSC (and also for the LHC). In this program, the input (or control) parameters and the derived parameters are linked by equations that express the accelerator physics involved. A subgroup of parameters that are considered critical, or possible bottlenecks, has been highlighted under the category of "Flags". Given certain performance goals, one can use this program to "tune" the input parameters in such a way that the flagged parameters not exceed their acceptable range. During the past years, this program has been employed for the following purposes: a) To guide the machine designs for various operation scenarios, b) To generate a parameter list that is self-consistent and, c) To study the impact of some proposed parameter changes (e.g., different choices of the rf frequency and bunch spacing).

I. INTRODUCTION

The Superconducting Super Collider (SSC) consists of a linac and four synchrotrons (three boosters and a collider). There are a great number of machine and beam parameters that need to be adjusted in a coordinated manner in order to reach the specified goals of performance. For this purpose, a set of EXCEL spreadsheets, the Spreadsheets of SSC Parameters (SSP), has been developed as an integrated design tool to tune the machines.

In this program, there are two categories of parameters — the input (or control) parameters and the derived parameters. All are linked by equations that express the accelerator physics involved. A subgroup of derived parameters that are considered critical, or possible bottlenecks, has been highlighted under the category of "Flags". Critical levels have been assigned to each of the flagged parameters. The object of the game, given certain performance goals (usually luminosity and beam energy at collision), is to "tune" the input parameters in such a way that the flagged parameters not exceed their acceptable ranges.

A number of cases have been studied using SSP, including different operation scenarios and the choice of some important beam parameters such as the rf frequency and bunch spacing. A by-product of the program is the generation of the SSC Parameter List, which is now widely used

*Operated by the Universities Research Association, Inc., for the U.S. Department of Energy under Contract No. DE-AC35-80ER40486.

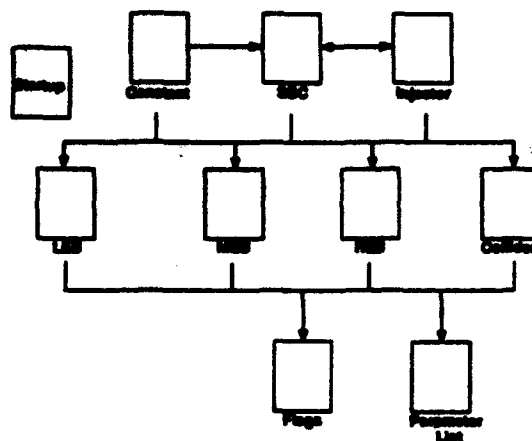


Figure 1. The worksheets in the SSP program.

in the laboratory as a quick design reference.

II. THE SSP PROGRAM

The SSP program is in the form of 10 linked spreadsheets, using the Microsoft EXCEL software as shown in Figure 1. At present it contains about 100 input, 280 derived, and 35 flagged parameters, linked to each other by about 160 equations.

1. The spreadsheets:

Top-level parameters are in the "SSC" worksheet, which appears as a "window" on the computer screen. Overall injector parameters are in the "Injector" worksheet. Specific machine parameters are generally listed in the corresponding worksheets. There is also a worksheet that contains all the physical constants used by the program. The "Flags" worksheet is set up to monitor the values of critical parameters. There are a total of 35 flagged parameters at this moment as listed in Table 1. Values in column B within safe operating ranges are indicated in column D with a "Green" flag; those outside acceptable ranges are flagged "Red". "Yellow" is used to indicate values near expected performance limits, which are described in Columns E and F. The macro-sheet, "Startup", can be used to open all the worksheets.

2. The input parameters:

The input parameters are entered individually in the various worksheets. All are possible tuning "knobs",

Table 1. The Flags worksheet (nominal case)

	A	B	C	D	E	F
1	Tune shift/spread:					
2	Total Head-on Tune Shift	0.0038		Green	0.01	0.02
3	Total Long-range Tune Shift	0.0087		Yellow	0.006	0.01
4	Total Long-range Tune Spread	0.0020		Green	0.006	0.01
5	Space Charge Tune Shift, LEB	0.383		Green	0.4	0.7
6	Space Charge Tune Shift, MEB	0.078		Green	0.2	0.4
7	Power loss:					
8	Synch Radiation	9.0	kW/beam	Green	11	22
9	Parasitic heating	1.26	kW/beam	Green	3	9
10	Refrigerator usage factor	1.01		Green	1.25	2.5
11	Collective Instabilities:					
12	Z.long.thresh, collider	3.7	ohm	Green	0.68	0.34
13	Z.trans.thresh, collider	247.1	Mohm/m	Green	40	20
14	Z.long.thresh, HEB	1.4	ohm	Yellow	1.9	0.95
15	Z.trans.thresh, HEB	16.6	Mohm/m	Green	10	5
16	Z.long.thresh, MEB	22.7	ohm	Green	1.4	0.7
17	Z.trans.thresh, MEB	34.1	Mohm/m	Green	1.9	0.95
18	Z.long.thresh, LEB	27.7	ohm	Green	2	1
19	Z.trans.thresh, LEB	18.4	Mohm/m	Green	0.76	0.38
20	Res wall growth time, collider	106	turns	Green	50	20
21	Dynamic aperture:					
22	Dyn aper, collider, Inj	13	sigma	Green	10	6
23	Dyn aper, collider, IR	11	sigma	Green	10	7
24	Dyn aper, HEB, Inj	11	sigma	Green	10	6
25	Energy depo./rad. damage:					
26	Peak energy depo, IR quads	0.104	mW/g	Green	4	8
27	Rad damage lifetime, collider	15.2	yr.	Green	5	2
28	Lifetime:					
29	Intrabeam lifetime, horiz emit	211.2	hr	Green	96	48
30	Intrabeam lifetime, long emit	120.2	hr	Green	96	48
31	Bucketbeam ratio, collider, Inj	30.4		Green	12	6
32	Bucketbeam ratio, collider, Op	25.1		Green	12	6
33	Lum lifetime, beam-beam	78.0	hr	Green	48	24
34	Lum lifetime, Residual gas	1378	hr	Green	48	24
35	Vacuum:					
36	H2 monolayer buildup time	5.7	day	Yellow	8	4
37	Re-desorption pressure rise time	4.1	day	Yellow	8	4
38	Others:					
39	Lum reduction, IR1	0.91		Green	0.85	0.7
40	Events per crossing	1.8		Green	3	30
41	HEB Dwell	20.1	s	Green	30	60
42	Collider Dwell	74.9	min	Green	80	160
43	Equatorial pressure quenching	18.8	psi	Green	200	300

but those commonly varied are the beam and performance input parameters as listed in Table 2, in which E is the beam energy, \mathcal{L} the luminosity at one interaction point (IP), S_B the bunch spacing, ϵ_N the normalized rms transverse emittance, ϵ_L the rms longitudinal emittance, β^* the β -function at the IP, P_{linac} the momentum of the protons extracted from the linac and p the vacuum pressure. The machine and lattice input parameters have tended to be relatively fixed, so that there has been less incentive to vary them. The input parameters are distinguished in the worksheets by appearing in bold type.

3. The formulae:

Most of the formulae are familiar to accelerator physicists. Some of them are valid only for the SSC. These

are either obtained from computer simulations (e.g., the dynamic apertures) or derived specifically for the SSC (e.g., the filling factor and the cycle times).

III. APPLICATIONS

A. Operation Scenarios

SSP has been used to study a number of cases. Among them are:

- Case A - Nominal;
- Case B - Commissioning;
- Case C - High luminosity, $\mathcal{L} = 10 \times 10^{33}$;
- Case D - High energy, $E = 23$ TeV.

The input parameters of each case are listed in Table 2. The results are not included here because of the lack of

space. In general one sees that, when the input parameters vary, the color of some flagged parameters will change to red. This indicates specific care is needed in order to adjust their values such that the color will turn back to green or yellow.

Table 2. Input Parameters

Case	A	B	C [†]	D
E (TeV)	20	20	20	23
\mathcal{L} ($10^{33} \text{ cm}^{-2} \text{ s}^{-1}$)	1	0.4	10	1
S_B (m)	5	20	10	5
ϵ_N (π mm-mrad)	1	3	2	1
ϵ_L (π eV-s)	0.233	0.233	0.466	0.233
β^* (m)	0.5	1	0.5	0.5
P_{linac} (GeV/c)	1.219	1.219	1.7	1.219
p (10^{-8} Torr)	1	5	1	1

[†]In Case C, two medium luminosity IP's are turned off to avoid large beam-beam tune shifts.

B. Parameter List

An on-line parameter list has been generated by the SSP program. The advantage of maintaining the list in such a way is that it is self-consistent and easy to update. The parameter list is on the node SSCVX1.SSC.GOV. One can have access to the list through a computer network either inside or outside the laboratory, by typing *SSCLAB* as the username [1]. The parameter list serves as a quick reference guide and is consistent with the Level 3 Specifications of the machine designs.

C. Impact of Parameter Changes

In the parameter space, when one changes, the others will follow suit. The SSP program is useful for this kind of study. Here we present two examples.

1. The choice of the rf frequency:

The program has investigated the impact of the rf frequency when it varies from 180 MHz to 480 MHz. It shows that the changes of most beam parameters are small [2]. It is thus concluded that the choice should be based on other factors, such as the beam transfer from the HEB to Collider, the cost, and market availability.

2. The bunch spacing:

The baseline bunch spacing in the SSC is 5 meters, which is mainly determined by the requirement of the detectors. But a larger bunch spacing is advantageous to the luminosity. In order to accommodate the flexibility of different bunch spacings in the accelerator design, the program has been employed to study the impact on the beam parameters when the spacing is increased to a multiple of 5 meters, using either the bunch coalescing scheme or the rf chopping scheme [3]. The possible bottlenecks are identified immediately by the program and a follow-up study is now under way.

IV. DISCUSSION

1. SSP is easy to use. By clicking the mouse a few times, one may readily make a judgment on whether or not a proposed operation scenario or parameter change would work. But SSP is neither robust nor bug-free. Care must be taken before drawing conclusions.
2. The present list of the flags is by no means complete. More flags will be added to the future version when the necessary information becomes available (e.g., vacuum, coupled-bunch instabilities, transition crossing, etc.).
3. SSP is not written for optimization. In other words, the control parameters need to be adjusted manually rather than by a computer search. Implementation of a search procedure should be straightforward but may be premature at this time.
4. A similar program has been developed for the LHC and its injectors (PS Booster, PS and SPS).

V. REFERENCES

- [1] T. Barts and W. Chou, "SSC Parameter List," SSCL internal technical note PMTN-073P (May 1993).
- [2] W. Chou and G. Schaffer, "Comments on the Collider rf Cavity in the SSC," SSCL internal technical note PMTN-036C (January 1992).
- [3] W. Chou, "Comments on Bunch Spacing in the SSC," SSCL internal technical note PMTN-0060P (March 1993).

Lattice Studies for KAON Factory Accumulator and Booster Rings

A. I. Iliev *, A.V. Budzko *

INR, 7-A 60th October Anniversary Prospect, Moscow, Russia 117312

R. V. Servranckx

TRIUMF, 4004 Wesbrook Mall, Vancouver, B.C., Canada V6T 2A3

Abstract

Some results of systematic studies of alternative lattices for the TRIUMF KAON Factory Accumulator and Booster rings are presented. The aim has been to seek lattices of a compatible form for both rings which have the following features: simple structure, dispersion-free straight sections, high transition energy for the Booster and a straight section of about 7 m with finite dispersion for H^- injection into Accumulator.

I. INTRODUCTION

The development of the racetrack Booster lattice [1] stimulated a search for a compatible racetrack design for the Accumulator ring. The lattices for the Booster and for the Accumulator, sharing the same tunnel, have different requirements which prevent to designing Accumulator as an emptier variant of the Booster ring. The main constraints for A-ring optics are induced by the requirements for H^- painting [2], i.e. providing about ≈ 7 m long drift unobstructed by quadrupoles for placement of the injection septum, bump magnets and centrally located stripping foil; achieving momentum resolution $\eta_n \equiv \eta/\sqrt{\beta_x}$ of about $1.3 \sim 1.5 \text{ m}^{1/2}$ and $\eta'_n = 0$ at the foil location, depending on the size of painted area; and minimising $\beta_{x,y}$ at stripping foil.

A number of alternative lattices for the Booster were considered with the aim of overcoming the weaker features of the standard [1] lattice, i.e. a rather large number of quadrupole families and lack of space in the arcs for momentum collimation.

II. ACCUMULATOR

Two approaches have been investigated: 1) lattices with injection in the long straight sections, 2) lattices with injection into the arc. Our study [3] indicates that the lattice with injection in a straight section is flexible for altering the momentum resolution, though it requires retuning their straight section and/or arcs, and exhibits good incoherent properties w.r.t. linear space charge. However, the finite dispersion required in both straights makes the transfer from Accumulator to Booster more difficult, involving both horizontal and vertical bending. It looks better to provide H^- injection in an arc rather in a long straight.

The sample lattice investigated (ARS4.v22) has the same number of cells and superperiods per arc as the standard Booster racetrack lattice ($S = 4, N = 3$) but has

a different structure in the superperiod: the first half-cell of each superperiod being empty creates a double waist for injection. The tune of each superperiod is 0.5, and hence the dispersion vanishes after passing two superperiods. The overall tunes are just above 5 in both planes. Fig. 1 shows the lattice functions for this lattice. The difference in shape compared to the B-ring seems to be acceptable (< 1 m) and has a bonus of leaving more room for the A-to-B transfer line. The momentum resolution at

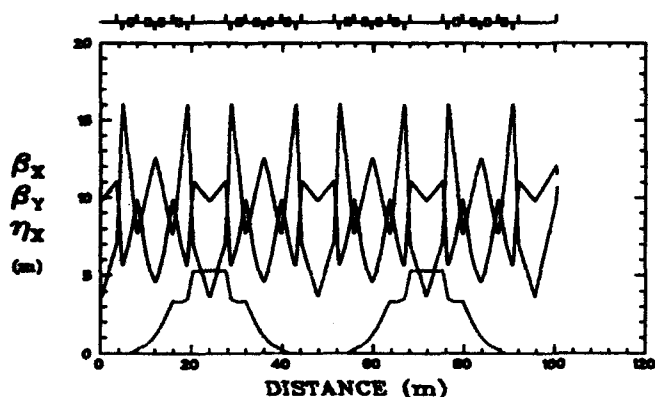


Figure 1: Lattice functions for racetrack Accumulator ARS4.v22.

the foil $\eta/\sqrt{\beta}$ is about 1.58, that is near the optimum value for the 40 Hz Booster scenario. However painting a smaller transverse area, required smaller momentum resolution, is more difficult — only small changes in η_n can be achieved, and even at the expense of a higher beta-function at the stripping foil.

For potential chromaticity correction four sextupoles are arranged in each arc in non-interleaved 180° pairs and placed in high dispersion regions with extreme $\beta_{x,y}$ to reduce coupling between the pairs. This scheme perfectly cancels sextupole-induced geometric aberrations, resulting in a quite large dynamic aperture for on-momentum particles (d.a. $> 1000 \pi \text{ mm mrad}$), though the chromatic aberrations are noticeable: off-momentum distortion in the β -functions is about 2 m in both planes.

During accumulation the peak current will increase from 0 to design value of $\approx 6.5 \text{ A}$ (depending on the beam distribution). To study the dependence of the lattice functions on linear space charge we have developed code *LinSp* [4] which is able to find a matched solution of envelope equations and then calculates Twiss parameters, dispersion, transition energy and chromaticity, as well as providing the stability analysis by computing eigenvalues λ_i of linearised envelope equations. We have found that the lattice is quite sensitive to integer resonances, leading to blow

*On leave at TRIUMF, Vancouver, B.C., Canada

up of either amplitude function and/or dispersion. Thus the bare tunes were chosen far from integers (5.28, 5.32), so crossing of an integer occurs only at higher intensity (about 16 A); for lower currents (up to 14 A) dispersion and amplitude functions change only a little (see Fig. 2).

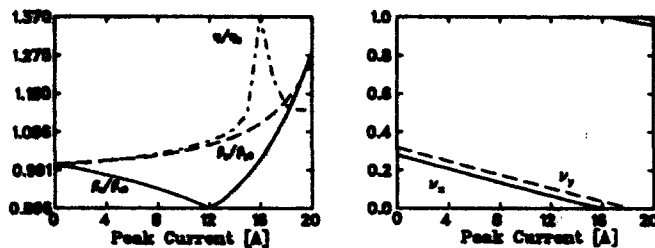


Figure 2: $\frac{\beta_{x,y}^{sp.ch.}}{\beta_{x,y}^{sp.0}}, \frac{\eta_x^{sp.ch.}}{\eta_x^{sp.0}}$ (dot-dashed), tunes vs. peak current for sample lattice *ARS4_v22* with gradient errors 0.1% rms.

The lattices considered so far for the Accumulator and Booster have a relatively large number of quadrupole families (four families in the arcs). G. Rees [5] has proposed an alternative racetrack lattice for the Accumulator ring, which has a remarkable feature of having only two quadrupole families. Unfortunately the divergence from the geometry of the racetrack Booster is unacceptable. Rees's attempt at designing a racetrack lattice without matched insertions has, however, prompted us to look at alternative designs for Accumulator and Booster.

The alternative lattice for the A-ring has a triplet focusing structure. Each arcs are made of 3 superperiods. Each superperiod consists of 3 cells with the central cell being empty to provide an ≈ 8.7 m-long drift for injection. Due to this structure and the phase advance per cell of 90° , the dispersion vanishes over one superperiod with a local peak of ≈ 3 m, and the corresponding momentum resolution is near the optimum $\approx 1.3 \text{ m}^{1/2}$. Advantages include the need for only two quadrupole types, and the same focusing structure in the long straight sections and the arcs, making the lattice easier to commission and run. Disadvantages include the shorter straights, which result in a potential problem of lack of space for the A-B transfer line, and larger divergence of the ring shape from the current standard racetrack Booster.

III. BOOSTER

The alternative lattice investigated, *NEWBR*, has 5 cells and two superperiods per arc, the tune of each superperiod being 1.5. Two empty cells are provided in each superperiod: one at the ends and one in the centre. Such an arrangement is required in order to push up γ_t . Transition is at $\gamma_t \approx 13$ and the peak dispersion is about 5.3 m. The straight sections are built from the same FODO cells as the arc's superperiods. The nominal working point is (7.83, 6.74).

The lattice functions for this lattice are shown in Fig. 3. Since canceling the dispersion at the ends of the arcs together with raising γ_t required a rather high phase advance

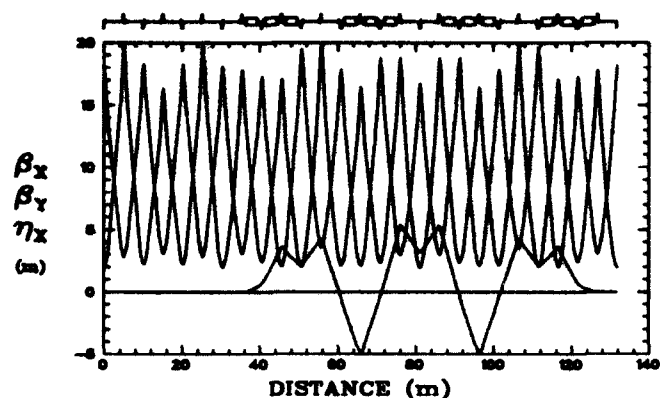


Figure 3: Lattice functions for alternative racetrack Booster *NEWBR*.

per cell (108 degrees) the lattice has a higher peak beta-function in the arcs (≈ 20 m) than the standard racetrack design. Since the arcs are not second-order achromats chromaticity correction is more difficult. A comparative study of closed orbit corrections indicates that both lattices (alternative and standard) have similar good stability against misalignments and field setting errors: the maximum residual orbit excursion after correction does not exceed 3 mm. However, the variation of the peak dispersion in the arcs and the amount of spurious dispersion in the straight sections were found to be less in the standard lattice: $\sigma_d < 1\%$ against $\sigma_d < 4.5\%$, $\eta_{ss} < 0.015$ m against $\eta_{ss} < 0.034$ m.

Particle tracking for the chromaticity-uncorrected lattices, with misalignments, field and systematic multipolar errors, have shown that d.a. for the standard lattice *BRS4* is in the range of about 750-950 π mm mrad with dips near $\Delta p/p = 0$ and 0.3%. The dynamic aperture for the alternative lattice lies in the range of about 350-750 π mm mrad with two dips in acceptance near $\delta p/p = 0.2\%$ and 0.4%. For low-amplitude motion the dominating resonances in both lattices are the coupling resonances $\nu_x \pm \nu_y$, which can be corrected by skew quadrupoles, but as the amplitude of the particles is increased, odd order coupling resonances (mainly $\nu_x - 2\nu_y$ and $3\nu_x - 2\nu_y$) become stronger, resulting in a quick loss of stability in the *NEWBR* lattice. We found that for both lattices the d.a. dropped very fast with increasing multipolar harmonics B_4 and B_6 up to about $3 \cdot 10^{-4}$.

Both lattices exhibit similar momentum dependence of tunes and beta-functions, but the higher order off-momentum dispersion is much larger for the *NEWBR* lattice: $\eta_{eff} = dx_{co}/d\delta \approx -0.018$ m, also leading to a noticeable momentum dependence of the γ_t . The effect on beam stability will have to be carefully evaluated.

To reduce number of quadrupole families a modified standard lattice has been considered (*b-feb10*). The lattice has the same 8×3 FODO structure of arcs, but the empty cell in each superperiod is not shortened anymore. Each long straight is simply 3 regular empty cells which are similar to those in the arcs. Hence only 2 quadrupole families are required, while space for momentum collima-

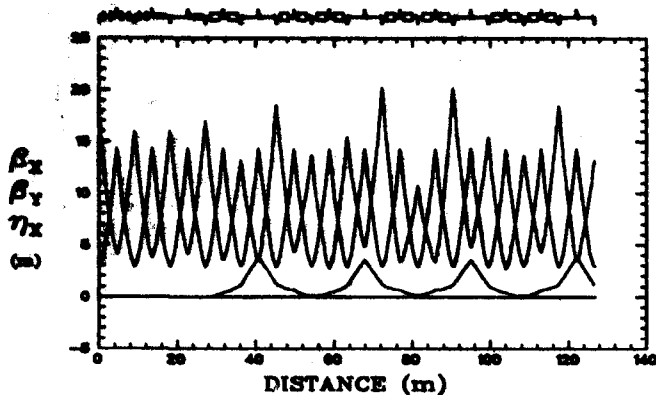


Figure 4: Lattice functions for alternative racetrack Booster b-feb10.

tion is created, though at the expense of shortening each straight by ≈ 10.5 m. The available space in the straights is still sufficient for rf cavities and beam transfer systems. Some of the features of the lattice: 1) slightly higher peak vertical beta-function in the arcs (18.5 m) due to β_y mismatch in the empty cells (this can be eliminated by trim quads); 2) working points either below half-integer $\rightarrow \gamma_t \approx 9$, or above half-integer $\rightarrow \gamma_t \approx 11-12$ (in both cases dispersion in the straight differs only slightly from zero); 3) good stability under space-charge conditions; 4) less room available for the A-B transfer line.

This lattice seems to be an interesting alternative to the standard design and has to be investigated in detail for placement of all the necessary hardware.

IV. SPACE-CHARGE EFFECTS IN THE BOOSTER

Self-consistent space-charge effects of the unbunched beam in the standard racetrack Booster have been studied by using a particle-in-cell computer code developed at INR [6]. Several runs have been performed for 2-D initially K-V and Gaussian distributions at a bare tune close to the half-integer (7.65, 5.6). *LinSp*'s prediction of envelope instability for beam with the phase-space density ($J = \bar{I}/\epsilon_{rms}$) of $\approx 0.5 - 1.25$ A/ π mm mrad has been confirmed by observing emittance blow-up for an initially K-V beam in the ideal lattice, while an initially Gaussian distribution has shown a smaller growth of rms emittance. After introducing rather strong quadrupole imperfections ($\sigma_{AQ}/Q = 0.3\%$) we have observed large rms and full size emittance growth in the x-plane in the range $J \approx 0.72-1.3$ (see Fig. 5, where the core width, i.e. 38% of all particles, widths of middle (68%) and tails (95%) are plotted versus phase-space density I/ϵ_0). This can be compared with the results of a *LinSp* run for a lattice with quadrupole errors (Fig. 6). Here we clearly see a point of bifurcation ($J \approx 0.853$), where a unique (unstable) equilibrium splits into two branches. Bifurcation of equilibrium produces changes in the topological structure of the phase-space distribution, which have been observed in computer simulations.

V. ACKNOWLEDGMENTS

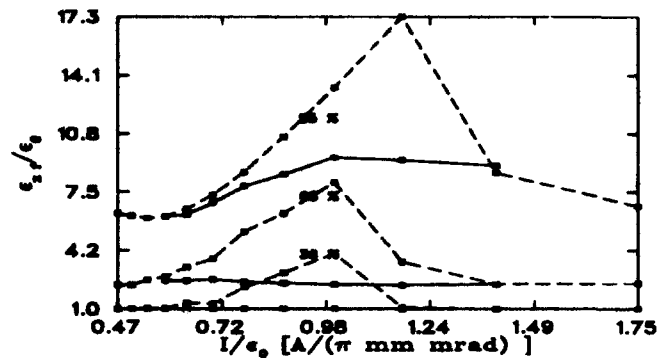


Figure 5: Core, middle and tail widths against phase space density (dashed/solid line — with/without quad. errors).

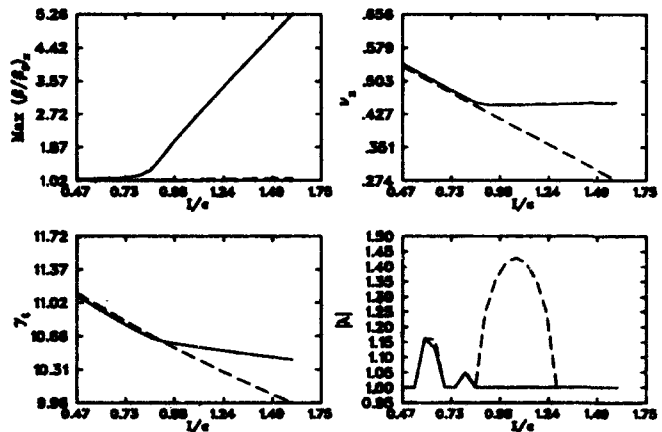


Figure 6: $\frac{\partial \epsilon_{ch}}{\partial \epsilon_0}$, ν_y , γ_t and $|\lambda|$ vs. phase space density for lattice w/ quadrupole errors.

We would like to thank Prof. M. Craddock for hospitality during our (A.I., A.B.) stay at TRIUMF. We are grateful to him for his support and encouragement during this work. We have benefited from discussions with U. Wienands, G. Mackenzie, R. Baartman, S. Koscielniak, Yu. Senichev. Some of the work in the lattice designs has been aided by the suggestions and insight of G. Rees.

VI. REFERENCES

- [1] U. Wienands *et al.*, "A Racetrack Lattice for the TRIUMF KAON Factory Booster," in *proc. of XVth Int. Conf. on High Energy Accel.*, Hamburg, 1992, p. 1073
- [2] C. W. Panner, G. H. Rees, G. H. Mackenzie, "A separated H⁻ Injection System in a Modified Accumulator Lattice for the TRIUMF KAON Factory," TRI-DN-89-K98, TRIUMF, December 1989
- [3] A. Iliev, "Lattice Studies for Accumulator ring," TRIUMF, 1993, (in preparation)
- [4] A. I. Iliev, "LinSp code for lattice parameters computation in presence of linear space charge," TRIUMF, 1993, (in preparation)
- [5] G. Rees (private communication)
- [6] A. V. Budsko, Yu. V. Senichev, "Passing Through Half-Integer Resonance due to space-Charge Under Different Initial Distributions," these proceedings

Reducing the Coupled-Bunch Oscillation in the Fermilab Booster by Optimizing RF Voltage

J.P. SHAN, D. MCGINNIS, R. TOMLIN

Fermi National Accelerator Laboratory * P.O. Box 500, Batavia, IL 60510

Abstract

In the Fermilab Booster, the coupled bunch oscillation is excited between transition and extraction by parasitic high order modes (HOM) in 17 RF cavities. The growth rate is determined by the coherent frequency shift and natural Landau damping due to nonlinearity of RF waveform. The passive damping and active feedback are normally used to reduce coherent frequency shift. Here we report that Landau damping can be enhanced through careful programming of RF voltage through the acceleration cycle. It is very effective during ramping where synchronous phase is big and bucket area is very sensitive to the RF voltage. In the case of a stationary bucket, the Landau damping is not sensitive to RF voltage.

1 Introduction

The Fermilab Booster is a fast cycling synchrotron, accelerating protons from 200 MeV to 8 GeV in 33 ms. The 8 GeV beam extracted from the Booster will be injected into the Main Ring (MR), which has a very limited transverse aperture. To achieve high transmission in the MR, it is desirable that the Booster beam has small momentum spread. Also the beam accelerated in the MR will either be used to produce antiprotons, or coalesced to single bunch. Both the antiproton stacking and the proton coalescing prefer beam from the Booster with small longitudinal emittance.

In the Booster the longitudinal emittance growth is due to transition crossing and longitudinal coupled bunch instability after transition. Some years ago the γ_t jump system [1] was implemented to increase effective transition crossing speed, thus reducing the longitudinal emittance blow up through transition. Although the γ_t jump did reduce emittance growth due to transition crossing, the smaller bunch after transition resulted in more pronounced longitudinal coupled bunch instability. So the γ_t jump system was not used operationally. So it is coupled bunch oscillation that limits the longitudinal performance in the Booster.

The individual coupled bunch oscillation mode has been identified to be strongly correlated to the parasitic modes in the RF cavities [2]. There are mainly two clusters of

coupled bunch mode, one around mode 16 and another around mode 36. Following the installation of resistive dampers [3] [4] in the RF cavities, modes around mode 16 are successfully damped. Modes 34, 35 and 36 still persist. The narrow band active damper is able to damp any one of three modes, but not all of them simultaneously. The wide band system is under design [5]. The coupled bunch oscillation is still the limitation of longitudinal performance. Operationally the coupled bunch oscillation is reduced by mistuning transition timing. If we try to operate at nominal (optimized) γ_t jump timing and phase jump timing, very strong CBM is excited.

We report the coupled bunch oscillation can be reduced by careful programming of RF voltage after transition. The nominal RF voltage curve has bucket area larger than 0.2 eV-s, which is much larger than the beam emittance (about 0.06 eV-s). So one way to increase the synchrotron tune spread is to let beam fill the bucket by the reduction of RF voltage [6].

2 Review of Sacherer Theory

The rule of thumb for coupled bunch instability is [7]

$$\frac{S}{\Delta\omega_m} > \frac{4}{\sqrt{m}} \quad (1)$$

where S is the synchrotron tune spread inside the bunch, and $\Delta\omega_m$ is the coherent frequency shift of mode m caused by a resonator shunt impedance R_s and quality factor Q

$$\Delta\omega_m = \frac{\omega_s R_s I D F_m(\Delta\phi)}{2\pi V_{rf} B} \quad (2)$$

where I is beam current, ω_s synchrotron frequency at the center, $F_m(\phi)$ is the form factor which specifies how efficiently the resonator can drive a certain mode m . The term D depends on the attenuation of the resonator signal between two bunches, and is about 1 for high Q resonator.

The quantity we want to maximize is

$$\frac{S}{\Delta\omega_m} \propto \frac{S}{w_s} V_{rf} B \frac{1}{NR_s} \quad (3)$$

The role of mode damping and the active feedback is to reduce the effective shunt impedance. The RF voltage should be programmed to maximize the figure of merit

$$FOM = \frac{S}{w_s} V_{rf} B \quad (4)$$

*Operated by the Universities Research Association Inc., under contract with the U.S. Department of Energy.

assuming the form factor is a constant. When ϕ_s is big, we reduce RF voltage by little to end up increasing the fractional synchrotron tune spread dramatically. But for a stationary bucket, the bunch length changes as $V_{rf}^{-1/2}$. To the first order approximation, $\frac{s}{w_s}$ is proportional to the square of bunch length. So

$$FOM \propto V_{rf}^{1/2}, \quad (5)$$

which has a very weak dependence on V_{rf} .

3 Result in the FNAL Booster

By reducing the RF voltage after transition as shown in Fig. 1, the coupled bunch oscillation is successfully reduced. Comparing the spectrum in Fig. 2 (triggered at 34ms, 1.5ms before extraction), coupled bunch mode has been lowered by 8 Db on the average of 32 pulses. Upon inspection, all three primary modes (34, 35 and 36) have been damped. With this new RF curve, there is couple bunch oscillation till roughly 32ms in the cycle. After that the synchrotron tune spread is not big enough to suppress coupled bunch instability entirely. The mountain range plot is shown at extraction with old RF curve at Fig. 3 and with the new one at Fig. 4.

As a result, the longitudinal emittance is further reduced and the transmission efficiency is increased. A new MR intensity record is created 2.17×10^{12} for 6 Booster turns (2.5×10^{12}), which is helpful to improve the antiproton stacking rate. For 7 Booster turns, the booster can accelerate 2.6×10^{12} , of which (2.53×10^{12}) injected to MR and 2.20×10^{12} accelerated to 120 GeV.

4 Discussion

The result in the booster verifies that the RF voltage reduction is a very effective way to increase landua damping when ϕ_s is bigger and becomes ineffective when synchrotron phase is small at extraction.

The reason for big variation of coupled bunch oscillation amplitude from pulse to pulse is not well understood. Good understanding of this variation may provide us better way to of controlling.

With upcoming 400 MeV upgrade, the intensity in the Booster will be doubled. So the coherent frequency shift will also be doubled if the longitudinal emittance is the same as now. Hopefully the wideband active feedback will come to the action. But the feedback system is only sensitive to the coherent dipole oscillation. Once dipole oscillation comes under control, the potential higher order (likely quadrupole) oscillation will become a concern.

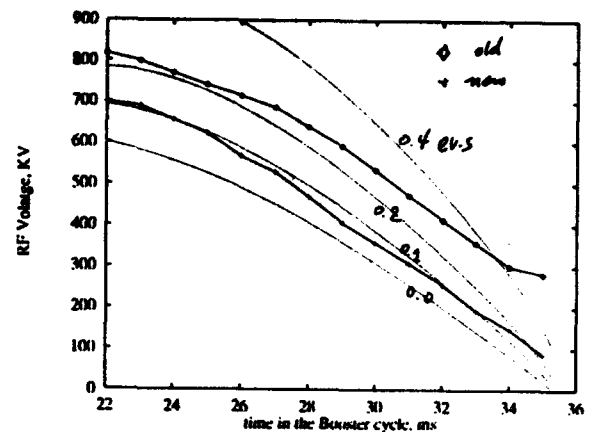


Figure 1: The RF voltage curve after transition in the Booster. The old curve starts with a bucket area 0.2 evs and increases to larger than .4 evs at extraction. The new starts with .1 evs and increases to 0.2 evs.

DSA 602A DIGITIZING SIGNAL ANALYZER
date: 23-FEB-93 time: 17:48:59

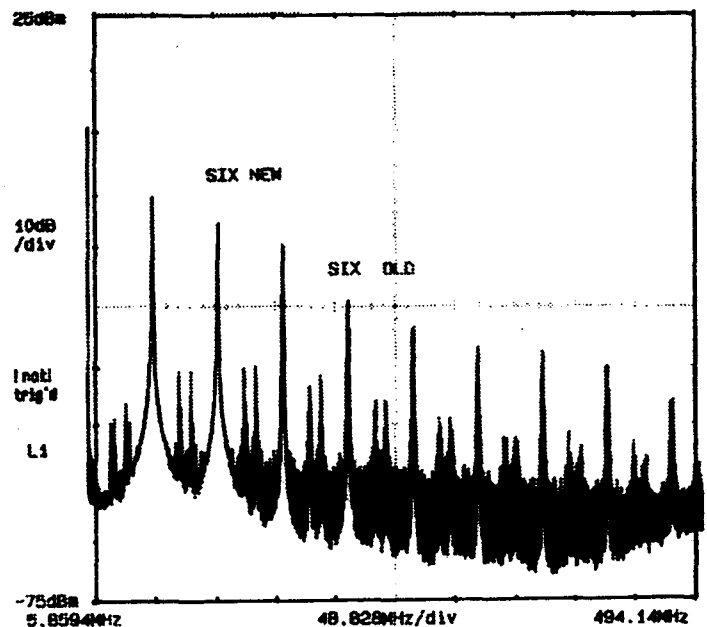


Figure 2: The beam spectrum in the Booster at 34.5ms averaged with 32 pulses. The reduction of 8 Db in coupled bunch modes with new RF rf curve is visible.

Acknowledgements

We want to thank J. Garety to tell us the successful story in the CERN PS. And one of us Shan want to thank the member of the Booster group for the support.

References

- [1] W. Merz, K. Koepke, and C. Ankenbrandt. γ_t jump system in the Fermilab Booster. In *PAC 87*, pages 1343-, 1987.
- [2] V. Bharadwaj et al. Coupled bunch instability and longitudinal emittance growth in the Fermilab Booster. In *Proc. XIVth Int. Conf. on High Energy Accelerators*, 1989.
- [3] D. Wildman and K. Harkay. HOM rf cavity dampers for suppressing coupled bunch instabilities. In *these proceedings*, 1993.
- [4] K. Harkay, P. Colestock, and A. Gerasimov. Comparison of the coupled bunch mode theory to experimental observations in the Fermilab Booster. In *these proceedings*, 1993.
- [5] J. Steinel and D. McGinnis. Damping in the Fermilab Booster. In *these proceedings*, 1993.
- [6] D. Boussard and J. Gareyte. Damping of the longitudinal instability in the CERN PS. In *Proc. VIIIth Int. Conf. on High Energy Accelerators*, pages 317-320, 1971.
- [7] F. Sacherer. A longitudinal critier for bunched beam. *IEEE Nul.*, 20(3), June 1973.

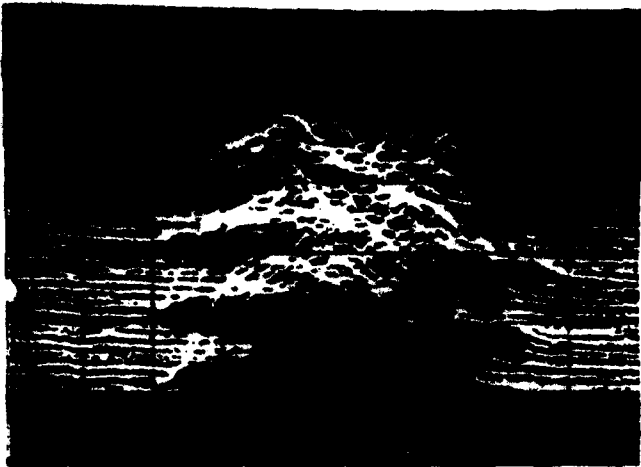


Figure 3: The typical mountain range display at extraction (33.5-35.5 ms) with old RF curve. The intensity is 2.2×10^{12} , the swip is 1 ns/div. The γ_t jump trigs at 18.72 and the transition phase jumps at 18.76ms.

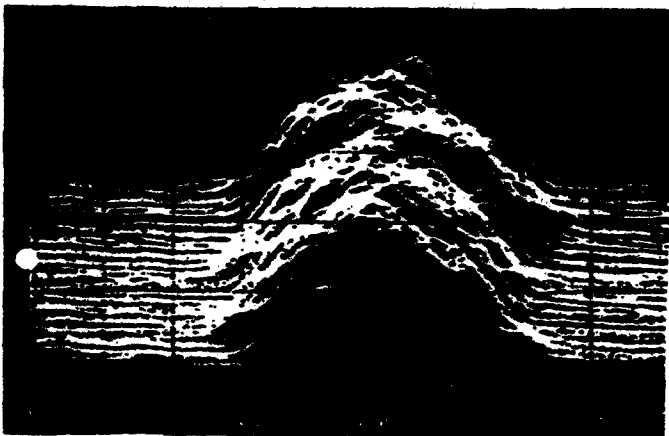


Figure 4: The same mountain range plot with new RF curve.

Beta Measurements And Modeling The Tevatron

Norman M. Gelfand

Fermi National Accelerator Laboratory*

P.O. Box 500, Batavia IL 60510, USA

Abstract

The Tevatron is currently operating as a collider with two low- β ($\beta^* = 0.25-0.5\text{m}$) interaction regions denoted as B0 and D0. This lattice allows independent operation of the interaction regions which required that the previous collider lattice, used in 1988-89, had to be modified. In order to see how well the lattice conforms to the design measurements of the β function have been carried out at 15 locations in the new Tevatron collider lattice. Agreement can be obtained between the measurements and a computer model for the Tevatron, based on the design, only if the strengths of the gradients in the quadrupoles in the low- β triplet are allowed to differ from their design values. It is also observed that the lattice is very sensitive to the precise values of the gradients in these magnets.

I. INTRODUCTION

The Tevatron is currently operating as a collider with two low- β ($\beta^* = 0.25-0.5\text{m}$) interaction regions denoted as B0 and D0. This lattice was designed to allow independent operation of the interaction regions so that the previous collider lattice, used in 1988-89, had to be modified. The design of these new low- β insertions required the construction of new, strong, quadrupoles to get to the desired value of $\beta^* = 0.25\text{m}$. In addition new quadrupole correctors are required outside of the triplet to match the lattice functions of the low- β insertion with the values in the lattice arcs at the matching point, an essential requirement if operation of the interaction regions is to be independent.

In addition to a new interaction region at D0, the closed orbit is a helix produced by electrostatic separators in order to reduce the beam-beam interaction between the colliding protons and anti-protons. This allows us to run with smaller proton emittances and thus increase the luminosity. Additional separators are used to make the beams collide head on at the interaction points. This complicates operations but has only a small effect on the lattice functions.

As with any new facility it is very desirable to test how well the actual performance matches the design expectations. With this as our objective, the lattice function β was measured at locations within the insertion, and also at one point in the arc, and the results compared to the calculations of β based on the design lattice. This note describes the results of that comparison.

II. METHOD

The method used to measure the amplitude function β was proposed by Courant and Snyder in their original paper on the Alternate Gradient Synchrotron[1]. The procedure is to

*Operated by Universities Research Association Inc., under contract with the United States Department of Energy.

vary the strength of a single quadrupole, at a point in the lattice where it is possible to do so, and measure the resulting change in the tune in both planes. The change in tune is related to the value of β at that point according to the following formula:

$$\beta = 4\pi \Delta w / (\Delta k^2)$$

where $\Delta k^2 = \Delta B' / [B\rho]$ and $\Delta B'$ is the change in the gradient of the quadrupole.

Because this relation is true only in the limit of very small $\Delta B'$, at which the change in tune is not measurable, tune changes were measured over a range of $\Delta B'$ and the data were fit to a second order polynomial. The slope of the fit at $\Delta B' = 0$ gives the desired value of β .

The measurements of β , using this procedure, were made at 7 locations on both sides of the interaction regions at B0 and D0 and at the location of a tuning quadrupole at B17. During these measurements there were only protons in the Tevatron.

It is obvious that no measurements, using this approach, can be made at the interaction points since those points must be left clear for the experiments. Further the low value of β there means that even if a quadrupole could be placed at the interaction point large changes would have to be made in the gradient to observe any tune shift. Knowledge of the values of the lattice functions at the interaction point must come from a model of the lattice.

III. COMPARISON WITH A MODEL FOR THE TEVATRON

An accurate model of the Tevatron would be able to reproduce the measurements made of the β function described above. As is seen the agreement between the measurements and the model using the design values for the the quadrupole gradients is not good (see figure 1a,1b,1c). The reason for the discrepancy came from inadequate knowledge of the transfer functions (the relationship between the current in the magnet and the resulting gradient) of the strong quadrupoles in the magnetic triplet.

The β function in the present low- β Tevatron lattice is very sensitive to small changes in the strengths of the quadrupoles in the low- β triplet. Figure 2 shows the change in the β function in the arcs when the gradients of the 232" quadrupoles at B0 are changed by 0.1%. In order to predict the behavior of the β function in the Tevatron it is necessary to know the transfer constants, i.e. the relationship between the current through the quadrupole and the resulting gradient, for the magnets in the triplet to better than 0.1%.

The fabrication methods used to construct these quadrupoles would lead us to expect magnet to magnet variations in the transfer constant of 0.05% for the 232" quadrupoles and 0.07% for the 132" quadrupoles. Thus the manufacturing tolerances are not good enough to enable us to predict the characteristics of the lattice. The other new

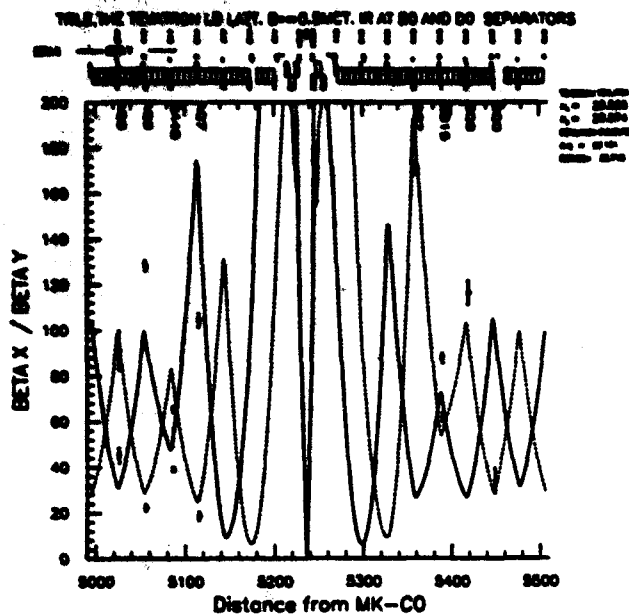


Figure-1a

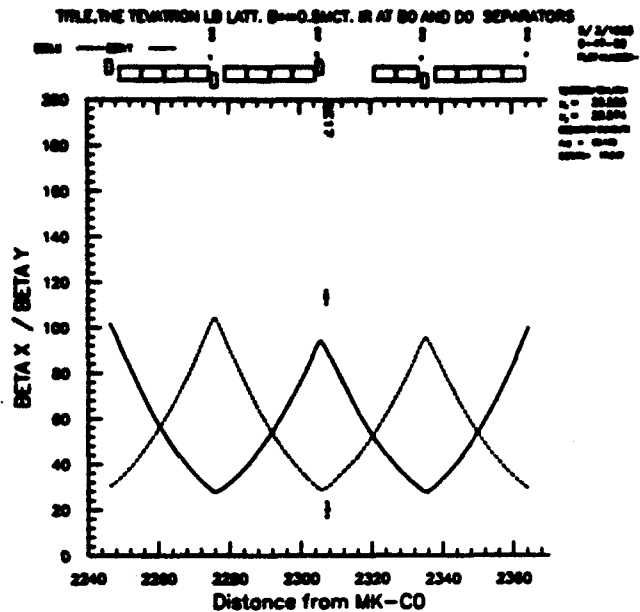


Figure-1b

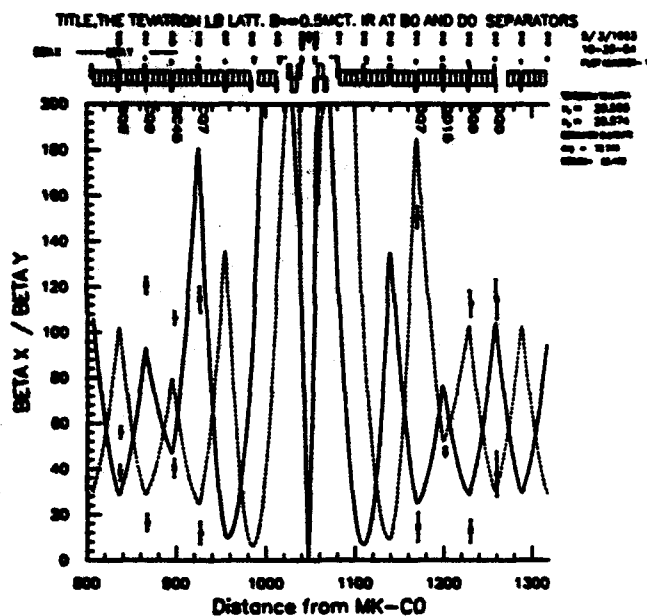


Figure-1c

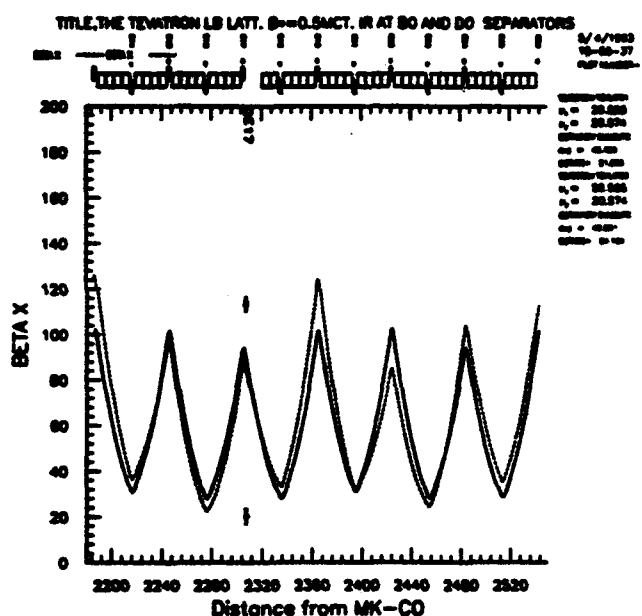


Figure-2

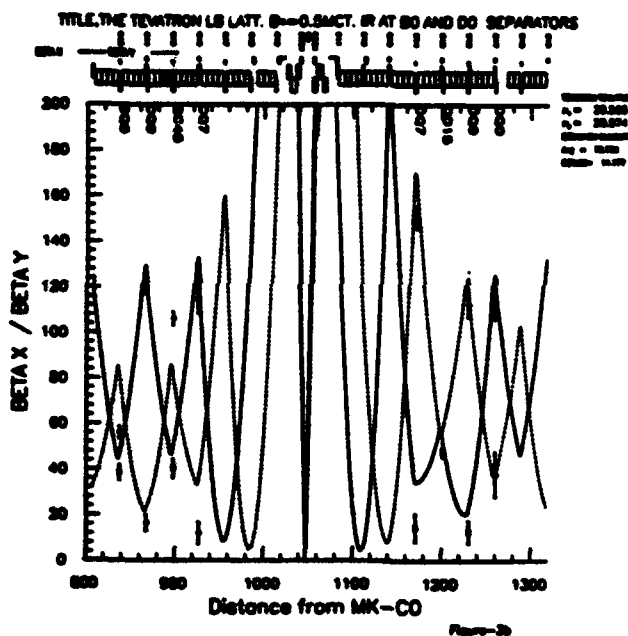
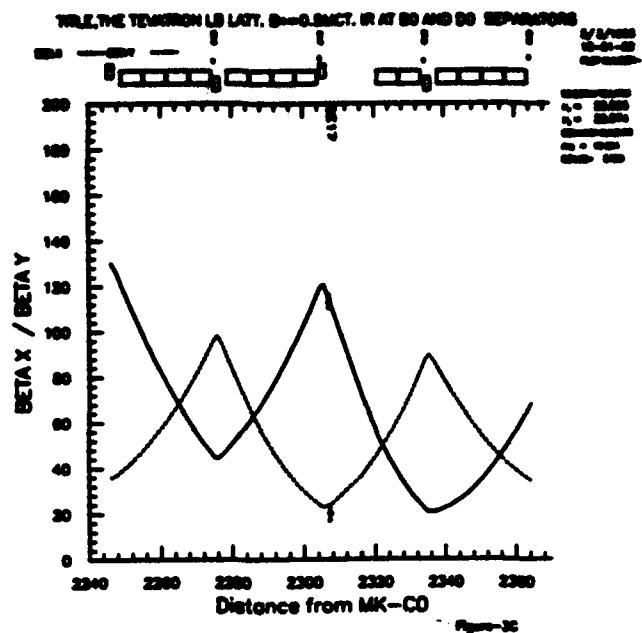
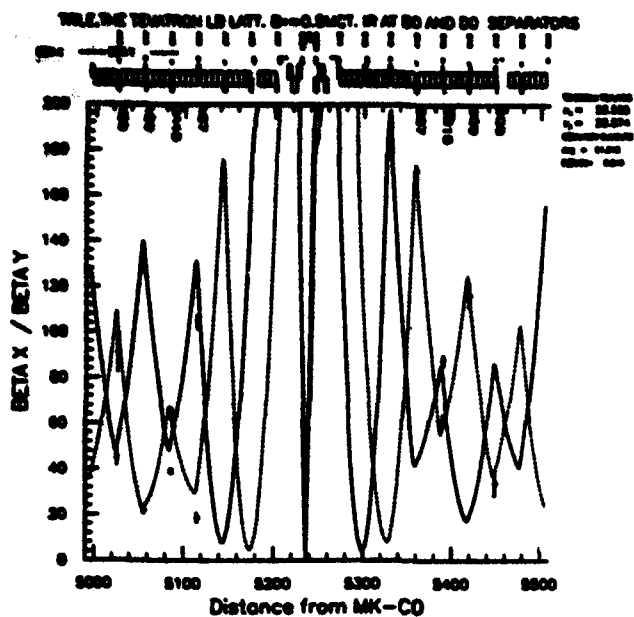
quadrupoles in the low- β insertions have larger uncertainties ($\sim 0.1\%$) but are weaker and are also at points in the lattice where they are less critical in determining the values of β .

An attempt was made to measure the transfer constants at the Fermilab Magnet Test Facility (MTF). Unfortunately there were serious problems with the measuring techniques which made the absolute values of the measured transfer constants unreliable, and therefore they have not been used in our model calculations.

Despite the fact that we could not measure, at MTF, the absolute values of the transfer constants we should be able to make use of the relative strengths of the magnets as measured at MTF to account for the variance in quadrupole gradient due to manufacturing tolerances. These relative measurements have been incorporated into our model.

We have attempted to fit the measured values of β varying, in our computer model, the strengths of the magnets in the triplet. Unfortunately the properties of the triplet are such that the three quadrupoles are at essentially the same phase. This means that we are unable to extract meaningful values only for the strength of the triplet and not for the individual elements.

We find reasonable agreement between the model and the data with reasonable changes in the nominal values of the quadrupoles in the triplet (figure 3a,3b,3c). Because of the correlation between the fitted transfer constants this procedure does not yield the values of the transfer constants for the individual quadrupoles but the procedure does give a reasonable model of the lattice.



IV CONCLUSIONS

The β function in the Tevatron collider lattice is very sensitive to the precise values of the strengths of the quadrupoles in the low- β triplet. Changes in the integrated gradients by 0.1% can produce significant changes in β in the arcs as well as in the low- β insertions.

We have been able to get reasonable agreement between the measured values of β and our model by making reasonable changes in the nominal values of the strengths of the magnets in the triplets producing the low- β interaction point.

V. REFERENCES

- [1] E. D. Courant and H.S. Snyder, "The Theory of the Alternating Gradient Synchrotron", *Ann of Phy* Vol 3, No 1, 1(1958).

The Status of the Fermilab Main Injector Project

D. Bogert, W. Fowler, S. Holmes, P. Martin and T. Pawlak
Fermi National Accelerator Laboratory*
P. O. Box 500, Batavia, IL 60510

Abstract

The Fermilab Main Injector Project is a new 150 GeV synchrotron now under construction at the Fermi National Accelerator Laboratory. The FMI has been designed to support a luminosity in excess of $5 \times 10^{31} \text{ cm}^{-2} \text{ sec}^{-1}$ in the Tevatron proton-antiproton collider while simultaneously providing a 2 microAmp resonantly extracted 120 GeV beam which will present unique capabilities in the realm of rare neutral K decays and long baseline neutrino oscillation experiments. Expected performance characteristics of the Main Injector will be reviewed, and the status of the project and the schedule for completion will be discussed.

The Fermilab Main Injector is the final piece of a program, known as Fermilab III, which is designed to produce an approximate factor of 10 increase in the Tevatron Collider luminosity as compared with the current performance of $6 \times 10^{30} \text{ cm}^{-2} \text{ sec}^{-1}$. [1] In itself, the Fermilab Main Injector (FMI) is designed, and expected, to yield a factor of 5 increase over the luminosity achieved by all the other modifications installed in the Tevatron complex prior to the commissioning of the Main Injector. The primary design goal is to achieve an operating luminosity in the Tevatron Collider of at least $5 \times 10^{31} \text{ cm}^{-2} \text{ sec}^{-1}$. All components of the Fermilab III program built and commissioned to date have met or exceeded their design performance, yielding a hope of not only achieving the $5 \times 10^{31} \text{ cm}^{-2} \text{ sec}^{-1}$ luminosity, but perhaps reaching a level of performance up to $1 \times 10^{32} \text{ cm}^{-2} \text{ sec}^{-1}$. The exact expectation can be more precisely stated after operation of the Tevatron Collider with the Linac Upgrade (an earlier part of Fermilab III) is achieved in late 1993.

The FMI project goal is to functionally and physically replace the operation of the 150 GeV accelerator (the original Fermilab conventional magnet "Main Ring") which presently shares the 6.3 km circumference main tunnel of the Fermilab accelerator complex with the superconducting Tevatron. The 150 GeV accelerator is the third accelerator of the four accelerator cascade at Fermilab (Linac, 8 GeV Booster, 150 GeV accelerator, Tevatron). After the aforementioned Linac Upgrade Project is operational, protons will be injected at 400 MeV into the Booster.

The FMI is an approximately circular (rather more elliptical due to siting considerations) accelerator 28/53 the circumference of the present "Main Ring." Twelve (12) "Booster batches" are presently used to fill the Main Ring and transferred to the Tevatron for injection and acceleration for

fixed target physics. Two FMI acceleration cycles will be required to fill the Tevatron for fixed target physics at Tevatron energies. The FMI will permit several operational scenarios which either do, or would, conflict with collider operations at present. The production of antiprotons, for example, requires the repeated excitation of the present Main Ring to 120 GeV on a 2.5 sec cycle. Small, but annoying proton losses during the acceleration cycle require the 'blanking' of the D0 collider detector for brief periods of time each cycle. This results in an approximately 15% loss of available collider luminosity at D0, as compared to CDF at B0. This is a result of the fact that the Main Ring runs partially through the D0 detector (only avoiding the central portion of the detector), rather than completely over the CDF detector at B0.

The critical justification for replacing the Main Ring with the FMI, however, is the very small admittance of the present configuration of the Main Ring (approximately $12 \pi \text{ mm.mrad}$ at 8 GeV). This limitation (which is a distinct reduction of the original admittance of the Main Ring when it was commissioned 20 years ago) is the result of the introduction of vertical dispersion from the CDF and D0 'overpasses', even though the D0 overpass is only a few feet in vertical dimension. Also, the increase in the number of Main Ring injection and extraction devices has further limited the aperture. The FMI is designed with an admittance at 8 GeV in excess of $40 \pi \text{ mm.mrad}$. Great care has been taken to place injection and extraction devices at advantageous locations in the lattice. Also, a 1.5 second cycle time to 120 GeV for antiproton production and a 1.8 second cycle time for neutrino production is envisioned. These requirements have implied the necessity of designing new conventional copper and iron magnets of good field quality over a large aperture with cost effective high rate ramping characteristics. Power supplies and rf capabilities to match these specifications are also critical. On the other hand, certain items may be 'recycled' from the existing Main Ring to the extent that quantities are available and the expected lifetimes are reasonable. Main Ring quadrupoles are such an example of devices planned for re-utilization. Other items can be used for different purposes; for example, the 8 GeV transfer line from the Booster to the Main Injector is approximately 750 meters long and will utilize one type of Main Ring dipole.

An active Research and Development program, expected to cost \$16.7M, is nearing completion. All the R&D program is expected to be concluded in approximately 18 months. This program has included the development and testing of new FMI dipole magnets, the associated dipole magnet power supplies, specialized quadrupole and sextupole magnets, and rf power amplifiers. The first two prototype

*Operated by the Universities Research Association, Inc., under contract with the U.S. Department of Energy

dipoles were completed in 1991 and extensively measured while 'endpack' designs were developed. In conformance with a U.S. Department of Energy (DOE) business strategy recommendation in 1992, a program to execute the majority of the dipole magnet construction using outside commercial vendors was developed. Twelve (12) additional R&D dipole magnets are now under construction, with Fermilab acting as the general contractor for the work, but with only final assembly (and less than 10% of the value added) being accomplished at Fermilab. Contracts, some with options to extend to production quantities, have been bid and negotiated (some using Source Evaluation Boards) for copper coils, coil insulation, magnet lamination steel, and steel 'half-core stacking.'

A prototype dipole power supply is under construction and nearing completion at site E4R where a ground level tunnel enclosure was created for an SSC magnet test string operated at Fermilab. The SSC testing is complete, and the equipment has been removed, and the site is available for a FMI test string utilizing the R&D dipole power supply powering a string of the R&D dipoles. A second R&D dipole power supply will also be built. The rf R&D program has included a comparison of commercially available components with the performance requirements. Units will be load tested this year.

Congress first appropriated funding for the FMI in FY92 in the amount of \$15M. This was later reduced by Congressional rescission to \$11.65M. For FY93 an additional \$15M was appropriated, bringing the total appropriated to date to \$26.65M. The latest approved FMI total project estimated cost (TEC), completed for the Title I review, is \$194M in \$FY\$91, which translates to \$222.5M in \$FY\$Then Year with the presently assumed Office of Management and Budget (OMB) schedule for funding and escalation. The Total Project Cost (TPC) including R&D, spares, and Pre-Operating is \$FY\$91 220.5M and \$FY\$Then Year 252.5M.

No part of the FY92 appropriation was released by DOE until late in FY92, and then only for very limited purposes. The development of FMI conceptual designs, FMI environmental assessment documents, approval of wetlands mitigation designs, and the selection of an outside A&E firm (Fluor Daniel) has been previously reported [2]. These efforts were directed towards obtaining DOE Acquisition Executive approval of the first Key Decisions (KD's) in May 1992 and the acceptance by DOE of the FMI Environmental Assessment as indicated by the publication of a "Final FONSI" (Finding Of No Significant Impact) in the Federal Register. The FONSI was published in early July 1992. At that time, based upon a very limited approval from the Acquisition Executive, civil work began on the wetlands mitigation. The May 1992 KD's (KD-0 and KD-1) accepted the project baseline based upon the latest conceptual design report (CDR 3.1) and authorized the release of FMI Project funds for the development of Title I. This was the first federal funding spent on the FMI at the A&E firm; all earlier work in support of the Environmental Assessment and the Wetlands Mitigation bid package was performed using State of Illinois

Challenge Grant funding. On August 15, 1992, the Title I package (in five volumes: technical systems, civil construction, technical components cost estimates, civil cost estimates, and an energy conservation report) was submitted to DOE. After review, this material was accepted and in September 1992 the Acquisition Executive approved KD-2 (develop civil and technical Title II - i.e. bid packages - for the entire project) and a limited KD-3 (start project construction) which was further augmented (but is still limited) in April 1993. As a result, almost all of the available FMI appropriations are now under contract; the exception being that to date no annual contingency funding has been required or requested. As soon as the planned FY93 bidding activity is complete, some of the contingency may be requested for schedule advancement. It will also be necessary to have an 'unlimited' KD-3.

Under the authority of the Acquisition Executive, several major contracts have been awarded. A fixed-price contract (\$5.6M) has been signed with the architectural and engineering firm Fluor Daniel for the delivery of all the civil Title II by April 1994. The point of closest approach of the FMI to the Tevatron (near tangency) is known as MI-60 in the FMI lattice. This is the location of the FMI rf straight section. It is also, above ground, the location of the largest of the FMI service buildings, housing the FMI rf and power supplies for one-sixth of the FMI. It is also the location of the 'drop hatch' and associated underground labyrinth for FMI component delivery. Because of its proximity to the existing Tevatron, and the necessity to operate the Tevatron during construction, it is a complex civil construction project. Significant amounts of sheet piling need to be driven in a line parallel to the existing Tevatron rf straight section labeled F0. Radiation shielding must be maintained. The structural integrity of the Tevatron enclosure and F0 buildings must be maintained. The pile driving must not disrupt the operation of the Tevatron with colliding beam. It was decided to work on this complicated project first. The civil work was divided, after discussion, into two pieces (mostly below grade and mostly above grade) and bid separately, with the above grade work to follow the labyrinth construction. Advantageous bids, below the Title I and Title II estimates, were obtained. These were for approximately \$3.6M for the below grade and \$2.5M for the above grade construction. The below grade construction began in March 1993, and by the first week of May 1993 approximately one-third of the sheet piling area was driven to grade (of an expected total of about 7,000 square meters [1.75 acres] steel surface). Excavation had begun to the level of below grade bracing. All construction at the MI-60 area should be complete by April 1994. The next civil package to be prepared for bids is for site preparations, including most of the underground electrical and control cable conduit construction, various water systems around the FMI, and provision for temporary power on aerial lines. Also, construction roads for access for enclosure construction, located over the utilities, is required. This bid period closes at the end of May, with award and construction expected to begin in June 1993. In FY94 construction on the FMI Ring

Enclosure, in a counter-clockwise (viewed from above) fashion from MI-60 should commence, contingent upon Acquisition Executive approval and funding.

Also, consistent with Acquisition Executive approvals received in April 1993, contracts for the first production quantities of dipole magnet copper coils and magnet steel will shortly be signed. It is already known, however, that as in the case of civil contracts to date, the pricing for these first technical component contracts is very favorable.

Additional accomplishments of the past year include the approval of the FMI Preliminary Safety Analysis Report (PSAR) and DOE concurrence with the classification of the facility as 'Low Hazard.' A Technical Safety Review Committee concurred with the PSAR and accompanying presentations. As recommended by the Technical Safety Review, a Civil Safety Implementation Plan was written and approved, based upon the Fermilab Civil Safety Procedures. As suggested by the Technical Safety Review panel, a document to address the non-civil construction safety considerations of the FMI is under draft. The Project Management Plan was approved by DOE March 15, 1993. The Configuration Management Plan and a Project Control System are in various stages of draft and circulation and review with DOE. Advanced Procurement Plans were written and approved for the FMI dipoles and dipole power supplies, including the procedures for using Source Evaluation Boards. A FMI Project Specific Quality Implementation Plan (SQIP) was written, and associated SQIPs for various support organizations were prepared. These are under review. A DOE audit of the FMI Project Quality Assurance (QA) plans and procedures was held in late April 1993.

The specifications for the FMI were prepared by the staff of the Fermilab Accelerator Division. Based upon these specifications, staff from the Main Injector Department and the Accelerator Physics Department of the Accelerator Division have done a large amount of simulation (tracking) to confirm that the dipole magnet design and lattice design are acceptable. These studies have included confirmation of the injection and extraction system design specifications, so that technical component design may proceed. Also, staff from these departments have worked to ensure that a variety of fixed target physics options based upon research with protons

originating directly from the FMI will be available, and that technical and civil designs are consistent with these requirements.

The project schedule is, at present, completely funding limited. An example of this statement is the fact that based upon the actual commitment of over \$20M for civil and technical contracts in FY93 (using funds from FY92 and FY93) the latest DOE/ER review of the FMI project in March 1993 agreed that not only could the FMI project responsibly commit \$52M as proposed in the DOE worksheets provided at that review; the review committee wrote in its report that the FMI could easily and responsibly commit \$75M in FY94. The President's budget request shows \$25M for FY94, which severely limits progress towards the FMI and is estimated to add about 13 months to the schedule. Unless some relief of this constraint is obtained project completion could extend to late in 1998.

FMI project management is very encouraged by the progress of the project to date. Formal groundbreaking was held on March 22, 1993. Progress on all civil and technical design and R&D efforts has been rapid given the available funding and Acquisition Executive approval rate. Actual contracts have been placed at very favorable pricing. The physics priority of this project (second only to the SSC) for the national program has been repeatedly endorsed. These endorsements are found in the HEPAP subpanels reports known as "Sculli" and "Witherell" reports. Project management is anxious to complete the job and to provide the research community the advantages of this excellent research facility.

REFERENCES

- [1] S. D. Holmes, "Achieving High Luminosity in the Fermilab Tevatron," *Conference record of the 1991 IEEE Particle Accelerator Conference, San Francisco, California, May 6-9, 1991*, pp. 2896.
- [2] D. Bogert, W. Fowler, S. Holmes, and P. Martin, "The Status of the Fermilab Main Injector," *XVth International Conference on High Energy Accelerators, Hamburg, Germany, Vol. 1*, p. 492, (July 20-24, 1992).

Constructing High Energy Accelerators Under DOE's "New Culture" for Environment and Safety: An Example, the Fermilab 150 GeV Main Injector Proton Synchrotron

W. Fowler
Fermi National Accelerator Laboratory*
P. O. Box 500, Batavia, IL 60510

Abstract

Fermilab has initiated construction of a new Main Injector (150 GeV proton synchrotron) to take the place of the current Main Ring accelerator. "New Culture" environmental and safety questions have been addressed. The paper will detail the necessary steps that were accomplished in order to obtain the permits which controlled the start of construction. Obviously these depend on site-specific circumstances, however, some steps are universally applicable. In the example, floodplains and wetlands were affected and therefore the National Environmental Protection Act (NEPA) compliance was a significant issue. The important feature was to reduce the relevant regulations to a concise set of easily understandable requirements and to perform the work required in order to proceed with the accelerator construction in a timely fashion. The effort required and the associated time line will be presented so that other new accelerator proposals can benefit from the experience gained from this example.

I. INTRODUCTION

The paper[1] "Designing High Energy Accelerators Under DOE's "New Culture" for Environment and Safety: An Example, the Fermilab 150 GeV Main Injector Proton Synchrotron," given at the 1991 conference described the NEPA requirements that were being more stringently adhered to since February 1990 when Admiral Watkins (Ret.) the new Secretary of Energy placed into effect his "New Culture."

In his February notice, Watkins reiterated how, in forming his initiatives, "I found that many of the Department's activities under NEPA had been carried out in a decentralized non-uniform and self-defeating manner. I also state my intention to become personally involved in NEPA decision making and to ensure that NEPA actions are more closely coordinated with the governors of the states which host DOE facilities..."

"Indeed," Watkins continued, "mission goals are best served by early and adequate NEPA planning, which avoids the delays that often follow 11th-hour consideration of NEPA requirements, the resulting failure to comply fully with those requirements and ultimately, the necessity to cure NEPA-related deficiencies before an important project may proceed. If the Department is to err in its judgment as to the extent to NEPA review required of new projects, it should err on the side of full disclosure and complete assessment of environmental impact."

*Operated by the Universities Research Association, Inc., under contract with the U.S. Department of Energy

The NEPA legislation besides setting forth a national policy for the environment, established the Council on Environmental Quality (CEQ). The CEQ issued Regulations for Implementing the Procedural Provisions of NEPA. These rules are found in the Code of Federal Regulations (40 CFR Parts 1500-1508). This is where the methodology of Environmental Impact Statements (EIS) with the final action of a Record of Decision (ROD) was established. Also, the simpler process of an Environmental Assessment followed by a Finding of No Significant Impact (FONSI) or a determination that an EIS is required was outlined.

As Watkins' emphasized, it is important to start the NEPA process as early as possible; however, it is obvious that the design has to have progressed sufficiently that enough information is available that environmental studies are feasible. In the case of the Fermilab Main Injector (FMI), this point was reached in the fall of 1989.

The FMI will be a 150 GeV accelerator with a circumference of about one-half that of the existing Main Ring. The FMI would be situated tangent to the Tevatron at the F0 straight section[2] in the southwest corner of the Fermilab site. The FMI is being constructed using newly designed (iron and copper) dipole magnets.

The FMI, whose location is shown in Figure 1, must serve a number of purposes. It must function as a bi-directional injector into the Tevatron. This means it must be near and approximately tangent to the Tevatron. Secondly, it must receive 8 GeV protons from the Booster and 8 GeV antiprotons from the Antiproton Source. It must also provide 120 GeV protons to the antiproton target. Finally, the FMI must provide a 120 GeV beam to the present Fermilab fixed target facility hardware.

The principal housing of the FMI utilizes below grade enclosures. The FMI ring enclosure is an oval-shaped, below grade structure, approximately 10,900' long, with a 10' wide by 8' high cross section. The floor of the enclosure will be level and at an elevation of 713'6" above sea level, 18' to 33' below existing grade. Earth shielding berms over the FMI enclosure provide the required 21' of earth equivalent shielding.

Details concerning the "Status of the Fermilab Main Injector Project," V.D. Bogert et al, are contained in paper Gc22[3] of this conference.

II. ENVIRONMENTALLY SIGNIFICANT ACTIONS

Beginning in April 1990, \$200,000 of Illinois Challenge Grant funds became available to conduct environmental studies and preliminary design. The first activity was to prepare the application for the joint permit for

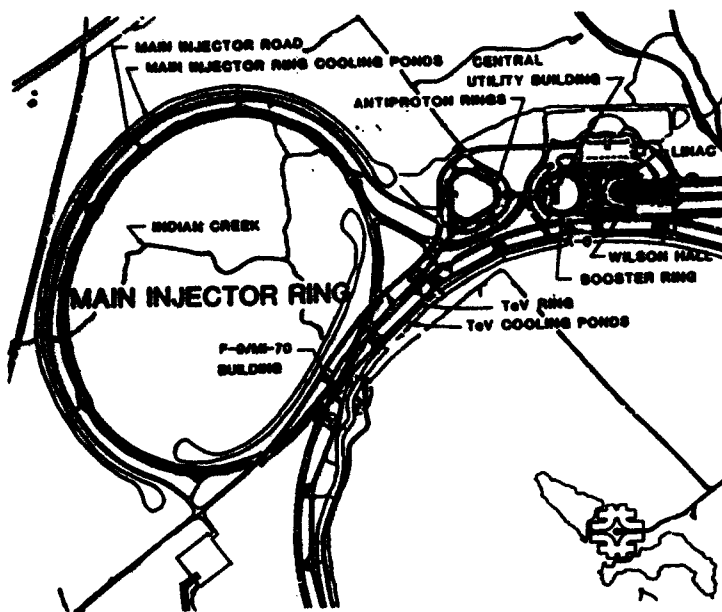


Figure 1. Fermilab Main Injector location. Indian Creek crosses the ring at several points. Approximately 100 acres of wetland is adjacent to the creek. The area of wetland that has been permanently filled is six acres.

filling of the wetlands and the modification of the floodplain of Indian Creek. The application was submitted in September 1990.

The U.S. Army Corps of Engineers (COE) issued the permit for filling the wetlands on June 26, 1991. Special conditions were included which required their approval of construction drawings prior to initiating construction.

In parallel, an Environmental Assessment (EA) was prepared which required several drafts. The submission to the environmental part of DOE occurred in April 1991. After publication for public comment the EA was found acceptable and a FONSI was issued on July 6, 1991. Of particular importance to the FMI Project was that this action included the finding that no EIS was required. If this had not been the case, the EIS process would have added an estimated 1 1/2 years to the project's duration. Illinois provided an additional grant of \$2,000,000 in the spring of 1991 of which \$500,000 was specified for environmental efforts.

Using the above plan, the funds expended for the environmental effort for the FMI is estimated to be \$1,400,000 since Fermilab has matched the funds of the State of Illinois as required by the terms of the Grant.

Because of the availability of Illinois funds it was possible to hire the architect/engineering firm of Fluor Daniel who prepared construction drawings and specifications for the wetland/floodplain construction. These were submitted to the COE who approved the package on February 5, 1992, and on July 15, 1992 the COE was notified in accordance with another special condition that construction would start on July 22, 1992.

The Illinois Department of Transportation/Division of Water Resources also had to approve the work, which included the creation of 22 acre-feet of floodwater storage, in the floodplain of Indian Creek. Their permit, based on the

Fluor Daniel drawings and specifications, was issued on April 3, 1992 so that this was in hand when the DOE released the funds for the wetland/floodplain construction work.

Due to favorable weather conditions in the fall of 1992, all the wetland/floodplain work was completed without incident with the exception of planting of the newly created 8 acres of wetland area. Spring planting is now underway and a five year monitoring program required by the COE is being put in place.

The great blue heron rookery which had been located in the approximate center of the new ring, was abandoned prior to the start of the FMI construction. This was due to the presence of a red-tailed hawk which decided to nest in the same tree and drove off the herons as they arrived. The herons took advantage of an alternate site in the center of the existing accelerator ring where the trees had reached a height suitable for heron nests and have not returned to the old site in subsequent seasons.

Another important event occurred on October 1, 1992 when a new provision of the "Clean Water Act" was brought into enforcement. The Illinois Environmental Protection Agency (IEPA) took on the task of enforcing the requirement for permits for stormwater discharges associated with construction activities in the State of Illinois. Since the FMI was under construction at that time a National Pollutant Discharge Elimination System (NPDES) stormwater discharge permit was required. The procedure adopted by IEPA was that they issued a general permit on October 20, 1992. Fermilab on September 24, 1992 based on an earlier draft issued a Notice of Intent (NOI) to qualify under the Illinois general permit.

Requirements include that Fermilab must have on file a Stormwater Pollution Protection Plan which is kept up-to-date by revisions as details of construction activities become firm. In addition, an Environmental, Safety and Health Procedures for Soil Erosion and Sediment Control for Construction Activities was prepared. Of interest is that each contractor signs a Certification that he understands the terms and conditions of the NPDES permit.

Figure 2 shows an air view of the Fermilab site with a white oval indicating the position of the tunnel. The FMI construction is entirely within the Fermilab site and, with the exception of the wetlands referred to in the above, involves previously farmed, almost flat areas.

III. ACKNOWLEDGMENTS

While it is true that I played a major role in the NPDES activity before the stormwater permit was required beginning on October 1, 1992, the work associated with this new requirement was carried out by Rod Walton and Linda Even.

IV. REFERENCES

- [1] William B. Fowler, "Designing High Energy Accelerators Under DOE's "New Culture" for Environment and Safety: An Example, the Fermilab Main Injector Proton Synchrotron," *Conference Record of the 1991 IEEE Particle Accelerator Conference*, Vol 2, p. 854.



Figure 2. Air view of the Fermilab site with heavy white oval indicating the location of the new accelerator tunnel.

- [2] The Main Ring and Tevatron Accelerators are designed with six straight sections, where the beam travels a short distance in a straight line, alternative with six arc sections where it follows the path of a circle with a radius of one kilometer. These 150-m long straight section are labeled A0, B0,.....F0, and are spaced equally around the ring.
- [3] D. Bogert et al, "The Status of the Fermilab Main Injector Project", paper Gc22 of this conference.

Performance and Comparison of the Different Coalescing Schemes Used in the Fermilab Main Ring.

I. Kourbanis, G. P. Jackson, X. Lu

Fermi National Accelerator Laboratory,*P.O. Box 500 Batavia, Illinois 60510

Abstract

The two different coalescing schemes used in the Fermilab Main Ring during the last collider run are compared using the ESME [1] simulation program. The simulation results are compared with the operational data. Finally, possible improvements are suggested.

INTRODUCTION

Two types of coalescing are being used in the Main Ring during this collider run. The first is the traditional type of coalescing which was used before [2], and the second is the so called "SNAP" coalescing used for protons. The voltage waveform vs. time for the two types of coalescing is shown in Fig.1. In the regular type of coalescing 11-15 $h=1113$ (53 Mhz) bunches are accelerated to 150 GeV in the Main Ring and the RF voltage is adiabatically reduced by paraphasing to a low value (depending on the beam emittance) until the beam area fills the rf bucket. Then the bunches are coalesced by a rotation in a 2.5 plus 5.0 MHz bucket and recaptured in a 53 MHz bucket. The whole coalescing process in this case takes about 1 sec.

In SNAP coalescing the paraphasing has been replaced with a rotation. The 53 MHz voltage is suddenly reduced to 30-50 kV (depending on the beam emittance) where the bucket height equals the beam height. Then the beam is left to rotate for a quarter of a period in order to achieve the minimum ΔE . The rest of the coalescing process is the same as in the regular coalescing. The SNAP coalescing process takes about 200 msec.

ESME COMPARISON

The program ESME was used to compare the two coalescing schemes. We considered 11 bunches with variable longitudinal emittance rotated in a bucket formed by 20.6 kV of 2.5 MHz and 4.12 kV of 5.0 MHz. These values were chosen because they are the maximum voltages available.

*Operated by the Universities Research Association under contract with the U. S. Department of Energy

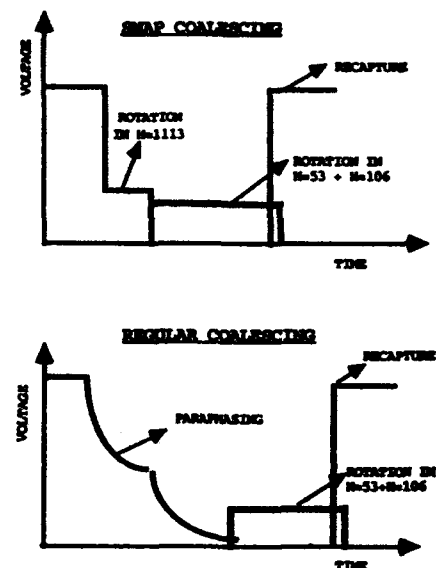


Figure 1: Voltage vs time for Regular and SNAP Coalescing

TABLE 1: MINIMUM ΔE vs. EMITTANCE FOR REGULAR AND "SNAP" COALESCING COMPARED WITH THE IDEAL CASE			
EMITTANCE (eV-sec)	REGULAR COALESCING ΔE (MeV)	"SNAP" COALESCING ΔE (MeV)	IDEAL ΔE (MeV)
0.10	4.60	6.00	2.60
0.15	6.70	8.50	4.00
0.20	8.60	11.10	5.30
0.25	10.70	13.10	6.60
0.30	12.90	16.00	7.90

The capture voltage used was 800 kV, resulting in a final longitudinal emittance of 3.78 eV-sec. It turns out that even in regular coalescing where the 53 MHz rf voltage is reduced till the beam fills the bucket, the maximum bucket height achieved is still larger than the ΔE of a rectangle with base equal to the 53 MHz bucket width of 18.9 nsec and area equal to the beam emittance. In SNAP coalescing, due to nonlinearities in the rotation, the beam does not extend to the edges of the bucket. As a result, the ΔE after the rotation is larger than the ΔE in the regular coalescing. Table 1 contains the 95% ΔE of the beam as

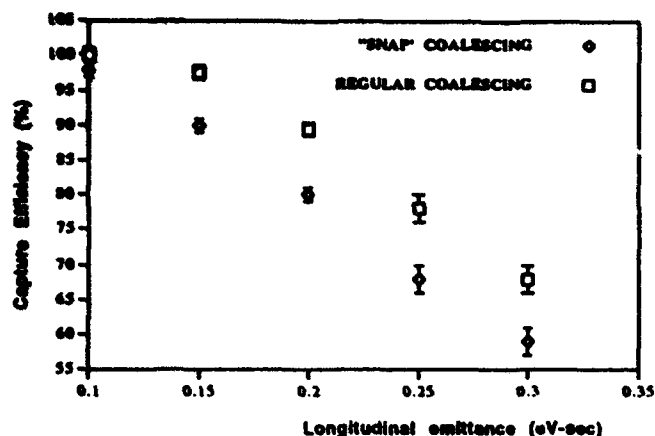


Figure 2: Capture efficiency vs long. emittance for Regular and "SNAP" Coalescing computed by ESME

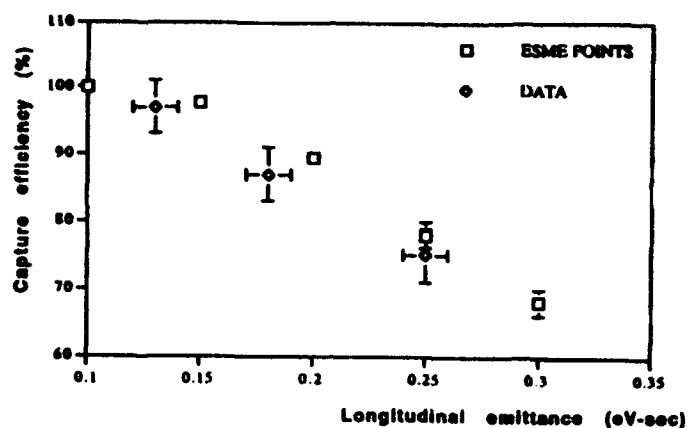


Figure 4: Capture efficiency vs long. emittance for Regular Coalescing

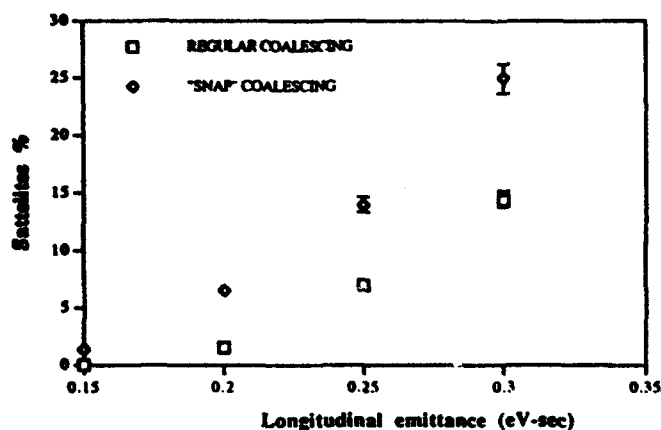


Figure 3: Fraction of beam captured in satellites vs longitudinal emittance for Regular and "SNAP" Coalescing computed by ESME

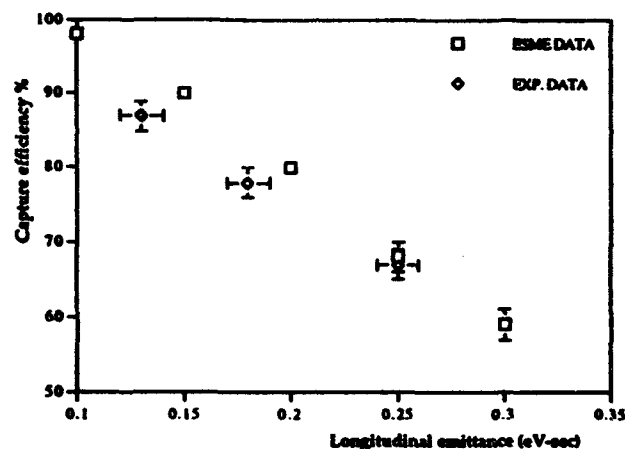


Figure 5: Capture efficiency vs long. emittance for "SNAP" Coalescing

OPERATIONAL EXPERIENCE

calculated from ESME at the end of paraphasing for regular coalescing and at the end of the 53 MHz rotation for SNAP coalescing, compared at different beam emittances. Also shown in the same table is the ΔE for the equivalent rectangle. As shown in Table 1, the paraphasing in regular coalescing leads to a blowup in the beam emittance of a factor of 1.6, while the rotation in SNAP coalescing leads to a blowup of about 2.0. The capture efficiency for both coalescing schemes versus long. emittance as calculated by ESME is plotted in Fig. 2. As expected the efficiency varies linearly with long. emittance. The fraction of the beam captured in the two nearest satellite buckets as a function of the longitudinal emittance for the two coalescing schemes is plotted in Fig. 3.

ESME simulation results were compared with experiment by using a Main Ring cycle with low intensity (to avoid emittance blowup at transition) and using an injection phase mismatch to vary the longitudinal emittance. The results of this comparison are plotted in Fig. 4 and Fig. 5. From these figures we see that the experimental data agree fairly well with the ESME simulation predictions. The data also show that the capture efficiencies achieved with regular coalescing are about 10% higher than SNAP coalescing for the same emittance. The problem with regular coalescing is that at higher intensities the bunches become unstable during the adiabatic debunching, having as result the blowup of the longitudinal emittance and the eventual deterioration of the coalescing efficiency. This is the reason that regular coalescing is used only for the low intensity antiprotons while SNAP co-

leaving is used for the protons. During collider operations we coalesce 13-15 proton bunches with typical intensities of 2×10^{10} ppb and emittances of 0.28-0.30 eV-sec. The capture efficiency varies between 54 % for 15 bunches to 61 % for 13 bunches with about 20 % of the beam captured in the two neighboring satellites. Typical coalesced proton bunches have intensities of $130 - 150 \times 10^9$ ppb, while a few bunches have been observed with 165×10^9 ppb. These values agree with ESME predictions which are 58% for 15 bunches and 62% for 13 bunches. Antiprotons have a parabolic bunch intensity and emittance profile, i.e the intensity and emittance is larger for the central bunches. The typical longitudinal emittance of the central antiproton bunches is 0.23-0.25 eV-sec and the coalescing efficiency is about 85-88% in agreement with the ESME values of 89-92%. Typical coalesced antiproton intensities are 65×10^9 .

CONCLUSION

A new method of coalescing called SNAP has been successfully tried in the Fermilab Main Ring in order to avoid the instability problems happening during adiabatic debunching at high intensities. In the future we plan to add a second harmonic cavity (106 MHz) in order to linearize the rotation in the 53 MHz bucket. This will make SNAP coalescing as efficient as regular coalescing.

REFERENCES

- [1] S. Stahl and J. MacLachlan, "Users Guide to ESME v.7.1", Fermilab internal note TM-1650(2/90).
- [2] P. Martin, K. Meisner, H. Miller, G. Nicholls, D. Wildman, "Performance of the RF Bunch Coalescing in the Fermilab Main Ring" *IEEE Trans. Nucl. Sci. NS-32*, No. 5, 1684 (1985).

Operational Experience with Collimators in the Tevatron Collider

S. M. Pruss

Fermi National Accelerator Laboratory
P.O. Box 500, Batavia, IL 60510

ABSTRACT

During the last year the Tevatron Collider has been running not only with two new low beta insertions and electrostatic separators to keep the protons and p-bars from colliding anywhere except where desired, but also with a new collimator system. We report on this system, including sensitivity of halo evolution to Tevatron operating point

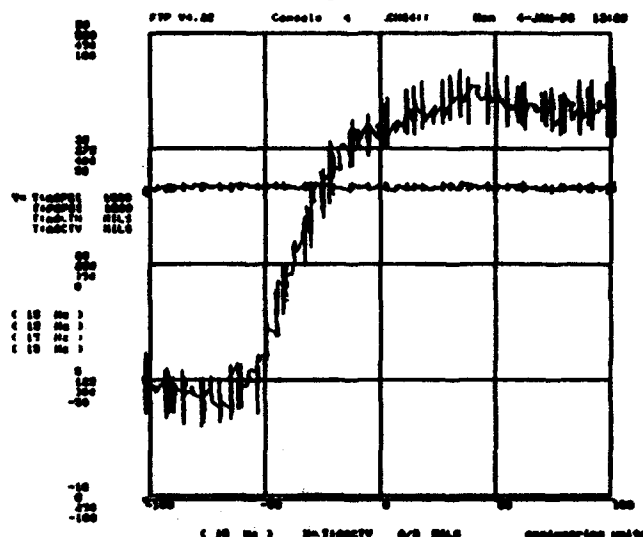
INTRODUCTION

In a previous paper¹, I reported on the design for the halo scraper system to be used in the present Tevatron Collider run. In this system, eight scrapers are available. Because of the separated orbits, protons and anti-protons must be scraped independently. There are scrapers for both vertical and horizontal planes. For every primary scraper, there is a secondary scraper to catch particles scattered back out of the edge of the primary scraper. This design has not been required for operations, however. Of the eight scrapers installed, only four are normally used. The design provided for the possibility of using the scrapers to localize beam loss away from the experiments and thus use scrapers during colliding running as shields for the experiments. Just as in the 1989 run however², it is only necessary to scrape away the initial large amplitude halo at the start of a store, and then withdraw the collimators about three beam sigma. If the machine parameters have been set to keep the particle betatron tunes well away from resonance lines, then once the large betatron amplitude (halo) particles have been scraped away, the background loss rates at the two experiments are tolerable for them - 2 to 10 kHz.

SINGLE BEAM EXTINGUISH DATA

The most significant change from the 1989 collider run for the scraper system is the separated orbits of the protons and anti-protons. It is no longer normally possible to scrape the halo of both beams with a single scraper. The single exception to that statement is any beam that has been lost from the RF bucket and is losing energy by synchrotron radiation. These particles, both protons and anti-protons, gradually drift toward the radial inside of the machine and can be removed by a single scraper at a high dispersion point. Figure 1 below shows the effect of moving the primary anti-proton vertex collimator down from above into and through the anti-proton beam. The anti-proton intensity signal is somewhat noisy, but can be seen to decrease from $\sim 40E9$ to 0 as the collimator moves from right to left from about 40 mils to about -60 mils. The proton signal remains at about $350E9$ all during this process. Finally, just below -100 mils, the proton signal began to drop. This is consistent with the flying wire measure of the beam sigma of 25 to 30 mils and a beam separation of about 5 sigma.

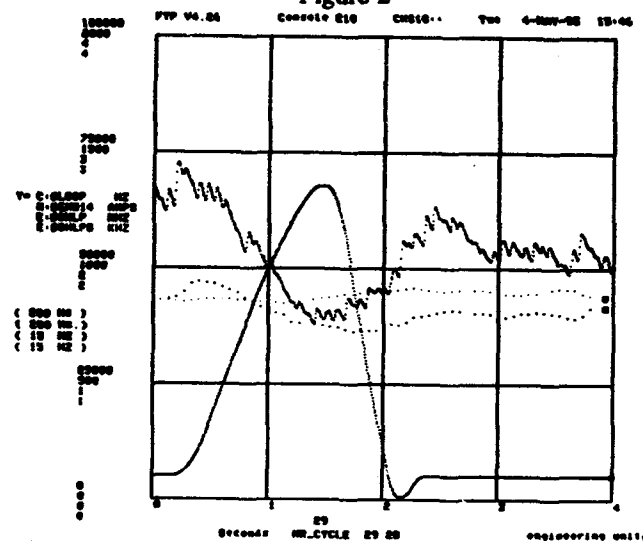
Figure 1



EFFECT OF MAIN RING RAMP

It is fortunate that it has proved not necessary to use the collimators to shield the experiments from losses during their data-taking, since the Main Ring ramp stray field has a large effect on losses and reduces the efficiency of the secondary collimator to clean up particles scattered from the primary. This is illustrated in Figure 2.

Figure 2



References

- (1) S.M.Pruss, "A Design for a Beam Halo Scraper System for the Tevatron Collider," in 1991 IEEE Particle Accelerator Conference, San Francisco, Calif., May 1991, pp. 2340-2341.
- (2) S.M.Pruss, C.Crawford, D.Finley and M.Harrison, "Operational Experience with Using Collimators to Remove Halo in the Tevatron Collider," in 1989 IEEE Particle Accelerator Conference, Chicago, IL., March 1989, pp. 439-440.

Reliability of the Fermilab Antiproton Source

E. Harms, Jr.
Fermi National Accelerator Laboratory*
P. O. Box 500, Batavia, IL 60510 USA

Abstract

This paper reports on the reliability of the Fermilab Antiproton source since it began operation in 1985. Reliability of the complex as a whole as well as subsystem performance is summarized. Also discussed is the trending done to determine causes of significant machine downtime and actions taken to reduce the incidence of failure. Finally, results of a study to detect previously unidentified reliability limitations are presented.

I. INTRODUCTION

The Fermilab Antiproton source consists of two storage rings, the Debuncher and Accumulator, which operate at a nominal energy of 8 GeV, a production target station, and beam lines connecting the rings and the target station to each other as well as the Fermilab Booster and Main Ring. During the current Tevatron Collider run, the source has achieved an all-time peak stacking rate of 4.54×10^{10} pbars per hour and a record peak Accumulator intensity of 1.61×10^{12} antiprotons. Typically, 2.7×10^7 antiprotons are produced and stacked in the Accumulator based on a flux of 1.8×10^{12} 120 GeV protons striking the production target every stacking cycle.

Since its first operation in 1985 the Antiproton source complex has provided antiprotons for three Tevatron Collider runs. During fixed target periods it has served the needs of E760 studying the spectroscopy of charmonium states produced by pp collisions in the Accumulator [1].

Table 1
FNAL Pbar Source Operations History
for Physics Runs

DATE	DURATION (WEEKS)	PURPOSE OF RUN
2 Feb., 1987 to 15 May, 1987	14	Tevatron Collider
4 July, 1988 to 4 June, 1989	48	Tevatron Collider
1 July, 1991 to 20 Jan., 1992	30	E760
4 May, 1992 to present	50 (to date)	Tevatron Collider

* Work supported by the United States Department of Energy under Contract No. DE-AC02-76CHO3000.

Table 1 lists the dates and duration of physics runs of the Pbar source. Data for this paper is limited to that gathered during these periods. The time between runs has been spent on machine improvement beam studies or shutdowns for system improvements and additions.

II. RELIABILITY

Reliability was studied in three ways: by means of recorded downtime, a Equipment Failure Report (EFR) system maintained by Pbar source personnel, and analyzing the frequency and reasons behind losses of stacks in the Accumulator.

A. Downtime

Machine downtime is recorded by an applications program resident on the Fermilab Accelerator controls consoles. Main Control Room operators log items that cause any program interruption. Every entry provides the identity of the device causing the downtime, the subsystem to which it belongs, the duration of the interruption, and detail of the problem. Off-line analysis capability is also provided. Table 2 summarizes recorded Pbar source downtime since 1 February, 1987.

The 1255.85 hours of recorded downtime is 7.6% of the total accelerator complex downtime during the period. The two major contributors of Antiproton source downtime are the antiproton production target station and beam transport line power supplies. Both deserve further mention.

Antiprotons produced by targeting 120 GeV protons are collected by the Lithium lens. Failures of this device account for 245 of the 300 recorded hours that the target station was not operational. There were eleven instances where repair or replacement of a lens/transformer assembly was necessitated by failures of the cooling water channels during the 1988-89 Collider run. This period was the worst in terms of lens problems. During those 48 weeks of operation an average of nearly 3 hours of target station downtime was accrued per week of source operation. An average of 1.5 hours per week is the norm for the run in progress. Thanks to improvements in lens/transformer design and manufacture, the lens problems of 1988-89 have not been repeated [2].

The second leading cause of target station downtime is failures of the pulsed magnet that bends 8 GeV negatively charged particles into the AP2 line. Whereas five pulsed magnets failed between April 1987 and October of 1991, there has yet to be a

failure since a magnet of new design was installed in January 1992. The new magnet is a single-turn, water-cooled, radiation hard device.

Table 2
Summary of FNAL Pbar Source Downtime

SYSTEM	HOURS OF DOWNTIME ACCRUED	PERCENTAGE OF PBAR TOTAL
Vacuum systems	9.02	1.0
Beam line power supplies	276.52	22.0
Accumulator power supplies	95.43	7.5
Debuncher power supplies	122.13	9.7
Accumulator RF systems	90.21	7.2
Debuncher RF systems	38.29	3.0
Accumulator stochastic cooling systems	82.15	6.4
Debuncher stochastic cooling systems	25.41	2.0
Production target station	299.70	23.9
Diagnostics	13.25	1.1
Correction elements and supplies	3.15	0.3
Miscellaneous	168.51	13.4
Controls	32.08	2.5
Total	1255.85	100.0

The largest single contributor to beam line supply downtime both in terms of hours accumulated and number of occurrences was the original power supply for the pulsed extraction septum (Lambertson) magnets from the Main Ring to the production target. This device accounted for over a quarter of the total for this category. In the summer of 1988 the power supply was replaced by that of a different design which to date has accumulated only 15.8 hours of downtime.

More recently, overheating magnets in the AP2 line connecting the target station to the Debuncher have contributed approximately 30 hours of downtime scattered over more than 90 such incidents. The frequency of such occurrences has been minimized in part by ramping those magnet strings most prone to overheating rather than running them DC. Plans are being formulated to mitigate such problems in the future by flushing out the entire Pbar source water system and adding filtering during the upcoming scheduled shut down.

B. Equipment Failure Reports

Another reliability indicator is Equipment Failure Reports (EFR's). EFR's are written reports filled out by technicians making repairs to or replacing faulty components. The Pbar EFR system in its current configuration has been in place since May 1990 [3]. EFR's are filled out only on components which fail

during normal operating periods; repairs and replacements made during extended scheduled maintenance periods are not so documented. Figure 1 is a summary of EFR data.

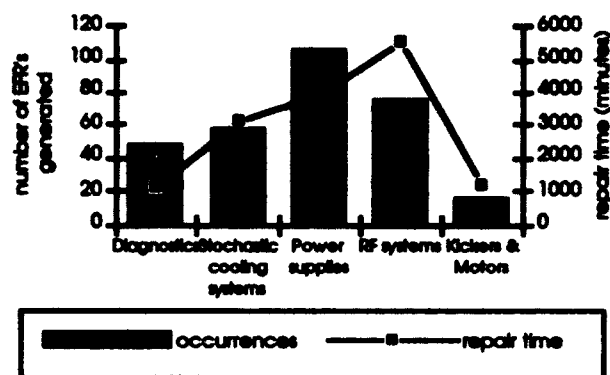


Figure 1
Summary of FNAL Pbar source
Equipment Failure Reports

In general, three classes of power supplies are used to excite Pbar source rings and beam line magnets: those with output less than 1 kW for dipole correctors, those with output in the 1 to 80 kW range for beam transport elements and ring quadrupoles and sextupoles, and those with output more than 1 MW for ring dipoles and major beam line dipole strings. The low power supplies contribute the second leading number of incidents, yet the least amount of repair time because these supplies are more often replaced rather than repaired in the field. The middle class has the most failures, though problems usually lie with instrumentation or metering rather than actual internal problems. Devices comprising the third class, while having the fewest failures, generally take the longest time to repair. A fourth class of devices, shunts for fine control of individual elements in series strings of dipoles or quadrupoles, have their share of failures as well.

The Accumulator and Debuncher each contains three radiofrequency systems. DRF1, the Debuncher 53 MHz bunch rotation and debunching system, has generated the greatest number of EFR's in the RF system category. This is primarily due to the larger number of components in this system than in the five others. DRF1 is comprised of eight cavities generating up to 1 MV each while the five other RF systems combined total six cavities generating substantially less voltage with a lower duty factor.

Traveling Wave Tube (TWT) power supplies dominate the Stochastic Cooling generated EFR's. Seventy-five such supplies drive the final stage of amplification of the stochastic cooling kickers for the nine cooling system used in the Antiproton source. No single mode of failure dominates [4].

Microprocessor-based scanners for the beam line Secondary Emission Monitor (SEM) grids are the most troublesome diagnostics component. Many of these devices are installed in the beam line enclosures and

are sensitive to the radiation found in those areas. Some scanners, specifically those in the 120 GeV line from the Main Ring to the target station and near the major bends in the injection and extraction lines, have been moved to the quieter environment of adjacent service buildings. The rate of failure of devices so moved has dropped significantly. Additional scanners will be moved out of the tunnels as resources permit.

C. Lost Stacks

A third measure of reliability is the frequency of loss of particles stored in the Accumulator, known colloquially as 'dumping a stack'. Figure 2 summarizes the frequency and reasons for dumped stacks over the history of the Pbar source. On average, a stack is dumped once per two weeks of operation. The longest sustained stack was 39.4 days achieved during November and December of 1988.

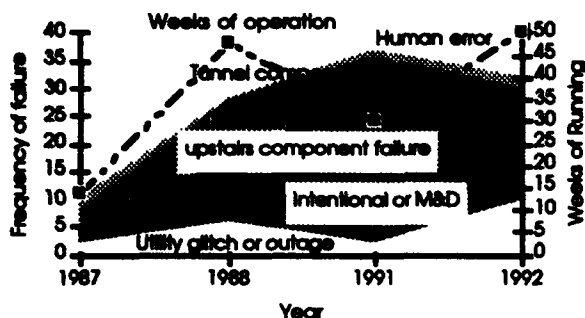


Figure 2

Summary of Dumped Stacks 1987 to present

Dumped stack data from 1991 is unique in that the Accumulator was used as an experimental area for E760. A typical week consisted of 42 hours of antiproton stacking, 92 hours of data taking and time for experimental set up and scattered downtime. Since most stores required decelerating the antiproton beam to an energy less than the accumulation energy of 8 GeV, what was left of the stack at the end of a store was dumped, an access made if necessary, then the Accumulator turned back on for antiproton stacking. Fewer component failures were encountered due to less stacking time per week compared to Collider operation and because unneeded loads were turned off once set up for a store was begun.

Over the history of the Pbar source, most dumped stacks have been due to failure of a component in the Debuncher/Accumulator tunnel. Failure of a pulsed septum or kicker magnet module was the culprit in thirteen of the twenty-nine such cases.

Utility glitches or outages have contributed twenty instances. Most such losses are traceable to glitches on the transmission grid of the electricity utility supplying Fermilab.

Only a handful of dumped stacks can be attributed to human error.

III. SUMMARY

The Fermilab Antiproton source has been in operation for nearly seven years. As a whole, it has proved to be a reasonably reliable complex. The best measure of stand-alone up time has come during periods of running for E760 when 80% of the time was accounted for either by antiproton stacking or data taking. Such a measurement for Collider operation is complicated by set up time for antiproton transfers to the Main Ring/Tevatron and a generally greater reliance on the other machines in the Fermilab complex. There has been an average of 91 stacking hours per week during the present Collider run which compares favorably with past operation.

An analysis of the data has yielded no surprises as far as uncovering previously undetected reliability limitations.

Known unreliable components are replaced or upgraded as resources permit. Notable changes to date include replacement of the power supply energizing the pulsed extraction septa from the Main Ring to the target station, improved design and manufacture of Lithium lenses, a target station pulsed magnet of better design, improvements to the design of pulsed magnetic septum magnets, more reliable capacitors in the kicker magnet modules, replacement of RG-220 coaxial cable for the kicker magnet systems [5], and relocation of selected SEM grid scanners from the beam enclosures to service buildings.

IV. ACKNOWLEDGMENTS

The author thanks past and present members of the Fermilab Accelerator Operations department for providing down time information and Bernard Wisner of the Fermilab Pbar source department for EFR summaries.

V. REFERENCES

- [1] S. Werkema, private communication
- [2] S. O'Day, private communication
- [3] J. Marriner, Fermilab Pbar source internal memo
- [4] W. Mueller, private communication
- [5] J. Petter, "Improved High Voltage Coax for Antiproton Source Kicker Pulse Forming Networks and Pulse Transmission", *Proceedings of the 1989 IEEE Particle Accelerator Conference*, Vol. 3, pp. 1951-1953.

Multibunch Operation in the Tevatron Collider

J. A. Holt, D. A. Finley and V. Bharadwaj
Fermi National Accelerator Laboratory[†]
P. O. Box 500, Batavia, IL 60510, USA

Abstract

The Tevatron Collider at Fermilab is the world's highest energy hadron collider, colliding protons with antiprotons at a center of mass energy of 1800 GeV. At present six proton bunches collide with six antiproton bunches to generate luminosities of up to $9 \times 10^{30} \text{ cm}^{-2} \text{ s}^{-1}$. It is estimated that to reach luminosities significantly greater than $10^{31} \text{ cm}^{-2} \text{ s}^{-1}$ while minimizing the number of interactions per crossing, the number of bunches will have to be increased. Thirty-six bunch operation looks like the most promising plan. This paper looks at the strategies for increasing the number of particle bunches, the new hardware that needs to be designed and changes to the operating mode in filling the Tevatron. An interactive program which simulates the filling of the Tevatron collider is also presented. The time scale for multibunch operation and progress towards running greater than six bunches is given in this paper.

I. INTRODUCTION

The long range Fermilab program requires fully capitalizing on the world's highest energy accelerator, the Tevatron, throughout the decade of the 90's. The program calls for increasing the collider luminosity with each successive run until peak luminosities of $> 5 \times 10^{31} \text{ cm}^{-2} \text{ s}^{-1}$ with the Main Injector and integrated luminosities of in excess of 100 pb^{-1} per run are achieved, effectively doubling the mass range accessible for discovery.

The present collider operates with 6 proton and 6 antiproton bunches colliding at the two detectors, CDF and D0. For the present configuration, the minimum spacing between bunches is 185 buckets. For the present typical initial luminosity, $5 \times 10^{30} \text{ cm}^{-2} \text{ s}^{-1}$, the number of interactions in the detectors per bunch crossing is 0.79 (assuming a cross section of 45 mbarns). For the upcoming collider run, the typical initial luminosities are

expected to exceed $1 \times 10^{31} \text{ cm}^{-2} \text{ s}^{-1}$. Since the number of bunches per beam will remain at 6 for that run, the number of interactions per crossing will exceed 1.57. Certain types of physics - not including the discovery of the top quark - are done more efficiently if the number of interactions per crossing is kept well below one. For the subsequent collider run, the typical initial luminosity is expected to remain near $1 \times 10^{31} \text{ cm}^{-2} \text{ s}^{-1}$. However, the number of bunches per beam will be increased to 36, in order to reduce the number of interactions per crossing to 0.26. For this configuration, the minimum spacing between bunches will be 21 buckets. With the Main Injector, the typical initial luminosity will exceed the Fermilab III goal of $5 \times 10^{31} \text{ cm}^{-2} \text{ s}^{-1}$, and the number of interactions per crossing will be 1.31, again exceeding one. If necessary for the types of physics to be done, some modest improvements to the Antiproton Source and the Tevatron can provide 99 bunches per beam with 7 bucket spacing. This would keep the number of interactions per crossing near one for luminosities of $1 \times 10^{32} \text{ cm}^{-2} \text{ s}^{-1}$.

II. TEVATRON INJECTION SIMULATION

An interactive X Window program has been developed to model the Tevatron multibunch injection process. The program consists of three windows. The first window is a control window which has a list of which proton and antiproton buckets are filled, a display of the number of crossings at the two experimental areas B0 and D0, and a menu bar. In the menu bar there are controls to inject a single bunch, a batch of bunches, clear bunches, and RF cog bunches for both protons and antiprotons. The kicker rise time, flattop time, and fall time can also be adjusted interactively. The resulting bunch configuration can be saved to a file and recalled for later use. Figure 1 shows the control window with a thirty-six bunch bucket configuration.

There are two types of graphical displays provided. The first one is a snapshot of the Tevatron at the moment of time when proton and antiproton buckets number one are crossing F0 (the RF straight section). The inner "hash"

[†] Operated by the Universities Research Association, Inc., under contract with the U.S. Department of Energy



Figure 1: Bunch Injection Control Window

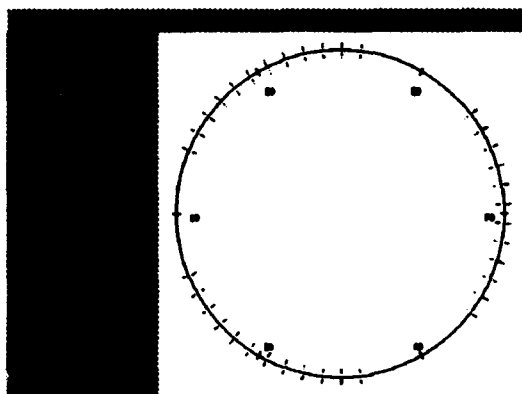


Figure 2: Snapshot in Time of the Tevatron

marks represent protons, the outer "hash" marks represent antiprotons. The second display is a space-time [1] diagram of the Tevatron. Space (distance around the ring) is plotted on the horizontal axis and time (in number of revolutions) is plotted on the vertical axis. Protons move diagonally up to the left, the antiprotons to the right. Figure 2 is a time snapshot of a 36x36 configuration. Figure 3 is a space-time diagram for the same configuration.

The program was used to simulate loading of the Tevatron under various constraints. One constraint is that there must be an equal number of crossings at both experimental areas (B0 and D0). Another important constraint is the abort gap length. There must be a large enough gap for the abort kicker rise time. A workable configuration calls for three batches of protons and antiprotons containing twelve bunches each. The three batches are spaced evenly around the ring. The protons can be loaded as three batches of twelve bunches each. The bunches within a batch are twenty-one buckets apart or 376 nsec. The antiproton loading scheme will be to load four bunches three times for each of the three batches. Under this scenario a kicker with a rise time of less than 376 nsec and a flat top of at least 1224 nsec (four antiproton bunches twenty-one buckets apart) is required. A kicker meeting these requirements is under development.

Some adjustments to the present abort kicker timing

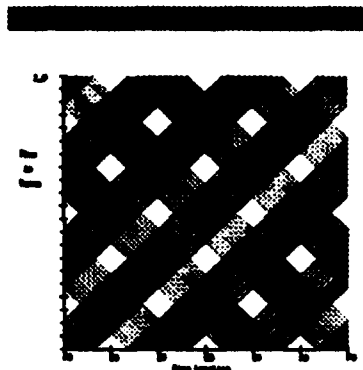


Figure 3: Space-time Diagram

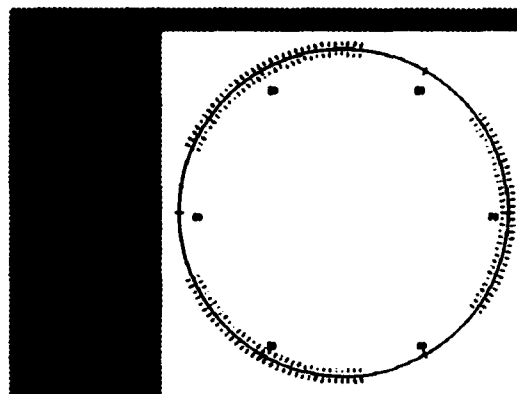


Figure 4: A Time Snapshot for 99x99

will have to be made for 36x36 operation. At present, the abort kicker rise time to full voltage is 4 μ sec. The present abort gap is 3.5 μ sec. The beam can be ejected when the kicker has reached 75% of its full value. With 36 bunches, the abort gap shrinks to 2.6 μ sec. Preliminary calculations [2] show that by changing the capacitance and moving the beam orbits downward, this requirement can be met.

In the ninety-nine bunch scenario, the required antiproton injection kicker rise time would be 112 nsec but the abort gap would be larger than that for thirty-six bunches. Figure 4 shows a time snapshot for the 99x99 configuration.

REFERENCES

- [1] G. Dugan. *Considerations of Bunch-Spacing Options for Multi-Bunch Operation of the Tevatron Collider*. Fermilab, TM-1637, December 1989.
- [2] Bruce Hanna, private communication.

Operational Experience with the Tevatron Collider using Separated Orbits

G. Annala

Fermi National Accelerator Laboratory*, PO Box 500, Batavia, Illinois 60510

Abstract

This paper will discuss the operation of the Tevatron for the 1992 collider run. Operation and commissioning of electrostatic separators, new low beta insertions, a new abort system, feeddown sextupoles, and new features of the control system will be discussed.

I. INTRODUCTION

During the 1989 collider run there was a single major experiment at B0. Six proton bunches and six antiproton bunches traveled on the same closed orbit, giving rise to 12 beam crossings per turn. The beam-beam tune shift caused the antiprotons to fill the available tune space of .025 units with proton intensities of 80 E9 given a transverse emittance of $25 \pi \text{ mm mrad}$. The proton emittances were intentionally blown up to this level to allow for the survival of the antiprotons. Separating the beams everywhere but at the two interaction points allows a factor of six higher proton densities while the beams are colliding. The beams are separated everywhere at injection.

Adding a second major interaction point required the addition of second low beta insertion. The insertion used in the 1989 run was not matched to the lattice, so two identical new insertions were installed.

Table 1 shows relevant parameters to compare the 1989 run with the goals for collider run 1A.

	1989	run 1A
Protons per bunch	$7.0\text{E } 10$	$1.2\text{E } 11$
Pbars per bunch	$2.9\text{E } 10$	$3.6\text{E } 10$
Proton emittance	$25\pi \text{ mm-mrad}$	$16\pi \text{ mm-mrad}$
Pbar emittance	$18\pi \text{ mm-mrad}$	$16\pi \text{ mm-mrad}$
Pbar tune spread	.025	.011
Proton tune spread	.014	.003
Luminosity	$1.6\text{E } 30$	$5.37\text{E } 30$

Table 1.

*Operated by the Universities Research Association, Inc., under contract with the U.S Department of Energy.

II. IMPACT ON THE TEVATRON

The arrangement of electrostatic separators chosen called for vertical separator to be placed where the antiproton abort kicker used to reside. Because of this, a new abort system was designed and installed elsewhere in the accelerator (A0 straight section).

Separating the beams requires that the particles go off center through devices with nonlinear fields. This gives rise to a differential tune shift of the two beams. To compensate for this, a distribution of sextupoles (feeddown sextupoles) were installed to differentially control the tunes and coupling.

The feeddown sextupoles were installed in pairs with opposite polarity to leave the chromaticity unchanged. The entire system consisted of 46 sextupoles of which 38 were already installed in the Tevatron. 8 spool pieces needed to be changed to a type containing skew sextupoles. 28 power supplies were added to run the feeddown system.

The low beta insertion called for special quadrupoles to extend back 600 feet into the arcs. 24 spool pieces had to be replaced by new low beta spools. The upstream correction packages in the spools, consisting of a steering dipole, a tune quadrupole, and a chromaticity sextupole, remained, but the secondary correction packages were replaced by a low beta quadrupole. Six skew quadrupoles and a single octupole (used only for fixed target) were only active elements eliminated. In addition to the spool replacement, 8 low beta quadrupoles were removed from the old insertion at B0 and 10 new quadrupoles were installed at both B0 and D0.

The process of putting a new store into the Tevatron is done in many distinct sequences. This is an operationally complex process, so much of the Tevatron control system was upgraded [1]. In the past, the fill sequence was halted in several places to reload waveforms needed for the next step. The Tevatron front end for the Camac link and the control console computers were PDP-11s. It was difficult to write and maintain the large application programs needed to run the collider. To solve these problems, a new waveform generator was designed to allow all the necessary waveforms to be preloaded and then triggered on event. The control consoles were upgraded to VAX work stations and many of the application programs were written to take advantage of these upgrades. The front

and computer was changed to a Multi-bus II multiprocessor system to improve performance.

III. IMPLEMENTATION

A. Separators

The nominal design separation of the beams was 5 transverse beam sigma's. This corresponded to about 100 KV for some of the separator modules. There was a problem with the physical aperture near the new abort dump early in the run, so the system was initially turned on to 60% of nominal separation. This separation was adequate for the beginning of the run as the antiproton lifetime was several hours at injection. As the proton intensities increased, the antiproton lifetime began to suffer during the injection front porch. The separators were eventually turned up to 115 % of their design value at 150 GEV to improve the beam lifetimes.

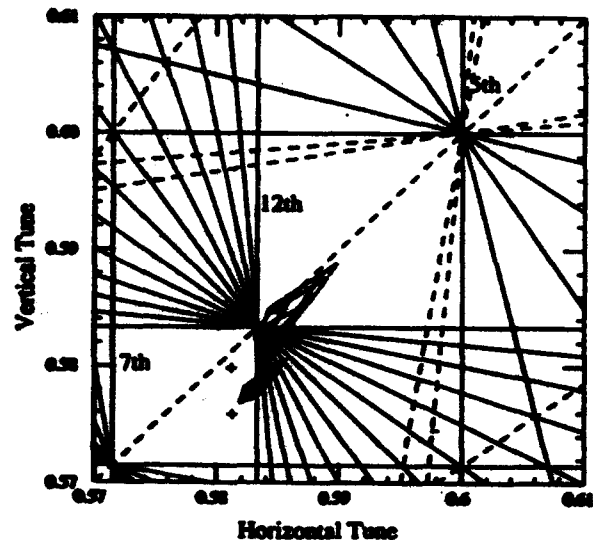
The performance of the separators has been excellent. There is one separator module that sparks at lower a voltage when its polarity is reverse. This is only a problem when attempting to run protons on the antiproton orbit by reversing the separator polarities. This is an activity during studies and the problem is handled by increasing the voltage on one electrode, and decreasing the voltage on the electrode susceptible to sparking. At this point in time, only one separator spark has been observed during normal operation and it had little impact on the quality of the store.

B. Feeddown Sextupoles

The feeddown sextupoles have been powered at low energies where the physical separation is large. At higher energy, the actual separation becomes smaller and the differential tune shift is small enough to fit inside the working space. These sextupoles have been adjusted during stores to study the effect on luminosity lifetime and background rates but they normally run at zero current during physics runs. Figure 1 shows the where in tune space where the beams actually exist with both the differential tune shift (.002 units vertically) and the tune spread caused by beam-beam forces.

The horizontal proton tune sits on the 7/12 resonance, but this is not destructive to the low amplitude particles. The high amplitude particles are affected by this high order resonance, but they are tune shifted less and stay below the resonance. The antiprotons are shifted above the protons, so they can reside between the 3/5 and the 7/12 resonances. The vertical

tunes for both the protons and antiprotons fit between the 7/12 and the 4/7 resonances. Details of beam-beam interactions around this working space can be found in reference [2] If the uncentered orbit does not go through the center of these sextupoles, tuning these circuits will cause the base tune to change. The normal tune quadrupoles can be adjusted in concert with the feeddown sextupoles, but since the separated tunes can result in acceptable lifetimes and background rates, the feeddowns are normally brought to zero during a store.



Three transverse beam sigma shown in this figure.
Proton intensity $1.2 \text{ E}11$ - Emittance $20 \pi \text{ mm-mrad}$
Antiproton intensity $5 \text{ E}10$ - Emittance $16 \pi \text{ mm-mrad}$
 σ/p of .0001 at 900 GEV.

figure 1

C. Low Beta Insertions

The installation of the new low beta inserts brought with it new quench protection systems and a larger burden on the cryogenic system. These complications have been managed successfully. It has been found however, that the magnet to magnet variation in transfer constants have introduced beta errors in the Tevatron of significant magnitude [3]. These errors have had many minor impacts on the operation of the collider. One adverse effect is that the maximum luminous point for the D0 experiment is not in the center of their detector. The collision point cannot be moved longitudinally to maximize the interaction rate at both experiments simultaneously. Trim power supplies are being added to quadrupoles within electrical circuits to be able to correct for the gradient errors.

The design beta * for collider run 1A is 1/2 meter. The quadrupoles and power supplies will allow further reduction of

beta *, but the beta errors have made this difficult. A small number of stores have been run at 1/4 meter beta *, but these were run with only a partial set of trim power supplies for the low beta quads.

D. A0 Abort System

The new abort system installed at A0 has operated with great success. The system was timed in and commissioned in a couple shifts and to date there has been only one prefire that ended a store. By comparison, the old abort system was responsible for ending 31 stores in the 1989 run because of kicker prefires. During the early weeks of run 1A, there were many quenches of the low beta quadrupoles caused by beam loss when the new abort system fired. It was found however that this was not caused by the abort system, but by an RF operation done in the Main Ring before beam was injected into the Tevatron. During bunch coalescing, small amounts of beam would actually be captured in buckets in the Tevatron abort gap.

E. Controls Improvements

The new waveform generator used by the collider is a Camac 465 card built in house. This card is driven by clock events and are loaded asynchronous with the operation of the collider. The 465 sums a time dependent waveform and a pair of machine parameter dependent waveforms. The operational code has been upgraded several times with only a change of prompts. The flexibility of this card has proven itself throughout the run.

Three major application programs were written specifically to control the upgraded Tevatron collider. The waveform generator and loader fills all of the 465s and does complex manipulations of ramp tables during special operations[4]. The orbit smoothing program was written to take care of all steering dipole corrections needed. This program has worked very successfully to globally correct the Tevatron orbit. The third program that was written was the Sequencer. This is used to orchestrate the operations needed for collider operation. The sequencer was written so the user can interactively change the sequence of operations performed, but still contain enough structure to allow for reliable execution of the fill sequence. Each of these three programs replaced programs that were limited by the old controls hardware.

IV. CONCLUSIONS

The upgrade to the Tevatron has allowed the collider to operate at Luminosities above the goal. Table 2 shows the goals next to the actual performance of the accelerator. The ACHIEVED column are the best done during the run. The only entry that

falls short of the goal is the proton emittance. 16 π mm-mrad protons have been achieved, but not with proton intensities as high as shown in table 2.

The improvements in the controls system permitted the Tevatron collider to be turned on with a minimum of difficulty. Improvements in the other accelerators have allowed higher intensity beams to be injected into the Tevatron. The Tevatron upgrade to separated orbits has made it possible to turn this increased intensity into increased luminosity.

	RUN 1A GOALS	ACHIEVED
Protons per bunch	1.2E 11	1.5E 11
Pbars per bunch	3.6E 10	8.0E 10
Proton emittance	16 π mm-mrad	20 π mm-mrad
Pbar emittance	16 π mm-mrad	16 π mm-mrad
Weekly integrated Luminosity	1000 nb ⁻¹	2300 nb ⁻¹
Total integrated Luminosity	25 pb ⁻¹	30 ⁻¹
Luminosity	5.37E 30	8.97E 30

Table 2

IV. REFERENCES

- [1] P. Lucas, "Updated Overview of the Tevatron Control System", Proc. of the 1987 conference on Control Systems for Experimental Physics, Villars-sur-Ollon, Switzerland, Cern 90-08.
- [2] D. Siegiej and G. Goderre, "Beam-Beam Experiments in the Tevatron", Presented at the IEEE Particle Accelerator Conference, Washington, DC, May 19, 1993.
- [3] G. Goderre, W. Marsh, and G. Annala "Beta Measurements in the Tevatron Using the Beam Position Monitors", Presented at the IEEE Particle Accelerator Conference, Washington, DC, May 17, 1993.
- [4] D. Johnson, G. Goderre, B. Hendricks, R. Johnson, and R. Joshi, "Control of the Time and Energy Dependent Parameters of the Upgraded Tevatron Collider", Proc. of the 1991 Particle Accelerator Conference, IEEE 91CH3038-7.

Fermilab Antiproton Accumulator in the Main Injector Era

Vladimir Visnjic
Fermi National Accelerator Laboratory*
Batavia, IL 60510, USA

Abstract

I review the demands on Fermilab Antiproton Accumulator in the Main Injector era and show that a major upgrade of the stochastic cooling systems is necessary. The main possibilities for the design of the new lattice are outlined. Three lattice designs are presented and discussed.

1 Introduction

Presently, the Fermilab Antiproton Accumulator accepts for stacking 3×10^7 antiprotons every 2.4 seconds. With the advent of Main Injector, the number of antiprotons injected into Fermilab Antiproton Accumulator is expected to increase about three times, while at the same time the period between injections should decrease to 1.5 sec. Since the cooling rate is proportional to the bandwidth of the system and inversely proportional to the number of particles in the beam, this will inevitably lead to slowing down the rate at which the antiproton beam is cooled.

Since the flux Φ_0 increases, while the energy aperture of the Accumulator does not, the voltage profile of the machine

$$E_d = -\frac{\beta p \Lambda \Phi_0}{TW^2 |\eta|} \quad (1)$$

must stay the same. Here, $\beta = v/c$, $\Lambda = \ln f_{\max}/f_{\min}$, T the revolution period, W the bandwidth of the stochastic cooling system, and η the momentum compaction factor

$$\eta = \frac{1}{\gamma_T^2} - \frac{1}{\gamma^2}.$$

Among these, β , p , Λ , T cannot change. If Φ_0 is to increase, E_d will remain unchanged if W and η scale such that their product remains constant. This can be seen as follows. W and η are related by the requirement that Schottky bands not overlap in the passband of the system. The width of n -th Schottky band is $n\Delta f_{rev}$, where $\frac{\Delta f_{rev}}{f_{rev}} = \eta \frac{\Delta p}{p}$, thus the width of the highest harmonic in the passband is $f_{\max} \eta \frac{\Delta p}{p}$. This must be smaller than the spacing between the bands f_{rev} .

This defines the relation between f_{\max} and η for a given lattice, i. e. f_{rev} and the momentum aperture $\frac{\Delta p}{p}$:

$$f_{\max} \eta \leq f_{rev} \left(\frac{\Delta p}{p} \right)^{-1}$$

From this we conclude that

$$\Phi_0 \eta = \text{const.} \quad (2)$$

Summarizing, if the stacking rate is to increase by a factor x , the momentum compaction factor η must scale as η/x . In core, the cooling rate is proportional to η and W has to scale as xW .

Presently, the stack tail systems use the 1-2 GHz band, while the core whose smaller frequency spread permits the use of higher bandwidth uses 2-4 GHz. There is also a 4-8 GHz core momentum cooling system. An upgrade to twice these values requires decreasing η to half the present value. γ_T presently has the value 5.43, which gives $\eta = 0.023$. Since only the absolute value of η is important, we have two possible values, ± 0.011 . The solutions are $\gamma_T = 6.74$ for positive η and $\gamma_T = \infty$ for negative one. The latter value would lead to too low dispersion for the purpose of stochastic cooling and will not be considered further.

γ_T is determined by the values of the dispersion function in the dipoles,

$$\frac{1}{\gamma_T^2} \approx \frac{1}{C} \sum_{\text{dipoles}} \langle \eta_x \rangle_i \theta_i, \quad (3)$$

where $\langle \eta_x \rangle_i$ is the average dispersion in a given dipole and θ_i its bend angle. From this expression it follows that in order to increase γ_T we have to decrease values of dispersion in the dipoles. At the same time, dispersion in the straight sections where the pickups and the kickers are located (high and low dispersion, respectively) must not change significantly. The lattice functions of one sextant (half of the superperiod) of the present Accumulator are shown in Fig. 1. On top of the picture is a schematic representation of the lattice, with the height of the boxes representing the field gradient.

*Operated by the Universities Research Association, Inc. under contract with the U.S. Dept. of Energy.

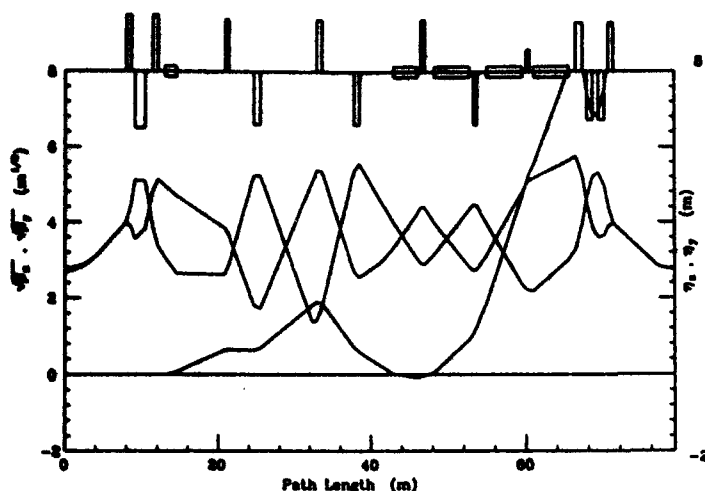


Fig. 1 The present lattice functions of one sextant of the Accumulator.

The following table lists the stochastic cooling systems in the Accumulator with their present and future bandwidths.

SYSTEM	Present	MI era
STACK TAIL Δp	1-2 GHz	2-4 GHz
STACK TAIL β	1-2 GHz	2-4 GHz
CORE Δp	2-4 GHz	4-8 GHz
CORE β	4-8 GHz	8-16 GHz
CORE Δp	4-8 GHz	8-16 GHz

TABLE 1 Bandwidths of stochastic cooling systems in the Accumulator.

2 Options For New Accumulator Lattice

We shall consider only the possibilities which retain the geometry of the present Accumulator lattice. In order of increasing complexity, we can

1. Change only the quadrupole gradients;
2. Change the gradients and allow quadrupoles to move;
3. Add new focusing elements and change the existing quadrupole gradients.

In what follows, we shall examine these possibilities.

3 Examples of Lattices

1. Change only the quadrupole gradients

Here one uses a lattice design program with optimization capability (here MAD¹ was used) to vary the fields in the quadrupoles in order to decrease the dispersion in the region of large dipoles, subject to the constraints of

- (1) maintaining its value in the high- and low dispersion sections,
- (2) maintaining the values of beta functions within reasonable limits, and
- (3) keeping the beta functions in low-beta regions as small as possible.

Similar investigation was done by G. Dugan in 1989².

The lattice obtained in this way is shown in Fig. 2 together with its lattice functions. A detailed description of this lattice can be found in Ref. 3. (Small negative dispersion in zero-dispersion straight section was added to counter the small residual dispersion of the lattice.)

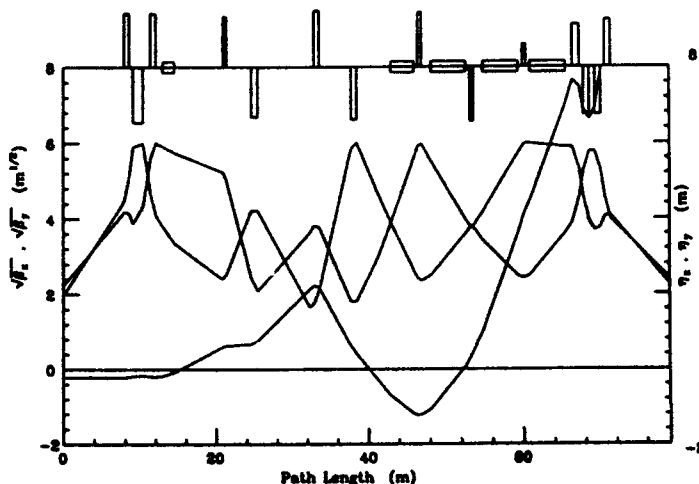


Fig. 2 The lattice functions of one sextant of the new Accumulator lattice obtained by varying the focusing strength.

The lattice has excellent properties regarding the stochastic cooling needs and is technically simple to realize. Feasibility issues are discussed in detail in Ref. 3. Possible disadvantage of this kind of solution might be a deterioration of field quality, as some quadrupoles run in the saturation region. This problem motivated the following two designs.

2. Change the gradients and allow quadrupoles to move

The problem of achieving stronger focusing in certain regions of the machine may be solved by moving quadrupoles, in addition to changing their strength. The resulting lattice together with its lattice functions is shown in Fig. 3. The problem of the field quality is much less severe than in the previous lattice.

3. Add new quadrupoles and vary gradients

Here we want to avoid operating in the saturation regime altogether. The basic requirement is thus that the field in the large quadrupoles should remain at its present value. The additional focusing needed to obtain higher γ_T is obtained by adding a new quadrupole, as seen in Fig. 4, where the lattice is shown. There is no change in the positions of the lattice elements with respect to the present lattice.

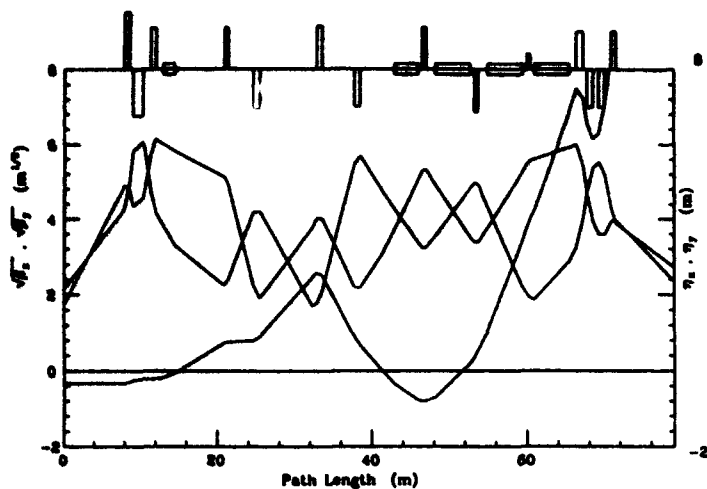


Fig. 3 The lattice functions of one sextant of the new Accumulator lattice obtained by changing positions of quadrupoles and varying their focusing strength.

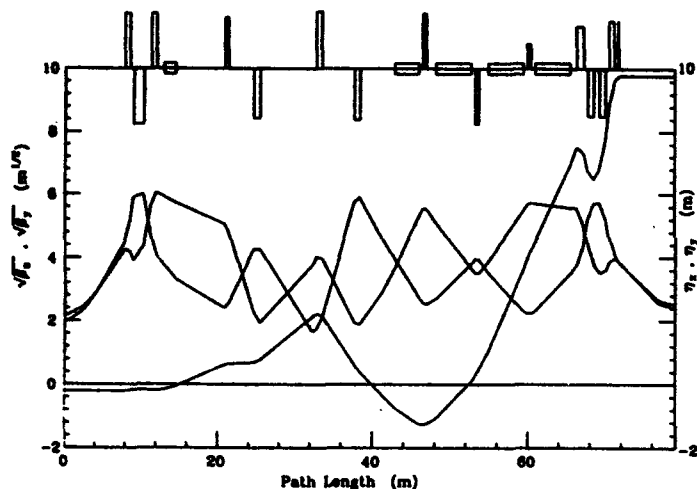


Fig. 4 The lattice functions of one sextant of the new Accumulator lattice obtained by adding one new quadrupole and varying the focusing strengths of small quadrupoles. The large quadrupoles are not changed.

It turns out that one new thin large quadrupole is sufficient. The gradient changes in existing quadrupoles are small, therefore there is no concern about the field quality. This lattice and the related feasibility issues are discussed in detail in Ref. 4.

References

- ¹ Methodical Accelerator Design, CERN, 1990.
- ² G. Dugan, Fermilab report PBAR Note 484, Fermilab, 1989.
- ³ V. Visnjic, Fermilab report TM-1797, Fermilab, 1992.
- ⁴ V. Visnjic, Fermilab report TM-1812, Fermilab, 1992.

Study of Betatron Stochastic Cooling in Fermilab Antiproton Debuncher

V. Visnjic and M. Halling
Fermi National Accelerator Laboratory*
Batavia, IL 60510, USA

Abstract

Results are shown of calculations and measurements of the effectiveness of the betatron stochastic cooling systems in the debuncher ring of the antiproton source at Fermilab. This system cools each batch of injected antiprotons from $\approx 8 \pi$ mm mrad to less than 1π mm mrad rms emittance in the 2.4 seconds between production cycles. The conclusions concerning future improvements are summarized.

1 Introduction and Theory

The Fermilab Antiproton Debuncher presently accepts 4×10^7 antiprotons every 2.4 seconds and prepares them for injection into the Accumulator for stacking. Besides the RF bunch rotation, the stochastic cooling (both longitudinal and transverse) of the antiproton beam is the essential part of this process. In particular, the task of the transverse cooling systems is to decrease the betatron amplitudes of the beam by about an order of magnitude during these 2.4 seconds. With the advent of the Main Injector, the number of antiprotons injected into the Debuncher is expected to increase about threefold, while the period between injections should decrease to 1.5 sec. Since the cooling rate is inversely proportional to the number of particles in the beam, this means slower cooling rate in addition to shorter time available for cooling. It will thus be necessary to upgrade the present systems. To this goal we study here the effectiveness of the betatron stochastic cooling systems in the Debuncher.

The process of betatron cooling is described by the differential equation (throughout the paper emittance is to be understood as the r.m.s. emittance)

$$\frac{d\epsilon}{dt} = -g \frac{W}{N} \left(2 - g \left(M + \frac{\epsilon_{th}}{\epsilon} \right) \right) \epsilon, \quad (1)$$

where W is the amplifier bandwidth, N is number of particles in the beam, g is the system gain, M is the mixing factor, and ϵ_{th} is a quantity with the dimension of emittance which represents the thermal noise of the system. Due to the rapid change of emittance during the cooling

process the noise term $\frac{\epsilon_{th}}{\epsilon}$ becomes the dominant limiting factor toward the end of the cooling cycle. We measure the emittance of the beam 2.3 seconds after the injection, and in order to compare the measurement results with the model we need ϵ for finite times, i.e. we have to solve the differential equation (1). This can be done analytically and the solution is

$$\epsilon(g, t) = \left(\epsilon(g, t') - \frac{g}{2 - gM} \epsilon_{th} \right) e^{g \frac{W}{N} (2 - gM)(t' - t)} + \frac{g}{2 - gM} \epsilon_{th}, \quad (2)$$

where t' is an arbitrarily chosen time. Actually, because $\epsilon(g, 0) = \epsilon(0, t)$ it is advantageous to choose $t' = 0$. We are interested in ϵ at the time $t = 2.3$ seconds as a function of gain. In the Debuncher $W = 2$ GHz and $N = 4 \times 10^7$. We use the calculated value of $M \approx 10$ and leave ϵ_{th} to be determined from the measurement. Also, since we measure ϵ as a function of power rather than the gain we will substitute $g = \text{const.} \times \sqrt{P}$ and determine the proportionality constant from the measurement.

2 Measurement Results

We measured both transverse emittances at $t = 2.3$ seconds after the injection. The measurement was done in the following way. The beam was injected and cooled at a given power for 2.3 seconds at which moment the cooling was turned off. By moving the horizontal (vertical) scraper into the beam and observing the beam current on the logarithmic plot (for increased sensitivity), the closed orbit position x_0 (y_0) was determined. Typical plot is shown in Fig. 1. At each cooling power setting the scraper was moved in and at the same time the beam current was monitored. For the Gaussian beam the current as a function of the scraper position x_s is

$$I(x_s) = I(\infty)(1 - e^{-x_s^2/2\beta\epsilon}),$$

where $I(\infty)$ is the initial beam current and β the amplitude function at the position of the scraper. The typical

*Operated by the Universities Research Association, Inc. under contract with the U.S. Dept. of Energy.

measured curve $I(x_s)$ is shown in Fig. 2.

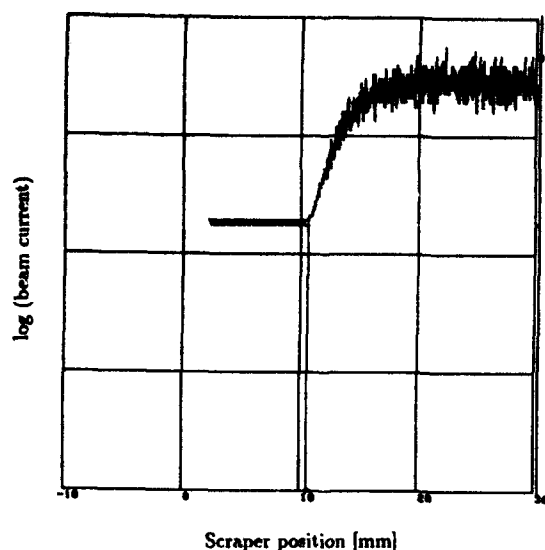


FIGURE 1 Determination of the closed orbit.

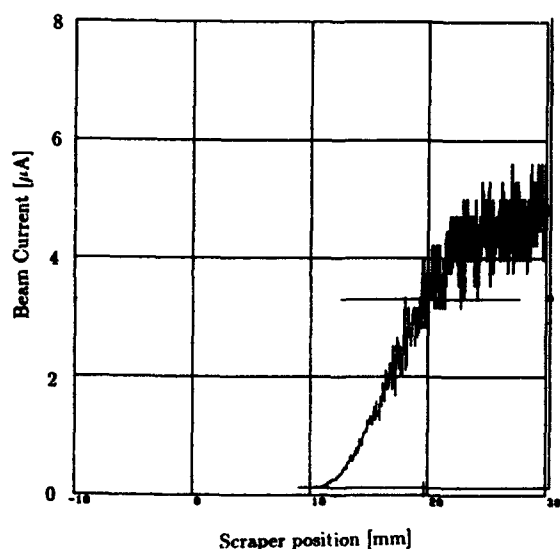


FIGURE 2 Typical measurement of the beam current as a function of the scraper position (x_s)

The results of the measurement are shown in Figs. 3 (horizontal) and 4 (vertical). In each measurement, the "other" power was kept constant throughout the measurement. We fit the function $\epsilon(P)$ at $t = 2.3$ s to the data points. The best fit is obtained for

$$\epsilon_{th} = 72.2 \pi \text{ mm mrad}$$

for the horizontal plane, and

$$\epsilon_{th} = 75.9 \pi \text{ mm mrad}$$

for the vertical plane. For the relation between power and

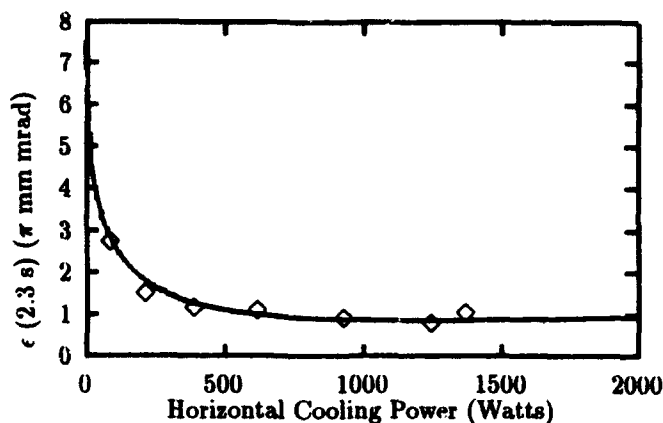


FIGURE 3 The measured values of the horizontal emittance after 2.3 s of cooling for various values of horizontal power. The power in the vertical system was 1117 W. The curve is the fit of Eq. (2) to the data.

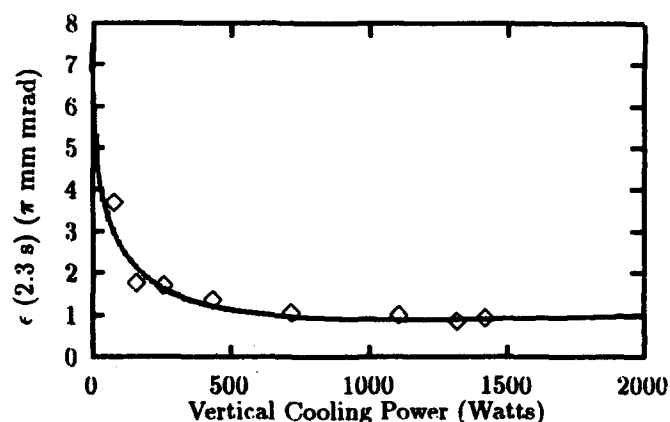


FIGURE 4 The measured values of the vertical emittance after 2.3 s of cooling for various values of vertical power. The power in the horizontal system was 1250 W. The curve is the fit of Eq. (2) to the data.

gain we obtain

$$P(\text{Watts}) = 4.44 \times 10^6 g^2.$$

Our figures for ϵ_{th} are higher than those given in the Design Report¹ ($\approx 24 \pi$ mm mrad) and those measured by M. Church² ($\approx 36 \pi$ mm mrad).

3 Debuncher in the Main Injector Era

The experimental results shown in Figs. 3 and 4 suggest that presently the optimal cooling power is about 1100–1200 W in each plane. The question is what we can expect in the Main Injector era with three times more antiprotons in the beam and the repetition rate of 1.5 seconds. The top curve in Fig. 5 shows the theoretical prediction for

the horizontal emittance of the beam consisting of 1.2×10^8 particles with the present system. The optimal power turns out to be 9083 W in the horizontal plane, leading to the emittance of 1.2π mm mrad, to be compared with 0.85π mm mrad for the present system, Fig. 3. The possibility of running at such high power is due to the fact that ϵ_{th} is inversely proportional to the number of particles N . It is clear that the present system will have to be modified. Besides increasing the power by an order of magnitude, we mention here two more possibilities. So far we have considered the gain to be constant in time and this is how the optimal gain was obtained (both in this paper and in the real machine). The optimal gain, however, is a function of the emittance,

$$g_{opt} = \frac{\epsilon}{M\epsilon + \epsilon_{th}} \quad (3)$$

and changes significantly during the cooling cycle, becoming smaller as the beam size decreases. The reason for this is that an increasing fraction of the power goes into the noise when the beam emittance becomes small. By shaping the gain such that it always follows the optimal curve, Eq. (3) we can achieve optimization throughout the cycle. By replacing the constant optimal gain by the gain shaped according to Eq. (3), while keeping all other parameters of the system unchanged, the final emittance is decreased by 25 % to 0.9π mm mrad.

The other possibility is doubling the amplifier bandwidth to 4–8 GHz. This increases the cooling rate and decreases the mixing by a factor of two. For the horizontal emittance

as a function of cooling power (no gain shaping) for these values of parameters we obtain the bottom curve in Fig. 5. The optimal power in this case is reduced to 7333 W, while the final emittance is 0.7π mm mrad. More extensive study of various options for the Debuncher upgrade will be published elsewhere.³

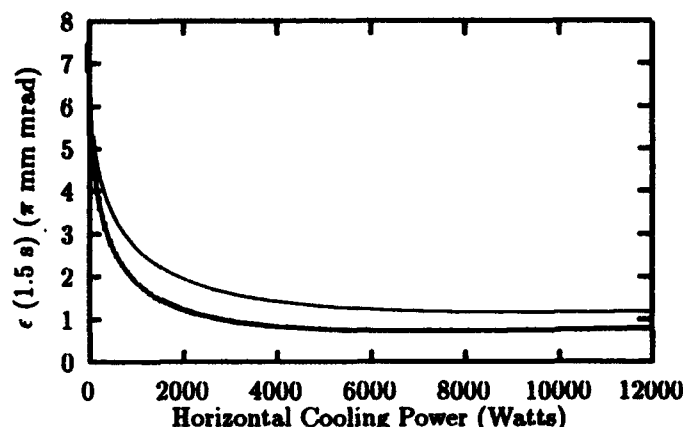


FIGURE 5 Theoretical predictions for emittance 1.5 seconds after injection for Debuncher in the Main Injector era (1.2×10^8 particles). The top curve is for the present cooling system, the bottom one for the 4–8 GHz stochastic cooling system.

References

- ¹ Tevatron1 Design Report, Fermilab 1984.
- ² M. Church, private communication.
- ³ V. Visnjic, Fermilab report TM-1845.

ENERGY AND LUMINOSITY LIMITS OF HADRON SUPERCOLLIDERS

William A. Barletta

Lawrence Berkeley Laboratory
and

Dept. of Physics, University of California at Los Angeles

ABSTRACT:

Extending the frontiers of experimental high energy physics in a manner that maximizes discovery potential requires the building accelerators of ever higher particle energies and luminosities. Both hadron and e^+e^- colliders have been proposed for this role. Based on a self-consistent computational model, this paper explores the features of hadron supercolliders beyond the SSC. The application of the presently available accelerator technologies embodied in the designs of the LHC and SSC to an ELOISATRON operating at 100 TeV per beam would yield a collider with a luminosity of $10^{34} \text{ cm}^{-2} \text{ s}^{-1}$. Even higher energies and luminosities are clearly possible. The paper concludes with an examination of the ultimate potential of synchrotron-based colliders to explore PeV energies.

I. GENERAL CONSIDERATIONS

The continuing search for understanding the nature of mass and the dynamical principles underlying the physical universe has led particle physicists to explore phenomena at the energy frontier particle interactions. The modern tools for the experimental explorations are colliders with ever higher beam energies and ever higher luminosities. Fig. 1 illustrates the performance trends for present and future hadron colliders. What are the energy dependences of the physics and technology that determine these trends?

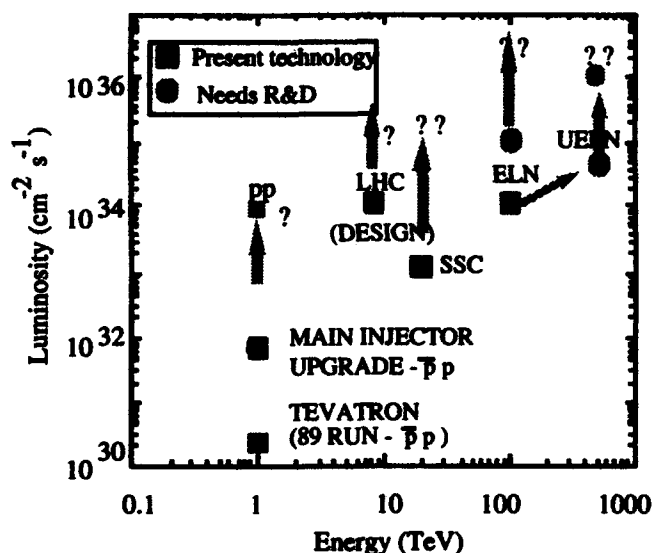


Figure 1. Luminosity goals of present and future hadron colliders

For simplicity, assume that both beams have bunches of equal population, N_B with a spacing S_B . In terms of the

normalized emittance, ϵ_n , the relativistic factor γ and the β -function at the interaction point, β^* , the luminosity is

$$\mathcal{L} = \frac{N_B^2 c \gamma}{4 \pi \epsilon_n \beta^* S_B} = \frac{1}{e r_p} \left(\frac{N_B r_p}{4 \pi \epsilon_n} \right) \left(\frac{\gamma I}{\beta^*} \right) \quad (1)$$

$$= \frac{1}{e r_p} \xi \left(\frac{\gamma I}{\beta^*} \right)$$

In eq. (1) I is the average current; r_p is the classical proton radius; ξ is the tune shift. The luminosity rises naturally with increasing beam energy at the "price" of increased practical difficulties in machine design. The difficulties of increasing the luminosity faster than linearly with energy are associated with increasing the beam current.

In analyzing the energy and luminosity limits of supercolliders one looks to choose N , S_B , β^* , and ϵ_n as a function of energy, E , subject to the following design constraints: 1) Detector limitations – electronics cycling and event resolution; 2) Beam physics – tune shifts, beam lifetimes, emittance growth; 3) Accelerator technology – magnets, fault modes handling of synchrotron radiation, beamline impedance, radiation damage of components.

II. SYNOPSIS OF SELECTED CONSTRAINTS

Constraints deriving from the interaction region reflect problems of event resolution and challenges of detector survival. For adequate event reconstruction, one ideally chooses the current per bunch and the bunch spacing so that the mean number of events per crossing, $\langle n \rangle$, is sufficiently low that the luminous region contains fewer than 1 event/cm. $\langle n \rangle$ depends on E via the inelastic cross-section, σ_{inel} :

$$\langle n \rangle = \frac{\mathcal{L} \sigma_{inel} S_B}{c} \quad (2)$$

Furthermore, cycling of the data acquisition electronics requires ≥ 10 ns between crossings. In a general sense the difficulties of dealing with the radiation from the collision point are most simply expressed by the power in charged particle debris (per side); namely,

$$P_{debris} = 350 \text{ W} \left(\frac{\mathcal{L}}{10^{33}} \right) \left(\frac{\sigma_{inel}}{90 \text{ mb}} \right) \left(\frac{E}{20 \text{ TeV}} \right) \quad (3)$$

The fundamental beam-beam effect that limits luminosity is the tune shift due to the space charge of the colliding beams. Although tune shifts as high as 0.06 have been measured in e^+e^- colliders, the experience with hadron beams at the CERN SppS and at the Tevatron indicates

that the maximum total tune shift is 0.024 with several interaction points. This observation might suggest that the luminosity can be maximized with a single high luminosity interaction point. Unfortunately, the validity of such an extrapolation is unknown. A more conservative assumption is that the maximum value of ξ per interaction point is 0.01 and that $\xi_{\text{tot}} \leq 0.024$.

Supercolliders will have to cope with a phenomenon that has been previously unimportant to proton colliders, i.e., the production of intense synchrotron radiation in the vacuum UV to hard X-ray range. The radiation will heat the walls of the vacuum chamber and desorb gas from the chamber. The synchrotron radiation power generated per meter of bend, P_{sync} , is proportional to the energy lost per turn, U_0 , to the beam current, I , and is inversely proportional to the radius of curvature of the bends, ρ :

$$U_0 = 6.03 \times 10^{-18} \text{ GeV/turn} \frac{\gamma^4}{\rho \text{ (meters)}} \quad (4)$$

As the radiation is deposited onto the cold walls of the vacuum chamber, the heat must be removed with a efficiency that is limited by the Carnot efficiency of the compressors which supply the cryogenic coolant. To limit operating power to practical levels the SSC design limits P_{sync} to 0.13 W/m on the magnet bore (at 4.2 °K). The LHC design incorporates a radiation shield at 20 °K inside the vacuum chamber, permitting 1 W/m. For supercollider operation at the highest possible energy or luminosity, P_{sync} must be allowed to exceed 1 W/m. To limit the power consumed, one also must increase the temperature of the surface on which the radiation is deposited; e.g., one might operate the radiation shield to 70 °K. Unfortunately, raising T_{wall} leads to serious consequences for collider luminosity due to the transverse resistive wall instability.

Transverse displacements of the beam from the centerline of the beam chamber will grow due to the finite conductivity of the wall, σ_{wall} . The growth time [1] of the instability in a beam pipe of radius, b , is

$$\tau_{\text{RW}} = \frac{N_B M r_p \beta_{\text{ave}} \omega_0 c}{(2 \pi \sigma_{\text{wall}} \omega_0 \delta v)^{1/2}} \frac{\text{Im}[(1+i)\zeta]}{2 \pi \gamma b^3} \quad (5)$$

M is the number of bunches, σ_{wall} is the conductivity of the inner layer of the beam tube, ω_0 is the revolution frequency, δv is the fractional tune, $v-n$, (use 0.1), and ζ is a correction for the multiple metallic layers (equal to $2.87 + 2.87i$ for SSC). The residual resistivity ratio (R_w) for copper plated onto stainless steel varies as

$$\ln(R_w) = 3.1 \left[1 + \frac{41.6 T_{\text{wall}}^{-0.93} - 0.24 T_{\text{wall}}^{0.93}}{41.6 T_{\text{wall}}^{-0.93} + 0.24 T_{\text{wall}}^{0.93}} \right] + 0.24 \quad (6)$$

where R_{wall} is normalized to its value at 300 °K, ($1.6 \times 10^{-6} \text{ ohm cm}^{-1}$).

As the resistive wall is an absolute instability, its growth cannot be Landau damped by spreading the betatron

frequencies in the beam. Hence, controlling the instability will require the use of a digital, bunch-by-bunch feedback system. The limits of such a system have not been established. However, many experts consider $\tau_{\text{RW}} \sim 6 T_0$ to represent the limits of available feedback electronics. Similar feedback electronics can also control emittance growth due to injection errors, coupled-bunch modes, and ground vibrations.

At energies $>10 \text{ TeV}$, for which copious radiation is generated, maximizing the luminosity while keeping $\tau_{\text{RW}} \gg T_0$ places an upper limit on the T_{wall} and a lower limit on the vertical aperture of the dipoles. Both T_{wall} and b are functions of B_{dipole} . The consequences of the constraints on T_{wall} and the beam pipe radius are both the operating costs of supplying power to the compressors and the capital cost of providing for a large magnetic field volume.

The most expensive sub-system of the supercollider is the magnetic transport. In evaluating the prospects for a 100 TeV ELN, the maximum value of B_{dipole} was taken to be 10 T. For the longer term future values as high as 15 T were considered. In that a 13.5 T dipole is presently under development at LBL, the assumption for the long term is not just wishful thinking.

III. PARAMETER STUDIES

Self-consistent characteristics of supercolliders at the highest energies and luminosities are explored most easily with a simple computer code for performing parameter searches. ELOSCALE is a spreadsheet-format design code based on the scaling relations described ref. [2]. The input variables are the injection and maximum beam energies, the normalized emittance and the bunch spacing. A critical characteristic is the maximum permissible tune shift per interaction point – taken to be 0.01. The inputs describing the storage rings are as follows: the maximum dipole field, and dipole fraction, and the vertical dipole aperture, the radiation power on the walls and the temperature of the beam tube, the number of interaction points, the crossing angle, the distance from the collision point to the septum, the scale value of β^* at 20 TeV, and the rf-system frequency. The injection chain consists of a linac and four intermediate boosters. All other characteristics of the collider and the injector chain are computed in the code.

Table 4. Possible sets of characteristics of ELOISATRON

	ELN34	ELN35	2ELN
Circumference (km)	355	355	355
B_{dipole} (T)	7.7	7.7	13
Maximum energy (TeV)	100	100	170
Beam current (mA)	100	400	50
Mains power (GW)	2	0.33	0.33
$\langle P_{\text{sync}} \rangle$ (W/m)	5	20	20
Crossing angle (μrad)	70	120	70
Interaction regions (IR)	2	2	2
Tune shift per IR	0.003	0.01	0.006
Events/cm/crossing	1.2	9	2.4
Luminosity ($\text{cm}^{-2} \text{ s}^{-1}$)	10^{34}	10^{35}	10^{34}

A parameter exploration with ELOSCALE indicates an approach to construct a 100 TeV proton supercollider (ELN-34) with a luminosity $>10^{34} \text{ cm}^{-2} \text{ s}^{-1}$ at $P_{\text{sync}} = 5 \text{ W/m}$ by using the same technologies that are being realized for the LHC. Raising P_{sync} to 20 W/m yields $10^{35} \text{ cm}^{-2} \text{ s}^{-1}$ (ELN-35). Parameters for both of these cases are given in Table 4. The variation of the luminosity of ELN with P_{sync} and operating energy are shown in Fig. 2. Fig. 3 displays two examples of cost and operational sensitivities such as those dependent on B_{dipole} .

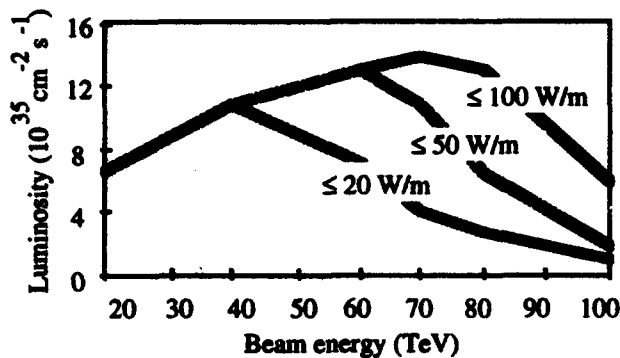


Figure 2. The luminosity ELN as a function of beam energy for radiation loads from 20 – 100 W/m.

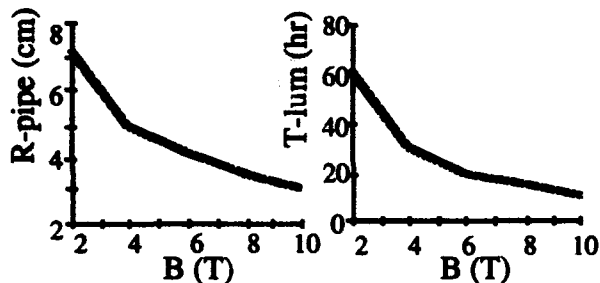


Figure 3. Variation of dipole aperture and luminosity lifetime with B_{dipole} for ELN35.

IV. ULTIMATE SUPERCOLLIDER

For the long term, ELOSCALE studies suggest the ultimate potential of conventional storage ring technology in the exploration of the high energy frontier of elementary particle physics. If the vacuum chamber of the storage ring operates at room temperature, then one could construct a hadron collider with a center of mass energy of 1 PeV and a luminosity $> 10^{36} \text{ cm}^{-2} \text{ s}^{-1}$. With a circumference twenty times SSC's and consuming $\approx 2 \text{ GW}$ of mains power, this proton synchrotron may well be the ultimate supercollider.

As the survival of detector components is doubtful at such a high luminosity, a more probable scenario for UELN is to keep the luminosity at $10^{34} \text{ cm}^{-2} \text{ s}^{-1}$. In that case all of the technical sub-systems are much closer to the present state of technology. In particular the vacuum sub-system should be fairly close in character to that of the ELN. The walls could be kept at 150 °K to limit the power to the compressors to 500 MW. Table 5 compares the high and "low" luminosity options.

Table 5. Two possible sets of characteristics of an Ultimate ELOISATRON (UELN)

Center of mass energy	1 PeV	
Circumference (km)	1500	1015
B_{dipole} (T)	8	13.5
Beam energy	500 TeV	
Beam current (mA)	800	10
Mains power (GW)	2	0.5
$\langle P_{\text{sync}} \rangle$ (W/m)	1400	55
Interaction regions (IR)	2	2
Limiting technology	IR survival	Management
Tune shift per IR	0.01	0.006
Luminosity ($\text{cm}^{-2} \text{ s}^{-1}$)	$\approx 10^{36}$	10^{34}

V. CONCLUSIONS

A systematic parameter search with the ELOSCALE code shows that conventional proton synchrotrons are a suitable technology for hadron supercolliders with an energy and luminosity much higher than those of the SSC. In particular, an ELOISATRON operating at 100 TeV per beam with a luminosity $>10^{34} \text{ cm}^{-2} \text{ s}^{-1}$ (ELN-34) could be constructed by using technologies now available. Assuming moderate advances in accelerator technology during its design cycle, one could expect to operate ELN at luminosities $\approx 10^{35} \text{ cm}^{-2} \text{ s}^{-1}$ at 100 TeV/beam (ELN-35). Such a hadron supercollider based on conventional technology would have the physics reach and discovery potential at least as great as a 10 TeV e^+e^- linear collider, for which no reasonable design concept now exists. With further advances in a few key technologies, a PeV collider based upon conventional proton synchrotron approaches would be technologically possible.

If existing technologies are extended into new regimes (e.g., given practical, high T_c superconductors suitable for magnet windings), one could extend the luminosity at 100 TeV/beam to $\approx 10^{36} \text{ cm}^{-2} \text{ s}^{-1}$. Such a supercollider would contain $\approx 500,000$ bunches with associated beam crossing rates approaching 1 GHz yielding several tens of collisions per crossing. As detectors are unlikely to accommodate or even survive extremely high luminosities, a more fruitful upgrade of a 100 TeV class collider would be a 70% energy increase in the existing tunnel (ELN-Up in Table 4).

ACKNOWLEDGMENTS

The author thanks Prof. A. Zichichi for his kind hospitality at the Ettore Majorana Centre for Scientific Culture. The author's participation in the 19th and 25th ELOISATRON Workshops provided a broad source of the physics embodied in ELOSCALE. This work was partially supported by Lawrence Berkeley Laboratory for the U. S. Dept. of Energy under contract No. DE-AC0376SF00098.

References:

- [1] SSC Site-specific Conceptual Design Report, 1990
- [2] W. A. Barletta, "Maximizing The Luminosity Of Hadron Supercolliders At 10 - 100 TeV", in Supercolliders and Superdetectors, W. Barletta and H. Leutz, ed. World Scientific, 1993

Ion Acceleration in the Synchrotrons with Constant RF of Electrical Field

V.P. Balov, Yu.P. Severgin
D.V. Efremov Scientific Research Institute
of Electrophysical Apparatus
189631, St.-Petersburg, Russia

Abstract

The way of protons and heavy ions acceleration in ordinary proton synchrotrons with constant RF of an electrical field is proposed. It is carried out, if acceleration is realized with high harmonic number q , and RF voltage V is changed so, that the particles hit the new neighboring separatrix on the following turn. This way requires the application of RF systems providing the high acceleration rate 100 MeV/m, and working with the constant frequency approximately several tens of GHz.

1. ACCELERATION WITH CONSTANT RF

With protons or heavy ions accelerated in synchrotrons up to high energies, their speed varies in a wide range making it necessary to change by several fold the frequency of RF-voltage. But it is not an easy task to perform. Currently, RF-systems providing a high rate of acceleration, up to 100 MeV/m and operating at a constant frequency of about several tens of GHz are under development. Such RF-systems are supposed to be used, for example, in the project VLPP [1]. They may be used as well, and we intend to show it, to accelerate protons and heavy ions in conventional - proton synchrotrons. We mean another alternative method, when RF - frequency may be kept constant in case the acceleration is realized at a high multiplicity q , and RF-voltage, V , is changed so that every one cycle the particles fall within a new neighboring separatrix.

Really, a gain in the ion energy with the charge Ze every one return amounts to

$$dE = eVZ \cos \phi$$

and, hence, the period of its return reduces by the value

$$\Delta T = -\frac{1}{\omega} \frac{\delta \omega}{\delta E} dE = \frac{K}{\omega E} eVZ \cos \phi,$$

where $\omega = v/\Pi$ is the frequency of ion return with the velocity v , K is the autophasing factor, Π is the synchrotron circumference. Requiring that the beam within one return should enter the neighboring separatrix: $\Delta T = T_{\text{ret}}/q = 1/q\omega$, we find the necessary RF-field voltage per turn

$$V \cos \phi = \frac{E}{eZqK}. \quad (1)$$

It depends on the autophasing properties of a synchrotron and is to vary with a change in the ion energy.

The transition to the neighboring separatrix requires a high rate of energy gain and high growth rate of the leading magnetic field:

$$\frac{1}{\langle B \rangle} \frac{\partial \langle B \rangle}{\partial t} = \frac{\beta c}{\Pi q \alpha}. \quad (2)$$

It follows from Eqs. (1) and (2), that the multiplicity q of the RF-field should be high enough for the voltage V and growth rate $(\frac{\partial \langle B \rangle}{\partial t})$ to be technically realizable. But in this case the energetic size of the separatrix is decreased and, hence, the momentum spread

$$\frac{dP}{P} = \pm \frac{2}{qK\beta^2} \sqrt{\frac{\tan \phi_s - \phi_s}{2\pi}} \quad (3)$$

will be small in the beam captured into the acceleration regime. This difficulty may be avoided by cooling down the stored beam or injecting the beam having been cooled down. Ratios (1), (2), (3) impose certain requirements for the selection of the structure of a synchrotron ring-shaped electromagnet, in particular, it can not be isochronous, the coefficient α of the orbit expansion and the perimeter Π should be as large as possible and special straight section suitable for the electron cooling-down system to be arranged are to be provided.

As an example, consider a synchrotron with a circumference $\Pi = 150\text{m}$, $\alpha = 0.5$, $B_{\text{max}} = 1.5\text{T}$, accelerating heavy ions with $A/Z = 2$ from $W = 50\text{MeV/n}$ up to $W = 2.8\text{GeV/n}$ ($\gamma = 4$). Then the parameters of the RF-systems will be the following: the RF-amplitude varies during acceleration cycle from 9.7kV to 0.32MV, ($\cos \phi_s = 0.5$), $q = 10^5$, $\omega = 62\text{GHz}$, $(\frac{\partial \langle B \rangle}{\partial t})_{\text{max}} = 58\text{T/s}$. A beam with a momentum spread of $(dP/P)_{\text{max}} = \pm 1.6 \cdot 10^{-5}$ is maintained in the synchrotron. The criterion [2] of betatron oscillation stability at a high multiplicity q is satisfied.

At $W = 2.8\text{GeV/n}$ $\beta = 0.79$ and, hence, circulation frequency changes slowly with the increased particle energy. The acceleration up to higher energies is reasonable with standard RF-station at a low q within a small range of frequency changes. That is why, the acceleration method proposed may be used in proton and heavy-ion synchrotrons:

1. to obtain a practically monoenergetic beam with an energy of several GeV/n bunched into q bunches with small dimensions;
2. to pre-accelerate protons or heavy ions from a low energy to an energy of several GeV/n at a constant

frequency of RF-voltage. In this case obtained is a higher acceleration rate, no frequency change is required, and RF-stations are small-sized and take up not much space in the ring-shaped electromagnet of the synchrotron.

II. REFERENCES

- [1] V.B. Balakin et al., "Isledovanie Predelnogo Tempa Ushoraniya v Lineinym Ushoritale VLRF", Proc. of the 13 Int. Conf. on High-Energy Particle Accelerators. Novosibirsk, 1987. vol.1, p.144.
- [2] S.A. Khaifets, Yu.F. Orlov, "Nenatochivost Dvisheniya Chastits v Sinkhrotrone pri Bolshikh Chastotakh Ushoryayushchego Pulsa", Preprint NFI-TP-4(88), Novosibirsk, 1988.

Ion Storage Ring of the INR Storage-Accelerating Complex

A.V. Dolinsky, A.I. Papash, S.N. Pavlov, A.T. Radchik,
A.B. Val'kov, I.N. Vlahovskiy, A.V. Zhmendak
Institute for Nuclear Research
262026, Kiev, Ukraine

V.P. Belov, A.A. Kapustin, V.S. Kashikhin, A.M. Kohorin, A.A. Makarov, B.G. Mad'yagin,
B.V. Rogdestvenskiy, Ya.P. Severgin, I.A. Schukhlo, M.N. Tarovik
D.V. Efremov Scientific Research Institute
of Electrophysical Apparatus
189631, St.-Petersburg, Russia

Abstract

The Storage - Accelerating Complex (SAC) of heavy ions is intended for the storage of ions up to Neon, their acceleration up to an energy of 300 MeV/u ($A/Z=2$), and physical experiment on an internal target with the electron cooling used at a high energy. The experiments can be performed both with narrow and wide beams on the targets. The stored current is about $10^9 - 10^{11}$ particles, the luminosity is expected to be $10^{28} - 10^{30} \text{ cm}^{-2} \cdot \text{sec}^{-1}$, the ion beam life-time - several tens of seconds.

I. THE STRUCTURE OF THE COMPLEX AND ITS MAIN PARAMETERS

The Storage-Accelerating Complex of heavy ions at the Institute for Nuclear Research (Kiev, Ukraine) comprises the isochronous cyclotron U-240 used as an injector, fast booster and storage synchrotron. Two stages are anticipated for the SAC development. The storage synchrotron is planned to be constructed in the first stage to store an ion beam up to Ne with the RF-stacking and electron cooling system used to accelerate ions to 300 MeV/u ($A/Z=2$) and to operate on to the inner target at a continuous electron cooling. In the second stage a multiturn recharging injection into the storage synchrotron from U-240 will be implemented, a fast cycling 200 MeV/u ($A/Z=2$) booster with a repetition frequency of 5 Hz will be constructed and repeated single-turn injection from the booster to the storage synchrotron will be realized.

The SAC will make it possible to operate with intensive beams of radioactive nuclei and ions in a wide range of masses (from proton to xenon) with an energy of up to 300 MeV/u ($A/Z=2$) at a high luminosity. The SAC scheme is shown in Fig.1. Its main parameters are given in the table 1.

II. RING ELECTROMAGNET OF THE STORAGE SYNCHROTRON.

It comprises two superperiods with a triplet focusing and includes eight 45 bending magnets, 36 quadrupole lenses

and 8 sufficiently long rectangular sections of 3 different types. Two of them with a zero dispersion and $\beta_{x,s} \approx 2-5 \text{ m}$ are intended for the installation of the electron cooling system (C30) and acceleration stations (VC). Another two of them with a zero dispersion and low $\beta_{x,s} < 0.8 \text{ m}$ are designed specially for physical experiments on the target M1. The beam is focused on M1 by two triplets of the quadrupole lenses JIK 4-6. The arrangement and parameters of the lenses are selected so that their switching-on changes the characteristic functions only in the section, where they are installed. The rest 4 sections with the dispersion different from zero are intended to perform physical experiments on the target M3 ($\beta < 4 \text{ m}$, $\phi \approx 3 \text{ m}$) and to implement 3 different types of injection into the storage synchrotron, i.e. single and multiturn recharging injection from U-240 with the electron cooling and RF-stacking used and single-turn injection from the booster. Eight sextupole lenses are used for chromaticity correction.

III. INJECTION AND STORAGE.

An average current of ion beams from the cyclotron U-240 varies from 0.2 μA (Ne) to 10 μA (P). With the ECR-source used the ion heavier than Xe can be accelerated in cyclotron. The operating cycle of the storage synchrotron (without the booster) is the following:

1. the single-turn injection of light element nuclei or multiturn recharging injection (of about 40 μA duration) of heavy ions;
2. RF-stacking (of 10-20 ms duration) with an increase in the energy of the injected beam by 2.5% (single-turn injection) or by 1.2% (multiturn recharging injection). The RF-stacking is used to eliminate the cooled beam travel through the input kicker-magnet or the stripping target M2 with, respectively, these two types of injection used;
3. electron cooling of the injected beam during 40-1400 ms;
4. storage resulting from the multiple repetition of the operation according to the above points 1, 2, 3 (duration of up to 10 s and more);

Table 1: The SAC parameters

	storage-synchrotron	booster
Perimeter, m	106.275	67.452
Number of betatron oscillations	3.709/3.406	1.3/1.288
Magnet field induction, T	1.5	1.5
Maximum magnet rigidity, T-m	5.4	4.3
Injection energy from U-240, Mev/a		
light ions	25 - 70	25 - 70
C - Ar	5 - 10	5 - 10
Kr - Xe	3	3
Maximum energy, Mev/a		
protons	930	660
ions with $A/z=2$	300	200
ions with $A/z=3$	144	94
Vacuum, Torr	lower than 10^{-10}	10^{-9}

5. acceleration with a duration of 1 s;
6. a physical experiment (≥ 10 s) with the electron cooling at high energy;
7. preparation of a new cycle of ≈ 1 s.

To store light ions in the storage synchrotron the single-turn injection is used. It is used as well to inject the beam into the booster. The injection of not completely stripped ions with $A/z = 3 - 5$ is implemented with the stripping on the foil. The beam is injected onto the closed orbit in the septum-magnet area. After 10-15 turns the disturbance is removed for about a period of revolution and electron cooling system is switched on [1]. The beam is compressed. With a special RF-resonator used, its energy is increased by 1.2% and the closed orbit is displaced outwards by 3.7 cm. Then, RF is rapidly reset, the cooled beam leaves the resonance with the RF-field and moves along the displaced orbit, where $\phi = 0$. The injection cycle is repeated.

The life time of the ions heavier than Ne is 1 s at a

pressure in the vacuum chamber of $< 10^{-10}$ Torr and energies achievable on the cyclotron U-240. That is why, their storage is possible only with the booster used. The total storage time in this case amounts to 46 s (Kr), 20 s (Xe). With the operation on the inner target the ion life time is determined mainly by a single scattering on the target and the electron capture by the target atoms, as the multiple processes are suppressed by the electron cooling. The target thickness should not exceed $2.6 \cdot 10^{-10}/s$, cm^{-2} so as to compensate energy losses in the target by the electron cooling. A typical life time of heavy ions with a platinum target is about 20 s. The cooled beam with a maximum energy has an emittance of 2.4π mm-mrad for protons ($N = 10^{11}$) and 0.3π mm-mrad for Ne ions ($N = 10^9$) and a size on the target of 2.8 mm and 0.6 mm for P and Ne ions, respectively.

IV. REFERENCES

- [1] N.S. Dikansky et al. "Predelnye vozmozhnosti elektronogo okhlazhdeniya", Preprint N 88-61, IYaF SO AN SSSR, Novosibirsk, 1988.

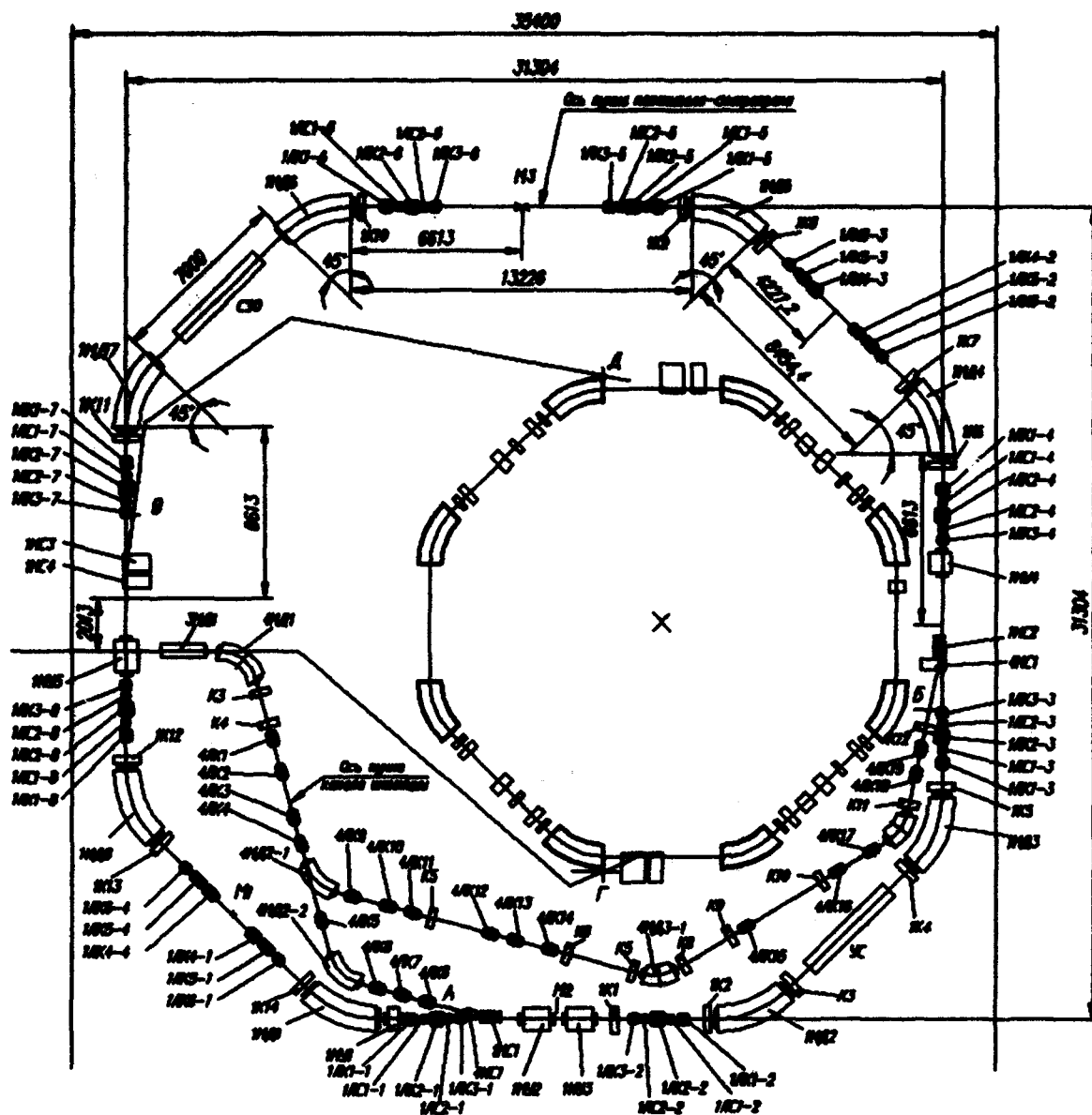


Fig.1. The INR (Kev) Storage-Accelerating Complex

A Compensated Dispersion-free Long Insertion for an FFAG Synchrotron*

Philip F. Meads, Jr.

7053 Shirley Drive, Oakland, CA 94611-1631 USA

Abstract

An FFAG synchrotron differs from a synchrocyclotron by having a large radial field gradient; this large gradient greatly reduces the magnet volume while maintaining stable orbits for all energies, but it does induce substantial nonlinearities. A decade ago, the author proposed a dispersion-free insertion for an FFAG that provides regions of small volume for rf cavities, strippers, and injection and extraction elements, similar to a normal synchrotron.¹ Here we exploit this insertion to provide compensation of the lower order nonlinear driving fields, thereby greatly increasing the dynamic aperture as compared to an FFAG without insertions. The correction fields may be programmed to track the momentum or may be static, providing full compensation at the injection energy.

I. INTRODUCTION

The proposed European spallation source requires an accelerator that can deliver 5 MW protons to the spallation target in a short pulse. In order to deliver such a large beam power with acceptable losses, the accelerator should be dc with a high repetition rate. An FFAG synchrotron would appear to be an ideal solution.² The inherent nonlinearities of an FFAG (e.g. $\langle B \rangle \propto \langle R \rangle^k$) overly limit the dynamic aperture for this application, particularly for compact and higher energy machines where the field index, k , is large. All essential resonances are strongly driven. However, if the FFAG were to have dispersion-free insertions, it would be feasible to place a number of correction elements within these insertions to compensate the limiting resonances. This would greatly increase the dynamic aperture.

One of the very nice features of an FFAG is the capability of stacking a number of injected pulses to deliver the beam to the target at a much lower rate than the repetition rate of the accelerator. A problem with stacking at such high currents is the development of tails in the particle distribution. These tails, although stable, would be expected to lead to increased activation through scattering. With a dispersion-free insertion, it becomes feasible to add cooling to damp these damaging tails.

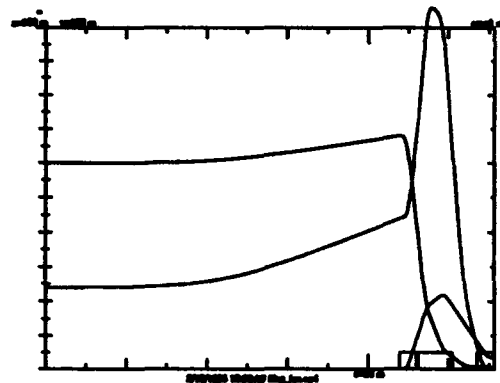
One would normally expect the correction magnets to be programmed to follow the acceleration cycle (in the absence of a stacked beam), thereby providing the maximum dynamic aperture throughout that cycle. However, the dynamic aperture needed is greatest at injection, and the time spent at that energy is relatively long, particularly if adiabatic trapping is employed. So one could consider static correction elements

optimized for the injection energy. As the energy increases, the total tune spread is reduced, and the amount of required correction is also reduced. This means that a dc correction may prove to be entirely adequate.

Should a dc correction entirely within the dispersion-free drift not be adequate, then one could use the drift spaces immediately adjacent to the central dispersion-free drift space. In these drift spaces, there is dispersion, but the overall width of the beam is still relatively small. Multipole magnets placed in these drift spaces with small, but not zero dispersion, will result in a correction that changes with momentum.

II. THE FFAG DISPERSION-FREE INSERTION

The example shown in the 1983 paper on the insertion for an FFAG is very symmetrical. The central dispersion-free drift space is twice as long as the drift spaces at either end. As is the case with π - 2π insertion for normal synchrotrons, it is possible to distribute the total drift space as desired.³ For example, it is possible to place all of the drift space, except what is needed between magnets, in the central dispersion-free portion. As we approach such a configuration, we are forced to increase the focusing strengths, and the amplitude functions vary more wildly, making it difficult to match the insertion to the remainder of the FFAG. An example of such an asymmetric insertion using rectangular bending magnets is shown in Fig. 1, where the Courant and Snyder beta functions and the dispersion are shown for one half of the insertion.



Cost considerations will surely limit the number of insertions to three or so, and thus the periodicity will be low. This is acceptable because of the compensation. My first

*Supported in part by the Forschungszentrum Jülich (KFA), Germany

approach was to start with a symmetrical insertion, adjust it to move all of the magnets toward the ends, add the FFAG section (50° net bends at each end of the insertion for three-fold periodicity) and then try to combine the FFAG magnets and the end magnets to yield a machine with a total of 15 radial bending magnets (no spiral), each of which is assumed to be superconducting, where the coil assemblies would be the major cost item.

Recognizing that a scaling FFAG running at its space charge limit is, in reality, not scaling because of the self fields, and knowing that we have the compensation available in the insertions, there does not seem to be any reason to keep the FFAG portion of the machine at all. A fresh start would be to use the minimum number of magnets to achieve the linear solution, including the required net bend, aperture considerations, and betatron phase advances in the dispersion-free drift and then adjust the higher order field components to keep the tunes fixed and maintain the dispersion-free property of the insertion over the entire energy range from injection to extraction.

III. DESIGN APPROACHES

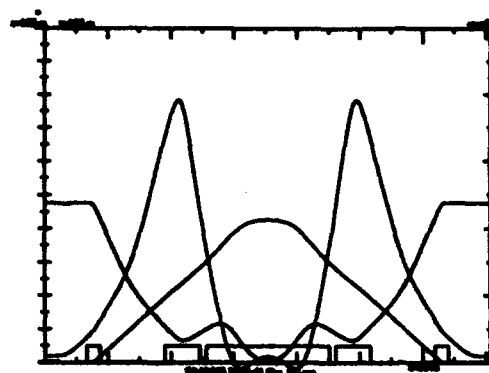
The first approach tried with the three-magnet symmetric lattice was to parameterize the three general magnets and then obtain algebraic expressions for the tunes and the slope of the off-energy orbit at the plane of symmetry—all in terms of the particle rigidity. Having these, we would use an algebra-manipulating program to adjust the parameters such that the dependence on rigidity is eliminated.

The second approach considered was to use an orbit integration program to simultaneously calculate the closed orbits and tunes about those closed orbits for several widely separated momenta and to fit the magnet parameters to minimize (eliminate) the differences with momenta.

The third approach, which is relatively simple, is to solve the linear problem with a matrix program with good online graphics and then use Martin Berz's code, COSY INFINITY,⁴ to extend the solution systematically to higher and higher orders in $\Delta p/p$. This is the approach adopted.

My version of the LATTICE code was used to adjust three gradient magnets with normal entry and exit to achieve the desired tunes and the desired dispersion-free drift space, subject to minimizing the maxima for the Courant and Snyder beta functions. The bends in the three magnets were arbitrarily chosen to be 10° in, 20° out, and 70° in, respectively, for a net bend of 60°. The three gradients and the magnet locations were adjusted by the code to meet the specified conditions. Although this approach suffices to show the feasibility of the method, one would want to consider different bending angles and the use of edge angles and, perhaps, edge curvature in a real design. Separating the big bend into two magnets, perhaps with reverse "gully" fields is another consideration. Once a solution has been obtained, LATTICE can be instructed to write an input file for the COSY INFINITY code. An

example, which is by no means optimized, is shown in Fig. 2.



The COSY INFINITY code reads the LATTICE deck and produces the same linear results. The next step is to have COSY INFINITY adjust the radial second derivatives of the magnet fields to obtain zero chromaticity and zero second order chromatic dependence of the displacement of the closed orbit in the dispersion-free insertion.

Extending the solution to other momenta requires that we expand each of the linear matrix elements in a power series in the displacements, slopes, and relative momentum shift. However, by starting the sector at the center of the dispersion-free drift space, the displacements and slopes at that point are, by definition, zero. This is an important point because we thus need only consider the pure chromatic derivatives. Moreover, because of the symmetry of the lattice, the Courant and Snyder α functions vanish at the center of the dispersion-free drift space. Thus, in order to achieve a dispersion free drift space with fixed tunes over the entire range of momenta from injection to extraction, we need to achieve the following conditions:

$$\frac{\partial^n M_{11}}{\partial p^n} = 0; \quad \frac{\partial^n M_{33}}{\partial p^n} = 0; \quad \frac{\partial^n M_{16}}{\partial p^n} = 0;$$

$$n = 1, 2, 3, 4, \dots$$

Here, the M_{ij} are the matrix elements in TRANSPORT notation.

Then, systematically, COSY INFINITY is set to calculate to the next higher order and requested to zero the pure chromatic derivatives at that order by optimizing the next higher order radial derivative of the magnetic fields. This process is repeated until we are sure that the order for which we have full correction is adequate for the total momentum spread to be accommodated (injection through extraction).

The procedure can be written as follows:

$$\frac{\partial^2 B_k}{\partial x^2} \rightarrow M_{11k} = 0; M_{33k} = 0; M_{1kk} = 0;$$

$$\frac{\partial^3 B_k}{\partial x^3} \rightarrow M_{11kk} = 0; M_{33kk} = 0; M_{1kkk} = 0;$$

$$\frac{\partial^4 B_k}{\partial x^4} \rightarrow M_{11kkk} = 0; M_{33kkk} = 0; M_{1kkkk} = 0...$$

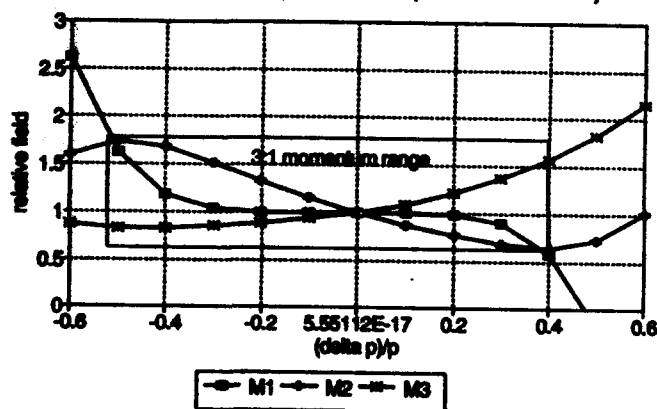
Here, the index k represents the three (or more) different bending magnets whose field we have at our disposal. We have this flexibility because we have dropped the requirement that the field scale with $\langle R \rangle^k$. Having the field and its radial derivatives, we can, of course, obtain its radial profile. The solution, which yields fixed tunes and dispersion-free drifts through the fifth order in the relative momentum shift is:

$$\frac{B_1}{B_0} = 1 + 2.4 \frac{x}{\rho} - 78.7 \left(\frac{x}{\rho} \right)^2 - 1.83 E5 \left(\frac{x}{\rho} \right)^3 - 8.49 E7 \left(\frac{x}{\rho} \right)^4 - 3.43 E10 \left(\frac{x}{\rho} \right)^5 + ...$$

$$\frac{B_2}{B_0} = 1 - 7.77 \frac{x}{\rho} + 35 \left(\frac{x}{\rho} \right)^2 - 144 \left(\frac{x}{\rho} \right)^3 - 785 \left(\frac{x}{\rho} \right)^4 + 5.1 E4 \left(\frac{x}{\rho} \right)^5 + ...$$

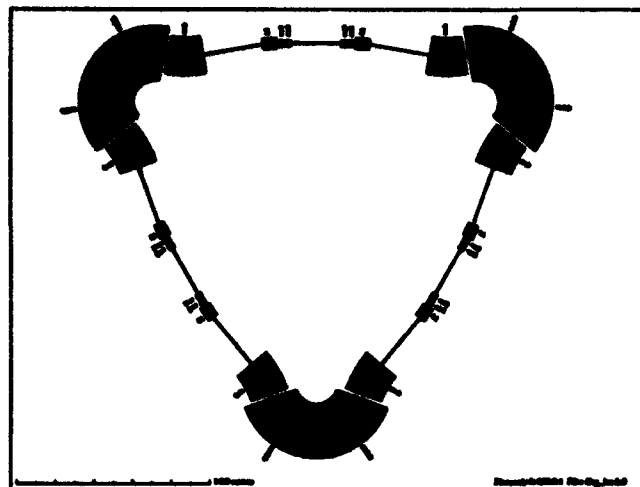
$$\frac{B_3}{B_0} = 1 + 1.4 \frac{x}{\rho} + 3.7 \left(\frac{x}{\rho} \right)^2 + 7.5 \left(\frac{x}{\rho} \right)^3 + 12 \left(\frac{x}{\rho} \right)^4 - 17.3 \left(\frac{x}{\rho} \right)^5 + ...$$

Three Magnet Dispersion-free Cell Field
Relative Magnetic Field (from COSY INF)



When graphed over the magnet region used by a momentum range of 3:1, the field profiles are as shown in Fig. 3. This

example, which is by no means optimized, has a circumference of 106.1 meters and radial and vertical tunes of 2.25 and 2.30, respectively. The floor plan for this ring is shown in Fig. 4.



The magnets close to the dispersion-free straight section are small, whereas those well away from the insertion are large because of the dispersion there.

The solution sequence can be modified so that COSY INFINITY determines the multipole components for the corrections magnets after the corresponding components for the bending magnets have been determined. This is yet to be done.

We have created a simple ring with fixed fields that contains a wide momentum range of 3:1 from injection to extraction with fixed tunes and dispersion-free insertions. The multipole correction magnets in the insertions can correct several resonances thereby providing a large dynamic aperture.

IV. REFERENCES

- [1] P. F. Meads, Jr., "A Dispersion-Free Long Straight Section for an FFAG Synchrotron", *IEEE Trans. Nucl. Sci.* NS-22, 2448 (1983)
- [2] D. W. Kerst, K. R. Symon, L. J. Laslett, L. W. Jones, and K. M. Terwilliger, "Fixed Field Alternating Gradient Particle Accelerators", *CERN Symposium*, 32 (1956)
- [3] P. F. Meads, Jr., "An 'Invisible' Long Straight Section for Synchrotrons", *Nucl. Instrum. Meth.* 96, 351 (1971)
- [4] M. Berz, "Computational aspects of design and simulation: COSY INFINITY", *Nucl. Instrum. Meth.*, A298, 473 (1990)

Vacuum Technology for Superconducting Colliders

A. G. Mathewson
AT Division, CERN, 1211 Geneva 23, Switzerland

Abstract

In high energy proton-proton colliders such as the CERN Large Hadron Collider (LHC) project with a centre of mass collision energy of over 14 TeV and the American Superconducting Super Collider (SSC) where the centre of mass collision energy reaches 40 TeV the relativistic protons lose energy in the form of synchrotron radiation. For adequate beam-residual gas lifetimes in these machines the pressure should typically be in the 10^{-10} Torr range. However the synchrotron radiation impinging on the walls of the vacuum chamber desorbs gas and may result in large pressure increases detrimental to the operation of the collider. To achieve the required strong bending in these machines it is necessary, in the case of the LHC, to employ dipole fields up to 9.0 T which need superconducting magnets operating at 1.9 K. The vacuum chamber is therefore at cryogenic temperature and functions as a cryopump. At first sight this free cryopumping may appear beneficial but in practice introduces several liabilities—for example, only a few monolayers of cryopumped H_2 already has a vapour pressure at 5 K in excess of 10^{-6} Torr. These and other effects and constraints on the design of the cold vacuum system will be described in detail.

I. INTRODUCTION

In high energy accelerators such as the CERN Large Hadron Collider (LHC) and the American Superconducting Super Collider (SSC) protons will be accelerated and stored at energies up to 7.2 TeV and 20 TeV respectively in a vacuum chamber at cryogenic temperatures. The relativistic protons, when accelerated in the magnetic fields of the bending magnets, will emit synchrotron radiation with a critical energy of 51.2 eV in the LHC and 284 eV in the SSC. The synchrotron radiation photons impinge on the walls of the vacuum chamber and desorb tightly bound gas which can give gas loads several orders of magnitude above the normal thermal outgassing. Although the vacuum chamber at cryogenic temperatures is a very efficient cryopump with a very large pumping speed for the desorbed gases, the combination of the photon induced gas desorption and the pumping surface may turn out to be somewhat of a liability.

It is these effects associated with gas desorption by synchrotron radiation from cold surfaces and other effects which place severe constraints on the vacuum engineer concerned with the design and understanding of these vacuum systems that will be described in this paper.

II. PRESSURE REQUIREMENTS

What interests the proton storage ring vacuum system builder is the molecular density encountered by the circulating

particles since it is these residual gas molecules which scatter the circulating particles and, with time, gradually reduce the beam intensity. In order that the beam lifetime is not unduly reduced by this process low pressures are required.

Since the vacuum chambers in these machines are at cryogenic temperatures the meaning of pressure has to be clearly defined.

Although most vacuum gauges measure the molecular density, conventionally we always refer to pressure, which is a force per unit area. For a given gas density the pressure is proportional to the temperature. For example at 293 K 1 Torr contains $3.3 \cdot 10^{16}$ mol cm^{-3} and at 5 K 1 Torr contains $1.93 \cdot 10^{18}$ mol cm^{-3} . Thus, when converting a gauge reading to molecular density the gas temperature must be known.

In the case of the LHC, CO pressures in the low 10^{-10} Torr range at 5 K are required for beam-gas lifetimes in excess of 24 hours.

III. SYNCHROTRON RADIATION

The characteristics of the synchrotron radiation in the two machines, such as the critical energy, power density and the number of photons per second incident on the vacuum chamber wall along with the machine parameters which determine them are given in Table 1.

Table 1
LHC and SSC Parameters

	LHC	SSC
Bending radius (m)	2700.27	10100
Energy (TeV)	7.3	20.0
Beam current (mA)	851.0	71.7
Critical energy (eV)	51.2	284.0
Photon flux ($s^{-1} m^{-1}$)	$1.6 \cdot 10^{17}$	$1.0 \cdot 10^{16}$
Synchrotron Radiation	0.41	0.14
Power loss ($W m^{-1}$)		

In both the LHC and the SSC the required dipole magnetic fields of 9.0 T and 6.76 T respectively are provided by superconducting magnets. In the case of the SSC the magnets run at 4.35 K but to obtain the 9.0 T in the LHC the magnets must operate at 1.9 K and hence the vacuum chamber is also at that temperature.

To absorb the synchrotron radiation power at 1.9 K would require an excessive amount of refrigeration thus a separate inner screen, a so-called beam screen, is necessary to absorb the power at a higher temperature.

The more than a factor of 10 higher beam current in the LHC means that many effects such as the power loss and the coupling impedances are more important. It is for this reason that we have concentrated on a collider with the LHC parameters.

IV. BEAM SCREEN

To minimize the coupling impedance of the beam screen the interior surface must have a high electrical conductivity and suitable materials would be Al or Cu. However, it must be remembered that the beam screen is in a large dipole magnetic field which decreases the conductivity because of the magnetoresistive effect. An additional effect arises in the case of magnet quenches where the rapidly changing decreasing magnetic field induces large currents and hence large forces in the beam screen. This is shown schematically in Figure 1 for the LHC where the proposed rectangular cross-section optimises the horizontal and vertical apertures available for the beam.

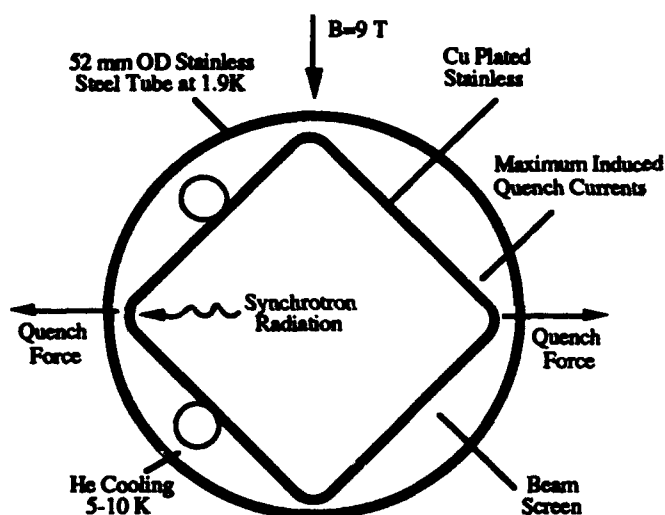


Figure 1. A schematic cross-section of the beam screen in the 1.9 K vacuum chamber.

For example in the LHC it is estimated that, during a quench, the magnetic field would decrease at about 30 T s^{-1} and would induce forces of 15 tons m^{-1} in a 1 mm thick Cu beam screen causing permanent deformation. The magnitude of these quench induced forces excludes the use of thick layers of such high conductivity metals as Al and Cu. The beam screen, therefore, will consist of an inner layer of Cu of sufficient thickness compatible with impedance requirements but sufficiently thin to minimise quench induced forces deposited on an outer tube of a low magnetic permeability material such as stainless steel to provide the necessary mechanical strength.

Since the conductivity of the Cu decreases with increasing temperature, a practical upper limit based on impedance considerations is 30 K.

V. SYNCHROTRON RADIATION INDUCED GAS DESORPTION

Synchrotron radiation photons impinging on the side wall of the vacuum chamber can desorb large quantities of gas. The desorption mechanism is complicated in that it is a two stage process whereby the primary photons produce photoelectrons which subsequently desorb gas by electron stimulated desorption [1], [2]. Also the primary photons are scattered and reflected thus producing desorption from all over the vacuum chamber surface although the primary photons hit along only one side of the chamber [3].

The photon induced neutral gas desorption yields at 63.5 eV critical energy, close to that of the LHC, for an unbaked Cu plated stainless steel chamber at room temperature as a function of the photon dose [4] are shown in Fig. 2. There it can be seen that the gases desorbed initially, in order of importance, are H_2 , CO_2 , CO , H_2O and CH_4 .

All gases during the long exposure to photons exhibited the same behaviour, increasing their yields with dose until they reached a maximum and then decreasing with dose. Although H_2O showed the largest increase with dose before decreasing, the final yield measured after a dose of 1.25×10^{21} photons/m was still above the initial by a factor of about 2.7.

After the maximum photon dose all desorption yields were decreasing and showing no signs of levelling off.

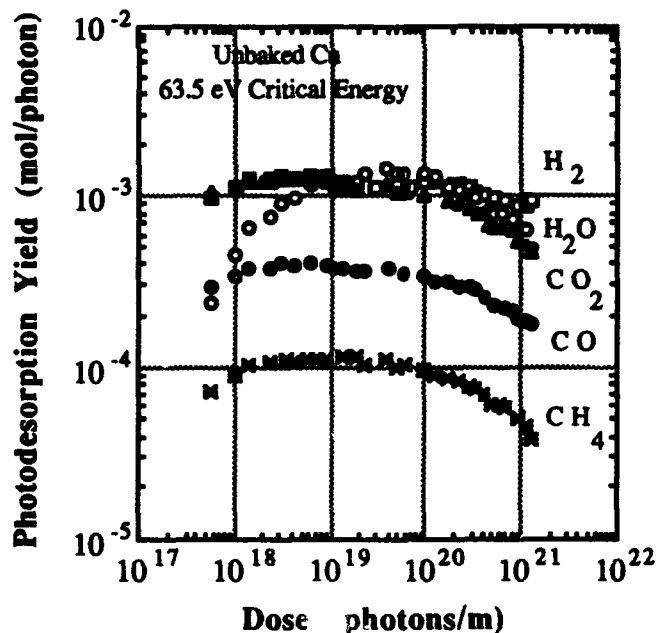


Figure 2. The photon induced gas desorption yields from an unbaked, 100 mm diameter, Cu plated stainless steel chamber as a function of photon dose at 63.5 eV critical energy.

In the critical energy range of ϵ between 12 eV and 284 eV the initial desorption yields scale as ϵ^a [4] where a lies between 1.08 and 1.33 depending on the gas species.

By integration of Figure 2 the total quantity of each gas desorbed was obtained and this is shown in Figure 3. The equivalent of about 0.5 monolayers of H_2 , H_2O and CO_2 were desorbed after a photon dose of 1.25×10^{21} photons/m followed by 0.1 monolayers of CO and 3×10^{-2} monolayers of CH_4 .

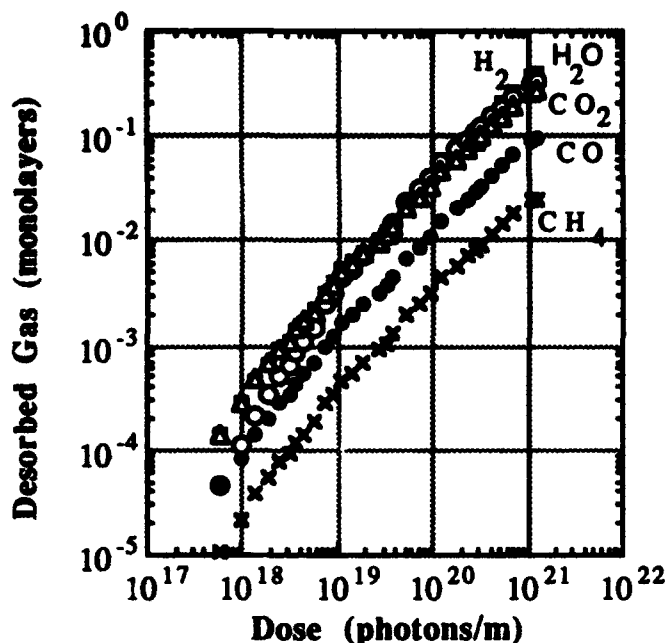


Figure 3. The total quantity of desorbed gas as a function of the photon dose.

Since the beam screen will operate at around 10 K, these desorbed gases will be pumped (physisorbed) by its large condensing surface and slowly build up thick layers.

The gas which is physisorbed on the cold screen surface has a thermodynamic vapour pressure. For temperatures < 10 K only the vapour pressure of H_2 will be significant. Initially, when the surface coverage is less than a monolayer, the pressure will be very low and completely insignificant.

But, as the first monolayer becomes completed, the vapour pressure rises dramatically [5] and exceeds 10^{-6} Torr at 5 K as shown in Figure 4. Such a high pressure is unacceptable in a storage ring such as the LHC or the SSC since the beam-gas lifetime would be several minutes instead of the required 24 hours.

It is important, therefore, that the screen surface be as clean as possible initially so that the photon induced gas desorption is small and the time to build up a thick layer is long.

Since it is not pure H_2 which is cryopumped but a mixture containing H_2 , CH_4 , H_2O , CO and CO_2 , it is uncertain what the vapour pressure of this composite layer will be. If the vapour pressure of the H_2 component is suppressed then this will be an advantage but another effect which is the pressure instability due to the ion bombardment will not be affected.

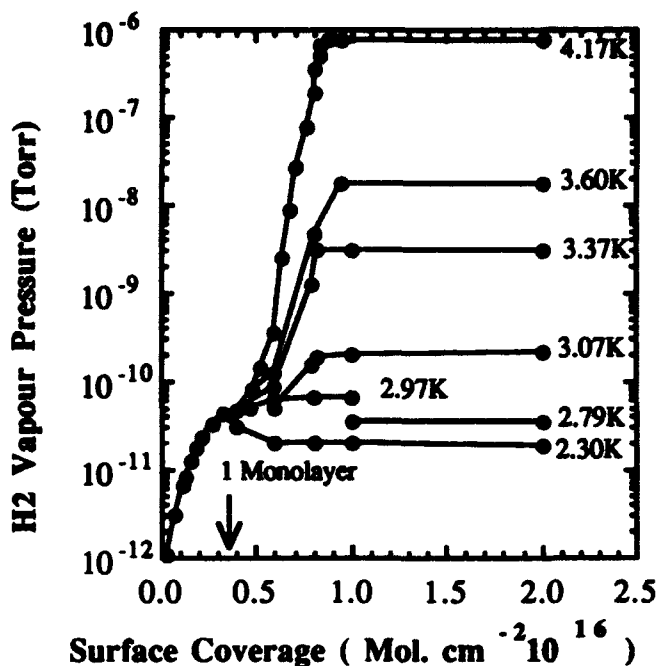


Figure 4. The vapour pressure of H_2 as a function of surface coverage for different temperatures.

VI. ION INDUCED PRESSURE INSTABILITY

The circulating proton beam will ionize the molecules of the residual gas which will then be accelerated towards the screen wall by the repetitive effect of the positive potential of the bunches of protons (~ 300 eV for 851 mA in the LHC). These relatively energetic ions will then desorb all species of gas from the accumulated layer. The resulting increase in pressure leads to an increase in the ion bombardment and hence the gas desorption. This gives another dynamic pressure component: the notorious "pressure bump" mechanism of the CERN Intersecting Storage Rings (ISR) which led to unstable runaway pressures for beam currents in excess of a certain critical value.

Here, as in the case of synchrotron radiation above, there will be a progressively increasing effect as the desorption coefficients increase with beam dose and the accumulated surface gas coverage. At a certain threshold value of the product of beam current and desorption coefficient an avalanche will occur resulting in a pressure run-away and loss of the beam [6].

Fortunately, the high linear pumping speed of the cold surfaces in the LHC and in the SSC vacuum systems helps to raise the threshold and, for H_2 , stability will be assured in the LHC if the product of the ion induced gas desorption yield η and the beam current I does not exceed 1300 A. The corresponding figure for CO is 700.

Since the η for 300 eV ions bombarding a 'clean' metal surface is typically ~ 5 mol. ion $^{-1}$, it is clear that, initially, the product ηI is well below the stability limit.

However as the coverage of gas increases on the pumping surface, so does the desorption yield and for thicknesses of many monolayers it can have values as high as 10^4 mol ion $^{-1}$.

[7] as shown in Figure 5. Thus it is important that this build-up of gas on the screen surface be as slow as possible i.e. the synchrotron radiation induced gas desorption be a minimum. This implies that the inner screen surface should initially be as free of desorbable gas as possible.

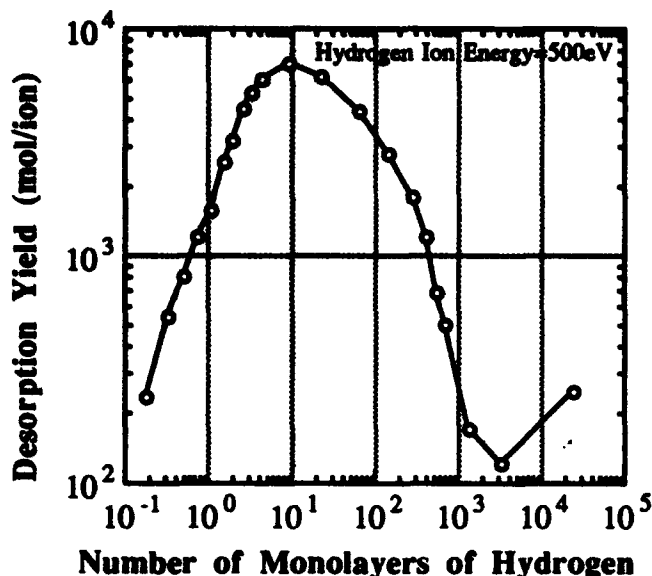


Figure 5. The desorption yield for 500 eV H₂ ions incident on thick condensed H₂ layers.

An obvious way of reducing the amount of adsorbed gas is by heating. However, any heat treatment must not increase the electrical resistivity of the Cu layer above certain limits. Thus once more the vacuum engineer faces constraints in his options.

VII. ELECTRON MULTIPACTORING

With bunched proton beams, pressure rises can occur due to electron multipactoring driven by the electric field of the passing proton bunches [8]. An electron is accelerated towards the bunch, traverses the vacuum chamber and produces secondary electrons from the opposite wall which in turn are accelerated towards the next bunch. If the secondary electron yield is greater than unity, and if the time between bunches is correct, a resonance condition is fulfilled -multipactoring- and large electron currents bombard the chamber walls. These electrons can desorb gas from the surface causing large pressure increases.

A simple calculation with the LHC parameters reveals that the threshold currents for multipactoring are in the range of the LHC beam currents.

VIII. PERFORATED BEAM SCREEN

The major problems, limitations and unpredictable behaviour of the LHC vacuum system all stem from the build-up of the condensed gas layer. The much praised super cryo-pump becomes, even if not a nightmare, a long term liability. A modification of the screen temperature will not change the situation. Operating the screen at 1.9 K for example would

only reduce the thermodynamic vapour pressure of H₂ while temperatures higher than 30 K are excluded for beam stability reasons. All other effects seem unaffected by temperature changes within this range.

The introduction of distributed pumping holes in the screen will, however, dramatically modify the LHC vacuum behaviour [9]. Suppose that 1% of the screen surface is considered to be perforated with holes which communicate to the magnet vacuum tube at 1.9 K - holes which are assumed to be perfectly gas transparent and perfectly opaque to synchrotron radiation. If the total pumping speed of the inner beam screen surface is $S \text{ ls}^{-1}$ then for 1% holes their pumping speed $s=S/100 \text{ ls}^{-1}$ (Figure 6).

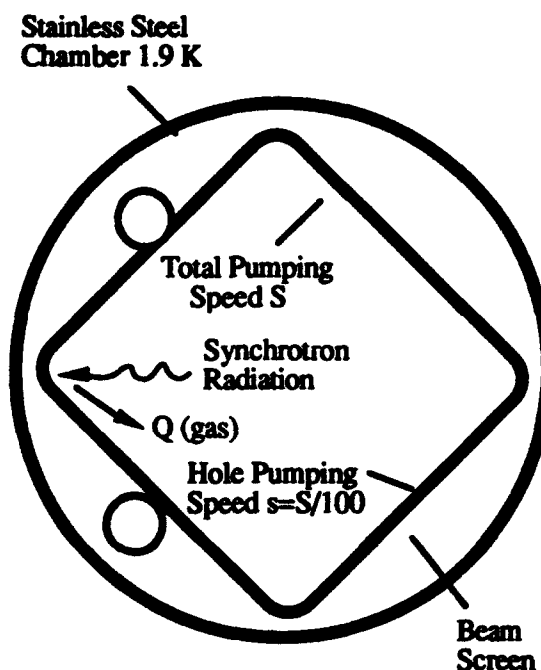


Figure 6. A schematic of the beam screen showing the desorbed gas and the wall and hole pumping speeds.

When the machine is first put into operation the initial pressure will be $Q/S \text{ Torr}$ where Q is the quantity of each gas desorbed by the synchrotron radiation (Torr ls^{-1}) and S is the pumping speed of the surface for each particular gas. The amount of gas pumped by the holes is $P.s \text{ (Torr ls}^{-1}\text{)}$ i.e. it increases as the pressure increases.

If we consider only H₂, then as the H₂ slowly builds up on the beam screen surface the thermodynamic vapour pressure of H₂ will slowly increase and, if there were no holes, it would increase to its value corresponding to the temperature of the screen e.g. 10^{-6} Torr at 4.2 K. The holes, however, will pump a fraction of this H₂ and an equilibrium will be reached when the quantity of desorbed gas equals the quantity swallowed by the holes i.e. $Q=P.s$. With the holes the equilibrium pressure of H₂ is therefore given by Q/s which is, for 1% holes, a factor of 100 above the initial H₂ pressure and the extra gas load condenses continually on the 1.9 K surface where its vapour pressure is negligible.

For the other gases their pressures remain unchanged at Q/S since their vapour pressures at the temperature of the beam screen are not dependent of the layer thickness.

The temperature and temperature uniformity of the screen become unimportant. They only affect the equilibrium coverage on the screen and, of course, the time to achieve this. However the temperature should be kept constant and, in particular, not be allowed to rise during machine operation. The condensing cryo-surface of the magnets may operate at any temperature which keeps the thermodynamic vapour pressure of H₂ low enough, e.g. 3 K for 10⁻¹⁰ Torr after the build-up of several or more monolayers.

However, should the photon induced gas desorption be such that the pressure increase of 100 is too high and decreases the beam-gas lifetime, there will be a need for periodic warming up and cleaning of the screen. However, the screen should at all times be kept warmer than the magnet bore to prevent contamination by retro-diffusion, especially when the machine is not operating.

IX. BEAM-PERFORATION INTERACTIONS

The vacuum engineer is not free to choose either the number or the diameter of the perforations in the beam screen since he must bear in mind that the holes represent discontinuities for the image currents of the beam and result in a beam coupling impedance.

An additional effect comes in the high frequency range from the real part of the impedance. Power is coupled through the holes into the coaxial space between the beam screen and the vacuum chamber and propagates in synchronism with the beam, gradually building up in strength and leaking back into the beam screen further adding to the real part of the coupling impedance [10].

This power is dissipated in both the outer beam screen wall and the 1.9 K inner vacuum chamber wall. For example, in the LHC, with both walls in stainless steel i.e. the same resistivity, for 5% of the surface covered with 2.5 mm diameter holes and 1 mm beam screen wall thickness the power dissipated per metre in the 1.9 K surface is 0.12 W/m whereas the calculated heat leak into the 1.9 K is 0.1 W/m. Thus 5% of 2.5 mm diameter holes more than doubles the heat load on the cryogenic system. For 5% of 1 mm diameter holes the power dissipation in the 1.9 K surface is negligible.

The beam screen must be supported in the 1.9 K tube, and the presence of dielectric and preferably lossy support structures in the coaxial space could reduce considerably the power dissipated at 1.9 K. The supports would, of course, be tied thermally to the beam screen.

The supports must be designed with care since it must be remembered that if there are any conducting loops there may be sufficiently large induced voltages during a quench and hence the risk of spot welding the support structure to the 1.9 K tube.

Possibly more critical is the low frequency imaginary (inductive) part of the impedance coming from the holes. An advantage may be gained by having short slots rather than round holes. For example, a slot 10 mm x 1 mm has an inductive impedance about a factor of 2 less than 10 holes each of 1 mm diameter [11].

X. CONCLUSIONS

It has been shown that, when designing vacuum systems in which synchrotron radiation is incident on surfaces at cryogenic temperatures, the vacuum engineer may not be completely free to choose the parameters.

Because of the power radiated by the synchrotron radiation, a screen at a higher temperature than the vacuum chamber may be necessary to intercept this radiation.

Beam stability criteria impose strict upper limits on the electrical resistivity of the beam screen inner wall, and hence the temperature, and also the diameter of the pumping holes in the beam screen.

It is imperative that the vacuum engineer must ensure that the surfaces hit by the synchrotron radiation are as clean as possible so that the pressure increases, which are determined by the diameter and number of the pumping holes, are consistent with the required beam-gas lifetimes and the time to build up thick layers of condensed gas is long i.e. months not days.

XI. ACKNOWLEDGEMENTS

The author is indebted to F. Caspers and E. Jensen for the impedance measurements and to his colleagues in the AT Division Vacuum Group at CERN whose professional efforts in the field of UHV applied to large accelerators over many years have greatly contributed to this paper. The expertise of J.-P. Potier and the CERN Electron Positron Accumulator operations crew in running the machine at energies outwith its normal operating range to provide the synchrotron radiation induced gas desorption data is also gratefully acknowledged.

XII. REFERENCES

- [1] G.E. Fischer and R. A. Mack, J. Vac. Sci. Technol., 2, 123, (1965).
- [2] M. Bernardini and L. Malter, J. Vac. Sci. Technol., 2, 130, (1965).
- [3] O. Gröbner, A.G. Mathewson, P. Strubin, E. Alge and R. Souchet, J. Vac. Sci. Technol., A7(2), March/April (1989).
- [4] J. Gómez-Gofi, O. Gröbner and A. G. Mathewson, Vacuum Group Technical Note 93-01, February, 1993.
- [5] C. Benvenuti, R.S. Calder and G. Passardi, J. Vac. Sci. Technol., 13, (1976), 1172.
- [6] E. Fischer and K. Zankel, CERN Divisional Report ISR-VA/73-52 (1973).
- [7] N. Hilleret and R.S. Calder, Proc. 7th Intern. Vac. Cong. & 3rd Intern. Conf. Solid Surfaces, R. Dobrozemsky et al., Vienna, 1977, 227.
- [8] O. Gröbner, Proc. Workshop on p p bar in the SPS, Geneva 1980 (CERN Divisional Report SPS-p p bar-1, Geneva, 1980), 130.
- [9] Design Study of the Large Hadron Collider (LHC), The LHC Study Group, CERN 91-03, 2 May, 1991.
- [10] F. Caspers, E. Jensen and F. Ruggiero, Third European Particle Accelerator Conference, Berlin, Germany, 24-28th March, 1992.
- [11] E. Ruiz, L. Walling, Y. Goren and N. Spayd, CAP 93, Pleasanton, California, 22-26th February, 1993.

Dynamic Vacuum in the Beam Tube of the SSCL Collider - Cold Beam Tube and Liner Options*

William C. Turner

Superconducting Super Collider Laboratory

2550 Beckleymeade Avenue

Dallas, Texas 75237-3997 USA

Abstract

In this paper model equations are derived for calculating the beam tube density of molecules desorbed by synchrotron radiation in the SSCL 20TeV proton Collider and the supporting simulation experiments at synchrotron light sources. Cold 4.2K beam tube and arbitrary temperature liner or distributed pump systems are considered. Physical effects included are; direct desorption, cryosorption, desorption of physisorbed molecules, the H₂ equilibrium isotherm, axial diffusion and distributed pumping. Convenient formulas are given for extracting the relevant physical variables from the simulation experiments and calculating the anticipated beam tube density in the Collider. A numerical example illustrating the important physical effects is presented.

I. INTRODUCTION

The new generation of proton colliders - SSC and LHC - are the first that will encounter significant synchrotron radiation in the cold bore tube of superconducting magnets. The vacuum systems of such colliders require taking into account the gas desorbed by synchrotron radiation to insure adequate beam lifetime and machine availability. Although the cold magnet bore tube can in principle serve as a cryopump its effectiveness can be limited by two effects. Firstly cryosorbed gas is rather weakly bound to the surface and may be easily desorbed, so the effective pumping speed may be severely reduced. Secondly, in the case of the SSC, the saturation vapor density of H₂ at the 4.2K magnet operating temperature exceeds the cryogenic/magnet quench limit by a factor of fifty, so accumulation of a monolayer of H₂ anywhere in the beam tube must be avoided.[1] The function of a liner is to intercept the photon flux and to pump the photodesorbed gases in a way that shields them from the synchrotron radiation. It will turn out that specifying a liner configuration that will work depends on far less information than qualifying a simple beam tube without a liner, if indeed such a tube exists. The situation with LHC is that because of the low 1.8K magnet operating temperature a 10-20K liner has been designed in from the beginning to intercept the synchrotron radiation heat load.[2] For the SSC it is reasonable to intercept the synchrotron heat load at 4.2K so whether to install a liner is an open question. Furthermore the temperature of the liner could be chosen to correspond to any of the available refrigeration systems 4.2K, 20K or 80K and each choice has its particular advantages and disadvantages.

Some basic synchrotron radiation parameters for the SSC are photon critical energy = 284eV, photon intensity = 1×10^{16} photons/m/s at 20TeV and 72mA and synchrotron power = 140mW/m. The photons hit the vacuum chamber wall at an incidence angle ~2mrad at a distance ~20m from their point of emission on the proton orbit. The FWHM of the

directly illuminated stripe on the beam tube wall depends on the photon energy and is ~4mm for the median photon energy .08E_{crit} = 23eV. The vacuum design goals are 300hr beam lifetime due to nuclear scattering and beam tube warm up interval of the order once per operational year (~ 2×10^{23} photons/m). The 300hr beam lifetime requirement corresponds to an average H₂ density 3×10^8 /cm³ or CO density 5×10^7 /cm³. The cryogenic limit 0.6W/m[3] corresponds to local density limits 4×10^{10} /cm³ for H₂ and 7×10^9 /cm³ for CO. Accumulation of less than one monolayer of H₂ in an operational year corresponds to an average photodesorption coefficient $\leq 2 \times 10^{-5}$ H₂/photon.

II. BASIC EQUATIONS

We begin by writing down equations describing the volume density n and surface density s of H₂ inside a 4.2K beam tube of radius a exposed to synchrotron radiation. Some comments on the treatment of other gases (CO, CO₂, CH₄) and tube temperatures (20K, 80K) will be made below. The equation for volume density is;

$$V \frac{\partial n}{\partial t} = \eta_1 \dot{\Gamma} + \eta' \dot{\Gamma} - \sigma_w S_w * (n - n_e) - C * n + A_c D \frac{\partial^2 n}{\partial z^2} \quad (1)$$

In eqn.(1) $V = \pi a^2$ is the beam tube volume per unit axial length. The first two terms on the right describe photodesorption of molecules. The desorption coefficient η_1 molecules per photon is for chemically bound matter not previously desorbed and is a function of the integrated photon flux per unit length Γ and perhaps the photon intensity $\dot{\Gamma}$. The second term allows for the desorption of relatively weakly bound physically sorbed molecules with desorption coefficient η' which is a function of the surface density s of cryosorbed molecules. At low surface coverage one would expect η'

depends linearly on the surface density s ; $\eta' = \eta'_0 \left(\frac{s}{s_m} \right)$ where

s has been normalized to the monolayer density s_m . The third term on the right of eqn.(1) accounts for the cryosorption of molecules incident on the surface; σ_w is the sticking probability per wall collision, $S_w = \bar{v} A_w / 4$ is the ideal wall pumping speed and n_e is the equilibrium isotherm density of molecules with surface density s . The fourth term allows for a liner or distributed pump with pumping speed C per unit axial length. The last term allows for the axial diffusion of molecules out the ends of a finite length tube; $A_c = \pi a^2$ is the tube cross section area and $D = \frac{2}{3} \bar{v} \lambda$ is the Knudsen

*Operated by the URA for the US DOE under Contract No. DE-AC02-89ER-40486.

The submitted manuscript has been authored by a contractor of the U.S. Government under Contract No. DE-AC35-89ER40486. Accordingly, the U.S. Government retains a nonexclusive, royalty-free license to publish or reproduce the published form of this contribution, or allow others to do so, for U.S. Government purposes.

diffusion coefficient. The equation for the surface density s of cryosorbed molecules is;

$$A_w \frac{\partial s}{\partial t} = \eta_2 \dot{\Gamma} + \sigma_w S_w (n - n_e) - \eta' \dot{\Gamma}. \quad (2)$$

The first term in eqn.(2) allows for the possibility of direct production of physisorbed molecules by the incident photon flux. The second and third terms are the same as in eqn.(1) but with opposite sign. All the terms on the right of eqn.(2) define the effective pumping of the beam tube surface which we note is reduced by the equilibrium isotherm and by the photodesorption or recycling of cryosorbed molecules. One more equation is needed to describe the equilibrium isotherm relating n_e to s . Here we choose to represent the isotherm by a BET equation;

$$x = \frac{\alpha y}{(1-y)(1+(\alpha-1)y)} \quad (3)$$

where $x = s/s_m$ and $y = n_e/n_{sat}$ and $\alpha = e\Theta/T$ is a dimensionless parameter. Eqn.(3) has the saturation property $y \rightarrow 1$ as $x \rightarrow \infty$. For any particular surface the equilibrium isotherm must be measured experimentally to determine s_m and α . Hydrogen isotherms have been measured on stainless steel by Benvenuti et al[4] and the 4.2K isotherm can be reasonably fit with $s_m = 6 \times 10^{15}$ H₂/cm³ and $\alpha = 1.37 \times 10^4$. In ref.[2] the saturation density of H₂ was also determined to be $n_{sat}(\text{cm}^{-3}) = 6.84 \times 10^{22} e^{-95.8/T/T}$. For our purposes s_m , which depends on the particular surface, and n_{sat} are the most important parameters and results are not too sensitive to uncertainty in α .

III. SOLUTIONS

The equations in Sec. II will be applied to tubes of length L with $-L/2 < z < L/2$ and the boundary condition $n(\pm L/2) = 0$ applied at the ends. In practice the density at the ends of a tube will be determined by the gas flow rate and pumping speed, which here we take to be infinite compared to the tube conductance. It is straightforward to add a finite density boundary condition to the solutions given below. Here we are

only interested in quasi-static solutions $V \frac{\partial n}{\partial t} = 0$ so the time dependence (slow) of n enters through the behavior of the desorption coefficients with increasing photon flux and increasing isotherm density due to the build up of surface density on the beam tube. We characterize the length of a tube without a liner according to whether the surface density reaches a quasi-steady state $A \frac{\partial s}{\partial t} = 0$ due to diffusion out the ends or continues to build up due to cryosorption and η_2 . Tubes with a surface reaching steady state are deemed to be "short", others "long". We first give the solutions for short and long tubes without liners and then give a criterion for short or long. The solution is then given for an arbitrary length tube with a liner. The presence of liner pumping again allows the surface to reach a quasi steady state $A \frac{\partial s}{\partial t} = 0$.

A. Short 4.2K beam tube without a liner

The solution to eqn.(1) for density $n(z)$ with $V \frac{\partial n}{\partial t} = 0$,

$C = 0$ and $A \frac{\partial s}{\partial t} = 0$ is;

$$n(z) = \frac{1}{2} \frac{(\eta_1 + \eta_2) \dot{\Gamma}}{A_c D} \left(\frac{L}{2} \right)^2 \left[1 - \frac{z^2}{\left(\frac{L}{2} \right)^2} \right]. \quad (4)$$

Given the density $n(z)$, the surface density $s(z)$ is obtained by solving the following implicit equation for s ;

$$\eta'(s) = \eta_2 + \frac{\sigma_w S_w}{\dot{\Gamma}} (n(z) - n_e(s)). \quad (5)$$

If $n_e \ll n(z)$ and $\eta_2 \ll \eta'(s)$ then

$$\eta'(s) = \frac{\sigma_w S_w}{\dot{\Gamma}} n(z). \quad (6)$$

If we make the further substitution $\eta' = \eta_0 \left(\frac{s}{s_m} \right)$ the surface density is given explicitly by

$$s(z) = \left[\frac{\sigma_w S_w}{\eta_0 \dot{\Gamma}} n(z) \right] s_m. \quad (7)$$

We note that the diffusion out the ends of the tube is driven by isotherm evaporation and η' desorption. If there is no η' process then isotherm evaporation alone drives the diffusion and s is given implicitly by;

$$n_e(s) = n(z) + \frac{\eta_2 \dot{\Gamma}}{\sigma_w S_w}. \quad (8)$$

B. Long 4.2K beam tube without a liner

The solution to eqn.(1) for $n(z)$ with $V \frac{\partial n}{\partial t} = 0$, $C = 0$ and

$A \frac{\partial s}{\partial t} \neq 0$ is;

$$n(z) = \left[\frac{\eta_1 \dot{\Gamma}}{\sigma_w S_w} + \frac{\eta' \dot{\Gamma}}{\sigma_w S_w} + n_e \right] x \left[1 - \frac{\cosh\left(\frac{z}{\lambda}\right)}{\cosh\left(\frac{L}{2\lambda}\right)} \right] \quad (9)$$

where $\lambda^2 = \frac{A_c D}{\sigma_w S_w} = \frac{4}{3} \frac{a^2}{\sigma_w}$ and we neglect possible z dependence of η' and n_e . The mean square axial distance a molecule travels before sticking to the wall is $2\lambda^2$ and L^2/λ^2 is equal to the wall pumping speed divided by the conductance of a tube of length L . Evidently as long as we are a few tube diameters from the end of the tube the cosh term is negligible and we have;

$$n = \frac{\eta_1 \dot{\Gamma}}{\sigma_w S_w} + \frac{\eta' \dot{\Gamma}}{\sigma_w S_w} + n_e \quad (10)$$

which is the solution obtained with axial diffusion neglected, $A_c D \frac{\partial^2 n}{\partial z^2} = 0$. Inserting eqn.(10) into eqn.(2) we obtain for the surface density;

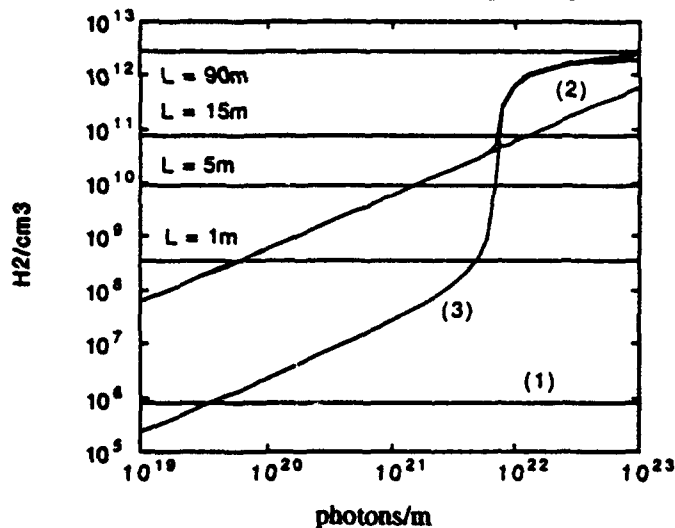
$$s = \frac{1}{A_w} \int_0^{\Gamma} (\eta_1 + \eta_2) d\Gamma \quad (11)$$

which just says all the desorbed gas winds up on the surface.

C. Numerical example for 4.2K beam tubes

In this section we give an example to illustrate the content of the equations. The measurement of a complete set of parameters at 4.2K is incomplete so we take the following assumed values: $\eta_1 = \eta_2 = 4 \times 10^{-4}$, $\eta_0' = 10$, $\sigma_w = 0.5$, $\bar{v} = 2.1 \times 10^4$ cm/sec, $a = 1.5$ cm, $s_m = 3 \times 10^{15}$ H₂/cm², $\alpha = 1.3 \times 10^4$ and $\Gamma = 10^{16}$ photons/m/sec. The short tube solution eqn.(4) depends on the tube length which we take to be $L = 1, 5, 15$ and 90 m. These lengths correspond approximately to: a typical beam tube sample for photodesorption experiments, a Collider quadrupole magnet or spool piece, a Collider dipole magnet and a Collider half cell. The long tube solution eqn.(10) depends on the integrated photon flux which we take to be $\Gamma = 1 \times 10^{19}$ to 1×10^{23} photons/m, corresponding to 1000sec to 100days of Collider operation. The long tube solution is independent of length and is plotted versus Γ in Fig. 1. The three components of the long tube solution are also shown: (1) the η_1 term, (2) the η' term and (3) the isotherm. The short tube solutions are independent of Γ and are indicated by the horizontal lines in Fig. 1 that are labeled with $L = 1, 5, 15$ and 90 m. For a given tube length it is the lower density of the long and short tube solutions which pertains. For this reason one always starts out at low Γ on the long tube solution and follows it until it intercepts the short tube solution for the chosen length.

Fig. 1: Short and long tube H₂ density



From the results in Fig. 1 we make several observations for the assumed parameters. The long tube solution is dominated by the η' desorption of cryosorbed H₂, which increases linearly with Γ , until the isotherm density takes over at $\Gamma \sim 8 \times 10^{21}$ photons/m. The η desorption of H₂, which drives everything, dominates the density only at very low accumulated photon flux not shown in Fig. 1. We also see that $L = 1$ and 5 m tubes reach maximum densities of 3.4×10^8 and 8.4×10^9 due to pumping at the ends and do not reach the region of rapid rise due to the isotherm. The relevance of this is that short tube photodesorption experiments at synchrotron light sources with tube lengths 1 to 5 m may not observe the

rapid isotherm density rise although the parameters may be the same as those which would lead to such a rise in a much longer tube. The 15m tube reaches the region of rapid isotherm rise, but pumping at the ends clamps the density at 7.6×10^{10} H₂/cm³. The 90m case reaches the isotherm saturation region before intercepting the short tube solution. For the particular parameters chosen, pumping at the ends of a 5m long quadrupole or spool piece would keep the density from reaching the value 4×10^{10} H₂/cm³ which would lead to a beam loss induced cryogenic overload/magnet quench, but fall short for a 15m dipole by a factor of two. Pumping at 1m intervals would be required to keep the density at the 300hr beam lifetime goal level of 3×10^8 H₂/cm³.

D. Beam tube length criterion

In this section we summarize a criterion for whether to use the long or short tube solutions to calculate $n(0)$. For a given set of parameters calculate $n(0)$ using the long tube solution eqn. (10). Then evaluate the expression;

$$S = \frac{16\pi a^2}{3 L^2} \frac{n(0)\bar{v}a}{\eta\Gamma} \quad (12)$$

If $S \leq 1$, use the long tube eqn.(10), if $S > 1$ use the short tube eqn.(4).

E. Beam tube with a liner

The case of a beam tube with a liner is only interesting when $Cn \gg A_c D \partial^2 n / \partial z^2$. In that case, and with the quasi

static approximations $V \frac{\partial n}{\partial t} = 0$ and $A \frac{\partial s}{\partial t} = 0$, the solution to for the density is;

$$n = \frac{(\eta_1 + \eta_2)\Gamma}{C} \quad (13)$$

The solution for the surface density is the same as eqns.(5) to (8). Eqn.(13) is remarkable in its simplicity compared to eqn.(10). It depends only on the desorption coefficient $\eta = \eta_1 + \eta_2$ to specify a conductance C that will meet the beam lifetime criterion. Eqn.(13) is valid for any temperature liner and is independent of whether or not there is cryosorption on the liner surface. The conductance C is related to the holes in the liner by $C = pN_h A_h \bar{v} / 4$ where p is the transmission probability, N_h the number of holes per unit axial length, A_h the area per hole and \bar{v} the mean molecular speed. Although the mean speed \bar{v} may be higher than that corresponding to equilibrium with the liner, a conservative estimate of the conductance may be made by assuming the molecules and liner are in thermal equilibrium. When using eqn.(13) to estimate the conductance it is important to include desorption of all the molecules since the heavier molecules have slower speeds and higher scattering cross sections. The calculational details cannot be given here, but at present it seems possible to specify liners with $T = 4.2, 20$ or 80 K which will meet the 300hr beam lifetime requirement with an effective open hole area of $\sim 3\%$. This is small enough to allow a comfortable safety margin for transverse beam instabilities.

IV. REFERENCES

- [1] A. Maschke, SSCL-Preprint 86. Mar. 1992
- [2] A. Mathewson, this conference
- [3] R. Carcagno et al, Proc. of Supercollider-4, New Orleans, 1992 pg. 897
- [4] C. Benvenuti et al, J. Vac. Sci. Technol., 13, 1172. 1976

Distributed Ion Pump Testing for PEP-II, Asymmetric B-Factory Collider

M. Calderon, F. Holdener, W. Barletta, D. Petersen
Lawrence Livermore National Laboratory

C. Foerster
Brookhaven National Laboratory

INTRODUCTION

At its design level, PEP-II will circulate asymmetric beams at 9 GeV and 1.5 A in a High Energy Ring and 3.1 GeV with 2.1 A in a Low Energy Ring. In addition, the vacuum systems of both rings will be designed to operate at a maximum current of 3 A to provide for higher current operation in the future. Pumping for both rings is provided by sputter ion pump systems.

In the High Energy Ring, high gas loads, deriving from the intense photon radiation, are calculated at 1.06×10^{-6} Torr liters $s^{-1} m^{-1}$ using a desorption coefficient (η) of 2×10^{-6} molecules $photon^{-1}$.

To maintain an average pressure of 5 nTorr or less in the arc cells, lumped ion pumps are used in the 2 m long straight sections and distributed ion pumps are used in the 6 m long dipole chambers where the conductance of the vacuum chamber is prohibitively low.

To achieve these pressures, the distributed ion pump system is required to have pumping speeds of 110 liters $s^{-1} m^{-1}$ however, a design level of 165 liters $s^{-1} m^{-1}$ has been set to provide a factor of safety of 50% based on pumping alone.

PUMP DESIGN

Ion pumps, using plate-type anodes, have been chosen to achieve these pumping speeds. The five plate anode shown in Fig. 1, contains four rows of pump cells in a staggered arrangement to produce a cell-area density of 68%. Cells, with a 1.8 cm diameter, intercept a dipole magnetic flux varying from 1800 gauss at the magnet pole center to about 1450 gauss at the pole edges. Although understood that cell diameter should increase with lowering field, we have elected to maintain a uniform cell diameter in order to maximize the total number of cells in the pump.

Contact fingers, between the titanium cathodes and chamber walls provide conduction cooling for the cathode plates. These spring contacts, spaced along the length of the cathode, are designed to remove a heat flux of $0.01 W cm^{-2}$ and the cathode plates have been shaped to provide the necessary stiffness to carry the contact spring force. A formed screen-plate, separating the beam tube from the pump chamber, contains 6 lines of slots pitched at 10 cm. The slots, 0.25 cm high by 9 cm wide, provide a calculated conductance of 1400 liters $s^{-1} m^{-1}$ through the screen. Where possible, the slots in the screen have been aligned



Figure 1. Distributed ion pump with screen-plate

with the spaces between the anode plates to improve the overall conductance of the pump-screen combination. Also, the height of the slot has been selected to keep the impedance contribution to a negligible level and the height-to-length ratio of the slot has been chosen to minimize the effects of RF interference during operation. Anode designs will have either five or seven plates and the slot patterns in the matching screen plates will correspond to the anode geometry.

TEST PLAN

To validate the pumping speeds described above, we are preparing to test a series of ion pump designs with varying pump parameters that include cell diameter, spacing between anode plates, B field, B field uniformity and voltage. A tube-type anode, similar to the former PEP design, will also be tested and a concluding experiment will test a module as used on the VuV and x-ray beamlines at the National Synchrotron Light Source to provide a comparison. Initial testing will begin with N_2 gas, however, the final design will be tested with the CO , CO_2 , H_2 , CH_4 , and H_2/CO gas mixtures.

TEST STAND

To test these designs, a test stand, that closely simulates actual ring conditions, was designed using a 12 control-volume model, as shown in Fig. 2, to establish pressures in the chamber.

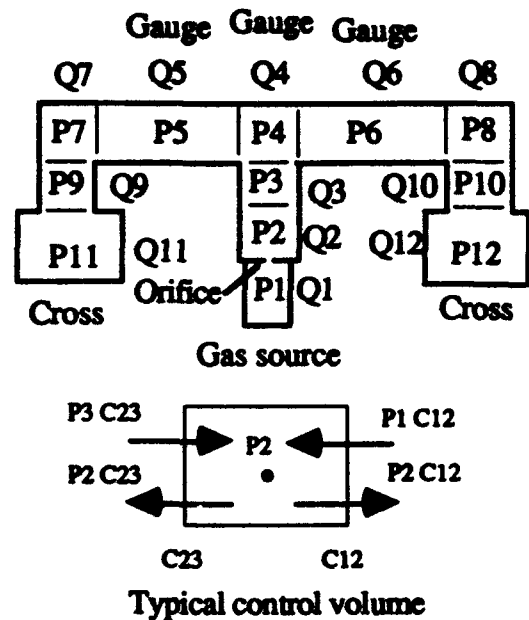


Figure 2. Pumping system schematic model.

The test chamber, shown inserted in the dipole magnet in Fig. 3, is sized to test pump modules 1 m long that are installed from the right. The system is pumped down with a

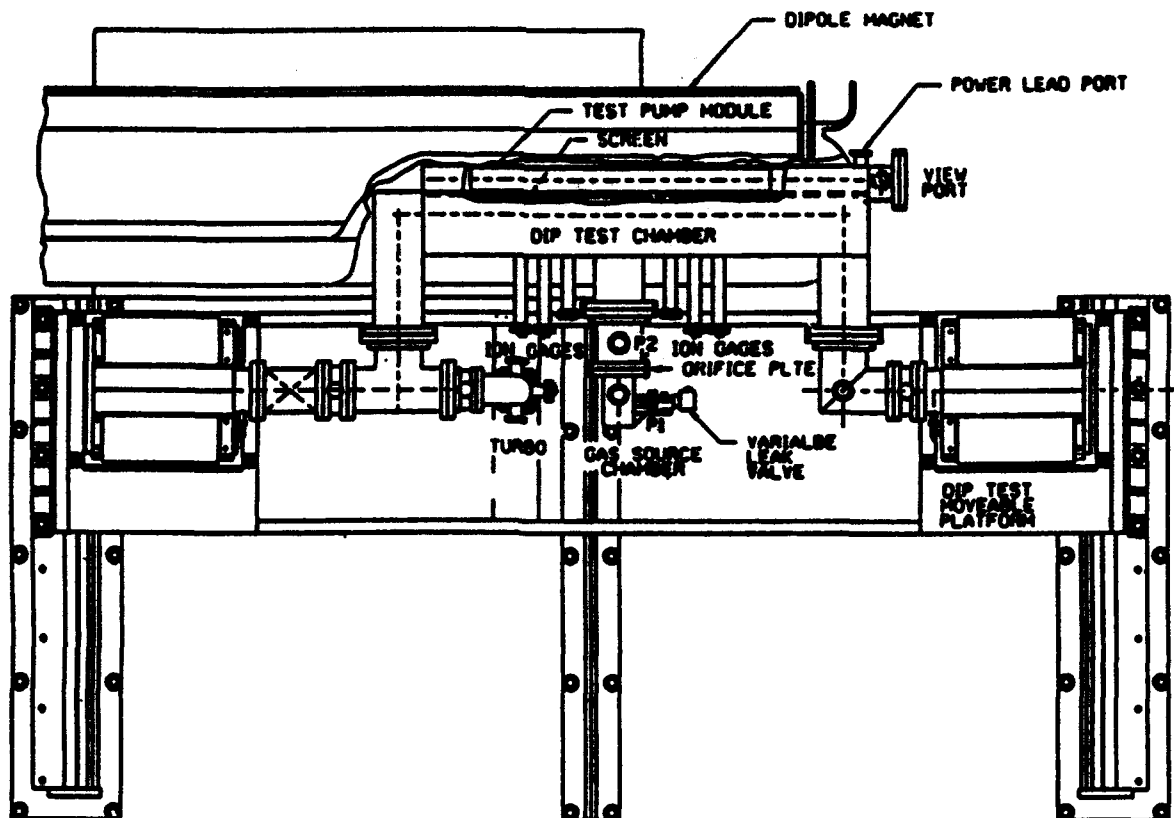


Figure 3. Dip test stand plan view.

1000 liters s^{-1} turbomolecular pump after which two, 400 liters s^{-1} ion pumps are used to bring the system into the 10^{-10} Torr range. A heating system, installed in the narrow space between the chamber and magnet pole faces bakes the chamber at 200°C during the high voltage conditioning of the module. Gas flow into the chamber will be determined by measuring the pressure difference across an orifice of known conductance. Once installed in the magnet, a programmable high voltage power supply conditions the module to 7 kV in a nominal field of 1800 gauss while at temperature. During a typical test run, a data acquisition

system is programmed to monitoring pressures and to display gas flows into the chamber, pressure differences at the pump before and after gas injection, and pumping speeds, all as a function of time. The test stand, now nearing completion at LLNL, is shown under construction in Fig. 4.

This work was performed under the auspices of the U.S. Department of Energy by the Lawrence Livermore National Laboratory under contract W-7405-Eng-48.



Figure 4. Dip test stand construction.

Paolo Manini, Massimo Marino, Fortunato Belloni, Mario Porro
SAES GETTERS S.p.A., Via Gallarate 215, 20151 Milano, ITALY

Abstract

UHV pumps based on non evaporable getter coated strips find widespread use in particle accelerators, synchrotron radiation machines and nuclear fusion experimental devices. Depending on the geometric constraints, pressure operation conditions and the foreseen gas loads, optimized getter structures, such as modules and cartridges, can be designed and assembled into a high-efficiency pump. In the present paper, the design and performance of a newly conceived High Capacity Getter Pump (HOGP) based on sintered getter bodies, in the shape of blades instead of strips, is illustrated. The porosity and the specific surface area of the blades and their arrangement in the cartridge have been optimized to significantly increase sorption capacity at a given speed. These pumps are well suited for those applications where a very high gas load is expected during the machine operation. The sintered getter bodies increase surface area and capacity, requiring less frequent reactivation and facilitating greater overall life of the pump. A discussion of the experimental results in terms of sorption speed and capacity for various gases is presented.

I. INTRODUCTION

Non Evaporable Getter (NEG) pumps find widespread use for maintaining vacuum in a variety of UHV experimental machines such as storage rings, synchrotrons, particle accelerators, nuclear fusion devices. At present, commercially available NEG pumps make use of metallic strips upon which the getter powder is deposited and mechanically anchored by compression. These strips can be inserted in suitable regions connected to the vacuum chamber to provide an effective distributed pumping system [1],[2],[3]. Alternatively, they can be shaped in more complex structures, such as cartridges and modules [4][5], which can be assembled into high efficiency pumps to

provide discrete pumping capabilities, as required for example in the crotches and absorbers regions of storage rings or synchrotron machines [6]. Some advantages of NEG pumps are high pumping speed, especially for hydrogen, absence of mechanical moving parts, no interference with the particle beam, low power consumption, low cost. Their main drawback is the finite sorption capacity for active gases, such as CO, N₂, CO₂ and H₂O, which requires periodical getter conditioning at moderate temperature (400 °C) to clean the surface by diffusion of the contaminants into the bulk. The frequency of getter conditioning depends on the gas load and the operating pressure conditions required for running the experiments. With this respect, next generation machines, such as high performances storage rings and B factories, will be characterized by increased thermal outgassing from the walls of the vacuum chamber and increased dynamic loads due to photon induced desorption [7]. Operating vacuum requirements will also become more stringent and pressure value lower than 1×10^{-9} torr necessary. In the present paper, the design and sorption characteristics of a newly conceived NEG pump, which can overcome above cited problems, are illustrated. This pump, which is based on the use of porous sintered getter, shows significantly larger sorption capacity and higher pumping speed per unit volume than NEG pumps making use of the coated strip. It is therefore particularly well suited for maintaining UHV standards under high gas load conditions.

II. DESIGN OF THE HIGH CAPACITY GETTER PUMP

NEG pumps based on modules and cartridges are highly optimized structures in which the surface area of the deposited getter material, as well as the effective sticking probability, i.e. the probability for a molecule entering into the gettering structure to be captured, are maximized. To further increase the sorption capacity per unit volume an approach has been pursued

which is based on the use of porous sintered getter bodies instead of the coated strip. A sketch of the high capacity getter pump (HCGP) prototype, having the same size and flanges of a standard SAES GP 200 pump is shown in fig.1.

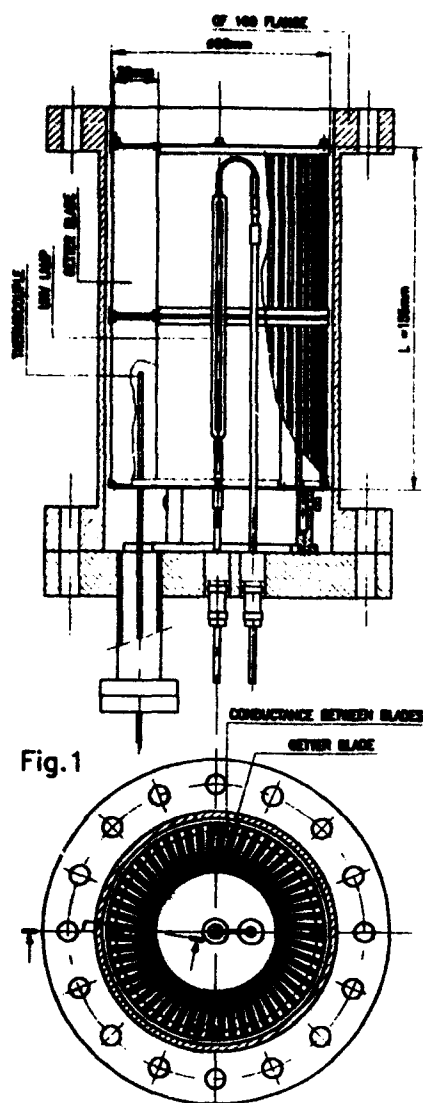


FIG. 1 - Cut and top views of the high capacity getter pump prototype

The getter cartridge is composed of a cylindrical array of nearly parallel rectangular porous blades which are inserted in a stainless steel retaining structure and act as the gettering elements. Gas molecules reach the gettering structure directly from the top surface of the pump or from the large central inner conductance. The blades are prepared by mixing and sintering proper amount of St 707 (Zr70%- V24.5%- Fe 5.5%) and zirconium powder. The microstructure of the sintered

getters has been specifically optimized during the manufacturing process to enhance porosity, thus providing a better accessibility for the gas molecules to the available gettering surface area. The geometrical arrangement of the blades inside the cartridge, as well as their number and size, has also been optimized in order to ensure both large gas conductance between adjacent blades and high trapping efficiency for the molecules which have entered the gettering structure. Knowing the intrinsic sorption properties for the sintered getters and applying a mathematical model based on Pisani's method [8], a quite accurate prediction of the sorption performances for HCGP can be made as a function of several parameters of interest, such as pump size and geometry, number and dimension of blades. This approach can be followed for designing high capacity pumps of specific desired performances. A detailed discussion of these aspects will be presented elsewhere. It is also worthwhile noticing that the use of porous getters allows to allocate a quantity of getter material inside the pump which is about 3.5 times higher than that available in a comparable size GP 200 (600 vs 180 grams). Moreover, the arrangement in blades of the getter material is such that the bigger amount of alloy, while remarkably increasing sorption capacity and speed, does not pose specific handling problems. Heating of the getter material during the activation process and the pump operation is accomplished in the prototype of fig.1 by means of a UHV lamp. The getter operating temperature is controlled by means of a thermocouple. Thanks to the relatively limited amount of getter material full activation to 500°C only requires 250 watts. External heating, even though less attractive, can be also provided.

III. PERFORMANCES OF THE HIGH CAPACITY GETTER PUMP

The HCGP has been tested according to the dynamic flow method, as described in detail in reference [9]. Activation of the getter material was carried out at 500°C for 60 minutes. Purity of the test gases, admitted to the getter pump through the known conductance was better than 99.99%.

Since hydrogen can be reversibly sorbed by the getter alloy, the pump was first tested for this gas and then, after successive

ACTIVATION 300 C x 60 min

DESORPTION TEMP 25 C

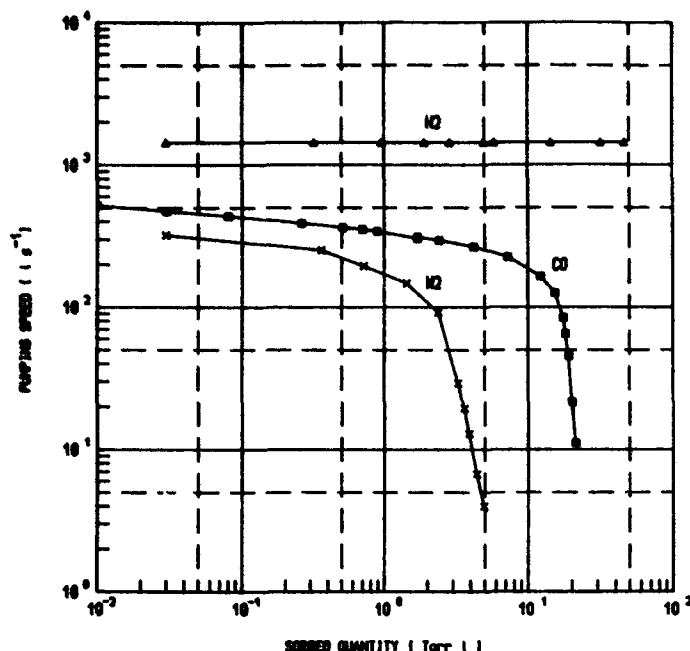


FIG.2 room temperature sorption curves (CO, N₂ and H₂) for the HOGP prototype

regenerations, for CO and N₂. Sorption tests were carried out at room temperature. Experimental results are shown in fig.2. Initial pumping speeds of the HOGP for CO, N₂ and hydrogen are about 500, 300 and 1300 l/s respectively. The CO sorption curve decreases slowly with the sorbed quantity up to about 10 torr l and then it rapidly drops. This behaviour is a clear indication of the porous nature of the getter blades and the high conductance of the cartridge structure. The optimization of these two parameters results in a continuous and efficient sorption process which goes on till the getter surface is nearly saturated. For higher gas load, an abrupt decrease in pumping speed takes place, since only few active sites are still available for chemisorption and room temperature diffusion is negligible. Similar behaviour is shown by nitrogen. Differently from CO and N₂, and in agreement with literature data, no decrease in the pumping speed for hydrogen has been measured up to the test dose. In fact thanks to the high diffusivity of hydrogen into the alloy lattice, the pump capacity

for this gas is extremely high, being practically limited by the embrittlement value only. A comparison between the sorption curves for CO, N₂ and H₂ of the present HOGP [10] and those of the GP 200 pump, based on the pleated strip concept [11], indicates a substantial increase in pumping speed (a factor two) and capacity (a factor fifteen at 100 l/s). This pump is therefore particularly well suited for those applications where a high gas load or prolonged machine operating cycles are foreseen.

IV. REFERENCES

- [1] B. Ferrario, "Non-evaporable getters in plasma and particle physics experiments", Int. Symp. on Vacuum Tech. & Nuclear Applications, Bombay, pp. 175-188, (1983).
- [2] C. Benvenuti, "A new pumping approach for the large electron positron collider (LEP)", Nuclear Instruments and Methods No. 205, pp. 391-401 (1983).
- [3] H.F. Dylla, D.M. Manos, J.C. Citrolo, A.G. Mathewson, A. Poncet, F. Mazza "Vacuum system design for a 1.2 GeV electron storage ring with non-evaporable getter pumping" Proc. AVS Topical Conf. on Vacuum Design, of Synchrotron Light Sources, Argonne, p. 389-403 (1990).
- [4] A. Barosi, T.A. Giorgi, L. Rosai "Characteristics of SORB-AC non-evaporable getter cartridges and their potential use in fusion reactors" Proc. of the Int. Conf. on radiation Effects and Tritium techn. for fusion reactors, pp. 213-216 (1975).
- [5] M. Audi, L. Dolcino, F. Doni, B. Ferrario, "A new ultrahigh vacuum combination pump", J.Vac.Sci.Technol. A 5(4), pp. 2587-2590 July/Aug (1987).
- [6] S.R. In, T. Maruyama, S. Yokouchi, S.H. Be, "Performance characteristics of lumped nonevaporable getter (NEG) pump" Journal of Vacuum Society, Vol.34, N° 12, pp. 882-893 (1991).
- [7] N.B. Mistry, AIP Conf. Proc. No. 171, 1, (1988).
- [8] C. Pisani, "Problems of gas kinetics in systems with adsorbing walls", Vacuum 18, No.6. pp. 327-334 (1968).
- [9] ASTM procedures F798-82.
- [10] Italian Patent Application N° MI92 A 001753
- [11] SAES internal Report N° 20 (1988)

ELETTRA Vacuum System

M. Bernardini, F. Daclo, F. Giacuzzo, R. Kersevan*, J. Miertusova, F. Pradal

Sincrotrone Trieste, Padriciano 99, 34012 Trieste, Italy

* SSC Laboratory, 2550 Beckleymeade Ave, Dallas, TX 75237, USA

Abstract

Elettra is a third-generation synchrotron light source which is being built especially for the use of high brilliance radiation from insertion devices and bending magnets. The UHV conditions in a storage ring lead to a longer beam lifetime - one of the most important criterion. The Elettra vacuum system presents some peculiarities which cannot be found in any already existing machine. The final version of bending magnet vacuum chamber is presented. After chemical and thermal conditioning the specific outgassing rate of about 1.5×10^{-12} Torr. $1 \text{ sec}^{-1} \text{ cm}^{-2}$ was obtained. A microprocessor-controlled system has been developed to perform bake-out at the uniform temperature. The etched-foil type heaters are glued to the chamber and Microtherm insulation is used. UHV pumps based on standard triode sputter-ion pump were modified with ST 707 NEG (Non Evaporable Getter) modules. A special installation enables the resistive activation of getters and significantly increases pumping speed for hydrogen and other residual gases (except methane and argon). All these technological innovations improve vacuum conditions in Elettra storage ring and consequently also the other parameters of our light source.

I. INTRODUCTION

Third generation light sources are dedicated machines to be built especially for the use of radiation from insertion devices rather than from bending magnets. High brilliance exceeds that of the previous generation by at least an order of magnitude, but high beam currents require a sophisticated ultra high vacuum system.

Elettra light source, which is being built on Carso hills near Trieste, Italy, consists of three main parts:

1. The 1.5 GeV full-injection linac already installed and tested *in situ* (in future can be upgraded to 2.0 GeV).
2. The transfer line (TL) from linac to storage ring. TL is 93 m long pumped by thirteen 60 l/s sputter-ion pumps which can obtain and maintain the average pressure 2×10^{-8} mbar.
3. The 260 m long storage ring which is divided into six sectors. The ring contains 24 bending magnets and 12 straight sections, one is for beam injection, 11 are for insertion device radiation beam lines.

In the storage ring the UHV conditions are necessary to drastically reduce the elastic Coulomb gas scattering and bremsstrahlung which strongly affect the beam lifetime. Stored beam lifetime due to gas density must be more than 10

hours and must be achieved soon after start up (short conditioning time).

Machine parameters characterizing the Elettra vacuum system are as follows:

Beam energy, E	1.5 (2.0)	[GeV]
Beam current, I	400	[mA]
Bending radius, ρ	5.5	[m]
Circumference	260	[m]
Required pressure with beam	2×10^{-9}	[Torr]

II. VACUUM COMPONENTS AND MATERIALS

For Elettra storage ring it has been decided to adopt the ante-chamber solution, which is very attractive from the vacuum point of view because of the efficient removal of desorbed gas far away from the electron trajectories where the small dimensions of the beam chamber limit the conductances and then the pumping effectiveness.

The electron beam chamber has a rhomboidal cross-section - $80 \times 56 \text{ mm}^2$ internal dimensions and 2 mm thickness - in order to fit all of the magnetic elements, its specific conductance is 30 l/s. The rhomboidal shape is obtained by cold-rolling a round pipe of suitable diameter.

The bending magnet vacuum chamber is made by coupling the rhomboidal chamber to the ante-chamber obtained by machining a 6.5 cm thick stainless steel sheet. The rhomboidal chamber is bent to the appropriate bending radius, 5.5 m on axis, and connected to the ante chamber via a 1 cm high slot, which is machined on the outer part of the chamber in order to let the synchrotron radiation photons go to experimental beam lines.

A non-standard sealing technique has been applied in a number of vacuum chamber's connections. It is based on VATSeal-type gaskets made of silvered copper with a small edge on both sides. These gaskets have been extensively tested in laboratory up to 300 °C without leaking problems. They required about 8 Nm of sealing torque and due to their geometry, there is no clearance between the coupled flanges and therefore the beam impedance contribution is minimum.

Another important device to be installed in the vacuum system is the photon absorber (or crotch absorber). It should be installed in each bending magnet vacuum chamber in order to absorb about 70% of the synchrotron radiation. Our design of the absorber is based on an OFHC copper block on which an OFHC copper pipe is brazed for cooling water. A second brazing to a stainless steel flange with feedthroughs for water assures the vacuum tightness and facilitates the assembly.

A 4.8 m long vacuum chamber has been designed for IDs installation. It has an elliptical cross-section with a cylindrical ante-chamber. All system will be pumped by four 60 l/s SIPs, if it will be necessary, NEG modules can be inserted inside.

An austenitic stainless steel ESR AISI 316 LN has been chosen, for its very low magnetic permeability, its high yield stress and well known welding and cleaning procedure. Internal surfaces and welds exposed to the vacuum must be free of microinclusions and cracks. Surface roughness must be less than 1 μm and free of oxides or impurities.

All vacuum components were carefully cleaned and finished to obtain the required vacuum level ($<1.e-10$ mbar without the beam). A complete surface treatment included the following phases:

- i) Organic solvent degreasing - all principal contaminations were eliminated by means of organic solvents as the acetone or the benzol; for components contaminated by oil an additional cleaning with perchlorethylene at 120 °C was necessary.
- ii) Ultrasonic washing - a bath in phosphateless alkaline solution at about 60 °C for minimum 4 hours.
- iii) Two phases rinsing - the first with normal water which eliminated detergent residues, the second in demineralized water, which removed the impurities from the normal water.
- iv) Drying - a hot air flow dries the walls and prevents dust deposition on them.

Cleaned vacuum components were than pre-baked and degassed in the high vacuum oven. This treatment is believed by a number of authors to give a lower desorption yield. The vacuum oven is 6 m long and 0.9 m of diameter cylindrical vessel made of stainless steel. It can be pumped by three oil-free turbo pumps, fore-vacuum is obtained by means of a 500 l/s piston pump.

Pre-baking was performed at 350 °C for 24 hours, while the pressure in the oven decreased down to $e-7$ mbar range. Cooling procedure took of about 36 hours and on the end the pressure was better than $1.e-9$ mbar. Before opening, the oven was saturated with dry nitrogen. The components were then taken out from the oven and immediately covered with flanges. One of the flanges had a small pipe to flush inside dry nitrogen. All flanges were closed, the pipe was cutting off and as fast as possible cleaned and pre-baked vacuum components were stored in anti-dust bags under overpressure atmosphere of dry nitrogen.

III. PUMPING AND MEASURING SYSTEM

Eight moveable roughing pumps are used to obtain fore-vacuum up to $1.e-7$ mbar in the storage ring. We have also developed a new kind of UHV pumps based on standard triode sputter-ion pumps (SIPs) combined with Non Evaporable Getter modules (NEG) St 707 (SAES Getter, Milano). Pumping speeds of such modified SIPs were measured for gases H_2 , N_2 and CO in our laboratory [1].

The installation of additional 12 lumped NEG pumps (LNPs) was inevitable in a straight section between two magnets where a SIP of comparable pumping speed cannot be fitted. This pump is based on NEG module inserted in a rectangular vacuum chamber, UHV feed-through is used to connect the NEG module with an external power unit for activation of the getter. Pumping speeds of LNPs, also developed in our laboratory, were measured at different experimental conditions, as well [2].

Totally 108 of 120 l/s and 24 of 400 l/s Varian StarCell pumps modified with St 707 NEG modules are used.

The total pressure in our vacuum chamber is measured by cold cathode (Penning) gauges TPG 300.

The analysis of residual gas mixtures and partial pressure measurements are performed by 6 quadrupole mass analyzers Balzers 421 (one for each sector). Linearity, sensitivity and stability tests of this instrument were done in our laboratory [3]. Spectrometers can be used for leak checking, bake-out monitoring and local surface outgassing, when radiation hits a surface.

IV. BAKE OUT PROCEDURE IN SITU

A microprocessor-controlled bake out system has been developed. The heaters are of the resistive deposit over a Kapton foil, which are glued to the chamber. The Microtherm insulation 3 mm of thickness guarantees the uniform temperature of 180 °C in all parts of vacuum chamber. The outside temperature does not exceed 95 °C (measurements were performed without magnets around the chamber).

Two control systems for both the sputter-ion pumps and the bake out heaters have been developed. The first enables to power four SIPs with only one power unit. There is a possibility of individual reading of the absorbed current and automatic current to pressure conversion. The second allows us to obtain a very uniform bake-out temperature by ramping of 23°C per hour.

V. RESULTS OF TESTS

All tests were measured on the prototype of bending magnet vacuum chamber. Bake-out procedure were performed at two different temperature: 150 and 180 °C. As it is illustrated in fig. 1 - the lowest ultimate pressure was reached after bake-out at 180 °C.

Our prototype was pumped by two 120 l/s and one 400 l/s SIPs and one LNP. All getter modules were activated at 450 °C for 45 min. The quadrupole mass analyzer has detected peaks 2 (H_2^+), 16 (CH_4^+), 28 (CO^+) and 44 (CO_2^+) as usual for a baked UHV system. Water peak 18 could be observed only after a bake-out procedure at 150 °C.

The outgassing rate measurements have been performed connecting the bending magnet vacuum chamber light port to a standard test-dome for measuring pumping speeds - fig. 2.

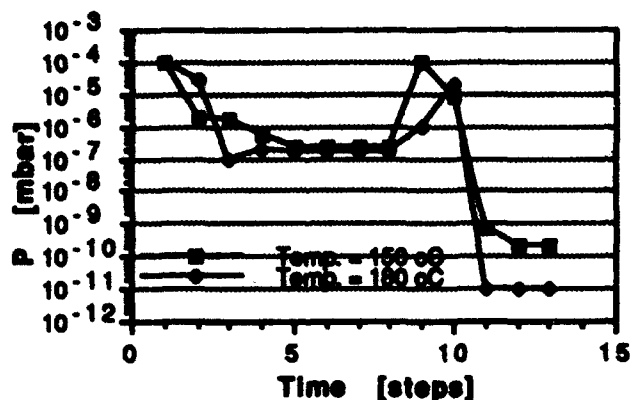


Figure 1. Pressure decrease after bake-out at 150 and 180 °C.

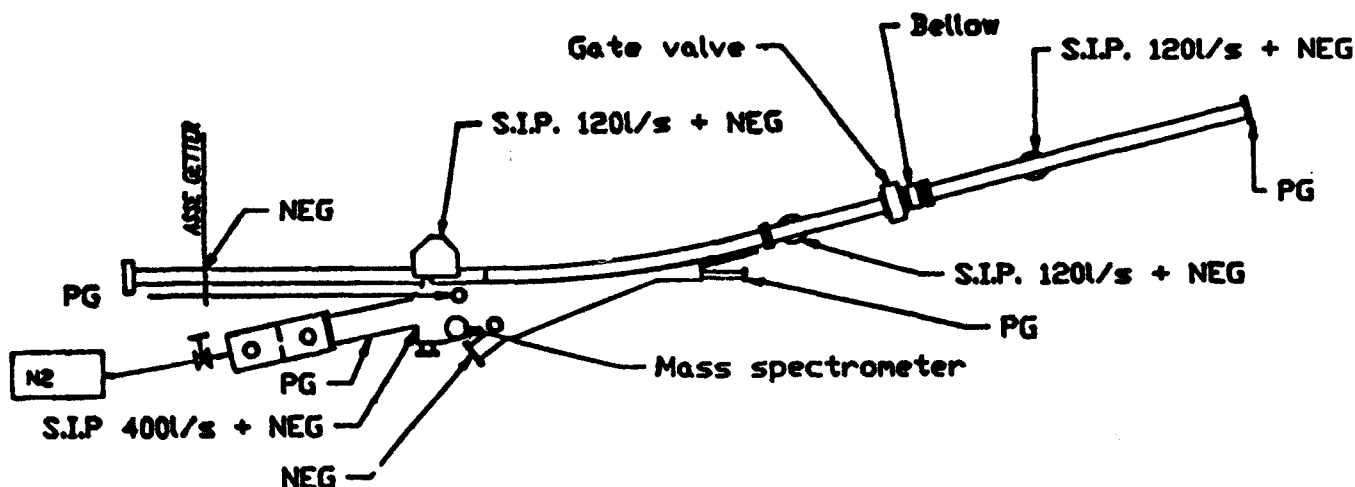


Figure 2. Bending magnet vacuum chamber outgassing rate measurements.

The prototype was pumped only by 520 l/s turbo pump. Outgassing rate was evaluated by the throughput method, pressures P_1 and P_2 in the upper and lower part of the test-dome were measured with Bayard-Alpert gauges. The specific outgassing rate was determined after both bake-out procedures, corresponding values are $1.5 \cdot 10^{-12}$ Torr.l.sec⁻¹.cm⁻² and $5 \cdot 10^{-13}$ Torr.l.sec⁻¹.cm⁻² at 150 and 180 °C, respectively.

Special bellows with internal RF sliding contacts have been successfully leak-tested subjecting them to many thousands mechanical cycles at temperatures higher than that foreseen for the bake-out in situ [4].

A non standard flanging technique has been used for connecting the beam position monitors (BPM) to the vacuum chamber. In fact, there are more than 100 BPMs distributed around the machine's circumference. Many of them are

situated between the magnetic elements so a reliable installation is very difficult if standard CF flanges are to be used. Therefore we have developed and tested rhomboidal-shaped flanges with flat surfaces where a special gasket ensures vacuum tightness even after prolonged bake-out procedures at higher temperatures.

VI. CONCLUSIONS

All presented technological innovations and measurements led to improve conditions in the Elettra vacuum system. We are confident that our light source and, particularly our UHV system will meet all the specifications before machine's start up in september 1993.

VII. REFERENCES

- [1] R. Kersevan, J. Miertusova, F. Pradal, "Pumping Speed of Sputter Ion Pump Modified with NEG Modules", *Int. rep. Sincrotrone Trieste*, ST/M-92/8.
- [2] J. Miertusova, R. Kersevan, M. Bernardini, "Pumping Speed of a NEG St 707 module at Diff. Temp. Cond.", 3rd - *European Vacuum Conference*, Wien, 1991.
- [3] F. Daclon, J. Miertusova, F. Pradal, "Comp. Test of Small Commercial QMA", *Proceedings of XII. Congresso Naz. sulla Scienza e Technol. Vuoto*, Bolzano, 1993.
- [4] F. Pradal, "Riassunto dei Test di Qualificazione Soffietti con Contatto RF per la Camera a Vuoto di Elettra", *Sincrotrone Trieste*, ST/M-TN-91/21.

Vacuum Chamber and Crotch Absorber for the SPring-8 Storage Ring Vacuum System

K.Watanabe, S.H.Be, Y.Oikawa, H.A.Sakaue, CY.Xu, S.Yokouchi,
Y.Wang, S.Takahashi*, M.Tsuchiya**, Y.Yanagi***

RIKEN-JAERI Joint Team

2-1 Hirosawa, Wako-shi, Saitama, 351-01 Japan

Abstract

The whole vacuum system for the SPring-8 storage ring is planning to be completely installed in the ring by October 1996. The vacuum chamber for the straight sections consists of a beam chamber and a slot-isolated antechamber in which NEG strips are installed. To suppress the chamber deformation at the BPM station due to the pressure difference between the atmospheric pressure and the vacuum, ribs are mounted on the chamber. In the bending magnet chamber, a distributed ion pump is also installed. The crotch and absorber have been designed to reduce their RF impedances and the radiation level outside the vacuum chamber. In this paper we present details of the final design for the vacuum chamber, crotch and absorber. The chamber supporting system and the structure of ribs are also described.

I. INTRODUCTION

The SPring-8 [1] is a highly brilliant synchrotron radiation source which is presently under construction, and scheduled for completion in 1997. The vacuum system [2] forms a ring of 1436m in circumference and consists of two differently shaped aluminum-alloy chamber extrusions, crotches, two types of absorbers and various chamber components such as bellows and gate valves.

To achieve a beam lifetime of approximately 24 hours, the vacuum chamber with its pumping system should be designed so as to maintain the beam-on pressure of 1nTorr or less with a circulating current of 100mA. The main pumping system is based on non-evaporable getter (NEG) strips [3] which are used in the straight and bending chambers.

In addition to the NEG strips a distributed ion pump is installed in a bending magnet chamber. Lumped NEG (LNP) [4] and sputter ion pumps are used at the crotch and absorber locations.

In our vacuum system, synchrotron radiation (SR) is almost intercepted by the crotches and absorbers placed just downstream and upstream of bending magnets. An only photon emission for energies less than 10eV with a angular spread larger than 1.5mrad in the vertical plane is intercepted by a slight part of 10mm photon beam slot walls of chambers. The important tasks for the vacuum system should be considered as 1) the design [5] of crotches and absorbers a)

in which photo-electrons, reflected photons and SR-induced outgasses are efficiently trapped and b) which can withstand the high photon beam power, and 2) the design of the chamber supports which can ensure the displacement and deformation of the chamber within the accuracy of 0.03mm or less for a beam position monitor (BPM), even after repeated bake cycles. To avoid the excessive production of ozone and corrosives in the air surrounding the vacuum chambers, synchrotron radiation shielding is considered in the crotch and absorber design.

We are planning to manufacture only one cell to estimate the performance of the vacuum system from various points of the view in advance of manufacture of the whole vacuum system composing of 48 cells. The manufacture of the one cell has already been started.

In this paper the crotches, absorbers, vacuum chambers and their supporting structures are described.

II. CROTCH AND ABSORBER

Crotches (CR) are placed just downstream of bending magnets (BM), and absorbers (AB2,3) just upstream of BM's and AB1,4 at both ends of the straight section for insertion devices to absorb the radiation that passes between the CR and the electron beam. An about 50% of the bending magnet radiation is absorbed by the absorbers [2]. Thus synchrotron radiation is almost intercepted by CR's and AB's, and not intercepted by vacuum chambers. Isometric views of the CR and AB1,2 are shown in Figs. 1 and 2, respectively. Structure of the AB3,4 following the CR is similar to that of the CR.

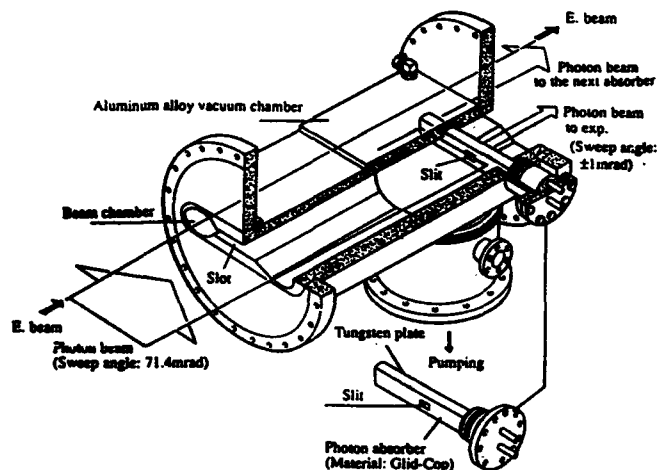


Fig1. Isometric view of the crotch

* The Kobe Steel, Ltd.

** Isikawajima-Harima Heavy Industries
Co., Ltd.

*** Hitachi, Ltd.

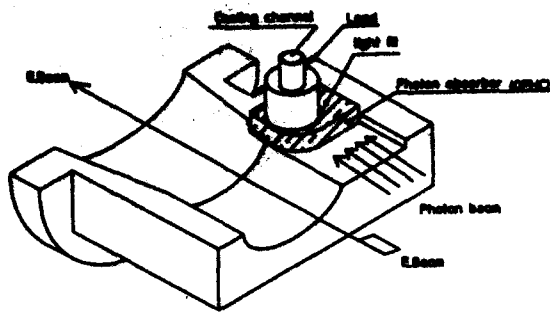


Fig2. Isometric view of the absorber

An initial design for main bodies of the AB3,4 and CR was based on OFHC copper. This initial design was abandoned and present one changed to be an Al-alloy extrusion. As the body materials the copper is better than the Al-alloy because of lower photodesorption rate compared to that of the Al-alloy. Regardless of this matter, the reason that we choose the Al-alloy is reduction of the cost due to an easiness of fabrication. If we compare two cases, an activation interval of the LNP to be used at the crotch and AB3,4 locations becomes shorter than that in the case of using the copper because of an earlier decrease of pumping speeds due to higher photodesorption rate of the Al-alloy. This brings an increase of the pressure. At the beginning of the machine operation, this becomes some problem but would not cause a critical one.

The number of photon absorber inserted in the CR was also changed from two photon absorbers to one. This is for reducing the SR power and its density irradiated at the CR by increasing the SR that passes between the CR and the electron beam. Thus the thermal load, in particular power density that was a critical problem in the initial design is relaxed, and we can make the CR design easy.

The photon absorbers are made of Glid Cop (Al and Al_2O_3 dispersion strengthened copper) because of the high allowable thermal stress of 60 kg/mm^2 , compared to 10 kg/mm^2 of OFHC. The thermal analysis results of the crotch have been described elsewhere by Y.Morimoto et. al.[6].

The crotch and absorber have the structure in which particles such as reflected photons, photo-electrons and SR-induced outgasses are efficiently trapped, and are also designed to reduce their RF impedances. SR-induced outgasses are evacuated locally by the high capacity pumping system before the outgasses have a chance to bounce into the beam chamber. The pumping system is composed of a lumped NEG pump ($\sim 500 \text{ l/s}$ at the CR and 350 l/s at the AB for CO) for evacuating H_2 and CO gasses, and a sputter ion pump (60 l/s) for CH_4 and inert gasses.

The photon-beam power (or maximum power density) per a crotch is of about 5 kW ($\sim 30 \text{ kW/cm}^2$) and the energetic photon spectrum is extended to energies in the several 100 keV range. To avoid the formation of ozone and nitrogen oxides in the air surrounding the vacuum chamber, the crotches and absorbers have been designed to be shielded against synchrotron radiation. As mentioned above, the

photon absorbers are of approximately 3-cm thickness. The photons of energies less than 80 keV are almost stopped at the photon absorbers, but those higher than about 100 keV are escaped from the crotches and absorbers. Owing to the normal incidence of the synchrotron radiation on the photon absorber, the attenuation along the direct photon path traversing the 3-cm thickness is of the order of 10^{-3} at the photon energies of 200 keV. To reduce further the radiation level outside the vacuum chamber, additional shielding is necessitated. The shielding for the crotches is provided with tungsten of a 3-mm thick plate on the photon absorber as shown in Fig.1, and the lead shielding with a 4-mm thick plate for the absorbers is provided (see Fig.2). The attenuation with the additional shielding becomes of the order of 10^{-6} for the same photon energies.

III. VACUUM CHAMBER AND ITS SUPPORTING SYSTEM

A. Vacuum Chamber

The vacuum chamber for the straight sections consists of a beam chamber and a slot-isolated antechamber in which NEG strips are installed.

The bending magnet chamber includes a rectangular pump channel, a beam chamber and a slot-isolated antechamber in which NEG strips are installed. The separation wall between the beam chamber and the pump channel is perforated, allowing the chamber to be evacuated by means of a pump, the so-called distributed ion pump (see Fig.3).

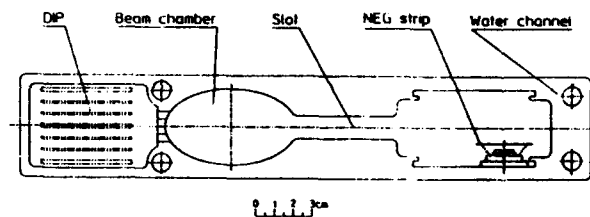


Fig.3 Cross section of the bending magnet chamber

These chambers are 6063 T5 aluminum extrusions and contain water channels for cooling and bakeout. A 150°C bakeout is achieved with portable water-heating units. The chamber is covered with thermal insulation to reduce heat losses. The LNP, gauges and bellows are baked with heating electrical tapes, and valves baked with mantle heaters.

The aluminum end flanges are joined to the chamber extrusion with incomplete penetration weldments not to appear the weld bead on an inside surface of the beam chamber for low RF impedance.

Chamber deformation at the locations of BPM's due to the pressure difference between the atmospheric pressure and the vacuum is about 0.14mm, while the deformation required for the BPM's must be within the accuracy of 0.03mm or less. To suppress the deformation, two ribs are mounted just beside the BPM on the chamber as shown in Fig.4. The BPM is installed to the chamber with a laser beam welding (Fig.5).

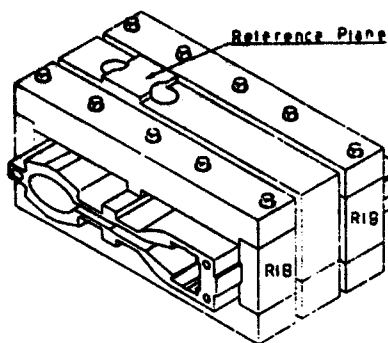


Fig.4. Chamber with ribs at the BPM station

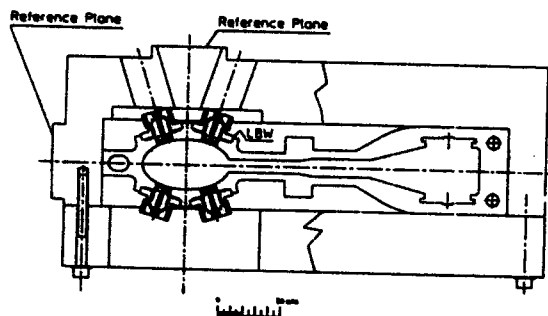


Fig.5 Mount of the BPM

Part Name	Qty	Part No.
1. Support	1	1000000
2. Support	1	1000000
3. Support	1	1000000
4. Support	1	1000000
5. Support	1	1000000
6. Support	1	1000000
7. Support	1	1000000
8. Support	1	1000000
9. Support	1	1000000
10. Support	1	1000000
11. Support	1	1000000
12. Support	1	1000000
13. Support	1	1000000
14. Support	1	1000000
15. Support	1	1000000
16. Support	1	1000000
17. Support	1	1000000
18. Support	1	1000000
19. Support	1	1000000
20. Support	1	1000000
21. Support	1	1000000
22. Support	1	1000000
23. Support	1	1000000
24. Support	1	1000000
25. Support	1	1000000
26. Support	1	1000000
27. Support	1	1000000
28. Support	1	1000000
29. Support	1	1000000
30. Support	1	1000000
31. Support	1	1000000
32. Support	1	1000000
33. Support	1	1000000
34. Support	1	1000000
35. Support	1	1000000
36. Support	1	1000000
37. Support	1	1000000
38. Support	1	1000000
39. Support	1	1000000
40. Support	1	1000000
41. Support	1	1000000
42. Support	1	1000000
43. Support	1	1000000
44. Support	1	1000000
45. Support	1	1000000
46. Support	1	1000000
47. Support	1	1000000
48. Support	1	1000000
49. Support	1	1000000
50. Support	1	1000000
51. Support	1	1000000
52. Support	1	1000000
53. Support	1	1000000
54. Support	1	1000000
55. Support	1	1000000
56. Support	1	1000000
57. Support	1	1000000
58. Support	1	1000000
59. Support	1	1000000
60. Support	1	1000000
61. Support	1	1000000
62. Support	1	1000000
63. Support	1	1000000
64. Support	1	1000000
65. Support	1	1000000
66. Support	1	1000000
67. Support	1	1000000
68. Support	1	1000000
69. Support	1	1000000
70. Support	1	1000000
71. Support	1	1000000
72. Support	1	1000000
73. Support	1	1000000
74. Support	1	1000000
75. Support	1	1000000
76. Support	1	1000000
77. Support	1	1000000
78. Support	1	1000000
79. Support	1	1000000
80. Support	1	1000000
81. Support	1	1000000
82. Support	1	1000000
83. Support	1	1000000
84. Support	1	1000000
85. Support	1	1000000
86. Support	1	1000000
87. Support	1	1000000
88. Support	1	1000000
89. Support	1	1000000
90. Support	1	1000000
91. Support	1	1000000
92. Support	1	1000000
93. Support	1	1000000
94. Support	1	1000000
95. Support	1	1000000
96. Support	1	1000000
97. Support	1	1000000
98. Support	1	1000000
99. Support	1	1000000
100. Support	1	1000000

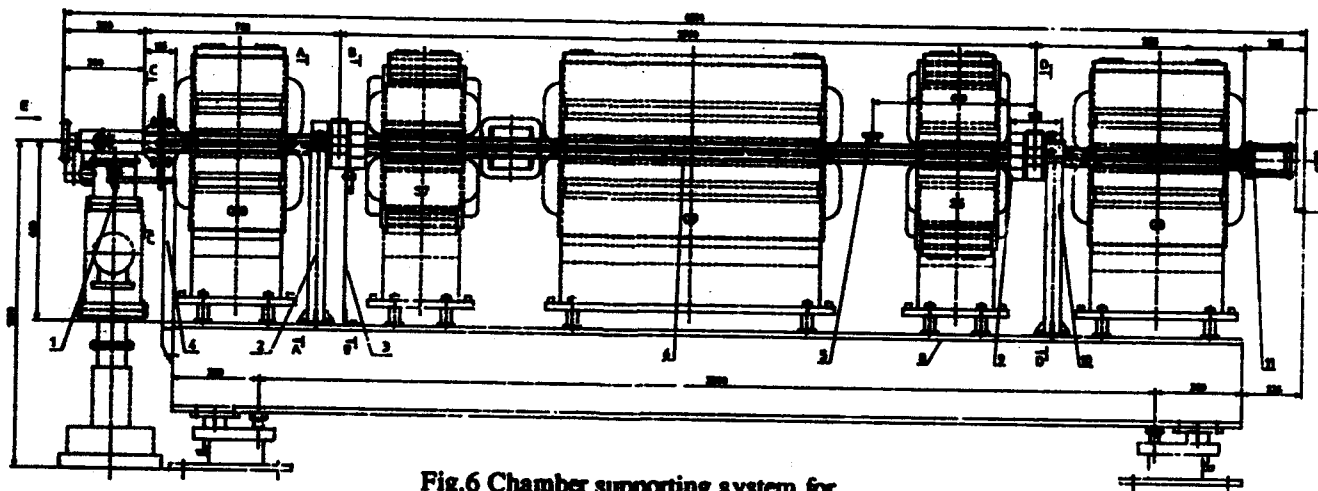
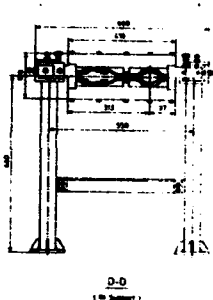


Fig.6 Chamber supporting system for the typical straight section

B. Chamber Supporting System

A chamber supporting system for the typical straight section is shown in Fig.6. Two or three supports per a section depending on the place of the section are used. One support is rigid and does not allow chamber motion in any direction. It is located near the end of the chamber. One of other two supports is composed of a leaf spring and the support with a rotational bearing allowing a chamber thermal expansion along the electron beam direction during the chamber bake cycle. Its position is located near the another end of the chamber.

The last one, which is used for the longest one of three straight sections, is located approximately at the both center of the section and for supporting the chamber weight. The performance of the supporting system has experimentally been confirmed [7]. The bending magnet chambers use three supports. Two sliding slot guides are located at the ends of the chamber to allow thermal expansion in the approximate beam direction. The center support is rigid one and constrains the chamber in any direction during the bake cycle.

REFERENCES

- [1]H. Kamitsubo, Rev. Sci. Instrum, 63, 1586(1992).
- [2]T. Nishidono et al, Conference Record of the 1991 IEEE Particle Accelerator Conference, Vol.4, PP.2298-2300.
- [3]Y. P. Lee. et al, J. Vac. Soc. Jpn, 33 154(1990).
- [4]S. R. In et al, J. Vac. Soc. Jpn., 34, 882(1991).
- [5]K. Watanabe et al, to be published in Proc. of XVth Intern. Conference on High Energy Accelerators, Hamburg, Germany, July 2024, (1992).
- [6]Y. Morimoto et al, Proc. of Topical Conference on Vacuum Design of synchrotrons Light Source, Argonne, Nov.(1990) PP.110-117.
- [7]S. H. Be et al, ibid PP.102-109.

SYNRAD, a Montecarlo Synchrotron Radiation Ray-Tracing Program

Roberto Keresvan
Superconducting Super Collider Laboratory*
2550 Beckleymeade Avenue, Dallas, TX 75237 USA

Abstract

A new module, SYNRAD, has been added to the MOLFLOW [1] software package, allowing the Montecarlo (MC) simulation of synchrotron radiation (SR) emission. The geometrical three-dimensional (3D) distribution of the photons, power and energy, and spectra can be calculated. A model of the vacuum chamber is generated, and the profiles of SR-induced desorption are obtained by means of SYNRAD. These desorption profiles are then embedded in the vacuum chamber model and the MC program for the calculation of UHV molecular flow is used for obtaining relevant quantities such as, among others, pressure profiles, pumping speed efficiencies and conductances. Results of the application of SYNRAD and MOLFLOW, and comparison with some published data will be given.

I. INTRODUCTION

A source of SR can be described giving the kind of particle, electron or proton, and its energy E , beam emittance and beta functions, together with the magnetic field distribution [2]. SYNRAD calculates the trajectory of the beam for the given magnetic field and generates photons, in a selected energy range (ϵ_{\min} , ϵ_{\max}), according to the real distributions [2, 3]. A ray-tracing algorithm is implemented which follows the photons' trajectories and keeps track of their scoring on planar facets. These planar facets can be defined using an editor program [1] by means of which 3D models of any shape can be analysed. Analytical formulas describing the emission of SR do exist, but their application to real life geometries is not always straightforward. For instance the assumption of infinite distance from the source point, in order to use tabulated angular spectral distributions, isn't applicable in general. In addition to that, the spectral distributions are usually given only for the vertical angle Ψ [2] (i.e. the emission angle measured in a plane orthogonal to the local plane of the orbit), and little or no mention of the horizontal distribution angle χ can be found [4], since usually an integration over χ is considered.

II. THEORY OF SR AND COMPUTATIONAL ALGORITHM

With reference to Fig. 1, four angles θ , ϕ , Ψ , and χ can be defined, and will be used in the following. For a given beam energy, the local radius of curvature ρ as a function of the magnetic field B is computed at each point of the beam trajectory, and the critical energy ϵ_c is obtained by using the

formula $\epsilon_c [\text{eV}] = 2.960 \cdot 10^{-7} \gamma^3 / \rho [\text{m}]$, where γ is the relativistic factor. Then the normalized energy ϵ/ϵ_c is generated following the real SR distribution, according to the function ($d\alpha$ is the trajectory arc element)

$$\left\{ \frac{dF}{d\alpha} = 2.457 \cdot 10^{10} E [\text{GeV}] G_1(y) \right. \quad (1)$$

$$\left\{ G_1(y) = y \int_y^\infty K_{5/3}(\eta) d\eta \quad y = \epsilon/\epsilon_c \right. \quad (2)$$

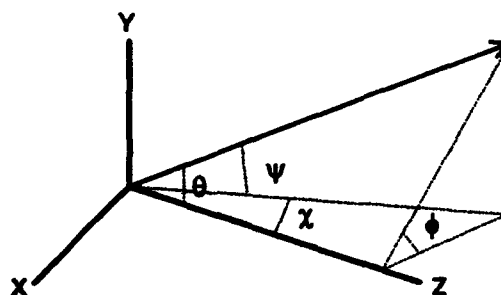


Fig. 1. Definition of the angles θ , ϕ , Ψ and χ .

in units of $\text{photons} \cdot \text{s}^{-1} \cdot (\text{mrad})^{-1} \cdot \text{mA}^{-1} \cdot (0.1\% \text{ bandwidth})^{-1}$, and the vertical angle Ψ is generated with distribution [3]

$$F(\Psi) = F_p + F_o \quad (3)$$

$$F_p(\Psi) = (1 + \gamma^2 \Psi^2)^2 K_{2/3}^2 \left\{ \frac{\epsilon}{2\epsilon_c} [1 + (\gamma^2 \Psi^2)^2]^{3/2} \right\} \quad (4)$$

$$F_o(\Psi) = (\gamma^2 \Psi^2)^2 (1 + \gamma^2 \Psi^2)^2 K_{2/3}^2 \left\{ \frac{\epsilon}{2\epsilon_c} [1 + (\gamma^2 \Psi^2)^2]^{3/2} \right\} \quad (5)$$

where F , F_p and F_o are the functions giving the vertical distributions for the total SR emitted at ϵ/ϵ_c and for the two components whose polarizations are parallel and orthogonal to the local plane of the orbit, respectively [2]. At this point the horizontal angle χ is needed. To obtain it, the following formula [3] giving F_o as a function of θ and ϕ is used

$$F = (1 + \gamma^2 \theta^2)^{-4} \left[(1 - \gamma^2 \theta^2 + 2\gamma^2 \theta^2 \sin^2(\phi))^2 + \gamma^4 \theta^4 \sin^2(\phi) \cos^2(\phi) \right] \quad (6)$$

where θ and ϕ are converted to Ψ and χ using the equations

*Operated by URA, Inc., for the U.S. Dept. of Energy under Contract No. DE-AC02-89ER40486

$$\begin{cases} \theta = \cos^{-1}(\cos(\Psi)\cos(\chi)) \\ \phi = \tan^{-1}(\tan(\Psi)/\sin(\chi)) \end{cases} \quad (7)$$

$$(8)$$

This algorithm allows the generation of each photon after calling two routines which generate the vertical and horizontal distributions separately, instead of setting the values for χ and Ψ from a bi-dimensional distribution. This procedure is faster, and gives good agreement with the figures reported in literature. If a cone with angular aperture $|\theta| < 1/\gamma$ about the tangent to the point of emission is considered, 7/32 of the total intensity should be emitted out of it; 17/112 for the parallel polarization and 11/16 for the orthogonal one [3]. In a benchmark run, SYNRAD generated some 300,000 photons, in about 5 hours running on a 50 MHz 486 personal computer, and the SR power emitted out of the cone was 0.22403 of the total, a factor 1.024 times greater than the theoretical value of 7/32.

Fig. 2 shows the scoring of the SR flux, in the photon energy interval $(10^{-4}, 10)e_c$, on a facet orthogonal to the beam trajectory, at a distance of 1000 cm. The horizontal and vertical width of the figure covers angular intervals of ± 4.6 for both $\gamma\chi$ and $\gamma\Psi$. Note the presence of two minima in the plane $\Psi=0.0$, at $\gamma\chi = \pm 1.0$, according to Ref. 5, pag. 39.

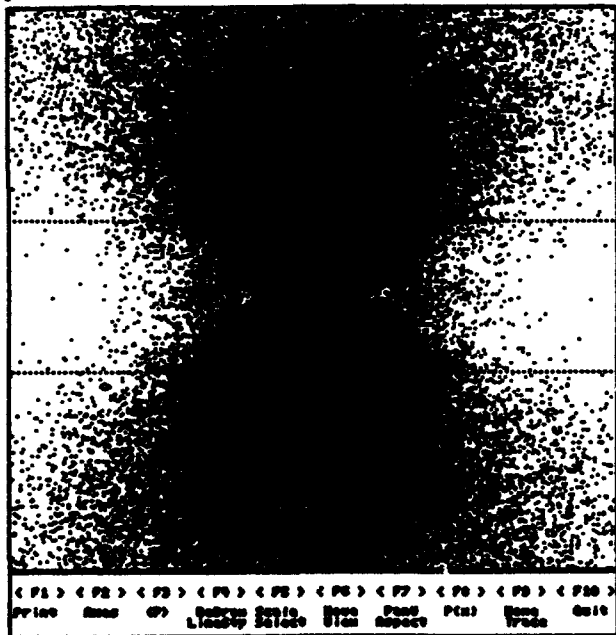


Fig. 2

Usually only the vertical power distribution can be found in literature. It is easy to calculate the spectral distributions, i.e. at selected photon energies s_i , just choosing the photon energy interval about s_i , with appropriate bandwidth. Each facet in the model can record one out of four different quantities relevant to the photon energy interval (s_{min} , s_{max}): the SR power, the SR flux, the SR power spectrum and the SR flux spectrum. This is obtained setting appropriately some attributes of the facet called transparency and sticking.

III. APPLICATIONS

Fig. 3 shows two different SR flux spectra for the SSC at a proton beam energy of 20 TeV, and a magnetic field of 6.6 T, in the photon energy interval $(10^{-4}, 10)e_c$, $s_c = 284$ eV.

Fig. 4 shows the SR power spectra for the same parameters.

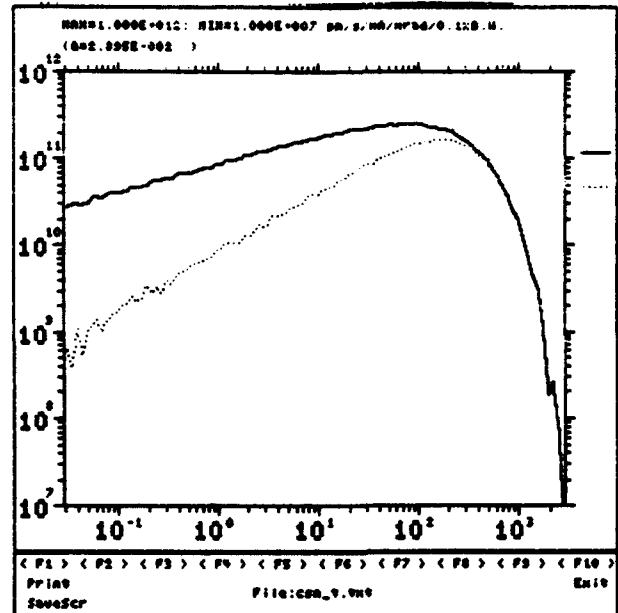


Fig. 3 Solid line: total spectrum; dotted: within $1/\gamma$ cone.

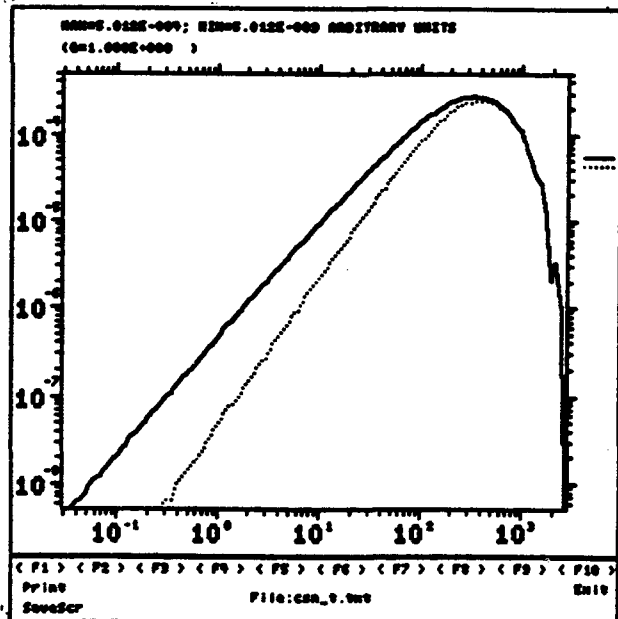


Fig. 4 Solid line: total spectrum; dotted: within $1/\gamma$ cone.

Fig. 5 and Fig.6 give the normalized horizontal and vertical distributions for the SR flux and the SR power, respectively. The angular intervals are ± 2.5 mrad for both χ and Ψ . The small decrease in the horizontal distributions around $\chi=0$ is under investigation. Nonetheless, the overall accuracy of these results is good when compared to analytical calculations [6].

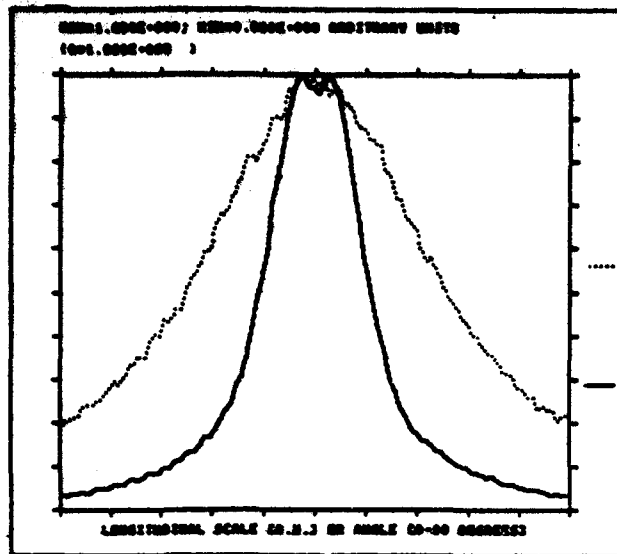


Fig. 5 Normalized SR flux spectrum in (0.0284, 2840) eV.
Solid:horizontal; dotted:vertical

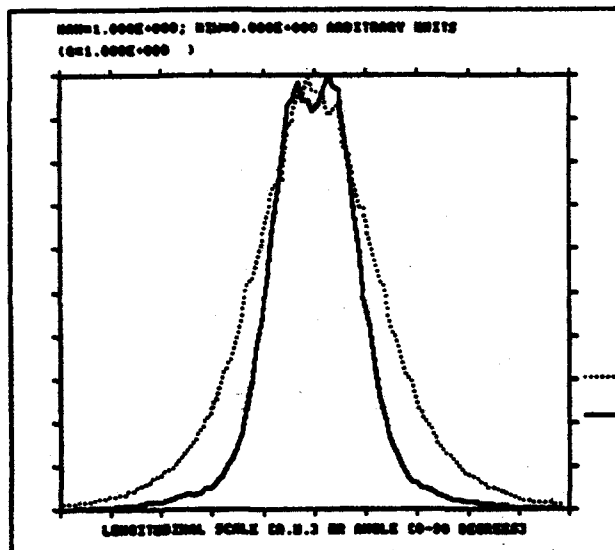


Fig. 6 Normalized SR power spectrum in (0.0284, 2840) eV
Solid:horizontal; dotted:vertical

The emission of SR in a two meter long section of the SSC bore tube in the arc section [7] has been simulated, Fig.7, in order to calculate the height of the strip which is directly illuminated by SR photons. The subtended arc is 0.198 mrad, and the 3D model is given by two one meter long straight sections placed with a small angle, 0.099 mrad, between them, in order to simulate the SSC's radius of curvature of 10100 m, with the Z axis coincident with the proton beam direction. Photons exiting from the second section re-enter the first section, with proper direction.

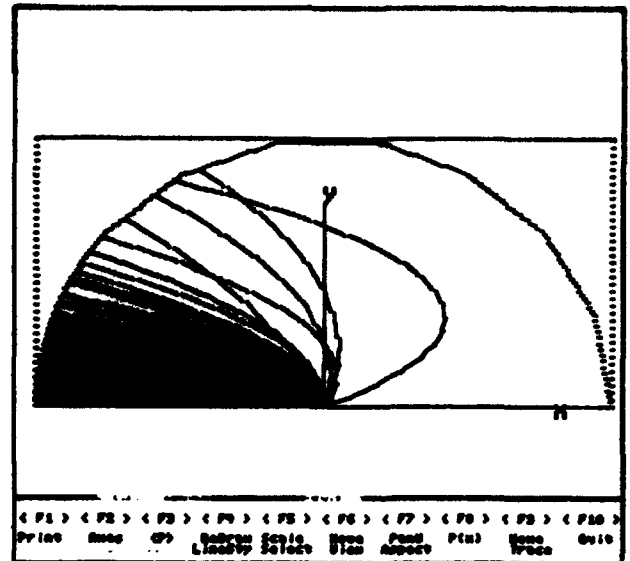


Fig. 7 XY-view of the model. XZ=symmetry plane.

IV. CONCLUSIONS

Some of the possibilities of a novel program for the calculation of SR-related quantities have been described.

SYNRAD runs on 486-based personal computers under DOS. Its speed has not been optimized so far, and translation into FORTRAN language for portability to faster processors will be implemented in the future.

SYNRAD allows a simple determination of SR fluxes and powers under different assumptions for the photon source, and when used in conjunction with MOLFLOW provides a unique tool for the analysis of SR-induced pressure profiles.

V. ACKNOWLEDGMENTS

The author gratefully acknowledges H. Humsttter for providing a fast routine, based on Chebyshev polynomials, for the evaluation of the SR spectrum.

VI. REFERENCES

- [1] R. Kersevan, "MOLFLOW User's Guide", Sincrotrone Trieste Technical Report, ST/M-91/17 (1991).
- [2] G. K. Green, BNL Report BNL 50522, April 1976.
- [3] R. Coisson, "Angular-spectral distribution and polarization of synchrotron radiation from a short magnet", Phys. Rev. A20, 524 (1979).
- [4] J. Schwinger, "On the Classical Radiation of Accelerated Electrons", Phys. Rev. 75, 1912 (1949)
- [5] A. Sokolov, I. Ternov, "Synchrotron Radiation", Pergamon Press Ltd., London, 1968.
- [6] K-J. Kim, "Angular Distribution of Undulator Power for an Arbitrary Deflection Parameter K", Nucl. Instr. and Meth. A246 (1986) 67-70.
- [7] J. Zbasiak et al., "Design of the Superconducting Super Collider Beam Tube: Baseline and Liner Approaches, this Conference.

Vacuum System Design of the MIT-Bates South Hall Ring

E. Ihloff, R. Averill, J. Flanz, K. Jacobs, S. Sobczynski
D. Wang, A. Zolfaghari
MIT-Bates Linear Accelerator Center
Box 846 Middleton MA 01949

Abstract

The MIT-Bates Linear Accelerator Center is now in the commissioning stage for the new South Hall Ring (SHR). The SHR is a 1 GeV electron storage/stretcher ring with a 190 meter circumference and is designed for circulating beams of 80 mA. The SHR vacuum system was completed in January 1993 with commissioning starting in February. This paper describes the design of the vacuum system, hardware developed and operational performance during commissioning.

I. INTRODUCTION

The vacuum system for the SHR is an all metal system which is designed and constructed to operate in the Ultra High Vacuum (UHV) regime. The following parameters have been used in the design of the vacuum system:

1. Energies from .3 to 1 GeV, maximum circulating currents of 100 mA, bending radius of 9.14 m. This yields a maximum synchrotron power loss of approximately 1 kW.
2. Design goal of static pressures less than 5×10^{-10} torr. Dynamic pressures of 2×10^{-9} torr with a stored beam after 100 Ah of operation.
3. Ability to recover one quadrant of the ring in a 24 hr period from planned or accidental venting.
4. Ability to monitor pressures with a computer interface and to log data. Use of residual gas analyzers (RGA) to

leak check and diagnose problems.

5. Minimum service life of 10,000 cycles or 10,000 hours on all equipment.

6. Use of 316L stainless steel and Conflat type flanges in most construction. Very large flanges use Helicoflex Delta Seals.

7. Ability to perform in situ bakeout to 150 C.

8. All vacuum equipment including pumping ports, chambers, valves, beam monitors, bellows, and transition sections are designed with a smooth internal bore to limit beam induced RF wake fields.

II. OPERATION

From atmosphere, only one quadrant at a time may be roughed out. First, a dry diaphragm pump is used to get to 27 in. Hg and then a large liquid nitrogen cooled sorption system with capacity of 1.7 million torr-liters is used to provide a totally oil free pump out from atm. to 5×10^{-4} torr. At this pressure, the starcell triode ion pumps easily start and quickly achieve 5×10^{-7} torr. All dipole ion pumps and dipole vacuum chambers have a direct current heated ST 707 non-evaporable getter pumps (NEGs). We then activate the NEGs for one hour at 400 C while monitoring the Ion pump current to keep the entire system in the 10^{-5} torr range. After all the ion pumps and NEGs are operating, the base static pressure

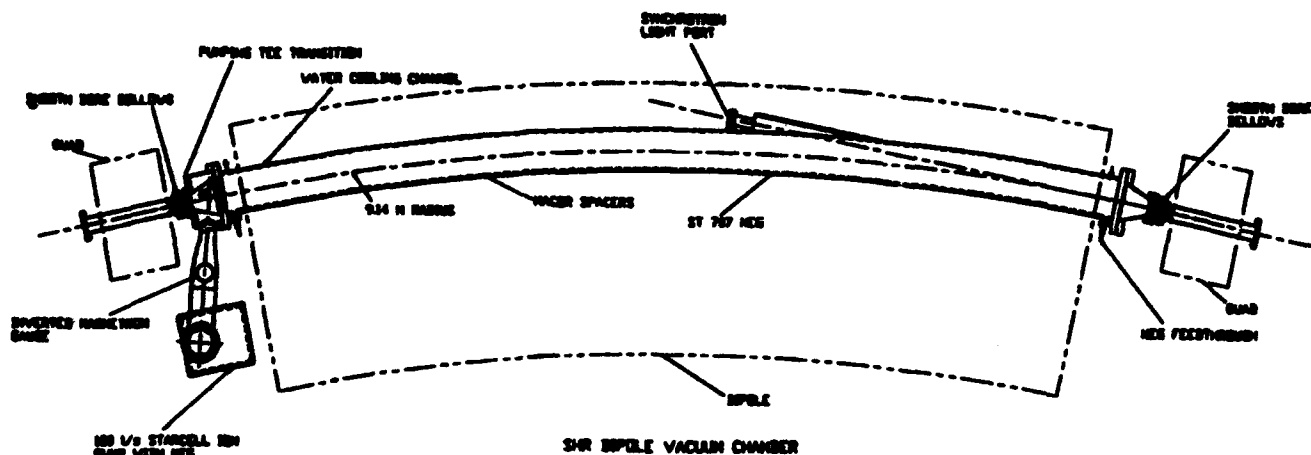


Figure 1.

quickly drops to 5×10^{-9} . After about a week, the pressure decreases to between 3×10^{-9} and 8×10^{-10} unbaked.

III. DIPOLE VACUUM CHAMBERS

There are sixteen 22.5° dipole vacuum chambers in the SHR lattice (see Figure 1). They are fabricated from commercially available 6" x 2" x .120 wall 316L stainless steel rectangular tubing. 316L was chosen for its low magnetic permeability. The tubing is bent the hard way in 20 foot sections to a radius of 9.14 m. The bent tube is then machined for the NEG electrical feedthroughs, synchrotron light ports and to final length. After a chemical cleaning, the flanges and ports are TIG welded using argon as a backing gas. After a final clean, all the chambers were mounted to test setup where they were pumped down, leak and RGA checked, and baked at 200 C for 48 hr. All chambers reached 5×10^{-10} torr before being removed from the test setup and installed in the ring.

Incorporated into the dipole vacuum chambers is a NEG strip which gives localized pumping to desorbed getterable gases (for example H_2, N_2, O_2, Co). The strips are held to the inside radius of the chamber on Macor spacers and connected to the outside by two high current feedthroughs. The NEG is a non-magnetic Constantan strip with a Zr-V-Fe composition sintered on to it. The NEG is activated by passing 50 A through it causing resistive heating to 400 C. The strips have a high pumping speed of .7 l/s/cm² for H_2 . At pressures envisioned in the ring, activation will only be needed twice a year.

Attached to the exterior of the dipole chamber are water cooling channels to dissipate the thermal load caused by synchrotron radiation. The cooling is provided to limit the temperature rise caused by the very localized heating. With a synchrotron power loss of 1 kW distributed around the ring, the linear power flux would be .17 W/cm. With a minimum beam height of 1.15 mm, the local power flux is 1.5 W/cm². The water cooling channel is capable of dissipating this load.

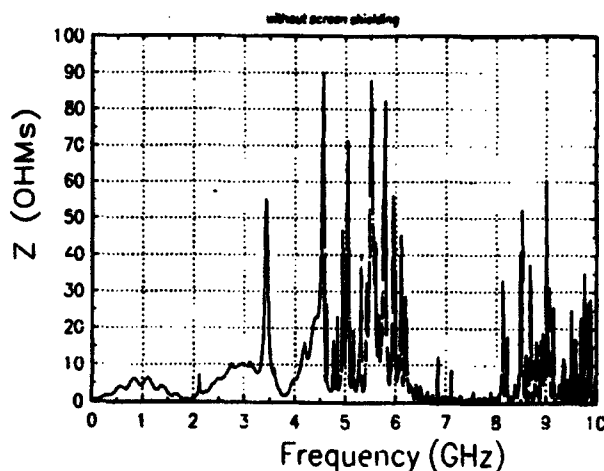
IV. VACUUM HARDWARE

This section gives a brief summary of hardware in the SHR vacuum system as well as operation experiences. The ion pumps were purchased on the basis of cost. The Starcell ion pumps are three different sizes, 60 l/s for straight sections, 120 l/s with direct heated ST 707 NEG for the arc sections and 230 l/s for the septum magnets and kickers. There are a total of 51 ion pumps in the ring. These pumps are extremely easy to start off a sorption pump. Ion pumps are started with large power supplies and then switched to 3 mA holding power supplies developed for MIT by a local company, Keruco Inc. All power supplies are monitored and controlled by a computer in the ring control room. Twenty eight HPS inverted magnetron gauges monitor the vacuum and provide setpoints to operate the valves. These gauges read

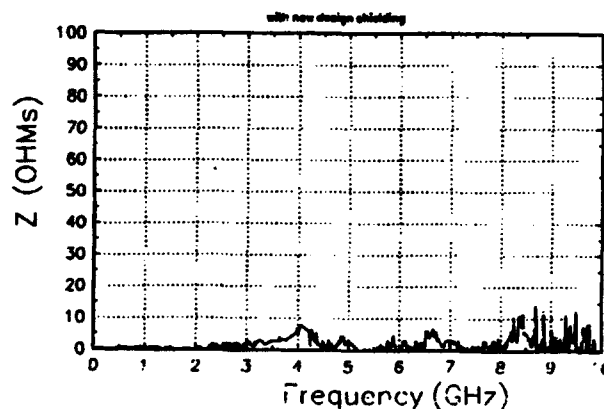
from 1×10^{-3} to 5×10^{-10} torr. These units have performed well. Ten RGA heads are also installed in the ring.

A large amount of detailed engineering effort was put into developing smooth bore hardware which meets the requirements of low higher order mode losses. The hardware includes: 16 smooth bore pumping tee transition which allows for ion pumping in a region which switches from 6" x 2" rectangular to 2 1/2" circular cross section, 14 smooth bore intercepting beam targets, 22 button beam position monitors (BPMs), 12 smooth bore stripline BPMs, 6 RF shielded gate valves, 60 smooth bore bellows and a RF cavity collimator pumping tee. Some designs were modeled by accelerator physics using MAFIA⁽¹⁾ to study unwanted modes which could lead to coupled bunch instabilities. Also, all hardware was measured for longitudinal impedance on a test setup which looked at frequencies to 10 GHz. Figures 2 and 3 below show measurements of bellows without shield and with shield.

Coupling Impedance of Bellows



Coupling Impedance of Bellows



Figures 2 and 3.

The smooth bore bellows (Figures 2,3,4) is similar in design to a unit designed by Duke University² at the FEL lab. It features a welded bellows which is shielded by an inner tube which makes solid contact on both ends with a beryllium copper Amp Products Louvertac strip which make a solid RF contact on both ends. RF tests showed the contact on both ends to be the most important criteria for a good design.

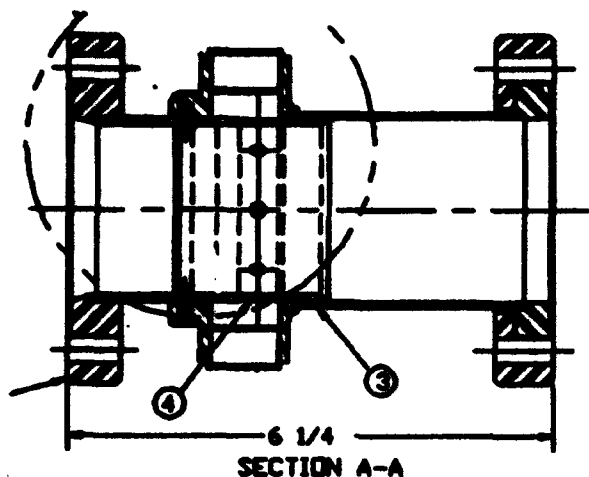


Figure 4.

Other detailed vacuum design work was on the Energy Compression System dipole vacuum chambers. They were modeled using SDRC Ideas FEA code (Figure 5). The parts were CNC laser cut from 316L stainless steel and TIG welded together.

ECB DIPOLE VACUUM CHAMBER, REV 1.
 .SAD SET: 1 - VAC LOAD
 DISPLACEMENT - NORMAL MIN: 0.00 MAX: 0.00000

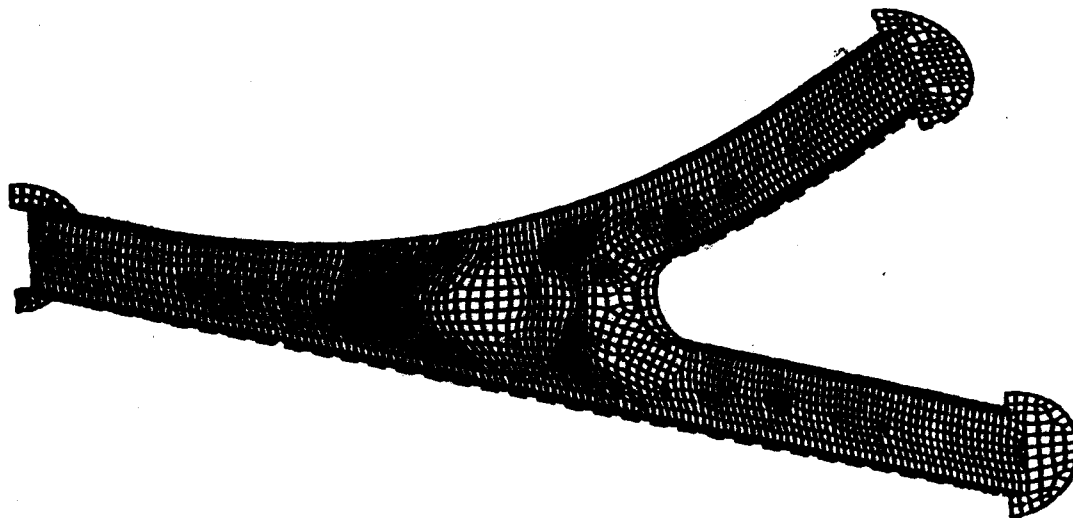


Figure 5.

V. COMMISSIONING TESTS

The vacuum system for the SHR was completed in January 1993 and commissioning started in February. Base vacuum around the ring was in the high 10^{-10} - low 10^{-9} torr range. Initial operation was at 300 MeV with very low currents at 1-3 mA, in the storage mode without RF. Storage times were limited by losses due to synchrotron radiation. The vacuum remained unchanged throughout these tests. After successful storage at low currents, the ring was brought to 40 mA, half the design current, and the vacuum in the arc sections rose to about 2×10^{-8} torr. Base pressures continued to improve after beam was shut off. Although the vacuum system is designed for in situ bakeout, we have not baked any components after installation. More section vacuum valves are to be installed so to limit the amount of beamline which needs to be vented to work on a section.

VI. ACKNOWLEDGEMENTS

The authors wish to give special thanks to the Mechanical/Vacuum technicians who helped in design, construction and testing. They are R. Capodilupo, S. Ciacara, B. Edgecomb, D. Fitch, M. Humphrey, D. Latons with J. Grenham, supervisor. Also, thanks to D. Nicoll for all the detail drafting and P. Krippendorf for testing chambers.

VII. REFERENCES

- [1] T. Weiland, Particle Accelerators, 17, 227 (1985).
- [2] N. Hower, Free Electron Laser Lab, Duke University.

Design of Vacuum Chambers for Experimental Regions of Colliding Beam Machines

C. Hauviller
CERN, CH-1211 Geneva 23

Abstract

During the last twenty years, highly transparent vacuum chambers adapted to the requirements of the detectors have been installed in the experimental regions of the CERN colliders: ISR, SPS and LEP. The general method of design of the chambers is described: criteria for the choice of materials, methods of determining the mechanical parameters, manufacturing methods, environmental constraints, ... An overview of possible future concepts is also presented, in particular the use of new materials.

I. INTRODUCTION

The vacuum chambers for the experimental regions of the colliding beam machines are the main physical interfaces between machine and detectors. Consequently, their design is determined by sometimes conflicting requirements, but drawbacks for the particle detection due to the necessary presence of the pipe could be minimized by a carefully optimized approach. No unique solution exists, but the aim of this paper is to try to give general guidelines based upon experience acquired during the last twenty years on CERN colliders: ISR, SPS and LEP [1], [3], [5]. After recalling the requirements, design strategy will be followed by general hints on shapes and materials and some remarks on manufacturing and an extrapolation to future machines.

II. REQUIREMENTS

General constraints from a collider together with those from an experiment lead to the main design parameters, but more factors specific to the machine type or to the detectors have to be added.

On the machine side, the vacuum chamber should obviously have an aperture large enough to allow the beam envelope, including all running conditions (injection, stable beams, ...), to go through and a sufficient conductance to keep the required ultra-high vacuum. A perfect electrical continuity is also a prerequisite. But one must also add specific requirements such as, for an electron-positron machine:

- protection against synchrotron radiation, either large aperture, in order that no particle hits the wall, or masks, to limit the particle interactions to local zones;
- smooth section transitions to minimize high-frequency losses.

The beam pipe should be compatible with the rapidity coverage of the experiment. The main parameter is its transparency to emerging particles but other phenomena have to be taken into account: shielding against electromagnetic noise, unwanted background created by collisions with residual gases or, in electron-positron machines, by synchrotron radiation photons. A sufficient

clearance between the external envelope of the beam pipe and the inner layer of the vertex detector is also very often a prime parameter for the installation.

Finally, it should be borne in mind that adequate supports are of prime importance in the design of a vacuum chamber and that forgetting this fact in the conception of an experiment may lead to rather uncomfortable situations.

III. BEAM PIPE SECTION

Having established the boundary conditions of the design problem, it is now possible to determine the general shape of the beam pipe. A lot of imagination can be incorporated at that stage, but the solutions are usually variants of basics. For example, all the vacuum chamber types ever installed in the ISR have been already determined in the early days of the machine[1].

The first question is the section: either circular or elliptical. An elliptical section can be matched more closely to the beam envelope and allows a minimization of the distance between the first layer of detection and the interaction point. But the increase of the wall thickness, a consequence of a weaker non-circular section, hampers considerably the above advantages and leads usually to the relinquishment of this more complex option.

Circular tubes which could be cylindrical or conical with various wall constructions will be detailed below.

IV. DESIGN

The very large quantity of beam pipe types leads to an impossibility to provide a fully general design method. Guidelines will be given for the simplest beam pipe, a smooth circular cylindrical tube. After definition of the main parameters, it becomes possible to optimise the project in analysing their sensitivity to any variation. Vacuum and mechanical behaviours are treated separately but they interfere one against the other during all the design process.

A. Vacuum

The static pressure in the beam pipe is affected by the outgassing rate of the material, the conductance of the tube and the location and type of the pumps. It can be demonstrated that the pressure difference between the centre (P_{\max}) and the extremities (P_0) of a cylindrical tube of a diameter D and of length $2L$ with two end pumps is independent of the pumping speed. Based upon LEP experience on aluminium tubes, a conservative approximation of this difference is

$$P_{\max} - P_0 = 1.3 \times 10^{-12} (L/D)^2 \quad (P \text{ in Torr}) .$$

The base pressure P_0 , dependant of the available pumping speed, is determined by background considerations. Figure 1 shows the pressure curves for two typical values of L . As an example, to run at a maximum pressure of about 10^{-9} Torr, a practical upper limit for the pressure difference would be half of this value.

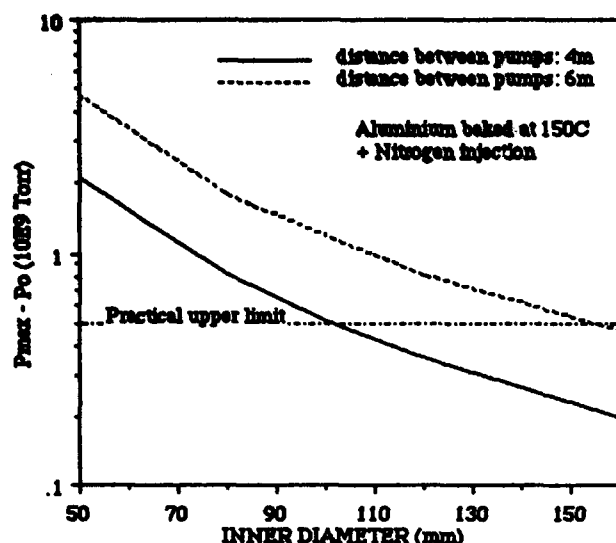


Figure 1. Pressure difference between interaction point (P_{max}) and pumps (P_0)

B. Mechanical behaviour

The main loads applied on a beam pipe are the external pressure due to vacuum and the own weight of the tube. They lead to buckling and bending.

For a long smooth cylindrical tube, the minimum thickness t required to avoid linear buckling (non-linear bifurcation before yielding) under vacuum is

$$t = 58 \sqrt{\frac{1 - \nu^2}{E}} D,$$

with a safety factor of 4, E and ν being respectively Young's modulus and Poisson ratio of the material (S. I. units).

But too long a distance between supports may cause a coupling between buckling and bending (ovalisation called the Brazier effect) leading to an earlier failure. Bending behaviour depends considerably upon the supporting method; an example is given below to illustrate this phenomenon. For a beam pipe simply supported only at the level of the pumps, assuming that the maximum deformation should be less than the wall thickness, the minimum value of t is

$$t = \frac{5}{3} \frac{\rho g L^4}{E D^2}$$

where ρg is the specific weight.

Figure 2 summarizes the application of this method to cylindrical beryllium tubes. However, it should be noted that this is the worst supporting case and that an extra support point improves significantly the situation.

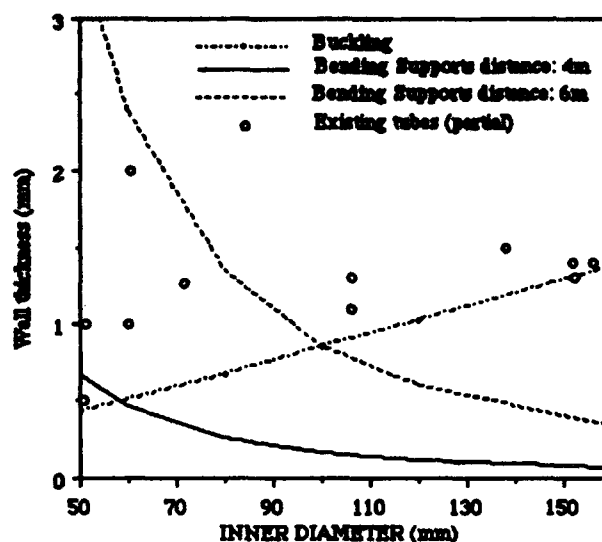


Figure 2. Geometry of beryllium beam pipes

Therefore, after having defined the vacuum pressure in running conditions based upon background considerations and after having defined the location of the pumps and the support points, geometrical and material parameters can be discussed.

V. SHAPES

A circular tube could be, in the order of manufacturing complexity, smooth, ring-stiffened, conical (simple or multiple), corrugated, a skin in tension between rings, ... The transparency of the first three options is compared in Fig. 3. (The ring-stiffened tube is a 0.5mm thick cylinder reinforced by ribs 0.5mm thick, 4.5mm in height, evenly spaced by 60mm).

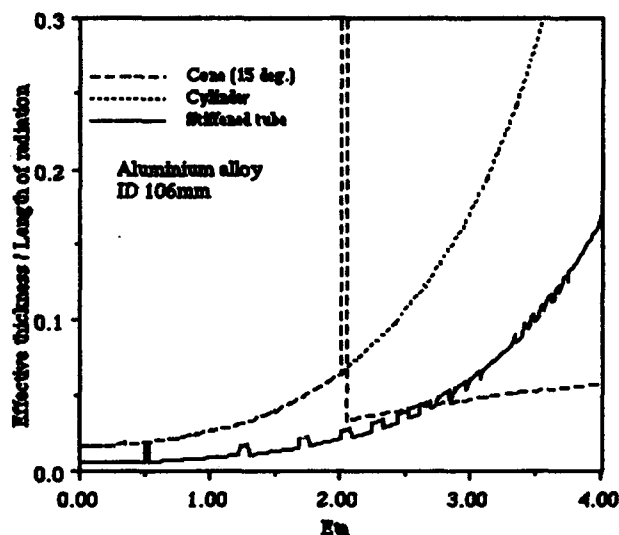


Figure 3. Transparency versus pseudo-rapidity

The smooth circular tube is the simplest beam pipe but its performances at high rapidity are very poor. The ring-stiffened tube is a way to minimize the wall thickness while keeping the smoothness of the internal wall. A way

to open a window at high rapidity is a cone but the allowable transition angles are limited in some machines (15° at LEP) and the path length inside the conical wall (corresponding to the big jump) becomes arbitrarily large; the latter drawback is even amplified by the fact that the interaction zone is not a point but finite and that charged particle tracks are curved in a magnetic field. A corrugated tube is an elegant way to minimize the wall thickness at low rapidity but at higher rapidity the number of wall crossings becomes prohibitive and this sort of tube is unacceptable in electron-positron machines. All attempts to manufacture a skin under tension have shown that the ring mass becomes prohibitive and the transfer of the large forces involved to the supports is a problem, especially with nowadays light trackers.

VI. MATERIALS

For the same design, the gain in transparency obtained in using one material instead of another can be determined in a rationalized way [2]. Considering the elastic buckling as usual failure mode of a circular tube loaded by an external pressure, it can be shown that if X_0 is the radiation length and E the Young's modulus, a non-dimensional parameter $X_0 E^{1/3}$ gives a figure of merit of materials. Table 1 allows to compare the principal ones.

Material	Be	CFC	Al	Ti	Fe
E (GPa)	290	200	70	110	210
X_0 (m)	0.353	0.27	0.089	0.036	0.018
$X_0 E^{1/3}$	2.34	1.58	0.37	0.17	0.11

Table 1

Beryllium gives uncontestedly the best performance but tube geometry has been limited up to now to smooth cylindrical shapes. It has three major drawbacks: safety hazards, manufacturing difficulties and, consequently price. Beryllium particles, generated in the case of an implosion or a fire, is highly carcinogenic. Obtained only through powder metallurgy, beryllium is considered not to be weldable at UHV standards. Tubes are presently produced from a hot formed sheet brazed on a longitudinal splice joint (Figure 2 shows dimensions of the longer vacuum tubes produced). Extruded tubes, proposed but not yet qualified, would permit more complex shapes. Heavy transition ends, either in aluminium or stainless steel, have to be brazed at both ends for welding to the other tubes.

A large number of wall constructions can be called composite [4]. Only two families will be mentioned: sandwich and carbon fibre reinforced plastics (CFRP).

A honeycomb sandwich made in Nomex honeycomb glued to two aluminium skins has been installed in a collider and further development work has shown the viability of this option, unfortunately presently asleep.

CFRP tubes have been used with more or less success. The composite structure itself was always up to the expectations and new fibres arriving on the market next year will double the Young's modulus value of Table 1, therefore superseding beryllium. When a problem appeared, it was always caused by the inner metallic liner and its connections to the transition end

pieces. But, if this continuous liner can be replaced by a sputtered metal, then fully reliable optimized vacuum chambers could probably be obtained at a very competitive price.

Aluminium alloys are light metals which provide the best cost-effective solutions. Almost any shape can be produced by precise machining, in particular ring-stiffened tubes as thin as 0.5 mm, which could be adapted to any detector acceptance. Their design is complex but present day analysis programs are able to handle any buckling problem. However, a great care is required to successfully weld thin aluminium alloy parts to UHV standards.

Titanium or stainless steel tubes could only be competitive with a very thin wall. The common solution is therefore to corrugate them but then a lower bending rigidity means more supports and, at high rapidity, the number of wall crossings increases quickly above an acceptable level. If the vacuum bake-out temperature can be limited to 150°C , then aluminium alloys are preferable.

VII. FUTURE COLLIDER BEAM PIPES

Beryllium is still considered to be the best option, especially for the central part, but carbon fibre reinforced plastics become very competitive with the arrival of new rigid fibres and reliable enough with the development of new resins and coating methods.

A cheaper option is to choose parts with fancy shapes machined in aluminium alloys, especially for the forward parts: ring-stiffened or cone, the latter being more transparent at high rapidity at the expense of an important "shadowed" zone.

But other ideas should not be forgotten, even if they need more development: honeycomb sandwich or even machined beryllium-aluminium alloy, ... once tubes become available.

VIII. REFERENCES

- [1] J.-C. Brunet, J.-C. Godot - Chambres à vide pour régions d'expériences ISR-CERN-ISR-GE/71-25 (1971)
- [2] C. Hauviller, I. Wilson - What materials should we use to make the vacuum chambers in the ISR experimental intersections? - CERN ISR-GE/74-52 (1974)
- [3] O. Gröbner, C. Hauviller - Design aspects of LEP experimental vacuum chambers - IEEE 1987 Particle Accelerator Conference (1987)
- [4] C. Hauviller - Development of composite tubes for experimental vacuum chambers of colliders - 1988 European Particle Accelerator Conference (J1988)
- [5] O. Gröbner, C. Hauviller - LEP vacuum chambers for experimental regions: experience with the first generation, prospects for the second generation - 1990 European Particle Accelerator Conference (1990)

Distributed Non-evaporable Getter Pumps for the Storage Ring of the APS*

R. Dortwegt and R. Benaroya
Argonne National Laboratory
Advanced Photon Source
9700 South Cass Avenue
Argonne, IL 60439

Abstract

A pair of distributed Non-evaporable Getter (NeG) strip assemblies is installed in each of 236 aluminum vacuum chambers of the 1104-m storage ring of the Advanced Photon Source. Distributed pumping is provided to remove most of the gas resulting from photon-stimulated desorption occurring along the outer walls of the chambers. This is an efficient way of pumping because conductance is limited along the beam axis. The St-707 NeG strips are conditioned at 450°C for 45 min. with 42 A. Base pressures obtained are as low as 4×10^{-11} Torr. The NeG strip assemblies are supported by a series of electrically isolated, 125-mm-long, interlocking stainless steel carriers. These unique interlocking carrier elements provide flexibility along the vacuum chamber curvature ($r=38.96$ m) and permit removal and installation of assemblies with as little as 150 mm external clearance between adjacent chambers.

I. INTRODUCTION

The Advanced Photon Source (APS), currently under construction at Argonne National Laboratory, is a synchrotron radiation research facility. It incorporates a 7-GeV positron storage ring (SR) designed to maintain a pressure less than 1

nTorr with a circulating current of 300 mA. The low pressure is critical to enabling the machine to deliver long beam lifetimes. The SR has 240 chambers over its 1104-m circumference. Each one of 236 aluminum chambers contains a pair of St-707 Non-evaporable Getter (NeG) [1, 2] strips, allowing for distributed pumping. This is an ideally suited pumping method over conductance limited chambers whose cross section is shown in Fig. 1. Test results indicate that the combination of sputter ion pumps and NeG strips achieve the desired chamber pressure. The NeG strips are designed to be effective over a 20-year period. However, should one or more of the strips require replacement (e.g., due to greater than anticipated exposure to gases while in a pumping mode or accidental damage), it would be desirable to accomplish the task without removing chambers. Therefore, unique interlocking stainless steel (SS) carriers for the NeG strips were designed and built to allow removal and installation of NeG assemblies between two adjacent chambers.

II. NEG PUMP TEST

Tests were made [3] to determine the effectiveness of the NeG strips even before the novel replacement design, using the interlocking carriers, had been incorporated. A 10-ft-long

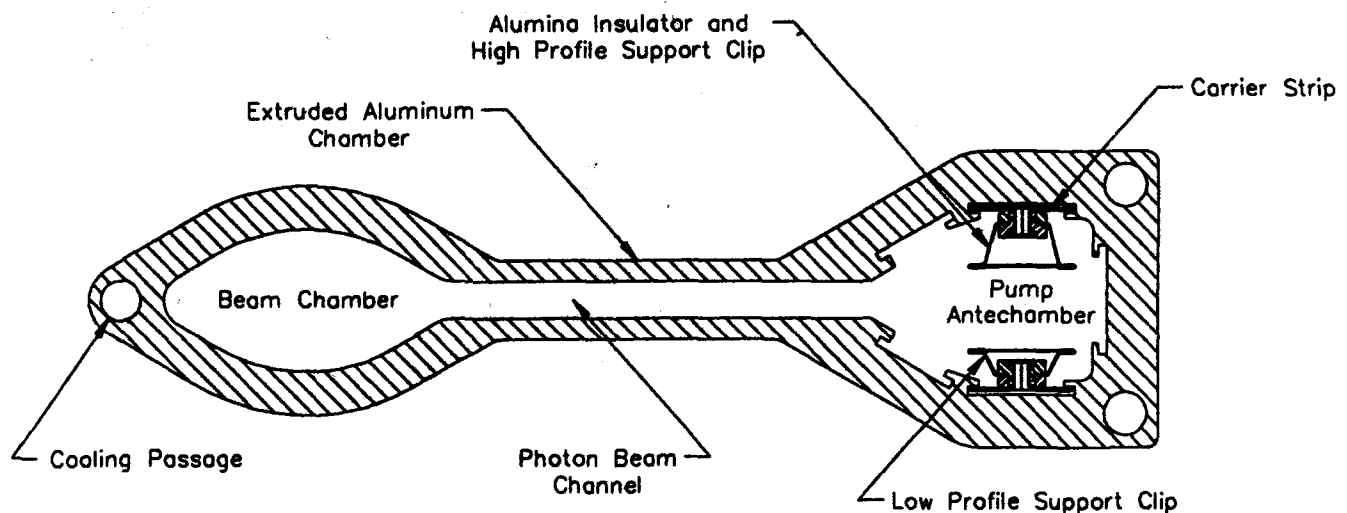


Figure 1. Storage Ring Vacuum Chamber Cross Section.

*Work supported by U.S. Department of Energy, Office of Basic Energy Sciences under Contract No. W-31-109-ENG-38.

The submitted manuscript has been authored by a contractor of the U.S. Government under contract No. W-31-109-ENG-38. Accordingly, the U.S. Government retains a nonexclusive, royalty-free license to publish or reproduce the published form of this contribution, or allow others to do so, for U.S. Government purposes.

straight chamber, similar to a section 1 type in a SR sector [4], was cleaned and installed with two 30-l/s sputter ion pumps, an angle valve for isolating the turbo molecular rough pumping complex, a nude ion gauge, and a residual gas analyzer. A pair of St-707 NeG strips was mounted on SS continuous carrier strips that were electrically isolated from the NeGs by means of ceramic insulators. The strips were constrained to the top and bottom antechamber walls within the grooved tracks that follow the straightness of the chamber. The NeGs were electrically joined in series at the end opposite to the entrance feedthroughs. The entrance junction was made with a banana jack-type connector, enclosed in a multicontact band, which solidly engaged the feedthrough with the Conflat seal closure action. The chamber was pumped with a turbomolecular pump. This was followed by a bakeout at 150°C which lasted until a stable pressure of 4×10^{-9} Torr was reached 36 hours later. The NeG strip was then activated at 450°C for 45 min. This was achieved with a current of 42 A through the NeGs. The expended power in the NeG strip was sufficient to retain the temperature of the insulated aluminum walls at 150°C without requiring additional baking power. During the initial phase of activation, the pressure increased to 1×10^{-5} Torr while the activation current was slowly raised towards its maximum. At the conclusion of the activation, the ion pumps were started. Finally, the turbo isolation valve was closed and, when the chamber walls cooled down to ambient temperature, the pressure stabilized at 4×10^{-11} Torr.

III. INTERLOCKING CARRIER SYSTEM

Mechanical support for the NeG strips is accomplished through the use of 0.75-mm-thick x 125-mm nominal length SS

strips (which have been termed "links"). A typical installation of one of the NeG assemblies is shown in Fig. 2. The links are snapped together during installation of the NeG assembly and inserted into the corresponding 2.5 x 32-mm slots which run the length of the vacuum chamber. The links are provided with fastening support clips and 99.5% alumina insulators to support the NeG at regular intervals while maintaining electrical isolation from the vacuum chamber.

The use of an interlocking set of links for a carrier strip is found to have the following advantages: (1) When installed, the assembly has sufficient flexibility in the horizontal plane to follow the 39-m radius of curvature possessed by some of the vacuum chambers. (2) The required space between chambers during removal of an assembly is less than 150 mm. As the NeG assembly is removed, each carrier link is disengaged from its neighbor immediately upon exit from the chamber. This permits bending of the NeG strip by itself to a radius less than 150 mm in the vertical plane, avoiding any adjacent hardware (see Fig. 3). (3) The force required to pull the assembly through the slot in the vacuum chamber is reduced significantly compared to a continuous strip (from approximately 10 kg down to the order of 1 kg or less on prototype units).

A detail of one of the typical links with fastening clip and insulators is shown in Fig. 4. The SS link, including the curled pin at one end, is stamped from flat sheet material. A hole of corresponding diameter is punched in the other end of the link. During installation, the curled pin of one link is snapped into the hole of the adjacent link. The curled pin detail was required since approximately 33% of the vacuum chambers are curved in the horizontal plane. For applications where only straight chambers are employed, the curled pin can be replaced with a vertical tab and the mating hole replaced with a slot.

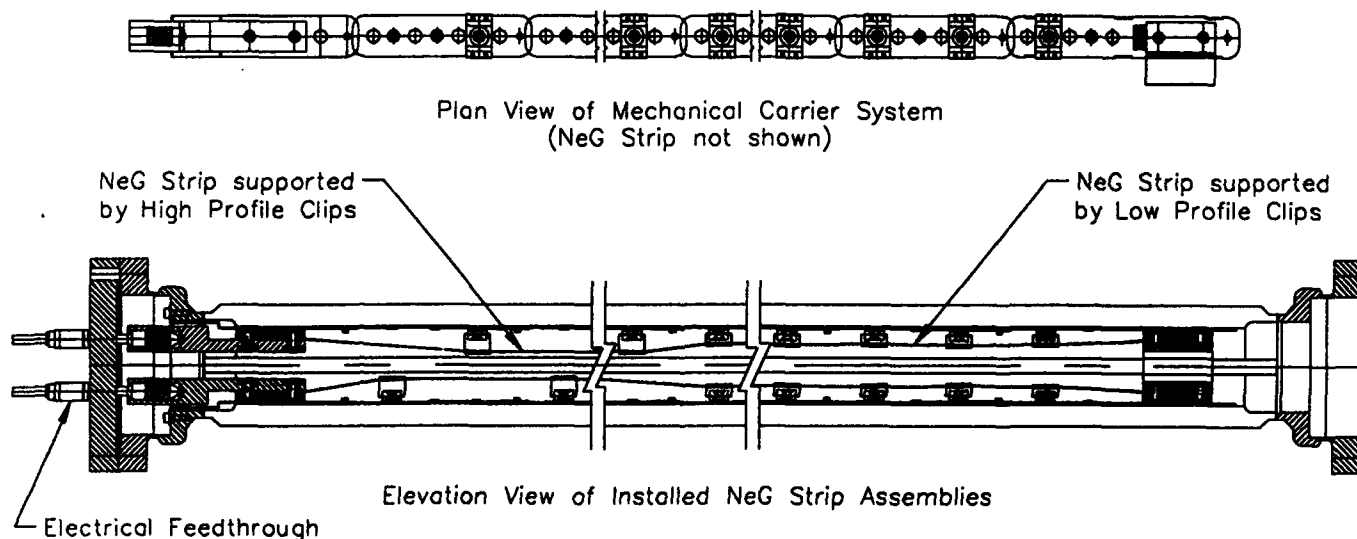


Figure 2. Typical Installation of NeG Assembly.



Figure 3. NeG Assembly Removal.

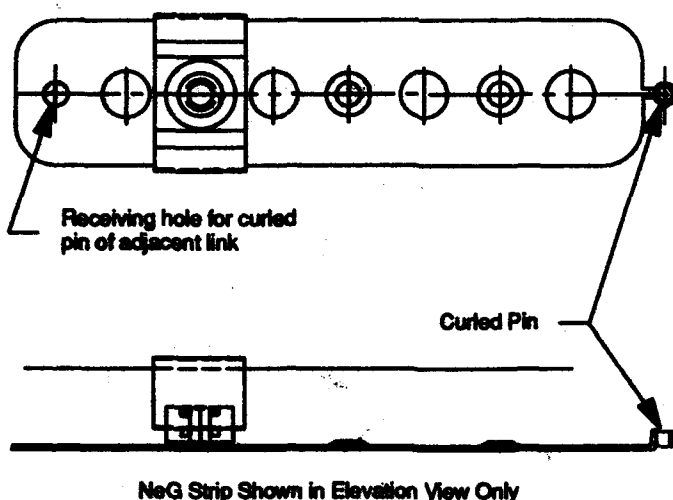


Figure 4. Typical Link.

Two types of fastening support clips (high and low profile types) are employed to support the NeG strip. As illustrated in Fig. 2, the low profile clips support the NeG strip further away from the beam axis than the high profile clips. The low profile clips are employed in regions where synchrotron radiation passes between the NeGs. In these regions, the NeG resides in the shadow of the vacuum chamber, preventing damage to the NeG in the event of beam missteering. The low profile clips are not used throughout since the force required to install the NeG assemblies increases significantly when the low profile clips are used. This is due to the reduced spacing between low profile clips (i.e., two clips per link). A reduced spacing between clips is required for the low profile supports so that the NeG is prevented from contacting the vacuum chamber during activation when the strip expands between clips due to differential thermal expansion (NeG at 450°C and carrier at 150°C).

When high profile clips are employed at the 125-mm interval (i.e., one clip per link), the system is assembled so that clips are staggered from top to bottom (see Fig. 2). This permits sagging of the top NeG strip without contacting the bottom strip which itself may coincidentally expand upwards.

Other manufacturing considerations include the use of 316 SS, which remains non-magnetic even when work hardened during forming and punching operations, and the removal of all burrs from carrier links prior to assembly.

IV. ACKNOWLEDGMENTS

The authors wish to thank R. Prien for his technical assistance, A. Salzbrunn for the preparation of the manuscript, and C. Eyberger for editing.

V. REFERENCES

- [1] C. Boffito, B. Ferrario, et al., *J. Vac. Sci. Tech.*, 18(3), 1981.
- [2] H. J. Halama and Y. Guo, *J. Vac. Sci. Tech.*, A9(3), 1991.
- [3] R. Benaroya, B. J. Roop, "Storage Ring Vacuum Chamber Section 1 Evaluation," unpublished.
- [4] R. C. Niemann, R. Benaroya, et al., *AIP Conf. Proc. No. 236*, pp. 84-101, 1991.

Test Fabrication of a Copper Beam Duct for the KEK B-Factory

Yusuke Suetsugu and Ken-ichi Kanazawa
National Laboratory for High Energy Physics
1-1 Oho, Tsukuba-shi, Ibaraki, 305, Japan

Abstract

A trial model of copper beam duct for the KEK B-Factory was fabricated and gas desorption rates were measured. The duct consists of a cooling channel, a beam channel and a pump channel, which were extruded separately and welded each other by the electron beam welding. The duct received only ultrasonic cleaning in a freon bath. The ultimate total pressure was about 4×10^{-10} Torr after a baking at 150°C for 48 hours and the thermal gas desorption rate was calculated as about 1.5×10^{-12} Torr. $l/(s \cdot \text{cm}^2)$ in N_2 equivalent. The measurement of the photon stimulated gas desorption rate was performed using the synchrotron radiation with a critical energy of 26.3 keV from the TRISTAN Accumulation Ring. The photo-desorption coefficients in the order of 10^{-2} molecules/photon were observed for main gases desorbed at the initial stage. These high gas desorption rates indicate that more careful surface preparation must be necessary.

I. INTRODUCTION

For the purpose of achieving a high luminosity, KEK B-Factory rings are operated with high current beams. Intensity of synchrotron radiation (SR) emitted from beams consequently becomes higher than any other existing e^-e^+ collider. How to treat this intense SR is a major subject in designing the vacuum system [1].

The choice of duct material, among others, has been the most important R&D point confronting us. Prospective materials are copper and aluminum alloy. Copper has many excellent properties, i.e. a high thermal conductivity, a high melting point and a low photo-desorption coefficient. Our little experience on fabricating copper ducts on a large scale, however, was one problem compared to aluminum case.

We have made a trial model of copper duct to see the capability of the existing fabrication technique and to get a base for the final duct design. The thermal gas desorption rate and the photon stimulated gas desorption (PSD) rate were measured using the model duct. The fabrication was successful but large gas desorption rates were observed. We outline here the fabrication of the copper duct and report the experimental results.

II. FABRICATION OF A COPPER DUCT

A plan of the copper duct manufactured is presented in Figure 1. The duct consists of a beam channel, a pump channel and a cooling channel like a conventional beam

duct. The duct is straight and the total length is 3.7 m. The aperture of the beam channel is 100 mm in width and 50 mm in height. The thickness of the duct wall is 6 mm. The pumping channel has three pumping ports for lumped ion pumps. The duct material is the Class 1 OFC (Oxide Free Copper) provided from HITACHI Cable, Ltd. The flanges are made of 304 stainless steel.

Each channel was independently extruded at first in a circular pipe with a proper size and then extracted to its design shape. They were welded each other by EBW (Electron Beam Welding). The length of the beam duct was limited by the volume (length) of EBW chamber at present. Due to the small total input power of EBW, the hardness of copper was not degraded except just near the welding point. The bend and the twist were also both less than 0.5 mm/m. The flanges were welded by TIG welding in Argon atmosphere inserting Inconel-625 between OFC and 304 stainless steel.

Since we had no definite idea to specify what surface treatment is the most appropriate for a copper beam duct, no special treatment was tried to the duct except for ultrasonic cleaning in a freon bath to get reference data for future studies. The roughness of the surface is less than $10 \mu\text{m}$, but we can see many narrow lines on the surface along the duct marked in the extraction process.

After assembly, the duct received two cycles of baking up to 180°C and no air leak was detected. Constructing the vacuum system of copper beam duct has basically no technical problem.

III. MEASUREMENTS OF GAS DESORPTION RATES

A. Thermal gas desorption

The duct was evacuated by a turbo-molecular pump (300 l/s) and two ion pumps (130 l/s) combined with NEG pumps (100 l/s). Two B-A gauges measured the total pressures in the beam channel and the pump head. The pump down curve is shown in Figure 2. After a baking at 150°C for 48 hours, the pressure reached to about 1×10^{-10} Torr at the beam channel in N_2 equivalent. The main residual gas was H_2 . Ar was hardly detected. Assuming the total effective pumping speed of 300 l/s at the base pressure, the thermal gas desorption rate was calculated as about 1.5×10^{-12} Torr. $l/(s \cdot \text{cm}^2)$. This desorption rate is not so good value as a vacuum chamber. Carefully treated vacuum chambers of aluminum alloy or stainless steel give the thermal gas desorption rate in the order of or less than 10^{-13} Torr. $l/(s \cdot \text{cm}^2)$.

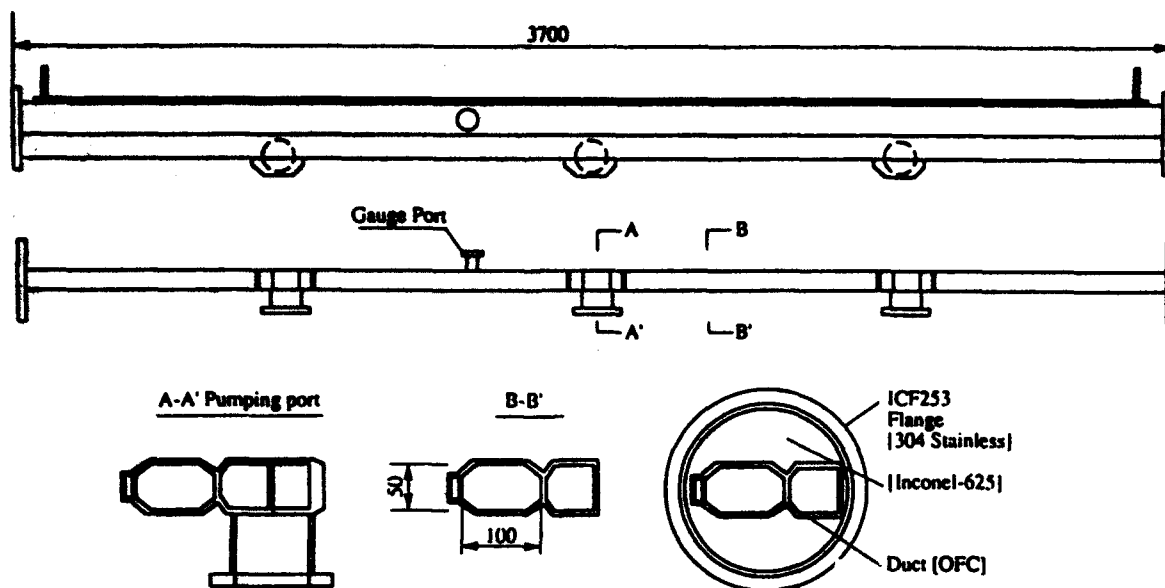


Figure 1. Plan of the copper duct.

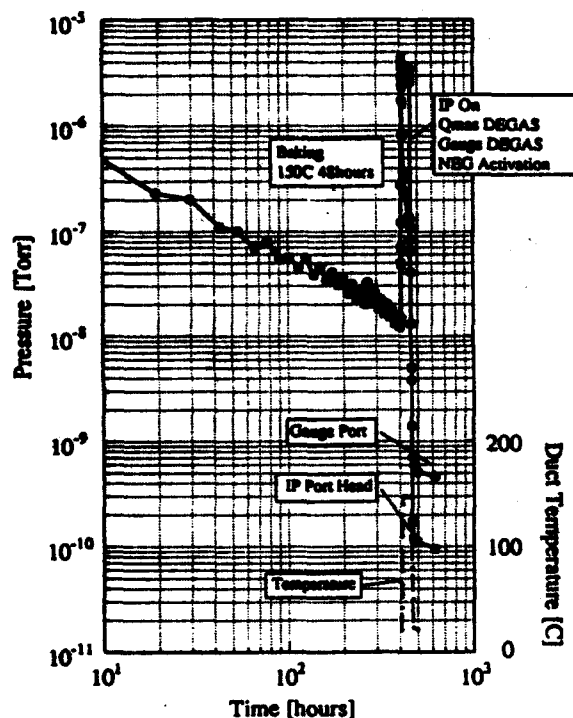


Figure 2. Pump down curve of the copper duct.

B. Photon stimulated gas desorption (PSD)

The photon stimulated gas desorption rate was measured using the synchrotron radiation (SR) from the TRISTAN Accumulation Ring (AR) having a critical energy of 26.3 keV. Schematic diagram of the beam line is shown in Figure 3. The duct received the photon directly from the source at a 14.8 mrad incident angle. The x-y slit limited the photon beam vertical and horizontal opening

angle to 0.50 mrad and 2.4 mrad, respectively. About 3 m out of 3.7 m long duct was directly irradiated by the SR with a height of about 8 mm. The incident photon flux N_p per beam current per second was about 1.54×10^{15} photons/(mA.s). The total pressures and partial pressures at the upstream and downstream side of the orifice (O_r) were measured by two extractor gauges (EXG1 and EXG2) and two quadrupole mas analyzer (QMA1 and QMA2), respectively. The photo-desorption coefficient η_i for i -th gas species is given by

$$\eta_i = 3.3 \times 10^{19} \frac{C_i \Delta P_i}{N_p I_b} \quad \text{molecules/photon,}$$

where ΔP_i is the pressure difference between the upstream and downstream side of the orifice in Torr, C_i is the conductance of the orifice (50 mm wide \times 12 mm height) in l/s and I_b is the beam current in mA. The downward beamline from the valve GV2 was baked up to 130°C for 48 hours. The base pressure of the copper duct was about 1×10^{-9} Torr.

Main gases desorbed was H_2 , CH_4 , CO and CO_2 . The η for these gas species as a function of photon dose are presented in Figure 4. The η at the initial stage is in the order of 10^{-2} molecules/photon. The η decreases with photon dose with an average slope of $-\frac{2}{3} \sim -1$ beyond 1×10^{20} photons/m. The desorbed gas reached up to 1 Torr. l at 1×10^{21} photons/m.

The η and the total quantity of desorbed gases are larger by about one order of magnitude than the data of copper ducts reported so far by O.Gröbner et al.[2], A.G.Mathewson et al.[3], R.Gavaggio et al.[4] in DCI, and H.J.Halama et al. [5] in NSLS, and almost the same order as those of aluminum-alloy ducts [3,4,5]. All of copper duct referred, however, had received chemical etching be-

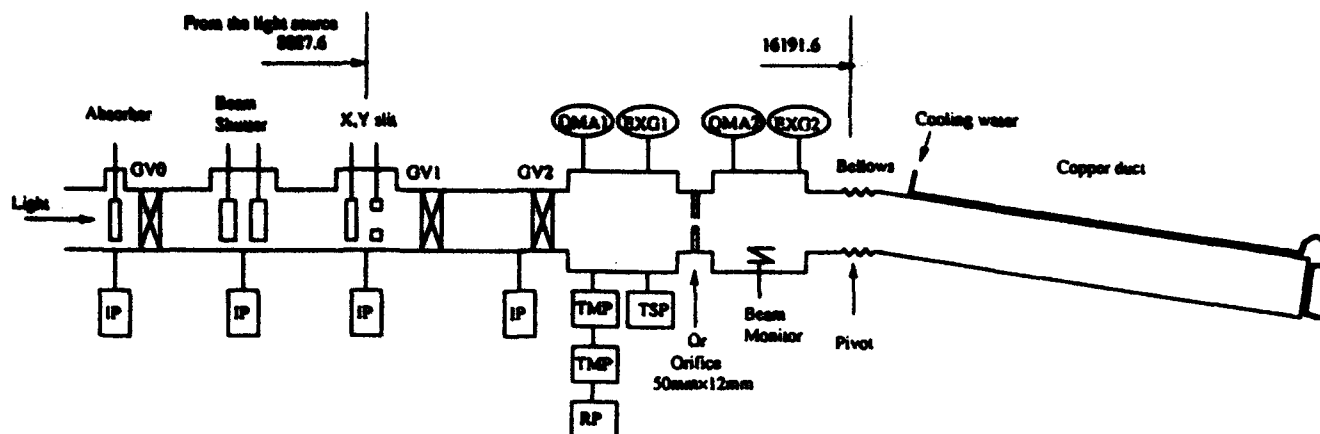


Figure 3. Schematic diagram of the beamline for PSD measurement.

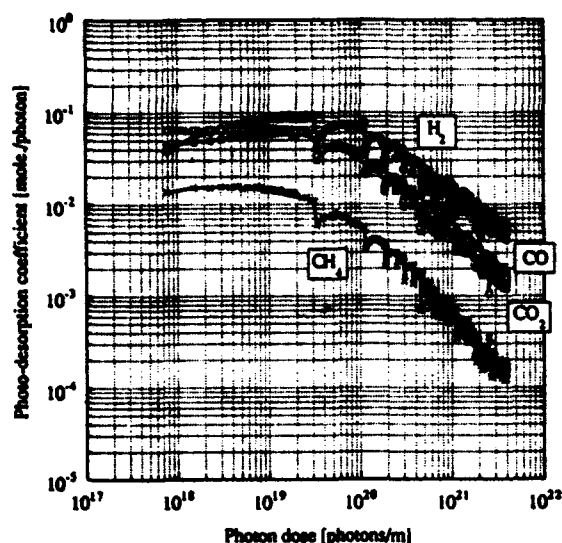


Figure 4. Photo-desorption coefficients for H_2 , CH_4 , CO and CO_2 as a function of photon dose.

fore the experiments. The large gas desorption from our model copper duct, therefore, will be due to the insufficient surface treatment.

IV. SUMMARY

A trial model of copper duct was fabricated with no mechanical problem. Constructing the vacuum system based on copper beam duct for the KEK B-Factor has no technical problem. The measured gas desorption rates were not good due to the insufficient surface treatment. Chemical surface cleaning will decrease the gas desorption rates. We are now planning to make several copper ducts

with different surface treatments and to compare the η this year.

ACKNOWLEDGMENTS

The authors would like to thank Prof. S.Kurokawa for his continuous encouragement and the staffs of the TRISTAN Vacuum Group for their technical help in the experiments. They would thank Mr.M.Katane, Mr.T.Torii, Dr.S.Kakiuchi, Dr.T.Kobari (Hitachi Works, Hitachi, Ltd.) for their help in designing and fabricating a trial copper duct.

REFERENCES

- [1] Y.Suetsugu and K.Kanazawa, "Vacuum Design for KEK B-Factor", *Proc. Int. National Workshop on B-Factor: Accelerator and Experiments*, KEK, Nov.17-20, 1992.
- [2] O.Gröbner, A.G.Mathewson and O.C.Marin, "Extended Study of Photon Stimulated Gas Desorption from OFHC Copper by 3.75 keV Critical Energy Photons", *EPAC-92*, Berlin, 1992.
- [3] A.G.Mathewson, O.Gröbner, P.Strubin, P.Marin and R.Socshet, "Comparison on Synchrotron Radiation Induced Gas Desorption from Al, Stainless Steel and Cu Chambers", *American Vacuum Society Series 12*, 325 (1990).
- [4] R.Gavaggio, A.G.Mathewson, P.Strubin and P.Marin, "Photon Induced Gas Desorption from A Cu Test Chamber", *Vacuum Technical note*, CERN, 2nd Nov., 1990.
- [5] H.J.Halama and C.L.Foerster, "Comparison of Photo-desorption Yields from Aluminum, Stainless and Cu Plated Beam Tubes", *Vacuum 42* No.3, 185 (1991).

FNAL* Main Injector Quadrupole Vacuum Chamber

Larry Sauer
Fermi National Accelerator Laboratory*
PO Box 500, Batavia, IL 60510 USA

Abstract

Recycling the existing Main Ring quadrupoles presented engineering with an array of technical and environmental problems. The solution addressed the higher Main Injector vacuum requirements, maximization of the horizontal aperture, longitudinal space limitations, magnet recycling time constraints, tooling costs, and minimizing radioactive debris. Inserting a newly processed oval tube inside the existing star shaped tube eliminated the need to separate the welded and epoxied half cores, thus satisfying all the criteria.

I. INTRODUCTION

Within the existing Main Ring enclosure some 200 quadrupoles provide focusing functions for the 22 year old synchrotron. Currently 127 of these quadrupoles are scheduled for installation into the Main Injector Ring. All Main Ring quads possess a star shaped vacuum chamber formed from 304 stainless steel sheet which is sandwiched between welded half cores and are epoxy vacuum impregnated into place during the coil impregnation process. The vacuum chamber stainless is unprocessed except for superficial cleaning at the time of fabrication and at magnet installation. Today, after two decades of pumping, the average Main Ring vacuum pressure is approximately 8×10^{-8} Torr while the desired Main Injector pressure is 1×10^{-8} Torr. In an effort to achieve the desired Main Injector pressure rapidly (on the order of six months) the newly fabricated dipoles will contain an oval chamber made of electropolished and chemically cleaned 316L stainless steel assembled using established ultra high vacuum techniques. Therefore it becomes important to "do something" with the quad chambers to upgrade their vacuum performance nearly a Torr-decade.

II. CONSTRAINTS

The Main Ring is scheduled to provide protons to the Tevatron until Main Injector civil construction begins at the RF hall. At this time the final Main Ring shutdown will begin and is scheduled to conclude seven months later. This time frame provides ample time to remeasure the 127 quads and perform cosmetic upgrades to each magnet prior to installation into the Main Injector Ring. However, it is impossible to separate the half cores, "burn" the epoxy, remove the vacuum chamber, rewrap the coils, assemble and remeasure the magnet with a new vacuum chamber installed within the time allowed. Additionally, a substantial amount

of radioactive debris would be generated causing severe control and disposal problems.

In principle, the existing quad chambers could be salvaged by cutting the end flanges from the tubes and creating equipment and procedures required to polish and clean the tubes within the magnets. Once again radioactive debris would be generated in the form of stainless chips (not particularly severe) and many gallons of cleaning solutions, alcohol, and distilled water. In all probability this procedure would result in chambers somewhat inferior to the newly fabricated dipole chambers due to the limited space and awkward length to cross section ratio.

Finally, it has been determined that the horizontal and vertical apertures in the new dipoles are also sufficient for the quadrupoles.

III. SOLUTION

The solution chosen which satisfies all the constraints also is the most economical. It is planned to slip a new tube, identical in cross section to the dipole tube, through the existing star shaped chamber after the Main Ring style flanges have been removed. The economy results from purchasing additional lengths of the dipole tube which incurs no additional tooling or set up costs. After the tube has been positioned, aligned, and welded within the quad, one end flange is added prior to final leak check. It needs to be mentioned that the new quad chamber will also house a beam position monitor approximately one meter long. The final cross sectional configuration is shown in Fig. 1.

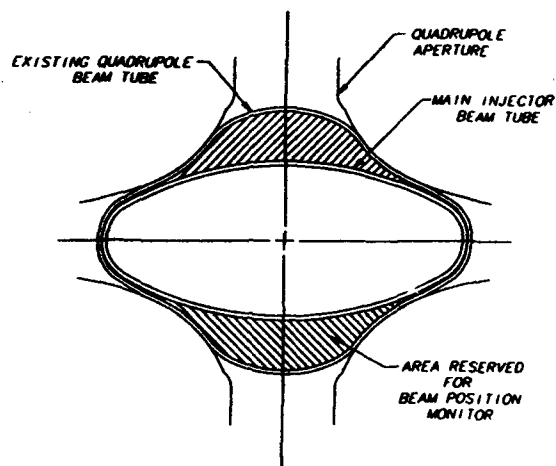


Fig. 1

*Operated by the Universities Research Association, Inc. under contract with the U. S. Department of Energy.

FNAL* Main Injector Dipole Installation Equipment

Keith Moravec, Fritz Lange, Jerry Leibfritz, Larry Sauer
Fermi National Accelerator Laboratory
P.O. Box 500, Batavia, IL 60510 USA

Abstract

The Main Injector (MI) construction schedule requires the use of several magnet installation vehicles concurrently. During the interval when MI dipoles are to be installed, both existing magnet installation vehicles will be used in the Main Ring (existing accelerator) to support machine operations. This necessitates the development of a new magnet installation system designed for use with the MI dipole magnets. Because all magnet installation vehicles will be available for MI installation following the decommissioning of the Main Ring, the system should be as inexpensive as possible. The chosen solution for MI dipole magnet installation is as follows: a tugger / towmotor (the Tevatron vehicle could be drafted) will tow the Main Injector dipoles to their installation site on dollies, then lift them slightly from the dollies and move them onto their magnet support stands.

I. INTRODUCTION

Main Injector dipole installation will be a refined version of the technique developed for the installation of several large magnets in P - bar. This is in contrast to the traditional magnet installation equipment currently used in the Main Ring and Tevatron. The traditional magnet installation vehicles are elaborate, self contained units with the ability to tow the magnets through the tunnel and place the magnets on their magnet support stands. The MI dipole installation equipment is not self contained, and requires two separate systems. A tugger and dolly combination will be used for towing the dipole magnets through the MI tunnel to the installation site. A pair of specialized machines will be used for lifting the magnet from the dollies and moving the magnet onto the magnet support stands.

The spatial considerations of the magnet installation were the driving factors in the magnet installation plan and installation machinery design. The primary physical parameter to be considered is the magnet size. The MI dipole magnets will be built in 20 and 13 foot lengths. A common cross section, 22 in. tall and 32 in. will be used. The larger magnets will weigh 20 tons. In addition, the access to the tunnel is restricted. Only the main service building has the capacity to lower the magnets from ground level into the tunnel. The tunnel circumference is 10,000 feet. Therefore, the maximum distance any single magnet must be moved is 5000 feet.

*Operated by the Universities Research Association, Inc. under contract with the U.S. Department of Energy.

Based upon the magnet installation requirements and parameters described above, a magnet installation plan and installation equipment design have been developed. They have been developed to be user friendly. In addition, they have been designed to be durable and withstand heavy use during the 28 month magnet installation period, and light use for the remainder of the Main Injector's operational life.

II. INSTALLATION SCENARIO

The most challenging aspect of the Main Injector dipole magnet installation is working within the physical parameters of the tunnel. Careful planning is required because of the small tunnel dimensions. Therefore, a detailed plan for the installation of the MI dipole magnets has been developed and is outlined on the following page in six different steps.

In step 1, the magnet installation equipment is shown in its storage location underneath two 20 foot dipole magnets. When stored, the magnet installer will not block the MI tunnel aisle. This is shown in Fig. 1 (Note that the cross hatched rectangles represent the magnet mover rails.)

In step 2, the magnet installer must be removed from its storage location underneath the dipole magnet and rolled into the tunnel aisle (see Fig. 2)

In step 3, the dipole magnet will be towed through the tunnel aisle to the installation site by the tugger. The magnet is supported by two dollies. See Figure 3 for illustration.

In step 4, the magnet installers are moved into position as shown in Figure 4. The magnet installers can be slid underneath the dipole magnet because of their low profile with the hydraulic jack in the collapsed position.

In step 5, the dipole magnet is lifted, moved over the magnet support stands and then lowered onto the stands. See Figure 5 for illustration.

In step 6, the second dolly is temporarily attached to the first dolly and towed back to the main service building to pick up another magnet. Also, the rails are stored underneath two of the 6m dipoles to allow normal operations to continue in the tunnel.

III. MAGNET INSTALLER DESIGN

The sole function of the magnet installer is to lift the magnet off the dollies and then move the magnet to the magnet support stands. The design shown in Figure 7 is the current version of the magnet installer. It is approximately 100 in. long, 29 in. wide, and 13 in. tall. Simplicity and ease of operation are the primary design features. All three primary axes of the magnet installer are capable of controlled

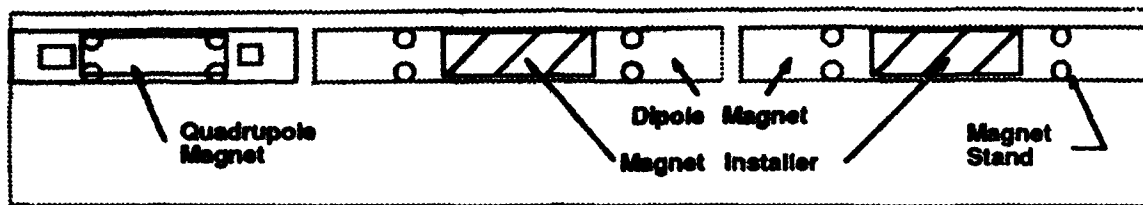


Figure 1 Magnet Installation Step 1

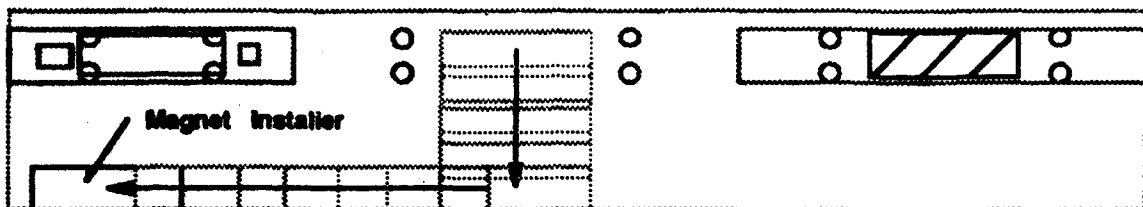


Figure 2 Magnet Installation Step 2

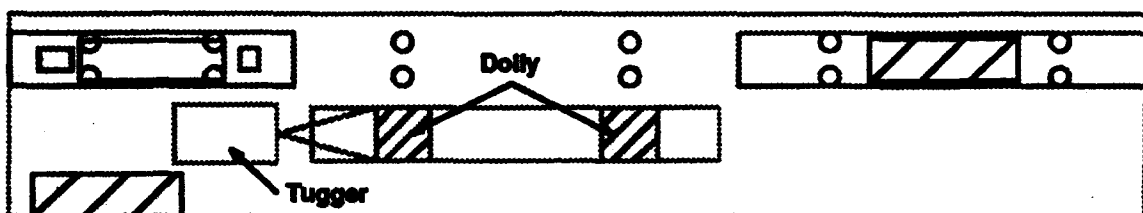


Figure 3 Magnet Installation Step 3

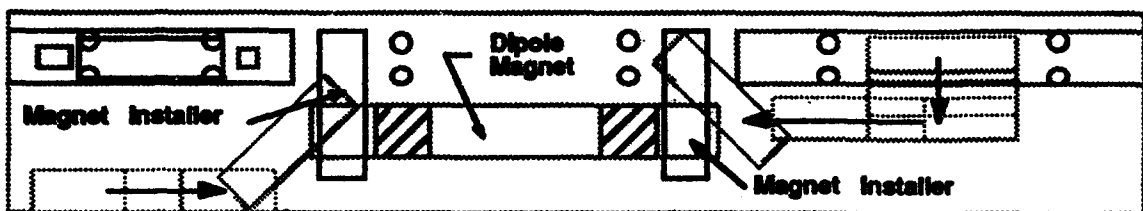


Figure 4 Magnet Installation Step 4

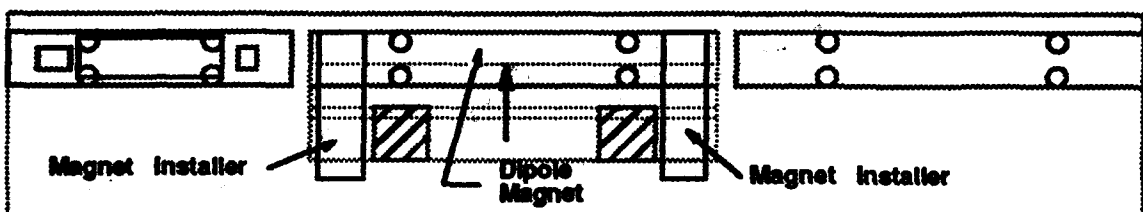


Figure 5 Magnet Installation Step 5

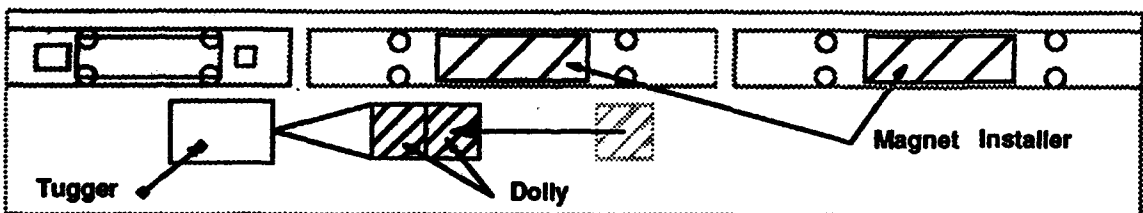


Figure 6 Magnet Installation Step 6

movement through hydraulic cylinders. Because the two magnet installers are used in coordination with each other, the potential for binding of the bearings is high, should the magnet installers be even slightly skew. Therefore, only one of the two magnet installer rails will have position control along the z - axis of the tunnel (axis along the particle path), while the other will be free floating to allow the magnet installers to be skew. In addition, the top plate of the magnet installer also serves as a turntable to allow for independent operation of each magnet installer rail.

To allow the magnet installer to be moved easily, it will be equipped with polyurethane wheels with needle bearings. The front wheel is a caster design and the rear wheels turn on an axle independently of each other. This design allows for good maneuverability of the magnet installer near the installation site as shown in figures 1 - 6 and also provides good towing characteristics.

The torsion spring suspension on the magnet installer is designed to support the installer during towing and to collapse during magnet installation. This allows the magnet installer to be agile under most conditions, however, during magnet installation (when the magnet installer is lifting the dipole magnet) the suspension will collapse and the magnet installer will be supported by the tunnel floor, rather than the wheels. This will increase durability, stability, and allow smaller wheels and box beam to be used in the design.

The hydraulic system consists of a main circuit: pump, reservoir, booster cylinders, and most valves, as an independent assembly. Some of solenoid actuated valves will be located on the magnet installer itself. In addition, a remote control panel, connected to the main circuit by a cable, will allow the operator freedom to position himself in the best place possible to observe the magnet installation. This design limits the number of hydraulic connections to each magnet installer rail to four. A hose recoil mechanism (not shown) will be used to keep the hydraulic lines orderly.

In addition, there will also be an electrical connection to each magnet installer rail for the solenoid activated control valves. As a safety precaution, spring centered solenoid valves will be used so that the magnet will remain idle in case of a power failure.

IV. CONCLUSION

A functional magnet installation plan and magnet installer have been developed to meet the requirements of the Main Injector dipole magnet installation. The magnet installation plan and equipment design are both economical and user friendly without sacrificing safety or installation efficiency.

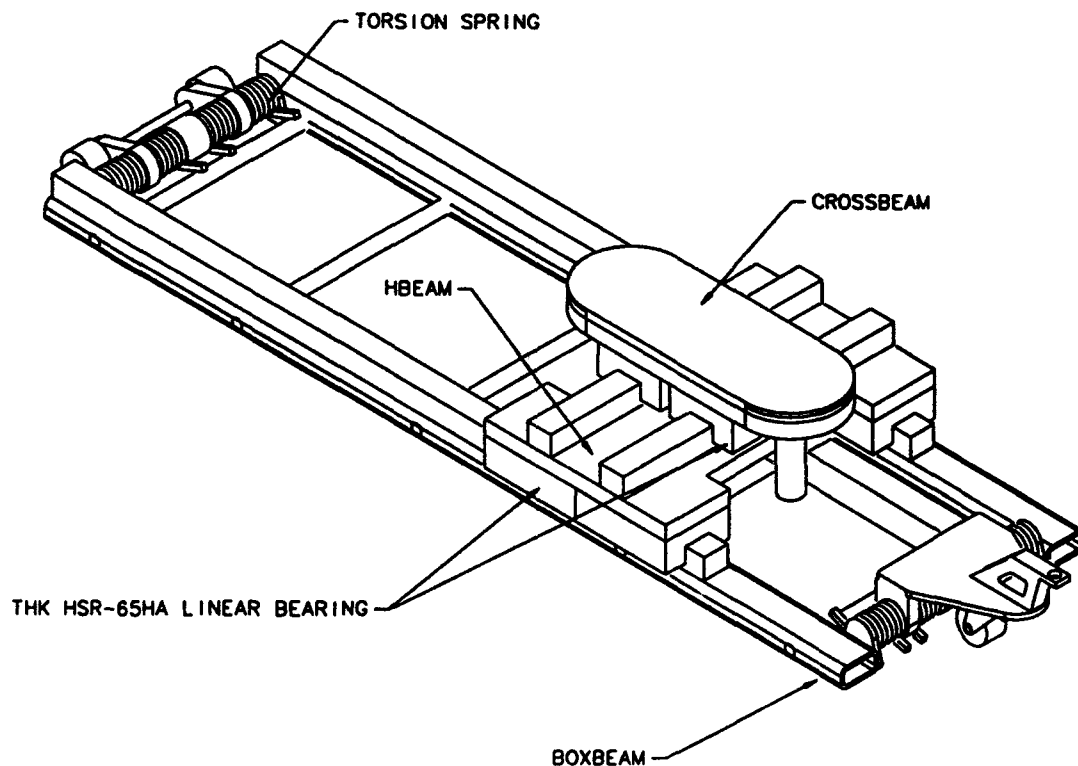


Figure 7 Isometric View of Magnet Installer

Solvents and Pumpdown Characteristics of SRF Nb Cavities*

M. G. Rao, P. Kneisel and H. F. Dylla

Continuous Electron Beam Accelerator Facility

12000 Jefferson Avenue, Newport News, Virginia 23606 USA

Abstract

High-performance superconducting radio frequency (SRF) cavities are placed under UHV and low particulate conditions when they go through the surface treatment process, and are kept under these conditions permanently thereafter, both before and during use in the accelerator. The outgassing of the gasket material in the gate valves and the outgassing of the solvents that come in contact with the gasket and the cavity surfaces determine the ultimate pressure that can be obtained in the cavity. A systematic study of gaskets and various solvents was undertaken in order to understand the conditions that lead to a low ultimate pressure in a short period of time. The results with Kalrez, Viton O-rings and solvents like methanol, acetone, isopropyl and freon will be presented in this paper. Also, we discuss the effect of a slow or fast initial pumpdown in order to prevent the settlement of particulates due to condensation.

I. INTRODUCTION

Superconducting accelerator cavities made from high-purity niobium are presently limited in their high-gradient performance by either field emission loading or thermal-magnetic breakdown at microscopic defects. It is generally accepted that field emission is either caused by artificial contamination of the sensitive cavity surfaces due to handling and assembly procedures or by intrinsic emitters embedded in the surface. There are in addition indications that the condensation of residual gases in the evacuated cavities can contribute to field emission loading.

Several precautions have been taken at CEBAF to minimize the potential for artificial contamination [1]: CEBAF's basic building block—the cavity pair—consists of two 5-cell 1500 MHz cavities, which are hermetically sealed when assembled in a class 100 clean room after chemical surface treatment and final solvent rinsing.

During this assembly procedure two ceramic rf windows are mounted onto the fundamental power coupling waveguide, the beam-pipe ends of the cavity pair are closed off with high-vacuum O-ring sealed gate valves and the higher-order-mode couplers are attached to the HOM-waveguide openings. The outgassing of all these components and in particular the outgassing of the O-ring materials that come in contact with solvent vapours or solvents used for final rinsing of the cavities and the cavity surfaces themselves determine the ultimate pressure attainable in the cavity pair.

Results of a systematic study [2] of the outgassing characteristics of O-ring materials such as Kalrez and Viton and solvents such as methanol, acetone, isopropyl and freon

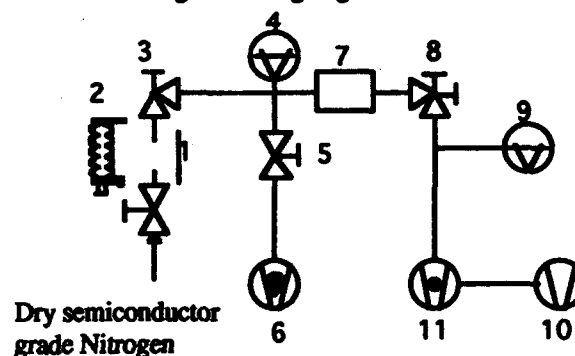
are reported in the following sections.

In addition we have investigated the influence of the solvents, viz. methanol and isopropyl, on the removal of water from the 5-cell Nb cavity. Further, the effect of pumpdown speed during the initial evacuation process of the cavities on particulate generation (which is well known in the semiconductor industry) is also studied.

II. EXPERIMENTAL SETUP

A. Outgassing Experiments

For the pumpdown characteristics studies a small UHV system as shown schematically in Figure 1 was assembled. A 50 l/sec turbomolecular pump was used for a short time for rough pumping the UHV system, consisting of a 60 l/sec star cell ion pump (Varian), a residual gas analyzer (RGA, Hiden) and a standard UHV nipple as the vacuum chamber holding the O-ring. At the beginning of each test, the UHV system was baked at 425 K for 12 hours to reach an ultimate pressure of $p \sim 2 \cdot 10^{-10}$ torr as indicated by the RGA with the dominant residual gas being H_2 . Prior to loading the chamber with the O-ring material, it was vented with dry 99.999% semiconductor grade nitrogen gas.



1. Nipple 2. Cavity 3, 5. All metal valves 4. RGA
 6. Ion pump 7. Particle counter 8. Two stage valve
 9. Ion gauge 10. Rotary pump 11. Turbomolecular pump
- Figure 1. Schematic of experimental setup.

B. Cavity Pumpdown and Particle Generation Experiments

For this type of experiments the same arrangement as shown in Figure 1 was used with the exception that a 5-cell cavity was the vacuum chamber and a 170 l/sec turbomolecular pump replaced the smaller pump.

* This work was supported by DOE contract DE-AC05-84ER40150.

In the particle generation experiments the pumping speed was regulated by a two-stage valve (HPS) consisting of a small by-pass valve made out of an aperture and a regular valve. A commercial particle detection system (TSI, Inc.) was placed between the cavity and the pump to monitor the amount of particles generated during evacuation.

III. RESULTS AND DISCUSSION

A. Kalrez and Viton O-Rings

A virgin Kalrez O-ring was placed in the nipple and the UHV system was pumped down to $2 \cdot 10^{-5}$ torr with the turbo pump, and the getter-ion pump was turned on after isolating the turbopump. On reaching a pressure of $1 \cdot 10^{-9}$ torr, the O-ring was removed from the nipple and soaked in methanol for 5 minutes. The pumpdown procedure was repeated with the methanol-soaked O-ring. The same procedure was also adapted with the Viton O-ring. Figure 2 shows the pumpdown characteristics of the virgin and methanol-soaked O-rings. The same ultimate pressure was obtained with both the Kalrez and Viton O-rings after 50 hours of pumpdown. The residual spectra for each O-ring indicate that besides H_2 , fluorine is the major residual component for Kalrez, and water in the case of Viton.

The methanol soaked O-rings were not baked during the first 50 hours of pumpdown except for one minute of hot air exposure onto the nipple. A final pressure of $1 \cdot 10^{-9}$ torr was reached with the Kalrez O-ring in 50 hours, whereas the Viton O-ring needed to be baked for 2 hours with 425 K hot air exposure onto the nipple to reach an ultimate pressure of $2 \cdot 10^{-9}$ torr in 175 hours. The RGA spectra indicate that methanol is the major residual gas component besides hydrogen with both of the O-rings. Fluorine is still the dominant residual gas in the case of Kalrez and water in case of the Viton. Since surface areas of both the O-rings are similar ($\sim 30 \text{ cm}^2$), one can directly compare their pumpdown characteristics. It appears that the Viton O-ring absorbs larger amounts of methanol and it needs to be baked out to desorb methanol. So the pumpdown characteristics of Kalrez are superior to those of Viton gasket material.

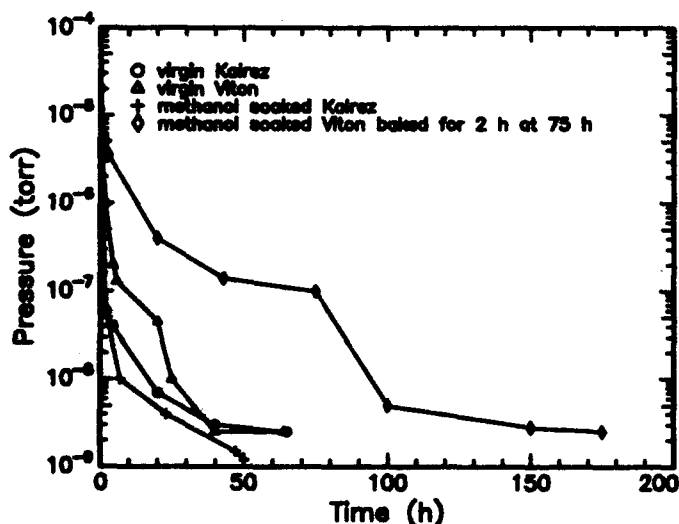


Figure 2. Pumpdown characteristics of O-rings.

A similar procedure was carried out with ethanol-soaked Kalrez and Viton O-rings, but the pressure in the system remained at $1 \cdot 10^{-8}$ torr even after pumping for a month. Similar results were obtained with freon-soaked O-rings. It appeared at this time that the slow outgassing of ethanol and freon themselves may be the reason for such results. So it was decided to carry out the pumpdown characteristics of the solvents in the absence of any gasket material.

B. Solvents

As usual, the UHV system was baked to reach a pressure of $2 \cdot 10^{-10}$ torr and the nipple was vented with the dry nitrogen. The inner surface of the nipple was wiped with a clean cloth wetted by the solvent under investigation. The pumpdown followed the same procedure as described above. Figure 3 shows the pumpdown characteristics of the solvents methanol, ethanol, isopropyl alcohol, acetone and freon. As can be seen the pumpdown times for methanol and acetone are much shorter to reach a pressure of $2 \cdot 10^{-9}$ torr compared to ethanol, isopropyl alcohol and freon. In fact, it is very difficult to reach ultimate pressures of less than 10^{-8} torr with ethanol, isopropyl alcohol and freon without a proper bake-out.

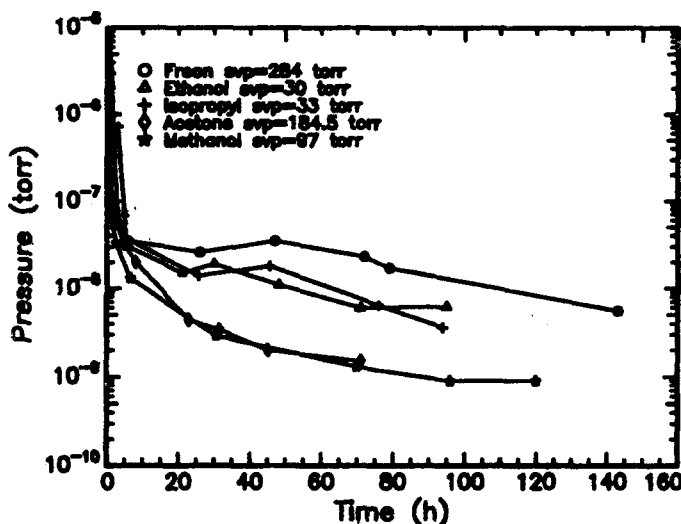


Figure 3. Pumpdown characteristics of solvents [saturated vapor pressure at $20^\circ\text{C} = \text{svp}$].

C. Cavity Pumpdown

At CEBAF a 5-cell Nb cavity is first rinsed with ultrapure water after the chemical surface treatment followed by a twofold solvent rinse with methanol or isopropyl alcohol to remove the water from the surface. Two cavities are assembled into a pair with all the auxiliary components and pumped down with a turbo pump for a period of 15 minutes; then further pumping is done with ion pumps. This procedure was adopted to minimize the contamination of the cavity surfaces with hydrocarbons from the pumping system. Figure 4 shows the partial pressure (PP) of water in a 5-cell cavity as a function of pumpdown time with the turbo pump and ion pump systems for methanol and isopropyl alcohol solvent rinses. The turbo pump system reduces the PP of water to the 10^{-8} torr range within a period of 7.3 hours. The PP of water in the methanol-rinsed cavity is lower than the isopropyl-

rinsed cavity. In the case of the ion pump pumped cavity the pressure never improves to the 10^{-8} torr range even after pumping for more than 13 hours. Again the PP of water is higher in the case of the isopropyl-rinsed cavity.

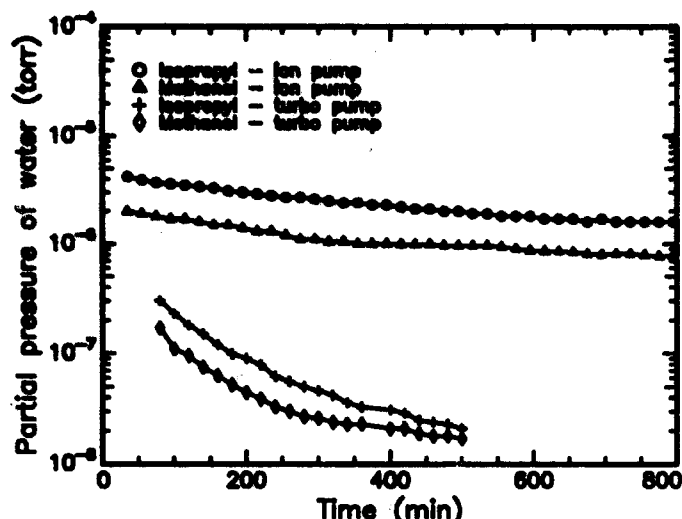


Figure 4. Partial pressure of water in a 5-cell cavity.

D: Particle Generation

The artificial contamination of the sensitive cavity surfaces during the handling and assembly procedures is recognized as one of the mechanisms responsible for the field emission loading of the cavities, despite precautions like assembly in a class 100 clean room and the use of high-purity chemicals and solvents.

Entrainment of residual particulates from condensation of solvents has been identified as the major source of contamination in the silicon wafer processing technology [3,4] mainly originating from particulate-laden process vacuum chambers and load locks.

Since the cavity surfaces are chemically cleaned and rinsed with very clean solvents, the reentrainment of particulates is drastically reduced in comparison. Furthermore the cavities have low relative humidity conditions due to the rinsing with solvents, and the formation of liquid particles due to fast initial evacuation is reduced.

Measurements have been done to verify these assumptions: the number of particles measured during the unthrottled pumpdowns is less than 4 per 25 liters of solvent vapour removed from the cavity pair. Further, this fast (2 minutes to reach 10^{-2} torr from atmospheric pressure) removal of solvent from the cavity surfaces is expected to drag away the remaining water molecules from the surface, leaving a drier surface behind. Slow (20 minutes to reach 10^{-2} torr from atmospheric pressure) pumpdowns through the orifice appear to have produced more particles due to the expansion and also seem to have inhibited the removal of water from the cavity surfaces in a short period.

IV. CONCLUSIONS

In the absence of baking, solvent-soaked Viton O-rings are prolonging the pumpdown time to reach lower pressures in comparison to Kalrez O-rings. In addition, pumpdown times are much shorter for methanol and acetone compared to ethanol, isopropyl alcohol and freon for achieving low pressures. Methanol removes water more effectively from the cavity surfaces in comparison to isopropyl alcohol, thereby facilitating better cavity pumpdowns with ion pumps to lower pressures. Neither slow nor fast pumpdown of the cavities contributes to particulate reentrainment or particle generation in cavity pairs. However, fast pumpdown is likely to remove more water from cavity surfaces.

V. ACKNOWLEDGMENTS

We would like to thank J. Mammosser and K. Yopp for their help with cavity rinsing and the drawing of the sketch respectively.

VI. REFERENCES

- [1] P. Kneisel *et al.*, "Superconducting Cavities from High Thermal Conductivity Niobium for CEBAF," Proc. of the Conf. on Electron Beam Melting and Refining, Reno 177 (1990) Bakish Materials Corporation.
- [2] M. G. Rao, "Outgassing of Kalrez, Viton O-rings and Solvents," CEBAF Report TN0185 (1989.)
- [3] John F. O'Hanlon, "Advances in Vacuum Contamination Control for Electronic Materials Processing," *J. Vac. Sci. Technol. A5*, 2067 (1987).
- [4] Degang Chen *et al.*, "Vacuum Particle Generation and Nucleation Phenomena During Pumpdown," *J. Vac. Sci. Technol. A8*, 933 (1990).

Leak Checker Data Acquisition System

John Payne, Jeffery Gannon

SSC Laboratory¹, Accelerator Systems Division
Electrical Engineering Department
2550 Beckleymeade Ave. MS 4004
Dallas, Texas U.S.A. 75237-3946

Abstract

A portable, high speed, computerized, data logging system. The primary function of this system is to collect 'Helium Readings' from mass spectrometers. This system monitors up to 14 mass spectrometers, operating from as far away as 1 kilometer, or clustered to isolate a helium leak within 20cm. Data logging enables technicians to witness the flight of the helium through the magnet string by a graphical plotting of every channel within microseconds of when the helium was released into the vacuum. The readings are used to locate vacuum leaks and provide acceptance testing of the vacuum system for a string of superconducting magnets. The secondary functions of this system are the documentation of test conditions, archiving data sets for future reference, and providing a real-time display of all channels as the string of magnets approach critical test conditions.

I. INTRODUCTION

By far the most time consuming aspect of magnet installation is leak hunting. In a completed machine (i.e. Tevatron²) there are 1,200 cryogenic interfaces. A typical interface consists of a beam tube seal, several liquid helium and nitrogen connections, and a room temperature insulating vacuum seal. Each of the cryogenic seals must be able to be verified at room temperature with sufficient sensitivity to assure that it will not leak liquid helium. On the average it takes only one-half hour to physically place a magnet, one hour to align it, and four man-hours to complete an interface. However, it takes a total of 40 to 50 man-hours to install and leak check each one. A pumpout port is supplied on each magnet, near the downstream interface of that magnet. A helium leak detector is put on each one of the four available interfaces and on the beam tube, and the cryostat is pumped down. The first pumpdown on a fresh cryostat typically takes 3 hours to reach a pressure sufficiently low so that the roughing pumps can be valved off and the leak detector opened fully to the cryostat. When the leak detector is able to be put on its most sensitive scale, leak hunting can proceed.

Previous systems used individual chart recorders to record the results of the leak check process. The scale of the SSC project required a computerized system for recording, analyzing, and documenting the leak check process. Existing commercial systems were not able to meet the requirements of this process.

This system utilizes digitizers daisy chained with a single twisted pair cable. A portable computer connects to this system and both controls and monitors the leak check process. The digitizers do not require special addressing, setup, or field adjustments as existing systems do. The system is user friendly and requires minimal training for use by technicians.

The computer used for this system, is a portable IBM-AT type clone. This PC is equipped with 4 Mb of RAM, 120 Mb hard disk, VGA color (flat screen) monitor, math co-processor, mouse, and 5 I/O expansion board slots. One of these I/O

slots contains the data acquisition board custom designed for the Leak Checker System. The leak checker software can run on a PC without the I/O interface installed. This feature allows the engineers to examine the data files on a different computer, from the computer used in the test. For instance the data from a recent test can be up-loaded, from down in the accelerator tunnel, across a network, to an office computer. Analysis of the data can be done in an area where the archived files are located.

II. THEORY OF OPERATION

The 'Recorder Output' on the leak detector is an analog output that would typically be connected to a multichannel chart recorder. This output is a very small voltage (0 to -50mV) and the great distances between leak detectors means that leak detector data could be distorted or attenuated depending on the chart recorder location for each test. Since these chart recorder printouts have been archived as a permanent record for acceptance testing, retesting at a later date could indicate slightly different characteristics for a section of the machine. This new system for monitoring the leak detectors replaces the multichannel chart recorder with a computer. The 'Recorder Output' of the leak detector gets digitized right at the leak detector and is transmitted to the computer on a serial data bus. The digitizer module has a direct analog input for monitoring any make of leak detector. The leak detectors currently in use at the SSC Laboratory have an auto-ranging feature and have been modified for this new system, to transmit the range setting associated with the digitized 'Recorder Output'.

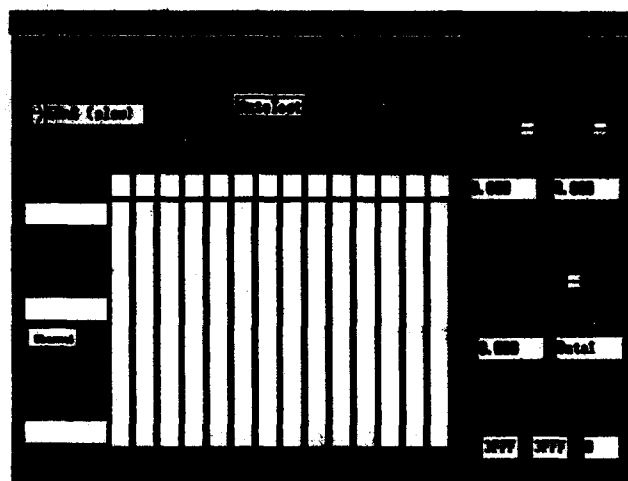


Figure 1

The application program uses three basic screens to work in. The main program screen will only be displayed if the I/O expansion board is present in the computer. Otherwise the program jumps right into the 'XYPlot' screen. The 'notes' screen can be launched from either the 'main' or the 'XYPlot' screen. Each of the three screens share a common menu

selection bar along the top of the monitor. These menu items will display help messages, open other screens, exit from screens to previous screens, invoke screen dumps, and handle the chores of printing and copying the data files.

Leak Detector monitoring begins with the screen shown in figure 1. This is the main screen of the application program. From this screen the operators can monitor the status of all the leak detectors simultaneously with incoming data displayed in the thermometer like rectangular windows. These windows represent the 'fine' measurement of the leak detectors, and corresponds to an analog meter movement. As the magnitude of the signal from the leak detector increases, the shaded area of the corresponding window rises upward. Directly above each of the 'fine' windows is a 'Range' window that corresponds to the 'coarse' tune of the Mass Spectrometer. This 'coarse' tune is the power of ten multiplier, 0 to -10. To the left of channel 1 the upper and lower range limits are displayed along with the actual value of the selected channel, scaled in the engineering units of the leak detector 'Standard CC Helium per Air Equivalent'. Any active channel can be directly monitored by clicking the mouse on the 'Channel' button.

The FileName 'data1' is the default name for data logging. A unique file name should be selected before enabling the data logging, AutoTest, or ScreenDump features. The 'Files' option in the menu bar opens a window showing all the existing files. Select any one of these or create a new file by entering the new name to use. Any errors with opening 'FileName' results in opening the default 'data1' file. One of the safe guards used to protect archived data is to make them a 'read-only' file. The 'Duration' is an indicator showing the elapsed time while data logging is active.

The ScreenDump feature acts as a frame grabber. Operators can create up to 100 printable files of the computer screens. The files are in the format of the HP LaserJet III printer. An option in the 'Files' menu will sequentially send all these files to the printer.

The sample period control determines how often the leak detector digitizes its reading. The period of the start pulse ranges from 200 μ S (5Khz) to 50mS (20hz). When reading leak detectors spaced 90 meters apart, the suggested period is 50 milliseconds. This value is derived from the fact that helium travels close to the speed of sound in a vacuum, and the time of flight down 90 meters is ~250 milliseconds. The 50mS sample rate provides 5 times over sampling to better capture a difference between adjacent leak detectors. When isolating a leak within a 1/2 cell, if the shortest distance is ~1/3 meter, the time of flight will be 1 millisecond and the suggested sample rate should be 200 microseconds (x5).

The Auto-Test mode causes the system to automatically sequence through a pre-defined number of settings. The AutoTest sequence is as follows:

- 1.) Set the period for 50mSec (Slow).
- 2.) Enable data logging to 'FileName'.
- 3.) Save 20 seconds worth of data.
- 4.) Set the period for 200 μ Sec (Fast)
- 5.) Open the Helium valve.
- 6.) Save 5 seconds worth of data.
- 7.) Close the Helium valve.
- 8.) Set the period for 50mSec (Slow).
- 9.) Save 5 seconds worth of data.
- 10.) Disable data logging.

The Helium Valve selection opens or closes the mass flow control valve. This feature is currently not functional until more information is available on the type of valve to be used for testing. This feature still serves a useful purpose if the valve is controlled manually at or about the time the computer selection is toggled. If data logging is active, an 'OPENED' time stamp is saved every time the switch is toggled, for reference during an XY PLOT.

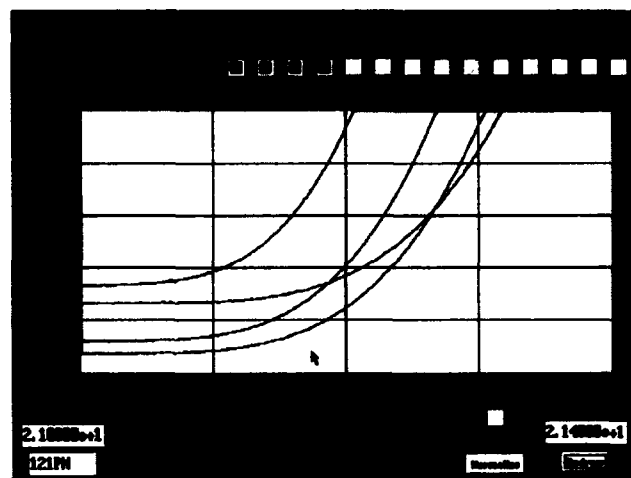


Figure 2

After a leak hunt test, with data logging, evaluating the data begins. The XYPlot selection in the menu bar, will launch a new screen (figure 2) and read the data file named. In this case the FileName is '121pm'. The plot will start at time zero and continue to the end of the data file. The operator can zoom in to any point in time during the plot by manually entering the desired start / stop times. As the plot is expanded the data points will be represented as stars to differentiate between actual data and the connecting lines between points. Along the top of the plot are channel numbers in a color that corresponds to the trace color for that channel. Individual channels can be de-selected in a plot if the data is obscuring other channels, or just want to make screen dumps of some of the channels. The 'Files' option brings up a choice of different files to plot. Operators can view the latest test data or data from previous tests. The 'Helium Valve Status', indicates all the times that the helium was released into the system. The 'Pump Out' display shows all the times that a pump out took place. Each channel can be plotted along with a 'flat base line'. This line helps to determine when the helium reading starts to rise above this point of reference. A rising trend indicates the presence of helium at that point in time. The 'Normalize Point' is the point in time to be used for normalization and for drawing the 'baseline' shown with each channel. By clicking on the 'Normalize' button, the 'Reading' at the 'Normalized Point' in time is subtracted from every 'Reading' in the block (for each channel).

The last program feature is the 'Note Book'. Selecting this launches a new window to display a text file for general purpose documentation. When the data file is re-examined at a later date, observations noted here will be used as a reminder of configurations, and the circumstances of this particular test.

III. HARDWARE DESCRIPTION

The PC initiates an analog to digital conversion by transmitting a START pulse to all leak detectors

simultaneously. The leak detectors send their own data, and all data from the leak detectors further away from the leak detector. Data can travel great distances without degradation. Each leak detector module starts its A/D conversion at the same time ($+2\mu\text{s}$ propagation delays), and it takes 13 microseconds to convert (using an ADC912 12 bit A/D converter). Every interface module takes 8 microseconds, plus 1.5 to 2 μs delay between interface transmissions, to send the data back to the PC. Therefore $13 + (\text{number of modules} * 10) = \text{maximum sample rate}$. The present application program limits the sample period to $200\mu\text{s}$, so all 14 channels can be monitored, at this rate, without concern of losing data. The transmitted serial data consists of 12 bits of digitized analog input and 4 bits of range setting.

The diagnostics area is useful in troubleshooting hardware problems. The computer I/O board has two storage buffers, each buffer is 32k by 8bits, for the incoming data. One buffer is filled with incoming 16 bit data while the other is transferred to the PC main memory by the DMA controller. After the transfer, the role of buffers is switched. The A/D conversions can take place with a precise frequency, while only the average frequency matters when the buffer is transferred. The 'Buff1' and 'Buff2' windows are references to the two memory buffers in the acquisition hardware. The hex values displayed are the number of voltage readings accumulated before they get transferred to the IBM main memory. As the value displayed approaches '0x3FFF' (16k words), an overflow may occur causing a loss of data. The system has been successfully bench tested in the fastest mode ($100\mu\text{s}$) with 7 input channels, and Data Logging enabled, without the loss of data. This $100\mu\text{s}$ mode should never be necessary, it serves only to demonstrate the limits of this system. A screen dump during high speed ($200\mu\text{s}$) transfers of 7 leak detectors showed an average of '0x1730' values accumulated before being transferred to the PC main memory. This indicates the system can easily read 7 leak detectors for isolating a vacuum leak within inches. The 'Errors' window displays the running total of the number of times the number of input channels is not equal to the same number of input channels of the previous block of readings. This can occur if digitizing modules are added or removed while the system is running, or if one of the digitizing modules becomes faulty.

The A/D module dimensions are $12 \times 7 \times 4$ and sits on top of the Mass Spectrometer. The future plans are to mount the digitizer modules inside the Mass Spectrometers to eliminate the extra power requirements and reduce the number of interface cables. Digitizing modules may be configured many ways depending on the test desired. Two bus ports are provided on each digitizing module. Connection must always be made to the 'Primary Bus' port of any sending module. Connection to the 'Secondary Bus' port is an option, for 'close proximity' applications. Any combination of sending modules is allowable, providing that the 'Primary' port of each A/D module is used. For instance if six digitizing modules were operating, each 90 meters apart, and an additional A/D module

was connected to the 'Secondary' port of the 3rd module. That new A/D module would become #4, and what was 4th, 5th, and 6th, would then become 5th, 6th, and 7th modules on the computer monitor.

The asynchronous data transmission on the differential twisted pair is accomplished by sending a synchronizing bit with every data bit. The suggested cable for this system is 'shielded twisted pair' (Belden DataLene), although 'ribbon' cable can be used for short ($<10\text{ft}$) runs. The cable is driven in a differential mode terminated in 100 ohms, with 1500 ohm pull-up and pull-down resistors to compensate for the capacitance of long cable lengths. The bit rate is 4Mhz, and was successfully tested at 8Mhz on 500' (150 meters) of cable. The PC uses a programmable clock timer to transmit the START signal, at a regular interval. After transmitting the START the PC listens for responding leak detectors. Each leak detector module monitors the data bus. If no data is moving in the bus, the module will switch to the receiver mode to wait for the START signal from the PC. The leak detector module looks for the rising edge of the START pulse to start a conversion, and transmits data after the falling edge of the START pulse. When the Leak Detector module is listening and waiting for a start pulse, it is standing ready to transmit a START pulse to the next Leak Detector module further away from the computer. The leading edge of the start pulse from the PC initiates a data conversion in all Leak Detector modules. The falling edge of the start pulse is the signal for a Leak Detector to transmit its data. After a Leak Detector module transmits its data, it will drop the start pulse to the next leak detector, and act as a repeater to relay the data from leak detectors further away from the PC, back to the PC. The computer determines how many channels to display, by how many leak detectors respond to the start pulse. Errors will be indicated in the diagnostic window if the number of leak detectors changes during operation.

IV. DOCUMENTATION

The software for this application is written in ANSI C, with some IBM assembly code. Procedures for modifying and compiling the code are documented within the code.

Data files created and associated with each test:

- <FileName>.dat -> raw block of 16 bit data.
- <.ctl -> block sizes, # of channels, and sample rate
- <.txt -> documentation file
- <.val -> helium valve log file
- <.lpo -> pump out log file
- <.pxx -> ScreenDump files (up to 100 may exist)

V. CONCLUSIONS

This system could have applications in other areas where a simple, low cost, portable data acquisition system is required. Battery operation could be used for systems requiring complete portability.

¹ Operated by Universities Research Association, Inc., for the US Department of Energy under contract No. DE-AC35-89ER40486.

² The Fermilab Tevatron: Vacuum for a superconducting storage ring (1983)
C.L. Bartelson, H. Jostlein, G.M. Lee, P.J. Limon, and L.D. Sauer

Theoretical and Experimental Study of Sorption Processes on Non Evaporable Getters St 707

J. Miertusova, F. Dacian
Sincrotrone Trieste, Padriciano 99, 34012 Trieste, Italy

Abstract

Non evaporable getters (NEG) are sorption materials widely used in vacuum technology to obtain and to maintain UHV conditions. For its optimal utilization it is important to know what types of interactions are dominant during the sorption process. Theoretical study on the sorption process of molecules H_2 , N_2 , Ar and CH_4 on the NEG St 707 surface has been performed. By the method of empirical potentials the total interaction energy was calculated as the sum of dispersion, repulsion, electrostatic and inductive part of the energy. The NEG surface was represented as a cubic $MgCu_2$ structure. The energetic profile of approaching of gas molecules to the surface model is evaluated. Theoretical values of sorption energies are in good agreement with experimental values obtained by the method of thermal desorption spectroscopy (TDS). Trapping effect of argon during adsorption of other residual gases was also observed. A low sorption probability of methane molecules on the NEG surface was also theoretically explained.

I. INTRODUCTION

Non evaporable getters are widely used to obtain HV or UHV conditions in particle accelerators, plasma machines, evacuated solar collectors and other vacuum systems. St 707 wafer module strip manufactured by SAES Getters S.p.A. is a ternary alloy consisting of [1]: Zr = 70%, V = 24.6% and Fe = 5.4%. The optimum performance of the St 707 getter is obtained after activation at a temperature of 300-500 °C under dynamic vacuum conditions. For its optimal utilization it is important to know what types of interactions during the sorption process are dominant, these ones can be evaluated according to values of sorption energy.

Theoretical studies of the elementary process of interactions between the surface and gaseous molecules are only at the beginning. If during the interaction of two systems the long range forces are dominant, the interaction energy might be calculated according to the method of empirical potentials.

Values of sorption energies obtained by the method of empirical potentials could be compared by experimental values measured by the method of thermal desorption spectroscopy (TDS). TDS provides the easiest way of predicting outgassing effect inside a vacuum chamber. From the Arrhenius' equation which describes the desorption from the surface a simple expression for calculation of sorption energies was derived [2]. Sorption characteristics of H_2 , N_2 , CO_2 , Ar and CH_4 were measured in the temperature range of 20 - 500 °C. During adsorption of CO_2 on St 707 NEG surface a production of methane was observed.

II. THEORETICAL CALCULATIONS OF SORPTION ENERGIES

A. Methods of empirical potentials

The combination of attractive and repulsive terms give the most types of empirical potentials but they are valid only for the unpolar and uncharged systems. To calculate interaction energies between more complicated systems the terms describing the coulombic and inductive part of interaction energy are added. However, this addition "abolishes the equilibrium" of attractive and repulsive terms but in this time only this is the simplest way to calculate the interaction energy between large polar and charged systems.

The total interaction energy between the sorbent and the gaseous molecule can be approximately divided into the individual contributions of dispersion, repulsive, inductive and coulombic forces:

$$E = E_D + E_R + E_I + E_C \quad (1)$$

The contribution of dispersion (attractive) forces is [3]:

$$E_D = - \sum_i \sum_j C_{ij} r_{ij}^{-6} \quad (2)$$

Where C_{ij} is the Kirkwood-Muller [4,5] constant

$$C_{ij} = - \frac{3mc^2}{8\pi^2\epsilon_0} \frac{\alpha_i\alpha_j}{\chi_i + \chi_j} \quad (3)$$

m is the mass of electron, c is the velocity of light, α_i , α_j are the polarizabilities of interacting particles, χ_i , χ_j are their molar diamagnetic susceptibilities, ϵ_0 is the dielectric permittivity of vacuum, r is the distance of the particles i and j .

The repulsion term is expressed [3]

$$E_R = \sum_i \sum_j B_{ij} r_{ij}^{-12} \quad (4)$$

B is a constant determined by conditions of minimal energy for nonbounded interactions

$$B_{ij} = \frac{1}{2} r_0^6 C_{ij} \quad (5)$$

r_0 is the equilibrium distance equal to addition of Van der Waals' radii of interacting atoms.

Induction part of interaction energy is approximated [6]

$$E_I = \sum_j \frac{\alpha_j}{2} e_f^2(r) \quad (6)$$

α_j is the polarizability of a gas molecule and $\epsilon_j(r)$ is the intensity of electrostatic field created by the surface.

The electrostatic (coulombic) part of interaction energy is given by interaction between the charge distribution in the sorbate q_i and the charge distribution q_j of the sorbed molecules [7]

$$E_C = \frac{1}{4\pi\epsilon_0} \sum_i \sum_j \frac{q_i q_j}{r_{ij}} \quad (7)$$

If the sorbed molecule has no permanent dipol moment but has a quadrupole moment, the electrostatic part of interaction is given

$$E_C = \frac{1}{16\pi\epsilon_0} \sum_i \sum_j q_i q_j (3 \cos^2 \delta - 1) r_{ij}^3 \quad (8)$$

where angle δ gives the orientation of the molecule quadrupole moment versus the positional vector r_{ij} .

B. Surface Model and Calculations

The structure of Zr-V-Fe alloys was studied by XPS analysis [8]. These structures could have the cubic structure $Zr(V_xFe_{1-x})_2$ of $MgCu_2$ type with lattice parameters $a = b = c = 0.745, 0.734$ or 0.708 nm. There are 8 $MgCu_2$ molecules in the face centered lattice. Mg atoms are uniformly placed in the distance of 0.291 nm, Mg - Cu distance is 0.305 nm. The surface of St 707 NEG was represented by the known surface of $MgCu_2$, Mg atoms were replaced by Zr atoms and Cu was substituted by V.

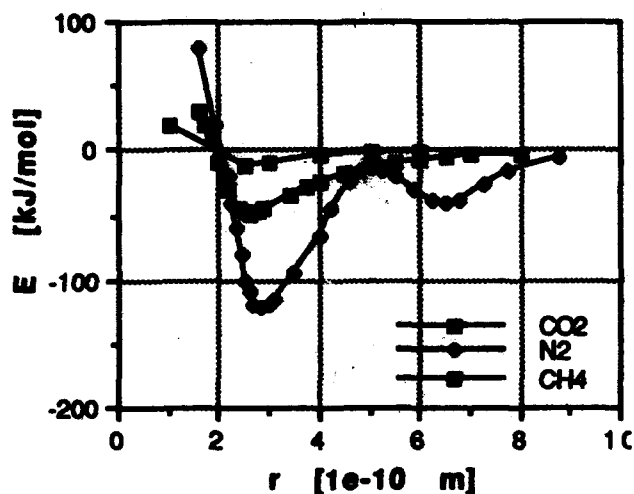


Figure 1. Total energy curves of interactions between the NEG surface and CO_2 , N_2 and CH_4 molecules.

Computer program ADNEG gives a series of curves for dispersion and repulsion part of the interaction energy. Induction and coulombic parts were not evaluated yet, there are no data about the NEG charge distribution published in the literature. Values of atomic polarizabilities, molar diamagnetic susceptibilities and van der Waals' radii of interacting atoms were taken from ref. [9].

There are shown in fig. 1 the curves of total interaction energy with NEG surface for gases CO_2 , N_2 and CH_4 . The value of sorption energy corresponds to the total energy in the deepest minimum of the sorption path.

III. EXPERIMENTAL INVESTIGATIONS OF SORPTION ON THE NEG SURFACE

A. Experimental Apparatus and Procedure

A WP 950 module with the St 707 NEG alloy was installed in the rectangular stainless steel vacuum chamber. Total pressure changes were measured by cold cathode TPG 300 Penning gauges.

A quadrupole mass analyzer Balzers 420 was used to monitor the thermal desorption of gases, as well as the composition of residual gases in the UHV system. The mass spectrometer was connected to an IBM PS/2 computer through its RS232 interface. Mass selection and scanning was then performed from the computer. During the thermal desorption experiment several masses were selected and their signal intensities as a function of temperature were stored in the computer.

The vacuum system was baked-out at 350 °C for 24 hours while the NEG module was passively activated at 260 °C. The pressure equilibrium after cooling was reached in the range of 10^{-9} mbar. Then the NEG module was resistively heated up to 500 °C and the desorption and mass spectra were measured.

After obtaining well reproducible results, the NEG was exposed to the desired amount of test gases at room temperature. When the pressure in the chamber was lower than $5 \cdot 10^{-10}$ mbar, the NEG was heated up to 500 °C at a constant heating rate. Selected masses and pressure changes were simultaneously monitored.

The sorption energy was evaluated according to expression [2]

$$E = RT_m \left(\ln \frac{v T_m}{a} + \ln \frac{1}{\ln \frac{v T_m}{a}} \right) \quad (9)$$

where R is the gas constant, $v = kT/h$ is a rate constant; k, h are the Boltzmann's and Planck's constants, respectively.

B. Results and Discussions

A typical desorption spectrum is shown in fig. 2, together with the curve of the temperature increase.

This desorption spectrum comprises two peaks: the first at the temperature of 78 °C (351 K), the second at 348 °C (621 K). The analysis of residual gases gives the highest intensity for masses 2 (H_2^+), 16 (CH_4^+ , NH_2^+ , O^+), 20 (Ar^{++} , HF^+), 28 (CO^+ , N_2^+), 40 (Ar^+) and 44 (CO_2^+).

Sorption energies calculated according to expression (9) for both peaks are 96 kJ/mol and 176 kJ/mol, respectively. The lower energy corresponds to the weakly sorbed molecules or atoms which are desorbed from the polymolecular layers.

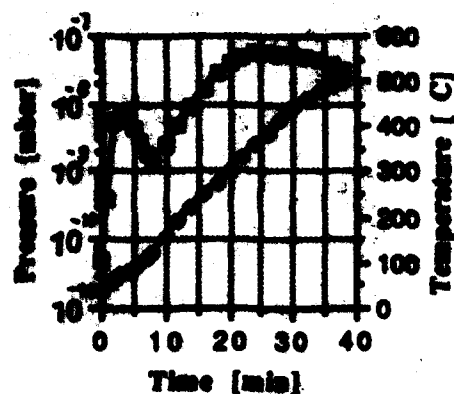


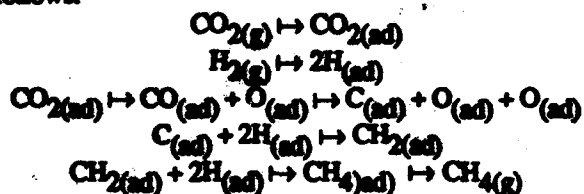
Figure 2. Thermal desorption spectrum and temperature increase.

Desorption and mass spectra after NEG exposure to H_2 did not show significant changes. The first peak was only slightly higher than one on the background TDS spectrum, while the second peak, monitored for mass 2 was always over the measured range of QMA (>5 A) because of a large amount of desorbed hydrogen. It can be concluded that only a small amount of hydrogen is physisorbed and a major part diffuses into the bulk of the getter where is chemisorbed.

After NEG exposure to nitrogen the second TDS peak was unchanged, masses 14 and 28 corresponded to the first TDS peak and were much higher than the ones in the background spectrum. Therefore it could be deduced that nitrogen is mostly weakly sorbed with the energy of ~ 91 kJ/mol.

After NEG exposure to CO_2 the first desorption peak together with masses 44 (CO_2^+), 28 (CO^+) and 22 (CO_2^{++}) were somewhat higher than those in background spectra, but masses 44 and 22 significantly increased also at the temperature of $250^\circ C$. It could be supposed that CO_2 desorbs through two different desorption features, corresponding sorption energies are 93 and 146 kJ/mol.

During injection of CO_2 into the vacuum chamber the increase of masses 13 (CH^+), 15 (CH_3^+) and 16 (CH_4^+) was observed, which corresponds to methane ion fragments. A plausible scheme of methane production may be formulated as follows:



A dependence of methane production on NEG's temperature surface was also studied. The NEG module at temperatures of 50, 100, 150, 200 and $250^\circ C$ was exposed to the same amount of CO_2 . No significant influence of NEG temperature on methane production was observed - see fig. 3.

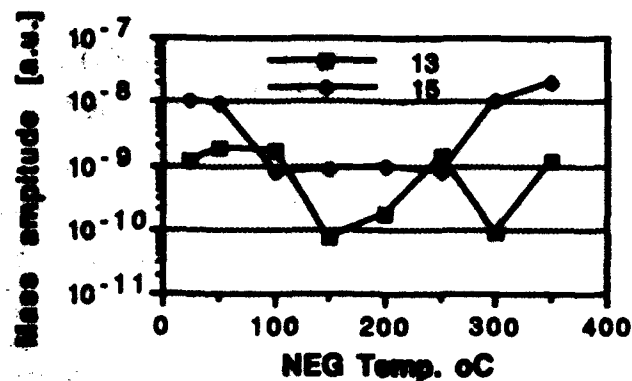


Figure 3. Quantity of CH_4 produced at different NEG temperature.

It is well known that the NEG does not affect noble gases. But in all measured desorption and mass spectra an increase of masses 20 and 40 has been observed. After the NEG exposure to Ar at the temperature of $200^\circ C$ and consequent cooling down to $20^\circ C$, the decrease of masses 20 and 40 was also significant. After flashing the NEG to $500^\circ C$ also masses 20 and 40 were comprised in the first peak of TDS spectrum.

IV. CONCLUSIONS

A desorption process from the St 707 NEG alloy passes in two steps. In the first desorption peak all masses of residual gas mixture are observed and the trapping effect of Ar could occur. Theoretical values, in spite of rough approximations, are in quite good agreement with experimental ones. The low sorption probability of methane was confirmed by the shallow minimum on the curve of total interaction energy.

V. REFERENCES

- [1] SAES Getters S.P.A., Non Evap. Getters Prospect, (1989).
- [2] M. Bernardini, R. Kersevan, J. Miertasova, "Adsorption and Desorption Phenomena on NEG during Activation", *Int. Rep. Sincrotrone Trieste*, ST/M-91/5.
- [3] M. Born, J.E. Meyer, *Z. Phys.* 75, 1 (1932).
- [4] J.G. Kirkwood, *Phys. Z.* 33, 57, (1932).
- [5] A. Muller, *Proc. Royal Soc. A* 154, 624, (1936).
- [6] A.G. Bezus, C.E. Dobrova, *Koloidnyj zurnal* 37, 1045 (1975).
- [7] J. Miertasova, *PhD Thesis*, Com. Univ. Bratislava (1982).
- [8] F. Welz, Z. Scheng, I. Vedel, L. Schlappbach, *Vacuum* 41 7-9, (1990).
- [9] J.O. Hirschfelder, C.F. Curtiss, R.B. Bird, *Molecular Theory of Gases and Liquids*, J. Wiley & sons, N.Y. (1954).
- [10] G. Xi, J. Liu, S. Li, T. He, *J. Vac. Sci. Technol.* A8 (3) 2528 (1989).

Photodesorption Experiments on SSC Collider Beam Tube Configurations*

I. Maslennikov, W. Turner

SSC Laboratory 2550 Beckleymeade Av. Dallas, TX 75237, USA

V. Anashin, O. Malyshev, V. Osipov, V. Nazmov, V. Pindyurin, A. Salimov
Institute of Nuclear Physics, Novosibirsk, Russia

C. Foerster, C. Lanni

Brookhaven National Laboratory Upton, New York 11973, USA

Abstract

Experimental measurements of photodesorption coefficients of H_2 , CH_4 , CO and CO_2 are being done to obtain data necessary to predict the vacuum performance of the Collider. Experiments have been done or are planned for warm tubes (i.e. room temperature), cold tubes (i.e. 4.2 K) and liner configurations (i.e. 4.2 K, 20 K and 80 K). Two synchrotron radiation beamlines have been constructed on the VEPP-2M storage ring at BINP, Russia. The photon critical energy is 284 eV, as in the SSC Collider, angle of incidence is 10 mrad. To date approximately fifteen warm beam tubes have been tested, including electrodeposited Cu, high purity bulk Cu and Nitronic 40 SS, several cleaning procedures, with and without in-situ baking and with and without magnetic field. The maximum integrated photon dose was achieved was $2 \cdot 10^{22}$ photons/m on the high intensity beamline. Several experiments have been done on the VUV ring at BNL to check a subset of the BINP data and to extend the integrated photon flux up to 10^{23} photons/m, or 100 days of SSC operation. The data from the warm experiments will be used to evaluate the best tubes to be used in the more time consuming cold experiments.

I. INTRODUCTION

Density increase in the beam tube due to photon-simulated desorption (PSD) can be a problem for achieving desirable beam current and lifetime in the SSCL 20 TeV proton Collider.[1] This problem may be significantly reduced if appropriate material and proper pretreatment procedures for the beam tube can be found. In order to test the selection of both the appropriate material and proper cleaning technique, we have exposed about fifteen potential candidates for collider beam tubes to synchrotron radiation on the two beamlines assembled in BINP, Russia and on the U10B beamline of the NSLS VUV ring. Each sample is 1 m long and 33 mm inside diameter(ID). Three basic materials for tubes have been tested so far: electrodeposited Cu (Silvex and Fluhmann), bulk Cu (Hitachi 10100) and Nitronic 40 SS (ASTM2169). These tube samples were cleaned following two ultrahigh vacuum cleaning proce-

dures used at BNL and at CERN. Photodesorption measurements were also made for different experimental conditions, such as "in situ" bake of the tested sample and with the presence of 500-1000 G magnetic field.

II. EXPERIMENTAL DETAILS

Basic parameters of the three beamlines used for experiments are given in Table I, where E - particle energy; I - beam current; γ - relativistic factor; E_{cr} - critical energy of photons; dI/dt - photon flux; ϕ - angle of incidence; $w_{1/2}$ - FWHM strip height of photons with the median energy $E_{1/2} = 23$ eV; D - distance from source point.

The BNL experimental setup has been described in detail previously.[2] Here we give some details of the BINP beamlines. The main difference between the two BINP beamlines is the distance from the source point of synchrotron radiation to the beam tube under test. The photon flux on the SSC1 beamline is collimated in both the vertical and horizontal directions in order to expose only the test tube. There is a loss of approximately 25% of low energy photons due to vertical collimation. On SSC2 beamline there is no vertical collimation due to very short distance from the source point. A calorimeter/electrometer is installed on the end of the SSC1 beamline to measure the power and intensity of reflected photons leaving the tube.

The vacuum systems of SSC1 and SSC2 are the same. The main part of these systems is a SS fixture which contains a calibrated RGA and ion gage installed at the center of the fixture. Tubes to be tested are inserted into the fixture from one end. This setup allows using the tube conductance to calculate photodesorption coefficients instead of the conductance of a specially made orifice placed at one end of the tube, as in the experimental setups used at CERN[3] and BNL. At each end of the fixture there is a combination ion and titanium sublimation pump with total pumping speed about 1000 l/s for H_2 . Two all-metal gate valves located on the ends of the fixture and small valve installed between the measurement unit and the fixture allow isolation of the beamline, pumps and measuring equipment during mounting of another sample. Each vacuum system was initially baked at 300°C for 24 hours. After a sample is installed it is usually pumped for 48 hours and the base pressure is about $2 \cdot 10^{-9}$ torr in the center

* Operated by the Universities Research Association Inc. for the US Department of Energy under Contract No. DE-AC35-89ER40486.

Table 1
Synchrotron radiation beamline parameters

Beamline	E, MeV	I, mA	γ	E_{cr} , eV	$d\Gamma/dt$, ph/m/s	ϕ , mrad	$w_{1/2}$, mm	D, m
SSC1	534	300	1045	284	$1.1 \cdot 10^{16}$	10	52	11.65
SSC2	534	300	1045	284	$8.4 \cdot 10^{16}$	10	8	1.75
U10B	740	600	1448	490	$1.2 \cdot 10^{17}$	12	16	5.07
SSC	$2 \cdot 10^7$	70	21322	284	$1.0 \cdot 10^{16}$	2	4	20

before beginning experiments.

Each tube sample is engraved with a number and chemically treated before experiments. Most of the tubes have been cleaned at the NSLS cleaning facility at BNL by using a standard procedure for this facility. To compare photodesorption results several tubes were cleaned at the CERN cleaning facility. Generally no strong etch treatment was applied to the tubes. The one exception was at CERN where two bulk Cu tubes were treated by a strong acid etch.

Three types of experiments were performed: (a) no bake, no magnetic field; (b) vacuum bake at 150°C or 350°C for 24 hrs, no magnetic field; (c) no bake, with magnetic field.

III. BASIC RESULTS

A. Silvex Electroplated Cu

So far eleven experiments have been done with Silvex electroplated Cu tubes; eight samples at BINP - three on the SSC1 beamline and five on SSC2 - and three samples at BNL.

(a) no bake, no magnetic field

Five tubes have been tested under these experimental conditions, four at BINP and one at BNL. Generally results of all these experiments are almost the same and have a small difference in initial η 's. Initial η 's differ by $\pm 50\%$, integrated desorption yields at 10^{22} photon/m by $\pm 20\%$. A typical plot of photodesorption yield versus integrated photon flux is shown in Figure 1.

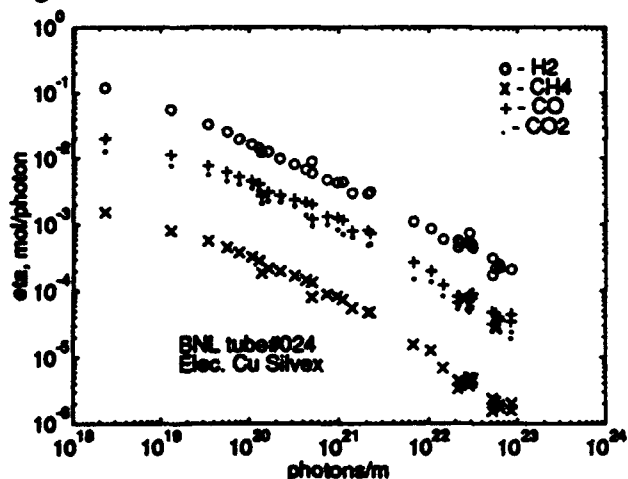


Figure 1. Photodesorption coefficients for unbaked Silvex electroplated Cu.

(b) vacuum bake, no magnetic field

Tube #003 was baked at 150°C for 24 hrs and then was exposed to photons on SSC1 beamline up to 10^{21} photons/m. We did not notice any significant difference in photodesorption coefficients compared with an unbaked sample (tube #002) exposed to the same photon flux in SSC1. For example the integrated amounts of desorbed H₂/CO were: $1.0 \cdot 10^{19}$ / $2.6 \cdot 10^{18}$ molecules/m for tube #003 with bake and $7.0 \cdot 10^{18}$ / $1.3 \cdot 10^{18}$ for tube #002 without bake.

Tube #032 was baked at 350°C for 24 hrs and then was exposed to photons on U10B line at BNL. Results of this experiment are shown in Figure 2. The initial η 's for main peaks are reduced approximately an order of magnitude compared to the unbaked tube in Figure 1. However due to a smaller rate of cleanup of the baked tube the desorption coefficients are almost the same at $\sim 10^{23}$ photons/m for the baked and unbaked tubes.

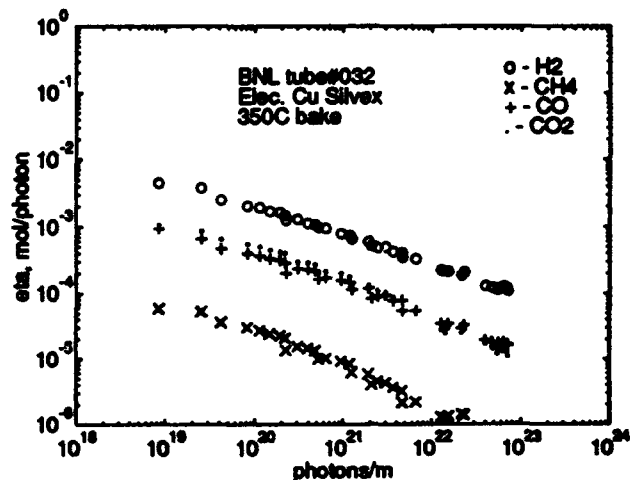


Figure 2. Photodesorption coefficients for *in situ* 350°C baked Silvex electroplated Cu.

(c) no bake, with magnetic field

Two experiments have been done with magnetic field, one on the SSC2 beamline at BINP and one on the U10B beamline at BNL. At BINP we used an electromagnet with ~ 500 G vertical magnetic field. The experimental data are shown in Figure 3. Most of the time the magnetic field was switched "on" and for short periods it was "off". Only slight differences between "on" and "off" periods were noted and are not visible in Figure 3 (i.e. no initial difference in photodesorption coeffi-

coefficients and approximately 10% higher photodesorption of H_2 with field "off" compared to field "on" at the conclusion of the experiment). This indicates a rather small role on photodesorption for photoelectrons which leave the surface. A similar experiment at BNL, used a permanent magnet with average vertical magnetic field about 1000 G and also showed a very small magnetic field effect.

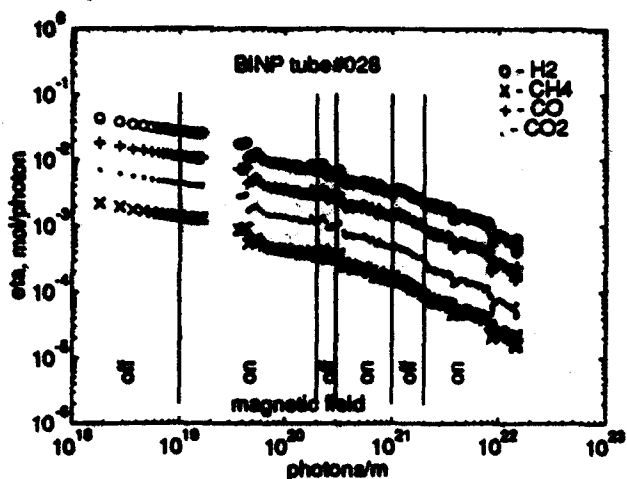


Figure 3. Photodesorption coefficients for Silvēx electroplated Cu with magnetic field.

B. Fluhmann Electroplated Cu

One sample of Fluhmann electroplated Cu has been tested at BNL. Comparing with Silvēx tubes the only essential difference is in the initial η for H_2 which is about five times less for the Fluhmann tube than the Silvēx tube shown in Figure 1. However at 10^{23} photons/m the Fluhmann and Silvēx tubes have essentially the same magnitude of photodesorption coefficients for all gases.

C. OFHC bulk Cu

Three OFHC bulk Cu samples have been tested on SSC1 at BINP and one at BNL. Generally the initial photodesorption coefficients obtained from these experiments are approximately 2 to 5 times less than for electroplated samples with the same cleaning procedure. In addition a rather large decrease in initial desorption coefficient was obtained with the CERN strong acid etch procedure compared to the BNL procedure with slight acid etch.

D. Nitronic 40 SS

Experiments on stainless steel tubes have been done at BINP on SSC1 beamline to compare results with earlier data from BNL experiments performed by Halama and Foerster.[4] Good agreement between the new and earlier data give confidence in the experimental procedures.

IV. SUMMARY

In Table 2 we summarize the results of this paper with a comparison of desorption coefficients and amount of desorbed gas at 10^{23} photons/m for H_2 and CO. Leaving the 350°C bake aside, at 10^{23} photons/m Silvēx and Fluhmann electrodeposited

Cu and bulk Cu have roughly the same magnitude of photodesorption coefficients and of photodesorbed gas (i.e. within a factor of two). The 350°C bake decreased the amount of H_2 desorbed at 10^{23} photons/m by a factor of three and CO by a factor of five. Magnetic field has no effect on initial photodesorption coefficients and there is approximately 10% higher photodesorption of H_2 with field "off" compared to field "on" at 10^{23} photons/m. Differences in cleaning procedures, baking versus no baking and materials are most pronounced in the initial desorption coefficients and tend to decrease to less than a factor of two by the time a photon flux $\sim 10^{23}$ photons/m has been reached.

Table 2

Photodesorption coefficients and amount of photodesorbed H_2 and CO for different test samples at 10^{23} photons/m

Tube sample	molecules/photon at 10^{23} photons/m		molecules/m	
	H_2	CO	H_2	CO
Elec Cu(S [*])	$1.7 \cdot 10^{-4}$	$4.4 \cdot 10^{-5}$	$5.1 \cdot 10^{19}$	$1.3 \cdot 10^{19}$
Elec Cu(S), 350°C bake	$9.3 \cdot 10^{-5}$	$1.4 \cdot 10^{-5}$	$1.7 \cdot 10^{19}$	$2.8 \cdot 10^{18}$
Elec Cu(S) with B	$1.4 \cdot 10^{-4}$	$3.0 \cdot 10^{-5}$	$3.3 \cdot 10^{19}$	$8.1 \cdot 10^{18}$
Elec Cu(F)	$1.3 \cdot 10^{-4}$	$2.8 \cdot 10^{-5}$	$2.8 \cdot 10^{19}$	$5.8 \cdot 10^{18}$
Bulk Cu	$9.2 \cdot 10^{-5}$	$2.0 \cdot 10^{-5}$	$2.4 \cdot 10^{19}$	$7.4 \cdot 10^{18}$

* S - Silvēx, F - Fluhmann

V. ACKNOWLEDGEMENTS

The authors would like to thank A. G. Mathewson for his assistance with the test samples cleaned at CERN and for fruitful discussion of photodesorption experiments.

VI. REFERENCES

- [1] A. Maschke, "Hydrogen desorption and the Search for the Higgs," SSCL-Preprint 86. Mar. 1992.
- [2] T. Kobari and H. Halama, *J. Vac. Sci. Technol. A* 5, 2355 (1987).
- [3] O. Grobner, A.G. Mathewson, H. Stori and P. Strubin, *Vacuum* 33, 397 (1983).
- [4] C. Foerster, H. Halama and C. Lanni, *J. Vac. Sci. Technol. A* 8 (3), 2856 (1990).

The Heat Load of an 80 K Liner for the SSC

J. Maddocks and A. Yücel
Superconducting Super Collider Laboratory*
2550 Beckleymeade Avenue, Dallas, TX 75237

Abstract

The Superconducting Super Collider (SSC) will be the first proton machine in which synchrotron radiation significantly affects the cryogenic system and the beam tube vacuum. Synchrotron radiation represents the single largest heat load on the 4 K single-phase helium. It also provides a mechanism by which hydrogen can be desorbed from the beam tube wall, gradually worsening the vacuum. Insertion of a perforated and heated liner into the cold beam tube, together with a strip of cryosorber, effectively creates a distributed cryopump. Such an arrangement is an attractive solution to possible vacuum problems, provided it does not increase the heat load on the single-phase helium. In this paper, the primary mechanisms of heat transfer from an 80 K liner are considered, and the results of measurements on heat conduction through prototypical mechanical supports are presented.

I. INTRODUCTION

Synchrotron radiation desorbs hydrogen from the beam tube of the super collider, reducing the vacuum and adversely affecting the luminosity lifetime [1]. One solution to this problem is to place a distributed cryopump within the beam tube which will trap desorbed gasses.

A distributed cryopump can be effected by attaching cryosorber to the cold (4 K) magnet bore tube. A concentric tube, or liner, centered within the magnet bore tube shields the cryosorber from the synchrotron radiation, and becomes the beam tube. By perforating a fraction of the liner surface with small (on the order of 1-3 mm) holes, the liner/cryosorber assembly becomes a distributed pump. The liner temperature may be allowed to equilibrate at a temperature close to that of the 4 K bore tube. However, actively stationing the liner at 80 K is of interest because the synchrotron radiation heat load can then be removed to the liquid nitrogen system. This, at least partially, decouples the allowable beam current from the helium cryogenic system. Active control is accomplished by means of 80 K helium flowing through a trace tube attached to the outside of the liner. A cross section of the magnet bore tube with an 80 K liner is shown in Figure 1.

II. HEAT LOADS

The SSC is the first proton machine in which the synchrotron radiation heat load is significant. At baseline operation the synchrotron load is 10.85 W per half-cell. (A half-cell, which

is the basic unit of the collider, is 90 m long and consists of five dipoles, one quadrupole, and one spool piece). The synchrotron radiation represents about 40% of the total 4 K heat load. With an 80 K liner, however, the 4 K synchrotron radiation load is replaced by a fixed heat load associated with the liner, while the intercepted synchrotron load is transferred to the LN2 system. This fixed or static liner heat load is independent of the collider beam current.

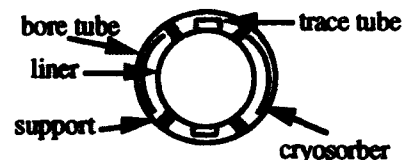


Figure 1. Cross-section of magnet bore tube with liner.

For an 80 K liner to be practical, it must not impose a heat load on the single-phase helium that is greater than the baseline dynamic heat load of the synchrotron radiation. A conservative budget for the static heat load has been set at 5 W per half-cell, which is less than half the nominal baseline synchrotron radiation heat load. Details are shown in Table 1. Non-negligible contributions to the static heat load arise from conduction through mechanical supports, blackbody radiation, end conduction through interconnect pieces where the trace tube penetrates the 4 K bore tube, and conduction through the beam position monitor (BPM).

Table 2
Static Liner Heat Load (W per component)

	Dipole	Quad	Spool	Half-cell
Support	0.50	0.50	0.30	3.30
IR radiation	0.20	0.06	0.04	1.10
Interconnect	0.05	0.05	0.05	0.35
BPM			0.26	0.26
Total	0.75	0.61	0.65	5.01

One BPM is located at the lead end of each spool piece, and represents a major portion of the heat load attributed to the spool. However, since there is only one per half-cell, its contribution to the total is small. The case is similar for interconnect contributions, in that they are discrete not dependent on length. There are seven interconnects per half-cell, one associated with each component. Trace tube penetrations of the 4 K bore tube have been carefully designed to keep the heat load associated with each one small. Thus the

* Operated by the Universities Research Association, Inc., for the U.S. Department of Energy under Contract No. DE-AC35-89ER40486.

The submitted manuscript has been authored by a contractor of the U.S. Government under Contract No. DE-AC35-89ER40486. Accordingly, the U.S. Government retains a nonexclusive, royalty-free license to publish or reproduce the published form of this contribution, or allow others to do so, for U.S. Government purposes.

sum of the interconnect heat loads is only 7% of the total heatload per half-cell. BPM and interconnect designs are generally considered to be within budget.

Blackbody radiation from the 80 K liner to the 4 K bore tube and conduction through mechanical supports combine to generate the largest portion of the heat load, with conduction through the supports being the greater of the two. Radiation is difficult to reduce to budgeted levels when the cryosorber, which is likely to have an emissivity near 1, is taken into account. Conduction through the supports, however, is the most difficult heat load to reduce, since long path lengths are difficult to achieve given the limited radial space available. Both radiation and support conduction are discussed in the following sections.

III. BLACKBODY RADIATION LOAD

Radiant heat exchange between the liner and bore tube is given by,

$$Q = \sigma E(T_H^4 - T_C^4), \quad (1)$$

where,

$$E = \{(1/A_L \epsilon_L) + (1/A_B)(1/\epsilon_B - 1)\}^{-1}. \quad (2)$$

The subscripts refer to the liner (L) and bore tube (B), ϵ is the emissivity (in this case both surfaces are stainless steel) and A the surface area.

In general the emissivity of a material is a function of temperature and surface preparation. The heat transferred by radiation between a stainless steel surface at 77 K and one at 4.2 K has been measured by Obert et.al. [2]. The results for a variety of surface preparations are reported in terms of emissivities, and reproduced in Table 2.

Table 2
Emissivity of Stainless Steel [2]

Surface preparation	Emissivity from 77 K to 4.2 K
As found	0.120 \pm 5%
Mechanically polished	0.074 \pm 5%
Electro-polished	0.065 \pm 5%
Silver plated	0.013 \pm 5%

To determine the radiation heat load of an 80 K liner, it is necessary to include the effect of holes in the liner tube and cryosorber on the bore tube. To account for these effects, average emissivities for the liner (ϵ_L) and bore tube (ϵ_B) are defined. Each is taken to be the weighted average of the appropriate stainless steel emissivity (ϵ_{ss}) and the hole (ϵ_h) or cryosorber (ϵ_c) emissivity. The liner holes are assumed to have an emissivity of 1, and the cryosorber an emissivity between 0.8 and 1, depending on the particular cryosorber.

The resulting average emissivity of each tube is a linear function of the fraction of surface coverage (f_h) or (f_c).

$$\epsilon_L = (1 - \epsilon_{ss})f_h + \epsilon_{ss}, \quad (3)$$

$$\epsilon_B = (\epsilon_c - \epsilon_{ss})f_c + \epsilon_{ss}. \quad (4)$$

While this is a rather simplistic model, more detailed numerical calculations indicate that it gives an accurate estimate of the total heat transferred by radiation.

To evaluate eq. (1) it is necessary to know the bore tube and liner tube diameters, the surface preparation of the stainless steel, the number and size of holes in the liner and the surface area of cryosorber. The last two numbers are not well known. The fraction of holes may vary up to 0.05, while the fraction of cryosorber coverage may be as high as 0.15. If (f_h) and (f_c) turn out to be near the maximum of their respective ranges, they will dominate the radiated heat leak. This is especially true in the case of the cryosorber.

As an example, assume a 33 mm liner with $f_h = 0.05$, and a 42 mm bore tube with $f_c = 0.15$. This arrangement will radiate 0.6 W/dipole with as found stainless, and 0.4 W/dipole with electro-polished stainless. For the same geometry, with $f_h = 0.03$ and $f_c = 0.10$ the heat leaks are reduced to 0.5 W/dipole and 0.3 W/dipole respectively. This last number is probably achievable, but is still 50% greater than the budgeted amount. Still, since radiation is only budgeted at 20% of the total load to begin with, this is considered acceptable.

IV. SUPPORT CONDUCTION LOAD

A prototype support, shown in Figure 2, consists of four stainless steel legs, bent in the middle, with a rectangular cross-section of 6 mm x 1.2 mm thick. To provide the necessary rigidity, support legs are less than 17.2 cm long, have both ends welded to the liner, and are spaced at 2 m intervals.



Figure 2. Mechanical support

The resistance to heat flow of each leg is the sum of the stainless steel resistance and the contact resistance between the support and bore tube. Neglecting contact resistance, the heat leak through a single leg is

$$Q = (2A/L) \int k dT \quad (5)$$

where A is the cross sectional area of a support leg, L is half the leg length and k is the thermal conductivity of stainless steel. Evaluation of the integral from 4 K to 80 K predicts a heat load of 0.06 W per leg. If all four legs are in contact with the bore tube, this results in a heat load of 1.9 W per dipole. This is less than the baseline synchrotron radiation load but nearly four times the static heat load budget.

The material and geometry of the support are more or less fixed by mechanical stability considerations and radiation resistance, so that contact resistance becomes the primary

design parameter with which to reduce the heat load. Contact resistance can be expressed as

$$R_{\text{contact}} = f(\Delta T, k, F, G), \quad (6)$$

where ΔT is the temperature difference across the contact, k is the mean thermal conductivity of the materials in contact, F is the force with which the contacts are pressed together, and G is a geometric factor related to surface roughness. In general, R_{contact} is not well known. For this reason, tests were conducted to measure both the heat leak of a prototypic support and the average resistance of a stainless-to-stainless contact [3]

The total heat leak as a function of liner temperature for a number of cases is shown in Figure 3.

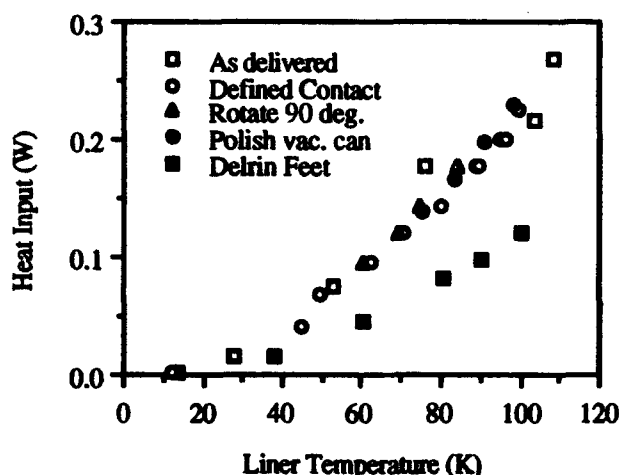


Figure 3. Results of heat leak test on mechanical support

Contact conductance generally obeys a power law dependence on temperature of the form

$$h_c = \alpha T^n, \quad (7)$$

where α is a function of applied force and surface roughness. In addition,

$$Q_i = A_c \int h_c dT, \quad (8)$$

with A_c the nominal contact area. Substituting eq. (7) into eq. (8) and integrating gives,

$$T_{\text{contact}} = [(n+1)Q_i / \alpha A_c + T_{\text{bath}}^{n+1}]^{1/(n+1)} \quad (9)$$

T_{bath}^{n+1} is much less than the leading term and can be neglected, so that average values of α and n can be extracted from a log-log plot of T_{contact} versus Q_i . The value of n measured in this way is 1.5 and compares favorably with stainless to stainless conductances published in the literature [4]. The value of α was determined from the largest values of Q_i so the data could be used to predict an upper bound for the heat leak. Its measured value of 0.75 is about two orders of magnitude lower than published data [4] for smooth stainless-to-stainless contacts under similar applied load, and indicates the potential sensitivity of the heat load to surface roughness.

In a final run, each contact point of a second support was fitted with a Delrin button. The buttons were attached by press fitting into holes drilled at the points of contact. Only the total heat leak and liner temperature were measured, so that no conductance can be extracted from the data. The data are included in Figure 3. Although Delrin is an unacceptable material for use in the bore tube, the data give an indication of the effect of attaching plastic buttons to the supports should an acceptable material be identified.

V. DISCUSSION

Blackbody radiation and conduction through the support system are the primary sources of 4 K liner heat load. In the case of radiation, hole and cryosorber coverages would have to be reduced to zero and electro-polished stainless used in order to meet the budget. However, the radiated heat load is a relatively small fraction of the total heat load. Thus, it is concluded that expensive surface treatment of the liner for the purpose of reducing the radiated power is unnecessary.

The heat load due to conduction through the supports is a strong function of the force applied at the contact. The applied contact force in the Collider will be determined by three factors: preloading by compression of the supports at the time of insertion in the bore tube, further loading or unloading of support legs due to differential contraction during cooling, and compression of the lower legs and unloading of the upper legs due to the weight of the liner. A simple model of the differential contraction predicts a net reduction in the applied contact force after cooling to 4 K, and no preloading is required. Thus, only the lower two support legs will be in contact with the bore tube when the Collider is in operation. Under these circumstances, the support heat leak will only be 0.7 W per dipole.

Finally, it appears that the contact resistance can also be increased by the addition of insulating buttons, though more work is required to identify an acceptable material and confirm that such is the case.

VI. REFERENCES

- [1] I. Maslennikov, et al., Photodesorption Experiments on SSC Collider Beam Tube Configurations, these proceedings.
- [2] Obert et al., Emissivity Measurements of Metallic Surfaces Used in Cryogenic Applications, *Adv. Cryo Eng.*, 27:293 (1982).
- [3] J. Maddocks, et al., Heat Leak Measurements and Thermal Modeling of a Mechanical Support for a SSC Beam Tube Liner, *Proceedings of the Fifth International Industrial Symposium on the Superconducting Super Collider*.
- [4] D.N. Lyon, and W.R. Parrish, Low Temperature Thermal Conductivities of Two High Compressive Strength Materials, *Cryogenics*, 7:21 (1967).

DESIGN OF LARGE APERTURE, LOW MASS VACUUM WINDOWS*

W. J. Leonhardt and M. Mapes

AGS Department, Brookhaven National Laboratory

Associated Universities, Inc.

Upton, New York 11973

Abstract

Large vacuum vessels are employed downstream of fixed targets in High Energy Physics experiments to provide a long path for particles to traverse without interacting with air molecules. These vessels generally have a large aperture opening known as a "vacuum window" which employs a thin membrane to preserve the vacuum environment yet allows the particles to pass through with a minimal effect on them. Several large windows have been built using a composite of Kevlar/Mylar including circular windows to a diameter of 96.5 cm and rectangular windows up to 193 cm x 86 cm. This paper describes the design, fabrication, testing and operating experience with these windows and relates the actual performance to theoretical predictions.

I. INTRODUCTION

Some experimental beam lines at Brookhaven National Laboratory require large aperture, low mass vacuum windows to minimize beam loss and reduce background radiation in close proximity to beam detectors. These vacuum windows are essentially a wall or membrane separating a vacuum space from atmosphere through which the beam passes, and they exhibit a vacuum integrity which allows them to be used in vacuum systems with a pressure of 10^{-4} Torr. The material used for the windows must be thin and light enough so as to have the minimum effect on the beam, and, at the same time, be thick and strong enough to operate reliably and safely. In the past, small aperture windows used Mylar as the window material. Mylar has a reasonably high tensile strength, good vacuum properties, and its density is acceptable for the thicknesses required in small aperture windows. As the apertures get larger, the thickness of the window material must increase, so Mylar becomes less attractive. In addition, Mylar is not available in thicknesses greater than 0.36 mm; therefore, if used in large aperture windows, multiple layers would be required.

To create a window with a mass lower than Mylar, designs have emerged which use a composite of a thin sheet of Mylar and a reinforcing fabric. Reinforcing fabrics are available with tensile strengths an order of magnitude greater than Mylar; therefore, smaller thicknesses are required for a given aperture. However, Mylar in thin sheets is still used since the fabrics cannot achieve any sort of a vacuum seal. Various reinforcing fabrics have been tried including carbon (graphite)[1], polyester fiber (Dacron)[2][3], and aramid

fiber (Kevlar)[3][4], and, after reviewing the results, it was judged that Kevlar was the best candidate to develop for designs at Brookhaven National Laboratory (BNL). Typical window materials are shown in Table I. To date, four large aperture windows have been constructed and tested at BNL including two circular windows of 91.4 cm and 96.5 cm diameter and two rectangular windows measuring 61 cm x 122 cm and 86 cm x 193 cm.

II. DESIGN AND FABRICATION

Current window designs used at BNL generally follow the technique first introduced by Fermi National Accelerator Lab.[4] The window composite is a combination of Kevlar 29 and Mylar type A sized appropriately for the specific window aperture. Components of a typical window assembly are shown in Fig. 1.

In assembling the window, a Viton O-ring is inserted into the vacuum window flange. Next an annular sheet of Mylar (Mylar ring) is used whose inner and outer dimensions are the same as the window clamp flange. Over the Mylar ring goes a full sheet of Kevlar and a full sheet of Mylar. Next comes the window clamping flange which also has an O-ring groove. In this groove is an O-ring of 1100-T0 aluminum. This aluminum O-ring aids in clamping the composite window materials since earlier windows experienced premature failure due to pullout from the flange. When assembling the window, the area opposite the Viton O-ring is marked on both the Kevlar and Mylar pieces. The Mylar is roughened with sand paper on the surface facing the Kevlar and the Kevlar is painted with a bead of epoxy in the same area. Care must be taken so that the epoxy doesn't spread appreciably in the plane of the window. The window assembly is then bolted together and properly torqued. When the epoxy cures, a vacuum tight seal is formed which prohibits edge leaking of the composite material. The epoxy mix used is formulated to be flexible and to soak well into the Kevlar providing a vacuum seal with no problems.[5] The final sizes of the materials used in the windows at BNL are as follows:

	Kevlar	Mylar	Composite
Aperture	Thickness	Thickness	Mass
φ91.4cm	0.43mm	0.13mm	0.05g/cm ²
φ96.5cm	0.43mm	0.13mm	0.05g/cm ²
122x61cm	0.30mm	0.05mm	0.03g/cm ²
193x86cm	0.43mm	0.05mm	0.04g/cm ²

The circular windows represent the earliest use of this type of window at BNL and thus the thicknesses and composite mass reflect a very conservative design. The material thicknesses for the φ91.4 window were determined by testing and, since

* Work performed under the auspices of the U.S. Department of Energy.

a large enough safety margin was present, these thicknesses were judged adequate for #96.5 window as well. Confidence gained with the use of the circular windows allowed the rectangular windows to be designed with a lower composite mass. As a comparison, if the 122 x 61 cm window was made only of Mylar, its thickness would be 1.4 mm and its mass would be 0.19 g/cm²; therefore, the composite window has a mass only 15% of a pure Mylar window.

II. SAFETY CONSIDERATIONS

Safety regulations require that a vacuum window shall be cycled three times at 50% over operating pressure to demonstrate its integrity in going from load to no load conditions; however, since the behavior of Kevlar fabric does not follow theoretical predictions, a cycling pressure of 100% over operating pressure is used. These vacuum windows are typically used on large vacuum vessels, and considerable shock wave would result in the event of a total window failure. When Mylar is used alone as a window material, experience has shown that failure of the Mylar is similar to a balloon breaking and the resulting shock wave a sizeable threat to life and property. All composite window designs used at BNL are hydrostatically tested to failure to indicate the margin of safety present in one atmosphere operation; however, it was felt that a hydrostatic test might not correctly model a catastrophic failure so a full scale test was conducted. The $\phi 91.4$ cm window assembly was attached to a vacuum vessel with an internal volume of over 3100 liters and the vessel pumped down to 10^{-3} Torr. A weighted pendulum with a sharp point was positioned in front of the window and swung in puncturing the window in the center. While the Mylar split across the full aperture, the Kevlar only suffered a hole the size of the puncturing elements and the tank bled up to atmosphere in a slow, gentle fashion.

III. TESTING

All window designs have been hydrostatically tested to failure in addition to the cycle test described in the previous section using a test fixture. The window assembly was bolted to the fixture as shown in Fig. 2 so that when pressurized with water, the window is stressed in the same direction as it is in experimental use. A pressure gauge was used to monitor the pressure applied to the window, and a dial indicator was placed in the center of the window to record the deflection of the window as pressure was applied to it.

Tests were conducted for various combinations of Kevlar and Mylar on the $\phi 91.4$ cm circular and both rectangular windows. The results are summarized in Table II. All the tests were carried out using a Kevlar 29 fabric except the one where the Kevlar thickness is 0.25 mm. This thickness was Kevlar 49 since it was not available in Kevlar 29. Kevlar 29 is preferred over Kevlar 49 since it has a lower elastic modulus while having the same tensile strength. This is more desirable in window applications where the greater deflection

aids in lowering the slippage or pull out forces. The test windows using Kevlar 29 had no short term creepage. Long term creepage needs more study.

Window failure in both the circular and rectangular windows was of the classic thin membrane failure type, with the windows rupturing along their edges.

IV. THEORETICAL PREDICTIONS

Classical equations used in predicting window performance are given by Timeoshenko[6] as:

$$S = Z \left[E \left(\frac{pa}{l} \right)^2 \right]^{1/3} \quad (1)$$

$$w = K \left[\frac{pa^4}{E_t} \right]^{1/3} \quad (2)$$

[illegible]

Using these equations has shown that they do not predict actual performance very closely, and testing is required to safely size and optimize the window materials. For example, looking at the Kevlar alone, catalog values of initial material properties give window deflection calculations that are lower than observed while measured values of material properties give calculations higher than observed. Several factors may contribute to the analytical and material property uncertainties and it is believed that most of them are due to the woven nature of the Kevlar.[5]

The above analytical expressions have been used with some success, however. If Eq. (2) is used to compute an "apparent pressure" using the deflection at failure and the properties for Mylar, that value can be used in Eq. (1) to compute an "apparent stress" on the Mylar at failure, again using Mylar properties. This apparent stress at failure compares reasonably well to the tensile strength of the Mylar; therefore it is felt that at actual operating deflections, the stress level in the Mylar can be computed, and an operating factor of safety can be determined.

V. OPERATING EXPERIENCE

Both circular windows have been installed in experimental beam lines. The ϕ 9.41cm window was used in an experiment which ran about six months. The vacuum was maintained at less than 10^{-3} Torr and, although the window was cycled about five times, no problems were encountered. The ϕ 96.5cm window ran for four six month periods. Initial

problems were encountered when the window was cycled since, after a few cycles, the window developed slow leaks. The leaks appear to have been caused by an older epoxy formulation which was not as flexible as the one currently used. Since the formulation has been changed, the window has run without problems at vacuum levels of 10^{-5} Torr. The rectangular windows are a new design and operating experience is not yet available.

In summary, the design of the Kevlar/Mylar composite windows has been further developed at BNL. These windows have been effectively used as a low mass alternative to Mylar alone and have been shown to be both safe and reliable.

V. REFERENCES

- [1] Takao Inagaki, National Laboratory for High Energy Physics (KEK), Japan, private communication, 1992.
- [2] J.E. Walter, "Large Rectangular Vacuum Windows," Trans. IEEE, 1973, p. 125.
- [3] R.M. Reimers, J. Porter, J. Meneghetti, S. Wilde, and R. Miller, A 344cm x 86cm Low Mass Vacuum Window, Lawrence Berkeley Lab. Report No. LBL-15991, 1983.
- [4] S. Sobczynski, E732/E621 Cloth Vacuum Window Design Report, Fermi National Accelerator Laboratory, private communication, 1986.
- [5] M. Mapes and W.J. Leonhardt, "Design of Large Aperture, Low Mass Vacuum Windows," to be published in *Vacuum Science and Technology A*, Vol II, Aug. 1993.
- [6] S. Timoshenko and S. Woinowsky-Krieger, *Theory of Plates and Shells*, McGraw Hill, N.Y., 2/e, 1959.

Dacron and Kevlar are registered trademarks of E.I. Dupont DeNemours and Co., Inc.

TABLE I - Typical Window Materials

Material	Tensile Strength MPa	Modulus* MPa	Density g/cm ³
Kevlar 29	2,760	62,000 (8,200)	1.44 (0.736)**
Kevlar 49	2,760	117,000 (18,000)	1.44 (0.736)
Dacron	1,120	13,800	1.38
Stainless Steel 304	580 - 1,276	200,000	7.83
Aluminum 6061 T6	310	69,000	2.70
Mylar	172	3,450 (5000)	1.40

*Catalog values shown; actual measured values—parenthesis.

**Density given is for individual strands and values in parenthesis are apparent density for woven material.

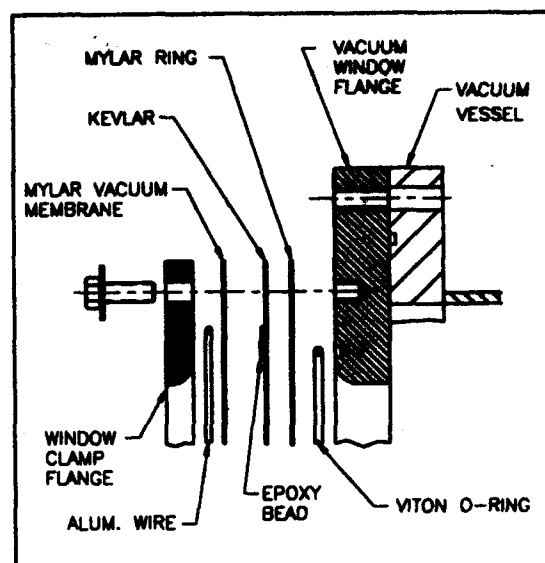


Figure 1 TYPICAL WINDOW ASSEMBLY

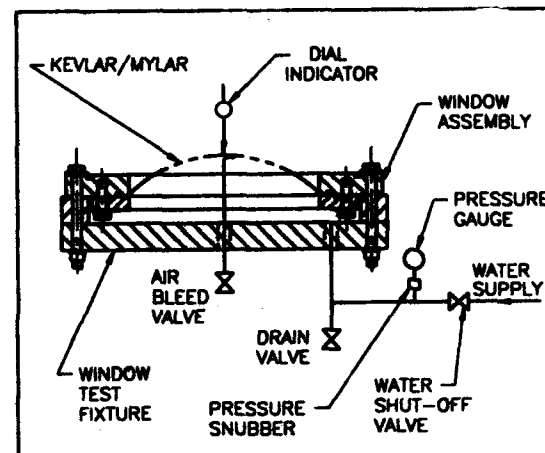


Figure 2 HYDROSTATIC TEST SETUP

TABLE II

Test No	Window Size	Thickness, Kevlar/Mylar	Pressure at Failure
1	91.4 circular	0.58/0.13mm	4.1 atm
2	"	0.43/0.13	4.1
3	"	0.30/0.13	2.0
4	122x61 rect.	0.38/0.13	3.2
5	"	0.30/0.13	2.5
6	"	0.30/0.05	2.3
7	"	0.25/0.13*	1.5
8	"	0.30/0.05	**
9	193x86 rect.	0.43/0.13	2.7
10	"	0.43/0.05	2.5
11	"	0.30/0.05	1.4

* Kevlar 49 used this test only; all others Kevlar 29.

** Not taken to failure, long term cycle test.

Observation and Analysis for Motions of Trapped Microparticles in the TRISTAN Accumulation Ring

Hiroshi Saeki*, Takashi Momose**, and Hajime Ishimaru
National Laboratory for High Energy Physics
1-1 Oho, Tsukuba-shi, Ibaraki-ken, 305, Japan

Abstract

Signals of high-energy bremsstrahlung in the TRISTAN accumulation ring was observed with lead-glass counters, accompanied by a sudden decrease in the electron beam lifetime which occurred due to microparticle trapping in the electron beam. The observation showed a trapped microparticle made a periodic oscillation; the period was 1s. The observation coincides with the result based on our newly developed theory for vertical oscillation of a trapped microparticle. Furthermore, the calculated variation in the beam lifetime also coincides with the actual variation in the beam lifetime.

I. INTRODUCTION

Observations of microparticle trapping phenomena in the TRISTAN accumulation ring with lead-glass counters have been carried out previously. It was found that microparticles in the beam chamber were actually trapped in the electron beam.[1-2] From signals of bremsstrahlung detected during microparticle trapping, the results of our theory developed giving the motion of a trapped microparticle and results of observations trapped microparticle motions with a wire simulating the electron beam, we expect that a trapped microparticle makes a periodic oscillation around the electron beam, as shown in References [2] and [3].

But it is difficult to find precisely the motion of a trapped microparticle using the complicated theory based on many assumptions. Therefore, we carried out simple theoretical analysis for a trapped microparticle motion, using our newly developed theory based on a vertical oscillation only. We also compared results of the observation and the analysis.

II. OBSERVATION OF TRAPPED MICROPARTICLE MOTIONS IN THE TRISTAN ACCUMULATION RING

Motions of trapped microparticles in the ring were observed with lead-glass counters, as shown in Reference [2]. If microparticles are trapped in the electron beam, signals of high-energy bremsstrahlung can be detected at the interacting location with intensity much greater than that of residual gases.

A. Measuring Instruments to Observe Motions of Trapped Microparticles

Four lead-glass counters were used to observe bremsstrahlung. High-energy bremsstrahlung generated at each source area corresponding to three bending magnets is

detected with each of the three lead-glass counters. The other one is set at a straight chamber.

The bremsstrahlung is detected with the lead-glass counter set behind plates made of lead (thickness 10 mm). Each lead-glass counter is constructed with a lead-glass block (360 mm × 120 mm × 100 mm) and a photomultiplier. The lead-glass counters are shielded with lead blocks (thickness 100 mm) except for the detecting slit. The amplified signals from the lead-glass counters are transmitted to a digital storage oscilloscope synchronized with bunch signals from a single bunch electron beam as it passes a position monitor.

B. Observations of High-energy Bremsstrahlung Accompanying a Sudden Decrease in the Beam Lifetime

If a trapped microparticle makes a periodic oscillation, it is expected that signals of high-energy bremsstrahlung corresponding to the motions of the trapped microparticle could be observed.

Figure 1 shows signals from the lead-glass counter at the straight chamber during microparticle trapping. The initial injected beam current of the single-bunch electron beam was 30 mA and the beam energy was 6.5 GeV. The beam current suddenly decreased at 25 mA. The beam lifetime also decreased from 125 min to 72 min and did not recover. At the beam current of 21 mA, signals of high-energy bremsstrahlung synchronized with the bunch signals from the electron beam and signal of 0.15 ms duration were also observed with the other counters. From results of test of lead-glass counters using a internal target, it was found that the voltage of signals detected with the lead-glass counters was 15-17 times higher than that of an electron with 6.5 GeV. Such signals can be detected very little, during a sudden decrease in the beam lifetime.

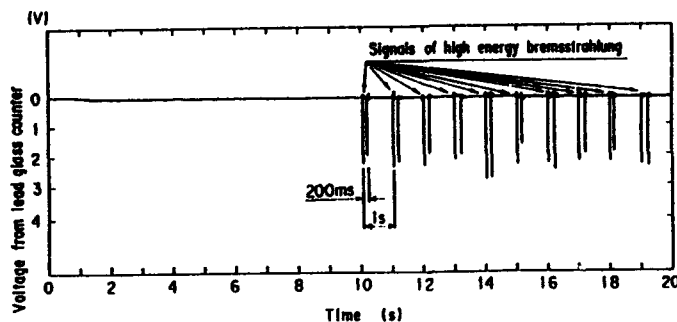


Fig. 1 Signals of high-energy bremsstrahlung caused by a microparticle oscillating around the electron beam orbit, at the beam current of 20 mA. The horizontal time scale is 1 s/division.

* Japan Synchrotron Radiation Research Institute, Minato-nakamachi 6-9-1, Chuou-ku, Kobe-shi, 650, Japan

** Miyagi National College of Technology, Miyagi, Natori-shi, 981-12, Japan

III. THEORETICAL ANALYSIS OF MOTIONS OF A TRAPPED MICROPARTICLE

Assuming that a microparticle to be trapped is just under the electron beam as shown in Figure 2, it is expected that the trapped microparticle makes a vertical oscillation only, in both a magnetic field and no magnetic field. In Figure 2, Z is the vertical direction and Z_0 is the distance from the bottom of the beam chamber to the center of the electron beam.

Considering the continuous vertical oscillation as shown in Figure 2 and the basic equation in Reference [4], the average vertical acceleration \bar{Z} , where Z is the distance between the microparticle and the bottom of the chamber wall, is given by

$$\bar{Z} = \frac{Q E_z t_1}{m t_2} - g \quad (1)$$

Here Q is the charge deposited on the microparticle through the photoelectric effect, E_z the electric field in the vertical direction, m the mass of the microparticle, t_1 the time interval while the electron bunch is over the microparticle, t_2 the revolution time of the electron bunch and g the acceleration due to gravity.

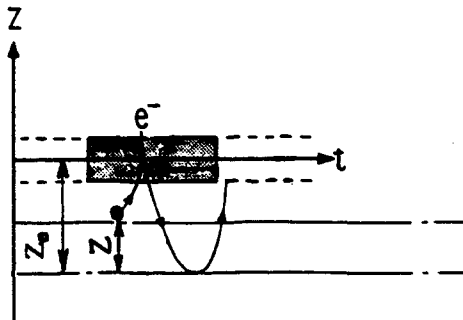


Fig. 2 A model for vertical oscillation of a trapped microparticle.

Assuming that the electrons in the bunch are formed into Gaussian distribution, the electric field E_{z0} at the vertical distance Z is given by

$$E_{z0} = \frac{Z_0 E_z [1 - e^{-\frac{(Z_0-Z)^2}{2L_b^2}}]}{Z_0 - Z} + E_z e^{-\frac{Z_0^2}{2L_b^2}} \quad (2)$$

where E_z is the electric field at $Z = 0$ and L_b is the bunch length. Substituting Equation (2) into E_z in Equation (1), the vertical acceleration at Z is given by

$$\bar{Z} = \frac{Q E_z t_1}{m t_2} \left[Z_0 \frac{1 - e^{-\frac{(Z_0-Z)^2}{2L_b^2}}}{Z_0 - Z} + e^{-\frac{Z_0^2}{2L_b^2}} \right] - g \quad (3)$$

Therefore, the solution of Equation (3) shows the vertical motion of the trapped microparticle.

Figure 3 shows a result of approximation for the vertical oscillation of the trapped microparticle corresponding to time duration, when QE_z/m is 1.85×10^5 Newton/kg of the trapping condition in the TRISTAN accumulation ring shown in Reference [1], $t_1 = 6.67 \times 10^{-11}$ s, $t_2 = 1.26 \times 10^{-6}$ s, $Z_0 = 0.024$ m, $L_b = 0.02$ m and the initial vertical velocity of the microparticle at the initial position is set to be 0.00005 m/s. As shown in Figure 3, the time interval of the vertical oscillation is about 0.7 s. Considering that the calculated vertical velocity at the electron orbit is about 1.1 m/s, the transit time of the microparticle passed through the electron beam is calculated as about 1.3 ms.

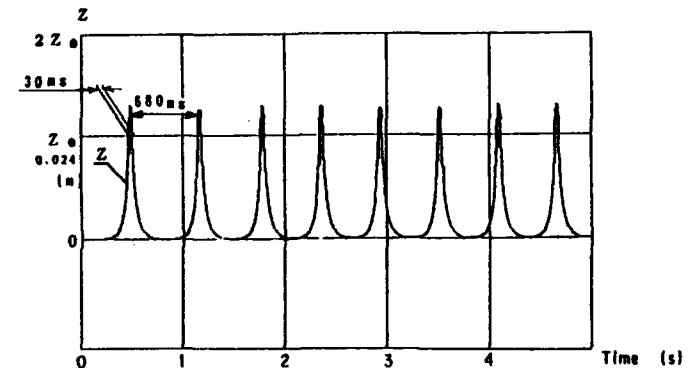


Fig. 3 A result of approximation for the vertical oscillation of the trapped microparticle. The horizontal time scale is 1 s/division.

IV. DISCUSSION

If a trapped microparticle makes a vertical oscillation as shown in Section III, it can be said that Figure 1 shows that the microparticle made the vertical oscillation and that the time interval is 1 s. It can be also said that signal of 0.15 ms duration shows the interaction time per pass of the microparticle. It can be seen that the observation coincides with the calculated result based on our newly developed theory, in spite of the simplified electric field and simplified motion of the trapped microparticle.

When the energy loss caused by a trapped microparticle becomes more than 0.1 % of the energy of an accelerated electron, it is assumed that the electron is lost. Generally, the beam lifetime τ is given by

$$\frac{1}{\tau} = \frac{N_p \sigma f \Delta t}{4\pi \sigma_x \sigma_y} \quad (4)$$

where N_p is the total number of atom in the microparticle, s the total cross-section, f the revolution frequency, Δt the transit time in a second, σ_x the width of the electron beam and σ_y the bunch length. Setting the diameter of the trapped microparticle made of Al is to be 0.1 mm, as shown in Reference [1], the calculated beam lifetime is 72 min. When the microparticle is made of Ti, the lifetime is calculated as 61 min. Compared results of the observation and the theoretical analysis show that our theory for motions of a trapped

microparticle is useful.

In near future, three dimensional precise analysis for motions of a trapped microparticle will be carried out. Furthermore, precise observations in the TRISTAN accumulation ring will be carried out using an automatic observation system with lead-glass counters.

V. ACKNOWLEDGEMENTS

The authors would like to thank Professor Y. Kimura and Professor H. Kobayakawa for their helpful suggestions. The authors also wish to thank Technicians Mr. M. Shimamoto, Mr. M. Sato, and Mr. M. Nakagawa for their generous support.

VI. REFERENCES

- [1] H. Saeki, T. Momose, and H. Ishimaru, "Observations of dust trapping phenomena in the TRISTAN accumulation ring and a study of dust removal in a beam chamber", Rev. Sci. Instrum. 62, 874 (1991).
- [2] H. Saeki, T. Momose, and H. Ishimaru, "Motions of trapped dust particles around the electron beam in the TRISTAN accumulation ring", Rev. Sci. Instrum. 62, 2558 (1991).
- [3] H. Saeki, T. Momose, and H. Ishimaru, "Experiments to trap dust particles by a wire simulating an electron beam", Rev. Sci. Instrum. 62, 2568 (1991).
- [4] P. Marin, LURE, RT/90-01, Orsay (1990).

OVERVIEW OF AN 80 K LINER DESIGN FOR SYNCHROTRON LIGHT INTERCEPTION IN SSCL COLLIDER

Q. S. Shu, W. Chou, D. Clark, W. Clay, Y. Goren, R. Kersevan, V. Kovachev, P. Kraushaar, K. Leung, J. Maddocks, D. Martin, D. Meyer, R. Mihelic, G. Morales, J. Simmons, G. Snitchler, M. Tuli, W. Turner, L. Walling, K. Yu, and J. Zbasnik

Superconducting Super Collider Laboratory*
2550 Beckleymeade Avenue, Dallas, TX 75237-3997

Abstract

The paper reports the efforts that develop a viable design for an SSC 80K Synchrotron Radiation Liner System. The liner is one method under consideration to minimize the presence of photodesorbed gases in the particle beam line vacuum in order to assure an acceptable, operational availability of the SSC Collider. Also the 80K liner is aiming at improving the Collider cryogenic thermal efficiency which would allow a potential luminosity upgrade. The trade studies, engineering analyses, concept evaluation and detailed design are introduced. This paper also briefly discusses the preliminary consideration of lower temperature liners.

I. INTRODUCTION

The Superconducting Super Collider (SSCL) is the first proton superconducting accelerator designed to operate at 20 TeV (each beam) and beam current of 72 mA in which synchrotron radiation is a significant design factor. The Collider will produce a synchrotron power of 0.14 W/m and 18 kW total at 4.2 K. This synchrotron light will produce considerable photodesorbed gases in the beam vacuum. The photodesorbed gases may greatly reduce the beam lifetime and scattered beam power may lead to quenching of superconducting magnets. The Collider availability may be unacceptable without properly addressing this concern. A liner is one method under consideration to minimize the presence of photodesorbed gases. An 80 K liner also replaces the 4 K dynamic heat load of the synchrotron radiation with a static heat load, independent of the beam intensity, and transfers the intercepted heat to the liquid nitrogen system that may improve Collider cryogenic thermal efficiency. It would allow a potential luminosity upgrade.

Operated by the URA, Inc., for the U. S. Department of Energy under Contract No. DE-AC35-89ER40486.

The liner operational temperature was required to be 80 K based on photodesorption data available from the CDG and SCDG measurements [1]. Those data showed that liners at lower temperatures 20 K or 4.2 K had either unacceptable impedance margins or excessively long conditioning periods. However, in January of 1993 new photodesorption data also indicated the viability of 4 K and 20 K systems [1].

The Collider Liner System Design addresses photodesorption, particle beam stability, magnetic field quality, beam induced wake fields, RF impedance, cryogenics, magnet quenching (especially quenches induced Lorentz pressure), and many other interdisciplinary technical problems.

II. ASST LINER TUBES CONFIGURATION

As shown in Figure 1, an 80 K liner tube consists of a perforated tube located coaxially inside the 4.2 K magnet bore tube. The ASST Dipole Magnet (CDM) liner temperature is maintained at 80 K by high pressure GHe loops of 0.25 g/s, as (A). The GHe flow is recooled by LN₂ in the cooling pipe of a magnet cryostat. A special end conducting cooling structure is designed to cool the ASST Quadrupole Magnet liner as Figure 1, (B)

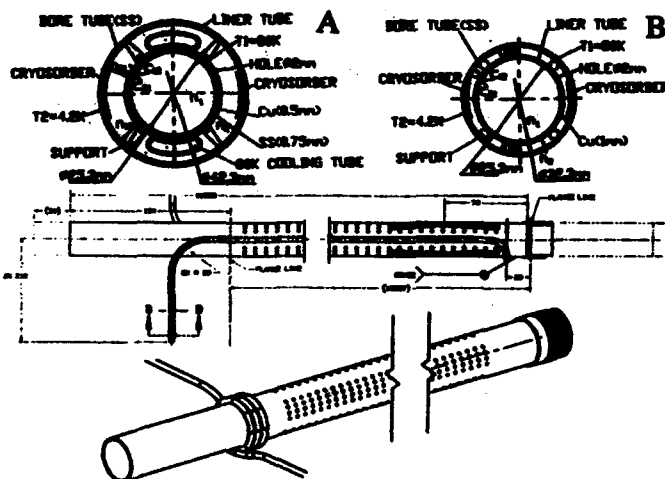


Figure 1. The CDM and CQM liner tubes.

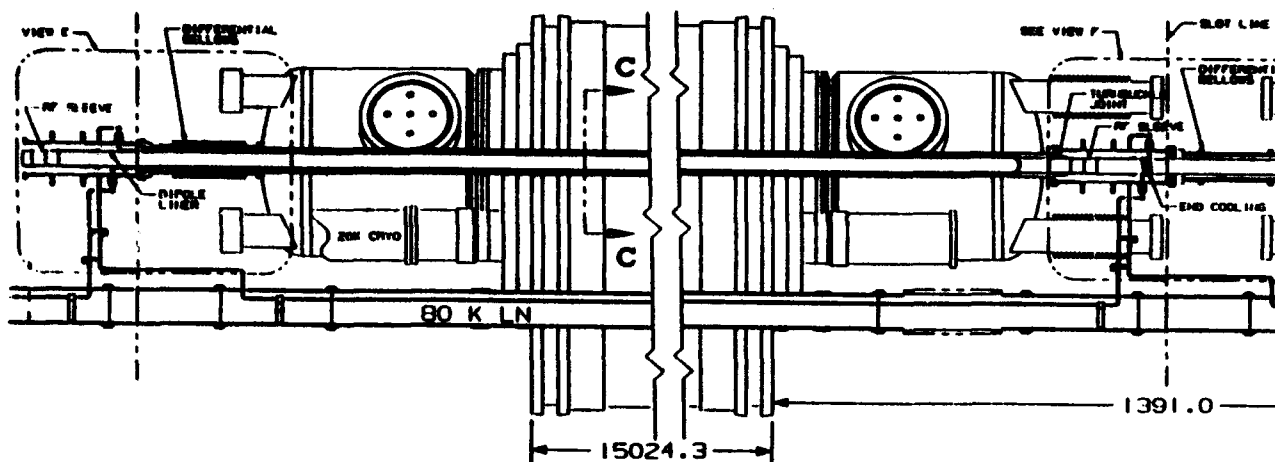


Figure 2. A CDM liner assembly in a CDM magnet.

since the (CQM) beam tube ID (32.3 mm) is much smaller than an ASST dipole ID (42.3 mm). Low heat leak supports hold the liner in the center of the beam tube. A thin layer of cryosorber (0.5 mm) on the inner surface of the 4.2 K beam tube pumps the photodesorbed gases through the holes on the liner tube (1300 holes/m, $D=2$ mm for CDM liner; 2400 holes/m, $D=1.5$ mm for CQM liner). The CQM liner tube is made of 1 mm thickness copper. The CDM liner is 1.25 mm bimetallic tube of an inner 0.5 mm copper and outer 0.75 mm stainless steel.

III. ASST LINER STRUCTURE

A liner system prototype has been developed for testing at the Accelerator System String Test (ASST) facility since the half cell (five dipoles, one quadrupole and one spool piece with a beam position monitor) is an existing basic unit of the Collider.

An extensive trade study has been performed to develop a retrofit 80 K liner structure and flow return cooling loop, Figure 2. If an 80 K liner is chosen for collider upgrade, the structure will help its insertion into magnets to be retrofitted in the tunnel. Figure 3 shows that a CQM liner is

refrigerated through thermal conduction by 80 K GHe in a compact heat exchanger at the end of the liner tube outside the CQD cold mass. The maximum temperature increase ΔT could be less than 5 K for a Spool Piece liner, and 10 K for a CQM. The total heat load from a liner system in a half cell to 4K is 5 - 6 W that is much smaller than a Collider baseline design.

The RF joint and a good thermal contact joint assure the continuity of the image current and aid assembly and maintenance. The magnet interconnect with these joints, and a compact heat exchanger are included in a cryogenic box. The cryogenic box also allows each liner to have up to a 54-mm thermal contraction during cooldown and warmup, as Figure 4. However, the liner is discontinuous when routed through the Beam Position Monitor (BPM). Two options of BPM designs have been carried out. One is an 80K BPM which is easy to connect with an 80K liner, but not to a Spool Piece. Another option is a 4K BPM, which is easy to connect to the Spool Piece, but not easy to a liner. Figure 5 shows a 4 K BPM.

IV. ANALYSES AND TRADE STUDY

A uniform and maximum possible liner inner diameter (ID) is needed due to: (1) particle beam commissioning, (2) particle beam dynamic stability, and (3) safety margin. However, the maximum liner ID is constrained by: (1) the available magnet beam tube inner diameter (ID), and (2) the minimum liner radial space. Using cooling, the minimum liner radial space is 6 mm and using end conducting cooling, the radial space needs to be 3.5 mm. Tables 1 and 2 show the maximum liner ID and the liner impedances in various options, respectively.

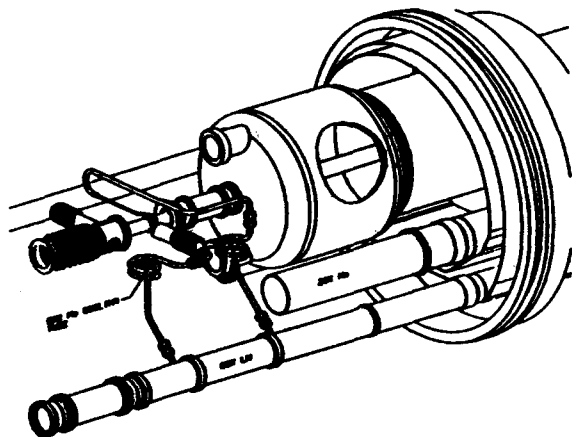


Figure 3. The end structure of a CQM liner.

Table 1. Possible maximum liner ID in various cases.

Object	Dipole Beam tube ID, mm	Magnet Liner ID, mm	Quad Beam tube ID, mm	Magnet Liner ID, mm	Spool Beam tube ID, mm	Piece Liner ID, mm
ASST	42.3	25.3	32.3	25.3	32.3	25.3
GD, B & W	32.3	20.2	32.3	20.2	32.3	20.2
Desired	42.3	31	42.3	31	42.3	31

Table 2. Comparison of impedances.

Case	Liner ID, mm	Hole/Slots Coverage	Z (liner) M ohm/m	Z (other) M ohm/m	Z (total) M ohm/m	Safety margin
Baseline	32.3			40	40	6.7
With liner	25.3	2 mm, 2%	22	112	133	2
With liner	25.3	2 mm, 4%	44	112	156	1.7
With liner	25.3	2 x 6, 2%	8	112	120	2.2
With liner	33	2 mm, 4%	15	40	55	4.9

Besides, the liner tube design also must meet the following requirements:

- | | |
|---|---|
| 1. Inner wall conductivity and thickness | $\sigma \delta > 2 \times 10^5 \text{ Ohms}^{-1}$ |
| 2. Liner impedance | $Z_L/n < 0.34 \text{ Ohm}, Z_T < 20 \text{ M Ohm/m}$ |
| 3. Inner wall photodesorption coefficient | $\eta = 0.02, \alpha = 0.3 \text{ for H}_2$ |
| 4. Liner pump speed | 600 l/m/s for H ₂ |
| 5. Total liner heat leak to 4 K | < 1 W for dipole |
| 6. Cryosorber pump speed | 1200-3000 l/m/s for H ₂ |
| 7. Cryosorber pumping capacity | 30 Torr l/m at 294K |
| 8. Cryosorber activation temperature | 294 K; regeneration < 80 K H ₂ ,
< 294 K all Gases; recovery fraction > 98% |
| 9. Liner quench survivability and ASME code | 100 quenches in 25 yrs |
| 10. Radiation dose tolerance | 1400 MRad in 25 yrs |

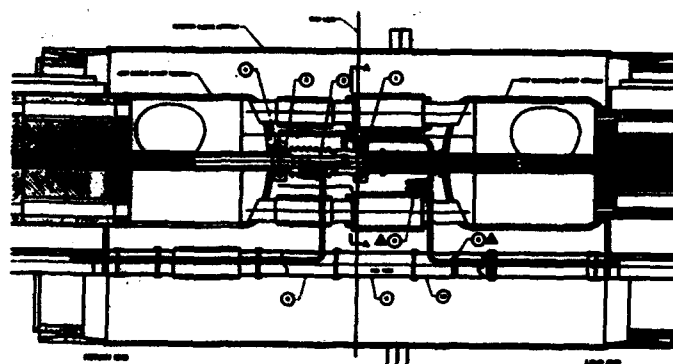


Figure 4. The liner interconnects.

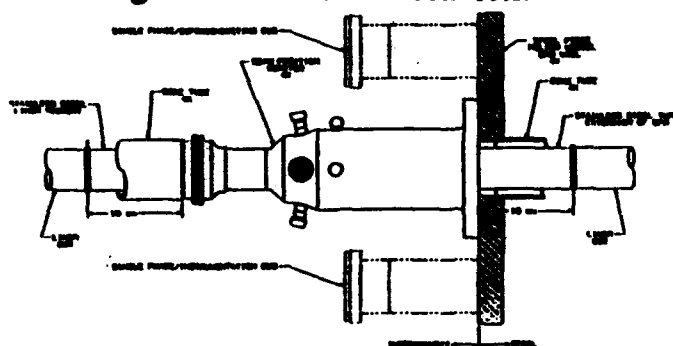


Figure 5. A schematic of a 4K BPM

V. LOWER TEMPERATURE LINERS

Several concepts of 4.2 K and 20 K Liners have been studied as a result of the new photodesorption tests. Concept A had a complex extruded shape with three supports integral to the liner tube. Concept B showed a circular beam tube with three brazed hat shaped supports running the full length of the tube (to ensure even thermal distribution between liner and bore tube). Concept C showed the same support system as proposed for 80 K liner, i.e., discrete supports located every 1 m. All three concepts would be optimized for good thermal contact between the liner and beam tube. In the three concepts, the cryosorber is located on the liner outer surface. Concept D considered addition of a 4.2 K channel on the liner tube to boost cooling capacity. The 20 K liner system concept is very similar to the 80 K system, but with the option of cryosorber on liner outer surface.

REFERENCES

1. 80 K ASST Liner Design Report, edited by Q. S. Shu, in preparation.

Thermal Model and Associated Novel Approach for Synchrotron Radiation Liner with End Cooling

Quan-Sheng Shu, Kun Yu, Wayne Clay
Jim Maddocks, Gilberto Morales and Jon Zbasnik

Superconducting Super Collider Laboratory
2550 Beckleymeade Ave. MS 8001, Dallas TX 75237 USA

Abstract

An end conductive cooling approach has been developed to reduce the radial space budget of a synchrotron radiation liner to permit the maximum possible liner tube inner diameter (ID). A thermal model has also been developed to analyze the thermal performance of such liners. This approach is found to be acceptable for a liner in a 5 m long quadrupole magnet and 3 m long spool piece, but not for a longer 15 m dipole. The heat transfer and temperature distribution were calculated respectively along the axis of two different liner model: 20K and 80K liner with different thicknesses (0.5 - 2 mm) of liner tubes and different emissivities (0.05 - 0.3) of liner surface for a variety of magnets. The thermal model is also applied to the case of an 80K liner connected directly to a 4K beam position monitor (BPM). In order to utilize the end cooling, a good thermal joint and a compact heat exchanger are designed.

I. INTRODUCTION

A uniform and maximum possible liner inner diameter (ID) is needed due to: (1) particle beam commissioning, (2) particle beam dynamic stability, and (3) safety margin of impedance. However, the maximum liner ID is constrained by: (1) the available magnet beam tube inner diameter (ID), and (2) the minimum liner radial space. Using regular cooling, the minimum liner radial space is 6 mm and using end conducting cooling, the radial space needs to be 3.5 mm. The 80K synchrotron radiation liner prototype was designed to be tested at the SSCL Accelerator System String Test (ASST) facility. In the case of the 80K ASST liner, the 25.3 mm design was chosen for the maximum liner ID.

Since the magnet quench induced Lorentz pressure on a CQM liner is much smaller than that on a CDM liner, the pure copper tube was chosen for the CQM liner material. The RRR and thickness

of the copper tube must be of sufficient value due to both requirements (1) resistance wall: conductivity \times Thickness $> 2 \times 10^5 \Omega^{-1}$ and (2) conducting heat transfer requirement. However, the RRR and thickness shall not be too larger in order to reduce the Lorentz pressure. This paper will focus on a thermal model used to predict the thermal performance of an end cooling liner for different cases.

II. THERMAL MODEL FOR END CONDUCTIVE COOLING

An end conductive cooling approach for the Spool Piece and CQM is shown in Figure 1. The 80K GHe flows through a compact heat exchanger located at each end of the liner tube outside of the CQM cold mass. The rest of the liner tube is refrigerated by thermal conduction. A compact heat exchanger & a good thermal conducting joint is designed to utilize the end cooling approach and to assure an easy assembly.

A thermal model to analyse the end conductive cooling was developed by Q.S.Shu and K.Yu [1][2], assuming: Q_r synchrotron radiation, 0.14 W/m ; Q_L (heat leak through support)/ $2L$; Q_r (heat leak by radiation)/ $2L$; L half length of the CQM or Spool Piece; A the cross section area of the liner tube; $\lambda(T)$ the heat conductivity; $\lambda(80)_{Cu} \approx 5.50 \text{ W/(cm.K)}$; $\lambda(80)_{\text{ins}} \approx 0.045 \text{ W/(cm.K)}$; ϵ_1, ϵ_2 the emissivity.

$$Q_r = \sigma A (T_1^4 - T_2^4) \epsilon_1 \epsilon_2 / (\epsilon_1 + \epsilon_2 - \epsilon_1 \epsilon_2)$$

$$dQ_c = (Q_r - Q_L - Q_r) dx$$

$$\text{if } q = (Q_r - Q_L - Q_r)$$

$$Q_x = -\lambda(T) A dT/dx$$

$$\text{and } Q_{x+dx} = -\lambda(T) A d[T + (dT/dx) dx] / dx$$

$$= -\lambda(T) A [dT/dx + (d^2T/dx^2) dx]$$

$$\text{we know } Q_{x+dx} = dQ_c + Q_x$$

$$d^2T/dx^2 = -q/[\lambda(T)A]$$

$$T(x) = (q/[2\lambda(T)A])x^2 + C_1x + C_2$$

boundary conditions:

$$T(x)|_{x=L} = 80 \text{ K}; \quad T(x)|_{x=-L} = 80 \text{ K}$$

we have,

$$T(x) = - (q/[2\lambda(T)A])x^2 + (q/[2\lambda(T)A])L^2 + 80$$

(1)

Operated by the URA, Inc., for the U. S.
Department of Energy under Contract No.
DE-AC35-89ER40486.

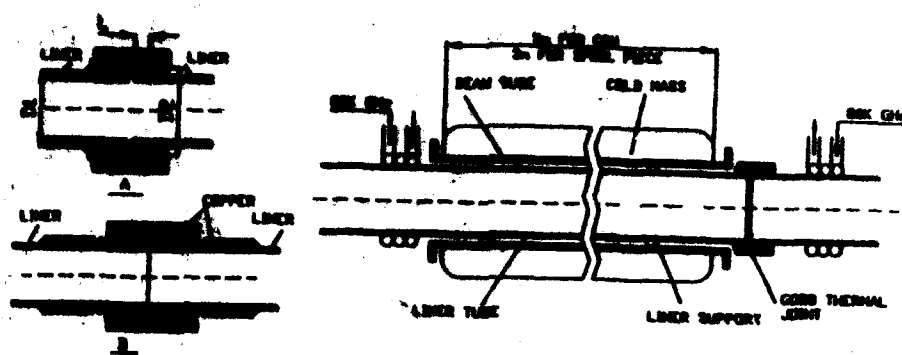


Figure 1. A schematic drawing of a liner with the end conducting cooling.

Using the model: 1) The temperature distribution along the liners as functions both of the emissivities and of the tube thicknesses were calculated. 2) The maximum ΔT could be less than 5K for Spool Piece liner, and 10K for CQM. 3) A temperature difference between the Spool Piece pipe ends and the middle of the liner is 2K when copper layer of 2 mm is used and 10K with copper layer of 0.5 mm was used. 4) For CQM ΔT of 6K is obtained when copper layer of 2 mm, and 26K when copper of 0.5mm. 5) The correction of the effect of the magnetic field on copper thermal conductivity is considered. Figures 2, 3, and 4 show some of the calculated results.

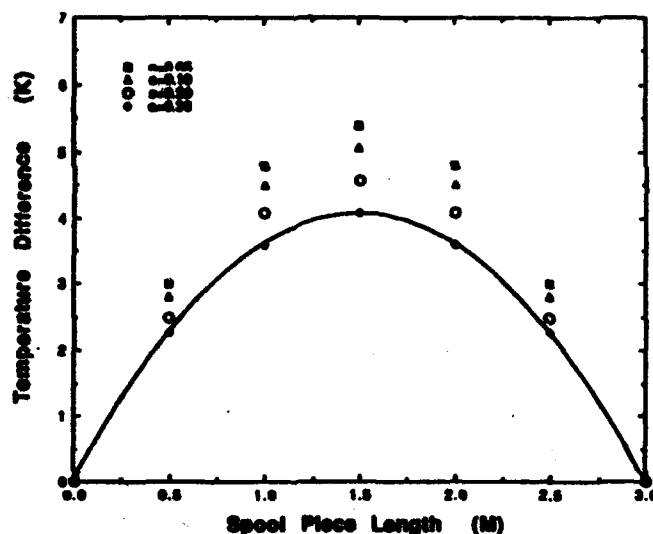


Figure 3. Temperature distribution of 80K liners as function of liner surface emissivities.

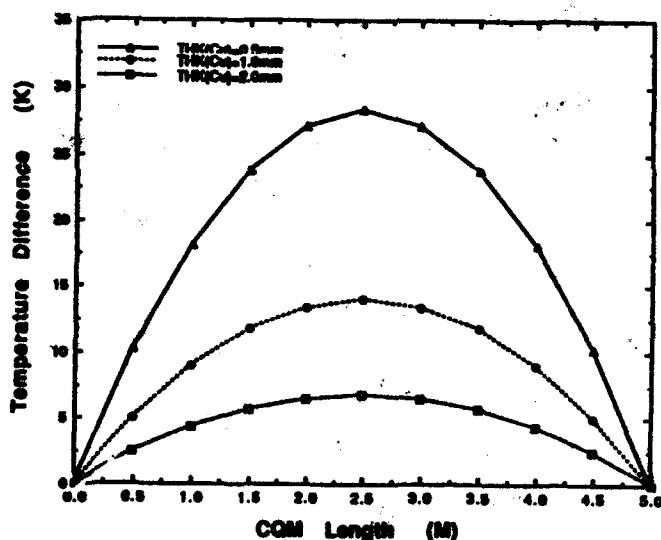


Figure 2. Temperature distribution of 80K liners as function of liner tube thicknesses.

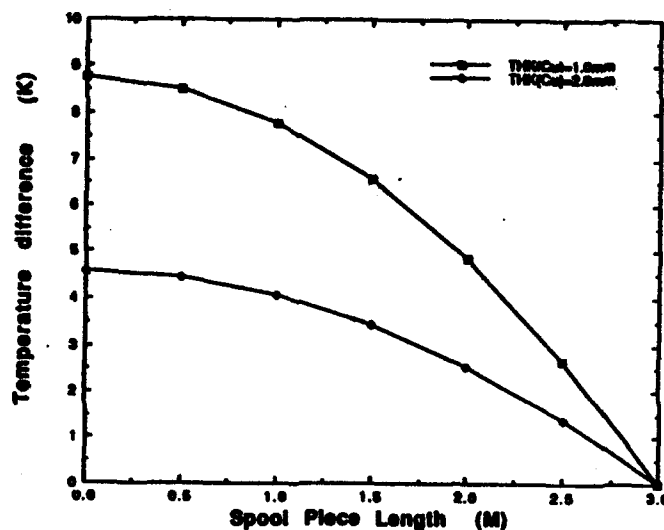


Figure 4. Temperature distribution of 20K liners with one end cooling only.

III. THERMAL MODEL FOR 80K LINER WITH A 4K BPM

If a 4K BPM is used, the 80K liner end conductive cooling becomes more complicated. As shown in Figure 5. To reduce the heat leak through the copper liner tube from 80K to 4K BPM, a 10 - 20 cm long piece of stainless steel tube is insert between the BPM and copper liner tube. The synchrotron radiation, the heat leak from liner to BPM, the heat leak from liner to 4K beam tube and the heat exchange between the liner and the 80K GHe must meet the law of conservation of energy .

First, we calculate a temperature distribution along the S. S Liner tube;
when $0 \leq X \leq L$, we have,

$$T_s(X) = -qx^2/(2\lambda_s A_s) + S_1 X + S_2 \quad (2)$$

The temperature distribution along the copper tube shall satisfy Eq.(3) if $L \leq X \leq L_0$.

$$T_c(X) = -qx^2/(2\lambda_c A_c) + C_1 X + C_2 \quad (3)$$

Eq. (2) & (3) must meet the following boundary conditions:

$$T_s(0) = 4$$

$$T_c(L_0) = 80$$

$$\lambda_c A_c (\partial T_c(X)/\partial X)|_{X=L} = \lambda_s A_s (\partial T_s(X)/\partial X)|_{X=L}$$

$$T_s(L) = T_c(L)$$

The C_1 , C_2 , S_1 and S_2 can be determined:

$$S_2 = 4$$

$$S_1 = [\lambda_c A_c / (\lambda_s A_s)] [80 + qL_0^2 / (2\lambda_c A_c) - qL^2 / (2\lambda_c A_c) + qL^2 / (2\lambda_s A_s) - 4] / [\lambda_c A_c L / (\lambda_s A_s) - L + L_0]$$

$$C_1 = [80 + qL_0^2 / (2\lambda_c A_c) - qL^2 / (2\lambda_c A_c) + qL^2 / (2\lambda_s A_s) - 4] / [\lambda_c A_c L / (\lambda_s A_s) - L + L_0]$$

$$C_2 = 80 + qL_0^2 / (2\lambda_c A_c) - L_0 [80 + qL_0^2 / (2\lambda_c A_c) - qL^2 / (2\lambda_c A_c) + qL^2 / (2\lambda_s A_s) - 4] / [\lambda_c A_c L / (\lambda_s A_s) - L + L_0]$$

Using Eq. (2) and (3) the temperature distribution can be calculated & shown in Figure 6.

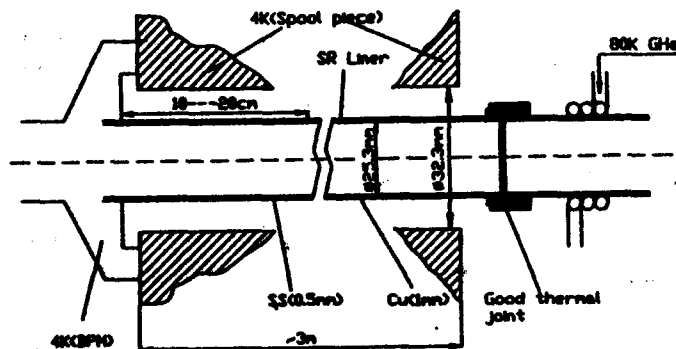


Figure 5. A schematic drawing of an 80K liner with a 4K BPM

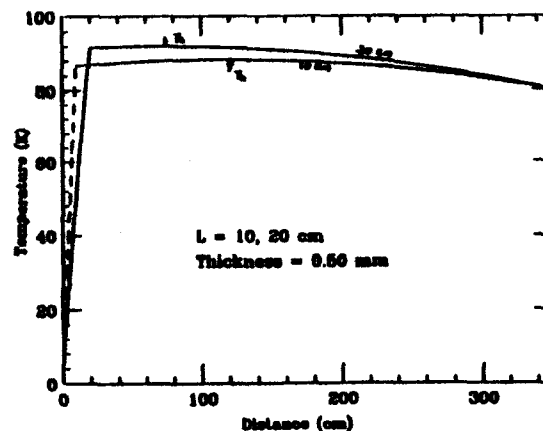


Figure 6. Temperature distribution along an 80K liner with a 4K BPM.

IV. GOOD THERMAL CONDUCTING JOINT

A good thermal conducting joint concept, as shown figure 1, was proposed by Q.S. Shu & K. Yu. The joint makes liner assembly easier. Assume synchrotron radiation of a quadrupole to be 1 W. The heat transferred at each liner end is 0.5 W. If the pressure on the Cu-Cu machined contact is 7 MPa, thermal conductance of the contact (at temperature range 5—25K) is $h(T) = 0.13T$ (W / cm² K). The temperature across the joint ΔT (at 80K) ≤ 1 K.

V. COMPACT HEAT EXCHANGER

To make end cooling work, a compact heat exchanger with a length of less than 5 cm was developed. The total heat to be transferred by the heat exchanger is $Q=2$ W. Design parameter used were: Copper cooling tube ID=0.25 cm, mass flow rate of the 80K GHe, $dM/dt = 0.25$ g / sec. the temperature increase of GHe is ΔT . $Re = GD/\eta = 31812$, $Pr = \eta C_p / \lambda = 0.357$, $h = 0.023 C_p G^{0.8} \eta^{0.2} / (Pr^{0.6} De^{0.2}) = 0.0345$. If three turns are used, $L = 28.75$ cm, $\Delta T < 1$ K.

ACKNOWLEDGEMENTS

The authors sincerely thank A. Yucel, D. Clark, D. Martin and W. Turner of the SSCL for their contribution to the work.

REFERENCES

- [1] Q. S. Shu, Status Report on the ASST Liner System Design, SSCL-N-805, November, 1993.
- [2] 80K ASST liner Design Report, prepared by Q. S. Shu, (in preparation)

DESIGN OF ECR ION SOURCE VACUUM SYSTEMS

Juraj Pivarč *

Joint Institute for Nuclear Research, FLNR, Dubna
Head Post Office, P.O.Box 79, 101 000 Moscow, Russia

Abstract

The present work has been motivated primarily by the discussions and results reported by M.CAVENAGO [1] and K.HATANAKA et al., [2] who indicate the requirements for vacuum systems of ECR ion sources. To use such source as a possible source of high charge state ions is very interesting on upgrading present heavy particle accelerators. The relevance of ion induced pressure instability and neutral gases processes is given.

I. INTRODUCTION

The vacuum system of the ECR ion source is one of the main component of the source. Whereas, operating pressure ranges for vacuum systems of accelerators are $10^{-4} - 10^{-9}$ Pa [3], the required operating pressure range for the vacuum system of the ECR ion source is $10^{-2} - 10^{-5}$ Pa, respectively. Basically, it consists of stainless steel, cooper beam tubes pumped with turbomolecular, cryosorption, getter - Ti - sublimation, NEG pumps combined with sorption and rotary pumps. The combination of turbomolecular and rotary pumps is being used for the time in the DECRIS ion source [4]. The other suitable combinations of vacuum pumps as well as the pressure measuring gauges are shown in Figure 1.

The paper is mainly oriented to more detail description of influence of gas desorption process (ion induced pressure instability) and neutral gases on the vacuum system design of the ECR ion sources.

II. DESORPTION OF GASES

The pressure of 10^{-5} Pa must be maintained inside the ECR ion source and its beam pipe despite of i) the thermal outgassing of surfaces, ii) outgassing due to the desorption of weakly bounded molecules on the walls of the vacuum system, iii) the ions induced by extracted and accelerated ions, iv) the diffusion of hydrogen from the walls of the vacuum system, iiv) the neutral gases produced inside the plasma of the ECR ion source, as well as ivv) the desorption of molecules generated by a roentgen radiation. There are also observed direct thermal effects produced by the radiation. The radiation is also penetrating to the region of the beam pipe of the

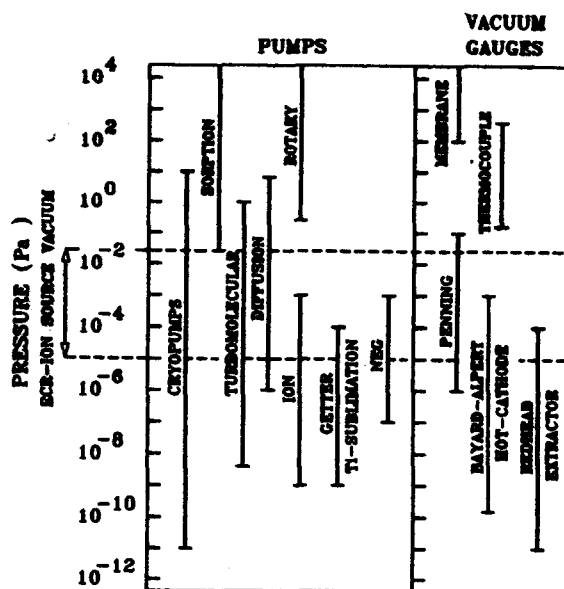


Figure 1. Vacuum pumps and gauges used for pumping and pressure measurement in ECR ion sources.

ECR ion source through the orifices in the anode and the extraction system of the source. Therefore, even water-cooling parts of the first and second stages and other small areas of the source, as for example the input flange of the high frequency generator, can be above ambient temperature by 80 °C or more with a corresponding increase in their thermal outgassing rate by an order of magnitude or more [5-6]. To establish the given pressure for the given pumping speed the average thermal outgassing rate and the total average desorption rate must be below certain definite values.

A. Ion - induced pressure instability

The ions induced by extracted and accelerated beam can produce desorption of strongly bound molecules. The desorption flow rate n_1 , Q_1 can be expressed by [7]

$$n_1 = \eta \sigma L (I/e) n \text{ or } Q_1 = \eta \sigma L (I/e) p \quad (1)$$

where η is the molecular desorption yield [molecules ion⁻¹], σ is the ionisation cross-section of extracted and accelerated ions [m²] (for example for high energy protons $\sigma = 1.2 \times 10^{-22}$ m² and for CO [3]) L is the length of beam section [m], I is the beam intensity [A], e is the

* Home address : Institute of Physics, Slovak Academy of Sciences, Dúbravská cesta 9, 842 28 Bratislava, Slovakia.

electron charge [As], n is the number of molecules in unit volume [m^{-3}] and p is the pressure [Pa]. Note, if ions are taken from the restgas, hence η will represent a net desorption yield. For $\eta < 0$ "beam pumping" can be observed, i.e. the system acts like an ion pump. In the presence of the ion induce - desorption is $\eta > 0$ and the equilibrium pressure can be expressed as

$$p = Q/S_{\text{eff}} = \frac{\eta\sigma(I/e)p + qA}{S_{\text{eff}}} \quad (2)$$

which gives

$$p(I) = \frac{P_0}{1 - \frac{\sigma \eta I}{e S_{\text{eff}}}} \quad (3)$$

where $p_0 = qA/S_{\text{eff}}$.

By introducing

$$(\eta I)_{\text{crit}} = \frac{e}{\sigma} S_{\text{eff}} \quad (5)$$

we obtain

$$p = \frac{P_0}{1 - \frac{\eta I}{(\eta I)_{\text{crit}}}} \quad (6)$$

Hence, the "critical current" product for $S \rightarrow \infty$ cannot exceed

$$(\eta I)_{\text{crit}} = \frac{e 6w}{\sigma L^2} \quad (7)$$

Therefore, the pressure p is a function of the beam current I . The higher is the current I , the higher is the equilibrium pressure p . The conductance of the beam pipe and the pump distance are also crucial parameters for vacuum stability. The remedy "defect" caused by the pressure bumps in the vacuum system of the source can be reduced by adding cryogenic, getter -Ti -sublimation, or NEG pumps, respectively [8-9]. By 300 °C bakeout and argon glow discharge cleaning of the source stages and beam pipes we can also reduce the molecular desorption yield η . By the way the required ion dose on the beam pipe is typically 10^{18} cm^{-2} and result in that $\eta \leq 0$.

The glow discharge cleaning could be done as shown in Figure 2. The discharge gas argon gives efficient sputtering and desorption of strongly adsorbed gas molecules. On the other hand the addition of oxygen produces from carbon contaminants on the surface CO and CO₂ which can easily be pumped out.

The other very important sources of gases in the ECR ion sources are neutral gases.

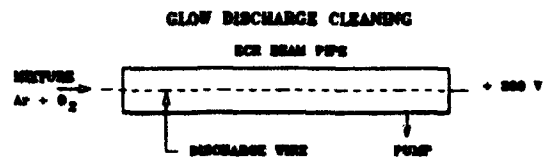


Figure 2. Layout of the glow discharge cleaning [3].

III. NEUTRAL GASES

The neutral gases can arise for example by recombinations of ions with electrons. The efficiency of the process is very high at the low energy of electrons and sufficiently long time of interactions of produced ions with electrons. At the low electron temperature the neutral gases strongly influence on the balance of the plasma which is created from charge particles.

The ion - loss rate due to the recombination process can be described by the following equation [10]

$$\frac{\partial n^+}{\partial t} = -\alpha n^{+2} \quad (8)$$

where n^+ is the concentration of the ions [cm^{-3}], t is the time [s] and α is the coefficient of recombination [$\text{cm}^3 \text{ s}^{-1}$]. The coefficient α may be approximated by

$$\alpha \approx \frac{10^{-13}}{\sqrt{T_e}} \quad (9)$$

where T_e is the temperature of electrons into the plasma [eV]. For the typical values reached in the ECR ion source is $n^+ \approx 5 \times 10^{10} \text{ cm}^{-3}$ [11], $T_e \approx 5000 \text{ eV}$ [12], $\alpha \approx 1.4 \times 10^{-15} \text{ cm}^3 \text{ s}^{-1}$, and at the volume of the second stage of the ECR ion source of 1500 cm^3 (DECRIS), the

desorption rate $\frac{dQ^{\text{ng}}}{dt}$ will be given by

$$\frac{dQ_1^{\text{ng}}}{dt} = 2 \times 10^{-8} \text{ Pa l s}^{-1} \quad (10)$$

The neutral gas is also generated as a residual gas from the usage gas flow rate. The usage rate for the solid and gas materials is varied depending on a variety of parameters. It has generally been confirmed by most of tests that the usage rates for many solid materials are approximately 1 mg h^{-1} [13]. It corresponds to consumption of

$$\frac{dQ_2^{\text{ng}}}{dt} = 2.5 \times 10^{-3} \text{ Pa l s}^{-1} \quad (11)$$

The lowest usage rate has been obtained 0.1 mg h^{-1} for a calcium run. The usage rate for gaseous materials are

approximately $0.06 \text{ cm}^3 \text{ (STP) min}^{-1}$ [14]. It corresponds to a maximum consumption of

$$\frac{dQ_3^{ns}}{dt} = 0.1 \text{ Pa l s}^{-1}. \quad (12)$$

So, the total neutral gas $\frac{dQ_1^{ns}}{dt}$ for the gaseous materials operation is given by

$$\frac{dQ_1^{ns}}{dt} = \frac{dQ_1^{ns}}{dt} + \frac{dQ_3^{ns}}{dt} \approx 0.1 \text{ Pa l s}^{-1}. \quad (13)$$

In order to obtain suitable operation vacuum inside the beam pipe of the ion source of 10^{-4} Pa the effective pumping speeds for the solid material (S_{eff}^s) and the gaseous (S_{eff}^g) operations have to be related by $S_{\text{eff}}^s \approx 25 \text{ l s}^{-1}$ and $S_{\text{eff}}^g \approx 1000 \text{ l s}^{-1}$, respectively.

IV OUTGASSING OF THE BEAM PIPE

For every vacuum system the size of the required pumps is directly related to the outgassing. The first imported source is the static and thermal outgassing of weakly adsorbed molecules and diffusion of H_2 from the bulk of the material. The standard procedure to reduce the thermal outgassing is the well known bakeout of the beam pipe. The pressure inside an unbaked system is mainly determined by water vapour. In a clean and well baked system H_2 will be the dominant residual gas constituent. Typically total specific outgassing rate q for unbaked 100 h pump down beam pipe constructed by stainless steel is $10^{-7} \text{ Pa l s}^{-1} \text{ cm}^{-2}$ at 293 K (q for baked 30 - 150 h pump down beam pipe constructed by the same material at 573 K is $10^{-10} \text{ Pa l s}^{-1} \text{ cm}^{-2}$) [3].

The second important source of gas in ion source is the so called "dynamic" outgassing in presence of the beam. Here, strongly bound molecules can also be desorbed.

The quantity of the outgassing rate very strongly also depends on the finished treatment with used materials. However, in order to obtain the outgassing rate less as $10^{-8} \text{ Pa l s}^{-1} \text{ cm}^{-2}$ the vacuum system is not allowed to be constructed by rubbers, polyamids, epoxy, viton and PTFE materials, respectively.

V. CONCLUSION

In practice, it is very difficult to construct very effective, reliable and cheap vacuum system for the ECR ion source. The vacuum system of the source have to be designed with respect of obtaining the vacuum of 10^{-5} Pa , for about 10 h with a leak rate lower than $10^{-3} \text{ Pa l s}^{-1}$

and the outgassing rate of the vacuum exposed surfaces lower than $10^{-7} \text{ Pa l s}^{-1} \text{ cm}^{-2}$. The plasma tubes and beam tubes must be made of stainless steel, steel with stable structure and with a low relative magnetic permeability. The aluminium and copper can also be successfully used because of good mechanical properties, availability and very low desorption rates.

As, it is practically impossible to separate the effects of diffusion, outgassing, and permeation which are manifold higher in polymers as in metals [15], it is not recommended to use polymers for clean interior surfaces of the ECR ion source vacuum system.

VI. REFERENCES

- [1] M. Cavenago, "Operation of the Legnaro ECR ion source," *Proc. of the 3rd European Part. Acc. Conf. (EPAC 92)*, Vol. 2, Berlin, 24 - 28 March, 1992, pp. 984 - 986. Editors: H. Henke, H. Homeyer and Ch. Petit-Jean-Genaz. Printed in Singapore by Fong and Sons Printers Pte. Ltd., 1992.
- [2] K. Hatanaka and H. Nonaka, "Status of the RIKEN ECRIS," *Proc. of the Int. Conf. on the Physics of Mult. Charged Ions and Int. Workshop on ECR IS*, Grenoble, Sept. 12 - 16, 1988, pp. 827 - 838.
- [3] O. Gröbner, "Vacuum systems," *Report CERN 85-19*, Geneva 1985, pp. 489.
- [4] A.A. Efremov, A.I. Ivanenko, V.B. Kutner, J. Pivarč and K.D. Tumanov, "Vacuum system for the Dubna ECR ion source DECRIS-14," *Proc. of the 3rd European Part. Acc. Conf. (EPAC 92)*, Vol. 2, Berlin, 24 - 28 March, 1992, pp. 1567 - 1569. Editors: H. Henke, H. Homeyer and Ch. Petit-Jean-Genaz. Printed in Singapore by Fong and Sons Printers Pte. Ltd., 1992.
- [5] G. Egelmann, M. Genet and W. Wahl, *J. Vac. Sci. and Technol. A*, 5, 2337 (1987).
- [6] B.A. Trickett, *Vacuum* 28, 471 (1978).
- [7] J. Pivarč, *Jemná mechanika a optika* 4, 121 (1988) (in Slovak).
- [8] F. Donni, C. Boffito and B. Ferrario, *J. Vac. Sci. and Technol. A*, 4, 2447 (1986).
- [9] M. E. Malinowski, *J. Vac. Sci. and Technol. A*, 3, 483 (1985).
- [10] J.P. Rajzer, *Fizika gazovogo razrjada* (Moscow, Science, Main Redaction of the Physics-Mathematics Literature, 1987, pp. 130) (in Russian).
- [11] R. Becker, E.D. Donets and G.D. Schirkov, "The ion cooling in EBIS", *Report E - 9 - 91 - 382*, JINR Dubna, Russia.
- [12] R. Geller, B. Jacquot and M. Pontonnier, *Rev. Sci. Instr.* 56, 1505 (1985).
- [13] R.C. Pardo and P.J. Billquist, *Rev. Sci. Instr.* 61, 239 (1990).
- [14] V.B. Kutner, private communication (1991) (in Russian).
- [15] R.N. Peacock, *J. Vac. Sci. and Technol. A*, 17, 330 (1980).

DEVELOPMENT OF DISTRIBUTED ION PUMPS FOR g-2 BEAM VACUUM SYSTEM*

H. C. Hsueh, M. Mapes and L. Snyderstrup
AGS Department, Brookhaven National Laboratory
Associated Universities, Inc.
Upton, New York 11973

Abstract

Distributed ion pumps (DIPs) will be used for the beam vacuum system of the g-2 muon storage ring. The magnetic field intensity and alignment angle at the DIP locations are not uniform. The pumping behavior of several different ion pump elements under this non-uniform magnetic field has been studied. The results are compared with the theoretical predictions. Based on these results, the optimum design of the g-2 DIPs has been developed.

I. INTRODUCTION

For the precision measurement of the muon g-2 value, a muon storage ring [1] is being constructed at Brookhaven. The principle equipment of the storage ring is the continuous superconducting magnet with a B of ≈ 1.45 Tesla and a diameter of 14m. Field homogeneity of 1 ppm is required in the muon storage region which rules out the use of the conventional lumped ion pumps for the beam vacuum. DIPs have been used extensively in the bending magnet chambers of the electron storage rings as the main high vacuum pumps. With the existing bending field and the vacuum chambers, only Penning discharge cells are needed. In the g-2 beam chambers, an area of 5cm by 50cm has been identified for the installation of the DIPs. The magnetic field at this location ranges from 12 to 15 kilogauss and the alignment angles (between the direction of B and the DIP anode axis) from 0° to 9° . The pumping behavior of the Penning cells in this non-homogeneous field has to be characterized before the implementation of the DIPs.

The pumping speed of the Penning cells is a function of B, the anode voltage V and the geometry of the cells. To prevent high voltage breakdown, V is usually limited to around 5 kilovolts. With the known B and V, we can maximize the pumping speed S by optimizing the geometry of the pump elements. Empirical formulae have been used by accelerator scientists to derive the optimum dimensions, such as the cell radius R, the cell length L and the gaps, δ , between the anodes and the cathode plates of the DIPs and to estimate the achievable S. The details of these formulae can be found in References 2, 3 and 4, and will not be repeated here.

*Work performed under the auspices of the U.S. Department of Energy.

Maleve [2] proposed the first practical formulae for deriving the geometry of the Penning cells. Based on his formulae, S increases with increasing B, R, L and V. Hartwig and Kouptsidis [3] pointed out later that S peaks at a transition magnetic field, B_{tr} . They proposed different formulae for S at B below and above B_{tr} . For $B < B_{tr}$, S is a function of L, R, B and the pressure P. For $B \geq B_{tr}$, S is independent of R and B. However several recent studies [5,6,7] indicated that S increased with R even at high B. To explain the dependence of S on R at high B, Suetsugu and Nakagawa [4] introduced the cell length and radius dependent total charge intensity Q and anode sputtering efficiency J. Good agreement with experimental data was achieved when S was modified by Q and J.

An additional variable for DIPs in the g-2 chamber is the alignment angle θ . No systematic study of the dependence of S on θ in the Penning cells has been reported. Hartwig [3] suggested that the effect of the misalignment on the pumping speed can be estimated by replacing R with the effective radius $R(\theta)$ ($= R \cos\theta - 0.5 L \sin\theta$).

II. DEVELOPMENT OF DIPs FOR g-2

The DIP locations in the g-2 beam chambers has B ranging from 12 to 15 kilogauss and θ from 0° to 9° . We have measured the pumping speeds of four ion pump elements at B from a few hundred gauss to 15 kilogauss and θ from 0° to 13° . The dimensions of the elements tested are listed in Table I. Elements A1 and A2 have the same R and L while B and C have larger cell radii. The results are summarized and compared with the predictions of the existing empirical formulae.

Table I.
DIMENSIONS (in cm) OF THE ELEMENTS TESTED

Element	R	L	# Cells
A1	0.6	1.9	92
A2	0.6	1.9	140
B	0.9	1.5	32
C	1.2	2.5	57

A bending magnet with a pole gap of 13 cm high, 25 cm wide and 120 cm long was used to supply the required B . A pumping speed measurement system was constructed for this study. It consists of a gas inlet chamber and a pumping chamber separated by an orifice with a conductance C of 0.9 l/sec for nitrogen. The ion pump element was mounted in the pumping chamber centered in the magnet gap. Ion gauges were used to measure the pressures at both chambers. The pumping speed measurements were carried out at a pressure of low 10^{-7} Torr. Nitrogen was used as a test gas. It was bled into the gas chamber through a variable leak valve and pumped by the element through the orifice. The elements would pump gas at either 1.4 Tesla or 0.2 Tesla for a few hours before the measurement began. The magnet was then ramped to the desired B . The gauge readings were recorded after a steady state was reached at the selected B , which usually occurred in a few minutes. The above steps were then repeated for the next B . To test the effect of the alignment on the pumping speeds, the pumping chamber was tilted to an angle Θ relative to the direction of B . The speed measurements were then taken at this angle. Pumping speeds at the following angles were studied: 0° , 3° , 6° , 9° , 11° and

13° . The pumping speeds were derived as $S = C(P_{\text{gas}} - P_{\text{pump}})/P_{\text{pump}}$.

The measured S of each element at different Θ are plotted versus B in Figure 1. As predicted by the empirical formulae, S increased with increasing B and peaked at B_{tr} . At $B \geq B_{\text{tr}}$ when Θ was small, S of elements A1 and A2 remained constant with increasing B . At large Θ , S dropped off initially then levelled off. For elements B and C, S dropped off rapidly with increasing B at all the angles. This dependence of S on B for the large cells is not predicted by the empirical formulae. The calculated S for elements A1 and C, using Suetsugu's modified formulae [4] are compared with the measured S in Figure 2 for $\Theta = 0^\circ$ and 9° . Reasonable agreement between the measured S and the calculated S was obtained for element A1.

The effects of alignment on S are illustrated in Figure 3, where S is plotted versus Θ for $B = 0.2$ and 1.45 Tesla. The results were compared with the calculated results using Suetsugu's formulae and $R(\Theta)$. Reasonable agreement between the calculated S and the measured S was obtained for

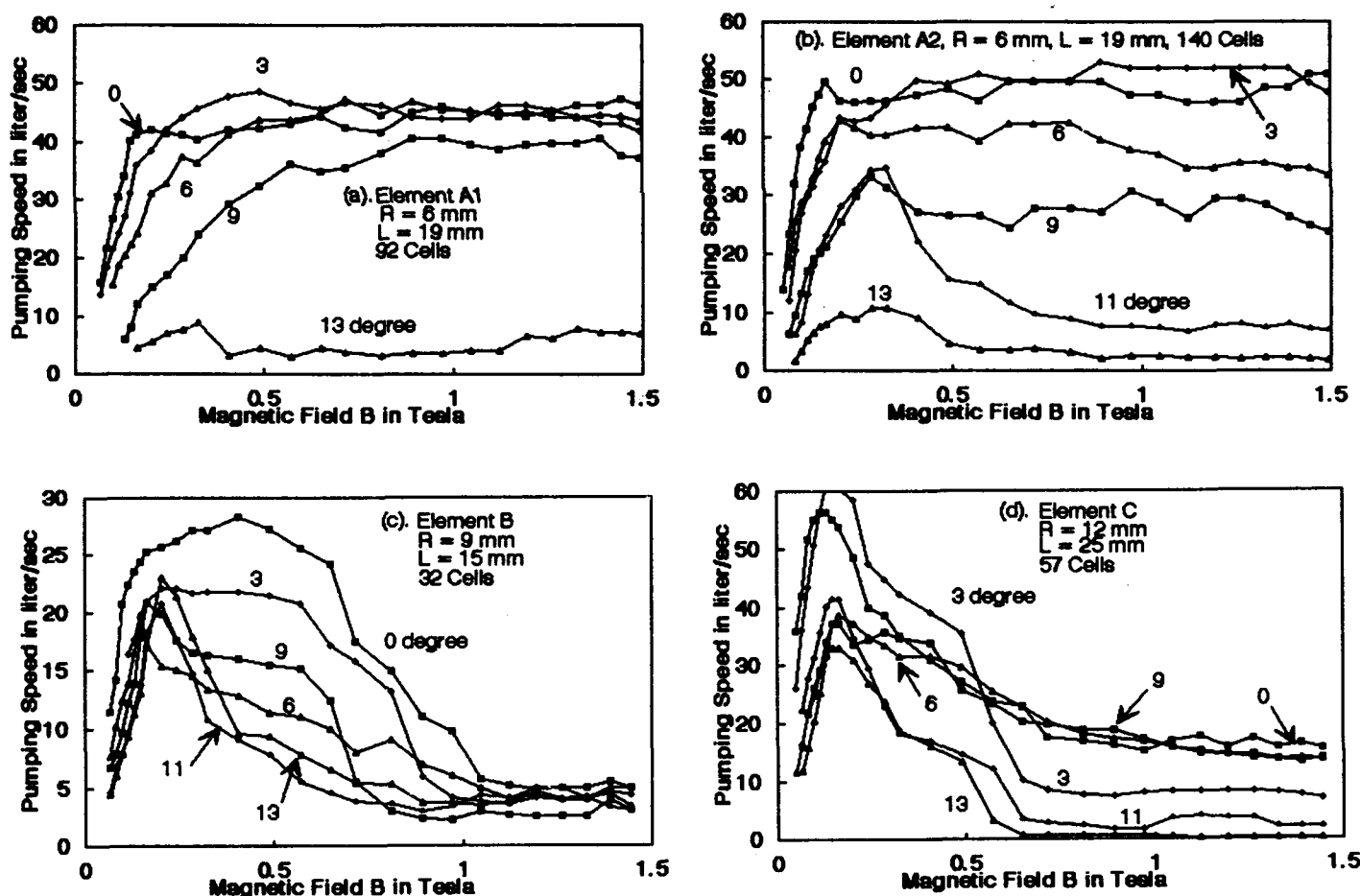


Figure 1. Measured pumping speeds of several ion pump elements as a function of the magnetic field. The numbers above are the alignment angles.

element A1 at 1.45 Tesla; and for elements B and C at 0.2 Tesla.

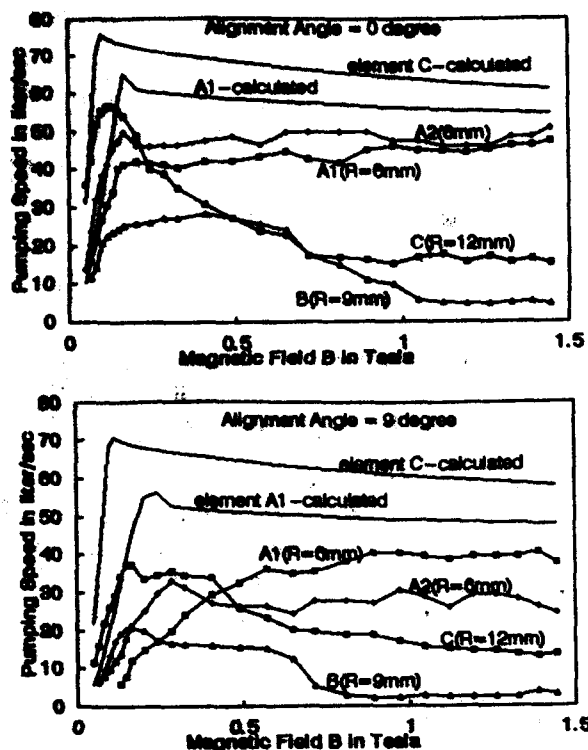


Fig. 2. Comparison between the calculated pumping speeds and the measured pumping speeds at alignment angles of 0° and 9°

In summary, at high B, the measured pumping speeds of the elements of small cells are substantially higher than those of the elements of large cells even at 9°. These results are in reasonable agreement with the calculated results. The pumping speeds of the elements of large cells decreased rapidly with increasing B, which are not predicted by the existing empirical formulae. At high B, the effect of misalignment on the pumping speeds of elements with small cells is in reasonable agreement with those calculated using $R(\Theta)$.

III. OPTIMUM DIP DESIGN FOR g-2

The results of our study indicate that the pumping speed of the elements with $R \geq 9\text{mm}$ dropped off rapidly with increasing B and Θ , which sets the upper bound for the cell radius of the g-2 DIPs. The minimum cell radius can be estimated from P_{\min} , the minimum operating pressure as defined by Maleve [2]. At a P_{\min} of 1×10^{-5} Torr, the smallest radius of the pseudo cells (the space between the regular cells that gives extra pumping) should be 1.5mm and that of the regular cells 4mm. Other measurements [5,6,7] at high B gave a minimum radius of 5mm, below that the pumping speed dropped off. This is consistent with the fact that the total discharge intensity Q [4] decreases with R.

Taking all these facts into consideration, the optimum cell radius seems to be around 6mm.

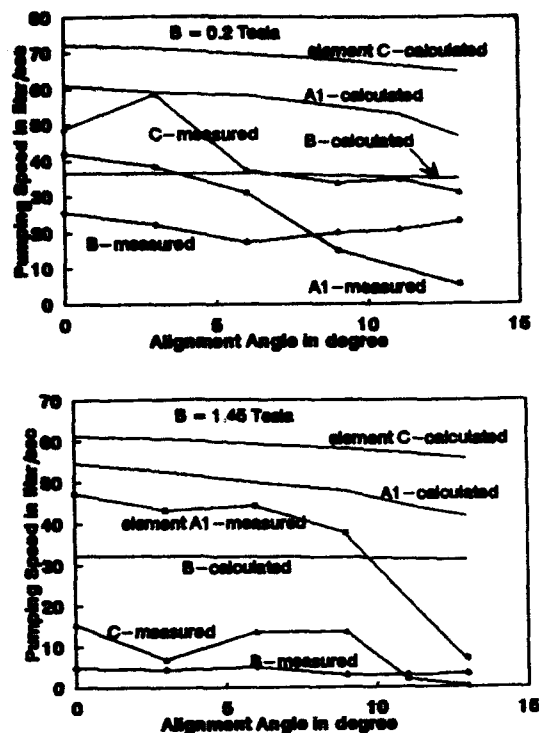


Fig. 3. The dependence of the pumping speeds on the alignment angle Θ at B = 0.2 T and 1.45 T for elements A1, B, and C.

To limit the pumping speed loss due to the conductance restriction to less than 10%, Maleve [2] proposed that the cell length L should be between 3-4 times of R, or around 20mm. The gaps δ between the cells and the cathode plates must be reasonably large for conductance purposes and to prevent high voltage breakdown. Gaps of 5mm will meet these requirements.

A total of 250 cells of the above geometry in three layers can be packed at each g-2 DIP location. Based on Suetsugu's formulae, as well as the performance of elements A1 and A2, pumping speed of over 100 l/sec can be realized from each g-2 DIP.

IV. REFERENCES

- [1] V.W. Hughes, in Particle, Strings & Cosmology, World Scientist, Singapore, p.868, 1992.
- [2] M.D. Maleve and E.M. Trachtenberg, Vacuum, **23**, 403 (1973).
- [3] H. Hartwig and J.S.Kouptsidis, J. Vac. Sci. Technol., **11**, 1154 (1974).
- [4] Y.Suetsugu and M. Nakagawa, Vacuum, **42**, 761 (1991).
- [5] T.S. Chou, J. Vac. Sci. Technol., **A5**, 3446 (1987).
- [6] Y.Suetsugu and M. Nakagawa, Vacuum, **42**, 625 (1991).
- [7] B.A. Trickett, Vacuum, **28**, 471 (1978).

WHAT JOINING METHOD FOR THE NEW GENERATION OF ACCELERATORS (SSC and LHC)

R. GILLIER

Helicoflex Company

PO Box 9889 Columbia SC 29290

J.MONTUCLARD, M.LEFRANCOIS, CH.ROUAUD

Le Carbone-Lorraine Cefilac Etanchéité

90, Rue de la Roche du Geai - 42029 Saint Etienne Cedex - FRANCE

Abstract

More than 8600 Superconducting magnets will equip the SSC (Superconducting Super Collider) accelerator and about 3000 will be used for the LHC (Large Hadron Collider). Those magnets require a specific piping system with about 10 different lines ranging in diameter from 43 to 150 which are meant to provide ultra-high vacuum and helium cooling down to 1.8°K.

One of the joining method under consideration is welding.

We have developed another solution which allows a quick and ultra-clean joining method, using a chain-clamp on tapered flanges sealed with a HELICOFLEX® resilient metal seal.

I. OPERATING CONDITIONS OF THE LHC PROTON COLLIDER MAGNETS.

Those magnets will be installed above the existing LEP accelerator built in a 27 km tunnel in Geneva-Switzerland.

To be reached, the 7.7 TeV beam energy implies the use of magnets allowing a magnetic field of about 9.5 T, which have to operate at 1.8°K.

A magnet is built with 2 tubes which are located inside the magnet body and have a 43 mm inner diameter where ultra-high vacuum is created, such configuration being known as the "two-in-one design". The required vacuum level is, for a beam lifetime of 24 hours :

$< 2 \cdot 10^{-9}$ Torr at 5°K for hydrogen

$< 2 \cdot 10^{-10}$ Torr at 5°K for carbon monoxide

All around the magnet body, in order to help reaching superconducting mode, there are:

2 tubes of 50 mm inner diameter containing a cryogenic fluid at about 80°K for cooling purposes

2 tubes of 50 mm inner diameter for thermal exchange
2 times 2 tubes of 65 mm and 150 mm inner diameter to carry superfluid helium at 2.2°K and 1.8°K.

All together there are 10 tubes ranging in diameter from 43 to 150 mm which, once joined, must comply with operating conditions as extreme as $< 1 \cdot 10^{-12}$ Torr ($< 1.33 \cdot 10^{-10}$ Pa) initial vacuum, 1.8°K superfluid helium, and 20 bar helium pressure when a magnet quenches.

II. EXPECTED NUMBER OF JOINING OPERATIONS

Each one of the junctions is expected to be assembled 3 times over the life of the machine:

-the first time by the magnet manufacturer in order to allow final inspection in terms of performance, i.e. vacuum, superconductivity, and magnetic field

-the second time during construction of the accelerator.

-the third time for eventual modifications of the accelerator which are likely to be decided over an expected operating life of 20 years.

III. TWO JOINING METHODS CAN BE CONSIDERED

A. Welding

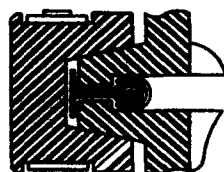
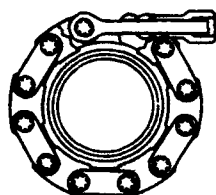
The TIG-ORBITAL welding process is probably one of the most commonly used methods in industry for joining 2 tubes end-to-end in a reliable way.

Without rejecting totally such a solution, it still must be remembered that connecting superconducting magnets implies specific requirements which this method makes it difficult to comply with. For example testing the magnets means having to weld all junctions and plugs which then have to be cut-off for final installation on the machine. The cut in that case can only be performed in

accordance with UHV requirements, that is to say without cutting oil and without any particle getting inside the piping system. Furthermore the welding operations must be carried out without oxidization in order not to have to perform afterwards chemical cleaning of the surfaces. Over the life of the machine similar difficulties will also be encountered whenever on-site modifications are necessary.

B. A demountable metallic junction: (fig.1)

In order to overcome the difficulties mentioned earlier regarding the welding and cutting operations, we have developed and tested in collaboration with the CEA (Commissariat à l'Energie Atomique) a joining system the principle of which is already well-known in UHV applications (chain-clamp, tapered flanges, and seal), which allows disassembling-reassembling cycles without ever having to cut the tubes.



IV. TESTS

A. Description of the tested system : (Fig 2 and 3)

A tested junction consists of :

2 - 63 mm- 304L stainless steel tapered flanges,

1 Helicoflex seal having aluminium gr-1050 sealing jacket,

1 stainless steel chain-clamp.

The chain-clamp when being tightened brings the tapered flanges together therefore compressing the seal.

The Helicoflex seal centered by means of metal cups ensures the required tightness by the plastic deformation of its aluminium jacket against the flange faces, the inner spring providing the elasticity needed to keep the performance steady over the operating life .

One of the major aspect of the test is to check the reliability of the system at LHC operating conditions. Tests were carried out at the CENG (Centre d'Etudes Nucléaires de Grenoble)[2] and CEA [1].

B. Test set-up and procedure:

Phase 1:

The 3 junctions are installed inside a cryostat having a 300mm inner diameter. The cryostat is successively filled with liquid nitrogen, then liquid helium, then pumped using a turbomolecular pump in order to reach the 1.8K superfluid helium temperature.

The inner volume of the junctions is evacuated to 10^{-5} atm at $\Delta P=1$ bar and connected to an ASM52 Alcatel leak detector which features a sensitivity better than 1.10^{-11} Pa.m³.s⁻¹. The leak rate is permanently monitored over the 300°K/1.8°K/300°K temperature cycle which is repeated 6 times in a row, thus giving test data from 18 different samples. The results are shown in Table 1.

TABLE 1
PHASE 1
CENG Test results

TEST CONDITIONS	JUNCTION TYPE	SEAL TYPE	CYCLE NUMBER	300°K	77°K	4°K	1.8°K
Liquid Helium outside $\Delta P = 1$ bar	ND 63 3 Junctions in series	Helicoflex HL 290 P Aluminium 3.2 mm C.S.	1	Et	Et	Et	Et
			2	Et	Et	Et	Et
			3	Et	Et	Et	Et
			4	Et	Et	Et	Et
			5	Et	Et	Et	Et
			6	Et	Et	Et	Et

Et = Performance equal or better than 1.10^{-11} Pa m³ / s
 1.10^{-11} Pa m³ / s = 1.10^{-10} atm cm³ / s

Phase 2:

In order to check further the behaviour of those junctions, an inverted testing arrangement has also been used.

This arrangement, even more stringent than the first one, is such that the junctions are pressurised with cryogenic fluid and installed inside a vacuum chamber connected to a leak detector. Liquid nitrogen is first introduced until 77°K temperature is measured at the thermocouple. Gaseous helium is then brought in instead, while the leak detector is monitoring the vacuum chamber for eventual leak. Then helium pressure is increased up to 25 bar, the leak rate being monitored over the whole temperature cycle (300°K/77°K/300°K) which is repeated 30 times in a row. The results are shown in Table 2.

TABLE 2
PHASE 2
CEA Test results

SEAL CONFIGURATION	JUNCTION TYPE	SEAL TYPE	CYCLE NUMBER	MPa	MPa	MPa	MPa
Orange Helium leak	Symmetrical grooved flange faces with metal-to-metal contact	Helicoflex AL 300 P Aluminium 4.8 mm C.S.	1	20	20	20	20
			30	20	20	20	20
	Flat flange-faces with compression stopped by the Helicoflex internal compression limiter	Helicoflex AL 300 P Aluminium 4.8 mm C.S.	1	20	20	20	20
			30	20	20	20	20
	Flat flange-faces with compression stopped by a metal ring located in the void space between Helicoflex inner diameter and tube inner diameter	Helicoflex AL 300 P Aluminium 4.8 mm C.S.	1	20	20	20	20
			30	20	20	20	20

20 = Performance equal or better than 1. 10-11 Pa·m³/s (1. 10-10 atm cm³/s)

V. DISCUSSION

Before all, it must be noted that it was decided to use aluminium as sealing material for 2 major reasons which are:

- firstly, pure aluminium is a very ductile metal which, except for indium which finds itself limited by some major drawbacks such as sticking, creeping, quick oxidation,...., has no equal for UHV applications,
- secondly, it was meant to check that this material is compatible with superfluid helium conditions. In that respect, no leak has been observed using aluminium under test conditions i.e. 1.8°K/liquid helium outside junction (see phase 1 results).

In phase 2 (liquid nitrogen + gaseous helium inside junction), we have checked the behaviour of 3 different configurations, using in each case a CEFILAC® newly-designed light-weight chain-clamp and an aluminium Helicoflex seal having a 4.8 mm cross-section diameter which features high springback capacity to compensate for differential expansion during thermal transients especially during the cooling phases.

The 3 configurations were:

- a) symmetrically grooved flange-faces with metal-to-metal contact as close to tube inner diameter as possible



- b) flat flange-faces with compression stopped by the Helicoflex internal compression limiter-



- c) flat flange-faces with compression stopped by a metal ring located in the void space between Helicoflex inner diameter and tube inner diameter-



In all 3 configurations, no leak has been observed (see phase 2 results)

As a conclusion, we can say that those demountable metallic joining systems are a perfectly suitable solution for the future in the new accelerators using superconducting magnets.

Complying with the most stringent reliability and cleanness requirements, they also allow a much shorter assembling time and make easier any further modification of the machine.

VI. REFERENCES

- [1] CEA : Nuclear Research Center- Rhone Valley -Dpt DCC/DTE/SLC
- [2] CENG : Nuclear Research Center- Grenoble -Dpt Cryogenics

Surface Treatments and Photodesorption of Oxygen Free Copper used in an Accelerator

Toshiaki Kobari, Masabu Matsumoto, and Shinjiro Ueda
Mechanical Engineering Research Laboratory, Hitachi Ltd.

302 Kandatsu, Tsuchiura, Ibaraki 300,
and

Masanori Kobayashi and Yoichiro Hori
National Laboratory for High Energy Physics
1-1 Oho Tsukuba, Ibaraki 305 JAPAN

Abstract

Test samples of machined oxygen free copper (OFC) were exposed to synchrotron radiation from the Photon Factory (PF) of KEK for a critical energy of 4 keV. In experiments, we measured the photoelectron yield and the photodesorption yield due to synchrotron radiation. The irradiated surfaces were also analyzed by AES.

I. INTRODUCTION

Oxygen Free Copper (OFC) has good properties as the material for vacuum components in an accelerator. Such properties include high conductivity and good shield characteristics that are effective against high energy radiation. OFC also shows lower photodesorption yields[1-3]. Photodesorption in accelerators is affected by the photon energy, the photon flux, and the surface treatments, etc. Some studies focusing on a photodesorption process[4-10] have shown that photoelectrons emitted from irradiated surfaces are the main cause of photodesorption.

The purpose of this experiment is to study the effects of irradiation of synchrotron radiation on OFC in terms of photoelectron production, surface changes, and desorption. While OFC samples are irradiated by synchrotron radiation photocurrent and desorption are measured. The irradiated surfaces are also analyzed by AES.

II. EXPERIMENT

A. Experimental setup

The apparatus at the BL21 of PF is reported in detail in

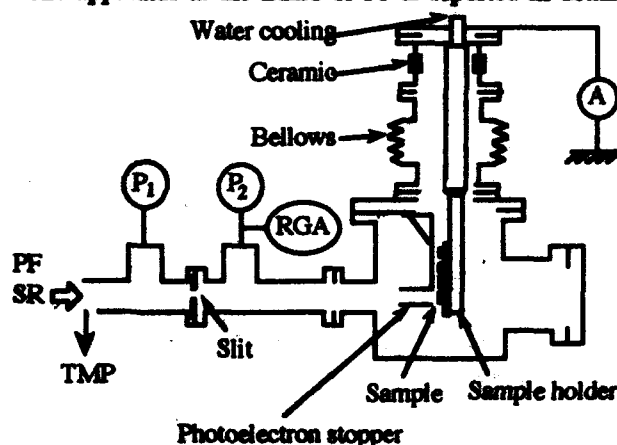


Fig. 1 Experimental set up for the measurement at BL-21 of the Photon Factory, KEK.

Reference[8]. The experimental set up for this experiment is shown in Figure 1. Synchrotron radiation from the PF ring enters the chamber after being collimated at the slit. The size of the photon beam is 5 mm in both directions. The slit also works as an orifice of 3 l/s conductance (N_2 equivalent).

OFC samples (max. of four) are first attached to the sample holder. The sample holder is then set in a chamber made of stainless steel through a ceramic chamber, the sample holder is floating. At this point, we can measure the photocurrent produced in samples. A photoelectron stopper made of OFC in front of the irradiated samples to possibly reduce the desorption from the chamber due to irradiation of secondary particles, such as secondary electrons and reflected photons.

B. OFC samples

All samples are made of high-purity oxygen free copper (ASTM-F68 Class-1)[11]. Table 1 lists the samples. Except for Sample 1-2 (extruded), the average roughness (R_a) of a machine finished[1] samples is either $R_a=12.5 \mu\text{m}$ or $0.5 \mu\text{m}$. Acetone is used for degreasing with ultrasonic agitation for 30 min. HNO_3 of 45% concentration by volume (from HNO_3 of 65% concentration by weight) is used for acid cleaning, after acid cleaning deionized water is used for rinsing, methanol and dry nitrogen are used for drying. There are two series of experiments: one series is indicated by "Sample 1-" and the other is "Sample 2-". The samples were irradiated serially in each series without exposure to air.

Table 1. OFC samples

Sample #	Roughness(R_a : μm)	Treatment	Dose($\text{mA}\cdot\text{h}$)
0	12.5(machining)	degreasing	0
1-1	12.5(machining)	degreasing	50
1-2	raw(extrusion)	degreasing	6,090
1-3	12.5(machining)	degreasing	1,020
1-4	12.5(machining)	degreasing	4,880
2-1	0.1(machining)	degreasing	790
2-2	0.1(machining)	degreasing	12,590
2-3	0.1(machining)	acid cleaning	27,340
2-4	12.5(machining)	acid cleaning	49,390

III. RESULTS AND DISCUSSION

A. Photoelectron yield

Figure 2 and Figure 3 show photoelectron yields in the first series and in the second series, respectively. The horizontal axis represents the integrated photon dose which is initialized after each direct irradiation on to a sample. A beam dose of $1 \text{ mA}\cdot\text{h}$

is equivalent to a cumulated photon dose of 1.75×10^{17} photons/slit introduced into the chamber through the slit, the order of irradiation is serial from Sample1-1 through Sample1-4. Note that degreasing is a common treatment in Figure 2. The photoelectron yields are similar for Sample1-3 and Sample1-4; these samples are machine finished and have the same roughness. Sample1-2 with an extruded surface has a smaller yield. Due to a data acquisition system error, the photoelectron yields in Figure 2 are shown from a point midway through irradiation of Sample1-2. The difference in photoelectron yields is attributed to the difference in surface conditions. It is considered that Sample1-2 still contains an impurity giving the lower photoelectron yield, e.g., carbon produced in the extrusion process.

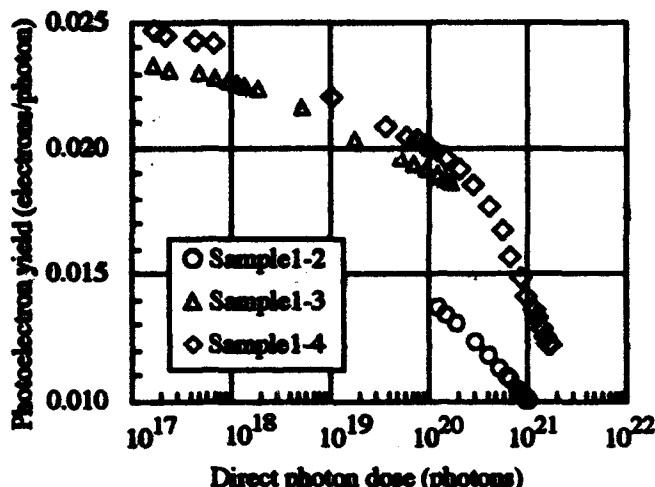


Fig. 2 Photoelectron yield in the first experimental series as a function of direct photon dose.

The photoelectron yields in the second series are shown in Figure 3. The average roughness for Samples 2-1, 2-2, and 2-3 is $0.1 \mu\text{m}$ and that of Sample2-4 is $12.5 \mu\text{m}$. Samples 2-1 and 2-2 are degreased with acetone, and Samples 2-3 and 2-4 are treated with HNO_3 . The tendency of decreasing photoelectron yields with increasing photon dose for Samples 2-1 and 2-2 is similar to that for Samples 1-3 and 1-4 in Figure 2. The common factor here is acetone degreasing. However the yields for Samples 2-1 and 2-2, each whose average roughness is $0.1 \mu\text{m}$, are smaller than those of Samples 1-3 and 1-4.

The decreasing tendency for the samples treated with HNO_3 differs from that for Samples 2-1 and 2-2, at photon doses higher than 10^{19} photons. Samples 2-3 and 2-4 experience a smaller slope. The yield of Sample2-3 begins decreasing again like the yield of the Sample2-2, but the yield of Sample2-3 is higher than that of Sample2-2. The yield of Sample2-4 is almost constant and maintains a high value. It is presumed that these behaviors of photoelectron yields for samples treated with HNO_3 are due to an oxide layer produced in the acid cleaning stage. This oxide layer possibly increases the photoelectron yields. The difference in yields between Samples 2-3 and 2-4 at photon doses higher than 10^{21} photons means that surface roughness affects the oxide layer production in the acid cleaning stage. The total dose, i.e., the integrated dose from the beginning of the experiment, is different for each irradiation. In spite of this difference, the yields are not so different among the

samples at lower photon dose. This means that photoelectron yield is not clearly influenced by the total dose.

In comparison with the photoelectron yield of aluminum alloy[9] at 2×10^{21} photons under normal incidence, the yield of Sample2-2 is almost one and half times higher.

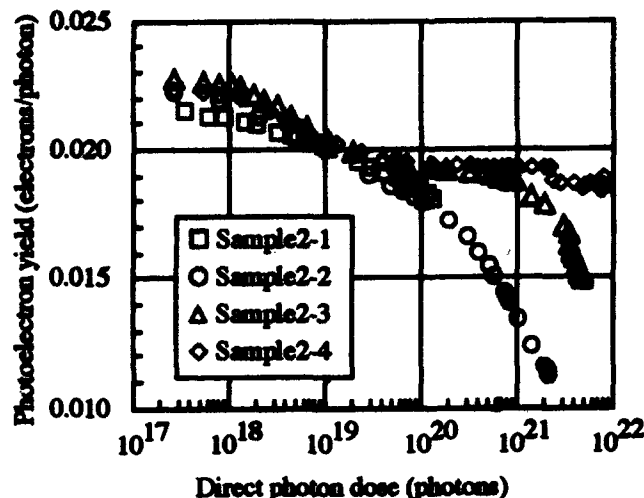


Fig. 3 Photoelectron yield in the second experimental series as a function of direct photon dose.

B. Surface analysis

The surface concentrations of the machine finished samples in the first experiment are shown in Figure 4. These results are obtained from AES analysis. The term "Others" includes Cl, S, N impurities. Sample 0 was not exposed to synchrotron radiation. The carbon ratio decreases for a small dose (Sample1-1), but increases with increasing photon dose (Samples 1-3 and 1-4). Consequently, the decrease in photoelectron yield with increasing photon dose in Figure 2 is probably caused by this carbon ratio increase on the surface. The ratio for carbon of Sample1-3 to Sample1-4 is almost same as the ratio for photoelectron yield of Sample1-4 to Sample1-3 at the last photon dose respectively. The pressures at this conditions were 10^{-8} Torr range.

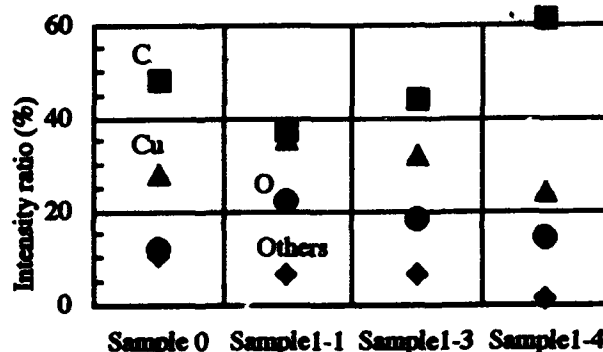


Fig. 4 Surface concentration of Carbon, Oxygen, and Copper by AES analysis.

Figure 5 shows Auger depth profiles obtained by 3 keV argon ion sputtering. The sputtering rate is 120 \AA/min (SiO_2 equivalent). The oxide layer becomes thick after photon irradiation.

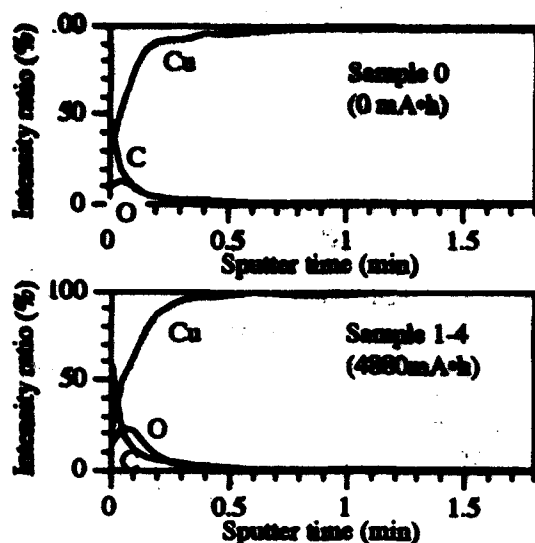


Fig. 5 Auger depth profiles of OFC before and after photon irradiation.

C. Photodesorption yield

Figure 6 shows the photodesorption yield (total photodesorption yield: N_2 equi.) in the second series. As shown in Figure 1, the size of samples is small and the area of the chamber inner surface is more than 50 times larger than that of the samples. Therefore, this photodesorption yield includes the effects of photodesorption from other components. Figure 6 also shows other yields [1] measured using a test duct. The total photodesorption yield in the second series is close to the yield of stainless steel duct (SUS duct); it is slightly higher due to a complicated room within the chamber and a large surface area; in spite of these conditions, however, the yields are not so high. It is assumed that the high density region of photoelectrons is surrounded by the samples and stopper made of OFC.

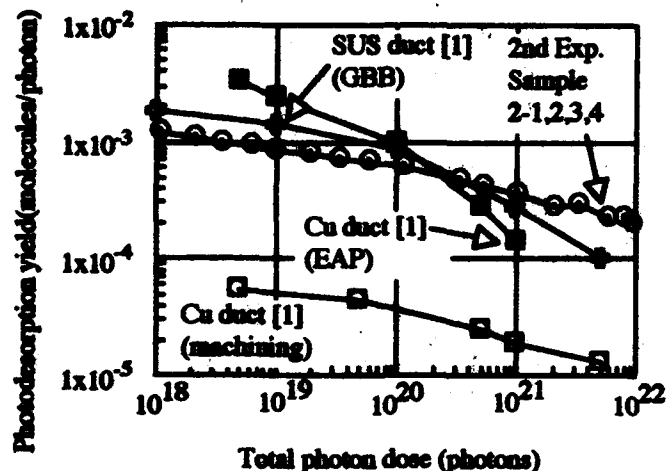


Fig. 6 Photodesorption yield of the second experimental series as a function of total photon dose. The yields are compared with those in Ref. [1].

Figure 7 shows the same yields as shown in Figure 6, but the horizontal axis represents the direct photon dose initialized at the beginning of each irradiation. At the beginning of each irradiation, each yield is higher than that of previously irradiated

sample. The difference probably includes the characteristics for photodesorption of samples.

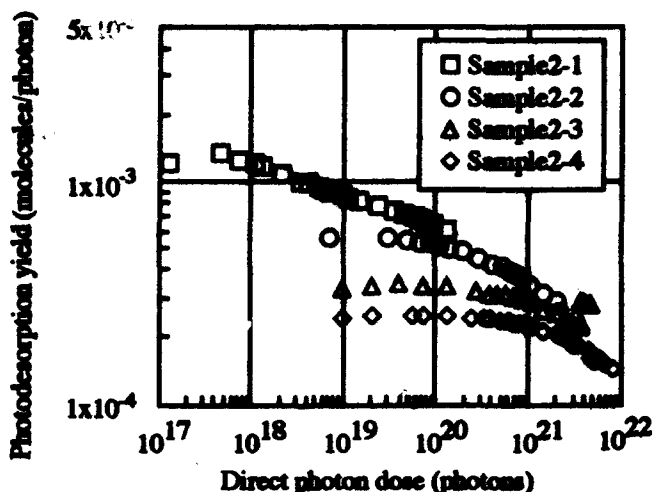


Fig. 7 Photodesorption yield in the second experimental series as a function of direct photon dose.

IV. CONCLUSION

Irradiation of synchrotron radiation to OFC increases the carbon concentration on the irradiated surface. The photoelectron yield which affects photodesorption is changed by the photon dose and the surface treatment; surfaces with acid cleaning in particular maintain a high yield.

Acknowledgment

The authors are indebted to Dr. Kanazawa (KEK) for supplying the extruded OFC sample.

V. REFERENCES

- [1] S. Ueda, M. Matsumoto, T. Kobari, T. Ikeguchi, M. Kobayashi, and Y. Hori, *Vacuum*, 41(7-9), 1928(1990).
- [2] H.J. Halama and C.L. Forester, *Vacuum*, 42(3), 185(1991).
- [3] W.A. Barletta, M. Calderon, C. Foerster, H. Halama, and G. Korn, *Int. Conf. on High Energy Acc.*, 358(1992).
- [4] M. Kobayashi, M. Matsumoto, and S. Ueda, *JVST*, A5(4), 2417(1987).
- [5] T. Kobari, H.J. Halama, *JVST*, A5(4), 2335(1987).
- [6] M. Andritschky, O. Gröbner, A.G. Mathewson, F. Schumann, and P. Strubin, *Vacuum*, 38(8-10), 933(1988).
- [7] O. Gröbner, A.G. Mathewson, P. Strubin, E. Alge, and R. Souchet, *JVST*, A7(2), 223(1989).
- [8] T. Kobari, M. Matsumoto, T. Ikeguchi, S. Ueda, M. Kobayashi, and Y. Hori, *AIP Conf. Proc.* 236, 347(1990).
- [9] Y. Hori, M. Kobayashi, M. Matsumoto, and T. Kobari, presented at IVC-12, 1992.
- [10] O. Gröbner, A.G. Mathewson, P.C. Marine, *EPAC92 proceedings*, 132(1992).
- [11] Y. Nagai, S. Sakai, Y. Saito, N. Matsuda, and G. Horikoshi, *Vacuum*, 41(7-9), 2100(1990).

The DAΦNE Main Ring Vacuum System

V. Chimenti, A. Clozza, H. Hsieh, G. Raffone, C. Vaccarezza
INFN-Laboratori Nazionali Frascati - C.P.13 - 00044 Frascati (Roma) - Italy

Abstract

The DAΦNE Main Ring Vacuum System is designed for an mean operating pressure of 1 nTorr with a circulating current of about 5 A/beam. Finite elements calculations have been carried out to check the maximum possible deformation for the Bending Quadrant vacuum chamber that will be made of Al 5083-H321. Water cooled copper absorbers are employed to cope with the Synchrotron Radiation, (SR), produced in the wigglers and dipoles. The total gas load due to SR is $Q=2.6 \times 10^{-5}$ Torr l/s per arc for CO, with a photodesorption rate $\eta=1 \times 10^{-6}$ molec/ph, (after ~40Ahr of commissioning), as measured at NSLS-BNL. Nine sputter ion pumps and nine titanium sublimation pumps are located in each arc to provide, respectively, the 15% and the 85% of the required pumping speed.

I. INTRODUCTION

The DAΦNE Φ -factory [1] is a twin ring 510 MeV e^+e^- collider facility under construction at INFN-LNF in Frascati. To reach the desired luminosity value of $L = 5 \times 10^{32} \text{ cm}^{-2} \text{ s}^{-1}$, at $\gamma = 1000$, a stored beam of 5.3A and a mean pressure of 1×10^{-9} Torr are required in each ring. Four 10-meter-long vessels constitute the vacuum chamber of the bending sections of each ring. The selected material is Al 5083-H321. A 10+20 mm slot divides the beam channel from an antechamber where the absorbers and the pumping stations are located. The maximum possible deformation of the vacuum chamber has been checked via a finite elements method as reported in section II. Water-cooled copper absorbers are provided to cope with the high photon flux produced in the Bending Quadrants, (BQ). The total gas load has been estimated from a photodesorption rate of $\eta \approx 1 \times 10^{-6} \text{ molec/ph}$ for CO, after ~40 Ahr of beam conditioning, as reported in section III. This η value is the result of an experiment on the U10B beam line

at NSLS [2]. Nine Sputter Ion Pumps, (SIP), and nine Titanium Sublimation Pumps, (TSP), are located in each arc, for a total required pumping speed of $S = 1.3 \times 10^4 \text{ l/s}$. The TSP is designed taking into account the operating needs of DAΦNE. A full scale prototype has been built and tested. The results of the measurements and the routine performance of our vacuum system are reported in section IV.

II. MAIN RING VACUUM CHAMBER MECHANICAL ANALYSIS

The Main Ring vacuum chamber is geometrically designed in such a way that most of the Synchrotron Radiation is stopped in the antechambers by water cooled copper absorbers. The generated gas load will be pumped out by the pumping stations located close to the absorbers which are perpendicularly oriented with respect to the photon direction. Each BQ chamber will be machined, inside and outside, from two Al 5083-H321 plates and welded along the median plane.

Several cross-sections of the DAΦNE Main Ring have been analyzed by means of a finite-element code [3] in order to check the maximum deformation. Both two and three dimensional (wherever possible) computations show, under the atmospheric pressure and the bakeout temperature, a maximum vertical displacement less than 0.3 mm in most cases, and the stress field is far from critical conditions. In the quadrupole section longitudinal ribs are advisable, as first calculations show a vertical displacement of the order of 0.5 mm. The stress concentration has been investigated around the fillets of the chamber, and the adaptive-mesh algorithm methodically used. Due to several improvements and changes in the shape of the chamber, a final finite-element analysis will be carried out, via a CAD interface, as soon as the geometry will be frozen.

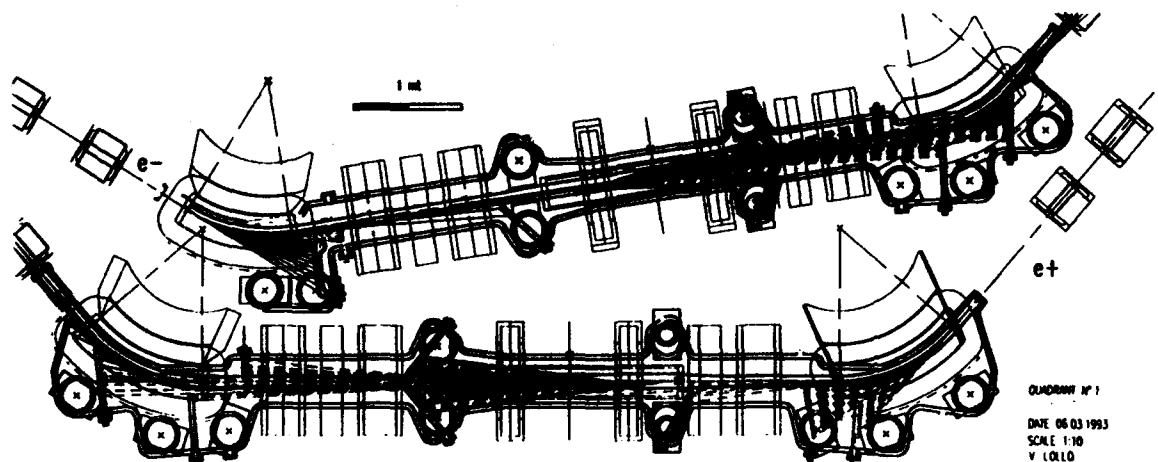


Figure 1 The DAΦNE Bending Quadrant layout.

III. SYNCHROTRON RADIATION INDUCED DESORPTION

Four wigglers and eight bending magnets constitute the bending sections of the Main Ring. The total number of ph/s emitted from the bending magnets is:

$$\frac{dN}{dt} = 8.08 \times 10^{20} \cdot E(\text{GeV}) \cdot I(\text{A}) = 2.2 \times 10^{21} \text{ ph/s.}$$

From the wigglers about 1.3×10^{21} ph/s are emitted, and the total photon flux per arc is:

$$N_{\text{tot}} = 8.8 \times 10^{20} \text{ ph/s.}$$

The total gas load is related to the photon flux by:

$$Q = \frac{N_{\text{tot}} \cdot \eta}{3.4 \times 10^{19}} = 2.6 \times 10^{-5} \text{ Torr} \cdot \text{l} \cdot \text{s}^{-1},$$

where η (molec/ph) is the photodesorption rate of the vacuum chamber. In order to estimate the right value of η we set up an experiment on the U10B beamline at the VUV ring in Brookhaven [2], having critical energy $\epsilon_c = 490\text{eV}$. Since the DAΦNE beam chamber and antechamber are made of

Table 1
Photodesorption coefficient η for H_2 , CH_4 , CO , CO_2 , after N_2 glow discharge, for different values of accumulated photon dose [2].

	η (molecules/photon)		
photon dose	1×10^{23} ph / m	5.5×10^{23} ph / m	$*1 \times 10^{24}$ ph / m
H_2	1×10^{-5}	7×10^{-6}	6×10^{-6}
CH_4	$< 1 \times 10^{-7}$	$\sim 1 \times 10^{-8}$	1×10^{-8}
CO	6×10^{-6}	2.5×10^{-6}	$< 2 \times 10^{-6}$
CO_2	1.5×10^{-6}	6×10^{-7}	4×10^{-7}
*extrapolated	After N_2 glow $1 \times 10^{18} \text{ atom/cm}^2$		

Table 2
Comparison of U10B and DAΦNE parameters

	VUV	DAΦNE	WIGGLERS	
E_c Crit. Energy	490	208	330	eV
Flux correction	1	0.84	0.92	
Low energy cut-off	5	0	0	eV
Angle of inc. on absorber	5.7	80-90		degrees
correction*	1	0.59		
Total correction on η		0.52		

*from electrical measurements.

aluminium and most of the Synchrotron Radiation is incident on a copper absorber, an aluminium tube containing a copper bar was exposed to a white photon beam and desorption coefficients were measured. In Table 1 the results obtained for the photodesorption rate of H_2 , CH_4 , CO , CO_2 , after N_2 glow discharge cleaning, are reported. Due to the differences between DAΦNE and U10B parameters, listed in Table 2, the values obtained at the U10B beamline have to be multiplied by a factor of 0.52, (see ref. [1]), in order to get the appropriate $\eta = 1 \times 10^{-6}$ molec/ph for the DAΦNE vacuum system.

IV. TITANIUM SUBLIMATION PUMP DESIGN AND TESTS

To reach the required average pressure of 1 nTorr, the pressure in the BQ has to be about 2 nTorr, since the straight sections must operate at pressures in the low 10^{-10} Torr range. For the pumping speed this constraint yields:

$$S_{\text{BQ}} = \frac{2.6 \times 10^{-5}}{2 \times 10^{-9}} = 1.3 \times 10^4 \text{ l/s.}$$

This pumping speed can be achieved by employing TSP's, which are well suited to pump a large quantity of Hydrogen at low pressures [4], [5] and [6], together with sputter ion pumps. In Figure 1 the BQ layout is shown where nine 200 l/s SIP's and nine TSP's are provided. In this way the required pumping speed for each TSP is:

$$S_{\text{TSP}} \approx 1.2 \times 10^3 \text{ l/s.}$$

To test the capacity of a TSP to pump such a high gas load for a reasonable time, i.e. to guarantee the desired mean pressure for a duration of two weeks without being switched on, a first TSP prototype, simulating the operating conditions in the BQ antechamber, has been built and tested at Frascati.

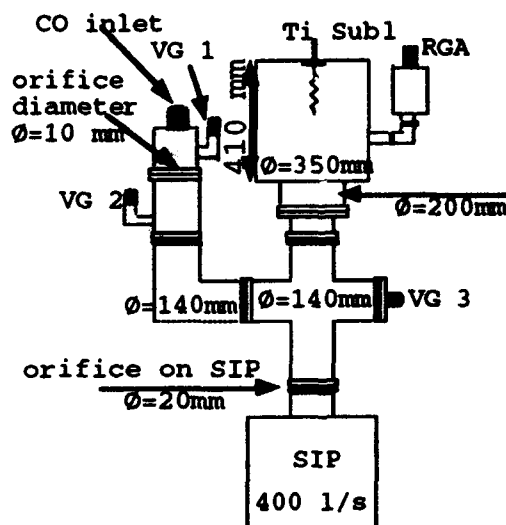


Figure 2 Experimental set-up.

In Figure 2 the experimental apparatus is shown. A Varian Titanium Filaments Cartridge was employed as Ti source. Three filaments are available in the standard cartridge for 3 grams of total evaporable Ti. Three Varian B.A. vacuum gauges were used, two for the CO throughput determination with the orifice method, VG1 and VG2, and the third, VG3, to record the pressure in the experimental chamber. A Vacuum Generator SX-200 Residual Gas Analyzer was used to determine the partial pressures of the gas species. The pumping speed S_G of a getter film of area A is [6]:

$$S_G/A = 3.64 f(T/M)^{1/2} l \cdot s^{-1} \cdot cm^{-2}$$

The data available in literature [4] for the sorption characteristics of flashed Ti films give $f \approx 0.38$ as the sticking coefficient of freshly deposited Ti, and $23 \times 10^{15} \text{ atom/cm}^2$ of CO as the total amount pumped by $\sim 1900 \times 10^{15} \text{ atom/cm}^2$ of Ti. In Figure 3 the curve of our TSP's pumping speed vs. the total amount of CO pumped is reported, for 500 nominal monolayers of deposited Ti, ($T=293 \text{ K}$). In this prototype the area actually covered by Ti is about 2400 cm^2 , leading to an initial sticking coefficient for CO of about $f \approx 0.6$. This value is higher than the sticking coefficient quoted in literature, but this can be attributed to a greater area actually covered by Ti, due to a deep sand-blasting of the surface. Furthermore, in this preliminary prototype, the presence of a short pipe, with different cross sections, between the TSP and the location of the vacuum gauge affects the accuracy of the measurements. However this uncertainty is easily avoided directly connecting the TSP to the experimental chamber, without limiting conductance between the two, as planned for a second prototype. As far as the sorption capacity is concerned, 1 Torr-l of CO corresponds to about 14 monolayers of gas, in relative agreement with Harra's results considering that the thickness of our Ti film is only ~ 500 monolayers. A second full scale prototype of TSP

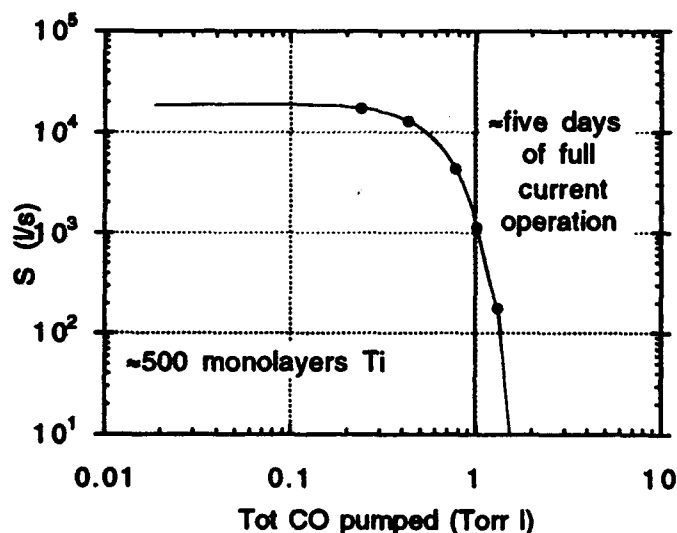


Figure 3. TSP's pumping speed vs. the total amount of CO pumped for 500 nominal monolayers of deposited Ti.

has been built and is now under testing, see Figure 4. In the new set-up the TSP pump is directly connected with a full scale prototype of a dipole vacuum chamber, in order to avoid any conductance between the TSP and the antechamber. Furthermore, an internal sawtooth shaped structure has been added to the TSP to increase the surface covered by the getter film. Accurate measurements are now in progress at Frascati to test this method of increasing the sorption capacity of the pump, in order to operate in an experimental set-up reproducing the actual operating conditions of DAΦNE.

V. SUMMARY

A vacuum system has been designed for the DAΦNE Main Ring. Due to the high Synchrotron Radiation load in the bending quadrants, a slot divides the beam channel from the copper absorbers and pumping stations locations. Based on the photodesorption yield of the Al vacuum chamber, after the commissioning, nine SIP's and nine TSP's will be provided in each BQ in order to guarantee an average pressure of 1 nTorr for about two weeks of full current operation.

VI. REFERENCES

- [1] Vignola G., these proceedings
- [2] Vaccarezza C., Halama H., Foerster C., to be published.
- [3] ANSYS, Swanson Analysis System Inc., Houston, Pennsylvania, 15342 (USA)
- [4] Harra D. J., J. of Vac. Sci. & Tech., 13, 471-4 (1976).
- [5] Clausing R. E., Trans. of the 8th Nat. Vac. Symposium & 2nd International Congress, 345 (1961)
- [6] Foerster C. L., Chou T. S., Halama H., Lanni C., AIP Conference Proceedings, 171, 334-41 (1988)
- [7] Roth A., "Vacuum Technology" 3rd ed., N.Holl. 1990

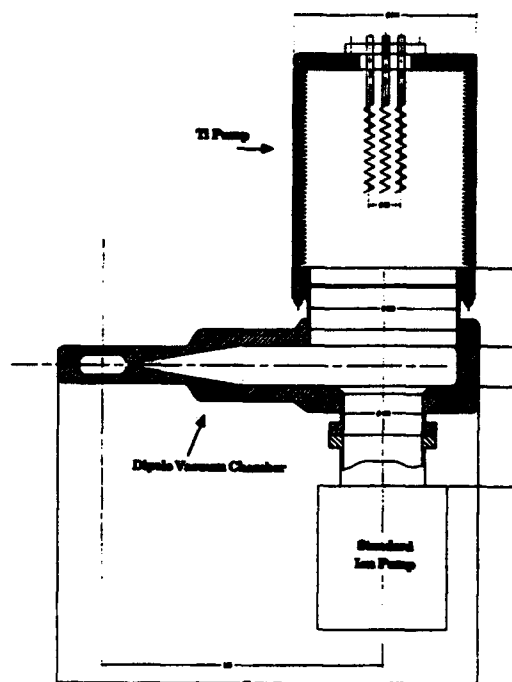


Figure 4. Final full scale prototype of DAΦNE TSP and Dipole Vacuum Chamber.

Vacuum Tracking

V. Ziemann
Stanford Linear Accelerator Center
Stanford University
Stanford, Ca. 94309

Abstract

A method to determine longitudinal pressure profiles in the presence of pumps and outgassing elements in conductance limited vacuum systems by a transfer matrix formalism is discussed. The algorithm is capable of dealing with multiple connected vacuum systems. An implementation of this method in the computer codes VAKTRAK and VAK-LOOP is briefly described.

I. INTRODUCTION

The longitudinal pressure profile $P(z)$ in a conduction limited vacuum system obeys the following linear differential equation in the presence of pumps and outgassing elements [1]

$$c \frac{d^2 P}{dz^2} - sP = -q \quad (1)$$

where the symbols are explained in table 1. We stress that the presented method is only applicable in the molecular flow regime, where the mean free path of the molecules is much larger than the dimensions of the pipes and manifolds such that the viscosity of the gas is negligible.

Under the assumption that the specific conductance c , the specific pumping speed s , and the specific outgassing rate q are piecewise constant, equation 1 is an ordinary differential equation with (piecewise) constant coefficients. Thus it can be solved by the method of transfer matrices.¹ The general transfer matrix can be easily found from the sum of homogeneous and inhomogeneous solution of eq. 1, namely

$$P(z) = C_1 e^{\alpha z} + C_2 e^{-\alpha z} + \frac{q}{s} \quad (2)$$

with $\alpha = \sqrt{s/c}$. Solving for initial conditions we obtain a transfer matrix R for the pressure P and the gas flow

Table 1: Definitions of symbols used.

Quantity	Units	Explanation
P	[Torr]	pressure
Q	[Torr l/s]	gas flow
z	[m]	longitudinal position
c	[ml/s]	specific conductance
s	[l/s m]	linear pumping speed
q	[Torr l/s m]	specific outgassing rate
S	[l/s]	integrated pump speed
L	[m]	element length

$Q = -c dP/dz$, assembled in a state vector $(P, Q, 1)$ which reads

$$\begin{aligned} R_{11} &= \cosh(\sqrt{s/c}L) \\ R_{12} &= -\frac{L \sinh(\sqrt{s/c}L)}{c \sqrt{s/c}L} \\ R_{13} &= -\frac{qL^2 \cosh(\sqrt{s/c}L) - 1}{c (s/c)L^2} \\ R_{21} &= -c\sqrt{s/c} \sinh(\sqrt{s/c}L) \\ R_{22} &= \cosh(\sqrt{s/c}L) \\ R_{23} &= qL \frac{\sinh(\sqrt{s/c}L)}{\sqrt{s/c}L} \\ R_{33} &= 1, R_{31} = R_{32} = 0 \end{aligned} \quad (3)$$

From eq. 3 we can now deduce special cases for elements which do only outgassing or pumping. A piece of beam line which neither pumps or outgasses is given by eq. 3 in the limit $q \rightarrow 0$ and $s \rightarrow 0$. A long pump is given by $q \rightarrow 0$. A very short pump can be described by eq. 3 with $L \rightarrow 0$ but constant integrated pump strength $S = sL$. The transfer matrix of a long outgassing element is given by eq. 3 in the limit of $s \rightarrow 0$.

Given the transfer matrices it is possible to track a given pressure profile through a vacuum lattice if the initial values P_0 and Q_0 are known. Another option is to find the initial values under the assumption of periodicity, i.e., if one considers a sequence of equal vacuum cells. Given a

⁰work supported by the Department of Energy Contract DE-AC03-76SF00515.

¹This approach was originally initiated by the author at the Universität Dortmund and led to the development of a PC based program CLOBIVAC [2] by M. Michel.

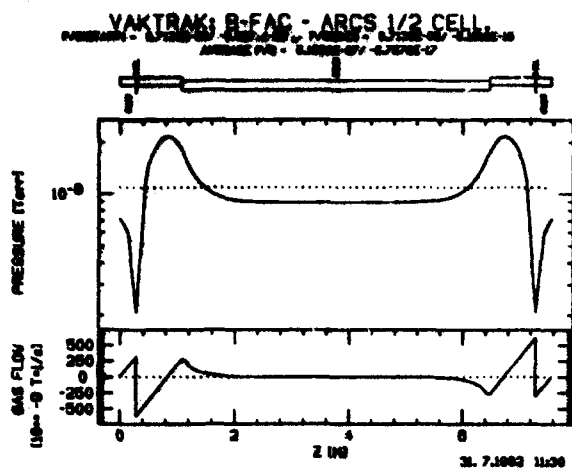


Figure 1: Longitudinal Pressure Profile

cumulative transfer matrix \tilde{M} through a vacuum structure

$$\tilde{M} = \begin{pmatrix} M & \vec{v} \\ 0 & 1 \end{pmatrix}, \quad (4)$$

where $M_{ij} = \tilde{M}_{ij}$ for $i, j = 1, 2$ and $v_i = \tilde{M}_{i3}$ for $i = 1, 2$, the periodic solution \vec{P}_0 is given by

$$\vec{P}_0 = (1 - M)^{-1} \vec{v}, \quad (5)$$

where \vec{P}_0 stands for the vector (P_0, Q_0) .

Observe that a transfer matrix represents two equations that relate two components of the input vector \vec{P}_0 to two components of the vector at the end of the vacuum beam line. By specifying two of the four values the system can be solved for the other two. In this way more general boundary conditions can be taken into account.

As an example consider a synchrotron radiation beam line. At one end it is linked to the storage ring which can be assumed to be held at constant pressure and at the other end it is closed off, such that the gas flow is zero. If the vacuum components in the beam line are specified the system can be solved for the incoming gas flow from the storage ring and the pressure at the closed off end.

II. VAKTRAK

The code VAKTRAK contains an implementation of the matrices given by eq. 3. It first reads an input file that contains the sequence of elements and their corresponding properties like length, conductance, pump speed and outgassing rate and constructs the transfer matrices. The code then prompts for the boundary conditions and continues to calculate the pressure profile and the gas flow. Finally it writes a TOPDRAW [3] file that displays the vacuum lattice, the pressure profile, and the gas flow as shown in fig. 1. The details of operating VAKTRAK are explained in ref. 4.

One has to keep in mind that this method is numerically touchy and the calculation of the solution for very long vacuum lattices is numerically unstable, so the user must be careful in interpreting the output. This problem is alleviated as far as possible by using REAL*16 variables in internal calculations. It should be noted that this problem mainly arises in systems with large pumps and small conductance, i.e. systems, which are physically not well designed.

The beam-gas scattering lifetime in a storage ring is determined by the average of the pressure and the beta function over the circumference of the ring [5]. VAKTRAK provides the option to specify a magnet lattice in TRANSPORT style input [6]. This file is read and the periodic solution for the beta functions is determined. Then the averages of β , P , and βP are calculated and displayed. Using this routine it is easy to optimize the placement of pumps in a vacuum system, and taking the detailed behavior of the beta functions into account.

III. MULTIPLE CONNECTED VACUUM SYSTEMS

So far we are dealing with single segments of beam line. Using periodic boundary conditions is equivalent to either an infinite array of such segments or a circular segment. In order to take more complex geometries into account such as pump manifolds connected to beam pipes at various locations, we have to generalize the concept of periodic boundary conditions.

This generalization is based on Kirchhoff-like rules for vacuum systems [7]. They are based on the observation that in vacuum systems the pressure plays the same role as the voltage in electric circuits and the gas flow behaves analogously to the current. Using these observations we can state two rules:

1. the sum of gas flows into a node is zero,
2. the sum of pressure differences around a closed loop is zero.

These rules now take the place of periodic boundary conditions.

A further complication arises from the number of unknowns we have to solve for. For our purposes we choose the pressure at each of the n nodes and the gas flows into and out of a link. In this way we have to deal with $n + 2l$ unknowns, where l is the number of links. Now we have to find the same number of relations among the unknowns in order to find the systems' equilibrium configuration.

The first of the above rules relates the fluxes flowing into and out of each node, thus yielding n equations among the unknowns. The second rule allows us to use the transfer matrices for each of the links j to relate the pressure at the starting node of a link P_j and the gas flow into that

link $Q_{e,j}$ to the pressure of the ending node of link P_e and the gas flow out of the link $Q_{e,j}$ according to

$$\begin{pmatrix} P_e \\ Q_{e,j} \end{pmatrix} = \begin{pmatrix} M_{11}^j & M_{12}^j \\ M_{21}^j & M_{22}^j \end{pmatrix} \begin{pmatrix} P_s \\ Q_{s,j} \end{pmatrix} + \begin{pmatrix} v_1^j \\ v_2^j \end{pmatrix} \quad (6)$$

In this way we obtain $2l$ more equations for a total of $n+2l$ linear equations among the pressures at the nodes and gas flows into and out of the links. The solution of this system is a simply accomplished by any routine that solves linear equations, e.g., those using a Gauss-Jordan algorithm. One should, however, pay attention to numerical instabilities, because the transfer matrix elements can become very large. The cure is to use the highest available precision on the computer implementation.

The described algorithm is implemented in the code VAKLOOP, which reads an input file that contains the segments (links) element by element just as VAKTRAK does with the exception that the segments are separated by input lines that specify the starting and ending node of the following segment. VAKLOOP then calculates the transfer matrices for each segment and sets up the linear equations as described in the previous section and solves them. Furthermore the code generates plots like those shown in fig. 1 for each of the segments. After the calculation is done a few consistency checks are performed (also needed for accuracy) to test whether the solution actually solves the linear system.

IV. CONCLUSIONS

We presented a method to calculate longitudinal pressure profiles in very general conduction limited vacuum networks. The method is implemented in computer codes which allow fast and simple evaluation of the pressure in such systems.

This method is closely related to a matrix formalism treating charged particle beams in magnetic systems. The pressure takes the role of the transverse position x and the gas flow that of the angle x' . Some of the transfer matrices discussed in the second section of this note can be directly identified with magnetic elements. Pressing this analogy a little further we can identify vacuum gauges with beam position monitors. It needs to be investigated in the future whether this can be used to determine the position of leaks in vacuum systems.

In this note the pumps are assumed to be linear ($S = Q/P$). However, this restriction can easily overcome. The equations in this case will become weakly nonlinear, but can still be solved iteratively [2].

Furthermore, the codes currently deal with one gas at a time and the pressures are partial pressures for that gas. It is easy, at the expense of a lot of bookkeeping, to improve the codes to allow to deal with different pressures at the same time.

ACKNOWLEDGEMENTS

Discussions with M. Michel, Univ. Dortmund are gratefully acknowledged. I have profited greatly from discussions with and suggestions for improvement in both the codes and this note from the first users of VAKTRAK and VAKLOOP, B. Scott, SLAC/SSRL, G. Bowden, SLAC and J. Rifkin, SLAC.

REFERENCES

1. O. Gröbner, *Vacuum Systems*, in CERN 85-19. p. 489.
2. M. Michel, *Überlegungen zum Ultrahoch-Vakuumsystem für DELTA*, Diploma Thesis, Universität Dortmund, 1988.
3. R. Chaffee, *TOPDRAWER*, SLAC-CGTM 178, 1989 rev.
4. V. Ziemann, *Vacuum Tracking*, SLAC-PUB 5962, 1992.
5. J. LeDuff, *Current and Density Limitations in Existing Electron Storage Rings*, Nucl. Instr. Meth. A239, 83, 1985.
6. K. Brown, et. al., *TRANSPORT Manual*, SLAC-91, 1977.
7. G. Horikoshi, Y. Saito, K. Kakiyara, *An analysis of complex network of vacuum components and its application*, KEK-Preprint-89-138, 1989.
8. H. Hirano, Y. Kondo, N. Yoshimura, *Matrix calculation of pressures in high-vacuum systems*, J. Vac. Sci. Technology A6, 2865, 1988.

Future Accelerators in Japan*

Nobu Toge
National Laboratory for High Energy Physics
1-1 Oho, Tsukuba-shi, Ibaraki 305, Japan

Abstract

This paper presents a brief report on the present status of future accelerator projects at the National Laboratory for High Energy Physics (KEK), Japan.

I. INTRODUCTION

The KEK laboratory has been successfully operating the TRISTAN accelerator complex since 1986. It consists of a 2.5 GeV electron / positron linac, an 8 GeV Accumulation Ring (AR) and a 29 GeV Main Ring (MR). Concurrently with this operation, in response to recommendations by the Japanese High Energy Physics Committee, survey studies have been continued on new accelerator facilities at KEK. We have two major future projects, namely, the asymmetric e^+e^- B-factory based on TRISTAN (TRISTAN-II) and the Japan Linear Collider (JLC). The purpose of this paper is to outline those research activities and to present an update on their status.

II. TRISTAN-II (B-Factory)

A. Overview

The eventual goal of a B-factory is to allow studies of CP violation interactions in weak decays of b-mesons. The KEK version of a B-factory aims to serve this purpose by providing e^+e^- collisions at the $\Upsilon(4S)$ resonance with asymmetric energies of 8 GeV (e^-) and 3.5 GeV (e^+) [1, 2].

After considerable discussions on the ring parameters, our present working assumption has converged to build two new rings within the existing TRISTAN tunnel. Best efforts will be made to use existing infrastructures and facilities.

Table 1 summarizes pertinent parameters of TRISTAN-II for its low energy ring (LER) and high energy ring (HER). The numbers shown are for the Phase-I operation where every fifth RF bucket is filled. We aim to deliver a peak luminosity of $2 \times 10^{33} \text{ cm}^{-2}\text{s}^{-1}$. Later in the Phase-II operation, by filling all buckets, while maintaining the same particle intensity per bunch, the final peak luminosity may reach $10^{34} \text{ cm}^{-2}\text{s}^{-1}$. Experiences to accumulate during the Phase-I will be essential in reaching the Phase-II goal.

B. Injector

The present KEK linac (S-band, 400 m long) produces 2.5 GeV electron and positron beams at 25 Hz (maximum 50 Hz). It is currently used as the injector for the TRISTAN accelerator complex and for the Photon Factory (PF) ring. To eliminate the need for accelerating beams in the TRISTAN-II rings, the linac will undergo an energy upgrade [3], starting

	LER	HER	unit
Energy	3.5	8.0	GeV
Circumference	3018	3018	m
Tune shifts (x/y)	0.05 / 0.05	0.05 / 0.05	
Beta at IP (x/y)	1.0 / 0.01	1.0 / 0.01	m
Beam current	0.52	0.22	A
Energy spread	0.078	0.073	%
Bunch length (1σ)	5	5	mm
Bunch spacing	3.0	3.0	m
Bunch population	3.3	1.4	10^{10}
Emittance (x/y)	19 / 0.19	19 / 0.19	nm.rad
Synchrotron tune	0.014	0.070	
Betatron tune	~ 43	~ 39	
Energy loss / turn	0.84	4.1	MeV
Momentum compaction	2.0×10^{-4}	1.0×10^{-3}	
RF voltage	4.4	47	MV
RF frequency	508	508	MHz
Energy damping decrement	2.4×10^{-4}	5.1×10^{-4}	
Bending radius	16.2	91.3	m
Length of bend magnet	0.85	2.56	m

Table 1. Parameters of TRISTAN-II B factory

1994.

The upgrade involves replacement of existing 30 MW klystrons with 60 MW types and installation of SLAC-style pulse compression systems (SLED) which will amplify the accelerating power. It will increase the accelerating gradient from 9 MeV/m to 25 MeV/m. With a modest extension of accelerating structures, the total energy of 8 GeV for electrons will be achieved. The positron target will be relocated so that the positrons will be produced by 4 GeV electrons, resulting in a factor 20 increase of positron intensity to 3.2×10^9 / pulse.

To provide beams to the TRISTAN-II with improved stability and good optical matching, enhanced beam diagnostic tools and improved timing control systems will be built and implemented.

C. Ring Lattice

An important consideration in the lattice design is to maintain a sufficiently large dynamic aperture. This is to eliminate the need to alter the optics during injection, and to obtain a long beam lifetime during collisions. The very small β^* would create a large chromaticity which needs to be compensated without much compromising the operability of the ring. Our choice is a non-interleaved sextupole scheme [4], where each pair of sextupole magnets is placed π apart. The cancellation of geometric aberrations helps maintain a dynamic aperture with a good margin for the injection time.

Another ingredient in our lattice design is the use of a low momentum compaction of $\sim 2.4 \times 10^{-4}$ at LER (factor

*Talk presented at the 1993 Particle Accelerator Conference, May 17 - 20, 1993, Washington, D.C., U.S.A.

1/4 reduction), and possibly, at HER. This allows to lower the RF voltage V_c , without increasing the bunch length. It helps to reduce coupled-bunch instabilities, particularly the ones due to the fundamental mode of the accelerating cavities.

Very detailed simulation work is under way to evaluate the ring characteristics in the presence of various construction errors. Specification on beam position monitors for closed orbit corrections, optics studies and beam-based magnet alignment is examined. Our estimations of dynamic apertures mainly rely on the SAD code which has been developed at KEK [5]. Tests to explore its validity have been repeated in the machine study time at TRISTAN [6] and will continue.

The non-interleaved sextupole lattice will be tested at the TRISTAN MR in the fall of 1993. This will be done by temporarily rewiring power-supply connections of the existing sextupoles.

D. RF System

The RF system at TRISTAN-II must be carefully built to reduce the growth rate of transverse and longitudinal coupled-bunch instabilities, where there are two types: (1) higher-order-mode (HOM) coupling (transverse and longitudinal) and (2) fundamental / accelerating mode coupling (longitudinal).

Superconducting cavities theoretically offer a good solution to both of these. Up to 28 cavities have been operated at maximum fields of 7 MeV/m for 12 mA beams at TRISTAN MR. For TRISTAN-II a new aluminum test model has been designed and built [7]. The cold test has shown good results. A full-size Nb model has been recently completed. In the initial cooling test an accelerating gradient of 10 MV/m was obtained with $Q \sim 10^9$. The studies on HOM absorbing materials are also on-going. The IB-400 ferrite made by TDK Co. Ltd. is currently tested in various aspects such as outgassing rates, mechanical characteristics and capabilities to handle high RF powers.

To acquire full confidence over the superconducting cavity technology, we feel it is important to exercise them in actual beam environments. While we plan some beam experiments at the present TRISTAN rings in the near future, the complete final design may have to wait for experiences at real-life TRISTAN-II. Therefore, our strategy is to support the initial runs of TRISTAN-II with normal conducting RF cavities. A candidate design is based on the damped cavity idea [8], which was originally proposed by Palmer [9]. The first 2-cell prototype cavity has been completed and a low-power test is under way with and without RF absorbers. Measured damping of TM110 and TM011 modes agrees with expectations. High power testing is planned later this year.

Another idea of HOM damping (Choke-mode cavity) came out through efforts on the linear collider R & D, which also need to deal with multi-bunches [10]. It is equipped with a "choke" structure which traps the RF fundamental mode, while the HOM components are allowed to escape radially towards outside the accelerating region. A cold test has shown good HOM damping characteristics.

Beam tests of those cavities (both normal- and superconducting) are scheduled for 1995 at the TRISTAN AR. Existing hardware in the RF section will be replaced by test modules. A high beam current of 500 mA will be stored in the ring by filling 128 bunches at 3.1 GeV. It is anticipated that normal-conducting cavities allow to bring the growth

rates of HOM instabilities in the range that can be controlled by using bunch feedback systems in the Phase-I operation. Our plan is to encourage efforts on different cavity ideas simultaneously and to make the final decision on the normal conducting type cavity within two years. Component testing of the bunch-to-bunch feedback is also presently under way [13]. The full system will be exercised during the high-current AR run.

When the commissioning and operation of the TRISTAN-II progresses, the beam intensity will be continually increased. Eventually the fundamental mode instabilities will become intolerable. At that time a transition to the superconducting cavities will be made. Yet another new idea which came out recently is to build a large energy storage cavity and attach it to the accelerating (normal conducting) cavity [11]. It will increase the Q value and reduce the cavity de-tuning frequency. The overall system can act like a superconducting cavity. Pilot studies on this possibility are also beginning [12].

E. Interaction Region

During the injection time, because of the large beam emittance, it is preferred to introduce a finite crossing angle to reduce parasitic crossing beam-beam effects. However, a large crossing angle could lead to excitations of synchro-beta resonance during the collision time [14].

Our present choice is driven by the desire to satisfy those conflicting requirements, with emphasis on the initial-stage runs where the bunch spacing is relatively large (3 m). We have adopted a beam separation scheme based on a combination of a small crossing angle (half crossing angle $\theta_c = 2.8$ mrad) at the collision point and a pair of separation bend magnets which are superconducting [15]. The final focusing is obtained with superconducting final quadrupole magnets which are housed in the same cryostat enclosure as the separation bends [16].

This design allows certain flexibility to alter the crossing angle up to 6 - 7 mrad without a major beam-line reconstruction, when the bunch spacing is made smaller in the future. At that time, a Crab crossing scheme may be required. The beam line space for Crab RF cavities will be set aside and the Crab R&D efforts will be continued [17].

Our current discussions are centered on detailed planning of the mechanical construction and evaluations of interface and interference with the experimental facility.

F. Other Activities

The vacuum system to achieve 10^{-9} Torr throughout the ring under the strong synchrotron radiation power up to 10 kW/m will use copper as the chamber material [18]. The time profile of vacuum baking process has been estimated and the predictions appear promising. Assuming the presence of 100 l/s NEG vacuum pump, the vacuum pressure distribution has been simulated for a proposed beam-line layout. A trial model (3.7 m long) of the full-size OFC vacuum chamber (although straight) has been built. Studies to improve the surface treatment process are under way.

Ground motions over short (10 ms) and long time (days) period have been monitored in the TRISTAN tunnel [19]. It appears that the seismic vibrations in the 10 - 100 Hz range is sufficiently small (the vibration amplitude is about 1 μ m at 1 Hz) so that their effects on the beam tuning is

manageable. However a mid-term(hours) to long term (weeks) ground motion of an order of 100 ~ 200 μm has been observed. It is likely due to the tidal wave, but it is also mildly correlated with the weather. This could cause a problem for the tuning stability of the ring. Some kind of feedback may need to be developed using signals from hydrostatic leveling systems.

G. Outlook

We are hoping to obtain a government grant of the TRISTAN-II this year, which would allow us to begin construction in the Japanese fiscal year of 1994 (to start April 1994). If this turns out to be the case, the accelerator will be commissioned sometime in 1998. Detailed schedules on the transition from the present TRISTAN configuration to the TRISTAN-II, machine study programs, and the detector de-commissioning / commissioning are being worked out.

III. JAPAN LINEAR COLLIDER (JLC)

A. Overview

Our motivation stems from the notion that it is a sensible thing to start the next-generation electron - positron linear collider from the energy range near $E_{\text{CM}} = 500 \text{ GeV}$ with the luminosity $10^{33} \sim 10^{34} \text{ cm}^{-2}\text{s}^{-1}$ [20]. The first primary physics target is a detailed study on productions and decays of the (yet to be discovered) top quark. A search for light Higgs mesons, which are strongly suggested by SUSY-based Grand Unified Theories (GUT), is another important menu. We also believe that the construction of a linear collider of this energy range will give us important experiences to help develop even higher energy linear colliders in the distant future.

Pioneering work has been done on the nature of beam interactions to occur at the collision point [21]. Theoretical studies on the final focusing optics [22], beam dynamics in the linear accelerator [23], and simulations of backgrounds to the experimental facility [24] followed.

Extensive work has been done to search for good machine parameters to use for the JLC [20]. The parameter set for the X-band (11.424 GHz) linac case is shown in Table 2.

The current major R&D activities at KEK include construction efforts of the Accelerator Test Facility (ATF), participation in the Final Focus Test Beam at SLAC, R & D on the RF power source, accelerating structures and others

B. Accelerator Test Facility (ATF)

The eventual goal of KEK ATF is to demonstrate ultra-low emittance (flat beam, $\gamma_e/\gamma_x \sim 5 \times 10^{-8}/5 \times 10^{-6} \text{ rad.m}$), required for future linear colliders, for a train of bunches (up to 20 bunches per train) at 1.54 GeV [25]. The beam energy is somewhat smaller than what we anticipate for the real-life JLC, due to the constraints of the size of the available experimental hall. However, many parameters have been chosen so as to follow the JLC configuration.

The planned ATF consists of multi-bunch electron guns, a buncher system, the beam transport line, a 1.54 GeV test damping ring, a bunch compressor and the emittance measurement section.

Creation of multi-bunches is the very first step in building the basis of the next linear collider. As the most

Parameter		unit	
Beam energy	E	150	250 GeV
Particles/ bunch	N	0.7	0.7 10^{10}
Bunches / pulse	N_b	90	90
Rep. frequency	f_{rep}	150	150 Hz
Bunch length	σ_z	85	67 μm
Accel. gradient	G_0	40	40 MeV/m
Active linac length	L_{ac}	5.0	8.5 km
Iris radius/wavelength	a/λ	0.18	0.18
Filling time	T_f	75	75 ns
Total average power into cavities		11	20 MW
Total wall-plug power		75	135 MW
Peak power / cavity		50	50 MW
Normalized damping	γ_e/γ_x	3000	3000 nm.rad
ring emittance	γ_y	30	30 nm.rad
Beta* at IP	β_x	10	10 mm
	β_y	100	100 μm
Beam size at IP	σ_x	335	260 nm
	σ_y	3.92	3.04 nm
Crossing angle		9.0	7.2 mrad
Beam diagonal angle	σ_y/σ_z	4.0	3.9 mrad
Disruption parameter	D_x	0.09	0.007
	D_y	7.7	6.0
# of beamstrahlung (BSM) photons	n_γ	0.8	0.95
Maximum upslon		0.15	0.39
Energy loss by BSM	δ_{BS}	1.8	4.5 %
Geometrical luminosity		0.63	0.70
reduction factor			
Pinch enhancement	H_D	1.71	1.72
Luminosity	L	3.5	6.3 10^{33}
			/cm ² /s

Table 2. The parameter set for the JLC-I, based on X-band linear accelerators (Parameters with S- and C-band cases also exist [20]).

orthodox approach a thermionic gun driven by a grid pulsar for multi-bunch beam generation has been developed [26]. The second approach, which may eventually take over for the real-life JLC, is the RF-gun technology. By flashing the Sb-Cs target with a YAG laser light (0.15 mJ, 532 nm), synchronized to a S-band RF, electron population of 2.3×10^{10} has been obtained [27]. Also polarized electron guns have been developed in collaboration with a group from Nagoya University [28]

The 1.54 GeV injector linac at ATF will use S-band RF. New S-band klystrons have been developed which outputs 85 MW peak power for 4.5 μs long pulses (100 MW for 1 μs). To deliver the required accelerating field of 33 MeV/m (this comes from the site constraint), a dual-iris SLED cavity has been developed. A stable peak SLED output of 380 MW has been achieved for an input power of 80 MW with 4.5 μs pulse width [29]. An R&D on RF windows has been carried out with a resonant ring, which has been specifically built for this purpose. By a careful selection of raw alumina, sintering binders and by using the hot isostatic pressing method, it has been shown that alumina windows could be built to survive

up to 310 MW of S-band RF power [30]. The entire 1.54 GeV linac will be completed early 1994.

Parameters for the ATF test damping ring are summarized in the table below.

Parameter		Unit
Beam energy	1.54	GeV
Repetition rate	25	Hz
Circumference	138.6	m
Harmonic number	330	
# of bunch trains	5	
# of bunches / train	20	
# of particles / bunch	$(1-3) \times 10^{10}$	
Energy loss / turn	0.173	MeV
# of FoBo cells	36	
Longitudinal Impedance threshold	0.30	Ω
Bending field strength	0.896	T
Momentum compaction	1.97×10^{-3}	
Natural emittance	1.34×10^{-9}	rad.m
Wiggler pitch	40	cm
Damping time (x / y / s)	6.32 / 8.26 / 4.88	ms
Tune (x / y)	16.2 / 8.3	
Wiggler field strength	1.88	T
RF frequency	714	MHz
# of cavity cells	4 + 1	
Bunch length	4.73	mm
RF voltage	0.77	MV
Energy spread	0.0773	%
Touchek lifetime	89	s
Emittance with intra-beam (x / y)	4.47×10^{-6}	rad.m
	4.47×10^{-8}	rad.m
Phase advance/cell (x / y)	140 / 52	deg.
Damping partition number (x / y / s)	1.3068 / 1.000 / 1.6932	

Table 3. Parameters of the ATF test damping ring.

The optics of the ATF damping ring uses an FoBo lattice where the horizontal defocusing is provided by combined function bend magnets. This lattice creates a low dispersion with relatively weak bend fields, and it helps to reach a low beam emittance. To control the damping time, wiggler magnets (21 m long) are introduced in the straight section where dispersion is absent. Allowed magnet construction errors and alignment errors have been evaluated. The magnet support system with 5 μ m accuracy with five degrees of freedom has been developed, and it is currently tested.

The vacuum chamber design has been refined to reduce the impedance of the entire vacuum system, including the beam diagnostic devices. Synchrotron photon absorbers are arranged so that they are not directly seen by the beam. The design value of longitudinal impedance of $\sim 0.1 \Omega$ appears possible [31].

Beam extraction from the damping ring will be done with a pair of two kicker magnets that are placed 180 degrees apart in phase advance [32]. This should reduce extraction orbit errors significantly. A detailed simulation work on the bunch compressor is in progress, taking into account the effects of the beam loading due to the multi-bunch nature of the beam [33]. The present design will occupy about 40 m of length. It is expected to compress the bunch length by a factor 1/10.

Development efforts are being made on beam instrumentation devices such as wire scanners, beam profile monitors, fast signal processing electronics, beam position monitors [34]. The wire scanner and a few other new instruments have been tested earlier this year in collaboration with a group from Tohoku University, using their electron linac facility. Synchrotron radiation monitor to use at the damping ring will be developed with a group at Institute for Nuclear Study, University of Tokyo.

Detailed EGS simulations and heat calculations on the positron production target has been on-going [35]. A prototype is planned to use 1.54 GeV electrons from the ATF linac.

C. Participation in Final Focus Test Beam (FFTB) at SLAC

As part of the U.S.-Japan collaboration program in High Energy Physics, KEK has been part of the Final Focus Test Beam (FFTB) collaboration based at SLAC. The goal of FFTB is to exploit the high energy (47 GeV) low emittance beam available at SLC, and explore the feasibility of extremely tight focusing at the interaction point required at future linear colliders. The beam commissioning has recently started. A bulk of beam time is scheduled for summer this year.

At the early stage of the project, physicists from KEK participated in the optical design and error analyses in the FFTB beam line [36]. Later, KEK has taken the responsibility for fabricating the doublet of small-bore (13 ~ 20 mm diameter) normal conducting final quadrupole magnets [37]. While those magnets have to create 140 ~ 180 T/m field gradient over up to 1.1 m of length, the higher-pole field components must be less than 0.01 % for sextupoles and below 0.1 % for octupoles. The fabrication accuracy, presently possible at 2 ~ 3 μ m, allows to satisfy the octupole requirement, but it is not sufficient for the sextupole errors. Remaining errors will be corrected by using trim windings.

The support system of the magnets has an adjustable table which is driven by high-power stepping motors and Piezo-electric devices. Position controls with the full six degrees of freedom are featured. The magnet position will be monitored with a laser interferometer and micro-sensors. The fabrication of magnets has been finished earlier this year, with complete magnet measurements. They have been delivered to SLAC and the installation in the beam line has been recently completed.

A novel idea on measuring the small beam spot parameters at the beam focal point has been proposed by a physicist at KEK [38]. It utilizes an interference pattern of two laser beams as a fine strip target to place at the beam focal point. The laser photons interact with the beam through Compton scattering process. Beam spot size parameters are deduced by knowing the width of the laser interference pattern and by measuring the modulation of the rate of Compton-scattered photons. The monitor based on this concept is presently under construction. Creation of laser interference pattern has been confirmed. It will be installed at the FFTB early summer this year, and will be tested.

D. RF Power Source Research and Development

The linear accelerator at JLC will be based on some sort of disk-loaded accelerating structure driven by high power RF klystrons. From the wall-plug power efficiency point of

view, it is advantageous to use a higher RF frequency such as X-band (11.424 GHz).

In early days of JLC efforts, a new simulation code FCI was developed to study behaviors of electrons in klystrons [39]. The first X-band klystrons built were 30 MW class XB-50K series tubes. Studies were made on high-voltage behaviors of electron guns and klystron windows. After achieving up to 26 MW output power, efforts were shifted to the XB-72K series klystrons (100MW class). The maximum output power of 79 MW has been achieved for 50 ns pulses. The peak electron voltage is 600 kV [40]. With improved high voltage performance of the output window, we hope to raise the output power to 100 MW or more. Possible use of superconducting coils for the beam focusing in the klystrons is contemplated.

The first high gradient tests of accelerating structures were conducted at S-band by combining the RF power from two klystrons (total 160 MW) on a 60 cm structure. An average accelerating field of 91 MV/m was achieved [41]. Subsequent studies have been made on 20 cm traveling wave structures at X-band with 100 ns pulses from an XB50K klystron. Dark currents and conditioning characteristics were studied. The average accelerating gradient reached 68 MV/m in runs over 600 hours for one structure sample, and 85 MV/m (limited by the klystron) within 50 hours for another. Efforts are being made to improve the fabrication process such as machining accuracy and brazing [42].

At JLC where multi-bunch trains are accelerated, it is essential to reduce the effects due to higher order mode fields within the accelerating structure. Studies on the damped mode cavity, choke-mode cavity and a detuned structure are in progress [43, 10]. Fine fabrication of X-band structures is being studied to achieve alignment of cells within a few microns, and to eliminate need for tuning after the brazing. A multi-cell choke mode cavity is being designed to prove the high power operation at S-band.

Review work of the JLC parameters in the past year has shown that a linear collider at 300 ~ 500 GeV ECM could be also designed using C-band (5.712 GHz) and S-band (2.856 GHz) linacs [20]. It appears possible to expand them in a higher energy range. At the present stage we defer final decision on the RF frequency, and we will let development efforts on those possibilities cross-fertilize.

E. Outlook

The immediate goal of the JLC development group is to construct the ATF and demonstrate the feasibility of multi-bunch flat beam with adequately low emittance. Development efforts on the RF power source and accelerating structure, studies on beam dynamics and collimation, refinement of the final focus optics and overall system design will continue. During this process various technical possibilities will be sorted out. We hope to submit a technical design proposal of the JLC in 1996 - 97.

IV. ACKNOWLEDGMENTS

The author wishes to thank many researchers at KEK who helped him prepare the materials presented in this paper, in particular, Prof. S. Kurokawa and Prof. K. Takata.

V. REFERENCES

- [1] "Accelerator Design of the KEK B-Factor", ed. by S. Kurokawa et al, KEK Report 90-24 (1991).
- [2] "Proc. of Int'l Workshop on B-Factories: Accelerators and Experiments", KEK, 1992 ed. by S. Matsuda et al., to be published. In particular, the articles by S. Kurokawa and K. Satoh therein.
- [3] S. Enomoto, in [2].
- [4] H. Koiso, in [2].
- [5] K. Oide and H. Koiso, KEK-preprint 92-45 (1992).
- [6] Y. Funakoshi in [2].
- [7] K. Kubo et al., in "Proc. of HEACC92", Hamburg (1992), p. 691. S. Mitsunobu, in [2].
- [8] M. Suetsugu in [2].
- [9] R.B. Palmer, SLAC-PUB-4542, 1988.
- [10] T. Shintake, Jpn. J. Appl. Phys. 31 (1992) p.1567.
- [11] T. Shintake, KEK-preprint 92-191 (1993). T. Shintake, PAC93
- [12] Y. Yamazaki and T. Kageyama, KEK-preprint 93-15 (1993).
- [13] E. Kikutani, H. Ishii and M. Tejima, private communications.
- [14] K. Hirata in [2].
- [15] K. Satoh in [2].
- [16] T. Kobayashi in [2].
- [17] K. Akai et al., "Proc. of HEACC92", Hamburg (1992), p.757.
- [18] Y. Suetsugu and M. Kobayashi in [2].
- [19] R. Sugahara in [2].
- [20] "JLC-I", ed. by JLC group, KEK Report 92-16 (1992).
- [21] K. Yokoya and P. Chen, "Beam-Beam Phenomena in Linear Colliders", Lecture Notes in Physics 400, Springer Verlag, (1991) p.414.
- [22] K. Oide, Nucl. Instr. and Method A276 (1989) p.427.
- [23] K. Yokoya DESY 86-084 (1986). Also, [20].
- [24] T. Tauchi et al, KEK-preprint 90-181.
- [25] "Proceedings of the SLAC/KEK Linear Collider Workshop on Damping Ring", ed. by J. Urakawa and M. Yoshioka, KEK Report 92-6 (1992).
- [26] T. Naito et al., KEK-preprint 92-97 (1992).
- [27] M. Yoshioka et al., KEK-preprint 92-63 (1992).
- [28] T. Nakanishi et al., Phys. Lett. A158 (1991) p.345. T. Omori et al., Phys. Rev. Lett. 67 (1991) p.3294.
- [29] H. Matsumoto et al., KEK-preprint 92-179 (1993), to be published.
- [30] A. Miura et al., KEK-preprint 92-215 (1993), to be published.
- [31] S. Terunuma, "Proc. of 3rd Workshop on JLC", KEK (1992).
- [32] H. Nakayama in [25].
- [33] M. Kikuchi, presented at "Int'l Workshop on Emittance Preservation in Linear Colliders", KEK (1993).
- [34] H. Hayano et al., KEK-preprint 90-117 (1990), also Nucl. Instr. and Method A320 (1992) 47, KEK-preprint 92-118 (1992). M. Ross et al., SLAC-PUB-6015 (1993).
- [35] H. Ida et al., KEK-preprint 92-56 (1992).
- [36] J. Irwin et al., SLAC-PUB-5539.
- [37] H. Nakayama, contributed to LC91 Workshop, Protvino (1991). N. Ishihara et al., "Proc. of HEACC-92", Hamburg (1992), p.945.
- [38] T. Shintake, Nucl. Instr. and Method A293 (1990) 206.
- [39] T. Shintake, "Proc. of IEEE PAC-89", Chicago (1992), p.94.
- [40] H. Mizuno et al., KEK-preprint 92-101 (1992).
- [41] H. Matsumoto et al., KEK-preprint 92-84 (1992).
- [42] T. Higo et al., "Proc. of HEACC-92", Hamburg (1992), p.836.
- [43] T. Taniuchi, KEK-preprint 92-122 (1992). M. Yamamoto, KEK-preprint 92-130 (1992).

LHC PROGRESS AND STATUS

The LHC Machine Group reported by G. Brianti
CERN, European Organisation for Nuclear Research
1211 - Geneva 23, Switzerland

Abstract

The LHC is a superconducting collider to be installed in the LEP tunnel for high energy pp, Pb ions and ep collisions. An overall machine optimization, including a new lattice arrangement and an increased dipole aperture (56 mm), will be presented. The increased energy to field ratio is (0.81 TeV/T). Recent results from a magnet model with industrially produced coils assembled at CERN reached 10 T with a limited training and ultimately attained 10.5 T, demonstrating that operational fields in excess of 9 T can be obtained.

Results from previous models and a 10 m-long prototype will be given. In total seven of these prototypes are being constructed by industry. In December 1991, the CERN Council unanimously adopted a resolution stating that the LHC is the right machine for the future of CERN and requesting a final proposal in 1993, which is being actively prepared and is summarized in this report.

1. INTRODUCTION

The general design of the collider, which essentially consists of a ring of high-field superconducting magnets to be installed above LEP in the 27 km tunnel, was described in the last International Conference in Hamburg[1]. A Design Study [2] was published in May, 1991.

The magnets are of the so-called 'two-in-one' structure, namely incorporating two beam channels in the same mechanical structure and cryostat (Fig. 1).

Such a magnetic structure added to LEP can provide three types of collisions, namely proton-proton, heavy ions (Pb-Pb) and electron-proton by colliding the LEP electron beam with one of the proton beams.

The most important parameters of these collisions are given in Table 1.

Emphasis is put on luminosity since the point-like nature of quark-quark interactions implies that the cross sections decrease as the collision energy E increases. To maintain equally effective physics programmes, the luminosity should increase as E^2 , and thus, to explore rare processes such as $Higgs \rightarrow ZZ \rightarrow 4\mu$, the LHC is designed to provide luminosities in excess of $10^{34} \text{ cm}^{-2} \text{ s}^{-1}$.

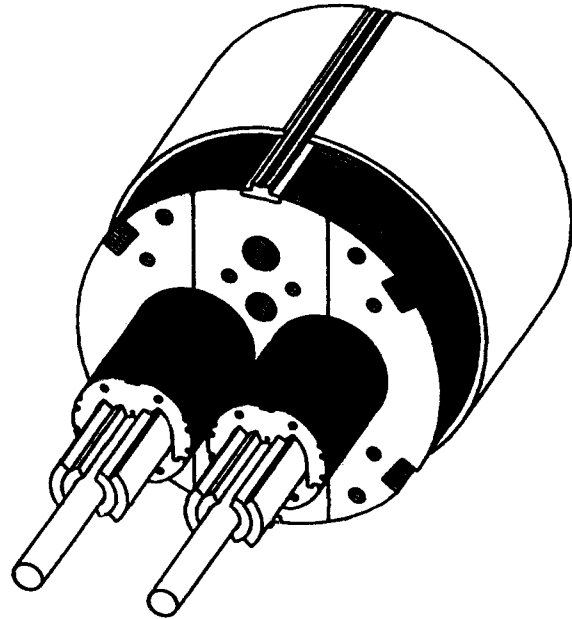


Fig. 1 Perspective view of a 'two-in-one' dipole

Table 1 : LHC Main Parameters

		pp	e-p	Pb-ions
C.m.energy for B=8.7 T	[TeV]	14.0	1.3	1150
Luminosity	[$\text{cm}^{-2} \text{ s}^{-1}$]	10^{34}	$2.5 \cdot 10^{32}$	$1.8 \cdot 10^{27}$
Number of bunches		2835	508	560
Bunch spacing	[ns]	25	164.7	135
Particle/bunch	(p)	10^{11}	$3.0 \cdot 10^{11}$	$9.4 \cdot 10^7$
" "	(e)		$9.2 \cdot 10^{10}$	
Particles/beam	(p)	$4.7 \cdot 10^{14}$	$1.5 \cdot 10^{14}$	$5.2 \cdot 10^{10}$
" "	(e)		$4.7 \cdot 10^{13}$	
Number of experiments		2		1
β at intersect. point ($\beta_x \beta_y$)	[m]	0.5	0.85, 0.26	0.5
			32.7, 3.05	
r.m.s. radius at intersection point (x,y)	[μm]	15	120 / 37	15.9
r.m.s. collision length	[cm]	5.3	3.8	5.3
Crossing angle	[μrad]	200	0	200

2. INJECTORS

The basic injection scheme is unchanged (Fig. 2) and makes use of all existing accelerators, namely Linac, Booster, 26 GeV PS and 450 GeV SPS for pp operation with only relatively minor modifications and additions.

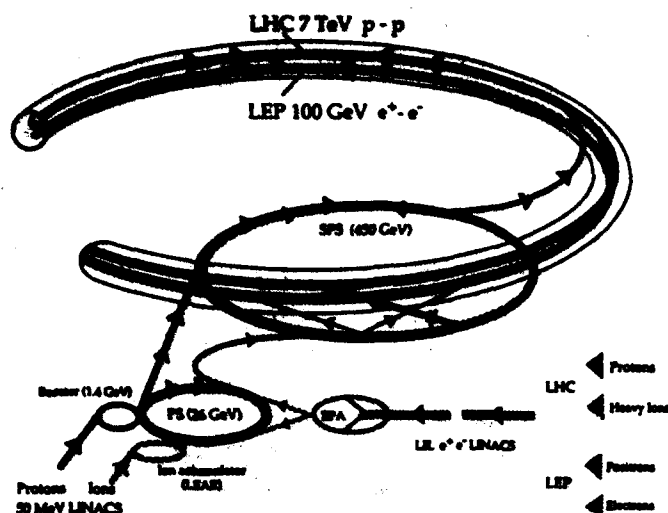


Fig. 2. The LHC injection complex

The nominal high luminosity operation requires two Booster cycles to fill the PS circumference, with the injected beam first accelerated by the existing RF system on $h = 8$, debunched and recaptured by a new 40 MHz RF system, to form a bunch train with 25 ns bunch spacing. The bunches are then compressed using an 80 MHz system and transferred to the SPS. Three such bunch trains are captured in the SPS and compressed to fit into the standard 200 MHz buckets by a new 80 MHz system, accelerated to 450 GeV and finally transferred into the LHC, via two new transfer lines. The whole operation is repeated 12 times to fill the entire LHC circumference.

The New developments are

In the Linac/Booster complex beams within 10% of the nominal parameters have been obtained after the installation of the new RFQ in front of the linac. A test of the LHC pre-injector, up to PS extraction energy, using prototypes in a configuration close to the final version, is scheduled for the end of the year 1993. In the SPS, a prototype of the 400 MHz LHC superconducting cavities will also be installed this year in order to test the bunch compression technique which will be required before transfer of the proton bunches into LHC.

3. GENERAL LAYOUT

The two interlaced LHC rings are placed 1.21 m above the LEP ring. The LHC lattice must follow very closely the LEP geometry, in particular the two machines must have the same revolution time in order to allow a later

conversion of LHC and LEP into an e-p collider. The constraints on the compatibility of the two machines has been reduced with the decision that LEP will be stopped as an e^+e^- collider before LHC is installed; the e-p collisions will anyway require a rearrangement of both LHC and LEP insertions.

The LHC lattice is, like LEP, made of 16 half-octants (about 1.7 km long) in which one finds successively the 24 regular half-cells of the arc, the 4 pseudo-half cells of the dispersion suppressors and the long straight section. Each octant has been separately equipped with its own cryogenic plant, its own power converter set, etc. so that it can be independently installed, tested and maintained.

Two of the eight long straight sections have been reserved for the machine: SS5 for beam dumping and SS3 for beam cleaning. Four straight sections will be equipped with low-beta insertions: SS1 and SS2 reserved for large LHC experiments, the injection of the clockwise circulating beam is in SS1; SS4 (or 6) for ions collisions and SS8 where the injection of the anti-clockwise circulating beam will be made in a detuned low-beta. The two remaining straight sections, SS6 and SS7, are kept in reserve as possible alternatives or for not yet specified applications (B-physics or gas-jet experiments). This layout is detailed in Fig. 3.

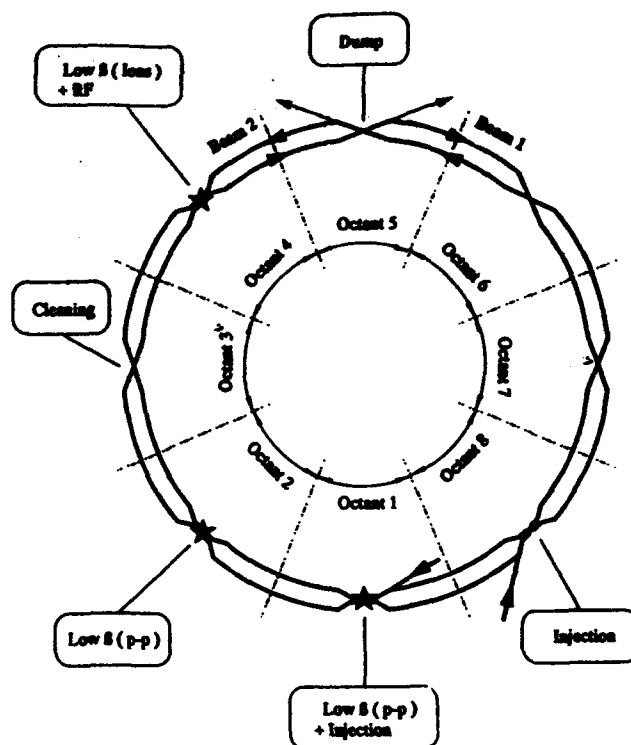


Fig. 3 LHC schematic layout

3.1. The arc half-cell

As indicated in Fig. 4 the 51 m long arc half-cell contains three 13.15 m long bending magnets and a 6.5 m long short straight section. In the straight section are

installed: the 3.05 m main quad., a beam position monitor and two corrector magnets, one with a combined dipole sextupole corrector and the other one with a tuning quadrupole and an octupole corrector. A set of sextupole and decapole correctors are attached to each main dipole to compensate the field errors introduced by these superconducting magnets. The effect of these field errors on the dynamic aperture has been reduced by enlarging the dipole aperture from the previous 50 mm to 56 mm (inner coil diameter).

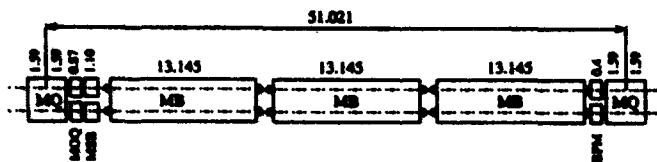


Fig. 4 The LHC half-cell
(new layout with three long dipoles)

The main magnets (dipole and quadrupole) of both rings are powered in series, one supply per half-octant, while the tuning quadrupoles allow an independent control of the tune of each ring over two integers in both planes.

A beam screen placed as shown on Fig. 5, inside the vacuum chamber allows the evacuation of synchrotron radiation power at about 10°K rather than at the 1.9°K of the superconducting magnet and vacuum chamber. The cryopumping is still ensured by the 1.9°K vacuum chamber through holes in the beam screen. The design of this screen has raised a number of interesting problems detailed in a companion paper [3].

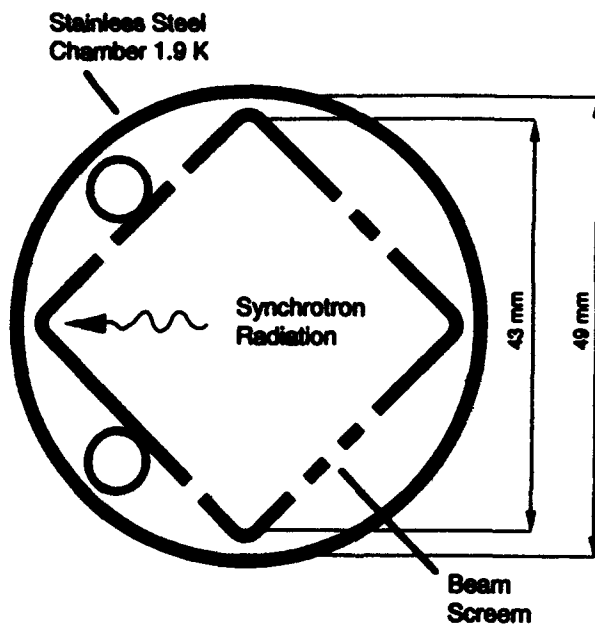


Fig. 5 Vacuum chamber cross-section

3.2. Dispersion suppressors

The dispersion suppressors are made of 4 pseudo half-cells. One half-cell contains a shortened magnet in order to

match the LEP tunnel curvature. The matching to the long straight section induces larger beta values which have imposed an enlargement of a number of quadrupoles. For the same reason the quadrupoles are not equipped with beam screen.

3.3. Low-beta insertions

The low beta insertions in SS1, 2, 4 and 8 use two triplets. The outer triplet made of two-in-one quadrupoles matches the dispersion suppressor to the inner triplet. In between those triplets a set of two separator magnets is used to install the two beams in the same vacuum chamber, so that the inner triplet uses single bore quadrupoles. These low beta superconducting quadrupoles are enlarged to 70 mm (inner coil diameter). In SS1 and 2, a collimator is placed between the interaction point and the quadrupoles of the inner triplet in order to protect them against the secondaries coming from the high luminosity interactions. In spite of this protection the heat deposition in these quadrupoles is about 30 to 40 W per quadrupole at luminosities of $10^{34} \text{ cm}^{-2} \text{ s}^{-1}$.

During injection and acceleration the low beta's are detuned to values of β^* of 15 m. In pp mode the low beta's are squeezed in straight sections 1 and 2 down to 0.5 m. In ion collisions mode only SS4 is squeezed to the same value of β^* .

3.4. Cleaning insertions

The superconducting magnets working at 1.9°K cannot stand the flux of about 10^9 protons per second which, at maximum luminosity, diffuses toward the vacuum chamber due to the scattering in the collisions and the combined effect of non-linearities and power converter ripple. A study of the heat deposition process due to these losses indicates that the localized losses must be limited to a few 10^6 protons per second at high energy, while about 30 times more are acceptable at injection. The diffusion of particles must be stopped before it reaches the superconducting elements; this is achieved in a dedicated insertion placed in straight section 3 and called the cleaning insertion.

In this crossing point, the lattice is arranged so that the beta values (and therefore the phase advance) are the same in both planes. For each beam, a set of four collimators, one primary and three secondaries are installed between the two separator magnets with the aim of trapping the large amplitude particles and absorbing them and their secondaries. The very high capture efficiency requested is achieved by installing the collimators very precisely around the beam at amplitudes not larger than about 6σ of the transverse distribution. The inefficiency results from small beam impact parameters, alignment and mechanical errors. The computer programs to simulate the cleaning process, including errors, are being prepared. The proper operation of the cleaning system will be part of the learning process during the build up of luminosity after running in.

3.5. Beam dump

In various operation conditions it will be necessary to dump the beams under clean conditions so that the superconducting elements are not deteriorated. Also, a

number of calorimeters placed on the magnet coils or beam loss detectors will require an emergency dumping of the beams in case losses in the ring exceed acceptable values.

The beam dump section mainly consists of powerful kickers capable of deflecting the beams into separate channels leading to dedicated absorber blocks. The two circulating beams are foreseen to have a 'hole' in the bunch train in which the beam dump kickers will be fired.

The beam dump must be able to absorb the 550 MJ of each beam. A central core of graphite surrounded by aluminium and shielded by massive iron blocks is proposed.

4. MAGNETS

The detailed results of the R&D programme obtained so far are summarized here for completeness.

- A 10 m-long twin dipole, in which two sets of HERA coils are incorporated into an LHC two-aperture structure, was tested at CEA-Saclay both at 4.5 K and at 1.9 K.

At 4.5 K it behaved exactly as good HERA single magnets, while at 1.9 K it reached the short sample field of 8.3 T in five quenches.

- A few 1 m-long models of full cross-section reached their short-sample field of ~ 8 T in two to three quenches at 4.2 K; they also reached the short-sample field of 9.8 to 10 T but after a long training above 9 T. The great majority of the quenches are located in the ends. In particular only three quenches occur in the central part before the short sample field is reached. A single aperture magnet built by KEK - Japan, with different cables, collars and steel structure on the basis of their own design, gave very similar results [4].

- In all magnets there is no sign of any negative influence of the 'two-in-one' structure.

These results give confidence that final magnets operating satisfactorily close to the maximum field of 9.5 T could be built.

Recently, a new model with the same industrially made coils, but separate stainless steel collars, was assembled at CERN and gave excellent results. At 4.3 K it reached the short-sample field of 8.1 T at the second quench and at 1.8 K ultimately reached 10.5 T (Fig. 6). Fields in excess of 10 T are readily obtained in current operation. It incorporates excellent 17 mm-wide cables with 5 μ m filaments. It is believed that the improved behaviour with respect to the previous models is due to the higher compression on the coil obtained by design and actually achieved at mounting.

Seven 10 m-long prototypes [5], all with the same set of coils but with three different mechanical structures are being built in industry. They will start to be delivered to CERN in the second half of 1993.

After an individual test, four of them will be mounted, together with a lattice quadrupole, to form a half-cell for extensive cryogenic tests.

The final dipoles will have an inner coil diameter of 56 mm and a magnetic length of 13.15 m. Maintaining the same short-sample field of 10 T would imply a somewhat larger cold mass and intra-beam distance and hence an increased cost. Therefore, as an alternative, we are

considering to use narrower cables (~ 13 mm) made of strands very similar to those used for the SSC. In such a case, the cold mass and intra-beam distance remain the same as for the 50 mm aperture, the superconductor volume decreases considerably and the field is reduced by ~ 5%.

At CERN new models are being built to optimize the coil design (especially ends) and mechanical structure.

The lattice quadrupole has been designed by CEA-Saclay and two full-scale units are being built. The first one is being tested at cryogenic temperature.

Prototypes of various correctors have also been built and some of them satisfactorily passed first tests.

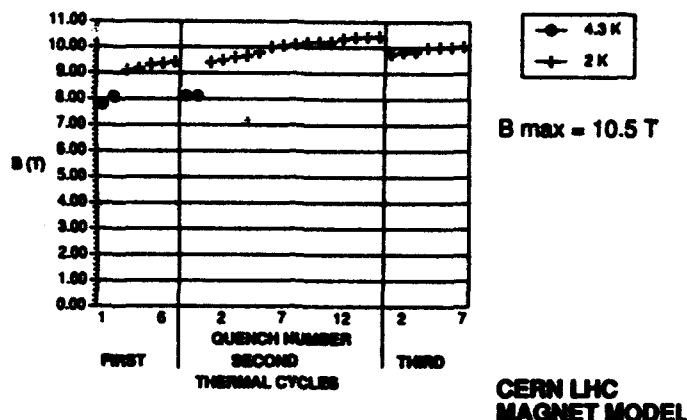


Fig. 6 Training curve of magnet model

5. CRYOGENICS

The block diagram of the cryogenic refrigeration system which corresponds to a half-cell (~ 51 m) is shown in Fig. 7.

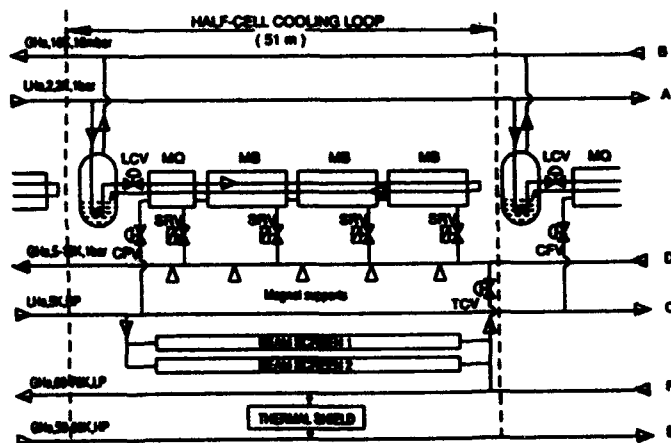


Fig. 7 Block diagram of cryogenic refrigeration

The magnets are immersed in static pressurized superfluid He at 1.9 K and cooled by heat exchange with saturated superfluid He flowing in a tube passing through the magnets and running all along the length of the half-cell. In this way the heat transfer path is streamlined from

the magnet windings to the linear cold source constituted by the heat exchanger tube. Moreover, the magnet baths are hydraulically decoupled from each other, as well as from the cooling circuit.

An important advantage of this system is that the working temperature of each magnet is little dependent on its location in the machine, with respect to the octant cryoplant.

To test this scheme in realistic conditions, a cryoloop model was built [5] in which the magnets are replaced by 10 m-long cryostat modules with an almost full scale heat exchanger tube. The actual magnet heat loads are provided by electrical heaters.

The experimental results have demonstrated correct operation of this cooling scheme, with excellent heat transfer capability, extracting the nominal heat load of 0.3 W/m across a temperature difference of a few mK between static baths and the flowing helium.

Each octant of the LHC will be cooled by its own refrigerator, with an installed capacity of:

- 1.8 kW isothermal refrigeration at 1.8 K,
- 8.5 kW non-isothermal refrigeration at 4.5-10 K
- 30 g/s liquefaction at 4.5 K
- 30 kW non-isothermal refrigeration at 50-75 K.

The four 12 kW cryoplants at 4.5 K already acquired for LEP 200 and installed at the even points, suitably boosted to 18 kW by additional compressors, will be used for LHC.

Four additional plants for the odd points and suitable cold boxes for lowering the temperature from 4.5 K to ~1.8 K will have to be installed in order to complete the refrigeration system.

6. EXPERIMENTAL AREAS

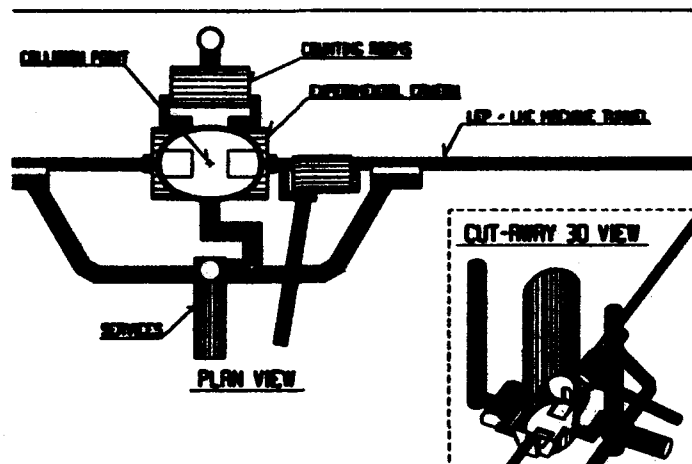


Fig. 8 Example of LHC underground experimental area

The design of the new LHC areas is actively pursued in close collaboration with proponents of experiments.

LHC experiments will be about twice the size of the LEP detectors and weigh between 10,000 and 30,000 tons. A design study for a suitable underground cavern, with a

40 m x 28 m elliptical section access shaft directly over the collision point is shown in Fig. 8. Relatively modest alcoves are added along the beam-line to allow the forward detectors to slide along the beam pipe and give access to the central region for repair and maintenance. In this way the underground handling of heavy components will be minimised. The counting room for the experiment and machine services are housed in separate caverns.

7. TIME TABLE AND CONCLUSION

The basic design of all machine components and the layout of equipment in the LEP tunnel are completed. They will form the basis of the final project proposal which is being prepared.

The construction schedule is based on the completion of the installation by the year 2000. It is therefore envisaged to complete the experimental programme with the LEP collider before the commissioning of the LHC, thus offering the opportunity of using very rationally the considerable infrastructure which exists in and around the LEP tunnel. Of course, the LEP machine itself will be fully preserved in view of a future ep operation.

The experimentation with both pp and ion collisions could start in the year 2001.

REFERENCES

- [1] Status report on the CERN Large Hadron Collider (LHC). The LHC Machine Group reported by G. Brianti at the XVth Intern. conf. on High Energy Accelerators, Hamburg, Germany, July, 1992. CERN/AC-DI/92-03 (LHC)
- [2] The LHC Study Group. Design Study of the Large Hadron Collider. A multiparticle collider in the LEP tunnel. CERN 91-03.
- [3] Vacuum technology for superconducting colliders. A. Mathewson. (this Conf.)
- [4] CERN/AC-DI/92-03 (LHC)
- [5] Design concept and first experimental validation of the superfluid helium system for the Large Hadron Collider (LHC) project at CERN. J. Casas, A. Cyvoct, PPh. Lebrun, A. Marquet, L. Taviani and R. van Weelden. LHC Note 191 and Proc. ICEC 14, Cryogenics Vo. 32, ICEC Supplement. Butterworth-Heinemann (1992).

Status of the SSC

Richard J. Briggs
Superconducting Super Collider Laboratory*
2550 Beckleymeade Ave., Dallas, TX 75237

Abstract

The Superconducting Super Collider (SSC) is a proton-proton colliding beam accelerator which, when completed, will provide collision energies of 40 TeV in the center-of-mass, at a luminosity of $10^{33}/\text{cm}^2/\text{sec}^{-1}$. This paper will describe the current status of the design and construction of the project.

I. INTRODUCTION

The basic concept for the Superconducting Super Collider goes back over ten years, to the DPF summer study of 1982. Based on technical successes in high field superconducting magnet developments for the Tevatron, a 40 TeV center-of-mass proton-proton collider was proposed as the next major step in the high energy physics (HEP) program. In 1983 HEPAP recommended that the SSC be built as the highest priority in the USA HEP program.

In the following years, detailed conceptual designs established the basic feasibility of the approach, leading to a presidential decision to proceed with the project. A site in Texas near Waxahachie was selected from over 43 proposals in 25 states. In 1989, a contract was signed with Universities Research Association to build and operate the SSC, marking the formal beginning of this ambitious construction project.

Over the past four years, enormous progress has been made in the construction of the SSC, and in the establishment of a new scientific laboratory on a "green field" site. At the present time, the staff working in Texas exceeds 2000 people, and civil construction activities, including the completion of over five miles of tunnel for the collider, are well underway.

In this paper, we present a brief overview of the current status of the accelerator design, development, and construction activities. A recent SSC publication can be consulted for additional details, including the status of the overall SSC program [1].

II. BASIC PARAMETERS AND THE SSC COMPLEX

The requirements established at the outset of the SSC project call for

- 20 TeV on 20 TeV proton-proton collisions
- a luminosity of $10^{33} \text{ cm}^{-2} \text{ sec}^{-1}$ at two or more interaction regions
- four interaction regions provided for experiments (initially), and
- a design reference mission of 4500 hours/year,

The baseline parameters of the colliding beams that meet these objectives are those given in Table 1. The individual bunch intensities and beam-beam tune shifts are conservative

by comparison with current practice. The transverse emittance represents a significant advance over currently achieved performance. The very large number of bunches, and the stored energy in the beams, is a major step beyond current experience (in beam stored energy, by about two orders of magnitude). The large size of the ring also leads to low revolution frequencies, and very low frequency ($< 1 \text{ kHz}$) resonances with the betatron motion.

Table 1
SSC Colliding Beam Parameters

Protons per r.f. bunch	0.75×10^{10}
Bunch spacing/rep rate	5 meters/60 MHz
Emittance (RMS)	$1\pi \text{ mm-mrad}$
Beam radius at interaction point (RMS)	5 micrometers
(S*=0.5M)	
Average number of events per bunch crossing	1.5
Beam-beam tune shift (total)	.007
	head-on = .003 long range = .004
Ring circumference	87.12 KM
Rotation frequency	3.44 kHz
Total number of bunches	17,424
Total particle energy/ring	418 megajoules
Cycle time	24 hours
Synchrotron radiation power/ring	8.75 kilowatts

An important influence on this choice of parameters is the desire for a limited number of proton-proton collisions for each beam pulse crossing (average of about 1.5 at the design luminosity). This parameter and the bunch rate of 60 MHz strongly influence the design of the experimental detectors.

At a particle energy of 20 TeV, the synchrotron radiation is becoming an important factor in the collider design. The synchrotron radiation heat load of about 18 kW is about half of the total 4.2-K cryogenic load. In addition, the irradiation of the vacuum wall by the energetic photons ($E_{\text{crit}} = 288 \text{ eV}$) will cause gas desorption, as in high energy electron rings. The 4.2-K beam tube may not provide adequate pumping capacity for hydrogen; an R&D program is underway to evaluate the desorption phenomenology and to investigate approaches for its mitigation.

The choice of a peak bending magnet field of about 6.6 T in the collider dipole magnets lead to a ring circumference of 87 km. A schematic of the collider is shown in Figure 1. On the west side, the injector complex is located on about 10,000 acres of land. Two interaction regions are also located on the west side. The large general purpose detectors will be located

*Operated by the Universities Research Association, Inc.,
for the U.S. Department of Energy under Contract No.
DE-AC35-89ER40486.

on the east side of the ring, to take advantage of the more favorable geological conditions in that area.

The main parameters of the various machines in the injectors are given in Table 2. The two collider rings and the bipolar HEB ring use superconducting magnets.

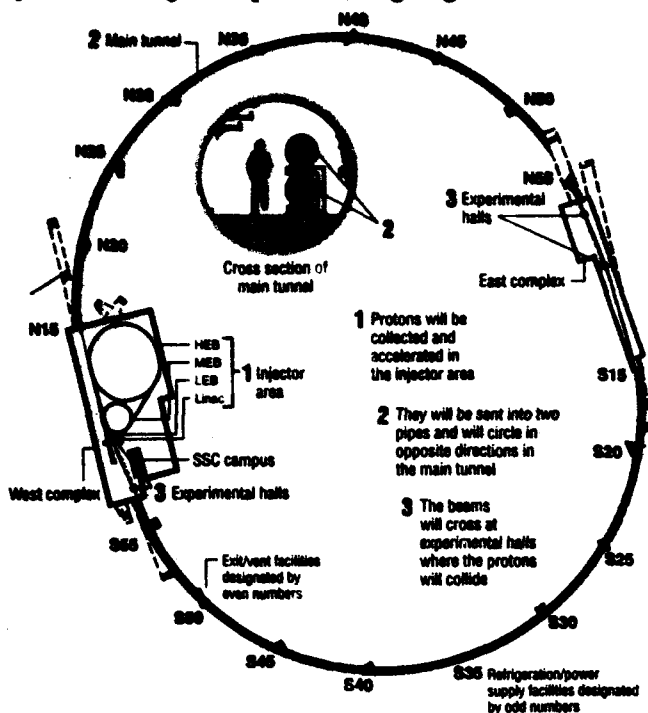


Figure 1. The overall layout of the SSC with the injector and west complex located on the left and the east complex on the right of the diagram.

III. SUPERCONDUCTING MAGNETS AND THE ACCELERATOR SYSTEM STRING TEST

The superconducting magnets represent the most costly single element in the SSC project, and it is also a relatively new technology compared to the other technical systems. A major R&D program was established at FNAL, BNL, and LBL to develop SSC superconducting magnets, following the 1983 decision by HEPAP. When the SSC Laboratory was established in 1989, a major effort was undertaken to acquire the capability on site (in people and facilities) to continue this R&D effort, and to create the industrial capability to do high rate production of the magnets.

In January 1990, the SSC Laboratory decided to increase the aperture of the collider dipole magnets from 40 mm to 50 mm to meet the dynamic aperture requirements during the injection phase. This change required significant changes in the collider dipole development plan. At this time the Laboratory committed to a system demonstration of one collider half-cell (the Accelerator System String Test) using industrially-assembled dipole magnets, to be completed by October 1992. The half-cell consists of five dipole magnets, one quadrupole magnet, a spool piece, and prototypical quench protection and sensor data acquisition systems.

The development of dipole magnets for this demonstration was carried out by FNAL and BNL, in collaboration with the SSC Laboratory. Once the industrial contracts were in place, General Dynamics sent a team to FNAL, and Westinghouse sent a team to BNL, to build the dipole magnets for the test. These magnets all demonstrated excellent performance, and the system test was successfully completed in August 1992, six weeks ahead of schedule.

Table 2.
Injector/Collider Parameters

Parameters	Linac	LEB	MEB	HEB	Collider
Kinetic Energy	0.6 GeV	11.1 GeV	180-200 GeV	2 TeV	20 TeV
Circumference (km)	(110 m long)	0.57	3.96	10.80	87.12
Cycle time	0.1 sec	0.1 sec	8 sec	2x4.3 min	~24 hours
Proton/ cycle	—	10^{12}	8×10^{12}	2×10^{12}	1.3×10^{14}
Protons/ bunch	—	10^{10}	10^{10}	10^{10}	0.75×10^{10}
Normalized rms emittance (π mm mrad)	<0.4	0.6	0.7	0.8	1

Tests of individual dipole magnets were run at temperatures below 4.2K, to explore the mechanical limits of these magnets. At a temperature of 1.8K, the quench current increased to almost 10 kA, as expected if it followed the theoretical short sample limit. This corresponds to a magnetic field of about 9.5 T, lowered somewhat from the 1 T/kA scaling because of iron saturation at these higher fields.

At this point, over 20 full-length 50-mm prototype collider dipole magnets have been tested. About 25 of the earlier 40 mm versions were also constructed and tested. Magnetic multipoles of the 50 mm dipoles are well within the range required by the collider. With this highly successful prototype development work completed, the superconducting magnet program is now beginning the transition to industrial production capability, aimed at high rate production (10 magnets/day). General Dynamics, the collider dipole magnet "lead" contractor for development, is well advanced in the construction of their production plant in Hammond, Louisiana. A full length prototype magnet should be available for testing in a few months. Westinghouse, the "follower" for the collider dipole and principal contractor for HEB dipoles, is constructing a plant in Round Rock, Texas. Babcock and Wilcox, contractor for the collider quadrupole magnets, is outfitting their facility in Lynchburg, Virginia.

One issue remaining in the superconducting magnet program is the observation of relatively large ramp rate dependencies of the quench current in some recent prototypes. This is not expected to be an issue for the collider, which ramps at about 4 A/sec, but it is a potential problem for the high energy booster magnets which ramps at about 60 A/sec. A program to resolve this issue is underway, as a collaborative effort involving Westinghouse and the SSC Laboratory, with cooperation from BNL and FNAL.

IV. STATUS OF THE INJECTOR AND COLLIDER

The basic parameters of the machines are given in Table 2. A description of these machines and their design features can be found in a recent conference paper [2] and in the SSC Annual Report [1]. In this summary, only a few highlights of recent accomplishments will be given.

To achieve the emittance goal of the SSC, we must start with a very high brightness beam out of the ion source and through the Linac. The design goal for the Linac emittance is several times smaller than that achieved at FNAL, BNL, or LAMPF. An additional challenge is the very high level of reliability required to meet the overall availability goals for the SSC.

An RF-driven negative ion volume source built by LBL for the SSC has operated at normalized transverse emittances less than 0.12π mm mrad (RMS) at 30 ma. A dual Einzel lens is used for the low energy beam transport (LEBT) section, to match into the RFQ. This lens has introduced aberrations that limit the transport through the RFQ to about 18 mA (in agreement with particle simulation). The RFQ section was built by Los Alamos National Laboratory, and it has recently been operated, accelerating the H^- beam to about 2.5 MeV. Very recent measurements of the emittance out of the RFQ indicate an emittance around 0.25π mm mrad at 18 mA, very close to the design goal [3].

The next acceleration stage is the Drift Tube Linac, which will accelerate the beam to 70 MeV. The first DTL tanks should be delivered around January 1994. The DTL consists of four tanks (supplied by Accelerator Systems Technology, Inc.) each powered by a 4 MW klystron (from Thompson CSF). The Coupled Cavity Linac tanks are being manufactured by IHEP, Beijing. Commissioning of the first CCL module is scheduled for October 1994, and the Linac commissioning is currently expected to be completed by April 1995.

The LEB magnets (resistive) are part of a collaboration with BINP in Novosibirsk. Delivery of the first production magnet is scheduled for October 1993. BINP is also collaborating on the correction magnets, the energy storage inductors, and the RF system. Two tuner designs are currently being tested, since this element is one of the higher risk items in the LEB.

The MEB is a large, normal conducting synchrotron similar to those at Fermilab and CERN. A model dipole magnet has been built by FNAL, and is currently beginning the testing phase. An agreement has been reached with Moscow Radio Technical Institute to provide the dipole and quadrupole magnets, following a successful prototype demonstration phase.

The HEB is a superconducting synchrotron, using superconducting magnets similar to those used in the collider. The novel feature of the HEB is its bipolar operation, required to inject oppositely-directed proton beams in the two collider rings. Bipolar tests of magnets at FNAL and KEK have not indicated any difficulties. The main issue in the HEB is the ramp rate dependence of the dipole magnet quench current mentioned in the previous section.

Significant advances have been made in a number of areas in the collider design and development activities, besides the superconducting magnets. The Utility Regions include components such as injection magnets, beam abort systems, and RF systems. These components are currently undergoing detailed design. The Interaction Region optics has received extensive review, and detailed design of the numerous specialty magnets required for this region is underway.

As mentioned in Section 2, the gas desorption from synchrotron radiation in the collider arcs is an outstanding issue. An extensive R&D program is underway to evaluate the impact of this phenomenon on collider operation, and to study various approaches for mitigating its effects [4]. Studies of gas desorption in cold tubes have been carried out at BINP. The most recent data indicates strong reductions in the desorption rate at lower temperatures, in disagreement with SSC-CDG experiments in the late 1980's. Mitigation effects include optimizing the copper plating process, coating the tube with thin layers of gold, and using cryosorbent materials to increase the local pumping capacity.

V. CIVIL CONSTRUCTION

The first major civil construction on the permanent "campus" site is at the N-15 area, on the northern edge of the west campus. The Magnet Development Laboratory (MDL), an 82,000 square foot building, is currently being used to fabricate prototype superconducting magnets. It will be used in the future to make the small quantities of specialty magnets used in the cluster regions of the collider. Adjacent to MDL

are buildings which house the cryogenic facilities for the N-15 section of the collider, and the Accelerator System String Test. Another nearby building, the Magnet Test Laboratory (MTL), is complete and equipment is currently being installed. It will have ten test stands for cold testing of full length magnets, and it also contains a three magnet test string. Cable winding equipment and numerous short magnet test areas and are also provided in the MTL.

The first vertical shaft down to the collider tunnel was excavated at N-15 (about 250 ft.). This oval shaped shaft, 30 ft. by 60 ft., provided access for the first tunnel boring machine. In the future, this shaft will be used for the delivery of magnets and other components to the tunnel. Four other shafts of this size will be spaced around the collider ring.

Several other shafts in the northern half of the ring have been completed, and four tunnel boring machines are in operation. At the present time, over five miles of tunnel has been excavated, about 10% of the collider ring. The construction crews have broken a number of world records for the tunneling "rate of advance" for four to five meter class hard rock tunnel boring machines (best day, best week, and best month). The aggregate tunneling progress has been close to one mile per week from all four machines.

The construction of the tunnels and buildings for the first machines in the booster chain is also well underway. Beneficial occupancy of the Linac tunnel is imminent, and installation of equipment will begin this summer. The LEB tunnel excavation is complete, and the LEB-MEB transfer line tunnel has been constructed. Beneficial occupancy of the LEB tunnel is scheduled for January 1994. Bids have been received on the MEB tunnel, and an award is expected soon.

VI. CONCLUSIONS

The SSC construction is underway. There has been excellent progress in the superconducting magnet program, now undergoing a transition to industrial production, and in the civil construction (tunneling at the rate of about one mile per week). Since these activities are the critical path for completion of the project, the technical progress still supports a date of October 1999 for first beam to experiments. The required funding levels in the past two years, and the current guidelines from the Administration for the next four years, do not support this schedule. The project is currently in the process of replanning its activities, in accord with current budget guidance. It is expected that the schedule will slip by 2-3 years relative to the original baseline.

VII. ACKNOWLEDGMENTS

This paper is a report on the work of several national laboratories, including SSC, and a large number of industrial contractors. The author hopes that their collective accomplishments are accurately portrayed in this brief report.

VIII. REFERENCES

- [1] Superconducting Super Collider - Laboratory Status Report-1992 (March 1993).
- [2] G. Dugan, "Status of the SSC," XVth International Conference on High Energy Accelerators (Hamburg, Germany July 1992).
- [3] K. Saadatmand, "Performance of the SSC Volume H- Source, Preaccelerator, and RFQ System" (May 1993, this conference).
- [4] W. Turner, "Dynamic Vacuum in the Beam Tube of the SSC Laboratory Collider: Cold Beam Tube and Liner Options" (May 1993, this conference).

Design for Low Beam Loss in Accelerators for Intense Neutron Source Applications

Robert A. Jameson
Accelerator Technology Division
Los Alamos National Laboratory, Los Alamos, NM 87545

Abstract

Control of beam loss in intense ion linacs involves keeping beam spill below parts in 10^{-5} - 10^{-8} /m by preventing total beam size from extending to the limiting apertures. Starting from good rms design practices, new analysis of the machine architecture is described in terms of space-charge effects on the machine tune, free-energy constraint, and halo-producing mechanisms. It is shown that halos are produced by the time- (or position-) varying nature of common linac aspects (such as misalignment, mismatching, acceleration, and construction techniques) through collective core/single-particle interaction dynamics plus resonances.

I. INTRODUCTION

High-intensity neutron sources can provide solutions to society's requirements for defense and commercial radioactive actinide and fission-product waste disposal and generation of electric power without a long-term waste stream [1-2], a pulsed neutron research facility [3], production of tritium and other special materials [4], conversion of plutonium, and the development of advanced materials [5]. These neutron sources are driven by large linear accelerators, with 30-300 mA proton current at energies of 1-2 GeV and 10-100% duty factors for the applications in [1-4], and modules of up to 250 mA cw deuteron current at 40 MeV for the materials development program.

These accelerators would have up to a few hundred megawatts of beam power, a large factor above the ~1 MW capability presently available at LAMPF. However, the power extrapolation is not fundamentally difficult; a factor of ~64 would be realized if LAMPF ran cw and all the rf buckets were filled. The major challenge is to keep residual activation of the linac by stray beam loss low enough that remote manipulator maintenance is not required; i.e., average losses should not exceed present LAMPF levels, translating to a rule-of-thumb of <1 nA/GeV/m. Dealing with more particles per bunch is the main challenge of the extrapolation. Most of the proposed configurations require within 2-3 times more particles per bunch, with the maximum scenario at 4-5. Acceleration of peak currents of these magnitudes has been achieved, but attainment of the required low loss must be demonstrated.

Typically, in real linacs and in multiparticle simulations of them, a high-intensity beam will develop a diffuse outer "halo" that can contain as much as a few percent of the beam current. If this halo extends to the bore radius, particles will be scraped off. There is presently no analytical guidance to performance at such low levels, and the physics in the simulation tools is also not accurate enough. Present design practice [3-5] concentrates on controlling the transverse and longitudinal rms beam sizes in ways that insure maximum "aperture factors" (or safe stay-clear ratios of bore-to-rms-beam-radius and accelerating-bucket-to-rms-beam-length) within various constraints. Reference design work for the new

applications avoids abrupt transitions such as those that cause "hot spots" at LAMPF, and achieves rms aperture factors from 2-3 times larger than the LAMPF design. New designs, including an anticipated error budget, are checked by simulation with up to a few hundred thousand particles, and are judged satisfactory if no particles are observed to hit the bore.

The simulations do show growth of the total beam size. The intent of this paper is to discuss aspects of total beam size, the control of which is the true goal of loss minimization.

II. ARCHITECTURE OF PRESENT DESIGNS

Two dominant features characterize the essentials of a typical RFQ accelerating section, a DTL, or a long coupled-cavity high-beta ion linac (CCL). Typically the accelerating gradient is held constant, because of rf power cost or sparking constraints. This results in rather small longitudinal focusing that decreases with energy, so the longitudinal zero-current phase advance per period decreases. The longitudinal tune depression from the beam space-charge then stays about constant with energy, typically ~0.4, a value at which the space-charge and emittance have approximately equal effect. There is phase damping with acceleration and the beam rms phase width shrinks, resulting in a larger rms longitudinal aperture factor [6].

Strong transverse focusing is relatively easy to obtain. With constant transverse focusing per unit length, the external focusing effect increases with energy as the space-charge forces weaken. The rms beam size shrinks, increasing the rms transverse aperture factor. The transverse tune depression, which may be strong (~0.4) at low energy, rapidly weakens.

In terms of the plasma period of the beam, the 1-2 GeV linac is long — of order 100 plasma periods.

The emittance and aperture factor behavior reflect the architecture, as shown in Fig. 1 for a typical 140 mA, 20-1500 MeV proton linac. In this typical simulation, the error-free linac is smoothly varying and the input beam is a mathematical, clean-edged distribution injected on-axis and rms-matched.

The tune trajectories are plotted on Hofmann's beam instability chart [7], Fig. 2, to check whether the observed growth can be explained in this way. The longitudinal/transverse rms emittance ratio stays at ~2. At 20 MeV, the trajectories are initially below the 4th-even mode thresholds and a rapid equilibration occurs in 1/4 plasma period (~1-2 tanks). The trajectory is above the 3rd-odd thresholds, and the 3rd-even is not excited because the transverse tune is not under its threshold. So the lower-order Hofmann modes do not explain the growth.

It is clear from Fig. 2 that the transverse/longitudinal energy balance (or partitioning) is not equal through most of the linac [8,9] and thus free energy is available that can be converted via nonlinear processes to size/emittance growth. A major phase of present research now in progress is to modify the machine tune so that various degrees of equipartitioning

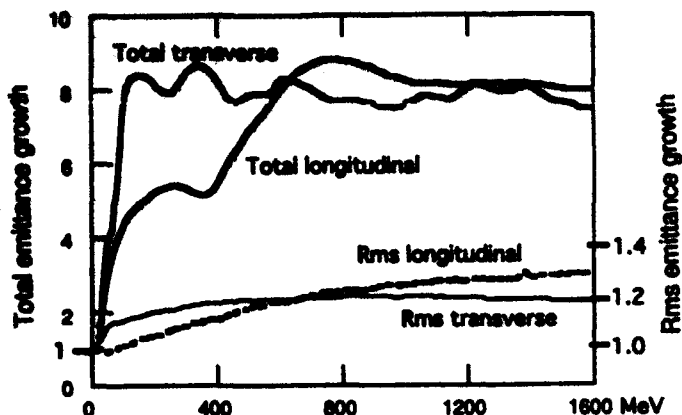


Fig. 1.a. Emittance growth in a typical CCL.

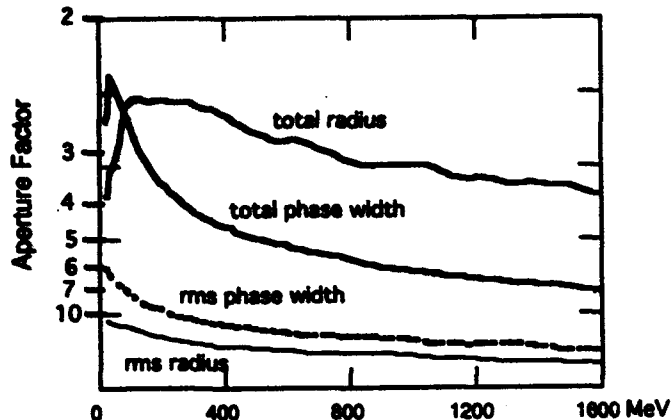


Fig. 1.b. Aperture factors in a typical CCL.

can be studied. Because the architecture economics specified the longitudinal tune, equipartitioning means a decrease in the transverse focusing with energy. Growth in rms beam size (perhaps a factor of 3-4) will occur along the machine, but if total beam size growth is reduced, an overall improvement may result. This work requires a self-consistent simulation code [8,9], which is being updated. These future studies of beam-involved machine tunes may result in a hybrid tune, with better energy balance at low energies where space-charge is more dominant, and stronger focusing at higher energies.

A superconducting (sc) linac could allow the accelerating gradient to increase with energy, allowing equipartitioning with smaller transverse beam size. This may be a major argument for sc linacs, along with larger aperture and shorter length from higher gradient.

Using the rms matching equations and the equipartitioning relationship, scaling and optimization equations for the aperture factors can be formulated [6]. Unfortunately, they are highly coupled and nonlinear and thus are not solvable except under special circumstances, such as constant equipartitioning ratios. In that case, the aperture factors are always larger at lower frequency. In other cases, optimum frequencies are evidenced in numerical studies, and some very strong relationships are indicated, such as that the maximum aperture factor always occurs at an almost constant tune depression. Some aspects of these kernel relationships have been discovered, but their basic forms remain elusive. Finding these kernels would help greatly in understanding the scaling and optimization of low beam-loss designs, so the search continues.

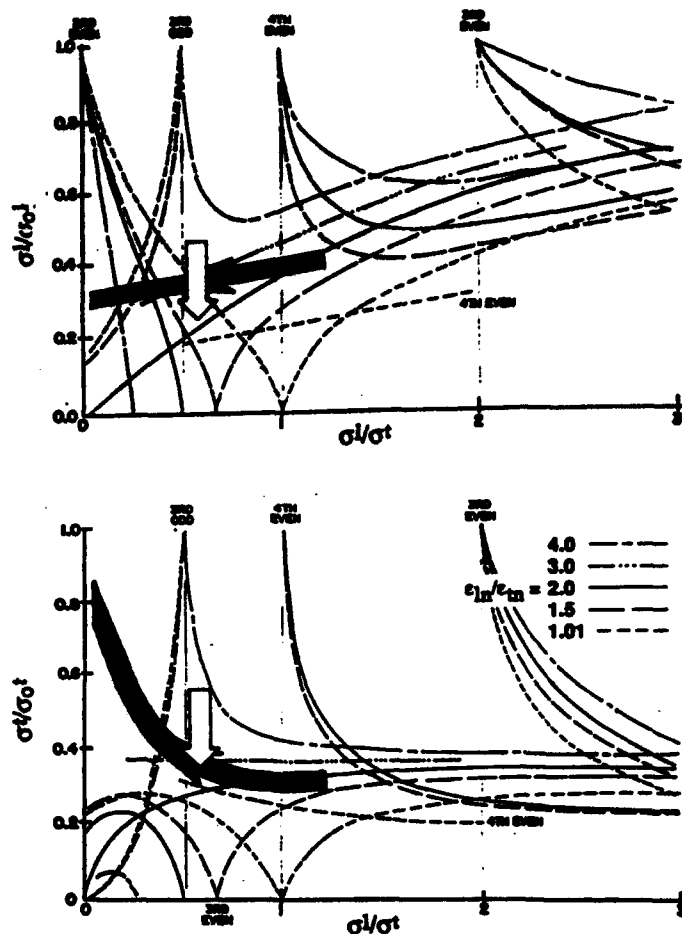


Fig. 2. CCL tune trajectories on Hofmann instability chart. Typical 140 mA, 20-1500 MeV CCL (black arrows), and equipartitioned tune (white arrows).

III. PHYSICS OF HALO BEAMS

Preventing halo formation a priori is the point-of-view of the research thrusts of this paper. We know that this means keeping nonlinearities small in both the external fields and in the beam space-charge, keeping the beam well matched, well aligned, and energy balanced, as much as possible within the many constraints. The latter make it hard; for example, strict equipartitioning is difficult to achieve practically, especially with the need to change accelerator structure and use a higher harmonic rf at higher energy. Thus we do have to search for the mechanisms causing halo formation and how they affect allowable error budgets.

The lower-order Hofmann instability modes did not explain the results in this case. Other analyses [10-12] have related nonlinear field energy and diffusion to asymptotic rms growth (from errors of energy imbalance, misalignment, rms mismatch, and input distribution mismatch) in transport systems, but these are not easy to apply to an accelerator, and all of these methods deal in a macro-effect on the beam bunch that does not reveal what really happens to particles that may form a halo. It had long been observed that particles originally in a well-sheathed beam core could later appear in a halo, meaning that substantial energy had to be acquired by that particle, but the mechanism was not known. There were

many questions — are halos generated continuously; will they reappear if scraped; why do different error conditions produce different halo effects?

Substantial new insight has been obtained by looking at detailed single-particle behavior in computer experiments [13]. The key mechanism is very simple, and the phenomenology is elucidated in the experiments described below. Development of the corresponding theory and analytical relation to total beam size and machine tolerances is now required. As indicated schematically in Fig. 3,

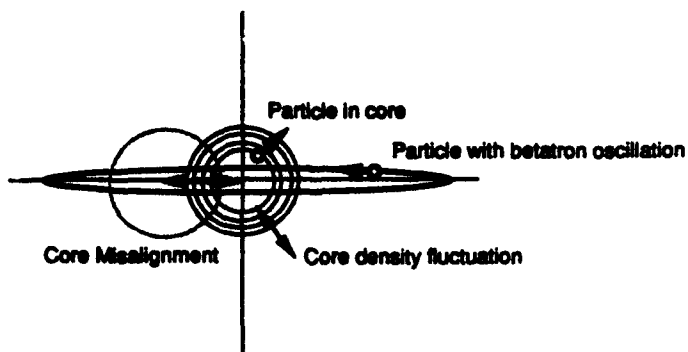


Fig. 3. Schematic of collective core/single-particle halo-producing mechanism.

the collective interaction of single particles with the beam core, when a density change in the core or a relative motion between the particle and the core occurs within an appropriate time, is a major halo-producing mechanism. Large energy transfers can occur in a single interaction; e.g., a particle with initial betatron motion can be slowed, stopped, reversed, or be accelerated by a "slingshot" effect analogous to a spacecraft passing a body in space. A particle initially at rest inside the core can receive a strong push from a nearby density

fluctuation. The accelerator is an essentially periodic system, so core fluctuations that are excited will oscillate periodically, and when a single-particle tune moves into resonance with the core oscillation, resonant interactions result in large orbits. Thus can particles move from the center of the core into the outer halo. The resonances tend to self-limit as the particle tune changes when its orbit changes. The core/single-particle interactions give a unifying insight into the halo-forming contributions of mismatching, misalignment, energy unbalance, alternating-gradient focusing, constant-beta linac sections, bunching, acceleration and other causes of beam core fluctuation. Some of the features of the mechanism are briefly summarized in the following.

The time-varying dynamics were first understood by observing the behavior of an initially round, continuous, zero-emittance, strongly mismatched, 3- σ Gaussian beam launched into a linear continuous radial focusing channel. Fig. 4 shows its evolution. (When x or y change sign, the sign of r is reversed, and r' adjusted, to aid the eye.) At $z/wp = 0.375$ plasma periods, some particles are still at rest near the origin. Then the outer tail sweeps through the origin, causing a local density anomaly there that repels nearby particles, and also slows or speeds up particles in the tail. This can be observed at $z/wp = 0.5$ and subsequently. Repeated interactions of this type result in folding of segments into a beam core ($z/wp = 3.875$), from which new tail segments begin to emerge. By $z/wp = 9.750$, the new tail extends almost as far as the original tail. The result of an abrupt scraping of the halo at $z/wp = 50$ can now be easily anticipated by considering the mechanism as described above — a strong central density oscillation is still present, so halo continues to form.

Fig. 5 shows the central density fluctuation induced by launching a warm (initial tune depression ~ 0.4) mismatched Gaussian beam, and the rr' radius of the six particles (from a set of 10K) that had the largest rr' radii at $z/wp = 10$. The sharp dip in rr' indicates a passage through the core, and it

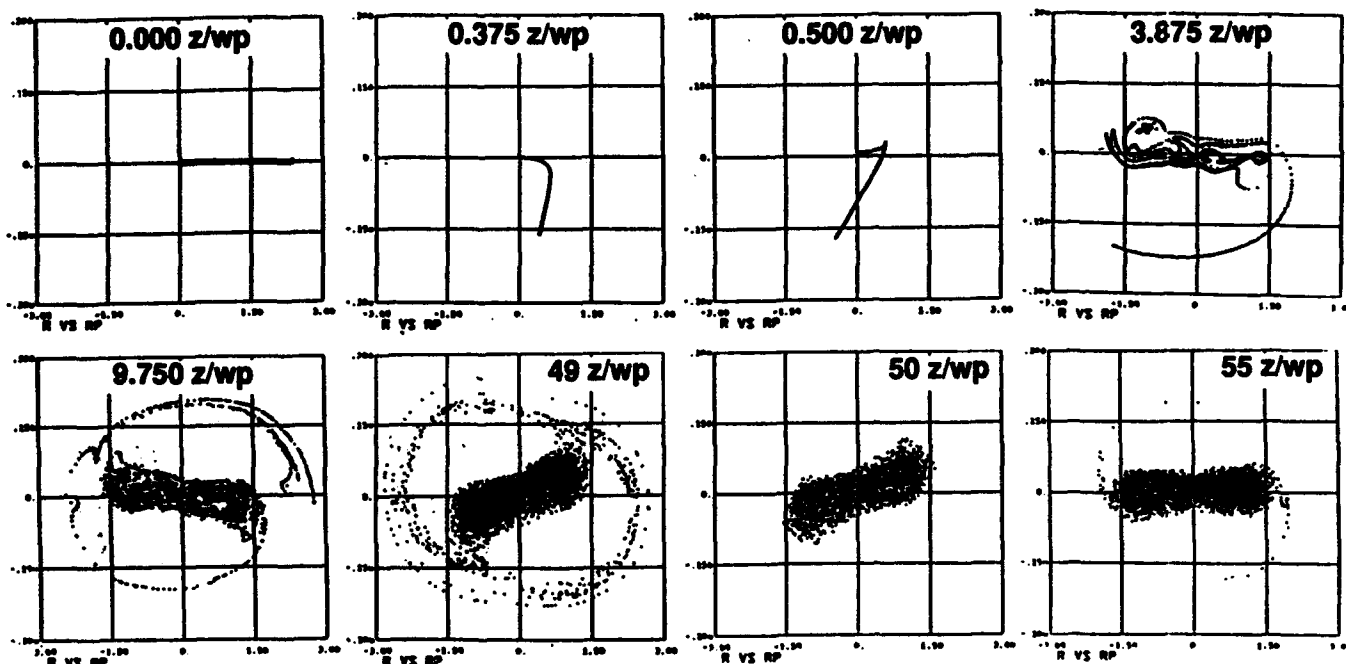


Fig. 4. Initially zero-emittance, mismatched beam in radial channel; scraped at $z/wp = 50$.

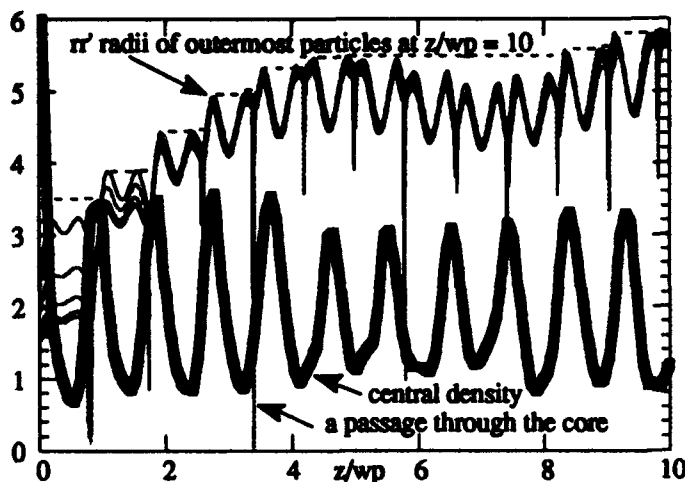


Fig. 5. Warm mismatched beam in radial channel.

will be noted that the peak in rr' following each of these interactions with the core is larger (if the interaction occurred when the central density was rising), or smaller (if the central density was falling). There is a resonant buildup during the first 5 interactions, with a change in single-particle tune that causes a slip to the falling density phase, resulting in loss of energy and change of tune back into resonant growth again at the end.

Stationary distributions can be formed [14] for the time-independent continuous radial focusing system using functions of the single-particle Hamiltonian (including space-

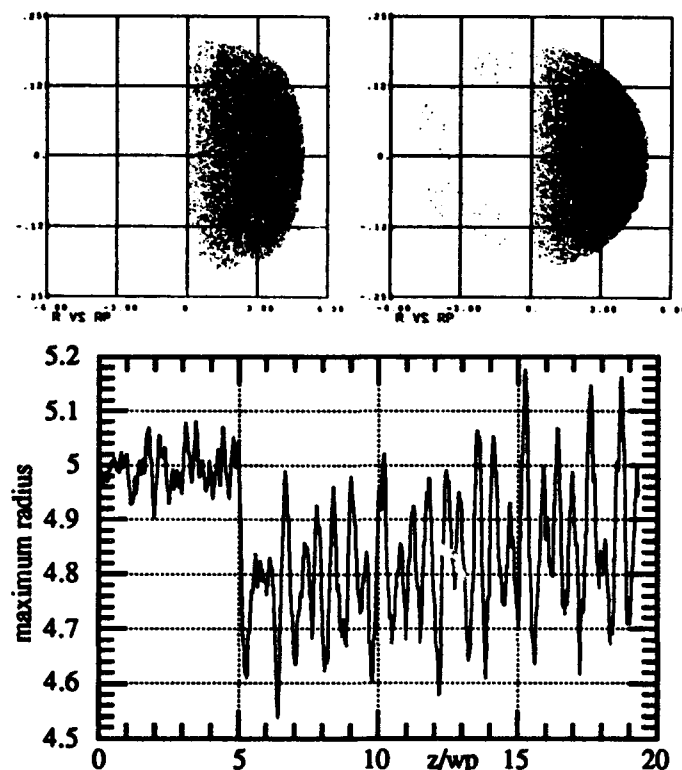


Fig. 6. (a.) Hamiltonian $\sigma/\sigma_0 = 0.4$ initial distribution. (b.) Scraped at $z/wp = 5$. (c) regrowth of maximum radius.

charge). The beam radius and focusing strength are chosen, giving the tune depression. In $r-r'$ phase space, the distribution has a squarish shape that sharpens with more tune depression (Fig. 6.a.) An initial distribution with tune shift $\sigma/\sigma_0 = 0.4$ was scraped with an elliptical rr' filter after 5 plasma periods (Fig. 6.b.). This excited a central density oscillation, and the maximum beam radius grew back larger than the initial value (Fig. 6.c.). As expected, the largest radius particles were driven as described above.

The stationary $\sigma/\sigma_0 = 0.4$ distribution was given an initial mismatch of 1.5 in radius. After 20 plasma periods, rms emittance had grown only 2-3%, the maximum rms radius remained unchanged, but the maximum radius grew by a factor of ~ 2.4 (times the matched radius - includes all the mismatch) via a strong resonant interaction on the rising side of the central density during the period from 8-14 z/wp .

With an initial 50% beam radius misalignment (in x) of the $\sigma/\sigma_0 = 0.4$ Hamiltonian distribution, the rms emittance oscillated to a peak of $\sim 15\%$ growth, damping to 3-4% at 10 z/wp . The maximum radius grew about 5% beyond the shift introduced by the misalignment. Only a small oscillation was excited in the central density over this distance. There was about 20% damping of the x -centroid oscillation, with growth in the y -centroid motion. The reason for the small total growth is that there is no resonant effect because of the wide separation between the particle tunes (near 0.4) and the undepressed betatron motion of the beam centroid. We would then expect more disturbance to a beam with less tune depression, and this was indeed the case. A 50% x -misalignment of a $\sigma/\sigma_0 = 0.83$ distribution resulted in 12% rms emittance growth over the first 6 z/wp . The maximum beam radius grew 20% beyond the misalignment shift (or to 1.8 times, including the misalignment, the radius of the on-axis beam). The x -centroid oscillation (Fig. 7) damped about a factor of 10, with excitation of a central density oscillation during the strongest part of the centroid oscillation damping, that then continued at roughly constant amplitude and a frequency slightly higher than that of the decaying centroid oscillation. Fig. 7 also shows the rr' radius of the particle that was largest at $z/wp = 10$, achieved by resonating with the σ_0 position-oscillation on the rising edge of $\text{abs}(x_{\text{mean}})$ during the first 6 z/wp . From 6-15 z/wp , the particle's rr' radius decreases as it interacts with the admixture of centroid and central density oscillations. From 15-20 z/wp , the centroid oscillation is small and the particle moves out again in resonance with the rising edge of the central density oscillation. This evidence that misalignment effects are worse for a beam with small tune depression is another reason to explore the equipartitioned tune of Fig. 2.

Energy equilibration via equipartitioning was demonstrated by injecting an unbalanced beam using the xx' distribution from a $\sigma/\sigma_0 = 0.1$, and yy' from a $\sigma/\sigma_0 = 0.83$ distribution. In 10 z/wp , the rms emittance growth was damping out at $\sim 7-8\%$, but the maximum radius growth was about 25% and still growing almost linearly. A strong central density oscillation was excited, with an increase in maximum radius on every rise in central density.

The 60-cell bunching section of a high-current RFQ was also studied [13]. In this section, the beam is at injection energy and encounters a steadily rising bunching voltage. The forming bunch makes a time-dependent density distribution.

A few (order 0.2%) particles were anomalously repelled longitudinally far from the bunch point, in some cases into the next bucket. It was found that these extraordinary orbits were

strongly correlated with very close encounters with the transverse $xx'yy'$ origin.

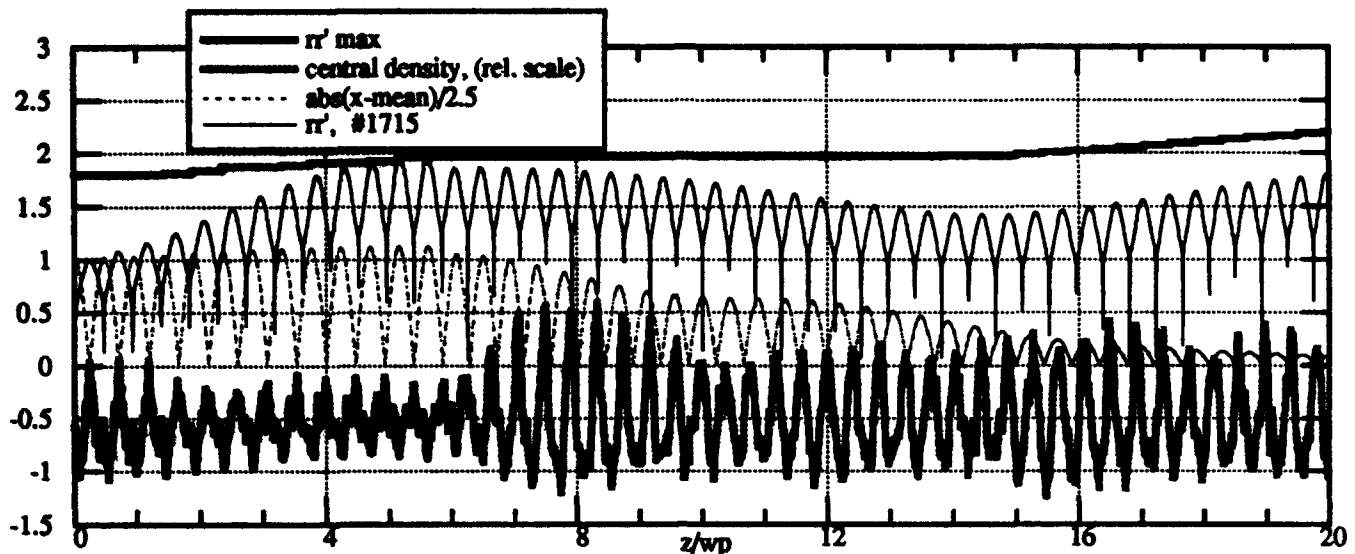


Fig. 7. Hamiltonian $\sigma/\sigma_0=0.83$ distribution misaligned 50% of beam radius in x .

IV. SUMMARY

Better knowledge of how halos are actually formed gives specific rationale for modeling descriptions of total beam behavior, development of space-charge tune architecture, and scaling/optimization procedures. In future work, it is of interest to explore the features (e.g., the relative growth of core vs. halo, limiting behavior, addition of multiple errors) of each type of perturbation, plus others such as alternating gradient focusing, constant-beta sections of accelerator cells, and graded-beta acceleration – all sources of time-dependent behavior. There are many practical aspects, e.g., tune strategy regarding misalignment, determination of adequate aperture factors, and error tolerances, that need to be worked out. P. Channell has begun theoretical modeling of the core/single-particle interactions, and R. Gluckstern has sketched a model for the resonance crossing with self-limiting behavior. We must tie these together, describe the tune spread of beams under various conditions, and relate the tune spread to the various resonances and number of particles that will be excited. We hope to use this new insight into the actual halo growth mechanism to accomplish macro-modeling of the total beam size.

V. ACKNOWLEDGMENTS

The able assistance of G. Boicourt with the simulations is gratefully acknowledged. The studies and ideas herein are the work of the author. The evidence was presented during its evolution to stimulate theoretical development. Discussions with P. Channell and R. Gluckstern, who are now working on the theory, and C. Bohn were very stimulating.

VI. REFERENCES

[1] C.D. Bowman, E.D. Arthur, et. al., "Nuclear Energy Generation and Waste Transmutation Using an Accelerator-Driven Intense Thermal Neutron Source", *NIM in Phys. Res.*, (Sec. A), Vol. A320, Nos.1,2, Aug. 15, 1992, pp. 336-367.

[2] F. Venneri, C. Bowman, R. Jameson, "Accelerator-Driven Transmutation of Waste (ATW) - A New Method for Reducing the Long-Term Radioactivity of Commercial Nuclear Waste", LA-UR-93-752, Los Alamos Natl. Lab., sub. for publ. to *Physics World*, Bristol, England.

[3] A. Jason, et. al., "Los Alamos Design Study for a High Power Spallation Neutron Source Driver", these proceedings.

[4] "Accelerator Production of Tritium", JASON Report JSR-92-310, The Mitre Corporation, McLean, VA (1992).

[5] R.A. Jameson, "Accelerator-Driven Neutron Sources for Materials Research", *NIM in Phys. Res.* B56/57 (1991) 982-986.

[6] R.A. Jameson, "On Scaling & Optimization of High Intensity, Low-Beam-Loss RF Linacs for Neutron Source Drivers", LA-UR-92-2474, Los Alamos Natl. Lab., *Proc. 3rd Workshop on Adv. Accel. Concepts*, 14-20 June 1992, Port Jefferson, Long Island, NY, American Institute of Physics.

[7] I. Hofmann, I. Bozsik, "Computer Simulation of Longitudinal-Transverse Space Charge Effects in Bunched Beams", 1981 *Linac Conf.*, LA-9234-C, Los Alamos, Natl. Lab., pp.116-119.

[8] R.A. Jameson, "Beam Intensity Limitations in Linear Accelerators", *IEEE Trans. Nucl. Sci.*, Vol. NS-28, No. 3, June 1981, pp. 2408-2412.

[9] R.A. Jameson, "Equipartitioning in Linear Accelerators", 1981 *Linac Conf.*, LA-9234-C, Los Alamos, Natl. Lab., pp.125-129.

[10] T.P. Wangler, et. al., "Relation Between Field Energy and RMS Emittance in Intense Particle Beams", 1985 PAC, *IEEE Trans. Nucl. Sci.*, Vol. NS-32, No. 5, October 1985.

[11] M. Reiser, "Emittance Growth in Mismatched Charged Particle Beams", 1991 IEEE PAC, 91CH3038-7 Conf. Record, p. 2497.

[12] C.L. Bohn, "Transverse Phase-Space Dynamics of Mismatched Charged-Particle Beams", *Phys. Rev. Letters*, Vol. 70, No. 7, 15 Feb. 1993, p. 932.

[13] R.A. Jameson, "Beam Halo From Collective Core/Single-Particle Interactions", LA-UR-93-1209, Los Alamos National Laboratory, March 1993.

[14] R. Gluckstern, R. Mills, K. Crandall, "Stability of Phase Space Distributions in Two Dimensional Beams", *Proc. Linac Conf.*, National Accel. Lab. (FNAL), September 1970, p. 823.

IS THERE A FUTURE FOR HIGH ENERGY ACCELERATORS?

M. Tigner,
Floyd R. Newman Laboratory of Nuclear Studies,
Cornell University, Ithaca, NY 14853-5001

Abstract

The question of continuing viability of high energy accelerators as instruments of fundamental physics is discussed. It is seen that the next decade in elementary CM energies beyond SSC may be achievable with accelerators that can be imagined now. Beyond that there is room for doubt that accelerators will be the instrument of choice. History teaches that there is a good likelihood that our perspective on the matter will be much different when we see the results from the few TeV region of elementary collision energies.

I. IMPERATIVES

The frontier of elementary particle physics has always been defined by the smallest distance scale achievable in the laboratory, i.e., the highest achievable collision energies. This inverse relationship between spatial resolution and momentum implies that the cross sections of interest will descend as the inverse square of the achievable CM collision energies. Known and projected cross sections for our current and near future parameter space are shown in Figure 1.

II. GOALS

In the "near term" we need to find and explore the t , the Higgs mechanism, the gauge structure of the Standard Model and what ever else might crop up in the range between 100's of GeV and a few TeV. The vehicles will be SSC/LHC and perhaps a 1/2 TeV or more electron positron linear collider (LC). These we will consider here to be more or less in hand.

In the "mid term" we have the energy decade beyond that, say a few hundred TeV for pp and 10 TeV for electron positron collisions. Perhaps we'll be deep into supersymmetry and the final expose of the SU_3 or seeing the first manifestations of strings or more likely something that we haven't imagined yet.

*This work was supported in part by the NSF.

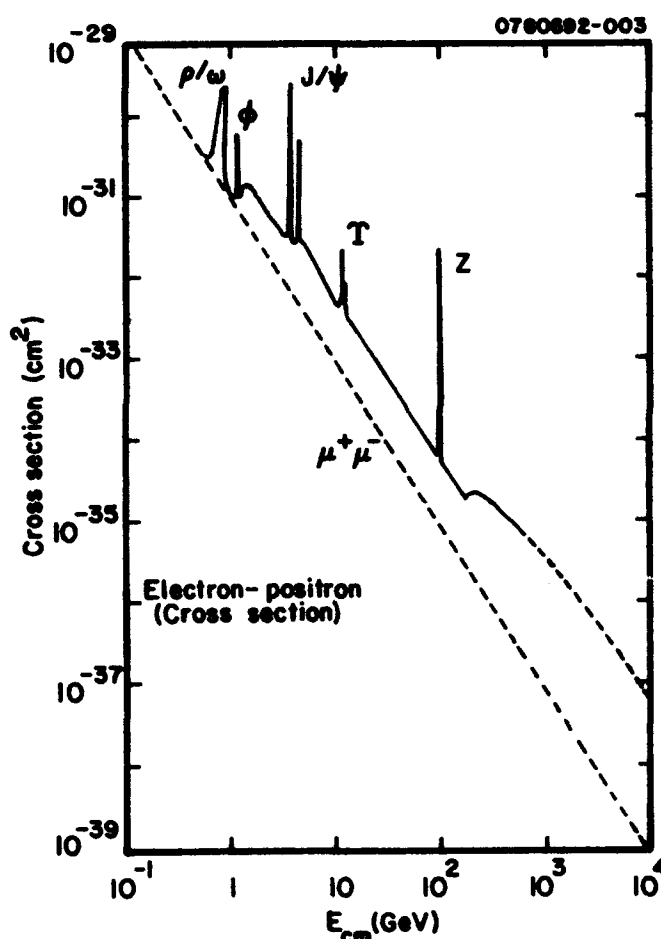


Figure 1: The elementary cross section as a function of collision energy

While our imaginations are not really capable of dealing with the "far term" at all we do have the notion that something manifesting the unification of all the known interactions may come to pass at the 10^{19} GeV level, the Planck scale.

We have to ask, are these energies and the luminosities implied even thinkable today? For the regions just beyond SSC there is already a body of literature which grapples with some of the important issues[1, 2, 3, 4]. In trying to see even further beyond we need to study some basic constraints on accelerators that play together with the imperatives of energy and luminosity.

III. FURTHER ACCELERATOR CONSTRAINTS

Important but not to be considered here are continuing world interest in elementary particle physics, world economy, other human factors and accelerator and detector technology. Here we will focus narrowly on energy(power) requirements. While the details are different for PP and e^+e^- collisions the overall conclusions are similar.

In the case of pp we note that a certain amount of energy is dissipated through lost particles at the IP. This is basic and is characterized by the total inelastic cross section. (For purposes of illustration we shall assume for a moment that the wall plug to beam power efficiency of the machine is 100%.) The minimum power spent, or dissipated, is

$$\dot{P}_{\text{dis}} = \dot{N}_{\text{lost}} \cdot E_{\text{cm}}; (\sim 1 \text{ kW at SSC}). \quad \dagger \quad (1)$$

Putting that together with

$$\dot{N}_{\text{lost}} = \mathcal{L} \cdot \sigma_{\text{inel}} \quad (2)$$

and the fact that luminosity must scale as energy squared we find immediately that the dissipated power is roughly proportional to the cube of the energy. If we assume that the luminosity is 10^{33} in cgs units at 40 TeV in the CM and use the high energy limit of the Particle Data Book formula for the inelastic cross section we get a formula for the dissipated power as a function of energy

$$\dot{P}_{\text{dis}} [W] \sim 3.5 \times 10^{-5} E_{\text{cm}}^3 \ln^2 [5 \times 10^5 E_{\text{cm}}^2]; E_{\text{cm}} [\text{TeV}]. \quad (3)$$

IV. CONSEQUENCES FOR PP

If for the moment we assume that we need, for economic reasons, to limit the dissipated power to O(1 GW) then we can solve our equation for center of mass energy to find

$$E_{\text{cm}} \sim 0(4000 \text{ TeV}) \text{ or } 100 \times \text{SSC/LHC}, \quad (4)$$

an interesting technical challenge for both detector and accelerator but far short of the Planck scale.

V. FURTHER ACCELERATOR CONSTRAINTS FOR e^+e^-

While this situation is a bit more complex in detail for e^+e^- we can begin with similar considerations. The first basic phenomenon to be considered is beamstrahlung the radiation of colliding particles in the collective field of the oncoming bunch. This process is characterized by an rms fractional energy loss

$$\delta = \left\langle \frac{\Delta E}{E} \right\rangle \simeq \frac{0.22 r_e^3 N^2 \gamma}{\sigma_l} \cdot \left(\frac{2}{\sigma_h + \sigma_v} \right)^2. \quad (5)$$

For physics utility this energy spread must be kept more or less constant at the few % level. The specific luminosity is thus limited. (A similar phenomenon occurs in pp collisions but only at energies well beyond those considered above.)

For single pass linear colliders such as are now being considered

$$P_{\text{dis}} = \delta \cdot P_{\text{beam}}. \quad (6)$$

Also, as is well known, basic relations lead to

$$\mathcal{L} \propto \frac{P_B \cdot \delta^{1/2}}{\gamma \epsilon_{v,n}^{1/2}}. \quad (7)$$

(Ideal focusing is assumed, i.e., no Oide limit). Remembering that luminosity must rise with energy squared

$$P_B \propto \gamma^3 \epsilon_{v,n}^{1/2} \delta^{1/2}. \quad (8)$$

Again the cube of energy appears in a difficult place.

VI. CONSEQUENCES FOR e^+e^-

Before converting into a scaling formula for max. energy in terms of available power we should take account of accelerator efficiency

$$P_B = \eta_{\text{ac-beam}} \cdot P_{\text{ac}}. \quad (9)$$

If we take for our luminosity calibration point a figure of 10^{34} cgs at 1 TeV CM and use beam power from the highest specific luminosity version of LC(1/2 TeV), [O(1 MW)], together with the efficiency from the highest efficiency version (0.2) we can get and use a scaling formula for E as a function of ac power

$$E [\text{TeV}] \simeq \frac{1}{2} \left[\frac{P_{\text{ac}}}{10^6} \cdot \left(\frac{\epsilon_n(\frac{1}{2})}{\epsilon_n(E)} \right)^{1/2} \cdot \left(\frac{\delta(E)}{\delta(\frac{1}{2})} \right)^{1/2} \cdot \frac{\eta(E)}{\eta(\frac{1}{2})} \right]^{1/3}. \quad (10)$$

Assuming that, for fixed energy spread, that in the future we can get 10 fold improvement in emittance and 2 fold improvement in efficiency and that again we are limited to about 1 GW in ac power, we find the maximum allowed energy of about 5 TeV.

In that great beyond you might imagine that, since energy spread due to beamstrahlung is small that we might recover beam energy with some efficiency, $[\eta_R]$ which is defined to include energy lost to beamstrahlung. Our formula is then modified in a transparent way to

$$E_{\text{Rec}} = E_{\text{noRec}} \cdot \sqrt{\frac{1}{1 - \eta_R}}. \quad (11)$$

For a 90% recovery efficiency we get a CM energy of about 11 TeV.

These examples are beamstrahlung limited. Suppose that we are able to apply some sort of beam neutralization using, for example, 4 beams $(e^+e^-e^+e^-)$ [5] and thus avoiding beamstrahlung to a large degree. We still have the individual particle collisions (Bethe-Heitler cross section) to make radiation which will be lost from the system. The power dissipated at the assumed luminosity at 1 TeV will be about 2kW. This leads to an ultimate limit of 85 TeV if we restrict ourselves to 1 GW dissipation.

Before leaving this subject one might note that the EM process we're confronted with would be much eased if we could collide muons. This has not been included because the problem of production and damping seem too daunting the face of the need for energy squared scaling of the luminosity. Perhaps the future will show this too dim a view. Also there are proposals for photon colliders but from the present perspective the energy requirements seem even more restrictive than cases mentioned. Again, perhaps the future will find a way around this restriction.

VII. FURTHER CONSIDERATIONS

We have somewhat, but not completely, arbitrarily chosen 1 GW as our allowed power consumption limit. Noting that

$$\dot{E} \propto P_{\text{ec}}^{1/3}, \quad (12)$$

we see that a large change in allowed power would be needed for even a modest change in top energy. Nevertheless, perhaps we're thinking too small. In the Amateur Scientist column of the April 1989 Scientific American[6] it is suggested, albeit tongue in cheek, that the power from the sun might be the appropriate limit for a Planck mass accelerator at 10^{26} W. However using our third power scaling law we'd need something like 10^{54} W to have the scaled luminosity it appears we would need. Perhaps an intergalactic collaboration is needed to do the job.

VIII. OUTLOOK

One should not take the details of such predictions too seriously nor should one be overly discouraged by them. After all our forbears have spent the last 50 years building what was seen by the sages of each generation as "the last machine". Our visions are clouded by the limitations of

current understandings and can only be used as a hint in which direction we should try to progress. It does seem from the above considerations that one strong emphasis needs to be energy consumption per important discovery. Perhaps we could help ourselves focus on energy or integrated power, IP, by rating our designs with an integrated power factor, IPF, giving the energy needed to produce one interesting event. One would use some standard elementary cross section like the annihilation cross section into muon pairs at the CM energy of momentary interest. For example, at 0.5 TeV our most optimistic "design" for scaling required about 5 MW at 10^4 mu pairs per 10^7 s year or 5^{15} J per 10^4 events for an IPF of 5 GJ/event.

In closing, let's borrow an analogy from Prof. Okun[7]. He sees the progress of physics as the building of a cathedral of physical understanding. Accelerator based scientists are building up from the foundation and the cosmologists and "theoretical" theorists are building from the top down. We can hope that they will actually be able to meet somewhere inbetween in a region accessible to accelerators. In this way we might hope to complete the cathedral even though accelerators can only carry us part way to the Planck scale.

REFERENCES

- [1] M. Tigner. Hadron Colliders Beyond the SSC, 1989 SLAC Summer Institute on Physics at the 100GeV Mass Scale. Stanford Linear Accelerator Center 1989.
- [2] W. Barletta and H. Leutz, editors. Supercolliders and Superdetectors. Ettore Majorana Centre for Scientific Culture, Erice, Sicily, 1993.
- [3] R. Palmer. Prospects for High Energy e+e- Linear Colliders. Annu. Rev. Nucl. Part. Sci. 1990.49: 529-92
- [4] M. Tigner. Imperatives for Future High Energy Accelerators, 4th Workshop on Advanced Accelerator Concepts, 1992, to be published as an AIP Conference Proceeding.
- [5] J. Rosenzweig, B. Autin and P. Chen. Instability of Compensated Beam Beam Collision, 1989 Lake Arrowhead Workshop on Advanced Accelerator Concepts. APS Conference Proceedings 1993.
- [6] A. Akihito. Scientific American, April 1989, p 112.
- [7] L. Okun. Proceedings of the 1993 ICFA Seminar, DESY 1993.
- [†] In the formulae I have followed the common notations also used in refs. 1-4.

List of Participants

ABE, DAVID E.
BERKELEY RESEARCH ASSOC
PO BOX 852
SPRINGFIELD, VA 22150
PHONE: 301-405-8009

ABELL, DAN TYLER
DEPT OF PHYSICS-UNIV OF MD.
COLLEGE PARK, MD 20742
PHONE: 301-405-6188

ACERBI, EMILIO
MURST-INFN
VIA FRATELLI CERVI 201
SEGRATE (MI), 20095
ITALY
PHONE: 022-392-571

ADAMS, FRED P.
ABCL RESEARCH
STR 111 CHALK RIVER LABS.
CHALK RIVER, ON K0J-1P0
CANADA
PHONE: 613-584-3311

ADAMS, GARY
US ARMY
106 WYNN DRIVE
HUNTSVILLE, AL 35807
PHONE: 205-955-4667

ADAMSKI, JOHN L.
BOEING DEFENSE & SPACE
PO BOX 3999
MAIL STOP 2150
SEATTLE, WA 98124
PHONE: 206-544-5986

ADOLPHSEN, CHRIS E.
SLAC
BIN 65
2575 SAND HILL RD
MENLO PARK, CA 94025
PHONE: 415-926-3560

AHRENS, LEIF A.
BROOKHAVEN NATIONAL LAB
911B
UPTON, NY 11973
PHONE: 516-282-4568

AHELLO, ROBERTO G.
SSCL
2550 BECKLEYMEADE AVE
MS-4005
DALLAS, TX 75237
PHONE: 214-708-3468

ALBERTI, STEFANO G.
MIT, PLASMA FUSION CENTER
167 ALBANY STREET
NW16-170
CAMBRIDGE, MA 02139
PHONE: 617-258-9179

ALLEN, CHRISTOPHER
LAB FOR PLASMA RESEARCH
UNIVERSITY OF MARYLAND
COLLEGE PARK, MD 20742
PHONE: 301-405-4967

ALLEN, MATTHEW A.
STANFORD LINEAR ACCELERATOR
P.O. BOX 4349
MD 84
STANFORD, CA 94309
PHONE: 415-926-2820

ALLEN, STEVEN L.
LAWRENCE LIVERMORE NATL LAB.
PO BOX 808 L-637
LIVERMORE, CA 94550
PHONE: 619-455-4137

ALLISON, PAUL
LANL
P 942
LOS ALAMOS, NM 87544
PHONE: 505-665-6233

ALPER, BOB
PRODUCT MANAGER
VARIAN ASSOCIATES INC.
811 HANSEN WAY
PALO ALTO, CA 94304-1031
PHONE: 415-424-6984

ALTON, GERALD
OAK RIDGE NATIONAL LAB
PO BOX 2008
OAK RIDGE, TN 37831-6368
PHONE: 615-574-4751

AMIRY, ALI A.
UCLA PHYSICS DEPT
405 HILGARD AVE
LOS ANGELES, CA 90024
PHONE: 310-825-1214

ANASHIN, VADIM V.
BINP
ACADEMICIAN LAVRENTYEV, 11
NOVOSIBIRSK, 630090
RUSSIA
PHONE: 011-738-32353901

ANDERSON, DANIEL R.
IUCF
2401 MILO SAMPSON LANE
BLOOMINGTON, IN 47405
PHONE: 812-844-2919

ANDERSON, DAVID
URA/SSC LABORATORY
2550 BECKLEYMEADE
MS 9000
DALLAS, TX 75237
PHONE: 214-709-4542

ANDERSON, LOUIS W.
UNIV OF WISCONSIN-MADISON
1150 UNIVERSITY AVE
DEPT OF PHYSICS
MADISON, WI 53706
PHONE: 608-262-8962

ANDREEV, V.A.
ITEP MOSCOW
B. CHEREJOMUSHKINSKAJA 25
117259 MOSCOW B-259,
RUSSIA

ANDREWS, MIKE C.
LINAC SYSTEMS
1132 OAK DRIVE
KELLER, TX 76248
PHONE: 817-431-3242

ANERELLA, MICHAEL
BROOKHAVEN NATIONAL LAB
BLDG 902
UPTON, NY 11973
PHONE: - -

ANALA, GERALD E.
FERMILAB
PO BOX 500
BATAVIA, IL 60510
PHONE: 708-840-4380

ANTAYA, TIMOTHY
MICHIGAN STATE UNIVERSITY
SOUTH SHAW LANE
E. LANSING, MI 48824
PHONE: 517-355-3309

ARCHIE, CHAS N.
IBM ALF
EAST FISHKILL FACILITY
ROUTE 52
HOPEWELL JUNCTION, NY 12533-0999
PHONE: 914-892-3821

ARCONI, PAOLO M.
UNIVERSITY OF PAVIA
DEPT OF ELECTRONICS
VIA ABBATEGRASSO 209
127100 PAVIA,
ITALY
PHONE: 39-382-391 200

ATWOOD, THOMAS D.
KTECH CORP.
901 PENNSYLVANIA NE
ALBUQUERQUE, NM 87110
PHONE: 505-268-3379

AVERILL, ROBERT J.
MIT
PO BOX 846
MIDDLETON, MA 01949
PHONE: 617-245-6600

AYVAZIAN, HENRIK
ION BEAM APPLICATION LAB
10821 DELIBAN AVE
TUNJUNGA
LOS ANGELES, CA 91042
PHONE: 818-353-6783

BAARTMAN, RICK A.
TRIUMF
4004 WESBROOK MALL
VANCOUVER, BC V6T-2A3
CANADA
PHONE: 604-222-1047

BAILEY, JAMES D.
NSCL/MSU
NSCL, MICHIGAN STATE UNIV
E. LANSING, MI 48824
PHONE: 517-355-9671

BAILEY, ROGER
CERN
1211 GENEVA, 23
SWITZERLAND
PHONE: 227-677-500

BAIRD, SIMON
CERN
CH-1211 GENEVA, 23
SWITZERLAND
PHONE: 767-259-0

BAJARD, MARCEL
GANIL
BP 5027
F-14021 CAEN, CEDEX
FRANCE
PHONE: 314-545-99

BALANDIN, VLADIMIR
INSTITUTE FOR NUCLEAR RESEARCH
60TH OCT ANNIVERSARY PROSPECT
7A
MOSCOW, 117312
RUSSIA

BALLEYGUIER, PASCAL
CEA-PTN
BP 12
BRUYERES LE CHATEL, 91680
FRANCE
PHONE: 133-169-266061

BALTRUSAITIS, ROSE M.
LOS ALAMOS NATIONAL LAB
LANL, MS D410
LOS ALAMOS, NM 87545
PHONE: 505-665-9933

BAND, ALAN H.
NIST
ROOM B206 BLDG 220
GAITHERSBURG, MD 20899
PHONE: 301-975-3764

BANE, KARL L.F.
SLAC
PO BOX 4349
BIN 26
STANFORD, CA 94309
PHONE: 415-926-2026

BANGERTER, ROGER O.
LAWRENCE BERKELEY LABORATORY
1 CYCLOTRON RD, MS 47-112
BERKELEY, CA 94720
PHONE: 510-486-6376

BARBIER, MARCEL M.
MARCEL M. BARBIER INC.
3003 RAYJOHN LANE
HERNDON, VA 22071
PHONE: 703-860-1275

BARLETTA, WILLIAM L.
LAWRENCE BERKELEY LABORATORY
1 CYCLOTRON RD.
50-149
BERKELEY, CA 94720
PHONE: 510-486-5408

BARLOW, DAVID B.
LOS ALAMOS NATIONAL LAB
MS H808, LANL
LOS ALAMOS, NM 87545
PHONE: 505-665-2813

BARNARD, JOHN J.
LLNL
PO BOX 5508
L-440
LIVERMORE, CA 94550
PHONE: 510-423-0675

BARNES, MICHAEL J.
TRIUMF
4004 WESBROOK MALL
VANCOUVER, BC V6T2A3
CANADA
PHONE: 604-222-1047

BAROV, NICK
UCLA
PO BOX 624
TOPANGA, CA 90290
PHONE: 310-206-5584

BARRY, WALTER C.
LAWRENCE BERKELEY LABORATORY
1 CYCLOTRON RD, MS 71-239
BERKELEY, CA 94720
PHONE: 510-486-6705

BARTON, DON
BROOKHAVEN NATIONAL LAB
BUILDING 911A
UPTON, NY 11973
PHONE: 516-282-7925

BATCHELOR, KENNETH
BROOKHAVEN NATIONAL LABORATORY
BLDG 725C
NATL SYNCHROTRON LIGHT SOURCE
UPTON, NY 11973
PHONE: 516-282-4674

BE, SUCK HEE
RIKEN
2-1 HIROSAWA
WAKO
SAITAMA, 351-01
JAPAN
PHONE: 814-846-21111

BEDAU, JUERGEN
BRUKER
13 WIKINGERSTREET
KARLSRUHE 21, 7500
GERMANY
PHONE: 497-215-967173

BEGG, MICHAEL C.
TESLA ENGINEERING LTD.
WATER LANE
STORRENTON, RH20 3EA
UNITED KINGDOM
PHONE: 449-037-43941

BEN-ZVI, ILAN
BROOKHAVEN NATIONAL LABORATORY
BLDG 725C
NATL SYNCHROTRON LIGHT SOURCE
UPTON, NY 11973
PHONE: 516-282-5143

BENESCH, JAY
CEBAF
12000 JEFFERSON AVE
NEWPORT NEWS, VA 23606
PHONE: 804-249-7085

BENSON, STEPHEN V.
CEBAF
12000 JEFFERSON AVE. MS16A
NEWPORT NEWS, VA 23606
PHONE: 804-249-5026

BERG, J. SCOTT
SLAC
PO BOX 4349
STANFORD, CA 94309
PHONE: 415-926-4732

BERKNER, KLAUS H.
LAWRENCE BERKELEY LABORATORY
1 CYCLOTRON RD
50A-5104
BERKELEY, CA 94720
PHONE: 510-486-4178

BERNSTEIN, DOREL R.
STANFORD LINEAR ACCELERATOR
P.O. BOX 4349
SLAC-BIN 50
STANFORD, CA 94309
PHONE: 415-926-3197

BEROUD, YVES
SICN
BP 1
VIEUREY-VOROIZE, 38113
FRANCE
PHONE: 337-686-9000

BERTSCHE, KIRK J.
SSCL
2550 BECKLEYMEADE AVE
MS 9000
DALLAS, TX 75237
PHONE: 214-708-4231

BERZ, MARTIN
MICHIGAN STATE UNIVERSITY
DEPT OF PHYSICS
E. LANSING, MI 48224
PHONE: 517-353-0899

BHANDARI, RAKESH K.
SSCL
2550 BECKLEYMEADE AVE
MS # 1043
DALLAS, TX 75237
PHONE: 214-708-4305

BIAT, CHANDRA M.
FERMI NAT'L ACCELERATOR LAB.
MS 323, PO BOX 900
BATAVIA, IL 60510
PHONE: 708-840-4821

BIATIA, TARLOCHAN S.
LANL/DOE
MS H811 LANL
LOS ALAMOS, NM 87545
PHONE: 301-903-5228

BIAGINI, MARIA ENRICA
INFN
CP 13
FRASCATI,
ITALY
PHONE: 396-940-3435

BICKLEY, MATTHEW H.
CEBAF
12000 JEFFERSON AVE
NEWPORT NEWS, VA 23606
PHONE: 804-249-7347

BIENIOSEK, FRANK M.
FERMILAB
MS 341, PO BOX 500
BATAVIA, IL 60510
PHONE: 708-840-

BIERI, ROBERT L.
W.J. SCHAFER ASSOCIATES, INC.
303 LINDBERGH AVE.
LIVERMORE, CA 94550
PHONE: 510-447-05555

BIGHAM, C. BRUCE
AECL
BOX 523
DEEP RIVER, ON K0J-1P0
CANADA
PHONE: 613-584-2198

BILLEN, JAMES H.
LOS ALAMOS NATIONAL LABORATORY
AT-1, MS H817
LOS ALAMOS, NM 87545
PHONE: 505-667-6627

BELLING, MICHAEL G.
LAB OF NUCLEAR STUDIES
CORNELL UNIVERSITY
DRYDEN RD
ITHACA, NY 14853
PHONE: 607-255-8788

BISCARDI, RICHARD
BROOKHAVEN NATIONAL LAB
NSLS, BLDG. 725 C
UPTON, NY 11973
PHONE: 516-282-7760

BISCARI, CATERINA
INFN
CP 13
FRASCATO ROMA, 00044
ITALY
PHONE: 39 - 61403435

BISOGNANO, JOSEPH J.
CERAP
12000 JEFFERSON AVE.
NEWPORT NEWS, VA 23606
PHONE: 804-249-7521

BIXIO, ANGELO
ANSALDO GIE
ANSALDO GIE STR
DEPT PMA PRMA
VIA N LORENZI 8, GENOVA
ITALY
PHONE: 391-065-56355

BLACK, MURRAY
GEORGE MASON UNIV
ELEC & COMP ENGR
FAIRFAX, VA 22030
PHONE: 703-993-1571

BLASCHE, KLAUS W.
GSI
PUB 110352
D6100 DARMSTADT,
GERMANY
PHONE: 004-961-51359383

BLASKIEWICZ, MICHAEL M.
BROOKHAVEN NATIONAL LAB
BNL 911 C
UPTON, NY 11973
PHONE: 516-282-7049

BLESER, EDWARD J.
BROOKHAVEN NATIONAL LAB.
BUILDING 911B
UPTON, NY 11973
PHONE: 516-282-7181

BLEWETT, JOHN P
BNL RETIRED
310 W 106 ST
NEW YORK, NY 10025
PHONE: 212-866-5767

BLIND, BARBARA
LOS ALAMOS NATIONAL LAB.
AT-3, MS HB11
LOS ALAMOS, NM 87545
PHONE: 505-665-2607

BLISS, KENNETH A.
ROCKWELL
PO BOX 263
WELLSVILLE, UT 84399
PHONE: 801-777-8240

BLUM, HANS P.
LSU-CAMD
6980 JEFFERSON HIGHWAY
BATON ROUGE, LA 70806
PHONE: 504-925-7071

BLUM, ERIC B.
BROOKHAVEN NATIONAL LABORATORY
BLDG 725C
NATL SYNCHROTRON LIGHT SOURCE
UPTON, NY 11973
PHONE: 516-282-2438

BLUMBERG, LEROY N.
BROOKHAVEN NATIONAL LAB.
NSLS BLDG 725C BNL
UPTON, NY 11973
PHONE: 516-282-4600

BOCCARD, PAUL
OLD DOMINION UNIV
PHYSICS DEPT
NORFOLK, VA 23529
PHONE: 804-683-3484

BOGACZ, ALEX S.
FERMI NAT'L ACCELERATOR LAB
PO BOX 500, MS 345
BATAVIA, IL 60510
PHONE: 708-840-3873

BOGE, MICHAEL
DESY
NOTKESTR 85
2000 HAMBURG, 52
GERMANY
PHONE: 040-899-82756

BOGERT, V. DIXON
FERMILAB
MS 323, PO BOX 500
BATAVIA, IL 60510
PHONE: 708-840-4010

BOHN, COURTLANDT L.
ARGONNE NATIONAL LAB.
EP-207
9700 S. CASS AVE.
ARGONNE, IL 60439
PHONE: 708-252-4871

BORDOLEY, MORDECHAI
BROOKHAVEN NATIONAL LAB
BLDG 725 B
UPTON, NY 11973
PHONE: 516-282-4768

BORDUA, MICHAEL G.
LAWRENCE BERKELEY LABORATORY
1 CYCLOTRON RD, MS 64-121
BERKELEY, CA 94720
PHONE: 510-486-7709

BORLAND, MICHAEL D.
ARGONNE NATIONAL LAB.
BLDG. 360
9700 S. CASS AVE.
ARGONNE, IL 60439
PHONE: 708-252-4205

BOSCH, ROBERT A.
SYNCHROTRON RADIATION CENTER
3731 SCHNEIDER DR.
STOUGHTON, WI 53589
PHONE: 608-877-2197

BOSSER, JACQUES
CERN/PS
1211 GENEVE, 23
SWITZERLAND
PHONE: 767-378-6

BOURIANOFF, GEORGE L.
SSCL
2550 BECKLEYMEADE AVE
DALLAS, TX 75237
PHONE: 214-708-3453

BOWLING, BRUCE A.
CEBAF
12000 JEFFERSON AVE
NEWPORT NEWS, VA 23606
PHONE: 804-249-7240

BOYCE, RICHARD M.
SSRL/SLAC
MS 69, 2575 SAND HILL RD
MENLO PARK, CA 94025
PHONE: 415-926-3441

BOYD, JOHN K.
LLNL
P.O. BOX 808 L-35
LIVERMORE, CA 94550
PHONE: 510-422-6783

BOZOKI, EVA
BROOKHAVEN NATIONAL LABORATORY
BLDG 725C
NATL SYNCHROTRON LIGHT SOURCE
UPTON, NY 11973
PHONE: 516-282-3701

BRENNAN, JOSEPH M
BROOKHAVEN NATIONAL LAB.
AGS DEPT. 911 B
UPTON, NY 11973
PHONE: 516-282-3755

BRESSLER, VINCENT E.
SLAC
2575 SAND HILL RD
BIN 21
MENLO PARK, CA 94301
PHONE: 415-926-4010

BRIANTI, GIORGIO
CERN
AC DIV.-CH-1211
23 GENEVA, CH 1211
SWITZERLAND
PHONE: 412-276-73153

BRIDGES, JAMES F.
ARGONNE NATIONAL LAB.
9700 S CASS AVE
371T
ARGONNE, IL 60439
PHONE: 708-252-3966

BRIGGS, RICHARD J.
SSC LABORATORY
2550 BECKLEYMEADE MS 1072
DALLAS, TX 75237
PHONE: 214-708-5403

BROUK, VICTOR L.
SSC LABORATORY
2550 BECKLEYMEADE AVE.
DALLAS, TX 75237

BROWMAN, M. JEAN
LOS ALAMOS NATIONAL LAB
MS H825 GROUP AT-7
LOS ALAMOS, NM 87544
PHONE: 505-667-3108

BROWN, NATHAN A.
UNIVERSITY OF MARYLAND
LAB FOR PLASMA RESEARCH
COLLEGE PARK, MD 20742
PHONE: 301-405-4967

BROWNE, MICHAEL J.
SLAC/STANFORD UNIVERSITY
P.O. BOX 4349
PALO ALTO, CA 94309
PHONE: 415-926-2680

BRUHWILER, DAVID L.
GRUMMAN CORP. RES.
4 INDEPENDENCE WAY
PRINCETON, NJ 08540
PHONE: 609-520-1807

BRUNS, WARNER
TU-BERLIN
EINSTEIN UFE 1Y
1000 BERLIN, 10
GERMANY
PHONE: 49-30-31423441

BUDNICK, JOHN E.
IND. UNIV. CYCLOTRON FACILITY
2401 MILO SAMPSON LANE
BLOOMINGTON, IN 47408
PHONE: 812-855-2932

BURNETT, DANIEL A.
TEKTRONIX, INC.
PO BOX 6026
GAITHERSBURG, MD 20884-6026
PHONE: 301-990-7548

BURNHAM, BENTLEY H.
DUKE UNIVERSITY
BOX 90319
DURHAM, NC 27708-0319
PHONE: 919-660-2644

BUSSE, WINFRIED W.R.A.
HAHN MEITNER INST BERLIN GmbH
BEREICH SCHWERIONENPHYSIK
BERLIN, D-14109
GERMANY
PHONE: 493-080-092330

BYERS, BOB
CEBAF
12000 JEFFERSON AVE
MS 16A
NEWPORT NEWS, VA 23602
PHONE: 804-249-7127

BYRD, JOHN M.
LAWRENCE BERKELEY LABORATORY
1 CYCLOTRON RD, MS 71 259
BERKELEY, CA 94720
PHONE: 510-486-6929

CAL, SHAO-YANG
UNIVERSITY OF MARYLAND
LAB FOR PLASMA RESEARCH
COLLEGE PARK, MD 20742
PHONE: 301-405-1605

CAL, YUNHAI
SSCL
2550 BECKLEYMEADE
DALLAS, TX 75237
PHONE: 214-708-4533

CALABRETTA, LUCIANO
INFN
VIALE A DORIA ANG S SOFIA
CATANIA, 95125
ITALY
PHONE: 955-422-59

CALAME, JEFF P.
UNIVERSITY OF MARYLAND
ENERGY RESEARCH BLVD
COLLEGE PARK, MD 20742
PHONE: 301-405-4962

CALDERON, MANUAL
LLNL
7000 EAST AVENUE
LIVERMORE, CA 94550
PHONE: 510-422-9800

CALLAHAN, DEBRA
LLNL
PO BOX 808 L-794
LIVERMORE, CA 94550
PHONE: 510-424-4066

CALLIN, RICHARD S.
STANFORD LINEAR ACCELERATOR
P.O. BOX 4349
MS 30
STANFORD, CA 94309
PHONE: 415-926-4478

CALVERT, JACK
LAWRENCE BERKELEY LABORATORY
1 CYCLOTRON RD BLDG 64/220
BERKELEY, CA 94720
PHONE: 510-486-5595

CAMERON, PETER R
BROOKHAVEN NATIONAL LAB
BLDG 830
UPTON, NY 11973

CAMPISI, ISIDORO
CEBAF
12000 JEFFERSON AVE.
NEWPORT NEWS, VA 23606
PHONE: 804-249-7650

CAPORASO, GEORGE J.
LLNL
PO BOX 5508
L-440
LIVERMORE, CA 94550
PHONE: 510-422-2752

CAREY, DAVE
FEMILAB
PO BOX 500
BATAVIA, IL 60563
PHONE: 708-840-3639

CARLSON, RANDOLPH L.
LOS ALAMOS NATIONAL LAB
GROUP M-4, MS-P940
LOS ALAMOS, NM 87545
PHONE: 505-667-9754

CARLSTEN, BRUCE E.
LOS ALAMOS NATIONAL LAB
MS H825, AT-7
LOS ALAMOS, NM 87544
PHONE: 505-662-3980

CARLTON, LINDA
CEBAF
12000 JEFFERSON AVE
NEWPORT NEWS, VA 23606
PHONE: - -

CARR, ROGER G.
SLAC
PO BOX 4349
STANFORD, CA 94309
PHONE: 415-926-3965

CARROLL, LEWIS
CTI, INC.
810 INNOVATION DR
KNOXVILLE, TN 37932
PHONE: 615-966-7539

CARTER, ANTHONY
MIT
PO BOX 846
MIDDLETON, MA 01949
PHONE: 617-245-6600

CARTER, HAMILTON B.
BOX 2767
BIG SPRING, TX 79721
PHONE: 915-267-6717

CARUS, BRIAN F.
AMERSHAM/MEDI-PHYSICS
3350 N RIDGE AVE
ARLINGTON HGTS, IL 60004
PHONE: 708-398-8400

CARWARDINE, JOHN A.
AEA TECHNOLOGY, CULHAM
7722 STEVENS ST.
DARIEN, IL 60561
PHONE: 708-789-8011

CARYOTAKIS, GEORGE
SLAC
PO BOX 4349
MS-33
STANFORD, CA 94309
PHONE: 415-926-2442

CASPI, SHLOMO
LAWRENCE BERKELEY LABORATORY
1 CYCLOTRON RD, MS 46-161
BERKELEY, CA 94720
PHONE: 510-486-7244

CASSEL, RICHARD
STANFORD LINEAR ACCELERATOR
2575 SAND HILL RD, MS 49
MENLO PARK, CA 94025
PHONE: 415-926-2299

CASTRO GARCIA, PEDRO
CERN
CH-1211
GENEVA 23,
SWITZERLAND
PHONE: 04 -22 -7675217

CAUSSYN, DAVID D.
IND. UNIV. CYCLOTRON FACILITY
2401 MILO B. SAMPSON LANE
BLOOMINGTON, IN 47408
PHONE: 812-855-5196

CAVALLARI, GIORGIO
CERN
CH 1211 GENEVA,
SWITZERLAND
PHONE: - -

CAYLOR, ROBERT
LAWRENCE BERKELEY LABORATORY
1 CYCLOTRON RD BLDG 46/161
BERKELEY, CA 94720
PHONE: 510-486-6483

CELATA, CHRISTINE M.
LAWRENCE BERKELEY LABORATORY
1 CYCLOTRON RD, MS 47-112
BERKELEY, CA 94720
PHONE: 510-486-7740

CERVELLERA, FEDERICO
INFN-LABORATORI NAZ DI LEGNARO
LAB NAZIONALI DE LEGNARO
CO
LEGNARO, I-35020
ITALY
PHONE: 003-949-8292351

CHAMPION, MARK S.
FERMILAB
WILSON & KIRK
RECEIVING DEPT
BATAVIA, IL 60510
PHONE: 708-840-3160

CHAN, CHUN FAI
LAWRENCE BERKELEY LABORATORY
1 CYCLOTRON RD
4-230
BERKELEY, CA 94720
PHONE: 510-486-7912

CHANG, CHENG HSIANG
SYNCHROTRON RADIATION RES CTR
NO 1, R & D ROAD VI
HSINCHU SCI-BASED INDUST PARK
HSINCHU, 30077
TAIWAN, R.O.C.
PHONE: 886-357-80281

CHANG, CHU RUI
SSCL
2550 BECKLEYMEADE AVE
MS 1043
DALLAS, TX 75237
PHONE: 214-708-4305

CHAO, ALEX W.
SSC LABORATORY
2550 BECKLEYMEADE
DALLAS, TX 75237
PHONE: 214-708-5361

CHAO, YU-CHIU
CERAP
12000 JEFFERSON AVE
MS: 12A
NEWPORT NEWS, VA 23606
PHONE: 804-249-6292

CHAPMAN, GERALD
SSCL
2550 BECKLEYMEADE AVE
STE 125
DALLAS, TX 75237
PHONE: 214-708-6330

CHARGIN, ANTHONY E.
LLNL
PO BOX 808 L-644
LIVERMORE, CA 94550
PHONE: 510-422-5196

CHARLTON, GORDON R.
US DEPT OF ENERGY
19901 GERMANTOWN ROAD
GERMANTOWN, MD 20874
PHONE: 301-903-4801

CHASE, BRIAN E.
FERMILAB
MS 308, PO BOX 500
BATAVIA, IL 60510
PHONE: 708-840-3040

CHATTOPADHYAY, SWAPAN
LAWRENCE BERKELEY LABORATORY
1 CYCLOTRON RD, MS 871H
MS-71-259
BERKELEY, CA 94720
PHONE: 510-486-7217

CHEL, STEPHANE
CEA/SACLE
DAPNIA/SEA
91191 GIF-SUR-YVETTE
GIF/YVETTE, 91191
FRANCE
PHONE: 331-690-87420

CHEN, BO
SSCL
2550 BECKLEYMEADE AVE
MS-1042
DALLAS, TX 75237
PHONE: 214-708-4511

CHEN, CHIPING
MASSACHUSETTS INST. TECHNOLOGY
MIT PLASMA FUSION CENTER
CAMBRIDGE, MA 02139
PHONE: 617-253-8506

CHEN, CHUNG-HSIN
UNIV OF MARYLAND
LAB FOR PLASMA RESEARCH
COLLEGE PARK, MD 20742
PHONE: 301-405-4998

CHEN, PISIN
STANFORD LINEAR ACCELERATOR
PO BOX 4349, MS-26
STANFORD, CA 94309
PHONE: 415-926-3384

CHEN, SENYU
SSCL
2550 BECKLEYMEADE AVE
MS 9000
DALLAS, TX 75237
PHONE: 214-708-3516

CHEN, SHIENCHI
MIT
NW16-176, MIT
CAMBRIDGE, MA 02139
PHONE: 617-253-0833

CHEN, TUNG
SLAC
SLAC MS2B,
P.O. BOX 4348
STANFORD, CA 94309
PHONE: 415-826-2527

CHEN, YU-JUAN
LAWRENCE LIVERMORE NATL LAB
PO BOX 808, L-440
LIVERMORE, CA 94550
PHONE: 510-422-9850

CHENG, JACK C.
UNIVERSITY OF MARYLAND
LABORATORY FOR PLASMA RESEARCH
COLLEGE PARK, MD 20742
PHONE: 301-405-5010

CHENG, WEN-HAO
UNIVERSITY OF MARYLAND
DEPT OF PHYSICS
COLLEGE PARK, MD 20744
PHONE: 301-405-6188

CHENG, YAO
SYNCHROTRON RADIATION RES CTR
NO 1, R & D ROAD VI
HSINCHU SCI-BASED INDUST PARK
HSINCHU, 30077
TAIWAN, R.O.C.
PHONE: 886-357-80281

CHESNEY, PHILIPPE
CEA-CEN/SACLAY-INS
GIF SUR YVETTE, 91191
FRANCE
PHONE: 331-690-84435

CHIANG, I-HUNG
BROOKHAVEN NATIONAL LAB.
BUILDING 911B
UPTON, NY 11973
PHONE: 516-282-7903

CHIN, JOHN W.G.
LAWRENCE BERKELEY LABORATORY
1 CYCLOTRON RD BLDG 46/161
BERKELEY, CA 94720
PHONE: 510-486-7236

CHIN, YONG HO
LAWRENCE BERKELEY LABORATORY
1 CYCLOTRON RD, MS 871H
BERKELEY, CA 94720
PHONE: 510-486-5614

CHIOU, TZENG-CHIH
U.S.C.
POWELL HALL
UNIVERSITY OF SOUTHERN CAL
LOS ANGELES, CA 90089

CHO, MOO-HYUN
PAL/POSTECH, KOREA
PO BOX 125
POHANG
SOUTH KOREA
PHONE: 825-627-92075

CHO, YANGLAI
ARGONNE NATIONAL LAB
9700 S CASS AVE D-360
ARGONNE, IL 60439
PHONE: 708-252-6616

CHO, YONG SUB
SEOUL NATIONAL UNIVERSITY
DEPT OF NUCLEAR ENGINEERING
SEOUL, 151-742
KOREA
PHONE: 028-807-213

CHOI, JINHYUK
PAL
PO BOX 125
POHANG KYUNGBUK, 790600
SOUTH KOREA
PHONE: 825-627-92993

CHOJNACKI, ERIC
ARGONNE NATIONAL LAB
9700 S CASS AVE
ARGONNE, IL 60439
PHONE: 708-252-6099

CHOU, WEIREN
SSCL
2550 BECKLEYMEADE AVE
MS-1042
DALLAS, TX 75237
PHONE: 214-708-4524

CHOW, CARSON C.
UNIVERSITY OF COLORADO
DEPT. OF APAS
UNIVERSITY OF COLORADO
BOULDER, CO 80309-0391
PHONE: 303-492-5659

CHUNG, KIE-HYUNG
SEOUL NATIONAL UNIVERSITY
NUCLEAR ENG DEPT
SEOUL, 151-742
SOUTH KOREA
PHONE: 028-830-904

CHUNG, YOUNGJOO
ARGONNE NATIONAL LAB
BLDG. 362-ASD
9700 S. CASS AVE.
ARGONNE, IL 60439
PHONE: 708-252-4601

CIAPALA, EDMOND
CERN
SL DIVISION
1211 GENEVA, 23
SWITZERLAND
PHONE: 022-767-4387

CIULLO, GIUSEPPE
INFN
PHONE: 498-292-425

CLARK, DAVID J.
LAWRENCE BERKELEY LAB.
1 CYCLOTRON ROAD
BLDG. 88
BERKELEY, CA 94720
PHONE: 510-486-7812

CLAYTON, CHRISTOPHER
UCLA
56-125B ENGR IV BUILDING
LOS ANGELES, CA 90024
PHONE: 310-206-2039

CLAYTON, THOMAS M.
SSC LAB.
MS 1040
2550 BECKLEYMEADE AVE.
DALLAS, TX 75237
PHONE: 214-708-4566

CLENDENIN, JAMES E.
SLAC
PO BOX 4349-BIN 66
STANFORD, CA 94309
PHONE: 415-926-2962

CLINE, DAVID
UCLA
405 HILGARD AVE
LOS ANGELES, CA 90024

CLOUT, PETER N.
VISTA CONTROL SYSTEMS INC.
134 EASTGATE DR #B
LOS ALAMOS, NM 87544
PHONE: 505-662-2484

COGHILL, CORTLANDT
BABCOCK & WILCOX
PO BOX 785
LYNCHBURG, VA 24502
PHONE: 804-522-6330

COKRAGAN, AHMET
IBA
CHEMIN DU CYCLOTRON, 2
B-1348 LOUVAIN-LA-NEUVE
LOUVAIN,
BELGIUM
PHONE: 321-047-5890

COLE, BEN H.
SSC LABORATORY
2550 BECKLEYMEADE AVE
MS 4011
DALLAS, TX 75237
PHONE: 214-938-0003

COLE, MICHAEL D.
GRUMMAN AEROSPACE & ELECTRONIC
MS AO1-26 GRUMMAN CORP
BETHPAGE, NY 11714
PHONE: 516-346-8976

COLEMAN, DALE P.
SSCL
2550 BECKLEYMEADE AVE
MS 4010
DALLAS, TX 75237
PHONE: 214-708-3766

COLTON, EUGENE P.
U.S. DEPT OF ENERGY
2550 BECKLEYMEADE, MS 1020
DALLAS, TX 75237
PHONE: 214-708-2421

CONDE, MANOEL E.
LAWRENCE BERKELEY LABORATORY
1 CYCLOTRON RD, MS/71-H
BERKELEY, CA 94720
PHONE: 510-486-5076

CONSTANT, TED
SLAC
PO BOX 4349
MS-50
STANFORD, CA 94309
PHONE: 415-926-3505

COOPER, RONALD G.
BO&G/EM
130 ROBIN HILL RD
GOLETA, CA 93117
PHONE: 805-681-2325

CORBETT, WILLIAM J.
SLAC/SSRL
P.O. BOX 4349
MAIL STOP 99
STANFORD, CA 94309
PHONE: 415-926-3645

CORLETT, JOHN N.
LAWRENCE BERKELEY LABORATORY
1 CYCLOTRON RD, MS 71-259
BERKELEY, CA 94720
PHONE: 510-686-5228

CORNACCHIA, MAX
SLAC
PO BOX 4349, MS 69
STANFORD, CA 94309-0210
PHONE: 415-926-3906

CORNELIUS, WAYNE D.
SAIC
4161 CAMPUS POINT CT.
SAN DIEGO, CA 92128
PHONE: 619-458-3793

CORNELIUSSEN, STEVE
CEBAF
12000 JEFFERSON AVE
NEWPORT NEWS, VA 23606
PHONE: - -

CORONIS, SUSAN D.
DEPARTMENT OF ENERGY
2586 GLENGYLE DR
VIENNA, VA 22181-5511
PHONE: 703-281-9194

COSTRELL, LOUIS
NATL INST OF STDS & TECHNOLOGY
245/C229
GAITHERSBURG, MD 20899
PHONE: 301-975-5608

COUTRAKON, GEORGE
LOMA LINDA UNIV MEDICAL CENTER
11234 ANDERSON ST
DEPT RADIATION MEDICINE
LOMA LINDA, CA 92373

COYNE, J. JOSEPH
SSC LABORATORY
2550 BECKLEYMEADE AVE.
MS 9000
DALLAS, TX 75237
PHONE: 214-708-4535

CRADDOCK, MICHAEL
TRIUMF/UBC
4004 WESBROOK MALL
VANCOUVER, BC V6T2A3
CANADA
PHONE: 604-222-1047

CRAFT, BEN C
LSU-CAMD
3990 W LAKESHORE DR
BATON ROUGE, LA 70803

CRAWFORD, JOHN F.
P.S.I.
CH-5234 VILLIZEN,
SWITZERLAND

CRAWFORD, KENNETH W.
CEBAF
12000 JEFFERSON AVE.
NEWPORT NEWS, VA 23606
PHONE: 804-249-7409

CRIST, CHARLES E.
SSCL
2550 BECKLEYMEADE AVE
MS-1043
DALLAS, TX 75237-3997
PHONE: - -

CURRY, BILL
ARGONNE NATIONAL LABORATORY
9700 SOUTH CASS AVE
ARGONNE, IL 60439
PHONE: 708-252-7683

CURTIN, MARK S.
ROCKWELL INTL
4429 LUBBOCK DR
SIMI VALLEY, CA 93063

CUKRTIS, CHRIS
CEBAF
12000 JEFFERSON AVE
NEWPORT NEWS, VA 23606
PHONE: - -

CUTLER, ROY L
SSC LABORATORY
2550 BECKLEYMEADE AVE
DALLAS, TX 75237
PHONE: 214-708-4221

D'AURIA, JOHN M
SIMON FRASER UNIVERSITY
DEPARTMENT OF CHEMISTRY
BURNABY, BC V5A1S6
CANADA
PHONE: 604-291-4607

BARROWELL, JOHN
BROOKHAVEN NATIONAL LAB
BLDG 725 B
UPTON, NY 11973
PHONE: 516-282-4632

BAHL, PER F.
SSC LABORATORY
2330 BECKLEYMEADE AVE
MS 1870
DALLAS, TX 75237
PHONE: 214-708-1080

DAINELLI, ANTONIO
INFN-LABORATORI NAZ DI LEGNARO
LAB NAZIONALI DE LEGNARO
CO
LEGNARO, I-35020
ITALY
PHONE: 003-949-8292352

DALENO, LEO ROBERT
LOS ALAMOS NATIONAL LABORATORY
P.O. BOX # 1663
MS H820
LOS ALAMOS, NM 87545
PHONE: 505-667-3414

DANARÉD, HAKAN
MANNE SIEGBAHN INST OF PHYSICS
S-10405 STOCKHOLM,
SWEDEN
PHONE: 468-161-038

DANLY, BRUCE G.
MET, PLASMA FUSION CENTER
MIT, NW16-172
CAMBRIDGE, MA 02139
PHONE: 617-253-8454

DAVIS, PEPE G.
UCLA/EE
ENG IV, RM 56-125B
LOS ANGELES, CA 90024
PHONE: 310-825-6012

DAVIS, TIMOTHY
CORNELL UNIVERSITY
909 MITCHELL ST
ITHACA, NY 14850
PHONE: 607-255-3352

DE JONG, MARK S.
ABCL RESEARCH
CHALK RIVER LABORATORIES
CHALK RIVER, ON K0J-1J0
CANADA
PHONE: 613-584-3311

DE MASCUREAU, JEAN
CEA
CEA/CESTA BP2
LE BARP, 33144
FRANCE
PHONE: 566-847-72

DEADRIK, FREDERICK J.
LLNL
PO BOX 5508
L-440
LIVERMORE, CA 94550
PHONE: 510-422-8511

DEATON, JAMES D.
US ASSDC
PO BOX 1500
HUNTSVILLE, AL 35807
PHONE: 205-935-4779

DEBENHAM, PHILIP H.
DEPT. OF ENERGY
19901 GERMANTOWN RD.
GERMANTOWN, MD 20874
PHONE: 301-903-5228

DEBIAK, TED W.
GRUMMAN CORPORATION
STEWART AVE., M/S B29-25
BETHPAGE, NY 11714
PHONE: 516-575-2691

DECKER, FRANZ-JOSEF
SLAC
P.O. BOX 4349
MAIL STOP 66
STANFORD, CA 94309
PHONE: 415-926-3645

DECKER, GLENN
ARGONNE NATIONAL LABORATORY
9700 S. CASS AVE.
ARGONNE, IL 60439
PHONE: 708-252-6635

DEFORD, JOHN F.
LLNL
PO BOX 5508
L-440
LIVERMORE, CA 94550
PHONE: 510-423-5118

DEITINGHOFF, HORST
INST FUR ANGEWANDTE PHYSIK
ROBERT MAYER STR. 2-4
D-60325 FRANKFURT,
GERMANY
PHONE: 069-798-2807

DELAYEN, JEAN
ARGONNE NATIONAL LAB.
9700 S. CASS AVE.
ARGONNE, IL 60439

DELHEZ, CARLO
EINDHOVEN UNIVERSITY
PO BOX 513
5600MB EINDHOVEN,
NETHERLANDS

DELIKARIS, DIMITRI
CERN A.T. CR CRYOGENIC GRP.
CH 1211 GENEVA,
SWITZERLAND
PHONE: - -

DELL, GEORGE F.
BROOKHAVEN NATIONAL LABORATORY
BLDG. 1005S
UPTON, NY 11973
PHONE: 516-282-2348

DEN HARTOG, PATRIC K.
GRUMMAN AEROSPACE CORPORATION
C/O ARGONNE NATL LAB
9700 S CASS AVE, BLDG 367 TR1
ARGONNE, IL 60439
PHONE: 708-739-8010

DENARD, JEAN-CLAUDE R.
CERAF
MS 16A, 12000 JEFFERSON AVE
NEWPORT NEWS, VA 23606
PHONE: 804-249-7555

BENG, DONG-PING
BROOKHAVEN NATIONAL LAB.
BUILDING 1806S
UPTON, NY 11973
PHONE: 516-282-3197

BERNINIV, YAROSLAV S.
UNIVERSITY OF MICHIGAN
RANDALL LAB
ANN ARBOR, MI 48109-1120
PHONE: 313-764-2534

BERWENT, PAUL F.
UNIVERSITY OF MICHIGAN
FERMI LAB MS318
PO BOX 500
BATAVIA, IL 60510
PHONE: 708-840-4965

DESMOND, EDMOND J.
BROOKHAVEN NATIONAL LAB
BLDG 72SB
UPTON, NY 11973
PHONE: 516-282-4768

DESPE, OSCAR D.
ARGONNE NATIONAL LAB.
9700 S. CASS AVE.
BLDG. 368T
ARGONNE, IL 60439
PHONE: 708-257-7140

DESTLER, WILLIAM W.
UNIV OF MARYLAND
EE DEPT
COLLEGE PARK, MD 20742
PHONE: 301-405-3683

DEWALD, MARY ANN
IEEE

DIAMOND, WILLIAM
ATOMIC ENERGY OF CANADA
CHALK RIVER, ONTARIO, K0J 1J0
CANADA
PHONE: 613-584-3311

DICKY, CARL E.
DUKE UNIVERSITY
FEL LAB, BOX 90319
DURHAM, NC 27708-0319
PHONE: 919-660-2645

DIMARCO, JOSEPH N.
LOS ALAMOS NATIONAL LABORATORY
AT-1, MS H817
LOS ALAMOS, NM 87545
PHONE: 505-665-1974

DIMASSA, GIUSEPPE
DES
UNIVERSITY OF CALABRIA
REUDE, 87036
ITALY
PHONE: 398-172-53330

DIVIACCO, BRUNO
SINCROTRONE TRIESTE
PADRICIANO 99
TRIESTE, 34012
ITALY
PHONE: 60-375-8 224

DOHAN, DONALD A.
SSCL
2550 BECKLEYMEADE AVE.
DALLAS, TX 75237
PHONE: 214-708-3736

DONAHUE, JOEY B.
LOS ALAMOS NATIONAL LABORATORY
P.O. BOX 1663
MP-7 MS H840
LOS ALAMOS, NM 87545
PHONE: 505-667-2856

DONALDSON, ANTHONY
STANFORD LINEAR ACCELERATOR
2575 SAND HILL RD, MS 49
MENLO PARK, CA 94025
PHONE: 415-926-2219

DONALDSON, RENE
SLAC
12000 JEFFERSON AVE
NEWPORT NEWS, VA 23606
PHONE: - -

DOOLING, JEFFREY C.
GRUMMAN
BLDG. 367-TRI
9700 S. CASS AVE.
ARGONNE, IL 60439
PHONE: 708-739-8015

DORTWEGT, ROBERT J.
ARGONNE NATIONAL LAB
9700 S CASS
BLDG 378T
ARGONNE, IL 60439
PHONE: 708-252-6058

DOUGLAS, DAVID ROSS
CEBAF
12000 JEFFERSON AVE.
NEWPORT NEWS, VA 23606
PHONE: 804-872-7045

DOWE, R. MICHEL
TITAN
3033 SCIENCE PARK RD
SAN DIEGO, CA 92121
PHONE: 619-552-9533

DRAGT, ALEX J.
UNIVERSITY OF MARY' AND
DEPARTMENT OF PHYSICS
COLLEGE PARK, MD 20742
PHONE: 301-405-6053

DROZHDIN, ALEXANDER
SSCL
2550 BECKLEYMEADE
DALLAS, TX 75237
PHONE: 214-708-5504

DRURY, MICHAEL
CEBAF
12000 JEFFERSON AVE.
NEWPORT NEWS, VA 23606
PHONE: 804-249-7493

DUDAS, ALAN J.
SIEMENS MEDICAL LABS.

DUDNIKOV, VADIM
OAK RIDGE NATIONAL LABORATORY
PO BOX 2005
BLDG 9201-2 MS 8071
OAK RIDGE, TN 37831-8071
PHONE: 615-574-1123

DUGAN, GERALD F.
SSCL
2550 BECKLEYMEADE AVE MS-1047
DALLAS, TX 75237-3997
PHONE: 214-708-4577

BUTT, SAMIR K.
SSCL
2550 BECKLEYMEADE AVE
DALLAS, TX 75237
PHONE: 214-708-4517

BUTTO, GERARDO
TRIUMF
4004 WEBBROOK MALL
VANCOUVER, BC V6T-2A3
CANADA
PHONE: 604-222-1047

DUVALL, BRUCE W.
KAMAN INSTRUMENTATION
PO BOX 7413
COLORADO SPRINGS, CO 80933
PHONE: 719-599-1889

DWINELL, ROGER
LAWRENCE BERKELEY LABORATORY
1 CYCLOTRON RD BLDG 46/161
BERKELEY, CA 94720
PHONE: 510-486-7701

DYKES, MICHAEL D.
SERC DARESBURY LAB.
DARESBURY
WARRINGTON
CHESHIRE, WA4 4AD
UNITED KINGDOM
PHONE: 092-560-3142

DYLLA, H. FREDERICK
CEBAF
12000 JEFFERSON AVE.
NEWPORT NEWS, VA 23606
PHONE: 804-249-7450

DYMIKOV, ALEXANDER D.
MARC, PHYSICS DEPT.
UNIVERSITY OF MELBOURNE
PARKVILLE
VICTORIA, 3052
AUSTRALIA
PHONE: 613-344-5433

EARLY, RICHARD A.
SLAC/STANFORD UNIVERSITY
PO BOX 4349
STANFORD, CA 94309
PHONE: 415-926-2951

ECKLUND, STAN
SLAC
PO BOX 4349
STANFORD, CA 94309
PHONE: 415-926-3182

EDIGHOFFER, JOHN
LAWRENCE BERKELEY LAB./ALS
1 CYCLOTRON RD. 71H
BERKELEY, CA 94720
PHONE: 510-486-5107

EDWARDS, DONALD A.
FERMILAB
MS 345, PO BOX 500
BATAVIA, IL 60510
PHONE: 708-840-8489

EDWARDS, HELEN T.
FERMI NAT'L ACCELERATOR LAB.
MS 341, PO BOX 500
BATAVIA, IL 60510
PHONE: 708-840-4424

EDWARDS, JOHN WM
NICHOLS RESEARCH CORP.
1604 SPRING HILL
SUITE 200
VIENNA, VA 22182
PHONE: 703-893-9720

EICKHOFF, HARTMUT
GSI
PLANCKSTR 1
6100 DARMSTADT,
GERMANY
PHONE: 061-5 -359368

EINFELD, DIETER
FORSCHUNGSZUENTR ROSSENDORF
BO. 19, 8051 DRESDEN
DRESDEN, 8051
GERMANY
PHONE: 493-515-913301

EISENBERG, YEHEDA
DESY/WEIZMANN INST.
DESY F1, NOTKESTR. 85
HAMBURG,
GERMANY
PHONE: 494-089-983092

EKDAHL, CARL A.
LOS ALAMOS NATIONAL LAB
P-14, MS D410
LOS ALAMOS, NM 87545
PHONE: 505-665-2470

ELLISON, MICHAEL
IUCF
2401 MILO B SAMPSON LN
BLOOMINGTON, IN 47408
PHONE: 812-835-9916

ELLISON, TIM J.
INDIANA UNIV. CYCLOTRON FAC.
2401 MILO SAMPSON LANE
BLOOMINGTON, IN 47405
PHONE: 812-835-0934

ELSNER, KONRAD
CERN
SL-DIVISION
GENEVA, CH-1211
SWITZERLAND
PHONE: 41 -22 -7676111

EMERY, LOUIS
ARGONNE NATIONAL LABORATORY
9700 S. CASS AVENUE
ARGONNE, IL 60439
PHONE: 708-252-7756

EMMA, PAUL J.
SLAC
P.O. BOX 4349
STANFORD, CA 94305
PHONE: 415-926-2438

EMSLEY, JOSEPH S.
BURLE INDUSTRIES, INC.
1000 NEW HOLLAND AVE
LANCASTER, PA 17601
PHONE: 717-295-6025

ENEGREN, TERRY A.
SSCL
2550 BECKLEYMEADE
DALLAS, TX 75237
PHONE: 214-708-3767

ENGWALL, DAVID
UNIV OF ILLINOIS
12000 JEFFERSON AVE
NEWPORT NEWS, VA 23606
PHONE: 804-249-7097

EFFLEY, KENNETH R.

SLAC
BIN 26
P.O. BOX 4349
STANFORD, CA 94309
PHONE: 415-926-3381

ERICKSON, ROGER

SLAC
P.O. BOX 4349
STANFORD, CA 94309
PHONE: 415-926-3381

ESAREY, ERIC

NAVAL RESEARCH LABORATORY
CODE 6791
WASHINGTON, DC 20375
PHONE: 202-404-7720

ESHELMAN, JAMES A.

BURLE INDUSTRIES, INC.
1000 NEW HOLLAND AVE.
LANCASTER, PA 17601
PHONE: 717-295-2057

ESIN, S.K.

INR MOSCOW
60TH OCT. ANNIVERSARY PROSPECT
117312, MOSCOW
RUSSIA

EVANS, ALBERT E.

US DEPT OF ENERGY
15005 CARRY BACK DR
GAITHERSBURG, MD 20878
PHONE: 301-903-4896

EVANS, LYNDON R.

CERN
SL DIVISION
CH-1211 GENEVA, 23
SWITZERLAND
PHONE: 412-276-74823

EVANS JR., KENNETH

ARGONNE NATIONAL LAB.
ASD-360
9700 S. CASS AVE.
ARGONNE, IL 60439
PHONE: 708-252-5110

EYHARTS, PHILIPPE

CEA
SERVICE DT/PE/MP-BF #2
LE BARP, 33114
FRANCE
PHONE: 566-840-00

FACCO, ALBERTO

INFN LEGNARO
VIA ROMEA 4 LEGNARO
PADOVA, 35020
ITALY
PHONE: 049-829-2311

FAHMIE, MICHAEL

LAWRENCE BERKELEY LABORATORY
1 CYCLOTRON RD BLDG 46/125
BERKELEY, CA 94720
PHONE: 510-486-4030

FARKAS, ZOLTAN D.

SLAC
P.O. BOX 4349
STANFORD, CA 94309
PHONE: 415-926-3381

FARKHONDEH, MANOUCHEHR

RESEARCH SCIENTIST
MIT-BATES
MIT-BATES LINEAR ACCELERATOR
PO BOX 846
MIDDLETON, MA
PHONE: 617-245-6600

FATHIZADEH, MASOUD

ARGONNE NATIONAL LAB
9700 S CASS AVE D-360
ARGONNE, IL 60439
PHONE: 708-252-6543

FAURE, JEAN

CEA-CEN/SACLAY-LNS
GIF SUR YVETTE, 91191
FRANCE
PHONE: 331-690-84952

FAWLEY, WILLIAM M.

LAWRENCE BERKELEY LABORATORY
1 CYCLOTRON RD, MS 47-112
BERKELEY, CA 94720
PHONE: 510-486-6229

FAZIO, MICHAEL V.

LOS ALAMOS NATIONAL LAB
MS H851
LOS ALAMOS, NM 87545
PHONE: 505-667-3281

FEDELE, RENATO

INFN SEZIONE DI NAPOLI
MOSTRA D'OLTREMARE PAD.20
NAPOLI, 80125
ITALY
PHONE: 398-172-53330

FEINBERG, BENEDICT

LAWRENCE BERKELEY LAB./ALS
1 CYCLOTRON RD.
MS 80-101
BERKELEY, CA 94720
PHONE: 510-486-7725

FERGER, FRITZ

CERN
CH-1211
GENEVA,
SWITZERLAND
PHONE: 022-767-2978

FERGUSON, PATRICK

MDS COMPANY
1955 MOUNTAIN BLVD, STE 101
OAKLAND, CA 94611
PHONE: 510-339-0957

FERIANIS, MARIO

SINCROTRONE TRIESTE
PADRICIANO 99
TRIESTE, 34012
ITALY
PHONE: 40-375-8 545

FERNOW, RICHARD C.

BROOKHAVEN NATIONAL LABORATORY
PHYSICS, 901A
UPTON, NY 11973
PHONE: 516-282-3741

FESCHEWKO, ALEXANDER V.

INR/SSCL
60TH OCTOBER ANNIVERSARY
PROSPECT
7a, MOSCOW, 117312
RUSSIA
PHONE: 214-708-5602

FESSENDEN, THOMAS J.
LAWRENCE BERKELEY LABORATORY
1 CYCLOTRON RD
47/112
BERKELEY, CA 94720
PHONE: 510-486-5356

FIEGUTH, THEODORE H.
SLAC
MS 20
P.O. BOX 4349
STANFORD, CA 94309
PHONE: 415-926-2539

FINK, CHARLES L.
ARGONNE NATIONAL LABORATORY
BLDG. 207
ARGONNE, IL 60439
PHONE: 708-252-6611

FINLEY, DAVID A.
FERMILAB
PO BOX 500
BATAVIA, IL 60510
PHONE: 708-840-4468

FIORITO, RALPH B.
NSWC DD
MS R36
10910 NEW HAMPSHIRE AVE
SILVER SPRING, MD 20901
PHONE: 301-394-1908

FISHER, ALAN
BROOKHAVEN NATIONAL LABORATORY
PHYSICS, 901A
UPTON, NY 11973
PHONE: . .

FISHER, AMNON
NRL
BEAM PHYSICS BRANCH
CODE 6793 NRL
WASHINGTON, DC 20375-5000

FLANNIGAN, JOHN
BROOKHAVEN NATIONAL LABORATORY
BLDG 725B
NATL SYNCHROTRON LIGHT SOURCE
UPTON, NY 11973
PHONE: 516-282-5190

FLANZ, JACOB B.
MASSACHUSETTS GENERAL HOSPITAL
149 13TH ST, RM 4022
CHARLESTOWN, MA 02129
PHONE: 617-724-9528

FOELSCH, HORST W.J.
BROOKHAVEN NATIONAL LAB.
BUILDING 1005
UPTON, NY 11973
PHONE: 516-282-2219

FOERSTER, CONRAD L.
BROOKHAVEN NATIONAL LABORATORY
BLDG 725C
NATL SYNCHROTRON LIGHT SOURCE
UPTON, NY 11973
PHONE: 516-282-4754

FOLEY, JOANN
IEEE

FOLEY, MICHAEL H.
FERMI NAT'L ACCELERATOR LAB.
MS 340, PO BOX 500
BATAVIA, IL 60510
PHONE: 708-840-2505

FONG, KENNETH S.
TRIUMF
4004 WESBROOK MALL
VANCOUVER, BC V6T-2A3
CANADA
PHONE: 604-222-1047

FONTANA, JORGE R.
UNIVERSITY OF CALIFORNIA
4375 VIA GLORIETA
SANTA BARBARA, CA 93110
PHONE: 805-682-3387

FOUAIDY, MOHAMMED
I.P.N. D'ORSAY
BAT. 100, BP1, CAMPUS D'ORSAY
91406 ORSAY, CEDEX
FRANCE
PHONE: 694-164-97

FOUGERON, CLAUDE
LAB NATL SATURNE/CE SACLAY
GIF SUR YVETTE, 91191
FRANCE
PHONE: 331-690-85969

FOWKES, WILLIAM RANDALL
STANFORD LINEAR ACCELERATOR
PO BOX 4349
STANFORD, CA 94309
PHONE: 415-926-4465

FOWLER, WILLIAM B.
FERMILAB
PO BOX 500
BATAVIA, IL 60510
PHONE: 708-840-3682

FOX, JOHN D.
SLAC
BIN 33, BOX 4349
STANFORD, CA 94309
PHONE: 415-926-2789

FRANZKE, BERNHARD J.
GSI
POSTFACH 110552, LIBRARY
D-6100 DARMSTADT, 11
GERMANY
PHONE: 615-135-9366

FRASER, JOHN S.
TRIUMF
4004 WESBROOK MALL
VANCOUVER, BC V6T-2A3
CANADA
PHONE: 604-222-1047

FRIEDMAN, AHARON
BROOKHAVEN NATIONAL LABORATORY
BLDG 725C
UPTON, NY 11973
PHONE: 516-282-5028

FRIEDRICH, JR., CARL C.
LOS ALAMOS NATIONAL LABORATORY
PO BOX 1663
MS: H827
LOS ALAMOS, NM 87545
PHONE: 505-667-8850

FRIESEL, DENNIS L.
IND. UNIV. CYCLOTRON FACILITY
2401 MILO B. SAMPSON LANE
BLOOMINGTON, IN 47401
PHONE: 812-855-2944

FRESCHE, JOSEF C.
SLAC
SLAC MS 66
STANFORD, CA 94309
PHONE: 415-926-2469

FRESCHEHOLZ, HANS W.
CERN
CH-1211 GENEVA, 23
SWITZERLAND
PHONE: 227-764-180

FRITSCH, CRAIG T.
ALLIED SIGNAL AEROSPACE CO.
PO BOX 419159
KANSAS CITY, MO 64141
PHONE: 816-997-5351

FUCHI, KYOKO
NSCL AT MSU
MASTERS OF PHYSICS
S. SHAW LANE
EAST LANSING, MI 48824-1321
PHONE: 517-353-5097

FUJA, RAYMOND E.
ARGONNE NATIONAL LABORATORY
9700 S. CASS AVE
ARGONNE, IL 60439

FULLETT, KENNETH
FERMI NATIONAL LAB
PO BOX 500 MS 341
BATAVIA, IL 60510
PHONE: 708-840-2507

FUNAKOSHI, YOSHIHIRO
KEK
OHO 1-1 TSUKUBA-SHI
IBARAKI-KEN, 305
JAPAN

FUNK, L. WARREN
SSC LABORATORY
2550 BECKLEMEADE AVE.
MS 1043
DALLAS, TX 75237
PHONE: 214-708-4300

GABELLA, WILLIAM E.
UCLA
FERMILAB MS 345
PO BOX 500
BATAVIA, IL 60510
PHONE: 708-840-2556

GAGNE, MICHAEL A.
SPANG POWER CONTROL
LAKE STREET
SANDY LAKE, PA 16145
PHONE: 412-376-2249

GAI, WEI
ARGONNE NATIONAL LAB
9700 S CASS AVE
ARGONNE, IL 60465
PHONE: 708-252-6560

GALAYDA, JOHN N.
ARGONNE NATIONAL LABORATORY
APS/ASD 360
9700 S. CASS AVE.
ARGONNE, IL 60439
PHONE: 708-252-7796

GALLARDO, JUAN C.
BROOKHAVEN NATIONAL LABORATORY
PHYSICS, 901A
UPTON, NY 11973
PHONE: 516-282-3523

GALLO, ALESSANDRO
INFN-FRASCATI
PO BOX 13
FRASCATI, 00044
ITALY

GAMMEL, GEORGE M.
GRUMMAN AEROSPACE CORP.
MS B29-25
1111 STEWART AVE.
BETHPAGE, NY 11714
PHONE: 516-575-0663

GANETIS, GEORGE
BROOKHAVEN NATIONAL LABORATORY
BLDG. 902
UPTON, NY 11973
PHONE: 516-282-4476

GARAVAGLIA, THEODORE
SSCL
2550 BECKLEYMEADE AVE
MS-1042
DALLAS, TX 75237
PHONE: 214-708-4526

GARDELLE, JACQUES
CEA
CEA/CESTA
PO BOX 2
33144 LE BARP,
FRANCE
PHONE: 566-840-00

GARDNER, CHRIS
BROOKHAVEN NATIONAL LAB.
BUILDING 911B
UPTON, NY 11973
PHONE: 516-282-4537

GARNER, JAMES L.
SML TECHNOLOGY
7180 LAMPSON AVE
GARDEN GROVE, CA 92641
PHONE: 714-898-1868

GARBY, ROLAND
CERN/PS
CH-1211 GENEVA, 23
SWITZERLAND
PHONE: - -

GARREN, AL
SSC
B-71H
LAWRENCE BERKELEY LAB
BERKELEY, CA 94720
PHONE: 510-841-8283

GELFAND, NORMAN M.
FERMILAB
PO BOX 500, MS 345
BATAVIA, IL 60510
PHONE: 708-840-3619

GEMME, GIANLUCA
INFN
VIA DODECANESO 33
GENOVA, 16146
ITALY
PHONE: 39 -10 -3536326

GERASIMOV, ANDREI L.
FERMILAB
PO BOX 500, MS 345
BATAVIA, IL 60510
PHONE: 708-840-8101

GERG, RODNEY
BNCL
2550 BECKLEYMEADE
MS 9000
DALLAS, TX 75237
PHONE: 214-708-4223

GETZ, DONALD
ARGONNE NATIONAL LAB.
BLDG. 360
9700 S. CASS AVE.
ARGONNE, IL 60439
PHONE: 708-252-4724

GHOSE, ARUP
BROOKHAVEN NATIONAL LABORATORY
BLDG. 902
UPTON, NY 11973
PHONE: 516-282-3974

GILAD, PINCHAS
RAFAEL
PO BOX 2250 (24)
HAIFA, 31021
ISRAEL

GILGENBACH, RONALD M.
UNIVERSITY OF MICHIGAN
NUCLEAR ENGINEERING DEPT
COOLEY BKDG, NORTH CAMPUS
ANN ARBOR, MI 48109-2104
PHONE: 313-763-1261

GILLESPIE, GEORGE H.
G.H. GILLESPIE ASSOCIATES INC.
12520 HIGH BLUFF DR, STE 330
SAN DIEGO, CA 92130
PHONE: 619-792-0222

GILPATRICK, J. DOUGLAS
LANL
MS: H808
LOS ALAMOS, NM 87545
PHONE: 505-667-3159

GIOVANNONI, PAUL P.G.
COMMISSARIAT A L'ENERGIE ATOM
C E SACLAY DSM/DAPNIA/STCM
GIF SUR YNETTE, 91191
FRANCE
PHONE: 169-087-6

GIOVE, DARIO
INFN
VIA FLII CERVI 201
SEGRATE (MILAN), 20090
ITALY
PHONE: 392-239-2559

GJAJA, IVAN M.
UNIVERSITY OF MARYLAND
DEPARTMENT OF PHYSICS
COLLEGE PARK, MD 20742
PHONE: 301-405-6053

GLASS, HENRY
FERMI NATIONAL ACCELERATOR LAB
P.O. BOX 500 - MS316
BATAVIA, IL 60510
PHONE: 708-840-8105

GLOCK, HANS-WALTER
INST FUR ANGEWANDTE PHYSIK
ROBERT MAYER STR. 2-4
D-60325 FRANKFURT,
GERMANY
PHONE: 069-798-2292

GLOVER, MIKE G.
SERC
RUTHERFORD APPLETON LAB.
CHILTON,
DIDCOT, OX110QX
UNITED KINGDOM
PHONE: 023-582-1900

GLUCKSTERN, ROBERT L.
UNIVERSITY OF MARYLAND
DEPARTMENT OF PHYSICS
COLLEGE PARK, MD 20742
PHONE: 301-405-6054

GODLOVE, TERRY F.
F M TECHNOLOGIES
9713 MANTEO COURT
FT WASHINGTON, MD 20744
PHONE: 301-567-3281

GOLD, SAUL L.
SLAC
PO BOX 4349
MS-33
STANFORD, CA 94309
PHONE: 415-926-4450

GOLD, STEVEN H.
NAVAL RESEARCH LAB
CODE 6793
4555 OVERLOOK AVE, SW
WASHINGTON, DC 20375
PHONE: 202-767-4004

GOLDBERG, DAVID A.
LAWRENCE BERKELEY LABORATORY
1 CYCLOTRON RD, MS 71 259
BERKELEY, CA 94720
PHONE: 510-486-7222

GOLDEN, JEFF
BERKELEY RESEARCH ASSOCIATES
PO BOX 852
SPRINGFIELD, VA 22150
PHONE: 703-750-3434

GOLDMAN, MICHAEL A.
BROOKHAVEN NATIONAL LAB
AGS DEPT 911B
UPTON, NY 11973
PHONE: 516-282-5090

GOLUBEVA, NINA
INSTITUTE FOR NUCLEAR RESEARCH
60TH OCT ANNIVERSARY PROSPECT
7A
MOSCOW, 117312
RUSSIA

GONCALVES DA SILVA, CYLON
DIRECTOR
LNLS/BRAZIL
CX P. 6192
CAMPINAS, 13083
BRAZIL
PHONE: 551-925-42624

GONICHON, JEROME
MIT
PLASMA FUSION CENTER
NW16-184
CAMBRIDGE, MA 02139
PHONE: 617-253-5132

GONZALEZ, RODOLFO E.
SSCL
2550 BECKLEYMEADE
DALLAS, TX 75237
PHONE: 214-708-4223

OREN, YEHUDA
IC LABORATORY
50 BECKLEYMEADE AVE
DALLAS, TX 75237
PHONE: 214-708-3769

OVIL, L.M.
PROFESSOR
ANIAB UNIVERSITY
DEPT OF PHYSICS
CENTER FOR ADVANCED STUDIES
HANDIGARH, 160 014
INDIA

RABER, JOEL H.
ORNELL UNIVERSITY
15 NEWMAN LAB
ITHACA, NY 14850
PHONE: 607-272-4951

RANATSTEIN, VICTOR L.
UNIVERSITY OF MARYLAND
LAB FOR PLASMA RESEARCH
COLLEGE PARK, MD 20742
PHONE: 301-405-4956

REEN, MICHAEL A.
SYNCHROTRON RADIATION CENTER
731 SCHNEIDER DR.
FOUGHTON, WI 53589
PHONE: 608-877-2159

RIESER, MANFRED
IPF FÜR KERNPHYSIK
P.O. BOX 103980
600 HEIDELBERG,
GERMANY

RIFFIN, JAMES E.
ERMILAB
BOX 261
/AYNE, IL 60184
PHONE: 708-584-2801

RIMM, TERRY
SSCL
550 BECKLEYMEADE AVE.
MS-4005
DALLAS, TX 75237
PHONE: 214-708-4232

GRIPPE, JAMES M.
SSCL
2550 BECKLEYMEADE AVE
DALLAS, TX 75237-3946
PHONE: 214-708-3781

GRUNDER, HERMANN A.
CEBAF
12000 JEFFERSON AVE
NEWPORT NEWS, VA 23606
PHONE: 804-249-7552

GUERRA, AL
CEBAF
12000 JEFFERSON AVE
NEWPORT NEWS, VA 23606
PHONE: 804-249-7636

GUERRA, EDUARDO
SLAC
2575 SANDHILL RD.
MENLO PARK, CA 94025
PHONE: 415-926-3409

GUHARAY, SAMAR K.
UNIVERSITY OF MARYLAND
LABORATORY FOR PLASMA RESEARCH
COLLEGE PARK, MD 20742
PHONE: 301-405-5013

GUIDEE, PHILIPPE
THOMSON TUBES ELECT
13 AVENUE MORANE SAULNIER
BAT CMAVEZ VELIZY ESPACE PO121
VELIZY VILLACOUBLAY, 78148
FRANCE
PHONE: 130-703-599

GUIGNARD, GILBERT F.
CERN/SL DIVISION
CH-1211 GENEVA, 23
SWITZERLAND
PHONE: 412-276-75975

GUO, ZHIYUAN
INST. OF HIGH ENERGY PHYSICS
P.O. BOX 918 100039
BEIJING,
P.R. CHINA
PHONE: 861-821-3374

GUPTA, RAMESH
BROOKHAVEN NATIONAL LABORATORY
BLDG. 902
UPTON, NY 11973
PHONE: 516-282-3974

GURD, DAVE
SSCL
2550 BECKLEYMEADE
MS 4002
DALLAS, TX 75237
PHONE: 214-708-3401

GUROL, HUSAM
GENERAL DYNAMICS SPACE SYSTEMS
PO BOX 85990, C1-8260
SAN DIEGO, CA 92185-5590
PHONE: 619-547-8032

GURR, JAMES RICHARD
USA SSCDC
PO BOX 1500
ATTN: CSSD-DE-N
HUNTVILLE, AL 35807-5722
PHONE: 205-955-1568

GUSEV, O.A.
EFREMOV INSTITUTE
POS METALLOSTRY
P.O. BOX 42
ST PETERSBURG, 189631
RUSSIA

GUSEWELL, DIETRICH
CERN
CH 1211 GENEVA,
SWITZERLAND
PHONE: 004-122-767

GUY, FRANK W.
SSC LABORATORY
2550 BECKLEYMEADE AVE
MS 1043
DALLAS, TX 75237
PHONE: 214-708-4313

HAAS, ALLAN K
SSCL
2550 BECKLEYMEADE AVE
MS 4001
DALLAS, TX 75237-3946
PHONE: 214-708-5444

BAKER, IRVING
NRL
CODE 6790 NAVAL RESEARCH LAB
WASHINGTON, DC 20375
PHONE: 202-767-3198

BAFIZI, BAHMAN
ICARUS RESEARCH
7113 EXPAIR RD
BETHESDA, MD 20814

HAHN, HARALD
BROOKHAVEN NATIONAL LAB
BLDG 100SS
UPTON, NY 11973
PHONE: 516-282-4683

HAHN, KYOUNG D.
LAWRENCE BERKELEY LABORATORY
1 CYCLOTRON RD, MS 47-112
BERKELEY, CA 94720
PHONE: 510-486-5286

HAIRAPETIAN, GARNICK
UCLA DEPT OF ELECT. ENGINEER.
56-125B ENGR IV BUILDING
LOS ANGELES, CA 90024
PHONE: 310-206-2039

HALBACH, KLAUS
LAWRENCE BERKELEY LABORATORY
1 CYCLOTRON RD BLDG 46/161
BERKELEY, CA 94720
PHONE: 510-486-5868

HAMILTON, BRETT J.
INDIANA UNIV. CYCLOTRON FAC.
2401 MILO B. SAMPSON LANE
BLOOMINGTON, IN 47408
PHONE: 812-855-5162

HAMM, ROBERT
ACCSYS TECHNOLOGY
1177 QUARRY LANE
PLEASANTON, CA 94566
PHONE: 510-462-6949

HAMMER, WILLIAM N.
GRUMMAN
STEWART AVE
BETHPAGE, NY 11714
PHONE: 516-346-3122

HANNA, SAMY M.
BROOKHAVEN NATIONAL LABORATORY
NSLS BLDG. 725C
UPTON, NY 11973
PHONE: 516-282-4635

HANSEN, SIGMUND
CERN
1211 GENEVA, 23
SWITZERLAND
PHONE: 767-340-1

HARDEK, THOMAS W.
LOS ALAMOS NATIONAL LAB.
MS-H838
LOS ALAMOS, NM 87545
PHONE: 505-667-9132

HARDEKOPF, ROBERT A.
LOS ALAMOS NATIONAL LAB
MS-H811
LOS ALAMOS, NM 87545
PHONE: 505-667-1289

HARDING, DAVID J.
FERMILAB
PO BOX 500, MS 323
BATAVIA, IL 60510
PHONE: 708-840-2971

HARGREAVES, THOMAS A.
LITTON ELECTRON DEVICES
960 INDUSTRIAL RD
SAN CARLOS, CA 94070
PHONE: 415-591-8411

HARKAY, KATHERINE C.
FERMILAB
PO BOX 500, MS 341
BATAVIA, IL 60510
PHONE: 708-840-4639

HARMS, MICHAEL G.
STANFORD LINEAR ACCELERATOR
P.O. BOX 4349
MS-50
STANFORD, CA 94309
PHONE: 415-926-2915

HARMS, JR., ELVIN R.
FERMILAB
PO BOX 500, MS 306
BATAVIA, IL 60510
PHONE: 708-840-4376

HARTMAN, SPENCER C.
UCLA
UCLA PHYSICS DEPT
405 HILGARD AVE
LOS ANGELES, CA 90024-1547
PHONE: 310-825-6012

HARTUNG, WALTER H.
CORNELL UNIVERSITY
NEWMAN LAB OF NUCLEAR STUDIES
ITHACA, NY 14853
PHONE: 607-255-4951

HARVEY, MARGE
FERMI LAB.
12000 JEFFERSON AVE
NEWPORT NEWS, VA 23606
PHONE: - -

HARWOOD, LEIGH H.
CEBAF
12000 JEFFERSON AVE
NEWPORT NEWS, VA 23606
PHONE: 804-249-7063

HASEBOTH, HELMUT D.
CERN
CH-1211 GENEVA, 23
SWITZERLAND
PHONE: 412-276-72503

HASS, MATHEW A.
FIELD EFFECTS
6 EASTERN RD
ACTON, MA 01720

HATTON, VINCENT
CERN
GENEVA,
SWITZERLAND
PHONE: 767- 4773

HAWORTH, MICHAEL D.
SSC LABORATORY
2550 BECKLEYMEADE AVE
MS 1043
DALLAS, TX 75237
PHONE: 214-708-4527

HERBERT, JOSEPH E.
SSC LABORATORY
2550 BECKLEYMEADE AVE
MS 1043
DALLAS, TX 75237
PHONE: 214-708-4516

HEEPNER, JAY

SSCL

2550 BECKLEYMEADE

MS 4002

DALLAS, TX 75237

PHONE: 214-708-3479

HEESE, RICHARD

BROOKHAVEN NATIONAL LABORATORY

BLDG 725C

NATL SYNCHROTRON LIGHT SOURCE

UPTON, NY 11973

PHONE: 516-792-4902

HEIFETS, SAMUEL

SLAC

BIN 26

P.O. BOX 4349

STANFORD, CA 94309

PHONE: 415-926-4600

HENDERSON, TOM F.

LAWRENCE BERKELEY LABORATORY

1 CYCLOTRON RD BLDG 46/161

BERKELEY, CA 94720

PHONE: 510-486-4672

HENDRICKSON, LINDA J.

STANFORD LINEAR ACCELERATOR

P.O. BOX 4349

MS 46

STANFORD, CA 94309

PHONE: 415-926-3913

HENDRICKSON, SCOTT

UNIV OF COLORADO

CAMPUS BOX 390

BOULDER, CO 80309

PHONE: 303-492-0312

HENKE, HEINO

TECHNISCHE UNIVERSITAET

EINSTEINUFER 17, EN-2

1000 BERLIN, 10

GERMANY

PHONE: 303-162-2690

HENNELLY, MICHAEL

AMERICAN INSTITUTE OF PHYSICS

HENNING, DALE L.

SSCL

2550 BECKLEYMEADE AVE

MS-9000

DALLAS, TX 75237

PHONE: 214-708-4571

HERMAN, HAROLD

ARGONNE NATIONAL LAB

9700 S CASS AVE

EP DIV-BLDG 207

ARGONNE, IL 60439

PHONE: 708-252-5317

HERR, WERNER F

CERN

SL DIVISION

CH 1211 GENEVA, 23

SWITZERLAND

PHONE: 767-463-5

HERRLANDER, CARL JOHAN

M.S.I.

FRESCATIVAGEN 24

S-10405 STOCKHOLM,

SWEDEN

PHONE: 46-816-1112

HERRMANNSFELDT, WILLIAM B.

STANFORD LINEAR ACCELERATOR

2575 SAND HILL RD

MENLO PARK, CA 94022

PHONE: 415-926-3342

HESELSON, STUART L.

EEV, INC.

4 WESTCHESTER PLAZA

ELMSFORD, NY 10523

PHONE: 914-592-6050

HEWETT, DENNIS W.

LLNL

PO BOX 505, L-418

LIVERMORE, CA 94550

PHONE: 510-423-6886

HIMEL, THOMAS M.

SLAC

SLAC MS-95

STANFORD UNIV

STANFORD, CA 94309

PHONE: 415-926-2004

HINDI, HAITHAM A.

SLAC

MS-33, BOX 4349

STANFORD, CA 94309

PHONE: 415-926-3546

HINKSON, JIM

LAWRENCE BERKELEY LABORATORY

1 CYCLOTRON RD BLDG 46/125

BERKELEY, CA 94720

PHONE: 510-486-4194

HIRAMOTO, KAZUO

ENERGY RES LAB. HITACHI, LTD.

2-1, OMIKA-CHO

7-CHOME HITACHI-SHI

IBARAKI-KEN, 319-12

JAPAN

PHONE: 029-453-3111

HIRATA, KOHJI

KEK

NATL LAB FOR HIGH ENERGY PHY

TSKUBA

IBARAKI, 305

JAPAN

PHONE: 298-641-1171

HIRSHFIELD, JAY

YALE UNIVERSITY

2008 YALE STATION

NEW HAVEN, CT 06520

PHONE: 203-288-6733

HISHITANI, EIJE

HITACHI ZOSEN CORPORATION

3-4, SAKURAJIMA 1-CHOME

KONOHANA-KU OSAKA, 554

JAPAN

PHONE: 064-653-061

HO, CHING-HUNG

ARGONNE NATIONAL LAB

807 S ADAMS ST, APT 1-D

WESTMONT, IL 60559

PHONE: 708-252-6148

HO, DARWIN D.

LAWRENCE LIVERMORE LABORATORY

PO BOX 5508, L-477

LIVERMORE, CA 94550

PHONE: 510-423-9786

BOAG, HAROLD A.
SLAC
PO BOX 4349
STANFORD, CA 94309
PHONE: 415-926-2444

BOFFMAN, BRUCE
MARKETING & SALES
THOMSON COMPONENTS & TUBES
40 G COMMERCE WAY
TOTONA, NJ 07511
PHONE: 201-812-9000

HOFFSTATTER, GEORG H.
MSU/NSCL
E. LANSING, MI 48824
PHONE: 517-355-1523

BOFLER, ALICIA S.
CEBAF
12000 JEFFERSON AVE.
MS 85A
NEWPORT NEWS, VA 23606
PHONE: 804-249-7171

HOGAN, MARK J.
UCLA DEPT OF PHYSICS
405 HILGARD
LOS ANGELES, CA 90024
PHONE: 310-825-6012

HORAN, DOUGLAS A.
ARGONNE NATIONAL LABORATORY
9700 S. CASS AVE-371T
ARGONNE, IL 60439
PHONE: 708-252-7565

HORELICK, DALE
SLAC
2575 SAND HILL RD
MENLO PARK, CA 94025
PHONE: 415-926-2337

HORN, PAUL M.
IBM T.J. WATSON RESEARCH
P.O. BOX 218
YORKTOWN HEIGHTS, NY 10598
PHONE: 914-945-2445

HORTON, CHRIS
PHONE: . .

HOUCK, TIMOTHY L.
LAWRENCE LIVERMORE NAT'L LAB
L-440 7000 EAST AVE.
LIVERMORE, CA 94550
PHONE: 510-423-7905

HOVATER, JAMES C.
SURA/CEBAF
12000 JEFFERSON AVE.
NEWPORT NEWS, CA 23606
PHONE: 808-249-7685

HOYER, EGON H.
LAWRENCE BERKELEY LABORATORY
1 CYCLOTRON RD BLDG 46/161
BERKELEY, CA 94720
PHONE: 510-486-7235

HSU, IAN C.
NATIONAL TSING HUA UNIVERSITY
TSING HUA UNIVERSITY
HSINCHU,
TAIWAN, R.O.C.
PHONE: 886-357-27303

HSUE, CHEN S.
SRRC
I R & D ROAD VI
HSIN-CHU, 300
TAIWAN, R.O.C.
PHONE: 035-721-450

HUANG, HAIKEN
INDIANA UNIV CYCLOTRON FAC.
2401 MILO B SAMPSON LANE
BLOOMINGTON, IN 47408
PHONE: 812-855-5196

HUANG, YUNXIANG
SSCL
2550 BECKLEYMEADE AVE
MS 9000
DALLAS, TX 75237
PHONE: 214-708-4225

HUBBARD, EDWARD L.
CONSULTANT
5527 CHELSEA AVE
LA JOLLA, CA 92037
PHONE: 619-454-8660

HUBBARD, ROBERT E.
MEDI-PHYSICS INC.
3350 N. RIDGE AVE
ARLINGTON HGTS, IL 60004
PHONE: 708-396-8400

HUDSON, CHARLES L.
EG&G/EM
130 ROBIN HILL RD
GOLETA, CA 93117
PHONE: 805-681-2325

HUDSON, TAMMY
CEBAF
12000 JEFFERSON AVE
NEWPORT NEWS, VA 23606
PHONE: . .

HUGHES, THOMAS P.
MISSION RESEARCH CORPORATION
1720 RANDOLPH RD, SE
ALBUQUERQUE, NM 87106-4245
PHONE: 505-768-7719

HUI, ZHONGXI
INSTITUTE OF ENGINEERING ELECT
BO 523-66
CHENGDU, 61003
CHINA
PHONE: 081-625-8395003

HUMPHREY, RUSTY
STANFORD LINEAR ACCELERATOR
P.O. BOX 4349
STANFORD, CA 94309
PHONE: 415-926-3197

HUMPHRIES, DAVID E.
LAWRENCE BERKELEY LABORATORY
1 CYCLOTRON RD BLDG 46/161
BERKELEY, CA 94720
PHONE: 510-486-6797

HURD, JAMES W.
SSCL
2550 BECKLEYMEADE AVE
DALLAS, TX 75237
PHONE: 214-708-4312

HURH, PATRICK G.
FERMILAB
PO BOX 500, MS 340
BATAVIA, IL 60510
PHONE: 708-840-2814

HUTSON, RICHARD
LOS ALAMOS NATIONAL LAB.
GROUP MP-5 MS-H838
LANL
LOS ALAMOS, NM 87545
PHONE: 505-667-8293/29132

HUTTON, ANDREW M.
CEBAF
12000 JEFFERSON AVE.
MS 12A
NEWPORT NEWS, VA 23606
PHONE: 804-249-7396

IAZZOURENE, FATMA
SINCROTRONE TRIESTE
PADRICIANO 99
TRIESTE, 34012
ITALY
PHONE: 40-375-8 504

IEIRI, TAKAO
KEK
KEK, ACC. DIV., OHO 1-1
TSKUBA
IBARAKI, 305
JAPAN
PHONE: 298-645-298

IHLOFF, ERNEST
MIT BATES LAB
MANNING ROAD
MIDDLETON, MA 01949
PHONE: 617-245-6600

ILIEV, ANDREI I.
TRIUMF
INR, 60TH OCTOBER ANNIVERSARY
PROSP 79
MOSCOW,
RUSSIA
PHONE: 604-222-1047

INGELS, SARAH
CEBAF
12000 JEFFERSON AVE
NEWPORT NEWS, VA 23606
PHONE: . . .

INGOLD, GERHARD
BROOKHAVEN NATIONAL LABORATORY
NSLS BLDG. 725C
UPTON, NY 11973
PHONE: 516-282-2379

IRELAND, JOHN
LOS ALAMOS NATIONAL LABORATORY
P.O. BOX 1663
MS K556
LOS ALAMOS, NM 87545
PHONE: 505-667-4344

IRWIN, JOHN
SLAC
BIN 26
SANFORD, CA 94305
PHONE: 415-926-2740

ISHIZUKA, HIROSHI
FUKUOKA INSTITUTE OF TECH
HIGASHI-KU
FUKUOKA, 811-02
JAPAN
PHONE: 092-606-3131

ISMAIL
UNIVERSITY OF TENNESSEE
1200 LAUREL AVE APT 3
KNOXVILLE, TN 37916
PHONE: 615-673-0493

IWASHITA, YOSHIHISA
ACCELERATOR LAB/ICK KYOTO UNIV
GOKANOSHO
UJI
KYOTO, 611
JAPAN
PHONE: 817-743-25806

JACH, CEZARY A.
SSC LABORATORY
2550 BECKLEYMEADE AVE.
MS: 4004
DALLAS, TX 75109
PHONE: 214-708-3310

JACHIM, STEPHEN P.
LOS ALAMOS NATIONAL LABORATORY
PO BOX 1663
MS: H827
LOS ALAMOS, NM 87545
PHONE: 505-667-9692

JACKSON, ALAN
LAWRENCE BERKELEY LABORATORY
1 CYCLOTRON RD BLDG 80/101
BERKELEY, CA 94720
PHONE: 510-486-6752

JACKSON, GERALD P.
FERMILAB
PO BOX 500, MS 341
BATAVIA, IL 60510
PHONE: 708-840-2317

JACKSON, L. TERRY
LAWRENCE BERKELEY LABORATORY
1 CYCLOTRON RD BLDG 46/125
BERKELEY, CA 94720
PHONE: 510-486-4803

JACOB, JR., RALPH W.
SLAC
PO BOX 4349, BIN 50
STANFORD, CA 94309
PHONE: 415-926-2927

JACOBS, EDWARD F.
MEDI & PHYSICS INC.
900 DURHAM AVE.
S. PLAINFIELD, NJ 07080
PHONE: 908-757-751E

JACOBS, KEN
MIT
PO BOX 846
MIDDLETON, MA 01949
PHONE: 617-245-6600

JAFFERY, TARIQ S.
SSC
2550 BECKLEYMEADE AVE MS-994
DALLAS, TX 75237
PHONE: 214-708-2283

JAHNEL, LUCIA
UNIV DE SAO PAULO
LAB NATL DE LUZ SINCROTRON
CAIXA POSTAL 6192
CAMPINAS, SAO PAULO, 13081-970
BRAZIL
PHONE: 551-925-42624

JAMES, MICHAEL F.
ATOMIC ENERGY CONTROL BOARD
P.O. BOX 1046 STE. B
OTTAWA, ON K2M-1A3
CANADA
PHONE: 613-995-2730

JAMESON, ROBERT A.
LANL
AT-DO MS H811
LOS ALAMOS, NM 87545
PHONE: 505-665-2275

JAMESON, GEORGES E.
SSCL
2550 BECKLEYMEADE AVE
DALLAS, TX 75237
PHONE: 214-708-3466

JAN, GWO-JEN
SYNCHROTRON RADIATION RES CTR
NO 1, R & D ROAD VI
HSINCHU SCI-BASED INDUST PARK
HSINCHU, 30077
TAIWAN, R.O.C.
PHONE: 886-357-80281

JAYAKUMAR, RAGHAVAN
SSCL
2550 BECKLEYMEADE
DALLAS, TX 75237
PHONE: 214-708-6884

JENNER, DAVID L.
IUCF
2401 MILO SAMPSON
BLOOMINGTON, IN 47408
PHONE: 812-855-9368

JENSEN, CHRIS C.
FERMILAB
PO BOX 500, MS 308
PINE ST & KIRK RD
BATAVIA, IL 60510
PHONE: 708-840-2674

JENSEN, KEN A.
TRIUMF
4004 WESBROOK MALL
VANCOUVER, BC V6T-2A3
CANADA
PHONE: 604-222-1047

JIANG, BING
INTEGRATED APPLIED PHYSICS
50 THAYER RD
WALTHAM, MA 02154
PHONE: 617-489-1818

JIANG, SCICHENG
UNIVERSITY OF MARYLAND
PHYSICS DEPARTMENT
COLLEGE PARK, MD 20742
PHONE: 301-422-4832

JOE, KIHUN
ARGONNE NATIONAL LAB
PHYSICS DIV BLDG 203
9700 S CASS AVE
ARGONNE, IL 60439
PHONE: 708-252-9114

JOHNS, RONALD A.
ARGONNE NATIONAL LAB APS
9700 S CASS
ARGONNE, IL 60439
PHONE: 708-252-6823

JOHNSON, BRANT M.
PHYSICAL REVIEW LETTERS
1 RESEARCH RD.
BOX 1000
RIDGE, NY 11961
PHONE: 516-924-5533

JOHNSON, CHRISTINE A.
DEPT OF ENERGY
1400 N. LAKE SHORE DR. #10-Q
CHICAGO, IL 60610
PHONE: 708-252-9483

JOHNSON, KENNETH F.
LOS ALAMOS NATIONAL LAB
AT-10 MS H818
LOS ALAMOS, NM 87545
PHONE: 505-665-2788

JOHNSON, ROLLAND P.
CEBAF
12000 JEFFERSON AVE.
NEWPORT NEWS, VA 23606
PHONE: 804-249-7420

JOHO, WERNER
PAUL SCHERRER INSTITUTE
PSI WURENLINGEN + VILLIGEN
CH 5232 VILLIGEN,
SWITZERLAND
PHONE: 004-156-993381

JONES, ALAN A.
SSCL
2550 BECKLEYMEADE AVE.
DALLAS, TX 75237
PHONE: 214-708-5616

JONES, CHARLES M.
OAK RIDGE NATIONAL LABORATORY
PO BOX 2008
OAK RIDGE, TN 37831-6368
PHONE: 615-574-4753

JONES, ROGER M.
SLAC/STANFORD UNIVERSITY
MS 26, SLAC, STANFORD UNIV
PO BOX 4349
STANFORD, CA 94309
PHONE: 415-926-2309

JONES, STEVEN A.
EG&G/EM
130 ROBIN HILL RD
GOLETA, CA 93117
PHONE: 805-681-2325

JORDAN, KEVIN C.
CEBAF
12000 JEFFERSON AVE.
NEWPORT NEWS, VA 23606
PHONE: 804-249-7644

JOSHI, CHAN
UCLA DEPT OF ELECT. ENGINEER.
56-125B ENGR IV BUILDING
LOS ANGELES, CA 90024
PHONE: 310-206-2039

JOUBERT, ALAIN R.
GANIL
BP 5027
F14021 CAEN, CEDEX
FRANCE
PHONE: 314-545-88

JOWETT, JOHN M.
CERN
SL DIVISION
CH-1211 GENEVA, 23
SWITZERLAND
PHONE: 412-276-76643

JOYCE, GLENN
NAVAL RESEARCH LABORATORY
CODE 6794
WASHINGTON, DC 20375
PHONE: 202-767-6785

JUNG, BOLAND
CERN
SL DIV
CH 1211 GENEVA, 23
SWITZERLAND
PHONE: 022-767-3295

KAAN, ALBERT P.
NIKHEP
POST BOX 41882
AMSTERDAM,
NETHERLANDS
PHONE: 020-592-2016

KADANTSEV, SERGEI G.
TRIUMF
4004 WESBROOK MALL
VANCOUVER, BC V6T-2A3
CANADA
PHONE: 604-222-1047

KAHN, STEPHEN
BROOKHAVEN NATIONAL LAB.
BUILDING 902
UPTON, NY 11973
PHONE: 516-282-2282

KALBFLEISCH, CARL
SUPER COLLIDER LABS
2550 BECKLEYMEADE AVE
DALLAS, TX 75237
PHONE: . . .

KALBREIER, WILHELM
SR. PHYSICIST
CERN
CERN-SL
1211 GENEVA, 23
SWITZERLAND
PHONE: 412-276-75278

KAMIYA, YUKIHIDE
ISP, THE UNIVERSITY OF TOKYO
3-2-1 MIDORICHO
TANASHI
TOKYO, 188
JAPAN
PHONE: 814-246-99564

KANG, BONGKOO
ASSOCIATE PROFESSOR
POHANG ACCELERATOR LAB.
PO BOX 125, DEPT OF EE
POHANG KYUNGPOOK,
KOREA
PHONE: 825-627-92286

KANG, YOON W
ARGONNE NATIONAL LAB
9700 S. CASS AVE.
ARGONNE, IL 60439

KARABEKOV, IVAN P.
CEBAF
12000 JEFFERSON AVE. N.
NEWPORT NEWS, VA 23606
PHONE: 804-299-6247

KARN, JEFF S.
SURA/CEBAF
12000 JEFFERSON AVE
NEWPORT NEWS, VA 23602
PHONE: . . .

KATO, RYUKOU
TOHOKU UNIVERSITY LAB.
1-2-1 MIKAMINE, TAIHAKU-KU
SENDAI, 982
JAPAN
PHONE: 812-224-52151

KATO, SYOHEI
LABORATORY OF NUCLEAR STUDIES
FACULTY OF SCI, OSAKA UNIV
TOYONAKA
OSAKA, 560
JAPAN
PHONE: 068-441-151

KATSOULEAS, TOM
USC
USC EE/EP DEPT
LOS ANGELES, CA 90089-0487
PHONE: 213-740-0194

KAUGERTS, JURIS E.
SR. STAFF PHYSICIST
DOE
EE-142
WASHINGTON, DC 20585

KAUFFILA, TODD J.
LOS ALAMOS NATIONAL LAB.
P.O. BOX 1663 MS P-940
LOS ALAMOS, NM 87545
PHONE: 505-667-8497

KAZIMI, REZA
CEBAF
12000 JEFFERSON AVE
MS 12A
NEWPORT NEWS, VA 23606
PHONE: 804-249-6250

KEANE, JOHN
BROOKHAVEN NATIONAL LABORATORY
BLDG 725C
NATL SYNCHROTRON LIGHT SOURCE
UPTON, NY 11973
PHONE: 516-282-4724

KEHNE, DAVID M.
CEBAF
12000 JEFFERSON AVE.
NEWPORT NEWS, VA 23606
PHONE: 804-249-4857

KEIL, EBERHARD
CERN
GENEVE 23, CH-1211
SWITZERLAND

KELLER, RODERICK
LAWRENCE BERKELEY LABORATORY
1 CYCLOTRON RD BLDG 80/101
BERKELEY, CA 94720
PHONE: 510-486-5223

KENNEDY, KURT D.
LAWRENCE BERKELEY LABORATORY
1 CYCLOTRON RD BLDG 46/161
BERKELEY, CA 94720
PHONE: 510-486-7238

KENNEDY, WILLIAM L.
ARGONNE NATIONAL LAB
5112 CENTER AVE
LISLE, IL 60532
PHONE: 708-252-6161

KERSEVAN, ROBERTO
SSCL
2550 BECKLEYMEADE AVE
DALLAS, TX 75237
PHONE: 214-708-4581

KERELICK, GRAHAM S.
CORNELL UNIVERSITY
HVL 909 MITCHELL STREET
ITHACA, NY 14850
PHONE: 607-255-3552

KEWISCH, JORG R.
CEBAF
12000 JEFFERSON AVE
NEWPORT NEWS, VA 23606
PHONE: 804-249-7669

KIM, CHARLES H.
LAWRENCE BERKELEY LABORATORY
1 CYCLOTRON RD.
MS 80-101
BERKELEY, CA 94720
PHONE: 510-486-7218

KIM, JIN-SOO
LAWRENCE BERKELEY LABORATORY
3146 BUNCHE AVE
SAN DIEGO, CA 92122
PHONE: 619-455-6607

KIM, JONATHAN M.S.
UNIVERSITY OF VICTORIA
DEPT OF BCE
PO BOX 3055
VICTORIA, BC V8W-3P6
CANADA
PHONE: 604-721-6028

KIM, KEEMAN
ARGONNE NATIONAL LABORATORY
9700 S. CASS AVE.
APS-362
ARGONNE, IL 60439
PHONE: 708-252-6027

KIM, KWANG-JE
LAWRENCE BERKELEY LAB.
MS-71-259
1 CYCLOTRON
BERKELEY, CA 94720
PHONE: 510-486-7224

KIM, SUK-HONG
ARGONNE NATIONAL LAB.
APS 362
9700 S. CASS AVE.
ARGONNE, IL 60439
PHONE: 708-252-4724

KIMURA, WAYNE D.
VICE PRESIDENT OF RESEARCH
STI OPTRONICS
2755 NORTHRUP WAY
BELLEVUE, WA 98004
PHONE: 206-827-0460

KIMURA, YOSHITAKA
KEK, NLHEP
KEK, ACC. DIV., OHO
TSKUBA-SHI
IBARAKI, 305
JAPAN
PHONE: 298-645-201

KIRBY, ROBERT E.
STANFORD LINEAR ACCELERATOR
MS 74
P O BOX 4349
STANFORD, CA 94309
PHONE: 415-926-2795

KIRCHGESSNER, JOSEPH L.
CORNELL UNIVERSITY
124 NEWMAN LAB
ITHACA, NY 14850
PHONE: 607-272-4951

KIRK, HAROLD G.
BROOKHAVEN NATIONAL LABORATORY
PHYSICS, 901A
UPTON, NY 11973
PHONE: 516-282-3780

KIRKMAN, GEORGE F.
INTEGRATED APPLIED PHYSICS
50 THAYER RD
WALTHAM, MA 02154
PHONE: 617-489-1818

KIRZ, JANOS
SUNY
PHYSICS DEPARTMENT
STONY BROOK, NY 11794
PHONE: 516-632-8106

KISHIMOTO, TAKESHI
SORTEC CORPORATION
16-1 WADAI
TSUKUBA-SHI IBARAKI, 300-42
JAPAN

KISHIRO, JUN-ICHI
NATL LAB FOR HIGH ENERGY PHY
1-1 OHO TSUKUHA
IBARAKI,
JAPAN

KISSLER, KARL-HEINZ
CERN
SL DIVISION
GENEVA 1211,
SWITZERLAND
PHONE: 412-276-74632

KITAMURA, HIDEO
KEK
1-1 OHO, TSUKUBA
IBARAKI, 305
JAPAN
PHONE: 029-864-5681

KLAISNER, LOWELL A.
STANFORD LINEAR ACCELERATOR
PO BOX 4349, MS-30
STANFORD, CA 94309
PHONE: 415-926-2726

KLEVEN, WILLEM YGM
EINDHOVEN UNIV. OF TECHNOLOGY
CYCL. 0214 BOX 513
5600 MB EINDHOVEN,
NETHERLANDS
PHONE: 314-047-4003

KLEIN, HORST
INST FUR ANGEWANDTE PHYSIK
ROBERT MAYER STR. 2-4
D-60325 FRANKFURT,
GERMANY
PHONE: 069-798-3489

KLEMAN, KEVIN J.
UNIV. OF WISCONSIN-SRC
3731 SCHNEIDER DR.
STOUGHTON, WI 53589
PHONE: 608-877-2147

KLOEPPPEL, PETER K.
CEBAF
12000 JEFFERSON AVE.
NEWPORT NEWS, VA 23606
PHONE: 804-249-7568

KNOWLES, HAROLD B.
H.B. KNOWLES, PHYSICS CONSULT.
4030 HILLCREST RD
EL SOBRANTE, CA 94805
PHONE: 516-758-5449

KO, IN SOO
ASSOCIATE PROFESSOR
PAL/POSTECH
PO BOX 125, POHANG
KYUNGBUK, 790-600
KOREA
PHONE: 825-627-94412

KO, SEUNG-KOOK
UNIV OF ULSAN
ULSAN, 680-749
KOREA
PHONE: 825-227-82321

KOBARI, TOSHIAKI
MERL HITACHI LTD.
502 KANDATSU
TSUCHIURA
IBARAKI, 300
JAPAN
PHONE: 298-32-4111

KOGA, JAMES K.
INSTITUTE FOR FUSION STUDIES
THE UNIVERSITY OF TEXAS
AUSTIN, TX 78712-1060
PHONE: 512-471-4315

KOONTZ, ROLAND F.
SLAC
BOX 4349
STANFORD, CA 94309
PHONE: 415-926-2528

KOSCIELNIAK, SHANE R.
TRIUMF
4004 WESBROOK MALL
VANCOUVER, BC V6T2A3
CANADA
PHONE: 604-222-1047

KOSEKI, TADASHI
ISSP, THE UNIVERSITY OF TOKYO
3-2-1 MIDORICHO
TANASHI
TOKYO, 188
JAPAN
PHONE: 814-346-99553

KOSTAS, CHRISTOPHER
SAIC
1710 GOODRIDGE DR.
MC LEAN, VA 22102
PHONE: 703-734-5805

KRAFFT, GEOFFREY A.
CEBAF
12000 JEFFERSON AVE.
MS 12A2
NEWPORT NEWS, VA 23606
PHONE: 804-249-7557

KRALL, JONATHAN
NAVAL RESEARCH LAB
CODE 6790
WASHINGTON, DC 20375-5346
PHONE: 202-404-7719

KRAMER, DIETER
BESSY
LENTZEALLEE 100
100 BERLIN, 33
GERMANY
PHONE: 493-063-924747

KRAUSHAAR, PHILIP F.
SSCL
2550 BECKLEYMEADE AVE.
SUITE 125
DALLAS, TX 75237
PHONE: 214-708-4571

KRAVCHUK, L.V.
INR MOSCOW
60TH OCT. ANNIVERSARY PROSPECT
117312, MOSCOW
RUSSIA

KREBS, GARY
LAWRENCE BERKELEY LABORATORY
1 CYCLOTRON RD BLDG 80/101
BERKELEY, CA 94720
PHONE: 510-486-7727

KREJCIK, PATRICK
SLAC
PO BOX 4349
MS 66
STANFORD, CA 94309
PHONE: 415-926-2790

KRINSKY, SAMUEL
BROOKHAVEN NATIONAL LABORATORY
BLDG 725B
NATL SYNCHROTRON LIGHT SOURCE
UPTON, NY 11973
PHONE: 516-282-4740

KRISHNASWAMY, JAYARAM
GRUMMAN AEROSPACE CORP
4 INDEPENDENCE WAY
PRINCETON, NJ 08546
PHONE: 609-520-1805

KROES, FRANS
NIKHEF
PO BOX 41882
1009DR AMSTERDAM,
NETHERLANDS
PHONE: 020-592-2055

KROGH, MICHAEL L.
ALLIED SIGNAL AEROSPACE CO.
PO BOX 419159
MC 2B35
KANSAS CITY, MO 64141
PHONE: 816-997-3699

KROLL, NORMAN M.
SLAC/ULSD
SLAC MS26
PO BOX 4349
STANFORD, CA 94309
PHONE: 415-926-4909

KRUPNICK, JIM
ALS/LAWRENCE BERKELEY LAB
1 CYCLOTRON RD M/S 80-101
BERKELEY, CA 94720
PHONE: 510-486-6480

KRYCUK, ANTON G.
CEBAF
12000 JEFFERSON AVE.
NEWPORT NEWS, VA 23606
PHONE: 804-249-7281

KUCHNIR, MOYSES
FERMILAB
934 PARKSIDE AVE.
ELMHURST, IL 60126
PHONE: 708-840-3368

KUMTER, BERENDE
CERN
CH-1211 GENEVA, 23
SWITZERLAND
PHONE: 412-276-72919

KULIKOU, ARTEM V.
SLAC
PO BOX 4349
STANFORD, CA 94309
PHONE: . .

KUMADA, MASAYUKI
NATL INST OF RADIOLOGICAL SCI.
9-1 ANAGANA
INAGE
CHIBA, 263
JAPAN
PHONE: 043-236-0122

KUO, THOMAS Y.T.
TRIUMF/UBC
4804 WESBROOK MALL
VANCOUVER, BC V6T-2A3
CANADA
PHONE: 604-322-1047

KURENNOY, SERGEY S.
SSCL
2550 BECKLEYMEADE AVE
MS-1042
DALLAS, TX 75237
PHONE: 214-708-5443

KUBOKAWA, SHIN-ICHI
KEK
NATL LAB FOR HIGH ENERGY PHY
ACCELERATOR DEPT, 1-1 OHO
TSUKUBA, 305
JAPAN
PHONE: 298-641-5691

KWAN, JOE W.
LAWRENCE BERKELEY LABORATORY
1 CYCLOTRON RD, MS 4/230
BERKELEY, CA 94720
PHONE: 510-486-5011

KWIATKOWSKI, SLAWOMIR
SSCL
2550 BECKLEYMEADE AVE
DALLAS, TX 75237
PHONE: 214-708-3709

KWOK, PATRICK T.
UCLA
405 HILGARD AVE
LOS ANGELES, CA 90024
PHONE: 310-825-1214

LACLARE, JEAN-LOUIS
DR
BSRF
BF202
38043 GRENOBLE, CEDEX
FRANCE
PHONE: 337-686-2002

LAHEY, TERRI E.
STANFORD LINEAR ACCELERATOR
P.O. BOX 4349
MS 46
STANFORD, CA 94309
PHONE: 415-926-3916

LAHTI, GEORGE
CEBAF
12000 JEFFERSON AVE
NEWPORT NEWS, VA 23606
PHONE: 804-249-7272

LAMPEL, MICHAEL
ROCKWELL INTERNATIONAL
PO BOX 7922 MS FA-38
CANOGA PARK, CA 91309-7922
PHONE: 818-586-3175

LANCASTER, HENRY D.
LAWRENCE BERKELEY LABORATORY
1 CYCLOTRON RD BLDG 64/220
BERKELEY, CA 94720
PHONE: 510-486-7261

LANDIS, ROBERT J
SSCL
2550 BECKLEYMEADE AVE
MS 4001
DALLAS, TX 75237-3946
PHONE: 214-708-3816

LANGE, FRITZ
FERMILAB
PO BOX 500
BATAVIA, IL 60510
PHONE: 708-840-4799

LAPITSKY, S.
IHEP SERPUKHOV
142284 PROTIVNO
MOSCOW,
RUSSIA

LARSON, DELBERT J.
SSCL
2550 BECKLEYMEADE AVE
MS-1040
DALLAS, TX 75237
PHONE: 214-708-3468

LASNIER, CHARLES J.
LLNL
L-637
LIVERMORE, CA 94550
PHONE: 619-455-4150

LATHAM, PETER E.
UNIVERSITY OF MARYLAND
LAB. FOR PLASMA RESEARCH
COLLEGE PARK, MD 20742
PHONE: 301-405-5020

LAU, Y.Y.
UNIVERSITY OF MICHIGAN
DEPT OF NUCLEAR ENGINEERING
ANN ARBOR, MI 48109
PHONE: 313-764-5122

LAWRENCE, GEORGE P.
LOS ALAMOS NATIONAL LABORATORY
MS 811 LOS ALAMOS LABS
LOS ALAMOS, NM 87545
PHONE: 505-667-9349

LAXDAL, ROBERT
TRIUMF
4004 WESBROOK MALL
VANCOUVER, BC V6T 2A3
CANADA
PHONE: 604-222-1047

LAZAREV, NIKOLAI
HEAD OF LINAL LAB
ITEP
INSTITUTE FOR THEORETICAL AND
EXPERIMENTAL PHYSICS
117259 MOSCOW,
RUSSIA
PHONE: 095-125-0292

LE DUFF, JOEL R.
LAB DE L'ACCELERATEUR LINEAIRE
BAT. 200 CENTRE D'ORSAY
91405
ORSAY, CEDEX
FRANCE
PHONE: 164-46-3430

LEE, BO
TEXAS A&M UNIVERSITY
PHYSICS DEPT
COLLEGE STATION, TX 77843
PHONE: 409-845-5490

LEE, KATE
UNIVERSITY OF MARYLAND
LAB FOR PLASMA RESEARCH
COLLEGE PARK, MD 20742
PHONE: 301-405-5010

LEE, S.Y.
INDIANA UNIVERSITY
DEPT OF PHYSICS
SW117
BLOOMINGTON, IN 47401
PHONE: 812-855-2809

LEE, SEUNGWHEAN
STEVENS INST OF TECHNOLOGY
DEPT. PHYSICS
HOBOKEN, NJ 07030
PHONE: 201-216-5671

LEE, TIM
CEBAF
12000 JEFFERSON AVE.
NEWPORT NEWS, VA 23606
PHONE: 804-249-7413

LEE, TONG-NYONG
POHANG ACCELERATOR LAB.
PO BOX 125
POHANG, 790 600
SOUTH KOREA
PHONE: 825-627-92062

LEE, YONG Y.
BROOKHAVEN NATIONAL LAB.
BLDG. 911B
UPTON, NY 11973
PHONE: 516-282-4663

LEEMANN, CHRISTOPH
CEBAF
12000 JEFFERSON AVE.
NEWPORT NEWS, VA 23602
PHONE: 804-249-7554

LEEMANS, WIM
LAWRENCE BERKELEY LABORATORY
1 CYCLOTRON RD.
MS-71H
BERKELEY, CA 94720
PHONE: 510-486-7788

LEHRMAN, IRA S.
GRUMMAN
4 INDEPENDENCE WAY
PRINCETON, NJ 08540
PHONE: 609-520-1808

LEIFESTE, GORDON T.
SSC LABORATORY
2550 BECKLEYMEADE AVE
MS 1043
DALLAS, TX 75237
PHONE: 214-708-4230

LEISS, JAMES E.
RT 2, BOX 142C
BROADWAY, VA 22815
PHONE: 703-896-5158

LENKSZUS, FRANK R.
ARGONNE NATIONAL LABORATORY
9700 S. CASS AVENUE
BLDG. 362
ARGONNE, IL 60439
PHONE: 708-252-6972

LENNOX, ARLENE J.
FERMILAB
PO BOX 500, MS 301
BATAVIA, IL 60510
PHONE: 708-840-3865

LENZ, JOHN W.
SSC LABORATORY
MS 1043
2550 BECKLEYMEADE AVE.
DALLAS, TX 75237
PHONE: 214-708-4574

LEONHARDT, WILLIAM J.
BROOKHAVEN NATIONAL LABORATORY
BLDG 911A
UPTON, NY 11973
PHONE: 516-282-2378

LEPELTIER, VINCENT
LAB DE L'ACCELERATEUR LINEAIRE
BAT. 200 CENTRE D'ORSAY
F91405
ORSAY, CEDEX
FRANCE
PHONE: 164-46-8375

LESSNER, ELIANE S.
ARGONNE NATIONAL LABORATORY
9700 S. CASS AVE.
ARGONNE, IL 60439
PHONE: 708-252-6466

LEUNG, KA-NGO
LAWRENCE BERKELEY LABORATORY
1 CYCLOTRON RD, MS 4/230
BERKELEY, CA 94720
PHONE: 510-486-7918

LEUNG, KENT K.
SSC
2550 BECKLEYMEADE AVE MS-1005
DALLAS, TX 75237
PHONE: 214-708-5927

LEVEL, MARIE PAULE
LURE-CNRS
BAT 209A
CENTRE UNIV PARIS-SUD
91405 ORSAY, CEDEX
FRANCE
PHONE: 644-682-50

LEVELING, ANTHONY F.
FERMILAB
PO BOX 500, MS 306
BATAVIA, IL 60510
PHONE: 708-840-4041

LEVERENZ, JULIE
CEBAF
12000 JEFFERSON AVE
NEWPORT NEWS, VA 23606
PHONE: - -

LEVINE, BARUCH
LABORATORY FOR PLASMA RES
UNIVERSITY OF MARYLAND
COLLEGE PARK, MD 20742
PHONE: 301-405-3012

LEWIS, STEPHEN A.
LAWRENCE BERKELEY LABORATORY
1 CYCLOTRON RD, MS 64-121
BERKELEY, CA 94720
PHONE: 510-486-7702

LI, DERUN
DEPT OF PHYSICS, INDIANA UNIV
BLOOMINGTON, IN 47405
PHONE: 812-855-5196

LI, MINGYANG
SSCL
2550 BECKLEYMEADE AVE.
MS-1040
DALLAS, TX 75237
PHONE: 214-708-4564

LI, NANYANG
SSCL
MS-9000
BECKLEYMEADE AVE
DALLAS, TX 75237
PHONE: 214-708-4212

LI, RUI
CEBAF
MS-12A
12000 JEFFERSON AVE.
NEWPORT NEWS, VA 23606
PHONE: 804-249-7069

LI, ZENGHAI
CEBAF
MS-16A
12000 JEFFERSON AVE.
NEWPORT NEWS, VA 23606
PHONE: 804-249-7069

LIANG, CHANGNIAN
CEBAF
12000 JEFFERSON AVENUE
NEWPORT NEWS, VA 23606
PHONE: 804-249-7654

LIEDL, JOHN
ELIN MAGNETIC TECHNOLOGY
6993 WOODMERE DR
WALKERTOWN, NC 27051
PHONE: 919-595-3541

LIMBERG, TORSTEN
SLAC
P.O. BOX 4349
STANFORD, CA 94309
PHONE: 415-926-2469

LIN, LEON
MIT
MIT NW16-219
CAMBRIDGE, MA 02141

LINCKE, ERIC
SUPER COLLIDER
2550 BECKLEYMEADE AVE MS9000
DALLAS, TX 75237
PHONE: 214-708-4226

LINNECAR, TREVOR P.
CERN
SL DIVISION
CH-1211 GENEVA, 23
SWITZERLAND
PHONE: 767-479-5

LIU, BONGLIN
RESEARCH ASSISTANT
UNIVERSITY OF S. CALIFORNIA
SSC ROOM 410, USC
LOS ANGELES, CA 90089-0484
PHONE: 213-740-4399

LIPPMANN, GERHARD
DORNIER GMGH
P.O. BOX 1420
FRIEDRICHSHAFEN, 7990
GERMANY
PHONE: 754-583-440

LISKA, DONALD J.
LOS ALAMOS NATIONAL LAB
GROUP AT-4 MS H821
LOS ALAMOS, NM 87544
PHONE: 505-667-3286

LITTMANN, BENGT
TU-BERLIN
EINSTEINUFER 17
1000 BERLIN, 10
GERMANY
PHONE: 49-30-31422490

LITVINENKO, VLADIMIR
DUKE UNIVERSITY
BOX 90319 FELL
DURHAM, NC 27708-0319
PHONE: 919-660-2638

LIU, CHENGJUN
VISITING RESEARCH ASSOCIATE
LAB FOR PLASMA RESEARCH
UNIVERSITY OF MARYLAND
PO BOX 523-56
CHENGDU,
P.R. CHINA

LIU, HONGXIU
SURA/CEBAF
12000 JEFFERSON AVE.
NEWPORT NEWS, VA 23606
PHONE: 804-249-6381

LIU, JIANYANG
UNIV OF WISCONSIN-MADISON
APS BLDG 360 E201
ARGONNE NATL LAB, 9700 S CASS
ARGONNE, IL 60439

LIU, KUO BIN
SYNCHROTRON RADIATION RES CTR
NO 1, R & D ROAD VI
HSINCHU SCI-BASED INDUST PARK
HSINCHU, 30077
TAIWAN, R.O.C.
PHONE: 886-357-80281

LIU, LIN
UNIV DE SAO PAULO
LAB NACIONAL DE LUZ SINCROTRON
CAIXA POSTAL 6192
CAMPINAS, SAO PAULO, 13081-970
BRAZIL
PHONE: 551-925-42624

LO, C.C.
LAWRENCE BERKELEY LABORATORY
1 CYCLOTRON RD BLDG 46/125
BERKELEY, CA 94720
PHONE: 510-486-5400

LOEW, GREGORY A.
SLAC
2575 SAND HILL RD, MS 33
MENLO PARK, CA 94025
PHONE: 415-926-2799

LOISELET, MARC G.
UNIV. CATH. DE LOUVAIN
2, CH DU CYCLOTRON
LOUVAIN-LA-NEUVE, B-1348
BELGIUM
PHONE: 321-047-3307

LOPEZ, FRED V.
ARGONNE NATIONAL LAB.
9700 S CASS AVE BLDG 362
C-189
ARGONNE, IL 60439
PHONE: 708-252-6092

LOPEZ, GUSTAVO
SSC LABORATORY
2550 BECKLEYMEADE
DALLAS, TX 75237
PHONE: 214-709-4542

LOU, WEIRAN
CORNELL UNIVERSITY
WILSON LAB
ITHACA, NY 14853
PHONE: - -

LOW, KENG
SUPER COLLIDER LABS
2550 BECKLEYMEADE AVE
DALLAS, TX 75237
PHONE: 214-708-3429

LU, XIANPING
FERMILAB
PO BOX 500, MS 341
BATAVIA, IL 60510
PHONE: 708-840-2549

LUBLINSKY, BORIS S.
FERMILAB
PO BOX 500, MS 307
BATAVIA, IL 60510
PHONE: 708-840-4726

LUCAS, PETER W.
FERMILAB
PO BOX 500, MS 307
BATAVIA, IL 60510
PHONE: 708-840-4950

LUCCIO, ALFREDO U.
BROOKHAVEN NATIONAL LAB.
BLDG. 911B
UPTON, NY 11973
PHONE: 516-282-7699

LUCHINI, KEN
LAWRENCE BERKELEY LABORATORY
1 CYCLOTRON RD BLDG 46/125
BERKELEY, CA 94720
PHONE: 510-486-4745

LUDEWIGT, BERNHARD A
LAWRENCE BERKELEY LABORATORY
1 CYCLOTRON ROAD
MS 64-121
BERKELEY, CA 94720
PHONE: 510-486-5788

LULJCKX, GUY
NIKHEF
KRUISLAAN 40G
1098 SJ AMSTERDAM,
NETHERLANDS
PHONE: 312-059-22121

LUJAN, RICHARD
LOS ALAMOS NATIONAL LAB
AT-4, MS H821
LOS ALAMOS, NM 87545
PHONE: 505-667-6979

LUMPKIN, ALEX
ARGONNE NATIONAL LABORATORY
9700 S. CASS AVE.
BLDG 362-ASD
ARGONNE, IL 60439
PHONE: 708-252-4879

LUO, GWO-HUEI
SRRC
NO 1 R&D ROAD VI
HSINCHU TAIWAN, 30077
CHINA

LYNCH, MICHAEL
LOS ALAMOS NATL LAB
LOS ALAMOS, NM 87845

MAAS, BOB
NIKHEF-K
PO BOX 41882
1009DB AMSTERDAM,
NETHERLANDS

MACEK, ROBERT J.
LOS ALAMOS NATIONAL LAB
MS H848, MP DIVISION
LOS ALAMOS, NM 87545
PHONE: 505-665-8877

MACHIDA, SHINJI
SSC LABORATORY
2550 BECKLEYMEADE AVE
DALLAS, TX 75237
PHONE: 214-708-4213

MACKAY, WILLIAM
BROOKHAVEN NATIONAL LABORATORY
BLDG 1005S
UPTON, NY 11973
PHONE: 516-282-3076

MADDOCKS, JAMES R
SSCL
2550 BECKLEYMEADE AVE.
MS 4003
DALLAS, TX 75237
PHONE: 214-708-3516

MADER, ED J.
E B & G SPECIAL PROJECTS
2450 ALAMO SE
ALBUQUERQUE, NM 87106
PHONE: 505-845-7352

MADEY, JOHN
DUKE UNIVERSITY
LA SELL EXTENSION
DURHAM, NC 27705
PHONE: 919-660-2643

MAGYARY, STEVEN B.
LAWRENCE BERKELEY LABORATORY
1 CYCLOTRON RD BLDG 46/125
BERKELEY, CA 94720
PHONE: 510-486-5376

MAHALE, NARAYAN K.
SSCL
2550 BECKLEYMEADE
MS 9000
DALLAS, TX 75237
PHONE: 214-708-4214

MAHONEY, KELLY L.
CEBAF
12000 JEFFERSON AVE
NEWPORT NEWS, VA 23606
PHONE: 804-249-7024

MAIN, WILLIAM T.
SUPER COLLIDER LABS
2550 BECKLEYMEADE AVE
MS-1043
DALLAS, TX 75237
PHONE: 214-708-4315

MAKI, AKI
JPS/KEK
1800 K ST. N.W. #920
WASHINGTON, DC 20000
PHONE: 202-659-8190

MAKO, FREDERICK M.
PRESIDENT
F M TECHNOLOGIES, INC.
10529-B BRADDOCK RD
FAIRFAX, VA 22032
PHONE: 703-425-5111

MALENFANT, JEROME R.
PHYSICAL REVIEW LETTERS
1 RESEARCH RD.
BOX 1000
RIDGE, NY 119612701
PHONE: 516-924-5533

MALITSKY, NIKOLAY D.
SSC LABORATORY
2550 BECKLEYMEADE AVE
MS 4011
DALLAS, TX 75237
PHONE: 214-708-3805

MAMMOSSER, JOHN
CEBAF
12000 JEFFERSON AVE
NEWPORT NEWS, VA 23606
PHONE: 804-249-7267

MANE, VIBHA
BROOKHAVEN NATIONAL LABORATORY
BLDG 1005S
UPTON, NY 11973
PHONE: 516-282-3077

MANINI, PAOLO
SAES GETTERS S.P.A.
VIA GALLARATE 215
MILAN, 20151
ITALY
PHONE: 39-2-30201

MANN, TOM
ARGONNE NATIONAL LABORATORY
9700 S. CASS AVENUE
BLDG. 360
ARGONNE, IL 60439
PHONE: 708-252-9187

MANWARING, WILLIAM A.
INDIANA UNIV. CYCLOTRON FACULTY
2401 SAMPSON LANE
BLOOMINGTON, IN 47405
PHONE: 812-855-5188

MAO, NAIFENG
SSCL
2550 BECKLEYMEADE
MS 9000
DALLAS, TX 75237
PHONE: 214-708-4559

MARA, GERHARD
ELIN
PENZINGERSTR. 76
VIENNA, A-1141
AUSTRIA
PHONE: 43-222-89100

MARIAM, FESSEHA G.
SSCL
2550 BECKLEYMEADE AVE
DALLAS, TX 75237
PHONE: 214-708-4557

MARKS, N.
SERC DARESURY LAB.
LONDON,
ENGLAND

MARKS, STEVE
LAWRENCE BERKELEY LABORATORY
1 CYCLOTRON RD BLDG 46/106
BERKELEY, CA 94720
PHONE: 510-486-5828

MARQUARDT, NIELS
UNIVERSITY OF DORMUND
DELTA, PO BOX 500500
4600 DORTMUND, 50
GERMANY
PHONE: 492-317-555391

MARRINER, JOHN P.
FERMILAB
PO BOX 500, MS 341
BATAVIA, IL 60510
PHONE: 708-840-4820

MARSH, KEN
UCLA DEPT OF ELECT. ENGINEER.
56-125B ENGR IV BUILDING
LOS ANGELES, CA 90024
PHONE: 310-206-2039

MARSHALL, JAMES
CEBAF
12000 JEFFERSON AVE
NEWPORT NEWS, VA 23606
PHONE: 804-249-7492

MARTI, FELIX
CYCLOTRON LAB, NSCL
MICHIGAN STATE UNIVERSITY
E. LANSING, MI 48824
PHONE: 517-353-8726

MARTIN, CHARLES
SALES & MKTG MGR
SPANG POWER CONTROL
PO BOX 457
SANDY LAKE, PA 16145
PHONE: 412-376-7515

MARTIN, EDWARD J.
CEBAF
12000 JEFFERSON AVE
MS TC164
NEWPORT NEWS, VA 23606
PHONE: 804-249-7006

MARTIN, RONALD L.
ACCTEK ASSOCIATES
901 S. KENSINGTON
LA GRANGE, IL 60525
PHONE: 708-252-6786

MARUYAMA, XAVIER
PROFESSOR
NAVAL POST GRADUATE SCHOOL
DEPT OF PHYSICS, CODE PH/MX
MONTEREY, CA 93943
PHONE: 408-656-2431

MARX, JAY N.
LAWRENCE BERKELEY LABORATORY
1 CYCLOTRON RD.
MS 70A-3307
BERKELEY, CA 94720
PHONE: 510-486-5244

MARZIALI, ANDRE
STANFORD UNIV
HENSEN LAB VIA PALOU
STANFORD, CA 94305
PHONE: 415-497-5510

MASCHKE, ALFRED
SSCL
2550 BECKLEYMEADE AVE.
DALLAS, TX 75237
PHONE: 325-708-5662

MASLENNIKOV, IGOR L.
SSCL
2550 BECKLEYMEADE
DALLAS, TX 75237
PHONE: 214-708-3622

MASULLO, MARIA ROSARIA
INFN
MOSTRA D'OLTREMARE PAD.20
NAPOLI, 80125
ITALY
PHONE: 398-172-53330

MATARRESE, ERIC ANDREA
THELMA S.R.L.
VIA ERMANNOWOLF FERRARI 15.
MILANO, 20141
ITALY
PHONE: 740-974-057400733

MATARRESE, GIOVANNI R.
MARTHA S.R.L. IMPIANTI
VIA ERMANNOWOLF FERRARI 15
MILANO, 20141
ITALY
PHONE: 025-740-9740

MATARRESE, ITALO KURT
MARTHA S.R.L. IMPIANTI
VIA ERMANNOWOLF FERRARI 15
MILANO, 20141
ITALY
PHONE: 025-740-9740

MATARRESE, SILVIO KURT
THELMA S.R.L.
VIA ERMANNOWOLF FERRARI 15
MILANO, 20141
ITALY
PHONE: 740-974-057400733

MATHEWSON, ALASTAIR C.
CERN A.T. DIVISION
CH 1211 GENEVA,
SWITZERLAND
PHONE: 412-276-75100

MATHIESON, DEREK
SUPER COLLIDER LABS
2550 BECKLEYMEADE AVE
DALLAS, TX 75237
PHONE: - -

MATTHEWS, BILL
UNIVERSITY OF MARYLAND
LABORATORY FOR PLASMA RES
COLLEGE PARK, MD 20742
PHONE: 410-405-5010

MAURY, STEPHAN
CERN
CH-1211 GENEVA, 23
SWITZERLAND
PHONE: -767-2635

MAZARAKIS, MICHAEL G.
SANDIA NATIONAL LABORATORIES
INTENSE BEAM RESEARCH DPT 1231
PO BOX 5800
ALBUQUERQUE, NM 87185
PHONE: 505-845-7138

MC CORMICK, DOUGLAS J.
STANFORD LINEAR ACCELERATOR
2575 SANDHILL RD.
BIN 66
MENLO PARK, CA 94025
PHONE: 415-926-2420

MC DOWELL, WILLIAM F.
ARGONNE NATIONAL LABORATORY
9700 S. CASS AVENUE
BLDG. 362
ARGONNE, IL 60439
PHONE: 708-252-6975

MC GILL, JOHN A.
SSC LABORATORY
MS 9000 Z.550 BECKLEYMEADE AVE
DALLAS, TX 75237
PHONE: 214-708-4560

MC GINNIS, KIMMIE "MAC" F.
ALLIED SIGNAL AEROSPACE CO.
PO BOX 419159
MC 2B35
KANSAS CITY, MO 64141
PHONE: 816-997-2101

MC INTURFF, ALBERT D.
SSC LABORATORY
2550 BECKLEYMEADE AVE.
SUITE 125
DALLAS, TX 75237
PHONE: 214-708-3468

MC INTYRE, PETER M.
TEXAS A & M UNIVERSITY
DEPT OF PHYSICS
TEXAS A & M UNIVERSITY
COLLEGE STATION, TX 77843-4242
PHONE: 408-845-7727

MC MAHAN, PEGGY
LBL
MS-88 1 CYCLOTRON RD.
BERKELEY, CA 94720
PHONE: 510-486-5980

MC NERNEY, ANDREW J.
BROOKHAVEN NATIONAL LAB.
BUILDING 911B
AGS DEPT.
UPTON, NY 11973
PHONE: 516-282-7693

MCALLISTER, BRIAN
MIT RATES LINAC
PO BOX 846
MIDDLETON, MA 01949
PHONE: 617-243-6800

MCCLAIN, WILLIAM L.
MEDI & PHYSICS INC.
900 DURHAM AVE.
S. PLAINFIELD, NJ 07080
PHONE: 908-757-0500

MCCUNE, EARL
VARIAN ASSOCIATES
811 HANSEN WAY
M/S B-118
PALO ALTO, CA 94304-1831
PHONE: 415-424-6332

MCMICHAEL, GERRY E.
CHALK RIVER LABORATORY
ABCL RESEARCH
CHALK RIVER, ON K0J-1J0
CANADA
PHONE: 613-584-3311

MEALS, P.J.
CEBAF
12000 JEFFERSON AVE
NEWPORT NEWS, VA 23606
PHONE: - -

MEDDAHL, MALIKA M.
LBL
LAWRENCE BERKELEY LABORATORY
1 CYCLOTRON ROAD MS71H
BERKELEY, CA 94720
PHONE: 510-486-5619

MEINKE, RAINER
SSCL
2550 BECKLEYMEADE AVE.
MS-1040
DALLAS, TX 75237
PHONE: 214-708-5506

MELIN, GERARD M.
CEA-CENG
DRPMC/PSI
SSX
GRENOBLE, 38041
FRANCE
PHONE: 33-768-84459

MELLOTT, ROBERT H.
KNIGHT ADV TECH FACILITIES GRP
549 W RANDOLPH ST
CHICAGO, IL 60661
PHONE: 312-346-2300

MENG, WUZHENG
BROOKHAVEN NATIONAL LAB
BLDG. 911B
UPTON, NY 11973
PHONE: 516-282-2121

MENOWN, HUGH
HEV
106 WATERHOUSE LANE
CHELMSFORD
ESSEX, CM12QU
ENGLAND
PHONE: 442-454-93493

MERMINGA, LIA
CEBAF
12000 JEFFERSON AVE.
NEWPORT NEWS, VA 23606
PHONE: 804-249-6281

MESTHA, L. K.
SSC LABORATORY
2550 BECKLEYMEADE AVE
DALLAS, TX 75104
PHONE: 214-708-3478

METZLER, JOHN E.
US DEPT OF ENERGY
1000 INDEPENDENCE AVE SW
ER-9111
WASHINGTON, DC 20585
PHONE: 202-586-7172

MEUTH, HERMANN
RESEARCH CENTER, JULICH, IKP
PO BOX 1913
D-5170 JUELICH,
GERMANY
PHONE: 492-461-614739

MEYER, DAVID
SSCL
2550 BECKLEYMEADE AVE
MS 4005
DALLAS, TX 75237
PHONE: 214-708-5614

MICHINE, ANDREI V.
SCHONBERG RADIATION CORP.
SANTA CLARA, CA 95054
PHONE: 408-980-9729

MIDDELKOOP, WILLEM C.
CERN
PE DIVISION
CH-1211 GENEVA, 23
SWITZERLAND
PHONE: 227-672-488

MIERTUSOVA, JANKA
SINCROTRONE TRIESTE S.P.A.
PADRICIANO 99
TRIESTE, 34012
ITALY
PHONE: 40-375-8 552

MILAM, JAMES K.
CTI, INC.
810 INNOVATION DR
KNOXVILLE, TN 37932
PHONE: 615-966-7539

MILLER, ROGER H.
SLAC MS26
P.O. BOX 4349
STANFORD, CA 94309
PHONE: 415-926-4457

MILLS, FRED
ARGONNE NATIONAL LABORATORY
9700 S. CASS AVE.
ARGONNE, IL 60439
PHONE: 708-252-6057

MILLS, MARK R.
SSCL
2550 BECKLEYMEADE AVE
MS 4005
DALLAS, TX 75237
PHONE: 214-708-3413

MINISTRINI, MARINA
INFN
FRASCATI ROME, 00044
ITALY
PHONE: 396-940-3336

MINTY, MICHIO
STANFORD LINEAR ACCELERATOR
MS26
P.O. BOX 4349
MENLO PARK, CA 94025
PHONE: 415-926-3690

MISHRA, C. SHEKHAR
FERMILAB
PO BOX 500, MS 323
BATAVIA, IL 60510
PHONE: 708-840-4094

MITCHEL, GARRY R.
AECL RESEARCH
TASCC STR. 49A
CHALK RIVER, ON K0S-1J0
CANADA
PHONE: 613-584-3311

MITRA, AMIYA K.
TRIUMF
4004 WESBROOK MALL
VANCOUVER, BC V6T-2A3
CANADA
PHONE: 604-222-1047

MIURA, ATSUSHI
GRADUATE UNIV FOR ADVANCED STD
1-1 OHO
TSUBUKA
IBARAKI, 305
JAPAN
PHONE: 029-864-1171

MIURA, IWAO
OSAKA UNIVERSITY
RES CENTER FOR NUCLEAR PHYSICS
10-1 MIHOGAOKA
OSAKA, IBORAKI, 567
JAPAN
PHONE: 068-775-111

MOATS, ANNE R.
SANDIA NATIONAL LABORATORIES
DEPT 1271, PO BOX 5800
ALBUQUERQUE, NM 87185
PHONE: 505-845-7293

MOBLEY, RICHARD M
40 UPPER RIVER RD
IPSWICH, MA 01938
PHONE: 508-356-4349

MODEER, YONAS HARALD
SCANDITRONIX AB
HUSBYBURG
UPPSALA, 75229
SWEDEN
PHONE: 461-818-0788

MOFFAT, DAVID L.
CORNELL UNIVERSITY
NEWMAN LAB
ITHACA, NY 14850
PHONE: 607-272-4951

MOKHTARANI, ABKAR
FERMI NATIONAL ACCELERATOR LAB
PO BOX 500 MS 316
BATAVIA, IL 60510
PHONE: 708-840-4200

MOLLER, SOREN P.
ISA, ARHUS UNIVERSITY
DK-8000 ARHUS C,
DENMARK
PHONE: 861-288-99

MONDELLI, ALFRED A.
SAIC
1710 GOODRIDGE DR.
MC LEAN, VA 22102
PHONE: 703-734-4066

MONTH, MELVIN
BROOKHAVEN NATIONAL LAB.
BLDG. 902
UPTON, NY 11973
PHONE: 516-282-7156

MONTJAR, BONNIE D.
CEBAF
MS-85A
12000 JEFFERSON AVE.
NEWPORT NEWS, VA 23606
PHONE: 804-249-7059

MORCOMBE, PETER H.
DUKE UNIVERSITY FEL LAB.
BOX 90319
DURHAM, NC 27708-0319
PHONE: 919-660-2661

MORGAN, DANIEL
NATIONAL RESEARCH COUNCIL
BOARD OF PHYSICS & ASTRONOMY
2101 CONSTITUTION AVE
WASHINGTON, DC 20418

MORI, WARREN
UCLA DEPT OF ELECT. ENGINEER.
56-125B ENGR IV BUILDING
LOS ANGELES, CA 90024
PHONE: 310-206-2039

MORI, YOSHIHARU
NLHEP
NATL LAB/HIGH ENERGY PHY KEK
ACC.DEPT, 1-1, OHO, TSUKUBA-SHI
IBARAKI-KEN, 305
JAPAN
PHONE: 812-946-41171

MORIN, JR., DORIS C.
622 JACOBSON AVE
MADISON, WI 53714
PHONE: 608-241-2322

MORRIS, WILLIAM A.
SERC
RUTHERFORD APPLETON LAB.
CHILTON
DIDCOT, OX11PQX
UNITED KINGDOM
PHONE: 023-582-1900

MORTAZAVI, PAYMAN
BROOKHAVEN NATIONAL LAB.
725 C NSLS
UPTON, NY 11973
PHONE: 516-282-4743

MOUAT, MICHAEL M.
TRIUMF
4004 WESBROOK MALL
VANCOUVER, BC V6T-2A3
CANADA
PHONE: 604-222-1047

MULLER, DIETER
GSI

MULLER, HENRY J.
CORNELL UNIVERSITY
NEWMAN LAB
ITHACA, NY 14853
PHONE: 607-255-4702

MURAKAMI, TAKERUHI
NAT'L INST OF RADIOLOGICAL SCI
4-9-1 ANAGAWA INAGAKU
CHIBA, 263
JAPAN
PHONE: 43-256-0122

MURROY, JOHN J.
SUNY AT STONY BROOK
ELECTRICAL ENGRG DEPT
STONY BROOK, NY 11794-2350
PHONE: 516-632-8413

MYERS, STEPHEN
CERN
SL DIVISION
CH1211 GENEVA, 23
SWITZERLAND
PHONE: 022-767-3406

MYNK, JOSEPH C.
SSCL/URA
2550 BECKLEYMEADE AVE
MS: 4010
DALLAS, TX 75237-3997
PHONE: 214-708-3780

NADAL, HELIOS
CERCA
1544 STICKNEY PT RD
SARASOTA, FL 34232
PHONE: 813-921-4288

NADJIL, AMOR
LURE-CNRS
BAT 209A
CENTRE UNIV PARIS-SUD
91405 ORSAY, CEDEX
FRANCE
PHONE: 644-682-46

NAGAITSEV, SERGHEI
IUCF
2401 MILO B SAMSON LANE
BLOOMINGTON, IN 47405
PHONE: 812-855-2919

NAGCHAUDHURI, ABHIJIT
DUKE UNIVERSITY
FEL, LASAELLE ST
DURHAM, NC 27708-0319
PHONE: 919-660-2647

NAKAMURA, KIYOTADA
UNIV OF SOUTH CALIFORNIA
C/O USHIO AMERICA, INC
20101 S VERMONT AVE
TORRANCE, CA 90502
PHONE: 310-539-7951

NAMKUNG, WON
POHANG ACCELERATOR LABORATORY
PO BOX 125, POSTECH
POHANG, 790 600
KOREA

NANTISTA, CHRISTOPHER
UCLA/SLAC
BIN 26, SLAC
PO BOX 4349
STANFORD, CA 94039
PHONE: 415-926-2302

NAPOLY, OLIVIER
CEA/SACLE
DAPNIA/SEA
91191 GIF-SUR-YVETTE
GIF/YVETTE, 91191
FRANCE
PHONE: 331-690-88452

NATION, JOHN A.
CORNELL UNIVERSITY
HVL 909 MITCHELL STREET
ITHACA, NY 14850
PHONE: 607-255-3552

NAWROCKI, GREGORY J.
ARGONNE NATIONAL LAB.
BLDG. 362
9700 S. CASS AVE.
ARGONNE, IL 60439
PHONE: 708-252-5891

NAWROCKY, ROMAN J.
BROOKHAVEN NATIONAL LABORATORY
BLDG 725B
UPTON, NY 11973
PHONE: 516-282-4449

NEIL, GEORGE R.
CEBAF
12000 JEFFERSON AVE
MS 12A
NEWPORT NEWS, VA 23606
PHONE: 804-249-7443

NEUFFER, DAVID V.
CEBAF
12000 JEFFERSON AVE
NEWPORT NEWS, VA 23606
PHONE: 804-249-2673

NEWBERGER, BARRY
SSCL
2550 BECKLEYMEADE AVE
MS 4001
DALLAS, TX 75237-3946
PHONE: 512-471-8865

NEWBERGER, BARRY S.
UNIV OF TEXAS-AUSTIN
IFS, RLM 11218, UT-AUSTIN
AUSTIN, TX 78712-1060
PHONE: 512-471-3726

NEWLAND, DELIA
SSC LABORATORY
12000 JEFFERSON AVE
NEWPORT NEWS, VA 23606
PHONE: - -

NEWTON, MARK A.
LAWRENCE LIVERMORE NATL LAB
PO BOX 5508, L-440
LIVERMORE, CA 94550
PHONE: 510-422-1861

NG, KING Y.
FERMILAB
PO BOX 500, MS 345
BATAVIA, IL 60510
PHONE: 708-840-4597

NGUYEN-TUONG, VIET
SURA/CEBAF
12000 JEFFERSON AVE. MS-58B
NEWPORT NEWS, VA 23606
PHONE: 804-249-2673

NICHOLLS, GILBERT L.
ARGONNE NATIONAL LABORATORY
EP BUILDING 207
9700 S. CASS AVE.
ARGONNE, IL 60439
PHONE: 708-252-4956

NECOL, THOMAS E.
FERMI NATIONAL ACCELERATOR LAB
PO BOX 500,
MS 316
BATAVIA, IL 60510
PHONE: 708-840-3441

NINAN, LUKOSE S.
CEBAF
MS 85A
12000 JEFFERSON AVE
NEWPORT NEWS, VA 23606
PHONE: 804-249-6283

NISHIMURA, HIROSHI
LAWRENCE BERKELEY LABORATORY
1 CYCLOTRON RD, BLDG 80-101
BERKELEY, CA 94720
PHONE: 510-486-5763

NOLEN, JERRY A.
ARGONNE NATIONAL LAB
9700 S CASS AVE
ARGONNE, IL 60439
PHONE: . .

NOLKER, KAREN S.
CEBAF
MS 85 A
12000 JEFFERSON AVE
NEWPORT NEWS, VA 23606
PHONE: 804-249-7594

NOOMEN, JACOB
NIKHEF
PO BOX 41882
1009DB AMSTERDAM,
NETHERLANDS
PHONE: 020-592-2097

NORDBY, MARTIN E.
STANFORD LINEAR ACCELERATOR
MS 21, P.O. BOX 4349
STANFORD, CA 94309
PHONE: 415-926-3415

NOREM, JAMES H.
ARGONNE NATIONAL LAB
9700 S CASS AVE
BLDG 362/HEP
ARGONNE, IL 60439
PHONE: 708-252-6548

NOSOVCHIKOV, YURI M.
SSCL
MS 4011 2550 BECKLEYMEADE AVE.
DALLAS, TX 75237
PHONE: 214-708-3847

NUSINOVICH, GREGORY S.
UNIVERSITY OF MARYLAND
LPR, UNIVERSITY OF MARYLAND
COLLEGE PARK, MD 20742
PHONE: 301-405-4917

O'CONNELL, JAMES S.
BAH
1725 JEFFERSON DAVIS HWY
ARLINGTON, VA 22202
PHONE: 703-412-7416

O'DAY, STEPHEN C.
FERMILAB
PO BOX 500
MS 341
BATAVIA, IL 60510
PHONE: 708-840-4827

O'SHEA, PATRICK
LOS ALAMOS NATIONAL LAB
MS H825
LOS ALAMOS, NM 87545
PHONE: 505-667-1956

OCHSNEV, JAMES P.
DUPONT
P30-2172, BAVLEY MILL PLAZA
WILMINGTON, DE 19880-0030
PHONE: 302-992-5388

ODERA, MASATO-HI
SUMITOMO HEAVY INDUSTRIES LTD.
2-5-15, YUTENJI, MEGUROKU
TOKYO, 153
JAPAN
PHONE: 033-713-1504

OEFITGER, UWE
DIPLOMAR PHYSICIST
CERN
1211 GENEVA, 23
SWITZERLAND

OGATA, ATSUSHI
KEK
OHO 1-1
TSUKUBA
IBARAKI, 305
JAPAN
PHONE: 298-645-255

OGAWA, YUJIRO
KEK
NATL LAB FOR HIGH ENERGY PHY
TSUKUBA
IBARAKI, 305
JAPAN
PHONE: 298-641-5691

OH, SAEWOONG
POSTECH
PO BOX 125
POHANG, 790600
KOREA
PHONE: 562-792-064

OHSAWA, SATOSHI
KEK
NATL LAB FOR HIGH ENERGY PHY
OHO 1-1, TSUKUBA-SHI
IBARAKI, 305
JAPAN
PHONE: 298-641-5692

OKAMOTO, HIROMI
UNIVERSITY OF MARYLAND
ACCELERATOR LAB, INST CHEM RES
GOKANOSHO, UJI
KYOTO, 611
JAPAN
PHONE: 301-405-6057

OKU, YASUNARI
KAWASAKI HEAVY INDUSTRIES, LTD
1-16-10 AMAKUBO
TUKUBA
IBARAKI, 305
JAPAN
PHONE: 812-985-28004

OLIVIER, MICHEL M.
C.E.A.
DSH/DIR
CE SACLAY
91191 GIF/YVETTE,
FRANCE
PHONE: 331-690-89231

OLSEN, DAVID
OSNL
OAK RIDGE, TN 37830
PHONE: 615-574-6122

OLSEN, ROLF
BROOKHAVEN NATIONAL LAB.
NELS BLDG. 725 C
UPTON, NY 11973
PHONE: 516-282-7335

ONESHENKO, LEONID M.
JOINT INST FOR NUCLEAR RES
MOSCOW REGION
141980 DUBNA,
RUSSIA
PHONE: 095-926-2251

OOTHOUDT, MICHAEL A.
LOS ALAMOS NATIONAL LAB.
PO BOX 1663 MS H812
LOS ALAMOS, NM 87545
PHONE: 505-667-4354

OREN, WILL
CEBAF
12000 JEFFERSON AVE
NEWPORT NEWS, VA 23606
PHONE: 804-249-7344

ORLOV, YURI F.
CORNELL UNIVERSITY
167 BESEMER HILL RD
ITHACA, NY 14850
PHONE: 607-273-3550

OTTER, ALAN J.
TRIUMF
4004 WESBROOK MALL
VANCOUVER, BC V6T-2A3
CANADA
PHONE: 604-222-1047

OYAMADA, MASAYUKI
LAB OF NUCL SCI, TOHOKU UNIV
1-2-1 MIKAMINE, TAIHAKU-KU
SENDAI, 982
JAPAN
PHONE: 81-22-245 2151

PADAMSEE, HASAN S.
CORNELL UNIVERSITY
NEWMAN LAB
ITHACA, NY 14850
PHONE: 607-272-4951

PALKOVIC, JOHN A.
URA/SSCL
2550 BECKLEYMEADE AVE
MS 9000
DALLAS, TX 75237
PHONE: 214-938-0003

PANG, PING
DUKE UNIVERSITY
5 CHURCHWELL CT
DURHAM, NC 27713
PHONE: 919-660-2669

PANG, YAOCHI
TEXAS A & M UNIVERSITY
DEPT. OF PHYSICS
TEXAS A & M UNIVERSITY
COLLEGE STATION, TX 77843-4242
PHONE: 409-845-5490

PANTAZIS, RICARDO D.
FREE ELECTRON LASER LAB-DUKE
PO BOX 0319
DURHAM, NC 27708-0319
PHONE: 919-660-2648

PAPASH, ALEXANDER I.
INSTITUTE FOR NUCLEAR RES.
252028 PR NAUKI, 47
INR OF UKR ACADEMY
KIEV,
UKRAINE
PHONE: 044-265-1465

PAPPAS, CHRIS
URA/SSC
2550 BECKLEYMEADE AVE
MS 4004
DALLAS, TX 75237
PHONE: 214-708-3334

PARDO, RICHARD C.
ARGONNE NATIONAL LAB
BLDG 203, ROOM F-153
ARGONNE, IL 60439
PHONE: 708-252-4029

PARK, GUN-SIK
NAVAL RESEARCH LAB
4555 OVERLOOK AVE SW
WASHINGTON, DC 20375
PHONE: 202-767-3936

PARK, SANGHYUN
FORP
UCLA
DEPT OF PHYSICS
LOS ANGELES, CA 90024-1547
PHONE: 310-206-4540

PARKER, BRETT L.
SSCL
2550 BECKLEYMEADE AVE
MS-1040
DALLAS, TX 75237
PHONE: 214-708-5501

PARKHOMCHUK, VASILY V.
SSCL
2550 BECKLEYMEADE AVE, S 500
DALLAS, TX 75237
PHONE: 214-708-3867

PARRY, RICHARD R.
SSCL
2550 BECKLEYMEADE
DALLAS, TX 75237
PHONE: 214-708-3867

PARSA, ZOHREH
BROOKHAVEN NATIONAL LAB
BLDG 901A
PHYSICS DEPT
UPTON, NY 11973
PHONE: 516-282-2085

PASOTTI, CRISTINA
SINCROTRONE TRIESTE
PADRICIANO 99
TRIESTE, 34012
ITALY
PHONE: 40-375-8 576

PASOUR, JOHN A.
MISSION RESEARCH CORPORATION
8560 CINDERBED RD
NEWINGTON, VA 22122
PHONE: 703-339-6500

PASQUINELLI, RALPH J.
FERMILAB
PO BOX 388
MS 341
BATAVIA, IL 60530
PHONE: 708-840-4734

PATERSON, J. ALAN
LAWRENCE BERKELEY LABORATORY
1 CYCLOTRON RD BLDG 46/161
BERKELEY, CA 94720
PHONE: 510-486-4198

PATERSON, JAMES M.
STANFORD LINEAR ACCELERATOR
P.O. BOX 4349 MS 24
STANFORD, CA 94309
PHONE: 415-926-2943

PAUL, MARILYN
FERMILAB

PAULSON, CARL C.
GRUMMAN CORPORATION
4 INDEPENDENCE WAY
PRINCETON, NJ 08540-6620
PHONE: 609-520-1802

PAULUHN, ANUSCHKA
DESY, HAMBURG
NOTKESTR 85
2000 HAMBURG, 52
GERMANY
PHONE: 040-899-82756

PAYNE, ANTHONY N.
LLNL
PO BOX 5508, L-440
LIVERMORE, CA 94550
PHONE: 510-423-0641

PAYNE, JOHN
URA/SSC
2550 BECKLEYMEADE AVE
MS 4004
DALLAS, TX 75237
PHONE: 214-708-3252

PEGGS, STEPHEN G.
BROOKHAVEN NATIONAL LAB.
BLDG. 1005S
UPTON, NY 11973
PHONE: 516-282-3104

PEI, ALEX
BROOKHAVEN NATIONAL LAB
BUILDING 911A
UPTON, NY 11973
PHONE: 516-282-7396

PEI, YUANJI
NSRL
NATIONAL SYNCHROTRON RADIATION
UNIV. OF SCI & TECH. OF CHINA
HEFEI ANHUI, 230029
P.R. CHINA
PHONE: 055-130-2011

PEINIGER, MICHAEL
SIEMENS AG
FRIEDRICH-EBERT-STRASSE
BERG. GLADBACH, 5060
GERMANY
PHONE: 492-204-843676

PELLEGRINI, CLAUDIO
UCLA
405 HILGARD AVE
LOS ANGELES, CA 90024-1547
PHONE: 310-206-1677

PELLEGRINO, LUIGI
INFN
INFN-VIA E. FERMI, 40
FRASCATI (ROMA), 00044
ITALY
PHONE: 011-390-69403510

PENNER, SAMUEL
10500 PINE HAVEN TERRACE
ROCKVILLE, MD 20852
PHONE: 301-468-1210

PEOPLES, JOHN
FERMILAB
PO BOX 500
BATAVIA, IL 60510
PHONE: 708-840-3211

PERELSTEIN, ELKUNO A.
JOINT INST FOR NUCLEAR RES
MOSCOW REGION
141980 DUBNA,
RUSSIA
PHONE: 095-926-2251

PERKINS, CHARLES W.
STANFORD LINEAR ACCELERATOR
2575 SAND HILL ROAD
MS-21
MENLO PARK, CA 94025
PHONE: 415-926-2970

PERRY, JOHN E.
CERAF
12000 JEFFERSON AVE.
NEWPORT NEWS, VA 23606
PHONE: 804-249-7249

PETERS, GERALD J.
US DEPT. OF ENERGY
DIV. OF HIGH ENERGY PHYS
ER224 GTN
WASHINGTON, DC 20585
PHONE: 301-903-5228

PETERSON, IVARS
SCIENCE NEWS
1719 N. ST. NW
WASHINGTON, DC 20036
PHONE: 202-785-2253

PETILLO, JOHN J.
SAIC
1710 GOODRIDGE DR.
MC LEAN, VA 22102
PHONE: 703-556-7146

PETIT-JEAN GENAZ, CHRISTINE
CERN
12000 JEFFERSON AVE
NEWPORT NEWS, VA 23606
PHONE: - -

PFUTZNER, HAROLD G.
EMR PHOTOELECTRIC
PO BOX 44
PRINCETON, NJ 08542

PHILLIPS, H. L.
CERAF
12000 JEFFERSON AVE.
NEWPORT NEWS, VA 23606
PHONE: 804-249-7607

PHILLIPS, ROBERT M.
SLAC
P.O. BOX 4349 MS 33
STANFORD, CA 94309
PHONE: 415-926-3754

FERNLEY, NAN
SLAC
STANFORD, CA 94309
PHONE: 415-926-2857

FICO, RANDOLPH E.
LAWRENCE LIVERMORE NATL LAB
7800 EAST AVENUE, L-380
LIVERMORE, CA 94550
PHONE: 510-425-6546

PIERCE, WILLIAM B.
SLAC
PO BOX 4349
STANFORD, CA 94305
PHONE: 415-926-2390

BEAUB, FRANCOIS P
MICHIGAN STATE UNIVERSITY

FLACINI, MASSIMO
CERN, SL DIVISION
CERN, SL DIVISION
GENEVA, CH1211
SWITZERLAND
PHONE: 412-276-7668

PLASS, GUNTHER
CERN
CERN-AC
CH 1211 GENEVA,
SWITZERLAND
PHONE: 767-292-067

PLATE, DAVID W.
LAWRENCE BERKELEY LABORATORY
1 CYCLOTRON RD BLDG 46/161
BERKELEY, CA 94720
PHONE: 510-486-7232

PLATT, ROBERT C.
URA/SSCL
2550 BECKLEYMEADE AVE
MS 9000
DALLAS, TX 75237
PHONE: 214-938-0803

FLINK, OLEG
MOSCOW RADIOTECHNICAL INST.
132 WARSZAWSKOE SHOSSE
113519 MOSCOW,
RUSSIA
PHONE: 095-314-0078

FLUM, MICHAEL
LOS ALAMOS NATIONAL LABORATORY
MP-S, MS H338
LOS ALAMOS, NM 87545
PHONE: 505-667-7347

FOERIER, ROGER L.
TRIUMF
4804 WEBBROOK MALL
VANCOUVER, BC V6T-2A3
CANADA
PHONE: 604-222-1047

POLLAK, PETER
DYNAPOWER CORPORATION
PO BOX 9210
S. BURLINGTON, VT 05407
PHONE: 802-880-7200

POLLOCK, DOUGLAS A.
SSCL
2550 BECKLEYMEADE AVE.
DALLAS, TX 75237
PHONE: 214-708-2905

POLLOCK, ROBERT E.
INDIANA UNIVERSITY
SWAIN HALL WEST
BLOOMINGTON, IN 47405
PHONE: 812-855-8306

POOLE, MICHAEL W.
SERC DARESBURY LAB.
DARESBURY
WARRINGTON, WA4 4AD
UNITED KINGDOM
PHONE: 092-560-3256

POPADIUK, JOANNA
PHYSICAL REVIEW E
1 RESEARCH RD.
BOX 1000
RIDGE, NY 11961
PHONE: 516-924-5533

PORTMANN, GREGORY J.
LAWRENCE BERKELEY LABORATORY
1 CYCLOTRON RD
BERKELEY, CA 94720
PHONE: 510-486-5924

POWER, JOHN G.
GRAD STUDENT PHYSICS
ITT
11134 S SPAULDING
CHICAGO, IL 60655
PHONE: 312-791-0307

POWERS, TOM
CEBAF
12000 JEFFERSON AVE.
NEWPORT NEWS, VA 23606
PHONE: 804-249-7660

PRELEC, KRSTO
BROOKHAVEN NATIONAL LAB.
AGS DEPARTMENT BLDG. 911B
UPTON, NY 11973
PHONE: 516-282-4777

PRICE, EDWIN J.
CEBAF
12000 JEFFERSON AVE
NEWPORT NEWS, VA 23602
PHONE: 804-249-6249

PROCH, DIETER
DESY
NOTKESTR 85
2000 HAMBURG, 52
GERMANY
PHONE: 494-089-944302

PROME, MICHEL A.
FRENCH ATOMIC ENERGY COMM.
DSM-CE SACLAY
GIF/YVETTE, 91191
FRANCE
PHONE: 331-690-87308

PROPP, ALAN D.
SSCL
2550 BECKLEYMEADE, MS 4008
DALLAS, TX 75237
PHONE: 214-708-3930

PRUSS, STANLEY M.
FERMILAB
PO BOX 500, MS 34L
BATAVIA, IL 60510
PHONE: 708-840-4427

QIAN, QIAN
PRINCETON UNIVERSITY
FTL PO BOX 451
PRINCETON, NJ 08540
PHONE: 609-343-3782

QINGHAI, ZHANG
CHINA INST OF ATOMIC ENERGY
PO BOX 275 17
BEIJING, 102413
P.R. CHINA
PHONE: 861-925-7244

QUARRIE, AVELL
CEBAF
12000 JEFFERSON AVE
NEWPORT NEWS, VA 23606
PHONE: - -

RABER, DOUG
NATIONAL RESEARCH COUNCIL
BOARD OF PHYSICS & ASTRONOMY
2101 CONSTITUTION AVE
WASHINGTON, DC 20418

RAJAGOPALAN, S.
UCLA
MS 26 SLAC FB 4349
STANFORD, CA 94309
PHONE: 415-926-2146

RAKOWSKY, GEORGE
ROCKWELL/ROCKETDYNE
683 WILDCREEK DR
THOUSAND OAKS, CA 91380
PHONE: 805-492-8619

RAMAMOORTHY, SUNEIL
BROOKHAVEN NATIONAL LABORATORY
BLDG 725B
NATL SYNCHROTRON LIGHT SOURCE
UPTON, NY 11973
PHONE: 516-282-2192

RANGANATHAN, RAJ P.
SSC LABS
MS 4006, SSC LABS
2530 BECKLEYMEADE AVE.
DALLAS, TX 75237
PHONE: 214-708-3642

RAPARIA, DEEPAK
SSCL
MS #1043
2530 BECKLEYMEADE AVE.
DALLAS, TX 75237
PHONE: 214-708-4310

RAUBENHEIMER, TOR O.
SLAC
P.O. BOX 4349
STANFORD, CA 94309
PHONE: 415-926-2474

REARDON, PAUL J.
SSC LABORATORY
2530 BECKLEYMEADE AVE.
DALLAS, TX 75237
PHONE: 214-708-3012

REECE, CHARLES
CEBAF
12000 JEFFERSON AVE.
NEWPORT NEWS, VA 23606
PHONE: 804-249-7645

REECE, R. KENNETH
BROOKHAVEN NATIONAL LAB.
AGS DEPT. - BLDG 911C
UPTON, NY 11973
PHONE: 516-282-4767

REES, DANIEL E.
LOS ALAMOS NATIONAL LABORATORY
PO BOX 1663
MS: H827
LOS ALAMOS, NM 87545
PHONE: 505-665-2802

REES, GRAHAME H.
SERC
RUTHERFORD APPLETON LAB.
CHILTON DIDCOT
OXON, OX110QX
UNITED KINGDOM
PHONE: 442-358-21900

REES, JOHN R.
SSCL
2530 BECKLEYMEADE AVE
DALLAS, TX 75237-3997

REEVES, STANLEY
ARGONNE NATIONAL LAB
9700 S CASS AVE
ARGONNE, IL 60439
PHONE: 708-252-6790

REGAN, AMY H.
LOS ALAMOS NATIONAL LABORATORY
PO BOX 1663
MS: H827
LOS ALAMOS, NM 87545
PHONE: 505-665-0658

REGINATO, LOUIS L.
LAWRENCE BERKELEY LABORATORY
1 CYCLOTRON RD, MS 47-112
BERKELEY, CA 94720
PHONE: 510-486-5352

REHAK, MARGARETTA
BROOKHAVEN NATIONAL LABORATORY
BLDG. 902
UPTON, NY 11973
PHONE: 516-282-4708

REICHERT, CRAIG R.
N.W.L. TRANSFORMERS
PO BOX 358
BORDENTOWN, NJ 08805
PHONE: 609-296-7300

REID, DON
LOS ALAMOS NATIONAL LABORATORY
P.O. BOX 1663, MS H827
LOS ALAMOS, NM 87545
PHONE: 505-667-3927

REIMUND, JAMES A.
SSC LABORATORY
2530 BECKLEYMEADE AVE.
DALLAS, TX 75237
PHONE: 214-708-3311

REINIGER, KLAUS
TRIUMF
4004 WESBROOK MALL
VANCOUVER, BC V6T-2A3
CANADA
PHONE: 604-222-1047

REHER, MARTIN P.
UNIVERSITY OF MARYLAND
LABORATORY FOR PLASMA RESEARCH
COLLEGE PARK, MD 20742
PHONE: 301-753-3946

REHSTAD, DAG
THE SVEDBERG LAB
BOX 533
75121 UPPSALA,
SWEDEN
PHONE: 018-183-177

REUSCH, MICHAEL F.
STAFF SCIENTIST
GRUMMAN CORPORATE RESEARCH
4 INDEPENDENCE WAY
PRINCETON, NJ 08540
PHONE: 609-520-1804

RHEE, MOON-JHONG
PROFESSOR
UNIVERSITY OF MARYLAND
ELECTRICAL ENGINEERING DEPT
COLLEGE PARK, MD 20742
PHONE: 301-405-1239

RICE, DAVID
CORNELL UNIVERSITY
WILSON LAB
ITHACA, NY 14853
PHONE: 607-255-8786

RICHARDSON, REX
SSCL
2550 BECKLEYMEADE
DALLAS, TX 75237
PHONE: 214-708-5306

RIFKIN, JEFF
SLAC
MS26
P.O. BOX 4349
STANFORD, CA 94309
PHONE: 415-926-2957

RIMMER, ROBERT A.
LAWRENCE BERKELEY LAB.
MS 71-299
1 CYCLOTRON RD
BERKELEY, CA 94720
PHONE: 510-486-6243

RJORDON, JAMES R
UNIVERSITY OF TEXAS
6707 DARBY RD.
LANDOVER HILLS, MD 20784
PHONE: 301-773-4116

RITCHIE, ARTHUR L.
LAWRENCE BERKELEY LABORATORY
1 CYCLOTRON RD, MS 46-125
BERKELEY, CA 94720
PHONE: 510-486-4785

ROBB, ALAN
LAWRENCE BERKELEY LABORATORY
1 CYCLOTRON RD, MS 10-110
BERKELEY, CA 94720
PHONE: 510-486-7321

ROBERSON, CHARLES W.
SCIENTIFIC OFFICER
OFFICE OF NAVAL RESEARCH
800 N QUINCY ST
ARLINGTON, VA 22217
PHONE: 202-696-4222

ROBERTS, THOMAS
TECHNOCO
PO BOX 4723
HUNTSVILLE, AL 35815-4723
PHONE: 205-883-8018

ROBERTSON, SCOTT H.
UNIV OF COLORADO
CAMPUS BOX 391
BOULDER, CO 80309
PHONE: 303-492-6453

ROBIN, DAVID S.
LAWRENCE BERKELEY LABORATORY
1 CYCLOTRON RD.
BERKELEY, CA 94720
PHONE: 510-486-6028

ROBINSON, WILLIAM
SSCL
2550 BECKLEYMEADE AVE.
SUITE 125
DALLAS, TX 75237
PHONE: 214-708-6908

RODGER, ERWIN
BROOKHAVEN LAB
BLDG 911 B
UPTON, NY 11973
PHONE: 516-282-4616

ROGERS, JIMMY D.
SSCL
2550 BECKLEYMEADE AVE
MS-4010
DALLAS, TX 75237-3997
PHONE: 214-708-3701

ROGERS, JOSEPH T.
CORNELL UNIVERSITY
232 NEWMAN LAB
ITHACA, NY 14850
PHONE: 607-255-4093

ROPERT, ANNICK
ACCELERATOR PHYSICIST
ESRF
BP 220
38043 GRENOBLE,
FRANCE
PHONE: 337-688-2038

ROSE, JAMES T.
BROOKHAVEN NATIONAL LAB
BLDG. 1005S
UPTON, NY 11973
PHONE: 516-282-7079

ROSENZWEIG, JAMES B
UCLA DEPT. OF PHYSICS
405 HILGARD AVE
LOS ANGELES, CA 90024
PHONE: 310-206-4541

ROSER, THOMAS
BNL
BLDG 91113
UPTON, NY 11973
PHONE: 516-282-7084

ROSS, MARC
SLAC
P.O. BOX 4349
L RD
STANFORD, CA 94043
PHONE: 415-926-3526

BORRA, EDOUARD
CERN/SL DIVISION
1211 GENEVA, 23
SWITZERLAND
PHONE: 412-876-7483

BOSSMANITH, ROBERT
CEBAF
12000 JEFFERSON AVE
NEWPORT NEWS, VA 23606
PHONE: 804-249-7621

BOSTAMZADEN, CYRUS
URA/SSC
2550 BECKLEYMEADE AVE
MS 4004
DALLAS, TX 75237
PHONE: 214-708-3382

BOTHMAN, JEFFREY L.
BNL/NSLS
BLDG 725A
UPTON, NY 11973
PHONE: 516-282-4914

BOUX, DANIEL
ESRF
BP 220
38043 GRENOBLE, CEDEX
FRANCE
PHONE: 337-688-2053

BOWE, EDNOR M.
SRC UNIVERSITY OF WISCONSIN
3731 SCHNEIDER DR.
STOUGHTON, WI 53589
PHONE: 608-877-2163

RUDOLPH, KLAUS
UNIVERSITY OF MUNICH
AM COULOMBWALL 1
GARCHING BAVARIA, 8046
GERMANY
PHONE: 004-989-32094080

RUFER, CHARLES E.
CERN
CH-1211 GENEVA, 23
SWITZERLAND
PHONE: 022-767-2635

RUGGIERO, ALESSANDRO G.
BROOKHAVEN NATIONAL LAB.
BLDG. 1005-S
UPTON, NJ 11973
PHONE: 516-282-4997

RUIZ, EVERARDO D.
SSCL
2550 BECKLEYMEADE AVE.
MS 4010
DALLAS, TX 75237
PHONE: 214-708-3716

RULE, DON W.
NAVAL SURFACE WARFARE CENTER
R36 NSWC 10901 NEW HAMPSHIRE
SILVER SPRING, MD 20903
PHONE: 301-394-2260

RUSSELL, THOMAS J.
ARGONNE NATIONAL LABORATORY
9700 S. CASS AVE
BLDG. 371T
ARGONNE, IL 60439
PHONE: 708-252-7829

RUSSO, DOMENICO
BROOKHAVEN NATIONAL LABORATORY
911A
UPTON, NY 11973
PHONE: 516-282-3412

RUTH, RONALD D.
STANFORD LINEAR ACCELERATOR
MS 26
P O BOX 4349
STANFORD, CA 94309
PHONE: 415-926-3390

RYAN, ANTHONY
BROOKHAVEN NATIONAL LAB
BUILDING 830
UPTON, NY 11973
PHONE: 516-282-3329

RYBAKOV, E.
EFREMOV INSTITUTE
METALLOSTROY
P.O. BOX 42
189631 ST. PETERSBUR, G
RUSSIA

RYBARCYK, LAWRENCE J.
LOS ALAMOS NATIONAL LAB
PO BOX 1663, MS-HB12
LOS ALAMOS, NM 87545
PHONE: 505-665-6697

RYNE, ROBERT
LANL
MAIL STOP H225
LOS ALAMOS, NM 87545
PHONE: 505-667-8111

SAAB, ALFREDO
STANFORD LINEAR ACCELERATOR
2575 SAND HILL RD, MS 49
MENLO PARK, CA 94025
PHONE: 415-926-3096

SAADATMAND, KOUROSH
SSCL
MS #1043
2550 BECKLEYMEADE AVE.
DALLAS, TX 75237
PHONE: 214-708-4311

SACCHI, GINA
IEEE

SACHTSCHALE, RICHARD J.
DUKE UNIVERSITY-FEL
BOX 90319
DURHAM, NC 27708-0319
PHONE: 919-660-2655

SAFRANEK, J.
BROOKHAVEN NATIONAL LABORATORY
BLDG 725C
NATL SYNCHROTRON LIGHT SOURCE
UPTON, NY 11973
PHONE: 516-282-7188

SAGALOVSKY, LEONID
ARGONNE NATIONAL LAB
EP 207
9700 S. CASS AVE.
ARGONNE, IL 60439
PHONE: 708-252-4305

SAGAN, DAVID
CORNELL UNIVERSITY
WILSON LAB
ITHACA, NY 14853
PHONE: 607-255-8062

SAKAMOTO, SUMIO
IBM
MECHATRONICS DEVELOPMENT CTR.
1-15 TOYOSU 3-CHOME, KOTO-KU
TOKYO, 135
JAPAN
PHONE: 033-534-3998

SALL, KENNETH E.
LAWRENCE LIVERMORE NAT'L LAB
L-41 7000 EAST AVE
LIVERMORE, CA 94550

SALISBURY, NENTON J.
UNIVERSITY OF SOUTH CAROLINA
706 S HOLLY ST.
COLUMBIA, SC 29208
PHONE: 803-777-8483

SAMPSON, WILLIAM
BROOKHAVEN NATIONAL LABORATORY
BLDG. 902
UPTON, NY 11973
PHONE: 516-282-2036

SANDBERG, VERN
LOS ALAMOS NATIONAL LAB
MS H846, MP-9 LANL
LOS ALAMOS, NM 87545
PHONE: 515-667-7268

SANDWEISS, JACK
YALE UNIVERSITY & PHYS. REV. LET
280 WHITNEY AVE.
P.O. BOX 6666
NEW HAVEN, CT 06511
PHONE: 203-432-3338

SANFORD, THOMAS W.L.
SANDIA NATIONAL LABORATORIES
INTENSE BEAM RESEARCH DPT 1231
PO BOX 5800
ALBUQUERQUE, NM 87185
PHONE: 505-845-7816

SARTEPE, SELCUK
SSCL
2550 BECKLEYMEADE
MS 1040
DALLAS, TX 75237
PHONE: 214-708-4588

SARKAR, SURAJIT
SSC LABORATORY
2550 BECKLEYMEADE AVE
MS: 4002
DALLAS, TX 75237
PHONE: 214-708-3439

SATOGATA, TODD
BROOKHAVEN NATIONAL LAB.
BLDG. 1005S
UPTON, NY 11973
PHONE: 516-282-5452

SAX, WERNER A.
STANFORD LINEAR ACCELERATOR
PO BOX 4349, MS 12
MENLO PARK, CA 94025
PHONE: 415-926-3077

SCANDALE, WALTER
CERN
GENEVE 23, CH-1211
SWITZERLAND

SCANLAN, RONALD M.
LBL
LAWRENCE BERKELEY LABORATORY
1 CYCLOTRON RD, MS46-161
BERKELEY, CA 94720
PHONE: 510-486-7241

SCHACHTER, LEVI
CORNELL UNIVERSITY
369 UPSON HALL
ITHACA, NY 14853
PHONE: 607-255-3552

SCHAFER, GEORG
SSC LABORATORY
SSCL, 2550 BECKLEYMEADE AVE.
DALLAS, TX 75237
PHONE: 214-708-3770

SCHAGHINGER, LINDSAY
LAWRENCE BERKELEY LABORATORY
1 CYCLOTRON RD BLDG 80/101
BERKELEY, CA 94720
PHONE: 510-486-5009

SCHAILLEY, RONALD
SSC LAB.
MS 1040
2550 BECKLEYMEADE AVE.
DALLAS, TX 75237
PHONE: 214-708-4565

SCHALLER, STUART C.
LOS ALAMOS NATIONAL LAB
MP-6, MS H852
LOS ALAMOS, NM 87545
PHONE: 505-665-2388

SCHLUTTER, ROSS
LAWRENCE BERKELEY LABORATORY
1 CYCLOTRON RD, BLDG. 46/161
BERKELEY, CA 94720
PHONE: 510-486-6705

SCHMIDT, CHARLES W.
FERMILAB
PO BOX 500, MS 307
BATAVIA, IL 60510
PHONE: 708-840-4414

SCHMIDT, FRANK
CERN
SL DIVISION
GENEVA 23, CH 1211
SWITZERLAND
PHONE: 767-463-5

SCHMOR, PAUL W.
TRIUMF
4004 WESBROOK MALL
VANCOUVER, BC V6T 2A3
CANADA
PHONE: 604-222-1047

SCHNEIDER, LARRY X.
SSC LABORATORY
2550 BECKLEYMEADE AVE.
DALLAS, TX 75237
PHONE: 214-708-3468

SCHNEIDER, WILLIAM J.
CEBAF
12000 JEFFERSON AVE MS 58B
NEWPORT NEWS, VA 23606
PHONE: 804-249-7173

SCHNELL, WOLFGANG
CERN
CH 1211 GENEVA,
SWITZERLAND
PHONE: 767-296-4

SCHORROW, PAUL
ARGONNE NATIONAL LAB
9700 S CASS AVE
ARGONNE, IL 60465
PHONE: 708-252-6280

SCHRAGE, DALE L.
LOS ALAMOS NATIONAL LABORATORY
AT-1, MS H817
LOS ALAMOS, NM 87545
PHONE: 505-667-1953

SCHRIEBER, STAN O.
LOS ALAMOS NATIONAL LAB.
PO BOX 1663, MS H811
LOS ALAMOS, NM 87545
PHONE: 505-667-5634

SCHUERMANN, MICHAEL
UNIVERSITY OF DORTMUND
DORTMUND, 44221
GERMANY
PHONE: 492-317-555380

SCHULTZ, SHELDON
UCSD
PHYSICS 0319
9500 GILMAN DR
LA JOLLA, CA 92093-0319
PHONE: 619-534-4078

SCHWANDT, PETER
IND. UNIV. CYCLOTRON FACILITY
INDIANA UNIV.
CYCLOTRON FACILITY
BLOOMINGTON, IN 47408
PHONE: 812-855-9365

SCHWARZ, HEINZ D.
SLAC
MS 33
P.O. BOX 4349
STANFORD, CA 94309
PHONE: 415-926-2081

SCHWEICKERT, HERMANN
KIK-KARLSRUHE
PO BOX 3640
WARLSRUHE 1, 7500
GERMANY
PHONE: 072-478-22433

SCHWEPPE, ERNST G.
PHILIPS RHW
STRESEMANNALLEE 101
2000 HAMBURG, 54
GERMANY
PHONE: 004-940-56133029

SCHWETTMAN, ALAN H.
STANFORD UNIVERSITY
DEPT OF PHYSICS
STANFORD, CA 94305

SCOTT, RON

SEARS, JAMES O.
CORNELL UNIVERSITY
LNS NEWMAN LAB
ITHACA, NY 14850
PHONE: 607-255-5537

SEBEK, JAMES J.
SSRL/SLAC
PO BOX 4349
STANFORD, CA 94309
PHONE: 415-926-3164

SEEMAN, JOHN T.
STANFORD LINEAR ACCELERATOR
2575 SAND HILL RD, MS 66
MENLO PARK, CA 94309
PHONE: 415-926-3566X4999

SEIDL, PETER
LAWRENCE BERKELEY LABORATORY
1 CYCLOTRON RD, MS 47-112
BERKELEY, CA 94720
PHONE: 510-486-7653

SELLY, WILLIAM C.
ARGONNE NATIONAL LAB
BLDG. 362-ASD
9700 S. CASS AVE.
ARGONNE, IL 60439
PHONE: 708-252-2857

SEN, TANAJI
SSC LABORATORY
2550 BECKLEYMEADE AVE
DALLAS, TX 75237
PHONE: 214-708-4522

SENICHEV, YURIJ V.
SSCL
2550 BECKLEYMEADE AVE
DALLAS, TX 75237
PHONE: 214-708-4305

SENSI, PERRY
IEEE

SERENO, NICHOLAS
UNIV OF ILLINOIS
12000 JEFFERSON AVE
NEWPORT NEWS, VA 23602
PHONE: 804-875-0276

SERVANCEKX, ROGER V.
TRIUMF
BOX 40
GABRIOLA IS., BC V0R-1X0
CANADA
PHONE: 604-247-9567

SESSLER, ANDREW M.
LAWRENCE BERKELEY LABORATORY
1 CYCLOTRON RD, MS B71H
BERKELEY, CA 94720
PHONE: 510-486-4992

SEVERGIN, Y.P.
EFREMOV INSTITUTE
METALLOSTROY
P.O. BOX 42
189631 ST PETERSBURG,
RUSSIA

SHAFFER, ROBERT E.
LOS ALAMOS NATIONAL LAB.
MS H808
LOS ALAMOS, NM 87545
PHONE: 505-667-5877

SHAN, JIANPING
FERMILAB
PO BOX 500, MS 341
BATAVIA, IL 60510
PHONE: 708-840-4670

SHAPERO, DON
NATIONAL RESEARCH COUNCIL
BOARD OF PHYSICS & ASTRONOMY
2101 CONSTITUTION AVE
WASHINGTON, DC 20418

SEAFINQ, GILBERT
LAWRENCE BERKELEY LAB
90-200
BERKELEY, CA 94720

SEARF, WILLIAM M.
LAWRENCE LIVERMORE NATL LAB
PO BOX 5508, L-440
LIVERMORE, CA 94550
PHONE: 510-422-1688

SHEA, TOM J
BROOKHAVEN NATIONAL LAB
BLDG 830
UPTON, NY 11973

SHEKHAN, JOSEPH F.
BROOKHAVEN NATIONAL LAB.
BLDG. 725-C
UPTON, NY 11973
PHONE: 516-282-4655

SHEFFIELD, RICHARD L.
LOS ALAMOS NATIONAL LABORATORY
PO BOX 1663
MS: H825
LOS ALAMOS, NM 87545
PHONE: 505-667-1237

SHEIKH, JAVID Y.
CHALK RIVER LABS., AECL
STN. 111 AECL RESEARCH
CHALK RIVER, ON K0J-1J0
CANADA
PHONE: 613-584-3311

SHELDON, BOB
URA/SSC LABORATORY
2550 BECKLEYMEADE, MS 7000
DALLAS, TX 75237
PHONE: 214-708-5350

SHELDRAKE, RONALD
REV
THYRATRON SECTION
106 WATERHOUSE LANE
CHELMSFORD ESSEX, CM1 2QU
ENGLAND
PHONE: 024-345-3547

SHENG, I. CHING A.
ARGONNE NATIONAL LAB
9700 S CASS AVE
ARGONNE, IL 60439
PHONE: 708-252-5837

SHEPARD, KENNETH W.
ARGONNE NATIONAL LABORATORY
9700 S CASS AVE
BLDG 203
ARGONNE, IL 60439
PHONE: 708-252-4085

SHEPPARD, JOHN C.
SLAC
MS 66, PO BOX 4349
STANFORD, CA 94309
PHONE: 415-926-3498

SHEYIN, SAM
SSCL
2550 BECKLEYMEADE AVE
MS 4006
DALLAS, TX 75237-3997
PHONE: 214-708-3629

SHI, JICONG
RESEARCH ASSISTANT
DEPT OF PHYSICS, UNIV HOUSTON
HOUSTON, TX 77206-5506
PHONE: 713-743-3531

SHIH, HSIUAN-JENG
SSCL
2550 BECKLEYMEADE AVE
MS-1042
DALLAS, TX 75237
PHONE: 214-708-4518

SHOAFE, HAMID
STANFORD LINEAR ACCELERATOR
PO BOX 4349, MS-46
STANFORD, CA 94309
PHONE: 415-926-2954

SHOGA, SAKANAKA
NATL LAB FOR HIGH ENERGY PHYS
OHO 1-1, TSUKUBA SHI
IBARAKI-KEN, 305
JAPAN
PHONE: 81-298-645630

SHRADER, MERRALD R.
18780 MONTE ESCONDIDO DR
BUENA VISTA, CO 81211
PHONE: 415-592-1221

SHU, QUAN-SHENG
SSCL
2550 BECKLEYMEADE AVE
MS 8001
DALLAS, TX 75237
PHONE: 214-708-6908

SHUKEYLO, B.A.
EFREMOV INSTITUTE
POS. METALLOSTROY
P.O. BOX 42
ST PETERSBURG, 189 631
RUSSIA

SIBLEY, COLES R
MIT BATES LINAC
PO BOX 846
MIDDLETON, MA 01949
PHONE: 617-245-6600

SIEMANN, ROBERT H.
SLAC
MS 26, PO BOX 4349
STANFORD, CA 94309
PHONE: 415-926-3892

SIERGIEJ, DONNA M.
FERMILAB
PO BOX 500, MS 304
BATAVIA, IL 60510
PHONE: 708-840-4823

SIMPSON, JIM
ARGONNE NATIONAL LAB
9700 S CASS AVE
ARGONNE, IL 60465
PHONE: 708-252-6587

SIMROCK, STEFAN N.
CEBAF
12000 JEFFERSON AVE
NEWPORT NEWS, VA 23606
PHONE: 804-249-7241

SIMS, WILLIAM P.
BROOKHAVEN NATIONAL LABORATORY
BLDG. 911B
UPTON, NY 11973
PHONE: 516-282-3271

SINCLAIR, CHARLES E.

CERAP

12000 JEFFERSON AVE MS 58B

NEWPORT NEWS, VA 23606

PHONE: 804-249-7672

SINGH, OM V.

BROOKHAVEN NATIONAL LABORATORY

BLDG 725B

UPTON, NY 11973

PHONE: 516-282-2994

SKARITKA, JOHN

SSCL

2550 BECKLEYMEADE AVE.

MS 4007

DALLAS, TX 75237

PHONE: 214-708-3654

SMITH, DAVID L.

SANDIA NATIONAL LABORATORIES

DEPT. 1239

PO BOX 5800

ALBUQUERQUE, NM 87185

PHONE: 505-845-7141

SMITH, DON

TAMU

2202 CASTER LAKE DR

COLLEGE STATION, TX 77845

PHONE: 409-690-0926

SMITH, GARY A.

BROOKHAVEN NATIONAL LABORATORY

BLDG. 911C

UPTON, NY 11973

PHONE: 516-282-3473

SMITH, H. VERNON

LOS ALAMOS NATIONAL LABORATORY

AT-10, MAIL STOP H818

PO BOX 1663

LOS ALAMOS, NM 87545

PHONE: 505-667-2667

SMITH, HAROLD E.

SLAC/STANFORD UNIVERSITY

1268 BLANEY AVE

SAN JOSE, CA 95129

PHONE: 415-926-3549

SMITH, JOHN R.

TITAN ADVANCED INNOVATIVE TECH

2309 RENARD SE, STE 200

ALBUQUERQUE, NM 87106

SMITH, JOHN

BROOKHAVEN NATIONAL LABORATORY

BLDG 725B

NATL SYNCHROTRON LIGHT SOURCE

UPTON, NY 11973

PHONE: 516-282-4734

SMITH, LLEWELLYN C.H.

CERN

1211 GENEVA 23,

SWITZERLAND

PHONE: 767-342-1

SMITH, STEVE

STANFORD LINEAR ACCELERATOR

2575 SAND KILL RD

PO BOX 4399

STANFORD, CA 94305

PHONE: 415-926-3916

SMITH, SUSAN L.

SERC DARESURY LAB.

KECHWICK LANE

WARRINGTON

CHESHIRE, WA4 4AD

UNITED KINGDOM

PHONE: 092-560-3760

SMYTHE, W. R.

UNIVERSITY OF COLORADO

CB446

BOULDER, CO 80309-0446

PHONE: 303-492-7770

SOLOMON, LORRAINE

BROOKHAVEN NATIONAL LABORATORY

BLDG. 725B

UPTON, NY 11973

PHONE: 516-282-5491

SONG, JOSHUA J.

ARGONNE NATIONAL LABORATORY

9700 S. CASS AVE. - 371T

ARGONNE, IL 60439

PHONE: 708-252-6537

SORTAIS, PASCAL

GANIL

BP 5027

F-14021 CAEN, CEDEX

FRANCE

PHONE: 314-545-29

SOUNDRANAYAGAM, RAYPFU

SSCL

2550 BECKLEYMEADE AVE

DALLAS, TX 75237

PHONE: 214-708-5502

SOUTHWORTH, BRIAN

CERN

CH-1211 GENEVA, 23

SWITZERLAND

PHONE: 41-22-767 3888

SPATARO, BRUNO

INFN-FRASCATI

PO BOX 13

FRASCATI, 00044

ITALY

PHONE: 694-032-53

SPECKA, ARND

ECOLE POLYTECHNIQUE

LPNHE

PALaiseau, 91128

FRANCE

PHONE: 33-69-333160

SPECKT, VICKI

UNIVERSITY OF MARYLAND

ENERGY RESEARCH BLDG

COLLEGE PARK, MD 20742

SPENCE, WM. L.

SLAC

SLAC MS 66

STANFORD UNIVERSITY

STANFORD, CA 94309

PHONE: 415-926-3386

SPENCER, JAMES E.

SLAC

P.O. BOX 4349

STANFORD, CA 94309

PHONE: 415-926-2081

SPRANGLE, PHILLIP A
NAVAL RESEARCH LAB
CODE 6790
WASHINGTON, DC 20375
PHONE: 202-777-3493

SREDNIAWSKI, JOSEPH J.
GRUMANN AEROSPACE CORP.
111 STEWART AVE.
MS-B29-25
BETHPAGE, NY 11714
PHONE: 516-346-9626

STACK, STEVE
US DEPARTMENT OF ENERGY
1000 INDEPENDENCE AVE SW
WASHINGTON, DC 20585
PHONE: 202-586-0791

STANEK, MICHAEL W.
SLAC
P.O. BOX 4349
BIN # 55
STANFORD, CA 94309
PHONE: 415-926-4340

STAPLES, JOHN W.
LAWRENCE BERKELEY LABORATORY
1 CYCLOTRON RD BLDG 64
BERKELEY, CA 94720
PHONE: 510-486-5788

STAPLETON, GEOFFREY B.
SSC LABORATORY
2550 BECKLEYMEADE AVE
MS: 9000
DALLAS, TX 75237
PHONE: 214-708-4573

STECK, MARKUS
GSI DARMSTADT
PLANCKSTR 1
POSTFACH 110552
6100 DARMSTADT,
GERMANY
PHONE: 061-5 -359406

STEGE, JR., ROBERT E.
SLAC
P.O. BOX 4349
STANFORD, CA 94309
PHONE: 415-926-3915

STEIMEL, JAMES M.
FERMILAB
PO BOX 500, MS 341
BATAVIA, IL 60510
PHONE: 708-840-4826

STEINBACH, CHARLES P.
CERN
PS DIVISION
CH-1211 GENEVA, 23
SWITZERLAND
PHONE: 417-673-483

STEINHAUER, LOREN C.
STI OPTRONICS
2755 NORTHUP WAY
BELLEVUE, WA 98004
PHONE: 206-881-9380

STEINHOFF, R. LEWIS
US DEPARTMENT OF ENERGY
1000 INDEPENDENCE AVE SW
WASHINGTON, DC 20585
PHONE: 202-586-3856

STEPANTSOV, SERGUEI V.
JOINT INST FOR NUCLEAR RES.
JINR, FLEROV LAB OF NUC REACT.
DUBNA, 141980
RUSSIA
PHONE: 709-597-52381

STEPHENSON, KENNETH E.
SCHLUMBERGER-DOLL RESEARCH
OLD QUARRY RD
RIDGEFIELD, CT 06877
PHONE: 203-431-5320

STESKI, DANNIE B.
BROOKHAVEN NATIONAL LAB.
BUILDING 901A
UPTON, NY 11973
PHONE: 516-282-4581

STEVENS, RALPH R.
LOS ALAMOS NATIONAL LABORATORY
PO BOX 1663
MS: H818
LOS ALAMOS, NM 87545
PHONE: 505-667-8850

STEVENSON, NIGEL R.
TRIUMF
4004 WESBROOK MALL
VANCOUVER, BC V6T-2A3
CANADA
PHONE: 604-222-1047

STILLMAN, ARNOLD N.
BROOKHAVEN NATIONAL LABORATORY
BLDG. 911B
UPTON, NY 11973
PHONE: 516-282-4944

STOLTZ, PETER H
UNIV OF COLORADO
DEPT OF PHYSICS
CAMPUS BOX 390
BOULDER, CO 80309
PHONE: 303-492-0312

STOVER, GREG D.
LAWRENCE BERKELEY LABORATORY
1 CYCLOTRON RD BLDG 46/125
BERKELEY, CA 94720
PHONE: 510-486-7706

STRAIT, JIM B.
FERMILAB
PO BOX 500
MS 316
BATAVIA, IL 60510
PHONE: 708-840-2240

STRAUSS, BRUCE P.
VICE PRESIDENT
COSINE, INC.
PO BOX 1078
BROOKLINE, MA 02146-0008
PHONE: 617-734-1649

STRIFFLER, CHARLES D.
UNIVERSITY OF MARYLAND
ELECTRICAL ENGINEERING
COLLEGE PARK, MD 20742
PHONE: 301-405-1238

STRINGFIELD, RAY M.
LOS ALAMOS NATL. LAB.
MS H851
LOS ALAMOS, NM 87545
PHONE: 505-667-1477

STRUBIN, PIERRE M.
CERN A.T. VACUUM GROUP
CH 1211 GENEVA,
SWITZERLAND
PHONE: 412-776-75100

STUPAKOV, GENNADY V.
SSCL
2550 BECKLEYMEADE AVE
DALLAS, TX 75237
PHONE: 214-708-4513

SUETSUGU, YUSUKE
NLHEP
NATL LAB/HIGH ENERGY PHY KEK
ACC.DEPT, 1-1, OHO, TSUKUBA-SHI
IBARAKI-KEN, 305
JAPAN
PHONE: 812-946-45253

SUGANO, TOMOI
MITSUBISHI HEAVY IND. LTD
5007 ITO ZAKI-CHO
MIHARA
HIROSHIMA, 729-03
JAPAN
PHONE: 084-867-2424

SUK, HYIYONG
UNIV OF MARYLAND
LAB FOR PLASMA RESEARCH
COLLEGE PARK, MD 20742
PHONE: 301-405-4567

SULLIVAN, CAROL A
NAVAL RESEARCH LAB
CODE 6793
WASHINGTON, DC 20375

SUN, NING
SSC LABORATORY
2550 BECKLEYMEADE AVE, MS 4011
DALLAS, TX 75237-3997
PHONE: 214-708-3848

SUNDELIN, RONALD M.
CEBAF
12000 JEFFERSON AVE MS 58B
NEWPORT NEWS, VA 23606
PHONE: 804-249-7545

SUSTA, JOSEPH T.
CEBAF
12000 JEFFERSON AVE MS 58B
NEWPORT NEWS, VA 23606
PHONE: 804-249-7653

SUTTER, DAVID
US DEPT OF ENERGY
ER-224, GTN
DIV OF HEP
WASHINGTON, DC 20585

SUZUKI, SHINSUKE
JAERI SPRING-8 PROJECT TEAM
2-4 SHIRAKATA SHIRANE
TOKAI-MURA, NAKA-GUN
IBARAKI-KEN,
JAPAN
PHONE: 812-928-26096

SWAIN, GEORGE
LOS ALAMOS NATIONAL LAB
PO BOX 1663 MS H847
LOS ALAMOS, NM 87545
PHONE: 505-667-4433

SWENSON, DONALD A.
LINAC SYSTEMS
115 MORENE AVE
WAYAHACHIE, TX 75165
PHONE: 214-937-3283

SYMPHERS, MICHAEL
SSCL
2550 BECKLEYMEADE AVE
MS-1042
DALLAS, TX 75237
PHONE: 214-708-4519

TACCONI, EUGENIO
URA/SSC
2550 BECKLEYMEADE AVE
MS 4004
DALLAS, TX 75237
PHONE: 214-708-3334

TAKEDA, OSAMU
TOSHIBA CORPORATION
2-4 SUEHIRO-CHO
TSURUMI-KU
YOKAHAMA, 230
JAPAN
PHONE: 045-509-6626

TALMAN, RICHARD
SSCL
2550 BECKLEYMEADE AVE
DALLAS, TX 75237
PHONE: 214-708-3452

TANABE, EIJI
AET ASSOCIATES, INC.
20370 TOWN CENTER LANE
#260
CUPERTINO, CA
PHONE: 408-996-1760

TANABE, JACK T.
LAWRENCE BERKELEY LABORATORY
1 CYCLOTRON RD BLDG 46/161
BERKELEY, CA 94720
PHONE: 510-486-4387

TANABE, TOSMYA
RIKEN, LASER SCIENCE RES. GRP.
2-1 HIROSAWA
WAKO
SAITAMA, 351-01
JAPAN
PHONE: 814-846-2111

TANAKA, MITSUYOSHI
BNL
AGS 911B
UPTON, NY 11973
PHONE: 516-282-7284

TANG, CHA-MEI
NAVAL RESEARCH LAB
11609 LAKE POTOMAC DR
POTOMAC, MD 20854
PHONE: 202-767-4148

TANG, HUAN
STANFORD LINEAR ACCELERATOR
MS 66, SLAC
PO BOX 4349
STANFORD, CA 94309
PHONE: 415-926-2487

TANG, Y.
BROOKHAVEN NATIONAL LABORATORY
BLDG 725B
NATL SYNCHROTRON LIGHT SOURCE
UPTON, NY 11973
PHONE: 516-282-7022

TANTAWI, SAMI
SLAC
KLYSTRON DEPT.
SLAC MS 33
STANFORD, CA 94309
PHONE: 415-926-4454

TATCHYN, ROMAN O.
STANFORD LINEAR ACCELERATOR
2575 SAND KILL RD
PO BOX 4399 BIN 69
STANFORD, CA 94305
PHONE: 415-926-2992

TAUSSIG, ROBERT T.
BECHTEL CORPORATION
P.O. BOX 1647
SAN FRANCISCO, CA 94119-3965
PHONE: 415-768-0159

TAYLOR, BRIAN
LAWRENCE BERKELEY LABORATORY
1 CYCLOTRON RD, MS 46-125
BERKELEY, CA 94720
PHONE: 510-486-4782

TAYLOR, CLYDE
LAWRENCE BERKELEY LABORATORY
1 CYCLOTRON RD, MS 46/161
BERKELEY, CA 94720
PHONE: 510-486-6236

TAYLOR, THOMAS
CERN
CH 1211 GENEVA,
SWITZERLAND
PHONE: . . .

TAZZIOLI, FRANCO
INFN
LABORATORI NAZ INFN
CP 13
00044 FRASCATI,
ITALY

TEMKIN, RICHARD J.
MIT
PLASMA FUSION CENTER
MIT NW16
CAMBRIDGE, MA 02139

TEMNYKGE, ALEXANDER
CORNELL UNIVERSITY
A. TEMNYKH NUCLEAR STUDIES LAB
ITHACA, NY 14850
PHONE: 607-255-4882

TEMPLE, LEWIS E.
ARGONNE NATIONAL LABORATORY
9700 S. CASS AVE.
BLDG 362-ASD
ARGONNE, IL 60439
PHONE: 708-252-3341

TENENBAUM, PETER
SLAC
MS 65 BOX 4349
STANFORD, CA 94309

TENG, LEE
ARGONNE NATIONAL LABORATORY
9700 S. CASS AVENUE
ARGONNE, IL 60439
PHONE: 708-252-3405

TEPIKIAN, STEVEN
BROOKHAVEN NATIONAL LAB.
BLDG. 1005S
UPTON, NY 11973
PHONE: 516-282-4845

THIAGARAJAN, V.
SSCL
2550 BECKLEYMEADE AVE
MS 1042
DALLAS, TX 75237
PHONE: 214-708-4579

THIEBERGER, PETER
BROOKHAVEN NATIONAL LABORATORY
PHYSICS, 901A
UPTON, NY 11973
PHONE: 516-282-4582

THIELHEIM, KLAUS OSWALD
UNIVERSITAT KIEL
INST REINE/ANGEWANDTE KERNPHYS
OTTO-HAN-PLATZ 3
W-2300 KIEL, 1
GERMANY
PHONE: 494-318-4989

THIVENT, MICHEL U.
CERN
DIVPS
1211 GENEVE, 23
SWITZERLAND
PHONE: 767-415-2

THOMAS, MANFRED G.
BROOKHAVEN NATIONAL LABORATORY
BLDG 725
NATL SYNCHROTRON LIGHT SOURCE
UPTON, NY 11973
PHONE: 516-282-4681

THOMPSON, KEVIN D.
CERCA
1544 STICKNEY PT RD
SARASOTA, FL 34232
PHONE: 813-921-4288

THOMPSON, PATRICK
BROOKHAVEN NATIONAL LABORATORY
BLDG. 902
UPTON, NY 11973
PHONE: 516-282-7635

THUOT, MICHAEL E.
LOS ALAMOS NATIONAL LABORATORY
PO BOX 1663
MS: H820
LOS ALAMOS, NM 87545
PHONE: 505-667-7947

TIEFENBACK, MICHAEL G.
CEBAF
12000 JEFFERSON AVE
MS-12A
NEWPORT NEWS, VA 23606
PHONE: 804-249-7430

TIGHE, RICHARD
SLAC
SLAC MS55,
P.O. BOX 4349
STANFORD, CA 94309
PHONE: 415-926-2151

TIGNER, MAURY
PROFESSOR OF PHYSICS
CORNELL UNIVERSITY
NEWMAN LABORATORY
ITHACA, NY 14853-5001
PHONE: 607-255-4951

TING, ANTONIO C.
RESEARCH PHYSICIST
US NAVAL RESEARCH LABORATORY
CODE 6795
WASHINGTON, DC 20375
PHONE: 202-767-3825

TKATCHENKO, ANDRE
LAB NATL SATURNE/CE SACLAY
GIF SUR YVETTE, 91191
FRANCE
PHONE: 331-690-83824

TODD, ALAN M.
GRUMMAN
4 INDEPENDENCE WAY
PRINCETON, NJ 08550
PHONE: 609-520-0220

TOGE, NOBU
KEK
1-1 OHO
TSUKUBA
IBARAKI, 305
JAPAN
PHONE: 029-864-5314

TOMIZAWA, MASAHIRO
INSTITUTE FOR NUCLEAR STUDY
UNIVERSITY OF TOKYO
3-2-1 SHIDORI-CHO
TANASHI, 188
JAPAN
PHONE: 424-614-131

TOMPKINS, PERRY A.
VANDERBILT UNIVERSITY
DEPT. OF PHYSICS & ASTRONOMY
NASHVILLE, TN 37235
PHONE: 615-343-8505

TOOKER, JOSEPH
SSCL
2350 BECKLEYMEADE AVE.
DALLAS, TX 75237
PHONE: 214-708-4570

TOSHIYUKI, SHIRAI
ACCELERATOR LAB/ICR KYOTO UNIV
GOKANOSHO
UJI
KYOTO, 611
JAPAN
PHONE: 817-743-25806

TOYAMA, SHIN'ICHI
PNC/OEC
4002 NARITA-CHO
OARAI-MACHI
IBARAKI-KEN, 311-13
JAPAN
PHONE: 029-266-3868

TRAKHTENBERG, EMIL M.
ARGONNE NATIONAL LAB
9700 S CASS AVE
ARGONNE, IL 60439
PHONE: 708-252-9400

TRAN, PHUONG
GRADUATE STUDENT
UCLA
DEPARTMENT OF PHYSICS
LOS ANGELES, CA 90024

TRAVISH, GIL
UCLA
DEPT OF PHYSICS
405 HILGARD AVE
LOS ANGELES, CA 90024

TRBOJEVIC, DEJAN
BROOKHAVEN NATIONAL LAB.
BLDG. 1005S
UPTON, NY 11973
PHONE: 516-282-3078

TREADO, TODD
VARIAN ASSOCIATES
150 SOHIER ROAD
BEVERLEY, MA 01915
PHONE: 508-922-6000

TREMBLAY, KELLY
CEBAF
12000 JEFFERSON AVE
NEWPORT NEWS, VA 23606
PHONE: 804-249-7155

TRIBENDIS, ALEXY G.
BUDKER INST OF NUCLEAR PHYSICS
SIBERIAN DEPT/RUSSIAN ACADEMY
11 LARENTIEV AVE
630 090 NOVOSIBIRSK, 90
RUSSIA

TRIPPE, ANTHONY P.
MAXWELL LAB, INC-BROBECK DIV.
4905 CENTRAL AVE.
RICHMOND, CA 94804
PHONE: 510-524-8664

TRONC, DOMINIQUE
GENERAL ELECTRIC
GEMS-RT, 283 RUE DE LA MINIERE
BP 34 BUC, CEDEX
FRANCE
PHONE: 139-564-135

TROST, HANS-JOCHEN
TEXAS A & M UNIVERSITY
DEPT. OF PHYSICS
TEXAS A & M UNIVERSITY
COLLEGE STATION, TX 77843-4242
PHONE: 409-845-7727

TRZECIAK, WALTER S.
SYNCHROTRON RADIATION CENTER
3731 SCHNEIDER DR.
STOUGHTON, WI 53589
PHONE: 608-877-2160

TSIANG, EUGENE
400 DAVEY GLEN RD # 4629
BELMONT, CA 94002
PHONE: 415-595-5026

TSOUPAS, NICHOLAOS
BROOKHAVEN NATIONAL LAB
BNL-923
UPTON, NY 11973
PHONE: 516-282-4979

TSYGANOV, EDWARD N.
SSCL
2550 BECKLEYMEADE
DALLAS, TX 75237
PHONE: 214-708-4541

TUCKER, PATSY
SSC LABORATORY
12000 JEFFERSON AVE
NEWPORT NEWS, VA 23606
PHONE: - -

TURKOT, FRANK
FERMI NAT'L ACCELERATOR LAB
PO BOX 500, MS 316
BATAVIA, IL 60510
PHONE: 708-840-4428

TURMAN, BOB N.
SANDIA NATIONAL LABORATORIES
PO BOX 5800, DEPT 1289
ALBUQUERQUE, NM 87185-5800
PHONE: 505-845-7119

TURNER, LARRY R.
ARGONNE NATIONAL LABORATORY
BLDG. 340
9700 S. CASS AVE.
ARGONNE, IL 60439
PHONE: 708-252-6257

TURNER, STUART
CERN, SL DIVISION
1211 GENEVA, 23
SWITZERLAND
PHONE: 022-767-3235

TURNER, WILLIAM C.
SSCL
2550 BECKLEYMEADE
DALLAS, TX 75237
PHONE: 214-708-4541

UHM, HAN
NAVAL SURFACE WARFARE CENTER
10903 NEW HAMPSHIRE AVE
WHITE OAK
SILVER SPRING, MD 20903-5640
PHONE: 301-394-1809

UNGRIN, JAMES
CHALK RIVER LABS., ABCL
STN. 111
CHALK RIVER, ON K0L-110
CANADA
PHONE: 613-584-3311

UNSER, KLAUS R.
CERN
CERN SL-DIV.
CH-1211 GENEVA, 23
SWITZERLAND
PHONE: 227-673-784

VACCAREZZA, CRISTINA C.
INFN-FRASCATI
VIA E. FERMI 40
FRASCATI, 00044
ITALY
PHONE: 396-940-3537

VACCARO, VITTORIO G.
DIPARTIMENTO DI SCI. FISICHE
UNIVERSITY OF NAPLES
MOSTRA D'OLTREMARE PAD 20
NAPOLI, 80125
ITALY
PHONE: 378-172-53458

VALBUENA, ROGER J.
CERN
MT DIVISION
CH-1211 GENEVA, 23
SWITZERLAND
PHONE: 412-276-72582

VALICENTI, RAYMOND A.
SSCL
2550 BECKLEYMEADE AVE.
MS 4008
DALLAS, TX 75237
PHONE: 214-708-3716

VAN ASSELT, WILLEM K.
BROOKHAVEN NATIONAL LAB
BUILDING 911B
UPTON, NY 11973
PHONE: 516-282-7778

VAN DEUSEN, ALAN L.
ALLIED SIGNAL AEROSPACE
2000 E BANNISTER
KANSAS CITY, MO 64141
PHONE: 816-997-2435

VAN HERP, LAURENS G.
HOLEC
P.O. BOX 23
HENGLO, 7550 AA
NETHERLANDS
PHONE: 317-446-28808

VAN STAAGEN, PETER K.
G.H. GILLESPIE ASSOCIATES INC.
PO BOX 4640
HUNTSVILLE, AL 35815
PHONE: 205-650-0509

VAN STEENBERGEN, ARIE
NATL SYNCHROTRON LIGHT SOURCE
BROOKHAVEN NATIONAL LAB
BLDG 725B
UPTON, NY 11973
PHONE: 516-282-4604

VAN ZEIJTS, JOHANNES
CEBAF, ACCEL
12000 JEFFERSON AVE.
NEWPORT NEWS, VA 23606
PHONE: 804-249-5034

VANDEPLASSCHE, DIK
IBA
CHEMIN DU CYCLOTRON, 2
B-1348 LOUVAIN-LA-NEUVE
LOUVAIN,
BELGIUM
PHONE: 321-047-5890

VANECEK, DAVID L.
LBL
LAWRENCE BERKELEY LABORATORY
1 CYCLOTRON RD, MS58-113
BERKELEY, CA 94720
PHONE: 510-486-7251

VARNEY, DOUGLAS L.
CTI, INC.
810 INNOVATION DR
KNOXVILLE, TN 37932
PHONE: 615-906-7539

VASSERMAN, ISAAC R.
ARGONNE NATIONAL LAB
9700 S CASS AVE
ARGONNE, IL 60439
PHONE: 708-252-9612

VENZANT, KENNETH L.
CEBAF
12000 JEFFERSON AVE
NEWPORT NEWS, VA 23606
PHONE: 804-249-7607

VERDIER, ANDRE
CERN
SL DIVISION
CH1211 GENEVA, 23
SWITZERLAND

VERNIER, GILLES M.
C.E.A.
PONTFAVERGER, 51490
FRANCE

VETTER, ARTHUR M.
BOEING DEFENSE & SPACE GROUP
PO BOX 3999
M/S 2T-30
SEATTLE, WA 98124
PHONE: 206-773-5801

VIGNOLA, GAETANO
INFN-LNF
CP 13
FRASCATI,
ITALY
PHONE: 396-940-3268

VIOLA, ROBERT J.
SSC LABORATORY
2550 BECKLEYMEADE AVE.
DALLAS, TX 75237
PHONE: 214-708-2065

VLEKX, ARNOLD E.
SLAC
2575 SAND HILL RD.
MS 33
MENLO PARK, CA 94025
PHONE: 415-926-2438

VOGT, MARK E.
ARGONNE NATIONAL LAB
BLD 376 T APS ANL
ARGONNE, IL 60439
PHONE: 708-252-6247

VONG, FREDERICK C.
ARGONNE NATIONAL LABORATORY
9700 S. CASS AVENUE
BLDG. 362
ARGONNE, IL 60439
PHONE: 708-252-5259

WAIT, GARY D.
TRIUMF
4004 WESBROOK MALL
VANCOUVER, BC V6T2A3
CANADA
PHONE: 604-222-1049/60422

WAKE, MASAYOSHI
SSCL
2550 BECKLEYMEADE AVE
DALLAS, TX 75237
PHONE: 214-708-6338

WAKUTA, YOSHIHISA
KYUSHU UNIV DEPT OF NUCL ENG
HAKOZAKI 6-10-1
HIGASHIKU
FUKUOKA, 812
JAPAN
PHONE: 092-641-1101

WALDNER, GIORGIO A.
MARTHA S.R.L. IMPIANTI
VIA ERMANNO WOLF FERRARI 15
MILANO, 20141
ITALY
PHONE: 025-740-9740

WALDNER, PATRIC LUCA
THELMA S.R.L.
VIA ERMANNO WOLF FERRARI 15
MILANO, 20141
ITALY
PHONE: 740-974-057400733

WALKER, NICHOLAS J.
SLAC
BIN # 66
PO BOX 4349
STANFORD, CA 94309
PHONE: 415-926-3677

WALLING, LINDA S.
SSCL
2550 BECKLEYMEADE AVE.
MS 4008
DALLAS, TX 75237
PHONE: 214-708-3771

WALTERS, DEAN R.
MECH ENGINEER
ARGONNE NATIONAL LAB
9700 S CASS AVE
ARGONNE, IL 60439
PHONE: 708-252-9377

WALZ, DIETER R
SLAC
PO BOX 4349
STANFORD, CA 94309

WAN, WEISHI
NSCL
E LANSING, MI 48823
PHONE: 517-355-1523

WANDERER, PETER
BROOKHAVEN NATIONAL LABORATORY
BLDG. 902
UPTON, NY 11973
PHONE: 516-282-3974

WANG, CHANGHAO
LAWRENCE BERKELEY LABORATORY
1 CYCLOTRON RD, MS 71H
BERKELEY, CA 94720
PHONE: 510-486-6731

WANG, CHUNXI
LAWRENCE BERKELEY LAB./ALS
MS 2-400
1 CYCLOTRON RD
BERKELEY, CA 94720
PHONE: 510-486-6024

WANG, DAN Y.
MAXWELL LABS. INC.
4905 CENTRAL AVE
RICHMOND, CA 94804
PHONE: 510-528-4808

WANG, DEFA
MIT/BATES
MIT/BATES P.O. BOX 846
MIDDLETON, MA 01949
PHONE: 617-345-6660

WANG, DX
UNIVERSITY OF MARYLAND
LAB FOR PLASMA RESEARCH
UNIVERSITY OF MARYLAND
COLLEGE PARK, MD 20742
PHONE: 301-405-4961

WANG, FUHUA
SSC LABORATORY
2550 BECKLEYMEADE
MS 9000
DALLAS, TX 75237
PHONE: 214-709-4542

WANG, GUANGWEI
UNIVERSITY OF HOUSTON
LB.P.P OF UNIV OF HOUSTON
HOUSTON, TX 77204-3506
PHONE: 713-743-3529

WANG, JIAN G.
LAB FOR PLASMA RESEARCH
UNIVERSITY OF MARYLAND
COLLEGE PARK, MD 20742
PHONE: 310-405-3026

WANG, JUWEN
SLAC
SLAC, MS-26
STANFORD, CA 94309
PHONE: 415-926-3713

WANG, TAI-SEN F.
LOS ALAMOS NATIONAL LAB
AT-7, MS H825
LOS ALAMOS, NM 87545
PHONE: 505-667-3183

WANG, XIHE
BNL
BLDG 725B, BNL
UPTON, NY 11973
PHONE: 516-282-5790

WANG, YUN
IND. UNIV. CYCLOTRON FACILITY
2401 MILO B. SAMPSON LANE
BLOOMINGTON, IN 47408
PHONE: 812-855-5190

WANGLER, THOMAS P.
LOS ALAMOS NATIONAL LABORATORY
AT-1, MS H817
LOS ALAMOS, NM 87545
PHONE: 505-667-3200

WARNER, DAVID A.
ARGONNE NATIONAL LAB
9700 S CASS AVE
ARGONNE, IL 60439-4814
PHONE: 708-252-9580

WARNOCK, ROBERT L.
SLAC/STANFORD UNIVERSITY
SLAC MS 26, P.O. BOX 4349
STANFORD, CA 94309
PHONE: 415-926-2870

WATERS, GRAHAM
TRIUMF
4004 WESBROOK MALL
VANCOUVER, BC V6T2A3
CANADA
PHONE: 604-222-1047

WATSON, JERRY M.
SSCL
MS 4000
2550 BECKLEYMEADE AVE.
DALLAS, TX 75237
PHONE: 214-708-3826

WATSON, SCOTT A.
LANL
MS P-940
LOS ALAMOS, NM 87544
PHONE: 505-665-6233

WEATHERUP, CLIFFORD R.
EEV
106 WATERHOUSE LANE
CHELMSFORD ESSEX, CM12QU
ENGLAND
PHONE: 024-535-3472

WEAVER, JAMES N.
SSRL/SLAC
SLAC, MS 69
PO BOX 4349
STANFORD, CA 94309
PHONE: 415-926-2027

WEAVER, JIM
UNIVERSITY OF MARYLAND
239-6 OLD LEONARDTOWN
COLLEGE PARK, MD 20742

WEBER, ROBERT C.
SSC LABORATORY
2550 BECKLEYMEADE AVE.
DALLAS, TX 75237
PHONE: 214-708-3451

WEBERS, GODFRIED A.
EINDHOVEN UNIVERSITY
PO BOX 513
5600MB EINDHOVEN,
NETHERLANDS

WEDEKING, MOIRA K.
INDIANA UNIV. CYCLOTRON FAC.
2401 MILO B. SAMPSON LANE
BLOOMINGTON, IN 47408
PHONE: 812-855-2927

WEI, JIE
BROOKHAVEN NATIONAL LAB.
BLDG. 1005S
UPTON, NY 11973
PHONE: 516-282-7183

WEISSE, EBERHARD
CERN
CH-1211 GENEVA, 23
SWITZERLAND
PHONE: 767-634-0

WEISZ, SYLVAIN
CERN
SL DIVISION
23 GENEVA, CH 1211
SWITZERLAND
PHONE: 767-463-5

WELBOURNE, LESLEY A.
SERC DARESBURY LABORATORY
KBECKWICK LANE, DARESBURY
WARRINGTON
CHESHIRE, WA4-4AD
UNITED KINGDOM
PHONE: 092-560-3267

WELCH, DALE R.
MISSION RESEARCH CORPORATION
1720 RANDOLPH RD, SE
ALBUQUERQUE, NM 87106-4245
PHONE: 505-768-7723

WELCH, JAMES J.
CORNELL UNIVERSITY
WILSON LAB
ITHACA, NY 14853
PHONE: 607-255-8777

WENG, WU-TSUNG W.
BROOKHAVEN NATIONAL LABORATORY
BLDG 911-B, BNL
UPTON, NY 11973
PHONE: 516-282-2135

WERKEMA, STEVEN J.
FERMILAB
PO BOX 500, MS 341
BATAVIA, IL 60510
PHONE: 708-340-2232

WEST, CHARLENE
CEBAF
12000 JEFFERSON AVE
NEWPORT NEWS, VA 23606
PHONE: 804-248-7394

WESTBROOK, EDWIN P.
7913 CLAUDIA DRIVE
OXON HILL, MD 20745-1417
PHONE: 301-839-3302

WESTENSKOW, GLEN ALAN
LLNL
LLNL-L-441
P.O. BOX 808
LIVERMORE, CA 94550
PHONE: 510-423-6936

WHEALTON, JOHN E.
OAK RIDGE NATIONAL LABORATORY
PO BOX 2009
9201-2 MS-8071
OAK RIDGE, TN 37831-8071
PHONE: 615-574-1130

WHITE, MARION M.
ARGONNE NATIONAL LAB
9700 S. CASS AVE
BLDG. 371 T
ARGONNE, IL 60439-4814
PHONE: 708-252-5552

WHITHAM, KENNETH
TITAN BETA
6700 R SIERRA CT
DUBLIN, CA 94507
PHONE: 510-828-0535

WIENANDS, ULRICH
SSCL
2550 BECKLEYMEADE AVE
MS 9000
DALLAS, TX 75237
PHONE: 214-708-6237

WIK, BJORN HARVARD
DESY
DESY-GD -NOTKESTR 85
2000 HAMBURG, 52
GERMANY
PHONE: 408-998-2407

WILDMAN, DAVID W.
FERMILAB
PO BOX 500, MS 306
BATAVIA, IL 60510
PHONE: 708-840-4619

WILKE, MARK D.
LOS ALAMOS NATIONAL LABORATORY
P.O. BOX 1663
MS D406
LOS ALAMOS, NM 87545
PHONE: 505-667-4415

WILKINSON, CAROL A.
LOS ALAMOS NATIONAL LABORATORY
MS H838
P.O. BOX 1663
LOS ALAMOS, NM 87545
PHONE: 505-667-8056

WILSON, DOUGLAS C.
LOS ALAMOS NATIONAL LABORATORY
X-1 MS P645, LANL
LOS ALAMOS, NM 87545
PHONE: 505-667-4370

WILSON, IAN
CERN
SL, DIVISION
CH-1211 GENEVA, 23
SWITZERLAND
PHONE: 767-327-4

WILSON, MARK
US DEPT OF ENERGY
ER-543
WASHINGTON, DC 20585
PHONE: 301-903-5048

WILSON, PERRY B.
SLAC
PO BOX 4349
BIN 26
STANFORD, CA 94309
PHONE: 415-926-3163

WINCHESTER, SUSAN
FERMILAB

WINICK, HERMAN
SSRL/SLAC
PO BOX 4349, BIN 69
STANFORD, CA 94309
PHONE: 415-926-3155

WINJE, RUM
URA/SSC
2550 BECKLEYMEADE AVE
MS 4804
DALLAS, TX 75237
PHONE: 214-708-3300

WINN, DAVID E.
FAIRFIELD UNIVERSITY
DEPT OF PHYSICS, BANNOU 118
FAIRFIELD, CT 06424-7524

WINTVESKY, DANIEL
LNLS
CX POSTAL 6192
CAMBRINAS, SP, 13084
BRAZIL
PHONE: 550-192-542634

WITKOVER, RICHARD L.
BROOKHAVEN NATIONAL LAB.
BUILDING 911B
UPTON, NY 11973
PHONE: 516-282-4607

WON, SANGCHUL
PAL
PO BOX 125
POHANG, 790 600
KOREA
PHONE: 562-792-221

WOODLEY, MARK D.
SLAC
SLAC MS66
P.O. BOX 4348
STANFORD, CA 94309
PHONE: 415-926-4081

WRIGHT, SCOTT
ALLIED SIGNAL AEROSPACE CO.
PO BOX 419159
KANSAS CITY, MO 64141
PHONE: 816-997-2549

WU, XIAOYU
SSCL
2550 BECKLEYMEADE AVE
SUITE 125, MS9000
DALLAS, TX 75237
PHONE: 214-708-4218

WU, YING
DUKE UNIVERSITY
FEL LAB BOX 90319
DURHAM, NC 27708-0319
PHONE: 919-680-2644

WURTELE, JONATHAN
MIT
NW06-238
CAMBRIDGE, MA 02139
PHONE: 617-253-8443

WUSTFELD, GODE
BESSY
LENTZBALLEE 100
100 BERLIN, 33
GERMANY
PHONE: 493-063-924638

WYSS, CARLO
CERN
CH 1211 GENEVA,
SWITZERLAND
PHONE: 767-292-067

XI, BOLING
EINDHOVEN UNIVERSITY
PO BOX 513
CYCLOTRON LAB 2.10
5600MB EINDHOVEN,
NETHERLANDS

YAMPOLSKY, JOSIF
INTEGRATED APPLIED PHYSICS
30 THAYER RD
WALTHAM, MA 02154
PHONE: 617-489-1818

YAN, YITON
SSCL
2530 BECKLEYMEADE AVE
DALLAS, TX 75237
PHONE: 214-708-4520

YANG, MING JEN
FERMILAB
PO BOX 500, MS 340
BATAVIA, IL 60510
PHONE: 708-840-4446

YAO, CHEN YUAN
SSC LABORATORY
2530 BECKLEYMEADE AVE
DALLAS, TX 75237
PHONE: 214-708-4531

YE, HUANCHUN
UNIVERSITY OF MARYLAND
DEPARTMENT OF PHYSICS
COLLEGE PARK, MD 20742
PHONE: 301-314-9525

YEN, EDWARD
SYNCHROTRON RADIATION RES CTR
NO 1, R & D ROAD VI
HSINCHU SCI-BASED INDUST PARK
HSINCHU, 30077
TAIWAN, R.O.C.
PHONE: 886-357-80281

YEN, YAN
TRIUMF
4004 WESBROOK MALL
VANCOUVER, BC V6T2A3
CANADA
PHONE: 604-222-1047

YOKOUCHI, NORIO
HITACHI ZOSEN CORPORATION
1-1 HITOTSUBASHI 1-CHOME
CHIYODAKU, TOKYO, 100
JAPAN
PHONE: 332-178-525

YONEHARA, HIROTO
JAERI SPRING-8 PROJECT TEAM
2-4 SHIRAKATA SHIRANE
TOKAI-MURA, NAKA-GUN
IBARAKI-KEN, 319-11
JAPAN
PHONE: 812-928-25269

YORK, RICHARD
CYCLOTRON LAB.
MICHIGAN STATE UNIVERSITY
EAST LANSING, MI 48824

YORK, ROB
LANL
MS: 5 MS. H838
LOS ALAMOS, NM 87545
PHONE: 505-667-4577

YOUNG, ANDREW
LOS ALAMOS NATIONAL LABORATORY
PO BOX 1663, MS H827
LOS ALAMOS, NM 87544
PHONE: 505-665-1773

YOUNG, JOYCE A.
LAWRENCE BERKELEY LABORATORY
1 CYCLOTRON RD, MS 10-110
BERKELEY, CA 94720
PHONE: 510-486-6724

YOUNG, LLOYD
LOS ALAMOS NATIONAL LABORATORY
AT-1, MS H817
LOS ALAMOS, NM 87545
PHONE: 505-667-1951

YOURD, RON
LAWRENCE BERKELEY LABORATORY
1 CYCLOTRON RD, MS 80-101
BERKELEY, CA 94720
PHONE: 510-486-4170

YU, DAVID
DULY RESEARCH INC.
1912 MAC ARTHUR ST
RANCHO PALOS VERDES, CA 90732
PHONE: 310-548-7123

YU, SIMON S.
LAWRENCE BERKELEY LABORATORY
1 CYCLOTRON RD, MS 47-112
BERKELEY, CA 94720
PHONE: 510-486-5477

YU, XIAO-TANG
MIT
NW16 223 MIT
CAMBRIDGE, MA 02139
PHONE: 617-258-9178

YUKINORI, KOBAYASHI
NATL LAB FOR HIGH ENERGY PHY.
OHO 1-1, TSUKUBA-SHI
IBARAKI-KOU, 305
JAPAN
PHONE: 812-986-45630

YULE, THOMAS J.
ARGONNE NATIONAL LAB
9700 S. CASS AVE.
BLDG. 207
ARGONNE, IL 60439-4814
PHONE: 708-252-6740

YUNN, BYUNG C.
CERAP
12000 JEFFERSON AVE
NEWPORT NEWS, VA 23606
PHONE: 804-249-7399

ZACH, MILOS A.
TRIUMF
4004 WESBROOK MALL
VANCOUVER, BC V6T2A3
CANADA
PHONE: 604-222-1047

ZANTE, TONY
TITAN BETA
6780 R SIERRA CT.
DUBLIN, CA 94568
PHONE: 510-828-0555

ZARCONI, MICHAEL JOSEPH
BROOKHAVEN NATIONAL LABORATORY
BLDG. 911A
UPTON, NY 11973
PHONE: 516-246-5070

ZELENSKI, ANATOLI
INR, MOSCOW/TRIUMF
4004 WESBROOK MALL
VANCOUVER, BC V6T-2A3
CANADA
PHONE: 604-222-1047

ZHABITSKY, VYACHESLAV M
JOINT INST FOR NUCL RESEARCH
141900 DUBNA
MOSCOW REGION,
RUSSIA
PHONE: 709-597-52381

ZHANG, PEILEI
SSCL
2550 BECKLEYMEADE
DALLAS, TX 75237
PHONE: 214-708-4563

ZHANG, SHOU-YUAN
BNL
911A AGS DEPT. BNL
UPTON, NY 11973
PHONE: 516-282-3412

ZHANG, XIAOHAO
BROOKHAVEN LAB.
NLS-725C, BNL
UPTON, NY 11973
PHONE: 516-282-5909

ZHOU, PING
FERMILAB
PO BOX 500, MS 341
BATAVIA, IL 60510
PHONE: 708-840-2383

ZINNEMAN, THOMAS E.
ARGONNE NATIONAL LAB
9700 S CASS AVE, BLDG 207
ARGONNE, IL 60439
PHONE: 708-252-6002

ZOBOV, MIKHAIL
INFN/LNF
INST NAZL DI FISICA NUCLEARE
FRASCATI
CP13-00044 ROMA,
ITALY
PHONE: 069-403-277

ZU, DONGLIN
BEIJING UNIV
DEPT OF TECH PHYS
BEIJING, 100871
CHINA
PHONE: 250- -1877

Conference Author Index

A

Aas, T. 2967
 Abbott, S. 3748
 Abe, I. 3087
 Abrahamsson, K. 1735
 Acerbi, E. 1524
 Ackerman, G. D. 3169
 Adam, S. R. 3639
 Adams, F. P. 829, 832, 835, 1039
 Adamaki, J. 2967
 Adler, R. J. 1306
 Adney, J. 3745
 Adolphsen, C. 414, 417, 543, 2019, 3342
 af Ugglas, M. 1735
 Ahrens, L. 3633
 Ahrens, L. A. 3763
 Aiello, G. R. 2322, 2367
 Aiello, R. 2118
 Aizawa, K. 1468
 Akai, K. 769, 992, 3450
 Akbari, H. 2492
 Akchurin, N. 32
 Akemoto, M. 1309
 Akre, J. 1572
 Alberti, S. 2656, 2690
 Aleksandrov, A. 3243
 Alessandria, F. 1524
 Alexandrov, V. 2042
 Alimov, A. S. 2059
 Allen, C. K. 3145, 3648
 Allen, L. J. 1689, 1691
 Allen, S. L. 1551, 1554
 Alley, R. 3045, 3047
 Alley, R. K. 2978, 3027, 3036
 Allison, P. 3172
 Allison, S. 1884, 2106
 Alton, G. D. 2979
 Amidei, D. 2199
 Amiranoff, F. 2450
 Amiry, A. 173
 Anami, S. 590, 1163, 1193, 1416, 3087
 Anamkath, H. 608, 611
 Anashin, V. 3876
 Anashin, V. V. 2022
 Anders, A. 1390
 Anders, S. 1390
 Anderson, D. 3745
 Anderson, D. E. 1354
 Anderson, K. 3096, 3163
 Anderson, R. R. 2919
 Anderson, S. 1421
 Anderson, T. 2835
 Andler, G. 1735
 Ando, M. 1468
 Andreev, V. A. 3121, 3124
 Andreev, V. G. 980
 Andreev, V. V. 297
 Anerella, M. 2744, 2766, 2790
 Annala, G. 3808
 Annala, J. 354
 Anne, R. 1789, 1792

Anthouard, P. 670, 697
 Antoine, C. 798
 Antropov, V. 2042
 Aoki, T. 2039
 Aoyagi, H. 2978, 3036
 Arai, S. 1780, 1783, 1786
 Arakaki, Y. 41
 Araki, M. 1518
 Arbique, G. 827, 3127
 Arbique, G. M. 2124, 2426, 2986
 Arbuzov, V. 1226
 Archie, C. N. 480
 Arcioni, P. 772, 1524, 1569
 Arinaga, M. 2292, 3552
 Arkhipov, O. 2042
 Arnaudon, L. 44
 Arnold, D. E. 989
 Arnold, N. D. 1957, 1960
 Artiominov, A. S. 2166, 2169
 Artru, X. 3093
 Asami, A. 3087
 Askew, D. R. 1336
 Assang, A. 2187
 Asseev, A. A. 315, 318, 320, 322, 324
 Assmann, R. 44
 Åström, J. 2068
 Atkins, W. H. 1669
 Aurerbach, E. H. 1872
 Ausset, P. 858
 Austin, R. H. 2970
 Averbukh, J. 824
 Averill, R. 1372, 2054, 2331, 2868, 2871, 2874, 3851
 Awaji, N. 1515, 1518
 Ayzanian, H. 1750
 Azuma, O. 1202

B

Baartman, R. 3330
 Baba, H. 959
 Babenko, E. 2423
 Baccaglioni, G. 1524
 Bachman, D. A. 3190
 Bachmor, R. 1178
 Badano, L. 32
 Bagge, L. 1735
 Baglin, V. 2720
 Bai, X. 3237
 Baier, T. 3093
 Baier, V. N. 3093
 Baik, K. H. 679
 Bailey, J. 3757
 Bailey, R. 1937, 2001, 2013
 Baiod, R. 2826
 Baishiev, I. S. 3109, 3772
 Bak, J. 581
 Bak, J. S. 593
 Balabin, A. I. 3675
 Balandin, V. 441, 444, 477
 Ball, M. 29, 224, 227, 420, 2289, 3745

Ball, M. S. 2243, 3536
 Balleyguier, P. 1136
 Baltrusaitis, R. M. 2400
 Band, A. 2240
 Bane, K. 543, 1445, 3240, 3375
 Bane, K. L. 596
 Bane, K. L. F. 3339, 3342, 3432
 Baptiste, K. 1238
 Baranovsky, A. E. 682
 Barbier, M. M. 3102
 Bardy, J. 670, 697
 Barklow, T. 2019
 Barletta, B. 2638
 Barletta, W. 2010, 3836
 Barletta, W. A. 775, 1524, 1988, 3817
 Barlow, D. 1703
 Barlow, D. B. 2480
 Barnard, J. 703, 706
 Barnard, J. J. 712, 715, 733, 3612
 Barnes, M. J. 1148, 1181, 1330, 3402
 Barnes, P. 763, 886, 889, 892, 918, 921, 977, 995, 1399
 Barov, N. 561, 2617, 2623, 3216
 Barr, D. S. 2163
 Barranco-Luque, M. 2956
 Barry, W. 2109
 Barsotti, E., Jr. 3294
 Barsotti, E. L. 2531
 Bartalucci, S. 778
 Bartelson, L. 918, 1342
 Barth, W. 3142
 Barts, T. 3444
 Bar'yakhtar, V. 1480
 Bassetti, M. 2048
 Batchelor, K. 2486, 3000, 3012
 Batishchev, O. V. 2620
 Batsikh, G. 2717
 Batsikh, G. I. 980
 Batygin, Y. K. 50
 Bazzani, A. 273
 Be, S. H. 3845
 Bearzatto, C. 1184
 Beaufait, J. 3103
 Beckert, K. 1645, 1738
 Beebe, E. 1735
 Beechy, D. 2118
 Behrsing, G. 83
 Belk, A. 1937
 Belkacem, A. 3751
 Bell, R. A. 1039, 2010
 Bellomo, G. 775, 1001, 1524
 Belloni, F. 3839
 Belomestnykh, S. 1226
 Belomestnykh, S. A. 3669
 Belomestnykh, S. E. 2022
 Beloshitsky, P. 2042
 Belov, V. 2042
 Belov, V. P. 3820, 3822
 Belova, N. G. 664, 3546
 Bemes, M. 2967
 Benaroya, R. 3857
 Benes, S. J. 1957
 Benesch, J. 1016

Benesch, J. F. 748, 781, 947
 Bengtsson, J. 567, 1488, 2272, 3312
 Benka, T. 1706
 Bennett, G. 2070
 Bennett, L. F. 667
 Bennett, M. 3748
 Bennett, P. 1916
 Benson, S. 3663
 Benvenuti, C. 806
 Ben-Zvi, I. 849, 1439, 1602, 2486, 2962, 3000, 3012
 Berg, J. S. 291
 Berg, W. 605
 Bergher, M. 3708
 Bergmann, U. 2145
 Bernard, D. 2450
 Bernard, M. 694
 Bernard, P. 806
 Bernardini, M. 3842
 Beroud, Y. 784
 Bertrand, P. 1789
 Bertsche, K. J. 1727
 Berz, M. 155, 164
 Bethel, S. 2967
 Bethke, S. 2172
 Betto, A. 1220
 Bhandari, R. 381
 Bharadwaj, V. 2228, 3806
 Bhat, C. M. 405, 787, 1223
 Biagini, M. E. 2048
 Bickley, M. 1835, 1895
 Bieniossek, F. 3096
 Bieniossek, F. M. 3163
 Bieri, R. L. 742
 Bieth, C. 1789
 Bijleveld, J. 2343
 Billan, J. 68
 Billen, J. 1712
 Billen, J. H. 790, 793
 Billquist, P. 1694
 Birattari, C. 1524
 Birnbaum, I. 2420
 Birnbaum, I. A. 3012
 Biscardi, R. 1419
 Biscari, C. 2048
 Bishop, D. 1148, 1181
 Bisoffi, G. 1747
 Bisognano, J. 512, 3663
 Bisognano, J. J. 179, 2364, 2929, 3246, 3473, 3515
 Bixio, A. 1063
 Bizek, H. 1485
 Blaker, G. 1300
 Blasche, K. 357, 3736
 Blaskiewicz, M. 3321, 3324
 Blell, U. 357
 Bleser, E. 3766
 Bleser, E. J. 3763
 Blewett, J. P. 2546
 Blind, B. 56
 Blockus, D. 2172
 Bloess, D. 806
 Blokland, W. 2528
 Blondel, A. 44
 Bloom, E. 3084
 Blum, H. 1451
 Blum, E. 3579
 Blum, E. B. 1599, 2246, 2307

Blumberg, L. N. 3579
 Bobin, J. L. 3202
 Bobyleva, L. 2042
 Bodan, A. 2051
 Boera, J. E. 327
 Boenf, J. P. 3039
 Bogacz, S. A. 74, 77, 2587
 Bogatov, N. 2769
 Bogaty, J. M. 1694
 Böge, M. 460
 Bogert, D. 3793
 Bohl, T. 2001
 Boha, C. L. 838, 1715, 3666
 Boiteux, J. P. 2358
 Bollinger, L. M. 1694
 Bolme, G. O. 1669, 3118
 Bondarev, B. I. 980
 Boni, R. 611, 778
 Bonifacio, R. 1524
 Bonin, B. 798
 Bonnafond, C. 670, 697, 2115
 Bordoley, M. 1867, 2313
 Bordry, F. 44, 2001
 Bordua, M. 3748
 Borer, J. 2103, 2492
 Borisov, O. N. 518
 Borland, M. 285, 2028, 3015
 Bosch, F. 1645
 Bosch, R. A. 3369
 Boscolo, I. 1524
 Bosotti, A. 1524
 Bossert, R. 2769
 Bossingham, R. 3751
 Botlo, M. 128
 Botman, J. I. M. 1072, 1820, 2062, 2065, 2892, 2927, 3423, 3645
 Bourg, F. 2997
 Bourgarel, M. P. 1789
 Bourianoff, G. 128, 203, 515
 Boussard, D. 2376, 2379
 Bovet, C. 2492
 Bowling, B. A. 1895, 2298, 2477
 Bowling, S. 1669
 Boyce, R. 1445, 1608
 Boyce, R. F. 543
 Boyd, J. K. 463
 Boyes, J. 667
 Bozoki, E. 105, 2284, 3636
 Brabson, B. 29, 224, 227, 420
 Bracco, R. 1587
 Bradley, S. 2054
 Brandeberry, F. 824, 880
 Brandt, D. 3429
 Branson, B. H. 1220
 Brau, C. A. 1448
 Brauer, S. O. 1217
 Braun, A. 354
 Bravar, A. 32
 Brennan, J. M. 1241, 3763
 Brennan, M. 2286
 Bres, M. 1184
 Bressan, M. 772, 1524, 1569
 Bressler, V. E. 2736, 2950
 Briand, P. 2997
 Brianti, G. 3917
 Bridges, J. 285, 1013
 Bridges, J. F. 766, 910, 913, 1157, 1408, 1906

Briegel, C. 1914
 Briggs, R. J. 3922
 Brindza, P. 3103
 Brinkgreve, P. 2892
 Brinkmann, R. 3742
 Brittain, D. L. 1169
 Broggi, F. 1524, 1569
 Brooks, T. 1154
 Broome, W. 1419
 Brouk, V. 2382
 Browman, A. 1683
 Browman, M. J. 3267
 Brown, B. 3757
 Brown, B. C. 351, 2829
 Brown, D. 2181
 Brown, D. J. 2664
 Brown, G. 2760
 Brown, I. 1390
 Brown, K. 384
 Brown, K. L. 333, 378
 Brown, N. 62
 Brown, P. 2358
 Brown, R. 2507, 3184
 Browne, M. 3045, 3047
 Brownman, M. J. 800
 Bru, B. 1789, 1792
 Brüttsch, E. 2748
 Bruhwiler, D. L. 59, 3624
 Brumwell, F. 3757
 Brunelle, P. 1465
 Bruns, W. 904, 1133, 3714
 Bryant, H. 369
 Bu, S. 1411
 Buchanan, E. 3533
 Buda, S. 1419
 Budlong, J. 3533
 Budnick, J. 29, 224, 227, 420, 2865
 Budzko, A. 3642
 Budzko, A. V. 3784
 Builta, L. 3055
 Bull, J. 1369
 Buller, T. L. 1075
 Bulos, F. 3084
 Bultman, N. 1712
 Bulyak, E. 300, 1480
 Bulyak, E. V. 3512
 Buon, J. 469, 2513
 Burgett, W. 2731, 2757, 2763
 Burke, D. 2019
 Burke, D. L. 543
 Burkhardt, H. 2001
 Burnham, B. 2889
 Burns, A. 2103, 2301
 Burns, M. 3055
 Burns, M. J. 2944
 Burtin, G. 2495
 Burton, R. J. 829, 832
 Busch, G. 2967
 Bushuyev, A. 1226
 Butterworth, A. 1903
 Büttig, H. 1477
 Byrd, J. 2349, 3315
 Byrd, J. M. 2109, 3318, 3408
 Byrne, T. 567

C

- Cai, S. Y. 3075
 Cai, Y. 209, 2781
 Calabrese, R. 3243
 Calame, J. P. 2667, 2670
 Calderon, M. 3836
 Callahan, D. A. 730, 733, 3660
 Callia, R. 543, 620, 1106
 Calloway, D. 2172
 Calo, A. 3127
 Calvert, J. 1160, 3748
 Camas, J. 2498
 Cameron, P. 1166
 Cameron, P. R. 2328
 Campbell, B. 1402
 Campisi, I. E. 1115, 1220
 Capista, D. 2252
 Caporaso, G. 703
 Caporaso, G. J. 712, 715
 Cappi, R. 3570
 Cardito, M. 2154
 Cardman, L. S. 3246
 Carey, D. C. 47
 Carlé, P. 1735
 Carlini, R. 2136, 3103
 Carlisle, L. 1718
 Carlson, R. L. 661
 Carlsen, B. 2675
 Carlsen, B. E. 2537, 2664
 Carmel, Y. 2714
 Carpenter, J. 3757
 Carr, R. 1596
 Carroll, F. E. 1448
 Carron, G. 1066, 3426
 Carson, J. 2769
 Carter, A. 2054
 Carwardine, J. 1709
 Carwardine, J. A. 3210
 Caryotakis, G. 543, 1106, 1259
 Casella, R. 1277
 Caspers, F. 2157, 3381
 Cassel, R. 543, 1318
 Castellano, M. 573
 Castro, P. 2103
 Catani, L. 573
 Caussyn, D. 3745
 Caussyn, D. D. 29, 224, 227, 420, 3536
 Cavallari, G. 806
 Celata, C. M. 724, 3748
 Cerniglia, P. 2310
 Chabert, A. 1789
 Chae, Y. 282
 Chae, Y. C. 182
 Chamberlain, O. 2172
 Champion, M. 809, 918, 1127
 Champion, M. S. 989
 Chan, C. F. 3157, 3160
 Chan, K. D. C. 2970
 Chanel, M. 2157
 Chang, C. H. 1943, 2886
 Chang, C. R. 122, 812, 3585
 Chang, H. P. 1943
 Chang, J. S. 1345
 Channell, P. J. 38
 Chao, A. 3781
 Chao, A. W. 29, 224, 227, 420, 3345, 3348
 Chao, Y. 587
 Chapman, L. 1914, 2249
 Chappelier, J. 158, 161
 Charruau, G. 858
 Chase, B. E. 2355
 Chattopadhyay, S. 83, 2638, 3042
 Chautard, F. 267, 2720
 Chechetenko, V. 1480
 Chehab, R. 3093
 Chel, S. 855
 Chen, B. 3345, 3348
 Chen, C. 2656
 Chen, H. 2151
 Chen, J. 1095
 Chen, J. R. 1635
 Chen, J. S. 1878
 Chen, P. 617, 2638
 Chen, S. 200, 3255
 Chen, S. C. 2575, 2696, 2699
 Chen, S. J. 1878
 Chen, T. 3479
 Chen, Y. 303, 718, 2841
 Chen, Y. J. 703, 706
 Cheng, J. 2659, 2667
 Cheng, W. 221
 Cheng, Y. 1262, 1398, 2269
 Chepurinov, A. S. 2059
 Chesnokov, Y. A. 454
 Chester, N. 2826
 Chester, N. S. 2823
 Chevallier, M. 3093
 Chiaveri, E. 806, 849
 Chida, K. 41
 Chimenti, V. 3906
 Chin, J. 1572, 1584
 Chin, Y. H. 3347, 3414
 Ching, C. H. 3351
 Chiou, T. C. 2635
 Chirkov, P. 2769
 Chmielewski, A. G. 1890
 Cho, C. 2151
 Cho, M. 581, 1521
 Cho, M. H. 593, 1315
 Cho, Y. 399, 3757
 Cho, Y. S. 679
 Choi, B. H. 679, 3196
 Choi, J. 2516, 3273
 Choi, J.-Y. 3087, 3705
 Chojnacki, E. 815, 1844, 2596, 3061
 Chou, P. J. 3363
 Chou, W. 818, 2281, 3444, 3609, 3781, 3888
 Christensen, K. 1712, 2947
 Christiansen, C. F. 1098, 2139
 Christianson, M. 2757
 Chu, C. 306, 2841
 Chubar, O. V. 1626, 2474, 2510
 Chubarov, O. V. 2059
 Chugun, T. 2205
 Chung, K. H. 679, 3196
 Chung, Y. 188, 1814, 2112, 2263, 2266, 2275, 2304
 Chupp, W. W. 703, 3199
 Church, M. 330
 Chuvilo, I. V. 1675
 Ciapala, E. 1903, 2358
 Ciardullo, D. J. 1241
 Ciarlette, D. 285
 Ciarlette, D. J. 1814
 Cifarelli, F. 3099
 Ciullo, G. 3243
 Claborn, G. 2222
 Clark, D. 369, 3888
 Clark, D. J. 1724, 1727
 Clark, S. L. 543
 Clarke, J. A. 1494, 1638, 3594, 3672
 Claudet, S. 2956
 Claus, J. 2895
 Clay, W. 3888, 3891
 Clayton, C. 2976, 3003
 Clayton, C. E. 558, 2551, 3543
 Clayton, T. 1369, 2781
 Clément, M. 1363
 Clendenin, J. 3033
 Clendenin, J. E. 2978, 3027, 3036
 Clerc, G. 1184
 CLIC Study Group 540
 Clift, B. E. 1694
 Cline, D. 2051, 2638
 Clout, P. 1801
 Clozza, A. 3906
 Coacolo, J. C. 3567
 Coadou, B. 798
 Cobb, J. K. 2838
 Codutti, A. 1587
 Cohen, S. 369
 Colby, E. 3021
 Colchester, R. J. 2495
 Cole, B. 128, 203
 Cole, M. 821, 3012
 Cole, R. 1669
 Coleman, P. 824
 Coleman, P. D. 1033, 1256, 3252
 Colestock, P. 3294
 Colestock, P. L. 3303, 3306, 3384, 3540
 Collet, G. J. 3030
 Collet, P. 1187
 Collier, P. 1937, 2001
 Collins, J. 29, 224, 227, 420
 Collins, J. P. 2823
 Colton, E. 3297
 Combs, C. 1703
 Combs, C. M. 846
 Concinauro, G. 1524, 1569
 Conde, M. E. 3042
 Condé, H. 1771
 Connolly, R. 1669
 Conte, M. 32, 438
 Conway, P. 2388
 Coombes, R. 2769
 Cooper, R. 3297
 Cooper, R. G. 2400
 Cooper, R. K. 3267
 Cooper, W. S. 3169
 Coosemans, W. 44
 Corbett, J. 173
 Corbett, W. J. 108, 114, 1483, 2275
 Cork, C. 1575
 Corlett, J. N. 2109, 3318, 3408, 3411
 Cornacchia, M. 173
 Cornelis, K. 2001, 3429

Cornelius, W. D. 2994
 Corredoura, P. 2370, 3240
 Corsini, R. 626, 1524
 Cottingham, W. B. 3118
 Courant, E. 3778
 Courant, E. D. 137
 Cover, R. 1605
 Craddock, W. 2638
 Crandall, K. R. 1042, 3585, 3657
 Crane, M. 1922, 1966
 Cravey, W. R. 739
 Crawford, A. 1223
 Crawford, C. 886, 918
 Crawford, C. A. 3540
 Crawford, J. F. 1771
 Crawford, K. 1925, 3757
 Crist, C. 2121
 Crist, C. E. 2124, 2130, 2426, 2456, 2501
 Croekford, G. 2504
 Crofford, M. 587
 Crofford, M. T. 2364
 Crosbie, E. 285, 1485
 Crosbie, E. A. 282, 506
 Crouch, R. 2199
 Cuevas, C. 1838, 3127
 Culwick, B. 1277
 Cuneo, M. E. 694
 Curbow, J. 941
 Curry, B. P. 375
 Curtin, M. 1154, 1244
 Cutler, R. 3509
 Cutler, R. I. 827, 1250

D

Dabrowski, J. 1274, 1855, 1858, 1861
 Daclon, F. 1378, 3842, 3873
 Dalesio, L. R. 1806
 D'Alsace, R. 1419
 Daly, R. 1960, 2142
 Damjanovich, R. 3175
 Damm, R. 1166
 Danared, H. 1735
 Danby, G. T. 2883
 Danilov, V. 3429, 3711
 Danly, B. G. 2575, 2656, 2690
 Dasbach, D. 1080
 Datte, P. 1703, 2118, 2483, 3127
 D'Auria, G. 953, 956, 1145
 D'Auria, J. M. 1641
 Dauvergne, J. P. 2739
 Davidson, A. D. 1175
 Davis, K. 2967
 Davis, P. 561, 2976, 3003, 3216, 3543
 Davis, T. J. 2653, 2687
 Dawson, J. 2462
 Dawson, R. 1733
 Deadrick, F. 703
 Debiak, T. 821
 Debiak, T. W. 2420, 3193
 Decker, C. 2635
 Decker, F. 3582
 Decker, F.-J. 414, 2019, 2278, 2435, 2507, 3234, 3240, 3576

Decker, G. 188, 2196, 2263, 2275, 2304
 Decker, G. A. 1814
 Deckers, R. 1820
 DeFord, J. 3450
 Degen, C. M. 2310
 DeHaven, R. 1021, 1683
 Dehen, J. 3142
 Dehning, B. 44
 Deitinghoff, H. 3139, 3142
 de Jong, M. S. 829, 832, 835, 1039
 Dekkers, E. 2892
 de Lamare, J. 1318
 Delaunay, M. 2997
 Delayen, J. R. 288, 838, 1715, 3666
 Delchamps, S. W. 2769
 Delcourt, B. 2513
 Delhez, J. L. 1820, 2062, 2065, 2423
 Delikaris, D. 2739
 Dell, G. F. 171
 Delmere, C. 2492
 Delsart, P. 670, 697
 de Mascureau, J. 670, 697, 2115
 de Menezes, D. 858
 Demmel, E. 1178
 Demos, P. T. 829, 832
 Demroff, H. 2711
 Demroff, H. P. 2705, 2708
 Demsky, M. I. 682
 Deng, D. P. 1172
 Denney, P. 1154, 1669
 Denney, P. M. 1232, 2391
 Depaola, F. 1013
 Derenchuk, V. 29, 224, 227, 420, 3184
 de Rijk, G. 1937, 2001
 Deruyter, H. 543, 620, 907, 986, 1121
 Derwent, P. F. 2199
 De Salvo, L. 1524
 Desforges, B. 2001
 Despe, O. D. 1864
 Destler, W. W. 685
 Devin, A. 670, 697, 2115
 Devred, A. 2769
 deVries, G. J. 3169
 Dewa, H. 1697
 Dey, J. 405, 1223
 Diamond, W. T. 1381
 Dickey, C. 1339
 Didelez, J. P. 3093
 Didenko, A. A. 2022
 Dienel, S. 1477
 Dikansky, N. 3243
 Dikansky, N. S. 2022, 3684
 DiMarco, J. 2769
 DiMarco, J. N. 1021
 Di Massa, G. 2154
 Dinkel, J. 1357
 Dinova, K. 1620
 Diviacco, B. 1587, 1590, 1593
 Dmitrieva, I. 2769
 Do, S. H. 3196
 Dobeck, N. 587
 Doble, N. 1363
 Doi, M. 1783, 1786

Dolinsky, A. V. 3822
 Dolique, J.-M. 3567
 Dombbeck, T. 2731, 2757, 2763
 Dombrowski, R. 2459
 Donahue, J. 369
 Donald, M. 131
 Dong, W. W. 1448
 Dooling, J. 1709
 Doolittle, L. R. 748
 Doose, C. 2802, 2805
 Doose, C. L. 2799
 Dorfman, J. M. 2010
 Dortwegt, R. 3857
 Douglas, D. 587, 1895
 Douglas, D. R. 584, 2929
 Dovbaya, A. 1480
 Dow, K. 2054, 2868
 Dow, K. A. 2935, 2938, 2941
 Dowell, D. 2967
 Dreher, K. 2748
 Drew, M. M. 2705
 Drobot, A. 3267
 Drozhdin, A. I. 1360, 3109, 3772
 Drury, M. 841
 Ducar, R. 2199
 Dugan, G. F. 3717
 Dunbar, A. 1166
 Dunn, A. 2199
 Dunnam, C. R. 578, 2394
 Dutt, S. 29, 224, 227, 267, 420, 3609
 Dutto, G. 2991
 Duval, M. 1789
 Dvornikov, V. A. 844
 Dwinell, R. 3748
 Dwyer, S. 2760
 D'Yachkov, M. 3330
 Dykes, D. M. 3594, 3672
 Dylla, H. F. 748, 3867
 Dymnikov, A. 206, 3618
 Dyskant, A. 454

E

Early, R. 620, 2025
 Early, R. A. 2880
 East, G. 29, 224, 227, 420
 Eaton, L. 1154
 Eaton, L. E. 2391
 Ebihara, K. 673
 Eden, J. R. 3485
 Edwards, D. A. 134
 Edwards, H. 918
 Edwards, H. T. 537
 Efimov, S. 300, 1480, 2057
 Egan-Krieger, G. V. 1887
 Ehrlich, R. 995
 Ehrnstén, K. 1735
 Eickhoff, H. 357, 1645, 1738
 Eidelman, Y. 450
 Einfeld, D. 149, 152, 1477
 Eisen, N. 2076, 2352
 Ekdahl, C. A. 2400
 Elayi, A. 3093
 Elia, R. 2172
 Elkins, J. 1160
 Elkonin, B. V. 849

Elliot, T. S. 2705
 Elliott, T. S. 2708, 2711
 Ellis, S. 1718
 Ellison, J. 423
 Ellison, J. A. 387, 3588
 Ellison, M. 29, 224, 227, 420
 Ellison, M. J. 3536
 Ellison, T. 29, 224, 420, 3745
 Ellison, T. J. P. 2243, 2289, 3536
 Elmgren, K. 1771
 Elsener, K. 1363
 Emery, L. 2266, 3360
 Emma, P. 116, 429, 635, 2019, 2160
 Emma, P. J. 98, 100
 Emoto, T. 546
 Endo, K. 1291
 Enegren, T. 846, 877, 941, 1703
 Enge, H. 2868
 Engels, O. 3139
 Engström, A. 1735
 Enomoto, A. 546, 590, 2516, 3087, 3705
 Eppley, K. 1106
 Eppley, K. R. 1190
 Erdman, K. 1733
 Erdt, W. K. 2956
 Erg, G. 1384
 Erickson, J. 1669
 Esarey, E. 2626, 2629, 2632
 Esin, S. 2426
 ESRF Project Team 1427
 Evans, D. 3127
 Evans, K., Jr. 188, 2263, 2275
 Evans, L. R. 1983
 Everett, M. 2551, 3003
 Evstigneev, A. 1384
 Eyharts, P. 670, 697
 Eyl, P. 670, 697
 Eylon, S. 703, 706, 709, 712, 3199

F

Fabbricatore, P. 1001
 Fabris, A. 953, 956, 1145
 Fabris, R. 1333, 1378
 Facco, A. 849
 Faehl, R. 2675
 Faehl, R. J. 2664
 Fahmie, M. 1869
 Faillon, G. 1184
 Fainberg, Y. B. 2620
 Faltens, A. 703, 721, 724
 Fan, J. Y. 1943
 Fan, M. 306, 1721, 2841
 Fang, J. 2578
 Fant, K. 543, 1106
 Fant, K. S. 620
 Farias, R. H. A. 1089
 Farkas, Z. D. 620, 1121, 1196, 1208
 Parkhondeh, M. 1372, 2054, 2868, 2935, 2938, 2941
 Fasanello, T. 2397
 Fathizadeh, M. 1288
 Faugier, A. 2001

Faure, J. 1465
 Faus-Golfe, A. 2045
 Fawley, W. M. 724, 1530
 Fazio, M. 2675
 Fazio, M. V. 2664
 Fedele, R. 209, 212
 Fedorov, V. 2769
 Fedotov, Y. S. 315, 318
 Feinberg, B. 2187, 3748, 3751
 Felker, B. 1551, 1554
 Fenstermacher, M. 1551
 Fenstermacher, M. E. 1554
 Ferguson, M. 1294
 Ferguson, S. W. 1551, 1554
 Ferioli, G. 2498, 2504
 Fero, M. 2172
 Ferrario, M. 573, 968, 3279
 Ferry, J. 3745
 Feschenko, A. 2426
 Fessenden, T. 703
 Ficklin, D. 1318
 Fieguth, T. 3084
 Fields, S. 1551
 Fields, W. F. 1554
 Filimonov, M. Z. 2208
 Filtz, M. 901, 1036
 Fink, C. L. 375
 Finley, D. A. 3721, 3806
 Fiorito, R. B. 1620, 2397, 2453
 Firebaugh, J. 1817, 1912
 Firjahn-Andersch, A. 3139
 Fischer, C. 2504, 3597
 Fischer, G. E. 44
 Fischer, J. 2929
 Fischer, R. 2632
 Fischer, W. 246, 2301
 Fisher, A. 2632
 Fisher, A. S. 2578
 Fishler, Y. 1297
 Fitzgerald, D. 366, 369, 2216, 2219, 3297
 Fitzgerald, D. H. 3739
 Flannigan, J. 1852
 Flanz, J. 2868, 2871, 2874, 3851
 Flanz, J. B. 1875, 2054, 2331
 Fleck, R. 1080
 Flora, R. 1914
 Flynn, T. 889
 Foelsche, H. W. 2895
 Foerster, C. 3836, 3876
 Foley, M. 852, 3294
 Fomin, M. 1226
 Fong, B. 1483
 Fong, K. 1139
 Fontana, J. R. 2614
 Force, R. 3748
 Forest, E. 131, 291
 Fortgang, C. M. 2480, 3118
 Fouaidy, M. 855
 Fougeron, C. 858
 Fowkes, R. 1106
 Fowkes, W. R. 620, 1259
 Fowler, W. 3793, 3796
 Fowler, W. B. 2823
 Fox, J. 2352
 Fox, J. D. 2076, 2109
 Fox, W. 995, 1712
 Fraivillig, J. 2790
 Franck, A. 2249, 2835

Franczak, B. 1645, 3736
 Frandsen, P. 2956
 Frandsen, P. K. 2739
 Frankle, S. 366, 369, 2216, 2219, 3297
 Franzke, B. 357, 1645, 1738
 Frias, R. 3748
 Friddell, K. 2967
 Friedman, A. 105, 703, 727, 730, 1599, 2284
 Friedrichs, C. 803, 824
 Friesel, D. 29, 224, 227, 420, 3184
 Frisch, J. 3045, 3047
 Frisch, J. C. 2978, 3027, 3036
 Frischholz, H. 1247, 2358
 Fritsche, C. T. 2501
 Fu, S. 1686
 Fugitt, J. 939, 1109
 Fuja, R. 605
 Fujita, H. 1697
 Fujita, Y. 2260
 Fukuda, S. 1193
 Fuller, R. 543
 Fullett, K. D. 3309
 Funakoshi, Y. 3497
 Funk, L. W. 812, 1700, 1706, 2130
 Funk, W. 1703, 1765, 3585
 Furman, M. A. 3485
 Furukawa, K. 2516, 3087, 3705
 Fuzesy, R. 2172

G

Gabella, W. 420, 2051, 2638
 Gabella, W. E. 233
 Gagliardi, P. 1063
 Gai, W. 2596, 3050
 Gallardo, J. C. 2578, 3012, 3081, 3615
 Gallo, A. 778
 Galloway, C. 620
 Galluccio, F. 209, 2154
 Galyaev, N. A. 454
 Gammel, G. 3193
 Ganetis, G. 2744, 2766
 Gannon, J. 1898, 2731, 2757, 3870
 Gao, J. 862, 865, 868
 Gao, S. 745, 3521, 3696
 Garavaglia, T. 3591, 3609, 3769
 Garber, M. 2744, 2766
 Gardelle, J. 626
 Garden, C. 3033
 Garden, C. L. 2978, 3027, 3036, 3039
 Gardner, C. 3633, 3763
 Gardner, M. 1439
 Gareyte, J. 246
 Garnett, R. 1712
 Garoby, R. 3570
 Garren, A. 2051, 3778
 Garren, A. A. 137
 Gath, B. 1572
 Gattignon, L. 1363
 Gattu, R. 2760

Gavrilov, N. 1226
 Gayot, P. 2956
 Gelsik, C. 3172
 Gelbart, W. Z. 3099
 Gelfand, N. 2835
 Gelfand, N. M. 3790
 Geller, J. 1277
 Gemme, G. 775, 1001, 1524
 Genasio, P. 806
 Genin, R. B. 3018
 George, M. J. 661
 Georges, P. 3033
 Gerasimov, A. 3276, 3291
 Gerig, R. 267, 3558
 Gerig, R. E. 333
 Geschonke, G. 2358
 Gevchuk, A. 1480
 Ghosh, A. 2744, 2766
 Ghosh, A. K. 2742, 2790
 Giacuzzo, F. 3842
 Giannini, M. 1378
 Giardino, G. 3202
 Gierman, S. M. 2970
 Giguët, E. 2656
 Gilgenbach, R. M. 2693, 3351, 3354
 Gillespie, G. H. 86
 Gillier, R. 3900
 Gilpatrick, J. D. 1669, 2163, 2316, 2334, 2480
 Giovannozzi, M. 246, 273, 500
 Giove, D. 1524
 Girard, M. 2997
 Gjaja, I. 3387
 Gladkikh, P. 1480, 2057
 Gladkikh, P. I. 194
 Gläser, W. 1477
 Glass, H. D. 351, 2829, 2856, 2859
 Glenn, J. W. 3633, 3763
 Glock, H.-W. 614, 623
 Gluckstern, R. L. 221, 1545, 3219, 3387, 3390
 Godden, D. 1709
 Goderre, G. 354, 3482
 Godfrey, G. 3084
 Godwin, R. P. 3090
 Goetz, T. 1477, 2534
 Golceff, P. 3018
 Gold, S. 1318
 Gold, S. H. 2644, 2647
 Goldberg, D. A. 871, 874
 Goldin, L. 1771
 Goldman, M. 1166
 Goldman, M. A. 2916, 2919
 Goldstein, J. C. 3090
 Golubeva, N. 441, 444
 Gonçalves da Silva, C. E. T. 252, 390, 1454
 Gonczy, I. 2769
 Gonichon, J. 2575, 2696, 2699
 Gonzalez, R. E. 2322
 Goodwin, J. E. 2835
 Goren, Y. 824, 846, 877, 880, 883, 1703, 3405, 3888
 Gormley, M. 1127
 Gorniker, E. 1226
 Gould, H. 3751
 Gourber, J.-P. 68

Gourlay, S. 2769
 Govil, I. M. 1753
 Gower, E. 1244
 Graber, J. 886, 889, 892, 918
 Grafström, P. 1363
 Granatstein, V. I. 2572
 Granatstein, V. L. 2667, 2670, 2673
 Gras, J. J. 2495, 2504
 Grau, M. C. 2528
 Gray, E. 1021
 Green, K. 998
 Greene, A. 2744, 2766
 Greenwald, Z. 3690
 Gregory, W. 3055
 Greiner, P. 798
 Greiner, M. 1747
 Grelick, A. 605, 2412
 Grenier, J. 626
 Gribov, I. V. 2059
 Griffin, J. 405
 Griffin, J. E. 408
 Grigor'ev, Y. 2057
 Grimm, T. 824, 1083
 Grimm, T. L. 3252
 Grippe, J. 827, 1250, 3213
 Grippe, J. M. 1169
 Grishanov, B. I. 2022
 Grossberg, P. 2106
 Grote, D. 703, 709
 Grote, D. P. 727
 Groupe d'Etudes des Cavités Supraconductrices 796
 Groves, T. 2249
 Grüneberg, H. 2748
 Grua, P. 670, 697
 Gruber, A. 1645
 Grudzien, D. M. 2213
 Grun, J. 2632
 Grusell, E. 1771
 Guharay, S. K. 3145, 3648
 Guidee, P. 1184, 1187
 Guidi, V. 3243
 Guigli, J. 1238
 Guignard, G. 3336, 3426, 3600
 Guirlet, R. 2450
 Guk, I. 2057
 Gulley, M. 369
 Gundersen, M. 3039, 3072, 3537
 Gundersen, M. A. 3066
 Günther, C. 3381
 Guo, Z. Y. 3237
 Gupta, R. 258, 2744, 2766
 Gupta, R. C. 2754, 2778
 Guratzsch, H. 1477
 Gurd, D. P. 1916
 Güzewell, D. 2956
 Gutscher, W. D. 1154
 Guy, F. 1703, 2986, 3585
 Guy, F. W. 122, 2124, 2127, 2426, 2483, 3130

H

Haas, A. 2222
 Haber, C. 2199

Haber, I. 724, 727, 730, 3612, 3627, 3660
 Haberichter, W. 2462
 Habs, D. 1747
 Haebel, E. 806, 898
 Haenni, D. 2757
 Hafizi, B. 1560, 1623, 2584, 2644, 2647
 Hage-Ali, M. 1363
 Hagedoorn, H. L. 1072, 2062, 2065, 2892, 2927, 3423, 3645
 Hahn, A. 2193
 Hahn, K. 3285
 Hahn, R. v. 1747
 Hairapetian, G. 561, 2976, 3003, 3216, 3543
 Halbach, K. 1445, 1581, 1599, 1608, 1727
 Halbleib, J. A. 691
 Halka, M. 369
 Hall, J. 32, 1244
 Hall, T. 2865
 Halling, A. M. 472, 474, 2193
 Halling, H. 1253
 Halling, M. 3814
 Halliwell, J. 3748
 Hamilton, B. 29, 224, 227, 420, 3745
 Hamilton, B. J. 2243, 2289, 3536
 Hamm, C. 962
 Han, H. S. 2796
 Hanaki, H. 590, 1163, 3087
 Hancock, S. 3570
 Hanft, R. 2769
 Hanna, B. 354, 1357
 Hanna, S. 1419
 Hanna, S. M. 895, 1118
 Hansberry, E. 1154
 Hansen, S. 1229
 Hanson, D. L. 694
 Haraguchi, M. 1518
 Hardek, T. 2319, 3297
 Hardek, T. W. 2240
 Hardekopf, R. A. 3760
 Harding, D. J. 2823, 2826, 2829
 Harfoush, F. A. 342, 345, 348, 351, 2829
 Harkay, K. 3258
 Harkay, K. C. 3306
 Harkewicz, R. 1694
 Harmer, P. 1916
 Harms, E. 3533
 Harms, E., Jr. 3803
 Harris, K. 1318
 Hart, R. 1901
 Hartley, R. 1527
 Hartman, S. 575, 2976, 3003, 3357, 3543
 Hartman, S. C. 561, 3216
 Hartmann, B. 1477
 Hartog, P. D. 1709
 Hartung, W. 898, 921, 3450
 Haseroth, H. 2720
 Hashimoto, Y. 1780, 1783
 Hassenzahl, W. 1572
 Hassenzahl, W. V. 1575, 1584
 Hatton, V. 2001
 Hattori, T. 1783, 1786, 3115
 Haug, F. 2739

Havviller, C. 3854
 Hawkins, S. A. 739
 Haworth, M. 1703, 2124, 2986
 Hayashi, S. 2039
 Hayes, T. 1241
 Haynes, W. 2675
 Hays, T. 3450
 Hayward, T. D. 1075
 Hayworth, M. D. 846
 He, A. 2775
 Hebert, J. 2986, 3151
 Hebert, J. E. 2483
 Heefner, J. 1838
 Heese, R. 608
 Heifets, S. 543, 3456, 3459
 Heifets, S. A. 3462
 Heinrichs, H. 995
 Hellborg, R. 206, 3618
 Heller, H. 2892
 Helm, R. 92, 131, 185
 Helser, A. 1399
 Hemmer, F. M. 2919
 Hendrickson, L. 1972, 2106
 Hendry, G. O. 1730
 Henestroza, E. 703, 709, 3199
 Henke, H. 549, 901, 904, 1133, 2593, 3288
 Henrichsen, K. 44
 Henriot, C. 798
 Herr, S. 2187
 Herriander, C. J. 1735
 Herrup, D. 2199
 Herrup, D. A. 2249
 Herz, P. R. 3190
 Hettel, R. 2275
 Heuer, R. 1439, 2420
 Heuer, R. L. 1527, 3012
 Hewett, D. 703
 Hewett, D. W. 706, 718
 Heydari, H. 411
 Hicks, J. 3184
 Higgins, C. S. 2298
 Higo, T. 1027, 3503
 Hildreth, M. 2019
 Hilke, J. 1735
 Hill, B. W. 86, 1762
 Hill, J. 1154
 Hill, N. 3050
 Hill, S. F. 3594, 3672
 Hiller, M. 921
 Hilleret, N. 806
 Himel, T. 1972, 1975, 2019, 2106, 2373
 Himeno, Y. 546
 Hindi, H. 2076, 2352
 Hinkson, J. 2097, 2109
 Hipple, R. 703
 Hiramatsu, S. 673
 Hiramoto, K. 309
 Hirano, K. 546
 Hirao, Y. 1291, 1686
 Hirata, K. 466, 3491
 Hirota, J. 309
 Hirshfield, J. L. 2584
 Hitz, D. 2997
 Ho, C. 1844, 2596, 3050
 Hoag, H. 543, 1106
 Hoag, H. A. 620, 907, 1121
 Hochadel, B. 1747

Hodgson, J. A. 1039
 Hoesberling, R. F. 2664
 Hoehn, M. 3739
 Hoffberg, M. G. 1957
 Hoffstätter, G. H. 164
 Hoffler, A. 587, 1895
 Hoffler, A. S. 2298
 Hofman, J. M. A. 3423
 Hofmann, A. 44, 173, 3429
 Hogan, B. 2667, 2670
 Hogan, M. 3494
 Hogrefe, R. 2799, 2802, 2805
 Holdener, F. 3836
 Holmes, S. 3793
 Holt, J. A. 80, 3806
 Holtzapple, R. 638
 Holtzapple, R. L. 3234, 3564
 Honaberger, D. 3055
 Honaberger, D. J. 2944
 Honma, H. 1416
 Hooper, E. B. 1551, 1554
 Horan, D. 1294, 3757
 Hori, T. 602
 Hori, Y. 3903
 Horton, T. E. 1413
 Hou, Y. 2841
 Houck, T. L. 2590, 2611
 Hourany, E. 3093
 Hovater, C. 587, 3515
 Hovater, J. C. 2364
 Howard, D. 1160, 3748
 Howell, J. 1497, 1500
 Hower, N. 2889
 Hoyer, E. 1572, 1575, 1581, 1584, 2850
 Hoyt, E. 3033
 Hoyt, E. W. 2978, 3036, 3039
 Hs, I. C. 2465
 Hseuh, H. C. 3897
 Hsieh, H. 611, 3906
 Hsu, I. 2151, 2638
 Hsu, K. T. 2031, 2091
 Hsu, T. 3066, 3072
 Hsue, C. S. 1943, 3369
 Hu, K. H. 2091
 Hu, Y. 2841
 Huang, H. 29, 224, 227, 420, 432
 Huang, T. H. 2465
 Huang, Y. 3558
 Hughes, E. 2172
 Hughes, E. A. 3594, 3672
 Hughes, T. 3055
 Hughes, T. P. 661
 Hui, M. 1160
 Hui, Z. 1557
 Hulsey, G. 803, 824, 877, 1083
 Hulsey, S. 1551
 Hulsey, S. D. 1554
 Hüllsmann, P. 614, 623
 Humphrey, R. 543
 Humphries, D. 1572, 1575, 1581
 Humphries, S. J., Jr. 1199
 Hunt, D. 3748
 Hunt, S. 128, 1823, 1826, 1829, 1838
 Hunter, T. 393
 Hur, J. 1327
 Hurd, J. 1703, 2986, 3127, 3509

Hurd, I. W. 122, 2124, 2127, 2130, 2426, 2444, 3130, 3585
 Hurh, P. 2148, 2459, 3533
 Husmann, D. 152
 Hutchison, R. M. 829, 832
 Hutson, R. 363, 366, 369, 2216, 2219, 3297
 Hutton, A. 527
 Hwang, C. 1393
 Hwang, G. J. 2886
 Hyodo, K. 1468

I

Ieiri, T. 2292, 2295, 3333
 Igarashi, Z. 1163
 Ihloff, E. 2054, 2331, 2868, 2871, 2874, 3851
 Iida, T. 1515
 Ikegami, M. 1697
 Ikezawa, M. 1614, 1617
 Iliev, A. 3784
 Imanishi, A. 1783
 Ingalls, W. 3118
 Ingalls, W. B. 1669
 Ingold, G. 1439, 1602
 Inoue, M. 1697
 Irwin, J. 92, 95, 116, 119, 131, 185
 Ishi, K. 1614, 1617
 Ishida, T. 2540
 Ishimaru, H. 3885
 Ishizuka, H. 676, 1566
 Ishkhanov, B. S. 2059
 Itano, A. 1291, 1686
 Ivanov, A. S. 555
 Ivanov, P. M. 2022
 Ivanov, S. 3561
 Ivers, J. D. 1312, 2687
 Iwashita, Y. 1697, 3154
 Izawa, M. 930

J

Jach, C. 1297
 Jachim, S. P. 1154, 1232, 2391
 Jackson, A. 1432
 Jackson, G. 402, 1366, 2148, 2418, 2525, 3021, 3363, 3366, 3533
 Jackson, G. P. 3799
 Jackson, J. W. 2883
 Jackson, L. T. 1265
 Jackson, M. C. 1554
 Jacobs, K. 3851
 Jacobs, K. D. 1875, 2054, 2331
 Jacobsen, R. 44
 Jacquet, F. 2450
 Jaenker, P. 1019
 Jaeschke, E. 1474, 1747
 Jaffery, T. S. 2769
 Jahnelt, L. 390
 Jain, A. 2744, 2766
 Jain, A. K. 2754, 2778
 Jakob, H. 2301

Jamason, R. 1683
 Jamason, R. A. 3926
 Jamieson, G. 1703, 2118, 2127
 Jan, G. I. 1878, 2091
 Jansen, D. 1477
 Jason, A. 1683
 Jason, A. J. 56, 3760
 Jean, P. 3093
 Jeanjean, J. 2513
 Jeansson, J. 1735
 Jejcic, A. 3093
 Jenner, D. 1421
 Jensen, C. 1357
 Jensen, D. R. 2838
 Jensen, K. 1300
 Jernag, D. 3757
 Jia, H. 2841
 Jiang, B. 1327, 3078
 Jiang, S. 3390
 Jiao, C. 2841
 Jiao, J. 2841
 Jin, J. T. 3196
 Joba, R. K. 2234, 2423
 Joh, K. 71, 89
 Johnson, A. 939
 Johnson, A. M. 1220
 Johnson, C. D. 626
 Johnson, D. 236, 378
 Johnson, J. 2109
 Johnson, K. F. 1669, 3118
 Johnson, P. 2967
 Johnson, R. P. 1451, 1949
 Johnson, R. R. 3099
 Johnstone, C. 1912
 Johnstone, J. 342
 Jones, A. 2118
 Jones, C. M. 1660
 Jones, R. M. 936
 Jones, T. A. 3063
 Jones, W. P. 29, 224, 227, 420
 Jonker, M. 2001
 Joshi, C. 561, 2551, 2976, 3003, 3216, 3543
 Jost, W. 998
 Jostlein, H. 2835
 Joubert, A. 1789, 1792
 Jowett, J. M. 2013
 Joyce, G. 1560, 2626
 Judd, D. 703
 Judkins, J. 3240
 Judkins, J. G. 1039
 Juillard, C. 3429
 Juillard, J. C. 2358
 Julian, J. 1238
 Junck, K. 3540
 Jung, J. 3654
 Jung, K.-S. 3196
 Jung, R. 2202, 2495, 2498, 2504
 Junk, T. 2172
 Junquera, T. 855
 Juras, R. C. 1660
 Jurgens, T. 852

K

Kadnikov, A. 564, 1348
 Kadokura, E. 2540

Kahana, E. 1814, 2112, 2237, 2304
 Kahn, S. 2744
 Kahn, S. A. 2754, 2766
 Kaiser, H. 944
 Kakigi, S. 1697
 Kakiyama, K. 3087
 Kako, E. 992, 1024
 Kalbfleisch, C. 1823, 1826, 1829
 Kalbreier, W. 2013
 Kallberg, A. 1735
 Kalnins, J. 3748
 Kaltchev, D. 2042
 Kamada, S. 1468
 Kamikubota, N. 3087
 Kamitani, T. 590, 2516, 3087, 3705
 Kamiya, Y. 930, 1509, 2260, 2295, 2337
 Kanai, T. 1614, 1617
 Kanazawa, K. 3860
 Kanazawa, M. 1291, 1686
 Kang, B. K. 2751, 2796
 Kang, H. 1521
 Kang, Y. G. 1268
 Kang, Y. W. 549, 766, 910, 913, 1057
 Kapchinskiy, I. M. 1675
 Kapustin, A. A. 3822
 Karabekov, I. P. 457
 Karas', V. I. 664, 2620, 3546
 Karl, F. X. 2919
 Karlner, M. 824
 Karnaukhov, I. 1480, 2057
 Kasha, D. 1166
 Kashihin, V. S. 3822
 Kasproicz, T. B. 2708
 Kasuga, T. 2409
 Katalev, V. 916
 Katayama, T. 41, 1783, 1786
 Katkov, V. M. 3093
 Kato, R. 1614, 1617
 Kato, S. 3518
 Kato, T. 1291
 Kato, Y. 2556
 Katsouleas, T. 2635, 2638, 3543
 Katsura, T. 2257, 2260, 2295, 2337, 2409
 Kauffman, S. 267
 Kauffmann, K. 3609
 Kauffmann, S. 2489
 Kauffmann, S. K. 137, 197
 Kauppila, T. 3055
 Kawakubo, T. 2540, 2556, 3552
 Kawamura, M. 1163
 Kawamura, Y. 3006
 Kawasaki, S. 676, 1566
 Kawazu, S. 3115
 Kazacha, V. 2042
 Kazarezov, I. 2650
 Kazarinov, N. 2042
 Kazimi, R. 599, 939, 1109
 Kazmark, D., Jr. 2919
 Keane, J. 608, 1118, 1419, 1852
 Keating, P. 369
 Keeney, D. S. 706
 Kehne, D. 62, 65, 3282, 3627
 Keller, F. 2811
 Keller, R. 2910

Kelley, E. 2790
 Kellogg, N. 1160
 Kelly, E. 2744
 Kennedy, W. L. 838, 1042
 Kerns, C. 1214
 Kerns, Q. 1127, 1214
 Kersevan, R. 3842, 3848, 3888
 Kerslick, G. S. 1312, 2687
 Kersteins, D. 1669
 Kewisch, J. 1835, 1895
 Kheifets, S. 543, 635
 Kheifets, S. A. 3462
 Kick, R. 233
 Kiehlmann, D. 1080
 Kijima, Y. 1518
 Killian, E. 2744
 Kim, C. H. 2036
 Kim, D. E. 2751, 2796
 Kim, G. H. 2564
 Kim, J. 2593
 Kim, J. M. S. 1112
 Kim, J. S. 3288
 Kim, K. 2799, 2802, 2805, 2808, 2814
 Kim, K.-J. 83, 1445, 1533, 3042
 Kim, S. H. 2799, 2802, 2805, 2808, 2814
 Kim, W. 3196
 Kimura, T. 2690
 Kimura, W. D. 2564, 2581, 2614
 Kimura, Y. 673
 Kincaid, B. 1572, 1575, 1578, 1581
 King, R. 2172
 Kinross-Wright, J. 2664
 Kinross-Wright, J. M. 2970
 Kinsho, M. 3181
 Kipper, A. 3139
 Kirbie, H. C. 739
 Kirby, R. E. 2978, 3030, 3036
 Kirchgessner, J. 763, 769, 886, 889, 892, 918, 921, 977, 995, 1399, 2953, 3450
 Kirchman, J. 2266
 Kirk, H. G. 3012, 3615
 Kirkman, G. 1327, 3066, 3072, 3078
 Kirsch, R. 3093
 Kiselev, V. A. 2022
 Kishimoto, T. 1515, 1518
 Kishiro, J. 673
 Kitagawa, A. 1291
 Kitagawa, S. 1686
 Kitagawa, Y. 2556
 Klaisner, L. 3033
 Klaisner, L. A. 2978, 3027, 3036
 Klamp, L. 3384
 Kleb, R. 3757
 Kleeven, W. J. G. M. 1072, 2065, 3423
 Kleffner, C. M. 1747
 Klein, H. 614, 623
 Kleman, K. J. 924, 1235
 Klepper, O. 1645
 Kloeppel, P. K. 2298
 Kneisel, P. 927, 947, 1010, 1016, 1060, 3867
 Knobloch, J. 889
 Knott, J. 2720

Knott, M. 1960
 Knowles, H. B. 1762
 Knox, A. 3757
 Knox-Seith, J. F. 255
 Ko, I. 581, 1521, 3654
 Ko, I. S. 593
 Ko, K. 936, 986, 1039, 1121
 Kobari, T. 3903
 Kobayashi, H. 3087
 Kobayashi, M. 3903
 Kobayashi, T. 3552
 Kobayashi, Y. 215, 1321
 Kobliaka, G. R. 2823
 Kocur, P. 236, 1369
 Kodaira, M. 1515, 1518
 Kodama, R. 2556
 Koechlin, F. 798
 Koepke, K. 918, 1127
 Kohno, T. 1291, 1686
 Koiso, H. 3497
 Kokorin, A. M. 3822
 Kolomiets, A. A. 1675
 Kondakov, A. 1226
 Konecny, R. 815, 2596
 Kong, S. H. 2970
 Kononenko, S. 1480, 2057
 Koo, Y. M. 2751, 2796
 Koontz, R. 543, 620
 Koontz, R. F. 1318
 Koop, I. 3711
 Koopman, J. 2504
 Korchuganov, V. 230, 564, 1384, 2793
 Korenev, I. L. 2543
 Koscielniak, S. R. 3506, 3639
 Koseki, S. 1291
 Koseki, T. 930, 1509, 2295
 Koshelkin, A. V. 1629, 1632
 Kostas, C. 3267, 3270
 Kosyakin, M. 2769
 Kot, N. C. 3243
 Kotov, V. I. 454
 Koujbida, R. P. 2853
 Koul, R. 2922
 Koul, R. K. 2924
 Kourbanis, I. 35, 405, 3630, 3799
 Koutchouk, J. P. 44, 68
 Kovachev, V. 3888
 Kowalski, S. 2054
 Kowitt, M. 2172
 Kozchekin, M. A. 2853
 Kozin, V. 1480, 2057
 Kozub, S. 2769
 Kozyrev, E. 2650
 Krafft, G. A. 426, 587, 599, 1895, 2298, 2364, 3246, 3515
 Kraimer, M. 1960
 Krall, J. 2626, 2629, 2632
 Krämer, D. 1436, 1474
 Krasnopolsky, V. 2717
 Krasnopolsky, V. A. 933
 Krasnykh, A. 552, 2042
 Kraus, R. 1669, 1703
 Kraushaar, P. 2731, 2757, 2763, 3888
 Krauter, K. 1922
 Krawczyk, F. 1712
 Krebs, G. 2187
 Kreiser, H. 32

Krejcik, P. 2019, 2370, 2373, 3240
 Kreutz, R. 2748
 Krinsky, S. 492, 1439, 1491, 1545, 1599, 1602, 1852, 3375
 Krishnaswamy, J. 1527
 Kroc, T. K. 1689
 Kroes, F. 1998, 2343
 Krogh, M. 2124, 2130
 Krogh, M. L. 2501
 Kroll, N. 620, 936, 1039, 1121, 2559
 Kroll, N. M. 543, 983, 1196, 3453
 Kropachev, G. N. 3675
 Krueger, W. 1004, 3267
 Krug, H. 1477
 Krupnick, J. 83, 2850
 Krycuk, A. 939, 1109
 Krylov, Y. 564
 Kryshkin, V. I. 454
 Kuang, E. 2687
 Kubo, H. 1291
 Kubo, K. 992, 1027, 2364, 3503, 3515
 Kubo, T. 1163
 Kubota, C. 1163
 Kuchair, M. 918
 Kudelainen, V. 3243
 Kudelainen, V. I. 2022
 Kudo, H. 1509
 Kudo, K. 1163
 Kudryavtsev, V. 916
 Kukhtin, V. P. 3205
 Kulikov, A. V. 2978, 3027, 3036
 Kulinski, S. 336, 573, 611, 968
 Kulipanov, G. 564, 1384
 Kulipanov, G. N. 2751
 Kumada, M. 1291, 1686
 Kumazawa, R. 2205
 Kunkel, W. B. 1727
 Kuo, C. C. 1635, 1943
 Kuo, C. H. 2091
 Kuo, T. 372
 Kuo, T. T. Y. 1730
 Kuprianov, A. P. 682
 Kuptsov, I. 1226
 Kuramoto, R. 1300
 Kurennoy, S. S. 3417, 3420
 Kurkin, G. 1226
 Kurochkin, I. A. 2190
 Kuroda, S. 2340
 Kurokawa, S. 294, 2004, 2073
 Kurz, M. 614, 623
 Kusche, K. P. 2564
 Kushin, V. V. 1798
 Kushnick, P. 1016
 Kuske, B. 1474
 Kuske, P. 1474
 Kustom, R. 285, 549, 1013, 1057, 1294, 3757
 Kustom, R. L. 766, 910, 913, 1217, 2213, 3393, 3396
 Kuzmin, I. A. 844
 Kuznetsov, G. 2650
 Kuznetsov, N. A. 2022
 Kuznetsov, S. 564, 1506, 1955
 Kvashonkin, I. 2042
 Kwan, C. M. 2385
 Kwan, J. W. 3169

Kwan, T. 2675
 Kwiatkowski, S. 824, 941
 Kwok, P. 2638
 Kwon, S. 1832
 Kwon, S.-I. 3042

L

Labrousche, J. 670, 697
 Lackey, J. 2228
 Lackey, S. 1912, 1914
 Laclare, J. L. 1427
 Lahey, T. 1969
 Lai, P. 2638
 Laird, R. J. 1814
 Lal, A. 2551
 Lamanna, G. 3243
 Lambert, G. 2376
 Lambertson, G. 1039
 Lambertson, G. R. 2109
 Lamm, M. J. 2769
 Lamont, M. 1937, 2001
 Lampel, M. 3009
 Lamzin, E. A. 3205
 Lancaster, C. 2967
 Landis, R. 2222
 Langdon, A. B. 730, 733, 3660
 Lange, F. 3864
 Langenbeck, B. 3736
 Langenbrunner, J. 1021
 Lanni, C. 3876
 Lanz, P. 1151
 Lapitsky, S. N. 2190
 Lapostolle, P. 3606
 Larsen, R. 2070
 Larsson, B. 1771
 Laslett, L. J. 724
 Lasnier, C. J. 1551, 1554
 Lath, A. 2172
 Latham, P. E. 2659, 2661, 2670, 2673
 Latushkin, S. T. 1795
 Lau, Y. Y. 3351, 3354
 Launspach, J. 670
 Launspach, J. 697
 Lavertv, M. 1139
 Lavine, T. 543
 Lavine, T. L. 620, 1121, 1196, 1208
 Lawson, W. 2667, 2670
 Lawson-Chroco, L. 44
 Laxdal, R. E. 372
 Lazarev, N. V. 1675
 Lebedev, V. A. 2022, 3243
 Leblond, B. 3053
 Le Diberder, F. 2513
 Le Duff, J. 2045
 Lee, B. 2705, 2708, 2711
 Lee, E. P. 3678
 Lee, H. 581
 Lee, H. K. 2796
 Lee, H. S. 593
 Lee, J. C. 1943
 Lee, M. 173, 1483
 Lee, M. J. 108
 Lee, M. K. E. 2667, 2670

Lee, S. Y. 6, 29, 102, 224, 227,
 430, 432, 435, 2845, 3291
 Lee, T. 841, 1106, 1457, 3273
 Lee, T. G. 1259
 Lee, Y. Y. 360, 3633
 Leemann, W. 83, 567, 2638
 Leffert, M. 3900
 Legg, R. 587
 Lehrman, I. 1439
 Lehrman, I. S. 1527, 3012
 Leibfritz, J. 3864
 Leifste, G. T. 2124, 2130, 2426
 Lemaitre, E. 798
 Lenisa, P. 3243
 Lenkzua, F. 1960, 2304
 Lenkzua, F. R. 1814
 Lennon, A. J. 1666, 1756
 Lens, J. 2986, 3133
 Lens, J. W. 3151
 Leonhardt, W. J. 3882
 Leonov, V. V. 1795
 Leontin, S. 1735
 Lepeltier, V. 2513
 Leroy, R. 1789, 1792
 Lessner, E. 1485, 3757
 Lessner, E. S. 399
 Le Taillandier, P. 670, 697
 Leung, K. 3888
 Leung, K. K. 1503, 2787
 Leung, K. N. 1727, 3169, 3190
 Leung, K.-N. 3042, 3160
 Level, M. P. 1465
 Levichev, E. 230, 564, 1384,
 1506, 2793
 Levin, M. 2757
 Levitt, S. 1969
 Levy, C. D. P. 2991
 Lewis, S. 3748
 Lewitowicz, M. 1792
 LHC Machine Group 3917
 Li, C. Y. 1727
 Li, D. 29, 224, 227, 420, 1439,
 2865, 3006
 Li, G. X. 3237
 Li, M. 38, 236
 Li, N. 2862
 Li, Q. 1620
 Li, R. 1909, 3473
 Li, T. 2841
 Li, X. 3527
 Li, Z. 179, 1721
 Liang, C. 2841
 Liang, C. F. 1792
 Liang, D. 3696
 Liebjörk, P. 2068
 Liebmann, J. 1747
 Lien, E. 1106
 Liger, P. 3663
 Likhachev, V. 1480, 2057
 Liljeby, L. 1735
 Lima, S. 1892
 Limberg, T. 429, 2019, 2025,
 2435, 3240
 Lin, K. K. 2031
 Lin, L. 252
 Lin, L. C.-L. 2575, 2696, 2699
 Lin, X. 3453
 Lindaer, A. 1160
 Lindaer, A. F. 2210

Linnecar, T. P. R. 2376
 Linnemann, J. 1477
 Linscott, I. 2076, 2352
 Liou, R. 2638, 3039, 3066, 3072,
 3537
 Liptin, I. M. 1675
 Lipnicky, M. 1151
 Lippmann, G. 944
 Lipeett, M. G. 1039
 Liska, D. 1718
 Littmann, B. 1133
 Litvinenko, V. N. 218, 1442, 2889
 Liu, B. 1611
 Liu, C. J. 688
 Liu, H. 279, 512, 1563, 3663
 Liu, H. C. 2886
 Liu, J. 182, 285, 2841
 Liu, K. 1262
 Liu, Y. 2151
 Liu, Y. C. 1635
 Liu, Z. 2070
 Lo, C. C. 1142, 1238, 3058
 Lobanov, N. R. 3187
 Lockner, T. R. 667
 Loew, G. 1445, 3084
 Loew, G. A. 543, 620, 644
 Logachov, P. 3243
 Loizelet, M. 1672
 Lom, C. 821, 2133
 Lombardi, A. 3121, 3606
 Lopez, F. 2922, 2924
 López, G. 200, 2784, 3255, 3467
 Lorello, M. 1709
 Lorenz, R. 1133, 2325
 Losito, R. 2154
 Low, K. 1823, 1826, 1829
 Lu, J. 2711
 Lu, J. J. 1303
 Lu, X. 3366, 3799
 Lu, X. P. 472
 Lublinsky, B. 1817, 2249
 Luccio, A. 438, 1872, 2175
 Luchini, K. 1265
 Ludewigt, B. A. 1759
 Ludmirsky, E. A. 315
 Ludwig, P. 2997
 Ludwig, T. 3139
 Luginsland, J. W. 3354
 Luijckx, G. 1998
 Lujan, R. 2947
 Lukasiewicz, J. 1890
 Lulevich, V. I. 2853
 Lumpkin, A. 2304
 Lumpkin, A. H. 2086, 2112
 Luo, G. 1211
 Lütkehaus, H. 2748
 Lutz, I. 1265
 Lyashchenko, V. 1480
 Lynch, D. 1439, 3000
 Lynch, M. T. 1683, 2391
 Lyons, S. 608, 611
 Lyssenko, A. 3711
 Lyssenko, W. P. 1669

M

Ma, Y. 1611

Maas, R. 1901, 1998
 Macak, R. 363, 366, 369, 2216,
 2219, 2319, 3297
 Macek, R. J. 3739
 Macek, R. W. 3760
 Macha, K. 2929
 Machida, S. 176, 255, 3224, 3558
 Maciga, B. 3243
 Maciszewski, W. 1890
 Mackenzie, G. H. 372
 Mackenzie, R. 1966
 MacKenzie, R. 1969
 Mackerrow, E. 369
 MacLachlan, J. 405
 Maddocks, J. 3879, 3888, 3891
 Madduri, V. B. 2711
 Madey, J. M. J. 218, 1442, 2889
 Madlung, J. 3139
 Maeda, H. 676
 Magyaray, S. 1811
 Mahale, N. 423, 3769
 Mahale, N. K. 877
 Mahoney, K. L. 2298
 Maier, K. 3093
 Maillard, J. 3093
 Main, W. 2714
 Maishev, V. A. 315, 322
 Majima, T. 1321
 Makarov, A. A. 3822
 Makarov, I. 2650
 Mako, F. M. 2702
 Makowski, M. 1551
 Makowski, M. A. 1554
 Makulkin, A. V. 3702
 Malitsky, N. 128
 Malone, R. 2486
 Malyshev, O. 3876
 Mammoser, J. 781, 947, 1016,
 2929
 Manarin, A. 2492
 Manca, J. 608, 611, 1244
 Mane, V. 3435, 3438
 Mangino, J. 2382
 Manheimer, W. M. 2644, 2647
 Manini, P. 3839
 Mankofsky, A. 3267
 Mann, J. 2498, 2504
 Mao, N. 333
 Mapes, M. 3882, 3897
 Mariam, F. G. 384
 Marin, M. 1063
 Marin, P. 1465
 Marino, M. 3839
 Markov, V. 1480, 2057
 Marks, N. 2898
 Marks, S. 1572, 1575, 1578, 1581
 Marnieris, I. 1277
 Maroli, C. 1524
 Marquardt, J. 3118
 Marquardt, N. 1471
 Marrufo, O. 827, 1169, 3213
 Marsden, E. 3127, 3213
 Marsden, S. 827
 Marsh, K. A. 558, 2551
 Marsh, W. 1912
 Marshall, J. 841, 1396
 Martens, M. 405
 Martens, M. A. 1963, 3300
 Martin, D. 1703, 2118, 3888

- Martin, K. 1914
 Martin, P. 3793
 Martin, R. 2913
 Martini, M. 3570, 3699
 Maruyama, T. 2172
 Maruyama, X. K. 1620, 2397
 Marzali, A. 950
 Mashiko, K. 602
 Maslennikov, I. 3876
 Massarotti, A. 953, 956, 1145
 Masuda, H. 1780, 1783
 Masullo, M. R. 2154
 Masunov, E. S. 1681, 2474
 Mathae, J. C. 2432
 Matheisen, A. 918
 Mathewson, A. G. 3828
 Mathieson, D. 1823, 1826, 1829
 Matsumoto, H. 959, 1124
 Matsumoto, S. 1291, 3491
 Matsuoka, M. 1024
 Matthews, H. W. 2667
 Matak, C. 83
 Matumoto, M. 3903
 Matveev, Y. 1348, 1384
 Matz, W. 1477
 Mavrogenes, G. 549, 605
 May, R. 2184
 Mayood, M. 44
 Mazarakis, M. G. 667
 Mazumdar, T. K. 2705, 2708, 2711
 Mazur, P. 2769
 Mazur, P. O. 2856
 McAllister, B. 2054
 McAllister, B. G. 1875
 McAshan, M. 2757
 McCammon, D. 1421
 McCauley, G. 1718
 McCormack, F. 2187
 McCormick, D. 1975, 2160, 2423
 McCrory, E. S. 1691, 1952
 McDonald, D. S. 3190
 McDowell, C. 2477
 McDowell, W. 1960
 McGhee, D. 1864, 3757
 McGhee, D. G. 1271, 2817
 McGill, J. 378, 381, 384
 McGill, J. A. 333
 McGinnis, D. 35, 2100, 2228, 2231, 2361, 3533, 3787
 McGinnis, K. 2124, 2130
 McInturff, A. 2731, 2763
 McInturff, A. D. 2757
 McIntyre, P. M. 2705, 2708, 2711
 McKenzie-Wilson, R. 1172
 McMahan, M. A. 2187
 McMichael, G. E. 1175
 McMurry, D. 1669
 McNerney, A. 1166
 McNerney, A. J. 1241
 McPherson, J. 32
 Meads, P. F., Jr. 3825
 Meddahi, M. 1488, 3312
 Medvedko, A. 1297
 Meigs, M. J. 1660
 Meinko, R. 203, 2468, 2489
 Meisner, K. 405, 2519, 2522, 2525
 Meitzler, C. R. 3148
 Melia, G. 2997
 Meller, R. E. 578
 Mellors, W. 1039
 Melnychuk, S. 3193
 Melton, J. G. 2944
 Mendelsohn, S. L. 1774
 Menegat, A. 543, 620, 1121, 1196, 1208
 Meng, W. 2883, 2904, 2907
 Meng, P. R. 2693, 3351
 Menninger, W. L. 2656
 Men'schikov, L. 552
 Mercier, E. 3202
 Merl, R. 2799, 2802, 2805
 Merle, E. 670, 697, 2115
 Merminga, L. 599, 2184, 2364, 3515
 Merz, W. 1841, 1898
 Meshcherov, R. 2717
 Mestha, L. K. 2382, 2385
 Meth, M. 1166, 1241, 2286
 Metty, P. 1244
 Metzger, D. 918, 995, 1399, 3450
 Meuth, H. 962, 1253, 3381
 Meyer, D. 3888
 Meyer, F. 1841, 1898
 Meyer, R. 1703
 Meyer, R. E. 2334, 2480
 Meyer, W. 1551
 Meyer, W. H. 1554
 Meyerhof, W. E. 3751
 Meyerhofer, D. D. 2638
 Mezentshev, N. A. 1494, 2751
 Michelotti, L. 80, 495
 Michizono, S. 1193
 Micklich, B. J. 1715
 Miele, G. 209, 212
 Miertusova, J. 3842, 3873
 Migdal, W. 1890
 Mihelic, R. 3888
 Milburn, J. E. 2796
 Miles, J. 44, 2001
 Militin, B. L. 2022
 Milityn, B. 3711
 Miller, E. 1972
 Miller, J. 3612
 Miller, R. 608, 608, 611, 611, 3084
 Miller, R. H. 543, 620, 3027, 3063
 Miller, W. 369
 Millich, A. 965, 3426
 Milliman, L. 2967
 Millo, D. 1587
 Mills, F. 285, 549, 3757
 Mills, F. E. 2817, 2922, 2924
 Mills, M. R. 2322
 Mills, R. S. 3657
 Millsom, D. 1966
 Milstead, I. 2301
 Milton, B. 1733
 Mimashi, T. 2340
 Miné, P. 2450
 Minestrini, M. 573, 968
 Minty, M. 224, 227, 447, 2019, 2370, 2373, 2435, 3240
 Minty, M. G. 29, 420
 Miram, G. 1106
 Mironov, V. 2042
 Mirzajan, A. 2426
 Mishin, A. V. 971
 Mishnev, S. I. 2022
 Mishra, C. S. 342, 345, 348, 351, 2829
 Mitchel, G. R. 2415
 Mitra, A. K. 974, 1303
 Mitsuhashi, T. 215
 Mitsui, H. 2205
 Minra, A. 959, 1124
 Minra, I. 1650
 Miwa, H. 1024
 Miyahara, Y. 653
 Mizuno, A. 602
 Mizuno, H. 1202, 1321
 Mocheshnikov, N. 1480, 2057
 Mock, R. C. 691
 Modder, J. 2034
 Moe, H. 3757
 Moe, H. J. 2213
 Moersel, J. 2892
 Moffat, D. 763, 769, 886, 889, 892, 918, 921, 977, 995, 3450
 Moffeit, K. 2172
 Moiseev, V. A. 3249
 Mokhov, N. V. 1360, 1369, 3090, 3109, 3772
 Moller, J. 1551
 Moller, J. M. 1554
 Møller, S. P. 1363, 1741
 Molodkin, V. 1480
 Momose, T. 3885
 Mondelli, A. 1004, 3267, 3270
 Montès, B. 2450
 Montuclard, J. 3900
 Morales, G. 3888, 3891
 Morales, H. 3018
 Morano, R. 2450
 Moravec, K. 3864
 Morcombe, P. 1339
 Morduev, A. 1672
 Moretti, A. 1127, 1214
 Morgan, G. 2744, 2766
 Morgan, G. H. 2754
 Morgillo, A. 2744, 2766
 Mori, W. B. 2635
 Mori, Y. 2991, 3181, 3754
 Morillo, J. 2450
 Morishita, O. 1686
 Moritz, G. 3736
 Morpurgo, G. 2103
 Morse, W. 2070
 Mortazavi, P. 1419
 Morton, P. 1445
 Moshhammer, H. 131, 2025
 Moskalenko, V. 1480, 2057
 Mosnier, A. 629, 855
 Mottershead, C. T. 1669
 Mourou, G. 2632
 Moz, S. 1063
 Mroczkowski, T. T. 2919
 Mudiugin, B. 2042
 Mud'jugin, B. G. 3822
 Mukugi, K. 1515, 1518
 Mulholland, G. 2757
 Muller, H. 889, 918, 995, 2953
 Müller, R. 1887
 Munson, F. H. 1694
 Murakami, T. 1291, 1686

Maratov, J. 2744, 2766
 Maria, B. P. 980
 Murphy, J. B. 1477
 Murphy, K. 2967
 Murray, D. 1838, 2737
 Murray, J. 1274, 1855, 1858, 1861
 Musenich, R. 1001
 Mustaine, R. E. 1033
 Myas, E. A. 318, 322
 Myak, J. 1250
 Mytarkov, A. 1480, 2057
 Mynnikov, K. 2769

N

Nadji, A. 1465
 Nagaenko, M. 2057
 Nagafuchi, T. 2039
 Nagaitsev, S. 29, 224, 227, 420, 3524, 3745
 Nagaitsev, S. S. 3536
 Nah, Y. G. 2796
 Nakagawa, S. 1468
 Nakahara, Y. 1566
 Nakajima, K. 2556, 2638, 3552
 Nakajima, S. 676
 Nakamura, H. 2260
 Nakamura, K. 3537
 Nakamura, N. 2257, 2295, 2337
 Nakamura, T. 3464
 Nakanishi, H. 2556, 2638, 3552
 Nakao, K. 1193
 Nakayama, H. 2340
 Nakazato, T. 1614, 1617
 Nam, S. 581
 Nam, S. H. 593, 1315
 Namkung, W. 581, 593, 1315, 1521
 Nantista, C. 543, 620, 983, 1196
 Napoly, O. 632, 3347
 Nassiri, A. 605, 2142, 2412
 Nation, J. A. 1312, 2653, 2684, 2687
 Natter, E. F. 1154, 2391
 Nawrocki, G. J. 1957
 Nawrocky, R. 2246
 Nawrocky, R. J. 2145
 Nazmov, V. 3876
 Neil, G. 279, 3663
 Neil, G. R. 1563
 Nelson, E. M. 983, 1086
 Nelson, J. 1916
 Nelson, W. R. 185
 Nemoshkalenko, V. 1480
 Neri, F. 56
 Nesterenko, I. 3711
 Nesterov, N. A. 1798
 Nett, D. 611
 Neuffer, D. 2136, 3297, 3663
 Neumann, W. 1477
 Neuschaefer, G. 1683
 Newberger, B. S. 387, 3588
 Newman, W. 2133
 Newton, M. A. 739
 Nexsen, W. 2468, 2489
 Nezhevenco, O. 564, 2650
 Ng, C. K. 986, 1039, 2638, 3432

Ng, K. Y. 29, 35, 102, 224, 227, 405, 420, 3300, 3630
 Ng, L. S. B. 1949
 Ng, Y. 2133
 Nguyen, D. C. 2970
 Nguyen, T. K. 2997
 Nguyen-Tuong, V. 1007
 Nick, W. 2748
 Nicol, T. 3021
 Nicol, T. H. 989
 Nielsen, R. 3757
 Nightingale, M. P. S. 1777
 Niki, K. 1780, 1783, 1786
 Nikiforov, A. 2650
 Nilsson, A. 1735
 Nilsson, B. 1771
 Ninan, L. 599
 Nishi, M. 309
 Nishida, Y. 2556, 2638, 3552
 Nishimura, H. 111
 Noda, A. 41, 1291, 1697
 Noda, K. 1291, 1686
 Nodarse, F. F. 1892
 Noguchi, S. 992, 1024
 Nolden, F. 1645, 1738
 Nolen, J. A. 71, 89, 1694
 Nomura, M. 546
 Noomen, J. 1998
 Noomen, J. G. 2343
 Nordberg, E. 995
 Norem, J. 2462, 2638
 Nortier, F. 3099
 Nosochkov, Y. 125, 143, 239, 3778
 Novak, J. 1021
 Novak, W. 2462
 Nuhn, H.-D. 173, 1445, 1608
 Nurushev, S. B. 315
 Nusinovich, G. S. 2572, 2659, 2661, 2673
 Nyman, M. 3748

O

Oasa, K. 1554
 Obert, J. 1792
 Obina, T. 2409
 Ochsner, J. 2790
 O'Connell, J. S. 3657
 O'Day, S. 330, 2459, 3096
 Oeftiger, U. 2157
 Oehme, W. 1477
 Oganessian, R. 1672
 Ogata, A. 2556, 2638, 3552
 Ogawa, H. 1291, 1686
 Ogawa, Y. 2516, 3087, 3705
 Ogitsu, T. 2769
 Ogiwara, N. 1566
 Ogloblin, A. A. 1795
 Ogren, H. 2172
 Ogura, K. 2714
 Oguri, Y. 3115
 Oh, J. S. 593, 1315
 Ohkuma, H. 1509
 Ohmori, C. 3297
 Ohnuma, S. 3148, 3603
 Ohsawa, S. 2516, 3087, 3705

Ohsawa, Y. 2205
 Oide, K. 466, 2340, 3339
 Oikawa, Y. 3845
 Okamoto, H. 221, 1545, 1697, 3390
 Okamura, M. 3115
 Okay, N. 2986, 3151
 Okay, N. C. 2483, 3133
 Oku, Y. 1468
 Okuda, S. 650
 Olchowski, F. 32
 Oldfather, D. E. 2210
 Oliphant, V. 1706
 Olivier, R. 44
 Olivo, M. 3190
 Ollis, C. W. 739
 Olsen, D. K. 1660
 Olsen, R. 44, 1274, 1855, 1858, 1861
 Olson, R. E. 667
 Onel, Y. 32
 Onillon, E. 2379
 Onischenko, L. 2042
 Onischenko, L. M. 518
 Ono, M. 546, 1024, 1163
 Oogoe, T. 3087
 Oothoudt, M. A. 3106
 Oren, W. 2929
 Orlov, Y. 3488
 Orr, N. 1792
 Orris, D. 2769
 Orthel, J. L. 1762
 Orzechowski, J. 3099
 Oshita, H. 546
 Osipov, V. 3876
 Ostiguy, J. 2901
 Ostiguy, J.-F. 2829
 Ostreiko, G. 564
 O'Sullivan, M. 1925
 Otis, A. 1241
 Otter, A. J. 2898
 Ovchinnikov, V. P. 555
 Owens, T. L. 1689, 1691
 Oxoby, G. 2076, 2352
 Oyamada, M. 1614, 1617
 Ozaki, T. 673, 2205

P

Paál, A. 1735
 Padamsee, H. 763, 769, 886, 889, 892, 918, 921, 977, 995, 998, 1399, 3450
 Page, T. 2459
 Page, W. 2222
 Palkovic, J. A. 21, 3261
 Palmer, D. 620
 Palumbo, L. 212, 778
 Pan, C. 44
 Pang, Y. 2705, 2708, 2711
 Papash, A. 372
 Papash, A. I. 3822
 Pappas, G. C. 1336
 Papureanu, S. 962, 1747
 Pardo, R. C. 1694
 Paris, P. 1792
 Parish, D. J. 2790

Parini, G. 3121, 3124
 Park, K. H. 2796
 Park, S. 561, 570, 2976, 3003, 3216
 Park, S. S. 593, 1315
 Parker, B. 1360, 3772, 3775
 Parkhomchuk, V. V. 2022, 2959
 Parodi, R. 775, 778, 1001, 1524
 Parry, R. 2222
 Parry, R. R. 2225
 Parsa, Z. 509, 2723
 Parshin, I. O. 1798, 3675
 Parzen, G. 483, 486, 489
 Pasotti, C. 953, 956, 1145
 Pasquinelli, R. 3533
 Pasquinelli, R. J. 2081, 2355, 2361
 Passardi, G. 2739
 Paterson, A. 2850
 Paterson, J. 1445
 Paterson, J. M. 543
 Patteri, P. 573
 Patterson, D. 2112
 Paulson, C. C. 1774
 Pauluhn, A. 270
 Pavlov, S. N. 3822
 Pawlak, T. 3793
 Paxson, V. 1940
 Payet, J. 1465
 Payne, A. N. 736
 Payne, J. 3870
 Pearce, W. J. 1949
 Pearson, C. 543, 907, 1106, 1259
 Pearson, C. C. 620
 Pedersen, F. 2370, 3240
 Peggs, S. 35, 168, 233, 258, 261, 351
 Peggs, S. G. 74
 Pei, X. 29, 224, 227, 420, 1421, 1424
 Peiniger, M. 1080
 Pekeler, M. 918
 Pellegrini, C. 173, 561, 570, 575, 1445, 1533, 1608, 2617, 2976, 3003, 3216
 Pelligrini, C. 3543
 Peadleton, R. P. 1039
 Penner, S. 381
 Penzo, A. 32
 Perelstein, E. 2042
 Perevedentsev, E. 3429, 3711
 Perkins, L. T. 3190
 Pergrini, L. 772
 Perret, R. 2202
 Perry, J. 587, 1925, 2184
 Persov, B. 2650
 Peschardt, E. 1903, 2358, 3429
 Peschel, H. 2748
 Pestrikov, D. 294
 Pestrikov, D. V. 3681, 3684, 3687
 Peter, W. 2702
 Peters, C. 703
 Petersen, D. 1551, 3836
 Petersen, D. E. 1554
 Peterson, D. 809, 3533
 Peterson, D. W. 3573
 Peterson, E. 2400
 Peterson, J. 203, 2281, 3769, 3781
 Peterson, T. 809

Petillo, J. 1004, 3267
 Petradza, M. 2172
 Petrov, E. 2042
 Petrov, S. 1297
 Petrov, V. 824, 1226
 Petrov, V. M. 877, 941
 Petrucci, G. 2820
 Pettersson, O. 1771
 Pewitt, E. G. 2823
 Peyromaure, J. 858
 Pfeffer, H. 918
 Philipchenko, A. 564, 1384, 2793
 Phillips, H. L. 1007
 Phillips, R. 543, 1106
 Phinney, N. 116, 2019
 Pianetta, P. 1445, 1536
 Picard, M. 1477, 2534
 Pickens, D. R. 1448
 Pierini, P. 1524, 1569
 Piestrup, M. A. 1620, 2397
 Pikin, A. 1735
 Pilat, F. 143, 203, 239, 515
 Pile, G. 1709, 3210
 Pimiskern, K. 944
 Pindyurin, V. 3876
 Pinkow, J. 357
 Piovella, N. 1524
 Pipersky, P. 1572
 Pirk, W. 1172, 1241
 Pirozhenko, V. M. 3112
 Pisent, A. 32
 Pistoresi, D. 2967
 Pitchford, L. 3039
 Pivarc, J. 3894
 Placidi, M. 44
 Plate, D. 1572, 1575
 Platt, R. C. 2456
 Plesca, L. 3133
 Plesko, M. 149, 152, 1477, 2534
 Plink, O. V. 3112
 Plotnikov, S. V. 1798
 Plotnikov, V. K. 1675
 Plouffe, D. 2736
 Ployard, G. 2115
 Plum, M. 366, 2181, 2319, 3297
 Pogorelsky, I. 2564, 2614
 Poilleux, P. 2450
 Poirier, R. L. 753
 Poizat, J. C. 3093
 Poliakov, R. V. 1892
 Poll, D. 3533
 Pollock, D. 2760
 Poloni, C. 1587
 Pontonnier, M. 2997
 Poole, M. W. 1494, 1638, 3594, 3672
 Popkov, Y. 1480, 2057
 Popov, A. 2042
 Popov, Y. 552
 Popovic, M. B. 1214, 1689, 1691
 Porro, M. 3839
 Porter, J. 2133, 2420
 Portmann, G. 1572, 2272
 Postiau, N. 1672
 Potter, J. 1004
 Potts, C. 3757
 Potukuchi, P. N. 1045
 Poukey, J. W. 667, 691, 694
 Power, J. 1669, 1844, 2596, 3061

Power, J. F. 2334
 Powers, T. 1007, 1010, 1016
 Ponomarev, E. 3711
 Pradal, F. 3842
 Preble, J. 841, 1396, 2929
 Preger, M. A. 2048
 Priest, D. H. 1103
 Prescott, C. 3033
 Prescott, C. Y. 2978, 3027, 3036
 Price, E. 587
 Price, R. R. 1448
 Primdahl, K. 766, 1013, 1294
 Pripstein, D. 2172
 Proch, D. 758
 Prodell, A. 2744, 2766
 Pröhl, D. 1477
 Propp, A. 824, 941
 Prosnitz, D. 1445
 Prusakov, V. 552
 Pruss, S. 2252
 Pruss, S. M. 3802
 Ptitsin, V. 3711
 Puech, V. 3039
 Pullia, M. 1524
 Pusterla, M. 32
 Putaux, J. C. 1792
 Puzo, P. 2513

Q

Qian, G. 745, 3521, 3696
 Qian, Q. 2670
 Qin, J. 3237
 Qin, Q. 3237
 Qiu, X. Z. 1439
 Quinn, P. D. 1638, 3594, 3672
 Qunell, D. 1357

R

Raabe, P. 1645
 Raffone, G. 2048, 3906
 Rahn, J. 1887
 Raimondi, P. 98, 100, 116, 2019
 Rajagopalan, S. 2638, 3555
 Rakowsky, G. 1605
 Ramamoorthy, S. 1849, 1852
 Ramaswamy, K. 685
 Rambaldi, S. 273
 Ramirez, G. 1419
 Ramseier, G. 44
 Ranganathan, R. 1402
 Rao, M. G. 927, 3867
 Raparia, D. 122, 1765, 2127, 2426, 2986, 3130, 3151, 3509, 3585
 Rathke, J. 1709
 Ratner, L. 432
 Ratti, A. 1166, 1172
 Raubenheimer, T. 417, 1445, 2019
 Raubenheimer, T. O. 11, 596, 635, 2025, 2880
 Rauchas, A. 3757
 Rawlins, A. 1727
 RD22 Collaboration 26

Recca, C. 1007, 1016
 Recca, R. K. 1277, 3763
 Reed, L. 2442
 Rees, D. 3213
 Rees, D. E. 1169, 1199, 1205
 Rees, G. 3297
 Rees, G. H. 3731
 Reeve, P. A. 2898
 Reeves, S. 2817
 Regan, A. 1683, 3213
 Regan, A. H. 1154, 2391
 Reginato, L. 703, 1351
 Reginato, L. L. 636
 Rehak, M. 2744, 2766
 Reich, H. 1645
 Reid, C. 809
 Reilly, R. 1357
 Reimund, J. A. 1280
 Reinhardt, N. 1327, 3078
 Reiniger, K. W. 1112, 1283
 Reiser, M. 62, 65, 685, 2667,
 2670, 3145, 3282, 3627, 3648,
 3660
 Reist, H. 1771
 Reistad, D. 1744, 3745
 Remelius, D. 2967
 Remillieux, J. 3093
 Remondino, V. 68
 Remy, M. A. 1089
 Rendon, A. M. 2480
 Renou, G. 3093
 Rensfelt, K.-G. 1735
 Repnow, R. 1747
 Reusch, M. F. 59, 1527, 3624
 Rhee, M. J. 688
 Ricard, C. 1789
 Rice, D. 1978, 3479
 Rice, D. H. 2007
 Richardson, R. D. 2456, 3772
 Richter, R. 1160
 Richter-Sand, R. J. 1306
 Ride, S. K. 1623
 Riedel, C. 3736
 Rietdyk, H. 2397
 Rieubland, J.-M. 2739
 Rifkin, J. 543
 Rimmer, R. 1039
 Rimmer, R. A. 871, 874, 3411
 Rinckel, T. 32
 Ringwall, A. 1703
 Ringwall, A. D. 846
 Riordon, J. 2118
 Risselada, T. 246
 Ritchie, A. L. 2210
 Ritson, D. M. 125, 143, 3778
 Riunaud, J. P. 3570
 Rivkin, L. 3429
 Rivoltella, G. 1524
 Rizzi, V. 1145
 Robb, A. 1575
 Robb, J. 2929
 Robertson, S. 2641
 Robin, D. 131, 173
 Robins, K. 1439, 1602
 Robins, K. E. 2742
 Robinson, W. 2731, 2757, 2763
 Roche, C. T. 1715
 Ródenas, J. 647
 Rodenburg, R. 2967

Rodenz, G. 2664, 3267
 Rodger, E. 2895
 Rodgers, J. 685
 Rodriguez, A. R. D. 1454
 Rodriguez, J. P. 798
 Rodriguez, R. 827, 1250
 Roedklein, J. C. 2919
 Rogdestvensky, B. V. 3822
 Rogers, J. D. 1033, 1256
 Romero, A. 128
 Rondan, G. 420
 Rönqvist, T. 1771
 Root, L. 372
 Ropert, A. 1512
 Roques, A. 670, 697
 Rose, C. 1669
 Rose, C. R. 2334
 Rose, J. 1172
 Rosengård, U. 1735
 Rosenthal, S. E. 694
 Rosenzweig, J. 233, 561, 1445,
 1548, 2623, 2638, 2976, 3024,
 3216, 3357, 3494
 Rosenzweig, J. B. 3021
 Roser, T. 2286, 3207, 3633, 3763
 Rosier, L. 3093
 Rosing, M. 815, 2596
 Ross, M. 522, 1975, 2019, 2234,
 2435
 Ross, M. C. 1972, 2160, 3564
 Rossa, E. 2432, 2492, 3429
 Rossi, C. 953, 956, 1145
 Rossi, L. 1524
 Rossmann, R. 32, 429, 457, 1477
 Rostamzadeh, C. 1405
 Rotela, E. 1497
 Roth, G. 3072
 Rothman, J. L. 2307
 Rouaud, C. 3900
 Roux, D. 2932
 Rowson, P. 2172
 Roy, A. 1045
 Rubin, D. 921, 3450, 3479
 Rubingh, M. J. A. 1072
 Rudchik, A. T. 3822
 Rudd, H. 65
 Rudenko, V. 552
 Rudolph, K. 1019
 Ruggiero, A. G. 700, 3530
 Ruggiero, F. 503
 Ruiz, E. 3405
 Ruland, R. E. 2736, 2950
 Rule, D. W. 1620, 2397, 2453
 Rullier, J. L. 2656
 Ruschman, M. 809
 Rusnak, B. 1021
 Russell, S. J. 2537, 2970
 Russell, T. 605
 Russell, T. J. 1324
 Russo, D. 2286
 Rusthoi, D. P. 1669, 3118
 Ruth, R. D. 291, 543, 620, 907,
 1196, 3693
 Rutkowski, H. 703
 Rutkowski, H. L. 706
 Ryan, W. A. 2310, 2328
 Rybakov, E. 2769
 Rybalko, V. 2717
 Rychagov, A. 2769

Rychkwaert, G. 1672
 Ryder, R. 3739
 Ryna, R. 3267
 Ryna, R. D. 3229
 Ryu, C. 581
 Rzaev, R. A. 454
 Rzezonka, B. 2748

S

Saadatmand, K. 2124, 2127,
 2426, 2483, 2966, 3127, 3130,
 3133, 3145, 3151
 Sacepe, B. 697
 Sachtschale, R. J. 1339
 Sacki, H. 3885
 Sáez, P. 3033
 Sáez, P. J. 2978, 3027, 3036
 Safranek, J. 1491, 2275
 Sagalovsky, L. 288, 838, 1715
 Sagan, D. 53, 3470, 3479
 Sage, J. 1838, 2444, 2483, 3127
 Saint Laurent, M. G. 1792
 Saito, K. 673, 1024
 Saito, Y. 1193
 Sajsev, V. 230
 Sakamoto, K. 1566
 Sakamoto, S. 676, 1321
 Sakanaka, S. 1027, 3503
 Sakae, H. A. 3845
 Sakawa, Y. 2556
 Saladin, V. 2763
 Sale, K. E. 1663
 Salimov, A. 3876
 Sampayan, S. E. 1554
 Sampson, W. 1439, 1602, 2744,
 2766
 Sampson, W. B. 2742, 2904
 Sandberg, J. 1277
 Sander, O. R. 1669, 3118
 Sanders, R. 1241
 Sanders, R. T. 1166
 Sandoval, D. P. 1669
 Sandweiss, J. 2578, 2617
 Sanford, T. W. L. 691
 Sannibale, F. 611
 Sapozhnikov, L. 2076, 2352
 Sapp, W. 1372, 2054
 Sapp, W. W. 2832, 2935, 2938,
 2941
 Saraniti, D. 921
 Saritepe, S. 354
 Sarkar, S. 1841, 1898, 1916, 1919
 Sasaki, Y. 2039
 Sass, R. 2106
 Sass, R. C. 1946
 Sathe, S. 1846, 1852
 Sato, H. 1291
 Sato, I. 546, 590, 1193, 1416,
 2516, 3087, 3705
 Sato, K. 1291, 1686
 Sato, Y. 1291, 1686
 Satogata, T. 261
 Satoh, K. 3115
 Sauer, L. 3863, 3864
 Saulter, Q. 841
 Saunders, C. 1864

Saversky, A. J. 1030
 Savord, T. 1914, 2731, 2757
 Sawada, K. 1686
 Sawyer, D. 2238
 Sazhin, V. 2717
 Scala, R. G. 2519
 Scandale, W. 16, 246
 Schachinger, L. 1940
 Schachter, L. 1312
 Schlichter, L. 2567, 2653, 2684, 2687
 Schaefer, J. 907
 Schiffer, P. 2748
 Schaffer, G. 1033, 1256
 Schailley, R. 236, 378, 1360, 1369
 Scharlemann, E. T. 1530, 1533, 1551
 Scharlemann, T. 1445
 Scheer, M. 1474
 Schegolev, L. 1384
 Schellekens, P. H. J. 2927
 Schempp, A. 3139, 3142
 Schimmel, F. 1901
 Schlenk, R. 1477
 Schlueter, R. 1572, 1575, 1581
 Schlueter, R. D. 1727
 Schmalzle, J. 2790
 Schmickler, H. 2001
 Schmid, J. 2739, 2956
 Schmidt, C. W. 1655, 1689, 1691
 Schmidt, F. 246, 500, 2301
 Schmidt, R. 44, 2103, 2133
 Schmitt, D. R. 3172
 Schmor, P. W. 2991
 Schmuesser, P. 886, 918
 Schnase, A. 962, 1253, 3381
 Schneider, J. D. 1669, 3166, 3172
 Schneider, L. X. 1354
 Schneider, W. 841, 1396
 Schneider, W. J. 2929
 Schoessow, P. 1844, 2596, 3050
 Scholz, T. 1036
 Schriber, S. O. 3760
 Schukeilo, L. A. 3822
 Schultz, D. 3033
 Schultz, D. C. 2978, 3027, 3036, 3039
 Schultz, S. 2559
 Schumm, B. 2172
 Schürmann, M. 264
 Schwalm, D. 1747
 Schwandt, P. 3184, 3745
 Schwarz, H. D. 1039
 Schweppe, E.-G. 1178
 Schwettman, H. A. 950
 Schwitters, R. 3781
 Sciutto, W. 1063
 Sears, J. 763, 769, 886, 889, 892, 918, 921, 977, 995
 Sebek, J. 3018
 Sedlacek, M. 3745
 Sedlyarov, I. 1226
 Seeman, J. 1445, 1608, 2019
 Seeman, J. T. 414, 596, 638, 2423, 2507, 3234, 3564
 Segalov, Z. 685
 Seidl, P. 721
 Seifrid, P. 3533
 Seleznev, V. S. 2190
 Selin, A. V. 2853
 Sellyey, W. 2112, 2237, 2304
 Selph, F. 83
 Semertzidis, Y. 2070
 Sen, T. 134, 137, 140, 143, 146, 239, 3778
 Senichev, Y. 3509, 3642
 Seo, H. S. 2751
 Serafim, P. 1560
 Serafini, L. 3024, 3279
 Serdobintsev, G. 564, 2650
 Serebrennikov, D. 2042
 Sereno, N. S. 3246
 Sergeeva, O. S. 2853
 Serio, M. 778, 2076, 2352
 Servranckx, R. 236, 255
 Servranckx, R. V. 167, 3784
 Sessler, A. 2638
 Sessler, A. M. 1530, 2593, 2608, 3288, 3527
 Sethi, R. 1703
 Settles, M. 2172
 Severgin, Y. 2057, 2769
 Severgin, Y. P. 2208, 3205, 3820, 3822
 Shafer, B. E. 1285
 Shafer, R. E. 2316
 Shaimerdenov, E. 564
 Shako, V. V. 2406
 Shalz, L. 3748
 Shan, J. 405
 Shan, J. P. 35, 74, 3787
 Shan'gin, V. 2769
 Shankland, L. W. 1175
 Shapiro, G. 2172
 Sharma, S. 1497, 1500
 Sharp, W. M. 733, 2593
 Shatunov, Y. 3711
 Shchedrin, I. S. 1030
 Shcherbakov, A. 1480, 2057
 She, K. 995
 Shea, T. 3438
 Shea, T. J. 2310, 2328, 2916
 Sheedy, E. 3012
 Sheehan, J. 1439, 1439, 1527, 3000
 Sheffield, R. L. 2970
 Sheikh, J. Y. 1175
 Shen, J. 2178, 2438
 Sheng, I. C. 1497, 1500
 Shepard, K. W. 1042, 1045, 1694
 Shephard, W. 821
 Sherman, J. D. 3166
 Sherwin, G. 1881
 Sheynin, S. 393
 Shi, J. 242, 243, 3603
 Shibata, H. 3552
 Shibata, Y. 1614, 1617
 Shidara, T. 590, 1416
 Shih, H.-J. 387, 3588
 Shiho, M. 676, 1566
 Shiltsev, V. D. 2959
 Shinoo, K. 1509, 2295, 2337
 Shintake, T. 1048, 1051
 Shiraga, H. 2556
 Shirai, T. 1697
 Shishido, T. 992, 1024
 Shiwaku, H. 1468
 Shoace, H. 1946, 2106
 Shofstall, D. 2967
 Shoji, T. 2556
 Shoji, Y. 3633, 376
 Shpak, A. 1480
 Shrader, M. B. 1103
 Shtirbu, S. 1934
 Shu, Q. S. 921, 2787
 Shu, Q.-S. 3888, 3891
 Shutt, R. 2744
 Shvedunov, V. I. 1069, 2059
 Shvets, G. 2635
 Sibley, C. 1372, 2054, 2868
 Siddons, D. P. 2145
 Siemann, R. 2019, 2370
 Siemann, R. H. 532, 2373, 3240
 Siergiej, D. 3482
 Sievers, W. 1916
 Siffert, P. 1363
 Sigov, Y. S. 2620
 Sikora, R. E. 2328, 2916
 Sillanoli, M. 2492
 Silva, J. 3093
 Sim, J. W. 2856
 Simmons, J. 3888
 Simpson, J. 815, 2596, 3050, 3061
 Simrock, S. 1925, 2184
 Simrock, S. N. 599, 1909, 2364, 3515
 Sims, R. E. 2769
 Sinclair, C. 3663
 Sinclair, C. K. 1109, 3246
 Singh, O. 2254, 2284
 Sissakian, A. 2042
 Skachkov, D. G. 3675
 Skachkov, V. S. 2853
 Skarpaas, K. 1039, 3030
 Sladen, J. P. H. 2346
 Sloan, T. 29, 224, 227, 420, 1421
 Sluijk, T. 2343
 Smellie, R. 2757, 2781
 Smirnov, Y. 2042
 Smith, B. H. 1175
 Smith, D. D. 2705, 2708, 2711
 Smith, D. L. 667
 Smith, D. R. 1075, 2559
 Smith, H. V., Jr. 3172
 Smith, J. 1852, 2222, 2284
 Smith, J. D. 1846, 1849
 Smith, J. R. 694
 Smith, K. S. 3178
 Smith, L. 3678
 Smith, M. 1669, 3118
 Smith, P. 1718, 2953
 Smith, S. L. 1494, 1638, 3594, 3672
 Smolucha, J. 1817, 1912
 Smolyakov, N. V. 1626
 Smythe, W. R. 1054
 Snee, D. 1013
 Snitchler, G. 3888
 Snyder, D. 1620
 Snyderup, L. 3897
 So, I. 2275
 Sobczynski, S. 1372, 3851
 Sohn, Y. U. 2751
 Sokolov, S. V. 318, 320
 Sokolowski, J. S. 849
 Solensten, L. 2133

Solheim, N. 2936
 Solomon, L. 1439, 1602, 1605
 Solomons, R. 3748
 Sommer, F. 2748
 Sommer, M. 1465
 Somov, L. 552
 Song, J. 1057, 2142
 Song, J. J. 2213, 3393, 3396
 Song, T. 2199
 Sortais, P. 1789, 1792
 Soukas, A. 1277, 3633
 Soukas, A. V. 1345
 Soundranayagam, R. 1360
 Spädtke, P. 1645, 1738
 Spalek, G. 1021
 Spanggaard, J. 2492
 Spata, M. 841
 Spataro, B. 611, 778
 Spataro, C. 2883
 Spayd, N. 880, 3405
 Specht, J. E. 1694
 Specht, V. 2670
 Specka, A. 2450
 Spence, W. 2019
 Spence, W. L. 3234, 3576
 Spencer, J. 543, 2025, 2638
 Spencer, J. E. 396
 Spencer, N. 1884, 1969, 1975
 Spencer, T. A. 2693
 Spinosa, F. 2757
 Spitz, R. 1166, 1241
 Sprangle, P. 1560, 2584, 2629, 2632, 2647
 Srodoniowski, J. 821, 2133, 3193
 Srinivasan-Rao, T. 3012
 Stagno, V. 775, 1524
 Stallard, B. 1551
 Stallard, B. W. 1554
 Stampke, S. 203, 2781
 Staples, J. W. 1759
 Stapleton, G. 2184
 Starker, J. 1735
 Starkovich, V. S. 1075
 Steck, M. 1645, 1738
 Steckmeyer, J. C. 1792
 Stefan, P. M. 895
 Stege, R. E., Jr. 2234
 Steimel, J. M., Jr. 2100, 2231
 Steinbach, C. 339
 Steiner, H. 2172
 Steinhauer, L. C. 2564, 2581, 2614
 Stelzer, J. E. 3172
 Stepanov, A. 2426
 Stepp, J. D. 1157, 1408, 1906
 Steski, D. B. 3178
 Stevens, J. 3357
 Stevens, R. R., Jr. 3166
 Stevenson, N. 1733
 Stevenson, N. R. 3099
 Stiening, R. 143, 239, 3778
 Stillman, A. 2471
 Stittsworth, D. 2124, 2130
 Stoker, J. 703
 Stover, G. 1351
 Strait, J. 2769
 Strakhovenko, V. M. 3093
 Strelkov, M. 1480, 2057
 Strelkov, M. A. 194

Striffler, C. D. 2667, 2670, 3075
 Stringfield, R. 2675
 Stringfield, R. M. 2664
 Struckmeier, J. 1645
 Stuart, M. E. 1727
 Stueck, H. 339
 Stupakov, G. V. 197
 Su, G. 1411
 Su, J. J. 2638
 Subbotin, S. 552
 Sudou, M. 1291, 1686
 Suemine, S. 650
 Suenaga, M. 2904
 Sueno, T. 1291
 Suetsugu, Y. 3860
 Sugahara, R. 2340
 Suhling, S. 587
 Sulgin, I. 916
 Suller, V. P. 1494, 1638, 3594, 3672
 Sullivan, C. A. 2644
 Sullivan, M. 131
 Sulyaev, R. M. 454
 Summers, L. K. 1220
 Sun, D. 1127
 Sun, H. 3696
 Sun, N. 515
 Sun, T. 1411
 Sundelin, R. M. 1092
 Sundquist, M. 3745
 Surma, I. V. 2059
 Susta, J. 1060
 Suwada, T. 2516, 3087, 3705
 Suzuki, H. 2039
 Suzuki, K. 2556
 Suzuki, S. 602
 Suzuki, T. 1024
 Svandrik, M. 953, 956, 1145
 Svinin, M. P. 555
 Swartz, M. 2172
 Swenson, D. 1703
 Swenson, D. A. 812, 846, 2426
 Swenson, D. R. 3175
 Sychev, V. 2769
 Symon, K. 285
 Syphers, M. 29, 203, 224, 227
 Syphers, M. J. 38, 134, 137, 140, 146, 420, 3588
 Sytchevsky, S. E. 3205
 Sytnikov, V. 2769

T

Tacconi, E. J. 1098, 2139
 Tadokoro, M. 309
 Tagawa, S. 3552
 Tajima, T. 1024, 2556
 Takada, E. 1291, 1686
 Takada, Y. 1291
 Takahashi, N. 546
 Takahashi, S. 3845
 Takahashi, T. 1614, 1617
 Takaki, H. 1509
 Takamuku, S. 650
 Takasaki, E. 1163
 Takayama, K. 673, 2205
 Takeda, O. 3115

Takeda, S. 1309
 Takeda, Y. 1783
 Takenaka, T. 1163
 Takao, T. 2409
 Tallorico, P. 1683
 Tallorico, P. J. 1199
 Talman, R. 203, 236
 Tamezane, K. 602
 Tamura, K. 2409
 Tanabe, J. 2850
 Tanabe, T. 1291, 3006
 Tanabe, Y. 3115
 Tanaka, M. 360, 2907
 Tang, C. 1623
 Tang, H. 2978, 3027, 3033, 3036, 3039
 Tang, Y. 1852, 2275
 Tang, Y. N. 492, 1846
 Tani, T. 2205
 Tantawi, S. 543, 936, 1106
 Tantawi, S. G. 620, 1121, 1130, 1196
 Tao, Q. 2841
 Taran, A. 2769
 Tarasenko, A. 1480, 2057
 Taratin, A. 2489
 Tarovik, M. N. 3822
 Tarrant, M. 1937
 Tatchyn, R. 1445, 1536, 1539, 1542, 1608, 2429
 Taylor, B. 1142, 1238
 Taylor, L. 824
 Tazzari, S. 573, 968
 Tazzioli, F. 573, 3279
 Tecchio, L. 3243
 Tecker, F. 2432, 3429
 Tekawa, M. 3748
 Telegin, Y. 1480, 2057
 Temkin, R. J. 2575, 2656, 2690, 2696
 Temnykh, A. B. 2007, 3476
 Tenenbaum, P. 2838
 Teng, L. 224, 285, 420, 1485
 Teng, L. C. 182
 Tepikian, S. 168, 420
 Terrien, J. C. 1187
 Terzi, F. 1063
 TESLA Collaboration 537
 Thern, R. E. 2471
 Thevenot, M. 670, 697
 Thiagarajan, V. 3372
 Thieberger, P. 3178
 Thielheim, K. O. 276
 Thiessen, H. 3297
 Thiessen, H. A. 1021, 3760
 Thivent, M. 339
 Thomas, M. G. 1419
 Thomas, P. 3053
 Thompson, K. 3757
 Thompson, K. A. 543, 3342, 3693
 Thompson, K. M. 2808, 2814
 Thompson, P. 2744, 2766
 Thompson, P. A. 2754
 Thorndahl, L. 1066, 3426
 Thuot, M. E. 1806
 Tidwell, S. C. 2564
 Tiefenback, M. 587
 Tiefenback, M. G. 426
 Tieger, D. 2054, 2871, 2874

Tieger, D. R. 2832, 2938
 Tighe, R. 2370, 2373
 Tigner, M. 769, 918, 921, 977,
 995, 3450, 3479, 3690, 3931
 Timmer, C. A. 2970
 Timmermans, C. J. 1072, 1820,
 2892, 2927, 3645
 Ting, A. 2629, 2632
 Titcomb, C. 2956
 Tiunov, A. V. 1069, 2059
 Tiunov, M. 2650
 Tkatchenko, A. 1465
 Tobiyama, M. 2409
 Todd, A. M. M. 1774, 1777
 Toge, N. 98, 100, 116, 3912
 Tojo, E. 1783
 Tokuchi, A. 676
 Tokuda, N. 1783
 Tokumoto, S. 1202
 Toldo, F. 1241
 Tolstun, N. G. 555
 Tomassini, D. 1477
 Tomizawa, M. 41, 1780, 1783,
 1786
 Tomkins, J. C. 2769
 Tomlin, R. 2228, 3787
 Tommasini, D. 1375, 1378, 2820
 Tompkins, P. A. 1448
 Tooker, T. F. 1706
 Tool, G. 1405, 2731, 2757
 Tornoe, R. N. 1103
 Tosolini, P. 1333, 1378
 Towne, N. A. 2415
 Toyama, S. 546
 Toyoda, K. 3006
 Tran, H. J. 3402
 Tran, P. 173
 Tran-Ngoc, T. 829, 832, 1039
 Travier, S. 3053
 Travish, G. 561, 1445, 1533,
 1548, 3216
 Trbojevic, D. 102, 168
 Treas, P. 608, 611
 Tribendis, A. 977, 3450
 Tribouillard, C. 1792
 Trifonov, D. E. 682
 Tron, A. M. 2403, 2406
 Tronc, D. 1768
 Trost, H.-J. 2705, 2708, 2711
 Trotsenko, V. 1480
 Trotz, S. 2575, 2699
 Trzeciak, W. 285
 Tsai, H. J. 1943
 Tsang, K. T. 3270
 Tsarik, S. V. 454
 Tschalaer, C. 2054
 Tsiang, E. Y. 3621
 Tsoupas, N. 2895
 Tsuchidate, H. 1515
 Tsuchiya, M. 3845
 Tsumori, K. 650
 Tsyganov, E. 2468, 2489
 Tuckmantel, J. 806
 Tuli, M. 3888
 Tupa, D. 3175
 Turchetti, G. 273
 Turlington, L. 939, 1109
 Turner, J. L. 2978, 3027, 3036

Turner, L. R. 2799, 2808, 2814,
 2817
 Turner, W. 3876, 3888
 Turner, W. C. 3833
 Tyrroff, H. 1477
 Tyson, E. 2967

U

Ueda, A. 215
 Ueda, S. 3903
 Ueda, T. 3552
 Ueng, T. S. 2031
 Ueyama, Y. 2039
 Uggerhøj, E. 1363
 Uher, T. 2382
 Uhm, H. S. 2599, 2602, 2605,
 2678
 Ulc, S. 2578
 Umezawa, H. 1024
 Umstadter, D. 2632
 Underwood, K. 1884, 1969
 Unser, K. B. 2394
 Urano, T. 2516, 3705
 Urasawa, S. 1614, 1617
 Ushakov, V. 564, 1384
 Ushkov, V. 564
 Utino, K. 1291
 Utterback, J. 1928, 1931

V

Vaccarezza, C. 3906
 Vaccaro, V. 2154
 Vaidya, M. 1010
 Vakhrushin, Y. P. 682
 Valbuena, R. 2202
 Valicenti, R. A. 3133
 Val'kov, A. E. 3822
 van Asselt, W. 3633, 3763
 van den Berk, F. 1820
 van der Heide, J. A. 1072
 van der Laan, J. 1901, 1998
 van der Stok, P. D. V. 1820
 Vandeusen, A. 2124, 2130
 Van Deusen, A. L. 2121
 van de Vijver, Y. 1820
 van Dyck, O. 369
 Vanecek, D. 703
 van Garderen, G. 1901
 van Laar, J. 3645
 van Oers, W. T. H. 2991
 VanOlst, D. 1884
 van Steenberg, A. 2578
 Van Straagen, P. K. 86
 Van Westrum, D. C. 1054
 van Zeijts, J. 587
 Variale, V. 775, 1524
 Varisco, G. 1524
 Vasil'ev, A. N. 315
 Vasiliev, A. 2717
 Vasserman, I. 3711
 Vaughn, G. 1669
 Vejck, S. 2199
 Vella, M. C. 3157

Verdier, A. 158, 161, 249
 Verdd, G. 647
 Vergamini, A. 1205
 Vescovi, M. 611
 Veshcherevich, V. 977, 1226,
 3450
 Vetter, A. M. 1075
 Vignola, G. 611, 1993, 2048
 Villate, D. 670, 697, 2115
 Vinnik, V. 1297
 Vinokurov, N. A. 1442
 Viola, R. 2913
 Vishnevsky, I. N. 3822
 Visnjic, V. 3811, 3814
 Vlieks, A. 543, 1106
 Vlieks, A. E. 620, 1121, 1196,
 1208
 Vobly, P. D. 2751
 Vodopianov, F. A. 1078
 Vogel, H. 1080
 Volk, K. 3139
 Volzhev, A. A. 682
 Vong, F. C. 1906
 Vormann, H. 3139
 Vorobjov, I. A. 1675
 Voroshilov, A. N. 2022, 3669
 Vos, L. 2301
 Voss, D. 285
 Votaw, A. 2112
 Votaw, A. J. 1814
 Vouillot, J. M. 2495
 Vretenar, M. 3121
 Vulcan, W. 3103
 Vylet, V. 543, 1445

W

Wadlinger, E. A. 1669
 Wagner, W. 2838
 Wait, G. D. 1148, 1181, 1330,
 3402
 Wake, M. 2769
 Walend, D. 2953
 Walker, N. 2019
 Walker, N. J. 92, 95, 98, 100,
 116, 119
 Walker, R. P. 1587, 1593, 2844,
 2847
 Wallace, J. D. 1033, 1256
 Walling, L. 824, 877, 880, 1083,
 3405, 3888
 Walstrom, P. 1021
 Walter, M. 3351
 Walter, M. T. 2693
 Walz, D. 185
 Walz, H. V. 2838
 Wan, W. 155
 Wanderer, P. 2726, 2744, 2766
 Wang, C. 1575, 1578, 2608
 Wang, C. J. 1878
 Wang, D. 2013, 2331, 3429, 3851
 Wang, D. X. 62, 3282, 3627, 3660
 Wang, D. Y. 1451, 1949
 Wang, F. 378, 381, 1360
 Wang, J. G. 62, 3282, 3627, 3660
 Wang, J. M. 1419

Wang, J. W. 543, 620, 907, 1086, 1208
 Wang, K. 3148
 Wang, M. H. 1943
 Wang, S. 1411
 Wang, T. 3297
 Wang, T. F. 883, 3500
 Wang, T.-S. 2319
 Wang, X. 2051, 2112, 2237
 Wang, X. J. 2486, 3000
 Wang, X. Q. 1033, 1256
 Wang, Y. 29, 224, 227, 420, 3845
 Wang, Y. L. 546
 Wangler, T. P. 1712, 3606, 3657
 Warn, C. E. 2400
 Warner, D. 2760
 Warnock, R. L. 291, 3378
 Warren, D. S. 2480
 Watanabe, A. 1566
 Watanabe, K. 3845
 Watanabe, M. 1515
 Watanabe, S. 41, 1291, 2714
 Watanabe, T. 41
 Waters, G. 1148, 1181
 Waters, J. W. 1448
 Watson, S. 3055
 Watson, S. A. 2447
 Weaver, H. J. 2959
 Weaver, J. 2714
 Weaver, J. N. 3018
 Webber, R. 2118
 Webber, R. C. 2094, 2382
 Weber, K. J. 1387, 2877
 Webers, G. A. 2062, 2065, 2927, 3423
 Wedekind, M. 3184
 Wei, J. 258, 3527, 3651
 Wei, K. 312
 Weihreter, E. 1474
 Weingarten, W. 806
 Weisend, J., II 2757
 Weiss, R. 1669
 Weissenburger, D. 1439
 Weisz, S. 26
 Welbourne, L. A. 1494, 1638, 3594, 3672
 Welch, D. R. 661, 3549
 Welch, J. J. 2007, 3476
 Wells, F. D. 2316
 Wells, R. P. 1727, 3169
 Weng, W. T. 3264, 3633, 3726, 3763
 Wenninger, J. 44
 Werkema, S. J. 3303, 3309, 3573
 Wesolowski, W. 605
 Westenskow, G. 2638
 Westenskow, G. A. 2611
 Wetherholt, D. M. 2483
 Wetzels, S. F. C. L. 2927
 Wheat, R. M. 2664
 Whelen, C. 2967
 White, G. R. 1881
 White, M. 605
 Whitham, K. 608, 611, 1244
 Whittenberg, W. A. 2483, 3130
 Whittum, D. 2638, 3552
 Whittum, D. H. 673, 3288, 3399
 Wismans, U. 255, 393
 Wiik, B. H. 1

Wildman, D. 405, 1223, 3258
 Wilke, M. D. 2480
 Wilkinson, C. 366, 369, 2216, 2219, 3297
 Willeke, F. 3742
 Willen, E. 2744, 2766, 2790
 Williams, R. 2638
 Williams, S. H. 2838
 Wilson, D. C. 3090
 Wilson, I. 641
 Wilson, P. 2681
 Wilson, P. B. 543, 620, 1208
 Winans, J. R. 1957
 Wines, R. 3103
 Wingate, C. A. 3090
 Winick, H. 173, 1445, 1608
 Winkler, G. 2956
 Wiseman, M. 841, 1060, 2929
 Wisnivesky, D. 1089, 1454
 Witherspoon, S. 599
 Witherspoon, S. D. 2364
 Won, S. C. 1832
 Wood, F. 2118
 Wood, R. 1551, 1712
 Woodbury, K. 1912
 Woodie, M. 1439, 2578, 3000
 Woodley, M. 92, 95, 119, 2019
 Woodley, M. D. 3576
 Woods, M. 2172, 2978, 3036, 3045, 3047
 Woods, M. B. 3027
 Woods, R. 3760
 Woodworth, E. 2184
 Worm, T. 1363
 Worth, G. T. 3118
 Wright, B. 998
 Wright, E. 1106
 Wright, E. L. 1259
 Wright, S. 2124, 2130
 Wu, B. 1611
 Wu, D. 173
 Wu, G. 2228, 2252
 Wu, X. 255, 393
 Wu, Y. 218, 1901, 1998, 2889
 Wuensch, W. 641, 2346
 Wuppertal, U. 995
 Wurtele, J. 2638
 Wurtele, J. S. 2575, 2635, 2699, 3327, 3399
 Wüstefeld, G. 1474
 Wyss, C. 2016

X

Xi, B. 2892, 3645
 Xie, M. 1445, 1533
 Xiu, L. 3148
 Xu, C. Y. 3845
 Xu, G. 3237
 Xu, Y. 3148

Y

Yakimenko, V. 450
 Yakovlev, S. 824

Yakovlev, V. 2650
 Yakovlev, V. P. 877, 941
 Yamada, S. 1291, 1686
 Yamada, T. 1291, 1686
 Yamaguchi, S. 959
 Yamakawa, T. 215, 1614, 1617
 Yamamoto, N. 466, 2340
 Yamamoto, T. 650
 Yamashita, Y. 676
 Yamazaki, Y. 3087
 Yampolsky, I. 1327
 Yan, C. 2136, 3103
 Yan, Y. 236, 3402
 Yan, Y. T. 29, 38, 224, 227, 242, 243, 420, 423, 515
 Yanagi, Y. 3845
 Yanagida, K. 602
 Yandon, J. C. 1916
 Yang, B. 3243
 Yang, X.-F. 2462
 Yao, C. G. 812
 Yao, C. Y. 122, 2444
 Yarba, V. 236
 Yarosh, V. E. 1795
 Yartsev, D. I. 1795
 Yelk, J. 2070
 Yen, E. 1460
 Yeremian, A. 543
 Yeremian, A. D. 2978, 3027, 3063
 Yeung, K. S. 2385
 Yin, Y. 2441
 Yokomizo, H. 602, 2039
 Yokota, M. 308
 Yokouchi, S. 38
 Yokoya, K. 3441
 Yoneda, C. 620
 Yonehara, H. 2039
 Yoneyama, S. 2039
 Yoon, J. R. 2796
 Yoon, M. 3273
 York, R. 236, 255, 393, 3739
 York, R. L. 3175
 Yoshida, K. 1780, 1783
 Yoshida, Y. 3552
 Yoshikawa, H. 602
 Yoshioka, M. 1614, 1617
 Yoshizawa, J. 1291, 1686
 Yoshizawa, M. 41, 1783, 1786
 Young, A. 1205, 1285
 Young, A. T. 1727, 3042
 Young, L. M. 790, 3136
 Youngman, B. 543
 Yu, D. 2388, 2681
 Yu, D. U. L. 936
 Yu, J. X. 1727
 Yu, K. 2787, 3888, 3891
 Yu, L. H. 1439, 1602
 Yu, S. 703, 709, 3199
 Yu, S. S. 712
 Yu, X. T. 3327, 3399
 Yuan, V. 1669
 Yücel, A. 3879
 Yudin, I. P. 191, 297, 1892
 Yudin, L. A. 2543
 Yudin, L. I. 1795
 Yugami, N. 2556, 3552
 Yule, T. 1709
 Yule, T. J. 1777
 Yunn, B. 3663

Yuan, B. C. 179, 1092, 1909
Yupiaov, Y. 564
Yvlov, T. 2042

Z

Zach, M. 1151
Zagel, J. R. 2193
Zakhvatkin, M. N. 2022
Zaltsman, A. 1241
Zangrando, D. 1587, 2844, 2847
Zante, T. 608, 611
Zapalac, G. 2172
Zapolsky, V. N. 454
Zapryagaev, I. 2650
Zarcone, M. J. 3178
Zarucheisky, V. G. 454
Zatopek, J. 2757
Zbasnik, J. 2787, 3888, 3891
Zelanzy, M. 1884
Zelazny, M. 1966
Zelenski, A. N. 2991

Zelinsky, A. Y. 194, 1480
Zelynsky, A. 2057
Zenkevich, P. 2073
Zhabitsky, V. M. 2543
Zhang, B. 1001
Zhang, C. 312, 3237
Zhang, H. 2841
Zhang, M. 1411
Zhang, P. 176
Zhang, P. L. 29, 224, 227, 420
Zhang, Q. 1411
Zhang, R. 561, 575, 3009, 3216
Zhang, S. Y. 1277, 3264
Zhang, T. 306, 2556, 2841
Zhang, W. 2841
Zhang, X. 312, 1439, 1599, 1721, 2841, 3081
Zhang, X. L. 3237
Zhang, Z. 303, 1611
Zhao, Y. 1033, 1256
Zhao, Z. 2841
Zhao, Z. T. 3237
Zhmendak, A. V. 3822
Zholents, A. 131

Zhou, C. 2841
Zhou, J. 3396, 3772
Zhou, P. 3303, 3309, 3540, 3573
Ziemann, V. 98, 100, 108, 114, 116, 498, 1483, 3909
Zinchenko, A. 2468, 2489
Zinkann, G. P. 1694
Zinneman, T. 1709
Zinneman, T. E. 3210
Ziomek, C. 1154, 3213
Ziomek, C. D. 2391
Zisman, M. S. 2010
Zolfaghari, A. 829, 832, 2331, 3851
Zolfaghari, Z. 2054
Zolotarev, M. 2172, 3027, 3045
Zolotarev, M. S. 2978, 3036
Zoni, G. 1063
Zotter, B. 3347, 3429
Zu, D. 1095
Zumbro, J. 1021
Zumbro, J. D. 2832, 2941
Zyngier, H. 1465

